Volume 13, Numbers 1/2/3, 1998

CODEN: JSGTEC
ISSN: 0928–0707

Journal of Sol-Gel Science And Technology

DISTRIBUTION STATEMENT A
Approved for Public Release
Distribution Unlimited

Editor-in-Chief
Sumio Sakka

19990315 031

Kluwer Academic Publishers

JOURNAL OF SOL-GEL SCIENCE AND TECHNOLOGY

EDITOR-IN-CHIEF

Sumio Sakka
Sakka Laboratory
2-7-30 Kuzuha-Asahi
Hirakata, Osaka-Fu 573
Japan

CO-EDITORS

Kanichi Kamiya
Mie University
Faculty of Engineering
Kamihama-cho, Tsu-shi, Mie-ken 514
Japan

Jacques Livage
Université Pierre et Marie Curie
Chimie de la Matière Condensée
4, place Jussieu, 75252 Paris Cedex 05
France

Lisa C. Klein
Rutgers University
Ceramics Department
P.O. Box 909
Piscataway, NJ 08854
USA

J.D. Mackenzie
University of California, Los Angeles
Department of Materials Science and Engineering
405 Hilgard Avenue
Los Angeles, CA 90024-1595
USA

EDITORIAL BOARD

Michel A. Aegerter
Institut für Neue Materialien (Germany)

Ilhan A. Aksay
Princeton University (USA)

David Avnir
Hebrew University of Jerusalem (Israel)

C. Jeffrey Brinker
Sandia National Laboratories (USA)

Giovanni Carturan
University of Trento (Italy)

Sandwip K. Dey
Arizona State University (USA)

Helmut Dislich
Consultant (Germany)

Dibyendu Ganguli
Central Glass & Ceramic Research Institute (India)

Massimo Guglielmi
University of Padua (Italy)

Larry L. Hench
University of Florida (USA)

Shin-ichi Hirano
Nagoya University (Japan)

P.F. James
University of Sheffield (United Kingdom)

Toshiyasu Kawaguchi
Asahi Glass Co., Ltd. (Japan)

William C. LaCourse
Alfred University (USA)

Tessy M. López
Universidad Autónoma Metropolitana (Mexico)

Akio Makishima
University of Tokyo (Japan)

Kensuke Makita
Central Glass Company (Japan)

R.C. Mehrotra
University of Rajasthan (India)

Gary L. Messing
The Pennsylvania State University (USA)

Felipe Orgaz Orgaz
Universidad Autónoma (Spain)

Edward J.A. Pope
Matech Advanced Materials (USA)

Michel Prassas
CORNING EUROPE Inc. (France)

Eliezer M. Rabinovich
AT&T Bell Laboratories (USA)

Angela B. Seddon
Centre for Glass Research (UK)

George W. Scherer
Princeton University (USA)

Helmut Schmidt
Universität des Saarlandes (Germany)

Donald R. Uhlmann
University of Arizona (USA)

Masayuki Yamane
Tokyo Institute of Technology (Japan)

Toshinobu Yoko
Kyoto University (Japan)

Bulent E. Yoldas
PPG Industries Inc. (USA)

J. Zarzycki
University of Montpellier II (France)

ISSN 0928–0707

© 1998 Kluwer Academic Publishers.

No part of the material protected by this copyright notice may be reproduced or utilized in any form or by any means, electronic or mechanical, including photocopying, recording or by any information storage and retrieval system, without written permission from the copyright owner.

Manufactured in The Netherlands.

JOURNAL OF SOL-GEL SCIENCE AND TECHNOLOGY

Volume 13—1998

1998 KLUWER ACADEMIC PUBLISHERS
Boston/U.S.A.; Dordrecht/Holland; London/U.K.

Preceding Page Blank

Journal of Sol-Gel Science and Technology **is abstracted and/or indexed in** *Current Contents®/Engineering, Computing & Technology (CC®/EC&T), SciSearch®, Research Alert®, Engineering Index, COMPENDEX PLUS, EiPageOne, Engineered Materials Abstracts, Metals Abstracts, Aluminum Industry Abstracts, Verre, and Glassfile Database.*

JOURNAL OF SOL-GEL SCIENCE AND TECHNOLOGY

SUBSCRIPTION RATE

The subscription price for 1999, Volumes 14–16 (9 issues) is: Institutions—US $787.50/NLG 1575.00
The subscription price for 1999, Volumes 14–16 (9 issues) is: Individuals—US $360.00/NLG 720.00

The above rates include postage and handling.

The individual rate is not available to institutions, libraries or companies.

For airmail delivery, please add US $9.50/NLG 22.00. The journal is shipped to the USA and Canada in bulk airfreight at no extra cost.

ORDERING INFORMATION/SAMPLE COPIES

Subscription orders and requests for sample copies should be sent to:

Kluwer Academic Publishers
P.O. Box 358–Accord Station
Hingham, MA 02018-0358
USA
PH: (781) 871-6600
FX: (781) 871-6528
EM: kluwer@wkap.com

or

Kluwer Academic Publishers
P.O. Box 322
3300 AH Dordrecht
THE NETHERLANDS

Subscriptions may also be sent to any subscription agent. Private subscriptions should be sent directly to the publisher at the above addresses.

ADVERTISING INFORMATION

For advertisement rates and other information, please write to:

Publisher
Journal of Sol-Gel Science and Technology
Kluwer Academic Publishers
101 Philip Drive
Assinippi Park
Norwell, MA 02061, U.S.A.

PHOTOCOPYING

In the U.S.A.: This journal is registered at the Copyright Clearance Center, Inc., 222 Rosewood Drive, Danvers, MA 01923, U.S.A. Authorization to photocopy items for internal or personal use, or internal or personal use of specific clients is granted by Kluwer Academic Publishers for users registered with the Copyright Clearance Center (CCC) Transactional Reporting Service, provided that the base fee of $9.50 per copy per article is paid directly to CCC. For those organizations that have been granted a photocopy license by CCC, a separate system of payment has been arranged. The fee code for users of the Transactional Reporting Service is 0928-0707/99/$9.50. This authorization does not extend to other kinds of copying, such as that for general distribution, for advertising or promotional purposes, for creating new collective works, or for resale. *In the rest of the world*: Permission to photocopy must be obtained from the copyright owner. Please apply to Kluwer Academic Publishers, P.O. Box 17, 3300 AA Dordrecht, The Netherlands.

Printed on acid-free paper.

© 1998 Kluwer Academic Publishers. Manufactured in The Netherlands.

ISSN 0928-0707

JOURNAL OF SOL-GEL SCIENCE AND TECHNOLOGY

Volume 13, Nos. 1/2/3, 1998

Guest Editors: Russell Hand, Peter James and Angela Seddon

Foreword ..... *Russell J. Hand, Peter F. James and Angela B. Seddon* 15

Sol-Gel Physical and Covalent Entrapment of Three Methyl Red Indicators: A Comparative Study ..... *Claudio Rottman, Avner Turniansky and David Avnir* 17

Structure Control in Sol-Gel Silica Synthesis Using Ionene Polymers—Evidence from X-ray Scattering .. *M.J. Adeogun, J.P.A. Fairclough, J.N. Hay and A.J. Ryan* 27

Synthesis and Structural Studies of Porous Organobridged Silicate Amorphous Powder ..... *Stuart W. Carr, Duan Li Ou and Alice C. Sullivan* 31

On the Existence and Hydrolytic Stability of Titanosiloxane Bonds in the System: Glycidoxypropyltrimethoxysilane-Water-Titaniumtetraethoxide ..... *Dagobert Hoebbel, Manfred Nacken and Helmut Schmidt* 37

Molecular Design of Novel Heterometallic Alkoxides as Precursors ..... *R.C. Mehrotra, A. Singh, M. Bhagat and J. Godhwani* 45

Spectroscopy and Structure of Sol-Gel Systems ..... *Rui M. Almeida* 51

Sulfide Gels and Films: Products of Non-Oxide Gelation ..... *L. Malier, J.P. Boilot and T. Gacoin* 61

Chemically Controlled Condensation of Polyoxovanadates ..... *J. Livage, L. Bouhedja and C. Bonhomme* 65

^{17}O-NMR of Sol-Gel Processes of TEOS and TMOS ..... *M.P.J. Peeters, T.N.M. Bernards and M.J. van Bommel* 71

NMR Studies on Hydrolysis and Condensation Reactions of Alkoxysilanes Containing Si—H Bonds ..... *Virginie Gualandris, Florence Babonneau, Michael T. Janicke and Bradley F. Chmelka* 75

On Aging of Acid-Catalyzed Silica Sols—A Dynamic Light Scattering Study ..... *B. Unger, M. Hähnert and R. Nitzsche* 81

On the Microstructure of Geyserites and Hyalites, Natural Hydrous Forms of Silica ..... *J. Göttlicher, H.J. Pentinghaus and B. Himmel* 85

Rheological and Coating Properties of Modified Silica Sols ..... *J. Marx, R. Lischewski, R. Schnabel, F. Apsel and H. Böttcher* 89

Fluorescence Probing of Composite Organic/Inorganic Transparent Matrices ..... *V. Bekiari, M. Ferrer, E. Stathatos and P. Lianos* 95

Inorganic Polymerization in a Non-Ionic Lyotropic Lamellar Phase ..... *L. Porcar, J. Marignan and T. Gulik-Krzywicki* 99

A Spectroscopic Study of an Anhydrous Tetraethyl Orthosilicate-Boric Acid-Ethanol System ..... *Congji Zha, G.R. Atkins and A.F. Masters* 103

Preparation of Inorganic Oxides via a Non-Hydrolytic Sol-Gel Route .. *John N. Hay and Hema M. Raval* 109

The Structure of Multicomponent (Titania/Zirconia) Nanoparticles ..... *J.R. Bartlett, D. Gazeau, Th. Zemb and J.L. Woolfrey* 113

Mechanism of Hydrothermal Synthesis of Zircon in a Fluoride Medium ..... *Rémi Valero, Bernard Durand, Jean-Louis Guth and Thierry Chopin* 119

Alkoxide Precursors for Er-Containing Glasses and Ceramics ..... *G. Westin, M. Wijk, M. Moustiakimov and M. Kritikos* 125

Fluoroalkoxides as Molecular Precursors of Fluoride Materials by the Sol-Gel Process ..... *O. Poncelet, J. Guilment and D. Martin* 129

Some Recent Developments in Aqueous Sol-Gel Processing ..... *A. Atkinson and D.L. Segal* 133

Inorganic-Organic Polymers with Barrier Properties for Water Vapor, Oxygen and Flavors ..... *S. Amberg-Schwab, M. Hoffmann, H. Bader and M. Gessler* 141

Design of Sol-Gel Coating Media for Ink-Jet Printing ..... *Bulent E. Yoldas* 147

Sol-Gel Science and Technology: Current State and Future Prospects .....*D.R. Uhlmann and G. Teowee* 153

Structure Design of Double-Pore Silica and Its Application to HPLC ..... *K. Nakanishi, H. Minakuchi, N. Soga and N. Tanaka* 163

Net-Shape Manufacture of Low-Cost Ceramic Shapes by Freeze-Gelation ..... *M.J. Statham, F. Hammett, B. Harris, R.G. Cooke, R.M. Jordan and A. Roche* 171

Refractive Microlens Fabrication by Ink-Jet Process ..... *S. Biehl, R. Danzebrink, P. Oliveira and M.A. Aegerter* 177

Industrial Application of Hybrid Sol-Gel Coatings for the Decoration of Crystal Glassware ..... *G. Schottner, J. Kron and A. Deichmann* 183

Sol-Gel Formation of Reticular Methyl-Silicate Materials by Hydrogen Peroxide Decomposition ..... *J. Gun, O. Lev, O. Regev, S. Pevzner and A. Kucernak* 189

Ceramic Foams from a Preceramic Polymer and Polyurethanes: Preparation and Morphological Investigations ..... *Paolo Colombo, Martina Griffoni and Michele Modesti* 195

Mullite-Alumina Composites Prepared by Sol-Gel ..... *A.M.R. Mendonça, J.M.F. Ferreira and I.M. Miranda Salvado* 201

Optical Sol-Gel Based Dissolved Oxygen Sensor: Progress Towards a Commercial Instrument ..... *C.M. McDonagh, A.M. Shields, A.K. McEvoy, B.D. MacCraith and J.F. Gouin* 207

Synthesis of Bi_2O_3 and $Bi_4(SiO_4)_3$ Thin Films by the Sol-Gel Method ..... *L. Armelao, P. Colombo and M. Fabrizio* 213

Sol-Gel Derived TiO_2/Lead Phthalocyanine Photovoltaic Cells ..... *S.M. Tracey, S.N.B. Hodgson and A.K. Ray* 219

Electrical Properties of Polycrystalline Lithium Chloroboracite Prepared by the Sol-Gel Method ..... *T. Nagase, K. Sakane and H. Wada* 223

Microstructures in High-Tc Bi-based Superconductors ..... *S. Horiuchi, M. Cantoni, Y. Tanaka, M. Ishizuka and L. Ben-dor* 229

Sol-Gel; Potential Creative Applications for the Artist, Focusing on the Colloidal Alkali Silicate Route ... *Ed Smy* 233

Bioactive Gel Coatings Derived from Vinyltrimethoxysilane ..... *Kanji Tsuru, Satoshi Hayakawa, Chikara Ohtsuki and Akiyoshi Osaka* 237

Direct Electrical Wiring of Oxidoreductase Enzymes to Silicate Based Electrodes ..... *S. Bharathi, S. Sampath, J. Gun, L. Rabinovich, Z. Wu, I. Pankratov and O. Lev* 241

Molecular Control of Bioactivity in Sol-Gel Glasses ..... *Larry L. Hench, Donna L. Wheeler and David C. Greenspan* 245

Nucleation of Hydroxyapatite on Silica-Gel: Experiments and Thermodynamic Explanation ..... *Patricia Teixeira da Costa, Tsuneharu Ogasawara, Maria Cecília de Souza Nóbrega and Luiz Cláudio Fernandes Lourenço Gomes* 251

Phase Formation in Gels of the Apatite-Anorthite System ..... *B. Samuneva, Y. Ivanova, P. Djambaski, S. Stefanova, Y. Dimitriev and M. Dimitrova-Lukacs* 255

Sol-Gel Derived Calcium Phosphate Coatings for Biomedical Applications..... *D.B. Haddow, P.F. James and R. van Noort* 261

Biodegradable Silica Fibers from Sols ..... *Monika Kursawe, Walther Glaubitt and Axel Thierauf* 267

Production of Valuable Drugs from Plant Cells Immobilized by Hybrid Sol-Gel SiO_2..... *G. Carturan, R. Dal Monte, G. Pressi, S. Secondin and P. Verza* 273

Sol-Gel Carrier Systems for Controlled Drug Delivery ..... *H. Böttcher, P. Slowik and W. Süß* 277

Encapsulation of Microbial Cells into Silica Gel ..... *Tomáš Brányik, Gabriela Kuncová, Jan Páca and Kateřina Demnerová* 283

The Application of a Sol-Gel Technique to Preparation of a Heavy Metal Biosorbent from Yeast Cells.... *János Szilva, Gabriela Kuncová, Milan Patzák and Pavel Dostálek* 289

Sol-Gel Immobilized Glucose-Oxidase: Calorimetric Investigations of Enzyme Activities..... *U. Georgi, H. Graebner, G. Roewer and G. Wolf* 295

Aerogels—Recent Progress in Production Techniques and Novel Applications ..... *J. Fricke and A. Emmerling* 299

Synthesis of Highly Porous Organic/Inorganic Hybrids by Ambient Pressure Sol-Gel Processing ..... *Guozhong Cao and Hang Tian* 305

Drying of Large Monolithic Aerogels between Atmospheric and Supercritical Pressures..... *Fikret Kirkbir, Hideaki Murata, Douglas Meyers and S. Ray Chaudhuri* 311

Thermal and Temporal Aging of Silica Gels in Monomer Solutions ..... *Mari-Ann Einarsrud and Elin Nilsen* 317

The Subcritical Preparation of Aerogels Based on Sodium Water Glass..... *Thomas Gerber* 323

Chemical and Structural Evolution of Silica Alcogels During their Formation: Acoustical Study..... *L. Forest, V. Gibiat and T. Woignier* 329

Mercury Porosimetry Applied to Low Density Xerogels; Relation between Structure and Mechanical Properties ..... *R. Pirard, B. Heinrichs, O. Van Cantfort and J.P. Pirard* 335

Parameters Involved in the Sol-Gel Transition of Titania in Reverse Micelles ..... *Nora François, Berta Ginzberg and Sara A. Bilmes* 341

Differentiation between the Green and Turkish Blue Solid Solutions of Vanadium in a Zircon Lattice Obtained by the Sol-Gel Process ..... *J.B. Vicent, J. Badenes, M. Llusar, M.A. Tena and G. Monrós* 347

Study of the Influence of Alkaline Ions (Li, Na and K) on the Structure of the Silicate Entities in Silico Alkaline Sol and on the Formation of the Silico-Calco-Alkaline Gel ..... *F. Gaboriaud, D. Chaumont, A. Nonat, B. Hanquet and A. Craeivich* 353

Preparation and Characterization of Forsterite (Mg_2SiO_4) Xerogels ..... *Matthew B.D. Mitchell, David Jackson and Peter F. James* 359

Room Temperature Densification of Aerogel by Isostatic Compression ..... *A. Hafidi Alaoui, T. Woignier, J. Phalippou and G.W. Scherer* 365

Structures, Properties and Potential Applications of Ormosils .... *John D. Mackenzie and Eric P. Bescher* 371

Structure Development in Simple Cross-Linked Organopolysiloxanes ..... *G.J. Gibbons, D. Holland and A.P. Howes* 379

FT-Raman-Spectroscopic Investigations of the System Glycidoxypropyltrimethoxysilane/Aminopropyltriethoxysilane ..... *B. Riegel, W. Kiefer, S. Hofacker and G. Schottner* 385

Encapsulation versus Tethering in the Incorporation of $C_5H_5Rh(CO)_2$ into Hybrid Inorganic-Organic Cubane $\{Si_8O_{12}\}$ Copolymers ..... *Philip G. Harrison and Christopher Hall* 391

The Sol-Gel Process for Nano-Technologies: New Nanocomposites with Interesting Optical and Mechanical Properties ..... *H.K. Schmidt, E. Geiter, M. Mennig, H. Krug, C. Becker and R.-P. Winkler* 397

Ceramers Based on Crosslinked Epoxy Resins-Silica Hybrids: Low Surface Energy Systems ..... *L. Mascia and T. Tang* 405

Coating of Tetraethylorthosilicate (TEOS)/Vinyltriethoxysilane (VTES) Hybrid Solution on Polymer Films ..... *Young-Joo Eo, Duk-Jun Kim, Byeong-Soo Bae, Ki-Chang Song, Tae-Young Lee and Seung-Won Song* 409

Porous Silica Obtained from Biodegradable and Biocompatible Inorganic-Organic Hybrid Materials ..... *D. Tian, S. Blacher, Ph. Dubois, J.P. Pirard and R. Jérôme* 415

Preparation of Saccharide-Silica Composites by a Sol-Gel Method and the Application for Optical Resolution of Metal Chelate Compounds ..... *Y. Akiyama, F. Mizukami, H. Izutsu, M. Sato, K. Maeda, Y. Kiyozumi and K. Sakaguchi* 421

Study of Hybrid Silica-Polyethyleneglycol Xerogels by Eu^{3+} Luminescence Spectroscopy ..... *S.J.L. Ribeiro, K. Dahmouche, C.A. Ribeiro, C.V. Santilli and S.H. Pulcinelli* 427

Hybrid Silica Gel-Polytetrahydrofuran Thin Films ..... *Alexandra Fidalgo and Laura Ilharco* 433

Photoluminescence Study of Functionalized Polysiloxane Gel ..... *R. Kalfat, N. Gharbi, S. Romdhane, J.-L. Fave, A. Chaïeb and M. Majdoub* 439

Processing and Properties of Inorganic-Organic Hybrids Containing Various Inorganic Components ..... *Noriko Yamada, Ikuko Yoshinaga and Shingo Katayama* 445

Microstructural and Mechanical Properties of Sono-Ormosils ..... *E. Blanco, M. García-Hernández, R. Jiménez-Riobóo, R. Litrán, C. Prieto and M. Ramírez-del-Solar* 451

Hybrid Xerogel Structure and Molecular Guest Dynamics.... *F. Cros, L. Malier, J.-P. Korb and F. Chaput* 457

X-Ray Diffraction Studies of Sol-Gel Derived ORMOSILs Based on Combinations of Tetramethoxysilane and Trimethoxysilane ..... *S.L.B. Lana and A.B. Seddon* 461

Thin ORMOSIL Films with Different Organics ..... *K.A. Vorotilov, V.A. Vasiljev, M.V. Sobolevsky and A.S. Sigov* 467

Leaching of the Anthraquinone Dye Solvent Blue 59 Incorporated into Organically Modified Silica Xerogels ..... *Jan-Christoph Panitz and Friederike Geiger* 473

Hybrid Pigments via Sol-Gel Processing ..... *S. Hofacker and G. Schottner* 479

Lignin-Silica-Titania Hybrids as Precursors for Si—Ti—C—O Fibers ..... *Isao Hasegawa, Yuka Fukuda, Tomohiro Okada and Meisetsu Kajiwara* 485

ORMOCER Coatings Based on Titanium and Poly(tetraethylene glycol malonate) ..... *C.S. Deng, P.V. Wright and P.F. James* 489

Vanadium-Based Organic-Inorganic Hybrid Materials Prepared by a Sol-Gel Method ..... *M. Mohseni, P.F. James and P.V. Wright* 495

SAXS and TEM Investigations on Thermoplastic Nanocomposites Containing Functionalized Silica Nanoparticles ..... *C. Becker, B. Kutsch, H. Krug and H. Kaddami* 499

CW and Pulsed EPR Study of Silver Nanoparticles in an SiO_2 Matrix ..... *G. Mitrikas, Y. Deligiannakis, C.C. Trapalis, N. Boukos and G. Kordas* 503

Development of the SC-RTA Process for Fabrication of Sol-Gel Based Silica-on-Silicon Integrated Optic Components ..... *R.R.A. Syms, A.S. Holmes, W. Huang, V.M. Schneider and M. Green* 509

Strip-Loaded High-Confinement Waveguides for Photonic Applications ..... *E.M. Yeatman, K. Pita, M.M. Ahmad, A. Vannucci and A. Fiorello* 517

Photocurable Sol-Gel Coatings: Channel Waveguides for Use at 1.55 μm ..... *P. Etienne, P. Coudray, Y. Moreau and J. Porque* 523

Structural and Optical Properties of Sol-Gel Derived Aluminosilicate Planar Waveguides Doped with Er^{3+} Ions ..... *M. Benatsou, B. Capoen, M. Bouazaoui, W. Tchana and J.P. Vilcot* 529

Fabrication and Characterization of Sol-Gel GeO_2-SiO_2 Erbium-Doped Planar Waveguides ..... *A. Martucci, G. Brusatin, M. Guglielmi, C. Strohhöfer, J. Fick, S. Pelli and G.C. Righini* 535

Hole Burning and Fluorescence Spectra of Sol-Gel Derived Sm^{2+}-Doped Glasses ..... *Masayuki Nogami and Yoshihiro Abe* 541

Sol-Gel Prepared Glass for Refractive and Diffractive Micro-Optical Elements and Arrays ..... *Y. Haruvy, I. Gilath, M. Maniewictz and N. Eisenberg* 547

Reversing Gels and Water Soluble Colloids from Aminosiloxanes ..... *T. Suratwala, K. Davidson, Z. Gardlund, D. Collins and D.R. Uhlmann* 553

Optical Nonlinearity of Hybrid and Nanocomposite Materials Prepared by the Sol-Gel Method ..... *Fuxi Gan* 559

Matrix Effects on Selective Chemical Sensing by Sol-Gel Entrapped Complexing Agents ..... *Nico A.J.M. Sommerdijk and John D. Wright* 565

Fabrication and Properties of Doped Porous Polysiloxane Sol-Gel Layers on Optical Fibers ..... *Daniela Berková, Miroslav Sedlář, Vlastimil Matějec, Ivan Kašík, Miroslav Chomát, Adnane Abdelghani, Nicole Jaffrezic-Renault and Monique Lacroix* 569

High Performance Varistor Discs Obtained from Chemically Synthesized Doped Zinc Oxide Powder..... *Ramón Puyané, Isabelle Guy and Renaud Metz* 575

Control of Dopant Adsorption from Aqueous Solution into Nanoporous Sol-Gel Films ..... *O. McCarthy and E.M. Yeatman* 579

Silicate Xerogels with Dopant-Induced Chirality ..... *Krzysztof Maruszewski, Marek Jasiorski, Witold Wacławek, Wiesław Stręk and Marek Lisowski* 585

Preparation of Ce^{3+}-Doped Inorganic-Organic Hybrid Materials Using Functionalized Silanes ..... *M. Iwasaki, J. Kuraki and S. Ito* 587

Qualitative and Quantitative Studies of Neodymium Doped Silica Gel-Glasses ..... *Carole C. Perry and Séverine Aubonnet* 593

Effect of Pr^{3+} Doping on the OH Content of Silica Xerogels ..... *C. Armellini, L. Del Longo, M. Ferrari, M. Montagna, G. Pucker and P. Sagoo* 599

Preparation and Optical Characterization of Organoeuropium-Doped Silica Gels ..... *Vilma C. Costa, Wander L. Vasconcelos and Kevin L. Bray* 605

Fluorescence and Absorption Probe of Metal Ion Centers in Silicates Obtained by the Sol-Gel Technique. ..... *J. Sokolnicki, K. Maruszewski, W. Stręk and J. Legendziewicz* 611

Sol-Gel Fabrication and Properties of Silica Cores of Optical Fibers Doped with Yb^{3+}, Er^{3+}, Al_2O_3 or TiO_2 ..... *Vlastimil Matějec, Ivan Kašík, Daniela Berková, Miloš Hayer and Jiří Kaňka* 617

CdSe Quantum Dot Doped Amine-Functionalized Ormosils..... *Angela B. Seddon and Duan Li Ou* 623

Sans Study of CdS and CdSe Quantum Dot Crystal Growth in a Silica Matrix by Sol-Gel ..... *N. de la Rosa-Fox, A. Santos, M. Piñero, L. Esquivias, L. Gago-Duport and E. Hoinkis* 629

Optical and Structural Properties of Doped ZnS Nanoparticles Produced by the Sol-Gel Method..... *D.U. Saenger, G. Jung and M. Mennig* 635

Optimization of Ormosil Films for Optical Sensor Applications ..... *P. Lavin, C.M. McDonagh and B.D. MacCraith* 641

Enhanced Second Order Non-Linear Optical Properties of Silica Sol-Gel Thin Films Through Photo-Induced Poling ..... *B. Abbas and G.R. Mitchell* 647

Aggregation Properties of Metallic Tetrasulphophthalocyanines Encapsulated in Sol-Gel Materials ..... *M.A. Garcia and A. Campero* 651

Photodegradation of Luminescence in SiO_2 : Rh B Gels Exposed to YAG : Nd Laser Pulses ..... *J. Garcia M., E. Ramirez J., M.A. Mondragon, R. Ortega, P. Loza and A. Campero* 657

Thermochromic Properties of Silver Colloids Embedded in SiO_2 Gels..... *V.M. Renteria, A. Campero and J. Garcia M.* 663

Sol-Gel Preparation of α-Fe_2O_3 Thin Films: Structural Characterization by XAFS and Raman ..... *C. Baratto, P.P. Lottici, D. Bersani, G. Antonioli, G. Gnappi and A. Montenero* 667

Characterization of Electrochromic WO_3 Layers Prepared by Sol-Gel Nanotechnology ..... *B. Munro, S. Krämer, P. Zapp and H. Krug* 673

Sol-Gel Deposited Sb-Doped Tin Oxide Films ..... *M. Guglielmi, E. Menegazzo, M. Paolizzi, G. Gasparro, D. Ganz, J. Pütz, M.A. Aegerter, L. Hubert-Pfalzgraf, C. Pascual, A. Durán, H.X. Willems, M. Van Bommel, L. Büttgenbach and L. Costa* 679

Synthesis and Optical Properties of Mn^{2+}-Doped ZnS Nanoparticles in Solutions and Coatings..... *U. Sohling, G. Jung, D.U. Saenger, S. Lu, B. Kutsch and M. Mennig* 685

Preparation of the TiO_2 Thin Film Photocatalyst by the Dip-Coating Process ..... *Nobuaki Negishi, Koji Takeuchi and Takashi Ibusuki* 691

Glass Strengthening Using Ormosil Polymeric Coatings ..... *R.J. Hand, F.H. Wang, B. Ellis and A.B. Seddon* 695

Sol-Gel Preparation of Coating Films Containing Noble Metal Colloids ..... *Sumio Sakka and Hiromitsu Kozuka* 701

Optical Viscometry of Spinning Sol Coatings ..... *F. Horowitz, A.F. Michels and E.M. Yeatman* 707

Aerial Oxidation of Tetraethyl Silicate and Effect on Ammonia Catalyzed Hydrolysis .... *Ian M. Thomas* 713

Investigation of Glass-Like Sol-Gel Coatings for Corrosion Protection of Stainless Steel Against Liquid and Gaseous Attack... *M. Mennig, C. Schelle, A. Duran, J.J. Damborenea, M. Guglielmi and G. Brusatin* 717

Sol-Gel Coatings on 316L Steel for Clinical Applications ..... *Pablo Galliano, Juan José de Damborenea, M. Jesús Pascual and Alicia Durán* 723

Organopolysiloxanes as Chemically Sensitive Coatings for Optical Fibers..... *Klaus Rose, Vlastimil Matějec, Milos Hayer and Marie Pospišilová* 729

Sol-Gel Processing of Organic-Inorganic Nanocomposite Protective Coatings ..... *Yunfa Chen, Lianming Jin and Yusheng Xie* 735

Synthesis of Transparent Mesoporous and Mesostructured Thin Silica Films ..... *J.M. Berquier, L. Teyssedre and C. Jacquiod* 739

Elaboration at 80°C of SiO_2 Layers Deposited by Aerosol-Gel Process..... *M. Langlet and C. Vautey* 743

The Effect of HF in a Two-Step Sol-Gel Process of TEOS..... *T.N.M. Bernards, M.J. Van Bommel and J.A.J. Jansen* 749

Inhibition of Pb-Leaching from Lead Crystal Glass by Coating with Films Prepared by the Sol-Gel Method ..... *A.A. Ahmed, I.M. Youssof, A.F. Abbas and O. Abou Eleinen* 753

Comparison of Different High and Low Index Materials in the Manufacture of High Laser Damage Threshold Mirrors at the 351 nm Wavelength ..... *N. Bazin, J.E. Andrew and H.A. Mcinnes* 757

Atomic Force Microscopy Study of NaOH Corroded Al_2O_3-TiO_2-SiO_2 Coatings on Glass..... *Yongjuan Du, Edda Rädlein and Günther Heinz Frischat* 763

Atomic Force Microscopy Study of TiO_2 Films Obtained by the Sol-Gel Method..... *Maria Zaharescu, Maria Crisan and I. Muševič* 769

Vanadium Doped Sol-Gel TiO_2 Coatings..... *Maria Crisan, Maria Zaharescu, D. Crisan, Rodica Ion and Mihaela Manolache* 775

Development of Heteropolysiloxane Coatings on Electrogalvanized Steel ..... *M. Mayrand, J.F. Quinson, V. Roisne and H. Guyon* 779

Multilayer SiO_2-B_2O_3-Na_2O Films on Si for Optical Applications ..... *N. Pellegri, E.J.C. Dawnay and E.M. Yeatman* 783

Synthesis of Nanocrystalline, Redispersable Antimony-Doped SnO_2 Particles for the Preparation of Conductive, Transparent Coatings ..... *Detlef Burgard, Christian Goebbert and Rüdiger Nass* 789

Improved Conductivity Induced by Photodesorption in SnO_2 Thin Films Grown by a Sol-Gel Dip Coating Technique ..... *Luis V.A. Scalvi, Fábio R. Messias, A.E. Souza, M. Siu Li, C.V. Santilli and S.H. Pulcinelli* 793

Phase Development in Sol Derived Microporous Membranes for Gas Permselectivity ..... *U. Stefan Björkert, Diane Holland and Mike H. Lewis* 799

Study of the Selectivity of SnO_2 Supported Membranes Prepared by a Sol-Gel Route..... *L.R.B. Santos, A. Larbot, C.V. Santilli and S.H. Pulcinelli* 805

Ferroelectric PZT Thin Films by Sol-Gel Deposition..... *Ian M. Reaney, David V. Taylor and Keith G. Brooks* 813

Preparation of Thick PZT Ceramic Film by an Interfacial Polymerization ..... *Masayuki Yamane* 821

Lead Zirconate-Titanate Films Prepared from Soluble Powders..... *Peer Löbmann, Susanne Seifert, Stefan Merklein and Dieter Sporn* 827

Acetic Acid Based Sol-Gel PLZT Thin Films: Processing and Characterization ..... *Barbara Malič, Nava Setter, Keith Brooks, Marija Kosec and Goran Dražič* 833

Chemistry-Crystallization-Microstructure Relations of Sol-Gel Derived Lanthanum Modified Lead Titanate Thin Films .....*M.L. Calzada, M. Algueró and L. Pardo* 837

Study by Rutherford Backscattering Spectroscopy of the Heterostructure of Lead Titanate Thin Films ....*M.J. Martín, M.L. Calzada, J. Mendiola, M.F. da Silva and J.C. Soares* 843

A Raman Scattering Study of $PbTiO_3$ and TiO_2 Obtained by Sol-Gel..... .....*D. Bersani, P.P. Lottici, T. Lopez and Xing-Zhao Ding* 849

The Effect of Barrier Layer Composition and Structure on the Crystallization of PZT Coatings on Silicon ..... *D.P. Birnie III, M.H. Jilavi, T. Krajewski and R. Naß* 855

Study of the Lead Environment in Liquid and As-Dried Precursors of PZ, PT and PZT Thin Films .... *Iztok Arčon, Barbara Malič, Marija Kosec and Alojz Kodre* 861

Preparation of PZT Film and Powder by Sol-Gel Technique Using Ti- and Zr-Alkoxides and a Novel Pb-Precursor; $Pb(NO_3)_2$1.5EO3..... *K. Lashgari and G. Westin* 865

Synthesis and Characterization of Highly Oriented Sol-Gel (Pb, La)TiO_3 Thin Film Optical Waveguides . ..... *Junmo Koo, Kwangsoo No and Byeong-Soo Bae* 869

Preparation of Transparent, Partially-Crystallized $BaTiO_3$ Monolithic Xerogels by Sol-Gel Processing ... . *Hirokazu Shimooka, Ken-Ichi Yamada, Seiji Takahashi and Makoto Kuwabara* 873

Sol-Gel Derived Barium-Strontium Titanate Films ..... *V.A. Vasiljev, K.A. Vorotilov, M.I. Yanovskaya, L.I. Solovjeva and A.S. Sigov* 877

$SrBi_2Nb_2O_9$ Ferroelectric Powders and Thin Films Prepared by Sol-Gel..... .....*J.H. Yi, P. Thomas, M. Manier, J.P. Mercurio, I. Jauberteau and R. Guinebretière* 885

Ferroelectric Thin Films of Bismuth Strontium Tantalate Prepared by Alkoxide Route ..... *E.P. Turevskaya, V.B. Bergo, K.A. Vorotilov, A.S. Sigov and D. Benlian* 889

Preparation and Characterization of Sol-Gel Derived Y_2O_3 Thin Films ..... *G. Teowee, K.C. McCarthy, F.S. McCarthy, T.J. Bukowski, D.G. Davis Jr. and D.R. Uhlmann* 895

Dielectric and Ferroelectric Properties of Sol-Gel Derived $YMnO_3$ Films ..... *G. Teowee, K.C. McCarthy, F.S. McCarthy, T.J. Bukowski, D.G. Davis Jr. and D.R. Uhlmann* 899

Preparation and Dielectric Properties of $YMnO_3$ Ferroelectric Thin Films by the Sol-Gel Method ..... *Kiyoharu Tadanaga, Hiroya Kitahata, Tsutomu Minami, Norifumi Fujimura and Taichiro Ito* 903

Investigation of New-Ion Conducting Ormolytes Silica-Polypropyleneglycol ..... *K. Dahmouche, P.H. de Souza, T.J. Bonagamba, H. Paneppucci, P. Judeinstein, S.H. Pulcinelli and C.V. Santilli* 909

Optical Switching in VO_2 Thin Films ..... *F. Béteille and J. Livage* 915

Electrochromic Properties of Peroxopolytungstic Acid Thin Films ..... *B. Pecquenard, H. Lecacheux, S. Castro-Garcia and J. Livage* 923

Metal (Fe, Co, Ni) Nanoparticles in Silica Gels: Preparation and Magnetic Properties ..... *T. Lutz, C. Estournès and J.L. Guille* 929

Role of Water on Fast Proton Conduction in Sol-Gel Glasses ..... *Masayuki Nogami, Ritsuko Nagao, Wang Cong and Yoshihiro Abe* 933

Sintering Aerogels ..... *George W. Scherer, Sylvie Calas and Robert Sempéré* 937

Silicon Oxycarbide Glasses Derived from Polymer Precursors ..... *K. Eguchi and G.A. Zank* 945

Crystallization of Gels in the Apatite-Mullite System ..... *B. Samuneva, V. Dimitrov, S. Kalimanova, E. Gattef and R. Hill* 951

Structural Efficiency and Microstructural Modeling of Wet Gels and Aerogels ..... *Joachim Gross and George W. Scherer* 957

Laser Sintering of SnO_2 : Sb Sol-Gel Coatings ..... *D. Ganz, G. Gasparro and M.A. Aegerter* 961

Silica Gels and Gel Glasses Containing Silver and Platinum Metal Particles ..... *B. Samuneva, Y. Dimitriev, V. Dimitrov, E. Kashchieva and G. Encheva* 969

Crystallization Behavior of SiO_2-TiO_2 Ceramics Derived from Titanosiloxanes on Pyrolysis ..... *Takahiro Gunji, Takayuki Kasahara and Yoshimoto Abe* 975

β-Eucryptite by a Sol-Gel Route ..... *Wafa I. Abdel-Fattah, M.SH. Fayed, SH.R. Gooda and W.F.F. Mekky* 981

Role of MnO on the Mullitization Behavior of Al_2O_3-SiO_2 Gels ..... *M.G. Ferreira da Silva* 987

Ultraviolet-Lasers-Induced Crystallization of Sol-Gel Derived Indium Oxide Films ..... *Hiroaki Imai, Atsushi Tominaga, Hiroshi Hirashima, Motoyuki Toki and Mamoru Aizawa* 991

Sol-Gel Synthesis and Microstructural Characterization of Silicon Oxycarbide Glass Sheets with High Fracture Strength and High Modulus ..... *N. Suyal, T. Krajewski and M. Mennig* 995

Sol-Gel Synthesis and Structure of Borosilicon Oxycarbide Glasses ..... *A.M. Wootton and M.H. Lewis* 1001

Influence of the Heating Rate on the Microstructure and on Macroscopic Properties of Sol-Gel SnO_2 : Sb Coatings ..... *J. Pütz, D. Ganz, G. Gasparro and M.A. Aegerter* 1005

Production of Titanate Microspheres by Sol-Gel and Spray-Drying ..... *E. Sizgek, J.R. Bartlett and M.P. Brungs* 1011

Preparation of Mullite Fibers by the Sol-Gel Method ..... *K. Chang Song* 1017

Synthesis and Characterization of PZT-Fibers via Sol-Gel ..... *O. Binkle and R. Nass* 1023

Effect of Solvent Diols and Ligands on the Properties of Sol-Gel Alumina-Silicas ..... *Fujio Mizukami, Yoshimichi Kiyozumi, Tsuneji Sano, Shu-Ich Niwa, Makoto Toba and Shigemitsu Shin* 1027

Application of ZrO_2-Al_2O_3 Aerogels to Catalysts ..... *K. Kohama, H. Imai, H. Hirashima, H. Hamada and M. Inaba* 1033

Preparation of Layer Structure-Controlled Ru-Sn-Al_2O_3 Catalysts and Their Reactivity ..... *M. Toba, S. Tanaka, S. Niwa, F. Mizukami, Z. Koppány and L. Guczi* 1037

Evidence for Lewis and Brønsted Acid Sites on MgO Obtained by Sol-Gel ..... *T. López, R. Gómez, J. Navarrete and E. López-Salinas* 1043

Chemical Microengineering in Sol-Gel Derived Fluoride and Lanthanide Modified Ceria Materials ..... *Philip G. Harrison, Adam Kelsall and John V. Wood* 1049

Structural and Chemical Modification of Polydiene Latexes by Gel Derived Silica ..... *I.A. Toutorski, T.E. Tkachenko and N.I. Maliavski* 1057

Thematic Index 1061

Author Index 1063

Subject Index 1069

9th INTERNATIONAL WORKSHOP ON GLASSES AND CERAMICS, HYBRIDS & NANOCOMPOSITES FROM GELS

'SOL-GEL '97'

Centre for Glass Research,
The University of Sheffield, UK
31 August–5 September 1997

JOINT CHAIRMEN
Peter F. James and Angela B. Seddon

DEPUTY CHAIRMAN
Russell J. Hand

Workshop Administrator
Jill Costello
Society of Glass Technology

Local Organisating Committee
Paul V. Hatton
William E. Lee
Rik van Noort
Ian M. Reaney
Mike L. Turner
Diane Holland
Alan Taylor

INTERNATIONAL ADVISORY BOARD

M.A. Aergerter (Germany)
R.M. Almeida (Portugal)
C.J. Brinker (USA)
A. Campero (Mexico)
L. Esquivias (Spain)
F. Gan (China)
M. Guglielmi (Italy)
L.L. Hench (UK)
J.L. Illinger (USA)
P.F. James (UK)
J. Livage (France)
J.D. Mackenzie (USA)
C.G. Pantano (USA)
S. Sakka (Japan)
H. Schmidt (Germany)
G.W. Scherer (USA)
A.B. Seddon (UK)
D.R. Uhlmann (USA)
M. Yamane (Japan)
J. Zarzycki (France)

SPONSORSHIP

We sincerely thank the following Organizations for their generous sponsorship of Sol-Gel '97:

- Dow Corning Ltd.
- Pilkington Technology Centre
- The Ravenhead Company Ltd.
- Zortech International Ltd.
- Centre for Glass Research, University of Sheffield
- European Commission,
  Directorate General XII
  Science, Research and Development,
  Directorate C:
  Industrial and Materials Technologies
- USARDSG,
  United States Army,
  European Research Office
- ONREUR,
  United States Navy,
  European Office of Naval Research
- EOARD,
  United States Airforce,
  European Office of Aerospace Research and Development
- Society of Glass Technology
- Sheffield City Council

P.F. James and A.B. Seddon

Journal of Sol-Gel Science and Technology 13, 15 (1998)
© 1998 Kluwer Academic Publishers. Manufactured in The Netherlands.

Foreword

The first day of Sol-Gel '97 was marked with sadness by the unexpected death of Princess Diana. This was compounded by the unusual monsoon-type weather in the UK on the 31 August 1997 as we welcomed our rather damp delegates to Sheffield.

The pro-Vice chancellor of the University of Sheffield Professor A.M. Gamble, on opening the Workshop, paid tribute to the Princess for her charity work and her compassion for AIDS sufferers, land mine victims and disadvantaged children the world over. Following on, Professor David Avnir, our Keynote Lecturer, also paid tribute to her on behalf of our overseas visitors.

Professor Avnir went on to present a superb, extended review of his excellent work in the area of encapsulation in sol-gel derived materials setting a high standard which was maintained for the rest of the week ensuring that Sol-Gel '97 lived up to its predecessor Workshops. The Sol-Gel Workshop is the premier forum for discussion of the latest developments in the rapidly growing, multidisciplinary field of sol-gel science and technology, which now includes the exciting new areas of organic-inorganic hybrid materials and nanocomposites via sol-gel. Indeed, lively, open debate followed many of the oral presentations during the week of the Workshop. There were 22 invited papers and 57 other oral papers, with no parallel sessions, and 184 poster papers. All papers subsequently accepted for publication here have undergone refereeing. About 300 delegates attended Sol-Gel '97 from 36 different countries.

We would like sincerely to thank our Local Organization Committee for all of their hard work; Jill Costello and her team from the Society of Glass Technology for the splendid conference administration and the International Advisory Committee for awarding us the honor of bringing the 9th Workshop to Sheffield. We are exceedingly grateful to our financial Sponsors, listed herewith, for making the Workshop possible.

As Chairmen of Sol-gel '97 we should like to wish the incoming Chairman, Professor Masayuki Yamane of the Tokyo Institute of Technology, Japan, much success with Sol-Gel '99 to be held in Yokohama, Japan.

Russell J. Hand
Peter F. James
Angela B. Seddon
Guest Editors of these Proceedings

Journal of Sol-Gel Science and Technology 13, 17–25 (1998)
© 1998 Kluwer Academic Publishers. Manufactured in The Netherlands.

Sol-Gel Physical and Covalent Entrapment of Three Methyl Red Indicators: A Comparative Study

CLAUDIO ROTTMAN, AVNER TURNIANSKY AND DAVID AVNIR
Institute of Chemistry, The Hebrew University of Jerusalem, Jerusalem 91904, Israel
david@granite.fh.huji.ac.il

Abstract. We report the results of a comparative study of the properties of three azo dyes from the methyl red indicator family, which were coentrapped with the surfactant cetyltrimethylammonium bromide within tetramethoxysilane-derived silica sol-gel matrices. Characteristic parameters studied were spectral shifts, shifts in indicating ranges and in pK_i values, isosbestic-point behavior, changes in the titration curves and stability to leaching. Physical entrapment of methyl red and para-methyl red (pMR) is compared to the covalent entrapment of a trialkoxysilane derivative of methyl red. High stability for leaching was found for all three entrapped indicators. The pK_i change in entrapped pMR is interpreted in terms of intracage motion induced by pH changes.

Keywords: entrapment pH indicators, surfactants, CTAB

1. Background

Chemical sensors are amongst the prime applications of organically doped reactive sol-gel materials [1]. In fact, the widest array of chemical reactions which has been carried out within sol-gel matrices was revealed while developing the doped sol-gel methodology for chemical sensing purposes [1–4]. They include proton-transfer reactions (such as pH indicators), redox reactions, complexations, ligand exchanges, enzymatic reactions and more [5]. Common to these reactions is their ability to sense chemical changes in the environment of the entrapped molecule, revealing it through color-developing reactions between the entrapped reagent and an external diffusable chemical species or through emission of light. In particular, the chemical inertness and the optical transparency of SiO_2 sol-gel matrices, have made the doping of this material quite suitable for sensor applications. The development of sol-gel pH sensors attracted several laboratories, employing various indicators and various techniques, based both on light absorption [4, 6] and fluorescence emission [7–9]. Configurations included simple monolithic discs embedded with various routinely used indicators [4, 6], thin films [10–12], fluorescent and absorbance fiber optics configurations [13], capillaries [14, 15] and miniaturized tips [16].

In a previous publication we reported the beneficial aspects of the coentrapment of the azo pH indicator methyl orange with the surfactant cetyltrimethylammonium bromide (CTAB) [6]. Here we extend it to a comparative study of the properties of methyl red, para-methyl red and a covalently bound methyl red within tetramethoxysilane (TMOS)-derived silica sol-gel matrices. Characteristic parameters studied were spectral shifts, shifts in indicating ranges and in pK_i values, isosbestic-point behavior, changes in the titration curves and stability to leaching. Very good stability from this point of view is reported.

2. Experimental Details

Chemicals. $Si(OCH_3)_4$ (TMOS) was from Aldrich. Cetyltrimethyl ammonium bromide (CTAB) was from Fluka. The indicators (Fig. 1) were methyl red (MR) from Aldrich and *p*-(*p*-dimethylaminophenyl-azo)benzoic acid sodium salt (pMR) from Kodak.

Synthesis of the Trimethoxysilylpropylamide Derivative of Methyl Red. MR was converted to the

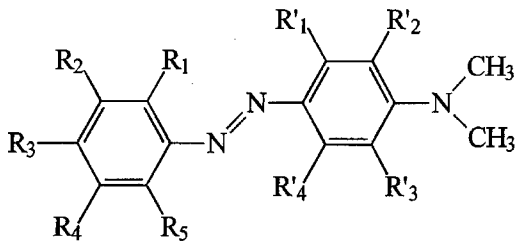

Methyl Red (MR): $R_1 = CO_2^-$; R_2, R_3, R_4, R_5, $R'_n = H$

p-Methyl Red (pMR): $R_3 = CO_2^-$; R_1, R_2, R_4, R_5, $R'_n = H$

Methyl Red Amidopropyltrimethoxysilane (MRAP):

$R_1 = C(O)N(H)(CH_2)_3Si(OCH_3)_3$; R_2, R_3, R_4, R_5, $R'_n = H$

Figure 1. Structures of the different MR indicators used in this study.

trimethoxysilylpropylamide derivative via dicyclohexyl carbodiimide (DCC) coupling between the amine residue of γ-aminopropyltrimethoxysilane (APTS) with the carboxyl residue of MR (2-[4-(dimethylamino)phenylazo]benzoic acid) (Fig. 1). 2.7 g (0.01 mole) of MR was placed in a three necked flask equipped with a magnetic stirrer and dissolved in 60 ml of dichloromethane (Frutarom, analytical, distilled and kept over molecular sieve 4). The reaction was performed under dry nitrogen (99.99%). 1.75 ml of APTS (ABCR, 99%, 0.01 mole) was added dropwise to the flask while cooling the flask in ice water. 2.27 g of DCC (Sigma, 0.011 mole) was added to the flask. After 30 min the cooling bath was removed and the mixture stirred for 7 h. The mixture was then filtered to remove the DCC-Urea and the solvent evaporated. The dark red residue was recrystallized from a methylenechloride-cyclohexane mixture (Merck, spectroscopic grade) to give the methyl red-amidopropyltrimethoxysilane, MRAP, as dark red-brown small needles (2.768 g, 64% yield, m.p. 95–96°C). Elemental analysis: Calculated C—58.58%, H—7.02%, N—13.01%; found C—59.01%, H—7.16%, N—13.19%; ^{1}H-NMR (ppm): 0.74 (2H, m), 1.79 (2H, m), 3.13 (6H, s), 3.53 (9H + 2H, s + m), 6.8 (2H, m), 7.49 (3H, m), 8.37 (1H, m), 9.11 (1H, s). ^{13}C-NMR (ppm): 6.86, 23.11, 40.25, 42.62, 50.54, 111.65 (strong), 115.86, 118.73, 125.69, 129.54, 129.78, 131.41, 131.49, 143.52, 150.44, 153.13, 166.13.

Physical Entrapment of MR and pMR. The following mixture was prepared in a 20 ml flask: 2.5 ml MeOH, 2.5 ml TMOS and 1.0 ml of a $8.2 \cdot 10^{-2}$ M methanolic solution of CTAB (CTAB : silane = $4.8 \cdot 10^{-3}$: 1). The mixture was sonicated for 5 min, after which 2.3 ml of water (water : silane = 7.6 : 1) and 0.1 ml solution of a 0.02–0.1% (w/w) of the indicator in water (pMR) or methanol (MR and MRAP) were added. The final mixture was sonicated for 10 more minutes and poured into a Petri dish (60 mm in diameter, 20 mm high), covered and left at room temperature for 5 days for the gelation and initial shrinkage. The wet gel shrank further, resulting in a transparent disc with typical dimensions of 26 mm in diameter and thickness of 2.5 mm.

Covalent Entrapment of MRAP. This was carried out as above using the following molar proportions: TMOS : water : methanol : MRAP : CTAB = 1 : 7.6 : 5.06 : 7.4×10^{-4} : 4.8×10^{-3}.

pH Indicating Performance. pH changes were affected with nonbuffered solutions. Isosbestic points were determined by taking full spectra within the cell of an HP 8452 diode array spectrophotometer each 5 or 15 s, depending on the observed response time of the different indicators tested. Full titration curves were obtained by taking the relative absorptions of the indicator basic/acidic forms, after the sol-gel glass had been immersed in solutions of different pH values, and

Table 1. Properties of the indicators.[a]

Indicator	Color change	pK_i glass	pK_i solution	λ_{max} (nm) glass	λ_{max} (nm) solution
MR	(A) R-Y (B)	4.9	5.05	(A) 522–422 (B)	(A) 518–436 (B)
pMR	(A) RO-Y (B)	0.9	2.10	(A) 506–430 (B)	(A) 510–464 (B)
MRAP	(A) R-OY (B)	3.2	3.30	(A) 518–472 (B)	(A) 514–466 (B)

[a]A: acidic form, B: basic form, R: red, RO: red-orange, OY: orange-yelow, Y: yellow.

after equilibrium was reached (about 15 min after the glass immersion).

Leaching Tests. Leaching tests were carried out by placing the sol-gel glass (with dimensions of about $8 \times 10 \times 1.5$ mm) in 50 ml of water at pH = 0.01.

3. Results

Spectral Shifts and Indicating Range Shifts. In Table 1 the observations made regarding the indicating ranges of the various entrapped molecules within the SiO_2 sol-gel glasses, along with their spectral characteristics and with comparison to solution values. It is seen that the indicating ranges of the entrapped MR dyes are shifted to more acidic values. As for the trimethoxysilane derivative of MR, MRAP (Fig. 1), as expected, the blockage of the carboxyl moiety in MR shifts the pK_i of MRAP in solution from 5.05 (which is the pK_i of MR in solution) to 3.30. This shift is an outcome of the inability to form zwitterionic forms of the type shown in Scheme B, because of the unavailability of the carboxylate moiety (see Section 4).

Since hydrolysis and polymerization may lead to non-homogeneous distributions and aggregations during the co-polymerization process of MRAP, we checked this point by testing whether Beer-Lambert behavior is maintained for aqueous solutions of MRAP at concentrations much higher than needed for the doped glass. As seen in Fig. 2, Beer-Lambert behavior is indeed maintained.

Isosbestic Points, Titration Curves and pK_i Values. Determination of isosbestic points within the porous glasses is shown in Fig. 3. Differences between the three MR pH indicators in the sharpness of their isosbestic points attest to changes in the homogeneity of the environment around the physically entrapped dyes as the pH of the solution change (see Section 4).

Titration curves in the glass are shown in Fig. 4. The resulting pK_i values are collected in Table 1. The shift in the behavior of MRAP due to the silylation, is again evident.

Stability to Leaching. Stability to leaching was analyzed as a pseudo first-order process. The results for

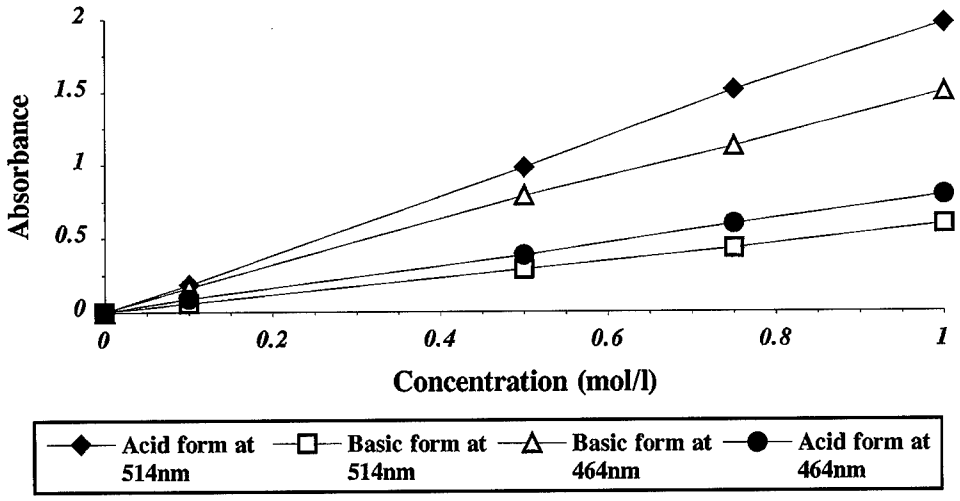

Figure 2. Beer-Lambert behavior of MRAP, the trimethoxysilane derivative of MR (Fig. 1).

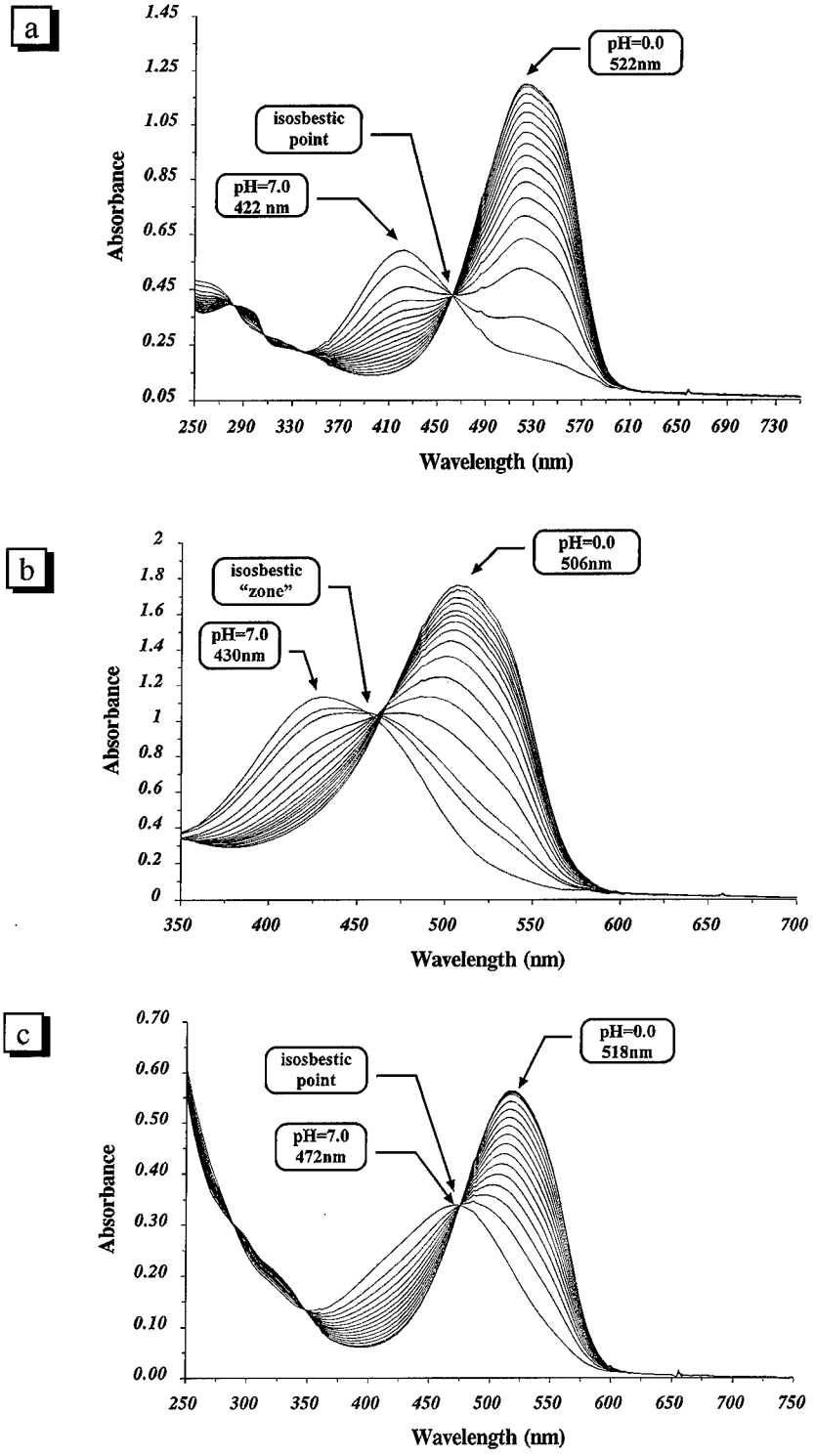

Figure 3. Comparison of isosbestic points behavior in physical sol-gel entrapment of MR (a) and pMR (b) with covalent-bond entrapment of MRAP (c).

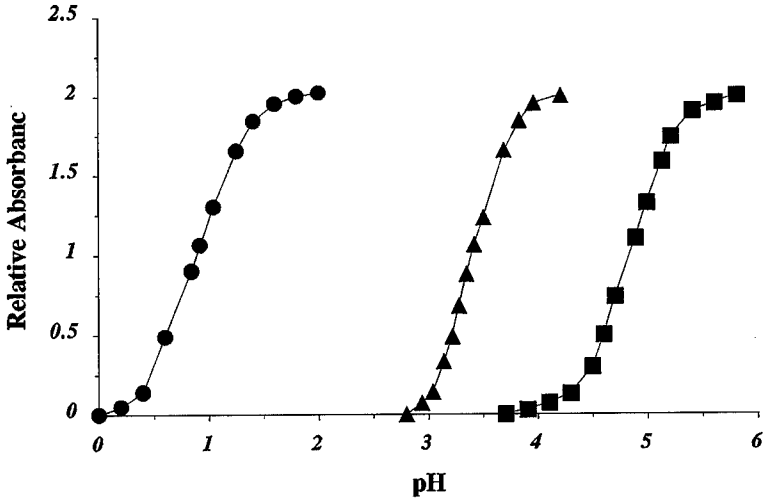

Figure 4. Titration curves of the entrapped pMR (●), MRAP (▲) and MR (■) in sol-gel glasses.

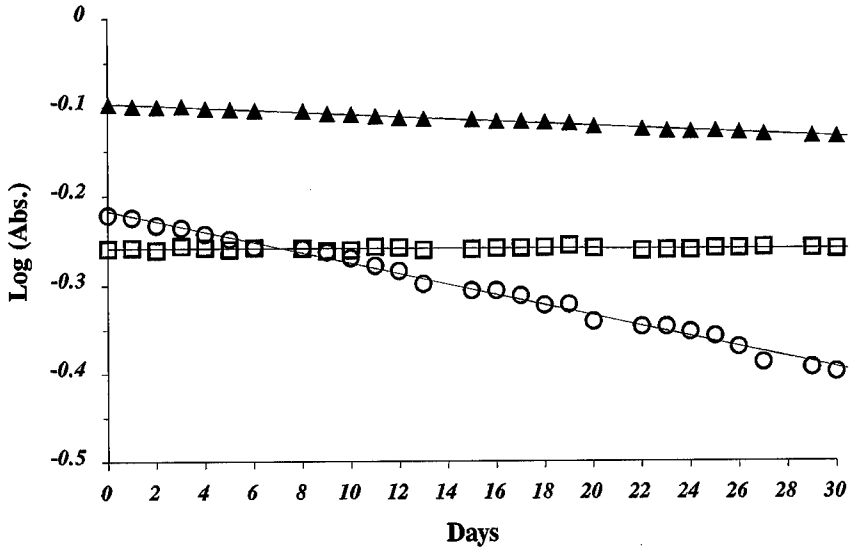

Figure 5. Leaching behavior of the MR series at pH = 0.01. The half lives are: 1.5 years ± 2 months for MR (▲); 57 years ± 2 years for MRAP (□); 4 months ± 12 days (○) for pMR.

MR series shown in Fig. 5, tested at the high acidity of pH = 0.01, were half lives of 4 months for pMR, 1.5 years for MR and about 60 years for the MRAP.

4. Discussion

CTAB is a single-chained cationic surfactant, the main properties of which originate from its amphiphilic nature. These properties are the ability of the polar residue to adsorb on the surface of silica and the ability of CTAB to form aggregates around the critical micelle concentration (cmc). The use of cationic surfactants such as CTAB has been reported for sol-gel systems and it was found that this additive has positive effects on the sol-gel processes due to its capability to homogenize the polymerizing system and to reduce the internal capillary pressure at the different stages of the porous glass forming process [6, 17, 18]. It was also reported that its coentrapment with molecules like pH indicators into the silica cage influences the main physical properties of those molecules, namely their pK_i and λ_{max} values [6, 10].

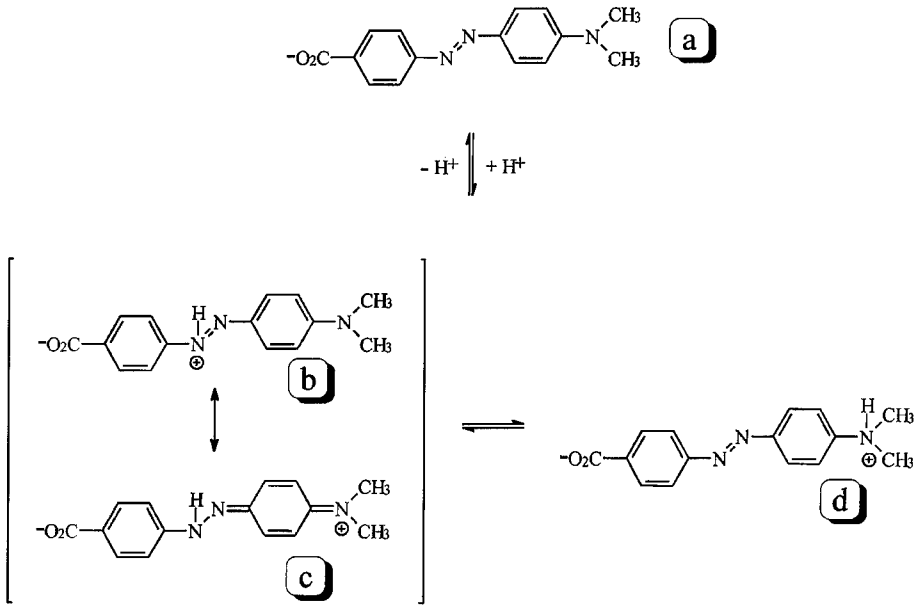

Scheme A. Representative structural changes causing the color transitions of the pMR indicator.

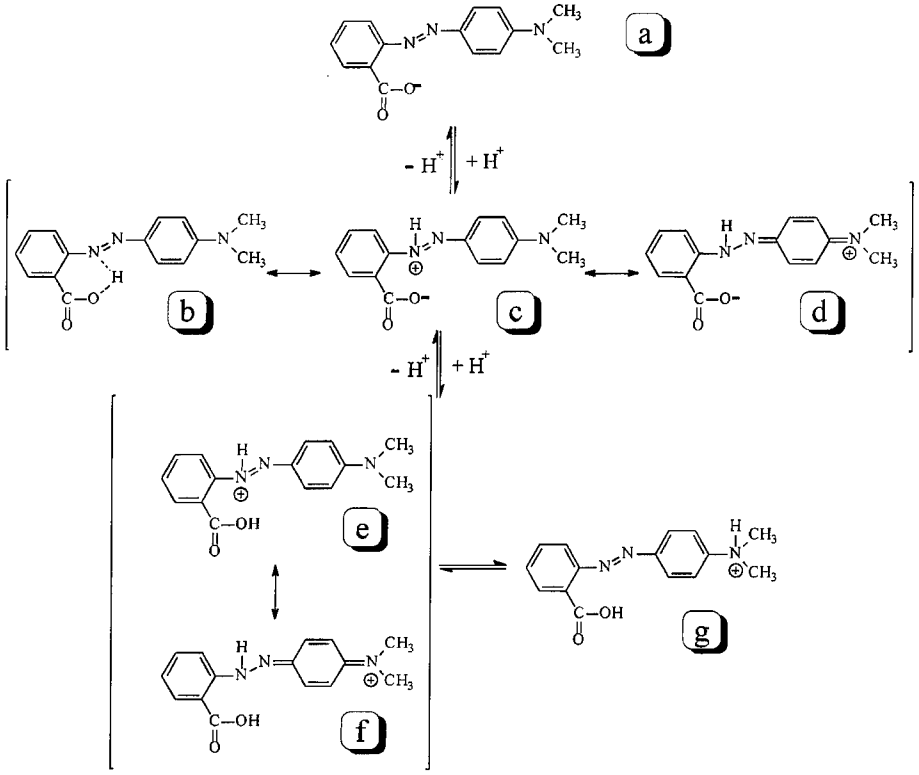

Scheme B. Representative structural changes causing the color transitions of the MR indicator.

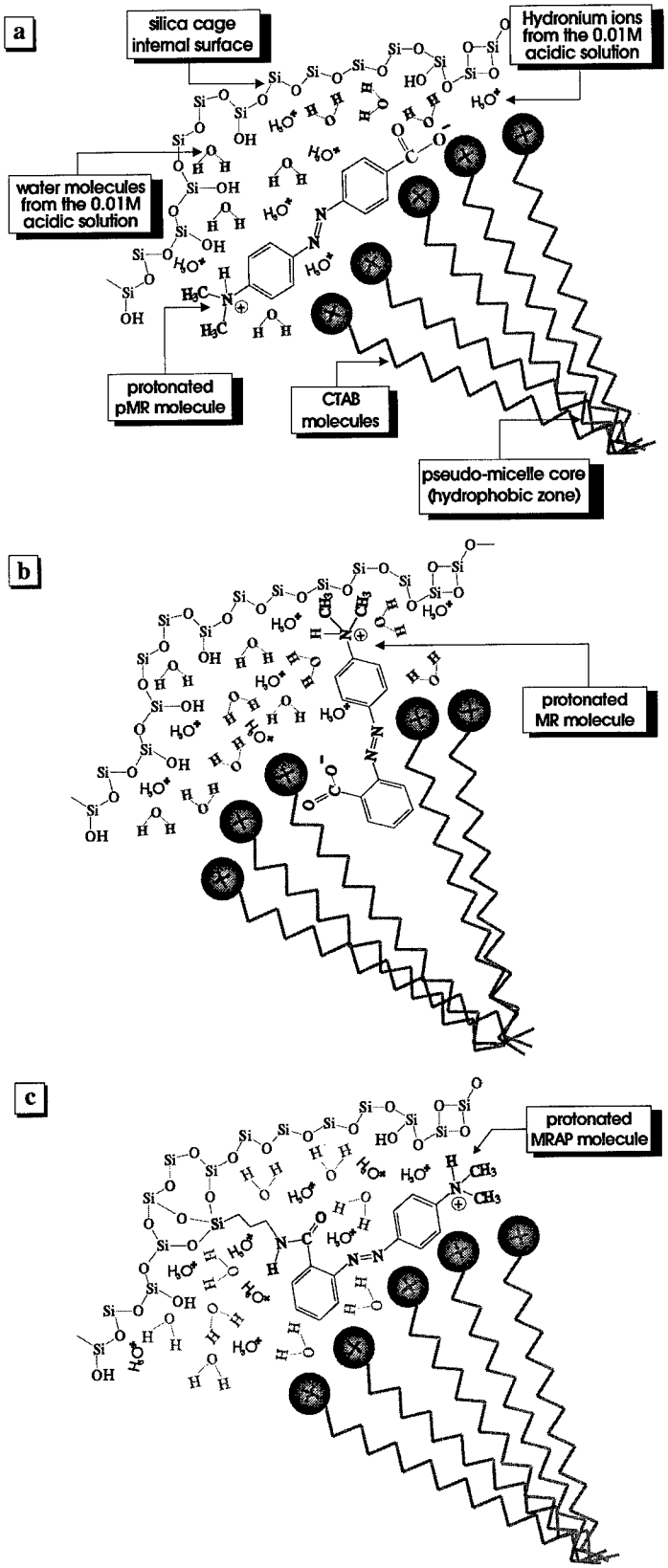

Scheme C. Schematic representation showing an estimated location of the entrapped (a) pMR, (b) MR and (c) MRAP molecules in the silica cage at pH = 0.01.

We now analyze the effects of the interaction between the surfactant CTAB and the three MR indicators and compare first sol-gel entrapment vs. aqueous solutions. In general, we shall ascribe the shifts in the λ_{max} and pK_i values to two main parameters: the free motion of the dye molecules in the silica cage, following the pH changes, and the electrostatic interactions developed between the charged Stern layer of the entrapped CTAB micellar environment with the charges existing on the indicator. The latter interactions are well known in aqueous micellar systems [19].

We begin with entrapped pMR for which a relatively large blue shift in the basic form of the λ_{max} as well as a pK_i acidic shift were observed, compared to solution. These can be understood by considering the orientation of species (a) and (b–d) (Scheme A) in the micellar environment (Scheme C(a)). The basic form (a) is contained fully within the surfactant micellar environment, because the negatively charged carboxylate group of the pMR associates with the positive quaternary ammonium group of the CTAB, whereas the noncharged dimethylaniline residue dissolves in the hydrophobic zone. Then, lowering the pH, the prototropic azo group is protonated and the dimethylaniline moiety becomes positively charged (forms (b–d)). This protonation forces the molecule to reorient fully into the polar micelle-silica cage, which is composed of residual water molecules and unoccupied silanol groups (Scheme C(a)). The spectral shift is therefore a reflection of the effect of hydrophobic vs. hydrophilic environments. Next, since the micellar interface is densely charged with the positive ammonium ions, a higher concentration of protons is required to reach a pK_i situation, i.e., the effective pK_i becomes more acidic. This dramatic environmental change which leads to molecular motions is nicely reflected by the fact that the isosbestic point is in fact smeared into an isosbestic zone (Fig. 3(b)). Indeed, for MR and MRAP the isosbestic points are sharper, indicating a lower degree of environmental change. This is also corroborated by the fact that the shifts for these two indicators is much smaller. For MRAP, which is covalently bound, restriction of molecular motion is obvious. The insensitivity of MR compared to pMR is due to the difference in the overall shape of the two molecules. The latter has a rod-like shape and the protonated/deprotonated dimethylamine group is far from the carboxyl functional group; the former is a folded, more compact molecule (Scheme B), which therefore stays always in the vicinity of the micellar polar interface, as demonstrated in Scheme C(b).

This folded structure of MR is also reflected by its relatively high pK_i value: Looking at both functional groups as isolated entities, one would expect the carboxylic acid group and the azo group in pure water to have pK_a values of the order of 4.2 and 3.2, respectively [19]. The fact that the pK_i of the MR molecule is 5.05 was attributed to the possible existence of an intramolecular interaction between the carboxylate and the azo moieties, originated by their close proximity (Scheme B(b–g)). On the other hand, the pK_i value of MRAP ($pK_i = 3.3$) is in good agreement with the pK_a of the isolated azo group in the phenylazobenzene molecule ($pK_a = 3.2$) [19], indicating that indeed, the azo group in the MRAP molecule is its only available prototropic group.

The results of the stability to leaching of the three indicators (Fig. 4) are also in agreement with this picture. We recall that the leaching was tested at the high acidity value of $pH = 0.01$. This value was selected because the azo indicators assume a hydrophilic zwitterionic form (Schemes A, B and C) which is therefore more prone to leaching problems. The somewhat higher leaching rate for the pMR may reflect the enhanced stabilization of the zwitterionic form due to its total molecular motion into the hydrophilic zone of the silica cage, as explained above (Scheme C(a)). The highest half-life as obtained for the MRAP molecules indeed proves that the trialkoxy groups incorporates the indicator covalently into the silica matrix. Although the ease of direct physical entrapment is given here away, for some specific applications, the covalent entrapment may be a method of choice. In all three cases the leaching stability is very good, showing that either physical coentrapment with a surfactant or covalent entrapment, may serve as good methods to improve durability and stability.

Acknowledgments

We thank the Israel Ministry of Science and Arts for a Special Infrastructure Fund and support of the German-Israel Foundation.

References

1. O.S. Wolfbeis, R. Reisfeld, and I. Oehme, Structure and Bonding **85**, 52 (1996).

2. O. Lev, M. Tsionsky, L. Rabinovich, V. Glezer, S. Sampath, I. Pankratov, and J. Gun, Anal. Chem. **67**, 22A (1995).
3. D. Avnir, L.C. Klein, D. Levy, U. Schubert, and A.B. Wojcik, in *The Chemistry of Organosilicon Compounds—Part 2*, edited by Y. Apeloig and Z. Rappoport (Wiley & Sons, Chichester, 1997), chap. 48.
4. R. Zusman, C. Rottman, M. Ottolenghi, and D. Avnir, J. Non-Cryst. Solids **122**, 107 (1990).
5. D. Avnir, Acc. Chem. Res. **28**(8), 330 (1995).
6. C. Rottman, M. Ottolenghi, R. Zusman, O. Lev, M. Smith, G. Gong, M.L. Kagan, and D. Avnir, Mater. Lett. **13**, 293 (1992).
7. C.K. Jorgensen and R. Reisfeld, *Optical and Electronic Phenomena in Sol-Gel Glasses and Modern Application* (Springer, 1996).
8. R. Gvishi, U. Narang, G. Ruland, D. Kumar, and P. Prasad, Appl. Organomet. Chem. **11**, 107 (1997).
9. F. Nishida, J. McKiernan, B. Dunn, and J. Zink, J. Am. Ceram. Soc. **78**, 1640 (1995).
10. S.C. Kraus, R. Uzolk, J. Reichert, and H.J. Ache, Sens. Actuators B **15/16**, 199 (1993).
11. B.M. Kubeckova, M. Pespisilova, and V.J. Matejec, Sol-Gel Sci. Technol. **2**, 513 (1994).
12. L. Yang and S.S. Saavedra, Anal. Chem. **67**, 1307 (1995).
13. J.Y. Ding, M.R. Shahriari, and G.H. Siegel, Electron. Lett. **27**, 1560 (1991).
14. M. Tsyonsky and O. Lev, Analyst **118**, 557 (1993).
15. I. Kuselman, B.I. Kuyavskaya, and O. Lev, Anal. Chim. Acta **256**, 65 (1992).
16. J. Samuel, A. Strinkovski, S. Shalom, K. Lieberman, M. Ottolenghi, D. Avnir, and A. Lewis, Mater. Lett. **21**, 431 (1994).
17. D. Avnir, V.R. Kaufman, and R. Reisfeld, J. Non-Cryst. Solids **74**, 395 (1985).
18. T. Murakata, S. Sato, T. Ohgawara, T. Watanabe, and T.J. Suzuki, Mater. Sci. **27**, 1567 (1992).
19. C.J. Drummond, F. Grieser, and T.W. Healy, J. Chem. Soc., Faraday Trans. 1 **85**, 561 (1989) and references therein.

Journal of Sol-Gel Science and Technology 13, 27–30 (1998)
© 1998 Kluwer Academic Publishers. Manufactured in The Netherlands.

Structure Control in Sol-Gel Silica Synthesis Using Ionene Polymers—Evidence from X-ray Scattering

M.J. ADEOGUN
Department of Chemistry, University of Surrey, Guildford, Surrey, England, GU2 5XH

J.P.A. FAIRCLOUGH
Materials Science Centre, UMIST, Manchester, Lancashire, England, M1 7HS

J.N. HAY*
Department of Chemistry, University of Surrey, Guildford, Surrey, England, GU2 5XH

A.J. RYAN
Materials Science Centre, UMIST, Manchester, Lancashire, England, M1 7HS

Abstract. Two polyviologens synthesized by the Menshutkin reaction were incorporated into silica networks using the sol-gel method. The effects of the incorporated polymers on the structure of the resulting organic-inorganic hybrid materials were investigated using X-ray scattering (small and wide angle). This provided evidence that the polyviologens in a lyotropic liquid crystalline state were causing the silica network to become more dense and less branched than sol-gel glasses synthesized without added polyviologen. Additional evidence for the templating effect of these polymers was obtained using FTIR spectroscopy and N_2 adsorption-desorption isotherms.

Keywords: sol-gel, structure control, X-ray scattering, polyviologen, lyotropism

Introduction

The sol-gel method represents a convenient low temperature route to convert metal or other alkoxides (via hydrolysis and condensation reactions) into the corresponding inorganic oxide (e.g., silica, titania, alumina) under relatively mild conditions [1]. It has the advantages of low processing temperatures, mixing at the molecular level to produce hybrid systems, and fabrication of novel materials [1].

There are many examples of the use of the sol-gel method to produce organic-inorganic hybrid materials, including systems where the organic component is a polymer [2]. Generally, the metal oxide formed can be regarded as an inorganic polymer having a three-dimensional network structure in which added polymer molecules can become entrapped. In principle, such hybrid systems allow an unlimited number of chemical and structural modifications to be made. Not surprisingly, there is a large amount of research geared to the synthesis of inorganic networks with specified and organized pore systems [3, 4], which could be of importance in catalysis, membrane technology and biomimetic technology.

The use of organic molecules to control the structure of inorganic networks is well known in the field of zeolite chemistry [5, 6]. Surfactants with a wide variety of sizes, shapes, functionalities and charges have been used to prepare zeolites [5] and sol-gel silicas [7]. Depending on the molecule used, different pore structures

*To whom correspondence should be addressed.

can be obtained within an organized network, once the organic component has been removed. The organic molecules direct the structure or fill space in the porous product via electrostatic, van der Waals and hydrogen-bonding interactions. Thus, materials are formed with tailored pore shapes and sizes. Recently, a number of researchers have looked at the possibility of using liquid crystal (LC) molecules as structure-directing agents [8, 9]. By using liquid crystal molecules it is possible to produce sol-gel silicates with ordered textures [9].

We have synthesized sol-gel hybrid materials with the aim of controlling the pore structure of a sol-gel silica network, using the ionene polymers known as polyviologens (PVs). These polymers (and also small-molecule viologens) have a wide range of properties including electrochromism [10], photochromism [11], and use as electron transfer catalysts [12].

It has been shown [13–15] that polyviologens containing ditosylate counterions are amphoteric liquid crystalline polymers, i.e., they exhibit LC behavior in solution (lyotropic) and when heat induced (thermotropic). Although polyviologens containing bromide counterions have been found to give birefringent gels at >85% polymer in water [13], we believe that this can be lowered by evaporating off some of the water from the polyviologen/water solution [16], while maintaining the lyotropic LC phase.

We have employed small and wide angle X-ray scattering (SAXS/WAXS) to determine the structure of these silica-PV sol-gel hybrids in terms of compatibility (between the inorganic and organic phases) and their fractal behavior. Additionally, preliminary results from FTIR spectroscopy, and nitrogen adsorption-desorption studies will be discussed briefly to provide further evidence for structure control in these materials.

Experimental

Polyviologen Synthesis

Poly(xylylviologen dibromide), (PXV-Br), was synthesized using the Menshutkin reaction as described by Adeogun and Hay [16]. Poly(hexylviologen ditosylate), (PHV-OTs), was synthesized using the method of Han and Bhowmik [15].

Silica-PV Synthesis

Tetramethylorthosilicate, TMOS (Aldrich), tetraethylorthosilicate, TEOS (Lancaster), methanol (Fisons), and glacial acetic acid (Fisons) were all used as received. Table 1 shows the systems synthesized with expts. 3 and 4 corresponding to expts. B1 and B6 respectively, in a previous publication [16]. The hybrid system containing PHV-OTs (expt. 2) was synthesized as follows: PHV-OTs (0.222 g, 0.37 mmol) was dissolved in methanol (0.166 g, 5.17 mmol), and to this solution was added TMOS (0.999 g, 6.56 mmol), glacial acetic acid (0.429 g, 7.15 mmol) and finally distilled water (0.594 g, 7.15 mmol). The pH was between 2.5 and 3.0, with gelation occurring after ca. 24 h. Two sol-gel silicas were prepared without added polyviologen for comparison with the hybrid systems.

Table 1. Sol-gel systems synthesized with calculated Porod slopes (P).

Experiment	PV incorporated	Alkoxide precursor	H_2O : Alkoxide, r	% PV[a]	P
1	None	TEOS	12.5	0	−1.5[c]
2[b]	PHV-OTs	TMOS	5.0	34	−1.83[d]
3	PXV-Br	TEOS	11.9	8	−0.5[d]
4[b]	PXV-Br	TEOS	15.4	34	−2.15[d]
5	None	TMOS	5.0	0	−0.9[d]

[a]Estimated value if complete hydrolysis and condensation of the alkoxide precursor occurs.
[b]Synthesized from lyotropic polyviologen solutions.
[c]P calculated from q range 0.05–0.2.
[d]P calculated from q range 0.06–0.2.

Characterization Analyses

SAXS-WAXS experiments were performed at the synchrotron radiation source (SRS) at the CLRC Laboratory (Daresbury, UK) at NCD station 8.2 [17]. The wet gels were studied approximately 1–2 h after gelation, and analyzed with Mylar (DuPont) windows. FTIR spectra of the sol-gel glasses were recorded on a Perkin-Elmer 2000 FTIR spectrometer. The samples were analyzed 1–2 h after gelation and also after 24 h at 80°C. Samples were prepared as KBr discs, and the data were acquired after 8 scans. N_2 adsorption-desorption isotherms at 77 K were obtained using a Coulter SA 3100 BET instrument. After gelation the sol-gel glasses were left at room temperature for two days, followed by a thermal treatment of 10 days at 80°C. The samples were then outgassed for 10 h at 110°C before analysis.

Results and Discussion

The study of the structure development in these silica-PV sol-gel hybrids was prompted by initial SAXS

results (not shown here) obtained for a fully cured (48 h at room temperature, followed by two weeks at 80°C) hybrid system (containing 8% PV) and a fully cured non-hybrid silica (from TEOS). It was found that the hybrid system displayed surface fractal behavior as opposed to the pure silica which showed mass fractal behavior, as expected for acid-catalyzed hydrolysis and condensation [18]. It was hypothesized that electrostatic interactions between the polyviologen N+ and silanol groups, Si—OH, and/or lyotropic liquid crystalline behavior of the polyviologens may be affecting the growth of the inorganic network. It was therefore decided to investigate how the structure of the silica network developed around the point of gelation in these hybrid systems, since at this stage the 3D network of siloxane bonds would be partially formed, but a relatively large number of silanol groups would still be present.

The SAXS data was obtained in the form of scattering profiles, which when plotted on a log-log scale, Porod plots can be obtained (see Fig. 1 and Table 1). These plots provide information on the fractal nature of the silicate domains i.e., whether the systems display mass or surface fractal behavior. This information can be obtained from the linear slope (Porod slope, P) of these plots [19]. Systems which show mass fractal behavior have slopes between $-1 \leq P \leq -3$, and for surface fractal behavior between -3 and -4. The fully cured systems mentioned previously gave Porod slopes of -3.2 for the hybrid system and -2.53 for the non-hybrid system. By using these values as a baseline and assuming that the fractal geometry develops in a consistent way, it can be seen that samples 2($P = -1.83$) and 4($P = -2.15$), which both display mass fractal behavior 1–2 h after gelation, are on the way to display surface fractal behavior. The slope of sample 4 is greater than its silica reference ($P = -1.5$), and over four times greater than sample 3($P = -0.5$). The slope of sample 2 was also found to be twice that of its silica reference ($P = -0.9$). It should be noted that the slopes for samples 3 and 5 are inconsistent with mass/surface fractal behavior, although it is assumed that these systems would display mass fractal geometry upon ageing. The differences described above indicate that samples 2 and 4 have more dense and less branched structures when compared with the other samples studied. Therefore, the presence, structure and the concentration of polyviologen in the hybrid systems, and also the possibility of the polyviologens in samples 2 and 4 being in a lyotropic liquid crystalline phase are affecting the growth of the inorganic network.

No ordering or crystallization was observed from the WAXS scattering profiles of the gels. Some degree of ordering was expected for the hybrid systems

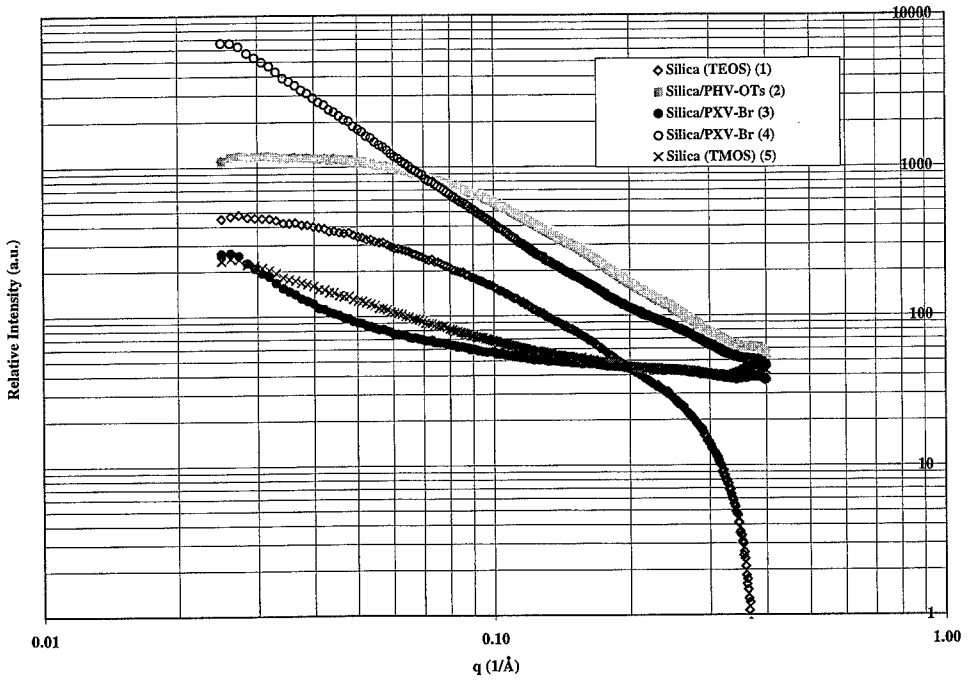

Figure 1. Porod plots for expts. 1–5.

containing polyviologen in a lyotropic LC phase. Work done by Coudurier et al. [20] and Burkett and Davis [21] indicates that the lack of observed crystallinity does not mean that the systems are not ordered. In fact, it was found that the presence of an IR peak at ca. 550 cm^{-1} indicates that there is some structure development and that the crystallites are probably too small to be observed by WAXS [20]. This peak is attributed to the deformation vibration of Si—O and is assigned to the presence of double rings of tetrahedra in the inorganic framework [20]. This peak, although observed in all the samples studied, was found to be much stronger and sharper in samples 2 and 3 (both synthesized from lyotropic polyviologen solutions). It therefore seems reasonable to conclude that the lyotropic polyviologen solutions used in the hybrid synthesis are directing the growth of the silica network.

Further information on the pore structure of the five samples was obtained from N_2 adsorption-desorption studies. It was found that both samples 2 and 4 gave type IV isotherms, compared to the type I isotherms obtained for samples 1, 3 and 5. Type IV isotherms are characteristic of "ink-bottle" shaped pores, whereas type I isotherms are characteristic of smooth and cylindrical pores [1, 22]. The presence of the polyviologens in samples 2 and 4 were found to cause changes in the pore structure (shape and size), a lowering of the BET surface area and the removal of micropores, when compared to their respective silica references. IR and pore analysis of these systems will be reported in more detail in a future publication.

Conclusions

Small and wide angle X-ray scattering has been used to provide evidence for structure direction or templating of two polyviologens on a growing sol-gel silica network. Differences observed in the fractal behavior of these materials were attributed to the presence of significant amounts of polyviologen in the hybrid materials and also to the use of lyotropic polyviologen solutions. FTIR spectroscopy provided further evidence of the affect of lyotropism in the hybrids. Additionally, N_2 adsorption-desorption studies indicate that the polyviologens have a dramatic effect on the pore structure of the silica network. These preliminary results provide evidence that the polyviologens of the ionene-type, have a templating effect on sol-gel silica networks. Although the mechanism of structure control is not fully understood in these materials, it is thought that electrostatic interactions are mediated by the presence of LC mesophases. By optimizing the conditions used and the polyviologens, tailored silicas may be produced for use in catalysis, membrane technology and biomimetic technology.

References

1. C.J. Brinker and G.W. Scherer, *Sol-Gel Science, The Physics and Chemistry of Sol-Gel Processing* (Academic Press, San Diego, 1990).
2. C. Sanchez and F. Ribot, New J. Chem. **18**, 1007 (1994).
3. S.A. Davis, S.L. Burkett, N.H. Mendelson, and S. Mann, Nature 385, (Jan. 1997).
4. S. Sato, T. Murahata, T. Suzuki, and T. Ohgawara, J. Mater. Sci. **25**, 4880 (1990).
5. M.M. Helmkamp and M.E. Davis, Annu. Rev. Mater. Sci. **25**, 161 (1995).
6. N.K. Raman, M.T. Anderson, and C.J. Brinker, Chem. Mater. **8**, 1682 (1996).
7. A. Julbe, C. Balzer, J.M. Barthez, C. Guizard, A. Larbot, and L. Cot, J. Sol-Gel Sci. and Tech. **4**, 89 (1995).
8. T. Dabadie, A. Ayral, C. Guizard, L.Cot, C. Lurin, W. Nie, and D. Rioult, J. Sol-Gel Sci. and Tech. **4**, 107 (1995).
9. T. Dabadie, A. Ayral, C. Guizard, L.Cot, J.C. Robert, and O. Poncelet, in *Better Ceramics Through Chemistry VI, Mat. Res. Soc. Symp. Proc.*, edited by K. Cheetham, C.J. Brinker, M.L. Mecartney, and C. Sanchez (Material Research Society, Pittsburgh, PA, 1994), Vol. 346, p. 849.
10. H. Kamagawa and S. Amemiya, J. Polym. Sci.: Polym. Chem. Ed. **23**, 2413 (1985).
11. C.L. Bird and A.T. Kuhn, Chem. Soc. Rev. **10**, 49 (1981).
12. A. Kameyama, Y. Nambu, and T. Endo, J. Polym. Sci.: Polym. Chem. Ed. **30**, 1199 (1992).
13. H. Han and P.K. Bhowmik, TRIP **3**(6), 199 (1995).
14. P.K. Bhowmik and H. Han, J. Polym. Sci.: Polym. Chem. Ed. **33**, 1745 (1995).
15. H. Han and P.K. Bhowmik, ACS Polym. Prepr. **36**(2), 330 (1995).
16. M.J. Adeogun and J.N. Hay, Polym. Int. **41**, 123 (1996).
17. W. Bras, G.E. Derbyshire, A. Devine, S.M. Clark, J. Cooke, B.E. Komanschek, and A.J. Ryan, J. Appl. Cryst. **28**, 26 (1985).
18. D.E. Rodrigues, A.B. Brennan, C. Betrabet, B. Wang, and G.L. Wilkes, Chem. Mater. **4**(6), 1437 (1992).
19. C.S. Betrabet and G.L. Wilkes, Chem. Mater. **7**, 535 (1995).
20. G. Coudurier, C. Naccache, and J.C. Vedrine, J. Chem. Soc., Chem. Commun. 1413 (1982).
21. S.L. Burkett and M.E. Davis, Chem. Mater. **7**, 1453 (1995).
22. S.J. Gregg and K.S.W. Sing, *Adsorption, Surface Area and Porosity*, 2nd edition (Harcourt Brace Jovanovich, London, England, 1982).

Journal of Sol-Gel Science and Technology 13, 31–36 (1998)
© 1998 Kluwer Academic Publishers. Manufactured in The Netherlands.

Synthesis and Structural Studies of Porous Organobridged Silicate Amorphous Powder

STUART W. CARR
Unilever Research, Quarry Road East, Bebington, L63 3JW, Merseyside, UK

DUAN LI OU AND ALICE C. SULLIVAN
Department of Chemistry, Queen Mary and Westfield College, Mile End Road, London, E1 4NS, UK

Abstract. Novel amorphous organobridged polysilsesquioxane porous powders have been prepared via hydrolytic precipitation from solutions of 1,4-bis(trichlorosilylmethyl)benzene. These new porous materials have been characterized by SEM, nitrogen sorption measurements and solid state ^{13}C and ^{29}Si NMR spectroscopy. The internal structure and porosity of the amorphous materials are correlated to the process conditions.

Keywords: amorphous powders, porous materials, structural studies

Introduction

The idea of tailoring the internal structures of organosilicates by inserting organic spacers into the siloxane network through the sol-gel processing of compounds with organobridged trifunctional silyl groups, X_3SiR-SiX_3, was originally reported by Shea [1]. A number of studies have focused on the relationship between the nature of the organic spacer and the microarchitecture of the derived organosilicate materials [1–5]. It was suggested that the intermolecular interaction between monomeric molecules during hydrolysis condensation processes may also direct the formation of the three-dimensional network [5]. This work mainly emphasizes the influence of the hydrolysis reaction conditions on the properties of the resulting materials. Sol-gel processing is a synthetic strategy for wet synthesis of inorganic oxide containing materials [6], and sometimes results in hydrolytic precipitation. Hydrothermal processes (hydrolysis in sealed vessels above the boiling point of the solvent) are widely used in the synthesis of zeolite materials. In this work, we applied hydrolytic precipitation (including hydrothermal processes) to solutions of 1,4-bis(trichlorosilylmethyl)benzene, in order to establish a correlation between the reaction conditions and the structure of the resulting organosilicates.

Experimental

Hydrolytic Precipitation from Solutions of 1,4-Bis(Trichlorosilylmethyl)Benzene

One aqueous and two non-aqueous reaction systems have been employed as reaction media for hydrolytic precipitation (including hydrothermal process) from solutions of 1,4-bis(trichlorosilylmethyl)benzene. Typical procedures used are as follows.

The hydrolysis agents were dissolved in the reaction media, and a solution of the precursor in a co-solvent was added and the reaction vessel loaded. A range of conditions were explored including variation of reaction temperature, time and pressure. The products were filtered, washed with H_2O and ethanol and dried overnight in an oven (50–60°C). The reaction conditions are collated in Table 1.

Samples A1 and A2 were obtained from the aqueous synthesis system at ambient pressure, A3 and A4 were obtained from the first non-aqueous synthesis system (Ethyleneglycol/Precursor/Pyridine/NaOH) under

Table 1. Formation of organobridged silicate powders by hydrolytic precipitations.

Ref	Precursor (g)	Medium (cm^3)	Co-solvent (cm^3)	Hydrolysis agents (g)	Time (day)	Temperature (°C)
A1	(1) 1.87	H_2O (40)		NaOH (1.2)	4	100
A2	(1) 1.87	Et_2O (25)		H_2O (5)	1(hr)	25
A3	(1) 0.94	EG (20)	Pyridine (10)	NaOH (0.3)	4	160
A4	(1) 1.87	EG (10)	Pyridine (10)	NaOH (0.08)	7	130
A5	(1) 0.94	EG (1) Bu^nOH (10)	THF (2.5)	NaOH (0.05)	30	180
A6	(1) 0.94	EG (1) Bu^nOH (10)	THF (2.5)	NaOH (0.05)	30	130

EG: ethylene glycol.

autogeneous pressure; A5 and A6 were obtained from the second non-aqueous system (*n*-Butanol/Precursor/Ethyleneglycol/THF/NaOH) under autogeneous pressure.

Scanning electron micrographs (SEM) were obtained using a JEOL JC 6300 microscope. Nitrogen sorption porosimetry was performed with a Micromeritrics ASAP 2400 instrument. The ^{13}C and ^{29}Si NMR spectra were acquired using cross polarization (CP) magic angle spinning (MAS) and high-power proton decoupling on a Bruker MSL-300 spectrometer. Spinning sidebands in the ^{13}C spectra were suppressed using the TOSS pulse sequence. The ^{13}C and ^{29}Si frequencies were 75.5 and 59.6 MHz, respectively.

Results and Discussion

Morphology and Pore Structure

Scanning electron microscopy (Fig. 1) reveals an amorphous assembly of small nodules (diameters several

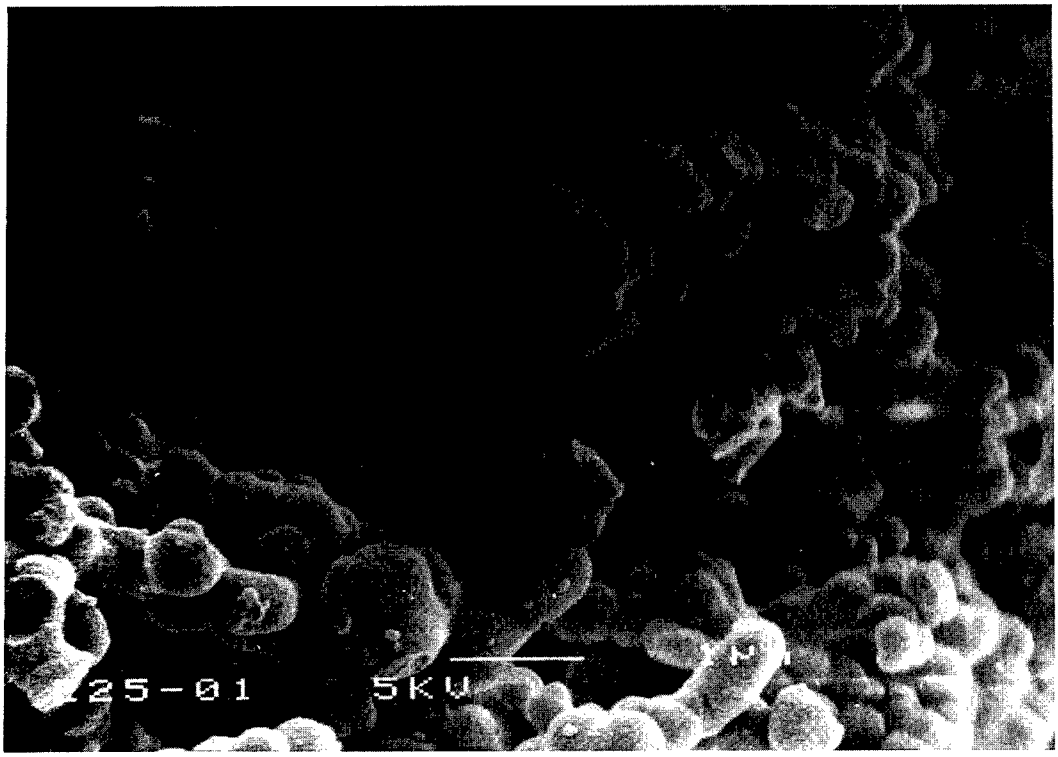

Figure 1. SEM of A2. Bar = 1 μm.

hundred nm). The pore structures of these samples were examined by nitrogen gas sorption. For the purpose of this study, the amorphous organosilicate samples were dried in the manner described previously [4].

There are three types of sorption isotherms observed in samples derived from the three reaction systems above. The isotherms are associated with three kinds of sorption behavior corresponding to three characteristic pore types [7].

A type 1 isotherm was found for the non-aqueous system 1 derived silicates A3 and A4 (see Fig. 2 for A4). A large portion of hysteresis loop covers a relatively high p/p_0 range but extends to the lower p/p_0 range, suggesting the pore structure is broad (overlapping both the micropore and mesopore region), and the existence of large interparticle voids [8]. The cumulative adsorption pore volume plot of A4 is shown in Fig. 3, and indicates that the pore sizes range from 17 to 2000 Å with

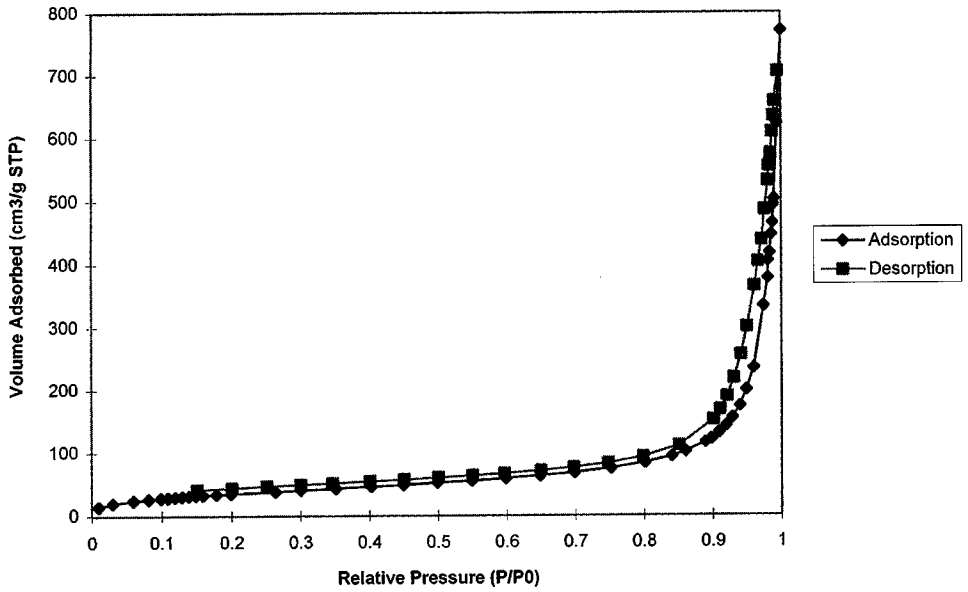

Figure 2. Nitrogen adsorption/desorption isotherm for A4.

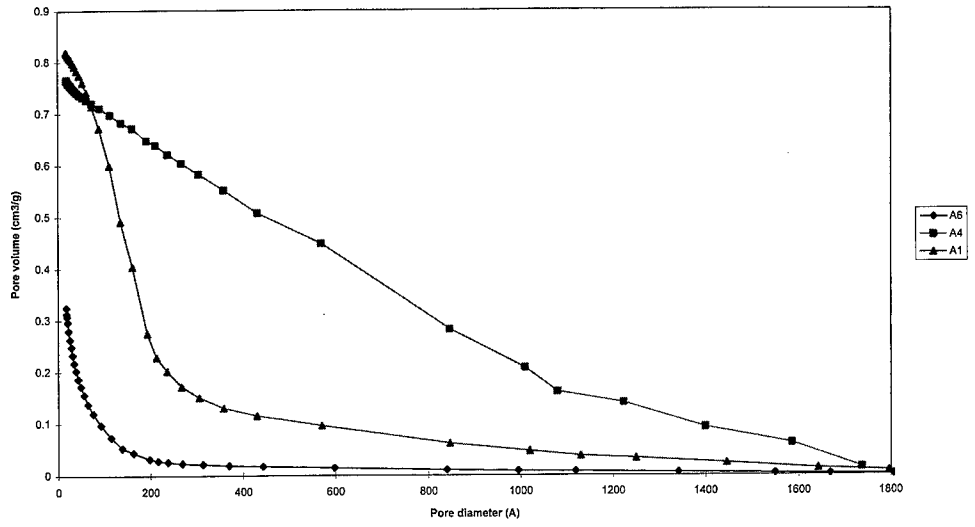

Figure 3. Cumulative adsorption pore volume plots for A1, A4 and A6.

over 90% of the pores having diameters greater than 50 Å. This contrasts with the sol-gel derived silicate xerogels from the same precursor, in which more than 70% of the pores have diameters less than 50 Å. The shape of the hysteresis loops suggests that A4 isotherms have Type B pore structures, which is a slit shaped pore with parallel plates. The hysteresis loop did not fully close, as with the corresponding sol-gel derived materials. The non-closure was suggested to result from the very slow desorption of N_2 in the low p/p_0 region [4]. This results from a reversible structural change which leads to some poorly accessible pores from which nitrogen is not readily desorbed at 77 K.

A type 2 isotherm was found for the non-aqueous system 2 derived silicates A5 and A6 (see Fig. 4 for A6), suggesting an ink bottle shape Type E pore structure [7]. The extent of non-closure of the hysteresis loop is much greater than for system 1 derived silicates and the previously reported xerogel [4]. There is also a marked step in the desorption curve between 0.4 and 0.5 p/p_0, which could be due to either the neck-size of ink bottle pores, or the natural instability of liquid nitrogen at this pressure. The cumulative adsorption plot (Fig. 3) shows a larger percentage of micropores than in the silicate materials derived from the other systems (over 50% less than 50 Å).

A type 3 isotherm with closed hysteresis loop was found for aqueous system derived A1 (see Fig. 5 for A1). It represents classical Type A cylindrical pore structure [7]. The loop is mainly in the higher p/p_0

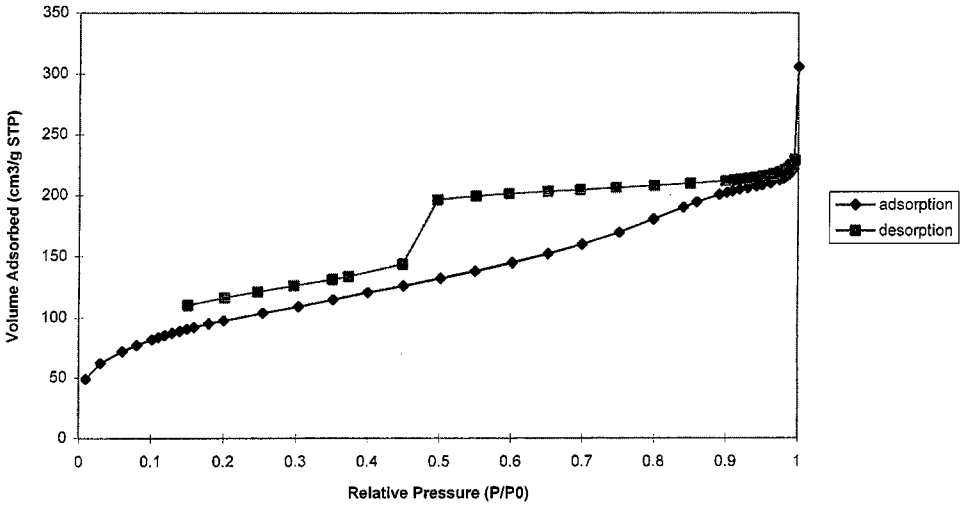

Figure 4. Nitrogen adsorption/desorption isotherm for A6.

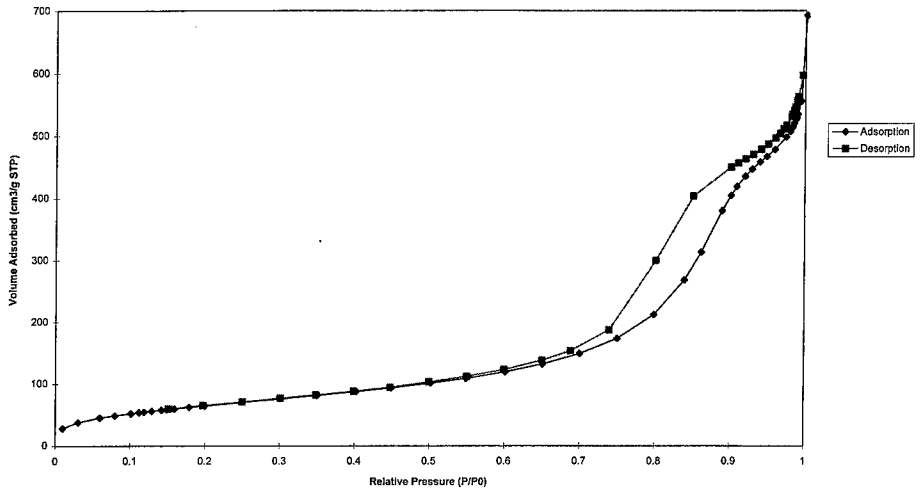

Figure 5. Nitrogen adsorption/desorption isotherm for A1.

Table 2. Porosimetry data for the amorphous organosilicates.

Ref	BET surface area (m^2/g)	BJH pore volume (cm^3/g)	Average pore diameter (Å)
A1	247.3	0.82	117
A2	15.4	0.04	63
A3	527.7	1.46	83
A4	137.0	0.77	90
A5	786.2	0.69	32
A6	369.5	0.32	34

region suggesting that there is a larger percentage of bigger interparticle or wider pores [8]. This is also shown in the cumulative adsorption pore volume plot (Fig. 3), with over 75% of the pores over 100 Å in size.

In the aqueous system derived samples, higher temperatures and higher alkaline concentration lead to a higher BET surface area. In the non-aqueous system 1 derived materials, reduction of the alkaline concentration (A3 and A4) did not affect the surface area of the resulting silicate materials. In the non-aqueous system 2 derived silicates, lower processing temperatures resulted in a lower BET surface area. The BET surface areas, total pore volumes and the mean pore diameters of these samples are summarized in Table 2.

^{29}Si CP MAS NMR Spectroscopy

^{29}Si solid state NMR is the major tool for providing structural information at the molecular level for the organobridged amorphous polysilsesquioxanes. T^1 to T^3 environments are found in all of these materials, while T^0 is found in some of them. The chemical shifts of T^0, T^1, T^2 and T^3 for a typical example of A6 are -17.5, -54.0, -64.0 and -69.9 ppm, respectively, similar to those in the related xerogels with same organic spacers.

The overall degree of condensation in these organobridged silicate amorphous materials has been evaluated by examining the contribution of the T^0 to T^3 species [3] in the manner previously used for the xerogels [4]. The overlapping T^1 to T^3 peaks were deconvoluted using a Linesim.3000 data system, and the results are collated in Table 3.

For the series of materials studied, A5 and A6, derived from non-aqueous system 2, are unique in retaining a substantial percentage of T^0 environments.

Table 3. Relative areas of T^n environments and degree of condensation of novel organobridged silicate amorphous materials measured from ^{29}Si CP MAS NMR spectra.

Ref	T^0	T^1	T^2	T^3	% condensation
A1		2.1	28.3	69.6	89.3
A2		19.1	62.8	18.1	66.5
A3		17.2	56.6	26.1	69.1
A4		16.6	61.5	21.9	68.0
A5	17.1	0.7	39.3	42.8	69.4
A6	12.1	7.5	44.1	36.3	68.4

It may be noteworthy that these materials were also unique in exhibiting Type E pore structure. The hydrophilic terminal T_0 group may block the entrance of these pores to create a narrow neck for the intrusion of liquid nitrogen during the sorption analysis. In addition, the distribution of T^n environments in A3 and A4 (non-aqueous system 1), with Type B pore structure, is very similar. Furthermore, we note that aqueous derived A1 has the highest relative percentage of $T^3 \sim 70\%$ ($T^3 < 50\%$ in all other cases) and that A1 was the only material with Type A pore structure.

^{13}C CP MAS NMR Spectroscopy

The ^{13}C CP MAS NMR spectra of these organobridged silicate amorphous materials are quite similar to the corresponding xerogels with the same organic spacers; two peaks were seen at around 129 and 135 ppm corresponding to the phenyl groups. Methylene carbons with T^1, T^2 or T^3 type silicon groups attached appear around 22 ppm. Methylene carbons with T^0 attached appear around 0 ppm. The latter resonance only appears in samples A5 and A6 (non-aqueous system 2), where substantial amounts of T^0 species remain.

Resonances due to alkoxy groups appeared in both of the non-aqueous system derived silicates, in which alcohol was used as the reaction medium. In the aqueous system derived samples, no such resonances appear; the T^1 and T^2 are connected with the hydroxy group.

Under non-quaternary suppression, the methylene carbons attached to T^1 to T^3 are totally suppressed and the CH resonances of the phenyl ring (around 129 ppm) reduced substantially. The quaternary phenyl carbon (around 133 ppm), and the resonances associated with highly mobile groups, such as residual alkoxy groups and methylene attached T^0, remain unaffected.

Conclusions

Our results show that 1,4-bis(trichlorosilylmethyl)benzene may be processed by hydrolytic precipitations (including hydrothermal processes) to give porous organosilicate amorphous powders. The degree of condensation of these amorphous silicate materials was not significantly higher than in the corresponding sol-gel derived silicates. The presence of hydrophilic end groups T^0 may somehow contribute to the formation of narrow neck pores in some of the organosilicates. The indications from porosimetry measurements are that the shape and size-distribution of pores depend upon the processing conditions, which raises the possibility of tailoring the pore structure of these organosilicate materials by controlling the processing conditions.

References

1. K.J. Shea, D.A. Loy, and O.W. Webster, Chem. Mater. **1**, 572 (1989).
2. D.J. Loy and K.J. Shea, Chem. Rev. **95**, 1431–1441 (1995) and references therein.
3. K.J. Shea, D.A. Loy, and O.W. Webster, J. Am. Chem. Soc. **114**, 6700 (1992).
4. P.J. Barrie, S.W. Carr, D.L. Ou, and A.C. Sullivan, Chem. Mater. **7**, 265–270 (1995).
5. R.J.P. Corriu, J.J.E. Moreau, P. Thepot, and M.W.C. Man, J. Mater. Chem. **4**, 987–989 (1992).
6. J. Livage, *Advanced Zeolite Science and Applications* (Elsevier, 1994).
7. S.J. Gregg and K.S.W. Sing, *Adsorption Surface Area and Porosity* (Academic Press London, 1982).
8. K.K. Unger, J. Rouquerol, K.S.W. Sing, and H. Kral, *Characterisation of Porous Solids* (Elsevier, 1988), p. 101.
9. M. Motevalli, D.L. Ou, A.C. Sullivan, and S.W. Carr, J. Mater. Chem. **7**, 865 (1997).

Journal of Sol-Gel Science and Technology 13, 37–43 (1998)
© 1998 Kluwer Academic Publishers. Manufactured in The Netherlands.

On the Existence and Hydrolytic Stability of Titanosiloxane Bonds in the System: Glycidoxypropyltrimethoxysilane-Water-Titaniumtetraethoxide

DAGOBERT HOEBBEL, MANFRED NACKEN AND HELMUT SCHMIDT
Institut für Neue Materialien, Im Stadtwald, 66123 Saarbrücken, Germany

Abstract. Heterometal materials based on glycidoxypropyltrialkoxysilane and titaniumalkoxide are used for optical applications and require a high homogeneity on the molecular level. The presence of heterometal titanosiloxanes, their distribution and hydrolytic stability should influence the homogeneity of these materials. ^{29}Si and ^{17}O NMR spectroscopy has been used to investigate sols with molar ratios Si : Ti = 1 and H_2O : OR (H) = 0.5–2.0 and their gels after heat treatment at 130°C. The presence of Si—O—Ti bonds in sols with a low water content (H < 0.2) and in the corresponding gels was identified by the high-field shift of the ^{29}Si NMR signals of T^1 and T^2 units of up to 2–3 ppm compared to corresponding signals of homo-condensed Si—O—Si bonds. The existence of Si—O—Ti bonds in the sols is supported by ^{17}O NMR spectra which show a characteristic signal around 340 ppm. A cleavage of the Si—O—Ti bonds occurs with increasing water/OR ratio in the sols. The cleavage of the heterometal bonds and the building up of homo-condensed species leads to a separation into areas with predominantly Ti—O—Ti and Si—O—Si bonds resulting in a decreased molecular homogeneity of the materials.

Keywords: heterometal bond, hydrolysis, condensation, ^{17}O and ^{29}Si NMR, titanosiloxane

1. Introduction

3-Glycidoxypropyltrimethoxysilane (GPTS) and titanium alkoxides are frequently employed for the preparation of heterometal hybrid polymers which are used for example as hard coatings on organic polymers and contact lens materials in the optical industry [1, 2]. A homogeneous distribution of structural units at the molecular level is a prerequisite for materials for optical applications and thus phase separations or inhomogeneities in composition should be kept at a level as low as possible [3, 4]. In this respect heterometal Si—O—Ti bonds, their distribution and their hydrolytic stability during sol-gel processing, play an important role in the preparation of highly homogeneous materials on a molecular scale. To date a detailed knowledge of the homo- and hetero-condensation reactions of GPTS and Ti-alkoxides during sol-gel processing is not available. The objective of this work is to attain a better insight into the reactions and interactions of the components of the system GPTS-H_2O-Ti$(OC_2H_5)_4$ in sol and gel states, mainly by means of ^{29}Si and ^{17}O NMR spectroscopy.

2. Experimental

Solutions of the system GPTS-H_2O-Ti$(OC_2H_5)_4$ were prepared at molar ratios Si : Ti = 1 and H_2O : alkoxide group = 0.5 to 2 (Table 1). 0.1 M HCl was used for all steps of hydrolysis. The time interval used was 0.5 h. The water content of the sols was determined by Karl-Fischer-titration [5] 0.5 h after their preparation. The gel samples were prepared from corresponding sols, after storage at room temperature for 24 h followed by heating to 130°C for 5 h. The solid products were then crushed and heated again for 2 h at 130°C.

The ^{29}Si and ^{17}O NMR spectra were obtained using a Bruker AC 200 spectrometer (4.7 T). ^{29}Si NMR: external reference: tetramethylsilane, internal standard: phenyltrimethylsilane, repetition time (r.t.): 40 s, pulse angle (p.a.): 63°, number of scans (n.s.): 45–1500. ^{17}O

Table 1. Flow chart of the preparation of solutions in the system GPTS-H_2O-$Ti(OC_2H_5)_4$ at room temperature. Water is always added as 0.1 M HCl.

Sol no.	C_{Si} (mole/l)	C_{HCl} (mmole/l)	H_2O/OR molar ratio		
					GPTS 4.52 mM
1	2.87	—	—	←	Ethanol 8.58 mM
				0.5 h	
2	2.66	7.2	0.5	←	H_2O 6.78 mM
				0.5 h	
3	1.26	3.4	0.21	←	$Ti(OC_2H_5)_4$/Ethanol 4.52 mM 16.12 mM
				0.5 h	
4	1.16	7.3	0.5	←	H_2O/Ethanol 9.0 mM 2.78 mM
				0.5 h	
5	1.01	12.7	1.0	←	H_2O/Ethanol 15.78 mM 4.88 mM
				0.5 h	
6	0.81	20.3	2.0	←	H_2O/Ethanol 31.56 mM 9.74 mM

NMR: single pulse, r.t.: 300 ms, p.a.: 90°, reference H_2O (1% ^{17}O), n.s.: 8000–20,000. The ^{17}O NMR measurements start from ^{17}O labelled GPTS-hydrolysate (sol 2) using 0.1 M HCl derived from ^{17}O (10%) enriched water. The subsequent hydrolysis steps (sol 4–6) were carried out with non-labelled 0.1 M HCl. The NMR measurements of solutions 2–6 were started 15 min after their preparation. The ^{29}Si NMR spectra were accumulated for 0.5 h (solution 2) or 15 h (solutions 3–6). The $^{29}Si\{^1H\}$ inverse gated sequence was used for solid state ^{29}Si NMR spectra. External standard: Q_8M_8, MAS: 3 kHz, p.a.: 63°, r.t.: 60 s, n.s.: 200–1000.

3. Results and Discussion

The data in Table 2 show that the amount of water in sol 2 decreases strongly from 0.5 to 0.13 H_2O/OR within 0.5 h of starting hydrolysis. The remaining water in sol 2 is small enough to prevent rapid homocondensation reactions of the Ti-ethoxide and precipitations [6]. Practically, the water in sol 2 is completely consumed by the added Ti-ethoxide for partial hydrolysis of its alkoxide groups (sol 3). The amount of free water in the sols 4–6 is increased by the stepwise addition of water. A nearly constant consumption of 0.46 H_2O/OR is obtained in the sols 5 and 6.

Table 2. Content of water in the standard sols 2–6 after 0.5 h reaction time.

Sol no. (Table 1)	Addition of water	Remaining water (0.5 h after addition)
2	0.50 H_2O/OR	0.13 H_2O/OR
3	(0.21 H_2O/OR)	0.02 H_2O/OR
4	0.50 H_2O/OR	0.12 H_2O/OR
5	1.0 H_2O/OR	0.54 H_2O/OR
6	2.0 H_2O/OR	1.53 H_2O/OR

^{29}Si and ^{17}O NMR Examination on Heterometal Bonds

The ^{29}Si NMR spectrum of the GPTS-prehydrolysate (sol 2) shows a variety of signals in the region of chemical shifts $\delta = -40$ to -44 ppm. This region is characteristic for monomeric silanes whose assignment

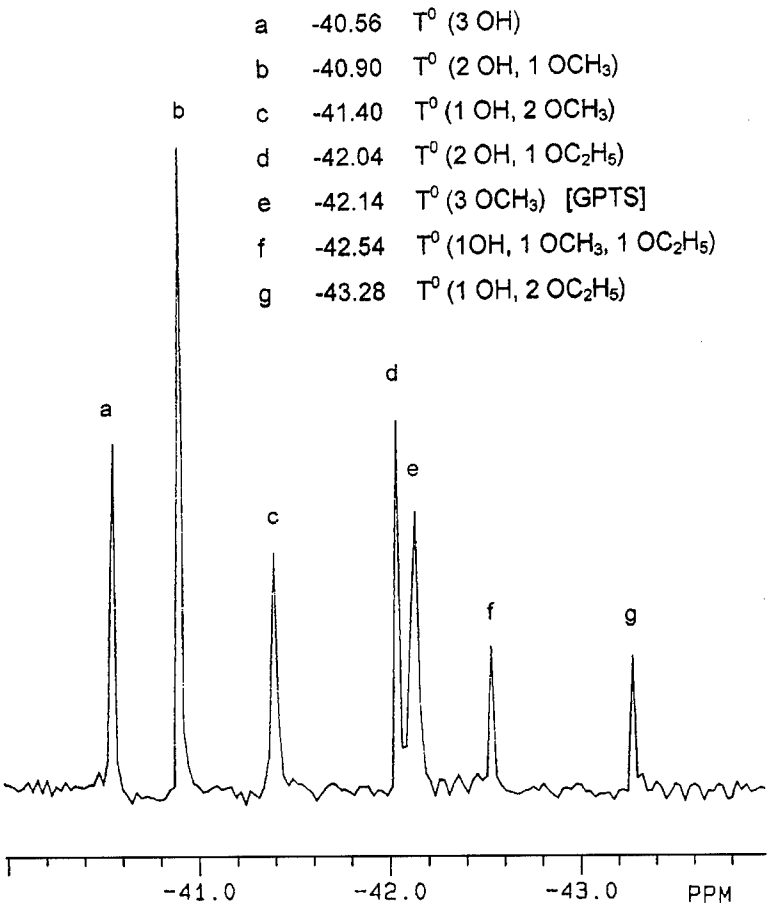

Figure 1. ^{29}Si NMR spectrum of the GPTS-hydrolysate (0.5 H_2O/OR, sol 2) and assignment of the signals.

follows from Fig. 1. Practically, the intensity of the seven visible signals represents the total content of Si-atoms so that condensed species can be neglected. From the spectrum it follows that about 50% of the alkoxy-groups are hydrolyzed. The dominant amount of monomeric silanols and the absence of condensed siloxanes gives a good basis to examine the reaction of these Si-species with the Ti-tetraethoxide.

The ^{29}Si NMR spectrum of solution 3 after addition of Ti-ethoxide shows three sharp signals at $\delta = -42.44$, -43.58, and -44.74 ppm which were identified as unreacted GPTS (4% of the total signal intensity) and the monomeric silanes T^0 (2 OCH_3, 1 OC_2H_5) (18%) and T^0 (1 OCH_3, 2 OC_2H_5) (13%) (Fig. 2, I). Furthermore, two broad signals at $\delta = -53.2$ (40%) and -61.1 ppm (25%) are visible in the region of T^1 and T^2 units implying that the predominant amount of Si in sol 3 is present as a condensed species. The stepwise addition of further water to sol 3 leads to the spectra of sols 4 and 6 shown in Fig. 2, II and III; no further signals of monomeric species are detected. The position of the three signals in the spectrum of sol 6 ($\delta = -49.7$ (14%), -58.0 (64%) and -65.6 ppm (22%)) is in accordance with homo-condensed Si-sites in T^1, T^2 and T^3 building groups of a long-term condensed GPTS hydrolysate (Fig. 2, IV). Comparing spectrum I with III a significant high-field shift of the T^1 and T^2 signals of up to 2–3 ppm can be seen. This shift cannot be caused by the influence of the Ti-atom on the chemical shift of the Si-atoms alone; this latter shift contributes 0.3 ppm at the most. It is very likely that the two signals in the spectrum of sol 3 reflect Si-atoms in hetero-metal Si—O—Ti bonds. Such a high field shift has been found for Si-atoms in Ti—O—Si—O—Ti bonds in previous works on titanodiphenylsiloxanes [7]. From the result it is concluded that after addition of water to sol 3 a degradation of the titanosiloxane bonds occurs in favor of homo-condensed siloxane bonds.

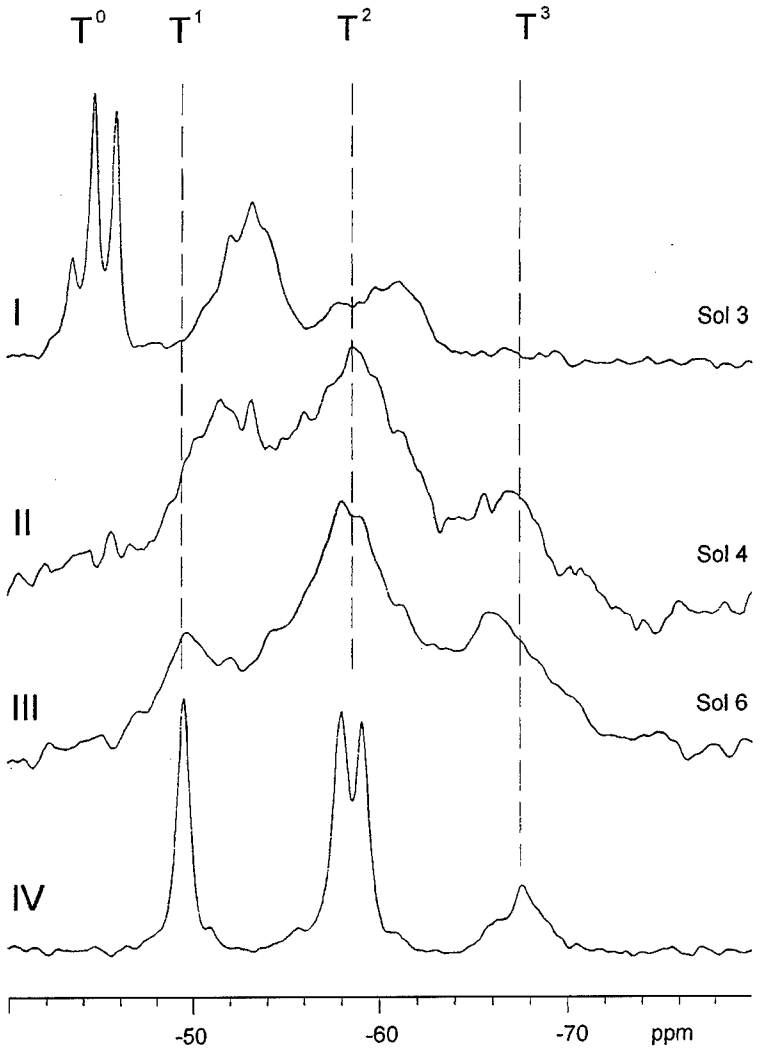

Figure 2. ^{29}Si NMR spectra of the sols 3, 4 and 6 (see Table 1) and of the GPTS-hydrolysate (2 H_2O/OR) after 15d.

The solid state ^{29}Si NMR spectrum of the Ti-containing gel 3 (Fig. 3, II) shows three broad signals with similar high-field shifts (−53.3 (32%), −60.3 (47%), −68.9 ppm (16%)) as those seen in the spectrum of the corresponding sol 3. This signal shift shows that species with Si—O—Ti bonds remain after the sol-gel transformation. The spectrum of gel 6 has two overlapped signals around $\delta = -58$ (56%) and −66 ppm (44%) whose maxima are in good agreement with those of the signals for homo-condensed Si—O—Si bonds of the reference gel (Fig. 3, IV).

^{17}O NMR was used to prove the existence of Si—O—Ti bonds. The ^{17}O NMR spectrum of the ^{17}O labelled GPTS hydrolysate (sol 2) shows strong signals at $\delta = 26$ and −8 ppm (Fig. 4, I) which are caused by the Si^{17}OH groups of the prehydrolyzed GPTS and by ^{17}O labelled water [8]. The signal at $\delta = 575$ ppm derives from deutero-acetone used as external lock and standard. A dramatic decrease in intensity of the SiOH and H_2O signal appears after the addition of Ti-ethoxide to sol 2. Meanwhile a broad asymmetrical signal centered around $\delta = 340$ ppm and signals at 540 and around 750 ppm develop (Fig. 4, II). The resonance at 340 ppm is attributed to O-atoms in Si—O—Ti bonds [7, 8], the signal at 540 ppm to μ_3- and those around 750 ppm to μ_2-Ti—O—Ti bonds according to [9]. It can be concluded from the ^{17}O NMR spectrum that the SiOH species in GPTS-hydrolysate are consumed

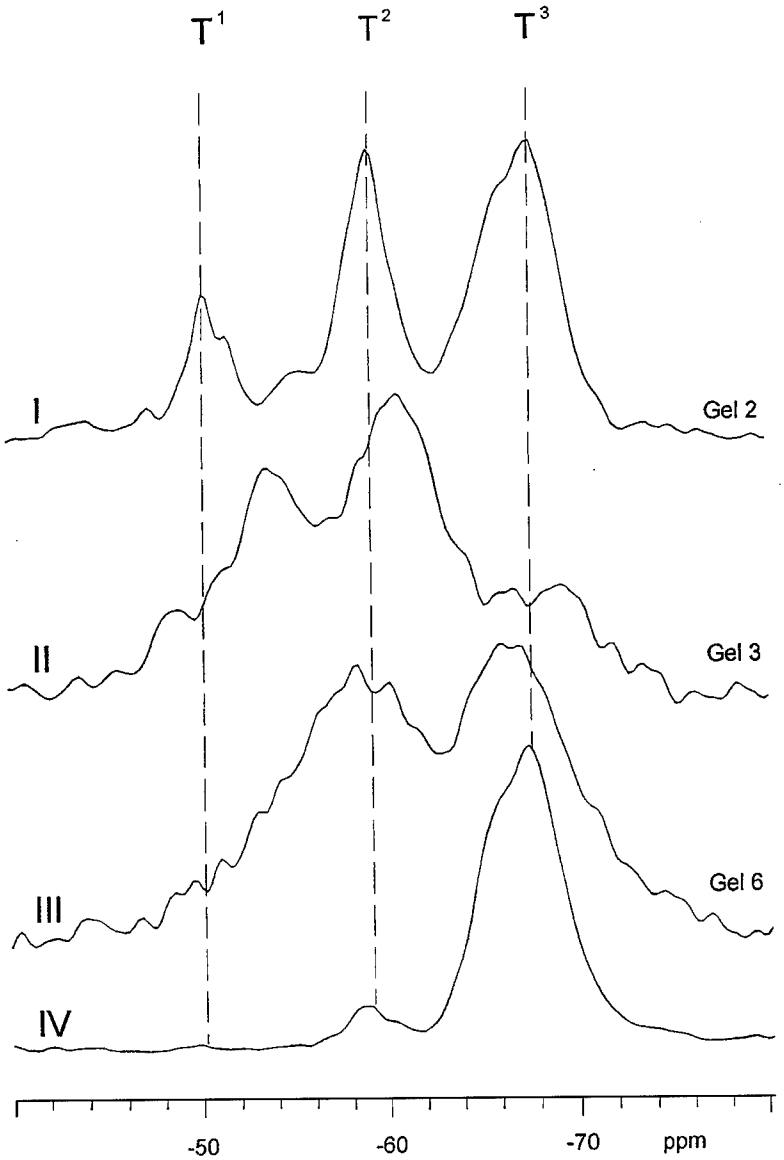

Figure 3. Solid state ^{29}Si NMR spectra of the gels 2, 3, 6 and the reference gel derived from GPTS-hydrolysate (2 H_2O/OR) by heat treatment at 130°C.

for hetero-condensation reaction with the Ti-ethoxide leading to Si—O—Ti bonds immediately after the Ti-ethoxide addition.

After repeated addition of 0.1 M HCl the intensity of the signals at 340 and 540 ppm decreases and a signal around 0 ppm appears (Fig. 4, III–V). This signal is mainly caused by ^{17}O labelled water and possibly some $Si^{17}OH$ groups but it can hardly be caused by condensed Si—^{17}O—Si species which should appear in the region at $\delta = 50$–80 ppm. The $H_2{}^{17}O$ signal mainly derives from ^{17}O-atoms in Si—^{17}O—Ti bonds. This means that the Si—^{17}O—Ti bonds undergo a quick isotope exchange during their cleavage with non-labelled water. The quick ^{17}O isotope exchange leads eventually to mostly non-labelled Si—O—Si bonds in the condensation products which cannot be detected in the ^{17}O NMR but they are detectable in the corresponding ^{29}Si NMR spectra. No significant signals can be found for homo-condensed Ti—^{17}O—Ti species. It is probable that the signals are overlapped by the broad oscillation bands or that the ^{17}O isotope is exchanged in favor of ^{17}O labelled water.

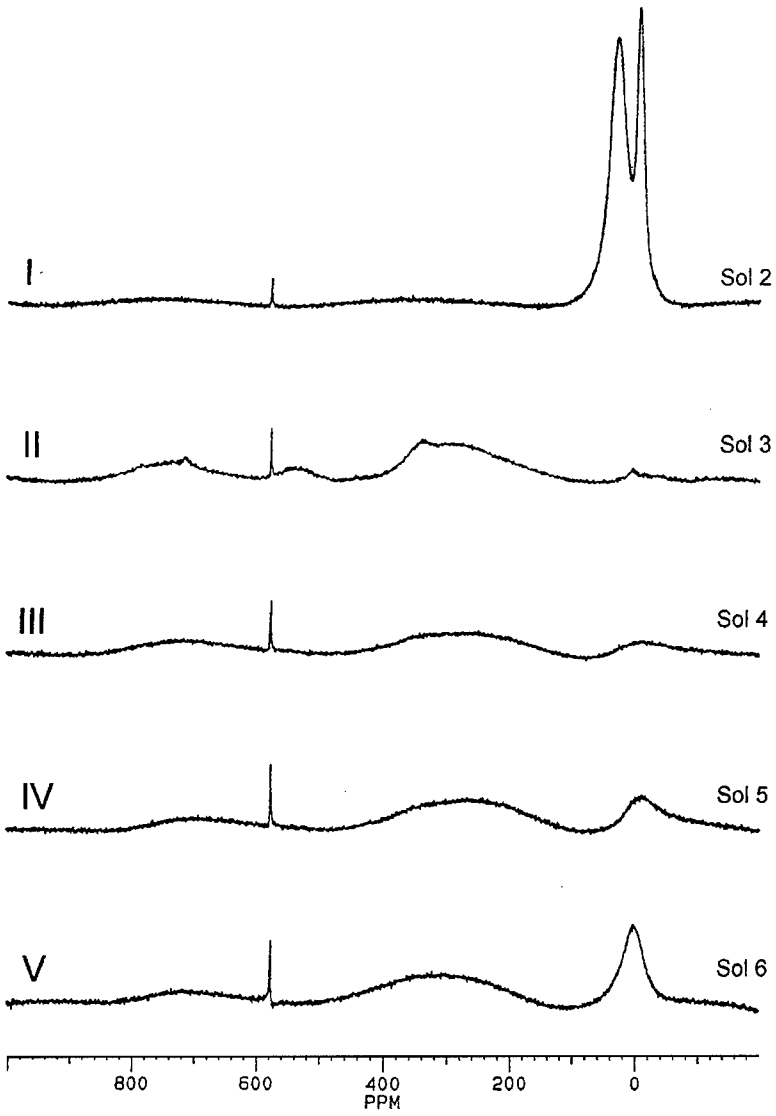

Figure 4. ^{17}O NMR spectra of the sols 2–6 (see Table 1).

4. Conclusions

GPTS-prehydrolysates which contain monomeric silanols and a low content of free water (0.13 H_2O/OR) react with titanium-tetraethoxide to form sols mainly consisting of titanosiloxane species. The heterometal bonds can be identified by the high-field shift of the T^1 and T^2 signals of up to 2–3 ppm in the liquid and solid state ^{29}Si NMR spectra of the sols and corresponding gels. The existence of titanosiloxane bonds is confirmed by the signal at $\delta = 340$ ppm in the ^{17}O NMR spectra. Considerable hydrolytic cleavage of the heterometal bonds can be detected with increasing amounts of water. Mainly species with homo-condensed Si—O—Si bonds appear in the sols and corresponding gels after the hydrolysis at molar ratio $H_2O/OR = 2$. The drastic cleavage of the heterometal bonds and the preferential building up of homo-condensed Si—O—Si species and probably also the species with Ti—O—Ti bonds lead to a separation in $(RSiO_{1.5})_x$ and TiO_2 rich areas which lower the homogeneous distribution of Si and Ti on a molecular scale. This result has to be considered for more controlled syntheses of highly homogeneous heterometal materials.

Acknowledgment

The authors gratefully acknowledge Ms. S. Carstensen for experimental work.

References

1. H. Schmidt, B. Seiferling, G. Philip, and K. Deichmann, in *Ultrastructure Processing of Advanced Ceramics*, edited by J.D. Mackenzie and D.R. Ulrich (J. Wiley, New York, 1988), pp. 651–660.
2. JP 6126637 in C.A. **105**, 80819 (1986).
3. J.D. Basil and C.C. Lin, in *Ultrastructure Processing of Advanced Ceramics*, edited by J.D. Mackenzie and D.R. Ulrich (J. Wiley, New York, 1988), pp. 783–794.
4. H. Schmidt, in *Chemical Processing of Advanced Materials*, edited by L.L. Hench and J.K. West (J. Wiley, New York, 1992), pp. 727–735.
5. E. Scholz, *Karl-Fischer-Titration* (Springer-Verlag, Berlin, 1984).
6. H. Schmidt, in *Structure and Bonding*, edited by R. Reisfeld and C.K. Jorgensen (Springer-Verlag, Berlin, 1992), pp. 119–151.
7. D. Hoebbel, M. Nacken, H. Schmidt, V. Huch, and M. Veith, submitted to J. Mater. Chem. (1997).
8. F. Babonneau, Mat. Res. Soc. Symp. Proc. **346**, 949–960 (1994).
9. V.W. Day, T.A. Ebersbacher, W.G. Klemperer, C.W. Park, and F.S. Rosenberg, J. Am. Chem. Soc. **113**, 8190–8192 (1991).

Journal of Sol-Gel Science and Technology 13, 45–49 (1998)
© 1998 Kluwer Academic Publishers. Manufactured in The Netherlands.

Molecular Design of Novel Heterometallic Alkoxides as Precursors

R.C. MEHROTRA, A. SINGH, M. BHAGAT AND J. GODHWANI
Chemical Laboratories, University of Rajasthan, Jaipur 302004, India

Abstract. In view of the advantages of employing heterometallic alkoxides as precursors for ceramic materials by the sol-gel process, efforts are being made to develop novel routes for their synthesis and to design single source precursors suited to the final targeted material. Three such new pathways are briefly presented in this paper: (i) varying the ratio of constituent metals; (ii) dissolution of metal chlorides in alkoxides of tetravalent metals; and (iii) reactions of acidic protons of metal glycolate derivatives with alkoxides of another metal yielding derivatives containing other alkoxometallates in cationic form.

Keywords: heterometallic alkoxide precursors, chloride alkoxide systems, cationic alkoxometallate components

1. Introduction

Although the advantages of using monometal alkoxides, either alone or as a mixture, had been well recognized since the early 1950s and the possibility of complexation reactions in the latter systems had been envisaged [1] in 1971, it was only in 1987 that ceramists learnt that a large number of such heterometallic complex alkoxides had actually been characterized [2]. Almost immediately afterwards (1988), Mehrotra [3] drew pointed attention to the advantages of the use of heterometal alkoxides as precursors and suggested a few such systems of potential applicability, even for aerogels. The successful synthesis [4, 5] of a variety of heterometal alkoxides with the general formula of the type $M\{Al(OPr^i)_4\}_x\ \{Ta(OPr^i)_6\}_y\ \{Zr_2(OPr^i)_9\}_z\ X_{n-x-y-z}$ (where M is a central element of valency n and X are simple ligands like alkoxide/β diketonate/carboxylate moieties) opened up the possibilities of designing a molecular precursor corresponding to the targeted material. Evidence has been accumulating [6, 7] on the greater homogeneity of the final materials from these presynthesized heterometallic derivatives compared to those obtained from the use of mixtures of component metal alkoxides.

As pointed out by Ulrich [8], a closer interaction between chemists and ceramists has benefitted the latter considerably. Moreover, the versatile applicability of metal alkoxides in general and heterometal alkoxides in particular has generated an unprecedented spurt in research activity in these fields as evinced by not only the publication of an increasing number of articles, but also of review articles [9–14]. In fact, even the identity of heterometallic alkoxides was looked upon with some scepticism till about a decade ago as the same was by and large based on elemental analyses, molecular weights in solution and spectroscopic (mainly NMR) data coupled with their volatilizability which could be perhaps ascribed to the "ion-pair" effect. Fortunately, almost all the structures envisaged on this basis are now being gradually confirmed [14, 15] by actual X-ray crystallographic studies.

The identity of the first heterotermetallic alkoxide $[\{Cd(OPr^i)_3\}Ba\{Zr_2(OPr^i)_9\}]_2$ derivative was established [16] in 1996. However, the synthesis of this termetallic product has revealed the transferability of the isopropoxometallate components as represented by the following steps employed in its synthesis:

$$CdI_2 + KZr_2(OPr^i)_9 \rightarrow ICd\{Zr_2(OPr^i)_9 + KI\downarrow$$

$$ICd\{Zr_2(OPr^i)_9\} + KBa(OPr^i)_3 \rightarrow \frac{1}{2}[\{Cd(OPr^i)_3\}Ba\{Zr_2(OPr^i)_9\}] + KI\downarrow$$

This observation is of special interest to the sol-gel ceramists, as it indicates possible rearrangement(s) of

the alkoxometallate moieties according to the oxophilicity of Ba(II) and its propensity for higher coordination numbers.

The structure of $[Er\{(\mu\text{-}OPr^i)_2Al(OPr^i)_2\}_3]$ envisaged as early as 1968 [17] was confirmed [18] in 1996. It should be relevant to mention that on hydrolysis, its rate is much faster at the aluminium centers, but the same could be reduced by reacting $[Ln\{(\mu\text{-}OPr^i)_2Al(OPr^i)_2\}_3]$ derivatives with acetylacetone (in a 1 : 6 molar reaction) when a volatile monomeric soluble product $[Ln\{(\mu\text{-}OPr^i)_2Al(acac)_2\}_3]$ is obtained [19]. Similarly, the reaction of the original $[Ln\{(\mu\text{-}OPr^i)_2Al(OPr^i)_2\}_3]$ with 6 moles of water under mild conditions yields a transient insoluble product $[Ln\{(\mu\text{-}OPr^i)_2Al(OH)_2\}_3]$, changing almost instantaneously into a soluble product $[Ln\{(\mu\text{-}OH)_2Al(OPr^i)_2\}_3]$, which is a much more convenient precursor for the sol-gel process. Hydroxo/oxo-alkoxides [20], which must be necessarily involved as intermediate entities in the hydrolysis of metal alkoxides during the sol-gel process, have been receiving unprecedented attention as stable species isolated sometimes during synthesis of alkoxy derivatives of metals and these have been reviewed recently by Mehrotra and Singh [20].

2. Recent Work on Novel Heterometallic Alkoxides

The main obstacle in more extensive applications of heterometallic alkoxides has been their commercial unavailability, difficulties in their synthetic procedures as well as difficulties in handling them due to their facile hydrolyzability. On the contrary, a suggestion from Mehrotra [21] during an international conference at Kuala Lumpur in 1993 that heterometallic alkoxides like $NaSn_2(OPr^i)_9$ can be more easily prepared by the direct reaction of $SnCl_4$ with $NaOPr^i$ in 2 : 9 molar ratio whereas $Sn(OPr^i)_4$ has to be generally obtained by a more complicated route involving intermediates like $NaSn(OPr^i)_9$, has already led to their wider applicability in the sol-gel process. The synthesis of the first volatile barium alkoxide $[Ba_2\{OC(CH_2OPr^i)_2Bu^t\}_4]$ by Herrmann et al. [22] in 1993 elicited the remark by Mehrotra and Singh [23] that "the bulky ligand with side-chains capable of donor functionality ... appears to combine the advantages of steric crowding as well as coordinative saturation within the same species." This remark has been quoted by Herrmann et al. [24] in an extensive review of the developments in this field of study and the same criteria are now being extended in our research school to cover heterometallic alkoxides also.

In this article, we limit ourselves to presenting a brief preview of mainly unpublished work accomplished in our laboratories during the last 2–3 years on the three types of heterometallic alkoxides mentioned in the abstract.

3. Heterometallic Alkoxides with Varying Ratios of Constituent Metals

Although alkoxides of most of the metals are soluble in organic solvents including parent alcohols, those of bivalent metals (like alkaline earths) are insoluble, limiting their applicability in the sol-gel process. Synthesis of soluble heterobimetallic alkoxides could be achieved [25] by the dissolution of alkaline earth metals "M" (Mg, Ca, Sr, Ba) in alcohols in the presence of two moles of alkoxides of other metals like Al, Nb, Ta and Zr. For example:

$$Mg + 2Pr^iOH + 2Al(OPr^i)_3 \xrightarrow{Pr^iOH} Mg\{(\mu\text{-}OPr^i)_2Al(OPr^i)_2\}_2 + H_2\uparrow$$

The crystal structure of $[(Pr^iOH)_2Mg][(\mu\text{-}OPr^i)_2Al(OPr^i)_2]_2$ was elucidated [26] in 1993.

In a recent publication [27], Gilje et al. described the synthesis of another product $Mg_2Al_3(OPr^i)_{13}$ by varying the ratio of magnesium to $Al(OPr^i)_3$:

$$2Mg + 3Al(OPr^i)_3 + 4Pr^iOH \xrightarrow{Pr^iOH} Mg_2Al_3(OPr^i)_{13} + 2H_2\uparrow$$

In a more recent study [28], novel tetra- and pentanuclear barium aluminium isopropoxides have been synthesized for the first time by the reactions (1 : 3 and 2 : 3) of barium and aluminium isopropoxide in isopropyl alcohol under refluxing conditions:

$$Ba + 3Al(OPr^i)_3 + 2Pr^iOH \xrightarrow{Pr^iOH} BaAl_3(OPr^i)_{11} + H_2\uparrow$$

$$2Ba + 3Al(OPr^i)_3 + 4Pr^iOH \xrightarrow{Pr^iOH} Ba_2Al_3(OPr^i)_{13} + 2H_2\uparrow$$

Heterobimetallic isopropoxides of aluminium and other alkaline earth metals M (Sr, Ca, and Mg) have

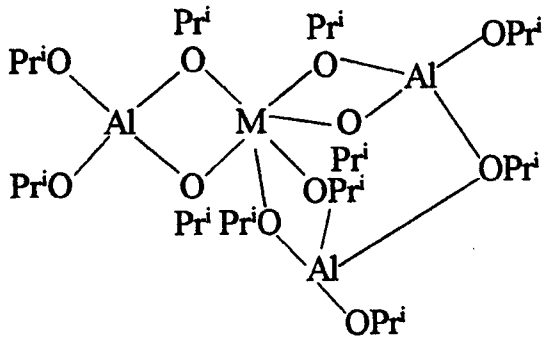

Figure 1. Structures of $MAl_3(OPr^i)_{11}$.

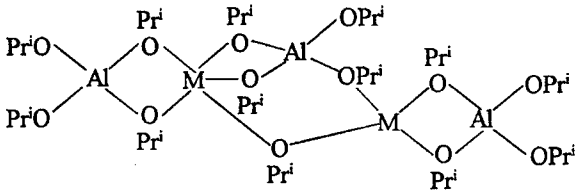

Figure 2. Structures of $M_2Al_3(OPr^i)_{13}$.

been synthesized with similar compositions $MAl_3(OPr^i)_{11}$ and $M_2Al_3(OPr^i)_{13}$. All these derivatives have been characterized by elemental analyses, molecular weight determinations and NMR (^1H, ^{13}C, and ^{27}Al) studies. Alcoholysis reactions with ramified alcohols like $Me_3COH(Bu^tOH)$, $Me_2EtCOH(Am^tOH)$, and $Et_3COH(TEC)$, respectively, gave derivatives with the compositions: $MAl_3(OPr^i)_3(OBu^t)_8$; $MAl_3(OPr^i)_3(OAm^t)_8$; $MAl_3(OPr^i)_6(TEC)_5$ from $MAl_3(OPr^i)_{11}$ and $M_2Al_3(OPr^i)_4(OBu^t)_9$; $M_2Al_3(OPr^i)_4(OAm^t)_9$; $M_2Al_3(OPr^i)_7(TEC)_6$ from $M_2Al_3(OPr^i)_{13}$, respectively. These alcoholysis data also support the following structures (Figs. 1 and 2) for the two types of heterobimetallic isopropoxides respectively.

4. Novel Heterometallic Chloride Alkoxides Obtained by Interaction of MCl_2 (M = Be, Mg, Zn, and Sn(II)) with $Zr(OPr^i)_4$

A number of heterometallic chloride alkoxides of zirconium with the general formula $M\{Zr_2(OPr^i)_9\}Cl$ (M = Mg, Zn, Cd, Sn(II), etc.) have been synthesized [14, 15] by the reactions (1 : 1) of MCl_2 with $KZr_2(OPr^i)_9$. Another series of title compounds have now been synthesized [29] by a novel route consisting of dissolution of MCl_2 (M = Be, Mg, Zn, and Sn(II)) in a solution of $Zr(OPr^i)_4$ in benzene:

$$MCl_2 + 2Zr(OPr^i)_4 \xrightarrow[\text{stir}]{\text{benzene}} MZr_2(OPr^i)_8Cl_2$$

The time required for dissolution varied with the metal: Be (5 h), Mg (15 h), Zn (10 h), and Sn(II) (20 h); this was followed by refluxing for about 4 h to ensure completion of the reaction. All these new compounds are colorless solids soluble is benzene in which they exhibit a dimeric behavior except the Be derivative which is monomeric when freshly prepared but dimerizes on ageing. The formation of these derivatives could be explained by the following reaction scheme:

$$2[Zr(OPr^i)_4]_3 \overset{\Delta}{\rightleftharpoons} 3[Zr(OPr^i)_4]_2$$

$$2[Zr(OPr^i)_4]_2 + 2MCl_2$$

$$\rightleftharpoons [Zr(OPr^i)_4]_2 \dashrightarrow M(Cl)_2M \dashleftarrow [Zr(OPr^i)_4]_2$$

$$\downarrow$$

$$[\{Zr_2(OPr^i)_8Cl\}_2M_2(\mu\text{-}Cl)_2]$$

All these products have been characterized on the basis of elemental analyses, molecular weight measurements and IR, as well as NMR{^1H, ^{13}C, ^{119}Sn} spectra, and could be assigned the following plausible structure in which $\{Zr_2(OPr^i)_8Cl\}$ moiety binds the central metal (M = Mg, Zn, and Sn(II)) in a tridentate manner (Fig. 3,

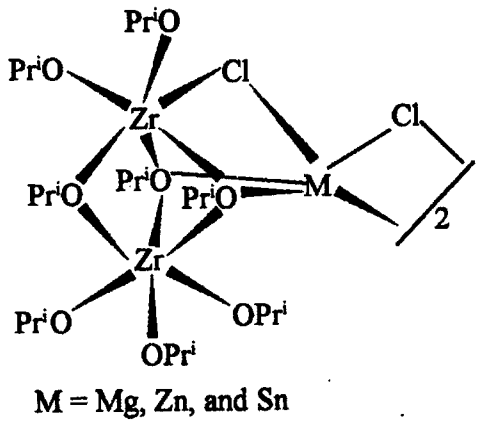

Figure 3. Proposed structures of $[\{Zr_2(OPr^i)_8Cl\}_2M_2(\mu\text{-}Cl)_2]$ (M = Mg, Zn, Sn(II)).

similar to that of X-ray crystallographically established Sn(II) derivative $[\{Zr_2(OPr^i)_9\}Sn(\mu\text{-}I)]_2$) with a sharp ^{119}Sn NMR signal at δ-299.9 comparable to δ-275 reported for the tin analogue [30]. In case of Be, the nature of bonding $\{Zr_2(OPr^i)_8Cl\}$ moiety may be changing [31] from tri- to bi-dentate on dimerization.

Similar types of heterometallic chloride isopropoxide derivatives of Nb as well as Al with bivalent metals have since been synthesized [32] by dissolution of MCl_2 in $Nb(OPr^i)_5$ and $Al(OPr^i)_3$ solutions:

$$MCl_2 + 2Nb(OPr^i)_5 \rightarrow \{(Pr^iO)_4Nb(\mu\text{-}Cl)(\mu\text{-}OPr^i)\}_2M$$

$$MCl_2 + 2Al(OPr^i)_3 \rightarrow \{(Pr^iO)_2Al(\mu\text{-}Cl)(\mu\text{-}OPr^i)\}_2M$$

5. Reactions of Acidic Protons of Metal Glycolate Derivatives with Alkoxides of Another Metal Yielding Heterometallic Alkoxides with the Other Alkoxometallate Moiety in Cationic Form

Compared to the extensive work on heterometallic alkoxides, the corresponding field of heterometallic glycolates is almost unexplored. These derivatives should be less prone to hydrolysis and could, therefore, be expected to yield homogeneous gels rather than precipitates of metal hydroxides due to rapid hydrolysis in the initial stages of the sol-gel process.

The synthesis of a series of monometal glycolates and their conversion into heterometallic complexes can be represented by the following reactions:

$$M(OPr^i)_4 + 3HO{-}G{-}OH \xrightarrow[\text{reflux}]{\text{benzene}} (OGO)_2M\leftarrow\overset{H}{O}GOH + 4Pr^iOH\uparrow$$

(1) soluble

(where M = Ti, Zr, Sn and G = $Me_2C{\cdot}CH_2{\cdot}CHMe$)

$$(1) + 2Al(OPr^i)_3 \xrightarrow[\text{reflux}]{\text{benzene}} \{Al(OPr^i)_2\}_2\{M(OGO)_3\} + 2Pr^iOH\uparrow$$

(2) soluble

(N.B.: 2-Methylpentane-2,4-diol (commonly known as hexylene glycol) has been chosen initially for such reactions, as it tends to give soluble monometal as well as heterometal derivatives.)

These products (**2**) are unique as the $\{Al(OPr^i)_2\}^+$ constituent is potentially in the cationic portion rather than the $\{Al(OPr^i)_4\}^-$ anionic component which is incorporated in almost all the heterometallic isopropoxides containing aluminium so far.

The isopropoxy groups on aluminium could be further replaced by glycolate (and if necessary by other groups like β-diketonates) by simple reactions of the type:

$$\{Al(OPr^i)_2\}_2\{M(OGO)_3\} \xrightarrow[\substack{\text{benzene}\\\text{reflux}}]{+2HOGOH} \{Al(OGO)\}_2\{M(OGO)_3\} + 4Pr^iOH\uparrow$$

(3) soluble

An alternative procedure for synthesis of an identical heterometallic titanium derivative of composition similar to that of (**3**) involves a reaction of the following type:

$$(OGO)_2Ti + (OGO)AlOGOAl(OGO) \xrightarrow[\text{reflux}]{\text{benzene}} \{Al(OGO)\}_2\{Ti(OGO)_3\}$$

soluble

All the above products have been characterized by elemental analysis, IR, NMR (^1H, ^{13}C, ^{27}Al, and ^{119}Sn) spectroscopic data, and simple plausible structures have been suggested for the same [33].

The technique could also be exploited for preparation of heterotermetallic glycolates by the following series of reactions:

$$(OGO)_2M\leftarrow\overset{H}{O}GOH + Al(OPr^i)_3 \rightarrow (OGO)_2M\leftarrow\overset{H}{O}GOAl(OPr^i)_2 + Pr^iOH\uparrow$$

(4)

$$(4) + Nb(OPr^i)_5 \rightarrow [\{Nb(OPr^i)_4\}\{Al(OPr^i)_2\}\{M(OGO)_3\}] + Pr^iOH\uparrow$$

The product (**4**) could be converted into heterotrimetallic glycolate (**5**) by treating it with glycol in a suitable molar ratio [34].

For shortage of space, we conclude this survey with the results obtained with another ligand diethanolamine, $HN(C_2H_4OH)_2$ among many others like triethanolamine $N(C_2H_4OH)_3$, the products of which

have been synthesized successfully so far [34]:

$$M(OPr^i)_4 + 3\begin{matrix}HOC_2H_4\\ \\ HOC_2H_4\end{matrix}\!\!\diagdown\!\!\diagup NH \rightarrow \underset{\text{insoluble(6)}}{H_2M\{OC_2H_4)_2NH\}_3} + 4Pr^iOH\uparrow \quad (M = Ti, Zr, Sn(IV))$$

$$(6) + 2Al(OPr^i)_3 \rightarrow \underset{\text{soluble}}{\{Al(OPr^i)_2\}_2M\{(OC_2H_4)_2NH\}_3} + 2Pr^iOH\uparrow$$

All these products have again been characterized adequately, the details of which would be published elsewhere in the journals of Chemistry as well as Sol-Gel Science.

6. Conclusion

In a number of recent publications on the hydrolysis of derivatives such as $Mg\{Al(OPr^i)_4\}_2$ [35, 36], $CaO_2Al_2(OPr^i)_4$ [37], and $Ba\{Zr_2(OPr^i)_9\}_2$ [38], it has been shown that the basic framework of the heterobimetallic alkoxides remains unaltered at least in the initial stages. However, detailed studies are still required to determine the occurrence of any phase separation on extensive hydrolysis and reasons for the same, which could indicate the possible steps for avoiding/minimizing such phase separation in the gel.

Acknowledgment

The authors are grateful to the Department of Science and Technology, New Delhi, for financial support.

References

1. H. Dislich, Angew. Chem. Int. Ed. Engl. **10**, 363 (1971).
2. R.C. Mehrotra, J. Non-Cryst. Solids **100**, 1 (1988); **121**, 1 (1990); **145**, 1 (1992).
3. R.C. Mehrotra, (a) Mater. Res. Soc. Symp. Proc. **121**, 81 (1988); (b) Chemtracts **2**, 389 (1990); (c) in *Sol-Gel Science and Technology*, edited by R. Reisfeld and C.K. Jorenssn, Structure and Bonding, Vol. 77 (Springer Verlag, Berlin, 1992), pp. 1–36; (d) in *Sol-Gel Processing and Applications*, edited by Y. Attia (Plenum press, New York, 1994), pp. 41–60.
4. R.C. Mehrotra, J. Sol-Gel Sci. and Tech. **2**, 1 (1994).
5. R.C. Mehrotra and A. Singh, in *Sol-Gel Processing of Advanced Ceramics*, edited by F.D. Gnanam (Oxford and I.B.H. Publishing Co., Delhi, 1996), pp. 11–36.
6. A. Nazeri-Eshghi, A.X. Kuang, and J.D. Mackenzie, J. Mater. Sci. **25**, 3333 (1990).
7. S. Hirano, T. Hayashi, K. Nosaki, and K. Kato, J. Am. Ceram. Soc. **72**, 707 (1989).
8. D.R. Ulrich, private communication.
9. R.C. Mehrotra, in *Sol-Gel Science and Technology*, edited by M.A. Aegerter, M. Jaffelicci, Jr., D.F. Souza, and E.D. Zanotto (World Scientific Publishing Co., Singapore, 1989), pp. 1–60, 421–431.
10. D.C. Bradley, Chem. Rev. **89**, 1317 (1989).
11. R.C. Mehrotra, J. Organometal. Chem. (Russian) **3**, 729 (1990).
12. K.G. Caulton and L.G. Pfalzgraf, Chem. Rev. **90**, 989 (1990).
13. R.C. Mehrotra, A. Singh, and U.M. Tripathi, Chem. Rev. **91**, 1287 (1991).
14. R.C. Mehrotra, A. Singh, and S. Sogani, Chem. Rev. **94**, 1643 (1994); Chem. Soc. Rev. **23**, 215 (1994).
15. R.C. Mehrotra and A. Singh, in *Progress in Inorganic Chemistry*, edited by K.D. Karlin (Wiley Interscience, New York, 1997), pp. 239–454.
16. M. Veith, S. Mathur, and V. Huch, J. Am. Chem. Soc. **118**, 903 (1996).
17. R.C. Mehrotra and M.M. Agrawal, J. Chem. Soc., Chem. Commn., 469 (1968).
18. M. Wijk, R. Norrestam, M. Nygren, and G. Wisten, Inorg. Chem. **35**, 1077 (1996).
19. R.C. Mehrotra, J.M. Batwara, and P.N. Kapoor, Coord. Chem. Rev. **31**, 67 (1980).
20. R.C. Mehrotra and A. Singh, Chem. Soc. Rev. **25**, 1 (1996).
21. R.C. Mehrotra, Proc. Ind. Nat. Sci. Acad. **61A**, 253 (1995).
22. W.A. Herrmann, N.W. Hüber, R. Anwander, and T. Priermeier, Chem. Ber. **126**, 1127 (1993).
23. R.C. Mehrotra and A. Singh, Chemtracts **6**, 27 (1994).
24. W.A. Herrmann, N.W. Hüber, and O. Runte, Angew. Chem. Int. Ed. Engl. **34**, 2187 (1995).
25. R.C. Mehrotra, S. Goel, A.B. Goel, R.B. King, and K.C. Nainan, Inorg. Chim. Acta **29**, 141 (1978), and references therein.
26. J. Sassmannshausen, R. Reidel, K.B. Plantz, and H. Chmiel, Z. Naturforsch **48b**, 7 (1993).
27. J.A. Meese-Marktscheffel, R. Weimann, H. Schumann, and J.W. Gilje, Inorg. Chem. **32**, 5894 (1993).
28. M. Bhagat, A. Singh, and R.C. Mehrotra, Main Group Metal Chem. **20**, 89 (1997).
29. M. Bhagat, A. Singh, and R.C. Mehrotra, Synth. React. Inorg. Met. Org. Chem. **28**, 997 (1998).
30. M. Veith, S. Mathur, and V. Huch, J. Chem. Soc. Dalton Trans. 2485 (1996).
31. R.C. Mehrotra and A. Singh, Symposium in Print Series, *Polyhedron* (1997) (in honour of Prof. D.C. Bradley).
32. M. Bhagat, A. Singh, and R.C. Mehrotra, unpublished results.
33. J. Godhwani, A. Singh, and R.C. Mehrotra, Polyhedron, (1997) (communicated).
34. J. Godhwani, unpublished results.
35. K. Jones, T.J. Davies, H.G. Emblem, and P. Parkes, Mater. Res. Soc. Symp. Soc. **71**, 111 (1986).
36. J. Rai and R.C. Mehrotra, J. Non-Cryst. Solids **152**, 118 (1993).
37. J. Rai and R.C. Mehrotra, J. Non-Cryst. Solids **134**, 118 (1991).
38. R. Kuhlman, B.A. Vaartstra, W.E. Streib, J.C. Huffman, and K.G. Caulton, Inorg. Chem. **32**, 1272 (1993).

Journal of Sol-Gel Science and Technology 13, 51–59 (1998)
© 1998 Kluwer Academic Publishers. Manufactured in The Netherlands.

Spectroscopy and Structure of Sol-Gel Systems

RUI M. ALMEIDA
Departamento de Engenharia de Materiais/INESC, Instituto Superior Técnico, Av. Rovisco Pais, 1000 Lisboa, Portugal

Abstract. Sol-gel derived glasses may differ from conventional melt-quenched glasses owing to the peculiar microstructures existing at the gel state, such that, even after gel densification, some differences may remain in their composition and molecular structure.

This paper discusses structural characteristics of thin film oxide gels and glasses, with a special emphasis on SiO_2-TiO_2 based systems, which are of particular interest for sol-gel integrated optics applications. Short range structure aspects are discussed based on infrared, X-ray photoemission and X-ray photoabsorption spectroscopies. The chemical homogeneity of sol-gel materials is evaluated, based on X-ray photoemission and nuclear magnetic resonance spectroscopies, dealing in particular with the issue of homo- vs. heterocondensation. Finally, some microstructural features of sol-gel derived films are analyzed, namely the relationship between infrared absorption and porosity and the structure of nanocrystalline sol-gel films, based on grazing incidence X-ray diffraction and micro-Raman spectroscopy. The types of structural information obtainable by each different technique are compared in detail.

Keywords: short-range structure, chemical homogeneity, nanocrystallization, silica-titania films, infrared spectroscopy

1. Introduction

The structure of sol-gel derived systems is a subject of considerable interest, not only in connection with the general problem of amorphous materials structure, but also because of possible differences between the structure of sol-gel derived glasses and that of their melt-quenched analogues [1]. In particular, silica-titania based films have important optical applications, which include antireflective coatings [2], passive [2, 3] and active [2, 4–6] optical planar waveguides. The structure of silica-titania based sol-gel derived materials has been the object of a number of spectroscopic studies, which include infrared (IR) [7–11], Raman [12, 13], Nuclear Magnetic Resonance (NMR) [14, 15], X-ray Photoelectron Spectroscopy (XPS) and X-ray Absorption Fine Structure (NEXAFS and EXAFS) [9, 16–18]. Some IR spectroscopy studies on silica sol-gel derived materials [19–21] are also relevant for understanding the structure of silica-titania compositions.

The available IR spectroscopy data [7, 8] have shown that, in silica-titania sol-gel films, the frequency of the dominant Si—O stretching at ca. 1070 cm^{-1} goes through a minimum for densification temperatures near 450°C (for 80 SiO_2-20 TiO_2 films, in mol%), or 400°C (for films with 30 mol% TiO_2), suggesting a minimum strength of the Si—O skeleton and, therefore, maximum porosity for such heat treatment temperatures. Also, the EXAFS and NEXAFS data [16, 17] have indicated that, in silica-titania sol-gel films, essentially all Ti^{4+} ions remain four-fold coordinated, both before and after thermal densification, contrary to what is found, e.g., in sodium-titanium-silicate glasses [22], where both five- and six-fold coordinated Ti^{4+} are believed to be present. This work describes specific structural features of silica-titania based sol-gel systems, including short-range order aspects dealing with near neighbor structures, the issue of chemical homogeneity, related to the occurrence of homo- vs. heterocondensation and the microstructural features of porosity and nanocrystallization.

2. Experimental

Silica-titania films containing 0–30 mol% TiO_2 were prepared on single crystal Si substrates by the sol-gel process, according to the procedure described in [23], from prehydrolyzed tetraethylorthosilicate (TEOS), titanium isopropoxide (TPOT) and, when doped with Al, P, or Er, with these elements added as Al nitrate, P pentoxide, or Er nitrate. Those films were subjected to different heat treatments in air. Pure silica films were also prepared from TEOS, as described in [19]. Film thickness was measured by ellipsometry at $\lambda = 633$ nm, with a Rudolph Instruments 444A spectroellipsometer.

Fourier transform infrared (FTIR) spectra were recorded for silica gel films with an IBM IR/98 spectrometer; for silica-titania films, a Nicolet 5DXC spectrometer was used. Raman spectra were recorded with a microspectrometer consisting of a Olympus BH2-UMA microscope, a SPEX Triplemate triple monochromator and a SPEX Spectrum One CCD detector. The 514.5 nm line of a Spectra Physics 2017 argon ion laser was used for excitation. XPS measurements were carried out with an Al Kα X-ray source (1486.6 eV) at an energy resolution of ca. 1 eV and NEXAFS spectra were measured with synchrotron radiation at the BESSY facility in Berlin, in the total electron yield detection mode. ^{17}O NMR spectra were recorded for ^{17}O-enriched silica-titania (2 : 1) ethanolic sols on a MSL-300 Bruker spectrometer, via Fourier transformation of time-domain data. Grazing incidence (2°) X-ray diffraction (XRD) was recorded for nanocrystallized films with a Siemens D-5000 diffractometer, using Cu Kα radiation.

3. Results

Figure 1 shows the FTIR absorption spectrum of a partially dense silica gel film, 150 nm thick, heat treated at 400°C (for 3 h). Four peaks are observed, plus a high frequency shoulder (Sh) at ca. 1200 cm^{-1}.

Figure 2 shows IR transmission spectra for a series of 90 SiO_2-10 TiO_{2-x} $PO_{2.5}$ (always in mol%) films densified at 900°C (for 2 min). In addition to the features found in the silica gel film spectrum, there is a more prominent peak near 940 cm^{-1}, whose intensity clearly decreases with the P content of the films.

Figure 3 shows the oxygen K-edge Near X-ray Absorption Fine Structure (NEXAFS) and the O 1 s XPS spectra for undensified SiO_2 and 70 SiO_2-30 TiO_2 gel films, dried at room temperature only. Figure 3(b) shows a nonlinear least squares Gaussian peak fit with

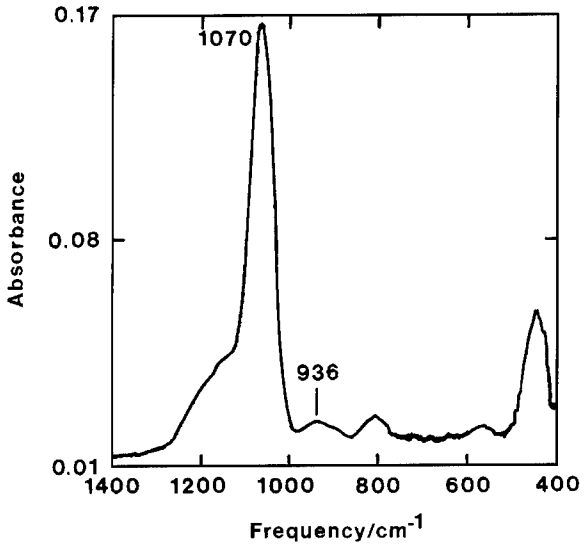

Figure 1. IR absorption spectrum of a SiO_2 gel film heat treated at 400°C. (Adapted from [19].)

three different components, which can be attributed to the presence of different structural types of oxygen atoms. Based on such results, Fig. 4 shows a plot of the fraction of nonbridging oxygen (NBO) atoms as a function of the TiO_2 content, for films densified at 900°C.

Figure 5 shows the ^{17}O NMR spectrum of a sol consisting of partially hydrolyzed TEOS and TPOT, after different reaction times. In both cases, a resonance is found at 263–266 ppm (relative to ^{17}O-enriched water), with FWHM = 23 ppm, which appears only after the addition of TPOT to the TEOS + ethanol + water solution.

Figure 6 is a plot of the IR absorbance of the Si—O stretching peak (ca. 1070 cm^{-1}) for SiO_2 sol-gel films (heat treated at 550°C) and 80 SiO_2-20 TiO_2 films (treated at 450°C). For each series of samples, several layers were deposited and immediately densified for 20 min, in sequence, on an Si wafer; therefore, each thickness value is cumulative.

Figure 7 shows the unpolarized micro-Raman spectrum and the XRD patterns of an 80 SiO_2-20 TiO_2 film nanocrystallized at 1100°C (for 60 min). Both graphs indicate the occurrence of anatase nanocrystals inside the amorphous film matrix.

4. Discussion

4.1. *Short-Range Structures*

In Fig. 1, the main peak at 1070 cm^{-1} is due to the transverse optic (TO) component of the asymmetric stretch

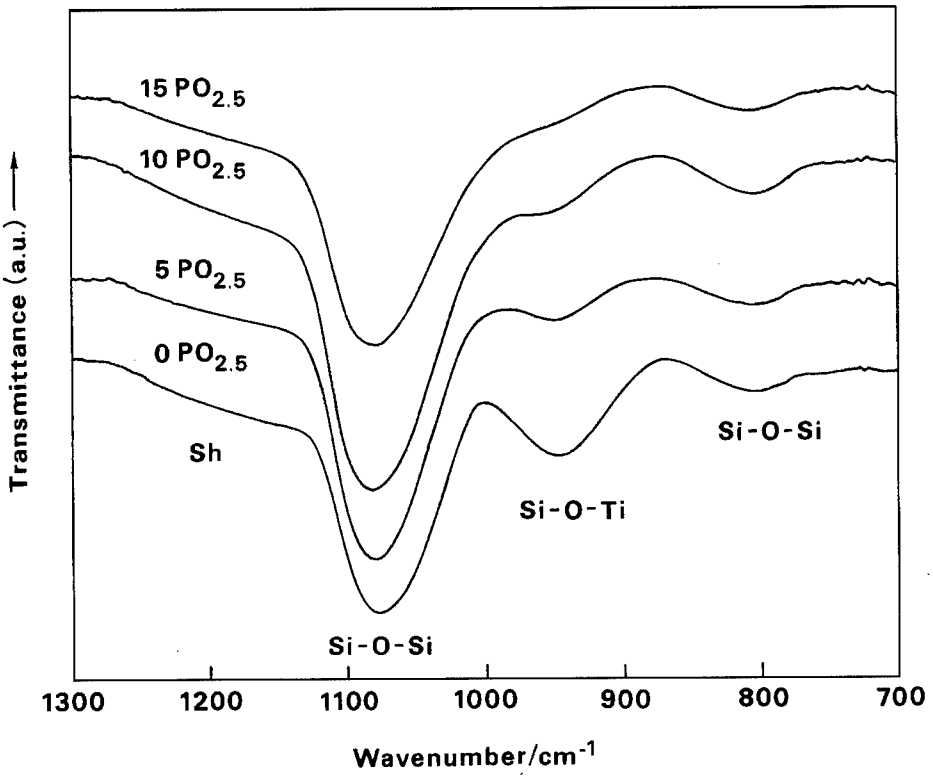

Figure 2. IR transmission spectra of 90 SiO_2-10 TiO_{2-x} $PO_{2.5}$ films, densified at 900°C.

of the oxygen atoms along a direction parallel to Si—Si (plus substantial Si cation motion [25]); the Sh feature near 1200 cm^{-1} is related to (but not coincident with) the longitudinal optic (LO) component of the same vibration [19, 25]. The main differences between the IR spectrum of the gel film and that of a silica glass film [19] are: (1) the FWHM of the TO peak is smaller in the gel film, suggesting the presence of strained Si—O—Si bonds near the surface of the gel pores; (2) the peak frequency is lower in the gel film, indicating the presence of longer Si—O bonds (with smaller vibrational force constants) near the pores; (3) the Sh feature is more intense for the gel film, due to the activation of the LO mode by its porosity [19]; (4) finally, the peak centered at 936 cm^{-1} in the silica gel film (absent in silica glass films) is due to the presence of Si—OH (or Si—O^-) species [19].

The main difference between the 90 SiO_2-10 TiO_2 infrared spectrum of Fig. 2 (0 $PO_{2.5}$) and that of Fig. 1 is a stronger peak near 940 cm^{-1} in the former, which is due to Si—O^- stretching in Si—O^-Ti^{4+} sequences involving tetrahedrally coordinated Ti^{4+} ions, but not to Si—OH, absent due to the full densification of the film at 900°C. On the other hand, the sharp decrease in the intensity of the 940 cm^{-1} peak of Fig. 2 as the P content increases up to 15 $PO_{2.5}$ shows that the presence of P atoms destroys the NBO species in Si—O^-Ti^{4+}, perhaps by forming Si—O—P—O^-Ti^{4+} bonding sequences. P atoms are usually added to silica based gels doped with Nd atoms, in order to help disperse the rare earth species, presumably through the formation of additional NBO species [9, 26]; according to the present results, these species are predominantly of a different kind and are formed at the expense of the Si—O^- NBO atoms which exist in P-free films.

The concentration of NBOs in sol-gel materials is a fundamental short-range structural feature, of special importance for the dissolution of rare earth elements in the amorphous matrix. Figure 3 shows how X-ray spectroscopy can be used to identify and quantify the presence of NBO species in silica-titania sol-gel films with 30 mol% TiO_2, in comparison with SiO_2, which does not have NBO species. Figure 3(a), with a clear pre-edge peak which is found to increase with the titania content between 0 and 30 mol% [18], indicates that, in terms of NEXAFS, a NBO of the Si—O—Ti or the Ti—O—Ti types has a photoabsorption edge at an energy

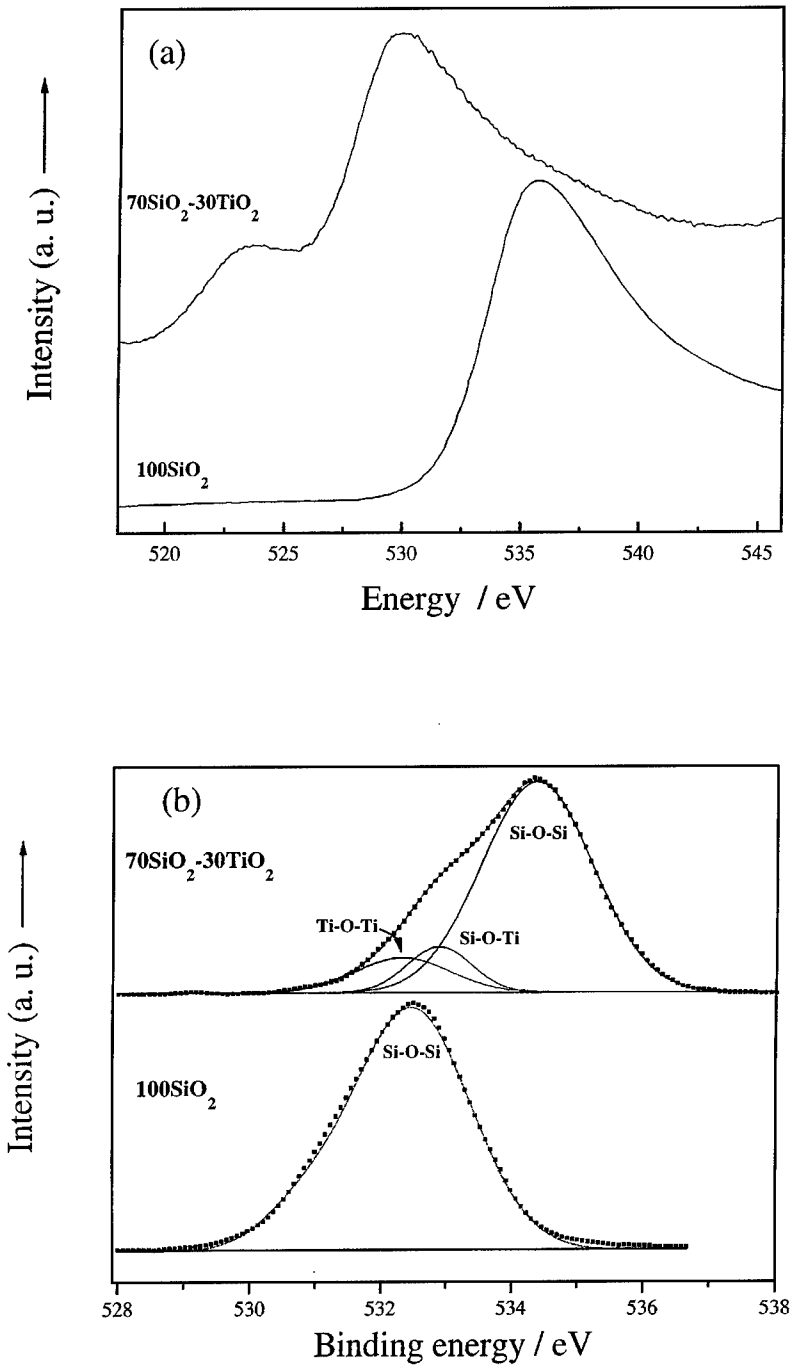

Figure 3. (a) Oxygen K-edge NEXAFS spectra and (b) O 1 s XPS spectra, of 70 SiO_2-30 TiO_2 and pure SiO_2 films, without heat treatment.

ca. 6 eV lower than the Si—O—Si bridging oxygens (main peak); however, the corresponding quantification is difficult. The XPS spectrum of Fig. 3(b) has a shoulder on the low binding energy (BE) side, which is not well resolved, but allows a better quantification of the fraction of NBO species present through peak-fitting and also permits a separation of the two types of NBO atoms, in Si—O—Ti and Ti—O—Ti bonds, which have a small BE difference of ca. 0.6 eV, but different chemical environments.

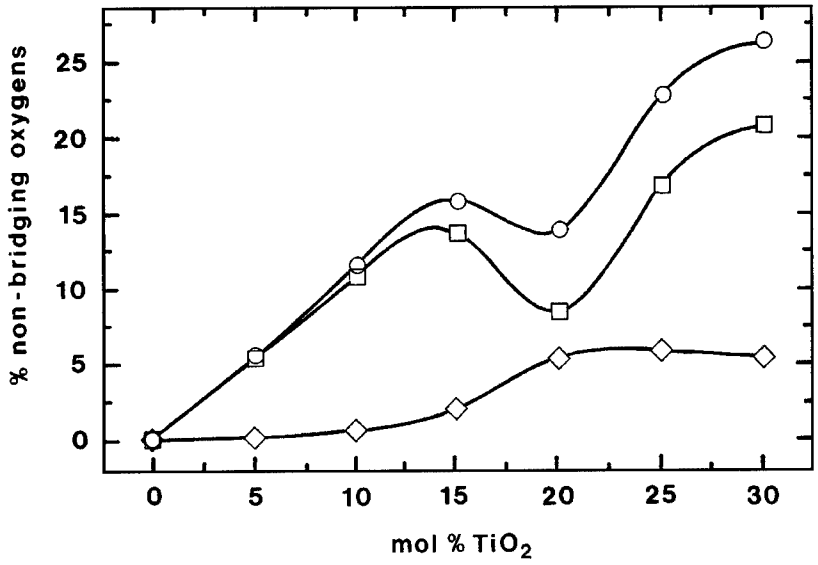

Figure 4. Fractions of different types of NBO atoms, from XPS results, for SiO_2–TiO_2 films with varying TiO_2 concentrations, densified at 900°C: (◇) Si–O–Ti, (□) Ti–O–Ti and (○) total NBO. (Adapted from [9].)

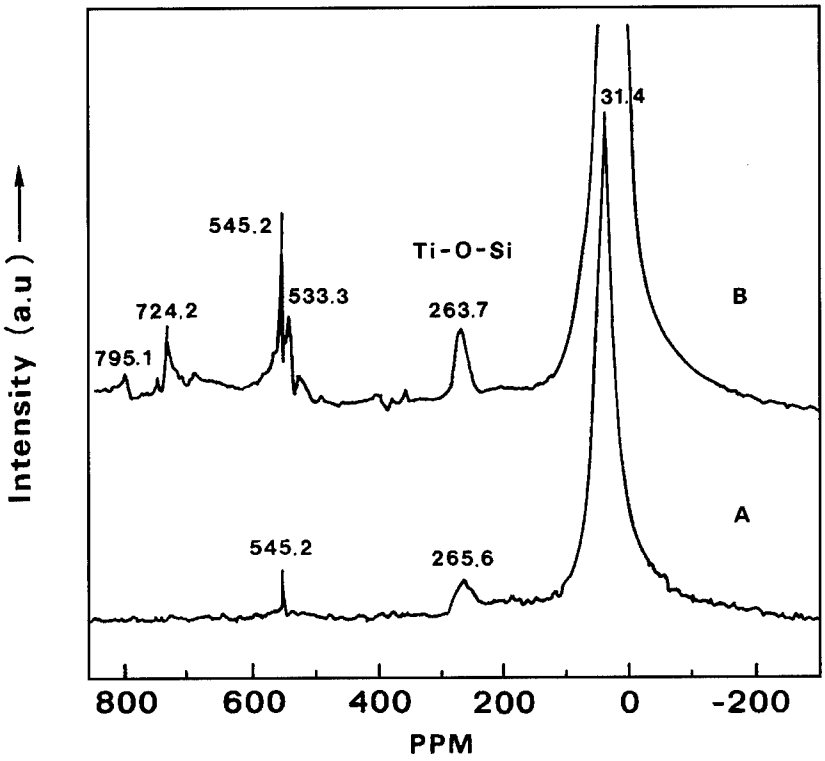

Figure 5. ^{17}O NMR spectra of partially hydrolyzed TEOS + TPOT sol after (A) 2 h and (B) 48 h of reaction time.

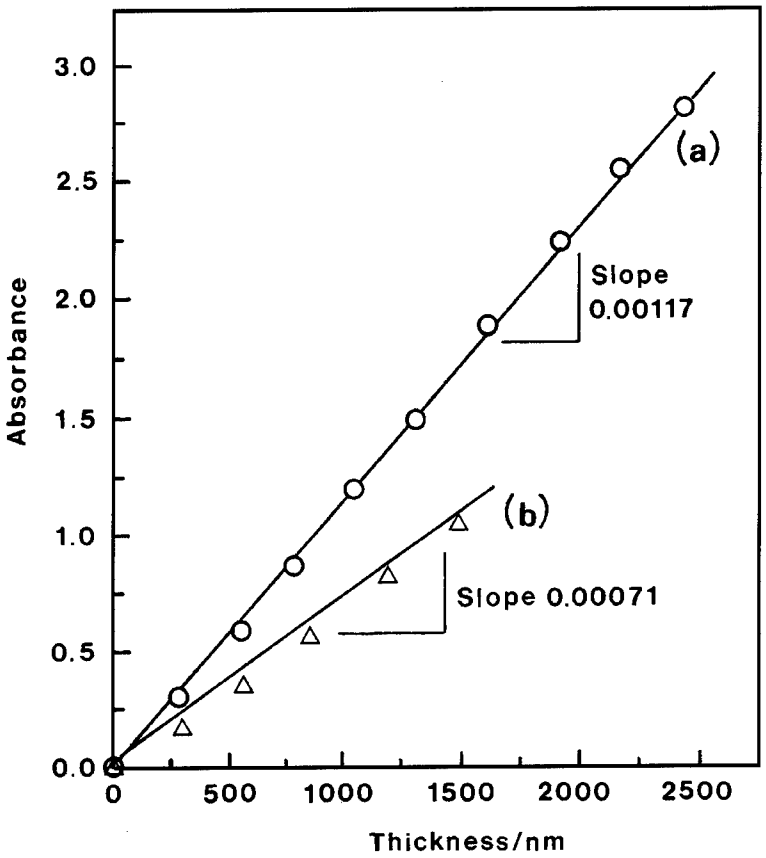

Figure 6. IR absorbance of dominant Si–O stretch in (a) porous SiO_2 and (b) 80 SiO_2-20 TiO_2 multilayer films, as a function of thickness. (Adapted from [7].)

4.2. *Chemical Homogeneity*

Figure 4, which shows the variation of the fractions of the two types of NBOs with the TiO_2 content, is an example of how XPS can be used to study the chemical homogeneity in sol-gel systems. The degree of heterocondensation (Si–O–Ti) is always less than that of homocondensation (Ti–O–Ti), indicating the presence of a titania-rich phase, but the latter reaches a local minimum at 20 mol% TiO_2, a titania concentration which has been used in active waveguides [6, 9].

Another spectroscopic tool well suited for investigating the chemical homogeneity of sol-gel systems, in particular, the degree of heterocondensation in silica-titania compositions, is NMR spectroscopy. Figure 5 shows a new resonance of ^{17}O at 264–266 ppm, which appears only when TPOT is added to partially hydrolyzed TEOS and may be assigned to Si–O–Ti linkages, in agreement with [27]. This NMR spectrum shows that, in addition to Si–O–Si bonds (main peak at 31.4 ppm), there are Si–O–Ti and also Ti–O–Ti bonds (Ti_2O units at 724–795 ppm [28]) simultaneously formed.

4.3. *Microstructure*

The porosity of sol-gel films is very important regarding their application in optical devices, but it is difficult to evaluate quantitatively, e.g., by surface acoustic wave gas adsorption or molecular probe ellipsometry [8], which are time-consuming. IR spectroscopy may be used as a quicker, indirect probe to monitor film porosity [7]. Defining *infrared thickness* of a porous film as the thickness x_{IR} that it would have after full densification, which is smaller than its actual thickness x, one may write the measured absorbance A in terms of Beer's law as:

$$A = \alpha x = \alpha_{std}\, x_{IR} \tag{1}$$

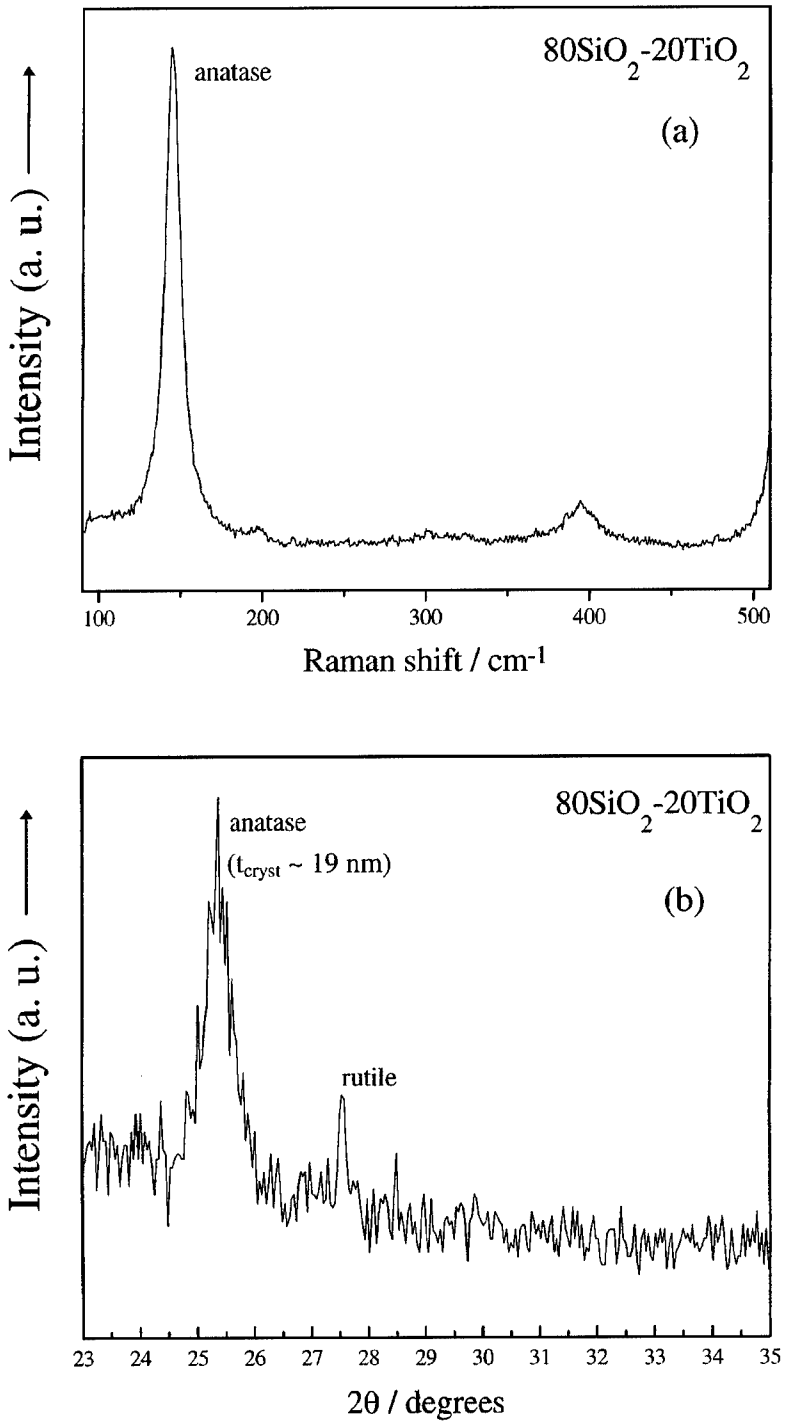

Figure 7. (a) Micro-Raman spectrum and (b) XRD patterns of 80 SiO_2-20 TiO_2 film nanocrystallized at 1100°C, for 60 min.

where α is the absorption coefficient of the porous film and α_{std} is the absorption coefficient of a standard, fully densified film. This leads to a porosity volume fraction given [7] by:

$$v_p = 1 - x_{IR}/x = 1 - \alpha/\alpha_{std}. \quad (2)$$

Therefore, if the value of α_{std} and the IR absorbance plus the sample thickness measurements are known, one can obtain α and thus the porosity v_p. The *infrared thickness* is simply the absorbance divided by α_{std}. Figure 6 shows the absorbance of partially dense films at the frequency of the dominant Si—O stretch (ca. 1073 cm^{-1} for pure silica and ca. 1056 cm^{-1} for silica-titania) as a function of multilayer film thickness. The straight line obtained shows that Beer's law holds without appreciable deviations [7] and also that the porosity is not varying significantly with the heat treatment time at the given temperature; the slope gives the value of α. For example, in the case of partially dense 80 SiO_2-20 TiO_2 films (heat treated at 450°C, the temperature of maximum porosity), the slope equals 0.00071 nm^{-1}, i.e., $\alpha = 7.1 \times 10^3$ cm^{-1}; for fully densified films, it was determined that $\alpha_{std} = 1.0 \times 10^4$ cm^{-1} and, from Eq. (2), one finds $v_p = 29\%$ for this temperature, in reasonable agreement with a value of 25% obtained from refractive index measurements [7].

Nanocrystallization is another aspect of microstructure, which may be used in order to improve the spectroscopic performance of rare-earth ions incorporated into an amorphous sol-gel matrix [29]. Figure 7 shows the particular example of anatase nanocrystals, with an average size near 19 nm, estimated by X-ray line broadening, which precipitated from an 80 SiO_2-20 TiO_2 matrix. In addition to this passive phase, other active phases containing rare-earth ions such as Er^{3+} may be precipitated as well [29]. Anatase is found both with XRD and micro-Raman spectrometry (through the peaks at 145, 200, and 399 cm^{-1} [30]), whereas a very small amount of rutile is also visible in the XRD plot, but not in the micro-Raman spectrum. In fact, due to the larger Raman scattering cross sections of anatase compared to rutile, small fractions of the former are easier to detect by Raman spectrometry, whereas rutile is easier to detect by XRD.

5. Conclusions

Different spectroscopic methods are shown to be powerful techniques for the elucidation of the short-range structures, the chemical homogeneity and the microstructure of sol-gel systems. In particular, for silica-titania based films, it was shown that the short-range atomic structures can be studied in detail by IR spectrometry and the identification of NBO species may be achieved based on IR, XPS and NEXAFS spectrometries. These two X-ray based techniques, as well as NMR spectroscopy, may also be used to study the chemical homogeneity of an oxide sol-gel system, through a quantitative evaluation of the different types of NBO species present; XPS is especially well suited for this. Finally, the porosity of the films may be evaluated, based on IR spectroscopy, and nanocrystallization may be followed by Raman spectroscopy and XRD.

Acknowledgments

I would like to acknowledge the financial support of the European Commission DGXIII, through ACTS project AC047 (CAPITAL), the support of ICEMS (Lisboa) and that of EC: HCM program, under contract No. CHGE-CT93-0027.

References

1. B. Roy, H. Jain, S.K. Saha, and D. Chakravorty, J. Non-Crystalline Solids **183**, 268 (1995).
2. H. Schroeder, in *Physics of Thin Films: Advances in Research and Development*, edited by G. Hass and R.E. Thun (Academic Press, New York, 1969), p. 87.
3. Y. Soreq, R. Reisfeld, I. Finkelstein, and S. Ruschin, Appl. Phys. Lett. **63**, 3256 (1993).
4. R.M. Almeida, X. Orignac, and D. Barbier, J. Sol-Gel Sci. Technol. **2**, 465 (1994).
5. D. Barbier, X. Orignac, X.M. Du, and R.M. Almeida, in *Proc. of Topical Symp. VII on Advanced Materials in Optics, Electro-Optics and Communication Technologies*, edited by P. Vicenzini (Techna Srl., Faenza, Italy, 1995), p. 33.
6. X. Orignac, X.M. Du, D. Barbier, and R.M. Almeida, Appl. Phys. Lett. **69**, 895 (1996).
7. R.M. Almeida, H.C. Vasconcelos, and L.M. Ilharco, SPIE **2288**, 678 (1994).
8. E.J.C. Dawnay, M.A. Fardad, M. Green, F. Horowitz, E.M. Yeatman, R.M. Almeida, H.C. Vasconcelos, M. Guglielmi, and A. Martucci, in *Proc. of Topical Symp. VII on Advanced Materials in Optics, Electro-Optics and Communication Technologies*, edited by P. Vicenzini (Techna Srl., Faenza, Italy, 1995), p. 55.
9. X. Orignac and R.M. Almeida, IEE Proc. Optoelectron. **143**, 287 (1996).
10. X.M. Du and R.M. Almeida, J. Sol-Gel Sci. Technol. **8**, 377 (1997).
11. T.M. Parril, J. Mater. Res. **9**, 723, 1994.
12. M.F. Best and R.A. Condrate, J. Mater. Sci. Lett. **4**, 994 (1985).
13. J. Cheng and D. Wang, J. Non-Crystalline Solids **100**, 288 (1988).

14. J.D. Basil and C. Lin, in *Better Ceramics Through Chemistry III*, edited by C.J. Brinker, D.E. Clark, and D.R. Ulrich (Materials Research Society, Pittsburgh, 1988), p. 49.
15. S. Dire and F. Babonneau, J. Non-Crystalline Solids **167**, 29 (1994).
16. M. Emili, L. Incoccia, S. Mobilio, M. Guglielmi, and G. Fagherazzi, J. Non-Crystalline Solids **74**, 129 (1985).
17. R.M. Almeida, M.I. de Barros Marques, and X. Orignac, J. Sol-Gel Sci. Technol. **8**, 293 (1997).
18. X. Orignac, H.C. Vasconcelos, and R.M. Almeida, J. Non-Crystalline Solids **217**, 155 (1997).
19. R.M. Almeida and C.G. Pantano, J. Appl. Phys. **68**, 4225 (1990).
20. M.C. Matos, L.M. Ilharco, and R.M. Almeida, J. Non-Crystalline Solids **147/148**, 232 (1992).
21. R.M. Almeida, Int. J. Optoelectronics **9**, 135 (1994).
22. C.W. Ponader, H. Boek, and J.E. Dickinson, Jr., J. Non-Crystalline Solids **201**, 81 (1996).
23. X.M. Du, X. Orignac, and R.M. Almeida, J. Am. Ceram. Soc. **78**, 2254 (1995).
24. R.M. Almeida, J. Non-Crystalline Solids **106**, 347 (1988).
25. F.L. Galeener, Phys. Rev. **B19**, 4292 (1979).
26. K. Arai, H. Namikawa, K. Kumata, T. Honda, Y. Ishii, and T. Handa, J. Appl. Phys. **59**, 3430 (1986).
27. F. Babonneau, in *Better Ceramics Through Chemistry VI*, edited by A.K. Cheetham, C.J. Brinker, M.L. Mecartney, and C. Sanchez (Materials Research Society, Pittsburgh, 1994), p. 365.
28. V.W. Day, T.A. Eberspacher, W.G. Klemperer, C.W. Park, and F.S. Rosenberg, in *Chemical Processing of Advanced Materials*, edited by L.L. Hench and J.K. West (John Wiley and Sons, Inc., 1992), p. 49.
29. R.M. Almeida and H.C. Vasconcelos, in *Proc. Fundamentals of Glass Science and Technology 1997* (Glafo, The Glass Research Institute, Vaxjo, Sweden, 1997), p. 110.
30. R.M. Almeida and E.E. Christensen, J. Sol-Gel Sci. Technol. **8**, 409 (1997).

Journal of Sol-Gel Science and Technology 13, 61–64 (1998)
© 1998 Kluwer Academic Publishers. Manufactured in The Netherlands.

Sulfide Gels and Films: Products of Non-Oxide Gelation

L. MALIER, J.P. BOILOT AND T. GACOIN
Laboratoire de Physique de la Matière Condensée, CNRS, URA 1254 D, Ecole Polytechnique, 91128 Palaiseau Cedex, France

Abstract. The preparation of concentrated sols and transparent stiff gels of II-VI semiconductors nanocrystals is reported. A two-step process for the production of cadmium sulfide is reported. Sol stabilization and gelation control are achieved through successive passivation and depassivation of the surface of the nanocrystals which are complexed with thiols. The mechanisms driving the aggregation and the gelation are explained on the basis of NMR and SAXS experiments. Thin films as well as monoliths can be produced. The general principles of the method presented are not restricted to chalcogenide systems and thus enlarge the domain of application of the inorganic sol-gel process.

Keywords: cadmium sulfide nanocrystals, sol-gel transition, aggregation, NMR, small angle X-ray scattering (SAXS), thin films

1. Introduction

The sol-gel process is a well-known synthetic route for the preparation of oxide materials. Starting from precursors in solution, it relies upon the successive formation and aggregation of molecular units or particles. Oxide systems are peculiarly well-suited to this process and represent most, if not all, of the systems on which the sol-gel synthesis has been applied. The hydrolysis and condensation reactions are controlled by many parameters (pH, stoichiometry or salinity of the solutions) and control of the relative rates of these reactions allows selective promotion of the growth, stabilization or aggregation of the particles. The formation of a gel—a three-dimensional solid network trapping solvent—requires the aggregation of units of limited surface reactivity [1]. This is fairly easily obtained in oxide sols.

This paper proposes a new sol-gel scheme, dedicated to chalcogenide systems and illustrated by cadmium sulfide gel synthesis. Our method relies on a multistep process which allow successive control of (a) the formation of nanocrystalline particles, (b) their stabilization by surface passivation, and (c) their aggregation by a limited increase of the surface reactivity of the particles [2]. Stable transparent gels are thus obtained, whose texture, network density or constitutive unit size can be controlled.

2. Experimental

The first step concerns the formation of the nanoparticles and their stabilization. Several procedures have already been published, all of which employ a complexing molecular agent for colloid stabilization [3]. Our synthesis schemes are adapted from these methods. By using a new fluorinated complexing molecule (4-fluorophenythiol), the maximum particle concentration has been enhanced by a factor of 10 and the systems are stable in most of the usual solvents. The particle size can be tuned from 1 to 6 nm and this paper will focus on the process leading to the smallest sizes.

This process consists of a precipitation of CdS in presence of a complexing agent. Under vigorous stirring, a solution of 4-fluorophenythiol (FPhiSH, 10^{-2} M), triethylamine (TEA, $2 \cdot 10^{-2}$ M) and H_2S ($5 \cdot 10^{-3}$ M) in deoxygenated acetone is added slowly into the same volume of acetone containing $Cd(NO_3)_2$ ($4 \cdot 10^{-3}$ M). After complete addition, a yellowish colloidal solution is obtained. The complete evaporation of the solvent gives a powder which is washed with ethanol and can then be dispersed in various solvents such as acetone, THF, DMF. This procedure thus gives a yellow sol whose cadmium concentration can be as high as 5 mol $\cdot l^{-1}$. From the absorption spectra of the sol, and following the correlation curve previously

published by Wang and Herron [4], the mean size of the particles is estimated to be around 1 nm.

3. Results and Discussion

Particle complexation was studied through liquid state ^{19}F and ^{113}Cd nuclear magnetic resonance (NMR) spectroscopy. The fluorine spectrum of the sol in acetone is shown in Fig. 1, the chemical shift being referred to $CFCl_3$. The sharp peak appearing at -118 ppm corresponds to dithiols in solution (FPhiS-SPhiF), that are not complexing species and that are used as an internal reference. Apart from this peak, the NMR signal exhibits two broad lines located at about -125 and -127.5 ppm, which account for 90% of the whole signal. These lines correspond to complexed thiols, either bridging two cadmium atoms (-125 ppm) or acting as terminal groups (-127.5 ppm). Such attributions are supported by Dance's studies of thiol-cadmium complexes [5] as well as by the ^{113}Cd NMR spectroscopy performed on our sols [2]. The latter reveals that cadmium atom environments are largely distributed over the range $CdS_x(SPhiF)_{4-x}$ where $0 \leq x \leq 4$. Such a distribution suggests that a competition takes place between the growth of the particles and their surface complexation by thiolate species, which is necessary to avoid uncontrolled aggregation. This competition is responsible for the limited size (1 nm) of the particles thus obtained.

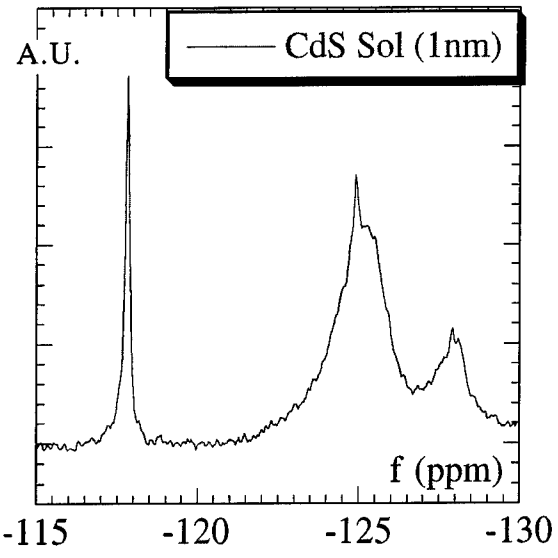

Figure 1. ^{19}F NMR spectrum of a cadmium sulfide sol. The crystalline particle size is 1 nm.

At the end of the step just described, the sol is perfectly stable, for periods longer than months, i.e., the particle surface is passivated by grafted thiolates. In order to obtain a gel, the particle reactivity has to be increased so that random aggregation can occur. This requires surface cadmium decomplexation. This can be achieved by controlled oxidation of a fraction of the capping thiolates using an oxidizer such as hydrogen peroxide. The oxidizer is slowly added under vigorous stirring at 0°C, in order to ensure a sufficient reactant dispersion. When treated with hydrogen peroxide in 0.2 molar ratio relative to the complexed thiol, a sol of 10^{-1} mol $\cdot l^{-1}$ in cadmium produces a gel after some hours at room temperature.

Figure 2(a) presents the ^{19}F NMR spectrum as measured 5 min. after H_2O_2 addition. When compared with Fig. 1, it shows an important increase of the dithiol concentration, together with a decrease of the complexed thiol contribution. This is in agreement with previous observations of dithiol as one of the possible thiol oxidation products [6]. Figure 2(a) also shows that the broad lines are slightly shifted towards the high fields, which we attribute to a change in charge density at the surface of particles. As the time passes, the capping thiol signal goes on decreasing without producing more dithiols (Fig. 2(b)). Thiol oxidation is then fast and the gelation rate is not controlled by the kinetics of the oxidation reactions. Once "reactivated," the particles slowly aggregate, the growing clusters tumbling more and more slowly into the solution. This accounts for the continuous fall of the signal of the complexed thiols, due to NMR dipolar broadening, in agreement with observations made in silica systems [7].

Small angle scattering is also well-suited to studying the growth of aggregates made of particles. Experiments were carried out using synchrotron radiation at LURE (Orsay, France). A one-dimensional position-sensitive detector was used to record the scattered X-ray intensity from the samples placed in capillary tubes. The parasitic scattering from air, slits and sample holder was substracted from the experimental SAXS intensity using standard methods. SAXS curves for the same system studied by NMR are presented in Fig. 3. Measurements were performed for scattering vectors q ranging from 0.02 to 4 nm^{-1}, at different times after the addition of hydrogen peroxide. Two very clear cutoffs are seen, one corresponding to particle size ($q = 2\ nm^{-1}$) and the other to the correlation length which increases as the clusters grow. Between these two limits, the scattered intensity clearly follows a power law, whose exponent equals 1.9, independent

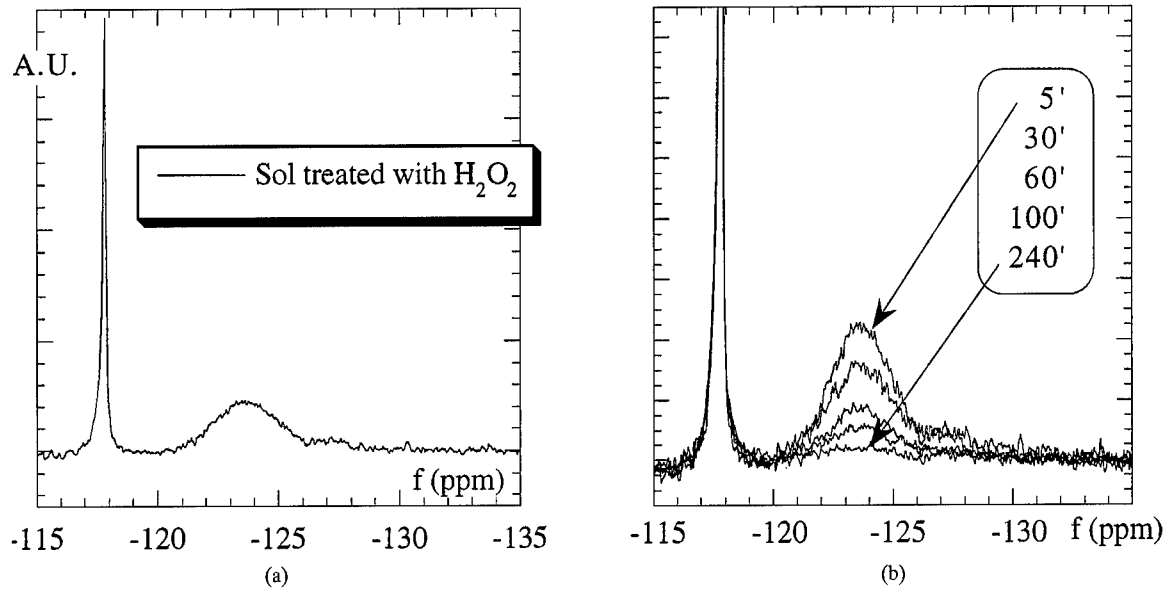

Figure 2. ^{19}F NMR spectrum of cadmium sulfide sol: (a) just after hydrogen peroxide addition, in 0.2 molar ratio relative to the grafted thiols (see text); (b) for different times after hydrogen peroxide addition.

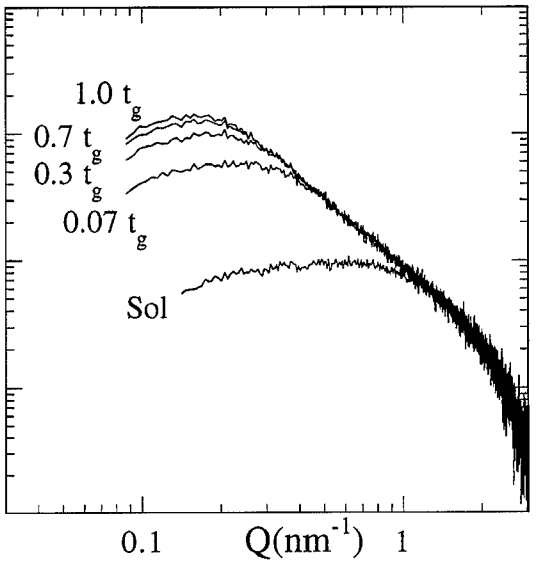

Figure 3. Small Angle X-ray Scattering (SAXS) curves for a cadmium sulfide sol of 1 nm particle size. The curves (from 0.07 t_g to the gelation time t_g) correspond to scattering of the destabilized sol after H_2O_2 addition.

of the correlation length. This exponent is characteristic of the structure and density distribution of the lacunar aggregates. Its value is consistent with reaction-limited cluster-cluster aggregation, as observed in some silica gels [8]. A decrease of the scattered intensity at low q, revealing interactions between clusters is also seen. This is due to the CdS concentration which was required to be at least 10^{-1} mol $\cdot$ l^{-1} for NMR sensitivity. Nevertheless, SAXS performed on much more diluted sols exhibited the same fractal dimension of 1.9.

Extensive parametric study of this chalcogenide sol-gel transition is under investigation; preliminary results are presented here. The first important parameter is the quantity of oxidizer, reported to complexed thiol. If too low, the particle surface remains passivated and there is no aggregation between particles. In the case of oxidizer in large excess (ratio > 1), the particle surfaces are totally depassivated and flocculation or precipitation occurs.

Our process can produce very diluted sols which can be destabilized in a similar way. Stiff gels have been obtained for CdS volume fraction as low as 1%. At that level of dilution, the gels remain transparent but slightly diffuse.

After gelation, syneresis occurs, with more than ten-fold contraction in the case of the most diluted gels. The dithiol concentration in the released liquid accounts for the whole dithiol content and proves that these molecules do not participate in the chemical bonding between particles. This has also been shown by transmission electron microscopy on partially oxidized sols with larger particle sizes (4 nm). CdS crystallites, observed in high-resolution transmission electron microscopy, are shown in Fig. 4. Collapsed particles are clearly observed. It can also be seen that the particles are highly crystalline.

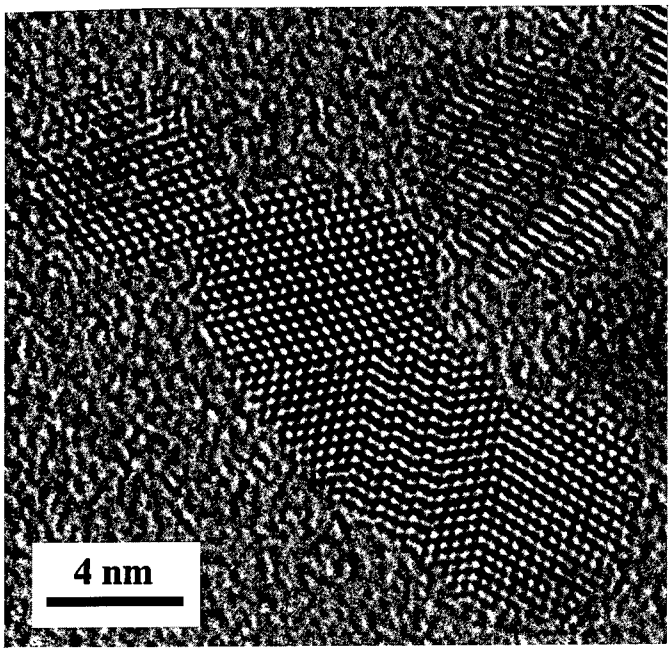

Figure 4. High resolution transmission electron microscopy for a destabilized cadmium sulfide sol of 4–5 nm particle size.

Lastly, thin films have been processed by spin coating partially oxidized CdS sols onto various substrates. The films are transparent and nanocrystalline. Their thickness is tunable by viscosity, over 100 nm. At 600 nm, the refraction index is 1.9.

4. Conclusion

A two-step sol-gel process applicable to chalcogenide systems such as cadmium sulfide has been reported. This process gives CdS sols in usual solvents, with a particle size ranging from 1 nm to 5 nm and concentration tunable up to 5 mol $\cdot l^{-1}$ ([Cd]). Sol stability is ensured through the formation of a surface complex involving thiolate species. The second step relies on a controlled destabilization of the sol by oxidizing the thiols. Transparent nanocrystalline gels are obtained, thanks to an aggregation phase whose mechanism is strongly reminiscent of RLCA. Starting from our process, production of ZnS, ZnSe or CdSe gels or films is straightforward. Moreover, we believe that the general principles of our method should apply to a large variety of non-oxide systems and allow future developments of the sol-gel technique.

Acknowledgment

We acknowledge C. Ricolleau, Laboratoire de Minéralogie-Cristallographie, CNRS URA 009, Universités Paris VI et Paris VII, 75252 Paris (FRANCE) for HRTEM observations on our samples (Philips EM 430 ST microscope working at 300 kV).

References

1. C.J. Brinker and G. Scherer, *Sol-Gel Science: The Physics and Chemistry of Sol-Gel Processing* (Academic Press, London, 1990).
2. T. Gacoin, L. Malier, and J.P. Boilot, J. Mat. Chem. **7**(6), 859 (1997); T. Gacoin, L. Malier, and J.P. Boilot, Chemistry of Materials **9**, 1502 (1997).
3. N. Herron, Y. Wang, and H. Eckert, J. Am. Chem. Soc. **112**, 1322 (1990); Y. Nosaka, N. Otha, T. Fukuyama, and N. Fujii, J. Colloid and Interf. Sci. **155**, 23 (1993); A. Fojtik, H. Weller, U. Koch, and A. Henglein, Ber. Bunsenges. Phys. Chem. **88**, 969 (1984); M.L. Steigerwald, A.P. Allivisatos, J.M. Gibson, T.D. Harris, R. Kortan, A.J. Muller, A.M. Thayer, T.M. Duncan, D.C. Douglass, and L.E. Brus, J. Am. Chem. Soc. **110**, 3046 (1988); P. Lianos and J.K. Thomas, Chem. Phys. Lett. **125**(3), 299 (1986).
4. Y. Wang and N. Herron, Phys. Rev. B **42**(11), 7253 (1990).
5. G.S. Lee, K.J. Fisher, A.M. Vassallo, J.V. Hanna, and I.G. Dance, Inorg. Chem. **32**, 66 (1993).
6. B.J. Evans, J. Takahashi Doi, and W.K. Musker, J. Org. Chem. **55**, 2337 (1990).
7. L. Malier, J.P. Boilot, F. Chaput, and F. Devreux, Phys. Rev. A **46**(2), 959 (1992).
8. D.W. Schaefer and D. Keefer, in *Fractals in Physics*, edited by L. Pietronero and E. Tosatti (Elsevier Science Publishers B.V., 1986), p. 39; R. Vacher, T. Woigner, J. Pelous, and E. Courtens, Phys. Rev. B **37**(11), 6500 (1988).

Journal of Sol-Gel Science and Technology 13, 65–70 (1998)
© 1998 Kluwer Academic Publishers. Manufactured in The Netherlands.

Chemically Controlled Condensation of Polyoxovanadates

J. LIVAGE, L. BOUHEDJA AND C. BONHOMME
Chimie de la Matière Condensée, Université Pierre et Marie Curie, 4, place Jussieu, 75252 Paris, France

Abstract. A wide range of polyvanadates can be synthesized from aqueous solutions. Vanadium oxide gels $V_2O_5 \cdot nH_2O$ are formed around the point of zero charge (pH $\approx$ 2). They exhibit a ribbon-like structure. Weak interactions between these ribbons lead to the formation of mesophases in which vanadium oxide gels or sols behave as nematic liquid crystals. Organic species can be easily intercalated between these oxide ribbons leading to the formation of hybrid nanocomposites made of alternative layers of organic and inorganic components. Hybrid materials can also be formed at a higher pH in the presence of large organic ions such as $[N(CH_3)_4]^+$. They exhibit layered structures in which organic cations lie between polyoxovanadate planes. Such layered structures are not obtained in the presence of anions such as Cl^- or I^-. Cluster shell polyvanadates are then formed. They are made of negatively charged polyvanadate hollow spheres in which the negative anion is encapsulated. In this case the organic cations behave as counter ions for the formation of the hybrid crystalline network.

Keywords: vanadates, hydrothermal syntheses, vanadium oxide gels, V^V precursors

1. Introduction

Vanadium, in its higher oxidation states, gives a large number of polyoxovanadates that exhibit a wide variety of structures such as chain metavanadates $[VO_3^-]_n$, layered oxides $[V_2O_5]$ or compact polyanions $[V_{10}O_{28}]^{6-}$. This is due to the ability of vanadium to adopt a variety of coordination and oxidation states (V^V, V^{IV}) [1].

The structure of these polyoxovanadates mainly depends on the pH of the aqueous solution. Vanadium pentoxide gels $V_2O_5 \cdot nH_2O$ are formed around the point of zero charge (pH $\approx$ 2). They exhibit a ribbon-like structure and have been shown to exhibit specific electronic and ionic properties. Therefore, they have been extensively studied for application in antistatic coatings on photographic films, reversible cathodes in lithium batteries, humidity sensors or electrochromic layers in display devices [2]. Vanadium pentoxide gels are currently synthesized via the acidification of aqueous solutions of metavanadate. Acidification can be conveniently performed with a proton exchange resin in order to get rid of all foreign ions so that the only ionized species in the aqueous solution are $[V_{aq}]^{5+}$, OH^- and H_3O^+ [3].

Completely different materials are obtained in the presence of foreign ions [4]. Positively or negatively charged precursors are formed below or above the point of zero charge. Counter ions are then required to form a neutral network. Supramolecular associations between ionic species may be formed in the solution. They are involved in the formation of V—O—V bonds via condensation reactions. Layered structures are formed in the presence of organic cations while hollow clusters have been synthesized when anions such as Cl^- or I^- are added to the solution [5].

This paper discusses the role of foreign ions (cations and anions) during the formation of a polyoxovanadate network from aqueous solutions of V^V.

2. Experimental

2.1. *Synthesis of Ribbon-Like Vanadium Oxide Gels*

Vanadium pentoxide gels $V_2O_5 \cdot nH_2O$ have been obtained via the acidification of aqueous solutions of sodium metavanadate $NaVO_3$ through a proton exchange resin [3]. The colorless solution turns pale

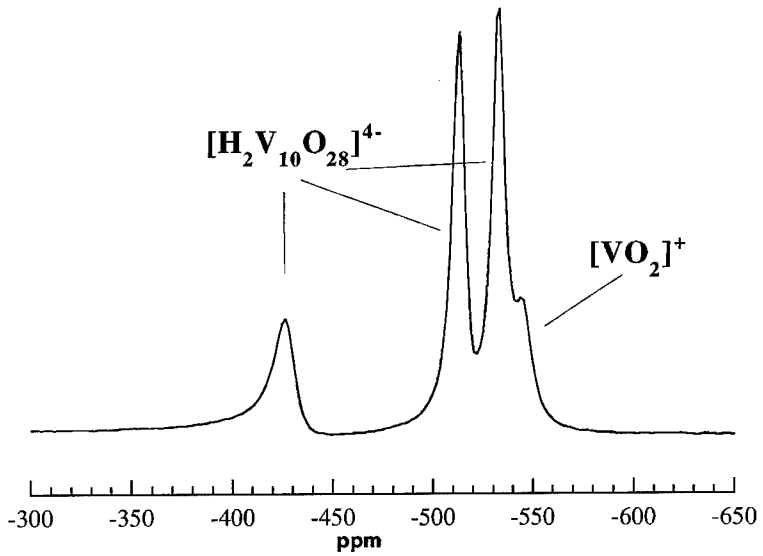

Figure 1. ^{51}V NMR spectrum of the solution formed upon acidification of a metavanadate solution (pH $\approx$ 2).

yellow as soon as the pH decreases. An acid solution (pH $\approx$ 2) is obtained at the bottom of the column that contains a mixture of decavanadic acid $[H_nV_{10}O_{28}]^{(6-n)-}$ and dioxovanadium cations $[VO_2]^+$ as shown by ^{51}V NMR spectra (Fig. 1). This clear solution polymerizes slowly within a few hours to give large condensed polymeric species. The color of the solution changes to dark red while its viscosity progressively increases, giving a colloidal solution or a $V_2O_5{\cdot}nH_2O$ gel.

Transmission electron microscopy shows that these gels are formed of flat ribbons about 0.1 μm long, 100 Å large and 10 Å thick [6]. The 1D Patterson map analyzed by Oka et al. suggests that V_2O_5 layers are made of two V_2O_5 sheets facing each other at a distance of 2.8 Å [7]. An ordered stacking of the ribbons is observed when these gels are deposited onto a flat substrate, giving an X-ray diffractogram made of a series of 00l peaks [8]. The basal distance between ribbons depends on the amount of water in $V_2O_5{\cdot}nH_2O$. It first increases by steps of about 2.8 Å, corresponding to the intercalation of one water layer ($d = 8.7$ Å, 11.5 Å, ...). A continuous swelling is observed beyond $d \approx 20$ Å [9].

Because of the acid dissociation of V—OH groups at the oxide-water interface, vanadium oxide ribbons are negatively charged (about 0.1 e^- per vanadium). Electrostatic repulsion prevents the precipitation of the vanadium oxide V_2O_5 and mesophases are formed as shown by Davidson [10]. When observed between crossed polarizers, vanadium oxide sols and gels display optical textures typical of liquid crystals. They actually behave like nematic solutions of semirigid polymers, confirming that the length of the ribbons is at least one order of magnitude larger than their width [11].

2.2. *Formation of Layered Polyvanadates in the Presence of Cations*

Vanadate compounds can be synthesized from negatively charged precursors at a pH higher than the point of zero charge (pH > 2). The formation of a neutral network then requires the presence of foreign cations [1].

In our experiments, V_2O_5 ($\approx$1 g) was dissolved in an aqueous solution (5 ml) of tetramethyl ammonium hydroxide TMAOH, $N(CH_3)_4OH$ (1 M). Dissolution occurs within half an hour upon gentle heating at 60°C as follows:

$$V_2O_5 + 6OH^- \rightarrow 2[VO_4]^{3-} + 3H_2O$$

The pH of the solution prior to dissolution is close to 13. Vanadate ions $[VO_4]^{3-}$ should then be formed at such a high pH, but according to the above equation, the pH of the solution decreases during dissolution. Vanadate species are then protonated $[H_nVO_4]^{(3-n)-}$, allowing condensation to take place via oxolation reactions. The ^{51}V NMR spectrum of the solution after dissolution (pH $\approx$ 7) exhibits two series of peaks corresponding to

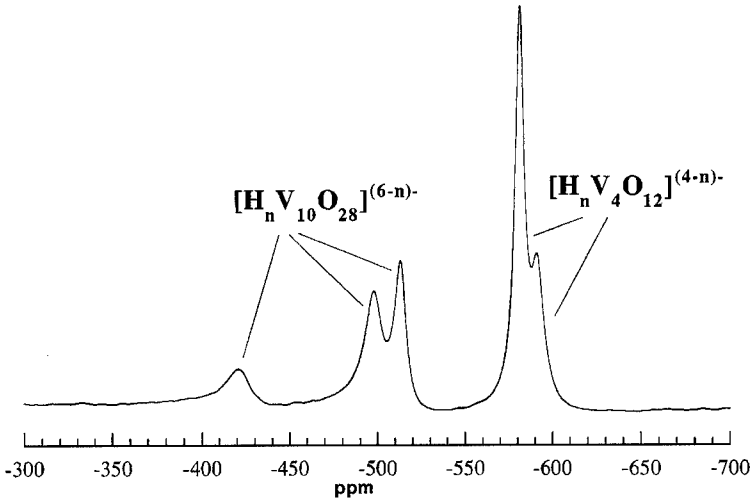

Figure 2. ^{51}V NMR spectrum of aqueous solutions formed via the dissolution of V_2O_5 in TMAOH (pH $\approx$ 7).

a mixture of metavanadates $[H_2V_4O_{12}]^{4-}$ ($\delta = -581$ and -591 ppm) and decavanadates $[V_{10}O_{28}]^{6-}$ ($\delta = -420$, -498 and -513 ppm) (Fig. 2). The intensity of metavanadate peaks decreases when the pH of the solution decreases and only decavanadates are observed below pH $\approx$ 6. The nature of precipitated phases then mainly depends on the final pH of the solution.

Large crystals of $N(CH_3)_4V_4O_{10}$ are obtained via the hydrothermal treatment of a mixture of V_2O_5 and TMAOH (200°C, 48 h). They exhibit a layered structure made of $[V_4O_{10}]^-$ anionic layers built of double chains of edge-sharing $[VO_5]$ tetragonal pyramids linked together by corners (Fig. 3). Large alkylammonium cations lie between the oxide layers where they interact weakly with the negatively charged terminal oxygen (V=O) [12]. They behave as counter cations and the structure of the oxide network is mainly governed by the dipolar interactions between adjacent V=O bonds.

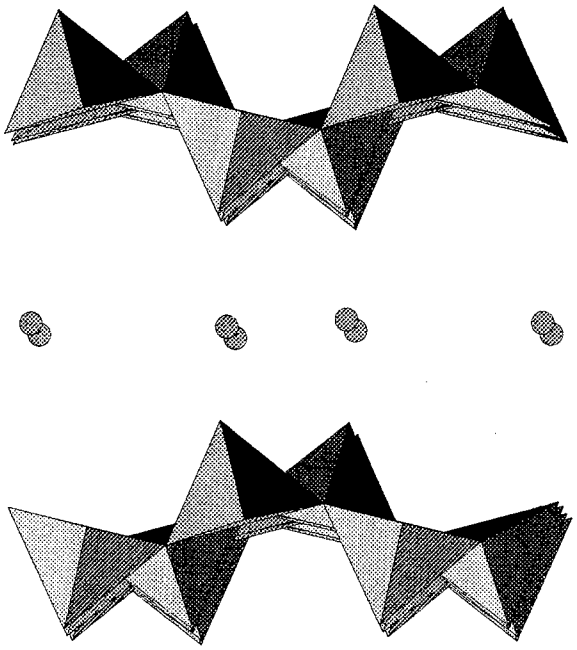

Figure 3. Crystal structure of $N(CH_3)_4V_4O_{10}$ (according to [12]).

2.3. *Formation of Polyvanadate Clusters in the Presence of Anions*

The nature and structure of solid phases precipitated from aqueous solutions of V_2O_5 and TMAOH are completely different when hydrothermal syntheses are performed in the presence of small amounts of anions. These anions can be conveniently introduced as $[N(CH_3)_4X]$ salts ($X^- = Cl^-, I^-$) dissolved in the aqueous solution. The ^{51}V NMR spectrum of the solution after hydrothermal treatment (200°C, 48 h) again shows the presence of both metavanadate and decavanadate species. Black shiny regularly shaped crystals are formed (hexagonal prisms for Cl^- and octahedra for I^-). These crystals obviously do not have a layered structure. X-ray diffraction performed on single crystals shows that they are made of hollow polyvanadate cages, $[V_{15}O_{36}Cl]^{6-}$ and $[V_{18}O_{42}I]^{13-}$ built of tetragonal $[VO_5]$ pyramids sharing edges and corners (Fig. 4.) [13, 14]. The X^- anion lies in the center of the cage;

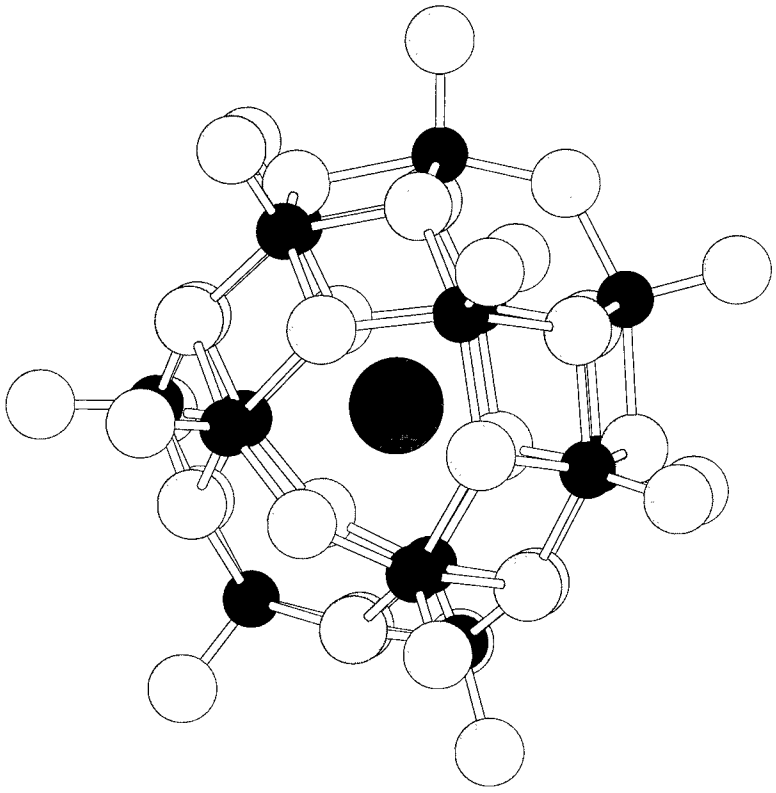

(a)

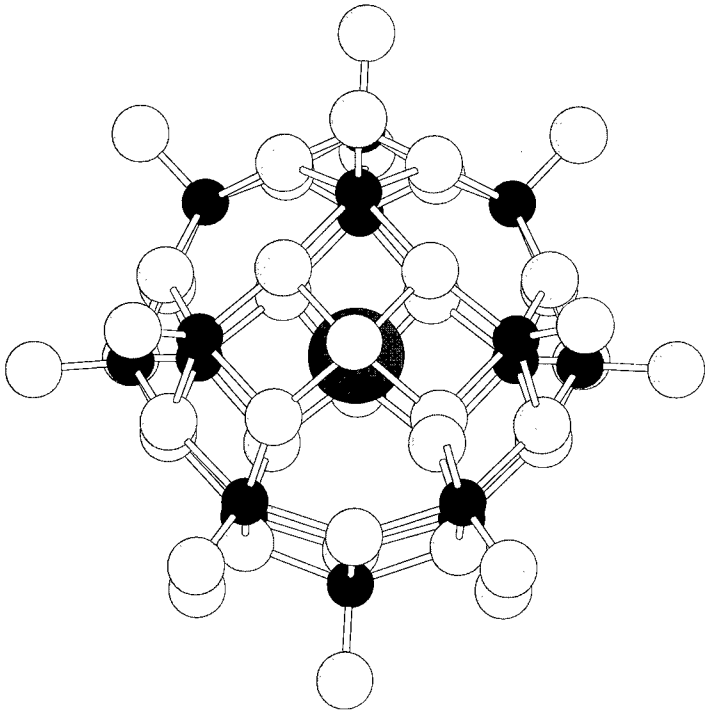

(b)

Figure 4. Molecular structure of polyoxovanadate clusters: (a) $[V_{15}O_{36}Cl]^{6-}$, (b) $[H_3V_{18}O_{42}I]^{10-}$ (according to [13, 14]). V = ●; O = ○; X = ●.

short V=O bonds are oriented toward the outside of the sphere and large organic cations just behave as counter ions. Some vanadium reduction occurs during the hydrothermal synthesis. The cage in $(NMe_4)_6[V_{15}O_{36}Cl]4H_2O$ contains both V^V and V^{IV} oxidation states, whereas the vanadium is completely reduced V^{IV} in $(NMe_4)_{10}[H_3V_{18}O_{42}I]3H_2O$.

3. Discussion

The aqueous chemistry of V^V mainly depends on pH. Fewer and fewer protonated species are formed when the pH increases. Positively charged octahedral $[VO_2(OH_2)_4]^+$ dioxo cations are observed at very low pH, whereas negatively charged tetrahedral species $[H_nVO_4]^{(3-n)-}$ are formed at high pH.

Vanadium pentoxide is precipitated from the neutral precursor $[VO(OH)_3(OH_2)_2]^0$ in which one water molecule lies along the z-axis opposite to the short V=O double bond (Fig. 5(a)). Condensation cannot proceed along this direction as there is no V—OH group. It occurs only in the xy-plane where one V—OH_2 and three V—OH bonds are formed. Oxolation along the HO—V—OH_2 direction proceeds faster than oxolation along the HO—V—OH direction, giving rise to a ribbon-like structure. X-ray diffraction experiments show that these ribbons are formed of double chains of edge and corner sharing $[VO_5]$ pyramids [7]. Dipolar interactions between neighboring V=O favor the formation of layered nanostructures. The V_2O_5 layer is stabilized because the V=O groups of edge-sharing pyramids are situated on different sides of the plane. Water molecules can be easily intercalated between these layers through hydrogen bonds. The acid dissociation of V—OH groups at the oxide-water interface leads to the formation of a negatively charged polyvanadic acid network. Electrostatic repulsion between oxide ribbons avoids precipitation and favors the formation of mesophases.

Layered polyvanadates are formed at higher pH (pH ≈ 7). They can be precipitated from the negatively charged precursor $[VO(OH)_4(OH_2)]^-$ (Fig. 5(b)). As before, condensation cannot occur along the O=V—OH_2 direction. Condensation in the equatorial plane where four V—OH bonds are observed then leads to layered polyoxovanadates. Two adjacent $[VO_5]$ pyramids are linked together via condensation of two V—OH groups directed by dipolar interactions between adjacent V=O bonds. The linkage of $[VO_5]$ pyramids is close to that observed in V_2O_5, leading to the formation of $NMe_4V_4O_{10}$ made of negative $[V_4O_{10}^-]_n$ layers. Large TMA^+ cations are situated between the planes where they interact with the negative V=O [12].

Cluster shell species are formed in the same pH range. The presence of X^- anions completely changes the way $[VO_5]$ pyramids are linked together. Encapsulated anions obviously behave as templates during the formation of cluster shell polyoxovanadates [15]. They appear to control the formation of the surrounding cluster shell. This should be due to the particular geometry of $[VO_5]$ pyramids in which the water molecule V···OH_2 opposite to the V=O bond is very labile. Negative anions X^- can then interact with the positive $V^{\delta+}$, favoring the formation of spherical species around a central anion. All V=O dipoles are then oriented toward the outside of the shell where they repel each other and interact with large organic counter cations.

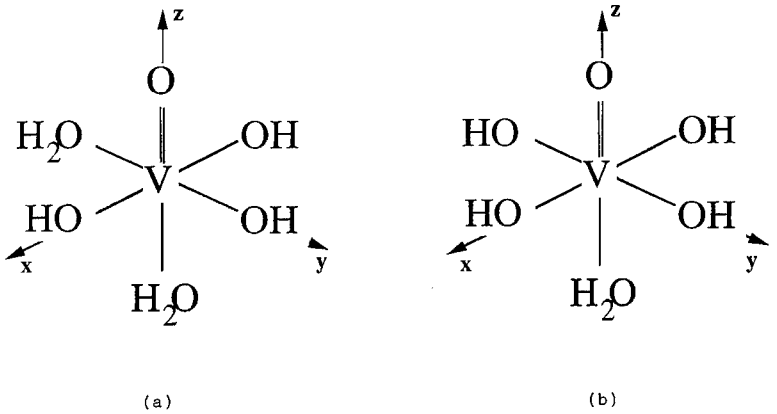

Figure 5. Possible V^V precursors in aqueous solutions in the pH range 2–7: (a) $[VO(OH)_3(OH_2)_2]^0$, (b) $[VO(OH)_4(OH_2)]^-$.

Electrostatic attractions between large anionic polyvanadates and large organic cations lead to the crystallization of hybrid "ionic" crystals with cell parameters of the order of 2 nm.

This work shows that small changes in the synthesis conditions can lead to completely different nanostructures. Several ionic species are always simultaneously present in aqueous solutions (H_3O^+, OH^-, M^{z+}, X^-, ...). The formation of a solid network depends on the nature of molecular precursor $[M(OH)_h(OH_2)_{6-h}]^{(z-h)+}$ but the way these primary building units self-assemble results from a competition between all the ionic species.

References

1. M.T. Pope, *Heteropoly and Isopolyoxometallates* (Springer-Verlag, Berlin, 1983).
2. J. Livage, Chem. Mater. **3**, 578 (1991).
3. N. Gharbi, C. Sanchez, J. Livage, J. Lemerle, L. Nejem, and J. Lefebvre, Inorg. Chem. **21**, 2758 (1982).
4. M.T. Pope and A. Müller, Angew. Chem. Int. Ed. Engl. **30**, 34 (1991).
5. J. Livage, L. Bouhedja, C. Bonhomme, and M. Henry, Nanophase and nanocomposite materials II, Mat. Res. Soc. Symp. Proc. **457**, 13 (1997).
6. J.J. Legendre and J. Livage, J. Colloids and Interface Sci. **94**, 75 (1983).
7. T. Yao, Y. Oka, and N. Yamamoto, Mat. Res. Bull. **27**, 669 (1992).
8. P. Aldebert, N. Baffier, N. Gharbi, and J. Livage, Mater. Res. Bull. **16**, 669 (1981).
9. N. Baffier, P. Aldebert, J. Livage, and H.W. Haesslin, J. Colloids Interface Sci. **141**, 467 (1991).
10. P. Davidson, A. Garreau, and J. Livage, Liq. Cryst. **16**, 905 (1994).
11. P. Davidson, C. Bourgaux, L. Schoutteten, P. Sergot, C. Williams, and J. Livage, J. Phys. II France **5**, 1577 (1995).
12. P.Y. Zavalij, M.S. Whittingham, and E.A. Boylan, Zeit. Krist. **211**, 1 (1996).
13. A. Müller, E. Krickemeyer, M. Penk, H.J. Walberg, and H. Bögge, Angew. Chem. Int. Ed. Engl. **26**, 1045 (1987).
14. G.K. Johnson and E.O. Schlemper, J. Amer. Chem. Soc. **100**, 3645 (1978).
15. A. Müller, H. Reuter, and S. Dilinger, Angew. Chem. Int. Ed. Engl. **34**, 2328 (1995).

Journal of Sol-Gel Science and Technology 13, 71–74 (1998)
© 1998 Kluwer Academic Publishers. Manufactured in The Netherlands.

^{17}O-NMR of Sol-Gel Processes of TEOS and TMOS

M.P.J. PEETERS
Philips CFT, Materials Analysis Department, Prof. Holstlaan 4, 5656 AA Eindhoven, The Netherlands

T.N.M. BERNARDS AND M.J. VAN BOMMEL
Philips Research Laboratories Eindhoven, Prof. Holstlaan 4, 5656 AA Eindhoven, The Netherlands

Abstract. Water consumption and formation in the acid catalyzed sol-gel processing of TEOS and TMOS can be followed using ^{17}O-NMR. By using ^{17}O-enriched water, insight into the hydrolysis and condensation in the acid step of the sol-gel process can be obtained. It is found that, after initially strong consumption of water due to hydrolysis, a steady state water concentration results. This amount of water increases upon dilution of the reaction mixture with alcohol. For a hydrolyzed TMOS-methanol-water system lower water contents are found than in a comparable TEOS-ethanol system. Addition of ethanol to a hydrolyzed TMOS methanol system enhances the condensation and a higher water concentration is found.

Keywords: ^{17}O-NMR, hydrolysis, condensation, sol-gel chemistry

1. Introduction

The sol-gel process is an attractive route for the preparation of pure silica glass and thin layers [1, 2]. The sol-gel process is based on the hydrolysis and condensation of, for instance, tetraethylorthosilicate (TEOS). In these reactions water is a dominant reactant.

It is possible to gain insight into the reactions occurring during the acid step of a two-step sol-gel process by using hydrolysis time versus gelation time curves [3]. For a system with a water to TEOS molar ratio of 2, a minimum gelation time was found. This minimum occurred at the moment when the water concentration also reached a minimum. For longer hydrolysis times a steady state water concentration was found.

Low temperature ^{29}Si-NMR has been shown to be a very efficient technique for the characterization of the sol-gel process [4]. However, the evolution of the water in the system cannot be followed directly. Using ^{17}O-NMR, the reactions of the oxygen-containing components in the hydrolysis mixture can be followed.

Geissberger and Bray used ^{17}O-NMR to determine the structure and bonding in amorphous SiO_2 [5]. However, ^{17}O-NMR has been little used in the characterization of the sol-gel processing of TEOS. Babonneau used ^{17}O-NMR to characterize the co-condensation reactions of methyl substituted silicon alkoxides [6–8]. She used this technique for a quantitative determination of the different oxygen species in a mixture of alkyl-alkoxy-silane, water, and titanium or zirconium alkoxides. A residual amount of free water during the pre-hydrolysis of the silicon-alkoxide precursor was observed, even if an under-stoichiometric amount of water was used. Although in this experiment the residual amount of water was found for an alkyl-alkoxy-silane compound, Babonneau claimed to observe even more residual water during the hydrolysis of TEOS [9].

By using ^{17}O-enriched water in sol-gel syntheses, it is possible to obtain a specific labelling of the M—O*H and M—O*M groups and thus greatly enhance their detectability compared to R—OH or M—OR groups.

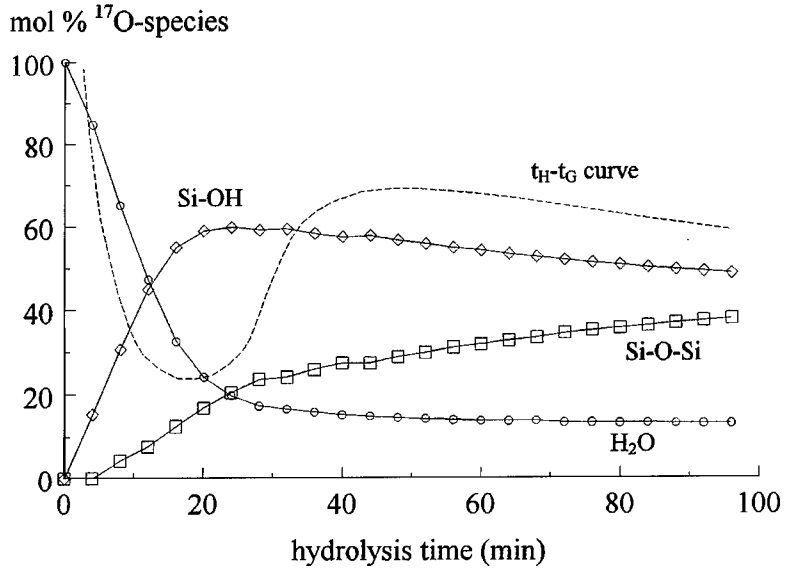

Figure 1. Evolution of the amount of water, silanols and siloxane of a hydrolyzing mixture of TEOS, ethanol and water (5×10^{-3} M HCl) in a molar ratio of 1 : 4 : 2 as measured with ^{17}O-NMR. The relation between the t_H and t_G is also indicated [11].

2. Experimental

To determine the amount of water in a hydrolyzing mixture, ^{17}O-NMR experiments are performed on a Bruker MSL spectrometer, equipped with a broadband probe operating at 40.7 MHz. During the measurements the samples are kept at a temperature of 50°C. For the hydrolysis of TEOS, 10 at.% ^{17}O-enriched water is used.

The NMR spectra are recorded in situ for a mixture of TEOS or TMOS, alcohol and ^{17}O-enriched water. The water fraction is acidified with HCl. After reaching a steady state water concentration, some samples are further diluted with alcohol and the measurements are continued.

3. Results

Figure 1 shows the results of ^{17}O-NMR measurements performed on samples of a mixture of TEOS, ethanol and water (5×10^{-3} M HCl) in the molar ratio of 1 : 4 : 2. The amount of water and silanols in the hydrolysis mixture is found by integration of the peaks around −5 ppm (H_2O^*) and between 10 and 30 ppm (≡Si—O*H), respectively [10]. The chemical shift of water is 0 ppm but, due to hydrogen bonding between water and ethanol, the chemical shift of water is shifted to a lower field. The peaks between 30 and 60 ppm belong to bridging oxygen atoms in ≡Si—O*—Si≡. In Fig. 1 the intensities of the ^{17}O species are plotted versus the hydrolysis time. In this figure the hydrolysis time versus gelation time is also plotted [11].

In Fig. 2 the residual amount of water in the steady state situation in the acid step is plotted as a function

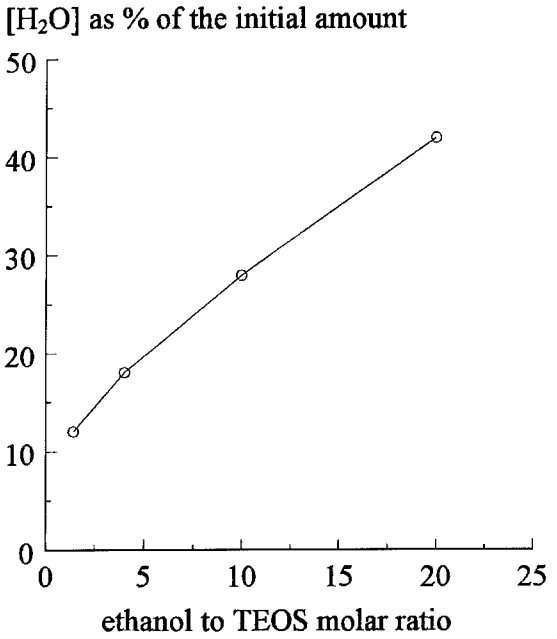

Figure 2. Amount of water in the steady state as a percentage of the initial amount of water of a hydrolyzing mixture of TEOS, ethanol and water (5×10^{-3} M HCl) in a molar ratio of 1 : x : 2 as a function of the molar ratio (x) of ethanol as measured with ^{17}O-NMR.

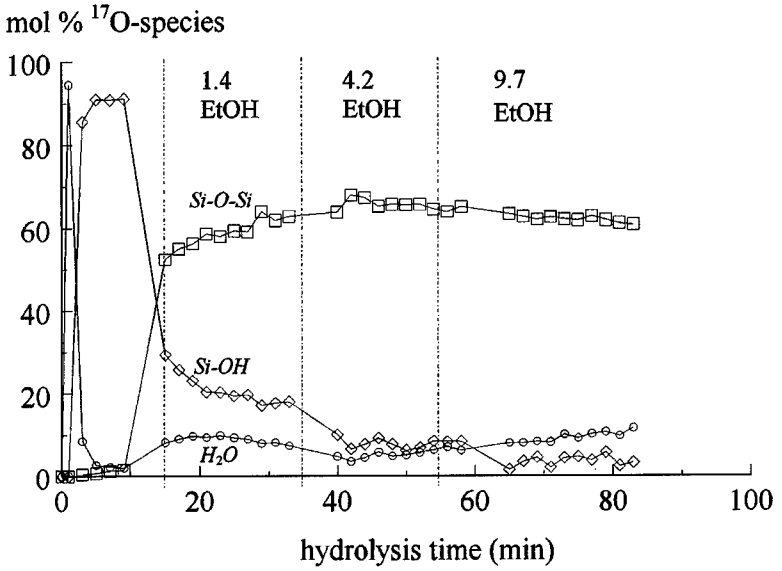

Figure 3. ^{17}O-NMR results as a percentage of the initial amount of water of a hydrolyzing mixture of TMOS, methanol and water (5×10^{-3} M HCl) in a molar ratio of 1 : 2 : 0.2. After 10, 55 and 62 min the system is diluted with 1.4, 4.2 and 9.7 mole of ethanol.

of the molar amount of ethanol. This graph shows that dilution of the system has a severe effect on the amount of water in the steady state.

Another parameter which influences the hydrolysis and condensation reactions, and thereby affects the water contents of the system in the steady state, is the nature of the solvent [13]. To this end a TMOS methanol water mixture (molar ratio = 1 : 1.4 : 0.2) was hydrolyzed. After a steady state water concentration has been reached, the hydrolysis mixture is diluted with 1.4, 4.2 and 9.7 moles of ethanol, respectively. The results are depicted in Fig. 3. After the addition of the extra ethanol, the amount of water in the system increases and the number of Si—OH groups diminishes in favor of the formation of Si—O—Si bonds. A similar experiment was performed for a TEOS-ethanol system. Methanol was added in the steady state. Besides a small decrease in water concentration, almost no change in the recorded species was observed.

4. Discussion

The consumption and formation of water during the hydrolysis and condensation of the silicon alkoxide gives insight into these reactions. Since ^{17}O-enriched water is used for the hydrolysis, the ^{17}O-NMR spectra give a direct insight into the reaction path of water and which bonds it was involved in. As also found by Babonneau, we observed that the total intensity of the ^{17}O signal did not change with time [7].

In the hydrolysis time versus gelation time curve, a minimum gelation time is found (Fig. 1). Comparing these data with the ^{17}O-NMR measurements given in this same figure, it appears that after the minimum gelation time a steady state water concentration occurs. The origin of the steady state water concentration is the equilibrium between the water consumption during hydrolysis and the water formation during condensation.

The increase in the amount of water with increasing dilution with ethanol, as depicted in Fig. 2, can be attributed to a reaction between ethanol and the silanols:

$$\mathrm{EtOH} + \mathrm{HO{-}Si{\equiv}} \rightarrow \mathrm{EtO{-}Si{\equiv}} + \mathrm{H_2O} \qquad (1)$$

However, with ^{29}Si-NMR no re-formation of alkoxysilanes is observed. Another explanation is that the residual water originates from water released by condensation and water not yet consumed during prolonged hydrolysis. The greater the reaction volume the hydrolysis reaction will proceed to a lesser extent and thereby more water remains in the solution. However, the above arguments only give a qualitative explanation of the intriguing data presented in Fig. 2. Further study and reaction kinetic considerations should give a more definitive description of the underlying mechanisms.

The hydrolysis and condensation reactions are highly influenced by changing the solvent [12]. In Fig. 3 the effect of the addition of ethanol on the evolution of the water, silanol, and siloxane concentration is presented for a tetramethyl orthosilicate (TMOS)-methanol-water system. The nature of the solvent has a considerable effect on the hydrolysis and condensation reactions [13]. For condensation in an acidic environment the presence of activated silanol complexes is necessary. Condensation occurs according to:

$$\equiv Si{-}OH + H_3O^+ \rightleftharpoons \equiv Si{-}OH_2^+ + H_2O \qquad (2)$$

followed by:

$$\equiv Si{-}OH_2^+ + HO{-}Si\equiv \rightleftharpoons \equiv Si{-}O{-}Si\equiv + H_3O^+ \qquad (3)$$

The relative amount of water and the presence of other species which have an affinity towards H^+ will have a strong influence on the condensation reaction.

Conway et al. [14] have observed that the nature of the alkyl group has a strong influence on the equilibrium reaction of an alcohol and a proton. It was found that the strength of the methanol H^+ complex is much higher than that of the ethanol complex and was higher than the equilibrium as given in reaction (2).

The effect of the nature of the solvent can be observed in Fig. 3. In a TMOS methanol system a high $\equiv Si{-}OH$ and low water concentration can be found, indicating that the condensation reaction hardly occurs in this system. However, after the addition of ethanol an exchange of methoxy groups (attached to the silicon) and ethoxy groups (of the ethanol) will occur. This will induce a redistribution of the protons and activated silanols are apparently formed. An enhancement of the condensation reaction which leads to an increase in the concentration of the $\equiv Si{-}O{-}Si\equiv$ and water concentration and a decrease in the $\equiv Si{-}OH$ is the result.

The effect is remarkable when comparing this TMOS ethanol system (Fig. 3) with a hydrolyzed TEOS system to which methanol is added. The condensation of the TMOS system starts immediately after the ethanol is added, whereas for the TEOS system hardly any condensation is observed after the addition of methanol. This is also an indication that the nature of the precursor, and thereby the nature of the formed silanols, is of importance. The hydrolyzed TMOS system is more reactive towards hydrolysis than the hydrolyzed TEOS system under comparable conditions, but less reactive towards condensation [13].

References

1. C.J. Brinker and G.W. Scherer, *Sol-Gel Science* (Academic Press, New York, 1990).
2. J. Zarzycki, in *Proceedings of the 8th International Workshop on Glasses and Ceramics from Gels*, J. Sol-Gel Science and Technology **8**, 17 (1997).
3. T.N.M. Bernards, Silicate Sol-Gel Chemistry as Studied by Hydrolysis-Gelation Time Curves, Thesis, University of Utrecht, 1997, chap. 3.
4. A.H. Boonstra, T.N.M. Bernards, and J.J.T. Smits, J. Non-Crystalline Solids **109**, 141 (1989).
5. A.E. Geissberger and P.J. Bray, J. Non-Crystalline Solids **54**, 121 (1983).
6. F. Babonneau, J. Maquet, and J. Livage, Chem. Mater. **7**, 1050 (1995).
7. F. Babonneau, New Journal of Chemistry **18**, 1065 (1994).
8. F. Babonneau, Mat. Res. Symp. Proc. **346**, 949 (1994).
9. F. Babonneau, in *Eighth Int. Workshop on Glasses and Ceramics from Gels* (Faro Porugal, September 1995), private communication.
10. U. Scheim, K. Rühlmann, J.W. Kelly, and S.A. Evans, Jr., J. Organomet. Chem. **375**, 33 (1989).
11. A.H. Boonstra and T.N.M. Bernards, J. Non-Crystalline Solids **108**, 249 (1989).
12. M.J. van Bommel, T.N.M. Bernards, and A.H. Boonstra, J. Non-Crystalline Solids **128**, 231 (1991).
13. T.N.M. Bernards, M.J. van Bommel, and A.H. Boonstra, J. Non-Crystalline Solids **134**, 1 (1991).
14. B.E. Conway, J. O'M. Bockris, and H. Linton, J. Chem. Phys. **24**, 834 (1956).

Journal of Sol-Gel Science and Technology 12, 75–80 (1998)
© 1998 Kluwer Academic Publishers. Manufactured in The Netherlands.

NMR Studies on Hydrolysis and Condensation Reactions of Alkoxysilanes Containing Si–H Bonds

VIRGINIE GUALANDRIS AND FLORENCE BABONNEAU
Chimie de la Matière Condensée, Université Pierre et Marie Curie/CNRS, 4 Place Jussieu 75252 Paris cedex 05, France

MICHAEL T. JANICKE AND BRADLEY F. CHMELKA
Department of Chemical Engineering, University of California, Santa Barbara, CA 93106-5080, USA

Abstract. Hydrolysis and condensation reactions of four organically modified alkoxides, used for the preparation of silicon oxycarbide gel precursors, have been followed by ^{29}Si NMR. Triethoxysilane ($HSi(OEt)_3$) and methyldiethoxysilane ($MeHSi(OEt)_2$) react extremely fast compared to methyltriethoxysilane ($MeSi(OEt)_3$) and tetraethoxysilane ($Si(OEt)_4$). Co-hydrolysis reactions between different pairs of precursors—$MeSi(OEt)_3/Si(OEt)_4$; $MeSi(OEt)_3/HSi(OEt)_3$; $MeHSi(OEt)_2/Si(OEt)_4$; and $MeHSi(OEt)_2/HSi(OEt)_3$—were investigated by solution state ^{29}Si and ^{17}O NMR. Despite significantly different reactivities between precursors, evidence for co-condensation reactions has been found for each system. Finally, two-dimensional ^{29}Si-^{1}H heteronuclear correlation MAS-NMR spectroscopy was used to probe the local environments of the various Si sites in the product hybrid networks.

Keywords: precursor chemistry, hydrolysis, condensation, solution NMR, solid state NMR

1. Introduction

Hybrid silica xerogels containing Si–H and $Si–CH_3$ groups have been reported to be good precursors for silicon oxycarbide glasses [1]. Such glasses exhibit improved physical and mechanical properties compared to silica glasses and are excellent candidates for high-temperature materials [2]. Introduction of Si–H groups together with $Si–CH_3$ groups in a silica gel network can favor, after pyrolysis under argon, the formation of a carbon-rich silicon oxycarbide network, and strongly reduce the presence of free carbon [3].

The preparation of these gels usually involves the co-hydrolysis of two organically modified alkoxides, which serve as sources for Si–H and $Si–CH_3$ groups. The homogeneous distribution of Si–C bonds within the silica gel network, required to minimize phase separation in the final glass, may strongly depend on the reactivity towards hydrolysis of the different precursors.

In this work, four systems were investigated, which have already been reported as precursors for Si–C–O glasses [3]: $MeSi(OEt)_3/Si(OEt)_4$ (MTES/TEOS); $MeSi(OEt)_3/HSi(OEt)_3$ (MTES/TREOS); $MeHSi(OEt)_2/Si(OEt)_4$ (MDES/TEOS); and $MeHSi(OEt)_2/HSi(OEt)_3$ (MDES/TREOS), all with a 1/1 molar ratio between the two precursors, so that the number of Si–Me bonds per Si was constant (0.5), while the number of Si–H bonds per Si varied from 0 to 1. Hydrolysis and condensation reactions of the four individual alkoxysilanes were followed by ^{29}Si NMR to compare their reactivities. Then, co-hydrolysis reactions between the different pairs of precursors were investigated by solution state ^{29}Si and ^{17}O NMR to detect the formation of any co-condensed species. Finally, it was demonstrated that two-dimensional (2D) ^{29}Si-^{1}H heteronuclear correlation MAS-NMR spectroscopy is a sensitive probe of the local environments of the various Si units in the product gel networks.

2. Experimental Section

All chemicals were used as received. Gels were prepared by co-hydrolyzing the corresponding two alkoxides in a 1/1 ratio under acidic conditions (EtOH/Si = 2; H_2O/OEt = 1; pH = 2(HCl)). The resulting solutions were aged in closed tubes at 60°C for 24 h, for gelation to occur. Then, the gels were dried at 100 °C for several days.

The solution state NMR spectra were recorded on a MSL400 Bruker spectrometer. The samples were held in an 8 mm tube which was in turn placed in a 10 mm tube with C_6D_6 in the annulus as lock solvent. The references for chemical shift were tetramethylsilane for the ^{29}Si experiments and tap water for the ^{17}O experiments. For the ^{17}O NMR, 10 at.% enriched water (Isotec, Saint Quentin, France) was used as reactant. The notation X_{xy} will be used to describe the Si sites where X designates the type of Si sites, x the number of oxo bridges and y the number of silanol groups. X will be Q for SiO_4, T for $MeSiO_3$, T^H for $HSiO_3$ or D^H for $HMeSiO_2$ sites.

The 2D ^{29}Si-^1H heteronuclear correlation MAS-NMR experiments were performed on a Chemagnetics CMX-500 spectrometer. Experimental parameters used were as follows: 5 kHz spinning rate; 2.5 ms contact time, 3 s repetition time; 128 individual experiments with 8 scans each.

3. Results

3.1. *Comparison of the Reactivities of the Various Precursors*

The hydrolysis and condensation reactions of the four organically modified alkoxides, were followed by solution state ^{29}Si NMR (EtOH/Si = 2; H_2O/OEt = 1; pH = 2). The extent of condensation reaction was calculated for each precursor, according to the equation:

$$c = \sum_i \left(\frac{i \cdot x_i}{f} \right) \quad (1)$$

where x_i is the relative concentration of the X_{ij} silicon site, derived from NMR spectrum simulation, and f is the functionality of the monomer (2 for MDES, 3 for MTES and TREOS and 4 for TEOS).

The variation of c during the first two hours for the various precursors (Fig. 1) showed an extremely fast condensation rate for MDES and TREOS, compared to MTES and TEOS. Within 10 min., condensation reactions were mostly completed for TREOS ($c > 80\%$) and MDES ($c > 90\%$), while they were in progress for MTES ($c \approx 15\%$) and just started for TEOS ($c \approx 5\%$). After 2 hours, c reached 40% for MTES and 20% for TEOS, and after 10 hours 55% for TEOS and 75% for MTES. These last results agree with previous report showing the higher reactivity of MTES, compared to TEOS, under acidic conditions [4]. Electronic inductive effects could be responsible for the high reactivity of the Si—H containing alkoxysilanes. However, the linear correlation existing between the paramagnetic screening factor and the net charge at the silicon atom in the [−40; −120 ppm] chemical shift range [5], indicates that the charge at the Si center in TREOS is intermediate between that of TEOS and MTES. Reactivity of TREOS would thus be expected to be intermediate between that of MTES and TEOS. Steric effects, with the presence of the very small H-substituent that will favor nucleophilic attack of the water molecule at the Si center, could therefore explain the differences in hydrolytic behavior. Similar observations have already been reported for alkoxysilanes with R groups of different sizes [6].

One point should be considered: due to the large difference in reactivities, co-hydrolysis of MDES and TEOS, or MTES and TREOS could lead to inhomogeneous distribution of the two types of Si units within the siloxane network, and thus of the Si—C bonds, that could promote the presence of C-rich regions in the final oxycarbide glass. Actually, Fig. 1 shows that addition of TREOS to MTES, or MDES to TEOS, leads to a marked increase in the extent of reaction of the less reactive units. Even if not a direct proof, this strongly suggests that co-condensation reactions between the two types of units occur.

3.2. *Evidence for Co-Condensation Reactions*

The four solutions (MTES/TEOS; MDES/TREOS; MDES/TEOS; MTES/TREOS) were hydrolyzed with a low amount of water ($h = 0.1$) and aged for 2 days. The resulting sols were characterized by ^{29}Si and ^{17}O NMR to investigate the formation of co-condensed species. The presence of short oligomers (monomers, dimers and trimers) facilitated high resolution of the ^{29}Si NMR spectra. On the other hand, ^{17}O NMR signals are always broad, and this is attributed to short relaxation times of the quadrupolar oxygen nuclei. Variable-temperature experiments were tried for increasing

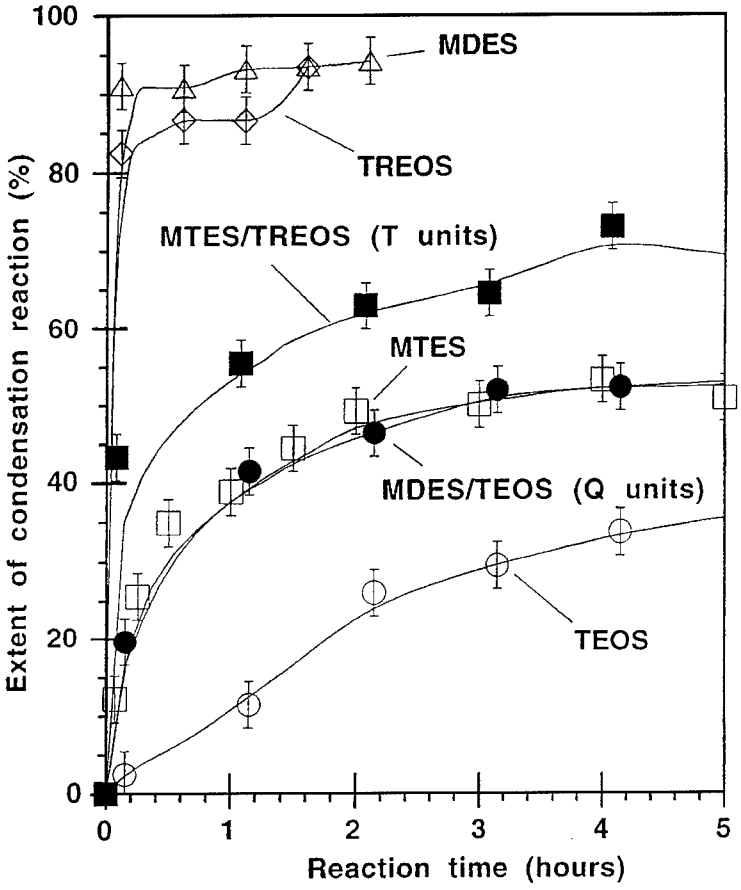

Figure 1. Evolution versus time of the extent of condensation reaction for MDES ($MeHSi(OEt)_2$), MTES ($MeSi(OEt)_3$), TREOS ($HSi(OEt)_3$) and TEOS ($Si(OEt)_4$), as well as MTES/TREOS (T units) and MDES/TEOS (Q units) mixtures. (EtOH/Si = 2; H_2O/OEt = 1; pH = 2).

resolution, but only a modest result was obtained on the MTES/TEOS system [7].

- *MTES/TEOS system*: evidence for co-condensation reactions between MTES and TEOS can be seen on the ^{29}Si and ^{17}O NMR spectra (Fig. 2(a)) as already reported in the literature [8–10].
- *MDES/TREOS system*: for the MDES/TREOS system, co-condensation could be clearly seen by the presence of new ^{29}Si resonance signals [11], but similar chemical shift values for (D^H)-O-(D^H), (T^H)-O-(T^H) and (D^H)-O-(T^H) sites prevented similar conclusions from the ^{17}O NMR experiments (Fig. 2(b)).
- *MDES/TEOS system*: formation of (D^H)-O-(Q) sites can be clearly seen on the ^{17}O NMR spectrum (Fig. 2(c)). The spectrum of the hydrolyzed solution of MDES presents mainly two peaks at 59.7 and 62.0 ppm assigned to D_1^H-D_1^H and D_1^H-D_2^H-D_1^H species. No clear evidence for (D^H)-OH groups was found. On the contrary, the spectrum of a solution of TEOS hydrolyzed under the same conditions, showed a main peak at 14.6 ppm due to (Q)-OH groups and a peak at 29.7 ppm due to (Q)-O-(Q) sites, confirming the much lower extent of condensation reaction. The hydrolyzed solution of the mixture of MDES and TEOS is characterized by a main peak at 46 ppm which corresponds to (D^H)-O-(Q) sites, with two additional peaks due to D_1^H-D_1^H and D_1^H-D_2^H-D_1^H species. No evidence for (Q)-OH or (Q)-O-(Q) sites could be found, suggesting that either TEOS does not hydrolyze, due to its much lower reactivity, and thus (D^H)-O-(Q) sites are formed as follows:

$$(D^H)\text{-OH} + \text{RO-(Q)} \rightarrow (D^H)\text{-O-(Q)} + H_2O \quad (2)$$

or TEOS hydrolyzes, but then reacts preferentially with (D^H)-OX groups (X = H or R).

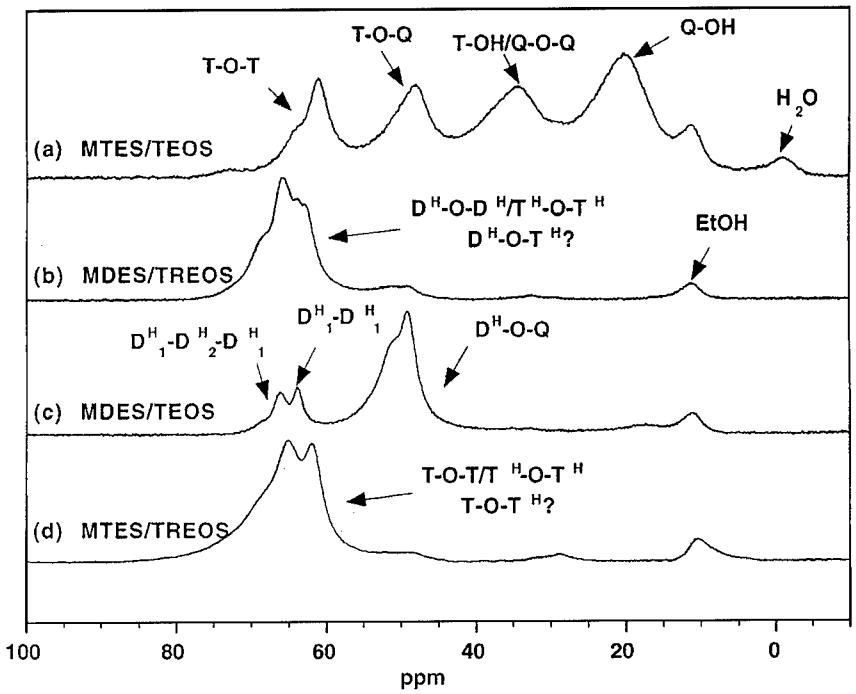

Figure 2. Solution state ^{17}O NMR spectra of hydrolyzed solutions of: (a) MTES/TEOS; (b) MDES/TREOS; (c) MDES/TEOS and (d) MTES/TREOS (EtOH/Si = 2; H_2O/OEt = 0.1; pH = 2).

Co-condensation reactions were also confirmed by ^{29}Si NMR experiments, with peaks at −87.1 ppm (Q^*_{10}-D^H) and at −93.5 ppm (Q^*_{20}-D^H). Peaks due to Q^*_{10}-Q and Q^*_{20}-Q, expected at −88.1 and −95.4 ppm, were not present.

- *MTES/TREOS system*: as for the MDES/TREOS system, ^{17}O NMR (Fig. 2(d)) is not a good technique to characterize the formation of (T)-O-(T^H) sites, because of the similarity between the chemical shift values of (T)-O-(T) sites ($\delta = 57$ ppm) [9] and (T^H)-O-(T^H) sites ($\delta = 58-60$ ppm) [11]. Evidence for the formation of co-condensed species was obtained from the ^{29}Si NMR spectrum with peaks at −49.7 ppm (T^*_{10}-T^H) and −57.3 ppm (T^*_{20}-T^H), instead of −50.2 ppm and −58.3 ppm for T^*_{10}-T and T^*_{20}-T, respectively. Similarly, to the MDES/TEOS, system, the less reactive units (i.e., T units) seemed to condense preferentially with the most reactive ones (i.e., T^H units). No signal due to T*-T species was seen.

At low hydrolysis ratio ($h = 0.1$), evidence for the formation of co-condensed species was found in all the four systems, even when a large difference in reactivity exists between the precursors, such as in the MDES/TEOS and MTES/TREOS systems. This suggests that the condensation mechanism, as described in Eq. (2), should occur to a large extent.

For a higher h value ($h = 1$), extensive condensation leads to a broadening of the ^{29}Si resonance signals, preventing any definitive conclusions on the formation of co-condensed species, and their stability versus time. For the MTES/TEOS system with $h = 0.5$, the condensation reactions were followed by ^{17}O NMR [10]: a peak due to (T)-O-(Q) sites was clearly identified around 45 ppm, whose intensity increased versus time. For the other three systems, a loss of ^{17}O NMR signal was observed for $h = 1$, preventing any site identification. This suggests that in the presence of a highly reactive precursor (MDES and/or TREOS), high molecular weight polymers are rapidly formed, incorporating through co-condensation reactions, the less reactive units, which cannot be detected.

3.3. *2D ^{29}Si-^1H Heteronuclear Correlation MAS-NMR Spectroscopy on Gel Networks*

Product gel networks can be investigated by 2D ^{29}Si-^1H heteronuclear correlation MAS-NMR spectroscopy.

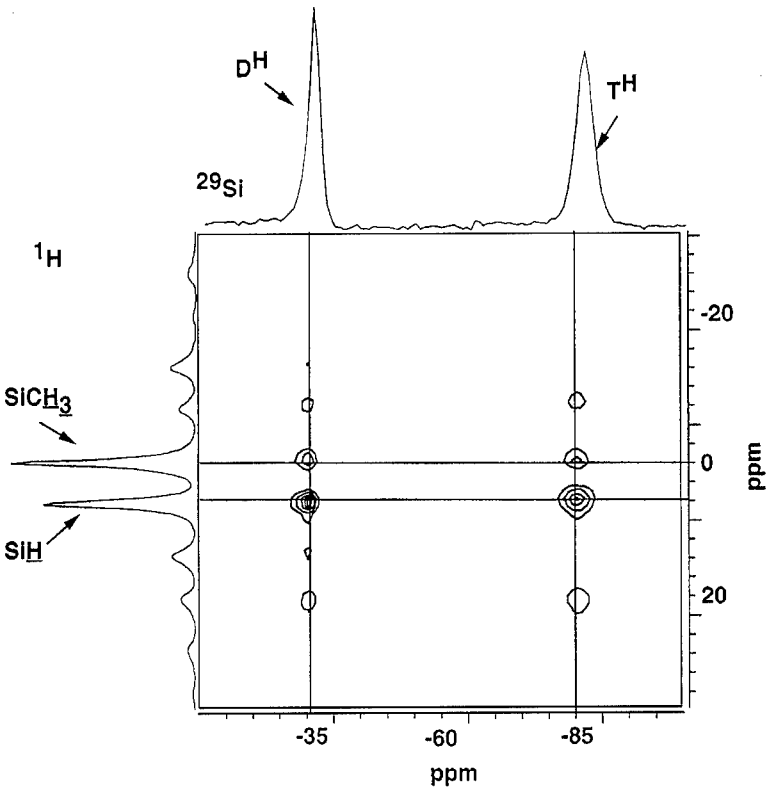

Figure 3. A 2D ^1H-^{29}Si heteronuclear correlation NMR spectrum (contour plot) obtained for a gel prepared from co-hydrolysis of MDES and TREOS in a 1/1 ratio (EtOH/Si = 2; H_2O/OEt = 1; pH = 2).

This sequence was first introduced to characterize surface species on silica and zeolite [12] and has already been applied to different siloxane-silica systems prepared from MTES and TEOS [13], or PhTES and TEOS [14].

Figure 3 shows the results of the ^{29}Si-^1H connectivity experiment carried out on a gel prepared by co-hydrolyzing MDES and TREOS. One should first note that MAS at 5 kHz gave good resolution on the one-dimensional (1D) ^1H NMR spectrum. This is related to the presence of motions that could partially average the strong ^1H-^1H dipolar couplings. In this particular system, the average functionality of the Si units was rather low ($f = 2.5$) and a glass transition temperature at $-43°C$ has been reported [11]. It was possible to distinguish clearly the Si—CH_3 ($\delta = 0$ ppm) and Si—H ($\delta = 4.5$ ppm) signals, and thus to identify the sources of polarization transfer. This is why this 2D sequence is so powerful compared to the equivalent 1D sequence: protons responsible for the polarization transfer to a given Si site can be identified, and thus spatial proximity established. In this example, there is, as expected, a connectivity between the D^H units and the protons of the methyl groups, but more interestingly, there is also a connectivity between these protons and the T^H units which indicates the proximity between the D^H units (bearing CH_3 groups) and the T^H units, and the absence of clearly separated domain structures.

4. Conclusions

The objective of this paper was to characterize with NMR techniques four different alkoxysilane systems, which have been reported as precursors for silicon oxycarbide glasses, $MeSi(OEt)_3/Si(OEt)_4$ (MTES/TEOS); $MeSi(OEt)_3/HSi(OEt)_3$ (MTES/TREOS); $MeHSi(OEt)_2/Si(OEt)_4$ (MDES/TEOS); and $MeHSi(OEt)_2/HSi(OEt)_3$ (MDES/TREOS). It is important to know whether the Si—C bonds are uniformly distributed within the product siloxane network, which could help the formation of a compositionally homogeneous oxycarbide network, after pyrolysis.

Hydrolysis and condensation reactions of the four organically modified alkoxides involved in the preparation of the starting gels, have been followed by solution state ^{29}Si NMR. Under acidic conditions (pH = 2) and with a hydrolysis ratio of 1 ($h = H_2O/OEt$), the alkoxysilanes with Si—H bonds (TREOS and MDES) reacted extremely fast compared to MTES and TEOS: this was attributed to steric, rather than electronic effects. The small H-group facilitated the nucleophilic attack of the water molecule at the Si center. However, despite large differences in reactivities that exist between several precursors, evidence for co-condensation reactions was found in all four systems hydrolyzed with a low amount of water ($h = 0.1$), using solution state ^{29}Si and ^{17}O NMR techniques. For a higher hydrolysis ratio ($h = 1$), the fast condensation reactions in MDES/TREOS, MDES/TEOS and MTES/TREOS lead to a broadening of the ^{29}Si resonance signals as well as a loss of the ^{17}O signal intensity, preventing any precise information concerning the formation and stability of co-condensed species in those systems.

Finally, two-dimensional ^{29}Si-^{1}H heteronuclear correlation MAS-NMR spectroscopy was found to be a sensitive probe of the local environments of the various Si sites in hybrid networks. It has been demonstrated that the two types of Si units in a gel prepared from MDES and TREOS were mixed in the product network. However, the details concerning the degree of mixing have not been established in a quantitative manner by the present results. Further investigations are in progress on the other systems.

References

1. G.D. Sorarù, G. D'Andrea, R. Campostrini, F. Babonneau, and G. Mariotto, J. Am. Ceram. Soc. **78**, 379 (1995).
2. G.D. Sorarù, V.M. Sglavo, S. Diré, G. D'Andrea, and F. Babonneau, in *Third Euro-Ceramics, V.2*, edited by P. Duràn and J.F. Fernàndez (Faenza Editrice Ibérica S.L. 1993), p. 1157.
3. F. Babonneau, G.D. Sorarù, G. D'Andrea, S. Diré, and L. Bois, Mat. Res. Soc. Symp. Proc. **271**, 789 (1992).
4. H. Schmidt, H. Scholze, and A. Kaiser, J. Non-Cryst. Solids **63**, 1 (1984).
5. G. Engelhardt and D. Michel, *High Resolution Solid State NMR of Silicates and Zeolites* (Wiley & Sons, New York, 1987), p. 125.
6. L. Delattre and F. Babonneau, Mat. Res. Soc. Symp. Proc. **346**, 365 (1994).
7. S. Prabakar, R.A. Assink, N.K. Raman, S.A. Myers, and C.J. Brinker, J. Non-Cryst. Solids **202**, 53 (1996).
8. S. Prabakar and R.A. Assink, J. Non-Cryst. Solids **211**, 39 (1997).
9. F. Babonneau, J. Maquet, and J. Livage, Chem. Mater. **7**, 1050 (1995).
10. F. Babonneau, V. Gualandris, and M. Pauthe, Mat. Res. Soc. Symp. Proc. **435**, 119 (1996).
11. G.D. Sorarù, G. D'Andrea, R. Campostrini, and F. Babonneau, J. Mater. Chem. **5**, 1363 (1995).
12. A.J. Vega, J. Am. Chem. Soc. **110**, 1049 (1988).
13. C.A. Fyfe, Y. Zhang, and P. Aroca, J. Am. Chem. Soc. **114**, 3252 (1992).
14. M.P.J. Peeters, W.J.J. Wakelkamp, and A.P.M. Kentgens, J. Non-Cryst. Solids **189**, 77 (1995).

Journal of Sol-Gel Science and Technology 13, 81–84 (1998)
© 1998 Kluwer Academic Publishers. Manufactured in The Netherlands.

On Aging of Acid-Catalyzed Silica Sols—A Dynamic Light Scattering Study

B. UNGER AND M. HÄHNERT
Bundesanstalt für Materialforschung und -prüfung, 12200 Berlin, Germany

R. NITZSCHE
MALVERN Instruments GmbH, Rigipsstr. 19, 71083 Herrenberg, Germany

Abstract. Dynamic light scattering experiments in acid-catalyzed silica sols are discussed. It is shown that in spite of limited parameter accuracy and limited absolute knowledge of the particle sizes, the scattering data from various experiments are comparable with one another and give information about structural differences. Measurements at various angles indicate changes between non-spherical and nearly spherical particles and allow the estimation of gelling times before gelation.

Keywords: acid-catalyzed silica sols, aging, structural development, dynamic light scattering

1. Introduction

Mathematical analyses of scattering data by Mie theory and its approximations are based on spherical particles. Consequently, dynamic light scattering (DLS) measurements for the characterization of alkoxide derived sol-gel processes are usually applied to base- or acid/base-catalyzed systems because of the sphere-like shape of their particles (e.g., [1, 2]). Non-spherical particles—as generally found with acid-catalyzed sols—should also be detectable. The calculated size will be between the smallest and the largest plane of projection because the scattering particles in a liquid dispersion is measured in all directions with a high statistical reliability, but the real particle size cannot be expected as result. This study shows that DLS can be applied to non-spherical particles.

2. Experimental

Sol Preparation and Measurement. The silica sols were made from $Si(OC_2H_5)_4$ (TEOS), C_2H_5OH, H_2O and HCl in molar ratios of 1 : (4–10) : 4.5 : 0.007 at 293 K and 350 K, respectively, and then kept at constant temperature (290 K) until gelation. They were investigated as prepared and diluted at different aging stages by means of DLS at 298 K.

DLS experiments were carried out with a "Zeta-Sizer 3" (MALVERN Instruments) equipped with an Nd:YAG laser (ADLAS 200 mW, 532 nm). The viscosity and refractive index (546.1 nm) of each DLS sample were measured separately at 298 K.

Interpretation of Sizing Results. The simplest way to analyze a correlation function is to take logs and fit a power series to the data:

$$Y(t) = A + Bt + Ct^2 \ldots \qquad (1)$$

with $Y(t) =$ log of the correlation function, after subtraction of the background, $t =$ delay time, $A, B, C =$ constants fitted by the analysis (*Cumulants method*). A divided by 100 gives the % "merit" which corresponds to the signal-to-noise ratio. B gives the "z-average mean" size which is weighted by the amount of light scattered by each size of particle in the sample. C/B^2 is the polydispersity. The degree of decay of the autocorrelation function to noise is indicated by the "in range" values (complete decay = 100%).

If more than one size of particles is present, the correlation function is a sum of many different exponentials.

MALVERN has chosen to use 24 sizes which represent the size distribution (*Exponential sampling method*). This number allows sufficient flexibility to describe complex distributions, without too long computation time. A least squares fit is carried out to find the mix of the chosen sizes which gives the best fit between the experimental data and the correlation function calculated from the mixture (iterative, 60 repeats). If the correct scattering theory is used, the weight and number average distributions should accurately describe the size distribution.

3. Results and Discussion

3.1. *Experimental Compromises Measuring Alkoxide Derived Sols*

Refractive Indices of the Particle. The refractive indices of the particles (real and imaginary parts) were not known. They can be neglected if the particles are small ($d < \lambda/2$) and transparent. In this case, the refractive index of the particles can be equated with that of the parent dispersion fluid and the analysis is carried using the Rayleigh-Gans-Debye approach. Particle size and transparency comply with that approximation but the divergence from a spherical shape requires an interpretation of the weight and number distributions with caution. Only analyses by intensity distribution are sensible.

Parameters of the Dispersion Fluid. The dispersion fluids used are ethanol/water solutions whose ratios are dependent on the degree of hydrolysis and condensation. These ratios are not known without using other costly analytical methods. Because of the smallness of the particles and the excellent formation of films, the separation of sample-typical dispersion fluids by centrifugation as a simple method for dilution of complex dispersions with unknown compositions is difficult or even impossible. Consequently, both the exact refractive index and the viscosity of the dispersion fluid cannot be used for the calculations.

In this study, the refractive indices and the viscosities of the (complex) sols at the appropriate temperature were measured for every sol, every aging time, and every dilution separately and were used as parameters of the respective dispersion fluid. The refractive indices of the DLS samples (1.362–1.366) and of the simulated dispersion fluids (1.362–1.364, ethanol/water, volume ratios 100 : 0–60 : 40) were in good agreement and allow this simplification. However, an automatic fitting of these parameters is impossible, in contrast to normal runs. The maximal deviation of the temperature in the measuring cell related to the temperature of the refraction and viscosity measurements was +0.3 K. The resulting errors are small (within the deviation between the single runs). A second error caused by measuring the refractive indices at $\lambda = 546.1$ nm as only an approximated wave length ($\lambda_{\text{Laser}} = 532$ nm) was ignored.

Sample Concentration. DLS measurements require optimal concentrations of the scattering particles. If the concentration is too small, fluctuations of the measuring signal are caused by input and output of particles into the scattering volume and from the one, respectively. If it is too high, smaller particle sizes are missed by multiple scattering because of interactions between the particles.

Measurements of sols as prepared are only possible in the early aging stages. The intensity of the scattering light increases with progressing aging of the sols. Consequently, the sols must be diluted gradually. Here, dilutions with absolute ethanol from 1 : 2 to 1 : 100 were used. Such a dilution causes an increase of the particle size due to aggregation induced by changing the surface charge of the particles. However, at volume ratios ethanol : sol ≥ 10 the influence of the added solvent is constant.

Considering these results, the development of the particle size during aging is interpreted as typical for this kind of sols. Differences of the absolute hydrodynamic diameters have to be included by dilution of the sols and divergence from the sphere geometry but not in the trend. The sols may be compared because all the samples have been kept at the same temperature, have similar dilutions with increasing aging and the measurements have been conducted in parallel.

3.2. *Sol Characterization*

Measurements at 90°. The complexity of hydrolysis and condensation leads to a mixture of different oligomer species and in the end to a broad spectrum of differently linked units. Thus, the high polydispersions between 0.4 and 0.6 are not surprising. However, analysis of the scattering data by exponential sampling method gives for all sols and during the whole period of aging a splitting of each broad distribution into two groups of particles, s1 and s2. Analyzing all data, the smaller particles, s1, were found to be the main particle kind. This result is confirmed by nearly identical values

of s1 and ZAve calculated at all stages. The particles s2 represent a small number of larger aggregates. In Fig. 1 the hydrodynamic diameters of these two kinds of particles as a function of the aging time for a boiled sol with $r_w = 4$ as example is given. The absolute gelling times, t_{gel}, are listed in Table 1.

Figure 1 shows three different ranges of the structural development of the sols until gelation, which are in agreement with measurements of viscosities and degradation of the polymer silica species by reaction with molybdate [3] also shown. The changes occur at about $t_r = t/t_{gel} = 0.25$ and 0.7, respectively, and are identical with the changes from Newtonian behavior (NB) to shear thinning (ST) to thixotropic behavior (TB). DLS, viscosity measurements, and the molybdate method indicate that analogous results occur with the other sols investigated.

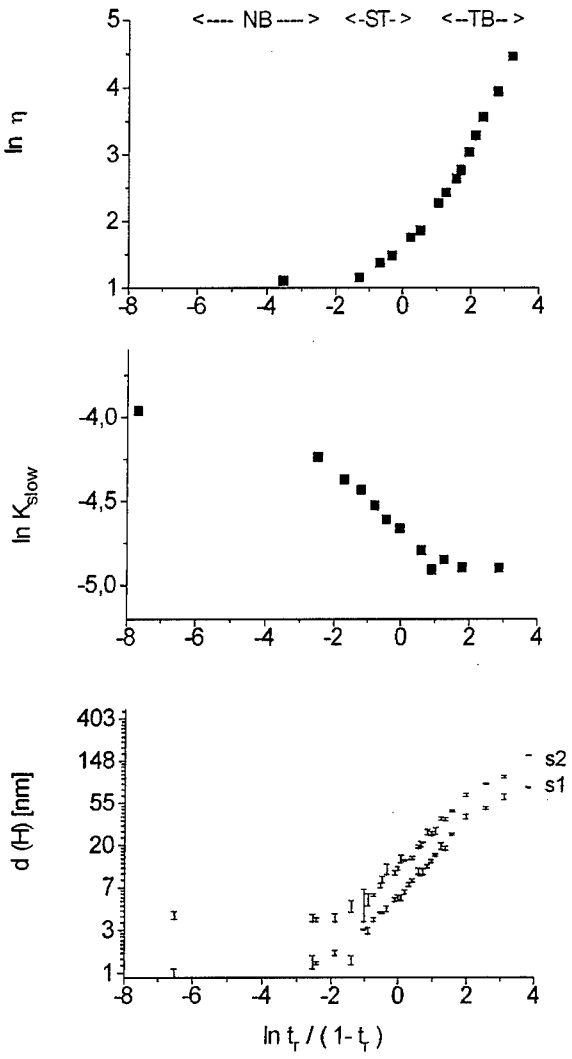

Figure 1. Viscosity, η, rate constant of the degradation of the slowly degradable (highly condensed) silica species by molybdate reagent, k_{slow}, and hydrodynamic diameters, $d(H)$, resulting from DLS measurements as a function of the aging time, shown as logarithm of the modified reduced time, $t_r/(1 - t_r)$, for a boiled sol with H_2O/TEOS = 4. NB = Newtonian behavior, ST = shear thinning, TB = thixotropic behavior. The DLS values result from 5–9 measuring series and 10 runs per series. The maximal and the minimal diameters are drawn for each aging time and each kind of particles.

Boiled sols show reliable scattering results at all aging stages (merit: 20–30%, in range: 90–99%). Additionally, they show a distinct increase of particle sizes as a function of the water/TEOS ratio at all aging stages demonstrated in Fig. 2 for sols with $r_w = 4$, 5 and 10. In contrast, for the analogous unboiled sols—independent of their starting water/alkoxide ratios—the particles are hard to detect (at $t_r = 0$–0.2 they cannot be detected) but although there is a nearly identical development of the particle sizes (see Fig. 2). This is in agreement with previous results [3, 4] which show that the influence of the temperature on the kind of species formed in the early stages is much greater than the influence of the starting water content. The greater reliability of the scattering data for boiled sols indicates that they have a more dense, less branched structure compared to unboiled sols. This deduction is confirmed by investigations on the degradation of the silica species by molybdate reagent: the boiled sols are degraded more slowly than the analogous unboiled ones [3]. Thus, in the final aging stages there is the possibility of forming smaller particles or aggregates in boiled sols than in the unboiled ones of the same starting composition (shown here for sols with $r_w = 4$, Fig. 2).

Measurements at 50–130°. At about $t_r < 0.75$ a slight increase of the scattering intensity with increasing detection angles is found which has not been explained yet. It may be supposed that the detected particles are non-spherical and orientated in a certain degree in the range before the ST → TB transition. However, at $t_r > 0.75$–0.85 the scattering intensity is totally independent of the angle. This isotropic behavior indicates spherical particles in the last aging stages. The onset of this behavior are given in Table 1. There are grounds to assume phase separation by spinodal decomposition as reported by Kaji et al. [5] for tetramethoxysilane-water-HNO_3-formamide systems. Those authors deduce that the silica-rich domains break-up and become spherical during the coarsening process of spinodal decomposition. The reported onsets of phase separation [5] occur at

Table 1. Gelling times of silica sols, t_{gel}, and some reduced aging times, t_r, at which rapid changes of the properties of the sols occur (u = unboiled, b = boiled, ST = shear thinning, TB = thixotropic behavior, I = scattering intensity, Θ = scattering angle).

H_2O/TEOS [molar]	t_{gel} (290 K) [d]	t_r (ST → TB) (viscosity)	t_r (ST → TB) (DLS/90°)	t_r (I = Θ-independent) (DLS/50–130°)
4_u	147	~0.7	~0.63	~0.85
5_u	113	~0.7	~0.7	~0.85
10_u	79	~0.7	~0.63	~0.85
4_b	136	~0.7	~0.68	~0.82
5_b	104	~0.65	~0.68	~0.83
10_b	49	~0.6	~0.63	~0.77

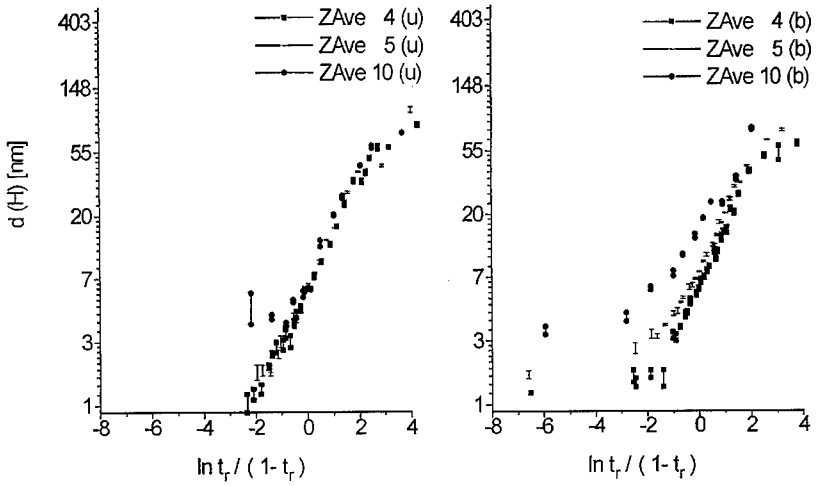

Figure 2. Development of the particle sizes of unboiled (u) and boiled sols (b) with H_2O/TEOS = 4, 5 and 10 demonstrated as z-average mean, ZAve, in dependence on the aging time (on measuring series see Fig. 1).

similar aging times as found for the change of the angle dependence of the scattering intensity in this study ($t_r \approx 0.8$). Those changes can be used for estimation of the gelling times before gelation because they occur at a defined stage and can be determined without knowledge of any parameter and the total structural development.

4. Conclusion

In spite of difficulties in determining the parameters for DLS and possible aggregation caused by necessary dilution, DLS experiments on acid-catalyzed silica sols give information about their structural development. The dependence of changes of the particle sizes on aging time are in perfect agreement with results of other analytical methods.

Acknowledgment

The authors gratefully acknowledge the financial support of the Deutsche Forschungsgemeinschaft (DFG) and thank Mr. Weber from MALVERN INSTR. for the excellent technical conversion of the ZetaSizer 3.

References

1. P. Strehlow, J. Non-Cryst. Solids **107**, 55 (1988).
2. A.H. Boonstra, T.P.M. Meeuwsen, J.M.E. Baken, and G.V.A. Aben, J. Non-Cryst. Solids **109**, 153 (1989).
3. B. Unger, P. Popp, U. Schade, and M. Hähnert, J. Non-Cryst. Solids **160**, 152 (1993).
4. B. Unger, H. Jancke, H. Stade, and M. Hähnert, J. Sol-Gel Sci. Technol. **2**, 51 (1994).
5. H. Kaji, K. Nakanishi, N. Soga, T. Inoue, and N. Nemoto, J. Sol-Gel Sci. Technol. **3**, 169 (1994).

Journal of Sol-Gel Science and Technology 13, 85–88 (1998)
© 1998 Kluwer Academic Publishers. Manufactured in The Netherlands.

On the Microstructure of Geyserites and Hyalites, Natural Hydrous Forms of Silica

J. GÖTTLICHER AND H.J. PENTINGHAUS
Forschungszentrum Karlsruhe GmbH, ITC-WGT, D-76021 Karlsruhe, Germany

B. HIMMEL
Universität Rostock, FB Elektrotechnik, D-18059 Rostock, Germany

Abstract. The submicron structures of two natural hydrous forms of silica (geyserites from Iceland, hyalite from Valec CS) have been studied by scanning electron microscopy, small-angle and wide-angle X-ray scattering. All geyserites investigated are particulate with a nonuniform size distribution. These particles are arranged in spherical agglomerates, in chains or in helical patterns. The average diameters of the colloidal particles range between 200 nm and 2 μm depending on the texture of the samples. SAXS experiments have revealed the porous nature of the particles with inhomogeneities smaller than 10 nm. Based on the structural pecularities of the geyserites their origin is discussed as the result of forced condensation of silicic acid in an aqueous environment, particle agglomeration and sedimentation. The structural development including the textures is determined by the dynamics of the underlying processes: fast decompression and cooling of the saturated parent solutions and their transport. By contrast, hyalite is characterized by a homogeneous microstructure.

Keywords: geyserite, hyalite, SEM, SAXS, microstructure

Introduction

There is a great variety of hydrous forms of silica which are either amorphous or microcrystalline. Numerous studies over decades now allow a minute differentiation which is expressed by a comprehensive nomenclature [1]. For the amorphous forms, geyserites and hyalites, however, we are still lacking in microstructural details and genetic mechanisms.

Hydrous silica glass, similar to hyalite, is formed experimentally when saturated, overheated fluidothermal SiO_2-solutions are transported over thermal gradients [2, 3]. For the formation of geyserites a transport scenario of silica as already described is assumed [4].

A thorough understanding of the low temperature behavior of oversaturated silica solutions is necessary, e.g., to quantify weathering of rocks and technical glasses or slags where beside secondary crystalline phases amorphous phases are also formed, apparently depending on the degree of silica oversaturation. An advantage of studying geyserites is that its formation can be observed in nature and reproduced experimentally.

The objective of this study is to describe the microstructure by scanning electron microscopy (SEM), small-angle X-ray scattering (SAXS) and X-ray diffraction (XRD).

Experimental

The geyserites studied were collected at the hot springs of Hveravellir in the central islandic highlands [5]. As there is no power generation in this area the silica deposition is not influenced by anthropogenic activities.

The geyserites from these locations show various macroscopic textures (Table 1). We have selected

Table 1. Macroscopic description of the geyserites and hyalite, T, pH.

Sample no.	Texture	T^* (°C)	pH*
GSPE1	Cover, earthy loose	?	?
GS13001	Cover, dense, solid	90	8.0
GS13053	Layered material, loose	?	?
GS12973	Layered material, solid	n.m.	m.m.
GS13008	Layered material, dense	n.m.	n.m.
Hyalite (Valec CS)	Dense material, zonal structure of the botryoidal aggregates	—	—

n.m.: not measured; ?: data not available; *17.07.1981 [5].

samples which represent their variety to check whether the microstructure corresponds to the macroscopic features.

Temperatures varied from 50°C to 95°C, pH values from pH 5 to pH 8 in different springs of this field [5]. The T, pH conditions were only known for sample GS13001 (Table 1). The hyalite came from Valec in the Czech Republic, well known for its transparent hyalites with botryoidal appearance up to 1 cm in diameter and its zonal growth structure.

Samples were investigated by scanning electron microscopy (DSM 960 from Zeiss) and by small-angle X-ray scattering (Cu-Kα radiation) with a Kratky camera (Anton-Paar Graz). X-ray diffraction experiments (Cu-Kα radiation, PSD 120° from INEL) were performed to check the presence of crystalline phases within the amorphous material.

Results and Discussion

SEM

All investigated geyserites consisted of colloidal SiO_2 particles with nonuniform size distribution. They were arranged either in spherical agglomerates or in chains. Some of the chains were helical with a repetition distance of about 50 μm (Fig. 1). The diameter of the colloidal silica spheres varied between 200 nm and 2 μm. Particle chains and helical aggregates were

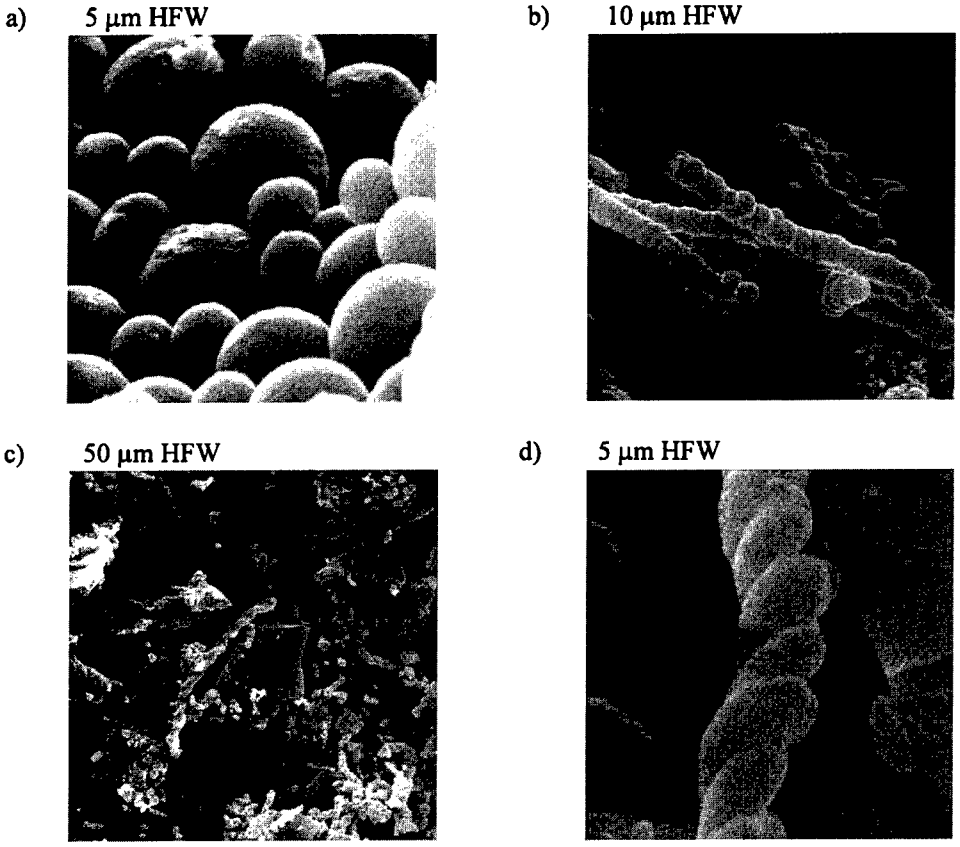

Figure 1. SEM images of geyserites showing different arrangements of colloidal SiO_2 particles (a) single particles (GS13008), (b) chains (GSPE1) and (c, d) helical shapes (GSPE1). HFW = horizontal field width.

mainly observed in the more loose and porous material. EDX spectra showed a signal of Si and O only.

The formation of spherical particles can be explained by a condensation process as a result of fast decompression and cooling of the saturated parent solutions. The random aggregation of particles in the effluents provided different shapes like chains or grapes. A biogenic origin of special shapes like the helical aggregates can be assumed via "encrustation" or "silicification" of microbes living around hot springs [6].

SEM investigation of the hyalite did not reveal any further details above those already known from light microscopy.

SAXS

SAXS experiments on geyserites showed a porous structure of the particles with inhomogeneities smaller than 10 nm inside resulting in the shoulder around $s = 0.9\ \mathrm{nm}^{-1}$ (Fig. 2). During the measurements, the intensity scattered from some samples (e.g., GS13008, GS12973) in that region increased gradually. This increased contrast inside the opaline matrix could be attributed to the desorption of volatile components, presumably water, because the samples were located in a vacuum for SAXS measurements. The process of gradual dehydration was accompanied by a slight increase of the average size of scattering entities indicating pores and not particles. For the other geyserites (GSPE1, GS13053, GS13001) these changes in the scattering contrast during measurement could not be detected. Pores present might have been closed.

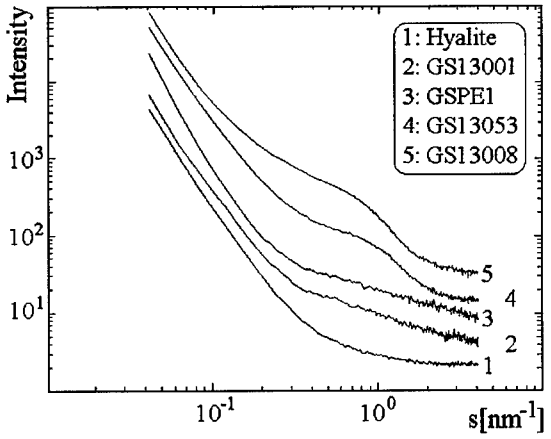

Figure 2. Comparison of the SAXS curves of hyalite and geyserites. The intensity of curve 1 is given in cps (counts per second). All other curves are shifted arbitrarily for clarity. ($s = 4\pi \cdot \sin(\Theta/2)/\lambda$ with λ is the wavelength and Θ is the scattering angle.)

The microstructure of the hyalite, however, was homogeneous inside the visual field of SAXS ($r_{\max} =$ 80 nm). The zoned macroscopic texture was due to a rhythmic growth.

The data in the low-angle region ($s < 0.1\ \mathrm{nm}^{-1}$) were approximated with the formula $\tilde{I}(s) \propto s^{-\tilde{b}}$ using the damped Newtonian method. With the exception of hyalite and GS13008 all other samples show deviations from the power-law scattering $I(s) \propto s^{-4}$ which is valid for systems with two phases separated by smooth boundaries. These inhomogeneities were larger than the visual field; however, their scattering tails indicated rough surfaces in the case of the geyserites (Table 2). A power-law exponent higher than 4 found for GSPE1 is rather unusual and was reported only for reversed phase silica gels [7]. It has been explained by a thin transition layer having a lower electron density composed probably of organic molecules.

WAXS

X-ray diffraction of the geyserites GS13001 and GS13008 show weak Bragg reflections. An identification of the crystalline phase has not yet been possible. The amount of crystallites in these samples was very small (Table 2). An influence on the microstructure of the amorphous part of the sample is excluded.

Table 2. Results of SEM and X-ray investigations.

Sample no.	SEM	XRD	SAXS (vd)	SAXS $\tilde{b}$	SAXS b
GSPE1	Helical structures, particle chains, agglomerates, single particles	a	No	3.89	4.89
GS13001	Agglomerates, single particles	a+c	No	2.88	3.88
GS13053	Agglomerates, particle chains, single particles	a	No	2.87	3.87
GS12973	Agglomerates, single particles	a	Yes	2.54	3.54
GS13008	Agglomerates, single particles	a+c	Yes	3.03	4.03
Hyalite	No particles	a+c	—	3.01	4.01

a—amorphous, c—small amounts of crystalline phases near the detection limit, vd—vacuum dehydration, $\tilde{b}$: negative slope of the SAXS curves (collimation condition "infinitely-long primary beam"); $b = \tilde{b} + 1$ (correction for point-like collimation).

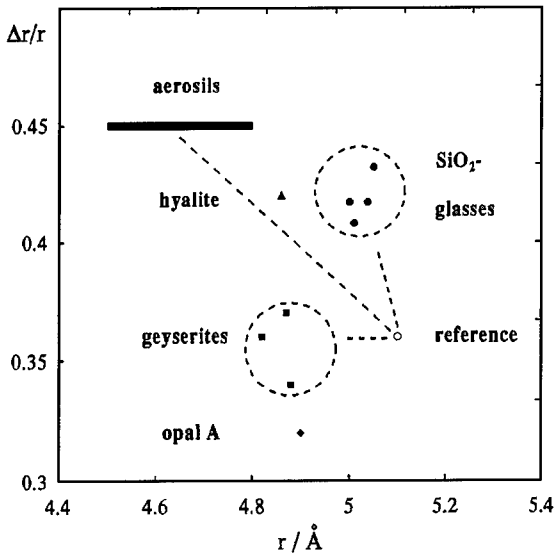

Figure 3. Fluctuation range $\Delta r/r$ versus mean size of typical MRO polyhedra (r) for different forms of (hydrous) silica. Each form of silica can be distinguished by the position on this map.

Besides the detection of crystalline phases WAXS experiments readily provide information on shapes and positions of the first sharp diffraction peak (FSDP). These in turn are strongly dependent on the composition of the silicate glass [8] or, if the composition is constant, on topological differences within the medium range order due to the kind of syntheses performed: melting or processing by a sol-gel route, including their individual thermal histories [9]. From a simple model of the structural origin of the FSDP, three parameters which were characteristic of the structure in the medium range order could be evaluated by describing the FSDP separated from the rest of the scattering function by an asymmetric peak: the mean size of a typical polyhedron of medium range order r, the fluctuation range $\Delta r/r$ of r and the correlation length l of the medium range order [10]. In a $\Delta r/r$ versus r plot different (hydrous) forms of silica could be distinguished (Fig. 3).

Conclusion

The development of the observed microscopic structures and macroscopic textures were determined by the dynamics of the processes of their formation: fast release of pressure, cooling of the parent solutions and their rapid transport. It is assumed that most important is the first step, the build-up of the oversaturation of monomeric H_4SiO_4 which forces rapid molecular condensation reactions at the pH of about 8. This determines the structure of the geyserites. The observed variety in textures was due to the conditions of nucleation and agglomeration of colloidal particles. Thereby even bacteria may provide heterogenous nucleation. Depending on the conditions between stagnant solution or fast flow also monomeric H_4SiO_4 will become involved and drive silicification of organic material or even growth of quartz. There is evidence for preserved bacterial microfossils in some of the geyserites' textures which should be investigated by further TEM investigations to look for bacterial relicts inside the helical aggregates [6].

Though imaging methods like light microscopy and electron microscopy in combination with SAXS are powerful instruments for describing the structures and textures of hydrous amorphous silica, an experimental set-up is currently operated to reproduce the structures determined in order to support our assumption.

Time dependent measures of the scattering intensities at an appropriate s-value (e.g., $s \approx 0.4$ nm^{-1}) might be useful to determine the kinetics of dehydration.

Acknowledgment

We gratefully acknowledge the provision of the geyserite samples by Prof. Dr. O. Flörke (University Bochum) which were collected by Dr. G. Oehlschlegel.

References

1. O.W. Flörke, H. Graetsch, B. Martin, K. Röller, and R. Wirth, N. Jb. Miner. Abh. **163**(1), 19–42 (1991).
2. O.W. Flörke, J.B. Jones, and E.R. Segnit, N. Jb. Miner. **H. 2**, 82–89 (1991).
3. O.W. Flörke, S. Flux, and B. Schröder, N. Jb. Miner. Abh. **151**(1), 87–97 (1985).
4. J.D. Rimstidt and D.R. Cole, Amer. J. Sci. **283**, 861–875 (1983).
5. G. Oehlschlegel, Unpublished report to the DFG, 1981.
6. B. Jones, R.W. Renaut, and R.M. Rosen, J. Sediment. Res. **67**(1), 88–104 (1997).
7. P.W. Schmidt, J. Appl. Cryst. **24**, 414 (1991).
8. J. Göttlicher and H.J. Pentinghaus, Ber. Bunsenges. Phys. Chem. **100**(9), 1563–1568 (1996).
9. H.J. Pentinghaus, J. Göttlicher, and B. Müller, Structural investigations of hyalite (Abstract), *Third Int. Conf. on Natural Glasses* (Jena, 1996).
10. B. Müller, personal communication, 1993.

Journal of Sol-Gel Science and Technology 13, 89–94 (1998)
© 1998 Kluwer Academic Publishers. Manufactured in The Netherlands.

Rheological and Coating Properties of Modified Silica Sols

J. MARX AND R. LISCHEWSKI
SynTec GmbH, Industriepark Wolfen-Thalheim, Werkstattstraße 188, D-06766 Wolfen

R. SCHNABEL AND F. APSEL
Martin-Luther-Universität Halle, Außenstelle Merseburg, Institut für Werkstofftechnologie, Geusaer Straße, D-06217 Merseburg

H. BÖTTCHER
Feinchemie GmbH Sebnitz, Höhenweg 9, D-01855 Sebnitz

Abstract. The rheological behavior of modified silica sols has been investigated by gel formation kinetics and dynamic flowing within the pH range 3–7 and the temperature range 20–50°C. The sols show pseudo-plastic behavior at low shear-rates, with Newtonian behavior below 100 s^{-1}. Oscillation measurements reveal that gelation starts with a significant decrease of phase difference <10°, because of a strong increase in elastic behavior. After solidification the values of phase difference increase, indicating a partial destruction of the gel structure due to stress. The relationship between the viscosity of the modified silica sols and their coating parameters was compared for both dip coating and continuous coating with a slide coating unit.

Keywords: sol-gel process, silica sol, rheology, gelation time, film coating

1. Introduction

Modern sol-gel techniques allow thin glass layers to be produced at room temperature on any required substrate. Such coatings have numerous technical applications, e.g., as special optical coatings [1]; to improve the mechanical properties of and to protect material surfaces [2]; as sensors [3] and as biologically active coatings following the incorporation of bio-chemical substances [4].

Modified silica sols (II) prepared by hydrolysis of tetraalkoxy-silane (I) were used to make the coatings:

$$\underset{(I)}{Si(OR)_4} \xrightarrow[-4ROH]{+2H_2O} \underset{(sol,\ II)}{(SiO_2)_n} \xrightarrow[gelation\ drying]{coating} \text{silica gel films}$$

There are many possible ways of modifying the silica matrix to adapt it for special applications:

(a) variation of the sol composition (concentration, water content, type of solvent),
(b) chemical modification of the silica gel by partial substitution of other elements (Ti, Al, Zr) or Si—R (R functional organic residues) for the silicon,
(c) physical modification with additives such as surfactants or polymers added either before or after the sol formation.

As all modifications of a silica sol significantly influence its rheological and coating behavior, comprehensive rheological characterisation is a necessary step in the technical production of sol-gel films. An example is given of an investigation into the rheological behavior of a silica sol. Various methods were employed to evaluate how the viscosity-enhancer hydroxypropylcellulose (HPC) affects rheological properties and layer parameters in the preparation of both dip coating and continuous coating.

2. Experimental

2.1. Preparation of the Standard Silica Sol A

10 ml tetraethoxysilane (TEOS), 40 ml EtOH and 20 ml 0.01 N HCl were stirred for 20 h at room temperature. The resulting silica sol A contains 4.0 wt% SiO_2 in 70 vol% EtOH. In order to provide a controlled increase in sol viscosity, HPC was dissolved in the sol solution and either 1 or 2% of low viscosity Klucel® E or 0.1 or 0.2% of high viscosity Klucel® H/Aqualon was added, see Table 1.

2.2. Rheological Investigations

The rotation rheometer MC 10/PHYSICA Meßtechnik GmbH was used to measure the viscosity of the sols. A constant deformation of $D = 30\ s^{-1}$ was used. The pH was adjusted by adding a solution of 3% ammonia in EtOH to the stirred sol, with simultaneous control by a pH meter. The gelling time t_g was obtained from the viscosity-time curves (the time at which the tangents to the curve branches intersect), see Fig. 1.

In a similar manner the flow curves (shear stress vs. shear rate behavior) were determined with a

Table 1. Viscosities of sol A modified with hydroxypropylcellulose.

Sol:	Sol A	+0.1% Klucel H	+0.2% H	+1% Klucel E	+2% E
η (mPas, 20°C):	3.25	11.47	37.60	8.46	19.30

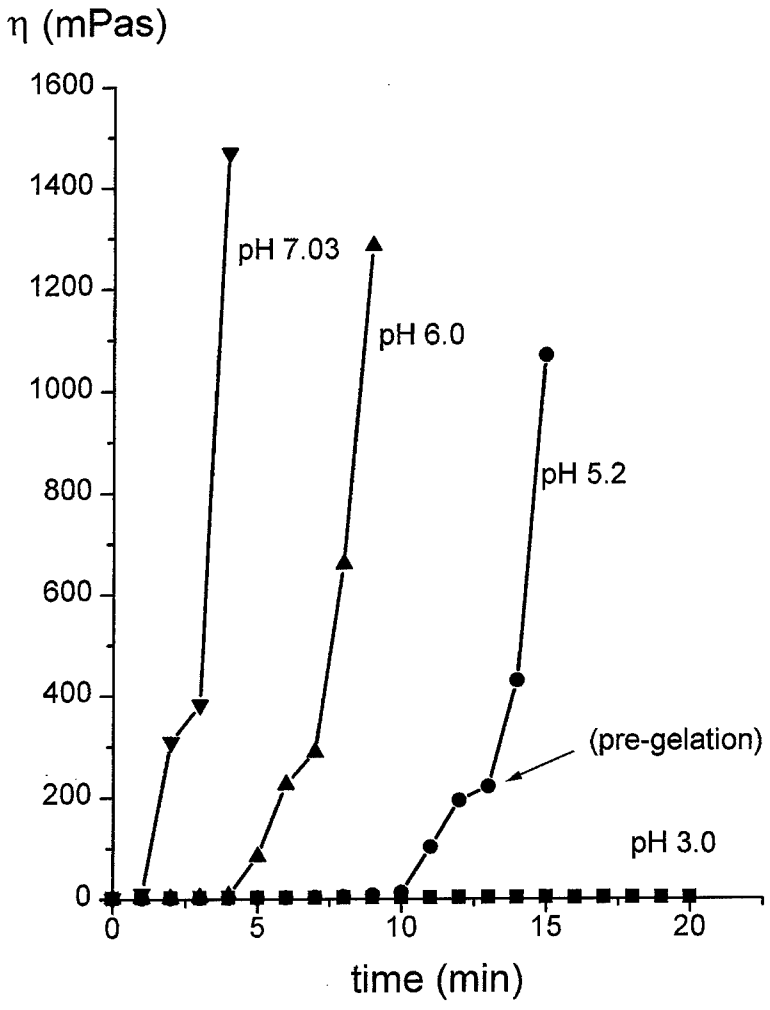

Figure 1. Viscosity-time curves of sol A at different pH values.

CSL 100/CarriMed rotation viscometer (plate-to-plate geometry, diameter 6 cm, slide 300 μm). For dynamic oscillation measurements a time-sweep was applied under the following conditions: amplitude 10% deformation, frequency 1 Hz (6.28 rad/s), shear stress 0.236 Pa, temperature 20–50°C, time 30 min.

2.3. *Coating*

Dip coatings were prepared by evenly pulling 140 μm cellulose acetate foils (75 × 25 mm^2) from a sol-filled tank at speeds of 15–30 cm/min.

The continuous coatings were prepared by casting the silica sols onto 140 μm cellite foils, using an LBM 70 lab coating device (MABA Spezialmaschinen GmbH Wolfen, Germany) equipped with a 70 mm slide coating unit and air drying. Layer thickness was controlled by the delivery of the coating solution, m, and by varying coating speed (speed of the polymeric support, v) between 1 and 6.5 m/min.

Layer thickness was determined by measurement of the optical interference of reflected white light with perpendicular incidence using a MCS 400/Carl Zeiss photodiode array spectrometer with the software program SDICKM. To reduce light reflection from the back, the layer surface was rubbed down with sandpaper.

When preparing continuous coatings, the sols were dyed with 0.16% Rhodamine 6G because some layers were slightly turbid. This allowed film thickness to be evaluated by means of proportional optical density at 533 nm.

3. Results and Discussion

The rheological behaviour of modified silica sols has been investigated by gel formation kinetics and dynamic flowing for the pH range 3–7 and the temperature range 20–50°C. The dependence of the gelling time of sol A on pH and temperature is shown in Fig. 2. The gelling time, as expected, decreases with increasing pH and temperature. Such graphic representations can be considered as the "identity card" of each sol, characterizing its pH thermal, and storage behavior and enabling the sol to be handled appropriately. It is necessary to prepare a new "identity card" when the SiO_2 or H_2O concentration or the solvent composition is altered, or when chemical or physical modifications are made to the sol.

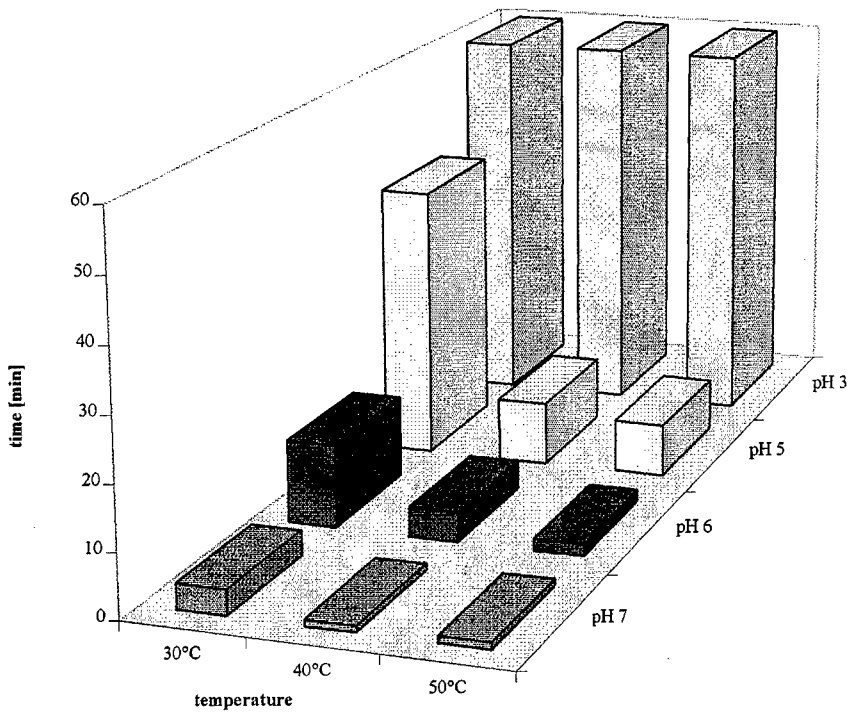

Figure 2. Gelling times of sol A at different pH values and temperatures.

To attain higher film thicknesses after coating, the viscosity η of the silica sol A can be increased by dissolving HPC in it, see Table 1.

The addition of HPC changes the rheological properties of sol A. Increasing additions of soluble HPC cause t_g to pass through a maximum at low polymer concentrations (at 0.1% Klucel® H and 0.5% Klucel® E in the sol A), beyond which the gelling time decreases continuously.

Additional information about the rheological behavior of the silica sols could be obtained from the flow curves (shear stress vs. shear rate). All the investigated sols had a similar behavior. The experimental values vary considerably at low shear rates, due to the high sensitivity of the viscometer in this region, but it is evident that at low shear rates the sols exhibit pseudo-plastic behavior and below 100 s^{-1} Newtonian behavior. The shear rates of practical interest fall within this region. In addition, oscillation measurements were made to evaluate the relationship between the viscous and elastic components of the modified silica sols. This ratio can be characterized by the phase displacement δ between the exciting and responding oscillation (purely viscous, Newtonian media $\delta = 90°$, elastic media $\delta = 0°$ and viscoelastic media $0 < \delta < 90°$). The δ-t curves reveal that after a small peak ("*pre-gelation*"; this peak corresponds to the stepwise increase of the viscosity-time curves in Fig. 1) the gelation starts with a significant decrease of phase difference $\delta < 10°$ due to a strong increase of the elastic components (see Fig. 3). The sol-gel transition is clearly recognizable and is completed in a very short time. After solidification the values of phase difference increase, indicating a partial destruction of the gel structure due to stress. The shapes of the curves are independent of concentration, temperature (up to 50°C) and modification of the sol, differing only in their position on the time scale. With increasing silica concentration in the sol, the δ value approaches zero because the gel strength increases. The addition of viscosity-enhancing hydroxypropylcellulose slows down gelation at low polymer concentrations by analogy with the t_g dependence.

Viscosity and gelling behavior are important parameters when manufacturing thin films. Both affect coating speed, drying conditions, film thickness and

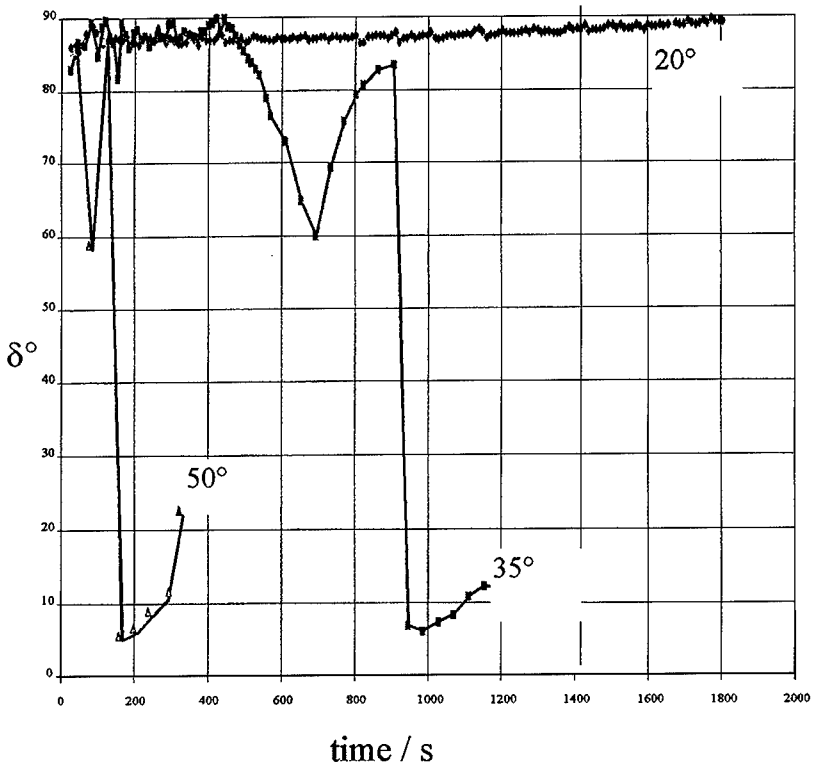

Figure 3. Time-dependence of the phase displacement δ of sol A at different temperatures.

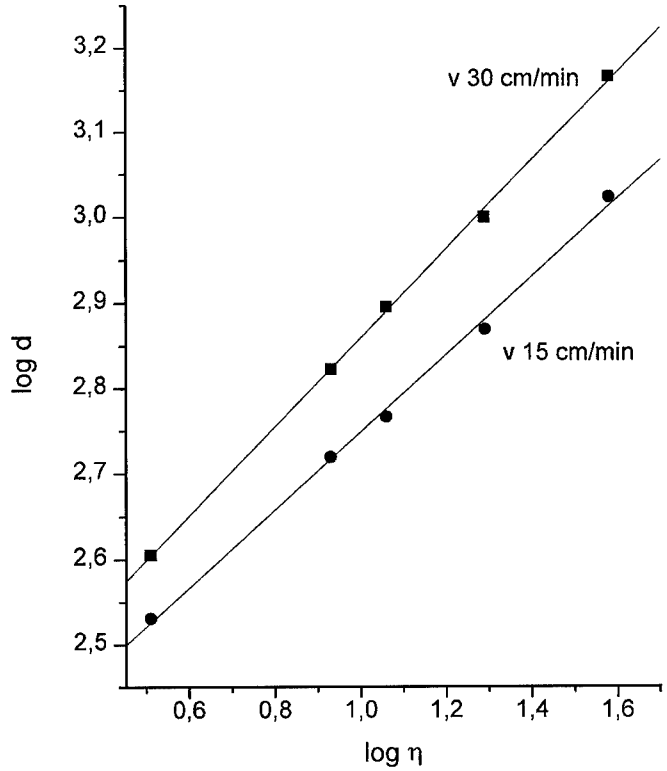

(a)

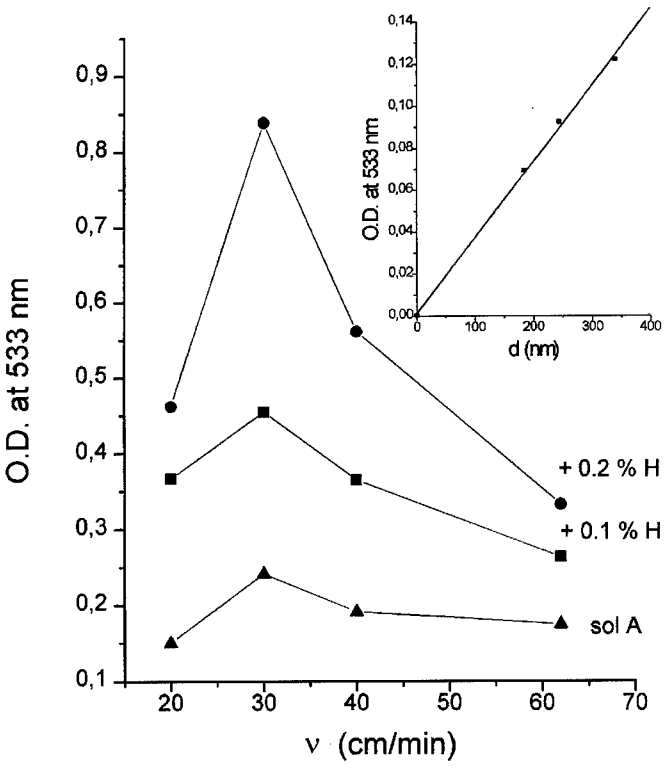

(b)

Figure 4. Relation between coating parameters and layer thickness of dried sol-gel films of sol A modified with hydroxypropylcellulose, see Table 1. (a) Layer thicknesses d (in nm) after dip coating of sols of different viscosities η in accordance with Table 1 (v = withdrawing speed, slope 0.52 and 0.45). (b) Optical density (O.D.) of the dyed film layers at 533 nm (which is proportional to the layer thickness d, see inset) after continuous coating of sol A modified with 0.1 and 0.2% Klucel H at different speeds v of polymeric support and $m = 0.7$ ml sol/min.

the mechanical and optical film properties. To date, detailed investigations into sol-gel film technology have only been carried out for the discontinuous dip-coating process [5, 6], where it was found that the relationships between the rheological and coating parameters are in accordance with those derived by Landau and Levich [7]. It could be confirmed that the thickness, d, of the silica films increases with the viscosity η of sol A and the withdrawing speed, v (Fig. 4(a)). Therefore, it is possible to control d by addition of polymeric viscosity enhancers to the sol. Knowledge of such relationships enables, e.g., the avoidance of interference effects (critical range $200 < d < 1000$ nm) in special optical sol-gel coatings.

The relationships are more complicated for continuous coatings made on a slide coating unit. Some characteristic features of the dependence of sol viscosity and the coating speed (determined by the speed of the polymeric support v) on the layer thickness are shown on the Fig. 4(b). Layer thickness d is determined by the ratio of the delivered coating solution, m, to the coating speed, v. When v is low, a surplus of coating solution is available on the coater surface, and d increases with v in the same manner as for dip coating. However, at increased speeds, d decreases with v as expected. Therefore, all correlations of d with v go through a maximum as shown in Fig. 4(b). Application of this knowledge would allow large-area sol-gel coatings on foils or paper to be made.

Conclusions

Discounting the pre-gelation effect, the rheological investigations reveal that modified silica sols do not show an extraordinary behavior compared with diluted polymer solutions. For a wide deformation range 10–600 s^{-1} the sols act as Newtonian liquids, i.e., their viscosity is independent of shear rate. Fine adjustments to sol viscosity can be made by adding hydroxypropylcellulose, allowing control of the film thickness not only for continuous coatings but also for dip coatings.

Acknowledgment

This work was carried out with financial support from the Deutsche Bundesministerium für Forschung and Technologie (Contract No. 03C3006A5).

References

1. R. Reisfeld and C.K. Jorgensen (Eds.), (a) *Chemistry, Spectroscopy and Application of Sol-Gel Glasses*, Structure and Bonding (Springer-Verlag, Berlin, 1992), Vol. 77; (b) *Optical and Electronic Phenomena in Sol-Gel Glasses and Modern Applications*, Structure and Bonding (Springer-Verlag, Berlin, 1996), Vol. 85.
2. H. Schmidt and H. Wolter, J. Non-Cryst. Solids **121**, 428 (1990); H. Schmidt, J. Non-Cryst. Solids **178**, 302 (1994); R. Kasemann and H. Schmidt, New J. Chem. **18**, 1117 (1994); J.E. Mark, Heterog. Chem. Rev. **3**, 307 (1996); M. Guglielmi, J. Sol-Gel Sci. Tech. **8**, 443 (1997).
3. O. Lev, Analusis **20**, 543 (1992); O. Lev et al., Anal. Chem. **67**, 22A (1995); D. Avnir, S. Braun, O. Lev, and M. Ottolenghi, Proc. SPIE **1758**, 456 (1992); Materials **6**, 1605 (1994).
4. D. Avnir and S. Braun (Eds.), *Biochemical Aspects of Sol-Gel Science and Technology* (Kluwer Acad. Publ. Group, Dordrecht, 1996).
5. S. Sakka, K. Kamiya, K. Makita, and Y. Yamamoto, J. Non-Cryst. Solids **63**, 223 (1984).
6. C.J. Brinker, A.J. Hurd, P.R. Schunk, G.C. Frye, and C.S. Ashley. J. Non-Cryst. Solids **147/148**, 424 (1992); C.F. Brinker and A.J. Hurd, J. Phys. III France **4**, 1231 (1994).
7. L.D. Landau and V.G. Levich, Acta Phys. Chim. URSS **17**, 41 (1942).

Journal of Sol-Gel Science and Technology 13, 95–98 (1998)
© 1998 Kluwer Academic Publishers. Manufactured in The Netherlands.

Fluorescence Probing of Composite Organic/Inorganic Transparent Matrices

V. BEKIARI, M. FERRER, E. STATHATOS AND P. LIANOS
Engineering Science Department, University of Patras, 26500 Patras, Greece
lianos@upatras.gr

Abstract. Transparent composite SiO_2/organic matrices have been made by the sol-gel method using tetramethoxysilane and either cetyltrimethylammoniumbromide (CTAB) or a polyethylene glycol oligomer (PEG-200) or a cationic polyelectrolyte. We have investigated conditions under which transparent xerogel matrices are possible and we have characterized them mainly by time-resolved fluorescence probing using stretched exponentials. CTAB creates a hydrophobic and PEG-200 a hydrophilic subphase in the matrix. An important property of these composite matrices is that they allow molecular diffusion contrary to matrices made in the absence of surfactants or polymers.

Keywords: sol-gel, composite, matrices, fluorescence, probing

Introduction

Silica-surfactant composites are a new class of materials which became popular when it was found that surfactants can be used as templates to fabricate ordered mesoporous structures [1–3]. Cetyltrimethylammonium halides are the chosen organic materials which match well with tetramethoxysilane or tetraethoxysilane, i.e., the alkoxides usually employed in sol-gel matrices [4]. Composite organic-inorganic matrices can also be made with polyelectrolytes and polyethylene glycol oligomers. Examples of such materials will be introduced in the present work. We have given emphasis to transparent matrices since they can be employed in photophysical applications.

Materials and Methods

Cetyltrimethylammonium bromide (CTAB, Fluka), tetramethoxysilane (TMOS, Aldrich), pyrene (Fluka), coumarin-153 (C-153, Aldrich), tris(2,2′-bipyridine) ruthenous dichloride hexahydrate ($Ru(bpy)_3^{2+}$, GFS Chemicals), methyl viologen (MV^{2+}, Aldrich), poly-(diallyldimethylammonium chloride) (PAC, Aldrich, high MW) and polyethylene glycol (PEG-200, Aldrich), were of the best quality available and used as received. Millipore filtered water was used in all experiments.

Composite silica-organic matrices were made at ambient conditions as follows: TMOS was partially hydrolyzed by mixing it with acidified water (pH 3.0) at a molar ratio of TMOS : water = 1 : 2. The mixture was continuously stirred for 1 hour. At the beginning it was turbid but in the course of hydrolysis it clarified. Then, to 1 ml of this original sol, we added 5.4 ml of an aqueous micellar solution of CTAB or an aqueous polymer solution under vigorous stirring. The sol obtained was transparent and homogeneous.

Transparent matrices (xerogels) were obtained by slowly drying the original colloidal solution at 40°C placed in plastic cuvettes covered with perforated aluminum foil.

Measurements were performed at ambient conditions. Fluorescence measurements were made with a home-assembled spectrofluorometer using Oriel parts and time-correlated fluorescence measurements with the photon-counting technique, using a home-made hydrogen flash and ORTEC electronics.

The luminescence decay profiles of $Ru(bpy)_3^{2+}$ in the presence of MV^{2+} as well as of pyrene, in the presence of pyrene excimer or coumarin-153, (which acts as energy acceptor of pyrene fluorescence) were analyzed

by a model of stretched exponentials given by the following equation [5, 6]:

$$I(t) = I_0 \exp(t/\tau_0) \exp[-C_1(t/\tau_0)^f + C_2(t/\tau_0)^{2f}] \quad 0 < f < 1. \quad (1)$$

The first-order quenching rate was calculated by:

$$K(t) = 1/\tau_0[fC_1(t/\tau_0)^{f-1} - 2fC_2(t/\tau_0)^{2f-1}]. \quad (2)$$

C_1, C_2 and f parameters were calculated by fitting Eq. (1) to the experimental decay profile and used to calculate the values of $K(t)$. τ_0 is the decay time in the absence of quencher and is measured by separate experiment. The model of Eq. (1) was shown in previous publications to fit decay profiles recorded with the photon-counting technique [5–7]. The model of Eq. (1) applies to any quenching reaction where an excited luminophore can, in principle, be quenched by any quencher present [6]. Thus, it applies to electron and energy transfer as well as to diffusion-controlled quenching. The restrictions imposed by geometry reflect on the value of the noninteger exponent f. f is smaller when the reaction is more restricted. The exponent of the second exponential in Eq. (1) should, in principle, be an infinite series [6, 8]. However, two terms are sufficient to fit the experimental decay profile [6].

The reaction rate is time-dependent in all cases where the model of Eq. (1) applies, since reaction rate then depends on the distance between the reacting species. Distance-dependence creates time-dependence which becomes even more intense in the case of restricted geometries. Thus, the value of K in Eq. (2) is time-dependent. Since it is difficult to tabulate any $K(t)$-value for any value of time, we usually choose to tabulate only its value K_1 at the first time channel and its value K_L at the last recorded time channel (total of 1000 channels at 2.6 ns/channel). Then K_1 represents the quenching rate at short times and K_L the quenching rate at long times.

Results and Discussion

Conditions for Preparation of Transparent Xerogels. As already explained, prehydrolyzed TMOS was mixed with an aqueous solution of either CTAB, PEG or PAC. The mixture was in most cases transparent but did not always stay so all through the drying process. Thus, in the case of CTAB, it was necessary to use a surfactant concentration lower than 0.2 M to obtain transparent xerogels. Anionic (sodium dodecylsulfate) surfactants did not give transparent gels. PEG-200 was found to mix with prehydrolyzed silica and give transparent gels even in the absence of added water. Of course, at high PEG-200 content, the matrix remained soft even at the end of the drying process. Mixture with other PEG oligomers was also possible for MW < 1000. This rule roughly applied also to nonanionic surfactants containing a polyethylene oxide group. Indeed Triton X-45 (with an average of 5 ethylene oxides per surfactant molecule) gave transparent gels but Triton X-100 (about 10 ethylene oxide groups per molecule) did not. Transparent gels and xerogels have also been obtained with the cationic polyelectrolyte up to 150 g/l. Anionic polyelectrolytes did not give transparent gels.

Fluorescence Probing. Composite silica/organic transparent matrices doped with fluorescent probes are characterized by an important property absent from pure silica sol-gel matrices. They allow diffusion of the probes within the matrix. This was demonstrated by the excimer formation kinetics of pyrene. As seen in Fig. 1, in a pure silica matrix, pyrene excimer forma-

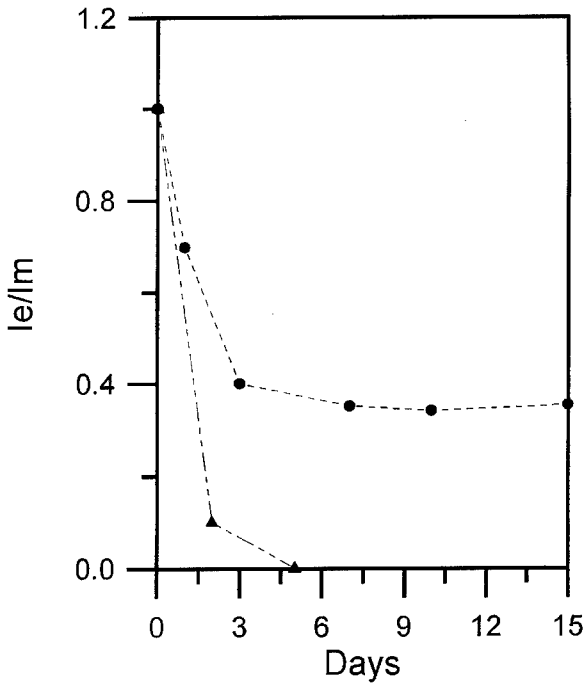

Figure 1. Plots of pyrene excimer over pyrene monomer fluorescence intensity in a silica xerogel (▲) and in a SiO_2/CTAB composite xerogel (●).

tion progressively decreased during the sol-gel transformation to disappear completely in the xerogel. On the contrary, in SiO_2/CTAB, excimer was still present in the xerogel. That this remaining excimer was due to diffusion and not to pyrene aggregation was concluded from examination of the form of the fluorescence spectra [9] and of the monomer and excimer fluorescence decay profiles [10]. It can be also concluded from the data of Table 1. There it is seen that excimer formation characteristics were similar in micelles and in xerogels save for the values of K_1 and K_L, which, naturally, decreased due to the viscosity increase in xerogels. f and the ratio of the long over the short-time reaction rate, i.e., K_L/K_1, stayed practically the same for both systems indicating similar excimer formation kinetics. Diffusion was also obvious from the resonance energy transfer kinetics between pyrene (donor) and C-153 (acceptor). In energy transfer kinetics, usually the noninteger exponent f is around 0.5 for three-dimensional systems and it may decrease in more restricted environments [6, 8]. The only possibility of getting f values larger than 0.5 in resonance energy-transfer quenching is by diffusion, where the spectral dimension of the reaction is increased by the increased probability of energy transfer due to reactant motion. The similar f-values between aqueous micelles and SiO_2/CTAB xerogels is obvious from Table 1, also for the above energy-transfer pair. K_1 and K_L was larger in the xerogel, since syneresis increased local concentration of the reacting species and, subsequently, increased energy-transfer probability. Matrices made with either CTAB, PEG or PAC were compared using a hydrophilic luminescence-quenching pair, since pyrene and C-153 are not sufficiently soluble in the aqueous polymer solutions. The data of Table 1 show the reaction kinetics between $Ru(bpy)_3^{2+}$ and MV^{2+} in the three different matrices and the three corresponding original aqueous solutions. Contrary to pyrene and C-153, the hydrophilic probes detected a different environment in aqueous micellar solutions from in xerogels. Thus f substantially decreased in the xerogel while K_1 increased and K_L decreased. Such behavior is suggestive of restricted motion in the xerogel. The hydrophilic probes, presumably, stayed outside the micellar subphase, because, among other reasons, of the repulsive charge of CTAB. Apparently, diffusion was possible only within the surfactant subphase whatever its geometry in the xerogel. Judging from the invariance of f for pyrene in the aqueous micellar phase and in the xerogel, the original micellar structure was most probably preserved in the xerogel. Similar behavior was also detected for the cationic polyelectrolyte, i.e., f and K_L decreased and K_1 increased in the xerogel. Apparently, the hydrophilic probes were not

Table 1. f, K_1, K_L values for pyrene and $Ru(bpy)_3^{2+}$ obtained through Eqs. (1) and (2) for composite SiO_2/organic materials.

Organic substance	Microenvironment	[F]* (mM)	[Q]+ (mM)	τ_0 (ns)	f	K_1 (10^6 s^{-1})	K_L (10^6 s^{-1})
	Pyrene diffusion-controlled excimer formation						
CTAB	Aqueous micelles	10		180	0.71	68	1.7
CTAB	Xerogel brick			218	0.72	37	0.9
	Pyrene/C-153 resonance energy transfer						
CTAB	Aqueous micelles	0.01	0.1	180	0.61	42	3.1
CTAB	Xerogel brick			218	0.63	70	3.5
	$Ru(bpy)_3^{2+}$ quenched by MV^{2+}						
CTAB	Aqueous micelles	1	10	430	0.69	36	1.3
CTAB	Xerogel brick			880	0.50	42	0.6
PAC	Aqueous solution	1	10	470	0.63	33	1.0
PAC	Xerogel brick			980	0.48	43	0.3
PEG-200	Aqueous solution	1	10	1100	0.78	24	10.3
PEG-200	Xerogel brick			1295	0.81	33	9.4

*[F]: fluorophore(luminophore) concentration in precursor solution.
+[Q]: quencher concentration in precursor solution.

associated with the polymer subphase and simply detected the restrictions imposed by the xerogel. The behavior of the probes, particularly in the presence of PEG-200. $Ru(bpy)_3^{2+}$ was obviously associated with the oligomer subphase both in solution and in the xerogel. This is concluded by the extensively long luminescence decay time T_0, apparently due to elimination of oxygen quenching in the PEG-200 subphase. Diffusion in the presence of PEG-200 was largely facilitated as indicated by the large f value, which, surprisingly, was even larger in the xerogel than in the aqueous phase. The particularly large values of K_L, observed only in the case of PEG-200, was a sound proof of existence of diffusion facilitated in the presence of this oligomer.

In Conclusion. Molecular diffusion in SiO_2/organic xerogels is possible for molecules associated with the organic subphase. CTAB facilitates diffusion of hydrophobic molecules and PEG-200 facilitates diffusion of hydrophilic species.

Acknowledgment

We acknowledge financial aid from NATO CR Grant 941146.

References

1. C.T. Kresge, M.E. Leonowicz, W.J. Roth, J.C. Vartuli, and J.S. Beck, Nature **359**, 710 (1992).
2. N.K. Raman, M.T. Anderson, and C.J. Brinker, Chem. Mater. **8**, 1682 (1996).
3. G.S. Attard, J.C. Glyde, and C.G. Goltner, Nature **378**, 366 (1995).
4. A. Firouzi, L.M. Kumar, T. Bull, P. Besier, P. Sieger, Q. Huo, S.A. Walker, J.A. Zasadzinski, C. Glinka, J. Nicol, D. Margolese, G.D. Stucky, and B.F. Chmelka, Science **267**, 1138 (1995).
5. P. Lianos and P. Argyrakis, J. Phys. Chem. **98**, 7278 (1994).
6. P. Lianos, Heterogeneous Chem. Rev. **3**, 53 (1996).
7. V. Bekiari and P. Lianos, J. Coll. Interf. Sci. **183**, 552 (1996).
8. J. Klafter and A. Blumen, J. Chem. Phys. **80**, 875 (1984).
9. F.W. Winnik, Chem. Rev. **93**, 587 (1993).
10. D. Papoutsi, V. Bekiari, E. Stathatos, and P. Lianos, Langmuir **11**, 4355 (1995).

Journal of Sol-Gel Science and Technology 13, 99–102 (1998)
© 1998 Kluwer Academic Publishers. Manufactured in The Netherlands.

Inorganic Polymerization in a Non-Ionic Lyotropic Lamellar Phase

L. PORCAR AND J. MARIGNAN
Groupe de Dynamique des Phases Condensées C. C. 26 (Unité Mixte de Recherche UM II/CNRS 5581), Université Montpellier II, F-34095 Montpellier Cedex 5
lionel@gdpc.univ-montp2.fr

T. GULIK-KRZYWICKI
Centre de Génétique Moléculaire-CNRS, 91190 Gif-sur Yvette, France

Abstract. Silicon tetramethoxide was polymerized within a nonionic lyotropic lamellar phase. After gelation, the birefringence of the sample is preserved and polarized light optical microscope observations reveal no segregation. High Resolution Small Angle X-ray Scattering patterns of the gel shows Bragg peaks characteristic of a layered structure. Freeze fracture experiments on the lamellar gel show stacks of parallel bilayers. The experimental observations indicate that the silica is located in the lamellar structure.

Keywords: inorganic gelation, lamellar phase, freeze fracture, small angle X-ray scattering (SAXS)

Introduction

The sol-gel process is a very attractive method for producing porous ceramic materials with controlled structure and composition [1]. Numerous research groups have focussed their attention on the synthesis of mesoporous (15–500 Å) materials [2–7] with a regular periodicity and high surface area, which have potential uses in biotechnology applications and large molecule selective catalysis. A challenging and a potentially rewarding approach for the synthesis of mesodimensioned porous media is to utilize an organized molecular array as a template for the condensation of inorganics species.

Particular advances have been made by performing the sol-gel reaction in organized surfactant media [8–12]. An interesting method is to use lamellar phases as a template to produce the inorganic polymerization in the water layers and to obtain, after calcination, a pure inorganic mesoporous network with a pore size of the order of the lamellar spacing, i.e., about 50–100 Å.

One attempt to produce "layered inorganic materials" through the sol-gel process by Dubois et al. [13] used a lamellar phase as a template. The main difficulty of this process is to conserve the smectic order during the hydrolysis and condensation reactions of the precursor:

$$\mathrm{Si(OR)_4 + 4H_2O \rightarrow Si(OH)_4 + 4ROH}$$

$$\mathrm{Si(OH)_4 + Si(OH)_4 \rightarrow (OH)_3Si{-}O{-}Si(OH)_3 + H_2O}$$

Indeed, these reactions create mechanical constraints which can destroy the organized mesophase [9, 14]. Friberg and Ma [14] attempted the synthesis of ceramic oxides in lyotropic liquid crystalline phases, but found that on hydrolyzing silicon alkoxide, the reaction mixtures turned isotropic. This problem is caused by the alcohol produced during the hydrolysis of the alkoxide which destroys the lyotropic phase.

In this paper, we investigate a lamellar phase in which silica polymerization occurs. The lyotropic phase we have studied is made from a mixture of nonionic surfactants, water and decane. The "lamellar gels," obtained after polymerization of the precursor, were characterized by Small Angle X-ray Scattering (SAXS), polarized light microscopy observations and freeze fracture experiments.

Experimental

The experimental starting system is a lamellar phase obtained from a ternary mixture of two nonionic commercial surfactants, Triton X100 (TX100) and Triton X35 (TX35), and water. The weight ratios are TX100/TX35 = 55/45 g/g and (TX100 + TX35)/H_2O = 1 g/g; both are kept constant. Decane is incorporated in order to make the solution fluid and to obtain a much better contrast in SAXS. It is inserted between the tails of the surfactants, increasing the bilayer thickness [15]. The quantity of decane is 26% of the weight of surfactant.

Silicon tetramethoxide $Si(OMe)_4$ (or TMOS) was added to the lamellar phase and stirred vigorously. The samples were left at 20°C and gelation was estimated by visual observation of the fluidity of the sample. Thus, a single phase and transparent lamellar gel with 10% by weight at TMOS was obtained. At the onset of the polymerization, the samples remained transparent and birefringent, indicating that the lamellar structure is preserved and not affected by the presence of alkoxide. To conserve the lamellar structure a water to TMOS molar ratio above 20 is required (henceforth, this ratio is referred to as h). For $h < 20$, the organized mesophase is destroyed during the polymerization and the obtained silica gel is opaque, not birefringent.

Results and Discussion

After the polymerization, the samples were studied by SAXS, polarized light microscopy and freeze fracture experiments.

The SAXS spectrum of the silica gel (Fig. 1) shows a series of diffraction peaks corresponding to the wave

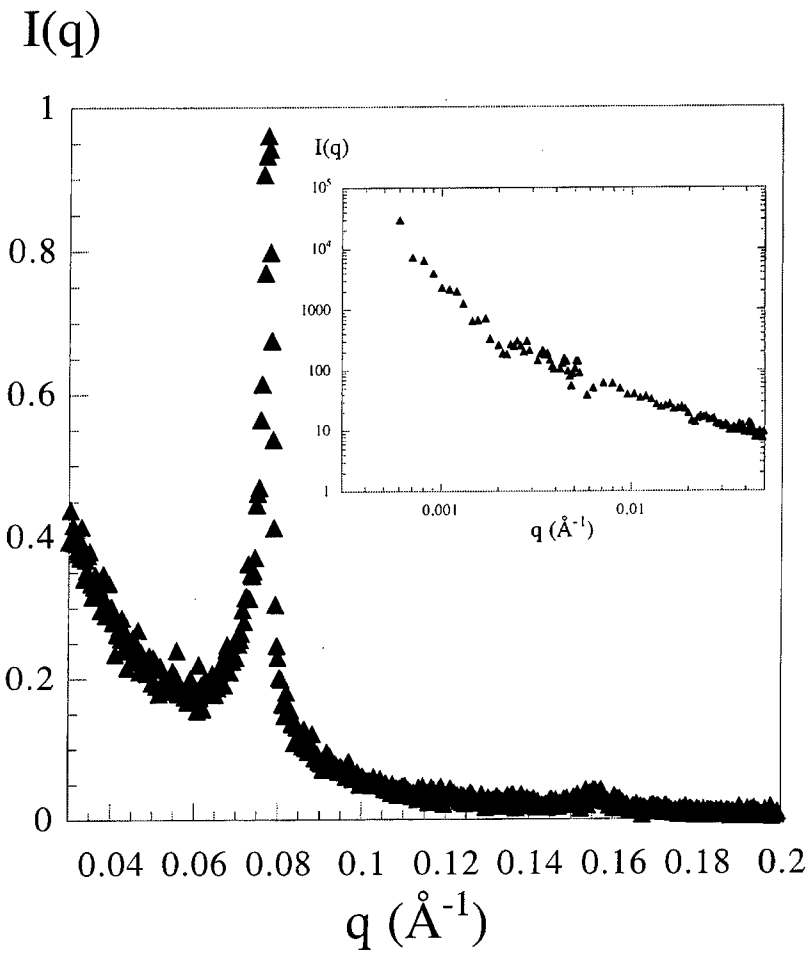

Figure 1. Small Angle X-ray Scattering spectrum of a lamellar gel in normalized units obtained for Triton X/water/decane solution (with 42.5 wt% TritonX and 15 wt% decane) and $h = 40$. The Bragg peak at $q_0 = 0.077$ Å^{-1} (scattering vector) corresponds to an interlamellar spacing of 81 Å. Inset: Log $I(q)$ vs. Log q at small wave vectors in absolute units for the lamellar gel. The samples are held in a 1 mm cell.

vectors q_0 and $2q_0$ characteristic of a lamellar structure, q_0 is related to the smectic periodicity d_p by $q_0 = 2\pi/d_p$. This indicates that the lamellar structure is maintained after the gelation process. Another feature of the SAXS spectra of the lamellar gel is the diffuse scattering as $Q \to 0$. For the pure lamellar phase this diffuse scattering is never observed. It is attributed to the scattering of a bushy silica structure which is the signature of a silica network.

Polarized light optical microscopy of the lamellar gel shows a marbled texture characteristic of a lamellar phase [16]. In the case of gelation out of the lyotropic

Figure 2. Freeze fracture electron micrograph of the lamellar gel corresponding to the sample in Fig. 1.

phase, a mixture of birefringent microdomains (pure lamellar phase) and isotropic microphase corresponding to the silica network would be seen between crossed polarizers. As shown in [16], an isotropic phase is never observed and a rotation of the sample of 90° lights the dark domains and quenches the others. This suggests that at the microscopic scale there is no segregation.

A freeze fracture experiment on the birefringent gel (Fig. 2) reveals a lamellar structure made of parallel bilayers which confirms that the inorganic polymerization occurs inside the smectic phase and does not affect the structure.

At this stage, we can affirm that the polymerization occurs inside the lamellar phase but we cannot specify where it is: on the polar heads of the surfactant bilayer or in the bulk of the water layer.

Conclusion

It is shown that gelation of silicon tetramethoxide in the lyotropic lamellar phase obtained from nonionic surfactants is possible, and that at the end of the polymerization, the lamellar structure of the sample is conserved. SAXS experiments, polarized light microscopy and freeze fracture experiments indicate gelation in the lamellar structure without segregation at the micrometer scale.

As shown in the literature, all of the related surfactant templated lamellar phases prepared to date collapse to an amorphous oxide upon template removal, but in each case, the inorganic walls are too thin to support the calcination process. In our experiments, the polymerization appears to occur in the bulk of the water layer which indicates a silica thickness of about 30 Å. Further work will consist in a study of the calcination process of these gels in order to obtain particular mesoporous materials.

References

1. C.J. Brinker and C.W. Scherer, *Sol-Gel Science* (Academic Press, New York, 1990).
2. A. Firouzi et al., Science **267**, 1138 (1995).
3. C.T. Kresge et al., Nature **259**, 710 (1992).
4. A. Monnier et al., Science **261**, 1299 (1993).
5. P.T. Tanev and T.J. Pinnavaia, Science **271**, 1267 (1996).
6. G.D. Stucky et al., Mol. Cryst. Liq. Cryst. **240**, 187 (1994).
7. T. Dabadie, Thèse de doctorat de l'université Montpellier II, 1994, (unpublished).
8. F.J. Arriagada and K. Osseo-Asare, Coll. Surf. **69**, 105 (1992).
9. S.E. Friberg, C.C. Yang, and J. Sjoblom, Langmuir **8**, 372 (1992).
10. K. Osseo-Asare and F.J. Arriagada, Coll. Surf. **50**, 321 (1990).
11. T. Abadie, A. Ayral, C. Guizard, L. Cot, J.C. Robert, and O. Poncelet, in *Better Ceramics and Through Chemistry IV*, Mater. Res. Symp. Proc., edited by K. Cheetham, C.J. Brinker, M.L. Mecartney, and C. Sanchez (Materials Research Society, Pittsburgh, PA, 1994), Vol. 346, p. 849.
12. S.E. Friberg and C.C. Yang, in *Innovations in Materials Processing Using Aqueous, Colloid, and Surface Chemistry*, edited by F.M. Doyle, S. Raghaven, P. Somasunaran, and G.W. Warren (The Minerals, Metals and Materials Society, Warrendale, PA, 1988), p. 181.
13. M. Dubois, T. Gulik-Krzywicki, and B. Cabane, Langmuir **9**, 673 (1993).
14. S.E. Friberg and Z. Ma, J. Non-Cryst. Solids **147/148**, 30 (1992).
15. L. Porcar, C. Ligoure, and J. Marignan, (in preparation).
16. L. Porcar, P. Delord, and J. Marignan, Langmuir **14**, 719 (1998).

Journal of Sol-Gel Science and Technology 13, 103–107 (1998)
© 1998 Kluwer Academic Publishers. Manufactured in The Netherlands.

A Spectroscopic Study of an Anhydrous Tetraethyl Orthosilicate-Boric Acid-Ethanol System

CONGJI ZHA
Australian Photonics Cooperative Research Centre, Optical Fibre Technology Centre, The University of Sydney, Australian Technology Park, Eveleigh, NSW 1430, Australia; and School of Chemistry, The University of Sydney, NSW 2006, Australia

G.R. ATKINS
Australian Photonics Cooperative Research Centre, Optical Fibre Technology Centre, The University of Sydney, Australian Technology Park, Eveleigh, NSW 1430, Australia

A.F. MASTERS
School of Chemistry, The University of Sydney, NSW 2006, Australia

Abstract. Hydrolysis and condensation reactions in an anhydrous sol-gel system comprising tetraethyl orthosilicate (TEOS, $Si(OC_2H_5)_4$), boric acid (H_3BO_3) and ethanol have been studied using X-ray diffraction and NMR spectroscopy, and similarities and differences with the more traditional aqueous system are discussed. Boric acid is able to hydrolyse TEOS directly, and subsequent condensation reactions form borosiloxane (=B—O—Si≡) and siloxane (≡Si—O—Si≡) linkages. In an aqueous system, borosiloxanes are unstable to hydrolysis and are formed only upon heat treatment of the gel, a restriction avoided with anhydrous conditions. The anhydrous mixture is stable indefinitely against gelation, but can be readily gelled by addition of NaOH in ethanol. This system may be useful for preparing borosilicate glasses at lower temperatures with good homogeneity.

Keywords: borosilicate sol-gel, anhydrous system, hydrolysis mechanism

1. Introduction

Although it has been known for many years that silicate glasses can be produced via sol-gel processing in the absence of water [1], only in the past five years have anhydrous systems received much attention. Such systems offer greater homogeneity in multicomponent systems with precursors of differing reactivity, such as silica/zirconia and silica/titania [2], or where hetero-linkages (M—O—M′) are unstable to hydrolysis, such as silica/phosphorus oxide [3]. Anhydrous halide/alkoxide [4] and alkoxide [5] silica systems have also been reported. In halide/alkoxide systems, oxygen bridges are produced directly with elimination of alkyl halides [2, 4], whereas in alkoxide-only systems, alkoxides are hydrolyzed by a weak acid such as oxalic acid, and oxygen bridges are formed by conventional condensation reactions [3, 5]. These alkoxide-only systems are not completely anhydrous, as water molecules produced by condensation may take part in subsequent reactions.

In aqueous borosilicate systems, borosiloxanes (=B—O—Si≡) are readily cleaved by hydrolysis, and significant incorporation of boron into the silica network occurs only when water is driven off by heating the gel to 450°C [6, 7], which is unacceptable if temperature sensitive substrates or dopants (such as optically nonlinear organic molecules) are incorporated in the system. This paper describes an anhydrous method for producing borosilicate glass at more

moderate temperatures, qualitatively similar to a phosphosilicate system [3], where Si—O—P linkages (also susceptible to hydrolysis) are produced with anhydrous phosphoric acid and TEOS.

2. Experimental

TEOS (Sigma Aldrich, 98%), ethanol (Biolab Scientific, 99.8%, <0.2% water) and boric acid (Sigma Aldrich, 99.9%) were used as received. Reactions were performed under nitrogen using standard Schlenk techniques, in a multistep process that was found to give a homogeneous product solution.

Step 1. Boric acid (2.7 g) and ethanol (5 ml) were heated to boiling (78°C) with stirring, then TEOS (10 ml) was added (whereupon the boric acid rapidly dissolved) and the mixture held at the same temperature for 30 min.

Step 2. Additional boric acid (2.7 g) was added, and the mixture heated to boiling (90°C) until the boric acid dissolved. TEOS (10 ml) was then added, and the mixture heated for a further 20 min.

Step 3. Step 2 was repeated four times, and the mixture cooled to room temperature to yield a transparent solution (**I**) containing 3.2/3.2/1 boric acid/TEOS/ethanol (by mole). Unlike aqueous silica sol-gel systems, in which condensation between hydrolyzed alkoxides usually leads to gelation, the anhydrous solution (**I**) was stable indefinitely at room temperature if protected from atmospheric moisture.

The susceptibility of borosiloxanes to hydrolysis was utilized to prepare several solid samples with variable =B—O—Si≡ contents:

(A) Addition of distilled water (1 ml) to solution (**I**) (10 ml) gave a white glue-like precipitate which was dried at 100°C to yield a white powder, solid (**A**).

(B) A sample of solid (**A**) was suspended in water for 1 h, then dried at 100°C. A white powder mixed with colorless particles was obtained, solid (**B**).

(C) Solvent was removed from the filtrate from which solid (**A**) had been separated, to yield a colorless material, solid (**C**).

(D) A NaOH/ethanol solution (1 ml, 4 wt%) was added to solution (**I**) (10 ml), and the mixture stirred for 20 min and sealed under nitrogen. A transparent gel was obtained after 20 h. The gel was dried at 100°C to yield a colorless material, solid (**D**).

(E) A powdered sample of solid (**D**) was immersed in water for 48 h, then dried at 100°C to yield solid (**E**).

^{13}C NMR spectra were obtained on a 200 MHz Bruker spectrometer. XRD data were obtained on a Siemens 5000 diffractometer with Cu Kα radiation, using silicon as an internal standard.

3. Results and Discussion

3.1. ^{13}C NMR Spectra

A proton-decoupled ^{13}C spectrum of a TEOS/boric acid/ethanol mixture after Step 1 of the sol preparation process is reproduced in Fig. 1. Resonances at approximately 57 ppm and 16 ppm (relative to TMS) are assigned to CH_2 and CH_3, respectively. A mixture of ethanol and TEOS has only two distinct CH_2 sites, and the complexity of the CH_2 signals in Fig. 1 indi-

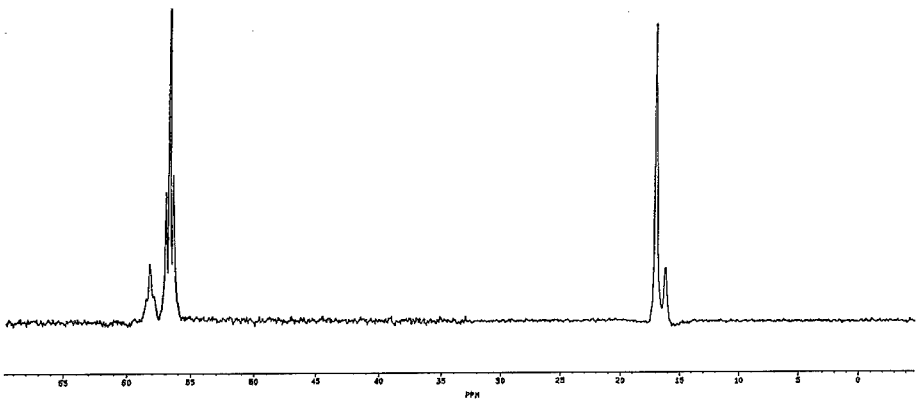

Figure 1. Proton-decoupled ^{13}C NMR spectrum of TEOS/boric acid/ethanol mixture after 30 min at 80°C.

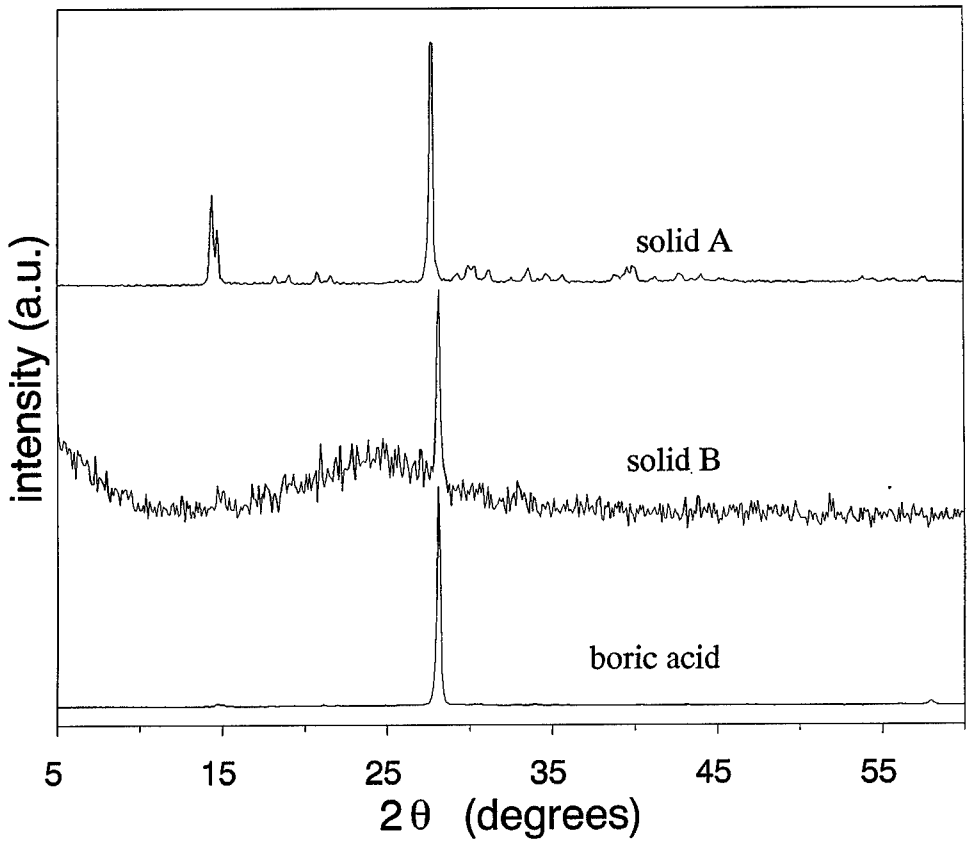

Figure 2. XRD patterns of solid (**A**), solid (**B**) and boric acid, scaled and offset for clarity.

cates that a reaction is occurring between TEOS and boric acid. ^{13}C NMR spectra on a 1 : 1 TEOS/boric acid mixture also indicated a reaction, but complete mixing could not be obtained without ethanol.

3.2. *XRD Patterns*

Figure 2 shows the XRD patterns of solids (**A**) and (**B**), with the pattern of boric acid (dominated by a strong peak at $2\theta = 28.1°$) for comparison. The resemblance between the patterns of (**A**) and boric acid suggests that a boron-rich phase was precipitated by addition of water to solution (**I**). It is hypothesized that borosiloxanes in solution (**I**) were cleaved into =B—OH and ≡Si—OH groups, and the phase with =B—OH terminal groups precipitated because of its lower solubility in ethanol. Solid (**C**), obtained from the solid (**A**) filtrate, is amorphous silica, with XRD pattern shown in Fig. 3.

Although the XRD patterns in Fig. 2 suggest that (**A**) and boric acid have similar structures, the decreased 2θ value of (**A**) (27.7° compared to 28.1°) and the different diffraction intensity distributions suggest that some silicon atoms are present in the lattice of (**A**). Since silicon has a larger ionic radius (42 pm) than boron (23 pm), incorporation of silicon into a boric acid lattice will increase the lattice plane spacing (d), thus reducing the scattering angle via the Bragg condition $n\lambda = 2d \sin\theta$. The other diffraction peaks from (**A**) are believed to arise from disruption of the planar structure of boric acid by tetrahedrally coordinated silicon atoms, implying that some of the borosiloxanes in solution (**I**) were not cleaved by the addition of water.

The hypothesis that solid (**A**) is essentially boric acid containing some silicon atoms can be verified by comparing the XRD patterns of (**A**) and (**B**). Solid (**B**) was obtained by suspending (**A**) in water, and the position of the diffraction peak ($2\theta = 28.1°$) and the occurrence of an amorphous phase (not present in (**A**)) indicate that any remaining borosiloxanes in (**A**) were cleaved by the re-hydrolysis process. The white and colorless particles in (**B**) were analyzed to be boric acid and silica, respectively.

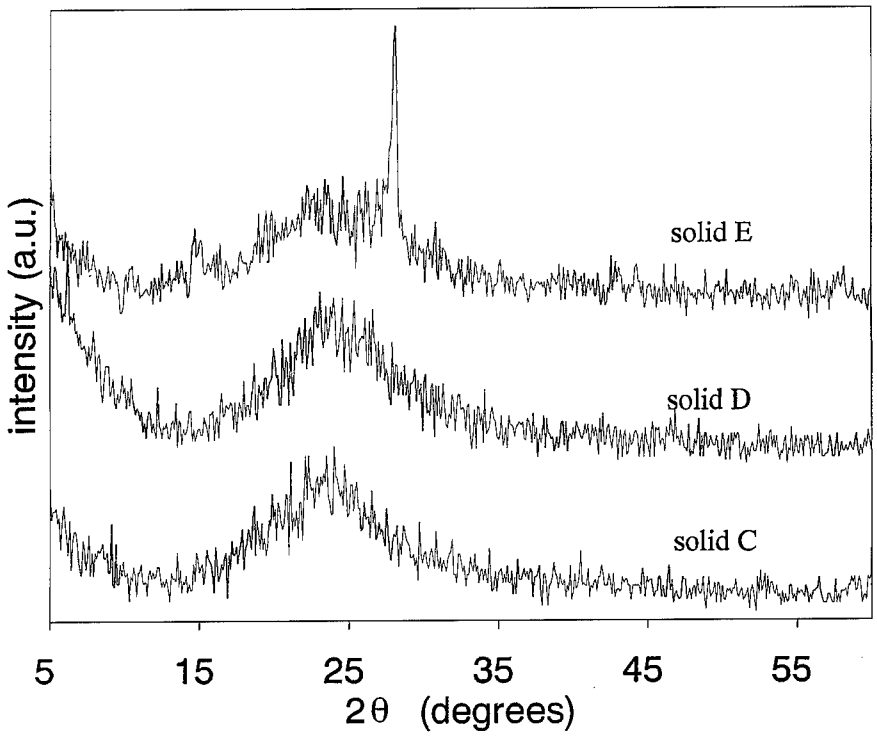

Figure 3. XRD patterns of solid (**C**), solid (**D**) and solid (**E**), scaled and offset for clarity.

In Fig. 3, the XRD patterns of solids (**D**) and (**E**), obtained by gelation of solution (**I**) with NaOH/ethanol, show that (**D**) is entirely amorphous, whereas (**E**) is partly crystalline. The amorphous nature of (**D**) indicates that boron and silicon have remained distributed after gelation, while the presence of a crystalline phase resembling boric acid ($2\theta = 28.1°$) in (**E**) suggests that some of the borosiloxanes in (**D**) were hydrolyzed to form a boron-rich phase. The low intensity of this peak and the observation that further hydrolysis of (**E**) did not increase its intensity indicate that the majority of borosiloxanes in (**D**) were stable against hydrolysis. From the diffraction peak areas, it was estimated that only 10–20% of the borosiloxanes in (**D**) were hydrolyzed, demonstrating that borosiloxanes are more resistant to hydrolysis in the gelled solid (**D**) than in solution (**I**).

3.3. *Possible Mechanisms*

Since water is absent from the initial mixture, the usual first step in a silica-based sol-gel reaction, hydrolysis of the silicon alkoxide, reaction (1), cannot occur.

$$\equiv Si(OR) + H_2O \rightarrow \equiv Si(OH) + ROH \qquad (1)$$

From the possible reactions in a silicon alkoxide/boric acid/ethanol/water system given in reference [6], the important reactions are expected to be:

$$\equiv Si{-}O{-}Et \quad H{-}O{-}B{=} \rightarrow \equiv Si{-}O{-}H{=} + {=}B{-}O{-}Et \qquad (2)$$

$$\equiv Si{-}O{-}H \quad {=}B{-}O{-}H \rightleftharpoons \equiv Si{-}O{-}B{=} + H_2O \qquad (3)$$

$$\equiv Si{-}O{-}H \quad \equiv Si{-}O{-}H \rightarrow \equiv Si{-}O{-}Si{\equiv} + H_2O \qquad (4)$$

$$\equiv Si{-}O{-}Et \quad {=}B{-}O{-}H \rightleftharpoons \equiv Si{-}O{-}B{=} + EtOH \qquad (5)$$

where (2) represents hydrolysis of TEOS by boric acid, equilibrium (3) represents a condensation reaction producing borosiloxanes, (4) represents the siloxane-producing condensation reaction, and equilibrium (5) represents the direct formation of borosiloxanes by a reaction between TEOS and boric acid; (3) and (5) are represented as equilibria because of the instability of borosiloxanes. In the initial mixture, only (2)

and (5) are possible, and the formation of silanols via (2) must be occurring for ≡Si—O—Si≡ bridges to be produced. Reaction (2) is more likely than (5) because the presence of ethanol would drive equilibrium (5) to the left, although the detection of ^{13}C signals assignable to ethanol and =B—O—Et species in a heated mixture of boric acid and TEOS suggests that both (2) and (5) are possible in the absence of ethanol.

Once silanol species have been produced by reaction (2), condensation reactions (3) and (4) can occur. Generation of water by reactions (3) and (4) does not limit borosiloxane formation, since it is consumed by hydrolysis of TEOS (reaction (1)) and the similar but more rapid hydrolysis of =B—O—Et species produced in the initiation reaction (2).

It is well established that the addition of hydroxide to a silica sol-gel mixture greatly increases the rate of silanol condensation (reaction (4)), probably via the formation of penta-coordinated silicon intermediates [8]; the initiation of gelation by adding anhydrous base to the present system is believed to be due to a similar process.

4. Conclusions

In this study, formation of borosiloxane (=B—O—Si≡) linkages in an anhydrous TEOS/boric acid/ethanol sol-gel system was investigated by XRD and NMR techniques. Following hydrolysis of TEOS by boric acid to form silanols, condensation of the silanols with each other and with boric acid forms a network of siloxane and borosiloxane linkages. The system did not gel spontaneously, but gelation could be induced by addition of a NaOH/ethanol solution, indicating that hydrolysis and gelation can be manipulated separately. Compared with aqueous systems, borosiloxanes formed in this anhydrous system have a higher resistance to hydrolysis, possibly because they are incorporated into a closed oxide network. These properties suggest that this system may be useful for improving the homogeneity of borosilicate glasses and ceramics, especially in cases where high temperatures cannot be used to drive the incorporation of boron.

Acknowledgments

The authors wish to thank the Director of the Australian Photonics Cooperative Research Centre for permission to publish this work. Zha and Atkins acknowledge the support of an AusAID scholarship and an Australian Research Council Postdoctoral Fellowship, respectively. Adam Sikorski of the Electron Microscope Unit, University of Sydney, is thanked for assistance with the X-ray diffraction measurements, and Dr. Ming Xie and Dr. Jacques Nemorin of the School of Chemistry are thanked for assistance with the NMR spectroscopy.

References

1. H. Dislich, Angewandte Chemie International Edition **10**, 363 (1971).
2. M. Andrianainarivelo, R. Corriu, D. Leclercq, P.H. Mutin, and A. Vioux, Journal of Materials Chemistry **6**, 1665 (1996).
3. C. Fernández-Lorenzo, L. Esquivias, P. Barboux, J. Maquet, and F. Taulelle, J. Non-Cryst. Solids **176**, 189 (1994).
4. R.J.P. Corriu, D. Leclercq, P. Lefèvre, P.H. Mutin, and A. Vioux, J. Non-Cryst. Solids **146**, 301 (1992).
5. Y. Sugahara, S. Sato, K. Kuroda, and C. Kato, J. Non-Cryst. Solids **147/148**, 24 (1992).
6. A.D. Irwin, J.S. Holmgren, T.W. Zerda, and J. Jonas, J. Non-Cryst. Solids **89**, 191 (1987).
7. A.D. Irwin, J.S. Holmgren, and J. Jonas, J. Non-Cryst. Solids **101**, 249 (1988).
8. L.L. Hench and J.K. West, Chemical Review **90**, 33 (1990).

Journal of Sol-Gel Science and Technology 13, 109–112 (1998)
© 1998 Kluwer Academic Publishers. Manufactured in The Netherlands.

Preparation of Inorganic Oxides via a Non-Hydrolytic Sol-Gel Route

JOHN N. HAY AND HEMA M. RAVAL
Department of Chemistry, University of Surrey, Guildford, Surrey, GU2 5XH, UK

Abstract. Inorganic oxides have been synthesized successfully under mild reaction conditions using a solvent-free non-hydrolytic sol-gel process based on the condensation reaction of "metal" chlorides with oxygen donors such as alkoxides, aldehydes and ethers. Iron(III) chloride was found to be an effective catalyst for the reactions. The order of reactivity of the halides was generally titanium > aluminium > silicon, but in some cases reaction was halted by premature gelation of intermediate species. Silica, alumina and titania were all prepared and characterized by various methods. Calcination studies on the silicas showed these materials to be amorphous up to at least 700°C, but devitrification occurred at 1000°C. Crystallization was studied by X-ray powder diffraction.

Keywords: inorganic oxide, sol-gel, non-hydrolytic, catalyst, calcination

1. Introduction

In recent years, much research activity has been aimed at the development of "soft chemistry" approaches to the synthesis of inorganic oxides. The most important of these remains the sol-gel process which, in its most common form, involves the hydrolysis and condensation of inorganic precursors such as alkoxides to produce a gel which can be converted by thermal treatment into a high purity inorganic oxide. The utility and advantages of this route have been well documented [1, 2]. The conventional hydrolytic route does, however, suffer from disadvantages associated with the use of water and the need for a compatible solvent. A non-hydrolytic approach which circumvents some of these difficulties has been developed, primarily by the group of Corriu [3–5]. In this route, a "metal" halide reacts with an oxygen donor to form the metal oxide in a thermal process. Most work to date has studied this process in solvent media, but the method is well suited to a solvent-free process [5]. Here we describe an extension of previous work to the solventless synthesis of inorganic oxides by the non-hydrolytic sol-gel route. Related work by us on binary oxides is described elsewhere [6].

2. Experimental

A Shimadzu Thermogravimetric Analyser-50 was used to determine sample weight loss over a temperature range of 25–490°C at a heating rate of 20 K min^{-1} under a nitrogen atmosphere (flow rate, 50 ml min^{-1}). A Perkin-Elmer TGA-7 interfaced with a Perkin-Elmer 7700 computer was used to measure sample weight loss over a temperature range of 40–900°C at a heating rate of 10 K min^{-1} under a nitrogen atmosphere with a flow rate of 50 ml min^{-1}. Calcinations were carried out in a Lenton UAF 16/21 furnace. An SMC 24127 calibrated digital K-type thermometer was used to control heating rates to ±5°C and the sample was contained in a mullite tube during the heating run. A Siemens D500 X-ray Diffractometer was used to determine sample morphology. Samples were ground into fine powders before being scanned with CuKα radiation at 40 kV 40 mA from 15 to 70° 2θ, with a step size of 0.02° and a count time per step of 10 s. Surface morphology and evidence of any microporosity in gold or carbon coated samples were evaluated using a CAMSCAM S4 Field Emission Scanning Electron Microscope with an accelerating voltage of 5 kV for the Secondary Electron Imaging (SEI) and 20 kV for

Table 1. Results of non-hydrolytic silica forming sol-gel reactions.

% by weight $FeCl_3$ catalyst	Gel-time and temperature	Yield (%)	Weight loss (%)[a]	Weight loss (%)[b]
1.0	5 min @ 90°C	104	—	15
0.8	20 min @ 90°C	117	21	16
0.4	60 min @ 90°C	93	19	14
0.2	70 min @ 90°C	105	18	11
0.8	20 min @ 110°C	107	19	15
0.8	45 min @ 60°C	100	22	11
0.8	4–24 h @ 40°C	105	17	14

[a]TGA weight loss between 40 and 900°C.
[b]TGA weight loss between 35 and 490°C.

the Energy Dispersive X-ray (EDX) analyses. EDX spectra were acquired from a number of areas to determine the elemental composition of the sample. Diffuse Reflectance Fourier Transform Infra-red (IR) spectra were recorded on a Perkin-Elmer 1750 FT-IR Spectrophotometer. Abbreviations used to describe peaks are as follows: vs = very strong; s = strong; m = medium; w = weak; vw = very weak; sp = sharp; b = broad; sh = shoulder.

Materials were either used as received or dried by standard methods before use. The synthesis of the inorganic oxides is illustrated by the following example. Silica syntheses are summarized in Table 1. Equimolar amounts of silicon tetrachloride (4.00 g, 2.70 cm^3, 0.024 mol) and tetraethylorthosilicate (TEOS) (4.91 g, 5.25 cm^3, 0.024 mol) were heated with ca. 0.8% by weight of iron(III) chloride catalyst (0.069 g, 0.77%) for 20 min at 90°C. The resulting dark brown monolith was washed in diethylether and the product dried in vacuo at 160°C for 3 days (117% yield, 3.30 g). The product showed a 21% weight loss by thermogravimetric analysis (TGA). The IR spectrum showed absorptions at ν_{max} (cm^{-1}): ~3500 (b, s), ~3000 (sp, m), 1630 (sp, m), 1220 (sp, vs), 1160 (m), 950 (m), 810 (m) and 525 (s). X-Ray diffraction (XRD) analysis produced a very broad peak at the low angle end of the scan indicating an amorphous material exhibiting some short-range order. The amorphous product was heated in air to 1000°C for 24 hours (25% weight loss) to leave a fine, matt-brown colored powder. XRD analysis suggested a large proportion of the sample had crystallized. A good fit was achieved with two types of silica phases—hexagonal quartz and tetragonal cristobalite. The IR spectrum exhibited absorptions at ν_{max} (cm^{-1}): ~2000 (b,vw), 1880 (w), 1620 (w), 1370 (sp, vs), 1200 (b, vw), 1030 (b, w), 814 (m), 616 (m), 570 (m) and 450 (vw).

3. Results and Discussion

Although the use of the non-hydrolytic sol-gel process for the preparation of inorganic oxides has been studied extensively recently by Corriu et al. [3–5], at the outset of this work little had been reported on the solvent-free synthesis of oxides by this route. In addition, most literature reports had used autogenous pressure in sealed tube systems. In the present work we proposed to extend these studies to ambient pressure (nitrogen) work on neat, solvent-free systems which were more practical for our ultimate aims. The oxides studied were silica, alumina and titania. At an early stage, it was realized that a catalyst was required to increase reactivity in many systems and, consequently, the Lewis acid catalyst iron(III) chloride was used, although this has not been utilized extensively in sol-gel systems [5, 7]. All reactions were carried out in the absence of solvent unless stated otherwise.

3.1. Silica

Our studies have confirmed earlier work by Corriu et al. [3, 7] that silicon tetrachloride is relatively unreactive towards diethylether, isopropylether and THF. In contrast to work by Zappel [8] and Corriu [4], but in agreement with that of Rochow and Gingold [9], benzaldehyde was found to be unreactive towards silicon tetrachloride after 8 days at 110°C; however, a catalytic amount of iron(III) chloride allowed this reaction to proceed and a black monolith was formed in ca. 45 min at 100°C. The apparent discrepancy with Corriu's work (gelation in 2 days at 110°C), could be accounted for by their use of a sealed tube which could generate an internal pressure providing more favorable reaction conditions.

A series of experiments was carried out to study the effect of catalyst level and reaction temperature on the reaction between silicon tetrachloride and TEOS. Earlier studies by Corriu et al. [7] found silicon tetrachloride to be unreactive towards TEOS, but silica could be obtained in the presence of a catalyst [10].

$$SiCl_4 + Si(OC_2H_5)_4 \xrightarrow{FeCl_3} 2SiO_2 + 4C_2H_5Cl$$

As the catalyst loading was reduced, gel-times increased as expected. IR analyses indicated production

of siloxane (Si—O—Si) vibration bands [2, 11, 12] at ~1220 (sp, vs), 1080 (m), 950 (m), 810 (m) and 525 cm^{-1} (s). The high yields, TGA results and IR spectra suggested the presence of unreacted precursors and/or trapped by-product, also indicated by a strong hydrogen chloride smell even after washing. The weight loss between 40 and 150°C probably arises from the evaporation of residual free organics. A larger weight loss observed between 300 and 450°C may arise from further condensation and/or thermal degradation of residual bound organics. As the catalyst loading was reduced, the weight loss due to residual organics was also reduced, but precise reasons for this are not known. Similar results were found in the study of the effect of reaction temperature on the sol-gel synthesis. As the reaction temperature was reduced, gel times increased, but there was no clear pattern in the weight loss figures. On the basis of these results it was concluded that a catalyst level of 0.8% by weight iron(III) chloride at 90°C reaction temperature offered the best balance between fast reaction and sufficient time to homogenize the reacting species.

XRD analysis before calcination of the 90°C/0.8% catalyst system showed a very broad peak at the low angle end of the scan, indicative of an amorphous material exhibiting some short-range order. EDX showed that the bulk of the surface appeared to be homogeneous with the silicon-to-oxygen ratio remaining relatively constant throughout. Both this system and the 1% catalyst system were calcined to investigate crystallization. The 1% catalyst system remained amorphous after 18 hours at 700°C, but crystallized to a mixture of hexagonal quartz and tetragonal cristobalite after a further 18 hours at 1000°C, although some vitreous silica was still present. The 0.8% catalyst system was crystallized directly to a mixture of quartz and cristobalite after 24 hours at 1000ºC. A temperature of 700°C is obviously too low for silica devitrification to occur and a further 18 hours at 1000°C failed to devitrify the silica completely. Increasing the calcination time to 24 hours increased the proportion of crystalline phase as a mixture of quartz and α-cristobalite, but this could not be quantified. No β-cristobalite was detected. The IR spectra after calcination showed that the strongest silica peaks normally found [2, 11, 13] at ~1220 and 950 cm^{-1} had shifted to slightly higher frequencies of 1370 and 1030 cm^{-1}, respectively, perhaps as a result of crystallization. The IR absorption band at ~618 cm^{-1}, characteristic of α-cristobalite [14, 15] has become clearer and sharper.

3.2. *Alumina*

A number of non-hydrolytic sol-gel alumina systems were investigated using aluminium trichloride at a molar ratio of 2:3 with the oxygen donor. Benzaldehyde reacted with aluminium trichloride to form a dark brown monolith in the absence of a catalyst, but a poor yield (27%) was obtained and TGA showed a weight loss of 22%, indicating incomplete reaction. IR analysis confirmed that an oxide had been formed.

$$2AlCl_3 + 3PhCHO \rightarrow Al_2O_3 + 3PhCHCl_2$$

Aluminium trichloride was found to be unreactive towards THF and diethylether in the absence of a catalyst, but addition of 1% iron(III) chloride produced a black solid in less than 24 hours at 110°C with THF, reflecting the higher reactivity of aluminium compared to that of silicon. The IR spectrum indicated alumina formation by the presence of absorption bands at 1100 and 800 cm^{-1} correlating to Al—O vibrations [16]; however, a poor yield (39%) was obtained and a large weight loss (54%) was observed by TGA.

Initial stoichiometric reaction of diisopropylether with aluminium trichloride in the absence of a catalyst gave a gel which dissolved in acetone on washing, perhaps because of formation of organochloroaluminates. In the presence of dichloromethane as solvent, a dark brown monolith was formed (cf. results of Corriu et al. [7, 17] in sealed tube experiments). The IR spectrum indicated the presence of alumina. This apparently surprising result may arise from premature solidification of intermediate species in the neat reaction, with consequent loss of mobility and reactivity.

3.3. *Titania*

Titania synthesis was evaluated using titanium tetrachloride with a number of oxygen donors. Since most of these reaction systems have been studied previously [5], the main interest was in assessing the effect of using an "open" reaction vessel instead of a sealed tube. The higher reactivity of titanium compared to that of silicon and aluminium was reflected in the results. Titanium tetrachloride is a powerful Lewis acid catalyst [5] and so no additional catalyst was required.

The reaction of titanium halide and benzaldehyde gave a dark brown-black monolith, which fumed when exposed to air, implying the presence of either

unreacted precursor, a reactive by-product or an intermediate product such as an organochlorotitanate. An exothermic reaction involving several color changes took place when the product was washed with acetone. Given that silicon tetrachloride reacts with benzaldehyde in the presence of a catalyst to form silica and aluminium trichloride forms an oxide with the same oxygen donor in the absence of a catalyst, the apparent lack of reactivity of titanium tetrachloride is surprising. This may, however, be another example of premature solidification of intermediates which would require higher reaction temperatures to melt and allow the reaction to proceed further. This reaction was not pursued further.

The final two reactions studied involved the etherolysis of titanium tetrachloride and gave results comparable to those of Corriu et al. [3]. The initial product from the diisopropylether reaction (apparent gelation in 6 hours at 110°C) was soluble in ethanol, but after drying at 150°C for 3 days in vacuo became insoluble. The drying process clearly completes the reaction in this case. In the case of both diisopropyl- and diethylether, yields were high (>90%) and TGA weight losses low (<16%) and IR analyses showed titania formation with Ti—O vibration bands [18] at 975 (sp, vs), 750 (b, sh, m) and 440 cm^{-1} (w).

4. Conclusions

The non-hydrolytic sol-gel route provides a practical route to inorganic oxides in solvent-free systems in an "open" reaction vessel. Iron(III) chloride is an effective Lewis acid catalyst for accelerating the reaction in sluggish cases. In general, the order of reactivity of the chlorides is titanium > aluminium > silicon. In some cases, however, complications arise from the formation of solid intermediate products which require elevated temperatures to convert further to the oxide.

Acknowledgment

The authors thank EPSRC and the Defence Evaluation and Research Agency (DERA) for award of a CASE studentship (to HR).

References

1. C.L. Bird and A.T. Kuhn, Chem. Soc. Rev. **10**, 49 (1981).
2. C.J. Brinker and G.W. Scherer, *The Physics and Chemistry of Sol-Gel Processing* (Academic Press Inc., San Diego, 1990).
3. P. Arnal, R.J.P. Corriu, D. Leclercq, P.H. Mutin, and A. Vioux, Mat. Res. Soc. Symp. Proc. **346**, 339 (1994).
4. R.J.P. Corriu, D. Leclercq, P. Lefèvre, P.H. Mutin, and A. Vioux, J. Non-Cryst. Solids **146**, 301 (1992).
5. P. Arnal, R.J.P. Corriu, D. Leclercq, P.H. Mutin, and A. Vioux, J. Mater. Chem. **6**, 1925 (1996).
6. J.N. Hay and H.M. Raval, submitted to J. Mater. Chem.
7. S. Acosta, P. Arnal, R.J.P. Corriu, D. Leclercq, P.H. Mutin, and A. Vioux, Mat. Res. Soc. Symp. Proc. **346**, 43 (1994).
8. A. Zappel, J. Am. Chem. Soc. **77**, 4228 (1955), and references therein.
9. E.G. Rochow and K. Gingold, J. Am. Chem. Soc. **76**, 4852 (1954).
10. L. Bourget, R.J.P. Corriu, D. Leclercq, P.H. Mutin, and A. Vioux, in *First European Workshop on Hybrid Organic-Inorganic Materials*, edited by C. Sanchez and F. Ribot (Paris, 1993), p. 308.
11. A.L. Smith (Ed.), *Analysis of Silicones* (Wiley-Interscience, New York, 1974).
12. R.K. Iler, *The Chemistry of Silica* (Wiley, New York, 1979).
13. R.B. Sosman, *The Phases of Silica* (Rutger University Press, New Jersey, 1965).
14. M.A. Saltzberg, S.L. Bors, H. Bergna, and S.C. Winchester, J. Amer. Ceram. Soc. **75**, 89 (1992).
15. L. Qi, J. Ma, H. Cheng, and Z. Zhao, J. Mater. Sci. Lett. **15**, 1074 (1996).
16. T. López, M. Asomosa, L. Razo, and R. Gómez, J. Non-Cryst. Solids **108**, 45 (1989).
17. S. Acosta, R.J.P. Corriu, D. Leclercq, P. Lefèvre, P.H. Mutin, and A Vioux, J. Non-Cryst. Solids **170**, 234 (1994).
18. M. Schraml-Marth, K.L. Walther, and A. Wokaun, J. Non-Cryst. Solids **143**, 93 (1992).

Journal of Sol-Gel Science and Technology 13, 113–118 (1998)
© 1998 Kluwer Academic Publishers. Manufactured in The Netherlands.

The Structure of Multicomponent (Titania/Zirconia) Nanoparticles

J.R. BARTLETT
Materials Division, Australian Nuclear Science and Technology Organisation, Private Mail Bag 1, Menai, N.S.W., 2234 Australia

D. GAZEAU AND TH. ZEMB
Service de Chimie Moléculaire, CEA, CE Saclay, 91191 Gif sur Yvette Cedex, France

J.L. WOOLFREY
Materials Division, Australian Nuclear Science and Technology Organisation, Private Mail Bag 1, Menai, N.S.W., 2234 Australia

Abstract. The local structure of titania/zirconia nanoparticles has been investigated using small-angle neutron scattering (SANS). The colloids were prepared either by hydrolyzing a mixture of titanium and zirconium alkoxides, and peptizing the resulting hydrolyzate with nitric acid (homogeneous) or hydrolyzing a titanium alkoxide, and peptizing the hydrolysate with zirconium(IV) nitrate (heterogeneous). The final titania/zirconia and metal oxide/nitrate mole ratios were 16.0 and 10.0, respectively. The nanoparticles were crystalline anatase (crystallite size ca.8 nm) and amorphous zirconia.

The results of SANS contrast-variation experiments are described. The minimum-contrast points for the homogeneous and heterogeneous colloids, determined using either the known analytic form of the scattering at $q = 0$ or the scattering invariant, gave similar results. Significant differences from the expected value were attributed to the sorption of nitrate counter-ions and hydroxyl species on the surface of the colloids. In both cases, the scattering at minimum contrast was consistent with a fractal network of uni-dimensional zirconia, with a typical diameter of ~1.5 nm. The results indicate that in the homogeneous colloids, the zirconia is segregated within the matrix of the titania crystallites (on ~1 nm scale), whereas in the heterogeneous colloids, the zirconia is segregated on the surface of the titania crystallites (on ~10 nm scale).

Keywords: SANS, nanoparticles, titania, zirconia, mixed oxide colloids

1. Introduction

The demand for ceramics with high purity, homogeneity and well-controlled, tailored properties has led to a renewed interest in sol-gel technology [1] to prepare colloidal nanoparticles. An inherent advantage in using a sol-gel process for the preparation of multicomponent particles is that mixing in the system occurs on a molecular, or at least nanometer, scale. In the preparation of multicomponent particles, it is essential to promote rapid co-hydrolysis of mixed precursor alkoxides, to obtain a homogeneous distribution of the components. However, this is not always possible due to the constraints of chemistry and cost.

In the present study, TiO_2/ZrO_2 nanoparticles were prepared by two different methods:

- hydrolyzing a mixture of titanium and zirconium alkoxides, and peptizing the resulting hydrolysate with nitric acid (homogeneous);
- hydrolyzing a titanium alkoxide, and peptizing the resulting hydrolyzate with aqueous zirconium(IV) nitrate (heterogeneous).

While co-hydrolysis of mixed alkoxides is to ensure homogeneity on a molecular scale, in the case of systems containing zirconia, the alkoxide precursors are very expensive. Alternatively, the hydrolysate of one of the materials (in this case titania) can be peptized with a hydrolyzable inorganic salts of the other component (in this case zirconium(IV) nitrate), e.g.,

$$xZr^{4+} + mH_2O \rightleftharpoons [Zr_x(OH)_m]^{(4x-m)+} + mH^+ \quad (1)$$

Such an approach leads to heterogeneous particles, that are no longer homogeneous on a molecular scale, but provides much cheaper materials.

This study investigates the differences in "homogeneity" and structure of ZrO_2 in TiO_2/ZrO_2 colloids prepared by the two different methods, using small-angle neutron scattering (SANS).

2. Experimental

Sol Preparation

TiO_2/ZrO_2 sols, with Ti : Zr and $[NO_3]^-$: (Ti + Zr) mole ratios of 16.0 and 0.10, respectively, were prepared as follows:

Homogeneous sol. Appropriate quantities of tetra-isopropyltitanate (TPT) and tetrabutyl-zirconate (TBZ) were mixed and rapidly added to a large excess of water (40 moles of H_2O per mole of alkoxide). The resulting hydrolysate was thoroughly washed with demineralized water, and peptized at 45°C with dilute nitric acid.

Heterogeneous sol. TPT was hydrolyzed and washed as above, and then peptized with an acidic zirconia sol at 45°C.

The sols were dried under ambient conditions, and the resulting gels re-dispersed in pure H_2O or pure D_2O, yielding stock solutions containing 5 vol% oxide. Homogeneous or heterogeneous sols containing 5 vol% oxide and 0 to 96 vol% D_2O-in-H_2O were subsequently obtained by mixing appropriate quantities of the stock solutions.

Characterization

SANS experiments were undertaken using the PAXE spectrometer at the Laboratoire Leon Brouillon, and are as detailed elsewhere [2]; the effective q range investigated was 6×10^{-3} to 6×10^{-1} Å^{-1}. The samples were held in 1 mm quartz cuvettes during analysis, and scattering intensities were normalized and scaled against the scattering of pure H_2O ($10/4\pi$ cm^{-1}) [3]. The densities of the sols were measured at 20.0 ± 0.1°C using a PAAR DMA 60 densitometer, equipped with a DMA 602 cell. The molecular volumes of the scattering species, Table 1, were calculated from their respective densities and molecular weights [4].

Table 1. Scattering parameters of species in the homogeneous and heterogeneous TiO_2/ZrO_2 sols.

Species	Scattering length (10^{-12} cm)	Density (g/cm^3)	Molecular volume (10^{-23} cm^3)	vol% D_2O in solvent phase to extinguish scattering
H_2O	−1.677	0.998	2.998	
D_2O	19.15	1.105	3.009	
TiO_2	8.172	3.84	3.454	42.1
ZrO_2	18.77	5.6	3.654	82.0
$[NO_3]^-$	26.68		4.900	86.4
$(TiO_2)_{0.94}(ZrO_2)_{0.06}$	8.797	3.95	3.466	44.6
$(TiO_2)_{0.88}(ZrO_2)_{0.06}(HNO_3)_{0.07}$				48.4
$(Ti_{0.88}Zr_{0.06})O_{1.975}(OH)_{0.09}(HNO_3)_{0.07}$				49.4
Homogeneous colloids				50[a]
Homogeneous colloids				52[b]
Heterogeneous colloids				49[a]
Heterogeneous colloids				51[b]

[a]Minimum-contrast point calculated using the Invariant method.
[b]Minimum-contrast point calculated using the Guinier method.

3. Results and Discussion

FT-Raman spectra of the sols, and XRD powder patterns from the gels, showed that the materials were crystalline anatase and amorphous zirconia. The TiO_2 crystallite size, measured by TEM, XRD line broadening and Guinier plots, was ca. 8 nm [2].

Contrast Variation and Determination of Minimum-Contrast Point

In the SANS contrast-variation experiment, scattering from the particles is investigated at different D_2O/H_2O volume ratios, to determine the ratio at which a minimum in the scattering intensity is observed. This minimum is generally determined by plotting the square root of the intensity at $q=0$ (I_0, obtained from a Guinier plot) against the volume fraction of D_2O. In the absence of long-range interactions, the intensity of scattering can be approximated by [5]

$$I(q) = \frac{I_0}{I^n} e^{-q^2 d^2}. \qquad (2)$$

The value of I_0 can be obtained from a plot of $\log\{I(q) \cdot q^n\}$ against q^2. Here, d is a characteristic dimension of the scattering species (e.g., radius-of-gyration of the crystallite or its cross section), and n is dependent on the geometry of the scattering species. Three cases are classically considered; globular particles ($n=0$), needle-like particles ($n=1$) and platelets ($n=2$). In the present study, the scattering diverged significantly from these standard models for both the homogeneous and heterogeneous sols at low q. However, an excellent linear fit was obtained when n was set equal to the fractal dimension of the scattering species, yielding an apparent minimum contrast at 50 ± 2 vol% D_2O for both sols. The validity of this novel approach, which involves dividing the scattering intensity by the dimensionality (following Teixeira [6]), has been discussed elsewhere [2].

An alternative method for locating the minimum-contrast point involves plotting the square root of the scattering invariant (Δ) as a function of the D_2O volume fraction [7]:

$$\Delta = \int_{q_{\min}}^{q_{\max}} I(q) q^2 \, dq. \qquad (3)$$

Both the invariant and Guinier extrapolations methods yield comparable minimum-contrast points for the homogeneous and heterogeneous colloids, Table 1. Identical minimum-contrast points would be expected due to their identical bulk compositions.

The measured minimum-contrast point (50 ± 2 vol% D_2O) is significantly different to that calculated for scattering from pure $(TiO_2)_{0.04}(ZrO_2)_{0.06}$ (44.6%), Table 1. Two factors contribute to this apparent discrepancy:

- Conductivity measurements indicate that ~70% of the HNO_3 initially added during peptization is sorbed on the $(TiO_2)_{0.94}(ZrO_2)_{0.06}$ particles. The calculated minimum-contrast point for such a colloid (i.e., $(TiO_2)_{0.88}(ZrO_2)_{0.06}(HNO_3)_{0.07}$) is 49.4% D_2O;
- Titration of the homogeneous gels with NaOH revealed that they also contained 0.05 moles of acidic-hydroxyl species per mole of $(TiO_2)_{0.94}(ZrO_2)_{0.06}$. The minimum-contrast point calculated for the hydroxylated colloid (i.e., $(Ti_{0.88}Zr_{0.06})O_{1.975}(OH)_{0.05}(HNO_3)_{0.07}$) is 48.9% D_2O, Table 1, in excellent agreement with the measured values for both the homogeneous and heterogeneous sols.

It is evident that sorbed species (such as nitrate anions) and surface hydroxyls can significantly influence the value of the minimum-contrast point in metal oxide colloids, which typically exhibit high solid/solution interfacial surface areas (and correspondingly high sorption capacities). To our knowledge, this is the first report of such effects in metal oxide systems.

Scattering at Minimum Contrast

The intensity of the residual scattering from the heterogeneous sol under minimum-contrast conditions, as a function of q, is illustrated in Fig. 1. Since the predicted intensity of scattering from the 8 nm TiO_2/HNO_3 crystallites is negligible under these conditions [2], the complex multicomponent scattering problem [8] is reduced to a simple two-component system (i.e., ZrO_2 and solvent). Hence, the residual scattering from the heterogeneous colloids was modelled using discrete ZrO_2 lamellae, spheres, and "infinite" cylinders, with the appropriate volume fraction and contrast for ZrO_2, Fig. 1:

- The lamella model provided a very poor fit to the experimental data, regardless of the thickness chosen, and can be rejected immediately;

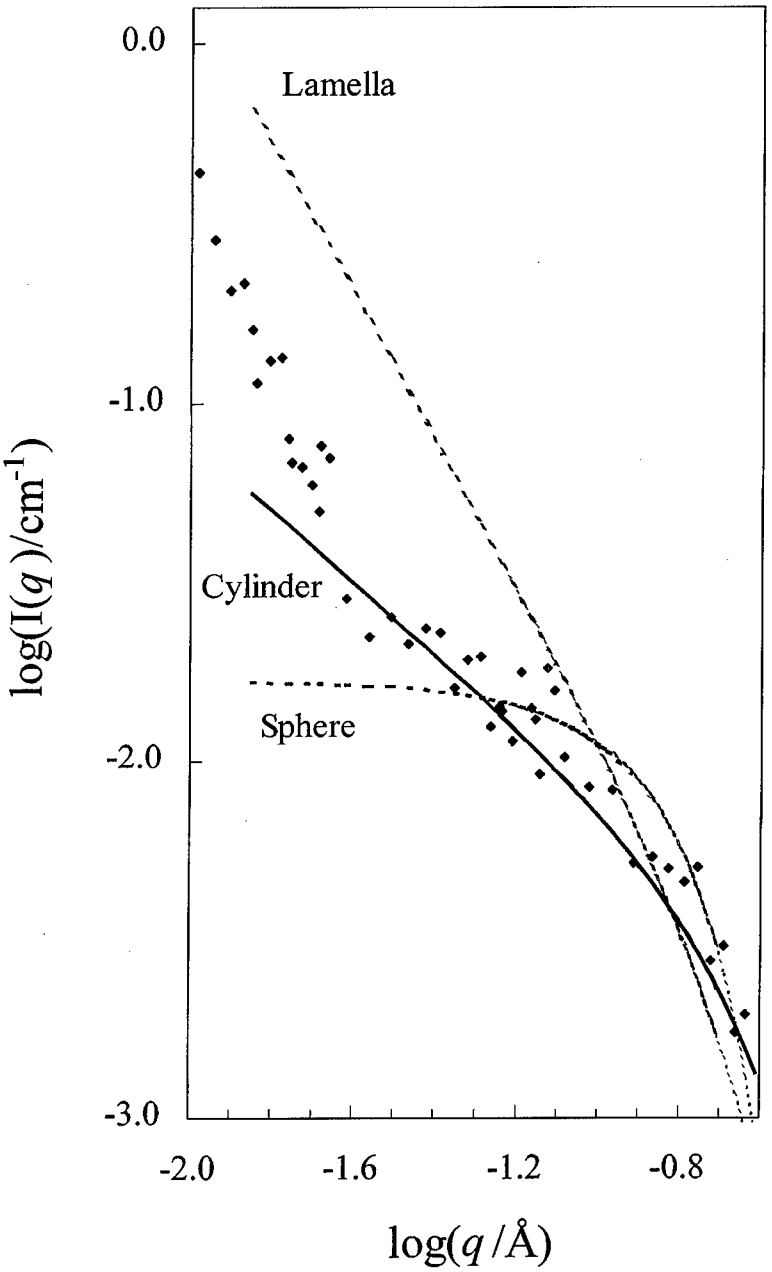

Figure 1. Variations in scattering intensity (I/cm^{-1}) with scattering wave vector (q/Å^{-1}) for heterogeneous TiO_2/ZrO_2 sols at the minimum-contrast point, modelled with ZrO_2 cylinders (radius 7.5 Å), spheres (radius 15 Å) and lamellae (thickness 7.5 Å).

- A better fit was obtained using spheres with a diameter of 15 to 30 Å, although significant differences are still evident;
- "Infinite" cylinders, with a diameter of 15 to 20 Å provided a very good fit to the data.

These data suggest that the residual scattering observed under minimum-contrast conditions, within the q range 10^{-1} to 10^{-2} Å^{-1}, is due to the presence of a network of ZrO_2 cylinders, with a diameter of 15 to 20 Å. Previous TEM studies of ZrO_2 particles produced

by forced hydrolysis of Zr(IV) salt solutions, and associated formation and polymerization of tetrameric $[Zr_4(OH)_8(H_2O)_{16}]^{8+}$ species, revealed similar dimensions in such systems [9].

It would be anticipated that a population of such small particles would exhibit a very low potential-energy barrier to aggregation [10]. This suggests that either the zirconia species would rapidly be sorbed on the surface of the larger titania crystallites, or would initially aggregate in solution to produce larger zirconia species. Modelling studies of the effect of unconstrained aggregation of such zirconia cylinders on the scattering intensity [2] demonstrate that the least-squares difference between the experimentally-observed scattering intensity and the model data increases significantly with increasing cylinder (or sphere) radius. The results suggest that the zirconia forms a fractal network of high aspect-ratio species, with an apparent radius of ~7.5 Å, on the surface of the larger (8 nm) titania crystallites.

The presence of a fractal network of zirconia cylinders on the surface of a titania core is also evident from the scattering behavior of the heterogeneous system under full-contrast conditions at high-q [2]:

- In pure H_2O, where $(\rho_{solvent} - \rho_{colloids})^2 \gg 0$, the scattering contains contributions from both titania and zirconia. Under such conditions, the scattering species (titania/zirconia) exhibit an apparent fractal dimension of 2.4 ± 0.02 [2];
- In D_2O/H_2O mixtures containing >80 vol% D_2O, the scattering from zirconia is essentially extinguished, Table 1. Under these conditions, the scattering species (titania) exhibit an apparent fractal dimension of 2.2 ± 0.02, consistent with a more loosely packed structure (since zirconia species filling the voids between titania crystallites are not detected) [2].

Under minimum-contrast conditions, the homogeneous colloids exhibited similar scattering behavior to that of the heterogeneous particles [2], suggesting that they also contain a fractal network of high aspect-ratio zirconia cylinders. This suggests that segregation also occurs during hydrolysis of the mixed TPT/TBZ alkoxide, leading to formation of a discrete zirconia network. However, the apparent fractal dimension of the homogeneous colloids did not change, and was 1.6 for all solvent compositions well removed from the minimum-contrast point [2]. This indicates that the zirconia particles are not located on the surface of the titania crystallites, but are distributed within the interior of the titania crystallite matrix.

Thus, segregation occurred even during hydrolysis of the mixed TPT/TBZ alkoxides, presumably due to the different rates of hydrolysis of the component alkoxides, but the zirconia particles were distributed within the interior of the titania crystallite matrix on ~1 nm scale. DLVO theory suggests that a relatively low barrier-to-aggregation would exist between the small TiO_2 and ZrO_2 particles initially produced in the homogeneous system, leading to rapid coagulation [11], and associated incorporation of the small ZrO_2 particles into the TiO_2 crystallite. This segregation could be minimized by using alkoxides based on the same alcohol (e.g., titanium and zirconium butoxides), which should hydrolyze at similar rates producing (Ti, Zr)O_2 species, rather than discrete TiO_2 and ZrO_2 particles.

4. Conclusions

The structure of titania/zirconia colloids has been investigated using small-angle neutron scattering (SANS). The colloids were prepared either by hydrolyzing a mixture of titanium and zirconium alkoxides, and peptizing the resulting hydrolyzate with nitric acid (homogeneous) or hydrolyzing a titanium alkoxide, and peptizing the hydrolyzate with zirconium(IV) nitrate (heterogeneous).

1. SANS contrast-variation experiments showed that the points of minimum contrast for the homogeneous and heterogeneous colloids differed significantly from the expected value, due to the sorption of nitrate counter-ions and hydroxyl species on the surface of the colloids.
2. In both cases, the scattering at minimum contrast was consistent with a fractal network of uni-dimensional zirconia (i.e., an open, chain-like aggregate structure) with a diameter of ~1.5 nm.
3. In the homogeneous colloids, the zirconia is segregated within the matrix of the 8 nm titania crystallites (on ~1 nm scale), whereas in the heterogeneous colloids, the zirconia is segregated on the surface of the crystallites (on ~10 nm scale).

References

1. In *Better Ceramics Through Chemistry I-VI*, Mater. Res. Soc. Proc. **32**, **73**, **121**, **180**, **271**, Mater. Res. Soc. Pittsburgh, Pennsylvania (1984, 1986, 1988, 1990, 1992, 1994).
2. J.R. Bartlett, D. Gazeau, Th. Zemb, and J.L. Woolfrey, Langmuir, (1997). To appear.
3. B. Jacrot and G. Zaccai, Biopolymers **20**, 2413 (1981).
4. *CRC Handbook of Chemistry and Physics*, 74th edition, edited by R.C. Weast (CRC Press, Inc., Boca Raton, FL, 1994).
5. A. Guinier and G. Fournet, *Small Angle X-Ray Scattering* (John Wiley and Sons, London, 1955), p. 25.
6. J. Teixeira, in *On Growth and Form*, edited by H.E. Stanley and N. Ostrowsky (Nijhoff, Dordrecht, 1986), p. 145.
7. H.B. Stuhrmann and A. Miller, J. Appl. Cryst. **11**, 325 (1978).
8. G. Beaucage, J. Appl. Cryst. **28**, 717 (1995).
9. A. Bleier and R.M. Cannon, in *Better Ceramics Through Chemistry II, Mater. Res. Soc. Proc., Vol. 73*, edited by C.J. Brinker et al. (Mater. Res. Soc. Pittsburgh, PA, 1986), p. 71.
10. J.R. Bartlett and J.L. Woolfrey, in *Better Ceramics Through Chemistry V, Mater. Res. Soc. Proc., Vol. 271*, edited by M. Hampden-Smith et al. (Mater. Res. Soc. Pittsburgh, PA, 1992), p. 309.
11. E.J.W. Verwey and J.Th. Overbeek, *Theory of Lyophobic Colloids* (Elsevier, Amsterdam, 1948).

Journal of Sol-Gel Science and Technology 13, 119–124 (1998)
© 1998 Kluwer Academic Publishers. Manufactured in The Netherlands.

Mechanism of Hydrothermal Synthesis of Zircon in a Fluoride Medium

RÉMI VALERO, BERNARD DURAND AND JEAN-LOUIS GUTH
Laboratoire de Matériaux Minéraux, URA 428 ENSCMu, 3 Rue Alfred Werner, 68093 Mulhouse Cedex

THIERRY CHOPIN
Centre de Recherches Rhône-Poulenc, 52 rue de la Haie Coq, 93308 Aubervilliers

Abstract. The hydrothermal synthesis of zircon in a fluoride medium leads principally to two kinds of zircons, differentiated by their morphology, chemical composition, thermal stability and solubility. Differences in the thermodynamic parameters of solution (pH, temperature, $[F^-]$) could explain the formation of these two kinds of zircons. The main hypothesis involves two crystallization mechanisms. Both include a step of gel dissolution with formation of soluble species that are responsible for the crystallization. In each case, the silicon species seem to be monomeric without fluorine. However, the nature of soluble zirconium species depends on the thermodynamic parameters of the solution. At acid pH and with fluoride ions, the reactive species for the crystallization seem to be fluoride rich zirconium complexes. In this case, the zircon obtained contains a large amount of fluoride presumably located in silicon sites (Zircon A). At basic pH, and whatever the concentration of fluoride, the reactive species for crystallization seems to be linear polymeric entities. In this case, the zircon obtained shows a typical morphology in the form of layered agglomerates and a high specific surface area (Zircon B).

Keywords: hydrothermal synthesis, zircon, crystallization mechanism, fluoride medium

Introduction

Caruba and Turco [1] previously obtained a fluoride-containing zircon by hydrothermal synthesis in acid fluoride media. More generally Colette and Frondel [2] proved that fluoride ions speed up the crystallization of zircon.

This paper is concerned with the influence of pH on the structure, morphology and chemical composition of zircons prepared by hydrothermal synthesis in a fluoride medium. Hypotheses concerning the mechanism of crystallization are proposed.

Experimental

Hydrothermal syntheses were performed in an autoclave at 150°C for 144 hours, under autogenous pressure. Precursors of dissolved reactive species were hydrous zirconia gel and amorphous silica. The hydrothermal medium was characterized by the following ratios: $F/(Si + Zr) = 1$, $Si/Zr = 1$ and $(Si + Zr)/H_2O = 2522$. XRD analysis was performed using a Philips PW 1800 diffractometer, and the lattice parameter calculation involved the Rietveld refinement.

Synthesis at Acidic pH

Synthesis was carried out at an initial pH of 2.5 and no significant pH change occurred during the thermal treatment. XRD analysis of the powder obtained (sample 1) lead to a diffractogram with peak intensities quite different from those of classical zircon (natural or solid-state reacted) (Fig. 1).

A small shift was also noticed in peak position leading to the following differences of tetragonal lattice parameters: sample 1: $a = 6.640$ Å $c = 5.926$ Å, natural $a = 6.616$ Å $c = 6.015$ Å. Chemical analysis revealed a significant depletion of silicon ($Si/Zr = 0.3$)

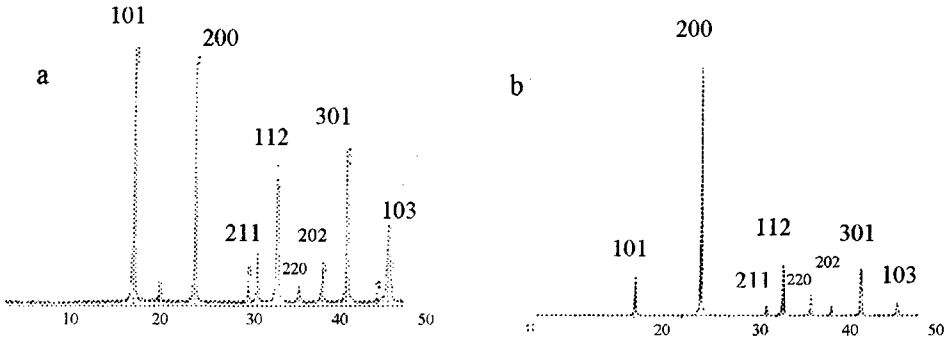

Figure 1. XRD patterns of zircon (2θ degree λCu K_α): (a) hydrothermal (sample 1), (b) classic.

and the presence of fluorine (F/Zr > 2). Zr—F bonds were detected by NMR ^{19}F MAS experiments. The deficient Si and the absence of Si—F bonds are interpreted by the replacement in the structure of some SiO_4^{4-} tetrahedra by $[F_{(4-x)}(OH)_x]^{4-}$ tetrahedra. Rietveld refinement, with an accuracy of 2%, and CRAMPS ^{1}H NMR results lead to the following formula:

$$Zr(SiO_4)_{0.3}[(F_4)_{0.3}(F_3OH)_{0.2}(F_2OH_2)_{0.3}(FOH_3)_{0.2}]_{0.7}$$

Sample 1 was characterized by a morphology of square plates with sizes in the range 1–5 μm (Fig. 2). Annealing of the powder at 800°C for 12 hours involved a weight loss of about 25% due to the release of SiF_4 and HF. The calcination residue was identified as monoclinic zirconia with an acicular morphology (Fig. 3). The needle size was about 100 × 10 nm and their orientation was related to the two main crystallographic directions of the original zircon plate.

Concerning the mechanism, the main hypothesis is that the reaction proceeds by dissolution of precursors (zirconia gel and silica) with formation of soluble species and crystallization. The reactive silicon species is probably a tetrahedral complex, like $Si(OH)_4$, that contains no fluorine. The zirconium species responsible for supersaturation must contain much fluoride [3, 4]. As a consequence of the strength of the Zr—F bond, heterocondensation reactions cannot easily occur and numerous silicon defects are present in the structure.

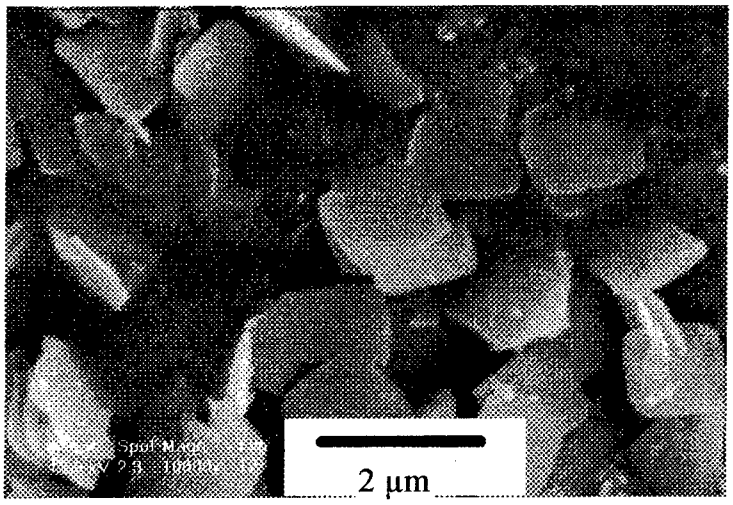

Figure 2. SEM of hydrothermal zircon obtained in acid pH (Sample 1).

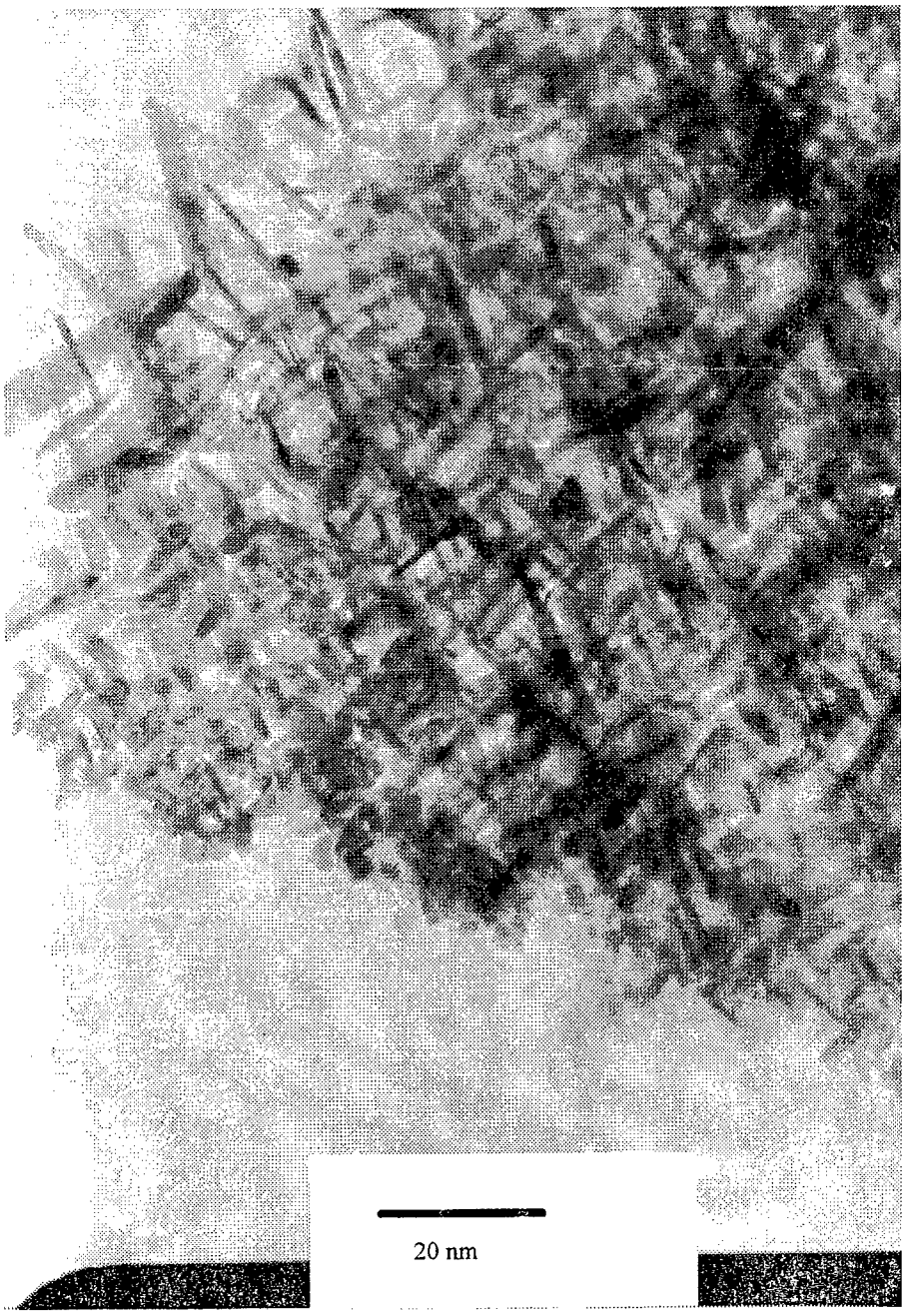

Figure 3. TEM of monoclinic ZrO_2 obtained by calcination of sample 1.

Synthesis at Basic pH

Synthesis was carried out at an initial pH 9 and, as in acid media, no significant pH fall occurred during the hydrothermal treatment. The XRD diffractogram of the powder obtained (sample 2) was different from the one of classic zircon by the significant broadness of all peaks except the 200 (Fig. 4). Chemical analysis revealed a molecular ratio Zr/Si = 1 and the absence of fluoride in the solid.

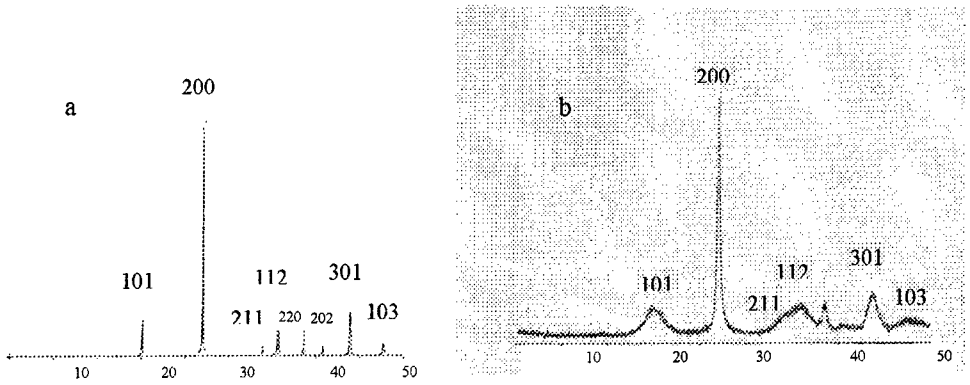

Figure 4. XRD patterns of zircon (2θ degree λCu K_α): (a) classic, (b) hydrothermal (sample 2).

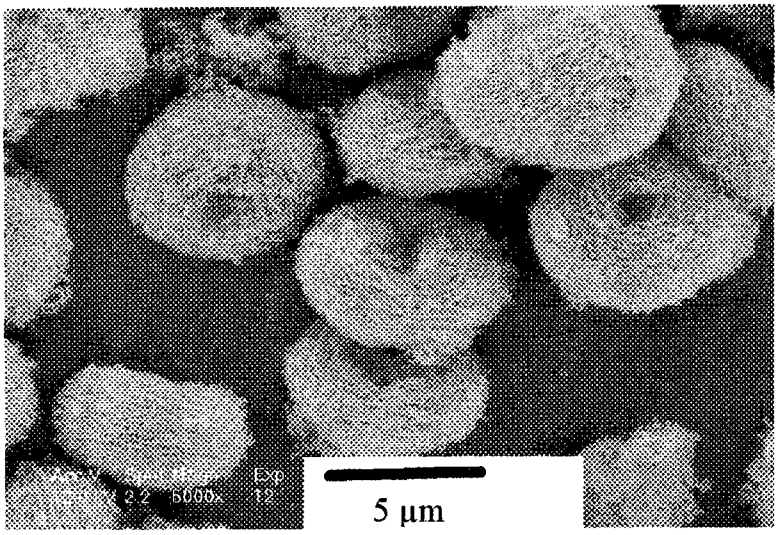

Figure 5. SEM of hydrothermal zircon obtained at basic pH (sample 2).

Scanning electron microscopy (Fig. 5) revealed that sample 2 was characterized by a very peculiar morphology in the form of ellipsoidal layered agglomerates. The texture of each ellipsoid was better observed by transmission electron microscopy (Fig. 6) which showed about 2 nm thickness layers. The broadness of XRD peaks is explained by layers with the main face 200.

Moreover, sample 2 was characterized by a specific surface area of about 200 m^2/g which exhibited an excellent thermal stability. Annealing at 800°C for 72 hours did not destroy the layered ellipsoidal agglomerates and 70% of the area was maintained.

Concerning the mechanism, it can be assumed that the silicon species responsible for supersaturation were the same as that in the former case, $Si(OH)_4$. The main difference came from the nature of zirconium dissolved species which were probably polymeric entities. These polymers are likely to form layers with surface heterogeneities as shown in Fig. 7. A heterogeneity can be the starting point for the growth of another layer with a different orientation leading finally to formation of ellipsoidal agglomerates.

Conclusion

In hydrothermal synthesis, the pH has a strong influence on the mechanism and consequently on the morphology of the solids obtained. A new morphology of

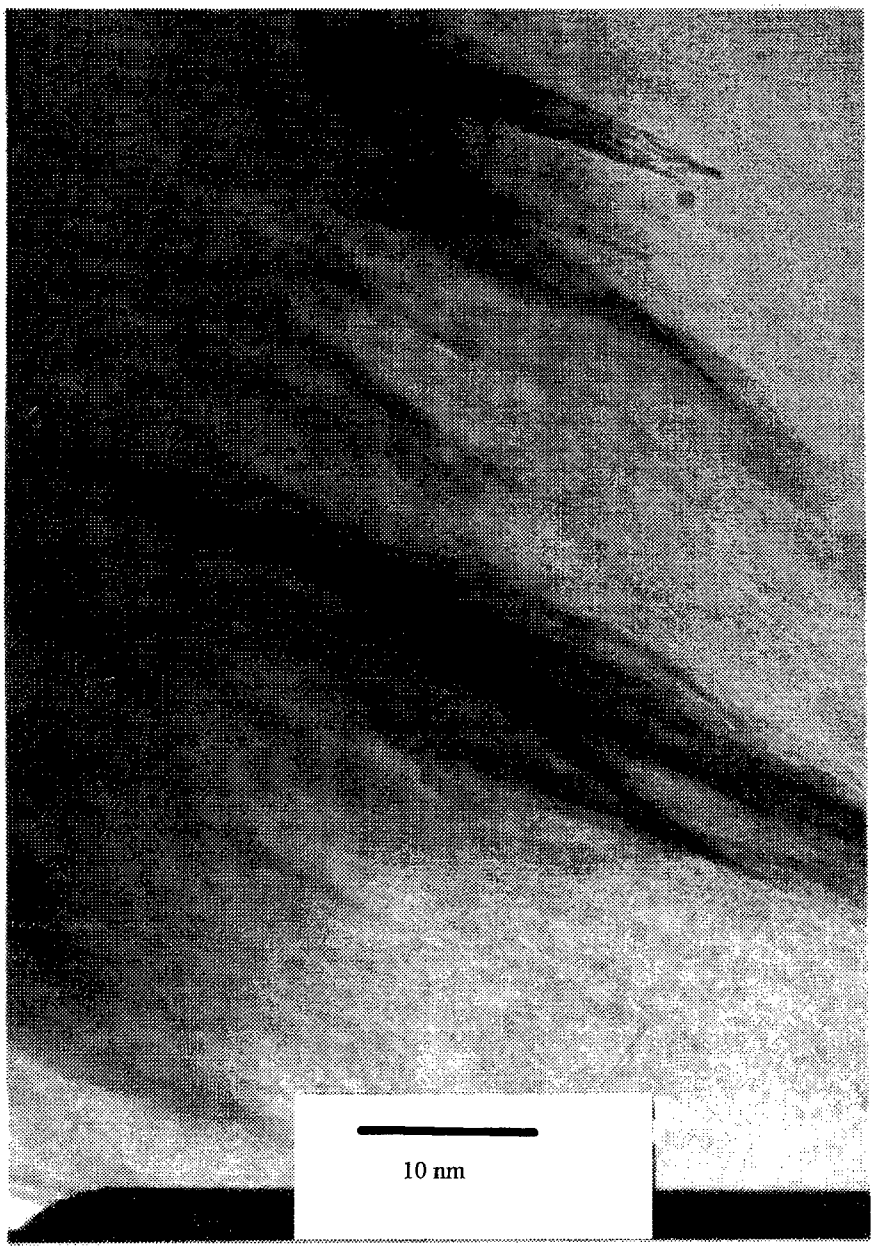

Figure 6. Transmission electron migrograph of zircon obtained at basic pH (sample 2).

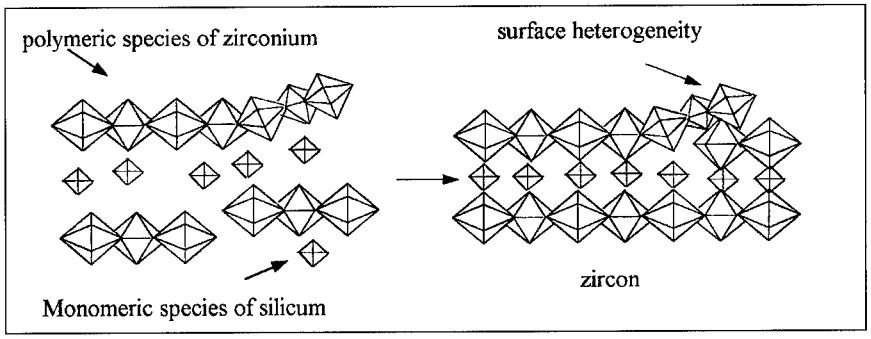

Figure 7. Surface heterogeneities formation.

zircon with a thermally-stable, large specific surface area has been found. The preparation and the application are covered by a Rhône-Poulenc patent [5].

Acknowledgment

The authors are indebted to Rhône-Poulenc for financial support.

References

1. R. Caruba and G. Turco, Bull. Soc. Fr. Min. Crist. **94**, 427 (1971).
2. R.L. Colette and C. Frondel, Amer. Miner. **42**, 759 (1957).
3. B. Noren, Acta. Chem. Scand. **21** (9), 2457 (1967).
4. P.A.W. Dean and D.F. Evans, J. Chem. Soc. A, 698 (1967).
5. R. Valero, B. Durand, J.L. Guth, and T. Chopin, French Patent No. 97 06733.

Journal of Sol-Gel Science and Technology 13, 125–128 (1998)
© 1998 Kluwer Academic Publishers. Manufactured in The Netherlands.

Alkoxide Precursors for Er-Containing Glasses and Ceramics

G. WESTIN, M. WIJK, M. MOUSTIAKIMOV AND M. KRITIKOS
Department of Physical, Inorganic and Structural Chemistry, Arrhenius Laboratory, Stockholm University, S-106 91 Stockholm, Sweden

Abstract. High yield synthesis of the stable Er-containing alkoxides $Er_5O(OiPr)_{13}$, $ErAl_3(OiPr)_{12}$, $Er_4TiO(OiPr)_{14}$, $Er_2Ti_4O_2(OEt)_{18}(HOEt)_2$ and $Er_2Zr_2O(OiPr)_{12}(HOiPr)_3$ is described. The solid state single-crystal X-ray determined structures are given and FT-IR spectroscopy is used to compare the structures of the solid and dissolved states. It was shown that all structures remained close to intact in solution.

Keywords: Er-alkoxides, FT-IR, structure

1. Introduction

Alkoxides are frequently used precursors in sol-gel processing of complex crystalline and glassy ceramics [1, 2]. The extreme homogeneity that can be obtained with hetero-bimetallic alkoxides makes it possible to obtain new low temperature modifications of crystalline materials and glasses of compositions that cannot be obtained by conventional melt-mixing techniques due to non-miscibility of the component oxides. Thus, it may be possible by choosing suitable multimetallic alkoxides, to produce glasses with compositions and properties changing smoothly over a wide range. One area where this might be of great benefit is that of Er-containing wave-guides for NIR-light amplification and frequency up-conversion. In these devices high Er-ion contents are desirable, but this often lead to the formation of Er-ion rich oxide clusters within the glass host, which in turn, reduces the optical gain through non-radiative pathways. We are investigating the preparation of heterometallic alkoxides containing besides Er-ions, optically silent metal ions to be used in various ceramic materials. In the preparation of optic materials we are searching for stable, well characterized heterometallic alkoxides containing single, isolated Er-ions and as low Er-to-M ratio as possible. In this article, we describe the syntheses and structures of one Er-oxo-isopropoxide and four Er-M-(oxo)-alkoxides with M = Al, Ti and Zr.

2. Experimental

The syntheses were performed in a glove-box with dry, oxygen-free argon atmosphere. The chemicals were used as purchased in anhydrous form, except for the $AlAl_3(OiPr)_{12}$, which was recrystallized before use. The solvents were dried by distillation over CaH_2. The syntheses of hetero-bimetallic alkoxides given in this section are those of the alkoxides of the lowest Er-to-M ratio that could be obtained as stable and isolable compounds the Er-M systems discussed. If lower Er : M ratios were used in the reactions, homometallic M-alkoxides were found together with the hetero-bimetallic ones. Analysis of the Er, K, Cl, Al, Ti and Zr contents was done with SEM-EDS on hydrolyzed and dried samples. The K and Cl contents can normally be detected down to ca. 0.3 mol% and the Er : M ratio be determined within ca. 2 mol% units. The contents of dried crystals and masses from the syntheses were in all cases close to those of the formulas of the alkoxides and the amounts of K and Cl were below the detection limit. The structures and formulas of the alkoxides have been obtained by single crystal X-ray diffraction for $Er_5O(OiPr)_{13}$ [3], $ErAl_3(OiPr)_{12}$ [4], $Er_2Ti_4O_2(OEt)_{18}(HOEt)_2$ [5] and $Er_2Zr_2O(OiPr)_{12}(HOiPr)_3$ [6], while the structure and formula of $Er_4TiO(OiPr)_{14}$ has been derived from the isostructural compound $(Tb_{0.9}Er_{0.1})_4TiO(OiPr)_{14}$ (see below) [7]. The detailed structure determinations

and structural features are or will be discussed elsewhere.

Synthesis of $Er_5O(OiPr)_{13}$. 0.429 g K dissolved in 16 ml of toluene : HOiPr (1 : 1) was slowly added 0.73 ml 1 M H_2O in toluene : HOiPr (1 : 1). One hour later, 1.000 g $ErCl_3$ was added and the KCl formed in the reaction was sedimented by centrifugation after 48 hours. The solution part was evaporated in vacuum to yield over 90 mol% of $Er_5O(OiPr)_{13}$. IR-data for $Er_5O(OiPr)_{13}$: 1009, 977, 974sh, 956sh, 952, 839, 832, 826, 546, 532, 498, 463, 448, 416, 393 cm^{-1}.

Synthesis of $ErAl_3(OiPr)_{12}$. 0.500 g $Er_5O(OiPr)_{13}$ and 0.945 g $AlAl_3(OiPr)_{12}$ were dissolved in 15 ml toluene : HOiPr (2 : 1) and heated at 80°C for 2 hours. Evaporation in vacuum yielded $ErAl_3(OiPr)_{12}$ as the sole product. IR-data: 1184, 1170, 1138, 1127, 1042sh, 1033, 955, 863, 856, 831, 704, 668, 612sh, 582, 540, 476, 449, and 400 cm^{-1}.

Synthesis of $Er_4TiO(OiPr)_{14}$. 0.500 g K dissolved in 20 ml toluene : HOiPr (1 : 1) was added 4.846 g $Ti(OiPr)_4$. Then, 4.26 ml 1 M H_2O in toluene : HOiPr (1 : 1) was slowly added followed, an hour later, by addition of 1.166 g $ErCl_3$. After 48 hours, the KCl formed was sedimented by centrifugation and the solution part was evaporated in vacuum to afford $Er_4TiO(OiPr)_{14}$ (yield ca. 90 mol%). IR-data: 1009, 999sh, 972, 947, 854, 837, 834sh, 823, 818sh, 615, 561, 530, 523, 501, 478sh, 445, and 408 cm^{-1}.

Synthesis of $Er_2Ti_4O_2(OEt)_{18}(HOEt)_2$. 0.493 g K dissolved in 70 ml toluene : EtOH (4 : 1) was added 1.92 g $Ti(OEt)_4$ and two hours later, 4.20 ml 1 M H_2O in toluene : EtOH (4 : 1) was slowly added. After another two hours, the solution was added 1.150 g $ErCl_3$ and 48 hours later it was centrifuged to sediment the KCl formed. Evaporation of the solution part in vacuum and addition of small amounts of ethanol produced $Er_2Ti_4O_2(OEt)_{18}(HOEt)_2$ (yield 70–80 mol%). IR-data: 1195, 1158, 1097, 1055, 925, 925, 898, 602, 561, 512, 512, 483, 467, and 420 cm^{-1}.

Synthesis of $Er_2Zr_2O(OiPr)_{12}(HOiPr)_3$. 0.600 g K dissolved in 24 ml toluene : HOiPr (1 : 1) was added 1.983 g $Zr_2(OiPr)_8(HOiPr)_2$, whereupon 2.55 ml 1 M H_2O in toluene : HOiPr was slowly added. One hour later, 1.399 g $ErCl_3$ was added and after another 48 hours, the KCl formed was sedimented by centrifugation. Evaporation of the solution in vacuum afforded $Er_2Zr_2O(OiPr)_{12}(HOiPr)_3$. (yield ca. 85 mol%). IR-data: 1171, 1150, 1129, 1063, 1018, 1006, 966, 889, 846sh, 835, 823sh, 606, 583, 550, 528, 448, and 410 cm^{-1}.

3. Results and Discussion

$Er_5O(OiPr)_{13}$. The combined metathesis and hydrolysis for preparation of $RE_5O(OiPr)_{13}$ has not been reported before, although metathesis only or dissolution of RE (Rare-Earth) or Y metal in isopropanol containing solvents have been reported to yield $(Re/Y)_5O(OiPr)_{13}$ [7–10]. If water was not added, another much less stable Er-isopropoxide, whose IR spectrum is shown in Fig. 1, was isolated as the sole alkoxide product in our experiments. This unstable alkoxide slowly converted to $Er_5O(OiPr)_{13}$ in solid form, but was rather stable in solutions containing HOiPr. $Er_5O(OiPr)_{13}$ and very soluble in toluene yet only slightly soluble in isopropanol. The other Er-isopropoxide was more soluble in isopropanol than in toluene. Thus this can be used for separation of the two alkoxides. The bands assigned as due to M—O and C—O vibrations (the region 1200–400 cm^{-1}) remained virtually unchanged on dissolution of $Er_5O(OiPr)_{13}$ in toluene-HOiPr solvents, showing that the molecular structure did not change (Fig. 1). The structure of the pentanuclear molecule is shown in Fig. 2.

$ErAl_3(OiPr)_{12}$. Metathesis of $ErAl_3(OiPr)_{12}$ from $ErCl_3$ and $KAl(OiPr)_4$ has been described before [11] and the structure has been determined by single crystal X-ray diffraction [4]. The IR spectra of the product of the acid-base reaction of $Er_5O(OiPr)_{13}$ and $AlAl_3(OiPr)_{12}$ described here and that of the structurally determined $ErAl_3(OiPr)_{12}$ prepared by metathesis according to [4] matched quite well, showing that the products were the same. The fate of the oxo-oxygen is not known, but if it is incorporated in the $ErAl_3(OiPr)_{12}$ molecule, then only one out of five molecules should contain it. The structure of an oxo-alkoxide should also be very close to that of the non-oxo alkoxide not to be detected by IR. $ErAl_3(OiPr)_{12}$ was quite stable both in the solid state and in toluene-isopropanol solutions. It was very soluble in toluene, but only slightly soluble in isopropanol. On dissolution in toluene-HOiPr, the IR-peaks due to the M—O and C—O bonds of the molecule were quite similar, as shown in Fig. 1, demonstrating that the molecular structure was close to unchanged. The molecular

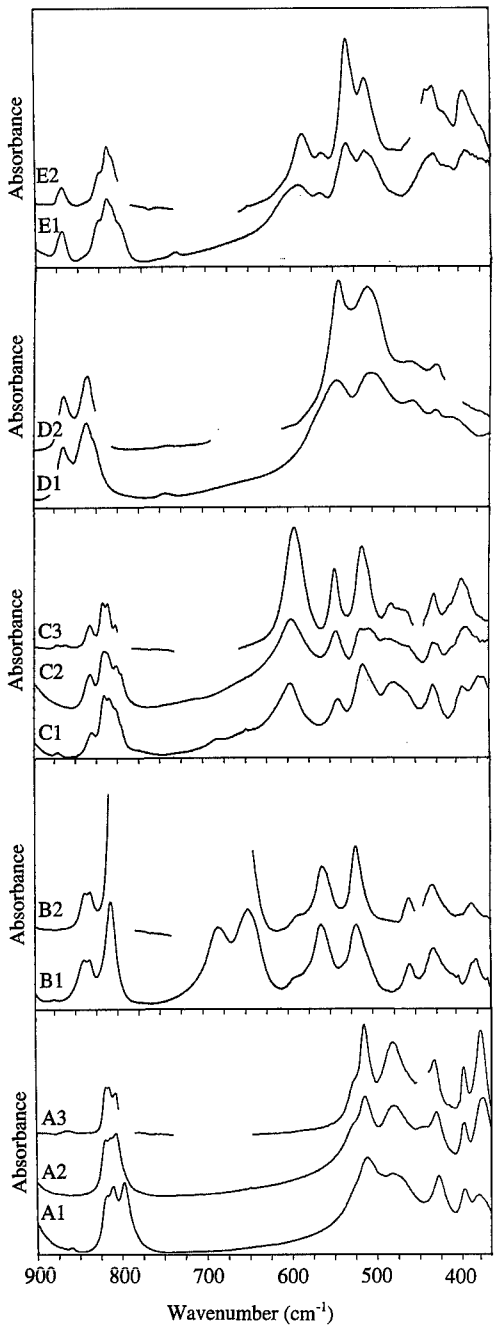

Figure 1. IR-Spectra of solid Er-isopropoxide formed without water addition (A1), $Er_5O(OiPr)_{13}$ (A2), $Er_5O(OiPr)_{13}$ dissolved in toluene : HOiPr (2 : 1 v/v) (A3), $ErAl_3(OiPr)_{12}$ (B1), $ErAl_3(OiPr)_{12}$ dissolved in toluene : HOiPr (2 : 1) (B2), $(Tb_{0.9}Er_{0.1})_4TiO(OiPr)_{14}$ (C1), $Er_4TiO(OiPr)_{14}$ (C2), $Er_4TiO(OiPr)_{14}$ dissolved in toluene : HOiPr (2 : 1) (C3), $Er_2Ti_4O_2(OEt)_{18}(HOEt)_2$ (D1), $Er_2Ti_4O_2(OEt)_{18}(HOEt)_2$ dissolved in toluene : HOEt (4 : 1) (D2), $Er_2Zr_2O(OiPr)_{12}(HOiPr)_3$ (E1), $Er_2Zr_2O(OiPr)_{12}(HOiPr)_3$ dissolved in toluene : HOiPr (2 : 1) (E2). The spectrum has been removed in areas where the solvent absorptions were too strong to be corrected for.

structure of $ErAl_3(OiPr)_{12}$ is shown in Fig. 2. No reaction between $Er_5O(OiPr)_{13}$ and $AlAl_3(OiPr)_{12}$ (Er : Al ratio 1 : 3) was observed at room temperature, but at 80°C, the reaction to form $ErAl_3(OiPr)_{12}$ was complete within 2 hours. This is important for the preparation of Er-containing glasses where Er- and Al-ions are often incorporated together with the role for the Al-ions to disperse the Er-ions. Thus, a good, stable precursor can easily be prepared in situ by heating, before addition of e.g., Si- and Ti-alkoxides. If this is not done one would on the other hand have a stable, clustered Er compound whose reactivity towards water is not synchronized with that of the Al compound and thus yields poor products for optics, but give possibilities to prepare metastable oxides with interesting magnetic coupling.

$Er_4TiO(OiPr)_{14}$. By metathesis of $ErCl_3$ and K-Ti-isopropoxide in combination with hydrolysis $Er_4TiO(OiPr)_{14}$ was formed. If water was not added unstable, liquid Er-Ti-isopropoxide(s) were formed. $Er_4TiO(OiPr)_{14}$ is stable both in the solid state and in solution. It was soluble in toluene, but only slightly soluble in isopropanol. The M—O and C—O IR-peaks changed very little on dissolution in toluene-HOiPr solvent, which shows that the molecular structure remains unchanged to a larger extent (Fig. 1). The structure of $Er_4TiO(OiPr)_{14}$ has not been determined, but its IR spectrum is quite similar to that of the structurally determined $(Tb_{0.9}Er_{0.1})_4TiO(OiPr)_{14}$, in which both the Er and Tb atoms are placed in the RE^{3+} positions [7], which shows that the structures are very similar. The structure of $(Tb_{0.9}Er_{0.1})TiO(OiPr)_{14}$ ($Er_4TiO(OiPr)_{14}$) is shown in Fig. 2. $Er_4TiO(OiPr)_{14}$ is also isostructural with $Sm_4TiO(OiPr)_{14}$, although the samarium compound was prepared from SmI_2 and $NaTi(OiPr)_5$ in a combined metathesis and redox reaction or Lewis acid-base reaction of $Sm_5O(OiPr)_{13}$ and $Ti(OiPr)_4$ [12].

$Er_2Ti_4O_2(OEt)_{18}(HOEt)_2$. As was the case with the Er-Ti-isopropoxide no stable isolable alkoxide was obtained by metathesis, if hydrolysis was not employed at the same time. With hydrolysis, $Er_2Ti_4O_2(OEt)_{18}(HOEt)_2$ was obtained in high yield as a relatively stable compound if stored or dissolved in presence of ethanol. The solubility was high in toluene and very low in ethanol. Its IR spectra in solid state and in toluene : ethanol were very similar showing that the molecular structure remained in solution (Fig. 1). The structure of $Er_2Ti_4O_2(OEt)_{18}(HOEt)_2$ is shown in Fig. 2.

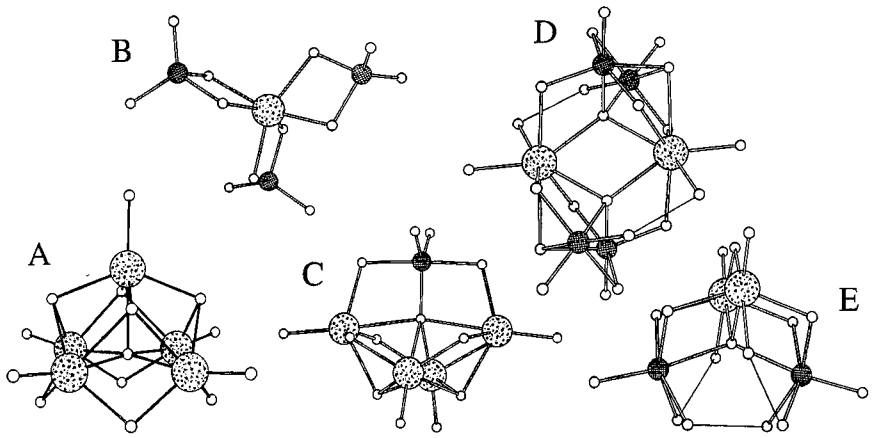

Figure 2. Molecular structure of $Er_5O(OiPr)_{13}$ (A), $ErAl_3(OiPr)_{12}$ (B), $(Tb_{0.9}Er_{0.1})_4TiO(OiPr)_{14}$ ($Er_4TiO(OiPr)_{14}$) (C), $Er_2Ti_4O_2(OEt)_{18}(HOEt)_2$ (D), and $Er_2Zr_2O(OiPr)_{12}(HOiPr)_3$ (E). The Er-atoms are represented by spotted circles, the M-atoms by grid circles and the oxygen atoms by small circles. The alkyl groups are not drawn out and the hydrogen bonds are represented by a single line.

$Er_2Zr_2O(OiPr)_{12}(HOiPr)_3$. The synthesis of $Er_2Zr_2O(OiPr)_{12}(HOiPr)_3$ was performed by metathesis and hydrolysis, but the compound also formed without hydrolysis, by autodecomposition in similarity with the formation of $Er_5O(OiPr)_{13}$. The oxo-isopropoxide was relatively stable both in solid state and in solution, especially if HOiPr was present. The solubility was high in toluene and very low in isopropanol. IR-spectra of the compound as solid and as toluene-HOiPr solution were very similar as shown in Fig. 1, demonstrating that the molecular structure was retained in solution. The molecular structure is shown in Fig. 2. Zirkonates are interesting materials for Er-containing optic materials due to their high refractive index and thermal stability, but also for a number of other applications e.g., oxygen conductors in sensors and fuel-cells. $Er_2Zr_2O(OiPr)_{12}(HOiPr)_3$ has the right composition for the $RE_2Zr_2O_7$ pyrochlore or fluorite structures and is thereby a very promising precursor for the preparation of such high quality materials.

4. Conclusions

High yield synthesis of stable Er-containing alkoxides has been given for $Er_5O(OiPr)_{13}$, $ErAl_3(OiPr)_{12}$, $Er_4TiO(OiPr)_{14}$, $Er_2Ti_4O_2(OEt)_{18}(HOEt)_2$ and $Er_2Zr_2O(OiPr)_{12}(HOiPr)_3$. In all cases but the Er-Al system, an assembling oxo-atom was needed for the preparation of stable compounds, which reflects lability of non-oxo alkoxides of RE-ions. The lability might stem from the weakly solvating alcohol ligands which leave the Er-ion coordinatively unsaturated when lost. Coordination can then be increased by decomposing alkoxo ligands to obtain the more donating and coordinating oxo-atoms. The oxo-alkoxides also have a rather high Er : M ratio, taking into account that the alkoxides studied here are the ones that have the lowest Er : M ratio that could be isolated as stable compounds. Only the Er-Al alkoxide, which is a non-oxo alkoxide, contains single, isolated Er-ions.

References

1. C.J. Brinker and G.W. Scherer, *Sol-Gel Science* (Academic Press, NY, 1990).
2. C.D. Chandler, C. Roger, and M.J. Hampden-Smith, Chem. Rev. **93**, 1205 (1993).
3. G. Westin, M. Kritikos, and M. Wijk, unpublished work.
4. M. Wijk, R. Norrestam, M. Nygren, and G. Westin, Inorg. Chem. **35**, 1077 (1996).
5. G. Westin, R. Norrestam, M. Nygren, and M. Wijk, submitted.
6. M. Wijk, M. Kritikos, and G. Westin, unpublished work.
7. M. Moustiakimov, M. Kritikos, and G. Westin, Acta Cryst. C. **54**, 29 (1998).
8. D.C. Bradley, H. Chudynzska, D.M. Frigo, M.E. Hammond, M.B. Hursthouse, and M.A. Mazid, Polyhedron **9**, 719 (1990).
9. O. Poncelet, W.J. Sartain, L.G. Hubert-Pfalzgraf, K. Folting, and K.G. Caulton, Inorg. Chem. **28**, 263 (1989).
10. L.M. Brown and K.M. Mazdiyasni, Inorg. Chem. **9**, 2783 (1970).
11. D.C. Bradley, R.C. Mehrotra, and D.P. Gaur, *Metal Alkoxides* (Academic Press, London, 1978).
12. S. Daniele, L.G. Hubert-Pfalzgraf, J.-C. Daran, and S. Halut, Polyhedron **13**, 927 (1993).

Journal of Sol-Gel Science and Technology 13, 129–132 (1998)
© 1998 Kluwer Academic Publishers. Manufactured in The Netherlands.

Fluoroalkoxides as Molecular Precursors of Fluoride Materials by the Sol-Gel Process

O. PONCELET, J. GUILMENT AND D. MARTIN
Kodak-Industrie, European Research Laboratory, Chalon-sur-Saône, France

Abstract. Numerous works have reported the preparation of pure oxide materials using the sol-gel process. The purpose of this paper is to show that it is possible to obtain pure fluoride homometallic or heterometallic materials at room temperature by the hydrolysis of tailored molecular precursors.

The work is focussed on alkaline-earth and lanthanide fluoroalkoxides ($[M(OR)n]n'$ where OR = fluoroalkoxo group) and the characterization of the final products of their hydrolysis. The molecular precursors were characterized by FT-Raman and the final powders by XRD and EDXRMA.

The formation of these fluoride materials involves fluoride organic by-products. The reactivity of these organic compounds on various substrates in terms of surface modification has been studied.

Keywords: fluoroalkoxides, fluoride material synthesis, sol-gel chemistry, hydrolysis, FT-Raman analysis

Introduction

The most common molecular precursors for sol-gel technology are alkoxides, which are known for a large part of the periodic table [1, 2]. Mainly developed for obtaining oxide materials, sol-gel technology has also been described for the preparation of oxynitrides and sulfides. Recently sol-gel synthesis of magnesium fluoride by the action of HF on magnesium ethoxide has been reported [3].

The purpose of this paper is to demonstrate the possibility of obtaining crystalline alkaline-earth or lanthanide fluoride materials at room temperature by hydrolysis of fluoroalkoxides: $M(OR_F)_n$, where M is an alkaline-earth or a lanthanide, OR_F is a fluoroalkoxo group.

Experimental

All reactions were carried out under purified argon at room temperature using Schlenk techniques. Metals were from Aldrich and Strem. All solvents were appropriately dried, distilled prior to use and stored under argon [4]. The alkaline-earth and/or lanthanide alkoxides were synthesized as described in the literature [1, 5]. The Raman Spectra of the alkoxide species and the reference materials were recorded at a resolution of 4 cm^{-1} on a FT-IR Bruker IFS66 spectrometer (FRA106 accessory). The XRD powder pattern of each fluoride sample was obtained with a Siemens D5000 diffractometer using filtered CuKα. Hydrolysis of fluoroalkoxides was made in dry ethanol, using four times the required stoichiometry of water in each case.

Results and Discussion

Alkaline-earth metals are electropositive, so the more convenient route to synthesize their alkoxides is the action of an alcohol on the metal (Eq. (1)). In the case of bromoalcohols, the reaction needs often to be catalyzed by addition of NH_3, Et_2NH or $(Me_3Si)_2NH$.

$$M + 2R_FOH \longrightarrow M(OR_F)_2 + H_2 \qquad (1)$$
$$(R_FOH = (CF_3)_2CHOH,\ CF_3CH_2OH)$$

The rare-earth fluoroalkoxides are obtained by alcoholysis of $Ln(OCH_2CH_2OCH_3)_3$.

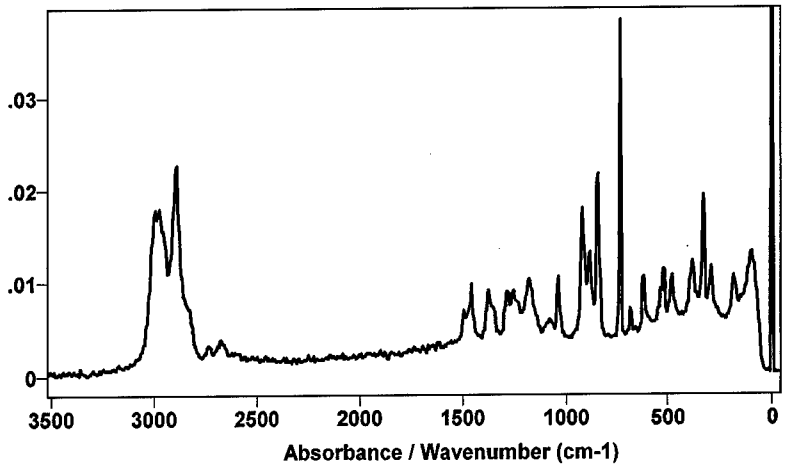

Figure 1. FT-Raman spectrum of $Ba(OCH(CF_3)_2)_2$.

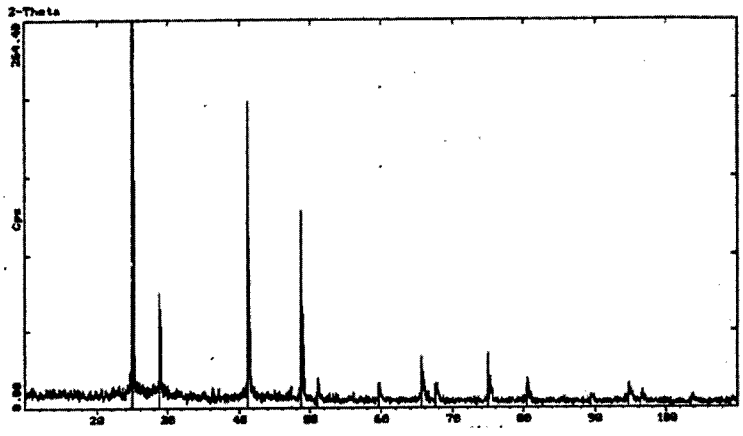

Figure 2. XRD spectrum of BaF_2 obtained by sol-gel technology.

Synthesis of BaF_2 and EuF_3

The reaction of hexafluoroisopropanol with barium led to formation of $Ba(OCH(CF_3)_2)_2$ which was characterized by FT-Raman spectroscopy (Fig. 1); the Ba—F interactions are indicated by a strong band at 739 cm^{-1}. The hydrolysis of $Ba(OCH(CF_3)_2)_2$ catalyzed by $HClO_4$ (the pH of the water was in the range 1 to 3) in dry ethanol produced BaF_2 which was identified by XRD (Fig. 2).

$Eu(OCH(CF_3)_2)_3$ exhibits strong Eu—F interactions (FT-Raman band at 743.2 cm^{-1}). Hydrolysis catalyzed by $HClO_4$ at room temperature gave EuF_3 as shown by XRD (see Fig. 3).

How Is it Possible to Explain the Formation of Fluorides Rather than Oxides by Hydrolysis of Fluoroalkoxides?

Homoleptic and heteroleptic fluoroalkoxides have been successfully used to obtain fluoride materials by MOCVD [6–8], but it is the first time to our knowledge that such fluoride materials were prepared by a sol-gel process without addition of HF to catalyze the reaction. Recent X-ray data recorded on monocrystals show that short M—F bonds appear to be a common feature for fluorinated alkoxide or β-diketonate derivatives, especially for large elements such as alkaline-earth metals and lanthanides [9–11]. For example, in the case

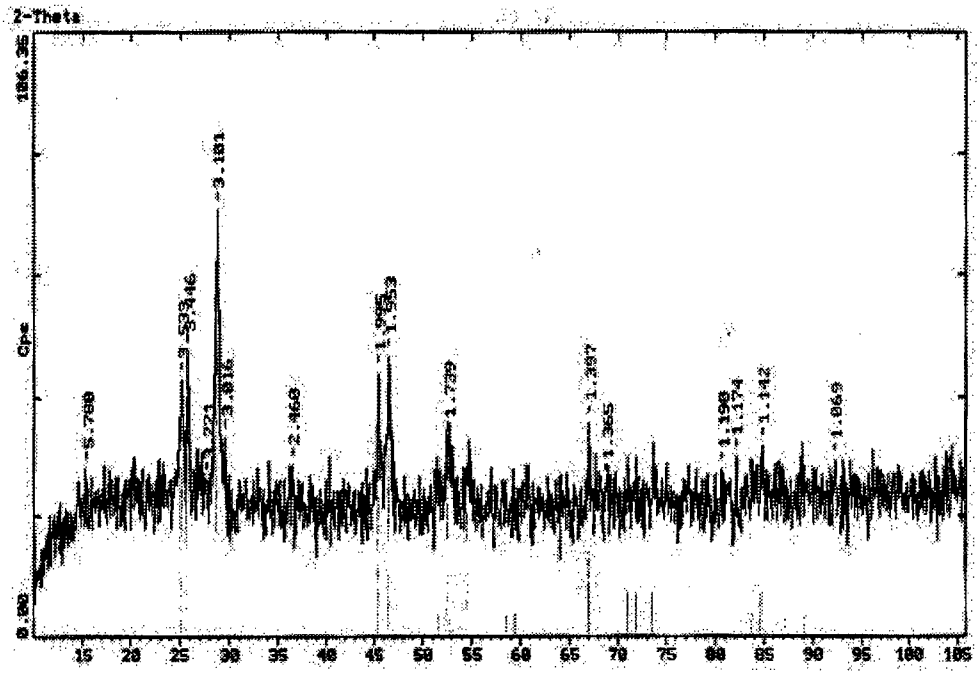

Figure 3. XRD spectrum of EuF_3 obtained by sol-gel technology.

of $BaY_2(OCH(CF_3)_2)_4$ $(THF)_4$ [12], the coordination polyhedron of the central barium atom formed by four alkoxide type oxygen atoms is supplemented by interactions with eight fluorine atoms (Ba—F: 2.9–3.16 Å). The sum of the van der Waals radii is 3.57 Å. These Ba—F interactions effectively act as secondary bonds leading to a final degree of coordination of twelve.

The observations on monocrystals show that such molecular fluoroalkoxides may be considered either as oxide or fluoride precursors depending on their hydrolysis conditions.

Our results confirm that it is possible to obtain fluoride materials by hydrolysis of fluoroalkoxides in alcohols. This shows that even in solution, for these compounds the metal centers keep in their coordination spheres some M—F bonds allowing fluoride materials to be obtained during hydrolysis. This strong "template" effect associated with the thermodynamic driving force probably explains the fact that fluoride can be formed instead of oxide. The hydrolysis reactions have to be catalyzed by an acid.

The formation of the M—X (X=F) bond involves the cleavage of a C—X bond. From thermodynamical data the bond strength C—F = 485 kJ/mole explains the need to catalyze the reaction in the case of the fluoroalcohols.

Conclusion

It is shown that fluoride materials may be synthesized at room temperature by a sol-gel process. The most attractive feature of the process is the possibility of directly obtaining lanthanide or alkaline-earth fluoride materials in various forms (thin films, fibers, bulk materials). Perfect control of the stoichiometry of the final fluoride materials is attainable using a mixture of homometallic fluoroalkoxides as starting materials. Thus it would be possible to use the sol-gel process to manufacture fluoride materials on heat sensitive organic substrates or HF sensitive inorganic substrates.

Fluoroalkoxides appear to be attractive as precursors for the sol-gel process of non-oxide materials. They are also of interest as tailor-made molecular precursors for specific applications.

References

1. D.C. Bradley, R.C. Mehrotra, and D.P. Gaur, *Metal Alkoxides* (Academic Press, London, 1978).
2. L.G. Hubert-Pfalzgraf, New J. Chem. **11**, 663 (1987).
3. A.A. Rywak and J.M Burlitch, Chem. Mater. **8**, 60 (1996).
4. D.D. Perrin and W.L.F. Armarego, *Purification of Laboratory Chemicals* (Pergamon Press, London, 1988).

5. O. Poncelet, L.G. Hubert-Pfalzgraf, J.C. Daran, and R. Astier, J. Chem. Soc., Chem. Com., 1846 (1989).
6. J.A. Samuels, E.B. Lobkovsky, W.E. Streib, K. Folting, J.C. Huffman., J.W. Zwanziger, and K.G. Caulton, J. Am. Chem. Soc. **115**, 5093 (1993).
7. J.A. Samuels, Wen-C. Chiang, Chung-Yu Yu, E. Apen, D.C. Smith, D.V. Baxter, and K.G. Caulton, Chem. Mater. **6**, 1684 (1995).
8. J.A. Samuels, K. Folting, J.C. Huffman, and K.G. Caulton, Chem. Mater. **7**, 929 (1995).
9. A.P. Purdy and C.F. George, Inorg. Chem. **30**, 1970 (1991).
10. H. Vincent, F. Labrize, and L.G. Hubert-Pfalzgraf, Polyhedron, 3323 (1994).
11. D.C. Bradley, H. Chudzynska, M.E. Hammond, M.B. Hursthouse, M. Motavelli, and W. Ruowen, Polyhedron **11**, 375 (1992).
12. F. Labrize, L.G. Hubert-Pfalzgraf, J.C. Daran, and S. Halut, J. Chem. Soc., Chem. Comm., 1556 (1993).

Journal of Sol-Gel Science and Technology 13, 133–139 (1998)
© 1998 Kluwer Academic Publishers. Manufactured in The Netherlands.

Some Recent Developments in Aqueous Sol-Gel Processing

A. ATKINSON
Department of Materials, Imperial College, London, SW7 2BP, UK

D.L. SEGAL
AEA Technology, F7 Culham, Abingdon, Oxfordshire, OX14 3DB, UK

Abstract. In this overview we describe the recent use of aqueous sol-gel processing for the preparation of ceramics that have very different end-uses. Zirconia nanofiltration membranes with 50% rejection of solutes at a molecular weight of about 1000 have been produced using zirconia sols containing inorganic polymeric "particles" and evaluated on the pilot-plant scale. Microporous alumina- and zirconia-pillared clays having a large and hydrothermally stable interlayer spacing (2 nm) and specific surface area (approximately 400 $m^2 g^{-1}$) have been prepared using similar polymeric sols. These have been produced on the 20 kg scale and evaluated for catalytic applications. Cathodoluminescent phosphor powders, based on the doped-yttrium aluminium gallium oxide system, have been synthesized for high resolution displays using a combination of aqueous sol-gel precursors and aerosol techniques to produce particles of controlled size and shape. Finally, ceramic stains for decorating ceramic bodies have been synthesized using this method, not only in powder form but also for direct application to ceramic ware by ink-jet printing. These examples illustrate the versatility of aqueous sol-gel processing for the preparation of a wide range of ceramic compositions and forms.

Keywords: membranes, catalysts, pillared clays, phosphors, pigments, ink-jet printing

Introduction

Most interest in sol-gel synthesis of ceramics in recent years has concentrated on the hydrolysis of metal alkoxides in organic media, but the alternative sol-gel processes in aqueous media can often be just as useful [1, 2]. The aqueous processes also offer advantages of cheaper precursors and, in many cases, more easily handled waste products. The aqueous sol-gel processes can be classified into four broad types: (1) colloidal dispersions of oxide particles that have been produced by another process (e.g., a vapor phase reaction); (2) colloidal dispersions of hydroxides or hydrated oxides produced by peptizing a precipitate; (3) polymerization of hydrolyzable cations (these polynuclear cations are usually regarded as "particles" when their "size" exceeds 1 nm); and (4) precipitation of hydrated oxide or hydroxide in the presence of an organic gelling agent (gel precipitation). The dispersions are usually electrostatically stabilized and are capable of forming gels by increasing concentration (loss of solvent water) or changing pH. The aqueous sol-gel route was pursued initially in the late 1950s as a method for making spherical particles of $(Th,U)O_2$ nuclear fuel by a controllable and dust-free process and has since been adopted by industry for a range of commercially successful products including: alumina abrasives, alumina-based fibers, chromatographic separation media (alumina and silica), zirconia plasma spray powders, membranes (alumina, titania and zirconia) catalyst supports (silica, alumina and ceria) and silica glass monoliths. Here we describe some recent examples from work undertaken at AEA Technology (Harwell) exploring the application of aqueous sol-gel processing to a range of materials.

Zirconia Nanofiltration Membranes

Inorganic membranes have better chemical and thermal durability and greater mechanical stiffness than organic membranes. The smallest pore-size available in the separation layer of commercial ceramic membranes is approximately 4 nm, corresponding to a molecular weight cut-off (MWCO) of about 10,000 (10 kD). There is now much interest in extending the pore diameter of the separation layer downwards into the microporous region (<2 nm). These so-called nanofiltration (NF) membranes have potential for applications in gas separations and liquid separations requiring lower MWCO. Zirconia was chosen as the preferred material for the separation layer in the work described here because it has better chemical resistance than silica, alumina or titania over a wide range of chemical conditions.

Ultrafiltration (UF) ceramic membranes are already produced commercially by slip casting from colloidal sols produced by alkoxide hydrolysis, and the same method can be extended to the NF range [3]. However, the aqueous sol-gel route is also suitable for NF membrane fabrication. In the case of zirconia membranes the aqueous polymerization route is attractive because zirconium salts readily form such polymeric ions [4]. For example, the basic cationic unit in zirconyl chloride solutions is the tetramer $[Zr(OH)_2 \cdot 4H_2O]_4^{8+}$. The tetramer undergoes further hydrolysis in aqueous solution and then OH groups and water molecules on neighbouring tetramers can condense to form more $=Zr=(OH)_2=Zr=$ linkages and so polymerize the units. Further loss of water by condensation converts the hydrated structure to an oxide with $-Zr-O-Zr-$ linkages. The type of anion and the hydrolysis conditions both influence the structure of the polymer, which can range from three-dimensional networks to two-dimensional sheets. Guizard et al. [5] have reported the fabrication of zirconia NF layers starting from zirconyl chloride precursor containing these species.

We have used a similar aqueous polymerization route [6], in which zirconia "nanosols" were prepared by the dissolution and hydrolysis of basic zirconium carbonate, $Zr_2O_2 \cdot CO_3 \cdot (OH)_2$, in aqueous nitric acid. These sols contain polymers of the type described above in which the degree of polymerization is controlled by the NO_3 : Zr ratio. The sols were then aged at temperatures up to 100°C to grow the particles (Fig. 1). X-Ray diffraction analysis of the calcined gels showed that the zirconia was stabilized in the tetragonal phase.

Nanofiltration membranes were fabricated using commercial UF membranes ("Kerasep", Tech Sep) as substrates having a zirconia UF separation layer with a nominal 15 kD MWCO. The NF layer was applied by slip casting from a zirconia sol with a particle size selected to avoid significant penetration of particles into the UF layer. The sol was modified by organic

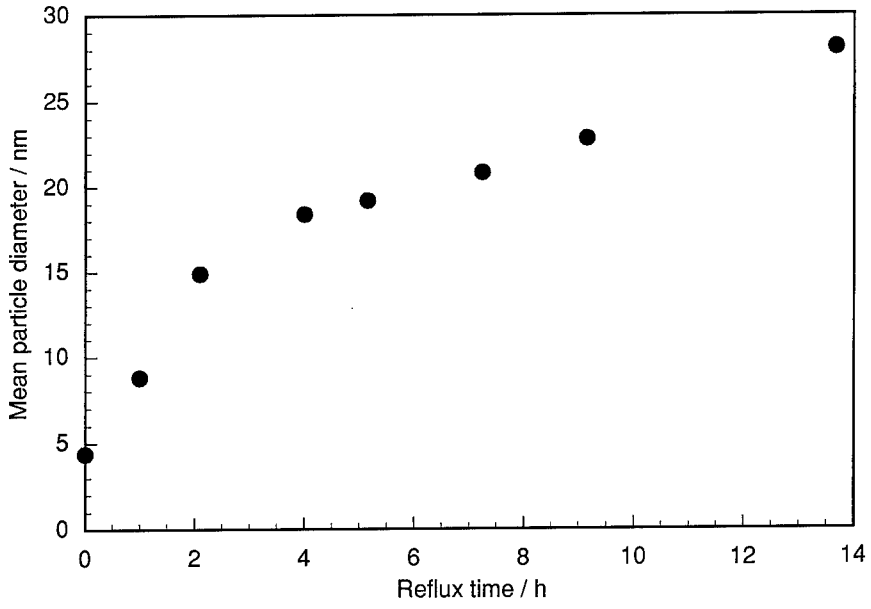

Figure 1. Hydrodynamic size, measured by light scattering, of particles in nitrate-stabilized zirconia sols as a function of refluxing time.

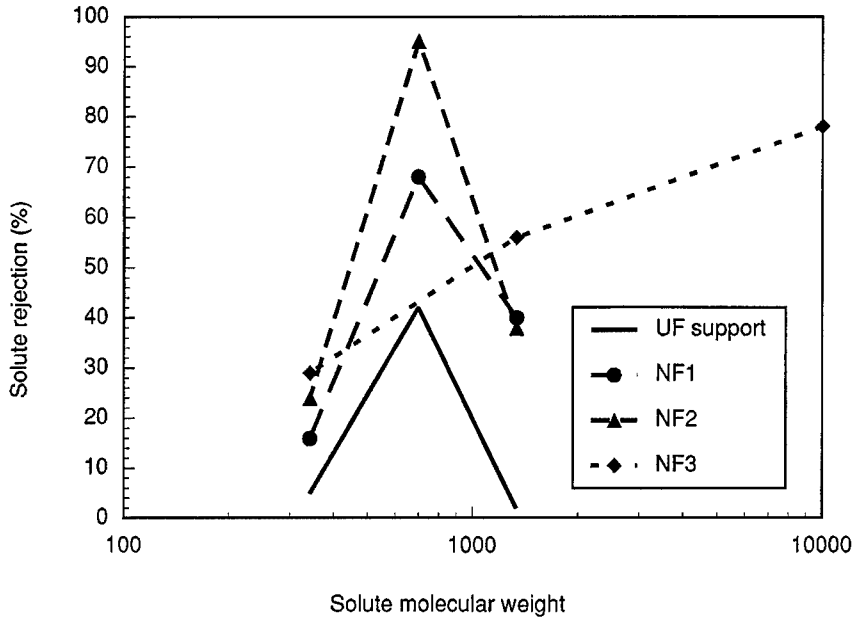

Figure 2. The retention characteristics for various solute molecules of zirconia NF membranes compared with the UF support. NF1, NF2 and NF3 are different examples of similar membranes.

additives to control viscosity and resistance to cracking of the NF layer during subsequent drying and calcination. The sol concentration, casting time, drying schedule and heat treatment were all adjusted to obtain a thin, crack-free NF layer approximately 0.5 μm thick.

The NF membranes had an average permeability at 10 bar of 35 ($\pm$10) $dm^3/h/m^2/bar$ which is significantly higher than other NF membranes [4, 5]. (The permeability of the UF support under the same conditions was 110 dm3/h/m^2/bar.) The separation characteristics of the membranes were investigated using the following solutes: dextran T10 (MW = 10,000); vitamin B12 (MW = 1355); bromocresol green (MW = 698); and sucrose (MW = 342). The solute retention characteristics of three of the NF membranes are summarized in Fig. 2 in comparison with the UF support. The NF membranes show increased retention of all the solutes with respect to the UF support and have a 50% retention in the region of 1000 molecular weight.

The separation performance is not quite as good as previously reported for gamma alumina NF membranes [5], but the permeability of the alumina membranes was almost an order of magnitude lower than the zirconia membranes described here. The separation characteristics of NF membranes are not determined solely by the molecular weight of the solute. This is evident from the high retention of the charged bromocresol green molecule by all the membranes in Fig. 2. Nevertheless, the retention as a function of molecular weight gives a semiquantitative guide to separation characteristics. The spread of performance in these membranes probably indicates that their performance is still being influenced significantly by residual defects and heterogeneities in both the NF layer and the UF support.

Pillared Clay Catalysts and Adsorbents

It is possible to exchange the alkali metal cations in some swelling clays by larger ions (organic or inorganic) to increase the interlayer spacing in the clay and form a so-called pillared clay. The attraction of pillared clays is that they have large micropore volumes with a characteristic size greater than can be achieved in a zeolite. This enables larger organic molecules to enter the pillared structure than can enter the cages of a zeolite and thereby absorb such molecules or carry out catalytic reactions involving them. The polynuclear cations, based on $[Al_{13}O_4(OH)_{24}(H_2O)_{12}]^{7+}$, present in aluminium chlorohydrate solutions, $Al_2(OH)_5Cl$, and sols and those based on $[Zr(OH)_2 \cdot 4H_2O]_4^{8+}$ in zirconyl solutions and sols are all capable of pillaring clays. In studies at AEA Technology such solutions and sols have been used to pillar sodium montmorillonite crystals in an American bentonite.

Table 1. Characteristics of pillared clays.

Specimen	Interlayer spacing from XRD (nm)		Nitrogen physisorption	
	d_{001}	"Free" spacing	BET surface area ($m^2\ g^{-1}$)	Micropore volume ($cm^3\ g^{-1}$)
Unpillared	0.972	0.000	37	
Al pillared (chlorohydrate)	1.911	0.939	245	0.100
Zr pillared (zirconyl chloride)	2.193	1.212	421	0.169
Zr pillared acetic acid sol	2.105	1.133	385	0.127
Zr pillared nitric acid sol	1.934	0.962	371	0.143

In the case of zirconia sols derived from zirconyl chloride the particle size in the sol was controlled in the range 1.3 to 90 nm by refluxing the aqueous dispersion. Zirconia sols were also prepared by dissolving basic zirconium carbonate in nitric or acetic acid. The particle size in the nitrate-stabilized sols varied from 1.3 nm at a $Zr:NO_3$ ratio of 1:3 to 4 nm at a ratio of 1:1. The particle size in the acetate-stabilized sol was 5 nm at Zr:acetate ratio of 1:1.5. The particles in some of the nitrate-stabilized sols were also grown by refluxing to as large as 90 nm. The clay was dispersed in a water/acetone mixture and then the sol was added to intercalate the expanded clay layers. After pillaring, the clays were dried and calcined at 400°C and then characterized by X-ray diffraction and nitrogen adsorption. The results are summarized in Table 1 and show that all the sols could produce a large and regular increase in interlayer spacing, a large surface area for nitrogen adsorption and a useful micropore volume. The hydrothermal stability of the pillared clays was tested by exposure to steam for 6 hours at 350°C and 700°C. After exposure at 350°C there was a slight reduction in surface area in all the pillared clays of about 30 $m^2\ g^{-1}$. After exposure at 700°C the surface areas were reduced significantly to the range 50 to 150 $m^2\ g^{-1}$ (depending on preparation method). The materials thus have reasonable hydrothermal stability.

Alternative routes were also developed to avoid the use of organic co-solvent. Although the resulting materials were not quite as good, the preparations were successfully scaled up to 20 kg batch size. The Al-pillared clay had suitable catalytic activity and selectivity for the hydration of ethylene to ethanol and the Zr-pillared clays were highly suitable for the synthesis of alkyl benzene.

Phosphors for High Resolution Displays

Phosphors are used widely in CRT and plasma displays for converting electron kinetic energy or UV energy into visible light. Typical phosphors are multicomponent ceramic crystal hosts doped with an active ion that is responsible for the energy conversion. The energy conversion efficiency is very sensitive to crystal quality and therefore in good phosphors powders each particle should be a single crystal, with a low density of dislocations and other defects and uniform concentration of the active ion. In order to improve the quality of small CRT displays and increase their resolution, phosphor powders having a uniform particle size in the range 1 to 2 μm are required. Here we summarize the synthesis of such a phosphor powder by a sol-gel route [10].

The particular phosphors that were synthesized were Tb-doped yttrium aluminium gallium garnets (YAGG), which emit green light on electron irradiation. The conventional synthesis method is to mill together the oxides of the phosphor constituents with up to 20% by weight of BaF_2 which acts as a flux [11, 12]. The powder mixture is reacted at about 1600°C and the phosphor crystals are finally extracted by dissolving the flux in nitric acid, milled to the required particle size and then annealed in the range 1500 to 1600°C to relieve damage from the milling process. This is the kind of synthesis route for which a sol-gel approach offers potential advantages in more readily achieving homogeneity. In a typical sol-gel preparation [10], Y_2O_3 and Tb_4O_7 were

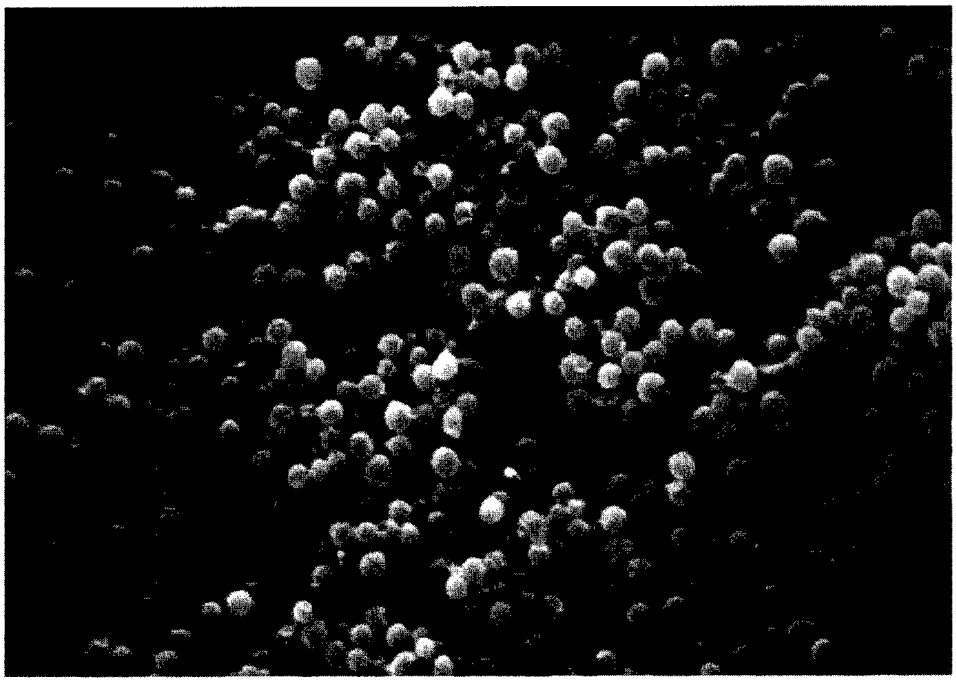

Figure 3. Scanning electron micrograph of Tb:YAGG phosphor particles produced by an aerosol sol-gel route with a maximum temperature of 1000°C.

dissolved in nitric acid and gallium nitrate was added to form a solution of Y, Ga and Tb nitrates. Aluminium chlorohydrate sol was then added to produce a stable mixed sol and up to 2% BaF_2 (by weight with respect to total oxides) added as a solution in nitric acid.

Freeze dried gels were calcined at 500°C to convert to oxide and then heated to 1500°C for 10 h to grow the YAGG crystals (which were shown by XRD to be of suitable quality) and residual flux was removed by washing with nitric acid. However, the crystals made in this way were strongly agglomerated by liquid phase sintering and the powder was not suitable for display fabrication.

To prevent agglomeration the sols were processed as aerosols produced by ultrasonic atomization of the sols. The aerosol dispersion was passed through a drying column to gel the droplets and then through a furnace at 1000°C (residence time 0.1 s) to calcine them. The calcined powder was collected in a cyclone and its morphology is illustrated in Fig. 3. The powder particles were uniform, spherical, unagglomerated and in the required target size range (1 to 2 μm). The particles were easily dispersed in water and their mean size was 1.3 μm. Sol feeds that gel on drying are preferable to solution feeds for the aerosol route since they readily form dense particles as opposed to hollow shells. Single crystal phosphor particles of the required size were grown from the powder at 1500°C, but the crystals were partially agglomerated by sintering. The aggregates were broken down by a brief milling and then evaluated as display screen phosphors. Their performance was found to be suitable, but elimination of the aggregation and final milling is required to improve them further. Similar sol-gel routes have been developed to synthesize a range of phosphors including Mn-doped zinc silicate and Eu-doped yttrium gadolinium borate.

Ceramic Pigments

Most ceramic pigments, used in the decoration of "traditional" ceramic artefacts such as tableware and tiles, are doped multicomponent oxides. The sol-gel process is thus well suited to their synthesis; offering the usual advantages of better homogeneity and lower processing temperature than pigments made by the traditional solid state reaction route. Furthermore, the ease with which sols can be gelled by spray drying enables free flowing pigment powders (as gels or oxides) to be produced having improved printing characteristics.

Sol-gel preparative routes for ceramic oxide pigments have been developed [13] similar to those

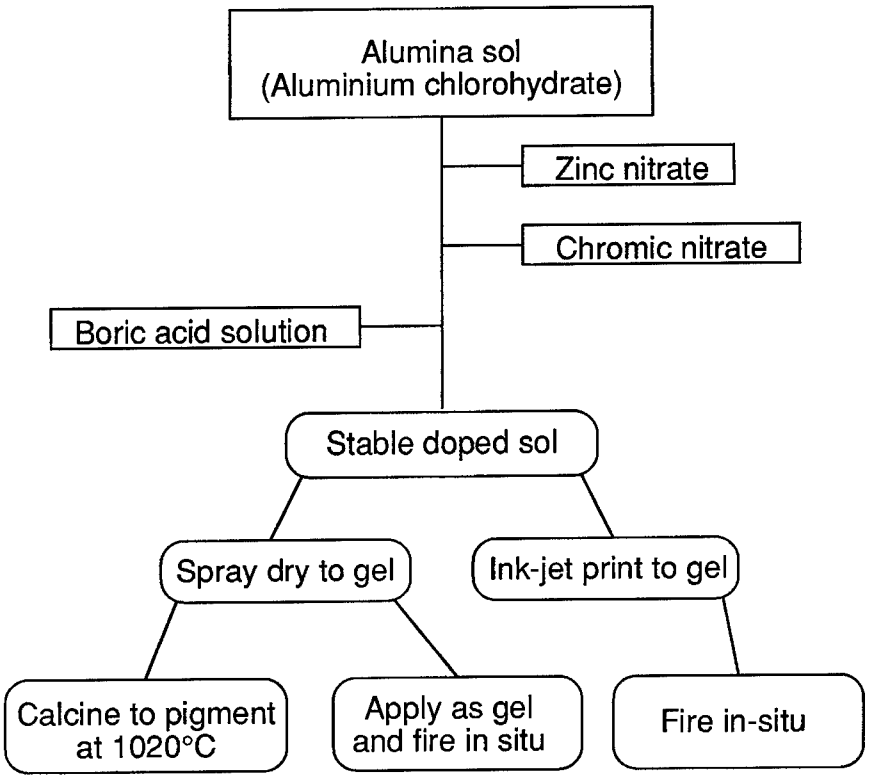

Figure 4. Example of a sol-gel pigment composition that can be applied to decorate ceramics in different ways.

described for phosphors and have been extended to encompass over 60 formulations. A typical example of a preparative route is illustrated in Fig. 4. Pigment compositions synthesized by the sol-gel route form the colored pigment oxide at significantly lower temperatures than in the conventional solid-state reaction process. The ceramic oxide pigments produced by the sol-gel routes have indeed proved to have "cleaner" color and wider firing tolerance than their conventional counterparts.

The high reactivity of the gels means that the "pigment" can be applied in the form of the sol or the gel such that the constituents react to form the color in-situ on the ceramic artefact when it is fired (Fig. 4). We have demonstrated the feasibility of this approach by formulating sol inks and applying them by continuous ink-jet printing to both glazed and unglazed tile and tableware substrates [14].

Concluding Remarks

The aqueous sol-gel processes constitute a very flexible set of potential routes for synthesizing a wide variety of oxide ceramics giving control over pore size on the nanometer scale in porous materials or compositional homogeneity in the case of multicomponent oxides. The degree of such control is probably not as great as can be achieved by the alkoxide sol-gel processes, but the precursors are much cheaper, and the environmental problems generated by handling large quantities of organic solvents can be avoided. Hence, it has been possible to scale up to reasonable trial production quantities (up to 20 kg) in some of the examples given here. For multicomponent oxides made by an aqueous sol-gel process it is usually necessary to have only one major component capable of gelation in order to achieve a successful synthesis. However, subsequent processing of the wet gel must be carried out in such a way (e.g., as spray dried or aerosol generated powder) to prevent redistribution of soluble components.

Acknowledgments

We would like to thank all our colleagues who helped to carry out this work at AEA Technology: Mr. G.B. Cole, Mrs. R. Evans, Mr. R.M. Guppy, Dr. R. Jones,

Dr. D.A.V. Morton and Mr. P.J. Russell. We would also like to thank the following companies who collaborated in these projects and evaluated the sol-gel products for particular applications: Tech Sep, Tate and Lyle Process Technology, BP Chemicals, Süd Chemie, Riedel de Haan, Thomson Tubes Electroniques, Portmeirion Potteries, H&R Johnson Tiles and Domino Amjet. We are grateful for financial support from AEA Technology, the Commission of the European Community (BRITE) and the UK Department of Trade and Industry (LINK Nanotechnology).

References

1. D.L. Segal, *Chemical Synthesis of Advanced Ceramic Materials* (Cambridge University Press, Cambridge, 1989).
2. C.J. Brinker and G.W. Scherer, *Sol-Gel Science* (Academic Press, London, 1990).
3. C. Guizard, C. Mouchet, R. Vacassy, A. Julbe, and A. Larbot, J. Sol-Gel Sci. Technol. **2**, 483 (1994).
4. A. Clearfield, J. Mater. Res. **5**, 161 (1990).
5. C. Guizard, A. Julbe, A. Larbot, and L. Cot, J. Alloys and Compounds **188**, 8 (1992).
6. A. Atkinson, P.J. Russell, and D.L. Segal, in *Proceedings of the 7th International Conference on Inorganic Membranes*, edited by D.E. Fain, Gatlinburg (1996).
7. P. Langer, B. Lintner, N. Arfsten, and R. Schnabel, Key Engineering Materials **61/62**, 33 (1991).
8. A. Larbot, S. Alami-Younssi, M. Persin, J. Sarrazin, and L. Cot, J. Membrane Sci. **97**, 167 (1994).
9. J.R. Butruille and T.J. Pinnavaia, in *Characterisation of Catalytic Materials*, edited by I. Wachs (Butterworth-Heinemann, Boston, 1992), p. 149.
10. D.L. Segal and A. Atkinson, Brit. Ceram. Trans. **95**, 103 (1996).
11. K. Ohno and T. Abe, J. Electrochem. Soc. **133**, 638 (1986).
12. K. Ohno and T. Abe, J. Electrochem. Soc. **134**, 2072 (1987).
13. A. Atkinson, J. Doorbar, D.L. Segal, and P.J. White, Brit. Ceram. Proc. **52**, 49 (1994).
14. A. Atkinson, J. Doorbar, A. Hudd, D.L. Segal, and P.J. White, J. Sol-Gel Science and Technology **8**, 1093 (1997).

Journal of Sol-Gel Science and Technology 1/2, 141–146 (1998)
© 1998 Kluwer Academic Publishers. Manufactured in The Netherlands.

Inorganic-Organic Polymers with Barrier Properties for Water Vapor, Oxygen and Flavors

S. AMBERG-SCHWAB AND M. HOFFMANN
Fraunhofer-Institut für Silicatforschung, Neunerplatz 2, D-97082 Würzburg, Germany

H. BADER AND M. GESSLER
Fraunhofer-Institut für Lebensmitteltechnologie und Verpackung, Giggenhauser Str. 35, D-85354 Freising, Germany

Abstract. With a new kind of barrier coating material, inorganic-organic polymers, it is possible to obtain high-barrier properties with respect to the permeation rates of oxygen, water vapor and volatile organic compounds.

The hybrid polymers are accessible via the sol-gel technique. The inorganic network is formed as a result of controlled hydrolysis and condensation of alkoxysilanes, organoalkoxysilanes, acryloxysilanes or metal alcoholates. The organic network results from subsequent thermal or UV-induced polymerization of organo-functional groups.

Due to the control of the inorganic and organic network densities and the insertion of specific functional groups to control the polarity of the resulting material, it was possible to develop high-barrier coatings with excellent adhesion properties on a wide variety of polymer films.

These high-barrier coatings are also suitable as adhesives which can be used in laminates. The properties of the processable multilayer structures are preserved to a much higher extent than with other comparable, commercially available materials even under high mechanical and thermal stress and storage in humidity.

Keywords: inorganic-organic polymers, barrier coating, barrier adhesive, laminating agent, water vapor barrier, oxygen barrier, flavor barrier

1. Introduction

In recent years polymeric packaging materials have become increasingly important, especially in the food packaging industry due to their numerous advantages over other materials with respect to convenience, economy and even ecology. However, unlike materials such as glass or metals, polymers are permeable to gases, water vapor and volatile organic compounds like hydrocarbons or food flavors. In order to meet the complex demands for packaging materials concerning the barrier properties as well as the mechanical stability and the stability against humidity, composite films containing different types of polymers generally have to be used in combination with aluminum-foil. In contrast to glass or metal, the disadvantages of any such laminated polymeric structures are the difficulties entailed in their recycling. More recently, they have come under criticism on this account and research into alternative packaging materials has been intensified [1–3].

New paths have been explored for the use of coatings combining different barrier functions. These materials, based on inorganic-organic polymers, may minimize the amount of packaging material. They will also reduce the number of different materials in such composite films, thereby improving the degree of reutilization and material recycling.

By systematically varying the inorganic and the organic network densities and the polarity of the hybrid polymer material matrices, it was possible to develop coating materials with barrier properties for water vapor, oxygen and flavors [4]. Furthermore, these materials proved to be suitable as laminating agents.

2. Experimental

The barrier properties of three different types of sol-gel derived coatings were investigated: a UV-curable (type 1), a thermally curable (type 2) and a thermally curable, water-based system (type 3).

The UV-curable system was synthesized by base catalyzed addition of 0.85 mol 3-mercaptopropyl-trimethoxysilane to 1.00 mol 1,1,1-tris-(hydroxy-methyl)-propan-triacrylate in 1000 ml ethyl acetate and subsequent hydrolysis of the intermediately formed acryloxysilane. After hydrolysis with 70% of the stoichiometric amount of water with respect to the hydrolyzable alkoxy groups, 700 ml ethyl acetate were evaporated and 0.18 mol 1-hydroxycyclohexyl-phenylketone were added. The sol, which had a solids content of 70%, was applied with a spiral applicator. UV-curing was performed with commercially available equipment (Beltron; type 22/III; UV contact time: 60 s, 80 mW/cm^2). The coating thickness was 9 μm.

The thermally-curable system (type 2) consisted of the following starting materials: tetramethoxysilane, zirconium propoxide, aluminum-sec-butylate, 3-glycidoxyproyl-trimethoxysilane and 3-aminopropyl-triethoxysilane. After hydrolysis with the stoichiometric amount of water with respect to the hydrolyzable alkoxy groups and cocondensation at 15°C the solution was stirred for two hours at 25°C. The sol, which had a solid content of 50%, was applied with a spiral applicator and cured for 1 hour at 130°C. The coating thickness was 5 μm.

The water-based coating material (type 3) consisted of the same starting compounds as type 2. After hydrolysis and condensation the resulting alcohols were evaporated and replaced by an equal amount of water. The samples were coated with a spiral applicator and cured for 1 hour at 130°C. The coating thickness was 5 μm.

To use these hybrid polymers as laminating agents the materials could be applied with a roller coating

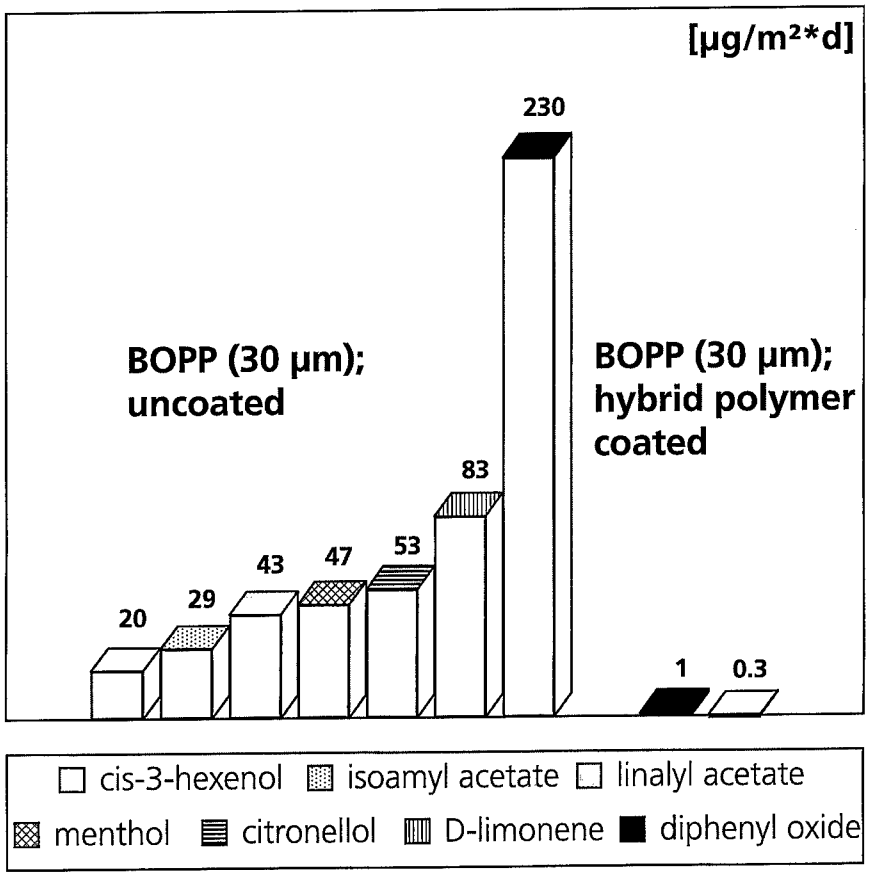

Figure 1. Permeation rates of seven different flavors for an uncoated and a hybrid polymer coated BOPP film.

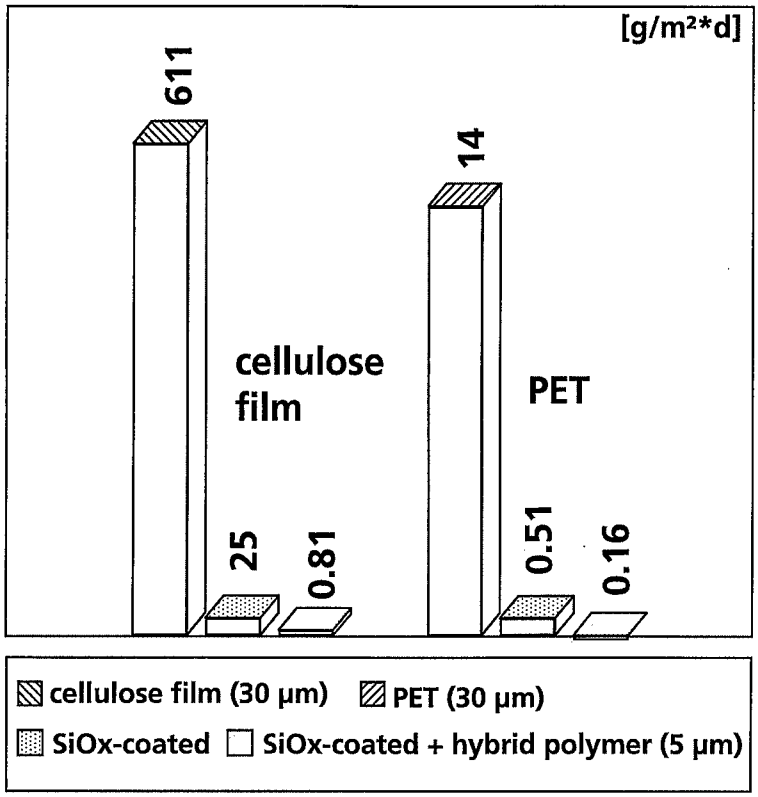

Figure 2. Water vapor transmission rates of uncoated and coated PET and regenerated cellulose films.

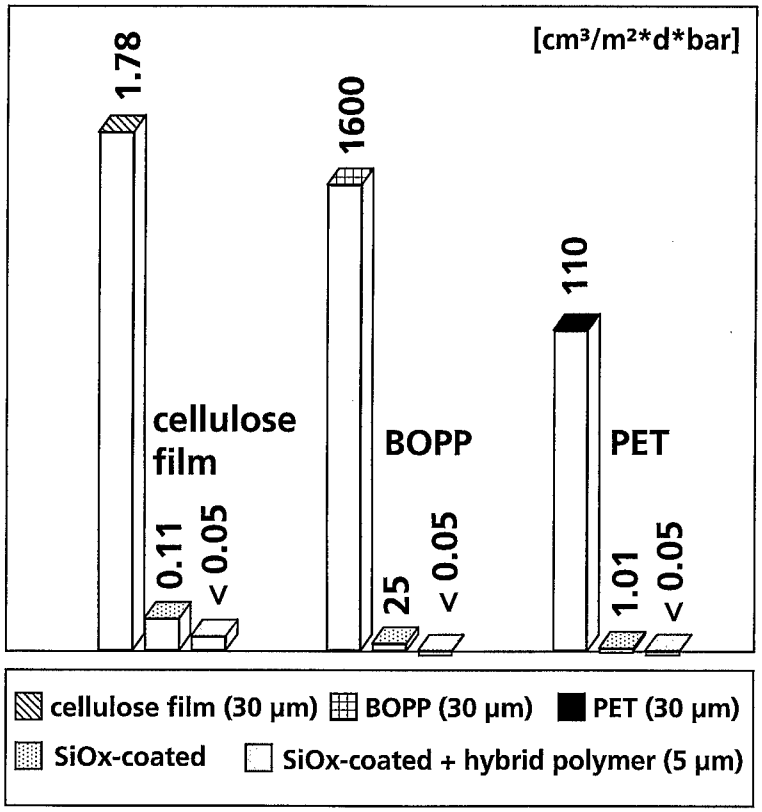

Figure 3. Oxygen transmission rates of uncoated and coated regenerated cellulose, BOPP and PET films.

process. The thickness of the resulting layer was about 2 μm.

3. Results and Discussion

3.1. Flavor Barrier Properties

With a new test method the permeation rates of seven different flavors were simultaneously measured by gas chromatography [5]. Flavor transmission rates were determined at 23°C and vapor pressures of the permeants ranged from 1.0×10^{-6} to 4.7×10^{-6} bar. The flavor permeation rates were obtained for both uncoated and hybrid polymer coated biaxially oriented polypropylene (BOPP) films.

Figure 1 shows that the permeation rates of the flavors were drastically reduced by the UV-cured hybrid polymer coating (type 1). For the coated BOPP film, the permeations of only two (diphenyl oxide and cis-3-hexenol) out of the seven flavors could be detected.

3.2. Barrier Properties for Water Vapor and Oxygen

The permeability of polymers with respect to water vapor, oxygen and flavors may be considerably reduced by vacuum deposition with thin inorganic coatings, for example with SiO_x. These techniques, however, cannot provide sufficient barrier in the field of high-barrier applications, a phenomenon that may be attributed to wetting defects or inadequate adhesion of the layers. It was therefore investigated to what extent the oxygen and water vapor permeation properties of SiO_x-coated PET (polyethyleneterephthalate) and regenerated cellulose films could be further improved by coating these materials with inorganic-organic polymers.

The water vapor permeation measurements were performed by an electrolytic technique according to DIN 53122 at 23°C and 85% relative humidity.

Figure 4. SEM of the multilayer structure: PET-SiO_x/hybrid polymer/PET.

Figure 2 shows the water vapor transmission rates of PET and regenerated cellulose, firstly untreated, secondly coated with SiO_x and thirdly with a combination of SiO_x and inorganic-organic hybrid polymer (type 2).

The application of this barrier material on SiO_x-coated PET films showed a three-fold increase of barrier property. For the SiO_x-coated regenerated cellulose film even an improvement factor of 30 could be attained.

The oxygen barrier properties of the inorganic-organic polymers were investigated in accordance with DIN 53380 at 23°C and 75% relative humidity. Figure 3 shows the oxygen transmission rates of regenerated cellulose, BOPP and PET again as single film, in combination with SiO_x and also in combination with SiO_x plus a thermally-cured water-based inorganic-organic polymer (type 3).

Applying a thermally curable, water-based hybrid polymer to the SiO_x-coated film reduces the resulting oxygen permeability for all material combinations below the detection limit of 0.05 $cm^3/m^2d \cdot bar$. For the polypropylene film, however, the permeation reduction effect is the most impressive one.

Further investigations showed that these materials can be used as laminating agents (Fig. 4).

The most remarkable features of these structures are their excellent adhesion and barrier properties even under high mechanical and thermal stress and storage in humidity (Table 1). The flex restistance of these materials was tested in accordance with ASTM F 392-74 (Gelboflex-Testing). The flexing action consists of a twisting, followed by a horizontal motion.

Table 1. Oxygen transmission rates of the multilayer structure PET-SiO_x/hybrid polymer/PET after being mechanically stressed.

		O_2-permeation/ cm^3/m^2 d · bar (23°C, 50% RH)
After strain		
PET-SiO_x/hybrid polymer/PET	0–5%	<0.05
PET-SiO_x/hybrid polymer/PET	6%	0.44
After Gelboflex-testing (50 cycles)		
PET-SiO_x/hybrid polymer/PET		0.37
Other commercially available laminates		2–10
After sterilization (20 min, 121°C)		
PET-SiO_x/hybrid polymer/PET		0.65

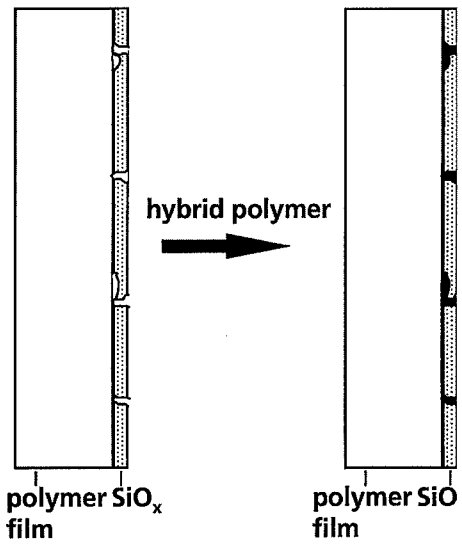

(a)

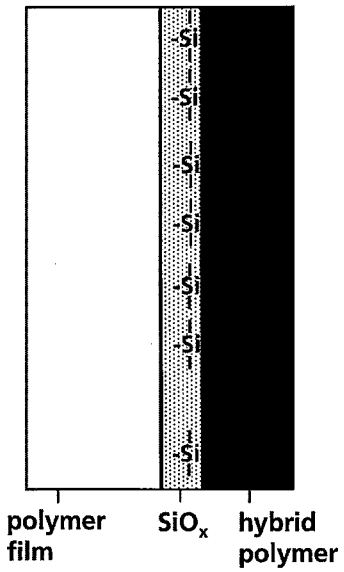

(b)

Figure 5. (a) Compensation of the macroscopic defects formed in the SiO_x layer. (b) Idealized scheme of interfacial bonding.

4. Synergistic Effects Through Combination of SiO_x-Vapor Deposited and Inorganic-Organic Hybrid Polymer Coating

The theoretically calculated transmission rates for a multilayer structure proved to be always far higher than

Table 2. Oxygen transmission rates of coated BOPP films.

	O_2-permeation/ cm^3/m^2 d · bar (23°C, 50% RH)
BOPP	1600
BOPP/hybrid polymer coated	34
BOPP-SiO_x	25
BOPP-SiO_x/hybrid polymer (calculated value) [6]	0.14
BOPP-SiO_x/hybrid polymer (measured value)	<0.05

the actual rate measured in the experiment (e.g., the oxygen transmission rate for BOPP-SiO_x/hybrid polymer, Table 2).

The difference between these rates can be explained as a synergistic barrier effect through combination of SiO_x- and hybrid polymer coating. This effect can be illustrated by two theoretical models (Fig. 5).

First, the macroscopic defects of the SiO_x coating are compensated by the hybrid polymer coating (Fig. 5(a)). Second, where SiO_x and hybrid polymer meet, covalent Si—O—Si bondings can be created. This could lead to an area of high inorganic network density, thus producing an additional barrier effect (Fig. 5(b)).

Both models are confirmed by the fact that the oxygen transmission rate of the BOPP-SiO_x/hybrid polymer film does not depend on hybrid polymer coating thickness. Thus, synergistic effects can be explained with the chemical and mechanical interaction at the SiO_x/hybrid polymer interface.

5. Conclusion

New developments based on inorganic-organic hybrid polymers can drastically improve the barrier properties of polymeric films, both as single coating (flavors) or in combination with SiO_x (water vapor and oxygen). Such materials can be used as coatings as well as high-barrier laminating agents in multilayered structures. Even after high mechanical and thermal stress and storage in humidity the composite film showed excellent oxygen barrier properties. The next step in the development will be the upscaling of the laboratory results into pilot plant dimension.

References

1. M. Boysen, Kunststoffe **77**, 522 (1987).
2. T.G. Krug, in *Proc. of the 33rd Annual Technical Conference* (Society of Vacuum Coaters, Washington, 1990), p. 163.
3. H.-C. Langowski and H. Utz, ZFL **43**, 520 (1992).
4. S. Amberg-Schwab, M. Hoffmann, and H.G. Bader, Kunststoffe Plast Europe **86**, 15 (1996).
5. Franz, Packag. Technol. Sci. **6**, 91 (1993).
6. W. Prins and J.J. Hermans, J. Phys. Chem. **63**, 716 (1959).

Journal of Sol-Gel Science and Technology 13, 147–152 (1998)
© 1998 Kluwer Academic Publishers. Manufactured in The Netherlands.

Design of Sol-Gel Coating Media for Ink-Jet Printing

BULENT E. YOLDAS
Carnegie Mellon University, Department of Chemical Engineering, Pittsburgh, PA 15213, USA

Abstract. Image transfer and storage is rapidly becoming one of the most important technologies in the communication age. Ink-jet printing by which multicolor images are transferred onto paper and transparencies is a major branch of this technology. In this technology electronic image transfer capabilities are often limited by the shortcomings in the materials used. The coating designed to receive the ink determines the ink-dry time, edge acuity or patterns, color fidelity, as well as light and water fastness of the print. These in turn govern the speed, resolution and quality of the image transferred. Chemical, structural and process parameters involved in the design of a transparent, single layer sol-gel coating media for ink-jet printing are discussed. Design goals include quick drying of the print, water resistance, edge acuity without bleeding, UV protection of color dyes, and being printer nonspecific.

Keywords: ink-jet, ink-jet coating, sol-gel coating, image transfer, dye immobilization, water absorption, water resistance, transparencies

1. Introduction

Ink-jet printing is increasingly used to print multicolor images on various substrates, e.g., on transparencies and photographic paper [1–4]. In the printer, droplets of ink, typically 20 μm radius, carrying 20–40 picoliter of ink are propelled from the printhead onto the surface of the recording media at a high speed. The recording media may receive as many as 600 droplets per inch (dpi) in a fraction of a second. Typically three principle colors, which are dye based, and a pigment black are used to produce various colors, and shades of colors. The present inks are water based, containing up to 95% water; the rest being color dyes and additives to control viscosity and surface tension. Since various colors, and shades of colors, are formed by blending three basic colors, it is necessary to strike the same precise dot location with different color droplets to form complex colors and shades. Thus the surface of the media receives a large flux of ink in a short period of time. The image "drying" process may take as long as 3–5 min for color prints, presenting a significant barrier to rapid production and handling of images. Some ink-jet printers incorporate heaters to accelerate this "drying" process. This has a limited effect since the "image drying" occurs not as a result of solvent evaporation, but by the diffusion and chemical immobilization of the solvent in the recording media. For rapid production of high-resolution images the challenge can be briefly stated as the quick removal of ink solvent without transporting the colorants outside of the targeted areas.

Recently, there have been attempts to apply substantially porous sol-gel films onto transparencies to accommodate this solvent removal [5–7]. These coatings typically incorporate a colloidal sol, e.g., alumina or silica, along with an organic binder, such as polyvinyl alcohol and various organic polymers and additives.

In addition to the "rapid drying" requirement, there are a number of requirements on print quality, on coating, and on the solution from which the coating is applied. Print quality includes: edge acuity; color fidelity; absence of ink coalescence, crystallization, bending, cracking, and bleeding. The image must be smear resistant, permanent, "waterfast" and "colorfast," i.e., substantially resistant to water and UV light. Coating related requirements includes the absence of "curle." For transparency applications, the coating must be transparent and substantially haze free and provide

high-density images with the versatility to accept different types of inks.

2. Experimental

The initial goal of the investigation was to reduce the "dry time" from around 3 to 5 min, to below 90 s for color prints printed on transparencies. This time was measured by placing a white paper over the freshly printed transparency and rolling a 2 in. thick four pound roller over it. The time when the printed color patterns did not leave any impression on the paper, was taken as the dry time. All other criteria related to print quality and coating properties mentioned earlier also had to be met or exceeded.

Necessary components of a sol-gel film, which would meet the minimum requirements of an ink-jet printing media, were first identified. Then candidate compounds which would provide these functions were selected. Using these compounds aqueous sols were formulated. Initially, a three-component coating system comprised of AlO(OH) sol, a cellulose ether, and a polyvinyl alcohol (PVA) was selected as the minimum starting point. In this system AlO(OH) provides the matrix of the film, cellulose ether provides chemical immobilization of aqueous solvent, and PVA plays the role of binder and provides abrasion resistance.

The AlO(OH) sol had to be produced from aluminum alkoxides by the method described by Yoldas [8, 9] in order for the coating film to be substantially haze free and transparent. The rheological properties of precursor sols were tested and adjusted for both high and low shear viscosity and stability. These sols were then applied by Meyer rods on polyethylene terephthalate transparency sheets and were dried at 100–130°C. Streamline potential measurements were carried out to determine surface charge characteristics (zeta potential). Printing of the coated transparencies was carried out by various color ink-jet printers: Hewlett-Packard's HP 310, HP 550, HP 855 and an Epson Color Stylist. Coated films and printed sheets were investigated for thickness, haze, curle, print quality, bleeding, water resistance, color fastness optical, and chemical stability.

3. Results and Discussion

3.1. Sol Composition and Application

One of the main considerations in the formulation of an ink-jet coating sol is its rheological characteristics. The solid concentration that would result in the required thickness of ink-jet coating film, e.g., 30 μm, must also have suitable sol viscosity, surface tension, wetting and drying characteristics to make commercial production feasible.

In these systems the viscosity is very sensitive to molecular weight of the organic polymers, as well as temperature; a precise control of viscosity can usually be attained by manipulating these noncompositional parameters, without affecting the film composition, e.g., by using a blend of various molecular weights. Consideration of various factors, led us to formulate a three-component system consisting of 10 parts AlO(OH) (produced from alkoxides), 2 parts hydroxypropyl cellulose, HPL, and 1 part polyvinyl alcohol, PVA, by weight in an aqueous sol with 9–15% solids.

Experimental results showed that use of hydroxypropyl cellulose, particularly in the molecular range of 200,000–400,000, was uniquely suited for ink-jet printing. Neither hydroxy ethyl cellulose nor hydroxy butyl cellulose (obtained from Aldrich) worked as well. PVA needed to be highly hydroxylated, e.g., 98%, and low molecular weight, e.g., 10,000 to 15,000. Substitution of polyvinyl pyrolidone (PVP) for PVA showed significant effects by enhancing drying time, and allowing printability by Epson printers. This effect was strongly molecular weight dependent. Molecular weight also affects haze. For example, additions of lower molecular weight K-17 and K-30 PVPs (BASF) did not have a significant effect, where as higher molecular weight K-80 and K-90 PVPs caused faster drying but also caused haze.

Further studies have shown that this enhancement on drying was directly related to the degree of haze formed. This meant that the phase separation that causes the haze also provides interfacial channels for rapid transfer of the solvent. For transparency coatings, the attainment of fast drying by introduction of PVP without forming haze was unsuccessful. It was also found that Epson printability could be obtained by increasing the HPC level in the original formulation. Thus, use of PVP was abandoned.

3.2. Recording Film and its Morphology

A series of experiments were conducted to establish the pore morphology of the recording film and the porosity changes with its formulation, particularly the porosity when the print quality is optimum. The recording

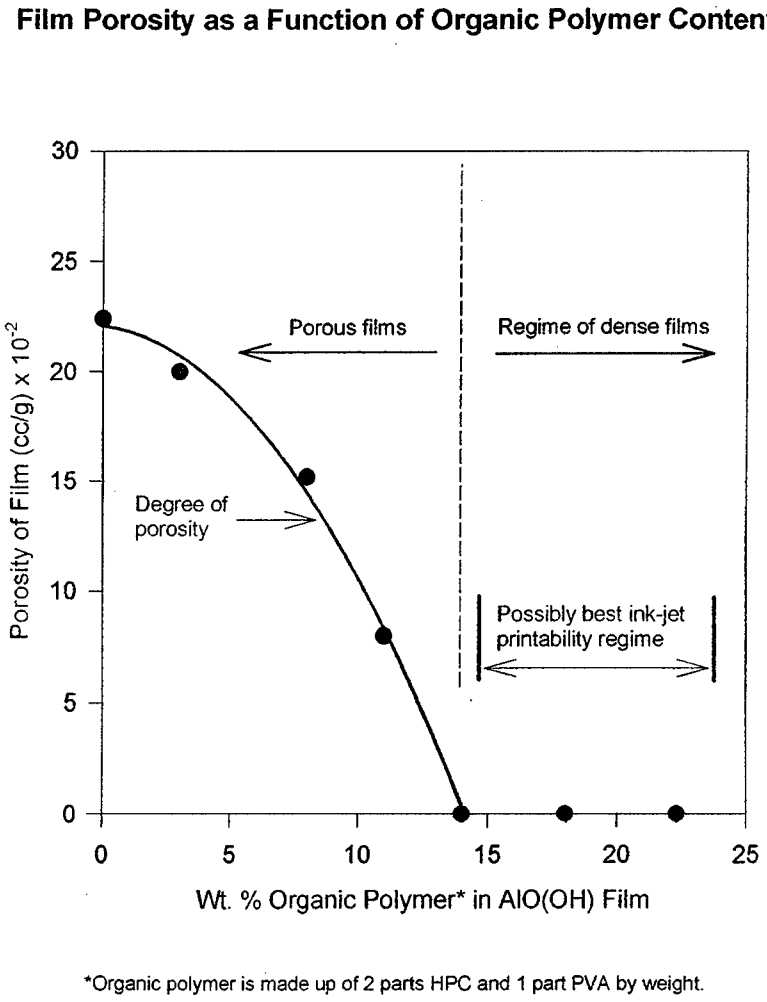

Figure 1. Porosity of organic polymer containing AlO(OH) films as a function of polymer content. (Organic polymer is a blend of 2 parts HPC, 1 part PVA by weight.)

film is essentially a three-component system, consisting of AlO(OH), HPC, and PVA; AlO(OH) making up most of the solid. AlO(OH) film by itself would be highly porous (40–60%) yet transparent. The effect of incorporating HPC and PVA into an AlO(OH) matrix was investigated. In these experiments, the films were cast over glass, peeled and the pore morphology was determined by the BET method utilizing nitrogen adsorption.

A polymer blend made up of 2 parts HPC and 1 part PVA were incrementally introduced into the AlO(OH) sol as to affect its pore morphology (Table 1) and to study the effect of this on print quality, and image drying. Figure 1 shows the resultant change in the pore morphology as a function of increasing organic polymer content and the region of the best print quality.

It is clearly evident from Table 1 and Fig. 1 that the porosity of the film decreases with increasing organic polymer content, and that porosity is entirely eliminated at around 13–14 wt% organic polymer. The

Table 1. Porosity of AlO(OH) films as a function of organic polymer content.

Polymer content (wt%)	Porosity (cm^3/g)	Surf. area (M^2/g)	% Porosity
0	0.2240	270	~43
3	0.2008	234	~37
7	0.1519	177	~30
11	0.0797	92	18
18	0.0007	0.7	0.2

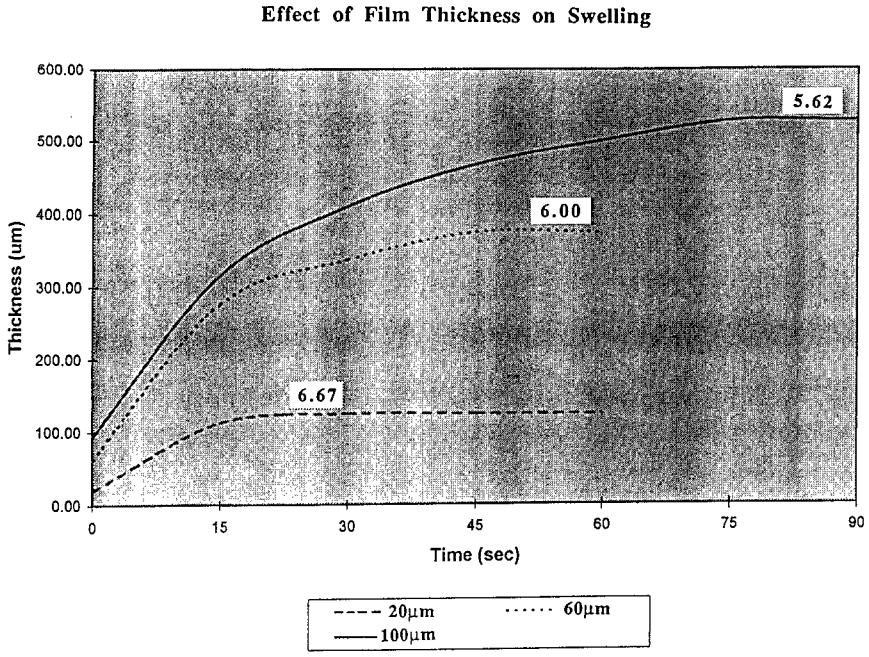

Figure 2. Swelling of ink-jet recording film of various thickness in water. (Note that thinner films swell more.)

best print regime occurs where the coating is dense. This is particularly significant since a recent sol-gel recording film patent [5–7] bases its claims on forming a highly porous layer in a similar ink-jet coating system.

3.3. Drying Mechanism and Film Swelling

In the ink-jet recording films described, the print "dries" not by evaporation of solvent, nor by its containment in the pores, but by chemically combining the water in the polymer structure. Since the recording film is originally dense, this "drying" process requires substantial *swelling* on the part of the recording film to accommodate the large amount of liquid in its structure. Calculations also show that the large amount of dye carrying liquid cannot be accommodated by the porosity without also causing unacceptable lateral diffusion of colors, i.e., bleeding.

Film swelling, up to 6 or 7 times the original thickness, depends on composition. This swelling is also a function of the film thickness as seen in Fig. 2. In these experiments, different thickness films were submerged in water exposing both sides. Thickness measurements were taken of the coating using the calibrated ocular in the stereomicroscope every 15 s while it was submerged in water, until the coating no longer increased in thickness. The experiments were repeated several times with excellent reproducibility.

As seen in Fig. 2, the swelling is not only a function of composition, but also a function of thickness. The swelling appears to take place in two stages: a rapid initial swelling within the first 20–30 s, followed by a gradual slower swelling to a final equilibrium, which may take several minutes for a film 100 μm thick. (This swelling is also affected by mordants and molecular weight of the polymers, which will be dealt with elsewhere.)

The swelling and its rate is a direct indication of the capability of the film to absorb ink and the rate of such absorption. Thus, it can be used to calculate required film thicknesses for a given flux of ink and dry time. Obviously, there is a minimum thickness below which the film cannot accommodate the volume of the liquid applied. (There is also a maximum thickness above which the coating flakes off, cracks, and causes curle on the substrate.) Calculations show that this thickness is around 20–30 μm for existing printers and printers under development. Below 15 μm thickness, the performance deteriorates significantly and bleeding occurs. With proper formulation and thickness, design color prints can be "dried" in less than 15 s.

3.4. *Water and Color Fastness*

Both the recording film and recorded image must be water resistant even though both are produced from aqueous systems, i.e., aqueous sol, and water-based ink. There are several ways to achieve this. The recording film consists of up to 60% AlO(OH) which can be made water resistant by one of the following methods:

- heat treatment above 150°C
- chemical combination with various silanes etc.
- combining with PVA, followed by heat treatment ~100°C
- by charge fixation

Usually heat treatment above 150°C is detrimental to the substrate, as well as to the organic components of the recording film is thus normally avoided. Chemical combination of γ-glycidoxypropyltrimethoxysilane and tetramethoxysilane at very low concentrations, e.g., as little as 1–3 wt%, induces water resistance on both the recording film and the image. However, these components also affect rheology and stability of the coating sol, as well as print quality and dry time of the image; thus, their overall effect must be carefully investigated.

Inclusion of 8–10% PVA followed by heat treatment of around 100°C is an effective method of imparting water resistance into AlO(OH) based coatings. Since PVA is a component of the coating formulation for other reasons and the heat treatment comes with the drying of the coating, this becomes an attractive alternative.

In the last method a series of compounds based on aziridine monomer chemistry are used as fixation agents for both the ink and the ink receiving film. In these products, known as polyethylenimines (PEI), protonated nitrogen groups show remarkable affinity for anionic sites, as well as for neutral surfaces, thus facilitating a charge-based fixation between particles and surfaces. The cationic charge density of nitrogen atoms in these compounds are strongly pH dependent. AlO(OH) based solutions with a pH of 3.5–4.5 provide a highly protonated environment for charge-based fixation. Ethoxylated polyethylenimines were the most effective. These compounds are highly basic, thus can only be added into the alumina based solutions after being diluted. AT 1–3 wt% they provide fixation against water in AlO(OH) and in the ink colorants.

The light fastness was investigated as a function of pH, mordant concentration, surfactant concentration, heat treatment and film thickness. The solution pH is found to be the most influential factor. The light fastness deteriorated significantly and rapidly with increasing acidity. Light fastness also decreased with increasing amount of mordants, especially above 2 wt%. At 3–10% mordant levels a significant deterioration of the light fastness is observed for all mordants investigated. The presence of nonionic surfactant FC 170-C appears to be beneficial to light fastness. Its concentration will be limited by other considerations, since this surfactant also causes haze at elevated levels. There appears to be a positive effect of thickness and a negative effect of heat treatment on light fastness.

3.5. *Haze and Transparency*

Haze, transparency and gloss are important considerations for ink-jet recording films. For overhead transparencies, complete elimination of haze is highly desirable. Haze is defined here as that percent of the transmitted light which in passing through the medium deviates from the incident beam more than 2.5° by forward scattering (ASTM D 1003-61). For the uncoated PET transparencies, the haze value is around ~2%. For the coated transparencies the haze value should be less than 8%.

Haze is associated with the presence of domains 1–100 μm in size and it appears to occur disproportionately in thicker films. The domain boundaries clearly visible on the optical microscopy are invisible on SEM, indicating it is primarily a subsurface structure. Strong haze formation often occurs as a result of drying conditions or aging. Thus, there appears to be at least two components of haze. An initial precursor for haze is formed in the sol when the ingredients are incompatible. This haze often manifests itself during drying. The second component of haze is created by crystallization and phase separation during aging. This is a kinetic phenomenon indicating structural instability with regards to the external conditions. Resolving a haze problem requires in depth understanding of both the chemistry and the kinetics of phase separation in the recording medium.

As mentioned earlier, haze formation appears to reduce the drying time significantly. It is believed that the grain boundaries created by the haze formation are responsible for the rapid transfer of the surface liquid into the interior of the coating. The challenge is to create these domains or channels at scales just below the visible range thus not significantly compromising the

optical clarity. We have formed stable coatings whose haze values are less than 3%, i.e., just 1% above the substrate.

4. Summary and Comments

Engineering of a sol-gel ink-jet recording film on transparencies by incorporation of strongly water absorbing polymers into the AlO(OH) matrix is discussed. The dense recording film described in this paper provides fast drying and prevents trailing or wicking of the ink by rapid incorporation of solvent into the polymer structure. The retainment of large volumes of solvent is accommodated by rapid swelling of the targeted area, e.g., as much as 600–700%, rather than by transporting it elsewhere. In this system, there are numerous requirements both on the rheology of the coating solution and on the coated film.

The system discussed here is a three-component system where water absorbing polymers, hydroxypropyl cellulose, and polyvinyl alcohol are incorporated into the AlO(OH) matrix. This system provides a clear coating, exhibits excellent receptivity to ink, and resists scratches. However, it also has shortcomings. Among these are substrate curle, poor blocking properties and being printer specific.

Recently, a new ink-jet coating system was designed that alleviates the weaknesses of the AlO(OH)-HPC-PVA system. This new system uses polyethylene oxide, $(-CH_2CH_2-O-)_n$ in a wide range of molecular weights as the water arresting agent. It gives a superior print quality with little tendency to curle. Most importantly, it is not printer specific. (This system will be discussed in detail in another paper; patent applied for.)

It has also been discovered that these ink-jet coating systems are very suitable for coating various types of surfaces, including textile, fabrics, plastics, etc., rendering them ink-jet printable. Some applications require further improvement on the performance of recording films, especially in the area of light fastness and stability under outdoor environmental conditions, and will have significant impact for the evolution of digital cameras, where the photographic images are produced by ink-jet printers.

References

1. *Chemical Technology in Printing and Imaging Systems*, edited by J.A.G. Drake (Royal Society of Chemistry, 1993).
2. L. Kuhn and R.A. Myers, Scientific American **240**, 120 (1979).
3. A. Atkinson, J. Doorber, A. Hudd, D.L. Segal, and P.J. White, J. Sol-gel Sci. Tech. **8**, 1093 (1997).
4. D.L. MacFarlane, V. Narayan, J.A. Tatum, W.R. Cox, T. Chen, and D.J. Hayes, IEEE **6**, 1112 (1994).
5. K. Misuda, S. Suzuki, T. Hasegawa, and H. Kiyimuta, U.S. Patent 5,264,275, 1993.
6. K. Misuda, H. Kiyimuta, and T. Hasegawa, U.S. Patent 5,104,730, 1992.
7. Y. Kurabayashi, M. Sakaki, and H. Sato, U.S. Patent 5,081,470, 1992.
8. B.E. Yoldas, Amer. Ceram. Soc. Bul. **54**(3), 289 (1995).
9. B.E. Yoldas, J. Mater. Sci. **10**, 1856 (1975).

Journal of Sol-Gel Science and Technology 13, 153–162 (1998)
© 1998 Kluwer Academic Publishers. Manufactured in The Netherlands.

Sol-Gel Science and Technology: Current State and Future Prospects

D.R. UHLMANN
Department of Materials Science and Engineering, Arizona Materials Laboratory, University of Arizona, 4715 East Fort Lowell Road, Tucson, AZ 85712 USA

G. TEOWEE
Advanced Technology Center, Donnelly Corporation, 4545 East Fort Lowell Road, Tucson, AZ 85712 USA

Abstract. This paper addresses the current state and future prospects of sol-gel processing. It summarizes responses to a questionnaire received from more than four dozen leaders of the sol-gel community. Overall, the respondents remain quite sanguine about the future prospects for the field, and with numerous areas where sol-gel processing can provide unique capabilities and novel materials. The present authors acknowledge this potential, but argue that its achievement will depend upon greatly increased involvement of the sol-gel community with applications, and carrying out a much larger fraction of sol-gel research in the context of applications.

Keywords: coatings, optics, electronics, processing, future prospects

1. Introduction

Two years ago, we presented an initial overview of the future prospects for sol-gel processing of glasses, ceramics and hybrid materials. Besides expressing our own views, we also presented the results of a questionnaire which had been sent out to leading practitioners of the sol-gel art.

Despite the authors indicating that they were generally positive—and for some areas even enthusiastic—about the future prospects for sol-gel processing, their comments were taken by some as painting a negative view of the field. In the words of one distinguished scientist, "Thank God the sponsors of research in the field were not present." Despite our admonition to the contrary, many participants seemed to believe that there must be another blockbuster—with the potential impact of nylon or aramid fibers or float glass—in the future of sol-gel technology.

This paper was undertaken to establish whether this view is correct, and to learn if any blockbuster application has been identified or to reinforce our original conclusion that the field should concentrate on expanding the range of products—some large, most small—for which this highly versatile approach to processing offers significant advantage.

Similar to the approach of two years ago, a questionnaire was sent to leading lights in the field from around the world. In particular, input was solicited from more than 100 individuals, about 2/3 from universities and 1/3 from industry. Responses were received from about half; and this paper summarizes their views, as well as those of the present authors. In many cases, quantitative evaluations were solicited, as rating on a scale of 0 to 10, with 10 being highest.

2. Views of Respondents

2.1. *Most Important Present Commercial Products*

When asked to identify the most important commercial products, more than 80% of respondents named films and coatings—including optical coatings generally, antireflection coatings, Schott-type coatings for architectural glass, release and water-repellent coatings, antiscratch and hybrid hard coatings for plastics, UV shielding coatings, coatings for heads-up

displays, and colored Ormosil coatings for containers.

The next most frequently cited commercial products, named by 20% of respondents, were ceramic fibers. Several respondents named 3M's Nextel fibers as specific examples. Approximately 10% named CO sensors, catalysts and abrasives; and the following products were cited by 1–3 respondents: TiO_2 flakes for cosmetics, aerogels, car mirrors, electric materials, ferroelectric materials, ultrafiltration membranes, materials for separations, chromatographic materials, oxide powders, spin-on glass, pyroelectric devices and zeolites.

Despite a request to give estimated sales of the products cited, only 4 of the 49 respondents provided such information. The authors have no knowledge whether this omission reflects a lack of insight into sales data generally, or the possibility that the listed products may have been commercialized by other companies, or a sensitivity about revealing commercial data. Of interest is the fact that among those who provided sales estimates, for no product did the estimated sales exceed $30 million annually.

2.2. *Most Important Commercial Products in Ten Years*

When asked to name the most important commercial products made by sol-gel processing in 10 years, nearly 35% of the respondents named coatings, especially functional coatings, providing capabilities such as antireflection, scratch and abrasion resistance, corrosion resistance, hydrophobic character, color, electrochromic or photochromic response and optical films generally. Of particular note for several respondents were coatings for plastics and coatings for architectural and automotive applications.

The next most frequently cited products, named by approximately 30% of respondents, were materials with high and tailored porosity, including aerogels, catalysts, microfilters and sensors.

Sensors for both chemical and biological applications, without mention of coatings, were cited by 10–15% of respondents, followed by carriers for drugs and enzymes which were cited by 10%. Listed by 1–4 respondents were abrasives, fibers, ceramic powders, catalysts, membranes, chromatographic materials, separations technology, memory materials based on dielectric properties, photonic devices, graded structures, nanocomposites, ferroelectric films for memory applications, nanotechnology, enzymatic catalysis for ceramics processing and encapsulation technology.

As was the case with present commercial products, few respondents provided estimates of commercial sales of listed products in 10 years. For no product where such estimates were given did the projected sales exceed $50 million annually.

2.3. *Sol-Gel Processing of Monoliths*

Respondents were generally pessimistic about the future of sol-gel processing to produce monoliths. The average score, on a scale of 0 to 10, for this area was 4.4, with no one rating it higher than 6. Reasons cited for negative views included cost (listed by 8); shrinkage, cracking and limited market (each listed by 6); and long processing times and porosity.

On the positive side, 10 respondents saw promise for small, net shape optical elements; 7 cited aerogels; 5 listed GRIN lenses; and 1–4 mentioned lenses, porous monoliths, Ormosils, special optical products, medical implants and rapid prototyping. The most positive note was sounded by one respondent, who cited a recent increase in knowledge regarding such processing as providing optimism for the future.

2.4. *Sol-Gel Processing of Powders*

The respondents were notably more optimistic about the future of sol-gel processing to prepare powders. The average score, on a scale of 0 to 10, was 7.2, with six respondents rating the area a 9/10. Reasons cited for positive views include high purity, high homogeneity, small and controlled particle size, ease of processing, and capability of synthesizing new powders. Reasons cited for negative views include cost (listed by six respondents), small production rate, agglomeration, and difficulty of purification.

Specifically-identified products included catalysts (listed by 11); electroceramics, SiO_2 and nanoparticles (each listed by 7); and the following powders, listed by 1–4 respondents each: cordierite, mullite, alumina, zirconia, barium titanate, phosphors, absorbents, aerogels, abrasives, pigments, encapsulated pigments, catalyst supports, ferroelectrics and specialty products.

2.5. *Sol-Gel Processing for Films and Coatings*

The respondents were even more positive about the future of sol-gel processing for films and coatings, rating

its prospects as 8.0/10. Ten respondents rated the potential here as 10/10. Reasons listed for positive views included compositions not obtainable by other methods; integrated multilayer fabrication; low cost relative to vacuum coating; uses small quantities of material; and can be combined with other systems with different properties. The only cited negative was long processing times. One thoughtful individual expressed the view that the future here will depend on two factors: (1) do sol-gel coatings offer better functions than other coatings (as those deposited by PVD or CVD); and (2) can efficient sol-gel coating methods, on-line on a commercial scale, be developed and coupled with readily-available coating materials?

Optical coatings (including reflecting, IR reflecting, antireflecting and the Schott architectural coatings) were cited by 28 respondents; and electrochromic windows, which include optically active coatings, were mentioned by an additional five. Coatings for filters, TV tubes, chemical protection, sensors, abrasion/scratch-resistant coatings, and ferroelectric devices were each listed by five or six respondents; while 1–4 respondents mentioned high porosity coatings, hybrid coatings, spin-on glass, low-ϵ dielectrics, selective absorbents, membranes, water-repellent coatings, protective coatings, coatings with new dielectric properties, magneto-optic coatings catalytic coatings, magnetic tapes, LCD devices, Li batteries, and oxide coatings on steels. One intriguing suggestion was for "ready-to-use" sprays.

Overall, the future of this area was summarized by one respondent, who stated: "I expect a great development in this field."

2.6. *Sol-Gel Processing of Ormosils*

The respondents were also highly optimistic about the future of Ormosils/Ormocers/Polycerams, also rating it as 8.0/10, with seven respondents rating its future as 10/10.

Attractive features of Osmosils were cited as materials which cannot be made by other methods, films and coatings with low temperature processing, and new and different functions which cannot be achieved for materials with homogenous microstructures (the last directed to nanocomposites). Also cited were tailored materials containing functional organic molecules and even living cells.

The most widely cited products were hard and abrasion-resistant coatings on plastics (listed by more than half of the respondents). This was followed by nanocomposites and protective coatings (each listed by 16%) and coated windshields (listed by 12%). Cited by 1–4 respondents each were materials for optical, chemical and biological applications, optical materials, optical coatings, antireflection coatings, optical components, photochromic coatings, smart materials, cladding on SiO_2 fiber waveguides, sensors, antiadhesion coatings, easy-to-clean coatings, corrosion-resistant coatings, high temperature rubbers and thick (multimicron) films.

Overall, the comments can be summarized by the words of one notable individual: "The possibilities are almost unlimited, in many cases with capabilities not possible until a few years ago."

2.7. *Sol-Gel Processing of Nanocomposites/Nanoparticles*

The potential of this area was regarded as less than that of sol-gel processing of coatings and Ormosils, and comparable to that of powders. The overall ranking was 7.4/10. Attractive features were variously listed as the ability to make novel materials and materials which are difficult to process by other methods, and the ability to combine functions. Several respondents regarded the areas as one of "great" or "nearly unlimited" potential; others felt there would be many uses if the materials could be produced using facile processing; while others regard nanocomposites as "mainly hype, with perhaps some optical applications" (in the words of one) or "may be hard to utilize/process" (in the words of another). Overall, the sentiments by the words: "Very interesting and promising, but practical applications have to be clearly demonstrated."

Cited products and applications covered a wide range, but tended to be rather nonspecific: nanoparticles in combination with polymers and Ormosils for special high-value applications, scratch-resistant coatings, electronics, UV-cured hard coatings, fillers, catalyst supports, abrasives, ceramic powders, thin film technologies, Ludox, Cab-o-sil, TiO_2 nanoparticles, photovoltaic coatings, photocatalytic coatings, quantum dots in glass matrices, nonlinear nanocomposites and nanocrystallized composites.

2.8. *Areas of Application*

Similarly, two years ago, the potential of sol-gel processing for various areas of application was explored.

This year, respondents were asked to quantify, on a scale of 0 to 10, their enthusiasm for each area.

2.8.1. Optical. Of the various areas of potential application for sol-gel processing, optical applications were ranked the highest. The overall rating was 8.0/10; and six respondents rated the potential of the area as 10/10. Cited benefits of sol-gel processing here included the ease of depositing films, the ability to provide coatings over large areas with high purity and homogeneity, the ability to tailor refractive index, low cost process, the ability to provide novel functionalities, small capital cost, and net shape processing—and even "no other methods available for some applications." A concern was, however, expressed that "Wet processes are more difficult to control than PVD."

Suggested products were dominated by coatings rather than bulk materials, with the notable exception of GRIN optical elements. Electrochromic films and devices were named by about 25% of the respondents; planar waveguides and antireflection coatings by about 18%; and spacers for LC displays, reflecting coatings, colored coatings, nonlinear optics, and transparent hard coatings for plastics were cited by about 12%. Mention by 1–4 respondents was made of electro-optics, filters, antifog coatings, sensors, quantum dots, Faraday rotators and photochromic coatings.

2.8.2. Electrical. Other areas of application also received generally favorable opinions by respondents, but were notably less positively viewed than optical applications. In the case of electrical applications, the overall rating was 6.6/10. Some respondents cited positively the ease of preparation of sol-gel coatings, and the capability (with appropriate apparatus) of making multilayered coatings; while others spoke of the difficulty of processing, especially multilayered structures, because of problems with the densification of individual layers, and the difficulty of making competitive transparent conductors by sol-gel processing.

Among specific applications, ferroelectric films received the most positive comments, being named by half of the respondents. Electrochromic films, antistatic coatings on plastics, and transparent conductors were each cited by about 12%; and 1–4 respondents listed dielectric films, multicomponent films, high dielectric constant films, porous silica low dielectric constant films, and electrode materials with high surface area for secondary batteries.

2.8.3. Mechanical/Wear. Mechanical/wear applications of sol-gel processing received an overall rating of 6.7/10, with three respondents rating the area a 10/10. Several respondents emphasized the importance of achieving dense films at low temperatures as important for success in this area; two noted the possible utility of radiation in promoting densification; and one respondent, after observing that ceramic coatings require high temperatures for densification, suggested that the situation can be improved using nanoparticulate systems and surface-limited firing methods. It was also noted that glass-like coatings on metals are too thin and cannot withstand abrasive loads, that it is difficult to make stronger/wear-resistant coatings on glass and that ceramic powders can be used to make strong, wear-resistant ceramics. One respondent commented that this property is meaningful only when combined with other useful properties, such as optical or water-repellent properties; another felt that there was low interest in this area by the research community; and yet another indicated a perception of decreasing interest in modifying the mechanical properties of substrates by coatings.

Among specific applications, protective/scratch-resistant/wear-resistant coatings on plastics was by far the most frequently cited (by more than one-third of respondents). Abrasives were noted by about 20%; and 1–4 respondents listed each of the following: high temperature rubbers, protective coatings on glass, nanocomposites, coatings on monument stones, and ZrO_2.

2.8.4. Thermal. The thermal applications of sol-gel processing received an overall rating of 6.4/10, but about 20% of respondents provided no input to this query. Aerogels received by far the most comments in this area, being noted by nearly one-third of respondents. Specific comments regarding aerogels included "monolithic aerogels for use as thermal insulation are and will be too expensive" and "mass production of aerogels without supercritical drying will be developed." These two comments are obviously interrelated.

Products identified by respondents included rubbery aerogels, thin film aerogels, IR reflective glazing, low-emissivity coatings, stabilized ZrO_2, inorganic foams, new materials for fire protection based on inorganic binders for glass wool, thermally resistant paints (with a concern regarding cracking), wood with increased thermal durability obtained by infiltrating sols, and, more generally, polymers with increased thermal

durability obtained by hybridization with inorganic substances.

2.8.5. Passivation. Passivation applications of sol-gel processing received an overall rating of 6.3/10; but more than one-third of respondents failed to respond to this query. Skepticism was expressed by some who felt that this function could be better provided by other methods, and by others concern about thickness limitations on films.

General suggestions were made regarding Ormosils, passivation of semiconductors, protective coatings on polymers and metals and even protection systems. Specifically noted were flaw-heating coatings on glass coupled with conservation of this state/as (via nanocomposites), and protection of functional coatings on glass by pre-coating with sol-gel SiO_2 or similar films (presumably referring to uses such as the protection of ITO when deposited on soda-lime-silicate substrates).

2.8.6. Release/Wetting. This area received an overall rating of 6.2/10, with only about half of the respondents providing input. It was noted that the thermal, mechanical and chemical stability of release/wetting coatings should be improved. It was also noted that one should be skeptical that the scratch resistance of hydrophobic coatings can be as good as that of other hard coatings. These points emphasize the importance of combinations of properties for meeting the demands of various applications.

For the area of release/wetting applications, specific mention was made by several respondents of biomedical applications, e.g., slow release of materials/drugs. Also noted were antistick coatings, easy-to-clean coatings, antigraffiti coatings, and antifouling coatings.

2.8.7. Sensors. Application of sol-gel processing to produce sensors received an overall rating of 6.8/10, with 80% of respondents providing a ranking. Some respondents suggested that this application would only lead to application in niche market; but others were more positive about a broader range of applications.

The most widely cited area was that of chemical sensors (listed by more than 20% of respondents). Applications listed by 1–4 respondents included SnO_2 and PZT-related materials, biosensors, thin film sensors, easily-formed microsensor elements, highly porous films synthesized without supercritical drying, nanocomposite and hybrid films containing functional molecules, pH sensors, temperature sensors, gas sensors, fiber sensors, photochromic sensors, IR detection using piezoelectric properties, selective adsorbents incorporating optical indicators, incorporation of enzymes and antibodies to produce powerful sensors and membranes/filters with tailored porosity.

2.8.8. Catalysis. The area of catalysis received an overall rating of 7.0/10; but only 40% of respondents provided input. A need for greater stability at high temperatures was noted; an opportunity for custom tailored porosity and interfacial chemistry was highlighted; and wash coats on monolithic substrates were viewed as offering good prospects. Specific mention was made of aerogel catalysts, catalyst supports, liquid chromatography elements, microfilters, and controlled pore materials.

2.8.9. Others. Suggestions in this area were not provided with numerical evaluations. Many of the cited products were included by others in previous categories. Specifically suggested were: biomedical applications, biomaterials (enzymes, etc.), biocatalysts, optical fibers, spacers for liquid crystal displays, aqueous solutions, controlled drug release capsules (e.g., for diabetics), membranes, filters, selective adsorbents, and colored thin coatings on glass bottles which can be recycled as colorless glass.

2.9. Does the Future of Sol-Gel Processing Depend on Improvements in Understanding?

About 80% of the respondents felt that improved understanding is important for the future of sol-gel processing; while the others (20%) felt that the key issue was further implementation, not more understanding.

Among those who viewed improved understanding as important/vital for the future of sol-gel processing the following areas were specifically identified: densification of gels and films, chemistry and cost of precursors, and manipulations and control of porosity (each named by nine respondents); improved processing generally, overall understanding of process, and reproducibility (each named by seven respondents); and thin film crystallization, process kinetics for improved homogeneity, aging, coating stability, photostability, non-silica systems, processing of transparent conductor layers, electrochromic systems, structure-property relations on Ormosils, and mechanism of densification/modification of gels by UV and other radiation (each named by 1–4 respondents). One respondent focussed attention on the gap between academics on the

one hand and engineers on production lines on the other with respect to wet chemically processed materials and fear regarding chemistry.

2.10. *Does the Future of Sol-Gel Processing Depend on Improvements in Ability to Control/Tailor the Process?*

The overwhelming majority (more than 85%) of respondents gave a positive response to this query. Four respondents expressed the view that improvements were needed in almost every aspect of sol-gel processing. The need for higher production rates and shorter production times was cited by 16 respondents; the need for greater reproducibility was listed by 11; and the need for improved control of porosity was noted by eight. Cited by 1–4 respondents each were the following: chemical processing of hybrids, production technology, alternative coating processes to spin and dip coating, heat treatment conditions, in situ means of monitoring the process, automation, aging, better homogeneity and nucleation of crystalline phases for low-temperature synthesis of ferroelectric films.

Expended and insightful comments were provided by one individual who noted: "The advantages of PVD/CVD coatings very much lie in technology. One can buy (at a high cost, admittedly) the whole technology, including quality control and process control. For sol-gel coatings, automatic, in situ control of thickness and quality (including inhomogeneities, dust, etc.) would be very useful."

2.11. *Principal Impediments to Wider-Scale Use of Sol-Gel Processing*

A clear majority of respondents (approximately 60%) were negative about the prospects for non-hydrolytic processing, expressing views such as: "academic," "not optimistic," "applicable to only a narrow area," "doubtful it will be important" and "a curiosity." The most positive comment noted: "very useful when one wants to avoid OH groups, such as in optics and electronics packaging."

In contrast, there was near unanimity in positive responses to aqueous-based processing (more than 90% positive). Many respondents cited environmental concerns as the principal driving force; some felt that the introduction of increased aqueous-based processing may not be all-or-nothing choice, and one may anticipate combined organic/aqueous processing; and one respondent suggested that aqueous-based processing would be particularly useful for large-area applications, provided one can meet the demands for properties.

2.12. *Overall Future of Sol-Gel Processing*

The overall future of sol-gel processing was rated as 8.1/10, with five respondents rating the prospects as 10/10 and no respondent providing a rating of less than 5/10. Among those who rated the futures as 10/10, two indicated that their ranking was based upon their own strong involvement with sol-gel processing, while three cited the potential for producing materials which are not obtainable using other methods (e.g., organic-inorganic hybrids, biologically-active gels, unique porous structures, low-temperature coatings and novel surface characteristics).

Many respondents (about 40%) cited the multiplicity of potential applications; many (about one-third each) mentioned ease or flexibility of processing, low cost processing, low cost equipment, low temperature processing, suitability for large area applications and ability to control structure at various levels.

Also noted by several respondents was the attractiveness of sol-gel processing for small companies; and the fact that many kinds of materials are prepared by chemists, and chemists can readily come to sol-gel processing. Several respondents noted that sol-gel processing poses challenges as well as opportunities. Some felt it offers promise only for niche areas. One noted that commercialization has been much slower than hoped for, and is likely to expand gradually rather than take off suddenly. Others mentioned concerns regarding long processing times, reproducibility, aging, problems with processing transparent conductors and the need for additional insight into film densification. Concern was also expressed about the ability to control sol-gel processing; the installed base of capital equipment for alternative processes, especially for coatings; and the need for improved, low cost, automated sol-gel processes. The potential for providing multifunctional materials—particularly coatings—was a bright spot on the horizon for several respondents.

3. Views of the Present Authors

3.1. *Present and Future Commercial Products*

Most of the views expressed by the present authors two years ago have, if anything, been reinforced by the developments since then and by the responses to the

present questionnaire. Sol-gel processing has still not launched or been critical to the formation of major new industries; nor does such processing appear to represent an enabling technology for large-scale new commercial products; nor has such processing supplanted existing technology in major areas of application.

Perhaps most disappointing was the fact that no respondents cited present commercial applications with annual sales exceeding $30 million annually, nor even the prospects for commercial applications with annual sales exceeding $50 million in 10 years. It must be acknowledged that the responses neglected areas whose current sales notably exceed these values—e.g., ferrite powders, zeolites, $SiO_2 + Al_2O_3$ coatings on pigmentary TiO_2 particles, and even roofing granules. Nevertheless, the absence of major new markets where sol-gel processing is expected to make important inroads during the coming decade seems noteworthy—and should convey an important message to practitioners in the field.

This message is as follows: it is unrealistic to expect blockbuster commercialization from a technology which is process-oriented rather than product-oriented (the only exception to this is the potential widespread introduction of electrochromic devices based on tungsten oxide—and even here sol-gel methods will face intense competition from vapor phase approaches to the deposition of coating layers). Rather, the opportunity lies in the progressively more widespread utilization of sol-gel methods to provide unique combinations of functionality, unique materials (including nanocomposites, coated particulate, materials with high and tailored porosity, gradient materials) which cannot readily be synthesized by alternative methods, and small capital, low cost, efficient approaches to a myriad of niche products. While no product may represent an important new industry, the sum of such "modest" advances may well represent a commercial development of considerable magnitude.

Besides the possibility of electrochromic panels and the likely expansion of already-important markets for products such as ferrites, zeolites, coatings on pigment particles and roofing granules, as well as ceramic fibers, abrasives, spin-on glass, flakes for cosmetics, spacers for displays, membranes, a variety of electronic ceramic powders and antireflection coatings, one may well anticipate the wide-scale introduction of hard coatings on plastics (which could become a large business, perhaps even a blockbuster business), passivation coatings, memory materials based on ferroelectric/dielectric properties, release coatings with mechanical durability, antifouling and antigraffiti coatings, GRIN optical elements, chromatographic and catalyst supports, a variety of sensors, new devices based on magneto-optic films, an expanded range of coated particulate and new particles (particularly multicomponent particles), embossed structures, active and passive optical elements, a range of nanocomposite and Ormosil products and very likely significant inroads made in the biological arena.

Also of note for applications of sol-gel processing during the coming decade is its use as a facile means of exploring compositional and heat treatment variations in development, even when the final production may be carried out using other methods. Not only are sol-gel methods efficient for such purposes, but also their use could help familiarize a broader industrial base with their use.

3.2. *Sol-Gel Processing of Monoliths*

The present authors continue to believe that the sol-gel processing of monoliths will be confined to producing (a) relatively small, high-value products such as GRIN lenses; (b) materials with tailored nanoporosity; and (c) the formation of particles rather than gelled masses, where the particles are subsequently processed by conventional (or unconventional) methods to form bulk products.

3.3. *Sol-Gel Processing of Powders*

In this area, sol-gel methods are already well-established on a commercial scale; and their use will almost certainly continue to grow. Compared with the processing of natural products, sol-gel produced materials are costly and hence must offer performance or processing advantages to compete effectively. As particulate materials of specific promise, the present authors are positive about composite particles incorporating, e.g., tailored coatings; and nanoparticles with tailored surface chemistry and dispersion aids.

3.4. *Sol-Gel Processing of Films and Coatings*

The authors agree with the consensus of the respondents that this represents an area of particular promise for the coming decade. Vital for success here will be the development of cost-effective, highly automated, integrated, likely in-line processing capability. Also of importance will be overcoming the effect of the sizable installed base of vapor phase coating equipment, the greater familiarity of industry with such methods,

and the concern of many about introducing wet chemistry into process lines.

Despite these concerns, the future appears quite bright for further expansion of chemically-deposited optical coatings of an expanded range of chemistry and function; for more widespread introduction of sol-gel coatings in electronics (including sensor applications), of hard coatings on plastics (almost sure to be a big winner), as well of a broad range of release and passivation coatings (many of which will represent hybrid and composite—and likely nanocomposite—formulations).

3.5. *Sol-Gel Processing of Ormosils/Ormacers/Polycerams and Nanoparticles/Nanocomposites*

The authors concur with respondents who pointed out that Ormosils represent materials which can only be synthesized using wet chemical methods. But this fact only has meaning if commercially attractive properties can be provided at competitive prices. The key here is functionality—and most likely a combination of functions; and in this regard adoption of a nanocomposite perspective is often advantageous. This approach has already been used successfully in developing products such as novel hard coatings and release coatings; and the future for combinations of nanoparticles with Ormosils will almost surely be bright. Even here, however, the present authors are enthusiastic about the prospects for films and coatings, but remain cautious about applications for bulk materials, in part because of the issue of solvent removal during processing.

3.6. *Areas of Application*

Among areas of application for sol-gel processing, the present authors are most positive about optical and mechanical applications. In nearly all cases—save products such as GRIN lenses—the applications will involve structures and devices utilizing sol-gel produced films and coatings. Among optical applications, the use of antireflection coatings will likely continue to increase, as will UV protecting and other optical coatings on plastics. Electrochromic panels represent an enormous potential market; but issues such as stability over many years and cycles, sealant performance and integrity, uniformity and reliability, and cost will have to be addressed successfully. Even then sol-gel processing will face intense competition from vapor phase methods. Planar waveguides, both active and passive, appear promising, as do embossed structures, colored coatings, magneto-optic devices, and possibly photochromic coatings. More problematic with respect to commercialization are quantum dot structures and solid state dye lasers (both of which have considerable scientific interest), NLO structures and Faraday rotators.

Transparent conductive films—particularly for application to plastics and as top layers on multilayer structures—represent another area of considerable potential. But to date sol-gel methods have failed to provide performance equivalent to that of vapor phase methods; and there already exists a considerable installed base of vapor phase deposition equipment, including two-sided, vertical, planar magnetion sputtering equipment, as well as CVD apparatus for deposition coatings within a float both.

Among electrical applications, ferroelectric films for memory applications will almost certainly see widespread commercial use during the coming decade; but it is by no means assured that these films will be prepared by sol-gel methods (as opposed to vapor phase processing). Devices based on pyroelectric and piezoelectric films are already being commercialized; and there is considerable commercial potential for films with both high and low dielectric constant, and for a range of electrode materials.

For mechanical applications, hard coatings on plastics represent a likely winner, and potentially big winner, particularly if plastic automotive glazing becomes important. The questions are how large will the market be on what time scale at what price, with what performance criteria. Already winners, but of much smaller magnitude, are spacer particles for LC displays.

Other mechanical applications strike the present authors as unlikely to be important commercially over the next decade.

Within the group of thermal applications, the present authors are positive about impregnated wood and plastics, and about new fire-resistant materials, but feel that more technical issues remain to be addressed in these areas. Solar control coatings represent an already-important commercial area; but to date the inroads of sol-gel produced coatings has been minimal, and it is not clear on what bases one may expect the situation to change during the coming decade. The development of effective non-supercritical processing of aerogels and the use of sodium silicate precursors could have a highly beneficial impact on the use of these materials in insulation.

The area of release/wetting coatings will almost certainly grow in importance during the coming decade,

at least in the opinion of the present authors. As with nearly all other areas, the key to the future will almost certainly involve combinations of properties and functionality; and success will likely involve a judicious trade-off among properties such as release and wear-resistance. Antistick, antigraffiti, anticorrosion and antifouling coatings can all be important; but nearly all such applications will demand other properties/functionality as well.

The authors are positive about the potential for sensors produced by wet chemical methods. The ability to tailor pore size, volume fractions and surface chemistry using inexpensive processing can be important for many applications. The key to success will be provided by interactions among device engineers, chemists/physicists, and sol-gel technologists.

The area of catalysis already benefits from wet chemical synthesis—witness the widespread use of such synthetic methods to prepare catalysts and supports ranging from zeolites to nanocrystalline spinel-like materials; and such uses will almost certainly continue to grow. The use of sol-gel derived materials and structures in various separation processes—from membranes and chromatographic supports to selective adsorbents and microfilters—appears quite attractive to the present authors.

Besides electrochromic devices and hard coatings on plastics, the great wild card for sol-gel processing may well involve biological/biomedical applications of the technology. The potential applications cover an enormous range; and the prospective impact on our societies is considerable; but it remains to be seen how much of this potential can be converted to commercially significant products. At the present time, most developments in this area seem quite distant from commercialization.

3.7. *Does the Future of Sol-Gel Processing Depend on Improvements in Understanding?*

At the present stage of its development, sol-gel processing seems to the present authors to have relatively little need of understanding which is unrelated to the development of products. Collectively, the world's technical community has made a considerable investment in sol-gel science and technology; and the time seems somewhat overdue for reaping a return on that investment.

This is not to suggest that we understand all that we could—or all that we would like—about the phenomena involved in sol-gel processing, but simply that with a few relatively rare exceptions—our attention should be focussed on implementation and commercialization. New understanding is certainly needed; but it should best be developed in the context of developments aimed at commercialization.

It should be noted that the present authors have modified their views from two years ago. At that time, we identified a number of areas where improvements in understanding and control of sol-gel processing seemed critical for future developments. These include the understanding and control necessary (1) to produce pinhole-free coatings of uniform thickness over large areas on both flat and curved surfaces; (2) to produce a spectrum of melt-processible organic-inorganic hybrid materials; and (3) to define general approaches to the synthesis and surface modification of nanoparticles with control of particle size and chemistry.

With respect to each of these critical areas, progress in general investigations has been minuscule. Where progress has been made, it has been in the context of commercialization/implementation of developments, hence our present suggestion, which represents a generalization from that experience.

3.8. *Does the Future of Sol-Gel Processing Depend on Improvements in Ability to Control/Tailor the Process?*

The present authors agree with the great majority that improvements in the ability to control/tailor the process will be vital to the future success of sol-gel processing; and improvement in production rates, reproducibility and control of porosity, as well as greater automation, homogeneity and ability to control phase development in films, all seem deserving of attention. But still more seems needed than this; and the respondent who cited the availability of the whole technology for PVD/CVD coatings raised an important issue. Sol-gel processing would greatly benefit from more of a systems approach, leading to the development, e.g., of in-line coating modules which provide automatic monitoring and control of the process coupled with low particulate contamination, whose nameplate capacity can be specified for a range of chemistries, where specifications can be placed on acceptable impurity levels in precursors, and where standard procedures can be cited for handling of waste streams. In other words, the field of sol-gel processing needs equipment manufacturers of a quality like Airco or Balzers, whose queries of sol-gel technologists and customers alike will push the boundaries of our knowledge.

3.9. Non-Hydrolytic and Aqueous-Based Processing

The present authors believe that non-hydrolytic processing is likely to remain a seldom-used tool, perhaps even a laboratory curiosity. This sentiment is closely related to the second part of this inquiry. Specifically, given the increasing importance of environmental concerns throughout the world, and the increasing cost of handling organic solvents both in the workplace and in waste streams, it seems clear that the future success of sol-gel processing will depend strongly on the development of aqueous routes using environmental-friendly precursors. Without the availability of such routes and precursors, sol-gel processing seems likely to face an unnecessarily uphill struggle with competing technologies.

3.10. Impediments to Wider Use of Sol-Gel Processing

Most of the principal impediments to the wider use of sol-gel processing, as seen by the present authors, have already been discussed. These include the lack of commercially available processing systems, or even commercial processing system suppliers; the lack of standard aqueous synthetic routes using environmental-friendly precursors; the lack of effective interactions between device technologists and sol-gel practitioners; the lack of a plethora of familiar success stories, large and small, where sol-gel processing has provided the key to commercial success; the magnitude of the installed base of capital equipment used for competing technologies; the fact that many applications involve small quantities of materials and use of relatively "strange" processes; and the fact that to the world at large, sol-gel processing remains largely a curiosity (and worse, a curiosity which depends on chemistry).

Among these impediments, the last may be the easiest to address. Rather than organizing meetings where sol-gel specialists talk to other sol-gel specialists, the community should organize teams of articulate enthusiasts for the technology to "spread the gospel" to other communities. These should be accompanied by effective information and case histories of notable commercial successes. Also notable is the series of topical meetings being organized by Drs. Schmidt, Sakka, Soga and Uhlmann, where past, present and prospective participants in commercial developments are brought together to share experiences, concerns and successes.

3.11. Overall Future of Sol-Gel Processing

The present authors rate the potential for sol-gel processing as quite high (exceeding 9/10), but rate the prospects for achieving this potential as quite modest (as 5/10 or less), and hence rate the overall future as in the range of 7/10. The likelihood of success will be increased by adopting the emphasis and approach suggested two years ago: (1) target *new* applications, where there is not so intense competition from established processes; (2) target applications which take advantage of the inherent capabilities of sol-gel processing (e.g., applications which depend on tailored high porosity, on the specific properties of hybrid materials, etc.) and (3) target applications where sol-gel processing offers clear advantages relative to competing technologies and is the natural approach (e.g., coating powders).

It is clear that practitioners of the sol-gel art today can synthesize a remarkably broad range of materials and structures—unique as well as conventional. The challenge of the coming decade will be to harness the potential power of this capability to advance a range of important areas of application. To have any realistic chance of accomplishing this objective, it seems important for the sol-gel community to devote a larger portion of their activities to research directed toward specific applications, to spend more time with their device colleagues, and to become more familiar with the demands on technological processes. We are, after all, dealing with a process—not with a new material or a new device structure; and process research is most effectively carried out in the context of learning how to process specific materials, and then generalizing from the sum of this experience.

We as a community simply must become much more involved with applications. Let's do it.

Acknowledgments

Financial support for the present work was provided by the Air Force Office of Scientific Research and by Donnelly Corporation. This support is gratefully acknowledged.

Journal of Sol-Gel Science and Technology 13, 163–169 (1998)
© 1998 Kluwer Academic Publishers. Manufactured in The Netherlands.

Structure Design of Double-Pore Silica and Its Application to HPLC

K. NAKANISHI, H. MINAKUCHI AND N. SOGA
Department of Material Chemistry, Graduate School of Engineering, Kyoto University, Yoshida, Sakyo-ku, Kyoto 60601, Japan

N. TANAKA
Department of Polymer Science and Engineering, Kyoto Institute of Technology, Matsugasaki, Sakyo-ku, Kyoto 606, Japan

Abstract. Utilizing the concurrence of polymerization-induced phase separation and sol-gel transition in the hydrolytic polycondensation of alkoxysilanes, a well-defined macroporous structure is formed in a monolithic wet gel. By exchanging the fluid phase of the wet gel with an appropriate external solution, the nanometer-range structure of the wet gel can be reorganized into structures with larger median pore size essentially without affecting the macroporous framework. The double-pore structure thus prepared is characterized by open pores distributed in discrete size ranges of micrometers and nanometers. A new type of chromatographic column (silica rod) has been developed using monolithic double-pore silica instead of packed spherical gel particles. Typical silica rod columns had significantly reduced pressure drops and improved analytical efficiencies which do not deteriorate even at higher sample flow rates, both arising from a greater macropore volume than particle packed columns.

Keywords: silica gels, phase separation, pore size distribution, liquid chromatography

1. Introduction

By combining the sol-gel reaction with phase separation and a subsequent solvent exchange treatment which enhances the Ostwald ripening of a finely textured wet gel matrix [1, 2], double-pore silica gel monoliths can be prepared to form well-defined micrometer-range pores with controllable volume fraction and median size [3] together with narrowly distributed mesopores [4]. The first key process is the hydrolysis and polycondensation of alkoxysilane, in the presence of water-soluble polymers or other additives, which can induce the phase separation to form micrometer-range co-continuous domain structures—parallel with the sol-gel transition of the system. Subsequent post-gelation treatments affect the nanometer-range pore distribution as appropriate for the specified application field of the gel materials. The present paper describes the principle of double-pore silica design emphasizing the importance of the post-gelation treatment. The rest of the paper demonstrates the application of double-pore silica to the high performance liquid chromatography (HPLC) columns in comparison with particle-packed columns.

2. Experimental

Tetramethoxysilane (TMOS) was hydrolyzed under acidic conditions in the presence of various additives such as water soluble polymers that induce a phase separation during the polymerization stage. In order to obtain well-defined co-continuous domains of gel- and fluid-phases, the starting compositions, including the catalyst concentration and the reaction temperature, were adjusted to induce the sol-gel transition and the phase separation concurrently. Wet gels thus formed were aged at the same temperature as the gelation stage and then immersed into aqueous solutions of higher pH than that of fluid phase for various periods at a range of

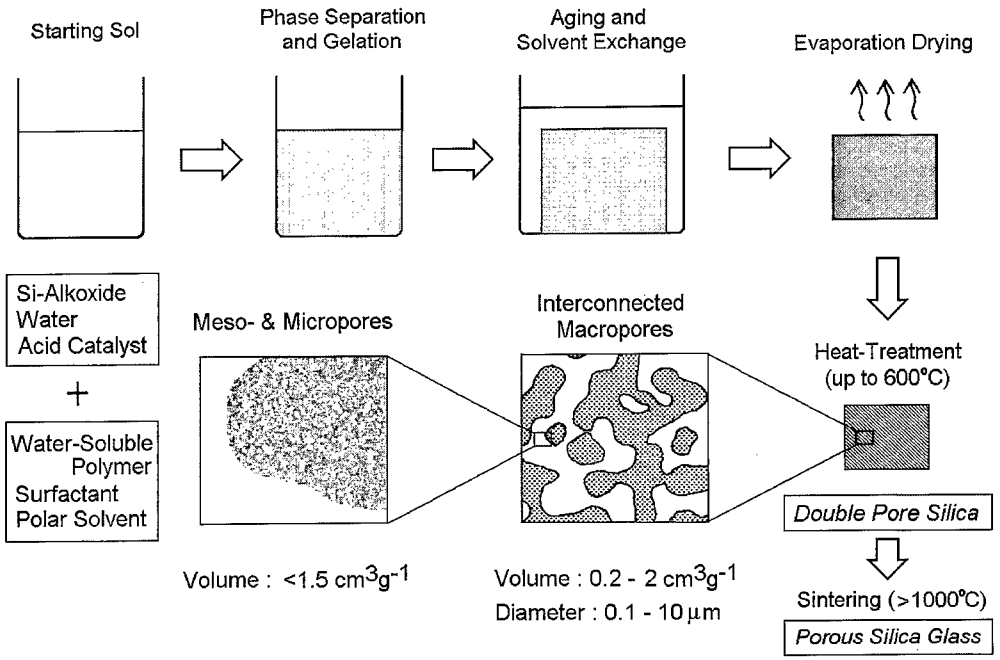

Figure 1. Schematic flow chart of the sample preparation procedure.

temperatures. Then the gels were dried and heat-treated at 600°C for 2 h (see Fig. 1).

The pore size distribution was determined by mercury intrusion porosimetry (Poresizer 9320, Micromeritics, USA) and nitrogen adsorption (ASAP 2000, Micromeritics, USA) using heat-treated gel samples. Preparation of silica rod columns for reversed phase HPLC and chromatographic evaluation of the columns were carried out as described in the literature [5, 6].

3. Results and Discussion

3.1. Choice of Macropore Forming System

There are two distinct types of phase relations among the systems which undergo polymerization-induced phase separation [4, 7]. In the first case, the attractive interaction between silica and the additive is low and the polymerizing silica and additive, respectively, comprise the gel- and fluid-phases with the solvent being distributed in both phases [8, 9]. In the other case the additive becomes strongly associated with polymerizing silica to form the gel-phase and the fluid phase is mainly composed of solvent. Since the ratio of additive to silica predominantly affects the onset of phase separation, it is the key parameter in determining the median pore size. The pore volume is largely determined by the volume fraction of the fluid-phase, which varies concurrently with the additive concentration in the former case. In principle the latter case, however, the fraction of fluid-phase can be varied independently of additive to silica ratio [4]. A starting composition containing poly(ethylene oxide), PEO, belonging to the latter category was adopted to fabricate gel monoliths with varied domain size and pore volume to be evaluated for chromatographic columns. The pore size distributions of gels with different pore volumes and/or median pore size obtained from the PEO-TMOS system [10] are shown in Figs. 2 and 3.

3.2. Choice of Mesopore Tailoring Condition

Since the macroporous gel domains are formed in the wet state, further tailoring of the smaller internal pore structure by exchanging the fluid phase can be performed more efficiently and in a less time-consuming fashion than with fully mesoporous gel monoliths. Detailed studies on the solvent exchange method revealed following the points [11]:

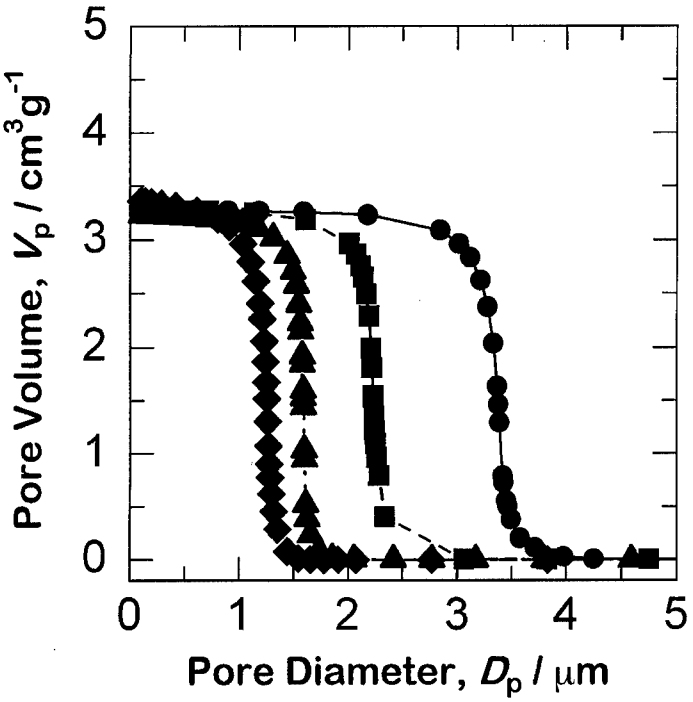

Figure 2. Pore size distribution of heat-treated gels determined by mercury intrusion measurements. Each starting composition consisted commonly of 0.01 M aqueous solution of acetic acid (100 ml) and TMOS (45 ml) with varied amounts of PEO which gelled at 40°C. ●: PEO 9.4 g, ■: 9.8 g, ▲: 10.2 g, ♦: 10.4 g.

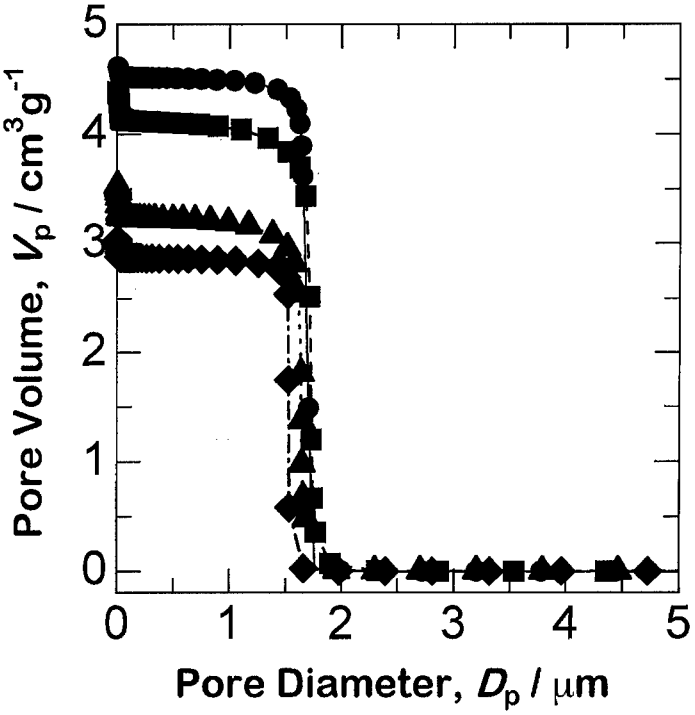

Figure 3. Pore size distribution of heat-treated gels determined by mercury intrusion measurements. Each starting composition consisted commonly of 0.01 M aqueous solution of acetic acid (100 ml) with varied amounts of PEO and TMOS which gelled at 40°C. ●: PEO 11.6 g and TMOS 40 ml, ■: 10.2 g and 45 ml, ▲: 8.8 g and 50 ml, ♦: 7.0 g and 55 ml.

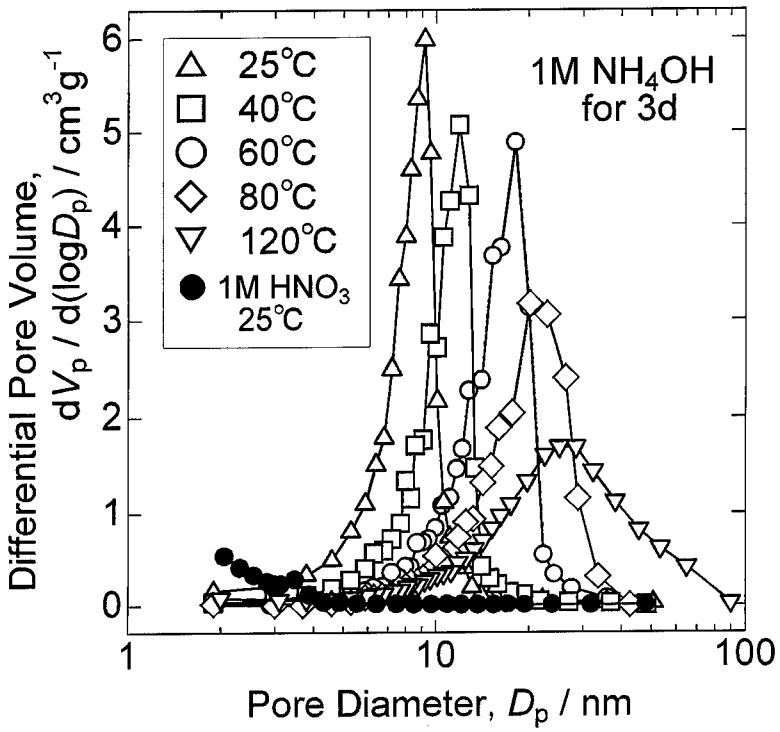

Figure 4. Pore size distribution of heat-treated gels in the mesopore range after immersion in various concentrations of ammonium hydroxide and/or at different temperatures determined with nitrogen adsorption-desorption measurements.

1. In acidic and neutral conditions where the hydrogen bonds between silanols and PEO molecules are relatively stable, the wet gel structure is little affected by the solvent exchange treatment. Subsequent drying and heat-treatment largely determines the pore structure. When the pH value of the external solvent becomes higher than ~8, mesopores are obtained with a median size larger than 5 nm, the structure of which was already formed in the wet state.
2. The equilibrium mesopore size corresponding to the pH of the external solution can be achieved earlier as the bath ratio and/or temperature becomes high. The distribution width tends to become broader as the temperature increases (Fig. 4).
3. The use of hydrothermal conditions enables one to prepare mesopores up to 50 nm but with significantly decreased pore volumes.

For the chromatographic columns described below, the treatment was performed with 0.01 M aqueous ammonium hydroxide solution at 80 and 120°C for 3 h to obtain mesopores 14 and 25 nm in size, respectively [8].

3.3. *Comparative Chromatographic Performance*

Conventional columns for HPLC usually consist of tightly packed silica gel particles as large as 5 μm in size [12]. Although a higher efficiency is expected for columns packed with smaller particles, the small particle size requires an increased back pressure, which is inversely proportional to the square of particle size, to obtain a constant sample flow rate. As this trade-off relationship stems from the geometry of particle packing, an essential solution should be found either with a completely different stationary phase geometry or a method other than mechanical pressing to drive a sample flow. Although monolithic chromatographic columns made of organic polymers have been reported, their advantage is relatively limited for separation of larger molecular mass substances [13, 14].

The double-pore silica gel monolith prepared for the rod column has substantially higher volume fraction of through-pores than the volume of interstitial void spaces in particle packed columns, which leads to the following features crucial to better analytical performance: (a) reduced pressure drop, (b) independent

Table 1. Volumes of through-pores and mesopores in a silica rod and a particle-packed column.

	Volume fraction of a column[a]		
	Silica rod		Particle-packed column
Pore volume	Before ODS	After ODS	Capcellpak C_{18}UG
Total porosity	0.86	0.81	0.60
Through-pore[b]	0.65	0.65	0.32
Mesopore	0.21	0.16	0.29
Bonded phase	—	0.05	—

[a]Measured by size-exclusion chromatography setting the total column volume as 1.0.
[b]Interstitial void volume in the case of particle-packed column.

design of skeleton size and through-pore size and (c) stable column structure. The pore characteristics of a representative particle packed column and of the ODS-modified rod column are numerically compared in Table 1.

The value HETP (Height Equivalent to Theoretical Plate) is a general measure of the efficiency of a column which is defined by the column length divided by the number of the theoretical plate [15]. As the plate number represents the frequency of distribution of a solute between stationary and mobile phases, the smaller the HETP the better the efficiency of a column. According to the Van Deemter formulation, the HETP shows a minimum around a relatively low mobile phase velocity u typically 1 mm s^{-1}, and the efficiency monotonously decreases with a further increase of mobile phase velocity. Figure 5 shows the u-dependences of HETP for amylbenzene with conventional and rod columns. The very weak dependence of the rod column can be attributed to the gel skeleton thickness being much thinner than the diameter of the particle packed column. The equilibrium distribution of solutes is rapidly attained with thinner stationary phases and is affected little by the flow rate of mobile phase. The pressure drops ΔP across the column length are comparatively plotted in Fig. 6. The pressure

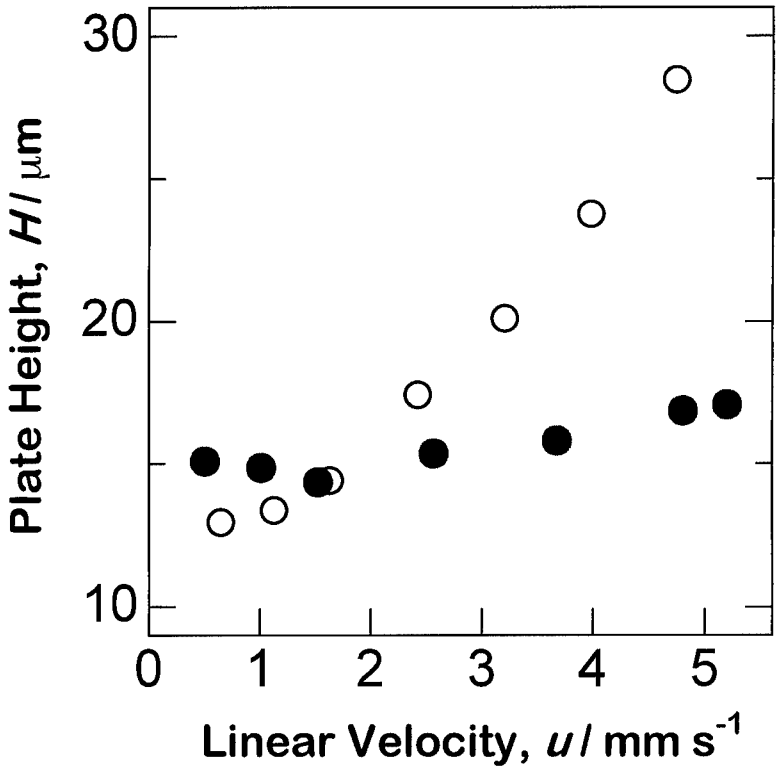

Figure 5. Dependence of HETP on the mobile phase velocity. Solute: amylbenzene, mobile phase: 80% methanol. ○: Capcellpack C_{18}UG, ●: Rod Column (ODS-modified, 1 μm of skeleton size and 1.6 μm of through-pore size).

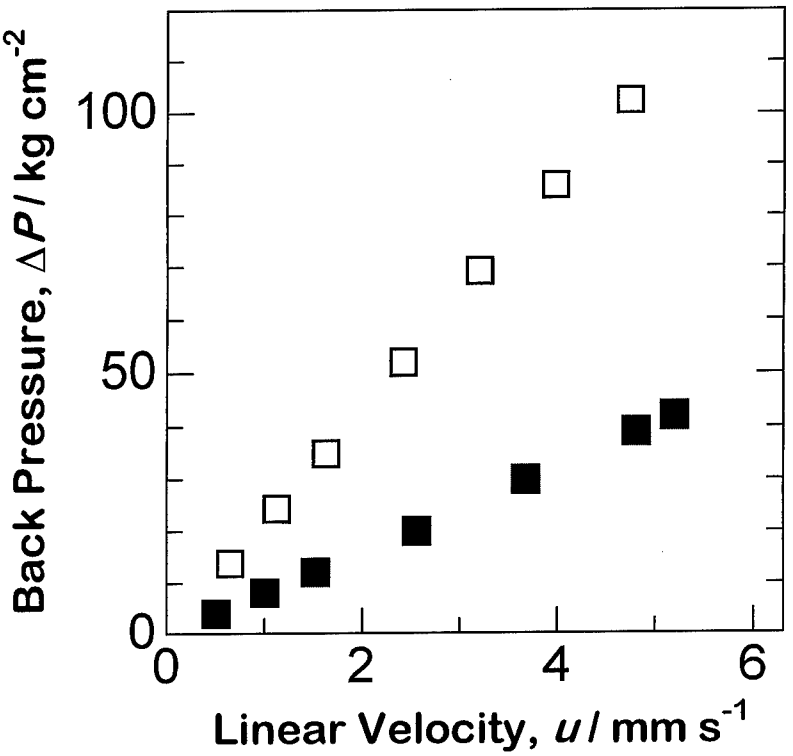

Figure 6. Dependence of back pressure ΔP on the mobile phase velocity. Mobile phase: 80% methanol. The data are normalized to the column length of 83 mm. □: Capcellpack C_{18} UG, ■: Rod Column.

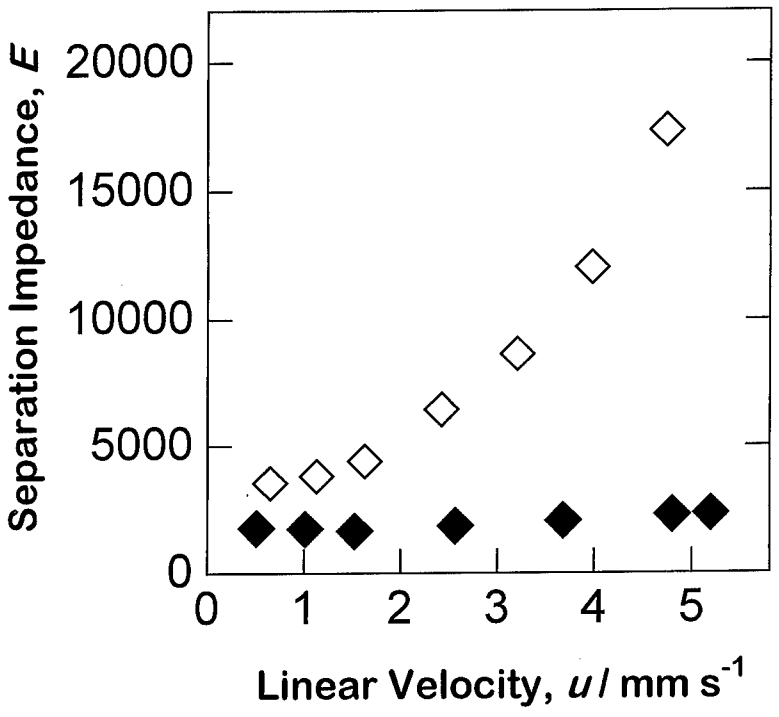

Figure 7. Dependence of separation impedence E on the mobile phase velocity. ◇: Capcellpack C_{18} UG, ◆: Rod Column.

drop of the rod column is 1/2 to 1/3 of that of conventional one, obviously due to the higher (>60%) volume fraction of through-pores. In order to evaluate the total column performance realizable in an ordinary HPLC apparatus, the standardized quantity called separation impedance E can be used [16]. It is defined as follows:

$$E = (\Delta P/N)(t_0/N)(1/\eta) \quad (1)$$

where t_0 denotes the unit time, N the number of the theoretical plate and η the viscosity of the mobile phase. The impedance quantitatively indicates the difficulty of obtaining theoretical plates against the pressure drop the loss of column efficiency at higher mobile phase velocity. As shown in Fig. 7, when evaluated by the separation impedance, the analytical performance of the rod column is about an order of magnitude better than the conventional ones.

4. Conclusion

The design principle of double-pore silica gel monoliths has been established. A monolithic silica gel column for HPLC has been developed. This column exhibits superior analytical performance to conventional columns especially at higher mobile phase velocities. Appropriate combinations of column structure, chemical modification and column geometry will open a new phase of high speed HPLC.

Acknowledgment

This work was supported in part by Grant-in-Aid for Scientific Research (No. 09554050 and No. 09750751) funded by the Ministry of Education, Science, Sports and Culture.

References

1. R.K. Iler, *The Chemistry of Silica* (Wiley, New York, 1979), chap. 5.
2. S. Liu and L.L. Hench, in *Sol-Gel Optics II*, edited by J.D. Mackenzie (SPIE—The International Society for Optical Engineering, Washington, 1992), Vol. 1758, p. 14.
3. K. Nakanishi, H. Kaji, and N. Soga, *Ceramic Transactions*—"Porous Materials," edited by K. Ishizaki et al. (The American Ceramic Society, Ohio, 1993), Vol. 31, pp. 51–60.
4. K. Nakanishi, J. Porous Mater. **4**, 67–112 (1997).
5. N. Tanaka, H. Kinoshita, M. Arakiand, and T. Tsuda, J. Chromatogr. **332**, 57–69 (1985).
6. H. Minakuchi, K. Nakanishi, N. Soga, N. Ishizuka, and N. Tanaka, Anal. Chem. **68**, 3498–3501 (1996).
7. K. Nakanishi, H. Komura, R. Takahashi, and N. Soga, Bull Chem. Soc. Jpn. **67**, 1327–1335 (1994).
8. K. Nakanishi and N. Soga. J. Am. Ceram. Soc. **74**, 2518–2530 (1991).
9. K. Nakanishi and N. Soga. J. Non-Cryst. Solids **139**, 1–24 (1992).
10. H. Minakuchi, K. Nakanishi, N. Soga, N. Ishizuka, and N. Tanaka, J. Chromatogr. A **762**, 135–146 (1997).
11. K. Nakanishi, N. Koheiya, and N. Soga, unpublished data.
12. G. Guiochon, in Cs. Horvath (Ed.), *High Performance Liquid Chromatography—Advances and Perspectives* Academic Press, New York, 1980), Vol. 2, pp. 1–56.
13. S. Hjerten, J.-L. Liao, and R. Zhang, J. Chromatogr. **473**, 273–275 (1989).
14. Q.-C. Wang, F. Svec, and J.M.J. Frechet, Anal. Chem. **65**, 2243–2248 (1993).
15. R.P.W. Scott, *Liquid Chromatography Column Theory* (John Wiley & Sons, Chichester, 1992), chap. 7.
16. P.A. Bristow and J.H. Knox, Chromatographia **10**, 279–289 (1977).

Journal of Sol-Gel Science and Technology 13, 171–175 (1998)
© 1998 Kluwer Academic Publishers. Manufactured in The Netherlands.

Net-Shape Manufacture of Low-Cost Ceramic Shapes by Freeze-Gelation

M.J. STATHAM, F. HAMMETT, B. HARRIS AND R.G. COOKE
Department of Materials Science and Engineering, University of Bath, Bath, Somerset, BA2 7AY, U.K.

R.M. JORDAN AND A. ROCHE
SDL, Singleton Park, Swansea, SA2 8PP, U.K.

Abstract. The use of freeze-gelation (or freeze-casting) overcomes many of the familiar limitations of sol-gel processing and permits the formation of low-cost, crack-free, essentially zero-shrinkage ceramic bodies of complex shape. There are many potential industrial applications for the manufacture of complex shapes by the freeze-gelation process. This paper presents the results of an investigation into the effects of materials and processing parameters on the performance, properties and microstructures of the ceramics produced. In particular, the effects on porosity and flexural strength of the type and composition of sol, filler particle size ranges, and variable freezing conditions, have been investigated.

Keywords: freeze-gelation, porosity, net-shape

1. Introduction

The sol-gel process offers a number of advantages over conventional ceramics processes; it may be carried out at low temperatures and involves wet processing to near-final shape. The initial forming stage may be followed by consolidation at relatively modest temperatures, but this is often unnecessary since the green strengths of sol-gel products can be very high. The disadvantage of the process is the inherently large shrinkage of typical gels, usually 20–25 vol%, but reducing to ~5% if appropriate proportions of fillers are used. However, the use of freeze-gelation [1] overcomes many of the familiar limitations of sol-gel processing and permits the formation of low-cost, crack-free, essentially zero-shrinkage ceramic bodies of complex shape.

The freeze-gelation method is eminently suitable for the manufacture of complex shapes for use in a wide variety of industrial applications. Factors affecting the quality of components produced by the freeze-gelation process include:

(i) The refractory nature of the materials and the robustness of surface and bulk characteristics under conditions of thermal shock (e.g., when exposed to sudden contact with molten metal).
(ii) Surface quality, including porosity, topography, and resistance to spalling of the surface under thermal shock.
(iii) Engineering tolerance and dimensional accuracy that can be achieved.
(iv) The ability to cast components to shape, in a mold, and the ability to extract complex cast shapes without damage.
(v) Green strength of the frozen and dried components.
(vi) The ceramic must be cheaply and easily manufactured.

These requirements can often be translated into profiles of mechanical and physical properties required for the manufacture of particular products, but in many cases the most important requirements very often relate to what might loosely be termed "surface quality." The current work has therefore examined the properties of surface porosity and strength in some detail in relation to various molten metal applications.

2. An Outline of the Freeze-Gelation Process

One of the greatest assets of the freeze-gelation process is its simplicity. A number of colloidal sols are freeze sensitive (i.e., they gel irreversibly if frozen), the majority of those investigated at the University of Bath are commercially available silica sols. Polymerization occurs because of the concentration of silica particles within the interstices between ice crystals. The formation of ice crystals within the sol occurs at 273 K, but freeze-gelation does not occur until temperatures a few degrees below freezing (~270 K) are reached. After freezing the gel is warmed to melt the ice crystals and then dried. The final article has a relatively high degree of continuous porosity (~35%), with pores duplicating the morphology and dimensions of the ice crystals formed during the freezing process. Control over the porosity in the ceramic may be achieved by controlling the nucleation and growth of the ice crystals during freezing. There are many similarities with the formation of freeze-cast ceramic fibres and particles from aqueous gels under controlled freezing conditions, this "freeze-forming" technique has been investigated by a number of workers [2–4].

At temperatures in the 270–273 K range full gelation does not occur despite the freezing of the bulk of the water due to the suppression of the freezing point of bound water. It is theorized that this acts as a barrier to the aggregation of the silica particles.

A range of different additions can be made to the sol prior to freeze-gelation, typical additives are refractory oxide or other ceramic powders. Incorporation of large mass fractions of filler can be achieved (up to ~85 wt%), and such additions are generally desirable because of the improvements to mechanical properties, and reduction in shrinkage which result.

After freeze-gelation, further processing may be carried out on the dried body if desired. Sintering occurs at very low temperatures due to the high reactivity of the homogeneously dispersed and finely divided components [5].

3. Materials and Processing Variables Studied

3.1. *Materials*

Three commercially available freeze-sensitive silica colloids have been investigated during this program, X30 and HT50 supplied by Morrisons and HS40 supplied by Du Pont. These sols contain 30, 50 and 40 wt% silica, with particles of a mean diameter of 25, 125 and 12 nm, respectively, and are all stabilized with sodium counter ions.

A number of different refractory oxide and other ceramic powders have been added successfully to freeze-cast materials. T-60 tabular α-alumina of three particle size ranges have been used for this study; $<300\,\mu$m, $<180\,\mu$m and $<63\,\mu$m.

Filler mass fractions of 80 to 85% have been investigated. Adjusting filler content within this narrow range has a large effect on the viscosity of the slurry, as does the size of the filler particles used. Shearthinning effects are evident in the more viscous slurries; a proportion of this behavior can be attributed to the quantity of air trapped in the slurry. Viscosity can be reduced by de-gassing the slurry in a vacuum, which results in better filling of mold details and fewer air bubbles and surface defects. Dispersion of the fillers in the sol is best achieved with a sigma-blade mixer.

3.2. *Processing Conditions*

A number of process variables have been investigated during the period of this study. Of primary importance for the resultant microstructure is the cooling rate applied to the slurry. Several different techniques have been used to chill the mold containing the slurry and cause freeze-gelation, which can be achieved at any temperature below around 270 K. Freeze-gelation has been carried out successfully in a standard household freezer and in a liquid nitrogen bath. For this study a stirred bath of silicone fluid cooled via a coil of liquid nitrogen was constructed, so that the effects of freeze-casting at a range of temperatures could be investigated. The cooling rate achieved can also vary according to the thermal conductivity and dimensions of the mold used to contain the slurry. A number of suitable mold materials have been investigated.

The effect of a number of freezing regimes on different slurries and the size and morphology of the ice crystals formed has been investigated with a simple mold designed for unidirectional freezing. The mold was manufactured from a nylon cylinder with a removable 8 mm thick base plate which can be replaced with different mold materials. During the freezing experiments this base plate was chilled to the desired temperature by immersion in the bath. Thermocouples were located in the slurry near the freezing face, the data from these being logged to allow the plotting of temperature-time profiles and estimation of values for

GR (cooling rate), *R* (freezing rate) and *G* (temperature gradient at freezing front) [6, 7].

The effects of a number of drying and sintering at a range of temperatures (323–1572 K), were investigated. The sintering cycle used a ramp rate of 5 $K \cdot min^{-1}$ and a holding time of 1 hour. Flexural strength was measured using three-point bend tests with specimen configurations of 8 mm × 8 mm × 100 mm and a span of 90 mm.

4. Results

Surface porosity, in terms of size and morphology, are the primary factors affecting both spalling (resistance to thermal shock) and replication characteristics. Bulk porosity affects mechanical properties including flexural strength of green and sintered products.

Cooling rate (*GR*) has a large effect on the size and morphology of the porosity formed. Three distinct sizes and morphologies are observed:

(i) A fine, irregularly shaped equiaxed ice crystal structure at rapid cooling rates.
(ii) A unidirectional columnar (cellular) ice crystal structure at intermediate cooling rates, cell diameter increasing at slower cooling rates.
(iii) A coarse irregularly shaped or dendritic ice crystal structure at slow cooling rates.

These different morphologies are illustrated in Fig. 1. Freezing in liquid nitrogen (~77 K) is rapid and results in very fine, evenly dispersed, equiaxed ice crystals. Freeze-gelation in a standard freezer (~253 K) results in a very slow cooling rate and the formation of large dendritic or irregularly shaped ice crystals. A single freeze-cast product may demonstrate two or more different morphologies and a range of crystal sizes owing to the changes in cooling rate as a function of distance away from the chilled mold surface.

During the current investigation values for *R* and *G* were estimated for a number of freeze-gelation experiments. Well developed columnar morphology was only noted for intermediate values of cooling rate *GR* and higher values of *G*/*R*. Results for freeze-cast substrates with a composition of 17.5 wt% X30 sol filled with a <180 μm alumina particle size range are presented in the Table 1.

Reduction of the mass fraction of filler in the slurry results in individual pores of similar dimensions and morphologies at the same cooling rate, but a greater overall porosity. A slight difference in pore size was

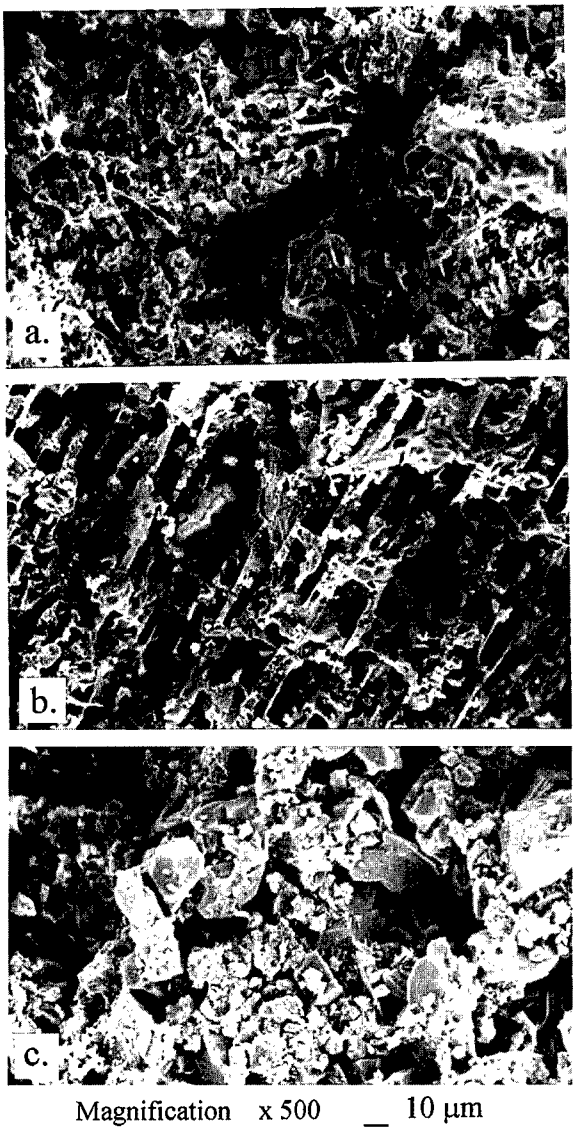

Figure 1. Scanning electron micrographs of fracture surfaces of freeze-cast, <180 μm alumina-filled ceramic (a) illustrating typical porosity resulting from fine equiaxed ice crystal growth, (b) illustrating typical porosity resulting from columnar ice crystal growth, and (c) illustrating typical porosity resulting from large coarse ice crystal growth.

observed for the sol types investigated, with overall porosity and pore size decreasing with increasing silica wt% (X30 < HS40 < HT50). The three different filler particle size ranges investigated result in large changes in pore dimension, the finer filler particles giving smaller pores at the same cooling rate.

The fracture stress of the freeze-cast ceramics increases with decreasing volume and extent of porosity

Table 1. Results for freeze-cast substrates.

GR (°C h^{-1})	*R* (cm h^{-1})	*G* (°C cm)	*G/R* (°C h cm^{-2})	Morphology	Diameter (μm)
1020	37.9	27	0.71	Equiaxed	~5
280	17.6	16	0.9	Cellular	10
120	12.7	9	0.74	Cellular	12
20	6.6	3	0.46	Irregular/dendritic	>20

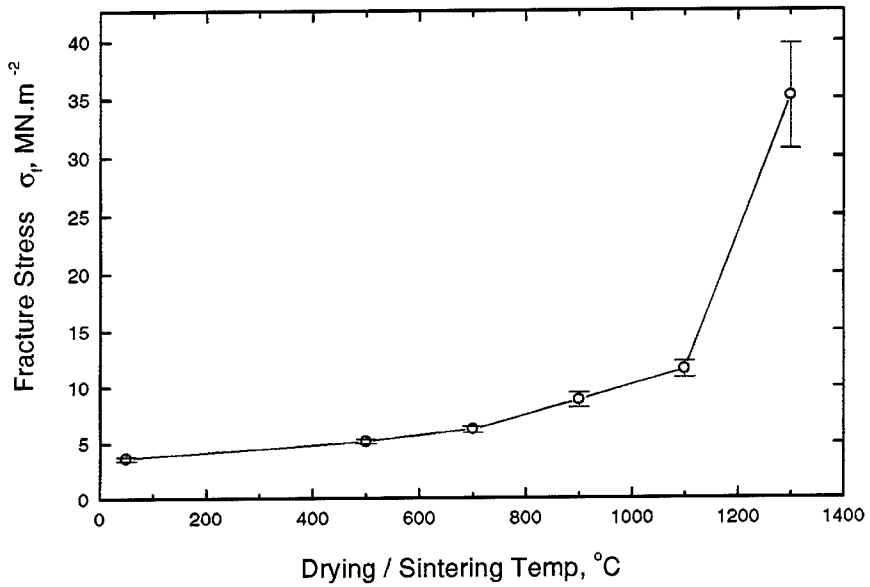

Figure 2. Fracture stress (σ) versus sintering temperature X30 sol with <180 μm alumina filler particle size range, $GR - 15.7°C \cdot min^{-1}$.

and increasing coherency. Thus, reductions in sol content, finer filler particle size ranges and increased cooling rates result in materials with better flexural strength properties. There is a gradual increase in flexural strength as a consequence of drying and/or sintering in the temperature range of 773–1373 K (Fig. 2). Beyond this point the increase in flexural strength is more rapid but is accompanied by increased shrinkage.

The rate of drying appears to have little effect on the physical properties of the freeze-cast substrate. However, directional drying, i.e., Infra-red lamps, can lead to warping and cracking as moisture is not uniformly removed from the surfaces of the substrate, also substrates with fine porosity often exhibit cracking owing to the difficulties in extracting moisture from narrow pores. Drying carried out in a convection oven at around 323 K is complete after about 24 hours. Drying has also been successfully carried out using a standard 650 W microwave oven in a greatly reduced time.

5. Conclusions

Freeze-gelation is a process with a wide range of potential industrial applications, offering an economic technique for the manufacture of near net-shape ceramics with controllable microstructures and physical properties. The properties of the freeze-cast product can be tailored to meet a variety of engineering applications.

The size of pores at the freeze-cast ceramic substrate surface can be modified by controlling the cooling rate and filler particle size range; morphology can be controlled by freezing under the correct conditions. The microstructure and hence the flexural strength of the ceramic substrate may be controlled by adjusting the cooling rates, mass fraction of filler particles, filler particle size ranges and sol type. Coherency and flexural strength may also be increased by sintering at modest temperatures.

Acknowledgments

The authors would like to acknowledge the support of the EPSRC in financing this research.

References

1. J. Laurie, C.M. Bagnall, B. Harris, R.W. Jones, R.G. Cooke, R.S. Russell-Floyd, T.H. Wang, and F.W. Hammett, Journal of Non-Crystalline Solids **147/148**, 320–325 (1992).
2. T. Maki and S. Sakka, Journal of Non-Crystalline Solids **82**, 239–245 (1986).
3. B.G. Muralidharan and D.C. Agrawal, Journal of Materials Science Letters **13**, 1017–1018 (1994).
4. W. Mahler and U. Chowdhry, *Ultrastructure Processing of Ceramics Glasses and Composites* (Gainesville Florida, USA, 1984), pp. 207–218.
5. R.K. Iler, *The Chemistry of Silica* (John Wiley and Sons, New York, 1979), p. 544.
6. M.C. Flemings, *Solidification Processing* (McGraw-Hill, New York, 1974).
7. W. Kurz and D.J. Fisher, *Fundamentals of Solidification* (Trans. Tech., Switzerland, 1989).

Journal of Sol-Gel Science and Technology 13, 177–182 (1998)
© 1998 Kluwer Academic Publishers. Manufactured in The Netherlands.

Refractive Microlens Fabrication by Ink-Jet Process

S. BIEHL, R. DANZEBRINK, P. OLIVEIRA AND M.A. AEGERTER
Institut für Neue Materialien-INM, Department of Coating Technology, Im Stadtwald 43, D-66123 Saarbrücken, Germany

Abstract. Microlenses made of hybrid organic-inorganic materials have been fabricated on glass substrates using a commercial drop-on-demand ink-jet printing system with a 50 μm diameter nozzle driven by a piezoelectric device. After deposition the drops have been polymerized by UV light irradiation. Viscosity, solvent evaporation, drop-substrate wetting condition and drop and substrate temperatures are the main parameters which govern the production of reproducible lens shapes. The shape and surface roughness of the lenses have been characterized by atomic force microscopy and profilometry. Their optical properties have been determined by light microscopy and spectrophotometric techniques. The printing technique can produce plano-convex spherical microlenses with diameters varying from 50 to 300 μm, focal lengths from 70 μm to 3 mm and f-numbers as low as 0.6.

Keywords: ink-jet printing, hybrid organic-inorganic, microlens

1. Introduction

Micro-optics technology is becoming increasingly important in the development of optical systems. Optical components such as diffractive and refractive microlenses are now being incorporated in many systems and commercial products. They are used, for example, for focusing in detector arrays, fiber optics and sensors, for illumination in flat panel displays, computers and for imaging in photocopiers and lithography [1–3]. Refractive microlenses provide an attractive low cost alternative to diffractive components and for devices using short wavelengths (<1 μm) requiring low f-numbers ($F < 4$) they are still the only available components. Refractive microlenses have been fabricated in various ways. In the photolithographic process a substrate is coated with a polymer and polymerized through a mask by UV light irradiation. Small cylinders are obtained by etching the unpolymerized part of the polymer. The substrate is then heated until the cylinders melt and flow forming a refractive lens profile by surface tension [4–6]. Other processes involve the filling of a negative form with a polymer, which after heating, transforms into small plano-convex lenses. The polymerized droplets must, however, be polished to reduce the surface roughness [1, 7, 8]. Reactive ion etching and ion milling can also be used [3]. Micro-optic systems can also be prepared using graded refractive technology. These lenslets are cylindrical rather than spherical [1].

The ink-jet process is commonly used in computer-controlled printing [9, 10]. To our knowledge sol-gel based inks have only been proposed to decorate ceramic tiles using a continuous process [11]. In this paper we describe the use of such a technology to manufacture microlenses on glass substrates using sols prepared from hybrid organic-inorganic materials.

2. Experimental

There are two classes of ink-jet printers: continuous [10] and drop-on-demand [12]. The equipment used here is a drop-on-demand printer (Microdrop, SP-K 130), composed of a piezoelectric ceramic nozzle (50 μm diameter), connected to a reservoir by a capillary tube (Fig. 1). The reservoir can be heated to lower the ink viscosity. A high frequency computer-controlled generator generates an electrical signal which squeezes the nozzle and generates a drop. The

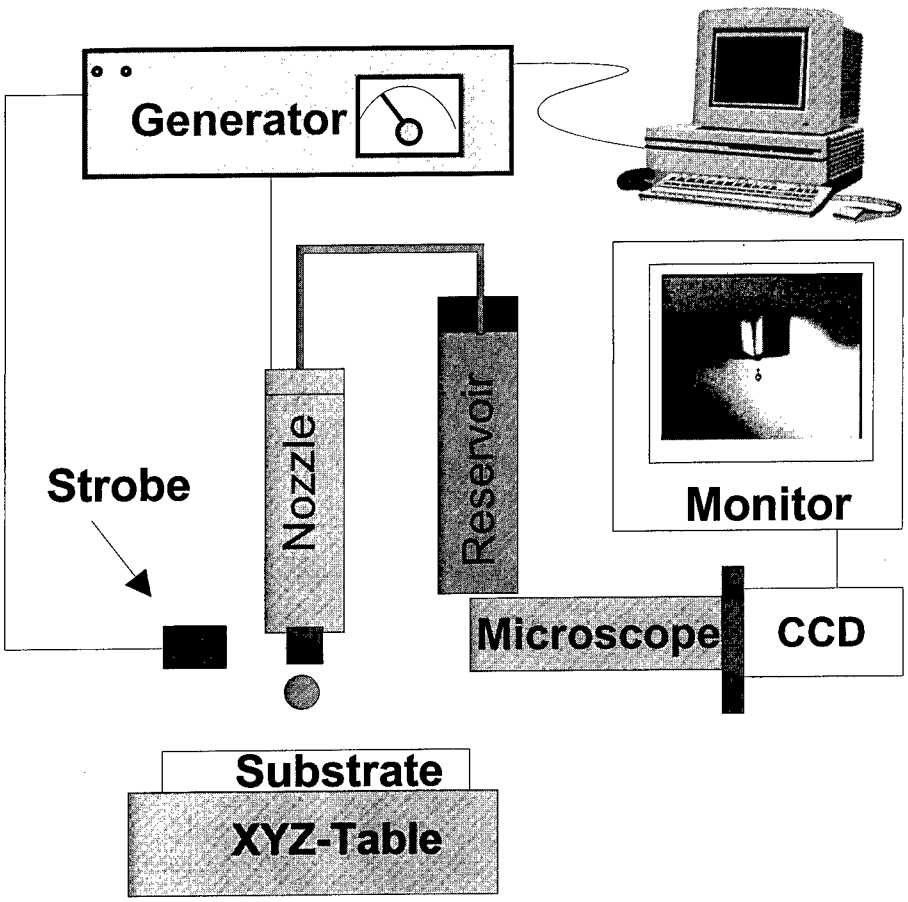

Figure 1. Scheme of the drop-on-demand ink-jet printing equipment.

rate can be varied from 1 to 2000 drops/s. The shape of the drops can be visualized by a CCD camera coupled to a stroboscope. After travelling a few millimeters at a speed of about 10 m/s, the drops become spherical, typically 50 μm in diameter. Single droplets have been deposited on clean glass substrates and glass substrates coated with a thin layer of a low surface energy perfluorated polymer (FTS/TEOS/MPTS/2-Propanol/Irgacure 184) [13] in order to vary the drop/substrate wetting conditions. The substrates can be moved in the XYZ-directions by stepper motors so that lines or arrays of drops can be printed.

Hybrid organic-inorganic sols have been prepared by hydrolysis of methacryloxypropyltrimethoxysilane (MPTS) mixed with an ethanolic solution of tetraethyleneglycoldimetacrylate (TEGDMA) and 1 to 10 wt% UV photoinitiator (Irgacure 184). After deposition, the drops have been polymerized by UV light irradiation (Kombistrahler Beltron). The polymerization of the sols during the UV irradiation has been followed by Fourier transform infrared spectroscopy (Bruker IFS 66V) particularly analyzing the C=C bonds band at 1636 cm^{-1}. The visible near-infrared optical transmission of the sol and polymerized material has been determined using a Varian Cary 5E spectrophotometer.

The shape and surface roughness of the lenses have been measured by atomic force microscopy (Topometrics Explorer 2000 AFM) and a Tencor P10 profilometer. The focal length of the plano convex lenses has been determined at $\lambda = 632.8$ nm using an optical microscope equipped with a scanning knife-edge device [14] and a silicon photodiode. The intensity image profiles of a parallel beam at the focus plane have been also recorded with a 3D Spiricon laser beam analyzer. The lens f-numbers have been calculated using the thick lens formula

$$F = \frac{1}{2z}\{n(1 - z^2) - [(1 - (nz)^2)]\}$$

where n is the refractive index (assumed $n = 1.5$) and $z = a/r$ with a the lens radius and r the radius of curvature.

3. Requirements

The sols used in ink-jet printing must satisfy particular requirements. As the flow velocity in the nozzle is very high (10 m/s) and the aperture very small (50 μm), the shear rates are very high (500 s^{-1}), and this places constraints on the rheological properties of the sols. For the preparation used here, the kinematic viscosity of the ink at room temperature cannot exceed 3 mm^2/s. In addition conventional sols, which gel through hydrolyzation and polycondensation processes, are difficult to handle with a drop-on-demand system as they rapidly block the fine nozzle. After arriving at the substrate, the final shape of the deposit depends essentially on the equilibrium $\alpha_{12} = \alpha \cos\theta$ between the van der Waals forces which act at the border of the drop/substrate interface and which correspond to the surface tension of the liquid α and the interfacial tension α_{12} (attractive forces between liquid and solid), θ being the contact angle. These vary rapidly as the solvent evaporates and depend on the substrate temperature and the composition of both the drop and the substrate. Moreover, the final lenses should be transparent over a large optical wavelength range and homogeneous. All these parameters considerably restrict the composition of the sol. A good compromise has been found with the compositions of the sols proposed here.

4. Results and Discussion

A typical sol prepared as above has a room temperature kinematic viscosity $\eta = 3$ mm^2/s. Its value decreases slightly with increasing temperature. The effect of the UV irradiation (17.5 J/cm^2 total energy in wavelength range 280–320 nm) on the network building (polymerization) was analyzed by studying the evolution of the infrared absorption band at 1636 cm^{-1} of the C=C bonds of MPTS and TEGDMA as a function of the irradiation time using a 0.1 μm thick film deposited by spin coating on a Si-wafer. For 10 wt% photoinitiator, polymerization is completed after 200 s. For smaller amounts of the time exposure should be longer. The lenses have been obtained with photoinitiator concentrations of 1 to 10 wt%. Figure 2 shows the visible/near-IR optical transmission of precursor sols with and without photoinitiator and of the UV polymerized layer. The UV absorptions of irgacure 184 at 244 nm and at 285 nm are clearly visible for the sol. After polymerization the bands practically disappear and the final material is highly transparent in the region 375 nm $< \lambda <$ 2.7 μm. Its optical properties are therefore adequate for the preparation of lenses.

Typical shapes of lenses obtained with different sols and substrates are illustrated in Figs. 3, 4 and 5. Figure 3 shows the effect of excess ethanol in the sol (>40 wt%). The sol wets the glass substrate and spreads on it. The inorganic-organic material is transported to the border of the drop and creates a ring shaped lens due to capillary effects.

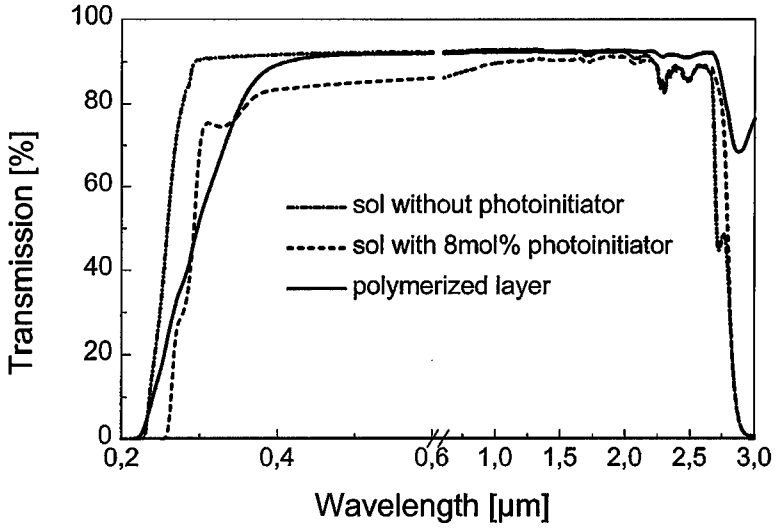

Figure 2. Optical transmission spectra of (———) polymerized layer, (------) sol with 8 mol% photoinitiator, (·-·-·-) sol without photoinitiator.

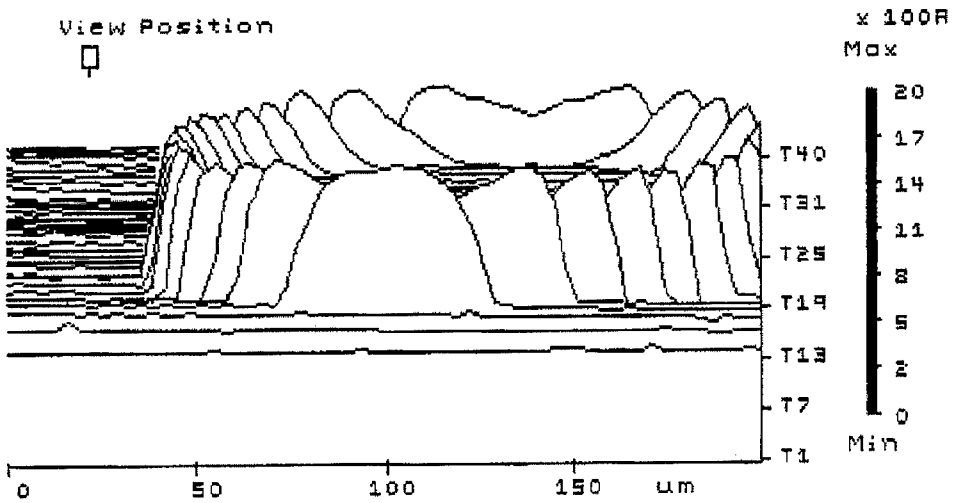

Figure 3. Ring shape of a lens obtained on a glass substrate measured by profilometry. The sol has a high ethanol content (40 wt%).

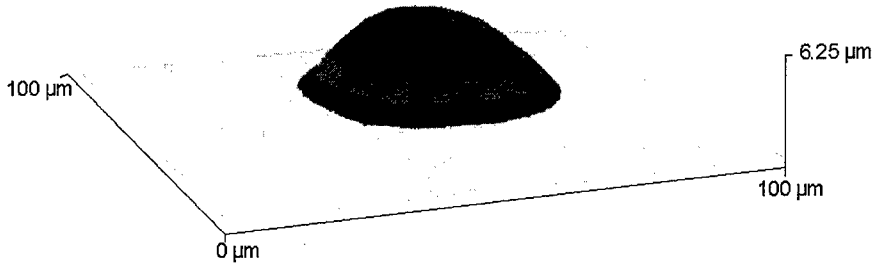

Figure 4. AFM micrograph of a lens obtained on a glass substrate with optimized ethanol content (30 wt%).

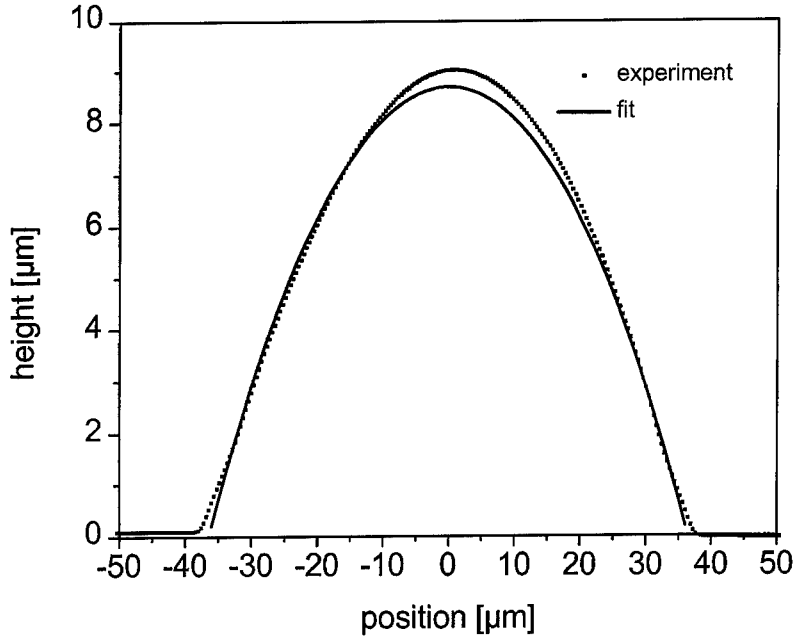

Figure 5. Profilometer plot of the shape of a lens deposited a modified glass substrate.

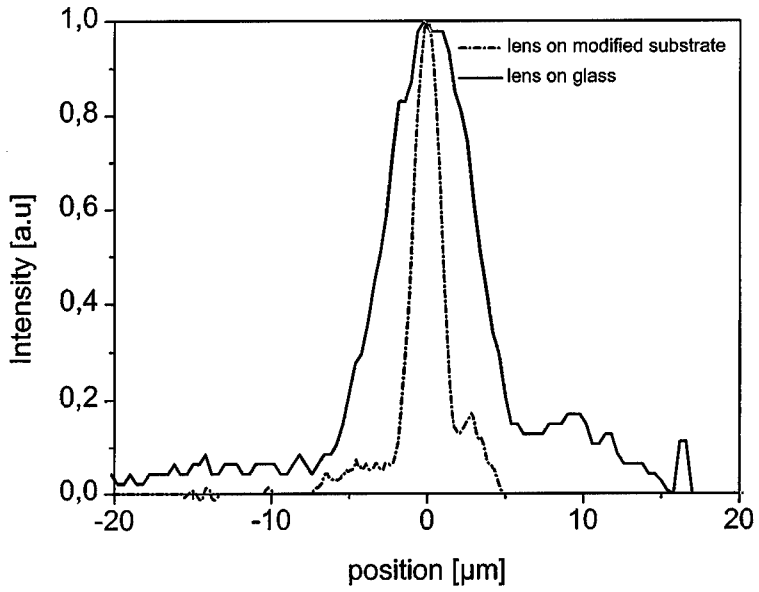

Figure 6. Fit of a vertical cross-section of a lens deposited on a perfluorided glass substrate showing the spherical shape.

Sols containing less than 30 wt% ethanol have a high viscosity $\eta > 5\,\text{mm}^2/\text{s}$, and tend to block the piezoelectric nozzle. Spherical lens formation was obtained on glass substrates with a mixture of 50 mol% MPTS and 50 mol% TEGDMA is 30 wt% ethanol fraction (Fig. 4).

This lens is spherical and has the following properties: radius $a = 25\,\mu$m, height $h = 6.25\,\mu$m, radius of curvature $r = 53.1\,\mu$m, focal length (at 632.8 nm) $f = 100\,\mu$m, lens power $F = 0.62$ and a surface roughness $R_a = 40$ nm.

In order to reduce the effect of the spreading of the high ethanol content sols lenses have been fabricated on a substrate whose interface has been coated with a thin layer ($0.1\,\mu$m) of a low surface energy polymer. Figure 5 shows a fit of a vertical cross-section passing through the center of the lens by a semicircle. The agreement is good.

This lens has the following properties: radius $a = 37.5\,\mu$m, height $h = 9\,\mu$m, radius of curvature $r = 82.6\,\mu$m, focal length at 632.8 nm $f = 125\,\mu$m, lens power $F = 0.72$, surface roughness $R_a = 40$ nm.

Two-dimensional intensity profiles of the light spot created at the focal plane by a collimated 632.8 nm laser beam travelling on the substrate side of the lenses are shown in Fig. 6.

Their shapes are practically Gaussian with a full width at half maximum (fwhm) equal to $1.8\,\mu$m and $6.2\,\mu$m, respectively. These values are small and can be compared to those calculated for a perfect diffraction limited lens (fwhm $\sim 0.7\,\mu$m). The smallest fwhm value was obtained for the lens deposited on the modified surface substrate.

5. Conclusion

A drop-on-demand ink-jet process has been successfully used to fabricate refractive microlenses on glass substrates from an organic-inorganic sol containing MPTS, TEGDMA and a photoinitiator. These components have been polymerized by UV-irradiation at room temperature and are transparent from 375 to 2700 nm and have a refractive index $n = 1.5$. Plano-convex spherical shapes have been obtained for optimized sol composition and drop/substrate wetting conditions with a diameter and f-number as small as $50\,\mu$m and $0.62\,\mu$m, respectively, and a surface roughness $R_a = 40$ nm. The fabrication of one and two dimensional closely spaced microlens arrays should be possible.

References

1. N.J. Phillips and C.A. Barnett, Miniature and micro-optics: Fabrication and system applications SPIE **1544**, 10 (1991).
2. H.M. Presby and C.R. Giles, IEEE Photonics Technology Letters **5**, 184 (1993).
3. M.E. Motamedi, M.C. Wu, and K.S.O Pfister, Optical Engineering **36**, 1282 (1997).

4. D. Daly, R.F. Stevens, M.C. Hutley, and N. Dacies, J. Phys. **E1**, 759 (1990).
5. M.C. Hutley, J. Mod. Optics **37**, 253 (1990).
6. K.-H. Brenner, M. Kufner, S. Kufner, J. Moisel, A. Müller, S. Sinzinger, M. Testorf, J. Göttert, and J. Mohr, Applied Optics **32**, 6464 (1993).
7. L. Erdmann, D. Efferenn, Opt. Eng. **36**, 1094 (1997).
8. D.L. Kendall, W.P. Eaton, R. Manginell, and T.G. Digges, Jr., Optical Eng. **33**, 3578 (1994).
9. M. Döring, Philips Tech. **40**, 192 (1982).
10. L. Kuhn and R.A. Myers, Scientific American **240**, 120 (1979).
11. A. Atkinson, J. Doorber, A. Hudd, D.L. Segal, and P.J. White, J. Sol-gel Science and Technology **8**, 1093 (1997).
12. D.L. MacFarlane, V. Narayan, J.A. Tatum, W.R. Cox, T. Chen, and D.J. Hayes, IEEE **6**, 1112 (1994).
13. J. Bersin, R. Kasemann, G. Jonschker, and H. Schmidt, Annual Report INM, 134 (1995).
14. D.U. Cohen, B. Little, and F.S. Luecke, Applied Optics **23**, 637 (1984).

Journal of Sol-Gel Science and Technology 13, 183–187 (1998)
© 1998 Kluwer Academic Publishers. Manufactured in The Netherlands.

Industrial Application of Hybrid Sol-Gel Coatings for the Decoration of Crystal Glassware

G. SCHOTTNER, J. KRON AND A. DEICHMANN
Fraunhofer-Institut für Silicatforschung, Neunerplatz 2, D-97082 Würzburg, Germany
schotty@isc.fhg.de

Abstract. The coloration of glass via melting techniques presents some unique problems with respect to the reproducibility, toxicology and economics of certain colors, especially if the market demands are highly variable. This is also the case for consumer products such as crystal glass and tableware. Traditionally, the decoration of crystal glasses is performed by laborious manual techniques, which are costly and do not meet modern market requirements. Alternatively, spraying of colored lacquers is a highly flexible and valuable tool for the development of new products. Sol-gel type hybrid coatings provide several advantages compared to conventional organic systems like high abrasion resistance, almost perfect adhesion, refractive index matching and sufficient stability in dishwashing procedures. The solubility of organic dyes in the hybrid matrix is sufficient for intense colors even at rather low layer thicknesses, which on the other hand convey the high brilliance of the base material. The development of transparent, translucent and opaque hybrid coatings for crystal glass has been completed in the last few years and the production of partially coated articles has started recently. The synthesis and properties of the coating material are reviewed and the industrial process and first market results are also outlined.

Keywords: hybrid sol-gel coatings, crystal glass, dishwashing resistance, lead release, spraying procedure

1. Introduction

Before the invention of English crystal by Ravenscroft in 1675, the use of lead oxide in glass to achieve clarity and brilliance was virtually unknown [1]. Today, the manufacture of crystal glasses is of major importance throughout Europe. In Germany, around 80,000 t was produced in 1995. The increasing globalization of all markets is affecting this highly traditional industry. Therefore, new developments replacing laborious and costly techniques are needed to assure international competitiveness. The industrial fabrication of inorganic sol-gel systems for various purposes has been important for many years [2]. In the last decade applications of hybrid sol-gel coatings for the protection of transparent plastics or metals have been developed [3, 4]. Now the investigation of colored coatings on crystal glasses has led to an industrial process that will be described in the following overview.

2. State of the Art

2.1. Colored Glass and Crystal Glass

The coloration of glasses is well known and has been extensively described elsewhere [5]. There are principally three different methods to achieve intense colors in bulk glasses. One route is incorporating transition metal cations into the glass network, which absorb visible light due to electronic transitions in their atomic orbitals. Metal salts of Au, Ag or Cu can also be added, which are reduced to the metallic state during melting and segregate from the glass matrix while cooling (colloidal coloration by small metal particles). Similar phase segregation processes take place after the addition of CdS or CdSe to the glass batch, which are used to obtain yellow, orange and red colors. It is obvious that these additives present toxicological problems during production and recycling.

An extensive survey of the properties and applications of lead in glass-making was published in 1963 [1]. The latest changes in the European regulation for the notation, composition and necessary properties of crystal glasses have been summarized recently [6], defining high lead crystal glass (min. 30% Pb, $n_D = 1.56$, $\rho = 3000$ kg/m^3), lead crystal glass (min. 24% Pb, $n_D = 1.545$, $\rho = 2900$ kg/m^3) and crystal glass (max. 10% Pb, $n_D = 1.52$, $\rho = 2500$ kg/m^3).

2.2. *Hybrid Sol-Gel Coatings*

The synthesis and structure-property relationships of hybrid sol-gel materials have been extensively reviewed in recent years [7, 8]. In addition, the incorporation of organic dyes and their photochemical behavior [9, 10] as well as spectroscopic investigations of hybrid sol-gel materials [11] have already been published. Therefore, only the main aspects of the synthesis procedure used will be described in the next section.

3. Development of Colored, Hybrid Sol-Gel Coatings for Crystal Glassware

3.1. *Material Preparation*

The synthesis procedure for abrasion resistant, colored hybrid coatings is outlined in Fig. 1 and mainly comprises the cohydrolysis and co-condensation of organo(alkoxy)silanes and metal alkoxides in appropriate amounts. On glass surfaces a mixture of phenyltrimethoxysilane, 3-glycidoxy propyltrimethoxysilane, 3-aminopropyltriethoxysilane and aluminum-*sec*-butoxide was proved to meet the requirements quite closely. The experimental details of the synthesis, exact composition and the development steps have already been described [12]. Important aspects are the adaptation of the reactivities of the metal and silicon alkoxides to avoid precipitation and phase segregation and to improve chemical resistance against alkaline media. The respective techniques—complexation of metal alkoxides and addition of hydrophobic epoxy resins—have also been described elsewhere [12, 13]. They have been used to develop formulations that have a shelf lifetime of at least three months, if they are stored at low temperatures. Coloration of the sols can be achieved by dissolving commercial organic dyes (e.g., ORASOL^{TM}, Ciba-Geigy) in small amounts (1–3%) or incorporating

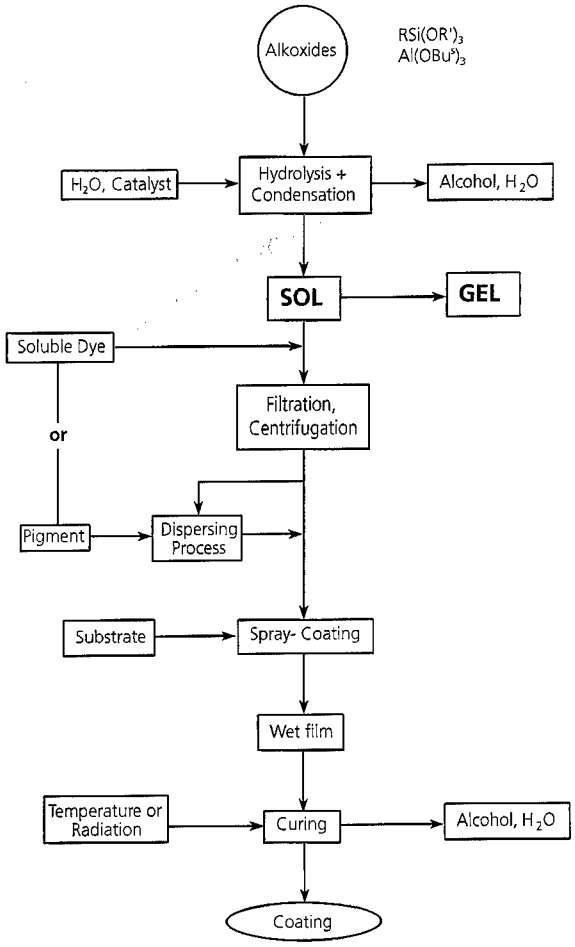

Figure 1. Synthesis and application of colored hybrid sol-gel coatings.

organic or inorganic pigments via conventional dispersing techniques.

3.2. *Application of Sols and Properties of Coatings*

A selection of the resulting properties of the sols and of the cured coatings as well as the application parameters are summarized in Table 1.

The application of the sols to the glass articles is done with conventional spraying equipment, wherein the spray nozzle is placed above the horizontally rotating glass goblet and the residual parts of it are protected from the spray fog by the application of metal shutters (Fig. 2).

The coated pieces are placed on a conveyor belt afterwards and cured at 180°C for 30 min in a conventional

Table 1. Properties of sols and cured coatings and application parameters.

Property	Value	Method
Viscosity	10.5–12.0 mm^2/s (clear-coat)	Ubbelohde
Solids content	42–45% (clear-coat)	DIN 52316-A
Density	1.002 kg/m^3 (clear-coat)	Pycnometer
Flash point	301 K	DIN-ISO 3676
Spraying parameters	Nozzle diameter 0.2–1.4 mm Pressure 1.5–3 bar	
Drying conditions	433 K/2 h to 473 K/600 s	
Layer thickness	8–12 μm	Interferometer
Adhesion	B 5-4	ASTM D 3359
Abrasion resistance	1.3–2.3% (clear-coat, related to epoxide content)	ASTM D 1044
Refractive index	1.5218–1.5240 (clear-coat, related to epoxide content)	Abbé-Refractometer

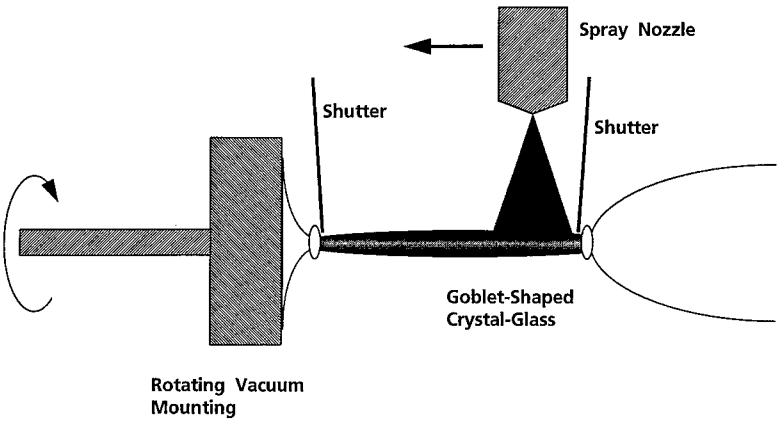

Figure 2. Spraying procedure for crystal glass goblets.

heater. Quality assurance and testing of colorimetric aspects are performed by conventional methods.

3.3. *Reduction of Lead Release and Stability Against Foodstuff*

An important aspect in the use of crystal glass is the leaching of lead from the glass network into liquids contained in cups or jars [14]. Several means to avoid lead leaching are recommended and used [15]. In this respect the hybrid sol-gel coating cannot only be applied to decorate exterior surfaces of crystal glassware, but also to avoid lead leaching from interior surfaces of cups or bowls. Table 2 demonstrates that the migration of lead into the test liquid (4% acetic acid, DIN 51031) is far below the admissible limits. In contrast to other treatments (acid polishing, ammonium sulfate treatment) this is also true after 100 cycles in the dishwashing machine.

A further concern is the migration of constituents of the coatings into foodstuffs in contact with them. Here, the appropriate investigations have shown that

Table 2. Lead release from coated bowls (A: white pigmented, B: blue transparent).

Bowl	Volume (ml)	Extraction volume (ml)	Lead leaching (mg Pb/l)
A_1 (white)	770	710	0.002
A_2 (white)	760	700	0.002
B_1 (blue)	770	710	0.001
B_2 (blue)	770	710	0.002

Figure 3. Coated crystal glass goblets.

with respect to German standards and to the US FDA regulations (§175.300) for resins there is no relevant migration into acidic (3% acetic acid) or lipophile solvents (Isooctane).

3.4. Dishwashing Resistance

The stability of the coatings in the dishwashing machine was determined in accordance with the European standard procedure CEN/TC 194 N 107 in a standardized dishwashing device G 540 (Miele & Cie, Germany). In contrast to the cleaning and rinse agents described in the standard, commercially available products (Somat™, Henkel KG, Germany) were used, because the latter are phosphate-free and contain no chlorine and are therefore more in line with current practice. The transparent, colored coatings were stable for at least 200 cycles, whereas the pigmented layers showed stabilities up to 400 cycles. Commercial organic glass coatings based on epoxy resins lost their color already after 150 cycles at best. Some luster colors were stable for only about 20 cycles.

3.5. First Market Results

Pilot production startet in 1994. In 1996 260,000 coated glasses were sold and the necessary amount of

lacquer was 150 l. This corresponds to approximately 0.6 ml/glass including overspray. The production volume increased further in 1997. An example of a coated crystal glass goblet is shown in Fig. 3.

4. Conclusion

The development of colored, hybrid sol-gel coatings for crystal glass objects has been completed in the last few years. The coatings show almost perfect adhesion, high abrasion resistance, variable colorability and high stability against alkaline media. Pilot production started in 1994 and was stable in the years 1995 and 1996. In 1997 the increase in the consumption of coating solution marked the successful establishment of the new product in the crystal glass market.

Acknowledgment

This work was supported by the Bavarian Ministry of Economic Affairs, Transport and Technology under Contract No. AA 415 950 494. The cooperation of F.X. Nachtmann Crystal AG and of Kristallglasfabrik Spiegelau is greatfully acknowledged.

References

1. C.F. Leiser, Glass Ind. **44**, 509 (1963).
2. H. Dislich, J. Non-Cryst. Solids **57**, 371 (1983).
3. H. Schmidt, B. Seiferling, and K.-J. Deichmann, in *Ultrastructure Processing of Advanced Ceramics*, edited by J.D. Mackenzie and D.R. Ulrich (J. Wiley & Sons, New York, 1988), p. 651.
4. K. Greiwe, farbe + lack **97**, 368 (1991).
5. H. Scholze, *Glas—Natur, Struktur und Eigenschaften*, 3rd edition (Springer-Verlag, Berlin, 1988), p. 217.
6. G. Weinmann, Sprechsaal **122**, 821 (1989).
7. C. Sanchez and F. Ribot, New J. Chem. **18**, 1007 (1994).
8. U. Schubert, N. Hüsing, and A. Lorenz, Chem. Mater. **7**, 2010 (1995).
9. G. Schottner, K. Rose, and U. Schubert, in *Intelligent Materials and Systems*, edited by P. Vincenzini (Techna Srl, Florenz, 1995), p. 251.
10. N. Böhm, A. Materny, W. Kiefer, H. Steins, M.M. Müller, and G. Schottner, Macromolecules **29**, 2599 (1996).
11. U. Posset, M. Lankers, W. Kiefer, H. Steins, and G. Schottner, Appl. Spectrosc. **47**, 1600 (1993).
12. J. Kron, G. Schottner, and K.-J. Deichmann, Glastech. Ber. Glass Sci. Technol. **68C1**, 378 (1995).
13. C. Sanchez, J. Livage, M. Henry, and F. Babonneau, J. Non-Cryst. Solids **100**, 65 (1988).
14. J.H. Graziano and C. Blum, The Lancet **337**, 141 (1991).
15. M. Rada, L. Sasek, and M. Mika, Glastech. Ber. Glass Sci. Technol. **68C1**, 541 (1995).

Journal of Sol-Gel Science and Technology 13, 189–193 (1998)
© 1998 Kluwer Academic Publishers. Manufactured in The Netherlands.

Sol-Gel Formation of Reticular Methyl-Silicate Materials by Hydrogen Peroxide Decomposition

J. GUN AND O. LEV
Fredy and Nadine Herrmann School of Applied Science, The Hebrew University of Jerusalem, Jerusalem 91904, Israel

O. REGEV AND S. PEVZNER
Chemical Engineering Department, Ben Gurion University of Negev, Beer Sheva 84105, Israel

A. KUCERNAK
Department of Chemistry, Imperial College of Science, Technology and Medicine, London, SW7 2AZ, UK

Abstract. A new method for the formation of reticular silicate and organically modified silicate is introduced. Monoliths were prepared by incorporating a few percent hydrogen peroxide in the sol-gel starting solution. For example, incorporation of 6–10% (*v*) hydrogen peroxide in base catalyzed sol-gel precursors of methyl-Ormosil yielded macroporous monoliths with a bi-modal pore size distribution. The average characteristic pore diameters were approximately 1.2 nm and 0.7 μm, depending on the sol-gel precursors used and the preparation protocol. The specific surface area was approximately 160 m^2/g, contributed mainly by the microporous structure. A similar preparation procedure without hydrogen peroxide yielded only fractured or powdery materials. Presumably, the decomposition of the hydrogen peroxide yielded microbubbles, which formed templates for the polycondensation reaction. SEM, nitrogen adsorption isotherms and small angle X-ray spectroscopy were used to characterize the reticular materials.

Keywords: chromatography, foams, macroreticular

Introduction

There is considerable scientific and technological interest in macroreticular ceramic materials, which exhibit a bi-modal pore size distribution. Such materials benefit from the large specific surface area contributed by the micro- or mesopores and from the high accessibility and permeability contributed by the macroporous structure. These materials are especially useful as supports for chemical catalysts and for separation and chromatographic applications. Additionally, the large void fraction of such materials results in low bulk density and low thermal expansion coefficient, which are favorable for dielectric materials.

The most useful method of preparation of such materials involves impregnation of organic polymer sponges (e.g., poly(urethane), poly(styrene) or latex) with a slurry containing the ceramic precursors [1]. Macroreticular or foamy materials are formed after drying, sintering and evaporation or thermal degradation of the organic material. Another synthesis pathway includes the production of inorganic or organically modified aerogels by freeze-drying or supercritical drying of sol-gel derived metal oxide gels [2]. These methods are quite expensive and involve high pressure or extreme temperature conditions. The preparation of chromatographic media in the form of monoliths or thick films, suitable for thin layer chromatography,

is a newly developed area and several teams are pursuing sol-gel methodologies for preparation of such media [3–5]. The ability to produce organically modified surfaces (Ormosils) by single step sol-gel processing is especially attractive for the formation of reversed phase chromatographic media. Thick macroporous Ormosil films were recently prepared [4] by incorporation of cluster-forming materials along with the precursors of sol-gel films. After film formation and leaching the organic compounds out of the film a macroporous thick film (ca. 10–60 μm), suitable for thin layer chromatography was produced. Nakanishi and co-workers introduced sol-gel derived monoliths for high pressure liquid chromatography [5]. These were prepared by incorporation of poly(ethylenglycol) during the sol-gel process and subsequent derivatization of the macroporous xerogels with alkyltrimethoxysilane [6].

This paper introduces, for the first time, a one-step preparation method for the production of organically modified ceramic monoliths with a bi-modal pore size distribution. The material is prepared by a base catalyzed sol-gel process in the presence of hydrogen peroxide. Decomposition of the hydrogen peroxide forms miniature bubbles, which serve as templates for the inorganic polymerization. The characteristics of these materials are presented in the following sections.

Experimental Details

Four type of materials were compared: A, base catalyzed methyl silicate; B, base catalyzed methyl silicate prepared in the presence of hydrogen peroxide; C, acid catalyzed methyl silicate; D, acid catalyzed methyl silicate prepared in the presence of hydrogen peroxide.

Preparation conditions of base catalyzed methyl silicate in the presence of hydrogen peroxide (Sample B) are as follows: 2.0 ml methyl trimethoxysilane, 2.0 ml methanol and 0.10 ml 3M NaOH catalyst, were mixed, then 2 ml hydrogen peroxide was added, properly mixed and allowed to dry to reach a constant weight (ca. 1.0 g) at 41°C for approximately one week. The same preparation protocol was used for the preparation of sample A but with addition of distilled water instead of hydrogen peroxide.

Preparation conditions of the acid catalyzed methyl silicate in the presence of hydrogen peroxide

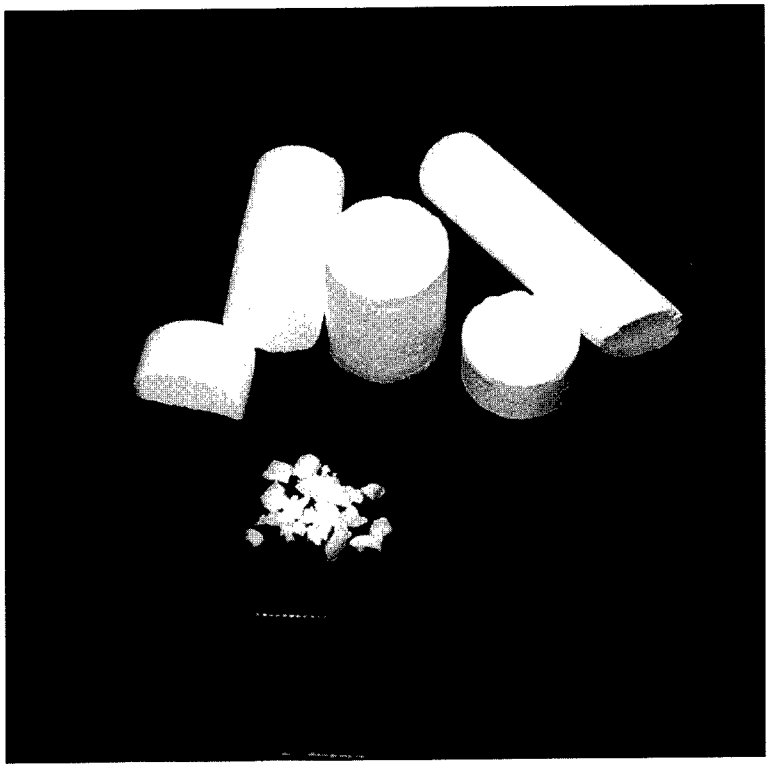

Figure 1. Base catalyzed sol-gel monoliths prepared with hydrogen peroxide (Sample B) and fractured material prepared under similar conditions but without hydrogen peroxide (Sample A).

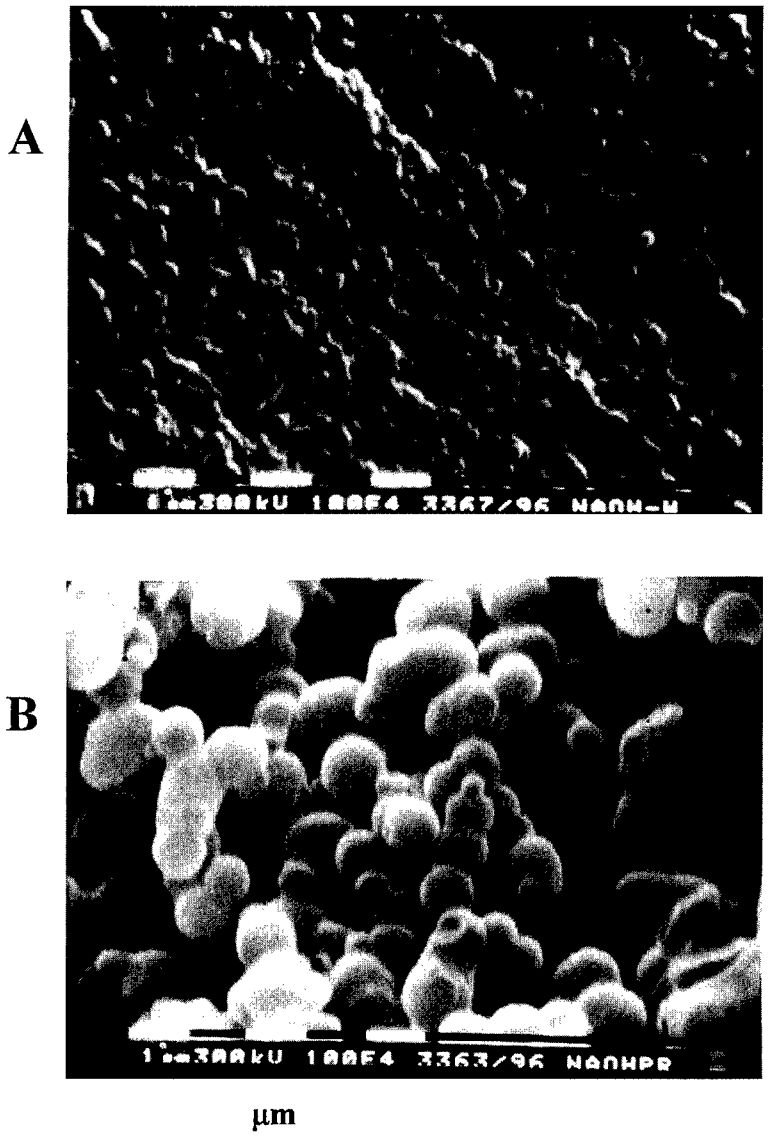

Figure 2. SEM micrographs of sample A and sample B (bar = 1 μm).

(Sample D) were similar to that of sample B with one exception: 0.1 ml of concentrated HCl was added instead of NaOH. The same preparation protocol was used for the preparation of sample C but with addition of distilled water instead of hydrogen peroxide.

Results and Discussion

Table 1 summarizes the composition and pertinent physical parameters of the four types of materials (A–D) described above. Figure 1 presents photographs of typical products of base catalyzed xerogels, that were prepared with and without hydrogen peroxide addition (Samples B and A, respectively). Large monoliths (e.g., 20 cm long × 0.5 cm in diameter rods) that almost did not shrink or crack during sol-gel processing could be prepared in the presence of hydrogen peroxide. The material maintained the original dimension of the reaction beaker and did not shrink during aging. In contrast, sample A was highly fractured during the drying step. The materials produced by acid catalysis were rather similar in appearance to that of sample A and therefore are not shown in Fig. 1. However, these

Table 1. Physical characteristics of samples A–D.

	A	B	C	D
Sample	Basic/H_2O	Basic/H_2O_2	Acid/H_2O	Acid/H_2O_2
Composition (Si : H_2O : H_2O_2) (molar)	1:8:0	1:5:2.5	1:8:0	1:5:2.5
Bulk density (g/cm^3)	0.6	0.22	0.34	0.31
Skeletal density (g/cm^3)	2.2	2.1	2.2	2.1
Void fraction	0.73	0.90	0.85	0.85
Surface area (BET) (m^2/g)	90	158	1.7	6.4
Radius of gyration (nm)	1.7	1.9	2.0	2.1
Fractal mass dimension	2.3	2.5	2	2
Average macroparticle size (μm)	—	0.7	3	3
Average micropore size (nm)	0.9	1.1	1.2	1.1

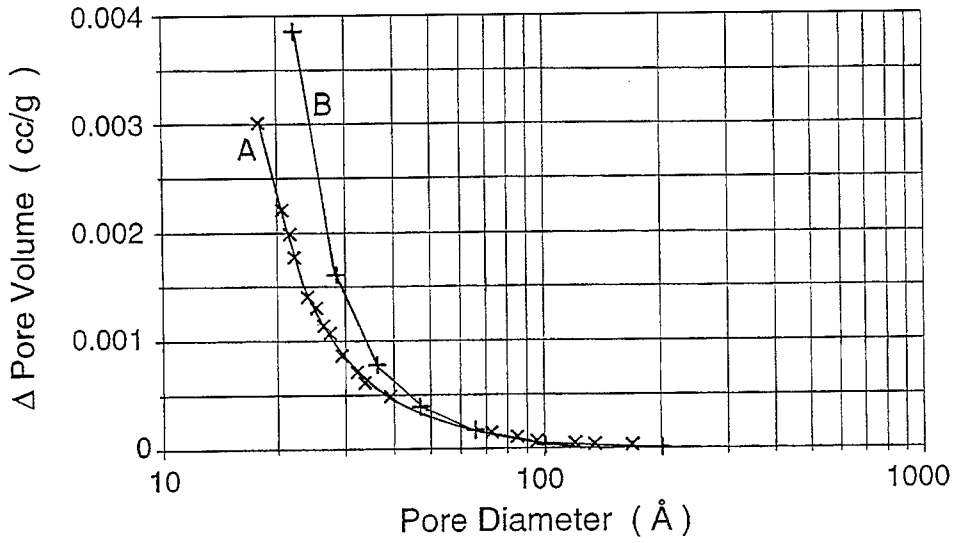

Figure 3. Pore size distribution, based on nitrogen adsorption isotherm of sample A and B.

materials shrank to approximately 85% of the dimension of the casting beaker.

Figure 2 depicts SEM micrographs of samples A and B. It is clear that the macrostructure of the two materials is very different. Sample B is comprised of approximately 0.7 μm spheres that often agglomerate to form tubular structures or more complex networks. Sample A exhibits a rather featureless structure, at least on the 0.01–100 μm scale that can be discerned by SEM.

The microporous structures of all four materials were examined by nitrogen adsorption isotherms and small angle X-ray scattering (SAXS). The average pore size of the two samples A and B were comparable (1.1 and 1.2 nm) and the specific surface area determined by multipoint nitrogen adsorption BET calculation are 90 and 158 m^2/g for samples A and B, respectively. However, Fig. 3 and the corresponding BET result should be taken with caution, since the adsorption isotherm did not form a closed loop even when long (15 min/N_2 addition) equilibration times were attempted. Such nonequilibrium behavior is usually encountered in microporous materials. In these cases the actual surface area far exceeds the area estimated by nitrogen adsorption tests [6].

SAXS spectra of the four samples A–D are depicted in Fig. 4. The mass fractal dimension was rather similar

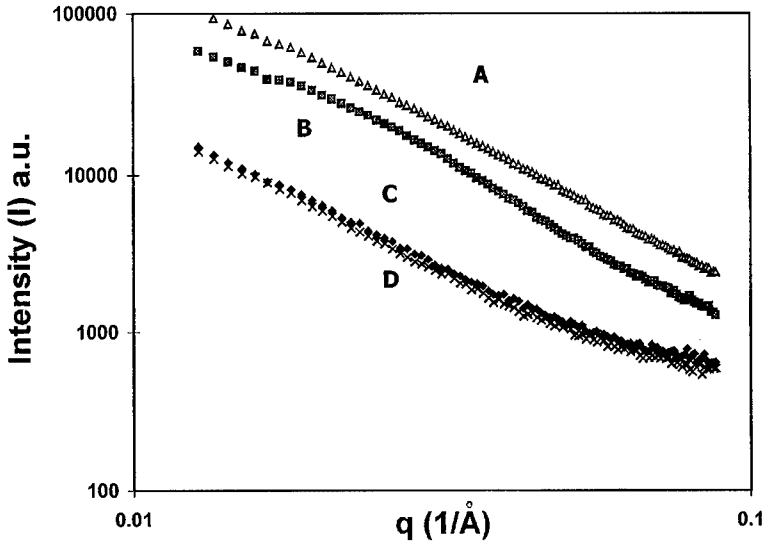

Figure 4. SAXS spectra of samples A–D.

for samples A and B, with fractal dimensions $D = 2.3$ and 2.5, respectively. The intensity (I) dependence of the scattering vector (q) obeyed the Guinier law over a large range (0.002–0.005) and permitted estimation of the radius of gyration, R, by Eq. (1),

$$I(q) \sim \exp(-R^2q^2/3) \quad (1)$$

The radius of gyration was found to be very similar for samples prepared with and without hydrogen peroxide ($R = 1.8 \pm 0.2$ and $R = 2.0 \pm 0.1$ for the base and acid catalysis, respectively).

Conclusions

Addition of hydrogen peroxide during the catalyzed sol-gel synthesis of methyl silicate materials yielded macroreticular materials with a bi-modal pore size distribution. The addition of hydrogen peroxide did not affect the micro- and mesoporosity of the materials.

Acknowledgment

We thankfully acknowledge the financial help of the Scientific Infrastructure Program of the Ministry of Science, Israel. J.G. thankfully acknowledges the Junior Scientists Scholarship endowed by the British Council.

References

1. J. Saggio-Woyansky, C.E. Scott, and W.P. Minnear, American Ceramic Society Bulletin **71**, 1682 (1992).
2. J. Brinker and G.W. Scherer, *Sol-Gel Science* (Academic Press, San-Diego, 1990).
3. M. Tsionsky, A. Vanger, and O. Lev, J. Sol-Gel Sci. Tech. **2**, 595, (1994).
4. O. Lev and M. Tsionsky, US Patent application no. 08/376,646 (1995).
5. K. Nakanishi, H. Minakuchi, N. Soga, and N. Tanaka, J. Sol-Gel Sci. Tech. **8**, 547 (1997).
6. Y. Polevaya, J. Samuel, M. Ottolenhi, and D. Avnir, J. Sol-Gel Sci. Tech. **5**, 65 (1995).

Journal of Sol-Gel Science and Technology 13, 195–199 (1998)
© 1998 Kluwer Academic Publishers. Manufactured in The Netherlands.

Ceramic Foams from a Preceramic Polymer and Polyurethanes: Preparation and Morphological Investigations

PAOLO COLOMBO AND MARTINA GRIFFONI
Dipartimento di Ingegneria Meccanica—Settore Materiali, Università di Padova, via Marzolo 9, 35131 Padova, Italy

MICHELE MODESTI
Dipartimento di Processi Chimici dell'Ingegneria, Università di Padova, via Marzolo 9, 35131 Padova, Italy

Abstract. Open-cell ceramic foams were obtained from a preceramic polymer (silicone resin) and blown polyurethanes. The preceramic polymer, which is crosslinked by condensation of silanol groups, was dissolved in CH_2Cl_2 and added to a liquid polyol containing the surfactant and the amine catalyst. Isocyanate was then added to the mixture and the foam was obtained through a twofold blowing mechanism (physical and chemical blowing). The morphology of the expanded polyurethane, which can be flexible or semirigid, characterized the final structure of the ceramic foam. The materials obtained were pyrolyzed in a nitrogen flux at temperatures of 1000–1200°C, thus allowing for the polymer-to-ceramic transformation to occur in the preceramic polymer. The ceramic foams produced in this way consisted of an amorphous silicon oxycarbide ceramic (SiOC). They presented a density ranging from 0.1 to 0.3 g/cm^3. The average pore diameter ranged from 200 to 400 μm and they possessed 80 to 90% open porosity.

Keywords: preceramic polymers, foams, silicon oxycarbide

1. Introduction

Cellular ceramics are divided into two general categories consisting of either open or closed cells. They possess a number of favorable properties, like low density, low thermal conductivity, thermal stability, high specific strength and high resistance to chemical attack, which make them suitable for a variety of applications. In fact, porous ceramics can be used in exhaust filters, molten metal filtration, catalyst supports, refractories, thermal insulation, and lightweight structures [1]. Recently they have been proposed as three-dimensional reinforcement in interpenetrating phase composites (IPC) [2].

Ceramic foams are commonly processed by impregnation of an open-cell polymeric foam by immersion into a ceramic slurry, and subsequent pressureless sintering at elevated temperatures [3]. Other possibilities are foaming of a suspension containing ceramic particles and a polyol-isocyanate mixture [4], direct foaming of a sol-gel solution [5], CVD/CVI deposition of various refractory materials on a foamed carbon skeleton [6], or siliciding of carbon preforms [7].

In this paper, foaming of a homogeneous solution containing a preceramic polymer and a polyol-isocyanate mixture is reported. Preceramic polymers are organoelement polymers, generally containing silicon, which undergo a polymer-to-ceramic conversion when heated at temperatures greater than 800°C. Despite their versatility, owing to the fact that conventional polymer processing techniques could be employed for obtaining various ceramic products, their use has been so far somewhat limited to the preparation of ceramic fibers. This is mainly due to the high volume shrinkage, accompanied by the formation of gases, experienced during the conversion from polymer

to ceramic, that limits the production of dense ceramic materials to small dimensional objects [8]. Therefore, thin-walled foams are, in principle, among the most favorable structures which could be successfully converted into a ceramic product by pyrolysis of preceramic polymers.

2. Experimental

By choosing expanded polyurethanes (PU) as sacrificial templates for the preparation of ceramic foams, a large variety of structures can be obtained. In particular, in flexible PU foams the polyurethane morphology is designed to be completely open-celled. By preparing semirigid PU foams, structures with pores (pin holes) in cell windows are obtained. Evidently, different structures attribute different physical-mechanical properties to the ceramic foam.

Flexible PU foams were prepared starting from a polyether polyol, amine catalysts, surfactants, blowing agent, TDI isocyanate (2,4-2,6-toluene-diisocyanate). Instead, semirigid PU foams were obtained from a polyether polyol, amine catalysts, surfactants, blowing agent, MDI (4-4′-diphenyl-methane-diisocyanate).

The preceramic polymer used was a thermosetting methyl-hydroxyl-siloxane (SR350, General Electric Silicone Products Div., Waterford, NY), which can crosslink at room temperature through the amine-catalyzed condensation of Si—OH groups [9].

Dichloromethane, which is compatible with the polyurethane precursors and the preceramic polymer, was chosen as solvent, and was used also as physical blowing agent (PBA) for the PU system.

A solution of SR350 in CH_2Cl_2 is added to the polyol mixture (polyol + amine catalysts + surfactant) and excess dichloromethane is evaporated. Isocyanate is added to this solution for polymerization in a quantity slightly greater than the stoichiometric amount. Due to the presence of amine catalysts, a more or less complete crosslinking of the silicone resin occurs (Eq. (1)), with release of water.

$$-\text{Si}-\text{OH} + \text{HO}-\text{Si}- \rightarrow -\text{Si}-\text{O}-\text{Si}- + H_2O \quad (1)$$

Two different mechanisms produce foaming: (1) CH_2Cl_2 evaporation (physical expansion) due to PU polymerization reaction heat and (2) CO_2 formation (chemical expansion) from the reaction between excess isocyanate and water from the crosslinking of the silicone resin, yielding disubstituted urea (Eqs. (2) and (3)).

$$-\text{R}-\text{NCO} + H_2O \rightarrow -\text{R}-\text{NH}-\text{CO}-\text{OH} \rightarrow -\text{R}-\text{NH}_2 + CO_2 \quad (2)$$

$$-\text{R}-\text{NH}_2 + -\text{R}-\text{NCO} \rightarrow -\text{R}-\text{NH}-\text{CO}-\text{NH}-\text{R}- \quad (3)$$

An accurate control of temperature, catalyst and therefore reaction rate is of utmost importance for regulating the expansion process and, as a consequence, the final foam density.

All foams were conditioned for 24 h at room temperature before heating them for 1 h at 1000°C and 1200°C in a N_2 flux (heating rate = 2°C/min).

The foams were characterized using Scanning Electron Microscopy (SEM), X-Ray Diffraction (XRD) and Fourier-Transformed Infrared Spectroscopy (FTIR); the pyrolsis process was investigated using thermogravimetry (TGA).

3. Results and Discussion

Figure 1 plots thermogravimetric curves for different samples heated in flowing N_2 or air. As received SR350 shows an ~7% weight loss at 180–300°C, due to release of water formed by the condensation reaction of silanols. A further weight loss at 650–800°C is due to the polymer-to-ceramic conversion of the silicone resin [9]; total weight loss is about 16%. Blank, merely-polyurethanic foams are completely burned out or decomposed by high temperature treatment in air or Ar. For the purpose of our work it is noteworthy to observe that heating a material comprised of a preceramic polymer and a polyurethane to temperatures above 900°C will thus yield a pure ceramic material with virtually no graphite residues from the organic phase. The possibility of effectively performing heat treatments in an inert atmosphere is obviously crucial for the development of carbide or nitride ceramics from preceramic polymers (polycarbosilanes, polysilazanes).

Thermogravimetric analysis of a foam prepared from a solution in which the weight ratio of SR350 to polyurethane precursors is 1 : 1 should show an approximate total weight loss of 66%. Since in our experiments (see dashed line in Fig. 1) the measured total loss is lower (about 60%), this indicates that the silicone resin in the foam not yet subjected to a thermal treatment is crosslinked. This is definitely due to the presence of amines (as a catalyst for PU polymerization) in

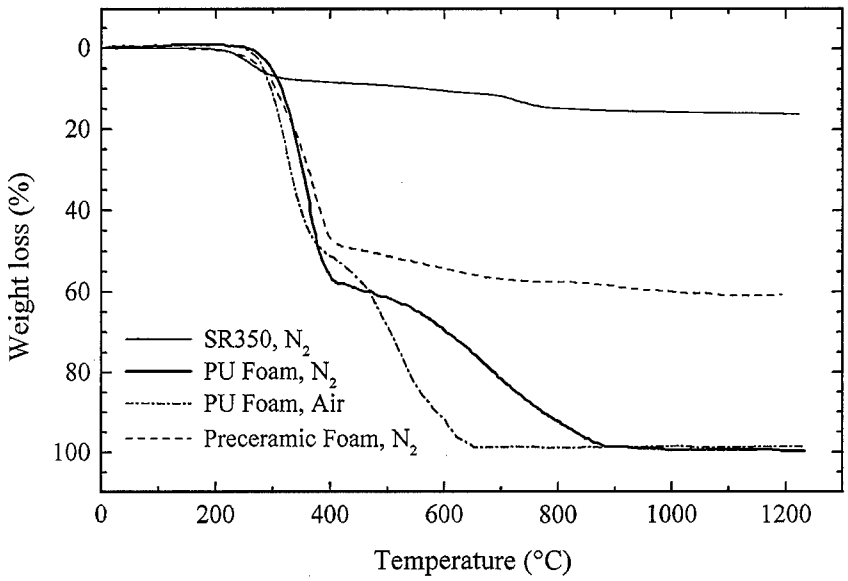

Figure 1. TGA curves for different semirigid foams and pure SR350 heated in nitrogen or air.

the starting solution. Direct pyrolysis of such a foam will thus allow the material to maintain its original morphology, because melting of the thermoplastic preceramic polymer is hindered by chemical curing. In this way, unlike reported experiments with other precursors [2], no specific curing step is to be included in the process, thus producing evident advantages.

This result is further supported by FTIR and SEM investigations and blowing experiments performed on an SR350/polyol mixture.

In Fig. 2, FTIR spectra for semirigid foams and pure SR350 before pyrolysis are reported. A detailed attribution of all the bands present in the patterns, related both to the polyurethane and the silicone resin, can be

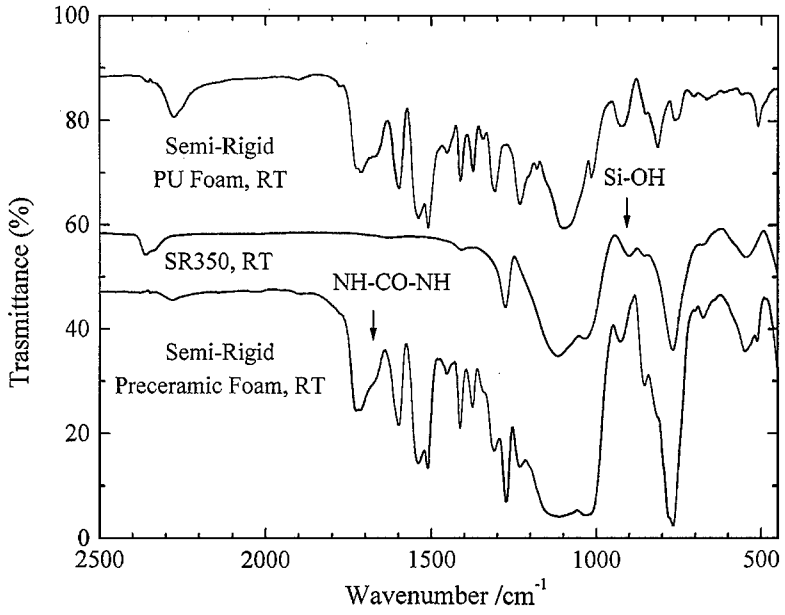

Figure 2. FTIR spectra for semirigid foams and pure SR350 before pyrolysis.

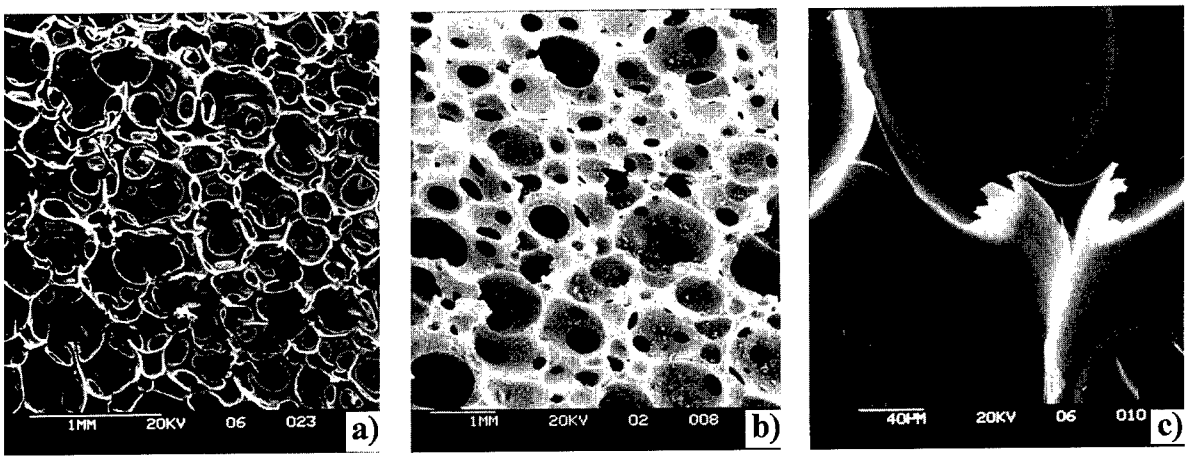

Figure 3. SEM micrographs of foams. (a) Flexible preceramic foam pyrolyzed at 1200°C in N_2 for 1 h. (b) Semirigid preceramic foam pyrolyzed at 1200°C in N_2 for 1 h. (c) Flexible preceramic foam pyrolyzed at 1200°C in N_2 for 1 h: detail of the struts.

found in [9, 10]. It is important to observe that Si—OH groups, which can be found in the as-received silicone resin (see band at about 900 cm^{-1}), completely disappear in the foamed material, confirming the cross-linking of the preceramic polymer. A direct indication of the chemical expansion mechanism which is operating in our system, involving the participation of water according to Eq. (2), comes from the presence of a band related to the formation of carbonyl ureic groups (Eq. (3)) in the preceramic foam pattern (shoulder located at about 1650 cm^{-1}). The same band appears in the spectrum of the PU material, which was foamed by adding water to the polyol solution. As a final confirmation for the proposed twofold blowing mechanism, we can report that we were able to expand amine-catalyzed solutions of SR350 and polyols to which no physical blowing agent was added. In this case, evidently, the foam was formed only due to the occurrence of reactions (1), (2) and (3).

In Fig. 3 are reported SEM micrographs for flexible and semirigid preceramic foams. Untreated foams present some thin membranes partially closing the pores in the structure. After high temperature pyrolysis, ceramic foams maintain the same morphology as the untreated samples, and during the polymer-to-ceramic conversion most of the observed thin membranes disappear, thus increasing the percentage of open cells in the material.

Foams from flexible PU acquire a rather homogeneous fully open structure, with an average cell and pore diameter of about 400 and 200 μm, respectively (Fig. 3(a)). For semirigid preceramic foams the final morphology consists of partially open cells with an average diameter of about 1 mm, and a pore diameter of approximately 400 μm (Fig. 3(b)). The ceramization of the preceramic foams occurs with a 20% linear shrinkage.

Since the produced foams are self-supporting during the polymer-to-ceramic conversion process (in the 600 to 800°C temperature range), this indicates that the preceramic polymer forms a homogeneous and continuous structure within the polyurethanic template. In fact, SEM investigations of foams in which virtually all the PU matrix is burned away by pyrolysis at 650°C in air (not reported here) show that their morphology is indistinguishable from that of the as prepared foams, and no signs of melting of the preceramic polymer could be found. It is noteworthy to observe that fully dense struts can be obtained with the proposed procedure (see Fig. 3(c)), which can be expected to yield optimal mechanical properties.

Finally, we can report that a fairly complete investigation of the physical and mechanical characteristics of these foams was performed. Depending on the structure of the polyurethanic foam (flexible or semirigid), values for important properties like elastic modulus, compression strength or density varied considerably. As an example, σ_{max} (compression) and elastic modulus ranged from 0.7–1.5 and 15–40 MPa, respectively, for foams from flexible PU, to 2.7–5.0 and 40–180 MPa for foams from semirigid PU. Apparent densities could be varied from 0.12 to 0.30 g/cm^3 and foams possessed 80 to 90% open porosity. Coefficient of thermal expansion (20–1000°C) for samples pyrolyzed at 1000 or 1200°C was $1.1 \cdot 10^{-6}\ K^{-1}$, and the foams were dimensionally stable up to their heat treatment temperature.

4. Conclusions

Open-cell preceramic foams can be successfully prepared from homogeneous mixtures of a thermosetting silicone resin and polyurethane precursors. They can be converted into a fully SiOC ceramic material, which maintains the same morphology of the PU template, by high temperature pyrolysis. By varying PU precursors nature and additives, foams with very different structures can be obtained.

References

1. E.J.A.E. Williams and J.R.G. Evans, J. Mater. Sci. **31**, 559 (1996).
2. T.J. Fitzgerald and A. Mortensen, J. Mater. Sci. **30**, 1025 (1995) and J. Mater. Sci. **30**, 1037 (1995).
3. F.F. Lange and K.T. Miller, Adv. Ceramic Materials **2**, 827 (1987).
4. W.P. Minnear, in *Ceramics Transactions 26, Forming Science and Technology for Ceramics*, edited by M.J. Cima (Am. Ceram. Soc., Westerville, OH, 1992), pp. 149–156.
5. T. Fujiu, G.L. Messing, and W. Huebner, J. Am. Ceram. Soc. **73**, 85 (1990).
6. A.J. Sherman, R.H. Tuffias, and R.B. Kaplan, Bull. Am. Ceram. Soc. **70**, 1025 (1991).
7. Y. Aoki and B. McEnaney, Brit. Ceram. Transactions **94**, 133 (1995).
8. P. Greil, J. Am. Ceram. Soc. **78**, 835 (1995).
9. G.M. Renlund, S. Prochaza, and R.H. Doremus, J. Mater. Res. **6**, 2716 (1991).
10. J.G. Dillon, *Infrared Spectroscopic Atlas of Polyurethanes* (Technomic Publisher, Lancaster, 1989).

Journal of Sol-Gel Science and Technology 13, 201–205 (1998)
© 1998 Kluwer Academic Publishers. Manufactured in The Netherlands.

Mullite-Alumina Composites Prepared by Sol-Gel

A.M.R. MENDONÇA, J.M.F. FERREIRA AND I.M. MIRANDA SALVADO
Departamento de Engenharia Cerâmica e do Vidro, Universidade de Aveiro, 3810 AVEIRO, Portugal

Abstract. Ceramic composite gels in the mullite-alumina system (with mullite phase contents ranging from 20 to 100 wt%) were prepared by sol-gel in acid media and using a water/alkoxide molar ratio of 4. Powders were uniaxially pressed to obtain discs.

The effect of heat treatment on the materials was followed by thermal analysis and X-ray diffraction (XRD). The crystalline phases formed from the gels were dependent upon the sample composition and the heat treatment temperature. For samples with composition close to the stoichiometric mullite composition the crystallization of mullite was observed after heat treatment at temperatures $\geq$900°C, and corundum appeared at higher temperatures. For samples with higher alumina contents mullite formation together with the spinel phase was observed at the lower heat treatment temperatures, while mullite, silimanite, corundum, and other transient phases of alumina were also detected at higher temperatures. The densities and microstructures of materials sintered at 1400°C were studied. Densification of the samples was low due to the agglomeration of the powders, as confirmed by scanning electron microscopy.

Keywords: mullite, mullite-alumina, composites, gels

1. Introduction

Composite materials in the mullite-alumina system are important for industrial production of electronic, and high-temperature materials due to their high strength, creep resistance, good thermal and chemical stability, and low dielectric constant [1, 2].

Mullite and mullite-alumina powders have been prepared by several methods and the mullitization and crystallization temperatures are dependent on the homogeneity attained during the preparation procedure, namely the degree of mixing of the Al and Si species in the precursors.

The temperature required to obtain the desired crystalline phases can be lowered from ~1700°C for conventionally prepared powders, to ~1000°C when the silica and alumina species are mixed at the molecular level [3, 4] as in the sol-gel process. Several authors used sol-gel based techniques to prepare mullite and mullite-alumina materials [5–7]. Diphasic or monophasic xerogels depending on the degree of mixing of silica and alumina were obtained by several authors [8, 9]. The presence of relatively sharp exothermic peaks at 960–980°C on DTA traces is related to a high degree of mixing and the production of a homogeneous phase at almost the atomic scale [10, 11].

The crystalline phases formed in gels with the stoichiometric composition of mullite are mullite and a spinel phase formed by the incorporation of silica into an alumina rich phase (γ-Al_2O_3). The mullite phase formed is often similar to the orthorhombic phase but with slight deviations. This can be observed by X-ray diffraction (XRD) where no splitting of the peaks with Miller indices (120), (240), (041) and (250) is observed. Some authors [12, 13] refer to this phase as a pseudo-tetragonal phase characterized by the fact that the lattice parameters a and b present the same value [14].

In the present study the sol-gel process was used to prepare composite gels in the mullite-alumina system, following a previous study of the influence of the preparation conditions on the crystallization behavior of mullite based compositions prepared by sol-gel [15].

Table 1. Sample composition (wt%) and designation.

Sample designation	Composition (wt%)
MG	71.8% Al_2O_3 28.2%SiO_2
MAG-20	76.5% Al_2O_3 23.5%SiO_2
MAG-40	79.9% Al_2O_3 20.1%SiO_2
MAG-80	84.3% Al_2O_3 15.7%SiO_2

2. Experimental

Samples in the composition range 20 to 100 wt% of mullite phase were prepared in the mullite-alumina system. Tetraethylorthosilicate (TEOS) and aluminium nitrate nona-hydrate were used as raw materials. Absolute ethanol was used as solvent for the nitrate. Water was added according to a water/TEOS molar ratio equal to 4 and hydrochloric acid was used as catalyst (HCl/TEOS molar ratio equal to 0.2). These experimental conditions were chosen from previous results of the authors [15]. In Table 1 the sample designation and compositions are presented.

For the preparation of all samples the clear sols were put in closed containers and kept at 60°C to promote gelation. After 7 days at this temperature the gels were dried for 48 hours at 120°C. The xerogels obtained were heat-treated at different temperatures (ranging from 900°C to 1400°C) with a heating rate equal to $10°C \cdot min^{-1}$. The xerogels were maintained for 2 hours at each heat treatment temperature.

In order to study the thermal evolution of the samples Differential Thermal Analysis (DTA) was performed. XRD studies were carried out with a computer controlled Rigaku XDMAX difractometer by using CuKα radiation in the range 10 to 70 $2\theta(°)$.

The powders were calcined at 900°C for 2 hours and then milled in an agate mortar, sieved through a ≤ 30 μm screen and pressed into disc-shaped compacts (0.5 cm diameter) at a pressure of 500 MPa and sintered at 1400°C for 2 hours.

Scanning electron microscopy (Hitachi S4100-1) was used to study the sintered samples MAG-20 and MAG-80. Density measurements were performed in a mercury balance using the Archimedes principle.

3. Results and Discussion

In Fig. 1 the DTA traces for samples with 20 and 80 wt% of alumina are shown. Both traces show endothermic effects in the range 100–350°C, these being more pronounced around 100–200°C. These effects

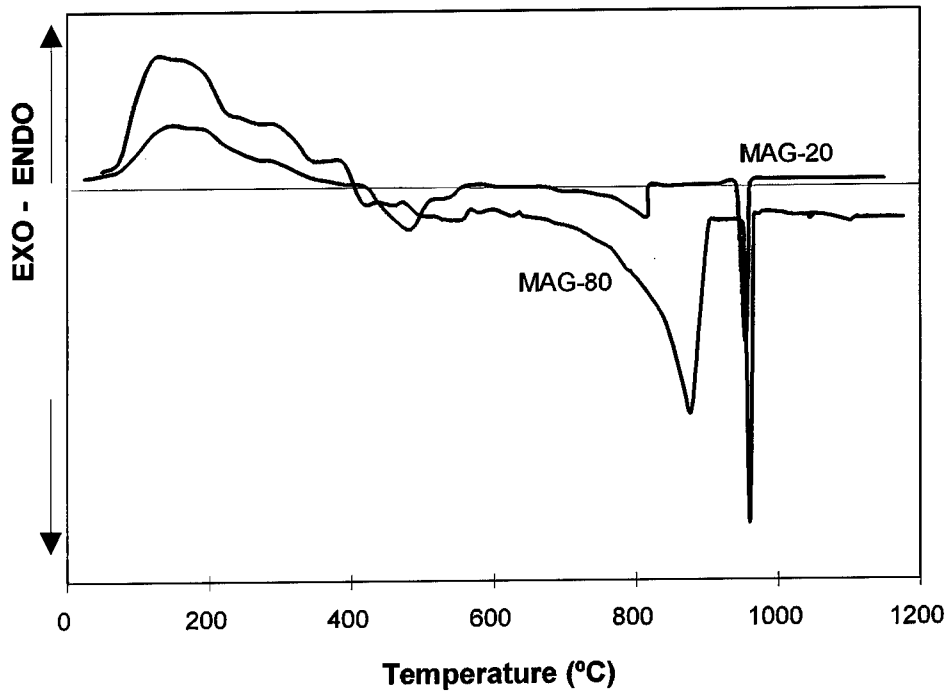

Figure 1. Differential thermal analysis traces for samples MAG-20 and MAG-80.

are attributed to the loss of physically adsorbed species such as OH^- groups and alcohol. In the region between ~350°C and 600°C several endothermic and exothermic effects due to the decomposition of nitrate and loss of residual organics are observed. For the sample MAG-20 a small exothermic effect at ~815°C and a sharp and well-defined exothermic peak are present at ~956°C. For the sample MAG-80 these peaks are slightly shifted to higher temperatures, ~876°C and ~958°C, respectively. The sharp peaks observed at the higher temperatures are attributed to the formation of mullite [9, 10], which agrees with the XRD results obtained for both samples heat-treated at 1000°C (Figs. 2 and 3). The broader DTA peaks observed at 815°C and

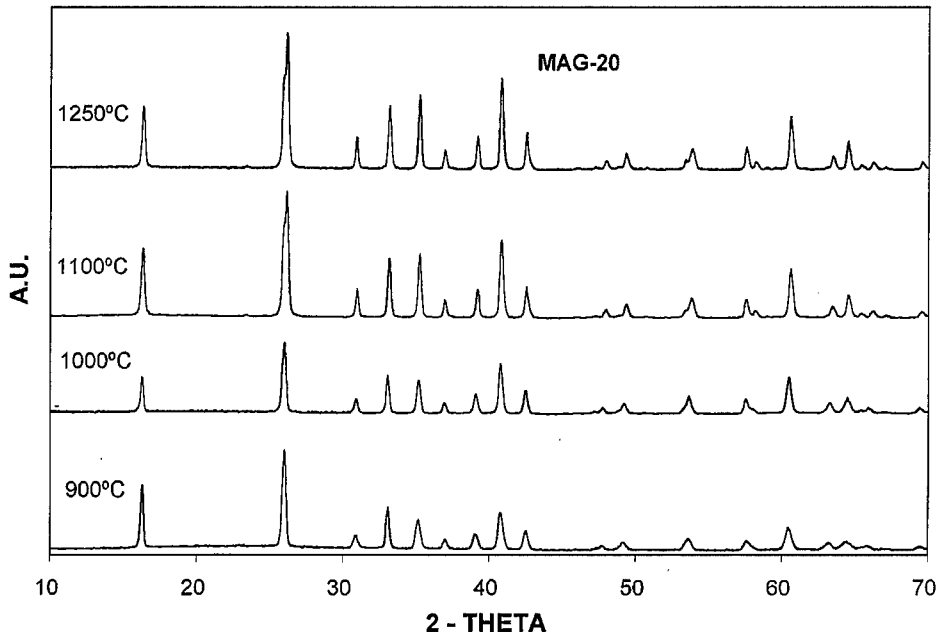

Figure 2. XRD patterns for sample MAG-20 heat-treated at different temperatures in the range 900–1250°C for 2 hours.

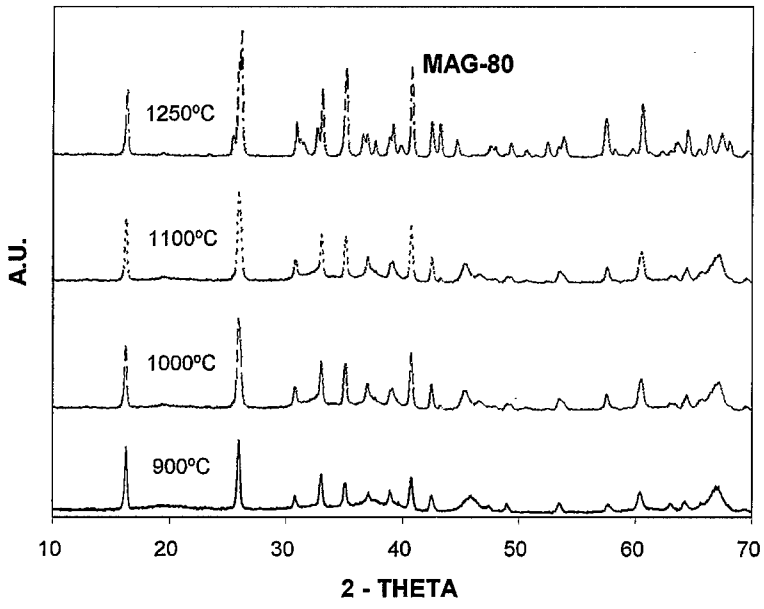

Figure 3. XRD patterns for sample MAG-80 heat-treated at different temperatures in the range 900–1250°C for 2 hours.

876°C might be due to the crystallization of a spinel phase (especially in the case of MAG-80) as well as to the formation of a pre-mullite phase [16, 17]. In fact, the X-ray spectra of both samples obtained at 900°C (Figs. 2 and 3) reveal a structure close to that of mullite. The presence of sharp peaks in the temperature range 950–960°C indicates that a high degree of homogeneity was obtained in the gels prepared in this study [8–10].

The pre-mullite phase was also observed in gels with the stoichiometric mullite composition heat-treated at 900°C (XRD results not shown). This distorted structure gradually approaches the orthorhombic mullite phase with the increase in heat treatment temperature. This is confirmed by the splitting of the peak at $2\theta^\circ \sim 26$ clearly observed for the samples MAG-20 and MAG-80 heat-treated at 1250°C, Fig. 4 [14].

The main differences between Figs. 2 and 3 are related to the compositions of the samples. Stronger evidence for the transient alumina phases at the lower heat treatment temperatures is observed for

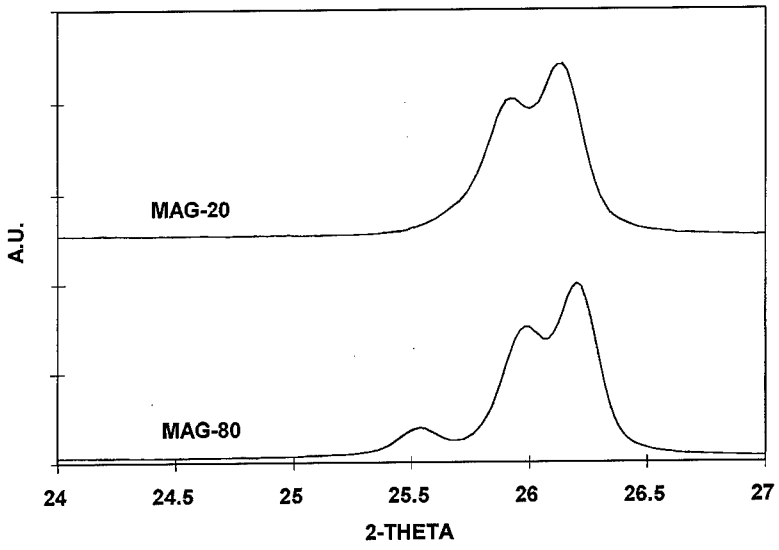

Figure 4. Splitting of the peak at $2\theta^\circ \sim 26$ observed for sample MAG-20 and sample MAG-80.

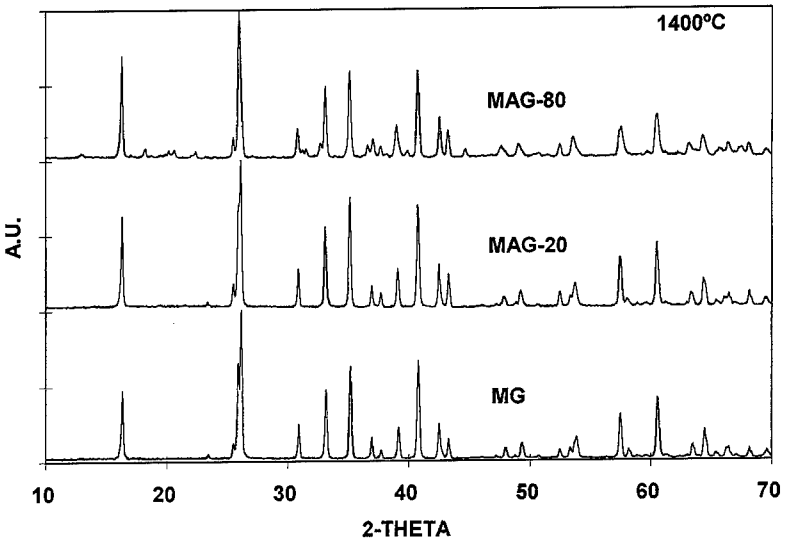

Figure 5. XRD patterns for samples MG, MAG-20 and MAG-80 heat-treated at 1400°C for 2 hours.

the sample richer in alumina, while for temperatures $\geq$1250°C this sample shows the formation of mullite and corundum together with silimanite, Fig. 5. For the samples MG and MAG-20 heat-treated at temperatures $\geq$1250°C the only identifiable phases are mullite and corundum.

The density of the compacts heat-treated at 1400°C (2 hours) was 64.5% and 61% of the theoretical density of the oxide mixtures. These relatively low density values can be attributed to the strong agglomeration of the powders and to the inefficiency of the milling procedure. This was confirmed by scanning electron microscopy observations.

4. Conclusions

Mullite and mullite-alumina composite materials were prepared by the sol-gel route. The crystalline phases formed were dependent upon the alumina content and the heat treatment schedule of the samples. Higher alumina contents favored the formation of transient phases of alumina at the lower heat treatment temperatures and the crystallization of corundum and silimanite at higher temperatures.

Further work is in progress in order to improve the densification of the compacts by controlled milling of the powders.

References

1. S. Somiya, R.F. Davis, and J.A. Pask (Eds.), *Mullite and Mullite Matrix Composites* (Am. Ceram. Soc., Westerville, OH, 1990), Vol. 6.
2. J. Wu, M. Chen, F.R. Jones, and P.F. James, J. European Ceramic Society **16**, 619 (1996).
3. J. Huling and G.L. Messing, J. Non-Cryst. Solids **147/148**, 213 (1992).
4. C.J. Brinker and G.W. Scherer (Eds.), *Sol-Gel Science. The Physics and Chemistry of Sol-Gel Processing* (Academic Press, San Diego, CA, 1990).
5. B.E. Yoldas, J Mater. Sci. **27**, 6667 (1992).
6. I. Jaymes and A. Douy, J. Am. Ceram. Soc. **75**, 3154 (1992).
7. M. Sales and J. Alarcón, J. European Ceramic Society **16**, 781 (1996).
8. D.W. Hoffman, R. Roy, and S. Komarneni, J. Am. Ceram. Soc. **67**, 468 (1984).
9. A.K. Chakraborty, J. Mater. Sci. **29**, 1558 (1994).
10. A.K. Chakraborty and D.K. Ghosh, J. Am. Ceram. Soc. **71**, 978 (1988).
11. I. Jaymes, A. Douy, M. Gervais, and J.P. Coutures, J. Sol-Gel Sci. Tech. **8**, 415 (1997).
12. T. Ban and K. Okada, J. Am. Ceram. Soc. **75**, 227 (1992).
13. W.E. Cameron, Am. Mineral. **62**, 747 (1977).
14. H. Schneider, K. Okada, and J. Pask, *Mullite and Mullite Ceramics* (John Wiley & Sons, 1994).
15. A.M.L. Marques Fonseca, J.M.F. Ferreira., I.M. Miranda Salvado, and J.L. Baptista, J. Sol-Gel Sci. Tech. **8**, 403 (1997).
16. A.K. Chakraborty and D.K. Ghosh, J. Am. Ceram. Soc. **61**, 170 (1978).
17. J.S. Moya, C.J. Serna, and J.E. Iglesias, J. Mater. Sci. **20**, 32 (1985).

Journal of Sol-Gel Science and Technology 13, 207–211 (1998)
© 1998 Kluwer Academic Publishers. Manufactured in The Netherlands.

Optical Sol-Gel-Based Dissolved Oxygen Sensor: Progress Towards a Commercial Instrument

C.M. MCDONAGH, A.M. SHIELDS, A.K. MCEVOY, B.D. MACCRAITH AND J.F. GOUIN
School of Physical Sciences, Dublin City University, Glasnevin, Dublin 9, Ireland

Abstract. A dissolved oxygen sensor based on fluorescence quenching of the oxygen-sensitive ruthenium complex, [Ru(II)-tris(4,7-diphenyl-1,10-phenanthroline]$^{2+}$, which has been immobilized in a porous silica sol-gel-derived film, is reported. Ormosil sensing films were fabricated using modified silica precursors such as methyltriethoxysilane (MTEOS) and ethyltriethoxysilane (ETEOS) and were dip-coated onto planar glass substrates. Tailoring of the films for dissolved oxygen (DO) sensing is described whereby sensor response is optimized by maximizing film hydrophobicity by the use of the modified precursors. Sensor performance parameters such as limit of detection and sensor resolution are reported. Issues such as dye leaching and photobleaching are discussed. Progress towards a commercial instrument is reported.

Keywords: optical sensors, sol-gel films, dissolved oxygen

1. Introduction

Dissolved oxygen (DO) sensing is of major importance in environmental, industrial and medical applications. The amount of oxygen dissolved in water is an indication of the quality of the water, and careful control of oxygen levels is important in fermentation processes and in food preparation. A knowledge of oxygen levels in blood is necessary for physiological and other medical studies. Optical DO sensors [1] are attractive as they do not consume oxygen or require stirring unlike the conventional Clark electrode method. Optical oxygen sensing is usually based on collisional quenching of a fluorophore embedded in a support matrix. The quenching process is described by the Stern-Volmer equations:

$$I_0/I = I + K_{sv} pO_2 \qquad (1)$$

where I is the fluorescence signal, I_0 is the signal in the absence of oxygen, pO_2 is the oxygen partial pressure and K_{sv} is the Stern-Volmer constant which is proportional to the oxygen diffusion coefficient in the matrix.

The sol-gel process lends itself very successfully to thin film production either by dip or spin coating. In this laboratory optical sensors for both gas phase and dissolved oxygen have been developed based on sol-gel coatings incorporating the oxygen-sensitive ruthenium complex $Ru(Ph_2\ phen)_3^{2+}$, whose fluorescence is quenched in the presence of oxygen [2, 3]. This paper reports further development and performance parameters of a sol-gel-based dissolved oxygen sensor based on ormosil films. Tailoring of the films for DO sensing is discussed and progress towards a commercial instrument is reported.

2. Film Fabrication and Characterization

Tetraethoxysilane (TEOS), methyltriethoxysilane (MTEOS), ethyltriethoxysilane (ETEOS) and ethanol were purchased from Aldrich. Glass microscope slides were cleaned sequentially using deionized water, methanol, acetone followed by a final deionized water rinse. A typical sol contained precursor, water at pH = 1 (using HCl as catalyst) 2.5 g/l of the ruthenium complex and ethanol. Water : precursor molar ratios of 2 and 4 were used. Sols were stirred magnetically for one hour. Films were dip-coated in a draught-free environment at a speed of 1 mm/s, using a computer-controlled

dip-coating apparatus. Coated films were dried for 17 hours at 70°C and then stored in ambient conditions.

Sensor instrumentation consisted of a high-brightness blue LED (Ledtronics, USA) with peak wavelength at 450 nm to match the absorption of the ruthenium complex, and a silicon photodiode detector. The coated slide is placed in a sealed cell through which water containing controlled concentrations of oxygen, is circulated. Further details of the system have been published previously [3].

3. Results and Discussion

3.1. *Tailoring of Films for DO Sensing*

Optical oxygen gas sensors based on TEOS-derived films have been reported by us previously [2]. While TEOS films produce excellent sensor response in gas phase, this is not the case in dissolved phase. The quenching response of the sensor is defined in terms of the parameter Q, where Q_{DO} is given by

$$Q_{DO} = (I_{deoxy} - I_{oxy})/I_{deoxy} \quad (2)$$

where I_{deoxy} and I_{oxy} are the intensities in fully deoxygenated and fully oxygenated water, respectively. The quenching response in gas phase, Q_G, is similarly defined where the intensity limits are those in 100% nitrogen and 100% oxygen gas. Figure 1 shows the quenching response for $R = 2$ TEOS and $R = 2$ MTEOS films in water. It is clear that the TEOS response is greatly reduced relative to that of MTEOS. TEOS-derived silica is known to have a high surface coverage of hydroxyl groups, thus rendering the surface hydrophilic [4]. It is thought that the quenching mechanism for dissolved oxygen involves the oxygen partitioning out of the water and accessing the ruthenium complex in the film in the gas phase. This partitioning effect is much reduced for a hydrophilic film while it is enhanced in the case of a hydrophobic film surface. The addition of modified precursors such as MTEOS or ETEOS to the sol increases the hydrophobicity of these ormosil films by replacing some of the surface hydroxyl groups with alkyl groups which have low affinity for water [5]. The results of a systematic study of the influence of different amounts of organic precursor on the quenching response, both in gas and aqueous phase, are shown in Table 1. It is clear that Q_{DO} increases with organic precursor content, the largest value being obtained from ETEOS films which are more hydrophobic than MTEOS films. Q_G values, on the other hand, show a decrease in response with increasing organic precursor content. This is consistent with a decrease in gas diffusion coefficient as the larger alkyl groups gradually replace the hydroxyl groups on the film surface. Hence, for gas-phase quenching, the quenching response of ormosil films decreases slightly as a function of organic precursor content due to decreased diffusion coefficients, while for DO quenching, response is vastly increased due to the increase in hydrophobicity. These conclusions are corroborated by FTIR data where the intensities of the water band at 3400 cm^{-1} and the SiOH band at 910 cm^{-1} were observed to decrease as a function of increasing MTEOS content for the mixed MTEOS/TEOS films [5, 6].

Table 1. Gas-phase and DO quenching response of ormosil films.

	Q_G	Q_{DO}
MTEOS/TEOS 1 : 1	93%	56%
MTEOS/TEOS 2 : 1	92%	62%
MTEOS/TEOS 3 : 1	89%	70%
MTEOS	85%	73%
ETEOS/TEOS 1 : 1	92%	72%
ETEOS	87%	80%

3.2. *Sensor Performance*

It is clear from Fig. 1(b) that the MTEOS-based DO sensor exhibits good reproducibility and large signal-to-noise ratio. For ETEOS films the quenching response is even higher due to increased surface hydrophobicity as seen in Table 1. Measured response times of the order of 10 s are typical, although the intrinsic response time is expected to be considerably less than this as the measured value includes the contribution of gas delivery and cell filling times. Limits of detection (LOD) and sensor resolution values for MTEOS and ETEOS films fabricated with $R = 2$, are shown in Table 2. Both calculations were based on three times the relevant standard deviation and could be improved by further averaging. Dye leaching is a common feature of sensors based on entrapped dyes. In this work, two strategies were employed to

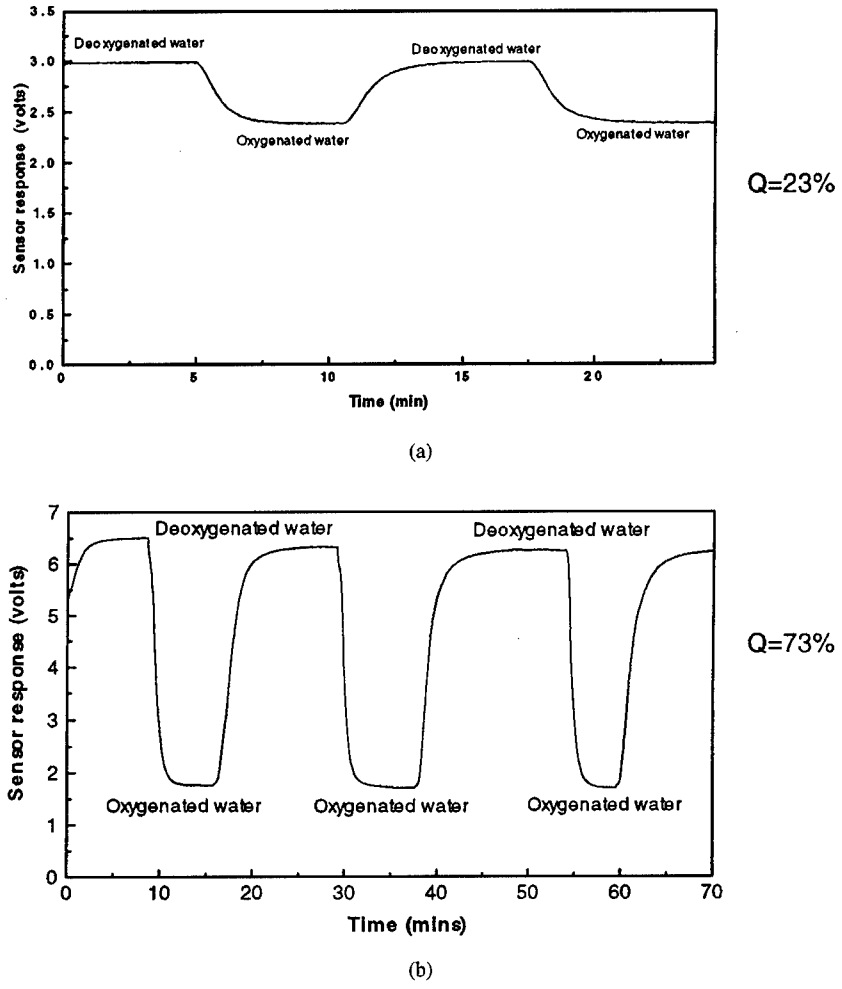

Figure 1. DO quenching response of (a) TEOS films and (b) MTEOS films.

minimize leaching. Leaching can be reduced by increasing the R value. For example, $R = 4$ MTEOS shows very little leaching (1%) due to the smaller average pore size and resulting improved dye entrapment. The small decrease in quenching response for $R = 4$ films compared with $R = 2$ films can be tolerated due to the excellent signal-to-noise ratio. Figure 2 shows a reduction in leaching from 12% to 1% between $R = 2$ and $R = 4$ films. These results are corroborated by other leaching studies carried out in this laboratory on pH-sensitive dyes [7]. The leaching experiment was carried out over 3 days in continuously flowing water. Dye leaching can also be minimized by coating the film with a silicone rubber barrier layer. Preliminary work indicates a reduction in leaching from 12% to 5% for an unoptimized coating as seen in Fig. 2. This rubber coating, as well as minimizing leaching, also serves to prevent fouling. It has also been established that photobleaching of the ruthenium fluorescence does not occur in these films. Having established that ormosil films exhibit excellent quenching characteristics in DO, the long-term quenching stability

Table 2. DO performance parameters of MTEOS and ETEOS films.

	LOD	Sensor resolution
$R = 2$ MTEOS	15 ppb	0.23 ppm
$R = 2$ ETEOS	5 ppb	0.18 ppm

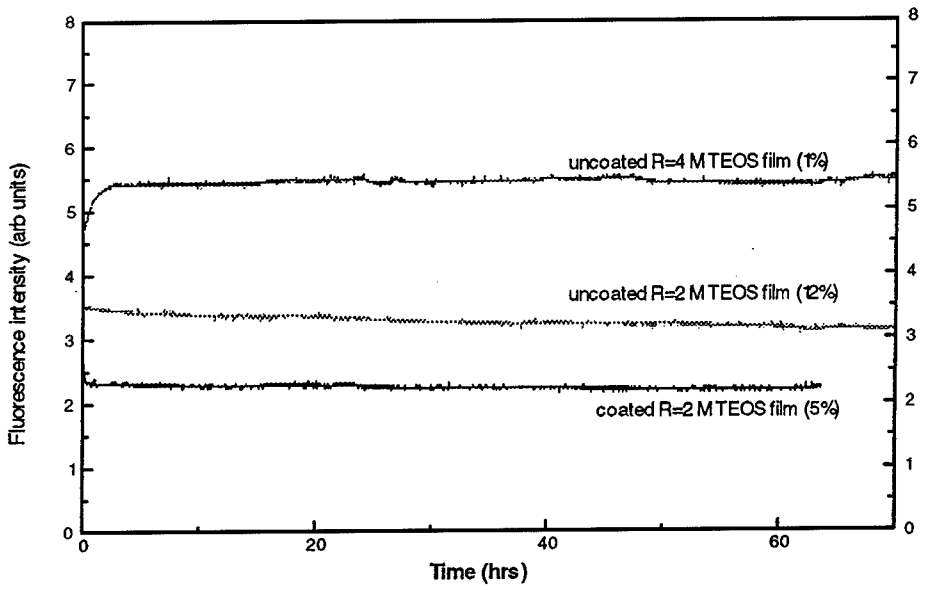

Figure 2. Dye leaching study of MTEOS films.

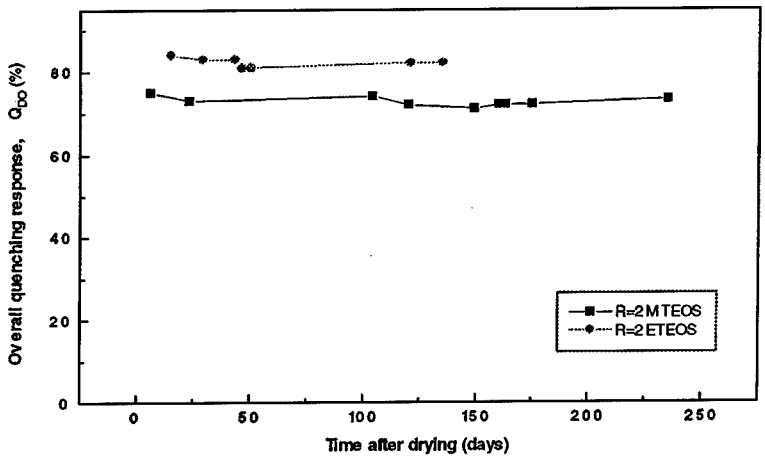

Figure 3. Long-term stability of sensor response for MTEOS and ETEOS films.

was also investigated. Figure 3 shows quenching response over a 6-month period for $R = 2$ MTEOS and ETEOS films. The stability of the response is clear. A prototype DO sensor based on a dipstick probe configuration is being built in the laboratory, and field tests will be carried out in the near future. A calibration protocol based on single-point calibration is also being implemented. The performance parameters quoted above emphasize the significance of the sol-gel approach for commercially viable optical sol-gel sensors.

4. Conclusions

High performance sol-gel based DO sensors have been reported. Tailoring of the films for DO was discussed in terms of the use of ormosil films in order to optimize the hydrophobicity. The feasibility of sol-gel-based optical sensors has been established. The commercial potential of these sensors is enhanced by their compatibility with low-cost optoelectronic components. The sensors exhibit low LODs and high calibration stability. Issues that remain to be addressed include temperature

compensation and the scaling up of the fabrication process for large-scale production.

References

1. K.E. Chung, E.H. Lan, M.S. Davidson, B.S. Dunn, J.S. Valentine, and J.I. Zink, Anal. Chem. **67**(9), 1505 (1995).
2. B.D. MacCraith, G. O'Keeffe, A.K. McEvoy, C.M. McDonagh, J.F. McGilp, B. O'Kelly, J.D. O'Mahony, and M. Cavanagh, Opt. Eng. **33**, 3861 (1994).
3. A.K. McEvoy, C. McDonagh, and B.D. McCraith, Analyst **121**, 785 (1996).
4. K. Matsui, M. Tominaga, Y. Arai, H. Satoh, and M. Kyoto, J. Non-Cryst. Solids **169**, 295 (1994).
5. P. Innocenzi, M.O. Abdirashid, and M. Gugielmi, J. Sol-gel Sci. Tech. **45**(3), (1994).
6. V. Murphy, M.Sc. Thesis, Dublin City University, 1996, unpublished.
7. T. Butler, Ph.D. Thesis, Dublin City University, 1996, unpublished.

Journal of Sol-Gel Science and Technology 13, 213–217 (1998)
© 1998 Kluwer Academic Publishers. Manufactured in The Netherlands.

Synthesis of Bi_2O_3 and $Bi_4(SiO_4)_3$ Thin Films by the Sol-Gel Method

L. ARMELAO
CSSRCC, CNR, via Marzolo 1, Padova, Italy

P. COLOMBO
Dipartimento di Ingegneria Meccanica, Settore Materiali Università di Padova, via Marzolo 9, Padova, Italy

M. FABRIZIO
IPELP, CNR, corso Stati Uniti 4, Padova, Italy

Abstract. Bi_2O_3 thin films were prepared by dipping silica slides in ethanolic solutions of tris(2,2′-6,6′-tetramethylheptane-3,5-dionato)bismuth(III) [$Bi(dpm)_3$] [1] and heating in air at temperatures $\leq$500°C. $Bi_4(SiO_4)_3$ homogeneous thin films were obtained from the reaction of the bismuth oxide coating with the silica glass substrate at temperatures higher than 700°C. For heat treatments at temperatures between 600°C and 700°C, Bi_2SiO_5 coatings were obtained. The composition and microstructure evolution of the films were determined by Secondary Ion-Mass Spectrometry (SIMS), X-Ray Photoelectron Spectroscopy (XPS) and Glancing Angle X-Ray Diffraction (GA-XRD). The synthesis procedure was reproducible and allowed the control of the Bi_2O_3 phase composition. Moreover, the thin film annealing parameters were correlated with the formation of bismuth silicates, among which $Bi_4(SiO_4)_3$ (BSO) is very appealing for the production of fast light-output scintillators [2].

Keywords: bismuth oxide, bismuth silicate, thin film, sol-gel, surface techniques

Introduction

Bismuth oxides show many properties which make them interesting for the development of sensor devices [3]. Moreover, amorphous or polycrystalline Bi_2O_3 films show remarkable catalytic activity in oxidation reactions which seems to be related to the existence of variable oxidation states of bismuth and with the high oxygen mobility at the surface [4].

The Bi-O system is rather complicated since it can have at least four main crystalline forms, usually indicated as α, β, γ and δ, each showing different chemical-physical properties [5]. Therefore, much effort has recently been devoted to the synthesis and characterization of Bi_2O_3 thin films. In particular, the choice of the synthesis methods should include an accurate control over stoichiometry, morphology, microstructure and phase composition of the coatings. Bi_2O_3 films can be prepared by several chemical and physical deposition techniques [4]. Thermal evaporation of the oxide is technologically unfavorable since molten Bi_2O_3 attacks almost all crucible materials. Thermal oxidation of bismuth films often yields a mixture of the various phases. On the contrary, reactive evaporation of Bi and activated reactive evaporation have been successfully employed to produce single-phase Bi_2O_3 films. Good quality Bi_2O_3 coatings have also been prepared by reactive sputtering in atmosphere of oxygen and argon. Recently, metal-organic chemical vapor deposition (MOCVD) has been used to prepare bismuth oxide coatings ranging from pure α- to pure β-phase by a proper combination of pressure and flow rate of the carrier gas (O_2). To our knowledge, the sol-gel method has never been employed to obtain bismuth oxide coatings. The use of the sol-gel route has gained great scientific interest during the last years for making advanced materials and in particular to prepare oxide-based coatings. The mild conditions of synthesis

("soft chemistry") make this method particularly suitable for yielding thin films with good control over composition and microstructure.

The chemical interaction between Bi_2O_3 and SiO_2 leads to the formation of various bismuth silicates [6], an interesting class of compounds, among which $Bi_4(SiO_4)_3$ (BSO) has been proposed as an alternative candidate to the analogue bismuth germanate (BGO) for the production of fast light-output scintillators for nuclear and high energy physics experiments [2]. Usually, inorganic scintillators are obtained as single crystals and also BSO has been recently grown in this form by the Czochralski method.

In this paper the sol-gel synthesis and characterization of Bi_2O_3 thin films on silica slides obtained by the dipping method in ethanolic solutions of tris (2,2′-6,6′-tetramethylheptane-3,5-dionato)bismuth(III) [$Bi(dpm)_3$] is reported. In particular, the aims of this study were at least two. First, to investigate if the adopted synthetic procedure was reproducible and allowed the control of the Bi_3O_3 phase composition, and secondly, to correlate variations of the experimental conditions, i.e., heating time and temperature, with BSO thin film formation.

Experimental

The starting solution was obtained by mixing ethyl alcohol (C_2H_5OH) as solvent and tris(2,2′-6,6′-tetramethylheptane-3,5-dionato)bismuth(III) [$Bi(dpm)_3$], synthesized and fully characterized in the laboratory, as oxide precursor. The choice of this compound was made taking into account that under heating organic compounds decompose more easily with respect to other inorganic salts like $Bi(NO_3)_3$ or $BiCl_3$, without leaving residual contaminants inside the coatings (i.e., Cl^-). $Bi(dpm)_3$ was dissolved in ethanol in order to obtain an oxide concentration of 20 g l^{-1}. The as prepared precursor solution was used for the film deposition.

The bismuth oxide based films were obtained by the dipping procedure (10 successive dippings without any heat treatments between them). Silica slides were used as substrate. Before use, they were cleaned in an ultrasonic bath, rinsed both in doubly distilled water and isopropanol and dried at room temperature. The film deposition was carried out at room temperature with a controlled withdrawal speed of 12 cm min^{-1}. Due to the high sensitivity of $Bi(dpm)_3$ to water, the preparation of the starting solution and the dip-coating operations were performed in an N_2-atmosphere drybox. After dipping, each sample was treated in a programmable oven at various temperatures (200°C $\leq T \leq$ 800°C) for 1 hour, obtaining homogeneous, transparent and colorless coatings.

The composition of the films at the surface and in the bulk was obtained by XPS. The spectra were run on a Perkin-Elmer Φ 5600ci spectrometer using non-monochromatized Mg-Kα radiation (1253.6 eV). The working pressure was $<5 \times 10^{-8}$ Pa. The spectrometer was calibrated by assuming the binding energy (BE) of the Au($4f_{7/2}$) line at 83.9 eV with respect to the Fermi level. The standard deviation for the BE values was 0.15 eV. The reported BEs were corrected for the charging effects, assigning a value of 284.8 eV to the C(1s) line of adventitious carbon. Survey scans were obtained in the 0–1100 eV range. Detailed scans were recorded for the Bi($4f_{7/2}$), O(1s), C(1s) and Si(2p) regions. Depth profiles were carried out by Ar^+ sputtering at 2.5 keV with an Argon partial pressure of 5×10^{-6} Pa.

A custom-built instrument described elsewhere [6] was used for SIMS analysis. A 2 keV O_2^+ ion beam collimated to 50 μm was generated in a mass-filtered duoplasmatron ion gun (model DP50B, VG Fisons). The secondary ion optics were of three-lens design with a central stop interfaced with a Balzers QMA 400 quadrupole mass analyzer (mass range 2048 u). A secondary electron multiplier (90° off-axis) was used for positive- and negative-ion detection in the counting mode. Lens potentials, quadrupole electronic control units and the detection system were controlled by a Balzers QMG 421 unit. For depth analysis of positive and negative fragments, sputtering of the coatings was carried out with a 2 keV O_2^+ primary ion energy at an ion current between 400 and 800 nA.

The crystallinity of the films was detected by X-Ray Diffraction (XRD) performed using a Philips diffractometer (CuKα radiation, 35 kV, 40 mA) equipped with a PW1820 thin film attachment (glancing angle = 0.5°). The average crystallite size was calculated using the Scherrer equation; for the microstructural characterization an improved profile fitting method using a pseudo-Voigt representation for the line profiles was used [7].

Results and Discussion

The goal of this work was to achieve pure Bi_2O_3 thin films with a good control over their microstructure.

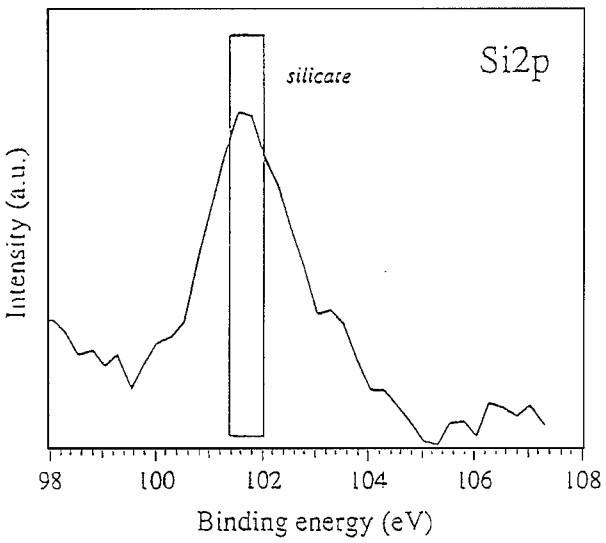

Figure 1. XPS Si(2p) region for the coatings annealed at 600°C.

Moreover, taking into account the technological potentiality of Bi silicates, the interaction of Bi_2O_3 coatings with the silica substrate was also investigated.

By XPS analysis, the coatings appeared to be very pure since no spurious peaks were found. An important peculiarity to be discussed is the amount of residual carbon within the films originating from incomplete removal of the degradation products of the organic residues. This was estimated by analyzing the C(1s) region during an etching process with 2.5 keV Ar^+ ions. Annealing at $T \geq 400°C$ was necessary to minimize (<1%) the carbon content. The Bi($4f_{7/2}$) and O(1s) peaks were found at BE values typical of Bi_2O_3 [Bi($4f_{7/2}$) = 159.5 eV, O(1s) = 530 eV] for heat treatments up to 500°C. Starting from 600°C, the Si(2p) line appeared at the surface with a position characteristic of silicates (Fig. 1), indicating the occurrence of a chemical interaction between the Bi_2O_3 coatings with the silica substrate.

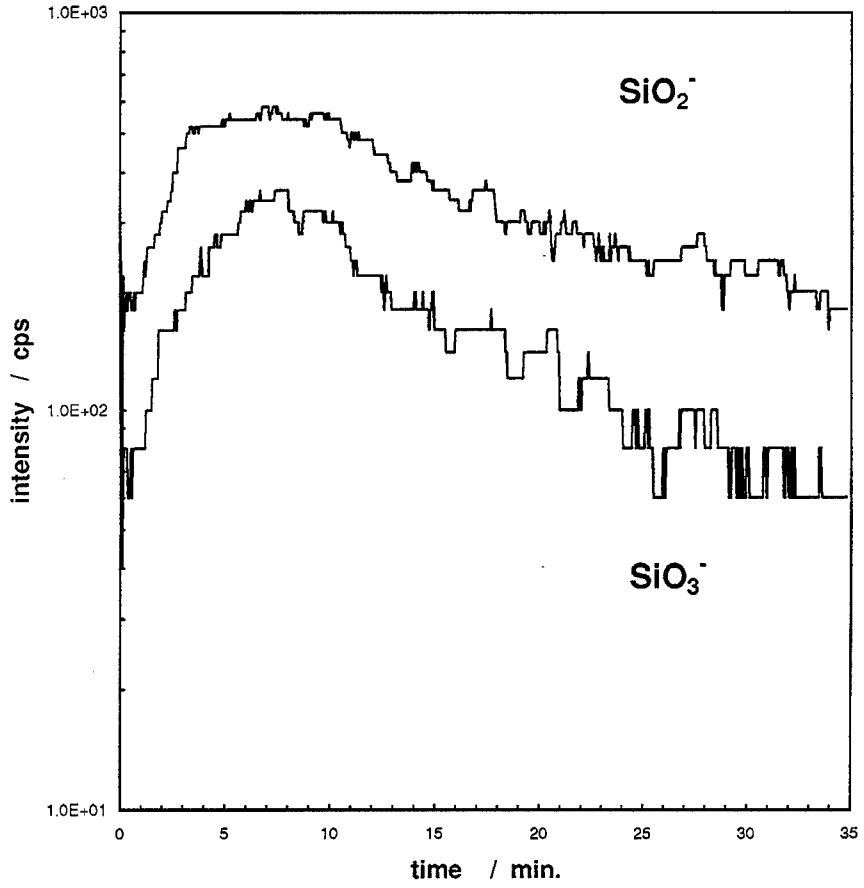

Figure 2. SIMS depth profiles of the intensities of SiO_2^- and SiO_3^- ions for a sample annealed at 700°C.

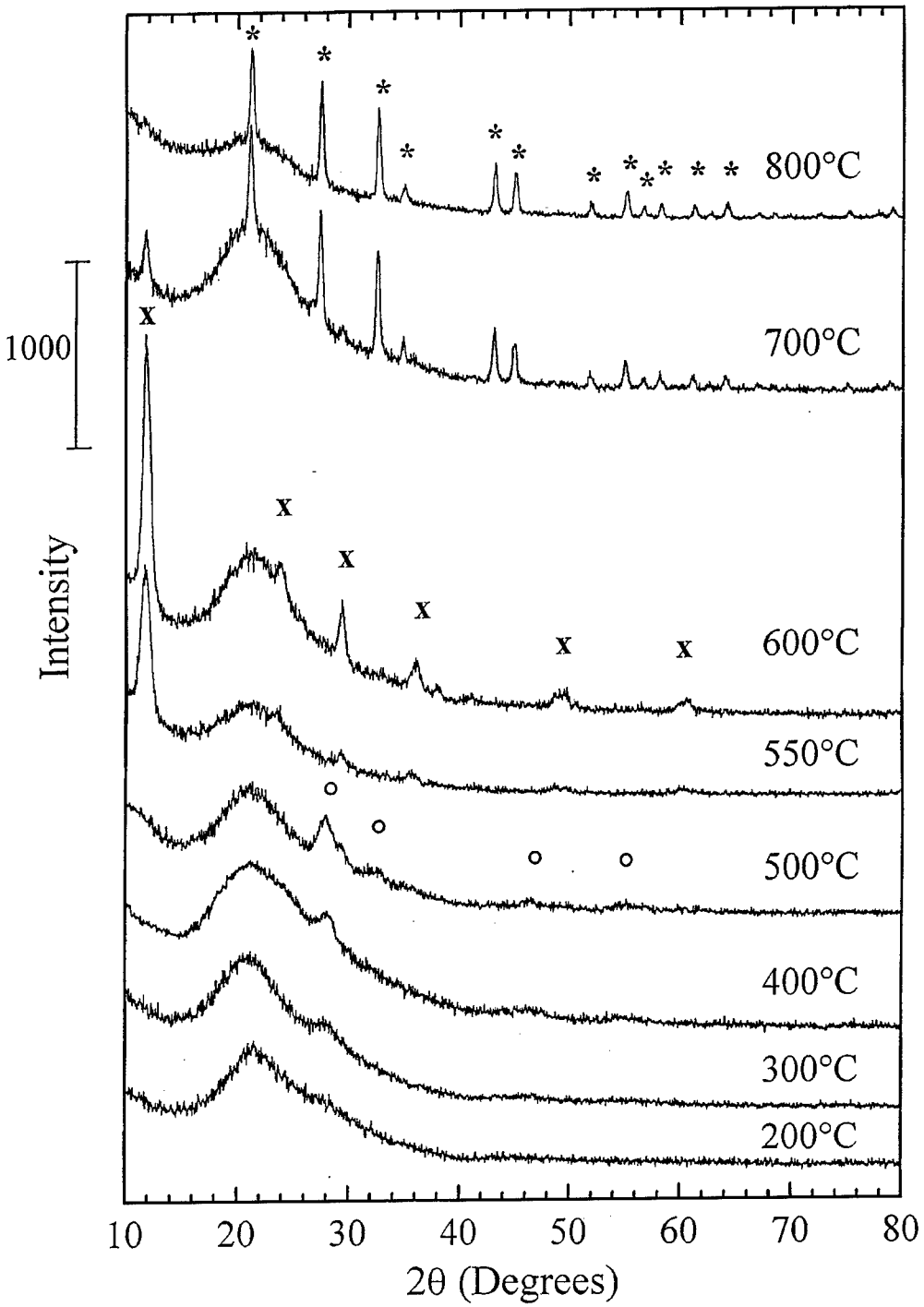

Figure 3. XRD patterns for samples heated at different temperatures (○ = Bi_2O_3; X = Bi_2SiO_5; ∗ = $Bi_4(SiO_4)_3$).

Silicate formation for samples annealed at 700 and 800°C was also analyzed by SIMS. Surface species were investigated by means of positive and negative ions spectra which were qualitatively similar for both the heating temperatures. Usual contaminants, characterized by high ionic yield signals (C^-, m/z = 12, Cl^-, m/z = 35, Na^+, m/z = 23, K^+, m/z = 39), were nearly absent, according to XPS analysis. As far as the composition is regarded, several clusters were observed and identified for both the samples: $Bi_xO_y^+$, $(1 \leq x \leq 2, 0 \leq y \leq 3)$, $BiSiO_y^-$ $(0 \leq y \leq 4)$ and finally $Si_xO_y^-$ ions $(1 \leq x \leq 3,\ 1 \leq y \leq 3)$, which are expected fragments from silica- and silicate-based materials. In particular, depth profiles of SiO_2^-, and SiO_3^- signals were carried out in order to evidence silicate and silica distribution across the coatings. In fact, if the sample composition is unvarying, the signal intensity ratio SiO_3^-/SiO_2^- remains constant from surface to inner layers, while its modification suggests a variation in Si-species concentration. Figure 2 shows depth profiles of SiO_2^- and SiO_3^- ions for the 700°C heated sample. The signal ratio SiO_3^-/SiO_2^- was constant for a sputtering time of about 15 min and successively dropped to a lower value. At 800°C the SiO_3^-/SiO_2^- ratio maintained a constant value across the film thickness. Taking into account the previous considerations, it can be stated that at the lower temperature silicates are localized first of all in the outer regions, while, at the higher temperature, the SiO_3^-/SiO_2^- ratio was constant, indicating that the silicate distribution was uniform from surface to inner layers.

In Fig. 3 are reported the XRD patterns for samples heat treated at different temperatures, which indicate that strong microstructural changes occurred in the films as a function of the treatment temperature.

After heating at 300°C, a peak attributable to bismuth oxide appeared at about 27.9°, which developed into a more definite Bi_2O_3 nanocrystalline structure at 500°C; average crystallite size increased from about 3 nm at 300°C to 7 nm at 500°C. Considering the quite large peak broadening due to the small crystallite size, a clear attribution of this pattern to either β-Bi_2O_3 (tetragonal, JCPDS card no. 27–50) or δ-Bi_2O_3 (cubic, JCPDS card no. 27–52) is not straightforward.

Heat treatment at 600°C caused the transformation of bismuth oxide. The diffraction pattern of the new phase resembled that of Bi_2SiO_5 (orthorhombic, JCPDS card no. 26–287), but with some degree of orientation with the predominance of the reflection from the plane (200) (at 11.6°). The reason for this orientation is not clear and it is still under investigation.

It was noticed that a small shoulder located at 29.3° was present in the 500°C-heated sample, which might indicate that the bismuth silicate phase formation already started at that temperature.

After heating at 700°C, the formation of a new phase, $Bi_4(SiO_4)_3$ (eulytite, cubic, JCPDS card no. 22–215), which became the only one at 800°C, was observed. No trace of this phase was observed in a 600°C-heated sample (not reported here).

Conclusions

Bi_2O_3 thin films were prepared by dip-coating procedure from an ethanolic solution of $Bi(dpm)_3$. Composition and microstructure showed strong dependence on the annealing temperature. The amount of hydrocarbon in the film due to incomplete pyrolysis of organic residuals was lower than 1% after thermal treatment over at least 400°C. Bi_2O_3 films were obtained for annealing at temperatures ranging between 300°C and 500°C, while reaction of the Bi_2O_3-coating with the silica substrate was detected at over 500°C.

Crystalline structure evolution was followed by XRD, while the samples were chemically characterized by XPS and SIMS analysis.

References

1. L. Armelao, G. Bandoli, M. Casarin, G. De Paoli, E. Tondello, and A. Vittadini, submitted.
2. M. Kobayshi, M. Ishii, K. Harada, and I. Yamaga, Nucl. Instr. and Meth. in Phys. Res. A **372**, 45 (1996).
3. N. Nicoloso, Phys. Chem. **94**, 731 (1990).
4. G. Bandoli, D. Barreca, E. Brescacin, G.A. Rizzi, and E. Tondello, Chem. Vap. Deposition **2**, 238 (1996).
5. H.A. Harwing and A.G. Gerards, J. Solid State Chem. **26**, 265 (1978).
6. C. Pagura, S. Daolio, and B. Facchin, in *Secondary Ion Mass Spectrometry SIMS* VIII, edited by A. Benninghoven, K.T.F. Jansen, J. Tumpner, and H.W. Werner (John Wiley, Chichester, 1992), p. 239.
7. S. Enzo, S. Polizzi, and A. Benedetti, Z. Kristallogr. **170**, 275 (1985).

Journal of Sol-Gel Science and Technology 13, 219–222 (1998)
© 1998 Kluwer Academic Publishers. Manufactured in The Netherlands.

Sol-Gel Derived TiO_2/Lead Phthalocyanine Photovoltaic Cells

S.M. TRACEY
University of Humberside and Lincolnshire, School of Engineering and Information Technology; and Sheffield Hallam University, School of Engineering Information Technology

S.N.B. HODGSON
University of Humberside and Lincolnshire, School of Engineering and Information Technology

A.K. RAY
Sheffield Hallam University, School of Engineering Information Technology

Abstract. Transparent TiO_2 films were deposited onto a base electrode comprising an $InSnO_2$ glass substrate using the (alkoxide) sol-gel technique. Lead phthalocyanine was subsequently vacuum sublimed onto the TiO_2 surface. The resulting $InSnO_2/TiO_2$/PbPc/Au heterojunction cell was investigated for its illuminated current density/voltage, and spectral characteristics. The ideality factor (m) and saturation current (J_o) were determined from current density/voltage $J(V)$ measurements. Photoelectrical measurements were conducted under both simulated solar radiation and within a wavelength range of 300–900 nm. This allowed calculation of open circuit voltage V_{oc}, short circuit current J_{sc}, fill factor FF, quantum efficiency Z and the overall conversion efficiency. Typical photovoltaic characteristics were obtained indicating the potential of the device for solar cell applications. The power conversion efficiency η was $\sim$0.001%; improvements are therefore required.

Keywords: heterostructures, solar cells, titanium dioxide, lead phthalocyanine

1. Introduction

The principle drawbacks of conventional Si-based cells are the high material and manufacturing costs. Consequently, a number of alternative material and device structures have been considered, including both organic [1] and hybrid organic/inorganic systems [2]. The main aims of these investigations are to improve overall conversion efficiency while also reducing production costs. Research has shown that organic dyes can be successfully used to spectrally sensitize wide band gap metal oxide semiconductors, resulting in a low cost photoelectrochemical cell [3]. Such devices incorporate a liquid electrolyte and there are significant concerns regarding their long-term stability. Consequently there is considerable interest in the development of solid state inorganic/organic heterostructures as low cost photovoltaic devices. This paper describes the development and results obtained from such a cell, which is in the form: Au/lead phthalocyanine (PbPc)/TiO_2/$InSnO_2$.

PbPc and TiO_2 can be considered to be p-type and n-type semiconductors, respectively. Therefore, the contact formed between the PbPc and TiO_2 will produce an inorganic/organic (IO) p-n heterojunction. The nature of the charge transfer and transport mechanisms in IO heterojunctions of this type remains the subject of some debate with a direct electron transfer mechanism being the most favored to explain the observed photovoltaic behaviour. Within the heterostructures the organic layer absorbs light, generating excitons which diffuse to the heterointerface and dissociate. Electrons transfer to the TiO_2 layer which provides electron transport, and the holes remain within the organic layer

and are transported therein [4]. The electrical current is supported only by majority charges. Therefore, such devices drastically differ from conventional *p-n* semiconductor devices in which the electrical current is supported by minority carriers [5], and would be anticipated to be less sensitive to surface and bulk defects obviating the need for the supertechnology and costs associated with most semiconductor device manufacture.

The fabrication of such devices entails the need to manufacture thin films of the organic and inorganic components. The fabrication of the inorganic layer, in particular, requires a relatively low cost, low temperature process capable of providing an optically transparent, electrically semiconducting, mechanically and chemically stable thin film, with good electronic contact with the substrate electrode. The sol-gel process is thus ideally suited for this application.

Titanium dioxide is an *n*-type semiconductor, easily formed by the sol-gel method and has the advantage of both chemical and thermal stability. Added to this it possesses economical and environmental advantages over some of the more prominent photovoltaic materials such as CdS, Si and GaAs. Lead phthalocyanine, (PbPc) belongs to a class of organic materials that have over the years received considerable attention [6]. This is mainly due to their semiconductive properties. Added to this they are abundant, stable and relatively cheap. However, attempts to produce substituted phthalocyanine solar cells have consistently shown low overall conversion efficiencies and in most cases this has been attributed to their low quantum efficiency and/or low charge carrier mobility [6]. They are, however, good photogenerators of free charge carriers.

2. Experimental Procedures

2.1. *Device Fabrication*

The device comprised a sandwich structure of an $InSnO_2$ glass electrode and substrate, transparent sol-gel derived TiO_2, PbPc dye and Au counter electrode. The complete device structure is shown in the inset of Fig 1.

Optically transparent TiO_2 films were deposited onto ultrasonically cleaned $InSnO_2$ glass substrates by dip coating at a withdrawal rate of 250 mm/min. The dip coating solution consisted of 12.6 vol% of

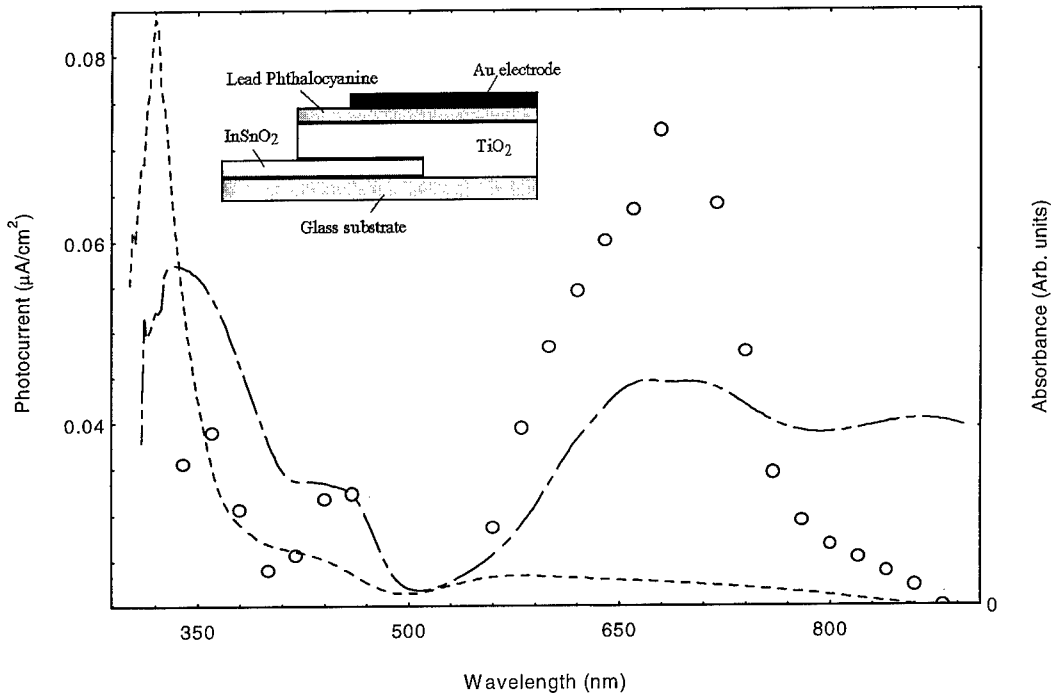

Figure 1. Photocurrent density action spectra (○) of a Au/PbPc(500 nm)/TiO_2(50 nm)/$InSnO_2$ cell. Absorbance of TiO_2 and PbPc film given by (---) and (-———), respectively. Device schematic shown in inset.

titanium isopropoxide (TIP) in ethanol, stabilized with glacial acetic acid additions in a molar ratio 4.16 : 1 TIP : ACID.

The entire procedure was carried out under atmospheric conditions. The films were left to dry in air for 24 hours then heated under atmospheric conditions to 500°C for 5 hours. X-Ray diffraction analysis carried out on residues of the sol mixture revealed that for gels heated to 500°C anatase is the predominant physical structure. The thickness of the TiO_2 films were measured using a planar surfometer and estimated to be in the order of 50 nm.

Films of lead phthalocyanine (PbPc) were prepared by vacuum sublimation. The TiO_2 coated substrates were held at room temperature and under a vacuum of $\sim 10^{-5}$ mbar during the sublimation process. A deposition rate of 1–10 A/s was used. The final film thickness was in the order of 500 nm, determined by a quartz crystal monitor in situ. Electrical connections were provided by evaporation of Au contacts onto the PbPc surface.

2.2. *Photoelectrical Measurements*

The performance of the cell was assessed using both the wavelength-dependent short circuit phototcurrent density J_{sc}, and the illuminated current density/voltage, $J(V)$ characteristics under simulated solar radiation.

Comparison of the PbPc absorption spectra with the $J_{sc}(\lambda)$ action spectra allowed calculation of the quantum efficiency (Z) defined as the ratio of photocurrent collected at each wavelength to the number of photons incident on the surface at that wavelength according to the following equation:

$$Z = \frac{Rhc}{e\lambda} \tag{1}$$

Where R is the device responsivity given by (J_{sc}/ϕ), ϕ is the incident intensity level in W/m^2, h is Planck's constant, c the speed of light, λ the wavelength of the incident monochromatic radiation and e the electronic charge. Comparison of the PbPc absorption spectra with the J_{sc} action spectra is also a direct indication of the ability of the dye to spectrally sensitize the TiO_2 to wavelength regions outside its intrinsic sensitivity.

The illumination for wavelength-dependent measurements was provided by a Spex 1681 0.22 m spectrometer in conjunction with a SPEX 1682A broad band radiation source. A 1683L tungsten/halogen incandescent lamp provided illumination over the wavelength range 300–900 nm. The V_{oc} and J_{sc} of the cell were measured as a function of wavelength (λ) in this range. The monochromator intensity level (ϕ) was found to be in the order of 32 μW/cm^2. A UV/Vis Unicam spectrometer was used to provide optical absorption spectra of the PbPc and TiO_2 films for comparison with the action spectra.

Illuminated $J(V)$ characteristics were used to determine the performance of the cell under white light conditions. The following photovoltaic cell parameters were obtained; open circuit voltage (V_{oc}); short circuit current density (J_{sc}); the fill factor (FF) or the fraction of the product of J_{sc} and V_{oc} available as power output given by:

$$FF = \frac{V_{mp}J_{mp}}{V_{oc}J_{sc}} \tag{2}$$

where V_{mp} and J_{mp} represent the voltage and current at the maximum power point respectively [5]. $\eta\%$, the overall conversion efficiency may then be calculated according to:

$$\eta = \frac{V_{oc}J_{sc}FF}{P_{in}} \tag{3}$$

where P_{in} is the power of the incident intensity (W/m^2).

Illuminated $J(V)$ measurements were performed under atmospheric conditions, using an electrometer. In all measurements the polarity of the forward voltages was positive at the Au electrode. For all illuminated $J(V)$ measurements, irradiation of the TiO_2/PbPc junction was directed through the $InSnO_2/TiO_2$ face. An Applied Physics, model 9500 solar simulator provided AM2 radiation at an intensity level of 1.52 mW/cm^2.

3. Results and Discussion

3.1. *Action Spectra*

To demonstrate photosensitization of the TiO_2 photocurrent action spectra were obtained over the range of visible light. Figure 1 displays the $J_{sc}(\lambda)$ action spectra obtained for the PbPc/TiO_2 cell in comparison with both the PbPc and TiO_2 absorption spectra. The PbPc film exhibits appreciable absorption in the 320–500 nm and ~580–900 nm ranges, typical of that observed in sublimed thin films of the material [7]. The TiO_2 films were highly transparent over the visible wavelength range.

Good agreement between the absorption spectra of the PbPc film and the spectral dependence of J_{sc} was observed for most of the visible region. Anomalies were observed for wavelengths below ~400 nm, most

probably due to a combination of optical absorption effects in TiO_2 and the $InSnO_2$ glass substrate. The similarity of the absorption spectra to the action spectra indicates that sensitization of the TiO_2 sol-gel layer with PbPc dye molecules occurred resulting in the extension of the absorbance of TiO_2 into the visible region. The observed wavelength dependence of J_{sc} must therefore be a consequence of photocarrier excitation in the PbPc and a subsequent transfer mechanism to the TiO_2 film.

The calculated quantum efficiencies (Z) at PbPc absorption maxima were $Z \sim 0.42\%$ at the lower maxima (~360 nm) and $Z \sim 0.41\%$ at the higher maxima (~680 nm). The corresponding J_{sc} were 0.031 μA/cm^2 and 0.072 μA/cm^2, respectively. This is an interesting observation, since a lower measured J_{sc} at 360 nm did not give rise to a lower value of Z; in fact, little difference in Z was observed. Two possible arguments are proposed to account for this effect. First, the increase in absorption of the PbPc film may contribute to a higher density of excitons within the organic layer. Secondly, the onset of absorption in the TiO_2 film at these wavelengths may result in an increase in charge carrier generation. This is in agreement with recent studies on ZnPc/TiO_2 cells which have shown that UV absorption in TiO_2 results in an increase in carrier density and conductivity of the TiO_2 film and that the UV absorbed in the space charge layer of the TiO_2 contributes to the photovoltaic effect [8]. It is anticipated, therefore, that both of these mechanisms result in the observed $Z(\lambda)$ dependence.

The quantum efficiencies obtained for this device were low. However, such efficiencies are not atypical of similar devices, the low efficiency having been previously attributed to recombination centers at the heterojunction interface [8], which may be present at the TiO_2 surface. The TiO_2 film was not treated in any way and as a consequence surface states could be present which can act as recombination centers. Impurities in the PbPc layer or grain boundaries within the TiO_2 or PbPc, polycrystalline films would also act as trapping sites for charge carriers.

3.2. *Illuminated J(V) Characteristics*

From the illuminated characteristics under simulated AM2 radiation, the following values were obtained for typical solar cell parameters. $V_{oc} = 200$ mV, $J_{sc} = 4.67 \times 10^{-7}$ A/cm^2, and FF (fill factor) $= 0.162$. These values corresponded to an overall power conversion efficiency of $\eta \sim 0.001\%$, according to Eq. (3). The relatively low values obtained for the conversion efficiency can be attributed both to interfacial and bulk effects as follows:

The presence of defects at the TiO_2/PbPc interface would be expected to result in a reduction of the power conversion efficiency, as explained in the previous section. In addition the overall conversion efficiency would be anticipated to be a function of the electrical resistance of the cell. The low electrical conductivity of the PbPc films would be expected to cause a high series resistance. This was confirmed from measurements of the series resistance (R_s) which under illuminated conditions was found to be $R_s \sim 57.5$ kΩ/cm^2. Such a high R_s indicates the disadvantage of the low conductivity of the organic semiconductor.

4. Conclusions

A low cost photovoltaic cell based on a p-PbPc/n-TiO_2 thin film heterojunction has been successfully produced utilizing the sol-gel technique.

The results indicate that a sol-gel derived TiO_2 film can be sensitized to wavelengths outside its intrinsic sensitivity. The observed response is anticipated to be a consequence of light absorption in the dye layer and the separation of photoexcited carriers at the PbPc/TiO_2 heterointerface.

The high series resistance caused by the organic layer is believed to be responsible for the low conversion efficiency of the cell and efficiency improvements are required. Preliminary investigations on devices incorporating thinner and/or more conductive organic layers are currently ongoing, and are yielding encouraging results with conversion efficiencies of at least an order of magnitude higher than reported here.

References

1. H. Yanagi, M. Imamura, and M. Ashida, Journal of Applied Physics **75**(4), 2061 (1994).
2. S. Antohe, Revue Roumanie de Phys. **37**(3), 309 (1992).
3. B. O'Regan and M. Grätzel, Nature **353**, 737 (1991).
4. Y, Shen, L. Wang, Z. Lu, Y. Wei, Q. Zhou, H. Mao, and H. Xu, Thin Solid Films **257**, 144 (1995).
5. M.S. Tyagi, *Introduction to Semiconductor Materials and Devices* (John Wiley & Sons, 1991), p. 340.
6. J. Simon and J.J. Andre, *Molecular Semiconductors* (Springer, 1983), p. 73.
7. D. Schmeißer, A. Rager, K. Thonke, M. Pilkuhn, D. Fröhlich, G. Gauglitz, M. Schäfer, and D. Oelkrug, Synthetic Metals **41–43**, 1457 (1991).
8. K. Kajihara, K. Tanaka, K. Hirao, and N. Soga, Japanese Journal of Physics **35**, 6110 (1996).

Journal of Sol-Gel Science and Technology 13, 223–227 (1998)
© 1998 Kluwer Academic Publishers. Manufactured in The Netherlands.

Electrical Properties of Polycrystalline Lithium Chloroboracite Prepared by the Sol-Gel Method

T. NAGASE, K. SAKANE AND H. WADA
Shikoku National Industrial Research Institute, 2217-14 Hayashi, Takamatsu 761-03, Japan

Abstract. The electrical properties of polycrystalline lithium chloroboracite, $Li_4B_7O_{12}Cl$, prepared by the sol-gel method were investigated in connection with their structure. $Li_4B_7O_{12}Cl$ pellets were prepared with different amounts of hydrochloric acid or ammonium chloride. The kind and amount of the chlorine source affected the formation of by-products ($Li_2B_4O_7$, LiCl, a glass phase) and the morphology of the $Li_4B_7O_{12}Cl$ pellets. Thus their conductivity, which is dominated by grain boundary response owing to the high porosity of the materials, was also affected. The formation of $Li_2B_4O_7$ as a by-product led to a higher activation energy and lower conductivity. In those pellets in which $Li_2B_4O_7$ did form, an increase of the amount of glass phase led to higher conductivities.

Keywords: lithium boracite, lithium-ion conductor, complex impedance method, by-products, morphology

1. Introduction

Lithium chloroboracite, $Li_4B_7O_{12}Cl$, is a lithium-ion conductor which has a high conductivity of 1×10^{-2} $S \cdot cm^{-1}$ at 573 K [1]; it is stable in air and insoluble in water. Therefore, $Li_4B_7O_{12}Cl$ has potential applications as a solid electrolyte in batteries and electrochromic displays. Such applications, however, require $Li_4B_7O_{12}Cl$ to be present either as a monolith or a film. $Li_4B_7O_{12}Cl$ powder and pellets have been already prepared by flux, hydrothermal [2] and sealed tube methods [1]. Among various preparation methods, the sol-gel method has advantages for the easy formation films. Using this method, $Li_4B_7O_{12}Cl$ powder and film were successfully prepared with hydrochloric acid or/and ammonium chloride as a chlorine source [3]. The kind and amount of the chlorine source affected the formation of both $Li_4B_7O_{12}Cl$ and by-products.

The conductivity of crystalline ionic conductors is generally affected by many factors, such as their crystalline structure, impurities, porosity, and preparation methods and conditions. Therefore, a detailed investigation of the electrical properties of polycrystalline $Li_4B_7O_{12}Cl$ prepared by the sol-gel method may enable improvements in the conductivity of $Li_4B_7O_{12}Cl$.

In this work, the electrical properties of polycrystalline $Li_4B_7O_{12}Cl$ pellets prepared by the sol-gel method have been measured using the complex impedance method. The effect of the kind and amount of chlorine source on the by-product formation and morphology is also described. The electrical properties are discussed in relation to the by-product formation and material morphology.

2. Experimental

Precursor powders for pellets were prepared in a way similar to that developed for $Li_4B_7O_{12}Cl$ powder preparation [3]. Lithium hydroxide monohydrate and boric acid were dissolved in methanol at a concentration of 0.6 M for lithium and 1.05 M for boron. Water and various amounts of hydrochloric acid or ammonium chloride were then added to the methanol solution. The molar ratio [total water]/([Li] + 3[B]) was fixed at 5. The [Cl]/[Li] molar ratio (R_{Cl}) was varied in steps from 0.6 to 0.68 to 0.9 for hydrochloric acid, and from 0.6 to 0.68 to 0.75 for ammonium chloride. The resulting solutions were dried at 373 K. The remaining residues were calcined at 773 K for 1 hour to obtain the precursor powders. The powders were pressed into pellets (ca. 10 mm diameter and 2 mm

thickness) under 6 MPa pressure and sintered at 973 K for 1 hour in air. Pellets prepared with hydrochloric acid with R_{Cl} of 0.6, 0.68 or 0.9 are referred to as HCl-0.6, HCl-0.68, and HCl-0.9 pellets, respectively, while pellets prepared with ammonium chloride with R_{Cl} values of 0.6, 0.68 or 0.75 are called NH_4Cl-0.6, NH_4Cl-0.68, and NH_4Cl-0.75 pellets, respectively.

The structure of the pellets was determined using an X-ray diffractometer (RINT-1200, Rigaku). Sections of the pellets were examined with a scanning electron microscope (S-2460N, Hitachi) equipped with an energy dispersive X-ray spectrometer (DX-4, EDAX International). The conductivity was measured using a frequency analyzer (HP4800, Hewlett Packard) in the frequency range of 1 Hz to 20 kHz. Measurements were carried out in an argon atmosphere at temperatures varying between 623 K and 423 K.

3. Results and Discussion

3.1. *Identification of Structure*

XRD results showed that the composition of the pellets consisted of essentially $Li_4B_7O_{12}Cl$ with some by-products such as lithium tetraborate ($Li_2B_4O_7$), lithium chloride (LiCl) and a glass phase. The formation of the glass phase was recognized from the presence of a broad peak around 20–40° 2θ(CuKα). The formation of these by-products depended on the kind and amount of the chlorine source. A small amount of LiCl appeared only in the HCl-0.9 pellet. Figure 1 shows the diffraction intensity of the strongest $Li_2B_4O_7$ peak at 21.78° and the integrated intensity of the broad band between 15° and 43°. $Li_2B_4O_7$ appears in the NH_4Cl and HCl-0.6 series, but its amount is small as the intensity of the strongest $Li_4B_7O_{12}Cl$ peak was at least 51 times stronger than that of $Li_2B_4O_7$. In the HCl-0.68 and HCl-0.9 pellets, the formation of $Li_2B_4O_7$ was barely observed. Among the NH_4Cl series, the amount of the glass phase increased as the added amount of ammonium chloride increased.

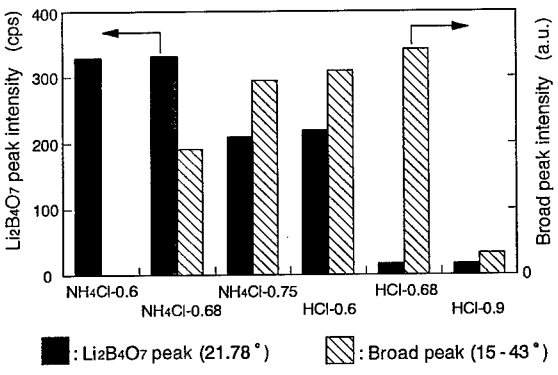

Figure 1. Formation of $Li_2B_4O_7$ and the glassy phase in various $Li_4B_7O_{12}Cl$ pellets.

SEM observation showed that all pellets except NH_4Cl-0.6 included a glass-like phase. EDX analysis showed that the glass-like phase contained chlorine as well as oxygen. The electroneutrality principle requires the presence of cationic elements, i.e., lithium and boron, which are not detectable with EDX analysis. Therefore, it is reasonable to assume that the glass phase is composed of B_2O_3-Li_2O-LiCl. Figure 2 shows SEM images of the NH_4Cl and HCl-0.68 series. The SEM images of the NH_4Cl series show that the sintering increased with the R_{Cl} ratio and with the amount of the glass phase formed, suggesting that the glass phase acts as a flux during the sintering process. The morphology of the HCl-0.68 pellet shows small grains buried in the glass phase and is different from the NH_4Cl series. The morphology of the HCl-0.6 and HCl-0.9 pellets was rather similar to that of HCl-0.68 pellet.

All the sintered pellets have a low bulk density of about 1.36–1.44 g/cm^3 corresponding to 56–59% of the theoretical density of $Li_4B_7O_{12}Cl$ [4], suggesting that all the samples have a high porosity of about 40%. This would scarcely be affected by the by-product formation, considering the densities of $Li_2B_4O_7$, LiCl and the B_2O_3-Li_2O-LiCl glasses [5].

3.2. *Electrical Properties*

Impedance plots for all the pellets showed similar behavior in response to temperature. At 423 K one arc was clearly observed for all the pellets except the HCl-0.6 pellet. As the temperature was increased the arc transformed into a spike. At 623 K the spike only was observed. The impedance plots were interpreted with reference to the literature [6]. The arc observed at 423 K was approximated by a semicircle which, if extended, would pass through the origin, and gave capacitance values of about 0.8 to 2.0 nF (Table 1). This suggests that the observed arc can be ascribed to a grain boundary response and that the total resistance

Table 1. Electrical properties of various $Li_4B_7O_{12}Cl$ pellets.

Pellet	Capacitance at 423 K (nF)	Conductivity at 573 K ($S \cdot cm^{-1}$)	E (eV)
NH_4Cl-0.6	0.9	1.8×10^{-4}	0.61
NH_4Cl-0.68	0.8	2.6×10^{-4}	0.62
NH_4Cl-0.75	0.9	3.4×10^{-4}	0.61
HCl-0.6	—	3.6×10^{-4}	0.61
HCl-0.68	0.8	7.9×10^{-4}	0.54
HCl-09	2.0	6.8×10^{-4}	0.56

— not detectable.

of the polycrystalline materials (a combination of grain boundary and bulk crystal resistances) is dominated by grain boundary response at 423 K.

Arrhenius plots of the conductivity calculated from the total resistance for the various pellets are shown in Fig. 3. The values of the activation energy for each

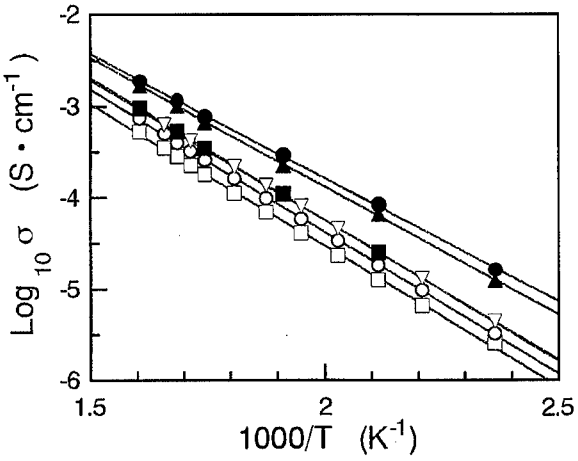

Figure 3. Arrhenius plots of conductivity for various $Li_4B_7O_{12}Cl$ pellets prepared with hydrochloric acid or ammonium chloride at various [Cl]/[Li] molar ratios. ■, ● and ▲ denote the HCl-0.6, -0.68 and -0.9 pellets, respectively. □, ○ and ▽ denote the NH_4Cl-0.6, -0.68 and -0.75 pellets, respectively.

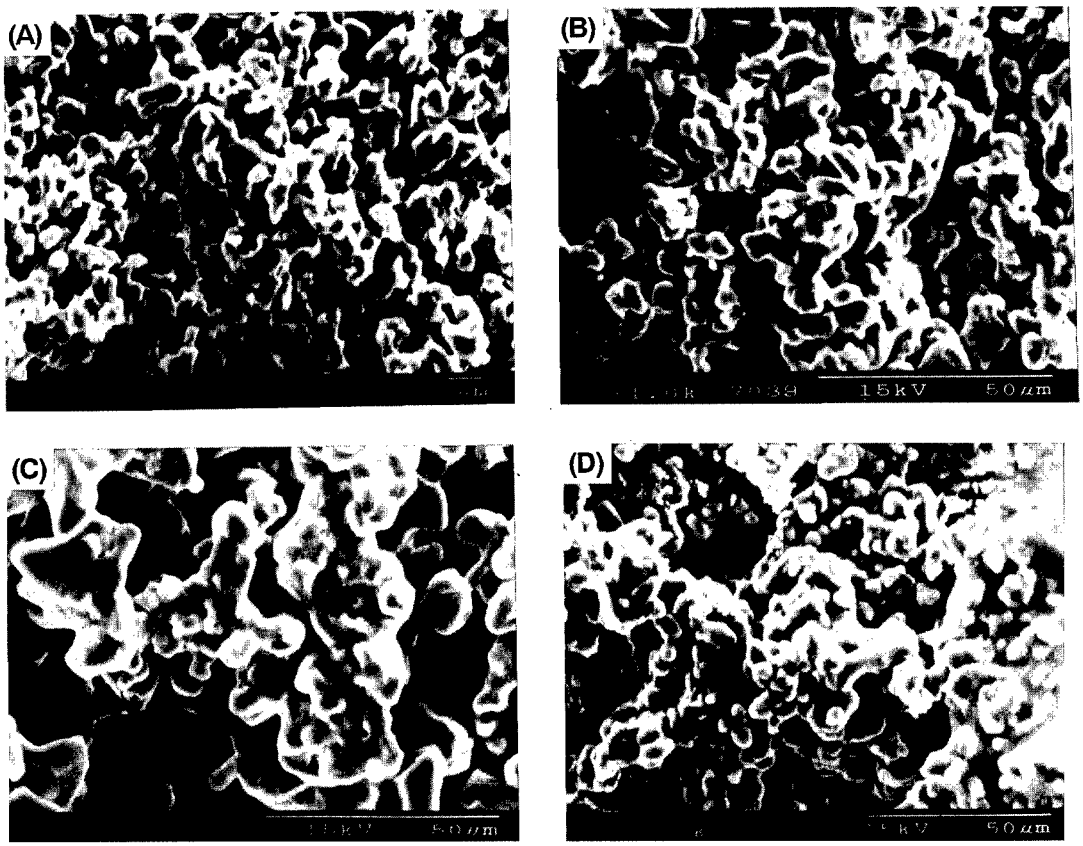

Figure 2. SEM images of NH_4Cl-0.6 (A), NH_4Cl-0.68 (B), NH_4Cl-0.9 (C), and HCl-0.68 (D) pellets.

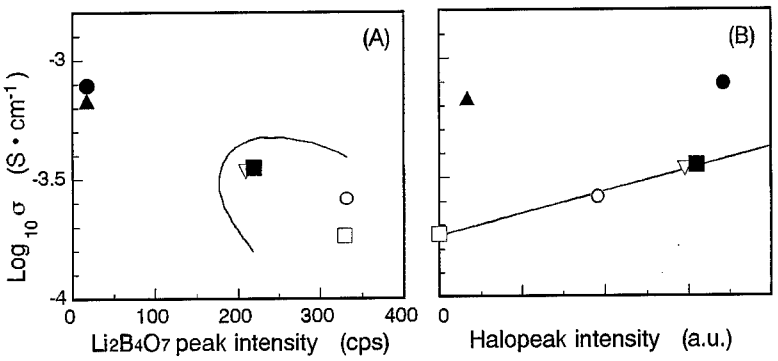

Figure 4. Relationship between conductivity and by-product formation of $Li_2B_4O_7$ (A), and the glassy phase (B). ■, ● and ▲ denote the HCl-0.6, -0.68 and -0.9 pellets, respectively. □, ○ and ▽ denote the NH_4Cl-0.6, -0.68 and -0.75 pellets, respectively.

pellet (Table 1) are independent of temperature in the range 423–623 K, suggesting that the total resistance was dominated by a grain boundary response and that the activation energy can be ascribed to a grain boundary response caused by the high porosity of the samples. Figure 3 and Table 1 both show that the pellet conductivity increases in the following order: NH_4Cl-0.6 < NH_4Cl-0.68 < NH_4Cl-0.75 $\leq$ HCl-0.6 $\ll$ HCl-0.9 < HCl-0.68. The best value is, however, about one order of magnitude lower than that reported for polycrystalline $Li_4B_7O_{12}Cl$ (85% theoretical density) prepared in a sealed tube [1], because of the higher porosity of the current samples.

Table 1 indicates that the HCl-0.68 and HCl-0.9 pellets showed lower activation energy than the others. This suggests that these pellets have a different grain boundary response. This is most probably related to the formation of $Li_2B_4O_7$, which is an insulator. Figure 4 shows the relationship between conductivity and amounts of $Li_2B_4O_7$ (A) and the glass phase (B) by-products, estimated by XRD measurements (see Fig. 1). Figure 4(A) shows that $Li_2B_4O_7$ formation depressed the conductivity. The presence of this by-product is likely to cause differences in the composition and morphology of the grain boundaries, affecting the conductivity and activation energy.

For the four pellets in which $Li_2B_4O_7$ formed, a comparison between Fig. 4(A) and (B) shows that their conductivity correlates more linearly with the amount of the glass phase than with the amount of $Li_2B_4O_7$. This is probably related to the improvement of the sintering of $Li_4B_7O_{12}Cl$ grains assisted by the glass phase. Furthermore, the glass phase itself should contribute to their conductivity, because in the B_2O_3-Li_2O-LiCl system it is known to possess a high lithium-ion conductivity [7].

4. Conclusions

Polycrystalline $Li_4B_7O_{12}Cl$ pellets were prepared by the sol-gel method with various amounts of hydrochloric acid or ammonium chloride. The kind and amount of the chlorine source affected the formation of $Li_2B_4O_7$, LiCl and glass phase by-products, the morphology of the pellets, and hence their conductivity. The conductivity was dominated by a grain boundary response, owing to the high porosity of the materials. $Li_2B_4O_7$ did not form when the samples were prepared with hydrochloric acid with [Cl]/[Li] molar ratios of 0.68 or 0.9. This resulted in a lower activation energy and higher conductivity. Among pellets in which $Li_2B_4O_7$ did form, an increase in the amount of glassy phase produced higher conductivity. This is most likely related to improvements in the sintering of $Li_4B_7O_{12}Cl$ grains and to the high conductivity of the glass phase itself.

5. Acknowledgment

We thank Dr. Y. Saito, Dr. T. Takeuchi and Dr. H. Kageyama (Osaka National Research Institute) for the measurement of conductivity and discussions.

References

1. B. Calès, A. Levasseur, C. Fouassier, J.M. Rèau, and P. Hagenmuller, Solid State Communications **24**, 323 (1977).
2. W. Jeitschko, T.A. Bither, and P.E. Bierstedt, Acta Cryst. **B33**,

2767 (1977).
3. T. Nagase, K. Sakane, and H. Wada, in *Proc. 2nd Int. Conf. on Borate Glasses, Crystals & Melts* (Abingdon, U.K., 1996), in press.
4. A. Levasseur, C. Fouassier, and P. Hagenmuller, Mat. Res. Bull. **6**, 15 (1971).
5. W. Soppe, F. Aldenkamp, and H.W. den Hartog, J. Non-Cryst. Solids **91**, 351 (1987).
6. A.R. West, Solid State Chemistry and its Applications (John Wiley & Sons, Chichester, 1984), p. 482.
7. A. Levasseur, J.C. Brethous, J.M. Reau, P. Hagenmuller, and M. Couzi, Solid State Ionics **1**, 177 (1980).

Journal of Sol-Gel Science and Technology 13, 229–232 (1998)
© 1998 Kluwer Academic Publishers. Manufactured in The Netherlands.

Microstructures in High-Tc Bi-based Superconductors

S. HORIUCHI AND M. CANTONI
National Institute for Research in Inorganic Materials, Tsukuba, 305, Japan
horiuchi@nirim.go.jp

Y. TANAKA
National Institute for Metals, Tsukuba, 305, Japan

M. ISHIZUKA
Res. & Dev. Center, Sumitomo Heavy Industries, Ltd., Hiratsuka, 254, Japan

L. BEN-DOR
Dept. Inorg. & Analyt. Chem., Hebrew Univ., Jerusalem 91904, Israel

Abstract. Microstructures of high-Tc Bi-based superconductors in a disk form and a tape form sheathed by Ag are examined by SEM and TEM. The disk specimens were prepared by the sol-gel method and are compact with few cavities. Bi-2212 or Bi-2223 grains grow with short heating times leading to rapid increases in magnetization. However, magnetization drops with further heating due to the formation of 2201 areas in the 2212 matrix or 2212 areas in the 2223 matrix together with the amorphization within the matrix. In the tape specimens prepared by conventional powder processing methods, thin plate-like grains grow large with some cavities among them. The Jc increases together with the grain growth and then drops slowly as the amorphization of the grains occurs.

Keywords: microstructure, high-Tc Bi-based superconductor, electron microscopy, sol-gel, preparation, amorphization

1. Introduction

In order to use high-Tc (critical transition temperature) superconductors practically, high Jc (critical current density) is necessary. From this viewpoint it is important to have strong linkages among the superconducting grains and to introduce pinning sites for the magnetic flux. The strong linkage requires the compactness of the substance with less cavities and impurity phases, and the preferred orientation of grains. Possible pinning sites for magnetic flux include lattice defects, precipitates, irradiation-induced defects, etc. We have recently found that in Bi- or Tl-based high Tc superconducting tapes [1, 2] high Jc is obtained when subgrain boundaries of pure-tilt type are formed.

In the present study we examine the microstructures in superconducting materials, which are prepared either by sol-gel processing or by conventional ceramic processing.

2. Experimental Procedure

Bulk specimens of $Bi_{1.8}Pb_{0.2}Sr_2Ca_2Cu_3O_x$ (Bi(Pb)-2223) or $Bi_{1.8+y}Pb_{0.2-y}Sr_2CaCu_2O_x$ (Bi(Pb)-2212) were prepared by sol-gel processing [3]; precursors were dried and preheated to obtain powders, which were then molded into a disk form (7 mm diameter $\times$ 1 mm thickness). The pellets were heated in air at 870°C. The dependence of the magnetic

susceptibility on temperature was measured. Alternatively, powders of the phases were prepared by conventional ceramic processing using component oxides and carbonates which were mixed together and heated. They were put into an Ag tube, which was drawn (powder-in-tube method) and finally rolled to a tape (2.5 mm width × 0.15 mm thickness). Their Jc values were obtained by conventional magnetic measurements [4].

The bulk and tape specimens obtained were examined by scanning and transmission electron microscopy (SEM and TEM). Thin plates were cut out from the specimens. After polishing the surface they were thinned by ion-thinning using Ar ions.

3. Results and Discussion

Figure 1 shows the measured magnetization for the bulk specimens of Bi(Pb)-2223 prepared by sol-gel processing [5]. The specimens were heated at 870°C for 56 h (curve 1), for 90 h (curve 2) and for 95 h (curve 3). The magnetization strongly depends on the heating time; strong magnetization is achieved after short heating times (curve 2). Deterioration of the magnetization occurs on further heating (curve 3). The similar results have been obtained from sol-gel prepared specimens of Bi(Pb)-2212 [6].

Figure 2(a) is a backscattered-electron SEM image of the Bi(Pb)-2212 specimen, which shows strong magnetization. Few cavities are present in the specimen. Bi(Pb)-2212 grains are the major phase, while many impurity phases are seen with dark contrast. Large grains are marked by arrows. Figure 2(b) is another SEM image of the specimen, in which deterioration of the magnetization has occurred. Thin plate-like bright areas, marked by arrowheads, are from the 2201 phase. The formation of the 2201 areas in the 2212 matrix is one of the reasons for deterioration of the magnetization. A similar observation has been obtained in sol-gel prepared Bi(Pb)-2223 bulk specimens, in which areas of Bi(Pb)-2212 phase occur [5].

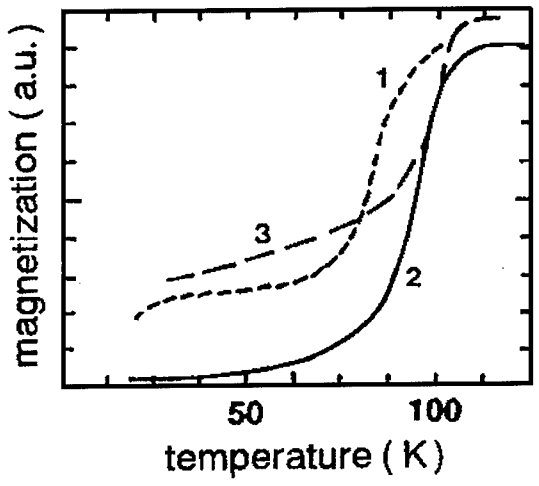

Figure 1. Relationship between the magnetization and temperature for the bulk specimens of Bi(Pb)-2223 prepared by the sol-gel method. The applied magnetic field is 15 Oe.

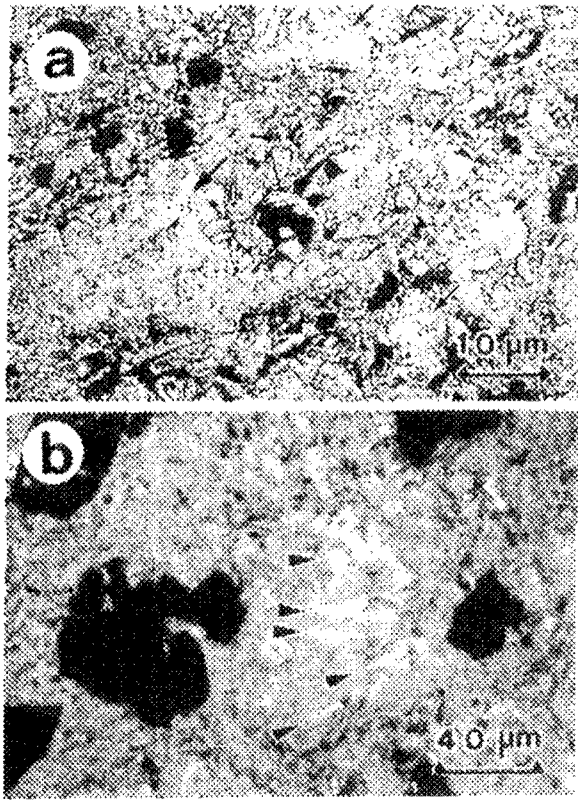

Figure 2. Backscattered-electron SEM image of sol-gel prepared specimens, with high magnetization (a) and reduced magnetization (b).

Figure 3 is a TEM image of the same specimen as Fig. 2(b), showing the formation of amorphous areas, as marked by arrows. According to the phase diagram the formation of a liquid phase is expected [7]. The amorphous phase in Fig. 3 may be due to the formation of a liquid phase on heating.

Figure 4 shows the relationship between Jc and the heating time of the Ag-sheathed Bi(Pb)-2223 tapes.

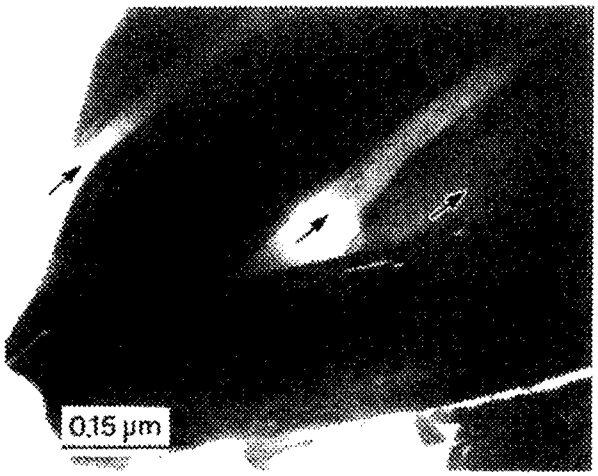

Figure 3. TEM image of the specimen in Fig. 2(b), showing the formation of amorphous areas marked by arrows.

A slight amount of additional elements was doped in the sheathing Ag; Hf for curve 1, Ti for curve 2 and Cu + Hf for curve 3. For each curve Jc reaches a maximal value after heating for long times (150–200 h) and subsequently deteriorates on further heating [1].

Figure 5(a) is a TEM image of the cross-section for the tape with the maximal Jc (after 150 h) in the curve 2 of Fig. 4. Thin, large plates of Bi(Pb)-2223 are formed, closely linked together. The plates are almost parallel to the tape plane. Cavities are also present. Figure 5(b) shows another TEM image for the tape, in which deterioration of Jc has occurred (after 400 h) along the curve 3. The amorphization starts mostly inside the 2223 grains, as marked by arrows. Its area is still limited so that the Jc is rather high even after heating for 400 h.

Therefore, in the specimens prepared by the sol-gel method, superconducting grains are small and compact. This is contrary to the specimens prepared by the conventional ceramic method. The magnetization and the Jc value first increase and then decrease on prolonged heating. The reason for the deterioration is the precipitation of other phases as well as the amorphization of the grains in the sol-gel specimens; in the powder processed specimens only amorphization occurs. A liquid phase may occur when the composition deviates from the exact Bi(Pb)-2223 or Bi(Pb)-2212 compositions in the equilibrium state. The faster amorphization in the sol-gel specimens is because of

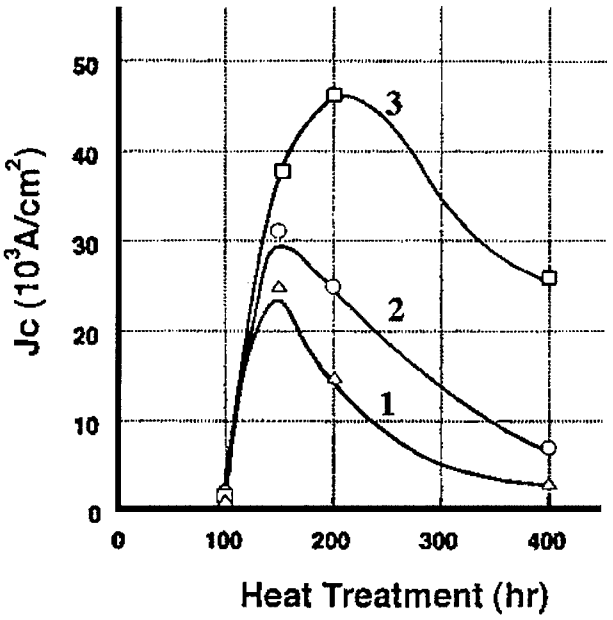

Figure 4. Relationship between Jc and the heating time of Bi(Pb)-2212 tape, for which powders of superconducting phase have been prepared by conventional ceramic processing. Different elements are doped in the sheathing Ag for each curve.

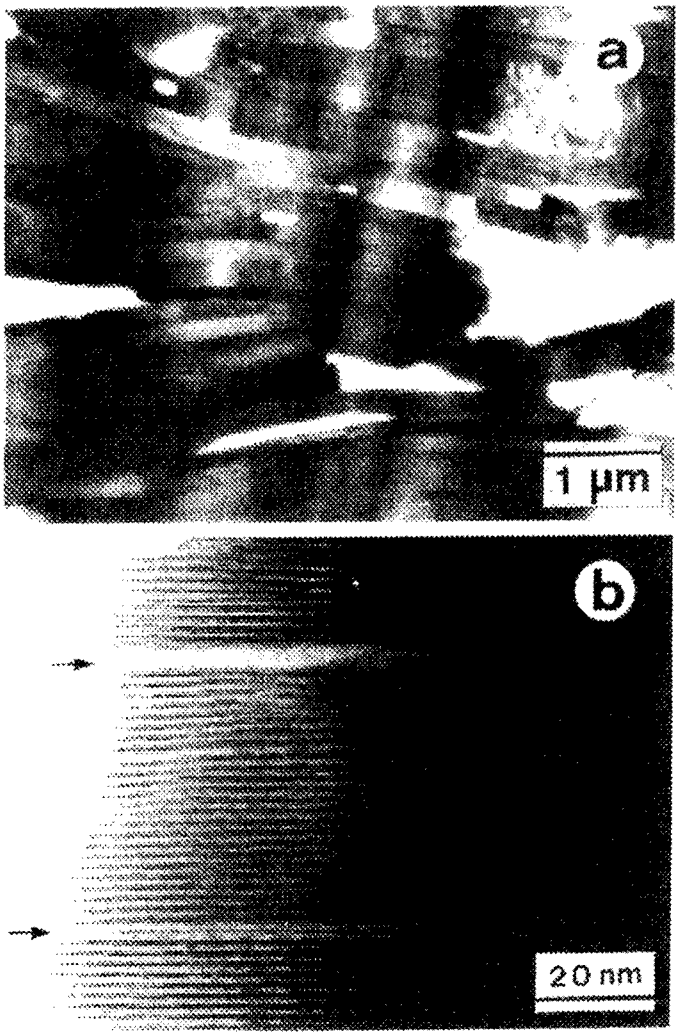

Figure 5. TEM images of the cross-sections of tapes, which show the maximal Jc in the curve 2 in Fig. 4(a) and the deterioration of Jc in the curve 3(b).

easier liquid phase formation as the equilibrium state is achieved more rapidly.

References

1. M. Cantoni, T. Tanaka, M. Ishizuka, and S. Horiuchi, Physica C **276**, 259 (1997).
2. D.Y. Jeong, M.H. Sohn, H.S. Kim, L.L. He, M. Cantoni, and S. Horiuchi, Physica C **296**, 279 (1996).
3. L. Ben-dor, H. Diab, and I. Felner, J. Sol. State Chem. **88**, 183 (1990).
4. Y. Tanaka, M. Ishizuka, L.L. He, S. Horiuchi, and H. Maeda, Physica C **268**, 133 (1996).
5. X.J. Wu, S. Horiuchi, L. Ben-dor, and H. Diab, J. Sol. State Chem. **97**, 82 (1992).
6. S. Horiuchi, M. Hirasaka, M. Tsutsumi, K. Kosuda, M.Y. Szerer, and L. Ben-dor, Micorsc. Res. Tech. **30**, 258 (1995).
7. H. Komatsu, Y. Kato, S. Miyashita, T. Inoue, and S. Hayashi, Physica C **190**, 14 (1991).

Journal of Sol-Gel Science and Technology 13, 233–236 (1998)
© 1998 Kluwer Academic Publishers. Manufactured in The Netherlands.

Sol-Gel; Potential Creative Applications for the Artist, Focusing on the Colloidal Alkali Silicate Route

ED SMY*
Department of Ceramics and Glass, University of Hertfordshire, Herts, UK

Abstract. The development of the colloidal alkali silicate gelation process (the Shoup Method) has established that intricately shaped large size monolithic glass samples are achievable without the need for long drying procedures or the use of a critical drying process. The ability to fabricate gels with large pores (diameter range of 100–300 nm) and the ability to dry them simply and quickly (with the help of a microwave oven) has made Sol-Gel technology accessible to the artist. The ability to cast from flexible molding compounds, to cast without major finishing, to dope and color directly with metal oxides, establishes new possibilities for the artistic forming of glass.

Keywords: casting, flexible molding, dissolvable substrates

Introduction

An important challenge for the artist whose aims are to mold and cast glass is to find a way of achieving some creative control over the molten state. The glass blower has developed a repertoire that is defined by the parameters of the equipment and constrained by the loss of heat and plastic malleability. The glass kiln worker has the element of time, a restricted component for the glass blower, at his disposal. This enables him to adapt and make changes at different stages in the forming process, an advantage offset by the need to engage complex molding process. Both approaches have a need to process the glass through a liquid stage, but both have limited access to molten glass, placing restrictions on potential creative directions. The Sol-Gel process provides a means for the glass artist to overcome this restriction by enabling a more direct and intimate relationship with the material at the crucial forming stage.

Advantages of the Sol-Gel process include:

- direct control over the liquid/sol stage, allowing for flexibility of choice in the composition and character of the glass;
- control over the gel stage, both wet and dry gels, allowing the artist to shape and form more spontaneously;
- a potential to form a glass at relatively low temperatures;
- minimal finishing to the final glass.

*In conjunction with Department Engineering Materials, University of Sheffield, UK

Background

Colloidal Alkali Silicate Route

Multicomponent aqua-sols have provided a basis for a range of Sol-Gel applications, primarily as precursors for powder formation. An early route involving the hydrolysis of specific metal salts was demonstrated by Roy [1]. The Shoup method [2] uses combinations of silica solutions and/or colloidal dispersed silica in the presence of an amine, e.g., Formamide.

The advantage for the artist offered by this route can be summarized as follows:

- easier to achieve homogeneous mixing;
- able to achieve large pore sizes;
- able to dry without use of critical drying process;
- able to speed up drying through use of microwave oven.

Disadvantages

- high temperatures needed to sinter into a glass (typically 1350–1750°C).

Monoliths

Homogeneous mixing, controlled drying and sintering management are critical factors in achieving a successful glass via the Sol-Gel process. This contrasts with traditional glass forming, where cullet preparation, heat transformation and annealing underpin practice. In initially concentrating on the forming of monolithic gels, an area of interest common to both scientist and artist, the following experiments attempt to combine the forming skills of the artist with selected knowledge developed by the sol-gel scientist.

In the initial comparison of the two main routes to produce a silica gel

- colloidal method involving gelation of colloidal silica combined with glass formers;
- hydrolysis and polycondensation of organometallic compounds.

It was seen that both routes were able to produce gel networks that could establish a basis for the forming of monolithic silica glasses.

Work by Rabinovich [3] Scherer and Luong [4] into colloidal silica gels had established that monolithic castings were possible. Work by Scherer [5] into the effects of syneresis established fundamental principles that need to be addressed if cracking is to be avoided. Shoup [2] and Hench [6] emphasized the requirement for large and evenly distributed pore formation, in Shoup's case preferably held within 100–300 nm. As a result the drying of these gels could be achieved without the need for long drying times or the use of super critical drying equipment. It was claimed that [7] gels formed through an alkali silicate route could be dried with the help of a microwave oven if the pore size averaged 240 nm. Yamane [8] concluded that it was easier to achieve homogeneous mixing of the sol components with the colloidal route while Zarzycki [9] claimed that particulate gels were more resistant to capillary forces than alkoxide derived ones and underwent less drying shrinkage.

Table 1.

Example	Sodium silicate	Lithium polysilicate	Water	Gelation time	Working period
1	40 g	10 g	6 g	5 h 15 min	23 min
2	40 g	10 g	12 g	6 h 10 min	35 min
3	40 g	10 g	18 g	8 h 15 min	75 min

Casting with the use of Silicone Rubber and Thick Coatings on Dissolvable Substrates

It has been demonstrated that alkali silicate gels can be cast and released from both glass and plastic molds. However, work to date has been restricted to simple castings [10], further shaping being achieved with the use of cutting and shaping equipment [7].

In the Sol-Gel process the sol to wet gel stage is undertaken at ambient temperature, enabling the use of non-refractory mold materials, e.g., silicone rubber, gelflex. Silicone rubber, with its cold cure properties, enables casts to be taken from organic/inorganic material and from found/formed objects opening up a wide range of casting possibilities. The flexible nature of the rubber also allows for the casting of glass shapes that have undercut detail, a problem that would normally require a waste or piece mold to conclude successful casting.

Initial experiments with the Shoup route to alkali silicate gels had found that the gelation period could be extended (working period) proportional to the % of water in the starting sol, without any loss of structural integrity (Fig. 1). This extended period allowed for the gel to be poured into molds or, alternatively, a series of dippings/coatings could be undertaken manually, each coating averaging 0.5–1 mm. As bonding to the substrate was not required a range of dissolvable substrates (chalk, salt, wax) could be considered. Each material providing a substrate that can be carved and/or shaped prior to dipping into or coating with the viscous gel (see Table 1).

Experimental Procedures

Shoup had established that gelation time, pore size and distribution were dependent on the ratio of silicate solutions and/or colloidal silica. In attempting to achieve a stable gel that could be cast into molds or onto dissolvable substrates it was found that sodium silicate

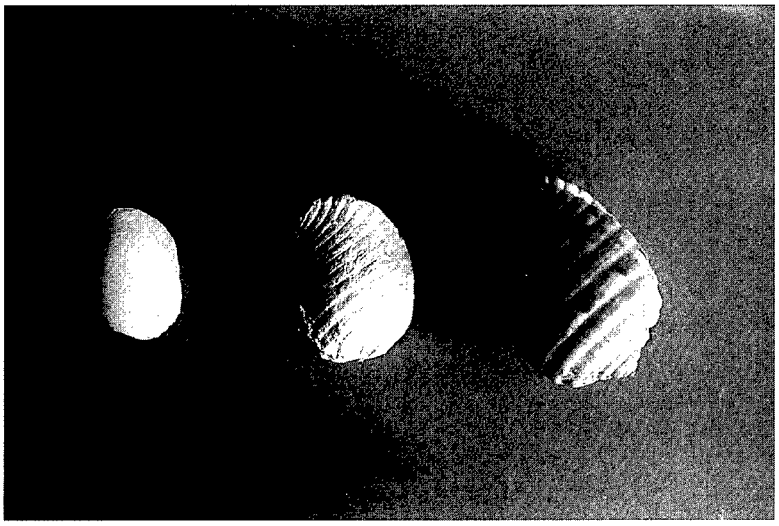

Figure 1. Original shell, cast/dried gel, consolidated form sintered at 1600°C.

combined with lithium polysilicate provided the most successful combination for homogeneous mixing. To explore the potential of these starting components in achieving crack-free castings three different compositions were undertaken (Fig. 2). Each were based on mixtures of *sodium silicate* (Na_2O SiO_2 H_2O)—composed of 9.4% Na_2O, 29.9% SiO_2, balance H_2O, *lithium polysilicate* (Li_2O SiO_2 $2H_2O$)—composed of 2.6% Li_2O, 18.7% SiO_2, balance H_2O with additions of *distilled water* and *formamide* as the organic catalyst.

Each sample was prepared by first mixing the sodium silicate and the water, then formamide was added slowly to achieve homogeneous mixing. Finally, the lithium polysilicate was added. All mixing was at ambient temperature.

Three different materials were chosen to prepare the coating of dissolvable substrates (the third was not dissolvable at the wet gel stage but would be combustible at the sintering stage): (1) chalk, (2) salt, and (3) cotton lace.

At the initial point of gelation (composition no. 3) the three test substrates were dipped into the viscous gel, the stability of the gel being dependent on; degree of gelation (the thickening of the gel due to chain-like networks being formed) surface of the substrate, absorbency of substrate.

The next stage was to allow the gel to give up some residual water and organics and this was accompanied by shrinking and a hardening of the gelled mass. At this point the substrates were either dissolved by relevant solvents, HCl for chalk, H_2O for salt, or left in place (cotton) for leaching with weak acids [2] (Shoup method) and then dried with the help of a microwave oven.

Consolidation of the porous, resultant structures was undertaken at temperatures between 1450°C and 1600°C.

Results

There were major differences in the gelling time, at ambient temperature. Sample 1 gelled within 3.3 h. Sample 2 within 2.6 h. Sample 3 within 5.4 h. Heating the gel at 40°C could reduce gelling time by at least 45–60 min. Importantly, gelling at ambient temperature resulted in an extended viscous stage. Conversely, heating the gel shortened the time available for coating or pouring into molds. Measurement of the pore sizes, using SEM indicated that a higher % of sodium silicate produced larger pores, a higher proportion of lithium polysilicate produced relatively smaller (see Table 2).

Table 2.

Example	Sodium silicate	Lithium polysilicate	Water	Formamide	Average pore size
1	25 g	25 g	6 g	5 g	60–80
2	10 g	40 g	6 g	5 g	10–20
3	40 g	10 g	6 g	5 g	160–180

In drying tests it was seen that samples 1 and 3 had low incidence of cracking but sample 2 was prone to cracking, especially when placed within a microwave oven. The average quality of the casting was good, with detail from the mold transferred to the wet gel successfully. Timing the removal of the soft gel from the mold was crucial to maintain a balance between retention of detail and dissolution in dispelled water/organics. It was observed that finer detail was recorded when the % of lithium polysilicate was higher than the sodium silicate.

All the dissolvable substrates accepted coatings ranging from 0.5 to 4 mm. These could be applied as either one thick coating or a series of 0.5 mm layers. When coating the salt it was observed that thick coatings over 1–2 mm were more successful than thin ones (under 0.5 mm). This could be achieved by coating towards the end of the gelation period, when the gel was more viscous. It was advantageous to allow the wet gel to consolidate partially before dissolving away the substrate; however, if shrinking was substantial major cracking would take place.

In sintering tests cracks appeared consistently in samples 1 and 2. Sample 3 produced some crack-free glass forms; however, these were opaque and some degree of distortion was always present.

Conclusion

At the present time there is a wide gap between the aims of the sol-gel scientist and the glass artist. However, the successful casting, drying and sintering of detailed monolithic shapes (Fig. 1), without the need for sophisticated drying equipment, has opened up possible directions for the glass artist. The sympathetic handling and behavioral properties offered by the colloidal alkali silicate gels establishes a positive foundation for future work. Advantages include having direct control over the forming process and the opportunity to employ inexpensive, innovative and reusable molding materials.

It is difficult to achieve intricacy of form at this higher range (1350–1600°C) as distortion is a problem and overall shrinkage, ranging from 40 to 60%, can make calculations for the finished form difficult. However, with transparency not being a critical criteria for the glass artist, the avoidance of leaching out the sodium salts and the addition of other metals would conceivably bring down the sintering temperatures without loss of the casting advantages.

References

1. R.J. Roy, Am. Ceram. Soc. **52**, 344 (1969).
2. R.D. Shoup and W.J. Wein, U.S. Patent 4,059,658 (1977).
3. E.M. Rabinovich, D.W. Johnson, J.B. McChesney, and E.M. Vogel, J. Non-Cryst. Solids **47**, 435 (1982).
4. G.W. Scherer and J.C. Luong, J. Non-Cryst. Solids **63**, 163 (1984).
5. G.W. Scherer, J. Non-Cryst. Solids **108**, 28 (1989).
6. L.L. Hench, in *Science of Ceramic Chemical Processing*, edited by L.L. Hench and D.L. Ulrich (John Wiley and Sons, New York, 1986), p. 52.
7. R.D. Shoup, Ceramic Bulletin **70**, 1505 (1991).
8. M. Yamane, *Sol-Gel Technology for Thin Films, Fibers, Preforms, Electronics and Speciality Shapes* (Noyes Publishers, NJ, 1988), p. 200.
9. J. Zarzycki, J. Non-Cryst. Solids **100**, 359 (1988).
10. R.D. Shoup, *Ultrastructure, in Processing of Advanced Ceramics*, edited by J. Mackenzie and D. Ulrich (John Wiley and Son, New York, 1988), p. 347.

Journal of Sol-Gel Science and Technology 13, 237–240 (1998)
© 1998 Kluwer Academic Publishers. Manufactured in The Netherlands.

Bioactive Gel Coatings Derived from Vinyltrimethoxysilane

KANJI TSURU, SATOSHI HAYAKAWA, CHIKARA OHTSUKI AND AKIYOSHI OSAKA
Biomaterials Laboratory, Faculty of Engineering, Okayama University, Tsushima, Okayama-shi 700-8530 Japan

Abstract. An ethanol (EtOH) solution of polymerized vinyltrimethoxysilane (VTMS), about 20-mers, was mixed with an aqueous solution of calcium acetate ($Ca(OAc)_2$) and refluxed in N_2 for 1 h to give sols of a typical composition $VTMS : H_2O : EtOH : Ca(OAc)_2 = 1 : 9 : 8 : 0.05$ (mol). Homogeneous films could be produced, by dip-coating, on Nylon6® and soda-lime glass, but not on polypropylene or polytetrafluoroethylene. The gel films did not deposit apatite within 14 days of soaking in a simulated body fluid whereas films abraded with emery paper as well as bulk gels deposited apatite on the surfaces within 7 days, indicating the present gel was suitable for bioactive coatings on Nylon6®.

Keywords: coating, bioactivity, apatite, Ca incorporation, silianol groups

1. Introduction

Implant materials may be as soft and strong as tissues to be substituted as well as bioactive, or they can bond to them spontaneously in the body environment. Kokubo and his co-workers [1] found that glass or glass ceramics with lime and silica as major ingredients formed a silica gel layer on their surface in the body environment, and that the layer served as nucleating sites for crystallization of calcium-deficient apatite which formed a bond with bone. However, they are too hard and brittle to be used as implants for softer tissue and for clinical materials such as tubes for which flexibility and softness of polymer materials are optimum. It is highly probable that organic polymers are bioactive if incorporating silanol groups and calcium ions since these are believed to play important roles in bioactivity [1]. Indeed, in a preliminary study [2], we have prepared such organic-inorganic composite gels, starting from vinyltrimethoxysilane, by sol-gel processing and have confirmed their bioactivity. It is expected that coatings of such bioactive gels may widen the biomedical use of organic polymer materials. In the present study we prepared such gels in a modified procedure, studied optimum conditions for developing homogeneous films on the polymers, and examined changes in bioactivity of the gels after coating.

2. Experimental

Vinyltrimethoxysilane was polymerized to 20-mers (PVTMS) with tertiary butyl peroxide as an initiator using refluxing for 2 h at 150°C in flowing nitrogen. An ethanol solution of PVTMS was mixed with an aqueous solution of calcium acetate and tetraethoxysilane and refluxed for 1 h at 80°C. Table 1 shows the final mixing ratios of the chemicals.

The sols prepared in this way were poured into polystyrene boxes sealed with wrapping film and were kept in an oven at 40°C to form bulk gels. The sols were dip-coated on substrates (15 × 10 × 1 mm in size) of commercially available polymers such as polyamide (Nylon6®), silicone, ABS, polyvinylchloride (PVC), polypropylene (PP), polytetrafluoroethylene (PTFE), and soda-lime glass (glass slides) where the pull-up speed was 1 mm/s. The coated substrates were kept at 25 or 40°C in atmospheres of 80 to 100% relative humidity. After dip-coating five times they were placed in an oven for 2 days at 40°C and for 2 days at 60°C.

The bulk gels and gel-coated substrates were soaked for up to 14 days in a simulated body fluid (SBF) with the Kokubo composition [3, 4]: it has an inorganic ion composition similar to that of human blood plasma, and in vitro experiments can reproduce well the reactions that may take place in vivo.

Table 1. The compositions of the organic-inorganic composite gels (mol) and their gelation times (day).

Gel	Mixing ratios (mol)[a]					Gelation time (day)	Description of bulk gel[b]
	VTMS	TEOS	EtOH	H_2O	$Ca(CH_3COO)_2$		
1	1.0	0	8.0	3.0	0.05	2	Op, htrg
2	1.0	0	8.0	9.0	0.05	1	Tr, hmg
3	1.0	0.5	8.0	9.0	0.05	1	Op, htrg
4	1.0	1.0	8.0	9.0	0.05	1	Op, htrg

[a]VTMS: vinyltrimethoxysilane, TEOS: tetraethoxysilane, EtOH: ethanol.
[b]Op: opaque, Tr: transparent, htrg: heterogeneous, hmg: homogeneous.

It was kept at 36.5°C and buffered at 7.4 in pH with tris(hydroxymethylaminomethane). The samples treated with SBF were examined with thin-film X-ray diffraction, Fourier transform infrared (FT-IR) reflection spectroscopy, and scanning electron microscopy (SEM).

3. Results and Discussion

Bulk Gels and Dip-Coated Gel Films

Table 1 describes the appearance of typical bulk gels. Addition of TEOS decreased homogeneity while greater water content depressed segregation and lead to a homogeneous gel (gel 2). Figure 1 showed thin film X-ray diffraction patterns for bulk gel 2, indicating deposition of apatite in 1 day of soaking in SBF. The composition of gel 2 was thus considered suitable for coating because of transparency, homogeneity, and bioactivity.

Homogeneous gel films could be developed from the final sols when they were kept in a 100% humid atmosphere 40°C after each dip-coating, whereas the films were cracked or easily peeled off when they were kept in atmospheres of relative humidity <80% after coating. For optimization we attempted to produce coatings from three sols with different ageing histories: (i) the sols (sol A) just after refluxing, (ii) those (sol B) kept at 40°C for half of the gelation time (12 h), and (iii) those (sol C) about to gel (aged ~1 day at 40°C). Sol A could be used successfully to coat substrates such as Nylon6®, ABS, PVC, polystyrene, and glass slides while only segregated films were obtained for PP, PTFE, and silicone due probably to less wetting of the substrate. The films on Nylon6® were 0.01, 0.07, and 0.12 mm thick for sols A, B, and C, respectively.

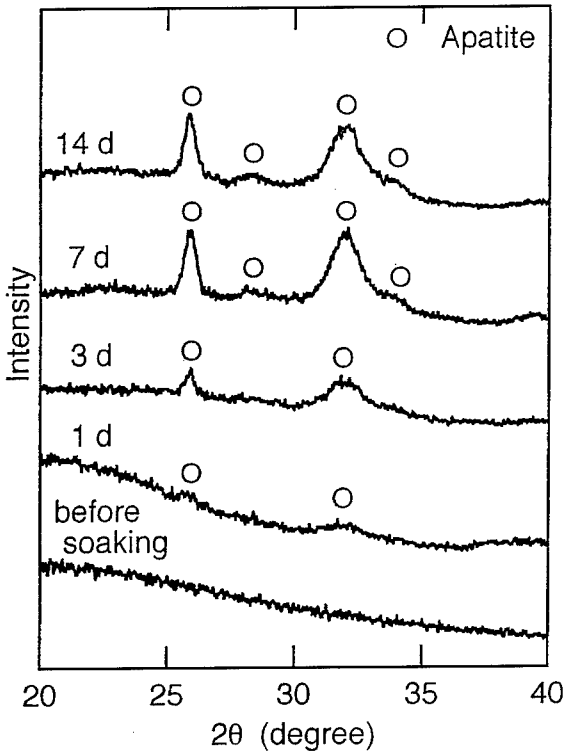

Figure 1. Thin film X-ray diffraction patterns for bulk gel 2. Apatite deposited in 1 day of soaking in SBF.

Thus a longer ageing time gave a thicker film since polymerization continued on ageing and increased the viscosities of the sols. From the above results we selected sol B of the gel 2 composition in Table 1 for developing coating films on Nylon6® substrates, and examined the bioactivity of the films.

Reflection FT-IR spectra did not suggest apatite deposition for the gel coatings on Nylon6® even after 14 days. Thin-film X-ray diffraction patterns also did

not indicate apatite formation. Thus, the coated gel films were not as bioactive as the corresponding bulk gels, indicating that the dip-coating process suppressed the bioactivity. Figures 2(a) and (b) show SEM photographs of the dip-coated gel films on Nylon6® after soaking in SBF for 14 days. The soaked film Fig. 2(a) was very similar in porous microstructure to the as-developed film. However, Fig. 2(b) indicates flaky crystallites near the cracks that grew in the gel film during the soaking in SBF. They mainly consisted of Ca and P from energy dispersive X-ray analysis. Moreover, the morphology of these crystallite aggregates was similar to the apatite crystals observed on bioactive glass surfaces after soaking in SBF [1, 3–5]. This indicated that the inner part of the gel coatings was bioactive, and it was only the outer surface of the films that lost bioactivity. Indeed, Fig. 3 indicates apatite crystals covering the whole gel film surface when the Nylon6® substrate with a gel film was soaked in SBF after abrading with emery paper.

Differences in the Bulk Gels and Coated Gel Films

Apatite formation requires dissolution of calcium ions into the SBF and nucleation sites provided by silanol

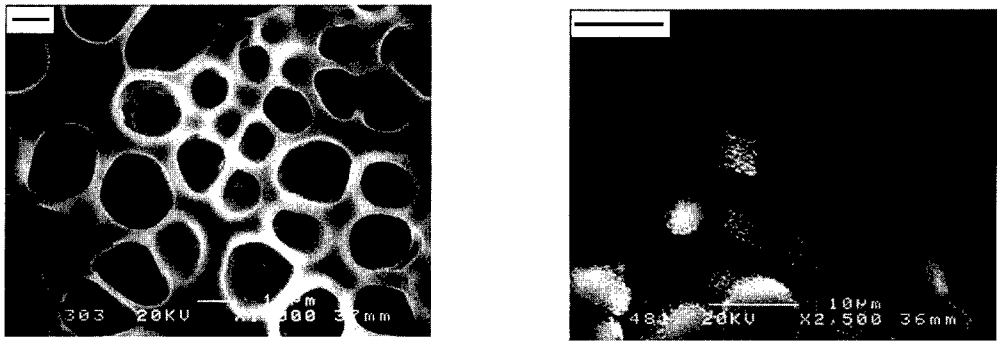

(a) (b)

Figure 2. SEM photographs of (a) the gel 2 film from solution B on Nylon6® after soaked in SBF for 14 days similar in microstructure to the as-coated gel 2 film, and (b) apatite crystallites near cracks in the gel 2 film after 14 days in SBF. Bar: 10 μm.

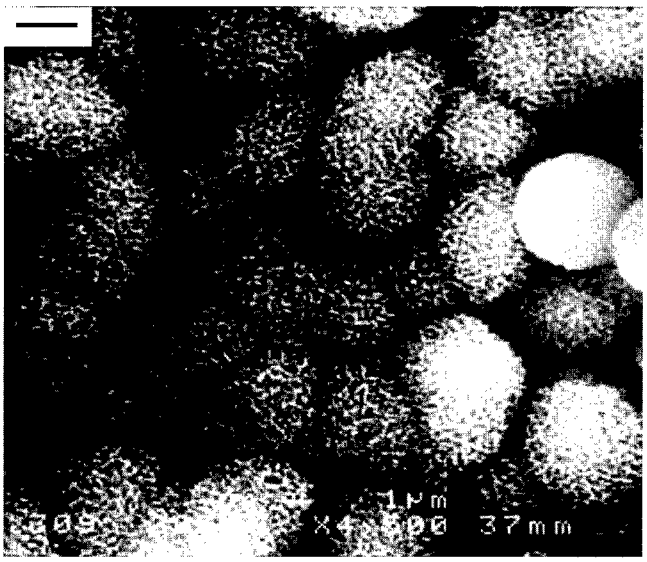

Figure 3. An SEM photograph of apatite grown on the gel 2 film scratched with emery paper on the surface before soaked in SBF for 14 days. Bar: 2 μm.

groups in direct contact with the SBF [4]. Moreover, the coated gel films were apparently hydrophobic and the bulk gels were hydrophilic. It follows that the gel film surface differs in structure from the inside of the film or the bulk gels: the film surface cannot provide nucleation sites consisting of silanol groups. The porous structure of the surface of the gel films in Fig. 2 indicates that the solvents may rapidly evaporate from the films during coating. On the other hand, in the bulk sols undergoing gelation there is enough solvent for the polymerizing species always to be in contact with each other and they can move around more freely. This leads to a stable polymerized Si—O—Si skeleton and to syneresis that takes place homogeneously in the whole gel body. Thus, we conclude that the present gel coating is suitable for application to polyamide since the inner film structure is favorable for depositing apatite.

4. Summary

An ethanol (EtOH) solution of polymerized vinyltrimethoxysilane (VTMS), about 20-mers, was mixed with an aqueous solution of calcium acetate ($Ca(OAc)_2$) and refluxed in N_2 for 1 h where a typical composition of the mixture was: $VTMS : H_2O : EtOH : Ca(OAc)_2 = 1 : 9 : 8 : 0.05$ (mol). The resultant sol was heated for 24 h at 40°C to produce a transparent bulk gel. The sol was also dip-coated on polyamide and gelled at 40°C. The bulk gel and the coated substrate were soaked in a simulated body fluid at 36.5°C: the bulk gel deposited apatite on the whole surface in 1 day while the gel coating with abraded surfaces deposited apatite within 7 days. It was concluded that the present gel was bioactive and suitable for bioactive coatings on polyamide.

Acknowledgment

Financial support to C. Ohtsuki by the Mazda Foundation was gratefully acknowledged.

References

1. T. Kokubo, J. Ceram. Soc. Japan. **99**, 965–973 (1991).
2. A. Osaka, C. Ohtsuki, and K. Tsuru, in *Bioceramics 8*, edited by J. Wilson, L.L. Hench, and D. Greenspan (Pergamon/Elsevier, New York, 1995), pp. 441–445.
3. C. Ohtsuki, T. Kokubo, and T. Yamamuro, J. Non-Cryst. Solids **143**, 84–92 (1992).
4. S.B. Cho, K. Nakanishi, T. Kokubo, N. Soga, C. Ohtsuki, T. Nakamura, T. Kitsugi, and T. Yamamuro, J. Am. Ceram. Soc. **78**, 1769–1774 (1995).
5. C. Ohtsuki, H. Kushitani, T. Kokubo, S. Kotani, and T. Yamamuro, J. Biomed. Mater. Res. **25**, 1363–1370 (1991).

Journal of Sol-Gel Science and Technology 13, 241–244 (1998)
© 1998 Kluwer Academic Publishers. Manufactured in The Netherlands.

Direct Electrical Wiring of Oxidoreductase Enzymes to Silicate Based Electrodes

S. BHARATHI, S. SAMPATH, J. GUN, L. RABINOVICH, Z. WU, I. PANKRATOV AND O. LEV
Division of Environmental Sciences, School of Applied Science, The Hebrew University of Jerusalem, Jerusalem, 91904, Israel

Abstract. Three types of reagentless glucose biosensor based on composite graphite-ormosil materials are described: (1) a redox modified silicate-graphite electrode doped with glucose oxidase, (2) a methyl silicate-graphite material doped with redox modified glucose oxidase, and (3) a methyl silicate and redox modified graphite composite material doped with glucose oxidase.

Keywords: chromatography, foams, macroreticular

Introduction

Sol-gel bioceramics are attracting increasing scientific and technological attention due to the compatibility between the inorganic support and the encapsulated biochemical species, making it possible to utilize both the biochemical reactivity and the favorable physical properties of inorganic materials. The optical transparency of silicates and other oxides directed most of the initial research efforts to optical sensing. The unique advantages of these materials for electrochemistry and electrochemical biosensing have only recently been recognized [1]. Notable advantages include the porosity, inertness and the mechanical and chemical stability of the supporting matrix. The encapsulation of bulky proteins can be very effective, resulting in zero leaching. Judicial selection of the characteristics of the porous surface can increase the stability and activity of the encapsulated enzyme compared to their native form [2–4]. Several sol-gel approaches for electrochemical biosensing have been proposed [3–8], all of which, except one [8], are dependent on the diffusion of either a mediator, reaction by-product or a reactant from the enzyme active center to the electrode surface. Thus, the electrochemical measurement can perturb the analyzed media, e.g., by depletion of oxygen in the vicinity of the probe or by leakage of a mediator from the support. The ultimate remedy to this problem is to provide alternative means of communication between the redox center of the enzyme and the electrode, e.g., by encapsulating mediators that have limited mobility but can still transport electrons by self-exchange mechanism. These are so-called reagentless electrodes, which are said to involve "direct wiring" of enzymes [1, 9]. The first attempts to facilitate direct electron transfer from the active enzyme center to electrode surfaces involved adsorption of enzymes on electrodes [10]. However, only few enzymes facilitate unmediated electron tunnelling from their redox centers to a conductive support. Glucose oxidase, the most useful oxidoreductase, is a bulky protein containing two flavin groups located far beyond the tunnelling distance. Encapsulation of active enzymes in conductive salts, conductive polymers and redox hydrogels [11–13] was suggested to circumvent the leaching problem and to improve enzyme-electrode communication. Heller and co-workers covalently bound redox moieties onto enzymes, which could then mediate the transfer of charge to the solid electrode by an electron hopping mechanism [1]. Willner and co-workers [14] designed mediator self-assembled monolayers, attached through a thiolate bond to a gold electrode. This system shuttled the charges from the enzyme to the electrode effectively. However, it was still restricted to planar geometry and thus had only limited enzyme loading and sensitivity.

This paper demonstrates recent designs of reagentless sol-gel biosensors. The different approaches are exemplified by glucose oxidase doped carbon-ceramic electrodes. Glucose sensing was selected because of the stability of the enzyme and its analytical significance. Composite carbon-silicate electrodes (CCEs), developed by our group [15] are made of a dispersion of carbon powder in organically modified or nonmodified sol-gel derived silicates. The electrodes are prepared by mixing an appropriate amount of graphite powder with the sol-gel precursors. Porous and brittle composite matrices are formed after gelation and drying. The composite electrodes benefit from the mechanical properties of the silicate backbone, the electron percolation conductivity through the interconnected carbon powder and the ability to manipulate the physicochemical characteristics of the matrix by incorporation of suitable monomer precursors or sol-gel dopants. Glucose oxidase based tetrathiafulvalene and ferrocene mediated glucose CCEs have also been reported [15–18]. Slow leaching of the mediator was, however, observed during prolonged operation.

Experimental

Preparation of Redox Silicate Biosensors. N(3-trimethoxy-silylpropyl)-ferrocenyl-acetamide was synthesized by DCC catalyzed amidization of 3-aminopropyltrimethoxysilane and ferroceneacetic acid in dichloromethane as described previously [19]. The electrode material was prepared by copolymerization of methyltrimethoxysilane, 3-aminopropyltrimethoxysilane and N(3-trimethoxysilylpropyl)-ferrocenylacetamide. The composite electrodes were prepared by mixing 0.08 ml methanol, 0.02 ml hydrochloric acid (0.01 M) catalyst, 1 ml methyltrimethoxysilane and 0.15 ml of ferrocene modified methoxysilane containing a ratio of 5 : 1 ferrocene to amine groups. The sol-gel precursors were sonicated for 1 min, followed by the addition of 100 mg glucose oxidase (G.O.D) (250,000 units/g, Aldrich). 1.0 g graphite powder (PP-200, Bay Carbon, MI, USA) was subsequently added and mixed thoroughly. The electrodes were prepared by filling 3 mm length of 1 mm inner diameter capillaries with the sol-gel-graphite mixture. The electrodes were then allowed to gel and dry in a refrigerator.

Preparation of 3D Organized Self-Assembled Monolayer Glucose Biosensors. The electrodes were prepared as described previously [20]. Graphite powder (pp-300, Bay Carbon, MI, USA) was mixed with $HAuCl_4 \cdot 3H_2O$ (Aldrich, USA) to yield 10 wt% of gold with respect to graphite. After drying at about 60°C overnight, reduction to Au metal was carried out in a 700°C hydrogen stream for 3 hours. The resulting gold-coated graphite powder was washed thoroughly and stored in a desiccator. Just before use, the gold-coated graphite powder was rinsed with concentrated HNO_3 and the acid was washed away with distilled water. The coated graphite powder was immersed in 0.02 M cystamine solution for 2 hours. It was then thoroughly rinsed in flowing distilled water to remove weakly absorbed cystamine. To attach a decaalkyl spacer, the cystamine modified powder was treated with 10% aqueous glutaraldehyde solution for about half an hour. The powder was thoroughly washed and treated with 0.05 M 1,10-diaminodecane. After washing with distilled water, ferrocene was attached to the SAM by overnight immersion of the powder with 10 mM solution of ferrocene acetic acid in 0.01 M HEPES buffer (pH 7.3) containing 10 mM of the water soluble carbodiimide coupling agent (1-ethyl-3-(3-dimethylaminopropyl)carbodiimide). The resulting material was washed and dried. Subsequently, G.O.D was absorbed onto the material by mixing aqueous enzyme solution with the modified powder to yield a loading of 25 wt% of the enzyme with respect to modified graphite. This was left in a desiccator at 4°C. The sol used in the present study was prepared by mixing 0.8 ml methyltrimethoxysilane with 0.5 ml water and 0.1 ml of 0.1 M HCl and sonicating for 10 min. The mixed sol was stored in a refrigerator overnight. A required amount of the sol was then mixed with the SAM modified, G.O.D adsorbed powder to yield 40% (w) graphite and molded in glass capillaries of 3–4 mm diameter.

Encapsulation of Ferrocene Modified Glucose Oxidase in Carbon Methyl-Silicate Composite Material. The derivatization of glucose oxidase was carried out according to the procedure of Degani and Heller [1]. 80 mg of ferrocene-carboxylic acid was dissolved in 4 ml of Na-HEPES buffer and the pH was adjusted to be between 7.2 and 7.3. DEC (100 mg) was added followed by urea (810 mg). Subsequently, 60 mg of G.O.D was added after adjusting the pH of the solution to 7.2. The solution was maintained on an ice bath for about 24 hours. The turbid mixture was then centrifuged and the clear liquid passed through a 0.2 mm membrane filter. Subsequently, the modified

enzyme was separated by passing the liquid through a sephadex column. The separated enzyme solution was then lyophilized to produce a powder of ferrocene attached glucose oxidase. The modified enzyme CCEs were prepared by the following method: 25 mg of the lyophilized enzyme was dissolved in distilled water (4°C) and immediately mixed with 100 mg graphite. This mixture was kept in a desiccator at 4°C. The silica sol and the electrode were prepared by the procedure described earlier.

All experiments were conducted in pH 5.6 at ambient temperature (210°C) and the potential is reported versus saturated calomel electrode (SCE).

Results and Discussion

Figures 1B–D demonstrate cyclic voltammograms of the three types of ferrocene mediated, reagentless electrodes, with and without dissolved glucose, compared to the response of a glucose oxidase doped CCE without any mediator or catalyst (Fig. 1A). The mediatorless glucose electrode operates at high overvoltage, approximately 1.0 V, and its response is sensitive to the level of dissolved oxygen in the sample. The other reagentless electrodes could operate at 0.2 V/SCE, which is determined by the choice of mediator (ferrocene). This makes the electrodes less susceptible to the presence of reducing agents in the solution. All three reagentless electrodes are almost indifferent to the oxygen content of the solution, in contrast to the mediatorless electrode, which is totally inhibited in the absence of dissolved oxygen. The three reagentless electrodes were stable for several months when kept in a refrigerator. Unlike the ferrocene doped electrodes all four electrodes depicted in Fig. 1 did not exhibit any leaching of the mediator or the enzyme during prolonged immersion in water. Detailed metrological comparison between the characteristics of the three mediatorless electrodes is beyond the scope of this short review because these were highly dependent on the thickness of the wetted active section, which in turn, depends on the composition and preparation conditions of the biosensors.

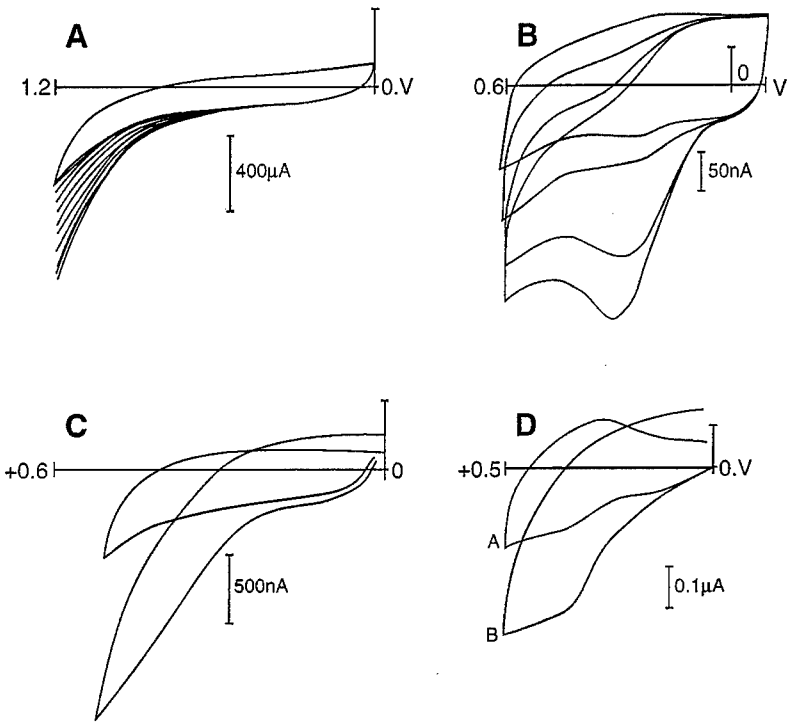

Figure 1. Cyclic voltammetry of unmediated and reagentless CCEs. (A) Nonmediated biosensors, curves correspond to 0 to 20 mM glucose at increasing additions of 2 mM each; $v = 5$ mV/s; (B) redox modified graphite CCE (blank, 5, 10, 20 mM of Glucose; $v = 10$ mV/s); (C) redox modified silicate CCE (blank, 20 mM of Glucose, $v = 5$ mV/s); (D) redox modified enzyme CCE (blank, 6 mM of Glucose; $v = 5$ mV/s).

There are basically three ingredients in the CCE biosensors: (a) ormosil backbone; (b) graphite powder and (c) enzymes. This paper has demonstrated that each of these components can be modified with a charge mediator that can shuttle electrons between the active center of the enzyme and the interconnected graphite network. In principle, for all three types of electrodes, the current is mediated by electron hopping between adjacent ferrocenyl groups. In the redox modified silicate biosensor methylsilane is added to grant hydrophobicity and the aminosilane is added to buffer changes in hydrophobicity caused by the oxidation/reduction of the ferrocene/ferrocinium couple. In the SAM CCE gold coating was added to support the self-assembled monolayer and a decyl spacer served as an extended arm that can reach the active center of the enzyme. Of the three approaches described above encapsulation in redox modified silicate is the most promising because practically all the enzymes in the network are effective. In the other two types of reagentless electrodes discussed only the enzymes that are in close contact with the percolating carbon powder can contribute to the charge transfer.

Acknowledgment

We thankfully acknowledge the support of the GBF-MOS.

References

1. A. Heller, Acc. Chem. Res. **23**, 128 (1990).
2. M.T. Reetz, A. Zonta, and J. Simpelkamp, Angew. Chem. Int. Ed. Engl. **34**, 301 (1995).
3. D. Avnir, S. Braun, O. Lev, and M. Ottolenghi, Chem. Mater. **6**, 1605 (1994).
4. S. Braun, S. Rappoport, R. Zusman, D. Avnir, and M. Ottolenghi, Mat. Lett. **10**, 1 (1990).
5. Y. Tatsu, K. Yamashita, M. Yamaguchi, S. Yamamura, H. Yamamoto, and S. Yoshikawa, Chemistry Letters, 1619 (1992).
6. P. Audebert, C. Demaille, and C. Sanchez, J. Chem. Mater. **5**, 911 (1993).
7. V. Glezer and O. Lev, J. Am. Chem. Soc. **115**, 2533 (1993).
8. T.M. Park, E.I. Iwuoha, M.R. Smyth, and B.D. MacCraith, Anal. Commun. **3**, 271 (1996).
9. I. Willner and A. Riklin, Anal. Chem. **66**, 1535 (1994).
10. R.M. Iannielo, T.J. Lindsay, and A.M. Yacynych, Anal. Chem. **54**, 1098 (1982).
11. W.J. Albery, P.N. Bartlett, and D.H. Craston, J. Electrochem. Chem. **194**, 223 (1985).
12. M. Pravda, C.M. Jungar, E.I. Iwuoha, M.R. Smyth, K. Vytras, and A. Ivaska, Anal. Chim. Acta. **304**, 127 (1995).
13. P.D. Hale, L.I. Boguslavsky, T. Inagaki, H.I. Karan, H.S. Lee, and T.A. Skotheim, Anal. Chem. **63**, 677 (1991).
14. I. Willner, A. Riklin, and N. Lapidot, J. Am. Chem. Soc. **112**, 6438 (1990).
15. M. Tsionsky, G. Gun, V. Glezer, and O. Lev, Anal. Chem. **66**, 1747 (1994).
16. S. Sampath and O. Lev, Anal. Chem. **68**, 2015 (1996).
17. M. Tsionsky and O. Lev, Anal. Chem. **67**, 2409 (1995).
18. I. Pankratov and O. Lev, J. Electroanal. Chem. **393**, 35 (1995).
19. J. Gun and O. Lev, Anal. Lett. **29**, 1933 (1996).
20. S. Sampath and O. Lev, Adv. Mater. **9**, 410 (1997).

Journal of Sol-Gel Science and Technology 13, 245–250 (1998)
© 1998 Kluwer Academic Publishers. Manufactured in The Netherlands.

Molecular Control of Bioactivity in Sol-Gel Glasses

LARRY L. HENCH
Department of Materials, Imperial College of Science, Technology and Medicine, London, England

DONNA L. WHEELER
Orthopaedic Research Laboratory, Oregon Health Sciences University, Portland, OR, USA

DAVID C. GREENSPAN
US Biomaterials Corporation, Alachua, FL, USA

Abstract. Bioactive materials can be divided into: Class A bioactive glasses which exhibit rapid bonding to bone and soft connective tissue and are osteoproductive, and osteoconductive; and Class B bioactive ceramics, which bond slowly only to bone and are only osteoconductive. Bioactive sol-gel glasses composed of SiO_2-CaO-P_2O_5 have Class A behavior in vitro and in vivo and also resorb as they enhance the proliferation of new trabecular bone.

Keywords: bioactivity, bone growth, porosity, osteoconduction

Introduction

Bioceramics are special compositions of ceramic materials in the form of powders, coatings, or bulk devices that are used to repair, augment or replace diseased or damaged tissues, usually bones, joints or teeth [1, 2]. Clinical use of bioceramics is rapidly expanding because of the increasing rate of failure of metallic or polymeric prostheses [3]. Bioceramics exhibit all four types of tissue response; (1) nearly inert, (2) porous ingrowth, (3) bioactive, (4) resorbable, depending on composition, crystallinity, and thickness of coatings or size of particulates [4]. Bioactive ceramics, glasses and glass-ceramics comprise a special group of biomaterials that form a mechanically strong bond to bone by means of a series of chemical reactions at the bone-tissue interface [1, 7]. There is increasing clinical use of bioactive implant materials because they offer the possibility of improving long-term clinical survivability of prostheses and improved repair of aged, diseased or damaged bone [3].

Class A and Class B Bioactivity

There are two classes of bioactivity, which depend upon the rate of tissue response to the implant [3, 6, 7]. Rate of bonding depends greatly on the composition and microstructure of the bioactive materials. Glasses with the most rapid bone bonding, termed Class A bioactivity, also bond to soft connective tissues, such as the tympanic membrane (eardrum). Characteristics of Class A, *osteoproductive*, bioactive materials are compared with Class B, *osteoconductive* materials in Table 1 [4, 6, 7]. Kinetics of surface reactions and ion dissolution influence the response of cells and determine whether Class A or Class B bioactivity occurs. Figure 1 summarizes the stages of material reactions and the biochemical responses that occur at the interface of a Class A bioactive implant with bone [4, 6]. Note the logarithmic time scale of the reaction stages; also note that reaction Stage 6, adsorption of biological molecules, overlaps Stages 3 through 9. The rate of formation of an inorganic silica gel layer (Stage 3), and development

Table 1. Bioactive materials.

Class A	Class B
Osteoproductive and osteoconductive	Only osteoconductive
Rapid bonding to bone	Slow bonding to bone
Enhanced bone proliferation	No enhancement of bone proliferation
Bonding to soft connective tissues	No bonding to soft connective tissues

of a hydrated hydroxyl carbonate apatite (HCA) layer (Stages 4 and 5) affect the attachment and differentiation of osteoprogenitor stem cells (Stages 8 and 9) and therefore the rate of growth and proliferation of bone [7].

Materials that exhibit Class A bioactivity have improved long-term survivability of implants due to both soft and hard tissue bonding which prevents micromotion of the implant. Prostheses that replace the bones of the middle ear are an excellent example of the difference in survivability of Class A bioactive implants compared with bioinert (polyethylene) or Class B bioactive implants (synthetic hydroxyapatite, HA) [3, 4]. Class A bioactive glass implants used to replace the roots of teeth for patients wearing dentures also have superior long-term survivability compared with Class B synthetic HA implants [3, 4].

When particles are implanted in bone to fill a bone defect, Class A bioactive glasses produce bone throughout the particulate array. This behavior is termed *osteoproduction*, defined by Wilson as "The process whereby a bioactive surface is colonised by osteogenic stem cells free in the bone defect environment as a result of surgical intervention" [1, 4, 7]. A Class A bioactive material exhibits both osteoproduction and osteoconduction. *Osteoconduction* is defined as "The process of bone migration along a biocompatible surface" [1]. A material with Class B bioactivity, such as synthetic HA, exhibits osteoconduction but does not exhibit osteoproduction. Thus, a Class B bioactive material leads to a very slow bond to bone and slow and incomplete proliferation of bone throughout a particulate array.

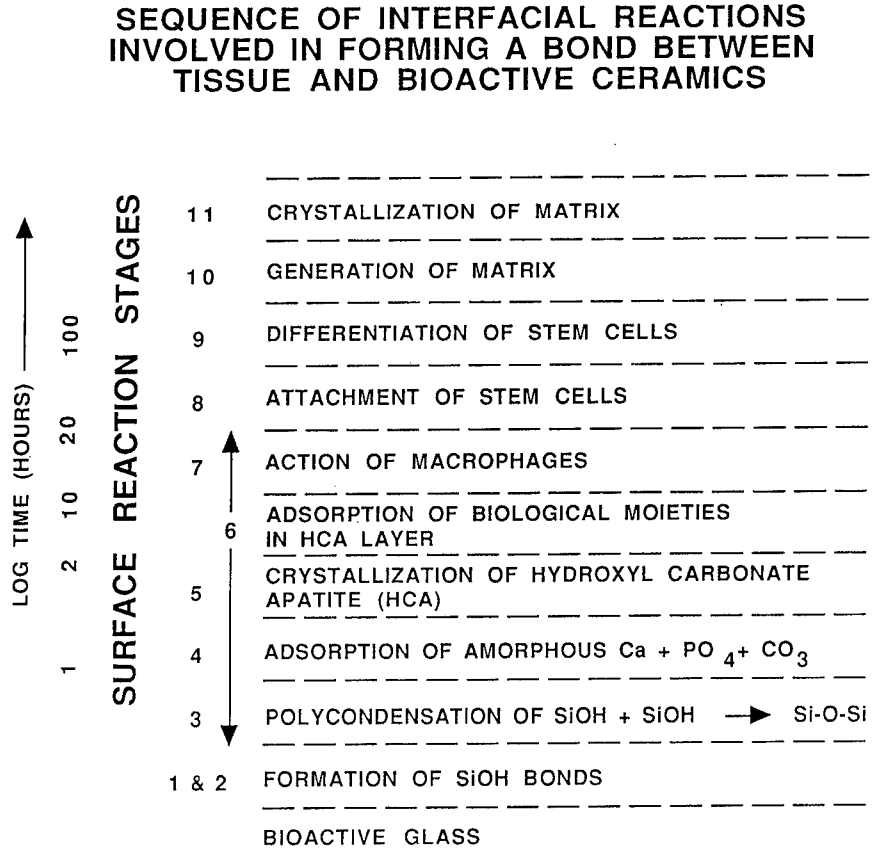

Figure 1. Sequence of interfacial reactions involved in forming a bond between living tissue and bioactive glasses.

Table 2. Glass and gel-glass compositions in mol%.

Sample	SiO_2	Na_2O	CaO	P_2O_5
45S5 Bioglass®	46.1	24.4	26.9	2.6
58S	60	0	36	4
77S	80	0	16	4

Structure, composition and surface chemical kinetics determine whether a material will exhibit Class A or Class B bioactivity. The rate of formation of the inorganic silica gel and HCA layer is more rapid for Class A bioactive materials than Class B materials, Fig. 1. The HCA layer develops as crystallized carbonated hydroxyapatite crystals within 2–6 hours on the most bioactive glass, 45S5 Bioglass® (Table 2). On materials with Class B bioactivity 2 to 30 days are required for the HCA layer to nucleate and crystallize.

Importance of Silica Gel Formation

On Class A bioactive glass surfaces the mechanism of formation of the hydrated silica gel layer (Stage 3 in Fig. 1) is polycondensation of silanols created during the ion exchange of protons for Na^+ ions from the glass [4]. The silica gel layer forms within minutes of exposure of a Class A bioactive material to water and is fully polymerized within 2 hours. The silica gel layer grows to 30 μm by 30 days on 45S5 Bioglass®. The growing silica gel layer serves several functions. The high surface area and low isoelectric point provide chemisorption sites for Ca and P ions which nucleate HCA crystals. Understanding the behavior of biological molecules within silica gel matrices has become a field of intense research. The porous 3D network of a gel is completely interpenetrated with a pore liquid and a wide range of inorganic, organic and biological molecules can be incorporated within the pore liquid networks [8–14]. This makes the sol-gel process attractive for producing controlled interactions between inorganic materials with biological molecules and living organisms as well as for implants and drug delivery.

Sol-Gel Chemistry and Biochemistry

Exploiting the overlap between sol-gel chemistry and biochemistry is a fruitful area of recent research [8–16] leading to the following generalizations:

(1) Most organic or biomolecules can be entrapped within sol-gel networks and retain their conformation and physical characteristics, including biological activity.
(2) Entrapped molecules are accessible to external reagents by diffusion through the pore network which enables chemical reactions to occur between reagent and the entrapped molecules.
(3) Many gel matrices are transparent to UV and visible wavelengths of light, which makes it possible to couple optics and photochemistry with entrapped molecules.
(4) Net shape and net surface components can be made by casting the sol into precision molds.
(5) Hybrid optics with biomolecular and catalytic capabilities are possible by incorporating organic molecules in the sol prior to casting or by impregnating the molecules into a preformed gel matrix following drying and stabilization.
(6) Sol-gel coatings can be applied to films, fibers, capillaries and devices to produce a controlled interface with biological molecules. It is possible to coat bioinert polymeric materials with inorganic layers to render them bioactive.
(7) Particulates can be made with controlled size and shape and controlled size, distribution and connectivity of porosity.
(8) Porous sol-gel networks can provide heterogenous nucleation sites for growth of biological apatite layers leading to controlled surface chemistry, isoelectric points and the adsorption/desorption of biological molecules while maintaining their conformation.
(9) Bioactive glasses with Class A bioactivity can be made by the sol-gel process.
(10) Bio sol-gel systems can be combined to create hierarchical substrates and matrices that mimic the nanometer to micrometer range of structures of biological systems.

Bioactive Sol-Gel Coatings

Common to all known bioactive materials is formation of a biologically active HCA layer (Stages 4 and 5 in Fig. 1) in the presence of in vivo body fluids or in vitro simulated body fluids (SBF). Bioactive sol-gel coatings of HCA have been made on various substrates; porous sol-gel silica [17–20], sol-gel organically modified silicates [21] sol-gel titania [22–24] Ti-HA composite [25], sol-gel zirconia [26, 27]. Mechanisms of nucleation and growth of HCA on silica gel substrates are controversial. The relative importance of surface silanol groups, surface structural defects [17,18] (such

as trisiloxane rings), pore size and pore volume [17] and adsorption of silicate ions dissolved from the silica gels [19] on the rate and structure of HCA from SBF have been considered. Evidence favors heterogeneous nucleation of HCA crystals in the nanometer size pore networks of the silica gels [17]. Chemical treatment of Ti with NaOH aqueous solutions also creates surfaces that grow HCA layers and form a strong bond to bone [28].

Bioactive Sol-Gel Glasses

Sol-gel processing can be used to make bioactive gel glasses containing SiO_2-CaO-P_2O_5 [29–31]. The seven processing steps are equivalent to making pure silica gels; however, temperature of stabilization and densification is lower due to the network modifiers in the silica gel network [7, 29–31]. Densification temperature increases with the silica content in the system. The amount of silica in bioactive sol-gel glasses can be higher than in melt-derived glasses and still exhibit bioactivity (Fig. 2). Rate of HCA formation and index of bioactivity is higher for the sol-gel glasses [29–31], attributed to more release of soluble silica that nucleates HCA crystals in the nanometer sized pores of the gel glass [32, 33].

Table 3. Composition and texture of sol-gel bioglass®.

ID	Composition	Bulk density (g/cm^3)	Pore diameter (Å)	Surface area (m^2/g)
SGl	77S	1.23	40	389
SG2	58S	0.99	86	207
BG	45S5	2.65	N/A	0.02

Evidence of in vitro bioresorption of 58S and 77S gel glasses (compositions and textures are in Table 3) correlates with animal data [34, 35]. Enhanced degradability of bioactive gel glasses gives control over in vivo resorption when used as a bone graft material. This is important because the ideal synthetic bone graft is one that is completely replaced with newly formed bone without loss in strength during bone remodelling. Control of texture of bioactive gel glasses by varying the ageing and thermal processing steps makes it possible to tailor the rate of degradability.

Figure 3 compares the amount of soluble silicon released into a simulated body fluid at 37°C over 10 days for a 45S5 melt-derived particulate array versus particles of gel glass of the same particle size (300–710 μm). The physical characteristics of the two materials are compared in Table 3. The 58S gel glass was prepared by acid hydrolysis of tetraethoxysilane with additions

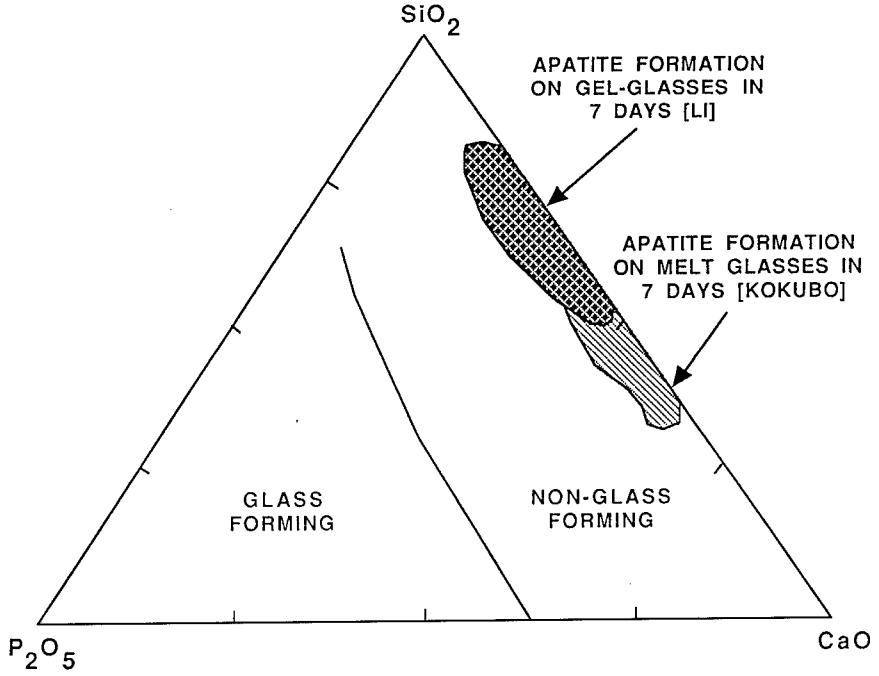

Figure 2. Compositional range of bioactivity of sol-gel glasses versus glasses made by melting and casting.

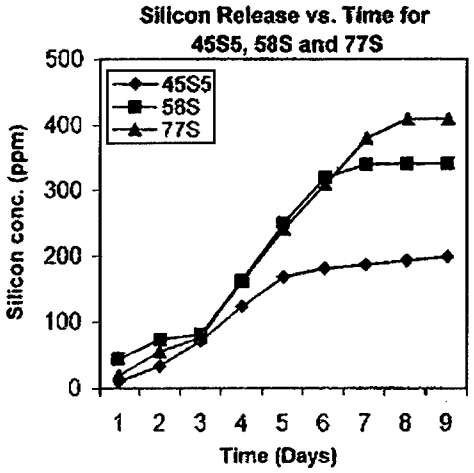

Figure 3. Release of Si from 58S and 77S bioactive gel glasses versus 45S5 melt-derived glass.

of triethylphosphate and calcium nitrate as previously described [29, 36]. The 58S gel was heat-treated in air at 700°C in ambient atmosphere. The resulting average pore radius, based on N_2 adsorption isotherm analysis, was 43 Å, Table 3. Powders were exposed to simulated body fluid (SBF 9) in an orbital shaker for 1 hour to 28 days [37].

Both materials leach silica rapidly during the first few hours in solution (Fig. 3). After 6 hours the gel glasses continue a high leach rate whereas the leach rate of the melt-derived particles decreases and levels off at 180 ppm. The gel glasses leach silica until a level of 340 and 400 ppm are reached. The higher leach rates for the gel glasses are interesting even though they have higher contents of silica network former compared with the melt glass. The enhanced in vitro resorbability of the sol-gel glass particles is attributed to interconnected pore structures, high surface areas and low density of the particles. A high surface area material with interconnected pore network increases rates of ion exchange and especially network dissolution of a glass which releases all constituent ions into solution. Soluble silica is required for bone mineralization [7]. Thus, it is possible to design a gel glass for specific rates of silica release by controlling composition and thermal history and thereby affect rate of bone mineralization and resorption of the implanted particles.

In vivo Behavior of Bioactive Gel Glasses

Animal tests of sol-gel glasses containing CaO-P_2O_5-SiO_2 demonstrate osteoproduction and osteoconduction; i.e., Class A bioactivity. The bioactive gel-glasses exhibit a greater rate of resorption than melt-derived 45S5 Bioglass® particles.

Histological and biomechanical evaluations of bone formed within rabbit distal femoral cancellous bone defects filled with 45S5 Bioglass® particulates (BG), and 77S and 58S bioactive sol-gel glass particulates were compared with normal cancellous bone and unfilled control defects [34, 35]. At four weeks extensive bone grew in 6 mm holes drilled in rabbit femurs when the holes were filled with bioactive gel glass [34]. Active mineralization occurs throughout the grafted defects with osteoblasts lining the new bone formed around the gel glass particulates [34].

All grafted defects had more bone within the area than unfilled controls. Average size of the BG particles was initially smaller than the 58S and 77S particles; however, the gel glass particles significantly resorbed by 12 weeks when compared with the Bioglass® particles ($p < 0.05$). There were also significantly more BG particles within the defect after 12 weeks when compared with 58S and 77S particles ($p < 0.05$). Both sol-gel glasses resorbed with time whereas there was little change in size of Bioglass® particles. BG-filled defects exhibited greater early bone growth than gel glass-filled defects. By the end of 12 weeks the amount of bone within the gel glass-filled defects was equivalent to BG sites. Because the gel glass particles exhibited greater resorption than BG particles, the bone-to-graft ratio was higher for the gel glass-grafted defects.

The compressive strength of the graft site, composed of a mixture of new bone and partially resorbed gel-glass particles, was significantly greater than the control defect [35]. Mechanically, all grafted defects had equivalent compressive modulus to normal cancellous bone. The effect of the enhanced compressive modulus on ability to bear in vivo loads is an especially important factor in the long-term behavior of bone grafted sites.

Conclusions

As the average age of people increases there is a growing demand for materials that enhance the repair and regeneration of bone. Bioactive sol-gel glasses provide a new approach to control the rate of bone repair and offer the advantage of controlled rate of resorption while being replaced by newly regenerated bone. Mechanical properties of bone produced through resorption of the bioactive gel glasses appear equivalent to normal cancellous bone. Molecular tailoring of bioactivity of

the gel glasses is possible by using composition, texture and thermal processing to control rates of surface reactions and network dissolution.

References

1. L.L. Hench and J. Wilson (Eds.), *Introduction to Bioceramics* (World Scientific, Singapore 1993).
2. B.D. Ratner, A.S. Hoffman, F.J. Schoen, and J.E. Lemons (Eds.), *Biomaterials Science: An Introduction to Materials in Medicine* (1996), p. 484.
3. L.L. Hench and J. Wilson (Eds.), *Clinical Performance of Skeletal Prostheses* (Chapman and Hall, London, 1996).
4. W. Cao and L.L. Hench, Bioactive materials, *Ceramics International* **22**, 493–507 (1996).
5. T. Kokubo, A/W Glass-ceramic: Processing and properties, in *Introduction to Bioceramics*, edited by Hench and Wilson (World Scientific, Singapore, 1993), pp. 75–88.
6. L.L. Hench, Bioactive ceramics: Theory and clinical applications, in *Bioceramics 7*, edited by O.H. Andersson and A. Yli-Urpo (Butterworth-Heinemann Ltd., Oxford, England, 1994), pp. 3–14.
7. L.L. Hench and J.K. West, Biological applications of bioactive glasses, *Life Chemistry Reports* **13**, 187–241.
8. J. Livage, Sol-gel processes, *Current Opinion in Solid State & Materials* **2**, 132–138 (1997).
9. R.M. Almeida and L.M. Ilharco (Eds.), *Journal of Sol-Gel Science and Technology* **8** (1–3), (1997).
10. D. Avnir, L.C. Klein, D. Levy, U. Schubert, and A.B. Wojcik, Organo-silica sol-gel materials, in *The Chemistry of Organosilicon Compounds—Part 2*, edited by Y. Apeloig and Z. Rappoport (Wiley & Sons, Chichester, 1997).
11. S. Braun and D. Avnir (Eds.), *Journal of Sol-Gel Science and Technology, Special Issue; Biochemical Aspects* **7**(1/2), (1997).
12. C.J. Brinker, N.K. Raman, M.N. Logan, R. Sehgal, R.A. Assink, D.W. Hua, and T.L. Ward, Structure-property relationships in thin films and membranes, *Journal of Sol-Gel Science and Technology* **4**, 117–135 (1995).
13. L.L. Hench and R. Orefice, Sol-gel technology, *Kirk-Othmer Encyclopedia of Chemical Technology*, 4th edition (J. Wiley & Sons, New York, 1997), Vol. 22, pp. 497–528.
14. J. Livage, C. Roux, J.M. da Costa, I. Desportes, and J.F. Quinson, Immunoassays in sol-gel matrices, *Journal of Sol-Gel Science and Technology* **7**, 45–51 (1996).
15. J. Zarzycki, Past and present of sol-gel science and technology, *Journal of Sol-Gel Science and Technology* **8**(1–3), (1997).
16. T.J. Pinnavaia and M.F. Thorpe (Eds.), *Access in Nanoporous Materials* (Plenum Press, New York, 1995).
17. M. Pereira and L.L. Hench, Mechanisms of hydroxyapatite formation on porous gel-silica matrices, *Journal of Sol-Gel Science and Technology* **7**, 45–51 (1996).
18. S.B. Cho, K. Nakanishi, T. Kokubo, N. Soga, C. Ohtsuki, and T. Nakamura, Apatite formation on silica gel in simulated body fluid: Its dependence on structures of silica gels prepared in different media, *Journal of Biomedical Materials Research (Applied Biomaterials)* **33**, 145 (1996).
19. S.B. Cho, F. Miyaji, T. Kokubo, K. Nakanishi, N. Soga, and T. Nakamura, Apatite-forming ability of silicate ion dissolved from silica gels, *Journal of Biomedical Material Research* **32**, 375–381 (1996).
20. P. Li, T. Kokubo, K. Nakanishi, and K. de Groot, Induction and morphology of hydroxyapatite, precipitated from metastable simulated body fluids, on sol-gel prepared silica, *Biomaterials* **14**, 963–968, (1993).
21. K. Tsuru, C. Ohtsuki, and A. Osaka, Bioactivity of sol-gel derived organically modified silicates, *Journal of Materials Science: Materials in Medicine* **8**(3), (1997).
22. P. Li, C. Ohtsuki, T. Kokubo, K. Nakanish, N. Soga, and K. de Groot, Bonelike hydroxyapatite induction by sol-gel derived titania coating on a titanium substrate, *Journal American Ceramic Society* **77**, 1307–1315 (1994).
23. D.B. Haddow, S. Kothari, P.F. James, R.D. Short, P.V. Hatton, and R. van Noort, Synthetic implant surfaces, *Biomaterials* **17**, 501–507 (1996).
24. D.B. Haddow, P.F. James, and R. van Noort, Characterisation of sol-gel surfaces for biomedical applications, *Journal of Materials Science: Materials in Medicine* **7**, 250–260 (1996).
25. P. Li, K. de Groot, and T. Kokubo, Bioactive $Ca_{10}(PO_4)_6(OH)_2$-TiO_2 composite coating prepared by sol-gel process, *Journal of Sol-Gel Science and Technology* **7**, 27–34 (1996).
26. M.J. Filiaggi, R.M. Pilliar, R. Yakubovich, and G. Shapiro, Evaluating sol-gel ceramic thin films for metal implant applications. I. Processing and structure of zirconia films on Ti-6A1-4V, *Journal of Biomedical Material Research (Applied Biomaterials)*, **33**, 225–238 (1996).
27. M.J. Filiaggi, R.M. Pilliar, and D. Abdulla, Evaluating sol-gel ceramic thin films for metal implant applications. II. Adhesion and fatigue properties of zirconia films on Ti-6AI-4V, *Journal of Biomedical Materials Research (Applied Biomaterials)* **33**, 239–256 (1996).
28. H.-M. Kim, F. Miyaji, T. Kokubo, and T. Nakamura, Preparation of bioactive Ti and its alloys via simple chemical surface treatment, *Journal of Biomedical Materials Research* **32**, 409–417 (1996).
29. R. Li, A.E. Clark, and L.L. Hench, Effect of structure and surface area on bioactive powders made by sol-gel process, in *Chemical Processing of Advanced Materials*, edited by L.L. Hench and J.K. West (J. Wiley and Sons, New York, 1992), pp. 627–633.
30. M.M. Pereira, A.E. Clark, and L.L. Hench, Homogeneity of bioactive sol-gel derived glasses in the system CaO-P_2O_5-SiO_2, *Journal of Materials Synthesis and Processing* **2**(30), 189–196 (1994).
31. M.M. Pereira, A.E. Clark, and L.L. Hench, Calcium phosphate formation on sol-gel derived bioactive glasses in vitro, *Journal of Biomedical Materials Research* **18**, 693–698 (1994).
32. D.C. Greenspan, J.P. Zhong, G.P. LaTorre, and M. Booher, The in-vitro degradability of sol-gel Bioglass®, *Transactions 23rd Annual Meeting of the Society for Biomaterials* (New Orleans, LA, 1997).
33. H. Oonishi, S. Kutrshitani, E. Yasukawa, H. Iwaki, L.L. Hench, J. Wilson, E. Tsuji, and T. Sugihara, Particulate Bioglass® and hydroxyapatite as a bone graft substitute, J. Clinical Orthopaedics and Related Research **334**, 316–325 (1997).
34. D.L. Wheeler and K.E. Stokes, In vivo evaluation of sol-gel Bioglass®. Part I: Histological findings, *Transactions 23rd Annual Meeting of the Society for Biomaterials* (New Orleans, LA, 1997).
35. D.L. Wheeler, R.G. Hoellrich, S.W. McLoughlin, D.L. Chamerland, and K.E. Stokes, In vivo evaluation of sol-gel Bioglass®—Biomechanical findings, in *Bioceramics 10*, edited by L. Sedel (Elsevier, Oxford, 1997).

Journal of Sol-Gel Science and Technology 13, 251–254 (1998)
© 1998 Kluwer Academic Publishers. Manufactured in The Netherlands.

Nucleation of Hydroxyapatite on Silica-Gel: Experiments and Thermodynamic Explanation

PATRICIA TEIXEIRA DA COSTA, TSUNEHARU OGASAWARA, MARIA CECÍLIA DE SOUZA NÓBREGA AND LUIZ CLÁUDIO FERNANDES LOURENÇO GOMES
Federal University of Rio de Janeiro, COPPE, PEMM, P.O. Box 68505 Ilha do Fundão, 21945-970 Rio de Janeiro-RJ, Brazil
ogasawat@metalmat.ufrj.br

Abstract. Silica-gels prepared from ethanol, TEOS and water, using a hydrochloric acid as catalyst, were slowly dried and heated in air up to 900°C. Plate-like pieces of heat treated silica-gel were used for hydroxyapatite nucleation experiments in a simulated body fluid (SBF) medium since sol-gel processing gives the silica an active surface. The SBF was changed every 3 days.

After 9 days in the SBF, hydroxyapatite was observed by SEM on the surface of the silica-gel samples. The presence of hydroxyapatite was confirmed by FTIR. Subsequent growth of hydroxyapatite was evaluated after 12 and 21 days total soaking time in SBF. A thermodynamic analysis was made in order to explain the nucleation and growth of the hydroxyapatite on the silica-gel.

Keywords: nucleation of hydroxyapatite on silica-gel, hydroxyapatite coating, bioceramics, thermodynamic explanation

Introduction

At present, researchers who have investigated the formation of hydroxyapatite on the surface of silica-gel and/or other biomaterials containing silica-gel as an important component, such as bioglasses, are convinced that the favorable anion sites available in the silica-gel are responsible for the good bioactivity of the silica-gel as a hydroxyapatite nucleating substrate [1–8]. Some of these authors believe that the same phenomenon governs the formation of hydroxyapatite on titania-gel; in this way, hydroxyapatite nucleation and growth on titanium metal is accelerated by a gel-forming thermochemical pretreatment. Similar features could be associated with the coating of biocompatible metals and alloys from aqueous solutions containing calcium phosphates.

The present paper reports the results of preparing silica-gel from alkoxides and then sintering it so as to obtain a substrate for hydroxyapatite from aqueous solutions containing calcium and phosphorus. Thermodynamic analysis was carried out in order to obtain a fundamental explanation on how the anionic sites in silica-gel give rise to chemical bonded hydroxyapatite crystals.

Experimental

Materials and Methods

To prepare silica-gel, TEOS, ethanol and twice distilled and dionized water were used. Hydrochloric acid was used as the catalyst for gel formation. Two molar ratios of TEOS/H_2O (that is, 1 : 32 and 1 : 16) were employed to produce silica-gels which were then dried and sintered at 1000°C. Some silica-gels prepared with a 1 : 16 TEOS/water ratio were sintered at 1100°C for comparison. Samples of sintered gel were then submitted to contact with SBF at pH 7.5 at 37°C for three different periods of time (9, 12 and 21 days).

Results

Figure 1 shows SEM micrographs of the hydroxyapatite formed by a SBF solution on the surface of the silica. FTIR analysis of the material on the silica-gel

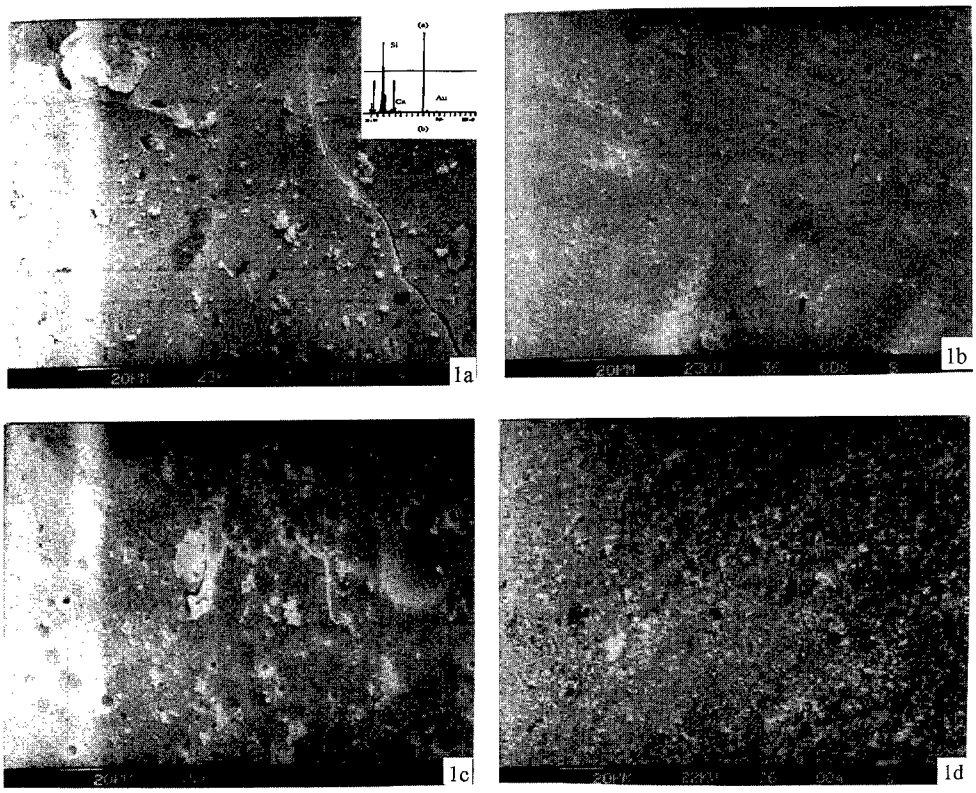

Figure 1. SEM photomicrographs of silica-gel substrate prepared with a 1/16 TEOS/water molar ratio; after 9 days in SBF, dried and sintered at (a) 1000°C (with EDS of the deposits) and (b) 1100°C; after (c) 9 days and (d) 12 days in SBF a sintered at 1100°C.

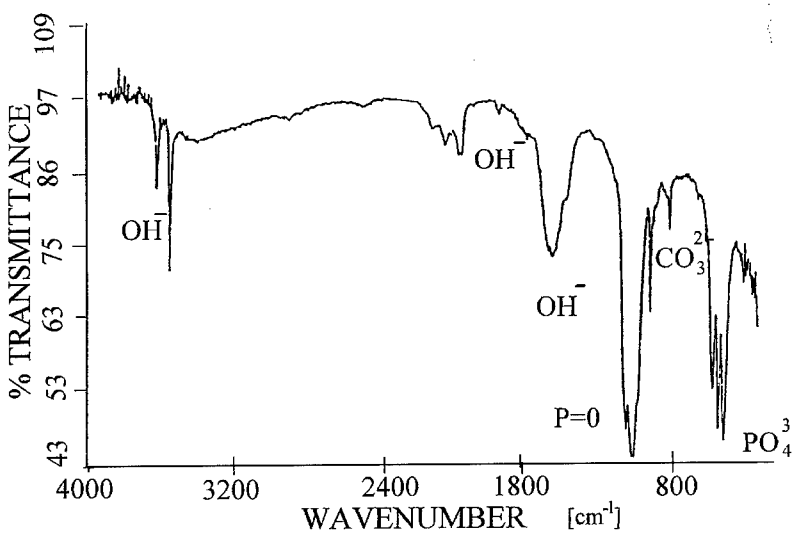

Figure 2. Infrared spectra of silica-gel substrate sample after 12 days in SBF.

surface confirmed that it was calcium phosphate in the form of hydroxyapatite (Fig. 2).

It is clear from the micrographs that at a constant TEOS/water molar ratio and soaking time of the silica-gel in SBF, the number of active sites for the nucleation and subsequent growth of the hydroxyapatite decreases with increasing sintering temperature from 1000 to 1100°C (Fig. 1(a) compared with 1(b)). On

the other hand, keeping constant the TEOS/water molar ratio and the sintering temperature (1100°C, in the present case), and increasing the time of soaking of the silica-gel in the SBF from 9 to 12 days increases the number of hydroxyapatite crystals (Fig. 1(c) compared with 1(d)).

Discussion and Thermodynamic Explanation

It is reasonable to assume that a cationic complex of calcium phosphate is electrostatically attracted by the anionic silicate surface, thereby giving rise to chemical bonding, and that a calcium silicate phosphate phase first forms on the gel surface. The micrographs show that only part of the silicate substrate was covered by the hydroxyapatite crystals. This means that for rapid and complete coverage of the silicate substrate it is necessary to optimize the substrate preparation conditions by choosing the right sintering temperature that leads to maximum surface activity.

Once every anionic site is bonded to the calcium phosphate cation there will be no active sites remaining on the silica substrate. The micrographs revealed that the hydroxyapatite crystals grew significantly far apart on the silica substrate, which means that the calcium silicate phosphate nuclei act as heterogeneous sites for subsequent nucleation and growth of hydroxyapatite.

The experimental evidence indicates that a chemical bonding is set up during the nucleation of the hydroxyapatite on the silica-gel, in agreement with the literature. However, it remained desirable to determine the stability domain for the chemical bonding compound or phases which form at the silica/hydroxyapatite interface, as an interphase. This was done by thermodynamic calculations as follows.

Consider the reactions (1) $3Ca_3(PO_4)_2 + Ca(OH)_2 = Ca_{10}(PO_4)_6(OH)_2$ and (2) $3Ca_3(PO_4)_2 + CaSiO_3 = Ca_{10}(PO_4)_6SiO_3$. A mathematical expression describing the apparent similarity between these reactions is suggested: $\Delta G^0_{R(1)}/[3\Delta G^0_f\, Ca_3(PO_4)_2 + \Delta G^0_f\, Ca(OH)_2] = \Delta G^0_{R(2)}/[3\Delta G^0_f\, Ca_3(PO_4)_2 + \Delta G^0_f\, CaSiO_3]$, from which $\Delta G^0_{R(2)}$ the free energy of formation of calcium silicate phosphate, that is "silica apatite" can be estimated at 25°C. Conventional methods gave the free energy values of the "silica apatite" for temperatures up to 300°C. The sources of the thermodynamic data used are references [9–19].

Figure 3(a) presents the pi-pH diagrams (with i = Ca, P and S, in the stoichiometric proportions for silicate apatite), at 25°C, showing the domains of stability for the important solids, calcium-deficient hydroxyapatite ($Ca_9H_2P_6O_{25}$) and silicate apatite [$Ca_{10}(PO_4)_6SiO_3$], and for the dissolved species [Ca^{2+}, $CaOH^+$, $Ca(OH)_2$(aq), H_3PO_4(aq), $H_2PO_4^-$, HPO_4^{2-} and PO_4^{3-}]. Figure 3(b) is the pi-pH equilibrium diagram at 25°C for the Ca-P-H_2O system, that is, the diagram applicable after the silica substrate has been completely deactivated by the formation of silicate apatite nuclei and the aqueous calcium phosphate sees this new substrate as pure hydroxyapatite.

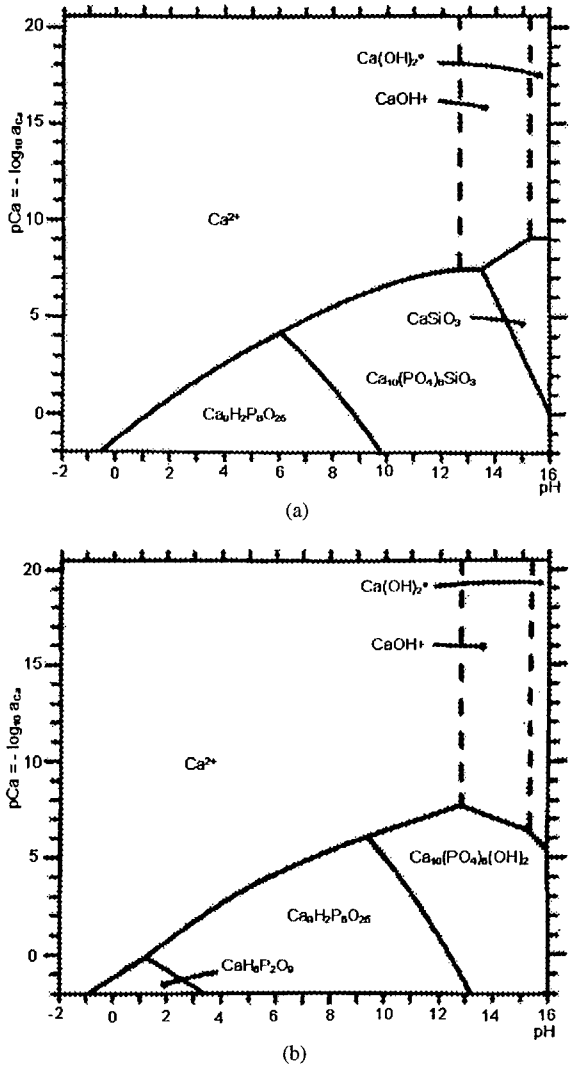

Figure 3. (a) pCa-pH diagram of the Ca-Si-P-H_2O system at 25°C for $a_{Si} = 10^{-4}$ molal and $a_P = 0.6\,a_{Ca}$ and (b) pCa-pH diagram of the Ca-P-H_2O system at 25°C for $a_P = 0.6\,a_{Ca}$; both in aqueous solution in equilibrium with 0.21 atm of oxygen.

Conclusions

(a) To prepare an active silica-gel surface, it is necessary to know the appropriate gel preparation conditions, which can be obtained by trial and error, and to perform subsequent tests with the gel in SBF solution. This must be followed by final characterization of the hydroxyapatite coating formed.

(b) The p*i*-pH diagram developed in the present work indicates the conditions under which the silicate apatite interphase, which provides the strong chemical bonding sites for the hydroxyapatite to the silica-gel substrate, can be formed.

(c) The p*i*-pH diagram can be applied only to the active sites of the silica-gel. Once these have been totally converted into silicate-apatite, the calcium phosphate SBF solution will only see the new substrate of hydroxyapatite crystals, and so the p*i*-pH diagram for the Ca-P-H_2O compound must be used subsequently to interpret the behavior of the system.

Acknowledgments

The authors would like to acknowledge the CNPq, CAPES, FINEP, PADCT and UFRJ for the support to the present work.

References

1. P. Li, I. Kangasniemi, K. Groot, T. Kokubo, and A.U. Yli-Urpo, Journal of Non-Crystalline Solids **168**, 281 (1994).
2. M.M. Pereira and L.L. Hurich, Journal of Sol-Gel Science and Technology **7**, 59 (1996).
3. T. Kokubo, S. Ito, Z.T. Huang, T. Hayashi, S. Sakka, T. Kitsugi, and T. Yamamuro, Journal of Biomedical Mater. **24**, 331, 731 (1990).
4. V.M. Castaño, D. Suarez, E. Rivera, M. Estevez, and J.C. Hernandesz, Ceramic Transactions **63**, in *Bioceramics: Materials and Applications II*, edited by Richard P. Rusin and Gary S. Fischman (The American Ceramic Society, Westerville, 1996), p. 49.
5. P. Li, C. Ohtsuki, T. Kokubo, K. Nakanishi, N. Soga, T. Nakamura, and T. Yamamuro, Journal of the American Ceramic Society **75**, 2094 (1992).
6. P. Li, C. Ohtsuki, T. Kokubo, K. Nakanishi, N. Soga, T. Nakamura, and T. Yamamuro, Journal of Applied Biomaterials **4**, 221 (1993).
7. P. Li, C. Ohtsuki, T. Kokubo, K. Nakanishi, N. Soga, T. Nakamura, and T. Yamamuro, Journal of Materials Science: Materials in Medicine **4**, 127 (1993).
8. Y. Abe, T. Kokubo, and T. Yamamuro, Journal of Materials Science: Materials in Medicine **1**, 233 (1990).
9. I. Barin, O. Knacke, and O. Kubaschewski, *Thermodynamic Properties of Inorganic Substances* (Springer-Verlag, Berlin and New York, 1973), Supplement 1977.
10. D.D. Wagman et al., *Selected Values of Chemical Thermodynamic Properties of the Alkaline Earth Elements* (NBS 270-6, Washington, DC, 1973).
11. I. Barin, *Thermodynamical Data of Pure Substances* (VCH Verlags Gesellschaft, 1993).
12. I. Barin, *Thermochemical Data of Pure Substances* (VCH Verlags Gesellschaft, Weiheim, 1989).
13. O. Knacke, O. Kubaschewski, and K. Hesselmann, *Thermodynamical Properties of Inorganic Substances* (Springer-Verlag, Berlin, 1991).
14. R.A. Robie et al., Thermodynamical properties of minerals and related substances at 298.15 K and 1 bar pressure at higher temperatures, U.S. Geological Survey Bull. **1452**, (1979).
15. S.M. Bailey, K.L. Churney, and R.L. Nuttal, Journal of Physical and Chemical Reference Data **11**, 1 (1982).
16. M.W. Chase et al., Journal of Physical and Chemical Reference Data **14**, 1 (1985).
17. G.V. Samsonov, Fiziko-khimischeskie svoistva okislov, Metallurgiya, Moscow, 1978.
18. L.P. Ruzinov and B.S. Guljanickij, Ravnovesnye Prevrasoenija Metallurgiceskin Reaktseij, Moskva, 1975.
19. H.C. Helgeson et al., Am. J. Sci., **278-A**, 1 (1978).

Journal of Sol-Gel Science and Technology 13, 255–259 (1998)
© 1998 Kluwer Academic Publishers. Manufactured in The Netherlands.

Phase Formation in Gels of the Apatite-Anorthite System

B. SAMUNEVA, Y. IVANOVA, P. DJAMBASKI, S. STEFANOVA AND Y. DIMITRIEV
University of Chemical Technology and Metallurgy, Sofia-1756, Bulgaria

M. DIMITROVA-LUKACS
ALUTHERY-FKI., Hungary

Abstract. Phase formation in heat-treated composites containing anorthite gel and fluorapatite has been investigated. For the sol-gel synthesis TEOS, $Al(NO_3)_3 \cdot 9H_2O$, $Ca(NO_3)_2 \cdot 4H_2O$, $(NH_4)_3PO_4 \cdot 3H_2O$, NH_4F and CaF_2 were used as precursors. The gel mixtures were treated from 200 to 1250°C. It was found that the gels remain in an amorphous state up to 900°C. From X-ray diffraction structural analysis of anorthite gel-glasses heat treated at 600°C and 800°C it was found that a shift of the first maximum occurred from 1.85 to 1.77 Å, which could be interpreted as a transformation of the gel-glass structure with increasing temperature. During the heat treatment of the mixed gels from the apatite-anorthite system it was found that fluorapatite is present as a major crystal phase at 950°C. At 1250°C anorthite and gehlenite are the major crystalline phases.

Keywords: composites, gel-glass, glass-ceramics, apatite, anorthite

Introduction

Recently sol-gel synthesis of apatite/anorthite glass-ceramics has been carried out by the crystallization of homogeneous gel derived glasses from the SiO_2-P_2O_5-Al_2O_3-CaO-F system without a melting process [1]. It is well known that the successful synthesis of pure anortite glass-ceramics from gels strongly depends on the heat treatment regimen and the type of precursors [2–4]. The production of hydroxyapatite $Ca_5(PO_4)_3OH$ by the sol-gel method is also well described in several papers [5–7]. Taking into account the peculiarities of these phases in the gel state we attempted to develop new composite materials on the basis of these two precursors.

The purpose of the study is to investigate the phase formation in mixtures containing fluorapatite and anorthite gel at different ratios and to establish the conditions for the production of monophase or multiphase glass ceramics without melting.

Experimental

The stoichiometrical anorthite composition was synthesized according to a simple scheme [4]. $Si(OC_2H_5)_4$ (TEOS), $AL(NO_3)_3 \cdot 9H_2O$ and $Ca(NO_3)_2 \cdot 4H_2O$ were used as starting materials. The salts were dissolved in absolute ethanol and TEOS was added and mixed to obtain hydrolysis and gelation without catalysts. The gels were dried at 100°C for 24 hours. The anorthite gel-glass powder, obtained after heat treatment at 600°C, was used for preparing composites. The starting materials for hydroxyapatite were: a water solution of $(NH_4)_2HPO_4$ and $Ca(NO_3)_2 \cdot 4H_2O$. The pH of the solution was ensured to be 10–12 by addition of NH_4OH. The hydroxyapatite was reacted with NH_4F at 500°C for 2 hours. The composite samples were prepared by mixing and homogenization of the anorthite gel-glass and fluorapatite in the concentration range 20–80 mol% anorthite. Heat treatment was performed at 900, 950, 1050, 1150 and 1250°C for 2 hours at each temperature.

Phase formation was studied using X-ray diffraction analysis (Diffractometer DRON-UM 1, CuK_α radiation) and IR-spectroscopy (Spectrometer Specord M-80). The intensity curves for X-ray diffraction structural analysis of anorthite gel-glasses were obtained from amorphous samples in the range $2\theta = 4$–$120°$. The scanning rate was $0.5°/min^{-1}$ with a curved monochromator for the beams and scintillation counter connected to a pulse height analyzer. Full details of the data analysis procedures adapted for IBM-PC are described in [8].

A gel of the composition $1.5SiO_2 \cdot 0.5P_2O_5 \cdot 1.0Al_2O_3 \cdot 1.0CaO \cdot 0.5CaF_2$ was obtained for comparison following the scheme proposed in [1] using the heat treatment described above.

Results and Discussion

A well-defined maximum at about 13° θ is observed in the intensity curves of anorthite gel glasses. The total pair correlation functions $T(r)$ are presented in Fig. 1. A well resolved first distance (r_1) was found which shifts with increasing temperature to lower values. The position of this maximum after heat treatment at 600°C is 1.85 Å and corresponds to the distances of the Si—O and Al—O atomic pairs established in multicomponent silicate glasses [9, 10]. Similar distances are found for the crystalline anorthite [12]. The slight decrease in r_1 to 1.77 Å of the amorphous anorthite gel treated at 800°C may be interpreted as a densification of the structure with the increase in temperature. It is mainly due to changes in the short-range order of the network as a result of Al—O polyhedra adjustments. The second well defined maximum at 3.15 Å for the gel treated at 600°C shifts to 3.00 Å for the gel treated at 800°C and may be assigned mainly to Si—Si distances. In the structure of binary glasses and melts from the CaO-SiO_2 system this peak lies at 3.23 Å [12]. The distances Ca—O do not appear because of the smaller CaO content. The O—O distances are also not found. This is a typical phenomenon when CuK_α radiation is used.

The XRD patterns of a sample containing 20 mol% anorthite gel-glass and 80 mol% fluorapatite are given in Fig. 2(a). During heat treatment from 950 to 1250°C the fluorapatite crystalline phase remains. At higher temperatures the gehlenite and anorthite crystalline phases are formed. In the sample heat treated at 1050°C all three crystalline phases are present in approximately equal amounts. The phase formation during heat treatment of the sample, containing 40 mol% anorthite gel-glass and 60 mol% fluorapatite is similar (Fig. 2(b)). There is only a difference in the amount of the fluorapatite and anorthite phases at 1250°C. With increasing anorthite gel-glass content in the starting samples, there is a tendency for an increase in the amount of anorthite crystalline phase at 1050, 1150

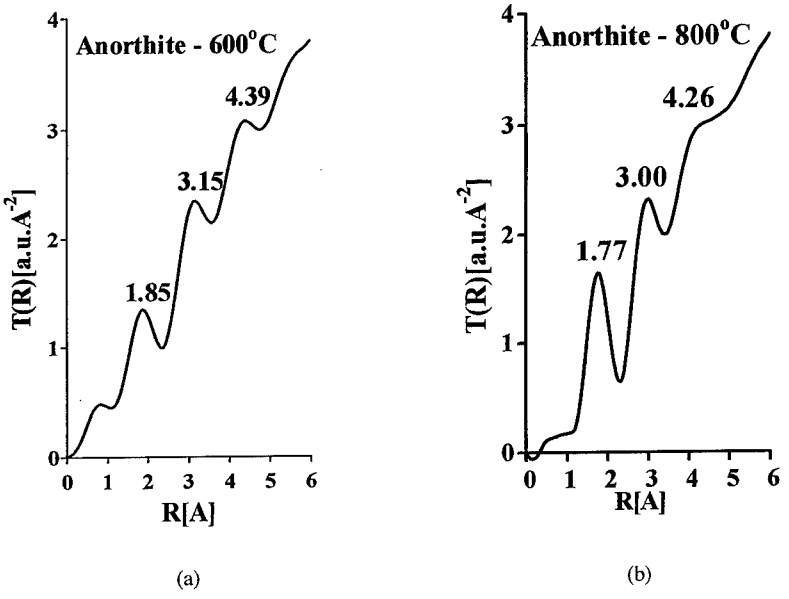

Figure 1. Total pair correlation function $T(r)$ of thermally treated gel-glass anorthite at 600°C and 800°C.

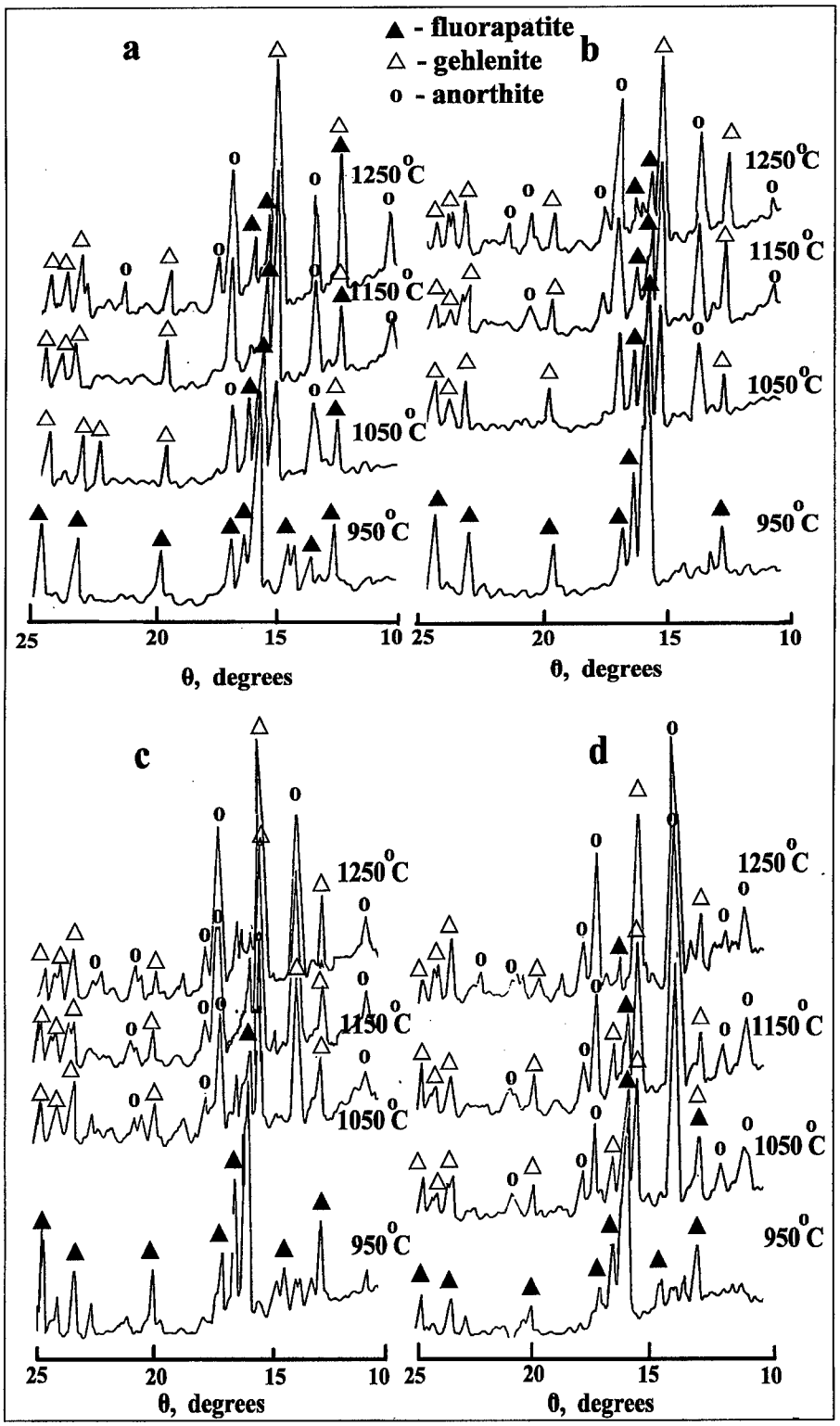

Figure 2. XRD patterns of thermally treated mixtures of anorthite gel-glass and fluorapatite: (a) 20 mol% anorthite, (b) 40 mol% anorthite, (c) 60 mol% anorthite, and (d) 80 mol% anorthite.

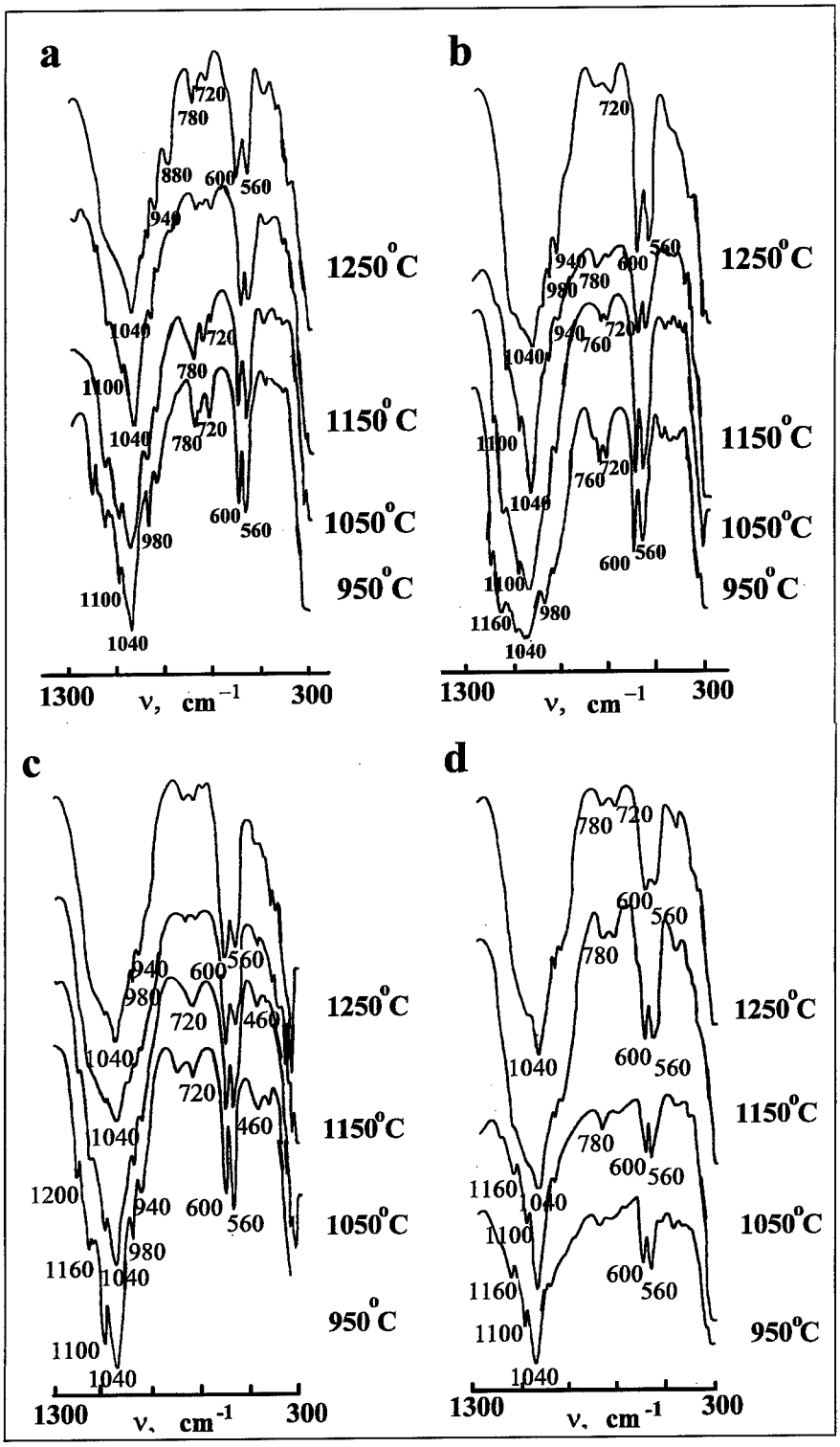

Figure 3. IR-spectra of thermally treated mixtures of anorthite gel-glass and fluorapatite: (a) 20 mol% anorthite, (b) 40 mol% anorthite, (c) 60 mol% anorthite, and (d) 80 mol% anorthite.

and 1250°C (Figs. 2(c) and (d)). In this way it is possible to synthesize glass-ceramics containing anorthite and gehlenite crystalline phases, without fluorapatite.

The IR-spectra are presented in Fig. 3. The spectra are complex due to the overlapping of the bands corresponding to the vibrations of different structural units. The analysis of the IR-spectra could be made on the basis of known spectral data of the stoichiometric phases and melt glasses in this system. The IR-spectrum of pure fluorapatite is characterized by a triple absorption band in the high frequency range at 1100, 1050 and 970 cm^{-1} and one well-defined doubled band at 607 and 577 cm^{-1} [13]. These bands are interpreted as stretching and bending vibrations of PO_4 groups. On the other hand, IR-spectrum of the pure crystalline anorthite is characterized with a wide absorption triple band at 1100, 1020 and 940 cm^{-1}, as well as with broad bands around 780 and 460 cm^{-1} [4]. The triple absorption band could be assigned to the antisymmetrical stretching vibration of SiO_4 tetrahedra, while low-frequency bands could be interpreted as corresponding bending vibrations. The bands corresponding to the vibration of AlO_4 units are observed in the spectra of alumosilicate glasses near 700 cm^{-1} [14].

The spectra of the specimens treated at 950°C are similar to the spectrum of the fluorapatite and changes are found with an increase in temperature. A broadening of the main peak takes place and simultaneously an increase in the number of the bands is observed at 1200, 1160, 1100, 1040, 970, 940 and 880 cm^{-1}. This means that aluminosilicate crystalline phases are formed in the materials. It is known that in the IR-spectra of the silicates with a lower degree of polymerization a strong band appears around 600 cm^{-1} ($\nu^{S}_{Si-O-Si}$) [15]. That is why the increase in the intensity of this band in our spectra can be assigned to the increase in Si—O—Si bonds instead of P—O—P.

The scheme proposed for the synthesis by sintering of mixed powders of fluorapatite and amorphous anorthite gel is suitable for the production of different glass-ceramics. Using this method it is possible to control precisely the amount and the type of the crystalline phases.

Conclusion

From the X-ray diffraction structural analysis of anorthite gel-glasses heat treated at 600°C and 800°C it has been established that a transformation of the short-range order of the gel-glass structure occurs with increasing temperature.

During the thermal treatment in the range 950–1250°C of the glass-ceramic materials it is possible to obtain: (1) glass-ceramics with only one crystalline phase-fluorapatite and an amorphous phase; (2) glass-ceramics containing three crystalline phases: fluorapatite, gehlenite and anorthite; (3) glass-ceramics containing two crystalline phases: gehlenite and anorthite, without crystalline fluorapatite.

Acknowledgment

We are very grateful for the financial support from the EU under Copernicus project 'ERB 3512PL 94 05 83 Contract' CIPA-CT94-0145.

References

1. B. Samuneva, M. Dimitrova-Lukacs, Y. Ivanova, P. Djambaski, and S. Stefanova, in *Proc. Inter. Symp. on Glass Problems* (Istanbul, 1996), Vol. 2, p. 302.
2. P. Panorazi, J. Phalippou, F. Sorrentino, and J. Zarzicki, J. Non-Cryst. Solids **63**, 81 (1984).
3. B. Zelinski, B. Fabes, and D. Uhlman, J. Non-Cryst. Solids **82**, 307 (1986).
4. B. Samuneva, Y. Dimitriev, Y. Ivanova, V. Dimitrov, and P. Djambaski, in *Proc. 10 Ibausil* (Weimar, 1988), Vol. 4, p. 289.
5. M. Yarco and C. Bolen, J. Mat. Sci. **11**, 2027 (1976).
6. E. Shor and R. Holmes, *Porous Hydroxyapatite, Introduce of Bioceramics* (1995), chap. 10, p. 181.
7. S. Dimieva, A. Montenero, and B. Samuneva, in *Proc. 12th Conf. on Glass and Ceramics* (Varna, AP 49, 1996).
8. N. Zotov, V. Dimitrov, and Y. Yanev, Phys. Chem. Miner. **16**, 774 (1989).
9. S. Urnes, Phys. Chem. Glasses **13**, 77 (1972).
10. M. Takahiko, Yoguo-Kyokai-Shi **78**(12) (1970).
11. L. Bragg and G. Claringbull, Crystal structures of minerals, Mir, Moskva (1967) (russ.).
12. Y. Waseda, The Structure of Non-Crystalline Materials (McGraw-Hill Int. Book Company, N.Y., 1980), chap. 5, p. 136.
13. R. Zinuk, A. Balikov, I. Gavrilenko, and A. Scheviakov, IR-spectroscopy in inorganic technology, Chimia, Leningrad (1983) (russ.).
14. C. Huang and E. Behrman, J. Non-Cryst. Solids 310 (1991).
15. A. Lazarev, Vibrational spectra and silicate structures, Nauka, Leningrad (1968) (russ.).

Journal of Sol-Gel Science and Technology 13, 261–265 (1998)
© 1998 Kluwer Academic Publishers. Manufactured in The Netherlands.

Sol-Gel Derived Calcium Phosphate Coatings for Biomedical Applications

D.B. HADDOW AND P.F. JAMES
Department of Engineering Materials, The University of Sheffield, Sir Robert Hadfield Building, Mappin Street, Sheffield, U.K.

R. VAN NOORT
Department of Restorative Dentistry, The University of Sheffield, Claremont Crescent, Sheffield, U.K.

Abstract. Hydroxyapatite (HA) coatings have received considerable attention because they exhibit bone bonding capabilities. Unfortunately the common forms of coating production result in cracking and degradation of HA due to the thickness of the coatings and the elevated temperatures employed. This study demonstrates the production of sub-micron, crack-free calcium phosphate coatings on quartz glass substrates using a sol-gel dip-coating technique and firing temperatures below 1000°C.

Coatings fired at 1000°C comprised a mixture of hydroxyapatite (HA) and tricalcium phosphate (TCP). XPS analysis of the coating surface showed that the Ca/P ratio lay in the range 1.5–1.67, and that there was a contribution from carbon in the form of carbonate.

It is proposed that the sol-gel coatings comprising a resorbable (TCP) and an insoluble (HA) phase have potential benefits in certain implant applications.

Keywords: bioactive coatings, hydroxyapatite, XPS, tailored surfaces, implants

Introduction

In order to utilize the special biological properties of hydroxyapatite a variety of approaches have been adopted which seek to overcome its limitations as a structural implant arising from its inherent brittleness and low tensile strength. Surface coatings of hydroxyapatite on tough biocompatible metallic substrates have received considerable attention [1–5]. Such coatings must be pure, crystalline and adherent to serve as effective implants and this has proved difficult to achieve, with coatings being heterogeneous, cracked and poorly bonded. The possibility of harnessing the accelerated bone healing and bone bonding of HA coatings, while diminishing the risk of mechanical failure at either the bone/coating or coating/substrate interface, would improve the engineering design of bone implants, while opening up the possibility of using a wider range of materials than are currently in use.

Sol-gel coating potentially offers a useful method of preparing tailor-made surfaces with properties suitable for specific applications, via surface engineering. Such processing allows control over the composition and properties of surface coatings [6] and lends itself to the production of ultrathin coatings, which will be less susceptible to cracking and delamination.

Materials and Methods

Coating sols were prepared using triethyl phosphite (Sigma Aldrich, U.K.), and calcium ethoxide (Gelest, Germany) using a Ca/P ratio of 1.67. 1 g calcium ethoxide was refluxed with 100 ml ethanediol until the calcium precursor had dissolved. Preparations were carried out in a nitrogen atmosphere glove box. The viscosity of the coating solutions was altered by adding various volumes of ethanol to the sol.

Powders were prepared from the solutions by drying in an oven at 200°C. Powders were then fired in air up to 1100°C using a heating rate of 3°C/min and a 2 hour dwell at the firing temperature, followed by a

furnace cool. Coatings were prepared by dip-coating quartz substrates, followed by firing in an air furnace up to 1100°C for time periods up to 5 hours using a heating rate of 3°C/min.

XRD was used to obtain data on changes in powder crystallinity with heat treatment. X-ray spectra were obtained on a Philips PW 1710 diffractometer using CoK_α radiation. Scans were performed at 40 kV and 30 mA with a step size of 0.02 deg and a speed of 0.02 degree/s over a 2θ range of 20–65 degrees. Data analyses were carried out using Sietronics PW1710 diffractometer software. Electron microscopy of coatings was performed using a Camscan Series 2 scanning electron microscope with an accelerating voltage of 20 kV. X-ray photoelectron spectra were recorded on a VG Scientific spectrometer using Mg K_α X-rays and a take-off angle of 30° with respect to the sample surface.

Results and Discussion

XRD data from powders fired at 1000°C showed that a two-phase mixture was formed, comprising hydroxyapatite and tricalcium phosphate.

After withdrawal from the sol, the liquid films dried to form a white coating. Addition of ethanol to the sol allowed thinner coatings to be produced because the viscosity of the coating sol was lowered. Figure 1 shows that for sol containing no ethanol additions, the coating thickness appears to be independent of withdrawal speed U. All the coatings were fired at 1000°C, and at this temperature they can be considered densified. Increasing quantities of ethanol added to the sol allows the coating thickness to be controlled by the withdrawal speed. For the most dilute solution the thinnest coating produced was just over 100 nm.

A micrograph for a sample prepared with 1.0 M ethanol added to the sol and fired at 1000°C is shown in Fig. 2. The diphasic nature of the coatings is confirmed by the SEM micrograph which shows light colored islands surrounded by a dark colored matrix. Quantitative EDS showed that the relative amounts of Ca and P were different for the dark and light regions in the coatings.

Peak signals for C, Ca, O and P are clearly seen in the XP spectra for a coating fired at 1000°C (Fig. 3(a)). The nature of the C core line for a coating fired at 1000°C is shown in Fig. 3(b).

The Ca/P ratios for unfired coatings lay in the range 1.3–1.4, with a mean value of 1.34 (determined from five samples). This ratio was unchanged after firing at 600°C but after a treatment at 1000°C the mean value had risen to 1.64. Calcium concentrations lay in the range 8–10 at.%, with 6–7 at.% P at the surface.

The nature of the coating surface has been determined by XPS, and also by SEM. As discussed earlier, the XRD data indicate that the two phases present were hydroxyapatite and tricalcium phosphate. The diphasic coating appearance is similar to that observed by Qiu et al. [7] who fabricated hydroxyapatite films based upon a colloidal sol-gel route utilizing calcium nitrate and ammonium dihydrogen phosphate.

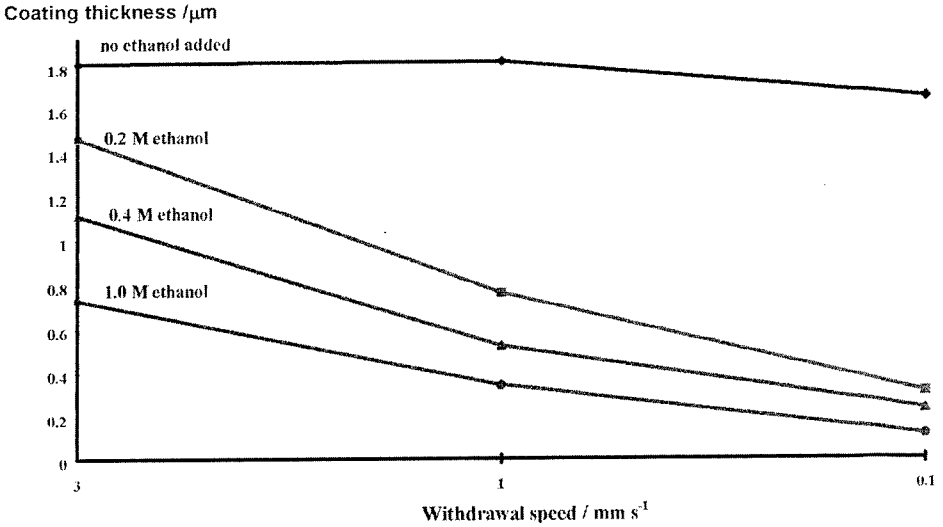

Figure 1. Variation in coating thickness with withdrawal speed U, and alcohol content.

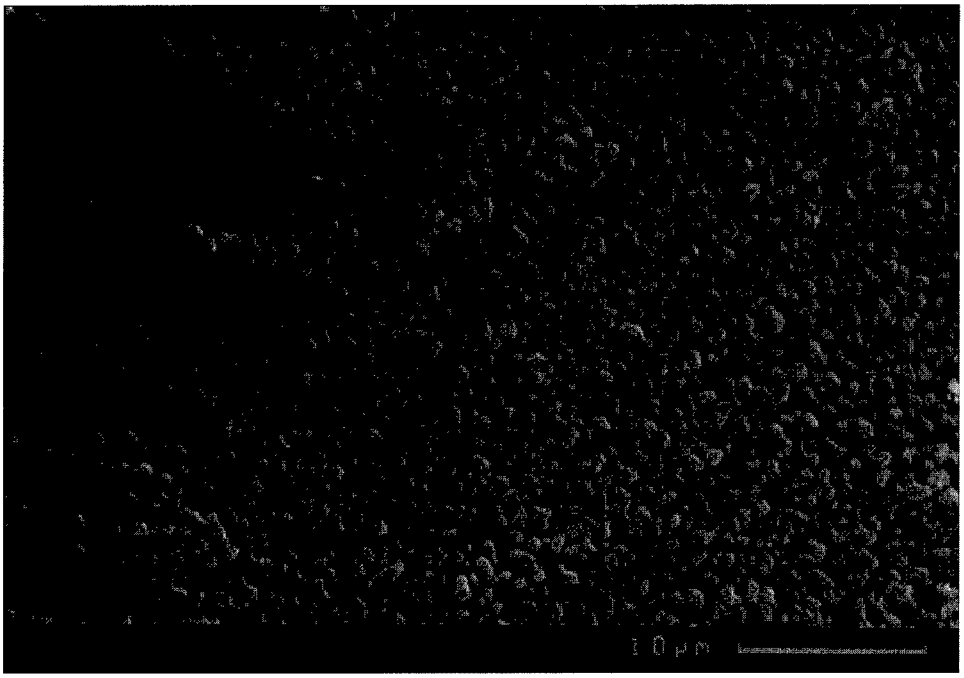

Figure 2. SEM micrograph of CaP coating fired at 1000°C.

Control over the coating process is obtained if ethanol is added to the sol. The solvent evaporation across the whole sample is uniform and control over the coating morphology is achieved. The typical grain size at high firing temperatures is about 1 μm, similar to that reported by Qiu et al. [7].

XPS analysis of the coatings showed the expected loss of carbon from the films as the firing temperature was raised. The atomic % C in the unfired film was ~62%, which was reduced to below 10% after firing at 1000°C for 60 min. The tail at the high binding energy side of the core line in Fig. 3(b) indicates that some of this carbon exists as carbonate material [8]. There is also a contribution from hydrocarbon arising from surface contamination. The presence of the carbonate signal at higher binding energy indicates the presence of a possible carbonate substituted apatite. However, no direct evidence for the formation of this particular phase was found in the XRD patterns for powders prepared under the same conditions as the fired coatings.

XPS has shown that the surface of the material is carbonate containing and that the binding energies for Ca, P and O are consistent with those found in commercial hydroxyapatite.

Qiu et al. [7] have claimed to have produced HA coatings from a colloidal sol-gel route. However, this type of deposition offers no mechanism of bonding to the substrate material. In addition, microscopy of Qiu's coatings show them to be very similar to those coatings produced in the present study, which have been characterized as a mixture of TCP and HA.

Besides the use of different Ca and P precursors, there are other factors which could influence the final CaP phase produced in sol-gel studies. Chief among these are post-heat treatments involving differences in temperature, time and surrounding atmosphere [9, 10]. Water molecules in the firing atmosphere could promote HA recrystallization, whereas in a dry atmosphere TCP and tetracalcium phosphate (TTCP) are more stable than HA. TCP and TTCP could be converted to HA by hydrolytic reactions if heated in a humid atmosphere.

Although recent coatings developed by Russell et al. [11] were analyzed to be pure HA rather than a mixture of TCP and HA as produced in the current work, both types of coatings may have their advantages. It has been reported [12] that the different crystalline and non-crystalline phases found in plasma-sprayed 'HA coatings' are characterized by different extents of dissolution in acid and neutral media. The formation of apatite, and in particular carbonate apatite on the surface of CaP materials is believed to be related

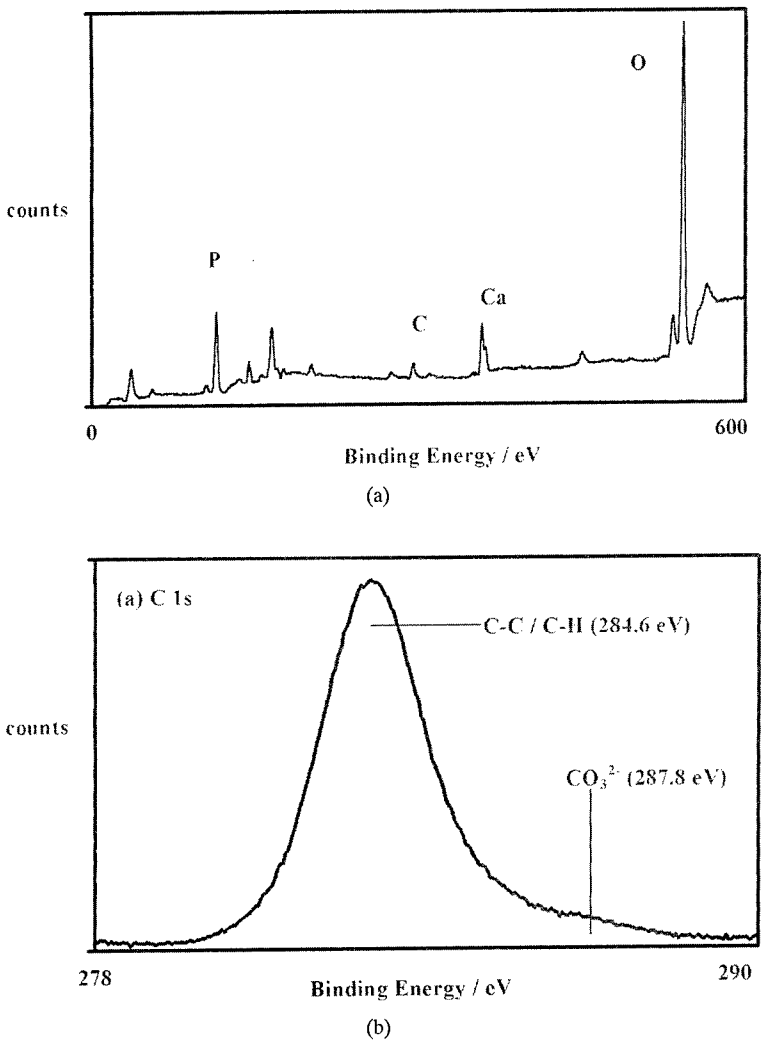

Figure 3. (a) XP survey scan for CaP coating fired at 1000°C and (b) XP C1s core line spectrum for CaP coating fired at 1000°C.

to the bioactivity of the materials, and results from the combined processes of dissolution and precipitation. Calcium phosphates in the coating partially dissolve, thus increasing the local calcium and phosphate ion concentrations leading to the precipitation of carbonate-apatite. The CO_3^{2-} ions can be incorporated in the newly formed depositing phase. If soluble phases can stimulate the deposition of apatite in this way, the question arises whether a coating of pure hydroxyapatite is the preferred composition. It is probable that HA would provide the ideal coating for substrates which are inert in the biological environment, because the biodegradation of HA is slower than amorphous apatite and TCP. However, in the case of titanium implants, another composition comprising a partially soluble coating may be more suitable. The present work has described the development of a thin CaP coating containing HA and TCP. Such a coating on titanium implants would promote a rapid response in terms of bone deposition on the coating, and a mixture of a highly resorbable phase with an insoluble phase could be beneficial in promoting a rapid bone response [13].

Conclusions

XRD of fired powders/coatings showed a diphasic β-TCP/HA mixture after firing at greater than 900°C. SEM of the coatings showed that coating morphology was uniform provided that sol viscosity was controlled.

XPS of the coatings showed that the Ca/P ratio was 1.64, lying in the expected range for an HA/TCP mixture. More than one C and O environment existed at the coating surface. The C1s core line comprised hydrocarbon and carbonate species, and the broadness of the O1s core line reflected the numerous bonding states of O present in the coating. Coating thicknesses after firing at 900°C were significantly less than 1 μm for solutions containing 1.0 M ethanol, with the thinnest coating being 0.15 μm thick.

References

1. K. de Groot, Journal of Biomedical Materials Research **21**, 1375 (1987).
2. E. Ruckenstein, S. Gourisankar, and R.E. Bayer, Journal of Colloid and Interface Science **63**, 245 (1983).
3. J.L. Ong and L.C. Lucas, Biomaterials **15**, 337 (1994).
4. H. Oguchi, K. Ishikawa, S. Ojima, Y. Hirayama, K. Seto, and G. Eguchi, Biomaterials **13**, 471 (1992).
5. H. Hero, H. Wie, R.B. Jorgensen, and I.E. Ruyter, Journal of Biomedical Materials Research **28**, 343 (1994).
6. D.B. Haddow, S. Kothari, P.F. James, R.D. Short, P.V. Hatton, and R. van Noort, Biomaterials **17**, 160 (1996).
7. Q. Qiu, P. Vincent, B. Lowenberg, M. Sayer, and J.E. Davies, Cells and Materials **3**, 351 (1993).
8. D. Briggs and M. Seah, *Practical Surface Analysis by Auger and X-Ray Photoelectron Spectroscopy* (Wiley, London, 1983).
9. S. Zhang and K.E. Gonsalves, Journal of Materials Science: Materials in Medicine **8**, 25 (1997).
10. J. Chen, W. Tong, Y. Cao, J. Feng, and X. Zhang, Journal of Biomedical Materials Research **34**, 15 (1997).
11. S.W. Russel, K.A. Luptak, C.T.A. Suchicital, T.L. Alford, and V.B. Pizzicone, Journal of the American Ceramic Society **19**, 837 (1996).
12. J.D. Santos, L.J. Jha, and F.J. Monteiro, Biomaterials **16**, 521 (1995).
13. R.Z. LeGeros, J.P. LeGeros, Y. Kim, R. Kijkowska, R. Zheng, C. Bautista, and J.L. Wong, in *Bioceramics: Materials and Applications*, edited by G. Fischman, A. Clare, and L.L. Hench (The American Ceramic Society, Westerville, 1995), p. 285.

Journal of Sol-Gel Science and Technology 13, 267–271 (1998)
© 1998 Kluwer Academic Publishers. Manufactured in The Netherlands.

Biodegradable Silica Fibers from Sols

MONIKA KURSAWE, WALTHER GLAUBITT AND AXEL THIERAUF
Fraunhofer-Institut für Silicatforschung, D-97082 Würzburg, Germany

Abstract. Biodegradable silica fibers for reinforcement of medical implants were successfully prepared by sol-gel processing. The spinnable precursor is based on TEOS and shows a characteristic, non-Newtonian rheological behavior in the presence of sol-particles of size 4 to 5 nm. This property suggests a non-covalent, supramolecular structure of the spinnable silica sol.

The fibers obtained were characterized using IR, NMR and thermal analysis as well as biological and mechanical testing. The degradation rate of fibers was tested in continuous flow experiments. The results demonstrate a good potential of the fibers for medical applications.

Keywords: fibers, biodegradable material, silica, spinnability, sol-gel structure

1. Introduction

Resorbable materials for medical implants provide a good alternative to conventional metal implants, because they degrade in the body and decompose. A second operation for removal of the implants after regeneration of tissue is unnecessary in this case. The majority of degradable biomaterials are organic polymers such as PLA (polylactid) or PG (polyglycolid), which are already used for small implants in certain bone surgery. The disadvantages of degradable polymers are their low mechanical strength and Young's modulus which do not allow their use for weight-bearing bones. Therefore, biodegradable polymers need reinforcement.

Such strengthening has been attempted by preparing fiber reinforced composites using several types of biodegradable fibers incorporated into organic polymer matrices. In all cases an effective reinforcement was not observed either due to low fiber quality of biodegradable organic fibers [1, 2] or due to too high degradation rates of biocompatible calcium phosphate glass-fibers [3]. However, there is still a need for new types of fibers for reinforcement of biopolymers. The development of degradable fibers in the SiO_2 system could be a possibility. The expected biocompatibility of SiO_2 and the known possibility to fiberize sols provided the motivation for the development of degradable SiO_2-based silica gel fibers using the sol-gel technique.

Although the chemistry of silica sols and gels is well known [4], the preparation of continuously drawn silica fibers remains a difficult task [5]. In this study the preparation of biocompatible, degradable silica fibers by sol-gel-processing is reported.

2. Experimental

A three-step synthesis was developed for preparation of the spinnable precursor. First, TEOS, EtOH, H_2O and HNO_3 were stirred at room temperature for several hours. In the second step EtOH was removed from the solution by heating at 70°C. After filtration of the resulting sol, a third step which involved a sol ripening process was carried out for several days at low temperature. The resulting sol showed spinnability for several hours (up to 24 h), providing good handling and homogeneity.

By extruding the spinnable sol through an orifice (100 μm), fibers were spun and wound up on a rotating drum. The silica gel fibers were taken from the drum and dried at room temperature until all the EtOH had been evaporated.

3. Results and Discussion

3.1. Characterization of the Spinnable Sol

In order to get highly viscous, spinnable sols, TEOS must be hydrolyzed and partially condensed without the formation of gels. Therefore, the sols had to be stabilized against gelation during the three reaction steps.

To avoid gelation during reaction step 1, the solvent ethanol was used in excess. Investigations using small-angle-X-ray-scattering (SAXS) showed that the particle radii of the dispersed phase did not exceed $R = 0.5$ nm in this case. The formation of small particles implies that during step 1 mainly hydrolysis reactions took place.

During reaction step 2, the solvent ethanol was evaporated. This entailed an initiation of particle growth due to the starting of condensation reactions, which could be controlled by the amount of EtOH remaining in the sol (Fig. 1). Again, the particle size was monitored by SAXS combined with dynamic light scattering. With decreasing amounts of EtOH in the sol we found an exponential increase of the particle radii for all tested stochiometric proportions (Fig. 1). If the particle radius exceeded 2.5 nm, then within a short time aggregation of particles led to formation of a gel.

However, the third reaction step prevented premature gelation. When the particles of the dispersed phase had reached radii of 0.8 nm to 1.8 nm, evaporation of EtOH was stopped and the particle growth was strongly slowed down by cooling the sol (reaction step 3: sol ripening).

During sol ripening we observed an abrupt increase of viscosity with ripening time, whereas the particle size only showed a minor increase up to $R = 2.5$ nm when the sol became spinnable. According to the rise of viscosity, a change of flow behavior from Newtonian to shear-thinning of the sol was observed. This is illustrated by Fig. 2.

The state of spinnability as a temporary phenomenon in sol evolution can be sufficiently described by the particle size of the dispersed phases and the flow behavior of the sol:

1. Spinnable sols in the system TEOS/EtOH/H_2O/HNO_3 exhibited particle radii from 2.0 nm to 2.5 nm.
2. Spinnable sols in the present system showed viscosities between 5 Pa · s and 13 Pa · s at shear rates $\dot{\gamma} = 18\ s^{-1}$.
3. The shear thinning flow behavior followed the empirical Ostwald relation [6] $\tau = k \cdot \dot{\gamma}^n$ (k = constant, τ = shear stress) with an exponent $n = 0.70$ to 0.95.

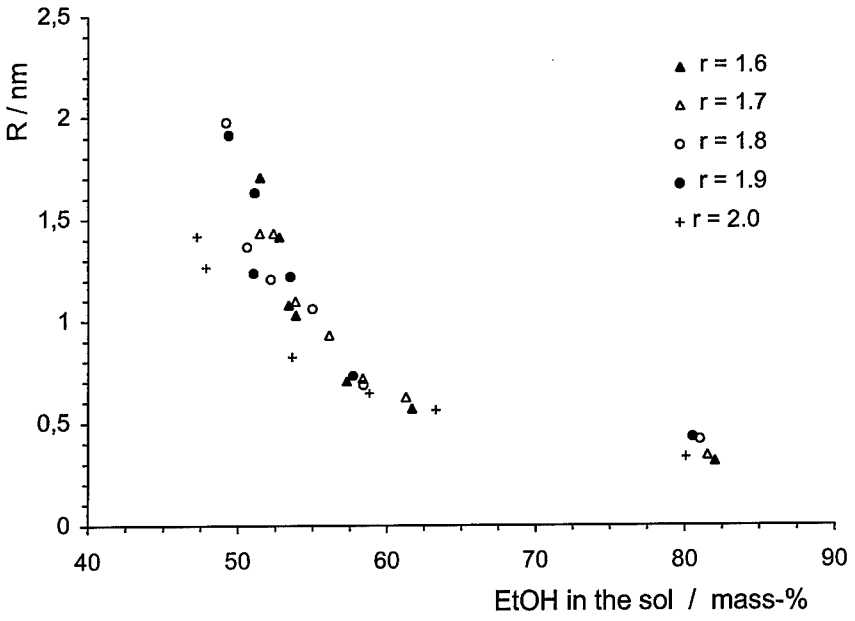

Figure 1. Reaction step 2: Plot of particle radii measured via SAXS versus amount of EtOH in the sol. Evaporation of EtOH leads to an increase of the particle size for all examined sols with different r, r = mol H_2O/1 mol TEOS.

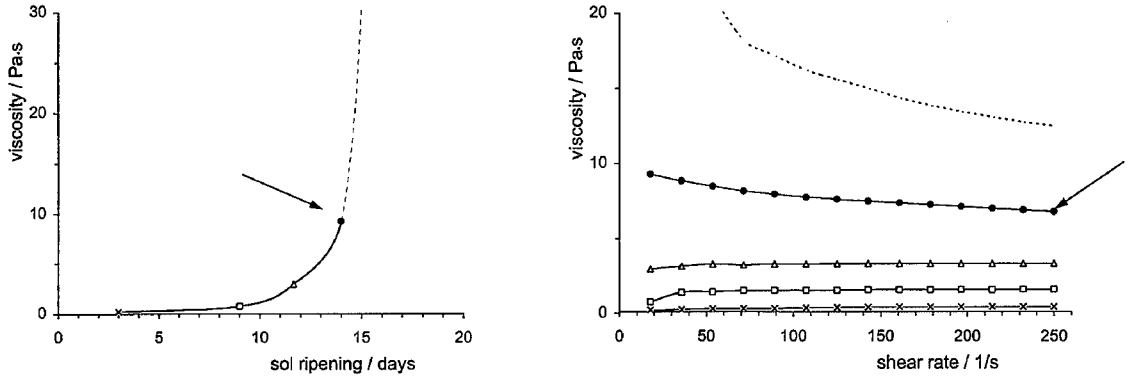

Figure 2. Reaction step 3: Increase of viscosity during sol ripening (left) and change of flow behavior from Newtonian to shear thinning (right). Spinnability of the sol is marked by an arrow.

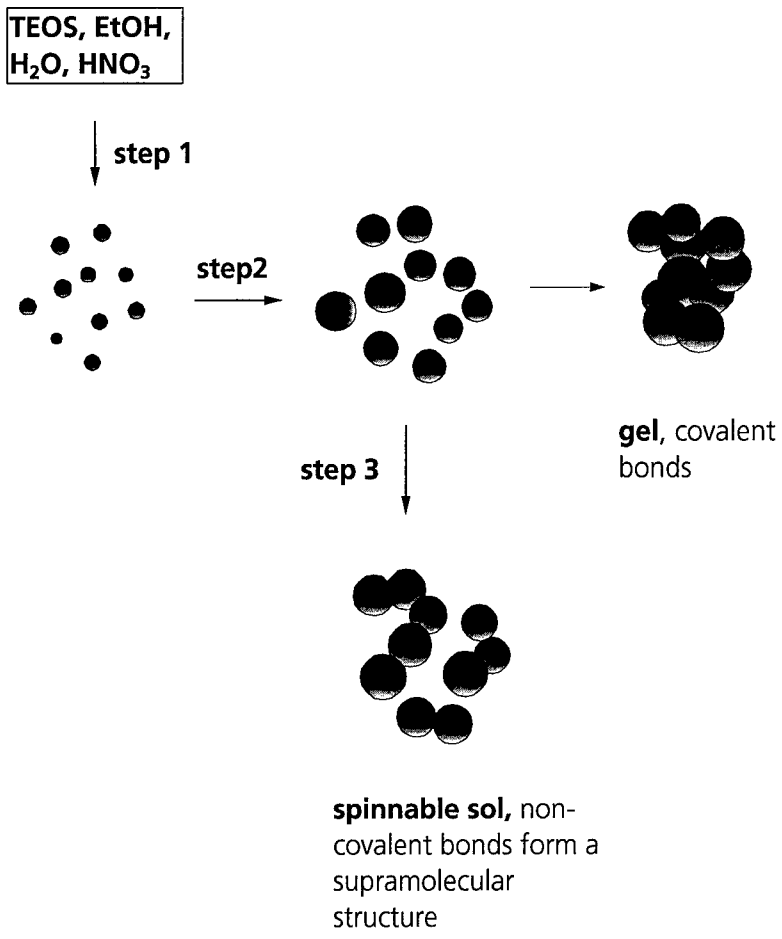

Figure 3. Suggested sol evolution during the preparation of spinnable precursors using the three-step synthetic route. A non-covalent, supramolecular structure is characteristic for the spinnable sol.

The exponent n is a measure of the deviation from Newtonian flow, where $n = 1$.

We found this dependence of spinnability on the above described rheological behavior in the presence of small particles ($R < 2.5$ nm) in all investigated compositions. There was strong evidence that this connection is typical for the system. It describes a general, characteristic pattern of the sol which can be correlated to a certain sol structure. Since the complex, non-Newtonian flow behavior cannot be caused by particles with radii up to $R = 2.5$ nm, we conclude that the particles formed a supramolecular, non-covalent network which caused this flow behavior. Figure 3 schematically illustrates the sol evolution and formation of a spinnable silica sol.

3.2. *Characterization of Silica Fibers*

3.2.1. Chemical Composition and Morphology. IR-spectra revealed the chemical composition of the fibers after spinning as $[Si(EOt)_x(OH)_yO_{2x/2-y/2}]_n$. Removal of EtOH led to silica fibers with the composition $[Si(OH)_yO_{2-y/2}]_n$. The OH-content was calculated by thermal analysis suggesting the chemical composition of silica gel fibers to be $[Si(OH)_{0.2}O_{1.9}]_n$. Figure 4 shows a photograph of silica gel fibers.

Table 1. Structural properties of silica gel fibers.

Measurement	Data
Density	1.755 g/cm^3
Fracture surface area	150–700 μm^2
$A_{specific}$ (DIN 66144)	0.117 m^2/g
OH-content	~5%
^{29}Si-NMR $Q^2 : Q^3 : Q^4$	10% : 43% : 47%

The cross-sections of the fibers varied from circular to oval and bone-shaped depending on the amount and velocity of solvent-evaporation during the spinning procedure, which has been described before [5, 7]. Unlike the results in [5, 7], our silica gel fibers did not show wavy surfaces and also exhibited much smaller cross-sectional areas (between 150 μm^2 and 700 μm^2).

3.2.2. Structural and Mechanical Data. For structural investigations ^{29}Si-NMR measurements provide a good method to evaluate the Si—O network in the silica fibers by calculating the relative amounts of Q^2, Q^3 and Q^4 groups. The results are summarized in Table 1, as well as fiber density, cross-sectional area and specific surface area of the fibers.

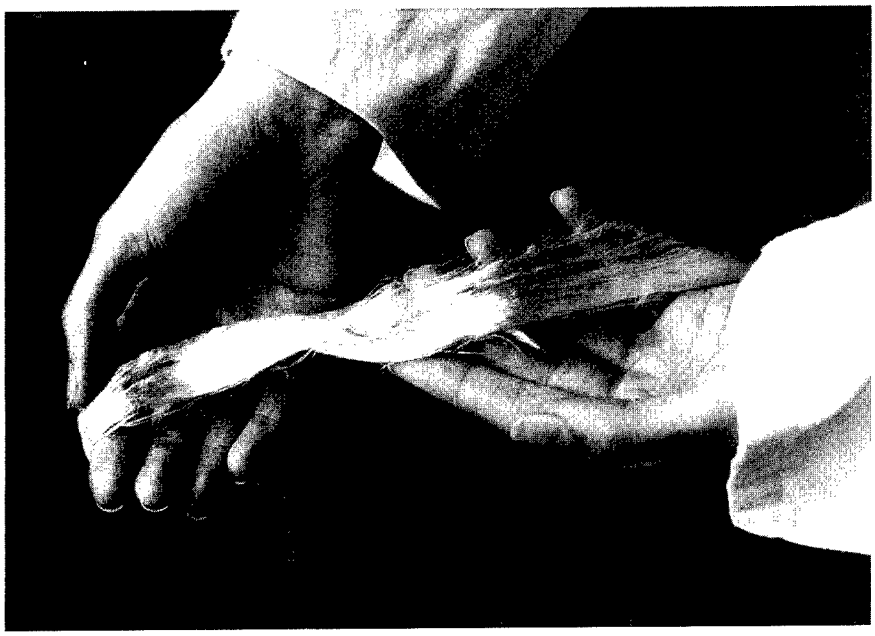

Figure 4. Photograph of silica gel fibers.

Besides the structural data given in Table 1, the two main requirements for the silica fibers applicable as reinforcements for biodegradable implants are the mechanical strength and the dissolution rate. We found tensile strengths of the silica fibers up to 300 MPa and Young's modulus up to 20 GPa. The dissolution rate of the fibers was tested by a continuous flow degradation test using a physiological medium (GAMBLE-solution) according to a literature description [8]. The silica fibers dissolved with a rate of 10 nm to 100 nm fiber radius per day. Mechanical strength and dissolution rate of the silica gel fibers fitted the requirements of a degradable fiber for reinforcement applications. To evaluate the biocompatibility of the fibers, basic cytotoxical tests were carried out. The results did not preclude medical applications of the silica fibers. We also observed a fast settlement of cells on the silica fibers, which is a good indication for the use of the fibers as medical material.

4. Conclusions

In an attempt to establish biodegradable silica gel fibers, we succeeded in developing a novel synthetic route for reproducibly preparing spinnable sols which were stable for several hours and provided good handling for the subsequent continuous spinning procedure. The spinnability of sols was characterized by a certain non-Newtonian rheological phenomenon in the presence of small particles in the sol, which indicated a supramolecular, non-covalent structure of the sol. Due to mechanical and biological testing we expect good potential of the fibers for medical applications.

Encouraged by the promising results we shall try to incorporate the gel fibers into poly(l)lactid (PLA) matrices using an injection molding technique.

Acknowledgments

The authors are grateful to Ms. M. Kapuschinsky for her help in fiber preparation. We also should like to thank Ms. P. Rehak from University of Jena for NMR examinations as well as Dr. C. Blau from IBMT St. Ingbert for the realization of the cytotoxical testings.

References

1. L. Fambri, A. Pegoretti, M. Mazzurana, and C. Migliaresi, J. Mater. Sci.: Materials in Medicine **5**, 679 (1994).
2. P. Ylinen, J. Mater. Sci.: Materials in Medicine **5**, 522 (1994).
3. S.T. Lin, S.L. Krebs, S. Kadiyala, K.W. Leong, W.C. LaCourse, and B. Kumar, Biomaterials **15**, 1057 (1994).
4. C.J. Brinker and G.W. Scherer, *Sol-Gel Science* (Academic Press, Boston, 1990), chap. 3.
5. W.C. LaCourse, *Sol-Gel Technology for Thin Films, Fibers, Preforms, Electronics and Specialty Shapes*, edited by L.C. Klein (Noyes Publications, Park Ridge, NY, 1988), p. 184.
6. F.R. Eirich, *Rheology* (Academic Press, NY, 1960), p. 465.
7. S. Sakka, *Sol-Gel Technology for Thin Films, Fibers, Preforms, Electronics and Specialty Shapes*, edited by L.C. Klein (Noyes Publications, Park Ridge, NY, 1988), p. 140.
8. K. Sebastian, Glass Sci. Tech. **68 C1**, 215 (1995).

Journal of Sol-Gel Science and Technology 13, 273–276 (1998)
© 1998 Kluwer Academic Publishers. Manufactured in The Netherlands.

Production of Valuable Drugs from Plant Cells Immobilized by Hybrid Sol-Gel SiO_2

G. CARTURAN
Department of Materials Engineering, 38050 Mesiano (Trento)

R. DAL MONTE, G. PRESSI, S. SECONDIN AND P. VERZA
R & C Scientifica, 36077 Altavilla Vicentina, Italy

Abstract. *Catharantus roseus* cells are supported on a polyester fiber mat and encapsulated by a porous layer of SiO_2 modified by Si—CH_3 and Si—H bonds. This layer is obtained by reaction of Si-alkoxides in the gas phase with H_2O adsorbed on the cell surface or with exposed —OH groups of cellulosic cell membrane. Viability and alkaloid production of cells are maintained after encapsulation. An experimental reactor allows study of secondary metabolite productivity, which is increased by two orders of magnitude with respect to that of free cells.

Sucrose consumption kinetics are also studied and related to the viability of encapsulated cells.

Keywords: sol-gel biotechnology, cell encapsulation, production of *Catharantus* alkaloids

Introduction

In vitro cultivation of cells affording calli and suspensions of undifferentiated cells may supply large quantities of cell masses of specific plants for the preparation of drugs [1]. This method allows preventive selection of stable and productive cell lines and appears to be suitable for improvements, such as the expedient of using the cell load immobilized on a solid support. The advantages of immobilization are known [2]: continuous production, control of the bioreactor, and reduction of volumes and by-products. In the specific case of plant cell immobilization coupled with undifferentiated cell availability, one crucial aspect is the independence of metabolite production of season cycle, even for plants, and of climatic trends or territorial habitat.

Among the various immobilization methods, the entrapment of single vegetable cells by a layer of porous SiO_2 modified by Si—CH_3 and Si—H moieties has been successfully applied [3]. This approach, called the Biosil® method [4, 5], involves the following steps:

(1) Adhesion of single cells, or small aggregates, to a "scaffold" [6] of various supports providing surface development much larger than the geometric surface, and sufficient stiffness to bear the loads resulting from reactor stirring and medium circulation.
(2) Incubation of the cell mass, which is fed allowing cell reproduction in the pores or network fibers.
(3) Encapsulation of wet cells by a flux of air saturated by a suitable mixture of silicon alkoxides holding Si—OC_2H_5, Si—H, and Si—CH_3 bonds. This latter step affords a porous network of Si—O—Si groups on the surface of the cell membrane.

In this work, we studied the production of *Catharantus roseus* metabolites by cells of these species immobilized by the above method. The aim of this research consisted in defining the experimental parameters useful for detecting the limitations of the technique, as compared with the native productivity of plants and that of ordinary bioreactors fed by free cells.

Experimental Section

Cell Cultures. Cell cultures of *Catharantus roseus* were prepared from leaves, sterilized by NaOCl and

Tween 20. Vegetable material was cultivated in solid B_5 basal medium, supplemented with 30 g/dm^3 of sucrose, 1.3 mg/dm^3 of 2,2-dichloro-phenoxy acetic acid, 0.25 mg/dm^3 of kinetin and 0.25 mg/dm^3 of α-naphthalene acetic acid. Calli were subcultured every 4 or 5 weeks; stable cell lines of pale yellow or ivory materials characterized by easy friability were selected. The calli of the MA cell line were used to prepare cell suspensions in liquid medium: 30 g of wet cell mass was stirred in 300 ml of B_5 liquid into a 1 dm^3 Ehrlenmeyer flask with a rotatory stirrer operating at 80 rpm at 25°C in the dark. Suspensions were subcultivated every 3 weeks.

Cell growth was monitored by measuring cell concentrations while detecting the stationary growth interval, which corresponds to the maximum productivity of secondary metabolites. This interval was reached in 3 weeks and cell concentrations were 20% of the wet cell weight, corresponding to 1 g of dry weight per 100 g of suspension.

Immobilization and Encapsulation of Cells. 100 ml of cell suspension in the stationary growth interval were used to seed polyester fiber mats as cylinders (2.5 cm diameter × 0.7 cm depth; fiber diameter = 10 μm) arranged in a pile inside a glass reactor so that the free volume was 15–20% of the container capacity. After 24 hours the medium was removed and wet cells were reacted with a flux of air saturated with $Si(OEt)_4$ and $CH_3SiH(OEt)_2$ by bubbling into a solution, kept at 80°C, having a molar ratio of $Si(OEt)_4/CH_3SiH(OEt)_2 = 80/20$. Flux was 0.8–0.9 dm^3/min at room temperature and atmospheric pressure. This treatment, prolonged for 30 min, was followed by a 10-minute treatment with an identical flux obtained by bubbling air in H_2O at 80°C. The reactor was filled with the B_5 liquid medium supplemented with 0.025% of tryptophan.

Production Kinetics. A static 1.2-dm^3 cylindrical reactor was provided with service ports for aeration (6 dm^3/day), drawing of samples and medium substitution. The process was monitored every 4 or 5 days by measuring pH, sucrose consumption and total alkaloid concentration. The sucrose concentration was directly measured by the enzymatic method (Boehringer Mannheim), affected by a ±0.2 g/dm^3 uncertainty. Alkaloids were extracted from a 10-cm^3 medium sample and monitored according to the described procedure [7].

Results and Discussion

The gaseous flux of silicon alkoxides affords a permanent deposit of amorphous SiO_2 on the living cell surface, upon reaction with H_2O adsorbed on the cellulose membrane of vegetable cells. The process does not exclude possible condensation between exposed hydroxides of the cellulose and the alkoxides. Layer thickness may be controlled by exposure time. The advantages of this encapsulation procedure are numerous. The gas phase process allows the elimination of ethanol as the building deposit progresses, avoiding poisoning as a result of alcohol produced by alkoxide hydrolysis. Even though the surface may be uneven, the reactive alkoxide flux can bear a homogeneous layer thickness on cells irregularly arranged over the "scaffold." The process can be performed within the reactor for the production of metabolites, avoiding manufacture trains and thus favoring fortuitous contamination by bacteria and spores.

The introduction of $Si—CH_3$ units in the sol-gel SiO_2 network gives rise to a variety of physical

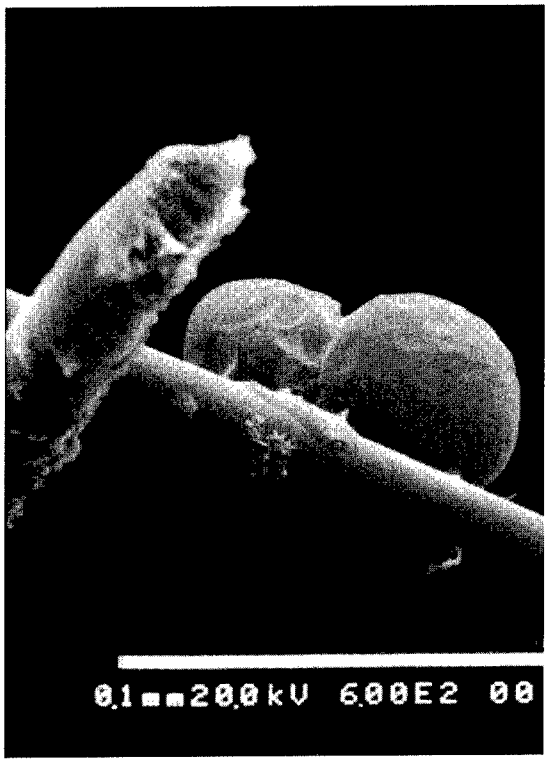

Figure 1. Micrograph of *Catharantus roseus* cells after encapsulation (Philips 515 equipped with EDAX DX4).

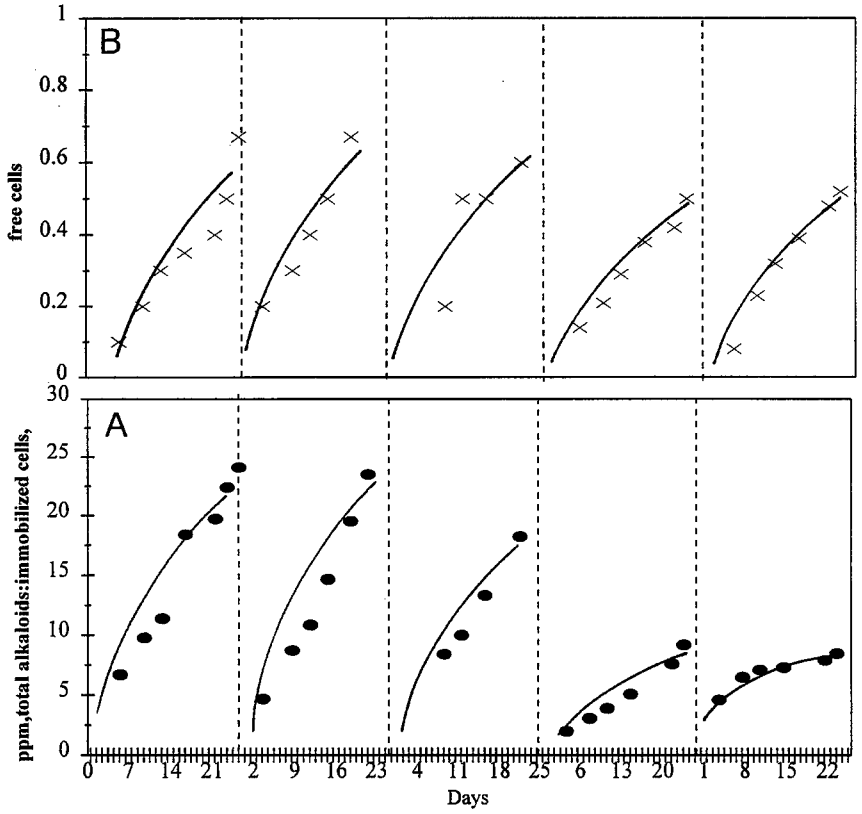

Figure 2. Total alkaloid production of 1 g of dry cell mass over time: productivity of encapsulated and free cells.

properties, accounting for intermediate behavior between SiO_2 and silicone polymers. In our case, this behavior can be controlled by changing the gas phase $Si(OEt)_4/CH_3SiH(OEt)_2$ molar ratio, modifying the original precursor solution from which the alkoxides were evaporated. The layer obtained by 30-minute treatment is strong enough to avoid cell reproduction and release in the medium over more than 15 weeks, i.e., the living time of our encapsulated cells. The layer allows 99% of cell viability measured 24 hours after encapsulation, and maintenance in the B_5 medium by Triphenyl Tetrazol Chloride (TTC) test. This result allows us to consider the living cell mass after encapsulation as equal to that calculated during stationary growth. One example of *Catharantus roseus* cell encapsulated by the SiO_2 layer and supported on polyester fibers is shown in Fig. 1.

The productivity of our encapsulated cells was determined in a research reactor holding 1.0 g of encapsulated dry cell mass. Total alkaloid production was monitored in time by analysis of the medium,

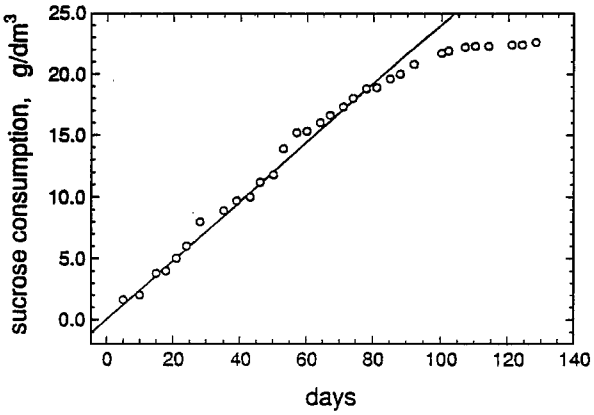

Figure 3. Sucrose consumption of 1 g of dry cell mass over time. Linear regression equation: $y = 0.24057x$, $R = 0.994$.

which also allows measurement of sucrose consumption: data are reported in Figs. 2 and 3 for total alkaloid production and sucrose consumption, respectively. As a result of the trend of Fig. 2, which parallels the

secondary metabolite production of free cells [8], the medium was substituted after 26 ± 2 days, corresponding to a total alkaloid concentration of 25 mg/l, for the first cycle (see Fig. 2A).

The results of Fig. 2 are compared as regards total alkaloid production of encapsulated and of free cells of the same cell line. The productivity of encapsulated cells is two orders of magnitude higher than that of free cells: the daily maximum output of 1 mg of alkaloids per gram of dry cell mass appears to be sufficiently high to compensate for processing costs.

Linear sucrose consumption (Fig. 3) indicates a daily requirement of 0.24 g per gram of dry cell mass over an interval of 77 ± 5 days. Lowering of consumption parallels the observed lowering of alkaloid productivity. This fact may first be associated with cell aging, since tests performed after 80 days indicate that viability is 95%, and then with cell mortality.

Considering the difference, Δ, between the consumption of sucrose calculated from the slope of Fig. 3 and the experimental value as a parameter proportional to inactive cells, we obtained a linear trend on plotting $\ln\Delta$ vs. time, for time $>77 \pm 5$ days. Treatment of data, according to a first-order functionality decay, gives a first-order rate constant of 0.0424 ± 0.0016 day^{-1}. Evaluation of total inactivity after $t = 77 \pm 5 \pm 3t_{1/2}$, the entire lifetime of our cell load is 126 ± 5 days, which agrees with the natural vegetative cycle of *Catharantus roseus*.

During the 5-cycle production, the recovered alkaloid mass is 0.1 g per gram of dry cell mass. This result may be improved further, since it was obtained with cell line productivity of one-tenth of the best productivities reported in the literature [9].

HPLC analysis of the medium after each production cycle indicates quantities of 35–42% of vincristine and vinblastine with respect to total alkaloids.

Conclusion

The Biosil method appears to be feasible for the industrial production of secondary metabolites; in the case studied here, it is shown that 100 days of continuous production affords a daily solution release of 1 mg of alkaloids per gram of dry cell mass.

References

1. G.F. Payne, V. Bringi, C.L. Price, and M.L. Shuler, *Plant Cell and Tissue Culture in Liquid Systems* (Hanser Press, Munich, 1992).
2. C. Vandrey, in *Immobilized Cells: Basics and Applications*, edited by R.H. Wijffels, R.M. Buitelaar, C. Bucke, and J. Tramper (Elsevier, 1995), p. 3.
3. R. Campostrini, G. Carturan, R. Caniato, A. Piovan, R. Filippini, G. Innocenti, and E.M. Cappelletti, J. Sol-Gel Sci. Tech. 7, 87 (1996).
4. E.M. Cappelletti, G. Carturan, and A. Piovan, PCT Intern. Publication No. WO 96/36703, 21 November 1996.
5. G. Carturan, M. Muraca, and R. Dal Monte, PCT International Application No. EP 96/02265, international filing date: 28 May 1996.
6. J. Kohn, MRS Bull., 18 (1996).
7. W.I. Taylor and N.R. Farnsworth, *The Vinca Alkaloids* (Marcel Dekker, New York, 1973).
8. A. Stafford and L. Smith, *Secondary Metabolism in Plant Cell Cultures* (University Press, Cambridge, 1986), p. 250.
9. J.P. Kutney, B. Aweryn, L.S.L. Choi, T. Honda, P. Kolodziejczyk, N.G. Lewis, T. Sato, S.K. Sleigh, K.L. Stuart, B.R. Worth, W.G.W. Kurz, K.B. Chatson, and F. Constabel, Tetrahedron **39**, 3781 (1983).

Journal of Sol-Gel Science and Technology 13, 277–281 (1998)
© 1998 Kluwer Academic Publishers. Manufactured in The Netherlands.

Sol-Gel Carrier Systems for Controlled Drug Delivery

H. BÖTTCHER
Feinchemie GmbH Sebnitz, Höhenweg 9, D-01855 Sebnitz, Germany

P. SLOWIK AND W. SÜß
Universität Leipzig, Institut für Pharmazie, Pharmazeutische Technologie, Schönauer Str. 160, D-04207 Leipzig, Germany

Abstract. Embedding of the well-known coronary therapeuticum nifedipine into a modified silica matrix by the sol-gel technique allows its releasing behavior to be controlled to a high degree. The liberation rate is proportional to temperature and is increased by the addition of penetration agents such as sorbitol, but is inversely proportional to particle size and is decreased by modification of the silica matrix with methyl-triethoxysilane or polyethyleneglycol. It is presumed that the drug is dispersed in the gel matrix and that diffusion occurs through solvent-filled capillary channels. The liberation rate is governed by the relationship between the rates of dissolution and diffusion.

Keywords: silica, composites, nifedipine, polyethyleneglycol, controlled release

1. Introduction

The controlled release of active agents from an inert matrix has become increasingly important for oral, transdermal or implantable therapeutic systems, due to its advantages of safety, efficacy and patient convenience [1]. Examples of fields where such controlled release systems may be applied are consumer products with encapsulated flavors, vitamins and minerals as well as agrochemicals and biocidal products [2].

The recently developed sol-gel technique offers new possibilities for embedding organic compounds within silica and other modified inorganic oxides [3], and for controlling their release from the host matrix into a surrounding medium. As yet, such sol-gel carrier systems for drug delivery systems are not widely known, despite their obvious advantages. The technology is simple and versatile, with the oxide matrix being cheap, inert and stable to light and heat without being hazardous to humans or the environment. Nevertheless, only a few investigations into embedding drugs within polycondensates of poly-ethoxysiloxans [4] and the release of steroids [5], flavors [6, 7] and biocidal substances [7] from a silica sol-gel matrix have been published.

Hence, it is interesting to evaluate the suitability of modified silica gels as the carrier matrix for pharmaceutical controlled release systems, and to investigate the influence of sol-gel parameters, grain size and temperature on releasing behavior. For these model investigations, the calcium antagonist nifedipine (dimethyl-[1,4-dihydro-2,6-dimethyl-4-(2-nitrophenyl)-3,5-pyridine-dicarboxylate]) was used. This well-known drug is commonly used to treat hypertension and angina pectoris. To deliver a constant plasma concentration over 24 hours, different galenic retard forms of nifedipine are already available (e.g., Procardia XL®30 as the first trade product in USA). The development of new improved retard forms for this drug is of great practical interest.

2. Experimental

2.1. *Preparation of Nifedipine-Silica Composites*

5.25 g nifedipine (I) (Arzneimittelwerk Dresden GmbH, Germany) were dissolved in 500 ml of sol A (prepared by stirring together 100 ml $Si(OEt)_4$, 400 ml

ethanol and 200 ml 0.01 N HCl for 20 hours at room temperature). After neutralization with 1% ammonia at 50°C, pale yellow transparent homogeneous gels formed within a few minutes. The minced light-sensitive gel was dried at 50°C in a light-protected drying oven, until the weight was constant (26.2 g). This prepared composite powder contains 20 wt.% (I). In the same way, 2.33 g (I) and 500 ml sol A yield 23.3 g of a composite powder with a content of 10 wt.% (I).

2.2. *Liberation Investigations*

The composite powder was ground and classified by sieving (sieve tower RETSCH AS 200 basic, Retsch GmbH Haan, Germany, 10 min with an amplitude of 45 μm). The liberation rates into water of (I) from the sieve fractions of the nifedipine-silica composites were determined by soaking samples (all with an absolute content of 5 mg (I)) in one liter of water under standard conditions of 20–60°C, 50 rpm (after DAB 1996) in a light-protected paddle device (Erweka DT 6, ERWEKA GmbH, Heusenstamm, Germany). The resulting solutions were analyzed by HPLC (HPLV 2200, BISCHOFF GmbH, Leonberg, Germany; column RP-18, solvent MeOH/water (80/20), UV detector at 238 nm). The deviations between two measurements were smaller than 5%.

3. Results and Discussion

It was shown that the releasing behavior of nifedipine from the silica matrix can be controlled to a high degree by the sol-gel technique. The rate of gel formation has a considerable influence on composite structure and releasing behavior. Higher sol concentrations and gelling temperatures (i.e., high gel formation rates) yield more porous composites with amorphously incorporated (I), which show a faster rate of release of (I) than comparable composites prepared at lower temperatures. DSC measurements and polarization microscopy proved that the nifedipine exists entirely in an amorphous state in composites with 10 wt.% (I) after a fast gelation at more than 50°C, whereas partially crystalline areas were found after a slow gelation (lasting more than 45 min) at room temperature. Therefore, it is necessary to use identical preparation conditions in order to obtain comparable measurements.

Two well-known general factors affecting the releasing behavior of drugs were confirmed to apply to the (I)-silica composites: the mean grain size and the releasing temperature.

As shown in Fig. 1, the rate of liberation of (I) from the composite is inversely proportional to the mean grain size, d. The smaller the grain size, the greater the rate of liberation. The more rapid release of (I) from smaller grain fractions was also confirmed by the

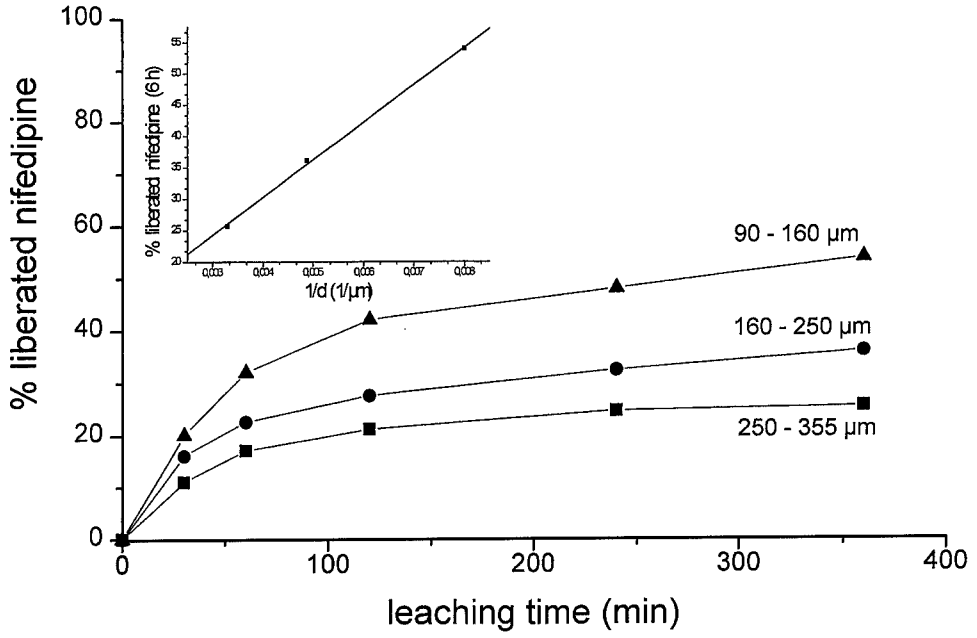

Figure 1. Liberation into water of (I) from silica composites of different mean grain size d (40°C, 20 wt.% nifedipine). Insert: Correlation of the wt.% liberated (I) vs. reverse mean grain size $1/d$.

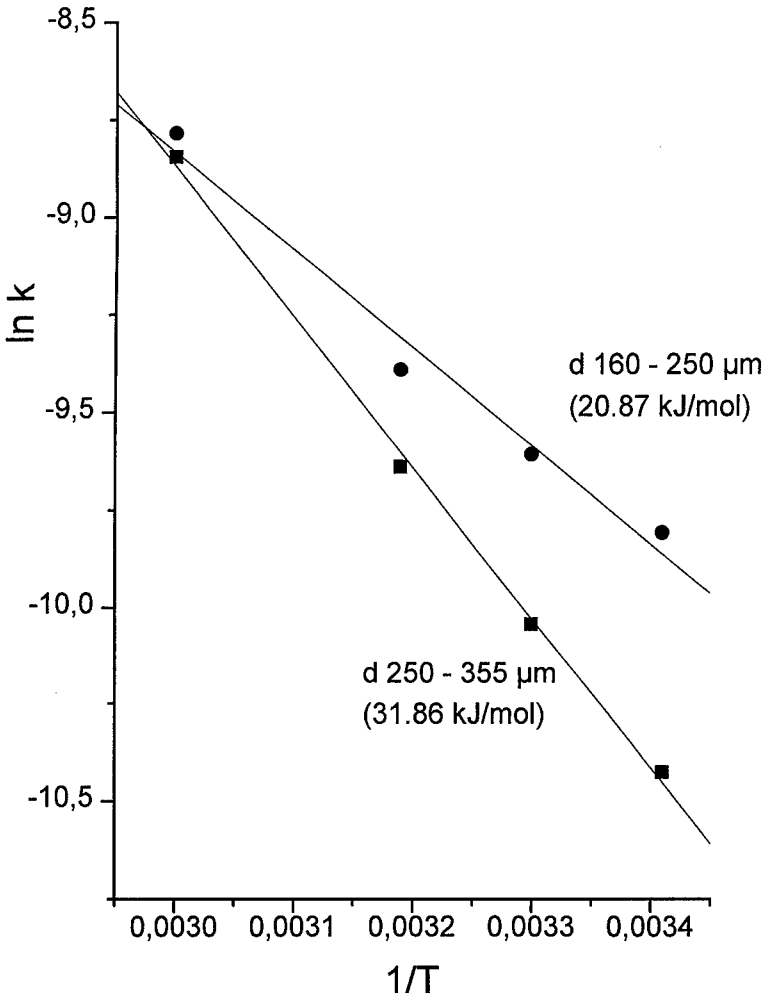

Figure 2. Arrhenius plot and activation energies of the liberation into water of (I) from silica composites (20 wt.% nifedipine) for different mean grain size d (k is calculated from the initial rates).

decrease in the activation energies, calculated from the Arrhenius plot in Fig. 2. This is caused by a reduced surface-to-bulk ratio as the grain size increases. Before liberation of the drug can occur, it must diffuse from within the increasingly large grain volume to the composite surface.

The releasing rate of (I) is also influenced by chemical or physical changes to the silica matrix. One possible chemical change is the modification by organofunctional metal alkoxides or trialkoxysilanes during the sol preparation, for example, by the co-hydrolysis of $Si(OEt)_4$ with $MeSi(OEt)_3$ during sol preparation. Partial substitution of $Si(OEt)_4$ with 10, 30 and 50 vol% $MeSi(OEt)_3$ during the sol preparation results in a successive slowing of the nifedipine liberation from the corresponding composites (Table 1).

This effect could be due to various causes, for example, the increasing hydrophobic character of the matrix and a diminished ratio of mesopores and nanopores within the matrix. However, Table 1 also shows that for films prepared by coating the same (I)-containing sols onto cellite foils there was a different relationship between $MeSi(OEt)_3$ content and liberation rate (with

Table 1. Relative liberation rates into water : EtOH (7 : 1) at 25°C of nifedipine from modified silica composites containing 20 wt.% (I).

% Co-hydrolyzed $MeSi(OEt)_3$	0	10	30	50
Composite bulk ($d < 500\,\mu m$)	1	0.87	0.77	0.62
Composite film	1	0.55	0.21	1.86

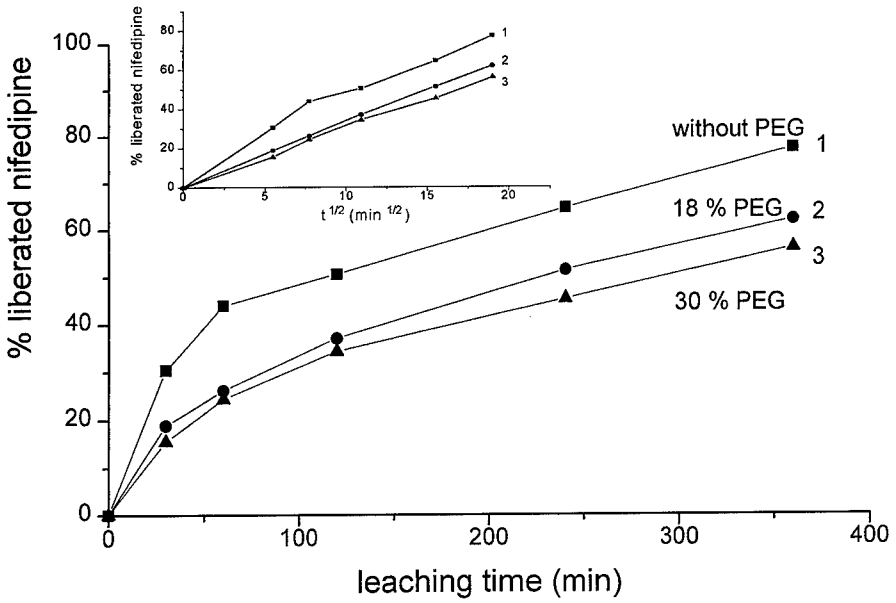

Figure 3. Liberation into water of (I) from different (I)-silica-PEG composites (37°C, 10 wt.% nifedipine, *d*: 180–250 μm). Insert: Correlation of the wt.% liberated (I) vs. the square root of leaching time, $t^{1/2}$.

minimum liberation at 30 vol% $MeSi(OEt)_3$), due to different mechanisms in the gelation and drying processes. Thus, to achieve reproducible release rates, the grain size as well as the gelling and drying conditions of the composites must be defined.

The composite structure can also be physically altered by the addition of external additives such as sol-soluble low or high molecular weight compounds during composite preparation. Substituting the effective penetration agent sorbitol at 20 wt.% for silica causes the liberation rate of (I) from the silica composite with 10 wt.% (I) to increase from 66% to 83% (I). Alternatively, the silica matrix may be modified without any problems by the addition of up to 50 wt.% of the liquid polyethyleneglycol, PEG 600. The resulting (I)-silica-PEG composites are also dry, stable, pale yellow granulates but exhibit surprising liberation behavior. Figure 3 shows that liberation from these composites is retarded in comparison to that from the pure silica composite. The progressive liberation process is connected with two interesting effects: firstly, the destruction of the composite particles and secondly, the formation of crystalline areas in non-destructed particles.

Generally, the (I)-composites can be considered as matrix systems in which the drug is to a large measure uniformly distributed within the gel matrix. Liberation of the drug occurs through penetration of solvent into the pores, cracks and interparticular spaces of the matrix. The drug slowly dissolves into the permeating fluid phase and diffuses from the system along the solvent-filled capillary channels. For such matrix systems there are four general categories, differing in the method of solution of the drug within the matrix and in the mechanism of diffusion. For example, for the (I) composites, the drug diffusion occurs through pores rather than directly through the matrix (as could be the case for some polymeric matrices). For each category, the equation which can be used to predict the initial release rates [1] is a form of the general solution (1) with differing values of the constant K:

$$a = Kt^{1/2} \tag{1}$$

where a is the liberated quantity of the drug and t represents the leaching time. For the category when the drug is dispersed in the matrix and diffusion occurs through solvent-filled pores, the constant is

$$K = [(D_s\varepsilon/\tau)c_s(2c_d - \varepsilon c_{sw})]^{1/2}. \tag{2}$$

From Eqs. (1) and (2) it can be seen that the liberation rate depends on the diffusion constant D_s of the drug in the solvent, and increases with (a) the ratio of porosity ε to tortuosity τ for the matrix, (b) the solubility c_s

of the drug in the solvent used and (c) the initial drug content c_d within the composite.

The insert in Fig. 3 shows that there is good correlation between a and $t^{1/2}$ for the (I)-silica-PEG composites, following Eq. (1). The small deviations from linearity after long leaching times are caused by the observed destruction of the composite grains. Due to the higher viscosity of the PEG-water mixture, diffusion occurs more slowly than for pure water and the releasing rates are lower than in PEG-free composites.

In polymer-free (I)-silica composites, Eq. (1) is only valid for the initial period (see Fig. 3). The course of further liberation can be described by zero-order kinetics. Because the diffusion rate of (I) is lower than its dissolution rate, after one hour a saturated solution of (I) is formed within the pores and the drug is able to form crystalline precipitates in the pores. Therefore, liberation is only controlled by the diffusion constant and is directly proportional to the leaching time. From a pharmaceutical point of view, it is desirable that a drug should have such a pattern of releasing behavior.

4. Conclusions

It has been proved that the liberation of nifedipine from sol-gel composites can be controlled to a high degree. The liberation rate is influenced by the grain size of the composites, by modification of the silica matrix with methyl-triethoxysilane and by low or high molecular weight sol-soluble additives (sorbitol, polyethyleneglycol). In this way it is possible to produce composites giving uniform drug release over a long period of time and to adapt the releasing behavior to the pharmacokinetic demands.

References

1. R. Langer, Acc. Chem. Res. **26**, 537 (1993); J. San Roman, A. Gallardo, and B. Levenfeld, Adv. Mater. **7**, 203 (1995); D. Lohmann, Macromol. Symp. **100**, 25 (1995).
2. S.J. Risch and G.A. Reineccius (Eds.), *Encapsulation and Controlled Release of Food Ingredients*, ACS Symp. Series 590 (Amer. Chem. Soc., Chicago, 1993).
3. S. Sakka, J. Sol-Gel Sci. Tech. **3**, 69 (1994); C. Sanchez and F. Ribot, New J. Chem. **18**, 1007 (1994); D. Avnir, Acc. Chem. Res. **28**, 328 (1995).
4. K. Unger, H. Rupprecht, B. Valentin, and W. Kirchner, Drug Developm. Ind. Pharm. **9**, 69 (1983).
5. L. Sieminska and T.W. Zerda, J. Phys. Chem. **100**, 4591 (1996).
6. G. Carturan, E. Pagini, R. Campostrini, and R. Ceccato, J. Sol-Gel Sci. Tech. **8**, 1115 (1997).
7. H. Böttcher, K.-H. Kallies, and H. Haufe, J. Sol-Gel Sci. Tech. **8**, 651 (1997); H. Böttcher, C. Jagota, K.-H. Kallies, and H. Haufe, Chem. Mater., submitted for publication.

Journal of Sol-Gel Science and Technology 13, 283–287 (1998)
© 1998 Kluwer Academic Publishers. Manufactured in The Netherlands.

Encapsulation of Microbial Cells into Silica Gel

TOMÁŠ BRÁNYIK AND GABRIELA KUNCOVÁ
Institute of Chemical Process Fundamentals, Academy of Sciences of the Czech Republic, Rozvojová 135, 16502 Praha 6-Suchdol, Czech Republic
kuncova@icpf.cas.cz

JAN PÁCA AND KATEŘINA DEMNEROVÁ
Institute of Chemical Technology Prague, Technická 5, 166 28 Praha 6, Czech Republic

Abstract. This work deals with changes in microbial phenol degradation and cell proliferation caused by immobilization into silica gel. Mixed microbial culture and the yeast *Candida tropicalis* were immobilized in silica layers and pieces prepared by mixing of prepolymerized tetraethoxysilane with cell suspension. The phenol degradation rate of cells entrapped in silica gel was compared with those immobilized into an organic polymer-polyurethane. The phenol degradation efficiency decreased in the following order: free cell suspension > cells entrapped into polyurethane foam > cells entrapped into prepolymerized TEOS. Inside the silica there was no growth observed by optical microscope. The immobilization of bacterium *Pseudomonas species 2* into silica gel, cells which co-metabolize PCBs with biphenyl, did not result in substantial change of intermediate concentration.

Keywords: sol-gel method, cell encapsulation, phenol biodegradation, PCB biodegradation

1. Introduction

Decontamination of waste waters containing phenols and polychlorinated biphenyls (PCBs) is of a great practical importance. Some microorganisms are able to utilize phenol as a sole carbon and energy source [1]. PCBs are co-metabolized with biphenyl [2]. Biodegradation is often complicated by unexpected difficulties and immobilized cells offer solutions via increasing and retention of bioreactors catalytic activity, protection of cells against wash out and substrate inhibitory effects, separation ease and storage stability. Among the common immobilization materials used in biodegradations [3] silica gels belong to those with high chemical and biological resistance. Microbial cells, plant cells and pancreatic islets [4–6] have been successfully incorporated into silica gel derived materials.

The aim of this work was to investigate the influence of immobilization into silica gel by sol-gel processing on phenol and PCB degrading cells. The phenol degrading cells were an undefined mixed culture and pure microbial culture of yeast *Candida tropicalis*. The PCB degrading cells were the bacteria *Pseudomonas species 2*. The applicability of biocatalysts formed by encapsulation of cells into silica gel and into polyurethane foam commonly used in environmental technologies was studied.

2. Experimental Part

2.1. Microorganisms and Medium

A mixed culture adapted to phenol was used. The microbes were cultured under aerobic conditions (rotary shaker, 120 rpm) at 30°C for 72 h in a mineral medium. 175 mg/l of phenol was added at the beginning of the cultivation 350 mg/l after 24 h and 525 mg/l after 48 h.

Yeasts *Candida tropicalis* were cultured under aerobic conditions (rotary shaker, 120 rpm) at 30°C for 120 h in a mineral medium. 250 mg/l of phenol was added daily. Bacterium *Pseudomonas species 2*

was cultured under aerobic conditions (rotary shaker, 120 rpm) at 30°C for 120 h in a mineral medium. Substrate (biphenyl) was added at the beginning of the cultivation at a concentration of 20 mg/l. The mineral medium contained in 1 liter: 4.3 g of K_2HPO_4; 3.4 g of KH_2PO_4; 2.0 g of $(NH_4)_2SO_4$; 0.34 g of $MgCl_2 \cdot 6H_2O$ and 1 ml of trace element solution.

2.2. *Chemicals and Analytical Methods*

The following chemicals were used: colloidal SiO_2 (250 g/l), 4-aminoantipyrene (Aldrich), tetraethoxysilane (TEOS) (Fluka Chemie AG), polyurethane (Hypol 2002; Hampshire Chemical Limited, Middlesbrough, UK), Biphenyl (Lachema, Brno) and polychlorinated biphenyls (PCBs) that were mixtures of approximately 40 congeners containing 2–6 chlorine molecules (Chemko, Strazske, Czech Republic).

Phenol content was determined by the photometric method [7]. Yellow intermediates (chlorinated derivates of 2-hydroxy-6-oxo-6-phenylhexa-2,4-dienoic acid) [2] of the PCB biodegradation were followed by UV-Vis spectrophotometer Hewlett Packard 8452A at 600 nm. The influence of light losses by cells and medium was eliminated by subtraction of the absorbance measured at 400 nm ($A_{600} - A_{400}$). The concentration of cells in suspension (optical density, OD) was determined by measuring the absorbance at 400 nm (*Pseudomonas species 2*) and 500 nm (mixed culture, *Candida tropicalis*). The growth of individual cells or colonies was observed by optical microscopy (Leitz Wetzlar).

2.3. *Immobilization*

Biomass was harvested by centrifuging the cell suspension for 10 min at 10,000 rpm, after which the recovered microorganisms were resuspended in appropriate amounts of distilled water. The microorganisms were then immobilized by one of the following methods:

(a) *Immobilization of cells into TEOS*: TEOS (3.5 ml) was vigorously mixed with 2.8 ml of slightly acid distilled water (pH 2.8) until the turbid mixture became a clear solution. The solution was then kept at 4°C for approximately 72 h until a viscous (ca. 1000 cP) solution, containing 25–27 wt.% Si, was formed. 1.5 g of the viscous solution was then transferred into a polyethylene test tube where the cell suspension (1 ml, ca. 25 g/l dry cell weight of the mixed culture or *Candida tropicalis*, ca. 15 gl/l dry cell weight of *Pseudomonas species 2*) and 0.1 ml of KOH solution was rapidly added and mixed. Gelation occurred within a few seconds. The gels were then dried at room temperature for 20 min and subsequently cut into pieces, approximately $3 \times 3 \times 4$ mm in size, which were dried at 4°C for 120 min.

(b) *Immobilization of cells into polyurethane (PU)*: 1.5 g of polyurethane was mixed with 1 ml of cell suspension (ca. 25 g/l dry cell weight) and allowed to polymerize in a silicone tube at 25°C. The resulting foam was cut to obtain cylinders with an average volume of 0.66 cm^3 in the swollen state.

2.4. *Batch Experiments*

Immobilized cells were placed into 250 ml Erlenmeyer flasks with 100 ml of mineral medium and the experiments were carried out under aerobic conditions on a rotary shaker (120 rpm) at 30°C. After phenol depletion in the medium and before starting a new cycle, the carriers with cells were rinsed several times with sterile distilled water and then transferred into a sterile medium together with an appropriate amount of phenol. In the first batch the newly prepared polyurethane with entrapped cells floated until it soaked up the medium.

Batch experiments with free cells and with PCB degradation were carried out under the same conditions. *Pseudomonas species 2* were entrapped into prepolymerized TEOS and placed into mineral medium with 0.1 g biphenyl and 4 μl PCB.

3. Results and Discussion

The influence of the encapsulation on phenol consumption and cell outgrowth is shown in Fig. 1. The mixed culture was immobilized either into prepolymerized TEOS (TEMC) or into polyurethane (PUMC). The most significant difference between the biocatalysts was in the duration of the phenol degradation lag phase. Twelve hours were observed for PUMC and less then one hour for TEMC. This means that cells suffered greater stress during the PU formation probably caused by toxic isocyanate groups present in the PU prepolymer [8]. The immediate phenol consumption in TEMC implies that the alcohol concentration in prepolymerized TEOS was below critical and

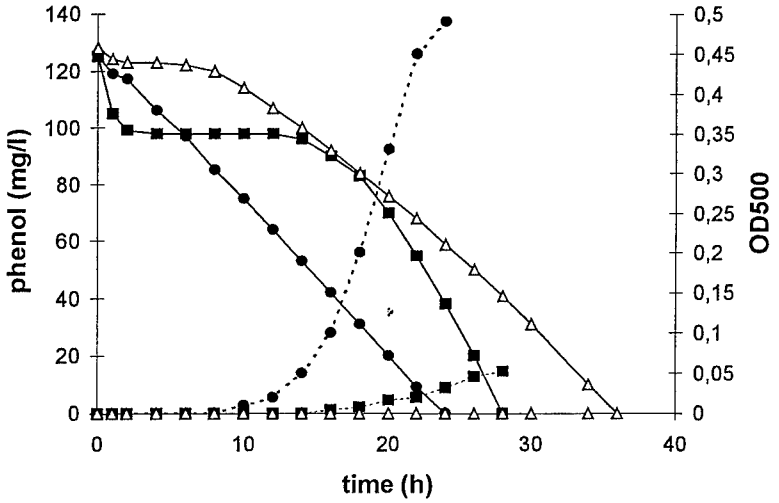

Figure 1. Biodegradation of phenol after immobilization by TEMC (—●—), PUMC (—■—) and yeast *Candida tropicalis* entrapped into prepolymerized TEOS (—△—). The outgrowths of cells are indicated with appropriate dotted lines.

therefore did not cause serious cell damage. Nevertheless, the average phenol degradation rate (APDR) for PUMC, after the lag phase, is higher (6.25 mg/l · h) than in TEOS (5.2 mg/l · h). Immobilization of *Candida tropicalis* into prepolymerized TEOS caused an 8-hour lag phase followed by a phenol degradation rate of 4.36 mg/l · h. The highest outgrowth was observed for TEMC probably as a result of partial gel dissolution during the first batch operation (Fig. 1). In subsequent batch operations the values of the outgrowth are similar for TEMC and PUMC. *Candida tropicalis* in TEOS showed no outgrowth due to the disadvantageous medium composition reducing its growth to a minimum and making the cultivation sensitive towards contamination.

The APDR of PUMC increased during the subsequent batch operations while for TEMC the maximum APDR was reached after three batch operations (Fig. 2). It is thought that the rigidity of the silica gel did not allow a significant growth of the biomass inside the silica gel. By contrast the flexibility of the polyurethane allowed cell growth in the polymer itself, and the macroscopic pores on the surface enabled the cells to colonize the surface and thus increase the biomass content.

The effect of initial phenol concentration on APDR is shown in Fig. 3. Two concentrations of cells in

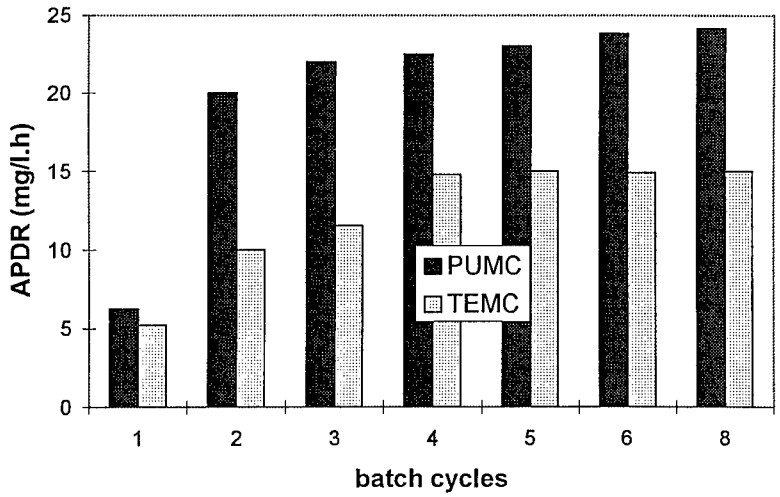

Figure 2. The growth of APDR at 150 mg/l initial phenol concentration during subsequent batch cycles.

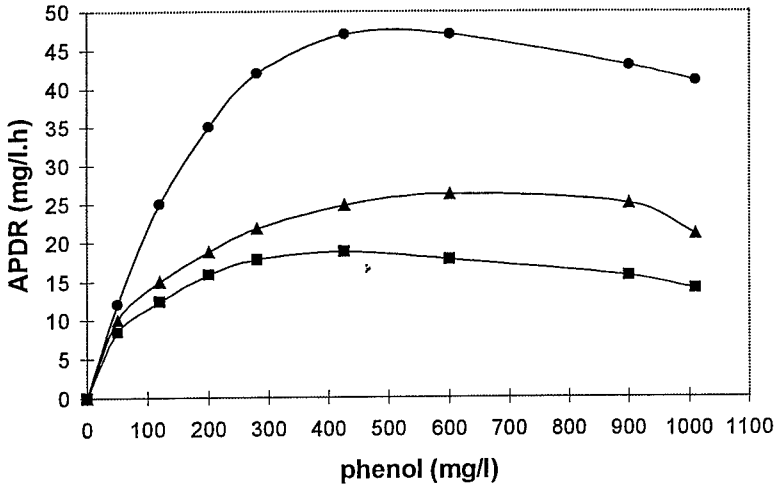

Figure 3. The effect of initial phenol concentration on APDR. —●— free cell suspension (OD_{500} = 0.5), —■— free cell suspension (OD_{500} = 0.04), —▲— TEMC.

suspension ($OD_{500} = 0.5$, $OD_{500} = 0.04$) were compared with TEMC. The higher cell concentration represents the same level of cells that were entrapped into TEMC. The free cells exhibited a much higher APDR in the whole concentration range compared to TEMC. Ignoring cell damage caused by immobilization, the lower oxygen and substrate supply to the cells inside the particles, compared to cells near surface, could decrease the effectiveness of the phenol oxidation. This limitation could be the result of the diffusion resistance of the silica gel, or could be caused by complete oxygen and substrate consumption by cells near the surface. Moreover, inside the rigid silica gel the growth of cells coupled with phenol consumption is considerably restricted and this could also lead to decreased degradation rate. The lower cell concentration is an average concentration of cells that outgrew from the TEMC during the degradation of approximately 150 mg/l phenol. The lower APDR of this cell suspension proved that other cells than just those that had escaped from the TEMC into the medium, consumed phenol.

The evolution of the yellow intermediate products of PCB degradation and the cell outgrowth is depicted in Fig. 4. Equal initial amounts of bacteria *Pseudomonas species 2* were compared in immobilized form and in cell suspension. The time of the greatest

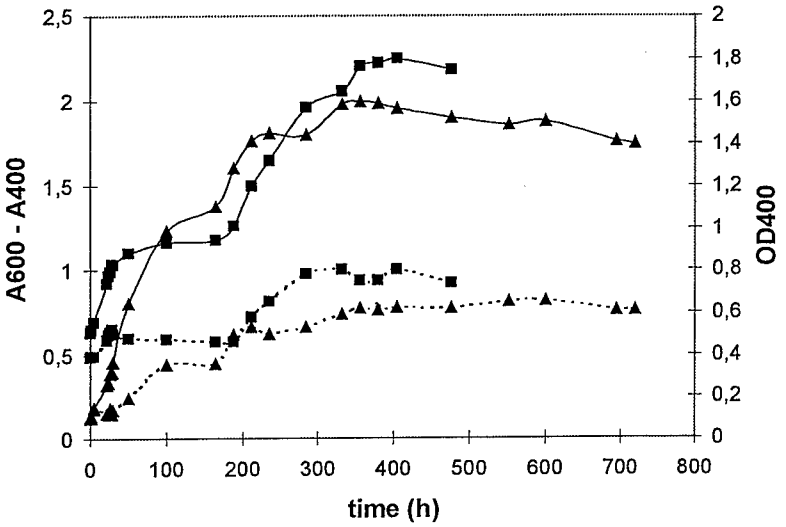

Figure 4. The evolution of yellow intermediates ($A_{600} - A_{400}$) during the degradation of PCBs by *Pseudomonas species 2* (—■— free cell suspension, —▲— cells immobilized into prepolymerized TEOS). The growth of cells (OD_{400}) is indicated with appropriate dotted lines.

increase in the intermediate concentration differed. However, there was no evidence of changes in the rate of biodegradation due to immobilization. This experiment, which was repeated several times using the initial silica gel with immobilized bacteria, also proved that co-substrates such as PCB were effectively metabolized.

Observation of living cells in silica layers, made of colloidal SiO_2 [9], showed that neither single cells nor groups of cells grew in the direction parallel to the silica layer. Under experimental conditions, there was no formation of colonies observed in silica gel pieces, unlike what happens in organic polymers [10]. It could be an effect of the material tensile strength that prevented cell reproduction [11]. The cell growth into the medium was probably a consequence of the cell leakage from the surface and/or the outgrowth in the direction vertical to the silica layer. However, local cell accumulations were observed in silica gel during PCB degradation. Air bubbles in the sol, which appeared after stirring, were captured by the rapid gelation. These open spaces were often filled with growing bacteria, giving dark spots inside the transparent silica gel.

4. Conclusions

The immobilization of living microbial cells into prepolymerized TEOS and polyurethane foams proved that the sol-gel process influenced the mixed culture by providing a less stressful environment than the cross-linking of the polyurethane prepolymer. The rigidity and the small pore size of the silica gel did not allow the cell growth inside the silica material. Cell proliferation was possible only on the surface of the carrier. The biodegradation capacity decreased in the order free cells > encapsulation in polyurethane foam > encapsulation in prepolymerized TEOS. The total volume of the swollen polyurethane foam with cells is at least six times larger than that of the silica gel with cells. This means that use of silica gel would enable an increase in biocatalyst concentration in a bioreactor. High densities of living cells, and the chemical and biological stability of the silica material also makes these biocatalysts attractive for in situ bioremediation of contaminated soil and water.

Acknowledgments

Financial support by the Czech Grant Agency (Grant 104/96/0459 and 104/97/1212) is gratefully acknowledged.

References

1. M. Krug, H. Ziegler, and G. Straube, Journal of Basic Microbiol. **2**, 103 (1985).
2. K. Furukawa, N. Tomizuka, and A. Kamibayashi, Applied and Environmental Microbiology **38**, 301 (1979).
3. M.B. Cassidy, H. Lee, and J.T. Trevors, Journal of Industrial Microbiology **16**, 79 (1996).
4. E.J.A. Pope, Journal of Sol-Gel Science and Technology **4**, 225 (1995).
5. R. Campostrini, G. Carturan, R. Caniato, A. Piovan, R. Filippini, G. Innocenti, and E.M. Cappelletti, Journal of Sol-Gel Science and Technology **7**, 87 (1996).
6. E.J.A. Pope, K. Braun, and C.M. Peterson, Journal of Sol-Gel Science and Technology **8**, 635 (1997).
7. R.W. Martin, Anal. Chem. **21**, 1419 (1949).
8. J. Klein and F. Wagner, Appl. Biochem. Bioeng. **4**, 11 (1983).
9. T. Brányik, G. Kuncová, J. Páca, K. Jurek, and F. Kaštánek, in *Immobilized Cells: Basics and Applications*, edited by R.H. Wijffels, R.M. Buitelaar, C. Bucke, and J. Tramper (Elsevier, Amsterdam, 1996), p. 757.
10. L.E. Huskens, J. Tramper, and R.H. Wijffels, in *Immobilized Cells: Basics and Applications*, edited by R.H. Wijffels, R.M. Buitelaar, C. Bucke, and J. Tramper (Elsevier, Amsterdam, 1996), p. 336.
11. L. Inama, S. Diré, G. Carturan, and A. Cavazza, Journal of Biotechnology **30**, 197 (1993).

Journal of Sol-Gel Science and Technology 13, 289–294 (1998)
© 1998 Kluwer Academic Publishers. Manufactured in The Netherlands.

The Application of a Sol-Gel Technique to Preparation of a Heavy Metal Biosorbent from Yeast Cells

JÁNOS SZILVA AND GABRIELA KUNCOVÁ
Institute of Chemical Process Fundamentals, Academy of Sciences of the Czech Republic, Rozvojová 135, 165 02 Prague 6-Suchdol, Czech Republic
kuncova@icpf.cas.cz

MILAN PATZÁK AND PAVEL DOSTÁLEK
Department of Fermentation Chemistry and Bioengineering, Institute of Chemical Technology, Technická 5, 166 28 Prague 6, Czech Republic

Abstract. In this work we compared biosorbents obtained by encapsulation of polysaccharides, isolated from waste brewing biomass, in sol-gel derived silicates and an organic polymer. Biosorbents were prepared by mixing cross-linking-agents—organic or siliceous—with dried cells envelopes. Siliceous prepolymers were synthesized via transesterification and hydrolysis from tetraethoxysilane (TEOS) and methanol. Sorption of Cd^{2+}, Cu^{2+} and Ag^{+} by biosorbent granules (0.25–0.6 mm) was examined in batch and in a packed column. The biosorbent prepared by interesterification of TEOS showed a 2–3 times higher intensity of sorption than the biosorbent cross-linked with epichlorohydrin (the most effective cross-linking organic agent) while the sorption capacity of both biosorbents was equal. The specific surface area of the silica matrix was 597 m^2/g but only traces of metals were sequestered from solution with a concentration of Cd^{2+} of 50 mg/l. The biosorbent with a silica matrix is a heterogeneous material containing microporous matrix inclusions of thin cell walls. Its high sorption intensity and good mechanical strength will be useful in continuous metal uptake of low concentrations of metals.

Keywords: sol-gel, metal biosorption, polysaccharide encapsulation, column sorption

1. Introduction

Metal accumulation by the cells of certain microorganisms in solution has been used with good results in recent years for environmental protection or metal recovery [1]. Thousands of tons of dead cell biomass, low cost residues, are produced each year by the fermentation industries. With this denaturated biomass, heavy metal accumulation has been clearly demonstrated on cell walls even though no particular molecules were found as specific sites for metal chelation [2]. The natural biomass is very soft and difficult to use. An effective sorption process needs a biosorbent of controlled size particles of certain durability, hardness and porosity. Methods of improving the stability and mechanical properties of biopolymers are: grafting into synthetic polymers (e.g., polystyrene), binding to a suitable carrier (e.g., cross-linking with epichlorohydrin) and entrapment into organic or inorganic material [3]. Advantages of inorganic matrices are their chemical stability and mechanical strength.

In this study we investigated immobilization of cell walls isolated from waste brewing biomass *Saccharomyces cerevisiae* in a silica matrix by a sol-gel method. Rates and capacity of sorption of Cd^{2+}, Cu^{2+} and Ag^{+} on biosorbents with silica and cross-linked with epichlorohydrin were compared to determine the effect of immobilization in a silica matrix on the properties of the biosorbent.

2. Experimental

2.1. *Materials*

Saccharomyces cerevisiae was obtained from Prague Breweries as a suspension containing 15% yeast as dry weight. The tetramethoxysilane (TMOS) and tetraethoxysilane (TEOS) used are commercial products of Fluka. The analytical grade $CdSO_4$, $CuSO_4 \cdot 5H_2O$, $AgSO_4$, HCl (35%) and ether were commercial products of Lachema Brno. NaOH, acetone, ethanol, were purchased from Penta Chrudim Czech Rep. The $AlCl_3$ and the aqueous solution of sodium silicate (80 g Si/l) were commercial products of STYL Praha. The epichlorohydrin (1-chlor-2,3-epoxypropane) was a product of Merck-Schuchardt, München BRD.

2.2. *Isolation of Cell Wall Envelopes from Yeast*

The suspension of cells (*Saccharomyces cerevisiae* 15% yeast weight) was boiled in 1 M NaOH (1 : 2; v/v) at 100°C for 4 hours to facilitate protein removal. The suspension was centrifuged for 20 min at 3000 rpm. The sediment was washed by deionized distilled water and centrifuged (20 min, 3000 rpm) twice. The crude biomass, cell envelopes, was then resuspended in 1 M NaOH and the procedure of protein removal was repeated (boiling time 2 hours). The cell envelopes were washed in ethanol, acetone and finally in ether three times and then dried for 24 hours at 25°C [4]. The resulting biomass, containing polysaccharides of cell wall envelopes (elemental analysis: 35.6% C, 6.3% H, 0.2% N, P traces) is a soft, light-brown powder (see Fig. 1). The calculated content of the rest of the protein was 1.2%. The yield of cell wall envelopes was 50% of the initial yeast weight.

2.3. *Immobilization of Cell Envelopes*

The compositions of the precursor solutions are listed in Table 1. All solutions were prepared with a volume of 10 ml. The biosorbent **A** was prepared by mixing the cooled (−5°C) components with the cell walls [5]. After 30 min a gel pellet was obtained which was dried at 90°C for 1 day. The biosorbent of composition **B** was prepared by mixing the components for 4 hours at 25°C. After addition of the cell walls the gel pellet formed within 1 hour. It was dried for 2 days at 25°C and for 1 day at 100°C. The components of **C** after mixing at room temperature were kept for 2 days at −5°C. After adding cell walls the pellet, which formed within 20 min, was dried for 1 day at 90°C. The sample **D** was prepared from aluminum chloride and sodium silicate by a previously described procedure [6]. The biosorbent **D** obtained consisted of brown particles (10–500 μm). The percentage content of the size range 250–600 μm was 60%. The components of biosorbent **E** were mixed for 2 hours and 70% of methanol was allowed to evaporate for 2 days at 25°C. Cell walls were added and the sample was dried at 90°C. The sample **E*** (without cell walls) was prepared, by an identical procedure to sample **E**, to evaluate the sorption capacity of the silica matrix.

Figure 1. SEM micrograph of the cell wall envelopes.

Cell walls immobilized with epichlorohydrin—biosorbent **F**—were prepared by the previously described procedure [7].

The dried brown pellets of biosorbents **A**, **B**, **C**, **E** and the white silica monolith of **E*** were crushed and sieved. Particles of size 250–600 μm were collected and used in sorption experiments. The surfaces of the biosorbents were observed by optical microscopy,

Table 1. The compositions of precursor solutions.

Sample	Composition of precursor solutions (weight ratio)				
A	TMOS	Methanol	H_2O	NaOH	Polysaccharide
	6.84	4.74	2.4	10^{-4}	1
B	TEOS		H_2O	HCl	Polysaccharide
	5.3		4.34	0.24	1
C	TEOS	Ethanol	H_2O	HCl	Polysaccharide
	5.2	4.34	0.4	0.75	1
D	Sodium silicate	$AlCl_3$	H_2O	NH_4^+	Polysaccharide
	0.25	0.25	15.85	0.15	1
E	TEOS	Methanol	H_2O		Polysaccharide
	9.5	20	6.73		1
E*	TEOS	Methanol	H_2O		Polysaccharide
	9.5	20	6.73		0
F	Epichlorohydrin		H_2O	NaOH	Polysaccharide
	0.177		0.119	0.079	1

SEM and a JOEL JXA-733 X-ray microanalyzer. Nitrogen adsorption-desorption (Digisorb 2600 V4.02, BET) was used to determine the specific surface area of the xerogels.

2.4. *Metal Uptake*

Sorption in Flasks. Biosorbent, containing 0.1 g of cell walls, and 100 ml aqueous solution of metal ($CdSO_4$, $CuSO_4$, $AgSO_4$) were contacted for 16 hours in 250-ml Erlenmeyer flasks on a rotary shaker (100 rpm) at 25°C. Equilibrium sorptions were followed in the experiments with an initial concentration of metal in solution in the range 5–300 mg/l. The concentration of metal remaining in solution was determined by polarography. The metal uptake (q) was determined as follows:

$$q_x = V(C_i - C_f)/M$$

where q is the metal uptake ($mg_{metal}/g_{biomass}$), x is the index of the initial concentration (mg/l) of the metal solution, V is the volume of solution in the batch flask (1), C_i is the initial concentration of the metal in the solution (mg/l), C_f is the final concentration of metal in the solution (mg/l), and M is the mass of cells (g).

Column Experiments. Glass columns (1 cm diameter × 20 cm length) were packed with 3.8 g biosorbent **E**, or 1.1 g biosorbent **F**, size fraction of 250–600 μm). Solutions of the metals ($CuSO_4$, $CdSO_4$) were pumped at a rate of 0.5 ml/min upflow in the column with a perestatic pump. The void space fraction of the bed was $\varepsilon = 0.36$ in the case of the biosorbent **E**, and $\varepsilon = 0.50$ in the case of the biosorbent **F**. The breakthrough point (volume V_b) for the column operation was defined as the volume when the effluent concentration of metal reached 0.03 $mg_{metal}/1$. The residual concentration of metals was determined by polarography.

3. Results and Discussion

Table 2 shows the cadmium uptake by cell walls encapsulated in silica material (**A–E**) and cross-linked by epichlorohydrin (**F**). The highest amount of cadmium by 1 g of cell walls was sequestered by biosorbents **E** and **F**. These materials were prepared without addition of acids (**B**, **C**), bases (**A**, **D**) or metal containing agents (**D**). The lowest cadmium uptake was observed by matrix **C** which formed with polysaccharides of cell wall envelopes a glassy nonporous material. Biosorbent with silica matrix **E** had a substantially larger specific surface area (597 m^2/g) in comparison with that

Table 2. Cadmium uptake by polysaccharides encapsulated in silica material (**A–E**) and cross-linked with epichlorohydrin (**F**).

	A	**B**	**C**	**D**	**E**	**F**
q_{50} (mg g^{-1})	17.6	12.63	2.94	15.27	24.13	18.4
q_{100} (mg g^{-1})	33.5	18	7.3	27.73	41.81	32.1

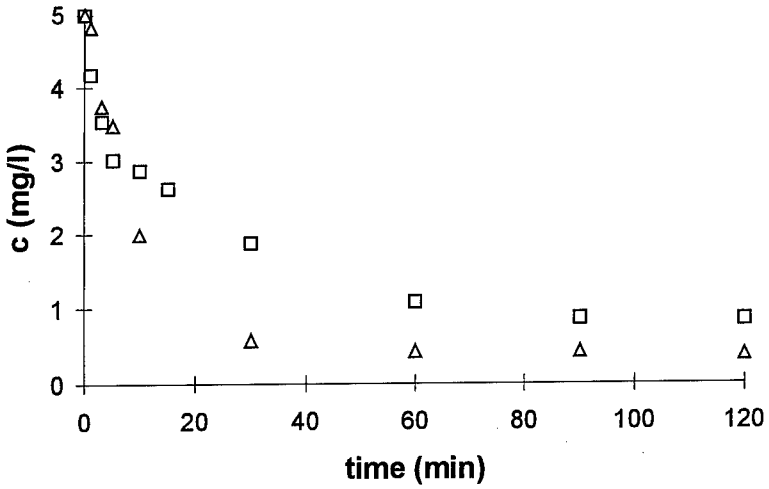

Figure 2. Sorption rate of Cd^{2+} by biosorbent **E**, cell walls encapsulated in silica matrix (-Δ-), and biosorbent **F** (cross-linked with epichlorohydrin, -□-); initial concentration of Cd^{2+} was 5 mg/l; batch experiment.

cross-linked by epichlorohydrin (**F**) (2.6 m^2/g). The difference in uptake values cannot be attributed to the difference in specific surface area. The specific surface area of biosorbent **E** with cells was only 10% higher than that of the biosorbents without cells (**E***) but in a test with an initial concentration of Cd^{2+} of 50 mg/l, the sorption capacity of **E** was 6.3 $mg_{Cd}/g_{biosorbent}$ in contrast to 0.1 mg_{Cd}/g_{matrix} for **E***. In flask tests with higher initial concentrations (100 and 300 mg/l) the differences in sorption capacity between these materials became lower by a factor of (3–5×).

Figure 2 shows the sorption rate of Cd^{2+}, for biosorbent **E** (cell walls encapsulated in silica matrix) and **F** (cross-linked with epichlorohydrin). The measured sorption rates of Cu^{2+} and Ag^{+} were similar. All tested metals were sorbed by **E** with higher rates. Both biosorbents reached similar maximum sorption capacities. These observations could be ascribed to better availability and higher intensity of sorption centers in **E**. This was confirmed also by sorption isotherms in which the intensity parameters were higher for biosorbent **E** and capacity parameters were alike for both biosorbents tested.

Figure 3 exhibits the results of sorption of Cd^{2+} and Cu^{2+} in columns filled by **E** and **F**. The breakthrough volume (l) of Cd^{2+} was 2.8 and that of Cu^{2+} was 2.1

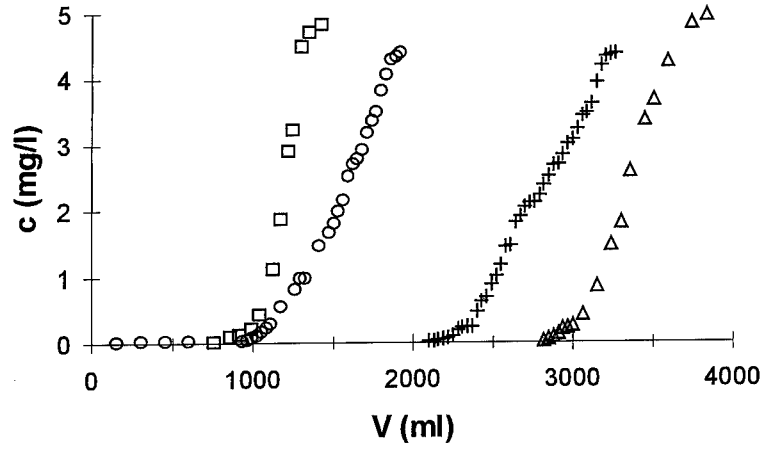

Figure 3. Sorption of Cd^{2+} and Cu^{2+} in column experiment. Initial concentration of metals was 5 mg/l, upflow rate 0.5 ml/min, diameter of the column 1 cm. Bed depth of biosorbent **E** was 16.1 cm, the void space was $\varepsilon = 0.36$. Bed depth of biosorbent **F** was 6.2 cm, $\varepsilon = 0.5$. Sorption of Cd^{2+} by biosorbent **E** (-Δ-), biosorbent **F** (-□-). Sorption of Cu^{2+} by biosorbent **E** (-+-), biosorbent **F** (-o-).

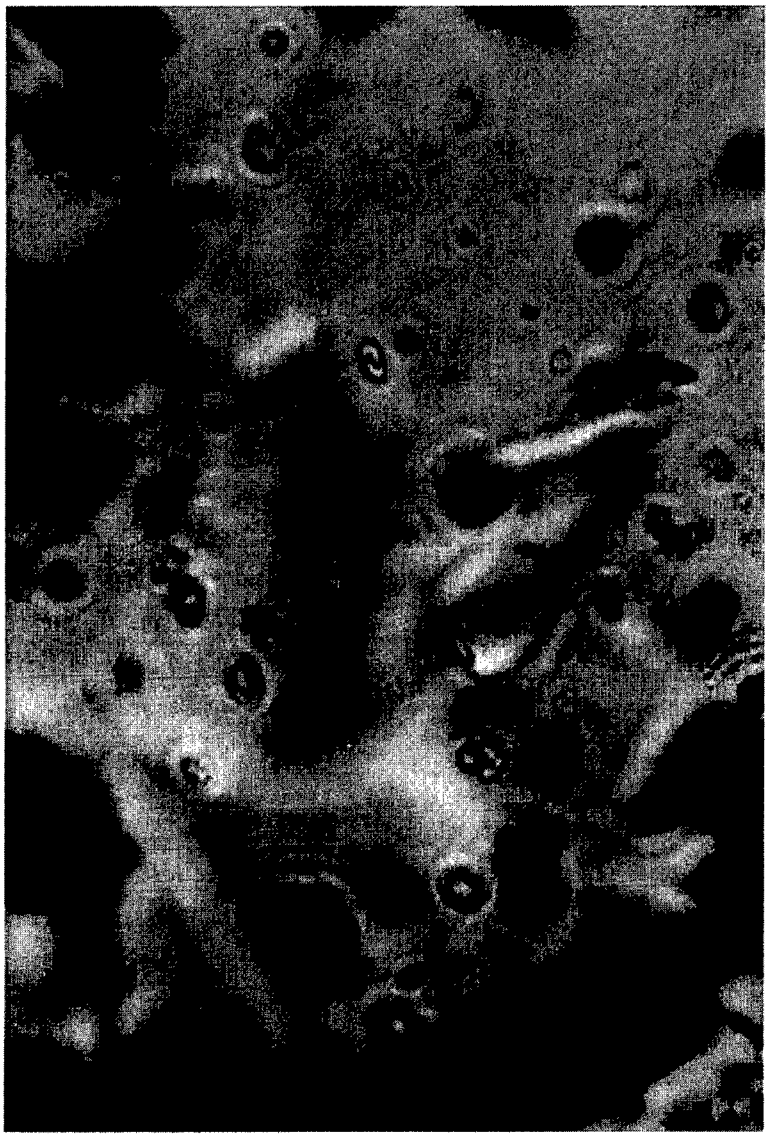

Figure 4. Optical photomicrograph of surface of the silica matrix with encapsulated cell walls, biosorbent **E** (magnification 480×).

for a column filled by **E**. In experiments with a column filled by **F** the breakthrough volume was 0.91 for Cd^{2+} and 0.9 for Cu^{2+}. The higher breakthrough volumes in the column filled by **E** were probably achieved due to the better availability of sorption centers and the result of the higher bed depth of **E**.

Microscopy showed that silica biosorbent **E** is a heterogeneous material formed by a microporous silica matrix with inclusions of cell walls (Fig. 4) Detection of sorbed metals on the cell walls could not be made by electron microprobe because immobilized cell walls were several times thinner than the penetration depth of the electron beam. The very high intensity of sorption by the biosorbent with the silica matrix showed that a positive effect of the specific interactions of the silica matrix and the cell wall polysaccharides on the sorption of metals cannot be excluded. Further investigation of the swelled biosorbents is necessary.

4. Conclusions

New biosorbent materials derived from yeast cell wall envelopes immobilized in silica matrix were prepared by a sol-gel process. The biosorbent exhibited

good mechanical strength. Therefore, the likelihood of blocking of the column by crumbled particles is reduced. A high intensity of sorption will be useful in the continuous removal of low concentrations of metals at high flow rates. The non-toxic composition of the biosorbent makes its application possible in the pretreatment of drinking water.

Acknowledgment

A financial support by the Czech Grant Agency (Grant 104/97/1212) is gratefully acknowledged.

References

1. G.M. Gadd and C. White, Trends in Biotechnology **11**, 353 (1993).
2. J.M. Tobin, D.G. Cooper, and R.J. Neufeld, Appl. Environ. Microbiol. **47**, 821 (1984).
3. Z.R. Holan, B. Volesky, and I. Prasetyo, Biotech. and Bioeng. **41**, 819 (1993).
4. M. Patzak, P. Dostalek, R. Fogarty, J. Tobin, and I. Safarik, Biotechnol. Tech., in press.
5. S. Braun, S. Rappoport, R. Zusman, D. Avnir, and M. Ottolenghi, Materials Letters **10**, 1 (1990).
6. Lakshman et al., U.S. Patent 5,084,389, 1992.
7. Sandula et al., CS Patent 221747, 1985.

Journal of Sol-Gel Science and Technology 13, 295–298 (1998)
© 1998 Kluwer Academic Publishers. Manufactured in The Netherlands.

Sol-Gel Immobilized Glucose-Oxidase: Calorimetric Investigations of Enzyme Activities

U. GEORGI
Freiberg University of Mining and Technology, Institute of Inorganic Chemistry, Leipziger Str. 29, D-09596 Freiberg

H. GRAEBNER
Freiberg University of Mining and Technology, Institute of Physical Chemistry, Leipziger Str. 29, D-09596 Freiberg

G. ROEWER
Freiberg University of Mining and Technology, Institute of Inorganic Chemistry, Leipziger Str. 29, D-09596 Freiberg

G. WOLF
Freiberg University of Mining and Technology, Institute of Physical Chemistry, Leipziger Str. 29, D-09596 Freiberg

Abstract. Using the sol-gel process, the enzyme glucose-oxidase was immobilized in modified SiO_2 layers. The tetraethoxysilane based sol was varied by veratrylaldehyde, aminopropyltriethoxysilane and an azomethine compound, which was synthesized from both molecules. Changes in reaction kinetics of the sol-gel process by addition of veratrylaldehyde were observed by ^{29}Si NMR measurements. The fixation of this additive in the final gel was clarified by FTIR spectroscopy.

The influence of inserted functional groups on the enzyme activity was determined by calorimetry. The Enzyme Thermistor is a fast and uncomplicated method to obtain comparative results of sol-gel immobilized enzyme activity. Differences in immobilization effects were found dependent on structure and concentration of additives.

Keywords: precursor chemistry, calorimetry, enzyme immobilization

1. Introduction

Stabilization of enzymes can be achieved by sol-gel immobilization in thin silica layers, which are applicable for biosensors [1]. The stimulation of enzyme efficacy should be possible by modification of sol-gel layers with certain functional groups. In this paper the influence of veratrylaldehyde on the kinetics of the sol-gel process, on the resulting gel properties and on the immobilization tendency of glucose-oxidase (GOD) is shown.

Further investigations were done by addition of aminopropyltriethoxysilane (APTS) and azomethine functionalized APTS. The inserted functional groups allow a better fixation of GOD in the gel matrix as the results of calorimetric measurements exhibit. A flow calorimeter [2] was used for the determination of enzyme activity. The enzymatic effects can be followed directly. It is not necessary to use consecutive reactions, additional enzymes or dyes. The enzyme activity can be judged by this method in a fast and efficient way [3].

2. Experimental

The silica sol was prepared by a two-step method. At first tetraethoxysilane (TEOS), ethanol, water and hydrochloric acid were stirred in the molar ratio 1 : 8 : 18 : 0.004 for 10 h. The enzyme solution was prepared from 30 mg GOD (E.C. 1.1.3.4., from Aspergillus niger, Biozyme, 180 U/mg) in 2 ml phosphate buffer solution ($KH_2PO_4 + Na_2HPO_4$, pH 5.8). In the second step 0.06 or 0.08 mol (to 1 mol TEOS) of veratrylaldehyde were mixed with the enzyme solution and added to 8 ml sol. The system was adjusted to pH 7 by 0.05 M NaOH solution.

The same sol composition was used for the preparation of systems containing APTS and azomethine (0.1 mol to 1 mol TEOS). The samples were filtered and pH adjusted by HCl. The azomethine precursor was prepared from 1 mol veratrylaldehyde dissolved in 200 ml toluol on a molecular sieve to bind reaction water and 1 mol APTS in 200 ml toluol added drop by drop, Eq. 1. After 2 days' stirring the solvent was drawn off by vacuum (130 Pa) [4].

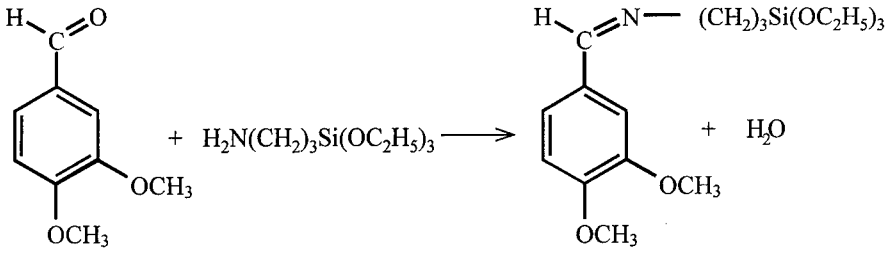

(1)

For the layer preparation SIRAN® (macroporous glass beads, bead diameter 1–2 mm, pore diameter 60–300 μm, Schott Mainz, Germany) were dipped into the different sols and dried at room temperature.

^{29}Si-NMR spectra were recorded on a Bruker AVANCE DPX 400 at 79.495 MHz using Teflon sample tubes. Tetramethylsilane was applied as external reference and chromium(III) acetylacetonate as relaxation reagent. The FTIR spectra were obtained by means of a Nicolet 510 FTIR spectrometer using pressed KBr pellets.

Enzyme activities on the SIRAN® samples were determined in a split-flow Enzyme Thermistor. Measurements were carried out at 25° with a flow velocity of 1.2 ml/min. Glucose solution (10 mmol/l) was introduced as substrate for enzymatic reaction with an injection valve using a 0.5 ml sample loop. The temperature difference occurring between the exits of enzyme column and reference column, respectively, is proportional to the quantity of exchanged heat in the flowing medium. The released heat is proportional to turnover of substrate in the column. The heights of resulting signals (ΔT_{max}, peak heights) can therefore be used as measuring parameter for catalytic or enzyme activities [5].

For all investigated systems calorimetric blank experiments (gel without GOD) were carried out.

3. Results

Figure 1 shows the ^{29}Si-NMR signal behavior of systems without and with veratrylaldehyde depending on reaction time (for signal assignments see [6]). The aldehyde was added in the second step to a 30 min old sol at pH 4.8. After this period the main part of TEOS was hydrolyzed already. The intermediate silicon species seem to be the same in both cases, but the kinetics exhibit obviously great differences. After a 10 min reaction time the spectrum of additive-free system showed already Q^2 groups, contrary to the modified system. Using veratrylaldehyde, all of the four possible monomeric hydrolysis products (−72 to −80 ppm region of the spectra) could be observed after 6 h. The unmodified sol gave only weak signals for monomeric species and more intensive signals of Q^2 and Q^3 groups.

After 14 h all monomeric species still existed using the additive. In comparison to the 6 h spectrum, a decrease in Q^1 group intensity and an increase in the broad and unspecific Q^3 signal were observed. The sol contained more cyclic intermediates, represented through signals between −82 and −84 ppm. In the unmodified system, fewer Q^1 groups and very small amounts of

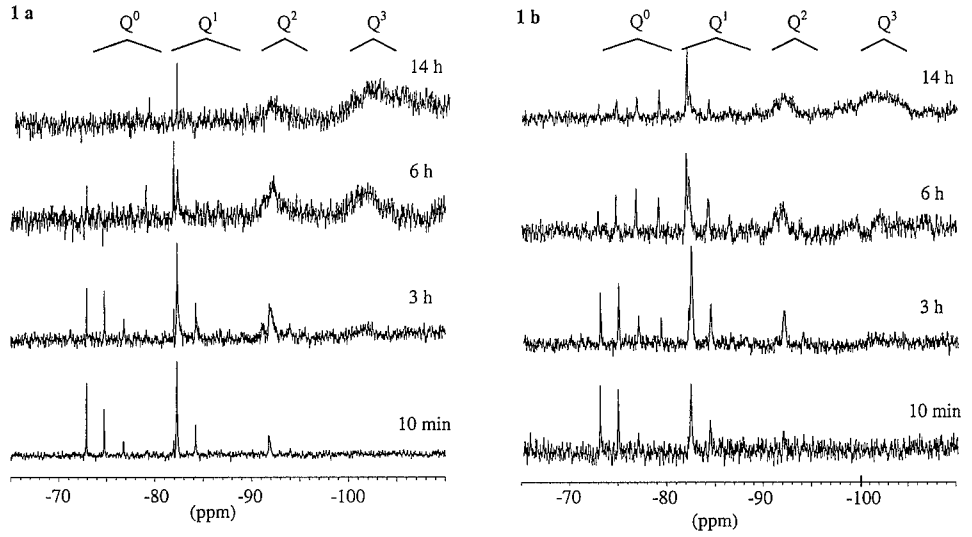

Figure 1. ^{29}Si-NMR spectra: (a) silica sol and (b) with veratrylaldehyde.

monomeric species were found after this period, caused by faster condensation reactions. Interactions between aldehyde and reactive sol groups reduced the number of cross-linkages during the gel formation. In this case the hydrolysis was much slower. It represented the rate-determining step in the conversion of precursor to gel.

The dried gel was investigated by FTIR spectroscopy. Characteristic bands of SiO_2 gel and veratrylaldehyde were detected, Fig. 2. The observed C=O stretching vibration at 1676 cm^{-1} is an important indicator of incorporated veratrylaldehyde, which should anchor the enzyme. In comparison to data of the free aldehyde, a bathochromic shift of this vibration band resulted [7]. This effect could be caused by interactions of the aldehyde group with silica gel via hydrogen bridging. Furthermore, we have to take into account the possibility of the aldehyde to enable hydrolysis and condensation reactions of methoxy groups within the sol.

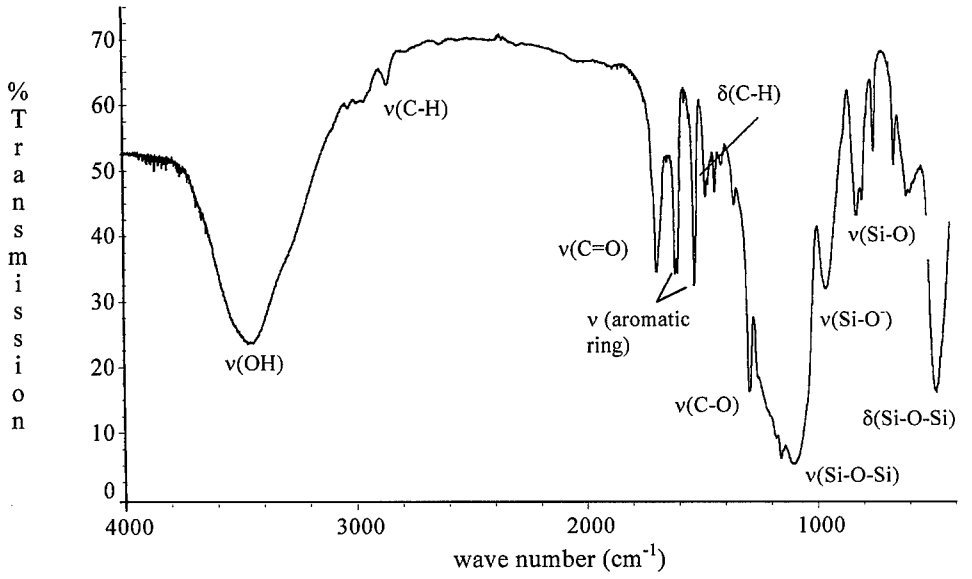

Figure 2. FTIR spectrum of SiO_2 gel with 0.08 mol veratrylaldehyde (to 1 mol TEOS).

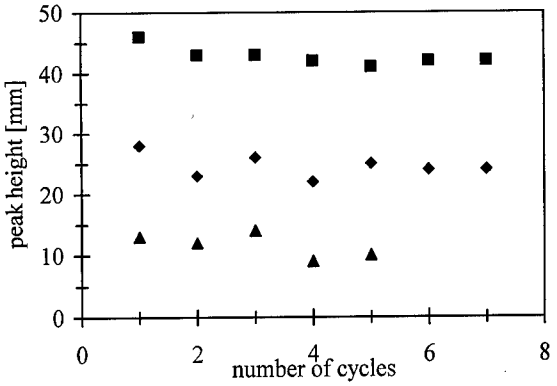

Figure 3. Calorimetric investigations on sol-gel immobilized GOD ▲) no additive, ♦) 0.06 mol veratrylaldehyde, ■) 0.08 mol veratrylaldehyde.

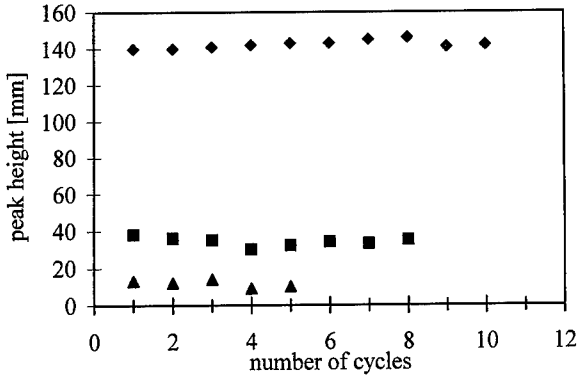

Figure 4. Calorimetric investigations on sol-gel immobilized GOD ▲) no additive, ■) 0.1 mol azomethine, ♦) 0.1 mol APTS (to 1 mol TEOS).

The enzyme activity of the incorporated GOD was measured by calorimetry, Fig. 3. Glucose was injected to the thermistor, starting the enzymatic reaction (number of cycles). The expected relationship was found between concentration of veratrylaldehyde and the intensity of thermal effects of enzymatic reaction. Increase of the additive concentration led to an improvement of the activity of the enzyme carrier complexes, Fig. 3. The addition of 0.08 mol aldehyde related to a higher enzyme activity than 0.06 mol additive. The enzyme activity did not decrease during observed reaction cycles.

Aminopropyltriethoxysilane is a well-known precursor of reactive gels to produce selective enzyme immobilization [8]. Via hydrolysis and condensation reactions of the ethoxy groups a direct coupling between the silica matrix and the additive can be realized. Our results of the calorimetric investigations confirm this proposal, Fig. 4.

The azomethine resulting from the reaction of APTS with veratrylaldehyde offers new possibilities to immobilize enzymes. At first the azomethine bond operated as a protective group for the highly reactive aldehyde function. The hydrolytic splitting of the formed azomethine bond lead to two functional groups in the sol. Besides the strong basicity of NH_2 function was reduced in this way. By means of the addition of this compound to silica sol the properties of the layers could be varied; for instance, an improved adhesion in comparison to APTS was observed. First immobilization experiments verified an enzymatic effect, see Fig. 4. Systematic experiments of enzyme fixation and reaction mechanism are goals for further investigations.

4. Conclusion

Veratrylaldehyde is a useful additive to get a better fixation of GOD in a gel layer. This aromatic aldehyde retards the hydrolysis and condensation reactions of the sol-gel process. Interactions between silica matrix and additive mask cross-linking sites.

Aminopropyltriethoxysilane and its azomethine compound with veratrylaldehyde are also promising compounds to immobilize glucose-oxidase. The resulting enzyme carriers can be judged comparatively by calorimetry in a fast and efficient way.

References

1. (a) B.C. Dave, B. Dunn, and J.S. Valentine, Anal. Chem. **66**, 1120A–1127A (1994); (b) O. Lev, M. Tsionsky, L. Rabinovich, and S. Glezer, Anal. Chem. **67**, 22A–30A (1995).
2. B. Danielsson, Appl. Biochem. Biotechnol. **7**, 127 (1983).
3. H. Graebner, U. Georgi, R. Hüttl, and G. Wolf, Thermochim. Acta, to be published.
4. F. Mucha, G. Roewer, and S. Lehr, in *Organosilicon Chemistry III*, edited by N. Auner and J. Weis (Wiley-VCH, Weinheim, 1997), in press.
5. B. Danielsson and K. Mosbach, FEBS Letters **101**, 47 (1979).
6. L.W. Kelts, N.J. Effinger, and S.M. Melpolder, J. Non-Cryst. Solids **83**, 353 (1986).
7. Ch.J. Pouchert, *The Aldrich Library of FTIR Spectra* (Aldrich Chemical Company, Milwaukee, 1998), p. 1299.
8. R. Collino, J. Therasse, P. Binder, F. Chaput, J.-P. Boilot, and Y. Levy, J. Sol-Gel Sci. Tech. **2**, 823 (1994).

Journal of Sol-Gel Science and Technology 13, 299–303 (1998)
© 1998 Kluwer Academic Publishers. Manufactured in The Netherlands.

Aerogels—Recent Progress in Production Techniques and Novel Applications

J. FRICKE AND A. EMMERLING
Physikalisches Institut der Universität, Am Hubland, D-97074 Würzburg

Abstract. Aerogels are sol-gel derived nanostructured materials with extraordinary properties according to their high porosity. Though first prepared more than 60 years ago, silica aerogels became widely known only in the late 1980s when they were used in Cerenkov detectors and their potential was recognized as high performance thermal insulants. Nowadays, aerogel research has attracted many scientists from different fields, resulting in some 100 publications per year and the fifth aerogel symposium (ISA 5) in Montpellier/France in September 1997. This review will focus on recent developments in fast supercritical and ambient pressure drying processes. The state of the art with respect to structural characterization and measuring the material properties is reported including nondestructive techniques and alterations induced by invasive methods. A brief survey is given on modeling the aerogel structure and simulating properties. Special attention will be given to carbon aerogels and their organic precursors. Due to the high electrical conductivity of their graphitic backbone and the large specific inner surface areas, carbon aerogels can be considered ideal electrodes in supercapacitors and fuel cells.

Keywords: aerogels, nanostructured materials, porosity, thermal insulant, supercapacitor

1. Introduction

Aerogels were fist made by Samuel Kistler in the early 1930s. He dried his waterglass-derived silica gels, employing a solvent exchange and using supercritical conditions to remove the pore fluid (methanol) nondestructively [1]. In the 1950s Monsanto adapted Kistler's process and produced silica aerogel under the trade name Santocel® [2]. The milled aerogel was tested as thickening agent in paints and as thermal insulant. A lower cost fumed silica process using tetrachloride brought Monsanto's aerogel project to a halt.

Renewed interest in aerogels occurred in 1962. Teichner and co-workers in Lyon invented a much faster method: they hydrolyzed and gelled a tetramethoxysilanemethanol solution by a molar excess of water in the presence of an acid or a base. They also used supercritical extraction. Their method was employed in the 1970s to make several cubic meters of monolithic highly transparent silica aerogel tiles for Cerenkov detectors [4, 5]. The Cerenkov detector application stimulated aerogel research and development. In the 1980s enough sample material became available to investigate the optical transmission [6], the low thermal conductivity [7] and the fascinating mechanical properties [8] of SiO_2 aerogels as a function of density and other parameters. Aerogels also became interesting as fractal systems [9]. Applications of aerogels as highly efficient transparent/translucent thermal insulants for passive solar usage [10] were promoted by BASF's R&D efforts and the production of granular SiO_2 aerogels in a pilot plant in quantities of several hundred cubic meters using water glass and mineral acids as cheap starting materials [11]. The process involves the formation of granular SiO_2 gel beads and supercritical drying with respect to methanol or CO_2. In 1996 BASF decided to discontinue the production of aerogels in its pilot plant in Ludwigshafen, despite the increasing number of potential applications.

2. New Production Methods

Several research groups have contributed ideas to further improve the production process, making it either

faster or running it at less extreme pressures and temperatures.

The Lawrence Livermore National Laboratory (LLNL) group has invented a rapid supercritical extraction process [12], which is similar to injection molding and is most suitable for the production of monolithic and large pieces of aerogel. In this process the sol is injected into a two-piece sealed high pressure steel mold which—after injection—is rapidly heated. During the rapid heating phase the sol gels and ages. Strains of the gel network upon heating are prevented by the mold. Once the liquid, which is under high pressure, becomes a supercritical fluid, it is rapidly decompressed. The whole process can be done in as little as 1 hour. Clear and large pieces of aerogel can be made. Due to the improved connectivity of the gel network obtained in the high temperature process the elastic moduli of the aerogels are about three times higher than for conventionally made aerogels.

Subcritical evaporation of the pore liquid of silica gels results in capillary pressures of the order of 100 bar caused by the surface tension of the receding liquid menisci. This leads, at best, to a greatly reduced porosity and, at worst, to a cracked gel body. This is why Kistler used supercritical extraction in the first place. However, there are other means to prevent the gel collape:

- Einarsrud and colleagues [13] aged their wet gels in an alkoxide/alcohol solution; the thus obtained addition of solid material to the necks and small pores of the gel stiffens the microstructure considerably. The wet gels are now strong enough to withstand the capillary pressures upon drying. Aerogels with densities as low as 240 kg/m^3 have been made.
- Smith and Brinker [2] took another approach. Upon drying a gel shrinks. As neighboring Si—OH groups condense and form an Si—O—Si bridge the shrinkage becomes irreversible. Thus they silylated the gel surface. Upon drying-induced shrinkage the chemically inert surface groups come into contact with each other. However, when the liquid phase starts to form isolated droplets and surface tension ceases, a "springback" effect is observed: since neighboring surface silyl groups can detach with little activation energy, the gel body is able to reexpand. Aerogels with densities as low as 100 kg/m^3 can be obtained. Due to the silyl groups on the inner surface the material is highly hydrophobic.

This ambient pressure drying method may become an industrial large scale process for aerogels at Hoechst/Frankfurt [14].

3. Aerogel Characterization

At the aerogel symposium in 1994 in Berkeley G.W. Scherer reported on the deformation of the aerogel network induced by the use of mercury porosimetry, thermoporometry and nitrogen sorption [15]. As a result of their low elastic moduli aerogels already show large strains at small stresses, which lead to systematic errors in the determination of pore volume and pore size distributions if these techniques are employed. It has clearly been demonstrated that even at highest pressures almost no intrusion of mercury can be detected. On the other hand, porosimetry may serve as a measuring tool to derive the bulk modulus upon isostatic compression [16]. Thermoporometry uses the depression of the freezing point upon freezing of a liquid inside the porous body to determine the pore size distribution. Systematically smaller pore sizes are obtained than are present, which is a consequence of a contraction of the tenuous gel body. This is due to the nucleation of crystals outside the gel body, which grow by draining liquid from the pores and causing a shrinkage of the network. Even by a technique such as gas sorption, which is supposed to be gentle, a contraction of about 50% of the initial volume during desorption has been observed. The forming of menisci upon pore condensation generates capillary pressures, which contract the fragile network, until unit relative pressure is approached. Here, the menisci become flat and the pressure is released and the gel body should expand to its initial dimension if no plastic deformation has occurred. The contraction reoccurs upon desorption for the same reason, however it is much more pronounced since more pores are filled. Thus, as a consequence of this shrinkage the (meso)pore volume is significantly underestimated. In the literature the difference to the total pore volume determined from the macroscopic density is generally attributed to macropores (which are therefore overestimated). The surface area determined via the BET method, however, can be regarded as accurate as it is not seriously affected by contraction. Disregarding these inherent errors all three techniques are still widely used for characterizing the aerogel pore structure. Only for high density aerogels (e.g., 300 kg/m^3), which are mechanically stable

enough to withstand these forces, reliable results can be expected. A further effect upon nitrogen adsorption has been observed: partial filling (about 50% of the total pore volume) may occur as a result of zero curvature of the adsorbate/vapor interface in the pore space, even if the maximum pore size is only 35 nm [17].

Gas diffusion and transport through an aerogel network, which is important for filter, catalytic and sensors applications, has been studied by several groups during the past years. Reichenauer et al. established the dynamic gas expansion (DGE) technique, which allows a simultaneous measurement of the diffusion coefficient and the skeletal density as well as adsorption features with respect to different gases [18]. This method was employed to a variety of silica, RF and carbon aerogels. Comparison to SAXS data and N_2-sorption showed that DGE provides additional information on the connectivity of the interconnected pore network. Gas flow through partially sintered aerogels has been studied by Beurroies et al., who find that Knudsen molecular diffusion is the dominant mechanism for these high density gels [19]; with increasing pore size laminar viscous flow becomes more and more important [20].

Nondestructive techniques such as SAXS, SANS and light scattering (LS) are well established to explore the nanostructure of aerogels. During the past years it has been shown that the scattering cross sections of SAXS and LS match when plotted on an appropriate scale, i.e., LS probes the same correlation function as small angle scattering, only at a different length scale [21]. This enables one to predict the level of light scattering and thus the optical transparency from the nanostructural features of the gel network as determined by SAXS. To reduce the optical extinction due to Rayleigh scattering for a silica aerogel of a given density, small primary particles and diffusion limited growth with a small fractal dimension are advantageous. This is fulfilled, e.g., for base-catalyzed samples at very high pH. An extensive study of radiation transport and image transmission through aerogels has been given by Beck et al. [22]. They found that small micron sized imperfections and inhomogeneities, contribute significantly to the total scattering cross section and cause image distortions as their scattering is strongly forward oriented.

The structure of RF and carbon aerogels has been and still is one important topic. Schaefer et al. presented the first detailed study on the texture of RF aerogels in the high catalyst regime (R/C = 50–300) [23]. Their results indicate that nanoscale phase separation might be the structure forming mechanism rather than kinetic growth. This has recently been corroborated by gelation studies at high R/C performed by Saliger et al. [24], which propose spinodal decomposition and domain growth in the early stages and "freezing" of this structure by condensation during the last (high temperature) steps of gelation. A structural study of RF and carbon aerogels over a vast range of R/C ratios from 100 to 1500 has been completed by Bock et al. [25]. One of the major findings was the creation of micropores during pyrolysis [24–27]. This yields an extremely high but well accessible inner surface area for the resulting carbon aerogels, even for high R/C-gels with large primary particles and pores. Since these gels can be dried at ambient pressures without shrinking and cracking, they are favored for applications in fuel cells and supercaps.

With respect to multicomponent aerogels contrast variation techniques become more and more important. In the case of neutron scattering, the aerogel can be filled with an appropriate H_2O/D_2O-mixture to match the scattering power of one of the constituting phases and thus allows the scattering of the other fraction(s) to be investigated. Disregarding (destructive) alterations of the gel network upon refilling, this method is used to investigate RuO_2-TiO_2 aerogels [28]. In the case of X-rays the anomalous dispersion of the atomic scattering coefficient near an absorption edge can be used to vary the scattering contribution of one element. From measurements at different energies close to the absorption edge, the scattering contributions can be separated and thus information on the structure of each phase and their mutual structural arrangement is obtained. An example are fractal ZnO-clusters in a silica aerogel matrix [29]. This method requires a synchrotron source and is limited to elements (Ti and higher atomic numbers) having an absorption edge in the available energy range.

4. Modeling of Aerogel Structure and Properties

Modeling the aerogel structure to match the experimental findings of small angle scattering, dynamic techniques (e.g., Brillouin scattering) and processes such as sintering have been extensively addressed. Numerical simulations of diffusion limited cluster-cluster growth gave a good agreement with short- and long-range correlations of the SANS spectra of base-catalyzed colloidal aerogels [30] as well as with the time evolution of those systems [31]. Using different reactivities as a function of the degree of condensation in these simulations, almost all structures can be generated that are

observed in reality, from weakly branched DLA clusters over highly branched reaction limited aggregates to compact precipitates [32, 33]. Assuming simple models to describe mechanical and transport properties of such a cluster network, good agreement is achieved between the predicted scaling behavior of thermal (or electrical) conductivity and elastic modulus and the experimental findings for a variety of aerogel series [33]. Diffusion limited aggregation has also been studied by Chandler [34]. Pohl et al. have carried out molecular dynamics simulations [35], which focused on the structure close to the molecular level. Another recent approach has been the modeling of organic aerogels by the superposition of two two-level cut Gaussian random fields, which may be suited to account for phase separation growth and can be used for simulating conductivity phenomena [36]. Model calculations of the electrical conductivity as a function of porosity are studied by Tarafdar [37].

Using a fractal scaling concept to account for the structural changes upon sintering, Jullien et al. have been able to describe the densification behavior of aerogels disregarding any sintering kinetics [38]. Although this approach seems to work well for acid-catalyzed or neutrally reacted gels with a wide fractal regime, sintering of colloidal gels exhibits an unusual behavior. During the initial densification a large loss of pore volume accompanied by a relatively small reduction in specific surface area is observed. This behavior, which holds up to a density where particles and pores become comparable in size, can be ascribed to a scale-length dependent viscosity which has been experimentally shown by our group [39]. A different approach to model dense aerogels is done by random close packing of spheres with interstices [40]. Another important subject is the mechanical, elastic and plastic behavior of aerogels upon compression [41–45].

5. Applications

The use of Cerenkov detection continues to be an intriguing application of monolithic, highly transparent silica aerogels. Ultralow density aerogels [46] have been made by distilling off the reaction-generated alcohol and replacing it with an aprotic solvent. This fascinating material has been used on NASA space shuttle flights to capture cosmic dust particles [47]. The particles are gradually decelerated and caught in the low density target. Easy visualization of track and particle is possibly due to the high transparency of the aerogel. A space mission to the comet Wild 2, scheduled for take-off from Earth in 1999, will carry a panel equipped with a variety of low density aerogel blocks designed to capture dust and particles in deep space nondestructively. Sample return is expected in 2006 [48]. Aerogel is also used to thermally insulate the rover 'Sojouner' which explores Mars since its landing in July 1997 [49].

Another interesting application is the use of aerogels as molds for alloy casting [50]. Due to the excellent thermal insulation a nearly one-dimensioned cooling and solidification process is achieved. The high optical transparency of the aerogel molds allows monitoring of this process via IR- and video techniques.

Passive use of solar energy and daylighting are among the most promising applications of silica aerogels [51]. Translucent aerogel beads can be filed between two glass panes and thus improve thermal insulation, redirect solar radiation due to scattering and provide privacy. Applications are in attic windows, bathroom windows, and walls of staircases of factory halls or of administrative buildings. An important factor in such applications is that the aerogel is immobilized, for example, by partial evacuation of the window spacing, and settling thus is prevented.

Opacified silica aerogels are most suitable as thermal superinsultants. The integration of infrared absorbers, such as carbon black reduces the radiative heat transfer through the tenuous system efficiently. Additional evacuation leads to a reduction of the thermal conductivity to about 0.003 W/mK for powdered aerogels. The German car maker BMW is building aerogel-superinsulated heat storage devices, which are loaded with the waste heat of the engine. The storage can be used to defrost the wind shield and preheat the engine on cold winter days.

Carbon aerogels are the first electrically conductive aerogels [52]. Their large surface area and nanostructure make them promising electrode materials for supercapacitors [52]. Capacities of up to 50 F/cm^3 have been measured for C-aerogel supercaps. Last but not least C-aerogels can also be used in deionization systems. For a stack of 192 electrode pairs, with an applied voltage of 1 V and a flow rate of 15 ml/min, effective removal of NaCl (100 ppm) occurred for 10 hours before the electrodes saturated [53].

References

1. S.S. Kistler, Nature **127**, 741 (1931).
2. D.M. Smith, D. Stein, J.M. Anderson, and W. Ackermann, J. Non-Cryst. Solids **186**, 104 (1995).

3. G.A. Nicolaon and S.J. Teichner, Bull. Soc. Chim. France **1900**, 1906 (1968); US Patent No. 3,672,833, 1972.
4. G. Poelz, in *Aerogels*, edited by J. Fricke, Springer Proc. in Physics (Springer, Berlin, 1986), Vol. 6, p. 176.
5. S. Henning, ibid, p. 38.
6. W. Platzer, V. Wittwer, and M. Mielke, ibid, p. 127.
7. J. Fricke, ibid, p. 94.
8. M. Gronauer, A. Kadur, and J. Fricke, ibid, p. 167.
9. R. Vacher, T. Woignier, J. Phalippou, J. Pelous, and E. Courtens, Rev. de Physique Appl. **C4-24**, 127 (1989).
10. A. Goetzberger and V. Wittwer, ibid, p. 84.
11. F.J. Broecker, W. Heckmann, F. Fischer, M. Mielke, J. Schroeder, and A. Stange, ibid, p. 160.
12. J.F. Poco, P. Coronado, R.W. Pekala, and L.W. Hrubesh, in *Proceedings MRS Spring Meeting* (San Francisco, 1996), in press.
13. S. Hæreid, M.-A. Einarsrud, and G.W. Scherer, J. Sol-Gel Sci. Tech. **3**, 199 (1994).
14. M. Reiß, Die Kälte und Klimatechnik Nr. **3**, 154 (1997).
15. G.W. Scherer, D.M. Smith, and D. Stein, J. Non-Cryst. Solids **186**, 309 (1995).
16. G.W. Scherer, D.M. Smith, X. Qiuo, and J.M. Anderson, J. Non-Cryst. Solids **186**, 316 (1995).
17. G.W. Scherer, Adsorption in gel networks, J. Non-Cryst. Solids **225**, 192 (1998).
18. G. Reichenauer, C. Stumpf, and J. Fricke, J. Non-Cryst. Solids **186**, 334 (1995).
19. I. Beurroies, D. Bourret, R. Sempéré, L. Duffours, and J. Phalippou, J. Non-Cryst. Solids **186**, 328 (1995).
20. B. Hostika, P.M. Norris, J.S. Brenizer, and E.E. Daitch, Gas flow through aerogels, J. Non-Cryst. Solids **225**, 293 (1998).
21. A. Emmerling, R. Petricevic, P. Wang, A. Beck, H. Scheller, and J. Fricke, J. Non-Cryst. Solids **185**, 240 (1995).
22. A. Beck, J. Linsmeier, W. Körner, H. Scheller, and J. Fricke, J. Non-Cryst. Solids **186**, 232 (1995).
23. D.W. Schaefer, R.W. Pekala, and G. Beaucage, J. Non-Cryst. Solids **186**, 159 (1995).
24. R. Saliger, V. Bock, R. Petricevic, T. Tillotson, S. Geis, and J Fricke, Carbon aerogels from dilute catalysis of resorcinol-formaldehyde, J. Sol-Gel Sci. Tech., to be published.
25. V. Bock, A. Emmerling, R. Saliger, and J. Fricke, Structural investigations of RF and carbon aerogels using SAXS and BET, J. Porous Mater, accepted for publication.
26. R. Petricevic, G. Reichenauer, V. Bock, A. Emmerling, and J. Fricke, J. Non-Cryst. Solids **225**, 41 (1998).
27. G. Reichenauer, A. Emmerling, J. Fricke, and R.W. Pekala, J. Non-Cryst. Solids **225**, 210 (1998).
28. C.I. Merzbacher, K.E. Swider, D.R. Rolison, and J. Barker, J. Non-Cryst. Solids **225**, 234 (1998).
29. C. Lorenz, A. Emmerling, J. Fricke, T. Schmidt, M. Hilgendorff, L. Spanhel, and G. Müller, Aerogels containing strongly photoluminescing fractal zinc oxide quantom dots, *Fifth Intern, Symp. Aerogels*, J. Non-Cryst. Solids, to be published.
30. A. Hasmy, M. Foret, E. Anglaret, J. Pelous, R. Vacher, and R. Jullien, J. Non-Cryst. Solids **186**, 118 (1995).
31. A. Hasmy and R. Jullien, J. Non-Cryst. Solids **186**, 342 (1995).
32. A. Hasmy and R. Jullien, J. Non-Cryst. Solids, to be published.
33. A. Emmerling and J. Fricke, J. Sol-Gel Sci. Tech. **8**, 781 (1997).
34. E. Chandler and D.F. Calef, J. Non-Cryst. Solids **186**, 356 (1995).
35. P.I. Pohl, J.L. Faulon, and D.M. Smith, J. Non-Cryst. Solids **186**, 349 (1995).
36. A.P. Roberts, Phys. Rev. E **55**, 1286 (1997).
37. S. Tarafdar, Conductivity variation with porosity in superionic aerogels, *Fifth Intern. Symp. Aerogels*, J. Non-Cryst. Solids, to be published.
38. R. Jullien, N. Olivi-Tran, A. Hasmy, T. Woignier, J. Phalippou, D. Bourret, and R. Sempéré, J. Non-Cryst. Solids **188**, 1 (1995).
39. A. Emmerling, W. Lenhard, J. Fricke, and G.A.L. van de Vorst, J. Sol-Gel Sci. Tech. **8**, 837 (1997); Scale-length dependent viscosity controls isothermal sintering of base-catalyzed aerogels, *Fifth Intern. Symp. Aerogels*, J. Non-Cryst. Solids, to be published.
40. L. Esquivias, J. Rodriguez-Ortega, C. Bartura, and N. de la Rosa-Fox, J. Non-Cryst. Solids **225**, 239 (1998).
41. T. Woignier, Comparison of textural changes induced by sintering, and compression, *Fifth Intern. Symp. Aerogels*, J. Non-Cryst. Solids, to be published.
42. S. Calas and R. Sempéré, J. Non-Cryst. Solids **225**, 215 (1998).
43. C. Levelut, J. Pelous, and E. Anglaret, Brillouin scattering investigation of elastic properties, and phonon-farcton crossover in uniaxially pressure identified, *Fifth Intern. Symp. Aerogels*, J. Non-Cryst. Solids, to be published.
44. E. Anglaret, I. Beurroies, L. Duffours, P. Word, C. Levelut, M. Foret, T. Woignier, J. Phalippou, and J. Pelous, J. Non-Cryst. Solids **225**, 248 (1998).
45. S. Calas, C. Levelut, T. Woignier, and J. Pelous, J. Non-Cryst. Solids, **225**, 244 (1998).
46. T.M. Tillotson and L.W. Hrubesh, J. Non-Cryst. Solids **145**, 44 (1992).
47. P. Tsou, J. Non-Cryst. Solids **186**, 415 (1995).
48. Stardust mission; http://pdc.jpl.nasa.gov./stardust/home.html
49. Jet Propulsion Laboratory, press release Jan. 1995.
50. J. Alkemper, T. Buchholz, K. Murakami, and L. Ratke, J. Non-Cryst. Solids **186**, 395 (1995).
51. V. Wittwer, J. Non-Cryst. Solids **145**, 233 (1992).
52. R.W. Pekala, S.T. Mayer, J.L. Kaschmitter, and F.M. Kong, in *Sol Gel Science and Applications*, edited by Y.A. Attia (Plenum Press, New York, 1994), p. 369.
53. J. Farmer and R.W. Pekala, Internal Document Lawrence Livermore National Laboratory, Livermore, CA 94550, 1995.

Journal of Sol-Gel Science and Technology 13, 305–309 (1998)
© 1998 Kluwer Academic Publishers. Manufactured in The Netherlands.

Synthesis of Highly Porous Organic/Inorganic Hybrids by Ambient Pressure Sol-Gel Processing

GUOZHONG CAO AND HANG TIAN
Department of Materials Science and Engineering, University of Washington, Seattle, WA 98195

Abstract. This paper reports the synthesis of highly porous organic/inorganic hybrids by a two-step acid-base catalyzed sol-gel process and ambient pressure drying. In the method organic and inorganic precursors are copolymerized so as to incorporate organic ligands into the solid network. The two-step acid-base catalyzed process was used to prevent phase segregation during the hydrolysis and co-condensation of organic and inorganic precursors. The organic ligands incorporated into the solid gel network modify the surface chemistry. Thus, the wetting angle is significantly increased so that the collapse of the gel network is greatly reduced upon the removal of pore fluid during drying. Organic/inorganic hybrids with BET surface areas above 1250 m^2/g, porosities above 75% and pore sizes of ~8 nm have been synthesized.

Keywords: organic-inorganic hybrids, highly porous hybrids, ambient pressure drying

1. Introduction

Supercritical drying is the typical method for making aerogels that possess high surface areas (>1000 m^2/g) and large porosities (>75%), leading to unique physical properties for many important applications [1, 2]. Supercritical drying is used to eliminate the capillary forces from the pore fluid exerted on the solid network during fluid extraction, that otherwise leads to the collapse of the porous structure of a wet gel that typically consists of over 90% pore fluid [3]. However, supercritical drying is energy intensive, time-consuming, and often dangerous. In addition, it is not applicable for continuous film fabrication. Therefore, there is an obvious need in developing alternative ambient pressure processes for synthesis of highly porous materials by which the capillary force is minimized, without employing supercritical conditions.

The capillary pressure P_c developed in the liquid during drying is given by [4]:

$$P_c = -2\gamma_{LV}\cos\theta/r_p, \quad (1)$$

where γ_{LV} is the liquid-vapor surface tension, θ is the wetting angle, and r_p is the pore radius. The capillary pressure developed during drying is supported by the solid network causing it to shrink. Shrinkage stops when the capillary pressure exerted by the liquid is balanced by the network modulus. Strategies to minimize drying shrinkage therefore include increasing the network modulus, decreasing the surface tension, and increasing the wetting angle. A solvent exchange process was developed recently [5–8] to deposit organosiloxane polymers onto the inner surfaces of pores, so as to change the surface chemistry and reduce the capillary forces. Bulk aerogels [5, 6] and aerogel films [7, 8] were synthesized under ambient pressure by solvent exchange. Up to now, this approach has proved to be the most effective and probably also the cheapest method; however, this approach suffers drawbacks such as it is labor intensive and involves consumption of a large quantity of chemical solvents. Efforts have also been made to synthesize hybrid organic/inorganic aerogels by direct incorporation of organic ligands into the gel network while the gel forms, but supercritical drying was employed [9–11]. Both pendant [9, 10] and bridging [11] organic ligands were investigated. Such organic/inorganic aerogels possess a high surface area and are hydrophobic, but much more work is needed to get a better understanding and to synthesize

Table 1. Inorganic and organic precursors used in the present study.

Precursors/chemical formula	Organic ligands	Pendant/bridging
Tetraethoxysilane (TEOS) $Si(OC_2H_5)_4$	NA	NA
Methyltriethoxysilane (MTES) $(H_5C_2O)_3Si{-}CH_3$	$-CH_3$	Pendant
Triethoxypropylsilane (TEPS) $(H_5C_2O)_3Si{-}CH_2CH_2CH_3$	$-CH_2CH_2CH_3$	Pendant
1,2-bis(triethoxysily)ethane (BTESE) $(H_5C_2O)_3Si{-}CH_2{-}Si(OC_2H_5)_3$	$-CH_2-$	Bridging
1,2-bis(trimethoxysily)ethane (BTMSE) $(H_3CO)_3Si{-}CH_2{-}Si(OCH_3)_3$	$-CH_2-$	Bridging

highly porous hybrids using ambient pressure drying. According to the Laplace equation (Eq. (1)), hybrid organic/inorganic aerogels could be synthesized under ambient pressure, if the surface chemistry is modified such that the wetting angle is increased significantly, e.g., above 90°. It has been demonstrated that highly porous hybrid gels can be synthesized by a base-catalyzed sol-gel process through direct incorporation of organic ligands [12, 13].

In the present study, we investigated the synthesis of highly porous organic/inorganic hybrids by two-step acid-base catalyzed sol-gel processing and ambient pressure drying. The effects of both pendant and bridging organic ligands on the wetting angles and porous structure have been studied, and the relations between processing conditions, type of organic ligands, surface chemistry, and porous structure are discussed.

2. Experimental

Table 1 summarizes the organic and inorganic precursors (all from Aldrich, Milwaukee, WI) used in the present study. Other chemicals are absolute ethanol (EtOH, 200 proof), hydrochloric acid (HCl) and ammonium hydroxide (NH_4OH, 28–30%). The hybrid organic/inorganic sols were prepared by copolymerizing TEOS and organic precursors using a two-step acid-base catalyzed sol-gel process. The first step is to mix TEOS, MTES (or other organic precursors), ethanol, deionized water, and HCl in a molar ratio of $1:1:7.6:2.2:1.4\times10^{-3}$ at 60°C under stirring at 200 RPM for 90 min. At the second step, NH_4OH and more water were added into the sol to adjust the pH values and water concentration for the final sols which were stirred for 15 min. The Si/H_2O molar ratio of the final sols was kept at approximately 1 : 5, the ethanol/H_2O ratio was 3 : 4, and the pH values varied from 8 to 9. The sols were allowed to age at 50°C in closed bottles until gelation. The liquid-containing gels were further aged for 60–200 h and then solvent was allowed to evaporate at 50°C by opening the bottles (i.e., under ambient pressure). The gels were then heated up to 200°C in air for 2 h to remove all residual solvent.

Hybrid organic/inorganic gels were characterized by nitrogen sorption porosimetry at 77 K (Micromeritics ASAP 2000M, Norcross, GA, and Quantasorb, Quantachrome, Syosset, NY). A VCA-200 (AST, Billerica, MA) sessile drop system was used for (advancing) contact angle measurements. Surface hydroxyl groups in hybrid organic/inorganic gels were analyzed by Fourier Transform Infrared (FTIR) spectroscopy (5DXB, Nicolet, Madison, WI).

3. Results and Discussion

A two-step acid-base catalyzed process was employed for the preparation of homogeneous hybrid organic/inorganic sols. In the first step, both organic and inorganic precursors were partially hydrolyzed, but the condensation process was suppressed due to the deficient amount of water available in the system and low pH (typically ~3) [3]. More importantly, this deficiency of water prevented and/or retarded phase segregation that has a strong tendency to occur due to the hydrophobic nature of organic ligands introduced into the systems. At the second step, a high pH value, ranging from 8 to 9, and excess water resulted in a rapid condensation reaction. Typically, gelation occurred in less than 50 min, depending on the organic precursors used. In

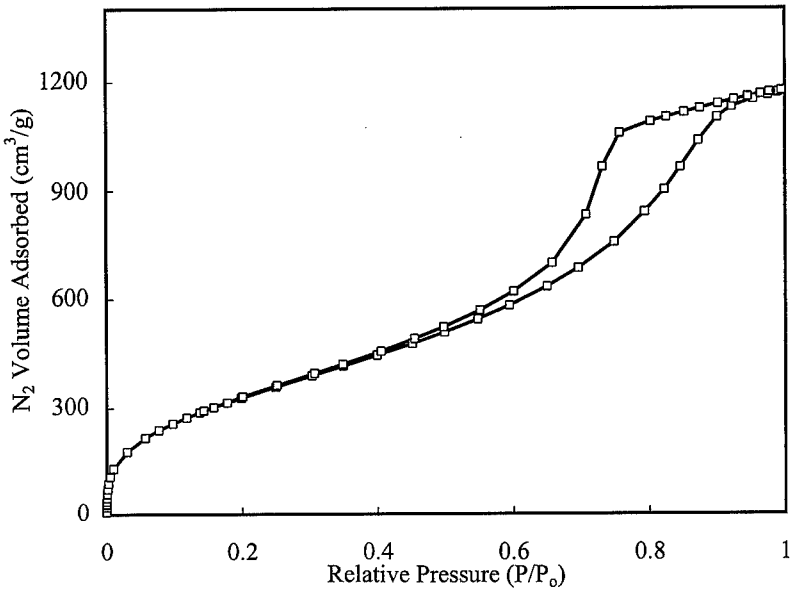

Figure 1. Typical nitrogen sorption isotherm (at 77 K) of hybrid organic/inorganic gels made from TEOS and MTES by two-step acid-base catalyzing process and ambient pressure drying. pH = 9 at the second step and gel was further aged for 60 h. BET surface area is above 1250 m^2/g, porosity above 75%, and average pore size about 8 nm in diameter.

this approach, homogeneous hybrid organic/inorganic sols, i.e., no detectable phase segregation, were prepared and organic ligands were incorporated into solid network while gel forms. High pH values were used to form relatively dense clusters, so as to achieve high porosities and BET surface areas for the hybrid organic/inorganic gels [3].

Dried hybrid gels are highly porous. Figure 1 shows a typical nitrogen sorption isotherm (at 77 K) of a hybrid gel made from TEOS and MTES that has a BET surface area above 1250 m^2/g, pore volume of 1.95 cm^3/g (estimated porosity of ~75%) and average pore size of ~8 nm. BET surface areas and pore volumes of other hybrid organic/inorganic gels made from other organic precursors are presented in Fig. 2. It is clear that different organic precursors resulted in different pore volumes and BET surface areas, though the processing conditions were kept the same.

The incorporation of organic ligands into the solid network will modify the surface chemistry. The pendant organic ligands will preferentially locate on the surface and make the surface hydrophobic [9, 10]. Upon the removal of pore fluid that consists of ethanol and water, ethanol is removed preferentially from the wet gel in the early stage of drying and thus the pore fluid becomes water-rich at the late stage of drying. The surface covered with hydrophobic organic ligands will have a drastically reduced capillary force because of an increased wetting angle, due to the change of solvent composition. The collapse of the porous structure of the wet gel during drying is, therefore, reduced. Contact angle measurements reveal that the gel made solely from TEOS has a wetting angle of 0° for DI-water, while the hybrid TEOS/MTES gel has a wetting angle of 69°. According to the Laplace equation (Eq. (1)), a high wetting angle will certainly result in a reduced capillary pressure and thus reduce the collapse of the porous structure of the wet gel during drying. The high wetting angle of the hybrid gel probably contributes to the high pore volume and BET surface area after ambient pressure drying. Compared to pendant ligands, bridging ligands would enhance the connectivity of the solid network and thus increase the network modulus. An increased network modulus would also reduce the collapse of the network. However, bridging ligands are less likely to be exposed to the surface as compared to pendant ligands, so the surface modification by incorporation of bridging ligands is less effective. The small contact angle, 13°, of the hybrid gel made from bridging organic precursor (BTESE) supports this hypothesis, though more experiments are needed to verify this hypothesis.

It is noteworthy that no "springback" phenomenon was observed in the present study as reported in

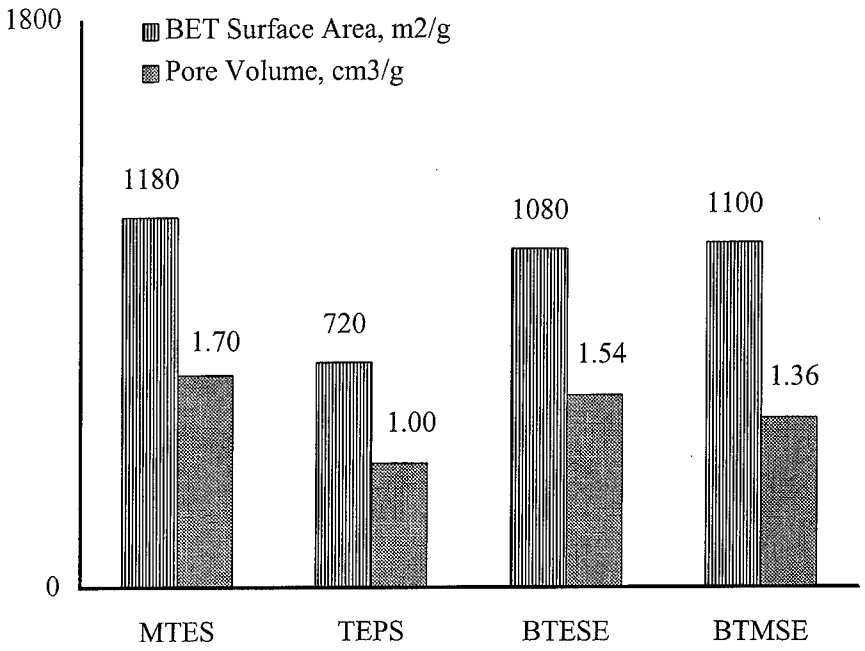

Figure 2. Comparison of BET surface areas and pore volumes of organic/inorganic hybrids prepared from various organic precursors. The ratio of TEOS/organic precursors was kept at 1:1 and all processing conditions (two-step acid-base catalysis) were also kept the same. pH = 9 at the second step and after gelation, gels were further aged for 60 h at 50°C in closed bottles before drying at ambient pressure.

solvent exchange studies [5–8]. If the organic ligands introduced into the system preferentially locate on the surface of the porous gel network, during drying the chemically inert organic ligands will not react to form chemical bonds and, thus, shrinkage is reversible. The lack of "springback" phenomenon could be attributed to the partial coverage of the organic ligands. The remaining hydroxyl groups on the gel network would condense and form an Si—O—Si bridge during drying, so that the shrinkage becomes irreversible and no "springback" occurs.

Prolonged aging and increasing pH values of the final sols enhance the pore volume of the organic/inorganic hybrids, regardless of the organic precursors used. The enhancement of pore volume could be attributed to the structural evolution due to network coarsening during aging [3], that increases the network modulus and thus reduces the collapse of the porous structure during drying. The SEM photographs revealed that prolonged aging resulted in structural coarsening in organic/inorganic hybrids similar to that observed in silica aerogels [14]. Prolonged aging and high pH values have two opposite influences on surface area. Structural coarsening would result in a decrease in surface area; however, an enhanced network modulus would reduce structural collapse and, thus, preserve surface area of the solid network.

Although high surface area and pore volume have been obtained, there was always some gel shrinkage observed during drying. This observation indicates the existence of a capillary force and agrees well with the contact angle measurements. Compared to the literature [12, 13], the organic/inorganic hybrids synthesized through direct incorporation of organic ligands into the solid network in the present study (except that made from TEPS) possess a much higher BET surface area and porosity. However, porosity of the organic/inorganic hybrids synthesized in the present study is lower than that synthesized through solvent exchange. This probably indicates the surface modification through direct incorporation of organic ligands is less effective compared to the solvent exchange. FTIR analyses reveal the existence of hydroxyl groups in the hybrid organic/inorganic gels, despite the high ratio of organic ligands incorporated into the gel network. That implies that part of the organic ligands are buried into the gel network. The FTIR results are consistent with the interpretation proposed above for the lack of "springback" phenomenon in the present study. The contact angle measurements also agree with the FTIR

results, i.e., the surface of the gel network is partially covered by hydrophobic organic ligands and partially covered by hydroxyl groups.

In comparison with the aerogels prepared by the supercritical drying process, the pores in the organic/inorganic hybrids prepared by ambient drying are much smaller, due to a partial collapse of the gel network during drying. Such highly porous hybrid monoliths demonstrate a better optical transparency due to less light scattering than one would expect from the relatively larger pores in supercritically dried aerogels (which typically have a milky appearance). In addition, highly porous organic/inorganic hybrids have much improved mechanical properties due to the incorporation of organic components.

4. Conclusions

Highly porous organic/inorganic hybrids with a BET surface area of above 1250 m^2/g and pore volume of 1.95 cm^3/g have been synthesized using a two-step acid-base catalyzed sol-gel process and ambient pressure drying. The two-step processing results in the formation of homogeneous hybrid organic/inorganic sols by preventing phase segregation. The homogeneous incorporation of organic ligands results in modification of the surface chemistry of the solid network as evidenced by the change of contact angles and, thus, reduces the capillary pressure upon the removal of solvent during drying. However, it remains a challenge to locate hydrophobic organic ligands on the surface of the solid gel network, so as to completely prevent the capillary pressure driven collapse of the solid gel network upon drying at ambient pressure.

Acknowledgment

We are grateful for the partial financial support from the Royalty Research Fund.

References

1. R.W. Pekala and L.W. Hrubesh, J. Non-Crystalline Solids **186** (1995).
2. R.W. Pekala, C.T. Alviso, F.M. Kong, and S.S. Hulsey, J. Non-Crystalline Solids **145**, 90 (1992).
3. C.J. Brinker and G.W. Scherer, *Sol-Gel Science: The Physics and Chemistry of Sol-Gel Processing* (Academic Press, Inc., San Diego, CA, 1990).
4. F.A.L. Dullien, *Porous Media, Fluid Transport and Pore Structure* (Academic Press, New York, NY, 1979).
5. R. Deshpande, D.M. Smith, and C.J. Brinker, U.S. Patent Application, 1992.
6. D.M. Smith, R. Deshpande, and C.J. Brinker, in *Better Ceramics Through Chemistry V*, edited by M.J. Hampden-Smith et al. (MRS Symp. Series 271, Pittsburgh, PA, 1992), p. 567.
7. S.S. Prakash, C.J. Brinker, and A.J. Hurd, J. Non-Crystalline Solids **188**, 46 (1995).
8. S.S. Prakash, C.J. Brinker, A.J. Hurd, and S.M. Rao, Nature **374**, 439 (1995).
9. F. Schwertfeger, W. Glaubit, and U. Schubert, J. Non-Crystalline Solids **145**, 85 (1992).
10. H. Yokogawa and M. Yokoyama, J. Non-Crystalline Solids **186**, 23 (1995).
11. D.A. Loy, G.M. Jamison, B.M. Baugher, E.M. Russick, R.A. Assink, S. Prabakar, and K.J. Shea, J. Non-Crystalline Solids **186**, 44 (1995).
12. W.G. Fahrenholtz, D.M. Smith, and D.W. Hua, J. Non-Crystalline Solids **144**, 45 (1992).
13. W.G. Fahrenholtz and D.M. Smith, in *Better Ceramics Through Chemistry V*, edited by M.J. Hampden-Smith et al. (MRS Symp. Series 271, Pittsburgh, PA, 1992), p. 705.
14. G.M. Pajonk, A. Venkateswara Rao, B.M. Sawant, and N.N. Parvathy, J. Non-Crystalline Solids **209**, 40 (1997).

Journal of Sol-Gel Science and Technology 13, 311–316 (1998)
© 1998 Kluwer Academic Publishers. Manufactured in The Netherlands.

Drying of Large Monolithic Aerogels between Atmospheric and Supercritical Pressures

FIKRET KIRKBIR, HIDEAKI MURATA, DOUGLAS MEYERS AND S. RAY CHAUDHURI
YTC America Inc., 550 Via Alondra, Camarillo, CA 93012, USA

Abstract. The objectives of this investigation are to show the feasibility of producing large monoliths with minimal shrinkage at subcritical conditions, and to understand the drying behavior. Crack-free SiO_2 monoliths (5.6 cm in diameter and 25 cm in length) were repeatedly dried with little shrinkage (<2%). Some gels showed increasing shrinkage with decreasing pressure. However, this shrinkage was reduced to negligible levels at conditions considerably less than supercritical pressure by increasing both the pore size and the gel strength. This moderate pressure drying (MPD) process may make aerogel fabrication economically more feasible due to reduced pressure chamber costs.

Keywords: silica, monolith, drying, subcritical, aerogel

1. Introduction

Wet gels are usually dried by two fundamental processes. In the first, the liquid in the gel pores is slowly evaporated at atmospheric pressure to yield so-called xerogels. The formation of capillary pressure during this process causes shrinkage of the gel network and thereby reduces the pore size.

In the second process, the wet gel is rapidly dried above the supercritical pressure and temperature of the pore liquid to minimize the shrinkage and to obtain so-called aerogels. Under these conditions, there is no interface between vapor and liquid and the destructive effects of capillary pressure are therefore avoided. Therefore, the gel does not collapse during drying. However, the supercritical pressures are usually so high (e.g., 6.4 MPa at 243.1°C for ethanol) that expensive autoclaves are necessary for this process.

It is of interest to investigate whether gels can be dried between atmospheric and supercritical pressures with minimal shrinkage to allow pores to remain large and open after drying. This helps the sintering process by allowing easier diffusion of gases through the gel. Also, since these gels can have low bulk density and high surface area, they can be used in the manufacturing of thermal insulation materials, catalysts, adsorbents, fuel cells, etc. Equipment costs may also be reduced substantially because of low pressure and/or lower temperature drying operation.

Considerable research efforts have been directed towards understanding drying phenomena at atmospheric pressures and above the critical conditions. However, there is little published research conducted specifically to understand the drying behavior of gels between atmospheric and critical conditions. Boonstra and Baken [1] and van Lierop et al. [2] did report drying of SiO_2 monoliths at subcritical conditions, but with considerable shrinkage. Woignier et al. [3] obtained monoliths slightly below critical conditions, but observed cracking at lower pressures. Deshpande et al. [4] dried gels in CO_2 and also found that shrinkage occurred at subcritical conditions. (Only standard gel preparation processes as reviewed by Brinker and Scherer [5] were considered in these studies. Special gel surface treatments, e.g., by Deshpande et al. [6] or TEOS aging processes, e.g., by Hærid et al. [7] which were carried out to obtain aerogels at atmospheric conditions were not the subject of the current and cited investigations above).

The aim, in this study, is to dry crack-free SiO_2 monoliths with minimal shrinkage at pressures substantially lower than supercritical pressures and to understand the drying behavior under these conditions.

Table 1. Gel strength and microstructure of gels dried at subcritical conditions.

	Wet gel		Drying			Dry gel		
Sol comp.	Rupture modulus (MPa)	Shear modulus (MPa)	Temperature (°C)	Pressure (MPa)	Shrinkage (%)	Average pore size (Å)	Pore volume (cm^3/g)	Surface area (m^2/g)
HF/HCl	0.76	5.47	250	4.4	9	48	2.06	863
HCl/NH_3	0.45	3.81	232	3.2	<1	91	3.20	705
HF	0.07	0.43	246	4.5	20	124	3.23	519

2. Experimental

Sols were prepared from tetraethyl orthosilicate, ethanol, water and catalysts such as HF, HCl and NH_3 (Table 1). After gelation and aging, the pore liquid was exchanged with ethanol. Then, the gels were placed in a pressure chamber for drying. The chamber was heated to a final temperature between 230°C and 260°C. The linear shrinkages of the gels were measured manually. The chamber pressures given are the maximum pressures reached at the end of heating. Details of gel preparation and analysis procedures have been reported in previous publications [8].

3. Results

For all of the experimental conditions, dry crack-free monoliths were obtained from gels typically 2.9–3.4 cm in diameter and 17–22 cm in length.

Figure 1 compares the vapor pressure-temperature curve of pure ethanol [9] with experimental pressures observed during heating of the chamber. Supercritical drying was achieved by loading the chamber with a quantity of ethanol sufficient to exceed the critical conditions. When loaded with an amount less than that required for the critical conditions, the chamber pressure first followed the vapor pressure-temperature curve and

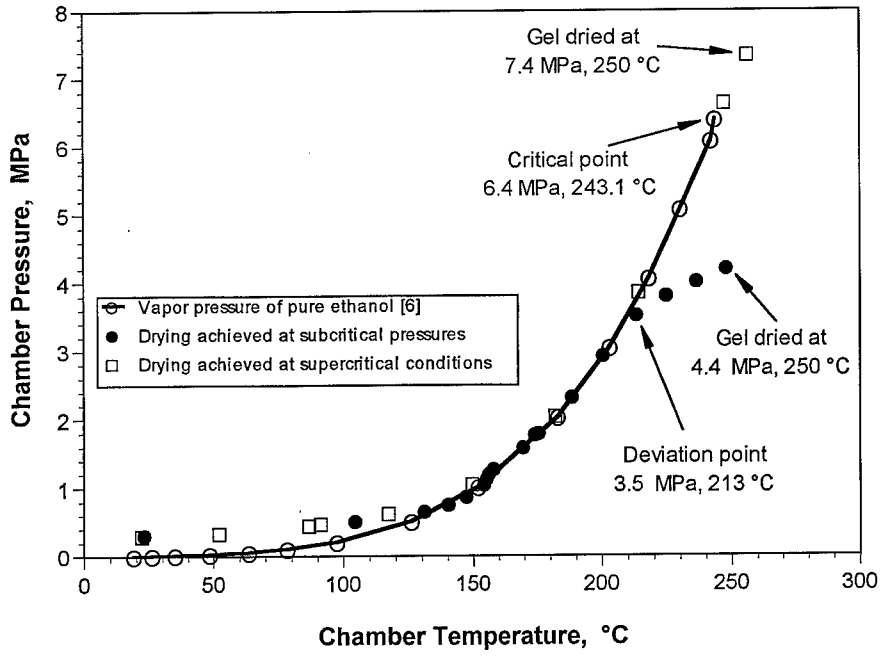

Figure 1. Vapor pressure-temperature curve for ethanol vs. experimental pressures. Gels were prepared from sol composition 1. The chamber was prepressurized to 0.3 MPa by using N_2 gas.

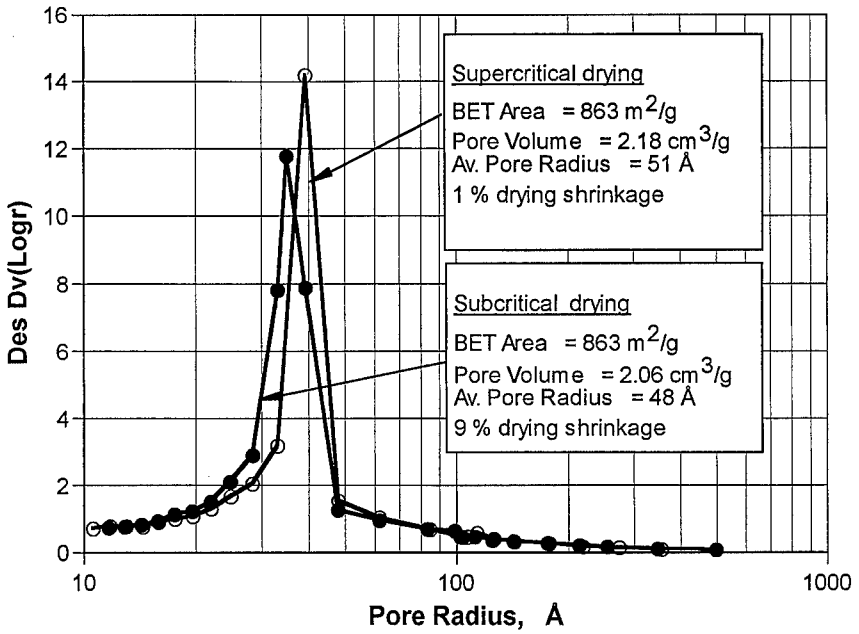

Figure 2. Microstructure of the gel dried at supercritical conditions vs. at subcritical pressures. Gels were prepared from sol composition 1.

then started to deviate. At the deviation point, virtually all ethanol was in vapor form and therefore, any further pressure increase could not be supported by liquid evaporation. The chamber pressure did increase further with temperature due to thermal expansion of the vapor, however, without reaching the critical levels.

Figure 2 shows the microstructures of the gels dried at conditions given in Fig. 1. The shrinkage of the supercritically dried gel was negligible. About 9% shrinkage occurred in the gel dried at the subcritical pressure. Their microstructures were similar.

Gels prepared from three different sol compositions were dried at subcritical pressures (Table 1). The HF/HCl catalyzed gels with the smallest pore size were the strongest. These gels showed some shrinkage, approximately 9%, under subcritical drying. As the pore size was increased by adjusting the sol composition, the shrinkage was reduced substantially, to <1% for HCl/NH_3 catalyzed gels, although the strength was lower than that of HF/HCl gels. The microstructure of this gel was very close to that of the supercritically dried sample (Fig. 3). Also, monoliths were obtained with this sol composition at temperatures below the critical value for ethanol, 243.1°C (Table 1). As the pore size was increased further (HF catalyzed gels), the gels were much weaker, and shrinkage was considerable.

For gels prepared from HF/HCl and HCl/NH_3, shrinkage increased and pore size decreased with decreasing chamber pressure (Figs. 4 and 5). However, there appears a threshold subcritical pressure above which the shrinkage was negligible. Below this threshold, the shrinkage was considerable. Also, the threshold pressure depended on sol composition. For gels with smaller pore size (HF/HCl), the threshold pressure was about 4.7 MPa (Fig. 4) and for gels with larger pores (HCl/NH_3), about 3.2 MPa (Fig. 5).

The yield was found to be about 95% for experiments repetitively done under similar conditions. In this study, 40 gels, 5.6 cm in diameter and 25 cm in length were dried with negligible shrinkage and without cracks.

4. Discussion

This study clearly shows that monoliths can be obtained over the entire range of pressure from atmospheric to supercritical conditions. The drying temperature can also be reduced below the critical value.

More interestingly, the results indicate the existence of a threshold subcritical pressure above which gels will undergo minimal shrinkage. Therefore, if aerogels are defined as wet gels dried with negligible shrinkage, this study showed that aerogels can be produced subcritically, over a range of pressure and temperature conditions. The subcritical operating domain depends

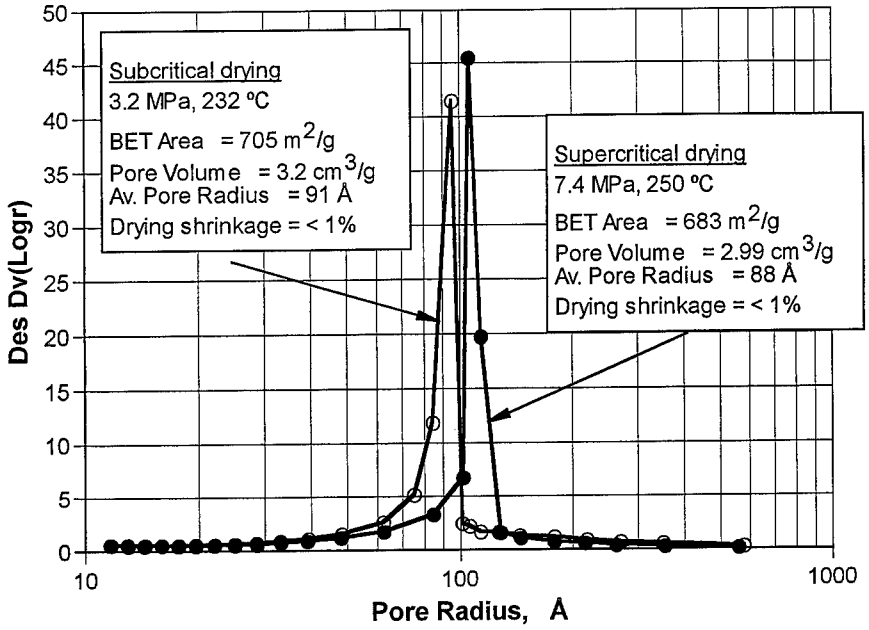

Figure 3. Microstructure of the gel dried at supercritical conditions vs. at subcritical pressures. Gels were prepared from sol composition 2.

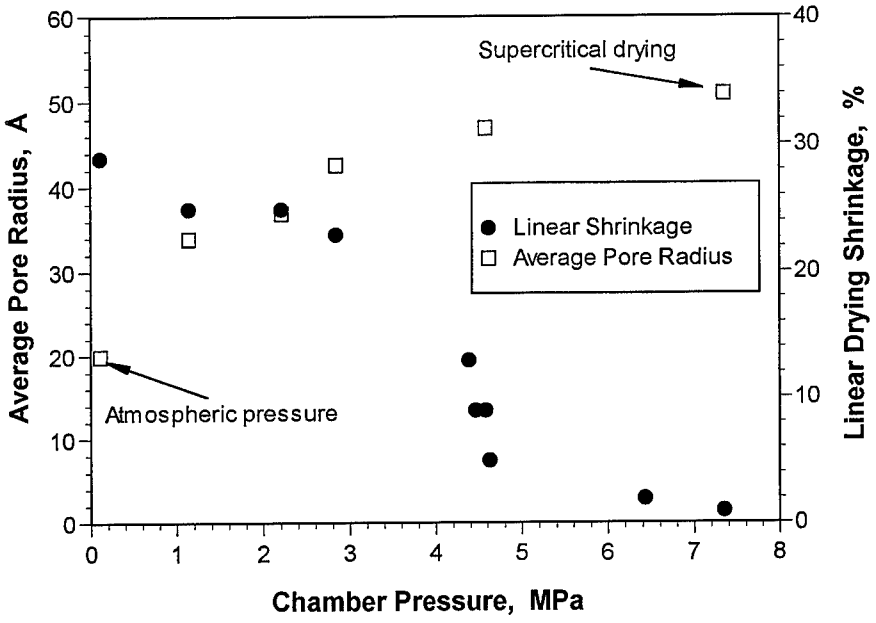

Figure 4. Shrinkage behavior of small pore size gels (sol composition 1).

on the pristine wet gel microstructure and the capillary pressure.

Kistler [10] had argued that drying shrinkage could be avoided only if the drying operation was carried out at supercritical conditions, so that capillary pressure at the vapor-liquid interface was eliminated. The results of this study contradict Kistler's theory. They clearly show that monolithic aerogels with minimal shrinkage can be produced repeatedly under subcritical conditions, even with the presence of substantial capillary forces.

It may be hypothesized that the shrinkage during subcritical drying is the net effect of capillary forces versus the inherent gel strength acting against each

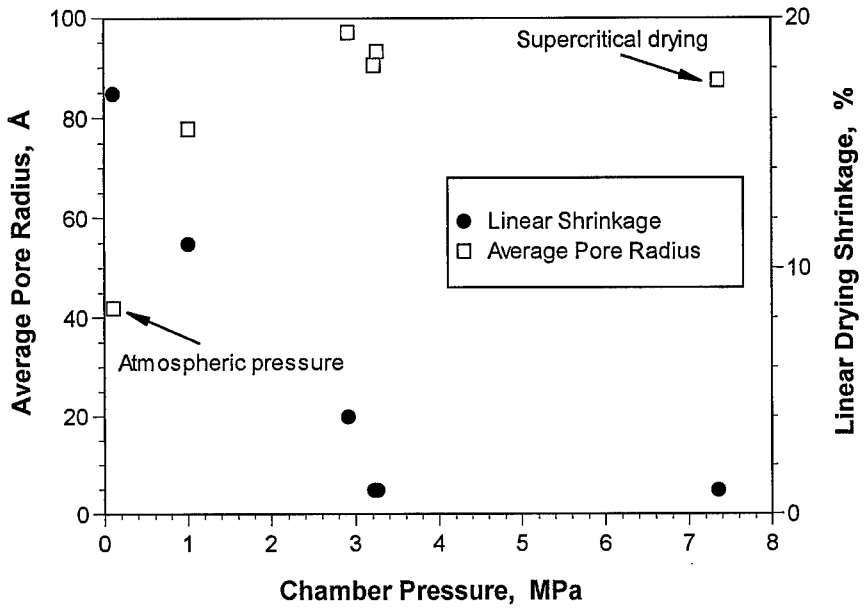

Figure 5. Shrinkage behavior of large pore size gels (sol composition 2).

other. This hypothesis implies that the pristine solid structure is not fully compliant to the capillary force exerted by the pore liquid. At the threshold point, the strength and the capillary pressure have equal but opposite value. Below the threshold point, the capillary pressure overcomes the strength and the solid structure collapses. Above the threshold point, since the strength is always higher than the capillary pressure, the shrinkage becomes negligible.

The smaller pore size gels (HF/HCl gel) had a higher shrinkage threshold pressure than gels with relatively larger pores (HCl/NH_3 gel): 4.7 MPa vs. 3.2 MPa. This might be explained by the fact that at any given pressure, the smaller pore size gels would experience a higher capillary force.

The capillary pressure was lowest for the gel with the largest pores (HF gel). However, since these gels were very weak, they shrunk considerably during drying. It is possible that the same phenomenon caused substantial shrinkages in the gels used in previous studies [1–4].

This shrinkage could be avoided by utilizing strong gels. However, very strong gels may have extremely small pores, for which the increased capillary pressure may cause some shrinkage.

This process was mainly developed to dry aerogels for manufacturing of dense synthetic silica. For this reason, the current investigation is focused on drying of high density aerogels (0.23–0.39 g/cm^3). However, this study can be extended to low density aerogels for production of insulation materials. Furthermore, since this development concerns only the subcritical drying process, rather than gel preparation or modification, it can be applied to drying of other type of aerogels (single or multicomponent ceramics, organic aerogels etc.).

In summary, we demonstrated that monolithic porous aerogels can be produced at subcritical conditions repeatedly and reliably. Subcritical drying operations can reduce the chamber costs substantially. This may lead to a commercially viable process for manufacturing aerogel monoliths for a variety of industrial applications.

5. Conclusions

The main conclusions of this research are:

1. Crack-free gels can be dried at pressures between atmospheric and supercritical pressures.
2. At such moderate pressure drying (MPD) conditions, the shrinkage can be completely prevented by synthesizing gels with large pores and sufficiently high strength.
3. The drying temperature can also be reduced below the critical value.
4. The MPD process yields large size monoliths reliably and repeatedly.

5. This process may be extended to dry aerogels with different chemical compositions, single or multi-component ceramics, organic aerogels etc.
6. The MPD process can reduce drying chamber cost significantly, which may lead to an economical process for the manufacture of aerogel monoliths with large pore size, high surface area, and low density.

References

1. A.H. Boonstra and J.M.E. Baken, J. Non-Cryst. Solids **109**, 1–8 (1989).
2. J.G. van Lierop, A. Huizing, W.C.P.M. Meerman, and C.A.M. Mulder, J. Non-Cryst. Solids **82**, 265–270 (1986).
3. T. Woignier, J. Phalippou, J.F. Quinson, M. Pauthe, and F. Laveissiere, J. Non-Cryst. Solids **145**, 25–32 (1992).
4. R. Deshpande, D.W. Hua, D.M. Smith, and C.J. Brinker, J. Non-Cryst. Solids **144**, 32–44 (1992).
5. C.J. Brinker and G.W. Scherer, *Sol-Gel Science: The Physics and Chemistry of Sol-Gel Processing* (Academic Press, New York, 1990).
6. R. Deshpande, D.M. Smith, and C.J. Brinker, U.S. Patent 5,565,142, 1996.
7. S. Hærid, M. Dahle, S. Lima, and M.-A. Einarsrud, J. Non-Cryst. Solids **186**, 96–103 (1995).
8. F. Kirkbir, H. Murata, D. Meyers, S. Ray Chaudhuri, and A. Sarkar, J. Sol-Gel Sci. Tech. **6**, 203–217 (1996).
9. R.H. Perry, D.W. Green, and J.O. Maloney, *Perry's Chemical Engineers' Handbook*, 6th edition (McGraw-Hill, New York, 1984), pp. 3–55, 3–63.
10. S.S. Kistler, Nature **127**, 741 (1931).

Journal of Sol-Gel Science and Technology 13, 317–322 (1998)
© 1998 Kluwer Academic Publishers. Manufactured in The Netherlands.

Thermal and Temporal Aging of Silica Gels in Monomer Solutions

MARI-ANN EINARSRUD AND ELIN NILSEN
Department of Inorganic Chemistry, Norwegian University of Science and Technology, 7034 Trondheim, Norway
Mari-Ann.Einarsrud@chembio.ntnu.no

Abstract. In previous work we have introduced the idea of preparing ambient pressure dried silica aerogels by increasing the wet gels' stiffness by aging in a TEOS solution until shrinkage during drying is almost eliminated. The present work elucidates the possibilities to obtain ambient pressure dried aerogels employing this idea, however, cheap water soluble sodium silicate (water glass) precursors have been used to increase the economic feasibility of the process.

We have shown how the G modulus of water glass based gels can be increased by aging in TEOS solution and gels with a density down to ~0.2 g/cm^3 can be obtained. These wet gels show a higher reactivity towards TEOS compared to TEOS based gels. We have also introduced the idea of aging wet gels in a solution where the monomers are provided from water glass instead of TEOS and some initial results on G modulus and density are included.

Keywords: silica xerogel, thermal aging, temporal aging, water glass

Introduction

After the gel formation, the properties of the wet gel like strength and stiffness can be altered by aging the gel either in the mother liquor or in another pore liquid [1–5]. The changes in the wet gel structure and properties have a profound effect on the subsequent drying process, i.e., reducing cracking and shrinkage during drying. Also during aging, the nanostructure of the wet gels will be altered, which is of interest for design of dried gels with desired properties.

In previous work, we have shown that gels can be strengthened and stiffened by providing new monomers to the alcogel giving ambient pressure dried aerogels [1, 4]. The new monomers have been provided through aging the wet gels in a solution of rather expensive alkoxide precursors. Recently, we have initiated work to study the use of water soluble sodium silicates (water glass) as precursors for the preparation of ambient pressure dried gels [6]. The present work elucidates the possibilities to obtain ambient pressure dried aerogels (i) made from wet water glass based gels or (ii) by aging alkoxide based gels in a water glass solution. An elevated pH is necessary to provide monomers during the aging in water glass solution [7]. However, it has been shown that aging at elevated pH might cause a decrease in the strength of wet gels [3]; hence, we have also studied the pH and temperature range for where aging in water glass solution can be performed. Finally, the G modulus of the wet gels will be reported together with properties of ambient pressure dried gels.

Experimental

The two-step TEOS based alcogels were prepared by a similar method as described by Brinker et al. (B2) [8]. For the preparation of sodium silicate (water glass) based gels, water glass (Akzo PQ, silica content 10 wt%, $SiO_2 : Na_2O = 3.4$) was exchanged using an ion exchanger (Amberlite IR-120, pH 2.3) and then added 1 M NH_4OH until pH equal to 4.6. The gels were cast into Teflon® tubes with an inner diameter of 8.6 mm and kept at 40°C (TEOS) or 50°C (water glass) for 1 h for gelation.

For the aging in a TEOS solution, gels of both types were first soaked into a washing solution of 20 vol% H_2O/ethanol for 24 h at 60°C followed by aging in a solution of 70 vol% TEOS/ethanol at 70°C for various lengths of time.

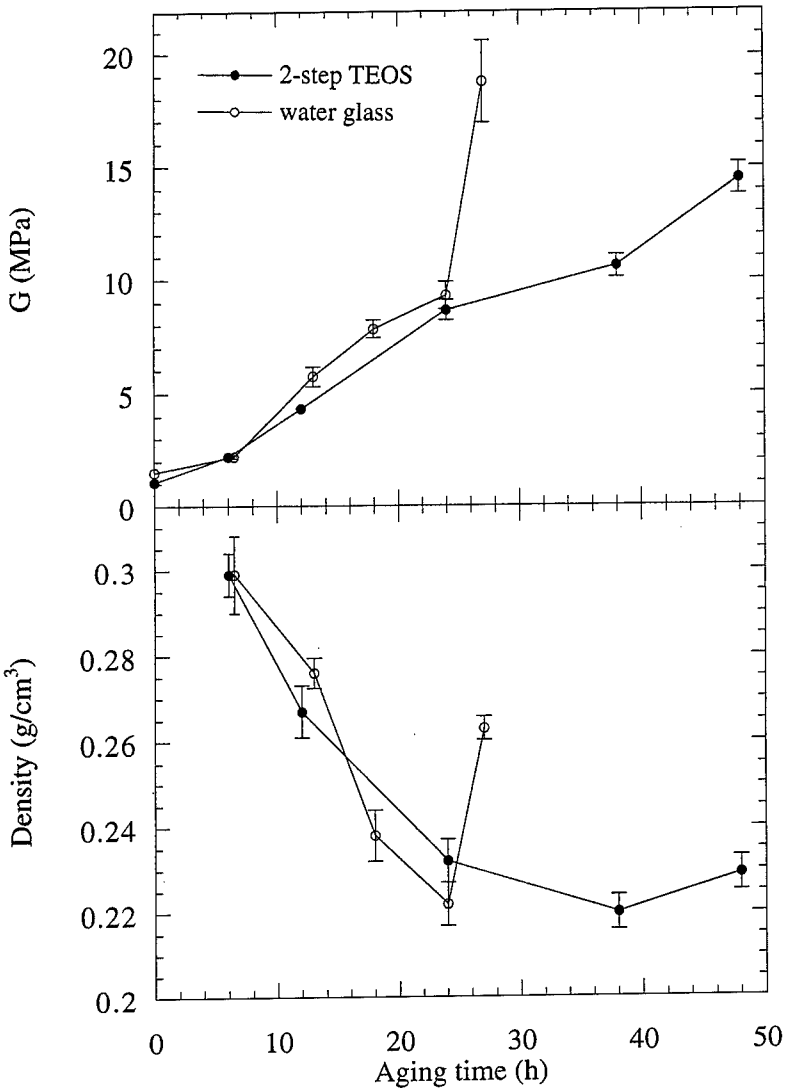

Figure 1. Development in G modulus and xerogel density after drying from *n*-heptane for water glass based gels and two-step TEOS based gels aged in 70 vol% TEOS/ethanol solution at 70°C for various time intervals. Prior to the aging, the gels were washed in 20 vol% water/ethanol solution for 24 h at 60°C.

Due to the fact that the aging in water glass solution has to take place at elevated pH [7], some of the two-step TEOS gels were soaked in solutions of water/methanol with different vol% water (20, 80 or 100 vol% H_2O) at pH = 9.00 for different times at different temperatures to determine the effect of aging at this pH. The aging in the water glass solution was performed by soaking the two-step TEOS gels in a solution of 80 vol% H_2O/methanol with water glass (Akzo PQ) corresponding to 3 wt% SiO_2 at pH = 9.00. The Na concentration of the aging solution was 0.02 M. Due to the polymerization of the aging solution an exchange to a freshly prepared solution was performed every 4 h. The presence of monomers in the aging solution was checked by using molybdic acid [9].

After the different aging treatments the samples were washed in ethanol four times within 24 h at 50°C before measuring G modulus by using a procedure described previously [10]. The samples were further washed in *n*-heptane four times within 24 h at 50°C before drying at ambient pressure. During the drying performed in 24 h intervals at 90, 120 and 180°C, the gels were partly

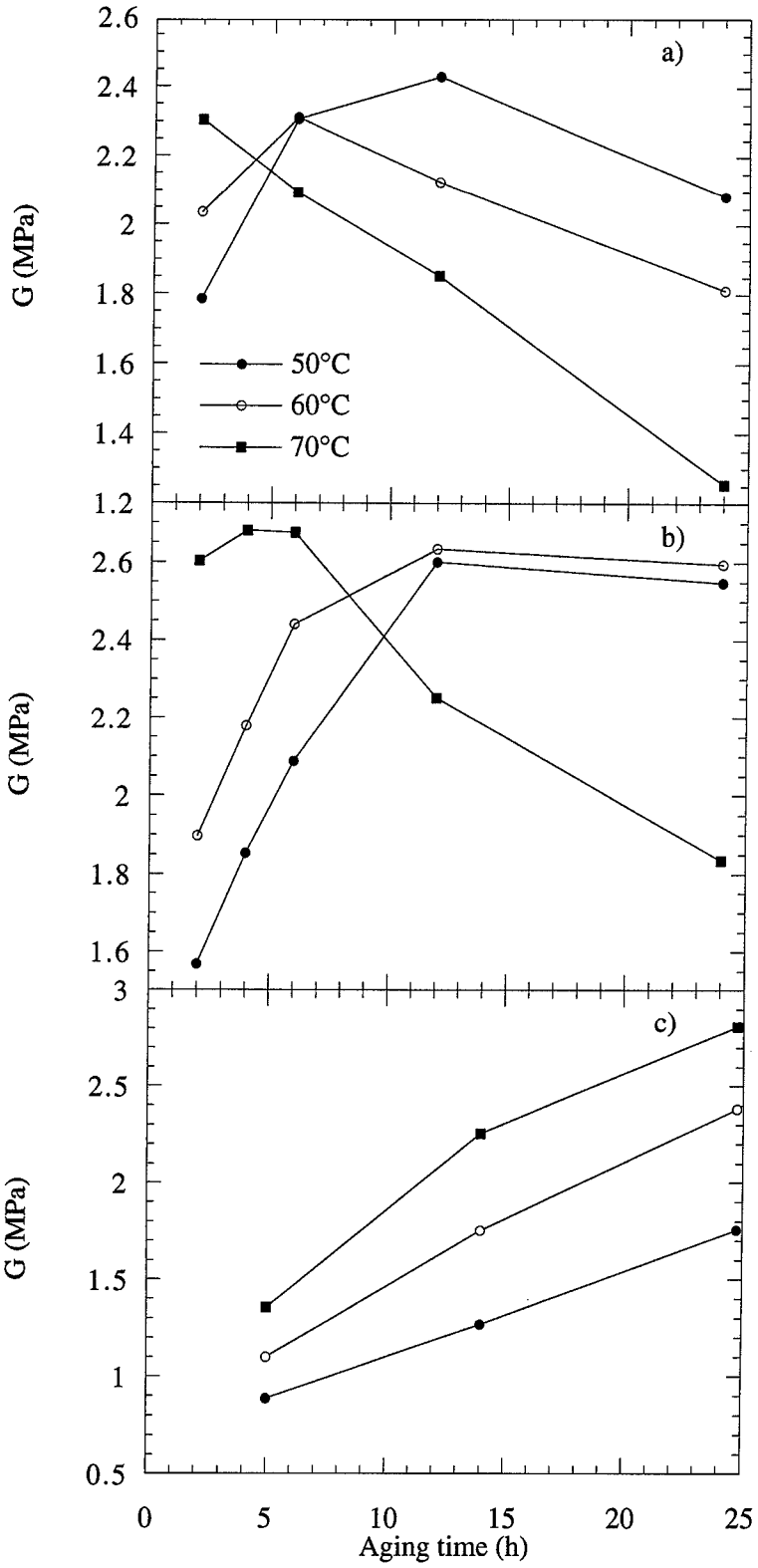

Figure 2. Development in G modulus (±0.08 MPa) of wet two-step TEOS gels aged at pH = 9.00 at different temperatures in (a) 100% water, (b) 80% water/methanol, and (c) 20% water/methanol.

covered. The xerogel bulk densities were calculated from the mass and the volume of the samples.

Results and Discussion

Figure 1 compares the increase in G modulus of two-step TEOS gels and water glass based gels during aging in TEOS solution at 70°C. Prior to the aging, the two types of gels had the same silica content corresponding to a density of 0.118 g/cm^3. The increase in G modulus for the water glass based gels is much sharper than for the two-step TEOS gels especially after ~20 h of aging showing a higher reactivity of these gels. One reasonable explanation for this increased reactivity is that the water glass based gels have a higher pore size (hydraulic radius of 18 nm compared to 15 nm for the two-step TEOS gels) and hence the diffusion rate of TEOS into the gel pore structure is higher, which is also giving a higher increase in weight gain for the water glass gels [6].

Figure 1 also includes the change in xerogel density as a function of increasing aging time in TEOS. The decrease in density for the shorter aging times is due to the increase in G modulus, while the increase observed at higher aging times is caused by the fact that the shrinkage has been eliminated while there still is a weight gain during the aging [1, 4]. A minimum density of ~0.2 g/cm^3 was obtained for both precursors.

To further expand this concept of using cheap raw materials we have initiated work on aging of wet gels in monomers provided from water glass. However, since the aging to provide monomers from water glass has to be performed at elevated pH [7], and it has been shown that aging of wet gels at elevated pH might decrease the strength of the wet gels [3, 5], we performed an initial study to check how aging at pH = 9.00 changes the properties of wet gels. Figure 2 shows the development in G modulus as a function of time for aging in different water solutions and a maximum in G modulus is observed for most of the experiments. However, for aging in 20 vol% water a maximum is expected for longer aging times and hence the maximum is shifted to higher aging times when the amount of water is decreasing. This maximum shows that the gels are first becoming stiffer by the dissolution/reprecipitation of silica into the necks between the particles, followed by a decrease in stiffness of the gel network probably due to a different particle size in the gels [3]. The smaller particles will be dissolved and the larger will increase in size.

The density of the corresponding xerogels aged in 80 vol% water/methanol is shown in Fig. 3; at 50 and 60°C the density is as expected decreasing with increasing G modulus [11]. However, for the gel aged at 70°C there is also a decrease in density even if the G modulus is decreasing after about 5 h of aging. We believe that this reduction is due to dissolution of the smaller particles of the gel network creating a larger

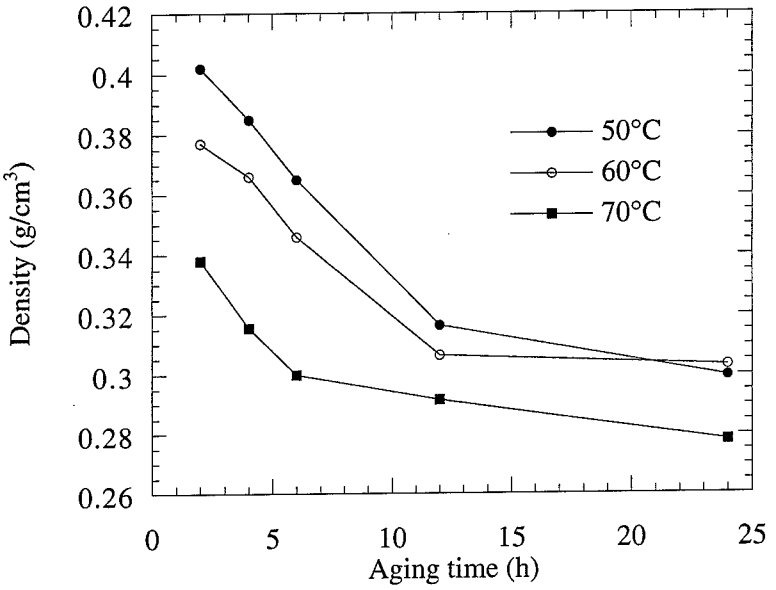

Figure 3. Development in xerogel density (± 0.007 g/cm^3) for two-step TEOS gels aged at pH = 9.00 at different temperatures in 80% water/methanol and dried from *n*-heptane.

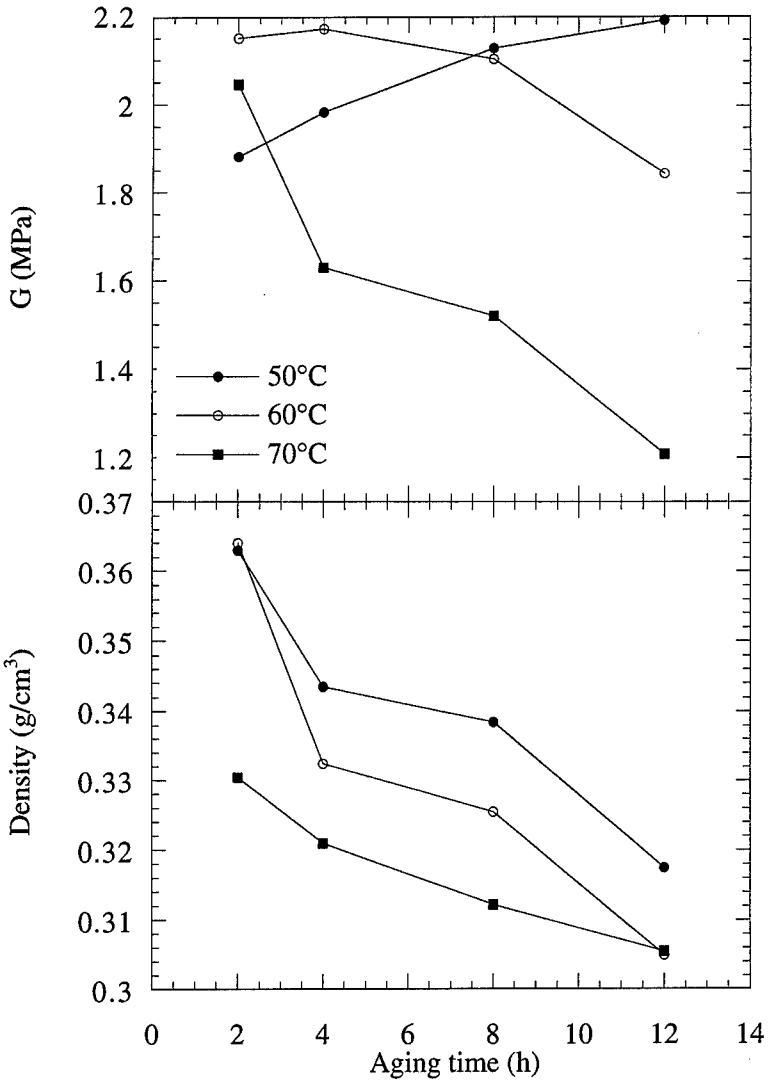

Figure 4. G modulus (±0.08 MPa) and xerogel density (±0.005 g/cm^3) for two-step TEOS gels aged in water glass solution (3 wt% SiO_2 and 80 vol% water) for different temperatures or 70 vol% TEOS/ethanol solution at 70°C.

pore size, and hence a smaller capillary pressure is developed during the drying causing less shrinkage [10]. From these results we decided to use 80 vol% water/methanol for the aging in monomers from water glass.

The change in the G modulus during aging in the water glass solution is displayed in Fig. 4. Compared to the data given in Fig. 2(b) where the aging was performed at similar conditions but with no monomers present, we observe that the G modulus is higher at short aging times for the water glass aging; however, for aging of more than ~4 h a lower G modulus is observed. A corresponding behavior is observed in density comparing aging without and with monomers because a lower density is observed for short aging times while a higher density is obtained for aging times exceeding ~4 h. These results show that we have obtained an effective aging for the first few hours, which was also confirmed by gravimetrical measurements of dried gels. However, for efficient aging of more than ~4 h the pH and Na content has to be more thoroughly controlled.

Conclusion

Wet gels obtained from water glass precursors have been aged in TEOS solutions and quite low density

xerogels ($\sim$0.22 g/cm^3) have been obtained. Compared to gels prepared from TEOS the water glass based gels show a higher reactivity to TEOS for the same aging time.

By aging in a solution providing monomers from water glass a density down to $\sim$0.3 g/cm^3 is obtained. However, the same density can also be obtained by aging in a water solution at elevated pH. At the conditions used in this work, the aging in a TEOS solution is more effective in order to increase stiffness of wet alkoxide based gels compared to aging in a solution providing monomers from water glass.

Acknowledgment

This project was supported from German Federal Ministry for Research and Technology under the code 00335004 and BASF AG, Ludwigshafen.

References

1. S. Hæreid, M. Dahle, S. Lima, and M.-A. Einarsrud, J. Non-Cryst. Solids **186**, 96 (1995).
2. S. Hæreid, M.-A. Einarsrud, and G.W. Scherer, J. Sol-Gel Sci. Tech. **3**, 199 (1994).
3. S. Hæreid, J. Anderson, M.-A. Einarsrud, D.W. Hua, and D.M. Smith, J. Non-Cryst. Solids **185**, 221 (1995).
4. S. Hæreid, E. Nilsen, and M.-A. Einarsrud, J. Porous Mater. **2**, 315 (1996).
5. S. Hæreid, E. Nilsen, V. Ranum, and M.-A. Einarsrud, J. Sol-Gel Sci. Tech. **8**, 153 (1997).
6. M.-A. Einarsrud and E. Nilsen, J. Non-Cryst. Solids **226**, 122 (1998).
7. C.J. Brinker and G.W. Scherer, *Sol-Gel Science: The Physics and Chemistry of Sol-Gel Processing* (Academic Press, New York, 1990).
8. C.J. Brinker, K.D. Keefer, D.W. Schaefer, R.A. Assink, B.D. Kay, and C.S. Ashley, J. Non-Cryst. Solids **63**, 45 (1984).
9. R.K. Iler, *The Chemistry of Silica* (Wiley, NY, 1979).
10. G.W. Scherer, J. Sol-Gel Sci. Tech. **2**, 199 (1994).
11. G.W. Scherer, S. Hæreid, E. Nilsen, and M.-A. Einarsrud, J. Non-Cryst. Solids **202**, 42 (1996).

Journal of Sol-Gel Science and Technology 13, 323–328 (1998)
© 1998 Kluwer Academic Publishers. Manufactured in The Netherlands.

The Subcritical Preparation of Aerogels Based on Sodium Water Glass

THOMAS GERBER
Universität Rostock, Fachbereich Physik

Abstract. A procedure is presented which involves working below the supercritical temperature and pressure and which conserves the structure of the wet gel. The fundamental step of the subcritical preparation of aerogels is the prevention of the condensation reaction of the $\equiv Si_{surface}OH$ groups at the inner surface of the gel during drying. The reaction

$$2 * \equiv Si_{surface}OH \rightarrow \equiv Si{-}O{-}Si\equiv + H_2O$$

is avoided by occupation of the surface with a stable chemical group which does not condense. An esterification $\equiv Si_{surface}OH + ROH \rightarrow \equiv Si_{surface}OR + H_2O$ is a simple method of sealing the inner surface. This reaction is an equilibrium reaction. The equilibrium is shifted in favor of $\equiv Si_{surface}OR$ by removal of the water. The best esterification was obtained by use of *n*-butanol. Densities of the aerogels prepared under subcritical conditions lower than 0.1 g cm^{-3} were obtained. The changes in the structure of the gel during all procedure steps were studied by small angle X-ray scattering, transmission- and scanning electron microscopy.

Keywords: aerogel, sodium water glass solution, subcritical preparation, fractal clusters, structure, SAXS

Introduction

Aerogels are a class of low density solid foams that are characterized by having open cell structures composed of particles in the nanometer range. Most aerogels are made from silica, but organic aerogels have also recently been made [1].

In general, aerogels are prepared by drying under hypercritical conditions with respect to alcohol or CO_2. In this way, the solid matter framework of the wet gel is conserved. The applications for aerogels are wide ranging and virtually unlimited, but the unacceptably high costs of the high-pressure process in autoclaves prevents the deployment of aerogels in the commercial marketplace [2].

Successful attempts to dry aerogels at ambient pressure were made by Haereid et al. [3]. They showed that by aging tetraethoxysilane (TEOS)-based alcogels in a solution of TEOS/ethanol the shrinkage during drying at ambient pressure can be reduced. Densities lower than 0.24 g cm^{-3} are not obtained. The relative high density and especially the cost of the starting material speak out against the manufacture of aerogels by this procedure.

The breakthrough in gel preparation at ambient pressure was made by Smith et al. [4]. TEOS gels were used as a model system. A methylating of the inner surface of the wet gel through a reaction with chlorotrimethyl silane produced a large effect during drying. The shrinkage of the gel with a surface modification during drying is equal to the shrinkage of a gel without surface modification. But the methylated silica gel shows a "spring back" or relaxation to the original size when drying is complete. The reason of the "spring back" was not discussed.

In the present work the structural changes during drying are examined by SAXS experiments. The mechanism of the "spring back" is discussed. Esterification is used as a surface modification technique.

Experimental Procedure

A sodium water glass solution with a constant Na : Si ratio of 0.6 and an Si-concentration of 1.7 mol/l was

used as a low-cost precursor. The Wofatit KPS ion exchanger (Chemie AG Bitterfeld Wolfen) was applied in order to achieve a substitution of sodium ions by protons. The ion exchange was carried out at pH 2 for 10 min. The pH 5.8 was obtained by adding small amounts of NH_4OH. The gelation takes place in a few minutes [5].

The whole gel body (200 ml) was heated in a closed vessel to 95°C for 1 hour. The gel body was granulated to reduce the timescale for the solvent exchange from water to *n*-butanol. The solvent exchange and an esterification of the inner surface take place by an azeotropic distillation. The gel was held at a temperature between the boiling point of pure butanol and the boiling point of the butanol/water azeotrope for 15 hours to complete the esterification. Gaseous HCl was used as a catalyst. A washing with acetone followed. The wet gel was placed in a preheated vessel in a furnace at 260°C for about 20 s. The gel granulate shrinks and becomes white. If the acetone is evaporated, a "spring back" takes place, and the granulate looks like a typical aerogel. The sample has a bulk density of 0.09 g cm^{-3}, and it is hydrophobic. A second sample was prepared in the same manner but without a catalyst. The dried gel is hydrophilic and has a bulk density of 0.35 g cm^{-3}.

All SAXS experiments were performed on a Kratky compact camera (Anton Paar, Graz) using Ni-filtered CuKα radiation (sealed tube, 2 kW X-ray generator). A position sensitive proportional counter (Braun 50M) filled with a gas mixture of 90% argon and 10% methane was used in the measurements. At the expense of a smaller visual field $r_{max} = \pi/s_{min} = 30$ nm, where $s = 4\pi/\lambda \sin(\Theta)$, Θ is the scattering angle and λ is the wavelength. The collimation conditions were selected so as to obtain as high an intensity as possible. The "infinite-slit" collimation condition was always fulfilled. The electron microscopy was carried out on EM 912 Zeiss Oberkochen.

Results

Figure 1 shows a typical result of the SAXS experiments. The scattering curve for the hydrogel prepared

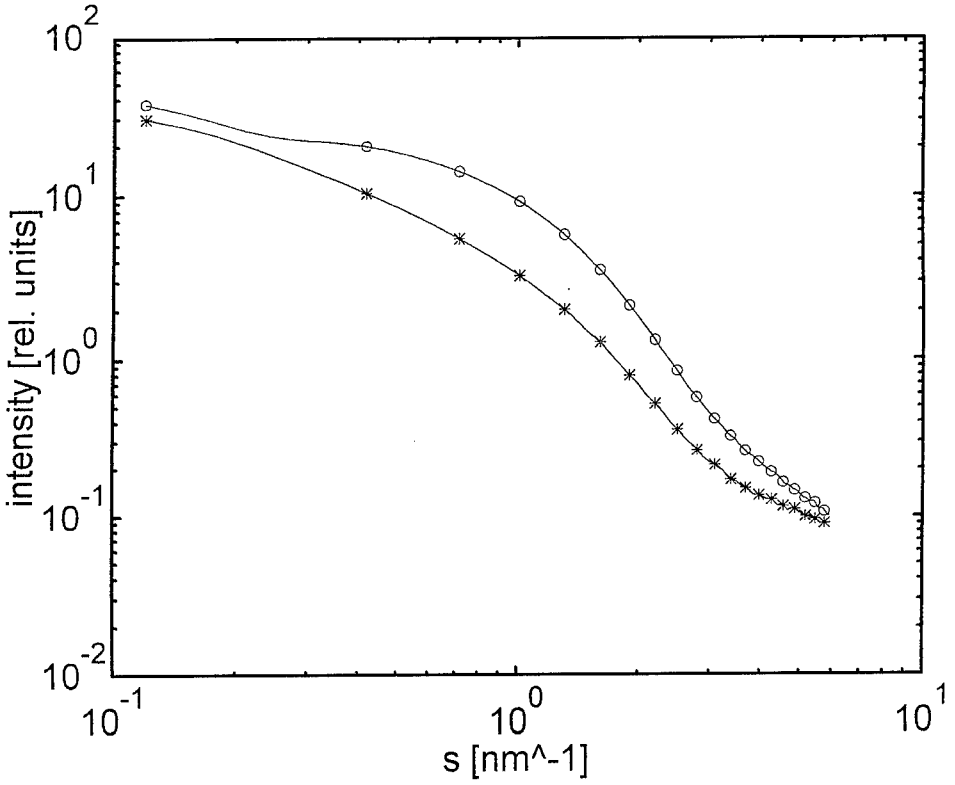

Figure 1. SAXS curves of a wet gels prepared at 18°C at pH 5.8 (*----*----*) and the corresponding xerogel (o----o----o).

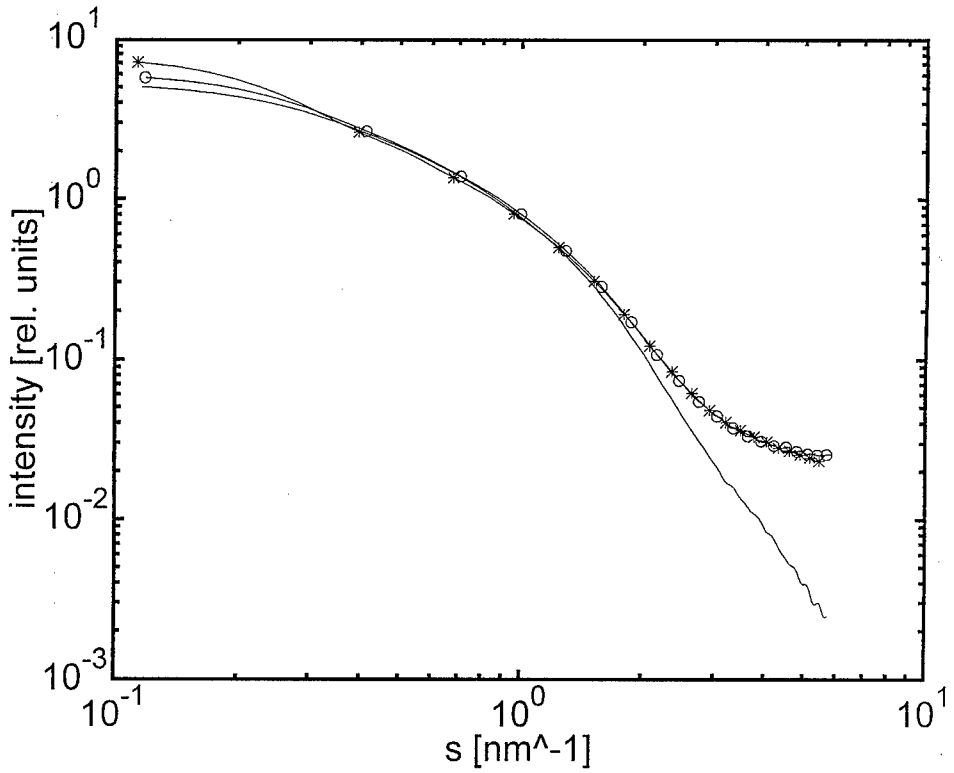

Figure 2. SAXS curves of an aged hydrogel (*-----*----*), the gel after solvent exchange and esterification (o-----o-----o), and the dried gel (aerogel) (— —).

at pH 5.8, directly after the gelation, and the scattering curve of the gel dried at 20°C are presented. The curve of the wet gel is typical for fractal clusters [6]. The size of the clusters are larger than the visual field $\pi/s_{\min}$ of the experiment. The Guinier region of the primary particles are seen at 1 nm^{-1}.

With the drying the fractal clusters collapse due to the capillary pressure, and a denser SiO_2 structure with pores of nearly 8 nm in diameter emerges. The pores originate from the condensation of the $\equiv Si_{surface}OH$ groups at the inner surface.

Figure 2 is a comparison of the SAXS curves of the aged hydrogel, the wet gel after esterification and the low density hydrophobic aerogel. Only small differences are seen. The solid matter framework does not change during the whole process. The primary particles of the framework have an average diameter of 3.2 nm which is determined by the ageing process. The differences in the tail of the scattering curves of the wet and the dried gel are caused by the fluctuation scattering from the solvent. The intensity decrease of the low s values in the scattering curves after drying shows a collapsing of the larger pores. The solid-state framework, seen clearly in the TEM micrograph in Fig. 3, of the aerogel prepared at ambient pressure is identical with one prepared at supercritical conditions.

Scanning electron microscopy results are shown in Figs. 4 and 5. The bulk of the aerogel is a close packing of "particles" of 100–150 nm in diameter (Fig. 4). The surface of the aerogel granulate has a denser structure. The pores between the "particles" are closed (Fig. 5).

The structural investigation of the sample prepared without a catalyst is presented in Fig. 6. The dried gel has a relatively high density. The framework of the wet gel is preserved up to a length scale of 12 nm. The large pores are destroyed.

Discussion

The gel formation can be explained by means of cluster-cluster aggregation. Therefore, the primary particles forming fractal clusters have a fractal dimension of 2.2. During gelation the more or less dense packing

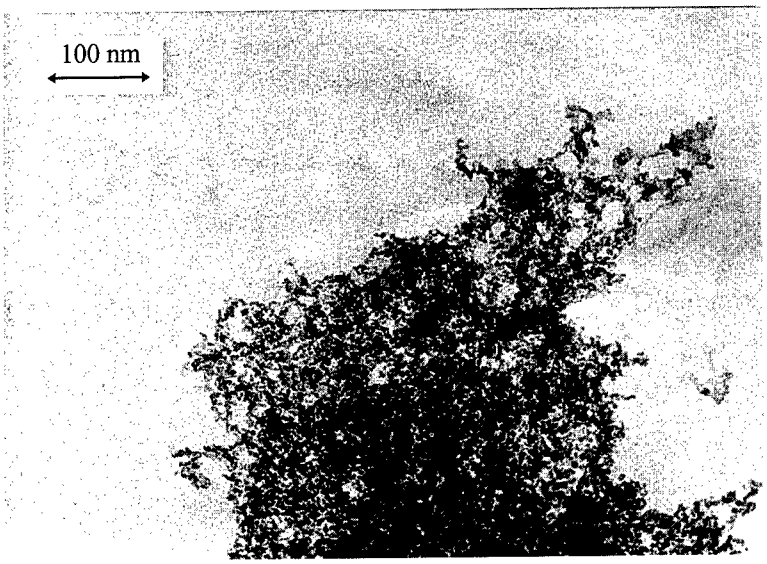

Figure 3. Transmission Electron Microscopy picture of an aerogel for which the SAXS curve is shown in Fig. 2.

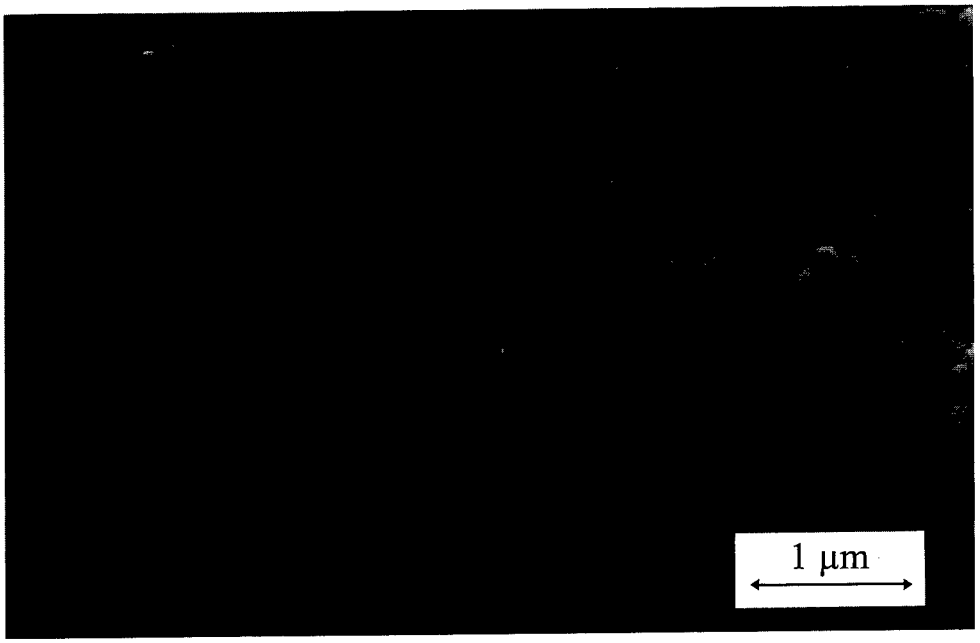

Figure 4. SEM micrograph of aerogel bulk prepared at ambient pressure.

of the clusters fill up the vessel. The primary particles inside the fractal clusters grow by Ostwald ripening during the aging process. The large pores in the clusters collapse simultaneously and the packing of the clusters becomes denser. Clusters of about 150 nm in diameter are observed in the aged gel. The clusters are fractal up to a length scale of 30 nm. The drying procedure described, which involves working at ambient pressure, conserves the structure of the wet gel as well as using supercritical drying.

The SAXS experiments show that the prevention of the condensation reaction of the $\equiv Si_{surface}OH$ groups at the inner surface of the gel during drying is important for the structure and the density of the dried gel. An

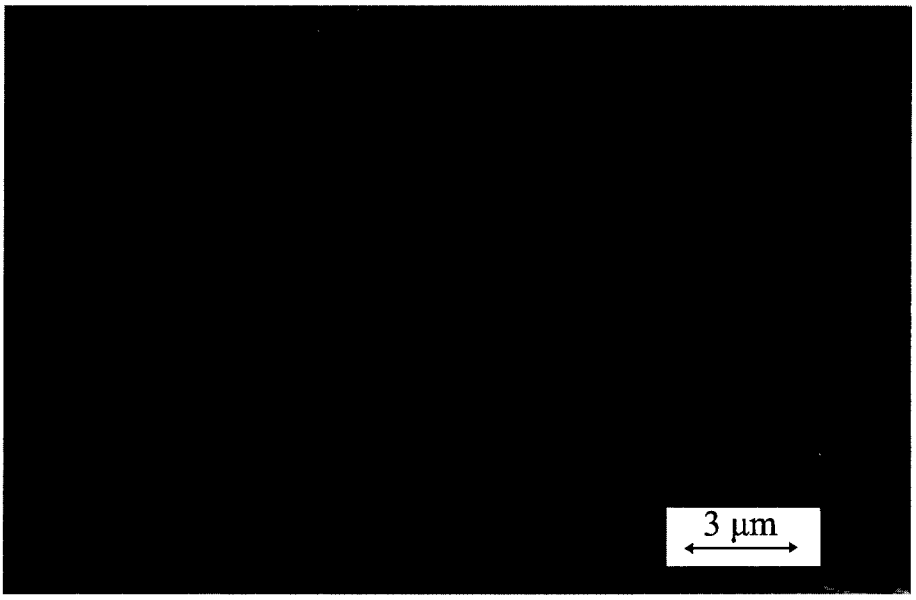

Figure 5. SEM micrograph of surface of the aerogel granulate prepared at ambient pressure.

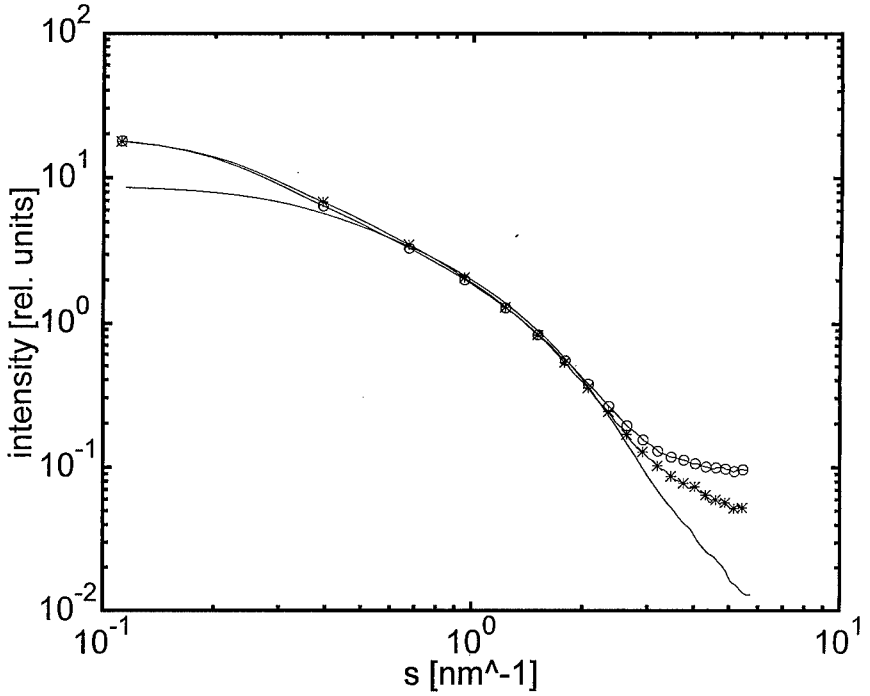

Figure 6. SAXS curves of an aged hydrogel (*-----*----*), the gel after solvent exchange (o-----o-----o), and the dried gel (— —) which is hydrophilic with a density of 0.35 g cm^{-3}.

esterification $\equiv Si_{surface}OH + ROH \rightarrow \equiv Si_{surface}OR + H_2O$ is a simple method of sealing the inner surface. This reaction is an equilibrium reaction. The equilibrium is shifted in favor of $\equiv Si_{surface}OR$ by removal of the water. The reverse reaction, hydrolysis, has been extensively investigated [7]. The esterification inside the nanoscaled pores is intricate because the reaction water must be transported across the pores, which are

hydrophobic after esterification. However, the very fast drying of the wet gel, which was washed in acetone and placed in an environment at 260°C, also prevents the condensation. This is shown by the second hydrophilic sample. A shrinkage and a collapsing of the large pores are seen, but the solid-state framework with a scale smaller than 15 nm remains.

Conclusions

The extent of drying shrinkage is governed by one main parameter, the condensation of $\equiv Si_{surface}OH$ groups at the inner surface. For a prevention of this condensation by an exchange of the $-OH$ group by $-OR$ or $-R$, the density increase upon drying is nearly 0. A variety of surface reactions to obtain $Si_{surface}OR$ or $Si_{surface}R$ coatings was explored by Iler [8]. The *n*-butanol esterification is shown to be a simple surface modification technique which employs a minimum of low-cost solvents.

References

1. R.W. Pekala, J. Mater. Sci. **24**, 3221 (1989).
2. G. Carlson, D. Lewis, K. McKinley, J. Richardson, and T. Tillotson, J. Non-Cryst. Solids **186**, 372–379 (1995).
3. S. Haereid, M. Dahle, S. Lima, and M.-A. Einarsrud, J. Non-Cryst. Solids **186**, 96–103 (1995).
4. D.M. Smith, D. Stein, J.M. Anderson, and W. Ackerman, J. Non-Cryst. Solids **186**, 104–112 (1995).
5. Th. Gerber, B. Himmel, and C. Hübert, J. Non-Cryst. Sol. **175**, 160–168 (1994).
6. D.W. Schaefer, J.E. Martin, P. Wiltzius, and D.S. Cannell, Phys. Rev. Lett. **52**, 2371 (1984).
7. C.J. Brinker and G.W. Scherer, *Sol-Gel-Science* (Academic Press, Inc., Boston, 1990).
8. R.K. Iler, *The Chemistry of Silica* (Wiley, New York, 1979).

Journal of Sol-Gel Science and Technology 13, 329–333 (1998)
© 1998 Kluwer Academic Publishers. Manufactured in The Netherlands.

Chemical and Structural Evolution of Silica Alcogels During their Formation: Acoustical Study

L. FOREST AND V. GIBIAT
Laboratoire Ondes et Acoustique URA CNRS 1503, ESPCI, 10 rue Vauquelin, 75005 Paris, France

T. WOIGNIER
Laboratoire des Verres URA CNRS 1119, Université Montpellier II, Place Eugène Bataillon, 34095 Montpellier, France

Abstract. Silica aerogels are materials of very high porosity obtained through a sol-gel process. Since their structural properties greatly influence their acoustical and mechanical properties, it is important to follow how the different chemical reactions occur during this process. We present a study of these evolutions for two different types of alcogels through acoustical measurements in the ultrasonic range. These samples have been chosen because of the significantly different behavior of the derived aerogels. The data obtained during gelation show fluctuations of the velocity that can be interpreted in terms of chemical changes. The absence of major changes in the velocity before and after gelation is explained with the aid of Biot's theory of acoustic propagation in porous media.

Keywords: gelation mechanism, acoustical measurements, alcogel structure, chemical changes

1. Introduction

It has been previously shown that the acoustical properties of silica aerogels exhibit an unexpected behavior for small bulk density materials ($\rho < 100$ kg $\cdot$ m^{-3}); in particular, sound velocities lower than that in air have been measured [1, 2]. Although the mechanical and acoustical properties of silica aerogels have been widely studied [1–3], there is, to our knowledge, a lack of literature on the acoustical properties of silica alcogels. In particular, the evolution of the acoustical properties during the gelation process has never been studied. These properties are important for understanding the physical processes which govern wave propagation in such media, and also because they can be related to chemical changes during the formation of the gel. The aim of our work is to follow the evolution of the acoustical characteristics of a TetraMethOxySilane solution during a base catalyzed sol-gel process.

2. Chemical Reactions in Alcogels and Acoustical Characteristics

2.1. *Chemical Reactions*

Although the following reactions are known, it is important to recall the chemical changes that occur in each reaction, in order to analyze the resulting sound velocity evolution. Silica alcogels are synthesized through an organic process with silicon alkoxide liquid precursor TetraMethOxySilane (TMOS) : $Si(OCH_3)_4$. This process involves two major steps [4] :

- hydrolysis yielding the generation of a metal hydroxide $Si(OH)_4$ and methanol:

$$Si(OCH_3)_{4(liq.)} + 4H_2O_{(liq.)} \longrightarrow Si(OH)_{4(solid)} + 4H_3C{-}OH_{(liq.)} \quad (1)$$

- polycondensation:

$$\equiv Si{-}OH_{(solid)} + HO{-}Si{\equiv}_{(solid)} \longrightarrow \equiv Si{-}O{-}Si{\equiv}_{(solid)} + H_2O_{(liq.)} \quad (2)$$

During the second step, a spontaneous polymerization occurs, creating oxide species whose molecular mass increases continuously. As these clusters grow, they link together in a three-dimensional solid network, the gel.

Moreover, if the hydrolysis is not complete, then a second kind of polymerization occurs with the remaining TMOS:

$$\equiv Si{-}OH_{(solid)} + H_3C{-}O{-}Si{\equiv}_{(liq.)} \longrightarrow \equiv Si{-}O{-}Si{\equiv}_{(solid)} + H_3C{-}OH_{(liq.)} \quad (3)$$

Nevertheless, because this reaction is usually considered as marginal, it is neglected here. These reactions are usually performed in a solvent (methanol or ethanol). In our experiments, ethanol was used.

2.2. *Parameters Influencing the Chemical Reactions*

The cluster size of the alcogels and aerogels varies inversely with the concentration of silicon alkoxide TMOS in the initial solution [5, 6]. The kinetics of the above reactions are slow at room temperature, requiring several days to complete. For this reason, acid or base catalysts are generally added to the solution. The amount and type of catalyst used greatly influence the chemical reactions and the microstructural, physical and optical properties of the final aerogel product.

For low pH (<2), the rate of hydrolysis is large compared to the rate of condensation; at high pH (>8), the hydrolysis is expected to be complete, and the condensation reaction (2), involving deprotonated silanol (SiO^-) [7], decreases with increasing pH. A dissolution reaction occurs in this pH domain. In the intermediate pH domain ($3 < pH < 8$) different behavior is expected: the hydrolysis rate goes through a minimum at approximately neutral pH and in the same pH range condensation goes through a maximum.

Thus, in the pH range 7–9 of interest, the hydrolysis rate increases while the condensation rate decreases [7].

Concerning the structural properties, in the case of an acid pH, the gel network turns out to be ramified and made up of little clusters. For the same rate of TMOS and a basic pH, the network is less ramified and made up of dense clusters [8], so the mechanical properties of the gel are significantly different from the previous case [9].

Table 1. Sound velocity in the different liquids in the solution.

	Sound velocity ($m \cdot s^{-1}$)
Methanol	1103
TMOS	1140
Water	1497

2.3. *Acoustical Characteristics*

Knowledge of the sound velocities in the different liquids in the solution is required to analyze the results. Table 1 indicates these velocities at 20°C and 1 bar. While the velocities in methanol and water are taken from a Handbook [10], the velocity in TMOS has been determined by a pulse technique with ultrasonic longitudinal transducers in emission-reception, with the experimental setup described below.

3. Experimental

3.1. *Measurement Set-Up*

The formation of alcogels during the sol-gel process has been studied in emission-reception in the frequency range 20–200 kHz using longitudinal and transverse transducers of resonance frequency 500 kHz. The measurement setup is shown in Fig. 1.

To take into account shrinkage of the gel, both transducers are partially immersed into the solution. Moreover, this method ensures a good contact between transducers and gel during the whole experiment. The emitted signal is a pulse of 1–5 μs duration. The distance between the transducers (around 30 mm) can be adjusted with an accuracy of 0.1 mm; the sample frequency of the scope is 2 MHz, allowing a temporal accuracy of 0.5 μs. Thus, a global accuracy less than 2% for the velocity measurement is obtained. This accuracy is improved to 0.2% by considering the third echo instead of the first one.

In a second step, after having recorded the emitted and received signals on the digital oscilloscope with an accuracy of 12 bits, one can obtain the evolution of longitudinal and transverse velocities in the solution.

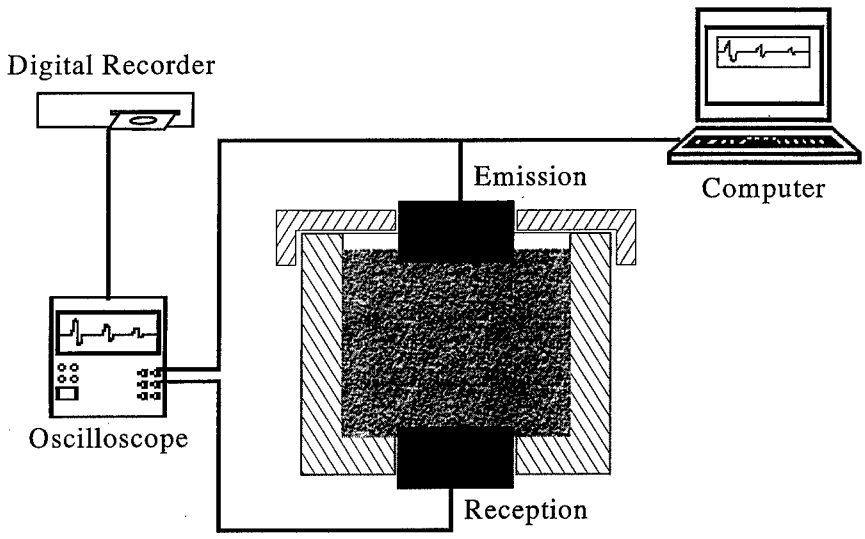

Figure 1. Measurement setup.

3.2. *Description of the Samples*

Two types of alcogels have been studied: B46 and B18. The numbers "46" or "18" indicate the volume percentages of TMOS in the solutions while "B" means that base catalyst (ammonia solution) has been used. Table 2 indicates the volume percentages of the components. The concentrations of the ammonia solutions, were for B46 5×10^{-3} M (pH $\approx$ 7.8) and for B18 1.7×10^{-2} M (pH $\approx$ 8.7). These two solutions were selected such that the gel formation time remains compatible with acoustic control. Gel formation times, reported in Table 2, correspond approximately to a state of no tendency to flow.

4. Results

Figure 2 shows the evolution of the longitudinal sound velocity in the B46 and B18 solutions between 2 min and 6 hours.

Table 2. Volume percentages in the solutions and gel times.

	B46	B18
TMOS	47%	18%
Ethanol	29%	73%
Catalyst solution	24%	9%
$[NH_4OH]$	5×10^{-3} M	1.7×10^{-2} M
Gel time	5 hours	3 hours

With sample B46, there is a rapid increase in the velocity during the first hour, but it becomes constant around 1285 $m \cdot s^{-1}$. B18 shows the opposite behavior: the velocity first decreases and becomes constant around 1197 $m \cdot s^{-1}$.

Using transverse waves, the received signal is too weak to determine the transverse velocity, even when gel formation has occurred. The only measurement that could be made was for the B46 sample with a completely formed gel, exhibiting a very low velocity (around 35 m/s).

5. Discussion

During the first hour, the reactions proceed but the solution is still liquid. Thus, the increase in the velocity can be interpreted in terms of the chemical changes in the solution.

When the solution is essentially water, alcohol addition leads to an unexpected increase in the velocity; however, when the solution is essentially alcohol, the velocity decreases as the volume ratio of alcohol increases. Consequently we can expect that reaction (1) yields a decrease in the velocity because of methanol formation. On the other hand, reaction (2) yields an increase in the sound velocity because of the water formation (cf. Table 1). The results in Fig. 2 suggest that, starting with the first data at $t = 2$ min, reaction (2) has been favored in the B46 case and reaction (1) in the B18 case. These results are in agreement with

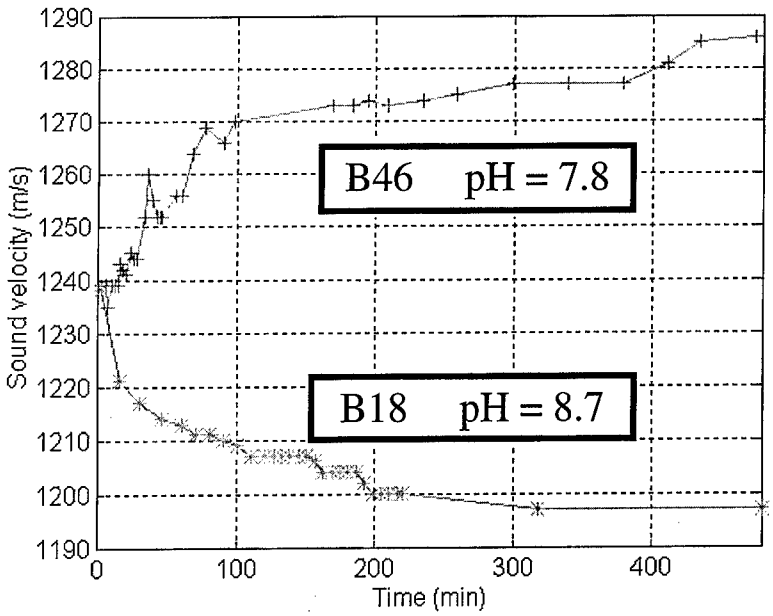

Figure 2. Evolution of sound velocity during B46 (+) and B18 (∗) gelation.

the evolution expected due to the pH of each solution (cf. Section 2.2):

- The higher pH of the B18 solution (compared to B46) favors the hydrolysis reaction (1) leading to alcohol formation and to the sound velocity decrease.
- On the other hand, for the pH close to 7 (solution B46) the hydrolysis rate is lower and the larger polycondensation rate leads to water formation as $Si(OH)_4$ is created by the hydrolysis. A rationale in term of volume ratios of TMOS, methanol and water shows that the water percentage increases at the expense of the TMOS concentration. Thus, this leads to a sound velocity increase.

Finally, when a gel network is formed, both samples do not exhibit significant sound velocity changes. This unexpected behavior is explained by Biot's theory of acoustic propagation in porous media [11, 12]. In the kHz frequency range, the longitudinal propagation is governed by the simplified expression of the velocity V_L [13]:

$$V_L \cong \sqrt{\frac{\left(K_{sk} + \frac{K_{fl}}{\phi}\right) + \frac{4}{3}\mu_{sk}}{\rho}} \qquad (4)$$

where K_{sk} is the bulk modulus of the skeletal frame, K_{fl} is the bulk modulus of the fluid phase alone, μ_{sk} is the shear modulus of the skeletal frame, and ρ is the bulk density of the whole sample.

Because of the weak bulk modulus of the skeletal frame, the alcohol bulk modulus is predominant in (4) and the medium behaves as a fluid, although it contains 10% solid. The further evolution of the curves can be interpreted in term of chemical changes: both the creation of water and the exothermic behavior of reaction (2) lead to the small increase in the velocity in the B46 case; the evolution of the velocity for B18 shows that hydrolysis, even if favored, is not completed once the solution is gelled since the small decrease in the velocity can only be interpreted as creation of methanol. After a long time (one week), we should also expect in this case an increase in the velocity as the hydrolysis will be completed and the polycondensation will be the major reaction. Unfortunately, this has not been verified because of shrinkage and evaporation.

6. Summary and Conclusions

Acoustical measurements during the gelation of two types of alcogels have revealed information about the chemical processes: the main chemical changes are followed during the first hour of the alcogel formation. Unexpectedly as the solution gels, the gel network formation neither produces significant longitudinal

velocity changes nor emergence of a transverse velocity; this was observed for both samples. After gel formation is complete, the evolution of the longitudinal velocity is also analyzed from a chemical point of view. Since gelation does not have a significant influence on the propagation of the longitudinal wave, the transverse measurement must be improved to obtain an acoustical analysis of gel formation.

References

1. J. Gross, G. Reichenauer, and J. Fricke, Journal of Physics D: Applied Physics **21**, 1447 (1988).
2. V. Gibiat, O. Lefeuvre, T. Woignier, J. Pelous, and J. Phalippou, Journal of Non-Crystalline Solids **186**, 244 (1995).
3. B. Nouailhas, F. Michard, R. Gohier, and A. Zarembowitch, in *Proceedings 11th Int. Cong. On Acoustics* (Paris, 1983), Vol. 2, p. 179.
4. C.J. Brinker and G.W. Scherer, *Sol-Gel Science* (Academic Press, New York, 1990).
5. R. Vacher, T. Woignier, J. Pelous, and E. Courtens, Physical Review B **37**, 6500 (1988).
6. P. Lourdin, J. Appell, J. Pelous, and T. Woignier, in *Proceedings of the 2nd Int. Symp. on Aerogels*, edited by R. Vacher (Revue de Physique Appliquée 24 C4, 1989), p. 197.
7. C.J. Brinker, Journal of Non-Crystalline Solids **100**, 30 (1988).
8. K.D. Keefer, in *Better Ceramics Through Chemistry II*, edited by C.J. Brinker, D.E. Clark, and D.R. Ulrich (Mat. Res. Soc., Pittsburgh, PA, 1986), p. 295.
9. T. Woignier, J. Phalippou, J.F. Quinson, M. Pauthe, and F. Laveissiere, Journal of Non-Crystalline Solids **145**, 25 (1992).
10. *Handbook of Chemistry and Physics*, 57th edition (C.R.C. Press, Cleveland, 1976/77).
11. M.A. Biot, J. Acoust. Soc. Am. **28**(2), 168 (1956).
12. M.A. Biot and D.G. Willis, J. Appl. Mech. **24**(4), 594 (1957).
13. L. Forest, V. Gibiat, and T. Woignier, Journal of Non-Crystalline Solids **225**, 287 (1998).

Journal of Sol-Gel Science and Technology 13, 335–339 (1998)
© 1998 Kluwer Academic Publishers. Manufactured in The Netherlands.

Mercury Porosimetry Applied to Low Density Xerogels; Relation between Structure and Mechanical Properties

R. PIRARD, B. HEINRICHS, O. VAN CANTFORT*AND J.P. PIRARD
Université de Liège, Laboratoire de Génie Chimique, Institut de Chimie (B6) Sart-Tilman, B-4000, Liège, Belgium

Abstract. Samples of low density xerogels were submitted to mercury porosimetry at pressures up to 200 MPa. These samples show an unusual behavior: they are first crushed by the isostatic mercury pressure without mercury intrusion and are then intruded by the mercury above a certain pressure. This transition allows the easy determination of the one constant found in the buckling model that is used to interpret the crushing part of the mercury porosimetry experiment. The relation between this constant and the structure of the xerogels determined by TEM and nitrogen adsorption is discussed.

Keywords: mercury porosimetry, xerogel, structure, buckling, stiffness

1. Introduction

Usually, the interpretation of mercury porosimetry data is made using Washburn's equation which is based on the hypothesis that the observed volume variation is due to the progressive intrusion of mercury into the pores [1]. Most porous materials are indeed penetrated under an isostatic mercury pressure. However, some materials among the most porous, such as aerogels, show no trace of trapped mercury after a mercury porosimetry experiment and, in that case, the reality of the intrusion mechanism is dubious. Moreover, if the volume variation is very small or nonexistent during the depressurization, it is certain that the actual mechanism is an irreversible mechanical shrinking under the isostatic mercury pressure [2].

Mineral aerogels have been extensively studied during the last decade [3, 4]. Those materials have obviously a very weak mechanical compressive strength. Aerogels submitted to mercury porosimetry are not intruded by mercury but are irreversibly compacted by the isostatic mercury pressure.

In a previous work [5], the pore size distribution of aerogels first compacted under various mercury pressures was measured by the nitrogen adsorption-desorption method. It has been shown that during compaction, the isostatic mercury pressure P crushes completely pores of size larger than a limiting size L, and leaves the smaller size pores unaltered. The relation between L and P has been determined as $L = k/P^{0.25}$. The collapse mechanism of the pores has been modeled as the buckling of the brittle filaments of mineral oxide under an axial compressive strength. The pressure which causes the buckling of a cubic structure is given by Euler's law:

$$P = \frac{n\pi^2 EI}{L^4} \text{ with } I = \frac{\pi d^4}{64} \qquad (1)$$

The k value is therefore a function of E the elastic modulus of the mineral oxide filaments, d the diameter of filaments and n, which varies with the geometry of the structure and its stiffness. Experimentally, in the case of an aerogel made of 50% SiO_2 and 50% ZrO_2, the k constant was estimated to be 47 nm · $MPa^{0.25}$.

In the case of aerogels which collapse under the isostatic mercury pressure, the knowledge of the k value allows determination of the pore volume distribution in relation to the pore size. To a first approximation, and if it is certain that the buckling is responsible for the volume variation in the whole pressure range until

*Aspirant FNRS.

200 MPa, the above value (47 nm · $MPa^{0.25}$) can be used for the k constant. However, it is preferable to determine k in each particular type of aerogel composition. This determination needs measurement of the limiting size L of the largest pore of aerogels first submitted to mercury isostatic pressure P, and it generally involves a great deal of hard work.

Recently, a new type of materials, the so-called "low density xerogels," has been synthesized [6, 7]. These materials have a pore volume larger than 2 cm^3/g, which is similar to the pore volume of aerogels, but they have a much tougher resistance against crushing. These materials can show a particular behavior when submitted to mercury porosimetry. The pressurization curve has an unusual aspect: the slope abruptly changes at a certain pressure (26 MPa in the sample investigated at this time). Below this pressure, the shape of the curve is as usually observed for aerogels. Above this pressure, the curve is characteristic of strong materials having small size pores. The curve corresponding to the pressure decrease, can also be divided into two distinct parts separated by a sudden change of slope. The first part, at high pressure, shows a large volume variation with, however, a clear hysteresis. The second part at low pressure shows, on the contrary, a very small volume variation. By performing mercury porosimetry, first limited to pressures below this critical pressure, it was concluded that in the first part of the pressurization curve, the mercury did not intrude the xerogel, mechanical crushing and shrinking occurs, while in the second part of the curve, the xerogel is indeed intruded by mercury.

These changes of mechanism allow an easy determination of the constant k in materials that exhibit this behavior. Immediately below the critical pressure P_c, the buckling law can be used:

$$L = k/P^{0.25}, \tag{2}$$

while immediately above the critical pressure, Washburn's law [1] is applicable:

$$L = -4\sigma \cos\alpha / P = 1500/P, \tag{3}$$

where P is expressed in MPa and L in nm. At P_c, we can equate these two relations, and we obtain:

$$k = 1500/P_c^{0.75} \tag{4}$$

The value of k, which is necessary for the correct interpretation of the first part of the mercury porosimetry curve, can be directly obtained from the pressure at which mercury intrusion begins [6].

In this paper, we examine a set of samples that exhibit this behavior. The different samples show different k values. The relation between the value of k and the structure of the samples will be discussed.

2. Experimental

The samples considered are five low density Pd-Ag/SiO_2 xerogels used as catalysts. The gels were formed by hydrolysis and condensation of tetraethyethoxysilane (TEOS). The metals were added as complexes containing a silane able to react with the TEOS: a mixture of palladium acetylacetonate and [3-(2-aminoethyl)aminopropyl]trimethoxysilane (EDAS) in ethanol and a mixture of silver acetate and 3-(aminopropyl)triethoxysilane (AS) were prepared. They were then mixed together and TEOS was added. Hydrolysis water was added as a solution of aqueous 0.18N NH_3 in ethanol. The gels were aged for 3 days at 70°C. The gels were then dried in a vacuum oven: they were first heated at 80°C, and the pressure was decreased to 1200 Pa in 20 h. These conditions were maintained 24 h, then they were heated to 150°C for 72 h. After this, the xerogels were calcined at 400°C for 12 h and then reduced under H_2 at 350°C for 3 h. A detailed explanation of the preparation of these xerogels can be found elsewhere [7].

The designation of the samples refers to the overall atomic percentage of silver in the Pd-Ag blend. The five samples contain 0% (palladium only), 33%, 50%, 67%, and 100% silver, respectively. In all samples, except the one containing only silver, the palladium loading was kept constant at 1.5 wt%. For the silver only sample, the silver loading was also 1.5 wt%.

The mercury porosimetry experiments were conducted on a Carlo Erba Porosimeter 2000 from atmospheric pressure up to 200 MPa. The samples were also examined by nitrogen adsorption at 77 K on a Fisons Sorptomatic 1990 and micrographs were taken on a Siemens Elmiskop 102 transmission electron microscope (TEM). Samples for TEM were impregnated with an epoxy resin (Eurepox 710) and 60 nm slices were cut using a Reichert Supernova ultramicrotome. The detailed results of these structural investigations are presented elsewhere [7].

3. Results and Discussion

Figure 1 shows the porosimetry curves obtained on the two extreme samples X0 and X100. Both curves have

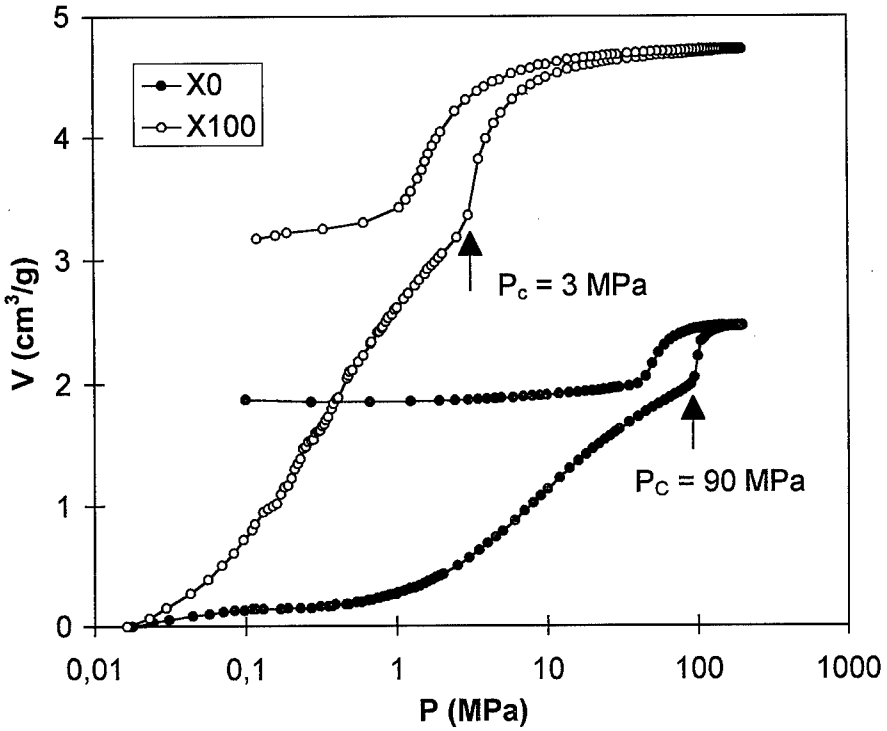

Figure 1. Mercury porosimetry curves of the two extreme samples X0 and X100.

a similar appearance. On the pressurization curve, we can easily distinguish a shoulder which corresponds to the pressure P_c at which mercury begins to intrude the xerogels instead of crushing the mineral network. On the depressurization curve, there is virtually no volume variation under a certain pressure. The volume stays at the level corresponding to P_c on the pressurization curve, indicating the irreversible nature of the crushing phenomena during pressurization. P_c is equal 90 MPa for sample X0 and 3 MPa for sample X100. Other samples show results that scale between X0 and X100.

Table 1 summarizes the results obtained from mercury porosimetry on the five samples. V_{Hg} represents the maximum volume variation; P_c, the pressure at which intrusion begins and k is the constant to use in the buckling law deduced from P_c.

Table 1. Mercury porosimetry results.

Sample	V_{Hg} (cm^3/g)	P_c (MPa)	k ($nm \cdot MPa^{0.25}$)
X0	2.5	85	54
X33	4.3	40	94
X50	4.7	18	171
X67	6.1	10	266
X100	4.9	3	656

From relations (1) and (2), the value of the k constant should be related to the structure and the geometry of filaments forming the network of the gel. In the cubic model used in relation (1) k is proportional to the diameter of the filaments.

In order to assess the existence of a relation between k and a characteristic dimension in the xerogel samples, sample sections were examined by transmission electron microscopy (TEM). The mean diameter of the particles composing the gels were determined by direct measurement on the micrographs. However, the particles themselves may not provide a good comparison as they are not a good indicator of the structure of the network and they cannot be subjected to buckling. Buckling or crushing occurs at the aggregate level and the aggregates could be considered as the real building blocks of the three-dimensional network of the gel. So, the mean size of the aggregates was assessed visually from the photographs.

Due to the difficulty of performing precise measurements on the TEM photographs, nitrogen adsorption was also used to determine a characteristic dimension

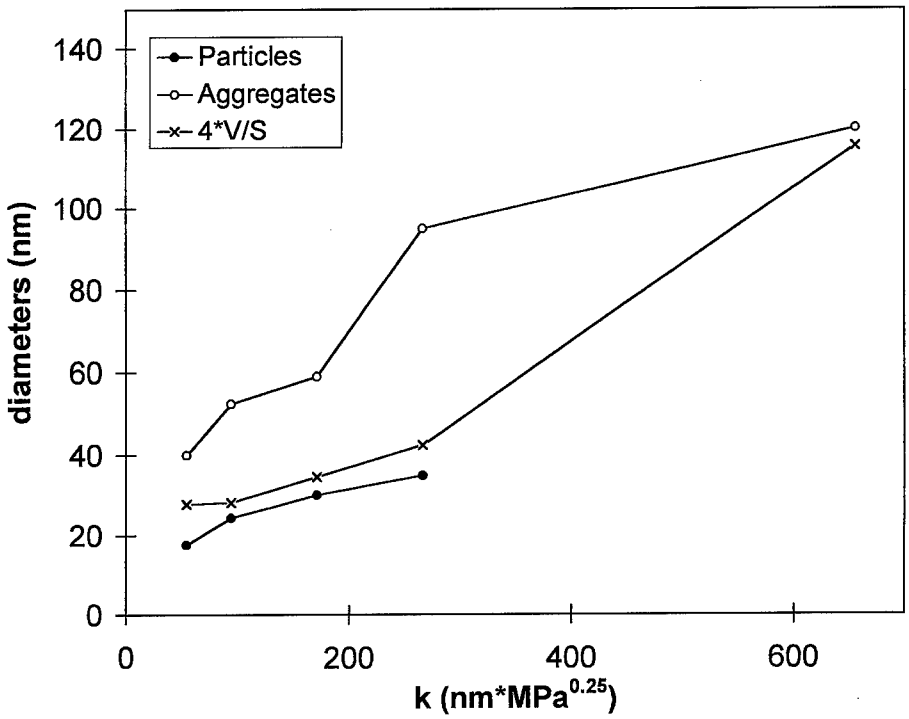

Figure 2. Relation between the buckling model constant and geometric diameters measured by TEM and nitrogen adsorption.

of the aggregates. The diameter of the filaments of the network is proportional to the ratio of their volume V to their surface S. The proportionality factor would be 4 for a long cylinder and 6 for a sphere. The value 4 was chosen to model the strings of particles. This choice is also more coherent with the buckling model.

The volume V was obtained from helium pycnometry and the surface area from nitrogen adsorption. However, the particles obtained by the condensation of TEOS are porous, and pores can also exist between several joined particles in an aggregate. It is necessary to subtract these contributions from the measurements of volume and surface. The surface was thus measured in the last linear part of the t-diagram calculated from the nitrogen adsorption-desorption isotherm. This linear part corresponds to the surface of the material when all the micropores and mesopores are already filled with nitrogen. The volume used was that obtained from helium pycnometry, with the addition of the volume occupied by all the pores with a diameter smaller than 10 nm. This value was chosen arbitrarily and is of the same order as the particle size. The volume of these pores was obtained from the nitrogen adsorption isotherm by the addition of the microporous volume calculated by the Dubinin-Radushkevich method and a part of the Broekhoff-de Boer mesopore volume distribution [1].

Figure 2 shows the particle mean diameters, the aggregates mean diameters and the value $4 * V/S$ determined as above plotted against the k constant of the different samples. This figure shows the relation between the value of the k constant and the dimension of the building units of the gel: the thicker the particles and aggregates, the higher the value of k. This behavior is consistent with that expected from relation (1).

Indeed the k constant of the buckling law gives an indication of the stiffness of the network in the xerogel. As the chemical compositions of the calcined samples are similar, the differences in stiffness should not be due to the material of the network, but to the geometry of the network. This geometry is strongly affected by the chemistry of the initial mixture. For example, the increased width of the particles and aggregates from samples X0 to X100 can be partly explained by the increased basicity of the initial mixture [7].

4. Conclusions

The complexity of the geometry of the network in gels and xerogels is such that a complete description is

impossible. Therefore, it is not expected that the measurement of the size of the particles and aggregates can allow prediction of the value of the k constant in the buckling law. However, the relation existing between the measured value of k and measured geometric parameters provides evidence of the soundness of the buckling model.

References

1. A.J. Lecloux, in *Catalysis Science and Technology*, edited by J.R. Anderson and M. Boudart (Springer, Berlin, 1981), Vol. 2, p. 171.
2. L. Duffours, T. Woignier, and J. Phalippou, J. Non-Cryst. Solids **194**, 283–290 (1996).
3. C.J. Brinker and G.W. Scherer, in *Sol-Gel Science: The Physics and Chemistry of Sol Gel Processing* (Academic Press, San Diego, CA, 1989).
4. J. Fricke, in *Aerogels, Proc. 1st. Int. Symp.* Würzburg, edited by J. Fricke (Springer, Berlin, 1986), p. 13.
5. R. Pirard, S. Blacher, F. Brouers, and J.P. Pirard, J. Mater. Res. **10**, 2114–2119 (1995).
6. R. Pirard, B. Heinrichs, J.P. Pirard, accepted in *Characterization of Porous Solids IV* (The Royal Society of Chemistry, in press).
7. B. Heinrichs, P. Delhez, J.P. Schoebrechts, and J.P. Pirard Journal of Catalysis (accepted).

Journal of Sol-Gel Science and Technology 13, 341–346 (1998)
© 1998 Kluwer Academic Publishers. Manufactured in The Netherlands.

Parameters Involved in the Sol-Gel Transition of Titania in Reverse Micelles

NORA FRANÇOIS AND BERTA GINZBERG
Facultad de Ingeniería, Universidad de Buenos Aires, Paseo Colón 850; (1043) Buenos Aires, Argentine

SARA A. BILMES
INQUIMAE; Departamento de Química Inorgánica, Analítica y Química-física, Facultad de Ciencias Exactas y Naturales, Universidad de Buenos Aires, Ciudad Universitaria Pab. II; (1428) Buenos Aires, Argentine

Abstract. Titania nanoparticles and gels are synthesized in reverse micelles with either an ionic (AOT) or a non-ionic (Triton X-100) surfactant in alkanes with low water contents. Acids were in some cases dissolved in the aqueous phase. Whereas the size of the sol nanoparticles is independent of the micellar composition, the kinetics of the sol-gel transition are not. The gelation time is shorter for the non-ionic surfactant and becomes longer as the acid content in the water increases, and for smaller anions of equal charge.

Keywords: titanium dioxide, nanoparticles, sol-gel

Introduction

The properties of semiconductor nanoparticles and gels can be successfully tailored by controlling the first step of the process; the hydrolysis of the metal alkoxide. A promising way to achieve this control is using reverse micelles which serve as compartmentalized polar microenvironments. In this case the alkoxide hydrolysis is controlled by the limited mobility of the water molecules which are bounded to the surfactant [1]. The sol formed is composed of the hydroxylated metal surrounded by surfactant molecules [2] that may be stable or may undergo further gelation depending on the probability of growth by the polycondensation reaction. Several materials such as $BaCO_3$ nanowires, SiO_2, and TiO_2 [3, 4] have been obtained in this way.

In previous work [3] it has been demonstrated that the structural and textural properties of the gel can be modified by the growth process. Improved knowledge of the gelation process will allow the optimization of the material properties.

Here we describe the influence on the kinetics of the sol-gel transition in the titania system when the chemical nature of the surfactant structure and the acid contents of the water core for different anions of equal charge are changed. UV-vis transmission spectra were used for the determination of the particle radius of the initial sol as well as for monitoring the sol-gel transition kinetics. The radius of the sol nanoparticles was estimated from the absorption edge spectra below 3.3 eV, according to the Brus equation [5]. The time evolution of the optical density OD, at $\lambda > 600$ nm has been used as an alternative method for the comparison of the gelation kinetics [6].

Experimental

Titania gels were prepared by mixing a reverse micelle microemulsion formed by water, a surfactant (anionic: sodium bis(2-ethylhexyl) sulfosuccinate = AOT and non-ionic, polyoxyethylene tetramethylbutyl-phenyl ether = Triton X-100), and organic solvent (cyclohexane, isooctane) with a solution of titanium butoxide diluted in the organic solvent. In some experiments, inorganic acids ($HClO_4$; HNO_3; HCl) were added to the water. All measurements were performed at

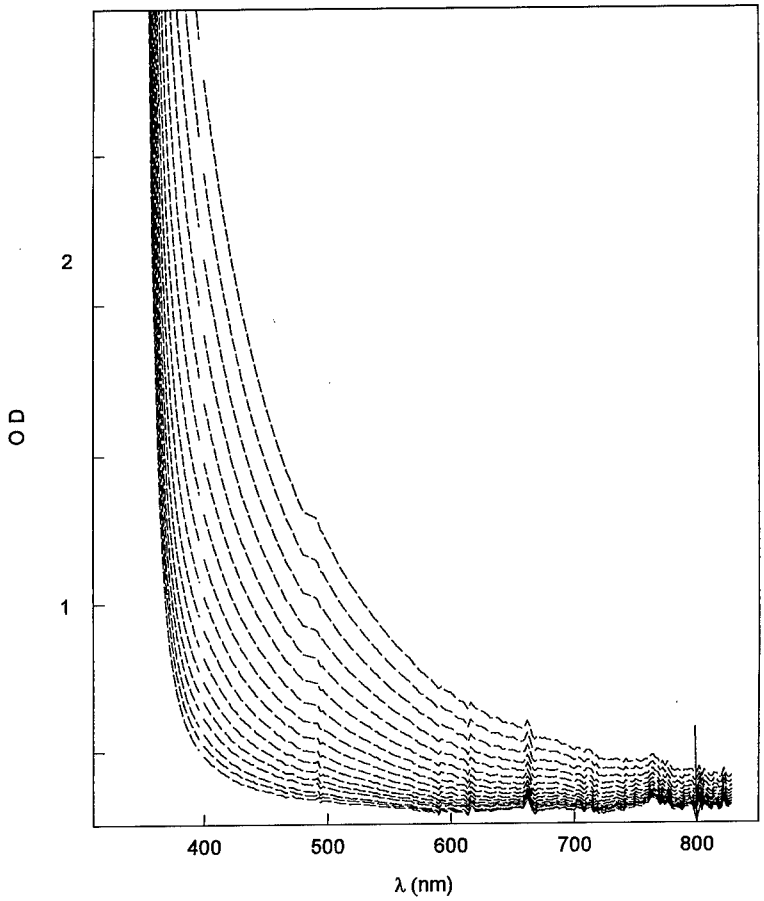

Figure 1. Absorption spectra of titania sols in reverse micelles of water in cyclohexane for [AOT] = 0.36 M, [$Ti(BuO)_4$] = 0.27 M and H_2O = 0.54 M.

(30 ± 0.1)°C. All reagents were p.a. or better and water was distilled and further purified by a Milli-Q system. The absorption spectra were taken with a diode array absorption spectrophotometer (Hewlett-Packard, 8452A).

Results

The sol-gel transition was monitored by measuring the optical density of the samples as a function of time.

Figure 1 shows UV-visible absorption spectra of titania sols synthesized with AOT as surfactant taken at time intervals of 100 s.

At the beginning of the process the particle size may be derived from absorption measurements; at longer times, however, scattering effects become very important, and further evolution of the particle size may not be followed. Figures 2 to 4 show the OD_{800} vs. time plots, which may be used to monitor the sol-gel kinetics.

In Fig. 2, reverse micelles prepared with AOT and Triton X-100 in cyclohexane are compared for the same [H_2O]/[surfactant] molar ratio of 1.5.

Figure 3 shows the dependence of titania sol-gel kinetics in micellar systems with water containing different amounts of HNO_3 for AOT in isooctane (Fig. 3(a)) and different amounts of $HClO_4$ for Triton X-100 in cyclohexane (Fig. 3(b)).

Figure 4 shows the influence of the anion size in the gelation of titania sols in AOT/isooctane micellar systems.

Discussion

As is well known the first stage of the reaction is the hydrolysis of Ti-alkoxide, which is controlled by the

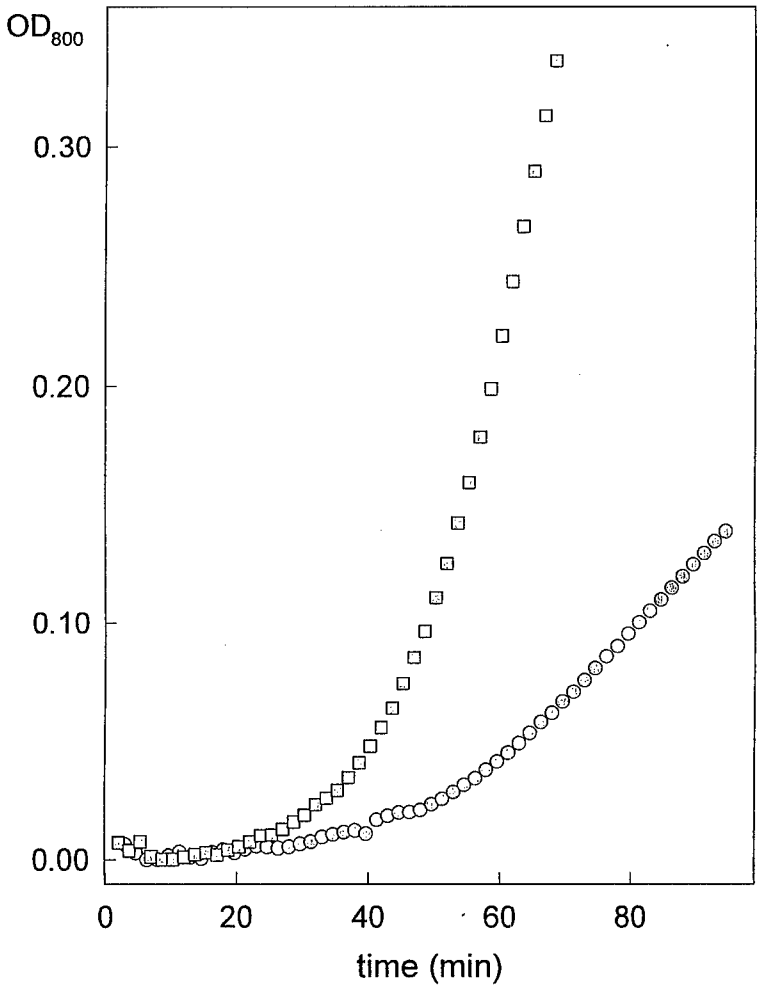

Figure 2. Optical density at 800 nm, OD_{800}, vs. time from the spectra of titania sols in reverse micelles of water in cyclohexane. [surfactant] = 0.36 M, $[Ti(BuO)_4] = 0.27$ M and $[H_2O] = 0.54$ M. (□) AOT, (○) Triton X-100.

$[H_2O]$/[surfactant] molar ratio defined as w [6, 7]. The w value determines the size and shape of the micellar cavity [8], but for the very low w values used in this work, every water molecule participates in the solvation of the counterions Na^+ or interacts with the polar heads [1, 8]. In this case, the aggregates behave like rigid spheres. On the other hand, for Triton X-100 micellar systems with $w \geq 1$, water is bounded to terminal hydroxyl groups of the surfactant monomer and to some of the oxyethylene groups with the hydrocarbon penetrating into the polar core of the micelle until water bridges the polar segments of adjacent surfactant molecules [9]. Within this picture, both for AOT and Triton X-100 micellar systems there is no free water in the polar cavity, and when the alkoxide is added the hydrolysis competes with the affinity of water to the surfactant. This leads to a high control of nucleation, and further growth proceeds slowly by reaction between hydroxylated titania clusters which are stabilized against aggregation by adsorption of surfactant molecules [10].

Although it is not possible to achieve a complete picture about the composition and structure of the nanoparticles formed by reaction of $Ti(OBu)_4$ and H_2O, it is reasonable to assume that they may be considered as "TiO_2 nanocrystals," irrespective of whether they contain OH, *n*-Butoxide and/or surfactant bound to the Ti(IV).

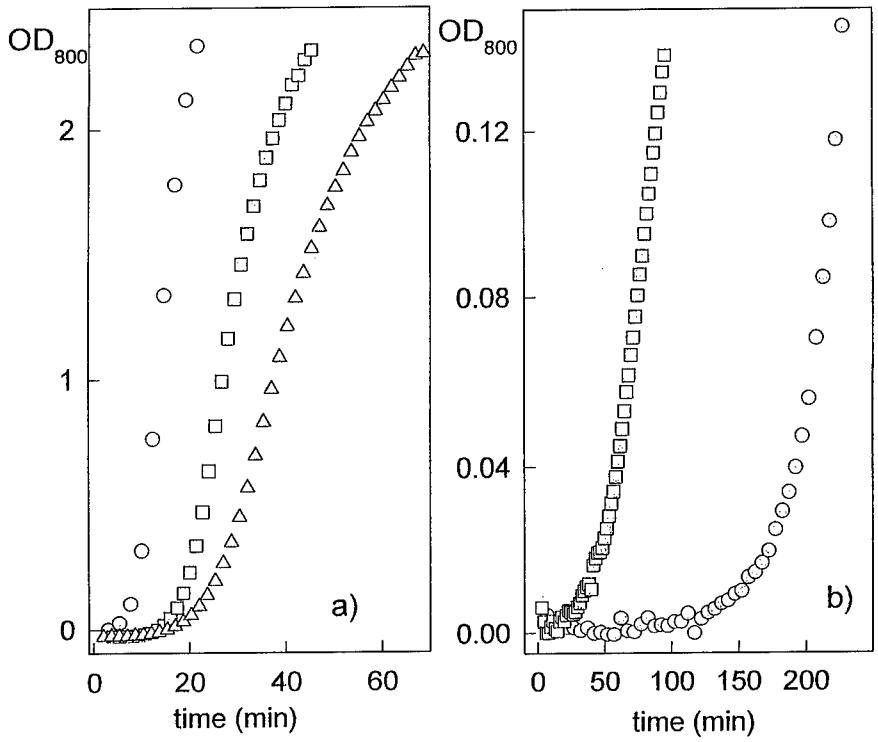

Figure 3. Optical density at 800 nm, OD_{800}, vs. time for sol-gel transition in (a) [AOT]: $[H_2O + x\text{M } HNO_3]$: $[Ti(BuO)_4]$ = 0.12 M : 0.29 M : 0.147 M in isooctane. (○) $x = 0$, (□) $x = 10^{-4}$ M, (△) $x = 10^{-1}$ M. (b) [Triton X-100]: $[H_2O + x\text{M } HClO_4]$: $[Ti(BuO)_4]$ = 0.36 M : 0.54 M : 0.27 M in cyclohexane. (□) $x = 0$, (○) $x = 10^{-4}$ M.

The radius (R) of the particles was estimated from the onset of the absorption by using the equation:

$$E^* \cong E_g + (h^2/8R^2)[(1/m_e^*) + (1/m_h^*)] - (1.8e^2/\varepsilon R)$$

with the following parameters: $[(1/m_e^*) + (1/m_h^*)]^{-1} = 1.63m_e$ [6] ($m_e = 9.1 \times 10^{-28}$ g) is the electron rest mass); $\varepsilon = 184$ [6], and $E_g = 3.2$ eV for anatase [6].

From the linear extrapolation of the steep part of the UV absorption towards the base line the energy of the lower excited state is determined.

Figure 5 shows the time evolution of the calculated radii of the nanoparticles for both surfactants: AOT and Triton X-100.

It can be seen that the TiO_2 particles synthesized in reverse micelles have calculated radii between 8 and 10 Å. These values represent a rough approximation, taking into account the ambiguity in the determination of the absorption onset, and the 50% spread of values for the effective masses reported in the literature [6].

As far as we know there is no rigorous theoretical expression for the calculation of the nanoparticle radii for our experimental conditions.

The calculated size of these "nanocrystals," and the fact that they remain in a narrow range suggests that the first stage of the hydrolysis is independent of the surfactant and the chemical nature of the oil.

The formation of a titania network implies that there is material exchange and polycondensation upon collisions between clusters of the partially hydrolyzed titanium alkoxide. The abrupt change of the OD_{800} is related to the growth of these clusters.

The gelation kinetics are slower for the non-ionic surfactant, as the concentration of acids increases and as the anion radius decreases (Figs. 2–4).

The fact that the gelation kinetics are slower in Triton X-100 than in AOT micellar systems, as shown in Fig. 2, reflects the influence on the reaction of the chemical nature of the surfactant. As water is more tightly bonded in Triton X-100 systems by the water bridges between two oxyethylene groups the breakdown of the micelle giving material

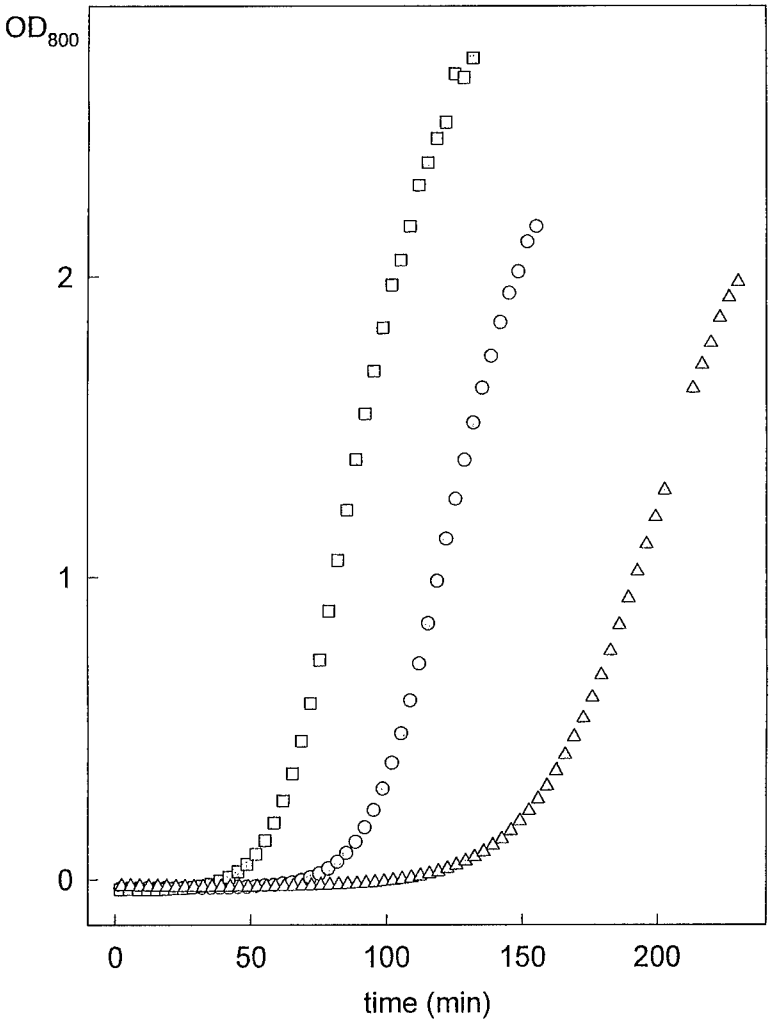

Figure 4. Optical density at 800 nm, OD_{800}, vs. time for sol-gel transition in reverse micelles of water in isooctane. [AOT] = 0.12 M, $[Ti(Bu)_4] = 0.147$ M and $[H_2O)^+ \times 10^{-1}$ M] = 0.29 M. (□) $x = [HCl]$, (○) $x = [HNO_3]$, (△) $x = [HClO_4]$.

exchange is more restricted in the Triton X-100 systems.

The addition of acids leads to the formation of more rigid micellar structures [11] by ion-water interactions which are stronger for smaller anions of equal charge, in good agreement with the results in Figs. 3 and 4.

Conclusions

Micellar systems are very useful for the control of the kinetics of the sol-gel transition by changing the microemulsion parameters.

In the Ti-alkoxide hydrolysis stage, water availability is determined by its affinity for the surfactant, and the gelation time is longer in Triton X-100, where water is more strongly bonded (by two oxyethylene groups) than in AOT.

Also in the hydrolysis stage, the increase in the acidity produces a decrease in the rate of hydrolysis.

The gelation time is longer when the aqueous phase is highly structured. The addition of acids leads to the formation of more rigid micellar structures by ion-water interactions. The ion-water interactions are stronger for smaller anions of equal charge.

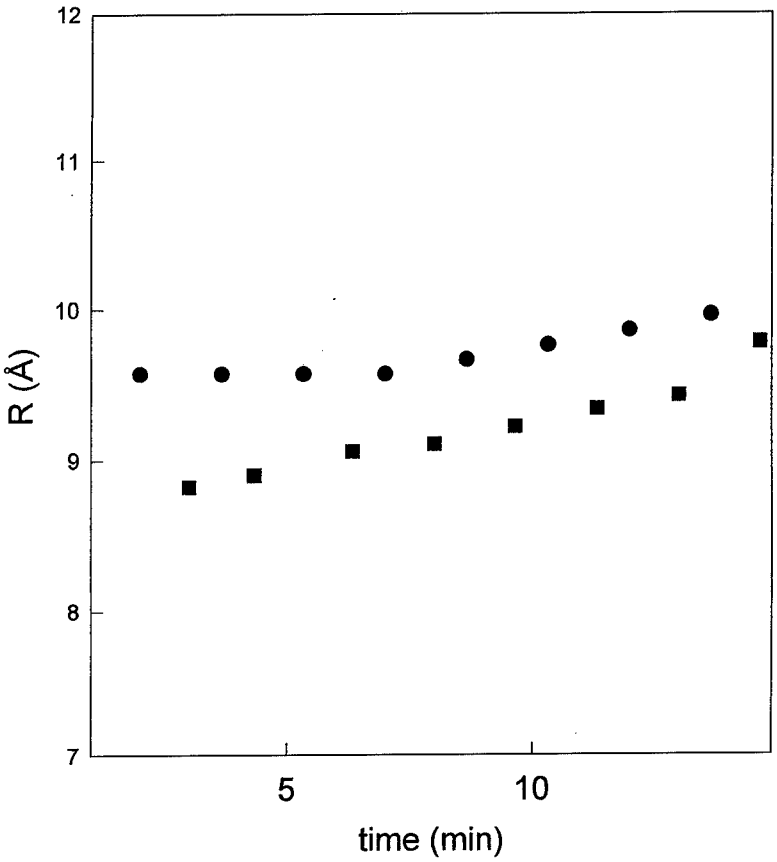

Figure 5. Radius of titania nanoparticles in the time window of sol stability for: [surfactant] = 0.36 M, $[Ti(BuO)_4] = 0.27$ M and $[H_2O] = 0.54$ M. (●) AOT, (■) Triton X-100.

Acknowledgments

Work supported by the University of Buenos Aires through grants: UBACyT Ex022 and UBACyT IN-023.

References

1. M. Wong, J.K. Thomas, and T. Nowak, Journal of the American Chemical Society **99**(14), 4730 (1977).
2. J.F. Quinson, J. Dumas, M. Chatelut, J. Serughetti, C. Guizard, A. Larbot, and L. Cot, Journal of Non-Crystalline Solids **113**, 14 (1989).
3. J. Marignan, C. Guizard, and A. Larbot, Europhysics Letter **8**(7), 691 (1989).
4. C.J Brinker and G.W Scherer, *Sol-Gel Science* (Academic Press, New York, 1989); L. Qi, J. Ma, H. Chen, and Z. Zhao, J. Phys. Chem. **101**, 3460 (1997); L. Auvray, Faraday Discuss **100**, 101 (1995); V. Chhabra, V. Pillai, B.K. Mishra, A. Morrone, and D.O. Shah, Langmuir **11**, 3307 (1995); E. Joselevich and I. Willner, J. Phys. Chem. **98**, 7628 (1994).
5. L. Brus, Journal of Physical Chemistry **90**, 2555 (1986).
6. B. Ginzberg and S.A. Bilmes, Progr. Colloid Polym. Sci **102**, 51 (1996).
7. S. Lebon, J. Marignan, and J. Appell, Journal of Non-Crystalline Solids **147/148**, 92 (1992).
8. C. Cabos and J. Marignan, Journal de Physique Lett. **46**, 267 (1985).
9. D.M. Zhu, K.I. Feng, and Z.A. Schelly, Journal of Physical Chemistry **96**(5), 2382 (1992).
10. J.M. Barthez, A Ayral, N. Hovnanian, C. Guizard, L. Cot, and J. Marignan, Journal of Sol-Gel Science and Technology **2**, 283 (1994).
11. B. Valeur and E. Bardez, *Structure and Reactivity in Reverse Micelles* (Elsevier Sciences Publishers B.V., Amsterdam, 1989), p. 103.

Journal of Sol-Gel Science and Technology 13, 347–352 (1998)
© 1998 Kluwer Academic Publishers. Manufactured in The Netherlands.

Differentiation between the Green and Turkish Blue Solid Solutions of Vanadium in a Zircon Lattice Obtained by the Sol-Gel Process

J.B. VICENT, J. BADENES, M. LLUSAR, M.A. TENA AND G. MONRÓS
Département de Química Inorgànica i Orgànica, Universitat Jaume I, Ap. Correos 224, 12080-Castelló, Spain

Abstract. In this communication, zircon containing vanadium samples which gradually turn greenish have been prepared by controlling the composition (fluoride addition) and the method of preparation (sol-gel, ceramic and solid impregnation) in order to investigate how to affect the shape and size of the vanadium particles, and their location, clustering and distribution. The level of green color, and consequently the amount of V^{5+} in the sample, could be associated with the development of an Si—O—Si network in the zircon lattice, bonding with the highly reactive zirconium precursors.

Keywords: Turkish Blue pigment, solid solution, solid impregnation, sol-gel

1. Introduction

The Turkish Blue vanadium pigment was patented in 1948 [1]. It was the first of the most successful ceramic pigment family, based on the structure of zircon, together with the Pink Koral (iron in zircon) and the Praseodymium Yellow pigment (praseodymium in zircon lattice). The necessary presence of halides as mineralizers and optimization of the experimental conditions were studied by Seabright [2] and Booth and Peel [3]. Batchelor [4] claims that in order to produce the pigment, three mineralizing ions are required: alkali metal ions, fluorides and a second halide (chloride or bromide). The role played by mineralizers in the formation of the color has been something of a mystery and probably still is.

Vanadium-zircon blue stain is assumed to be the solid solution, V-$ZrSiO_4$, but three types of solid solutions of V in zircon can be obtained at high temperature: (I) V^{4+}-$ZrSiO_4$ blue solid solution obtained with vanadium amounts lower than 0.03 mols per formula weight; (II) V^{4+},V^{5+}-$ZrSiO_4$ green solid solution, when vanadium exceeds 0.03 mols per formula weight, and (III) F^-,V^{4+}-$ZrSiO_4$ commercial Turkish Blue, synthesized by addition of fluorides [5, 6].

Using the hydrolysis-condensation of alkoxides and the colloidal gel method, tetragonal zirconia crystallizes in the silica matrix prior to zircon formation [5]. In this tetragonal zirconia-silica matrix composite, vanadium clustering has been observed by EPR studies. This clustering can be avoided by addition of fluoride or by using slow drying methods [7].

On the other hand, optical and EPR spectra of blue vanadium solid solutions in zircon have been studied widely and a controversy exists about whether such solid solutions can be accounted for by conventional crystal theory or not [9–11]. The localization of V^{4+} ion in D_{2d} symmetry sites (fourfold substituting Si^{4+} or eightfold changing Zr^{4+} in the zircon lattice) is the basis of this controversy. Demiray [8] considered that vanadium does not occupy a tetrahedral coordination, yet Di Gregorio [9] and Xyayou [10] presented evidence that such occupation is possible. However, Di Gregorio did not observe vanadium clustering in V-$ZrSiO_4$ single crystals, grown using the flux technique. The absence of V^{4+}-V^{4+} pairs in the EPR spectra of the single crystal is another piece of evidence against the dodecahedral site. Neighboring dodecahedral sites share an oxygen ligand, while tetrahedral sites do not.

It is well established that the relative amount of V^{4+} : V^{5+} of the sample is the deciding factor regarding the color obtained: when V^{4+} prevails, the color becomes blue, and as the V^{5+} content increases the

color becomes greenish [5, 6]. Fluoride stabilizes V^{4+} and substitutes O^{2-} in the zircon lattice, and consequently the unit cell size of zircon decreases [6, 7]. However, fluoride addition does not guarantee the blue color. This blue solid solution has become an important commercial ceramic pigment, and its greenish behavior must be avoided in industrial manufacture. In this communication samples which gradually turn greenish have been prepared by controlling the composition (fluoride addition) and the method of preparation (sol-gel, ceramic and solid impregnation) in order to investigate how to affect the shape and size of vanadium particles, and their location, clustering and distribution.

2. Experimental

F^-,V^{4+}-$ZrSiO_4$ solid solution in the commercial molar composition of $0.84ZrO_2 \cdot SiO_2 \cdot 0.16NH_4VO_3 \cdot 0.7$ NaF has been prepared by three different methods: the ceramic method (CE), the impregnation method (IMO and IMZ) and a polymeric gel route (PG without NaF addition and PGF with NaF).

In the ceramic method (CE), the precursors from PANREAC were mixed and homogenized in a planetary ball mill for 20 min at 800 rpm.

In the impregnation method (IM), two kinds of samples were processed: IMZ and the IMO samples. For IMO samples, NH_4VO_3 was chelated in an aqueous solution of tartaric acid, 0.5 M, giving an orange solution. Zirconium(IV) oxychloride 8-hydrate, as the zirconium precursor, was added into the continuously stirred solution, then concentrated ammonia solution was added until gelation occurred (pH = 1, 5–2). The greenish blue gel was dried in an oven at 110°C, producing a green powder. The powder was mixed with the mineralizer (fluorides) and quartz in a ball mill, using an acetone medium.

In the IMZ sample, zirconia from PANREAC was added to a 0.5 M tartaric acid aq. solution containing the NH_4VO_3. Impregnation of the solid dispersion was maintained for 1 hour. Then, concentrated ammonia was added dropwise until pH = 5.70 was reached and the solution was dried in an oven at 110°C. The dried material had a thin black layer on the surface. The powder was mixed with the mineralizer (fluorides) and quartz in a ball mill, using an acetone medium.

The polymeric gel (PG) was obtained by the hydrolysis-condensation of alkoxides. Vanadium(IV) oxyacetylacetonate, from FLUKA, was the vanadium precursor, and was refluxed in ethanol media, acidified with HNO_3 (molar ratios H^+ : TEOS = 1 : 0.05 and ethanol : TEOS = 22 : 1). Then tetraethylorthosilicate (TEOS) was added to the refluxing solution, with continuous stirring at 70°C. Acetylacetone and water were added (molar ratios : water : TEOS = 4 : 1; acetylacetone : TEOS = 1 : 1) and refluxed for 24 h. Then zirconium(IV) *n*-propoxide was added and gelation of solution occurred immediately. A homogeneous blue gel was obtained, which when aged and dried in the open air for 4 months, became a greenish blue, homogeneous, dried gel. Two kinds of samples have been prepared: the PG sample without mineralizer addition and the PGF sample with fluorides. As for all samples, for PGF the mineralizer was milled in order to avoid differences in fluoride homogenization.

All samples were studied by DTA-TG analysis, which led to a choice of firing schedule involving ramping at 5°C/min and dwelling at 750°C for 2 h. Fired samples were washed two times in a ball mill (weight ratio : solid : water = 1 : 1). The amount of vanadium in the washing water was measured by H_2O_2 colorimetry in a sulphuric acid medium and $FeSO_4 \cdot 7H_2O$ addition for $V^{5+} \rightarrow V^{4+}$ reduction. The washed sample was enamelled in a commercial borosilicate glaze at 5% by weight in order to check its coloring properties.

Samples have been studied by XRD, IR and optical UV-Vis-IR spectra, CIE-La*b* measurements of enamelled samples, magnetic susceptibility measurements and SEM-EDX microstructural characterization.

3. Results and Discussion

DTA and TG measurements were carried out by ramping at 5°C/min up to 1000°C for the PG samples. For the PGF sample, a sharp exothermic peak at 250°C, associated with burning of acetylacetonate, and a broad exothermic peak at 350°C, assigned to other absorbed organics, and a weak peak at 630°C, probably due to the crystallization of zirconia, have been observed. The three DTA bands have associated mass loss on the TG spectra of 21%, 12% and 5%, respectively. Features of the DTA-TG analysis of the PG sample were similar, but the band at 630°C was not detected and the 250°C band was less intense. However for TG, the mass losses were similar: 21%, 16% and 2%, respectively. XRD diffractograms performed on the TG residue indicated a total crystallization of zircon in the samples (Table 1). Only for the PGF sample were there weak XRD peaks associated with residual monoclinic zirconia. From

Table 1. XRD, CIE-L*a*b* results, V^{4+} leaching and magnetic susceptibility.

	CE	IMZ	IMO	PG	PGF
XRD					
750°C/2h	Z(vs)M(w)	Z(vs)M, Q(w)	Z(vs)M, Q(w)	T(w)	Z(s)M(w)
750°C/4h	—	—	—	T(s)M(w)	—
800°C/2h	—	—	—	Z(vs)M(m)	—
TG waste (1000°C)	—	—	—	Z(vs)	Z(vs)M(w)
CIE-L*a*b* (750°C/2h)*					
L	71.3	67.9	71.4	66.3	72.2
a*	−17.8	−17,9	−16.5	−13.6	−18.9
b*	−21.0	−22,9	−5.2	−5.5	−9.4
V^{4+} washed (750°C/2h)* (mgV^{4+}/g)	14.3	22.9	20.3	1.7	15.2
χ $(emu/g)\cdot 10^{-6}$	−1.395**	−1.055	−0.988	−2.26***	

(*) Except PG sample performed at 800°C/2h. (**) undoped zircon from SIBELCO S.A., (***) raw gel. CRYSTALLINE PHASES: Z(zircon), M(monoclinic zirconia), T(tetragonal zirconia), Q(quartz). PEAK INTENSITY: vs(very strong), s(strong), m(medium), w(weak), vw(very weak).

these results, a thermal firing treatment of 750°C/2 h was designed in order to produce the blue solid solution.

XRD and CIE-L*a*b* [11] parameters of all samples are shown in Table 1. XRD results reveal a lot of crystallized zircon at 750°C for all samples except the PG sample, which stabilized nanoparticles of tetragonal zirconia. It is necessary to fire the PG sample at 800°C/2 h in order to reach an adequate level of zircon crystallization. All samples had residual monoclinic zirconia and for the impregnation route quartz was also detected. From the CIE-L*a*b* analysis L is the lightness axis (black (0) → white(100)), a* is the green(−) → red(+) axis and b* is the blue(−) → yellow(+) axis. It is observed that CE, IMZ produced a neat true blue color ($b^* = -20$), the PGF sample had an intermediate blue level ($b^* = -9$) and IMZ and PG samples were green ($b^* = -5$). When the gel route was applied without fluoride addition, the greenish phenomenon increased, which means that the vanadium clustering (avoided by using the sol-gel route and the presence of fluoride [7]), as the cause of green coloration. Thus, V^{+5} formation is associated with highly reactive powders (the type of zirconium precursor is a decisive factor as indicated by the colors from the impregnation route and fluoride absence).

Vanadium analyses carried out on the washing water are shown in Table 1. Results indicate that the PG sample fired at 800°C exhibited a weak leaching of vanadium. Data were similar for the other samples.

IR spectra of the fired and raw samples were carried out by the conventional KBr pellet technique between 4000 and 200 cm^{-1}. The spectral features of the CE, IMZ and IMO raw samples are similar: a double and broad band centered at 3400 and 3160 cm^{-1}, associated with O—H stretching and CO_2—H stretching of the tartaric acid; a double band at 1623 (molecular water) and 1580 cm^{-1} (C=O group); a sharp band at 1400 cm^{-1} associated with ZrO^- (O^- signifying non-bridging oxygen ions) bands at 1080 and 1200 cm^{-1} (LO and TO modes of Si—O—Si asymmetric stretching vibration); 800 cm^{-1} (Si—O—Si symmetric stretching); 460 cm^{-1} (Si—O—Si bending) and 750 cm^{-1} (Zr—O stretching) have been observed. Bands at 580 and 526 cm^{-1} could be assigned to mineralizing fluorides [12, 13]. No spectral difference was found between the IM samples. The CE sample did not exhibit CO_2—H and C=O bands, and the region between 300 and 600 cm^{-1} was broadened. Polymeric samples exhibited different features: Si—O—Si, Zr—O and Si—O low intensity bands were present, and C=O, OH and molecular water associated bands increased in intensity.

The IR spectra were similar for all fired samples: five bands at 900, 620, 420, 380 and 310 cm^{-1}, associated with $ZrSiO_4$ were detected. In addition, bands

at 1400 (ZrO^-), 1100 (Si—O), 980 and 800 cm^{-1} were observed. The bands at 1100 and 800 cm^{-1} appeared more intense and sharper for green samples (PG and IMO), which could indicate the development of an Si—O—Si network in the green material.

Magnetic susceptibility measurements were performed at room temperature using an ELECTROSCAN magnetosusceptometer. Data shown in Table 1 indicate that vanadium in IM samples have diminished diamagnetic susceptibility compared with undoped zircon, and the green sample (IMO) exhibited the lower value. The PG dried gel showed more diamagnetic behavior than the undoped and fired IM samples. This behavior could be interpreted as a distortion effect of a small amount of V^{5+} (0.59 Å versus 0, 74 for V^{3+} Pauling ionic radius) according to the higher amount of V^{5+} in green samples.

UV-Vis-IR spectra of the more intense blue sample (IMZ) and the green samples (IMO and PG) are depicted in Fig. 1. The spectra show a broad band at 1400 nm (assigned to tetrahedrally coordinated V^{4+} $^2B_1 \rightarrow {}^2B_2$ transition) [5–7, 11]; the band at 640 nm is assigned to the tetrahedral, or dodecahedral, coordinated V^{4+} $^2B_1 \rightarrow {}^2E$ transition and the band centered at 300 nm is associated with the dodecahedral coordinated V^{4+} $^2B_1 \rightarrow {}^2A_1$ transition. Shoulders at 210 and 800 nm can be observed which are associated with forbidden transitions. Green samples were characterized by broadening of the band at 4000 nm and the shoulder of 800 nm. The band at 640 nm is slightly more intense for the blue samples. This behavior could be interpreted by the entrance of V^{5+} in the green zircon lattice [11].

SEM-EDX studies have been carried out using a Zeiss-Leica electron microscope coupled with the Link Isis EDX system from Oxford Instruments. Microstructural features of the pigment particles are depicted in Fig. 2. CE and IM samples have a similar microstructure: cubic particles, 3 μm sized. The polymeric gel samples contain 30% of big, monolithic particles of 10 μm, and 70% of particles with an average size of 3 μm. The latter small particles aggregate into agglomerates. No difference in shape or particle size could be detected between green and blue samples.

EDX semiquantitative analysis indicated a similar content of V_2O_5 in fired samples: about 5.5% in CE;

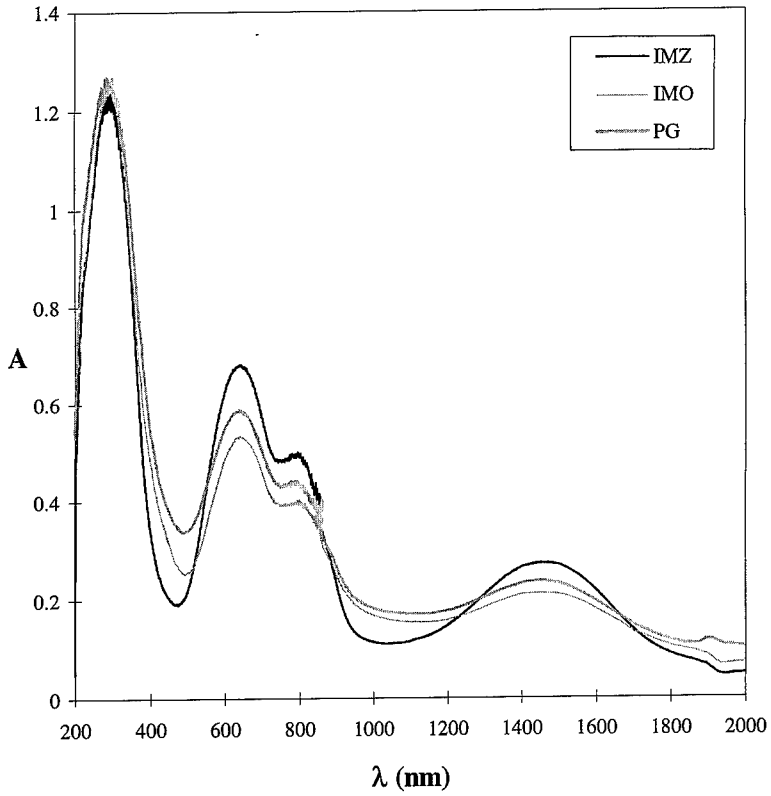

Figure 1. UV-Vis spectra.

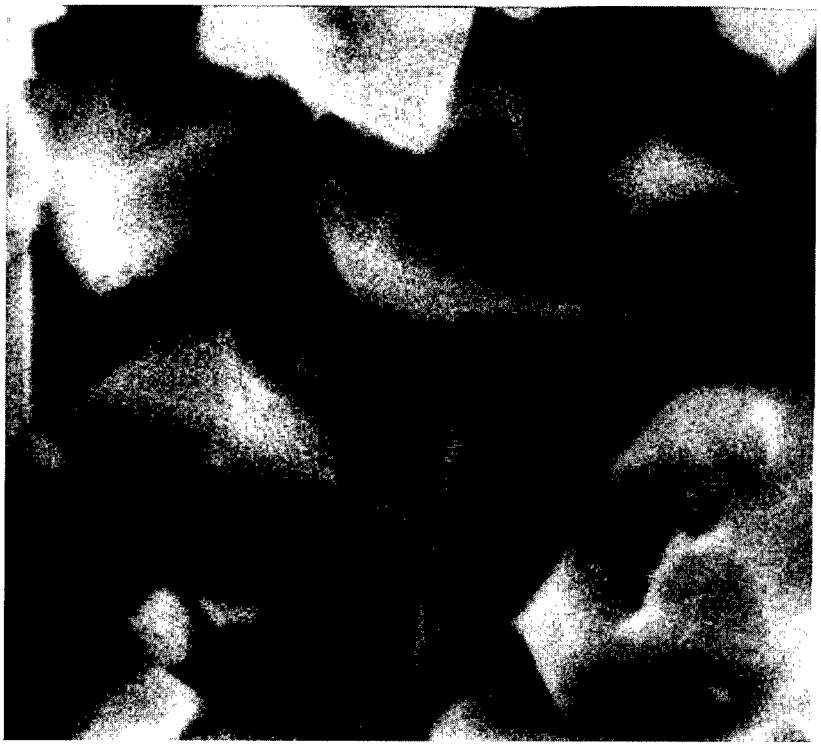

(a)

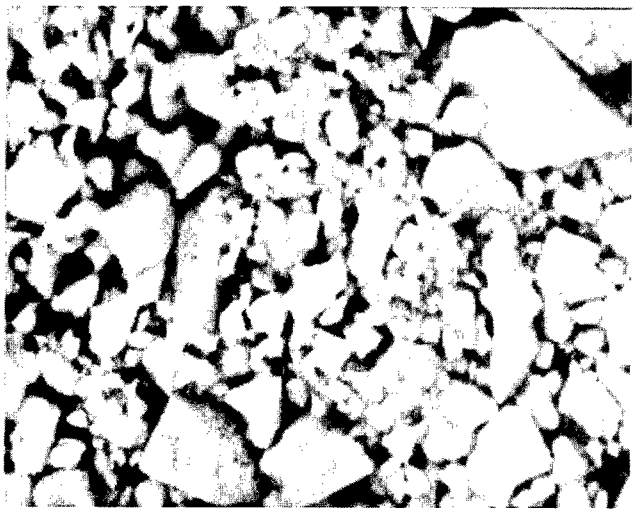

(b)

Figure 2. SEM micrographs: (a) IMO secondary electrons; (b) PG backscattering electrons.

5.2% in IMZ; 4.5% in IMO; 8.0% in PG and 6.3 in PGF. The relatively larger amount of vanadium in the PG sample is due to the addition of halide mineralizers in all of the other samples. It was found that a blue color was not associated with vanadium content in the sample. Spot, and mapping, EDX analysis indicated the presence of free zirconia, quartz and mineralizer agent in CE, IMZ and IMO samples. The analysis indicated a homogeneous vanadium distribution in the IMO, PG and PGF samples. In the CE sample, vanadium appeared to be associated with zirconia, while in the IMZ sample spot analysis indicated an association with quartz. Therefore, an association cannot be made between color and microstructural vanadium distribution in the samples.

4. Conclusions

The appearance of V^{5+} and the undesirable greenish coloration to the F^-,V^{4+}-$ZrSiO_4$ commercial Turkish Blue cannot be associated with microstructural parameters such as the shape or particle size of the pigment powder, the vanadium amount or its distribution in the particles. However, the level of green color, and consequently the amount of V^{5+} in the sample could be associated with development of the Si—O—Si network within the zircon lattice, associated with highly reactive zirconium precursors.

Acknowledgments

Authors are grateful to Fundación Caixa Castelló (PIA95-10 project) for financial support. M. Llusar is grateful to Conselleria Educació Valenciana for his grant.

References

1. C.A. Seabright, U.S. Patent, 2,441,707, May 1948.
2. C.A. Seabright and H.C. Draker, Amer. Cer. Soc. Bull. **40**, 1 (1961).
3. F.T. Both and G.N. Peel, Trans. Brit. Ceram. Soc. **61**, 359–400 (1962).
4. Ferro Corporation, Brit. Pat, 1,214,794, 1970.
5. G. Monrós, M.C. Martí, J. Carda, M.A. Tena, and P. Escribano, Journal of Material Science **28**, 5852 (1993).
6. G. Monrós, J. Carda, M.A. Tena, P. Escribano, V. Cantavella, and J. Alarcón, Material Research Bulletin **27**, 753 (1992).
7. G. Monrós, J. Carda, M.A. Tena, P. Escribano, F. Ribot, and C. Sanchez, Solid State Ionics **63–65**, 218 (1993).
8. T. Demiray, Journal of American Ceramic Society **53**, 1 (1970).
9. S. Di Gregorio, Journal Chemical Physics **15**, 2931 (1982).
10. H. Xiaoyu, Journal Physical Chemistry Solids **46**, 719 (1985).
11. CIE, Recommendations on Uniform Color Space, Color Difference Equations, Psychometrics Color Terms. Supplement No. 2 of CIE Publ. No. 15 (E1-1.31)1971. Bureau Central de la CIE, Paris (1978).
12. M. Nogami, Journal of Non-Crystalline Solids **69**, 415 (1985).
13. L.J. Bellamy, *The Infra-red Spectra of Complex Molecules* (Wiley, New York, 1958).
14. G. Monrós, J. Carda, M.A. Tena, P. Escribano, M. Sales, and J. Alarcón, Journal of European Ceramic Society **11**, 77 (1993).

Journal of Sol-Gel Science and Technology 13, 353–358 (1998)
© 1998 Kluwer Academic Publishers. Manufactured in The Netherlands.

Study of the Influence of Alkaline Ions (Li, Na and K) on the Structure of the Silicate Entities in Silico Alkaline Sol and on the Formation of the Silico-Calco-Alkaline Gel

F. GABORIAUD, D. CHAUMONT AND A. NONAT
LRRS, UMR 5613, Université de Bourgogne, BP 400-21011 Dijon Cedex, France

B. HANQUET
LSEO, UMR 5632, Université de Bourgogne, BP 400-21011 Dijon Cedex, France

A. CRAEIVICH
LNLS, Caixa Postal 6192, 13083-970 Campinas, SP, Bresil

Abstract. The study of silico-calco-alkaline gel is essential to warn against the degradation of concrete due to the alkali-silica reaction. In the laboratory, those gels are simulated by the destabilization of a silico-alkaline sol by calcium ions. Their speed of formation depends on the alkali species. The influence of alkaline ions (Li, Na and K) on the structure of silicate entities in sol and on the gel formation has been studied. The state of polymerization of the silico-alkaline sol was determined by NMR and depends on the alkali species and the molar ratio ($Rm = [SiO_2]/[A_2O]$ with A = Li, Na or K). It appears that lithium enhances the polymerization. By scattering techniques (SAXS and ELS), the evolution of size and number of scattering particles during gelation can be determined from scattering curves with Guinier approximation. The mechanism of gelation appears like a hierarchic structure composed with several discrete sizes.

Keywords: silicate, alkaline, gelation, kinetics

Introduction

Concrete is a porous material comprised of aggregates immobilized in a cement paste. If the aggregates contain reactive silica, the interaction between these aggregates and the various ions present in the concrete pore solution (hydroxide, alkaline, calcium,...) induces the formation of calcium alkaline silica gel which can subsequently lead to cracking of the concrete. This reaction is commonly called the alkali-silica-reaction (ASR).

In our laboratory, this system is simulated by destabilization of alkaline silicate sols by a calcium salt ($Ca(OH)_2$ portlandite). The preparation of these gels consists of two stages:

(1) Dissolution of the silica by hydroxide ions leading to the formation of a concentrated silico-alkaline solution. The maximum silica concentration is defined as the pessimum condition ($[SiO_2]_{max} = 1.5\ mol \cdot l^{-1}$) [1].
(2) Destabilization of the alkaline silicate solution by calcium ions leading to the formation of a silico-calco-alkaline compound (gel or precipitate).

Other works [2, 3] have shown that, when the molar ratio ($Rm = SiO_2/A_2O$; A = Na or K) is low, the silico-alkaline solution contains weakly polymerized silicate entities. Increasing the molar ratio strongly enhances the degree of polymerization of these solutions. When the ratio is higher than 2, Iler [4] and Harris [2] have shown that the solution can be considered to be colloidal one (entities of between size 10 and 1000 Å). When such sols ($Rm > 2$) are destabilized by calcium ions, the compound formed is a gel, while if $Rm < 2$,

it is a precipitate. Calcium ions act as a "catalyst" by bringing together two silicate entities and then being replaced by a siloxane bond.

There is a great disparity in gelation times depending on the alkali species and the molar ratio. Gels formed with sodium have the shortest gelation time, at constant calcium concentration, independent of the molar ratio (2 or 3).

The aim of this study is to explain these differences by determining, first, properties of sols by ^{29}Si Nuclear Magnetic Resonance (NMR) and then to determine the structure of gel by Small Angle X-ray Scattering (SAXS) and Elastic Light Scattering (ELS).

Experimental

Sols are obtained by mixing silica (silicagel, Merck chromatography), an alkali (Li, Na or K) oxide and water for several days, until thermodynamic equilibrium is reached (no filtration). For both molar ratios of 2 and 3, the silica concentration is maintained constant at 1.5 mol $\cdot$ l^{-1}.

^{29}Si NMR spectra of the sols were recorded on a Bruker DRX500 spectrometer operating at 99.36 MHz (the silicon-29 frequency resonance). PTFE sample tubes were used (4 mm o.d.), held vertically a 5 mm o.d. glass tube. Heavy water (10%) was added to the samples to lock the spectrometer. A pulse width of 90° (10.8 μs) was used with a repetition time of 90 s. FIDs were acquired over a sweep width of 20 kHz (200 ppm) using 32 K data. A "blank" FID was acquired, corresponding to the background of the probe, and was subtracted from each data set. A line broadening of 8 Hz was applied, giving a satisfactory signal-to-noise ratio.

The samples were sonicated after calcium hydroxide was added to the sols. The samples were then centrifuged so as to obtain homogeneous destabilized sols. The gelation time was determined by observing when the meniscus in a container no longer remained horizontal when the container was tilted. These gelation time results were very reproducible (~5%).

Kinetics of gelation have been followed in situ by two scattering techniques. SAXS curves have been obtained by LURE (Orsay) and those of ELS in our laboratory (LRRS-Dijon). They measure the angular dependence of the intensity scattered by a sample with heterogeneities in electron density (SAXS) and in refraction index (ELS). The domain studied is not the same because the wavelength used is different. The SAXS technique scattering vector domain observed was: 5×10^{-3} Å$^{-1} < q_{SAXS} < 7 \times 10^{-2}$ Å^{-1} and the ELS one was 4×10^{-4} Å$^{-1} < q_{ELS} < 2 \times 10^{-3}$ Å^{-1}. There is a blind zone (5×10^{-3} Å$^{-1} < q < 2 \times 10^{-3}$ Å^{-1}) which could be reached by SANS. The SAXS curves of the samples were treated by subtracting the background and the corresponding nondestabilized sol curve.

Results and Discussion

Analysis of Sols

^{29}Si NMR was performed on silico-alkaline sols. It gives information about the degree of connectivity of silicon atoms. The usual notation is Q^n where Q represents a silica tetrahedron and n is the number of tetrahedra connected to this one. Structural distributions for those solutions are presented in Table 1.

A mean degree of connectivity was calculated using:

$$\bar{n} = \frac{\sum_n n \times Q^n}{\sum_n Q^n}$$

to account for the state of polymerization of the silico-alkaline solutions. The evolution of n as a function of the alkali ion present and the molar ratio is shown in Fig. 1.

For all the alkali ions, the mean degree of connectivity increases with the molar ratio. This is in agreement with the results for sodium reported by Harris [4].

Table 1. Structural distributions for aqueous silico-alkaline sols with different molar ratios (2 and 3); constant silica concentration ([SiO_2] = 1.5 mol $\cdot$ l^{-1}).

Structural unit (%)	$SiO_2/Li_2O = 2$	$SiO_2/Li_2O = 3$	$SiO_2/Na_2O = 2$	$SiO_2/Na_2O = 3$	$SiO_2/K_2O = 2$	$SiO_2/K_2O = 3$
Q^0	9.72	2.85	9.62	7.39	10.3	10.03
Q^1	12.47	7.15	17.73	14.55	13.8	11.28
Q^2	18.53	12.01	28.43	11.43	35.7	13.5
Q^3	59.28	53.83	44.22	66.63	40.2	65.19
Q^4	0	24.16	0	0	0	0

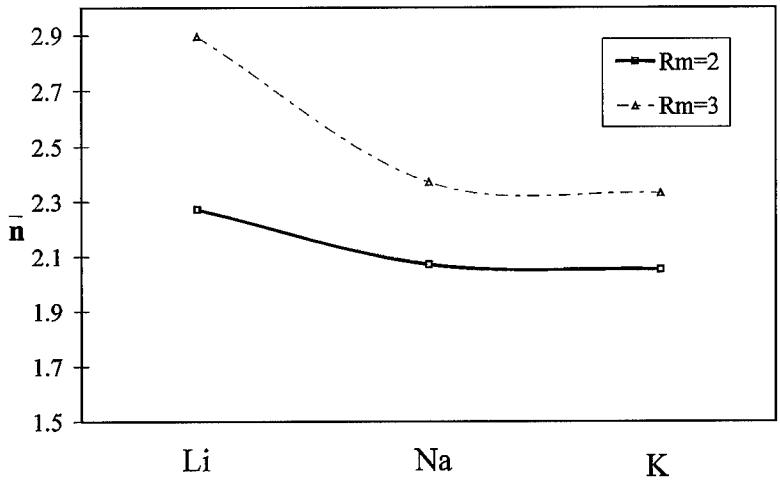

Figure 1. Evolution of mean degree of connectivity of silico-alkaline solutions ($[SiO_2]$ =1.5 mol·l^{-1}) as a function of alkali ion and molar ratio ($Rm = [SiO_2]/[A_2O]$ with A = Li, Na and K).

Moreover, it appears that with lithium, the degree and polymerization is higher than in the case of sodium or potassium, independent of the molar ratio.

Gelation Time

The influence of the alkali species and the molar ratio on the gelation time is shown in Fig. 2.

At a constant calcium concentration and independent of the molar ratio, gelation time with sodium is shorter than the gelation time with lithium and potassium.

When the molar ratio increases, the gelation time increases, except if potassium is present. For a molar ratio of 2, the gelation time with potassium is the greatest; whereas for a molar ratio of 3, the gelation time with lithium is the greatest.

Structure of Gels

Figure 3 represents scattering curves by SAXS and ELS at different times (times normalized by gelation time) for one gelation condition.

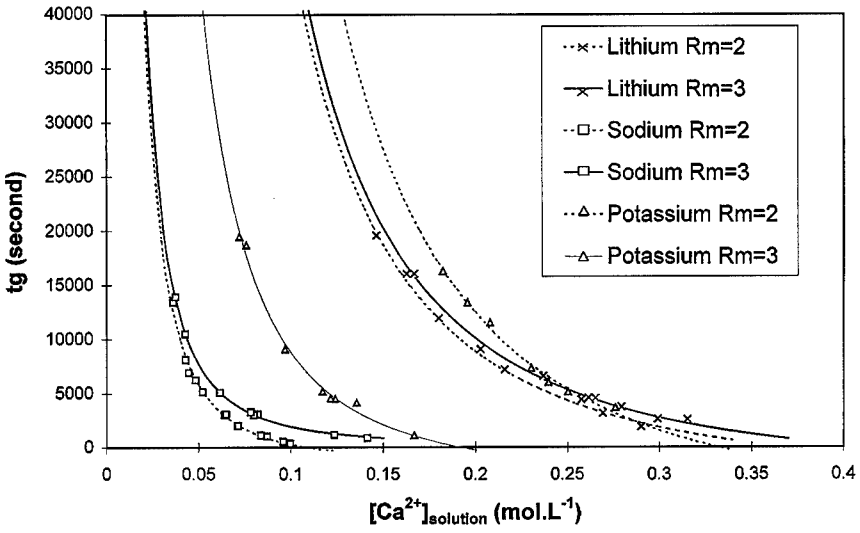

Figure 2. Evolution of gelation time as a function of calcium concentration in solution (after centrifugation).

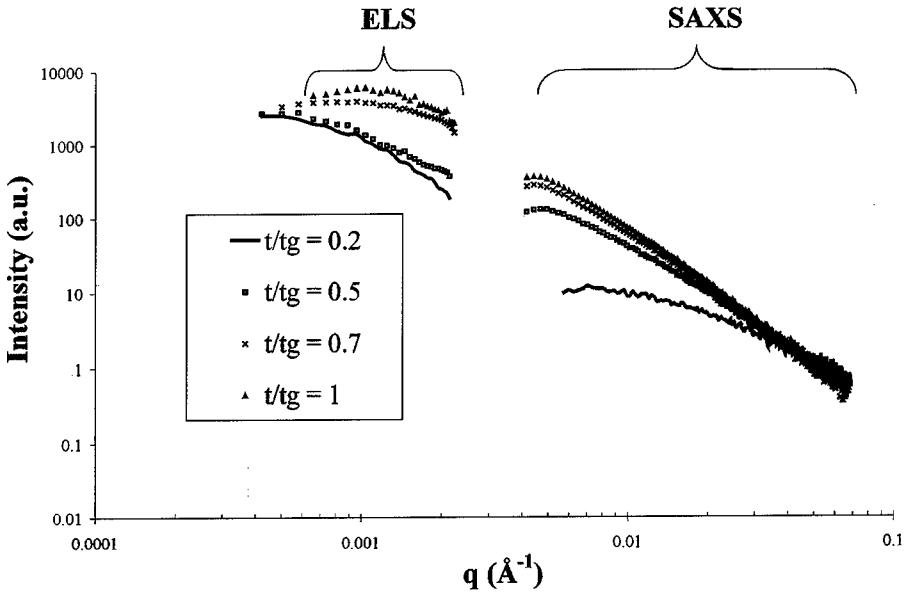

Figure 3. SAXS (Small Angle X-ray Scattering, LURE Orsay) and ELS (Elastic Light Scattering) curves for a silico-calco-sodium gel ($Rm = 2$; $[Ca(OH)_2] = 0.08$ mol $\cdot$ l^{-1}). Measurements made in situ; time normalized by gelation time.

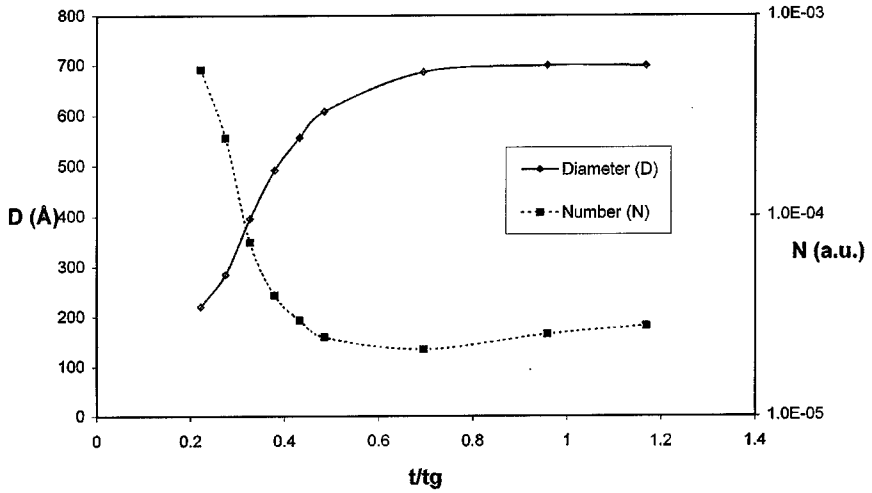

Figure 4. Evolution of size and number of particles by SAXS as a function of time (normalized by gelation time) for a silico-calco-sodium gel ($Rm = 2$; $[Ca(OH)_2] = 0.08$ mol $\cdot$ l^{-1}).

In each case, the intensity scattered has a plateau at low angles which can be approximated by Guinier's law [5]:

$$I_{\text{scattered}} = I_0 \times \exp\left(-\frac{q^2 \times Rg^2}{3}\right)$$

$$\text{with } D = 2 \times \sqrt{\frac{5}{3}} \times Rg.$$

Using these relationships, information on the size (D = diameter) of particles is obtained from scattering curves for qRg smaller than 1. The evolution of particle number N (qualitative) is deduced from I_0 (the extrapolated intensity to $q = 0$) by the relation:

$$I_0 \propto NR^6.$$

After the Guinier zone (in SAXS and ELS), the scattered intensity does not follow a power law as seen with

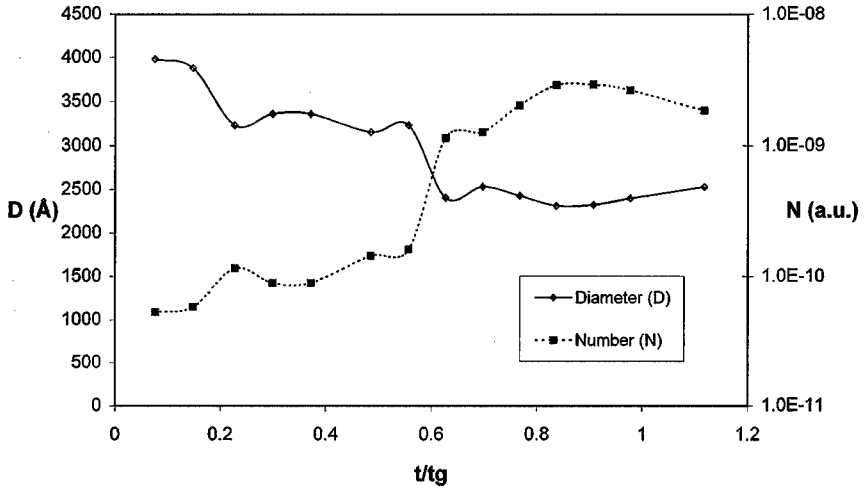

Figure 5. Evolution of size and number of particles by ELS as a function of time (normalized by gelation time) for a silico-calco-sodium gel ($Rm = 2$; $[Ca(OH)_2] = 0.08$ mol $\cdot l^{-1}$).

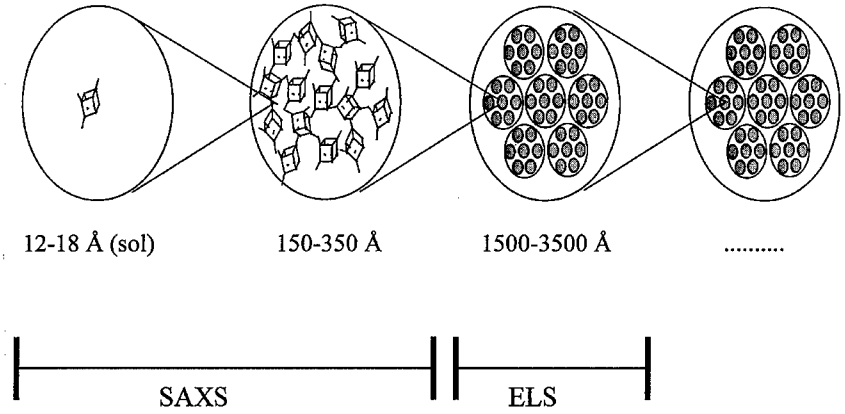

Figure 6. Hierarchic structure for the mechanism of gelation.

fractal systems. Porod's law ($I \sim q^{-4}$)[7], for large angles, is also not observed in this study.

Figures 4 (SAXS) and 5 (ELS) show the evolution of particle size and particle number during silico-calco-sodium gel formation.

It can be seen that particles reach an equilibrium size in the "two windows of observation." The number of smaller particles decreases (shown by SAXS), while the number of larger particles increases (shown by ELS). Smaller particles appear to be absorbed by larger particles. The reaction kinetics are similar and they are independent of the alkali present, meaning that the mechanism of gelation is the same.

These results show that three or more discrete sizes of particles are present: particles with the same size of initially sols, particles detected by SAXS and particles detected by ELS.

A hierarchic structure (Fig. 6) can be proposed as the structure of silico-calco-alkaline gel.

Conclusion

This study shows the influence of alkali ions on silico-alkaline sols; most notably lithium ions increase the degree of polymerization of silicate entities.

When calcium ions are added, we observe some variation of the gelation time dependent on the alkali ion and the molar ratio. However, the variations in gelation time do not follow the variations in the degree

of connectivity. Therefore, the gelation time is independent of the structure of the silicate entities in sol.

If the interaction between silicate entities and alkali ions is strong, calcium ions cannot readily replace the alkali ions [6]. The observed differences in gelation time are probably due to this interaction.

The mechanism of gelation induces a hierarchic structure of discrete sizes. More experiments must be done to examine the unobserved domain between SAXS and ELS experiments.

References

1. L.S. Dent Glasser and N. Kataoka, Cement and Concrete Research **11**, 1 (1981).
2. R.K. Harris, E.K.F. Bahlmann, K. Metcalfe, and E.G. Smith, Magnetic Resonance in Chemistry **31**, 743 (1993).
3. A.V. McCormick, A.T. Bell, and C.J. Radke, Studies in Surface Science and Catalysis **28**, 247 (1986).
4. P.K. Iler, *The Chemistry of Silica* (John Wiley & Sons, 1979).
5. O. Glatter and O. Kratky, *Small Angle X-Ray Scattering* (Academic Press, New York, 1982).
6. A.V. McCormick, A.T. Bell, and C.J. Radke, Journal Physical Chemistry **93**, 1733 (1989).

Journal of Sol-Gel Science and Technology 13, 359–364 (1998)
© 1998 Kluwer Academic Publishers. Manufactured in The Netherlands.

Preparation and Characterization of Forsterite (Mg_2SiO_4) Xerogels

MATTHEW B.D. MITCHELL
Department of Engineering Materials, University of Sheffield, Sir Robert Hadfield Building, Mappin St., Sheffield S1 3JD, UK

DAVID JACKSON
Zortech International, Hadzor Hall, Hadzor, Droitwich, Worcestershire WR9 7DJ, UK

PETER F. JAMES
Department of Engineering Materials, University of Sheffield, Sir Robert Hadfield Building, Mappin St., Sheffield S1 3JD, UK

Abstract. Mg_2SiO_4 gels were prepared from alkoxide precursors, and the formation of the forsterite crystal phase was studied after heat treatments up to 1200°C. Prehydrolyzed TEOS in solution with 2-methoxyethanol was mixed with $Mg(OEt)_2$, and the solution was hydrolyzed using excess water. The resultant gels were dried at 100°C to form xerogels which were subsequently powdered. These powders were characterized using thermal analysis (DTA and TGA), surface area analysis (BET), X-ray diffraction (XRD) and transmission electron microscopy (TEM).

DTA and XRD indicated that forsterite crystallized at 770°C, and by 1000°C the powders were predominantly crystalline. BET gave powder surface areas between 400 and 550 $m^2 g^{-1}$. TEM revealed angular particles with sizes between 0.2 and 2 μm. The low temperature of crystallization of forsterite indicates a high degree of intimate mixing between the precursor alkoxides, although XRD indicated some degree of inhomogeneity.

Keywords: forsterite, alkoxides, prehydrolysis

Introduction

Pure forsterite ($MgSiO_4$) can be prepared by heating MgO and SiO_2 powders together at temperatures up to 1525°C. However, the sol-gel process offers a low temperature route to form amorphous powders of the composition $2MgO{\cdot}SiO_2$ which, due to the more intimate mixing of SiO_2 and MgO, could crystallize to form pure forsterite at much lower temperatures. Low density, high surface area forsterite powders have potential high temperature applications.

Kazakos et al. [1] produced dense pellets of forsterite by pressing and heating powders prepared from TEOS and $Mg(NO_3)_2{\cdot}6H_2O$. Bansal [2] found that a maximum of 15 mol% magnesia may be incorporated into a silica network if $Mg(NO_3)_2{\cdot}6H_2O$ is used as the source of MgO, and it is therefore unlikely that the as-produced powders prepared in [1] were fully homogeneous. Burlitch et al. [3] prepared forsterite powders from TEOS and $Mg(OMe)_2$, and found crystallization of forsterite at 850°C. Park et al. [4], using similar preparation methods, found that the addition of chromium reduced the temperature of crystallization by as much as 50°C. The low temperature of crystallization of forsterite indicates that the powders produced in [3, 4] were an intimate mixture of SiO_2 and MgO.

Recent studies have produced magnesia-silica oxides from magnesium diethoxide $Mg(OEt)_2$ and TEOS [5, 6]. The compositions studied had a much lower magnesia content than that of forsterite, but it was considered possible that a similar route could

be employed to produce homogeneous powders of $2MgO{\cdot}SiO_2$.

Experimental

1 M solutions of $Mg(OEt)_2$ were prepared by stirring $Mg(OEt)_2$ in 2-methoxyethanol at 80°C for 1 hour. 1 M solutions of TEOS in 2-methoxyethanol and HCl were prepared with a TEOS : H_2O : HCl ratio of 1 : 2 : 0.1. These solutions were prehydrolyzed by stirring at room temperature for times between 1 and 120 hours before mixing with the $Mg(OEt)_2$ solution in the required ratio to produce $2MgO{\cdot}SiO_2$. Excess water : alkoxide (20 : 1) was added to complete hydrolysis and condensation and the resultant gels were aged for 24 hours before drying. These gels were termed P*n*, where *n* is the prehydrolysis time in hours. Gels were also made by prehydrolyzing the TEOS for 24 hours before mixing with $Mg(OEt)_2$ solutions and subsequently ageing them for times between 0 and 120 hours. These gels were termed A*n*, where *n* is the aging time in hours. In addition to these, a further gel, termed PR, was prepared by refluxing the TEOS solution for 24 hours to achieve prehydrolysis before mixing with the $Mg(OEt)_2$ solution. Table 1 summarizes the three preparation methods for the gels.

The gels were all oven dried at 100°C for 24 hours before powdering with a pestle and mortar. Samples were heated at 10°C min^{-1} to 400°C or 1200°C and held for 1 hour. The resultant powders were characterized using DTA and TGA (Stanton Redcroft DTA 673-4 and TG 750/770), BET surface area analysis (Gemini 230), XRD (Philips diffractometer) and TEM (JEOL 400). XRD was also performed on A24 after heating to 20°C above and below any exothermic peaks observed in the DTA.

Table 1. Summary of preparation conditions for A and P series of gels.

Gel	Prehydrolysis of TEOS/hrs	Ageing/hrs
A	24	0, 2, 6, 24, 48, 120
P	1, 2, 5, 24, 48, 120	24
PR	24	24

Results

DTA results for as-produced PR and A24 are given in Fig. 1. TGA for P2, P24 and P48 (Fig. 2) showed weight losses of between 37 and 40% up to 800°C, compared with 44% for all the A powders, regardless of ageing time. Table 2 presents the specific surface areas obtained for degassed samples, which were previously heated to 400°C for 1 hour to drive off residual organics. XRD showed that all the as-produced powders were amorphous. On heating to 400°C some small, broad

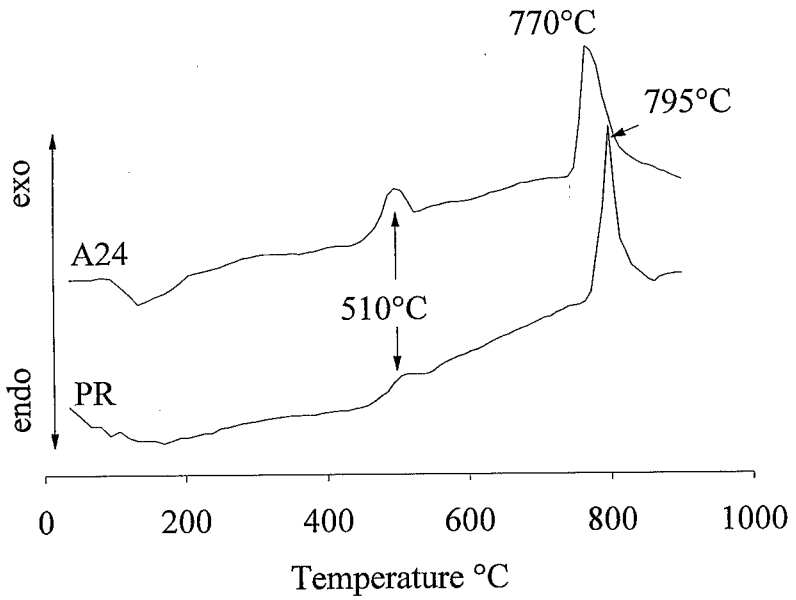

Figure 1. DTA trace of as-produced PR, heated at 10°C min^{-1} in air.

Table 2. BET surface areas of selected samples after heating to 400°C for 1 hour (±5%).

Sample	Surface area ($m^2\ g^{-1}$)
A1	527
A24	520
A48	509
A120	504
P1	480
P24	501
P48	492
PR	432
PR heated at 1200°C for 1 hr	5

peaks corresponding to MgO were observed. Figure 3 shows the crystalline phases observed by XRD when A24 was heated in the DTA equipment. On heating to 1200°C all the powders were predominantly forsterite with some MgO present (Fig. 4). TEM micrographs of as-produced P1 and A120 are given in Fig. 5.

Discussion

The first exothermic peak observed in the DTA (Fig. 1) at 510°C was initially thought to be crystallization of MgO. However, XRD clearly shows (Fig. 3) that MgO is present at 490°C and the size and width of the peaks have not altered after heating to 530°C. The exotherm was not reversible, suggesting that the peak is not a glass transition temperature. However, the peak remained when DTA was performed in N_2, indicating that the exotherm is not due to an oxidation reaction. XRD shows that A24 heated to 750°C has a small amount of forsterite present (Fig. 3), and at 790°C the forsterite peaks are well developed, suggesting that the exotherms observed at 770°C are due to the crystallization of forsterite. This occurs 80°C lower than the temperature reported in [4]. Increasing the heating rate to 20°C min^{-1} did not affect the position of either peak, and so the reduction in temperature may be explained by a greater degree of intimate mixing between MgO and SiO_2 in the powder.

TGA (Fig. 2) shows weight losses of up to 40%, which occur in three main stages. The first stage occurs below 100°C and is probably caused by removal of residual water. The second stage, between 100 and 350°C, can be ascribed to the removal of residual organic groups, which would leave behind traces of carbon. Removal of residual carbon from pores is a slow process, and contributes to the third, steady weight loss observed above 400°C. This continues to around 800°C above which no further loss is observed. Removal of surface OH groups also contributes to the losses observed. The amount of weight loss reduced slightly as the time of prehydrolysis increased, suggesting a greater degree of condensation in the gel before drying. However, altering the ageing time of the gels (A0 to A120) had no discernible effect.

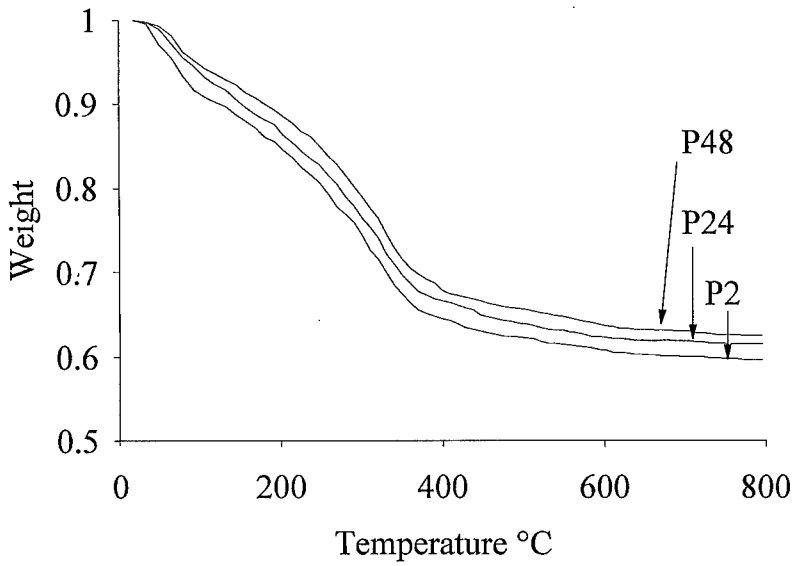

Figure 2. TGA traces for as-produced P2, P24 and P48 heated at 10°C min^{-1} in air.

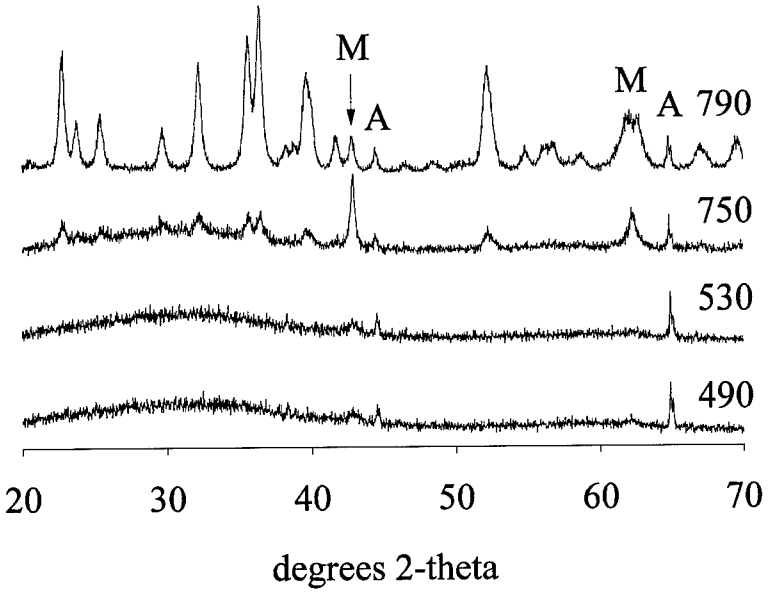

Figure 3. XRD traces of A24 after heating in the DTA equipment at 10°C min^{-1} to 490, 530, 750 and 790°C. All the peaks are characteristic of forsterite except M; MgO and A; and Al from the sample holder. Scan speed 2°/min, step 0.02°, CuK_{α}.

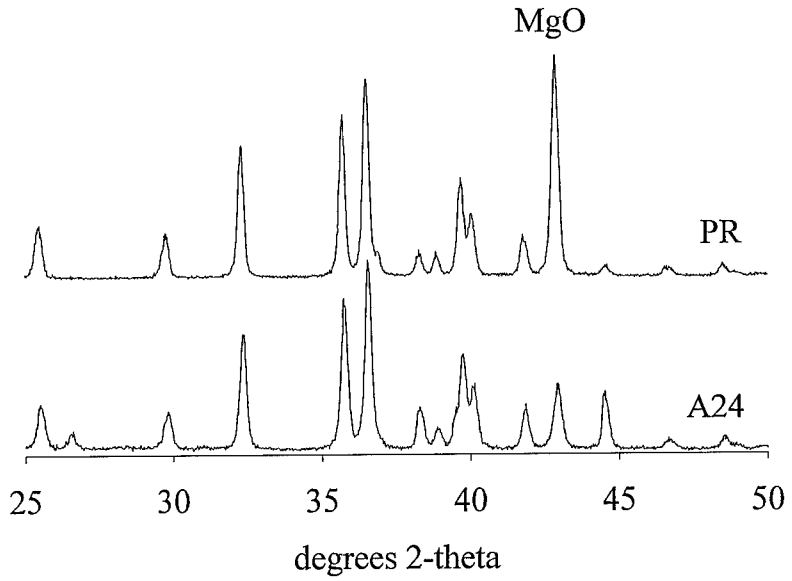

Figure 4. XRD traces of PR and A24 after heat treatment at 1200°C for 1 hour. All peaks are characteristic of forsterite except those indicated. Scan speed 2°/min, step 0.02°, CuK_{α}.

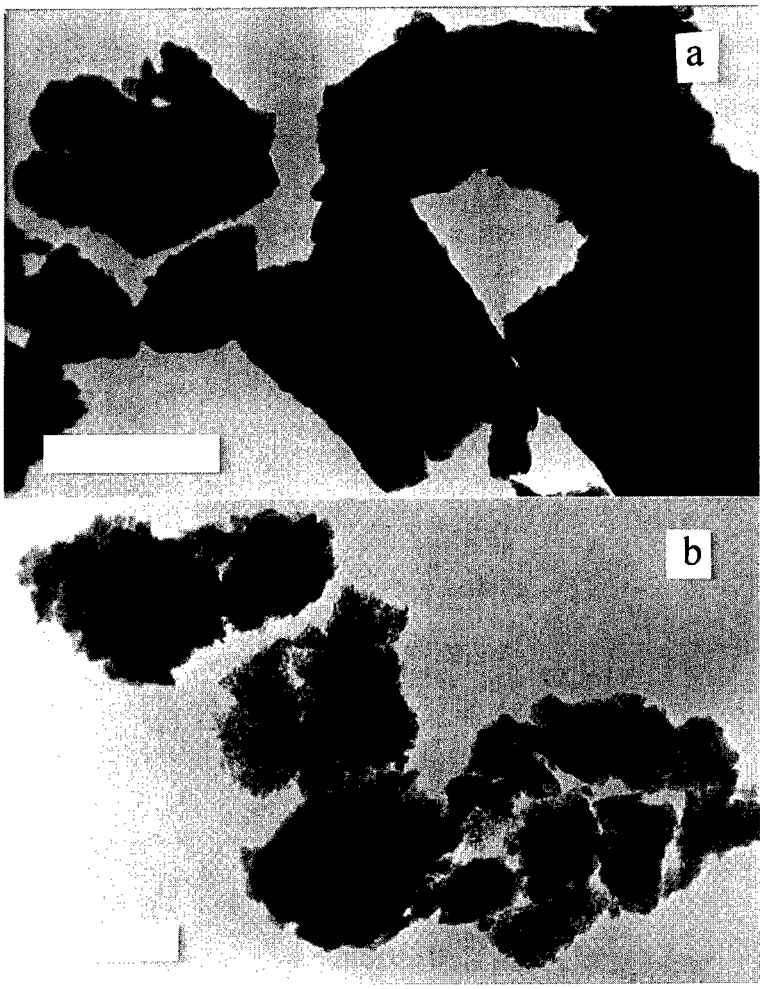

Figure 5. Bright field transmission electron micrographs. (a) As-produced A1. Bar = 0.5 μm. (b) As-produced P120. Bar = 0.5 μm.

The surface areas of all the powders produced were between 400 and 550 $m^2\ g^{-1}$, which dropped to 5 $m^2\ g^{-1}$ on heating to 1200°C. The high weight losses observed would lead to the high surface areas, as pyrolysis of organics would leave tiny 'holes' in the particles. The first crystal phase to form on heating the powders was MgO, which was present in small quantities when the powder was held at 400°C for 1 hour before cooling. On further heating, forsterite formed between 770 and 795°C. XRD (Fig. 4) shows that when PR was heated to 1200°C for 1 hour, a significant amount of MgO had formed in addition to forsterite. MgO was also observed in the A and P series of powders, but in smaller amounts, suggesting that these powders were more homogeneous. This is supported by the lower temperature of crystallization of forsterite of A24 compared to PR. Increasing the ageing time for the A powders did not significantly alter the amount of MgO formed.

From TEM observations (Fig. 5), the as-produced powders consisted of angular particles with dimensions of between 0.2 and 2 μm. The uniform contrast in thin areas of the particles suggests that phase separation has not occurred on a scale greater than 10 nm and therefore that the MgO and SiO_2 are intimately mixed. Fine scale porosity within the powders could account for the high surface areas observed. The P gels which had been prehydrolyzed for longer times (Fig. 5(b)) also showed similar sized angular particles but some of these were composed of fine primary subparticles of diameters of less than 10 nm, indicating a lesser degree of homogeneity. Longer times of prehydrolysis

of TEOS could lead to more condensed SiO_2 in the system before addition of $Mg(OEt)_2$, which would in turn lead to a more particulate, less homogeneous gel. A crude primary particle packing model of the xerogel assuming spherical, non-porous primary particles, would indicate a primary particle diameter of $\approx$5 nm from a surface area of 500 $m^2\ g^{-1}$. This is consistent with the observations in Fig. 5(b).

Conclusions

Prehydrolysis of TEOS by stirring at room temperature produced more homogeneous gels than refluxing. All of the powders contained significant amounts of residual organic compounds, which were reduced slightly by increasing the time of prehydrolysis. Ageing the gels had little effect on the surface areas or homogeneity of the powders. Intimate mixing of the precursors gave rise to the crystallization of forsterite at temperatures as low as 770°C. However, the presence of crystalline MgO after heat treatments indicated a degree of non-homogeneity. It is expected that the temperature of crystallization could be reduced further if a method of producing a more fully homogeneous gel of $2MgO{\cdot}SiO_2$ could be developed.

Acknowledgments

This work was jointly funded by the EPSRC and Zortech International.

References

1. A. Kazakos, S. Komarneni, and R. Roy, Materials Letters **9**, 405 (1990).
2. N.P. Bansal, Journal of the American Ceramic Society **71**, 666 (1988).
3. J.M. Burlitch, M.L. Beeman, B. Riley, and D.L. Kohlstedt, Chemistry of Materials **3**, 692 (1991).
4. D.G. Park, M.H.E. Martin, C.K. Ober, and J.M. Burlitch, Journal of the American Ceramic Society **77**, 33 (1994).
5. T. Lopez, M.E. Llanos, J. Navarrete, I. Schifter, P. Salas, and R. Gomez, Journal of Sol-Gel Science and Technology **8**, 321 (1997).
6. M.E. Llanos, T. Lopez, and R. Gomez, Langmuir **13**, 974 (1997).

Journal of Sol-Gel Science and Technology 13, 365–369 (1998)
© 1998 Kluwer Academic Publishers. Manufactured in The Netherlands.

Room Temperature Densification of Aerogel by Isostatic Compression

A. HAFIDI ALAOUI
Faculté des Sciences et Techniques de Tanger, B.P. 416, Tanger, Maroc

T. WOIGNIER AND J. PHALIPPOU
Laboratoire des Verres, UMR 5587 Université Montpellier II, Place E. Bataillon, 34095, Montpellier Cedex, France

G.W. SCHERER
Civil Eng. & Operations Res., Princeton University, Princeton, NJ 08544, USA

Abstract. An alternative to the sintering process in densifying aerogels is the compaction by isostatic compression at room temperature. A porosimeter is used to compress the aerogel and to measure the amplitude of the shrinkage. We focus our study on the time dependent mechanisms such as densification kinetics and relaxation effects. These two mechanisms respectively increase or decrease the total densification.

The densification kinetics is followed by the evolution of the volumetric shrinkage and stiffening with time. Hydroxylated and esterified aerogels show almost the same shrinkage evolution but the hydroxylated aerogels stiffen during compaction while the elastic bulk modulus of esterified aerogels decreases. Shrinkage is due to two opposing mechanisms: formation of new siloxane bonds that freeze the strained network, but also breakage of links between clusters which allows the restructuring of the solid phase.

Relaxation is caused by the disentanglement of the clusters when the pressure is released (40% of the shrinkage can be recovered). However, if during the compression run a large quantity of siloxane bonds are formed, relaxation is not observed.

Keywords: aerogel, elastic properties, plasticity

1. Introduction

Owing to their large compliance, when subjected to isostatic pressure aerogel networks deform irreversibly. Previous work has shown that this phenomenon can be easily studied using mercury porosimetry [1–3] which provides the shrinkage amplitude and also the elastic modulus (K) of the network.

The main parameters of this densification by compression are the elastic properties of the solid and the pore volume but also the silanol content. Previous work [2] has shown that the replacement of the organic species by silanols amplifies the densification and the stiffening. This shows clearly that the condensation reaction of silanols are partly responsible for the irreversible shrinkage.

We attribute the plastic shrinkage to three types of mechanisms. First, the rearrangement of the clusters by breakage of links between them; second the freezing of the strained structure by formation of siloxane bonds, and third, a relaxation effect. This relaxation effect has been recently observed [4] and has been attributed to the entanglement of the clusters under pressure. When the pressure is released the disentanglement which requires structural changes (like random cleavage of bonds or frictional effects associated with steric hindrance) on the microscopic scale is time dependent.

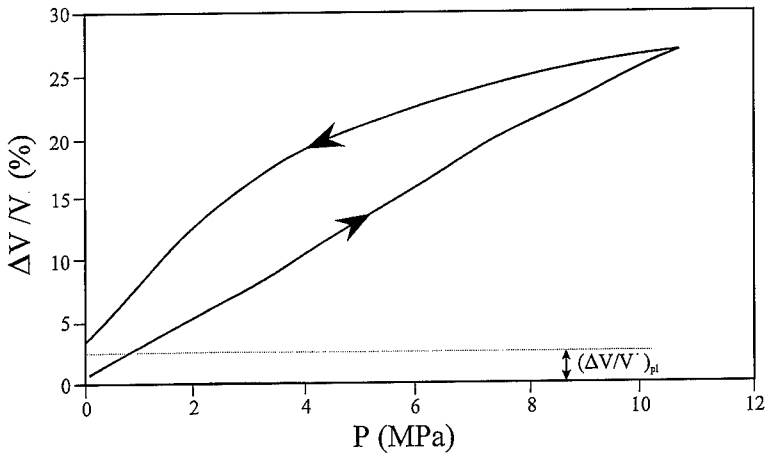

Figure 1. Strain $\Delta V/V$ versus P for the B40 sample.

The densification by compaction at room temperature is thus affected by this relaxation that modifies the final density of the compressed aerogel. To control and limit this effect, we propose to increase the links between clusters by varying the time of reaction (silanol condensation) at a given pressure. For this purpose the densification kinetics of aerogels will be characterized by the time evolution of the volume shrinkage and bulk modulus.

2. Experimental

Silica gels used in this study were made from tetramethoxysilane (TMOS, Fluka Chemical, grade assay 98%, cat No. 87682) hydrolyzed under basic conditions (10^{-2} M NH_4OH). The molar ratio of the hydrolyzing solution to TMOS was equal to 4. Ethanol (R.P. Normapur Analytical Reagent, 99.85%) was used as solvent. The TMOS constitutes 46 vol% of the total solution (designated as B40). The TMOS-ethanol solution was stirred and aged one week at room temperature.

According to a procedure previously reported [5], the alcogels were transformed into aerogels by supercritical drying. The conditions of the supercritical drying were 305°C and 13 MPa. As-prepared aerogels are oxidized by a heat treatment in air at 350°C for 15 h. The samples are labelled B40 OX; OX represents the oxidative heat treatment in air.

Isostatic compression experiments were done using a Hg porosimeter (Carlo Erba porosimeter 2000) on outgassed monolithic aerogels. Hg pressure can be varied from 0.1 to 200 MPa [2, 4].

3. Results

Figure 1 shows the typical curve which is obtained on the samples between 0.1 MPa and 25 MPa. $\Delta V/V$ corresponds to the volumetric strain in percent. The sample volume shrinks with pressure, but when the pressure is released the sample dilates partially and the volume after depressurization is lower than the initial value.

This curve gives us the plastic shrinkage just after the pressure release. If the applied pressure increases, this shrinkage is enhanced and Fig. 2 shows the evolution

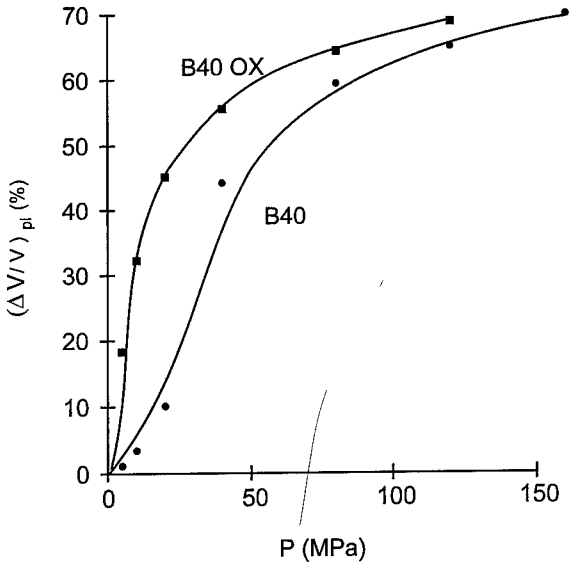

Figure 2. Effect of oxidation treatment on the plastic shrinkage $(\Delta V/V)_{pl}$ versus P for samples with 40% TMOS concentration.

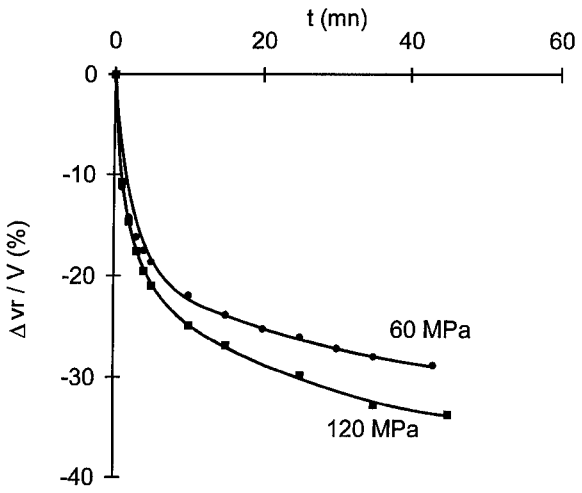

Figure 3. Relaxation effect for B40 after pressure release versus time. $\Delta V_r/V$ is the relative expansion during relaxation. The two curves correspond to two pressure runs 60 and 120 MPa. At $t=0$, $\Delta V_r/V=0$.

of the irreversible strain as a function of the applied pressure for the B40 and the B40 OX. Figure 2 shows clearly that the oxidation treatment favors the volumetric shrinkage at low pressure. In that case, the arms of the clusters are chemically active. They may react if silanol groups are close enough to condense, leading to the freezing of the strained structure. Figure 2 corresponds to the plastic shrinkage just after the pressure release. As mentioned in Section 1, after the pressure release samples expand, corresponding to a delayed elastic effect.

Figure 3 shows that the relaxation is very fast. One hour after the pressure release the shrinkage has lost 30–35% of its magnitude. On the B40 sample, the two curves corresponding to 60 MPa and 120 MPa compression runs show that the relative expansion is higher for the 120 MPa compressed sample, owing to its larger volumetric shrinkage compared to the sample compressed at 60 MPa (Fig. 2).

Table 1 underlines the effect of the OH content on the relaxation effect. To explain this difference we can assume that the lower expansion of the B40 OX is related to its more connected network.

Table 1. The bulk density evolution after a 120 MPa compression run (ρ_c) and the relaxation step (ρ_r).

Sample	Initial bulk density, ρ_i (g/cm^3)	ρ_c	ρ_r
B40	0.21	0.61	0.53
B40 OX	0.21	0.66	0.63

4. Discussion

The strong influence of the oxidizing heat treatment on the further relaxation effect indicates the role of the siloxane bond formation. To confirm this assumption we investigated the kinetics of densification at a given pressure. In Fig. 4, we plot the time evolution of the relative volumetric shrinkage at 10 MPa. For B40 and B40 OX, the evolution is quite similar and low. After 2 hours at 10 MPa, the shrinkage gain is less than 2%. Thus, it is tempting to conclude that the network evolves slightly with time regardless of surface chemistry. However, as mentioned in Section 1 the porosimeter data give also information on the bulk elastic modulus. As mercury cannot penetrate the pores, pressure increase induces an isostatic pressure on the aerogel. In the elastic (reversible) part of the curve, the volumetric strain is due to its compressibility. Thus, the slope of the curve at low pressure is related to the elastic bulk modulus $K(P)=-V(P)(dP/dV)$, where $V(P)$ is the volume of the sample at the pressure P [2–4]. In the elastic region, $K=$ constant. The time evolution of the bulk modulus will characterize the connectivity change in the solid network.

Figure 5 shows the curves $\Delta K/K$ as a function of time for the samples B40 and B40 OX at 10 MPa ($\Delta K/K$ corresponds to the relative increase with time of the elastic bulk modulus). The data prove clearly that in the case of the esterified sample (B40) shrinkage is accompanied by a weakening of the network. The bulk modulus which is 7 MPa at $t=0$, shows a 25% decrease. For the same shrinkage, B40 OX stiffens by 30%, the bulk modulus being 30 MPa at $t=0$.

These results confirm that during the compression runs, two opposing phenomena exist. First, the breakage of siloxane bonds which allows the moving of the clusters and the restructuring. Second because clusters interpenetrate, the formation of links by silanol condensation is possible.

The change in network connectivity (measured by the K evolution) is the result of the competition between these two mechanisms. For esterified aerogels (B40) densification is due to the action of pressure which forces clusters to interpenetrate, but only a few siloxane bonds are created at this pressure. On the other hand, for B40 OX, owing to the large silanol content, the formation of new siloxane bonds largely compensates for the cleavage of some of them.

The further relaxation effect is also a consequence of this competition. In the case of B40, pressure forces the clusters to interpenetrate but strained clusters are

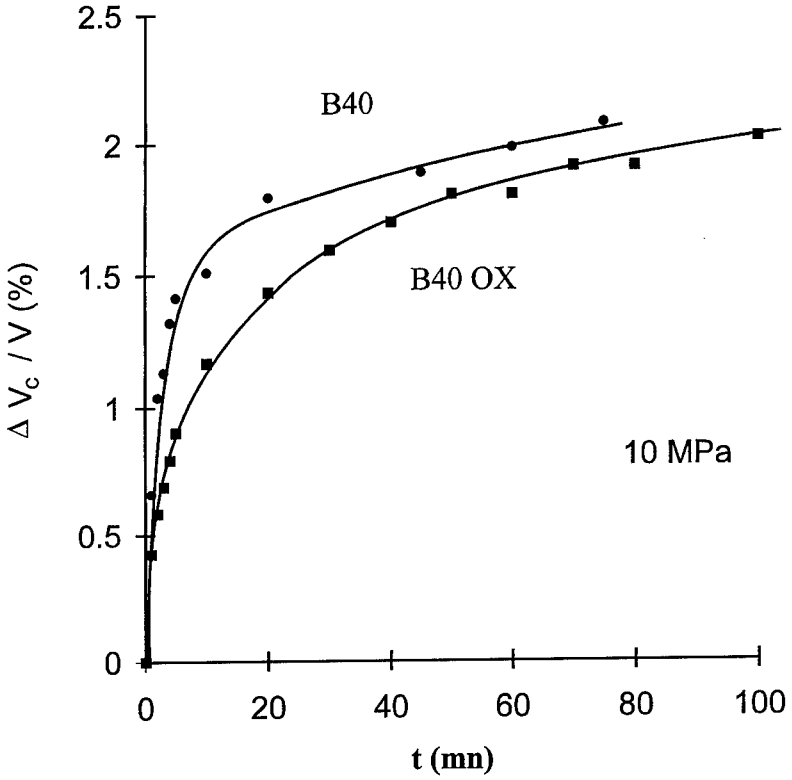

Figure 4. Densification kinetics for samples B40 and B40 OX at 10 MPa. $\Delta V_c/V$ is the relative shrinkage during the step time. At $t=0$, $\Delta V_c/V=0$.

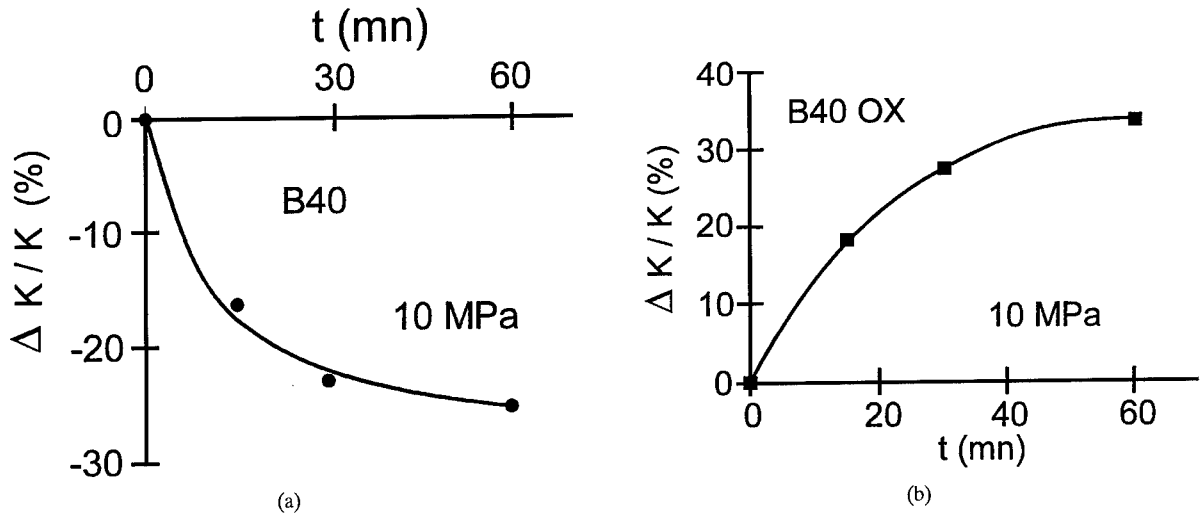

Figure 5. Relative stiffening $\Delta K/K$ versus time for samples: (a) B40, (b) B40 OX at 10 MPa at $t=0$, $\Delta K/K=0$.

poorly linked. During the pressure release the network tends to reduce its strain and consequently expands. The disentanglement is time dependent because of the friction effect within the solid. For the B40 OX aerogel, the clusters strained by the pressure are stuck to each other by the formation of new links. When the pressure decreases the high K value limits the expansion of the sample.

This analysis shows that, if the B40 OX is compressed with a step time at a given pressure, the relaxation effect will be lowered compared to the same experiment without the step time. So after a 120 MPa pressure cycle with a 5 hours step time the bulk density increases from 0.21 to 0.66 g/cm^3. The step time does not increase the ρ_c value (cf. Table 1) but after one week of relaxation ρ_r is still higher than 0.65 g/cm^3.

5. Conclusion

The volumetric shrinkage observed after a compression run can be partially annulled by a relaxation effect which expands the network. The reason for this expansion is the disentanglement of the clusters which has been constrained by the isostatic pressure. The reticulation increase by the formation of siloxane bonds acts as a glue between the constrained clusters. The sticking between the clusters is favored by a preliminary oxidation heat treatment which transforms the organic groups into reactive species (silanol), and a step time under pressure which amplifies the reticulation. The condensation reaction causes stiffening of the network. In this case the relaxation effect can be reduced and the final density is close to that measured just after the pressure release.

References

1. R. Pirard, S. Blacher, F. Brouers, and J.P. Pirard, J. Mater. Res. **10**, 1 (1995).
2. L. Duffours, T. Woignier, and J. Phalippou, J. Non-Cryst. Solids **186**, 321 (1995).
3. G.W. Scherer, D.M. Smith, X. Qiu, and J. Anderson, J. Non-Cryst. Solids **186**, 316 (1995).
4. T. Woignier, L. Duffours, I. Beurroies, J. Phalippou, P. Delors, and V. Gibiat, J. Sol-Gel Sci. Tech. **8**, 781 (1997).
5. J. Phalippou, T. Woignier, and M. Prassas, J. Mater. Sci. **25**, 3111 (1990).

Journal of Sol-Gel Science and Technology 13, 371–377 (1998)
© 1998 Kluwer Academic Publishers. Manufactured in The Netherlands.

Structures, Properties and Potential Applications of Ormosils

JOHN D. MACKENZIE AND ERIC P. BESCHER
Department of Materials Science and Engineering, School of Engineering and Applied Science, University of California, Los Angeles, CA 90095-1595, USA

Abstract. Ormosils are organic-inorganic hybrid solids in which the organic component may be chemically bonded to a silica matrix. Somewhat similar to inorganic silicate glasses, the structure of the silica network can be modified by the presence of organic groups. The resulting properties of the Ormosils are then governed by the type and concentration of organics used. Examples are presented in which the mechanical, electrical and optical properties of selected Ormosils can be influenced by organic groups. For instance, small amounts of polydimethylsiloxane (PDMS) added to a solution of TEOS will give an Ormosil about ten times harder than the hardest organic polymer. Larger amounts of PDMS (20%) will now yield an Ormosil which is as rubbery as organic rubber. Ormosils in which the organic and inorganic constituents are covalently bound to each other are the focus of this critical review. The potential applications of such Ormosils are discussed.

Keywords: Ormosils, review, applications, rubbery Ormosils

1. Introduction

One of the attractive features of the sol-gel process is that it enables the preparation of numerous types of new organic-inorganic hybrid materials which are either impossible or are extremely difficult to synthesize by any other process. There are three ways to prepare such hybrids [1]. The first method involves the dissolution of an organic, such as a dye molecule in a sol-gel solution, e.g., TEOS in alcohol. On gelation the dye molecule is trapped in the porous silica matrix [2]. It is assumed that no chemical reactions have occured between the two constituents. In the second method, an organic solution is impregnated into a porous oxide gel. The organic phase is then solidified, for instance via polymerization, and a nanocomposite is formed as has been shown for PMMA in silica [3]. No chemical bonds usually exist between the organic and inorganic phases. In the third approach, the inorganic precursor either already has a chemically bonded organic group (for instance, $CH_3Si(OCH_3)_3$ or reactions occur in the liquid solution between the two components to form chemical bonds in the hybrid gel. The most common system in this class of hybrids is that of PDMS (polydimethylsiloxane) and TEOS [4, 5]. All these can be termed "Ormosils," that is, organically modified silicates. This report will be concerned with only the third type of Ormosils, namely, those in which chemical bonds exist between the organic and inorganic phases.

Since the pioneering research of Schmidt [4] and Wilkes [5] in 1985, more than 400 publications on this third type of Ormosil have appeared. The reason for such a level of activity is presumably twofold. One is that since these constitute a truly new family of materials, the synthesis of more and more new materials and the understanding of the reactions in solution and structures of the new hybrids are sufficient justification for the research. The other reason is that these new materials are predicted or expected to have uniquely useful properties and/or are less costly than existing materials to produce. Many of the more recent contributions have come from chemists and organic polymer scientists. It is evident that their increasing collaboration with the ceramists, who have been most active in the development of sol-gel science and technology, will now become necessary for the growth of science and technology of these new hybrid materials. The objective of this critical review is to present a

summary of the current status of these new materials including structures, important properties and potential applications.

2. New Materials and Structures

The simplest class of Ormosils are those formed from precursors such as $RSi(OCH_3)_3$ where R is an organic terminal group which does not form a bridge in the three-dimensional gel network (Fig. 1-A). Alternatively, one can start with $R_2Si(OCH_3)_2$ and mix in TEOS [6]. Thus, the subsequent 3D SiO_2 network will have a controllable number of terminal CH_3 groups. Such precursors with a more complex R group are exemplified by the molecule triethoxysilylpropyl 2,4-dinitrophenylamine (TDP, in short) shown in Fig. 1-B. The organic group is now optically active. Gels can be formed by mixing TDP with TEOS [7]. Other inorganic groups such as nanocrystals of the ferroelectric $BaTiO_3$ can also be contained in the SiO_2 resulting in even more interesting new gels for the study of organic-inorganic interactions [8]. The polyhedral oligomeric silsesquioxanes (POSS) are another new family of hybrids, a monomeric precursor of which is shown in Fig. 1-C. R is a non-reactive end group whereas Y is functionalized for polymerization [9]. Not only numerous new Ormosils of this family have been synthesized, but also POSSs have been blended with other organic polymers such as PMMA to produce yet larger number of new materials. Such cubic silsesquioxanes can be thought of as the smallest silica particles possible. Another family of somewhat different polysilsesquioxanes are the arylene-, alkylene- and

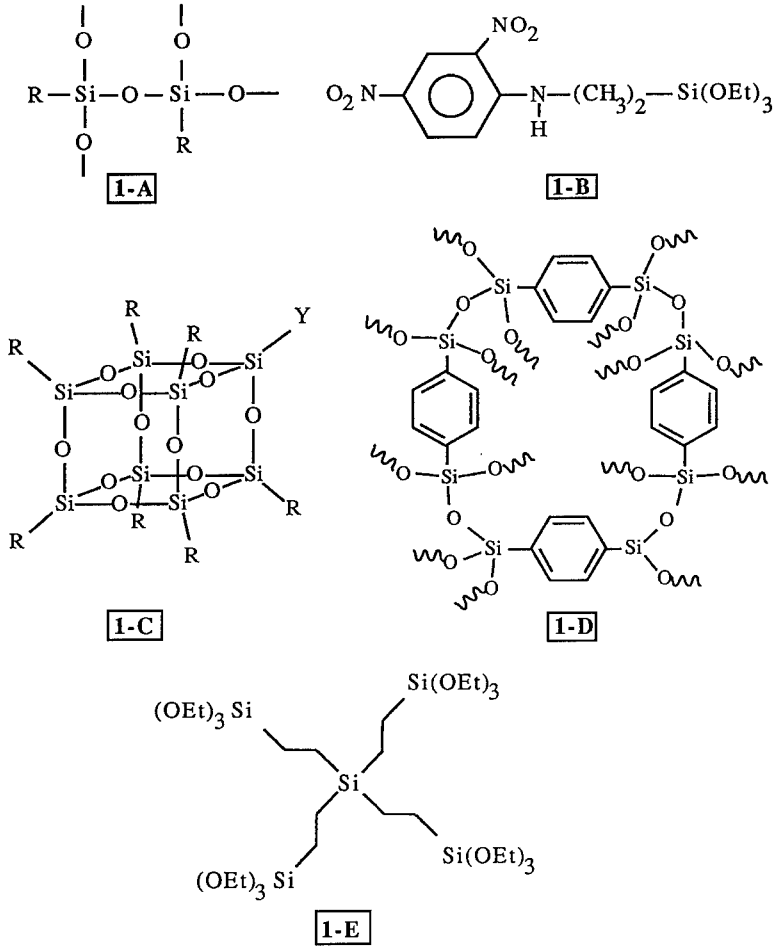

Figure 1. Examples of structures of Ormosils where the organic and inorganic constituents are chemically bonded.

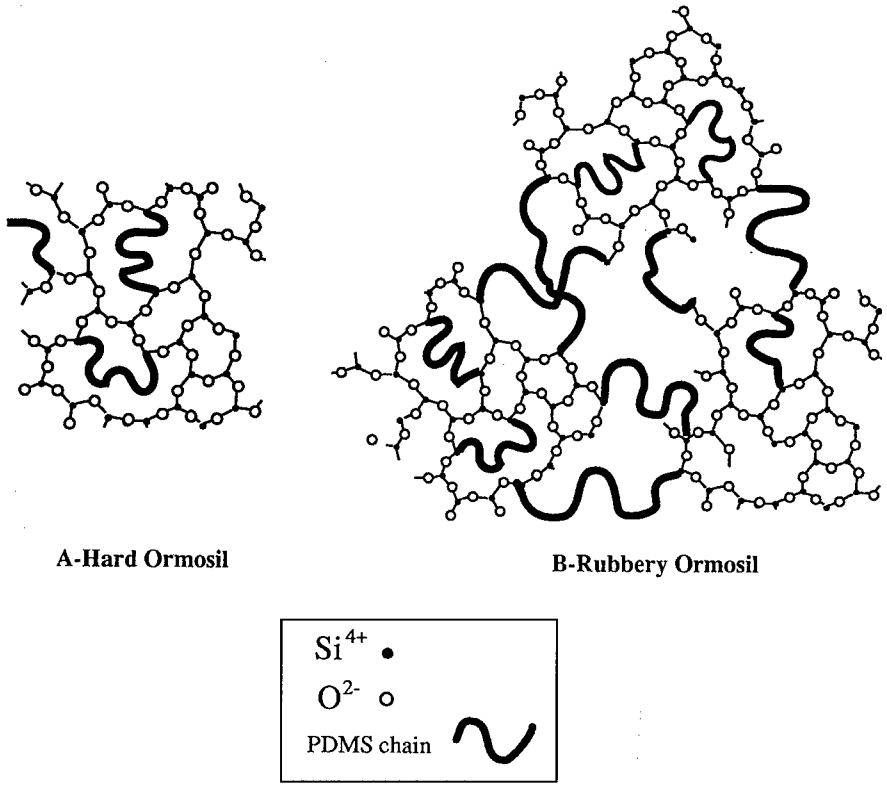

Figure 2. Proposed structures of SiO_2-PDMS hybrids for low (A) and high (B) PDMS content.

phenylene-bridged polymers, one example of which is shown in Fig. 1-D [10]. The phenylene group can form two as well as three bridges and can also be substituted by thiophene rings or chains to give numerous different materials. Yet another new family of Ormosils are the "star gels" [11]. These are formed from polyfunctional network precursors with a number of flexible arms radiating from a common atomic, linear or cyclic core and terminating in trialkoxysilane groups. The atomic core-type precursor is shown in Fig. 1-E. The original two component systems involving TEOS and OH-terminated PDMS chains first studied by Schmidt and Wilkes in 1985 have been re-examined in greater details in the present authors' laboratory. It is hypothesized that TEOS and small concentrations of PDMS react in solutions to form gels with a porous three-dimensional network as depicted in Fig. 2(A). The continuous Si—O—Si linkages continue to dominate the character of the gel. However, when the PDMS content increases, the structure consists of silica clusters linked by flexible PDMS chains as represented by Fig. 2(B). Somewhat similar to the inorganic silicate glasses the random network of the silica is now "modified" by the PDMS. Some of the properties, especially the mechanical properties, are now drastically altered. Many other new Ormosils have recently been reported in the Symposium "Better Ceramics through Chemistry VII: Organic/Inorganic Hybrid Materials" [12]. There are too many for inclusion in this short review. In general, most of the research reported has been in synthetic chemistry; frequently the precursors to Ormosils are not commercially available; materials characterization and testing are minimal. Utilization of many of these new Ormosils is clearly far into the future. We will select a few of those with interesting properties for discussion in the next section.

3. Some Important Properties

The most undesirable property of inorganic oxide gels is undoubtedly their brittleness. This, plus the high porosity usually accompanying gelation result in mechanically weak solids which can create great difficulties in subsequent densification or in the utilization of the porous gel after drying. The hitherto unsuccessful exploitation of the 99% porosity of the aerogels is

primarily due to their fragility. Clearly then, perhaps the apparent decrease of brittleness when the silica is modified by an organic would be one of the most important advantages of Ormosils. The presence of organic groups would unfortunately limit the use of Ormosils at elevated temperatures. Of course, if the Ormosils are to be used at ambient temperatures the problem of thermal stability no longer exists. One must now question the advantages of Ormosils, if any, over organic polymers.

Rubbery Behavior. It has been shown that in the PDMS-SiO_2 system, when the PDMS content exceeds about 30 wt%, the gel becomes rubbery. The resilience of rubbery Ormosils is similar to that of common organic rubbers and the densities are usually lower [13]. The structure shown in Fig. 2(B) suggests that further cross-linking under ambient conditions is unlikely and together with the high SiO_2 content would limit their environmental deterioration. However, rubbery Ormosils, at the present stage of their development possess relatively low tensile strengths because of the shortness of the PDMS chains linking the silica clusters, although their compressive modulus is comparable to that of common rubbers.

Hardness. When the PDMS content of Ormosils is less than about 10 wt% the Vickers Hardness of bulk samples is approximately 150 kg/mm^2 compared to the 25 kg/mm^2 value of the hardest organic plastics [14]. Since these hard Ormosils are prepared at room temperature and they are colorless and transparent they can possibly be useful as optical materials.

Optical Properties. Ormosils, similar to the inorganic oxide gels, can be the matrix for organic dyes and biological materials. One of their advantages would be their lower brittleness which makes the fabrication of samples easier. This area of investigation is still in its infancy. Ormosil matrices in which the organic is optically inactive have been investigated as matrices for rare-earth luminescence. The hydrophobicity and lower hydroxyl content was beneficial to radiation lifetimes [15, 16]. However, it was also determined that Ormosil matrices cause clustering of the rare-earth, resulting in lifetime decrease [17]. As far as optically active organics are concerned, the previous focus on "encapsulated" dyes has shifted to matrices of the type $RSiO_{3/2}$, where R is optically active. The shift in interest is due to the limitations of the encapsulation approach and the versatility of the "graft" approach. Such systems are ideal for the study of interactions between organic and inorganic moieties. Table 1 contains a list of some typical systems. For example, TDP-silica solutions containing certain alkali ions give yellow colored

Table 1. Examples of Ormosils in which organic and inorganic constituents are covalently bound.

	Potential applications	Reference
Organic as network modifier		
Triethoxysilyl 2,4 dinitrophenylaminosilane	NLO, organic/organic interactions	[7, 27]
Coumarin dyes	Solid state lasers	[41]
Carboxylate	White phosphors	[22]
ICTES-Red 17	NLO	[20]
DR1, DR17, DY7 dyes	Optical storage	[21]
Carbazole	Photorefractive materials	[19]
EDTA	Chromium removal from solution	[24]
Aminopropyltriethoxysilane	SO_2 sensor	[25]
CH_3	O_2 sensor	[23]
Perfluoroaryl silane	Low optical loss in the near IR loss	[42]
Low hydroxyl $(CH_3)_2SiO$	Rare-earth luminescence	[16]
Methacrylate-functionalized POSS	New copolymers	[9, 43]
Organic as network former		
SiO_2-PTMO	Flexible coating	[44]
SiO_2-Polyimide	Coating material	[45]
TEOS-PDMS	Organic/inorganic rubber	[13]

gels whereas those with some alkaline-earth ions are red due to the interactions of the metallic ions with the TDP. Such interactions have been observed by other researchers [18]. Photorefractive films with second-harmonic coefficients of 100 pm/V have been fabricated [19]. When grafted onto a siloxane network, the Red-17 dye gives a d_{33} value of 90 pm/V [20]. Optical storage has also been demonstrated in substituted azobenzene molecules grafted onto silica [21]. A recent report indicates that silicate-carboxylate gels exhibit phosporescent properties without metal activator ions [22]. Although no commercial applications have emerged, there is a consensus among researchers that optics is one of the most promising fields for applications of Ormosils.

Sensors, Corrosion Protection. The properties of grafted R groups can be exploited for sensing purposes. MacCraith et al. [23] used CH_3 groups as O_2 sensors. Recent work in the authors' laboratory has shown that when ethylenediamine tetraacetic acid (EDTA) is grafted onto silica, heavy metals such as Cr can be chelated within the gel [24]. If the EDTA molecule is not grafted, chelation occurs but the EDTA-Cr complex leaches out , and the gel cannot be used as a filter. This directly illustrates the usefulness of the grafting approach. Aminopropyltriethoxysilane (APTES) has been used for SO_2 detection via adsorption on the amine [25]. Ormosils have also been proposed as anticorrosion coatings [26] but such work is still very qualitative. Comparative studies with polymer coatings are needed.

Structural Investigations, Porosity, Phase Separation. The basic thermodynamic difference between organic and inorganic networks prompts researchers to investigate the homogeneity of hybrids and the extent of phase separation. Some indirect structural information such as T_g is available, abeit rare. For example, the T_g of the TDP-SiO_2 system increases from 60 to 80°C as the SiO_2 molar fraction increases from 0 to 60% [27]. Techniques such as NMR provide direct information on first neighbour environment. For example, ^{17}O NMR has shown that dimethyldiethoxysilane and TEOS cocondense to a large extent, leading to good homogeneity in such hybrids [28]. However, if TEOS is replaced with another metal alkoxide $M(OR)_x$, phase separation tends to occur, as Si—O—M bonds are unstable in these sytems [29]. Little is known of the structure of Ormosils beyond the first neighbor range of NMR. Scattering techniques such as LS and SANS may help, but much remains to be done in this domain. An original use of the segregation of organic and inorganic components is the use of organics as templates for the control of porosity. Corriu et al. [30] made silica with a pore structure reflecting the nature of the organic removed.

4. Potential Applications

In practically every published article in the field of sol-gel science and technology there is mention of potential applications for the materials under investigation. This is also the case for Ormosils. It is impossible to review all the "claims" and hence this section is selective by necessity. In 1984, Schmidt first discussed the potential applications of Ormosils [31] and since then has contributed more than anybody else towards the development of Ormosils as useful materials. Examples include new contact lenses, scratch resistant coatings [31], laser photopatternable components for optics [32], hosts for semiconductor quantum dots, organic dyes and metallic colloids [33], second-order nonlinear optically active nanocomposites, Fresnel lenses [34], photochromic coatings [35], porous solvent absorbers [36] and GRIN optical components [37]. Some other recent suggestions of potential applications are discussed below.

Hard Coatings. A variety of Ormosil coatings have been coated on the organic plastics Lexan and CR-39 and their abrasion resistance measured by the Taber abrasion test [38, 39]. After each abrasion cycle the optical transmission of the samples was measured. Typically, after 500 cycles, the transmission of the uncoated samples would decrease by about 27% whereas those with a 4 μm coating would decrease by 5–10%. It seems likely that this potential application will lead to improved transparent organic plastics for ophthalmic lenses and possibly even for automotive windows.

Aeromosils. It has been mentioned above that the utilization of aerogels as thermal insulation is curtailed by their fragility. Ormosil-based aerogel, or "Aeromosils," with porosity in excess of 97%, have been prepared which are rubbery [40]. Cylindrical samples of 1 cm diameter have been subjected to linear compression of 30% without fracture. If the process cost can be decreased Aeromosils will undoubtedly find practical applications.

Optical and Sensing Applications. Commercial applications of Ormosils in the field of optics have not emerged yet, but many new materials have been proposed and show interesting properties. Among those are waveguides, high near-IR transmission materials [42], GRIN materials [46], photorefractive coatings [19, 47]. The field is one of the most promising for Ormosil films and coatings.

Because of the number of claimed potential applications, it is difficult to distinguish between truly promising materials and mere laboratory curiosities. Ultimately, the technology will succeed on its true merits, not on claims of potential applications. Many of the proposed potential applications are unlikely to pass the first hurdles of commercial development. For example, it is not known if anticorrosion Ormosil coatings compare well with polymer coatings, since adhesion, thermal expansion and porosity have not really been evaluated. To some extent, such haste is an inherent flaw of our interdisciplinary field. It would be beneficial to be more rigorous in claims of potential applications. As for those truly promising applications, they face the challenge of the frequent inadequacy, and at times ineptness of technology transfer mechanisms between university and industry. They hamper commercialization of the most promising laboratory discoveries. A new funding-research-technology transfer paradigm is needed.

5. Summary and Conclusions

Since 1985, over 400 publications on hybrids have appeared. Many new Ormosils have been reported. The bulk of the work is concerned with chemical synthesis and short range structural investigations such as NMR. Characterization of the materials synthesized is frequently incomplete. Despite claims of potential applications, the only truly promising to date appear to be Ormosil scratch resistant coatings on organic plastics. The collaboration of chemists, polymer scientists and ceramic engineers will be necessary if new applications are to be developed in the future.

Acknowledgments

The authors are grateful to the Air Force Office of Scientific Research for the support of this work under Grants F49620-94-1-0071 and F49620-94-1-0339.

References

1. J.D. Mackenzie, J. Sol-Gel Sci. Tech. **2**, 81 (1994).
2. D. Avnir, D. Levy, and R. Reisfeld, J. Phys. Chem. **88**, 5956 (1984).
3. E.J.A. Pope, A. Asami, and J.D. Mackenzie, J. Mater. Res. **4**,1018 (1989).
4. G.L. Wilkes, B. Otter, and H. Huang, Polymer Prep. **26**, 300 (1985).
5. H. Schmidt, J. Non-Cryst. Solids **73**, 681 (1985).
6. F. Babonneau, C. Toutou, and S. Gavériaux, J. Sol-Gel Sci. Tech. **8**, 553–556 (1997).
7. E.P. Bescher, E. Hong, Y.-H. Xu, and J.D. Mackenzie, in *Better Ceramics through Chemistry VII: Organic/Inorganic Hybrid Materials*, edited by B.K. Coltrain, C. Sanchez, D.W. Schaefer, and G.L. Wilkes (Materials Research Society Symposium Proceedings, Vol. 435, Pittsburgh, PA, 1996), p. 605.
8. E.P. Bescher, Ph.D. Thesis, University of California, Los Angeles (1996).
9. J.D. Lichtenhan, C.J. Noel, A.G. Bolf, and P.N. Ruth, in *Better Ceramics through Chemistry VII: Organic/Inorganic Hybrid Materials*, edited by B.K. Coltrain, C. Sanchez, D.W. Schaefer, and G.L. Wilkes (Materials Research Society Symposium Proceedings, Vol. 435, Pittsburgh, PA, 1996), p. 3.
10. J.H. Small, K.J. Shea, and D.A. Loy, J. Non-Cryst. Solids **160**, 234 (1993).
11. K.G. Sharp and M.J. Michalcyzk, MRS Symp. Proc. **435**, 105 (1996).
12. *Better Ceramics through Chemistry VII: Organic/Inorganic Hybrid Materials*, edited by B.K. Coltrain, C. Sanchez, D.W. Schaefer, and G.L. Wilkes (Materials Research Society Symposium Proceedings, Vol. 435, Pittsburgh, PA, 1996).
13. J.D. Mackenzie, Q. Huang, and T. Iwamoto, J. Sol-Gel Sci. Tech. **7**, 151 (1996).
14. T. Iwamoto and J.D. Mackenzie, J. Sol-Gel Sci. Tech. **4**, 141 (1995).
15. N.I. Koslova, B. Viana, and C. Sanchez, J. Mater. Chem. **3**(1), 111–112 (1993).
16. S.K. Yuh, E.P. Bescher, F. Babonneau, and J.D. Mackenzie, Sol-gel Optics III, SPIE Proc. (1995).
17. B.T. Stone and K.L. Bray, in *Better Ceramics through Chemistry VII: Organic/Inorganic Hybrid Materials*, edited by B.K. Coltrain, C. Sanchez, D.W. Schaefer, and G.L. Wilkes (Materials Research Society Symposium Proceedings, Vol. 435, Pittsburgh, PA, 1996), pp. 617–622.
18. B. Lebeau, Ph.D. Thesis, U. Pierre et Marie Curie, Paris.
19. F. Chaput et al., in *Better Ceramics through Chemistry VII: Organic/Inorganic Hybrid Materials*, edited by B.K. Coltrain, C. Sanchez, D.W. Schaefer, and G.L. Wilkes (Materials Research Society Symposium Proceedings, Vol. 435, Pittsburgh, PA, 1996), pp. 583–588.
20. B. Lebeau et al., in *Better Ceramics through Chemistry VII: Organic/Inorganic Hybrid Materials*, edited by B.K. Coltrain, C. Sanchez, D.W. Schaefer, and G.L. Wilkes (Materials Research Society Symposium Proceedings, Vol. 435, Pittsburgh, PA, 1996), pp. 395–401.
21. Chaput et al., J. Sol-Gel Sci. Tech. **2**, 779–782 (1994).
22. W.H. Green, K.P. Le, J. Grey, T.T. Au et al., Science **276**(5320), 1826–1828 (1997).

23. B.D. Mac Craith et al., J. Sol-Gel Sci. Tech. **8**, 1053–1061 (1997).
24. Kris S. Oka, M.S. Thesis, 1997.
25. J. Lin, S. Moller, and E. Obermeir, Sensors and Actuators B, 219–221 (1991).
26. M. Pilz and H. Romich, J. Sol-Gel Sci. Tech. **8**, 1071–1075 (1997).
27. B. Lebeau, J. Maquet et al., J. Mat. Science **7**(6), 989–995 (1997).
28. F. Babonneau, C. Toutou, and S. Gaveriaux, J. Sol-Gel Sci. Tech. **8**, 553–556 (1997).
29. L. Delattre, M. Roy, and F. Babonneau, J. Sol-Gel Sci. Tech. **8**, 567–570 (1997).
30. P. Chevalier et al., J. Sol-Gel Sci. Tech. **8**, 603–607 (1997).
31. H. Schmidt and H. Wolter, J. Non-Cryst. Solids **121**, 428 (1990).
32. G. Philipp and H. Schmidt, J. Non-Cryst. Solids **63**, 283 (1984).
33. H. Schmidt, SPIE Proc. **1758**, 396 (1992).
34. P.W. Oliveira, H. Krug, H. Kunstle, and H. Schmidt, SPIE Proc. **2288**, 554 (1994).
35. L. Hou, M. Mennig, and H. Schmidt, SPIE Proc. **2288**, 328 (1994).
36. V. Gerhard, H. Schmidt, and U. Dreier, MRS Symp. Proc. **435**, 455 (1996).
37. P.W. Oliveira, H. Krug, P. Muller, and H. Schmidt, MRS Symp. Proc. **435**, 553 (1996).
38. J. Wen, V.J. Vasudevan, and G.L. Wilkes, J. Sol-Gel Sci. Tech. **5**, 115 (1995).
39. J. Wen, K. Jordens, and G.L. Wilkes, in *Better Ceramics through Chemistry VII: Organic/Inorganic Hybrid Materials*, edited by B.K. Coltrain, C. Sanchez, D.W. Schaefer, and G.L. Wilkes (Materials Research Society Symposium Proceedings, Vol. 435, Pittsburgh, PA, 1996), p. 207.
40. S.J. Kramer, F. Rubio-Alonso, and J.D. Mackenzie, in *Better Ceramics through Chemistry VII: Organic/Inorganic Hybrid Materials*, edited by B.K. Coltrain, C. Sanchez, D.W. Schaefer, and G.L. Wilkes (Materials Research Society Symposium Proceedings, Vol. 435, Pittsburgh, PA, 1996), p. 295.
41. T. Suratwala, Z. Gardlund, and K. Davidson et al., J. Sol-Gel Sci. and Tech. **8**, 973–978 (1997).
42. C. Roscher and M. Popall, in *Better Ceramics through Chemistry VII: Organic/Inorganic Hybrid Materials*, edited by B.K. Coltrain, C. Sanchez, D.W. Schaefer, and G.L. Wilkes (Materials Research Society Symposium Proceedings, Vol. 435, Pittsburgh, PA, 1996), pp. 547–552.
43. J. Lichtenham, Y. Otonari, and M. Carr, Macromolecules **28**, 8435–8437 (1995).
44. H.H. Huan, G.L. Wilkes, and J.G. Carson, Polymer **30**, 2001 (1989).
45. A. Morikawa, Y. Iyoku, M. Kakimoto, and Y. Imai, J. Mater. Chem. **2**(7), 679 (1997).
46. P.W. Oliveira, H. Krug, P. Müller, and H. Schmidt, in *Better Ceramics through Chemistry VII: Organic/Inorganic Hybrid Materials*, edited by B.K. Coltrain, C. Sanchez, D.W. Schaefer, and G.L. Wilkes (Materials Research Society Symposium Proceedings, Vol. 435, Pittsburgh, PA, 1996), pp. 553–558.
47. R. Burzynski, S. Ghosal, M.Casstevens, and Y. Zhang, in *Better Ceramics through Chemistry VII: Organic/Inorganic Hybrid Materials*, edited by B.K. Coltrain, C. Sanchez, D.W. Schaefer, and G.L. Wilkes (Materials Research Society Symposium Proceedings, Vol. 435, Pittsburgh, PA, 1996), pp. 595–603.

Journal of Sol-Gel Science and Technology 13, 379–383 (1998)
© 1998 Kluwer Academic Publishers. Manufactured in The Netherlands.

Structure Development in Simple Cross-Linked Organopolysiloxanes

G.J. GIBBONS, D. HOLLAND AND A.P. HOWES
Department of Physics, University of Warwick, Coventry CV4 7AL, UK

Abstract. ^{13}C CP and CPPI MAS NMR have been carried out on thermally cured samples of polymethylvinylsiloxane and polydimethylsiloxane. By varying the CP contact time, the α and β vinyl carbons and the methyl carbon of the CH_3—(SiO<)—CH=CH_2 species could be identified. A further methyl carbon was detected which was less mobile and which we assign to methyl groups attached to silicon species on which the vinyl group has reacted to form a cross-link. Resonance from —CH_2— carbons was observed in the 30–40 ppm range, and these species arise from methyl-vinyl cross-linking to give CH_3—(SiO<)—$\underline{C}H_2$—$\underline{C}H_2$—$\underline{C}H_2$—(SiO<)—CH=CH_2. Higher temperature curing promotes vinyl-vinyl cross-linking to give CH_3—(SiO<)—CH_2—$\underline{C}H$=$\underline{C}H$—CH_2—(SiO<)—CH_3 links between chains. Evidence for this comes from the insensitivity of the β carbon resonance under CPPI, indicating that it is in a —CH= rather than a =CH_2 environment. There was also evidence of —CH_2— carbons in the polydimethylsiloxane material, suggesting that thermally activated, methyl-methyl cross-linking can occur to give CH_3—(SiO<)—$\underline{C}H_2$—$\underline{C}H_2$(SiO<)—CH_3 links between chains.

Keywords: organopolysiloxane, solid-state NMR, cross-linking

1. Introduction

Novel polysiloxane interpenetrating polymer network (IPN) materials have been developed, for device encapsulation, with a view to obtaining hermeticity while retaining flexibility [1]. The systems consist of two interpenetrating networks, each based on a polysiloxane (Si—O—Si) backbone and each having separate organic cross-links. The mechanical properties of the IPN material are determined by the cross-link density of both the inorganic and the organic networks. The organic network is developed during a post preparation exposure to heat and a knowledge of the cross-linking mechanism is desirable. In the system considered here, a knowledge of the interactions that occur between methyl (—CH_3) and vinyl (CH_2=CH—) species is required. The mechanism of this interaction has been studied extensively but conflicting mechanisms have been proposed [2]. Classically, the interaction would be expected to occur predominantly between vinyl groups [3] although there is considerable evidence against this being the dominant mechanism [4–7], with the methyl-vinyl interaction being suggested as more likely. Previous investigations used peroxide as a catalyst for the cross-linking reaction but encapsulation material should be cured without catalysts, to avoid compromising the dielectric properties. We here report an investigation of the cross-linking mechanism operative within simple, catalyst-free, thermally cured, polysiloxane systems.

2. Experimental

2.1. *Sample Preparation*

Samples were prepared by the hydrolysis and condensation of dichlorodimethylsilane (DCDMS) or dichloromethylvinylsilane (DCMVS) in 50/50 v/v toluene/ethylacetate with an 8.0 M initial precursor concentration. After hydrolysis with a stoichiometric volume of distilled H_2O for a period of 30 min, the systems were controlled to pH 7 by the addition of 1.0 M solution of KOH in 50/50 v/v H_2O/EtOH. After further reaction for 24 h the KCl precipitate was

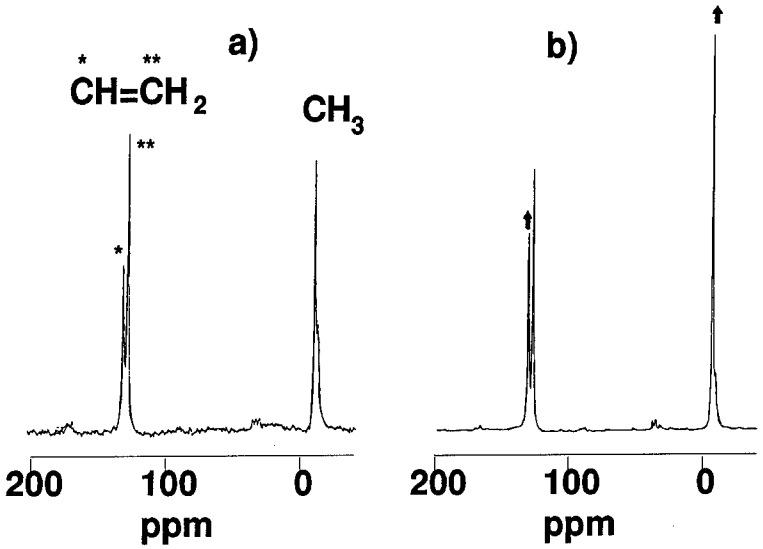

Figure 1. ^{13}C MAS DD CP NMR of PMVS heated at 200°C for 4 h. Contact times are (a) 2 ms and (b) 10 ms.

removed from the systems prior to final phase separation and desolvation at room temperature.

2.2. *Solid-State NMR Techniques*

^{13}C solid-state NMR experiments were performed on a Bruker 360 MSL spectrometer at 90.55 MHz. To eliminate dipolar broadening, samples were spun at ~3.5 kHz using zirconia rotors sealed with either Kel-F (ambient) or Delrin (high temperature) caps. Referencing was to tetramethylsilane (TMS). The solid-state NMR techniques employed included ^{13}C H-C dipolar-decoupled (DD) magic-angle-spinning (MAS) NMR, ^{1}H-^{13}C MAS cross-polarization (CP), variable temperature MAS CP and MAS cross-polarization-polarization-inversion (CPPI) [8] a spectral editing technique. The experiments are detailed elsewhere [9].

3. Results

^{13}C MAS DD CP spectra of polymethylvinylsiloxane (PMVS) cured at 200°C for 4 h are presented in Fig. 1 for CP contact times, τ_c, of 2 ms and 10 ms. The spectrum of a sample of PMVS cured at 220°C/4 h is given in Fig. 2. Spectra obtained using variable temperature CP are presented in Fig. 3. These spectra were obtained using a 10 ms τ_c and are thus comparable to Fig. 1(b). Spectra collected using the CPPI technique for a τ_{PI1}, $+\tau_{PI2}$ of 1, 20, 100 and 700 μs, respectively, are presented in Fig. 4.

4. Discussion

4.1. *Mas DD CP*

MAS DD CP was more effective than MAS or MAS DD, giving a low noise, high resolution spectrum for a

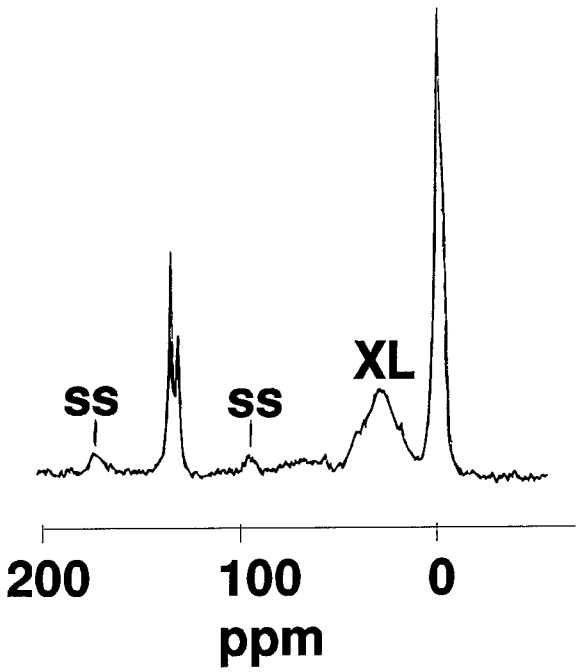

Figure 2. ^{13}C MAS DD CP NMR of PMVS heated at 220°C for 4 h.

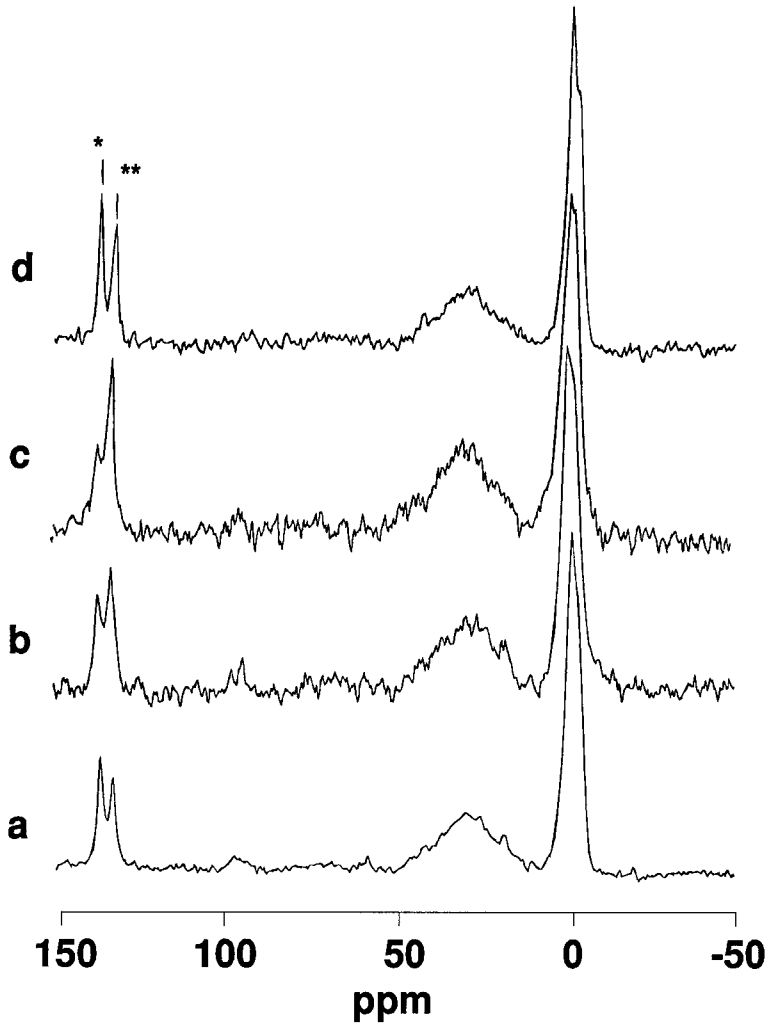

Figure 3. ^{13}C MAS DD CP NMR of PMVS heated at 220°C for 4 h. Spectra obtained at (a) 295 K, (b) 332 K, (c) 353 K and (d) 400 K.

sample of PMVS cured at 200°C for 4 h (Fig. 1). The efficiency of CP is dependent upon the strength of the static dipolar interaction [10], which is greater for a rigid system than in more mobile elastomers and liquids. The high S/N observed implies that the polymer systems investigated are indeed rigid, being below or very near to T_g and possessing a strong static component to the dipolar interaction. The narrow lines suggest that the system is amorphous since crystallinity would result in a broadening of the resonances [10].

Three main resonance groups are observed. The first group, of two peaks (124.7 ± 0.6, 138.4 ± 0.6 ppm) is assigned to the β and α carbons of the vinyl, based on assignments made by Schraml et al. [11] for $((CH_3)_3SiO)_2(CH_3)Si(CH{=}CH_2)$. By reference to literature [12] the three peaks at mid frequencies (40.7 ± 0.6, 37.5 ± 0.6 and 35.0 ± 0.6 ppm) may be tentatively assigned as $-CH_2-$ mid chain species, consistent with the formation of methyl-vinyl cross-links in $CH_3-(SiO<)-\underline{C}H_2-\underline{C}H_2-\underline{C}H_2-(SiO<)-CH{=}CH_2$. Vinyl-vinyl cross-linking would produce a single peak. The resonance at -4.9 ± 0.6 ppm is assigned to the $-CH_3$ group in PMVS, but is more shielded than the value of -0.2 ± 0.3 reported by Schraml [11]. The resonance at -5.9 ± 0.6 ppm would not be expected in an uncured PMVS system since only one $-CH_3$ environment would exist, it is thus proposed that this group is associated with the cross-linked silicon. A significant difference is seen between the spectrum acquired using a 2 ms contact time and that obtained using a 10 ms contact time. In particular, the α carbon resonance of the vinyl group and that of the $-CH_3$ attached

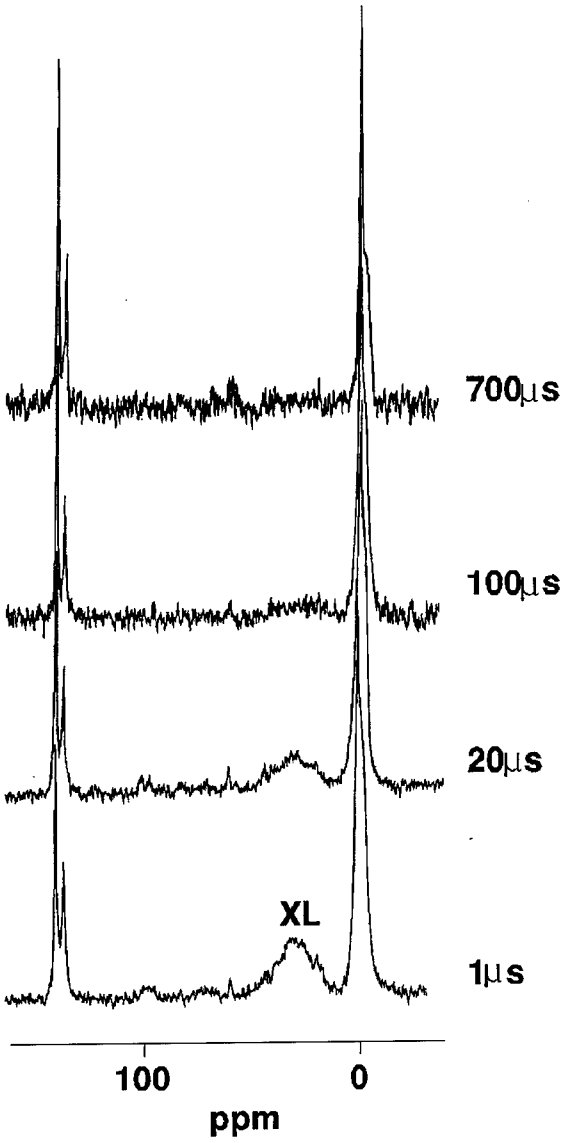

Figure 4. ^{13}C MAS DD CPPI NMR of PMVS for a range of polarization inversion times.

to a cross-linked silicon are both observed to increase in intensity, as indicated in Fig. 1. The former may be accounted for by the α carbon possessing fewer directly attached protons than the β carbon and thus receiving less magnetization transfer—a factor which becomes less important as contact time increases. The smaller magnetization transfer to the methyl group, is probably due to it being highly mobile, thus reducing the CP efficiency. The greater magnetization transfer to the lower intensity $-CH_3$ resonance (as inferred from its invariance to an increase in τ_c) suggests this to be less mobile than the slightly downfield $-CH_3$. It is proposed that this resonance is a methyl group attached to a silicon, upon which the vinyl group has been reacted to form a cross-link. Thus low-temperature curing is predominantly via methyl-vinyl cross-linking.

4.2. *Effect of Cure Temperature*

Curing of the PMVS at a higher temperature (220°C/4 h) results in a large increase in the intensity of the proposed cross-link resonance (Fig. 2) and a decrease in the vinyl β. The growth of the lower frequency CH_3 resonance, is commensurate with an increase in the number of PMVS units with reacted vinyl groups. The increased width of the cross-link resonance indicates greater rigidity but there is also the possibility of an additional contribution.

4.3. *Effect of Experiment Temperature*

MAS DD CP spectra were obtained at temperatures from 295 to 400 K for a sample cured at 220°C for 4 h (Fig. 3). The lineshape of the cross-link species is scarcely affected by increase in temperature, suggesting it may be partially crystalline, since the line width from an amorphous system would increase due to molecular motion [11]. The vinyl α carbon resonance halves in intensity (relative to the β carbon) over the temperature range 295–353 K which is unusual since both carbon atoms would be expected to have similar degrees of freedom. This results from a contribution to the "β" intensity from a second, less mobile species $Si-CH_2-\underline{C}H=C$ as suggested by Schraml [11]. The α carbon resonance for the cross-link structure may thus be the additional contribution to the broad group of resonances, indicated as XL of Fig. 2. The trend reversal seen at 400 K indicates the material has passed through T_g. The lower frequency $-CH_3$ resonance appears to increase in intensity with increasing temperature. Again, this is probably a result of an increased degree of cross-linking. Thus increasing the cure temperature promotes vinyl-vinyl cross-linking.

4.4. *CPPI*

Over the range of polarization inversion (PI) times 20–700 μs, all resonances are suppressed to some degree, with the most marked suppression being of the proposed cross-link species (Fig. 4) suggesting that these

resonances are from $-CH_2-$ species, as previously inferred. Suppression of the CH_3 resonances is much less pronounced, with a sizeable signal remaining after a 700 μs polarization inversion time. The absence of suppression of the β carbon is consistent with this being predominantly a CH group, which, according to Wu and Zilm [8], requires substantially longer PI times before significant suppression occurs providing confirmation that this is largely in the form $CH_3-(SiO<)-CH_2-\underline{C}H=\underline{C}H-CH_2-(SiO<)-CH_3$.

4.5. *PDMS*

Cross-linking also occurs within PDMS systems, as evidenced by the growth of the low intensity resonance at 30–40 ppm, commensurate with $-CH_2-$ species in $CH_3-(SiO<)-\underline{C}H_2-\underline{C}H_2-(SiO<)-CH_3$. However, higher temperatures (240°C) are required before the cross-link structure can be detected.

5. Conclusions

^{13}C CP MAS NMR of a 200°C cured sample of a simple $CH_3-(SiO<)-CH=CH_2$ siloxane gave well resolved, high signal-to-noise spectra, suggesting the sample to be both rigid (near to or below T_g) and amorphous. The α and β vinyl carbons and the methyl carbon of the $CH_3-(SiO<)-CH=CH_2$ species were all identified.

A single narrow resonance observed at a slightly lower frequency than the CH_3 resonance was confirmed, by CPPI and CP NMR to be from methyl groups in less mobile regions of the polymer, i.e., attached to silicon species on which reaction of the pendant vinyl group has resulted in the formation of a cross-link. A group of resonances observed in the region 30–40 ppm were assigned as $-CH_2-$mid-chain species $CH_3-(SiO<)-\underline{C}H_2-CH_2-\underline{C}H_2-(SiO<)-\underline{C}H=CH_2$. On curing at higher temperature this resonance broadened. A methene assignment was made on the basis of its ready suppression after short polarization times in CPPI spectra. Involvement of these species within a cross-link structure of the type $-SiCH_2CH=CHCH_2Si-$ was further supported by changes within the vinylic region of the spectra. The unusual insensitivity of the β carbon resonance under CPPI would result from the species being of the type $-CH=$ (cross-link) and not $=CH_2$ (vinylic).

A thermally created $-CH_2-$, commensurate with a methyl-methyl interaction, was observed in PDMS although the intensity of the species is very low. This requires further investigation.

Acknowledgments

We thank EPSRC and Nortel plc for financial support and Prof. R. Dupree for access to the solid-state NMR facilities.

References

1. G.J. Gibbons, Ph.D. Thesis, 1996.
2. D.R. Thomas, Cross-linking of poly-dimethylsiloxanes, in *Siloxane Polymers* (Prentice-Hall, London, 1993).
3. E.M. Barrall, R. Hawkins, A.A. Fukushima, and J.F. Johnson, J. Poly. Sci. Polym. Symp. **71**, 189 (1984).
4. W.J. Bobear, Rubber. Chem. Technol. **40**, 1560 (1967).
5. A.G. Tanner and W.G. Davies, Dow Corning Private Communication.
6. M.A. Lorente and J.E. Mark, Rubber. Chem. Tech. **53**(4), 988 (1980).
7. P.G. Bork and C.W. Rousch, *Vulcanisation of Elastomers* (Reinhold, New York, 1964), p. 369.
8. X. Wu and K.W. Zilm, J. Magn. Reson. **A 102**, 205 (1993).
9. G.J. Gibbons, D. Holland, and A.P. Howes, Solid State NMR, to be published.
10. R.A. Komoroski, in *High Resolution NMR Spectroscopy of Synthetic Polymers in Bulk*, edited by R.A. Komoroski (VCH, Florida, 1986), Vol. 7.
11. J. Schraml, V. Chvalovsky, M. Magi, and E. Lippmaa, Coll. Czec. Chem. Comm. **42**, 306–317 (1977).
12. G.C. Levy, R.L. Lichter, and G.L. Nelson, *Carbon-13 Nuclear Magnetic Resonance Spectroscopy*, 2nd edition (John Wiley & Sons, New York, 1980).

Journal of Sol-Gel Science and Technology 13, 385–390 (1998)
© 1998 Kluwer Academic Publishers. Manufactured in The Netherlands.

FT-Raman-Spectroscopic Investigations of the System Glycidoxypropyltrimethoxysilane/Aminopropyltriethoxysilane

B. RIEGEL AND W. KIEFER
Institut für Physikalische Chemie, Universität Würzburg, Am Hubland, D-97074 Würzburg, Germany
wolfgang.kiefer@rzroe.uni-wuerzburg.de

S. HOFACKER AND G. SCHOTTNER
Fraunhofer Institut für Silicatforschung, Neunerplatz 2, D-97082 Würzburg, Germany

Abstract. The base catalyzed sol-gel process in the system 3-glycidoxypropyltrimethoxysilane (GPTS)/ 3-aminopropyltriethoxysilane (APTS) is highly interesting for the synthesis of hybrid (inorganic-organic) polymers. FT-Raman spectroscopy with excitation in the near infrared as a versatile tool for in situ measurements was used to monitor the kinetic behavior of the hydrolysis reaction.

An unexpected slow-down of the hydrolysis of GPTS recorded at higher temperatures can be attributed to a decrease of the pH-value during hydrolysis caused by silanol groups. After condensation has started, the pH-value reincreases and forces hydrolysis to reaccelerate. The results strongly suggest the existence of a pentacoordinated transition state with a negative charge at the silicon atom during base catalyzed hydrolysis.

Keywords: hydrolysis, sol-gel kinetics, FT-Raman spectroscopy, hybrid sol-gel materials

1. Introduction

The sol-gel process [1] has been used to prepare inorganic as well as inorganic-organic materials from R'-Si$(OR)_3$ precursors. The appropriate choice of R' enables one to synthesize inorganic-organic polymers with a wide variety of properties [2–4]. One of the most widely applied organofunctional alkoxysilanes is 3-glycidoxypropyltrimethoxysilane (GPTS). 3-aminopropyltriethoxysilane (APTS) is frequently used in sol-gel coatings, as it works both as a network builder and as a base catalyst for the hydrolysis. Only a few investigations on the system GPTS and APTS have been performed so far [5, 6].

Raman spectroscopy has proven to be an outstanding tool for the investigation of the above mentioned processes, because it allows an in-situ measurement of the whole sol-gel reaction. Instead of the micro-Raman spectroscopy used in earlier experiments [6], we applied the Fourier-transform Raman technique with laser excitation in the near infrared region, because it offers several advantages, which were described elsewhere [7].

The Raman data provide information about the hydrolysis and condensation reactions of the silanes leading to the Silsequioxane-network as well as reactions of the organic moieties, e.g., the ring cleavage of the epoxy group [8]. In this contribution the hydrolysis of GPTS is described.

2. Experimental

The sol-gel reaction of the GPTS/APTS-system was performed in a tempered Raman-cell [7] attached to a "*Bruker RFS100*" Raman-spectrometer and a "*Bruker IFS120HR + FRA106*" IR-spectrometer with Raman-module. The spectral resolution of the presented spectra was 4 cm^{-1}. In the sol-gel reactions of GPTS and APTS we varied the GPTS/APTS molar ratio of the components from 95/5 to 70/30, the water amount from 1/4- to 2-stoichiometric and the temperature from 20°C

to 60°C. For the quantitative analysis of the spectra small amounts of cyclohexane were added as internal standard.

The pH-measurements were made with a glass electrode (Mettler Toledo InLab408), which was connected to a pH-meter.

The water amount present in the samples was determined by Karl-Fischer titration in a "701KF-Titrino" (Dt. Methrohm GmbH).

3. Results and Discussion

Figure 1 shows the Raman spectra of a GPTS/APTS 70/30 mixture during reaction. In the spectra a doublet at 643 cm^{-1} and 613 cm^{-1} is observed. These two bands can be assigned to the $\nu(SiO_3)$ stretching vibrations (symmetric and antisymmetric) of GPTS [6].

After starting the hydrolysis, the GPTS bands at 643 cm^{-1} and 613 cm^{-1} diminish and show the decrease of unhydrolyzed GPTS during formation of the inorganic network.

The 1035 cm^{-1} band can be assigned to the CO-stretching vibration of methanol, the band at 881 cm^{-1} to the CCO-stretching of ethanol. Both band intensities are growing due to the evolving alcohols during hydrolysis of GPTS and APTS.

For the kinetic curves the intensity of the 643 cm^{-1} Raman band, which is related to the residual GPTS, was determined and plotted against time. Since the $\nu(SiO_3)$-vibrations of APTS appear very close at 650 cm^{-1} and at 627 cm^{-1} (± 4 cm^{-1}) a curve fitting procedure was used for the determination of the intensity.

Measurements with different amounts of APTS show that an increase of the concentration of the basic catalyst APTS leads to an acceleration of

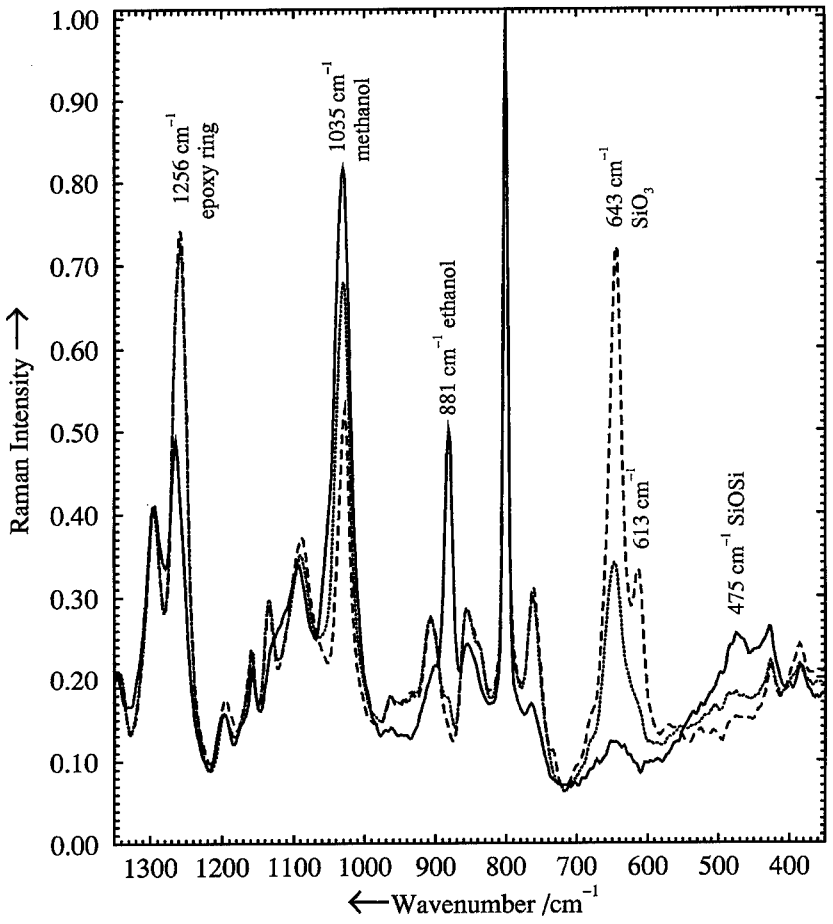

Figure 1. Raman spectra of the GPTS/APTS system with 30 mol% APTS during hydrolysis at 20°C, with the characteristic Raman bands indicated in the plot. The plots are recorded 0 min (dotted), 15 min (dashed) and 4 h (solid) after start of sol-gel reaction.

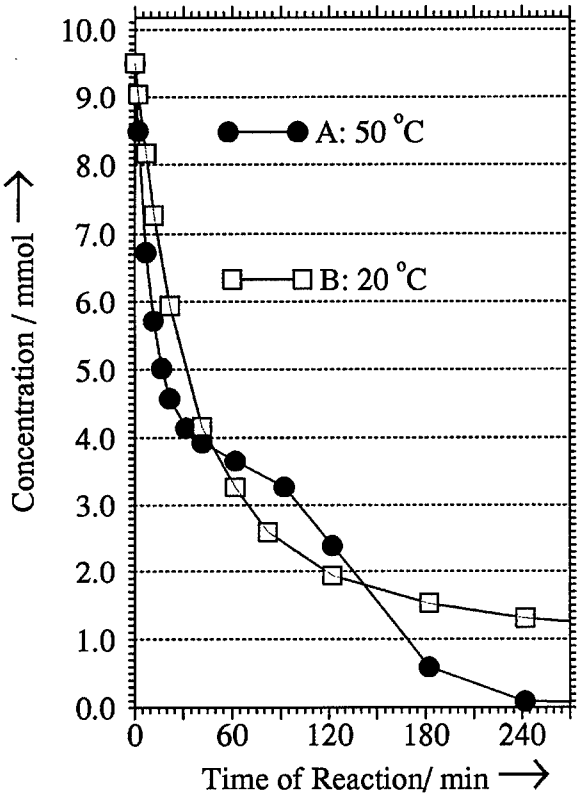

Figure 2. Kinetic plot of the GPTS hydrolysis for the 5% APTS samples at 20°C and at 50°C. The *y*-axis indicates the concentration of the residual GPTS (±0.3 mmol).

GPTS-hydrolysis as water dissociates under basic conditions to produce nucleophilic hydroxyl anions, which attack the alkoxysilane. This confirms the results obtained by other authors for base catalyzed hydrolysis of alkoxysilanes [1, 9].

The decrease of unhydrolyzed GPTS is shown in Fig. 2 for the GPTS/APTS ratio of 95/5 at 50°C and 20°C. The *y*-axis indicates the absolute amount of GPTS in mmol. The plots show a remarkable difference between the results obtained at 20°C and at 50°C. At 50°C one observes a decrease of the velocity of the hydrolysis for a certain time during reaction with a reacceleration afterwards. The resulting plateau appears very clear, whereas no plateau is detectable in the 20°C plot. A plateau was generally observed at elevated temperatures as could be shown by measurements at 40°C, 50°C, and 60°C.

At concentrations of APTS higher than 10% we could not observe any plateau, since the time resolution was not sufficient for the very fast hydrolysis at the given experimental conditions.

Before discussing these results, we have to point out, that the intensity of the GPTS Raman band at 643 cm^{-1} is only due to the amount of the totally unhydrolyzed trimethoxysilane-molecules ($-Si(OCH_3)_3$). If one methoxy-group is replaced, e.g., by a hydroxyl-group (OH^-), this molecule no longer contributes to the intensity at 643 cm^{-1}. The Raman bands of the partially hydrolyzed molecules cannot be observed under the experimental conditions. Because of the small amount of APTS (5%) in the sample and because of the slower hydrolysis of ethoxy-groups we neglect the hydrolytic reaction of APTS in our further discussion. Diffusion effects causing the slow-down can be excluded since the samples were stirred continuously during spectra recording until time of gelation. Moreover, we observed no relationship between the time of gelation and the appearance of the plateau. Therefore, we can furthermore exclude a hindered mobility of the molecules as the reason for this observation.

A first possibility to explain this behavior (see Fig. 3) is the following assumption: The active agent that is responsible for the hydrolysis is the hydroxyl anion which has to be formed by water and APTS. At the beginning of the reaction there is enough water for this equilibrium. The OH^- ions will react with the GPTS molecules to form hydroxy-alkoxy silane and alcohol (Eq. (1)). In the case of half-stoichiometric water addition, the quick hydrolysis at elevated temperatures leads to a lack of water resulting in a diminution of

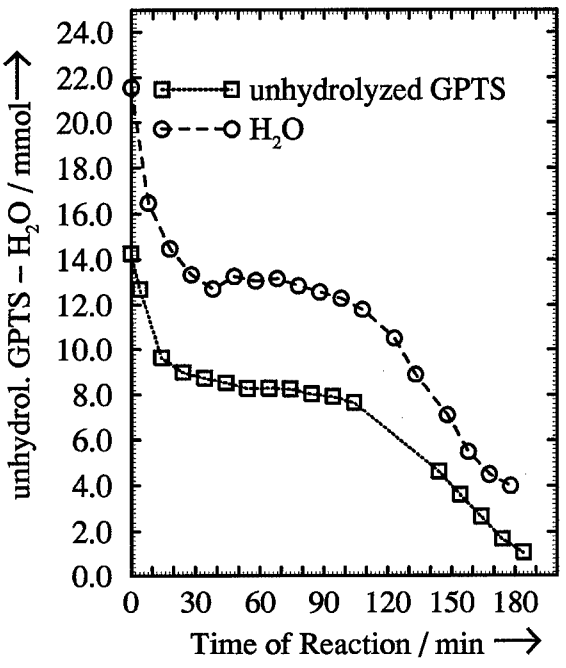

Figure 3. Plot of unhydrolyzed GPTS (±0.3 mmol) and water concentration (±4%) versus time at 60°C.

hydroxyl anions. Thereby, hydrolysis slows down, leading to the observed plateau. After a certain time (induction period), when enough Si—OH groups are formed, condensation sets in. The released water is then available for the generation of new hydroxyl anions, which hydrolyze the residual alkoxysilanes. The reason for this long induction period is the competitive reaction of alcohol condensation forming methanol, which is in general more probable than water condensation for under-stoichiometric additions of water [9]. That this effect is only observable at higher temperatures can be explained by a more accelerated hydrolysis compared to condensation.

$$R_GSi(OCH_3)_3 + nH_2O \overset{[OH^-]}{\rightleftharpoons} R_GSi(OCH_3)_{3-n}(OH)_n + nCH_3OH \quad n = 1-3 \tag{1}$$

$R_G = -(CH_2)_3-O-CH_2-\underset{\llcorner\!\lrcorner}{CHOCH_2}$

From this reasoning we would expect a minimum in the concentration of water related to the appearance of the plateau.

Therefore, we determined the water amount of the samples via Karl-Fischer titration parallel to Raman measurements. As displayed in Fig. 3 for a 60°C sample the amounts of water and of unhydrolyzed GPTS show the same courses at elevated temperatures. No minimum in water concentration is observed. Thus, the hypothesis of water shortage must be withdrawn.

The second approach for explanation takes into account the acidity of the silanol groups. As in the preceding hypothesis we suppose that hydrolysis is more accelerated at elevated temperatures than condensation under the given basic conditions. Therefore, the silanol groups produced in hydrolysis reaction are not immediately consumed by the condensation reactions and can accumulate.[1] As they are weak acids, they perform a neutralization reaction with the basic hydroxyl ions formed by the aminogroup of APTS (Eq. (2)). This results in a reduction of the pH-value. As the hydrolysis is strongly dependent on pH-value [1, 10, 11], it slows down and nearly stops in some cases. When the SiOH groups are decreasing due to condensation reactions afterwards the pH-value increases again and under the restored basic conditions the hydrolysis reaccelerates.

$$R_GSi(OCH_3)_{3-n}(OH)_n + nOH^- \rightleftharpoons R_GSi(OCH_3)_{3-n}(O^-)_n + nH_2O \quad n = 1-3 \tag{2}$$

This hypothesis could be verified by pH-measurements parallel to the recording of the Raman spectra of a 95/5 molar ratio GPTS/APTS sample at 50°C shown in Fig. 4. The pH plot clearly displays a decrease of pH at the beginning, a minimum corresponding to the plateau in the plot of unhydrolyzed GPTS and a reincrease of pH corresponding to the reacceleration of GPTS hydrolysis.

Thus, the plateau observed at elevated temperatures is caused by a decrease of pH-value due to a fast hydrolysis, which liberates silanol groups. The end of the plateau has its origin in the starting condensation releasing water, which reduces the amount of silanol functions present in the mixture.

At room temperature this effect is not observed. Obviously, condensation reactions are so fast at 20°C, that no silanol groups can accumulate and change the pH-value via neutralization. This is consistent with the result that condensation generally is very fast under basic conditions. At higher temperatures hydrolysis must be much more accelerated than condensation to explain this effect. Thus, the temperature dependence of hydrolysis is much stronger than that of the condensation reactions.

In the case of half-stoichiometric addition of water (1.5 mol H_2O/1 mol GPTS) it can be calculated from the plots, that 1 mol GPTS has reacted with 1.7–2.0 mol water when reaching the plateau. Therefore, multiple hydrolysis seems to be preferred over single hydrolysis for all GPTS molecules. This reasoning leads to the conclusion that the intermediate products of $-Si(OCH_3)_x(OH)_y$ with $y = 1, 2$ are more reactive concerning the hydrolysis than the initial $-Si(OCH_3)_3$. Because of the larger negative inductive effect of a hydroxyl group in comparison to a methoxy group [1], the attack of a second hydroxyl ion to a $-Si(OCH_3)_2(OH)$ is preferred which causes the observed multiple hydrolysis. This course of reaction therefore supports the model of a pentacoordinated transition state with a negative charge at the silicon atom during the base catalyzed hydrolysis as postulated by Pohl and Osterholtz [10] and Keefer [12].

4. Conclusions

Monitoring of the GPTS/APTS sol-gel reaction by means of Raman spectroscopy was used to analyze the inorganic hydrolysis and condensation of the trialkoxysilyl moieties. In the reaction at elevated temperatures we observed a slow-down in the velocity of

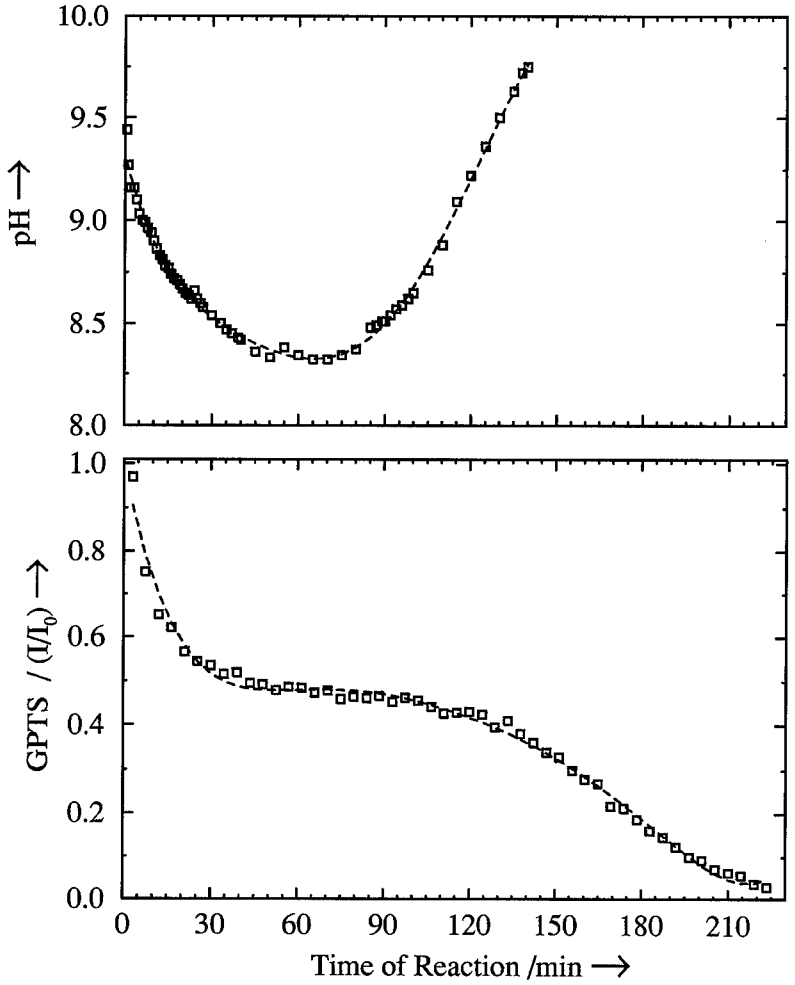

Figure 4. Plot of pH-value (±0.05) and unhydrolyzed GPTS concentration (±0.3 mmol) versus time at 50°C.

hydrolysis, which can be attributed to a neutralization reaction of acid silanol groups leading to a pH-decrease. From the resulting plateaux in the decrease of the $Si(OR)_3$-moieties we derived a multiple hydrolysis of GPTS, which strongly suggests a pentacoordinated silicon center as a transition state during hydrolysis, as proposed by Pohl and Osterholtz [10] and Keefer [12]. Moreover, it can be concluded, that the condensation processes are not as strongly dependent on temperature as the hydrolysis and that a dominance of alcohol condensation over water condensation exists for understoichiometric addition of water.

Acknowledgments

Financial support from the *Deutsche Forschungsgemeinschaft* as well as from the *Fonds der Chemischen Industrie* and from the *Bundesministerium für Bildung, Wissenschaft, Forschung und Technologie* (*BMBF*) are gratefully acknowledged.

Note

1. The accumulation of silanol groups is sufficient for changing the pH-value, but the amount is to small to be detected in the Raman spectra.

References

1. C.J. Brinker and G.W. Scherer, *Sol-Gel Science* (Academic Press, New York, 1990), p. 2.
2. C. Sanchez and F. Ribot, New J. Chem. **18**, 1007 (1994).
3. H. Scholze, J. Non-Cryst. Solids **73**, 699 (1985).
4. B.M. Novak, Adv. Mater. **5**, 422 (1993).

5. U. Posset, M. Lankers, W. Kiefer, H. Steins, and G. Schottner, in *Proc. XIV. Int. Conf. Raman Spectr.*, edited by N.-T. Yu and X.-Y. Li (John Wiley & Sons, Chichester, 1994), p. 576.
6. U. Posset, M. Lankers, W. Kiefer, H. Steins, and G. Schottner, Appl. Spectrosc. **47**, 1600 (1993).
7. B. Riegel, S. Blittersdorf, W. Kiefer, N. Hüsing, and U. Schubert, J. Mol. Struct., **410**, 157 (1997).
8. B. Riegel, S. Blittersdorf, W. Kiefer, S. Hofacker, M. Müller, and G. Schottner, J. Non-Cryst. Solids, to be published.
9. C.J. Brinker, J. Non-Cryst Solids **100**, 31 (1988).
10. E.R Pohl and F.D. Osterholtz, in *Molecular Characterization of Composite Interfaces*, edited by H. Ishida and G. Kumar (Plenum, New York, 1985), p. 157.
11. R. Aelion, A. Loebel, and F. Eirich, J. Am. Chem. Soc. **72**, 5705 (1950).
12. K.D. Keefer, in *Better Ceramics through Chemistry*, edited by C.J. Brinker, D.E. Clark, and D.R. Ulrich (North-Holland, New York, 1984), p. 15.

Journal of Sol-Gel Science and Technology 13, 391–396 (1998)
© 1998 Kluwer Academic Publishers. Manufactured in The Netherlands.

Encapsulation versus Tethering in the Incorporation of $C_5H_5Rh(CO)_2$ into Hybrid Inorganic-Organic Cubane $\{Si_8O_{12}\}$ Copolymers

PHILIP G. HARRISON AND CHRISTOPHER HALL
Department of Chemistry, University of Nottingham, University Park, Nottingham NG7 2RD, UK

Abstract. Copolymerization of cubane octavinylsilsesquioxane, $\{Si_8O_{12}\}(CH{=}CH_2)_8$, with the cubane silsesquioxane hydrides, $\{Si_8O_{12}\}H_8$ and $\{Si_8O_{12}\}(OSiMe_2H)_8$ in the presence of $C_5H_5Rh(CO)_2$ affords hybrid inorganic-organic copolymers incorporating monocarbonyl $\{C_5H_5Rh(CO)\}$ species. These are of two types, one containing Rh(III) and the other Rh(I). The Rh(III) species appears to be that formed initially, and can be converted into the Rh(I) species by photolysis. BET measurements show that a significant increase in surface area occurs when the copolymerization is carried out in the presence of the rhodium complex.

Keywords: silsesquioxanes, MAS-NMR, infrared, isotopic substitution, inorganic-organic copolymers, cyclopentadienylrhodium dicarbonyl

Introduction

Controlled pore inorganic solids play a key role in modern chemical technology as inter alia heterogeneous catalysts, adsorbents, and porous membranes. We have previously demonstrated that porous materials may be obtained by the copolymerization of cubane octavinylsilsesquioxane, $\{Si_8O_{12}\}(CH{=}CH_2)_8$ (D4R-vinyl[1]), with the cubane silsesquioxane hydrides, $\{Si_8O_{12}\}H_8$ (D4R-H) and $\{Si_8O_{12}\}(OSiMe_2H)_8$ (D4R-$OSiMe_2H$) under mild conditions [1] (Fig. 1). The copolymer (I) resulting from $\{Si_8O_{12}\}H_8$ exhibits a remarkably high BET surface area of around 500 $m^2\ g^{-1}$.

Experimental

The two hybrid copolymers (I) and (II) were synthesized according to procedures outlined previously [1]. Isotopomers (isotopically substituted variants) of cyclopentadienyl(dicarbonyl)rhodium, $(C_5H_5)Rh(^{12}CO)_2$, $(C_5H_5)Rh(^{13}CO)_2$, and $(C_5H_5)Rh(^{12}CO)(^{13}CO)$ were synthesized according to the procedure of McCleverty and Wilkinson [2].

Synthesis of $(C_5H_5)Rh(CO)_2$ Isotopomers $(C_5H_5)Rh(CO)_2$, $(C_5H_5)Rh(^{13}CO)_2$ and $(C_5H_5)Rh(^{12}CO)(^{13}CO)$

$[(CO)_2RhCl]_2$ was dissolved in diethyl ether (ca. 20 ml) and transferred slowly with stirring into a slurry of thallium cyclopentadienide (1.02 g, 3.78 mmol) also in diethyl ether (ca. 10 ml). The mixture was stirred under argon for 60 h, filtered and the solvent removed in vacuo yielding a brown oily solid. Purification by trap-to-trap distillation afforded $(C_5H_5)Rh(CO)_2$ as an orange/yellow liquid. NMR ($CDCl_3$): $\delta(^1H)$ 5.54 ppm (d, $^2J_{RhH} = 0.66$ Hz), $\delta(^{13}C)$ 87.84 ppm (d, $^2J_{RhC} = 3.5$ Hz) (C_5H_5), 191.29 ppm (d, $^2J_{RhC} = 3.5$ Hz) (CO). The same method was also employed for the synthesis of $(C_5H_5)Rh(^{13}CO)_2$ and $(C_5H_5)Rh(^{12}CO)(^{13}CO)$ starting from $[(^{13}CO)_2RhCl]_2$ and $[(^{12}CO)(^{13}CO)RhCl]_2$, respectively, with a stirring period for the reaction mixture of 90 h. Infrared showed 100% ^{13}C enrichment for $(C_5H_5)Rh(^{13}CO)_2$ and ca. 50% enrichment for $(C_5H_5)Rh(^{12}CO)(^{13}CO)$.

Copolymerization of Octahydrido- and Octavinylsilsesquioxane in the Presence of $(C_5H_5)Rh(CO)_2$, $(C_5H_5)Rh(^{13}CO)_2$ and $(C_5H_5)Rh(^{12}CO)(^{13}CO)$

Octahydridosilsesquioxane (0.1 g, 0.235 mmol) and octavinylsilsesquioxane (0.15 g, 0.235 mmol) were placed in a round-bottomed flask fitted with a reflux condenser. To this was transferred a solution of $(C_5H_5)Rh(CO)_2$ (ca. 50 mg, ca. 0.22 mmol) in dry, degassed toluene (10 ml) under argon, followed by 40 μl of a 5 mmol l^{-3} solution of H_2PtCl_6 in isopropanol (10^{-4} mol/mol of double bonds). The mixture was then heated to reflux with rapid stirring under a slow stream of argon. After 10 min the orange solution darkened to orange/brown then red/brown, and after a further 5 min gelation occurred yielding a deep red gelatinous solid. The mixture was heated for a further 2 h to ensure complete reaction. By this time the red gel, which had occluded most of the solvent, was collected on a Buchner funnel and washed with toluene (4 × 50 ml). The first washing produced a yellow solution, the infrared spectrum of which exhibited ν(CO) bands at 2042 and 1976 cm^{-1} due to $(C_5H_5)Rh(CO)_2$. Subsequent washings remained clear. The gel at this stage was uniformly clear indicating a homogeneous dispersion of rhodium complex throughout the polymer. The gel was then dried in vacuo for 3 h at 65°C to remove occluded toluene leaving a dark purple/brown glassy solid (233 mg). Similar procedures were employed for $(C_5H_5)Rh(^{13}CO)_2$ and $(C_5H_5)Rh(^{13}CO)(CO)$.

Reaction of Octahydridosilsesquioxane with $(C_5H_5)Rh(^{12}CO)_2$ and $(C_5H_5)Rh(^{12}CO)(^{13}CO)$

To octahydridosilsesquioxane (1.111 g, 2.62 mmol) dissolved in dry, degassed toluene (ca. 10 ml) in a round-bottomed flask was added $(C_5H_5)Rh(CO)_2$ (0.40 g, 0.18 mmol) and the mixture heated under reflux

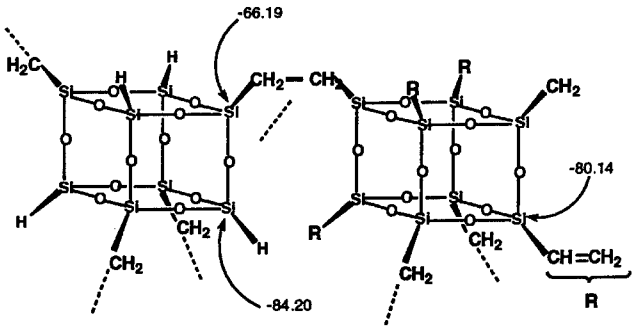

I D4R-H/D4R-vinyl

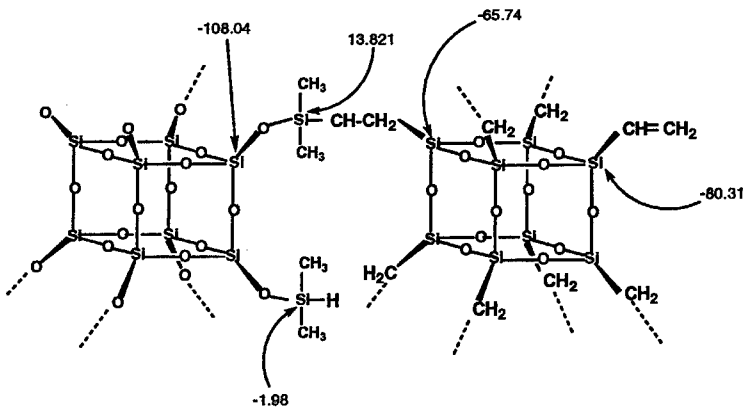

II D4R-OSiMe$_2$H/D4R-vinyl

Figure 1.

(*Continued on next page.*)

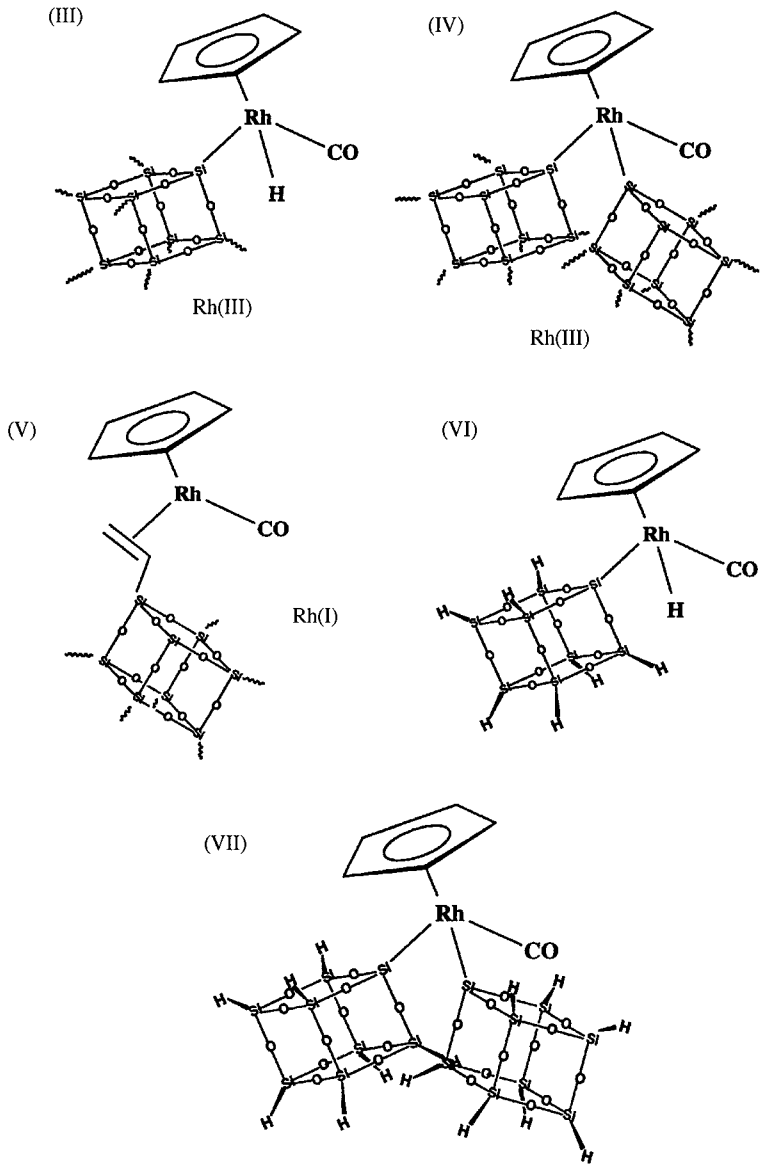

Figure 1. Schematic representations of the copolymers resulting from the polymerization of $\{Si_8O_{12}\}(CH{=}CH_2)_8$ with $\{Si_8O_{12}\}H_8$ (I) and $\{Si_8O_{12}\}(OSiMe_2H)_8$ (II). The numerical data refer to the solid state NMR chemical shifts (^{13}C or ^{29}Si as appropriate).

for 5.2 h under a slow stream of argon with vigorous stirring. After this time a white crystalline solid and a brown solution remained. The solution was filtered off and the solvent removed leaving a yellow/brown solid.

Copolymerization of Octakis(dimethylsilyloxy)- and Octavinylsilsesquioxane in the Presence of $(C_5H_5)Rh(^{12}CO)_2$ and $(C_5H_5)Rh(^{12}CO)(^{13}CO)$

Octavinylsilsesquioxane (0.402 g, 0.635 mmol) and octakis (dimethylsilyloxy)silsesquioxane (0.648 g, 0.637 mmol) were dissolved in dry, degassed toluene (20 ml) containing $(C_5H_5)Rh(^{12}CO)_2$ (30 mg, 0.132 mmol). A solution of H_2PtCl_6 in isopropanol (110 μl of a solution concentration 5 mmol l^{-3}; 10^{-4} mol/mol of C=C double bond), and the reaction mixture heated to reflux with vigorous stirring under a slow stream of argon. Gelation occurred after 10 min forming an orange gel which darkened to red/brown over the next 20 min. After heating for a further 2 h the resultant gel was collected by filtration and washed with toluene (4×50 ml). All the washings were clear indicating that all the rhodium complex was incorporated into the

copolymer. The gel was then dried in vacuo at 65°C for 3 h leaving a brown glassy solid (01.07 g, 99%). Found: C, 21.6; H, 4.74%. (D4R-$OSiMe_2H$/D4R-vinyl/0.25CpRhCO requires C, 23.6; H, 4.81%. A similar procedure was employed for $(C_5H_5)Rh(^{12}CO)(^{13}CO)$.

Discussion

Incorporation of the $(C_5H_5)Rh(CO)_2$ isotopomers was accomplished by carrying out the copolymerization in the presence of the rhodium complexes (Eqs. (4) and (5)) yielding colored gels:

$$n\{Si_8O_{12}\}H_8 + n\{Si_8O_{12}\}(CH{=}CH_2)_8 \xrightarrow[\text{Toluene, 115°}]{H_2PtCl_6} [\{Si_8O_{12}\}\text{-}CH_2\text{-}CH_2\text{-}\{Si_8O_{12}\}]_n \quad (1)$$

D4R-H + D4R-vinyl → D4R-H/D4R-vinyl

$$n\{Si_8O_{12}\}(OSiMe_2H)_8 + n\{Si_8O_{12}\}(CH{=}CH_2)_8 \xrightarrow[\text{Toluene, 115°}]{H_2PtCl_6} [\{Si_8O_{12}\}\text{-}OSiMe_2\text{-}CH_2\text{-}CH_2\text{-}\{Si_8O_{12}\}]_n \quad (2)$$

D4R-$OSiMe_2H$ + D4R-vinyl → D4R-$OSiMe_2H$/D4R-vinyl

Two possibilities exist as to the fate of the rhodium complexes when incorporated into the gel structure: (a) encapsulation as intact $(C_5H_5)Rh(CO)_2$ molecules with little or no interaction with the polymer framework, and (b) some type of chemical interaction with resulting in tethering of rhodium species to the gel framework. The observation from the solid state NMR spectra of a significant number of unused hydride and vinyl functionalities in the gels would facilitate such chemical interaction.

A distinction between these possibilities may be made by an examination of the infrared spectra of gels derived from the three isotopomer complexes, $(C_5H_5)Rh(^{12}CO)_2$, $(C_5H_5)Rh(^{13}CO)_2$, and $(C_5H_5)Rh(^{12}CO)(^{13}CO)$. Infrared carbonyl stretching frequencies for these complexes are listed in Table 1, and two strong bands are observed for the two monoisotopomers as expected. However, the infrared data show that the mixed $^{12}CO/^{13}CO$ complex actually comprises a mixture of all three isotopomers exhibiting six bands. Data for the three polymer gels are shown in Table 2. Again the spectra of the two monoisotopomer gels exhibit two bands, while the gel derived from the mixed $^{12}CO/^{13}CO$ complex exhibits three bands and is a superimposition of the spectra of the other two. These observations indicate unequivocally that the $(C_5H_5)Rh(CO)_2$ complex is not incorporated into the gel structure as an intact molecular species. Rather, the inference is that *two rhodium monocarbonyl* species have been formed. The positions of the observed bands indicate that the higher wavenumber band is due to a (cyclopentadienyl) rhodium(III) monocarbonyl species and that at lower wavenumber to a (cyclopentadienyl) rhodium(I) monocarbonyl species (cf. the model compounds $(C_5H_5)Rh(SiEt_3)(X)(CO)_2$ ν(CO) 2012 cm^{-1}, $(C_5H_5)Rh(C_2H_2)(CO)$ ν(CO) 1997 cm^{-1}). We, therefore, conclude that the rhodium(III) species present in the polymer gels is that shown in (III) in which the rhodium is linked to the gel framework by a direct Rh—Si bond, although a bridging species such as that illustrated in (IV) cannot be excluded. The structure of the rhodium(I) species is probably that shown in (V)

Table 1. Infrared carbonyl stretching frequencies (cm^{-1}) for $(C_5H_5)Rh(CO)_2$ isotopomers.

$(C_5H_5)Rh(^{12}CO)_2$[a]	$(C_5H_5)Rh(^{13}CO)_2$[a]	$(C_5H_5)Rh(^{12}CO)(^{13}CO)$[b]	Assignment[c]
2049(s)		2041(s)	$\nu(^{12}CO)_{sym}$ (12/12)
1984(s)		1975(s)	$\nu(^{12}CO)_{asym}$ (12/12)
	2032(vw)	2025(s)	$\nu(^{12}CO)$ (12/13)
		1945(s)	$\nu(^{13}CO)$ (12/13)
	2001(s)	1994(s)	$\nu(^{13}CO)_{sym}$ (13/13)
	1939(s)	1929(s)	$\nu(^{13}CO)_{asym}$ (13/13)
	1986(w)	1903(m)	$\nu(C^{18}O)_{sym}$
	1910(w)		$\nu(C^{18}O)_{asym}$

[a]Halocarbon oil mull.
[b]Liquid film.
[c]The nomenclature (12/12) refers to the $(C_5H_5)Rh(^{12}CO)_2$ complex, (13/13) refers to the $(C_5H_5)Rh(^{13}CO)_2$ complex, and (12/13) to the $(C_5H_5)Rh(^{12}CO)(^{13}CO)$ complex.

Table 2. Infrared carbonyl stretching frequencies (cm^{-1}) for D4R-H/D4R-vinyl copolymers incorporating $(C_5H_5)Rh(CO)_2$ isotopomer complexes prepared by copolymerization.

D4R-H/D4R-vinyl/ $(C_5H_5)Rh(^{12}CO)_2$ copolymer[a]	D4R-H/D4R-vinyl/ $(C_5H_5)Rh(^{13}CO)_2$ copolymer[a]	D4R-H/D4R-vinyl/ $(C_5H_5)Rh(^{12}CO)(^{13}CO)$ copolymer[a]	Assignment
2034(s)		2036(s)	$\nu(^{12}CO)$ [Rh(III)]
1992(s)		1990(s)	$\nu(^{12}CO)$ [Rh(I)]
	1990(s)	1990(s)	$\nu(^{13}CO)$ [Rh(III)]
	1947(w)	1946(w)	$\nu(^{13}CO)$ [Rh(I)]

[a] Very weak and broad.

Table 3. $\delta(^{29}Si)$ MAS-NMR data for D4R-H/D4R-vinyl copolymers incorporating $(C_5H_5)Rh(CO)_2$ isotopomer complexes prepared by copolymerization.

D4R-H/D4R-vinyl copolymer	D4R-H/D4R-vinyl/ $(C_5H_5)Rh(^{12}CO)_2$ copolymer	D4R-H/D4R-vinyl/ $(C_5H_5)Rh(^{13}CO)_2$ copolymer	D4R-H/D4R-vinyl/ $(C_5H_5)Rh(^{12}CO)(^{13}CO)$ copolymer	Assignment
−84.28	−83.57	−84.06	−84.47	*Si*-H
−80.32	−80.39	−80.57	−81.52	*Si*-vinyl
−66.46	−65.78	−66.22	−67.79	*Si*-CH_2-CH_2-*Si*
	~45[a]	~45[a]	~45[a]	*Si*-Rh?

[a] Very weak and broad.

Table 4. $\delta(^{13}C)$ MAS-NMR data for D4R-H/D4R-vinyl copolymers incorporating $(C_5H_5)Rh(CO)_2$ isotopomer complexes prepared by copolymerization.

D4R-H/D4R-vinyl copolymer	D4R-H/D4R-vinyl/ $(C_5H_5)Rh(^{12}CO)_2$ copolymer	D4R-H/D4R-vinyl/ $(C_5H_5)Rh(^{13}CO)_2$ copolymer	D4R-H/D4R-vinyl/ $(C_5H_5)Rh(^{12}CO)(^{13}CO)$ copolymer	Assignment
4.19	4.13	4.15	4.17	cage-CH_2-CH_2-cage
129.54	129.58	129.55	129.52	cage-CH=CH_2
135.46	134.06	134.49	134.34	cage-CH=CH_2
	89.09	89.07	89.06	C_5H_5 of "CpRh(CO)"
	190.27	190.21	190.25	CO of "CpRh(CO)"
	30.67	30.70	30.67	*Vinyl* coord. to Rh(I)

in which the $(C_5H_5)Rh(CO)$ moiety is bound to the framework via coordination involving a vinyl group.

Some corroboration is afforded from the ^{29}Si and ^{13}C MAS-NMR data (Tables 3 and 4, respectively). These in general are very similar to those of the unsubstituted polymer gel (Fig. 1). However, the former also exhibits a very weak and broad band at ca. 45 ppm due to silicon cage atoms bound directly to rhodium. Single resonances in the latter at ca. 89 ppm (C_5H_5) and ca. 190 ppm (CO) corroborate the presence of $(C_5H_5)Rh(CO)$ species, and that at 30.7 ppm is consistent with a vinyl group π-bonded to rhodium.

In comparison, no reaction occurs between $(C_5H_5)Rh(CO)_2$ with $\{Si_8O_{12}\}(CH{=}CH_2)_8$ under the conditions of the polymerization process (toluene, 115°). However, under the same conditions $(C_5H_5)Rh(CO)_2$ and $\{Si_8O_{12}\}H_8$ react to afford, after work-up, a yellow-brown solid exhibiting a $\nu(CO)$ band at 2036 cm^{-1} indicative of Rh(III). No corresponding band due to a Rh(I) species was detected. NMR spectra exhibited resonances at $\delta(^1H)$-12 ppm [Rh-*H*] and $\delta(^{29}Si)$-44.2 ppm [*Si*-Rh] (cf. $\delta(^{29}Si)$-48.3 ppm and 50.5 ppm for the silicon atoms bonded to cobalt in the complex $\{Si_8O_{12}\}[Co(CO)_4]_2$ [3]. These observations

are consistent with the formation of the rhodium(III) complex (VI), analogous to the rhodium(III) species (III) formed interaction of $(C_5H_5)Rh(CO)_2$ with the Si-H functionalities in the polymer framework.

Some information concerning the formation of the origin of the rhodium(I) species may be obtained by a photolytic study of the D4R-H/D4R-vinyl/"$(C_5H_5)Rh(^{12}CO)$" polymer gel. Before photolysis the infrared spectrum of this material exhibits ν(CO) bands at 2034 cm^{-1} (due to the Rh(III) species) and 1992 cm^{-1} (due to the Rh(I) species). However, after photolysis (220–380 nm) the intensity of the band at 2034 cm^{-1} decreases and that of the 1992 cm^{-1} band increases. The changes are more pronounced in the subtraction spectrum which shows a negative intensity (material consumed) band at 2034 cm^{-1} and positive band at 1996 cm^{-1} (material produced). Thus, it can be concluded that the rhodium(I) species observed in the polymer is generated from the rhodium(III) species, the net photolysis reaction being illustrated in Eq. (3).

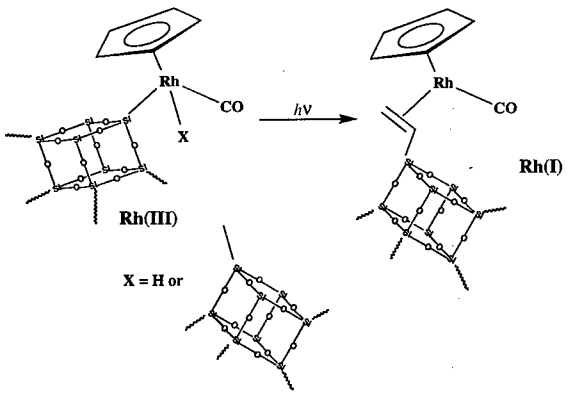

(3)

Copolymerization of D4R-$OSiMe_2H$ and D4R-vinyl in the presence of $(C_5H_5)Rh(^{12}CO)_2$ affords a brown gel which exhibits a single $\nu(^{12}CO)$ at 2019 cm^{-1} due to a [Rh(III)] species together with a weak band at 2255 cm^{-1} assigned as the ν(Rh-H) mode. The gel derived from $(C_5H_5)Rh(^{12}CO)(^{13}CO)$ exhibits two carbonyl bands at 2021 cm^{-1} [$\nu(^{12}CO)$] and 1974 cm^{-1} [$\nu(^{13}CO)$] two due the two monocarbonyl [Rh(III)] species in addition to the ν(Rh-H) band at 2254 cm^{-1}. As expected MAS-NMR spectra exhibit resonances at $\delta(^{13}C)$ 89.24 ppm ["$(C_5H_5)Rh(CO)$"] and 190.24 ppm ["$(C_5H_5)Rh(CO)$"]. Other $\delta(^{13}C)$ and $\delta(^{29}Si)$ resonances very similar to unsubstituted polymer (Fig. 1). In this system, therefore, it would appear that the rhodium complex is incorporated into the gel structure exclusively as the rhodium(III) species (VII).

Table 5. BET surface areas.

Material	BET surface area ($m^2\,g^{-1}$)
D4R-vinyl/D4R-H copolymer	479
D4R-vinyl/D4R-H/"$C_5H_5Rh(CO)$" copolymer	656
D4R-vinyl/D4R-H copolymer impregnated with $C_5H_5Rh(CO)_2$	275
D4R-vinyl/D4R-$OSiMe_2H$ copolymer	53.5
D4R-vinyl/D4R-$OSiMe_2H$/"$C_5H_5Rh(CO)$" copolymer	566

BET surface area data for the materials are listed in Table 5. Incorporation of $(C_5H_5)Rh(CO)_2$ into the two copolymers has a significant effect on the specific surface areas. That of the D4R-vinyl/D4R-H copolymer is 479 m^2g^{-1} rising to 656 m^2g^{-1} for the D4R-vinyl/D4R-H/"$(C_5H_5)Rh(CO)$" copolymer. A very similar material may also be obtained by impregnation of prepared D4R-vinyl/D4R-H copolymer using a toluene solution of $(C_5H_5)Rh(CO)_2$. Although very similar in appearance, these two materials differ substantially in their BET surface areas that measured for the impregnated polymer is much lower (275 $m^2\,g^{-1}$) reflecting the filling of the pore network. The increase in surface area is much more dramatic for the copolymer derived from $\{Si_8O_{12}\}(OSiMe_2H)_8$, where a tenfold increase is observed when the copolymer is prepared in the presence of the rhodium complex.

Acknowledgments

We thank the EPSRC for support and also Dr. Barbara Gore at UMIST for assistance in recording the solid state nmr spectra.

Note

1. ≡Double four ring.

References

1. P.G. Harrison and R. Kannengeisser, J. Chem. Soc., Chem. Commun. **3**, 415 (1996).
2. J.A. McCleverty and G. Wilkinson, Inorg. Synth. **8**, 211 (1966).
3. P.G. Harrison and R. Kannengeisser, J. Chem. Soc., Chem. Commun. **20**, 2065 (1995).

Journal of Sol-Gel Science and Technology 13, 397–404 (1998)
© 1998 Kluwer Academic Publishers. Manufactured in The Netherlands.

The Sol-Gel Process for Nano-Technologies: New Nanocomposites with Interesting Optical and Mechanical Properties

H.K. SCHMIDT, E. GEITER, M. MENNIG, H. KRUG, C. BECKER AND R.-P. WINKLER
Institut für Neue Materialien gem. GmbH, Saarbrücken, Germany

Abstract. Various nanocomposite systems have been synthesized by sol-gel routes. For this reason, prefabricated nanoparticles (SiO_2 sols or boehmite powder) have been dispersed after surface modification in sol-gel-derived organically modified or polymeric ligand matrices. In all cases, a significant effect on dispersibility by surface modification could be observed. After curing, the mechanical or optical properties depend strongly on the dispersion and surface modification. Using these results, composites to be used in chip coupling and as hard coatings on polycarbonate and CR 39 have been developed.

Keywords: nanocomposite, surface modification, hard coatings, transparent adhesives

1. Introduction

Sol-gel techniques for a long time have been used for the fabrication of glasses and ceramics [1–6]. The sols used for these investigations are made from alkoxides, and their stability was obtained by controlling the electric charges on the sol particles, which, in general, are in the range of several nanometers in diameter. The formation of these entities either in form of macromolecules or in form of spherical or non-spherical particles follow the established rules for nucleation and growth. For stabilization of the sols, the pH value is established in a range aside from the point of zero charge. The resulting surface charges reduce the particle-to-particle interaction to a level that no aggregation or agglomeration takes place. Thus, gelation can be prevented. Gelation takes place if the surface charges are decreased, for example, by pH change or if the particle-to-particle distance is reduced below the repulsing level [7], for example, by solvent evaporation, and the repulsion turns into attraction. If the particles grow too large, precipitation takes place. In sol-gel systems based on oxides, the particle-to-particle interaction is strong (oxide bridges accompanied by hydrogen bridges) so that, especially after drying, the agglomeration is irreversible.

As described elsewhere, the surface reactivity of the sol particles can be controlled by chemical surface modification. In this case, the concentration of uncontrollable chemically reactive groups can be reduced and substituted by a tailored reactivity, which now depends only on the reactivity of the modifiers (schematically shown in Fig. 1).

This leads to a type of stabilization which, in general, after a "gelation" provides redispersibility [8, 9]. The presence of any type of surface interacting agent during nucleation and growth, of course, interferes with the nucleation and growth process by itself. This has been described in detail elsewhere [9]. Using this approach, it is possible to fabricate sols with specific properties, not only depending on the properties of the core material but also depending on the properties of the surface modifier. This approach has been used meanwhile in many cases for the fabrication of various materials [9–14]. The change of surface properties of the small particles not only governs its chemical properties, but also influences the surrounding matrix when dispersed in liquid or solidified media. In this paper, some examples are investigated showing how sol-gel derived nanoparticles can interact with their environment and how this can be used for the development of the desired material properties.

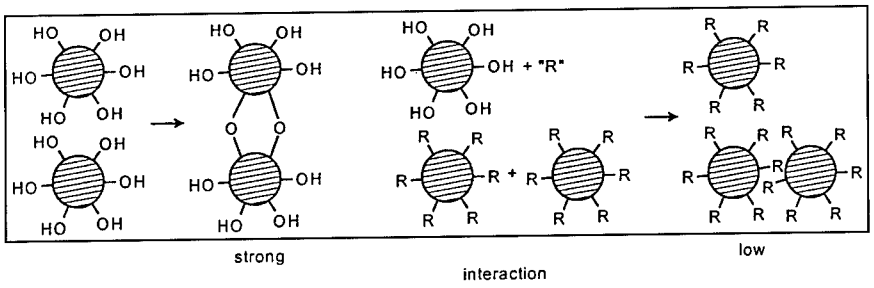

Figure 1. Effect of surface modification of sol particles on particle-to-particle interaction. "R": chemical groupings linked to oxidic particles, e.g., β-diketones, ether amines, acids.

2. Surface Modification

The basic principles of surface modification of nanoparticles have been shown elsewhere [9]. In Fig. 2, some selected examples are given [15, 16].

In general, if ceramic particle filled compounds with polymers are produced, the distribution of the particles in the matrix is obtained by mechanical forces, especially by the employment of high shear rates. With decreasing particle size, the effect of shear rate for dispersion is decreasing also, and with nanoparticles, the particle-to-particle interaction becomes the governing force. This is shown schematically in Fig. 3. In addition to this, the dispersion is more or less governed by the interfacial thermodynamics. As soon as the free energy of agglomeration is higher than the interfacial free energy, the system disperses by itself if the activation energy for given temperatures is low enough. This situation can be named as a thermodynamically stabilized dispersion and is schematically shown in Fig. 4.

One can postulate that in the case of (a), due to the strong interaction of the nanoparticles, this type of composite should show a higher viscosity, but should show a low viscosity in the case of (b), see Fig. 4. To demonstrate this phenomenon, composites have been synthesized [17] according to the following experimental route:

1 mole GPTS (glycidyloxypropyltrimethoxysilane) is hydrolyzed with 1.5 mole of water at 120°C for 24 h under reflux. Methanol is eliminated at 70°C at 20 mbar, to prepare a solvent free matrix. Colloidal silica sol (PIA-ST, Nissan Chemicals) with 20 wt% SiO_2 in isopropanol is mixed with 2 mg of tetrahexyl ammonium hydroxide (THAH) per g colloidal silica and stirred for 0.5 h. The solvent free GPTS condensate is mixed with different amounts of this colloidal silica solution and 1.5 wt% of a cationic photocuring catalyst (UVI 6974, UVI 6990) are added. Finally the solvent (isopropanol) is extracted at 50°C under 12 mbar.

These systems show a low viscosity since the crosslinking of the organic groupings has not yet taken place and can be used for photocuring of the composites. In Fig. 5 the viscosities of the surface-modified SiO_2 particle containing system is compared with the unmodified system. Even at low concentrations the unmodified system shows a rather high viscosity compared to the modified system. The effect is attributed to the modification of the SiO_2 surface by THAH, leading to a change in polarity so that no agglomeration takes place. HRTEM investigations showed that in contrast to the untreated SiO_2, the surface-modified composites show a perfect dispersion of the 7-nm particles.

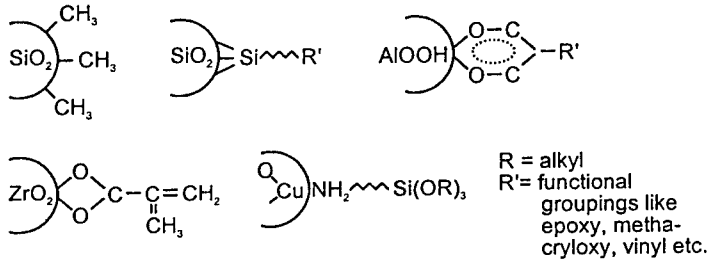

Figure 2. Some principles for surface modification of nanoparticles.

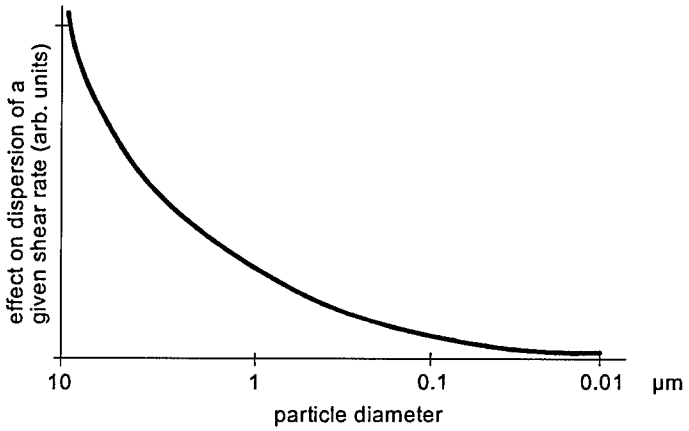

Figure 3. Significance of shear rates for a uniform dispersion of nanoparticles in nanocomposites.

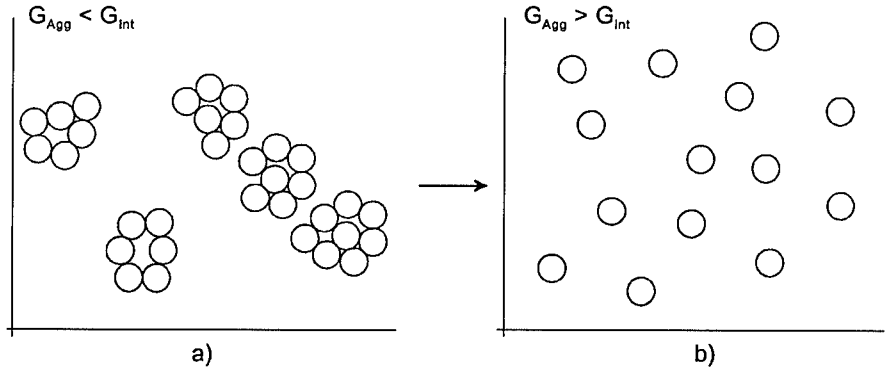

Figure 4. Effect of free energy levels on the dispersion of small particles in a low viscosity matrix: G_{Agg} = free energy of agglomeration; G_{Int} = interfacial free energy.

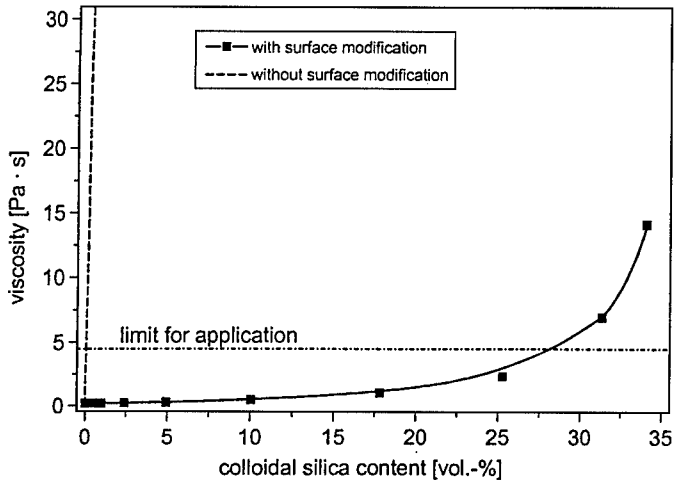

Figure 5. Viscosity of a nanomer optical glue as a function of colloidal silica content (with and without surface modification by THAH), measured after storage at 25°C for 8 days.

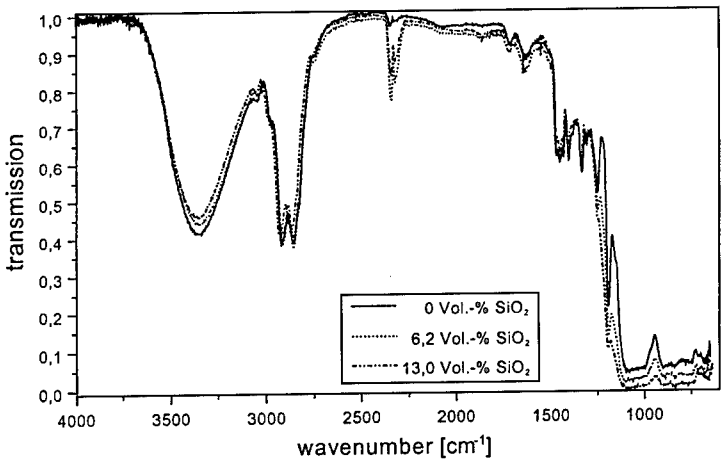

Figure 6. IR (liquid, ATR) of condensates with different colloidal silica contents.

Due to the residual number of OH groups in the system (Fig. 6), the composite, which is almost independent of the SiO_2 content, shows a very good adhesion on glass surfaces, and in combination with the overall properties of this material, a technology has been developed for using these systems for fiber-to-chip coupling. Compared to conventional sealants mainly based on epoxides or methacrylates, the thermal expansion coefficient is rather low ($30 \cdot 10^{-6}$ K^{-1}), the temperature stability is up to 250°C, and the volume shrinkage during curing is only in the range of 3.6% [18]. One of the surprising findings is that using the surface modification approach, high concentrations of nano-scaled fillers (up to 30 vol%) can be introduced into the systems without affecting the viscosity in an undesired way and without affecting the transparency, due to the perfect distribution. The high transparency is required to use these systems as an optical sealant. The use of fumed silica, for example, leads to unacceptable viscosities even in the range of 1 or 2 wt% filler.

Another example is shown with methacryloxy containing systems using SiO_2 nanoparticles and modifying them with various silanes. The experimental procedure is published elsewhere [19]. SiO_2 sols with a diameter ranging from 1000 to 10 nm were treated with two different silanes: A: Acetoxypropyltrimethoxysilane (a silane with a non-reactive grouping) and M: Methacryloxypropyltrimethoxysilane (polymerizable double bond), and introduced into a matrix consisting of 50% of methylmethacrylate and 50% of hydroxyethylmethacrylate (molar ratios). Stirring the monomer mixture with the SiO_2 sols and subsequent thermal curing including polymerization of the reaction mixture leads to transparent thermoplastic nanocomposites. Different measurements have been carried out after curing these systems. As shown in Fig. 7 the glass transition temperature T_g of the polymeric matrix obtained from differential scanning calorimetry (DSC) measurements can be varied over a wide range by introducing specially surface coated silica nanoparticles.

Whereas with 1000 nm, 250 nm and 100 nm particles no significant differences could be detected compared to the unmodified matrices; differences could be obtained for the systems with 10 nm particles, especially with those coated with modifier M. It clearly can be seen that only the modifier M, which is polymerized to the matrix shows an effect on T_g as a function of filler content and only in the nano-scale version. Covalent immobilization of matrix molecules on the surface of the M-coated 10 nm silica particles leads to a strong increase of the glass transition temperature of the polymeric matrix. This means that the interface plays an important role for the thermal properties of the composite as far as its volume fraction is large enough to play a sufficiently important role. Again one can see the influence of the particle size and the surface modifier. Modifier A cannot be polymerized and shows a far lower interface effect on the modulus than modifier M.

Information about the reinforcement behavior of nanoparticles with different surface modifications dispersed in the copolymer matrix given above can be obtained by examination of the storage modulus E′ from dynamic mechanical thermal analysis (DMTA) in the rubbery plateau region above the glass transition temperature of the polymeric matrix. The dependence of

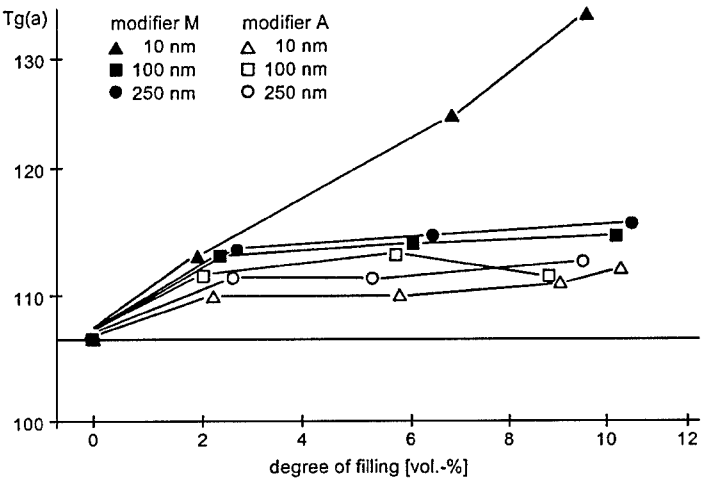

Figure 7. T_g values of SiO_2 particle filled composites (10–250 nm in diameter) with the modifiers A and M after polymerization obtained by DSC measurements.

the storage modulus on the filler surface modification and the filler content is shown in Fig. 8.

As shown in Fig. 8, the storage modulus can be increased by a factor 16 compared to the unfilled polymer matrix by introducing 10 vol% M-coated 10 nm SiO_2 particles.

Another interesting feature of surface modification is to use the surface modifier as an intermediate in order to make a sol compatible for processing purposes. In this case, the surface modifier should be easily removable so as not to disturb further processes. As shown elsewhere, nanoparticles have been used for reinforcing organic or hybrid matrices in order to increase their scratch resistance. A system based on boehmite and epoxysilanes has been developed to be used as scratch-resistant coatings for eye glass lenses [14, 20]. The detailed experimental process is described elsewhere [21]. For the preparation of the system, commercially available boehmite powder from Condea (Chemical Company) with 10–17 nm particle size has been used. These powders are stabilized with acetic acid and can be easily redispersed in diluted HCl. However, the viscosity of this system increases with time. This is attributed to the fact that the acetic acid is slowly substituted by electric charges as indicated in Fig. 9.

The viscosity increase of this system is shown in Fig. 10.

Using this type of stabilized sols directly after redispersion, quick hydrolysis and condensation reactions can be started in a mixture of GPTS (γ-glycidyloxypropyltrimethoxysilane) and TEOS (tetraethoxysilane) with a molar ratio of 5 : 3 [21]. In this first synthesis step the amount of aqueous boehmite sol corresponds to the theoretical amount of water necessary

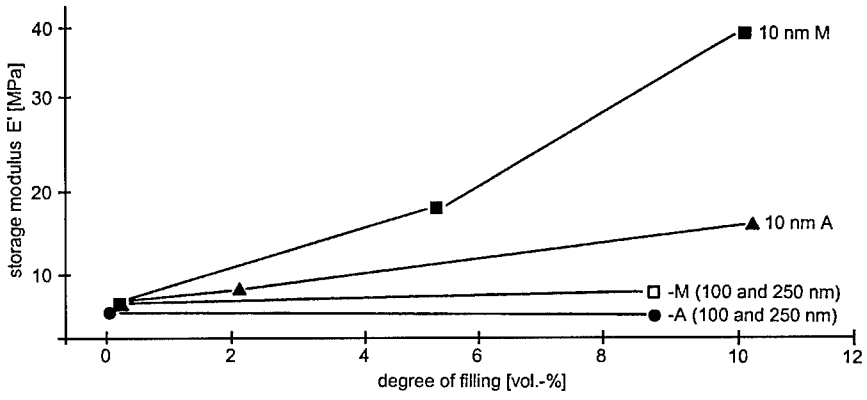

Figure 8. Storage modulus of filled MMA/HEMA composites with various filler diameters (10, 100 and 250 nm). $T = 170°C$ (rubbery regime).

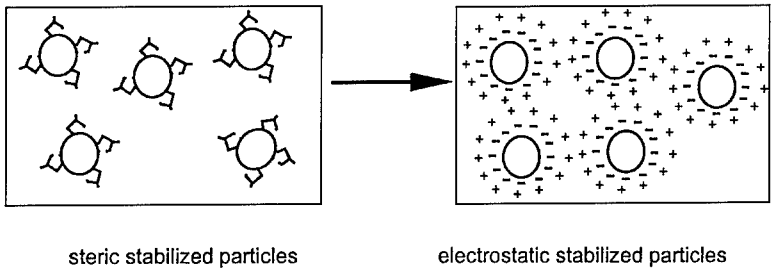

Figure 9. Change of stabilization mechanism of nano-scaled boehmite particles in aqueous media.

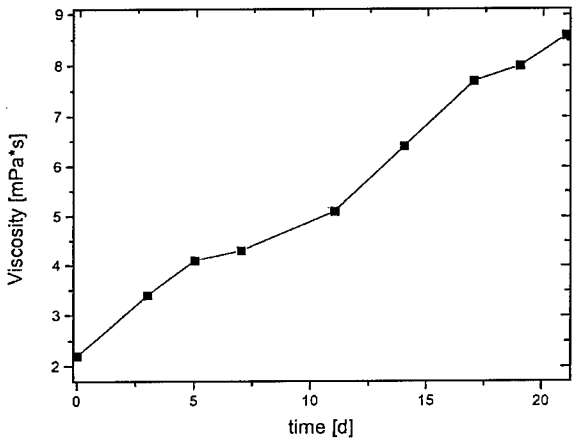

Figure 10. Changes in viscosity of an aqueous boehmite sol in dependence on the sol age.

for the half-stoichiometric hydrolysis of the silanes. After 2 h reaction time the amount of boehmite can be easily increased up to 10 wt% by a final addition of boehmite sol into the prehyrolyzed silane mixture.

It is assumed that during the mixing of the boehmite with the silanes, the acetic acid is substituted completely by the reaction of silanes to the surface. This can be demonstrated by an aluminum NMR spectroscopy (Fig. 11).

The ^{27}Al-NMR spectrum of a system containing silanes and nano-scaled boehmite particles is shown in Fig. 11. By line shape analysis of the measured spectrum a broad peak at 0 ppm and a smaller peak at 60 ppm can be detected. The peak at 0 ppm can be attributed to aluminium atoms with coordination number VI in Al—O—Al formations of the nanocrystalline boehmite particles, whereas the peak at 60 ppm results from the formation of Al—O—Si bonds, wherein the aluminium atoms show the coordination number IV. This result clearly proves the reactivity of the AlOH groups on the particle surface in regard to co-condensation reactions with the Si—OH or SiOR groups of the silanes.

If these liquids are used for coating purposes, for example, on polycarbonate, very high scratch resistances can be obtained, as shown in Fig. 12.

The superiority of the boehmite containing nanomer system in comparison to conventional siloxane coatings is demonstrated in taber abrasion and sand fall tests. After 1000 cycles of the taber abrasion test the nanomer coating shows very low haze values similar to those of glass. This result proves the extremely high scratch resistance of the coating material. Comparing the haze values after sand fall tests, it can be shown that the wear resistance of the nanomer system is even higher than the resistance of glass under this very abrasive stress (see Fig. 12).

Other investigations have been carried out to find out the role of the boehmite with respect to the formation of an organic network.

Using ^{13}C-Solid-NMR and NIR spectroscopy it was found that the characteristic signals of epoxide groups disappear during the thermal curing of GPTS-TEOS-boehmite systems (Figs. 13 and 14). In addition to this, new signals can be detected, attributed to the formation of polyethylene oxide chains. In comparison to the composite with boehmite no polymerization reactions of the expoxide groups in analogous GPTS-TEOS systems without boehmite can be detected. It can be supposed that the AlOH groups on the particle surface, which show a Lewis acidity, provoke the polymerization of the epoxides.

The experiments show clearly that an important catalytic activity of the boehmite particles can be detected. This catalytic activity contributes to the formation of an polyethyleneoxide network, which surrounds the boehmite particles (platelets and needles) and which is considered to be an important factor for the extremely high abrasion resistance of these coatings.

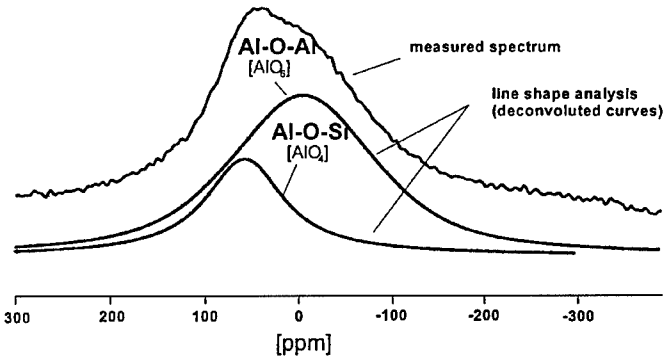

Figure 11. ^{27}Al-NMR spectra of the GPTS-TEOS-boehmite sol.

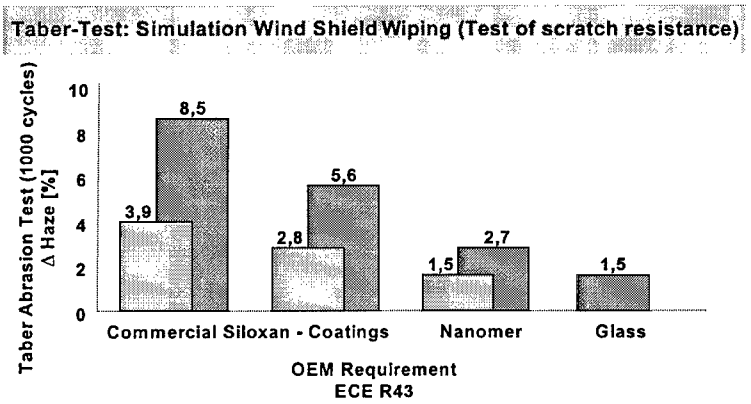

Figure 12. Abrasion properties of the boehmite type of hard coatings [21]. The boehmite/epoxysilane coating is indicator as Nanomer (*nano*particle reinforced poly*mer*).

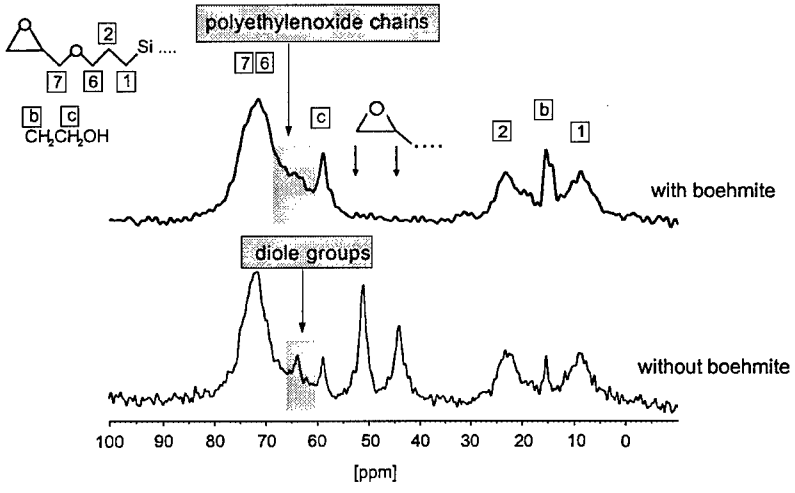

Figure 13.

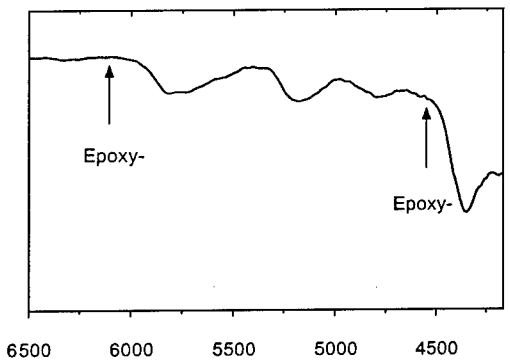

Figure 14. NIR spectrum of the boehmite containing nanomer after thermal curing.

3. Conclusion

As a conclusion it can be stated that the surface chemistry of nano-scaled particles can be considered as a key parameter for processing and properties of the materials produced with nanoparticles. Especially, if organic polymeric networks are present, the surface modifier can influence the surrounding molecular structure in a way that thermal and mechanical properties can be influenced. In addition to this, surface modifiers as intermediates can be used for improvement of the processing properties, and after the removal of the modifiers, other effects of nanoparticles such as catalytic effects can be used, for example, to improve organic cross linking.

References

1. C.J. Brinker, D.E. Clark, and D.R. Ulrich (Eds.), in *Better Ceramics through Chemistry I*, Materials Research Society Symposia Proceedings, Vol. 32 (North Holland, New York, Amsterdam, Oxford, 1994).
2. C.J. Brinker, D.E. Clark, and D.R. Ulrich (Eds.), in *Better Ceramics through Chemistry II, Materials Research Society Symposia Proceedings* (Materials Research Society, Vol. 73, Pittsburgh, PA, 1986).
3. C.J. Brinker, D.E. Clark, and D.R. Ulrich (Eds.), in *Better Ceramics through Chemistry III*, Materials Research Society Symposia Proceedings (Materials Research Society, Vol. 121, Pittsburgh, PA, 1988).
4. V. Gottardi (Ed.), J. Non-Cryst. Solids **48** (1982). North-Holland Physics Publishers, Amsterdam.
5. H. Scholze (Ed.), J. Non-Cryst. Solids **63** (1984). North-Holland Physics Publishers, Amsterdam.
6. Z. Zarzycki (Ed.), J. Non-Cryst. Solids **82** (1986). North-Holland Physics Publishers, Amsterdam.
7. O. Stern, Z. Elektrochem. **508** (1924).
8. R. Naß, S. Albayrak, M. Aslan, and H. Schmidt, in Processing and sintering of nanosized TiN, *Advanced Materials in Optics, Electro-Optics and Cummunication Technologies.* edited by P. Vincenzini (Techna Srl., Faenza, 1995), pp. 47–54.
9. H. Schmidt, Relevance of sol-gel methods for synthesis of fine particles, KONA Powder and Particle, **14**, 92–103 (1996).
10. S. Hirano, In-situ control of microstructures of ceramic composites, Funtai Oyobi Funmatsu Yakin **39**(12), 1093–1099 (1992).
11. H. Schmidt, in *Proc. Fourth International Conference on Frontiers of Polymers and Advanced Materials*, edited by P.N. Prasad, J.E. Mark, S.H. Kandil, and Z. Hafifi (Plenum Publishing Corporation, New York, USA), in print.
12. H. Schmidt, in *Proc. Symp. 9, "Neue Werkstoffkonzepte," Werkstoffwoche 1996*, edited by H. Schmidt, and R.F. Singer (DGM-Informationsgesellschaft mbH, Frankfurt/M., 1997), pp. 11–24.
13. C. Becker, M. Zahnhausen, H. Krug, and H. Schmidt, in *Ceramic Transactions: Sol-Gel Science and Technology*, edited by E. Pope, S. Sakka, and L. Klein (American Ceramic Society, 1995), Vol. 55, pp. 299–306.
14. R. Kasemann, H. Schmidt, and E. Wintrich, Mat. Res. Soc. Symp. Proc. **346**, 915–921 (1994).
15. H. Schmidt, R. Kasemann, T. Burkhart, G. Wagner, E. Arpac, and E. Geiter, in *ACS Symposium Series No. 585: Hybrid Organic-Inorganic Composites*, edited by J.E. Mark, C.Y.-C. Lee, and P.A. Bianconi (American Chemical Society, Washington, 1995), pp. 331–347.
16. C. Sanchez, oral presentation in *Organic/Inorganic Polymer Systems*, Division of Polymer Chemistry, Inc. (American Chemical Society, Napa Valley, 1995).
17. H. Krug, H. Schmidt, E. Arpac, M. Mennig, and Z. Ahmad, Verfahren zur Herstellung von Kompositmaterialien mit hohem Grenzflächenentail und dadurch erhältliche Kompositmaterialien, German Open DE 195 40 623 A1, 31-10-1995.
18. M. Mennig, private communication, details to be published later.
19. C. Becker, Ph.D. Thesis, University of Saarland, Saarbrücken, 1997, in print.
20. R. Kasemann, E. Geiter, H. Schmidt, E. Arpac, G. Wagner, and V. Gerhard, Verfahren zur Herstellung von Zusammensetzungen auf der Basis von epoxidgruppenhaltigen Silanen. German Open DE 43 38 361 A1, 10-11-1993.
21. E. Geiter, Ph.D. Thesis, University of Saarland, Saarbrücken, 1997.
22. Comparison of hard coating data on polycarbonate. Bayer Chemical Company, private communication.

Journal of Sol-Gel Science and Technology 13, 405–408 (1998)
© 1998 Kluwer Academic Publishers. Manufactured in The Netherlands.

Ceramers Based on Crosslinked Epoxy Resins-Silica Hybrids: Low Surface Energy Systems

L. MASCIA AND T. TANG
Institute of Polymer Technology and Materials Engineering, Loughborough University, Loughborough LE11 3TU, UK

Abstract. Ceramers based on silica and bisphenol-A epoxy resin cured with methyl nadic anhydride (MNA) and diamino diphenyl sulphone (DDS) were prepared in THF solutions. Compatibilization was induced through functionalization of the epoxy resin with amine trialkoxy silanes prior to mixing with a pre-hydrolyzed tetralkoxysilane solution (TEOS).

The epoxy ceramers were further modified by the addition of small amounts of a silane functionalized alkane perfluoroether oligomer.

A morphology consisting of very fine interpenetrating phases could be easily achieved through the silane functionalization of the epoxy resin. The final ceramer, however, always displayed a reduction in the glass transition temperature (T_g), resulting either from reactions of the anhydride hardener with the ethanol produced from the hydrolysis of TEOS or from the reaction of the acid catalyst with the epoxy groups.

The use of the perfluoroether oligomer produced a large reduction in surface energy due to migration of the fluorinated components to the outer layers of the films.

Keywords: epoxy, fluorine, surface energy, ceramers, organic-inorganic hybrids

Introduction

There are basically two ways of preparing organic-inorganic hybrids by the sol-gel method. These differ from each other with respect to the molecular state of the organic component, which can either be in the form of a linear polymer or as a network involving some of the metal oxide units from the inorganic component [1, 2].

Organic networks are produced from oligomers containing alkoxysilane terminal groups which are capable of reacting with the metal alkoxide, usually tetraethoxysilane. The morphology is controlled by adjusting the reaction/processing conditions [3].

There have been few reports to date on the preparation of epoxy resin/silica hybrids. Landry et al. [4] have prepared a hybrid material from a very high molecular weight epoxy resin ($M_w = 47{,}000$), functionalized with γ-aminopropyltriethoxysilane, and silica. A dioxane solution of the reactants catalyzed by 0.15 M HCl was cast in open air and subsequently allowed to gel and the solvent to evaporate over a period of 2 days. This was followed by further drying at 60°C for 2 h and a curing step at 150°C for 15 h.

Recently, Nishijima et al. [5] have reported the preparation of a hybrid material based on an epoxy resin/silica system, using tetraglycidyl-meta-xylenediamine (TGDA) as the resin and 1,2-cyclohexanedicarboxylic anhydride (HHPA) as curing agent. In this case, the hybrid was prepared by producing a silica filler, by the sol-gel method, containing N-β-aminoethyl-γ-aminopropylmethyldimethoxysilane as a coupling agent. This was subsequently incorporated in the epoxy resin mixture.

In the present study several epoxy resin-silica hybrids were prepared through telechelic functionalization of a bisphenol-A epoxy resin by means of secondary amine coupling agents based on both mono- and di-functional alkoxysilanes, using various molar ratios and always ensuring that a major amount of epoxy groups remained for crosslinking with the hardener.

The cross-linking agents, in this case, were methyl nadic anhydride (MNA) or diaminodiphenylsulphone (DDS).

A particular feature of this study is the large reduction in surface energy of the final product with the addition of small amounts of a silane functionalized perfluoroether oligomer.

Experimental

Functionalization of the Epoxy Resin

Bisphenol-A epoxy resins of different molecular weight were functionalized with varying molar amounts of phenylaminopropyltrimethoxysilane (Y-9669) and bis(γ-trimethoxysilyl propyl)-amine (A-1170), (both from OSI Specialities). The reaction was carried out at 90°C for 2 h and the progress was monitored by FTIR and ^{1}H-NMR analysis.

Preparation of Epoxy Ceramers

The silane functionalized epoxy resin was dissolved in THF at 25% concentration and measured amounts of water and TEOS at molar ratio of 3–4 : 1 were added, followed by a 32% HCl solution to bring the pH to 2–3. This precursor solution mixture was stirred for 24 h at room temperature and then cast in open PTFE molds, allowing 24 h for drying and gelation before curing at 80°C for 48 h and post-curing in steps consisting of 24 h at 120°C, 5 h at 150°C and 3 h at 180°C.

For low surface energy systems a perfluoroether oligomer corresponding to

$$HO{-}(CH_2{-}CH_2{-}O)_{1.5}{-}CH_2\{{-}(O{-}C_2F_4)_p{-}(CF_2O)_q\}_n$$
$$-CH_2{-}(O{-}CH_2{-}CH_2)_{1.5}{-}OH$$

(Fomblin ZDOL-TX, Ausimont) was telechelically extended through successive reactions with chlorendic anhydride and ε-caprolactone and then with γ-glycidoxypropyltrimethoxysilane according to previously described procedures [6, 7].

Various amounts of modified perfluoroether, after functionalization with a trialkoxysilane, were mixed with the functionalized epoxy resin and the hydrolyzed TEOS solution prior to adding the DDS hardener.

Characterization of the Ceramers

After visual inspection the morphology of the cured systems was examined by SEM (Cambridge, model 360) and TEM (JEOL, model 100CX) and the physical state was determined by thermal analysis using DSC (DuPont).

The surface energy was estimated from contact angle measurements (Kruss apparatus) and the chemical analysis of the surface layers was carried out at the Institute of Surface Science and Technology at Loughborough University, using XPS analysis at 30° and 90° incident angles to determine the approximate concentration gradient of the main elements in the outer layers.

Results and Discussion

The molar ratios of phenylaminopropyltrimethoxysilane (Y-9669) to epoxy resin (based on 50% conversion of the reactive amine groups), of different molecular weights that are required to produce a transparent ceramer film are reported in Table 1. These show that increasing the molecular weight of the resin reduces considerably the level of silane functionalization required to compatibilize the stated epoxy-silica hybrids. This can be attributed to the increased number of hydroxyl groups along the chains, which provides more favorable conditions for the formation of H-bonds between the organic phase and the silanol groups of the silica phase.

The morphology of a typical compatibilized epoxy ceramer, cured with DDS, is shown by the TEM micrographs in Fig. 1. These reveal the typical interpenetrating domains of the two phases with dimensions in the region of a few nanometers.

The data in Table 2 show that the various components of the alkoxysilane solution can interact with either the

Table 1. Effect of molecular weight of bisphenol-A epoxy resins on the amount of Y-9669 (50% conversion) for compatibilization of epoxy resin/silica hybrids, as indicated by the transparency of the films and SEM examinations.

Molecular weight epoxy resin	370	880	5000
Molar ratio of Y-9669 to epoxy resin	0.50	0.17	0.07

Table 2. Effect of nature of hardener on the T_g (°C) of the epoxy network in the resulting ceramer.

SiO_2 content (wt%)	MNA	DDS
0	103	124
2	80	93
10	63	89

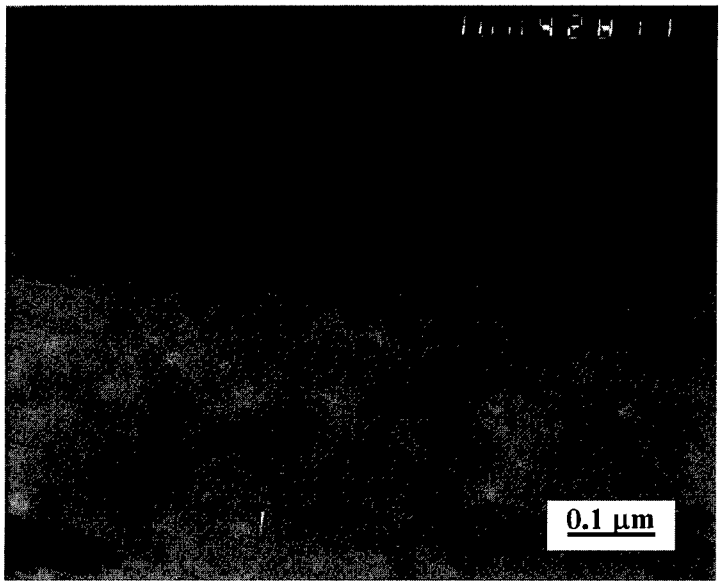

Figure 1. TEM micrograph of a typical compatibilized epoxy ceramer, cross-linked with DDS, containing 10 wt% SiO_2.

hardener or the epoxy resin in a manner that results in a reduction of the T_g of the cured resin.

An anhydride hardener will react with the alcohol produced from the hydrolysis of the alkoxysilane to produce the corresponding mono- and di-esters which have a plasticizing effect on the cured epoxy resin.

Through a series of control experiments it was established that the reduction in T_g that occurred with the use of the DDS hardener can be attributed to the reaction of HCl, used to hydrolyze the tetraethoxysilane, with epoxy groups and consequently resulting in a reduction in the crosslinked density of the organic network.

The implications are that it may be possible to minimize the reduction in crosslinking density with the use of anhydrides by removing the alcohol produced from the hydrolyzed alkoxysilane precursor solution before being mixed with the hardener. It is difficult to see, however, how this can be prevented altogether in view of the need to carry out the hydrolysis of the TEOS in acidic conditions to prevent rapid gelation of the resulting silica domains.

The surface energy results for ceramers containing different amounts of silane functionalized perfluoroethers are reported in Table 3. These results show that there is extensive migration of perfluoroether additive to the surface prior to the gelation of the silica phase, thereby considerably reducing the surface energy. It is noted that this is achievable even with levels of perfluoroligomer as low as 1%, and possibly even lower.

Table 3. Fluorine content (%) by XPS analysis and surface energy results for ceramers containing 10 wt% SiO_2 and modified with functionalized perfluoroether oligomer.

Perfluoroether (wt%)	% F at stated depth			Surface energy (mJ/m^2)
	Overall	3–5 nm	7–10 nm	
0	0	0	0	36.8
1	0.38	29.1	19.6	17.7
2	0.76	30.3	19.7	17.4
10	3.79	29.0	21.2	16.1

Table 4. Fluorine content (%) by XPS analysis of an epoxy ceramer film containing 5% functionalized perfluoroligomer cast on a glass slide.

	Air side	Glass slide side
% Fluorine		
(a) In bulk	1.90	1.90
(b) 3–5 nm depth	31.7	30.8
(c) 7–10 nm depth	27.0	28.2

The fluorine concentration on the two surfaces of a ceramer film, containing 5% functionalised perfluoroether, cast on a glass slide are reported in Table 4. The uniformity of the fluorine concentration on the two surfaces suggests that the migration of the fluoroligomer is diffusion controlled and is driven by both

the thermodynamic requirement of the system seeking to reduce its surface energy and the availability of a mechanism to allow it to do so.

Conclusions

The main conclusions that can be derived from this study are as follows:

(a) Increasing the molecular weight of the epoxy resin makes it possible to substantially reduce the extent of silane functionalization required for compatibilization with the silica domains.
(b) A large decrease in the T_g of the epoxide network is experienced even for small levels of silica in the final ceramer. This is attributed to reactions of the anhydride hardener with ethanol produced from the hydrolysis of TEOS and the reactions of the acid catalyst with the epoxy groups of the resin.
(c) A large reduction in surface energy of the final ceramer is achieved with the addition of even very small amounts of functionalized perfluoroether oligomer (i.e., 1% or less).

References

1. H.H. Huang, B. Orler, and G.L. Wilkes, Macromolecules **20**, 1322 (1987).
2. C.J.T. Landry, B.K. Coltrain, and B.K. Brady, Polymer **25**, 3715 (1992).
3. B.K. Coltrain, C.J.T. Landry, J.M. O'Reilly, J.M. Chamberlain, G.A. Rakes, J.S. Sedita, L.W. Kelts, M.R. Landry, and V.K. Long, Chem. Mater. **5**, 1445 (1993).
4. M.R. Landry, B.K. Coltrain, C.J.T. Landry, and J.M. O'Reilly, J. Polym. Sci., Polym. Phys. Ed. **33**, 637 (1995).
5. S. Nishijima, M. Hussain, A. Nakahira, T. Okada, and K. Nihara, *Mat. Res. Symp. Proc.* (Pittsburgh, PA, 1996), Vol. 435, pp. 245, 369.
6. L. Mascia, F. Zitouni, and C. Tonelli, J. Appl. Polym. Sci. **51**, 905 (1994).
7. L. Mascia and T. Tang, Polymer **39**, 3045 (1998).

Journal of Sol-Gel Science and Technology 13, 409–413 (1998)
© 1998 Kluwer Academic Publishers. Manufactured in The Netherlands.

Coating of Tetraethylorthosilicate (TEOS)/Vinyltriethoxysilane (VTES) Hybrid Solution on Polymer Films

YOUNG-JOO EO, DUK-JUN KIM AND BYEONG-SOO BAE
Department of Materials Science & Engineering, Korea Advanced Institute of Science and Technology (KAIST), Taejon 305-701, Korea

KI-CHANG SONG
Department of Chemical Engineering, Keun-Yang University, Chungnam 320-800, Korea

TAE-YOUNG LEE AND SEUNG-WON SONG
Taedok Institute of Technology, Yukong Ltd., Taejon 305-370, Korea

Abstract. Tetraethylorthosilicate (TEOS)/vinyltriethoxysilane (VTES) hybrid materials were prepared and the hydrolysis and condensation reactions during processing were investigated by means of ^{29}Si NMR solution spectroscopy. The variation of drying characteristics of the coating films was examined with respect to the tetraethylorthosilicate (TEOS)/vinyltriethoxysilane (VTES) ratio, as well as drying temperature, by FT-IR spectroscopy. It is shown that the TO mode of Si—O—Si stretching absorption was enhanced with increasing tetraethylorthosilicate (TEOS) content and drying temperature. Also, the wettability of the coating films on polymer films was independent of the solution composition but enhanced by the precoating of poly(4-hydroxystrene) (PHS) as a wetting agent. The adhesion between the coating and the films was also enhanced when the vinyltriethoxysilane (VTES) content in the coating solution was increased.

Keywords: TEOS-VTES, inorganic-organic hybrid, sol-gel coating, wetting, adhesion

1. Introduction

Inorganic-organic hybrid materials are a new type of composite material in which the inorganic and the organic components are combined at the molecular level [1, 2]. There has been much research on the application of these hybrid materials as functional coatings on glass and polymer substrates [3, 4]. In particular, coating such hybrid materials onto polymer films potentially produces a transparent, abrasion resistant coating. The organic part of the hybrid material can improve the adhesion between the coating and a polymer substrate, and the inorganic part can increase the hardness of the coating. The sol-gel method is now widely used for the preparation of hybrid material coatings, since it has the advantage of being a low temperature process and potentially giving highly homogeneous coatings.

The TEOS (tetraethylorthosilicate) and VTES (vinyltriethoxysilane) system can be used to make protective, hard, crack-free coatings on PET (polyethyleneterephthalate) film substrates [4]. It has been shown that the hardness of the PET can be increased when coated with TEOS-VTES. However, the reaction mechanisms and coating characteristics of the TEOS-VTES system have not been investigated in detail before. Therefore, the present study aims to examine the hydrolysis and condensation reactions of the TEOS-VTES system. Also, the wetting and adhesion behavior, and drying characteristics at low temperature were investigated for coatings on PP (polypropylene), and on PET.

2. Experimental

VTES (Aldrich) and TEOS (Aldrich) were used as-received with ethanol as the co-solvent, and HCl as the catalyst. Reactions were therefore conducted in the TEOS-VTES-ethanol-water-HCl system.

For NMR measurements, tetramethylsilane (TMS) was used as the reference, D_2O as the lock solvent, and chromium(III)acetylacetonate ($Cr(acac)_3$) was added to reduce the ^{29}Si spin-lattice relaxation time. The composition of the solution which was analyzed by NMR spectroscopy was TEOS : VTES = 5 : 5, EtOH/(TEOS + VTES) = 20, (water + D_2O)/(TEOS + VTES) = 10, and HCl/(TEOS + VTES) = 7×10^{-4}. Infrared spectra of coatings coated as to a Si wafer were measured using an FT-IR spectrophotometer. The compositions of this solution were TEOS : VTES = 1 : 9, 5 : 5, and 9 : 1 EtOH/(TEOS + VTES) = 2, water/(TEOS + VTES) = 4, and HCl/(TEOS + VTES) = 0.01. The solution was stirred for 1 h at room temperature and then spin coated onto a Si wafer at 1000 rpm for 30 s and dried at various temperatures for 30 min.

In order to investigate the coating ability of the solutions onto polymer films, the contact angle between the solution and PP and PET (Yukong) films was examined using the different solution compositions. Also, poly(4-hydroxystrene) (Aldrich) was precoated on the films as a wetting agent. The cross-section of the coating films was observed by SEM in order to investigate the adhesion between coatings and polymer films.

3. Results and Discussion

3.1. *NMR Spectroscopy*

The notation of Si environments in NMR spectroscopy is represented as follows. The silicon in VTES is represented by T_m^n and the silicon in TEOS is represented by Q_m^n where n denotes the number of Si—O—Si bonds surrounding the silicon and m denotes the number of —OH bonds.

Figure 1 shows ^{29}Si NMR spectra for the TEOS-VTES system. According to the chemical shifts, the

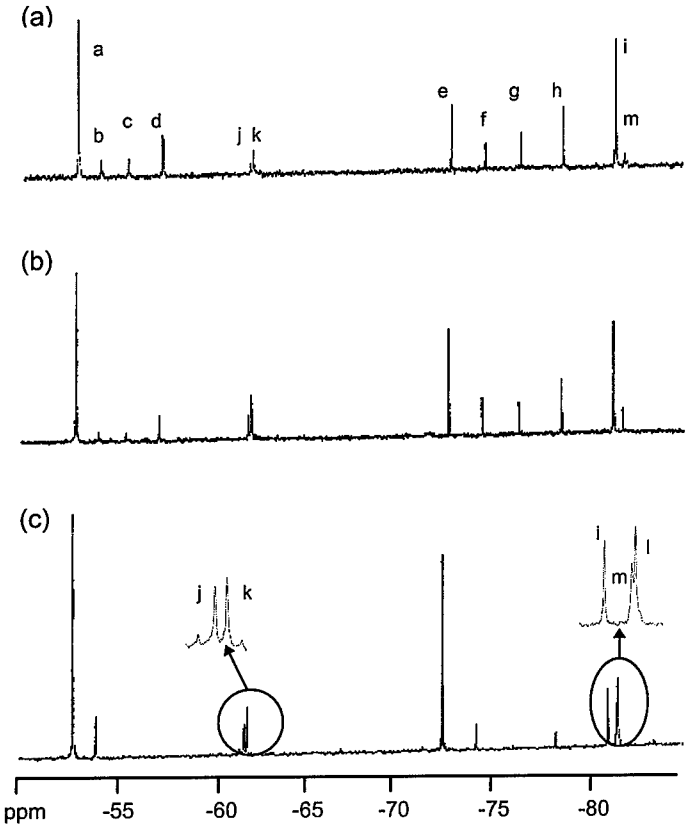

Figure 1. ^{29}Si NMR spectra of solutions of the TEOS-VTES system for reaction times: (a) 30 min; (b) 1 h and (c) 2 h.

peaks a, b, c, d are assigned to monomeric species of VTES: T_3^0, T_2^0, T_1^0, T_0^0, respectively, and the peaks e, f, g, h, i are assigned to monomeric species of TEOS: Q_4^0, Q_3^0, Q_2^0, Q_1^0, Q_0^0, respectively. In addition to the peaks of monomeric species, the peaks of dimeric species, peaks j and k in the T^1 region, and the peak m in the Q^1 region, are shown in the spectra for 30 min reaction. As the reaction proceeded, new strong dimeric species denoted peak l, in Q^1 region, appeared. Because these peaks are dependent on the structures of two silicons bonded to each other, they can provide assignment of the species produced by self-condensation and co-condensation. The assignments of dimeric species are based on the distribution of the monomeric species and the behaviour of signal intensities. Thus, the assignments are based on the assumption that two signals of dimeric species in the T^1 and Q^1 regions, having different environments of silicon, should have similar intensities in the spectra for the co-condensation reaction. One can expect two components of self-condensation and co-condensation in the T^1 region assuming perfect hydrolysis. One component for self-condensation, T_2^1 in T_2^1 T_2^1, will be independent of the intensity of any other resonance in the spectrum, while the other component for co-condensation, T_2^1 in T_2^1 Q_3^1, will always have the same intensity of one component for co-condensation, Q_3^1 resonance in Q_3^1 T_2^1, in the Q^1 region. The other component for self-condensation in the Q^1 region is Q_3^1 in Q_3^1 Q_3^1.

In the T^1 region, the intensity of peak k is stronger than that of peak j. Peak j has the same intensity as peak m, which is in the Q^1 region. Also, the T_3^0 species has the strongest intensity in the T^0 regions. Thus, peak k is produced by self-condensation of T_3^0 and can be assigned to T_2^1 T_2^1. It is also expected that peak j may be assigned to T_2^1 in T_2^1 Q_3^1 and peak m may be assigned to the Q_3^1 resonance in Q_3^1 T_2^1, both by co-condensation. As the reaction proceeded, peak l which is another component from self-condensation in the Q^1 region, Q_3^1 Q_3^1, appeared and grew very rapidly. Therefore, self-condensation of VTES was dominant in the initial condensation stage because of more rapid hydrolysis of VTES compared to that of TEOS. However, the co-condensation and the self-condensation of TEOS became the dominant reaction mechanisms as the reaction proceeded further.

3.2. *FT-IR Spectroscopy*

Figure 2 shows FT-IR spectra of the films coated on an Si wafer at various TEOS-VTES ratios as well as drying temperatures. The bonds around 1080 cm^{-1} and 1120 cm^{-1} are assigned to the asymmetric stretching absorption of the TO mode and LO mode of the Si—O—Si bond, respectively. The band at about 775 cm^{-1} is due to symmetric stretching of the Si—O—Si bond [5]. As the drying temperature and the TEOS content of the solution increased, the intensity of the absorption peak of the TO mode increased but that of the LO mode decreased. Thus, the more the Si—O—Si network was formed, the stronger the intensity of the band

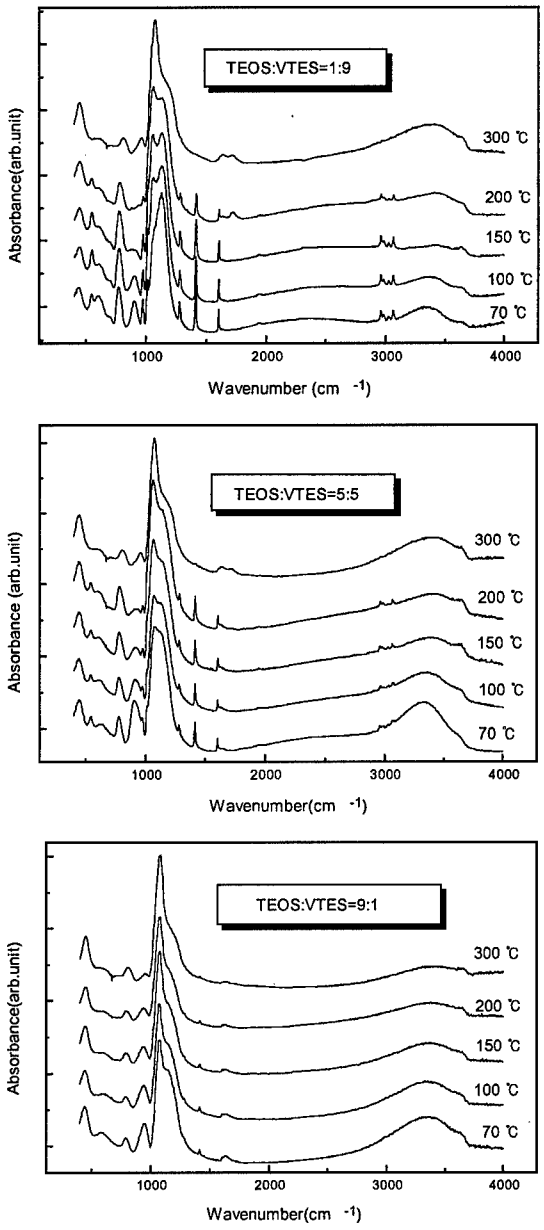

Figure 2. FT-IR spectra of the TEOS-VTES coating films dried at different temperatures for 30 mins.

Table 1. Contact angles between the solution and polymer films (±4°).

	Bare PP	Bare PET	PP on PHS	PET on PHS
TEOS : VTES = 0 : 10	39°	20°	Completely wet	Completely wet
TEOS : VTES = 1 : 9	39°	19°	Completely wet	Completely wet
TEOS : VTES = 5 : 5	42°	20°	Completely wet	Completely wet
TEOS : VTES = 9 : 1	38°	18°	Completely wet	Completely wet
TEOS : VTES = 10 : 0	41°	21°	Completely wet	Completely wet

due to the TO mode peak. The position of the TO mode band shifted to higher wavenumber and the intensity of the band at 910 cm^{-1}, assigned to the Si—OH bond, decreased with increasing drying temperature. This indicates that the polymerization of the Si—O—Si network by the condensation of Si—OH groups was enhanced. On the other hand, the band at about 1400 cm^{-1} related to the Si—C bond and that at 1600 cm^{-1} due to the C=C, bond, which were more intense for a higher content of VTES in the solution, were diminished with increasing drying temperature. Also, the other bands around 3000 cm^{-1} related with C—H bonds, which were more prominent with increasing VTES content, disappeared as the drying temperature was increased. This is due to the decomposition of these groups during the drying process.

3.3. *Wetting and Adhesion on Polymer Films*

Wetting is a necessary condition for solution coating. Solution coating onto polymer films is difficult due to the film hydrophobicity. Table 1 presents the composition dependence of the contact angles between coating solutions and PP and PET films. It is shown that the contact angles of the solution and PP were 38°–42° and for PET were 18°–21° regardless of the composition of the TEOS-VTES solution. Thus, the inorganic-organic hybridization does not effect the wetting on polymer films. However, all the films precoated with PHS, which is commonly used as a wetting agent, were completely wetted by the TEOS-VTES hybrid solution. This means that PHS can be used as a wetting agent for TEOS-VTES solution coating on polymer films.

Figure 3 shows the SEM photographs of cross-sections of ormosil coatings on PET films. It is shown that the coating films were uniform and had a very smooth surface regardless of their solution composition. However, the coatings containing a low VTES content were not attached sufficiently, but the coatings containing a high VTES content were fully attached to the PET substrate. Thus, VTES acts as an effective adhesive joint material between PET films and a SiO_2 network.

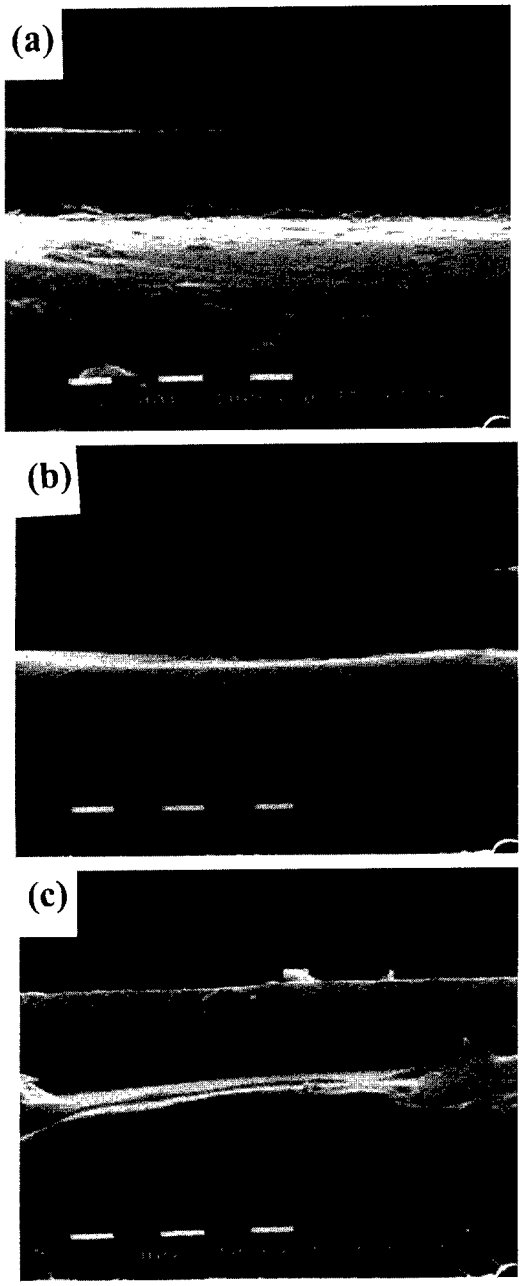

Figure 3. SEM micrographs of the cross-section of coating films on PET (a) TEOS : VTES = 1 : 9, (b) TEOS : VTES = 5 : 5, (c) TEOS : VTES = 9 : 1.

4. Conclusion

^{29}Si-NMR spectroscopy of the hydrolysis and initial condensation process of the TEOS-VTES hybrid solutions showed that TEOS and VTES are hybridized. In the FT-IR spectra, the intensity of the absorption band of the TO mode of Si—O—Si bond became dominant with an increasing degree of network connectivity; decomposition of the Si—C, the C=C and the C—H bond was found to occur during the drying process. The wettability of the solution was independent of the solution composition. However, the solution underwent complete wetting when a precoating of PHS was placed on the polymer films as a wetting agent. Adhesion between the TEOS/VTES solution coating film and the PET substrate was enhanced with increasing VTES content of the hybrid solution.

References

1. G. Phillips and H. Schmidt, J. Non-Cryst. Solids **63**, 283 (1984).
2. G.L. Wilkes, B. Orler, and H. Huang, Poly. Prepr. **26**, 300 (1985).
3. K. Tadanaga, K. Iwashita, and T. Minami, J. Sol-Gel Sci. Tech. **6**, 107 (1996).
4. T. Iwamoto and J.D. Mackenzie, J. Mat. Sci. **30**, 2566 (1995).
5. D.L. Ou and A.B. Seddon, J. Non-Cryst. Solids **210**, 187 (1997).

Journal of Sol-Gel Science and Technology 13, 415–419 (1998)
© 1998 Kluwer Academic Publishers. Manufactured in The Netherlands.

Porous Silica Obtained from Biodegradable and Biocompatible Inorganic-Organic Hybrid Materials

D. TIAN
Center for Education and Research on Macromolecules (CERM), University of Liège, Sart-Tilman, B6, 4000 Liège, Belgium

S. BLACHER
Service de Génie Chimique, University of Liège, Sart-Tilman, B6, 4000 Liège, Belgium

PH. DUBOIS
Center for Education and Research on Macromolecules (CERM), University of Liège, Sart-Tilman, B6, 4000 Liège, Belgium

J.P. PIRARD
Service de Génie Chimique, University of Liège, Sart-Tilman, B6, 4000 Liège, Belgium

R. JÉRÔME
Center for Education and Research on Macromolecules (CERM), University of Liège, Sart-Tilman, B6, 4000 Liège, Belgium

Abstract. Porous silicas have been successfully prepared from poly(ε-caprolactone) (PCL)-silica hybrid materials based on the template approach. The final texture of the porous silica can be tailored by the PCL template, i.e., molecular weight and molecular weight distribution, content, type and number of reactive end-groups per chain. Porosity has been investigated by nitrogen adsorption-desorption technique and small angle X-ray scattering (SAXS).

Keywords: porous silica, inorganic-organic hybrid, pyrolysis, texture characterization

1. Introduction

Porous materials, such as silica [1–3], are emerging as a new area of great technological and scientific interest. One method to obtain porous silica is the template-based approach [2, 5], in which porosity is created by removing the incorporated template from the silica network. The porosity is therefore tailored by the design of the template. Recently, we have reported on novel biodegradable and biocompatible inorganic-organic hybrid materials prepared by the sol-gel process [6–9]. Poly(ε-caprolactone) (PCL), well-known for its biocompatibility, permeability and biodegradability, has been successfully incorporated into silica network. The organic (PCL) and inorganic (SiO_2) constitutive components are associated not only by covalent bonds (in case of end-reactive PCL) but also by hydrogen bonding (between the carbonyl groups of PCL and the residual OH groups on silica) [8]. "In vitro" cell culture and biodegradation tests have demonstrated that these new inorganic-organic hybrid materials are biomaterials with biodegradable and

biocompatible properties [7]. Dynamic mechanical properties and the phase morphology of these new hybrid materials have also been reported elsewhere [9]. In this paper, we report on the preparation of porous silicas by the template approach involving the deliberate removal of the organic component, i.e., PCL chains.

2. Experimental

Synthesis of α,ω-hydroxyl PCL ($M_n = 2000$ and 4000) and α,ω-triethoxysilane PCL ($M_n = 2000$) has been detailed elsewhere [8]. PCL-diol ($M_n = 1250$) and PCL-triol ($M_n = 900$) (Aldrich) were used as received. PCL/TEOS (tetraethoxysilane (Janssen)) mixtures of various compositions were dissolved in THF (20 wt%) and hydrolyzed by a stoichiometric amount of water with respect to the alkoxide functions. HCl was used as a catalyst with a 0.05/1 HCl/TEOS molar ratio. A representative synthesis was as follows: 1.5 g TEOS was added to the α, ε-triethoxysilane PCL (0.5 g, $M_n = 2000$) solution in THF (10.0 ml) and thoroughly mixed until a homogeneous solution was formed. Then deionized water (0.54 ml), ethanol (0.80 ml) and HCl (0.01 ml) were added with rapid stirring at ambient temperature for ca. 10 min. The clear solution was then cast into a plastic Petri dish and covered with a Parafilm for several days, depending on the PCL end-groups (hydroxyl or triethoxysilane) [5]. The gelified material was then dried under ambient conditions for one week and finally cured at 100°C for 2 days. The usual film thickness was 0.1–1 mm. Porous silica was prepared by pyrolysis of the silica-PCL hybrid materials at 400°C under an air flow (100 ml/min) until no weight loss was detected by thermogravimetric analysis (TGA).

Nitrogen adsorption-desorption isotherms were measured at the boiling temperature (77 K) of liquid nitrogen (99.98%) with a Sorptomatic Carlo Erba 1900. Small-angle X-ray scattering (SAXS) measurements were carried out at the "Laboratoire pour l'Utilisation du Rayonnement Electromagnetique" (LURE; Orsay France) on DCI (D24 station). The size of the X-ray beam ($\lambda = 1.488$ Å) at the sample was smaller than 1 mm^2, so that no desmearing of the data was required. The scattered X-rays were detected with an Argon-CO_2 gas-filled, one-dimensional position-sensitive detector (with a resolution of 0.4444 mm). The sample-to-detector distance (1151 mm) allowed SAXS data to be recorded in the 0.02 to 0.8 nm^{-1} s range. These data were plotted as relative intensity versus s after correction for parasitic scattering and sample absorption. The background scattering was corrected in the standard manner.

3. Results and Discussion

The effect of molecular weight of the PCL template on the final texture of porous silica has been studied. Figure 1 shows the nitrogen adsorption-desorption

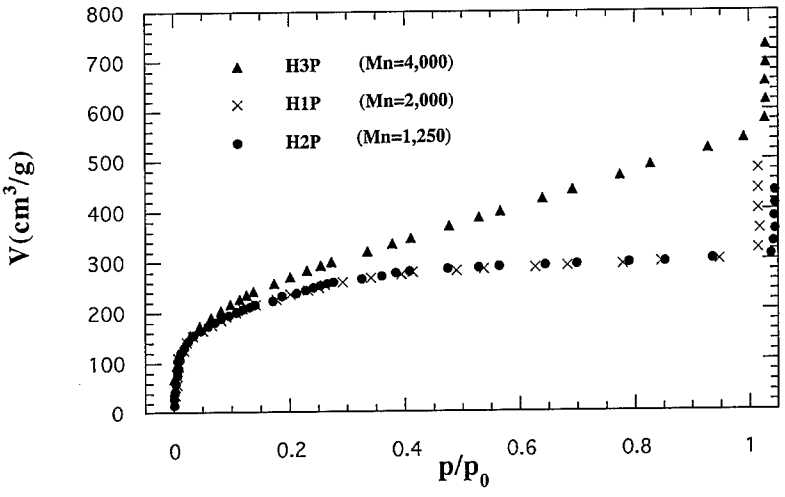

Figure 1. Nitrogen adsorption-desorption isotherms for the silica/α,ω-hydroxyl PCL samples after pyrolysis: effect of the PCL molecular weight.

Table 1. Main characteristics of the PCL-templated porous silica.

Samples	End-groups of PCL chains	M_n of PCL	M_n/M_n of PCL	PCL wt%	[a]S_{BET} (m^2/g)	[a]V_T (cm^3/g)	[a]W_{DR} (cm^3/g)	[a]r (nm)	[a]R_g (nm)	[a]P
H1	PCL-diol	1250	1.45	46.5	844	0.785	0.449	0.97 ± 0.22	6.70	2.90
H2	α,ω-hydroxyl	2000	1.50	46.5	876	0.634	0.452	0.93 ± 0.30	6.50	3.80
H3	α,ω-hydroxyl	4000	1.50	46.5	1017	1.132	0.668	1.49 ± 0.48	5.05	2.60
H4	α,ω-hydroxyl	4000	1.50	27.8	515	0.536	9.232	0.72 ± 0.16	3.60	2.50
H5	α,ω-hydroxyl	4000	1.50	15.5	94	0.390	0.043	—	—	—
H6	α,ω-triethoxysilane	2000	1.50	45.8	653	0.58	0.309	0.83 ± 0.21	4.95	2.70
H7	PCL-triol	900	1.40	46.5	870	0.626	0.415	0.67 ± 0.33	6.40	2.80
H8	α,ω-methyl	4000	1.25	46.5	872	0.640	0.544	0.89 ± 0.21	6.17	2.60

[a]Indicate textural characteristics after pyrolysis.

isotherms for samples H1P, H2P and H3P, that contain 46.5 wt% α,ω-PCL template of different molecular weights M_n, i.e., 1250, 2000 and 4000, respectively (Table 1). The isotherms of the H1P and H2P samples can be clearly identified as type I isotherm according to the BDDT classification [10], which is characteristic of microporous materials (pore width $w < 2$ nm). For the sample H3P, the isotherm cannot be clearly identified with one of the typical BDDT isotherms. t-Plots [11] (Fig. 2) exhibit downward deviations with respect to the straight line passing through the origin for the three samples. Nevertheless, the H3P deviation is more gradual and appears at a higher adsorbed volume than for H2P and H1P. This feature indicates that pores are larger and their size distribution is broader in H3P compared to the pores in the other two samples H2P and H1P. Table 1 shows the BET specific surface area (S_{BET}) obtained by the BET technique [11] in the classical range (0.05–0.20); the porous volume (V_T) calculated from the adsorbed volume at saturation; the microporous volume (W_{DR}) calculated by the Dubinin-Raduskevich equation [11] and the mean pore size and corresponding standard deviations calculated by the Brunauer's method [11]. These results show that pyrolysis of the H1P, H2P, H3P samples leads to very heterogeneous microporous materials, in which the mean pore size, the pore size distribution, the specific surface area, the microporous volume and the total volume, increase with the molecular weight of the PCL template.

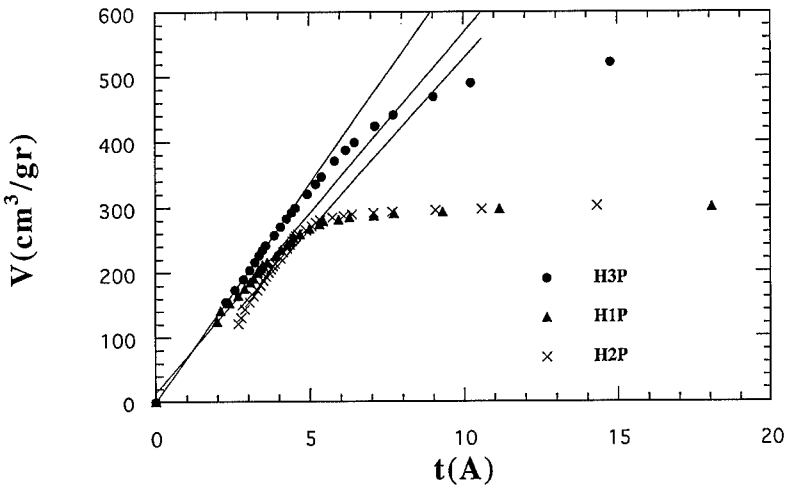

Figure 2. t-Plots for the samples H1P, H2P and H3P (see Table 1).

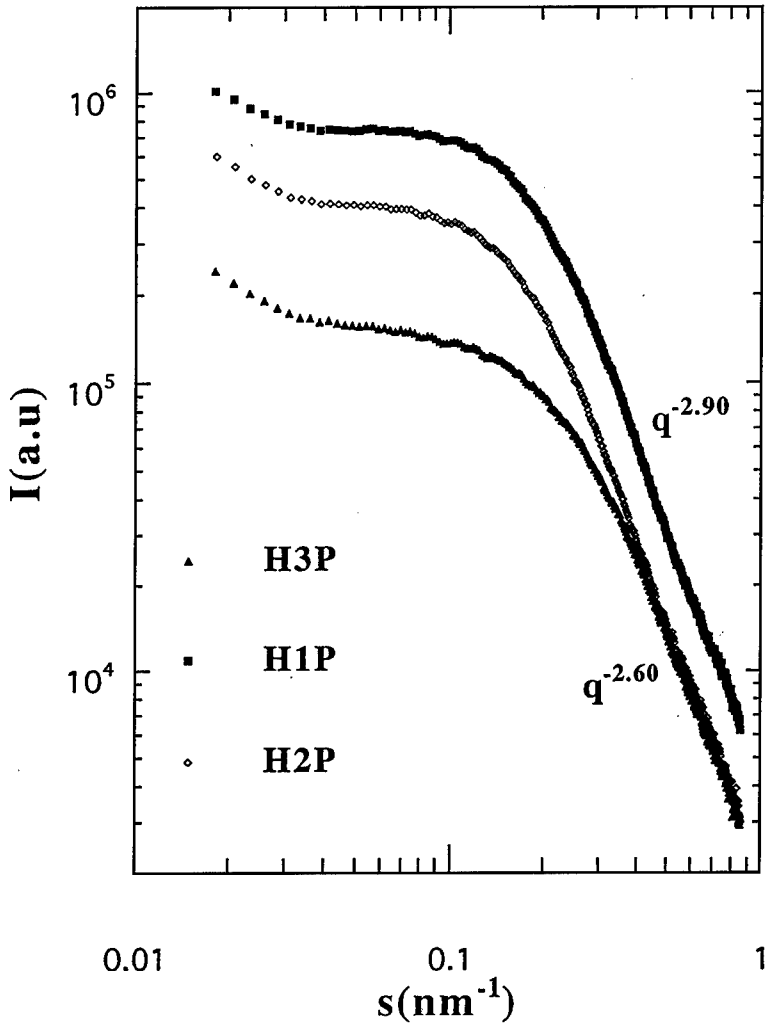

Figure 3. SAXS profiles for the samples H1P, H2P and H3P (see Table 1).

The scattered intensity, I, has also been measured over a range of scattering vectors s defined as $s = 2\lambda^{-1}\sin(\theta/2)$, where λ is the wavelength of the incident photons and θ is the total scattering angle. Porod's law, $I \alpha s^{-P}$, is valid for scattering between sharp surfaces. For $1 < P < 3$ the material has a mass/pore fractal structure of dimension $D_{m/p} = P$. If $3 < P < 4$, there is a surface fractal structure of dimension $D_s = 6 - P$ [12]. The limiting values $P = 3$ and 4 are characteristic of uniformly dense structures and smooth surfaces, respectively. Figure 3 compares the SAXS curves for pyrolyzed PCL-silica hybrid materials that originally contained PCL of different molecular weights (samples H1P, H2P and H3P). For the low s regime the SAXS curves are almost flat indicating the absence of any structure. From Guinier's law [12], the particulate radius of gyration, R_g, has been calculated (Table 1). For high s values, a linear regime extends over a length scale that depends on the molecular weight of the PCL template. Upon increasing molecular weight of PCL, R_g decreases from 7 to 5 nm and P from 2.90 to 2.60. These values agree with a mass/pores fractal structure. Finally, taking into account the pore size distribution for the samples as obtained from adsorption-desorption measurements and the R_g values (Table 1), we can infer that the microporosity is intra-particle in the H1P and H2P samples and it could be intra- and inter-particle in the H3P sample.

The amount of the PCL template ($M_n = 4000$) has also been varied (46.5, 27.8 to 15.5 wt% in samples H3P, H4P and H5P, respectively), see Table 1. For the non-porous H5P material (shown by the adsorption-

desorption isotherm), a decrease in the amount of PCL template yields microporous materials that contain less micropores. These micropores are smaller in size and have a narrower size distribution. This is consistent with the S_{BET}, V_T and W_{DR} data (Table 1). SAXS profiles confirm the adsorption results, since both the R_g and the fractal dimension value (P) decrease as the amount of PCL decreases.

The effect of the PCL template end-groups, and their number per chain, on the final texture of the porous silica has been studied by comparing the H1P, H2P, H6P, H7P and H8P samples (Table 1). As reported previously [8], when the amount of PCL is kept constant, an increase in the reactivity and number of the PCL end-groups favors the incorporation of PCL into the silica network. After pyrolysis, it is observed that increasing either the reactivity of the PCL end-groups or their number per PCL chain has the same effect on the final texture of the porous silica (see samples H2P and H6P, samples H1P and H7P in Table 1). The adsorption-desorption isotherms, the t-plots, and the SAXS measurements (not shown) indicate that the microporous silica templated with PCL α,ω-hydroxyl PCL rather than α,ω-α,ω-triethoxysilane PCL has a broader pore size distribution, which however excludes small pores and a possible sieve effect. The same conclusion holds when PCL-diol and PCL-triol are compared. Table 1 shows that all the experimental sizes are larger for samples H2P and H1P than for samples H6P and H7P, respectively, indicating a more open porosity. However, the reverse behavior is observed for samples H3P (α,ω-hydroxyl PCL template) and H8P (α,ω-methyl PCL template which is non-reactive in the sol-gel process), see Table 1. Indeed, a broader pore size distribution (at the exclusion of small pores with sieve effect) is promoted by the hydroxy terminated PCL in contrast to the α,ω-methyl PCL template. This indicates that the reactivity of the PCL template end-groups is not as important as the molecular weight distribution of the template (see Table 1, samples H3P and H8P). As expected, microporous silica templated with PCL of a narrower molecular weight distribution has a smaller microporous size with a narrow size distribution and, smaller S_{BET}, V_T and W_{DR} values (Table 1, samples H8P and H3P).

4. Conclusion

Porous silicas have been successfully prepared by pyrolysis of silica-PCL hybrid materials based on the template approach. This structure has been analyzed by two independent characterization methods. The silica microporosity can be tailored by the amount of the PCL template, molecular weight and molecular weight distribution of the PCL template and by the reactivity and number of the PCL end-groups.

Acknowledgment

The authors are very much indebted to the "Services Fédéraux des Affaires Scientifiques, Techniques et Culturelles" for general support to CERM in the frame of the "Pôles d'Attraction Interuniversitaires: Polymères." They warmly thank R. Sobry, B. Diez and P. Van den Bosshe for SAXS measurements (Laboratory of Experimental Physics, University of Liège, Belgium). Ph. Dubois is "Chercheur qualifié" by the Belgium FNRS.

References

1. C.T. Kresge, E.E. Leonowicz, W. Roth, J.C. Vartuli, and J.S. Beck, Nature **359**, 710 (1992).
2. N.K. Raman, M.T. Anderson, and C.J. Brinker, Chem. Mater. **8**, 1682 (1996).
3. C.J. Brinker, and G.W. Scherer, *Sol-Gel Science: The physics and Chemistry of Sol-Gel Process* (Academic Press, London 1980).
4. D.W. Schaefer, MRS Bull. **19**, 14 (1994).
5. J.S. Beck, J.C. Vartuli, G.L. Kennedy, C.T. Kresge, W. Roth, and S.E. Schramm, Chem. Mater. **6**, 1816 (1994).
6. D. Tian, Ph. Dubois, and R. Jérôme, Polymer **37**, 3983 (1996).
7. D. Tian, Ph. Dubois, Ch. Grandfils, R. Jérôme, P. Viville, R. Lazzaroni, J.L. Brédas, and P. Leprince, Chem. Mater. **9**, 871 (1997).
8. D. Tian, Ph. Dubois, and R. Jérôme, J. Polym. Sci., Polym. Chem. **35**, 2295 (1997).
9. D. Tian, S. Blacher, Ph. Dubois, and R. Jérôme, Polymer **39**, 855 (1998).
10. S. Brunauer, P.H. Emmet, and E. Teller, J. Amer. Chem. Soc. **60**, 309 (1938).
11. S.J. Gregg and K.S.W. Sing, Adsorption, *Surface Area and Porosity* (Academic Press, London, 1982).
12. J.E. Martin, A.J. Hurd, J. Appl. Cryst. **20**, 61 (1987).

Journal of Sol-Gel Science and Technology 13, 421–425 (1998)
© 1998 Kluwer Academic Publishers. Manufactured in The Netherlands.

Preparation of Saccharide-Silica Composites by a Sol-Gel Method and the Application for Optical Resolution of Metal Chelate Compounds

Y. AKIYAMA
Faculty of Science and Technology, Science University of Tokyo, 2641 Yamazaki, Noda, Chiba 278, Japan

F. MIZUKAMI AND H. IZUTSU
National Institute of Materials and Chemical Research 1-1, Higashi, Tsukuba, Ibaraki 305, Japan

M. SATO
Faculty of Science and Technology, Science University of Tokyo, 2641 Yamazaki, Noda, Chiba 278, Japan

K. MAEDA AND Y. KIYOZUMI
National Institute of Materials and Chemical Research 1-1, Higashi, Tsukuba, Ibaraki 305, Japan

K. SAKAGUCHI
Faculty of Science and Technology, Science University of Tokyo, 2641 Yamazaki, Noda, Chiba 278, Japan

Abstract. A novel organic-inorganic composite was prepared by a sol-gel process using hydrolysis and condensation of tetraethoxysilane (TEOS) reacted with a saccharide. During the process, ethoxy groups of the TEOS were replaced with hydroxyl groups of the saccharide and, consequently, saccharide molecules were combined with silica through their hydroxyl groups. Samples obtained under different reaction conditions were used for optical resolution of a metal chelate compound. The resolution ability of the composites was affected by the amount of water added for hydrolysis and of the saccharide. In particular, the amount of water drastically influenced the optical resolution performance. Composites obtained at the lower H_2O/TEOS ratio gave the metal chelate compound a higher optical rotation. Three types of composites with the same composition were prepared by kneading, impregnation and by the sol-gel method, and were compared. The sol-gel composite showed the best optical resolution ability. It was concluded that the optical resolution ability was closely related to dispersibility of saccharide in the silica matrix.

Keywords: inorganic-organic composite, saccharide-silica composite, D-fructose silica, molecular recognition, optical resolution

1. Introduction

Many composites of silica combined with optically active organic compounds have been prepared and used in chromatography [1–3]. Silica is used only as a support to fix an optically active compound on the surface because of its mechanical strength, stability and high surface area. We have suggested that composites with organic compounds dispersed in the silica matrix should have different properties from those with organic compounds fixed on the silica surface using spacer molecules. In previous reports [4], we showed that silica composites combined with L-tartaric acid and saccharide molecules by a sol-gel method

exhibit an optical resolution ability and that the molecular recognition ability is influenced by the reaction conditions. Here, in a further investigation of sol-gel saccharide silica composites, the D-fructose-silica composites were prepared by sol-gel, kneading and impregnation methods. The dispersibility of D-fructose molecules in the composites were evaluated on the basis of XRD and NMR together with the optical resolution of a racemic metal chelate compound.

2. Experimental

2.1. *Preparation of Three D-Fructose SiO_2 Composites*

Kneading D-fructose SiO_2 (Kned-fru) and impregnation D-fructose SiO_2 (Imp-fru) were prepared by the same procedure as described in a previous report [4]. Sol-gel D-fructose SiO_2 (SG-fru) was prepared as follows; TEOS (0.60 mol) was mixed with D-fructose (0.04–0.40 mol) in ethanol (0.20 mol) in the presence of acetic acid (0.20 mol) at 70°C for 2 h. Water (0.1–2.0 mol) was added to the reaction mixture at the same temperature and allowed to stand for 6–60 h to give a gel. The resulting gel was dried at 70°C under reduced pressure. In the sol-gel procedure, various composite samples were prepared by changing the ratios of D-fru/TEOS and H_2O/TEOS to investigate the effect of the reaction conditions on the resolution performance of the composites. The SG-fru samples obtained using 0.04, 0.08, 0.12, 0.20, 0.30 and 0.40 mol D-fructose were denoted as SG-fru004, SG-fru008, SG-fru012, SG-fru020, SG-fru030 and SG-fru040, respectively. Likewise, the SG-fru samples obtained using 0.10, 0.20, 0.40, 0.80, 1.20, and 2.00 mol water were denoted as SG-W01, SG-W02, SG-W04, SG-W08, SG-W12 and SG-W20, respectively.

2.2. *Packing and Elution*

All composites were finely ground to sizes smaller than 200 mesh and slurried with a benzene: *n*-hexane mixture (1 : 1 v/v). The slurry was packed in a glass tube (6 mm I.D. × 400 mm column length). Racemic $Co(acac)_3$(10 mg) dissolved in benzene was placed on the top of the packing and eluted with a benzene: *n*-hexane mixture (1 : 1 v/v).

2.3. *Measurements and Characterization*

The X-ray diffraction (XRD) patterns were recorded on a MAC Science MXP 18 instrument using CuK_α radiation with a nickel filter. The circular dichroism (CD) spectra were recorded on a JASCO J-600 spectropolarimeter. The first fraction eluted from the column, whose absorbance showed ca. 0.7, was taken for an evaluation of the optical resolution ability. The ^{13}C CP/MAS-NMR was measured on a Bruker AMX-500.

3. Results and Discussion

3.1. *Characterization of Sol-Gel D-Fructose Composites*

Figure 1 shows XRD patterns of sol-gel D-fructose SiO_2 obtained at different ratios of H_2O/TEOS when

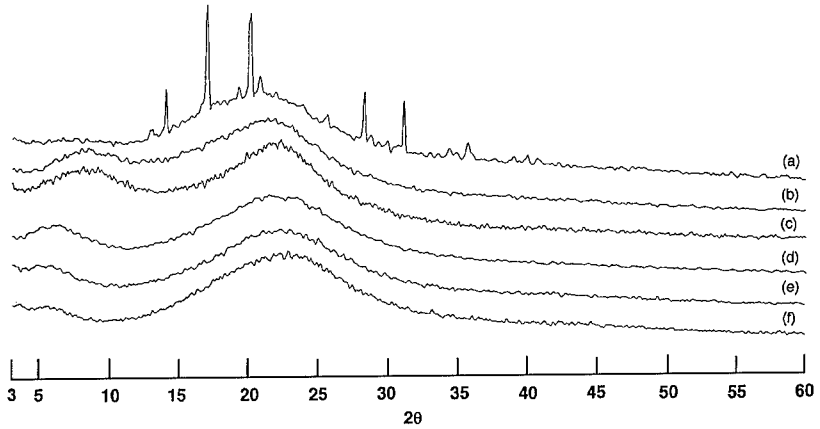

Figure 1. XRD patterns of sol-gel D-fructose SiO_2 composites obtained for different reaction conditions as shown in Table 3. (a) SG-W01; (b) SG-W02; (c) SG-W04; (d) SG-W08; (e) SG-W12; (f) SG-W20.

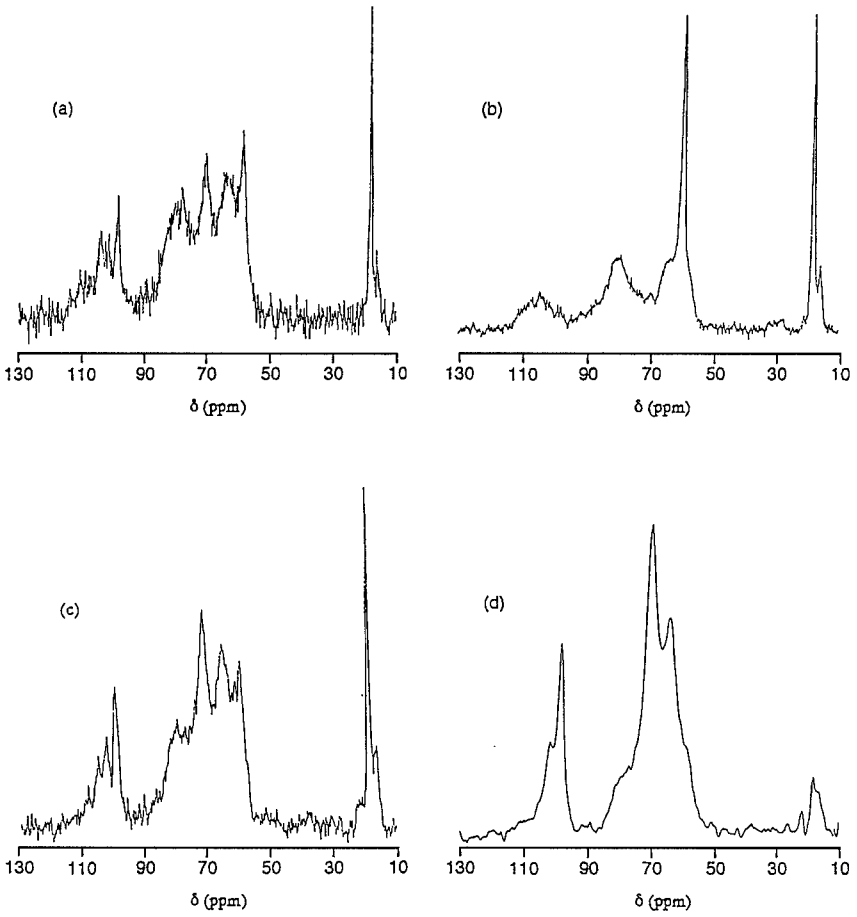

Figure 2. ^{13}C MAS-NMR spectra of sol-gel D-fructose SiO_2 composites as shown in Table 3. (a) SG-W01; (b) SG-W02; (c) SG-W08; (d) SG-W20.

the ratio of D-fru/TEOS was 0.2/0.6. Except for SG-W01, all the samples did not show clear XRD peaks, while SG-W01 showed sharp peaks assigned to crystalline D-fructose. This means that the D-fructose in SG-W01 is in the form of large crystals or 'lumps'.

Figure 2 shows ^{13}C MAS-NMR spectra of SG-W20 (a), SG-W08 (b), SG-W02 (c) and SG-W01 (d). Signals around 98.0, 70.0 and 64.0 ppm are assigned to C-2/C-4/C-5 and C-3/C-1 and C-6 sites of D-fructose, respectively, based on comparison with reported data [5]. Signals around 58.4 and 18.1 ppm in Figs. 2(a), (b), and (c) were assigned to the unhydrolyzed ethoxy group of TEOS. All the signals originating from D-fructose in the composites were broader than those of pure crystalline D-fructose. In particular, in SG-W08, the signals were much broader. This broadening suggests that D-fructose molecules exist in different states reflecting many possibilities in the connection of the hydroxy groups of D-fructose with silica, which, may reflect the high dispersion of D-fructose molecules in the silica matrix of SG-W08.

3.2. *Optical Resolution Ability of D-Fructose-Silica Composites*

Table 1 represents the molecular circular dichroism ($\Delta\varepsilon$) of the eluates obtained with Kned-fru, Imp-fru and SG-fru. The D-fru/SiO_2 ratios of these three composites were almost the same. As shown in Table 1, Kned-fru and Imp-fru showed little resolution of $Co(acac)_3$. As reported previously [4], D-fructose molecules were highly dispersed by the sol-gel method, probably at the molecular level in or on the silica matrix, while the kneading and impregnation methods gave less dispersed composites. This difference reflected the

Table 1. Optical resolution of $Co(acac)_3$ with different D-fructose silica composites.

	D-fructose (mol)	SiO_2 (mol)	$\Delta\varepsilon$ (328 nm)
Kneading D-fructose silica	0.2	0.6	+0.05
Impregnation D-fructose silica	0.2	0.6	+0.08
Sol-gel D-fructose silica[a]	0.2	0.6	+17.5

[a] H_2O/TEOS (mol/mol) = 0.2/0.6.

Table 2. Influence of the amount of water added on the optical resolution.

	H_2O (mol)	TEOS (mol)	D-fructose (mol)	$\Delta\varepsilon$ (328 nm)
SG-fru004	2.0	0.6	0.04	No elution
SG-fru008	2.0	0.6	0.08	No elution
SG-fru012	2.0	0.6	0.12	+13.7
SG-fru020	2.0	0.6	0.20	+17.5
SG-fru030	2.0	0.6	0.30	+3.35
SG-fru040	2.0	0.6	0.40	+0.61

respective optical resolution abilities. A racemic form of $Co(acac)_3$ was resolved into the enantiomers by the sol-gel D-fructose composites, giving at first eluates with positive $\Delta\varepsilon$.

Table 2 gives the $\Delta\varepsilon$ of eluates from the sol-gel composites with different D-fructose/SiO_2 ratios. $Co(acac)_3$ was not eluted from SG-fru004 and SG-fru008 because interaction between the complex and the silica surface was very strong. Except for these two samples, the optical resolution ability or $\Delta\varepsilon$ increased with an increase in the ratio of D-fru/TEOS, reaching a maximum (+17.5) with SG-fru020, and then suddenly decreasing with further increase in the ratio. On the other hand, although XRD patterns of SG-fru004, 008, 012, 020, 030 and 040 indicated an amorphous structure, a new halo appeared around $2\theta = 18°$ with an increase in the D-fructose content, as shown in Fig. 3. The halo probably corresponds to a D-fructose derived syrupy component. Thus, the decrease of $\Delta\varepsilon$ from +17.5 to +.335 or +0.61 may be due to the increase of the syrupy component, which may cover D-fructose molecules dispersed at the molecular level on the surface of the silica matrix.

Table 3. Influence of the amount of D-fructose added on the optical resolution.

	H_2O (mol)	TEOS (mol)	D-fructose (mol)	$\Delta\varepsilon$ (328 nm)
SG-W01	0.1	0.6	0.2	+24.0
SG-W02	0.2	0.6	0.2	+47.0
SG-W04	0.4	0.6	0.2	+5.30
SG-W08	0.8	0.6	0.2	+1.43
SG-W12	1.2	0.6	0.2	+3.20
SG-W20	2.0	0.6	0.2	+17.5

$\Delta\varepsilon$ of optically pure $Co(acac)_3$ seems to be −100.9 or +103.9 at 328 nm [4].

Next, at the D-fru/TEOS ratio of 0.2/0.6, the influence of added water was investigated (Table 3). Firstly, the optical resolution ability increased with an increase in the H_2O/TEOS ratio, reaching a maximum, then decreasing with increasing water content to give a minimum, and than increasing with the H_2O/TEOS ratio once again. This tendency was confirmed to be reproducible. At present, although it is difficult to understand the phenomenon, it is probably related to the substitution of ethoxy groups of TEOS with D-fru and the changes in hydrolysis-dehydration-condensation of

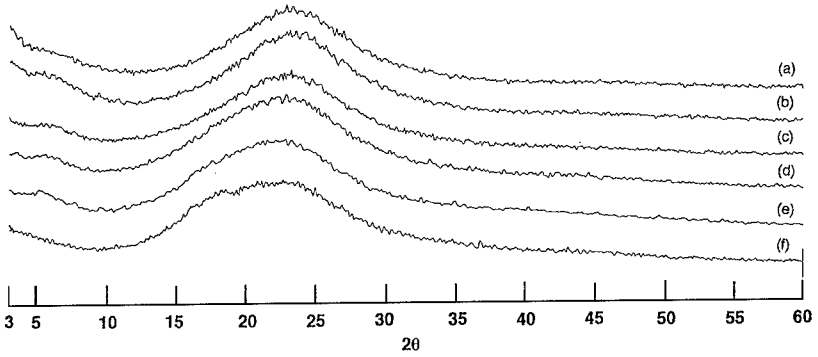

Figure 3. XRD patterns of sol-gel D-fructose SiO_2 composites obtained at different reaction conditions as shown in Table 2. (a) SG-fru004; (b) SG-fru008; (c) SG-fru012; (d) SG-fru020; (e) SG-fru030; (f) SG-fru040.

TEOS with the amount of water added, as discussed below.

3.3. *Inclusion Mechanism of D-Fructose into Silica Matrix*

In the system of TEOS, D-fru and water in the presence of acetic acid, the following reactions (1)–(6) are proposed to occur:

(1) $Si(OEt)_4 + \text{D-fru} \rightarrow Si(OEt)_x\ (\text{D-fru})_y + n\text{EtOH}$
(2) $Si(OEt)_4 + H_2O \rightarrow Si(OEt)_3(OH) + \text{EtOH}$
(3) $mSi(OEt)_2(OH) \rightarrow (EtO)_3Si(OSi(OEt)_2)_{m-1}$ $OH + (m\text{-}1)\text{EtOH}$
(4) $Si(OEt)_4 + 4H_2O \rightarrow Si(OH)_4 + 4\text{EtOH}$
(5) $zSi(OH)_4 \rightarrow zSiO_2 + 2H_2O$
(6) $Si(OH)_4 + \text{D-fru} \rightarrow -\text{Si}-\text{O}-\text{D-fru} + H_2O$

In the case of $[\text{D-fru}] \geq [H_2O]$ (SG-W01 and W02), the reaction (1) will be predominant with an increase in the water content because D-fru has six hydroxy groups and the solubility of D-fru increases with the water content. Thus, under this condition, D-fru will be fixed through the Si—O—D-fru bond, and dispersed at molecular level in the silica matrix. As the result, the composite will show a very high resolution ability.

When the amount of water is greater than that of the D-fru and comparable to that of the TEOS (SG-W04, SG-W08 and SG-W12), reaction (2) precedes (1) and predominates with increasing water content followed by (3). In this case, D-fru may tend to be enclosed in 'lump form' in the silica matrix.

In an excess of water, as the H_2O/TEOS ratio increases the reaction (4) predominates over (2) and (3) [6]. Subsequently, both reactions (5) and (6) proceed. In this case, the composite will contain D-fru which is, at the least partly, dispersed at the molecular level, although it is also in the form of syrupy lumps.

References

1. T. Fukushima, T. Santa, H. Homma, S.M. Al-kindy, and K. Imai, Anal. Chem. **69**, 1793 (1997).
2. N. Enomoto, S. Furukawa, Y. Ogasawara, H. Akano, Y. Kawamura, E. Yashima, and Y. Okamoto, Anal Chem. **68**, 2798 (1996).
3. M. Matsuoka, K. Banno, and T. Sato, J. Chromatogr., B: Biomed. Appl. **676**(1), 117 (1996).
4. F. Mizukami, H. Izutsu, T. Osaka, Y. Akiyama, N. Uiji, K. Moriya, K. Endo, K. Maeda, Y. Kiyozumi, and K. Sakaguchi, J. Chromatogr. A **697**, 279 (1995).
5. A. Ueki, *Seikagaku Data Book*, Vol. 1 (Tokyo Kagaku Dojin, 1979), p. 680.
6. C.J. Brinker and G.W. Scherer, J. Non-Cryst. Solids. **70**, 301 (1985).

Journal of Sol-Gel Science and Technology 13, 427–432 (1998)
© 1998 Kluwer Academic Publishers. Manufactured in The Netherlands.

Study of Hybrid Silica-Polyethyleneglycol Xerogels by Eu^{3+} Luminescence Spectroscopy

S.J.L. RIBEIRO, K. DAHMOUCHE, C.A. RIBEIRO, C.V. SANTILLI AND S.H. PULCINELLI
Institute of Chemistry—UNESP, P.O. Box 355, 14801-970 Araraquara, SP, Brazil
sidney@iq.unesp.br

Abstract. Good optical quality Eu^{3+}-doped silica-polyethyleneglycol hybrids were prepared by the sol-gel process. Thermomechanical analysis showed an increase of the glass transition temperature, due to the stiffness of the polymeric network, as the amount of Eu^{3+} increased. Europium luminescent properties were used to study structural evolution during the sol-gel transition. For lower doping concentrations dried gels present statistical distributions of Eu^{3+}, typical of an amorphous environment, while for higher concentrations a crystalline-like environment of Eu^{3+} was observed. A broad emission band was observed in the visible part of the electromagnetic spectrum and assigned to the intrinsic emission from the hybrid polymeric network.

Keywords: hybrid gels, Eu^{3+} spectroscopy, polymer electrolytes, optical probes, sol-gel

1. Introduction

The synthesis and characterization of organic-inorganic hybrid materials is a rapidly growing field of study, with applications expected in optics, electronics, mechanics and biology [1]. Most of the properties of these materials are related to the synergy between the organic and inorganic parts and to their biphasic structure at the nanometer scale, providing totally new properties [2]. In this context, recent studies deal with materials prepared by reacting silicon-alkoxide with polyethers [3, 4]. Polyethyleneglycol (PEG) presents certain liquid-like features, the polymer acting as an immobile solvent for many metallic salts, while the presence of a silica network allows the transparent materials to be obtained, presenting better mechanical properties than pure PEG systems.

Some reports [5, 6] have proposed that lanthanide salts could be dissolved in polyethers, although the complete coordination of lanthanide ions by the polymer has not been established. However, the possibility of using an organic-inorganic hybrid rather than a glassy matrix is of great interest for the development of low cost flexible luminescent films, opening new areas of application.

This work is concerned with a silica-polyethyleneglycol (SiO_2-PEG) hybrid material, in which the organic and inorganic network are covalently bonded. The presence of PEG allows the dissolution of large quantities of europium perchlorate and (SiO_2-PEG) bonds give the material a high chemical stability. The luminescence characteristics of the SiO_2-PEG nanocomposite doped with different concentrations of Eu^{3+} are examined to identify the local structure surrounding the europium ions.

2. Experimental

The triethoxysilicon end-capped polyethyleneoxide (abrreviated $(OEt)_3Si\text{-}PEG_{800}\text{-}Si(OEt)_3$, where 800 is the molecular weight of the polyethyleneglycol), used as molecular precursor, was synthesized by stoichiometric reaction of 3-isocyanatopropyltriethoxysilane and O,O′(2-aminopropyl)polyethyleneglycol. Tetrahydrofuran (THF) was used as solvent and the reaction was carried out under reflux at 80°C for 6 h. This hybrid precursor was obtained after evaporation of THF. Ammonium fluoride (NH_4F) dissolved in ethanol was used as a nucleophilic catalyst for the

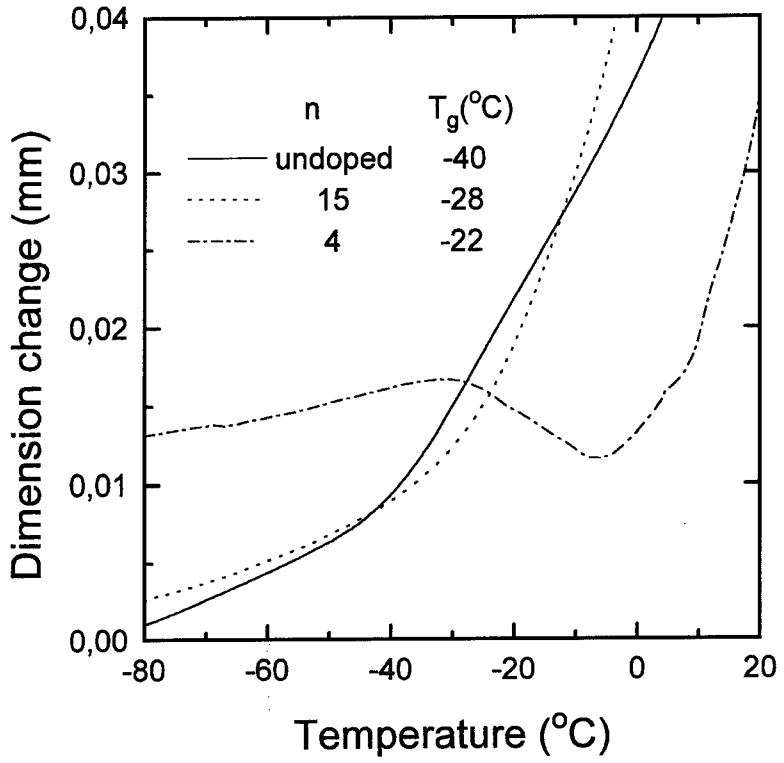

Figure 1. TMA curves for undoped and doped dried gels at 5°C/min heating rate under N_2 atmosphere. The glass transition temperature T_g is indicated.

hydrolysis reaction of the precursor ($NH_4F/Si = 0.005$). Finally, 0.2 ml of europium perchlorate aqueous solution was added with stirring allowing the formation of a clear monolithic wet gel in 4 h. Ethanol and water were then slowly removed at 50°C to give a rubbery and good optical quality transparent body. Samples were prepared for $n = 4$, 8, 15, 100 and 355 ($n = [O]/[Eu]$, where the oxygens considered are only those of the ether type).

Glass transition temperatures (T_g) of undoped and Eu^{3+}-doped SiO_2-PEG hybrids were determined from thermomechanical analysis (TMA) performed with an apparatus from TMA2940 TA-Instrument from −100 to 60°C (heating rate of 5°C/min) under an N_2 atmosphere.

Excitation and emission spectra were obtained under both continuous (450 W) and pulsed (5 mJ/pulse, 3 μs bandwidth) Xe lamps excitation with a SPEX Fluorolog F212I spectrofluorimeter. All measurements were obtained in the front face acquisition mode at room temperature. Decay curves were processed with the SPEX 1934 phosphorimeter.

3. Results and Discussion

Figure 1 presents the TMA curves of SiO_2-PEG hybrids prepared with different values of n. For $n > 8$ all curves show the same shape as the undoped SiO_2-PEG hybrid. A low thermal expansion coefficient ($\alpha \cong 3 \cdot 10^{-5}/°C$), characteristic of the glassy state, is observed at low temperature, while α values of the order of $10^{-3}/°C$ are observed at higher temperatures. This behavior characterizes the glass transition. The curve of the hybrid containing the highest amount of Eu^{3+} studied here ($n = 4$) shows a shrinkage just after T_g, which is a characteristic of the softening of the sample. Moreover, T_g increases from −40 to −22°C as the relative Eu^{3+} concentration increases. This effect may be due to the decrease in mobility of the PEG caused by the interaction among the Eu^{3+} ions and the polymer chains. A similar mobility decrease was observed by ionic conductivity measurements for Li^+ doped SiO_2-PEG or SiO_2-PPG samples [4, 7].

Figure 2 shows room temperature Eu^{3+} emission under 394 nm excitation for the sol and for the transparent

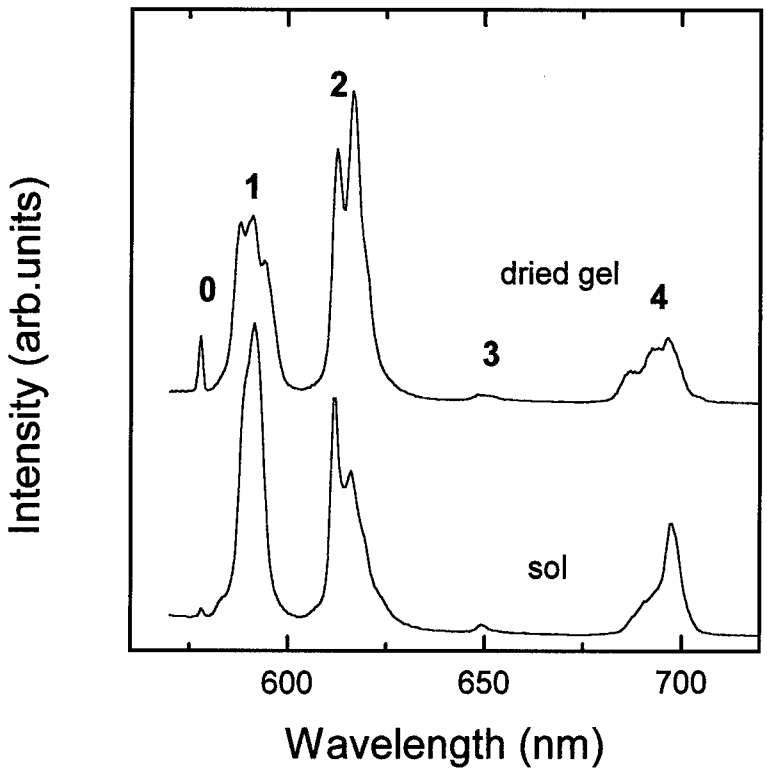

Figure 2. Eu^{3+} emission spectra ($\lambda_{exc} = 393$ nm) for the sol and the dried gel for $n = 8$. J levels for the observed $^5D_0 \rightarrow {}^7F_J$ transitions are assigned in the figure. The decay times are 120 μs and 180 μs for the sol and the dried gel, respectively.

gel ($n = 8$) dried for 4 h at 50°C. $^5D_0$ lifetimes are also presented in the figure caption. Transitions arising from the $^5D_0$ level of the $4f^6$ electronic configuration of Eu^{3+} are easily assigned. The first important observation concerns the relative transition intensities between the magnetic dipolar $^5D_0 \rightarrow {}^7F_1$ (≈590 nm) and the electric dipolar $^5D_0 \rightarrow {}^7F_2$ (≈610 nm) transitions. The higher this ratio, the closer the local symmetry around Eu^{3+} is to an inversion center [8]. The spectrum of the sol is similar to the spectrum obtained for Eu^{3+} in water, where Eu^{3+} ions are surrounded by 8.3 water molecules, as deduced from X-ray studies [8, 9]. About the same decay time is also obtained (107 μs for Eu^{3+} in water and 120 μs here) and may indicate that Eu^{3+} ions in these hybrid sols are in a water-like environment, similar to that observed for silica systems [10]. With drying, more asymmetrical local fields are revealed by the lowering in the ratio of band intensity between the transitions $^5D_0 \rightarrow {}^7F_1$ and $^5D_0 \rightarrow {}^7F_2$, denoting the interaction of Eu^{3+} with the polymeric network. The increase in the $^5D_0$ decay time from 120 to 180 μs is related to the loss of water molecules from the Eu^{3+} neighborhood.

Assuming that only radiative and non-radiative processes are involved in the depopulation of the $^5D_0$ level we may evaluate the total radiative contribution from relative intensities. The $^5D_0 \rightarrow {}^7F_1$ transition, being magnetic dipolar in character and therefore insensitive to change in the Eu^{3+} surroundings, may be taken as a reference with the radiative rate of 50 s^{-1} [11]. The other observed transitions arising from the $^5D_0$ level have electric dipolar character and from the intensity ratios the $^5D_0$ radiative lifetime is evaluated. Table 1

Table 1. Results for experimental (k_{EXP}), calculated radiative (k_{RAD}) and non-radiative ($k_{N\text{-}RAD}$) Eu^{3+} $^5D_0$ level decay rates (ms^{-1}) for dried gels with different Eu^{3+} concentrations ($n = [O]/[Eu]$).

n	k_{RAD}	k_{EXP}	$k_{N\text{-}RAD}$
8 (sol)	0.17	8.33	8.16
4	0.25	6.25	6.00
8	0.21	5.88	5.67
15	0.33	5.88	5.22
100	0.36	5.56	4.84
355	0.67	6.25	4.13

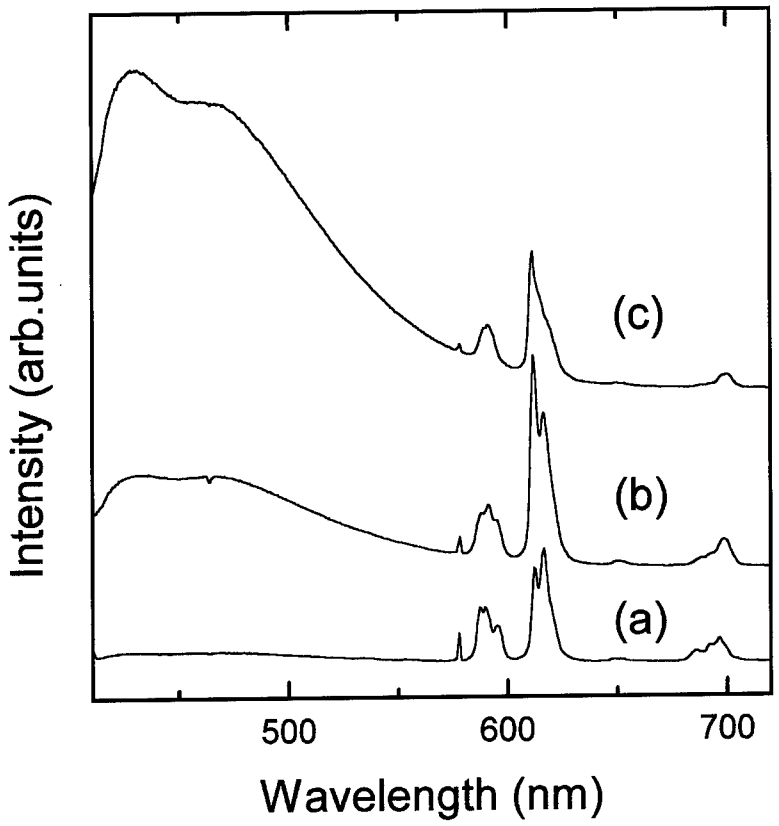

Figure 3. Emission spectra obtained under 394 nm excitation for doped dried gels: (a) $n = 4$, (b) $n = 15$ and (c) $n = 100$.

gathers the results obtained for the sol ($n = 8$) and for the dried gels. The experimental decay times are also shown and non-radiative decay times are calculated assuming that $\tau_{exp}^{-1} = (\tau_{RAD}^{-1} + \tau_{N\text{-}RAD}^{-1})$. The decrease in the experimental decay rate is a consequence of the decrease in non-radiative paths for $^5D_0$ depopulation on going from the sol to the gel. As mentioned above, this observation may be related to the loss of water molecules from the Eu^{3+} first coordination sphere. Experimental decay times change somewhat for gels with different concentrations of Eu^{3+} while radiative decay rates increase with dilution of Eu^{3+} in the hybrid matrix. We may then conclude that non-radiative rates increase with the increase in europium concentration.

The emission spectra obtained for gels with different values of n are displayed in Fig. 3. The broad bands at lower wavelengths will be discussed later. We focus our attention on the Eu^{3+} bands occurring above 570 nm and it is observed that spectra become more structured with decreasing n, with three clear components for the $^5D_0 \rightarrow {}^7F_1$ ($\approx$590 nm) and two components for the $^5D_0 \rightarrow {}^7F_2$ ($\approx$610 nm). For higher n values spectra are typical of Eu^{3+} in amorphous media. Eu^{3+} ions would be statistically distributed in the hybrid matrix. With increasing Eu^{3+} concentration some kind of stoichiometric compound could be formed involving europium perchlorate and the hybrid network, as observed for $EuBr_3$-containing poly(ethyleneoxide) [12]. Nevertheless, no visible segregation or phase separation seems to occur. Another hypothesis should be that the crosslinking via electrostatic interactions is favored with the increase of Eu^{3+} concentration. This interpretation agrees with the rise of T_g observed by TMA.

In Fig. 3 a broad emission band can be observed from 400 to about 600 nm. The relative intensity between this band and the Eu^{3+} lines decreases with the increase in Eu^{3+} concentration. It is also observed for samples not containing Eu^{3+} and it is also not observed for pure polyethyleneglycol, being therefore characteristic of the hybrid polymer. To go a little further in the spectroscopic characterization of this excited state we

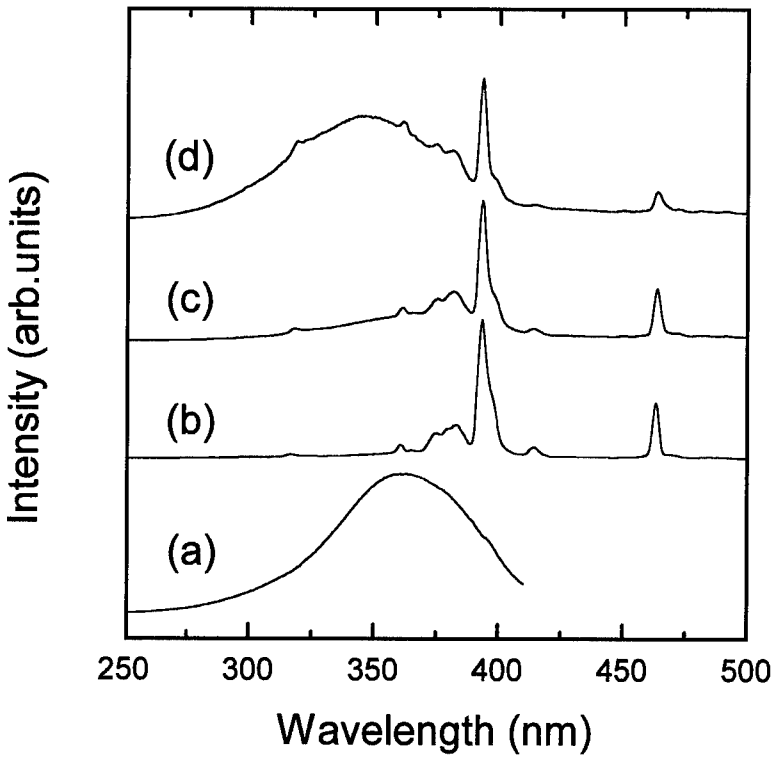

Figure 4. Emission excitation spectra for doped dried gels: (a) $n = 100$, $\lambda_{em} = 430$ nm; (b) $n = 4$, $\lambda_{em} = 611$ nm; (c) $n = 15$, $\lambda_{em} = 611$ nm and (d) $n = 100$, $\lambda_{em} = 611$ nm.

have obtained excitation spectra, displayed in Fig. 4. Curves (b)–(d) show Eu^{3+} emission excitation spectra ($\lambda_{em} = 611$ nm) obtained for different gels. A broad excitation band is observed at around 350 nm. In curve (a) the excitation spectrum was obtained with emission fixed at 430 nm. The Eu^{3+} emission is then excited by energy transfer from the matrix. With increase in Eu^{3+} concentration this excitation mechanism is less operative.

4. Conclusions

Hybrid silica-polyethyleneglycol xerogels containing different concentrations of Eu^{3+} were prepared. The increase in the electrolyte concentration decreases the mobility of the polymer chains due to strong Eu^{3+}-polymer interactions. Eu^{3+} emission characteristics strongly change on going from the sol to the gel and also with increasing concentrations of the metallic ion. The observation of decreasing radiative decay rates and spectral variations suggest the transformation of Eu^{3+} surroundings from amorphous-like to crystalline-like. A new strong emission in the visible region of the electromagnetic spectrum and assigned to the hybrid network is also observed. Efficient energy transfer from these excited states to the Eu^{3+} is observed. This efficiency decreases with the increase in Eu^{3+} concentration.

Acknowledgments

Authors acknowledge FAPESP and CNPq (Brazilian financial agencies).

References

1. H.K. Schmidt, J. Sol-Gel Sci. Tech. **8**, 557 (1997).
2. H.K. Schmidt, *Chemistry, Spectroscopy and Applications of Sol-Gel Glasses* (Springer-Verlag, Berlin, 1992), p. 117.
3. P. Judeinstein, J. Titman, M. Stamm, and H. Schmidt, Chem. Mater. **6**, 127 (1994).
4. K. Dahmouche, M. Atik, N.C. Mello, T.J. Bonagamba, H. Paneppuci, M. Aegerter, and P. Judeinstein, J. Sol-Gel Sci. Tech. **8**, 711 (1997).
5. A. Brodin, B. Mattsson, and L.M. Torell, J. Chem. Phys. **101**, 4621 (1994).

6. L.D. Carlos, and A.L.L. Vieira, Phys. Rev. B **49**, 11721 (1994).
7. K. Dahmouche, P.H. De Souza, T.J. Bonagamba, H. Paneppuci, P. Judeinstein, S.H. Pulcinelli, and C.V. Santilli, J. Sol-Gel Sci. Tech., in press.
8. S.J.L. Ribeiro, R.S. Hiratsuka, A.M.G. Massabini, M.R. Davolos, C.V. Santilli, and S.H. Pulcinelli, J. Non-Cryst. Sol. **147/148**, 162 (1992).
9. A. Habenschuss and F.H. Spedding, J. Chem. Phys. **73**, 442 (1980).
10. M. Ferrari, R. Campostrini, G. Carturan, and M. Montagna, Phil. Mag. B **65**, 251 (1992).
11. M.F. Hazenkamp and G. Blasse, Chem. of Materials **2**, 105 (1990).
12. M.M.S. Puga, L.D. Carlos, T.M.A. Abrantes, and L. Alcacer, Electrochimica Acta **40**, 2383 (1995).

Journal of Sol-Gel Science and Technology 13, 433–437 (1998)
© 1998 Kluwer Academic Publishers. Manufactured in The Netherlands.

Hybrid Silica Gel-Polytetrahydrofuran Thin Films

ALEXANDRA FIDALGO AND LAURA ILHARCO
Centro de Química-Física Molecular, Complexo I, Instituto Superior Técnico, Av. Rovisco Pais, 1096 Lisboa Codex, Portugal

Abstract. The sol-gel process has been used to prepare hybrid silica gel-polytetrahydrofuran (PTHF) thin films, using tetraethylorthosilicate (TEOS) as the precursor. The films were prepared by spin-coating, and characterized by profilometry, transmission FTIR and SEM. Film properties were conditioned by the preparation procedure as well as by the initial recipe, namely the solvent, polymer content and molecular weight. Evidence was obtained of the participation of the polymer in the condensation step of the process, interacting by hydrogen bonds with hydroxyl groups of the silicate network.

Keywords: hybrid films, polytetrahydrofuran, FTIR, SEM

1. Introduction

Since their initial development by Schmidt [1], hybrid organic-inorganic materials prepared by the sol-gel process have received a great deal of attention, given their attractive intermediate properties. The precursors are usually organically modified silicon alkoxides and metallic alkoxides [2, 3], but copolymerization of organic and inorganic precursors [4] and incorporation of organic polymers in the initial recipe of the sol [5] have also been used. In particular, silica films have been improved in mechanical strength [6], optical and electrical properties [7], by incorporation of polymers into the silica network. The most widely used has been polyethylene glycol (PEG), which, depending on the hydrolysis conditions, may have only electrostatic interactions with the silica network (van der Waals interactions or hydrogen bonds) [8], or participate in the hydrolysis process, forming Si—O—C chemical bonds [5, 9]. However, these bonds are not stable, being easily hydrolyzed in the presence of water or even water vapor [10].

With the aim of improving mechanical properties of protective films, we have, in the present work, incorporated the more hydrophobic polymer, polytetrahydrofuran [HO—(CH_2—CH_2—CH_2—CH_2—O)$_n$—H], in the initial mixtures, using different recipes and routes. The hybrid films obtained by spin-coating were characterized. The influence of the initial sols on the film thickness and uniformity and on the type of interactions between organic and inorganic components has been analyzed.

2. Experimental

Materials. TEOS, (Fluka, 99%) and PTHF with average molecular weights of 650 and 2900 (Aldrich), were used as purchased. Reagent grade ethanol (EtOH), from Merck, and tetrahydrofuran (THF), from Riedel-de Haen, were used without further purification. Distilled-deionized water and concentrated HCl, from Merck, were also used.

Preparation of Sols. Two different systems, PTHF : TEOS : EtOH : H_2O (named PTEH samples, after the initials) and PTHF : TEOS : THF : H_2O (PTTH samples) were investigated. The molar ratios were $x : 1 : 4 : 4$ in the former and $x : 1 : 11 : 4$ in the latter, where x varied from 0.01 to 0.06. The final pH was 1.2.

Three routes were investigated:

1. At room temperature, the relevant amount of PTHF was dissolved in the solvent and TEOS was diluted in half the amount of this solution. The remaining polymer solution was mixed with the specified amount of water and the pH adjusted. The aqueous mixture was then added dropwise to the TEOS

mixture, under vigorous stirring. After an additional 2 h stirring, the solutions were kept at ambient atmosphere, partially covered.

2. TEOS was previously mixed with PTHF in half of the non-aqueous solvent, acidified, and stirred for half an hour at 50°C. Water was dissolved in the remaining solvent and added to the non-aqueous mixture, as in route 1.
3. Same as route 2, but with no addition of water and the final sols were kept in sealed containers, to prevent contamination by atmospheric water.

Coating Method. Thin films were prepared by spin coating the sols at different ageing times onto silicon wafers, using a Headway Research photoresist spinner, model EC 101D, at 2500 rpm, for 3 min. The substrates were previously cleaned with distilled water and ethanol and blown with nitrogen just before film deposition. All the gel films were dried at room temperature for at least two weeks prior to characterization.

Characterization Methods. The gelation times for bulk sols, t_G, were visually determined. Film thickness was measured by a stylus instrument ALPHASTEP 200, from Tencor Instruments. Infrared spectra of the films were recorded in a Mattson RS1 FTIR spectrometer, in the range 400–4000 cm^{-1}, as the result of 100 scans at normal incidence, with resolution 4 cm^{-1}. Thin film texture was examined using a scanning electron microscope (SEM) Hitachi S4100-1, operating at 25 kV.

3. Results and Discussion

The water free samples (route 3) did not gel. This would be expected for pure silica systems, as no additives to promote the non-hydrolytic reaction of TEOS were used [8]. For hybrid systems, this result can be understood in terms of the hydroxyl groups of PTHF being too weak as nucleophilic agents to assist the solvolysis of TEOS. Therefore, we may conclude that if the polymer participates in any stage of the sol-gel process, it must be in the condensation reactions. The influence of the preparation procedure on gelation times is clear, since the samples that were pre-heated (route 2) systematically show shorter gelation times than those using procedure 1.

Incorporation of polymer induced an increase in the gelation time for all the samples prepared by route 1. Hybrid mixtures prepared with THF showed shorter t_G values than the corresponding ones with EtOH, explained by the faster evaporation of THF. The polymer average molecular weight did not play a dominant role on gelation time for THF samples, probably because this is such a good solvent for the polymer. However, due to the poorer solubility of PTHF in ethanol, it may form globules that render gelation more difficult in ethanolic samples, t_G increasing with the polymer average molecular weight.

The film thickness increased with constant roughness up to ageing times about 0.3–0.4 t_G, the roughness increasing there on. In Table 1, information on gelation times and film characteristics is summarized for selected samples.

Table 1. Compositions and gelation times of some selected samples. Average thickness (*Avg*), apparent roughness (*Ra*) and SEM observations for the films obtained after indicated ageing period (t/t_G).

				Best films obtained			
Samples	Pol. MW	x_{pol}	t_G (days)	t/t_G	*Avg* (kÅ)	*Ra* (Å)	SEM observations
TEH	—	0	10	0.4	7.9	273	Homogeneous, fractured edge of ~500 μm
PTEH650/0.01	650	0.01	15	0.3	8.9	398	Highly homogeneous, fractured edge of ~200 μm
PTEH650/0.01 (route 2)	650	0.01	10	0.4	11.2	330	Fractured, with some particles of a distinct phase on the surface
PTEH650/0.06	650	0.06	20	0.4	17.4	590	Concentric soft textured
PTEH2900/0.01	2900	0.01	21	0.3	21.0	1000	Regular, with no fractured edge
PTEH2900/0.03	2900	0.03	21	0.3	42.0	1300	Concentric waved textured
TTH	—	0	10	0.3	5.1	203	Highly homogeneous, fractured edge of ~200 μm
PTTH650/0.01	650	0.01	12	0.3	5.2	206	Highly homogeneous, fractured edge of ~50 μm
PTTH650/0.01 (route 2)	650	0.01	8	0.4	11.4	333	Fractured edge of ~200 μm, with some particles of a distinct phase on the surface.
PTTH2900/0.01	2900	0.01	12	0.3	7.2	440	Irregular soft textured

Using route 1 with ethanol as solvent, the increasing content of polymer in PTHF650 resulted in a significant increase in the film thickness, and only a slight increase in the apparent roughness. This was accompanied by reduction of the film fractured area at the edge of the substrate. The homogeneity of these films, analyzed by SEM, was excellent for molar ratio PTHF : TEOS of 0.01 : 1, but a very smooth texture appeared when it reached 0.06 : 1. The compromise between improved homogeneity and maximum thickness lies between these two concentrations, at about 0.03. The average molecular weight was determinant of the film thickness: incorporating PTHF2900, a completely homogeneous film, with no fractures at the borders and thickness 2.1 μm was obtained for a polymer : TEOS ratio of 0.01 : 1. A substantial thickness of 4.2 μm was measured for the 0.03 : 1 ratio. SEM micrographs of this film already showed a concentric wavelike texture (sample PTEH2900/0.03, Fig. 1(a)).

When THF was the solvent, the thickness of the films was systematically lower and very little influenced by the incorporation of polymer, because this is such a

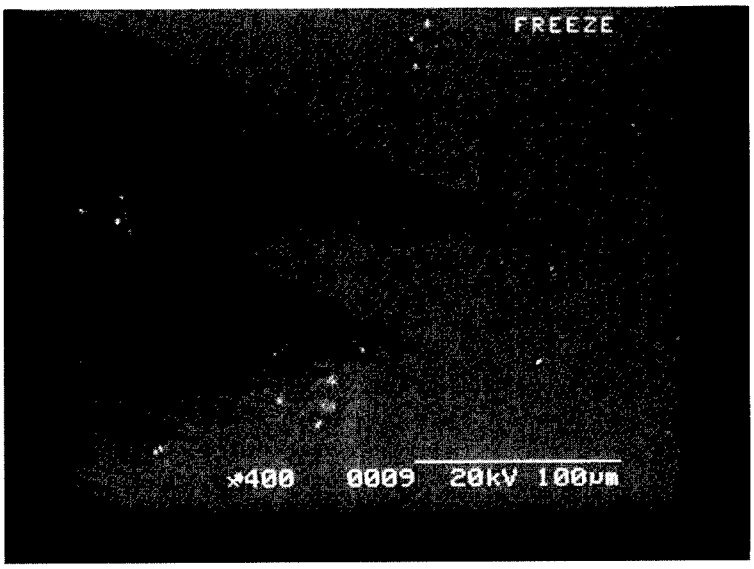

(a)

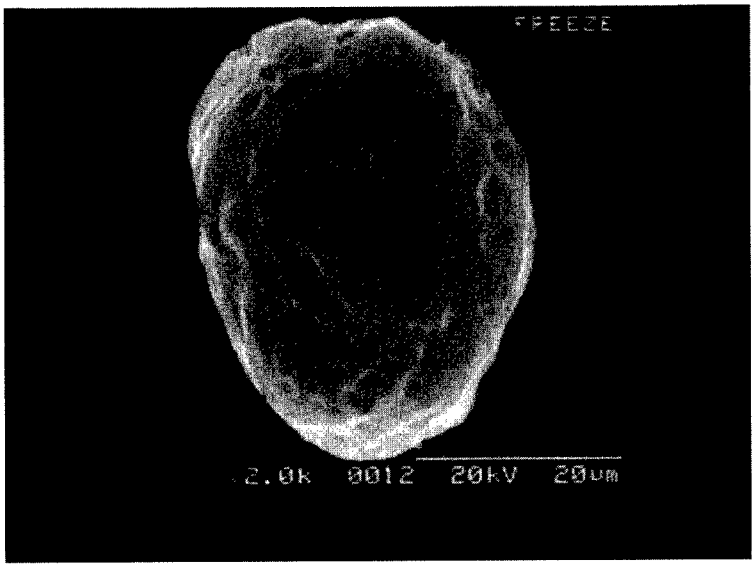

(b)

Figure 1. Scanning electron micrographs of the films obtained by spinning samples PTEH2900/0.03 (a) and PTTH650/0.01, route 2 (b).

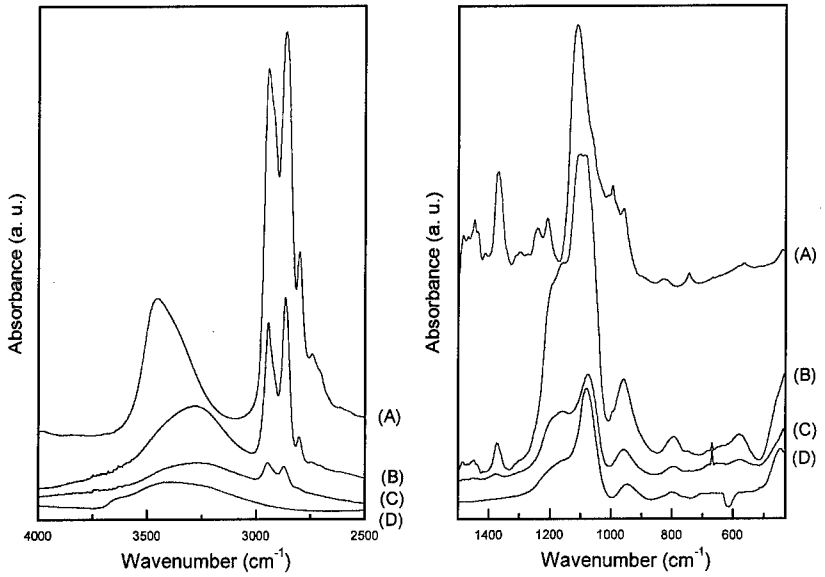

Figure 2. Two important wavenumber regions of the transmission FTIR spectra of selected films obtained from: (A) a PTHF reference solution not containing TEOS; (B) sample PTEH650/0.06; (C) sample PTEH2900/0.03; (D) sample TEH.

good solvent for PTHF. However, when PTHF650 was added, the fractured region at the edge of the films was much smaller than for the corresponding films with ethanol. Incorporating PTHF2900, even in low concentration, the films were slightly rougher, with an irregular texture and no fractured zone at the edges.

Route 2 yielded thicker films than route 1, showing a few nodules of about $\sim$15 μm diameter, with a porous structure, in SEM micrographs (Fig. 1(b)). These may correspond to large particles of a different phase, where Si—O—C chemical bonds could be involved. This is still under investigation by complementary techniques.

FTIR spectra of some films obtained from ethanolic sols by route 1 are shown in Fig. 2. Assignments are made in Table 2.

Table 2. Assignments of the main infrared bands in the spectra of Fig. 2.

Wavenumber (cm^{-1})	Assignment
3450	O—H str. (PTHF)
3200–3400	O—H str. (films)
2950	CH_2 asym. str. (PTHF)
2874	CH_2 sym. str. (PTHF)
1111	C—O—C asym. str. (PTHF)
1050–1200	Si—O—Si asym. str. (silica)
950–960	Si—OH str. (silica)

The dominant bands in spectrum 2D are those characteristic of pure, non-densified, silica gel films: ν_{as}(Si—O—Si), ν(Si—OH) and ν(OH). The effect of polymer incorporation (spectra 2B and 2C) is evident by the shift of $\sim$100 cm^{-1} to lower wavenumbers observed in the ν(OH) band of both silica and polymer. This shift increased with the polymer molecular weight and concentration, giving positive indication that, in hybrid films, the silica and polymer hydroxyl groups are involved in strong hydrogen bonds. Taking into account the small dimensions of the primary silica particles that form at this pH [11], we think that PTHF molecules remain in the solvent, either in globules (ethanolic sols) or in random coils (THF sols), as the systems age. During spinning, they form a large number of hydrogen bonds with the available silica hydroxyl groups. If only the terminal OH were involved, the polymer molecular weight would have no effect on the ν(OH) shift. To explain the observed effect, we suggest that the ether oxygens of the polymer must also be involved in these interactions. This could be observed by a shift in the ν_{as}(C—O—C) skeleton band. However, it is difficult to confirm, as the deconvolution of the broad band between 1050 and 1200 cm^{-1} has shown that it is the superposition of this polymer band with the ν_{as}(Si—O—Si) band of silica.

In order to prove whether Si—O—C covalent bonds are formed, further work is in progress.

4. Conclusion

Hybrid films were prepared by spinning, from sol mixtures using TEOS as precursor and containing different concentrations of polytetrahydrofuran of two molecular weights. The films were characterized by profilometry, FTIR and SEM. It has been shown that homogeneous, unfractured films with thickness $\sim 4\ \mu$m may be prepared in a single layer, once the adequate recipe and hydrolysis route are selected. Ethanol, not as good a solvent for PTHF as tetrahydrofuran, produced thicker films for corresponding procedures. The polymer only participates in the condensation steps of the process, strongly interacting (by hydrogen bonds) with hydroxyl groups of the forming silica structure.

Acknowledgments

One of the authors (Alexandra Fidalgo) is grateful to J.N.I.C.T. for a PRAXXIS XXI BM grant.

References

1. H. Schmidt and H. Scholze, German Patent, DE 27 58 415, 1972.
2. C. Sanchez and F. Ribot, New J. Chem. **18**, 1007 (1994).
3. D. Avnir, Accounts of Chem. Res. **28**, 328 (1995).
4. H. Schmidt and B. Seiferling, in *Better Ceramics through Chemistry II*, edited by C.J. Brinker, D.E. Clark, and D.R. Ulrich (Mat. Res. Soc., Pittsburgh, PA, 1986), p. 739.
5. D. Ravaine, A. Seminel, Y. Charbouillot, and M. Vincens, J. Non-Cryst. Solids **82**, 210 (1986).
6. S. Yarno, Polymer **32**(25), 5565 (1994).
7. C.J. Brinker and G.W. Scherer, *Sol-Gel Science—The Physics and Chemistry of Sol-Gel Processing* (Academic Press, Boston, 1990), p. 840.
8. P. Judeinstein, J. Titman, M. Stamm, and H. Schmidt, Chem. Mater. **6**, 127 (1994).
9. G. Zehl, S. Bishoff, F. Mizukami, H. Isutzu, M. Bartoszek, H. Jancke, B. Lucke, and K. Maeda, J. Mater. Chem. **5**, 1893 (1995).
10. C. Sanchez and M. In, J. Non-Cryst. Solids **147/148**, 1 (1990).
11. L.M. Ilharco, A.M. Santos, M.J. Silva, and J.M.G. Martinho, J. Sol-Gel Sci. Technol. **8**, 877 (1997).

Journal of Sol-Gel Science and Technology 13, 439–443 (1998)
© 1998 Kluwer Academic Publishers. Manufactured in The Netherlands.

Photoluminescence Study of Functionalized Polysiloxane Gel

R. KALFAT
Lab. Chimie de la Matière Condensée, IPEIT, 2, Rue Jawaher Lel Nehru, .BP 229, 1008, Montfleury, Tunisia; Fac. des Sc. de Bizerte, 7021-Zarzouna, Tunisia

N. GHARBI
Lab. Chimie de la Matière Condensée, IPEIT, 2, Rue Jawaher Lel Nehru, .BP 229, 1008, Montfleury, Tunisia

S. ROMDHANE*
Lab. Physique de la Matière Condensée Fac. des Sc.de Tunis 1060, Tunis, Tunisia; Fac. des Sc. de Bizerte, 7021-Zarzouna, Tunisia

J.-L. FAVE
Groupe de physique des solides, Univ. Paris 7 et 6, CNRS URA 17, Tour 23, 2 Place Jussieu, 75251 Paris Cedex 05, France

A. CHAÏEB AND M. MAJDOUB
Lab. Chimie des Polymères Fac. des Sc. de Monastir 5000 Monastir, Tunisia

Abstract. Photoluminescence of a polysiloxane gel film incorporating a partially conjugated copolymer polyether-polyphenylenevinylene (PEPPV) has been studied and compared with results obtained from bulk and vacuum evaporated films of the same starting material. The evaporation clearly affects the distribution of lengths of the conjugated parts, yet the incorporation in the gel matrix induces only slight changes in the spectroscopic properties of the polymer.

Keywords: photoluminescence, sol-gel, polysiloxane gel, conjugated polymer

Introduction

Conjugated polymers are an attractive alternative to inorganic semiconductors for use in optoelectronic devices [1–3]. They have been suggested for use in light emitting diodes (LEDs) [1, 4].

Several methods have been proposed to incorporate chromophores in thin films such as spin-coating from a solution of the chromophore dissolved in an appropriate solvent either mixed or copolymerized with an organic polymer [5–7]. Evaporation under vacuum can also be used. The sol-gel process offers a novel approach for the preparation of transparent thin films; the low temperatures involved in the process allow the incorporation of organic molecules in gel matrix [8]. The Si—H bonds of PMHS allows the grafting of organic chains that contains a double bond or hydroxyl end group [9].

Experimental

Polyether-polyphenylenevinylene (PEPPV) was synthesized by homopolycondensation of *p*-dihalo-genoxylene in a heterogeneous medium via a phase transfer catalysis route using potassium hydroxide solution (50%) as base. The PEPPV which precipitates in the reaction medium was separated by filtration.

PMHS was functionalized by hydrosilylation of the Si—H groups belonging to PMHS and hydroxyl end groups of the PEPPV polymer, promoted by platin catalyst $H_2PtCl_6 \cdot 6H_2O$ (0.1 ml from 10^{-2} M solution in THF). The reaction occurred at 50°C without stirring in a closed vessel. THF was used as solvent (5 ml/g PMHS). The sol, obtained after a few minutes, was spin-coated on glass slides. Films of polymer were also deposited on slides by evaporation at 300°C under vacuum (10^{-6} Torr). FTIR spectra were recorded on a Perkin-Elmer 1000 spectrometer using KBr pellets for solids and CCl_4 solution for PMHS. ^{13}C CP-MAS NMR was conducted on Bruker ASX 300 (75.45 MHz, with a contact time of 1 ms). Photoluminescence spectra of samples at 2 K were recorded using a Jobin-Yvon U1000, through a cooled photomultiplier. Low power excitation at various wavelengths (ranging from 457.9 to 514.5 nm) from an Argon ion laser Coherent Innova 90 was used.

Results and Discussions

Characterization of PEPPV

Figure 1 shows the ^{13}C CP-MAS NMR of PEPPV. The spectrum exhibits two groups of peaks: those corresponding to sp^3 carbon atoms (40–70 ppm) and to sp^2 carbon atoms (120–140 ppm). In the region of aliphatic carbons, the main peak appearing at 68.7 ppm corresponds to the carbons of the ether groups (C4). The broad peak at 44.9 ppm is assigned to the end chain $\underline{C}H_2$—Cl (C6). The shoulder present at the basis of the main peak appearing at 65 ppm may be attributed to $\underline{C}H_2$—OH terminal groups (C5).

Table 1. Elemental analysis of PEPPV.

	%C	%H	%O	%Cl
Found	80.50	6.04	10.24	3.21
Calculated	81.18	6.34	9.47	3.01

In the region of sp^2 carbons, three peaks are present showing the presence of ethylenic carbons (C3: 127.8 ppm) in addition to aromatic carbons (C2: 124.9 and C1: 138.1 ppm) [10]. This suggests that phenylenevinylene moities are present in the structure in addition to the expected ether sequences. These results are in agreement with IR results that show the presence of OH, aromatic, ethylenic and saturated C—H, conjugated C=C, C—O—C and CH_2—Cl groups.

Chemical analysis is presented in Table 1. Theoretical values are calculated from the structure deduced from IR and NMR results assuming that each polymer chain is terminated by CH_2—Cl at one end and CH_2—OH at the other. The best correlation between experimental and theoretical values is obtained when $x = 3$ and $y = 6$. The average molecular weight of the

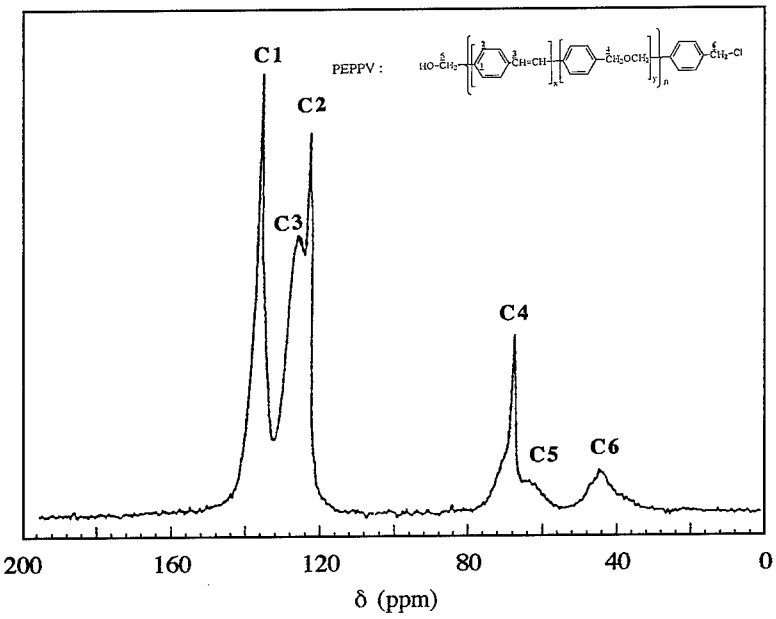

Figure 1. ^{13}C CP-MAS NMR spectrum of the copolymer (PEPPV).

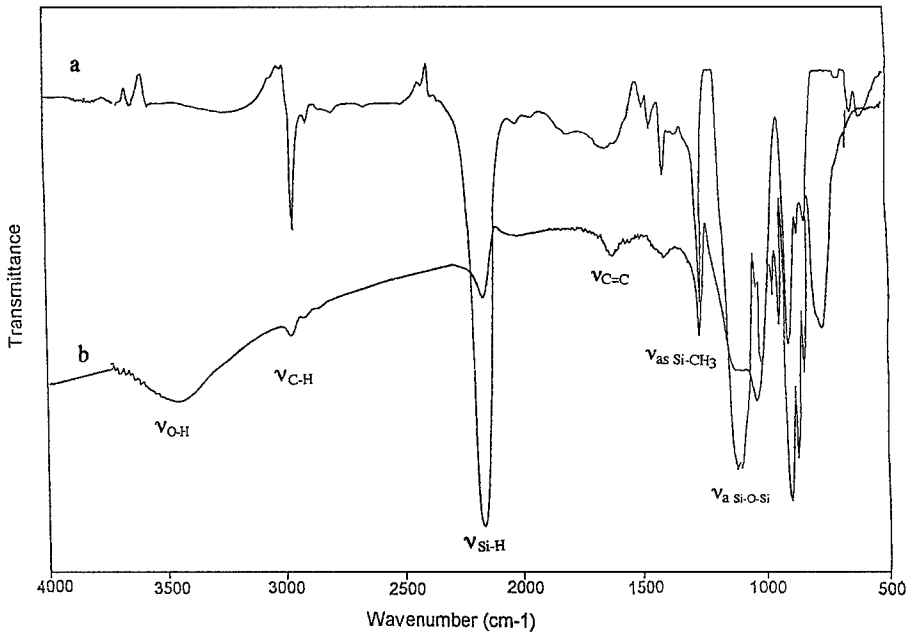

Figure 2. FTIR spectra of PMHS (a) and functionalized gel by PEPPV (b).

polymer according to the proposed formula is about 1100 g/mol.

Characterization of Functionalized PMHS

The reaction between PMHS and PEPPV was followed by monitoring the decrease of the Si—H IR band at 2160 cm^{-1}. The IR spectrum recorded after the end of the reaction (Fig. 2(b)) shows the presence of a weak band at 2180 cm^{-1} corresponding to Si—H groups which remain unreacted due to steric effects. The ν_{O-H} band at 3400 cm^{-1} is related to the unreacted OH groups of PEPPV. A similar behavior was observed in the reaction between PMHS and hexanediol [11]. The minor band appearing at 1646 cm^{-1} is ascribed to $\nu_{C=C}$. The sharp band situated at 1280 cm^{-1} is attributed to $\nu_{as(Si-CH_3)}$. The broad absorption between 1000 and 1100 cm^{-1} is related to $\nu_{a(Si-O-Si)}$. Complementary experiments have shown that PMHS does not react with conjugated alkenes. Thus, in the case of PEPPV C=C bonds, conjugated with phenyl, do not react.

Photoluminescence Study

Figure 3 presents the photoluminescence spectra of the PEPPV: bulk (a), evaporated (b) and introduced in a polysiloxane gel (c). These spectra are recorded at different excitation wavelengths, at a temperature $T = 2$ K.

For the bulk material (Fig. 3, I-a to VI-a), the emission spectrum shows three distinct bands (2.42, 2.26 and 2.10 eV). The peak positions are independent of the excitation wavelength for I-a to IV-a; for the low energy excitations (V-a and VI-a), the peaks move, become sharper and shoulders become sharper.

The total intensities have the same order of magnitude for the all spectra, but a continuous evolution of the relative heights of the different peaks is evident. This yellow-orange emission is similar to the well-known photoluminescence of polyphenylenevinylene (PPV) [1] and thus clearly comes from the conjugated part of PEPPV (Scheme 1).

A given excitation wavelength photoselects a subpopulation of chain lengths in the size distribution of these conjugated segments; this is especially evident in Fig. 3 (VI-a), where only the longest chains can be photoexcited and emit. Furthermore, the vibrational structure of this spectrum exhibits characteristic C—C stretching modes around 1250 and 1500 cm^{-1}.

Evaporated films (Fig. 3, I-b to VI-b) exhibit roughly the same peaks as those observed in the bulk. However, a slight blue shift is observed for the 0-0 peak (508 nm instead of 512 nm for the bulk), which

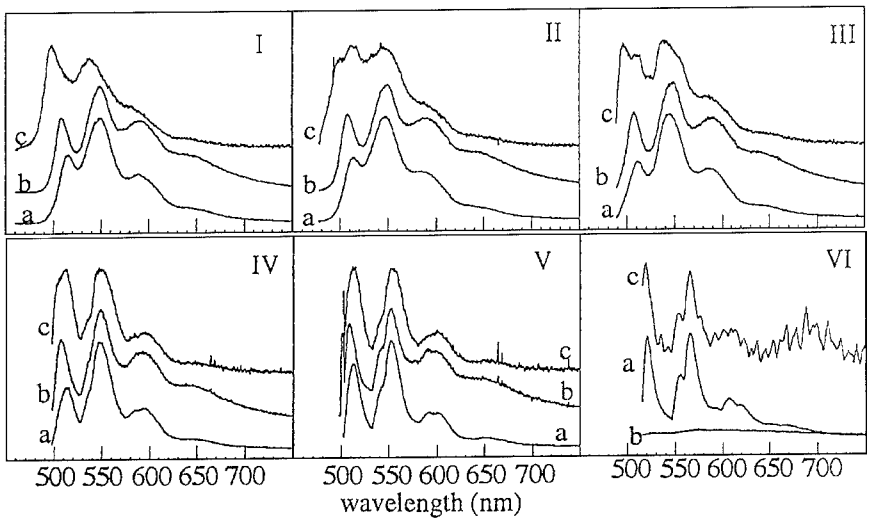

Figure 3. Photoluminescence spectra of bulk PEPPV (a), evaporated PEPPV (b), and PEPPV incorporated in the gel (c). Excitation wavelengths (I: 457.9 nm; II: 476.6 nm; III: 488 nm; IV: 496.5 nm; V: 5018 nm; VI: 514.5 nm).

is related to shorter average length of the PPV in the evaporated PEPPV [12]. The same phenomenon was observed in the case of vacuum evaporated poly(*p*-phenylene) [13]. The sharp peaks do not shift with excitation wavelength, indicating a small size dispersion, without the longest segments present in the bulk. This is confirmed by the lack of emission of the PEPPV film excited at 2.41 eV (VI-b), lower in energy than the level (2.43 eV) shown in the spectra I-b to V-b. The bands become broader when PEPPV is included in the gel (Fig. 3, I-c to VI-c). The new peak appearing at 498 nm with $\lambda_{exc} = 457.9$ nm decreases in favor of the peak at 512 nm, identical to the one observed in the bulk. The presence of these two peaks is evident in spectrum II-c and indicates the existence of an additional energy level when the PEPPV copolymer is confined inside the gel matrix. The vibrational structure is the same as observed in the bulk. At $\lambda_{exc} = 514.5$ nm, the emission spectrum obtained from the gel is very noisy (the ordinate had to be enlarged by a factor twenty), but shows the same sharp peaks as the bulk material (VI-a). This shows that, despite the low concentration of PEPPV in the gel, its spectroscopic properties are conserved when it is introduced in the gel.

A preliminary study (Marai [14]) allowed the determination of the width of the forbidden band (the gap energy Eg) from absorption measurements made on PEPPV thin films prepared by vacuum evaporation. Eg was obtained by a graphical method using the following equation: $\alpha h\nu = B(h\nu - Eg)^n$ [15]. Where α is the absorption coefficient, $h\nu$ the photon energy, B a constant, Eg the gap energy, n is taken equal to 2, a common value for amorphous compounds [16]. An approximate value of Eg equal to 1.8 ($\pm$0.1) eV was obtained by extrapolation from the curve of $\alpha h\nu^{1/2}$ against $h\nu$. This value of Eg is situated in the range 1–3 eV characteristic of semiconductors. Preparation of OLEDs from PEPPV is in progress. A Yellow-Orange luminescence is expected.

Conclusion

Sol-gel processing provides a simple and cheap method for the preparation of transparent thin films. The inclusion in the gel matrix does not alter the photoluminescence properties of the host polymer. The preliminary results show that PEPPV could be used as a probe for electroluminescence study. A luminescence in the yellow region is expected.

References

1. J.H. Burroughes, D.D.C. Bradley, A.R. Brown, R.N. Marks, K. Mackay, R.H. Friend, P.L. Burn, and A.B. Holmes, Nature (London) **347**, 539 (1990).
2. J. Bisberg, W.J. Cumming, R.A. Gandiana, K.D. Hutchinson, R.T. Ingwall, E.S. Kolb, P.G. Mehta, R.A. Minns, and C.P. Petersen, Macromolecules **28**, 386 (1995).

3. O. Lohst, J.L. Brédas, S.C. Graham, R.H. Friend, and D.D.C. Bradley, Synth. Met. **55–57**, 4308 (1993).
4. D. Braun and A.J. Heeger, Appl. Phys. Lett. **68**, 1991 (1982).
5. D. Mc Branch, I.H. Campbell, D.L. Smith, and J.P. Ferraris, Appl. Phys. Lett. **66**, 1175 (1995).
6. P. Frederiksen, T. Bjørnholm, H.G. Madsen, and K. Bechgaard, J. Mater. Chem. **4**, 675 (1994).
7. M. Aguiar, F.E. Karasz, and L. Akcelrud, Macromolecules **289**, 4598 (1995).
8. D.L. Logan, C.S. Ashley, R.A. Assink, and C.J. Brinker, SPIE Sol-Gel Optics II **1758**, 519 (1992).
9. R. Kalfat, N. Gharbi, H. Zarrouk, and F. Babonneau, J. Soc. Chim. Tunisie **3**, 533 (1994).
10. J.H. Simpson, N. Egger, M.A. Masse, D.M. Rice, and F.E. Karasz, J. Polym. Sci., Part B: Polymer Physics **28**, 1859 (1990).
11. R. Kalfat and N. Gharbi, J. Mater. Synth. Process **2**, 379 (1994).
12. A. Schmidt, M.L. Anderson, D. Dunphy, T. Wehrmeister, K. Müllen, and N.R. Armstrong, Adv. Mater. **7**, 8 (1995).
13. K. Miyashita and M. Kaneko, Macomolecular Rapid Communication **15**, 511 (1994).
14. F. Marai, Thesis Faculté des Sciences de Tunis, 1996.
15. N.F. Mott and E.A. Davis, *Electronic Process in Non Crystalline Materials*, 2nd edition (Clarendon, Oxford, 1979).
16. W. Hôrig, H. Neumann, and H. Sobotta, Thin Solid Film **48**, 67 (1978).

Journal of Sol-Gel Science and Technology 13, 445–449 (1998)
© 1998 Kluwer Academic Publishers. Manufactured in The Netherlands.

Processing and Properties of Inorganic-Organic Hybrids Containing Various Inorganic Components

NORIKO YAMADA, IKUKO YOSHINAGA AND SHINGO KATAYAMA
Advanced Technology Research Laboratories, Nippon Steel Corporation, 3-35-1 Ida, Nakahara-ku, Kawasaki 211, Japan

Abstract. Inorganic-organic hybrids containing various inorganic components have been synthesized from silanol-terminated polydimethylsiloxane (PDMS) and three different inorganic components: $Al(O\text{-}sec\text{-}C_4H_9)_3$, $Ti(OC_2H_5)_4$ and $Ta(OC_2H_5)_5$. The hybrids obtained were transparent and flexible. Dynamic mechanical measurements and stress-strain experiments were carried out in order to study the effect of inorganic component on the properties of the Metal-O-PDMS hybrids. The storage modulus at around room temperature increased in the order Al-O-PDMS, Ti-O-PDMS, Ta-O-PDMS hybrids, indicating that the three-dimensional network structure became denser in this order. The tensile strength increased in the order Al-O-PDMS, Ta-O-PDMS, Ti-O-PDMS hybrids. The difference in tensile strength is considered to be related to the strength of the interaction between the inorganic component and PDMS. The elongation at failure also depended on the inorganic component. Ti-O-PDMS hybrid exhibited the largest elongation of all the samples (more than 200%).

Keywords: inorganic-organic hybrid, storage modulus, Young's modulus, tensile strength, elongation

1. Introduction

The sol-gel method permits the introduction of organic components into an inorganic network, giving inorganic-organic hybrids with unique features [1–4]. These new materials provide the possibility of not only combining the properties of the inorganic and organic components but can also display novel properties.

The mechanical properties of the hybrids comprised of a ≡Si—O—Si≡ inorganic network modified with organic component have previously been studied [4–7]. They were synthesized from polydimethylsiloxane (PDMS) and tetraethoxysilane (TEOS) and showed a variety of rubbery properties depending on the process conditions. The use of various metal alkoxides instead of TEOS is expected to alter the structure and properties of PDMS-based hybrids reflecting the nature of the metal alkoxides. However, there have been few reports on the mechanical properties of the hybrids containing various different inorganic components derived from metal alkoxides [8, 9].

In this study, three different inorganic components, $Al(O\text{-}sec\text{-}C_4H_9)_3$, $Ti(OC_2H_5)_4$ and $Ta(OC_2H_5)_5$ were used to synthesize Metal-O-PDMS hybrids. The results of dynamic mechanical measurements and stress-strain experiments were investigated to elucidate the effect of the inorganic component on the properties of the hybrids.

2. Experimental

$Al(O\text{-}sec\text{-}C_4H_9)_3$, $Ti(OC_2H_5)_4$ and $Ta(OC_2H_5)_5$ were obtained from Kanto Chemical Co., Inc., Tokyo Chemical Industry Co., Ltd. and Kojundo Chemical Laboratory Co., Ltd., respectively. Silanol-terminated PDMS with an average molecular weight of 3000 was obtained from Shin-Etsu Chemical Co., Ltd. Ethyl acetoacetate (EAcAc) was used as a chemical modifier of the metal alkoxides in order to retard the hydrolysis reaction because metal alkoxides used in this study were reactive toward water. The modified alkoxides were separately mixed with PDMS in ethanol. The alkoxides in the solutions were hydrolyzed by addition of water. The hydrolyzed solutions were allowed to gel, and then heat-treated to yield monolithic hybrids. The molar

ratio of metal alkoxide, EAcAc and H_2O was 1 : 2 : 2. The molar ratio of metal alkoxide to PDMS (M/PDMS ratio) was changed from 1 to 4.

The microstructure of the hybrids was examined by transmission electron microscopy (TEM) using a Hitachi H-800 instrument with an acceleration voltage of 200 kV. The dynamic mechanical data were obtained with a Rheology DVE-V4 dynamic visco-elastic analyzer. The specimen size was about $5 \times 25 \times 1$ mm. Samples were tested at 110 Hz in the temperature range -150°C to $+300$°C with a heating rate of 3°C/min. Stress-strain experiments were carried out on an Orientec RTM-25. Dumbbell-shaped samples of 10 mm in length between chucks were used. The strain rate was 1 mm/min.

3. Results and Discussion

3.1. *Description of Samples*

The hybrids obtained were transparent, indicating that no visible particles were formed. TEM observations at a magnification of 75,000 also revealed that the hybrids were homogeneous and contained no aggregates or clusters. If inorganic particles such as metal oxides or hydroxides are formed from excess metal alkoxide, they must be smaller than 10 nm, the detection limit of TEM analysis. The hybrids were flexible and rubbery although the degree of flexibility differed according to the inorganic species and M/PDMS ratio. A large sample of 135 mm in diameter and 1 mm in thickness was obtained as shown in Fig. 1.

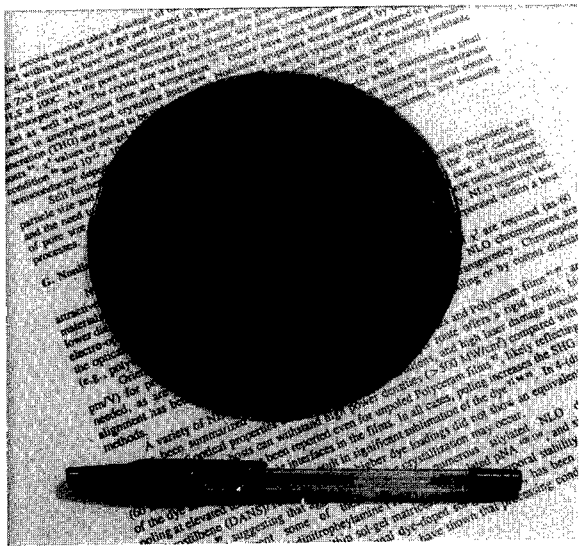

Figure 1. Photograph of Ti-O-PDMS hybrid with Ti/PDMS ratio of 2.

3.2. *Dynamic Mechanical Properties*

The dynamic mechanical properties of Al-O-PDMS, Ti-O-PDMS and Ta-O-PDMS hybrids with M/PDMS ratio of 4 are shown in Fig. 2. In the glassy region below -120°C, all of these hybrids had a storage modulus with a magnitude of 10^9 Pa. The storage modulus above -80°C was higher in the order Al-O-PDMS, Ti-O-PDMS, Ta-O-PDMS hybrids. The amount of inorganic phase in the hybrid is considered to be too small for the modulus of metal oxides or hydroxides to effect the results because no inorganic particles were observed in the hybrid even by using TEM. Thus, the difference in storage modulus is attributed to the inorganic-organic network structure which is formed by the reaction between hydrolyzed metal alkoxide and PDMS. As the number of bonds between the metal alkoxide and PDMS increases, the storage modulus becomes higher. Thus, the Ta-O-PDMS hybrid is thought to have a denser network structure in which many bonds are formed between the inorganic component and PDMS, whilst the Al-O-PDMS hybrid is believed to have a looser structure with fewer bonds.

The tan δ curve showed a peak in the glass transition region around -110°C. Although no significant difference was observed in the peak temperature of the tan δ curve, the peak height decreased in the order Al-O-PDMS, Ti-O-PDMS, Ta-O-PDMS hybrids. The decrease of the peak height means that energy loss accompanying glass transition decreases in this order. The origin of the energy loss is the friction between PDMS chains constituting inorganic-organic network. As the atomic weight of the metallic inorganic component becomes larger, the effect of restraint on the motion of PDMS becomes more significant. This results in lower friction between PDMS chains, and thus a lower energy loss associated with the glass transition.

3.3. *Stress-Strain Experiments*

Figure 3 shows the results of stress-strain experiments. The Young's modulus became higher in all the M-O-PDMS hybrids as the M/PDMS ratio increased. As the inorganic content in the hybrid increases, more bonds are formed between PDMS and

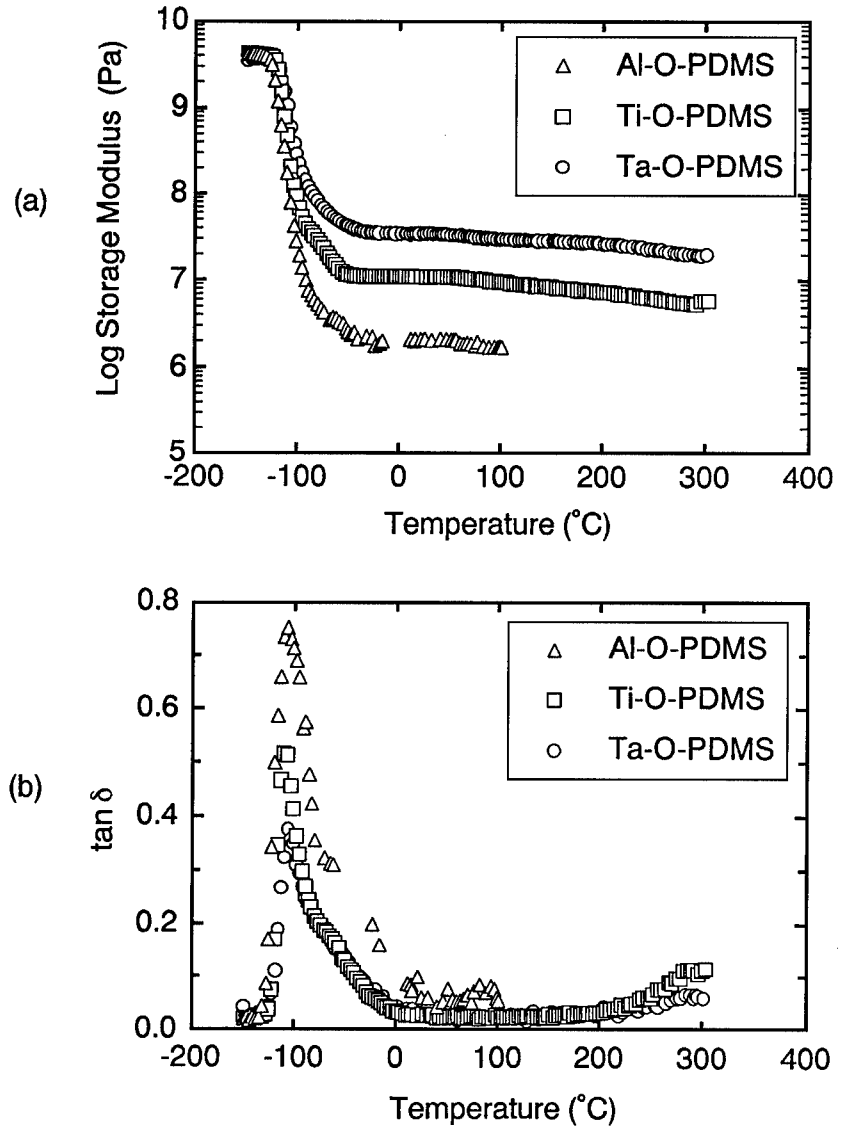

Figure 2. Temperature dependence of the dynamic mechanical properties of M-O-PDMS hybrids with M/PDMS ratio of 4: (a) storage modulus and (b) tan δ.

inorganic component, leading to a hybrid with a higher Young's modulus. The Young's moduli of M-O-PDMS hybrids with small M/PDMS ratios of 1 and 2 had little dependence on the inorganic component. In the case of hybrids with a large M/PDMS ratio of 4, the Young's modulus was strongly influenced by the inorganic component. It increased in the order Al-O-PDMS, Ti-O-PDMS, Ta-O-PDMS hybrids, which was consistent with the results of the storage modulus.

The tensile strength of Ti-O-PDMS hybrids was the highest and that of Al-O-PDMS hybrids was the lowest for all M/PDMS ratios. The tensile strength is affected by the interaction between PDMS and inorganic component. The interaction in Ti-O-PDMS hybrids seems to be stronger than the one in Ta-O-PDMS hybrids. However, the results of the Young's modulus suggests that Ti-O-PDMS hybrids have a smaller number of bonds between PDMS and inorganic components than Ta-O-PDMS hybrids. This means that the inorganic component derived from $Ti(OC_2H_5)_4$ formed much stronger chemical bonds with PDMS than the one derived from $Ta(OC_2H_5)_5$. Thus, the interaction between inorganic component and PDMS is related to the number and the strength of the bonds between

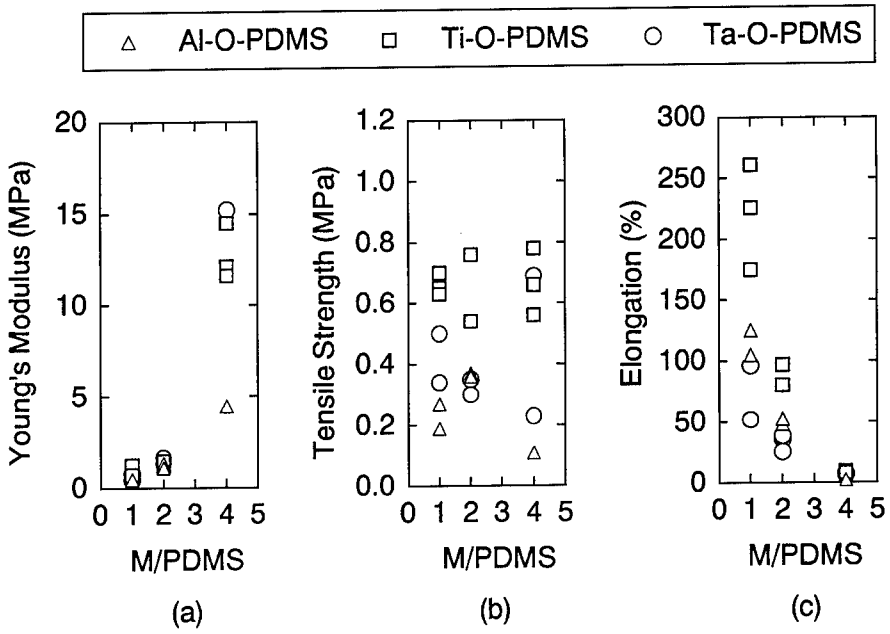

Figure 3. Effect of inorganic component on the stress-strain behaviors of the M-O-PDMS hybrids: (a) Young's modulus, (b) tensile strength and (c) elongation at break.

them. The interaction was found to increase in the order Al-O-PDMS, Ta-O-PDMS, Ti-O-PDMS hybrids.

Elongation at failure data clearly shows that the elongation depends on the M/PDMS ratio. The elongation of M-O-PDMS hybrids with a M/PDMS ratio of 4 was too small to show any difference in elongations between the M-O-PDMS hybrids. M-O-PDMS hybrids with M-PDMS ratio of 1 and 2 exhibited relatively large elongations. The elongation increased in the order Ta-O-PDMS, Al-O-PDMS, Ti-O-PDMS hybrids. The Ti-O-PDMS hybrid with a Ti/PDMS ratio of 1 had an especially high elongation of more than 200%.

The origin of the elongation is mainly attributed to the straightening of the PDMS helical chain [10]. The number of PDMS bonds to the inorganic component increases as the amount of the inorganic component increases. This hinders the straightening behavior of PDMS, leading to the decrease in the elongation. Among the M-O-PDMS hybrids with M/PDMS ratio of 1, the Ti-O-PDMS hybrid had a distinctly high elongation at break. This means that siloxane chains of PDMS in the Ti-O-PDMS hybrid are easily elongated as compared to the siloxane chains in other hybrids. The factors determining the elongation are the degree of a three-dimensional network formation and the strength of the interaction between inorganic component and PDMS. In the Ti-O-PDMS hybrids, these two factors are well balanced, leading to high elongation. The Ta-O-PDMS hybrids have a denser network structure, giving low elongation. The Al-O-PDMS hybrid is considered to have loose network structure in which siloxane chains are elongated easily. However, the low tensile strength of Al-O-PDMS hybrid due to the weak interaction between inorganic component derived from $Al(O\text{-}sec\text{-}C_4H_9)_3$ and PDMS seems to limit the elongation.

The results of stress-strain experiments has clarified some features of the mechanical properties of M-O-PDMS hybrids. The Young's modulus becomes higher as the number of bonds between inorganic component and PDMS increases to form a denser network structure. The tensile strength is influenced by the interactions between the inorganic component and PDMS which differs according to the inorganic present. The elongation at break is likely to be determined by the balance of the two factors, i.e., the degree of a three-dimensional network formation and the interaction between inorganic component and PDMS.

4. Conclusions

Mechanical properties of the hybrids differed according to which inorganic component was present reflecting the difference in network structure and strength of the interaction between the inorganic component and

PDMS. The storage modulus at around room temperature increased in the order Al-O-PDMS, Ti-O-PDMS, Ta-O-PDMS hybrids, indicating that the network structure becomes denser in this order. On the other hand, the tensile strength increased in the order Al-O-PDMS, Ta-O-PDMS, Ti-O-PDMS hybrids. The interaction between the inorganic component and PDMS is considered to increase in this order. Among the three different hybrids, Ti-O-PDMS hybrid showed the largest elongation at failure and Ta-O-PDMS hybrid, the smallest one.

Acknowledgment

This work was supported by NEDO as part of the Synergy Ceramics Project under the Industrial Science and Technology Frontier (ISTF) Program promoted by AIST, MITI, Japan. The authors are members of the Joint Research Consortium of Synergy Ceramics.

References

1. D. Avnir, D. Levy, and R. Reisfeld, J. Phys. Chem. **88**, 5956 (1984).
2. H. Schmidt, H. Scholze, and A. Kaiser, J. Non-Cryst. Solids **63**, 1 (1984).
3. G. Philipp and H. Schmidt, J. Non-Cryst. Solids **63**, 283 (1984).
4. G.L. Wilkes, B. Orler, and H. Huang, Polym. Prep. **26**, 300 (1985).
5. H. Huang, B. Orler, and G.L. Wilkes, Polym. Bull. **14**, 557 (1985).
6. H. Huang, B. Orler, and G.L. Wilkes, Macromolecules **20**, 1322 (1987).
7. J.D. Mackenzie, Y.J. Chung, and Y. Hu, J. Non-Cryst. Solids **147/148**, 271 (1992).
8. S. Katayama, I. Yoshinaga, and N. Yamada, in *Better Ceramics through Chemistry VII*, edited by B.K. Coltrain, C. Sanchez, D.W. Schaefer, and G.L. Wilkes (Mat. Res. Symp. Proc., 1996), Vol. 435, p. 321.
9. N. Yamada, I. Yoshinaga, and S. Katayama, J. Mater. Chem. **7**, 1691 (1997).
10. R.F.T. Stepto, in *Siloxane Polymers*, edited by S.J. Clarson and J.A. Semlyen (PTR Prentice Hall, Inc., 1993), p. 373.

Journal of Sol-Gel Science and Technology 13, 451–455 (1998)
© 1998 Kluwer Academic Publishers. Manufactured in The Netherlands.

Microstructural and Mechanical Properties of Sono-Ormosils

E. BLANCO
Departamento de Física de la Materia Condensada, Universidad de Cádiz, Apartado 40, 11510-Puerto Real, Cádiz, Spain

M. GARCÍA-HERNÁNDEZ AND R. JIMÉNEZ-RIOBÓO
Instituto de Ciencia de Materiales de Madrid, C.S.I.C., Cantoblanco, E-28049-Madrid, Spain

R. LITRÁN
Departamento de Física de la Materia Condensada, Universidad de Cádiz, Apartado 40, 11510-Puerto Real, Cádiz, Spain

C. PRIETO
Instituto de Ciencia de Materiales de Madrid, C.S.I.C., Cantoblanco, E-28049-Madrid, Spain

M. RAMÍREZ-DEL-SOLAR
Departamento de Física de la Materia Condensada, Universidad de Cádiz, Apartado 40, 11510-Puerto Real, Cádiz, Spain

Abstract. Monolithic pieces and films of ormosils were obtained from ultrasound-assisted polycondensation of tetraethoxysilane (TEOS) and polydimethylsiloxane (PDMS). These sono-ormosils were studied by means of high resolution Brillouin spectroscopy and their textures analyzed from adsorption isotherms. Evidence is given for the occurrence of organic and inorganic micro-phase separation in samples with high polymer concentrations. Nitrogen isotherms show that the texture of the samples is highly dependent on the composition.

Keywords: sono-ormosil, textural features, Brillouin spectroscopy, microstructural model

1. Introduction

In recent years, sol-gel scientists have dedicated a huge effort to study the unique properties of organically modified silicates (ormosils) [1, 2]. A full exploitation of the mechanical properties of these materials requires a deep understanding of the interplay between structural and dynamical correlations. However, investigations have been mainly focused on the macroscopic elastic features [3, 4] with little attention paid to their correlation with the dynamical elastic behavior. In this context, we have made use of Brillouin scattering which has been widely proven to be an essential technique in determining the relationship between structure and elastic properties [5].

Ormosils studied in this paper were prepared by the solventless sonogel route [6, 7] in order to extend the compositional range in which no microphase separation occurs [4, 8–10]. Elasticity results are correlated with the textural analyses performed on samples with different organic-inorganic ratios and the overall information is explained using a simple microstructural picture of the sono-ormosils network.

2. Experimental

Ormosils have been prepared by a solventless sol-gel route using tetraethoxysilane (TEOS) from Merck as inorganic precursor and polydimethylsiloxane (PDMS) from Hüls America Inc., with an average molecular weight of 550, as organic source. Hydrolysis and condensation reactions were carried out in an acid environment and promoted by a high power ultrasound probe (20 kHz, 15 W) [6].

In order to promote the copolycondensation reaction against self-polymerization of PDMS [7], samples were prepared as follow. First, TEOS-acidic water mixtures (2 mol H_2O/mol TEOS) were subjected to ultrasound radiation ($E_s = 60\ J \cdot cm^{-3}$). Then, amounts of PDMS, ranging from 0 to 40 wt%, referred to TEOS were added, and, finally, the mixtures were subjected to an additional ultrasonic dose to complete a total energy dose of 0.12 $kJ \cdot cm^{-3}$. The resulting transparent sols were poured into a plastic container and left to gel. After one week ageing and two weeks drying at room temperature, monolithic pieces of dried ormosils resulted. These were transparent for lower doses of organic component, but became milky for the highest dose.

Thick film samples of the same compositions were also prepared by deposition of the sols in a silicon rubber cell, obtaining free standing films of about 10 μm of thickness with plane parallel faces and transparency suitable for Brillouin spectroscopy [11].

For the sake of clarity, the organic fraction in the hybrid material will be expressed in the following as monomer molar fraction, that is: X = DMS mol/(TEOS mol + DMS mol), X being 0.24, 0. 0.41, 0.55 and 0.65 in the samples studied.

Pore size distribution, specific surface area [12] and porous volume, have been evaluated from nitrogen adsorption isotherms, performed in a Sorptomatic 1990 FISON equipment. Samples were previously evacuated, using a rotary pump, in order to remove the liquid from the pores. Complete adsorption-desorption isotherms were analyzed and pore size distributions were evaluated using the Horvath/Kawazoe method [13].

The density of the samples was estimated by pycnometry using two different probes. Thus, bulk density was measured by the Archimedes method using cyclohexane ($\rho = 0.78\ g \cdot cm^{-3}$), with negligible penetration into the pores. The density of the solid organic-inorganic network (skeletal density) was estimated from helium pycnometry.

The elasticity of materials was evaluated by Brillouin spectroscopy [14], performed with two different geometries: the backscattering (180°) and the special 90° scattering geometry [15]. The corresponding phonon wavelengths are: $\Lambda^{90A} = \lambda_0/\sqrt{2}$ and $\Lambda^{180} = \lambda_0/2n$, where λ_0 is the wavelength of the light source (514.5 nm), and n is the relevant refractive index of the sample. The elastic constant is derived from the spectra using: $c = \rho \cdot v^2$, where ρ is the density of the material and the sound velocity, $v = f \cdot \Lambda$, f being the corresponding Brillouin shift in frequency units. For our acoustic isotropic system there are only two independent elastic constants, c_{11} and c_{44}, corresponding to the longitudinal and shear polarized modes, respectively [16].

3. Results and Discussion

Textural features of the samples were inferred from the nitrogen physical adsorption on the free surface of the samples, at the liquid nitrogen temperature. On the basis of initial experiments, all the samples were previously evacuated at 60°C. The choice of this relatively low temperature, has been made in order to remove the residues from the pore walls, without noticeable changes in the textural features of the hybrid material. Adsorption-desorption isotherms for sono-ormosils with different DMS concentrations are shown in Fig. 1. Isotherms corresponding to the 0.24 and 0.41 DMS samples can be considered as IUPAC type I [17], characteristic of microporous solids. Both curves show that pore filling takes place at low relative pressure, above which a plateau occurs, indicating little additional adsorption. Nevertheless, for the isotherm corresponding to 0.55 of PDMS ormosil, the shape is much closer to those produced by adsorption on mesoporous materials, a type IV isotherm, with a hysteresis loop due to capillary condensation in the mesopores. Finally, the curve shape for the 0.65 DMS sample can be attributed to a macroporous network, where the absence of small pores in the sample causes no adsorption at low pressures.

Similar trends are found from the textural parameters derived from these experiments (Table 1). The main feature is that the surface area drastically decreases once the organic phase becomes the major component in the sample. Additional information about the influence of organic phase on the solid network can be inferred from the volume/surface ratio. The increase of this parameter with DMS concentration points to an

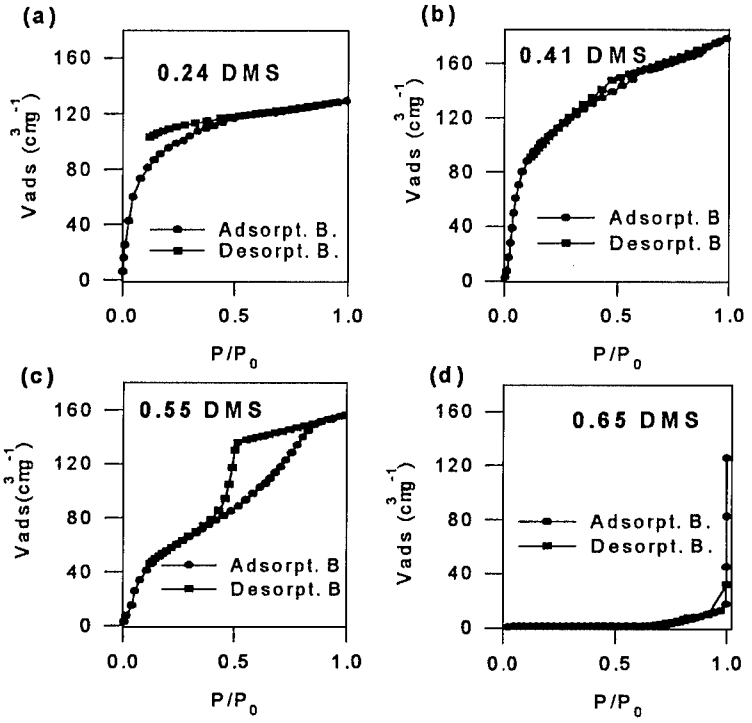

Figure 1. Adsorption-desorption isotherms for ormosils with different DMS molar concentrations, performed after samples were evacuated at 60°C.

enlargement of the pores. As noted previously, the highest DMS concentration studied ($X = 0.65$) leads to a hybrid network without noticeable porosity at the resolution level of the experiment. The BET method is not valid to estimate a specific surface value in this case where there is not adsorption at low relative pressure. It is important to notice that the density of the 0.65 sample, measured by He and C_6H_{12} pycnometries, is not significantly different (Table 1), supporting the absence of mesopores in this sample.

Table 1. Sono-ormosil textural parameters, obtained from nitrogen adsorption isotherms, and He and C_6H_{12} pycnometry, for samples with different DMS concentration (S_{BET}, surface area; V_p, pore volume).

X DMS	Bulk density ($g \cdot cm^3$)	Skeletal density ($g \cdot cm^3$)	S_{BET} ($m^2 \cdot g^{-1}$)	V_p ($cm^3 \cdot g^{-1}$)
0.24	1.39	1.45	350	0.20
0.40	1.14	1.32	372	0.27
0.55	1.07	1.18	220	0.24
0.65	~1.17	1.17	—	0.018

Pore size distributions corresponding to these four samples are shown in Fig. 2. The contribution of small pores to the total pore volume becomes lower as the PDMS concentration is increased, especially for the

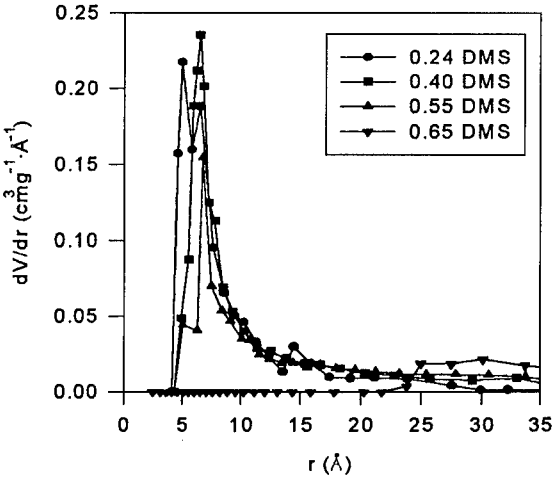

Figure 2. Pore size distributions obtained from the adsorption branch of the isotherms presented in Fig. 1. Notice that increasing the DMS concentration modifies the ormosil pore size distribution.

$X = 0.55$ and $X = 0.65$ DMS samples. In the latter, there are no pores with radius smaller than 25 Å.

From the analysis of the Brillouin spectra, valuable information about the influence of DMS content on the static and dynamic elastic properties is obtained (Fig. 3) [16]. The elastic constants were evaluated, from Brillouin shifts and bulk densities, for monolithic or thick film samples. As no transverse modes were noticeable from the spectra, probably because they are severely damped in these porous materials, only c_{11} values are presented in Fig. 3(a). The figure reveals a smooth decrease of the elastic constant with increasing DMS concentration, without any significant influence from the sample morphology. Calculated values tend asymptotically to the value for the pure PDMS (liquid), reaching this at a concentration close to 0.40. This indicates the influence of the polymeric phase concentration on the elastic properties of sono-ormosils.

A reliable estimation of the hypersonic attenuation (Γ) was obtained from the half width at half maximum (HWHM) of the Brillouin peaks, corrected for the Rayleigh value (Fig. 3(b)). The change of the DMS concentration dependence of the hypersonic attenuation should be noted, initially decreasing until a minimum is reached at about $X = 0.4$, and increasing for higher concentrations. Considering the inverse relation between the hypersonic attenuation and the phonon lifetime, it is possible to explain the attenuation behavior in terms of a changing number of interfaces in the medium (i.e., pores and segregated microphases). Thus, for low PDMS concentration, the organic phase links uniformly to the inorganic phase, leading to a homogeneous hybrid organic-inorganic network. The enrichment in DMS content of the solid network together with the increase in the average pore size, as demonstrated from the adsorption experiments, would lead to a reduction in the number of interfaces, which explains the hypersonic attenuation decay. However, it seems to be a limiting DMS concentration ($X \approx 0.4-0.5$) above which some polymer tends to adopt a globular form, leading to microphase separation and, consequently, increasing the attenuation.

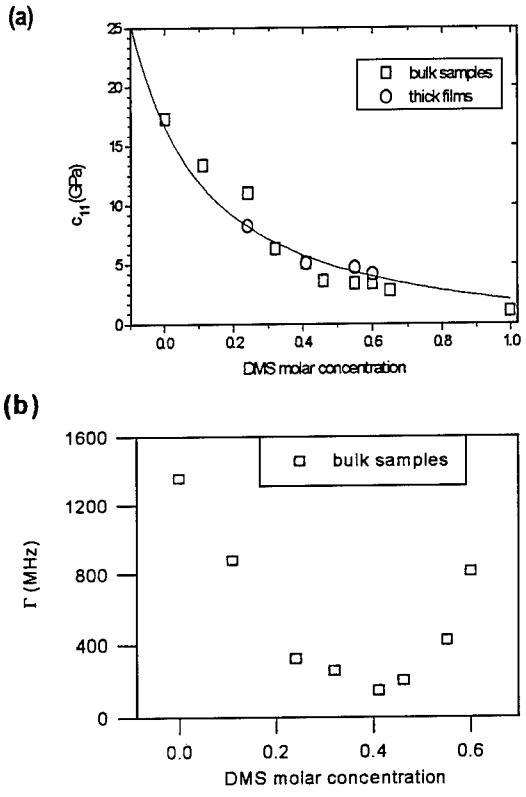

Figure 3. DMS concentration dependence of the longitudinal elastic constant (a) and the hypersonic attenuation (b). In both cases, a change in these parameters can be observed, for DMS concentrations higher than 0.40–0.50.

This interpretation of the elastic data in terms of two coexisting morphologies of PDMS (segment-like and globular) are clearly supported by previous NMR results. Evaluation of the optical properties points out that the refractive index is also sensitive to the existence of a characteristic DMS concentration [16].

The observed elastic behavior can be qualitatively explained in terms of a simple model based on those used by Mackenzie [3]. In agreement with our results, the model is based on the assumption of two different microstructures for PDMS, a segment-like configuration within the backbone of the sonogel network and a quasiglobular (liquid-like) configuration. Both forms are parallel branched while being branched in series to the silica structure. Normalizing their relative contributions to the sample elastic behavior according to the composition x, we obtain:

$$c_{11} = \frac{1}{\left(\frac{1-x}{c_1} + \frac{x}{c_2(1-x)+c_3 x}\right)} \tag{1}$$

where c_2 and c_3 are the elastic constants of PDMS in a segment-like and globular-like configuration, respectively, and c_1 is the elastic constant of the sonogel. Using the elastic constant of liquid PDMS for c_3, an estimation of c_1 and c_2 is obtained by fitting Eq. (1) to the experimental results. The continuous line in Fig. 3, corresponding to the best fit ($c_1 = 17$ GPa, $c_2 = 3$ GPa),

indicates that the model provides a semiquantitative description of the elastic behavior of the sonogels.

4. Conclusions

High resolution Brillouin spectroscopy and nitrogen adsorption have been used to investigate the elastic and textural properties of ormosils obtained by the sonogel method. These techniques allowed the evaluation of the DMS concentration effect on the elastic constant, c_{11}, the hypersonic attenuation, Γ, and pore size distribution. No appreciable difference in behavior between monolithic and film samples was observed. The concentration dependence of both the static and dynamic elastic parameters markedly changed around 0.4–0.5 DMS.

The inclusion of the polymeric phase in the sonogel network modifies the textural characteristics of these samples, increasing the pore size average and giving rise to microphase segregation when it reaches 50%.

A model, assuming two different configurations for the polymer, shows good agreement with the experimental results and supplies, as fitting parameters, the elastic constants of the sonogel backbone and that of the polymer embedded in it.

Acknowledgments

This work was supported by the CICYT (Proj. MAT-95-0040-C02-02) and Junta de Andalucía (TEP0015).

References

1. G. Philipp and H. Schmidt, J. Non-Cryst. Solids **63**, 283 (1984).
2. G.L. Wilkes, B. Orler, and H.H. Husng, Poly. Prep. **26**, 300 (1985).
3. Y. Hu and J.D. Mackenzie, J. Mat. Sci. **27**, 4415 (1992) and references therein.
4. T. Iwamoto and J.D. Mackenzie, J. Sol-Gel Sci. Tech. **4**, 141 (1995).
5. J. Kruger, in *Optical Techniques to Characterize Polymer Systems*, edited by H. Bassler (Elsevier, Amsterdam, 1989), p. 429.
6. L. Esquivias and J. Zarzycki, in *Ultrastructure Processing of Advanced Ceramics*, edited by J.D. Mackenzie and D.R. Ulrich (Wiley, New York, 1987), p. 255.
7. M. Ramírez-del-Solar, L. Esquivias, A.F. Craievich, and J. Zarzycki, J. Non-Cryst. Solids **147/148**, 206 (1992).
8. H. Huang, B. Orler, and G.L. Wilkes, Macromolecules **20**, 1322 (1987).
9. T. Iwamoto, K. Morita, and J.D. Mackenzie, J. Non-Cryst. Solids **159**, 65 (1993).
10. K. Morita, Y. Hu, and J.D. Mackenzie, J. Sol-Gel Sci. Tech. **3**, 109 (1994).
11. M. García-Hernández, R.J. Jiménez-Riobóo, C. Prieto, J.J. Fuentes-Gallego, E. Blanco, and M. Ramírez-del-Solar, Appl. Phys. Lett. **69**, 3827 (1996).
12. S. Brunauer, P.H. Emmett, and E. Teller, J. Amer. Chem. Soc. **60**, 309 (1938).
13. G. Horwath and K. Kawazoe, J. Chem. Eng. of Japan, **16**(6), 470 (1983).
14. J.R. Sandereock, Trends in Brillouin scattering, *Topics in Applied Physics* (Springer, Berlin, 1982), Vol. 51, p. 173.
15. J.K. Krüger, A. Marx, L. Peetz, R. Roberts, and U.G. Unruh, Col. Pol. Sci. **264**, 403 (1986).
16. R.J. Jiménez-Riobóo, M. García-Hernández, C. Prieto, J.J. Fuentes-Gallego, E. Blanco, and M. Ramírez-del-Solar, J. Appl. Phys. **81**(12), (1997).
17. R.W. Sing and Members of the Subcommitee on Reporting Gas Adsorption Data, Pure Appl. Chem. **57**(4), 603 (1985).

Journal of Sol-Gel Science and Technology 13, 457–460 (1998)
© 1998 Kluwer Academic Publishers. Manufactured in The Netherlands.

Hybrid Xerogel Structure and Molecular Guest Dynamics

F. CROS, L. MALIER, J.-P. KORB AND F. CHAPUT
Laboratoire de Physique de la Matière Condensée, Ecole Polytechnique, 91128 Palaiseau Cedex, France

Abstract. A new experimental approach to study the porosity of hybrid organic-inorganic glasses is reported. It relies upon nuclear magnetic resonance observation of molecular guest dynamics. It is shown that in MTEOS xerogels, there exists an interconnected organic-rich network in which organic guests are trapped and can eventually diffuse. The interpore translational diffusion is strongly activated and its spatial extension gives information on the pore connectivity, whose decay is characterized by the interpore jump probability given by the theoretical model.

Keywords: hybrid organic-inorganic materials, gel drying, molecular dynamics, NMR, sol-gel transition, confinement

1. Introduction

In the last ten years, the sol-gel process has been shown to be well-suited for preparing hybrid organic-inorganic materials in which trapped organic molecules provide specific and optimized optical functionalities [1]. For successful applications a number of requirements must be met: sufficient mechanical strength and chemical stability, shaping possibilities (including dicing or polishing), minimal association of the dyes, and control of the dye-matrix interactions. Preparation of dense materials with closed porosity addresses some of these points, but study of such materials is complicated as some characterization methods such as N_2 BET, thermoporosimetry or small angle scattering [2] cannot be applied and questions remain concerning the porosity texture of such materials or their local viscosity distribution [3].

The aim of this paper is to show how nuclear magnetic resonance spectroscopy (NMR) of organic probes trapped in a hybrid sol-gel matrix can provide valuable information concerning the pore network and its topology. We illustrate this new method with methyltriethoxysilane (MTEOS) matrices, but the same approach has been applied to other materials. The method relies upon the specific thermal behavior of the molecular dynamics, studied through NMR spectroscopy and interpreted in terms of diffusion in restricted geometries. For this study, the selected molecular probe was adamantane ($C_{10}H_{16}$), which is highly symmetrical and nonpolar.

2. Experimental

Silica-based xerogels were prepared by sol-gel synthesis from MTEOS in acetone, following a previously published procedure [4]. The hydrolysis was performed through water addition in a molar ratio (water/precursor) of 3 and catalyzed by addition of 3-aminopropyltriethoxy silane to control the base content. Fully deuterated adamantane was added to acetone at the start of the synthesis ($5 \cdot 10^{-3}$ M). After complete hydrolysis, the solution was divided into several containers and stored at 65°C for a variable ageing period after the gelation had occurred. For a sample aged a given time, the experiments consisted in NMR measurements of ^2H spectra and relaxation parameters over a large temperature range. NMR measurements were performed on the deuterium nuclei of adamantane molecules, at a Larmor frequency of 55 MHz, for temperatures ranging from −100°C to +100°C. The nonassociation of adamantane was deduced from the reproductibility of the results at various molecular concentrations. Drying and ageing times between 0.1 t_g and 6 t_g were studied after gelation (t_g is the

gelation time). Such a processing procedure leads to fairly dense matrices, with no residual solvent in the gel phase. Mercury porosimetry as well as Helium pycnometry gave an apparent density around 1.25 $g \cdot cm^{-3}$.

3. Results and Discussion

Typical results are presented in Fig. 1(a) and (b), for a xerogel aged for a time 3 t_g, showing the temperature dependencies of the adamantane deuterium spectra and relaxation times. The ^2H spectra broadens and its associated relaxation rate ($1/T_1$) increases as the temperature is lowered. The relaxation time T_1 reveals a regular activated behavior over the whole temperature range. On the other hand, the thermal evolution of the linewidth exhibit a sharp crossover between two regimes. While at low temperature the linewidth changes slightly, its variation appears strongly activated (18 kcal $\cdot$ mol^{-1}) at higher temperatures. Understanding the T_1 dependence is straightforward. As the relaxation is driven by quadrupolar mechanisms, it is related to molecular rotational motion [5] and the T_1 values indicate a rotational correlation time of 10 ps at room temperature, the evolution of which is activated with an energy of 2.1 kcal $\cdot$ mol^{-1}. In comparison, this last parameter equals 1.7 kcal $\cdot$ mol^{-1} [6] for adamantane in solution and 0.7 kcal $\cdot$ mol^{-1} [7] in crystalline adamantane. Due to its symmetry and weak polarity, the adamantane molecules rotate almost freely, even in the dry solid silica matrix.

In order to understand the origin of the linewidth, we performed proton decoupling experiments which consisted in exciting the proton nuclear spins while observing the ^2H and allowed the possible couplings between these spins to be averaged to zero. As shown in Fig. 2, the proton decoupling strongly reduces the linewidth when applied at low temperature. This decoupling effect thus clearly shows that the low temperature linewidth is due to residual dipolar interactions with protons. The linewidth value is consistent with pores of 10 Å radius covered with 8 to 10 methyl groups acting as cages for the adamantane molecule. The regular Gaussian lineshape also indicates that these pore features are narrowly distributed. As shown in Fig. 1(a), these dipolar interactions are progressively averaged when the temperature is raised. This indicates a translational diffusion of the adamantane. A theoretical model was developed to explain these experimental results [8]. It accounts for the low-temperature regime

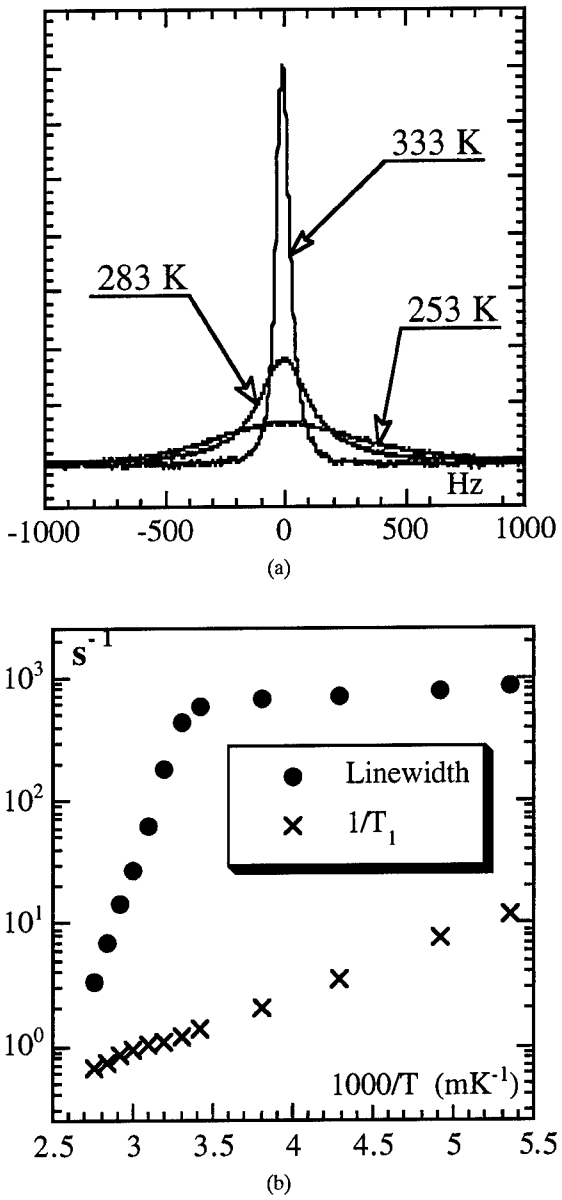

Figure 1. (a) 2D NMR spectra of a xerogel aged for a time 3 t_g, for various measurement temperatures. The chemical shift is arbitrarily referred to the center of the ^2H line which does not shift in the measurements conditions. (b) Temperature evolution of linewidths and tranverse relaxation rate for the same sample as Fig. 1(a).

through local diffusion within the pores, the higher temperature regime being due to diffusion through many cages. The more pores the molecules visit per unit time, the smaller is the linewidth. More precisely, our model gives the calculation of the lineshape at any temperature from the low-temperature lineshape and the rate of the interpore molecular jumps.

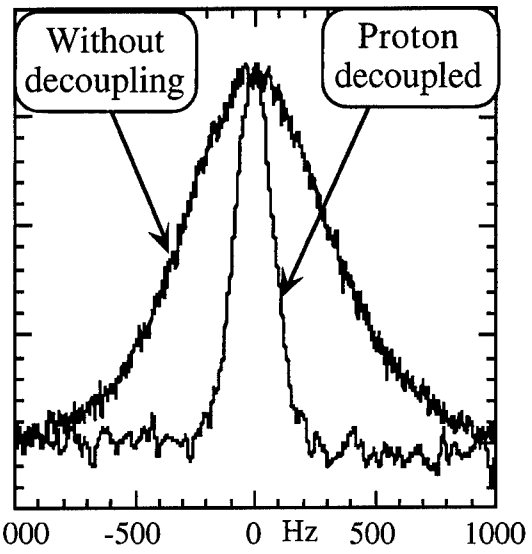

Figure 2. Deuterium spectrum at −20°C, with and without proton decoupling (same sample as in Fig. 1).

Thus, the overall conclusion at this stage is that there exists an interconnected organic-rich network in which the molecules are trapped and can diffuse. The low temperature NMR features give insights on the local geometry of this pore network while the behavior at higher temperatures gives information on the connectivity of this network. The experimental results indicate pores of 10 Å covered with methyl groups.

The evolution with ageing (Fig. 3) exhibits clear features. First, neither the value of the linewidth at low temperature nor the activation energy characterizing the adamantane translational diffusion are sensitive to ageing time. It is the same for the relaxation time T_1 which appears to be fixed as soon as the gel has been aged for 0.1 t_g, which is our earliest measurement. These experimental results are interesting since they reveal that in our system, the local geometry of the pores is fixed as soon as gelation occurs and does not vary with drying. This has to be the case for the pore size and organic content as well as for the geometry of the pore interconnection since these determine the activated diffusion.

The effect of ageing on the thermal evolution of the linewidth is striking and can be reduced to one parameter: ageing shifts the cross-over temperature towards higher values. As presented in Fig. 3, our model accounts for this effect perfectly, the different theoretical curves being defined by a parameter, the average number of access points per pore. These results can be interpreted in the following way. It is known that during ageing, new siloxane bonds are formed, although the gel volume scarcely decreases. When a siloxane bond is formed in an organic-rich channel (or in a pore interconnection), molecular diffusion becomes impossible at that point. This causes the average number of access points per pore to decrease but does not affect the local diffusion characteristics since in channels which are allowed for diffusion, the steric hindrance remains constant. In other words, only the connectivity of the organic network is affected by ageing and reduces with ageing time. Although it is difficult to

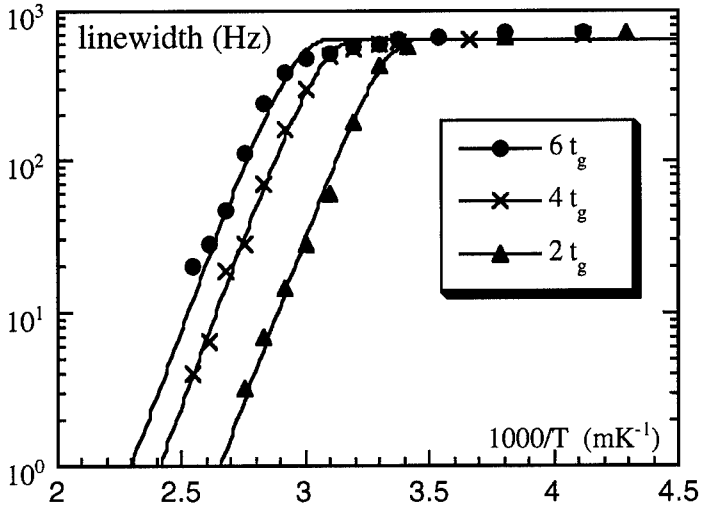

Figure 3. Thermal variations for initially identical xerogel samples with different ageing times (2 t_g, 4 t_g and 6 t_g,). The lines are the results of a fit based on our theoretical model.

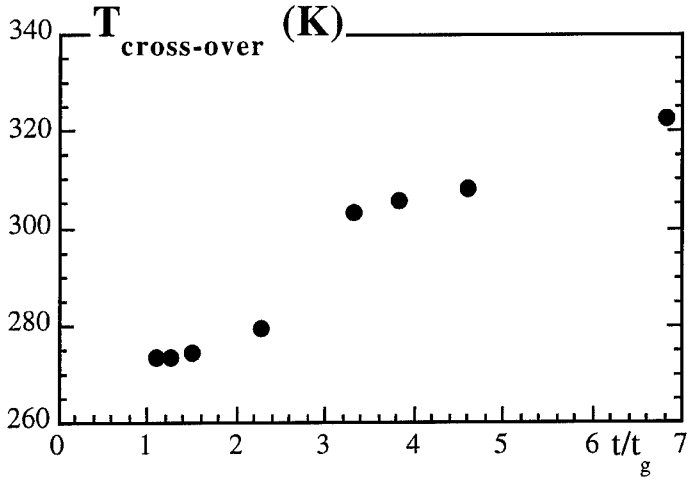

Figure 4. Variations of the cross-over temperature (see text for definition) with the ageing time of the xerogel.

define precisely the spatial extension of the interconnected pore network, our model indicates a diminution by a factor of 40 between the extrema of Fig. 3.

Figure 4 presents the evolution of the linewidth cross-over temperature when the ageing time increases. It is noticed that a sudden increase occurs around 3 t_g. It also interesting to compare this observation with the mechanical strength of our samples. Before the time 3 t_g, they remain rubber-like and cannot be diced or polished. After the time 3 t_g, their behavior is more glass-like and mechanical finishing becomes possible. From our observations, this could be correlated with a diminution of the mean distance between connecting siloxane bonds in a medium where a quasi-continuous organic phase prevents a classical gelation based on percolation of the siloxane bonds. This point remains the subject of theoretical and experimental investigations.

Conclusion

A new experimental approach to studying the porosity of hybrid organic-inorganic glasses is reported. Illustrated for MTEOS xerogels, the approach shows that these materials contain an interconnected organic-rich network in which organic guests are trapped and can eventually diffuse. The interpore translational diffusion is strongly activated and its spatial extension gives information on the pore connectivity, the decay of which is characterized by the interpore jump probability given by our theoretical model.

References

1. J.P. Boilot, F. Chaput, T. Gacoin, L. Malier, M. Canva, A. Brun, Y. Levy, and J.-P. Galaup, Comptes Rendus de l'Académie des sciences Ser. II **322**(1), 27 (1996).
2. D.P. Gallegos and D.M. Smith, J. Colloid Interface Sci. **122**(1), 143 (1987); G. Liu, Y. Li, and J. Jonas, J. Chem. Phys. **95**, 6892 (1991); K. Ishikiriyama, M. Todoki, and K. Motomura, J. Colloid. Interface Sci. **171**, 92 (1994).
3. U. Narang, R. Wang, P.N. Prasad, and F.V. Bright, J. Phys. Chem. **98**(1), 17 (1994); N.K. Raman, M.T. Anderson, and C.J. Brinker, Chem. Mat. **8**(8), 1682 (1996).
4. M. Canva, A. Dubois, P. Georges, A. Brun, F. Chaput, A. Ranger, and J.-P. Boilot, *SPIE Sol-Gel Optics III*, SPIE Proc. **2228**, 298 (1994).
5. A. Abragam, *The Principles of Nuclear Magnetism* (Oxford University Press, Oxford, 1961).
6. E. Rössler, J. Tauchert, and P. Eiermann, J. Phys. Chem. **98**(33), 8173 (1994).
7. M. Bee and J.-P. Amoureux, Mol. Phys. **40**, 617 (1980).
8. F. Cros, L. Malier, J.P. Korb, and F. Chaput, J. Chim. Phys. **95**, 264 (1998); M. Goldman, T. Tabti, C. Fermon, J.F. Jacquinot, and G. Saux, J. Magn. Res. Ser. A **103**, 288 (1993).

Journal of Sol-Gel Science and Technology 13, 461–466 (1998)
© 1998 Kluwer Academic Publishers. Manufactured in The Netherlands.

X-Ray Diffraction Studies of Sol-Gel Derived ORMOSILs Based on Combinations of Tetramethoxysilane and Trimethoxysilane

S.L.B. LANA* AND A.B. SEDDON
Centre for Glass Research, Department of Engineering Materials, University of Sheffield, Sheffield, S1 3JD, UK
Lana@oraculo.lcc.ufmg.br
a.b.seddon@sheffield.ac.uk

Abstract. ORMOSILs have been prepared in the series $TMOS_x \cdot MTMS_{(100-x)}$ (where TMOS is tetramethoxysilane; MTMS is methyltrimethoxysilane; x is mol% silane with respect to total silane for $0 \leq x \leq 100$) by means of acid catalyzed, sol-gel processing. After drying at 60°C, small bulk samples were obtained of excellent optical clarity. Powder X-ray diffraction (XRD) patterns, in the range of 5 to 60 °2θ, were compared with that of fused silica. All the prepared samples were amorphous. Fused silica exhibits one broad peak, d_2 centered at d-spacing 4.12 Å. For the $TMOS_{100}$ silica xerogel, the analogous broad peak had shifted slightly, to be centered at 3.88 Å; and remained in about the same position as x was decreased for the series $TMOS_x \cdot MTMS_{(100-x)}$. In addition, a second, broad peak, d_1, was observed for the ORMOSIL series centered at the d-spacing 8.7 Å for $MTMS_{100}$ (i.e., $x = 0$) and increasing smoothly as x was increased, reaching 11.3 Å for $x = 70$, and >11.3 Å for $x > 70$. The intensity of d_1 was found to have trebled, relative to the intensity of d_2, on increasing the organic character of the matrix from $TMOS_{70} \cdot MTMS_{30}$ to $MTMS_{100}$.

The d_2 peak appearing at about 4 Å for both fused silica and the ORMOSILs is assumed to be associated with the spacing between silicon atoms connected by means of an oxygen bridge. The Si—O—Si angle for silica xerogels is known to depend upon the nature of the sol-gel processing and is bigger than that of fused silica.

The d_1 peak may be associated with the spacing between silicons attached to methyl groups and indicative of channels of methyl groups in the structure. Alternatively, the d_1 peak may have its origin in a preferred, discrete structural unit in the matrix for instance cubane based on a octameric silicon arrangement.

Keywords: sol-gel, ORMOSILs, X-ray diffraction (XRD)

Introduction

ORMOSILs have been prepared via sol-gel type routes and are hybrid inorganic/organic materials. These materials are not only fascinating from a structural point of view but also have many potential applications including active optical materials.

We have begun work investigating systematically the synthesis and properties of a range of ORMOSILs systems. Here we briefly report powder X-ray diffraction (XRD) patterns, in the range of 5 to 60 °2θ, and compare them with that of fused silica.

Experimental

ORMOSIL samples have been prepared by combining monomethyltrimethoxysilane (MTMS) with tetramethoxysilane (TMOS) in varying proportions and hydrolyzing these under acidic conditions. After drying at 60°C, small bulk samples were obtained of excellent optical clarity [1]. Samples of the methyl-modified series ranging from 100% of TMOS to 100% of MTMS were analyzed by powder XRD using CuK_α radiation ($\lambda = 1.542$ Å).

Current address: Centre for Materials Research, Department of Chemistry, Federal University of Minas Gerais, Belo Horizonte, Brazil.

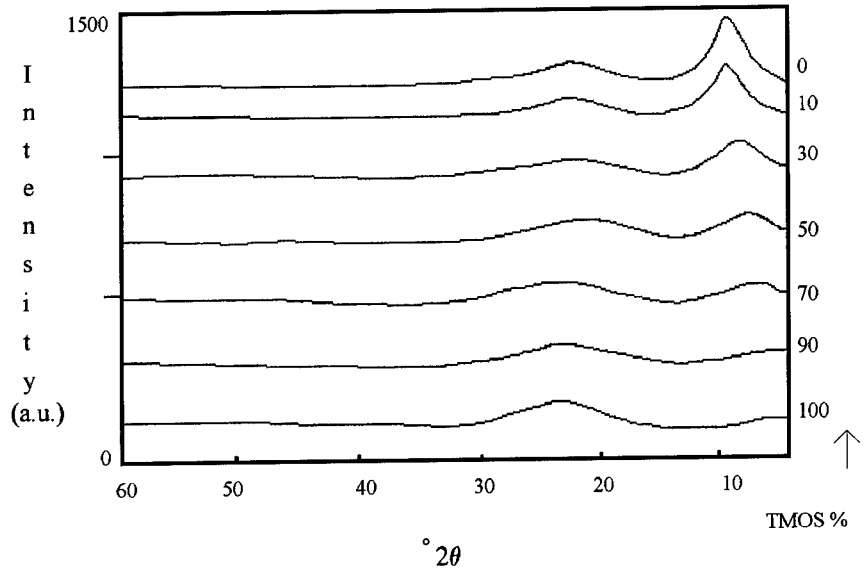

Figure 1. XRD patterns of samples from the $TMOS_{n\%}/MTMS_{(100-n)\%}$ series.

Results and Discussion

From Fig. 1 it can be seen that all the prepared samples were amorphous and that there are two broad haloes of maxima at: (a) $2\theta \sim 23°$ and (b) $2\theta \sim 7°$ to 10°. The latter, at the smaller angle, apparently moves off-scale for a TMOS content higher than 90 mol%.

Figure 2 shows the expanded X-ray patterns for the $TMOS_{x\%}/MTMS_{(100-x)\%}$ series from pure MTMS to pure TMOS. Patterns of the $TMOS_{30}{\cdot}MTMS_{70}$ and $TMOS_{90}{\cdot}MTMS_{10}$ samples have an overall greater intensity and this could be related with the packing of the powders onto the X-ray plates, or due to a different mass of samples.

The diffractogram made inhouse for fused silica, has a single broad diffraction band with a maximum at 21.16° (see Fig. 3). This is similar to that determined by Warren and Briscoe in 1938. For silica gel they

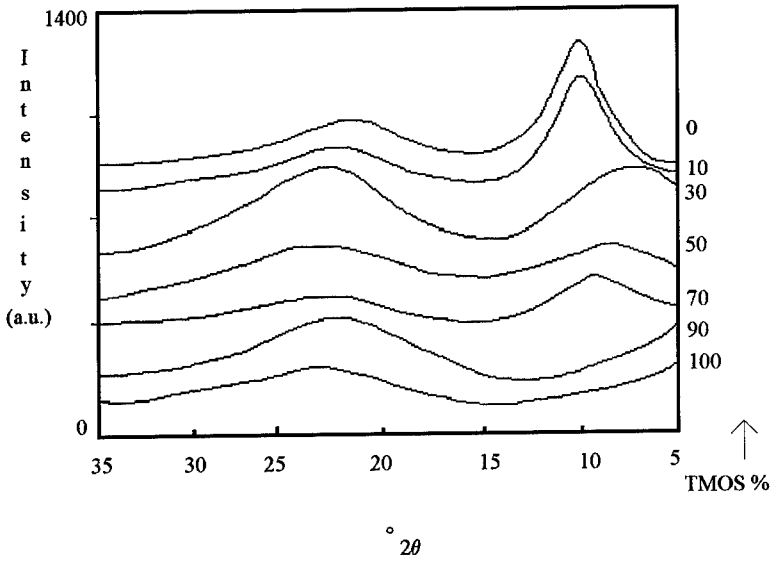

Figure 2. XRD patterns ($5° < 2\theta < 30°$) for samples from the $TMOS_{n\%}/MTMS_{(100-n)\%}$ series.

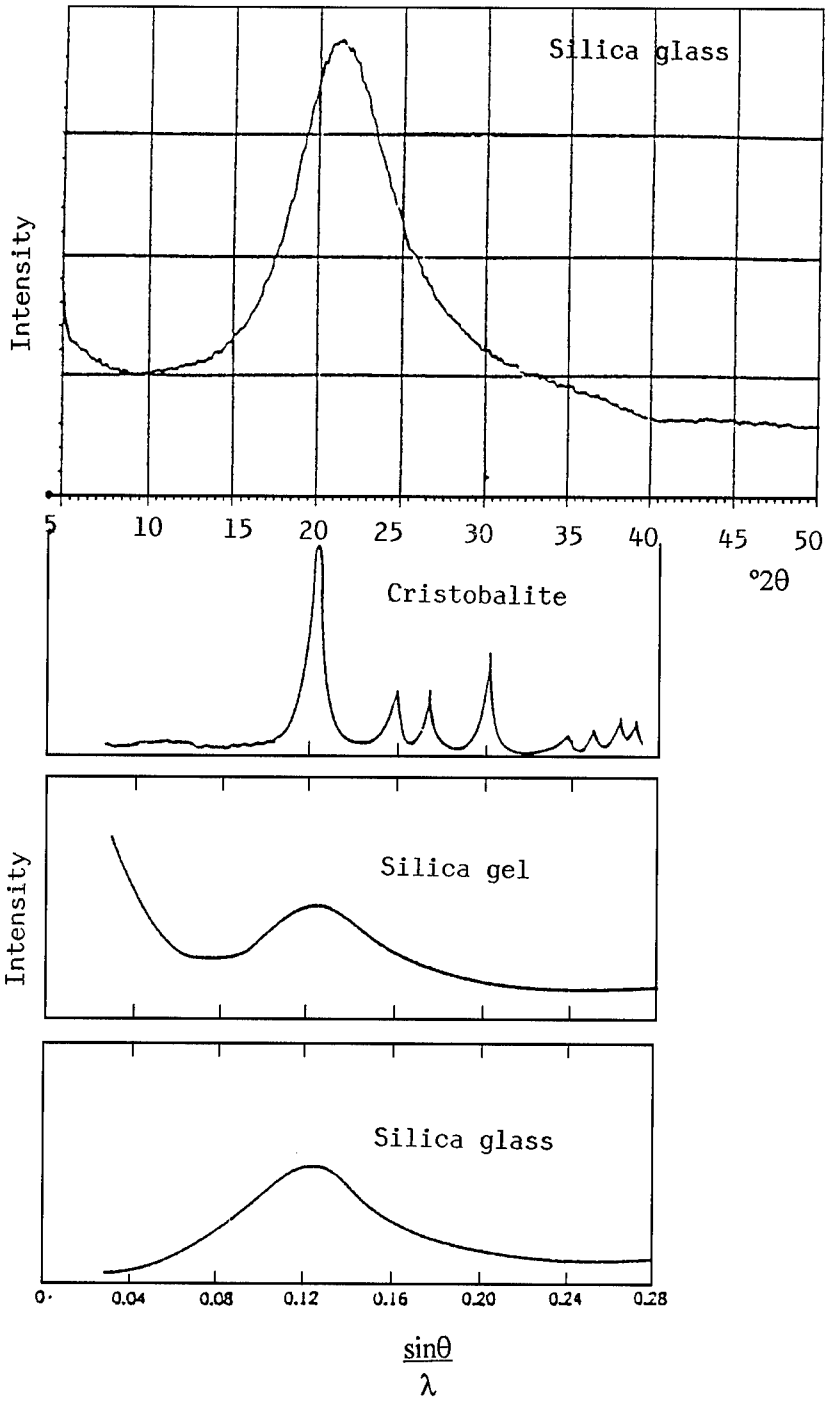

Figure 3. XRD patterns of: (a) vitreous silica analyzed inhouse and (b) crystobalite, silica gel, and vitreous silica [2]. Note: $(\sin\theta/\lambda) =$ 0.04, 0.08, 0.12, 0.16, 0.20, 0.24, 0.20 are $2\theta = 7.07°$; 14.2°; 21.3°; 28.6°; 35.9° and 43.4°, respectively.

found a second diffraction peak at $2\theta \leq 7°$, but it was incompletely resolved. However, this latter peak could correspond to the peak present here at low angle for the TMOS/MTMS ORMOSILs (compare Figs. 1 and 2). These diffuse diffractograms for fused silica, silica gel and ORMOSILs (Figs. 2 and 3) may be compared with the sharp reflections for crystobalite (Fig. 3), which is crystalline.

For the series of ORMOSILs prepared in the present study the values of $°2\theta_1$, the smaller angle, and $°2\theta_2$, the larger angle, together with their relative Bragg d-spacings, d_1 and d_2 and respective intensities Ir_1 and Ir_2, are compared with those for vitreous silica in Table 1.

The larger $°2\theta_2$ values are approximately constant at 22.96 ± 0.42, while the smaller $°2\theta_1$ appear to be a function of TMOS/MTMS molar ratio. The variation

Table 1. XRD results for $TMOS_{n\%}/MTMS_{(100-n)\%}$ series determined here compared with vitreous silica [2].

	$2\theta_1$(°)	Ir_1	d_1 (Å)	$2\theta_2$ (°)	Ir_2	d_2 (Å)	Ir_1/Ir_2
Vitreous silica	—	—	—	21.16		4.12	—
TMOS							
100	<7	—	>11	22.9	12	3.88	—
90	<7	—	>11	23.4	11	3.80	—
70	7.8	11	11.34	23.4	10	3.80	1.1
50	8.9	15	9.94	23.4	10	3.80	1.5
30	9.2	18	9.61	22.8	10	3.90	1.8
10	9.7	23	9.12	22.3	10	3.99	2.3
0	10.2	28	8.67	22.5	10	3.95	2.8

Note: Ir_1 and Ir_2 are the relative intensities of the peaks $°2\theta_1$ and $°2\theta_2$, respectively.

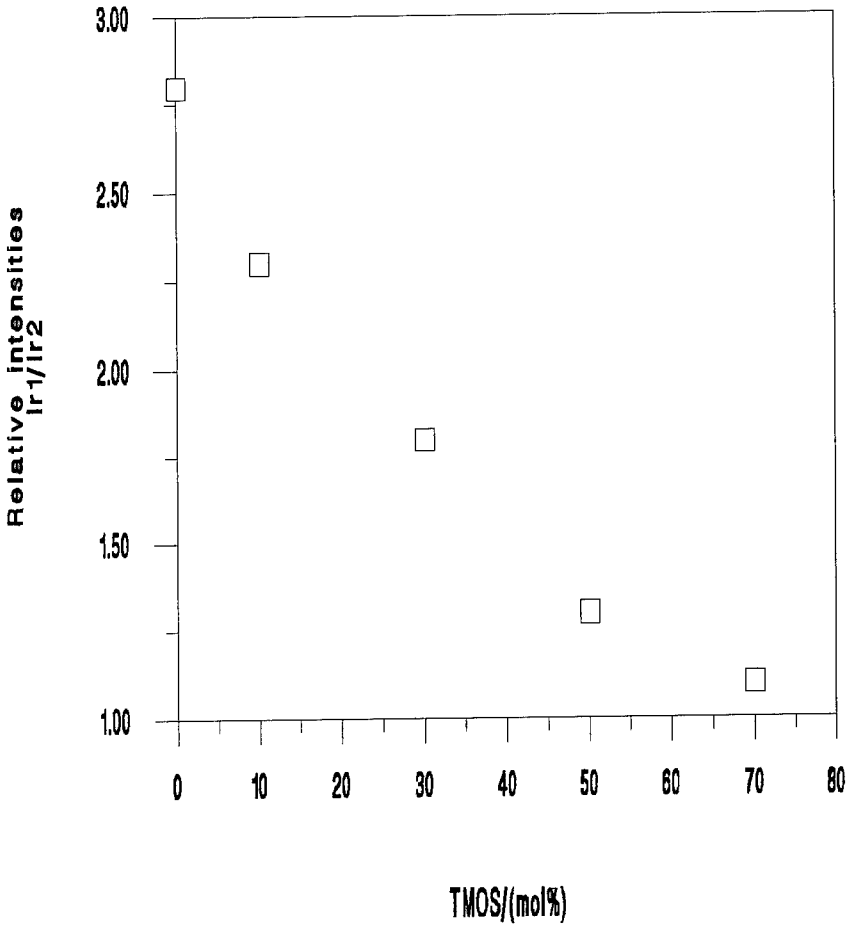

Figure 4. XRD relative intensities Ir_1/Ir_2 variation (where Ir_1 refers to peak $°2\theta_1 < 10°$ and Ir_2 refers to peak at $°2\theta_2$ at ~23°) with TMOS content for the $TMOS_{x\%}/MTMS_{(100-x)\%}$ series.

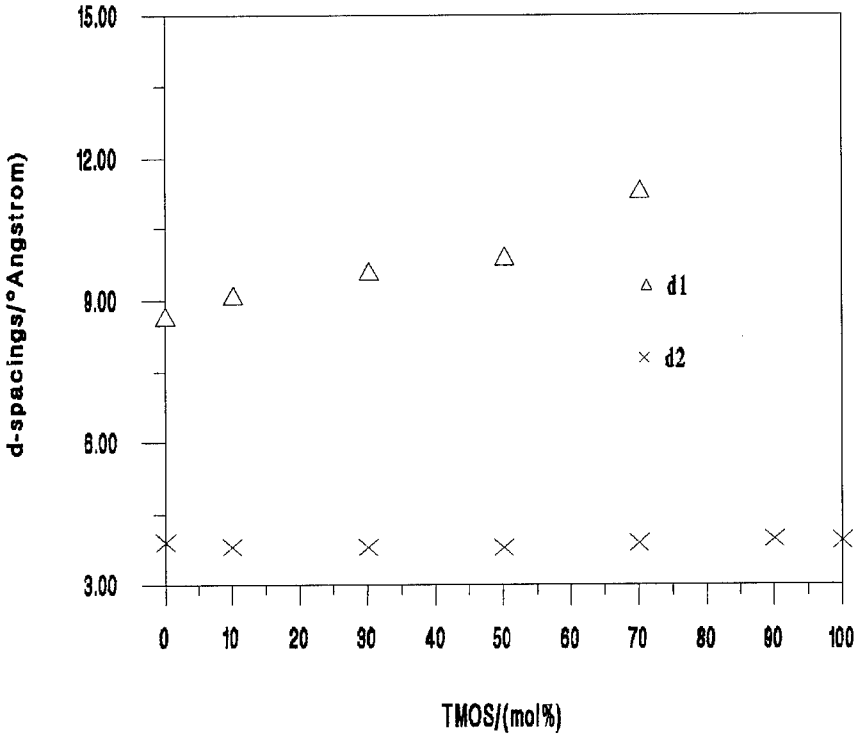

Figure 5. Variation of d-spacings d_1 and d_2 with TMOS content.

of: (a) the relative intensity of the bands at $°2\theta_1$ and $°2\theta_2$; the Ir_1/Ir_2 ratio and (b) the Bragg d-spacings, d_1 and d_2 with TMOS content are seen in Figs. 4 and 5, respectively.

The relative intensity ratio of the bands at $°2\theta_1$ and $°2\theta_2$ varies inversely with the TMOS content (see Fig. 4). The bands at $°2\theta_1$ and $°2\theta_2$ show a very near relative intensity of 1 for the 70% TMOS member of the series. Interestingly, as the content of methyl groups increases, the $°2\theta_1$ band reaches almost three times the intensity of the $°2\theta_2$ band. The variation of $°2\theta_1$ means that values of d_1 increase from about 9 to >11 Å with the increase in concentration of MTMS, according to Table 1 and Fig. 5. Yet $°2\theta_2$ and d_2 values are constant, at approximately 23° and 4 Å, respectively, i.e., they are unaffected by the relative concentration of the components. Since silicon atoms scatter more intensely than oxygen or carbon, an initial interpretation includes the nearest neighbor silicon atoms. The distance between silicon atoms may be estimated from the Si—O bond length and the Si—O—Si bond angle.

There is a big variation of the Si—O angle described in the literature both for vitreous silica [4, 5] and xerogel as the Si—O—Si angle is known to depend upon the nature of sol-gel processing and it is bigger than that of fused silica [6]. As defined earlier, d_1 is the smaller angle and thus it represents structural information at larger interatomic distances. As the amount of the organic component (MTMS) in the series is increased, the angle $°2\theta_1$ increases (see Table 1) and the relative intensity of the associated peak decreases; the peak may be diagnostic of the ORMOSIL modification of the silica. Thus, as the silica composition is approached this longer range structural order decreases, and is absent for fused silica, but interestingly not absent for silica gel.

The d_1 peak may be associated with the spacing between silicons attached to methyl groups and indicative of channels of methyl groups in the structure. Alternatively, the d_1 peak may have its origin in a preferred, discrete structural unit in the matrix for instance cubane, based on an octameric silicon arrangement where methyl groups tend to replace hydroxyl groups, as the non-bonding group on each corner silicon atom, as more of the methyl modified silane is incorporated in the precursor mix. This would account for evidence that the d_1 peak is already

present in non-organically modified, sol-gel derived silica.

Conclusions

- The organic component increases the longer range order in the structure, and that this feature might be diagnostic of the ORMOSIL modification of silica.
- The Si—Me bond does not affect the ≡Si—O—Si≡ angle, because to a first approximation the d_2 position is kept constant.
- The d_1 peak might be associated with the spacing between silicons attached to methyl groups and indicative of channels of methyl groups in the structure. Alternatively, the d_1 peak may have its origin in preferred, discrete structural units in the matrix which may already be present in sol-gel derived silica but have the capability of becoming increasingly organically modified.

Acknowledgment

The authors wish to thank B. Ellis for input into discussion of these results.

One of the authors (SLBL) is indebted to CNP_q/FAPEMIG-Brazil for provision of funds.

References

1. S.L.B. Lana, Ph.D. Thesis, Department of Engineering Materials, University of Sheffield, 1994, p. 146.
2. W.D. Kingery, H.K. Bowen, B.R. Uhlman, *Introduction to Ceramics* (John Wiley & Sons, NY, 1976), p. 91.
3. J.R. Fitzpatrick and B. Ellis, *The Physics of Glassy Polymers* (Applied Science Publishers Ltd., London, 1973), p. 108.
4. J. Bockrins, *The Vitreous State* (The Glass Delegacy of the University of Sheffield, 1955), p. 61.
5. C.E. Magrabi, Ph.D. Thesis, Department of Ceramics, Glasses and Polymers, University of Sheffield, 1970, p. 54.
6. C.J. Brinker and G.W. Scherer, *Sol-Gel Science: The Physics and Chemistry of Sol-Gel Processing* (Academic Press, NY, 1990), pp. 241, 577, 583.

Journal of Sol-Gel Science and Technology 13, 467–472 (1998)
© 1998 Kluwer Academic Publishers. Manufactured in The Netherlands.

Thin ORMOSIL Films with Different Organics

K.A. VOROTILOV, V.A. VASILJEV, M.V. SOBOLEVSKY AND A.S. SIGOV
Moscow State Institute of Radioengineering, Electronics and Automation, 117454, Vernadsky prosp., 78, Moscow, Russia

Abstract. Structural, optical and electrical properties of silicate films modified by structure fragments containing different organic groups were studied. The ORMOSILs were produced by a cohydrolysis of tetraethoxysilane with different types of alkyl (aryl) substituted alkoxysilanes. Film structure and its evolution during heat treatment were studied by ellipsometry and IR spectroscopy. For methyl- and phenyl-modified silicate films the shrinkage is lower than for silicate ones in the range of annealing temperature from 200 to 500°C. The shrinkage of phenyl-modified silicate film is more than three times lower than of methyl- and trimethyl-modified ones. The presence of single or double C=C bonds in the organic chain leads to an increase in the film shrinkage due to the thermodestruction of the bond as it is confirmed by IR data. In the case of phenyl- and methyl-modified silicate films this process starts from 500°C and it is accompanied by abrupt film shrinkage. The dielectric constant and the loss tangent of methyl and phenyl groups decrease due to reduction of hydroxyl content and film density. Other groups are not effective due to their thermodestruction at lower temperatures.

Keywords: organically modified silicates, thin films, structural properties, electrical properties

1. Introduction

Recent research on sol-gel science has focussed on inorganic-organic hybrid materials. In these materials organic fragments are built into silicon-oxide networks (organically modified silicates—ORMOSILs) or, in the general case, into metal-oxide networks (organically modified ceramics—ORMOCER). A typical method of producing such inorganic-organic hybrids is by a co-hydrolysis of an alkoxide and an alkyl(aryl)-substituted alkoxysilane (in the case of ORMOSILs). Alkyl(aryl) groups, in contrast to alkoxy ones, do not undergo hydrolysis and, as a result, are incorporated into growing silicon-oxide gel network.

A combination of inorganic and organic networks facilitates the design of new engineering materials with exciting properties for a range of applications (see, for example, [1–3]). In addition inorganic-organic hybrids are of particular scientific interest as a new solid-state medium.

Thin films and coatings were the earliest and remain so far one of the most important applications of the sol-gel technology. Recent years have been marked by a growing interest in sol-gel processed films in microelectronics, optics, and many other areas. One of the most important application of sol-gel films in microelectronics, discussed in this paper, is the process of planarization of multilevel metallization of very-large scale integration (VLSI) and ultra-LSI (ULSI) devices [4, 5].

It is clear that the type, concentration, and spatial arrangement of organic groups within the metal-oxide skeleton will substantially determine the material properties. Thus, practical applications of the inorganic-organic hybrids require fundamental understanding of their structural and physical peculiarities. The present work deals with the study of optical and electrical properties of silicate films modified by structural fragments containing different organic groups.

2. Solution Preparation and Film Coating Process

The ORMOSIL structures were produced by a co-hydrolysis in *n*-butanol of tetraethoxysilane with different types of alkyl(aryl) substituted alkoxysilanes:

Table 1. Some chemical and physical properties of solutions.

Organics R/Si = 0.5	Viscosity (cPs)	Density (g/cm^3)	Conductivity ($\Omega^{-1}cm$)	Refractive index	pH
Silicate	3.1	0.8615	$8.0*10^{-5}$	1.3938	1.1
Me	3.0	0.8546	$1.9*10^{-4}$	1.3959	0.9
3Me	2.8	0.8467	$3.6*10^{-5}$	1.3958	1.7
Et	3.4	0.8544	$3.1*10^{-5}$	1.3965	4.3
Vin	3.0	0.8596	$1.4*10^{-4}$	1.3985	1.0
Hex	3.4	0.8559	$3.0*10^{-5}$	1.4020	6.5
Ph	3.5	0.8696	$3.2*10^{-5}$	1.4058	5.6

methyltriethoxysilane, trimethylethoxysilane, ethyltriethoxysilane, vinyltriethoxysilane, allyltriethoxysilane, hexyltriethoxysilane, phenyltriethoxysilane (PTEOS), and diphenyl diethylhexyloxy diethoxy disiloxane (DPS). The equivalent silicon content in the solutions was 4 wt% and the molar ratio of components was $H_2O/HCl/[Si(OEt)_4 + R_xSi(OEt)_{4-x}] = 4/0.04/1$. The number of organically modified bonds of each silicon atom R/Si was varied between 0.15 and 0.6.

All solutions were clear after mixing and suitable for film deposition, except those with high allyl and hexyl content. Allyl-modified solutions had gelated after a few hours (12–15 h at R/Si = 0.3, and 3 h at R/Si = 0.6), whereas hexyl-modified ones (hexyl to silicon ratio 0.6) strongly sedimented immediately after mixing. No gelation was observed in all the other solutions for at least three months (the solutions remained clear, except for some sedimentation after 20 days in the methyl- and vinyl-modified ones). Some characteristics of the ORMOSIL solutions with an organic to silicon ratio of 0.5 are given in Table 1. These properties were measured 3 days after the preparation of solutions. It is important for film deposition that the nature of organic group has only a slight effect on the solution viscosity.

The films were deposited on silicon substrates by a spin-on technique and were annealed at temperatures from 200 to 900°C for 30 min. An important problem in ORMOSIL film deposition is a loss of film continuity as a result of nonwetting of the substrate surface. This problem usually arises in the case of high organic to silicon ratios and extended organic groups (see Table 2).

γ-Aminopropyltriethoxysilane was used as an adhesion promoter and gave good results in all cases except for solutions prepared with trimethylethoxysilane.

Table 2. Film covering properties of ORMOSIL solutions.

	R/Si		
	0.15	0.3	0.6
Silicate	Good		
Me	Good	Good	Good
3Me	Good	Good	Bad Bad with AP[a]
Et	Good	Good	Good
Vin	Good	Good	Good
Allyl	Middle	—	—
Hex	Good	Middle	Bad Good with AP[a]
Ph	Good	Middle	Middle Good with AP[a]
DPS	Good	Middle	—

[a]AP—adhesion promoter: γ-aminopropyltriethoxysilane $NH_2CH_2CH_2CH_2Si(OC_2H_5)_3$.

3. Evolution of Film Structure During Heat Treatment

Information concerning film structure and its evolution during heat treatment was obtained from ellipsometry and IR spectroscopy data. The film thicknesses and refractive indexes were measured at four points of each film (in a central part of the substrate) by multiangle ellipsometry at 632,8 nm and at incident irradiation angles from 45 to 70° [6]. The real and imaginary parts of the refractive index of the uncoated silicon substrate was determined to be 3.85 and −0.02, respectively. The measurement errors were ±0.0005 for the refractive index, and ±0.5 nm for the film thickness. The deviation in the refractive index and the film thickness for a given substrate were less than ±0.005 and ±5 nm, respectively.

Figure 1 presents the dependence of the film thickness of the ORMOSIL films as a function of annealing temperature. As described above, the initial solutions had the same concentration of silicon and practically same viscosity. Therefore, we can consider the change in the film thickness as an effect of the distortion of the silicon-oxide network by the organic groups. This suggestion is confirmed by the fact that after annealing at high temperature (800°C) all the films have practically the same thickness (an increase in the film thickness for the films annealed at 900°C is due to oxidation of silicon substrate). Therefore, distortion of silicate

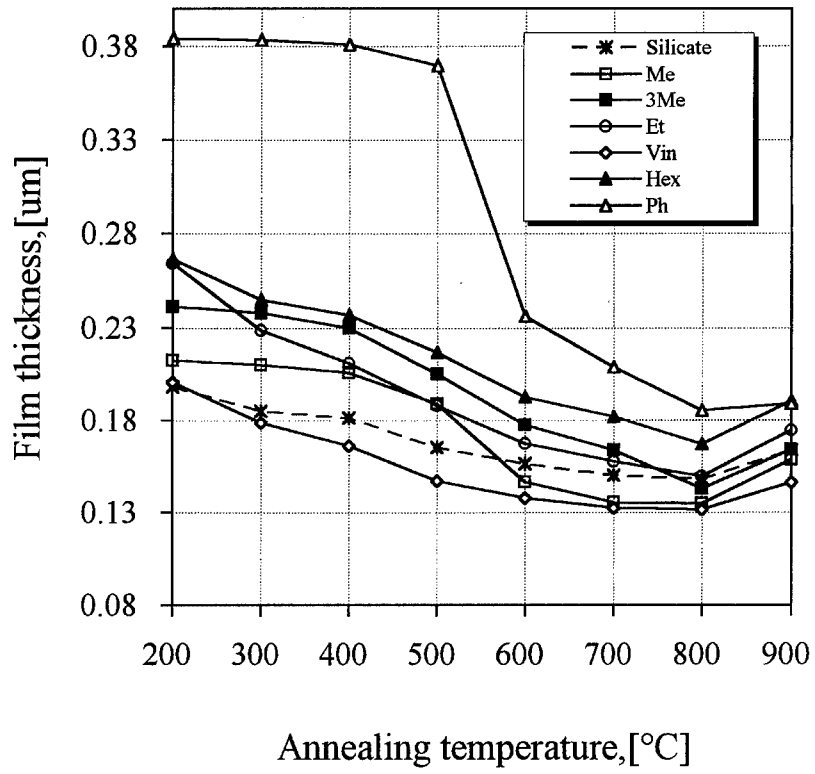

Figure 1. The dependence of the thickness of ORMOSIL films with different organic groups (R/Si = 0.5) as a function of heat treatment temperature.

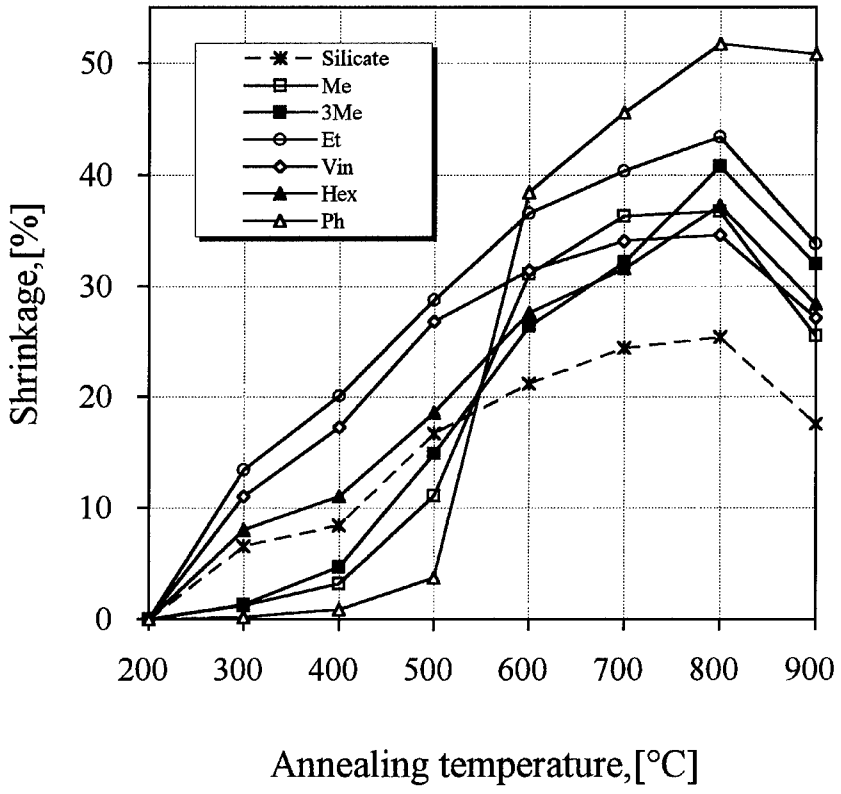

Figure 2. The shrinkage of ORMOSIL films with different organic groups (R/Si = 0.5) as a function of heat treatment temperature.

network is increased as the size of organic group increases (except in the case of vinyl-modified silicate). This effect is most pronounced in phenyl-modified silicate films the thickness of which are two times the thickness of unmodified silicate films.

Film shrinkage as a function of annealing temperature is shown in Fig. 2. Methyl- and phenyl-modified silicate films have lower shrinkages for annealing temperatures between 200 and 500°C than silicate films. The shrinkage of the phenyl-modified silicate film is more than three times lower than that of the methyl- and trimethyl-modified ones (less than 1% shrinkage from 200 to 400°C). The presence of single or double C=C bonds in the organic chain leads to an increase in the film shrinkage due to its thermodestruction, as confirmed by the IR data. In the case of phenyl- and methyl-modified silicate films this process starts at 500°C and it is accompanied by abrupt film shrinkage. The process of thermodestruction is illustrated by the IR spectra of phenyl-modified silicate films (see Fig. 3). An increase in the annealing temperature from 450 to 600°C leads to disappearance of the absorption peaks of phenyl groups (475, 705, 750, 1140, 1440, 3075 cm^{-1}), as well as the shifting of the Si—O band from 1075 to 1080–1085 cm^{-1}. The latter shift is indicative of a densification of the silicon oxide skeleton during destruction of phenyl groups. It should be noted that the IR spectra of phenyl-modified silicate films after the heat treatment at 600°C is different from the silicate spectra because of the presence of absorption

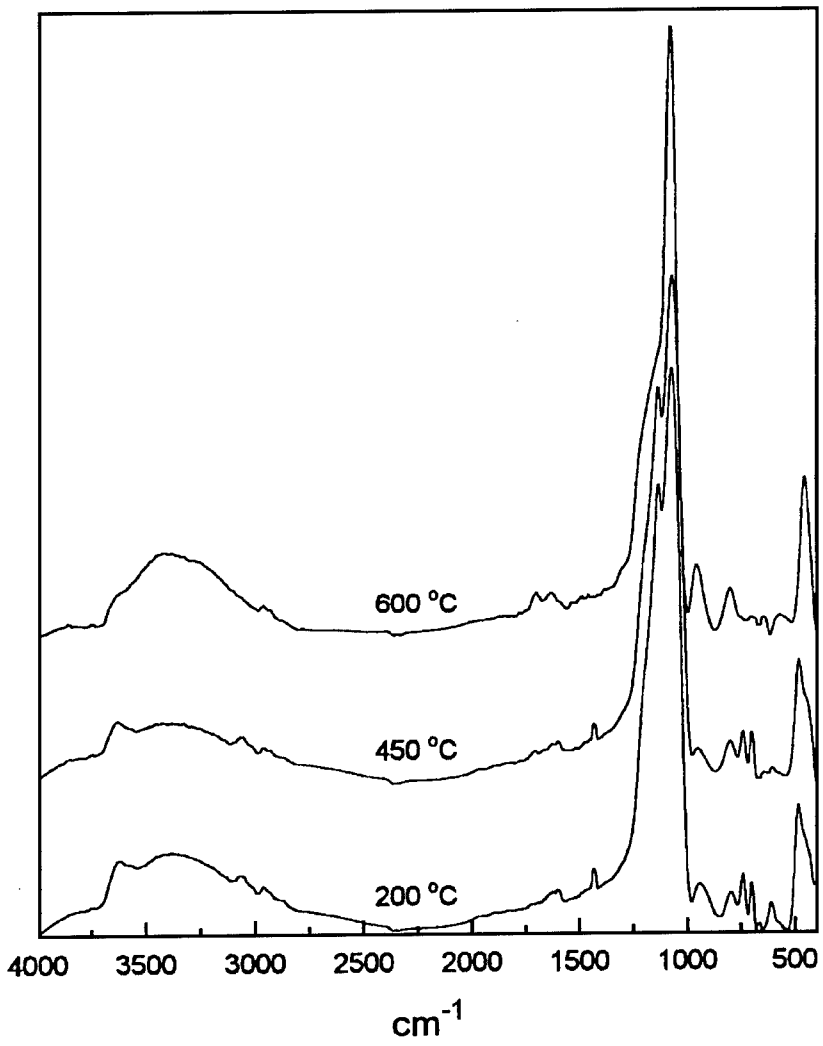

Figure 3. IR spectra of phenyl-modified silicate films annealed at different temperatures.

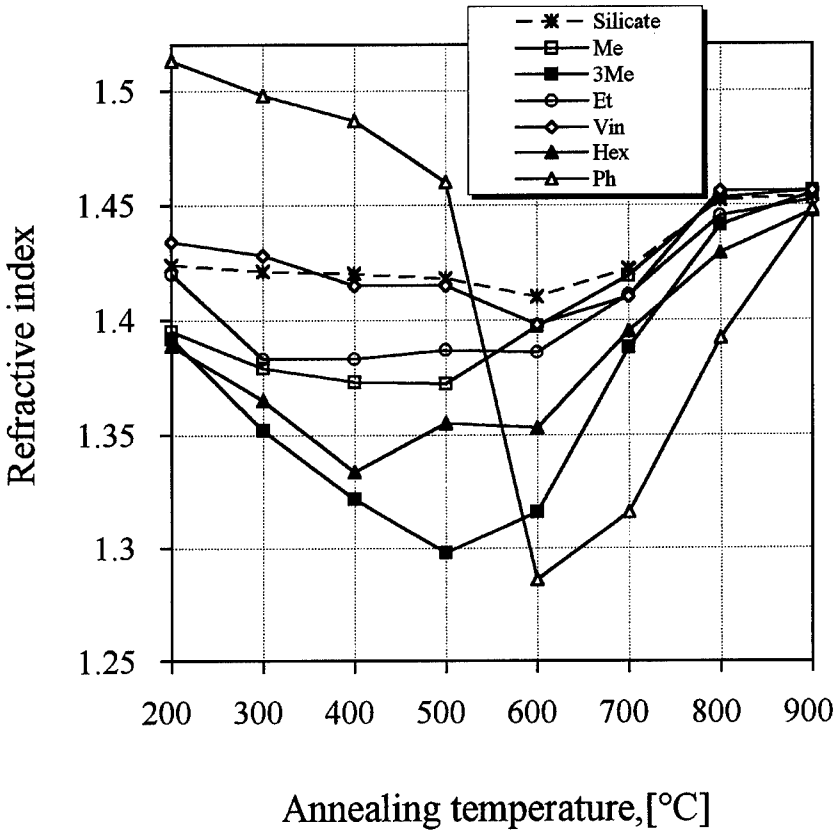

Figure 4. The dependence of the refractive index of ORMOSIL films with different organic groups (R/Si = 0.5) as a function of heat treatment temperature.

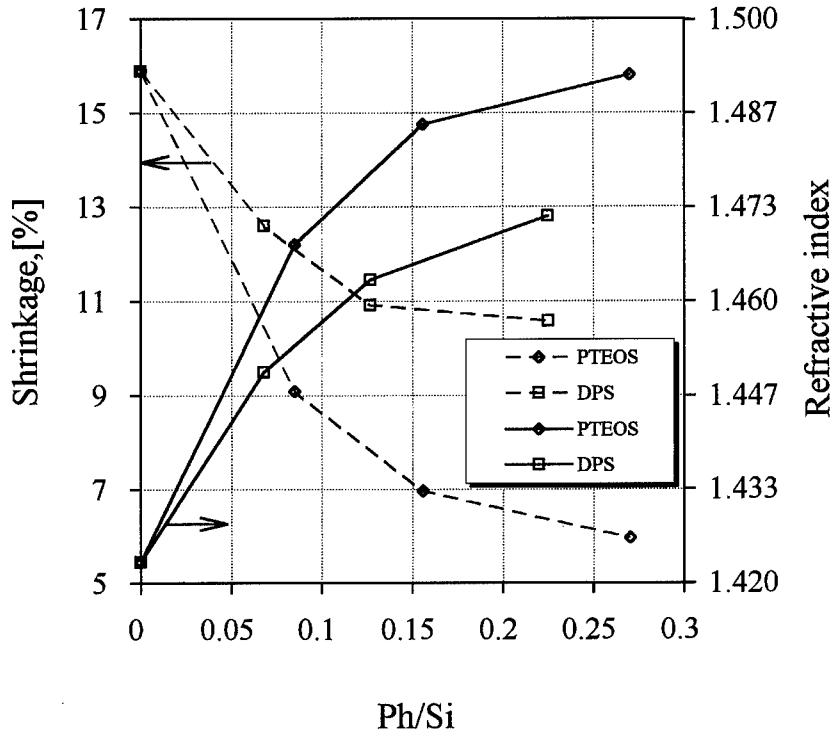

Figure 5. The shrinkage and the refractive index of phenyl-modified silicate films prepared from PTEOS and DPS.

peaks resulting from the thermodestruction of phenyl groups (e.g., absorption peaks at 1705 cm^{-1} and 1305 cm^{-1}, conceivably $CH_3COC_6H_5$ and C_6H_5CHO, respectively, [7]). A negative slope in the film shrinkage at 900°C is due to oxidation of the silicon substrate.

The process of elimination of organic groups as a result of thermodestruction is clearly seen in the temperature dependence of refractive index, especially, for phenyl-modified silicate films (see Fig. 4). The refractive index of this film dramatically falls at annealing temperature 600°C from 1.46 to 1.28 as a result of thermodestruction of the phenyl group and void production. Annealing at higher temperatures leads to densification of the film structure due to viscous sintering, so that the films annealed at 900°C have practically the same refractive index (1.45).

Figure 5 illustrates how the phenyl to silicon content and the spatial distribution of phenyl groups affect the refractive index and shrinkage of the films. The increase in silicon to carbon bonds in the films blocks the polycondensation reaction in some directions and thus reduces film shrinkage. Films prepared from PTEOS-based solutions have a more dense structure and lower shrinkage than ones prepared from DPS. After completion of hydrolysis of alkoxy-groups, the DPS molecule differs from the PTEOS one by the presence of two phenyl groups bonded with two silicon atoms. Although it is hard to obtain direct information concerning film structure, it would appear reasonable that lower shrinkage of the films prepared from PTEOS is due to their greater effectiveness in blocking the polycondensation reaction (at the same Ph/Si content the phenyl groups in the PTEOS precursor are more uniformly distributed in silicon matrix, and block higher numbers of polycondensation chains, than with the DPS precursor where the two phenyl groups are rigidly fixed.

Acknowledgments

The research described in this work was made possible in part by grant N 97-02-17822 from the Russian Foundation for Basic Research and grant 218/68/1–2 from the SSTP "Advanced Technologies and Devices of Micro- and Nanoelectronics."

References

1. H. Schmidt, J. Non-Cryst. Solids **73**, 681 (1985).
2. C.J. Brinker and G.W. Scherer, *Sol-Gel Science: The Physics and Chemistry of Sol-Gel Processing* (Academic Press, San Diego, CA, 1990).
3. J.D. Mackenzie, J. Sol-Gel Sci. Tech. **2**, 81 (1994).
4. A.S. Sigov, K.A. Vorotilov, A.S. Valeev, and M.I. Yanovskaya, J. Sol-Gel Sci. Tech. **2**, 563 (1994).
5. K.A. Vorotilov, V.A. Vasiljev, M.V. Sobolevsky, and N.I. Afanasyeva, Thin Solid Films **288**, 57 (1996).
6. V.K. Grigor'ev, V.I. Petrovsky, and I.A. Shapova, Izmeritelnaja Technicka **1**, 15 (1991) (in Russian).
7. L.J. Bellamy, *The Infra-Red Spectra of Complex Molecules*, (Methuen D Co., London, J. Wiley and Sons, NY, 1954).

Journal of Sol-Gel Science and Technology 13, 473–477 (1998)
© 1998 Kluwer Academic Publishers. Manufactured in The Netherlands.

Leaching of the Anthraquinone Dye Solvent Blue 59 Incorporated into Organically Modified Silica Xerogels

JAN-CHRISTOPH PANITZ AND FRIEDERIKE GEIGER
General Energy Research Department, Paul Scherrer Institute, CH-5232 Villigen PSI

Abstract. The effects of preparation method and precursor composition on the leaching behavior of the anthraquinone dye Solvent Blue 59 incorporated into silica based xerogels have been studied. Xerogels were prepared under acidic conditions from mixtures of 20 mol% of organically modified silicon alkoxides, $R'—Si(OR)_3$, in $Si(OR)_4$ (R = methyl or ethyl, R′ = methyl, vinyl, phenyl). The dye was added at the beginning of the sol-gel reaction. The reaction was carried out by either hydrolysis under acidic conditions or acidolysis by formic acid. The dye incorporated was leached with refluxing ethanol using a Soxhlet extraction procedure to simulate the long-term stability of the samples prepared. With increasing size of organic substituent (methyl < vinyl < phenyl), the amount of dye leached decreases. Results from nitrogen adsorption experiments show that all samples characterized have about the same average pore diameter, but they differ in total pore volume and BET surface area. With increasing size of the organic residue, the pore volume decreases by an order of magnitude. Therefore, it is concluded that the microstructure of the xerogels prepared determines the retention behavior of dyes incorporated during the sol-gel reaction.

Keywords: organically modified silica gels, leaching of dyes, formic acid-alkoxide route

Introduction

The sol-gel process offers the possibility of incorporating organic molecules into an inorganic gel network at low processing temperatures (200°C and below). Of special interest has been the incorporation of dyes [1–4], and the use of such dye-doped materials as chemical sensors [5, 6]. Another possibility discussed in the literature is the use of inorganic gels as carriers in drug-delivery systems [7] and as contrast enhancers for CRT devices [8]. Information about the stability of dye-doped gels against varying temperature, irradiation with light, humidity, or solvents capable of leaching out the incorporated dyes is important for any successful application of such materials. Here, we present an investigation of the leaching behavior of the anthraquinone dye Solvent Blue 59 (1,4 Bis-(ethylamino)-anthraquinone) entrapped during sol-gel synthesis. The properties of the gel network were modified by using organically modified silicon alkoxides in the sol-gel reactions. We have recently shown that the use of non-aqueous sol-gel reactions has benefits for the preparation of organically modified silica xerogels [9]. In order to compare this method against the standard preparation methods, xerogels were prepared using either hydrolysis or acidolysis of silicon alkoxides by formic acid [10]. The reduction of dye uptake by syneresis and the effects of grinding of the samples on the outcome of the leaching step will be discussed. Finally, the results presented will be discussed in conjunction with the pore size distribution characteristics and BET surface of the samples.

Experimental

Alkoxides [tetraethoxysilane (TEOS), tetramethoxysilane, TMOS, methyltrimethoxysilane, MTMS, phenyltrimethoxysilane, PTMS (all obtained from Fluka), phenyltriethoxysilane, PTES (Aldrich), vinyltriethoxysilane, VTES, (Strem)], all of synthetic grade, were used as received. Formic acid, HCOOH, and ethanol were of analytical grade (both from Merck). Water was

purified in a Christ Ministill and had a conductivity of $<0.2\,\mu S$. For the sol-gel reaction by hydrolysis, hydrochloric acid (Merck, analytical grade) was used as a catalyst. Reactions were carried out in closed containers made of borosilicate glass. Dye solutions were prepared by dissolving Solvent Blue 59 (Aldrich) in formic acid and ethanol, respectively. Dye concentration was adjusted to the 10^{-4} m range.

The preparation of the gel samples was performed according to the following procedure: After the silicon alkoxide or the silicon alkoxide mixture containing 20 mol% organically modified silicon alkoxide was placed in the container, the necessary amount of HCOOH or the usual water-HCl-ethanol-mixture was added. The reaction mixture was stirred at room temperature (294 ± 1 K) until gelation occurred. Table 1 gives the composition of the samples prepared.

After an aging period of 50 days, the syneresis liquid was drawn off in order to measure the dye concentration in the syneresis liquid. The syneresis liquid was removed by filtration. From the volume of the syneresis liquid recovered and the measured dye concentration, the uptake of dye in the gel network was calculated. UV-vis spectra of an aliquot were recorded on a single beam instrument (Philips PU8700). Then, the wet gels were kept under reduced pressure (20 mbar) for 4 h. The amount of liquid evaporated during this step was estimated by collecting the drawn off vapors in a cold trap. In a second step, drying was completed by transferring the gel samples to a drying chamber where they were stored at 313 K for 48 h.

Table 1. Precursor ratio used in the preparation of the dye-doped xerogels. The volume of exuded syneresis liquid is given as well. 'HCO' and H_2O refer to the use of Formic acid and H_2O-HCl-ethanol mixture, respectively.

Sample	Precursor ratio	Syneresis liquid (ml)
TEOS_H_2O	Neat TEOS	6.5
VTES_H_2O	VTES : TEOS/0.2 : 0.8	0.0
PTES_H_2O	PTES : TEOS/0.2 : 0.8	0.0
TMOS_H_2O	Neat TMOS	6.0
MTMS_H_2O	MTMS : TEOS/0.2 : 0.8	0.0
PTMS_H_2O	PTMS : TEOS/0.2 : 0.8	0.0
TEOS_HCO	Neat TEOS	16.0
VTES_HCO	VTES : TEOS/0.2 : 0.8	9.0
PTES_HCO	PTES : TEOS/0.2 : 0.8	7.5
TMOS_HCO	Neat TMOS	11.0
MTMS_HCO	MTMS : TEOS/0.2 : 0.8	7.5
PTMS_HCO	PTMS : TEOS/0.2 : 0.8	4.5

For the leaching experiments, about 1 g of xerogel was pulverized in a rotating blade grinder. After weighing, the sample was transferred to an extraction thimble that was placed in a Soxhlet extraction apparatus. The dye-doped xerogel was then leached with 80 ml ethanol over a period of 10 h. The extract was collected, and the amount of dye in the extract was determined using UV-vis spectroscopy. Again, this procedure allowed for the calculation of the loss of dye due to the leaching procedure. For a selected sample, leaching was performed with a xerogel sample not subjected to milling in order to check for possible effects of the grinding procedure. BET surface and pore size distribution measurements were performed on an ASAP 2000 (Micromeritics) device.

Results and Discussion

Details concerning the composition of the xerogel samples and the labelling adopted are given in Table 1. The amount of syneresis liquid exuded is also given in Table 1. With increasing size of the organic residue, the amount of syneresis liquid decreases. Comparing the two preparation methods used, we notice that the amount of syneresis is generally lower in the samples prepared by the hydrolysis method. All samples prepared with organically modified silicon alkoxides using the hydrolysis reaction show no syneresis after 50 days ageing, whereas no sample prepared using the acidolysis reaction is free from syneresis.

The effects of grinding the xerogel samples on the outcome of the leaching step is illustrated in Fig. 1 for the case of the PTES_HCO sample. The UV-vis spectrum of the leaching agent recorded for a ground sample is shown in trace (a), whereas trace (b) shows the spectrum recorded after leaching a non-ground sample. Data are corrected for the different masses of xerogel employed in the leaching experiments. Comparing the traces, we note that the amount of dye leached from the non-ground sample is substantially lower than that leached from a ground sample. Furthermore, the spectrum shown in trace (a) resembles the spectrum recorded from dye solutions in ethanol, whereas the spectrum in trace (b) resembles the spectrum recorded from dye solutions in formic acid. We infer from this result that the access of the leaching agent to the pores of the xerogel is assisted by the grinding step. Also, the different shapes of the spectra indicate that

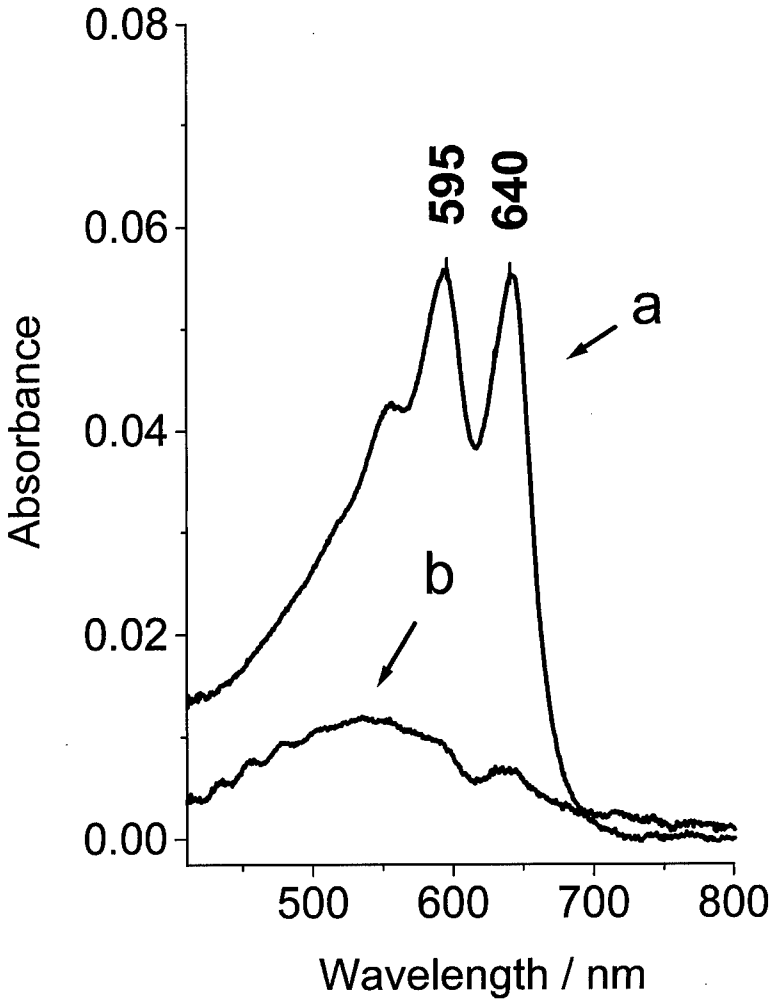

Figure 1. UV-vis spectra of leached out dye. Trace (a) was recorded from a PTES_HCO xerogel sample subjected to grinding, and trace (b) was obtained by leaching a nonmilled PTES_HCO xerogel.

the unprotonated form of the dye is leached from the inner pores, whereas a small fraction of protonated dye molecules resides on the external surface of the PTES_HCO sample.

The results of the leaching experiments performed on the dye-doped xerogels are depicted in Fig. 2. In this figure the fraction of dye remaining in the xerogel is given for each step. The white bars show the effects of syneresis and syneresis liquid removal on the relative dye content of the sample, whereas the hatched bar shows the relative amount of dye retained after the leaching. The final amount of dye retained in the xerogel, defined by the product of the fraction retained after syneresis and the fraction of dye remaining after leaching, is given by the black bar. Within the samples prepared, the range of dye retained varies between 3% and 88%. We observe that with increasing size of the organic residue, the amount of dye retained increases. This holds for the syneresis step as well as for the leaching step.

One might explain these results with the decrease in polarity imparted to the xerogel samples by the organic residues. To gain more insight, nitrogen adsorption experiments were performed on powdered samples subjected to the leaching step in order to investigate possible influences of the pore structure on the leaching process. The results are listed in Table 2. The introduction of the organic residues has no significant effect on the average pore size of the xerogels in the case of the xerogels prepared by acidolysis. On the other

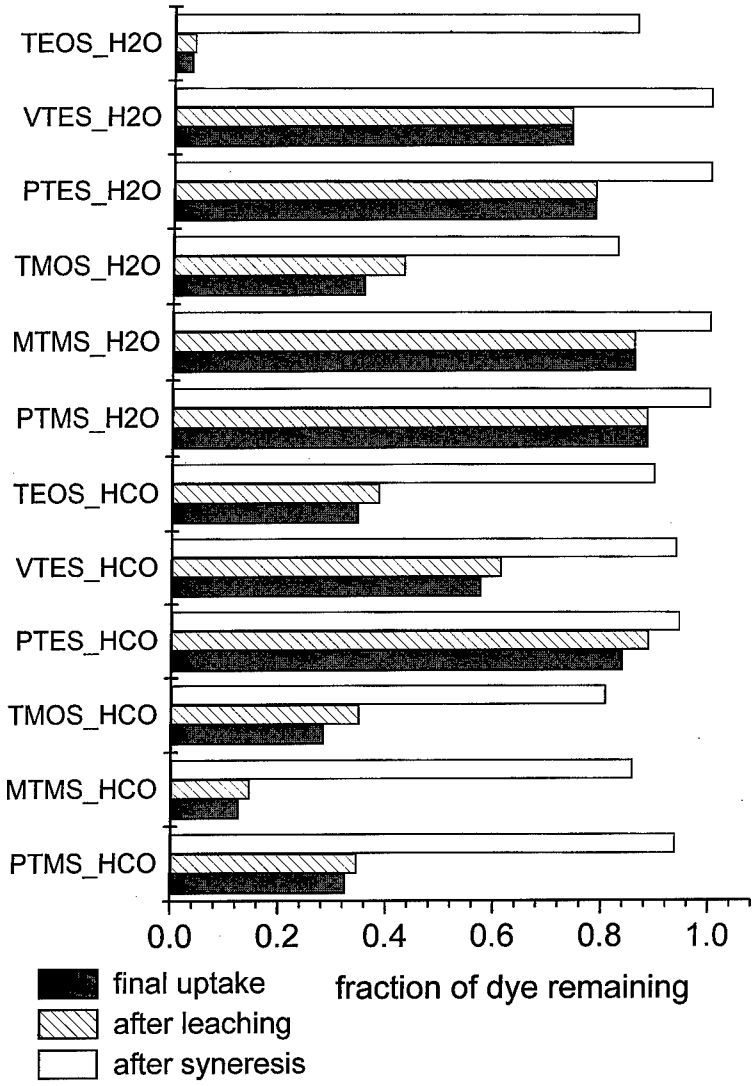

Figure 2. Fraction of dye remaining in the xerogel matrix after removal of syneresis liquid and leaching steps. The final amount of dye retained in the xerogel is given by the black bar.

hand, in the case of samples prepared by hydrolysis, the pore diameter increases with increasing size of the organic residue. All the samples can be classified as microporous solids, according to their nitrogen adsorption isotherm. However, both series of samples show marked trends in the surface accessible to nitrogen, and in the cumulative pore volume (cf. Table 2). With increasing size of the organic residue, the BET surface and the pore volume decrease. Therefore, we propose that for the samples prepared, the pore volume influences the leaching behavior observed. A larger pore volume will allow better penetration of the leaching agent, and so the loss of dye by leaching is more pronounced in these samples.

Conclusions

The results show that the incorporation of Solvent Blue 59 in silica xerogels is influenced by using organically modified silicon alkoxides in the sol-gel reactions. Both synthetic methods employed here show the same

Table 2. BET surface, cumulative pore volume and average pore size of dye-doped xerogels.

Sample	BET surface ($m^2\ g^{-1}$)	Pore volume ($cm^3\ g^{-1}$)	Pore size (Å)
TEOS_H_2O	532	0.087	34
VTES_H_2O	351	0.040	37
PTES_H_2O	2.3	0.005	96
TMOS_H_2O	498	0.045	27
MTMS_H_2O	371	0.028	30
PTMS_H_2O	2.1	0.004	93
TEOS_HCO	635	0.272	36
VTES_HCO	627	0.142	31
PTES_HCO	514	0.088	33
TMOS_HCO	569	0.285	39
MTMS_HCO	562	0.172	30
PTMS_HCO	452	0.062	29

trend that with increasing size of the organic residue, the amount of leachable dye decreases. It found that the dye retaining capacity of the xerogel decreases with increasing pore volume.

Acknowledgments

The financial support of Aldo Steinfeld of PSI's Solar Technology Section to this work is gratefully acknowledged.

References

1. D. Avnir, D. Levy, and R. Reisfeld, J. Phys. Chem. **88**, 5956 (1984).
2. U. Narang, R. Wang, P.N. Prasad, and F.V. Bright, J. Phys. Chem. **98**, 17 (1994).
3. R.A. Dunbar, J.D. Jordan, and F.V. Bright, Anal. Chem. **68**, 604 (1996).
4. W.P. Hsu, R. Yu, and E. Matijevic, Dyes and Pigments **19**, 179 (1992).
5. C. Rottman, M. Ottolenghi, R. Zusman, O. Lev, M. Smith, G. Gong, M.L. Kagan, and D. Avnir, Mater. Lett. **13**, 293 (1992).
6. O. Lev, M. Tsionsky, L. Rabinovich, V. Glezer, S. Sampath, I. Pankratov, and J. Gun, Anal. Chem. **67**, 22 A (1995).
7. L. Sieminska and T.W. Zerda, J. Phys. Chem. **100**, 4591 (1996).
8. I.J.M. Snijkers-Hendrickx and J. van den Ven, in *Proceedings of the XVIIth International Congress on Glass* (Chinese Ceramic Society, Beijing 1995), Vol. 4, p. 9.
9. J.-C. Panitz and A. Wokaun, J. Sol-Gel Sci. Tech. **9**, 251 (1997).
10. K.G. Sharp, J. Sol-Gel Sci. Tech. **2**, 35–41 (1994).

Journal of Sol-Gel Science and Technology 13, 479–484 (1998)
© 1998 Kluwer Academic Publishers. Manufactured in The Netherlands.

Hybrid Pigments via Sol-Gel Processing

S. HOFACKER AND G. SCHOTTNER
Fraunhofer-Institut für Silicatforschung, Neunerplatz 2, D-97082 Würzburg, Germany

Abstract. The incorporation of organic dyes into inorganic and hybrid sol-gel derived materials is a valuable method for the fabrication of colored layers for optical applications like filters, solar energy conversion, non-linear optical devices, and active laser media. There have been clear hints for photochemical stabilization of the organic dyes, therefore, our aim was to investigate the light stability of organic dyes within hybrid solids. Besides the traditional way of doping sol-gel coatings with dyestuffs, they were also covalently attached to the hybrid matrix and pigments were produced by spray-drying processes.

The resulting spherical powders were investigated with respect to their morphological, structural and photochemical properties. The results show that uniformly shaped and colored hybrid pigments can be synthesized. The spectroscopic studies demonstrate the fixation of the dye to the matrix and the high degree of crosslinking achieved in the composite. Additionally, the hybrid pigments drastically improve the resistance of the dye against bleeding from thermoplastic polymers. Furthermore, a higher photochemical stability of the dye is observed within the hybrid matrix compared to a solution, and purely organic or inorganic solid hosts.

Keywords: organic dyes, hybrid sol-gel material, pigments, photochemical stabilization

1. Introduction

In the last decade a lot of investigations with the aim of photochemical stabilization of organic dyes in sol-gel derived materials were performed [1–5]. In most cases it was tried to incorporate organic laser-dyes within a solid matrix to increase the lifetime of organic laser dyes [6–8]. Commercial tetra- and trialkoxysilanes like tetramethoxy- or tetraethoxysilane, methyl-, phenyl- or 3-glycidyloxypropyltrimethoxysilane, respectively, were co-hydrolyzed in the presence of the dyestuff and dried afterwards to form colored bulk materials. Those physically dissolved organic dyes in solid matrix were investigated with respect to their laser characteristics [4, 9, 10]. As a result it was found that the incorporation of an organic dye in a glass-like solid matrix improves the laser efficiencies and lifetimes [11–14].

Until now the integral light stability of organic dyes within a sol-gel derived matrix has not yet been evaluated. There are some hints for a photochemical stabilization of organic dyes in polymers but so far the underlying mechanisms of degradation or stabilization have not been fully investigated [15, 16].

Therefore, our aim was to investigate more closely the light stability of organic dyes within amorphous solids under defined conditions. Besides the traditional way of doping the sol-gel coatings by physically dissolving organic dyes, we first silylated our dyes to be able to attach them to the matrix during hydrolysis and condensation. It is anticipated that the rigidity and the residual free volume of the matrix have great influence on the translational, rotational and vibrational degree of freedom of the dye molecule and consequently its reactivity, e.g., with oxygen. To form such a rigid matrix, which on the other hand is flexible enough to homogeneously incorporate the organic dyes we co-hydrolyzed metal-alkoxides together with an epoxy functional trialkoxysilane to achieve a highly crosslinked inorganic network. Additionally, we initiated an organic crosslinking reaction of the epoxy functional silane during the following thermal treatment.

In this way we produced colored transparent layers as well as hybrid pigments by a spray-drying process; both

were investigated with respect to their photochemical stability.

2. Experimental

As organic dyes we used several species, like azo dyes (Disperse Red 1; DR1) (Fig. 1(a)) anthrachinon dyes (Disperse Blue 3; DB3) (Fig. 1(b)) or perylene dyes (Perylene Dicarboxylic Acid; PDA) (Fig. 1(c)).

These organic components, which have hydroxy or amino moieties, were silylated with 3-isocyanatopropyltriethoxysilane (IPTS) to form urethane or urea derivatives, respectively [17, 18]. The perylene dicarboxylic acid which is highly insoluble in alcohols or in alkoxysilanes, was modified by addition to 3-glycidyloxypropyltrimethoxysilane (GPTS) in the presence of *N*-benzyl dimethyl amine at 100°C for 2 hours (Fig. 2(a)).

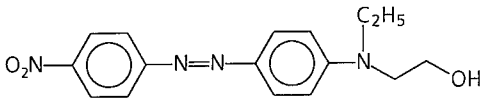

(a)

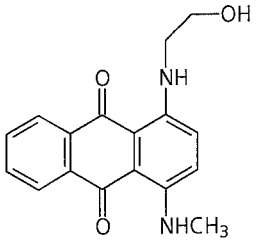

(b)

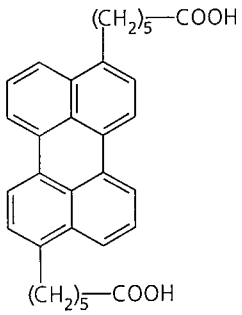

(c)

Figure 1. (a) Azo dye Disperse Red 1 (DR1), (b) anthrachinone dye Disperse Blue 3 (DB3) and (c) perylene dye Perylene Dicarboxylic Acid (PDA).

The silylated dyes, GPTS and aluminum-sec-butylate (ASB), which was complexed with ethylacetoacetate, were mixed in a molar ratio of 1 : 79 : 20 and cohydrolyzed with the stoichiometric amount of water with respect to the hydrolyzable alkoxy groups. After 2 hours stirring at 20°C and filtration, glass slides were spin coated and dried for 2 hours at 160°C. Hybrid powders were also produced by a spray-drying process at an inlet-temperature of 175°C.

The coated glass slides were irradiated in a Xenotest 150 S (Heraeus) with radiant flux density of 125 mW/cm^2 from 300 to 800 nm and with 103 mW/cm^2 from 400 to 800 nm for the perylene dicarboxylic acid (PDA), respectively. The absorption measurements were carried out with a Shimadzu UV-vis spectrometer UV-2501 PC. A Nicolet Magna 750 FT-IR-spectrometer was used for the infrared spectroscopic investigations and the ^{29}Si-CP-MAS technique (Bruker MSL 300) supplied information about the degree of crosslinking in the inorganic network. To determine the thermal and photochemical behavior of the hybrid pigments, the migration of the dyes out of the hybrid matrix was verified according to DIN 53775 part 3 and valued by DIN 54002. The light stability of the colored powder was determined in accordance with DIN 54003.

3. Results

Derivatization of PDA

Figure 2(b) shows the infrared spectra of PDA and the silylated PDA (PDA-Si). In the spectrum of PDA a very strong single band at 1705 cm^{-1} can be observed, which can be assigned to the ν(C=O) stretching vibration of the carboxyl function, whereas in the GPTS spectrum no remarkable absorption in this region can be recognized. In the spectrum of PDA-Si a strong band appears at 1737 cm^{-1} which is due to the ν(C=O) stretching vibration of the formed carboxylic ester (Fig. 2(b)). The band at 1705 cm^{-1} disappears completely. This proves the quantitative addition of PDA to GPTS.

Condensation Degree of the Inorganic Network

To examine the structure of the produced hybrid material we used solid state ^{29}Si-CP-MAS- and ^{27}Al-MAS-

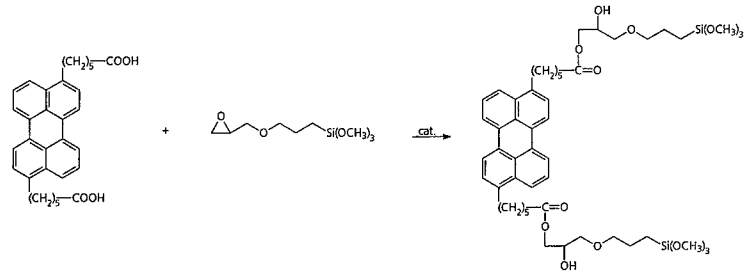

(a)

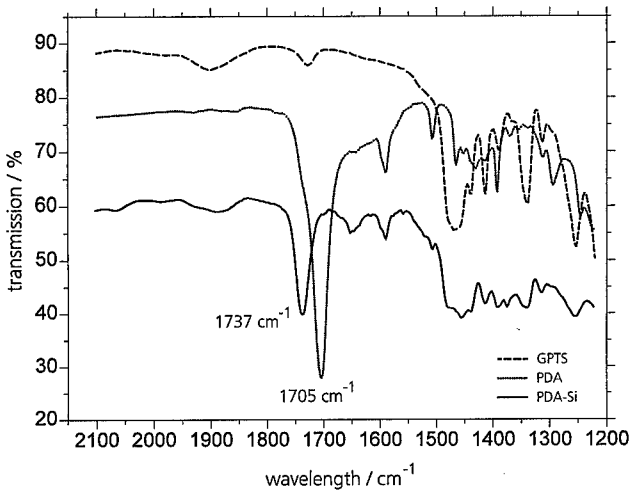

Figure 2. Reaction scheme (a) and IR-spectra (b) of the silylation of PDA.

NMR spectroscopy. Figure 3 shows a typical ^{29}Si-NMR spectrum with three peaks. The signals at −67 ppm and at −58 ppm can be assigned to T^3 and T^2 groups, respectively. The peak at −45 ppm can be assigned to Si—O—Al. These and Raman spectroscopic investigations, which will be described elsewhere [19], clearly illustrate the high degree of inorganic cross-linking.

Morphology of the Hybrid Pigments

The scanning electron micrograph in Fig. 4 shows the morphology and the particle size distribution of the synthesized hybrid pigment containing PDA-Si after spray-drying process. The resulting spherical powder has a particle distribution between 0.3 and 25 μm with a maximum at 10 μm. These results are representative for the pigments produced.

Photochemical Investigations

Table 1 shows the results of the migration behavior of PDA-Si, DR1 and DR1-Si containing hybrid pigments. The valuation of the investigations is in accordance with DIN 54002 where 1 is the poorest (high migration, high degree of bleeding) and 5 the best rating (no migration, no bleeding).

As can be seen from the diagram we found a great improvement of the resistance of the dyes against bleeding from thermoplastic polymers.

The light stability of the powders was determined according to DIN 54003 that is a coarse measurement and leads to light stabilities which are in the same range as those of the dyes themselves. In the case of light stability measurements on the coated glass slides (Fig. 5) we found distinct differences between the dyes attached to the network in a hybrid matrix, in solution and when physically dissolved in

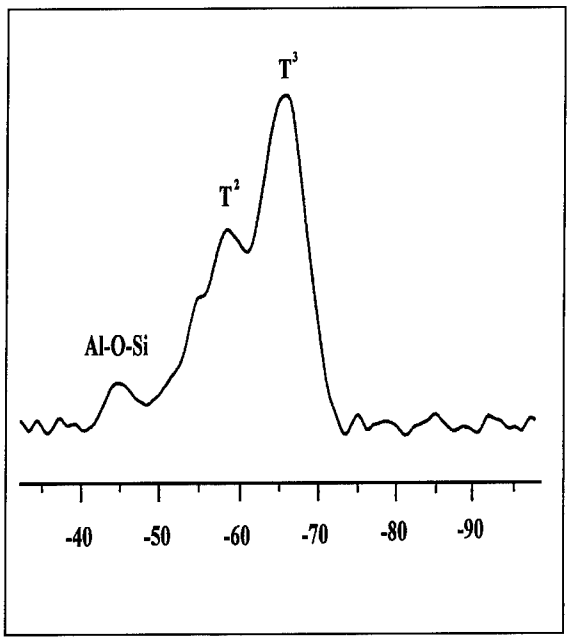

Figure 3. Typical ^{29}Si-CP-MAS NMR spectrum of the hybrid matrix resulting from GPTS and ASB mixture in a molar ratio of 80 : 20.

Table 1. Comparison of the migration behavior of dyes and hybrid pigments in thermoplastic matrices (PVC).

Dye/pigment	Migration rate[a]
Dye DR1	1
Dye DRI-Si	1
Pigment DRI-Si; hybrid matrix I	1.75
Pigment DRI-Si; hybrid matrix II	3.25
Dye PDA	to be determined
Dye PDA-Si	to be determined
Pigment PDA-Si; hybrid matrix I	5
Pigment PDA-Si; hybrid matrix II	to be determined

[a]Rating: 1 (very bad; high migration); 5 (very good; no migration).

other organic or inorganic polymers like polymethylmethacrylate (PMMA) or tetraethoxysilane (TEOS), respectively. As can be seen from the curves, there is a higher photochemical stabilization of the organic dye in a hybrid matrix than in a conventional organic polymer or in solution especially if the dye is covalently attached to the hybrid matrix.

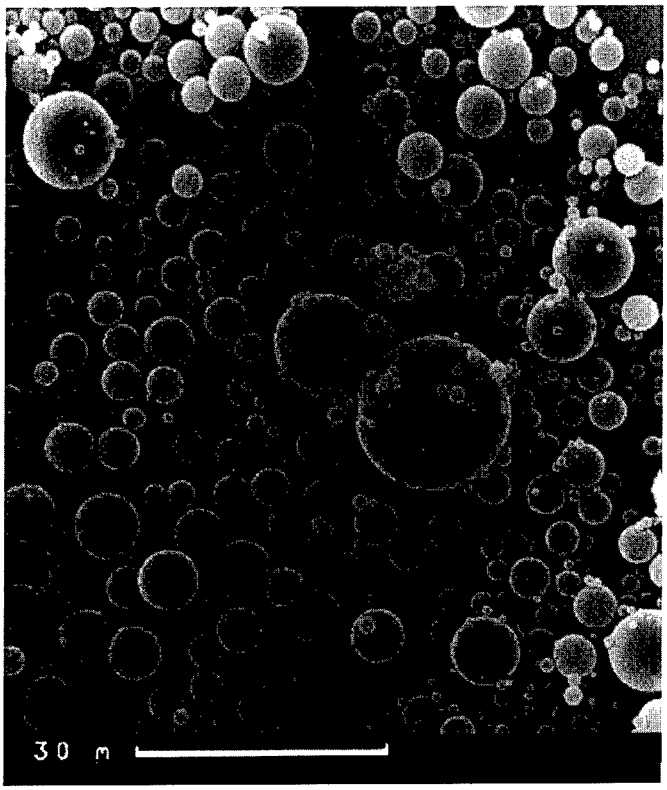

Figure 4. SEM of the hybrid PDA-Si doped pigment.

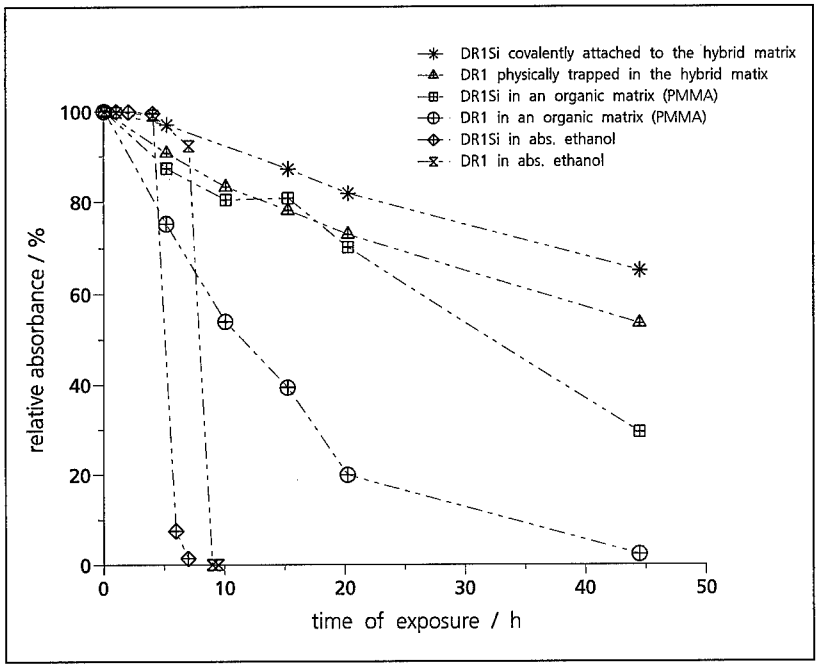

Figure 5. Comparison of the photochemical investigations of DR1 and DR1-Si in solution, organic matrix and in a hybrid polymer.

4. Conclusion

It is possible to produce hybrid pigments via sol-gel processing with defined physical appearance. Furthermore, we achieved a covalent attachment of the organic dyes to the hybrid matrix that results in a great improvement concerning the migration behavior of the dyes from thermoplastic matrices (PVC). In the case of coated glass slides we also achieved a higher photochemical stabilization in a hybrid matrix than in a conventional organic polymer. Further investigations to increase the photochemical stability of the hybrid pigments by variation of the hybrid matrix are under progress. Moreover, the physical properties of the organic dyes in the hybrid host materials are a matter of current investigation.

Acknowledgment

Financial support from the Bundesministerium für Bildung, Wissenschaft, Forschung und Technologie (BMBF) is highly acknowledged. We also express our thanks to Mr M. Templin at the Max-Planck-Institut für Polymerforschung, Mainz for performing the NMR-measurements.

References

1. B. Dunn, J.I. Zink, and J. Mater. Chem. **1**, 903 (1991).
2. C. Burgdorff, H.-G. Löhmannsröben, and R. Reisfeld, Chem. Phys. Lett. **197**, 358 (1992).
3. M.M.E. Severin-Vantilt and E.W.J.L. Oomen, J. Non-Cryst. Solids **159**, 38 (1993).
4. R. Reisfeld, Structure and Bonding **85**, 215 (1996).
5. S. Sakka, Structure and Bonding **85**, 1 (1996).
6. E.T. Knobbe, B. Dunn, P.D. Fuqua, and F. Nishida, Appl. Optics **29**, 2729 (1990).
7. K. Yagi, S. Shibata, T. Yano, A. Yasumori, M. Yamane, and B. Dunn, J. Sol-Gel Sci. Tech. **4**, 67 (1995).
8. M. Canva, A. Dubois, P. Georges, A. Brun, F. Chaput, and A. Ranger, Proc. SPIE-Int. Soc. Opt. Eng. (Sol-Gel Optics III) **2238**, 298 (1994).
9. Y. Kobayashi, Y. Kurukawa, Y. Imai, and S. Muto, J. Non-Cryst. Solids **105**, 198 (1988).
10. H.-T. Lin, E. Bescher, J.D. Mackenzie, and H. Dai, J. Mater. Sci. **27**, 5523 (1992).
11. R. Reisfeld, D. Brusilovsky, and M. Eyal, SPIE **1182**, 230 (1988).
12. J.C. Altmann, R.E. Stone, B. Dunn, and F. Nishida, IEEE Photo. Tech. Lett. **3**, 189 (1991).

13. B. Dunn, J.D. Mackenzie, J.I. Zink, and O.M. Stafsudd, SPIE **1328**, 174 (1990).
14. A.B. Wojcik. L.C. Klein, and S. Muto, Proc. SPIE-Int. Soc. Opt. Eng. (Sol-Gel Optics III) **2288**, 392 (1994).
15. D. Avnir, D. Levy, and R. Reisfeld, J. Phys. Chem. **88**, 5956 (1984).
16. R. Reisfeld, R. Zusman, Y. Cohen, and M. Eyal, Chem. Phys. Lett. **147**, 142 (1988).
17. P.-H. Sung, S.-L. Wu, and C.-Y. Lin, J. Mater. Sci. **31**, 2443 (1996).
18. F. Chaput, D. Riehl, J.P. Boilot, K. Cargnelli, M. Canva, and Y. Levy, Chem. Mater. **8**, 312 (1996).
19. B. Riegel, W. Kiefer, S. Hofacker, and G. Schottner, J. Non-Cryst. Solids, to be submitted.

Journal of Sol-Gel Science and Technology 13, 485–488 (1998)
© 1998 Kluwer Academic Publishers. Manufactured in The Netherlands.

Lignin-Silica-Titania Hybrids as Precursors for Si–Ti–C–O Fibers

ISAO HASEGAWA, YUKA FUKUDA AND TOMOHIRO OKADA
Department of Chemistry, Faculty of Engineering, Gifu University, Yanagido 1-1, Gifu-City, Gifu 501-11, Japan

MEISETSU KAJIWARA
Department of Applied Chemistry, Faculty of Engineering, Nagoya University, Furo-Cho, Chikusa-Ku, Nagoya-City, Aichi 464-01, Japan

Abstract. Lignin-silica-titania and lignin-titania hybrid fibers have been prepared by sol-gel processing from lignin, tetraethoxysilane, and titanium tetrakis(2,4-pentanedionate) using a mixture of 2,4-pentanedione and tetrahydrofuran as solvent and H_2SO_4 as catalyst. Amounts of H_2O and H_2SO_4, to add to the solutions with the Si-to-Ti atomic ratios of 0–1.0, were determined for achieving favorable spinnability of fibers from the solutions. The FT-IR spectrum of the fibers indicated the formation of hybrid fibers. The hybrid fibers, cured in air to avoid coalescense, could be converted into Si—Ti—C and TiC fibers upon pyrolysis at 1500°C in Ar.

Keywords: lignin, organic-inorganic hybrids, fiber, carbothermal reduction, carbide

1. Introduction

Organic-inorganic hybrids derived by sol-gel processing have been shown to be prominent precursors for non-oxide ceramics such as silicon carbide (SiC). Wei et al. [1] first reported synthesis of SiC powders from the hybrids with the aid of carbothermal reduction. Tanaka and Kurachi [2] produced sub-micron SiC powders with high purity from silica (SiO_2)-phenolic resin hybrids.

We have demonstrated that the hybrids can also be put into the fiber form and the hybrid fibers can further be converted into continuous SiC fibers by heating at 1500°C in flowing Ar without any pretreatment such as cure [3, 4]. Introduction of a titania (TiO_2) or zirconia component to the hybrids has also been possible, which give Si—Ti—C or Si—Zr—C fibers, respectively, by the heat-treatment [5–7].

Lignin is one of the main components of wood, which is a high-molecular compound consisting of the phenylpropane unit as the building block. Waste liquor formed upon the production of pulp contains a large amount of lignin. Its use, however, is limited. Recently, carbon fiber synthesis from lignin has been reported [8], which implies that lignin gives a considerable amount of carbonaceous residue upon pyrolysis under a non-oxidizing atmosphere. Consequently, this study has been aimed at investigating the use of lignin as a source of carbide fibers. Conditions for preparing lignin-SiO_2-TiO_2 hybrid fibers and their conversion into Si—Ti—C—O fibers have been studied.

2. Experimental

Lignin used in this study was that prepared by digestion of cedar with acetic acid [Composition: $C_9H_{8.33}O_{2.37}(OCH_3)_{0.96}$]. Tetraethoxysilane [$Si(OC_2H_5)_4$, TEOS] and a 65 wt% 2-propanol solution of titanium tetrakis(2,4-pentanedionate) [$Ti(C_5H_7O_2)_4$, TTP] were used as a SiO_2 and TiO_2 source, respectively. 2,4-Pentanedione and tetrahydrofuran (THF) were used as solvents, and H_2SO_4 as catalyst.

The lignin was added to 5 cm^3 of 2,4-pentanedione or a mixture of 2,4-pentanedione (5 cm^3) and THF (5 cm^3), followed by the addition of TEOS, the 2-propanol solution of TTP, distilled water, and H_2SO_4.

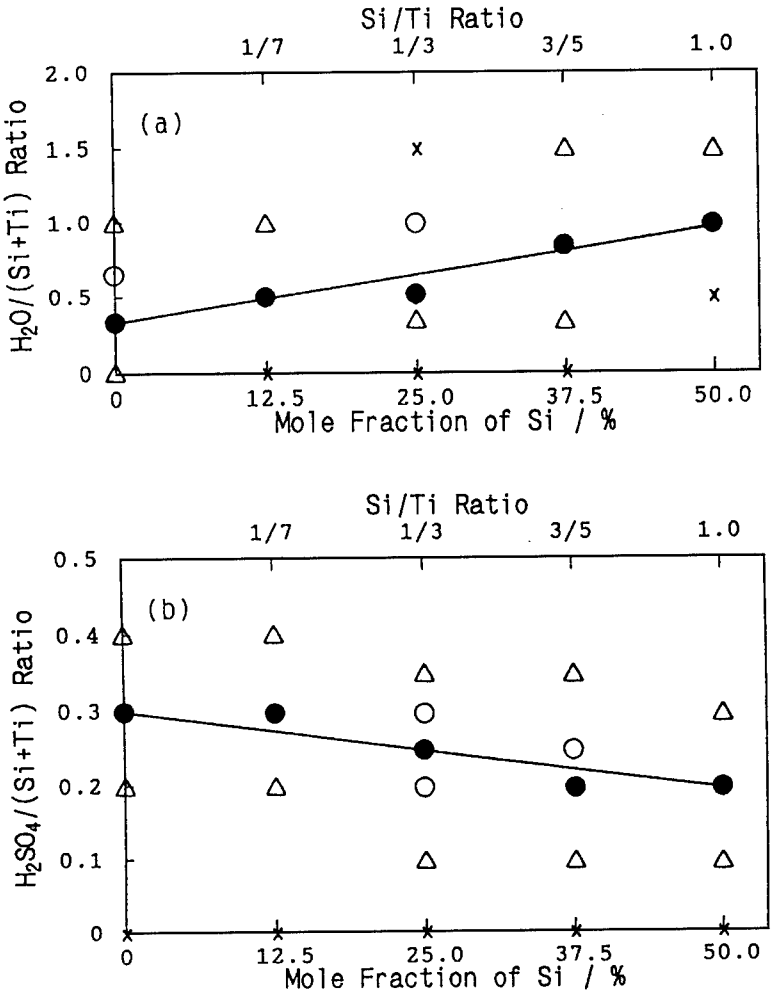

Figure 1. The effects of (a) $H_2O/(Si + Ti)$ and (b) $H_2SO_4/(Si + Ti)$ ratios of the starting solutions with Si/Ti ratios of 0–1.0 on spinnability of lignin-SiO_2-TiO_2 and lignin-TiO_2 hybrid fibers from the solutions. (●: optimal for spinning, ○: possible to spin, △: difficult to spin, ×: impossible to spin).

The mixtures had the following compositions: Si-to-Ti atomic (Si/Ti) ratio = 0–1.0, C*/(Si + Ti) ratio (the atomic ratio of C in the lignin to a total amount of Si and Ti) = 4.0, total amount of TEOS and TTP = 1.68×10^{-2} mole. The amounts of H_2O and H_2SO_4 added to the solutions are designated as the $H_2O/(Si + Ti)$ and $H_2SO_4/(Si + Ti)$ ratios, respectively.

The mixtures were stirred at room temperature for ca. 30 min to mix intimately, giving single-phase starting solutions. Fibers could be drawn from viscous sols which were formed by holding the solutions at 65°C. The fibers were characterized with a Perkin-Elmer SYSTEM 2000 FT-IR spectrometer.

The fibers were heated at 1500°C for 4 h in flowing Ar (100 cm^3 min^{-1}). The heating rate was 10°C min^{-1}. Products after the heat-treatment were analyzed with a Rigaku RINT 1100 X-ray diffractometer using Ni-filtered CuK_α radiation and a TOPCON ABT-60 scanning electron microscope.

3. Results and Discussion

Spinnability of SiO_2-TiO_2-phenolic resin hybrid fibers from TEOS-TTP-phenolic resin-H_2O-H_2SO_4-2,4-pentanedione solutions differed drastically with the Si/Ti, $H_2O/(Si + Ti)$, and $H_2SO_4/(Si + Ti)$ ratios of the solutions [6]. Then, 2,4-pentanedione solutions of the lignin, TEOS, and TTP with a fixed Si/Ti ratio of 1.0 and a C*/(Si + Ti) ratio of 4 were prepared as functions of added amounts of H_2O and H_2SO_4 in order

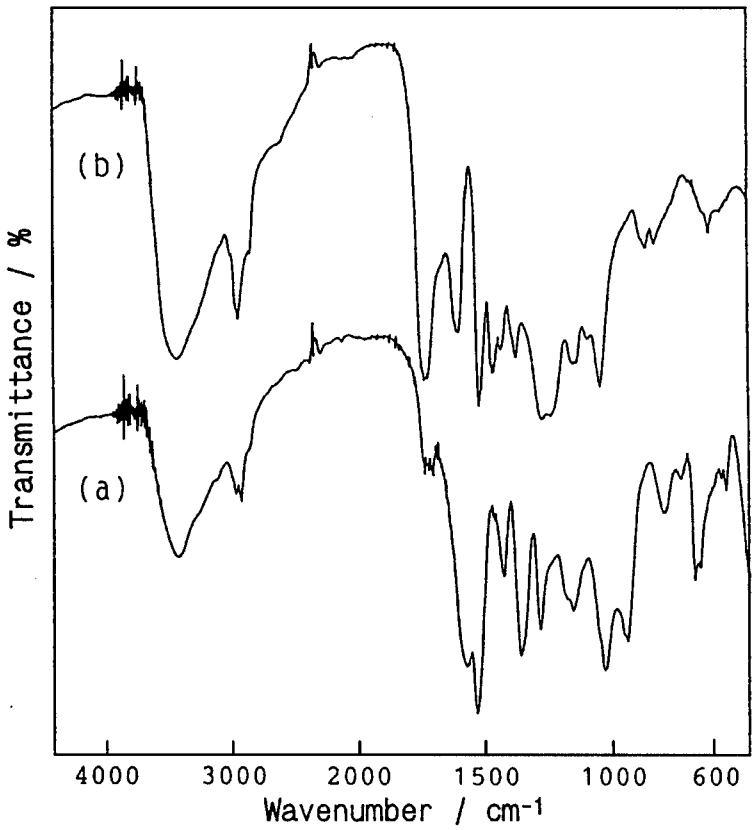

Figure 2. FT-IR spectra of (a) lignin-SiO_2-TiO_2 hybrid fibers prepared from the starting solution with a Si/Ti ratio of 1.0 and (b) the lignin employed in this study.

to estimate the H_2O/(Si + Ti) and H_2SO_4/(Si + Ti) ratios optimal for spinning fibers from the solutions just before gelation. The solution with a H_2O/(Si + Ti) ratio of 1.03 and a H_2SO_4/(Si + Ti) ratio of 0.22 gave fibers over 30 cm in length after holding at 65°C for 5–5.5 h, whose ratios were optimal for preparing the fibers. However, single-phase starting solutions with Si/Ti ratios lower than 1.0 could not be prepared using 2,4-pentanedione as solvent since the lignin did not dissolve in the solutions.

Since the solubility of the lignin is high in THF, the mixture of 2,4-pentanedione and THF was instead used as solvent. With the aid of the solvent, single-phase starting solutions with Si/Ti ratios of 0–1.0 could be prepared. And, fibers could be produced after 7.5– 15 h of holding at 65°C most favorably from the solutions with the H_2O/(Si + Ti) and H_2SO_4/(Si + Ti) ratios shown as closed circles in Figs. 1(a) and (b), respectively. It is noteworthy that the ratios of solutions at each Si/Ti ratio are the same as those found to be suitable for synthesizing SiO_2-TiO_2-phenolic resin hybrid fibers. This suggests that, despite the type of an organic compound, there is no difference in the H_2O/(Si + Ti) and H_2SO_4/(Si + Ti) ratios suitable for drawing fibers from the solutions with Si/Ti ratios of 0–1.0. In addition, these ratios are in proportion to the Si/Ti ratio, expressed in mole fraction, of the solutions. Using the linear correlations, fibers can be prepared from solutions with desired Si/Ti ratios in the range of 0–1.0.

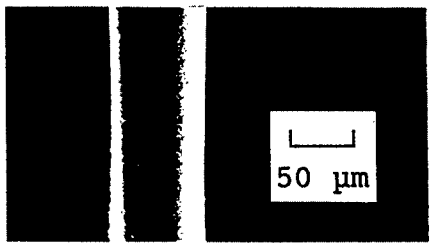

Figure 3. An SEM photograph of a Si—Ti—C fiber obtained by the heat-treatment at 1500°C in Ar for 4 h from the hybrid fiber prepared from the starting solution with a Si/Ti ratio of 1.0. The hybrid fiber was cured at 150°C in air for 1.5 h before the treatment.

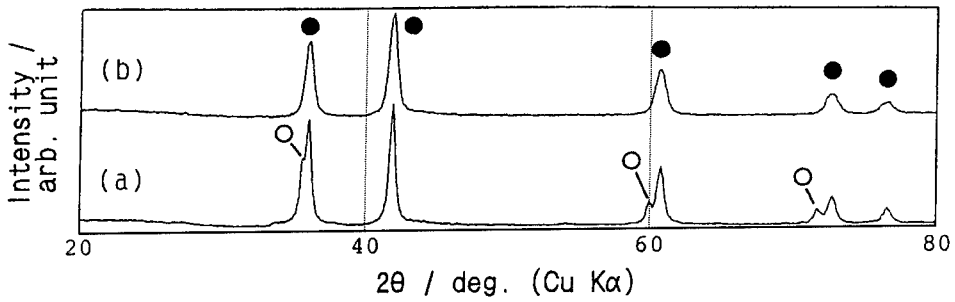

Figure 4. XRD patterns of fibrous products obtained by heating (a) lignin-SiO_2-TiO_2 hybrid fibers obtained from the starting solution with a Si/Ti ratio of 1.0 and (b) lignin-TiO_2 hybrid fibers at 1500°C in Ar for 4 h. (○: β-SiC, ●: TiC).

Figure 2 shows FT-IR spectra of (a) fibers obtained from the solution with a Si/Ti ratio of 1.0 and (b) the lignin. Assignments of bands due to lignin are well established [9], with which major bands seen in Fig. 2(b) are ascribable to each bond present in the lignin. Intense bands seen in Fig. 2(b) are also observed in Fig. 2(a), indicating the fibers obtained involve the lignin. Additional bands appear at 790, 936, and 1027 cm^{-1} in Fig. 2(a), which can be assigned to the Ti—O stretching in TiO_4 tetrahedra, Si—O—Ti stretching, and Si—O—Si stretching vibrations, respectively [5]. This implies that the SiO_4 and TiO_2 components are also involved in the fibers, suggesting that the fibers obtained are lignin-SiO_2-TiO_2 hybrid fibers. In the same manner, the solution with a Si/Ti ratio of 0 is found to give lignin-TiO_2 hybrid fibers.

The hybrid fibers were heated at 1500°C in an Ar flow, which gave a lump of fibers. This means that the hybrid fibers coalesced during the heat-treatment. Also, the fibers became thicker by the treatment. By investigating changes of the states of the hybrid fibers with temperature, it was found that the fibers begin to soften at ca. 150°C. Subsequently, the hybrid fibers were heated at 150°C in air for 1.5 h, and then heated at 1500°C in Ar. The products preserved the fiber form, although some of the thick hybrid fibers coalesced. This indicates that coalescence of the fibers is virtually preventable by curing at 150°C in air. Figure 3 shows a SEM photograph of one of fibers thus obtained, whose precursors were prepared from the solution with a Si/Ti ratio of 1.0. The XRD pattern of a powdered sample of the fibers is shown in Fig. 4(a). β-SiC and TiC phases give rise to peaks in the pattern, indicating that the lignin acts as a carbon source to give Si—Ti—C fibers. The lignin-TiO_2 fibers gave TiC fibers as shown in Fig. 4(b).

In conclusion, lignin-SiO_2-TiO_2 and lignin-TiO_2 hybrid fibers could be prepared by sol-gel processing from lignin, TEOS, and TTP using a mixture of 2,4-pentanedione and THF as solvent. The hybrid fibers had to be cured to avoid coalescence during heat-treatment. The cured thin fibers could be converted into Si—Ti—C or TiC fibers by firing at 1500°C for 4 h in Ar, indicating that lignin can be employed as a carbon source of the carbide fibers.

Acknowledgment

IH acknowledges financial support of this work by Nippon Sheet Glass Foundation for Materials Science and Engineering.

References

1. G.C. Wei, C.R. Kennedy, and L.A. Harris, Bull. Am. Ceram. Soc. **63**, 1054 (1984).
2. H. Tanaka and Y. Kurachi, Ceram. Int. **14**, 109 (1988).
3. I. Hasegawa, T. Nakamura, S. Motojima, and M. Kajiwara, J. Mater. Chem. **5**, 193 (1995).
4. I. Hasegawa, T. Nakamura, S. Motojima, and M. Kajiwara, J. Sol-Gel Sci. Technol. **8**, 577 (1997).
5. I. Hasegawa, T. Nakamura, and M. Kajiwara, Mater. Res. Bull. **31**, 869 (1996).
6. I. Hasegawa, Y. Fukuda, and M. Kajiwara, J. Eur. Ceram. Soc, **17**, 1467 (1997).
7. I. Hasegawa, Y. Fukuda, and M. Kajiwara, Ceram. Int., to be published.
8. K. Sudo, K. Shimizu, N. Nakashima, and A. Yokoyama, J. Appl. Polym. Sci. **48**, 1485 (1993).
9. *Rigunin no Kagaku* (*Chemistry of Lignin*), edited by J. Nakano (Yuni Koho, Tokyo, 1979), pp. 176–181 (in Japanese).

Journal of Sol-Gel Science and Technology 13, 489–493 (1998)
© 1998 Kluwer Academic Publishers. Manufactured in The Netherlands.

ORMOCER Coatings Based on Titanium and Poly(tetraethylene glycol malonate)

C.S. DENG, P.V. WRIGHT AND P.F. JAMES
Department of Engineering Materials, University of Sheffield, Mappin Street, Sheffield S1 3JD, UK

Abstract. Organically modified hybrid ceramic oxide coatings based on titanium and poly(tetraethylene glycol malonate) (PTEGM) have been prepared by sol-gel methods and the structure characterized by FT-IR spectroscopy and X-ray photoelectron spectroscopy. Results indicate that malonate units (TEGM) in PTEGM form a co-ordination bond with titanium, enabling titania to be homogeneously distributed in the polymer matrix. For molar ratios [TEGM] : [TIP] = 1 and 4 maximum crack-free thicknesses of 1.2 and 15 μm, respectively were achieved in a single dip. Ionic conductivity measurements were performed on coatings having molar ratios [TEGM] : [Ti] : [Li^+] = 5 : 1.25 : 1, with lithium perchlorate as the electrolyte, giving a relatively high solid-state ionic conductivity of ca. 10^{-5} S cm^{-1} at room temperature.

Keywords: ORMOCER coating, titanium isopropoxide, electrochemical properties

1. Introduction

There has been considerable interest in preparation of hybrid materials by sol-gel methods in recent years [1]. Introduction of organic polymers into inorganic networks formed by sol-gel process can bring about significant modification to the inorganic materials. However, most of the work on ORMOCERs has been devoted to silica-based systems [2], much less attention has been paid to systems based on the oxides of other metals, such as titanium [3]. Titanium-based ORMOCERs have potential applications in electrochemical areas such as electrochromic devices and batteries [4]. Polyethylene oxide (PEO) doped with alkali salts is a good ionic conductor [5] and the derivatives of this polymer have been incorporated into silica based networks by sol-gel methods [6]. In this report the ionic conductive properties of PEO-based polymer and the network-forming properties of titania are combined to prepare coatings with potential use in electrochemical devices.

2. Experimental

Titanium isopropoxide (TIP) (Aldrich) was used as received. Poly(tetraethylene glycol malonate) was synthesized using standard procedures [7]. After purification the polymer gave a peak molecular weight of 5000.

As an example of preparation of sols, 3.5 g of polymer was dissolved in 12.7 g of co-solvent of chloroform and isopropanol (50/50 wt%). To the polymer solution, 3.8 g of TIP was added. For conductivity measurements an appropriate quantity of $LiClO_4$ (based on the ether oxygen content) was added to the sol. The solution was then agitated and heated on a hot plate at 50°C for 24 hours in a sealed bottle. Microscope slides cleaned with acetone, distilled water and finally with isopropanol were used as coating substrates. Dip coating was performed in an anti-static coating rig, at a withdrawal speed of 0.2 to 2.5 mm s^{-1}. Coatings were left in air overnight, and heat treatments were carried out in a furnace at 120°C, typically for 1 h. The films

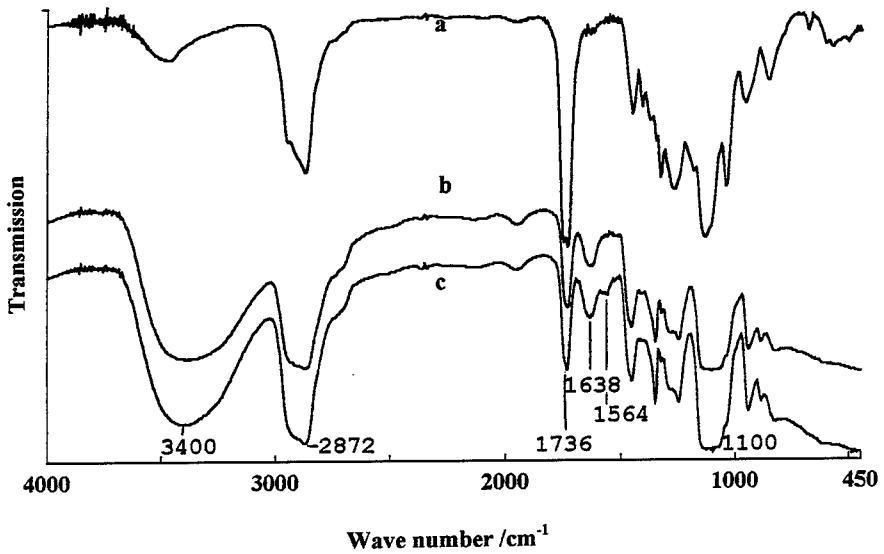

Figure 1. FT-IR spectra of PTEGM and coatings: (a) PTEGM, (b) coating dried at room temperature, and (c) coating after heat treatment at 120°C for 1 h.

for conductivity measurements were dried by storage in a desiccator under vacuum.

Fourier transform infrared spectroscopy (FTIR) was carried out on coatings using a Perkin-Elmer Spectrum 2000 spectrometer. XPS analyses were performed on a V.G. CLAM 200, using MgK_α X-ray (1253.6 eV) to excite the spectrum. The coating features were investigated with a Camscan scanning electron microscope. The coating thicknesses were determined by weighing the coating and assuming that the coating has the same density as a dried gel prepared from the same sol composition. Thermomechanical analyses (TMA) were performed using a DuPont 943 TMA. Ionic conductivity measurements of the coatings were performed between ITO electrodes over a temperature range from 20 to 120°C by complex impedance analysis using a Solartron 1286 Electrochemical Interface coupled to a 1250 Frequency response analyzer.

3. Results and Discussion

The coating thickness depends on the composition of the sols, particularly the polymer concentration. All the coatings prepared from sols with TIP concentration less than 20 wt% were crack-free and featureless in the SEM. Log-log plots of coating thickness, t against the withdrawal speed, U, give straight lines, indicating a $t \propto U^n$ relationship with $n = 0.88$ for coatings from the sol of 10 wt% TIP, 18 wt% PTEGM and $n = 0.35$ for a sol of 10 wt% TIP, 36 wt% PTEGM. For molar ratios [TEGM]:[TIP] = 1 and 4, maximum crack-free thicknesses of 1.2 and 15 μm, respectively were achieved in a single dip.

Figure 1 shows the FT-IR spectra of the polymer and hybrid coatings dried at room temperature and heated at 120°C for 1 h. The most noticeable feature is the decrease in intensity of the carbonyl stretch absorption (ca. 1736 cm^{-1}) in relation to the other strong bands at ca. 1100 cm^{-1} (C—O stretch) and 2872 cm^{-1}(C—H stretch) if the pure polymer and metal-containing systems are compared. These two "reference" bands appear to have approximately the same relative intensities as in the pure polymer. The O—H stretch band in the hybrid coatings in the region 3400 cm^{-1} remains

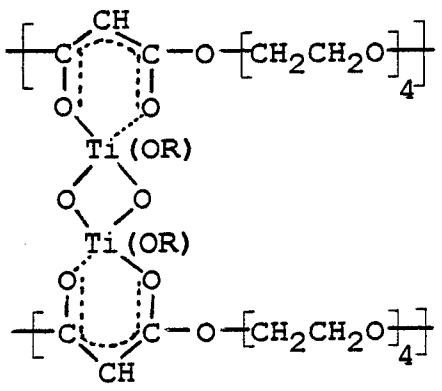

Figure 2. Proposed structure of the hybrid material.

appreciable even after heating at 120°C. Since free isopropanol should have been expelled at this temperature, it seems that the OH band arises from the water content of the hybrid. The peak at 1638 cm^{-1} may also be assigned to water and the band at 1564 cm^{-1} which increases with heat treatment may arise from the formation of unsaturated (C=C) groups generated within the malonate function as Ti—O—C bonds are formed. This region has medium to strong bands associated with metal chelates of ketoesters [8] whereas the bands at ca. 450–800 cm^{-1} are indicative of Ti—O—Ti network formation [9]. Following IR analyses of analogous ethyl acetoacetate complexes by Yamomoto and Kambara [8], a proposed structure of the hybrid material is shown in Fig. 2. However, TEM micrographs showing uniform distribution of particles of 2–5 nm in diameter suggest that "crosslinks" incorporating several more Ti atoms must also be present [10].

Figures 3(a) and (b) show the XP spectra of C1s for coatings dried at room temperature and after heat

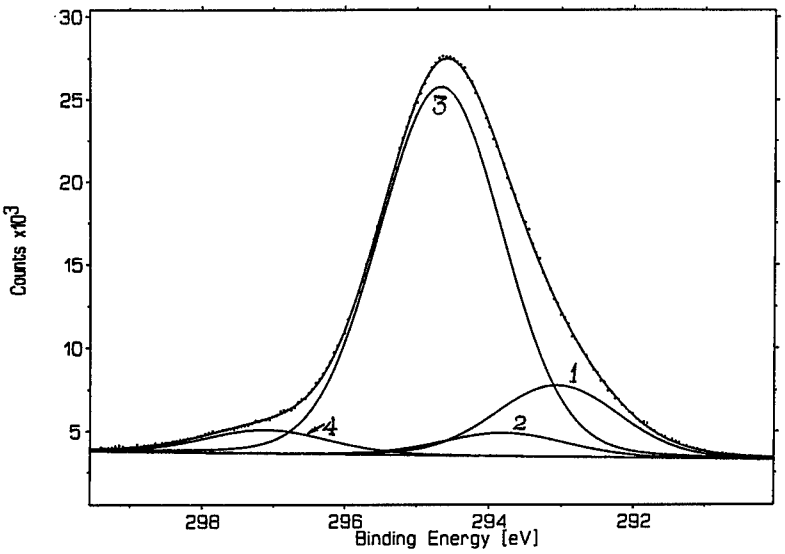

(a)

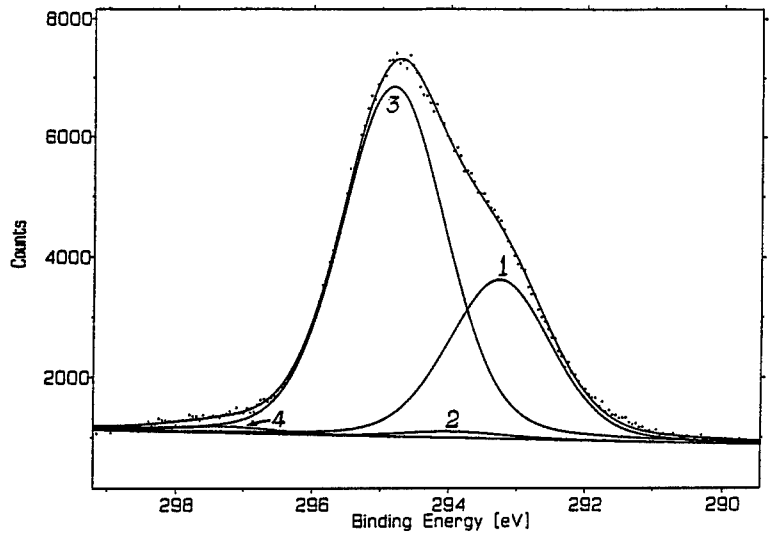

(b)

Figure 3. XP C1s spectra of coatings (a) room temperature dried, (b) after heat treatment at 120°C for 1 h.

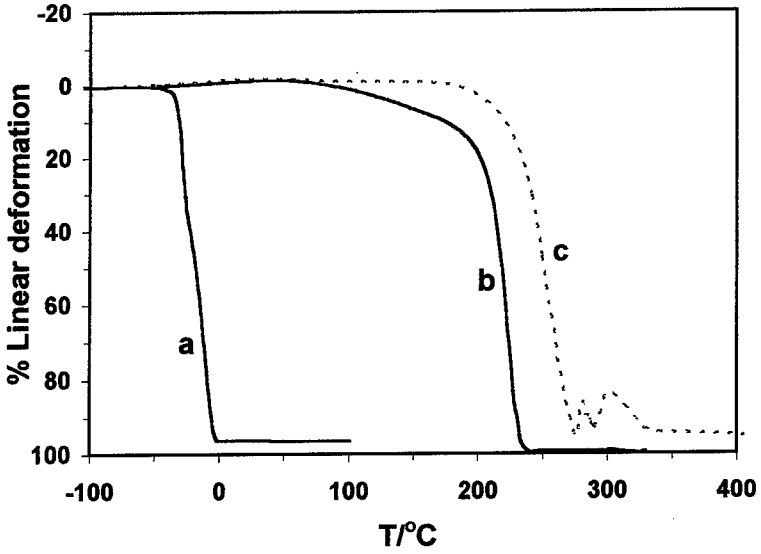

Figure 4. Thermomechanical analysis data of (a) the pure polymer and a gel having composition of [TEGM] : [TIP] = 1 : 1, (b) dried at room temperature, and (c) after heat treatment for 24 h at 120°C. % linear deformation against temperature; heating rate 10°C/min.

treatment at 120°C for 1 h, respectively. The spectra have not been corrected to C1s 285 eV. Curve fitting indicates that they comprise four components, which may be assigned to C—C/C—H (1), C—(CO)—OR (2), C—OX (3), and (C=O)—OH/OR (4), respectively, where X = alkyl, hydrogen or Ti [11]. It is noted that the (atomic) ratio between C (3) and C (4) changes from 17 : 1 for the room temperature dried coating to 57 : 1 for the coating after heat treatment at 120°C for 1 h, while the C : O ratio has only changed from 1.66 to 1.44. This apparent increase in C—OX and reduction in carbonyl groups of the ester is consistent with the chelation of titanium by the dicarbonyl group, involving the delocalization of the electrons of the C=O bonds, as suggested in the proposed structure (Fig. 2). On heating, additional C—H is seen, which may be assigned to hydrocarbon impurities from the oven/atmosphere and the spectrometer.

Figure 4 shows thermomechanical analysis data for the pure polymer (a) and a gel having a composition of [TEGM] : [TIP] = 1 after heat treatments (b and c). The data show a dramatic increase in deformation temperature brought about by the addition of TIP. The lower deformability as a result of the higher temperature heat-treatment indicates some enhancement of the network structure.

The ionic conductivities of hybrid coatings doped with $LiClO_4$ at concentration $[-CH_2-CH_2-O-]$: $[Li^+] = 20$, with molar ratios of [TEGM] : [TIP] = 4 and 1 are shown as $\log\sigma$ vs. 1/T plots in Fig. 5(b) and (c), respectively. The conductivity of an $LiClO_4$ doped PTEGM film free of TIP is shown in Fig. 5(a). The plots are curved and typical of amorphous systems in which the charge carrier mobilities are determined by free-volume mechanisms [12]. Complex impedance plots from the hybrid coatings show well-developed semicircles arising from the structural heterogeneity

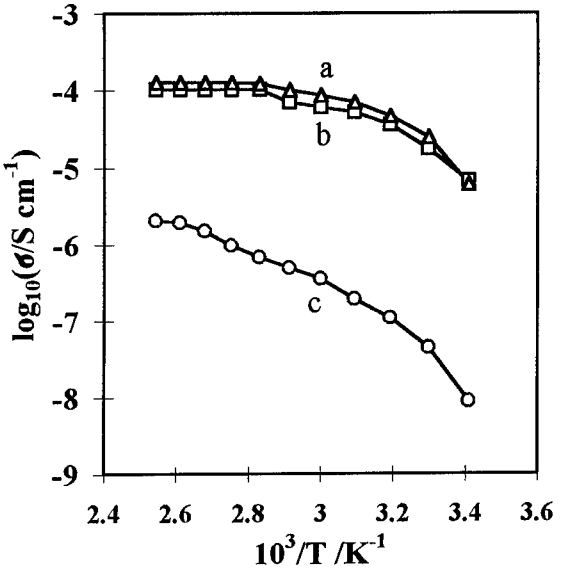

Figure 5. Ionic conductivity (σ) of PTEGM (a), and hybrid coatings having [TEGM] : [TIP] = 4 (b) and 1 (c) doped with $LiClO_4$ with [ether oxygen] : $[Li^+] = 20$.

in the samples even though the samples are optically transparent. The conductivity for [TEGM] : [TIP] = 4 is virtually identical to that of the TIP-free coating although the hybrid coating is quite "solid" and the pure polymer is liquid. However, a greater concentration of TIP brings about 2–3 orders decrease in conductivity (Fig. 5(c)) owing to the increase in crosslinking density and simultaneous reduced mobility of the network chains to which the ion mobilities are coupled. The opposite trend might be anticipated if the conductivity was principally electronic. Further characterization of the structure of the hybrid coatings is under way.

Acknowledgment

We thank SBFSS (Sino-British Friendship Scholarship Scheme) for financial support of this project. We are also grateful to our colleague Dr. R.D. Short for his help with the XPS.

References

1. C.J. Brinker and G.W. Scherer, *Sol-Gel Science* (Academic Press, Inc. Harcourt Brace Jovanovich, Publishers, London, 1994).
2. H. Schmidt, J. Sol-Gel Sci. Tech. **1**, 217 (1994).
3. C. Sanchez and F. Ribot, New J. Chem. **18**, 1007 (1994).
4. M.A. Macedo, L.H. Dall'Antonia, B. Valla, and M.A. Aegerter, J. Non-Cryst. Solids **147/148**, 792 (1992).
5. P.V. Wright, Brit. Polymer J. **7**, 319 (1975).
6. K. Dahmouche, M. Atik, N.C. Mello, T.J. Bonagamba, H. Panepucci, M.A. Aegerter, and P. Judeinstein, J. Sol-Gel Sci. Tech. **8**, 711 (1997).
7. A.C. Tang and K.S. Yao, J. Poly. Sci. **35**, 219 (1959).
8. A. Yamomoto and S. Kambara, J. Amer. Chem. Soc. **79**, 4344 (1957).
9. K.A. Mauritz and C.K. Jones, J. Appl. Polym. Sci. **40**, 1402 (1990).
10. C.S. Deng, P.F. James, and P.V. Wright, J. Mater. Chem. **8**, 153 (1998).
11. D.M. Brewis and D. Briggs, Polymer **22**, 7 (1981).
12. H. Cheredame and J.F. Le Nest, in *Polymer Electrolyte Reviews I*, edited by J.R. McCallum and C.A. Vincent (Elsevier, London, 1987), p. 103.

Journal of Sol-Gel Science and Technology 13, 495–497 (1998)
© 1998 Kluwer Academic Publishers. Manufactured in The Netherlands.

Vanadium-Based Organic-Inorganic Hybrid Materials Prepared by a Sol-Gel Method

M. MOHSENI, P.F. JAMES AND P.V. WRIGHT
Department of Engineering Materials, University of Sheffield, Mappin St., Sheffield S1 3JD, UK

Abstract. Synthesis and characterization of hybrid organic-inorganic nanocomposites based on reaction of vanadium *i*-propoxide with an organically functionalized poly(ethylene glycol) having di-carbonyl groups is reported. The bulk gels were characterized by thermal analyses (DSC, TGA and TMA) and FT-IR spectroscopy. The results revealed that the gels consist of vanadium-oxygen-vanadium groupings which are cross-linked with the functionalized polymer through the di-carbonyl groups. Gels doped with lithium salt show significant electrical conductivity.

Keywords: sol-gel, hybrids, vanadium, poly(ethylene glycol)

1. Introduction

The tendency for phase separation in organic-inorganic hybrid materials appears to be effectively reduced by covalently bonding the inorganic and organic constituents [1]. The flexibility of organic polymers may be combined with the rigidity of inorganic components without any phase separation. Various polymers have been used [2] in organically modified ceramics, most of which are based on Si. Transition metals have also been incorporated into organic-inorganic networks [3, 4]. Vanadium pentoxide has already been prepared [5] by the sol-gel method. It can be used in micro-ionic devices such as reversible cathodes or electrochromic layers [6]. "Class I" [7] organic-inorganic hybrids have been made by intercalating conducting polymers [8] into the layered structure of vanadium pentoxide. Poly(ethylene glycol), PEG, has been incorporated into hybrid materials by sol-gel procedures using $Si(OR)_4$ [9] leading to ionic conduction by introduction of a lithium salt into PEG. In this paper we have studied the feasibility of making "class II" [7] hybrid materials by reacting vanadium *i*-propoxide with a modified PEG having dicarbonyl groups appended ($CH_3COCH_2CO{-}O{-}[{-}(CH_2)_2{-}O{-}]_nCOCH_2COCH_3$).

2. Experimental

Vanadium *i*-propoxide, $VO(O^iPr)_3$ (Alfa products), ethylacetoacetate (Aldrich), PEG600 (Aldrich) were used as received. FT-IR spectroscopy was performed with a Perkin-Elmer Spectrum 2000 on samples dispersed in a KBr disc. Differential scanning calorimetry (DSC) and thermomechanical analysis (TMA) were carried out in air using a DuPont 910 DSC and 943 TMA at a heating rate of 10°C/min. A Stanton-Redcroft TG770 was used for thermogravimetric analysis. Samples were analyzed from 25 to 550°C at a heating rate of 10°C/min. AC conductivity measurements were performed with a Solarton 1286 Electrochemical Interface connected to a 1250 Frequency Response Analyzer.

Functionalized PEG600 (FPEG600) was prepared by an ester-interchange reaction in a round-bottom flask heated in an oil bath (170–180°C). The reaction was carried out under argon. The molar ratio of ethylacetoacetate to PEG600 was 2.2 : 1. Ethanol, as by-product, was removed from the flask. A viscous solution was obtained after 5 days which was pale brown in color. Gel permeation chromatography showed no species with molecular weight higher than 1000 suggesting that no condensation reaction occurred for PEG600. For the preparation of sols a known amount

of FPEG600 was dissolved in acetonitrile to which was added different amounts of vanadium isopropoxide. The molar ratio of vanadium to FPEG600, x, given by

$$x = \mathrm{VO(O^iPr)_3/FPEG}$$

was varied between 1 : 1 and 3 : 1. Sols were magnetically stirred for 24 h. Gels were made by casting the sols in plastic dishes and hydrolyzing in air. Bulk gels (green) were obtained after 2 days which were then heat-treated at 100°C. For conductivity measurements, Li $N(SO_2CF_3)_2$ was incorporated into gels by adding the salt to FPEG600-$VO(O^iPr)_3$ solutions in acetonitrile. The lithium salt was added in proportion [ether oxygen]/[Li]= 20. A gel film was deposited onto an ITO electrode with a sellotape spacer (~60 μm) and allowed to cure in the atmosphere at room temperature overnight. The films were then dried by storage in a vacuum dessicator for 48 h.

3. Results and Discussion

An indication of completion of esterification in FPEG is given by the disappearance of —OH groups of PEG located at 3500 cm^{-1} in its FT-IR spectrum. The small peak at 3500 cm^{-1} in Fig. 1(a) may indicate unreacted —OH termini. Gravimetric analysis of the reaction products indicated that at least 95% of esterification was achieved. Diketo groups are well known to show enol-keto tautomerism [10]. The keto form of the carbonyl group in ketoesters shows a peak at 1750–1740 cm^{-1} whereas that of the enol form is at 1700–1720 cm^{-1}. So the carbonyl groups in FPEG are mostly in the enol form. Sols which were made by reacting vanadium *i*-propoxide and FPEG600 were red in color indicating the formation of a complex. At x less than 0.5 gels were "sticky" indicating that the cross-linked network has only partially formed and the hybrid material behaves similarly to FPEG600. This was observed for all samples at ratios less than 0.5 containing different concentrations of FPEG600 in the solutions. At a greater ratio of vanadium to FPEG600, gels with good integrity were obtained. After storage the color of gels and coatings turned to green which is indicative of the presence of V^{+4} and V^{+5} ions [5]. A typical FT-IR spectrum of these gels is shown in Fig. 1(b). Vibrations located at 1621 cm^{-1} and 1525 cm^{-1} correspond to ν(C—C) + ν(C—O) of the enolic form of the chelated metals with diketones [10]. Infrared spectra of all the gels exhibit a broad band in the 500–600 cm^{-1} region which corresponds to the ν(V—O—V) [10]. These suggest that FPEG600 has covalently reacted with the vanadium-oxo network. There is also a band at 900–1000 cm^{-1} which shows the vibration of ν(V=O) [10].

An endothermic peak was observed in the DSC traces (not shown) of gels around 60–140°C which may be attributed to the removal of physically adsorbed

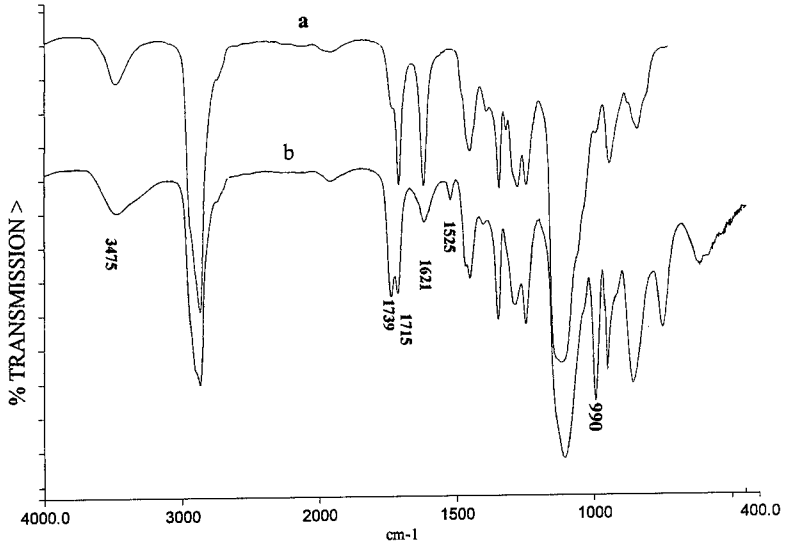

Figure 1. FT-IR spectrum of (a) functionalized PEG600 and (b) hybrid gel.

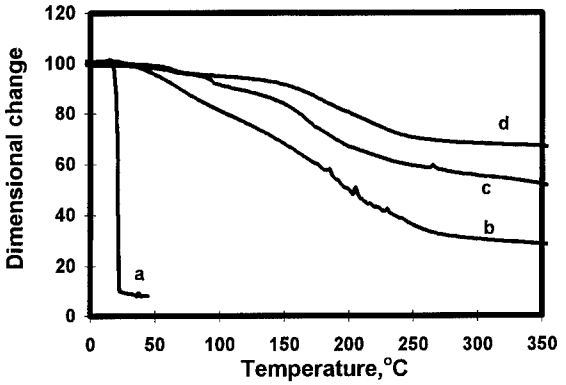

Figure 2. Thermomechanical analysis (TMA) of hybrid gels at different x: (a) 0, (b) 1, (c) 2 and (d) 3.

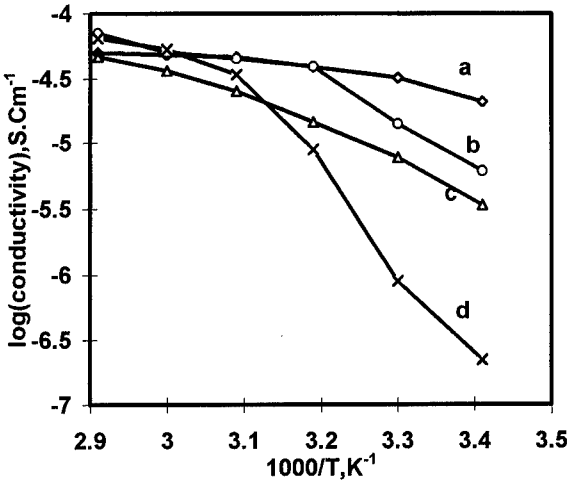

Figure 3. Temperature dependence of ionic conductivities of hybrid gels at different x ([O]/[Li] = 20) (a) 0, (b) 1, (c) 2 and (d) 3.

and trapped solvent since thermogravimetric analysis showed up to 15% weight loss at this temperature range. An exothermic peak with a maximum around 320–350°C which has a shoulder starting from 250°C may be assigned to the oxidation and removal of organics. This corresponds to a weight loss of about 60–70% in the materials. Another exothermic peak between 450 and 500°C is believed to be the crystallization of vanadium pentoxide as the gels are amorphous to X-ray below this temperature.

Thermomechanical analysis (TMA) shows that the deformation temperatures of the gels depend not only on the modification ratio but also on the initial concentration of the sols. Figure 2 shows that deformation occurs between ca. 20 and 150°C for $0 \leq x \leq 3$. This presumably arises from more extensive network formation in gels with increasing $VO(O^iPr)_3$ content.

Ionic conductivities of various FPEG(25 wt% in solution)-vanadium i-propoxide samples doped with Li $N(SO_2CF_3)_2$ are presented in Fig. 3. The plots are curved and typical of amorphous systems in which charge carrier mobilities depend on free-volume [11]. The highest ionic conductivity is observed for the vanadium-free sample. As vanadium is increased the ambient conductivities become smaller due to increasing crosslink density between the polymer segments. However, the sample with $x = 3$ shows significant rise in conductivity at higher temperatures. This behavior contrasts with that of similar network crosslinked with titania as reported by Deng et al. [12] in which the more titania-rich networks remain significantly less conductive throughout the temperature range. These observations could be explained by an electronic contribution to the conductivity of the gel via contacting vanadium particles [6]. This mixed conduction is under further investigation.

Acknowledgement

One of the authors (Mohseni) would like to thank the Iranian Government for financial support.

References

1. H. Hung, B. Order, and G.L. Wilkes, Macromol **20**, 1322 (1987).
2. A.B. Wojick and L.C. Klein, J. Sol-Gel Sci. Tech. **5**, 77 (1995).
3. M. In, C. Gerardin, J. Lambard, and C. Sanchez, J. Sol-Gel Sci. Tech. **5**, 101 (1995).
4. B. Wang and G.L. Wilkes, J. Polm. Sci. A, Part A: Polym. Chem. **29**, 905 (1991).
5. G. Guzman, R. Morineau, and J. Livage, Mat. Res. Bull. **29**(5), 509 (1994).
6. M. Nabavi, C. Sanchez, and J. Livage, Eur. J. Solid-State Inorg. Chem. **28**, 1173 (1991).
7. C. Sanchez and F. Ribot, New J. Chem. **18**, 1007 (1994).
8. M.G. Kantazidis and C.G. Wu, Am. Chem. Soc. **111**, 4139 (1989).
9. D. Ravaine, A. Semiel, Y. Charabouillot, and M.A. Vincess, J. Non-Cryst Solids **82**, 210 (1986).
10. G. Socrates, in *Infrared Characteristic Group Frequencies* (John Wiley and Sons, Ltd. London, 1980).
11. H. Cheredame and J.F. Le Nest, "Ionically conducting polyether networks," in *Polymer Electrolyte Review I*, edited by J.R. MacCallum and C.A. Vincent (Elsevier, London, 1989), p. 103.
12. C. Deng, P.F. James, and P.V. Wright, J. Sol-Gel Sci. Tech. **13**, 489 (1998). (These Proceedings).

Journal of Sol-Gel Science and Technology 13, 499–502 (1998)
© 1998 Kluwer Academic Publishers. Manufactured in The Netherlands.

SAXS and TEM Investigations on Thermoplastic Nanocomposites Containing Functionalized Silica Nanoparticles

C. BECKER, B. KUTSCH AND H. KRUG
Institut für Neue Materialien, Im Stadtwald, D-66123 Saarbrücken, Germany

H. KADDAMI
University CADI AYYAD, Faculty of Science and Technics-Gueliz, Avenue Abdelkarim Elkhattabi P.B. 618, Marrakech, Marocco

Abstract. Transmission electron microscopy (TEM) and small angle X-ray scattering (SAXS) were used to characterize the morphology of thermoplastic nanocomposites. These materials were based on a thermoplastic matrix of a copolymer of methylmethacrylate (MMA) and 2-hydroxyethylmethacrylate (HEMA) with spherical 10 nm silica particles as a filler (filler content 2, 5 and 10 vol%, respectively). Depending on the surface modification of the particles, it was possible to control the aggregation tendency of the primary filler particles. With uncoated particles large aggregates about 100 nm in size could be observed by TEM. For nanocomposites containing particles coated with methacryloxypropyltrimethoxysilane (MPTS), TEM showed that the particles were better dispersed in the polymer matrix only forming aggregates comprised of two or three primary particles. In comparison to the TEM results, the volume weighted particle size distribution calculated from SAXS for the systems with uncoated particles is monomodal and shows particle sizes in the range of primary particles whereas the systems with MPTS coated particles revealed a bimodal size distribution with particle sizes comparable to those measured with TEM. To obtain complete information about the morphology of the nanocomposites above the critical upper limit of detectable scattering vectors (particle sizes >50 nm) SAXS has to be supported by TEM, whereas in the nanosize range below the critical limit both methods exhibit an excellent correspondence.

Keywords: SAXS, TEM, nanocomposites, hybrid materials, surface modification

1. Introduction

The idea of combining inorganic networks and polymers has opened a wide field in materials science. A large family of hybrid organic-inorganic materials have been produced by sol-gel processing, where in both inorganic and organic parts contribute to the overall properties of the composite by their own specific properties. For this reason hybrid organic-inorganic materials offer various applications in different fields like nonlinear-optics [1], adhesives [2], selective membranes [3], coatings [4] and bulk-composites for optical applications [5]. Parameters such as the amount and type of catalyst and the amount of water affect the kinetics of the sol-gel reactions [6–8]. Consequently, the morphology and the final properties of the resulting hybrid organic-inorganic materials are strongly dependent on the reaction conditions. Controlled phase separation in the nanoscale range offers the possibility of forming transparent composite materials with interesting new mechanical properties. The use of coupling agents such as alkylalkoxysilanes can provide strong bonds between the inorganic and the organic nano-domains to avoid undesired macroscopic phase separation. A number of reports have appeared on the preparation of so called nanocomposites based on organic polymers as matrix materials filled with inorganic particles in the nanoscale range [9–11]. A homogeneous dispersion of

the nanoscale particles in the matrix can be achieved by proper control of the interfacial free energy, which has to be decreased by the use of compatibilizers [9]. Small angle X-ray scattering (SAXS) in combination with transmission electron microscopy (TEM) is a useful method to characterize the morphology of hybrid organic-inorganic materials. Many authors [12–17] have reported SAXS investigations on hybrid organic-inorganic materials to describe the morphology of hybrid materials over a broad scale in the nanosize range. This work presents SAXS and TEM investigations on hybrid materials based on thermoplastic polymers as matrices and nanosized silica particles as fillers. The aim was to characterize the morphology, i.e., the size of particle aggregates and the quality of particle segregation in the nanocomposites depending on the filler concentration and the surface treatment of the fillers.

2. Experiment

Nanosized silica particles (Nissan, mean diameter: $d = 10 \pm 3$ nm) were coated with methacryloxypropyltrimethoxysilane (MPTS) in a methanolic dispersion containing approximately 1 vol% of silica. MPTS was used to achieve covalent bonding between filler and matrix. The coating reaction was performed using an equimolar amount of silane compared to the calculated number of silanol groups. The dispersions with 10 nm particles were used without further centrifugation. The monomers methylmethacrylate (MMA) and 2-hydroxyethylmethacrylate (HEMA) were distilled in vacuum prior to use. Equal amounts of both monomers were mixed with predetermined amounts of the methanolic silica dispersions. After removal of methanol the monomer mixtures contained approximately 2, 5 and 10 vol% silica. These mixtures were cured with heating up to 120°C, by free radical polymerization using azobisisobutyronitril (AIBN) as initiator. The curing was performed in special reaction containers under oxygen-free conditions, resulting in plate-like poly(MMA-co-HEMA) (PMH) nanocomposites with a thickness of 4 mm. The unfilled PMH copolymer matrix was synthesized as reference system. For the TEM investigations, the nanocomposites were ultramicrotomed in a Reichert ultracut using a diamond knife. The resulting slices, with an approximate thickness of 100 nm, were prepared on 400 mesh copper grid. The dispersion of the filler particles was directly visible in TEM without further preparation. SAXS measurements were performed using a compact Kratky camera (Paar (Graz), Type KKK) with slit collimation and equipped with a linear position sensitive detector (Braun, 2048 channels). The X-ray wave length was 0.154 nm using monochromatized CuK_α radiation. Thus, the detectable scattering vectors q with $q = 4\pi/\lambda * \sin(\theta)$ where 2θ is the scattering angle, range from $q = 0.035$ nm^{-1} to 5 nm^{-1}. The SAXS spectra have been corrected for parasitic background scattering and for the background contribution of the organic polymer phase.

3. Results and Discussion

All nanocomposites synthesized in the manner described above were transparent indicating that macroscopic phase separation has not occurred. This was confirmed by TEM analysis. Figure 1 shows the results of the TEM investigation for the PMH nanocomposites with 5 vol% of silica fillers and different filler surface treatment.

For the system with uncoated filler particles aggregates up to $d = 100$ nm in diameter are visible. It can be assumed that the smaller aggregates are the result of aggregates which were cut perpendicular to their longer axis. The aggregates observed show an open structure, so a fractal behavior could be expected. In the case of the MPTS coating the particles were nearly homogeneously distributed in the matrix. Only a few small aggregates were detectable. The better dispersion in these nanocomposites is evident for the coated particles which have approximately the same functionality on the surface, as the matrix material along the polymer backbone. This result shows that the compatibilization concept of decreasing the interfacial free energy is valuable.

The differences in morphology between the nanocomposites filled with uncoated and MPTS coated particles found by TEM should also be manifested in the SAXS data. Figure 2 shows the dependence of the scattering intensity I on the logarithmic scattering vector $\ln(q)$ as determined from the SAXS experiments on samples with uncoated and MPTS coated silica, respectively.

At the lowest scattering angles an increase in intensity for the systems filled with uncoated particles can be observed and may be attributed to large sized silica domains. This observation is in agreement with the TEM results for this system, which show aggregates in the size range around $d = 100$ nm. On the other hand, one can observe a small shoulder in the SAXS spectra of the systems filled with MPTS which is not visible in the case of uncoated particles. This shoulder

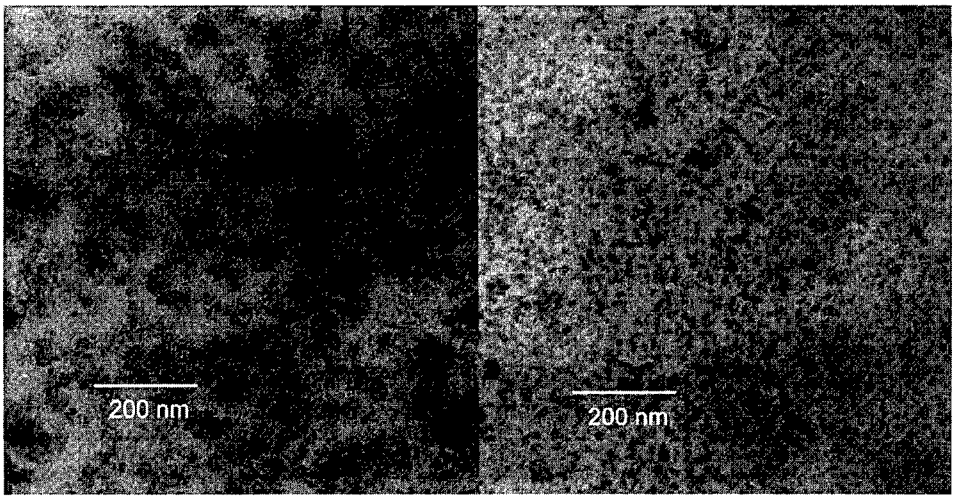

Figure 1. TEM micrograph of a PMH nanocomposite with (a) 59 vol% uncoated and (b) 55 vol% MPTS coated SiO_2 particles, $d = 10$ nm.

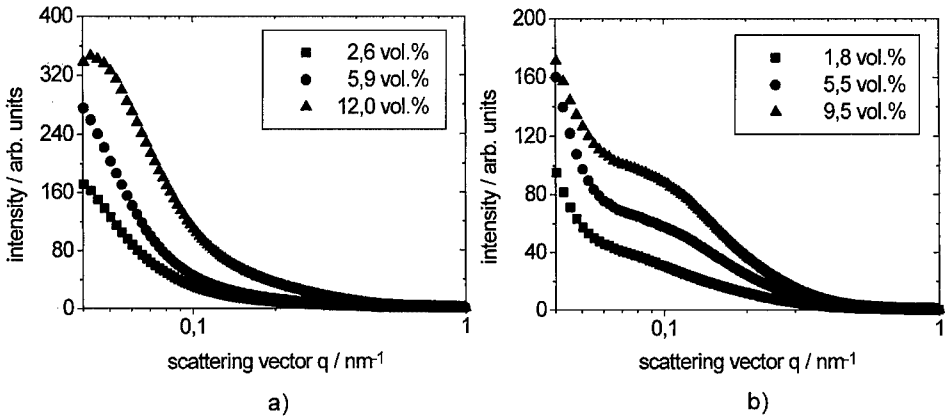

Figure 2. SAXS spectra of PMH nanocomposites with (a) uncoated and (b) MPTS coated 10 nm SiO_2 particles for different filler volume fractions.

becomes more pronounced in the SAXS spectra for the samples with 5.5 vol% and 9.5 vol% coated particles. The observed shoulder can be attributed to a correlation length given by a partial ordering of the dispersed particles in the composites.

The particle size distribution function $N(r)$ for particles with radius r can be calculated according to the method of Glatter [18] using the program package ITP 92. The calculation is based on the following equation [19]

$$I(q) = \int_0^\infty N(r) r^6 I_0(q, r)\, dr$$

where $N(r)$ is the particle size distribution function, r is the particle radius and $I_0(q, r)$ is the normalized form factor of a single particle with characteristic length r.

In order to calculate $N(r)$ information about the shape of the particles has to be available. According to the TEM results the SiO_2 particles with $d = 10$ nm are nearly spherical. The volume weighted particle size distributions $V(r)$ calculated from $N(r)$ ($N(r)$ calculated from the SAXS spectra) assuming spherical shape of the particles are shown in Fig. 3(a) and (b).

For greater values of r, the calculated size distributions given in Fig. 3 sometimes showed small oscillations around $V(r) = 0$. In this case, the size distribution was cut, when it reached 0 for the first time. From Fig. 3 it is evident that all samples have a particle size distribution of about $r = 7$ nm which corresponds to the size of the primary particles. Besides this the samples

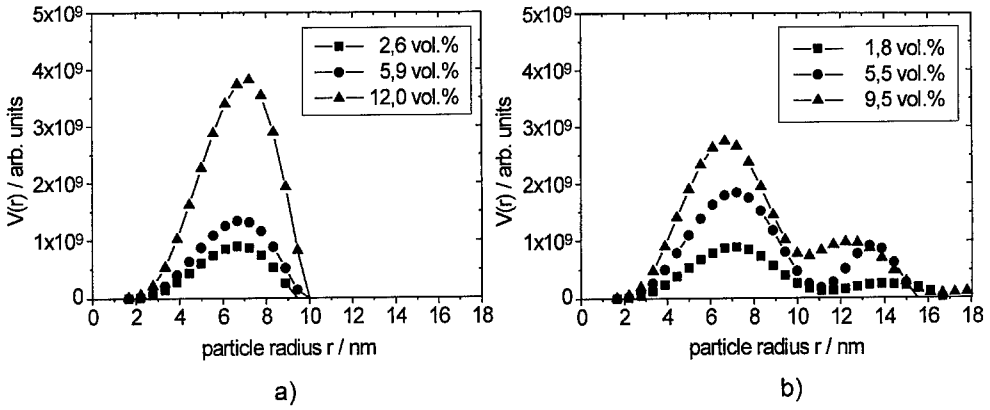

Figure 3. Calculated volume weighted particle size distributions $V(r)$ of the (a) uncoated and (b) MPTS coated SiO_2 particles from the SAXS spectra for PMH nanocomposites containing different volume fractions of silica using the program ITP 92 developed by Glatter [18, 19] assuming spherical shape and a limit of calculation of 50 nm.

filled with MPTS coated particles show a second population of particles with higher values of r between 11 nm and 16 nm. The calculation error in this range of radius r is usually high, but in agreement with the TEM results (Fig. 1) these samples contain primary particles and aggregates in the same size range. The lack of the second part of the distribution in the case of materials filled with uncoated 10 nm SiO_2 particles (Fig. 3(a)) is in agreement with the existence of larger aggregates in the size range above 50 nm which are visible in TEM, but not in SAXS, due to restricted upper limit of detectable scattering vectors.

4. Conclusion

Combined TEM and SAXS investigations on thermoplastic nanocomposites such as a PMH copolymer filled with 10 nm SiO_2 particles with different particle surface coatings have been shown to be important tools in gaining complete information about the morphology of the materials. TEM analysis gives visible information on the extent of particle separation in the nanocomposites depending on the surface modification over a broad scale range including especially large sized aggregates. On the other hand, SAXS analysis enables to receive more detailed information about size distributions of primary particles and "mean" size aggregates in the real nanosize range below 20 nm.

References

1. C. Sanchez and F. Ribot, New J. Chem., 1007–1047 (1994).
2. B. Wang and G. Wilkes, Pure Appl. Chem. **A31**, 249–269 (1994).
3. C. Guizard and P. Lancan, in *First European Workshop on Hybrid Organic-Inorganic Materials: Synthesis, Properties, Applications* (Château de Bierville, France, 1993), pp. 153–169.
4. R. Kasemann and H. Schmidt, in *First European Workshop on Hybrid Organic-Inorganic Materials: Synthesis, Properties, Applications* (Château de Bierville, France, 1993), pp. 171–180.
5. B. Abramoff and J. Covino, J. Appl. Polym. Sci. **46**, 1785–1791 (1992).
6. H. Kaddami, F. Surivet, J.F. Gérard, T.M. Lam, and J.P. Pascault, J. Org. Organomet. Polym. **4**, 183–198 (1994).
7. H.H. Huang, R.H. Glasser, and G.L. Wilkes, in *Inorganic and Organometallic Polymers*, edited by M. Zeldin, K.J. Mynne, and H.R. Allcock (Am. Chem. Soc., Washington, 1988), chap. 29, Vol. 4, pp. 1437–1446.
8. C.J.T. Landry, B.K. Coltrain, and B.K. Brady, Polymer **33**, 1486–1495 (1992).
9. C. Becker, H. Krug, and H. Schmidt, Mater. Res. Soc. Symp. Proc. **435**, 237 (1996)
10. C.J.T. Landry, B.K. Coltrain, M.R. Landry, J.J. Fitzgerald, and V.K. Long, Macromolecules **23**, 3702–3712 (1993).
11. E.P. Giannelis, Adv. Mater. **8**, 29 (1996).
12. H.H. Huang and G.L. Wilkes, Polym. Bull. **18**, 455–462 (1987).
13. H.H. Huang, B. Orler, and G.L. Wilkes, Macromolecules **20**, 1322–1330 (1987).
14. F. Surivet, T.M. Lam, and J.P. Pascault, Macromolecules **25**, 5742–5751 (1992).
15. B.K. Coltrain, C.J.T. Landry, J.M. Oreilly, A.M. Chamberlain, G.A. Rakes, J.S. Sedita, L.W. Kelts, M.R. Landry, and V.K. Long, Chem. Mater. **5**, 1445–1455 (1993).
16. H. Kaddami, Thèse INSA Lyon, p. 248; No. d'ordre 95ISAL, 1995.
17. M.R. Landry, B.K. Coltrain, C.J.T. Landry, and J.M. Oreilly, J. Polym. Sci., Part B: Polym. Phys. **33**, 637–655 (1995).
18. O. Glatter, J. Appl. Cryst. **13**, 7–11 (1980).
19. O. Glatter, *Small Angle X-Ray Scattering* (Academic Press, London, 1982), pp. 119–165.

Journal of Sol-Gel Science and Technology 13, 503–508 (1998)
© 1998 Kluwer Academic Publishers. Manufactured in The Netherlands.

CW and Pulsed EPR Study of Silver Nanoparticles in a SiO_2 Matrix

G. MITRIKAS, Y. DELIGIANNAKIS, C.C. TRAPALIS, N. BOUKOS AND G. KORDAS*
Institute of Material Science, NCSR Demokritos 15310, Aghia Paraskevi, Athens, Greece

Abstract. Metallic silver nanoparticles were prepared by the sol-gel method in an SiO_2 matrix. The process includes complexation of silicon alkoxides with metal salts, hydrolysis, polycondensation, formation of powder, and subsequent thermal treatment first in oxidizing and second in reducing atmospheres. The sizes of metallic particles were determined both by X-ray diffraction and transmission electron microscopy. These measurements revealed sizes of metallic particles between 1 and 20 nm, depending upon processing conditions. The magnetic properties were investigated using electron paramagnetic resonance spectroscopy in the temperature range between 4 and 300 K. The spin-lattice relaxation time T_1 was measured by pulsed EPR. The temperature dependence of T_1 is described by the relation $1/T_1 \propto T^n$, where $0.4 < n < 1$. This behavior is unusual and different from any well-known relaxation processes such as Raman, Direct or the Orbach-Aminov.

Keywords: silver nanoparticles, spin-lattice relaxation, pulsed EPR

Introduction

Small clusters of metallic atoms (nanoparticles) have interesting applications in a number of areas like heterogeneous catalysis [1] and fields of research where surface and interface properties are important such as in heat exchangers and thermometers at ultralow temperatures. In most of these cases, the basic properties of the nanoparticles are determined by their size and differ from the properties of the corresponding bulk material. From a more fundamental point of view, the study of these particles is very interesting since the physics of infinitely large systems is not applicable in the finite-size particles.

For small metal crystals the boundary conditions imposed on the conduction electrons cause the conduction energy levels to become discrete and the mean energy spacing between adjacent levels is given by

$$\delta = \frac{4E_F}{3N} \propto \frac{1}{V} \tag{1}$$

where E_F is the Fermi energy, N is the number of conduction electrons, and V is the volume of the particle [2]. This fact has important consequences at low temperatures. The thermodynamic properties, such as the specific heat and the magnetic susceptibility are significantly altered from their bulk values. Kubo [2] first noted that at low temperatures the unpaired spins of the particles with odd number of electrons exhibit Curie-low paramagnetism.

One of the main unresolved points is whether the energy levels are randomly distributed [2] or they follow a specific distribution function (orthogonal, symplectic or unitary) [3, 4]. In addition, the putative dependence of the energy levels on the size of the particles is not clearly understood.

In the case of paramagnetic nanoparticles the temperature dependence of the electron spin-lattice relaxation is sensitive to the energy levels that exist near the ground state and this can be used as a probe for the study of the energy level distribution.

Here, we present a study of the spin relaxation times (T_1) of Ag nanoparticles at temperatures between 4.2 and 100 K. The nanoparticles were embedded in an SiO_2 matrix prepared by the sol-gel method.

*To whom all correspondence should be addressed.

Experimental

The Ag particles were prepared by the sol-gel method [5, 6] which allows the preparation of samples with narrow particle size distributions and adjustable metal loadings. The procedure includes three steps. The first step includes complexation of the silicon alkoxide NH_2—$(CH_2)_3$—Si—$(OEt)_3$ with $AgNO_3$, hydrolysis of the Si—(OR) groups, and polycondensation. During the sol-gel processing, the organic groups —NH_2 coordinate to the metal ions and the resulting metal complexes are anchored to the silicate matrix. In this way, aggregation of the metal ions is prevented and a relatively homogeneous distribution throughout the SiO_2 matrix is obtained. In the second step the metal complex containing gel is dried and then heated in air (500°C) to oxidize all organic moieties. Thus, small silver oxide particles are formed. In the final step the powder sample is heated under hydrogen (500°C) which reduces the oxide to metal particles having diameters of a few nm.

The size of the particles was determined by transmission electron microscopy (TEM CM 20 Phillips). The bright-field micrographs with number 3 or 4 were taken for each sample. From these micrographs a representative number of nanoparticles (500–600) was measured in order to find their size distribution.

Continuous-wave (CW) EPR measurements were performed with a Bruker ESP 380 X-band spectrometer. The temperature was varied in the range 4.2–300 K using an Oxford liquid helium flow system. The microwave frequency and the magnetic field were measured with a microwave frequency counter HP 5350B.

Spin-lattice relaxation times, T_1 were measured by saturation recovery on a Bruker ESP 380 X-band spectrometer as described in [7]. The saturation recovery was monitored by recording the two-pulse echo intensity ($\pi/2 - 160$ ns $-\pi$; with $t_{\pi/2} = 16$ ns) as a function of the time after a saturating pulse sequence. The magnetic field corresponded to the maximum of field-swept spectrum. To minimize contributions from spectral diffusion a burst of N saturating pulses was employed [8, 9]. The pulse length was $t_p = 16$ ns; typically $N = 30$ pulses with an interpulse delay of 0.5 μs. The repetition rate was adjusted in every measurement in order to ensure complete magnetization recovery.

Results

The composite $Ag \cdot 12SiO_2$ (13 wt% Ag) was prepared using $x = 10$ equivalents of TEOS and $y = 2$ equivalents of NH_2—$(CH_2)_3$—Si—$(OEt)_3$. The resultant powder was heated in a horizontal tube furnace. DTA and XRD demonstrated that crystallization occurs at around 500°C, and based on this the oxidation was performed for 1 hour at this temperature in a pure oxygen atmosphere. In the reduction step the sample was heated at the same temperature for 2 hours, in the presence of a gas mixture H_2 4%-Ar 96%. After reduction the color of the sample changed from white to dark brown. Figure 1(A) shows a typical bright-field micrograph of a sample prepared by this way. The Ag particles can clearly be seen embedded in the SiO_2 matrix. The particles were spherical. Occasionally, ellipsoidal shape particles were observed for sizes greater than 8 nm.

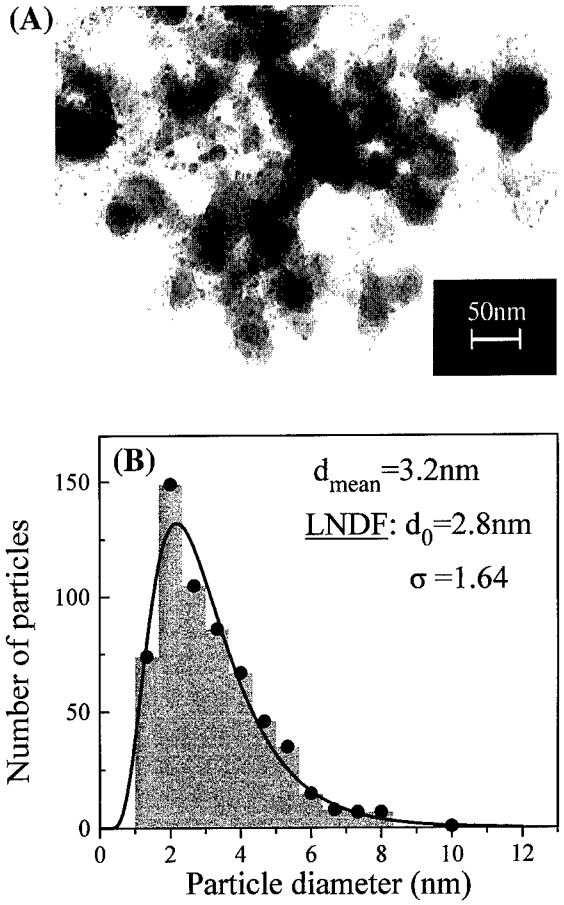

Figure 1. (A) TEM bright-field micrograph for sample $Ag \cdot 12SiO_2$ (13 wt% Ag) with the thermal treatment: 1 h O_2 500°C, 2 h H_2 500°C. Magnification 150,000×. (B) Size distribution for Ag particles. The filled circles denote midpoints in the size histogram with $\Delta d = 0.67$ nm and $N = 600$. The curve shows LNDF as defined by Eq. (2).

Figure 1(B) shows the size distribution of the particles derived from the TEM micrographs. The histogram

in this figure was obtained from the measurements of $N = 600$ particles. The mean diameter of particles in this sample is 3.2 nm and their size distribution is fairly narrow. The solid curve in Fig. 1(B) is fitted to the log-normal distribution function (LNDF) [10]:

$$\Delta N = \frac{N}{\sqrt{2\pi}\ln\sigma}\frac{1}{d}\exp\left[-\frac{1}{2}\left(\frac{\ln(d/d_0)}{\ln\sigma}\right)^2\right]\Delta d \quad (2)$$

where $\Delta N/N$ is the fraction of particles in the interval $\ln(d/d_0)$, $\ln(d/d_0)+\Delta\ln(d/d_0)$; d_0 is the peak diameter of the distribution, σ is a parameter that determines the width of the distribution, and N is the total number of particles in the sample. The fitting procedure gave $d_0 = 2.8$ nm and $\sigma = 1.64$.

Figure 2(A) shows the CW EPR signal recorded for the sample. The spectrum consists of a structureless derivative with $\Delta H_{pp} = 7.5 \pm 0.5$ G. No hyperfine splitting is observed and the signal is due to a spin state with $S = 1/2$ as was demonstrated by the Curie temperature dependence of the double integral of the signal (data not shown).

Progressive microwave saturation can be used to determine relative spin relaxation rates. The saturation curve is constructed by plotting the ratio of the signal amplitude to the square root of power versus the incident microwave power [11]. The saturation data are fit to the expression $I(P) = (1+P/P_{1/2})^{-b/2}$ where I is the normalized EPR amplitude divided by the square root of the incident microwave power, and P is the incident microwave power. The $P_{1/2}$, the power at which the signal attains half of its unsaturated value and b the inhomogeneity parameter, are the two fitting parameters. The progressive saturation study of the signal shows that the signal saturates easily with no changes in the lineshape. The fit of the data at 10 K, displayed in Fig. 2(B), yields $P_{1/2} = 20\ \mu$W and $b = 1.9$.

The spin-lattice relaxation was measured by monitoring the saturation recovery of the two-pulse echo at the field position corresponding to the maximum absorption. A typical echo-detected saturation recovery curve of Ag nanoparticles with mean diameter $d_{\text{mean}} = 3.2$ nm at 15 K is shown in Fig. 3(A). The recovery is well described by a single exponential; the residual from the fit is shown at the bottom of the transient (Fig. 3(A)). The fit at 15 K gives $T_1 = 11.9$ ms. The relaxation measurements were extended over the 5–100 K range; the observed spin-lattice relaxation rates were a single exponential over this range. The temperature dependence of the spin-lattice relaxation rate determined as described above is shown in Fig. 3(B) (filled circles). The power-law fit of relaxation rates gives a temperature dependence of the form $1/T_1 \approx 25.9\ T^{0.4\pm0.1}$. The saturation parameter $P_{1/2}$ depends rather weakly on the temperature. It is noticed that the temperature dependence of the $P_{1/2}$ (Fig. 3(B), filled squares) parallels that of T_1 (Fig. 3(B), open squares).

Discussion

The progressive saturation measurements showed that the inhomogeneity parameter is $b = 1.9$. For a spin system which is described by the Bloch equations $b = 1$ indicates a completely inhomogeneous broadening character while $b = 3$ is for a homogeneously broadened line. According to this the $b = 1.9$ implies that the CW EPR spectrum of the silver nanoparticles has a modest homogeneous broadening character [11]. Since $P_{1/2}$ is inversely proportional to the product T_1T_2 [11] the similar temperature dependence of the T_2 and the T_1 in Fig. 3(B) indicates that the T_2 for these silver nanoparticles is temperature independent. This implies the absence of temperature-dependent dynamic processes such as exchange or spin hopping as T_2-determining mechanisms.

The data show that the temperature dependence of the spin-lattice relaxation rate is described by an equation of the form $1/T_1 \propto T^{0.4\pm0.1}$. This behavior is rather unusual, because it does not agree with any of the well known spin-lattice relaxation processes such as Direct ($1/T_1 \propto T^1$), Raman ($1/T_1 \propto T^2, T^7, T^9$), or Orbach ($1/T_1 \propto \exp(-\Delta/kT)$) [12]. Moreover, the temperature dependence that we measure for silver nanoparticles in an SiO_2 matrix is different from the temperature dependence reported for silver nanoparticles in gelatin [13].

A theoretical model for the spin-lattice relaxation of conduction electrons in small metallic particles has been reported by Khaliullin et al. [14]. According to this, at $T < \Delta$ the recovery is non-monoexponential while at $T > \Delta$ it becomes exponential. The spin-lattice relaxation and its temperature dependence are governed by spin-orbit scattering of electrons by thermal vibrations and by inhomogeneities in the nature of the forces of interaction at the metal-matrix interfaces.

We have attempted to fit our data by using the equations of Khaliullin and Khusainov for each of the three models of level-statistics (orthogonal, symplectic, uncorrelated) and all the possible particle diameters [14]. No satisfactory fit could be obtained with these

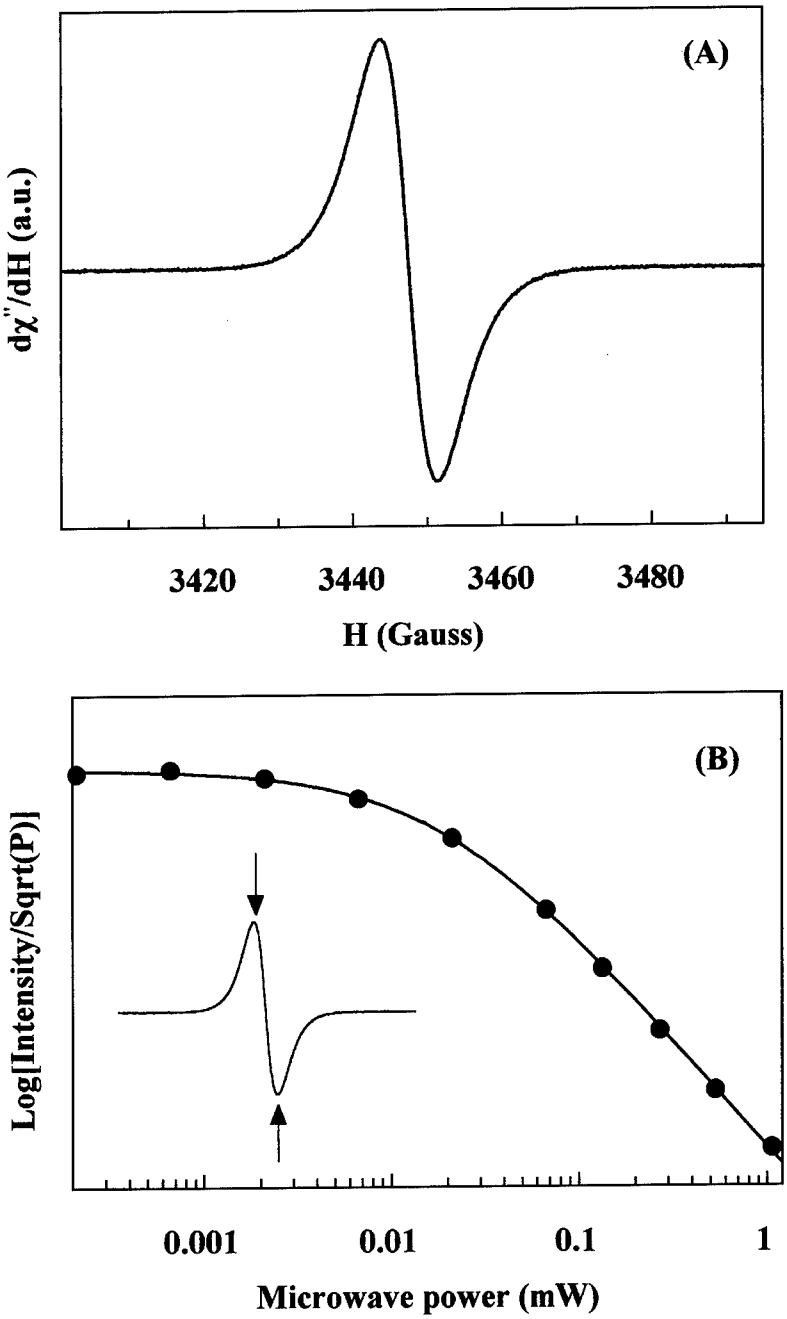

Figure 2. (A) CW X-band EPR spectrum of the sample $Ag \cdot 12SiO_2$ (13 wt% Ag) with the thermal treatment: 1h O_2 500°C, 2h H_2 500°C. Experimental conditions: temperature, 10 K; microwave frequency, 9.66 GHz; microwave power, 134 μW; modulation frequency, 1.6 kHz; modulation amplitude, 1.5 G. (B) Progressive microwave saturation for the same sample at 10 K. The solid line through the data points is the fit using the equation $I(P) = (1 + P/P_{1/2})^{-b/2}$, where P is the microwave power; for parameter values see text.

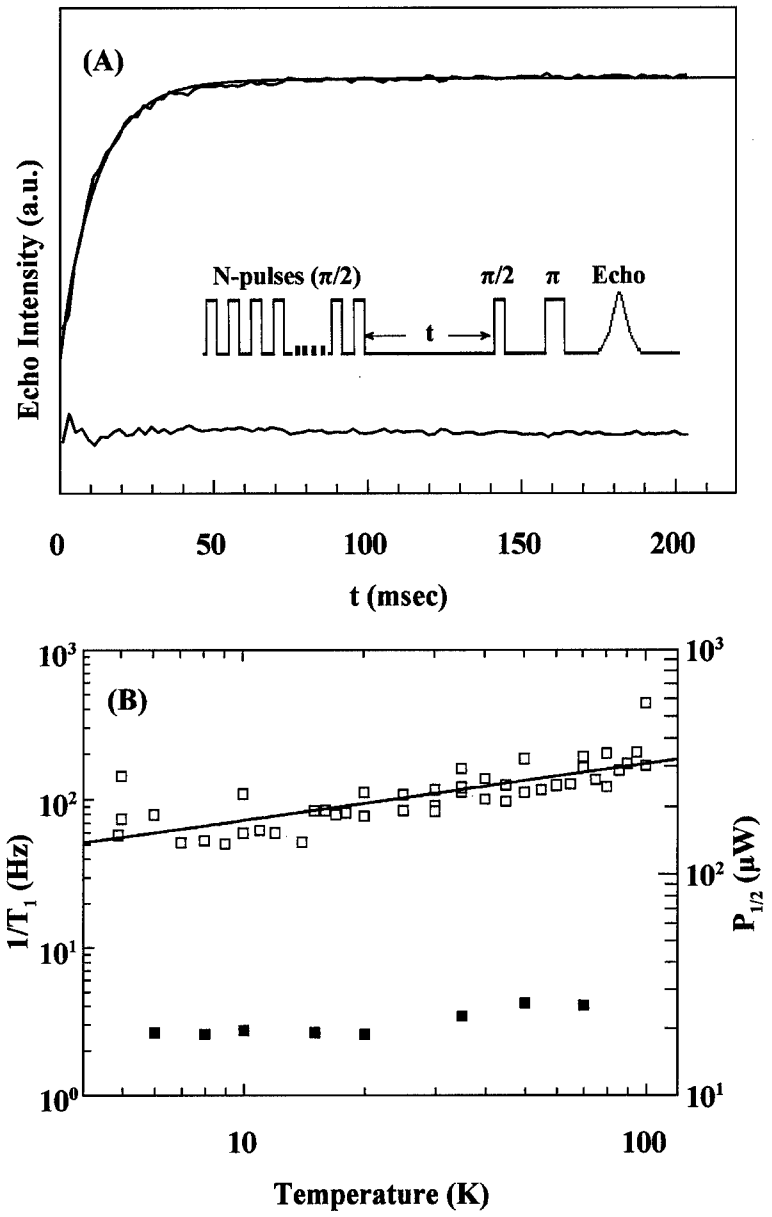

Figure 3. (A) Saturation recovery transient observed for the sample $Ag \cdot 12SiO_2$ (13 wt% Ag) with the thermal treatment: 1h O_2 500°C, 2h H_2 500°C. The single exponential fit is superimposed; the difference between the experimental and the fitted curve is shown at the bottom. The two-pulse echo intensity ($\pi/2 - 160$ ns $-\pi$, with $t_{\pi/2} = 16$ ns), was recorded after a sequence of $N = 30$ saturating pulses with interpulse separation of 0.5 μs. Experimental conditions: Temperature, 15 K; magnetic field strength, 3451 G; microwave frequency, 9.63 GHz. (B) Open squares: Temperature dependence of the spin-lattice relaxation rate for the same sample. The solid line show power-law fit to the experimental data ($1/T_1 \approx 25.9T^{0.4\pm0.1}$). Filled squares: Temperature dependence of the values of $P_{1/2}$.

equations and thus we conclude that the mechanisms suggested in [14] are not applicable in our system.

This analysis shows that the spin-lattice relaxation in metallic nanoparticles is not thoroughly understood at present. However, factors such as the particle diameters and the matrix might play important roles in the spin-lattice relaxation and experiments for the elucidation of their roles are presently in progress.

Acknowledgments

We thank EIIET II 296 for funding.

References

1. G.C. Bond, Surf. Sci. **156**, 966 (1985).
2. R. Kubo, J. Phys. Soc. Jpn. **17**, 975 (1962).
3. L.P. Gor'kov and G.M. Eliashberg, Sov. Phys. JETP **21**, 940 (1965).
4. K.B. Efetov, Sov. Phys. JETP **56**, 467 (1982).
5. B. Breitscheidel, J. Zieder, and U. Schubert, Chemistry of Materials **3**, 599 (1991).
6. U. Schubert, B. Breitscheidel, H. Buhler, C.C. Egger, and W. Urbaniak, Mat. Res. Soc. Symp. Proc. **271**, 621 (1992).
7. Y. Deligiannakis, A. Boussac, and W.A. Rutherford, Biochemistry **34**, 16030 (1995).
8. R.L. Dalton, L.A. Kwiram, and A.L. Cowen, Chem. Phys. Lett. **17**, 495 (1972).
9. F.W. Beck, B.J. Innes, and W.G. Brudvig, in *Current Research in Photosynthesis,* edited by M. Baltscheffsky (Kluwer Academic Publishers, Dordrecht, The Netherlands, 1990), p. 817.
10. C.G. Granqvist and R.A. Burhman, J. Appl. Phys. **47**, 2200 (1976).
11. C.P. Poole, *Electron Spin Resonance. A Comprehensive Treatise on Experimental Techniques* (Wiley, New York, 1983).
12. M.K. Bowman and L. Kevan, in *Time Domain Electron Spin Resonance*, chap. 3: *Electron Spin-Lattice Relaxation in Nonionic Solids*, edited by L. Kevan and R.N. Schwartz (Wiley, New York, 1979), p. 80.
13. V.A. Zhikarev, A.P. Staroverov, Yu.I. Talanov, F.G. Cherkasov, and S.F. Chernov, Sov. Phys. Solid State **29**, 981 (1987).
14. G.G. Khaliullin and M.G. Khusainov, Sov. Phys. JETP **67**, 524 (1988).

Journal of Sol-Gel Science and Technology 13, 509–516 (1998)
© 1998 Kluwer Academic Publishers. Manufactured in The Netherlands.

Development of the SC-RTA Process for Fabrication of Sol-Gel Based Silica-on-Silicon Integrated Optic Components

R.R.A. SYMS, A.S. HOLMES, W. HUANG, V.M. SCHNEIDER AND M. GREEN
Optical and Semiconductor Devices Section, Dept. of Electrical and Electronic Engineering, Imperial College, Exhibition Road, London SW7 2BT, UK

Abstract. The SC-RTA process for fabricating silica-on-silicon PLCs from sol-gel glass is described. A wide range of glasses has been deposited, process temperatures have been reduced, and components fabricated by reactive ion etching, reflow and burial of channel guides have shown steadily decreasing loss. Propagation losses are $\approx$0.2 dB/cm at $\lambda = 1.523$ μm in a high Δn system. Passive components demonstrated include tree-structured power splitters and thermo-optic switches.

Keywords: sol-gel glass, silica-on-silicon, integrated optics, planar lightwave circuit

1. Introduction

Several processes have been developed for depositing the thick silicate glass layers used in silica-on-silicon integrated optics, the most promising system for low-cost planar lightwave circuits (PLCs). The most advanced are flame hydrolysis (FHD) [1], chemical vapor (CVD) [2] and plasma-enhanced chemical vapor deposition (PECVD) [3].

The search for suitable glasses has paralleled work on silica-based fibers. In these, loss is dominated by Rayleigh scattering at short wavelengths, O—H absorption at near-infrared wavelengths and absorption from the vibrational bands of the dopants at long wavelengths. Scattering is minimized by avoiding dopants prone to crystallization (particularly, TiO_2); OH^- contamination by dehydration, and IR absorption by adopting the dopant whose band is furthest in the infrared, GeO_2.

O—H absorption occurs in PLCs, but can be removed by annealing. Other losses include coupling loss, substrate loss, scattering from core walls and bend loss. Low-loss coupling to single-mode fibers is only obtained with large (6–8 μm square) and weakly confining ($\Delta n/n = 0.25$–0.75%) cores. Minimization of substrate loss requires a thick buffer layer (20 μm in low Δn systems). Sidewall scattering is reduced by reflowing the core; this requires the core glass melting point to be lowered, e.g., by addition of P_2O_5. However, the P_2O_5 concentration is limited, and further temperature reduction requires addition of B_2O_3. Bend loss is reduced using smaller, more strongly confining cores. TiO_2, GeO_2 and As_2O_3 all allow a large index change. The best composition is unclear, but GeO_2-B_2O_3-P_2O_5-SiO_2 gives excellent results in FHD [1].

The sol-gel process is an alternative method of depositing glassy films, based on the hydrolysis and polycondensation of alkoxides. Three stages are involved: formation of a particulate suspension (a sol), processing to form a solid network permeated by liquid (a gel), and drying to form a porous glass. For silica, the overall reaction is $Si(OR)_4 + 2H_2O \rightarrow SiO_2 + 4ROH$, where "R" denotes an alkyl group. This reaction proceeds in steps. The alkoxide is first hydrolyzed, so that several OR groups are replaced by OH. Mixing the alkoxide with a quarter of the stoichiometric ratio of water and refluxing with a catalyst (e.g., HCl) will replace on average one group; repeating the process replaces two. These reactions may be slowed by dilution with solvent. When some groups have been hydrolyzed, polymerization can take place. The by-product is water, which causes further hydrolysis and

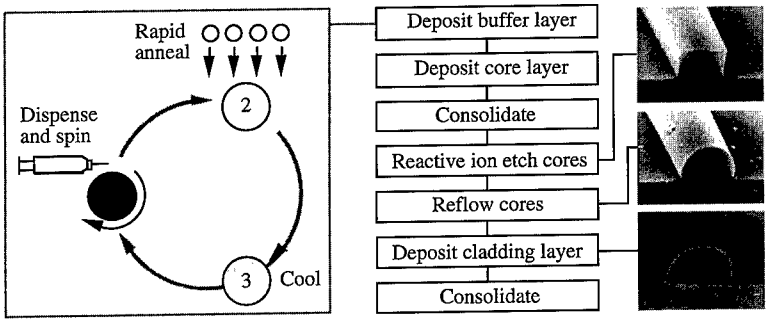

Figure 1. SC-RTA process for channel guide silica-on-silicon PLC fabrication.

polymerization. This reaction can also be slowed by dilution; however, when the sol is coated onto a substrate, the solvent is driven off, causing gelation. The gel is then baked to form a glass.

Sol-gel films have been used in antireflection coatings [4]. Planar waveguides have also been formed from sol-gel glass on SiO_2 substrates [5]. Porous material has been used as a host for sensing dyes [6], optically nonlinear organic [7] and semiconductor [8] materials, and rare-earth [9, 10] dopants. Channel guides have also been fabricated from planar layers by CO_2 laser irradiation [11] and by cross-linking an embedded photopolymer [12].

In sol-gel films, shrinkage often causes cracking when the thickness exceeds a few μm, especially on Si substrates. Cracking is avoided in thick (>30 μm) films using repetitive spin-coating and rapid thermal annealing (SC-RTA) [13]. These films have been formed into channel guide PLCs by the conventional topographic method. Figure 1 shows the process. A thick buffer of doped silica is first deposited, followed by a thinner layer of higher index material to act as the guide. These films are built up as multilayers. At each iteration, the wafer is spin-coated, heated by a rapid thermal annealer, and cooled. The bilayer is then consolidated. The cores are etched and reflowed; further spin-coating is used to bury them, and the cladding is consolidated. This paper describes the evolution of the process, and demonstrates the performance obtained using optimized materials.

2. Sol Preparation, Film Deposition and Glass Properties

Work has mainly been performed on proprietary sols, including silica-titania, and phosphosilicate, borosilicate, borophosphosilicate and germanophosphosilicate glass (PSG, BSG, BPSG and GPSG). The number of components has slowly been increased to optimize different glass properties.

Alkoxide precursors are used as sources of SiO_2, TiO_2 and GeO_2. Suitable Si alkoxides include silicon ethoxide (TEOS), silicon methoxide and methyl triethoxysilane; in our work, we have used TEOS. Ti alkoxides include titanium ethoxide, isopropoxide (TPOT) and butoxide; we have used TPOT. For GeO_2, we have used germanium ethoxide (TEOG) [14]. Trialkyl borates are suitable precursors for B_2O_3, while P_2O_5 can be derived from trialkyl phosphites and phosphates. However, we have used the alternative of oxide solutions in alcohol [15].

Sols are prepared using a two-step acid-catalyzed hydrolysis [6]. TEOS is first dissolved in alcohol. An HCl solution is added to achieve a water : alkoxide molar ratio of unity ($R = 1$), and the alkoxide is refluxed at 70°C for 2 hours. A similar mixture containing the primary dopant precursor is then added, together with sufficient HCl to take the water : alkoxide ratio to $R = 2$, and the solution refluxed again. An alcohol mixture containing the secondary dopant (if required) is then added. Since these solutions are often highly reactive, no further catalyst is used. For example, in a recent process for GPSG the primary dopant was P_2O_5 in IPA, and the secondary dopant a TEOG solution. The latter was so reactive that the sol required dehydration using a molecular sieve before its addition [16].

Films are deposited by spin-coating for 40 s, and heated for 10 s in O_2. The single-layer thickness t_f is determined by the spin speed ω and the sol viscosity, typically following the variation $t_f \approx k(1 - v_a)\omega^{-\gamma}$, where k is a constant, v_a is the volume fraction of solvent and $\gamma \approx 0.5$. Multilayers are built up from films with thicknesses of 2500 to 5000 Å. Below this range, the number of layers is excessive, while above it, beading of the wafer rim occurs. Good thickness

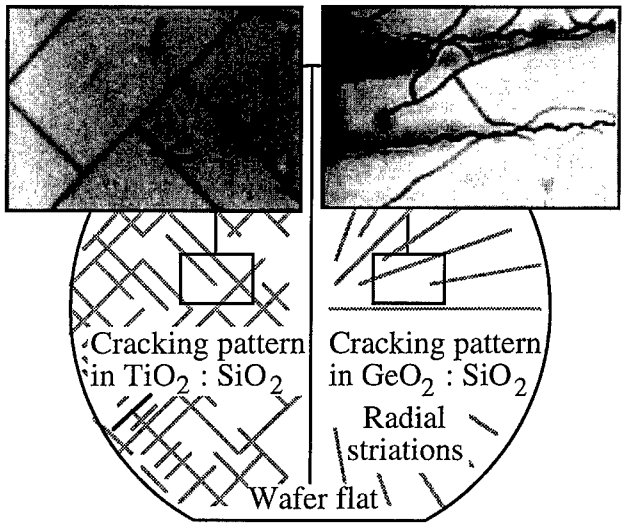

Figure 2. Cracking patterns in silica-titania (LHS) and germanosilicate glass on (100) Si.

uniformity is obtained, but there is a slow radial thickness variation and a faster angular variation due to striations [13].

Even thin (≈ 2 μm) films on Si tend to crack, due to tensile stress. For (100) wafers, the cracks are uniformly distributed and oriented at 45° to the intersection of {1 1 1} planes with the surface, as in the LHS of Fig. 2. Since the stress generally becomes compressive as the anneal temperature rises, it can be made compressive during annealing itself by careful control of the RTA temperature [17].

The stress at room temperature (σ_f) can be found from the wafer curvature, and the stress during annealing (σ_i) estimated from the mismatch in expansion coefficient between glass and substrate. Figure 3 shows the variation of σ_f and σ_i with anneal temperature T_A for a silica-titania glass [17]. σ_f is tensile below a critical temperature $T_{AC} \approx 1000$°C. Above this, it is compressive. However, σ_i is still tensile until $T_{AC'} \approx 1075$°C. Near $T_{AC'}$, there is a dramatic rise in the thickness to failure. The thickness is then limited by other factors. Silica-titania films are limited to ≈ 15 μm

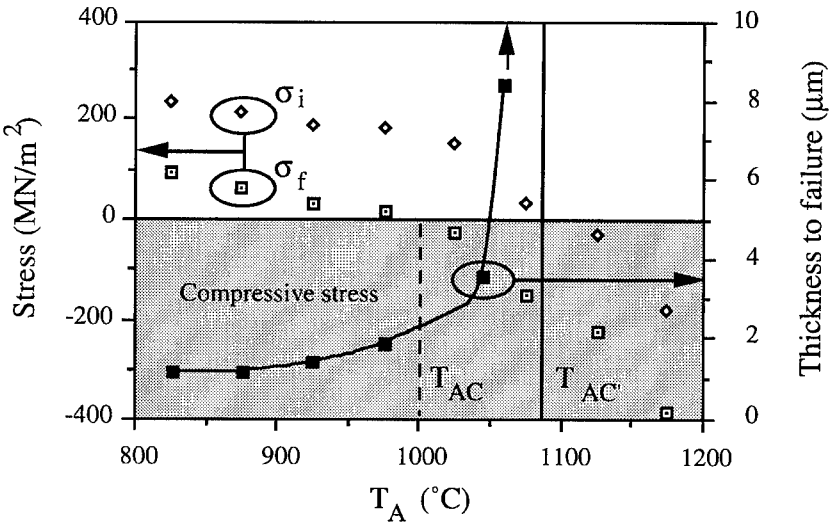

Figure 3. Variation of film stress, intrinsic stress and thickness with anneal temperature, for silica-titania.

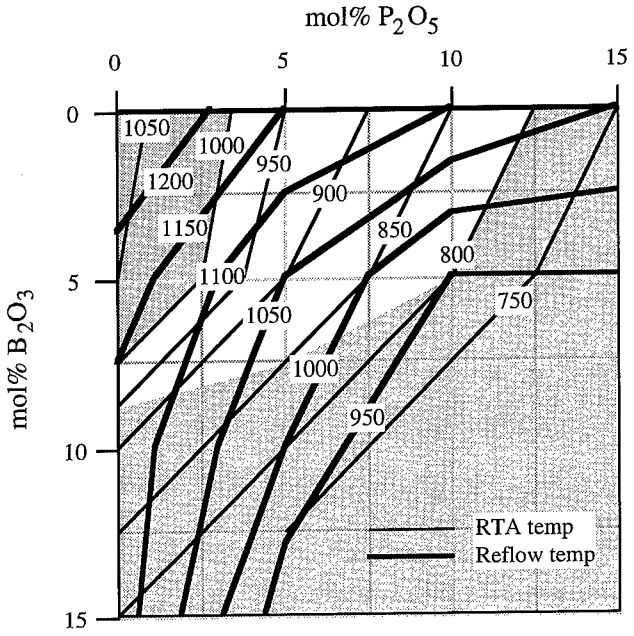

Figure 4. Variation of RTA and reflow temperature with composition, for the BPSG system.

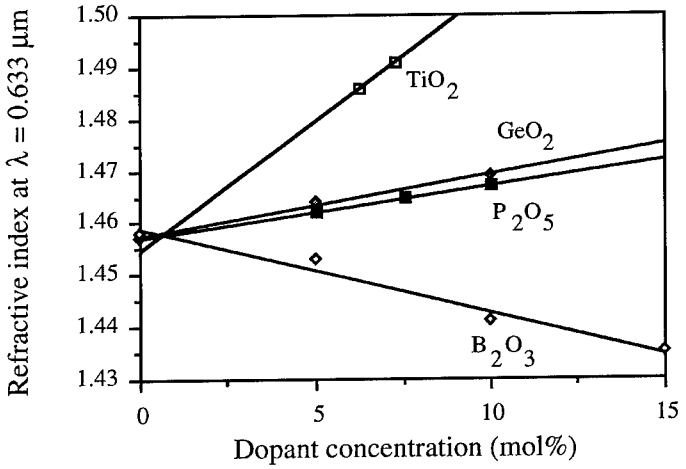

Figure 5. Variation of refractive index with composition for silica glass containing different dopants.

by the wafer distortion and lattice damage caused by cycling to ≈1100°C, which interferes with the formation of fiber alignment grooves by anisotropic etching.

P_2O_5 and B_2O_3 both lower the anneal temperature, allowing thicker (>30 μm) films to be made [18–20]. Figure 4 shows the anneal temperature for the BPSG system; a reduction of more than 300°C can be achieved by heavy doping. One explanation is that both dopants increase the expansion coefficient of SiO_2, reducing the thermal stress. Dopant concentrations are limited, however. Heavily-doped PSG is hygroscopic, and the maximum practical P_2O_5 content is ≈10 mol% [20]. Films containing more than 10 mol% B_2O_3 often appear milky after spin-coating, possibly due to the formation of polycrystalline B_2O_3. Films containing a high level of B_2O_3 and P_2O_5 can also become opaque at high temperatures. The optimum compositional range is the clear area in Fig. 4.

Additional annealing causes a gradual decrease in thickness and porosity, coupled with changes in stress [17]. Further processing is therefore required for consistent properties. Consolidation in a tube furnace

eliminates residual porosity, and forces the thickness and stress to stable values.

For waveguides, appropriate refractive index differences must be established between core and cladding. Figure 5 shows the variation of index with concentration for different dopants. TiO_2 and P_2O_3 increase the index, while B_2O_3 decreases it. GeO_2 also raises the index. Unfortunately, we have been unable to form thick films of pure germanosilicate glass, since the rapid reaction of TEOG causes uneven gelation and cracking. In contrast to silica-titania, the cracks are sinusoidal, and follow the radial striations as on the RHS of Fig. 2. This cracking mode can be controlled using P_2O_5 [16].

Channel guide cores are fabricated by reactive ion etching in a Plasma Technology RIE 80 using CHF_3, Ar and O_2, with a Cr mask. Silica-titania cores can be etched with almost vertical sidewalls [13]; however, some undercut occurs with PSG [18]. Generally, modest RF power (140 W) and pressure (50 mTorr) are used, but high power and low pressure are needed to avoid micromasking in glasses forming involatile by-products (e.g., GeO_2-SiO_2) [16].

Compositions are chosen so that cores can be reflowed without melting the buffer. Because TiO_2 has little effect on the viscosity of SiO_2, the reflow temperature of silica-titania is very high (1260°C), and core and cladding melt together. Furthermore, silica-titania crystallizes at high temperatures. However, P_2O_5 and B_2O_3 lower the melt temperature. Figure 4 shows data for the BPSG system, for a 5 minute reflow in O_2. Temperatures of 950°C can be achieved by heavy doping [20].

3. Passive Channel Waveguides and Devices

For low fiber-device-fiber insertion loss at near-IR wavelengths, all sources of loss must be systematically reduced. Low scatter requires avoidance of crystallization, and the ability to control melt temperature. Low absorption requires elimination of OH^- contamination. Low substrate loss requires a thick buffer (in turn needing low anneal temperatures) and a high core-cladding index difference Δn, so that the guided mode is well confined and spaced away from the substrate. High Δn is also needed for low bend loss. Low coupling loss actually requires low Δn; however, waveguide tapers may overcome this conflict. Low substrate damage is a prerequisite for V-groove etching.

Channel guides have been constructed from (1) silica-titania [13], (2) PSG [18], (3) BPSG [19, 20] and (4) GeO_2-B_2O_3-P_2O_5-SiO_2 (GBPSG) [16]. In each case, a core width of 7 μm was used; however, the layer thicknesses differ from system to system, typically being the largest practical. In the last two systems, different compositions have been used for all three glass layers; most recently, PSG has been used for the buffer, GPSG for the core, and BPSG for the cladding. Steadily improving optical performance has been obtained.

Losses are highest in silica-titania, with a significant differential between the TE and TM modes. The main loss is substrate absorption, due to the restriction on buffer thickness caused by the high RTA temperature. However, other losses are significant. Figure 6 shows a spectral loss variation for 3.5 cm length of

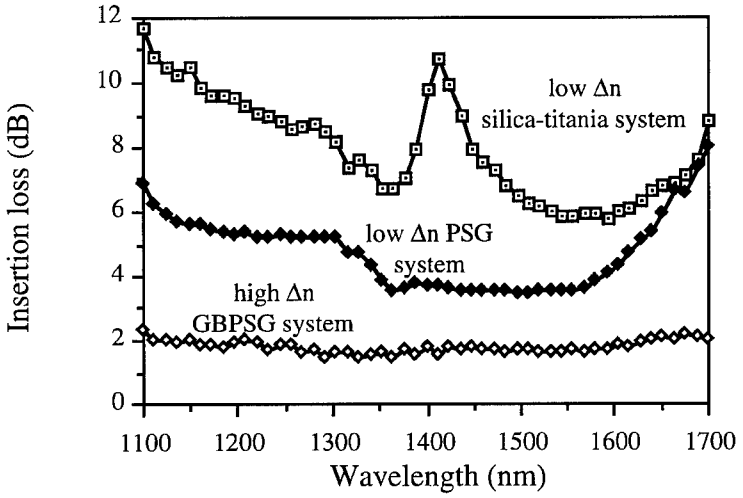

Figure 6. Spectral loss variation of guides formed in silica-titania, PSG and GBPSG.

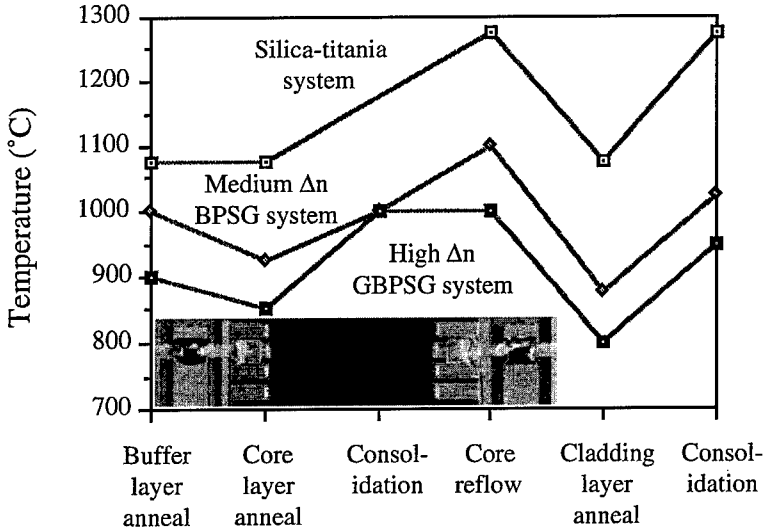

Figure 7. Process temperatures of guides formed in silica-titania, PSG and GBPSG.

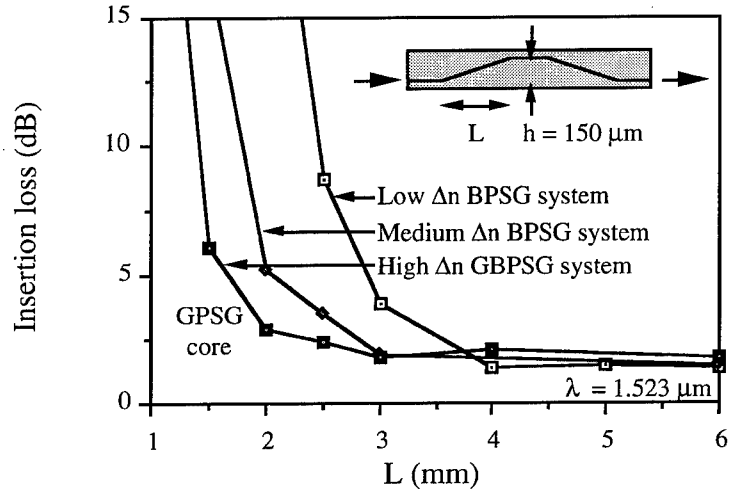

Figure 8. Variation of insertion loss with transition length for back-to-back S-bends with low and medium Δn cores formed in BPSG, and high Δn cores formed in GBPSG.

silica-titania guide [16]. The increase in loss at long wavelengths is due to substrate absorption, while the rise at short wavelengths is caused by scattering following from incomplete reflow. There is also significant O—H absorption near $\lambda = 1.39\ \mu$m.

In PSG, substrate and scattering losses are reduced due to the increased layer thickness allowed by a reduced RTA temperature, and due to improved reflow. Figure 6 shows a further advantage: there is no O—H absorption. One explanation is that excess water is retained in volatile phosphorus compounds, and driven off during the RTA step.

These characteristics are retained in BPSG, but substrate and scattering losses are reduced further because of temperature reductions. Polarization-independent losses of 0.2 dB/cm at 1.525 μm were obtained using this system [19]. However, the usefulness of both PSG and BPSG is limited by the small Δn achievable (due to restrictions on the doping level) and by deformation of the core during cladding. For higher performance, B_2O_3 and P_2O_5 must be relegated to controlling process temperatures, and a further dopant introduced to control the index. GeO_2 is the optimum candidate, since it avoids the problems associated with TiO_2.

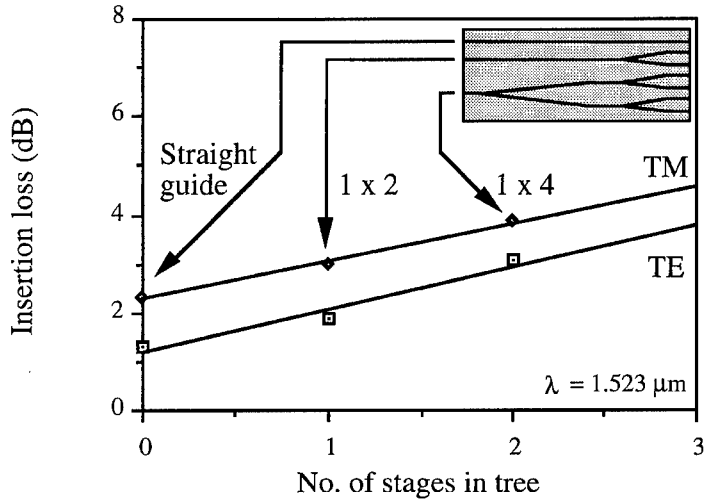

Figure 9. Variation of insertion loss with number of stages for tree-structured splitters with low Δn cores formed in BPSG.

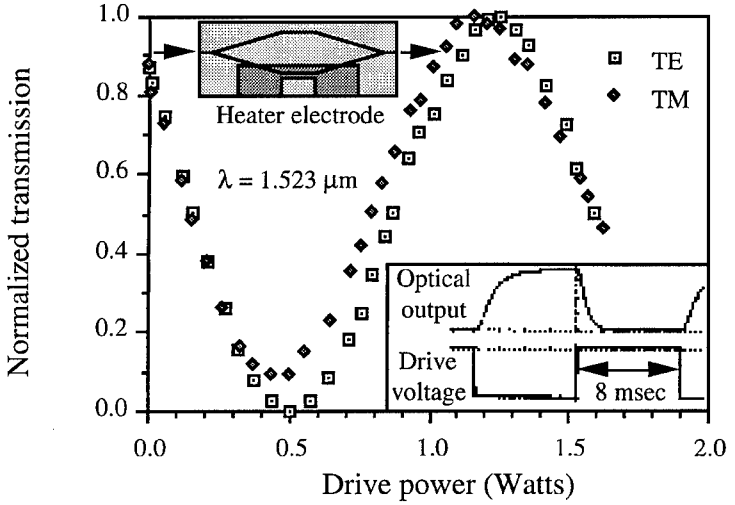

Figure 10. Transmission and switching characteristics of a thermo-optic Mach-Zehnder interferometer with medium Δn cores formed in BPSG.

Figure 6 shows the low, spectrally flat and polarization-independent performance obtained with GBPSG [16].

Figure 7 compares the temperatures used in the fabrication of silica-titania, BPSG and GBPSG PLCs, showing the reduction in temperature accompanying this improvement in performance. Low process temperatures also allow fabrication of integrated fiber alignment grooves by anisotropic etching. Figure 7 shows a packaged PLC formed in PSG with an 8-core single-mode ribbon fiber pigtail at each end. Using passive alignment, coupling losses were 1.3 dB/facet at $\lambda = 1.523$ μm.

The achievable Δn has great influence on bend losses. Figure 8 compares the loss of back-to-back sinusoidal S-bends in low and medium Δn BPSG systems and a high Δn GBPSG system. Shorter transitions, with smaller bend radii, can be achieved in the high Δn system. Limited work has been performed on passive components. Figure 9 shows the insertion loss of Y-junction based tree-structured power splitters. Although these were formed in low Δn BPSG, excess losses below 4 dB were obtained for 1 × 4 splitters. Similarly, Fig. 10 shows the performance of a Y-junction based Mach-Zehnder interferometer in medium Δn BPSG.

Switching is obtained by the thermo-optic effect, and a thick cladding is required to isolate the guided mode from the Ti heater electrode. A TE mode insertion loss of 3.5 dB was achieved for a length of 3.4 cm. Switching times of 2–4 ms were achieved using 0.5 W drive power [20].

4. Conclusions

Sol-gel glasses used to form silica-on-silicon PLCs by SC-RTA have been compared. Each material has shown significant improvement over its predecessor, and the main losses have been identified and eliminated. GBPSG allows low, polarization-independent and spectrally flat propagation loss to be combined with low bend loss. Improving performance has been accompanied by reduced process temperature. The most significant problem remaining is low process yield, caused by glass flakes originating from the wafer rim. Automated equipment is now needed to make SC-RTA competitive with FHD, CVD and PECVD.

References

1. M. Kawachi, IEE Proc. (Optoelectronics) **143**, 257 (1996).
2. Y.P. Li and C.H. Henry, IEE Proc. (Optoelectronics) **143**, 263 (1996).
3. S. Valette et al., Sensors and Actuators **A21**, 1087 (1990).
4. B.E. Yoldas and T.W. O'Keefe, Appl. Opt. **18**, 3133 (1979).
5. P.P. Herrmann and D. Wildmann, IEEE J. Quant. Elect. **QE-19**, 1735 (1983).
6. A. Martin and M. Green, Proc. SPIE **1328**, 352 (1990).
7. J-L.R. Noguès and M.V. Moreshead, J. Non-Cryst. Solids **121**, 136 (1990).
8. M.A. Fardad et al., IEE Proc. (Optoelectronics) **143**, 298 (1996).
9. D. Barbier, R. Almeida, and X. Orignac, *8th World Ceramics Cong.* (Florence, paper SVII-1 LO4, 1994).
10. X. Orignac and R.M. Almeida, "Silica-based sol-gel optical waveguides on silicon," IEE Proc. (Optoelectronics) **143**, 287 (1996).
11. M. Guglielmi, P. Colombo, L.M.D. Esposiți, G.C. Righini, and S. Pelli, Proc. SPIE **1513**, 44 (1990).
12. C.-Y. Li, J. Chisham, M. Andrews, S.I. Najafi, J.D. Mackenzie, and N. Peyghambarian, Elect. Lett. **31**, 271 (1995).
13. A.S. Holmes, R.R.A. Syms, Ming Li, and M. Green, Appl. Opt. **32**, 4916 (1993).
14. T.N.M. Bernards, M.J. van Bommel, E.W.J.L. Oomen, and A.H. Boonstra, J. Non-Cryst. Solids **147**, 13 (1992).
15. P.N. Kumta and M.A. Sriram, J. Mat. Sci. **A28**, 1097 (1993).
16. R.R.A. Syms, V.M. Schneider, W. Huang, and M.M. Ahmad, Elect. Lett. **33**, 1216–1217 (1997).
17. R.R.A. Syms and A.S. Holmes, J. Non-Cryst. Solids **170**, 223 (1994).
18. A.S. Holmes and R.R.A. Syms, *8th World Ceramics Cong.* (Florence, paper SVII-1 LO9, 1994).
19. R.R.A. Syms, V.M. Schneider, W. Huang, and A.S. Holmes, Elect. Lett. **31**, 1833 (1995).
20. R.R.A. Syms, W. Huang, and V.M. Schneider, Elect. Lett. **32**, 1233 (1996).

Journal of Sol-Gel Science and Technology 13, 517–521 (1998)
© 1998 Kluwer Academic Publishers. Manufactured in The Netherlands.

Strip-Loaded High-Confinement Waveguides for Photonic Applications

E.M. YEATMAN, K. PITA AND M.M. AHMAD
Department of Electrical and Electronic Engineering, Imperial College, London SW7 2BT, UK

A. VANNUCCI AND A. FIORELLO
Alenia, Via Tiburtina Km 12.4, 00131 Roma, Italy

Abstract. Sol-gel is a promising deposition technique for the fabrication of silica-on-silicon photonic components. Silica-titania compositions provide large index differences, and thus strong mode confinement, and are suitable hosts for Er-doped optical amplifiers. We have developed channel waveguides based on phosphosilicate strip loads over high index titania-doped guiding layers. Here we demonstrate that low propagation loss (0.3 dB/cm) can be obtained in such guides at optical communication wavelengths. Alumina co-doped guiding layers are shown to inhibit OH retention without causing titania segregation, and reduced humidity during spinning is shown to be necessary to achieve low propagation losses.

Keywords: integrated optics, silica-on-silicon, spin coating, silica-titania

1. Introduction

The use of sol-gel for fabrication of optical waveguides has attracted wide attention, much of which has focused on planar (slab) waveguides for use at visible wavelengths, where the requirements on performance and geometry are generally modest. Sol-gel integrated optics is also beginning to show potential for application in optical communications [1]; here, requirements include multi-micron thicknesses, and high transparency at near-infrared wavelengths, where residual organic or hydroxyl content may contribute excessively to propagation losses.

The sol-gel fabrication of buried channel waveguides was demonstrated by Holmes et al. [2] using SiO_2-TiO_2 glass deposited by an iterative spin coating/rapid thermal annealing (RTA) process. Guiding layers were deposited above lower index buffer layers, and formed into ridges using reactive ion etching (RIE). These ridges were buried by a lower index cladding material. Using high temperature reflow of the cores before burial, to improve shape and reduce surface roughness, this system was improved to give losses of 1.5 and 6 dB/cm for TE and TM propagation, respectively [3]. Other authors have reported low loss SiO_2-TiO_2 waveguides [4], but these have been planar, of modest thickness (<1.5 μm), and measured at visible wavelength. The buried channel technology has been adapted to other materials; losses have been reduced to 0.2 dB/cm (TE and TM) for borophosphosilicate compositions [5], and the index difference Δn increased to 1% using germania doping [6].

Silica-titania remains attractive, however, offering very large Δn and good spectroscopic potential for use in optical amplifiers [7]. Low loss channel waveguides have been reported using SiO_2-TiO_2 cores by Hitachi Cable [8]; the deposition technique for these materials was reported elsewhere as electron beam evaporation. Our aim was therefore to develop a sol-gel process for fabricating channel waveguides with SiO_2-TiO_2 guiding layers, having low, polarization-independent losses (<0.5 dB/cm) at 1.5 μm wavelength.

Silica-on-silicon is a very attractive format for photonic components, and is the basis for this work, as well as [3, 5, 6]. However, the high refractive index of Si means that a thick buffer layer is necessary to prevent leakage of the guided mode into the substrate. Since TM reflectivities are lower than TE below

the critical angle, polarization dependence of loss is a strong indication of insufficient buffer thickness. If the buffer material is SiO_2 or lightly doped SiO_2-TiO_2, the process temperatures required for multi-micron deposition, using the method of [2], are sufficiently high that progressive substrate damage occurs with each deposition cycle, limiting the maximum film thickness.

The materials in which the guided light propagates must avoid scattering losses and absorption mechanisms in the wavelength range of interest. Scattering may result from phase separation of the glass, crystallization, or residual porosity. For near-IR wavelengths a likely cause of absorption is the presence of water or hydroxyl groups. Roughness in the core-cladding interface will also contribute to scattering.

2. Fabrication Processes and Results

Titania in a silica matrix tends to crystallize to anatase or rutile at high temperatures, the tendency increasing with concentration. This is particularly likely during core reflow. Achieving sufficient surface quality during reactive ion etching to eliminate the need for reflow is difficult with this material, as Ti produces etch products with low volatility, which tend to redeposit and cause micro-masking. We therefore adopted a strip-loaded geometry, as shown in Fig. 1. Here the guiding layer is not etched; the waveguides are defined by etching the cladding layer to form guiding strips.

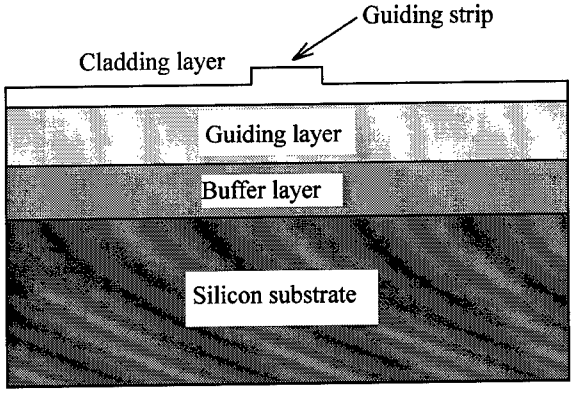

Figure 1. Geometry of strip loaded waveguides.

The process temperature of the buffer and cladding layers should be sufficiently low to avoid wafer damage and crystallization in the guiding layer. Initial tests were carried out using pure SiO_2 for these layers, and high losses were obtained (>1 dB/cm at 1310 nm), with a strong peak in the loss spectrum at 1400 nm indicating OH contamination. This may result from atmospheric water being absorbed into residual pores. Phosphosilicate glass was then adopted, with the molar composition $90SiO_2 : 10PO_{2.5}$, prepared as in [9]. The SiO_2-TiO_2 layers were prepared as in [2]. All sols were prepared by acid catalysis. A set of multilayer samples was fabricated as listed in Table 1 (IC50–IC55), using guiding layers with molar composition $90SiO_2 : 10TiO_2$.

Table 1. Passive waveguides: loss vs. fabrication parameters.

Sample No.	IC50	IC51	IC52	IC53	IC54	IC55	IC70	IC82
Buffer layer								
Thickness (μm)	5	5	3	3	5	5	>6	>6
Post heat treatment (°C)	—	—	—	—	1150	1150	1175	1150
Guiding layer								
Composition	A	A	A	A	A	A	B	B
Thickness (μm)	~2	~2	~2	~2	~2	~2	~2	~2
RH (%) during spinning	38	38	38	38	34	<11	40–50	25–27
Post heat treatment (°C)	—	—	—	—	—	—	—	1100
Cladding								
Thickness (μm)	~1	~1	~1	~1	~1	~1	~1.2	~1.2
Final heat treatment (°C)	1150	1050	950	1050	1050	1050	—	1100
Propagation loss (dB/cm)	1.96	0.65	1.84	1.82	0.74	0.43	2.0	0.3

Guiding layer composition A is 90Si10Ti, and B is 93Si7Ti10Al. All post heat treatments were 1 minute in RTA, except the buffer layer of IC70 (20 minutes in silica tube furnace).

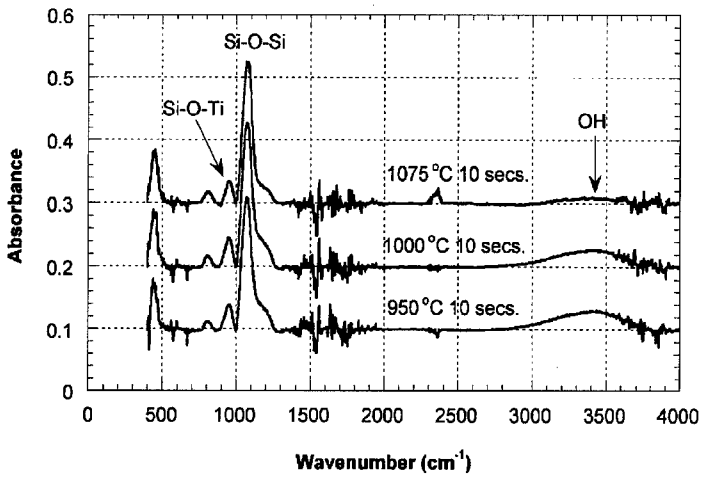

Figure 2. FTIR spectra of 93Si7Ti films annealed at various temperature for 10 s in RTA.

Waveguides were defined by standard photolithography (contact) using polymethylmethacrylate (PMMA) resist. Al was then deposited by electron beam evaporation and patterned by lift-off. This metallization formed the mask for RIE in a $CHF_3/CF_4/O_2/Ar$ mixture, after which it was removed.

Insertion losses in Table 1 were measured at 1550 nm wavelength. Mode profiles were measured at the waveguide exit, and used to calculate coupling losses, allowing propagation loss to be determined. Coupling loss to single mode fibre was typically about 3 dB per facet; this indicates that for practical use some mode tapering structure or coupling optics will be necessary.

A 3 μm buffer thickness is insufficient, as indicated by high losses for samples IC52 and IC53, for which the TM losses were approximately twice as high; for the others there was no significant polarization dependence. The higher loss of IC50 over IC51 suggests that 1150°C is sufficient to induce crystallization for this composition. For this reason, TiO_2 concentration was reduced to 7%.

No peak in the spectral loss was seen in these waveguides. Figure 2 shows the evolution of FTIR (Fourier transform infrared) spectra with heat treatment for $93SiO_2 : 7TiO_2$. The OH peak is reduced, but not completely even after 1075°C. We estimate the sensitivity

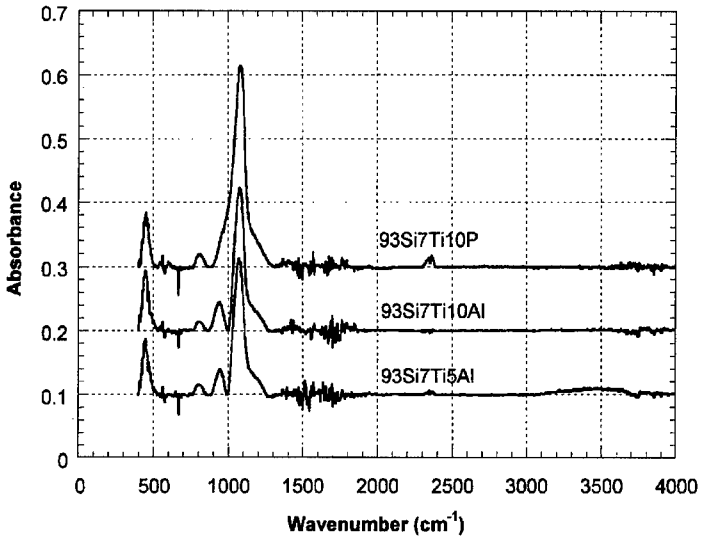

Figure 3. FTIR spectra of various film compositions annealed at 950°C for 10 s in RTA.

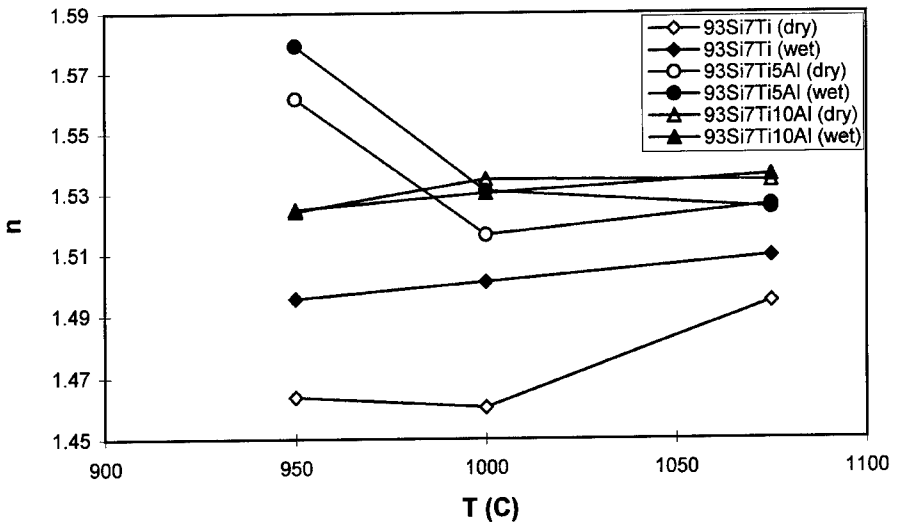

Figure 4. Refractive index of various compositions measured under dry and wet atmospheres as a function of annealing temperature.

of the FTIR measurements to OH to be higher than for the loss spectra, at about 100 ppm.

The guiding layers are intended as a host for Er^{3+} ions for optical amplification, and our collaborators' work shows that co-doping of silica-titania with either P_2O_5 or Al_2O_3 gives improved fluorescence performance and high doping levels [7]. Figure 3 shows the effect of these co-dopants on the FTIR spectra. Both inhibit the retention of OH. With increasing P_2O_5 concentration, however, the Si—O—Ti peak is diminished, possibly because of segregation. Al and P were added to sols as $Al(NO_3)_3$ and P_2O_5 dissolved in ethanol.

Nanoporosity of films can be studied by measuring refractive index in wet and dry atmospheres [10]. In Fig. 4, the densification temperature (at which the wet and dry indices converge) is shown to decrease with increasing level of Al_2O_3. We believe that the higher

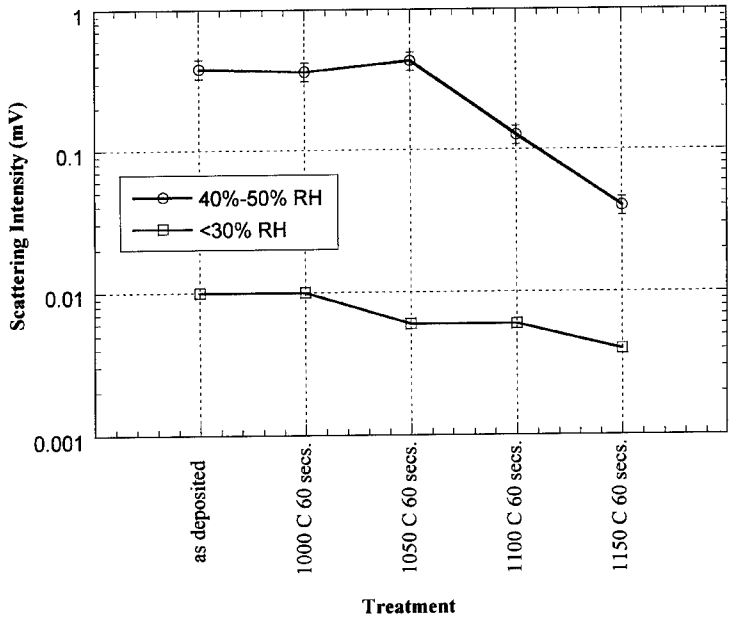

Figure 5. Variation of scattering intensity with heat treatment and relative humidity (RH) for the guiding layer (93Si7Ti10Al).

indices for 5% $AlO_{1.5}$ annealed at 950°C are anomalous, and result from polar effects of the hydroxylation of the pore surfaces. Films of $93SiO_2 : 7TiO_2 : 10AlO_{1.5}$ composition were inspected by Raman spectroscopy, and no crystallization was found for annealing (for 1 minute by RTA) up to and including 1150°C.

Sample IC55 indicates that reduced humidity during spinning may be important in improving homogeneity. This was studied for $93SiO_2 : 7TiO_2 : 10AlO_{1.5}$ by preparing films under normal and artificially reduced humidity, using an enclosed spinning chamber. The resulting films were observed by optical microscopy using dark field illumination, with the backscattered light measured by a photodetector on the camera port. The results are shown in Fig. 5. Although heat treatment can improve homogeneity, the importance of humidity is here strongly confirmed. For the phosphosilicate layers, we found that such humidity control was unnecessary; annealing for 1 minute at 1150°C was sufficient to remove visible inhomogeneity.

Finally, samples IC70 and IC82 were fabricated using the $93SiO_2 : 7TiO_2 : 10AlO_{1.5}$ composition for the guiding layer. Indices measured at 633 nm give a Δn for this system of 4.6%. The losses for IC70 were again high. IC82 combines all the knowledge gained on process requirements, including low humidity for guiding layer deposition, and densification of buffer and cladding layers. This gave losses of 0.3 dB/cm, well below the original target, with no strong polarization dependence.

3. Conclusions

We have shown that the silica-titania-alumina composition, previously shown to be a good spectroscopic host for Er-doping, can achieve low, polarization independent losses without reflow in strip-loaded channel waveguides. Important future goals are to improve the weak lateral confinement, and to devise mode tapering structures to allow low coupling loss to standard communication fibre.

Acknowledgment

We gratefully acknowledge support for this work by the European Commission under the project CAPITAL (ACTS AC047). We are grateful to Prof. Rui Almeida and Dr. Orlando Martin of INESC for providing the Raman measurements, and to Dr. Emma Dawnay for experimental assistance.

References

1. E.M. Yeatman, in *Sol-gel and Polymer Photonic Devices*, edited by S.I. Najafi and M. Andrews (SPIE Crit. Rev. Proc. **CR-68**, 1997), pp. 119–142.
2. A.S. Holmes, R.R.A. Syms, L. Ming, and M. Green, Appl. Opt. **32**, 4916 (1993).
3. R.R.A. Syms and A.S. Holmes, Phot. Tech. Lett. **5**, 107 (1993).
4. L. Yang, S.S. Saavedra, N.R. Armstrong, and J. Hayes, Anal. Chem. **66**, 1254 (1994).
5. R.R.A. Syms, V. Schneider, W. Huang, and A.S. Holmes, Electr. Lett. **31**, 1833 (1995).
6. R.R.A. Syms, V. Schneider, W. Huang, and M.M. Ahmad, Electr. Lett. **33** (1997).
7. R. A. Almeida, in *Sol-gel and Polymer Photonic Devices*, edited by S.I. Najafi and M. Andrews (SPIE Crit. Rev. Proc. **CR-68**, 1997), 172–191.
8. H. Uetsuka, T. Hakuta, H. Okano, N. Taketani, and T. Teraoka, IEICE Trans. Electron. **E80 C**, 134 (1997).
9. A.S. Holmes and R.R.A. Syms, in *Advances in Science and Technology 11:Advanced Materials in Optics, Electro-Optics and Communication Technologies*, edited by P. Vincenzini and G.C. Righini (Techna, 1995), p. 73.
10. E.M. Yeatman, Mino Green, E.J.C. Dawnay, M.A. Fardad, and F. Horowitz, J. Sol-Gel Sci. Tech. **2**, 711 (1994).

Journal of Sol-Gel Science and Technology 13, 523–527 (1998)
© 1998 Kluwer Academic Publishers. Manufactured in The Netherlands.

Photocurable Sol-Gel Coatings: Channel Waveguides for Use at 1.55 μm

P. ETIENNE
Laboratoire des Verres UMR No. 5587, Université de Montpellier II, Place Eugène Bataillon, 34095 Montpellier Cedex, France

P. COUDRAY, Y. MOREAU AND J. PORQUE
Centre d'Electronique et de Micro-optoélectronique de Montpellier, Université de Montpellier II, Place Eugène Bataillon, 34095 Montpellier Cedex, France

Abstract. The development and characterization of channel waveguides using wet-process, low temperature sol-gel chemistry is described. Two structures have been developed. The first one is a one-layer structure, composed of a sol-gel solution which is a mixture of photopolymerizable organosilicate and organozirconate precursors. The other is a multilayer structure with a buffer under the guide and a protective coating. The layers are deposited by the dipping technique. The devices are obtained by UV light exposure of the coating through a predefined mask (channel waveguides). The refractive index increase is sufficient enough to allow the use of waveguides in the 1.55 μm telecommunication window.

These waveguides are thick enough to reduce the coupling losses with an optical fiber below 0.5 dB. Also, because of our sandwich structure, the propagation losses are less than 0.1 dB.

Keywords: nanocomposite, sol-gel, photopolymerization, channel waveguides

1. Introduction

During the past few years, the fabrication of integrated optics devices using sol-gel precursors and photocurable polymers coatings has received an increasing amount of attention [1, 2]. Low cost and simplicity makes this process an attractive alternative to conventional technologies like ion exchange and plasma deposition [3]. These hybrid materials, made of organic, silica and zirconium precursors, are also good challengers in comparison to the more recent use of the sol-gel process alone [4].

The 3D surface waveguides are made in three steps [5]. First, the solution is coated on glass or silicon substrates and dried at a temperature, sufficient to stabilize the structure, but which allows photoreactive molecule movement. Secondly, the coating is cured through a mask by means of an UV light source. Finally, the coating structure is definitively frozen by a temperature treatment which ends the sol-gel polymerization. These waveguides are suitable for use at 1.55 μm wavelength.

However, many important problems still remain. First, as waveguide fabrication in a few minutes involves the UV light being close to the mask, waveguides are larger than the predefined mask aperture. Their refractive index is high compared to the refractive index of silica fiber. Moreover, UV penetration in the layer, limited to about 4 μm depth [6], does not allow waveguide fabrication with the same diameter as a single mode optical fiber. These two phenomena induce high coupling losses of about 5 dB [5].

The mechanical properties of the guiding layer are not good enough to avoid scratches during the mask installation or during manipulations and use. Moreover, the photocured areas inflate and then induce geometrical defects and propagation losses. Optical simulations demonstrate that channel-waveguide performances can

be enhanced by encapsulating the waveguide with a layer whose refractive index is close to the non-imprinted part of the guiding layer. That allows us to reduce the strong guiding effect due to the air cover and silicon substrate.

This paper deals with a dual approach. First, we modified the guiding layer precursors to improve waveguide definition by replacing the *Irgacure* 184 photoinitiator by the more effective *Irgacure* 1800 and reduced the basic refractive index by decreasing the zirconium concentration.

Then, we worked on a three-layer system. First, a buffer layer was deposited with the guiding layer solution without the photoinitiator. The refractive index was equal to the unimprinted guiding layer and was high enough to delete the strong guiding effect of the silicon substrate. The guiding layer with the photoinitiator was then deposited. Finally, it was immediately covered by a UV transparent layer which acts as a protective coating, avoids guide inflation during the photocuring and the risk of trapping dust, and reduces the strong guiding effect of air.

2. Experimental

2.1. *The Buffer Layer (BL)*

The buffer layer is a mixture of 3-(trimethoxysilyl) propylmethacrylate (MAPTMS, Fluka, Assay ~99%), zirconate *n*-propoxide ($Zr(OPr)_4$, Fluka, Assay ~70% in propanol) and methacrylic acid (MAA, Fluka, Assay >98%) in a ratio of 2.5 : 1 : 1. The complete procedure is detailed in Fig. 1. MAPTMS is hydrolyzed with an aqueous HCl 0.01N solution with a ratio of 1 : 0.75. Independently, MAA is added dropwise to $Zr(OPr)_4$ with a ratio of 1 : 1. MAA reacts on $Zr(OPr)_4$ as a chelating agent and decreases its reactivity with water. After 45 minutes, the partially hydrolyzed MAPTMS is added slowly to the zirconate complex. Following another 45 minutes, hydrolysis and condensation reactions of MAPTMS and zirconate complex are enhanced with a quantity of pH 7 water suitable to give a final ratio MAPTMS : MAA : $Zr(OPr)_4$: H_2O of 2.5 : 1 : 1 : 5.

2.2. *The Guiding Layer (GL)*

The guiding layer is the buffer layer solution to which 5% wt of *Irgacure* 1800 photoinitiator (Ciba) is added.

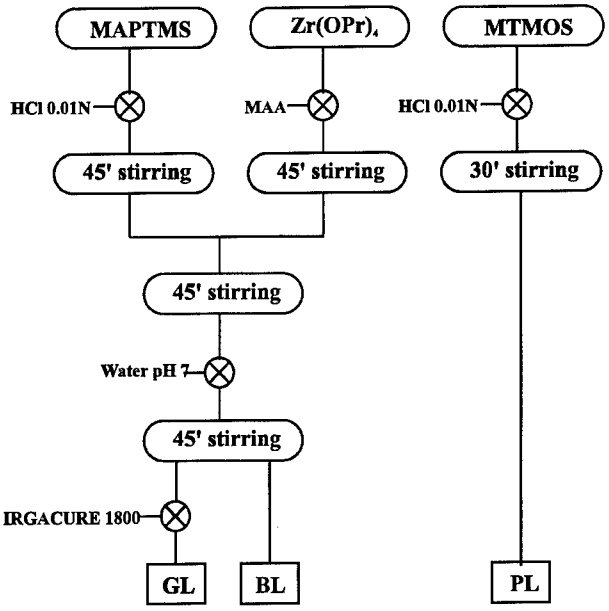

Figure 1. Synthesis flow chart for each layer.

2.3. *The Protective Layer (PL)*

It is known that hybrid coatings with high silica contents are scratch resistant [7, 8]. Moreover, silica glass is UV transparent [9]. Therefore, as a first approach, we chose to use methyl-trimethoxysilane (MTMOS, Fluka, Assay >98%) as a precursor. This organosilicate is an Ormosil®-network modifier. The methyl grouping softens the network by reducing the reticulation degree and allows denser and thicker crack-free coating fabrications than purely mineral precursors.

MTMOS is hydrolyzed with an aqueous 0.01N HCl solution (Fig. 1). After stirring for 30 minutes, films of about 1 to 3 μm can be deposited without any cracking or any dissolution of the photocurable coating.

2.4. *Sample Preparation*

Each solution was filtered through a Teflon filter (0.2 μm). They were deposited by the dip-coating technique. Glass substrates were used to perform thickness and refractive index measurement by means of reflection spectroscopy in the visible range [10]. Values are assumed to be unchanged from one substrate to another. The refractive index of the non-imprinted guiding layer (BL) was 1.479 $\pm$ 0.001 and increased up to 1.494 $\pm$ 0.001 when photocured (GL). The protective layer refractive index was 1.471 $\pm$ 0.001.

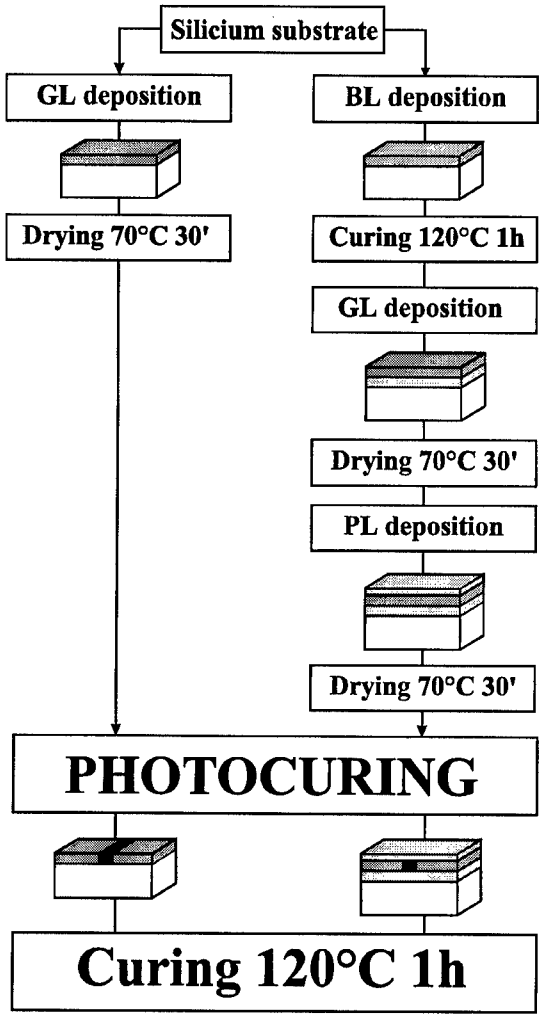

Figure 2. Sample preparation flow chart of each structure.

Transmission measurements in the UV range verified that this coating is transparent at the wavelength where the photoinitiator is active (300 to 350 nm).

The first sample structure was formed with the guiding layer solution deposited on silicon and dried at 70°C for 30 minutes. The deposition speed was about 2 mm/s giving a thickness close to 6 μm.

The second structure contained three layers. Using the measured refractive indexes of each layer, the thickness was optimized using customized software. The software used Galerkin's method with a Hermite-Gauss function expansion to resolve the scalar, semi-vectorial and vectorial wave equations [11]. A description of each region of the structure is easily obtained and the index gradient can be taken into account. The method allows small sized matrix products to simulate propagation in channel-waveguides and deals with coupling problems. A normalized effective index, B is calculated as a function of the thickness of each layer (Table 1). The guiding quality of each structure can be compared.

According to the computations, 5 μm thick buffer layers should be enough to insulate the guide from the silicon effect. To be safer, a 7.5 μm buffer layer was used. The protective layer reduces the strong guiding conditions at the surface. Its optimal thickness is 2.5 μm.

Consequently, a 7.5 μm thick buffer layer was deposited on silicon and cured at 120°C for 1 hour. It was then covered with about 6 μm of the guiding layer solution and baked at 70°C for 30 minutes. It was followed by a 2.5 μm thick protective layer deposition (1.5 mm/s speed) which was dried at 70°C for 30 minutes.

Each sample was imprinted through a mask by UV light for 30 minutes (Hg vapor source, 200 W power, 60 cm stand-off). Finally, the samples were cured at 120°C for 1 hour to freeze the structure.

The complete procedure for each structure is detailed in Fig. 2.

3. Results and Discussion

3.1. The One-Layer Structure

Scanning Electronic Microscopy of a cleaved sample (not presented here) shows that channel depth corresponds to the layer thickness ($\sim$7 μm). The use of Irgacure 1800 photoinitiator leads to a refractive index mismatch ($\Delta n = 0.015$) sufficiently high to develop new components where channels have sharp turns.

Both a decrease of exposure time and the stand-off distance of the UV source improve the channel-guide definition. The error which is measured with an optical microscope is less than 1% irrespective of the channel width.

Channel waveguides were tested using a 1.55 μm laser diode. Near-field pictures were taken at the output of the waveguides (Fig. 3(a)). Propagation losses are about 10 dB/cm which were much higher than those obtained with the initial composition [1]. This result can be explained by the higher efficiency of the new photoinitiator, which enables the photopolymerization of the layer down to silicon substrate. This phenomenon defines a quasi-step index waveguide in contact with the high-refractive index of the substrate. The result is an increase of the propagation losses by diffusion, and thus a buffer layer is required. Moreover, the channel

Table 1. Normalized effective index, B, as a function of PL and BL thickness. Grey columns correspond to the structures produced.

	PL (μm)	0	0	1	2	3	5	2	2	2	2
	GL (μm)	6	6	6	6	6	6	6	6	6	6
Structures	BL (μm)	0.1	∞	∞	∞	∞	∞	1.5	3	5	7.5
Normalized B	E_{x11}	0.554	0.568	0.602	0.609	0.610	0.610	0.600	0.607	0.609	0.609
	E_{y11}	0.549	0.561	0.601	0.608	0.610	0.610	0.600	0.606	0.608	0.608

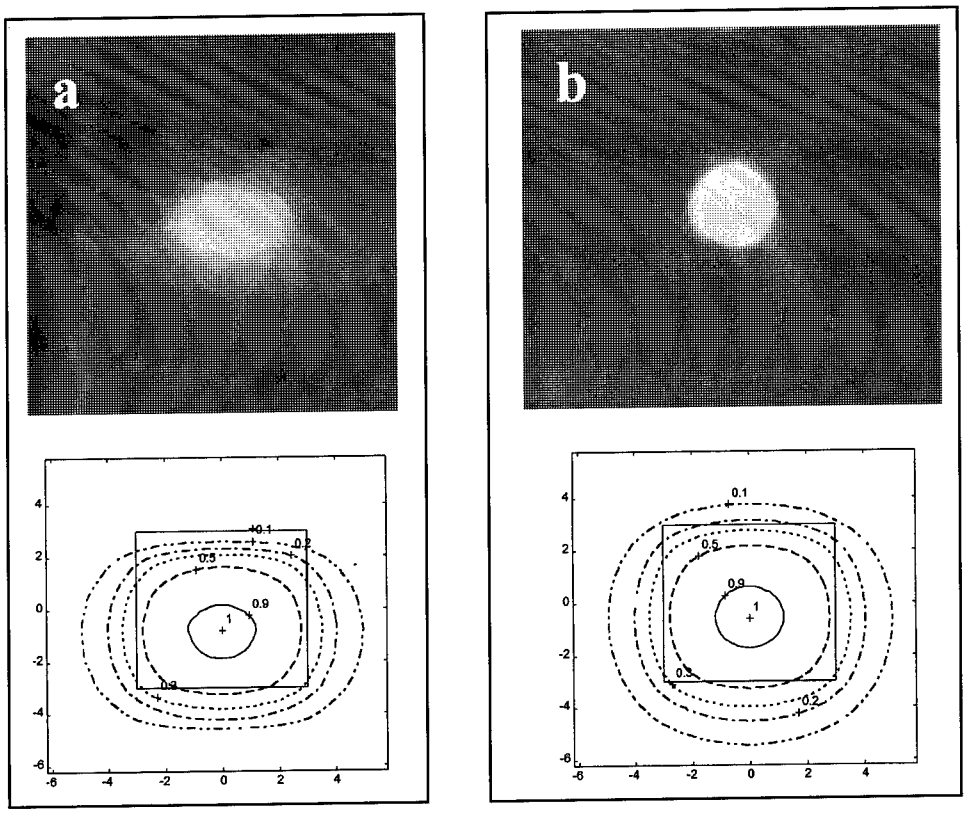

Figure 3. Near-field images and computed field contours of the one-layer (a) and the three-layer (b) structures.

waveguide inflation, seen by Atomic Force Microscopy (AFM), still remains [12]. This induces losses by scattering.

However, the increased channel depth compared to silica-fiber diameters is associated with a decrease in the refractive index. This acts mainly on coupling losses. Its value is less than 3 dB which corresponds to a very important reduction of a factor of 2.

3.2. *The Three-Layer Structure*

An AFM image of the three-layer structure shows only a slight inflation of the channel area [12]. The protective layer restricts expansion possibilities of the guiding layer and this should lead to internal stresses in the channel waveguide. However, the guiding layer did not show any cracks, nor did it debond with time.

The protective layer makes the structure scratch-resistant. No absolute measurement with a scratch test apparatus was performed, because our goal was only to create protection during the mask application and manipulations.

The channel waveguides were also tested using a 1.55 μm laser diode. Theoretical computations of light intensity are compared with near-field pictures at the output of each waveguide (Fig. 3(b)). The modifications in the field distribution induced by the sandwich structure are seen in both the experimental and computed field contours. A more symmetrical

guide was obtained. Losses were measured by the *cut-back* method. Propagation losses were estimated to be less than 0.1 dB/cm while coupling losses were below 0.5 dB for a 10 μm width guide.

4. Conclusion

The modified guiding layer inserted in a three-layer structure reduced both coupling and propagation losses respectively to a value of less than 0.5 dB and 0.1 dB/cm. This was due to an increase of the channel depth and better insulation from the air and the silicon substrate.

The optimized three-layer structure was used to fabricate more complex devices. Index modulation gratings, with a period of $\lambda = 500$ nm for use at 1.55 μm wavelength, were imprinted by a holographic set-up. The measure of the first-order diffraction efficiency gives 5.7%. A 1×8 beam splitter was also made by imprinting through a predefined mask. Finally, codirectional couplers with several coupling lengths have been produced.

Therefore, the inclusion of rare-earth compounds in the sol-gel guiding layer solution can be considered for the fabrication of active integrated optical devices such as lasers and amplifiers.

References

1. C.Y. Li, J. Chisham, M. Andrews, S.I. Najafi, J.D. Machenzie, and N. Peyghambarian, Electronics Lett. **31**, 271 (1995).
2. P. Coudray, J. Chisham, A. Malek-Tabrizi, C.Y. Li, M. Andrews, and S.I. Najafi, in *SPIE: Integrated Optoelectronics and Semiconductor Manufacturing* (San Jose, USA, 1996).
3. *Proceedings of Critical Review Conference on Glass Integrated Optics and Optical Fiber Devices*, edited by S.I. Najafi, SPIE Vol. CR53 (1994).
4. L. Yang, S.S. Saavedra, N.R. Armstrong, and J. Hayes, Anal. Chem. **66**, 1254 (1994).
5. P. Coudray, J. Chisham, A. Malek-Tabrizi, C.Y. Li, M. Andrews, N. Peyghambarian, and S. Najafi, Optics Commun. **128**, 19 (1996).
6. C.Y. Li, S.I. Najafi, J. Chisham, M. Andrews, P. Coudray, A. Malek Tabrizi, J.D. Mackenzie, and N. Peyghambarian, in *Proc. of Intern. Workshop on Advanced Materials for Multifunctional Waveguides* (Chiba, Japan, 1995).
7. H. J. Schmidt, Non-Cryst. Solids **73**, 681 (1985).
8. P. Etienne, J. Denape, J.Y. Paris, J. Phalippou, and R. Sempere, J. Sol-Gel Sci. Tech. **6**, 287 (1996).
9. D.R. Uhlmann and N.J. Kreidl, *Optical Properties of Glass* (The American Ceramic Society, NY, 1991).
10. P. Etienne, J. Phalippou, and R. Sempere, to be published.
11. A. Wesshaar, J.Li, R.L. Gallawa, and I.C. Goyal, J. of Lightwave Tech. **13**, 1795 (1995).
12. P. Coudray, Y. Moreau, P. Etienne, and J. Porque, "Sol-gel and polymer photonics devices," *International Conference SPIE*, CR No. 68 (San Diego, USA, Juillet 1997).

Journal of Sol-Gel Science and Technology 13, 529–533 (1998)
© 1998 Kluwer Academic Publishers. Manufactured in The Netherlands.

Structural and Optical Properties of Sol-Gel Derived Aluminosilicate Planar Waveguides Doped with Er^{3+} Ions

M. BENATSOU, B. CAPOEN AND M. BOUAZAOUI
Laboratoire de Spectroscopie Hertzienne, URA CNRS no. 249, Centre d'Etudes et de Recherches Lasers et Applications, Université Lille I, 59655 Villeneuve d'Ascq Cedex, France

W. TCHANA AND J.P. VILCOT
Institut d'Electronique et de Microélectronique du Nord, UMR CNRS 9929, Cité Scientifique, Avenue Poincaré-B.P. 69, 59655 Villeneuve d'Ascq Cedex, France

Abstract. Er^{3+} doped-aluminosilicate thin films were prepared on silica and silica/Si substrates by the sol-gel process and dip-coating. The sol-gel aluminosilicate planar waveguides were prepared from silicon and aluminium alkoxides. Their structural characterization has been carried out by Raman spectroscopy, Atomic Force and Scanning Electron Microscopies. The results indicated that these films present an amorphous structure until an annealing temperature of 900°C, while at temperatures higher than 1000°C, crystallization occurs. An estimate of microcrystallite sizes using Raman spectroscopy is given, which agrees with data from scanning electron microscopy. The optical properties have been investigated by Fluorescence spectroscopy in the visible region.

Keywords: sol-gel, aluminosilicate thin films, waveguides, erbium doping

1. Introduction

The sol-gel route using metal alkoxides is currently arousing increasing interest for the preparation of homogeneous multicomponent glasses and thin films for technological applications [1]. In this paper, we present the preparation of aluminosilicate planar waveguides doped with Er^{3+} ions. Their structural characterization has been investigated using Raman Spectroscopy, Scanning Electron Microscopy (SEM) and Atomic Force Microscopy (AFM). Fluorescence spectroscopy was used to demonstrate Er^{3+} incorporation and to probe the aluminosilicate gel network as a function of annealing temperature.

2. Experimental and Results

The method followed to prepare sol-gel aluminosilicate planar waveguides has been described in [2]. Thin films were deposited by a dip-coating technique onto SiO_2/Si substrates (75×25 mm^2 with 2 μm of SiO_2 on 500 μm thick Si wafers). The deposited film was first dried at 650°C under an O_2 atmosphere for 5 min. After 4 dipping cycles, the sample was heat treated to 900°C with a heating rate of 3°C/min and maintained at 900°C for 1 hour. Hence, the thickness of the film was built up by repeating the multiple dipping and firing cycles. In this case, the refractive index of film was measured by means of the "m-lines" technique, performed at 632.8 nm, was found to be equal to 1.548 for Al_2O_3-SiO_2 waveguides with a molar ratio Al/Si = 2. The film thickness for 25 layers was found to be 0.905 μm which implies deposition of 36.2 nm per dipping.

For these waveguides, optical loss, measured by detection of the scattered-light from the waveguide, was found to be around 0.2 dB/cm. Films of thickness ranging from 0.905 μm to 2 μm were made without cracks. The refractive index and the thickness of these films were found to depend on the annealing temperature and the solution ageing before the dip-coating process.

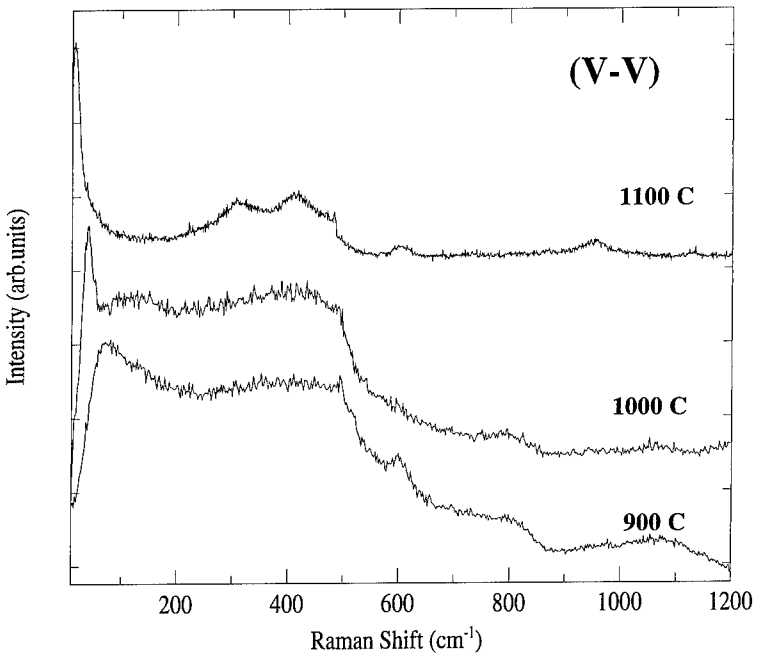

Figure 1. VV polarized Raman spectra of Al_2O_3-SiO_2 (Al/Si = 2) planar waveguides annealed at (a) 900°C, (b) 1000°C, and (c) 1100°C.

Indeed, the refractive index of films (Al/Si = 2) prepared using a 24 hours aged solution and annealing at 1100°C, following the heat-treatment described above, was equal to 1.601 (at $\lambda = 632.8$ nm) instead of 1.548 and the thickness of 25 layers was 0.839 μm instead of 0.905 μm, at 900°C. Furthermore, when the solution was four months aged the refractive index decreased and was equal to 1.525 (at $\lambda = 632.8$ nm) while the thickness per dipping increased to 45 nm.

Raman and fluorescence spectra were recorded using the experimental set-up described previously [2, 3]. The Raman spectra of undoped waveguides were recorded under excitation with the 488 nm line of an argon ion laser in order to avoid the weak fluorescence region which ranges from 520 to 600 nm and can overlap the Raman bands. This fluorescence is attributed to the presence of pentahedrally coordinated Al sites inherent in alumina systems obtained via polymeric condensation methods [4]. Figure 1 shows the "VV" polarized Raman spectra of an Al_2O_3-SiO_2 (Al/Si = 2) planar waveguide first annealed at 900°C (Fig. 1(a)), 1000°C (Fig. 1(b)) and then at 1100°C (Fig. 1(c)).

Figure 1(a) shows a typical Raman spectrum of an aluminosilicate glass (with a high alumina content). The very low wavenumber band centered near 80 cm^{-1} is usually called the "Boson peak" and is related to a maximum in the vibrational density of states. Such a low-frequency Raman band (50–100 cm^{-1}) has been observed for other glass systems and is characteristic of the vitreous state. Several models explain the "Boson peak" as a characteristic frequency of the presence of clusters or domains (structural inhomogeneities) within glasses of a size $\sim 2R$, where R is the radius of domains or blocks less disordered, in the 10–20 Å range [5–7]. The broad band observed around 450 cm^{-1} may be described as a symmetric motion of the bridged oxygens in the planes bisecting the Si—O—Si bonds [8]. Nevertheless, this band is broader than in vitreous silica. This broadening is generally attributed to the oxygen vibrations occurring at higher frequency for Si—O—Al linkages [8]. The bands in the region between 500 and 600 cm^{-1} are assigned to the vibrations of Al—O (bridging) vibrations [9]. The narrow band at 600 cm^{-1} is assigned to structural defects in the glass involving Si(Al)—O (nonbridging) vibrations [10]. It might also be associated with the 606 cm^{-1} defect line (D_2) of vitreous SiO_2 [11, 12]. The band group near 800 cm^{-1} is due to symmetrical motion of silicons in vitreous silica network. The high-frequency region consists of a broad asymmetric band between 880 and 1200 cm^{-1} with its maximum near 1050 cm^{-1}. This band was attributed to Si—O stretching vibrations of $SiO_{4/2}$ tetrahedron involving one, two, three, or four nonbridging oxygens [9].

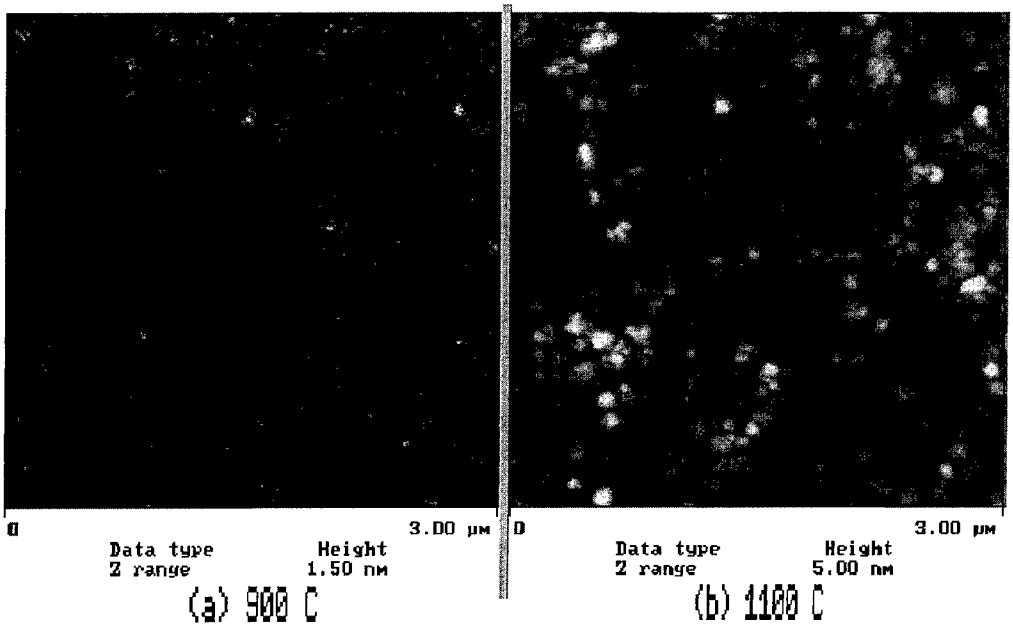

Figure 2. AFM images of the surface of Al_2O_3-SiO_2 (Al/Si = 2) planar waveguides annealed at (a) 900°C and (b) 1100°C.

Figure 2(b) shows the Raman spectrum of the Al_2O_3-SiO_2 (Al/Si = 2) film annealed at 1000°C. The "Boson peak" has disappeared and a new sharp peak at low frequency appears at 40 cm^{-1}. However, the rest of the spectrum shows slight changes indicating the presence of an amorphous structure discussed above. Figure 2(c) shows the Raman spectrum of the film annealed at 1100°C. The low-frequency peak shifts towards the Rayleigh line and appears at 16 cm^{-1}. Furthermore, the rest of the spectrum consists of narrow bands, which are characteristic of a crystalline structure that we have not yet identified. The very low-frequency peak is due to Raman scattering from spherical particles, or microcrystallites, and, according to the literature, their size is related to the band position by the relation [5, 7]:

$$2R = 0.7(v_l/\omega c) \qquad (1)$$

where $2R$ is the size or the diameter of the microcrystallite, v_l is the longitudinal sound velocity in a particle and c the vacuum light velocity. According to Eq. (1) taking v_l = 7020 m/s corresponding to the value of longitudinal sound velocity in glass [5] with a composition close to the mineral cordierite ((52 wt.%) SiO_2- (35 wt.%) Al_2O_3), which is a good approximation for our system, we find that the particle diameters $2R$ are equal to 4.7 and 11.7 nm, respectively, for films annealed at 1000 and 1100°C. The value obtained for the film annealed at 1100°C is in good agreement with the smallest diameters measured by Scanning Electron Microscopy (SEM). Indeed, the diameters determined by SEM were found to vary from 10 nm to 50 nm. Hence, we can deduce that the thin films heated at 1000°C contain an amorphous part and crystalline particles while at the curing temperature of 1100°C they are more crystallized and microcrystallites sizes increase with increasing annealing temperature.

We have also used Atomic Force Microscopy to investigate the structure of the waveguide surface and to measure its average roughness as a function of the annealing temperature. As an example, the AFM images of the surface of aluminosilicate waveguides annealed at 900°C and 1100°C are shown in Fig. 2(a) and (b), respectively. Hence, we observe a homogeneous and densified surface for a waveguide annealed at 900°C while nanocrystals appear at 1100°C. The average roughness measured for waveguides annealed at 900, 1000, 1100 and 1200°C were found to be equal to 0.173, 0.897, 1.047 and 3.960 nm, respectively. The high values obtained for films annealed at high temperatures (1100 and 1200°C) are due to the growth of the crystalline particles in these films.

Figure 3(a) shows the up-conversion fluorescence spectrum in the visible region of the 0.5-at.% Er^{3+}: Al_2O_3-SiO_2 (Al/Si = 2) planar waveguide annealed

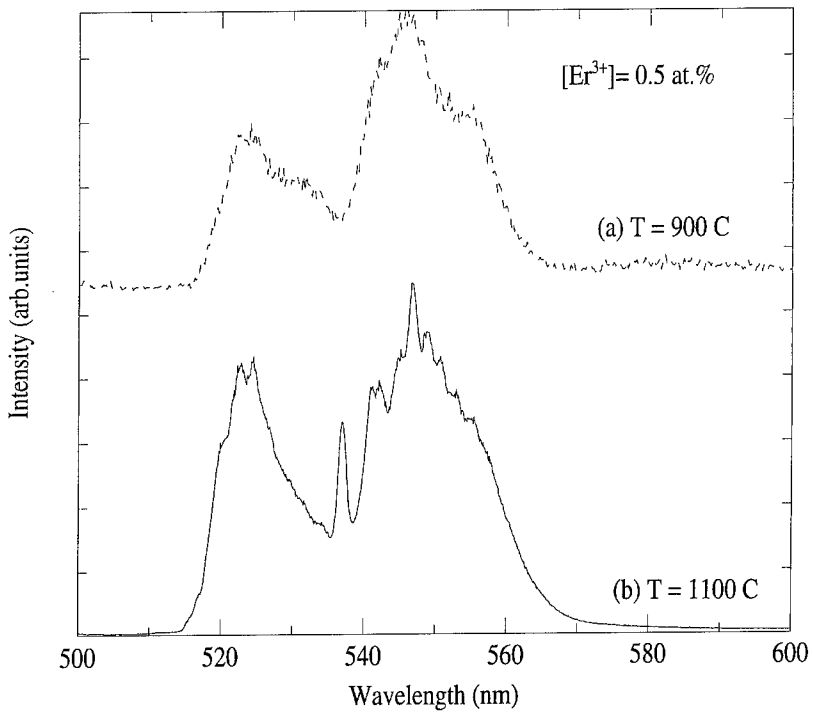

Figure 3. Up-conversion fluorescence spectra of 0.5-at.% Er^{3+}: Al_2O_3-SiO_2 (Al/Si = 2) planar waveguides obtained under excitation in the $^4I_{9/2}$ level (λ = 800 nm), annealed at (a) 900°C (dashed-line) and (b) 1100°C (solid-line).

at 900°C under excitation at λ = 800 nm. These up-conversion fluorescence broad bands, observed around 524, 548 are attributed, respectively, to $^2H_{11/2} \rightarrow {}^4I_{15/2}$ and $^4S_{3/2} \rightarrow {}^4I_{15/2}$ and are characteristic of Er^{3+} ions embedded in an amorphous structure. However, as the film is annealed at high temperature, the emission bands become narrower and split into several lines corresponding to transitions between the Stark sublevels of the excited and ground levels indicating a change in the rare earth environment evolving towards a crystalline structure. The fluorescence in the infrared region has been reported in [2].

The results reported above concerning the structural properties obtained via Raman, SEM, AFM and fluorescence spectroscopies are in good agreement with XRD investigations carried out by Yoldas [13] on aluminosilicate gels which showed that the crystallization process occurs at an annealing temperature higher than 980°C.

3. Conclusion

In summary, we have shown that thick aluminosilicate planar waveguides doped with rare earth ions can be prepared by the sol-gel method without cracks. These films can be easily densified into a glass. The structural and optical analysis via SEM and AFM, Raman, and fluorescence spectroscopies shows that sol-gel derived aluminosilicate films present an amorphous and homogeneous structure up to an annealing temperature of 900°C. Moreover, at this annealing temperature (900°C), the optical losses of these waveguides were found to be around 0.2 dB/cm and the surface roughness equal to 0.17 nm. We have also showed that crystallization of aluminosilicate thin films occurs at an annealing temperature of 1000°C and measured the size of crystalline particles.

Acknowledgment

The authors would like to thank Dr. Y. Pennec for AFM measurements. The Laboratoire de Spectroscopie Hertzienne is "Unité de Recherche Associé au C.N.R.S". The "Centre d'Etudes et de Recherches Lasers et Applications (C.E.R.L.A.)" is supported by the "Ministère chargé de la Recherche" the "Région Nord/Pas-De-Calais" and the "Fonds Européens de Développement Economique des Régions."

References

1. C.J. Brinker and G.W. Scherer, *Sol-Gel Science* (Academic, New York, 1990).
2. M. Benatsou, B. Capoen, M. Bouazaoui, W. Tchana, and J.P. Vilcot, App. Phys. Lett. **71**, 428 (1997).
3. M. Benatsou and M. Bouazaoui, Opt. Comm. **137**, 143 (1997).
4. B.E. Yoldas, J. Non-Cryst. Solids **147/148**, 614 (1992).
5. E. Duval, A. Boukenter, and B. Champagnon, Phys. Rev. Lett. **69**, 2052 (1986).
6. T. Pang, Phys. Rev. B. **45**, 2490 (1992).
7. E. Duval, A. Boukenter, and T. Achibat, J. Phys. Condens. Matter. **2**, 10227 (1990).
8. P. McMillan and B. Piriou, J. Non-Cryst. Solids **53**, 279 (1992).
9. J.T. Kohli, R.A. Condrate, Sr., and J.E. Shelby, Physics and Chemistry of Glasses **34**, 81 (1993).
10. S.K. Sharma, D. Virgo, and B.O. Mysen, Am. Min. **64**, 779 (1979).
11. F.L. Galeener, J. Non-Cryst. Solids **49**, 53 (1982).
12. F.L. Galeener and A.E. Geissberger, Phys. Rev. B. **27**, 6199 (1983).
13. B.E. Yoldas, J. Mater. Sci. **27**, 6667 (1992).

Journal of Sol-Gel Science and Technology 13, 535–539 (1998)
© 1998 Kluwer Academic Publishers. Manufactured in The Netherlands.

Fabrication and Characterization of Sol-Gel GeO_2-SiO_2 Erbium-Doped Planar Waveguides

A. MARTUCCI, G. BRUSATIN AND M. GUGLIELMI
Dipartimento di Ingegneria Meccanica—Settore Materiali, Università di Padova, Via Marzolo, 9, 35131 Padova, Italy

C. STROHHÖFER AND J. FICK
Laboratoire d'Electromagnétisme Microondes et Optoélectronique, ENSERG, BP 257, 38016 Grenoble, France

S. PELLI AND G.C. RIGHINI
I.R.O.E.-C.N.R., Via Panciatichi 64, 50125 Firenze, Italy

Abstract. GeO_2-SiO_2 sol-gel planar waveguides doped with Er were deposited by spinning on silica substrates. P_2O_5 or Al_2O_3 were used as co-dopants to improve erbium dissolution in the GeO_2-SiO_2 matrix. Multilayer amorphous films were obtained at 600 or 700°C.

Er ions in the planar waveguide pumped at 980 nm showed fluorescence features around 1530 nm. Narrow fluorescence spectra (~20 nm) and long lifetimes (~6 ms) were found in P_2O_5 co-doped samples, whereas Al_2O_3 co-doping gave wider spectra (~50 nm) with slightly lower lifetimes (~5 ms). The quenching concentration in the Al_2O_3 co-doped samples was 0.9 mol% Er.

Heat treatments in CCl_4 improve the active properties and the addition of Yb enhances the pump absorption efficiency.

Keywords: optical waveguide amplifiers, erbium, sol-gel, GeO_2-SiO_2

1. Introduction

Erbium-doped optical waveguides have received growing interest over the last decade due to their multiple applications, e.g., in integrated lasers or amplifiers for telecommunications [1].

Integrated optical amplifiers need a much higher Er-concentration with respect to erbium doped fiber amplifiers, in order to compensate the smaller interaction length. This high concentration is responsible for parasite effects caused by interactions between excited ions, notably cooperative up-conversion and quenching by energy transfer [2].

Special measures are needed to suppress clustering. This is usually done by the addition of oxides, such as Al_2O_3 and P_2O_5, which improve the miscibility of erbium in silica based matrices [2].

The performances of the amplifier are governed by the electronic and optical characteristics of the active ion, but are strongly influenced by matrix properties [2]. Among these, the phonon energy is a crucial aspect, because it affects the efficiency of an Er doped amplifier. In fact they lead to non-radiative relaxation of Er ions from the $^4I_{13/2}$ metastable level [2].

The maximum phonon energy in GeO_2 matrices, for instance, is 150 cm^{-1} lower than in SiO_2. Therefore, GeO_2-based glass matrices have the potential to improve the active properties of erbium. Its high refractive index allows easy fabrication of highly confined waveguides on silica buffer layers. Moreover, the

photosensitivity of GeO_2 glass allows the fabrication of confined waveguides by illuminating with UV-light [3].

From results reported on the sol-gel preparation of GeO_2-based glasses [4–6] it is known that a critical problem is the tendency of GeO_2 gels to crystallize. Another problem related to sol-gel is the presence of residual OH groups in the matrix which is the limiting factor for application in active devices. In fact the energy transfer to the OH complex is extremely effective at quenching excited rare earth ions [2] even for a few hundred ppm of OH.

Our work is focused on GeO_2-SiO_2 thin films doped with erbium and produced by the sol-gel technique. The $80GeO_2$-$20SiO_2$ system was optimized with respect to heat treatments, to avoid crystallization and to reduce as much as possible the OH content, and with respect to co-dopants to reduce Er clustering.

2. Experimental

$Ge(OEt)_4$ (TEOG) and $Si(OEt)_4$ (TEOS) were used as precursors for germania and silica, respectively. TEOS was dissolved in ethanol (EtOH) and pre-hydrolyzed with H_2O and HCl maintaining 15 hours at 80°C under reflux. TEOG was dissolved in ethanol, added to the TEOS solution and stirred for 3 hours. The following molar ratios were used: (TEOG + TEOS) : EtOH = 1 : 10; TEOS : H_2O = 1; HCl : TEOS = 0.01. For P and Al co-doped samples, P_2O_5 powder and $Al(OBu)_3$, respectively, were dissolved in ethanol, before adding it to the GeO_2-SiO_2 precursor solution. In the final solution $Er(NO_3)_3$ or $ErCl_3$ and/or $Yb(NO_3)_3$ dissolved in ethanol were added, with different molar ratios with respect to the total oxide concentration, which was 80 g/l. Pure GeO_2 (named G) and $80GeO_2$-$20SiO_2$ (molar, named G8S2) films were deposited on silica or silicon substrates by spinning, and co-doped with different amounts of Al_2O_3 or P_2O_5. Multilayer films with thickness up to 2 μm were obtained by heating each layer at 600°C or 700°C for 15 min. Details about chemical procedure are published elsewhere [7].

X-ray diffraction (XRD) analysis was performed on films (Philips PW 1740) using a grazing angle goniometer to enhance the signal to noise ratio.

FT-IR measurements were performed on films deposited on silicon (Perkin-Elmer System 2000). All the measurements were performed in the range 4000–400 cm^{-1} with a resolution of 2 cm^{-1}.

Refractive index was measured in films, along with thickness, using the linear m-line technique at the HeNe laser wavelength (632.8 nm). Propagation losses were evaluated by measuring the light scattered out of the plane of the film by means of a Hamamatsu camera with vidicon connected to a computer [8].

The active properties of the planar waveguide samples were characterized by fluorescence spectra and lifetime measurements. In both cases the erbium ions were pumped by a laser diode emitting at 980 nm. The pump was end-coupled into the samples, whose edges had been cleaved to obtain good coupling efficiency.

3. Results and Discussion

Monolayer G and G8S2 films were heat treated at increasing temperatures between 300 and 800°C with intervals of 100°C for 1 hour at each temperature. No crystallization was observed up to 600°C. For this reason multilayer films were obtained, heating each layer at 600°C. XRD, performed to verify the influence of the process on the crystallization behavior, showed that under the above conditions the films were amorphous to XRD at the end of the multiple deposition process. Multilayer films were heat treated also at 700 and 800°C for 1 hour. In multilayer films hexagonal GeO_2 peaks are evident at 700°C both for G and G8S2 samples. Even the samples co-doped with P_2O_5 crystallize above 600°C. On the contrary samples co-doped with Al_2O_3 crystallize above 700°C.

FTIR spectra of GeO_2 films show the strongest absorption bands typical of germanate glasses around 870 cm^{-1} with a shoulder at 960 cm^{-1} also visible in GeO_2-SiO_2 systems treated at $T > 500$°C (Fig. 1). The band at 1100 cm^{-1} is due to the Si—O—Si asymmetric stretching of the silicon oxide layer of the substrate.

The bands in this region can be assigned to asymmetric stretching motions of GeO_4 tetrahedral containing bridging (Ge—O—Ge bond) and non-bridging (Ge—O^- bonding) oxygen [9]. In GeO_2-SiO_2 systems also Si—O—Si vibrations are visible at 1070 cm^{-1}.

The second region of absorption of germanate glass lies between 500 and 600 cm^{-1}: the bands in this region may be related to mixed stretching-bending motions [9].

The appearance, with heat treatment, of sharp peaks (triplet) at 530, 560 and 590 cm^{-1} indicates the formation of crystalline GeO_2 (hexagonal); these peaks are clearly visible at 700°C only in the pure GeO_2 multilayer film spectra (Fig. 1) where also the formation of

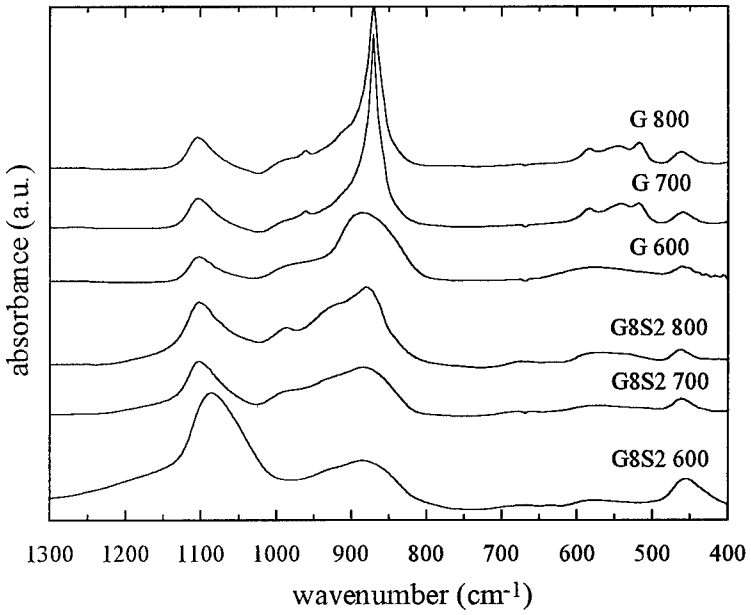

Figure 1. FTIR spectra of G (a) and G8S2 (b) multilayer films, treated at 600, 700 and 800°C.

a sharp Ge—O—Ge peak (at about 870 cm^{-1}), typical of a crystalline phase, is visible.

The IR investigation showed that the highest absorption frequencies are at 870 cm^{-1} for all GeO_2 based systems, with the exception of the silica containing matrices where a vibration at 1100 cm^{-1} is present. This however should not affect significantly the overall phonon relaxation process in G8S2, due to the low SiO_2 content.

As reported elsewhere [4–6, 10], the crystallization temperature of GeO_2 based sol-gel glass is affected by the amount of hydrolysis water used in the gel synthesis. For this reason no water was used for the hydrolysis of $Ge(OEt)_4$ in our procedure and the hydrolysis is performed by the atmospheric moisture and by H_2O impurity contained in the ethanol. The heat treatment at 600°C (i.e., slightly above the transition temperature of vitreous GeO_2) enables significant densification of the film, as shown by the high refractive index (see Table 1) without causing its crystallization. Using the Lorentz-Lorentz [11] equation and an index of 1.609 for GeO_2 glass [12], a porosity of about 1% was calculated. The formation of hexagonal GeO_2 occurs above 600°C, as demonstrated by both XRD and FT-IR measurements.

Optical losses of 2–3 dB/cm (at 630 nm) and 1.5 dB/cm (at 840 nm) were measured on $80GeO_2$-$20SiO_2$ multilayer films. Similar results were recently obtained by different authors [3, 6, 13]. The measured losses are probably mainly due to scattering arising from dust or other imperfections connected with the multideposition process that is not carried out in a clean room. Measurements at different wavelength (i.e., 1.3 and 1.5 μm) should help to understand better the nature of the scattering losses (Rayleigh or inhomogeneities) and will permit improved evaluation of the waveguide properties of the active films.

The fluorescence properties of GeO_2 and $80GeO_2$-$20SiO_2$ samples are reported in Table 1. It was found that a supplementary co-doping with P_2O_5 or Al_2O_3 is necessary to obtain satisfactory active properties.

Table 1. Optical properties of GeO_2-SiO_2 planar waveguides doped with 0.2 mol% of Er.

Glass matrix[a]	Heat treatments	Refractive index[b]	Lifetime (ms)	λ_{peak} (nm)	FWHM (nm)
G	600°C	1.60	—	—	—
G-P	600°C	1.60	1.5	1537	18
G-Al	700°C	1.58	4.0	1529	60
G8S2	600°C	1.56	3.0	1536	20
G8S2-P	600°C	1.58	5.1	1536	19
G8S2-P	CCl_4	1.59	6.1	1535	15
G8S2-Al	700°C	1.59	5.0	1530	53
G8S2-Al	CCl_4	1.57	5.6	1530	60

[a]Concentration of P and Al co-dopants are 10 mol% of P_2O_5 and Al_2O_3, respectively.
[b]Measured with m-line technique at 633 nm.

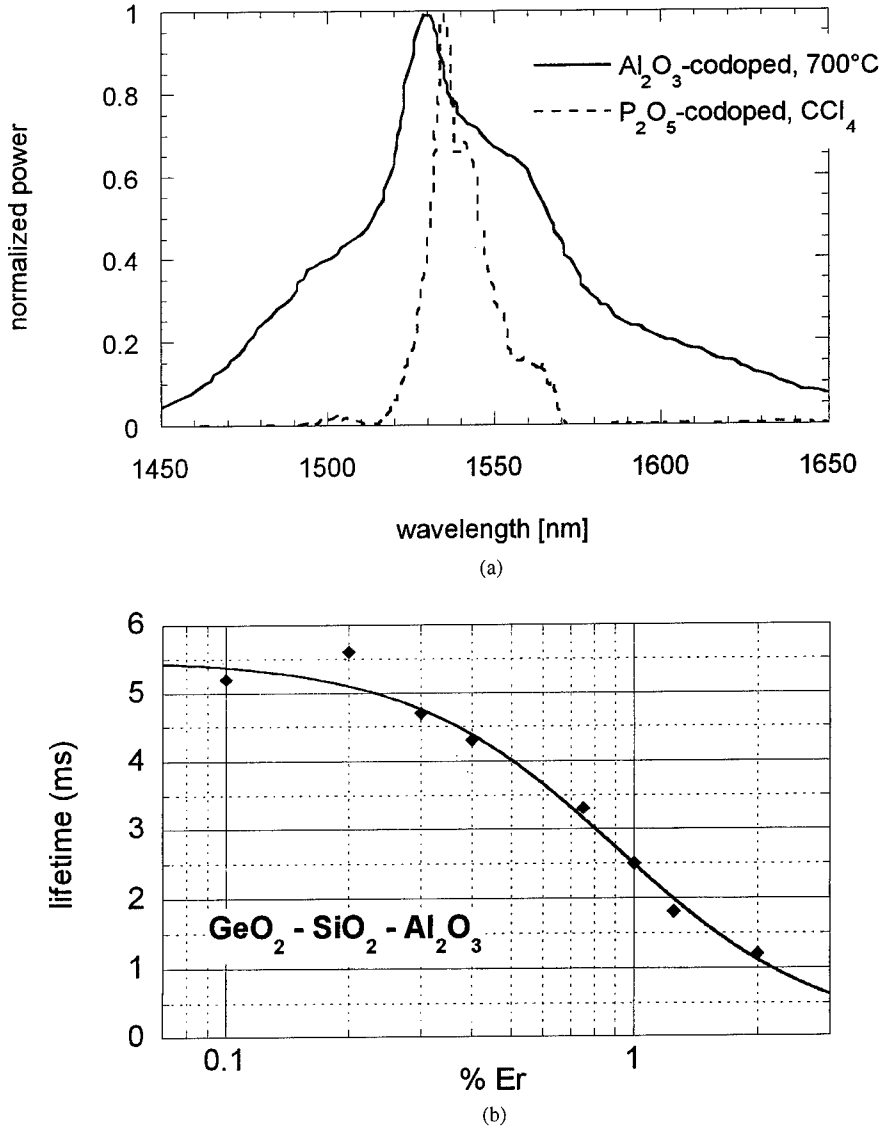

Figure 2. (a) Erbium fluorescence spectra of G8S2 films co-doped with 10 mol% of Al_2O_3 or P_2O_5. (b) Quenching curve for G8S2 films co-doped with 10 mol% of Al_2O_3. The values deduced for the maximum fluorescence lifetime and the quenching concentration are $\tau_0 = 5.5$ ms and $c_q = 0.9$ mol% [2].

Figure 2(a) shows the erbium fluorescence spectra in the GeO_2-SiO_2 matrix co-doped with P_2O_5 or Al_2O_3. In the first case a peak is observed at about 1535 nm with a half width of some 20 nm. A broad shoulder at the short wavelength side of the peak can be seen. The addition of Al_2O_3, on the other hand, broadens the spectrum for the other co-doped matrices. Since for optical amplifiers used in WDM-multiplexed systems a homogeneous amplification over a broad spectral region (~40 nm) is necessary, the Al_2O_3 co-doped material is more convenient for this application, even its lifetime being slightly shorter. On the other hand, the P_2O_5 co-doped material with its narrow fluorescence spectrum is more suited for laser or active filter devices.

A problem inherent in the sol-gel process in view of its use for fabrication of host matrices for active ions, is the contamination of the vitreous matrices by OH groups. A commonly used technique to reduce the hydroxyl concentration in the matrix consists of a special heat treatment in carbon tetrachloride (CCl_4) [14]. We studied the effects of such treatment at 500°C for a duration of 30 min. For the P_2O_5 co-doped samples the application of the treatment in CCl_4 increases the lifetime by 1 ms to 6.1 ms (0.2 mol% Er) (see Table 1).

Even for $80GeO_2$-$20SiO_2$ films co-doped with Al_2O_3 the heat treatments in CCl_4 gave higher lifetimes, even if the increase was lower with respect to the P co-doped samples (from 5 to 5.6 ms, obtained for 0.2 mol% Er, see Table 1).

The higher lifetime presented by the P_2O_5 co-doped samples could be related to a lower content of OH groups, as characteristic of other sol-gel phosphate glasses [15].

Co-doping an erbium-doped matrix with ytterbium enhances absorption of the pump and thus the inversion of the laser level [2]. We have tested the effect of Yb in G8S2 films co-doped with 10 mol% of Al_2O_3 or P_2O_5, doped with 0.5 mol% Er and the same amount of Yb. The fluorescence intensity increased by more than one order of magnitude, while the emission cross-section remained unchanged. These preliminary measurements show that there is still a large potential of optimization for our materials.

We also investigated the influence of different Er-precursors on the active properties of our films. They behave in different ways for the two investigated co-doped matrices. In the case of the Al_2O_3 co-doped matrices, $ErCl_3$ as erbium precursor leads to longer lifetimes, while in the case of P_2O_5 co-doping considerably longer lifetimes by up to 1 ms are achieved using $Er(NO_3)_3$.

To obtain the dependence of the lifetime on co-dopant concentration, we investigated G8S2 films co-doped with 5, 7.5, 10, and 12.5 mol% of Al_2O_3 and doped with 0.2 mol% Er. The results showed a sharp rise in lifetime between 7.5 mol% and 10 mol% Al_2O_3 concentration.

The quenching concentration in the Al_2O_3 co-doped system was determined, measuring the lifetime of samples doped with different erbium concentrations. The experimental results are reported in Fig. 2(b) from which a concentration quenching of about 1 mol% of Er was evaluated. We used the equation $\tau_0/\tau = 1 + (c/c_q)^p$ to deduce a quenching concentration of $c_q = 0.9$ mol% [2].

4. Conclusions

Amorphous GeO_2-SiO_2 multilayer films, doped with Er, were prepared by the sol-gel method. A film densification temperature of 600°C, was found to be suitable for multilayer deposition. Al_2O_3 and P_2O_5 co-dopants are necessary to obtain satisfactory active properties. We obtained narrow fluorescence spectra (~20 nm) and long lifetimes (~6 ms) for the P_2O_5 co-doped samples. In the case of Al_2O_3 co-doping the fluorescence spectra are wider (~50 nm), and the lifetimes are slightly lower (up to 5 ms). For the Al_2O_3 co-doped samples the concentration quenching was 0.9 mol% Er with a lifetime of 2.7 ms.

Heat treatment in CCl_4 and addition of Yb have a beneficial influence on the active properties of the films.

Acknowledgment

We acknowledge the support of the European Commission through the ACTS project "CAPITAL" (#AC047).

References

1. M. Federighi, I. Massarek, and P.F. Trwoga, IEEE Phot. Techn. Letters **5**, 227 (1993).
2. W.J. Miniscalco, in *Rare Earth Doped Lasers and Amplifiers*, edited by M.J.F. Digonnet (Marcel Dekker, New York, 1994), p. 19.
3. K.D. Simmons, G.I. Stegeman, B.G. Potter Jr., and J.H. Simmons, J. Non-Cryst. Sol. **179**, 254 (1994).
4. M. Yamazaki and K. Kojima, J. Mater. Sci. Lett. **14**, 813 (1995).
5. S. Shibata, T. Kitagawa, F. Hanawa, and M. Horiguchi, J. Non-Cryst. Sol. **88**, 345 (1986).
6. D.G. Chen, B.G. Potter, and J.H. Simmons, J. Non-Cryst. Sol. **178**, 135 (1994).
7. G. Brusatin, M. Gugliemi, and A. Martucci, J. Am. Cer. Soc. **80**, 3139 (1997).
8. S. Pelli and G.C. Righini, *Advanced in Integrated Optics* (Plenum Press, London, 1994), p. 1.
9. K.E. Lipinska-Kalita, J. Non-Cryst. Sol. **119**, 41 (1990).
10. S.P. Mukherjee, J. Non-Cryst. Sol. **82**, 293 (1986).
11. C.J. Brinker and G.W. Scherer, *Sol-Gel Science: The Physics and Chemistry of Sol-Gel Processing* (Academic Press, San Diego, 1990).
12. N.P. Bansal and R.H. Doremus, *Handbook of Glass Properties* (Academic Press, Orlando, 1986).
13. M. Banatsou and M. Bouazaoui, Optics Comm. **137**, 143 (1997).
14. J. Phalippou, T. Woignier, and J. Zarzycki, in *Ultrastructure Processing of Ceramics, Glasses and Composites*, edited by L.L. Hench and D.R. Ulrich (Wiley, New York, 1984), p. 70.
15. R.R.A. Syms, V.M. Schneider, W. Huang, and M.M. Ahmad, Elect. Lett. **33**, 1216 (1997).

Journal of Sol-Gel Science and Technology 13, 541–545 (1998)
© 1998 Kluwer Academic Publishers. Manufactured in The Netherlands.

Hole Burning and Fluorescence Spectra of Sol-Gel Derived Sm^{2+}-Doped Glasses

MASAYUKI NOGAMI AND YOSHIHIRO ABE
Nagoya Institute of Technology, Showa Nagoya, 466 Japan

Abstract. Sm^{2+}-doped glasses in the system of Al_2O_3-SiO_2 were prepared by sol-gel processing of metal alkoxides and reacting with H_2 gas at 800°C. The hole burning properties of these glasses were investigated. The holes were burned in the $^7F_0 \rightarrow {}^5D_0$ line of the Sm^{2+} ions using a DCM dye laser at 77 K. The hole depth increased with increasing the laser irradiation time, reaching up to ~15% of the total intensity within a few hundred seconds. The hole width was 3 cm^{-1} full width at half maximum. Fluorescence line narrowing spectra of the $^5D_0 \rightarrow {}^7F_1$ transition were analyzed to study the local structure surrounding the Sm^{2+} ion. It is concluded that the Sm^{2+} ions are closely coordinated with nine oxygens of the AlO_6 group in aluminosilicate glasses and that the addition of Al^{3+} ions into glass induces an increase in the coordination number of the Sm^{2+}.

Keywords: spectral hole burning, Sm^{2+}-doped glass, sol-gel, fluorescence line narrowing

1. Introduction

Persistent spectral hole burning (PSHB) phenomena, provide a powerful tool for low temperature spectroscopy with high resolution, and have been suggested as the basis for high-density frequency-domain optical data storage [1]. Many methods have been applied to the preparation of PSHB materials, although the PSHB operating temperature is limited to extremely low temperatures using liquid helium. Recently, room temperature PSHB was observed for the f-f transitions of Sm^{2+} ion-doped fluoride single crystals [2]. Since then, Sm^{2+}-doped crystals and glasses have attracted much interest for use in applications such as high density optical memories. Glasses are thought to be more suitable for high density memory devices than single crystals, because of their wide inhomogeneous width, high transparency and easy mass production. Sm^{2+} ions were doped in some fluoride and borate glasses by melting under a strongly reducing gas atmosphere [3, 4]. Previously we have successfully prepared Sm^{2+} ion-doped aluminosilicate glasses using a sol-gel method and observed PSHB at room temperature [5–7]. Since silicate glasses have superior chemical and mechanical durabilities compared to other glasses, they offer some advantages for practical applications.

Room temperature PSHB is observed in the excitation spectra for the $^5D_0 \rightarrow {}^7F_0$ fluorescence of Sm^{2+} ions. When designing PSHB memories, it is first necessary to develop glasses with a high Sm^{2+} ion fluorescence intensity. In the sol-gel process, Al_2O_3-SiO_2 glasses containing Sm^{3+} ions are prepared from an alkoxy-derived solution, then reacted with H_2 gas to reduce the Sm^{3+} ions to Sm^{2+} in the glass matrices. In previous papers, we have shown that the addition of Al^{3+} ions increases the dispersion and reaction of Sm^{3+} ions with the H_2 gas [7]. The fluorescence intensity of the Sm^{2+} ions was also strongly affected by the Al_2O_3 content preparation conditions. At present, however, the effect of Al^{3+} ions on the fluorescence of Sm^{2+} ions is not well understood.

In this paper, we report hole-burning measurements in the $^7F_0 \rightarrow {}^5D_0$ transition of Sm^{2+} ions and the analysis of the local structure surrounding Sm^{2+} ion using laser-induced fluorescence line narrowing (FLN) spectra of the Sm^{2+} ion-doped Al_2O_3-SiO_2 glasses.

2. Experimental Procedure

Using a sol-gel method, $x Al_2O_3$ $(100-x)SiO_2$ (x; 1–15 mol%) glasses containing nominally 2 wt% Sm_2O_3 were prepared. Commercially available starting materials were used $Si(OC_2H_5)_4$, $Al(OC_4H_9^{sec})_3$ and $SmCl_3 \cdot 6H_2O$. A detailed explanation of the gel preparation is given elsewhere [5–7]. The gels obtained were heated in air at 500°C and then allowed to react with H_2 gas at 800°C in a fused silica tube.

A hole was burned in the $^7F_0 \rightarrow {}^5D_0$ line near 14600 cm^{-1} by a cw Ar^+-laser-pumped DCM dye laser (Coherent CR599, band width of ~1 cm^{-1} full width at half maximum (FWHM)). The hole spectra were recorded by scanning the laser from 14,380 to 14,810 cm^{-1} while monitoring the fluorescence of the $^5D_0 \rightarrow {}^7F_2$ transition at 13,790 cm^{-1}. The laser power for reading the hole was attenuated by an ND filter to less than 0.1% of that for burning.

The FLN spectral measurement was performed using the Ar^+-laser-pumped DCM dye laser. The fluorescence intensity was measured at 77 K with a chopper that alternately opened the optical paths before and after the sample. The chopping frequency was 150 Hz. The fluorescence wavelength was selected using a Jobin Y von 32 cm monochromator.

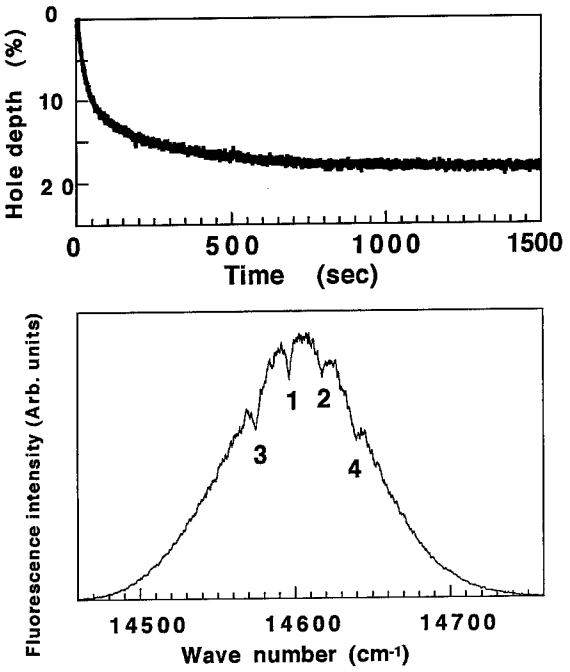

Figure 1. Hole-burning spectrum of the Sm^{2+} ion-doped $10Al_2O_3 \cdot 90SiO_2$ glass at 77 K. Holes were burned at four wave numbers in order of numbers shown. Hole depth burned as a function of burning time. The holes were burned using a DCM dye-laser at 14599 cm^{-1}.

3. Results and Discussion

3.1. *Hole Burning Measurement*

Hole burning was observed in the excitation spectrum of the $^7F_0 \rightarrow {}^5D_0$ transition. Figure 1 shows a typical hole spectrum at 77 K, where the laser was used to irradiate 14,599, 14,620, 14,577, and 14,641 cm^{-1} in order for 10 min. Four holes corresponding to the burning energies were found. It is evident that holes can be burned at wavelengths covering the range of the $^7F_0 \rightarrow {}^5D_0$ transition. The hole width (FWHM) and depth are 3 cm^{-1} and ~15%, respectively. We found that the hole width increased with increasing burning temperature. The excitation profile represents an inhomogeneous line shape with a width of 100 cm^{-1} FWHM, which is almost independent of temperature up to room temperature. This large width is due to the random structure of the glass and is much broader than that observed in crystals [8] and fluoride glasses [9], but is comparable to borate glasses [4]. The inhomogeneous width did not change after burning, and was again almost independent of temperature up to room temperature.

The hole depth dependence on time during burning at 77 K is also shown in Fig. 1. The hole depth, which is normalized to the excitation intensity before burning at the burning wavelength, increases with burning time up to about 15% within a few hundred seconds.

3.2. *FLN Spectra of Sm^{2+} Ion-Doped Glasses*

Figure 2 shows the FLN spectra due to the $^5D_0 \rightarrow {}^7F_1$ transition when $10Al_2O_3 \cdot 90SiO_2$ glass containing 2 wt% Sm_2O_3 was heated at 800°C in H_2 gas. Similar spectra were recorded for all the glasses containing 1–15 mol% Al_2O_3 prepared in this study. The three distinct peaks resulting from Stark splitting of the $^7F_1$ state appear in the energy range from 14,500 to 14,100 cm^{-1}. The full width of each band is about 80 cm^{-1}. The highest energy component of the $^5D_0 \rightarrow {}^7F_1$ transition is considerably sharper than the other two components and has a smaller shift in its peak position with decreasing excitation energy. The lowest

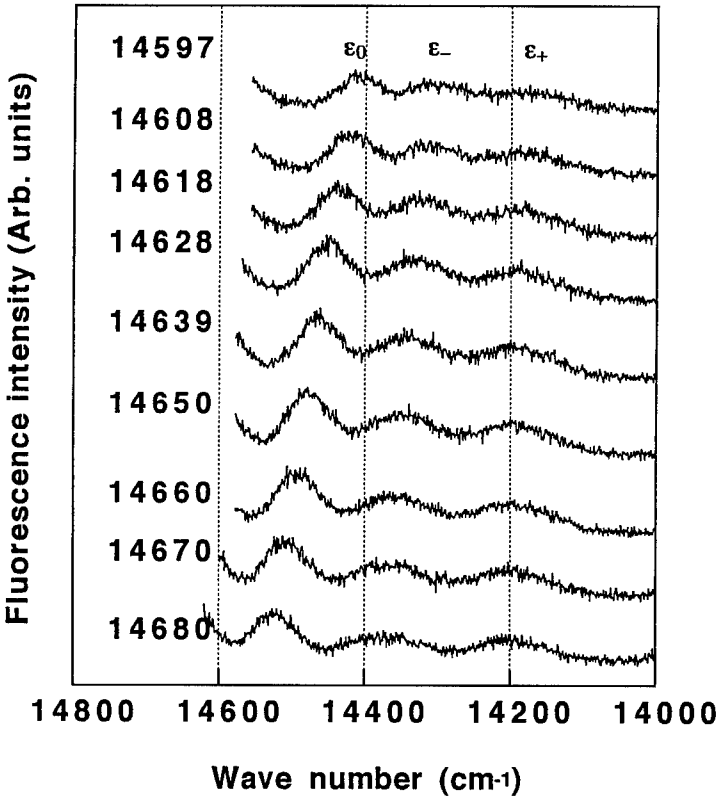

Figure 2. FLN spectra of the $^5D_0 \rightarrow {}^7F_1$ transition of Sm^{2+} in $10Al_2O_3 \cdot 90SiO_2$ glass. Spectra were measured at 77 K under dye-laser excitation into the $^7F_0 \rightarrow {}^5D_0$ transition line. The number indicates the wave number of the excitation laser beam.

energy component is less sensitive to the excitation energy.

As the fluorescence band due to the $^5D_0 \rightarrow {}^7F_1$ transition can be completely resolved into three components and all the lines continuously shift with the excitation energy, the Sm^{2+} ions at different sites in a glass are thought to have the same type of ligand structure. These FLN properties are similar to those of fluoride glasses containing Sm^{2+} ions, as measured by Tanaka and Kushida [6], who restricted the point symmetry of the Sm^{2+} ion in fluoride glasses to C_{2v}, C_2, or C_s symmetry. Following their assignment, we assume that Sm^{2+} ions doped in aluminosilicate glasses have the same point symmetry as in fluoride glasses. In the above point symmetries, it is thought that the lowest energy of the $^7F_1$ lines can be assigned to the $M_j = 0$ component of the $^7F_1$ levels, which has a large electron distribution along the z-axis. On the other hand, the other two high-energy components correspond to the electron distribution along the x-y plane. Under these conditions, the z-axial and x-y plane components of the second-order crystal field parameters, B_{20} and B_{22}, respectively, can then be estimated from the energies of the three $^7F_1$ lines as follows [10]:

$$B_{20} = \frac{5}{3}\{2E_{(\varepsilon_0)} - E_{(\varepsilon_+)} - E_{(\varepsilon_-)}\}$$

$$B_{22} = \frac{5}{\sqrt{6}}\{E_{(\varepsilon_+)} - E_{(\varepsilon_-)}\}$$

where $E_{(\varepsilon_+)}$, $E_{(\varepsilon_-)}$, and $E_{(\varepsilon_0)}$ are the wave numbers of the $^5D_0 \rightarrow {}^7F_1$ transition in order of energy. The calculated second-order crystal field parameters, B_{20} and B_{22}, are shown in Fig. 3 as a function of the excitation energy. The B_{20} value decreases as the excitation energy of the $^7F_0 \rightarrow {}^5D_0$ transition increases, while the B_{22} value increases only slightly with increasing excitation energy. In this figure, the crystal field parameters determined for Sm^{2+} doped in fluoride glass [11] are shown for comparison. Note that the B_{20} value depends on the excitation energy while the B_{22} value is almost independent of it. Although the values determined for

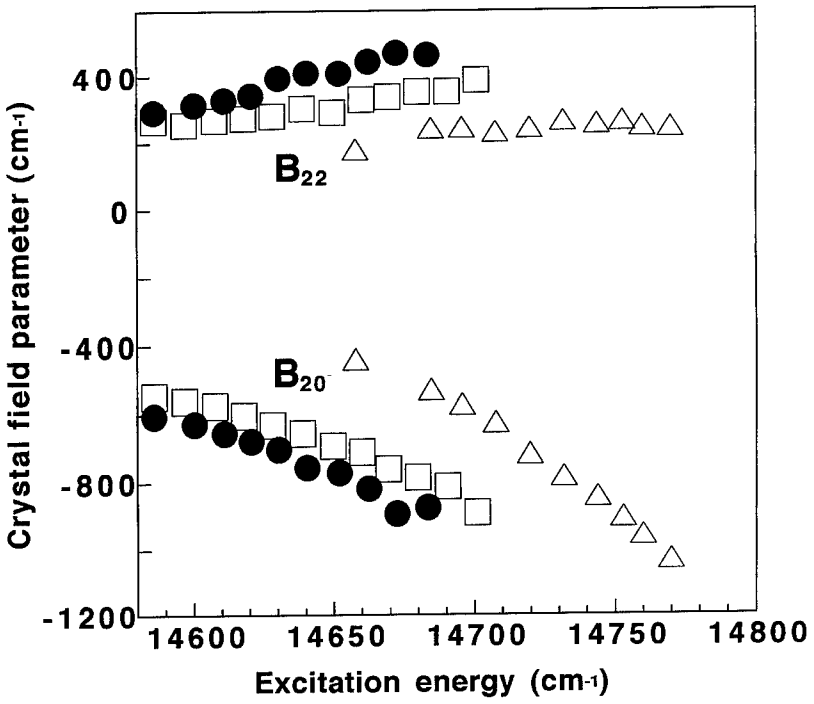

Figure 3. Ratio of second-order crystal field parameters, B_{22}/B_{20}, as a function of excitation energy.

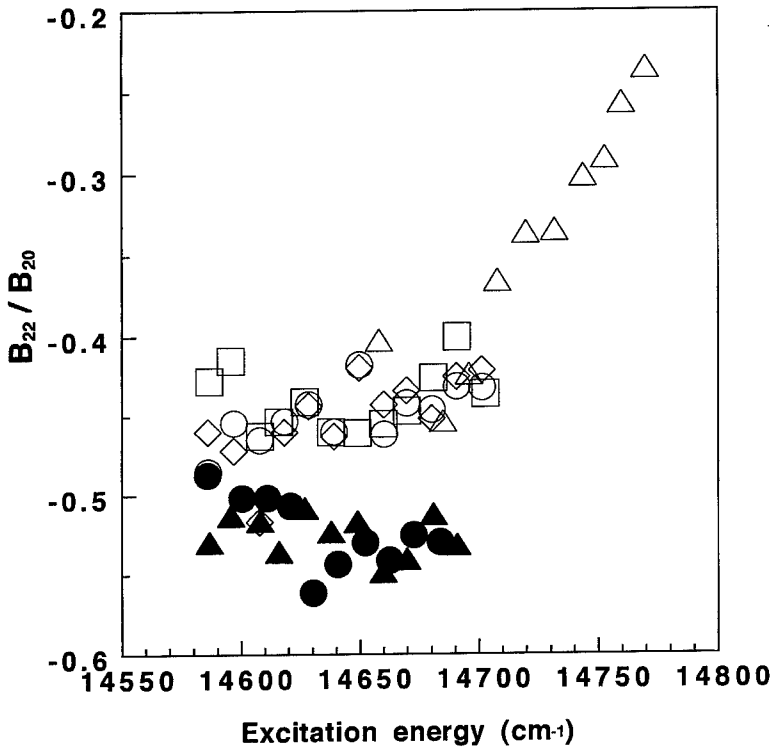

Figure 4. Second-order crystal field parameters, B_{20} and B_{22}, for Sm^{2+} in $xAl_2O_3 \cdot (100 - x)SiO_2$ glasses as a function of the $^7F_0 \rightarrow {}^5D_0$ transition. ●, ▲, □, ○, and ◇, denote glasses containing 1, 2, 5, 10, and 15 mol% Al_2O_3. △ is for Sm^{2+}-doped fluoride glasses [11].

glasses containing 2, 5, and 15 mol% Al_2O_3 are not plotted for clarity, the crystal-field-parameter dependence on the excitation energy can be categorized into two groups according to the Al_2O_3 content in the glass. One is for glasses containing more than 5 mol% Al_2O_3. In these glasses, the values are almost the same within the limits of the experimental error as those of a glass containing 10 mol% Al_2O_3. On the other hand, the values in glass containing 2 mol% Al_2O_3 are similar to those of the 1 mol% Al_2O_3 glass. Values of the B_{20} and B_{22} are related to the electron distribution along the z-axis and x-y-plane components, respectively [12]. The results in Fig. 3 show that the values of both B_{20} and B_{22} increase with increasing excitation energy, suggesting that oxygens surrounding the centered Sm^{2+} ion are distorted to decrease the distance between the Sm^{2+} and oxygen. Brecher and Riseberg measured the crystal-field parameters for Eu^{3+} ions in glasses and restricted the ratio of the crystal field parameters, B_{22}/B_{20}, to the coordination number of the Eu^{3+} ions, in which the B_{22}/B_{20} values of -2.05 and -0.23 correspond to the coordination values of 8 and 9, respectively [12]. Figure 4 shows the B_{22}/B_{20} value for the Al_2O_3-SiO_2 and fluoride glasses as a function of excitation energy. It is evident that in the fluoride glass the B_{22}/B_{20} value increases with the excitation energy, indicating the wide distribution of F_2-ions coordinated to the Sm^{2+} ions. On the other hand, the B_{22}/B_{20} value for the Al_2O_3-SiO_2 glasses is independent of the excitation energy, although the values for glasses containing more than 5 mol% Al_2O_3 are higher than those containing 1 and 2 mol% Al_2O_3. These results indicate that the Sm^{2+} ions are closely coordinated with nine oxygens of the AlO_6 group in aluminosilicate glasses and the addition of Al^{3+} ions into glass induces an increase in the coordination number of the Sm^{2+} ion.

4. Conclusions

Persistent spectral holes with the hole width and depth of 3 cm^{-1} FWHM and ~15%, respectively, were observed at 77 K in the Sm^{2+}-doped Al_2O_3-SiO_2 glasses prepared by sol-gel processing of metal alkoxides. It was concluded from the FLN spectra that the Sm^{2+} ions are closely coordinated with nine oxygens of the AlO_6 group in aluminosilicate glasses and the addition of Al^{3+} ions into glass induces an increase in the coordination number of the Sm^{2+}.

Acknowledgment

This research was partly supported by a Grant-in-Aid for Scientific Research (No. 09650734) from the Ministry of Education, Science, and Culture of Japan.

References

1. G. Castro, D. Haarer, R.M. Macfarlane, and H.P. Trommsdorff, U.S. Patent 41019761, 1978.
2. R. Jaaniso and H. Bill, Europhys. Lett. **16**, 569 (1991).
3. T. Izumitani, S.A. Payne, and J. Lumi. **54**, 337 (1993).
4. K. Hirao, S. Todoroki, D.H. Cho, and N. Soga, Opt. Lett. **18**, 1586 (1993).
5. M. Nogami and Y. Abe, Appl. Phys. Lett. **64**, 1227 (1994).
6. M. Nogami, Y. Abe, K. Hirao, and D.H. Cho, Appl. Phys. Lett. **66**, 2952 (1995).
7. M. Nogami, N. Hayakawa, N. Sugioka, and Y. Abe, J. Am. Ceram. Soc. **79**, 1257 (1996).
8. J. Zhang, S. Huang, J. Yu, and J. Lumin, **56**, 51 (1993).
9. A Kurita and T. Kushida, Opt. Lett. **19**, 314 (1994).
10. M. Tanaka and T. Kushida, Phys. Rev. B **49**, 16917 (1994).
11. M. Tanaka and T. Kushida, Phys. Rev. B **49**, 5192 (1994).
12. C. Brecher and L.A. Riseberg, Phys. Rev. B **13**, 81 (1976).

Journal of Sol-Gel Science and Technology 13, 547–551 (1998)
© 1998 Kluwer Academic Publishers. Manufactured in The Netherlands.

Sol-Gel Prepared Glass for Refractive and Diffractive Micro-Optical Elements and Arrays

Y. HARUVY AND I. GILATH
SOREQ NRC, Yavne 81800, Israel

M. MANIEWICTZ AND N. EISENBERG
JCT, Jerusalem 91160, Israel

Abstract. The fast sol-gel method enables facile preparation of siloxane-based glassy matrices, in which polymerization is completed within minutes and volume changes <5% take place upon curing. Single-face and two-face replication of micro-optical arrays have been obtained, as well as crack-free elements >10 mm thick. Minimizing shrinkage and enabling relaxation of the drying sol-gel are key factors in the elimination of cracking. These features and the resulting optical quality of the glass make this method technologically and economically attractive for replication-produced micro-lenses and micro-optical arrays.

Keywords: sol-gel, fast, micro-optics, patterning, replication

Introduction

Glass is the natural material for optical applications. Micro-optical elements and arrays are required to be produced at high dimensional accuracy, high optical quality, tailorable index of refraction and a competitive price. Hence, the sol-gel synthetic route seems appealing from both cost and technology considerations.

In the sol-gel synthetic route [1], hydrolysis of metal-alkoxide monomers and subsequent condensation result in macromolecular species, in the form of chains or particulate sol, that cross-link into a three-dimensional glassy matrix. Sol-gel fabrication of passive and active optical elements has been widely investigated [2–4]. The preparation of glass monoliths by these methods necessitates a cautious and prolonged process [1] to avoid cracking. Further, the matrix drying involves great shrinkage which complicates the preparation of optical elements.

The fast sol-gel method enables facile preparation of glassy materials in which polymerization is completed within minutes and curing within hours [4]. This synthetic route employs mixtures of alkyl-alkoxysilane monomers and provides crack-free films and monoliths. High concentrations of guest molecules can be encaged in these glassy matrices for various applications of nonlinear optics [5–6].

Cast-replication of optical components is preferred to cutting and polishing, especially for micro-lenses and micro-lenslet-arrays, where fabrication is complex and expensive [7]. The pioneering sol-gel industrial fabrication of micro-optical arrays by Gel-Tech [8] still involves overcoming a substantial shrinkage in the course of curing. The fast sol-gel method offers a facile process, minute shrinkage and optical clarity of the elements obtained that appears technologically and economically attractive for producing micro-optical elements and arrays.

Micro-optical arrays are densely patterned and hence, their replication imposes strict requirements on both the templates and the sol-gel prepared replicas. The chemical nature of the template must provide durability to swelling for dimensional accuracy, and surface polarity for adhesion to the gel throughout the curing. The chemical nature of the sol-gel must allow removal of volatile products prior to gelation, to

minimize shrinkage after gelation and mobility in the matrix after gelation, and to maintain the relaxation necessary for crack-free drying.

Here the problems related to these aspects of the replication are presented, and the solutions achieved by chemical manipulation of the template and the sol-gel processes are discussed.

Experimental

Methyltrimethoxysilane (MTMS), tetramethylorthosilicate (TMOS) (Aldrich, CP) and dimethyldimethoxysilane (Hulls, CP) were used as received. Glass slides and Kapton films were used as flat templates. Patterned templates were made of polycarbonate or PMMA and cured polyimide photoresist.

The sol-gel experimental setup and procedure are described elsewhere [4]. In a typical procedure 1 g MTMS and 0.2 g HCl 10^{-2} M are stirred vigorously for 5 min. In a capped reactor in a water bath ($\sim$100°C), Vacuum-assisted distillation to obtain a weight loss of 0.5–0.6 g is followed by casting and curing for 24 h at 65°C.

Surface analysis was carried out by FTIR (Nicolet: DX-5); XPS (Kartos Analytical: HS-AKIS); SEM (JEOL 6300; Phillips 525/535); AFM (Digital Instruments: Nanoscope-II) and ZYGO 3D Imaging Surface Nano-Structure Analyzer.

Results, Observations and Discussion

Photoresists commonly employed for the preparation of patterned templates were swollen by the sol-gel resins and hence replaced by polyimide photoresists that were highly cured following the photolithography.

A template for free standing elements must provide sufficient adhesion to the curing sol-gel, while allowing it to separate when cured. These requirements are met since in the course of curing, hydroxy and methoxy groups at the gel surface undergo condensation. The resulting enrichment of the surface with methyl-groups [5] decreases the gel-template adherence forces. To manipulate the timing of the adhesion/separation sequence we may modify the adhesion properties of either the template or the resin. It was found preferable, however, to tailor the *resin* to meet the needs of crack-free curing of the *sol-gel bulk*, and tailor the *template* to meet the needs of adhesion to the *sol-gel surface*.

To eliminate premature separation of glass films >500 μm in thickness, template chemical etching in 6N NaOH was effective yet difficult to regulate. Oxygen plasma oxidative etching was found effective and controllable for delicate manipulation of the template surface. The sol-gel adhesion/separation on a given template display a general trend: the thicker the element, the earlier it separates, and the more extensive the etching necessary for timing of the separation.

The above trend was verified by FTIR and XPS surface analysis, described in detail elsewhere [7]. The FTIR data indicates an incomplete hydrolysis of the methoxy-groups at the near-stoichiometric water-to-silane molar ratio (MR) employed. Nonetheless, this relatively low MR ratio allows the slow crosslinking necessary for facile casting, patterning and crack-free drying.

The XPS data in Table 1 shows the effect of the material in contact with the gel on the gel surface composition. The air-facing surface (001 and 007) is richer in carbon, i.e., methyl and methoxy groups, compared to the template-facing surface, although when cast, both surfaces have similar constitutions. During the gel curing, one side faces the polar template while the other faces the nonpolar air. The different concentrations of nonpolar groups at the two surfaces probably causes a surface-rearrangement of the gel to match the adjacent environments [5]. The different behavior of 019 results from a higher rate of condensation produced by the higher MR ratio. It is likely that the air-face of the gel became "glassy" so early it could no-longer rearrange.

SEM analysis of spin-cast films shows the defect-free surfaces of the matrix. AFM verified that these surfaces contain irregularities smaller than a few nm. SEM analysis of replicated Fresnel Lenses indicated an "improved" surface quality of the replica compared to the template. This was attributed to the inaccessibility of small defects to the viscous sol-gel resin. The

Table 1. XPS of MTMS derived sol-gel films.

Sol-gel composition	Concentration of atomic species (%)						Sample code
	Sol-gel: air-side			Sol-gel: kapton-side			
	C 1s	O 1s	Si 1s	C 1s	O 1s	Si 1s	
MR = 1.40	42.2	37.8	20.0	32.4	43.5	24.1	001
MR = 1.43	31.6	44.6	23.8	30.4	45.4	24.2	007
MR = 1.80	28.2	47.5	24.3	30.3	45.1	24.6	019

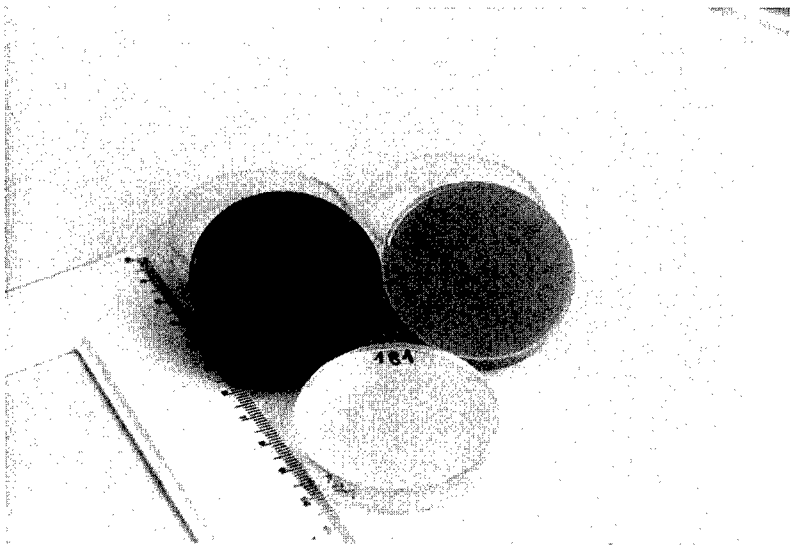

Figure 1. Photograph of fast-sol-gel derived discs. Thickness: 12 mm; diameter: ~40 mm; dyes: Rhodamine 6G, fluorescein and Macadole blue; [Dye] = 10^{-3} M in the glass.

apparent advantage of "mending" minor imperfections may become an obstacle leading to imprecise replication of tiny patterns in the template. The practical question is: how small can the radius of curvature in a pattern be and still become accurately replicated? The replication factor [7], defined as the ratio between radii of curvature of a replicated optical pattern and its template, is still to be studied experimentally. At present we know it is close to one for radii >20 μm.

The gel volume shrinkage following the distillation with weight loss of 0.60 g/g is currently smaller than 5%, with a corresponding lateral shrinkage smaller than 1% and highly accurate replication. High optical quality necessitates stress-free drying, since the elements produced do not undergo firing. The MR ratio used with slow drying and crosslinking permits the necessary relaxation.

Accurate replication necessitates tailoring of the template surface polarity to its specific patterning. The effective surface area of a densely patterned template may greatly exceed the nominal surface area (by a factor of $\times$2.4 for an array of half spheres). Hence, the larger the surface area, the smaller the etching needed. Furthermore, for micro-optical arrays of exceptionally fine patterning, tailoring of both the resin viscosity and template surface may be needed.

Single face replication was carried out, employing an array of negative micro-cylindrical elements, with a range of radii of 5–50 μm, photolithographically imprinted onto polyimide photoresist film. Replication was carried out by hot casting at (~100°C) a sol-gel resin with a 48% weight loss after distillation. The replicas thus prepared were 12 mm thick and 40 mm in diameter, as shown in Fig. 1, with the positive lenslet-array imprinted on the surface.

A ZYGO 3D Imaging Surface Structure Analyzer, which is an image-processing optical nanoscope, was employed to accurately study the replication, thus overcoming the poor stereoscopic resolution obtained by SEM.

The images of the sol-gel replica surface show that the cylindrical lenses are smooth and accurately replicated. The polyimide template after the replication appears identical to that before replication, implying the possibility of its multiple use. The differences in diameter between the template and the replica were found negligible in the entire range (5–50 μm), which is currently the most useful for micro-optical arrays. Ongoing research is aimed at studying the replication factor at diameters of 0.5–50 μm, for future needs.

Two-face replication was demonstrated employing two arrays of negative micro-cylindrical elements, ca. 48 μm wide and 2.2 μm deep, also photolithographically imprinted onto polyimide. Replication was carried out by hot casting (at ~100°C) a sol-gel resin (as described above) onto one template placed in a Petri dish, and embossing the gel with the other template one hour later. The template replicas thus prepared are

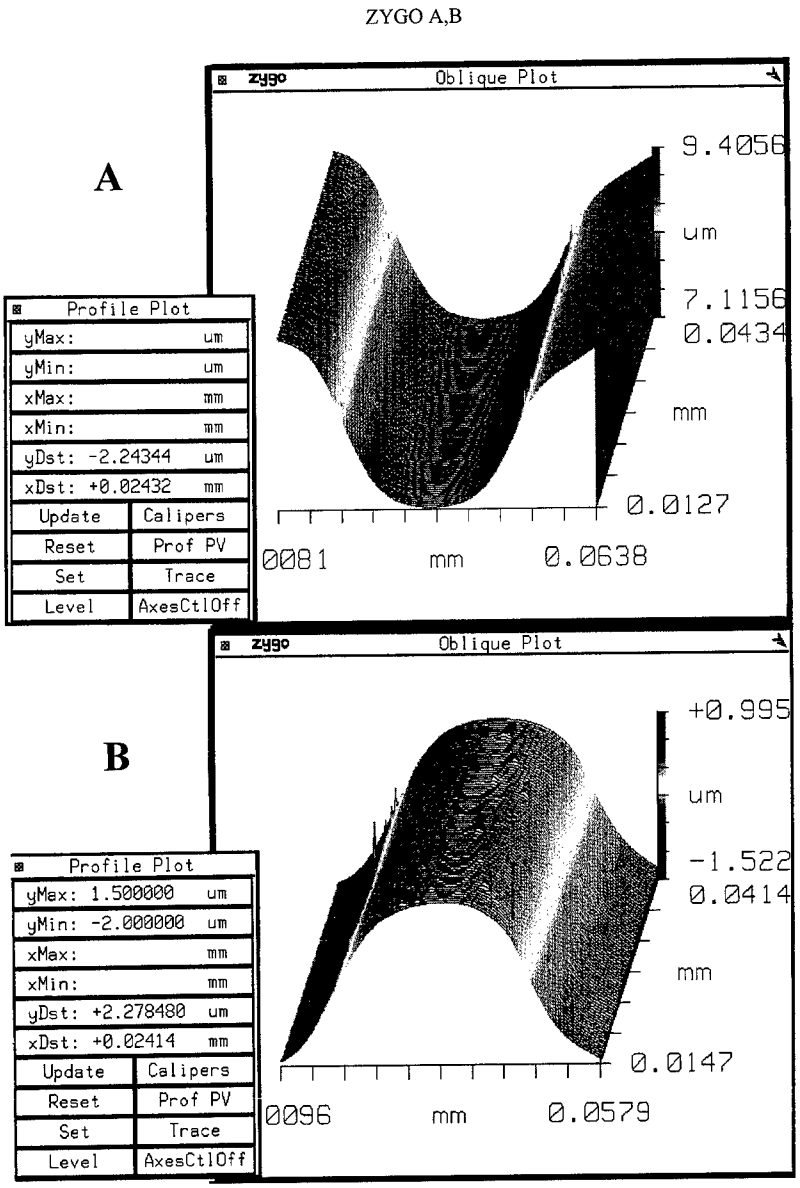

Figure 2. Two-face sol-gel replication of cylindrical micro-lenslet array: (A) template made of cured polyimide photoresist; (B) sol-gel derived replica.

shown in Fig. 2. The workability of the two-face replication, free of cracking or bubbles at the upper face, requires the complete removal of volatile species from the highly viscous resin cast onto the template. It is noteworthy that the tiny shrinkage in the width of the cylinders (0.4%) is accompanied by an *increase* in height (0.3%). The resulting change in optical performance may require adjustments to the process to correct this effect.

Evolution of the sol-gel route, enabling silicate films of thickness ≤ 1 μm to be produced [1], yielded the fast sol-gel route enabling preparation of organo-silicate films of thickness ≤ 100 μm [4–7]. This latter thickness permitted replication of micro-optical elements, yet with very limited mechanical strength. The current developments enable self-supporting, mechanically stable, >10 mm thick elements with imprinted replicas of <10 μm micro-optical elements.

This evolution of the fast sol-gel reaction was facilitated by both lowering the MR ratio and elevating the temperature. The latter is believed to increase the formation of linear ladder-like segments. Early results of on-going research on the molecular structures in the gels, carried out by time-domain microwave spectroscopy, verified the coexistence of polymer-like (probably ladder polymers) and particulate fractions in the matrix.

Conclusions

A fundamental study of the replication, using the fast-sol-gel derived glass, has led to several breakthroughs in this art:

- Controlled modification and quantitative analysis of the template surface, as a primary means for prompt timing of the glass-template sequence of attachment and detachment.
- Fine tuning of the sol-gel chemical constitution, polymerization and weight loss by distillation, specifically tailored to the patterning density and curvature, as the primary means to ensure the mechanical and optical features of the glass.
- As a result, a facile single-step replication of micro-optical arrays was achieved. Self-supporting sol-gel derived glass patterned elements with thicknesses up to 12 mm and diameters of up to 10 cm were thus prepared for various experiments and applications.

Acknowledgment

The authors wish to express their gratitude for the financial support of this research by the *Ministry of the Science and the Arts*, contract no. 8559-1-95.

References

1. C.J. Brinker and G.W. Scherer, *Sol-Gel Science: The Physics and Chemistry of Sol-Gel Processing* (Academic Press, San Diego, CA, 1990).
2. J.D. Mackenzie (Ed.), *Sol-Gel Optics. II*, Proc. SPIE **1758**, (1992).
3. J. Zyss (Ed.), *Molecular Nonlinear Optics* (Academic press, San Diego, CA, 1994).
4. Y. Haruvy and S.E. Webber, *Chem. Mater.* **3**, 501 (1991).
5. Y. Haruvy, A. Heller, and S.E. Webber, in *Submolecular Glass Chemistry and Physics*, edited by P. Bray and N.J. Kreidl, Proc. SPIE **1590**, 59 (1991).
6. Q. Hibben, E. Lu, Y. Haruvy, and S.E. Webber, Chem. Mater. **6**, 761 (1994); and references therein.
7. Y. Haruvy, I. Gilath, M. Maniewictz, and N. Eisenberg, in *Proc. 10th Meeting on Optical Engineering in Israel*, edited by I. Weismann (SPIE, 1997), Vol. 3110; and references therein.
8. Geltech, Corporate Profile and data package, available from Geltech, 3267 Progress Drive, Orlando, FL 32826, USA.

Journal of Sol-Gel Science and Technology 13, 553–558 (1998)
© 1998 Kluwer Academic Publishers. Manufactured in The Netherlands.

Reversing Gels and Water Soluble Colloids from Aminosiloxanes

T. SURATWALA, K. DAVIDSON, Z. GARDLUND, D. COLLINS AND D.R. UHLMANN
Department of Materials Science and Engineering, Arizona Materials Laboratory, University of Arizona, 4715 E. Fort Lowell, Tucson, AZ 85712

Abstract. The unique sol/gel behavior of an organic/inorganic hybrid material synthesized from 3-aminopropyltriethoxysilane (3AS) and tetramethoxysilane (TMOS) is discussed and examined. The addition of H_2O to a mixture of a basic (3AS) and an acidic (TMOS) alkoxide leads to rapid gel formation. This wet gel reverses to a sol upon heating which is attributed to the dissolution of siloxane bonds between the surfaces of colloidal particles in the gel. The reversed sol dries to an optically transparent solid which is water soluble. The water solubility and the stability of these colloidal particles are described by their aminopropyl/silanol surface and the electrostatic interactions between them using DLVO theory.

Keywords: water soluble silica, colloids, 3-aminopropyltriethoxysilane, tetramethoxysilane, reversible gel, DLVO theory

1. Introduction

The gelation of colloidal silica can be pictured as the collision between colloids with silanol surfaces resulting in condensation reactions to form siloxane bonds. The siloxane bonds are formed irreversibly, and the resulting gel/precipitate is water-insoluble. Silica gels can be made water soluble: (1) by including substituents in the composition which prevent siloxane bond formation or (2) by placing the material in a highly basic environment where dissolution of the siloxane bonds can take place. Alkali metal silicates such as Na and K silicates [1] and certain organically modified sols are known to be water soluble [1, 2]. At a high pH, the silica surface will have a negative surface charge, and the positive cations (Na, K, Li, etc.) will adsorb on the surface of silica. Particles will then be linked together by acid-base bonds rather than siloxane bonds, and these materials can be peptized to become water soluble [1]. Organically modified sols can also be water soluble by incorporating organic ions on the surface of the silica such as tetramethylammonium ions [1, 3, 4], again preventing siloxane bond formation.

In this study, we present a new organically modified silicate material and discuss its unique characteristics of reversible gelation and water solubility which is believed to be governed by the dissolution of silica and electrostatic interactions between silica colloids.

2. Experimental

Synthesis. The physical behavior of the 3AS : TMOS composition during processing is shown in Fig. 1. Typically, 3AS, TMOS, and H_2O (distilled or acidified) were mixed in a vial at a 5.5 : 1 : 3.9 mole ratio. Upon the addition of H_2O, rapid hydrolysis/condensation resulted in the formation of a wet gel (B) within 60 s of mixing with distilled H_2O and within 10 s of mixing with acidified H_2O. This wet gel (B) was optically transparent, often with a bluish color caused by Raleigh scattering. Upon heating the wet gel to 75°C for several hours, the gel would reverse back to an optically transparent solution (C). The reversed solution (C) was slightly more viscous than the original 3AS : TMOS solution (A). Solution (C) was very stable, since it would not gel upon sitting or cooling. The drying of solution (C) resulted in an optically

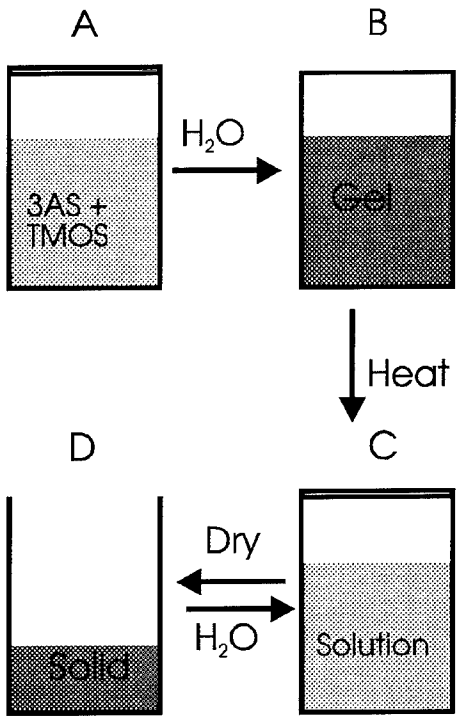

Figure 1. Schematic of the physical behavior of the 3AS : TMOS composition during processing.

transparent, crack free solid (D). The addition of water to the solid (D) returned the solid to a solution (C). The rate of dissolution was slow; it typically took several hours at 75°C.

Atomic Force Microscopy (AFM). The reversed solutions (C) were diluted in water and deposited and dried on mica. Images were taken in tapping mode on a Nanoscope III (Digital Instruments) AFM.

3. Results and Discussion

The formation of the wet gel (B) can be explained by examining the acid/base catalysis of the sol-gel reactions. As individual precursors, TMOS and 3AS hydrolyze rapidly within 30 s in the presence of water. Just after hydrolysis, these solutions are fluid, and do not form a gel as in the presently-studied (mixed) system. During typical sol-gel processing, treating an alkoxide in an acidic environment catalyzes both the hydrolysis and condensation reactions. The hydrolysis rate typically far exceeds the condensation rate, resulting in relatively long gel times [1, 5]. As the pH increases, the condensation rate increases, decreasing the gel time. 3AS is an alkoxide with a basic amine substituent, while TMOS is a relatively acidic alkoxide. The addition of H_2O to a mixture of an acid and a basic alkoxide results in rapid gel formation which is attributed to rapid catalysis of both hydrolysis (due to the acidic TMOS) and condensation (due to the basic 3AS).

The high optical transparency of the wet gel (B) suggests the rates of hydrolysis and condensation of the two alkoxides are closely matched and hence both of the alkoxides are being homogeneously incorporated into the matrix. By comparison, when H_2O is added to a mixture of tetraethoxysilane (TEOS) and 3AS, or to a mixture of TMOS and 3-aminopropyltrimethoxysilane (3AMS), a precipitate is formed, suggesting that the reaction rates of the two alkoxides are not matched. The hydrolysis/condensation rate of TEOS is much slower than that of TMOS and the reaction rate of 3AMS is faster than that of 3AS [5, 6]. However, when water is added to TMOS and 4-aminobutyltriethoxysilane, which should have similar reaction rates as 3AS, an optically transparent initial gel is formed that behaves like the 3AS : TMOS composition.

The wet gel (B) reverses to a solution which contains colloidal particles (i.e., forms a sol); an AFM image of the colloidal particles (10–15 nm in diameter) is shown in Fig. 2(a) for a composition at 3AS : TMOS = 5.5. The gel-to-sol transition is probably caused by the dissolution of the siloxane crosslinks (i.e., the break up of Si—O—Si bonds by hydrolysis or reesterification reactions where solvent has easy access). The solubility of silica is known to increase at high pH [1, 5], and the large amine concentration in the present composition makes the gel very basic (pH = 9–10). Also, silica solubility increases by a factor of three upon increase in temperature from 25°C to 75°C [1], which coincides with the fact that the wet gel reversal rate increases with temperature.

The addition of different solvents in solution (A) provides some further evidence that dissolution of the silica is occurring during the gel-to-sol transition. Ethanol (EtOH) was added to the 3AS : TMOS mixture (A), and a gel was still formed when water was added. The ethanol containing gels still reversed and behaved like compositions without added solvent (Fig. 1). In contrast, 3AS : TMOS solutions in tetrahydrofuran (THF), also form an optically transparent gel (B), but the gels were found to be irreversible. Protic solvents, such as EtOH, can hydrogen bond to hydroxyl

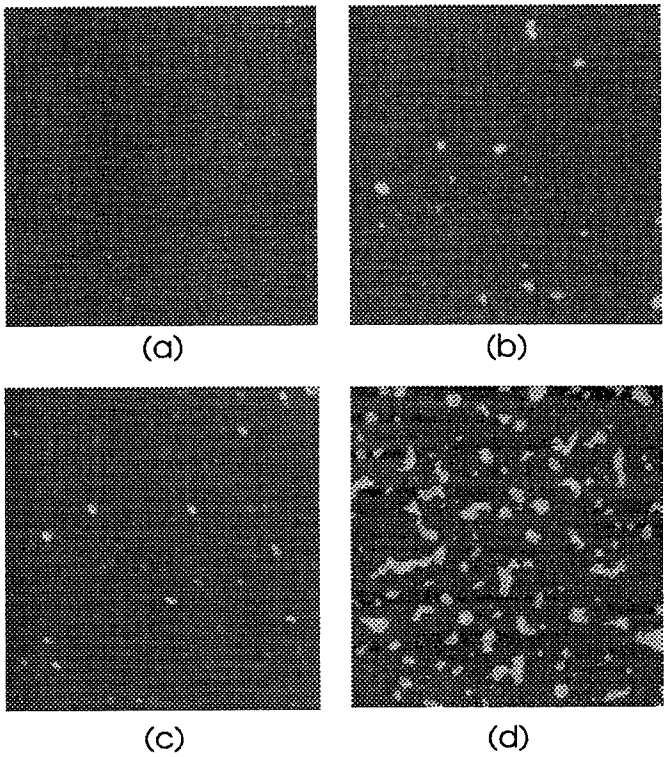

Figure 2. AFM images of diluted reversed solutions with (a) 3AS : TMOS = 5.5 at low concentrations, (b) 3AS : TMOS = 5.5 at higher concentrations, (c) 3AS : TMOS = 3 at low concentrations and (d) 3AS : TMOS = 3 at higher concentrations. The full scale for each image is 1000 nm.

ions or siloxanes to make them more electrophilic and can influence the reverse reactions as shown below [5]:

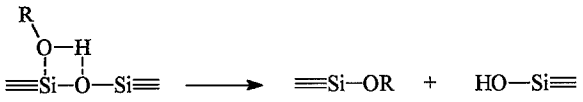

Aprotic solvents, such as THF or dioxane, are considerably more inert. They cannot form hydrogen bond with hydroxyl ions (or siloxanes) and cannot participate in the hydrolysis or reesterification of siloxane bonds. This supports the suggestion that the wet gel (B) formation is due to siloxane crosslinking as opposed to just hydrogen bonding, and the gel-to-sol reversal is due to the dissolution of silica.

A phase diagram for the 3AS + TMOS + H_2O system determined as a function of the acid content and the 3AS : TMOS ratio gives insight into the behavior of the gel (Fig. 3). In all cases, except at a 3AS : TMOS ratio of ∞, a wet gel (B) was formed. At lower acid contents and lower TMOS contents, the wet gels (B) were reversible. As the acid content increases, the degree of hydrolysis/condensation of the alkoxides increases, thereby increasing the number of crosslinks between the colloidal particles. High crosslink densities decrease the ability for dissolution to cause breakup of the colloids and to cause gel reversal to a sol. As the TMOS content increases, the number of crosslink sites between the colloids should also increase, because TMOS is four functional and the 3AS is only three functional. At very high TMOS contents (3AS : TMOS < 2), the wet gel (B) did not reverse.

The reversed solutions (B) became more viscous with increasing TMOS content. This is believed to be caused by the increase in the colloid size and colloid interaction at higher TMOS contents as indicated by the AFM images in Fig. 2. At a 3AS : TMOS = 5.5 : 1 (Fig. 2(a)), the dispersed colloid size was relatively small (10–15 nm), while at 3AS : TMOS = 3 : 1 (Fig. 2(c)), the size was much larger (40–100 nm). There was also greater interaction between the colloids at 3AS : TMOS = 3 : 1, because at higher colloid concentrations, the colloid size increases dramatically (Fig. 2(d)). In contrast, with the 3AS : TMOS = 5.5 : 1

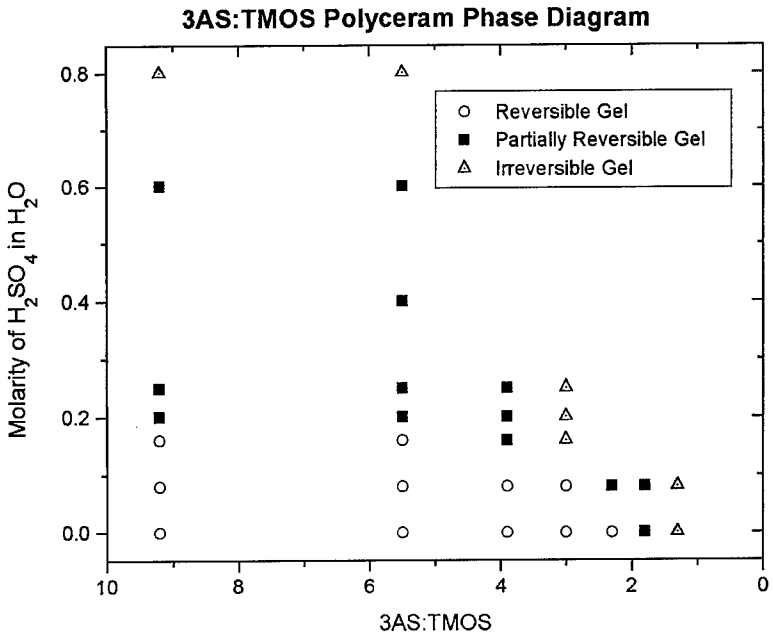

Figure 3. Phase diagram of 3AS : TMOS compositions as a function of H_2SO_4 content and TMOS content.

composition, the colloid size does not increase as much (Fig. 2(b)). The greater interaction between the colloids of the higher TMOS samples could stem from the larger concentrations of silanols at the surface which can undergo condensation reactions (i.e., there are fewer amine groups to block the surface silanols).

3AS alone hydrolyzed by H_2O is unusually stable in aqueous environments [7]. The unique water solubility stems from the formation of low molecular weight cage structures and from internal cyclization, where the propyl amine group wraps around and hydrogen bonds with the silanol groups [7, 8]. The propyl amine in this configuration blocks the silanol groups and hinders the condensation reactions, resulting in high stability in aqueous environments. The energy for cyclization has been reported to be -26.3 kcal/mole, which is much greater than the thermal energy [7]. When both 3AS and TMOS are hydrolyzed together, larger cage structures (colloids) are believed to be formed which are linked mostly by siloxane bonds in the wet gel (B). After dissolution, the reversed solution (C) does not return to a gel (B) upon cooling because: (1) the internal cyclization of the amine groups to the silanol groups on the surface of the colloids hinders inter-colloid condensation; and (2) the electrostatic interactions between the colloids contributes to the colloid-colloid repulsion (see discussion below). For these same reasons, the dried gel (D) is water soluble.

Two experiments confirm that the interaction of the colloidal particles is governed by electrostatic forces. First, the colloidal solution (B) precipated when $ZrCl_4$ was added to the solution. The addition of a multivalent salt contributed to the decrease in the electrical double layer and hence caused flocculation or coagulation. Second, the particles have a significant zeta potential of -30 to -40 mV as measured by electrophoresis, suggesting that a strong surface charge exists on the colloids.

Knowing this, Derjaguin-Landau-Verwey-Overbeek (DLVO) theory can be applied to confirm and predict conditions under which flocculation or dispersion of the colloids will occur [9]. DLVO theory takes into account electrostatic repulsion and van der Waals attraction and can be described by:

$$\kappa^{-1} = \left[\left(\frac{4\pi}{\varepsilon\varepsilon_0 k_B T}\right)\cdot\left[n_p Z_p^2 e^2 + n_\alpha Z_\alpha^2 e^2\right]\right]^{\frac{1}{2}}$$

$$U_A = -\frac{A}{6}\cdot\left(\frac{2a_p^2}{r^2-4a_p^2} + \frac{2a_p^2}{r^2} + \ln\left(\frac{r^2-4a_p^2}{r^2}\right)\right)$$

$$U_R = \frac{Z^2e^2}{\varepsilon\varepsilon_0}\cdot\left(\frac{\exp(\kappa a_p)}{1+\kappa a_p}\right)\cdot\frac{\exp(-\kappa r)}{r}$$

$$U_T = U_A + U_R$$

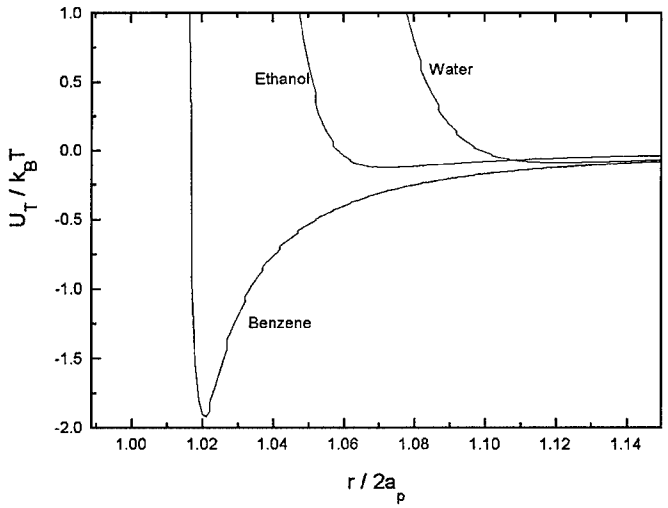

Figure 4. Interaction energy of two colloidal particles relative to the thermal energy predicted by DLVO theory (a) upon change in the dielectric constant of the solvent (for water $\varepsilon = 78$, $A = 0.323 * 10^{-20}$ J, for ethanol $\varepsilon = 26$ and $A = 0.181 * 10^{-20}$ J, for benzene $\varepsilon = 2$ and $A = 0.373 * 10^{-20}$ J) with the parameters $Z_p = 2500$, $a_p = 6$ nm, $T = 300$ K, $n_p = 10^{17}$ cm^{-3}, and $n_\alpha = Z * n_p$. Hamaker constants were estimated using equation 11.14 from Israelachvili [10].

where κ^{-1} is the screening length (approximately the double layer thickness), U_R is the Columbic repulsion energy, U_A is the van der Waals attraction energy, ε is the dielectric constant of the solvent, ε_0 is the permittivity of a vacuum, k_B is Boltzmann's constant, T is the temperature, n_p is colloid density, Z_p is valence of colloidal particle, e is the charge of an electron, n_α is the counterion density, Z_α is the counterion valence, a_p is the particle radius, r is the distance between particles and A is the Hamaker constant [9].

The reversed solution (C) was added to a variety of different solvents. In general, high dielectric solvents resulted in a stable colloid mixture, while low dielectric constant solvents result in flocculation of the colloidal particles. A decrease in the dielectric constant results in the decrease in the electrical double layer, and hence causes flocculation. Figure 4 is a plot of the energy between two colloids relative to the thermal energy for three solvents (H_2O ($\varepsilon = 78$), EtOH ($\varepsilon = 24$) and benzene ($\varepsilon = 2$)) as a function of the distance between the colloids in units of particle diameter as predicted by DLVO theory. The low dielectric constant solvent, benzene, has a minimum in the energy curve suggesting that the colloids should flocculate; the curves for the two other solvents do not have an energy minimum, suggesting that the particles should be dispersed. The predicted behavior in Fig. 4 matched the experimental results of adding the respective solvents, and therefore the behavior of the 3AS : TMOS colloids seems well predicted by DLVO theory.

4. Conclusions

A sol-gel material derived from 3AS and TMOS precursors has been characterized, and its unique properties of reversible gelation and water solubility have been described. The reversibility of the initial gel is caused by the dissolution of the Si—O—Si in the presence of a highly basic environment. This results in formation of colloidal particles with amine and silanol surfaces that are water soluble, and whose behavior is governed by electrostatic interactions.

Acknowledgment

The financial support of the Air Force Office of Scientific Research is gratefully acknowledged.

References

1. R. Iler, *The Chemistry of Silica* (John Wiley & Sons, New York, 1979).
2. J. Vail, *Soluble Silicates,* ACS Monograph Series (Reinhold, New York, 1952), Vol. 1/2.

3. R. Iler, U.S. Patent 2,692,863, DuPont, 1954.
4. D. Shaefer, U.S. Patent 3,625,856, Nalco Chemical Co., US, 1971.
5. C. Brinker and G. Scherer, *Sol-Gel Science* (Academic Press, Boston, 1990).
6. H. Schmidt, H. Scholze, and A. Kaiser, *Journal of Non-Crystalline Solids* **63**, 1–11 (1984).
7. E. Plueddemann, *Silane Coupling Agents* (Plenum Press, New York, 1982).
8. C. Chiang, H. Ishida, and J. Koenig *74* **2**, 396 (1980).
9. A. Sood, *Solid State Physics* (Academic Press, 1991), Vol. 45, pp. 1–73.
10. J. Israelachvili, *Intermolecular and Surface Forces* (Academic Press, San Diego, 1992).

Journal of Sol-Gel Science and Technology 13, 559–563 (1998)
© 1998 Kluwer Academic Publishers. Manufactured in The Netherlands.

Optical Nonlinearity of Hybrid and Nanocomposite Materials Prepared by the Sol-Gel Method

FUXI GAN
Shanghai Institute of Optics and Fine Mechanics, Academic Sinica, P.O. Box 800-211, Shanghai 201800, P.R. China

Abstract. In this paper the nonlinear refractive index, optical limiting effect, photoinduced and electroinduced second harmonic generation of dye-doped hybrid and nanoparticle-doped composite materials prepared by the sol-gel process have been reported. The origin of these nonlinear optical effects has been discussed.

Keywords: sol-gel, hybrid, nanocomposite, optical nonlinearity

1. Introduction

Nonlinear optical effects, such as nonlinear optical absorption, second and third optical nonlinearities, can be used for making optical limiters, optical modulators, as well as laser second and third harmonic generators. Thermal and light instabilities are the main problems for application of organic materials, although they possess high values of optical absorption and optical nonlinearity. To solve these problems research on doping an active organic phase into an inorganic host matrix to prepare hybrid materials has been intensified in recent years. Organic and inorganic hybrids are called Ormosils. Our recent experimental results of dye-doped Ormosils are reported.

Quantum-confined nanoparticles have been investigated extensively from the viewpoint of fundamental physics and also from interest in their application in optical and electronic devices. The preparation of nanocomposite materials by sol-gel is a promising alternative for obtaining new and competitive products for optical nonlinearity applications. New nanocomposite materials doped with CdSe, CuI, Sb_2S_3, Bi_2S_3 and Bi_2O_3, as well as fullerene, are reported. Their nonlinear optical susceptibility, optical limiting, photoinduced and electroinduced second-order harmonic generation were studied, and the origin of these optical nonlinear effects is discussed.

2. Experimental

2.1. Method of Preparation

Nonlinear optical hybrid and nanocomposite materials prepared by the sol-gel process have been paid more attention in recent years, due to the very low temperature involved in preparing this kind of nonlinear optical material. For preparation of dye-doped Ormosils, $Si(OC_2H_5)_4$ (TEOS), $(CH_3)_2Si(OC_2H_5)_2$ (DMDEOS), $CH_2(O)CH—CH_2—O(CH_2)_3—Si(OCH_3)_3$ (GPTMOS) and $CH_3Si(OCH_3)_3$ (MTMOS) were used as starting materials, in which ethanol (C_2H_5OH) was mixed with aq. HCl to form a sol. Dye dissolved in chloroethane was added to the above mentioned solution to form the precursor sol. For chalcogenide semiconductor doped Ormosils, TEOS was mixed with C_2H_5OH, HCl and H_2O for the first hydrolysis. Then $Cd(CH_3COO)_2 \cdot H_2O$, $Zn(CH_3COO)_2 \cdot 2H_2O$, $SbCl_3$, $Bi(NO_3)_3 \cdot 5H_2O$ and thiourea $SC(NH_2)_2$ in ethyl alcohol, were mixed to complete the hydrolysis. CuI was dissolved in CH_3CN. The detailed method of preparation has been reported in previous work [1–3].

The sol-gel derived hybrid materials doped with C_{60} were prepared as follows. In the $C_{60}—NH_2(CH_2)_3Si(OC_2H_5)_3$ (KH550) system, the fullerene has high reactivity to the primary and secondary amines through N-H addition reaction, thus the C_{60} can be bonded

chemically to the KH550 matrix and finally the system can be synthesized into a uniform gel through the hydrolysis and condensation reactions of the Si—OR groups. The maximum reaction ratio of C_{60}/Si is up to 1.6×10^{-3}. The mechanical strength of the gel can be modified by introducing some organic precursors, such as 3-glycidoxypropyltrimethoxysilane (KH560) and dimethyldiethoxysilane (DMDEOS). The method of preparation has been described in detail in [4].

2.2. *Measurement*

The third-order nonlinear optical susceptibility $\chi^{(3)}$ can be measured by four-wave mixing, third harmonic generation and the "z-scan" technique. The z-scan technique has great advantages of simplicity and high sensitivity; it has been used to make sensitive simultaneous measurements of the sign and magnitude of nonlinear refractive index and the two-photon absorption coefficient of nonlinear optical materials. The experimental arrangement has been described in [5]. The experiments were performed with a low power continuous-wave He-Ne laser, air cooled Ar^+ laser and high power Nd:YAG laser operating at different laser wavelengths and pulse duration.

The origin of the third-order optical nonlinearity comes from nonlinear refraction and nonlinear absorption. The third-order optical susceptibility $\chi^{(3)}$ can be expressed:

$$\chi^{(3)} = [(\mathrm{Re}\,\chi^{(3)})^2 + (\mathrm{Im}\,\chi^{(3)})^2]^{1/2} \quad (1)$$

$$\mathrm{Re}\,\chi^{(3)} = 2n_0^2\varepsilon_0 c\gamma, \quad \text{real part Re } \chi^{(3)} \quad (2)$$

$$\mathrm{Im}\,\chi^{(3)} = \beta\frac{n_0^2\varepsilon_0 c\gamma}{2\pi}, \quad \text{imaginary part Im } \chi^{(3)} \quad (3)$$

where n_0 is the linear refractive index, ε_0 is the permittivity of free space, and c is the velocity of light, γ is nonlinear refraction and β is nonlinear absorption. Both can be obtained from the z-scan measurement. The nonlinear refractive index n_2 at the non-resonant region is

$$n_2 = 16\chi^{(3)}/\pi^2 c\varepsilon \quad (4)$$

The optical nonlinearity is composed of an electronic part (short time response) and thermal parts (long time response); these can be separated by different method measurements.

The optical limiting effect is easily observed in nonlinear optical materials. A schematic of the method of measurement is given in [6].

The second-order nonlinear optical susceptibility $\chi^{(2)}$ can be measured by second harmonic generation or Maker fringes. The experimental setup for second-order harmonic generation was described in [7].

3. Results and Discussion

3.1. *Nonlinear Refractive Index of Organic and Inorganic Hybrid and Nanocomposite Materials*

A conjugated polymer with π-electron delocalization has a large third-order optical nonlinearity. 2D and 3D octupolar structures open new perspectives for third-order nonlinear optical media. Table 1 shows the nonlinear refractive index n_2 of a series of dyes in Ti-OM (TiO_2-Ormosil) prepared by us [2].

The data listed above were measured by the z-scan method using doubling frequency Nd:YAG laser with 0.5 μs pulse at wavelength of 532 nm (near-resonant). Figure 1 shows the measured z-scan of pyrylium-G doped Ormosil.

Phthalocyanine compounds have good physical properties, i.e., thermal and light stability. It is easy to get a thin film by spin-coating of the molecularly doped Ormosil. The n_2 value of vanadyl-phthalocyanine is larger than that of other phthalocyanine compounds. Figure 2 shows the measured z-scan of Pr_4VOPc-Ormosil film with a thickness of 80 nm. The shape of the pike-valley in the curve demonstrates the negative value of nonlinear refractive index (defocusing). The n_2-value is around 10^{-11} esu at wavelength of 532 nm and pulse duration of 100 ps.

The approaches for increasing optical nonlinearity of nanocomposite materials are as follows: increasing

Table 1. Nonlinear refractive index of dye-doped Ormosil-TiO_2.

Dye	Concentration	λ_{ab} (nm)	$n_2 \times 10^{-11}$ (esu)
DODCI	5×10^{-4}	591.0	9.21
MG	2×10^{-5}	629.6	13.13
Pyrylium-G	2×10^{-5}	577.4	12,900
Pyrylium-H	2×10^{-5}	550.0	3523
Fluorescein	4×10^{-5}	480.6	12,191
Acridine Orange	3×10^{-5}	491.0	3489

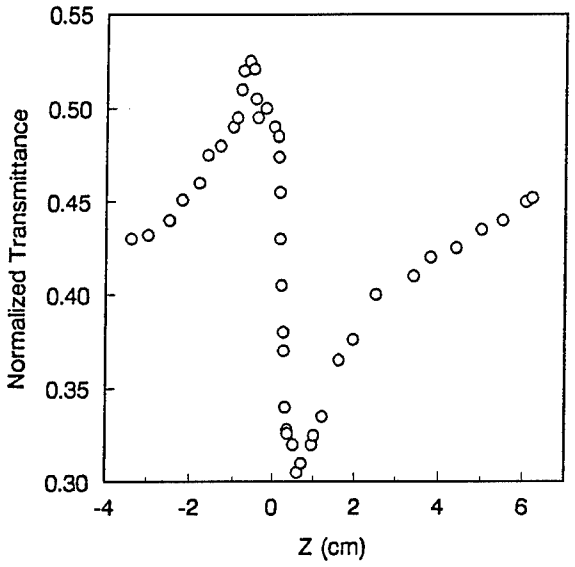

Figure 1. Measured z-scan of the pyrylium-G doped Ormosil.

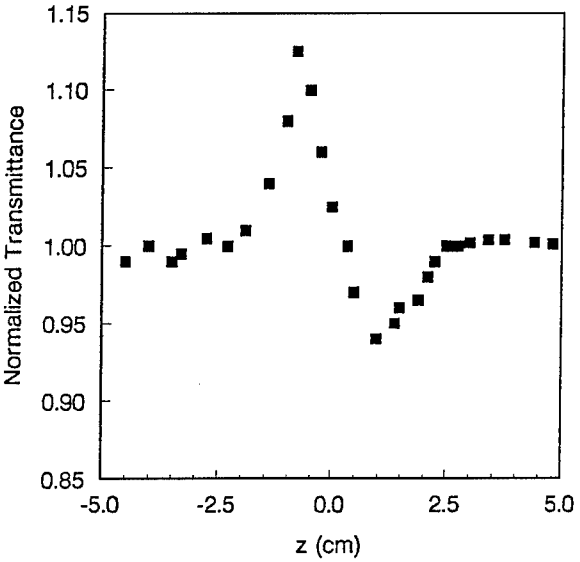

Figure 2. Measured z-scan of the Pr_4VOPc doped Ormosil.

particle concentration; working at near-resonant wavelength and adding dielectric confinement effect beside the quantum confinement effect.

The sol-gel method is quite suitable for increasing particle concentration. For example, using a conventional melting method under near-resonant conditions the $\chi^{(3)}$ of 2% CdS doped glass was estimated to be 1.5×10^{-10} esu (390 nm). Increasing the doping concentration up to 8 wt% of CdS by the sol-gel process, increased the $\chi^{(3)}$ value to 6.3×10^{-7} [8]. The nonlinear refractive index of Sb_2S_3, Bi_2S_3 doped Ormosils, measured by the z-scan method, gave 2.2×10^{-10} esu and 3.3×10^{-9} esu, respectively, at the near-resonant wavelength of 532 nm.

Using a 1.06 μm laser wavelength and 150 ps pulse duration, we measured the nonlinear refractive index of C_{60}-KH550 by the z-scan method. The nonlinear index of refraction (n_2) of the sol and gel was in the range of $5–6 \times 10^{-12}$ esu, corresponding to $\chi^{(3)} = 1.5–2 \times 10^{-11}$ esu (at 1.06 μm). The approximate magnitude of n_2 shows that fullerenes are located in a similar environment, surrounded by amino groups. This is the pure electronic contribution during ps laser pulse duration. It should be larger at ns and μs pulse duration, including the thermal contribution.

Optical nonlinearity can be enhanced by the dielectric confinement effect, which is a surface polarization effect induced by trapped state and atomic vacancy defects. This effect depends on the dielectric constant ratio ($\varepsilon_1/\varepsilon_2$) of microparticles and surroundings. There are two ways to intensify the dielectric confinement effect: nanoparticles with high refractive index, such as In_2O_3, SnO_2, Bi_2O_3, CdS, Bi_2O_3, PbS(Se) doped in a matrix with low refractive index, such as SiO_2, PMMA, PVA and nanoparticles with a high refractive index, coated with a low refractive index layer, such as: stearic acid (ST), sulfonic acid sodium salt (DBS), poly(vinyl alcohol) (PVA).

Recently, we have been successful in preparing colloidal PbS, Bi_2O_3, In_2O_3 and SnO_2 nanocrystallites coated with ST or DBS. Taking an example for coated Bi_2O_3 in a sol, Table 2 shows the experimental results comparing the $\chi^{(3)}$ value of nanoparticles of Bi_2O_3 coated with ST, bare particles of Bi_2O_3 and bulk Bi_2O_3.

Table 2. Experimental results of the z-scan measurements for bare Bi_2O_3 nanoparticles in a hydrosol, coated ones with toluene (±20%) and bulk Bi_2O_3.

Sample	Coated Bi_2O_3	Bare Bi_2O_3	Bulk Bi_2O_3
Band-edge (eV)	2.18	3.00	2.80
β (cm/GW)	0.23	0	0
$\mathrm{Re}\chi^{(3)}$ (esu)	3.47×10^{-11}	3.8×10^{-12}	4.2×10^{-13}
$\mathrm{Im}\chi^{(3)}$ (esu)	-2.61×10^{-12}	0	0
$\chi^{(3)}$ (esu)	3.48×10^{-11}	3.8×10^{-12}	4.2×10^{-13}

The difference in $\chi^{(3)}$ is about one order of magnitude. This shows strong evidence of the enhancement of optical nonlinearity by the dielectric confinement effect.

3.2. *Optical Limiting Effect*

Using a Nd:YAG laser with 10 ns duration and wavelength 532 nm, the optical limiting behavior of a C_{60}-KH550 Ormosil is shown in Fig. 3. With increase in the incident laser intensity, the increasing transmitted laser energy tended to saturate gradually. This was caused by the reverse saturation characteristic of the fullerene in the gel. No laser damage phenomenon in the sample was observed under the microscope even when the incident laser intensity rose to 5 J/cm^2. At low incidence, the transmittance of the two samples of C_{60}-KH550 were about 51% and 21%, respectively. Along with increasing the fluence in, the fluence out was limited at about 0.85 and 0.4 J/cm^2, respectively. The optical limiting parameters are decided by the absorption of C_{60} and the matrix, the reflection of the face and the scattering losses of the sample, etc. The absorption at 530 nm of undoped (blank) KH550 gel was very low; the optical limiting effect is mainly due to the nonlinear absorption of C_{60}. The absorption at 530 nm is in the tail of the broad band absorption of C_{60}; the peak wavelength is located at 280 nm in ultraviolet region.

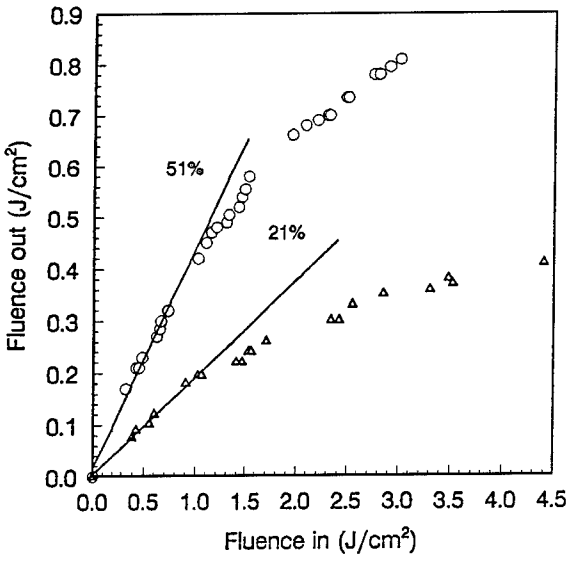

Figure 3. Optical limiting data of C_{60}-KH550 (0.5 mg/ml, 0.08 cm thickness) gel (○); C_{60}-KH550 (1 mg/ml, 0.12 cm thickness) gel (△).

We have observed the optical limiting effect in PbS- and Bi_2S_3-doped Ormosil films too.

3.3. *Photoinduced and Electroinduced Second Harmonic Generation (SHG)*

We have obtained the SHG signal from CuI, Sb_2S_3 and Bi_2O_3 doped Ormosils. The samples were preilluminated by a mode-locked Nd:YAG laser with the fundamental laser beam (1.06 μm) or fundamental and frequency-double laser beam (1.06/0.532 μm), and then photoinduced SHG was detected from the fundamental beam. It has been found that all the photoinduced SHG signals generated in the above samples show common characteristics, i.e., the SHG intensity increases with illuminating time and approaches saturation gradually. However, for different kinds of sample, the illuminating time needed for the SHG saturation is different. Figure 4 shows the quadratic dependence of SHG on input laser power for the CuI microcrystallite doped Ormosil; it was verified that a second-order process was indeed responsible for the signals from the semiconductor dots. In addition, the SHG is interrelated with both the power intensity of the preparation beam and the thickness of sample. The photoinduced second-order nonlinear optical effect of

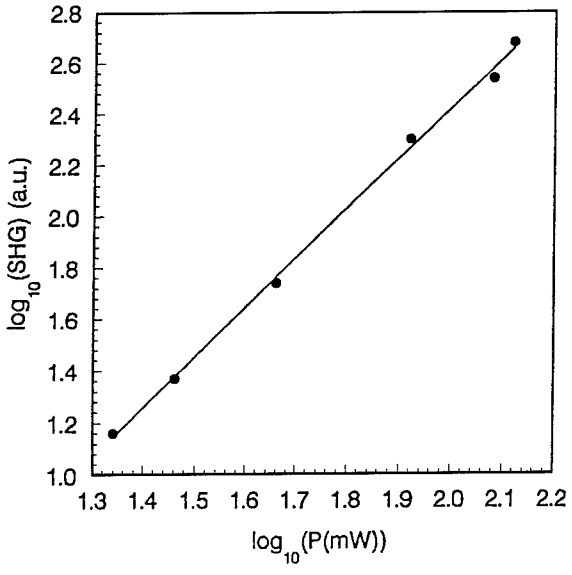

Figure 4. Log-log plot, displaying second harmonic power dependence on the input beam power squared for CuI microcrystallite doped silica glass.

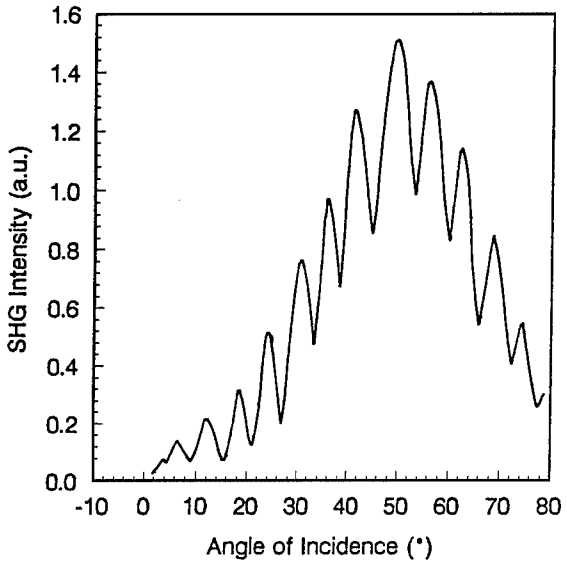

Figure 5. Variation of SHG intensity with incident angle for CuI microcrystallites doped borosilicate glass poled at 200°C and 4 kV.

Table 3. The second harmonic generation and the poling conditions of glasses.

Glasses	Poling conditions	$I_{max}(I/I_q)$
CuI-doped glass	200°C, 4 kV, 1 h	7.0×10^{-4}
CuBr-doped glass	200°C, 4 kV, 1 h	7.5×10^{-4}
CuCl-doped glass	200°C, 4 kV, 1 h	8.2×10^{-4}
$CdS_{1-x}Se_x$-doped glass	200°C, 5.2 kV, 1 h	1.0×10^{-3}
JGS_2	200°C, 7.5 kv, 1 h	4.4×10^{-4}

JGS_2—germanium-doped silica glass.

semiconductor microcrystallite doped glasses can be explained reasonably well by the dc field model [9].

The SHG signals of several kinds of semiconductor microcrystallite doped Ormosils were observed in experiment. As the samples were electrically poled under a dc field at elevated temperature, the electroinduced SHG was detected by the fundamental laser beam with wavelength 1.06 μm for the Q-switched Nd:YAG laser. Figure 5 shows the Marker fringe of the CuI microcrystallite doped Ormosil. Through measuring the Marker fringes of the samples electrically poled under certain conditions, it is found that the SHG intensity depends on the incident angle of the laser beam and the maximum SHG intensity is located around 50°. The relative value of maximum SHG intensity $(I_s/I_q)_{max}$ is in the range of 10^{-4} to 10^{-3}. Table 3 shows the second harmonic signal generation intensity and poling conditions. It is also found that the electroinduced second-order nonlinear polarization in glasses is stable at room temperature, but can be erased just by heating the samples. The experimental results can be explained qualitatively by the dipole orientation model [10].

4. Conclusion

The nonlinear refractive index of organic-inorganic hybrid and semiconductor nonocomposite materials has been systematically studied. The optical limiting effect of fullerene doped Ormosil and the photoinduced and electroinduced second harmonic generation of CuI, Sb_2S_3, Bi_2S_3 nanoparticle doped gels and glasses have been observed for the first time. The sol-gel derived materials have potential applications in the fields of optics and optoelectronics.

References

1. F. Tang, F. Gan, and C. Zhu, SPIE, Sol-Gel Optics III **2288**, 350 (1994).
2. Z. Jiang, H. Ye, and L. Hu, in *Proceeding on XVII International Congress on Glass*, edited by Fuxi Gan (Chines Ceramic Society, Beijing, 1995), Vol. 1, p. 203.
3. H. Chen, C. Zhu, and F. Gan, J. Sol-Gel Sci. Tech. (in press).
4. H. Xia, C. Zhu, and F. Gan, Fullerene Sci. Tech. (in press).
5. B. Yu, C. Zhu, and F. Gan, Opt. Mat. **7**, 103 (1997).
6. H. Xia, C. Zhu, and F. Gan, Chinese J. Laser **B-4**, 247 (1995).
7. H. Chen, C. Zhu, and F. Gan, Chinese J. Laser (in press).
8. T. Takada, T. Yano, and A. Yasumori, J. Non-Cryst. Solids **147/148**, 631 (1992).
9. R.H. Stolen and H.W.K. Tom, Opt. Lett. **12**, 585 (1987).
10. R.A. Myers, N. Mukherjee, and S.R.J. Brueck, Opt. Lett. **16**, 1732 (1991).

Journal of Sol-Gel Science and Technology 13, 565–568 (1998)
© 1998 Kluwer Academic Publishers. Manufactured in The Netherlands.

Matrix Effects on Selective Chemical Sensing by Sol-Gel Entrapped Complexing Agents

NICO A.J.M. SOMMERDIJK AND JOHN D. WRIGHT
Centre for Materials Research, Department of Chemistry, University of Kent, Canterbury, KENT CT2 7NH, UK

Abstract. Changes in the selectivity of molecular recognition systems on sol-gel entrapment are reported. Thermodynamic effects are exemplified by studies of the metal-ion complexing agent Eriochrome Cyanine R (ECR). In aqueous solution this binds strongly and selectively to Al^{3+}, whereas in a TMOS-based sol-gel matrix it is selective for Cu^{2+}. Thermodynamic effects, due to restricted translational freedom of water molecules or different solvent structure and isolation of ligands, can explain these observations. Effects of entrapment on molecular recognition by a large conformationally flexible molecule have been studied using a *tris*-terminated PAMAM dendrimer. The dendrimer conformation and its complexation with Cu^{2+} changes on entrapment, and binding of aromatic carboxylic acids such as ibuprofen can be detected by changes in visible absorption and surface plasmon resonance using spun films of the sol-gel composite. These effects show that in addition to providing a porous entrapment matrix of good optical quality, sol-gels may be used to alter the binding characteristics of the entrapped receptors.

Keywords: composites, chemical sensing, spectrophotometry, surface plasmon resonance

1. Introduction

Molecular recognition by complexing agents and selective receptors provides many opportunities for the development of chemical sensors. Sol-gel entrapment provides a convenient means of immobilization of such receptors in a matrix which is both porous to analytes and suitable for optical transduction of the recognition process [1]. This paper describes recent results which demonstrate that this entrapment matrix also modifies receptor selectivity, and that a proper understanding of these effects can lead to additional fine-tuning of sensor performance.

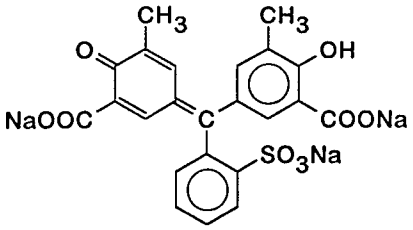

Ia

Eriochrome Cyanine R (ECR, **Ia**) forms a red-violet complex with Al^{3+} ions in aqueous solution, which provides the most sensitive spectrophotometric method for determination of $[Al^{3+}]$ [2]. To explore the possibility of using this system for optical sensing of aluminum ion contamination of water supplies, sol-gel monoliths have been prepared from precursor solutions containing appropriate amounts of ECR, and changes in their optical absorbance on exposure to metal ion solutions of controlled pH have been monitored.

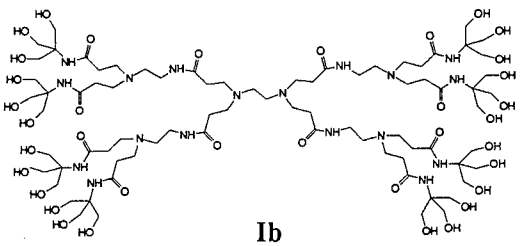

Ib

The *tris*-terminated PAMAM dendrimer **Ib** is a receptor for aromatic carboxylic acids, a class of compounds which includes common drugs like

ibuprofen [3]. This large flexible molecule was selected as an example of a system likely to reflect effects of conformational change as a result of sol-gel entrapment, and because of its potential diagnostic applications. Since the binding of ibuprofen would lead to no optical absorbance change, **Ib** was first complexed with Cu^{2+}, whose d-d transition energies are sensitive to the coordination environment. Electron spin resonance and solid-state NMR were used to provide information on molecular conformations in this system.

2. Experimental

Tetramethoxysilane (TMOS, 2.5 ml) was dissolved in 3.0 ml of an ethanol solution of ECR (5×10^{-8}–10^{-6} mol) and 1.6 ml of water and 2 drops HCl added (final pH 5.5). Mixtures were stirred for 30 minutes and sealed in petri dishes to gel. After 5 days, pinholes were made in the seals and after 10 days the gels were warmed slowly to 50°C for 4 days, then cooled to room temperature for 2 days before opening and aging for a further 2 weeks before use. Sol-gel composites of **Ib** were prepared by hydrolysis of TMOS using a 1.5% aqueous solution of the dendrimer, which acts both as a base catalyst and a surfactant to aid mixing of TMOS and the aqueous phase. The gels, either alone or spin-coated onto glass substrates covered with 50 nm silver films, were aged in a humid atmosphere at 50°C for 4 weeks. Pore size distributions were determined by thermoporometry using a Perkin-Elmer DSC7 following literature procedures [4]. Solid-state NMR data were obtained using a Chemagnetics CMX 300 Infinity spectrometer.

3. Results and Discussion

3.1. *Effects of Sol-Gel Entrapment on Metal-Ion Complexation by ECR*

Pieces of glass containing 0.17 μmol ECR per gram immersed in 0.1 mM aqueous $KAl(SO_4)_2$ solutions at pH 3, 4.5 and 6 showed almost no change in visible absorption spectra, in marked contrast to ECR in solution (Fig. 1). However, identically prepared composites containing the fluorescent Al(III) complexing agent 3,5,2′,7′-pentahydroxyflavone showed a response to Al(III) concentrations down to 10 ppm, establishing that Al^{3+} ions are not prevented from entering the gel

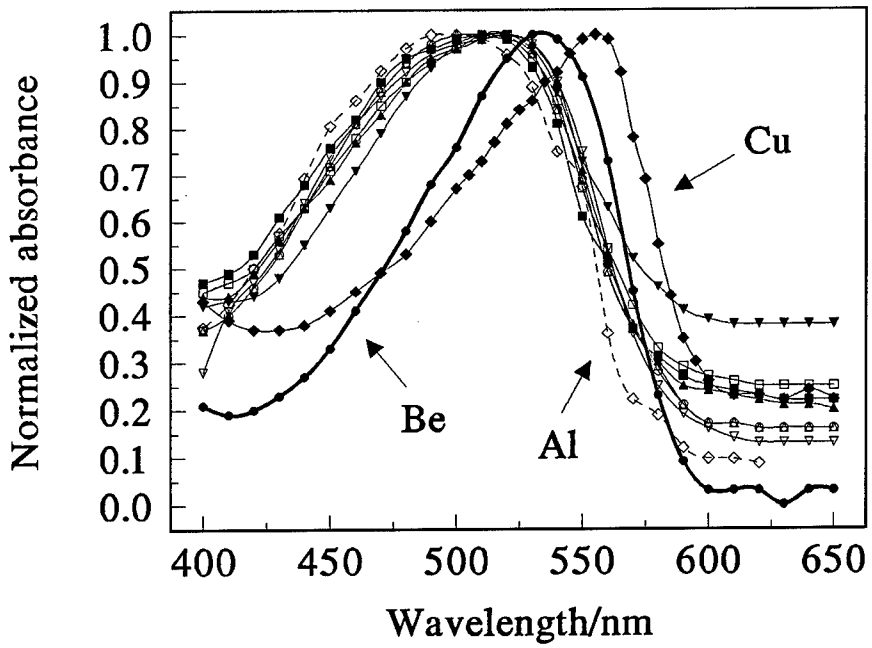

Figure 1. Normalized absorption spectra of **Ia**-doped gels at pH 4.5 in water (□) and in 10^{-3}M Fe(III) (■), Zr(II) (▲), Co(III) (▼), Cr(III) (▽), Ni(II) (△), Al(III) (◇), Be(II) (●), and Cu(II) (♦).

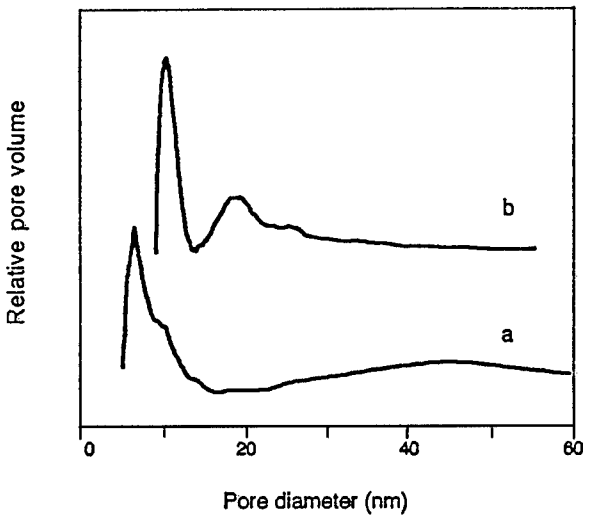

Figure 2. Pore size distributions determined by thermoporometry for (a) "thick" and (b) "thin" samples of **Ia**-doped gels (see text).

by strong complexation with surface hydroxy groups. The ECR composites were therefore exposed to 1 mM solutions of Cr(III), Fe(III), Zr(II), Be(II) and Cu(II) at pH 4.5, and visible spectral changes (Fig. 1) were observed only for Cu(II) and to a lesser extent Be(II). Experiments with different Cu^{2+} concentrations showed that the complexation was so strong that the final absorbance at $\lambda_{max} = 580$ nm was dependent only on the amount of entrapped ECR in the composite. However, the change in 580 nm absorbance was linear with $(\text{time})^{1/2}$ as expected for a diffusion-limited process, and the slopes of these plots increased linearly with the Cu^{2+} concentration, providing a quantitative optical sensing method for Cu^{2+} ions. Although these slopes were shown to be reproducible for a given Cu^{2+} concentration with a given piece of the composite, they were higher for thinner samples in which the pore size distributions (Fig. 2) had been modified as a consequence of the different drying stresses. In thinner glasses not only the analyte diffusion pathway is shorter but also the small pores are on average larger, aiding diffusion.

Entrapment of ECR in small sol-gel pores affects complexation with metal ions in two ways. First, the favorable entropy increase expected on displacement of the metal hydration sphere by ECR will be drastically reduced, since translational freedom is restricted in small pores. This effect will be particularly marked for small highly charged ions such as Al^{3+}. Second, the changed solvent structure arising from H-bonding with surface OH groups in small pores (reflected in changed freezing points observed in thermoporometry), and interactions of both ligand and metal ions with pore walls, affect the enthalpy of complex formation. Changing the pore size and pore wall chemistry, for example by replacing part of the TMOS with methyltriethoxysilane (MTEOS), in principle provides a means of fine-tuning these effects. However, initial experiments have led to either severe cracking or leaching of ECR from the enlarged pores, indicating that the range of parameters to be included in such fine-tuning is likely to be large.

3.2. *Sol-Gel Entrapped Dendrimer*

Despite large pore sizes (20–60 nm diameter, from thermoporometry and typical for base-catalyzed gels), no leaching of the entrapped dendrimer was observed. The 24 peripheral OH groups in **Ib** provide covalent immobilization by condensation reactions with surface OH groups of the gel pores. This is reflected in a new peak in the ^{13}C CPMAS NMR spectrum due to $Si{-}O{-}CH_2$ linkages. On complexation of **Ib** with copper chloride, the ^{13}C CPMAS NMR spectrum shows resonance shifts which are consistent only with complexing via nitrogen atoms of the dendrimer. Diffuse reflectance spectra of **Ib** and copper acetate (1–8 equivalents) showed a broad d-d band whose position varied between 620 and 680 nm depending on the Cu concentration. The complex formed after soaking the entrapped **Ib** in excess Cu^{2+} showed a different, broadened band at 680 nm. ESR spectra showed that the gel-entrapped complex ($g_\perp = 2.07$, $g_\parallel = 2.17$, $A_\parallel = 220$ G) has a different copper coordination environment from that of any of the free complexes ($g_\perp = 2.08 - 2.12$, $g_\parallel = 2.20$, $A_\parallel = 178$ G). On exposure of the gel-entrapped copper-dendrimer complex to 0.125 mM aqueous ibuprofen, the intensity of the d-d transition decreased, the decrease being linear with $(\text{time})^{1/2}$, confirming a diffusion-limited process. The shape and g values of the ESR spectrum also changed (although the g and A values could not be clearly determined), suggesting some modification of the copper environment by the ibuprofen. Surface plasmon resonance (SPR) curves recorded using the equipment described in [5] for the thin spun films of the composite on 50 nm silver on glass substrates (Fig. 3) showed significant shallowing and shifting of the resonance minimum on exposure to 0.1 M copper

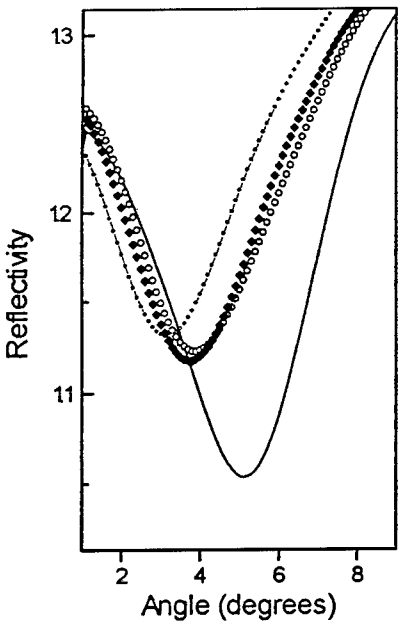

Figure 3. Surface plasmon resonance curves for **Ib**-doped gel film (solid line), after exposure to 0.1 mM $Cu(OAc)_2$ (◯), after subsequent exposure to 0.125 mM Ibuprofen (○) and after washing with 0.1 mM $Cu(OAc)_2$ (◆).

acetate. Subsequent exposure to 0.125 mM ibuprofen led to further significant shifts, which were readily reversed by washing the film with 0.1 M copper acetate solution, the free Cu^{2+} ions complexing the ibuprofen more strongly than the dendrimer-complexed copper.

4. Conclusions

Sol-gel entrapment of ECR changes its selectivity for complexation of different metal ions via thermodynamic effects arising from restricted translational motion in small pores and changed solvent structure due to pore wall interactions. Varying gel thickness and pore size provides control of analyte diffusion rates to the entrapped reagent, and hence of sensitivity. PAMAM dendrimer-copper complexes are insoluble in water and thus relatively inaccessible to analytes such as ibuprofen, whereas in gels the dendrimer is held in a highly porous matrix and retains sufficient conformational flexibility to complex copper and to display changes in the coordination environment on exposure to ibuprofen. The resulting optical absorbance and SPR sensing opportunities demonstrate the value of modifying the environment of such large receptors using sol-gel entrapment. As with the ECR system, controlled modification of the local sol-gel environment by changing the precursors and/or gel preparation conditions should provide opportunities for fine-tuning the sensing system.

Acknowledgments

We thank Miss R. Esfand and Dr. J.C. Mitchell for samples of the dendrimer, Dr. E.R.H. van Eck for NMR spectra, Miss A. Poppe and Miss C.A. Gibson for assistance with the ECR studies and the European Community Human Capital and Mobility program for financial support.

References

1. R. Zusman, C. Rotman, M. Ottolenghi, and D. Avnir, J. Non-Cryst. Solids **122**, 107 (1990).
2. Z. Marcenko, *Spectrophotometric Determination of Elements* (Halsted Press/Wiley, Chichester, 1976).
3. R. Esfand, A.E. Beezer, J.C. Mitchell, and L.J. Twyman, Pharm. Sci. **2**, 157 (1996).
4. J.F. Quinson and M. Brun, J. Non-Cryst. Solids **99**, 151 (1988); K. Ishikiriyama, M. Todoki, and K. Motomura, J. Colloid Interface Sci. **171**, 92 (1995).
5. J.D. Wright, A. Cado, S.J. Peacock, V. Rivalle, and A.M. Smith, Sensors and Actuators **B29**, 108 (1995).

Journal of Sol-Gel Science and Technology 13, 569–573 (1998)
© 1998 Kluwer Academic Publishers. Manufactured in The Netherlands.

Fabrication and Properties of Doped Porous Polysiloxane Sol-Gel Layers on Optical Fibers

DANIELA BERKOVÁ, MIROSLAV SEDLÁŘ, VLASTIMIL MATĚJEC,
IVAN KAŠÍK AND MIROSLAV CHOMÁT
Institute of Radio Engineering and Electronics, AS CR, Chaberská 57, 182 51 Praha 8, Czech Republic

ADNANE ABDELGHANI, NICOLE JAFFREZIC-RENAULT AND MONIQUE LACROIX
Laboratoire Ingéniérie et Fonctionnalisation des Surfaces, Ecole Centrale de Lyon, 69131-ECULLY Cédex, France

Abstract. Polysiloxane porous layers doped with TiO- and phenyl-groups were fabricated by the sol-gel method. Starting sols were prepared from alkoxides using catalysis by HCl or HF. Stable SiO-TiO-sols were obtained by using HF. Porous gel layers with thicknesses of 0.3–1.1 μm were coated on fiber surfaces or silicon wafers. Layers with the refractive index of 1.38–1.48 were prepared. The fractional porosity of the layers was estimated to be 0.1–0.35. The interactions of the layers with vapor or liquid chlorinated hydrocarbons, alcohols or aromatic hydrocarbons have been studied in immersing experiments by measuring the output light intensity from the fibers. The observed changes of the output intensity could be correlated to changes of the refractive index of the layer caused by the penetration of the tested chemicals into the layer pores.

Keywords: porous layers, chemical sensing, sol-gel, optical fiber

1. Introduction

In recent years there has been increased interest in the application of porous layers prepared by the sol-gel method to the development of fiber-optic chemical sensors. Employing the sol-gel technique, fiber-optic sensors for pH sensing or oxygen sensing [1, 2] or the detection of chlorinated hydrocarbons [3] have been developed. In these sensors, changes of the refractive index of porous sol-gel materials due to interaction with chemicals are measured [3]. Chemical transducers such as pH indicators [1] or Ru-complexes [2] are immobilized in porous sol-gel matrices and changes of their light absorption coefficients or fluorescence are detected.

Porous materials have been coated on the fiber tip or as the fiber jacket. In the latter case, the evanescent-wave detection principle is often used for the detection of chemicals [1–4]. The reversibility of these sensors is mainly controlled by the properties of porous materials and their sensitivity in addition depends on waveguiding properties of the fiber structure [1–4].

This paper deals with the preparation of porous siloxane layers coated on silica optical fibers, their doping with TiO- or phenyl-groups and changes in their optical properties due to the contact with liquid alcohols or gaseous chlorinated hydrocarbons. The paper is aimed at extending the basis for the development of evanescent-wave fiber-optic chemical sensors with increased sensitivity by lowering the refractive-index difference between the fiber core and cladding.

2. Experiment and Results

2.1. *Preparation of Input Sols*

Silica and titania stock sols based on tetrathoxysilane (TEOS), phenyltriethoxysilane (PhTS) and titanium isopropoxide (TiIP) were prepared at first. Their

compositions are shown in Table 1. The sols A and B were obtained by refluxing the alkoxides with the solvent and catalyst at 60°C for 40 min. By mixing the stock sols A and B or by mixing the sol C with TEOS, water, glycerol and HCl or HF acids as catalysts, input sols for the coating of porous layers were prepared (see Table 2). Hydrofluoric acid has been used for testing the possibility of increasing the porosity of the coated layers [5]. An extensive investigation has been done on the gelation of the Si/Ti sols. It has been found that the sols containing HCl are stable for several months, while the most stable sols containing HF and glycerol gelled already after two weeks from their mixing.

2.2. *Preparation and Characterization of Coatings*

The sols were coated on silicon wafers or silica fibers. Fiber substrates were fabricated from silica fibers with a core diameter of 400 μm coated with silicone rubber by decladding the rubber in a 10-cm long fiber segment in the central part of the fiber. Both substrates were cleaned in a detergent, rinsed with water and dried.

The substrates were dipped into the sols and withdrawn with a velocity of 10 cm/min. The multiple coating process was also used. In this case, the coating was dried at 70°C for 1 h after the application of the sol. The final coatings were thermally treated at 70°C for 24 h.

The thicknesses and refractive indices of coatings fabricated on silicon wafers were determined by ellipsometry and in the case of layers on silica fibers they were estimated from optical power measurements [3, 4] (see the results in Table 3). The fractional coating porosity P was estimated from the equation

$$n = \sqrt{n_s^2 \cdot (1 - P) + P}, \tag{1}$$

where n is the measured refractive index and n_s is the refractive index of the fully densified solid material. These values are given in Table 3.

The interaction of layers coated on optical fibers with liquid or gaseous chemicals was investigated in a cell by bringing the coated fiber into contact with chemicals and measuring the changes of the output optical power from the fibers. Using these values, the attenuation α was calculated as

$$\alpha = 10 \cdot \log\left(\frac{I_{\text{ref}}}{I_{\text{out}}}\right) \quad \text{(in dB)}. \tag{2}$$

In Eq. (2), I_{ref} is the output power from the same fiber measured under reference conditions. Both selective excitation of the fiber by a parallel beam incident at an angle of 20° [3] and homogenous excitation [4] have been used. The attenuation was determined with an accuracy better than 0.05 dB.

Mixtures of 1-butanol and benzyl alcohol with predetermined values of the refractive index were used in experiments with liquid chemicals. The results are

Table 1. Composition of the stock sols.

Sol	C (mol/dm^3)	R_w	R_s	R_{Me}	R_{Ac}	R_H
A-(TEOS)	1.0 (0.64)	5	6	0	0	0.5
B-(PhTS)	1.0	5	6	0	0	0.6
C-(TiIP)	1.39	0	0	4	1	0.0

R_w = C(H_2O)/C, R_s = C(ET)/C, R_H = C(HCl)/C, R_{Me} = C(Me)/C, R_{Ac} = C(Ac)/C.

Table 3. Refractive indices (n), thicknesses and porosity (P) of porous layers.

	n/Thickness (nm)/P	
Coating/sol/substrate	70°C (1 h)	After 30 days
Si/I (C = 0.64 mol/dm^3)/w	1.37/1000/0.22	1.47/110/N
Si/I (C = 1 mol/dm^3)/w	1.44/220/0.04	1.4/210/0.14
Si/I (C = 1 mol/dm^3)/f	N	1.39/800/0.17
Si(0.5)/Si(0.5)/IV/f	N	1.48/800/0.35
Si(0.8)/Si(0.2)/III/f	N	1.46/1100/0.22

w: silicon wafer, f: fiber, N: undetermined.

Table 2. Composition of sols for the preparation of porous layers.

Sol	C (mol/dm^3)	R_w	R_H	R_F	R_s	R_{Me}	R_{Ac}	R_G
I (Si-)	1.0 (0.64)	5.0	0.5	0.0	6	0.0	0.0	0.0
II (Si/SiPh)	0.5/0.5	0.0	0.5	0.0	6	0.0	0.0	0.0
III (Si/Ti)	1.0/0.2	4.7	0.1	0.0	0	3.4	0.9	0.0
IV (Si/Ti)	0.76/0.76	4.0	0.0	0.1	0	4.0	1.0	1.5

R_F = C(HF)/[C(Ti) + C(Si)] and R_G = C(G)/[C(Si) + C(Ti)].

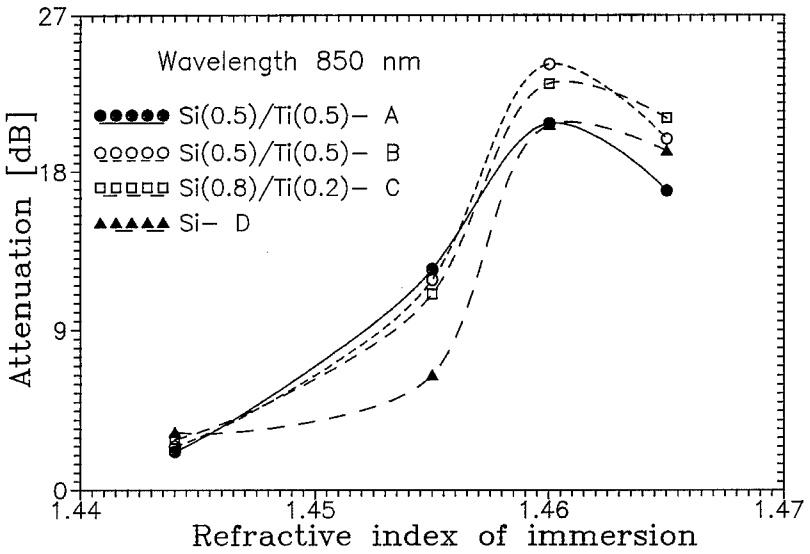

Figure 1. Effect of immersing the fibers with porous layers in solutions of 1-butanol and benzyl alcohol; the layer thicknesses: A: 300 nm, B: 800 nm, C: 1100 nm and D: 800 nm (Homogenous excitation. Reference: output power from the fiber in 1-butanol).

shown in Fig. 1. Gaseous mixtures of CCl_4, $CHCl_3$, benzene or toluene were used for the investigation of the effects of vapors (see the results in Figs. 2 and 3). The vapor mixtures were prepared by passing air or nitrogen through a flask with liquid chemicals at an air (nitrogen) flow rate of 100 cm^3/min. The time responses of the fibers during the interaction with the liquids or vapors have also been examined (see Fig. 4).

3. Discussion

The addition of 2-methoxyethanol and acetylacetone into the titania sols allowed us to make stable silica-titania sols under the catalysis of HF acid. It has been found that the stability of these sols decreases for increasing values of R_w. Glycerol, which was added to achieve a higher thickness of the coated layer, also decreases the sol stability (e.g., sols with Si/Ti = 0.8/0.2 could be prepared only if $R_G < 0.8$ and $R_w < 3$).

The values of the layer thicknesses in Table 3 show that there is a volume relaxation effect changing the thickness of the porous layers prepared from the sols with the lower silica content. A similar effect has been described for coating siloxane layers from sols with low values of R_w [1].

The layer porosity (see Table 3) calculated on the basis of the measured refractive indices and Eq. (1), represents only a rough estimate of this quantity. One reason is that when determining the refractive index of the layers using ellipsometry or optical power measurements, simplified models are used. In the case of thin and porous layers, such models may give unrealistic values of the refractive index of 1.47 for the siloxane layer (Table 3, the first row, measured after 30 days). The second reason is that for low-temperature processing of the layers, acetylacetone, 2-methoxyethanol or glycerol cannot be entirely removed from the coatings containing Ti. Therefore, they decrease the final value of the refractive index of porous coatings.

The results of the immersing experiments in Fig. 1 show that the liquid chemicals penetrate into the fiber coatings and change their refractive indices. The fibers coated with the porous layers prepared from titanium alkoxides exhibit, to some extent, higher sensitivity to this effect (higher values of the attenuation were measured with them) than the fibers coated with a pure siloxane porous layer. Because of the absence of absorption bands, the effect of the refractive index can also be directly deduced from the curves of the spectral attenuation in Fig. 2 where the modulations on the curves can be attributed to inaccuracy of the measurement. The penetration of liquids into the layers is relatively rapid; see Fig. 4 for immersing the fibers in 1-butanol, CCl_4 or $CHCl_3$.

The results of the immersing experiments with the vapors show that the fiber response depends on the compounds and their concentration (see Figs. 3 and 4). These curves can be explained by the effect of capillary condensation in the pores of the layer. Owing to

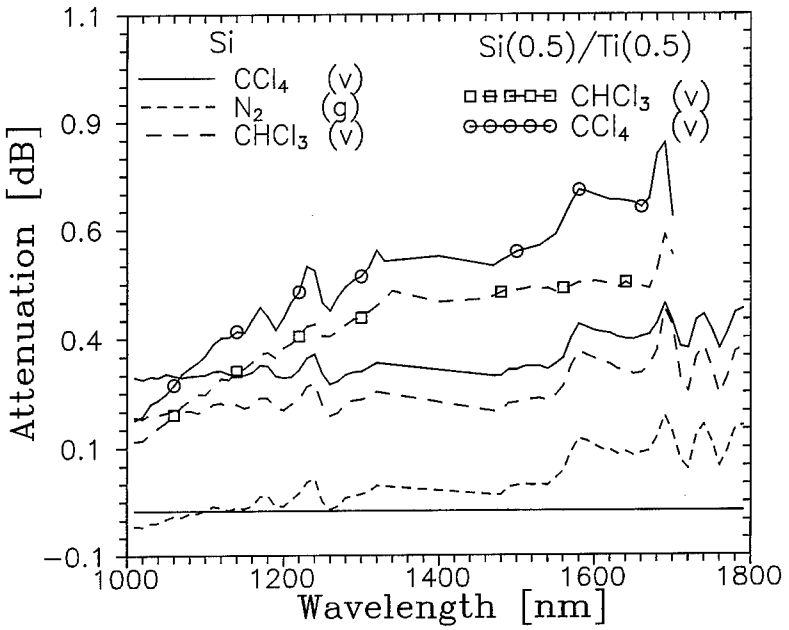

Figure 2. Changes of the spectral attenuation of the fibers coated with the porous layers (Si-t = 800 nm, Si/Ti-t = 800 nm) due to the contact with the CCl_4 and $CHCl_3$ vapors (v). Curve N_2 (g): effect of residual CCl_4 in the silica coating (Homogenous excitation. Reference: output power from the fiber in N_2).

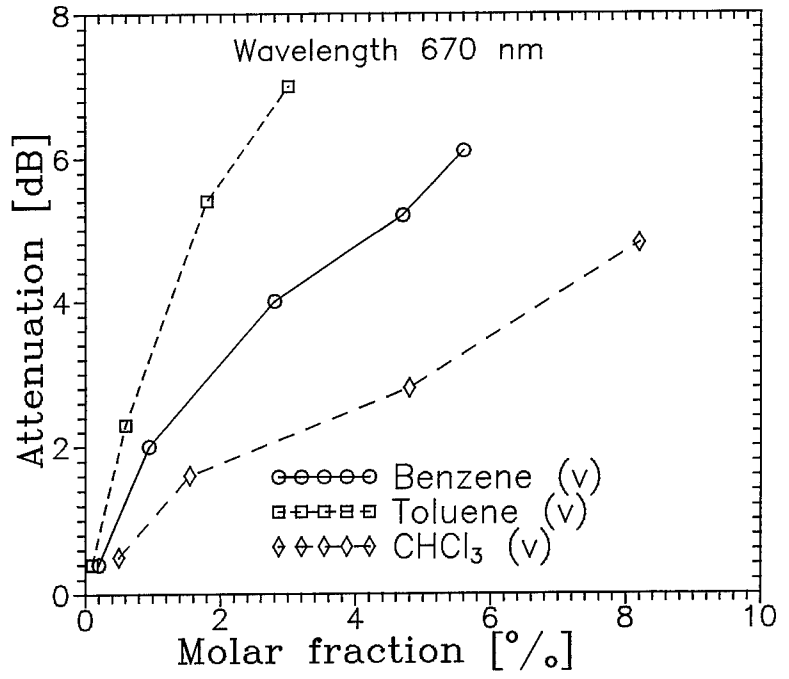

Figure 3. Effects of toluene, benzene and $CHCl_3$ vapors in air on the attenuation of the fibers coated with porous layers doped with phenyl-groups (Selective excitation. Reference: output power from the fiber in air).

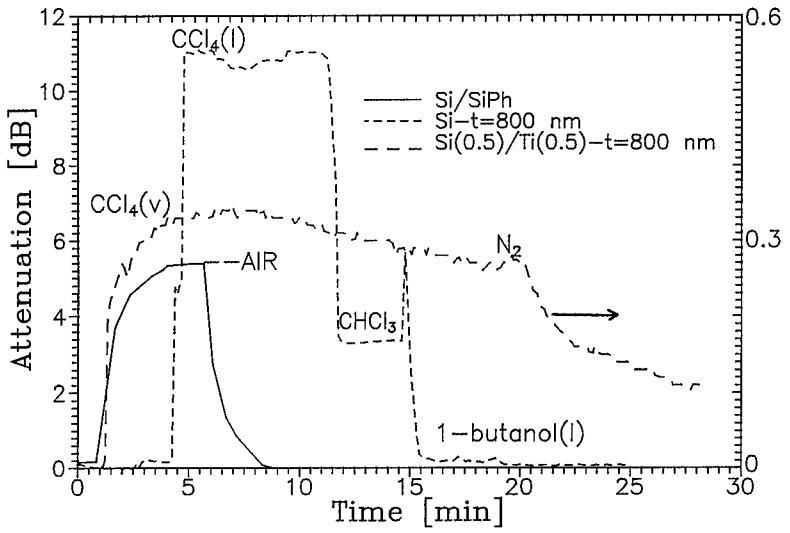

Figure 4. Time responses of the fibers—Si/SiPh layers: response to toluene vapor ($x = 1.8$ mol%) and air in 2 min and 4 min, respectively; Silica layers: effect of liquid CCl_4, $CHCl_3$ and 1-butanol in 4 min, 12 min and 14.5 min, respectively; Si/Ti layers: effect of CCl_4 vapors, decrease of the CCl_4 concentration and N_2 in 1 min, 5–20 min and 21 min, respectively.

differences in the vapor pressures, molar volumes and surface tensions of the liquids and dimensions of the pores, different amounts of liquids fill the layer pores and as a result affect the layer refractive index. However, in the case of the layers containing phenyl groups, the interaction of the liquid with the groups in the pore wall must also be taken into account for the explanation of the measured data.

In contrast with liquids, the penetration of vapors into the porous layer is a slower process, as shown in Fig. 4. In the case of vapors, transport properties of gases in the pores can be controlled by organic moieties remaining in the layers after the heat treatment. Future investigations will be focused on the control of the content of these substances in the layers and their effect on the selectivity and sensitivity of the layers. From Fig. 4 one can draw an important practical conclusion that the sensitivity of the measurements can be substantially enhanced by using selective excitation of the fibers [3].

4. Conclusion

Porous siloxane layers doped with TiO- or phenyl-groups with various refractive indices, thicknesses and sensitivities to liquid or vapor aromatic hydrocarbons, chlorinated hydrocarbons or alcohols were fabricated by the sol-gel method. A method of preparation of silica-titania sols using catalysis by HF acid was developed. The doping of porous siloxane layers with titania was found to be a convenient approach for increasing the detection sensitivity of the layers both to liquids and vapors. Detailed examination of the effects of acetylacetone and 2-methoxyethanol remaining in the layers after the heat treatment as well as practical implementation of the results into fiber-optic chemical sensors will be the objectives of further investigations.

Acknowledgment

This work was financially supported by the Grant Agency of the Czech Republic under contract Nos. 102/95/0871 and 102/96/0939.

References

1. O.S. Wolfbeis, R. Reisfeld, and I. Oeheme, *Structure and Bonding—Optical and Electronic Phenomena in Sol-Gel Glasses* (Springer, Berlin, 1996), Vol. 58, p. 51.
2. B.D. MacCraith, C. McDonagh, A.K. McEvoy, T. Butler, G. O'Keeffe, and V. Murphy, J. Sol-Gel Sci. Tech. **8**, 1053 (1997).
3. A. Abdelghani, J.M. Chovelon, N. Jaffrezic-Renault, M. Lacroix, V. Matejec, M. Chomát, M. Pospíšilová, C. Velias, and H. Gagnaire, in *Proc. of Eurosensors X* (Leuven, Belgium, 1996), p. 605.
4. V. Matějec, M. Chomát, M. Hayer, M. Pospíšilová, and D. Berková, in *Proc. SPIE—Photonics System for Ecological Monitoring* (Praha, Czech Republic, 1996), in print.
5. Y. Xi, Z. Liangying, and W. Sasa, Sensors and Actuators B **24/25**, 347 (1995).

Journal of Sol-Gel Science and Technology 13, 575–578 (1998)
© 1998 Kluwer Academic Publishers. Manufactured in The Netherlands.

High Performance Varistor Discs Obtained from Chemically Synthesized Doped Zinc Oxide Powder

RAMÓN PUYANÉ,
Cooper Industries, Cooper Power Systems Division, Olean, New York 14769, USA

ISABELLE GUY AND RENAUD METZ
Pharmacie Centrale de France, La Voulte-sur-Rhône, France

Abstract. The ceramic microstructure, the chemical homogeneity of specific dopants and the mechanical integrity of a varistor disc are critical parameters in determining the transient voltage suppression features of these devices. The material properties and overall quality of the starting ceramic powders used to produce such components are essential in achieving the desired properties. The present work describes a novel chemical method developed to produce doped zinc oxide powders and an industrial scale manufacturing process for the production of final varistor blocks for surge arrester applications. The results are compared with those obtained when using standard varistor powder made by the mixed oxide route is used. All the fundamental electrical properties of the discs have been determined and correlated with the relevant manufacturing steps.

Keywords: zinc oxide powder, spray dry, varistor, overvoltage transient, arrester

Introduction

Electrical equipment for electric power transmission and distribution is highly susceptible to dielectric damage by overvoltage transients generated by lightning discharges or line switching surges. Surge arresters using ZnO varistors are widely used to protect electrical equipment from transient overvoltages. The highly non-linear current-voltage behaviour of ZnO varistors is determined by the physical and chemical characteristics of the ceramic microstructure which in turn is strongly affected by the nature of the initial powder. The foremost important property of a ZnO varistor is its ability to reversibly switch practically instantaneously (close to picosecond time) [1] from a nonconducting state (with a conductivity of $\rho \leq 10^{12}\ \Omega\,\mathrm{cm}$) to a low resistivity state ($\rho \leq 1\ \Omega\,\mathrm{cm}$) above the switching voltage as well as being able to absorb power pulses and handle high peak currents densities ($\simeq 1\ \mathrm{kJ}/\mu\mathrm{s} \cdot \mathrm{cm}^3 = 1\ \mathrm{mW}/\mathrm{cm}^3$). An ideal varistor has a crystalline microstructure of uniform grain size, shape and composition as well as minimal presence of mechanical defects such as voids, porosity and cracks. Traditional ceramic fabrication methods are not usually adequate to produce these characteristics.

Experimental

Sample Preparation

Two type of varistor powders were produced. One was prepared following the conventional procedure of mixing single oxides and subsequent wet milling for several hours to produce a suitable slurry for spray drying to obtain a powder suitable for uniaxial compaction (MO powder). In the second case, doped zinc oxide was chemically synthesized by the oxalate precursor method (CS powder) [2–4]. Zinc oxalate was prepared by precipitation in an aqueous solution of zinc salts and an organic compound. Soluble salts of metal dopants such as bismuth, cobalt, manganese, nickel

and antimony were introduced during the oxalate precipitation achieving a high degree of sub-micrometer chemical homogeneity as a consequence of mixing at practically the molecular level. The resulting powder had a clear greenish colour. The particle size distribution of the raw powder (before spray drying) as measured by a laser scattering technique (Horiba LA500). The average particle size was 1.95 μm and the maximum particle size was below 8.8 μm.

This chemical synthesis method has been implemented at industrial scale. An appropriate thermal treatment for each precursor maintains the shape and grain size distribution of the precipitate. The specific surface area of the raw powder can be varied over a wide range (~5 to ~30 m^2/g) as a function of dopant formulation and precursor decomposition temperature. A drawback initially found with chemically synthesized spray dried powders is the lower flow and tap densities as compared with standard mixed oxide powders. This disadvantage can be greatly diminished or totally eliminated by proper thermal conditioning of the raw powder before spray drying.

Key processing operations considered for scale up procedures were the following:

- Coprecipitation parameters (salts concentration, temperature, solution pH amongst others);
- evaluation of separation techniques from mother liquor;
- precipitate drying stages;
- thermal decomposition (influence of surrounding atmosphere, thermal cycling, phase evolution and so on).

The real challenge presented in this case, was to reproduce at industrial scale the same physicochemical characteristics of the raw powders as obtained at laboratory scale. In other words, how to go from about 100 g sample to the production of a multi-ton batch.

Processing of ZnO Ceramics

A brief description is given here of the ceramic processing steps to obtain ZnO varistors from mixed oxides and chemically synthesized powder. The forming of ZnO varistors requires powders suitable for uniaxial compaction. Spray drying is an excellent process to produce ceramic powders with good flowability and

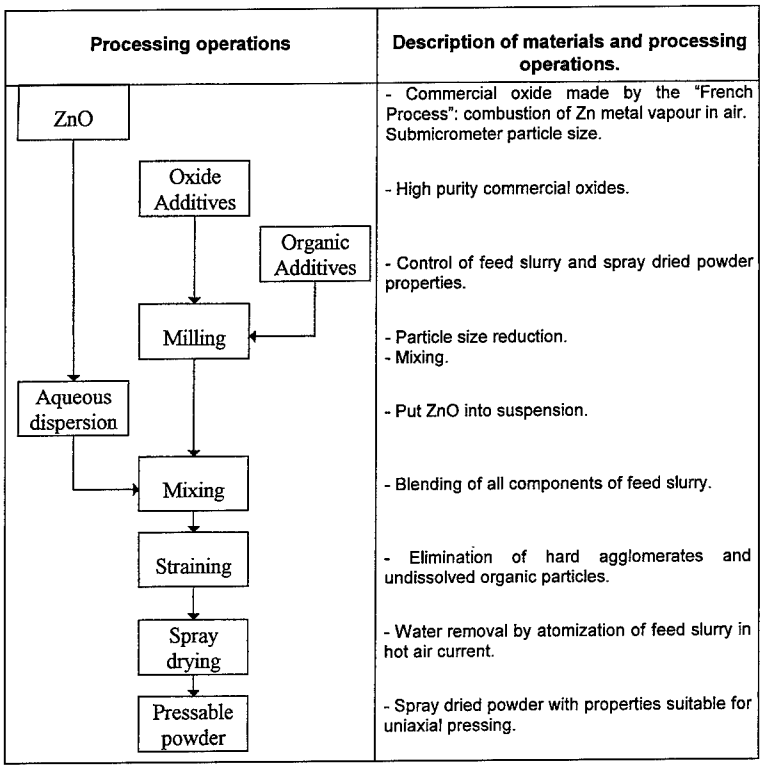

Figure 1. Production of "mixed oxide" ZnO varistor powder by spray drying.

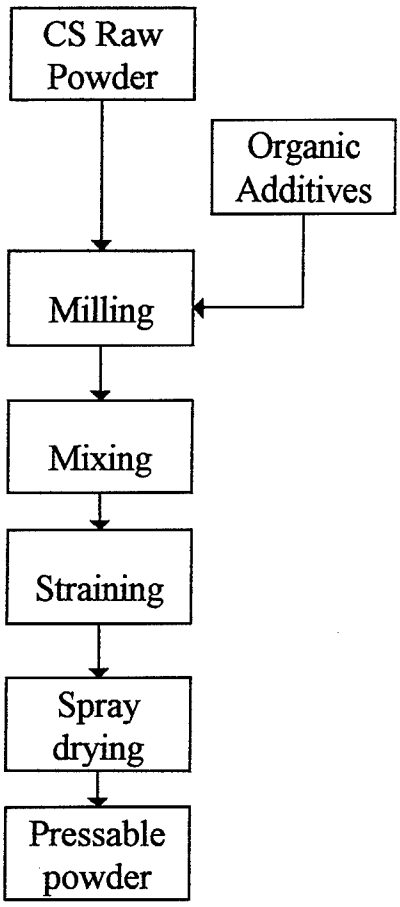

Figure 2. Production of "chemically synthesized CS" ZnO varistor powder by spray drying. (Same description of materials and related processing operations as for "mixed oxides" apply.)

compressibility. Spray drying is a single step unit continuous operation producing dried powders from solution or suspension. When contact between the spraying and drying medium (hot air in most cases) occurs, evaporation of water takes place and this continues until the desired level of moisture is reached in the dried powder. The elapsed drying time is only a few seconds due to the high surface to mass ratio. Flowability is improved when a more uniform particle size of the spherical agglomerates is obtained during spray drying. Desirable properties of the spray dried powder to improve its compressibility are high bulk and tap density; controlled moisture content as well as the lubricity and plasticity of the organic additives. Figure 1 shows schematically the processing steps involved in the production of spray dried mixed oxides powders. Also, Fig. 2 shows schematically the processing steps in the production of 'chemically synthesized' (cs) ZnO visitor powder by spray drying.

Both spray dried (MO and CS) powders were pressed into varistor discs suitable for surge arrester applications. These are discs of 39.08 mm diameter and 32 mm height with a green density of 3.25 g/cm^3. The compaction of these discs was carried out using a carbide die tooling in a double action hydraulic press at a maximum compaction pressure of 112 MPa. The discs were sintered in a continuous kiln following a temperature profile developed for commercial varistor discs. The shrinkage observed in the MO powder was 15.51% and for the CS powder was 15.67%.

Physical Properties of the Spray Dried Powders

The bulk properties of the spray dried powders, the compacting and ejecting properties of the powder in a die and the characteristics of the green compact were determined using a "Powder Testing Center" (Trade mark) instrument, model PTC-03DT manufactured by KZK, Powder Tech Corp. (Virginia, USA). A carbide testing die was chosen to simulate conditions as closely as possible as those found in the manufacturing equipment. The powder properties measured were the bulk (or apparent) and tap density; the angle of repose; the slide coefficient for test density, which is a measure of the frictional interactions between the powder particles and the die walls during compaction and the compactability coefficient for the test density, which quantifies the ability of the powder to be compacted. The cohesiveness of the green compact, C, represents the ratio between the strength of the green compact and the maximum friction forces between the compact and the die walls. This is an important parameter since it is directly correlated with the tendency of the powder compact to crack, delaminate or suffer other mechanical damage during ejection from the die. If C is less than 1 (friction forces larger than compact green strength) compact cracking during ejection from the die may occur. To avoid this, precautionary steps such as slow ejection, hold-down pressure and special die exit design, may be required as well as use of stronger binders and/or solid lubricants. The average ejection pressure, the total ejection energy and the axial and radial green strength of the compact were also measured. Table 1 shows the values obtained for the two batches of powder being compared.

Electrical Characteristics

The I–V characteristics of the varistor discs were measured at low and high current. Table 2 gives the average

Table 1. Physical properties of MO and CS spray dried ZnO varistor powders.

Powder type	Bulk density (g/cm^3)	Tap density (g/cm^3)	Angle of repose (degrees)	Slide coefficient for test denstiy (ρ)	Compactability coeff. for test density (α)
CS	1.501	1.581	35	0.527	0.127
MO	1.134	1.195	31	0.336	0.185

Powder type	Cohesiveness	Average ejection pressure (kg/cm^2)	Total ejection energy (J)	Axial green strength (MPa)	Radial green strength (MPa)
CS	0.595	1.491	1.65	2.74	0.248
MO	0.685	3.740	4.11	4.62	0.507

Table 2. Electrical characteristics of varistor discs made with CS and MO powders.

Powder type	$V_{1\,mA}$ (V)	Specific voltage (V/mm)	Leakage current (μA)	Resistive powder loss (W)	Capacitance (pF)	$V_{5\,kA}$ (kV)	$V_{5\,kA}$ (kV)	$V_{10\,kA}$ (kV)
CS	6850	259	7.7	0.73	170	11.62	12.36	13.71
MO	5810	215	19.3	0.110	183	9.39	9.97	11.05

values for nominal voltage ($V_{1\,mA}$), specific voltage, leakage current, resistive power loss, capacitance and residual voltages at 3, 5 and 10 kA. The results show that the powder obtained via the chemical synthesis route has a higher specific voltage. This feature makes it possible to produce a thinner disc. The low current characteristics have also been improved, i.e., the leakage current and the resistive power loss have been reduced. Capacitance values are similar for both type of devices. The residual voltage are higher for the CS discs due to their higher nominal voltage $V_{1\,mA}$.

Conclusions

A chemically synthesized varistor powder has been produced with shrinkage properties during sintering similar to those of a classical mixed oxide varistor powder. The CS powder showed improved bulk and tap density; together with similar compaction properties and mechanical strength as the MO powder.

The specific voltage of the CS varistor powder has been increased by over 20%. Leakage current and resistive power losses have been reduced while maintaining the high current characteristics.

References

1. R. Puyané, Journal of Materials Processing Technology **55**, 268–277 (1995).
2. French Patent No. 9303956, 1993.
3. I. Guy, R. Legros, A. Rousset, J.M. Laffargue, A. Loubiere, and A. Bui, Electroceramics **4** (1994).
4. I. Guy, Thèse No. 1971, University of Toulouse, France, 1995.

Journal of Sol-Gel Science and Technology 13, 579–584 (1998)
© 1998 Kluwer Academic Publishers. Manufactured in The Netherlands.

Control of Dopant Adsorption from Aqueous Solution into Nanoporous Sol-Gel Films

O. McCARTHY AND E.M. YEATMAN
Department of Electrical and Electronic Engineering, Imperial College, London SW7 2BT, UK

Abstract. The doping of porous sol-gel films by adsorption of cations onto silica from aqueous solutions is demonstrated. The films are fabricated using the sol-gel method, giving nanometer scale porosity, high surface area, and homogeneity on the scale of optical wavelengths. After deposition by spin coating and initial heat treatment, the films are soaked in a salt solution of the desired dopant, and then given a further consolidating heat treatment.

Doping with lead, aluminum and calcium has been demonstrated, and consistent and reproducible processes have been established. Results are presented showing control of doping level through pre-doping temperature and surface treatment, doping time and temperature, and doping solution pH. Potential applications in integrated optics are proposed.

Keywords: thin films, doping, silica, integrated optics

1. Introduction

The adsorption of ions from aqueous solution has long been known, and investigated in a wide variety of fields. Applications include the removal of unwanted materials from solution, as in the nuclear and water treatment industries; concentration of certain species from solution, in chemical analysis; and the deliberate introduction of dopants to the surface of a material, e.g., for the production of optical glasses. Our interest is in the doping of films for silica-on-silicon integrated optics [1], although we believe the results described herein are of wider applicability.

A potential advantage of solution doping of sol-gel glasses is that compositions may be attained that cannot be produced by melt techniques, because for instance they lead to crystallization. To benefit from this it is necessary that a product be obtained of sufficient homogeneity for the application without final processing at near melt temperatures. Solution doping of bulk sol-gel glasses was studied by Rabinovitch et al. [2], who used combined alkoxide-particulate methods to avoid stress cracking, leading to pore sizes of 10s of nm. We have found that solution doping can be achieved for films prepared by using acid catalyzed alkoxides, which have pore sizes below 10 nm [3], and that this doping can be patterned with high resolution [4]. Here we show that this doping process is reproducible and controllable.

Several models for adsorption at solid-solution interfaces have been proposed, all of which are based on the concept of a reaction between the ionic species in solution and the ionized surface sites. According to Yiacoumi [5], the surface complex formation model is the one most commonly used in the case of adsorption on hydrous oxide surfaces.

The basic reaction involves the substitution of one or more of the silanol groups on the surface with the adsorbing species. It is thought that the main reacting species is not the fully ionised cation, but one of the hydrolysis products [5]. The adsorption process can be modelled by Eqs. (1) and (2) below. The first step is the hydrolysis of the cation (M), here taken to be divalent, and the second is the adsorption of this species onto the surface site represented by the silanol group (SOH).

$$M^{2+} + yH_2O \Leftrightarrow M(OH)_y^{(2-y)+} + yH^+ \qquad (1)$$

$$\mathrm{SOH}_x^{(x-1)+} + \mathrm{M(OH)}_y^{(2-y)+} \Leftrightarrow \mathrm{SOH}_{(x-z)} - \mathrm{M(OH)}_y^{(1+x-y-z)+} + z\mathrm{H}^+ \quad (2)$$

The amount of dopant incorporated is determined both by the number of adsorption sites available, according to the surface area and surface morphology, and the number of these sites at which adsorption occurs, according to the process chemistry. The equilibrium conditions are determined by many parameters, including the solution pH, the number of surface sites, the cation valency, the oxide surface charge, the metal salt concentration, the presence of electrolytes, and other thermodynamic factors such as pressure and temperature.

2. Experimental Procedure

Film fabrication conditions were designed to maximize porosity while maintaining good optical quality. The main factors contributing to these properties, i.e., molar ratio R of water to TEOS (tetraethyl orthosilicate), type and concentration of catalyst, and heat treatment after spinning, were previously studied [6, 7]; from these results, optimum conditions were determined and used as the starting point for this work.

The silica sol was made by mixing TEOS and ethanol in equal volumes, and adding water, as 0.1 M HCl, to $R = 2$. The solution was then refluxed at 70°C for 2 hours while stirring continuously. The resulting sol was stored in a sealed container at room temperature for a maximum of two weeks before use. Thin films were fabricated by spin coating; sol was dispensed through a 0.1 micron PTFE filter onto a silicon wafer, which was spun at 3000 rpm for 30 s. This gel film was then immediately baked in air in an electric tube furnace at 500°C for 30 min.

Doping solutions were made by dissolving acetate salts in de-ionized water, to a molarity of 0.05 M. All chemicals were 99% pure and obtained from Sigma-Aldrich Ltd. Solutions were made no more than 2 hours before use, with pH adjusted with ammonia water and acetic acid as required. Films were doped by soaking in the salt solution, rinsed thoroughly in de-ionized water, and dried with a nitrogen gun. Where required, doping was carried out in a temperature controlled water bath. Unless otherwise specified, films were doped at room temperature. Pre-soak treatments were carried out immediately prior to doping; films were soaked in solutions of either ammonia water or acetic acid, and then dried without rinsing.

Finally, films were heated in an electric tube furnace until they reached densification; this was defined as the point at which there was no residual porosity, measured according to the method described in [3]. The densification temperature ranged between 800°C and 1000°C depending on the dopant concentration.

3. Results and Discussion

The three dopants investigated were Pb, Ca and Al, all common glass constituents extensively described in the literature. The thickness and index of films were measured using a Rudolph AutoEL ellipsometer with precision of ±0.002 in index and a few tens of Angstroms in thickness. Energy dispersion spectroscopy (EDS) was used to qualitatively determine the atomic constituents of the films. After initial experiments to establish approximate doping conditions, samples with the highest doping levels, as indicated by refractive index, were analysed by EDS. The presence of the desired dopants was confirmed, and no undesired species were detected. A summary of the results is shown in Table 1.

As Pb doping gave the largest index change, it was used for detailed characterization of the process. We believe that all the lead is in the form of PbO; the absorption spectrum of our material after annealing at 800°C, shown in Fig. 1, is similar to that of Magruder et al. [8], who found that for a similar Pb doping level, ion implanted silica films were almost identical to bulk lead silicate glass after annealing at 800°C. Based on this assumption the doping level can then be estimated from the refractive index, for the results that follow, by correlation with data from commercial lead silicate glasses [9], as shown in Fig. 2. In all results below, the measured index is given after lead doping and densification.

To test the effect of surface hydroxylation, doping was carried out on films pre-soaked in solutions

Table 1. Refractive indices of films doped with Ca, Al and Pb (index of pure silica is 1.459). EDS analysis confirmed the presence of each dopant.

Dopant	Doping solution	Doping time	Index	EDS
Ca	0.05 M CaAc, pH 8.75	30 min	1.472	✓
Al	0.05 M AlAc, pH 3.75	24 h	1.480	✓
Pb	0.05 M PbAc, pH 6.1	30 min	1.536	✓

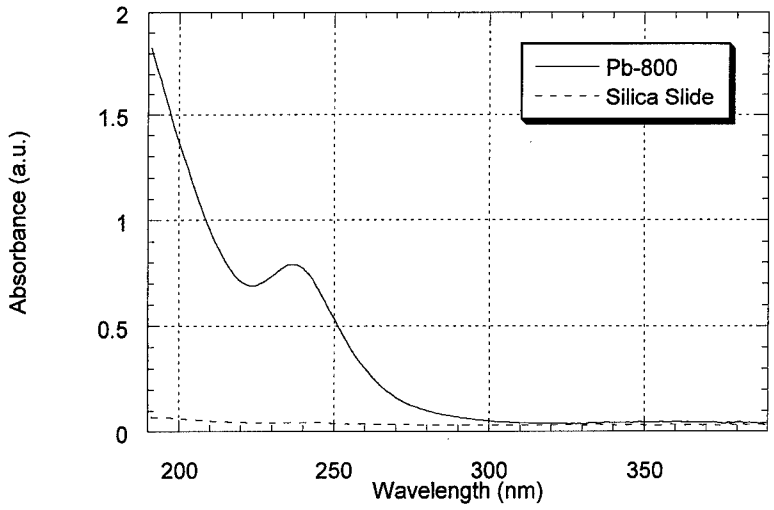

Figure 1. Absorption spectrum of Pb doped silica film, annealed at 800°C.

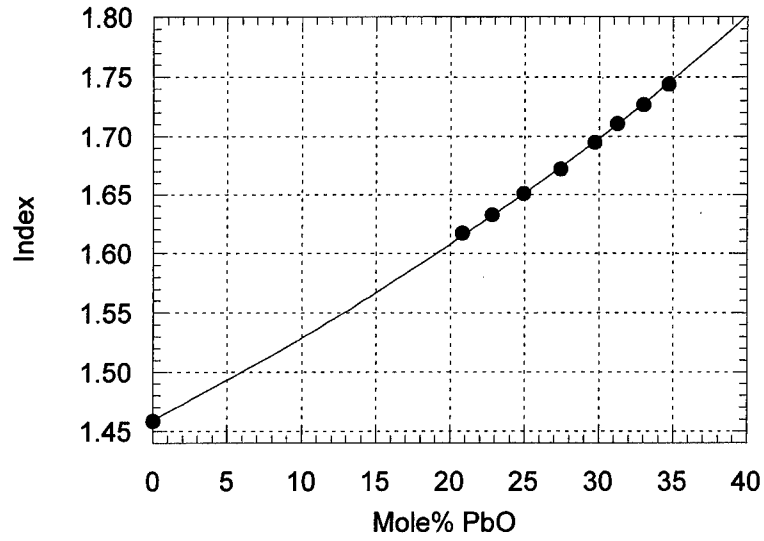

Figure 2. Refractive index vs. mole% PbO for lead silicate glasses, after [9]. The line shows a 3rd order polynomial fit to the data.

of different pH. As can be seen in Fig. 3, a marked increase in index was seen after pre-soaking in solutions above pH 6.0. This may be a consequence of increased hydroxylation, or of increased pore surface area by etching. Etching is indicated by the corresponding decrease in thickness, but significant etching of silica is not expected below pH 9 [10], so the effect of soaking in pH 7 seems to indicate increased hydroxylation.

In the following results, only the doping conditions were varied. Figure 4 shows the effect of pH on the doping solution. This is an important factor, due to both its effect on the surface charge and the degree of hydrolyzation of the dopant. According to Schindler et al. [11], the relationship between pH and adsorption is expected to be s-shaped, with a rapid transition over a narrow pH range. Figure 4 shows a linear relation in this transition region; below pH 5.3 doping was negligible, while above 6.3 precipitation of the solution occurred. To test repeatability, results were obtained for two equivalent sols; no difference is seen within the error range of the measurements.

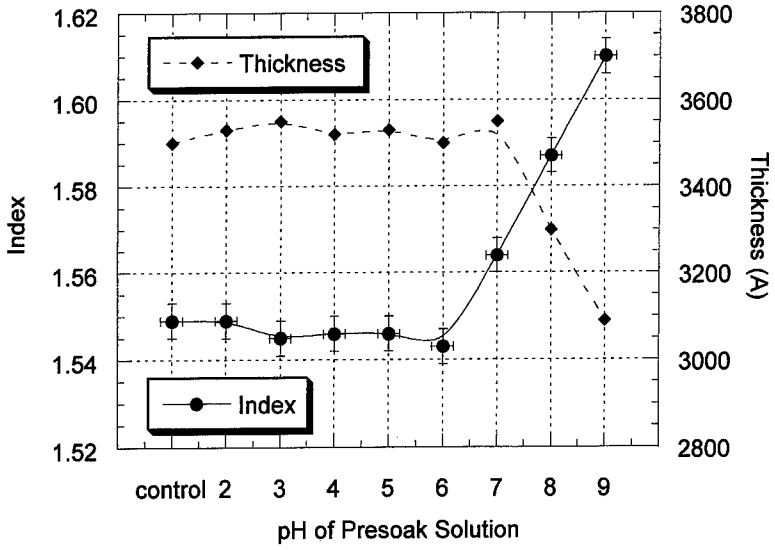

Figure 3. Effect of pre-soaking on index and thickness of doped films. The control sample had no presoak treatment before doping. Lines are for ease of viewing only.

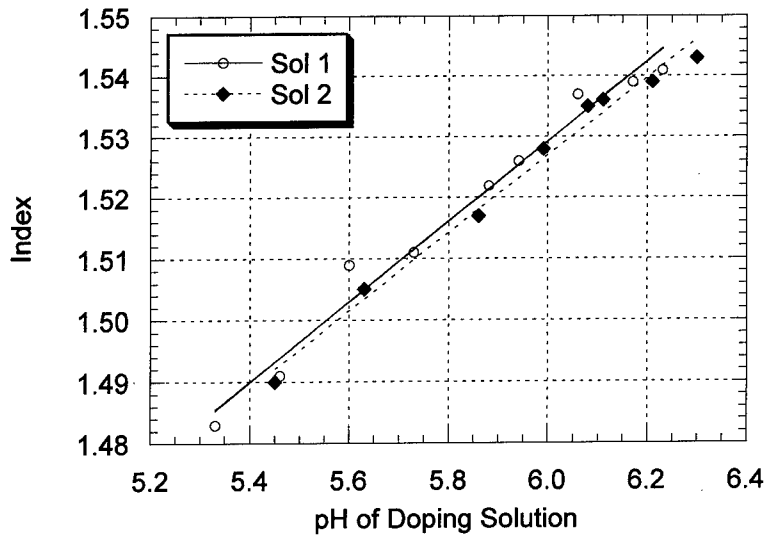

Figure 4. Refractive index vs. doping solution pH, for two equivalent sols. Doping time was ~15 min. Lines show best linear fit to data.

In Fig. 5 the logarithmic dependence of doping level on time is shown. In Fig. 6 an approximately linear dependence on doping solution temperature is indicated.

By isolating and controlling major factors, repeatability can be achieved. This is indicated by the correlation of the experiments of Figs. 4–6. For example, Fig. 6 for room temperature (22°C), gives an index $n = 1.52$, as does Fig. 5 for a time of 10 min. Figure 5 for 15 min gives $n = 1.53$, as does Fig. 4 for pH = 6.0.

4. Conclusions

Surface adsorption from aqueous solution can be used to dope nanoporous acid catalyzed sol-gel films. The doping level can be widely and systematically controlled by doping time, temperature and solution pH, and by treatment of the film prior to doping. A variety of dopants can be exploited. This method has potential applications in optical waveguide fabrication,

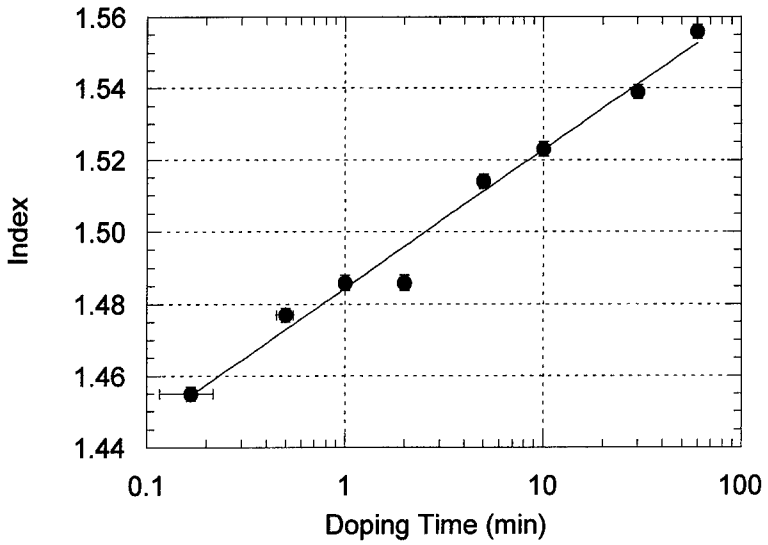

Figure 5. Refractive index vs. doping time. Line indicates best logarithmic fit to data. Doping conditions: pH 6.0, temperature 22°C.

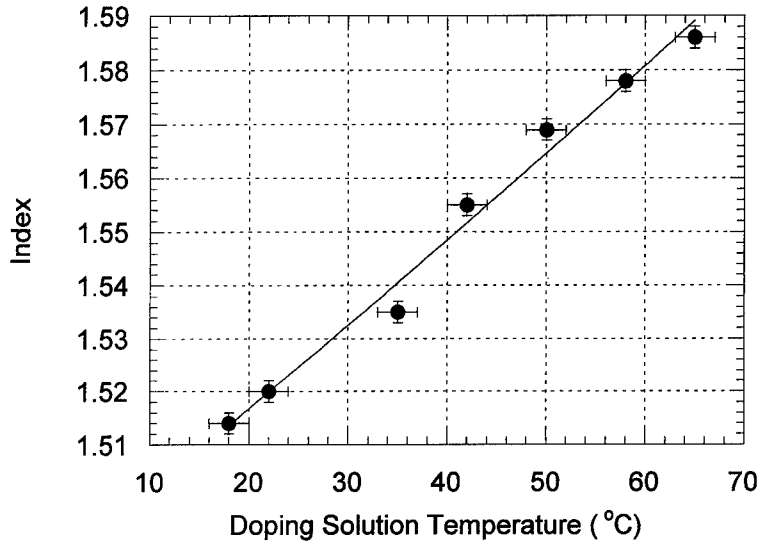

Figure 6. Refractive index vs. doping solution temperature. Line indicates best linear fit to data. Doping conditions: pH 6.0, time 10 min.

particularly as patterned doping can be obtained. Future work will include investigation of additional dopant species; one possible application is in the monolithic integration of passive and amplifying waveguides, by selective area doping with rare earth ions.

Acknowledgments

We are grateful to the European Commission for financial support, under the CAPITAL Project (ACTS AC047) and through a Human Capital and Mobility Fellowship for O. McCarthy, and to Drs. Emma Dawnay and Munir Ahmad for technical advice.

References

1. E.M. Yeatman, in *Sol-gel and Polymer Photonic Devices*, edited by S.I. Najafi and M. Andrews (SPIE Crit. Rev. Proc. **CR-68**, 1997), pp. 119–142.
2. E.M. Rabinovitch, A.J. Bruce, N.A. Kopylov, and P.L. Trevor, J. Non-Cryst. Solids **160**, 126 (1993).

3. E.M. Yeatman, M. Green, E.J.C. Dawnay, M.A. Fardad, and F. Horowitz, J. Sol-Gel Science and Technology **2**, 711 (1994).
4. O. McCarthy and E.M. Yeatman, Selected area doping of porous sol-gel films for integrated optics, Optics Letters **22**, 1864 (1997).
5. S. Yiacoumi and C. Tien, *Kinetics of Metal Ion Adsorption from Aqueous Solutions* (Kluwer Academic Publishers, Boston, 1995), chap. 2.
6. M.A. Fardad, E.M. Yeatman, E.J.C. Dawnay, M. Green, and F. Horowitz, J. Non-Cryst. Solids **183**, 260–267 (1995).
7. M.A. Fardad, Catalysts and the structure of silica sol-gel films, J. Materials Science, in press.
8. R.H. Magruder, D.O. Henderson, S.H. Morgan, and R.A. Zuhr, J. Non-Cryst. Solids **152**, 258 (1993).
9. N.P. Bansal and R.H. Doremus, *Handbook of Glass Properties* (Academic Press, New York, 1986), p. 547.
10. R. Iler, *The Chemistry of Silica* (Wiley, New York, 1979), chap. 1.
11. P.W. Schindler, B. Furst, R. Dick, and P.U. Wolf, J. of Colloid and Interface Science **55**, 469 (1976).

Journal of Sol-Gel Science and Technology 13, 585–586 (1998)
© 1998 Kluwer Academic Publishers. Manufactured in The Netherlands.

Silicate Xerogels with Dopant-Induced Chirality

KRZYSZTOF MARUSZEWSKI
Institute of Low Temperature Research and Structural Studies, Polish Academy of Sciences, 50-950 Wrocław 2, P.O. Box 937, Poland; Opole University, Chemistry Department, Oleska 48, 45-052 Opole, Poland

MAREK JASIORSKI AND WITOLD WACŁAWEK
Opole University, Chemistry Department, Oleska 48, 45-052 Opole, Poland

WIESŁAW STRĘK
Institute of Low Temperature Research and Structural Studies, Polish Academy of Sciences, 50-950 Wrocław 2, P.O. Box 937, Poland

MAREK LISOWSKI
Wrocław University, Chemistry Department, Wrocław, Poland

Abstract. A series of silicate xerogels with entrapped chiral amino acids have been obtained via sol-gel technology. The transparent, glassy samples obtained exhibit chirality in the bulk due to the presence of the entrapped asymmetric molecules. Measurements of the optical activity of the doped xerogel samples revealed that the entrapment did not significantly influence the optical activity observed for liquid solutions of the amino acids. Thus, the sol-gel method enables the preparation of amorphous optical materials exhibiting properties of strictly spatially defined molecular systems. Apart from the obvious optical applications, such porous materials with asymmetric centers might find interesting applications in chiral chemical syntheses and separations.

Keywords: sol-gel technique, optical activity, amino acid doping

Introduction

Sol-gel technology [1, 2] enables preparation of low-temperature transparent xerogels from liquid precursors. This enables doping of the xerogels with chemical molecules varying from simple inorganic salts [3] to proteins [4]. The doping procedure is relatively straightforward since solutions or suspensions of dopants can be admixed to the liquid hydrolyzates. After gelation the added dopant molecules are effectively immobilized within the solid matrix. In this way the sol-gel glass acquires the physical and chemical properties of the entrapped substances. This allows preparation of a virtually limitless variety of active glasses [2] with applications as sensors, optoelectronic elements, optical memories, graded refractive index (GRIN) glasses etc.

The optical activity of chemical molecules stems from their asymmetry, i.e., their own mirror images are not identical [5]. In the case of organic molecules this phenomenon is typically induced by the "asymmetric carbon atoms." Many biological molecules like sugars and amino acids possess such carbon atoms and are capable of rotation of plane-polarized light. In this work we report preparation of xerogels doped with chiral amino acids by the sol-gel method. The glasses obtained display optical activities comparable to those observed for free solutions of the amino acids used.

Experimental

The sol-gel samples were prepared according to the following procedure. Distilled water, tetraethyl orthosilicate $Si(OC_2H_5)_4$ TEOS (Fluka), ethanol and hydrochloric acid as a catalyst were mixed together in the molar ratio 20 : 1 : 4 : 0.001 and stirred for approximately 1 h. At this stage aqueous solutions of L-amino acids (methionine (Met)—SAS Scientific Chemicals; histidine (His), proline (Pro) and threonine (Thr)—Reanal, Hungary) were added to the hydrolysate and the mixtures were stirred for another 5 min. The slurries were then poured in to containers for gelation. The pH of the mixtures was brought slowly to approximately 7 by means of diluted ammonia solution. At pH $\approx$ 7 gelation occured after approximately 1 min. These gels were then air-dried for several days. The optical rotation measurements were performed on a JASCO DIP-1000 polarimeter at 28°C and the 589 nm excitation line.

Results and Discussion

The measured values of angles of optical rotation were used to calculate specific optical rotations, allowing comparison of the optical activities of samples with different concentrations of the chiral substances. Since the xerogels obtained by the sol-gel method undergo significant shrinkage upon drying, this procedure is necessary to compensate for different volumes of the samples obtained. The formula defining the specific optical rotation (α) at the excitation wavelength λ and temperature T is:

$$\alpha_\lambda^T = \frac{\alpha \cdot 100}{l \cdot c} \quad (1)$$

where α is the measured value of the optical rotation, l is length of the optical path (the sample thickness) and c is the concentration of the optically active substance (g/100 ml). Table 1 presents the calculated values of the specific optical rotations obtained for the L-amino acids in aqueous solutions and the sol-gel glasses containing molecules under investigation. As can be seen, the entrapment does not significantly influence the specific optical rotations compared to the free (aqueous) solutions of the optically active amino acids. Thus, the sol-gel matrix offers an ideal platform for preparation of modified glass-like materials with properties of the immobilized dopants. Since the doped xerogels are porous (the porosity can be, to some extent, chemically controlled), the immobilized chiral centers could interact with molecules small enough to be able to diffuse through the network of pores. This makes such composites promising materials for conducting chiral syntheses or separations.

Table 1. Specific optical rotations (deg) measured for L-amino acids in water solutions and entrapped in sol-gel glass.

	Specific optical rotation	
Amino acid	Water solution	Sol-gel glass
Methionine (Met)	−7.01°	−7.07°
Histidine (His)	−36.88°	−35.54°
Proline (Pro)	−79.24°	−72.31°
Threonine (Thr)	−27.59°	−25.85°

Conclusions

Silicate xerogels containing L-amino acids have been prepared by the sol-gel method. The amorphous matrix thus gains the property of rotating the plane polarized light. It has been shown that the immobilization procedure does not significantly change the specific optical rotations observed for aqueous solutions of the amino acids under investigation. Thus, the sol-gel method offers a promising way of preparation of modified, "active" glasses and glass-like materials.

References

1. *Chemistry, Spectroscopy and Applications of Sol-Gel Glasses*, edited by R. Reisfeld and C.K. Jorgensen (Springer-Verlag, Berlin, Heidelberg, 1992).
2. C.J. Brinker and G.W. Scherer, *Sol-Gel Science* (Academic Press, New York, 1989).
3. J.S. McCormack, Electron. Lett. **17**, 630 (1981).
4. L.M. Ellerby, C.R. Nishida, F. Nishida, S.A. Yamanaka, B. Dunn, J.S. Valentine, and J.I. Zink, Science **255**, 1113 (1992).
5. F.A. Cotton, *Chemical Applications of Group Theory* (John Wiley & Sons, New York, 1990).

Journal of Sol-Gel Science and Technology 13, 587–591 (1998)
© 1998 Kluwer Academic Publishers. Manufactured in The Netherlands.

Preparation of Ce^{3+}-Doped Inorganic-Organic Hybrid Materials Using Functionalized Silanes

M. IWASAKI, J. KURAKI AND S. ITO
Department of Applied Chemistry, Kinki University, 3-4-1 Kowakae, Higashi-Osaka, Osaka, 577 Japan

Abstract. Ce^{3+}-doped, inorganic-organic hybrid monoliths were prepared from $Si(OCH_3)_4$, $CH_3Si(OCH_3)_3$, $CeCl_3$ and various functionalized silanes (FSs) such as amino- (APTM), glycidyloxy- (GPTM), trifluoro- (TFTM) and chloro- (CPTM) silanes at 60°C by the sol-gel process. The functional groups of silane coupling agents coordinated with Ce^{3+} ions in the inorganic-organic materials. Ce^{3+}-doped materials were transparent under the preparation conditions of FS/Ce^{3+} ratio of 100 and 1.0×10^{-4} mol/cm^3 of Ce^{3+} concentration. Optical properties such as absorption spectra, emission spectra and fluorescence quantum yield for the Ce^{3+}-doped hybrid materials were strongly affected by the Ce^{3+} ion environment. Emission spectra were observed for the Ce^{3+}-doped materials below 400 nm. The emission intensities of the materials prepared from TFTM, CPTM and without FS were approximately 100 times as much as those of materials prepared from APTM and GPTM. The fluorescence quantum yield was highest (11%) for the material prepared from TFTM hybrid materials.

Keywords: functionalized silane, ligand, cerium, inorganic-organic hybrid material

1. Introduction

There is a growing interest in preparing inorganic-organic hybrid materials by the sol-gel process. These materials are especially desired for optical applications because of the advantages of transparency in the near-UV and visible region, low temperature processing below 100°C, ease of preparation of crack-free materials and high heat resistance up to 250°C [1, 2]. Doped materials prepared by the sol-gel method are also expected to have a wide variety of applications. Many kinds of dopants have been investigated such as transition metal ions, rare-earth metal ions, dyes and fine metal particles for fabricating optical materials, catalyst, membranes and electronic devices.

Recently, Ce^{3+}-doped fluoride crystals have attracted considerable attention for all solid-state laser materials with tunable emission in the ultraviolet wavelength region [3]. The biggest issue to overcome is the preparation of large single crystals, whereas large-scale inorganic-organic hybrid materials can be fabricated more easily. For laser materials, the first neighbor anions around the dopant cation such as the Ce^{3+} ion should be well-controlled.

In the present study, control of the first neighbors around Ce^{3+} ions in inorganic-organic hybrid materials was attempted using $-CF_3$ and $-CH_2Cl$ groups of functionalized silanes. Optical properties such as emission, excitation spectra and fluorescence quantum yield were also investigated for there Ce^{3+}-doped inorganic-organic hybrid materials.

2. Experimental

2.1. *Preparation of Ce^{3+}-Containing Methanolic Solutions and Inorganic-Organic Hybrid Materials*

Cerium(III) chloride ($CeCl_3$) was dissolved in methanol containing various functionalized silanes (FSs), and the methanolic solution was stirred for 1 h. 3-aminopropyl-trimethoxysilane ($(CH_3O)_3Si(CH_2)_3NH_2$: APTM), 3-glycidyloxypropyltrimethoxysilane

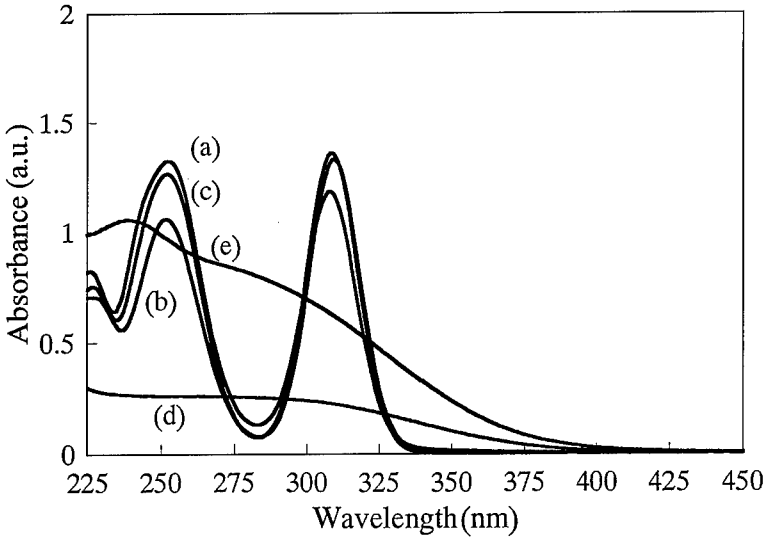

Figure 1. Absorption spectra of methanolic solutions containing $CeCl_3$ and functionalized silanes: (a) without FS, (b) CPTM, (c) TFTM, (d) APTM, (e) GPTM.

$((CH_3O)_3Si(CH_2)_3OCH_2CH(O)CH_2)$: GPTM), 3-chloropropyltrimethoxysilane $((CH_3O)_3Si(CH_2)_3Cl$: CPTM) and 3,3,3-trifluoropropyltrimethoxysilane $((CH_3O)_3Si(CH_2)_2CF_3$: TFTM) were used as functionalized silanes. The functionalized silane to cerium (III) chloride atomic ratio (Si/Ce) was 100.

Prehydrolyzed silica sols were prepared by stirring tetramethoxysilane ($Si(OCH_3)_4$: TMOS), methyltrimethoxysilane ($CH_3Si(OCH_3)_3$: MTMS) and distilled water adjusted at pH = 3 for 1 h. The molar ratio of MTMS and FS to total silane ((MTMS + FS)/(MTMS + FS + TMOS)) was varied from 0 to 1. The molar ratio of water to total silane was 2. After being stirred for 1 h, the prehydrolyzed silica sol was added to the $CeCl_3$-containing methanolic solution with (or without) functionalized silane. Then methanol in the mixture was evaporated at 50°C at 10 Torr for 30 min, and the viscous sol was poured into a teflon container. Finally, the Ce^{3+}-doped inorganic-organic hybrid material was obtained by drying the sol at 50°C for 1 week.

2.2. *Measurements*

Absorption spectra for methanolic solutions containing cerium(III) chloride and functionalized silanes, and Ce^{3+}-doped inorganic-organic hybrid materials were measured in the range 300–800 nm using the Hitachi U-4000 spectrometer. Excitation and emission spectra for hybrid materials were measured by a fluorescence spectrophotometer RF-1500 (Shimadzu Co., Ltd.) using a halogen lamp as the excitation source. Fluorescence quantum yield was determined from the excitation and emission spectra. Details of the measurement of quantum yield have been written elsewhere [4].

3. Results and Discussion

3.1. *UV-Vis Spectra of Ce^{3+}-Containing Methanolic Solutions*

Figure 1 shows the absorption spectra for methanolic solutions containing cerium(III) chloride (1×10^{-4} mol) and various functionalized silanes (FSs) (5×10^{-3} mol; FS/Ce = 50 in molar ratio) in the near-UV and visible ranges.

Broad absorption bands were seen in spectra of APTM- and GPTM-containing solutions in the wavelength range from 225 to 400 nm. On the other hand, two sharp bands were observed at 260 and 315 nm in spectra (a), (b) and (c), respectively. As the functionalized silanes used here have no absorption band between 250 nm and 400 nm, coordinate bonds seem to be formed between Ce^{3+} ion and functional groups of APTM and GPTM, respectively, and those surrounding the Ce^{3+} ion are totally different from those in the solution without functionalized silane. It is well known from the HSAB (hard-soft acid-base) effect that the

Ce^{3+} ion prefers hard base [5]. Oxygen and nitrogen donors are favored over halides. Therefore, the amino group of APTM and gem type hydroxy group, which is formed by the hydrolysis reaction of glycidyloxy group in GPTM, tend to coordinate the Ce^{3+} ions. On the other hand, the local environment of Ce^{3+} ions are similar in solutions (a), (b) and (c) since the two maxima band positions were the same for the three spectra.

3.2. *Various Properties of Ce^{3+}-Doped Inorganic-Organic Hybrid Materials*

Ce^{3+}-doped inorganic-organic hybrid materials were transparent when prepared with the FS/Ce^{3+} ratio of 100 and 1.0×10^{-4} mol/cm^3 of Ce^{3+} concentration. The color of the hybrid materials prepared from APTM and GPTM was yellow, but colorless for those prepared without FS, from CPTM and TFTM. The lower the ratio of MTMS and FS to total silanes, the more the hybrid material shrank. The linear shrinkage was ca. 15% in diameter for the hybrid materials prepared in the absence of MTMS, but was less than 5% for the materials prepared with a ratio greater than 0.5 of MTMS and FS to total silanes. The hybrid materials were crack-free when MTMS was used as the starting material, whereas the materials prepared from only TMOS broke into several pieces.

Emission spectra for various Ce^{3+}-doped hybrid materials are shown in Fig. 2.

Since non-doped material has no emission, the emission was due to Ce^{3+} ion. Emission intensities were different among the hybrid materials prepared from various functionalized silanes. The emission intensity of the material without functionalized silane (a) is ca. 100 times as large as that of the materials prepared from APTM (b) and GPTM (c). It is well known that less multiphonon relaxation results in greater emission intensity. Low emission intensity may be the result of the coordination bond between Ce^{3+} and amino or hydroxy group in the curves (b) and (c). Cl^- ions bonded to Ce^{3+} ions in the materials prepared without FS would exhibit a lower phonon energy of the Ce—Cl bond as compared with Ce—N and Ce—O. Emission intensity of the materials prepared from CPTM and TFTM were comparable to that of the material without FS (vide infra).

Figure 3 shows the excitation and emission spectra for the methanolic solution and hybrid materials without FS.

Two excitation maxima were observed in the spectra (a) and (b), and are located at 250 and 310 nm for the Ce^{3+}-containing methanolic solution and 275 and 300 nm for the Ce^{3+}-doped hybrid material, respectively. These bands are due to transitions to different crystal field components of the 5*d* excited states. The lowest excitation band of the solution shifted to longer wavelengths compared with the inorganic-organic hybrid material, and the second lowest peak of the solution shifts to shorter wavelengths. This result indicates that

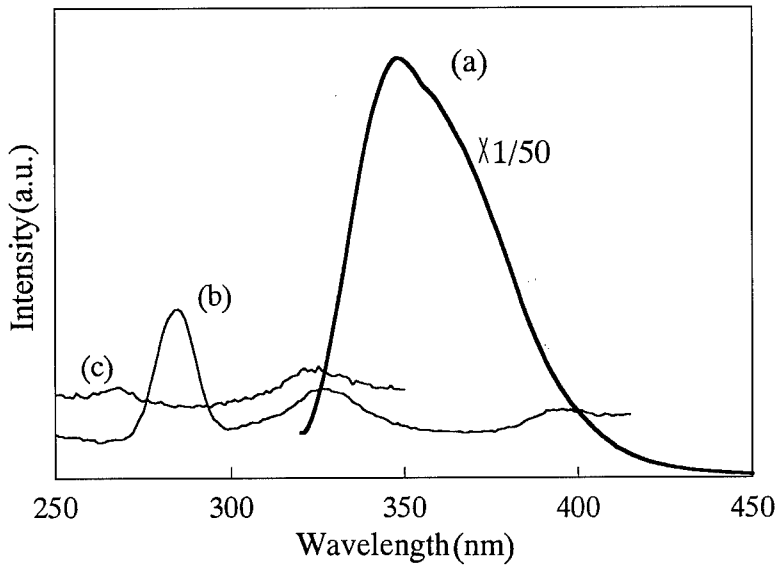

Figure 2. Emission spectra for inorganic-organic hybrid materials prepared without FS (a), from APTM (b) and GPTM (c).

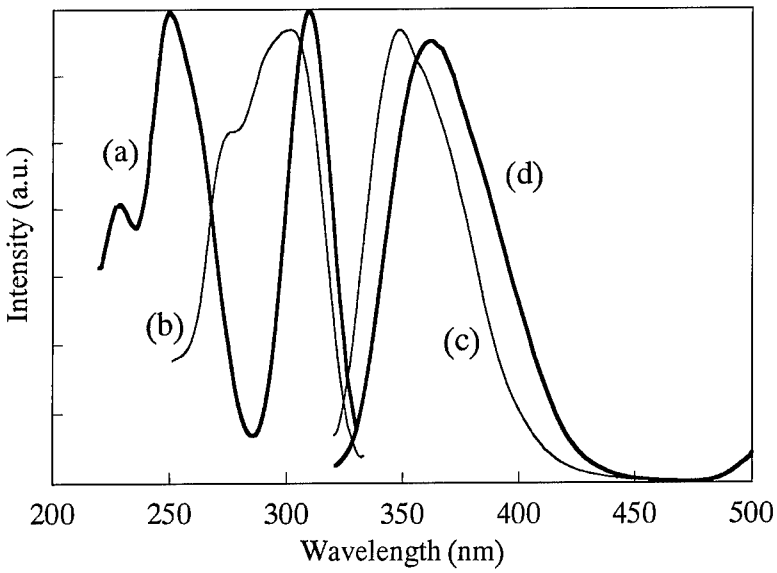

Figure 3. Excitation spectra of the Ce^{3+} ion in methanolic solution (λ_{em} = 360 nm) (a) and in hybrid material (λ_{em} = 348 nm) (b), and emission spectra in methanolic solution (λ_{ex} = 310 nm) (c) and hybrid material (λ_{ex} = 300 nm) (d).

the environment of Ce^{3+} ions in the material is different from that in the methanolic solution.

One emission peak and a weak shoulder were seen in the curves (c) and (d). These two emission peaks are due to transition from the lowest excited $5d$ level to the $^2F_{5/2}$ and $^2F_{7/2}$ levels of the $4f$ configuration, respectively [6]. The peak maximum of the hybrid material is shifted to shorter wavelength compared with that of the solution. The shift to shorter wavelength of the charge transfer band of Ce^{3+}-doped inorganic-organic hybrid materials can also be explained by a change in surroundings of the Ce^{3+} ion. Rio [7] has shown that the emission spectra shifts to shorter wavelength because of H_2O molecules in the primary coordination sphere of Eu^{3+} were replaced by SiO^- entities at SiO_2 surface. The present result suggests that some of Ce^{3+} ions in the material are bonded to SiO^- entities instead of OH^-. Moreover, the environments around the Ce^{3+} ions in both cases were somewhat different from those of silicate glass as the emission maximum of Ce^{3+}-doped silicate glass was ca. 400 nm [8]. Some Cl^- ions must coordinate with Ce^{3+} ions in both media.

Figure 4 shows the emission spectra for the hybrid materials prepared without FS, from CPTM and TFTM, respectively.

Emission intensity was normalized by the maximum band intensity of each spectrum. The band position in spectra (a) and (c) was ca. 350 nm, but located at 381 nm in spectrum (b). In the spectra (a) and (c), the ratio of the emission intensity due to $5d \rightarrow 4f$ ($^2F_{5/2}$) at 370 nm against $5d \rightarrow 4f$ ($^2F_{7/2}$) at 345 nm was 0.65 and 0.85, respectively.

Table 1 shows the optical data for the three hybrid materials. Each excitation spectrum was monitored at the emission peak position shown in the table, and each emission spectrum was also measured at the excitation band. Fluorescence quantum yield for the hybrid materials prepared from no-FS, CPTM and TFTM was 4.6, 8.3 and 11%, respectively. It is well known that fluorescence quantum yield increases with decreasing phonon energy of first neighbor anions around the emitting metal ion. Therefore, the environments of the Ce^{3+} ion are changed by functional groups in the silane coupling agents. It is commonly observed that a more ionic surrounding results in a blue shift of the emission spectrum [9]. The emission maximum was

Table 1. Optical data of Ce^{3+}-doped inorganic-organic hybrid materials.

Ce^{3+}-doped hybrid materials	Excitation peak position (nm)	Emission peak position (nm)	Quantum yield (%)
No-FS	305	348	4.6
CPTM	312	381	8.3
TFTM	308	352	11

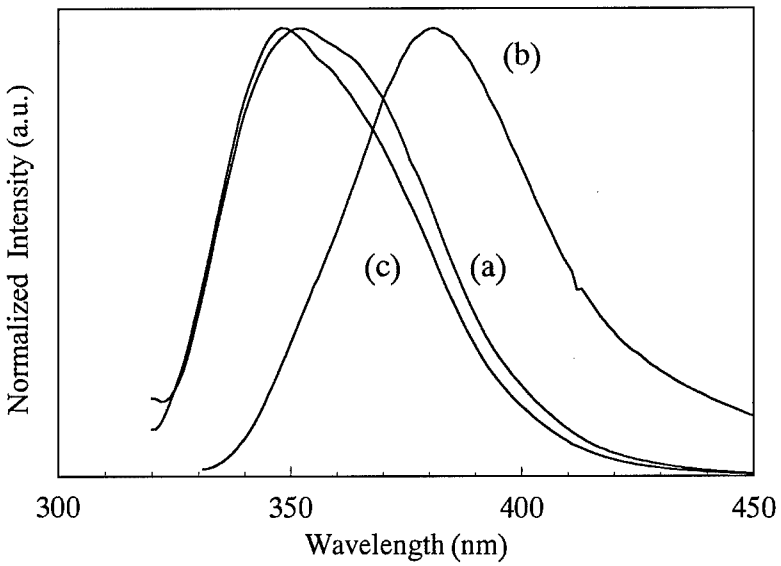

Figure 4. Normalized emission spectra for Ce^{3+}-doped materials prepared without FS (a), from CPTM (b) and TFTM (c).

at long wavelength in spectrum (b), indicating that the Ce^{3+} ion lies in rather covalent surroundings such as C—Cl entities because the electronegativity of Cl of CH_2Cl is much less than that of F in CF_3, Cl^- and OH^- ions. As fast nonradiative multiphonon relaxation is induced by coupling with the high frequency O—H oscillators, the high intensity ratio of $5d \rightarrow 4f$ ($^2F_{7/2}$) to $5d \rightarrow 4f(^2F_{5/2})$ for the CF_3-modified materials suggests that some CF_3 entities coordinate with Ce^{3+} ions instead of OH^- ions. However, the quantum yield of Ce^{3+} ions modified by the CF_3 group was much lower that that of Ce^{3+}-doped fluoride glasses, indicating that all first neighbor ligands of Ce^{3+} ion are not fluorines of a terminal $-CF_3$ group.

4. Conclusion

Transparent inorganic-organic hybrid monoliths doped with cerium(III) ions were prepared by the sol-gel process. Ce^{3+} ions became coordinated with the functional groups of silane coupling agents in the inorganic-organic hybrid materials. The affinity of functional groups of silanes for cerium(III) ion in the hybrid materials was linked to HSAB theory.

Optical properties such as absorption spectra, emission spectra and quantum efficiencies for the Ce^{3+}-doped materials were strongly influenced by the environment of the Ce^{3+} ions. Emission intensities of the materials prepared from TFTM, CPTM and without FS were approximately 100 times as large as that prepared from APTM, GPTM and MPTM. Fluorescence quantum yield in the near-ultraviolet region was highest (11%) for the material prepared from TFTM in all hybrid materials.

Acknowledgment

We gratefully thank Professor M. Nakatsuka (Institute of Laser Engineering, Osaka University) for measuring the fluorescence quantum yield of Ce^{3+}-doped hybrid materials.

References

1. H. Schmidt, J. Sol-Gel Sci. Tech. **2**, 895 (1994).
2. J.D. Mackenzie, J. Sol-Gel Sci. Tech. **2**, 81 (1994).
3. M.A. Dubinskii, V.V. Semashko, A.K. Naumov, R. Yu. Abdulsabirov, and S.L. Korableva, J. Modern Optics **40**, 1 (1993).
4. Y. Fujimoto and M. Nakatsuka, J. Non-Cryst. Solids **215**, 182 (1997).
5. J.R. Bowser, *Inorganic Chemistry* (Cole Publishing Company, Belmont, 1993), p. 675.
6. K.H. Yang and J.A. DeLuca, Appl. Phys. Lett. **31**, 594 (1977).
7. M.F. Hazenkamp, G. Blasse, and N. Sabbatini, J. Phys. Chem. **95**, 783 (1991).
8. J. Qui, N. Sugimoto, Y. Iwabuchi, and K. Hirao, J. Non-Cryst. Solids **209**, 200 (1997).
9. N. Sabbatini, S. Perathoner, G. Lattanzi, S. Dellonte, and V. Balzani, J. Phys. Chem. **91**, 6136 (1987).

Journal of Sol-Gel Science and Technology 13, 593–597 (1998)
© 1998 Kluwer Academic Publishers. Manufactured in The Netherlands.

Qualitative and Quantitative Studies of Neodymium Doped Silica Gel-Glasses

CAROLE C. PERRY AND SÉVERINE AUBONNET
Department of Chemistry and Physics, The Nottingham Trent University, Clifton Lane, Nottingham NG11 8NS

Abstract. The effect of neodymium ions on establishment of the sol-gel matrix and of the sol-gel matrix on the metal ion chemistry has been investigated by spectroscopic techniques including FTIR, FTNIR and UV/Vis. Materials were prepared by the pre-doping method and contained metal ions added as the chloride in either the aqueous or alcoholic phase at initial solution concentrations between 10^{-7} M and 1 M. The presence of the metal ions affects the rate of drying of the gel-silicas and can reduce the time required for weight stabilization by ca. 50%. Irrespective of the solvent system used for metal ion incorporation, the metal ions are found in 9-fold coordination sites in the as-prepared gels, in 8-fold coordination sites in gels where solvent has been removed by evacuation and for gels heated to 800°C, a highly symmetric environment (concentrations of 0.01 M and below) or 8-fold solid-state coordination where there is a degree of covalent character between the liganding atoms and the metal ions. Metal ion concentration and absorbance are related for gel-silicas prepared with dopants at initial concentrations of 0.01–1 M, although the absorbances measured depend on the solvent used for incorporation of the metal ion. Experimental data suggest that the matrix and metal ions interact at various stages in the formation of the doped gel-silica, however, we do not presently know if these interactions are transitory or permanent in nature.

Keywords: coordination chemistry, aging/drying, spectroscopic studies, neodymium

Introduction

Porous sol-gel materials provide an excellent vehicle for the incorporation of secondary phases including metal ions, organic molecules, biomolecules, e.g., enzymes and entire organisms such as yeast for a wide range of applications including lasers, sensors and chemical factories.These species may be doped into the gel-matrix as it is being formed (pre-doping) [1] or incorporated after the glass has been prepared (post-doping). We are studying the behavior of "dopants" in sol-gel matrices produced by both routes. In particular, we are interested in the effect of the "dopants" on the development of the gel-matrix and in the effect of the matrix on the behavior of the dopants themselves.The qualitative and quantitative solution and solid-state behavior of the example metal ion, neodymium, used in this study is established. In contrast, however, the behavior of the ions in sol-gel matrices is poorly understood particularly in respect of molecular interactions between the dopant phase, the developing sol-gel matrix and any solvent present.

In this paper we present results obtained from gel-glass monoliths prepared with varying concentrations of neodymium chloride. Glassy phases have been produced at low temperatures where the solid-state problems associated with ion migration to boundaries and phase segregation are minimized and it is likely that metal dopants will be more homogeneously distributed.

Experimental

Non-doped and Nd-doped silica gel-glasses were prepared in an identical fashion with the dopant being incorporated into the aqueous or alcoholic phase as appropriate. Tetraethylorthosilicate 98%, dry ethanol, 0.2 M HCl and $NdCl_3 \cdot 6H_2O$ at solution concentrations from 1 to 10^{-7} M were mixed at molar ratios of 4TEOS : 4EtOH : $1H_2O$: 0.04HCl and stirred for an

hour before being placed (4 ml) in petri dishes (3.4 cm diameter) covered with nescofilm in which 50.6 mm holes had been made before being placed in a fan assisted oven at 40°C to dry. Samples were weighed daily and when their weight had stabilized the matrix structure and silanol functionality were investigated using a Nicolet MAGNA 750 spectrometer with KBr beamsplitter and DTGS detector in the midIR region and a liquid nitrogen cooled InSb detector in the NIR region. The neodymium coordination chemistry was investigated using an ATI-UNICAM UV2 UV-Vis spectrometer operating between 190 nm and 1100 nm. Samples were investigated as dried pieces of glass, after dehydration by subjecting samples to a vacuum of 3 mBar for 48 hours and after thermal treatment at 800°C for 8 hours.

Results and Discussion

When salts of neodymium are used in the formulation to produce doped sol-gels they affect the rate at which the weight of the gel matrix stabilizes (Fig. 1). Sol-gels prepared without dopant show an essentially linear weight loss during the first period of aging/drying followed by a slower transition to a stable weight. The doped sol-gels show different behavior in that regardless of the concentration of dopant used (from 10^{-7} to 1 M) weight loss appears to occur in three distinct stages. In the first stage weight loss is less rapid than for the undoped gels. In the second period, weight loss is rapid with the effect being most pronounced for the samples prepared with neodymium chloride solutions between 0.01 and 0.1 M. After this rapid weight loss the samples stabilize much more rapidly that for the undoped samples. For the samples doped with neodymium chloride solutions at 0.01 M stabilization occurs in less than 50% the time required for the weight to stabilize in the undoped gel-silicas. Materials prepared with neodymium salt solutions from 0.3 to 1.0 M lose less of their original weight than for the undoped samples. The opposite effect is observed for samples prepared with lower concentrations of the neodymium salt solution. The presence of neodymium chloride clearly affects the way in which the gel structure is stabilized and solvent (alcohol and water) is lost to the environment. Similar behavior is observed if the salt solutions are added to the alcoholic phase rather than the aqueous phase. In principle, it could be expected that all doped samples would behave in an identical fashion with the solvent being retained by the structure because of the solvation of the additional cations and anions in the system. This perhaps is the effect observed at the start of the drying period for the doped sol-gels. However, this behavior is not observed throughout and the presence of the metal ions aids in the stabilization of the gel-structure and removal of the solvent phase, perhaps by building a more rigid network from which solvent can be lost more easily. The observation that samples prepared with concentrations of 0.3 M neodymium chloride and above leads to a reduction in weight loss tends to suggest that only a certain proportion of the neodymium salt solution added can act in this way. Whether these observations can be correlated with changes in molecular structure of the gel phase after weight stabilization is discussed below, but it is possible that structural features which might have been observed may no longer exist within the gel after the weight has finally stabilized. The results suggest that addition of the salt solutions affects the way in which the initial gel structure develops and ages and also alters the hydrophilicity/hydrophobicity of the gel. The changes in the gel network at the molecular level caused by the presence of the neodymium salt solutions are shown in the midIR spectra presented in Fig. 2. The silica network exhibits bands at ca. 1100 cm^{-1} (antisymmetric Si—O—Si stretch, transverse optic mode, with the shoulder at ca. 1200 cm^{-1} arising from the longitudinal optic mode), ca. 980 cm^{-1} (Si—OH), ca. 800 cm^{-1} (symmetric Si—O—Si stretch) and ca. 470 cm^{-1} (Si—O—Si bending). In addition, peaks at ca. 3400 and 1640 cm^{-1} arise from hydroxyl groups associated with the silica. A further peak at ca. 550 cm^{-1} can be attributed to siloxane ring structures. Low concentrations of the dopant phase

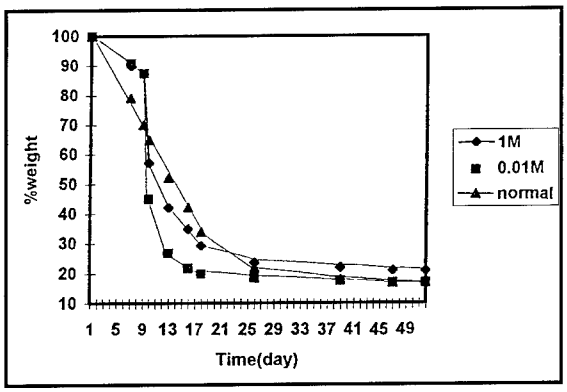

Figure 1. The effect of Nd on the time taken for weight stabilization for undoped and Nd doped sol-gel silicas.

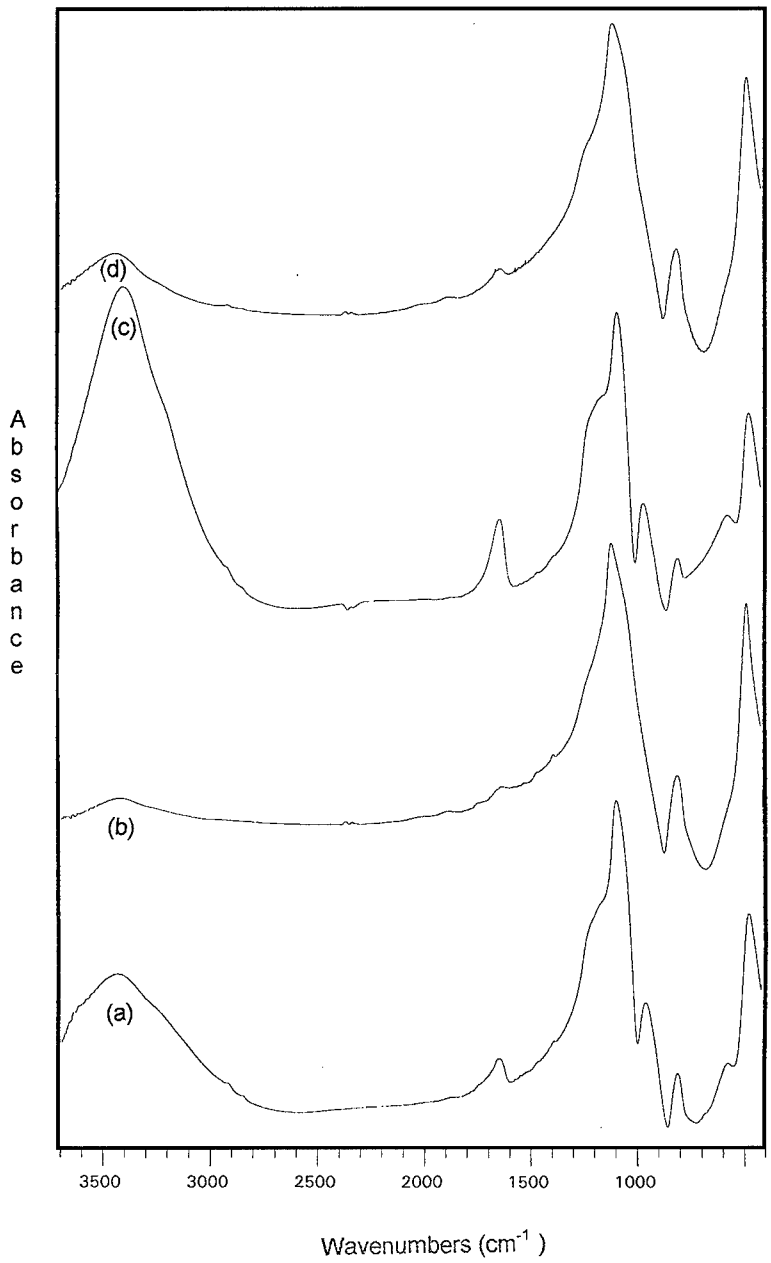

Figure 2. FTIR spectra of (a) normal sol-gel dried at 40°C, and (b) heated at 800°C, (c) Nd (1 M) pre-doped sol-gel dried at 40°C and (d) heated to 800°C.

(below 10^{-3} M) do not appear to show any gross effects on the molecular character of the gel phase. At concentrations above 10^{-2} M significant increases in bands due to siloxane ring and hydroxyl functionalities are observed (Fig. 2). In the near infrared these effects are seen as a broadening of the band at ca. 5240 cm^{-1} indicating the presence of hydrogen bonded silanol groups. When the samples are heated, Fig. 2(b) and (d), the bands due to cyclic species, Si—OH groups, —OH and H_2O disappear. The presence of the neodymium ions leads to increased levels of hydroxyl functionality in the gel-glass and increased significance of the transverse optic mode suggesting a molecular interaction between the gel-glass and the metal ions.

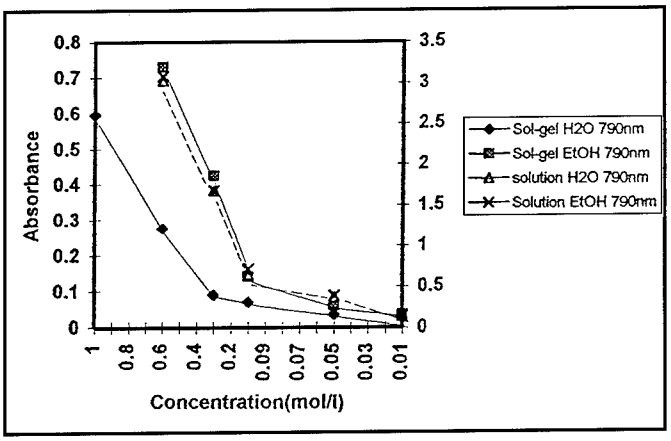

Figure 3. Variation in absorbance for the band at ca. 790 nm for Nd in ethanol and water and in pre-doped sol-gels. Left-hand legend: sol-gel, right-hand legend: solution.

The electronic configuration of Nd^{3+} is $4f^3$. The electric transitions in f^q configurations are parity forbidden but in crystals and solutions there arise weak so-called "forced" electric-dipole transitions [2]. As the observed spectra arise directly from crystal-field induced electric-dipole transitions, a change in neodymium environment [3, 4] may be expected to give rise to changes in observed spectral features. The spectra exhibit complex fine structure which arises directly from a number of transitions from the ground level ($^4I_{9/2}$) to various excited levels. The "*hypersensitive transitions*" are $^4I_{9/2} \leftarrow {}^4G_{5/2}, {}^2G_{7/2}$ (575 nm and 580 nm); the "*insensitive transitions*," with substantial sensitivity toward changes in the coordination environment of neodymium, are $^4I_{9/2} \leftarrow {}^4G_{7/2}$ (520 nm), $^4I_{9/2} \leftarrow {}^4S_{3/2}$, $^4F_{7/2}$ (740 nm), $^4I_{9/2} \leftarrow {}^4F_{5/2}$, $^2H_{9/2}$ (800 nm) [5, 6]. Solutions of neodymium chloride exhibit changes in peak shape, especially for the peaks at ca. 580 and 750 nm according to the solvent used. For solutions in dry ethanol the coordination number of neodymium is 8 and in water it is 9. It is suggested that water or ethanol [7] are the ligands in the first coordination sphere for these complexes, with chloride ions in the outer sphere having no direct effect on the coordination chemistry of the metal ions. There are no significant changes in intensity according to solvent but the intensity of the peaks decreases as dopant concentration is reduced (Fig. 3). Representative spectral traces for spectra recorded from 1 M and 0.01 M sol-gels predoped with neodymium chloride are given in Figs. 4 and 5. The coordination number of neodymium in the pre-doped sol-gels can be found

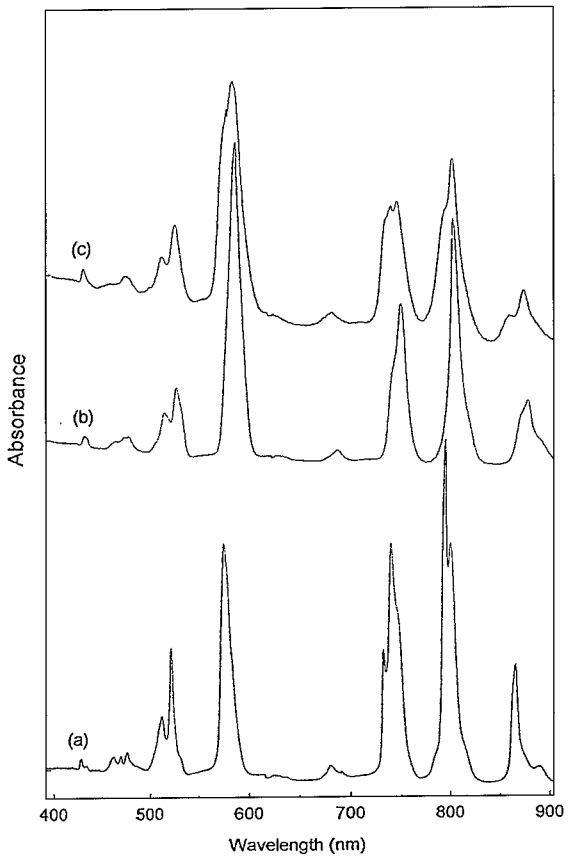

Figure 4. Visible spectra of a 1 M Nd-doped sol-gel: (a) as prepared, (b) after evacuation and (c) after heating to 800°C.

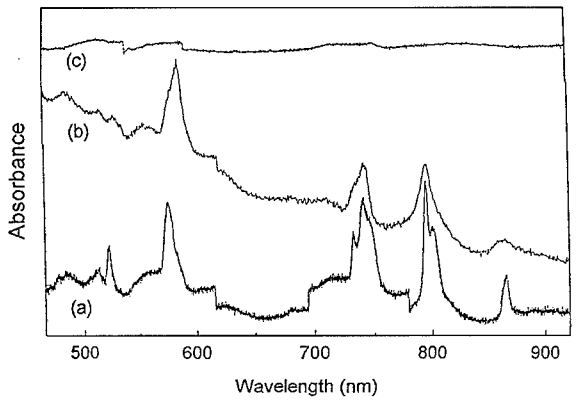

Figure 5. Visible spectra of a 0.01 M Nd-doped sol-gel: (a) as prepared, (b) after evacuation and (c) after heating to 800°C.

by studying the positions and line shape of the hypersensitive spectral transitions. In both solvents the coordination number of neodymium is 9 in the dried gels, similar to that found in solutions. On evacuation of the gels to remove solvent from the system, the line widths remain virtually the same but the relative intensities of the peaks change indicating a change in coordination environment to 8 (line shapes indicate coordination similar to solutions containing neodymium in 8-fold coordination). Similar effects are also observed after heating the gel-glasses to 800°C, although the spectral line shapes suggest an arrangement of atoms around the neodymium ions more in keeping with 8-fold coordination in the solid state. After thermal treatment, the bands due to the hypersensitive transitions are red shifted by ca. 4 cm^{-1} indicating that the Nd-O interaction has a higher degree of covalency than for the as prepared glasses. Figure 5 shows that as the concentration of the metal ions in the gel-glass are reduced there is a far greater reduction in spectral response for the thermally treated glasses than for the as prepared and evacuated glasses perhaps suggesting that at low concentrations, neodymium is in a more symmetrical environment within the gel-glass with a very weak spectral signature. The changes in relative intensity of the band at ca. 790 nm with dopant concentration are plotted in Fig. 3. Although spectral response is similar for the salt in dry ethanol or water (the band shapes suggest differences in cooordination geometry!) this is not the case for the gels prepared with the neodymium salt incorporated in the gel-silica via the aqueous or alcoholic phase. There is a linear relationship between the concentration of the salt solution used and absorbance but this differs according to the solvent used perhaps suggesting that the local environment around the metal ion in the gels prepared with the dopant in the alcoholic phase are less symmetric with a mixture of ligands in the first coordination sphere.

From the results presented it is apparent that neodymium salt solutions interact with the gel network as it ages and dries. At concentrations of ca. 0.01 M this has a beneficial effect and reduces the time required for weight stabilization by ca. 50%. The exact nature of the interactions between the gel-phase and the ions are not known and may be of a transitory nature during the development of the gel network. Alterations in coordination geometry of the metal ions on evacuation and thermal treatment suggest that the metal ions are accessible to the external environment and probably sit largely on the surfaces of the gel network.

References

1. O. Svelto, *Principles of Lasers* (Plenum Press, New York, 1989), p. 292
2. B.G. Wybourne, *Spectroscopic Properties of the Rare Earths* (Interscience Publishers, New York, 1965).
3. D.G. Karraker, Inorg. Chem. **7**, 473 (1968).
4. D.G. Karraker, Inorg. Chem. **6**, 1863 (1967).
5. S.N. Misra and S.B. Mehta, Bulletin. Chem. Soc. Jpn. **64**, 3653 (1991).
6. S. Davis, M.F. Reid, and E.M. Stephens, Inorg. Chem. **23**, 4607 (1984).
7. D.P. Graddon, *Co-ordination Chemistry* (Pergamon Press, Oxford, 1968).

Journal of Sol-Gel Science and Technology 13, 599–603 (1998)
© 1998 Kluwer Academic Publishers. Manufactured in The Netherlands.

Effect of Pr^{3+} Doping on the OH Content of Silica Xerogels

C. ARMELLINI, L. DEL LONGO AND M. FERRARI
C.N.R.-CeFSA via Sommarive 14, 38050 Povo-Trento, Italy

M. MONTAGNA, G. PUCKER AND P. SAGOO
INFM, Dip. Fisica, Univ. Trento, via Sommarive 14, 38050 Povo-Trento, Italy

Abstract. Pr_2O_3-SiO_2 xerogels doped with different Pr/Si concentrations were annealed at 900°C for 120 h and then investigated by FTIR, NIR absorption, Raman and luminescence spectroscopies. It is observed that the content of surface silanol groups is lower for higher Pr^{3+} concentrations. Luminescence measurements indicate that the amount of the residual OH plays an important role in the spectroscopic properties of the Pr^{3+} ion and in particular the quantum yield of the emission from the $^3P_{0,1}$ and $^1D_2$ states.

Keywords: silica xerogel, Pr^{3+}, OH contents, luminescence

1. Introduction

The interest in sol-gel glasses activated by rare-earth ions is mainly based on the possible applications for photonics and optoelectronics [1]. The main problems for successful applications were found to be the fluorescence quenching due to high hydroxyl (OH) content and rare-earth clustering. Moreover, the influence of the optical active ion on the densification process has to be considered. For instance, it is well known that chromium is a strong nucleating agent in silicate glasses prepared by the sol-gel route [2]. On the contrary, the role of the rare-earth ions is still not clear. It has been observed that a low content of Eu^{3+} makes the crystallization process less efficient in SiO_2 [3] and in SnO_2 [4] xerogels, whereas the devitrification tendency in gel-derived Er_2O_3-SiO_2 is found to increase with the erbium concentration [5].

In earlier studies on Pr^{3+} doped sol-gel glasses, emission from both the $^1D_2$ state and the $^3P_{0,1}$ [6] states or only from $^1D_2$ state was observed [7, 8]. The origin of these differences can be due to different OH content or Pr^{3+} clustering.

In this study we report on a preliminary investigation by optical spectroscopic techniques of silica xerogels doped with Pr^{3+}, spanning a wide range of concentrations.

2. Experimental

Silica gels were prepared, using as starting solution a mixture of tetramethylorthosilicate (TMOS), methanol, deionized water and nitric acid in the molar ratios 0.06 : 0.35 : 0.55 : 0.04, respectively, following the procedure given in a previous work [3]. Praseodymium was introduced as $Pr(NO_3)_3 \cdot 6H_2O$ in the initial solution. Samples with different Pr/Si concentrations ranging from 200 up to 100,000 ppm were prepared. Densification was achieved by thermal treatment in air at 900°C for 120 hours with a heating rate of 0.1°C/min. The final samples were monolithic square pieces of about 10 × 10 × 3 mm. The two highest Pr^{3+} doped samples (80,000 and 100,000 ppm) cracked during densification.

NIR spectra were taken with a Cary 14 spectrometer in the 700–2600 nm.

FTIR-spectra in the range 700–4000 cm^{-1} were measured on KBr-pellets using a Bio-Rad mod. FTS 185 spectrometer. The spectra of the KBr-pellets were corrected for the water content of KBr.

Raman spectra were taken in the standard 90° geometry, using the 514.5 nm line of an Argon-ion laser. The spectra were recorded by analyzing the scattered light with polarization parallel to that of the exciting beam.

Luminescence spectra under CW excitation were obtained, exciting with the 457.9 nm line of an Argon laser. The excitation power was 100 MW for all measurements. The fluorescence from the sample was analyzed using a double monochromator and photon counting technique.

All the measurements were performed at room temperature.

3. Results and Discussion

Figure 1(a)–(d) shows the FTIR spectra for samples containing 200, 500, 10,000 and 100,000 Pr/Si ppm, respectively. The bands in the region 700–1500 cm^{-1} are due to Si—O—Si vibrations [9, 10]. The shoulder at 980 cm^{-1} is assigned to silanol groups. The band at 1630 cm^{-1} is attributed to the bending vibration of H_2O, and the broad band in the range 3200–3650 cm^{-1} is due to an overlap of O—H stretching vibrations of both molecular water (3440 cm^{-1}) and hydrogen bonded Si—OH groups (3650 cm^{-1}) [11]. The fact that the maximum is observed at 3440 cm^{-1} and the presence of the band at 1630 cm^{-1} indicates that the main contribution is due to molecular water. The most interesting feature is the decrease of the intensity of the two bands with an increase of the Pr^{3+} concentration (Fig. 1(a)–(d)). This behavior is observed for all the samples. The water content in the samples 200 and 500 ppm is much higher than for the samples with high Pr^{3+} concentration.

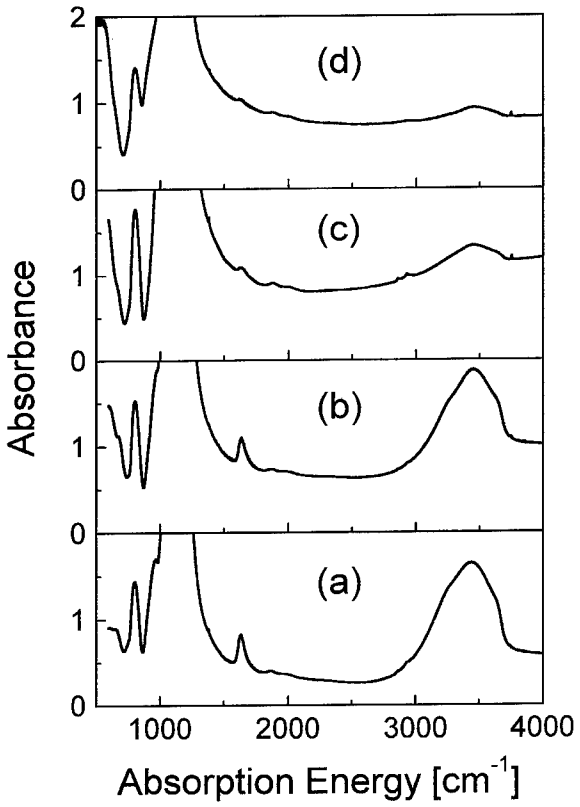

Figure 1. Room temperature FTIR absorption spectra of the 200 (a), 500 (b), 10,000 (c) and 100,000 (d) Pr/Si ppm doped samples.

The combination and overtones of vibrations related to Si—OH or H_2O observed in the NIR represent a further possibility to recognize changes in the OH content. Figure 2(a)–(d) shows the NIR spectra for the samples containing 200, 500, 10,000 and 40,000 Pr/Si ppm, respectively. For low Pr^{3+} content (Fig. 2(a) and (b)) the spectra show only bands at about 4550 and 7300 cm^{-1} due to Si—OH vibrations. The sharp band at 7300 cm^{-1} is the overtone of the O—H stretching vibration of the free silanol groups on the surface of the pores [12]. Additional absorption bands due to f-f transitions of Pr^{3+} can be observed for the more concentrated samples (Fig. 2(c) and (d)). The band centered at 5150 cm^{-1} and the one with the maximum at 6500 cm^{-1} are due to $^3H_4 \rightarrow {}^3H_6$, $^3F_2$ and to $^3H_4 \rightarrow {}^3F_{3,4}$ absorption transitions, respectively. The intensities of the bands assigned to Si—OH vibrations decrease with the increase of the Pr^{3+} concentration, as observed in the FTIR spectra.

In Table 1 the intensities of the FTIR and NIR bands related to the OH content are reported. The difference between low and high Pr^{3+} doped samples appears evident: the OH content is significantly lower for

Table 1. Absorbance of the IR bands related to the OH vibrations as a function of the Pr/Si concentration. The FTIR values are relative to pellets containing 5 mg sample. The NIR absorbances are normalized to a thickness of 1 cm.

Pr/Si (ppm)	FTIR		NIR	
	1630 cm^{-1}	3440 cm^{-1}	4550 cm^{-1}	7330 cm^{-1}
200	0.37	1.17	1.66	2.98
500	0.27	0.87	1.65	2.57
1000	0.03	0.09	1.25	1.29
10,000	0.06	0.21	0.49	0.34
20,000	0.03	0.08	0.56	0.11
40,000	0.07	0.22	0.45	0.39
80,000	0.02	0.03	0.50	0.61
100,000	0.04	0.12	0.32	0.38

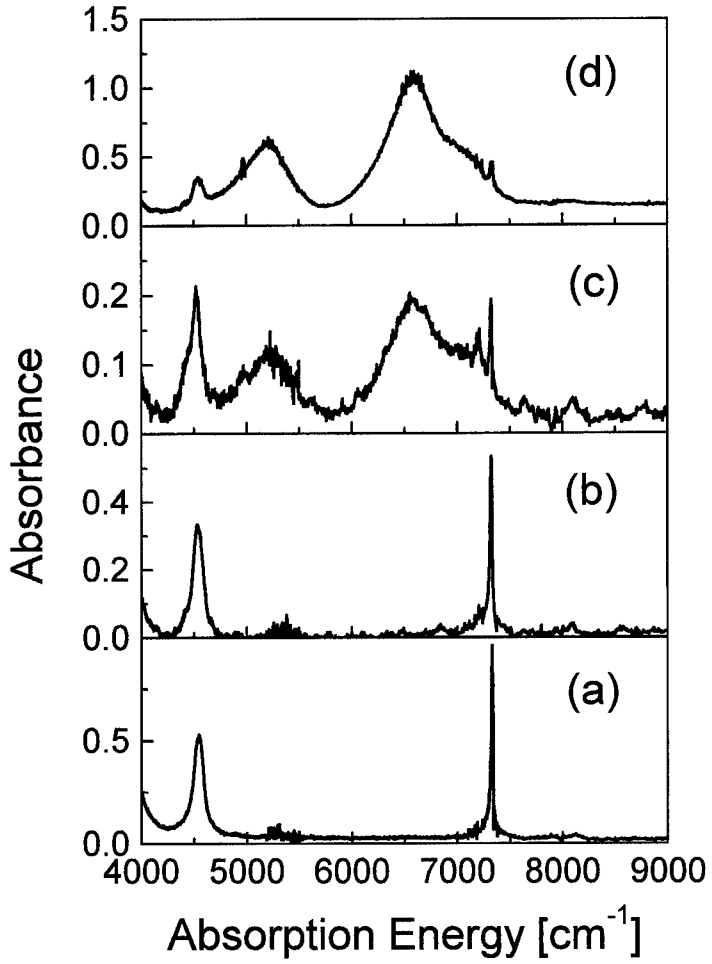

Figure 2. Room temperature NIR absorption spectra of the 200 (a), 500 (b), 10,000 (c) and 40,000 (d) Pr/Si ppm doped samples.

$Pr^{3+} \geq 10{,}000$ ppm. If one assumes that the OH-coverage within the series of investigated samples is approximately constant, the intensity of the surface silanol modes might be a measure for changes in the surface area [13]. Hence, samples with lower intensity of the 7300 cm^{-1} band of surface silanol groups may have a lower porosity, but this is a hypothesis as no textural studies have been undertaken here.

Figure 3(a)–(c) shows the Raman spectra of the samples containing 200, 500 and 20,000 Pr/Si ppm, respectively. The spectra show some remarkable differences in the intensities of SiOH modes and defect Raman bands. Samples with lower Pr^{3+} content (Fig. 3(a) and (b)) show Raman bands due to the SiO—H stretching vibrations of both free (3750 cm^{-1}) and hydrogen bonded (3650 cm^{-1}) silanol groups and a band due to the Si—OH vibration (980 cm^{-1}). Moreover, intense defect Raman bands D_1 and D_2 at around 495 and 610 cm^{-1}, respectively, are present [13, 14]. These observations suggest that, for the samples with low amount of Pr^{3+}, the densification may be far from complete. On the contrary, the Raman spectrum of the sample with 20,000 ppm of Pr^{3+} (Fig. 3(c)) looks very similar to that reported for a fully densified silica xerogel [3]. In particular, it is noted that the appearance of the Boson peak at about 60 cm^{-1} is a strong indication for the complete densification of the sample. However, the bands at 960 and 3680 cm^{-1} indicate that residual bulk OH groups are still present [13].

Figure 4(a)–(d) shows the luminescence spectra of the samples containing 500, 10,000, 20,000 and 100,000 Pr/Si ppm, respectively, obtained by exciting at 457.9 nm within the $^3H_4 \rightarrow {}^3P_2$ absorption band of Pr^{3+}. For the low Pr^{3+} concentrations (up to

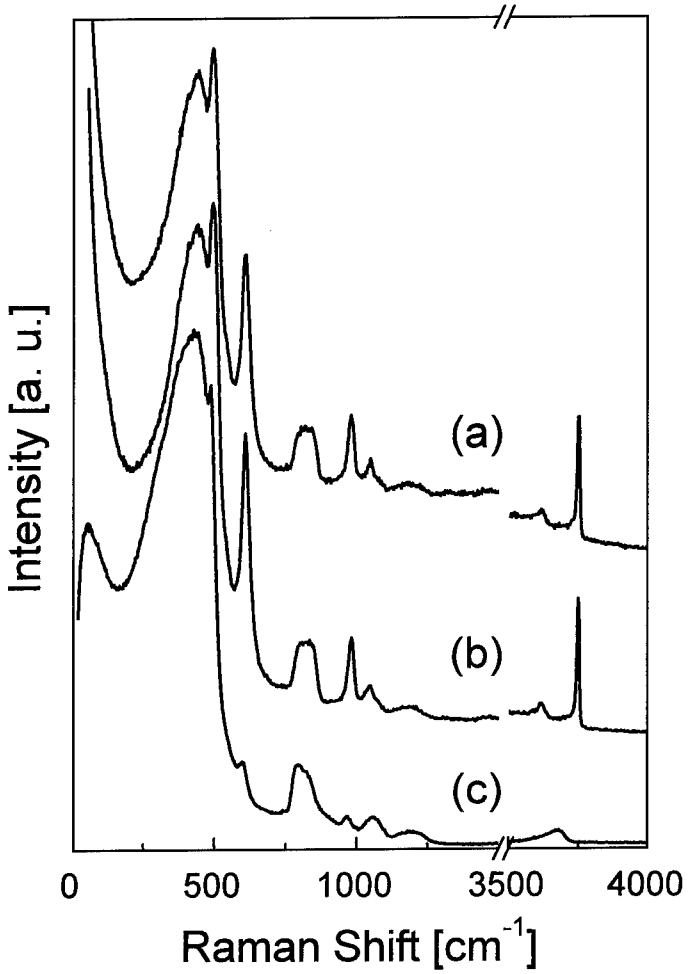

Figure 3. Room temperature Raman spectra in V-V polarization of the 200 (a), 500 (b) and 20000 (c) Pr/Si ppm doped samples.

1000 ppm Pr^{3+}), only emission from the $^1D_2$ state is observed. The intensity of the luminescence is low for all the investigated samples and is comparable to the intensity of the Raman band visible in the high energy part of the spectra. The $^1D_2$ emission can be best seen in the region of the $^1D_2 \rightarrow {}^3H_6$ transition around 11,500 cm^{-1}, since in this spectral region there is no overlap with the luminescence from the $^3P_{0,1}$ states. The $^1D_2$ emission increases with the Pr^{3+} concentration and reaches the maximum value for the sample with 10,000 ppm Pr^{3+}, whereas for higher concentrations it is strongly quenched by cross-relaxation to lower states and the spectra are dominated by the emission from the $^3P_{0,1}$ states. Luminescence from the $^3P_{0,1}$ states were found to be completely quenched for the samples with 200, 500 and 1000 Pr/Si ppm. The considerably higher OH content observed in the samples 200, 500 and 1000 ppm suggests that fast non-radiative relaxation from the $^3P_0$ to the $^1D_2$ state takes place. In samples with low Pr^{3+} and high OH content, the probability of this process is enhanced, since a single OH stretching mode instead of three Si—O stretching modes covers the energy gap.

4. Conclusions

The FTIR, NIR absorption and Raman spectra show that the investigated samples can be roughly divided into two groups according to their OH content: high content for the samples 200, 500 and 1000 Pr/Si ppm and considerably lower OH concentration for all the

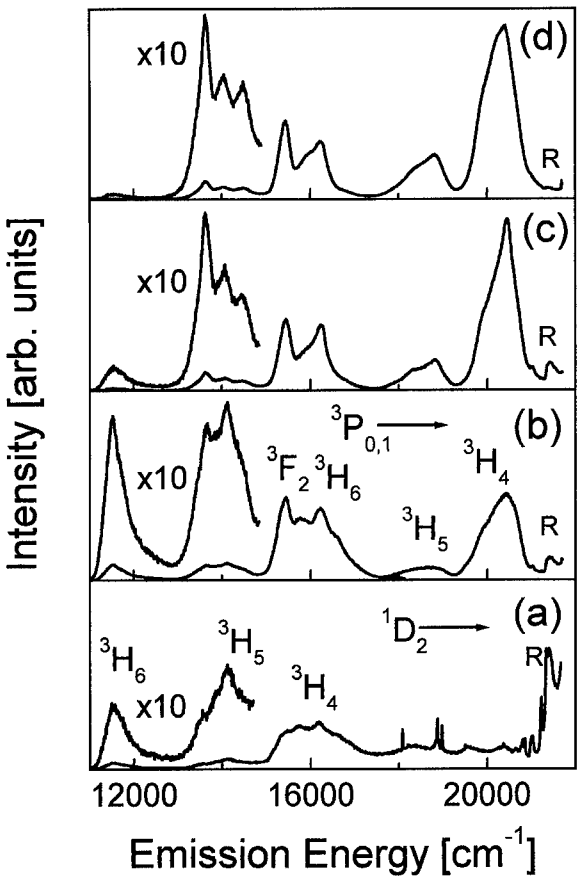

Figure 4. Room temperature luminescence spectra of the 500 (a), 10,000 (b), 20,000 (c), and 100,000 (d) Pr/Si ppm doped samples. Excitation was at 457.9 nm. The main emissions from the $^3P_{0,1}$ and $^1D_2$ states are indicated. R labels the Raman band at 430 cm^{-1}.

higher Pr^{3+} concentrations. The luminescence spectra show that, for the low concentrated samples, only emission from the $^1D_2$ state is observed. The luminescence from the $^3P_{0,1}$ states is completely quenched by fast non-radiative relaxation due to O—H stretching vibrations. At higher Pr^{3+} concentrations, when the samples are densified, emission occurs from both $^3P_{0,1}$ and $^1D_2$ states. Emission from the last one is strongly reduced in the samples doped with a Pr/Si concentration higher than 10,000 ppm, because the cross-relaxation process becomes very efficient.

Acknowledgment

This research was partially supported by the Coordinated CNR Special Project "Glass Waveguides for Non-Linear Optics." We are indebted to E. Moser for his invaluable technical support.

References

1. D.R. Uhlmann, J. Boulton, and G. Teowee, J. Non-Cryst. Solids **196**, 26 (1996).
2. W. Nie, G. Boulon, C. Mai, C. Esnouf, R. Xu, and J. Zarzycki, J. Non-Cryst. Solids **121**, 282 (1990).
3. A. Bouajaj, M. Ferrari, and M. Montagna, J. Sol-Gel Sci. Technol. **8**, 391 (1997).
4. G.E.S. Brito, S.J.L. Ribeiro, V. Briois, J. Dexpert-Ghys, C.V. Santilli, and S.H. Pulcinelli, J. Sol-Gel Sci. Technol. **8**, 261 (1997).
5. L.L. Lee and D.S. Tsai, J. Mater. Sci. Lett. **13**, 615 (1994).
6. G. De, A. Licciulli, and M. Nacucchi, J. Non-Cryst. Solids **201**, 153 (1996).
7. A.A. Boiko, E.N. Poddenezhny, E. Lukowiak, W. Strek, J. Sokolnicki, and J. Legendziewicz, J. Appl. Spectr. **62–64**, 629 (1995).
8. A. Biswas, J. Sahu, and H.N. Acharya, Mat. Sci. Eng. **B-41**, 329 (1996).
9. T.A. Guiton and C.G. Pantano, Colloids and Surfaces A **74**, 33 (1993).
10. H. Yoshino, K. Kamiya, and H. Nasu, J. Non-Cryst. Solids **126**, 68 (1990).
11. K.M. Davis and M. Tomozawa, J. Non-Cryst. Solids **201**, 177 (1996).
12. C.J. Brinker and G.W. Scherer, *Sol-Gel Science* (Academic Press, Boston, 1990), p. 627.
13. V. Gottardi, M. Guglielmi, A. Bertoluza, C. Fagnano, and M.A. Morelli, J. Non-Cryst. Solids **71**, 761 (1984).
14. C.J. Brinker, R.K. Brow, D.R. Tallant, and R.J. Kirkpatrick, J. Non-Cryst. Solids **120**, 26 (1990).

Journal of Sol-Gel Science and Technology 13, 605–609 (1998)
© 1998 Kluwer Academic Publishers. Manufactured in The Netherlands.

Preparation and Optical Characterization of Organoeuropium-Doped Silica Gels

VILMA C. COSTA
Centro de Desenvolvimento da Tecnologia Nuclear, CDTN, Rua Mário Werneck s/n, Cidade Universitária, Pampulha, Belo Horizonte, MG
vilma@prover.com.br

WANDER L. VASCONCELOS
Depto. Eng. Metalúrgica, UFMG, Rua Espírito Santo, 35-2° andar 30160-030, Belo Horizonte, MG

KEVIN L. BRAY
University of Wisconsin, Department of Chemical Engineering, Madison, WI, 53706, USA
holz_kb@physik.uni.paderborn.de

Abstract. Gels have been investigated as potential matrices for rare earth luminescence. The use of complexing ligands in the sol-gel synthesis of the rare-earth doped glasses has been suggested to improve the rare earth ion luminescence properties in these matrices due to the changes in the local environment experienced by the rare earth ion. In this work, transparent Eu^{3+}-doped gels were prepared from $Si(OCH_3)_4$ and fluorinated and/or complex-forming Eu^{3+} precursors $(Eu(fod)_3$, $(CF_3SO_3)_3Eu$, $(CF_3CO_2)Eu{\cdot}3H_2O$, $Eu(thd)_3$ and $Eu(acac)_3)$. Results of emission, fluorescence line narrowing and lifetimes studies of Eu^{3+}-doped gels derived from $Si(OCH_3)_4$ and fluorinated/chelate Eu^{3+} precursors are presented. The results were interpreted in terms of the evolution of the Eu^{3+} fluorescence in systems varying from solutions to the gels densified to 800°C. Analysis of the fluorescence decays of the $^5D_0$ state suggests that the use of the fluorinated Eu^{3+} precursors reduces the hydrophobic content in the silica gels matrices. FLN studies indicate that Eu^{3+} clustering occurred in all densified samples.

Keywords: Eu^{3+}, glasses, complex-forming precursors

Introduction

The rare earth ions have interesting emission properties for laser applications and have been studied as luminescent ions when incorporated inside sol-gel matrices. The optical spectroscopy of rare earth ions can be useful for characterization of glasses [1, 2]. Eu^{3+} has been most often used as an optical probe because of its particularly informative luminescence spectrum [3].

Hydroxyl quenching and dopant clustering are the two primary complications that currently limit the luminescence efficiency of rare earth ions in sol-gel host materials. Hydroxyl quenching is caused by residual water, solvents, and silanol groups present in sol-gel glasses and leads to an enhancement of non-radiative decay pathways of rare earth ions. Dopant clustering is deleterious because it leads to concentration quenching of luminescence through cross-relaxation and energy transfer processes. In recent work, an optical method for detecting rare earth clustering in sol-gel glasses based on Eu^{3+} fluorescence line narrowing spectroscopy has been shown to be effective [4].

In order to minimize the hydroxyl content of sol-gel matrices, the use of organically modified alkoxide sol-gel precursors [5], dopant ion encapsulation [6, 7] and the addition of fluorine as dehydroxylating agent [8],

have been attempted and demonstrated to reduce hydroxyl content in silica gel glasses.

In this work the spectroscopy of Eu^{3+} ions is used as a probe of structural changes in sol-gel silica glasses to investigate the effect of the use of different Eu^{3+} precursors, containing fluorinated and/or chelating ligands, on clustering and hydroxyl quenching of Eu^{3+} ions. Fluorescence and lifetime properties of Eu^{3+} are used to examine the effects of Eu^{3+} precursor characteristics on the luminescence efficiency of Eu^{3+} in densified sol-gel silica.

Experimental Procedure

Sample Preparation

The gels were prepared by mixing TMOS and the solutions in which the europium precursors were previously dissolved. The Eu^{3+} precursors (Aldrich) studied were: tris(6,6,7,7,8,8,8-heptafluoro-2,2-dimethyl-3,5-octanedionate) Eu(III) ($Eu(fod)_3$), Eu(III) trifluoromethanesulfonate ($(CF_3SO_3)_3Eu$), Eu(III) acetylacetonate hydrate ($Eu(acac)_3$), Eu(III) trifluoroacetate trihydrate ($(CF_3CO_2)_3\,Eu\cdot 3H_2O$), tris(2,2,6,6-tetramethyl-3,5-heptanedionate) Eu(III) ($Eu(thd)_3$) and $Eu(NO_3)_3\cdot 6H_2O$. DMF was used to dissolve the $Eu(fod)_3$ and methanol was the solvent for $Eu(thd)_3$ and $Eu(acac)_3$. The molar ratio solvent to TMOS was 4. The water to TMOS molar ratio was 16. HNO_3 was added to lower the pH to 1.5. The samples contained 1 and 5 wt% Eu_2O_3. After gelation, the gels were aged and dried at 60°C and 90°C for 2 days and ultimately heated to 800°C.

All precursors were studied in solution (precursor concentration of 0.1 M). Spectra are presented for the sol or initial mixing stage, the wet gel (corresponding to the material after aging at room temperature) and the gels heated to 90°C and 800°C.

Spectroscopic Measurements

The broadband emission spectra were obtained, at room temperature, by exciting samples with the 466 nm and 514.5 nm lines of a Coherent Innova Series 70-5 argon ion laser. Luminescence was collected on a 1-meter monochromator and detected by a photomultiplier tube.

Fluorescence line narrowing measurements were carried out using a pulsed tunable dye laser pumped by a Q-switched Nd : YAG. Spectra were normalized to the $^5D_0 \rightarrow {}^7F_1$ peak intensity and were collected at 77 K. Spectra normalization was completed because, to a very good approximation, the $^5D_0 \rightarrow {}^7F_1$ intensity is independent of the coordination environment of Eu^{3+}. As a result, the normalization provides a useful way to directly compare the environmentally sensitive intensities of the $^5D_0 \rightarrow {}^7F_0$, $^7F_2$ transitions in samples prepared from the different Eu^{3+} precursors. Luminescence decay measurements were recorded using a digital storage oscilloscope.

Results and Discussion

Fluorescence Spectra

Figures 1 and 2 present broadband fluorescence spectra for the 5.0 wt% Eu_2O_3 doped samples prepared from the different Eu^{3+} precursors at stages of the sol-gel reaction ranging from precursor solutions to mildly heated gels. The precursors used are indicated in the figures.

Important spectral differences in the relative intensities of the emission peaks of Eu^{3+} were observed with the different precursors. Weak $^5D_0 \rightarrow {}^7F_0$ and $^5D_0 \rightarrow {}^7F_2$ emission bands reflect a symmetric solvation shell of the Eu^{3+} ion and are indicative of ligand dissociation in solution and an Eu^{3+} inner coordination shell comprised primarily of water. Strongly coordinating monodentate and chelating ligands lead to asymmetric distortions of the Eu^{3+} bonding environment. These distortions are reflected in intensity increases for the $^5D_0 \rightarrow {}^7F_0$ and $^5D_0 \rightarrow {}^7F_2$ transitions.

The spectra of samples prepared from $Eu(fod)_3$ show pronounced interactions between Eu^{3+} and the fod ligands during the sol-gel reaction. The strong $^5D_0 \rightarrow {}^7F_0$ and $^5D_0 \rightarrow {}^7F_2$ transitions reflect a low symmetry Eu^{3+} inner coordination shell and provide evidence that fod chelation is preserved even after gelation and mild heating. The lowering of symmetry leads to stronger $f \rightarrow f$ transitions via ligand orbital mixing and relaxation of the parity selection rule. Similar, but less pronounced, considerations apply to $Eu(thd)_3$. Figures 1 and 2 reveal that the spectra of samples prepared from $(CF_3SO_3)_3Eu$, $(CF_3CO_2)_3Eu$ and $Eu(NO_3)_3\cdot 6H_2O$ are similar in appearance. Previous work [9] has shown that the NO_3^- ion has the ability to form an inner sphere complex with Eu^{3+}. In the nitrate solution, the coordination shell of Eu^{3+} will consist of one NO_3^- ion and 6–8 water molecules,

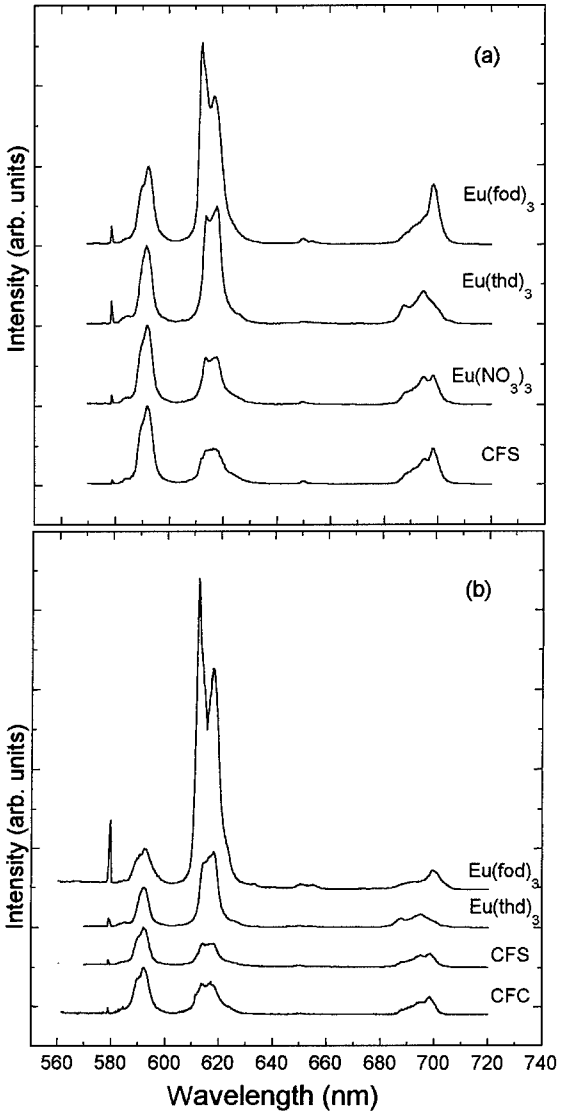

Figure 1. Fluorescence spectra (77 K) of some Eu^{3+} precursors: (a) solution, (b) sol. Intensities were normalized to the $^5D_0 \rightarrow {}^7F_1$ emission.

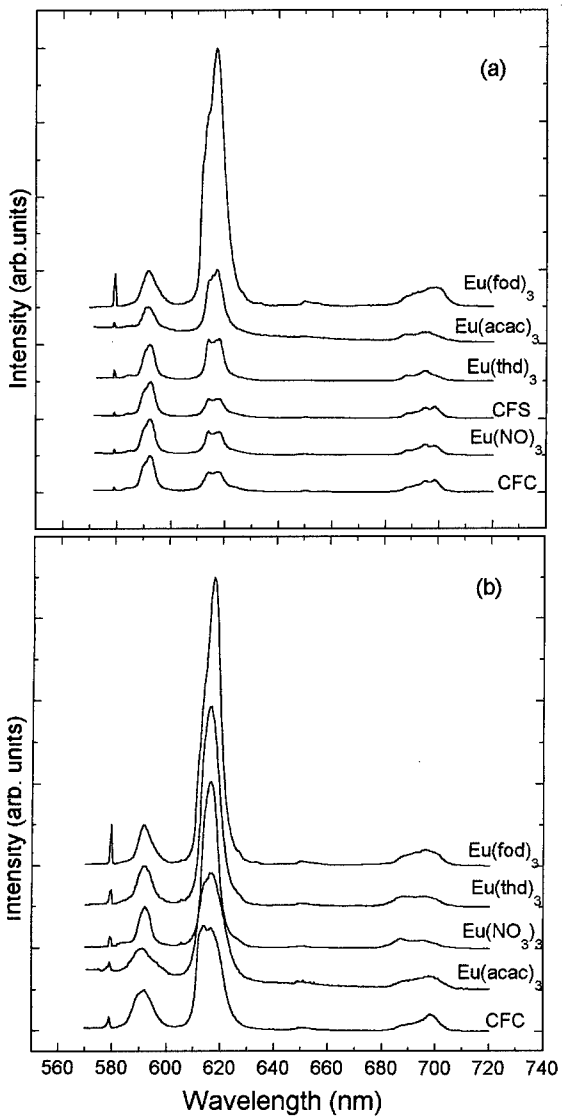

Figure 2. Eu^{3+} fluorescence spectra (77 K) of samples prepared with various Eu^{3+} precursors: (a) wet gel product, and (b) gel heated to 90°C.

resulting in increased asymmetry compared to coordination only by water. The $^5D_0 \rightarrow {}^7F_0$, $^7F_2$ intensities in the spectra for samples prepared from $(CF_3SO_3)_3Eu$ and $(CF_3CO_2)_3Eu$ indicate that the strength of interaction in solution between Eu^{3+} and the ligands $CF_3SO_3^-$ and $CF_3CO_2^-$ is intermediate, similar to the NO_3^- case, and weaker than that observed for the ligands fod and thd. Figure 2(b) shows the spectra after heating for 2 days at 90°C. Heating promotes evaporation of solvent and water, gel contraction, and an increase in the interaction between Eu^{3+} and the rigid gel network. The Eu^{3+} bonding environment undergoes a transformation from being essentially solution-like in the unheated wet gel to more solid-like in the mildly heated gel. This transformation to a lower symmetry, more amorphous bonding environment is reflected in the increased $^5D_0 \rightarrow {}^7F_0$, $^7F_2$ intensities and inhomogeneous line broadening.

Lifetime Measurements

Room-temperature luminescence lifetime of the $^5D_0$ state are presented in Table 1. Excitation was at the

Table 1. Room temperature Eu^{3+} lifetime values (μs).

Precursor	Solution	Sol	Wet gel	90°C
$Eu(NO_3)_3$	136.6	120.2	133.7	154.0
$(CF_3CO_2)_3Eu$	153.5	109.0	139.1	330.7
$(CF_3SO_3)_3Eu$		140.0	131.6	193.6
$Eu(acac)_3$	115.9	108.4	111.4	385.0
$Eu(thd)_3$	133.0	183.1	158.0	362.9
$Eu(fod)_3$	235.4	415.0	627.1	575.7

maximum of $^7F_0 \rightarrow {}^5D_0$ absorption band and $^5D_0$ luminescence was monitored at 617 nm.

The lifetimes observed for samples prepared from $Eu(thd)_3$ and $Eu(fod)_3$ at the sol and wet gel stages were longer than those obtained using the other precursors. In the case of $Eu(thd)_3$, partial chelation of the ligand reduces the concentration of coordinated water and consequently decreases non-radiative vibrational quenching. In $Eu(fod)_3$, chelation by fod leads to a similar effect and in addition, the presence of hydrophobic fluorine is expected to further protect Eu^{3+} from water. A general increase in lifetime was observed upon mild heating and is attributed to a reduction in hydroxyl concentration due to evaporation of water.

Eu^{3+}-Doped Silica Gel Partially Densified

Selectively excited fluorescence spectra measured at 77 K for the samples prepared from the fluorinated Eu^{3+} precursors revealed no line narrowing effect. Figure 3 shows broadband and selectively excited emission spectra for 1 wt% silica gel prepared from $Eu(fod)_3$. The FLN spectra of all precursors studied were very similar to those of the $Eu(fod)_3$ precursor and therefore are not presented. This result indicates that the use of fluorinated or chelated Eu^{3+} precursors does not inhibit Eu^{3+} clustering in densified samples [6].

The fluorinated precursors had a pronounced effect on the Eu^{3+} lifetime. Table 2 summarizes 77 K lifetime results of samples containing 5 wt% Eu_2O_3 heated to 800°C for two excitation (λ_{exc}) and two detection (λ_{em}) wavelengths. A clear increase in lifetime was observed when fluorinated precursors were used. Since the fluorescence line narrowing spectra indicate that appreciable clustering is present, the longer lifetimes indicate that the use of fluorinated Eu^{3+} precursors leads to lower hydroxyl content in the densified gels.

Table 2. Eu^{3+} ($^5D_0$) lifetime values (ms) measured at 77 K for 5 wt% Eu_2O_3-doped silica gels densified at 800°C.

λ_{exc} (nm)	577		579	
λ_{em} (nm)	610	625	610	625
$Eu(NO_3)\cdot 6H_2O$	1.17	1.14	1.16	1.17
Eu(CFC)	1.63	1.44	1.69	1.61
Eu(CFS)	1.63	1.63	1.74	1.67
$Eu(fod)_3$	1.60	1.63	1.67	1.64
$Eu(thd)_3$	1.52	1.48	1.52	1.49
$Eu(acac)_3$	1.22	1.12	1.26	1.22

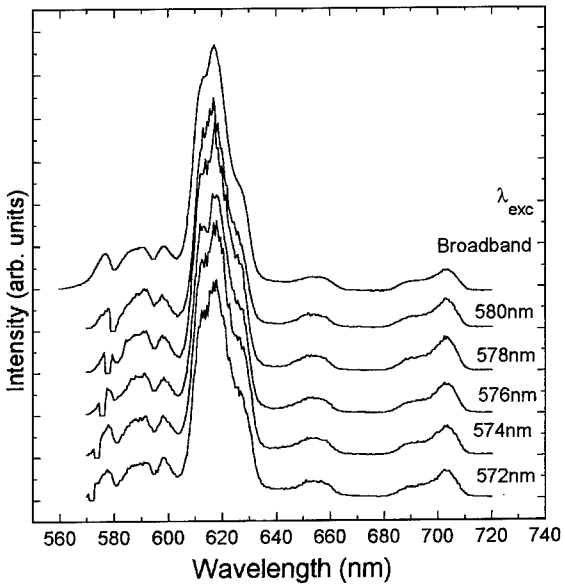

Figure 3. FLN spectra of 1 wt% silica gel prepared from $Eu(fod)_3$, densified to 800°C. Upper spectrum, fluorescence spectrum at 300 K.

Conclusions

Fluorescence, lifetime and fluorescence line narrowing (FLN) studies were presented at different stages of reaction for Eu^{3+}-doped TMOS silica gels prepared using different Eu^{3+} precursors, including those with chelating and/or fluorinated ligands. Much longer lifetimes, relative to samples prepared from $Eu(NO_3)\cdot 6H_2O$, were observed in gels densified at 800°C that were prepared from the fluorinated Eu^{3+} precursors. This result suggests that the presence of fluorine in the pores of the gel significantly facilitates the removal of water during heat treatment and that the use of fluorinated precursors may lead to rare-earth doped sol-gel materials with

higher luminescence efficiency. FLN studies indicate that significant Eu^{3+} clustering, however, occurred in all densified samples. When combined with previous work [4], the results suggest that compositions based on fluorinated Eu^{3+} precursors and non-fluorinated metal ion codopants such as Al^{3+} may provide densified sol-gel glasses with low hydroxyl quenching and uniformly distributed Eu^{3+} ions.

Acknowledgments

The authors acknowledge financial support from the U.S. National Science Foundation, the UW Graduate School, CNPq, Fapemig and FINEP/PADCT.

References

1. M. Ferrari, R. Campostrini, G. Carturan, and M. Montagna, Phil. Mag. B. **65**, 251 (1992).
2. L.R. Matthews, X. Wang, and E.T. Knobbe, J. Non-Cryst. Solids **178**, 44 (1994).
3. D. Levy and R. Reisfeld, Chem. Phys. Lett. **109**, 593 (1984).
4. V.C. Costa, M.J. Lochhead, and K.L. Bray, J. Chem. Mater. **8**, 783 (1996).
5. C. Sanchez, B. Lebeau, and B. Viana, in *Sol-Gel Optics III*, edited by J.D. Mackenzie (Bellingham, 1991), Vol. 2288, p. 227.
6. L.R. Matthews and E.T. Knobbe, Chem. Mater. **5**, 1697 (1993).
7. C. Brecher, H. Samelson, and A.J. Lempicki, Chem. Phys. **42**, 1081 (1965).
8. E.J.A. Pope and J.D. Mackenzie, J. Am. Cer. Soc. **76**, 1325 (1993).
9. P.J. Breen and W. Dew. Jr. Horrocks, Inorg. Chem. **22**, 536 (1983).

Journal of Sol-Gel Science and Technology 13, 611–615 (1998)
© 1998 Kluwer Academic Publishers. Manufactured in The Netherlands.

Fluorescence and Absorption Probe of Metal Ion Centers in Silicates Obtained by the Sol-Gel Technique

J. SOKOLNICKI
Faculty of Chemistry, University of Wrocław, Wrocław, Poland

K. MARUSZEWSKI AND W. STRĘK
Institute of Low Temperatures and Structure Research, Polish Academy of Sciences, Wrocław, Poland

J. LEGENDZIEWICZ
Faculty of Chemistry, University of Wrocław, Wrocław, Poland

Abstract. An optical probe of the structure of metal ion centers in sol-gel systems based on Eu^{3+} and Nd^{3+} emission and absorption measurements has been developed. The effects of the structure and composition of organic complexes of Eu^{3+} on the clustering processes and retention of water molecules in the gel and glasses were investigated. Mechanical properties of systems prepared with Triton detergent were also investigated. The studies have been performed for two types of complexes of lanthanides, with β-diketones as the precursor lanthanide salts. The emission, excitation and absorption spectra of the precursor salts, gels and glasses heated to 1100 K were measured. Splitting of the levels and electronic transition probabilities were analyzed. The IR spectra were used for the detection of the OH^- modes in the glasses.

Keywords: europium, neodymium, spectroscopy, sol-gel silicates

Introduction

Silica gels and glasses doped with lanthanide ions are of interest for a variety of technological applications such as fiber amplifiers, waveguides, tuneable solid-state lasers and many others [1]. The sol-gel process provides a convenient way of synthezing the optical materials since it gives an opportunity to control the macrostructure and composition of the host matrix [2]. The low processing temperatures allow incorporation of organic species into the silica gels [3].

In recent years, there has been an increasing interest in studies of lanthanide complexes with organic ligands due to their attractive emission features. The organic ligands can prevent the clustering of dopant ions [4, 5], isolate the metal ion from the deactivating group [6, 7] and reduce hydroxyl quenching by dopant ion encapsulation, which leads to increasing luminescence intensity [8].

In previous papers we reported successful incorporation of europium trichloroacetate [5] and europium β-diketonate salts [7] into a silica sol-gel matrix. It is well known that lanthanide complexes can absorb light by the ligand and that the energy may be transferred to the emitting metal ion, markedly increasing the luminescence efficiency. This was recently shown [9] for organic complexes of Eu^{3+} ions incorporated in silica gels.

In this paper we investigate the luminescent properties of Eu^{3+} and Nd^{3+} complexes with β-diketonates and 1,10-phenanthroline in silica gels.

Experimental

The Eu^{3+} complexes $Eu(AA)_3 \cdot 2H_2O$, $Eu(BA)_3 \cdot 2H_2O$ (further denoted as $Eu(AA)_3$ and $Eu(BA)_3$), $Eu(AA)_3Phen$, $Eu(BA)_3Phen$ (where HAA—acetyl-

acetone; HBA—benzoylacetone; Phen—phenanthroline were obtained according to the procedure described in [10, 11] and for mixed complexes the molar ratio Eu : HAA(HBA) : Phen was 1 : 3 : 1. $NaNdWo_4 \cdot H_2O$ (Wo = $CCl_3C(O)NP(O)(OCH_3)_2$) was prepared in a similar procedure to the europium compounds.

Ln^{3+}-doped silica sol-gel samples were prepared by the acid-catalyzed hydrolysis and condensation of tetraethoxysilane (TEOS) with deionized water. A methanolic solution of europium complexes was added. The molar ratio TEOS : water : methanol was 1 : 4 : 8. The sol pH reached approximately 1.5.

For comparison the sample with $Eu(BA)_3Phen$ was prepared using acetone instead of alcohol. The second sample with $Eu(BA)_3 \cdot 2H_2O$ was also prepared with Triton.

After homogenization, these sols were allowed to gel at room temperature, aged for one week, dried at 60°C and heated in air to 900°C. Transparent monolithic solid samples of cylindrical shape (diameter ~10 mm, thickness ~4 mm) were obtained.

Absorption spectra were measured by a Cary-Varian 5 spectrophotometer. Fluorescence and fluorescence excitation spectra were recorded at 293 and 77 K using a SLM Aminco SPF-500 spectrofluorometer. IR spectra were detected in the 300–4000 cm^{-1} range using a Brucker FS 88 FTIR spectrometer.

Results and Discussion

In the emission spectra of Eu^{3+} ions, transitions from the $^5D_0 \rightarrow {}^7F_J$ (where $J = 0, 1, 2, 3, 4$) levels are observed. The intensities of the 0-2 transitions in the systems under investigation are the highest. Intensities of the 0-1 transitions allowed by the magnetic dipole selection rule are less intense and for the mixed complexes with phenanthroline, their separated components are almost as intense as the 0-0 transition [12]. The luminescence properties of the europium ion are controlled by the energy gap, by the energy transfer from triplet or singlet states of ligands in the chelates, by a nonradiative quenching process promoted by OH vibrational modes of water molecules in the close environment of the metal ions and by other vibrational modes of the ligand molecules. Moreover, an important role in emission quenching may be played by the C-T ligand to europium ion transition, depending on their energy and the slope of the C-T state parabola. All the above processes can affect the intensities of the emission bands and the decay time of the emitted intra-ion states. The emission spectra for the complexes with BA and their phenanthroline derivatives obtained by us are comparable with those reported by Bünzli [13]. Comparison of the results obtained for chelates with AA and their phenanthroline derivatives indicate that the spectra of the latter

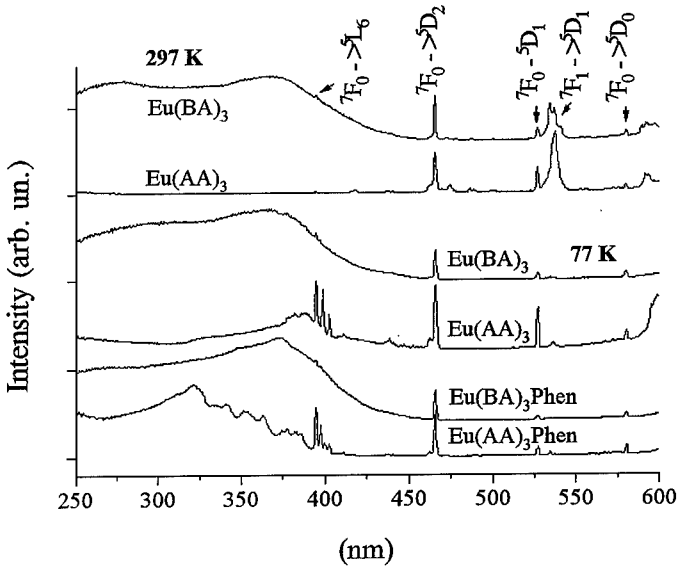

Figure 1. Fluorescence excitation spectra of Eu^{3+} complexes with β-diketones at room and 77 K temperatures.

are sharper and they essentially differ in the splitting of the 0-1 transition. Intensities of emission are strengthened by phenanthroline molecules as a result of the energy transfer from π-π^* levels of the ligand to metal ions levels. Comparison of the low and room temperature spectra reveals some differences which are probably caused by quenching processes promoted by both OH vibrations and/or by the C-T ligand to metal transition. Moreover, the transitions inside both type of ligands (AA and BA), as well as in the phenanthroline molecules overlap the metal states to different extents, which can affect the energy transfer process.

The drastic changes of intensities in the UV region in the splitting and in the relative intensities of the f-f transitions are indicated in the excitation spectra. In addition to the transition from the $^7F_0$ ground state, strong components were recorded from the $^7F_1$ excited level. An especially intense 0-0 transition was measured in the excitation spectrum of $Eu(AA)_3Phen$ at 293 K.

It is worth noting that a relatively high population of $^7F_1$ levels is preserved even at 77 K and even more in the $Eu(AA)_3 \cdot 2H_2O$ and $Eu(AA)_3Phen$ complexes.

Figures 2 and 3 show emission spectra of the complexes incorporated in the silica sol-gel matrixes. The splitting pattern of the Stark components in the

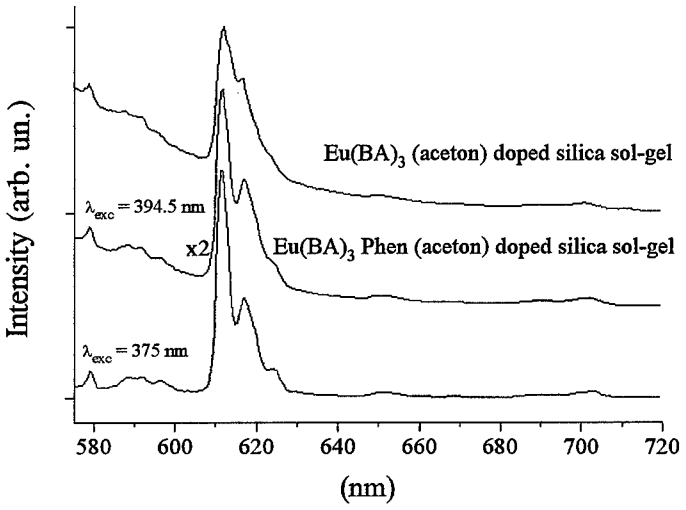

Figure 2. Fluorescence spectra of Eu^{3+} doped silica sol-gel at 77 K.

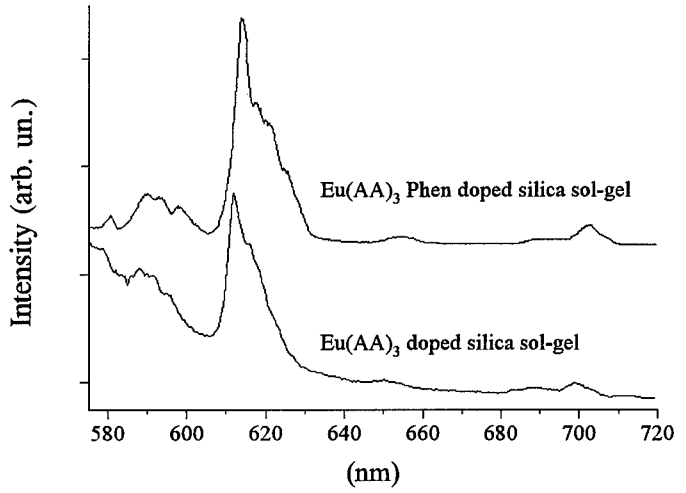

Figure 3. Fluorescence spectra of Eu^{3+} doped silica sol-gel at 77 K.

fluorescence spectrum of $Eu(AA)_3 \cdot 2H_2O$ in the silica gel indicates that the environment of the Eu^{3+} ion in the gel differs from that of the europium complex. This is most probably due to the exchange of water molecules by silica groups in the first coordination sphere of the Eu^{3+} ion. Investigations of the decay times of both systems can explain this phenomenon [14].

Only small changes of the shape of the emission bands were recorded in $Eu(AA)_3Phen$ doped silica gel. This could indicate partial coordination of phenanthroline, as well as competitive exchange of water molecules by silica. The situation is different in the case of the $Eu(BA)_3Phen$ complex prepared from the acetone solution. The similarity between the europium silica gel spectra and the pure complex suggests that the Eu^{3+} ion environment has not been changed and phenanthroline is still present in the first coordination sphere of the Eu^{3+} ion (Fig. 2 and in [12]). In contrast, the spectrum of the $Eu(BA)_3Phen$ doped silica sol-gel prepared without acetone is similar to that of the $Eu(BA)_3 \cdot 2H_2O$ doped silica sol-gel. This leads to the conclusion that synthesis from aqueous solution causes the phenanthroline molecules to be pushed out from the first coordination sphere of the Eu^{3+} ion by water molecules and furthermore, in the process, water is exchanged by silica groups.

The emission spectra in the region of the $^5D_0 \rightarrow {}^7F_{0\text{-}4}$ transitions for europium complexes and the doped silica sol-gel systems were measured for excitation of the ligand absorption bands. The intensity of the $^5D_0 \rightarrow {}^7F_0$ transition was found to increase both at room and at liquid nitrogen temperatures, which is directly related to the capacity of the ligands for absorbing and transferring energy to the Eu^{3+} ion levels.

Use of Triton in the preparation of the sol-gel improves the mechanical properties of the gels and glasses. Usually gels prepared according to the procedure described here can be used after drying at 60°C. Heating to 900°C leads to elimination of water molecules from the gel glasses, which is excellently confirmed from the IR spectra in the range of OH vibration frequencies (Fig. 4). This means that starting from the organics complexes, which can be entrapped in silica gels and glasses, water can be excluded from the final product. This effect is controlled primarily by the composition of the direct surroundings of the metal ions in the complexes which can help in the elimination of water.

Recent reports [5, 7] show how the concentration of active ions affects electronic transition probabilities in neodymium glasses and how this can be applied in the detection of clustering of ions and formation of aggregates in the glass structure. In the present paper we analyze the optical properties of neodymium glasses synthesized using a similar chelate to the europium compounds with composition $NaML_4 \cdot H_2O$; however, with phosphonic analogues of β-diketones. In this type of compound the strongest M—O bonds were observed [14]. Results of the intensity analysis of the f-f transition in the glasses and in the crystal spectra [14] are included in Table 1. Intensities of the hypersensitive band of the Nd^{3+} ion correspond reasonably well to the oscillator strength value calculated in the crystal spectra ($1769{,}26 \cdot 10^{-8}$ and $1837{,}7 \cdot 10^{-8}$,

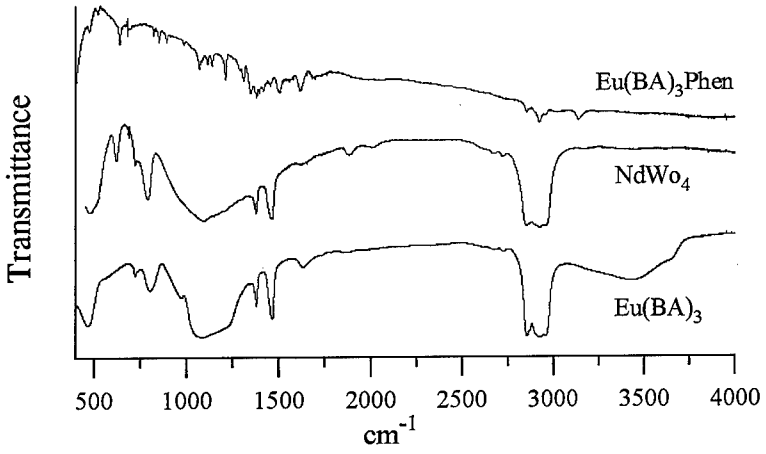

Figure 4. IR spectra of lanthanide complexes doped silica sol-gel glasses heated at 1200 K.

Table 1. $^5D_0 \rightarrow {}^7F_2/{}^5D_0 \rightarrow {}^7F_1$ intensity ratio and oscillator strength values ($P \times 10^8$).

	Complex $^5D_0 \rightarrow {}^7F_2/{}^5D_0 \rightarrow {}^7F_1$		Complex in sol-gel $^5D_0 \rightarrow {}^7F_2/{}^5D_0 \rightarrow {}^7F_1$	
	RT	77 K	77 K	
$Eu(AA)_3Phen$	9.62	12.40	4.74	
$Eu(BA)_3Phen$ (acetone)	13.71	11.97	11.18	
$Eu(AA)_3$	9.00	7.89	7.36	
$Eu(BA)_3$	9.03	9.54	7.74	
$NaNdWo_4 \cdot H_2O$	$^4I_{9/2} \rightarrow {}^2G_{7/2}, {}^4G_{5/2}$		Sol-gel	Complex
$P \times 10^8$			1769,26	1837,7

respectively), thus confirming that the structure of the metal centers in both these systems (crystal and gel) remain similar. After heating to 900°C, transformations of the structure occur, with the formation of silicate and almost complete elimination of water from the glasses. Again, the IR spectra confirm well the exclusion of water from the glasses.

Summary

1. Absorption, emission, excitation and IR spectra were applied in controlling the structure of active metal centers and OH vibrational modes in the glasses.
2. It was shown that the structure of the precursor complexes controls the structure of metal centers in the silica gel.
3. Elimination of water from the precursor salts (during chelation) prevents water retention in the glasses; chelation also affects formation of aggregates in the glasses.

Acknowledgments

The authors would like to thank Dr. T.A. Pavich for preparation of the lanthanide β-diketonate compounds.

This paper was supported by Committee for Scientific Research, grant 3T 09A 119 10.

References

1. R. Reisfeld and C.J. Jørgensen, Structure and Bonding **77**, 207 (1992).
2. C.J. Brinker and G.W. Scherer, *Sol-Gel Science* (Academic Press, Boston, 1990).
3. R. Reisfeld, J. Non-Crystalline Solids **121**, 254 (1990).
4. S. Chakraborti, J. Sahu, M. Chakraborty, and J.N.H. Acharga, J. Non-Crystalline Solids **180**, 96 (1994).
5. J. Legendziewicz, W. Stręk, J. Sokolnicki, B. Keller, and M. Borzechowska, Acta Physica Polonica A **90**, 241 (1996).
6. D.C. Lai, B. Dunn, and J.I. Zink, Inorg. Chem. **35**, 2152 (1996).
7. J. Legendziewicz, W. Stręk, J. Sokolnicki, B. Keller, and M. Borzechowska, Proc. SPIE, in press.
8. L.R. Matthews, X. Wang, and E.T. Knobbe, J. Non-Crystalline Solids **178**, 44 (1994).
9. O.A. Serra, E.J. Nassar, G. Zapparolli, and I.L.U. Rosa, J. Alloys and Compounds **207/208**, 454 (1994).
10. K. Utsunomiya and T. Shigematsu, Bull Chem. Soc. Japan **45**, 303 (1972).
11. T.A. Pavich and V.S. Khomenko, Functional Materials **3**(4), 521 (1996).
12. J. Legendziewicz, J. Sokolnicki, and K. Maruszewski, to be published.
13. J.-C.G. Bünzli, E. Moret, V. Foiret, K.J. Schenk, W. Mingzhao, and J. Linpei, J. Alloys and Compounds **207/208**, 107 (1994).
14. W. Amirkhanov, C. Jańczak, L. Macalik, J. Hanuza, and J. Legendziewicz, J. Applied Spectroscopy **62**(4), 5 (1995).

Journal of Sol-Gel Science and Technology 13, 617–621 (1998)
© 1998 Kluwer Academic Publishers. Manufactured in The Netherlands.

Sol-Gel Fabrication and Properties of Silica Cores of Optical Fibers Doped with Yb^{3+}, Er^{3+}, Al_2O_3 or TiO_2

VLASTIMIL MATĚJEC, IVAN KAŠÍK, DANIELA BERKOVÁ, MILOŠ HAYER AND JIŘÍ KAŇKA
Institute of Radio Engineering and Electronics, Academy of Sciences of the Czech Republic, Chaberská 57, 182 51 Praha 8, Czech Republic

Abstract. Optical cores of preforms for drawing optical fibers doped with Er^{3+} and Yb^{3+} were fabricated by the sol-gel method with the aim of increasing the thickness of glass layers coated in a single coating cycle and to determine the relation between the preparation conditions and optical properties of the fibers. Al_2O_3-P_2O_5-SiO_2 and TiO_2-P_2O_5-SiO_2 glasses have been studied as matrices for entrapping the rare-earth elements. Input sols have been prepared from silicon and titanium alkoxides, $AlCl_3$, $ErCl_3$, $YbCl_3$, $POCl_3$, water and a modifier under acidic catalysis of HCl. The sols were coated on the inner wall of a silica substrate tube and the gel layers were sintered at high temperatures up to 2000°C after which the tube was collapsed into the preform. Continuous and homogenous glass films with the maximum thickness of about 8 μm were fabricated. The influence of high-temperature heat treatment of the layers on their composition and optical attenuation was observed. The amplified stimulated emission of Er^{3+} around 1.55 μm was measured under the excitation of the fibers by an Nd : YAG laser at 1.064 μm.

Keywords: sol-gel, rare-earth doping, optical fibers

1. Introduction

In recent years, great interest has been paid to the development of novel optoelectronics structures based on glass and ceramic materials for communications and data transmission. For the manufacturing of such advanced glass structures novel technologies have been employed including chemical vapor deposition and the sol-gel method.

The sol-gel method has been used for the development of advanced coatings and their application in integrated optics. TiO_2-SiO_2 planar waveguides with low attenuation [1], semiconductor-doped waveguides with high nonlinear refractive-index coefficients [1, 2] or rare-earth doped waveguides [3] have been fabricated. In particular, Er^{3+} or Nd^{3+}-doped planar waveguides with SiO_2, TiO_2, P_2O_5, Al_2O_3 matrices have been intensively studied. A low fluorescence lifetime of Er^{3+} in comparison with materials prepared by the chemical vapor deposition has been measured in this case [3].

Similar approaches as those used in the fabrication of planar waveguides have been employed for the preparation of preforms for drawing silica optical fibers [4, 5]. There, a gel layer is coated on the inner wall of a silica tube. This layer is dried, densified and then the composite tube is collapsed into a preform. By this technique, fibers doped with Al_2O_3, TiO_2, P_2O_5 and/or codoped with Er^{3+} and Yb^{3+} have been fabricated and the fluorescence of Er^{3+} around 1550 nm has been observed.

Employing the above-mentioned approach [4, 5], this paper deals with the fabrication and investigation of glass layers doped with Yb^{3+} and Er^{3+} ions. These ions, suitable for high-power lasers generating ultrashort pulses [6, 7], are doped into Al_2O_3-P_2O_5-SiO_2 and TiO_2-P_2O_5-SiO_2 matrices. The effect of preparation conditions on optical properties of the prepared fibers is shown.

2. Experiment and Results

2.1. *Preparation of Sols and Coatings*

The sols for coating the layers were prepared by mixing stock sols. Tetraethoxysilane (TEOS), titanium

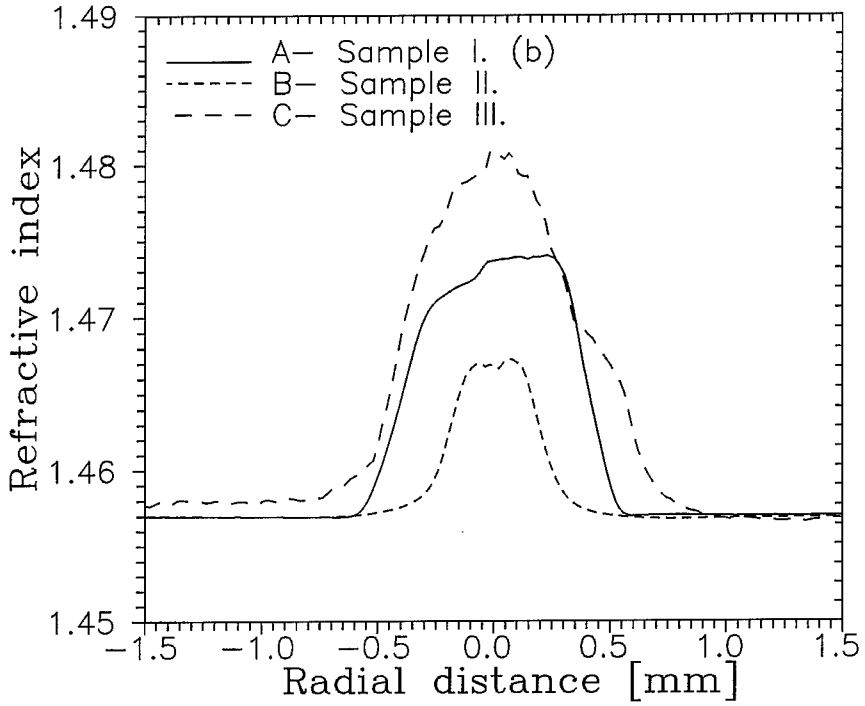

Figure 1. Refractive-index profiles of the fabricated preforms: Sample I.(b) single coating cycle and draining; Sample II. two coating cycles and draining; Sample III. gelation under $POCl_3$ and batching.

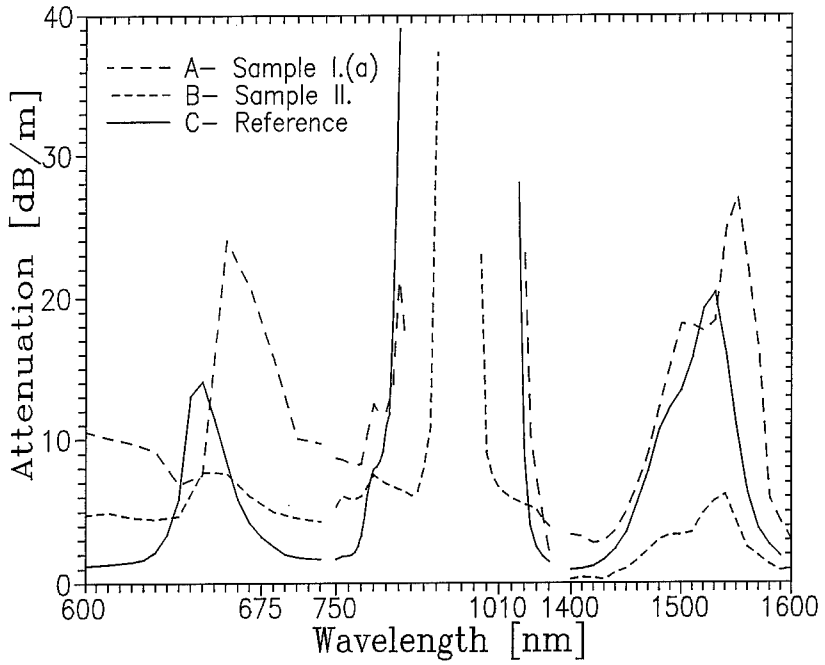

Figure 2. Spectral attenuations of the fibers: A. 39,000 ppm Yb^{3+}, 2900 ppm Er^{3+}—sol-gel method; B. 5600 ppm Yb^{3+}, 600 ppm Er^{3+}—sol-gel method; C. 26,000 ppm Yb^{3+}, 1600 ppm Er^{3+}—solution-doping technique.

Table 1. Compositions of the stock sols.

Sol	C (mol/dm^3)	R_s	R_w	R_H	R_{Ac}
A Si (TEOS)	3.7	0.8 (ET)	0.8	0.02	0.0
B Si (TEOS)	2.0	3.5 (IP)	1.5	0.0002	0.0
C Ti (TiIP)	0.4	2.7 (IP)	0.01	0.0	0.6
D Al/Yb/Er	1.4–1.8/0.3/0.018	3.9 (ET)	5.0	0.0	0.0
E P ($POCl_3$)	5.0	2.7 (ET)	0.2	0.0	0.0

$R_s = C(\text{solv.})/C$; $R_w = C(H_2O)/C$; $R_H = C(HCl)/C$; $R_{Ac} = C(Ac)/C$.

isopropoxide (TiIP) and $POCl_3$ were used as precursors of SiO_2, TiO_2 and P_2O_5, respectively. The stock sol containing $AlCl_3$, $ErCl_3$ and $YbCl_3$ was used for doping with Al_2O_3, Er_2O_3 and Yb_2O_3, respectively. Ethanol (ET) and isopropanol (IP) were used as solvents, acetylacetone (Ac) as a modifier and hydrochloric acid as catalyst. Typical compositions of the stock sols are given in Table 1. The stock sols A–D were prepared using refluxing at 60°C for 30–60 min. The sol containing $POCl_3$ was prepared under vigorous cooling.

The stock sols were stable for about 20–30 days. The period of stability substantially decreased after mixing the stock sols together. In particular, after the addition of the sol E into the mixture it decreased to 30 min—3 days depending on the R_w value.

The layers were coated on the inner wall of a substrate silica tube (HERALUX WG). The batching of about 10 cm^3 of the sols into the rotating tube inclined at an angle of about 3° to the horizontal was employed as one approach in the layer preparation [5]. Filling-in and lowering the column of the sol in the substrate tube at a controlled velocity of 10 cm/min was used as the second approach. In this latter case the multiple coating process was also utilized in which the gel layer was heat-treated at 200°C after every sol application. The final gel layer was heat-treated at 400°C for 20 min and then the tube temperature was gradually increased to 1600°C and the gel layer was densified. An atmosphere of $POCl_3$ in oxygen, and pure oxygen, were used during the sintering of layers containing Al_2O_3 and TiO_2, respectively. The tube with the coated layer was collapsed into the preform at about 2000°C. Fibers were drawn from the preforms [5].

2.2. *Characterization of the Preforms and Fibers*

The concentrations of doping oxides in the preform cores were determined by electron microprobe analysis with absolute errors of about 0.1%. On the basis of these measurements, relative contents of elements in the cores were calculated which are shown in Table 2. For comparison, relative contents of elements in the input sols are also shown. Maximum relative errors of these values are estimated to be about 10–15%.

The refractive-index profile of the preforms at a wavelength of 589.4 nm was determined from the measurement of the deflection angle by using a refractive-index profiler (York-Technology, UK). The measured refractive-index profiles are shown in Fig. 1. The thickness t of the glass layer coated on the inner wall of the tube with the diameter D was determined from the core radius r as $t = r^2 \cdot D^{-1}$.

The spectral attenuation of the fibers (see Fig. 2) was measured by the cut-back method [7]. The amplified stimulated emission (ASE) of Er^{3+} at 1.55 μm was measured when the fiber was excited at 1.064 μm by a CW Nd : YAG laser [7]. The typical measured ASE spectrum is shown in Fig. 3 where it is also compared with the spectrum measured on a fiber fabricated by the solution-doping technique [7].

Table 2. Relative contents of the elements in the input sols and glass cores (related to Al or Ti).

	Si, Al, Ti, Yb, Er, P											
Sample	Sol						Glass core					
I.(a)	0.0	1.0	0.0	0.18	0.012	2.6	1.9	1.0	0.0	0.17	0.014	0.8
I.(b)	0.0	1.0	0.0	0.18	0.012	2.6	3.2	1.0	0.0	0.16	0.012	0.4
II.(a)	19.0	0.0	1.0	0.15	0.011	1.0	22.0	0.0	1.0	0.13	0.015	0.3
III.(a)	0.0	1.0	0.0	0.18	0.012	0.0	1.8	1.0	0.0	0.16	0.013	0.9
IV.(a)	16.0	1.0	0.0	0.16	0.013	3.8	19.0	1.0	0.0	0.15	0.012	2.5

(a) Tube with a diameter of 18 mm, slow sintering and collapse used.
(b) Tube with a diameter of 6 mm, rapid sintering and collapse used.

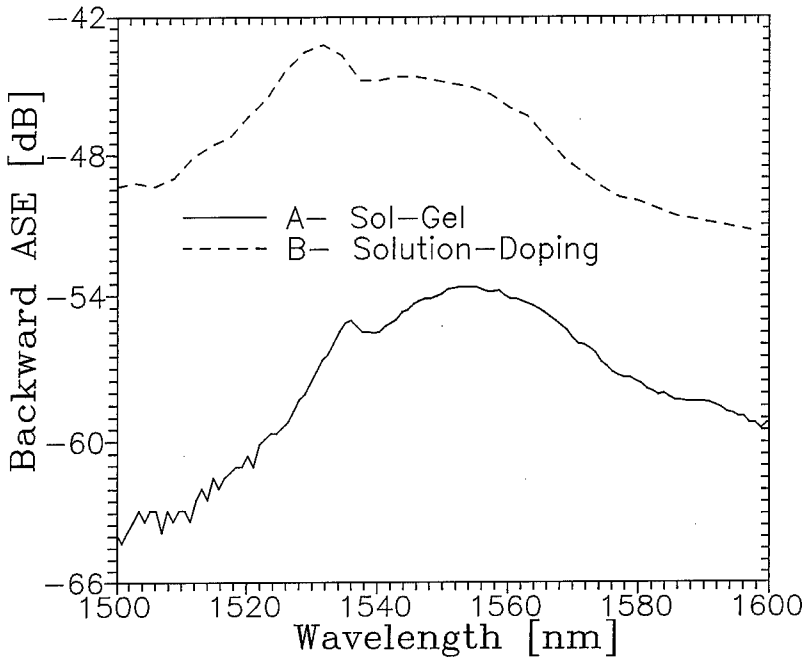

Figure 3. Spectrum of the backward amplified spontaneous emission of Er^{3+}-doped fibers excited by an Nd : YAG laser at 1064 nm.

3. Discussion

In comparison with the previously published results [5], the use of input sols with increased concentrations has enabled us to increase the homogeneity of the coated gel layer by suppressing the peeling off of the layer from the tube wall. The employment of sols which were prepared by mixing the stock sols D and E has enabled layers to be prepared with thicknesses of about 6 μm (Fig. 1, curve A) in a single coating cycle. This thickness has been further increased to about 8 μm by using the mixture of $POCl_3$ in oxygen (concentration of 2.7 mol%) for the gelation of the sol D prepared with a higher R_w value (equal to 7) and batched into the rotating tube (Fig. 1, curve C).

The method based on controlled lowering of the sol column in the substrate tube enabled an increase in the thickness of the prepared layer by using multiple coating. The result of this process is shown in Fig. 1 (curve B) for the case of two successive applications of the input sol prepared by mixing the stock sols B–E.

On the basis of the measured concentrations of dopants in the preform cores and in the input sols shown in Table 2, it is readily seen that there is a higher content of SiO_2 in the layers than in the sols. For the examination of this effect, a sol prepared by mixing the stock sols D and E was applied on the inner wall of the substrate tubes. The inner diameter of the substrate tube and period of the heat treatment were varied. A relatively high content of SiO_2 was found in the core (see Table 2, first and second rows).

From the data in Table 2 it can be deduced that there is a strong interaction of the substrate (silica) with the coated layers, probably due to viscous flow both in the substrate tube and in the coated layer. This interaction plays a role mainly at temperatures above the softening point of silica. It can be expected that this effect would be more important in the case of layers which are difficult to sinter.

The heat-treatment conditions also strongly influence the content of P_2O_5 which depends on the glass composition, sintering atmosphere and sintering times. In the layers doped with TiO_2 the decrease of the P_2O_5 content during the heat treatment can be related to the sintering in pure O_2 used for preventing the Ti^{4+} reduction. However, even when sintering the Al_2O_3-doped layers in the $POCl_3$ atmosphere, a relatively high decrease of the P_2O_5 content has been observed in layers coated from the sol D. In this case formation of glass layers with the $Al(PO_3)_3$ composition in the temperature range 1000–1300°C and the evaporation of P_2O_5 at higher temperatures may be expected. Taking into

account the actual compositions of the glass cores and the apparent refractive indices of SiO_2, Al_2O_3, TiO_2, Yb_2O_3 and P_2O_5 equal to 1.458, 1.59, 1.82, 1.48 and 1.5, respectively, agreement between the measured and calculated maximum values of the refractive index better than 0.002 can be obtained.

From the above results it is clear that high-temperature heat treatment during the preform fabrication influences the composition of the coated layer. Moreover, it may also increase the layer thickness because there is interaction of the substrate tube and the coated porous layer. Although no apparent macroscopic cracks have been observed, they may be, in principle, healed due to this interaction.

The spectral attenuation curves in Fig. 2 show some differences between the spectral bands of Er^{3+} and Yb^{3+} in both the studied matrices. In comparison with the previous results [5], much lower attenuation has been achieved in the case of fibers doped with TiO_2. This can be explained by the use of oxygen instead of CCl_4 during sintering the layers. These conditions prevent Ti^{4+} ions from reducing to Ti^{3+} ions.

The results of the ASE measurements show that there is an effect of energy transfer between Yb^{3+} and Er^{3+} ions because only Yb^{3+} ions are excited at 1.064 μm by the Nd : YAG laser. The green upconverted fluorescence, which was also observed, is in agreement with this effect. This green emission is typical for all efficient Er^{3+} and Yb^{3+}-doped fibers prepared by the solution-doping technique [7]. In comparison with these fibers, a lower intensity of the Er^{3+} fluorescence near 1.55 μm has been observed in the fibers prepared by the sol-gel method. These lower efficiencies can be attributed to Er^{3+} ion-ion interactions leading to concentration quenching and cooperative upconversion. Since in the fibers intensive upconverted fluorescence has been observed, cooperative upconversion may be important. The quenching induced by OH groups is a less probable cause, because it is known to be important at OH contents higher than 100 ppm [8] while the contents of OH groups in the cores of the fabricated fibers are below 5 ppm. For a detailed explanation of these effects, measurements of the fluorescence lifetimes are proposed.

4. Conclusion

Glass silica layers doped with Al_2O_3, P_2O_5, TiO_2, Yb^{3+} and Er^{3+} with thicknesses of 5–8 μm were prepared by increasing the concentration of the input sols. A strong interaction of the coated layers with the substrate tube was observed. The energy transfer between Yb^{3+} ions excited at 1.064 μm and Er^{3+} ions was observed. Owing to Er^{3+} ion-ion interactions, low fluorescence intensities at 1.55 μm were measured. The future research will be concentrated on the investigation of the latter two effects.

Acknowledgment

This work was financially supported by the Grant Agency of the Czech Republic under contract No. 102/95/0871.

References

1. G.C. Righini and S. Pelli, J. Sol-Gel Sci. Technol. **8**, 991 (1997).
2. L. Spanhel, M. Popall, and G. Müller, *Proc. Indian Acad. Sci. (Chem. Sci.)* **107**(6), 637 (1995).
3. D. Barbier, X. Orignac, X.M. DU, and R.M. Almeida, J. Sol-Gel Sci. Technol. **8**, 1013 (1997).
4. F. Wu, G. Puc, P. Foy, E. Snitzer, and G.H. Siegel, Jr., Mat. Res. Bull. **28**, 637 (1993).
5. V. Matějec, M. Hayer, M. Pospíšilová, and I. Kašík, J. Sol-Gel Sci. Technol. **8**, 889 (1997).
6. M.J. Guy, D.U. Noske, and J.R. Taylor, Opt. Lett. **26**(17), 1447 (1993).
7. I. Kašík, V. Matějec, J. Kaňka, and D. Berková, in *Proc. EOS—Materials for Nonlinear Optics*, edited by M. Bertolotti (EOS, Capri-Italy, 1997), p. 154.
8. V.P. Gapontsev, S.M. Matitsin, A.A. Isineev, and V.B. Kravchenko, Optics and Laser Technology **14**, 189 (1982).

Journal of Sol-Gel Science and Technology 13, 623–628 (1998)
© 1998 Kluwer Academic Publishers. Manufactured in The Netherlands.

CdSe Quantum Dot Doped Amine-Functionalized Ormosils

ANGELA B. SEDDON AND DUAN LI OU
Centre for Glass Research, Department of Engineering Materials, University of Sheffield, Sheffield S1 3JD, UK

Abstract. Nanosized phenyl-capped CdSe particles (quantum dots) were isolated, after preparation inside reversed micelles present in AOT/H_2O/heptane, and then successfully redispersed in amine-functionalized Ormosils derived from 3-aminopropyl(trimethoxy)silane (i.e., SA). Doped ormosils were formed into films of a few μm thickness or small bulk samples. Host ormosils were structurally characterized by means of absorption spectroscopy, in the near- and mid-infrared ranges, and by ^{29}Si and ^{13}C solid-state nuclear magnetic resonance (NMR) spectroscopy. Doped ormosils were prepared and investigated via visible spectroscopy. The size of CdSe particles dispersed into the amino-ormosil hosts was calculated using the Effective Mass Model.

Keywords: sol-gel, ormosil, nanosized CdSe particles, quantum dots, optical nonlinearity, solid-state NMR, near-infrared spectroscopy, visible spectroscopy

Introduction

In order to realize the potential of optical data transmission systems, the current electronic method of signal processing should be replaced by all-optical devices. A prime example is an all-optical switching device based on a nonlinear optical coupler. The material used to construct this device should exhibit a high nonlinear refractive coefficient and picosecond relaxation time [1]. Such materials also must be amenable to fabrication in waveguide form.

Recently, a large amount of research work on this kind of material has been focused on small sized semiconductor particles doped into glasses. Such particles are expected to show third-order optical nonlinearity [2]. The particle size of the semiconductor can determine the volume normalized oscillator strength, and the particle size distribution can determine the wavelength selectivity [3].

During the 1980s/1990s the development of semiconductor nanosized particles (quantum dots) doped into glass has comprised of two types: growth of these particles in either melt-derived or sol-gel derived amorphous oxide systems. In contrast, it is possible to pre-synthesize these particles inside the water pools of reversed micelles. The semiconductor particles may be chemically capped in situ with organic species to prevent aggregation. This allows isolation of the capped particles as powders, which may be redispersed into a suitable host.

Here, such CdSe particles have been successfully redispersed in amine-functionalized ormosils, as described below, which is attributable to the intrinsic basicity of both the host precursor and processing conditions, which involved only addition of adventitious water.

The aromatic nature of the phenyl capping groups, with their π electron clouds, makes for weak base characteristics [4] encouraging hydrogen bond formation between the hydrogen of the amine group ($-NH_2$), of the organic part of the ormosil network, and the phenyl-capped surface of the CdSe particle. Such bonding could help to anchor the particles into an amine-functionalized ormosil matrix inhibiting aggregation of the CdSe particles. We therefore believe that the chemical structure and conditions of processing of the host material are key factors in fulfilling the task of doping the nanosized particles.

In order to understand further the structure of the host amino-silicate materials, mid- and near-infrared (IR) spectroscopy, together with solid-state nuclear magnetic resonance spectroscopy (NMR), were used to

examine the undoped ormosils. Visible spectroscopy was employed to determine the size of the semiconductor particles.

Experimental

The phenyl-capped CdSe nanosized particles were prepared according to a procedure modified from that of Steigerwald et al. [5] and described elsewhere [6]. Three different sizes of CdSe nanosized particles (QD1/1.1, QD1/2.3 and QD1/4.3) were prepared using the reverse micellar method with different water/AOT ratios ($W = 1.1$, 2.3 and 4.3, respectively; AOT is the surfactant bis(2-ethylhexyl) sulfosuccinate). In addition, four other sizes of CdSe nanosized particles (QD6, QD10, QD15 and QD20) were prepared using the sequential layer build-up method with, in total, 6, 10, 15 and 20 sequential additions of Cd and Se reagents prior to the final capping process. The prepared CdSe particles were manually stirred into 3-aminopropyl(trimethoxy)silane ($NH_2CH_2CH_2CH_2Si(OCH_3)_3$, termed SA, supplied by Aldrich). Such a mixture can be fabricated into bulk samples and thin films of CdSe doped amino-ormosils in room temperature using only the ambient moisture. Undoped amino-ormosil bulk samples and films were prepared from the SA precursor under identical conditions.

The characterization procedures of prepared materials are also described in detail elsewhere [6]. Single point BET surface areas indicated apparent zero porosity. The maximum loading of CdSe particles in the amino-silicate matrix was measured to be 2.05 wt% $CdSe_{0.72}$, where the density of the amine-functionalized ormosils was about 0.5 to 0.7 of the density of a typical melt-derived silicate glass.

Results and Discussion

Mid-Infrared Spectroscopy

Mid-IR spectra of the undoped ormosil materials SA were typical of an hydroxylated silicate network, with the organic functionality and amine groups evident, and the band assignments are summarized in Table 1. The siloxane, silanol and water bands were identified with reference to previous work on inorganic sol-gel derived silicates [7, 8] and organically modified silicates [9]. Observed bands arise from vibration of O—H, Si—O, Si—C, C—H, C—N and N—H bonds.

Table 1. Selected mid-IR band locations (cm^{-1}) and assignments for ormosils derived from 3-aminopropyltrimethoxysilane.

Wavenumber (cm^{-1})	Mode	Structural unit
3500–3000 (s, br)	(O—H, H)	OH envelope
3342(w)	$\nu_{as}(NH_2)$	1° R—NH_2
3277 (w)	$\nu_s(NH_2)$	1° R—NH_2
2915 (ms)	ν_{as} (CH_2)	R—CH_2—R
2857 (ms)	$\nu_s(CH_2)$	R—CH_2—R
1601 (ms)	$\delta(NH_2)$	1° R—NH_2
1456 (m)	$\delta(CH_2)$	R—CH_2—R
1203 (s, sh)	wag(CH_2)#	Si—CH_2—R
1138 (vs, br)	ν_{as}(Si—O—Si)	≡Si—O—Si≡
1047 (vs, br)	ν_{as}(Si—O—Si)	≡Si—O—Si≡
960 (s)	ν_{as}(Si—OH)	≡Si—OH
801 (ms)	ν_s(Si—O—Si)	≡Si—O—Si≡

vs = very strong; m = medium; br = broad, ν_s = symmetric stretch; ν_{as} = asymmetric stretch; δ = deformation; (O—H, H) = hydrogen bonded O—H; 1° = primary amine; R = straight alkyl chain; # = where CH_2 is attached to silicon.

Near-Infrared Spectroscopy

Near-IR spectra are presented in Fig. 1 and the band assignments are summarized in Table 2. Vibrational groups in the mid-IR spectral region 3000 cm^{-1} to 2000 cm^{-1} (~3–5 μm) will give the most easily detectable overtone and combination bands in the near-IR [10–12], hence for amino-silicates the O—H, C—H and N—H fundamentals are of most importance. Making use of the detailed band assignment for the mid-IR, allows the near-IR bands due to the organic functionality of the matrix to be assigned with some confidence.

For bands due to O—H vibrations, unlike the previously reported propyl, vinyl and phenyl silicates [9], the 1940 nm polymeric water band dominates the spectra instead of the 1890 nm monomolecular water band. According to our assignments the C—H and N—H near-IR bands appear as "family groups." From low to high wavelength, the first region (2490–2295 nm) consists of bands due to combination modes involving the CH_2 fundamental stretching vibrations. The second region (2114–2000 nm) is based on combination bands involving the NH_2 fundamental stretching modes. At still higher energy (1765–1700 nm) the first overtone region of the CH_2 fundamental stretching vibrations occurs followed by the first overtone region (1620–1400 nm) for analogous fundamental bands of

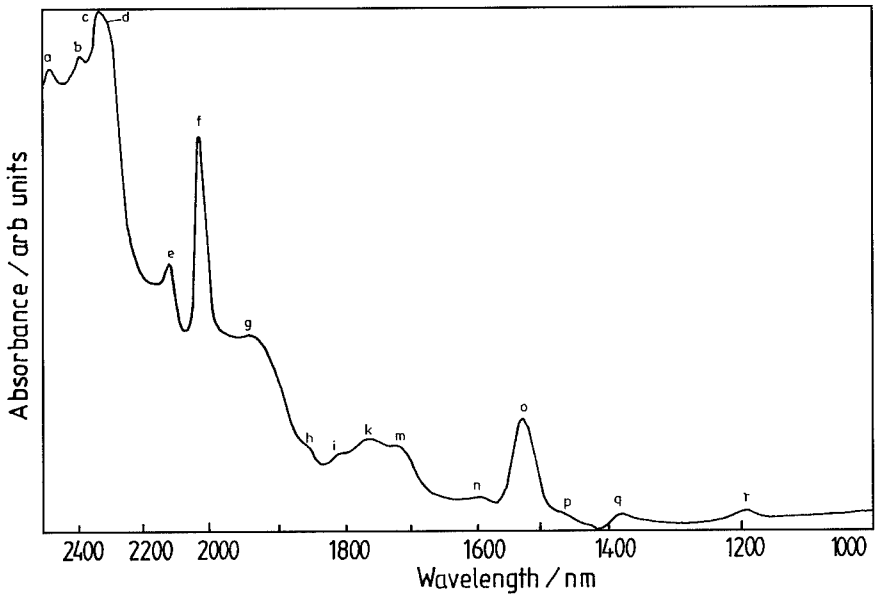

Figure 1. Near-infrared spectrum of undoped amine-functionalized ormosil host materials SA.

NH_2. It should be noted that the weak to medium amine absorption bands at 1500–1600 nm unfortunately coincide with the telecom signal wavelength of 1550 nm.

^{29}Si Direct Polarization (DP) Magic Angle Spinning (MAS) NMR

The peaks in ^{29}Si DP MAS NMR spectra of undoped ormosil SA are at −50.6, −59.5 and −67.8 ppm, respectively, corresponding to the T^1, T^2 and T^3 species. No uncondensed Si species (T^0) remain in the undoped ormosils, which is an advantage for the material chemical durability. The relative areas of T^1, T^2 and T^3 peaks are 4.8, 38.3 and 56.9%, respectively, and the resulting percentage of condensation efficiency is 84.2. The percentage of T^3 species in the aminosilicate materials is around 20% to 45% higher than in ormosils made from organo-bridged hexalkoxysilanes [13]. There is a surprisingly high overall condensation

Table 2. Selected near-IR band locations (nm) and assignments for ormosils derived from 3-aminopropyltrimethoxysilane (SA). Bands are based on Si—O, O—H, Si—C, C—H, C—N and N—H.

Wavelength (nm)			
Observed	Calc.	Mode	Structural unit
2469 (s) ***a***	2463	$wag(CH_2)_{1203} + \nu_s(CH_2)_{2857}$	R—CH_2—R
2295 (s, sh) ***d***	2288	$\delta(CH_2)_{1456} + \nu_{as}(CH_2)_{2915}$	R—CH_2—R
2114 (m) ***e***	2050 2082	$\delta(NH_2)1601 + \nu_s(NH_2)_{3277}$ or $3\delta(NH_2)_{1601}$	1° R—CH_2—NH_2
2016 (s) ***f***	2023	SA: $\delta(NH_2)_{1601} + \nu_{as}(NH_2)_{3342}$	1° R—CH_2—NH_2
1938 (m) ***g***		$\nu(H_2O, poly) + \delta(H_2O, poly)$	Polymeric H_2O
1529 (m) ***o***	1526	$2\nu_s(NH_2)_{3277}$	1° R—CH_2—NH_2

s = strong; m = medium; vw = very weak; sh = shoulder; ν_s = symmetric stretch; ν_{as} = asymmetric stretch; δ = deformation; 1° = primary amine; R = straight alkyl chain; 2ν is first overtone stretch; 3δ is second overtone deformation; $\nu_s(CH_2)_{2857}$ = fundamental at 2857 cm^{-1}.

of the matrix of the amine-functionalized ormosils, given that hydrolysis of the associated organosilane precursors depended only upon adventitious water.

^{13}C Cross Polarization (CP) Magic Angle Spinning (MAS) NMR

^{13}C CP MAS NMR of the ormosils potentially yields information on the organic group bound to silicon, residual alkoxy groups and alcohol. The 12.2, 26.3 and 44.8 ppm peaks observed [9] correspond to ^{1}C, ^{2}C and ^{3}C, respectively. ($\equiv Si-^{1}CH_2-^{2}CH_2-^{3}CH_2-NH_2$, where the carbon atoms are numbered consecutively with distance from the silicon atom.) As nitrogen is more electronegative than carbon, electrons are withdrawn from local carbon atoms and hence the chemical shift of these carbon atoms tends to move down-field. Thus, NMR peaks corresponding to the different carbons on the organic function may be readily assigned according to chemical shift. The carbon bonded to silicon in SA ormosils appears to be semi-rigid because the corresponding peak at 12.2 in the ^{13}C NMR spectra is almost totally removed by the non-quaternary suppression (NQS) treatment [9]. In contrast, the spectrum of the rest of the carbon chain is not affected by the NQS treatment, which indicates a high mobility for the rest of the carbon chain.

CdSe Doped Amine-Functionalized Ormosils

Figure 2 shows visible absorption spectra of thin films of samples of QD1/1.1/SA, QD1/4.3/SA, QD15/SA and QD20/SA. The absorption edges are blue-shifted compared with the optical band gap of bulk crystalline CdSe. This increase in the energy of the optical gap of the semiconductor is attributed to localization of the electron-hole carriers in a confined space, that is within the nanosized CdSe particle, which results in quantization of the electronic energy levels [14–16]. The absorption spectra show a well resolved shoulder which is due to the optical transition of the first excitonic state (E^*) and is indicative of a reasonably narrow size-distribution of CdSe particles formed by the reversed micellar route. The shoulder energy exhibited on spectra of the CdSe doped ormosils tends to decrease with increase of the H_2O/AOT ratio (W) employed during synthesis of the nanosized particles, as found by Steigerwald et al. [5] for isolated capped CdSe nanosized particles.

Premature flocculation occurred when $W > 4.5$, which limits the maximum size of CdSe particles achievable. In order to make bigger particles, we repeated the method used by Steigerwald et al. [5] involving building up sequential layers of CdSe inside the reversed micelle. For $W = 1.1$, nanosized particles were prepared with up to 20 sequential additions of CdSe and these particles were successfully doped into ormosils to produce samples: QD6/SA, QD10/SA, QD15/SA and QD20/SA. The absorption edge and first excitonic shoulder energy were found to decrease in energy with increase of the number of sequential layers added, and hence with increase in the particle size. We found that the CdSe particles were unstable and flocculated after 20 sequential additions at $W = 1.1$.

The absorption spectrum provides indirectly a quantitative measure of the CdSe particle radius (R) using the Effective Mass Model [15] based essentially on a "particle-in-a-box" approach to the electron-hole pair. We have taken E^* from the absorption spectra, of CdSe doped ormosils, as the range of energies associated with the plateau region of the shoulder due to the first excitonic transition as indicated by markers on Fig. 2. We adopted this method as there appears to be little consensus in the literature of a more exact method.

Samples QD1/1.1/SA were calculated to have a CdSe particle radius ranging from 1.56 to 1.60 nm and samples were yellow; samples QD1/4.3/SA have particle radius of 1.84 to 2.01 nm and were orange while samples QD20/SA have particle radius of range from 2.04 to 2.36 nm and were red. It is noticeable that the particle size range broadened as the mean particle size was increased. We conclude from this analysis that the reversed micelle means of synthesis can be used to create CdSe particles in the approximate range 1.5 nm to 2.4 nm. All of our attempts to increase the particle size either by adjusting the water/AOT ratio or by the sequential build-up method were limited by flocculation of the CdSe particles under the more extreme processing conditions.

We are currently pursuing third order nonlinear susceptibility (χ^3) measurements of the CdSe doped amine-functionalized ormosils.

Conclusions

1. From ^{29}Si DP MAS NMR, the siloxane matrix of the SA host is about 84% condensed suggesting a high level of silanols in the matrix, which is confirmed by absorption spectroscopy.

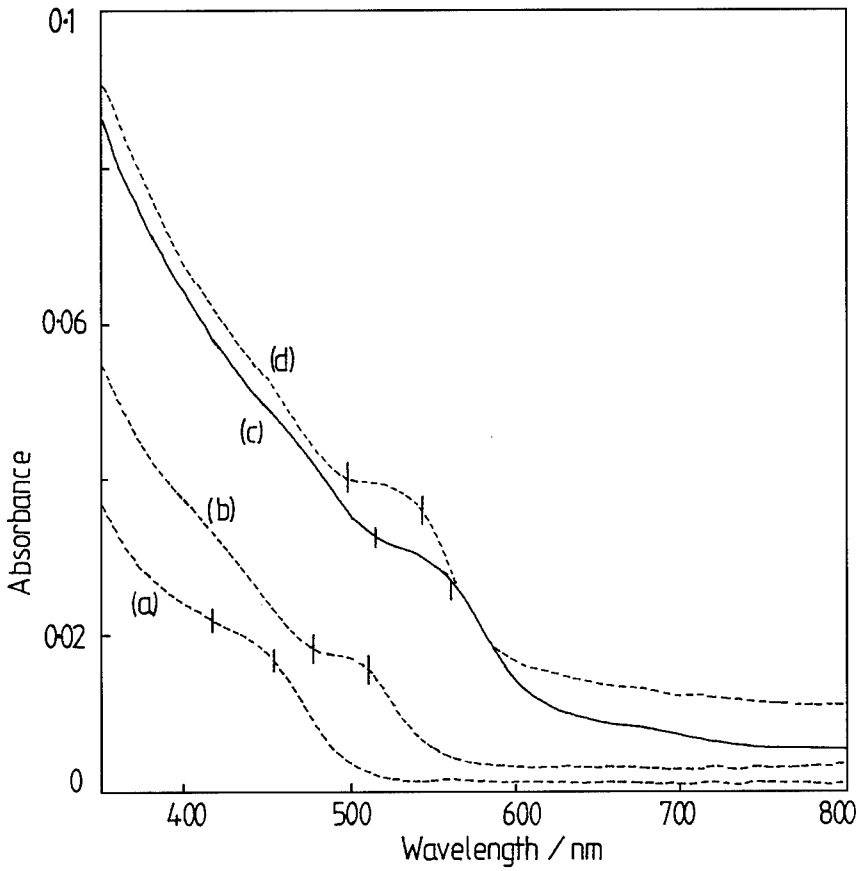

Figure 2. Visible absorption spectra of SA ormosil films doped with 0.5 wt% of phenyl-capped CdSe nanosized particles: (a) QD1/1.1/SA (yellow), (b) QD1/4.3/SA (orange), (c) QD20/SA (red), and (d) QD 15/SA (red). Colors cited are those of the corresponding bulk doped ormosils.

2. Evidence from ^{13}C NQS MAS NMR suggests mobility of the organic amine pendant chain in the ormosil matrix which could indicate aggregation of the chains to form relatively hydrophobic pockets in the matrix. Such pockets could also house the phenyl-capped CdSe nanosized particles.
3. Spectra of the doped films exhibit a good excitonic structure giving evidence of monodispersity of size of the particles. The apparent lack of porosity of the ormosil hosts should inhibit oxidation of the particles.
4. The doping levels achieved here were up to 2.05 wt% of $CdSe_{0.72}$ in the ormosils (whose density is around 0.5 to 0.7 of that of a typical silicate glass). Doped ormosils were prepared with CdSe particles whose radius ranged between about 1.5 to 2.4 nm going from yellow to red.

Acknowledgments

The authors sincerely thank Stephen Oliver of BT Labs., Martlesham Heath, Ipswich for drawing their attention to the reverse micelle synthetic method and for very helpful discussions and guidance in laboratory techniques at the beginning of this work. We also thank David Apperley of the EPSRC solid-state NMR Service at Durham University for the collection of NMR spectra and their deconvolution. The project was funded by the 21st Century Materials Initiative of EPSRC, grant No. GR/H62657.

References

1. S.R. Friberg, Y. Silberberg, and M.K. Oliver, Applied Physics Letters **51**, 1135 (1985).

2. M. Nogami, S. Suzuki, and K. Nagasaka, J. Non-Cryst. Solids **135**, 182 (1991).
3. L. Spanhel, E. Arpac, and H. Schmidt, J. Non-Cryst. Solids **147/148**, 657 (1992).
4. N.B. Colthup, L.H. Daly, and S.E. Wiberley, *Introduction to Infrared and Raman Spectroscopy*, 2nd edition (Academic Press, New York, London, 1975), p. 217.
5. M.L. Steigerwald, A.P. Alivisatos, J.M. Gibson, and L.E. Brus, J. Am. Chem. Soc. **110**, 3046 (1988).
6. D.L. Ou and A.B. Seddon, Phys. Chem. Glass **39**, 154 (1998).
7. C.C. Perry and X. Li, J. Chem. Soc. Faraday Trans. **87**(5), 761 (1991).
8. G. Orcel, J. Phalippou, and L.L. Hench, J. Non-Cryst. Solids **88**, 114 (1986).
9. D.L. Ou and A.B. Seddon, J. Non-Cryst. Solids **210**, 187 (1997).
10. R.F. Goddu, *The Handbook of Analytical Chemistry* (Polytechnic Institute of Broody, McGraw Hill Book Company, Luois Meiters, 1963), p. 146.
11. O.H. Wheeler, Chem. Rev. **59**, 629 (1959).
12. W. Kaye, Spectrochim. Acta **6**, 257 (1954).
13. P.J. Barrie, S.W. Carr, D.L. Ou, and A.C. Sullivan, Chem. Mater. **7**, 265 (1995).
14. R. Rosetti, J.L. Ellison, J.M. Gibson, and L.E. Brus, J. Chem. Phys. **80**(9), 4464 (1984).
15. L.E. Brus, J. Phys. Chem. **90**, 2555 (1986).
16. G. Hodes, A. Albu-Yaron, F. Decker, and P. Motisuke, Phys. Rev. B **36**(8), 4215 (1987).

Journal of Sol-Gel Science and Technology 13, 629–633 (1998)
© 1998 Kluwer Academic Publishers. Manufactured in The Netherlands.

SANS Study of CdS and CdSe Quantum Dot Crystal Growth in a Silica Matrix by Sol-Gel

N. DE LA ROSA-FOX, A. SANTOS, M. PIÑERO AND L. ESQUIVIAS
Dpto. Física de la Materia Condensada, Facultad de Ciencias, UCA, Aptdo 40, Puerto Real 11510, Cádiz, Spain

L. GAGO-DUPORT
UVIGO, Pontevedra, Spain

E. HOINKIS
Berlin Neutron Scattering Center, HMI, D-14109 Berlin, Germany

Abstract. Size and size distribution of the semiconductor nanocrystals embedded in a dielectric matrix play a dominant role in line broadening and the exciton quantum confinement level. The results show new aspects of the CdS and CdSe crystal growth as quantum dots using small-angle neutron scattering techniques (SANS). Thus, the crystal growth influences the aggregation process of the silica network. The intensity difference of the scattering between the silica matrix and the composite accounts for the crystal size and their volume fraction. Under similar conditions CdS nanocrystals grow faster and bigger than CdSe ones.

Keywords: quantum dots, II–VI crystal growth, silica gel, SANS

Introduction

Semiconductor nanocrystals embedded in a dielectric matrix is a standard example of a structure presenting quantum confinement effects [1]. These quasi zero-dimensional semiconductor structures, usually referred to as quantum dots (QDs), confine the photoexcited species, either an exciton (one electron-hole pair) or biexciton (two electron-hole pair); as a consequence the material exhibits non-linear optical properties [2]. Its performance is influenced by the small size of the crystals. In this way, the blue-shift of the optical absorption band caused by the nanocrystals varies with the crystal size R, as $1/R^2$. A transition frequency corresponds to each particle radius, producing the characteristic line broadening. Thus, the crystal size and their size distribution are critical parameters to improve the quantum confinement effects which take place when the crystal radius is in the range $a \ll R < a_B$, where a is the crystal lattice constant and a_B is the exciton Bohr radius [3].

CdS and CdSe nanocrystals in a glass matrix have been extensively investigated as QDs. The sol-gel method has been employed because these nanocrystals precipitate in silica gel with good optical transmission. The sol-gel process may improve critical parameters of both crystals and matrix. Thus, the dots have increased density, limited size, more homogeneous distribution and a smoother and more passivated surface. The matrix has increased optical purity and hybrid organic-inorganic matrices may be prepared to improve matrix densification [4, 5]. Moreover, the use of high power ultrasound in the early stages of the synthesis process produces many nucleation sites, helping to increase the number of crystals inside the matrix [6].

One powerful and non-destructive characterization technique to study the composite structure is small-angle scattering radiation (X-ray or neutron) [7], which permits nanometer resolution. In this work we present a study of the crystal growth in situ during the gelation process using small-angle neutron scattering (SANS).

The results reveal kinetic information about the CdS and CdSe crystal growth, and its influence on the aggregation process of the silica network.

Experimental

SANS experiments were carried out on sols prepared in quartz cells of 1 mm path from a mixture of TMOS : D_2O : formamide in a molar ratio of 1 : 4 : 7. Cadmium acetate (acCd) and thioacetamide (TAA) were used as the source of the Cd^{+2} and S^{-2} ions, and $SeCl_4$ for the Se^{-2} ions. Appropriate amounts of these precursors were diluted as an aqueous solution before reaction in order to obtain a CdS, or CdSe, crystal nominal concentration of 5 wt% of total silica.

SANS measurements were carried out in the V4 experimental station at the Berlin Neutron Scattering Center facility at the Hahn-Meitner Institut (Berlin, Germany) [8]. Three kinetic processes for silica matrix, CdS-doped silica and CdSe-doped silica were monitored every 30 min for each one and repeated six times, taking into account that gelation time is around 5 h. The neutron wavelength was 0.6 nm. Scattering data were obtained using sample-detector and collimator distances of 8 m to cover a q-range from 0.05 to 0.3 nm^{-1}. Standard programs were used for the data reduction, e.g., normalization of the efficiency of the two-dimensional detector, masking of the detector cells near the beam stop and subtraction of the scattering by the empty cell [9]. The macroscopic coherent scattering cross-section in cm^{-1} was calculated by using the scattering data from H_2O.

Results and Discussion

The coherent scattering cross-section, after data reduction, for the three kinetic studies are plotted in Fig. 1(a)–(c) for the silica matrix, CdS-doped silica and CdSe-doped silica, respectively. Increase in intensity runs parallel to the reaction time as a consequence of the increase in number of scattering centers, either crystals or silica aggregates. Both the matrix (160 min) and CdSe-doped silica (130 min) samples show similar features. Neverthless, the intensity scattered by the CdSe-doped silica sample was lower since it was measured 30 min before the matrix. Normalization of the intensities was possible because the same volume ($3.85 \cdot 10^{-2}$ cm^3) of the samples was irradiated with neutrons and the transmission of the empty quartz cell was 0.95. Therefore, the peak that appeared at around 0.09 nm^{-1} is assigned to the silica aggregates formation involving correlation distances of 11 nm, revealing low formation of CdSe crystals. The presence of such a peak for the CdSe-doped silica kinetic was more evident at 220 min. It remained as a knee at 580 min. This fact can be explained by the Se^{-2} ions influencing the liquid solution that slowed down the silica aggregation process.

The contrary seems to be the case for the CdS-doped silica kinetics which show a faster increase of intensity, even for lower reaction times (100 min). This fact reveals the onset of the nucleation and subsequent CdS crystal growth as well as its influence on the silica aggregation process, which masks the above-mentioned peak. The intensity curve for the CdS-doped silica (550 min) indicated a well-aggregated network which was produced by the contrast variations of both the CdS crystals and silica aggregates. This implies that both kinds of heterogeneity grow in the same size range.

Another structural characteristic comes from the asymptotic decay of the scattering curves. In all of the cases the slopes were close to -1, which is characteristic of linear polymer chains as the scattering objects. This picture seems to correspond to the silica network (acid catalyzed) as the crystal concentration is low enough to discard them as the cause of such behavior. The nanocrystals grew surrounded by a shell of the mother liquid (mainly D_2O) forming a transition region schematically represented in the inset of Fig. 2. If this was the case, positive deviations from Porod's law can arise because of scattering length density variations between the three levels. When the transition region width is of the same order as the crystal size, a $\mathrm{Ln}(Iq^4)$ vs. q^2 plot must show linear behavior in the high-q region. Such a linear region was found for the three kinetic studies (Fig. 2).

As a consequence, the above model permits consideration of the intensity difference, calculated as $|I_{\mathrm{matrix}}(q) - I_{\mathrm{composite}}(q)|$. This evaluation should lead to information on the crystal size and their spatial distribution. Some of them are shown in Fig. 3(a) and (b) for the CdS and CdSe, respectively. The results corroborate the above statement, that the crystal signal has been isolated from the silica matrix. In the case of the CdS kinetics, an asymptotic decay of -4 can be discerned at low angle (Fig. 3(a)) in agreement with Porod's law. Consequently, the signal must correspond to a great extent to the CdS nanocrystals. On the other hand, for the CdSe kinetics (Fig. 3(b)) the slopes are

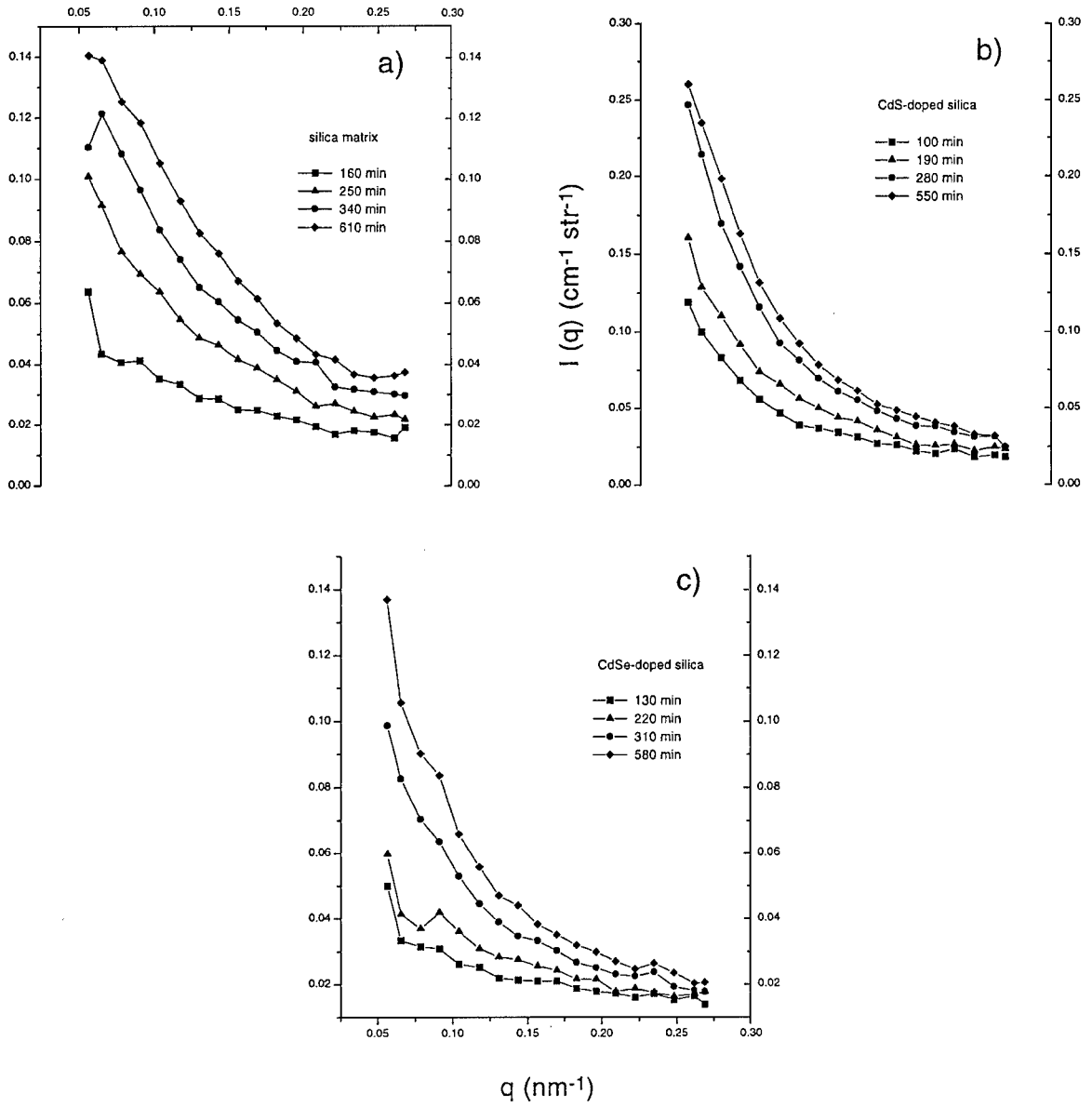

Figure 1. Scattering cross-section for the three kinetic studies of: (a) silica matrix, (b) CdS-doped silica, and (c) CdSe-doped silica. The reaction time is taken from the onset of obtaining the sol. (The lines are drawn as a guide to the eye.)

close to -2, indicating some fluctuation of the crystal boundary, probably due to the small size of the CdSe nanocrystals.

In order to estimate the crystal size and their spatial distribution, several classical models were used. Polydispersity was evident from Guinier plots (Ln $I(q)$ vs. q^2) which exhibited curved behavior in the high-q region. However, Debye plots ($I(q)^{-1/2}$ vs. q^2) showed a good near-linear region for estimating the average size of the scatterers of arbitrary shapes. The results from the slope are plotted in the inset of Fig. 3 (left axis) for the CdS (solid square) and for the CdSe (solid up triangle) intensity differences. It can be seen that there is a faster growth and bigger size for the CdS (ranging 12–21 nm) than that of the CdSe ones (ranging 4–4.5 nm). The size of CdSe nanocrystals remains stabilized.

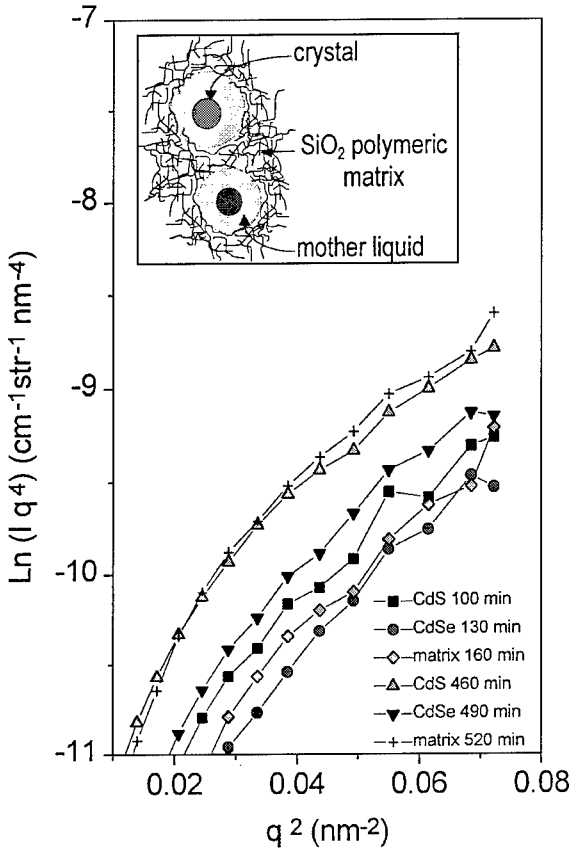

Figure 2. Ln (Iq^4) vs. q^2 of some outlined kinetics, first one (100, 130 and 160 min) and fifth one (460, 490 and 520 min). The inset shows schematically the structure of the crystal-doped silica.

Finally, the results of the crystal volume fraction, which was obtained by extrapolating the intensity to $q = 0$, are plotted in the inset of Fig. 3 (right axis). In the case of the CdS (open circle) the volume fraction increases as the nucleation centers increase. After this, the decrease implies a growth in size at the expense of smaller particles. For the CdSe (upside down triangle) a great number of nucleation sites were created and the subsequent spreading growth stabilized their sizes. For the same crystal nominal concentration the volume fraction of CdSe clearly reached smaller values, the same volume fraction being there from the beginning of the reaction ($\sim 1.47 \cdot 10^4$).

Conclusions

The study of crystal growth in situ revealed different kinetics for CdS and CdSe semiconductors when they

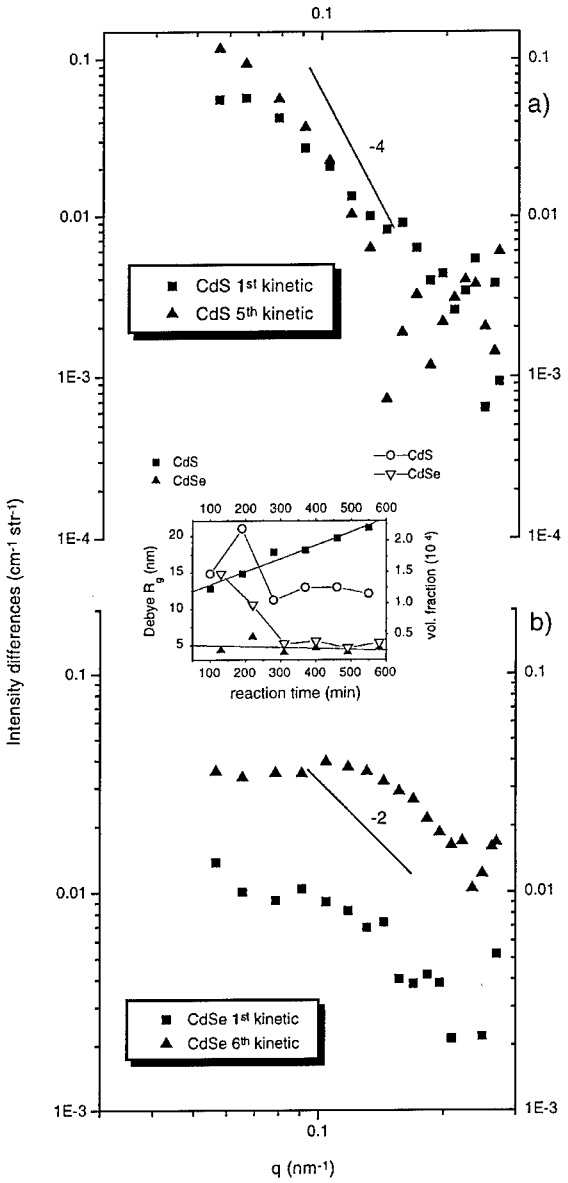

Figure 3. Scattering cross-section from the intensity differences: (a) CdS and (b) CdSe. The inset shows the results of size (left axis and solid markers) and crystal volume fraction (right axis and open markers) from the Debye plot. The straight line through the solid markers are linearly regressed whereas the line through the open markers are only a guide for the eye.

are embedded in a silica matrix. The sol-gel method proved its potential to make QDs of CdSe ($a_B = 6$ nm), but some chemical modifications are required to stabilize the size of the CdS QDs ($a_B = 3.2$ nm). The data treatment used permits an isolation of the nanocrystal signal. Thus, the sharp interface of the CdS crystal boundary should avoid surface trap sites, and the small

size (4 nm) of the CdSe nanocrystals gave rise to the scattering length density variations.

This work has been supported in Spain by the Junta de Andalucía (TEP 0015) and the neutron scattering measurements in Berlin by the TMR/LSF access program (ERBFMGE CT950060) of the European Commission.

References

1. N.F. Borrelli, D.W. Hall, H.J. Holland, and D.W. Smith, J. Appl. Phys. **61**, 5399 (1987).
2. N. Peyghambarian, S.W. Koch, and A. Mysyrowicz, *Introduction to Semiconductor Optics* (Prentice Hall, Englewood Cliffs, NJ, 1993).
3. L. Efros and A. Efros, Sov. Phys. Semicond. **16**, 772 (1982).
4. G. Banfi, V. Degiorgio, and B. Speit, J. Appl. Phys. **74**, 6925 (1993).
5. T. Takada, T. Yano, A. Yasumori, M. Yamane, and J.D. Mackenzie, J. Non-Cryst. Solids **147/148**, 631 (1992).
6. M. Piñero et al., J. Sol-Gel Sci. Tech. **2**, 689 (1994).
7. O. Glatter, in *Modern Aspects of Small-Angle Scattering*, edited by H. Brumberger (NATO ASI, Kluwer Academic Publishers, Dordrecht, NL, 1995), Vol. 451, p. 107.
8. N. de la Rosa-Fox, M. Piñero, A. Santos, P. Villar, L. Gago-Duport, and E. Hoinkis, BENSC Experimental Reports, HMI-B 536, 1995, p. 221.
9. E. Hoinkis, Langmuir **12**, 4299 (1996).

Journal of Sol-Gel Science and Technology 13, 635–639 (1998)
© 1998 Kluwer Academic Publishers. Manufactured in The Netherlands.

Optical and Structural Properties of Doped ZnS Nanoparticles Produced by the Sol-Gel Method

D.U. SAENGER, G. JUNG AND M. MENNIG
Institut für Neue Materialien, Im Stadtwald 43, 66123 Saarbrücken, Germany

Abstract. Optical and structural properties of Mn^{2+}-doped ZnS nanoparticles in an organic matrix are experimentally and theoretically studied. The nanoparticles, which were produced by the sol-gel method, are nearly monodisperse with a diameter of approximately 3 nm and show the characteristic orange-red luminescence of Mn^{2+} centers in a crystalline ZnS matrix. The absorption spectrum of the embedded ZnS nanoparticles is slightly blue shifted and broadened compared to the reference system containing ZnS microparticles. This blue shift is caused by quantum size effects, whereas the broadening is due to defects such as lattice distortions, and vacancies, which are probably located close to the surface in the case of small particles. With increasing temperature the absorption spectra shift to the red and are broadened due to thermal activated diffusion of ions close to the surface. In contrast, the spectral feature of the emission spectra via the Mn^{2+} center is nearly unchanged compared to the ZnS microparticles. Furthermore, the quantum efficiency is increased and the decay time of the electron-hole pairs is shortened to the nanosecond regime because of the enhanced probability of the electron-hole pairs to "see" the Mn^{2+} center. Therefore, the only effect of doping of ZnS nanoparticles with Mn^{2+} center is the suppression of the relaxation of electron-hole pairs via surface defects generating a highly efficient and fast relaxation of the electron-hole pairs via the Mn^{2+} center.

Keywords: luminescent properties of solids, nanostructured materials, optical properties, sol-gel chemistry

1. Introduction

Nanostructured materials such as systems containing semiconducting nanoparticles have attracted a lot of interest in the past decade [1] and are particularly interesting for their application as optoelectronic device materials.

These interests are governed by the possibility of observing quantum size effects such as enhanced oscillator strengths and faster relaxation times in the macroscopic properties of these systems in order to use them in future device applications. On the other hand, the reduction of the linear dimension of materials to the nanometer regime makes them very sensitive to defects such as lattice distortions, vacancies and interstitials, which are mainly located at the surface of the nanoparticles [2, 3]. These defects produce enlarged local fluctuations in the optical properties due to the individual realization of microscopic disorder in each nanoparticle. Due to the higher probability of electrons and holes to "see" disorder, these fluctuations can be detected in the macroscopic properties of the ensemble of nanoparticles.

The problem addressed in this paper is the origin of the fast relaxation time and the high quantum efficiency as measured in a dilute ensemble of Mn^{2+}-doped ZnS nanoparticles [4–6]. The important issue from the experimental and theoretical side is to achieve a consistent microscopic interpretation of the electron-hole dynamics in such an ensemble. Based on the extension of a recently developed theory [2, 3], experimental and theoretical evidence will be provided that these effects are not produced by the change of the electronic coupling of the Mn^{2+} center on the ZnS host lattice for small particles as usually assumed [4–6]. It is supposed that it is only an effect of the linear reduced dimension of the particles, which increases the probability of the excited electron-hole pairs to see the Mn^{2+} center. In order to

put the problem into proper context some important experimental and theoretical developments in this field will be reviewed first.

Bhargava et al. [4, 5] performed experiments on a dilute ensemble of Mn^{2+}-doped ZnS nanoparticles embedded in an organic polymer matrix. For small particles (approximately 3 nm) a relaxation time in the nanosecond range was measured. This relaxation time is much faster than the relaxation time for particles in the micrometer range, where it is about 1.5 ms. Furthermore, they measured a quantum efficiency between 10% and 20%, which is rather high for semiconducting nanoparticles due to the inefficient relaxation via surface states in undoped small particles [7]. As a possible explanation, they suggested that a stronger coupling of Mn^{2+} center on the ZnS lattice could produce such fast relaxation times and high quantum efficiencies.

In a recent contribution, the optical response of an ensemble of undoped semiconducting nanoparticles in the presence of microscopic disorder was computed using mode-coupling theory. As a result, it could be shown that microscopic disorder has a considerable influence on the macroscopic optical response of the system. The fluctuations in the level schemata induced by the individual realization of microscopic disorder broaden the absorption spectra considerably and a red-shift due to quantum mechanical level repulsion effects between one-particle states occurs. Additionally, surface states, which cannot be controlled by the growth process, generate a highly efficient radiative and non-radiative relaxation path for the electron-hole pairs. Therefore, the quantum efficiency of the light output in such a system is rather low [7]. The doping of the nanoparticles with luminescence centers reduces the probability of the relaxation via such surface paths and a highly effective and fast relaxation via luminescence centers located in the crystalline core is possible. For a review of this theory see [2, 3]. Note that within the formalism outlined in [2] small deviations from cubic structures and spherical particles are also modulated.

In this paper experiments are performed on the excitation and emission spectra, the relaxation times and the temperature dependence of the emission in order to clarify the contribution of the disordered surface to the optical response. In Section 2 the preparation of the samples and the experimental details are described. In the same section, the structural characterization is performed using high resolution transmission electron microscopy (HRTEM), grazing incidence small angle X-ray scattering (GISAXS) and wide angle X-ray scattering (WAXS). The optical properties of the system are outlined and discussed in Section 3. Section 4 contains the conclusions.

2. Experimental

2.1. *Preparation*

Mn^{2+}-doped ZnS nanoparticles were formed by precipitation with H_2S gas from a precursor solution containing 0.01 M $Zn(CH_3COO)_2$ in the presence of hydroxypropyl cellulose (HPC) as a stabilizer. Doping of Mn^{2+} ions into ZnS nanoparticles was realized in situ during the precipitation procedure. The Mn concentration was chosen as 2 mol% with respect to the cations. After dipcoating and drying at 423 K on soda-lime glass substrates, the sheets were transparent and colorless and had thicknesses of up to 50 μm [8].

Additionally, a system with dispersed Mn^{2+}-doped ZnS microparticles in ethanol, which is commercially available, with a diameter of approximately 10 μm was studied as reference. The dispersed microparticles were dried at 373 K on a soda-lime glass.

2.2. *Characterization*

For the structural characterization HRTEM (Philips CM 200), GISAXS (beam line D22 of the synchroton at Lure in Paris/Orsay [9]) and WAXS (Siemens D 5000) were used.

The size and size distribution of the ZnS nanoparticles were investigated by HRTEM and SAXS. Further information about the crystallinity was obtained by WAXS.

The optical characterization was performed by UV-VIS spectroscopy, using a Bruins Omega 20 spectrometer, and by excitation and emission spectroscopy with an Hitachi fluorescence spectrometer. Also, time resolved measurements were performed with an excimer (XeCl, 308 nm, 20 ns) and a Nd:YAG (266 and 355 nm, 8 ns) laser system. Furthermore, temperature dependent absorption and emission spectra measurements were done using a Xenon lamp as excitation source. The temperature was varied from 15 K to 300 K. All other measurements were carried out at room temperature.

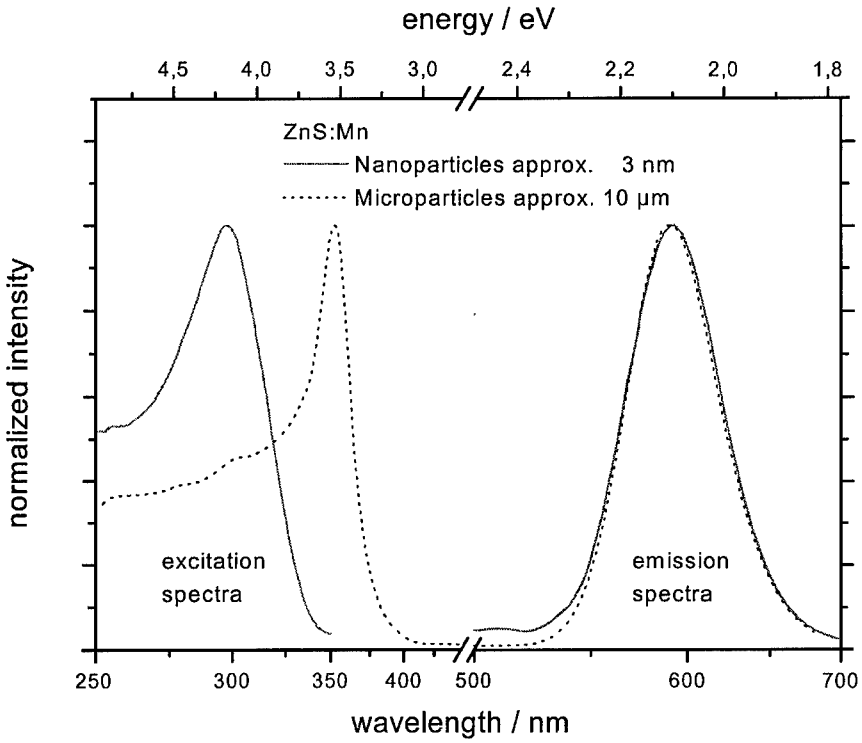

Figure 1. The solid line represents the excitation spectra (left scale) and the emission spectra (right scale) of a dilute ensemble of semiconducting ZnS nanoparticles. The dashed lines represent the same spectra for an ensemble of microparticles.

3. Results and Discussion

By SAXS measurements the mean radius of the ZnS nanoparticles was about 1.6 nm, resulting in a diameter of approximately 3 nm.

From HRTEM a mean diameter of the ZnS particles of about 2.5 to 3.5 nm was observed which is in good agreement with the SAXS results. By HRTEM and additionally by WAXS, the ZnS particles were found to be single crystals (for detailed description of the experiments, see [7, 8]).

In Fig. 1 the excitation and emission spectra of the layers containing Mn^{2+}-doped ZnS nanoparticles and the reference system containing Mn^{2+}-doped ZnS microparticles are shown. The excitation spectrum of the system with the nanoparticles is slightly shifted towards the blue and considerably broadened compared to that of the microparticles. On the other hand, the emission spectra is nearly unchanged. This observation is interpreted as follows. The blueshift of the excitation spectrum can be explained by quantum size effects, resulting in a more discrete energy spectrum of the individual nanoparticles and in a blueshift [2, 3]. The broadening of the excitation spectrum is mainly produced by the strongly disordered surface, generating an individual random potential in each nanoparticle. This random potential induces enhanced fluctuations in the energy levels between different nanoparticles. The fluctuations of the levels increase with decreasing size of the particles, i.e., the excitation spectra broaden with decreasing size. This effect is produced by the higher probability of smaller particles "seeing" the disordered surface.

In contrast to this result, the emission spectrum is nearly unchanged in comparison with the microparticle system. As a result, it is argued that the main radiative relaxation occurs via Mn^{2+} centers, probably located in the crytalline cores of the nanoparticles, and in a suppression of relaxation via surface states. These Mn atoms have a nearly unchanged local environment compared to the microparticles. Consequently, the spectral feature of the emission spectrum is nearly unaffected by the particle size. In a further experiment, the relaxation time of both systems was measured. In the

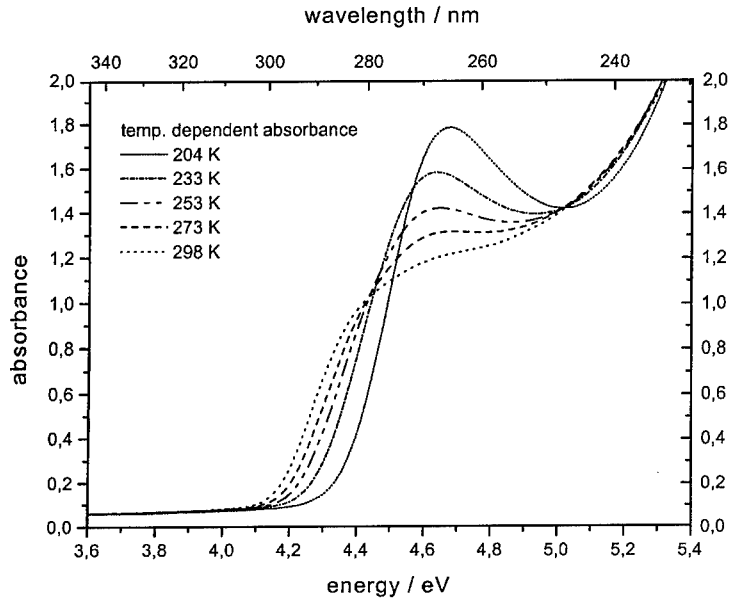

(a)

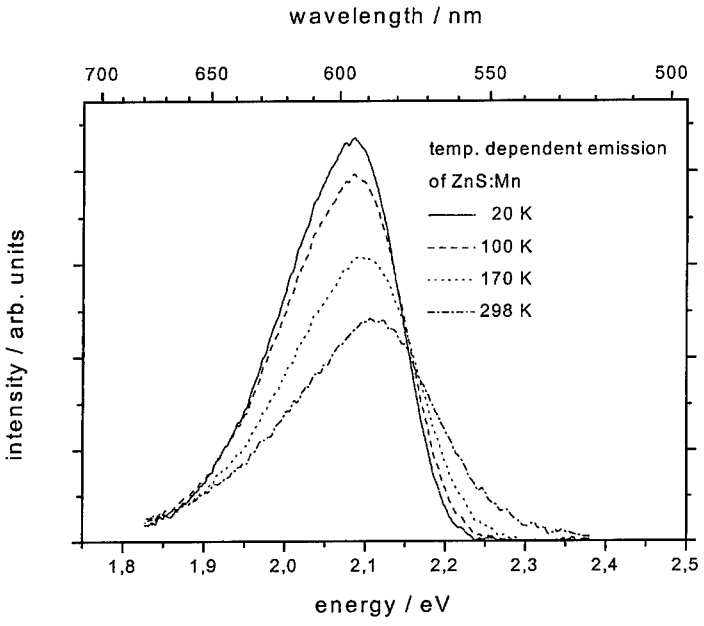

(b)

Figure 2. In (a) the absorption spectra of undoped ZnS nanoparticles for different temperatures are drawn, showing the broadening and the redshift of the spectra with increasing temperature. In (b) the emission spectra for different temperatures are given in order to demonstrate that the spectral feature of the emission spectra is nearly unchanged. The quantum efficiency, however, decreases with increasing temperature.

system with nanoparticles the relaxation time shortens into the nanosecond regime (10–20 ns), whereas in the microparticle system it was approximately 2 ms. This effect is produced by the higher probability to "see" the luminescent center, generating a fast relaxation via the luminescence center.

For a further clarification of the effect of the disordered surface the absorption and emission spectra, temperature dependent measurements were performed, which are shown in Fig. 2. Due to experiment difficulties it was not possible to measure both spectra at the same temperatures. The observed absorption spectra shift towards the red and broaden with increasing temperature. This effect can be attributed to a partial melting of the surface, generating thermal diffusion of ions close to the surface. In contrast, the peak position as well as the linewidth of the emission line (Fig. 2(b)) are only slightly changed. The quantum efficiency at lower temperatures is approximately larger by a factor of two, showing that thermally activated disorder at the surface enhances the relaxation via surface states for higher temperatures diminishing therefore the relaxation via Mn centers in the crystalline core.

4. Conclusion

In conclusion, temperature dependent optical spectroscopy was used in order to clarify the role of the surface in the electron-hole dynamics of Mn-doped ZnS nanoparticles.

As a result of these experiments, it is postulated that the fast and efficient relaxation is not produced by the change of the electronic coupling of the Mn^{2+} center on the ZnS host lattice for small particles as usually assumed [4–6]. It is only an effect of the linear reduced dimension of the particles, increasing the probability of the excited electron-hole pairs to "see" the Mn center and resulting in a partial suppression of the relaxation via surface states.

In future experiments, the size dependence as well as the dependence on the volume fraction of the electron-hole pair dynamics will be studied in order to give a deeper insight in the role of the surface or the grain boundaries, respectively, in the case of systems with higher volume fractions.

References

1. H. Gleiter, Progress in Materials Science **33**, 223–315 (1989).
2. D.U. Saenger, Phys. Rev. B **54**, 14604–14617 (1996).
3. D.U. Saenger, Nanostruct. Mater. **6**, 795–798 (1995).
4. R.N. Bhargava et al., Phys. Rev. Lett. **72**, 416–419 (1994).
5. Y.L. Soo et al., Phys. Rev. **50**, 7602–7607 (1994).
6. K. Sooklal et al., J. Phys. Chem. **100**, 4551–4555 (1996).
7. M. Danek et al., Chem. Mater. **8**, 173–179 (1996).
8. S. Lu et al., J. Sol-Gel Sci. Tech, to be published.
9. B. Kutsch et al., J. Appl. Cryst., (1997), in press.

Journal of Sol-Gel Science and Technology 13, 641–645 (1998)
© 1998 Kluwer Academic Publishers. Manufactured in The Netherlands.

Optimization of Ormosil Films for Optical Sensor Applications

P. LAVIN, C.M. MCDONAGH AND B.D. MACCRAITH
School of Physical Sciences, Dublin City University, Glasnevin, Dublin 9, Ireland

Abstract. Recent work has indicated that Ormosil films, fabricated from organically modified precursors, produce better sensor performance for some specific applications, compared to films fabricated from conventional sol-gel precurors such as TEOS or TMOS. This paper aims to compare film properties and sensor behavior for films fabricated from tetraethoxysilane (TEOS) and tetramethoxysilane (TMOS) silica precursors and both methyltrimethoxysilane (MTMS) and methyltriethoxysilane (MTES) organically modified precursors. Microstructural differences, for example, porosity changes due to the different precursor backbone structures, are interrogated by monitoring oxygen gas and aqueous-phase sensor response. Oxygen sensing using these films is enabled by incorporating in the films an oxygen-sensitive ruthenium dye whose fluorescence is quenched in the presence of oxygen. Film properties such as thickness, thickness stabilization time, as well as sensor response, are discussed in terms of relative hydrolysis and condensation behaviour for the different precursors. Film hydrophobicity, an issue which has been identified as being of crucial importance for optimum dissolved oxygen sensor response, is discussed and contact angle measurements are used to investigate the degree of hydrophobicity for different film types. The main motivation for this work is film optimization for optical gas-phase and dissolved oxygen sensors.

Keywords: hydrophobicity, dissolved oxygen, fluorescence

1. Introduction

Sol-gel-derived films are becoming increasingly important for optical sensor applications [1–3]. Analyte-sensitive dyes are easily entrapped in the porous films while remaining accessible to the analyte, and the nature of the sol-gel process lends flexibility to film fabrication, in particular, enabling tailoring of film properties for specific sensor applications. In this laboratory, sol-gel-based optical sensors have been developed for gaseous oxygen [1], aqueous phase oxygen [3], pH and ammonia monitoring [4, 5]. In particular, recent work [3] has indicated that for some sensor applications such as dissolved oxygen (DO) sensing, sensor response is greatly enhanced by the use of the organically modified precursor MTES compared to that of TEOS. In this paper we report the results of a comparative study of films fabricated from TMOS, MTMS, TEOS and MTES precursors. The work was motivated by the need to study ormosil films of varying composition in order to optimize optical oxygen sensor response. Films were characterized with respect to film thickness, optical quality, film stabilization time (which is manifest as the thickness behavior with time after coating), oxygen sensing behavior and film hydrophobicity. In order to investigate oxygen sensing behavior, films were doped with the oxygen sensitive dye Ru(II)-tris(4,7-diphenyl-1,10-phenanthroline) abbreviated to $Ru(Ph_2phen)_3^{2+}$, whose fluorescence is quenched in the presence of oxygen. Oxygen sensing was measured in both gas and aqueous phase and the enhanced DO sensor response measured from films fabricated from organically modified precursors, or ormosil films, was interpreted in terms of the increased hydrophobicity of the film surface.

2. Film Fabrication and Characterization Techniques

Tetraethoxysilane (TEOS), tetramethoxysilane (TMOS), methyltriethoxysilane (MTES) and methyltrimethoxysilane (MTMS) were purchased from

Aldrich and used without further purification. $Ru(Ph_2phen)_3Cl_2$ was synthesized and purified as described in the literature [6]. Glass microscope slides and silicon wafers were cleaned sequentially using deionized water, methanol and acetone, followed by a final deionized water rinse. Sols were prepared using the precursor, water at pH = 1 (using HCl as catalyst) and ethanol. Water : precursor $\{R\}$ ratios of 2 and 4 were used. The ruthenium compound was added to the sol with a concentration of typically 2.5 g/l in the precursor solution. The sol was stirred magnetically and aged at 70°C for varying times depending on the precursors used. Films were dip-coated in a draft-free environment at a speed of 1 mm/s, using a computer-controlled dip-coating apparatus. Coated films were dried at 70°C and stored in ambient conditions.

Film thickness was measured on an ellipsometer (Rudolph AutoEl III). Optical quality of the films was monitored using an optical microscope (Nikon Optiphot). Ellipsometric film thicknesses were corroborated by transmission measurements on a Shimadzu UV-Vis Spectrophotometer. All thicknesses quoted were averaged over six measurements with a standard deviation of approximately 20 nm.

The experimental system used to measure the sensor response has been published previously [3]. Briefly it consists of a high-brightness blue light emitting diode (LED) from Ledtronics, USA, as excitation source for the ruthenium fluorescence and a photodiode detector from Hamamatsu, UK. For gas phase measurements, oxygen and nitrogen were mixed and flowed via mass flow controllers to a sealed sample chamber. Water samples were prepared by flowing a gas mixture of nitrogen and oxygen from mass flow controllers into a sealed reservoir of deionized water. These solutions were then flowed into the sample chamber for measurement.

Contact angle measurements were made on a home-made system based on the Wilhelmy Plate technique and Young's equation [7].

3. Results and Discussion

3.1. Film Thickness and Stabilization Behavior

Film thickness is determined by such factors as coating speed, aging time before coating, sol pH, R-value and precursor type. For films fabricated using different precursors and with all other variables fixed, the thickness is largely determined by the relative hydrolysis and condensation behavior characteristic of the precursors. For films fabricated at pH = 1 and $R = 2$ it has been established in this laboratory [8] that the thickness of TEOS films gradually decreases after coating to give a stable thickness after some weeks. This behavior is correlated with continuing hydrolysis facilitated by atmospheric moisture. The effect is related to the relatively low R-value. At $R > 2$, the TEOS film stabilization time decreases. MTES films, on the other hand, have a relatively fast stabilization time due to the much larger hydrolysis and condensation rates compared to TEOS [9] and consequently have a much shorter stabilization time. Figure 1 shows the temporal behavior of the thickness for TEOS, MTES, TMOS and MTMS films. All films were doped with ruthenium.

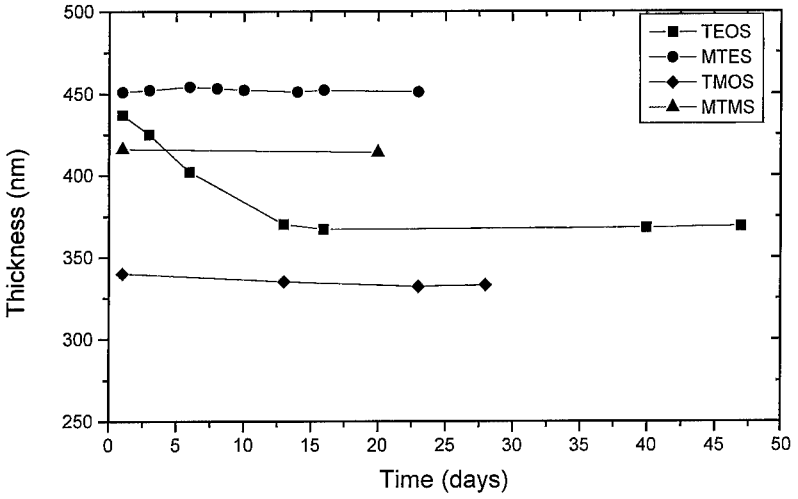

Figure 1. Thickness stabilization behavior of TEOS, MTES, TMOS and MTMS films.

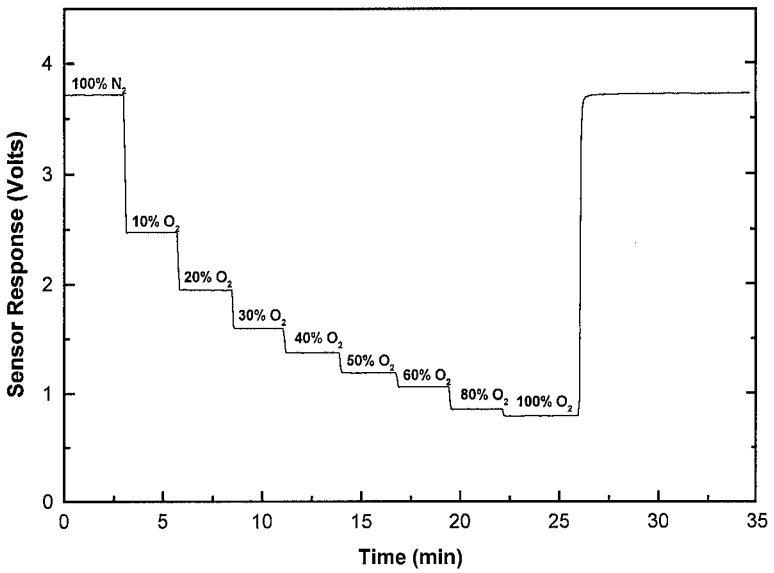

Figure 2. Typical gas-phase sensor response of an MTMS film.

In the course of this study, it has been observed that the presence of the ruthenium dye decreases the stabilization time compared with the undoped film. This is assumed to be due to an enhancement of the hydrolysis rate by the dye. The exact mechanism is as yet unexplained. It has been reported that the hydrolysis and condensation rates for TMOS are significantly greater than for TEOS [10]. This is to be expected due to the decreased steric hindrance for the TMOS molecule. The short stabilization time for TMOS, MTMS and MTES in Fig. 1 is consistent with increased reaction rates for these films compared with TEOS. This is consistent with the gel times observed for these sols when prepared under similar conditions whereby TEOS>MTES>TMOS>MTMS. It is indicated in the literature that ormosil films, due to enhanced reaction rates, are more dense and have smaller average pore size, than TEOS and TMOS films [11]. This is corroborated by quenching data presented in the following sections. Optical quality was monitored for all films and ormosil films were consistently of poorer quality than TEOS or TMOS films. However, optical quality or surface roughness does not appear to be correlated to the optical quenching response.

3.2. *Gas-Phase Quenching*

The oxygen sensing principle used in this work is the collisional quenching by oxygen of the $Ru(Ph_2phen_3)^{2+}$ molecule. The main factor governing sensor response is the oxygen diffusion coefficient in the sol-gel film. The quenching process is governed by the Stern-Volmer equation [3], which predicts a non-linear decrease in fluorescence intensity as a function of oxygen concentration. Typical quenching behavior in gas phase for a MTMS film is shown in Fig. 2. It is observed that the largest decrease in intensity occurs at low oxygen concentrations as predicted. The sensor response is quantified by defining a quantity $Q_G = (I_{N_2} - I_{O_2})/I_{N_2}$, where I_{N_2} and I_{O_2} are the intensities in 100% N_2 and 100% O_2, respectively. Table 1 shows Q_G values for films fabricated from the four different precursors. It is clear that TEOS has the largest gas-phase sensor response. Previous work [12] on MTES and ETEOS (ethyltriethoxysilane) films has indicated that gas phase response is reduced in ormosil films due to the reduction in gas diffusion coefficient

Table 1. Gas-phase and DO quenching response.

	Q_G (±2%)	Q_{DO} (±2%)
TEOS	94%	30%
MTES	85%	69%
TMOS	71%	0%
MTMS	78%	65%

as a result of the methyl and ethyl groups on the pore surface. However, as seen in Table 1, MTMS films have a larger gas-phase sensing response than that for TMOS. It is thought that may be related to the hydrophilic nature of the TMOS surface. This is discussed in Section 3.4.

3.3. *Dissolved Oxygen (DO) Quenching*

Table 1 shows the quenching response Q_{DO} in water for films fabricated from the four different precursors. Q_{DO} is defined in a similar way to Q_G in the last section except that the intensity limits are those for fully deoxygenated and fully oxygenated water. It is clear that there is no quenching response for TMOS in water while the response for TEOS is low compared to that for the ormosil films. It has been established that the large Q_{DO} for MTES is due to the hydrophobicity of the film [3, 12]. Surface hydroxyl ions, which largely cover the surface of TEOS and TMOS films, are replaced by hydrophobic methyl groups in MTES and MTMS films. It is thought that the mechanism for dissolved oxygen sensing in these films is via the partitioning of oxygen gas out of solution at the water/film interface. This partitioning is more efficient as the film hydrophobicity increases. Previous work [12] indicates that ETEOS (ethyltriethoxysilane) is even more hydrophobic than MTES due to C_2H_5 groups on the surface. Hence ETEOS film exhibit a higher Q_{DO}. From Table 1 it appears that MTMS and MTES have largely similar Q_{DO} values indicating the same degree of hydrophobicity. The lack of DO response for TMOS films indicates that TMOS is even more hydrophilic than TEOS. This would suggest that no gas partitioning occurs at the TMOS/water interface due to the large surface coverage of hydroxyl groups. These conclusions are corroborated by contact angle measurements in the next section.

3.4. *Contact Angle Measurements*

Contact angle measurements were made on the films using an apparatus as described in Section 2. Results are shown in Table 2. The larger the contact angle, the greater the degree of hydrophobicity. The results clearly differentiate between the hydrophobic surfaces of MTMS and MTES and the more hydrophilic TEOS and TMOS surfaces. Within the error, MTMS and MTES have a comparable degree of hydrophobicity which is consistent with the Q_{DO} data in Section 3.3. TMOS has the smallest contact angle corresponding to the most hydrophilic surface. This is consistent with the reduced gas-phase quenching response for TMOS compared to other films. While these measurements correlate well with the quenching data, more work is required in order to establish a reliable reference for low contact angle on the apparatus used.

Table 2. Contact angle measurements.

	Contact angle (±3°)
TEOS	47°
MTES	80°
TMOS	40°
MTMS	82°

4. Conclusions

For sol-gel-based optical sensors, it is clear that sensor response is dependent on the precursor used. In this study, the optimum oxygen gas-phase response was obtained with TEOS films. On the other hand, these films took a number of weeks for the thickness to stabilize while ormosil films, with lower gas-phase response, stabilized in a matter of days. For dissolved oxygen sensing, the increased hydrophobicity of the ormosil films resulted in enhanced sensor response. In this study MTES films gave the maximum response, but previous work in this laboratory indicates that extending the aliphatic group of the precursor further enhances hydrophobicity. Hence the quenching response, Q_{DO}, of ETEOS is even higher than for MTES. No DO quenching response was measured for TMOS films, and this result, correlated with contact angle measurements, is indicative of a very hydrophilic film surface which hinders the DO sensing mechanism. In this work it was found that TMOS/MTMS films offered no advantages for oxygen sensing over the TEOS/MTES family of films.

References

1. B.D. MacCraith, G. O'Keeffe, A.K. McEvoy, C. McDonagh, J.F. McGilp, B. O'Kelly, J.D. O'Mahony, and M. Cavanagh, Opt. Eng. **33**(12), 3861 (1994).
2. K.E. Chung, E.H. Lan, M.S. Davidson, B.S. Dunn, J.S. Valentine, and J.I. Zink, Anal. Chem. **67**(9), 1505 (1995).

3. A.K. McEvoy, C. McDonagh, and B.D. MacCraith, Analyst **121**, 785 (1996).
4. T.M. Butler, B.D. MacCraith, and C. McDonagh, *Proc. SPIE* **2508**, 168 (1995).
5. T.M. Butler, Ph.D. Thesis, Dublin City University, Ireland, 1996, unpublished.
6. R.J. Watts and G.A. Crosby, J. Am. Chem. Soc. **93**, 3184 (1971).
7. A. Adamson, *A Textbook of Physical Chemistry* (Academic Press, New York, 1979).
8. C. McDonagh, F. Sheridan, T.M. Butler, and B.D. MacCraith, J. Non-Cryst. Solids **194**, 72 (1996).
9. M.J. Van Bommel, T.N.M. Bernards, and A.H. Boonstra, J. Non-Cryst. Solids **128**, 231 (1991).
10. J.C. Pouxiel, J.P. Boilet, J.C. Beloeil, and J.Y. Lallemand, J. Non-Cryst. Solids **89**, 345 (1987).
11. P. Innocenzi, M.O. Abdirashid, and M. Guglielmi, J. Sol-Gel Sci. Tech. **3**, 45 (1994).
12. A.K. McEvoy, Ph.D. Thesis, Dublin City University, Ireland, 1996, unpublished.

Journal of Sol-Gel Science and Technology 13, 647–650 (1998)
© 1998 Kluwer Academic Publishers. Manufactured in The Netherlands.

Enhanced Second Order Non-Linear Optical Properties of Silica Sol-Gel Thin Films Through Photo-Induced Poling

B. ABBAS AND G.R. MITCHELL
Polymer Science Centre, The Department of Physics, The University of Reading, Reading RG6 6AF

Abstract. Sol-gel derived inorganic materials are of interest as hosts for non-linear optically active guest molecules and they offer particular advantages in the field of non-linear optics. Orientationally ordered glasses have been prepared using a sol-gel system based on tetramethoxysilane, methyltrimethoxysilane and a non-linear optical chromophore Disperse Red 1. The novel technique of photo-induced poling was used to generate enhanced levels of polar order. The level of enhancement is strongly dependent on the extent of gelation and an optimum preparation time of ~100 h led to an enhancement factor of ~5. Films prepared in this manner exhibited a high stability of the polar order.

Keywords: photo-induced poling, guest-host system, isomerization

Introduction

Sol-gel materials show a considerable promise for exploitation in many areas including, for example, waveguide devices, optical communications, and signal processing [1]. A number of studies have highlighted the possibility of embedding organic molecules in silica glasses through the sol-gel process [2–7]. Such materials may be used in the form of a guest-host system in which specific organic molecules with large non-linear susceptibilities are dispersed in the inorganic polymeric matrix. The polar order, necessary for second-order non-linear properties, is generated by the process of electric field poling. In a typical organic polymer-based guest-host system, the material is first heated to temperatures close to the glass transition. This imparts enhanced mobility to the chromophores and the ensuring orientational polar order is quenched in by subsequent cooling to room temperature. Of course, heating a freshly prepared sol-gel system will only serve to accelerate network formation and as a consequence chromophore mobility will be substantially limited. We have utilized an alternative technique to prepare highly ordered sol-gel based guest-host systems in which resonant interactions of the chromophores with an optical irradiation field are used to enhance chromophore mobility. This novel technique is called photo-induced poling (PIP) [8]. A dc electric field and light irradiation are applied simultaneously. Previous work on organic polymers has shown that although the application of a dc electric field at room temperature may produce very little polar order due to the non-ability of the trapped chromophores inside the polymeric matrix to rotate, irradiation with light at a suitable absorption band will invoke the guest molecules to rotate and align along the electric field direction [9]. The whole process can be explained in terms of a photo-induced *trans-cis-trans* isomerization cycle of the guest molecules, where the *cis* isomers can rotate more easily than the *trans* isomers due to their packed shape [9].

Photo-induced isomerization in sol-gel glass films has been reported by Ichimura and co-workers [5–7], but not the possibility of PIP. A particular advantage of the PIP technique is that it can be used to write patterns of polar order in thin films with obvious applications in optical devices [10]. In this paper we report the initial results of the application of PIP to a sol-gel based guest-host system.

Materials and Experimental Procedures

Thin optical quality films were prepared from tetramethyloxysilane (TMOS; $Si(OCH_3)_4$) and

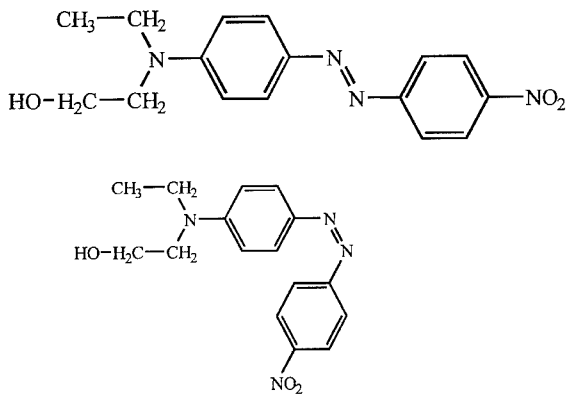

Figure 1. The *trans* and *cis* isomers of DSR1.

methyltrimethoxysilane (MTMS; $CH_3Si(OCH_3)_3$) using a procedure reported by Capozzi and Seddon [11] with some modification. A 42/58 mol% TMOS/MTMS mixture was mixed with methanol in the ratio 1 : 1 together with 0.04 M HCl. The amount of HCl was 0.7 M relative to the total number of methoxy groups. The solution was stirred for 1 h before Disperse Red 1 (DSR1) from Aldrich was added at a ratio of 7.5% w/w (see Fig. 1). This solution was stirred for a further hour and then filtered using 0.2 μm regenerated cellulose membrane filter. Thin films were prepared through dip-coating using Indium Tin Oxide (ITO)-coated glass substrates which served as electrodes enabling the electric field to be applied across the film. Samples were allowed to gel and dry at room temperature. Sandwich cells for electric field poling were constructed by placing a second ITO-coated glass slide over the polymer film. The polar order in these films was evaluated through measurement of the intensity of the frequency doubled light ($I_{2\omega}$) using a pulsed Nd : YAG laser (λ = 1064 nm) as the fundamental beam. The dc electric fields were generated using a Stanford programmable power supply. PIP was performed using an Ar-ion laser (λ = 514 nm) with a power density of 15 m W/cm^2 or a broad band arc-lamp coupled with a monochromator centerd at 514 nm with bandwidth of 20 nm which gives a power density of ~2.8 mW/cm^2. These arrangements allowed the intensity ($I_{2\omega}$) to be measured continuously as a function of time during the poling procedure. The experimental configuration is shown schematically in the inset to Fig. 2.

Results and Discussion

A series of films of 2.4 μm thickness containing 7.5% w/w of DSR1 were prepared. Figure 3 shows the results of a typical poling experiment at room temperature on a film prepared 48 h prior to the measurements. Initially an electric field of 100 V/μm was applied and a stable level of polar order rapidly develops. Subsequent irradiation of the film at 514 nm using the same electric field leads to a substantial increase in the value of $I_{2\omega}$ over a period of 1500 s. We attribute the increased level of polarity to the enhanced mobility of the chromophores during the PIP process. In the absence of the irradiation field, a significant fraction of the chromophores are trapped in the developing silicate network despite the application of the poling field. Irradiation with 514 nm light results in a photo-induced *trans-cis-trans* cycle in the chromophores, which enhances the mobility and increases the number of chromophores which can respond to the applied electric field. The *cis* isomer has a more compact shape which allows DSR1 molecules to rotate inside the matrix. Previous studies by Ichimura et al. have shown that *trans-cis* isomerization can take place in doped sol-gel systems. Hence, we use a chromophore which has strong acceptor and donor groups which reduce the life-time of the *cis* form to ~1 s [10]. This means that at any one time only a small fraction of *cis* isomers are present. This short life-time is essential for PIP to perform the *trans-cis-trans* cycle through enhancing the mobility of chromophores rather than making a shift in *trans/cis* population.

After 5000 s the irradiation field was removed and there is a slight increase in the value of $I_{2\omega}$. Removal of the applied electric field results in a slow reduction

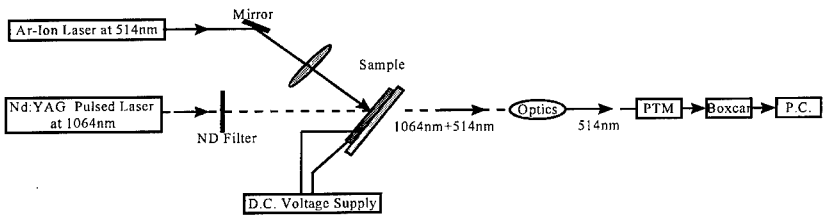

Figure 2. A schematic diagram of the experimental set-up for real-time SHG measurements.

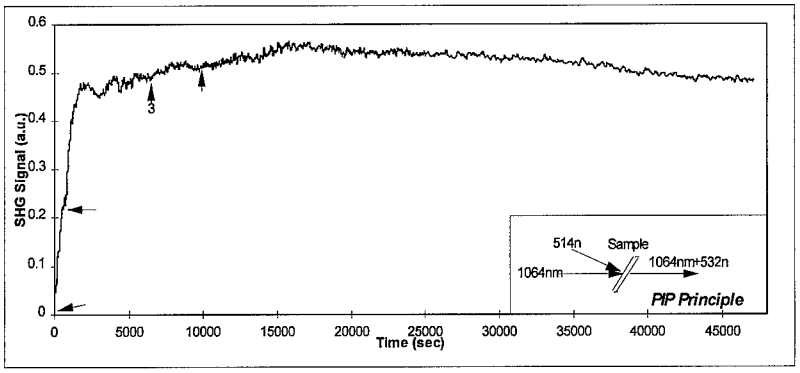

Figure 3. In situ SHG experiment of a sol-gel based thin film, where 1-denotes applying a dc electric field across the film at 100 V/μm; 2-Ar-Ion laser is on; 3-Laser is off; 4-E-field is off.

of the value of $I_{2\omega}$. Relaxation behavior often follows the Kohlrausch-Williams-Watts equation [12],

$$I(t) = I_0 \exp(t/\tau)^{\beta}$$

where I_0 is the signal at the beginning of the decay stage, $I(t)$ is the signal at time t, and β is a constant provides a measure of the distribution of free volume in the sample. Fitting this equation to the data after the field is removed in Fig. 3 gives $\beta = 0.67$ and $\tau \cong 1.1 \times 10^5$ s, indicating a high stability of polar order in contrast to a typical organic polymer based guest-host system [13]. Of course the sample for which Fig. 3 relates.

The Effect of Gelation Time

After preparation, the films are in a continual state of evolution towards a fully cross-linked system. As a consequence the response to the poling field may vary as the period of time since preparation increases. We have performed a series of experiments on a set of samples prepared at the same time in which each sample was subjected to a single poling after a specific period of time had elapsed since preparation. Pairs of samples were considered. One sample was used at a time for measurements with an applied electric field only (100 V/μm), and the second sample was used for simultaneous application of an electric field and the 514 nm light field. Figure 4 shows the results of this series of experiments. For the series of samples in which only the electric field is applied there is a suggestion of a small increase in $I_{2\omega}$ for a period of ~100 h. Over the equivalent period of time; the level of $I_{2\omega}$ generated using PIP is substantially higher and increases with time since preparation. In other words the effect of continued gelation is to enhance period of time; the level of $I_{2\omega}$ generated using PIP is substantially higher and increases with time since preparation. In other words the effect of continued gelation is

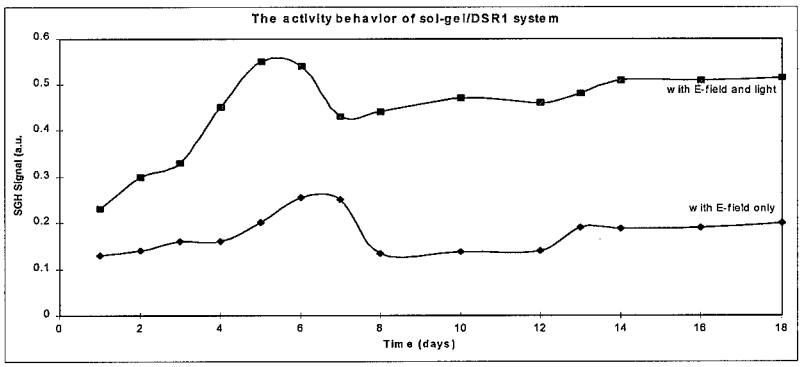

Figure 4. A plot of $I_{2\omega}$ for samples poled using (a) electric field and (b) electric field plus 514 nm laser light for different elapsed periods since preparation.

to enhance the effectiveness of the PIP technique. After a period of ~100 h following preparation the level of $I_{2\omega}$, which is obtained using PIP, reaches a steady value. Clearly an elapsed period of 100 to 125 h represents an optimum preparation time.

It is clear that PIP leads to enhanced levels of polar order. Moreover, such enhanced polar order has a high stability in contrast to equivalent but uncross-linked organic polymer systems prepared using PIP [9]. The use of PIP to prepare films with spatial variation in the non-linear optical activity requires a near-zero response to the poling field in the absence of the irradiating light field [10]. Although we have always observed some limited electric field response, the "contrast" factor between electric field alone and PIP poling is dependent upon the elapsed time following preparation. Experiments are in hand to evaluate the potential of PIP for patterning this type of film.

The level of polar order is substantially enhanced through the use of photo-induced poling and it is strongly dependent on the gelation period.

Acknowledgment

We would like to thank Dr. F. Davis from Chemistry Department for his valuable advice regarding the chemical side of this work and the Atomic Energy Commission of Syria for providing the financial support during this work.

References

1. Y. Sorek and R. Reisfeld, Appl. Phys. Lett. **63**, 24 (1993).
2. A. Slama-Schwok, D. Avnir, and M.Oyyolenghi, Photochemistry and Photobiology **54**(4), 525 (1991).
3. V.R. Kaufman, D. Levy, and D. Avnir, J. Non-Crystalline Solids **82**, 103 (1986).
4. Q. Hibben, E. Lu, Y. Haruvy, and S.E. Webber, Chem. Mater. **6**, 761 (1994).
5. M. Ueda, H.B. Kim, T. Ikeda, and K. Ichimura, J. Non-Crystalline Solids **163**, 125 (1993).
6. M. Ueda, H.B. Kim, and K. Ichimura, Chem. Mater. **6**, 1771 (1994).
7. M. Ueda, H.B. Kim, T. Ikeda, and K. Ichimura, Chem. Mater. **4**, 1229 (1994).
8. P.M. Blanchard and G.R. Mitchell, Appl. Phys. Lett. **63**, 15 (1993).
9. P.M. Blanchard and G.R. Mitchell, J. Phys. D: Appl. Phys. **26**, 500 (1993).
10. P.M. Blanchard and G.R. Mitchell, Optics Letters, in press.
11. C.A. Capozzi and A.B. Seddon, *Sol-Gel Optics III* (SPIE, San Diego, 1994).
12. G. Williams, IEEE Trans. Electr. Insul. **20**, 843 (1985).
13. S. Schussler, R. Richert, and H.Bassler, Macromolecules **27**, 4318 (1994).

Journal of Sol-Gel Science and Technology 13, 651–655 (1998)
© 1998 Kluwer Academic Publishers. Manufactured in The Netherlands.

Aggregation Properties of Metallic Tetrasulphophthalocyanines Encapsulated in Sol-Gel Materials

M.A. GARCIA AND A. CAMPERO
Department of Chemistry, Universidad Autónoma Metropolitana (Iztapalapa), P.O. Box 55-534, México, DF, 09340, México

Abstract. Metallic phthalocyanines exhibit, among many useful properties, the ability to protect sensors against short, intense optical pulses deleterious to efficient sensor operation. It is possible by means of low temperature sol-gel techniques to obtain porous monolithic materials encapsulating metallic ions, and all sorts of complex organic molecules. We report here the study of water-soluble metallic tetrasulphophthalocyanines (MTSPc) encapsulated in silica obtained by the sol-gel technique. These materials are transparent and stable and exhibit interesting optical properties. Absorption in the visible region of the spectrum reveals aggregation of the MTSPc species to form dimers which modify the optical absorption of excited states and the resulting optical properties. We investigate the relative importance of the various physicochemical parameters affecting dimer formation (dye concentration, pH, presence of species such as dimethylformamide, pyridine, etc.) in order to control and inhibit dimer formation. Two species are chosen as examples of the general behavior: CuTSPc, which shows a strong tendency to dimerize in water and in mixtures of solvents, and (OH)AlTSPc, which does not form dimers in aqueous solutions because of its hindering OH axial group. The experiments performed show that addition of dimethylformamide or pyridine does not inhibit aggregation in CuTSPc, simultaneously causing the blue color to disappear from the prepared gels. In the case of (OH)AlTSPc addition of relatively high concentrations of pyridine brings about the formation of non-monomeric species.

Keywords: metallic tetrasulphophthalocyanines, aggregation, monolithic gel, sol-gel

Introduction

Physical properties of many types, such as semiconductivity [1], photoconductivity [2], catalytic [3] and optical [4], have been found in metallic phthalocyanines (Pc) and porphyrins (P). The high chemical and thermal stability of these centrosymmetric macrocycles with an extensively delocalized system of conjugated p-electron double bonds induces large third-order nonlinear optical properties [5], useful in modern optoelectronic applications [6, 7].

The trapping of these organic macrocycles in the disordered three-dimensional networks of the gels normally obtained by the sol-gel method brings about a sharp deformation and a strong decrease [8] of the absorption bands of the UV-Vis spectrum of these species. This is due to the formation of aggregates of macrocycles (dimers, trimers, etc.). This phenomenon has been studied by a number of workers [9, 10], and it has been clearly found that this clustering is solvent dependent. In this work it is intended to make a contribution to a better understanding of the agglomeration phenomena of water soluble metallic tetrasulphophthalocyanines (MTSPc) in water, as well as in gels made from tetraethoxysilane (TEOS). For this purpose, we have chosen initially CuTSPc, forming one of the more stable dimers [11], and (OH)AlTSPc, which normally does not form aggregates due to the presence of an OH axial ligand hindering dimerization [12].

Experimental

Copper and aluminum tetrasulphophthalocyanines were synthesized following the methods of Weber and

Busch [3]. Monolith gels of MTSPc (M = Cu, Al) were prepared using the relative molar concentrations [TEOS/H_2O/HCl/MTSPc] = [1/19/2.5 $\times 10^{-5}$/1.5 $\times 10^{-6}$]. Immediately after preparation of these mixtures, and before gelation, then: (i) when M = Cu either (a) dimethylformamide (DMF) in various amounts (10, 20, 30, and 40% v/v with respect to the total volume of the mixture) or (b) pyridine (5%) was added, and (ii) when M = Al, sols with pyridine (0.1, 1, 5%) were prepared. These samples were put in plastic cells covered with parafilm paper. A similar set of samples was prepared, this time with small holes in the covering paper, in order to allow a more rapid solvent evaporation. Gelation time (t_g) was ordinarily around 200 h. The behavior of samples was followed by UV-Vis spectroscopy, using a Cary 5E instrument.

Results and Discussion

As a preliminary, we show in Fig. 1 the UV-Vis spectrum of CuTSPc dissolved in water. The two maxima, at 337 nm (Soret band), and 629 nm (Q band) are assigned to a transition common to all these macrocycles and to the dimeric species, respectively.

By dissolving the same species in DMF the spectrum changes. It now features bands at 349 nm (Soret, $a_{2u}(p^*) \rightarrow e_g(p^*)$), 608 nm ($Q_I$, vibronic) and 675 nm ($Q_{III}$, $a_{1u}(p) \rightarrow e_g(p^*)$), well known as characteristic of monomeric phthalocyanines [6]. We have found that if we add DMF in concentrations higher than 40% (v/v) to water solutions of CuTSPc, dimerization is completely inhibited. With pyridine, the same result is attained with concentrations higher than 5% (v/v). With (OH)AlTSPc, no dimerization is observed while in water solution.

Going now to the samples prepared by the sol-gel method, we give in Fig. 2 the rate of decrease of the 675 nm band of CuTSPc sols and gels with different amounts of DMF added.

It is seen that, with the exception of the sample with 40% DMF, after around 200 h the intensity of the band decreases to practically zero, close to the gelation time (t_g); interestingly, this time can be detected as a small bump in the curve. However, though the rate of decrease is remarkably slower using 40% (v/v) of DMF, the band intensity becomes zero after 1000 h. Gels then lose their blue color. All this suggests an interaction between DMF and CuTSPc; some sort of lactam ring may be formed, causing a disruption of the macrocycle conjugated double bond system, resulting in gel bleaching. Since the acidity of the medium is low (10^{-3} M), neither destruction of the macrocycle, nor its demetallization, are possible [13], thus the lactam ring formation is plausible. DMF accepts a proton, thus

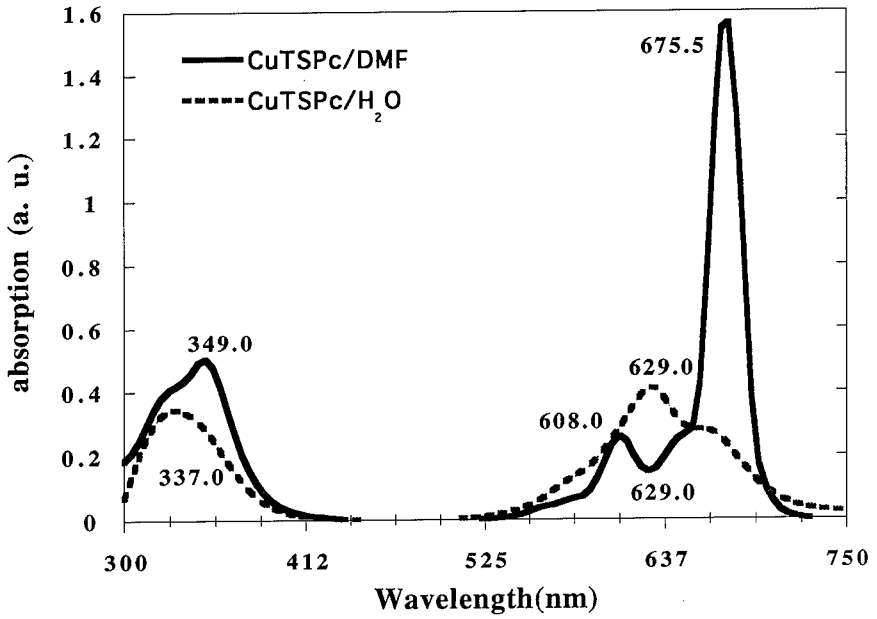

Figure 1. UV-Vis absorption spectra of CuTSPc in different solvents.

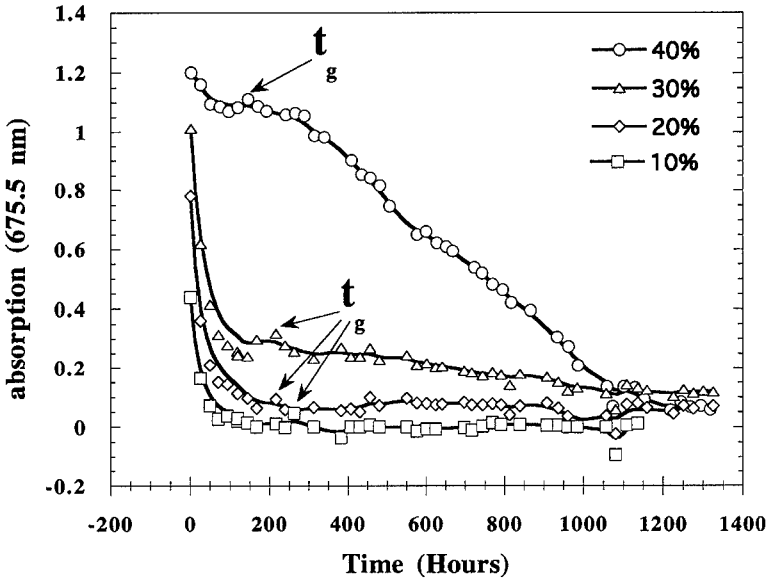

Figure 2. Rate of decrease of the 675 nm absorption band of CuTSPc gels at different concentrations of added DMF; t_g = gelation time.

acquiring a tautomeric structure which can be coupled below and above the plane of the CuTSPc macrocycle. We are at present trying to understand the nature of this phenomenon in order to explain the bleaching of these samples.

The absorption spectra of CuTSPc gels (5% pyridine, open cell), which gel within 5 min, are given in Fig. 3 at different times after mixing.

At the start, aggregation is inhibited, but at later times dimer formation increases noticeably, as witnessed by the increase in the band at 626 nm. With an ageing time of 335 h, we only see a small bump at 607 nm, assigned to a larger size aggregate.

Passing to (OH)AlTSPc gels, where various amounts of pyridine are added, Fig. 4 shows their absorption spectra. The intensity of the bands depends on the

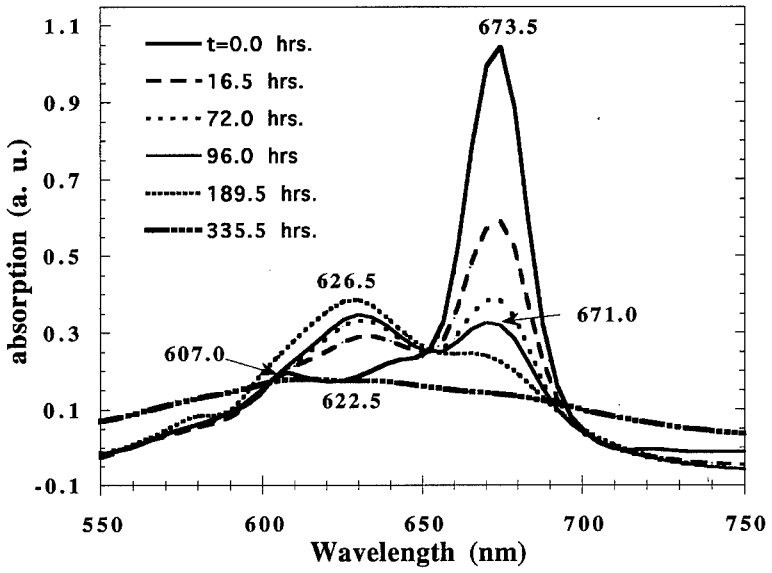

Figure 3. UV-Vis absorption spectra of a CuTSPc gel (5% pyridine added), at various times after mixing of initial reagents.

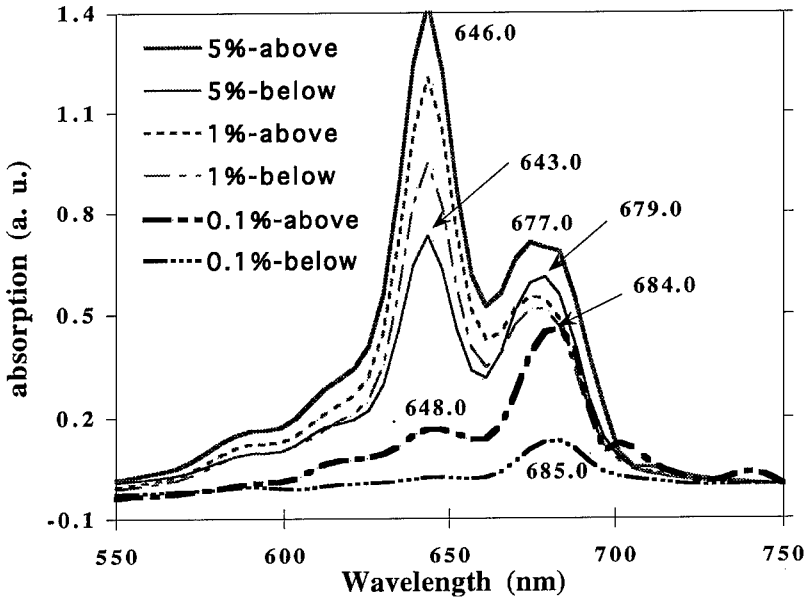

Figure 4. UV-Vis absorption spectra of (OH)AlTSPc gels with various concentrations of added pyridine. Spectra taken above and below of the monolithic gels in the sample cell.

position, above or below in the sample cell, which is exposed to the radiation beam of the spectrometer.

Sample monoliths with 5% and 1% pyridine have spectra with bands at 646 nm and 677 nm, assigned to a non-monomeric species (probably a dimer), and to the monomer, respectively. Whereas with lower concentrations of pyridine, the spectrum shows a very small or zero intensity of the 648 nm band and the band at 684 nm assigned to the monomer, in an environment suggestive of pyridine in a high concentration. This idea is supported by the results given in Fig. 5. As we see, the most intense band of (OH)AlTSPc in aqueous solution is found at 674 nm. However, after a rather high excess of pyridine is added (60%), this band shifts

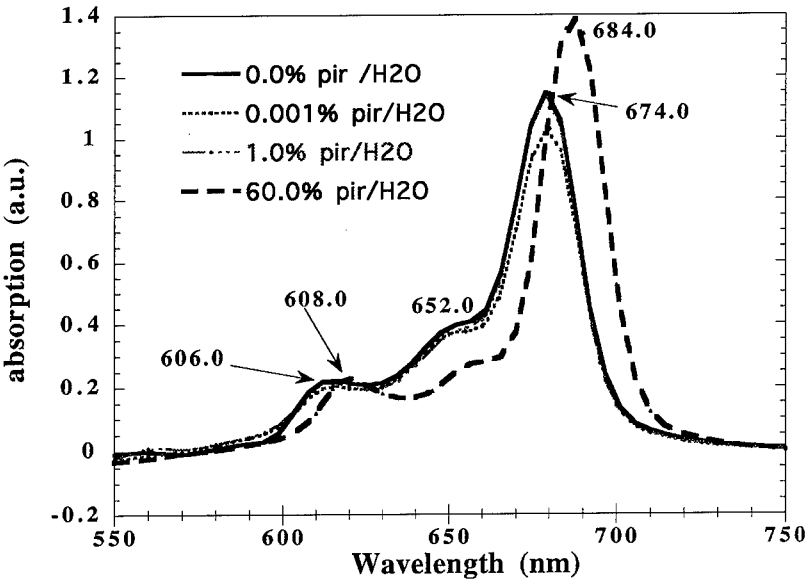

Figure 5. UV-Vis absorption spectra of aqueous solutions of (OH)AlTSPc, with different amounts of added pyridine.

to 684 nm. Probably, with a high concentration of pyridine, a non-monomeric species is formed. The excess pyridine tends to evaporate, increasing the size of upper pores in the gel, thus explaining the higher concentration of the non-monomeric species in the upper part of the sample cell. We have found that in pyridine-water solutions of the (OH)AlTSPc macrocycle, in the absence of TEOS, no dimeric species is formed, unless a strong base such as NaOH is used. We have to conclude then that in the gel, the environment encapsulating the (OH)AlTSPc, pyridine attacks the OH group in axial position, generating an anion which then attacks another macrocycle, forming a dimer via an *oxo* bridge.

Conclusion

Dimer formation is studied in gels of metallic tetrasulphophthalocyanines obtained by the sol-gel method. With CuTSPc, the higher the concentration of DMF used, the more efficient the dimer formation inhibition; the 675 nm band in the absorption spectrum disappears witnessing a strong interaction between N, O in DMF and N, Cu in CuTSPc. The extended system of conjugated double bonds of the macrocycle is ruptured, bringing about bleaching of the sample. With monoliths of (OH)AlTSPc where 1% and 5% pyridine is added, a non-monomeric species is formed which rises to the upper part of the sample cell inducing a concentration gradient. Proper understanding of these phenomena will provide metallic macrocycle sol-gel materials with higher quality and performance.

Acknowledgment

The authors wish to thank Conacyt (México) for the financing of project 30728.

References

1. J.K. Duchowski and D.F. Bocian, J. Am. Chem. Soc. **112**, 3312 (1990).
2. Y. Liu, K. Shigehara, and A. Yamada, Bull. Chem. Soc. Jpn. **65**, 250 (1992).
3. J.H. Weber and D.H. Buch, Inorg. Chem. **4**, 469 (1965).
4. L.A. Martarano, C.P. Wong, and W. de W. Horrocks Jr., J. Phys. Chem. **80**, 2389 (1976).
5. T.H. Wei, D.J. Hagan, M.J. Sence, E.W. Stryland, J.W. Perry, and D.R. Coulter, Appl. Phys. B, **54**, 46 (1992).
6. C.C. Leznoff and A.B.P. Lever, in *Phtcalocyanines Properties and Applications*, edited by C.C. Leznoff and A.B.P. Lever (VCH Publishers, Inc., New York, 1989).
7. M. Hanack and M. Lang, Adv. Mater. **6**, 819 (1994).
8. P.D. Fuqua, B. Dunn, and J.I. Zink, *Proceedings of the SPIE*, Vol. 2288, Sol-Gel Optics III (San Diego, USA, 1994).
9. E.W. Abel, J.M. Pratt, and R. Whelan, J. Chem. Soc. Dalton, 509 (1976).
10. Y.C. Yang, J.R. Ward, and R.P. Seiders, Inorg. Chem. **24**, 1765 (1985).
11. H. Sigel, P. Waldmeier, and B. Prijs, Inorg. Nucl. Chem. Lett. **7**, 161 (1971).
12. M.G. Lagorio, L.E. Dicelio, and E. San Roman, J. Photochem. Photobiol. A: Chem. **72**, 153 (1993).
13. B.D. Bezerin, Russ. J. Inorg. Chem. **7**, 11 (1962).

Journal of Sol-Gel Science and Technology 13, 657–661 (1998)
© 1998 Kluwer Academic Publishers. Manufactured in The Netherlands.

Photodegradation of Luminescence in SiO_2 : Rh B Gels Exposed to YAG : Nd Laser Pulses

J. GARCIA M., E. RAMIREZ J. AND M.A. MONDRAGON
Instituto de Fisica, UNAM, P.O. Box 20-364, 01000 Mexico, D.F., Mexico

R. ORTEGA AND P. LOZA
Centro de Instrumentos, UNAM, P.O. Box 70-186, 04511 Mexico, D.F., Mexico

A. CAMPERO
Departamento de Quimica, UAM (Iztapalapa), P.O. Box 55-534, 09340 Mexico, D.F., Mexico

Abstract. Silicate gels doped with organic dyes have been proposed as solid-state tunable lasers. Photobleaching of the dye under laser excitation is an important phenomenon in this application. The optical absorption and luminescence of SiO_2 silica gels doped with Rhodamine B exposed to the second harmonic pulses of a YAG : Nd laser have been studied. In addition to the characteristic exponential decay with the number of pulses, overlapping oscillations in the intensity were observed. This behavior is explained in terms of a long lived metastable electronic excited state of the dye molecules.

Keywords: luminescence, photostability, photobleaching, Rhodamine B, silica gels

Introduction

Organic dyes are commonly used to produce tunable laser action, but because they have to be dissolved, the handling and disposal of their solutions involves some potential hazards. The confinement of these laser dyes in matrices for use as optical gain media for lasers, has technological advantages. For instance, efficient laser output has been obtained from xanthene dyes impregnated into plastics [1]. The processing characteristics and versatility of preparation of sol-gel materials means that they are good alternative hosts for laser dyes. The first attempts to develop a sol-gel lasing gain media involved dye doped silica and sodium silicate gels [2]. Since then many dyes, including rhodamines, xanthenes and even IR dyes, have been used as lasing materials in sol-gel matrices [3–5]. One of the laser dyes from which successful laser action has been obtained in silica matrices is Rhodamine B [4]. In order to better understand the mechanisms involved in the degradation and photobleaching of the dyes, we have studied the optical response of silica gels doped with Rhodamine B when exposed to the second harmonic pulses of a YAG : Nd up to the point where the gel becomes bleached. Careful monitoring of the changes in the absorption, excitation and luminescence spectra of the dye in the silica gel was undertaken.

Experimental

Samples of silica gels were prepared by mixing and stirring tetraethoxysilane (TEOS), ethanol and distilled water in the molar ratio (2 : 4 : 1). Rhodamine B diluted in ethanol at two concentrations, 1×10^{-4} and 1×10^{-5} mol, was added to the solution. After drying at room temperature for four weeks, good optical samples were cut from the dried gel and polished. The

samples were irradiated with the 2nd. harmonic of a Continuum Surelite II YAG:Nd laser for a range of times. The energy per pulse was 47.6 mJ at 10 Hz with a pulsewidth of 6 ns. The absorption spectra were taken on a Milton Roy Spectronic 3000 spectrophotometer and the excitation and emission spectra were obtained using a Spex Flurolog-2 spectrofluorometer. The lamp emission and detector response were used to correct the luminescence data.

Results

Figure 1 shows the absorption, excitation and emission spectra for the low concentration sample, before and after being exposed to an energy of 4.2 J. Vertical arrows identify the absorption, excitation and emission peaks that were monitored. Figure 2 shows the absorption coefficient behavior of the band peaks at 550 nm, for both the low (lcs) and high concentration (hcs) samples. The low concentration sample (lcs) appears in the inset. An exponential decay in α is observed for both concentrations, but oscillations for hcs are also observed. The exponential decay was fitted with the equation $Y = Y_0 + A_1 e^{-x/t_1}$. The corresponding parameters for both concentrations are included in Table 1. The oscillations represent a partial periodic recovery of α as the irradiation proceeds. The t_1 value in Table 1 represents the energy required to change the initial Y value to $Y_0 + A_1/e$. As can be observed from the table, the hcs sample requires five times more energy to produce this decay than the lcs sample; this is due to the

Table 1. Fitting parameters.

Figure	Concentration (mol)	Parameters
2	10^{-4}	$Y_0 = 9.41517$
		$A_1 = 52.7348$
		$t_1 = 101.3822$
	10^{-5}	$Y_0 = 2.10791$
		$A_1 = 5.13475$
		$t_1 = 20.91658$
3	10^{-4}	$Y_0 = 0.10255$
		$A_1 = 1.0049$
		$t_1 = 268.38208$
	10^{-5}	$Y_0 = 0.12312$
		$A_1 = 0.20761$
		$t_1 = 12.87859$
4	10^{-5}	$Y_0 = 0$
		$A_1 = 2.98596$
		$t_1 = 24.72647$

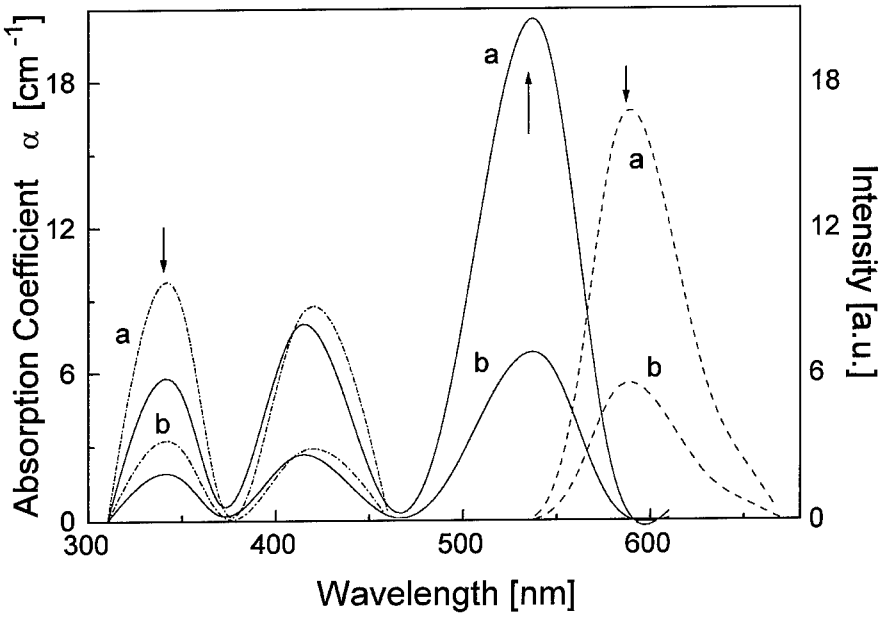

Figure 1. Absorption (continuous line), excitation (dashed-dotted), and emission spectra (dashed) of the SiO_2 gel with Rhodamine B. The emission spectra were obtained for $\lambda_{exc} = 550$ nm. Curves (a) correspond to nonirradiated samples, and (b) to spectra after 4.2 J of energy. The vertical arrows indicate the bands followed in this work.

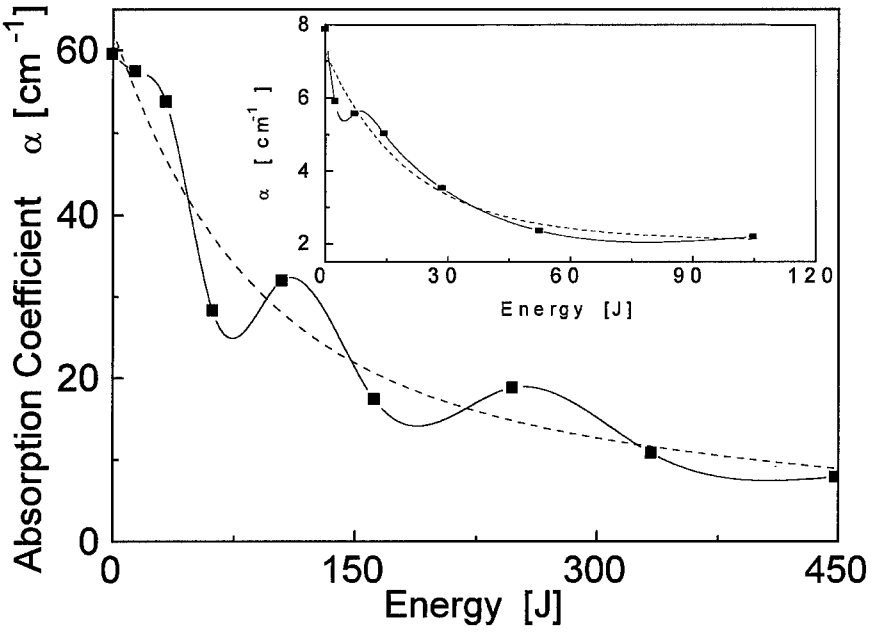

Figure 2. Evolution of the absorption coefficient α for the band at 550 nm as a function of the energy deposited in the sample. The inset shows the evolution for the low concentration sample.

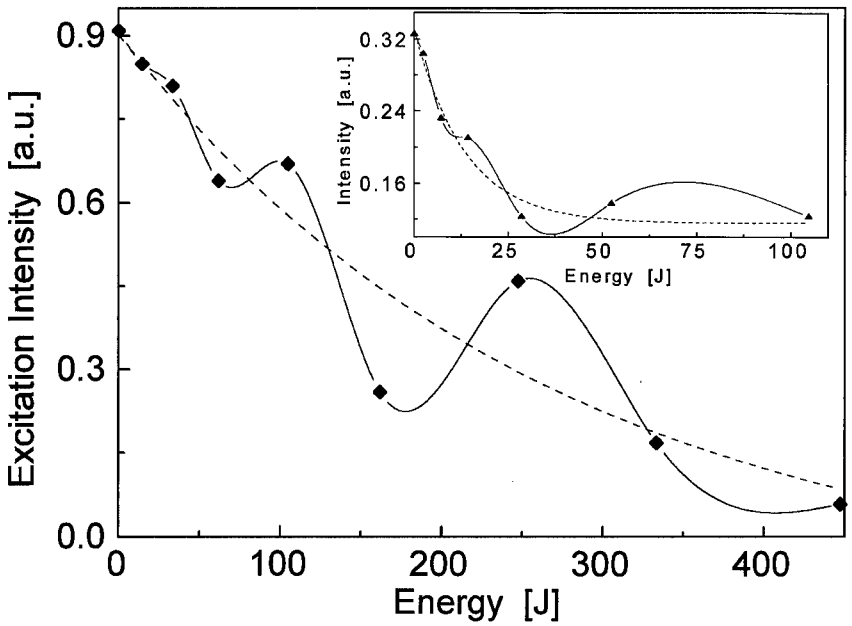

Figure 3. Excitation intensity as a function of the accumulated energy. The excitation wavelength was 360 nm detecting the emission at 590 nm.

excess in number of dye molecules in hcs compared with lcs. Figure 3 shows the evolution of the excitation peak intensity centered at 360 nm. The results are similar to those shown in Fig. 2. The exponential fit parameters are also included in Table 1. In this case t_1 for hcs is twenty times the lcs value. Figure 4 shows how the intensity of the emission peak changes with the irradiation. Again, the lcs behavior is fitted with

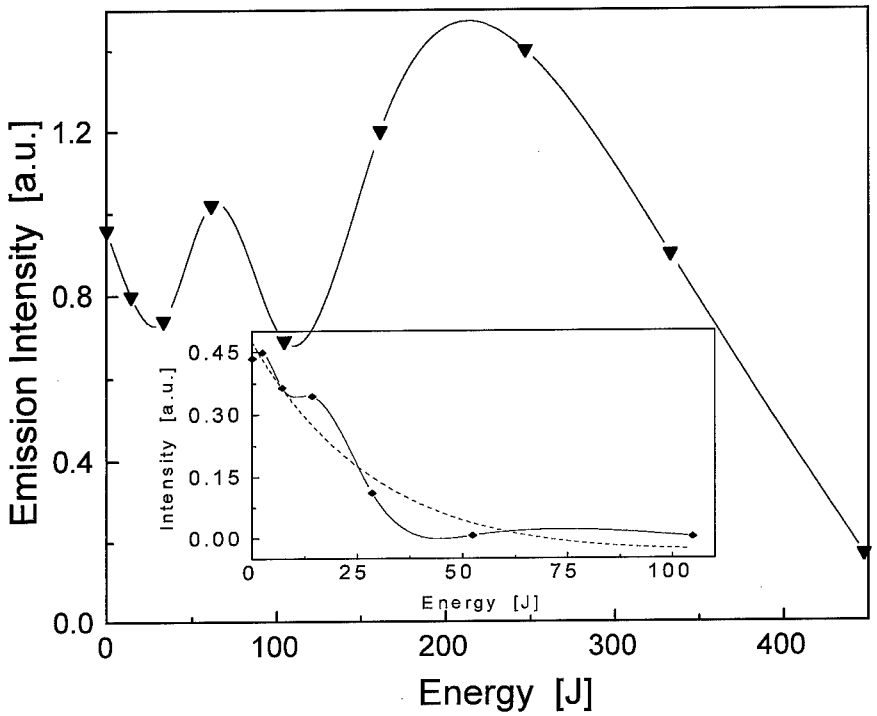

Figure 4. Emission intensity as a function of the accumulated energy. The excitation wavelength was 550 nm with an emission at 580 nm.

an exponential, and the corresponding parameters are included in Table 1. However, hcs has a very different behavior. Several oscillations are present, and a 45% enhancement of the luminescence as compared to the initial value is observed. In all cases the oscillations can be explained as being due to the periodic filling and emptying of the long-lived electronic lowest triplet excited state [6], populated by cross linking from the singlet excited states of the electronic levels of the dyes [7]. It is well established that the laser dyes have a concentration limit, depending on the specific dye. Concentrations in excess of this limit result in an inhibition of the luminescence (concentration quenching) due to energy migration between the molecules until a sink is reached. Taking this into account, the increment in the luminescence can be explained in the following way: as the irradiation proceeds the dye molecules are damaged, thus reducing their concentration, up to a point where there is no quenching of the luminescence and the increment is produced. Further irradiation induces more damage so the emission intensity is finally reduced considerably. In our emission spectra we observed an hypsochromic peak shift (to higher energies) of the lcs with respect to the hcs. A shift of the emission peak to shorter wavelengths is observed for both samples as the exposure energy increases. This confirms that the effective concentration is diminishing, as stated above.

Conclusions

SiO_2 : Rh B gels subjected to the second harmonic irradiation of a YAG : Nd laser show an exponential decay in both the absorption and excitation spectra as a function of the accumulated energy. This is due to the photodegradation of the dye molecules. The superposed oscillations in the intensity are related to the filling and emptying of the long-lived excited electronic triplet state. The exponential decay is faster for the low concentration samples. The high concentration samples show an enhancement of the emission at moderate deposition energy. This is explained by an inhibition of the concentration quenching of the luminescence caused by the photodestruction of the dye molecules. This is confirmed by the hypsochromic shift of the emission peak during irradiation.

Acknowledgment

Work supported by CONACyT 1072P-E9507 and DGAPA IN-105196.

References

1. D.A. Gromov, K.M. Dyumaev, A.A. Manenkov, A.P. Maslyukov, G.A. Matyushin, V.S. Nechitailo, and A.M. Prokhorov, J. Opt. Soc. Am. **2**, 1028 (1985).
2. G.B. Altshuler, V.A. Bakhanov, E.G. Dulneva, A.V. Erofeev, O.V. Mazurin, G.P. Roskova, and T.S. Tsekhomskaya, Opt. Spectroscopy (USSR) **62**, 709 (1988).
3. A. Charlton, I.T. Mckinnie, M.A. Meneses-Nava, and T.A. King, J. Modern Opt. **39**, 1517 (1992).
4. J.C. Altman, R.E. Stone, B. Dunn, and F. Nishida, IEEE Photonics Tech. Lett. **3**, 189 (1991).
5. B. Dunn, F. Nishida, R. Toda, J.I. Zink, T.H. Allik, S. Chandra, and J.A. Hutchinson, Mat. Res. Soc. Symp. Proc. **329**, 267 (1994).
6. J. Rickards, J. Garcia M., R. Garcia M., E. Ramirez, and K. Lopez, Nucl. Instr. and Meth. in Phys. Res. B **11413** (in press) (1977).
7. F.P. Schäfer, in *Dye Lasers*, edited by F.P. Schäfer (Spinger-Verlag, Berlin, 1973), p. 28.

Journal of Sol-Gel Science and Technology 13, 663–666 (1998)
© 1998 Kluwer Academic Publishers. Manufactured in The Netherlands.

Thermochromic Properties of Silver Colloids Embedded in SiO_2 Gels

V.M. RENTERIA AND A. CAMPERO
Depto. de Química, UAM-Iztapalapa, P.O. Box 55-534, 09340, México, DF

J. GARCIA M.
Instituto de Física, UNAM, P.O. Box 20-364,01000, México, DF

Abstract. By using the sol-gel process, colloids are prepared by the spontaneous reduction of silver ions, where the presence or absence of ethanol plays an important role. Thermochromic properties are observed in these gels in the temperature range between 15°C and 150°C. In the UV-Vis region the transmission spectrum red shift of the cut-off is employed to study these properties as a function of the temperature; a shift from 300 to 750 nm is observed. Originally, a broad shoulder centered at 435 nm is seen in gels prepared in the absence of ethanol and at 425 nm with ethanol, corresponding to surface plasmon resonances of the small silver particles in the colloids. These particles are responsible for the various colors observed in the gels. Additionally, the influence of temperature on the color stability, as well as on the influence shown by ethanol on the rate of displacement of the transmission cut-off wavelength, are studied.

Keywords: silver colloids, thermochromic glasses, optical properties

1. Introduction

Though there has been a good deal of interest in the preparation of silver doped glasses for many years, preparation of these materials by means of the sol-gel method has been attempted only in some recent work [1–5]. Among the potential applications of these materials, their use in thermochromic, photochromic and non-linear optics devices is most interesting. In addition, applications as photomurals, information storage devices, temperature sensors [6] and in holography [7] are worth mentioning. Frequently, thermochromic properties are observed in materials containing organic molecules [8], in liquid crystals [6] and in semiconductors [9]. The shift of the wavelength cut-off in the UV-Vis transmittance spectrum is commonly employed to study these properties [10]. The sol-gel technique is interesting for the preparation of these materials because of the high purity and optical transparency of the gels obtained, and for the simplicity of introduction of the soluble silver salt into the initial sol, prior to gel formation. Neither the behaviour of the cut-off wavelength shift in the transmission spectrum, nor the influence of ethanol on the stability and aggregation properties of these colloidal gels, has been previously reported, and this work aims at providing some results concerning these important factors.

2. Experimental

For the preparation of the silver-containing SiO_2 gels the following procedure was used: in plastic beakers, tetraethoxyorthosilicate (TEOS), H_2O and ethanol (EtOH) were mixed in the relative molar concentrations $[TEOS/H_2O/EtOH] = [1/4/x]$, with $x = 0$ (sample Ag-1) or $x = 3$ (samples Ag-2). Under strong agitation, 0.1 ml of concentrated HNO_3 was added and $AgNO_3$ was dissolved in this mixture, to give concentrations of 5.8×10^{-2} M and 7.3×10^{-2} M, respectively. Gelation times were 4 h and 24 h, respectively. The containers were covered with Al foil, and aged for 4 weeks. After ageing, the samples were put in an oven and heated at a rate of 2.5°C/min. Various samples were

obtained by raising the temperature to 30, 60, 90, 120 and 150°C, respectively, and holding these temperatures for 30 min. The UV-Vis spectra were obtained using a Cary 5E spectrometer, with air as a reference. The transmission cut-off wavelength was determined by measuring the intercept on the wavelength axis for the tangent line which could be drawn at half maximum of the transmission edge.

3. Results and Discussion

We show in Fig. 1 the absorption spectra of sample Ag-1 (no EtOH) for different temperatures. The absorption band at 300 nm increases in intensity as the temperature rises. At a temperature of around 90°C, a broad shoulder at 435 nm emerges. A similar shoulder is seen in sample Ag-2 (not shown), the gel prepared with ethanol, this time at 425 nm and 120°C.

The absorption bands appearing at 300 nm are due to clusters, precursors of colloids, similar to those in aqueous solutions containing silver ions which have been irradiated with electrons [11, 12]. The silver particles formed during the thermal treatment give rise to characteristic colors ranging from yellow to red as the temperature is increased. However, as seen in Fig. 1, for sample Ag-1 (no EtOH) an optical reversibility phenomenon is apparent at 120°C. Physically adsorbed water and ethanol evaporate at around 100°C, so the reversibility observed at 120°C is probably due to silver atom colloids which, having grown large enough, are oxidized to Ag_2O [1, 3]. At temperatures of around 150°C, the band is extremely wide and strong, suggesting a high concentration of silver particles. At this point, it is interesting to mention that no use has been made in this work of network-forming or reducing agents of the type employed in other works [1, 2]. At 150°C, thermal decomposition of the organic part of the gels is at a minimum, so the possibility of ethanol participating in the reduction of the Ag^+ ions can be safely disregarded.

As mentioned above, optical reversibility is attained at lower temperatures when samples are prepared in the absence of EtOH. Probably, the SiO_2 polymers formed in these conditions contain a larger proportion of OH (compared with OR groups), than in samples with EtOH. Thus, this increased number of OH groups, probably activated because of temperature, might be the cause of the easier reduction of Ag^+ ions in sample Ag-1. The role which the small amount of HNO_3 used in the preparation of the gels plays in the formation of the silver colloids cannot be neglected, and its influence is at present being investigated in the laboratory.

The wavelengths at the absorption maximum are longer than those normally observed in ordinary glasses (400 nm) [13]. This result shows that the sizes of the silver particles in our samples are larger than those reported for ordinary glasses; a similar result has been reported in irradiated gold-containing colloids in silica gel [14].

Figure 2 shows the energy cut-off shift (in eV) obtained from the transmission spectrum, as a function of temperature, for samples Ag-1 and Ag-2, prepared without and with ethanol, respectively.

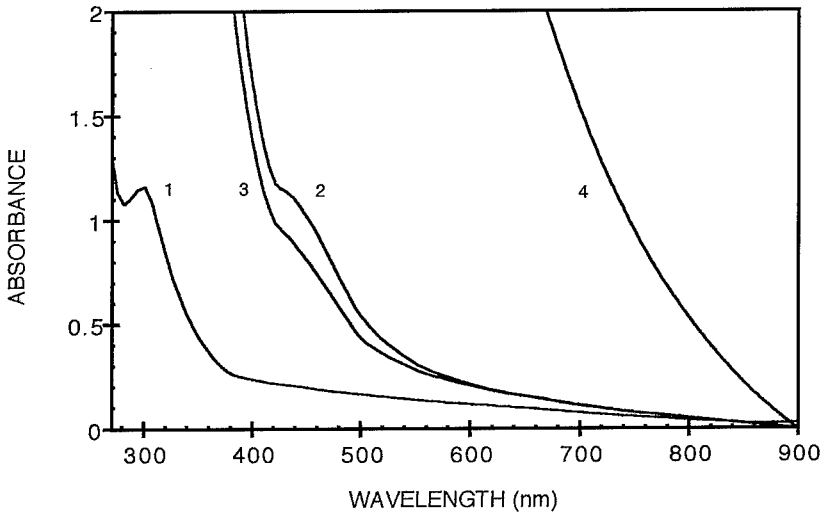

Figure 1. Absorption spectra of sample Ag-1 (no EtOH) at different temperatures: (1) 15°C; (2) 90°C; (3) 120°C and (4) 150°C.

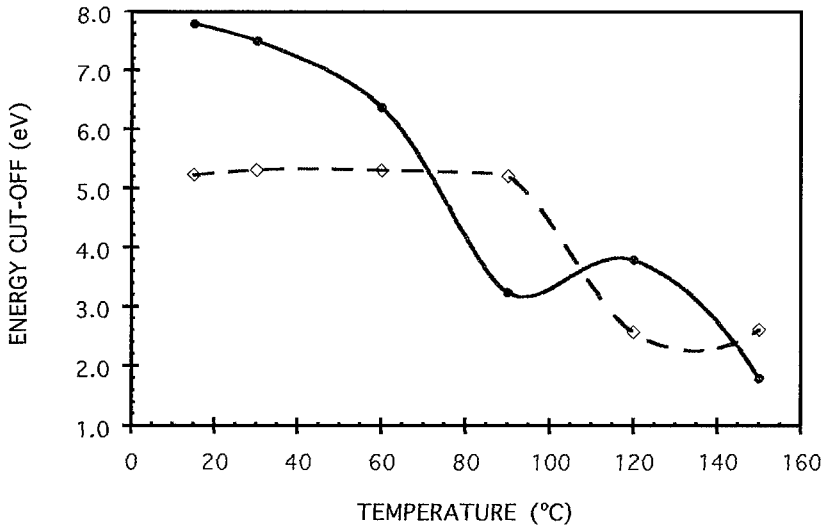

Figure 2. Energy cut-off shift (eV) as a function of temperature. (•) Sample Ag-1 (with no EtOH); (◇) Sample Ag-2 (with EtOH).

The more significant bathochromic shifts occur for the samples prepared without ethanol (Ag-1); also, the optical reversibility of the cut-off in these gels is more noticeable (90–120°C). As far as we know, this is the first time such low temperature values for the reversibility have been observed. At high temperatures (>400°C), this phenomenon has been explained in two different ways: (1) oxidation of the silver particles and (2) aggregation-collapse of the colloidal silver particles. At any rate, we see in Fig. 2 that the largest and most rapid cut-off shifts occur in the samples prepared in the absence of ethanol. Thus, we can conclude that ethanol is an inhibiting agent in the formation of silver colloids.

After generating the colloids at a certain temperature, the sample was taken to room temperature and the container was covered with Al foil. It was observed that the colors were not stable. The transmission spectra were similar to those of the heat-treated gels. We see in Fig. 3 the transmission spectra of sample Ag-2 recorded at different times after the heat treatment at 150°C; a bathochromic shift of the cut-off is observed.

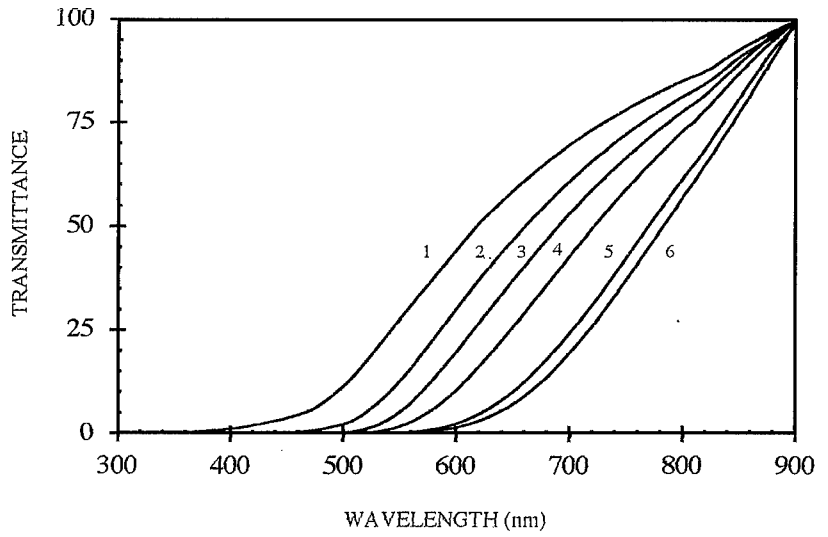

Figure 3. Bathochromic shift of room temperature transmission spectra of sample Ag-2 (with EtOH) heated at 150°C, recorded at different times after the thermal treatment: (1) 0 min; (2) 10 min; (3) 20 min; (4) 110 min; (5) 1380 min and (6) 2640 min.

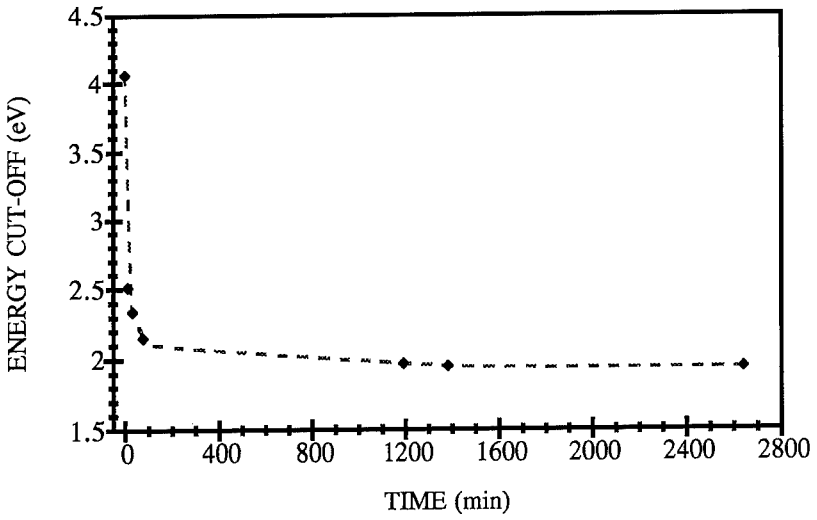

Figure 4. Cut-off wavelength (eV) of sample Ag-2, as a function of time.

The band in the absorption spectra of these samples (not shown), increases in intensity as well as width, probably due to the aggregation of the colloidal Ag particles, which takes place as far as the porosity of the matrix allows it [2].

Furthermore, for sample Ag-2 treated at 150°C we show in Fig. 4 the rate of shift at room temperature of the cut-off wavelength (eV) as a function of time.

An asymptotic curve is obtained, with a rather steep linear decrease in the cut-off during the first 100 min; in this time interval we calculate a rather high value of the slope, around 1.2×10^{-2} eV/min, suggesting the efficient aggregation of silver particles in these gels.

4. Conclusions

The thermal treatments carried out give rise to important thermochromic properties. The cut-off wavelength shift in the transmission spectrum varies from 300 to 750 nm in samples prepared in the absence of ethanol, and an optical reversibility phenomenon at low temperature is observed around 120°C. No reducing agents have been used in this work. The use of ethanol in the preparation is an inhibiting agent in the formation of silver colloids.

Acknowledgment

The authors wish to thank Conacyt (México) for financing of project 2115-30728, and DGAPA UNAM, for project IN105196.

References

1. M. Mennig, M. Schmitt, and H. Schmidt, J. Sol-Gel Sci. Tech. **8**, 1035 (1997).
2. B. Ritzer, M.A. Villegas, and J.M. Fernández Navarro, J. Sol-Gel Sci. Tech. **8**, 917 (1997).
3. G. De, A. Licciulli, C. Massaro, L. Tapfer, M. Catalano, G. Battaglin, C. Meneghini, and P. Mazzoldi, J. Non-Cryst. Solids **194**, 225–234 (1996).
4. S. Datta and G.C. Das, Bull. Mater. Sci. **15**, 363 (1992).
5. R. Reisfeld, M. Eyal, and D. Brusilovski, Chem. Phy. Letters **153**, 210 (1988).
6. U.S. Patents 3,114,836, 1963 and 3,440,882, 1969.
7. S.D. Stookey, G.H. Beall, and J.E. Pierson, J. Appl. Phys. **49**(10), (1978).
8. J.H. Day, Chem. Rev. **63**, 65 (1963).
9. J. Feinleib and W. Paul, Phys. Rev. **155**, 841 (1967).
10. S. Inoue, Y. Shimizugawa, A. Nukui, and T. Maeseto, J. Non-Cryst. Solids **189**, 36 (1995).
11. A. Henglein, Chem. Phys. Letts. **154**(5), 473 (1989).
12. B.G. Ershov, E. Janata, and A. Henglein, J. Phys. Chem. **97**, 339 (1993).
13. R.H. Doremus, J. Chem. Phys. **42**, 414 (1965).
14. I. Tanahashi and T. Mitsuyu, J. Non-Cryst. Solids **181**, 77 (1995).

Journal of Sol-Gel Science and Technology 13, 667–671 (1998)
© 1998 Kluwer Academic Publishers. Manufactured in The Netherlands.

Sol-Gel Preparation of α-Fe_2O_3 Thin Films: Structural Characterization by XAFS and Raman

C. BARATTO, P.P. LOTTICI, D. BERSANI AND G. ANTONIOLI
INFM and Dipartimento di Fisica, Università, Viale delle Scienze, 43100 Parma, Italy

G. GNAPPI
CORIVE, Viale delle Scienze, 43100 Parma, Italy

A. MONTENERO
Dipartimento di Chimica Generale ed Inorganica, Chimica Analitica, Chimica Fisica Università, Viale delle Scienze, 43100 Parma, Italy

Abstract. Films of Fe_2O_3 have been prepared by two different sol-gel syntheses, starting from inorganic salts as precursors, $Fe(NO_3)_3 \cdot 9H_2O$ or $FeCl_3 \cdot 6H_2O$. Differences in the local order between the two preparations are investigated by XAFS (X-Ray Absorption Fine Structure) and Raman measurements.

Keywords: Raman spectroscopy, XAFS, Fe_2O_3, thin films

Introduction

Iron oxide thin films are currently being investigated for applications in catalysts, sensors, optical and magnetic devices. Films of α-Fe_2O_3 (hematite) have been recently reported as a high $\chi^{(3)}$ material, with one of the highest third order susceptibilities among the inorganic oxides (5.8×10^{-11} esu) [1] and are receiving attention for their use in humidity sensors [2]. The sol-gel technique is largely used for the production of metal-oxide thin films, enabling an accurate control of the film morphology and purity [3, 4]. As is well known, the specific structural features of the final products depend on the nature of the precursor and on the thermal history. The starting precursor may be an organic or inorganic compound: this paper reports the synthesis of α-Fe_2O_3 films from two different sol-gel methods, both starting from inorganic salts diluted in organic solvents. To study their structure during the different heat treatments, in addition to XRD characterization, Raman spectroscopy has been employed, while the local environment around the Fe atoms has been investigated by X-Ray Absorption Spectroscopy.

Experiment

Two different processes have been followed to obtain α-Fe_2O_3. In the first process (hereafter called A) hydrate ferric nitrate $FeNO_3 \cdot 9H_2O$ was dissolved in a mixture of 2-methoxyethanol (MET) and acetylacetone in a molar ratio 20 : 2, by stirring the solution at room temperature (RT) for 2 hours. The best quality of the films was obtained for 0.3 M concentration of the nitrate.

In a second preparation (which will be called B), $FeCl_3 \cdot 6H_2O$ was dissolved in H_2O at a weight ratio 1 : 10. NH_3 (25%) was then added to the solution up to $pH \geq 9$, when $Fe(OH)_3$ precipitates. Peptization was attained with glacial acetic acid 60 mol%: the sol was stirred for about 12 hours and then kept in an ultrasonic bath.

For both preparations A and B, films were made by dip coating at room temperature on glass substrates, with a withdrawal speed of 11.6 cm/min for A and 4.2 cm/min for B, due to its higher viscosity. By a single dip, thin (40–100 nm) films were obtained, whereas films with 0.8–1 μm thickness were obtained

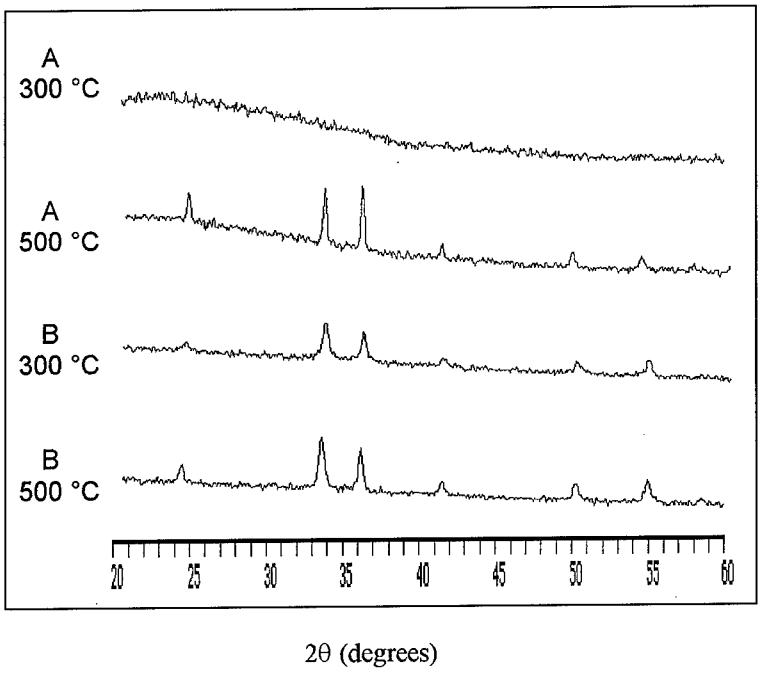

Figure 1. X-ray diffraction patterns of the films obtained by preparations A and B annealed at 300°C and 500°C.

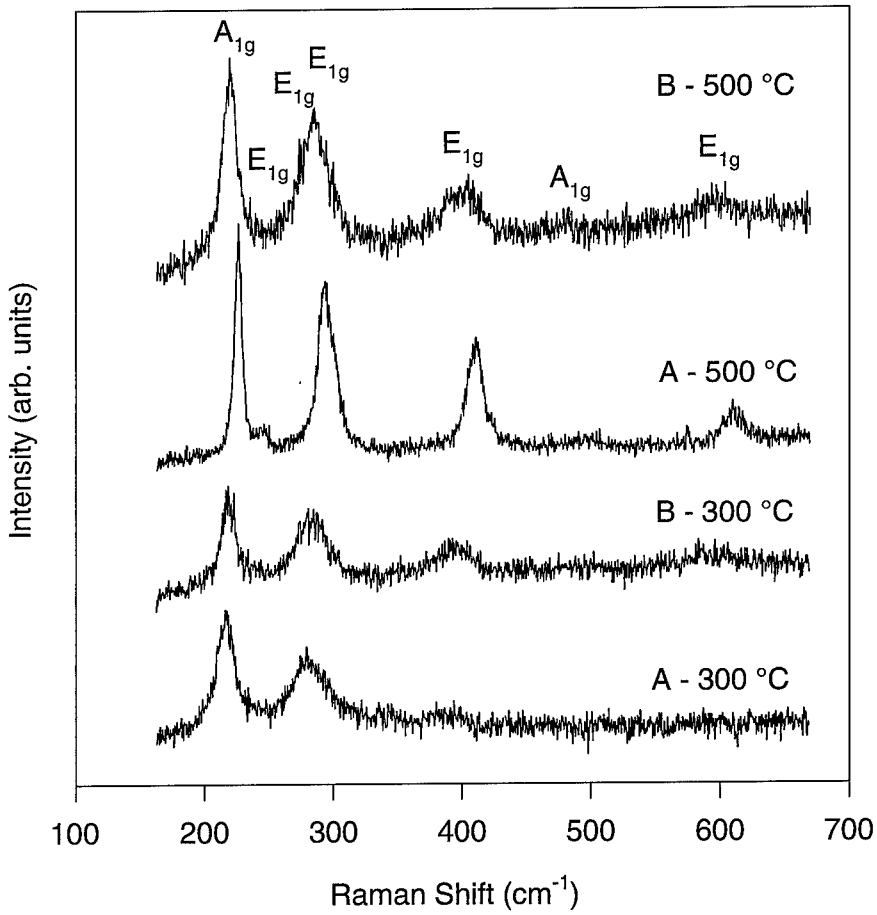

Figure 2. Raman spectra at RT taken with 488.0 nm excitation in films heat treated at 300°C and 500°C. The symmetry of the peaks in the hematite crystals is indicated.

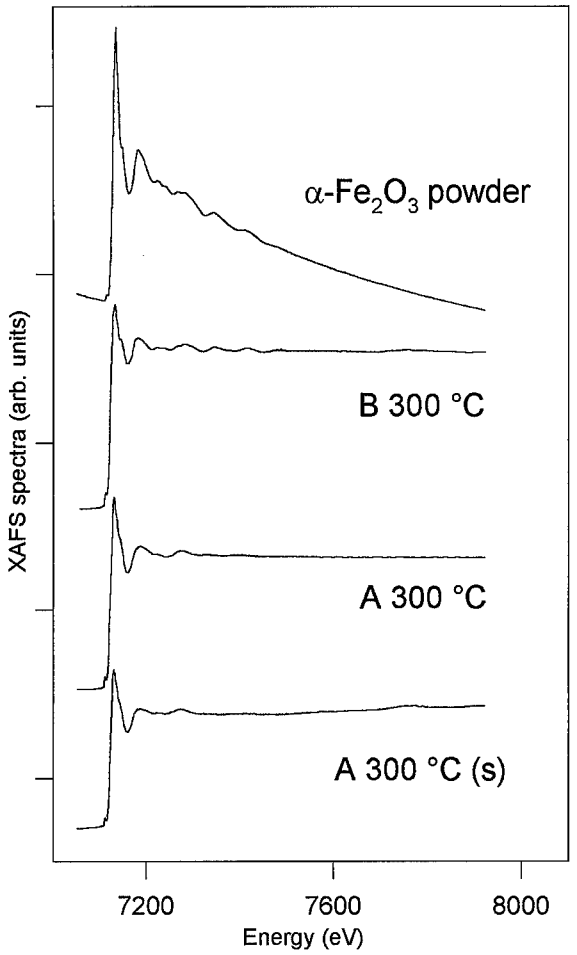

Figure 3. X-ray absorption (for the hematite powder) and fluorescence spectra for the films A and B at 300°C. (s) indicates the film obtained by a single dip.

by multiple (up to 15–18) dips. After each dip, thermal treatments were performed raising the temperature at approximately 100°C/h. Different samples were obtained, keeping the temperature at 300°C or at 500°C for 1 h. The temperature was kept constant for about 1 h at the boiling points of the organic solvents (124°C and 139°C for MET and acetylacetone, respectively, in A; 117°C for acetic acid in B) to prevent the formation of bubbles.

The degree of crystalline order of the films was studied by X-ray diffraction at RT using a Philips PW 3710 powder diffractometer at the CuK_α line. Their vibrational spectra were obtained by Raman spectroscopy at RT with the 488.0 nm line of a Ar^+ laser, using a Dilor XY spectrometer and multichannel CCD detector, in micro-Raman configuration at the Laboratoire de Physique des Solides, Toulouse.

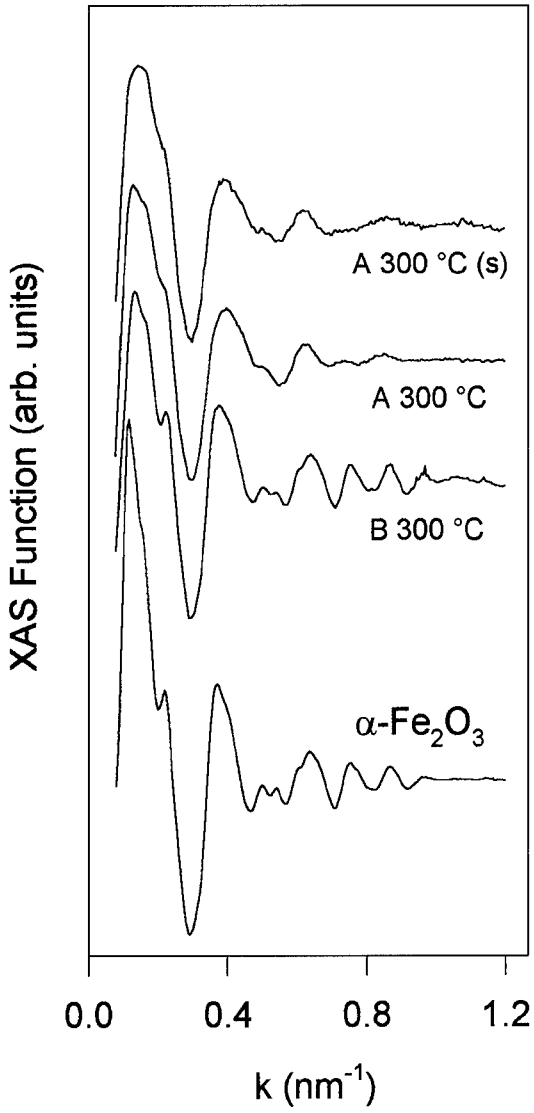

Figure 4. XAFS oscillations in k-space (photoelectron wavenumber), obtained from the data in Fig. 3. The film B 300°C shows medium-long-range crystalline order, as the α-Fe_2O_3 powders.

Information on the the local structure around the Fe atoms in films made both by single and multiple dips was obtained by X-Ray Absorption Spectroscopy. The XAFS experiments were performed with synchrotron radiation at the European Synchrotron Radiation Facility (ESRF), Grenoble, at the Italian GILDA beamline. The monochromator was equipped with 311 Si crystals [5]. The spectra at the Fe K-edge were taken in fluorescence mode for the films, using a Si photodetector, and in transmission mode for the reference α-Fe_2O_3 powder, using ionization chambers for the absorption measurements.

Results and Discussion

The results of the XRD measurements on thick samples are shown in Fig. 1. At 300°C, the sample A shows the diffraction pattern of an amorphous material, whereas in the sample B the characteristic hematite features [6] appear. The hematite peaks are clearly observed in the diffraction pattern at 500°C for both preparations. Slightly narrower peaks are found in sample A.

Raman spectra of hematite crystals or powders have been published [7, 8], but the data on iron oxide films are scarce [9]. In Fig. 2 the Raman spectra of the thick films are shown. Seven optical modes of even symmetry ($2A_{1g} + 5E_g$) are expected in the Raman spectrum of α-Fe_2O_3 and indeed these modes are observed in the films with the correspondence: A_{1g}: 221–499 cm^{-1}, E_{1g}: 244~290~298–401–605 cm^{-1}. The line at 290–298 cm^{-1} is usually reported as a doublet of E_{1g} symmetry and cannot be easily resolved.

No unambiguous signal from other iron oxide phases was observed in the Raman spectra. For the XRD data, the narrowest peaks are observed for preparation A at 500°C (a factor of two in the linewidths), indicating a higher degree of crystallization, i.e., greater crystallite sizes. A Raman signal is present also for the A film at 300°C, which should be amorphous according to the XRD pattern. Even if a greater sensitivity of the Raman probe to nanocrystals with respect to XRD has been reported [10], this fact could be due to the focussing (concentrating) of the laser light during the micro-Raman measurements and to an induced crystallization. Stokes and anti-Stokes measurements indicate, however, local temperatures not greater than 200°C.

With respect to the A sample annealed at 500°C, the Raman linewidths are larger and the frequencies are red-shifted: this could be due to phonon confinement effects in the nanocrystals [11]. The fluorescence spectra at the Fe X-ray absorption K-edge of the films annealed at 300°C of both preparations are reported in Fig. 3, compared with the absorption spectrum of the hematite. After the usual background removal and normalization [12], these are reported in Fig. 4 as a function of the photoelectron wavenumber k. These spectra were Fourier transformed and in the resulting functions in r-space (Fig. 5) the peaks correspond to the different coordination shells of Fe atoms, which are shifted with respect to the true crystallographic distances [6] by 0.03–0.04 nm due to phase-shift effects on the photoelectron wavefunction.

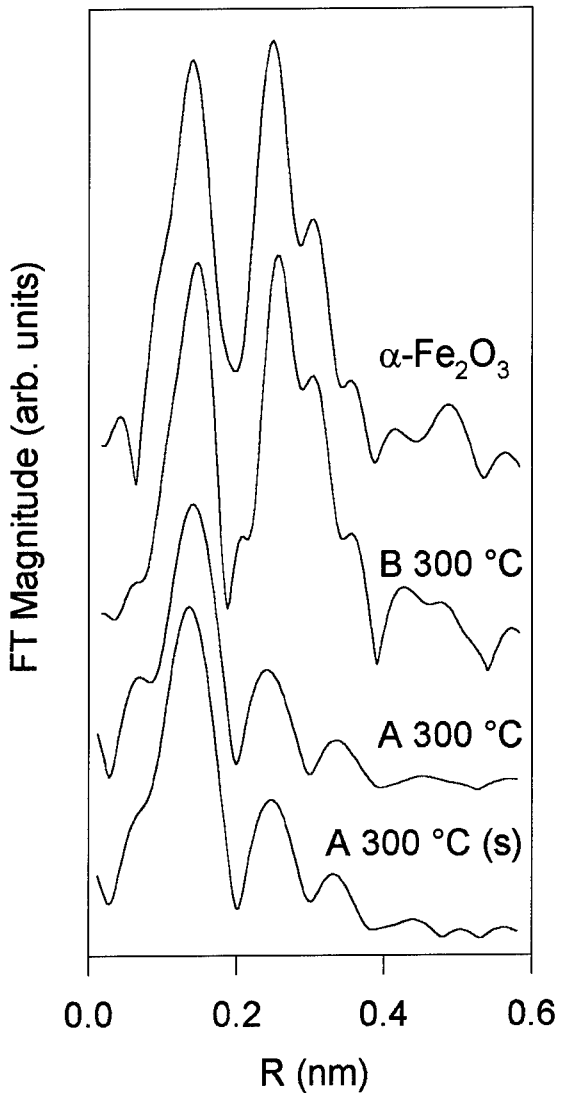

Figure 5. Radial distribution functions (magnitude of the Fourier transform) relative to the data in Fig. 4.

The crystalline order typical of the hematite [13] beyond the first coordination shell is clearly evidenced for sample B, whereas in the A film the peaks beyond the first shell are greatly reduced, probably due to a greater structural disorder of the higher coordination shells. This result is compatible with the XRD and Raman measurements and shows that in preparation B the films crystallize at lower temperatures. The XAFS data taken on the films annealed at 500°C confirm the results obtained by XRD. XAFS measurements were also possible on thin films obtained by a single dipping and for both preparations the result is similar to that found in the thicker sample A at 300°C.

Conclusions

Thin films of iron oxide have been synthesized by two different sol-gel procedures. In all samples, at 300°C, the first neighbor iron-oxygen coordination corresponds to that found in hematite; only the film obtained from $FeCl_3 \cdot 6H_2O$ clearly shows the hematite medium-long-range-order. Conversely, when the heat treatment is performed at 500°C, higher crystalline order is found for the films obtained starting with $FeNO_3 \cdot 9H_2O$ with respect to those made from $FeCl_3 \cdot 6H_2O$.

Acknowledgments

We are indebted to the staff of GILDA-CRG beamline (S. Pascarelli, F. D'Acapito) at ESRF, Grenoble, and to R. Carles and J. Groenen of the LPS, Universitè Paul Sabatier, Toulouse for technical support for XAFS and Raman measurements, respectively. This work was partially financed by C.N.R. under the Progetto Strategico "Materiali Speciali" and by the Joint Program Italy-France "Galileo."

References

1. T. Hashimoto, T. Yamada, and T. Yoko, J. Appl. Phys. **80**, 3184 (1996).
2. H.T. Sun, C. Cantalini, M. Faccio, M. Pelino, M. Catalano, and L. Tapfer, J. Am. Ceram. Soc. **79**, 927 (1996).
3. C.J. Brinker and G.W. Scherer, *Sol-Gel Science: The Physics and Chemistry of Sol-Gel Processing* (Academic Press Inc., San Diego, 1990).
4. L.C. Klein, Annu. Rev. Mater. Sci. **23**, 437 (1993).
5. F. d'Acapito, F. Gonella, E. Cattaruzza, S. Pascarelli, P. Mazzoldi, and S. Mobilio, Nucl. Instr. Meth. B **120**, 110 (1996).
6. R.L. Blake and R.E. Hessevick, Amer. Mineral. **51**, 123 (1966).
7. R.L. Farrow and A.S. Nagelberg, Appl. Phys. Letts. **36**, 945 (1980).
8. T.P. Martin, R. Merlin, D.R. Huffman, and M. Cardona, Solid State Commun. **22**, 565 (1977).
9. R.J. Thibeau, C.W. Brown, and R.H. Heidersbach, Appl. Spectrosc. **32**, 532 (1978).
10. P.P. Lottici, D. Bersani, M. Braghini, and A. Montenero, J. Mater. Science **28**, 177 (1993).
11. D. Bersani and P.P. Lottici, Phys. Stat. Sol. B **174**, 575 (1992).
12. P.A. Lee, P.H. Citrin, P. Eisenberger, and B.M. Kincaid, Rev. Mod. Phys. **53**, 769 (1981).
13. S. Quartieri, G. Antonioli, P.P. Lottici, and G. Artioli, Mineral. Mag. **57**, 249 (1993).

Journal of Sol-Gel Science and Technology 13, 673–678 (1998)
© 1998 Kluwer Academic Publishers. Manufactured in The Netherlands.

Characterization of Electrochromic WO_3-Layers Prepared by Sol-Gel Nanotechnology

B. MUNRO, S. KRÄMER, P. ZAPP AND H. KRUG
Institut für Neue Materialien, Im Stadtwald, Geb. 43, D-66123 Saarbrücken, Germany

Abstract. Stable tungsten oxide coating sols suitable for electrochromic applications were prepared by a modified peroxotungstic acid route. Layers up to 250 nm thickness could be deposited on ITO-coated and/or FTO-coated glass substrates in a single dip-coating process. Optoelectrochemical measurements were employed to determine the variation of the electrochromic properties (change in optical density (ΔOD) and switching times) of WO_3-layers, investigated as a function of coating parameters, such as chamber humidity and the temperature of heat treatment. High resolution transmission electron microscopy (HR-TEM) has shown that the optimized layers possess a partially crystalline morphology with nanocrystalline regions 2–3 nm in size.

Keywords: electrochromism, sol-gel, tungsten oxide, peroxotungstic acid, nanocrystalline

1. Introduction

In recent years, there has been a vast amount of research and development conducted at both university [1, 2] and company level [3–6] into electrochromism, due to the variety of potential applications, which exist for electrochromic devices, i.e., antiglare rearview mirrors [3, 4], sunroofs and smart windows. However, large area electrochromic devices are not yet commercially available. Sputtering, although it supplies coatings of a very high quality, involves high capital investment costs. The objective of this work, therefore, was to develop sol-gel electrochromic-layers for large-area applications with the inherent advantages of low cost thin films by conventional wet-chemical coating techniques and chemical flexibility.

The material of choice for the electrochromic layer is tungsten oxide, WO_3, due to its high coloration efficiency of between 40 cm^2/C (550 nm) and 130 cm^2/C (800 nm) [3] and several different sol-gel routes based on different starting compounds have been reported [7]. Sols based on the hydrolysis and condensation of tungsten alkoxides [8] may be employed to form WO_3-layers, however, the cost of the precursors limits the potential of this route for a commercial application. Layers prepared from tungsten oxychloride, $WOCl_4$, have also been reported [9] as having very good properties in laboratory investigations. However, sols have to be handled in a dry inert atmosphere and there may be problems with the long-term electrochemical stability of such layers due to residual chloride. Synthesis of WO_3-layers by a peroxotungstic acid [6] has several advantages in that the starting materials, namely tungsten metal powder and hydrogen peroxide solution, are inexpensive and that WO_3 layers can be obtained at low firing temperatures. Industrial procedures for the safe handling of syntheses involving hydrogen peroxide solution are already established.

Therefore, in this work a modified peroxotungstic acid route was developed under consideration of criteria such as sol stability and the potential for scaling-up, which are relevant for large area applications. The influence of pre-doping the sol with a lithium hydroxide to introduce lithium ions into the layers as a potential method for reducing swinging-in behavior [9] was also investigated. The properties of complete "all sol-gel" electrochromic devices constructed employing these WO_3-layers has already been reported [10].

2. Experimental

The synthesis route for WO_3 has already been described in detail elsewhere [10] and so will only be briefly described here. Stable tungsten oxide coating

sols were synthesized using a route based on the dissolution of tungsten metal powder in an excess of hydrogen peroxide solution (30%), in the presence of ethanol and glacial acetic acid, to give peroxotungstic acid.

Glass substrates with an ITO layer (Donnelly Applied Films, sheet resistance 12 Ω/□) or an FTO layer (Libbey-Owens-Ford: TEC-glass, sheet resistances 10 Ω/□ and 20 Ω/□) were coated by dip coating under controlled conditions of relative humidity and temperature.

The layer thicknesses were determined by partial etching of the WO_3-layers with 1 M KOH solution and measuring the step with a Tencor Profilometer. The variation in layer thickness was determined as a function of dipping speed and for different glass substrates (ITO, FTO).

Optoelectrochemical measurements were conducted on individual WO_3-coated ITOs in order to determine the long-term influence of doping with lithium ions on electrochromic properties such as the change in optical density (ΔOD) and the coloring and bleaching times. In order to study the coloration and bleaching kinetics of the WO_3-layers, WO_3-coated ITO-substrates were placed in three electrode cells containing liquid electrolyte ($LiClO_4$/propylene carbonate, PC) and switched at a variety of potentials as referenced against a $Ag/AgClO_4$ electrode. On switching, the average transmission over the wavelength range 380–800 nm was measured as a function of time, employing a multichannel UV-Vis spectrometer (ZEISS SPECORD S10). Coloring times were defined as the time between 90% of the initial transmission, T_0, and 110% of the final transmission, T_x; bleaching times were similarly defined. The change in optical density, ΔOD, was also taken as an important criterion for assessing the electrochromic layers, whereby:

$$\Delta OD_x^{(380-800\ nm)} = \log\left(T_0^{(380-800\ nm)}/T_x^{(380-800\ nm)}\right) \quad (1)$$

Samples for electron microscopy were prepared by coating ITO-coated glass substrates with subsequent thermal curing. The oxide layer was then removed by scratching and the splinters examined at an energy of 200 keV.

3. Results

By optimizing the concentrations of glacial acetic acid and solvent, and through the adjustment of technical parameters relevant to the synthesis, it was possible to obtain stable WO_3-coating sols on a liter-scale and thus substrates up to 0.1 m^2 could be coated to date. The sols had a storage life of at least 4 weeks at 6°C, as determined by monitoring the viscosity of the sol. Furthermore, the sols could be evaporated under reduced pressure to give a powder, which could be redispersed as required.

The determination of the layer thickness as a function of dipping speed and as a function of the type of substrate is important so that the correct thickness may be adjusted according to application requirements. Figure 1 clearly shows that the WO_3-layers on the FTO-coated glass substrates (TEC 10 and 20) are thinner than those deposited on ITO at the same speed of dipping. Cracks in the layers prepared on ITO at 6 mm/s caused additional errors in the measurements so that this point deviates somewhat from the anticipated value.

Coatings were prepared at two different chamber humidities (20% and 40%), with heating at 120°C or 240°C for either 1 or 2 h (see Fig. 2). The former temperature was chosen as being sufficient to remove physically adsorbed water, but not chemically bound water, with the expectation that a lower heating temperature would facilitate faster kinetics. The second heating temperature was selected to be as high as possible without leading to complete crystallization of the layers.

A small effect from the chamber humidity was observed but only for layers heated at 120°C. The effect of the relative humidity in the coating chamber on the coloration of the WO_3-layers in the first switching cycle did not seem to be significant. Only a modest increase of the speed of coloration was observed with increasing humidity, indicating the influence of H^+ as a charge carrier. The varying duration of the heat treatment had no noticeable effect, which would suggest that 1 h is sufficient to attain a constant water content. The initial differences in coloring disappeared, however, after several cycles.

Figure 3 shows the variation in ΔOD for WO_3-layers heated at 120°C and 240°C as a function of the number of switching cycles (positive values of ΔOD correspond to coloring and negative values represent bleaching). It can be seen from figure that the WO_3-films heated at only 120°C exhibit a gradual decrease in ΔOD with an increasing number of cycles, whereas those layers heated at 240°C, after an initial decrease in ΔOD, display an increase in ΔOD as a function of the number of cycles.

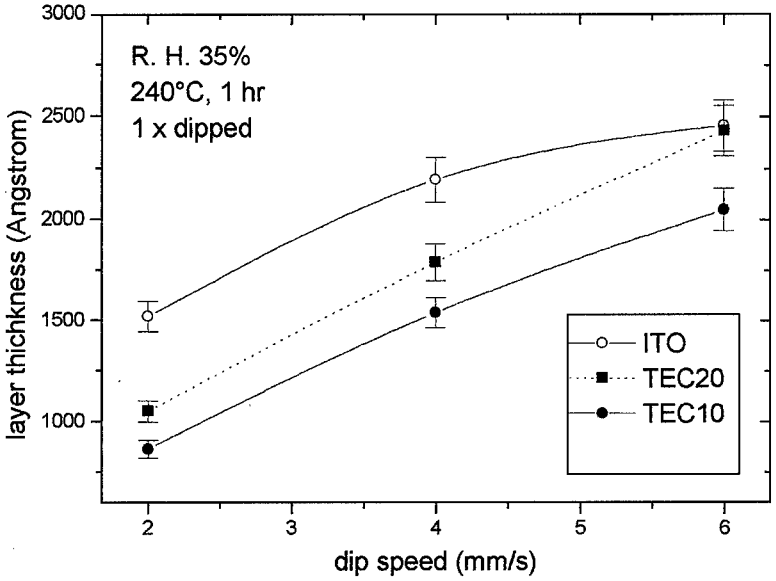

Figure 1. The variation in WO_3-layer thickness as a function of both dipping speed and glass substrate. The lines drawn serve only as guide for the eye.

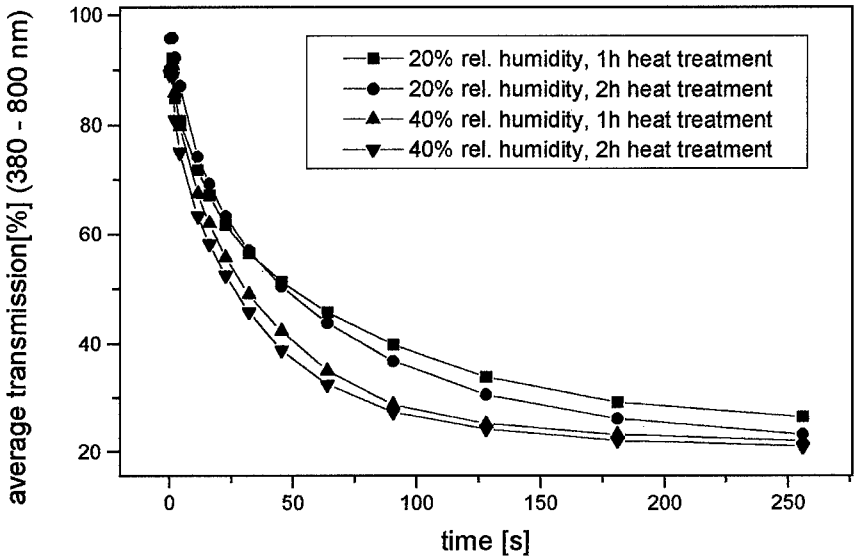

Figure 2. Time dependence of coloration for WO_3-layers prepared under varying conditions, on switching at a potential of -1.2 V as referenced against a $Ag/AgClO_4$ electrode in $LiClO_4$/PC electrolyte.

In Fig. 4 the dependence of switching times for coloration and bleaching as a function of the number of cycles is shown for WO_3-layers heated at 240°C with and without prior doping with lithium salt. The addition of lithium strongly reduces the time required in the initial cycles to achieve a degree of coloration comparable with that for the undoped layers. Switching times of less than 60 s could be measured after only 1 cycle whereas for undoped layers at least 100 cycles were necessary. The times for bleaching were slightly higher in layers with added lithium.

Figure 5 shows a HR-TEM micrograph of an WO_3-layer heated at 240°C. It can be seen that the layer is partially crystalline and that the crystalline areas have diameters between 2 and 3 nm.

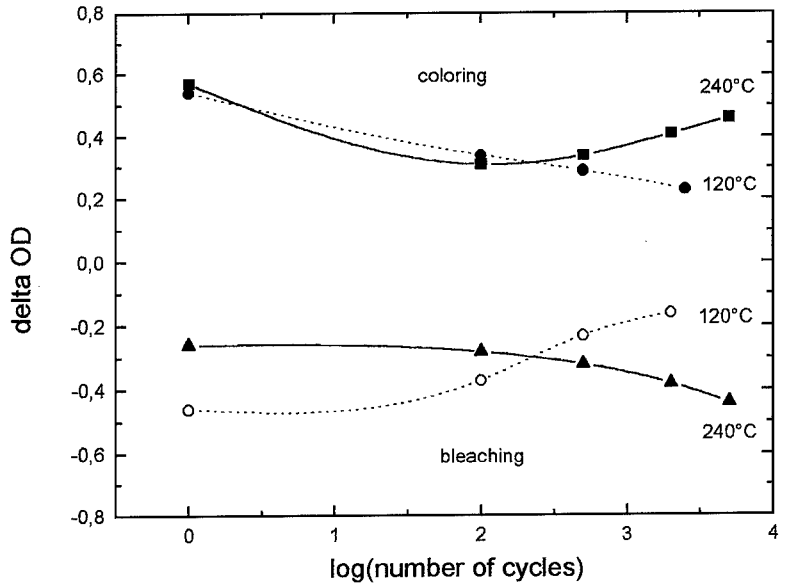

Figure 3. ΔOD plotted against the logarithm of the number of cycles for WO_3-layers heated at 120°C and 240°C. Each value is an average from measurements on eight different samples. The drawn lines are a guide for the eye.

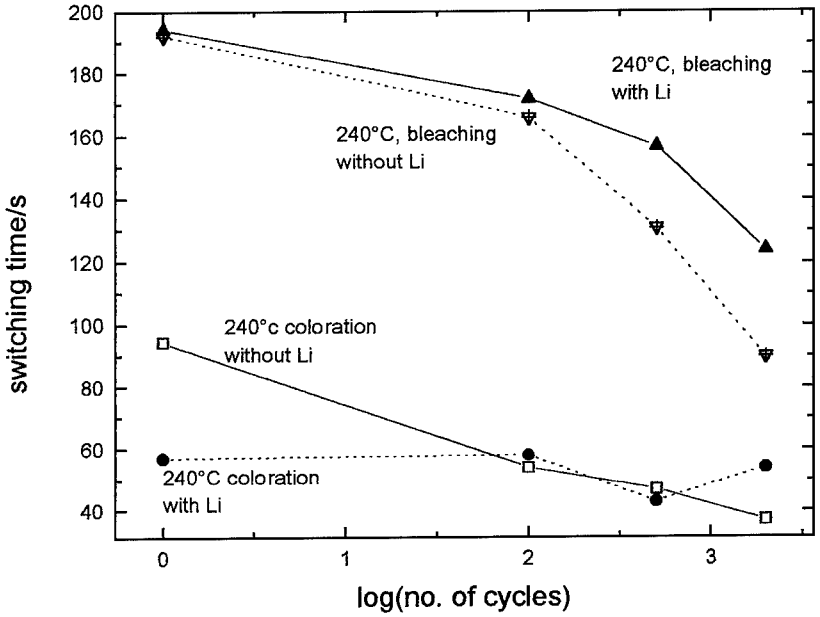

Figure 4. Switching times (coloration and bleaching) for WO_3-layers with and without pre-doping with lithium, heated at 240°C for 1 h. The lines are drawn as a guide for the eye.

4. Discussion

The gradual decrease in ΔOD with an increasing number of cycles for the WO_3-films heated at only 120°C is due to the poor chemical resistance of the layers to the electrolyte medium, especially as traces of water are present. The behavior seen after the 1st cycle, for the layers heated at 240°C, represents the swinging-in of the layers. It has been speculated that such behavior is due to the permanent incorporation of a

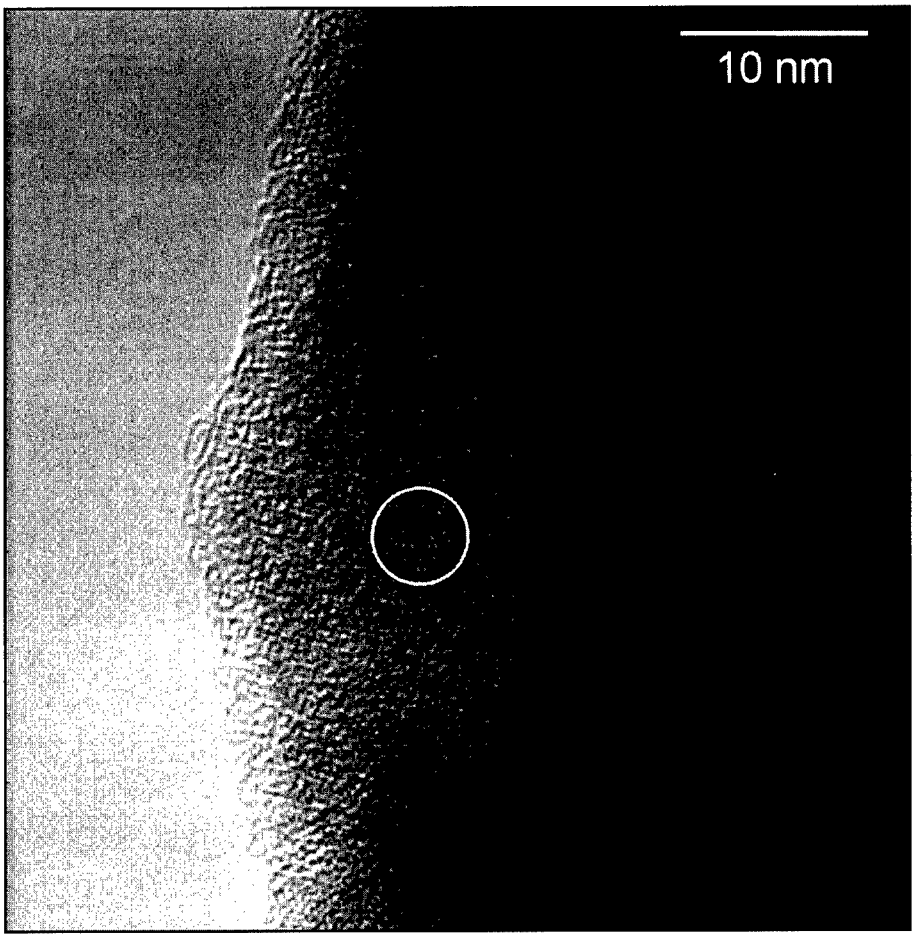

Figure 5. HR-TEM micrograph of a splinter of WO_3-sol-gel layer; heating conditions: 240°C, 1 h (E_0 = 200 keV). Circled area contains a crystalline region.

fraction of the lithium ions in the WO_3-layer, which do not lead to coloration. Indeed, previously reported investigations with electrochemical quartz microbalances seem to confirm that lithium ions are incorporated irreversibly [11]. The large value of ΔOD observed in the initial cycle is probably due to residual water in the WO_3-layers.

Another consequence of swinging-in is the decrease in switching times with repeated cycling. The experiments conducted to investigate the long-term effect of doping the lithium sols with lithium hydroxide show that near cycling-independent coloration times are obtained, through the incorporation of lithium ions during layer formation.

The partially crystalline structure observed by HR-TEM for the sample heated at 240°C is responsible for the stability of the layers in $LiClO_4$/PC, whereby the coloration efficiency remains high at 45 cm^2/C ($\lambda = 0.633$ μm). Completely amorphous films have a poorer chemical stability [6] and crystalline films have such a low coloration efficiency that they have been considered as a possible candidate for a non-coloring ion-storage layer in EC devices [1].

5. Conclusions

Sol-gel nanotechnology may be exploited to prepare electrochromic WO_3-layers with a partially crystalline morphology with the benefits of both high chemical stability and high coloration efficiency. The electrochromic properties of the layers may be optimized

with respect to the sol-gel coating parameters, such as heating temperature and duration and chamber humidity. Further, by doping the tungsten oxide sol with small amounts of a lithium-containing compound it was possible to reduce the swinging-in behavior of the cells. Layers were deposited on substrates up to 0.1 m^2 in size. These sol-gel WO_3-layers were used to construct electrochromic cells with excellent properties [10].

Acknowledgments

The authors would like to thank the German Ministry for Education and Research (BMBF) for their financial support of this project (3N2001A4) as part of the Matech program and partners Bischoff Glastechnik (BGT) and Donnelly HOHE for permitting the publication of these results. Thanks are also due to Dr. T. Krajewski for the HR-TEM measurements.

References

1. C.G. Granqvist, *Handbook of Inorganic Electrochromic Materials* (Elsevier, Amsterdam, 1995).
2. C.M. Lampert, Sol. Energy Mater. **11**, 1 (1984).
3. T. Gambke and B. Metz, Glastech. Ber. **62**(2), 38 (1989).
4. F.G. Baucke, K. Bange, and T. Gambke, Displays, **9**, 179 (1988).
5. T. Kamimori, J. Nagai, and M. Mizuhashi, Sol. Energy Mater. **16**, 27 (1987).
6. M. Denesuk, J.P. Cronin, S.R. Kennedy, K.J. Law, G.F. Nielson, and D.R. Uhlmann, in *Optical Materials Technology for Energy Efficiency and Solar Energy Conversion XIII*, edited by V. Wittwer, C.G. Granqvist, C.M. Lampert (SPIE, Bellingham, 1994), Vol. 2255, p. 52.
7. M.A. Aegerter, *Structure and Bonding* (Springer, Berlin, Heidelberg, 1996), Vol. 85, p. 149.
8. A. Takase and K. Miyakawa, Jap. J. Appl. Phys. **30**(8B), L 1508 (1991).
9. P. Judeinstein and J. Livage, J. Mater. Chem. **1**(4), 621 (1991).
10. B. Munro, P. Conrad, S. Krämer, H. Schmidt, and P. Zapp, in *Proc. Eurosun'96* (SPIE, Freiburg, 1996), to be published in Sol. Energy Mater.
11. S.J. Babinec, Sol. Energy Mater. **25**, 269 (1992).

Journal of Sol-Gel Science and Technology 13, 679–683 (1998)
© 1998 Kluwer Academic Publishers. Manufactured in The Netherlands.

Sol-Gel Deposited Sb-Doped Tin Oxide Films

M. GUGLIELMI AND E. MENEGAZZO
Dip. Ing. Meccanica, S. Materiali, Università Padova, 35100 Padova, Italy

M. PAOLIZZI
Istituto Giordano SpA, Bellaria (RN), Italy

G. GASPARRO, D. GANZ, J. PÜTZ AND M.A. AEGERTER
Institut für Neue Materialien INM, Im Stadtwald, D-66123 Saarbrücken, Germany

L. HUBERT-PFALZGRAF
Laboratoire de Chimie Moléculaire (URA-CNRS), F-06108 Nice Cedex 2

C. PASCUAL AND A. DURÁN
Instituto de Ceramica y Vidrio (CSIC), 28500 Arganda del Rey (Madrid), Spain

H.X. WILLEMS AND M. VAN BOMMEL
Philips Research Laboratories, NL-5656 AA Eindhoven, The Netherlands

L. BÜTTGENBACH
Fa. E. Merck, ZGE, D-64293 Darmstadt, Germany

L. COSTA
Gel Design and Engineering (GDE), I-28100 Novara, Italy

Abstract. The structural, electrical and optical properties of single sol-gel derived antimony-doped tin oxide (ATO) films sintered at 550°C have been measured. The reproducibility of both the preparation and the characterization procedures have been tested by a round-robin test involving eight laboratories within a Concerted European Action (CEA) project. The resistivity measured as a function of Sb content has been obtained by electric and reflectance and transmission measurements. Their differences are discussed in terms of structural and grain boundary effects. An increase of Sb content results in a decrease of the crystallite size (7.0 to 5.4 nm) and a greater influence of the grain boundary.

Keywords: thin films, transparent conductors, Sb-doped tin oxide, optical properties, electrical properties

1. Introduction

Conductive and transparent coatings are essential in the development of optic and optoelectronic devices [1], displays [2], heat shields [2], solar energy applications [3], gas sensors [4], conductive paint coatings [5] and catalysts [6].

Sol-gel deposited ATO coatings have been described in several papers [7–15]. These previous studies have shown that their performances are worse than those

reported for coatings deposited by other deposition techniques [1, 14, 16] and depend on several parameters, such as the chemical composition of the solution (precursors, catalysts, amount of water, hydrolysis control reagents, concentration), layer thickness, heating procedure, and treatment atmosphere. The effect of these parameters is not completely understood and it is difficult to correlate the optical and electrical properties to the structural and chemical features of the material.

The aim of a project developed in the frame of a Concerted European Action [17] was to realize a round-robin test with seven laboratories (Università Padova (UP), Istituto Giordano (IG), Instituto de Ceramica y Vidrio (CSIC), Institut für Neue Materialien (INM), Philips Research Laboratories (PRL), Fa. E. Merck, Gel Design and Engineering (GDE)) with the aim to verify the reproducibility in the preparation and characterization of ATO coatings in terms of thickness, structural features (crystalline structure, average grain size), electrical and optical performances and to study the effect of antimony concentration. Some results are described in this paper, but a more complete description will be published elsewhere [18].

2. Experimental Procedures

Tin tert-butoxide ($Sn(OtBu)_4$) was used as precursor for tin oxide. Following the indications of a preliminary study on its alcoholysis and hydrolysis reaction [19] a sol (SOL 1) was prepared by dissolving $Sn(OtBu)_4$ in pure, anhydrous ethanol (EtOH) at a concentration $[Sn] = 0.33$ mol/l; then 1 equivalent of acetylacetone (acacH) was added and reacted for 2 h at room temperature; 2 moles of H_2O per mole of alkoxide were finally added.

Sb(III) ethoxide was used as precursor for antimony oxide. It was dissolved in pure, anhydrous ethanol at a concentration $[Sb] = 0.33$ mol/l (SOL 2).

The final sols were prepared by mixing SOL 1 and SOL 2 in the proportions to get a Sb/Sn molar ratio of 0.15 for the first series samples, and ranging from 0.02 to 0.15 for the second series. The concentration of this sol was about 50 g/l of oxides.

Doped tin oxide layers were deposited by spinning on Corning 7059 glass slides (in order to avoid problems related to alkali contamination) following a common procedure and using the same sources. For the first series, seven samples were produced at PRL, INM and UP. For the second series, the samples were produced at PRL and distributed for characterization.

Heat treatment was performed in air. Samples were dried at 80°C for 2 h, heated to 550°C at 5 K/min, left for 10 min at 550°C and then cooled in the furnace down to 350°C.

The thickness of the films was measured by surface profilometry. The films were analyzed at UP by X-ray diffraction using a diffractometer equipped with a glancing-incidence X-ray optics. The average crystallite size was calculated from the Scherrer equation after fitting the experimental profiles.

A detailed optical study was performed on the second series of samples at IG where the spectral transmittance and reflectance were measured at normal incidence, in the range 0.25–2.5 μm. The optical constants n and k, thickness and resistivity ρ_{opt}, were obtained from these measurements assuming a homogeneous, isotropic layer texture and a Drude-Lorentz dispersion relationship.

Electrical resistivity measurements (ρ) were performed at room temperature by 4-point technique (INM, Merck, UP and PRL) and 4 point ac impedance spectroscopy (CSIS).

The details on the equipment and procedures used for characterization will be reported elsewhere [18].

3. Results and Discussion

X-ray diffraction was performed on all the samples. Tin oxide was present in its tetragonal form (cassiterite). No significant differences among the samples produced by different laboratories were found.

Crystallite size was calculated from the broadening of the (110) and (101) lines. A systematic decrease, from 7.0 to 5.4 nm, was observed with increasing antimony oxide content.

Table 1 presents the data of thickness for the first series of samples (15 at% Sb). There are significant

Table 1. Thickness d (nm) for samples of the first series measured by profilometer (*) and calculated from optical results (+).

	Source		
Measurement	UP	PRL	INM
UP*	73	75	78
INM*	63	67	75
IG+	63	71	79

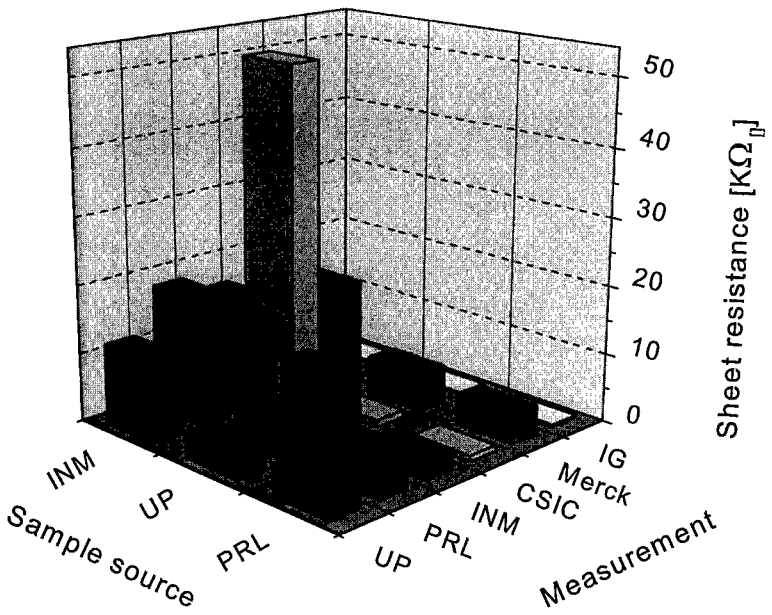

Figure 1. Sheet resistance for samples of the first series (15 at% Sb) measured by 4-point technique at UP, PRL, INM, Merck, 4-point ac impedance spectroscopy at CSIC and calculated from optical measurement at IG.

deviations in the measured values not only between the different source of preparation, but also from the measuring laboratories. The values calculated from optical data are close to those measured by profilometer.

Figure 1 shows the data of the sheet resistance ($R_\square$) for the same series. The electrical values measured by different laboratories on the samples coming from the same source show a large distribution, the differences being larger than those coming from the preparation of the samples in the various laboratories. These differences are certainly due to the conditions under which the measurements were performed and the time elapsed between the fabrication and the measurement. The ac measurements performed at CSIC under a dry atmosphere and controlled temperature showed, in fact, an instability of the electrical properties. For example, the resistance of the INM sample was found to decrease from 50 to 14 $k\Omega_\square$ after heating to 100°C. With PRL and UP samples the instability was observed also at room temperature: the PRL sample increased its resistance from 0.87 to 1.05 $k\Omega_\square$ after two days in the measurement cell and to 1.7 $k\Omega_\square$ after heating at 100°C and cooling down to room temperature. Therefore, the experimental conditions (humidity, atmosphere, temperature, geometry, etc.) should be defined more precisely. The values calculated from the optical data for samples prepared in 3 laboratories are in good agreement but are at least one order of magnitude smaller than the electrically measured ones.

The samples containing different Sb contents (second series) were analyzed in the same way and the results are summarized in Tables 2 and 3.

Table 2. Thickness d, mobility μ, carrier density n, resistivity ρ, and sheet resistance $R_\square$, measured at INM by the van der Pauw/Hall method (second series).

Sb content (at%)	t (nm)	ρ (10^{-3} Ωcm)	μ (cm^2/Vs)	n (cm^{-3})	$R_\square$ ($k\Omega/\square$)
2	68.8	38,7	1.1	1.5×10^{20}	5.8
4	73.2	33,1	0.9	2.2×10^{20}	4.5
6	69.2	26,7	0.8	3.0×10^{20}	3.8
8	69.4	20,2	1.0	3.1×10^{20}	2.9
10	70.0	21,0	0.8	3.7×10^{20}	3.0
15	69.3	19,0	0.8	4.5×10^{20}	2.7

Table 3. Thickness d, resistivity ρ_{opt}, and sheet resistance $R_\square$ calculated at IG from optical measurements (second series).

Sb content (at%)	d (nm)	ρ_{opt} (10^{-3} Ωcm)	$R_\square$ (k$\Omega/\square$)
2	70	11.1	1.57
4	70	4.4	0.62
6	69	2.8	0.40
8	70	2.6	0.37
10	69	2.4	0.35
15	69	2.3	0.34

The thickness determined by the two different methods are again in good agreement. As the Sb concentration increases by a factor 7, the already low values of the mobility slightly decrease and the carrier density increases by a factor 3 and seems to saturate for higher concentrations. As a consequence the resistivity decreases only by a factor 2 (Table 2).

On the other hand, the values of ρ_{opt} (Table 3) calculated from the optical spectra are again an order of magnitude lower than the ones measured electrically, except for the sample with 2 at% Sb. It should be remembered that the optical data have been taken at short wavelengths ($<2,5$ μm) which act as a microscopic probe from which mainly the intra-grain resistivity is extracted. On the other hand, the electric determinations probe macroscopic areas ($\approx$1 cm^2) averaging the response over a large number of grains. These are intersected by grain boundaries which introduce an effective electron scattering reducing the electron mobility and thus increasing the resistivity. The difference between the values obtained by these two methods should thus come essentially from the influence of the grain boundaries. This trend, evident in Fig. 2, seems to indicate that grain boundary scattering becomes more important for high Sb contents possibly due to the smaller grain size and/or a segregation of Sb(III) at grain boundaries [20]. Thus, the decrease in mobility cannot be completely attributed to ionized impurities scattering from the dopant. The index of refraction of the samples with different Sb content was evaluated at $\lambda = 500$ nm. It increased from 1.65 to 1.75 with increasing Sb content possibly indicating a denser packing of the crystallites [18].

4. Conclusions

The first series of experiments have shown that the preparation of the coatings has to be described more precisely in order to get a sufficient reproducibility. This involves the chemical procedures, the coating process, and the subsequent heat treatment. Furthermore, the electrical measurements and the storage of the samples have to be carried out under standardized conditions (humidity, temperature) to obtain comparable results.

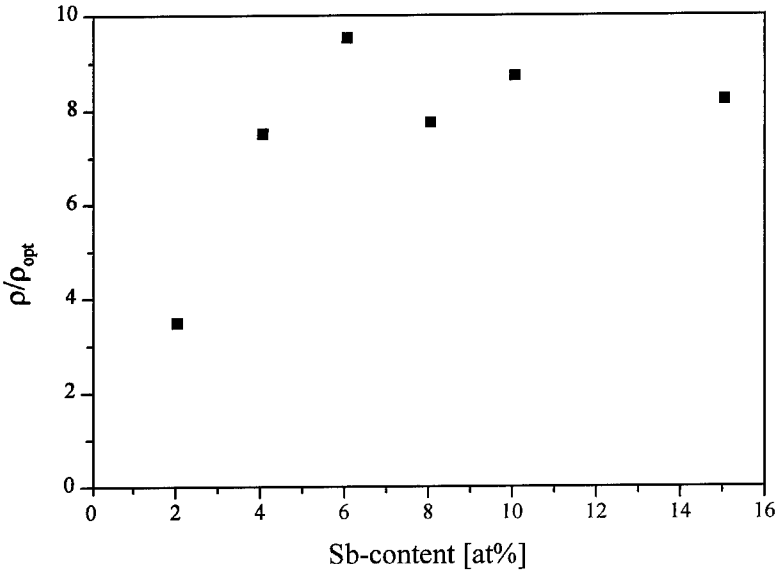

Figure 2. Ratio between resistivity values obtained from electrical measurements, ρ, and calculated from optical data, ρ_{opt}.

The combination of electrical and optical measurements proved to be a powerful means in the investigation of micro structural properties of the samples. In the second series it could be shown that the influence of the grain boundaries increase with increasing Sb content which was attributed to a reduction in crystallite size in combination with a possible segregation of Sb(III) on the surface of the crystallites.

Acknowledgments

This work was done in the frame of the Concerted European Action "Sol-Gel Processing for Advanced Industrial Material Technologies." The authors thank the European Commission of the European Community for their financial support.

References

1. K.L. Chopra, S. Major, and D.K. Pandya, Thin Solid Films **102**, 1 (1983).
2. C.G. Granquist, Thin Solid Films **193/194**, 730 (1990).
3. C.M. Lampert, Solar Energy Mater. **6**, 1 (1981).
4. W. Göpel and K.-D. Schierbaum, Sens. Actuators B **26/27**, 1 (1995).
5. Yoshizumi and K. Wakabayashi, Plastics Eng. 61 (1987).
6. Ono, T. Yamanaka, Y. Kubokawa, M. Komiyama, and J. Catal. **109**, 423 (1988).
7. C.J.R. Gonzales-Oliver and I. Kato, J. Non-Cryst. Solids **82**, 400 (1986).
8. G. Gowda and D. Nguyen, Thin Solid Films **136**, L39 (1986).
9. Y. Takahashi and Y. Wada, J. Electrochem. Soc. **137**, 267 (1990).
10. J.C. Giuntini, W. Granier, J.V. Zanchetta, and A. Taha, J. Mater. Sci. Lett. **9**, 1383 (1990).
11. B. Orel, U. Lavrencic-Stangar, Z. Crnjak-Orel, P. Bukovec, and M. Kosec, J. Non-Cryst. Solids **167**, 272 (1994).
12. J.P. Chatelon, C. Terrier, E. Bernstein, R. Berjoan, and J.A. Roger, Thin Solid Films **247**, 162 (1994).
13. S.-S. Park, H.X. Zheng, J.D. Mackenzie, Mater. Lett. **22**, 175 (1995).
14. C. Terrier, J.P. Chatelon, R. Berjoan, J.A. Roger, Thin Solid Films **263**, 37 (1995).
15. P. Olivi, E.C. Pereira, E. Longo, T.A. Varella, and L.O. de S. Bulhões, J. Electrochem., Soc. **140**, L81 (1993).
16. E. Shanti, V. Dutta, A. Banerjee, and K.L. Chopra, J. Appl. Phys. **51**, 6243 (1980).
17. Concerted European Action on "Sol-Gel Processing for Advanced Industrial Material Technologies."
18. M. Guglielmi, E. Menegazzo, M. Paolizzi, G. Gasparro, D. Ganz, J. Pütz, M.A. Aegerter, L. Hubert-Pfalzgraf, C. Pascual, A. Durán, H.X. Willems, M. van Bommel, L. Büttgenbach, and L. Costa, to be published.
19. S. Gaign and L.G. Hubert-Pfalzgraf, to be published.
20. D. Bélanger, J.P. Dodelet, B.A. Lombos, and J.I. Dickson, J. Electrochem. Soc. **132**, 1398 (1985).

Journal of Sol-Gel Science and Technology 13, 685–689 (1998)
© 1998 Kluwer Academic Publishers. Manufactured in The Netherlands.

Synthesis and Optical Properties of Mn^{2+}-Doped ZnS Nanoparticles in Solutions and Coatings

U. SOHLING, G. JUNG, D.U. SAENGER, S. LU, B. KUTSCH AND M. MENNIG
Institut für Neue Materialien, Im Stadtwald, Gebäude 43, D-66123 Saarbrücken, Germany

Abstract. Mn^{2+}-doped ZnS nanoparticles with different Mn-doping concentrations stabilized by hydroxypropyl cellulose (HPC) have been synthesized in ethanolic solutions and coatings. Their optical and structural properties have been characterized by means of UV-vis spectroscopy, luminescence spectroscopy, high resolution transmission electron microscopy (HRTEM) and small angle X-ray scattering (SAXS). Solutions and coatings exhibit a strong luminescence at 590 nm when excited with UV light showing that Mn^{2+} is incorporated into the ZnS nanoparticles. The highest luminescence intensity is obtained with an Mn^{2+} concentration of 2 mol%. HRTEM and SAXS investigations show that the particles are crystalline and are 3 ± 0.5 nm in size. Irradiation of the coatings with UV light leads to a photochemical oxidation of the particles, as shown by the decreasing absorption of the coating with irradiation time and a blue shift of the absorption maximum. Furthermore, the luminescence intensity first strongly increases and then decreases completely with UV-irradiation time. Both phenomena can be explained by the photochemical oxidation of the particles.

Keywords: zinc sulfide, nanoparticles, absorption spectroscopy, luminescence spectroscopy, coatings

1. Introduction

In recent years semiconducting nanoparticles have been investigated intensively because of their possible use in optoelectronic device materials [1–11]. Their optical properties depend on the particle size, producing for example fast relaxation times or changes in the electronic structure, respectively. On the other hand, their large surface area leads to a high chemical reactivity of the particles, which might give limitations in application.

Therefore, this paper addresses the chemical stability and the time dependence of the absorption and emission spectra of Mn^{2+}-doped ZnS nanoparticles during UV irradiation in a solvent-free environment. These particles are suitable model material to study the chemical stability by optical measurements, because the intensity of the luminescence of the Mn^{2+} center in the ZnS nanoparticles is very sensitive to chemical and structural changes of the host particles. It is known that micro sized Mn^{2+}-doped ZnS particles lose their luminescence properties within a few years under daylight UV irradiation [12]. In this paper, in the experimental section, it is shown that nanosized particles can degrade much faster due to their large surface area.

Considerable experimental work has been performed in the past in order to understand the physical and chemical properties of Mn^{2+}-doped ZnS nanoparticles. Bhargava et al. performed luminescence measurements on Mn^{2+}-doped ZnS nanoparticles as powders and in an organic polymer matrix [7, 13]. An increase in the luminescence intensity on irradiation with UV light was reported and it was hypothesized that passivation of the surface of the nanoparticles by photopolymerization of the stabilizer (methacrylic acid) leads to a decrease of surface related nonradiative processes and therefore to an increased luminescence intensity [7, 8, 13]. An activation of the luminescence in Mn^{2+}-doped ZnS nanoparticles, stabilized with polymethylmethacrylate (PMMA) in ethanol was also detected by Jin et al. after UV irradiation for 1 h [14]. On the other hand, it has been shown by absorbance measurements on undoped ZnS-nanoparticles 2 to 3 nm

in size that the particles are oxidized in the presence of oxygen within several minutes under UV irradiation from a 450 W Xenon lamp at stand-off distance of 30 cm [4, 5].

Systematic investigation of these phenomena on Mn^{2+}-doped ZnS particles by measuring time dependent absorption and luminescence spectra have not been performed to date. To investigate this in detail, Mn^{2+}-doped ZnS nanoparticles have been synthesized in solutions and coatings, and their optical and structural properties are characterized in this paper. Hydroxypropyl cellulose (HPC) was used as a stabilizer and as a viscosity-increasing agent in order to obtain coatings with thicknesses in the micro range to investigate the spectroscopic properties in a solvent-free surrounding. Absorption and luminescence properties of the nanoparticles in the coatings were measured as a function of the UV-irradiation time and a model for the time dependent spectroscopical behavior is presented.

2. Experimental

A 50 ml solution with a constant total cation concentration of 0.01 M and 4.0 wt% HPC was prepared by dissolving $Zn(CH_3COO)_2 \cdot 2H_2O$ (Fluka), $Mn(CH_3COO)_2 \cdot 4H_2O$ (>99%, Aldrich) and HPC (Aldrich, average molecular weight 100,000) in ethanol, with stirring, at room temperature. Doping concentrations of 1, 2, 3, 4, 6 and 8 mol% Mn^{2+} have been adjusted. Transparent solutions of Mn^{2+}-doped ZnS colloids were prepared by the injection of 15 ml H_2S gas from a 20 ml plastic syringe into the mixture within 2 min and during stirring. Coatings with thicknesses between 0.5 to 50 μm were obtained from the solutions by multiple dip-coating onto glass substrates. The coatings were dried at 120°C for 2 h in nitrogen atmosphere.

Absorption spectra were measured at room temperature using a Hitachi U3000 spectrophotometer and 2 mm fused silica cuvettes with air as a reference for the solutions. Emission spectra and excitation spectra were recorded with a Hitachi F-3010 fluorescence spectrophotometer. High resolution transmission electron microscopy (HRTEM) investigations were performed with a Philips CM 200 FEGTEM. Samples were prepared by dipping a copper grid coated with carbon film into the as-prepared solutions. The thickness of the coatings was measured with a Tencor P-10 surface profiler. UV irradiation of the samples has been performed under air using a Penray Hg-calibration lamp (Ultraviolet Products Inc; intense lines at 253, 312 and 365 nm; 14 W; 5 cm distance). Small angle X-ray scattering (SAXS) measurements were carried out under grazing incidence at the beam line D22 of the LURE synchrotron (Paris/Orsay) with an X-ray energy of 9500 eV. Details of the experimental setup and the data evaluation are described in [15, 16].

3. Results and Discussion

In Fig. 1 the absorption spectrum of a solution with a dopant concentration of 2 mol% is shown together with the spectra of the coatings before and after drying at 120°C. The spectra of the ZnS containing solutions have a peak at 273 nm, which can be assigned to an excitonic transition and proves the existence of ZnS nanoparticles [4, 5]. Compared with the solution, the peak measured for the coatings has a red shift of 0.11 eV and is broadened. As the absorption spectra of the coatings before and after heat treatment are nearly the same, it can be supposed that particles have slightly agglomerated during the dip coating. In addition, weak scattering effects of the HPC coating matrix have to be taken into account (see Fig. 1).

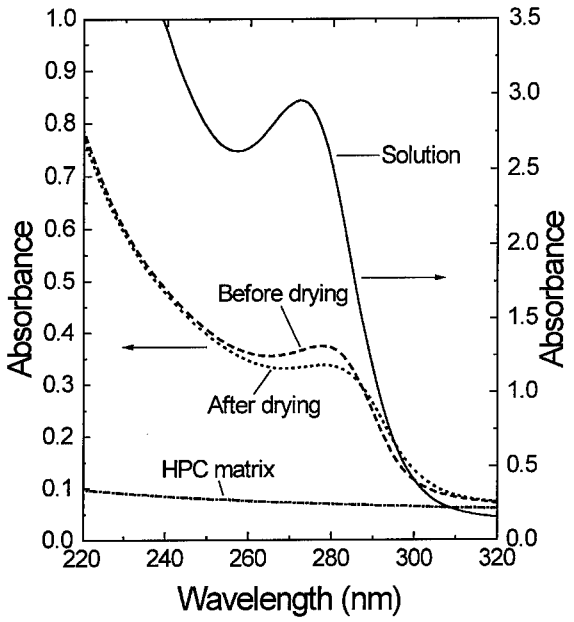

Figure 1. Absorption spectra of ZnS nanoparticles doped with 2 mol% Mn^{2+} with HPC as stabilizer in solution and corresponding coatings (thickness 0.5 μm) on fused silica glass before and after heating. For comparison, the spectrum of a pure HPC matrix coating is also shown.

In order to prepare Mn^{2+}-doped ZnS particles with maximum luminescence intensity emission spectra were measured for different Mn^{2+} concentrations with an excitation of 288 nm. All samples had an orange luminescence with a maximum at 590 nm which is characteristic for the $^4T_1 \rightarrow {}^6A_1$ transition of Mn^{2+} ions in a crystalline ZnS-matrix. The luminescence intensity showed a maximum at an Mn^{2+} concentration of 2% under the chosen experimental conditions. Therefore, this doping concentration was chosen for the further characterization and UV irradiation experiments. A further increase of the Mn^{2+} concentration leads to a decrease in the fluorescence intensity, which may be attributed to a concentration quenching of Mn^{2+} due to increasing crystal distortion [7], an enrichment of Mn^{2+} at the surface of the ZnS particles or the formation of separate MnS particles.

The ZnS particle sizes in the coatings were determined by SAXS and TEM. From the results of the SAXS measurements a mean diameter for the ZnS nanoparticles of 3.4 ± 1.0 nm was calculated. The TEM measurements showed that the particles are single crystalline and exhibit an average particle diameter of 3.0 ± 0.5 nm (determined from 90 individual particles) which is in good agreement with the SAXS results.

Next, the effect of UV irradiation on the spectroscopic properties of the coatings was investigated. The absorption spectra without and after 3 and 8 minutes of UV irradiation are depicted in Fig. 2(a). The corresponding luminescence spectra are shown in Fig. 2(b). After 8 minutes of UV irradiation the maximum of the absorption band is blue shifted from 278 nm to 273 nm. In addition, the absorption decreased from 0.32 to 0.24. The luminescence intensity is a factor of two larger after UV irradiation of 3 minutes and decreases again by 10% after 8 minutes of UV irradiation.

In addition, the time dependent emission behavior was also investigated by measuring the luminescence intensity at 590 nm as a function of time with an excitation at 300 nm and two different irradiation intensities

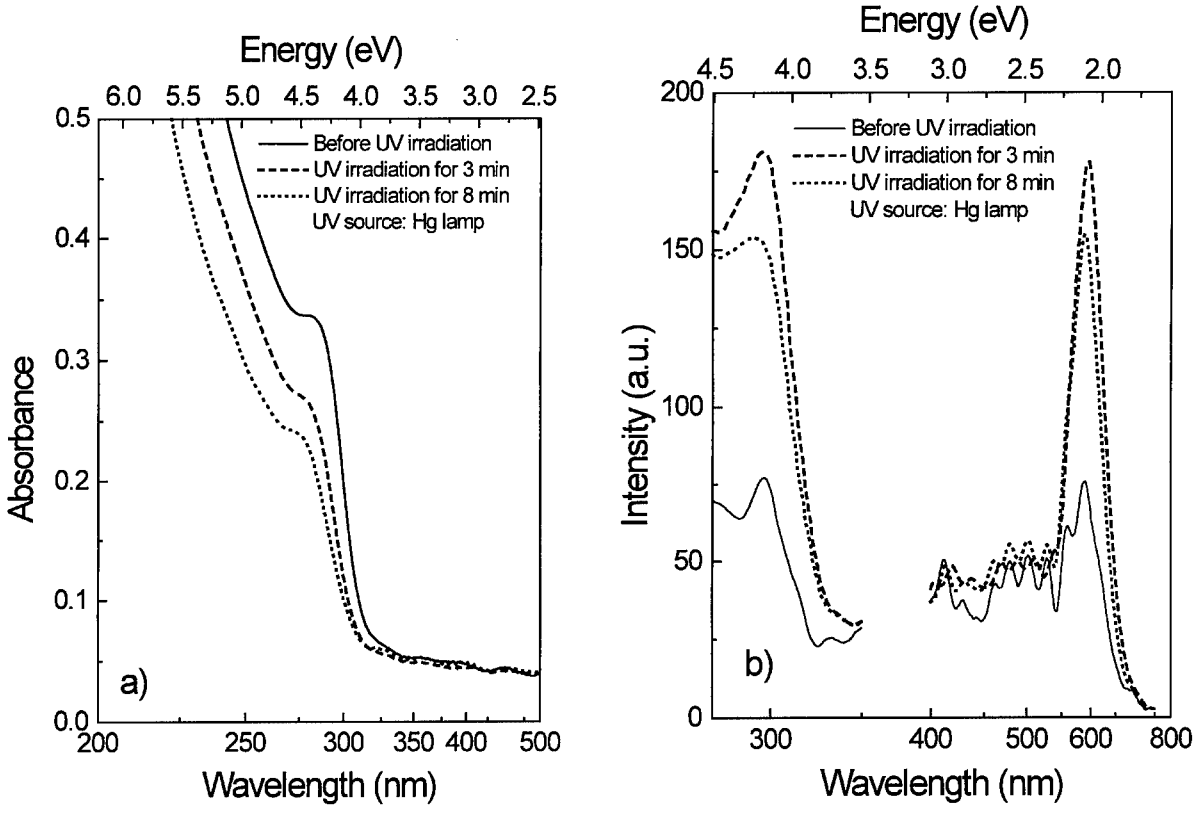

Figure 2. (a) Absorption spectra of a coating of 2 mol% Mn^{2+}-doped ZnS nanoparticles on fused silica glass slides (coating thickness 0.5 μm; dried at 120°C for 2 h in N_2 atmosphere) after different times of UV irradiation with a Hg lamp (14 W; 5 cm distance). (b) Luminescence and excitation spectra of the same sample after different UV-irradiation times (same conditions as under (a)).

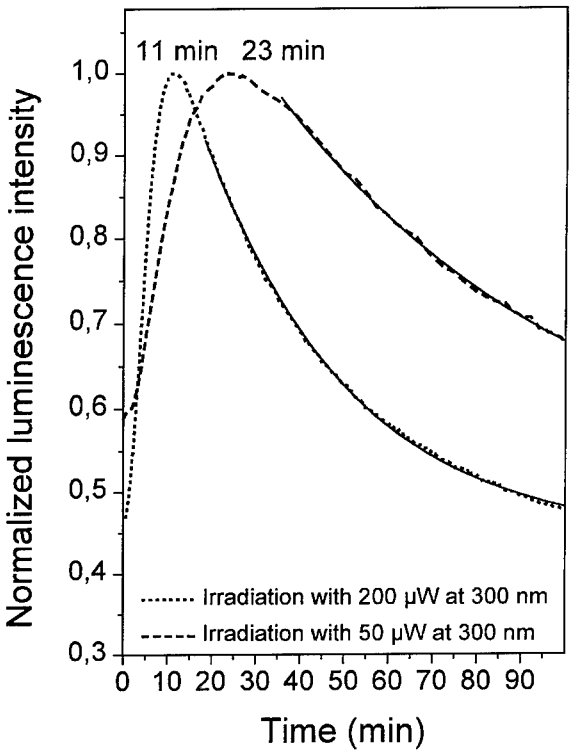

Figure 3. Luminescence intensity at 590 nm of Mn^{2+}-doped ZnS nanoparticles (Mn^{2+}-concentration: 2 mol%) on fused silica glass slides (coating thickness 0.5 μm; dried at 120°C for 2 h in N_2 atmosphere) on excitation at 300 nm as function of the irradiation time in the fluorescence spectrometer for two different irradiation powers. The decays in both curves were fitted by single exponential laws (solid lines).

as depicted in Fig. 3. For the lower UV-irradiation intensity the peak of the luminescence intensity is reached after 23 min; for the 4-fold irradiation intensity it is obtained after only 11 min. The difference in the initial values of both curves is attributed to large errors of measurements due to very low luminescence intensities in the non-irradiated state. In both cases the luminescence intensities strongly decrease for longer UV irradiation. The decay can be very well fitted by a single exponential law, as one can see from Fig 3.

As seen in Fig. 1, the HPC matrix does not absorb in the relevant UV range of the UV lamp used. Therefore, photochemical reactions of the coating matrix can be excluded in the interpretation of the spectra in Figs. 2 and 3. These spectra are therefore explained as follows. The changes of the absorption and luminescence spectra with UV-irradiation time are attributed to the UV induced degradation of the ZnS, which starts at the surface [4, 5]. The shift of the absorption maxima and the decrease of the absorbance with UV-irradiation time in Fig. 2(a) show that the ZnS nanoparticles become smaller and the total concentration of absorbing ZnS decreases. From investigation of the photochemistry of ZnS nanoparticles in solution, in the presence of oxygen, it is expected that $ZnSO_4$ is formed by this process [4, 5]. From Figs. 2(b) and 3 it is postulated that on oxidation of the surface of the ZnS-nanoparticles trap states, which are responsible for the nonradiative recombination of electron hole pairs, are removed. This can be detected by the luminescence via the Mn^{2+} center, because the possibility of relaxation of the electron-hole pairs via the Mn^{2+}-center is enhanced due to the better passivation of the surface, yielding an increasing emission intensity during the initial period of UV irradiation. It seems plausible that this process is faster for higher UV intensities and therefore the luminescence peak intensity is reached more quickly for the higher UV intensity (Fig. 3). It is assumed that by further irradiation Mn^{2+}-doped ZnS particles are successively oxidized and the concentration of Mn^{2+}-doped ZnS is lowered leading to the decrease in absorbance (Fig. 2(a)) and a strong decay of luminescence after long UV-irradiation times (Fig. 3).

4. Conclusion

From these results it is concluded that HPC is a suitable stabilizer for the preparation of monodispersed 3 nm sized Mn^{2+}-doped ZnS particles in alcoholic solutions and micrometer thick transparent coatings on glass. The intensity of luminescence via the Mn^{2+} center is a sensitive detector for surface passivation and degradation processes during UV irradiation. In the future, HR-TEM and XPS experiments will be performed in order to identify the photoreaction products of the ZnS nanoparticles.

References

1. L. Brus; Appl. Phys. **A53**, 465 (1991).
2. V.L. Colvin, M.C. Schlamp, and A.P. Alivisatos, Nature **370**, 354 (1994).
3. C.B. Murray, D.J. Norris, and G. Bawendi, J. Amer. Chem. Soc. **115**, 8706 (1993).
4. A. Henglein and M. Gutierrez, Ber. Bunsenges. Phys. Chem. **87**, 852 (1983).
5. H. Weller, U. Koch, M. Gutierrez, and A. Henglein, Ber.

Bunsenges. Phys. Chem. **88**, 649 (1984).
6. R.N. Bhargava, D. Gallagher, and T. Welker, J. Lumin. **60/61**, 275 (1994).
7. R.N. Bhargava, D. Gallagher, X. Hong, and A. Nurmikko, Phys. Rev. Lett. **72**, 416 (1994).
8. D. Gallagher, W.E. Heady, J.M. Racz and R.N. Bhargava, J. Cryst. Growth **138**, 970 (1994).
9. Y.L. Soo, Z.H. Ming, S.W. Huang, Y.H. Kao, R.N. Bhargava, and D. Gallager, Phys. Rev. **B 50**, 7602 (1994).
10. K. Sooklal, B.S. Cullum, S.M. Angel, and C.J. Murphy, J. Phys. Chem. **100**, 4551 (1996).
11. I. Yu, T. Isobe, and M. Senna, J. Phys. Chem. Solids **57**, 373 (1996).
12. A. Siggel, Riedel de Haen AG, private communication.
13. R. Bhargava, D. Gallager, and J. Racz; European Patent 0 622 439 A1; publication date 02.11.1994.
14. C. Jin, J. Yu, L. Sun, K. Dou, S. Hou, J. Zhao, Y. Chen, S. Huang, and J. Lumin. **66/67**, 315 (1996).
15. B. Kutsch, O. Lyon, M. Schmitt, M. Mennig, and H. Schmidt, J. Appl. Cryst. **30**, 948 (1997).
16. B. Kutsch, O. Lyon, M. Schmitt, M. Mennig, and H. Schmidt, J. Non-Cryst. Solids **217**, 143 (1997).

Journal of Sol-Gel Science and Technology 13, 691–694 (1998)
© 1998 Kluwer Academic Publishers. Manufactured in The Netherlands.

Preparation of the TiO_2 Thin Film Photocatalyst by the Dip-Coating Process

NOBUAKI NEGISHI, KOJI TAKEUCHI AND TAKASHI IBUSUKI
National Institute for Resources and Environment, 16-3 Onogawa, Tsukuba, Ibaraki 305, Japan

Abstract. Titanium dioxide (TiO_2) coated glass-plate thin film photocatalysts for elimination of air pollutants were prepared by the dip-coating process with titanium alkoxide including polyethylene glycol (PEG). The surface structure of these thin films changed drastically with the size of the PEG. They were either transparent or opaque. Nitrogen oxides (NO_x), one of the most hazardous of air pollutants, were found to be efficiently eliminated by the thin film photocatalyst. The photocatalytic activities of the transparent and opaque thin films were found to be almost equal. This may be due to the two films having the same surface area. The highest activity was obtained for thin films around 1 μm.

Keywords: elimination of air pollutant, thin film photocatalyst, TiO_2, dip-coating method

1. Introduction

Nitrogen oxides (NO_x), which are major air pollutants, can be effectively removed by photocatalytic oxidation using titanium dioxide [1]. Development of such a deNO_xifying photocatalyst is essential for the design of highly efficient photocatalytic environmental purification materials [2, 3]. The large surface area and high crystallinity of the thin film can be expected to lead to high photocatalytic activity. One strategy in increasing the surface area is to add polymer to the coating solution, since this leads to porosity after calcination [4–6]. The crystallinity can be controlled by using a ligand for the metal alkoxide [7, 8], and some kinds of polymer may work as the ligand. However, the effects of the polymer on dip-coated thin films are not well understood.

In this study, we have examined the effect of the polymer doping process on the surface structure as well as the photocatalytic activity of the thin films, and have thus developed an efficient photocatalyst for the deNO_x reaction.

2. Experimental

A starting solution for the dip-coating process was prepared by mixing tetrapropyl orthotitanate (TPOT), ethanol, 2-(2-ethoxyethoxy)ethanol (EEE) and poly-(ethylene)glycol (PEG) having an average molecular weight of 300, 600, 1000 and 1500. Approximately 700 ml of ethanol, 80 g of PEG and 80 ml of EEE were mixed together; 80 ml of TPOT was continuously added to the mixed solution at room temperature. Silica coated glass plates ($100 \times 100 \times 1$ mm) were dip-coated with the solution at <10% relative humidity. The withdrawing speed of the substrates was 1.5 mm/s. The dipping process was carried out five times, and calcined at 450°C for 1 h. This process was repeated to obtain a film of ca. 1 μm thickness. The thin film photocatalysts doped with PEG300, PEG600, PEG1000 and PEG1500 were designated as TiO_2-P300, TiO_2-P600, TiO_2-P1000 and TiO_2-P1500, respectively, and a film without doping as TiO_2-P0.

The transmittance spectra were recorded with a spectrophotometer. The surface structure of the thin films was observed by atomic force microscopy (AFM). The crystal structure of the TiO_2 coatings was identified by X-ray diffraction (XRD). The specific surface area was determined by the BET method. Differential Scanning Calorimeter (DSC) measurement was done in air with a heating rate of 7°C/min.

A flow type photoreactor was constructed to examine the photocatalytic activity of the films. The light intensity was about 0.38 mW/cm^2 ($\lambda = 365$ nm) at the photocatalyst surface. Dry air containing 1 ppm of NO was passed through the reactor at a rate of 1.5 l/min.

The NO_x concentration was monitored with a chemiluminescent NO_x analyzer, and the photocatalytic ability of the thin films was estimated by the amount of NO degradation achieved.

3. Result and Discussion

The thin films obtained were either transparent or opaque depending on the molecular weight of the doped polymer, the thin films doped with smaller sizes of polymer were transparent (TiO_2-P0, TiO_2-P300 and TiO_2-P600) while the PEG1000 and PEG1500 doped films were opaque. The transparency of these films did not decrease even when the number of dipping times was increased, and the transmittance of these films in the visible region was around 80%. These thin films generated an interference wave in the transmittance spectra, and the number of interference peaks increased with the dipping time. The increase in the number of interference peaks formed were closely related to the film thickness [9]. The film thickness obtained using this technique corresponded well with the scanning electron microscopy measurements.

The *d* values obtained from the main peaks of the thin films were 3.52, 2.38 and 1.89. These values correspond to the anatase phase of TiO_2. These results show that these thin films crystallized below 450°C. Nishide et al. [7] reported that the effect of the ligand for the titanium alkoxide depended strongly on the crystallization temperature of TiO_2. It is thought that EEE works in coordination with TPOT. In the case of TiO_2-P600, the exothermic peak associated with the baking of the organic compounds can be recognized from the DSC curves, as shown in Fig. 1. The EEE and PEG doped in the films were lost by calcination at the same time, since only a single exothermic peak could be detected. It might be that the TiO_2 thin film crystallized after the removal of the above organic compounds. A small exothermic peak was observed at around 430°C as shown in Fig. 1, and this small peak was found to be associated with the transformation of the amorphous phase to the anatase phase. An increase in the DSC curve at around 500°C may be attributed to the softening of the substrate (soda-lime glass). However, we could not observe the XRD pattern of the thin films under 430°C.

We observed quite different surface structures for the transparent and opaque films by AFM as is shown in Fig. 2. The surface of the transparent thin films appeared smooth, consisting of uniformly aggregated

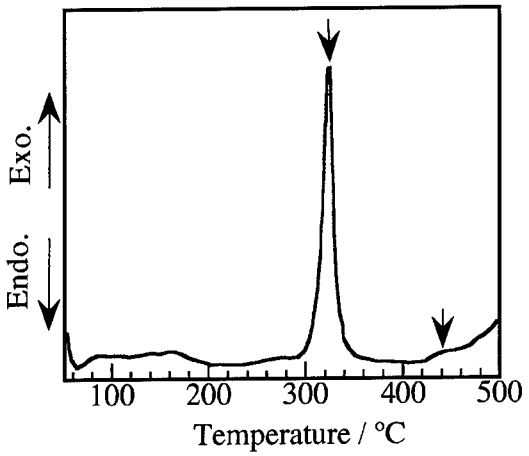

Figure 1. DSC curve of TiO_2-P600.

nanometer size TiO_2 single crystals, while the opaque thin films contained micron sized cubic TiO_2 crystals as can be seen in Fig. 2(A). With the transparent films, the fine structure did not change with an increase in the number of dipping times. The formation of the opaque thin films was completely different from that of the transparent films. After the first dipping, the film surface consisted of both the fine and large size TiO_2 particles. The number of large TiO_2 particle islands increased with the number of dipping cycles. Finally, the film surface was covered with the large TiO_2 crystals, as shown in Fig. 2(B). XRD showed that these large TiO_2 crystals were polycrystalline, while the fine TiO_2 crystals in the transparent film were single crystal.

This remarkable difference between the two samples can be explained by the hydrolysis rate of the titanium alkoxide. PEG becomes more hydrophobic with an increase in the molecular weight. During the withdrawing process of the thin films, the large molecular weight PEG (PEG1000 and PEG1500) rejects the adsorbed water. The water rapidly hydrolyzes TPOT, and the organic and inorganic phases are separated. Finally, the large TiO_2 particle islands are formed. On the other hand, the smaller molecular weight PEG (PEG600 and PEG300) is not strongly hydrophobic and the hydrolysis of TPOT was only mildly advanced after the withdrawing process. It is thought that this process is related to the spinodal phase separation [10]. However, the detailed mechanism behind the phase separation of the organic and inorganic components will be the subject of our future work.

Figure 3 shows the time dependence of the changes in NO concentration due to different film thicknesses

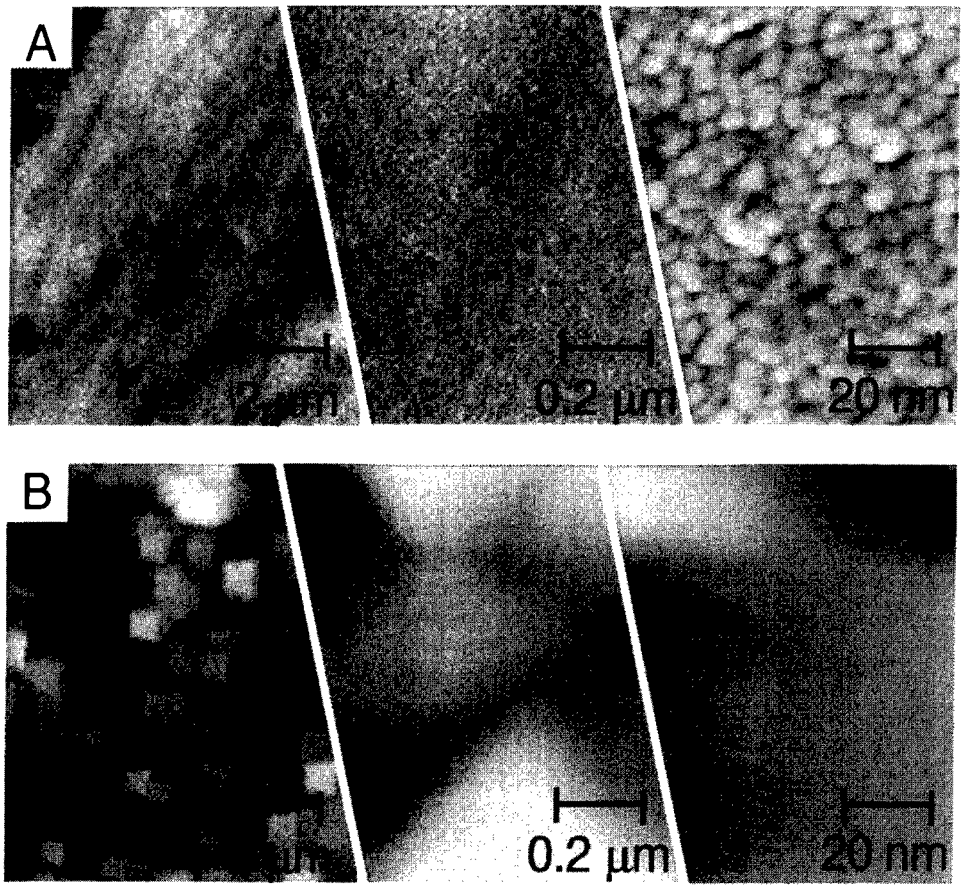

Figure 2. AFM image of the TiO_2-P600 (A) and TiO_2-P1000 (B).

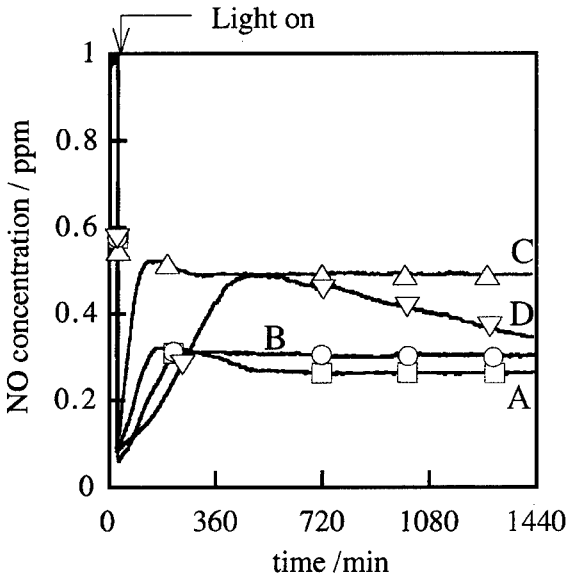

Figure 3. Time dependence of the changes in NO concentration due to the thin film photocatalyst. A(□): 1 μm, B(○): 0.5 μm, C(△): 0.25 μm and D(▽): P25 (60 mg).

of thin film photocatalyst. The film thicknesses of the photocatalyst for the oxidation of NO were 1, 0.5, and 0.25 μm. The photocatalytic activity of the thin films was markedly affected by the film thickness. As shown in Fig. 3, the greatest amount of NO was removed by the 1 μm thin film. The photocatalytic ability of the 1 μm thin film is higher than P25 of the same weight (ca. 60 mg) and illuminated area (100 cm^2). These results show that the photocatalytic activity of the thin films is closely related to the surface area of the photocatalyst. The amount of NO_2 formed by the 1 μm of thin film was lower than that formed with the other thin films. It is thought that most of the NO_2 was further oxidized to HNO_3 in the case of thick films, leading to the design of a desirable deNO_x photocatalyst since NO_2 is also an air pollutant.

On the other hand, we could not observe large differences in the photocatalytic activity of the transparent and opaque films. Therefore, measurements of the BET surface area of these thin film photocatalysts were carried out. The specific surface area of TiO_2-0, TiO_2-300,

TiO_2-600, TiO_2-1000 and TiO_2-1500 were 112, 104, 118, 140 and 93 m^2/g, respectively. It is thought that the small difference in photocatalytic activity between transparent and opaque films was related to the specific surface areas. However, these values were smaller than the differences anticipated from the differences in the surface structure of these films. This leads to the idea that the surface area of the opaque film can be attributed to the complex structure in the micrometer scale region, while the transparent thin films consist of many nanometer crystals and many pores, giving the large surface area.

References

1. T. Ibusuki and K. Takeuchi, J. Mol. Catal. **88**, 93 (1994).
2. M. Anpo, T. Nomura, T. Kitao, E. Giamello, D. Murphy, M. Che, and M.A. Fox, Res. Chem. Intermed. **15**, 225 (1991).
3. N. Negishi, M. Matsuoka, H. Yamashita, and M. Anpo, J. Phys. Chem. **97**, 5211 (1993).
4. N. Negishi, K. Takeuchi, and T. Ibusuki, Appl. Surf. Sci., **121**, 417 (1997).
5. N. Negishi, T. Iyoda, K. Hashimoto, and A. Fujishima, Chem. Lett. 841 (1995).
6. K. Kato, A. Tsuzuki, Y. Torii, H. Taoda, T. Kato, and Y. Butsugan, J. Mat. Sci. **30**, 837 (1995).
7. T. Nishide and F. Mizukami, J. Ceram. Soc. Jpn. **100**, 1122 (1992).
8. T. Nishide and F. Mizukami, J. Mat. Sci. Lett. **15**, 1149 (1996).
9. Y. Takahashi and Y. Matsuoka, J. Mat. Sci. **23**, 2259 (1988).
10. K. Nakanishi and N. Sogal, Bull. Chem. Soc. Jpn. **70**, 587 (1997).

Journal of Sol-Gel Science and Technology 13, 695–699 (1998)
© 1998 Kluwer Academic Publishers. Manufactured in The Netherlands.

Glass Strengthening Using Ormosil Polymeric Coatings

R.J. HAND, F.H. WANG, B. ELLIS AND A.B. SEDDON
Centre for Glass Research, Department of Engineering Materials, University of Sheffield, Sir Robert Hadfield Building, Mappin Street, Sheffield, S1 3JD, UK

Abstract. Ormosil polymeric coatings comprised of an epoxy resin, an amine hardener and a silane have been applied to glass samples containing large, controlled defects introduced by Vicker's indentation. The coatings can completely overcome these controlled defects. The strengthening effect is due to penetration of the defects by the coatings. Therefore, the reactions between the components of these hybrid materials and the glass substrate are of crucial importance in determining both the degree of strengthening that is achieved and the hydrolytic durability of the coatings. The maximum strengthening effect of these ormosil polymeric coatings is obtained when 25% of the active hydrogen is supplied by the silane (7.2 wt% silane). More than 7.2 wt% silane reduces coating cohesion and thus gives a reduced strengthening effect. Studies on silane primed systems show that both good coating adhesion and cohesion are required for significant strengthening. Coatings with good adhesion also have greater hydrolytic durability.

Keywords: coatings, strengthening, glass, hybrids

Introduction

The ubiquitous presence of surface flaws limits the strength of glass articles. No method exists for completely overcoming these flaws. However, coatings can, to some extent, counteract flaws in glass surfaces and thereby increase the strength of glass artifacts [1–3]. We have developed a series of hybrid ormosil polymeric coatings which may be used to strengthen glass [4, 5]. The coatings are synthesized from epoxy resin, amine hardener and silane mixtures (E/H/S coatings). We have previously shown that these coatings strengthen glass by penetrating pre-existing defects [6]; this paper discusses the effects that coating parameters have on the degree of strengthening achieved.

Experimental

The hybrid ormosil polymeric coatings are comprised of mixtures of MY753, a plasticized bisphenol A epoxy resin, HY951 amine hardener (triethylenetetramine—TETA) and aminoethylaminopropyltrimethoxysilane (Z6020). In addition to investigating the ormosil polymeric (E/H/S) coatings some work has been conducted on MY753/HY951 coatings applied to glass primed with Z6020 silane (S_p/E/H coatings).

The coatings were applied to commercial soda-lime glass slides with polished edges. Ten kg Vicker's indents were used to produce reproducible strength limiting flaws on the glass slides. Following indentation the samples were aged in air for 24 hours. This process resulted in large semi-elliptical cracks with a surface length, $2c$, of $950 \pm 14\,\mu$m and a depth, a, of $285 \pm 10\,\mu$m; failure normally occurred from the controlled damage rather than the edge of the microscope slide (for more details see [6]).

Both the hardener and silane can react chemically with the epoxy group (see below). Therefore, the relative amounts of hardener and the silane will affect the detailed structure of this network and thus the resulting properties of the coating. Five coating compositions were examined; the ratio of total active hydrogen from both the hardener and the silane to epoxy was maintained at stoichiometric for all of the coatings (see Table 1 for details). All of the coatings were prepared by mixing appropriate amounts of epoxy and hardener

Table 1. E/H/S coating compositions.

Composition	Percentage of active hydrogen from Z6020	Wt% of Z6020 (excluding solvent)	Wt% of HY951 (excluding solvent)
a	0	0.00	9.50
b	10	2.98	8.35
c	25	7.23	6.71
d	50	13.60	4.23
e	100	24.60	0.00

for 1.5 hours at $25 \pm 2°C$ followed by addition of the silane. The resultant mixture was diluted with acetone. To hydrolyze the silane half the stoichiometric amount of water was then added. The resulting solution was stirred for 4 hours. The coating was applied to the glass by dipping. The coated samples were cured at room temperature for 24 hours followed by a post cure at 100°C for 1 hour. Bulk samples ($40 \times 29 \times 2$ mm) were also cast from the above mixtures for dynamic mechanical thermal analysis (DMTA). DMTA measurements were conducted at a strain rate of 1% and a frequency of 1 Hz with a heating of rate of $5°C\,min^{-1}$ on a Polymer Laboratory Mark 2 DMTA. Glass transition temperatures were determined from the variation of glassy modulus with temperature using the intercept method [9].

Some silane primed samples were also prepared. In this case the glass samples were dipped into a 1 wt% Z6020 aqueous solution which had been mixed at room temperature for 0.5 hours. After dipping and before coating the samples were either (i) dried (S_p/E/H coatings); or (ii) immersed in distilled water at room temperature for 1 hour and then dried (S_p/W_{RT}/E/H coatings); or (iii) given treatment (ii) followed by immersion in distilled water at 60°C for 1 hour and drying (S_p/W_{60}/E/H coatings). In all cases drying was carried out at 120°C for 0.5 hours.

The failure stresses of coated and uncoated control samples were measured in 4 point bending using a Mayes SM200 universal testing machine. To assess the hydrolytic durability of the coatings coated samples were tested after an accelerated ageing treatment of 96% r.h. at 50°C for 7 days.

Results and Discussion

Figure 1 shows the variation of strength of the E/H/S coated samples with the concentration of the silane. Independent of the amount of silane, all coatings lead to significant increases in strength of coated samples compared to uncoated samples. Maximum strength was observed at 7.23 wt% silane (composition c) which is equivalent to 25% of the active hydrogen being supplied by the silane. As the amount of silane is further increased the strength sharply decreases. This reflects changes in the network structure at higher silane concentrations that also lead to reductions of both the glassy modulus and the glass transition temperature of the coatings, as obtained from DMTA (see Fig. 2).

Both an epoxy network and a siloxane network are formed during the curing process. The amine hardener has active hydrogen atoms which react with epoxy groups to form secondary amines:

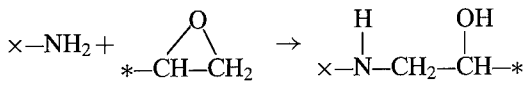

These in turn react with an epoxy group to form a tertiary amine [7]:

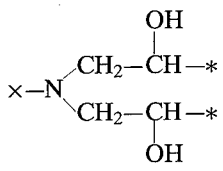

The rate of this latter reaction is slower than that of the primary amines. As well as the two primary amines there are, of course, two secondary amine hydrogens initially present on TETA and these again react more slowly than the primary amines. The silane Z6020 has initially one primary and one secondary amine group which also react with the epoxy groups. In addition, the silane forms a siloxane network through hydrolysis

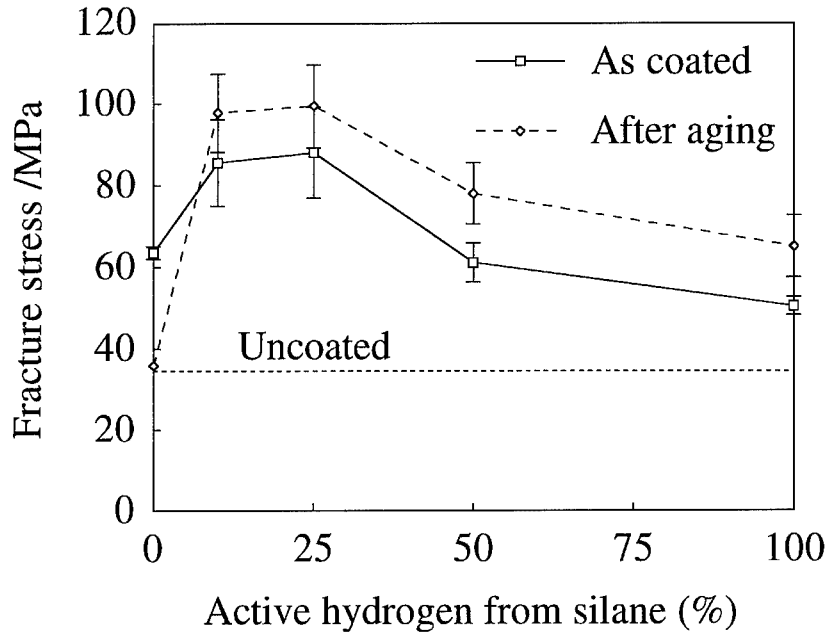

Figure 1. Fracture stress of E/H/S coated samples as a function of active hydrogen supplied by silane before and after ageing at 50°C/ 96% r.h. for 7 days.

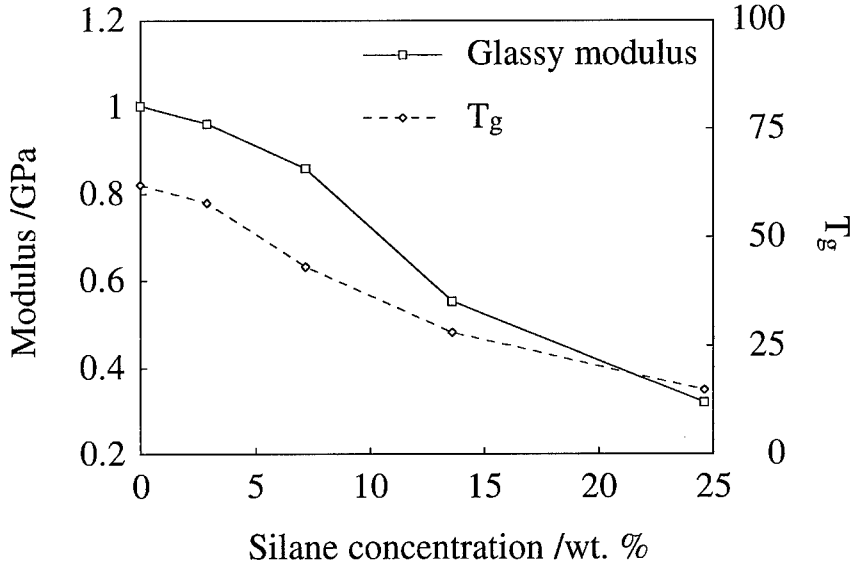

Figure 2. Glassy modulus and T_g as a function of silane concentration in E/H/S coatings.

of the methoxy groups on the silane followed by condensation of the silanol groups to form siloxane bonds. Thus, a covalently bonded interpenetrating network is formed because the silane participates in the formation of both the epoxy and siloxane networks [8]. The relative rates of formation of the epoxy and siloxane networks are significantly different with formation of the epoxy network being essentially complete after the standard curing treatment, although further changes can occur after a prolonged cure [6], whereas the siloxane network forms more slowly.

In fact the siloxane network continues to form with ageing and this can be seen in Fig. 1 where the effect of the accelerated ageing treatment on the strength of

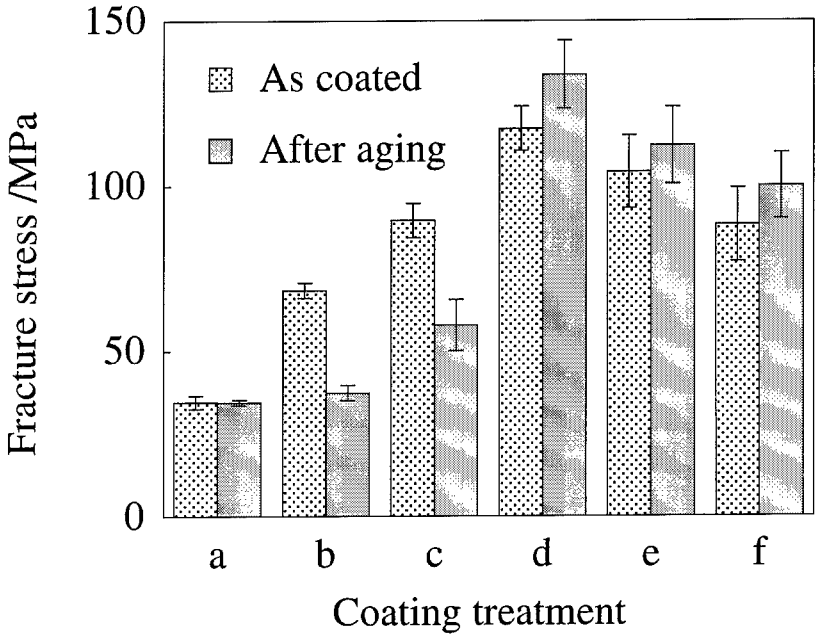

Figure 3. Fracture stress of various silane primed coatings systems before and after ageing at 50°C/96% r.h. for 7 days. (a) Uncoated, (b) E/H coating, (c) S_p/E/H coating, (d) W_{RT}/E/H coating, (e) W_{60}/E/H coating, and (f) E/H/S coating with 7.23 wt% silane.

E/H/S coated samples is also shown. The measured strengths increased following the accelerated ageing treatment except when the silane content was zero. The siloxane network is modified by the ageing treatment because only half of the stoichiometric ratio of water was used and therefore the hydrolysis of the methoxy groups may not be completed. Hence, during ageing under humid conditions hydrolysis of the remaining methoxy groups can take place. This hydrolysis may then be followed by condensation of the resulting silanol groups. The condensation reaction can, in theory, occur either between adjacent silane molecules in the coating or between the silane and the glass surface. The latter reaction is apparently limited because some debonding of the coating is seen during the ageing treatment. The former reaction increases the number of linkages within the siloxane network thereby leading to a tighter siloxane network structure. Studies of the locus of failure of these samples show larger regions of cohesive failure compared to the locus of failure seen on unaged samples [10], and thus it is thought that the tighter siloxane network produces a coating with improved cohesion.

The importance of both coating cohesion and coating adhesion in determining the overall strengthening is further demonstrated by the behavior of silane primed systems. Figure 3 shows the degree of strengthening achieved with silane primed systems. The maximum degree of strengthening was obtained with the S_p/W_{RT}/E/H coatings. Currently accepted models for a silane on glass state that there is a physisorbed silane layer overlaying a chemisorbed silane layer which in turn overlays a silane monolayer bonded to the glass surface [11, 12]. According to these models the room temperature water treatment (S_p/W_{RT}/E/H) removes the physisorbed layer of silane primer whereas the treatment at 60°C (S_p/W_{60}/E/H) also removes the chemisorbed layer. The chemisorbed layer is necessary to achieve good adhesion of the coating to the substrate and therefore to avoid adhesive failure during loading. However, the physisorbed layer has low cohesion, and if this layer has not been removed (S_p/E/H coatings) the coatings tend to fail cohesively at lower applied stresses.

We have previously demonstrated that good coating adhesion is required to achieve a strength increase with simple E/H coatings [5]. The current studies indicate that coating cohesion is also important. Silane is required to improve the adhesion of the coating to the glass and can be included either as part of a hybrid

coating or as a primer; both E/H/S and S_p/E/H give significantly greater increases in strength than simple E/H coatings (see Figs. 1 and 3). Although the primer route gives greater increases in strength, the hybrid approach will have greater commercial application as it involves less processing. Both the E/H/S and S_p/E/H coatings studied strengthen glass. However, if *excess* silane is present then the coating cohesion is relatively low and this reduces the strengthening effects that may be achieved with these coatings.

Conclusions

Studies on silane primed coatings (S_p/E/H) show that greater coating adhesion gives greater increases in strength. The maximum strengthening effect with the ormosil polymeric hybrid (E/H/S) coatings is obtained when 25% of the active hydrogen is supplied by the silane. Although more active hydrogen from the silane might lead to improved adhesion of the coating to the substrate it also creates a looser network which has a lower cohesive strength that more than offsets any improvements in adhesion. Therefore, the degree of strengthening obtainable from the hybrid ormosil polymeric coatings is dependent on both the cohesive strength of the coating and the adhesion of the coating to the glass.

Acknowledgments

This work was carried out while FHW was in receipt of a Research Scholarship from the University of Sheffield.

References

1. B.D. Fabes and G.D. Berry, J. Non-Cryst. Solids **121**, 357 (1990).
2. P.F. James, M. Chen, and F.R. Jones, J. Non-Cryst. Solids **155**, 99 (1993).
3. J.E. Ritter and M.R. Lin, Glass Technol. **32**, 51 (1991).
4. F.H. Wang, X.M. Chen, R.J. Hand, B. Ellis, and A.B. Seddon, Br. Ceram. Proc. **54**, 119 (1995).
5. F.H. Wang, X.M. Chen, B. Ellis, R.J. Hand, and A.B. Seddon, Mat. Sci. Tech. **13**, 163 (1997).
6. F.H. Wang, R.J. Hand, B. Ellis, and A.B. Seddon, Phys. Chem. Glasses **36**, 201 (1995).
7. B. Ellis, in *Chemistry and Technology of Epoxy Resins*, edited by B. Ellis (Blackie Academic and Professional, London, 1993), pp. 72–116.
8. X.M. Chen, B. Ellis, F.H. Wang, and A.B. Seddon, J. Non-Cryst. Solids **185**, 1 (1995).
9. B. Ellis, M.S. Found, and J.R. Bell, J. Appl. Polym. Sci. **59**, 1493 (1996).
10. F.H. Wang, Ph.D. Thesis, University of Sheffield, 1997.
11. H. Ishida and J.L. Koenig, J. Polym. Sci. Polym. Phys. Ed. **17**, 1807 (1979).
12. D. Wang and F.R. Jones, J. Mater. Sci. **28**, 2481 (1993).

Journal of Sol-Gel Science and Technology 13, 701–705 (1998)
© 1998 Kluwer Academic Publishers. Manufactured in The Netherlands.

Sol-Gel Preparation of Coating Films Containing Noble Metal Colloids

SUMIO SAKKA
Fukui Universitu of Technology, Gakuen, Fukui, 910, Japan

HIROMITSU KOZUKA
Institute for Chemical Research, Kyoto University, Uji, Kyoto-Fu, 611, Japan

Abstract. Coating films containing Au, Ag, Pt and Pd metal colloids have been prepared by sol-gel processing. It is shown that for oxide films the temperature where the metal particles are precipitated by heating in air depends on metal species: 200°C for Au, 600°C for Ag, 800°C for Pt and 1000°C for Pd. The use of reducing atmosphere lowers the temperature for formation of noble metal colloids. This procedure can be used for direct formation of metal colloids from metal ions in the film as well as reduction of oxide particles to metal particles in the film. For an organic-inorganic matrix, noble metal colloids are precipitated by thermal reduction or photo-reduction. Thermal reduction occurs as a result of reduction by decomposing organic matter. Photo-reduction occurs as a result of UV irradiation.

Keywords: coating films, noble metal colloids, photo-reduction, sol-gel preparation

1. Introduction

Coating films containing fine metal particles are attracting much attention because of their third-order nonlinear optical effects [1], optical absorption and reflective properties [2], photo-sensitization [3] and catalysis [4] etc. Sol-gel processing is suitable for preparing coating films containing dispersed fine metal particles. This method gives coating films of gel glass with much greater metal particle contents than glasses prepared by melt-quenching.

This paper reviews the present state of work on preparation of coating films containing noble metal particles: Au, Ag, Pt and Pd. Matrices for dispersing metals include oxides, such as SiO_2, TiO_2, AlOOH and organic-inorganic hybrids.

2. General Procedures for Preparing Coating Films Containing Noble Metal Colloids

Preparation of coating films containing fine noble metal particles commences with a starting solution, similar to those used in preparing coating films, with the addition of a metal particle source material. Acidic solutions are employed. The metal particle source is dissolved as ions in the starting solutions and possibly in the gel film. Formation of metal particles from metal ions is realized by one of the following treatments.

(1) Reduction of metal ions by heating the gel in air.
(2) Reduction of metal ions by exposing the gel to UV light.
(3) Reduction of precipitated metal oxide particles by heating in a reducing gas.

3. Coating Films Containing Gold Colloids

Figure 1 shows procedures for the preparation of coating films that contain fine particles of gold, silver, platinum and palladium. Matsuoka et al. [5] showed that silica coating films that contain dispersed fine gold particles, of about 4 nm in size, are obtained from a coating solution containing 1 mol% Au by procedure similar to that shown in Fig. 1(a). Fine Au particles

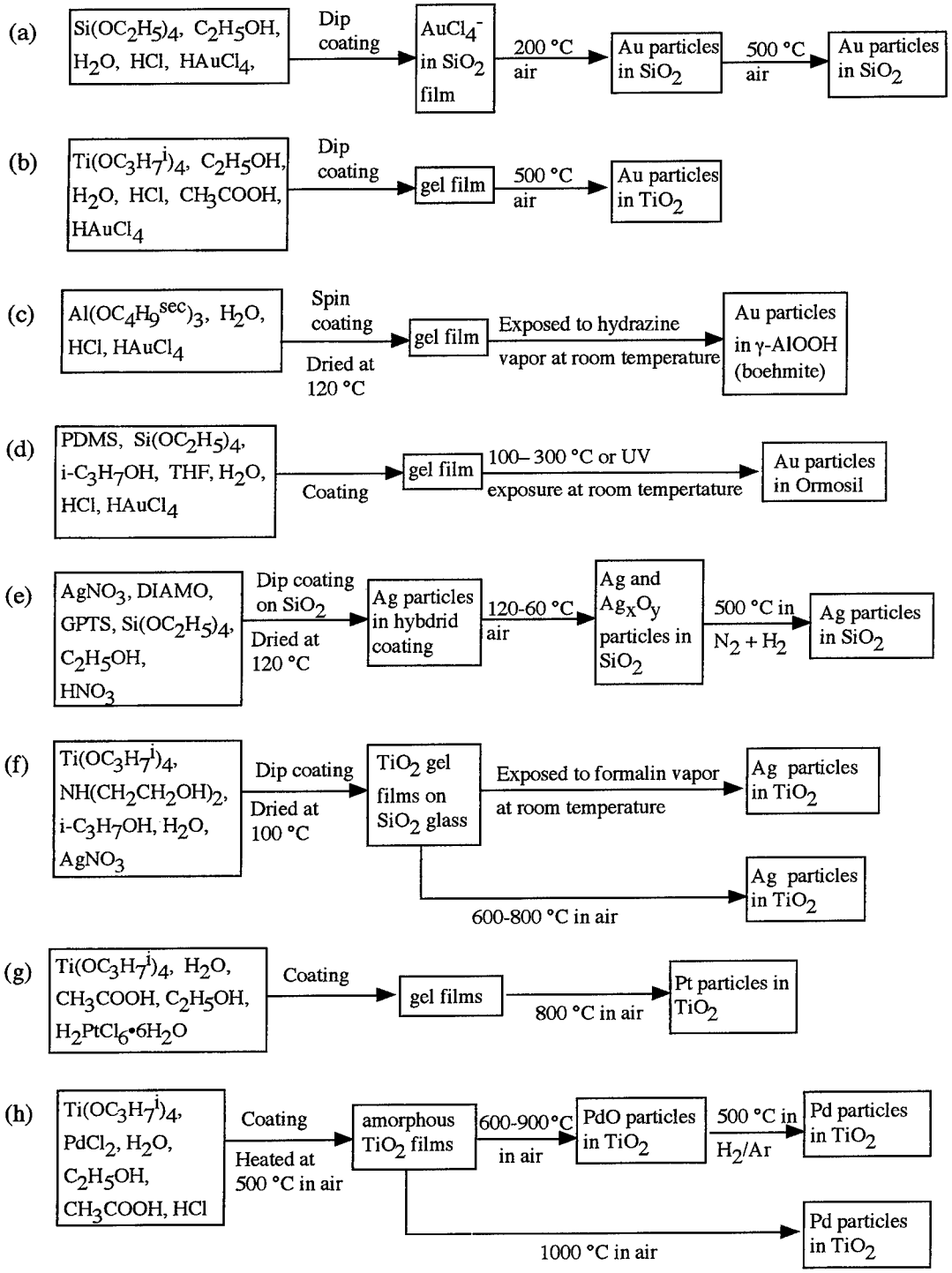

Figure 1. Preparation procedures for coating films containing fine particles of metals: gold, silver, platinum and palladium.

are precipitated when the film is heated at 300–400°C in air. No special procedure for reducing Au^{3+} ions proved necessary. Kozuka et al. [6] obtained silica films that contained dispersed fine Au particles by the procedure shown in Fig. 1(a). The Au content was 2.8 mol% (1 vol%). In as-coated films gold is present as $AuCl_4^-$ ions. After heating at 200°C in air, Au particles are precipitated. They are stabilized when the film is heated to 500°C in air. It is found that some gold particles are present on the surface of the film and are easily removed with tissue paper. This escape of gold species out of the coating film might be caused by syneresis during gelation. The escape of gold is minimized when as-prepared coating films are exposed to monoethanolamine vapor before heating. It is assumed that the amine treatment promotes formation of gel networks.

Partial substitution of $CH_3Si(OC_2H_5)_3$ (MTES) for $Si(OC_2H_5)_4$ (TEOS) in the solution for the silica film containing 4 mol% Au results in the reduction of the average size of Au particles [7]. The shape of particles is round at higher MTES contents and elongated at lower MTES contents. In addition, larger coating thicknesses, (up to 0.5–0.7 μm in one coating step) can be obtained without cracks.

Kozuka et al. [8] employed TiO_2 as matrix for dispersing fine Au particles, as shown in Fig. 1(b). 15 mol% of Au was included. Heating of the coating film at 500°C in air produced spherical gold particles of 20–30 nm size. The crystalline phase of TiO_2 is anatase. The optical absorption peak due to the surface plasma resonance of gold particles in this film is located at around 640 nm, which is about 100 nm longer than that of the Au/SiO_2 system (ca. 540 nm).

Gold particles of 6–20 nm size were precipitated in boehmite gels of the composition AlOOH [9] (Fig. 1(c)). A coating sol was obtained by adding $HAuCl_4$ to a pseudoboehmite sol prepared from $Al(OC_4H_9^{sec})_3$-H_2O-HCl solution of which Au content was 2.5 mol%. A gel film was deposited on a slide glass by spin coating at 3400 rpm, dried at 120°C and placed over a hydrazine in ethanol solution. Very thin coating films 20–25 nm thick were obtained. TEM shows that fine elongated gold particles of aspect ratios from 2 to 4 are aligned along the fibrous texture of boehmite matrix. It is assumed that reduction of Au^{3+} ions by hydrazine causes precipitation of gold particles at room temperature and that the fibrous texture of boehmite matrix causes alignment of elongated gold particles. When the gel film is exposed to hydrazine vapor without drying, spherical gold particles less than 20 nm in size are seen. The surface plasma resonance absorption is found at 660 nm for elongated particles and 600 nm for spherical gold particles of similar size, respectively.

Spanhel et al. [10] used coating solutions consisting of $HAuCl_4$, $NH_2[(CH_2)_2NH](CH_2)_3Si(OC_2H_5)_3$ (diamine silane), prehydrated methacryloxy-propyltrimethoxysilane and H_2O in which the Au/Si mol ratio was 0.05. Coating films on commercial glass substrates were exposed to UV radiation from a high pressure Hg-Xe lamp at 60°C. This treatment achieved both growth of the photo-induced gold metal particles and thermal curing of the film, that is, hybrid network formation, simultaneously. The resulting coating film had an absorption peak due to surface plasma resonance at about 550 nm. Crack-free thick films up to 8 μm thick were obtained in one-step coating. Spanhel et al. state that in this procedure diamine silanes act as ligands of gold particles, thereby preventing undesirable gold particle growth and at the same time modifying the optical properties of gold particles. If $NH_2[(CH_2)_2NH]_2(CH_2)_3Si(OC_2H_5)_3$ (triamine) was used as the gold colloid-stabilizing agent in place of diamine, photo-irradiation was not required. Reduction of Au^{3+} is caused by organic materials and fine gold metal particles are spontaneously precipitated.

Tseng et al. [11] employed polydimethylsilane to prepare inorganic-organic hybrid coating films containing fine gold particles. A solution silanol-terminated polydimethylsiloxane (PDMS), $Si(OC_2H_5)_4$, i-C_3H_7OH, tetrahydrofuran (THF), H_2O and HCl was refluxed at 80°C for 2 h and $HAuCl_4$ solution was added, in order to obtain a coating solution. 5 wt% gold was included in the Ormosil. As shown in Fig. 1(d), fine gold particles were precipitated in the film heated at 100–300°C or irradiated with UV. Gold particles of 2.5 nm in size were formed by heating the film at 200°C. UV exposure also gives fine gold particles.

Organic-inorganic hybrid materials (ormosils) have the following advantages over oxide matrices.

(1) Easy formation of films.
(2) Crack-free thick coatings possible.
(3) Transparency.
(4) High water durability.

It should be remembered that in general, photostability and thermal resistance are higher for oxides than organic-inorganic hybrids.

4. Coating Films Containing Silver Colloids

Mennig et al. [12] prepared coating films containing Ag colloids from solutions of $AgNO_3$, *N*-(2-aminoethyl)-3-aminopropyltrimethoxysilane (DIAMO), prehydrolyzed 3-glycidoxypropyltriethoxysilane (GPTS), tetraethoxysilane (TEOS), C_2H_5OH and HNO_3. The Ag content was 6.2 mol%. Films deposited on fused silica by dip coating and dried at 120°C were yellow colored due to presence of Ag colloids, as shown in Fig. 1(e). Formation of Ag colloids was attributed to reduction of Ag^+ ions by organic materials in the coating films. DIAMO in the coating solution acts as a stabilizing agent for Ag particles. When coating films are heated at 120–600°C in air for decomposition of organic materials and densification of the film, some of the Ag colloids were oxidized to Ag_xO_y. Heating of this film at 500°C reduced silver oxide particles to Ag metal colloids of 8 nm average size. When a soda-lime-silica glass substrate was used, heating of the coating films at 400–600°C oxidized all the Ag colloids to Ag_xO_y. Heating of these films at 500°C in 90% N_2-10% H_2 atmosphere reduced Ag_xO_y to Ag colloids, producing an Ag colloid-containing film similar to that applied to the SiO_2 substrate.

The effect of heating temperature on the color intensity due to silver colloids at 410 nm has been studied with silica sol-gel glass doped with 0.05 mol% silver [13]. This glass was prepared by gelling $Si(OC_2H_5)_4$-$AgNO_3$-C_2H5OH-HNO_3 solution at 60°C and then densifying the film at 600°C. When a darkened sample is heated above 400°C, reversible bleaching took place. This darkening-bleaching was attributed to aggregation-disaggregation of fine silver particles by Ritzer et al. [13]. Another explanation for this phenomenon is that Ag particles may be oxidized to Ag_xO_y above 400°C (but below 600°C), and reduced to Ag particles at 600°C. It is known that at high temperatures metal oxides are reduced to metals.

Kozuka et al. [14] prepared TiO_2 coating films containing fine Ag particles by sol-gel processing using a $Ti(OC_3H_7^i)_4$-$NH(CH_2CH_2OH)_2$-*i*-C_3H_7OH-H_2O-$AgNO_3$ solution (Fig. 1(f)). The Ag content was 6.2 mol%. Exposure of a gel film to formalin vapor at room temperature caused reduction of Ag^+ ions, forming Ag particles of 4–23 nm in size in the gel film. The gel film showed a sharp absorption peak at 441 nm due to surface plasma resonance of Ag metal particles. Heat treatment of the gel films at 600–800°C in air resulted in formation of anatase or rutile polycrystalline films containing Ag particles 5–45 nm in size (5–25 nm for 600°C and 13–45 nm for 800°C). These films had an absorption peak due to surface plasma resonance around 550 nm. The shift of the surface plasma resonance absorption of Ag particles from 441 nm for the coating film exposed to formalin vapor at room temperature to 550 nm for that heated at 600–800°C may be attributed to an increase in dielectric constant of the oxide matrix caused by its thermal densification and crystallization.

5. Coating Films Containing Platinum Colloids

Kozuka et al. [8] prepared TiO_2 coating films containing Pt colloid particles (7 mol% Pt) on silica substrate by the sol-gel processing. $Ti(OC_3H_7^i)_4$-H_2O-CH_3COOH-C_2H_5OH-$H_2PtCl_6 \cdot 6H_2O$ solutions were used to produce coating films. As shown in Fig. 1(g), platinum fine particles were precipitated by heating at 800°C in air. The films show a broad absorption ranging from 380 nm to 800 nm.

Silica based ormosil coating films containing Pt colloids were prepared by Tseng et al. [11]. Pt^{4+} ion-doped gel films were prepared from coating solutions consisting of silanol terminated polydimethylsilane, H_2O, HCl and $H_2PtCl_6 \cdot 6H_2O$. Thermal reduction by heating at 200°C and photoreduction by exposure to a high pressure mercury lamp reduced the Pt^{4+} ions, producing hybrid coating films containing Pt colloids of 3–5 nm in size. The color of the film was light brown.

6. Coating Films Containing Pd Colloids

Zhao et al. [15] prepared coating solutions from titanium isopropoxide, palladium(II) chloride, deionized water, ethanol, acetic acid and hydrochloric acid, to produce TiO_2 coating films containing 3 vol% Pd (7 mol% Pd). A transparent red-brown solution resulted. Heating TiO_2 coating films at 600–900°C in air produced PdO particles in the film (Fig. 1(h)). Reduction of this film by heating at 500°C in an H_2/Ar atmosphere gave films containing dispersed metal particles. The average diameter of Pd is 15–30 nm. The films containing Pd particles are brownish grey, showing optical absorption due to surface plasma resonance. As shown in Fig. 2, PdO particles grow with time at 800°C in air. Crystallite size of Pd metal particles as a function of heating time at 500°C in H_2/Ar atmosphere shows an increase similar to that of PdO

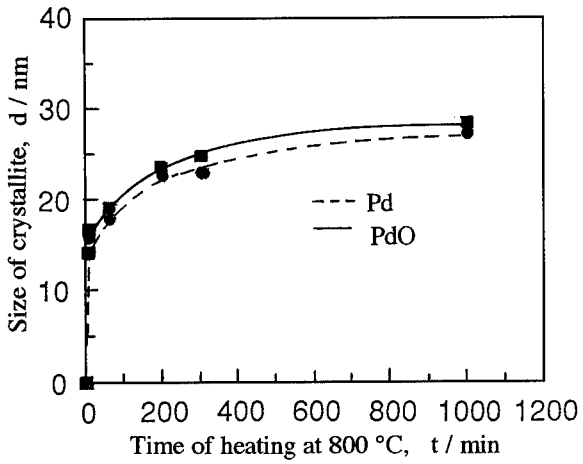

Figure 2. Crystallite size of PdO and Pd particles as a function of time of heat treatment at 800°C in air. The PdO particles were reduced to Pd particles by subsequent heat treatment at 500°C in H_2/Ar atmosphere [15].

particles, indicating that Pd particles are formed as a result of reduction of PdO particles. This indicates that particle size is controlled by selecting the heating time at 800°C. It should be noted that Pd metal particles are precipitated when TiO_2 coating films are heated at 1000°C in air.

7. Summary and Concluding Remarks

It was shown that sol-gel preparation of coating films containing noble metal colloids is based on reduction of metal ions in the films. The simplest way of reducing metal ions is to heat the films at high temperatures in air. It is known that redox equilibrium tends to move to reduction side as the temperature rises. The temperature of heating necessary for forming metal colloids in air is, approximately, 200°C for Au, 600°C for Ag, 800°C for Pt and 1000°C for Pd. When the appropriate organic compounds are present, the reduction of metal ions occurs at low temperatures, for example, room temperature. It was also shown that UV irradiation promotes reduction of metal ions to form colloidal particles. Alternatively, metal oxide particles can be precipitated by heating in air and then reduced to metal particles by heating the film in a reducing gas at lower temperatures. This method can be applied to metals other than gold.

Preparation conditions for the coating films, such as composition of starting solution, time and temperature of UV exposure, if any, and time of various heat treatments affect the size and the size distribution of precipitated noble metal particles, which in turn affect the optical and other properties of the coating film.

The average size of noble metal particles can be varied over a pretty wide range, but the size distribution is generally not very sharp.

References

1. D. Ricard, Ph. Roussignol, and Ch. Flytsanis, Opt. Lett. **10**, 511 (1985).
2. H. Dislich, in *Sol-Gel Technology for Thin Films, Fibers, Preforms, Electronics and Specialty Shapes*, edited by L.C. Klein (Noyes Publications, Park Ridge, 1988), p. 50.
3. G. Zhao, H. Kozuka, and T. Yoko, J. Ceram. Soc. Japan **104**, 164 (1996).
4. J. Papp, H.-S. Shen, R. Kershaw, K. Dwight, and A. Wold, Chem. Mater. **5**, 284 (1993).
5. J. Matsuoka, R. Mizutani, H. Nasu, and K. Kamiya, J. Ceram. Soc. Japan **100**, 599 (1992).
6. H. Kozuka and S. Sakka, Chem. Materials **5**, 222 (1993).
7. P. Innocenzi, H. Kozuka, and S. Sakka, J. Sol-Gel Sci. Tech. **1**, 305 (1994).
8. H. Kozuka, G. Zhao, and S. Sakka, J. Sol-Gel Sci. Tech. **2**, 741 (1994).
9. H. Kozuka, M. Okuno, and T. Yoko, J. Ceram. Soc. Japan **103**, 1305 (1995).
10. L. Spanhel, M. Mennig, and H. Schmidt, in *Proc. XVI International Congress on Glass*, Vol. 7 (1992), p. 9.
11. J.Y. Tseng, Chia-Yen Li, T. Takada, C. Lechner, and J.D. Mackenzie, SPIE Vol. 1758, Sol-Gel Optics II (1992), p. 612.
12. M. Mennig, M. Schmit, and H. Schmidt, J. Sol-Gel Sci. Tech. **8**, 1035 (1997).
13. B. Ritzer, M.A. Villegas, and J.M. Fernandez Navarro, J. Sol-Gel Sci. Tech. **8**, 917 (1997).
14. H. Kozuka, G. Zhao, and S. Sakka, Bull. Inst. Chem. Res. Kyoto Univ. **72**, 209 (1994).
15. G. Zhao, H. Kozuka, and S. Sakka, J. Sol-Gel Sci. Tech. **4**, 37 (1995).

Journal of Sol-Gel Science and Technology 13, 707–712 (1998)
© 1998 Kluwer Academic Publishers. Manufactured in The Netherlands.

Optical Viscometry of Spinning Sol Coatings

F. HOROWITZ AND A.F. MICHELS
Instituto de Fisica, UFRGS, Campus do Vale CP15051, 91501-970 Porto Alegre, RS, Brasil
flavio@if.ufrgs.br

E.M. YEATMAN
Department of Electrical and Electronic Engineering, Imperial College of Science, Technology and Medicine, London SW7 2BT, UK

Abstract. Optical interferometric monitoring of spin coating (optospinography) has allowed close observation of the temporal evolution of a thin silicate sol film (typically at 2000 rpm, 100 Hz data acquisition). The kinematic viscosity data obtained, using a simple analytical model, are validated with those from a mineral oil standard, with agreement well within the experimental uncertainties. For spin coating in open air, the influence of variations in refractive index, rheological properties and air flow are discussed. Inflections in the temporal evolution of the optical thickness of silicate sol films are analyzed, which indicate the usefulness of optospinography, particularly when applied in the proximity of the rotation axis and evaporation is minimized, to monitor time variations in the kinematic viscosity of these sols during spin coating.

Keywords: spin coating, kinematic viscosity, optical viscometry, monitoring of spin coating

1. Introduction

Sol-gel coatings, due to their wide flexibility in composition and microstructure, have increasingly been used in magnetic, opto- and microelectronics applications. The viscosity of the coatings during formation is a key parameter for process control and reproducibility. In addition, valuable information on the solution structure of a sol, and on its subsequent transition to a gel, is provided by determination of its viscosity dependence on time [1, 2].

When a sol is spin cast in open air, the optospinography technique, where an interferometric representation is obtained for the temporal variation of the optical thickness of the film during the process, has allowed us to distinguish four main stages of evolution: (I) pre-spinning oscillations in the sol, (II) ultrafast convective mass flow, (III) convection-evaporation, and (IV) limited evaporation [3], as can be seen in Fig. 1. We have recently proposed use of this technique for the measurement of viscosities during spin coating, and considered its potential and validity for spinning sols [4]. In this study, we examine temporal variation of the optical thickness, and its relationship with kinematic viscosity of the film of silicate sol.

2. Experimental

Analysis is made of a HeNe laser beam reflected from the liquid film on a silicon wafer or glass substrate, spinning at speeds in the range of 700–3000 rpm, in the experimental setup described in [3]. The ratio between the reflected and reference signals is computed after processing by an A/D converter, and readings are taken every 10 ms. Alignment of the system is critical, to ensure that the illuminated spot remains at the center of the substrate at all spinning times, which are typically up to 60 s. Conversion from optical to physical thickness was performed by index measurement using a commercial Abbe refractometer. For three different sets of process parameters, Fig. 2 shows the temporal evolution of the sol optical thickness, as inferred from the optospinogram data [3].

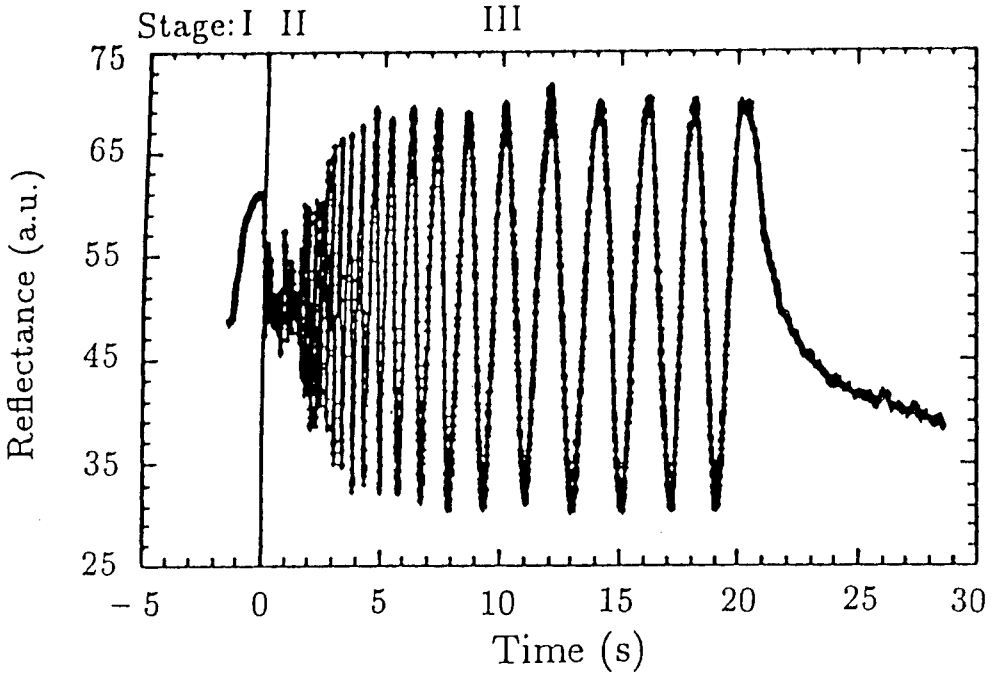

(a)

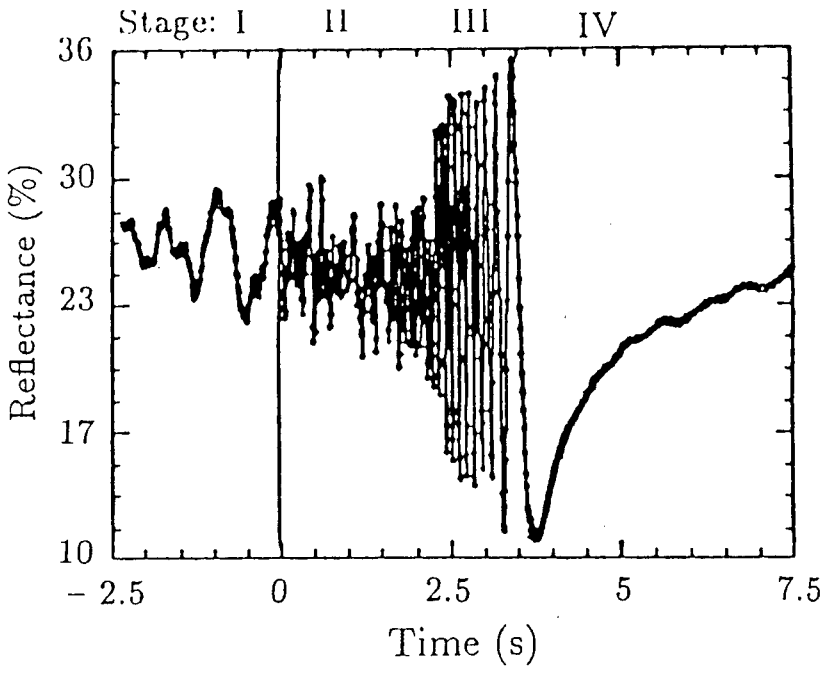

(b)

Figure 1. A typical "optospinogram" of a spinning sol (tetraethylorthosilicate precursor, 1 : 1 vol dilution in ethanol, pH = 1.0, 12 days old) at 2000 rpm: (a) saturated solvent atmosphere; (b) open-air.

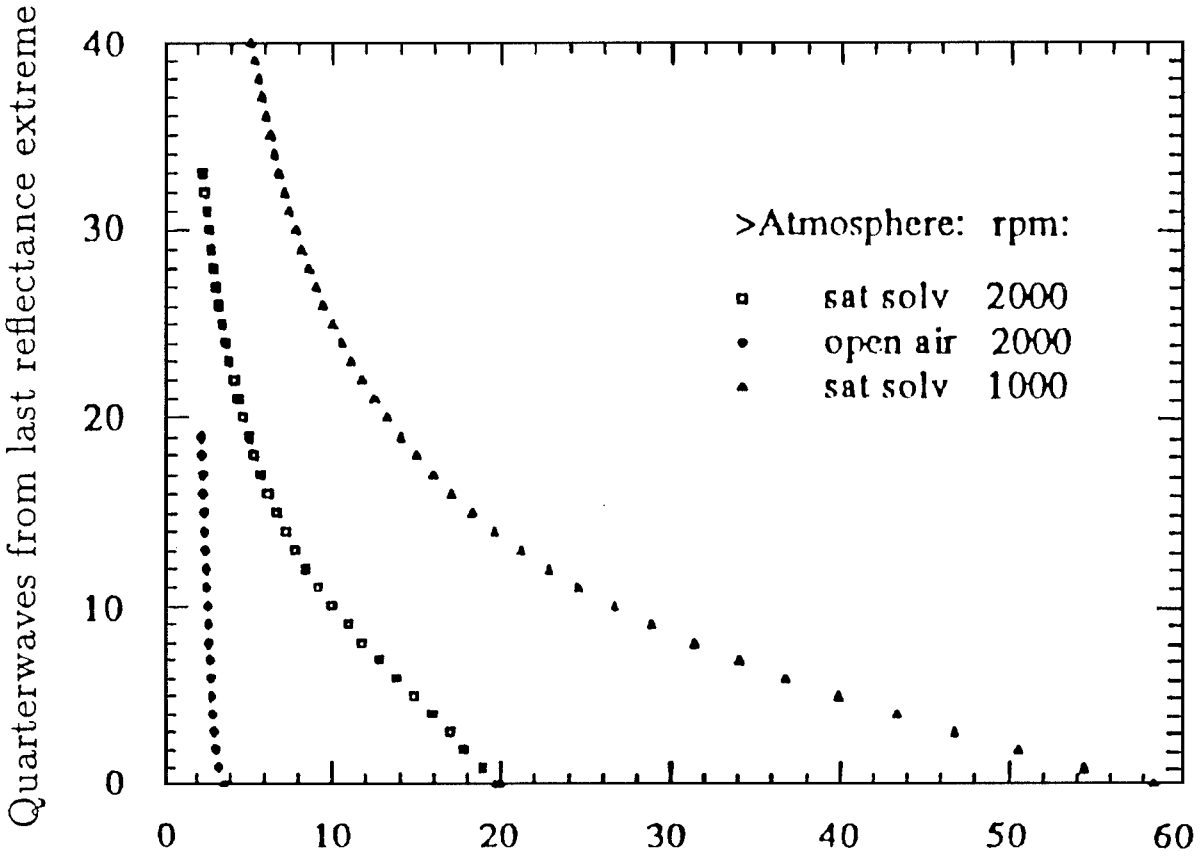

Figure 2. Optical thickness variation with time, in quarterwave units for a spinning sol at three different sets of process parameters. Counting of quarterwaves starts from the last reference extreme in each optospinogram.

3. Theoretical

Assuming an infinitely extended horizontal, rotating plane disk, and a thin liquid film with negligible Coriolis forces and Newtonian behavior, the Emslie, Bonner and Pack (EBP) model [5] predicts a thickness time dependence of the form:

$$d = d_0\left[1+\left(\frac{d_0}{b}\right)^2 t\right]^{-\frac{1}{2}}; \quad b^2 = \frac{3\nu}{4\omega^2}$$

where d_0 is the initial thickness, ω the angular speed, and ν the kinematic viscosity. For times $t \gg \frac{b}{d_0}$,

$$d \approx bt^{-\frac{1}{2}}.$$

It should be also pointed out that no mass loss is considered in this model, which therefore cannot be applied to situations where there is significant evaporation to the surrounding atmosphere.

4. Validation and Results

In order to validate the results obtained from optospinography [3], we applied our method to an oil standard with kinematic viscosity value $\nu_1^0 = 0.37 \pm 0.01$ S (mineral oil OP20) at 22°C. This value was obtained from interpolation, with a second degree polynomial fitting, starting from the supplier specifications at a set of temperatures; the uncertainties correspond to a temperature fluctuation of ±0.5°C in our experimental conditions. The measured and linear fitting for the temporal evolution of the oil optical thickness at 2000 rpm is shown in Fig. 3.

The fact that a straight line is obtained, corresponding to a constant ν, implies that the liquid is Newtonian and that the EBP model is valid in all measured ranges.

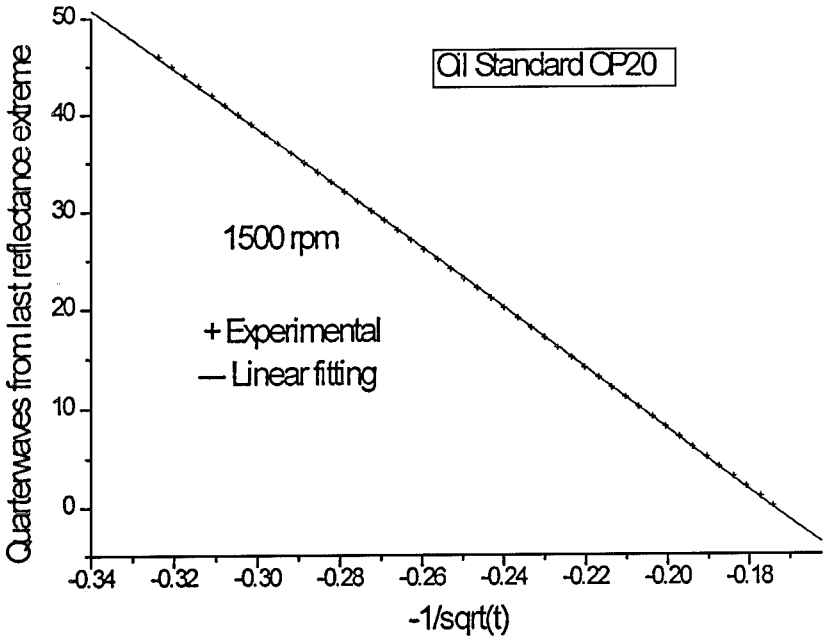

Figure 3. Optical thickness variation vs. $t^{-1/2}$, where the minus sign was used to plot variation with increasing time. Linear fitting corresponds to the EBP model prediction for a Newtonian fluid with $v_1 = 0.361$ S.

Conversion from optical to physical thickness is made possible by a direct measurement with an Abbe refractometer, giving $n_1 = 1.46 \pm 0.01$ (OP20). From this procedure, the experimental result for the oil standard is $v_1 = 0.361 \pm 0.001$ S, where the uncertainties correspond to the observed angular speed fluctuation of ± 5 rpm.

The agreement between the known kinematic viscosity of the oil standard and the result obtained by optospinography, within the experimental uncertainties, indicates the validity of the method. Application to our typical spinning sol at 2000 rpm, produced the optical thickness variation vs. $t^{-1/2}$, in saturated solvent and open air atmospheres, shown in Fig. 4.

5. Discussion and Concluding Remarks

For open-air sol-gel processing, application of this method could generally be useful as an alternative kinematic viscosity measurement, without need of additional instrumentation, and whose result is applicable to initial sol conditions. In terms of viscometry of the sols during spinning sols in open air, possible changes in refractive index and rheological properties need to be considered, as well as the influence of air flow.

For the sol composition we used in this work, (which gives silica films after subsequent heat treatment) the refractive index values of the initial sol, as measured by Abbe refractometry, were the same, up to the second decimal place, as those measured by ellipsometry right after spinning. Although this does not apply for all sol compositions (as opposed to the case of a saturated solvent atmosphere, where negligible loss by evaporation allows the refractive index to remain constant), it does indicate that the index contrast between the solvent and the partially dried porous medium was very small.

As to the implications of the rheological evolution of the sol during the process in open air, we rely on present models and the available experimental evidence. For resist and spin-on glass materials, Sukanek has shown that non-Newtonian effects are always accompanied by a variation of thickness with radial position, and that the film remains uniform up to a critical value of the radius, ξ^*, corresponding to the critical value of shear up to which the liquid viscosity is independent of shear rate [6]. In agreement with published data [7], silicate sol-gel films spun at 2000 rpm have shown nearly uniform thickness up to a radius larger than 10 mm; the radius of the spot illuminated by the laser beam was of the order of 0.1 mm.

Taking into account the influence of the air flow dynamics, Bornside and collaborators have identified a central region in the spinning disk where, for radii less than a critical value (corresponding to a Reynolds

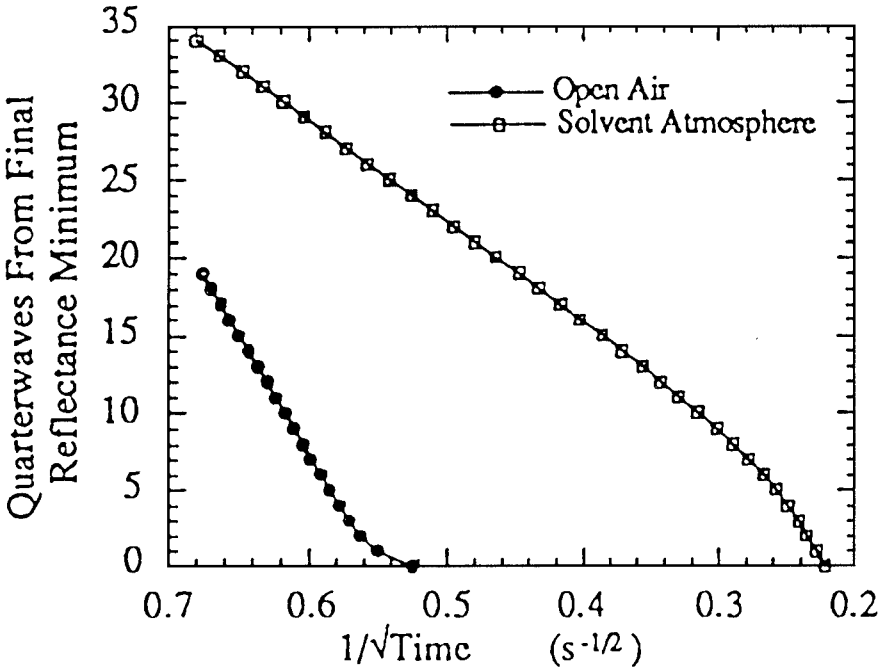

Figure 4. Optical thickness variation (in quarterwaves, at 632.8 nm and 2000 rpm) vs. inverse square root of spinning time ($s^{-1/2}$) for the sol described in Fig. 1, for open air and saturated solvent atmosphere. The latter case corresponds to a kinematic viscosity in the range 3–21 cS.

number of the order of 10^5), the flow is laminar, axisymmetric and steady state, and the mass transfer coefficient is independent of radial position [8]. Specifically for a colloidal system (polystyrene latex spheres suspended in water), Rehg and Higgins showed experimentally, by measuring the film thickness dependence on the inverse square root of the angular velocity, that shear rate thinning effects are unimportant in a region with radius up to 2.5 cm around the axis of rotation (the variation in film thickness was less than 0.3% at 1930 rpm) [9].

In Fig. 4, at the initial spin-off stage the slope is constant, and therefore the kinetic viscosity of the sol is essentially constant—a behavior similar to that of the oil standard. As the sol thins further, on the contrary, the kinematic viscosity of the sol changes significantly. In the case of saturated solvent atmosphere, if we assume that the evaporation of solvent is insufficient to account for this behavior, a possible explanation for the increase in viscosity (from 3 to 21 cS) is an attractive interaction with the substrate, which is consistent with the EBP boundary condition of zero fluid velocity with respect to the rotating disk in the limit of zero film height. The open-air film shows the opposite final behavior, with the thinning rate increasing beyond that predicted by the EBP model. This can be explained directly by mass loss through evaporation, which although continuous, only becomes significant as the spin-off decreases.

We therefore have good theoretical and experimental indications that, despite the simplifying assumptions in this study, useful measurements of viscosity evolution during spin coating of sols can be obtained, particularly for the case where mass loss through evaporation is minimized.

Acknowledgments

We are grateful to Eng. Leandro Galuska and Ms. Vanessa Dutra for their assistance, as well as to Ms. Lizette Peters for providing us the oil standard, under the supervision of Eng. Rogerio Auad at TINTAS RENNER S.A. This work was partially supported by CNPq, PADCT/FINEP and CAPES programs.

References

1. C.J. Brinker and G.W. Scherer, *Sol-gel science: the physics and chemistry of sol-gel processing*, (Academic Press, San Diego, 1990), chap. 3.
2. R. Xu, E.J.A. Pope, and J.D. Mackenzie, J. Non-Cryst. Sol. **106**, 242 (1988).

3. F. Horowitz, E.M. Yeatman, E.J.C. Dawnay, and M.A. Fardad, J. Phys. III France **3**, 2059 (1993); F. Horowitz, E.J.C. Dawnay, M.A. Fardad, Mino Green, and E.M. Yeatman, J. Nonlin., Opt. Phys. Mat. **6**, 1 (1997).
4. F. Horowitz, A. Bacchieri, A. Michels, E.M. Yeatman, and H.P. Grieneisen, SPIE Proc. **2861**, 164 (1996).
5. A.G. Emslie, F.T. Bonner, and L.G. Peck, J. Appl. Phys. **29**, 858 (1958).
6. P.C. Sukanek, J. Electrochem. Soc. **138**(6), 1712 (1991).
7. K. Vorotilov, V. Petrovsky, and V. Vasiljev, J. Sol-Gel Sci. Tech. **5**, 173 (1995).
8. D.E. Bornside, R.A. Brown, P.W. Ackmann, J.R. Frank, A.A. Tryba, and F.T. Geyling, J. Appl. Phys. **73**(2), 585 (1993).
9. T.J. Rehg and B.G. Higgins, AIChE Journal **38**(4), 489 (1992).

Journal of Sol-Gel Science and Technology 13, 713–716 (1998)
© 1998 Kluwer Academic Publishers. Manufactured in The Netherlands.

Aerial Oxidation of Tetraethyl Silicate and Effect on Ammonia Catalyzed Hydrolysis

IAN M. THOMAS
Lawrence Livermore National Laboratory, 7000 East Ave., Mail Stop L-483, Livermore, CA 94550

Abstract. Colloidal suspensions of SiO_2 in ethanol prepared by the ammonia catalyzed hydrolysis of tetraethyl silicate (TEOS) in ethanol have been routinely used for over 10 years to prepare antireflective (AR) coatings on the fused silica transmissive optical components of high power fusion lasers. Very high purity coatings are required to avoid laser damage and these are obtained when the TEOS is fractionally distilled under N_2 prior to use.

Recently we found that products from aerial oxidation of distilled TEOS, had a significant effect on the particle size of our coating suspensions to the detriment of the optical performance. We require particle sizes less than 20 nm to avoid light loss due to scatter and contaminated TEOS gave suspensions with much higher particle sizes. Oxidation products were identified by GC mass spectroscopy and included acetaldehyde, acetic acid, silicon acetates and reaction products of these compounds with ethanol.

Acetic acid and silicon acetates were found to be the major cause of large particle formation. These could be removed by careful redistillation preferably in the presence of a small quantity of magnesium ethoxide. Storage in sealed containers under N_2 avoided further problems.

Keywords: tetraethyl silicate, antireflective coatings, colloidal silica, silica particle size

1. Introduction

One of the most successful applications of the sol-gel process is in the preparation of AR coatings for high power fusion lasers. A colloidal suspension of silica in ethanol prepared by the ammonia catalyzed hydrolysis of TEOS (Stober process [1]) is used for coating fused silica transmissive optical components which can be up to 80 cm in diameter [4]. The suspension can be applied either by spin or dip at room temperature and, after evaporation of the ethanol, a coating consisting of a porous disordered array of silica particles is obtained. The refractive index of this coating is approximately 1.22 and it is therefore a near perfect quarterwave AR coating for fused silica substrates which have an index of 1.46. The process is illustrated in Fig. 1.

High power fusion lasers require maximum transmission through all optics, for maximum efficiency, and high laser damage threshold for all components for maximum power. Sol-gel porous silica coatings give near 100% transmission and have a laser damage threshold at least twice as high as any other AR coating prepared by other methods.

Fusion lasers in France [2], England [3], and the US [4] including the two most powerful ones in the world, the NOVA at LLNL in California and the OMEGA at LLE in Rochester, New York all use sol-gel AR coatings.

2. Discussion

The Nova laser at LLNL has been in operation for over 12 years. We prepare our own coating suspensions and have our own coating equipment.

High laser damage resistance is related to high purity. We have found that the purity level of commercial samples of TEOS varies and this is easily seen in their UV transmission spectrum. Figure 2 shows the UV spectra of four different commercial samples of "pure" TEOS. Sample (a) is obviously the best and there are various quantities of absorptive impurities in the others. At

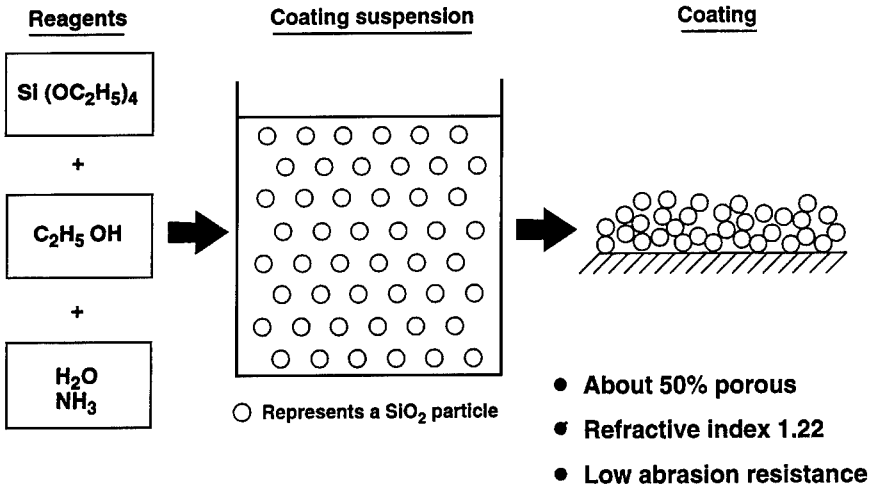

Figure 1. Coating from silica suspension prepared by ammonia catalyzed hydrolysis of TEOS.

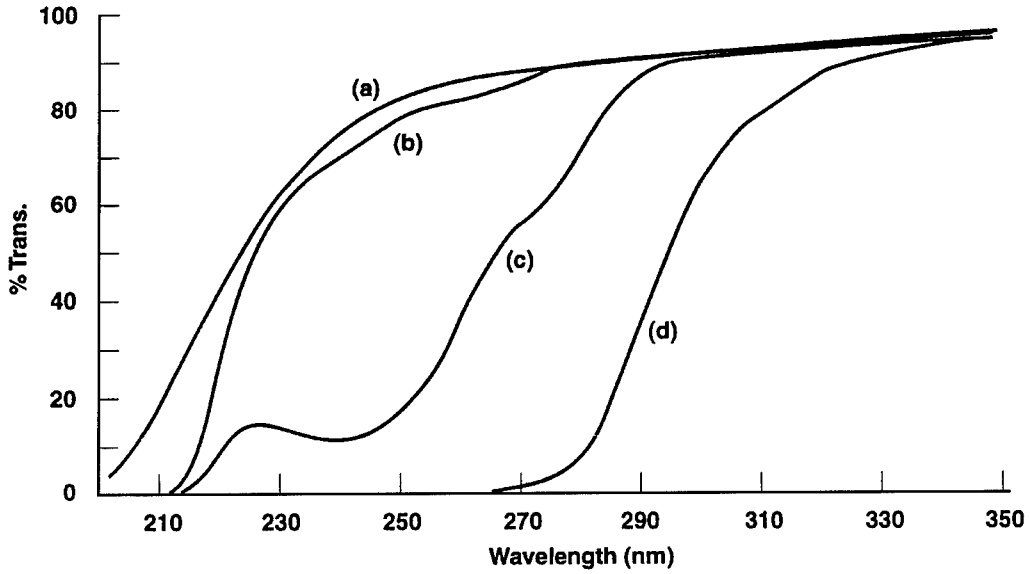

Figure 2. UV transmission spectra of four different commercial samples of TEOS (1-cm cell).

LLNL we fractionally distill TEOS from a 72-liter flask under N_2 at atmospheric pressure. We normally distill about four batches in succession and store the product in 20-liter glass carboys under N_2. We have used a boiling point specification of 166–167° and a "clean" UV transmission which is shown in Fig. 3. This has given a coating sol with particles in the 15–20 nm size range. Coatings prepared from particles much larger than this were found to cause scatter in the laser beam leading to power loss.

Recently we found that a carboy of distilled TEOS stored for about a year had changed and when used to prepare test batches of our standard colloidal suspension gave material with a particle size in the range of 70–80 nm. Container storage had been changed from a relatively constant temperature enclosure to one subject to daily fluctuations of up to 50°F. The carboy also had a leaking stopper. It was highly likely that air had cycled in and out on a daily basis for some time. Oxidation and hydrolysis were then suspected as being

Table 1. Analysis of improperly stored TEOS with probable sources of impurities.

Analysis	Impurity and source
0.09%	acetaldehyde—oxidation product
0.21%	acetic acid—oxidation product
0.64%	ethanol—hydrolysis product
0.09%	ethyl vinyl ether—acetaldehyde + ethanol
0.19%	ethyl acetate—ethanol + acetic acid
0.69%	1,1,diethoxyethane—acetaldehyde + ethanol
0.54%	diethoxyhydroxysilicon acetate—acetic acid + TEOS
0.17%	triethoxysilicon acetate—acetic acid + TEOS
0.43%	triethoxysilanol—hydrolysis product
0.43%	diethoxysilicon diacetate—acetic acid + TEOS
0.42%	triethoxyethyl silane—impurity
94.5%	TEOS

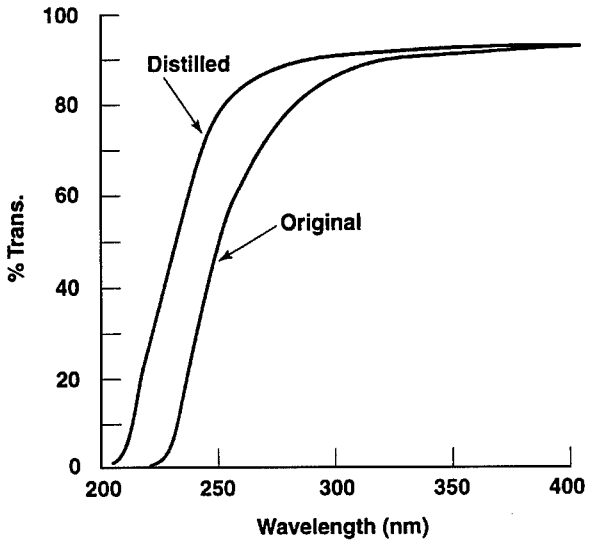

Figure 3. Typical before and after UV transmission spectra of LLNL distilled TEOS (1-cm cell).

a potential problem and this was confirmed by a GC mass spectroscopic analysis which is shown in Table 1. Almost all compounds identified can be accounted for by oxidation, hydrolysis and subsequent reactions.

GC mass spectroscopic analysis was also carried out on a number of different TEOS samples, both commercial and distilled, and the results are shown in Table 2. Most impurities can be accounted for from a small amount of hydrolysis and oxidation. These are strong UV absorbers and also account for the variation in the UV spectrum. The particle size variation is probably

Table 2. Analysis of different commercial and distilled TEOS samples.

Component	Comm. (a)	Comm. (b)	Comm. (c)	LLNL dist.	LLNL dist. over Mg
Ethanol	0.07	0.13	0.23	0.27	—
Triethoxyethylsilane	0.21	0.74	0.78	0.73	0.92
Diethoxyhydroxy silicon acetate	0.04	—	—	0.14	—
Tetraethylsilicate	99.5	98.4	98.6	98.4	99.1
Triethoxysilanol	—	0.27	0.12	0.20	—
Triethoxysilicon acetate	—	0.43	—	—	—
Unknown, higher boilers	0.02	—	0.16	0.21	—

caused by acetic acid and silicon acetates. Unlike other impurities these will form ionic products, i.e., ammonium acetate, in the subsequent colloidal suspension preparation and this should affect the nucleation and growth of the silica particles.

This was confirmed by suspension preparations under standard conditions using TEOS samples of varying acetate content and measurement of the particle size after reaction was complete. We also include samples which were deliberately doped with acetic acid. A convenient method for estimating small quantities of acetate involved nonaqueous titration of a sample of TEOS with 0.1 N ethanolic NaOH solution. The results are shown in Table 3 and the relationship between acetate content and particle size is immediately apparent.

While we found that very careful fractional distillation could be used to remove most of the acetates, a better method was developed. There is a well-known reaction first used to prepare metallosiloxanes

Table 3. Acetate content of various TEOS samples and particle size of sol.

TEOS sample	Acetate content (as acetic acid)	Particle size (dia. in nm)
Commercial (a)	0.01%	5
Commercial (d)	0.00%	3–5
LLNL (stored 1 yr and sealed)	0.03%	22
LLNL (distilled)	0.20%	58
LLNL (doped TEOS)	0.10%	29
LLNL (doped TEOS)	0.20%	(gelled)
LLNL (distilled over Mg)	0.00%	3–5

involving reaction between silicon acetates and metal alkoxides: [5]

$$\rightarrow\!\!\!

Journal of Sol-Gel Science and Technology 13, 717–722 (1998)
© 1998 Kluwer Academic Publishers. Manufactured in The Netherlands.

Investigation of Glass-Like Sol-Gel Coatings for Corrosion Protection of Stainless Steel Against Liquid and Gaseous Attack

M. MENNIG AND C. SCHELLE
Institut für Neue Materialien, D-66123 Saarbrücken, Germany

A. DURAN
Instituto de Ceramica y Vidrio, Madrid, Spain

J.J. DAMBORENEA
Centro Nacional de Investigaciones Metalurgicas, Madrid, Spain

M. GUGLIELMI AND G. BRUSATIN
Dip. di Ingegneria Meccanica, Universita di Padova, Italy

Abstract. Glass-like sol-gel coatings have been investigated as corrosion protective coatings on stainless steel. Magnesium- and borosilicate coatings with thickness of about 100–700 nm and methyl-modified SiO_2 coatings with a thickness of about 2 μm were deposited on stainless steel plates by dip-coating. The coatings were densified between 400°C and 500°C in different atmospheres (N_2, air) for 1 h. The corrosion protection against gaseous attack was investigated by accelerated corrosion tests at 800°C in air for 1 h. A corrosion protection factor was calculated from the relation Fe/Fe_2O_3, determined by XRD on the surface of coated and uncoated samples. Methyl-modified SiO_2 coatings showed a protection factor, which was 2 orders of magnitude higher than for the other coatings. Electrochemical investigations were performed on samples submerged in a NaCl solution for 200 h. The corrosion propagation, polarization resistance and impedance vector were measured. For accelerated corrosion tests, polarization intensity curves were determined for high potentials of up to 1 V. Again excellent results were obtained for the methyl-modified SiO_2 coatings, which remained passive for 200 h. Results of the salt spray corrosion test, however, showed no corrosion protection by the sol-gel coatings. After 2000 h in the salt spray chamber the steel was corroded and the coatings peeled off. It is concluded that for the further development of these coatings an improved interfacial passivation will be required.

Keywords: corrosion protective coatings, protection of stainless steel, magnesium silicate coating, borosilicate coating

1. Introduction

The mechanical and chemical performance of steel surfaces can be improved by glass-like or ceramic sol-gel coatings [1]. Coatings from SiO_2 [2–6], Y-doped ZrO_2 [7–10], alumino- and borosilicates [11–13] on steel are of special interest for the protection of metals against oxidation and acid corrosion at elevated temperatures ($T > 300$°C), due to their high chemical and thermal durability. However the protective function of these coatings is limited by the formation of cracks during their thermal densification at temperatures up to 600°C if the coating thickness exceeds several 100 nm [14]. Hence, such thin coatings may not be suitable for a complete covering of surface layer defects and they are very sensitive against mechanical impact or long

term chemical attack. An important reason for the poor coating performance is the low solid content of coating sols synthesized by common techniques. This leads to a high shrinkage during drying and sintering. Thus, enhanced crack formation in coatings thicker than several 100 nm is observed [14].

The objective of the present paper was to investigate thick (2 μm) SiO_2 coatings already developed for coatings on glass [15] in comparison with thin (<1 μm) magnesium and borosilicate coatings [11, 16] as protection on stainless steel.

2. Experimental

Two types of stainless steel (AISI 304, AISI 430, size: 100 × 100 × 2 mm^3) with one polished (p) and one brushed (r) side were used as substrates. Coatings were applied by dip-coating, coating thickness was measured after densification on the polished side by profilometry. The different coatings are listed in Table 1.

Two different sol synthesis routes are shown in Table 1. While SiO_2 coatings (INM) with thicknesses of about 2 μm were prepared by using a methyl modified nanoparticulate SiO_2 sol [15], B_2O_3-SiO_2 coatings (PD, MASBM) with a thickness up to 600 nm and MgO-SiO_2 coatings (FAAM) with a thickness of about 300 nm were synthesized by using aminosilane precursors [11, 16].

Protection against gaseous attack was investigated by oxidation tests performed at 800°C for 1 h. Special X-ray diffraction analysis [11] was performed on both coated and uncoated parts of the samples. Using the ratio of Fe_2O_3/Fe on the uncoated and coated part of the substrate, a protection factor (P.F.) was calculated according to Eq. (1).

$$\text{P.F.} = \frac{A_u(Fe_2O_3)/A_u(Fe)}{A_c(Fe_2O_3)/A_c(Fe)} \quad (1)$$

from the measured peak areas A_u (uncoated) and A_c (coated). This protection factor (P.F.) was used to compare the different coatings.

Electrochemical investigations were performed to measure the corrosion resistance of the sol-gel coatings against attack by NaCl solution (0.6 M, pH 7) on a test area of 1 cm^2. The electrochemical measurements were made on specimens submerged in the solution, every 24 h until 200 h, with additional measurements 30 min and 3 h after the start [17]. The corrosion resistance was characterized by measuring the current (A/cm^2). After the tests, the specimens were examined by optical microscopy.

First, a screening procedure, consisting of cyclic voltammetry for a fixed corrosion time (0.6 M NaCl solution, 5 h) was used and only the samples that had passed this pre-test were investigated by long term corrosion tests.

Corrosion behavior for long-term conditions (2000 h) was examined in a salt spray chamber with NaCl solution (ASTM B117-73). Before the corrosion test, the coatings were damaged by a 5 cm long scratch down to the substrate with a scratch pen to investigate possible decohesion effects of the coatings during corrosion. After the tests the samples were examined visually.

Table 1. Summary of the different coatings on stainless steel (AISI 304, AISI 430) with coating composition, thickness obtained by profilometer and densification parameters.

Sample	Stainless steel type	Coating composition (molar ratio)	Coating thickness (μm)	Densification temperature (°C)	Synthesis in
PD 1	AISI 430	0.25 B_2O_3-SiO_2	0.6	400	[11]
PD 2	AISI 304	0.25 B_2O_3-SiO_2	0.1	400	[11]
FAAM1	AISI 304	2 MgO-SiO_2	0.28	500	[16]
FAAM2	AISI 430	2 MgO-SiO_2	0.28	500	[16]
MASBM1	AISI 304	0.3 B_2O_3-SiO_2	0.32	500	[11]
MASBM2	AISI 430	0.3 B_2O_3-SiO_2	0.32	500	[11]
INM 1	AISI 304	SiO_2	2	500	[15]
INM 1N	AISI 304	SiO_2	2	500/N_2	[15]
INM 3	AISI 430	SiO_2	2	500	[15]

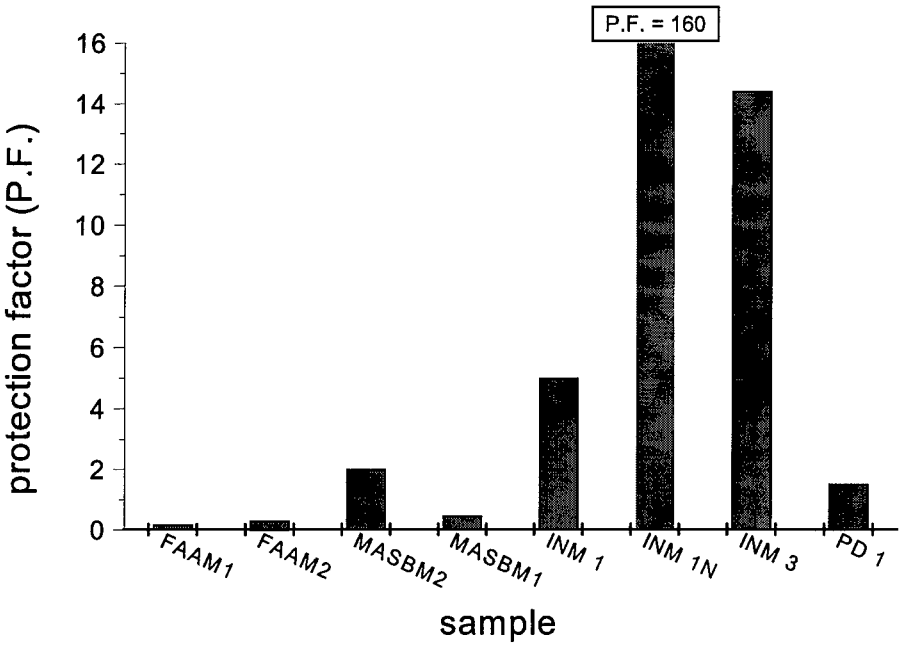

Figure 1. Comparison of the different coatings (Table 1) by protection factor calculated by Eq. (1) after thermal oxidation at 800°C 1 h on the polished side of stainless steel AISI 304 and AISI 430. High values indicate good protection.

3. Results

By performing static oxidation tests, electrochemical investigations and salt spray corrosion tests, the protection abilities of the different sol-gel coatings on stainless steel were investigated.

3.1. *Static Oxidation Tests*

The results of the static oxidation tests are shown in relation to surface structure of the substrates in Fig. 1 (polished surface, $R_a \approx 0.02$ μm) and Fig. 2 (brushed surface, $R_a \approx 2$ μm).

Comparing the protection factors of different coatings on polished steel showed (Fig. 1), that the thick SiO_2 coatings (INM) produced the highest protection factor against oxidation at 800°C. The figures illustrate qualitative differences. For quantitative discussions with statistical relevance, the error of measurement of the described method must be determined and a series of samples at different temperatures must be investigated, which was not possible in this study. The protection factors of the different coatings on the rough side are shown in Fig. 2.

As shown in Fig. 2, the 2 μm thick SiO_2 coatings (INM) provided the highest protection factor also on the rough side of the stainless steel. This may be explained by a decreased O_2 penetration which is diffusion controlled and therefore depending on the coating thickness and the exposure time. On the other hand, different surface passivation and oxygen penetration by coating defects could be evident. In order to give a final explanation further investigations with different coating thicknesses, exposure times and temperatures would be necessary.

3.2. *Electrochemical Corrosion Tests*

The results of the electrochemical investigations are presented in Fig. 3.

Figure 3 shows very good results for PD 2, INM 1 and INM 3, remaining passive after 200 h of electrochemical attack. As no corrosion was measured, these results indicate also that dense, nonporous coatings have been obtained at densification temperatures much lower than the T_g of comparable glasses. The coating on the polished side (INM 3) provided passivation, while on the rough side (INM 3r) attack was observed (Fig. 3). This last result confirms that polishing of the substrate surface strongly enhances the protection potential of any coating by decreasing the surface area for the corrosive attack. In Fig. 4

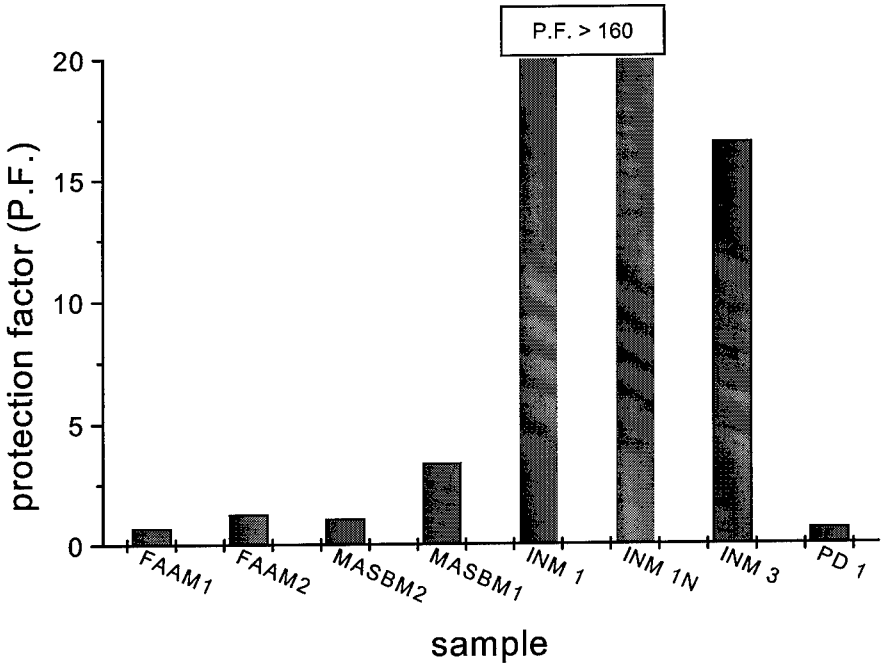

Figure 2. Comparison of the different coatings by protection factor (P.F.) calculated by Eq. (1) after thermal oxidation at 800°C for 1 h on the rough side of stainless steel AISI 304 and AISI 430 (Table 1). High values indicate good protection.

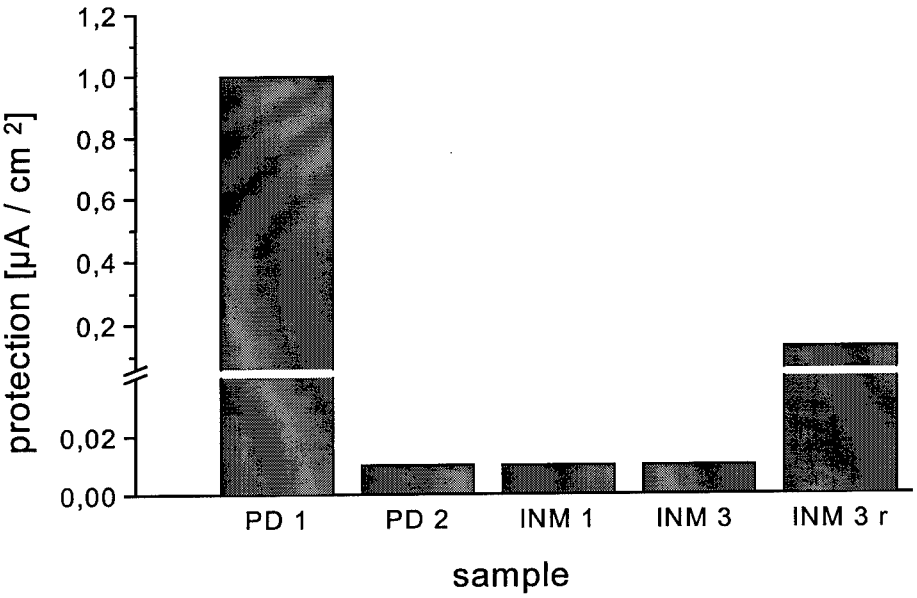

Figure 3. Results of the electrochemical investigations of the long time corrosion tests (200 h in 0.6 mol NaCl solution) on the different coatings (Table 1) on polished side of stainless steel (AISI 304, AISI 430) and on the rough side (INM 3r, AISI 430) at room temperature. Low values indicate good protection.

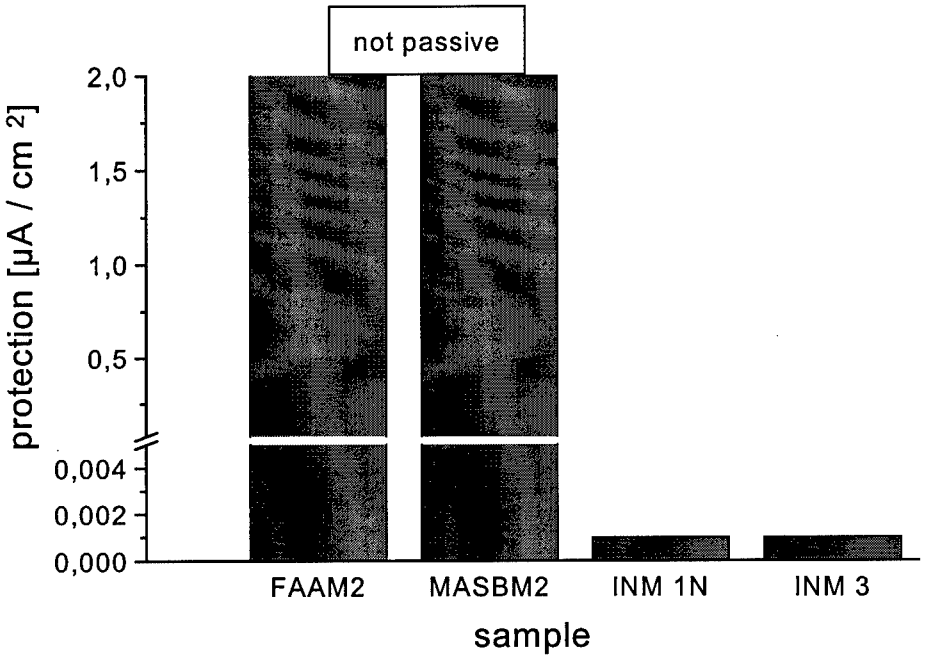

Figure 4. Results of the voltammetry corrosion tests performed for 5 h in 0.6 mol sodium chloride solution on different coatings (Table 1) on the polished side of stainless steel at room temperature. Low values indicate good protection.

the results of the voltammetry corrosion tests are shown.

The results in Fig. 4 show, that neither MASBM2 (B_2O_3-SiO_2) nor FAAM2 (MgO-SiO_2) provided passivation for the stainless surface (AISI 304). While MASBM2 did not show any passivation from the beginning of the test, FAAM2 behaved as a barrier up to nearly 100 mV, when pitting appeared. The thick SiO_2 coatings remained passive up to 700 mV (INM 1N) or 900 mV (INM 3). The bad performance of the coatings MASBM and FAAM (Fig. 4) is in agreement with the results of the oxidation tests (Figs. 1 and 2), where no protection against O_2 diffusion was provided by these coatings.

3.3. *Salt Spray Tests*

The results of the salt spray corrosion tests on coated and uncoated stainless steel samples are shown in Table 2.

The uncoated AISI 304 showed slight corrosion only on the brushed side because of the higher surface area on this side. The results in Table 2 show no

Table 2. The results of 2000 h salt spray corrosion test with SiO_2-B_2O_3 and SiO_2 coatings on stainless steel (Table 1) in comparison with uncoated stainless steel samples (AISI 304, AISI 430).

Sample	Coating	Steel	Corrosion behavior
—	Uncoated	AISI 304	Slight corrosion on brushed side
—	Uncoated	AISI 430	Slight corrosion on both sides
PD 1	SiO_2/B_2O_3	AISI 430	Strong corrosion on both sides
PD 2	SiO_2/B_2O_3	AISI 304	Strong corrosion on brushed side, Slight corrosion on polished side
INM 1	SiO_2	AISI 304	Strong corrosion on both sides
INM 3	SiO_2	AISI 430	Totally corroded on both sides
INM 1N	SiO_2	AISI 304	Strong corrosion on both sides

improvements in the corrosion resistance of stainless steel against corrosive attack in the salt spray chamber. For all samples the corrosion began at single spots on the coated substrates already present after 500 h. The spots grew in diameter until the whole coating flaked off.

The corrosion resistance of the steel AISI 304 was decreased remarkably by the coating; probably due to the thermal load of the substrate during the thermal densification of the coating, or due to chemical attack of the coating sol (acid catalysis). For the investigation of the mechanism further experiments are required.

4. Conclusions

The corrosion tests against gaseous attack at elevated temperatures have shown that SiO_2 coatings prepared from nanoparticulate sols show a rather high rate of densification, since they are an effective barrier against O_2 diffusion at 800°C. But the tests have only been carried out for 1 h. A long-term protection will only be possible if the interface is sufficiently passivated.

The electrochemical measurements with sodium chloride solution at room temperature also lead to the conclusion that dense layers were obtained with this sol. But from the salt spray tests it has to be concluded that the coatings are not free of defects and that the surface passivation obtained by acid catalyzed sols is not sufficient. Therefore, surface passivation seems to be the key for the development of coatings with long term corrosion protection.

References

1. M. Guglielmi, J. Sol-Gel Sci. Tech. **8**, 443–449 (1997).
2. O. de Sanctis, L. Gomez, N. Pellegri, P. Parodi, A. Marajofsky, and A. Duran, J. Non-Cryst. Solids **121**, 338–343 (1990).
3. K. Itzumi, H. Tanaka, Y. Uchida, N. Toghe, and T. Minami, J. Non-Cryst. Solids **147/148**, 483–487 (1992).
4. M. Murakami, K. Izumi, T. Deguchi, A. Morita, N. Tohge, and T. Minami, J. Ceram. Soc. Jpn. Inter. Ed. **97**, 86–89 (1989).
5. O. de Sanctis, L. Gomez, N. Pellegri, and A. Duran, Surf. Coat. Tech. **70**, 251–255 (1995).
6. K. Izumi, H. Tanaka, Y. Uchida, N. Tohge, and T. Minami, J. Mat. Sci. Let. **12**, 724–727 (1993).
7. P. de Lima Neto, M. Atik, L.A. Avaca, and M. Aegerter, J. Sol-Gel Sci. **1**, 177–184 (1994).
8. M. Shane and M.L. Mecartney, J. Mat. Sci. **25**, 1537–1544 (1990).
9. K. Itzumi, H. Tanaka, M. Murakami, T. Deguchi, A. Morita, N. Tohge, and T. Minami, J. Non-Cryst. Solids **121**, 334–347 (1990).
10. K. Itzumi, M. Murakami, T. Deguchi, A. Morita, N. Tohge, and T. Minami, J. Am. Ceram. Soc. **72**(8), 1465–1468 (1989).
11. M. Maliavski, E. Tchekounova, P. Innocenzi, D. Festa, M. Guglielmi, and L. Mancinelli, degli Esposti, J. Europ. Cer. Soc. **15**, 337–342 (1995).
12. A.R. Di Giampaolo, Conde Di Giampaolo, M. Puerta, H. Ruiz, and J. Lira Olivares, J. Non-Cryst. Solids **147/148**, 467–473 (1992).
13. M. Gulielmi, D. Festa, P.C. Innocenzi, P. Colombo, and M. Gobbin, J. Non-Cryst. Solids **147/148**, 474–477 (1992).
14. C.J. Brinker and G.W. Scherer, *Sol-Gel Science: The Physics and Chemistry of Sol-Gel Processing* (Academic Press, New York, 1990).
15. M. Mennig, G. Jonschker, and H. Schmidt, SPIE **1758**, 125–134, 1992.
16. M. Maliavski, O.V. Dushkin, E.V. Tchekounova, and J.V. Markina, J. Sol-Gel Sci. Techn. **8**, 571–575 (1997).
17. J. de Damborenea, N. Pellegri, O. de Sanctis, and A. Duran, J. Sol-Gel Sci. Techn. **4**, 239–244 (1995).

Journal of Sol-Gel Science and Technology 13, 723–727 (1998)
© 1998 Kluwer Academic Publishers. Manufactured in The Netherlands.

Sol-Gel Coatings on 316L Steel for Clinical Applications

PABLO GALLIANO
INTEMA (CONICET-UNMdP), 7600 Mar del Plata, Argentina

JUAN JOSÉ DE DAMBORENEA
Centro Nacional de Investigaciones Metalúrgicas (CSIC), 28040 Madrid, Spain

M JESÚS PASCUAL AND ALICIA DURÁN
Instituto de Cerámica y Vidrio (CSIC), 28500 Arganda del Rey, Spain

Abstract. SiO_2 and SiO_2-CaO-P_2O_5 coatings have been prepared by dipping electropolished stainless steel 316L samples and microscope glass slides in three different sol-gel solutions. Multilayered dense SiO_2 coatings, and thick silica films obtained from equimolar contents of TEOS and MTES were used. The latter were able to strongly reduce both the corrosion attack on the steel and the iron diffusion to the sample surface. SiO_2-CaO-P_2O_5 coatings were also obtained and applied onto the silica films, in order to provide a bioactive external surface for contact with living tissue. In-vitro evaluation of these coatings and films is discussed.

Keywords: SiO_2 coating, SiO_2-CaO-P_2O_5 coating, protection of 316L stainless steel, protection of implant

1. Introduction

Metallic implant materials such as 316L stainless steel, Co-Cr alloys and Ti are widely used as load-bearing prosthesis in orthopedics and dentistry due to their excellent mechanical properties. These implants, however, show two severe shortcomings: a limited corrosion resistance in the human body, especially critical in the case of stainless steel, and the lack of bioactivity, i.e., they are not able to bond to living tissue without cementation or external fixation devices. On the contrary, certain glasses and ceramics are bioactive, but they are not strong enough to be used for load-bearing applications.

Coating metallic prosthesis with bioactive glasses could be a route to combine both mechanical resistance and bioactivity in one material. Many attempts have been made in this direction by using different coating techniques such as enamelling, flame-spraying and rapid immersion in molten glass [1]. Some of the problems associated with these techniques are: poor adherence of coating to metal, interfacial strength reduction due to glass leaching, and contamination of the coating by metallic ions diffused from the substrate during firing. This last point is a critical one, since it is well known that a small percentage of certain metallic ions such as Fe^{3+} are enough to inhibit bioactivity [2].

Glass coatings can also be applied on metal surfaces using sol-gel methods. Promising results have been obtained with sol-gel SiO_2 coatings when used as barriers against oxidation and gaseous NH_3 corrosion of stainless steel [3–5]. Thus, sol-gel coatings could be an attractive way for improving the performance of metallic prosthesis. Furthermore, silica-based sol-gel systems usually have a high content of surface silanol groups, which have been reported to promote in-vitro and in-vivo nucleation of apatite on bioactive glasses and related materials [6, 7].

In this work, SiO_2 and SiO_2-CaO-P_2O_5 sol-gel coatings have been prepared by dipping electropolished stainless steel 316L samples in three different sol-gel solutions. Dense and thick SiO_2 coatings have been deposited in order to provide a first barrier able to strongly reduce both the corrosion attack of the steel and the iron diffusion to the sample surface. SiO_2-CaO-P_2O_5 coatings and self-supported films have also been obtained.

These coatings were applied onto the silica films to provide a bioactive external surface for contact with living tissue. Corrosion resistance, Fe^{3+} diffusion and in-vitro surface reactivity of these coatings were analyzed.

2. Experimental

Electropolished stainless steel 316L flat sheets of $50 \times 20 \times 1$ mm used as substrates were heat-treated at 350°C for 1 h to produce a slight surface oxidation that enhances the adhesion of the coating, and further cleaned and rinsed with ethanol. Microscope glass slides were also used as substrates after cleaning.

Two different solutions, A and B, were used for preparation of SiO_2 coatings. The first one was prepared from tetraethylorthosilicate (TEOS) using a two-step acid catalysis process [8] in order to control the degree of hydrolysis and the condensation rate. This preparation process allows high density SiO_2 coatings ($\sim$2.0 g/cm^3) to be obtained at temperatures lower than 600°C [9] with a maximum crack-free thickness of 300–400 nm in a single layer. The solution was stable for several weeks and the viscosity, measured using the Ostwald method, varied between 2 and 3 cP, for a constant concentration of SiO_2 of 60 g/l.

A second type of silica containing sol-gel solution (B) was obtained by mixing TEOS and methyltriethoxysilane (MTES) in a molar ratio 1:1. HCl (0.1 N) and AcH were added as catalysts and the ratio $(H_2O + AcH)/(TEOS + MTES)$ was 1.7. The solution was stirred under reflux for 2 h and used 30 min after preparation. It showed viscosities between 2 and 3 cP for a concentrations of 150 g/l and was stable for 1 week.

Coatings and films of composition $80CaO\text{-}16SiO_2\text{-}4P_2O_5$ were prepared from solution C. This solution was obtained from TEOS, triethylphosphate ($PO(OEt)_3$) and calcium methoxyethoxide, distilled water, HCl as catalyst, and EtOH as a solvent. The $H_2O/(TEOS + PO(OEt)_3)$ molar ratio was 2.5. The solution had an oxide concentration of 60 g/l and was stable for several months.

The coatings were obtained by dipping with withdrawal rates between 10 and 40 cm/min. After drying, they were heat treated at 500°C for 1 h. Multilayer coatings were obtained by repeating this process. Self-supporting films were prepared from solution C by pouring on a flat glass vessel. The films thus obtained were dried at room temperature and also heat-treated for 1 h at 500°C.

Coating thickness was measured with a Talystep profilometer on a step made by scratching the film after the deposition.

The electrochemical measurements were performed on three samples: the four-layer dense SiO_2 coating A2 and monolayer coated samples B1 and B2. Experiments were performed on the specimens immersed in the SBF solution every 24 h until the 200 h of the experiment were completed. The first measurement was made after 1 h of testing. The corrosion behavior was determined by means of the electrochemical impedance spectroscopy technique on samples of 1 cm^2. Data were taken using a Schumberger Potentiostat, 1286 Solartron model connected to a 1250 frequency response analyzer from the same manufacturer. The frequency sweep was between 5×10^4 and 10^{-3} Hz.

The surface composition of most of the steel coated samples after different thermal treatments was analyzed by X-ray photoelectron spectroscopy (XPS), determining the binding energies of Fe $2p^{3/2}$, Si 2p and O 1s electrons, and Fe/Si surface molar ratios.

Sol-gel silica coatings were soaked in SBF solution in simulated physiological conditions (37°C and pH = 7.25) to analyze their in-vitro bioactivity. This solution contains ion concentrations similar to those of human plasma, and is usually employed to reproduce in-vivo apatite formation on the surface of bioactive materials [2, 6, 7, 11]. Silicophosphate coatings and films were also tested in a Ca-enriched SBF solution (SBF150) [6, 11] in similar conditions. After several days, the surfaces were analyzed by SEM microscopy and FTIR reflectance spectroscopy.

3. Results and Discussion

3.1. *Silica Coatings*

Crack-free silica coatings up to 350 nm were obtained from solution A, after densification treatments at 500°C. Films of about 550 nm were also obtained by multilayer deposition. Thicker silica coatings up to 1400 nm were obtained from solution B. Coating characteristics are summarized in Table 1.

3.2. *Corrosion Resistance of the Coated Steel Samples*

The first point to note is the very low corrosion rate in the three tested samples, which is in agreement with previous results found by the authors for a sol-gel silica

Table 1. Compositions, metal-organic precursors and thicknesses of the coatings.

Coating	Metal-organic precursors	Coating composition	Coating thicknes (nm)
A1	TEOS	SiO_2	140
A2	TEOS	SiO_2	560
B1	TEOS + MTES (1:1)	SiO_2	600
B2	TEOS + MTES (1:1)	SiO_2	1400
C1	TEOS + $PO(Et)_3$ + Calcium metoxyethoxide	$80SiO_2 \cdot 16CaO \cdot 4P_2O_5$	400

coated 304 stainless steel in a 0.6 M NaCl solution. Figure 1 shows the evolution of the impedance diagrams for sample B2 at the beginning of the test (1 h) and at the end (200 h). This behavior was the same in all the samples studied, although they are omitted here. The frequency dependences of the impedance modulus and the phase angle (Bode plot) show a high resistant material with high scattering at frequencies below 1 Hz. This scattering is due to limitations of the experimental equipment, which is unable to reach the high impedances required by the coatings. There are no variations either in the shape or in the values reached by impedance modulus in the experimental time, which indicates a highly stable system.

Figure 2 shows the results obtained for the three samples after 200 h of immersion in the physiological solution. The phase angle variation is near 90 and the slope of the Bode plot is almost −1, which indicates a near pure capacitive behavior. In the present experimental conditions, it is not possible to elucidate

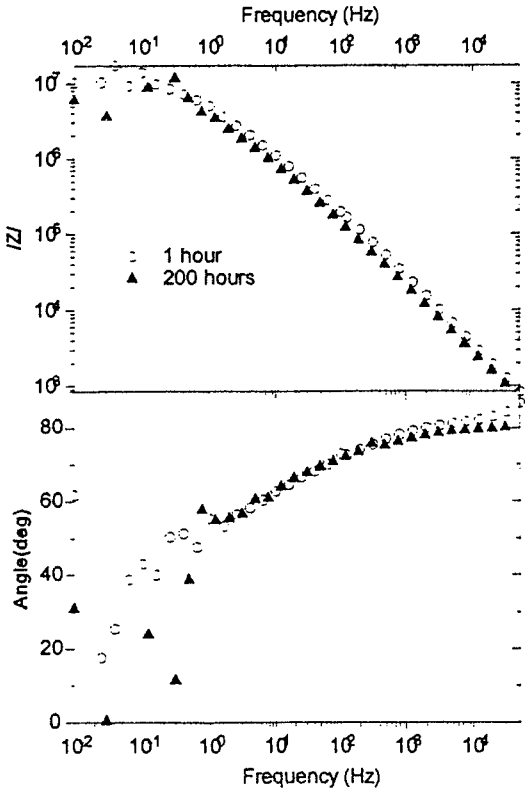

Figure 1. Impedance spectra for 1 and 200 h for the 1400 nm coating (B2) in SBF solution.

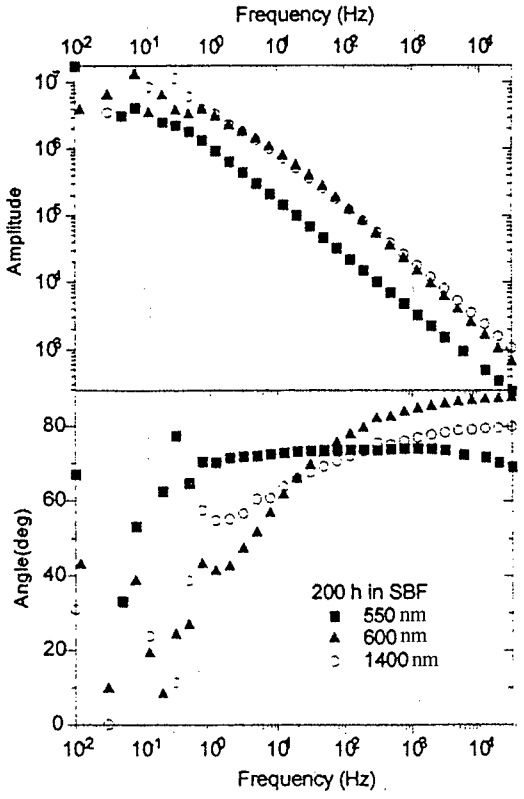

Figure 2. Bode plot after 200 h of electrochemical attack for the coatings A2, B1 and B2 (550, 600 and 1400 nm) in the physiological solution.

Table 2. Binding energy (eV) of internal electrons of O, Fe and Si in coating surfaces, and molar ratio Fe/Si.

Coating	O 1s	Si 2p	Fe $2p^{3/2}$	Fe/Si
A2	532.8	103.4	711.0	0.101
B1	532.9	103.4	710.6	0.024
B2	532.6	103.4	709.9	0.013

the values of the charge transfer resistance but, for the lowest value of the frequency, they are greater than $10^6\ \Omega \cdot cm^2$. In all cases impedance values are high enough to ensure a negligible corrosion rate of the base material, and show that the coatings of 600 and 1400 nm have the largest impedance modulus.

The results of the XPS analysis of coatings A2, B1 and B2 on the steel substrates are shown in Table 2.

No significant change is observed in the binding energy of Si and O. In the case of Fe, it is present on the surface, either as Fe_2O_3 or FeOOH [12]. The Fe/Si molar ratio is as low as 0.01 on coating B2, and twice this value in coating B1. The former value is lower than those reported for bioactivity inhibition [2]. When comparing these two monolayered coatings obtained from the same starting solution, it is observed that the thicker the coating, the better is its performance as an Fe^{3+} diffusion barrier. On the other hand, the Fe/Si surface molar ratios of sample A2 is about 5 times that of sample B1, although their thicknesses are nearly the same. However, in this case there is a difference, not only in the starting solution but also in the densification thermal treatments. Although both samples have been densified at the same final temperature, coating A2 is a multilayered one, and was subjected to four heat treatments at 500°C after each dip-coating step. Thus, a high Fe diffusion is expected in this case.

These silica coatings showed no in-vitro bioactivity after 30 days of immersion in SBF solution. Next, a second external bioactive coating was applied to improve the biological performance of this samples.

3.3. *Calcium Silicophosphate Films and Coatings*

Monolayered crack-free coatings of 400 nm were obtained from this solution after thermal treatments at 500°C. These coatings as well as self-supported films were soaked for 30 days in an SBF150 solution, and subjected to in-vitro evaluation. Sol-gel monolithic glasses of the same composition developed an apatite layer after 12 h of soaking in SBF [10]. In this case, self-supported films showed formation of apatite on their surfaces after only 20 days, while no apatite layer was formed on coating C1.

Silicophosphate sol-gel systems in a physiological medium are able to release Ca and P to the solution, favoring the supersaturation of apatite in the fluid. The high surface area (around 300 m^2/g) of the sol-gel bioactive monolithic glasses prepared by Pereira et al. [10] could be one of the reasons for their remarkable in-vitro bioactivity. Texture has also been reported to play an important role on the surface reactivity. Recently, Hench et al. [11] have suggested that bioactivity is not only a matter of surface area and/or composition, but also depends on the size and total volume of mesopores. The observed differences in the in-vitro behavior of films and coatings may be related to the textural differences among these samples.

4. Conclusions

- Thick sol-gel SiO_2 coatings obtained from equimolar contents of TEOS and MTES showed an excellent corrosion behavior in a simulated body fluid solution, remaining passive after 200 h of electrochemical attack.
- These coatings are able to act as efficient barriers against the diffusion of Fe, a bioactivity inhibitor, to the sample surface. The thicker the coating, the lower is the surface Fe content, the ratio Fe/Si being as low as 0.01 for a layer of 1400 nm.
- Dense SiO_2 multilayered coatings of 550 nm thickness also show a good corrosion resistance, but show a higher Fe content on their surfaces.
- Both types of SiO_2 coatings show no in-vitro bioactivity.
- Crack-free calcium silicophosphate sol-gel coatings and self-supported films were also obtained. Only the self-supported films showed some ability to induce apatite formation in-vitro, suggesting that bioactivity depends not only on surface composition but also on the textural characteristics of the samples.

Acknowledgments

The authors wish to thank Dr. J.L. García Fierro for performing XPS measurements and for helpful discussions. This work was partially financied by a bilateral grant of CSIC (Spain)—CONICET (Argentina).

References

1. L.L. Hench and O. Andersson, in *An Introduction to Bioceramics*, edited by L.L. Hench and J. Wilson (World Scientific, 1993).
2. Y. Ebisawa, T. Kokubo, K. Ohura, and T. Yamamuro, J. Mater. Sci. Mater. Med. **1**, 239–244 (1990).
3. O. de Sanctis, L. Gómez, N. Pellegri, C. Parodi, A. Marajofsky, and A. Duran, J. Non-Cryst. Solids **121**, 338–343 (1990).
4. O. de Sanctis, N. Pellegri, and A. Durán, Surface and Coating Technology **70**, 251–255 (1995).
5. J. de Damborenea, N. Pellegri, O. de Sanctis, and A. Durán, J. Sol-Gel Sci. Techn. **4**, 239–244 (1995).
6. P. Li. Ph.D. Dissertation, Leiden University, 1993.
7. P. Li, C. Ohtsuki, T. Kokubo, K. Nakanishi, N. Soga, T. Nakamura, and T. Yamamuro, J. Am. Ceram. Soc. **75**, 2094–2097 (1992).
8. D.W. Schafer and K.D. Keefer, Mat. Res. Soc. Symp. Proc. **32**, 1–7 (1984).
9. M. Guglielmi, G. Brusatin, and N. Tombolan, Riv. Staz. Sper. Vetro, 23sup (1993).
10. M.M. Pereira, A.E. Clark, and L.L. Hench, J. Biomed. Mater. Res. **28**, 693–698 (1994).
11. M.M. Pereira, A.E. Clark, and L.L. Hench, J. Am. Ceram. Soc. **78**, 2463–2468 (1995).
12. J.L. García Fierro, private communication.

Journal of Sol-Gel Science and Technology 13, 729–733 (1998)
© 1998 Kluwer Academic Publishers. Manufactured in The Netherlands.

Organopolysiloxanes as Chemically Sensitive Coatings for Optical Fibers

KLAUS ROSE
Fraunhofer-Institut für Silicatforschung, Neunerplatz 2, D-97082 Würzburg

VLASTIMIL MATĚJEC, MILOS HAYER AND MARIE POSPIŠILOVÁ
Institute of Radio Engineering and Electronics, ASCR, Chaberska 57, CZ-18251 Prague

Abstract. Various types of UV-curable organically modified siloxanes have been synthesized by the sol-gel method with the aim of fabricating chemically sensitive coatings for silica optical fibers. The refractive index of the coating material can be tailored in the range from 1.46 to 1.56, and sensitivity towards CO_2 is achieved by incorporation of amino groups. The interaction of the cured layers with CO_2 or with hydrocarbons has been studied in immersion experiments. Both the reaction of CO_2 with incorporated amino groups and the penetration of hydrocarbons into the layer induce changes of the light absorption coefficient and the refractive index of the coating which are detected by measuring the output light intensity from the fiber.

Keywords: hybrid materials, organopolysiloxanes, sol-gel synthesis, fiber optic sensor

1. Introduction

During recent years the sol-gel route has increasingly been extended to the preparation of inorganic/organic hybrid materials [1]. Owing to the wide range of possible combinations of inorganic and organic components, they have considerable potential for functional coatings [2]. Recently, they have been studied for changing the hydrophobicity of sensing layers in fiber-optic chemical sensors [3]. Moreover, sensitive layers for interdigital capacitors and integrated optical interferometers have been developed [4, 5] as well as UV-curable poly(acryloxy)siloxane coatings for silica fibers [6]. The influence of solvents and CO_2 dissolved in water on the light attenuation of these fibers has been reported elsewhere [7]. This paper describes the preparation and properties of UV-curable poly(acryloxy)siloxanes applied on silica optical fibers with respect to the special use as fiber-optic chemical sensor for CO_2 and hydrocarbons.

2. Experimental

2.1. *Material Synthesis*

Mercaptopropylmethyl-dimethoxysilane or aminopropylmethyl-diethoxysilane is added to an equimolar amount of a multifunctional acrylic compound (ethoxylated bisphenol-A-diacrylate, trimethylolpropane triacrylate, propoxylated or highly propoxylated glyceryl triacrylate) dissolved in ethylacetate or ethanol. After the addition reaction hydrolysis is carried out using the semimolar amount of water with respect to all hydrolyzable alkoxy groups. After sol-gel processing, the solvent is removed in vacuo and a viscous resin is obtained. For UV-curing, 3% by weight of a photocatalyst (Irgacure® 500) are added.

2.2. *Fabrication and Characterization of Coated Fibers*

Fibers were drawn from silica rods (Herasil, France) in a graphite furnace (Centor, USA). Acrylate polysiloxanes were continuously applied on fibers in a die and UV-cured using a lamp with an input power of 1.6 kW (Fusion, USA). The coating thickness was controlled by the output diameter of the die.

The spectral attenuation of coated fibers and its changes due to interaction with chemicals have been determined by measuring the output light power from the fiber. The experimental setup and measurement conditions have been described elsewhere [8].

The sensitivity of fibers to selected chemicals has been determined by immersing a fiber in a dispersion

of water with *n*-heptane or xylene, or bringing a fiber into contact with gaseous CO_2 in a gas cell.

The mechanical strength of fibers has been determined by using an axial load tester [9].

3. Results and Discussion

3.1. Material Preparation and Characterization

The synthesis of the coating materials in the first step comprises the Michael type addition reaction of $H_2N(CH_2)_3SiMe(OEt)_2$ or $HS(CH_2)_3SiMe(OMe)_2$ to one acrylic C=C-bond of a monomeric multifunctional acrylate compound. In the second step the resulting acrylate alkoxysilane reacts to the polysiloxane via hydrolysis and condensation (Fig. 1). The poly(acryloxy) siloxanes **1** and **2** bearing thioether moieties exhibit refractive indices of 1.56 and 1.52, respectively. Since these values are too high for evanescent-wave measurements using a silica optical fiber sensor system, we synthesized new acrylate functional polysiloxanes with lower refractive indices, which contained no aromatic structures and no thioether groups. Based on the addition of the amino silane to various acrylate compounds, the refractive indices of the resulting acrylate amino polysiloxanes **3**–**5** were in the range of 1.46–1.47.

The reaction of primary and secondary amines with CO_2 forming carbamic acid derivatives due to the insertion of CO_2 into the N—H-bond is well known [10] and can be observed by infrared spectroscopy. We chose this special reactivity for our approach of the manufacture of a CO_2 sensitive coating system. Using cured layers on glass slides, we observed the reaction of the incorporated N—H moiety with gaseous CO_2 by

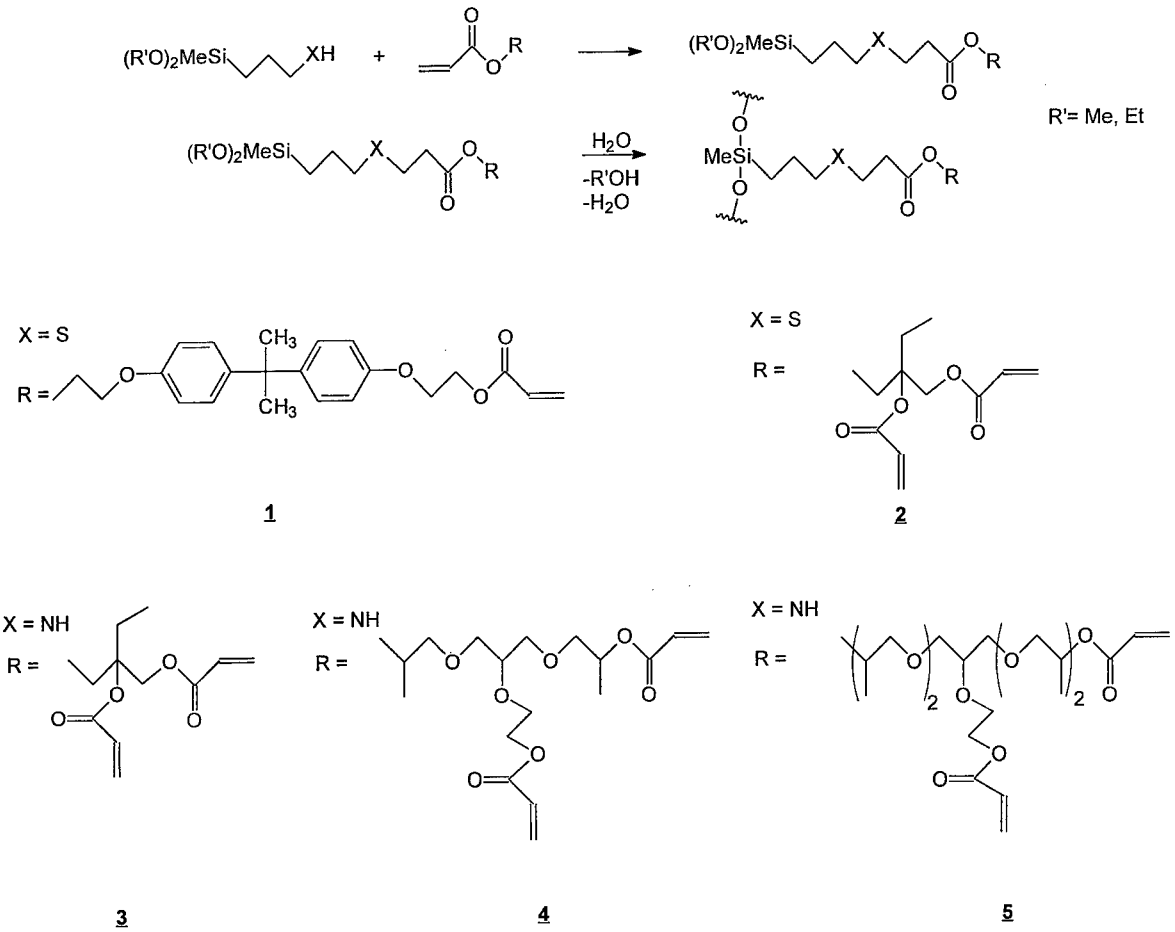

Figure 1. Synthesis scheme of various acrylate functional polysiloxanes.

infrared spectroscopy. The disappearance of the N—H-signal at 3321 cm^{-1} and the appearance of new signals of the C=O vibration at 1540 and 1560 cm^{-1} indicate the reaction of the secondary amino groups in the cured layer as outlined before.

3.2. *Properties of Coated Fibers*

Based on the observed reactivity of the N—H-groups incorporated in the polysiloxane we investigated the CO_2-sensitivity of fibers coated with siloxanes **3** and **5** during their contact with CO_2 at different flow rates (Fig. 2). In both cases a significant change of the fiber attenuation is observed which can be attributed to the change of the refractive index of the polysiloxane layer, due to the CO_2 insertion mentioned above. Higher attenuation is achieved using a higher flow rate and siloxane **3**.

Results of preliminary investigations concerning the influence of solvents on the attenuation of coated fibers have been described earlier [7]. Now we determined the sensitivity of fibers coated with polysiloxane **5** to selected hydrocarbons by immersing them into a dispersion of water with 10 vol% of *n*-heptane ($n_D = 1.387$) or xylene ($n_D = 1.497$). On the addition of xylene a significant higher increase of the attenuation was found in comparison to the influence of *n*-heptane due to the higher refractive index of the aromatic compound (Fig. 3). The changes of the fiber attenuation can also be explained by changes of the refractive index of the siloxane due to diffusion of the hydrocarbons into the layer. The washing-out of the hydrocarbons from the coatings and the effect of water penetration into them have been investigated by long-time immersion of the fiber into pure water after treatment with the hydrocarbons. As can be seen from the comparison of the curves measured after 10 and 800 min, xylene

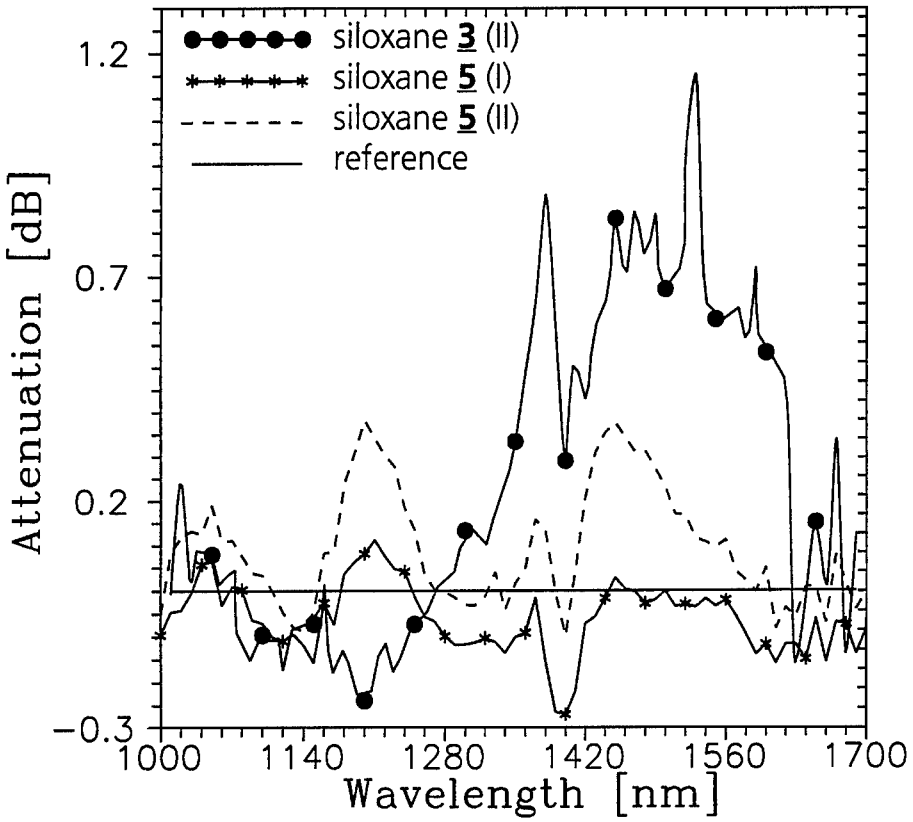

Figure 2. Effect of gaseous CO_2 on the attenuation of silica fibers coated with siloxane **3** and **5** measured at CO_2 flow rates of 10 cm^3/min (I) and 100 cm^3/min (II). Fibers with active lengths of 15 cm, silica diameter of 200 μm and coating thickness of 5 μm were used. The reference output power was measured with the fiber in air.

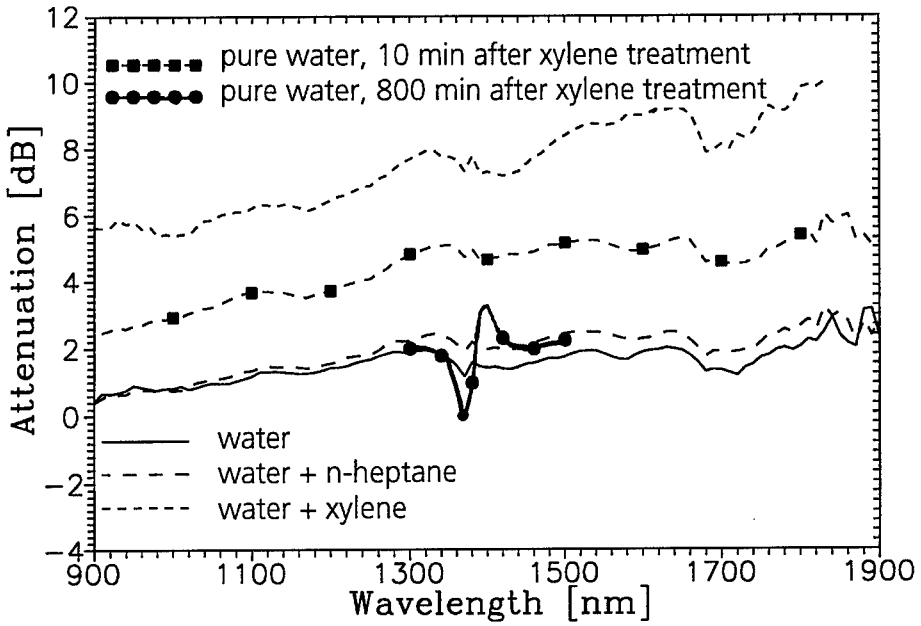

Figure 3. Changes in attenuation of fibers coated with siloxane **5** after immersion into water/*n*-heptane or water/xylene dispersion (10 vol% of the hydrocarbon) for about 10 min. Effects of washing-out of xylene by immersion in pure water measured 10 and 800 min after hydrocarbon treatment.

once having penetrated into the siloxane layer is also washed-out again, resulting in a decreased attenuation (Fig. 3). The spectral changes around 1400 nm observed after immersing the fiber for 800 min are attributed to a slow penetration of water into the siloxane layer.

An important aspect for the application of coated silica fibers is the resulting fiber strength. The mechanical strength of the fiber samples coated with polysiloxane **1** is comparable to that of fibers coated with a commercially available UV-curable acrylate resin (DeSotto, USA) (Fig. 4). The mechanical strength has been observed to be strongly dependent on the thickness of the siloxane layer. For coatings with thicknesses of 5 μm the fiber strength decreased to about 1.5 GPa.

4. Conclusion

Several samples of acrylate functional polysiloxanes with different values of refractive indices have been prepared by the sol-gel method. They can be applied on silica optical fibers using standard fiber drawing technology and can be used as protective coatings as well as sensitive layers. The sensitivity is based on changes of optical properties due to interaction with gaseous CO_2 or hydrocarbons. This sensitivity can be employed for the development of fiber-optic chemical sensors. The future development in this field will focus on the scaling-up of acrylate siloxane resins with a refractive index below 1.457 in order to prepare materials suitable for evanescent-wave chemical sensors.

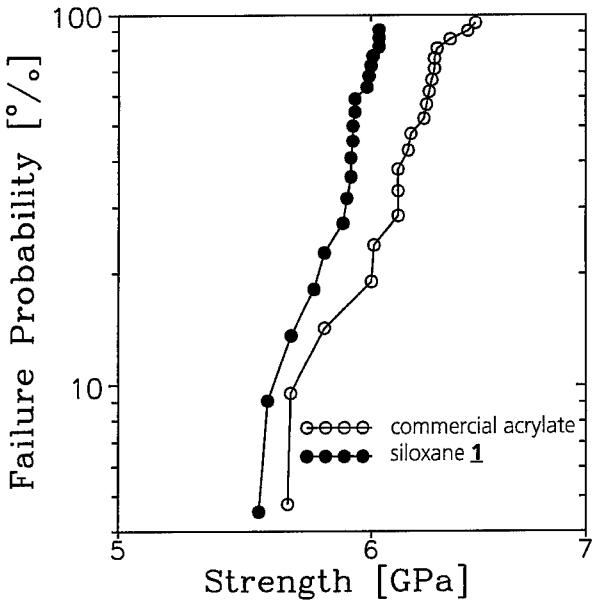

Figure 4. Weibull probability plots of silica fibers coated with siloxane **1** and a commercial UV-curable acrylate (DeSotto). Fibers with silica diameters of 125 μm and a coating thickness of 60 μm are used.

Acknowledgment

This work was financially supported by the European Community under contract No. CIPA-CT94-0140 and by the Grant Agency of the Czech Republic under Contract No. 102/95/0871.

References

1. B.M. Novak, Adv. Mater. **5**, 422 (1993).
2. U. Schubert, N. Hüsing, and A. Lorenz, Chem. Mater. **7**, 2010 (1995).
3. B.D. MacCraith, C. McDonagh, A.K. McEvoy, T. Butler, G. O'Keeffe, and J. Murphy, J. Sol-Gel Sci. Technol. **8**, 1053–1061 (1997).
4. H.E. Endres, S. Drost, and F. Hutter, Sens. Act. B **22**, 7 (1994).
5. A. Brandenburg, R. Edelhäuser, and F. Hutter, Sens. Act. B **11**, 361 (1993).
6. K. Rose, in *Organosilicon Chemistry II*, edited by N. Auner and J. Weis (VCH, Weinheim, 1996), p. 649.
7. V. Matějec, K. Rose, M. Hayer, M. Pospíšilová, and M. Chomát, Sensors and Actuators B **39**, 438 (1997).
8. G. Stewart, J. Norris, D. Clark, M. Tribble, I. Andonovic, and B. Culshaw, in *Chemical, Biochemical and Environmental Application of Fibers*, Proc. SPIE **990**, 188 (1988).
9. V. Matějec, M. Hayer, P. Pavlovič, M. Kubečková, G. Kuncová, and M. Guglielmi, J. Sol-Gel Sci. Technol. **5**, 193–199 (1995).
10. A. Diaf, R.M. Enick, and E.J. Beckman, J. Appl. Polym. Sci. **50**, 835 (1993).

Journal of Sol-Gel Science and Technology 13, 735–738 (1998)
© 1998 Kluwer Academic Publishers. Manufactured in The Netherlands.

Sol-Gel Processing of Organic-Inorganic Nanocomposite Protective Coatings

YUNFA CHEN, LIANMING JIN AND YUSHENG XIE
Institute of Chemical Metallurgy, Chinese Academy of Sciences, Beijing 100080, China

Abstract. Organic-inorganic nanocomposite protective coatings are prepared on aluminum substrates by the spinning technique with the concept of incorporating homogeneously nanosized particles (of AlOOH, Al_2O_3, ZrO_2, SiC) into molecular organic-inorganic hybrid matrices. The hybrid matrices are prepared from epoxysilane and bisphenol A with imidazol as catalyst. The AlOOH particles are derived from aluminum isopropoxide and introduced into the hybrid sols directly, and Al_2O_3, ZrO_2, SiC particles are first surface-modified with Si—OH from hydrolyzed TEOS. The coatings are dense, smooth and flexible and inhibit corrosion.

Keywords: sol-gel, organic-inorganic nanocomposite, protective coating, nanosized particles

1. Introduction

Sol-gel processing of new organic-inorganic hybrid materials has gained increased interest in the last decade. These materials are synthesized by chemically incorporating organic polymers into inorganic networks, resulting in excellent and even unique properties [1–3]. Due to avoidance of the disadvantages in processing of monoliths, such as the relatively high cost of precursors, drying stresses and effective removal of volatiles, sol-gel coatings have already been used in a wide variety of applications, in which organic-inorganic hybrid coatings constitute an important new family [4].

Particulate sols can be prepared using colloid chemistry and polymeric sols by hydrolyzing alkoxides [4]. Thus, incorporating particulate sols (nanosized particles) into the molecular hybrid structure normally derived from modified silicon alkoxides will open the possibility of achieving new multifunctional materials, especially those including non-oxide components [5].

In this work, organic-inorganic nanocomposite coatings are prepared by incorporating homogeneously nanosized particles (of AlOOH, Al_2O_3, ZrO_2, SiC) into molecular organic-inorganic hybrid matrices. The hybrid matrices are derived from epoxysilane and bisphenol A. AlOOH particles were introduced into the hybrid sols directly, and Al_2O_3, ZrO_2, SiC particles were first surface-modified with Si—OH from hydrolyzed TEOS. The coatings thus obtained are dense, flexible, inhibit corrosion and are chemically durable.

2. Experimental

Polymeric Sol Preparation

The precursors were 3-glycidoxypropyltrimethoxysilane (GLYMO) and bisphenol A, imidazol being used as a catalyst. The preparation procedure is as follows. First, GLYMO (1 mol) was prehydrolyzed with 6 molar equivalents of water (pH 5–6) at 40°C for 1 hour, bisphenol A (0.1 mol) was then added. After stirring for 10 min, imidazol was put into the mixture, increasing the temperature to 60°C, and stirring continued for another 30 min.

Particulate Sol Preparation

Boehmite (AlOOH) sol was prepared at 90°C by hydrolysis of Al-isopropoxide in excess water, and peptization with HNO_3 (molar proportion of $Al(OR)_3$/H_2O/HNO_3, 1/100/0.07), using the procedure reported by Yoldas [6]. The boehmite size in the sol was determined as <50 nm. The Al_2O_3, ZrO_2 and SiC powders were prepared in the laboratory using a coprecipitation

or plasma method, with an average size of 40 nm, 70 nm and 80 nm, respectively. In order to improve the distribution/bonding of the ceramic particles in the hybrid matrix, they were first surface-modified by hydrolyzed tetraethoxysilane (TEOS) using Sacks's method [7], using ~70 wt% powders/30 wt% SiO_2. The hydrolysis was stopped after stirring 4–6 hours at 40°C and monitored by IR spectral analysis.

The two kinds of sol prepared were subsequently mixed to produce nanocomposite (coating) sols. If boehmite, Al_2O_3 and ZrO_2 were used as the particulate phase, the mixed sols sometimes became turbid, but a little ethanol addition would cause the system to become transparent. In the case of SiC particles, the sol had the color of the SiC particles. The low viscosity nanocomposite sols could be stored for a long time and remain suitable for coating. Commercial aluminum plate (1.5 mm in thickness) was used as the substrate. The spinning technique was used for coating with a speed of 3000 rpm. The coatings were then dried at room temperature and subsequently heated very slowly (1°C/min) to 130°C and held at this temperature for 1 hour.

The characterization techniques used included viscosity measurement, thermal analysis (DTG-DTA), infrared spectroscopy (IR), surface profilometry, scanning electron microscopy (SEM) and corrosion inhibiting tests.

3. Results and Discussion

3.1. Viscosity Measurement

In order to obtain the most suitable time for carrying out the coating process, the viscosity of the nanocomposite sols was measured by a rotational viscometer at 60°C. In all the cases with different nanosized particles, the viscosity variation with time initiated from the moment when the polymeric sol was mixed with the particulate sol was similar and can be divided into three stages, as shown in Fig. 1 for the Al_2O_3 system. The first increase may be due to further polymerization and the interaction of the two kinds of sol. A constant viscosity of about 15 cP is subsequently obtained for almost 90 min, which is suitable for coating. The gelation begins in the third stage. However, some precipitate particles were observed if the particle size was larger than 50 nm.

In coating by the spinning method, only a small quantity of sol is normally needed, which leads the hot sol to cool down quickly. The viscosity measured at 60°C was therefore compared with that at room temperature but only a minor difference was detected. It is worth noting that the performance of coatings derived from the sol kept at room temperature is even better than those from the sol at 60°C. This will make the coating procedure more useful practically.

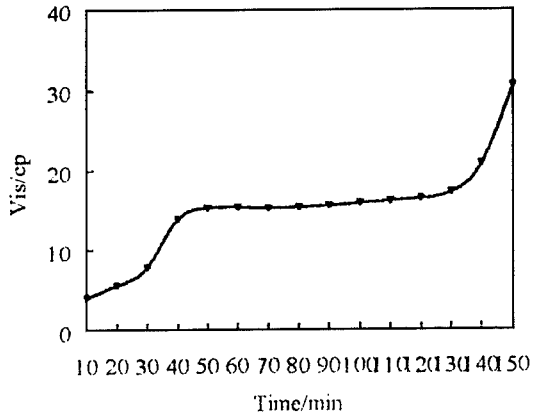

Figure 1. Variation of viscosity with time in sol containing Al_2O_3 particles (60°C).

3.2. Thermoanalysis

Thermal analysis was completed in an air atmosphere using a heating rate of 2°C/min. The samples were ground xerogels obtained by drying the sols at 40°C for 10 hours.

Figure 2 illustrates the TG-DTA curves recorded on the sample containing boehmite. The endothermic

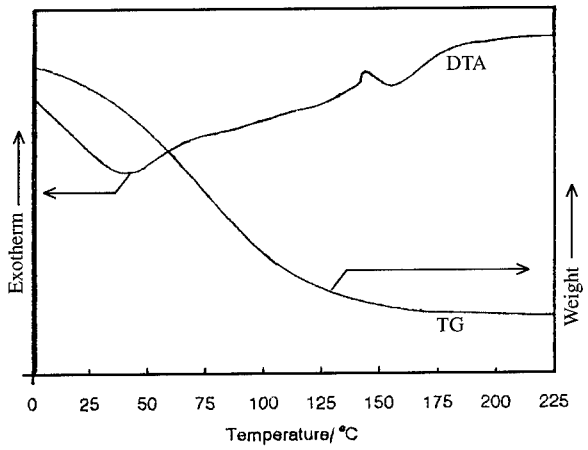

Figure 2. TG-DTA curves on the xerogels (boehmite, air atmosphere, 2°C/min).

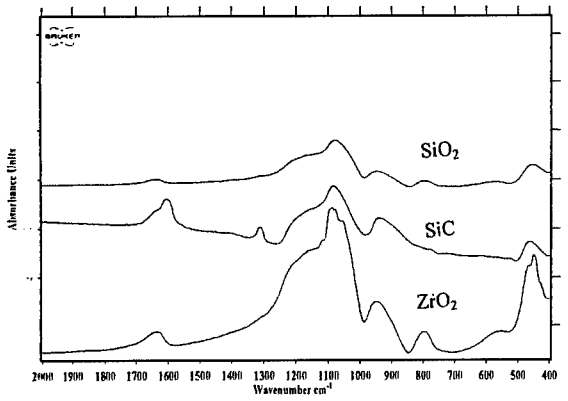

Figure 3. IR spectra of the surface modified particles by hydrolyzed TEOS.

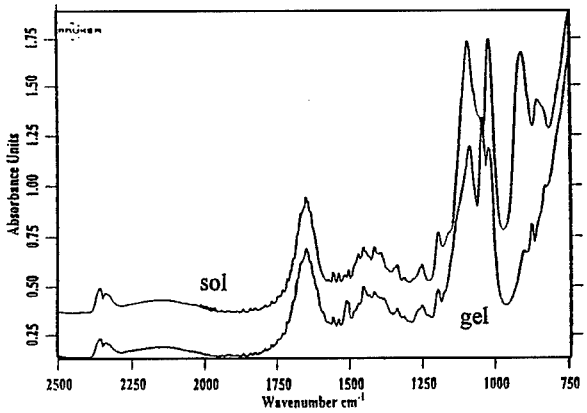

Figure 4. IR spectra of nanocomposite sol and gel (boehmite system).

peak accompanied by a weight loss is attributed to the removal of residual water and solvent. An exotherm at about 150°C appears to be the result of decomposition. If the coating was heated to 150°C, it became yellow. From the IR spectra, it is found that the Si—OH in the coating disappeared at 150°C. So the curing temperature in this system is normally fixed at 130°C.

3.3. *Infrared (IR) Spectroscopy [8]*

Figure 3 shows the IR spectra for the surface-modified ZrO_2 and SiC particles using hydrolyzed TEOS. For comparison, IR spectra of the SiO_2 gel obtained from TEOS under the same reaction conditions is also included. Figure 3 indicates that the ceramic particles were coated with a layer of Si—O groups, which is useful to assist bonding of the particles with the hybrid matrix.

The epoxy group in GLYMO is capable of forming either diol units by hydrolytic ring opening or polyethene oxide chains by polyaddition. To separate the two process with formation of the inorganic network and organic crosslinking, the introduction of bisphenol A and 1-methylimidazol (MI) into the system is normally necessary. MI acts as a catalyst for the condensation of silanol groups and also an initiator for the epoxide polymerization above 60°C [3]. However, It was found that the MI addition resulted in a light yellow color. The replacement of MI with imidazol in the present work avoided the color change until a slightly higher temperature.

Comparing the IR spectra of GLYMO before and after prehydrolysis, the epoxy ring (~1200 cm^{-1}, 930 cm^{-1} and 850 cm^{-1}) is clearly opened. After hydrolysis of Si—OR, the peak of Si—O (Si—OH) is near 860 cm^{-1}, $-CH_3$ in the form of $Si—OCH_3$ (~2817 cm^{-1}) has almost disappeared. Figure 4 shows the IR spectra for the nanocomposite sol and the cured coating. Bisphenol A is covalently connected with the chain and the C—O—C bond is detected near 1050 cm^{-1}, also the broad peak of Si—O—Si is clearly observed. From Fig. 5, the differences for IR spectra of the gels cured at 90°C and 150°C are related to the bands belonging to the Si—OH group. Above 150°C, the Si—OH disappeared as observed on the DTA curves.

3.4. *Coating Thickness and SEM Observation*

The coating thickness was measured using a surface profiler (Sloan Tech, Dektak-3ST). The thickness of coatings after a single spinning was 1–3 μm. If thicker

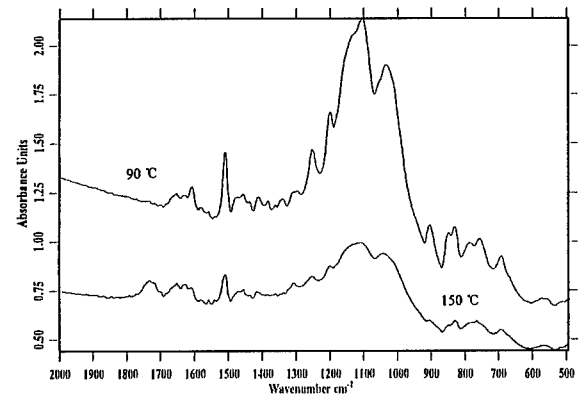

Figure 5. IF spectra of the cured gels at 90°C and 150°C (ZrO_2 system).

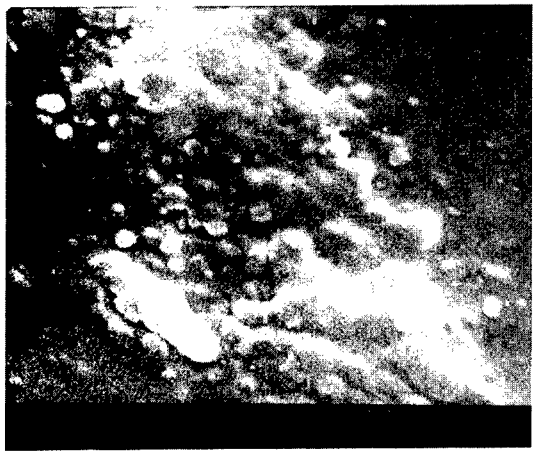

Figure 6. SEM micrograph of cured nanocomposite coating (Al_2O_3 system).

coatings were needed, repeated spinning could be used. In the present case, spinning for 2–3 times was necessary to obtain dense, smooth and flexible coatings with a thickness of about 7 μm.

The surface characteristics of the coatings were observed by SEM. Figure 6 shows the cured coating with Al_2O_3 particles, but it is representative of all the cases. The particles were observed to be homogeneously distributed in the coatings. The particle size on the SEM micrographs was slightly larger than that in the raw materials. This may be due to the particles being coated with Si—O or organic groups. If AlOOH was used, this phenomenon was less obvious.

3.5. Coating Performance

Coated aluminum samples were treated in 1 N HCl, 1 N NaOH and 1 N KCl solutions at room temperature for one month, but no corrosion took place. However, for treatment in concentrated HCl (37 wt%), corrosion was detectable after only 70 min.

If boehmite is added as a nanosized particle, Kassemann and Schmidt assumed that the interface is stabilized by the nanocomposite matrix through the heterocondensation of silanols with surface Al—OH groups. In the present case, a similar explanation can be applied due to the very similar corrosion behavior of the various nanocomposite coatings.

If the coated aluminum plate was subjected to bending for several times, the coating did not peel off, indicating that it was sufficiently flexible. In this system, the introduction of bisphenol A and boehmite sol should make the coating scratch resistant and the organic groups should improve the flexibility, although tests have not been completed.

4. Summary and Conclusions

Organic-inorganic nanocomposite protective coatings were prepared on aluminum substrates by a spinning technique. In the coatings nanosized oxide particles (AlOOH, Al_2O_3, ZrO_2, SiC) were incorporated homogeneously into a molecular hybrid matrix. The hybrid matrix was derived from epoxysilane and bisphenol A with imidazol as catalyst, which avoids the light yellow color found in the case of 1-methylimidazol. The AlOOH particles prepared from Al isoproxide were introduced directly into the hybrid sols, and the other particles were first surface modified with Si—OH groups. The coatings are dense, smooth and flexible and inhibit corrosion.

Acknowledgment

The authors are grateful for financial support by the Chinese Academy of Sciences (CAS) and Ministry of Human Affairs.

References

1. G. Philipp and H. Schmidt, J. Non-Cryst. Solids **63**, 283 (1984).
2. G.L. Wilkes, B. Orler, and H. Huang, Polymer. Prepar. **26**, 300 (1985).
3. S. Amberg-Schwab, E. Appac, W. Glaubitt, K. Rose, G. Schottner, and U. Schubert, in *High Performance Ceramic Films and Coatings*, edited by P. Vincenzini (Elsevier Science, B.V., 1991), p. 203.
4. C.J. Brinker and G.N. Scherer, *Sol-gel Science* (Academic Press, San Diego, 1990), p. 235.
5. R. Kassemann and H. Schmidt, in *First European Workshop on Hybrid Organic-Inorganic Materials* (Chateau de Bierville, France, 1993), p. 171.
6. B.E. Yoldas, J. Mater. Sci. **10**, 1856 (1975).
7. M.D. Sacks, N. Bozkurt, and G.W. Wchwiffele, J. Am. Ceram. Soc. **74**, 2428 (1991).
8. Y. Zhao and X. Sun, *Spectrum Analysis and Indentification of Organic Structure* (Press of University of Science and Technology, Hefei, China, 1992), p. 430.

Journal of Sol-Gel Science and Technology 13, 739–742 (1998)
© 1998 Kluwer Academic Publishers. Manufactured in The Netherlands.

Synthesis of Transparent Mesoporous and Mesostructured Thin Silica Films

J.M. BERQUIER, L. TEYSSEDRE AND C. JACQUIOD
Laboratoire CNRS/Saint-Gobain "Surface du Verre et Interfaces", 39 quai Lucien Lefranc, F 93303 Aubervilliers

Abstract. A novel method for obtaining crack-free transparent periodic mesoporous thin films is described. Such films are prepared by a simple sol-gel process using surfactants as templates, with a pre-treatment of the glass substrate. The silicate precursor (tetraethoxysilane) is pre-hydrolyzed under acidic conditions before dissolving directly cetyltrimethylammonium bromide (CTAB). The solution is then spin-coated on pre-treated glass substrate. After the film has been deposited, it is calcined in air. X-ray Diffraction (XRD) has been used to characterize the film before and after thermal treatment. The film consists of a nanocomposite material with a periodic structure. Before calcination the XRD pattern has a sharp peak at $d = 3.8$ nm, which is broadened and shifted by about 3.0 nm after calcination. Infrared transmission spectra have been performed on the films. Analysis of the free OH group stretching vibration indicates the removal of the surfactant after calcination in addition to an enhancement of the specific surface area.

Keywords: mesoporous materials, thin films, template, silicon compounds

Introduction

Since the synthesis of the ordered mesoporous silica material M41S [1], the use of surfactants as templates to prepare mesostructured materials has been widely studied [2]. The principal applications of these materials are as molecular sieves and in catalysis. Consequently, processing to data has concentrated on powder products obtained by hydrothermal synthesis. Interest in the synthesis of thin mesoporous films by molecular templating is recent. Several different approaches have been examined. Free standing oriented films have been produced by growth at the substrate/liquid or air/liquid interface for applications as membranes [3, 4]. For silica films on a substrate, the sol-gel process is suitable but the thermal treatment necessary to obtain porous materials is often critical for the quality of the final coating. Ogawa [5] reported the production of transparent nanostructured films on silica without release of surfactants by sol-gel processing. The only mesoporous films they obtained were self-supported. Anderson et al. described the preparation of homogeneous mesostructured, but light scattering, films [6]. It is noteworthy that good results have been obtained on porous silica substrates [7].

We report here a simple method for the synthesis of mesoporous, transparent and defect free nanocomposite films on dense glass substrates.

Experimental

A sol-gel process was employed for the preparation of the samples. The films were deposited from a solution of prehydrolyzed tetraethoxysilane (TEOS, Aldrich) on glass substrates (Pyrex).

A mixture containing TEOS : H_2O(HCl pH = 2.5) : C_2H_5OH in the molar proportions 1 : 10 : 6 was stirred overnight. The alcohol (Normapur Prolabo) was partially evaporated in order to obtain a solution with a 5 M silicate concentration. The surfactant cetyltrimethylammonium bromide (CTAB, Sigma) was then directly dissolved in this solution by vigorous stirring. The CTAB/Si ratio was 0.1. The films were then spin-coated at 2500 rpm for 30 s on pre-treated substrates. The pre-treatment consisted of precipitating a thin layer of aluminium hydroxide on the surface before depositing the silica gel. For this purpose, the substrate was immersed into a KNO_3-$Al(NO_3)_3$ solution before precipitating the aluminium hydroxide by addition of

KOH [8]. The thickness of the hydroxide layer determined by Atomic Force Microscopy (AFM) was about 5 nm.

After coating, the films were dried at 100°C for 12 hours in order to remove the residual alcohol and accelerate the condensation reactions. The porous materials were obtained after a calcination for 12 hours at 400°C in air with a slow heating rate (10°/hour). The thickness of the films was about 1 μm. The template free films are transparent in the visible wavelength region and defect free.

The films were characterized before and after calcination by low angle X-ray diffraction on a Siemens D5000 Diffractometer (θ–2θ mode) using CuK_α radiation. Infrared spectroscopy was used to confirm the departure of the surfactant molecules after calcination and to follow the evolution of hydroxyl groups in the film. IR spectra in transmission mode were recorded on Nicolet 710 FTIR spectrometer with a resolution of 2 cm^{-1}.

Results and Discussion

Small angle X-ray diffraction patterns (Fig. 1) of a film containing CTAB clearly indicates that the process leads to a mesostructured material. The XRD pattern shows a sharp peak at $d = 3.8$ nm and a weaker reflection at $d = 1.9$ nm that can be indexed on a lamellar phase respectively (100) and (200). The diffraction peaks at $d = 2.6$ and 1.3 nm are due to residual CTAB crystals that a water washing is sufficient to release. The less intense peak at smaller angles ($d = 4.2$ nm) could be attributed to randomly packed micelles as previous studies supported by TEM investigations have shown [7].

After calcination, the free template films have a similar structure with broadened diffraction peaks and a decrease in the relative intensity. This result demonstrates that even if the structural order is decreased by the calcination, the structure is maintained on coherent domains of about 30 nm according to the Scherer formula. The $d_{(100)}$ value of the template free sample (3.0 nm) is smaller that the value of the noncalcined sample. This reveals a contraction of the siliceous network during calcination.

Figure 2 shows the FTIR transmission spectra of the films prepared according to the same process. The spectrum obtained before calcination reveals several aspects of the organization of the CTAB contained in the film. This spectrum has two bands between 2800

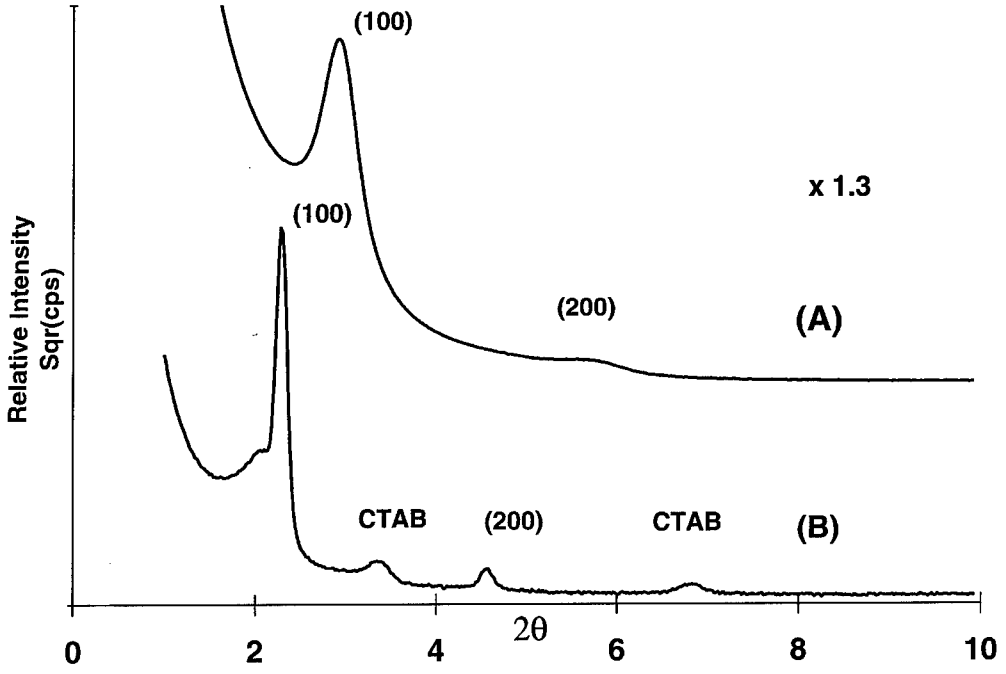

Figure 1. XRD pattern of silica thin film: (A) after calcination at 400°C and (B) before calcination.

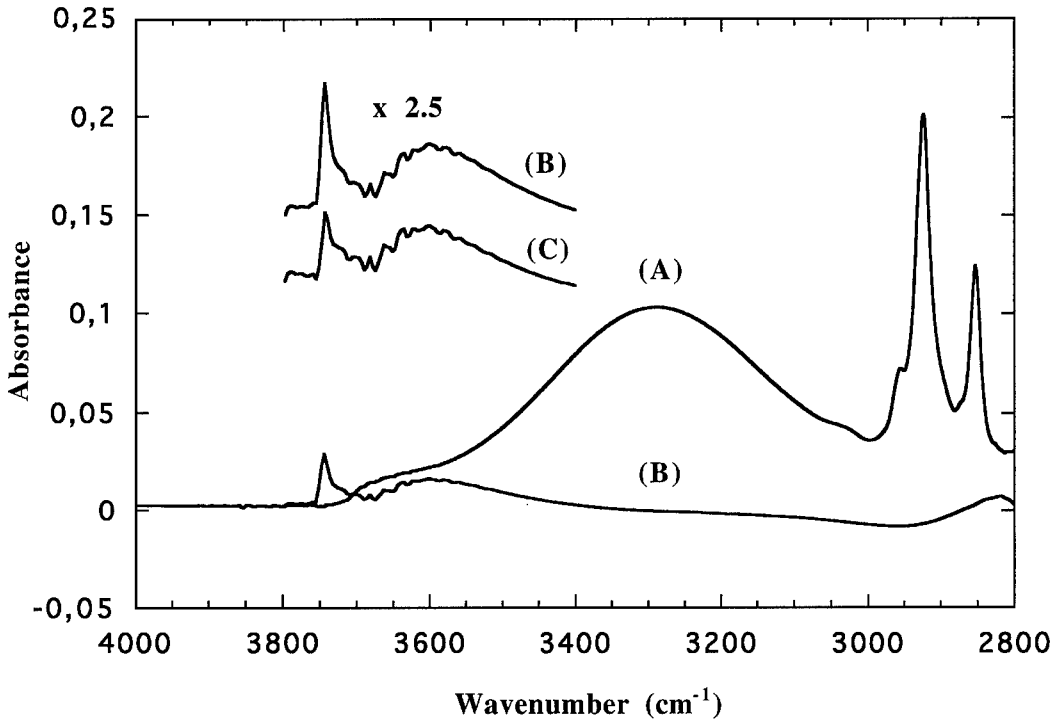

Figure 2. IR spectra of the silica film: (A) before calcination and (B) after calcination at 400°C. Inset, IR spectra with an intensity scale expansion of 2.5 of calcined film: (B) with CTAB/Si = 0.1 and (C) with CTAB/Si = 0.01.

and 3000 cm^{-1} due to CTAB and a large band between 3000 and 3600 cm^{-1} due to adsorbed water and to the silanols engaged in hydrogen bonding.

The bands due to CTAB consist of two intense and narrow bands corresponding to the CH_2-stretching vibrations (asymmetric at 2923 cm^{-1} and symmetric at 2853 cm^{-1}) and in two less intense bands, respectively at 2955 and 2872 cm^{-1} due to similar vibrations for the CH_3 groups. The frequencies of these vibrations are very dependent on the aggregation order of the CTAB molecules. According to Kung and Hayes [9], the observed values correspond to CTAB in micellar forms. The quantity of CTAB in crystalline form, visible on XRD patterns, should provide peaks at 2930 and 2860 cm^{-1} which are not detected. The reason is that this form is minor and the bands are probably merged in with more intense bands. The integrated intensities of the bands are consistent with the quantity of surfactant introduced in the film.

After calcination, a narrow band at 3740 cm^{-1} appears. This band corresponds to the stretching vibrations of the free silanols [10]. This band is characteristic of the surface sites of the pores created by the departure of the CTAB micelles. Its intensity is proportional to the initial quantity of CTAB. Figure 3 shows the spectrum of the film after condensation of water vapor on the surface. A broad band with a maximum around 3400 cm^{-1} appears to be due to ν(OH) of molecular water and to H-bonded silanols. On the other hand, the intensity of the band of free OH decreases considerably which proves that a large amount of pores are accessible to the water vapor and are hence interconnected.

These results show that it is possible to realize nanocomposite mesoporous films. Moreover, even though no mechanical tests have been performed, the mechanical behavior of these coatings is sufficient to resist thermal stresses and surfactant release. Hence the material is defect free. The improvement with respect to previous studies consists essentially in the pre-treatment of the substrate. The origin of the effect of the pretreatment is the modification of the isoelectric point (IEP) of the surface. Silica glasses present an IEP of the order of 2–3 which is lower than the pH of the synthesis medium. In these conditions the surface is negatively charged by preferential dissociation of the silanols in SiO^- sites. The cationic surfactants consequently adsorb on the substrate [11] hindering the condensation of the silicate species with the surface silanols. The resulting films do not resist thermal treatment because there is insufficient adhesion and therefore large crack

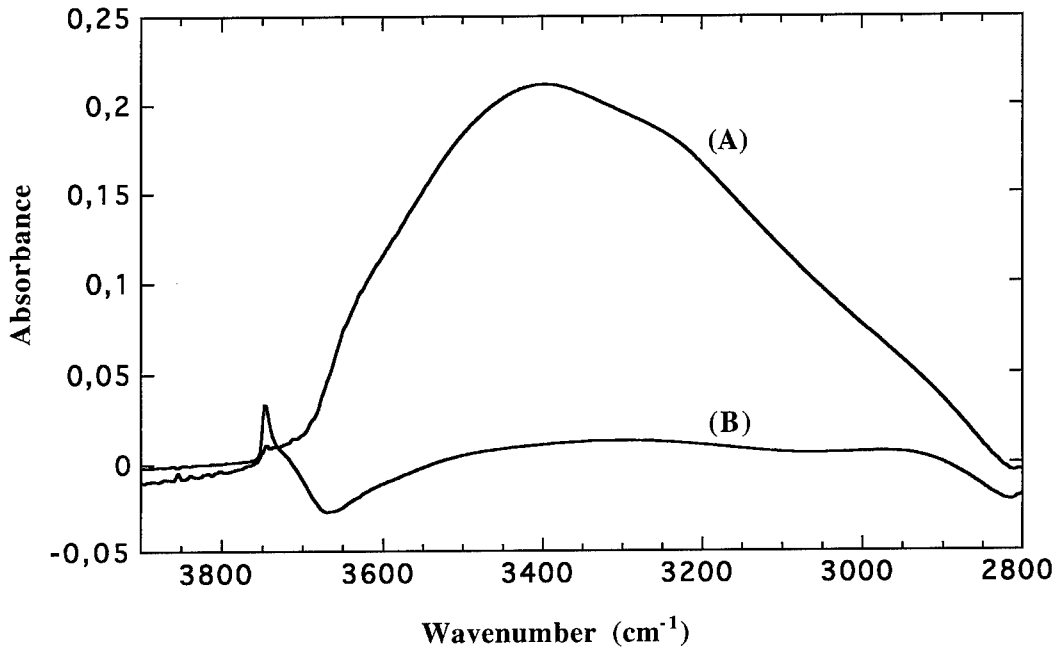

Figure 3. IR spectra of the calcined film: (A) with water condensation and (B) without water condensation.

develop. As the IEP of the alumina-treated substrate is higher (IEP ≈ 9 [12]), the affinity between the surfactant and the substrate vanishes, benefiting the covalent bonds between the glass surface and the film. Such a pre-treatment effectively results in crack free porous materials.

Conclusions

We have described a simple method to obtain transparent mesoporous and mesostructured silica films on glass substrates. To our knowledge this is the first time that such films have been obtained on dense substrates and could find developments in functional coatings requiring high specific area (e.g., catalytic activity, optical devices, etc.) for transparent materials like glasses.

Acknowledgments

We thank B. Germain for the XRD data.

References

1. C.T. Kresge, M.E. Leonowicz, W.J. Roth, J.C. Vartuli, and J.S. Beck, Nature **359**, 710 (1992).
2. N.K. Raman, M.T. Anderson, and C.J. Brinker, Chem. Mater. **8**, 1682 (1996).
3. H. Yang, A. Kuperman, N. Coombs, S. Maniche-Afara, and G.A. Ozin, Nature **379**, 703 (1996).
4. H. Yang, N. Coombs, I. Sokolov, and G.A. Ozin, Nature **381**, 589 (1996).
5. M. Ogawa, Chem. Commun. 10, 1149 (1996).
6. M.T. Anderson, J.E. Martin, J.G. Odinek, and P. Newcomer, MRS Proc. **431**, 217 (1996).
7. J. Liu, J.R. Bontha, A.Y. Kim, and S. Baskaran, MRS Proc. **431**, 245 (1996).
8. A. Doren, L. Lemaitre, and P.G. Rouxhet, J. Colloid. Interf. Sci. **130**, 146 (1989).
9. K.H.S. Kung and K.F. Hayes, Langmuir **9**, 263 (1993).
10. A. Corma, V. Fornes, M.T. Navarro, and J. Perez-Pariente, J. catal. **148**, 569 (1994).
11. R.B. Bjorklund, S. Zangooie, and H. Arwin, Langmuir **13**, 1440 (1997).
12. R.J. Hunter, *Zeta Potentiel in Colloid Science—Principles and Application* (Academic Press, London, New York, 1981).

Journal of Sol-Gel Science and Technology 13, 743–747 (1998)
© 1998 Kluwer Academic Publishers. Manufactured in The Netherlands.

Elaboration at 80°C of SiO_2 Layers Deposited by Aerosol-Gel Process

M. LANGLET AND C. VAUTEY
Laboratoire des Materiaux et du Génie Physique—UMR 5628 CNRS, ENSPG-INPG, BP 46, 38402 Saint Martin d'Hères, France
Michel.Langlet@inpg.fr

Abstract. The aerosol-gel process is a thin film deposition technique based on the sol-gel polymerization of a liquid film deposited from an ultrasonically sprayed aerosol. SiO_2 layers have been deposited by aerosol-gel process from TEOS solutions prepared using a two-step procedure. After a post-treatment at 80°C, the layers have a remarkable abrasion resistance and a high refractive index. In this paper, the chemical mechanisms involved in the formation of SiO_2 layers at low temperature are studied by FTIR spectroscopy and related to the processing conditions.

Keywords: sol-gel thin film deposition, silica layers, FTIR spectroscopy, ultrasonic pulverization of an aerosol

Introduction

The aerosol-gel deposition process, i.e., the deposition of sol-gel thin films from an ultrasonically sprayed aerosol, has been known for several years to be an attractive alternative to the sol-gel deposition of SiO_2 thin films [1, 2]. Recently, it was shown that the chemical stability of the sprayed droplets, during aerosol transport from the pulverization pot to the deposition chamber, was the most critical parameter for achieving deposition of homogeneous layers [3, 4]. Thus, we have developed a two-step preparation procedure of the TEOS solution, specifically to control this parameter. The aim of this procedure was to combine a low reactivity of the solution in the diluted state, so giving high chemical stability of the aerosol during transport, and a high reactivity of the chemical species once the solvent is vaporized, in order to allow a maximal sol-gel polymerization at low temperature. This new preparation route has enabled us to prepare SiO_2 layers with high refractive index (1.45) and excellent mechanical properties (adhesion, scratch resistance) with post-treatment temperatures as low as 80°C. These properties appeared closely related to the solution aging conditions and could only be obtained if the solution had been sufficiently aged before deposition, for instance several days at room temperature. In this paper, the two-step preparation procedure is described and the chemical mechanisms involved in the formation of SiO_2 layers at a low temperature are studied by FTIR spectroscopy with respect to the post-treatment conditions and solution aging time.

Experimental

Layers were deposited from acidic TEOS solutions. For the first preparation step, the TEOS : ethanol : water : HCl molar ratio was fixed at 1 : 0.3 : 10 : 0.0043. The solution pH was around 2. The elevated TEOS concentration ($C_{TEOS} = 2.35$ mol/l) and acidic conditions were chosen to promote a maximal hydrolysis of the TEOS. Moreover, the pH value was fixed close to the silica isoelectric point in order to prevent polycondensation of the hydrolyzed species in the solution [5]. Then the solution was diluted in ethanol in the presence of ammonia. The final TEOS : ethanol : water : HCl : NH_3 composition was fixed at 1 : 66 : 12 : 0.0043 : 0.0038. Due to the final dilution of the chemical species in ethanol ($C_{TEOS} = 0.235$ mol/l), polycondensation of the hydrolyzed species in the liquid solution was effectively prevented. The pH of the final solution was around 3.5. This value, significantly higher than the silica isoelectric point, was expected

to promote the polycondensation process during and after solvent evaporation [5]. Film deposition was performed on to silicon wafers using a previously described deposition reactor [3]. The deposition duration was fixed at 35 s leading to a film thickness of approximately 0.1 μm. Deposition experiments were carried out using solutions aged for various time at room temperature or at 60°C. After deposition, the films were heat treated at 80°C for 2 hours (except when mentioned in the text).

Results and Discussion

Figure 1 shows the typical IR spectrum recorded at 65° off-normal incidence on films heat treated at 80°C. The transverse optical modes of silica, TO_1, TO_2 and TO_3, are observed, respectively at 460, 800 and 1060 cm^{-1}, as well as a band located around 950 cm^{-1}. Oblique incidence intensifies the longitudinal optical mode LO_3 of silica (around 1200 cm^{-1}). The intensity of this vibration mode is closely related to the expansion of the silica network [4]. Figure 1 shows that the LO_3 mode emerges clearly after heat treatment at 80°C. It is significant that for films deposited from low reactivity solutions prepared using a single-step procedure [3, 4], the same observation could be done only after treatment at temperatures greater than 300°C. These data confirm that the composition and preparation procedure of our solution favour the completion of the polycondensation process at low temperature and the development of the silica network during the drying and post-treatment stages. The position and intensity of the longitudinal and transverse modes did not vary significantly for the whole range of experimental conditions investigated here.

The band located at 950 cm^{-1} depended significantly on the experimental conditions. Figure 2 shows the variations in wave number and absorbance of this band, with solution aging time at room temperature, for films heat treated at 80°C. Aging at room temperature or at 60°C led to the same effect, i.e., an increase of the wave number and absorbance with aging time. In a previous study [4], we showed that the band at 950 cm^{-1} is composed of two components: a low wave number component is related to silanol groups and a high wave number component is related to non-hydrolyzed alkoxy groups. Therefore, it

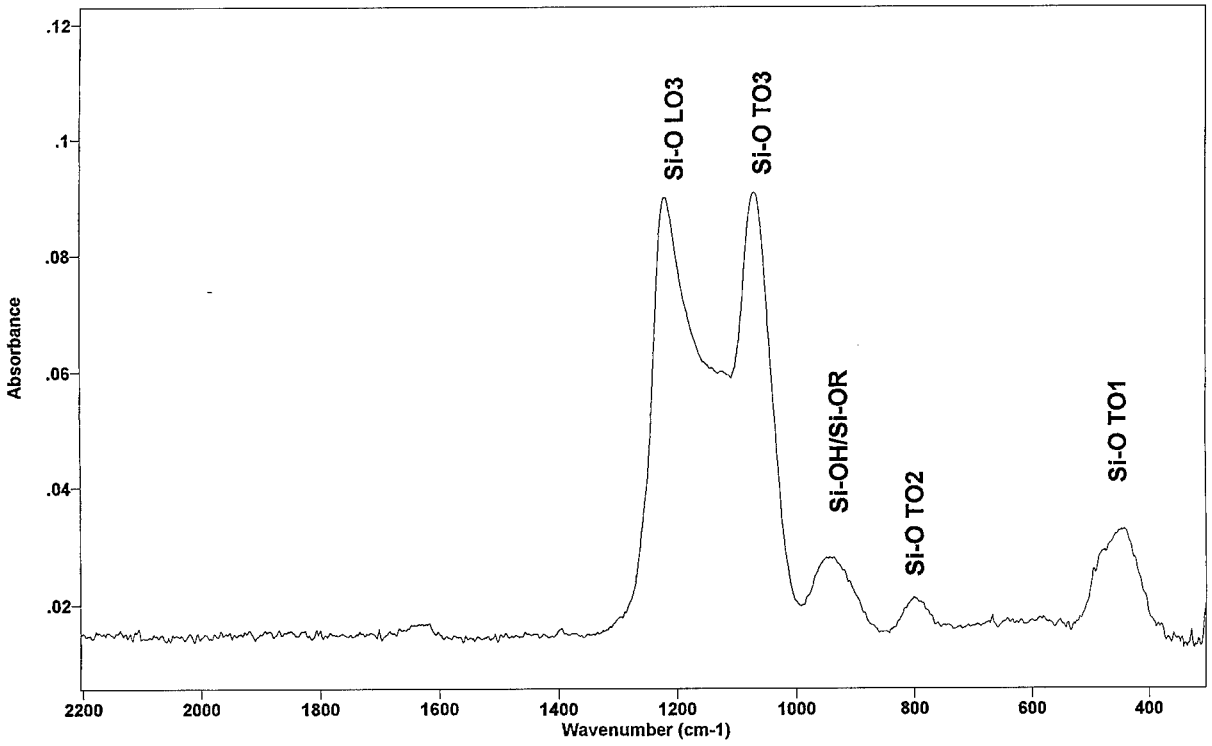

Figure 1. IR spectrum at 65° off-normal incidence of a layer heat treated at 80°C for 2 hours.

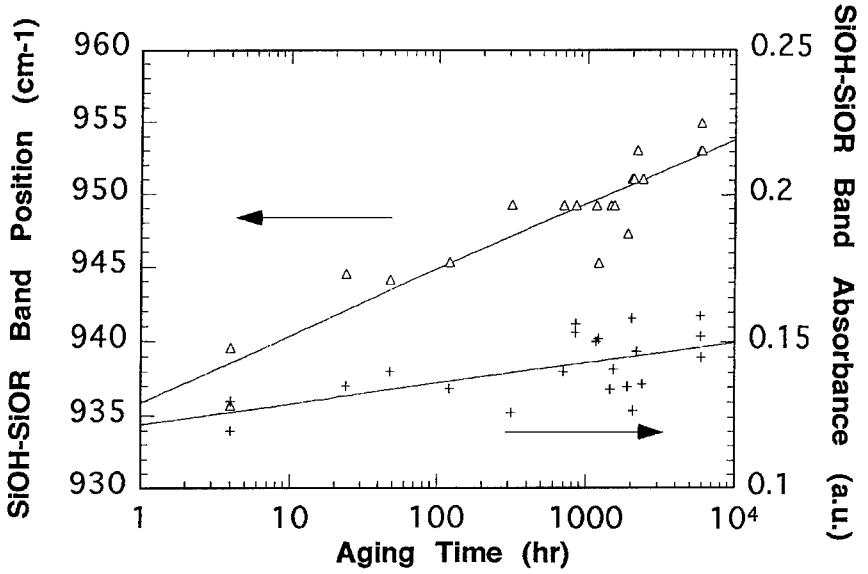

Figure 2. Influence of the solution aging time at room temperature on the SiOH-SiOR band position and absorbance for layers heat treated at 80°C.

can be concluded that a shift of this band towards high wave numbers corresponds to consumption of silanol species and/or the appearance of alkoxy groups. Silanol groups may be consumed by a classical polycondensation mechanism, in which case an intensity decrease of the band should be observed, in addition to the mentioned shift. Silanol groups may also be consumed by reesterification, i.e., the reverse of the hydrolysis reaction. In this case, formation of alkoxy groups is expected to occur. Figure 3 shows the effect of the post-treatment duration on the SiOH-SiOR band absorbance. The absorbance is clearly observed to decrease with time. This decrease is consistent with consumption of silanol groups by polycondensation

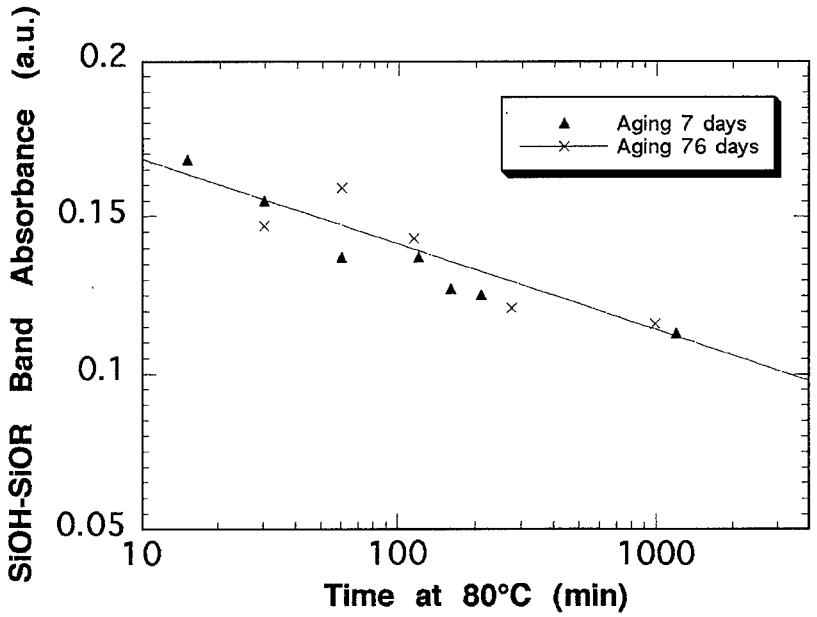

Figure 3. Influence of film post-treatment duration and solution aging at room temperature on the SiOH-SiOR band absorbance for films heat treated at 80°C.

and the progressive silica network expansion taking place during post-treatment.

Comparison between Figs. 2 and 3 shows that the chemical mechanisms related to solution aging cannot be discussed only in terms of polycondensation. In order to more fully investigate this idea, we have also studied the effect of solution aging on the film spectra before heat treatment (Figs. 4 and 5). In the high wave number spectral range (Fig. 4), a broad band is observed between 3600 and 3000 cm^{-1} and is assigned to different O—H stretching modes in H_2O and SiO—H [4]. This band did not vary significantly during solution aging. The set of peaks between 3000 and 2800 cm^{-1} is attributed to C—H stretching modes and is associated with the presence of alkoxy groups in the layer. The intensities of the C—H peaks increased strongly with solution aging time. In addition,

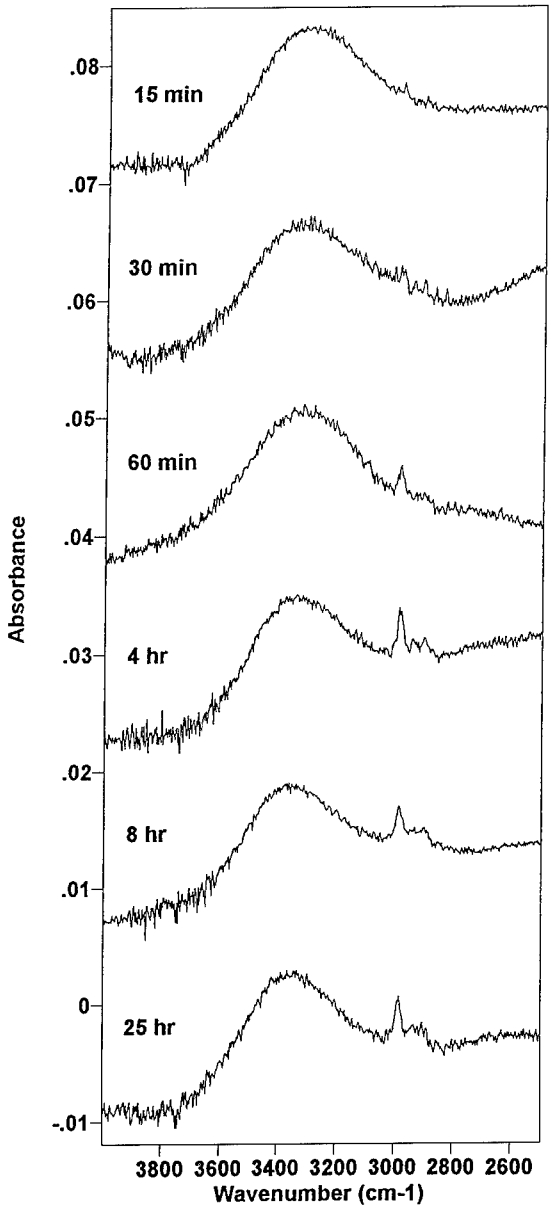

Figure 4. Influence of the solution aging time at 60°C on IR spectrum of as-deposited films (high wave number spectral range).

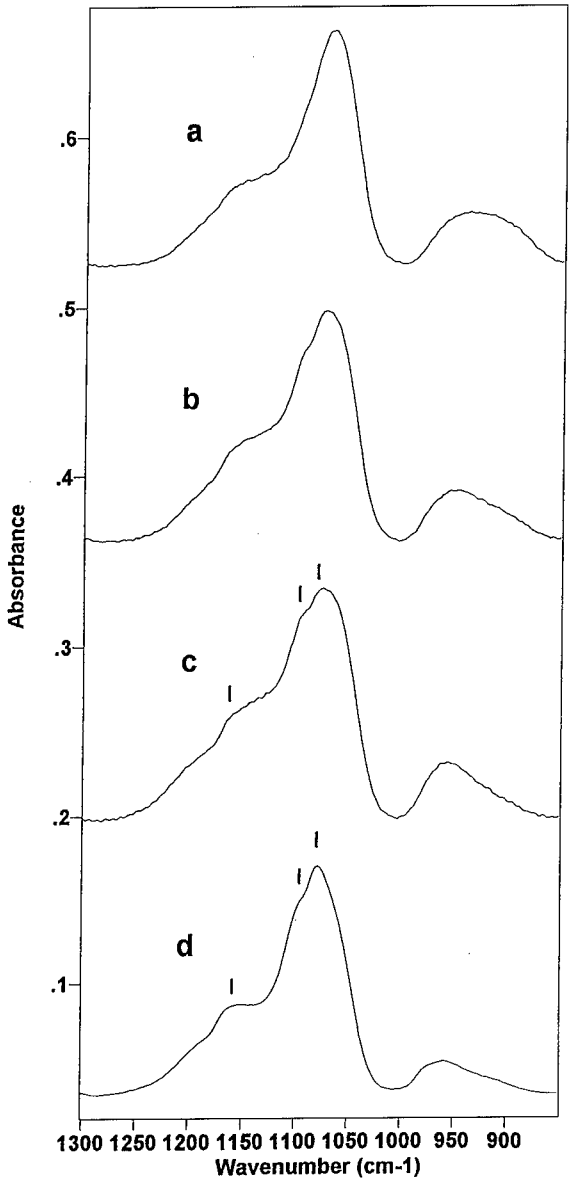

Figure 5. IR spectrum in the low wave number spectral range for as-deposited films obtained from a two-step solution aged at 60°C for 1 hour (a), 25 hours (b), 126 hours (c) and from a low reactivity solution with a small water to TEOS ratio (after [4]) (d). Alkoxy components are shown with a mark.

the SiOH-SiOR band was shifted towards higher wave numbers and three small shoulders appeared on the TO_3 peak, respectively at 1160, 1100 and 1080 cm^{-1} (Fig. 5). These shoulders were previously assigned to the CH_3 rocking and OC asymmetric stretching modes of alkoxy groups [4]. From Figs. 2, 4 and 5, we can conclude that solution aging promotes the formation of alkoxy groups. From that point of view, it is significant that the spectrum of the layer deposited from the most aged two-step solution (Fig. 5(c)) was very similar to the spectra of layers deposited from an incompletely hydrolyzed solution with a low water/TEOS ratio (Fig. 5(d) after [4]). The alkoxy group formation is consistent with a reesterification mechanism taking place during solution aging at room temperature or at 60°C. This mechanism is related to the ethanol excess in the solution (ethanol/water molar ratio = 5.5). As mentioned above, mechanically resistant layers were only obtained from sufficiently aged solutions. This suggests that the formation of layers with good mechanical properties at low temperature could be the result of a suitable balance between partial reesterification promoted by solution aging and silica network development at low temperature promoted by our solution composition and taking place during drying and post-treatment.

Conclusion

SiO_2 thin films have been deposited by the aerosol-gel process using a two-step TEOS solution. Dense and mechanically resistant layers were obtained after treatment at 80°C provided that the solution was suitably aged. This study shows that a partial silanol group reesterification takes place in the solution during aging. It is believed that the formation of mechanically resistant layers at low temperature can be discussed in terms of a balance between the effects of reesterification promoted by solution aging and the silica network expansion at low temperature promoted by the reactivity of our solution. Further experiments are in progress to evaluate the respective role of reesterification and polycondensation on the formation at low temperature of mechanically resistant layers.

Acknowledgment

The present research was performed under project number BE-7765 sponsored by the Brite Euram Programme 2.

References

1. M. Langlet, D. Walz, P. Marage, and J.C. joubert, Thin Solid Films **221**, 44 (1992).
2. P. Marage, M. Langlet, and J.C. Joubert, Thin Solid Films **238**, 218 (1994).
3. M. Langlet and C. Vautey, J. of Sol-Gel Sci. Tech. **8**, 347 (1997).
4. N. Primeau, C. Vautey, and M. Langlet, Thin Solid Films **310**, 47 (1997).
5. C.J. Brinker and G.W. Scherer, *Sol-Gel Science* (Academic Press, San Diego, 1990).

Journal of Sol-Gel Science and Technology 13, 749–752 (1998)
© 1998 Kluwer Academic Publishers. Manufactured in The Netherlands.

The Effect of HF in a Two-Step Sol-Gel Process of TEOS

T.N.M. BERNARDS AND M.J. VAN BOMMEL
Philips Research Laboratories Eindhoven, Prof. Holstlaan 4, 5656 AA Eindhoven, The Netherlands

J.A.J. JANSEN
Philips CFT, Materials Analysis Department, Prof. Holstlaan 4, 5656 AA Eindhoven, The Netherlands

Abstract. The addition of HF to a TEOS-ethanol-water mixture results in faster gelation compared to a system without HF. When HF is added in the basic step the effect is most pronounced. The addition of HF in the acid step only results in an enhancement of the condensation reactions. The effect of HF in the acid step is largely determined by the H^+ concentration due to the low acidity of HF. At low HF concentrations a maximum in gelation time is found as a function of the H^+ concentration. At low H^+ concentrations the F^- enhances gelation; at high H^+ concentrations the influence of F^- is negligible but gelation is enhanced by the protons.

Keywords: sol-gel chemistry, acid catalyst, IR

1. Introduction

The preparation of optical SiO_2 coatings by a sol-gel process is a very attractive technique because of its cost efficiency compared to physical vapor deposition techniques.

For the hydrolysis of a tetraethylorthosilicate (TEOS) solution an aqueous HCl solution is used. It has been found that the replacement of the HCl catalyst by HF in a sol-gel process will give rise to faster gelation and a gel structure with larger pores [1–3]. In this paper we report on the effect of the addition of HF to a TEOS solution. To gain more insight into the mechanism of the influence of HF on the sol-gel process of TEOS, gelation time versus hydrolysis time curves have been recorded. It has been shown that the relation between the hydrolysis time (t_H) in the acid step and gelation time (t_G) gives insight into both the hydrolysis and the condensation reactions of TEOS [4].

Besides the hydrolysis time versus gelation time curves, Horizontal Attenuated Total Reflectance (HATR) FT-IR is also used to study the effect of the addition of HF to a TEOS sol-gel system. Traces of HF have a remarkable catalytic effect on the polymerization rate of a sol-gel system. F^- has about the same size as OH^- and has the ability to increase the coordination of Si to above four. Corriu et al. [5] stated that the addition of F^- affects the hydrolysis of TEOS. The first step in the hydrolysis is a fast reversible formation of a pentavalent intermediate. This intermediate stretches and weakens the surrounding Si—OR bonds. The subsequent rate determining step is the nucleophilic attack of water on the hypervalent silicon leading to nucleophilic substitution by proton transfer and elimination of ROH.

Because F^- is more electron-withdrawing than OH^-, an alternative argument is that F^- substitution for OH^- reduces the electron density on Si, making it more susceptible to nucleophilic attack. This argument implies an enhancement of the condensation reactions.

2. Experimental

To study the influence of F^- on the hydrolysis and condensation of TEOS, t_H versus t_G curves are recorded for a mixture of TEOS, ethanol and water (molar ratio 1 : 4 : 2), with and without the addition of HF. The water fraction is acidified with $5 \cdot 10^{-3}$ M HCl. The 4 mol of ethanol are divided into three parts: one part is used

for the dilution of the acid-water fraction, another part in which NH_3 gas is dissolved is used as a basic fraction, and a remaining part in which TEOS is dissolved. Three different systems are studied: one to which no HF is added, one system to which the HF is added in the acidic step together with the addition of the water fraction, and in the third system the HF is added together with the basic fraction. A concentration of $1 \cdot 10^{-3}$ mol HF per mol TEOS is used.

The starting TEOS/alcohol mixture is kept at a constant temperature of 50°C and is stirred thoroughly. The acidic water fraction is added to the mixture within 30 s. To prevent evaporation of the alcohols the experiments are carried out in a closed vessel. The acidic water fraction is diluted with ethanol in order to avoid immiscibility during the addition. A sample is taken from the hydrolyzing mixture every few minutes. A specific amount of the basic ethanol fraction is added to this sample. The sample is stirred for 15 s and poured into a test-tube which is closed immediately. During the addition of the base, as well as during the gelation process, the sample is kept at a constant temperature of 50°C. The gelation time is determined visually with an accuracy of ±15 s. For each sample t_H is defined as the time interval between the addition of the acid fraction and the moment the basic fraction is added. t_G is defined as the time interval between the moment the basic fraction is added and the moment at which, when tilting the test-tube, no fluidity of the sol is observed.

Time-evolved FT-IR spectra are recorded in steps of 5 s at 8 cm^{-1} resolution on a Nicolet 800 with an MCT-B detector. A spectra-Tech HATR is used with a 45° ZnSe or Ge crystal. In order to follow the reactions as a function of reaction time (t_r), difference spectra between t_r and $t = 0$ are calculated. The spectra are recorded for mixtures of TEOS, ethanol and water (molar ratio of 1 : 4 : 2 and 0.01 M HCl). After a hydrolysis time of 30 min at room temperature the basic fraction is added. Two curves are recorded: one for a system without HF and one in which the HF is mixed with the basic fraction. A concentration of $1 \cdot 10^{-3}$ mol HF per mol TEOS is used.

At high HF concentration, gelation is observed without the addition of a basic fraction. We have investigated the effect of the HCl concentration on the gelation time at different TEOS to HF molar ratios. Mixtures of ethanol, water, HCl and HF are made and poured into test tubes. The proper amount of TEOS is added to these mixtures and the systems are homogenized. The samples are kept at a constant temperature of 25°C.

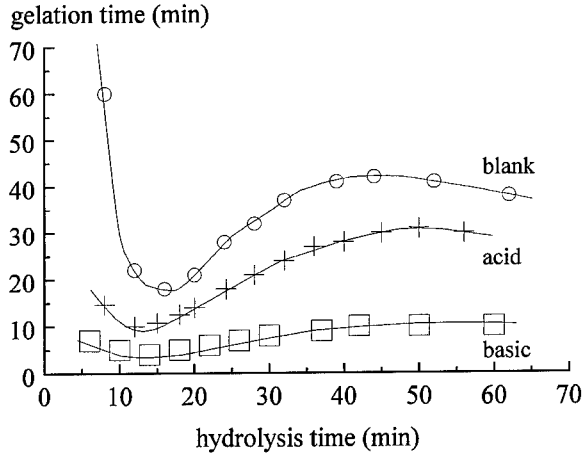

Figure 1. The gelation time, t_G, as a function of the hydrolysis time, t_H, of TEOS, ethanol and water mixtures with a final molar ratio of 1 : 4 : 2, (○) without and with the addition of $1 \cdot 10^{-3}$ mol HF in the (+) acid and (□) basic step.

3. Results and Discussion

In Fig. 1 the gelation time versus hydrolysis time curves are given of TEOS, ethanol and water mixtures (molar ratio of 1 : 4 : 2), without and with the addition of ($1 \cdot 10^{-3}$ mol) HF per mol TEOS in the acid step and in the basic step. The water fraction was acidified with HCl in a concentration of $5 \cdot 10^{-3}$ M. $0.25 \cdot 10^{-3}$ mol NH_3 per gram ethanol was used for the basic step. For the TEOS mixtures with HF, the complete curves are shifted to lower gelation times. For the system in which the HF was added in the basic fraction, this effect is more pronounced.

The differences in gelation times between systems without HF and with HF added in the acidic step and basic step indicate that in both steps the addition of HF has an effect. If the F^- only has an effect in the basic step, both curves with HF should coincide. If HF only has an effect in the acidic step, the curve obtained after HF addition in the basic step should coincide with the blank.

The addition of the HF in the acid step results in a retardation of gelation compared to the situation in which the HF is added in the basic step. However, when this curve is compared to the system where no HF is added, shorter gelation times are found.

The difference between the addition of HF in the acid and basic step can only be caused by a difference in silanol concentration at the moment the basic fraction is added to the system. The addition of F^- to

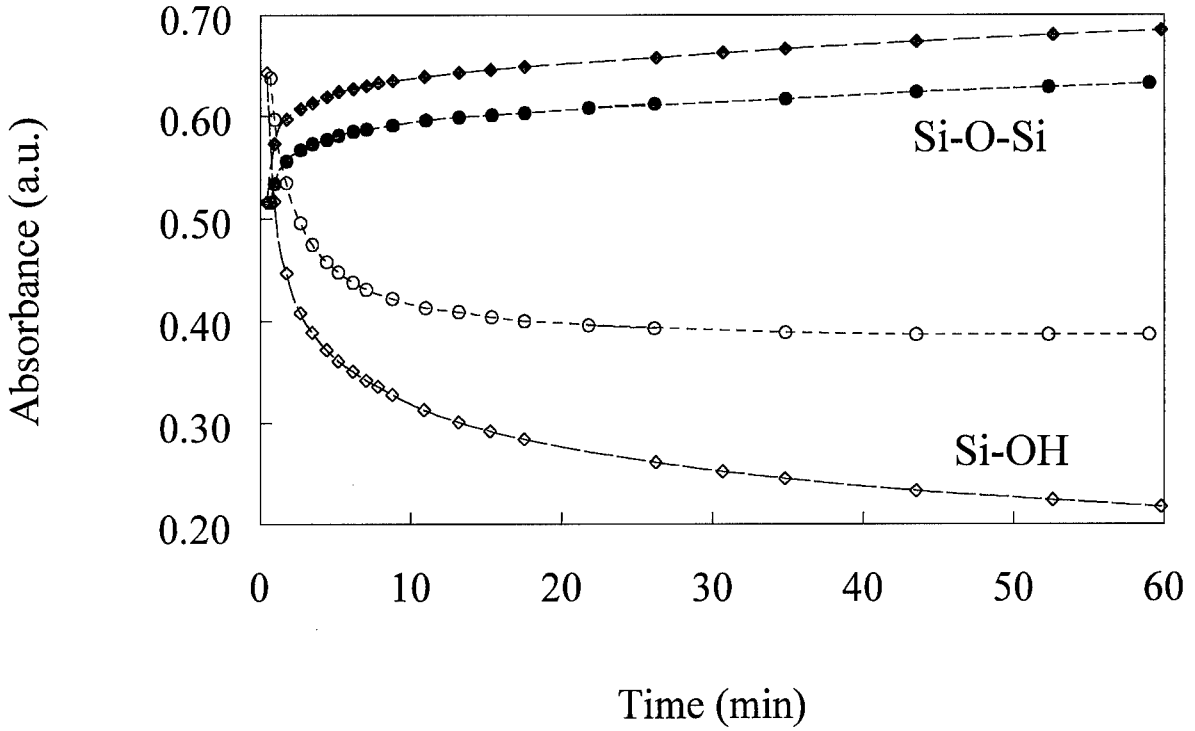

Figure 2. The absorbance of the Si—OH (938 cm^{-1}) and the Si—O—Si (1172 cm^{-1}) bands as a function of time after the addition of NH_3, (♦, ◇) with and (●, ○) without the addition of $1 \cdot 10^{-3}$ mol HF.

a sol-gel system will enhance the condensation reactions. If the F^- also enhances the hydrolysis reaction, it should result in a shift of the minimum in gelation time to lower hydrolysis times [4]. The addition of the F^- in the acid step will probably only enhance the condensation in the acid step. Therefore, compared to a system without F^-, a lower silanol concentration will be found at the same hydrolysis time. This ultimately results in an increase in gelation time.

HF is less effective in an acidic environment due to the low acidity of HF. Only F^- ions have an effect on the enhancement of the condensation reactions of the TEOS sol-gel system. The pK_a value of HF is 3.14. In addition, it can be expected that the dissociation of the HF will be further hampered in an alcohol-rich environment. In the acid step, at the conditions used for recording the curves, only a minor part of the HF will be dissociated. The non-dissociated HF in acidic environment will be completely dissociated in basic environment and will therefore only affect the condensation reactions in the basic step.

In Fig. 2 the absorbance of two characteristic IR bands are plotted as a function of time after the addition of NH_3 to hydrolysis mixtures as used for the

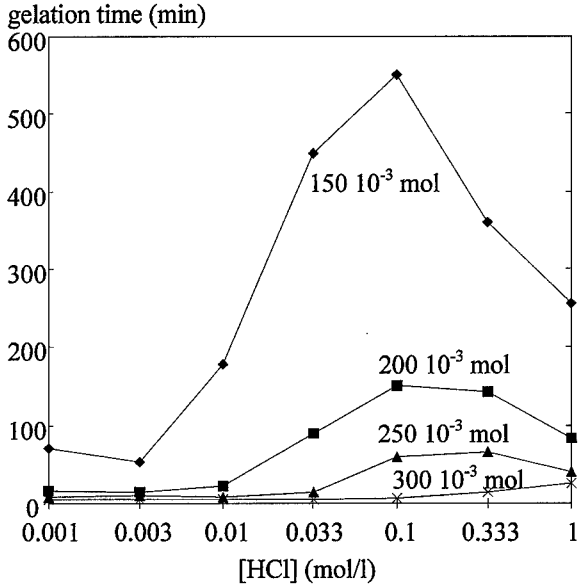

Figure 3. Gelation time, t_G, as a function of the HCl concentration of a mixture of TEOS, ethanol and water with a final molar ratio of 1 : 4 : 2 and with the addition of HF concentrations of (♦) $150 \cdot 10^{-3}$ mol, (■) $200 \cdot 10^{-3}$ mol, (▲) $250 \cdot 10^{-3}$ mol and (×) $300 \cdot 10^{-3}$ mol.

experiment in Fig. 1. The two bands are respectively the ≡Si—OH (938 cm^{-1}) and the ≡Si—O—Si≡ band (1172 cm^{-1}). The HF is added together with the basic fraction. The curves show that for the system with HF a lower Si—OH concentration and a higher degree of condensation is found. These effects are followed for the addition of HF in the basic step. Under these conditions the maximum available amount of F^- is present.

In an acidic environment the F^- concentration is largely determined by the H^+ concentration of the system. Based on the low acidity of HF, it can be concluded that the HCl concentration in the acid step will have an influence on the number of the F^- ions available during in the acid step. In order to investigate this influence in more detail, gelation times were recorded for TEOS systems with different amounts of HF for different HCl concentrations. In Fig. 3 the gelation times are given as a function of the HCl concentration for mixtures to which different HF amounts were added.

This figure shows that at high HF concentrations fast gelation is obtained irrespective of the HCl concentration used. For lower HF concentrations the amount of F^- will be highly influenced by the HCl concentration in the system. For low HCl concentrations, the HF will be dissociated to a large extent and the F^- will enhance gelation. On the other hand, for high HCl concentrations only a small amount of F^- will be present. However, a high H^+ concentration will also enhance the gelation process in an acid environment. Therefore, a maximum in gelation time is found in these low HF-containing systems. When a low HF concentration ($100 \cdot 10^{-3}$ mol per mol TEOS) is used, no gelation after several days was found for systems with a HCl concentration below 1 mol/l.

References

1. R. Winter, J.B. Chan, R. Frattini, and J. Jonas, J. Non-Crystalline Solids **105**, 214 (1988).
2. E.M. Rabinovitch, J. Non-Crystalline Solids **104**, 107 (1988).
3. A.M. Gadalla and S.J. Yun, J. Non-Crystalline Solids **143**, 221 (1992).
4. T.N.M. Bernards, *Silicate Sol-Gel Chemistry as Studied by Hydrolysis-Gelation Time Curves* (Thesis University of Utrecht, 1997).
5. R.J.P. Corriu, D. LeClerq, A. Vioux, M. Pauthe, and J. Phalippou, in *Ultrastructure Processing of Advanced Ceramics*, edited by J.D. Mackenzie and D.R. Ulrich (Wiley, New York, 1988), p. 113.

Journal of Sol-Gel Science and Technology 13, 753–756 (1998)
© 1998 Kluwer Academic Publishers. Manufactured in The Netherlands.

Inhibition of Pb-Leaching from Lead Crystal Glass by Coating with Films Prepared by the Sol-Gel Method

A.A. AHMED, I.M. YOUSSOF AND A.F. ABBAS
Glass Research Laboratory, National Research Center, Dokki, Cairo 12622, Egypt

O. ABOU ELEINEN
Glass Research Laboratory, National Research Center, Dokki, Cairo 12622, Egypt; and Petroleum Applications Department, Petroleum Research Institute, Nasr City, Cairo, Egypt

Abstract. The chemical durability of lead glass tumblers (24% PbO) in a 4% (v/v) acetic acid solution before and after coating with sol-gel derived SiO_2 films was assessed to determine the extent of reduction in Pb-leaching that can be achieved. It was found that by coating the internal surface of the glass tumblers with 1 ml of 10% TEOS solutions at 100°C and densifying the coating formed at 500°C for 1 h, it was possible to reduce Pb-leaching to about one quarter of that of the uncoated glass.

Keywords: lead crystal glass, sol-gel coating, lead leaching, durability improvement

Introduction

Lead oxide is used as an essential constituent in many types of glass. Lead crystal glass is probably the most commonly known lead containing glass. Lead oxide was used in this particular type of glass to cause a substantial increase in its refractive index and light dispersion giving the glass a notable brilliance. The chemical resistance of lead crystal glass toward attack by aqueous solutions is an important property [1]. A high degree of chemical stability, including no visible alteration, is required. Recently, the chemical durability of lead crystal glass has become a top priority subject for lead crystal glass manufacturers, users and standardization organizations. This is due to the toxic nature of the lead that migrates from lead crystal glassware, in conjunction with other cations, during their contact with food and drinks. Recent medical reports show that excessive exposure to lead and its accumulation in the human body can lead to kidney problems, raised blood pressure, changes in the nervous system, birth defects, anemia and death in severe cases [2]. This has led standards organizations to set limits for the allowable levels of lead release during standard testing conditions from lead crystal glassware intended for use in the preparation, storing or serving of food and drinks. The maximum permissible limits of lead release were revised downward to about one tenth of their previous values during the last 10 years [3]. Although the levels of lead release from commercially available lead crystal glassware designed to be used in contact with food and drinks were already low, they now have to be substantially reduced [4]. This necessitates either elimination of lead oxide entirely from lead crystal glass compositions or treatment of the surface of the glassware that will be in contact with food and drinks so as to substantially improve its chemical resistance. One of the possible treatments is to coat the glass surface with a sol-gel derived silica film that is known to possess extremely high chemical resistance to aqueous solutions of pH values lower than 9 [5].

In this work, the preliminary results of a study of the chemical durability of a commercially available lead crystal glass tumbler (24% PbO) before and after coating with sol-gel derived silica glass film are reported. This study was carried out to determine the extent of improvement of the chemical durability, i.e., the extent of reduction in lead leaching that can be achieved by such coating.

Experimental Procedure

A commercially available lead crystal glass (24% PbO) in the form of tumblers (240 ml size) was used in this work. The chemical composition and other characteristics of the glass tumblers are given elsewhere [6]. The internal surface of the glass tumblers was coated with tetraethoxy orthosilicate [TEOS] solutions. The coating solution was prepared by diluting the TEOS with the appropriate volume of ethyl alcohol to obtain the required concentrations of the TEOS solutions (from 1 to 20% v/v). A few drops of dilute acetic acid were added to the mixture which was mixed by stirring for 6 h at 60°C, after which the solution was held at room temperature for 24 h. The internal surface of the tumblers was coated by spraying 1 ml of solutions containing different concentrations of TEOS. Spraying was conducted on both cold and hot tumblers. The temperature of the tumblers was varied between 25°C and 200°C. After spraying, the tumblers were left at the same temperature for about 1 hour. The tumblers were then subjected to a heat-treatment in an electric muffle furnace at a temperature in the range 100–500°C for times in the range of 1 to 6 h.

The chemical durability of the glass tumblers before and after surface coating was determined after attack by 4% (v/v) acetic acid at 95°C for 6 h in a water bath. Previous studies [7] revealed that the quantity of lead ions extracted from these glass tumblers after attack by 4% (v/v) acetic acid for 24 h at room temperature was very small. Accordingly, in this work relatively severe conditions of attack, 6 h at 95°C were adopted in order to magnify the extent of leaching of lead from uncoated and coated glass surfaces by acetic acid. At the end of time of attack, the solution content of the tumblers was immediately transferred into plastic bottles. The extent of lead leaching was evaluated by determination of the concentration of Pb^{2+} ions extracted from glass by acetic acid solution. The accuracy of the results was better than 5%. The details of the experimental procedure are given elsewhere [6, 7].

Results and Discussion

In a previous study of the interaction between the same glass tumblers and acetic acid, Ahmed and Youssof [7] showed that Pb^{2+} is released in concentration <0.5 ppm by 4% (v/v) acetic acid solution at 22 ± 2°C for 24 h. It is evident that lead is released in concentration that is below the limit specified by the current international standards [3], i.e., these tumblers comply with the requirements of these standards.

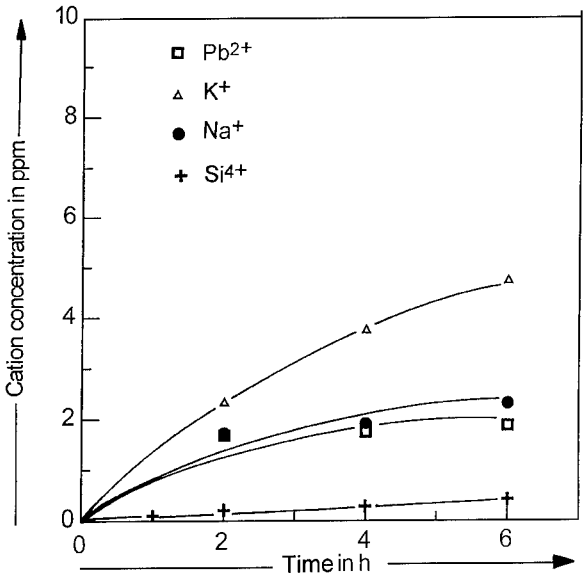

Figure 1. Effect of time of attack at 95°C on the extraction of K, Na, Pb and Si ions from glass tumblers by 4% acetic acid solution. Data were taken from [7].

The effect of time of attack at 95°C on the release of Pb^{2+} and other cations from the same type of glass tumblers by 4% acetic acid solution is shown in Fig. 1. It is clear that the extraction of Pb^{2+}, K^+ or Na^+ ions proceeds in a parabolic manner. This behavior is expected since the process of extraction of modifier cations K^+ and Na^+ as well as Pb^{2+}, which also occupies modifier sites [6], is diffusion-controlled.

Figure 2 shows the effect of concentration of TEOS in the spraying solution on the release of lead from the internal surface of the tumblers by the attack with 4% (v/v) acetic acid solution for 6 h at 95°C. Spraying was performed at 100°C and the tumblers were then heat-treated at 500°C for 1 h. The data for uncoated glass is also included for comparison. It is clear that the quantity of lead released from glass is dependent on the concentration of the TEOS in the coating solution. With increasing TEOS concentration the amount of Pb^{2+} extracted from the surface of the glass decreases. Lead extraction is reduced to about 50% of that of the uncoated glass by coating with 1% TEOS solution and ultimately to about 25% by coating with 20% TEOS solution.

Figure 3 shows the effect of the temperature of the glass during spraying on the extraction of lead from glass. The glasses were coated with 10% TEOS

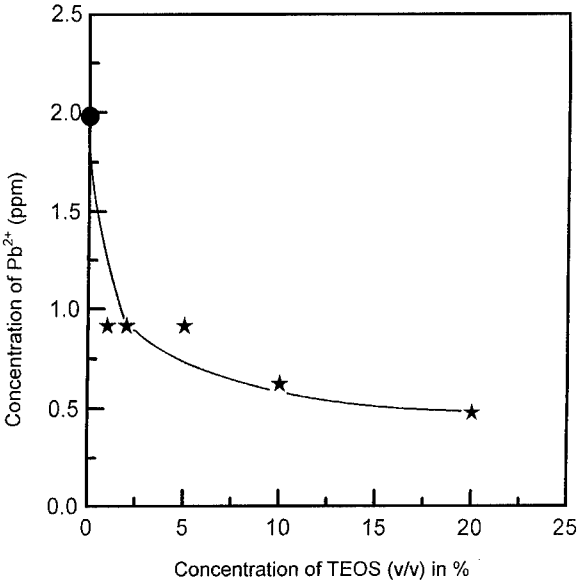

Figure 2. Effect of concentration of TEOS in the spraying solution on Pb-leaching from the internal surface of glass tumblers by 4% (v/v) acetic acid solution. The tumblers were heat-treated at 500°C for 1 h. • represents data for Pb-leaching from the uncoated glass.

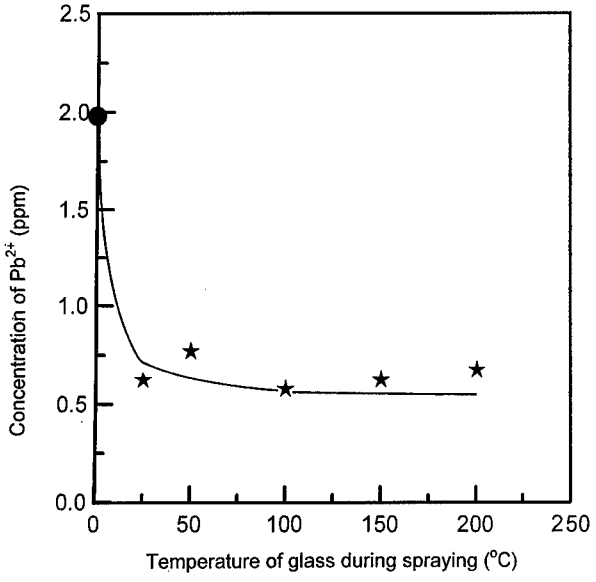

Figure 3. Effect of temperature of glass surface during spraying on Pb-leaching from the internal surface of glass tumblers by 4% (v/v) acetic acid solution. The tumblers were heat-treated at 500°C for 1 h. • represents data for Pb-leaching from the uncoated glass.

solution and heat-treated at 500°C for 1 h. It is evident that the concentration of lead extracted from coated glass is substantially reduced to about one third of that

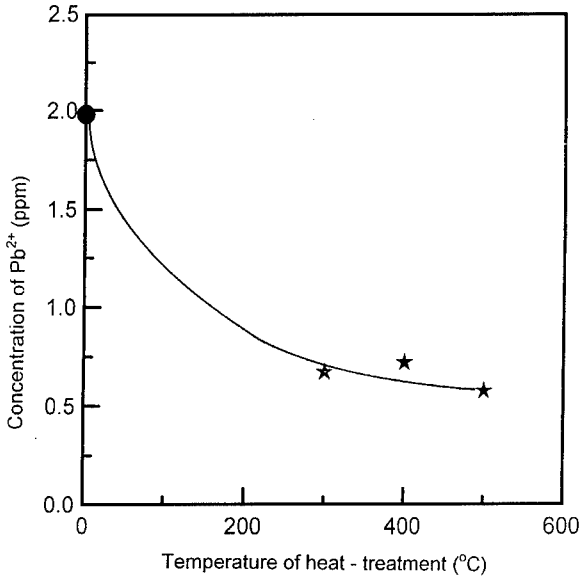

Figure 4. Effect of heat-treatment temperature on Pb-leaching from the internal surface of glass tumblers by 4% (v/v) acetic acid solution. The tumblers were heat-treated for 1 h. • represents data for Pb-leaching from the uncoated glass.

of uncoated glass. The figure also indicates that the temperature of glass surface during spraying has no significant effect on the efficiency of the protective layer formed on glass surface.

Figure 4 shows the effect of the 1 h heat-treatment temperature on the lead extraction from glasses coated with 10% TEOS solution at 100°C. It is apparent that lead extraction gradually decreases with increasing heat-treatment temperature. The time of heat-treatment at 500°C, Fig. 5, seems to have no significant effect on the extraction of lead from the glass surface.

The sol-gel formation route can simply be described by a number of processes [8–10]:

1. Hydrolysis and Condensation Polymerization. Hydrolysis and condensation polymerization of the TEOS by H_2O in the presence of an acid catalyst to control the rate and extent of the hydrolysis reaction. The hydrolysis reaction of the TEOS solution to produce silanols can be represented by the equation:

(Hydrolysis)

$$Si(OC_2H_5) + H_2O \rightarrow SiOH + C_2H_5OH$$

As soon as a silanol group is formed, condensation polymerization occurs simultaneously by which the

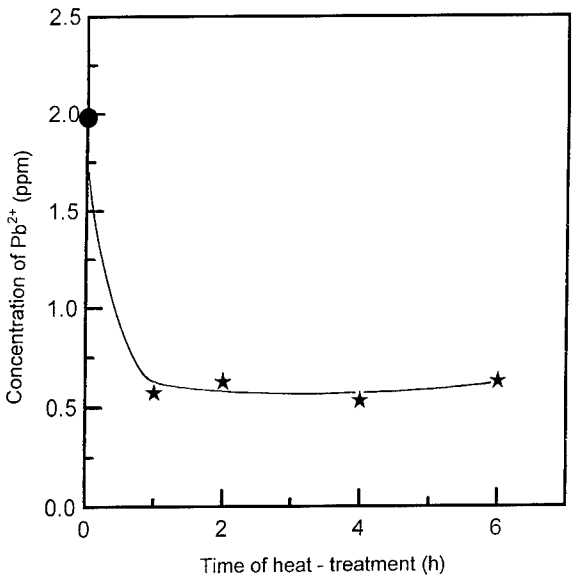

Figure 5. Effect of heat-treatment time on Pb-leaching from the internal surface of glass tumblers by 4% (v/v) acetic acid solution. The tumblers were heat-treated at 500°C. • represents data for Pb-leaching from the uncoated glass.

silanol group reacts with an ethoxy group to create siloxane bonds.

(Polymerization)

$$Si(OC_2H_5) + HO\,Si \rightarrow Si{-}O{-}Si + C_2H_5OH$$

2. Gelation. The transition from sol to gel due to the hydrolysis and polymerization of the TEOS precursor was carried at atmosphere pressure.

3. Drying. The sol produced was left to dry so that no further weight loss occurs over time.

4. Densification. Densification of the dried gel network requires heating. The processes that takes place as the temperature increases are: elimination of trapped water and ethanol, oxidation of residual organics, condensation of adjacent hydroxyls and viscous sintering.

Accordingly, the retardation of leaching from glass on increasing the concentration of TEOS in the coating solution (Fig. 2), can be attributed to the increase in thickness and coherence of the formed SiO_2 film which act as a protective layer or a barrier that insulates the glass surface from direct contact with the acetic acid solution.

The temperature of the glass surface during spraying is expected to affect the rate of evaporation of the TEOS solution as it contacts the glass surface. It could, also, yield discontinuous or discrete islands of the SiO_2 film after heat-treatment, i.e., inefficient film coverage Fig. 3 indicates that surface temperatures up to 200°C have no significant effect on the structure and homogeneity and thereby the ability of the SiO_2 film to retard Pb-leaching.

The densification of the SiO_2 film and its temperature-dependence, Fig. 4, show that the temperature of 500°C is sufficient for the SiO_2 film to attain a densified structure that is capable of reducing Pb-leaching to about 25% of that of the uncoated glass. The temperature of 500°C, which is the maximum temperature used in this work, was dictated by the Tg of the crystal glass used. Results shown in Fig. 5 also indicate that heating at 500°C for 1 h is sufficient for the SiO_2 film to attain good densification.

References

1. A.A. Ahmed and I.M. Youssof, in *Proc. 8th Int. Crystal Federation Tech. Exchange Conf.* (Int. Crystal Fed., Stourbridge, 1996), p. 99.
2. J.H. Graziano and C. Blum, The Lancet **331**, 141 (1991).
3. ISO Standard 7086, part 2 (1082); BS No. 7648 (1986), DIN No. 51031 (1986); Egyptian Standard no. 2060 (1991).
4. Anon, Bull. Am. Ceram. Soc. **73**, 93 (1994).
5. R.W. Douglas and T.M.M. ElShamy, J. Am. Ceram. Soc. **50**, 1 (1967).
6. A.A. Ahmed and I.M. Youssof, Glass Technol. **37**, 21 (1997).
7. A.A. Ahmed and I.M. Youssof, Glastech. Ber. Glass Sci. Technol. **70**, 173 (1997).
8. L.C. Klein, Annu. Rev. Mater. Sci. **15**, 237 (1985).
9. L.L. Hench and W. Vasconcelos, Annu. Rev. Mater. Sci. **20**, 269 (1990).
10. C.J. Brinker and G.W. Scherer, *Sol-Gel Science* (Academic Press, NY, 1990).

Journal of Sol-Gel Science and Technology 13, 757–761 (1998)
© 1998 Kluwer Academic Publishers. Manufactured in The Netherlands.

Comparison of Different High and Low Index Materials in the Manufacture of High Laser Damage Threshold Mirrors at the 351 nm Wavelength

N. BAZIN, J.E. ANDREW AND H.A. MCINNES
Radiation Physics Department, AWE plc Aldermaston, Reading, Berkshire, UK, RG7 4PR

Abstract. Sol-gel material based mirrors have been produced by forming alternate layers of high refractive index and low refractive index thin films. These mirrors have proven to have a high laser induced damage threshold [LIDT]. Using nitric acid stabilized zirconia derived from zirconium-*n*-propoxide and base catalyzed silica, a 16 layer mirror with a reflectivity of better than 94% at 351 nm and 45° angle of incidence was fabricated. This had an LIDT of 7.7 J/cm^2 at 351 nm with a 0.7 ns pulse width. Crazing prevented further layers being deposited. Both spin and dip coating were attempted with dip coating yielding the best results.

The coating structure has been analyzed using XPS depth profiling and AES. The bulk materials have been investigated using transmission electron microscopy (TEM), X-ray diffraction (XRD) and TGA. High refractive index layers using Hafnia with nitric or acetic acid have also been investigated as prospective high LIDT mirrors.

Alternative acidic routes to silica have been studied as a possible low index material and a route to preventing crazing.

Keywords: zirconia, laser damage, sol-gel, depth profiling, thin films

Introduction

The use of sol gels for the synthesis of thin film coatings has been expanding over the past few years in a broad range of applications [1–4]. In the high peak power laser field, base catalyzed colloidal silica with particles in the range of 10–20 nm are conventionally used as AR coatings [5]. These coatings can either be dip or spin coated and both techniques have been investigated [6–8]. Frequency tripled Nd-Yag/YLF ultraviolet lasers require the synthesis of ultraviolet mirrors which reflect only frequency tripled light and filter out any unconverted green or near IR light. The main criteria a mirror must adhere to is (1) high reflectivity, (2) high LIDT and (3) preservation of wave front quality. Here we have successfully made a high reflecting UV mirror by optically matching alternating layers of high and low index materials [9] with good LIDT relative to conventional UV mirrors [10]. Nitric acid stabilized zirconia paired with base catalyzed silica resulted in the highest LIDT.

Experimental

The silica component of the HR coatings was derived through the base [ammonium hydroxide] catalyzed hydrolysis and condensation of TEOS and water in ethanol, a now well established route [11, 12]. Zirconia and hafnia were made from ethanol, zirconium-*n*-propoxide or hafnium-*n*-propoxide (70% in *n*-propanol), respectively, and water, stabilized with nitric or acetic acid and methoxyethanol. The high index materials formed a light turbid blue solution after 48 h and were ready for coating. All chemicals were used as supplied without further purification. Before coating, the silica and high index sols were diluted and filtered through a 0.2 μm filter to remove particulates that enter from the atmosphere.

Initially, both spin and dip coating were attempted however, it was soon apparent that spin-coated stacks were cracking after less pairs had been applied than dip-coating study.

Dip coating was carried out using an in house dipping mechanism incorporating a counterbalance piston

running through a viscous oil at a dipping speed of 5 mm/s. After each coating the substrate (50 mm diameter fused silica) was heated under an IR lamp for 2 min to increase the evaporation rate of the ethanol. UV-Vis spectra were measured on a Cary 5 spectrophotometer.

Bulk sample analysis included XRD of the high index samples at a range of temperatures. TGA using a NETZSCH TG 90 and a heating rate of 10°C/min in air. TEM (not shown) as taken on a JOEL 2000FX.

The thin films were analyzed using AES and XPS on a Kratos XSAM800 and an SSI m-probe.

Results and Discussion

X-ray diffraction patterns (Figs. 1(a)–(d)) clearly show Hafnia forming the monoclinic phase for both nitric acid and acetic acid and the zirconia forming the tetragonal/cubic phases then the monoclinic phase. Up to 400°C, both the nitric acid and the acetic acid stabilized zirconia (Figs. 1(a) and (b)) were less crystalline than a methoxyethanol stabilized sample (not shown) and an unstabilized sample (direct reaction between zirconium-*n*-propoxide and water in ethanol). From 400°C to 600°C the HNO_3 sample showed that a cubic phase had emerged from the amorphous state. This changed to a mixture of cubic and tetragonal up to 800°C with the most stable monoclinic [baddeleyite] phase occurring between 800°C and 1000°C. The acetic acid stabilized zirconia began to show a tetragonal phase between 400°C and 600°C. At 600°C a mixture of cubic and tetragonal phase existed with the tetragonal phase dominating at 800°C. By 1000°C the monoclinic phase had formed. Both the HNO_3 and the acetic acid samples

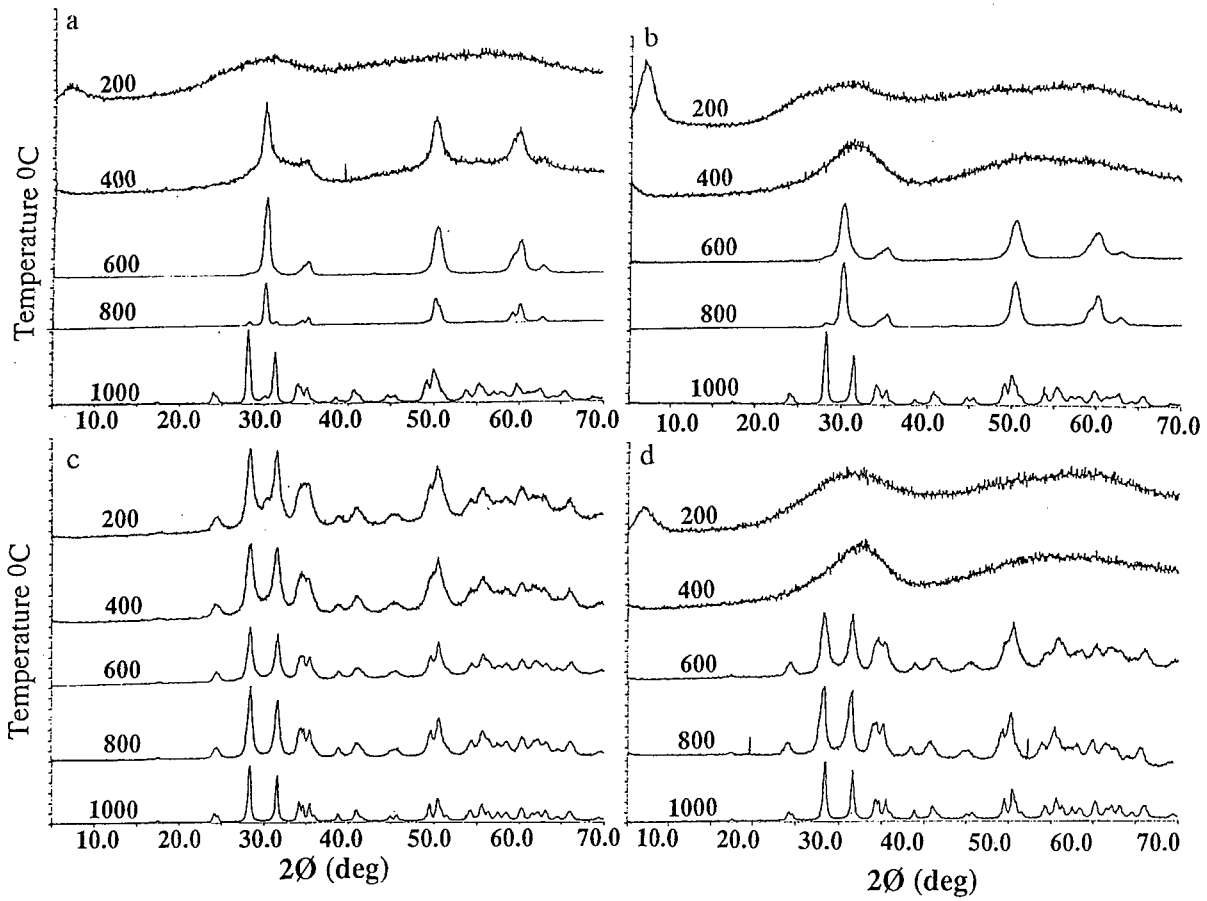

Figure 1. XRD analysis of: (a) HNO_3 stabilized ZrO_2, (b) CH_3COOH stabilized ZrO_2, (c) HNO_3 stabilized HfO_2 and (d) CH_3COOH stabilized HfO_2.

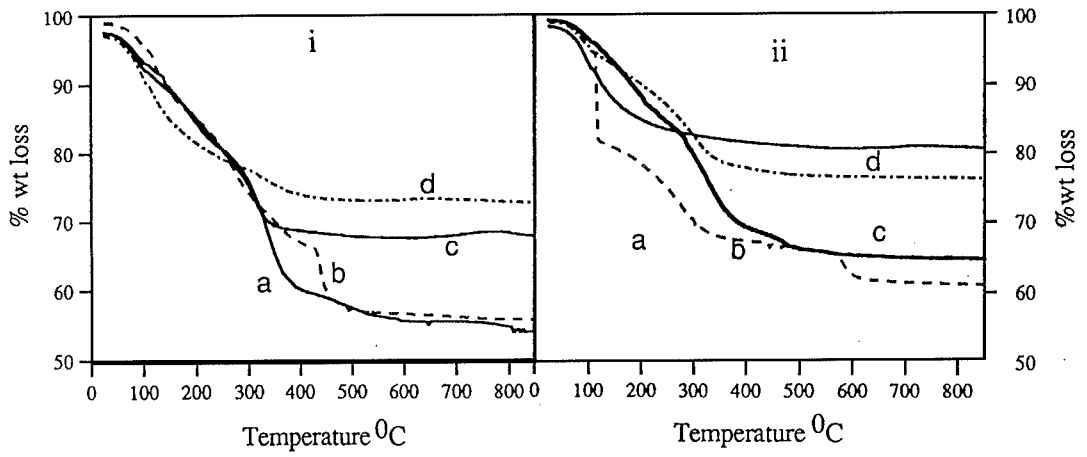

Figure 2. TGA plots of ZrO_2 and HfO_2 derived from HNO_3 CH_3COOH, MeOEt and water.

displayed a retardation of crystallinity relative to an methoxyethanol and un-stabilized sample. The hafnia samples all formed the monoclinic phase directly from the amorphous phase. The acetic acid stabilized hafnia again showing a higher crystallization temperature than the other samples (similar to that of zirconia).

TGA of zirconia derived from the nitric acid and acetic acid showed a similar total weight loss of 45% both of which were greater than the methoxyethanol sample and the unstabilized sample (Fig. 2(i)). The nitric acid stabilized sample showed the material bound to the zirconia up to 440°C; the acetic acid stabilized sample lost all its organic matter by 360°C. Organic matter contained in the methoxyethanol sample was released at a lower temperature than the others suggesting a weaker bound system. The TG's Hafnia (Fig. 2(ii)) are similar to those of zirconia except for the nitric acid stabilized Hafnia; here an almost instant loss of weight at 115°C occurred where 10% of the weight was lost. However, not until 580°C does this final loss take place (cf. 440°C for the zirconia sample).

The silica formed has been well characterized previously by TEM, light scatttering and BET [13]. These particles, stabilized in ethanol at pH 10.5 at a wt% of 2.25 gave a neflometric turbidity reading τ of 22 NTU. A stable acidic catalyzed silica for the low index layer has been made but as it gives a higher refractive index, more layers will be needed to yield similar reflectivities. A previous TEM of nitric acid stabilized zirconia showed only a darkening of the grid [14] suggesting the presence of a polymeric film, features of which were too small to be seen. The undiluted zirconia sol had a typical τ of 46 NTU.

The AES depth profile (Fig. 3) indicates very little intermixing of the silica into the zirconia layer (silicon content falls to 0%); however, zirconia has penetrated much further (zirconia has minimum of 7%) into the silica layer. This might not be wholly unexpected considering that silica is a highly porous colloidal layer about 5–6 particles thick and the zirconia layer is a dense polymeric film made from polymer species probably no more than 1 nm in diameter. It is unlikely that the zirconia has penetrated all the way through the silica layers as the figure indicates, as the nature of the AES analysis causes a degree of intermixing itself. Better resolution could be obtained using a rotating stage and smaller etch increments. The XPS analysis (Fig. 3) revealed less resolution than the AES with only the outer two layers being separated. Before, this analysis, however, the surface had cracked like crazy paving (either due to age or pre-sample treatment) such that the area of analysis required by the XPS was greater than any one paving. This resulted in analysis of cracks as well as pavings, thus, better resolution is hoped for with crack-free samples.

LIDT results from the best coating at AWE was an eight pair basic silica and HNO_3 stabilized zirconia dip coated mirror. Using an R on 1 test [15] this had a LIDT of 8.1 J/cm^2 with a 0.7 ns pulse length. This compared very favorably (as shown in Fig. 4) to commercially available 3ω mirrors tested (analysis of which has showed that at least some mirrors were composed of silica and zirconia).

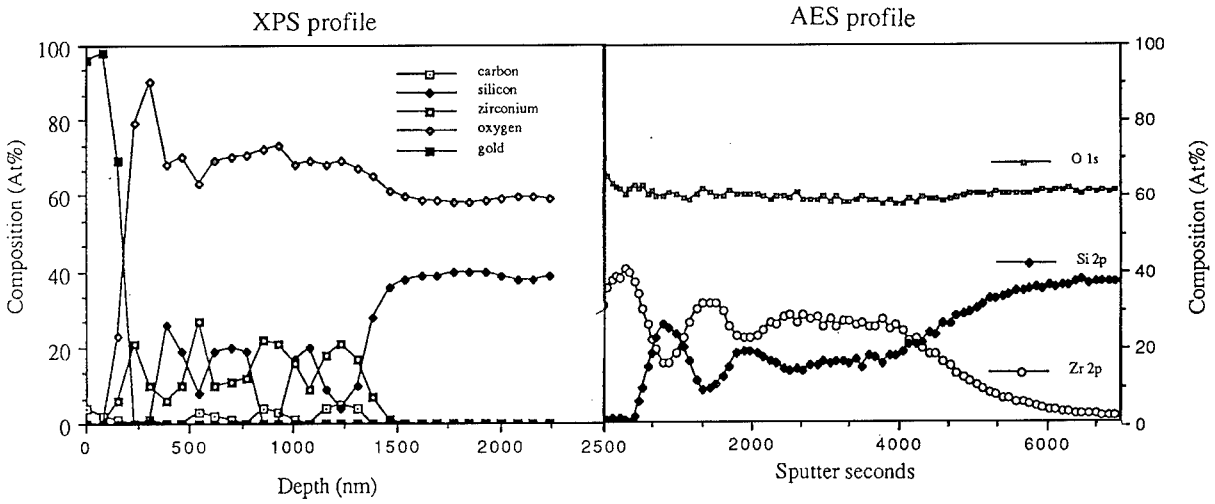

Figure 3. XPS and AES depth profile of a 4 pair silica/zirconia stack.

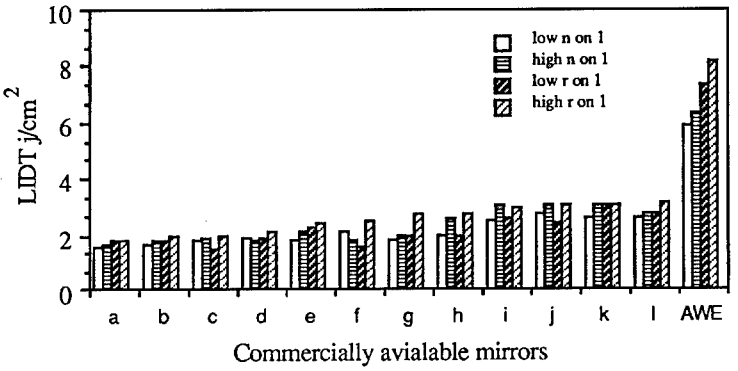

Figure 4. LIDT measurements of commercially available and AWE made mirrors.

Conclusion

High LIDT UV mirrors have been made using alternating stacks of silica and zirconia made by sol-gel processing. The best reflectivities and LIDT obtained were from using nitric acid to stabilize the zirconia, although acetic acid and methoxyethanol could also be used. Characterization of the bulk materials suggest that different routes between the high index materials yield different intermediate species (either more or less resistant to change during heating). These differences could be responsible for differences in the LIDT. Initial depth profiling of one sample showed intermixing to some degree between the silica and zirconia layers. This still needs to be quantified but does not appear to be a negative factor as this sample had a high LIDT.

Acknowledgments

The authors would like to thank the assistance of the EXAM section for their assistance with the XRD analysis and A.J. Morris for the dip coating.

References

1. S. Sakka, K. Kamiya, K. Makita, and Y. Yamamoto, Journal of Non-Crystalline Solids **63**, 223–235 (1984).
2. A. Matsuda, Y. Matsuno, S. Kataoka, S. Katayama, T. Tsuno, N. Tohuge, and T. Minami, Sol-Gel Optics, SPIE **1328**, (1990).
3. K. Vorotilov, V. Petrovsky, and V. Vasiljev, Journal of Sol-Gel Science and Technology **5**, 173–183 (1995).
4. Y. Yan, S.R. Chaudhuri, and A. Sarker, Journal of the American Ceramic Society **79**(4), 1061–1065 (1996).

5. I.M. Thomas, Applied Optics **25**(9), 1481–1483.
6. C.J. Brinker, G.C. Frye, A.J. Hurd, and C.S. Ashley, Thin Solid Films **201**, 97–108 (1991).
7. J.A. Britten and I.M. Thomas, Journal of Applied Physics **71**(2), 972–979 (1992).
8. C.J. Brinker, A.J. Hurd, G.C. Frye, P.R. Schunk, and C.S. Ashley, The Centiennial Memorial Issue of the Ceramic Society of Japan **99**(10), 862–887 (1991).
9. O.S. Heavens, *Thin Film Physics* (Methuen, Chapman & Hall, London, 1970).
10. H. Mc Innis, J.E. Andrew, N. Bazin, A.T. Morris, and K.T. Porter, Laser damage and optical properties of high index single layer and high/low index multilayer mirrors, submitted to the *29th Annual Boulder Damage Symposium* (1997).
11. W. Stober, A. Fink, and E. Bohn, Journal of Colloid and Interface Science **26**, 62 (1968).
12. M.T. Harris, R.R. Brunsen, and C.H. Byers, Journal of Non-Crystalline Solids **121**, 397–403 (1990).
13. M.S.W. Vong, N.J. Bazin, and P.A. Sermon, Journal of Sol-Gel Science and Technology **8**, 499–505 (1997).
14. D.M. Spriggs, J.E. Andrew, and N.J. Bazin, *SPIE Proceedings of the 28th Annual Boulder Damage Symposium.*
15. L. Sheehan, M. Kozlowski, C. Stolz, F. Genin, M. Runkel, S. Schwartz, and J. Hue, SPIE **2775**, 357–369 (1996).

Journal of Sol-Gel Science and Technology 13, 763–767 (1998)
© 1998 Kluwer Academic Publishers. Manufactured in The Netherlands.

Atomic Force Microscopy Study of NaOH Corroded Al_2O_3-TiO_2-SiO_2 Coatings on Glass

YONGJUAN DU*, EDDA RÄDLEIN AND GÜNTHER HEINZ FRISCHAT
Institut für Nichtmetallische Werkstoffe, Technische Universität Clausthal, Zehntner-straße 2A, 38678 Clausthal-Zellerfeld, Germany

Abstract. Atomic force microscopy (AFM) was used to study the performance of ≈80 nm thick Al_2O_3-TiO_2-SiO_2 sol-gel coatings on glass substrates following corrosion in 1 M NaOH solutions at 60°C. The as-prepared coatings were homogeneous on a nanoscale and displayed the "glass pattern" before corrosion. Layers with different compositions behaved differently during the corrosion process. Thus, TiO_2 or TiO_2-dominated layers had tetragonal-like crystals on their surfaces after corrosion, possibly of anatase composition. On the other hand, layers with a molar ratio $Al_2O_3 : SiO_2$ near 1 : 2 displayed a pseudo-hexagonal morphology, possibly with a nepheline ($Na_2O{\cdot}Al_2O_3{\cdot}2SiO_2$) composition. Layers of $5Al_2O_3$-$40TiO_2$-$55SiO_2$ were corroded is a stepwise fashion and had no special surface morphology.

Keywords: sol-gel, coatings, corrosion, morphology, atomic force microscopy

1. Introduction

Many glass properties are more or less strongly controlled by the surface state, i.e., the micro- or nanoscale morphologies. Of the techniques developed both to modify and to improve glass surfaces, the sol-gel method is one of the most attractive and effective ones. It can equally be used to improve classical properties such as chemical durability [1, 2], or to provide the glass surface with totally new characteristics [3, 4]. Recently the crystallization and the corrosion mechanisms of TiO_2 coatings on glass substrates were studied [5], and it was demonstrated that atomic force microscopy (AFM) is ideally suited for such an investigation. In the meantime the AFM method has been used to study the nanoscale performance of non-conducting glass surfaces [6–8].

This work is part of a program of NaOH corrosion studies on TiO_2 coatings [5]. Different Al_2O_3-TiO_2-SiO_2 sol-gel coatings on glass were prepared and their nanoscale topographies were studied by AFM, following corrosion in NaOH solutions.

2. Experimental

The compositions of the coatings prepared by dip coating on commercial microscope slide glasses are shown in Table 1. The coatings were ≈80 nm thick. Details of the solutions, the preparation and the dip coating processes are given in [5, 9, 10]. Table 1 also indicates the effects of annealing for 1 h at 550, 700, and 800°C. Annealing at 450 and 500°C resulted in totally X-ray amorphous (glassy) films. With increasing Al_2O_3 content the stability of the solutions decreased drastically, and solutions 7 to 10 contained some gel-like precipitates at the walls and the bottom of the container.

The coated substrate glasses were immersed in 1 M NaOH solutions at 60°C for times up to 48 h, then washed several times in warm distilled water and cleared ultrasonically for 1 min in acetone, before storage in a desiccator at 20°C. The topographies of the surfaces were investigated by AFM (Nanoscope II with

**Permanent address*: Research Institute of Glasses and Ceramics, East China University of Science and Technology, Shanghai, P.R. China.

Table 1. Compositions and crystallinity of the prepared sol-gel films.

	Composition (mol%)			Status		
Sample	Al_2O_3	TiO_2	SiO_2	550°C	700°C	800°C
0	0	100	0	a	a	a
6	5	40	55	am	am	a
7	20	40	40	am	am	a
8	20	50	30	am	a	a
9	30	40	30	am	a	a
10	20	60	20	am	a	a

a = anatase, am = X-ray amorphous.

A-head, Digital Instruments, Inc., Santa Barbara, CA, USA) with a maximum scanning range of 1 μm^2. Si_3N_4 tips were used. The measurements were made at 20°C and a relative humidity of 40%.

3. Results and Discussion

3.1. *TiO_2 and TiO_2-Rich Films*

NaOH corrosion of pure TiO_2 coatings has already been reported [5]. Crystalline TiO_2 (anatase) films were etched, although part of the surface retained its more

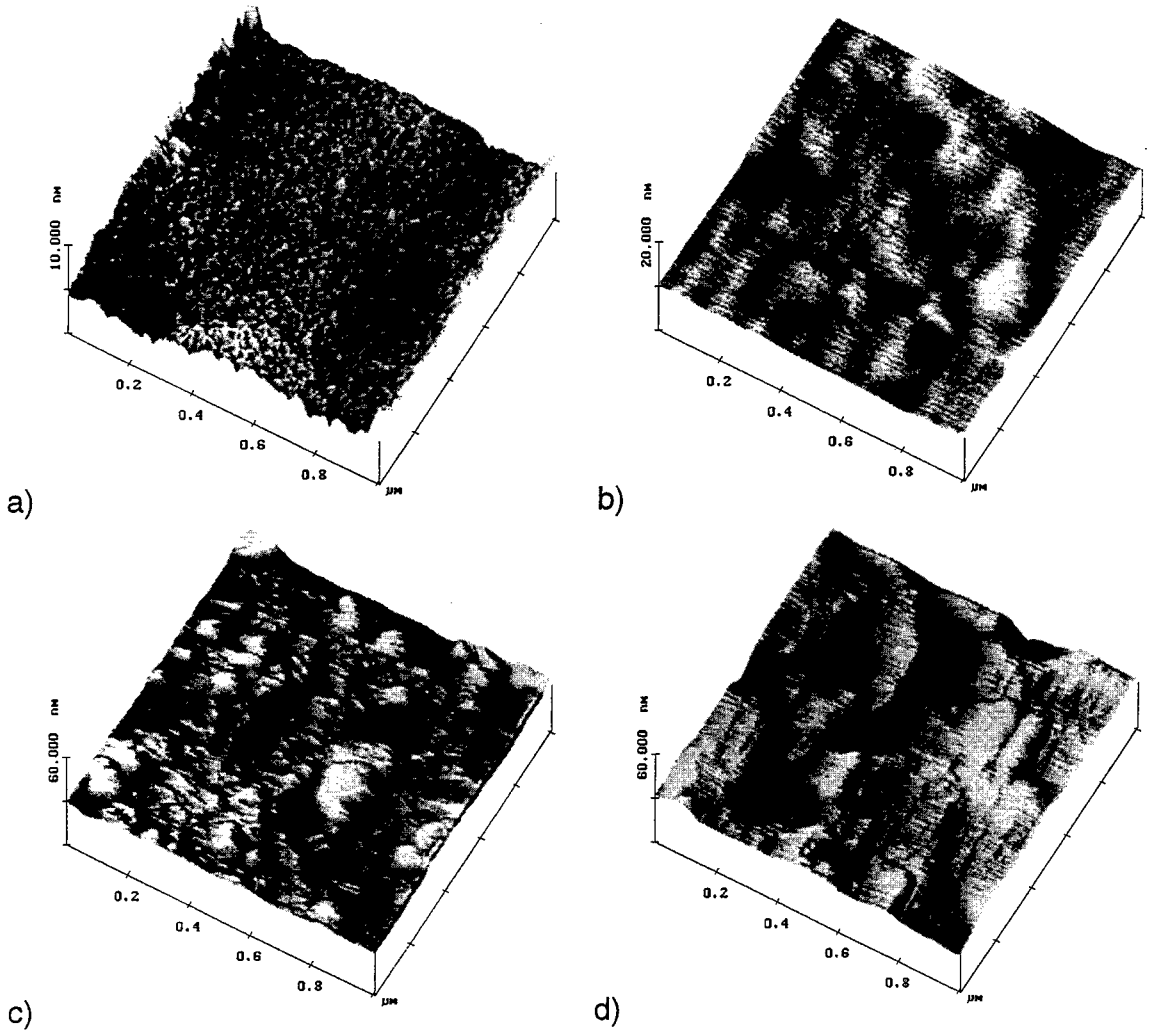

Figure 1. AFM height mode images of $30Al_2O_3$-$40TiO_2$-$30SiO_2$ coatings following corrosion in 1 M NaOH solutions at 60°C: (a) uncorroded, (b) after 6 h corrosion, (c) 12 h and (d) 24 h.

regular nanoscale morphology. The corrosion of glassy TiO_2 films proceeded differently. Probably due to a redeposition process, regularly shaped crystal-like features were formed at the surface. The glassy TiO_2 material was dissolved. With ongoing NaOH corrosion the solution at the surface was supersaturated with TiO_2, owing to the stationary nature of the dissolution process. Crystal formation may have been supported by the presence of some TiO_2 nuclei.

To some extent, glassy films with the compositions $20Al_2O_3$-$60TiO_2$-$20SiO_2$ and $30Al_2O_3$-$40TiO_2$-$30SiO_2$ behave like pure glassy TiO_2 films. Figures 1(a)–(d) show a set of AFM images following corrosion of the $30Al_2O_3$-$40TiO_2$-$30SiO_2$ coating in NaOH. Figure 1(a) displays the uncorroded film surface. The coating is very homogeneous and shows the usual surface "glass pattern", similar to other coatings and glasses [8–10]. The surface ripples have a diameter of 20 to 30 nm, a height of 0.5 to 1.5 nm, and the rms (root mean square) surface roughness is 0.77 ± 0.12 nm. After 6 h corrosion in NaOH solution at 60°C the previously reported [5] tetragonal-like surface features appear, see Fig. 1(b). They are between 150 to 200 nm wide and 1.5 to 2 nm high, with angles between two sides of 85° to 105°. The rms value of 0.75 ± 0.17 nm demonstrates that the surface is still smooth. With ongoing corrosion the surfaces become rougher and some cavities can be seen. Thus, Fig. 1(c) shows both residues of tetragonal surface features and etched cavities. The former are 60 to 180 nm wide and 3 to 8 nm high while the latter are 100 to 180 nm wide and 2 to 8 nm deep. Figure 1(d) displays that after 24 h corrosion the cavities, which are 90 to 220 nm wide and 4 to 14 nm deep, become dominant.

The $20Al_2O_3$-$60TiO_2$-$20SiO_2$ coating behaves similarly to the $30Al_2O_3$-$40TiO_2$-$30SiO_2$ coatings just discussed. Since this coating is chemically less stable, the corrosion process proceeds faster and the etched surface cavities are wider and deeper, e.g., 40 to 120 nm wide and 5 to 20 nm deep after 6 h corrosion. The tetragonal-like surface crystals, also formed after short corrosion times, disappear totally at longer times. The glassy film has been nearly totally dissolved.

3.2. *Films with an $Al_2O_3 : SiO_2$ Ratio Near 1 : 2*

The sol-gel films (annealed for 1 h at 500°C) having the composition $20Al_2O_3$-$40TiO_2$-$40SiO_2$ corrode in a different fashion. Their surfaces display a nearly regular hexagonal-like nanostructure (Fig. 2(a)). The lateral size of the pseudo hexagons is between 100 and 200 nm and the height is 15 to 30 nm, with angles between the sides varying from 110° to 125°. With longer corrosion times the hexagonal-like morphology is enhanced. Thus, for example, the surface in Fig. 2(c) shows hexagonal plates 100 to 250 nm wide and 10 to 40 nm high, with angles very near 120°.

To some extent the corrosion of glassy films of $20Al_2O_3$-$50TiO_2$-$30SiO_2$ is similar to the corrosion $20Al_2O_3$-$40TiO_2$-$40SiO_2$ films. Films prepared by 1 h annealing at 450 and 550°C, respectively, showed the same behavior. However, the typical hexagonal morphology disappeared when the corrosion time strongly exceeded 24 h. The surface then only contained pits and hillocks indicating very strong corrosion of the total layer.

What is the reason for the formation of the regular-shaped hexagons? One can suppose that during the corrosion process Na^+ and OH^- ions diffuse into the coatings, dissolve the TiO_2 and form crystals of nepheline-type composition, $Na_2O \cdot Al_2O_3 \cdot 2SiO_2$, which show a hexagonal habit. This process of nepheline formation is facilitated by those film compositions, where the molar ratio of $Al_2O_3 : SiO_2$ already is near 1 : 2. This is perfectly the case for sample 7, and approximately also for sample 8. When the molar ratio of $Al_2O_3 : SiO_2$ is too far from 1 : 2, nepheline formation is no longer the dominating process, e.g., as with the films of composition $30Al_2O_3$-$40TiO_2$-$30SiO_2$ (see Fig. 1).

3.3. *Films of Other Compositions*

NaOH corrosion of the glassy $5Al_2O_3$-$40TiO_2$-$55SiO_2$ coatings (annealed for 1 h at 500°C) proceeds in a different way. The rms surface roughness increases from 0.58 ± 0.08 (uncorroded film surface) to 1.24 ± 0.34 nm (3 h corrosion), 1.55 ± 0.19 nm (12 h), and 10.2 ± 1.8 nm (24 h). The height differences between peak and valley increase correspondingly from 0.5 to 1.5 nm, 4 to 6 nm, 6 to 8 nm, and 25 to 45 nm. The coating is increasingly etched away by the NaOH solutions and a special morphology is not observed during the corrosion process.

4. Conclusions

TiO_2 and Al_2O_3-TiO_2-SiO_2 films were prepared by sol-gel technology. 1 M NaOH solutions corroded

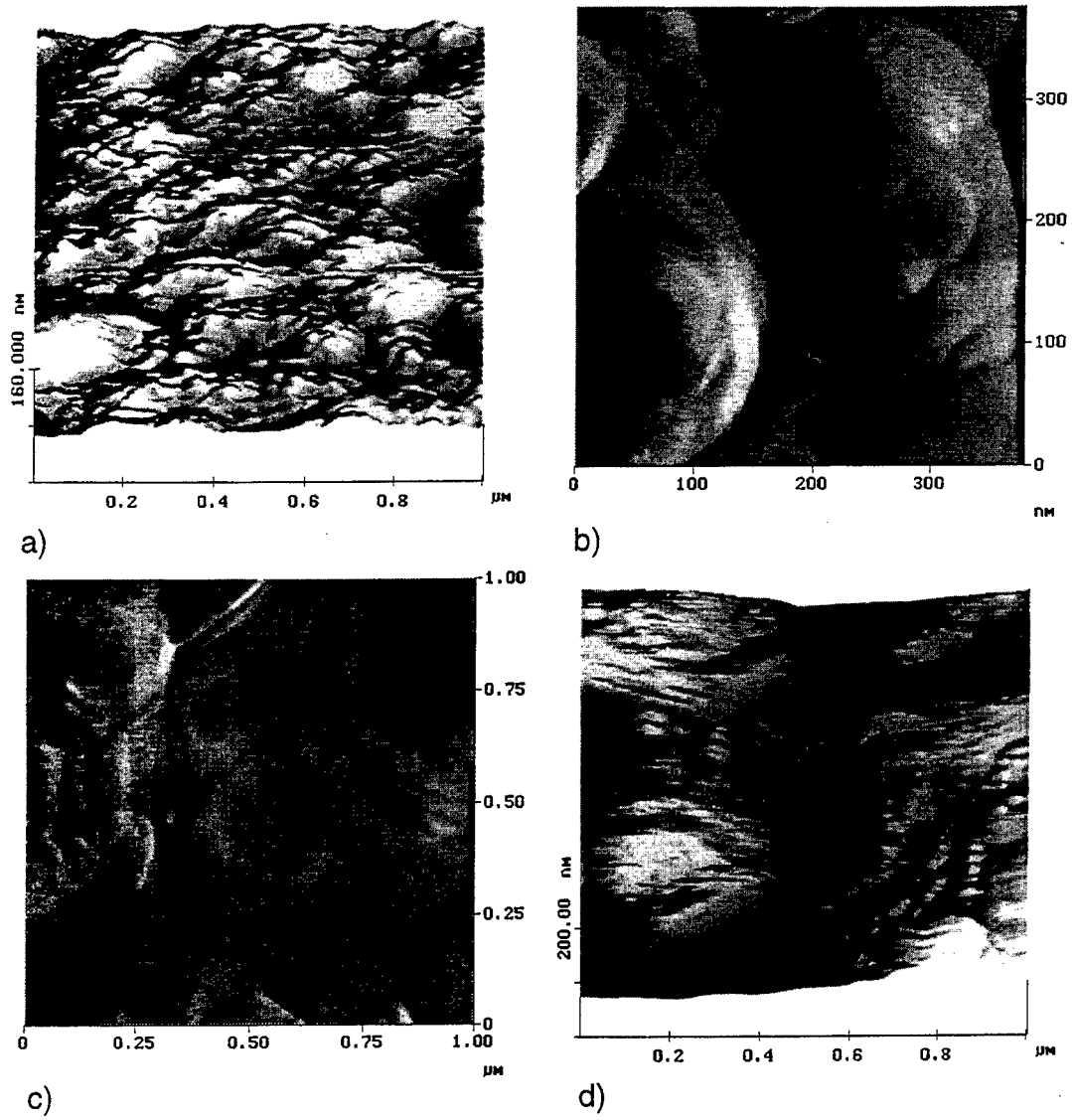

Figure 2. AFM images of $20Al_2O_3$-$40TiO_2$-$40SiO_2$ coatings following corrosion in 1 M NaOH solutions at 60°C: (a) after 3.5 h corrosion, (b) 12 h, (c) 24 h and (d) 24 h, (b) and (c) represent force mode images with the grey scale between 0 and 1.0 nN.

these films differently. Corroded glassy TiO_2 or TiO_2-dominated films had a tetragonal-like nanostructure with crystals showing the habit of anatase. Corroded films with molar ratios of $Al_2O_3 : SiO_2$ near 1 : 2 contained hexagonal-like nanocrystals, possibly with a nepheline composition. Other films, e.g., $5Al_2O_3$-$40TiO_2$-$55SiO_2$, were corroded without the formation of a special surface morphology.

References

1. W. Beier and G.H. Frischat, Materials Research Symposium Proceedings **121**, 827 (1988).
2. Q. Chen, G.H. Frischat, and J. Cheng, Journal of Sol-Gel Science and Technology **2**, 535 (1994).
3. C.J. Brinker and G.W. Scherer, *Sol-Gel Science* (Academic Press, Boston, 1990), p. 839.
4. H. Schmidt, Boletin de la Sociedad Espanola de Ceramica y Vidrio **31-C**, Vol. 1, 185 (1992).
5. Y. Du, E. Rädlein, and G.H. Frischat, in *Proceedings International Symposium on Glass Problems*, edited by R. Akcakaya, N. Erinc, G. Albayrak, and S. Isevi (Sisecam, Istanbul, 1996), Vol. 1, p. 462.
6. F. Creuzet, G. Ryschenkow, D. Abriou, F. Didier, and H. Arribart, Boletin de la Sociedad Espanola de Ceramica y Vidrio **31-C**, Vol. 7, 105 (1992).

7. E. Meyer, H. Haefke, H.-J. Güntherodt, O. Anderson, and K. Bange, Glastechnische Berichte Glass Science and Technology **66**, 30 (1993).
8. C. Wünsche, E. Rädlein, and G.H. Frischat, Glastechnische Berichte Glass Science and Technology **68 C1**, 275 (1995).
9. U. Wellbrock, W. Beier, and G.H. Frischat, Journal of Non-Crystalline Solids **147/148**, 350 (1992).
10. Y. Du and G.H. Frischat, in *Proceedings of XVII International Congress on Glass*, edited by F. Gong (International Acedemic Publishers, Beijing, 1995), Vol. 4, p. 187.

Journal of Sol-Gel Science and Technology 13, 769–773 (1998)
© 1998 Kluwer Academic Publishers. Manufactured in The Netherlands.

Atomic Force Microscopy Study of TiO_2 Films Obtained by the Sol-Gel Method

MARIA ZAHARESCU AND MARIA CRISAN
Romanian Academy, Institute of Physical Chemistry, 202, Splaiul Independentei, 77208 Bucharest, Romania

I. MUŠEVIČ
J. Stefan Institute, Jamova 39, 61111 Ljubljana, Slovenija

Abstract. Atomic Force Microscopy (AFM) was used to study the influence of thermal treatments on the structural and textural properties of the sol-gel TiO_2 films obtained from $Ti(OC_3H_7^i)_4$. X-ray diffraction (XRD), ellipsometric and porosity measurements have also been made.

The TiO_2 sol-gel films were homogeneous, transparent and amorphous. Heat treatments in the 400–600°C range indicate that the films have a strong tendency to crystallization. The high initial homogeneity of the TiO_2 films was preserved during the crystallization process. AFM shows that the thermally treated films exhibit uniform, monodispersed crystals.

Keywords: TiO_2 films, sol-gel method, AFM study

1. Introduction

The chemistry of the sol-gel process based on hydroxylation and condensation of molecular precursors has been extensively studied for silica. Transition metal alkoxides appear to be much more reactive than silicon alkoxides. This is due to the lower electronegativity of the transition metals compared with silicon and the ability of transition metal atoms to exhibit several coordination states [1, 2]. Among the transition metal alkoxides, those of titanium have been systematically studied both from experimental [3–11] and theoretical [2, 12–14] points of view. There are, however, unanswered questions concerning the influence of different experimental parameters on the properties of the materials.

We have previously published results on vitreous reflecting TiO_2 films on aluminized commercial glass [15], TiO_2 films containing transition metals [8] and TiO_2 films obtained from different Ti-alkoxides by sol-gel processing [16]. Here we present an AFM study of the influence of thermal treatments on the structural and textural properties of sol-gel TiO_2 films, as obtained from $Ti(O\text{-}C_3H_7^i)_4$.

2. Experimental

Tetraisopropyl orthotitanate (Merck) was used as the TiO_2 source. The composition of the starting solution and the experimental conditions are listed in Table 1. The hydrolysis reaction was carried out in a closed system, flushed with purified nitrogen, via a dropping funnel. During the reaction the system was vigorously stirred [17]. Titanium alkoxides were hydrolyzed using a small quantity of water while controlling the pH to prevent the formation of TiO_2 precipitates.

Non-supported porous material was formed from the TiO_2 solution by careful evaporation of the solvent at room temperature, followed by thermal treatments at 300 and 400°C for 1 hour. Supported TiO_2 films on silicon wafer substrates have been obtained by dip coating using the solution of composition given in Table 1. The films were deposited immediately after the reaction at 50°C has been completed (see Table 1). The TiO_2 films were thermally treated at 400, 500 and 600°C, respectively, according to previous DTA/TGA results [17].

Characterization of both TiO_2 gel and TiO_2 films was performed using X-ray diffraction; BET specific

Table 1. Solution composition and experimental conditions.

Solution composition	Molar ratio
i-$C_3H_7OH/Ti(O\text{-}C_3H_7^i)_4$	55
$H_2O/Ti(O\text{-}C_3H_7^i)_4$	1.5
$HNO_3/Ti(O\text{-}C_3H_7^i)_4$	0.912 (pH = 4.1)
Experimental conditions	
Reaction time (min)/temperature (°C)	30/50
Gelling time of unsupported gel (hours)	85
Gelling temperature of unsupported gel (°C)	20
Viscosity of solution at the moment of deposition η (mPa · s/20°C)	2.49
Withdrawal temperature (°C)/speed (cm/min)	20/5
Thermal treatment of the film (1 hour) at:	400–600°C

surface area; computerized volume and pore size measurements and Atomic Force Microscopy.

3. Results and Discussion

3.1. *Unsupported Gels*

X-ray diffraction patterns of the unsupported gels display the well known strong crystallization tendency of TiO_2 gels, (Fig. 1).

The structural and textural properties of porous unsupported materials are presented in Table 2.

The surface area and pore volume of the initial gel are high and decrease after heat treatment at 400°C because of the densification and crystallization of samples. The mean pore size shows a slight tendency to increase with the heat treatment, which is a result of crystallization.

3.2. *Supported Films*

The films, which were obtained under the conditions presented in Table 1, are homogeneous, transparent and amorphous. X-ray diffraction patterns of the supported gels (TiO_2 film on Si-wafer support) indicate that for all the treatment temperatures the films are amorphous. However, the XRD results could be influenced by the low thickness of the films. Previous ellipsometric measurements [16] on the initial films and films thermally treated at 400 and 500°C have shown a densification of the film (Table 3). The refractive index n increased and the film thickness decreased upon thermal treatment.

Table 3. Ellipsometric measurements (refractive index and thickness) of TiO_2 film on Si-wafer support [16].

Temperature (°C)	Refractive index (n)	Thickness (Å)
Initial	1.60	571
300	1.88	271
400	2.23	257
500	2.25	255

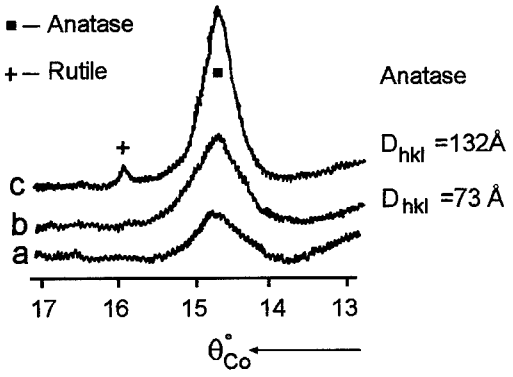

Figure 1. XRD patterns of the TiO_2 gels thermally treated for 1 hour at: (a) 300°C; (b) 400°C and (c) 500°C.

3.3. *Atomic Force Microscopy of the Surfaces of Deposited Films*

The surfaces were using a Nanoscope III Atomic Force Microscope operating in air and in the contact mode. Si_3N_4 cantilevers with a tip radius of 10 nm were used

Table 2. Some structural and textural properties of TiO_2 gels thermally treated at different temperatures.

Sample	Thermal treatment (°C)	S_{sp} (m^2/g)	V_p (0–300 Å) (cm^3/g)	D_p (Å)	D_{hkl} (Å)
	Initial	199	0.2826	28	Amorphous
I	300	199	0.4874	49	73
II	400	164	0.3440	42	71

S_{sp}—specific surface area; V_p—pore volume; D_p—mean pore size; D_{hkl}—crystallite size.

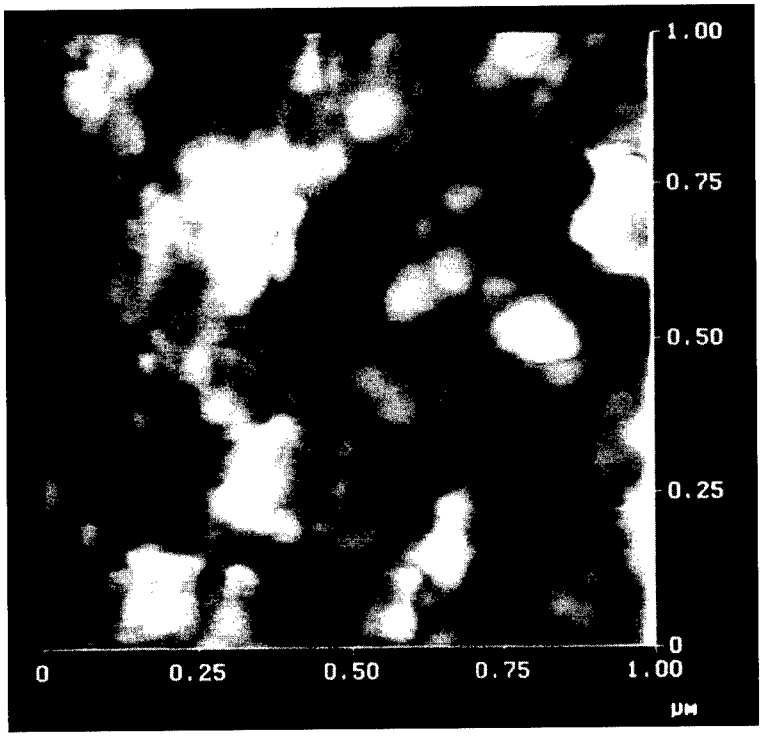

Figure 2. AFM image of the surface of the initial TiO_2 film.

in the experiments. The normal force of the AFM tip was 10^{-10} N. The resolution of the images was 512 × 512 points, and a typical image acquisition time was 1–2 min at a scanning rate of several lines per second. The scanning area was from several 100 μm^2 to 1 μm^2, where most of the characteristic features of the surfaces could be observed.

Figure 2 shows the surface of the initial, non-treated film. The surface is characterized by the presence of rather large particles, which could not be observed on treated films. The RMS surface roughness is of the order of 3 nm and no crystalline-like objects of a regular shape could be observed on the surface. One can, however, observe the presence of tiny aggregates of an amorphous shape. The dimension of these particles is between 50–100 nm and features of this size are also observed on the thermally treated films.

Figures 3–5 show the surfaces of the films, treated at 400, 500 and 600°C, respectively. The RMS roughness of these surfaces is close to 1 nm and seems to be independent of the treatment temperature. One can, however, see that by increasing the temperature of the treatment, grains of regular shapes develop on the surface. For example, the surface of the film treated at 600°C (Fig. 5), shows a regular surface structure, indicating a significant degree of surface order on the scale of several tens of micrometers. A typical dimension of these grains is again in the region 50–100 nm. This suggests, that during the thermal treatment above 500°C, the film recrystallizes. Moreover, one can clearly see in Fig. 5, there is a prefered orientation of these regularly-shaped grains, which suggests the growth of a microcrystalline film from the oriented substrate.

The AFM results are in good agreement with ellipsometric data which show film densification due to thermal treatment. Film densification takes place with film crystallization, as etablished by AFM. The differences between AFM results and XRD results on supported film are determined by the different sensitivities of the two methods.

4. Conclusions

Atomic Force Microscopy (AFM) was used to study the influence of the thermal treatment on the structural and textural properties of sol-gel TiO_2 films produced from $Ti(OC_3H_7^i)_4$. The thermally treated films exhibit

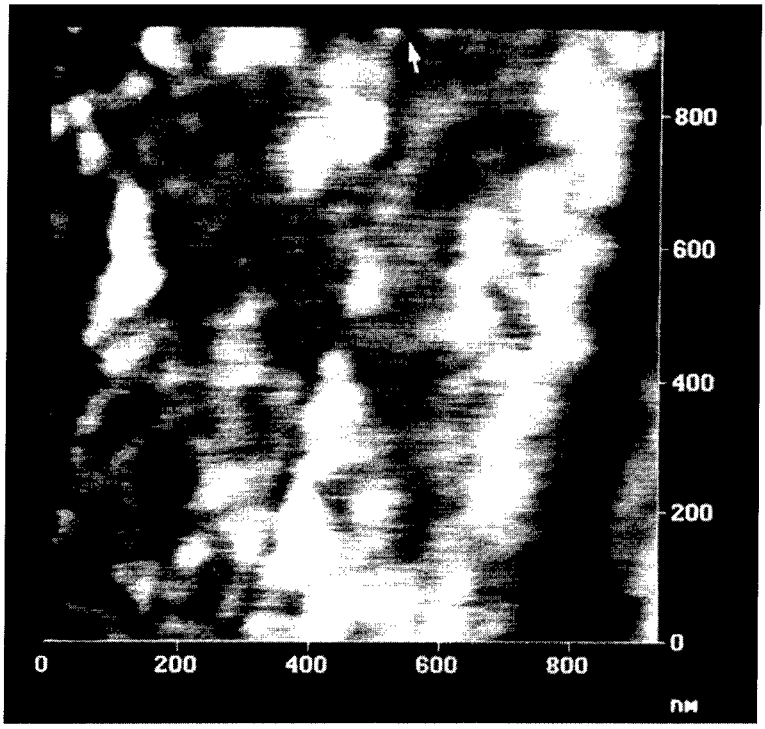

Figure 3. AFM image of the surface of TiO_2 film, thermally treated at 400°C.

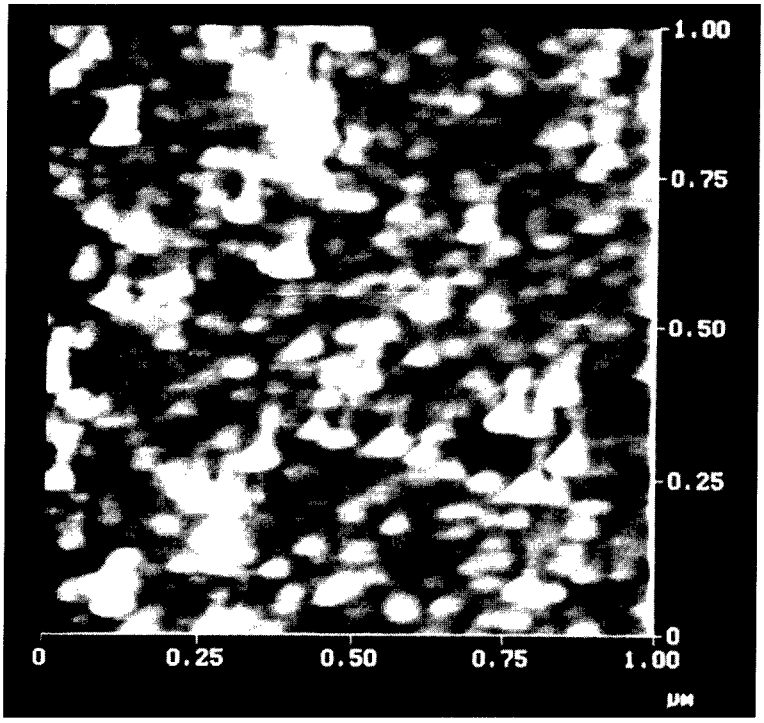

Figure 4. AFM image of the surface of TiO_2 film, thermally treated at 500°C.

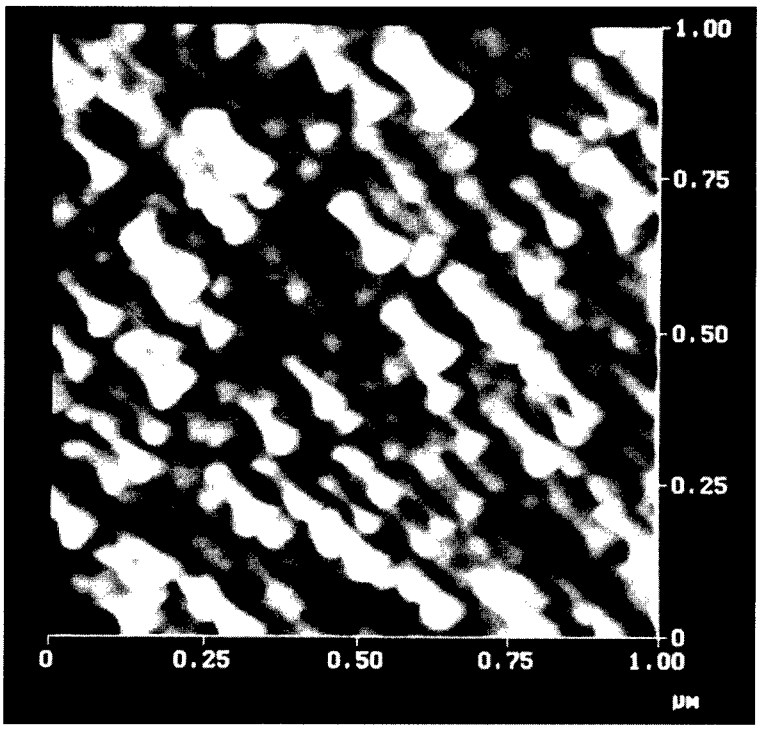

Figure 5. AFM image of the surface of TiO_2 film, thermally treated at 600°C.

uniform, monodispersed regularly-shaped grains, with preferred orientation, which suggests the growth of a microcrystalline film from the oriented substrate.

References

1. D.C. Bradley, R.C. Mehrotra, and D.P. Gaur, *Metal Alkoxides* (Academic Press, London, 1978).
2. J. Livage, M. Henry, and C. Sanchez, Progr. Solid State Chem. **18**, 259 (1988).
3. B.E. Yoldas and T.W. O'Keefe, Applied Optics **18**, 3133 (1979).
4. B.E. Yoldas, Applied Optics **19**, 1425 (1980).
5. B.E. Yoldas, Applied Optics **21**, 2960 (1982).
6. B.E. Yoldas, J. Mat. Sci. **21**, 1087 (1986).
7. K.A. Vorotilov, E.V. Orlova, and V.I. Petrovsky, Thin Solid Films **207**, 180 (1992).
8. M. Zaharescu, C. Parlog, M. Crisan, M. Gartner, and A. Vasilescu, J. Non-Cryst. Solids **160**, 162 (1993).
9. B. Samuneva, V. Kozhukharov, Ch. Trapalis, and R. Kranold, J. Mat. Sci. **28**, 2353 (1993).
10. Ch. Trapalis, V. Kozhukharov, B. Samuneva, and P. Stefanov, J. Mat. Sci. **28**, 1276 (1993).
11. V. Kozhukharov, Ch. Trapalis, and B. Samuneva, J. Mat. Sci. **28**, 1283 (1993).
12. C. Sanchez, J. Livage, M. Henry, and F. Babonneau, J. Non-Cryst. Solids **100**, 65 (1988).
13. C. Sanchez and J. Livage, New J. Chem. **14**, 513 (1990).
14. J. Livage and M. Henry, in *Ultrastructure Processing of Advanced Ceramics*, edited by J.D. Mackenzie and D.R. Ulrich (Wiley, New York, 1988), p. 183.
15. M. Zaharescu, C. Parlog, M. Crisan, M. Sahini, and D. Moraru, Silikattechnik **37**, 165 (1986).
16. M. Zaharescu, M. Crisan, D. Crisan, M. Gartner, and F. Moise, Rev. Roum. Chim. **40**, 983 (1995).
17. M. Crisan, M. Zaharescu, D. Crisan, and L. Simionescu, in *Proc. 8th CIMTECH, B.13.4.* (Faenza, Italy, 1994).

Journal of Sol-Gel Science and Technology 13, 775–778 (1998)
© 1998 Kluwer Academic Publishers. Manufactured in The Netherlands.

Vanadium Doped Sol-Gel TiO_2 Coatings

MARIA CRISAN, MARIA ZAHARESCU AND D. CRISAN
Romanian Academy, Institute of Physical Chemistry, 202, Spl.Independentei, 77208 Bucharest, Romania

RODICA ION
ZECASIN S.A., 202, Spl.Independentei, 77208 Bucharest, Romania

MIHAELA MANOLACHE
Chemical Research Institute ICECHIM, 202, Spl.Independentei, 77208 Bucharest, Romania

Abstract. A study of the experimental conditions required to obtain vanadium doped sol-gel TiO_2 coatings is presented. Tetraethyl orthotitanate was employed as the TiO_2 source and VCl_3, $VOSO_4 \cdot H_2O$ and $VOSO_4$ dissolved in H_2SO_4 were employed as vanadium sources.

Dip coating has been used to produce coatings on silicon wafers, spectral carbon electrodes and titanium electrodes. Both supported and unsupported films have been studied by UV-Vis spectra, IR spectroscopy and X-ray diffraction (XRD). The measurements have been made on samples as prepared and treated thermally at temperatures between 100°C and 300°C. The thermal treatment temperatures have been established from DTA/TGA measurements.

The vanadium doped sol-gel TiO_2 coatings have been tested as sensors for redox potential measurements in electrochemical processes. The influence of both the thickness of films and the nature of substrate has been investigated.

Keywords: vanadium doped TiO_2 films, sol-gel method, sensors, electrochemical properties, redox potential

Introduction

During the last decade, TiO_2 films doped with transition metal ions have been suggested as electrochromic materials for display devices [1]. In the case of vanadium doped TiO_2 films, these exhibit semiconductive or catalytic properties [2, 3] and also high electrochemical conductivity and have therefore been suggested for potential application as anti-static coatings or switchings [4].

A study of the experimental conditions required to obtain vanadium doped sol-gel TiO_2 coatings has been carried out. These coatings have been tested as sensors for redox potential measurements in electrochemical processes.

Experimental

Tetraethyl orthotitanate was employed as the TiO_2 source and VCl_3, $VOSO_4$ solution in H_2SO_4, and $VOSO_4 \cdot H_2O$ were employed as vanadium sources. The compositions of the solutions employed are listed in Table 1.

One can note that, with the exception of the vanadium source type, all the other reaction parameters were similar; e.g., water/alkoxide ratio, solvent/alkoxide ratio, pH, time and temperature of reaction.

Dip coating has been used to obtain coatings on silicon wafers, spectral carbon electrodes and titanium electrodes under the conditions shown in Table 1.

The characteristics of both supported and unsupported samples have been measured by UV-Vis absorption spectra, IR spectroscopy and XRD, for as prepared and samples treated thermally at temperatures between 100°C and 300°C.

Results and Discussion

XRD patterns (Fig. 1) showed that the initial gels were amorphous for sample V_3 and that there was a tendency for anatase to crystallize in samples V_2 and V_1 (more evident for sample V_1). In all the samples thermally treated at 300°C, poorly crystallized anatase is present. At 800°C well crystallized phases: anatase, rutile and V_2O_5 were identified. V_2O_5 is present only in sample V_3, while sample V_1 only contains rutile.

IR spectra (Fig. 2) of all initial gels contain a 1375 cm^{-1} band, the characteristic vibration of υ_{C-CH_3}, a 1640 cm^{-1} band, assigned to the molecular water vibration and a broad band at 3200–3300 cm^{-1} assigned

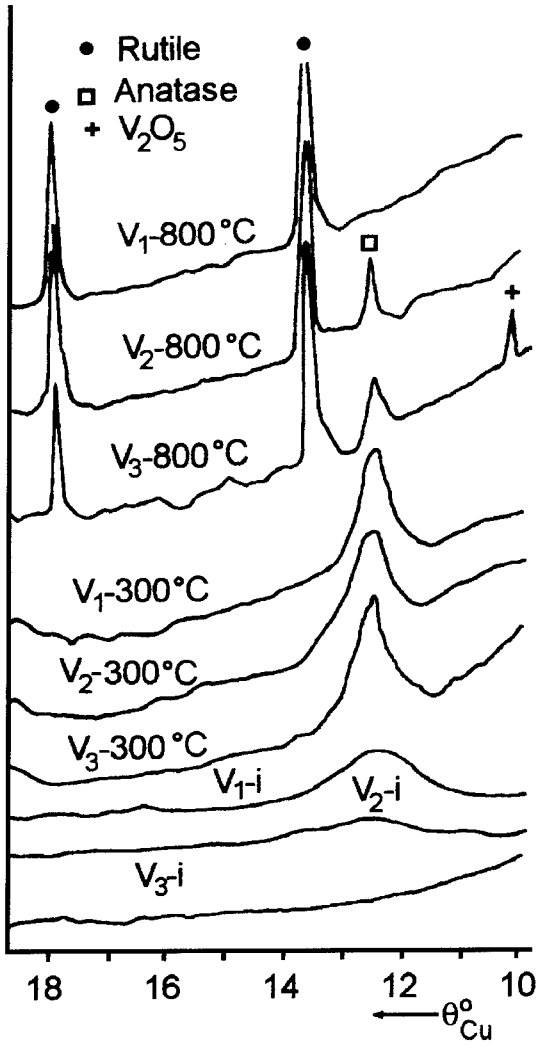

Figure 1. XRD patterns of the vanadium doped TiO_2 gels: as prepared and thermally treated at 300°C and 800°C.

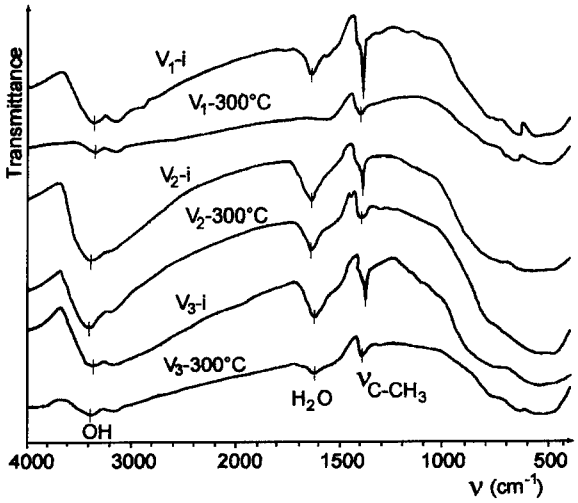

Figure 2. IR spectra of the vanadium doped TiO_2 gels: as prepared and thermally treated at 300°C.

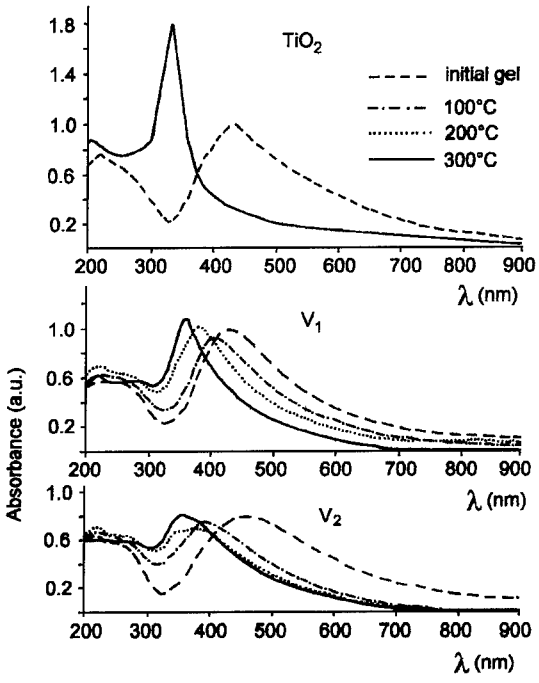

Figure 3. UV-Vis absorption spectra of the vanadium doped TiO_2 coatings, deposited on Si wafers, compared with a pure TiO_2 film: initial and thermally treated.

Table 1. Solution compositions and experimental conditions.

Solution		Solution composition	Molar ratio
V_1	Vanadium source: VCl_3	$[C_2H_5OH] : [Ti(OC_2H_5)_4]$	55
		$[H_2O] : [Ti(OC_2H_5)_4]$	1.5
		$[HNO_3] : [Ti(OC_2H_5)_4]$	0.057 (pH = 3 ÷ 3.5)
		$[V^{3+}] : [Ti(OC_2H_5)_4]$	0.02
V_2	Vanadium source: vanadyl sulphate solution $VOSO_4$ in H_2SO_4 (contained 3.03 g V_2O_5/l)	$[C_2H_5OH] : [Ti(OC_2H_5)_4]$	55
		$[H_2O] : [Ti(OC_2H_5)_4]$	1.5
		$[HNO_3] : [Ti(OC_2H_5)_4]$	0.023 (pH = 3.5)
		$[V^{4+}] : [Ti(OC_2H_5)_4]$	$1.399 \cdot 10^{-4}$
V_3	Vanadium source: vanadyl sulphate $VOSO_4 \cdot H_2O$	$[C_2H_5OH] : [Ti(OC_2H_5)_4]$	55
		$[H_2O] : [Ti(OC_2H_5)_4]$	1.5
		$[HNO_3] : [Ti(OC_2H_5)_4]$	0.034 (pH = 3.5)
		$[V^{4+}] : [Ti(OC_2H_5)_4]$	0.02
Experimental conditions			
Reaction time (min)/Reaction temperature (°C)			30/50
Withdrawal speed (cm/min)/Withdrawal temperature (°C)			5/20
Thermal treatment of the film			
Temperature (°C)/Time (h)			100–300/1

Table 2. Testing response of TiO_2-V^{3+}/Ti electrode at redox potential.

Test solution		F.E.M. (mV)		Composition of redox system (aqueous solutions)
Redox potential (mV)	pH	Ti/E.C.S.	Pt/Ti	
293	2.34	295	−2	Potassium ferrocyanide + potassium ferricyanide + potassium biphtalate + hydrochloric acid
230	2.48	231	−1	
208	2.45	208	+1	
234	3.89	226	+8	Potassium ferrocyanide + potassium ferricyanide + potassium biphtalate + hydrochloric acid
181	3.95	180	+1	
143	3.97	143	−1	
223	8.14	228	−6	Potassium ferrocyanide + potassium ferricyanide + potassium biphtalate + hydrochloric acid
170	8.37	170	0	
109	8.20	112	−3	
167	7.72	165	+2	Mercury + potassium iodide + nitric acid
164	7.70	160	+4	
−115	12.70	−143	−25	Copper + copper sulfate + ammonia + sodium hydroxide
−118	12.71	−159	−41	
−139	11.65	−133	−6	Mercury + sodium sulfide + nitric acid
−199	12.50	−145	+44	Copper + copper sulfate + ammonia
−412	11.70	−330	+84	Mercury + sodium sulfide
−471	12.10	−375	+98	
−531	13.50	−389	+146	

to OH structural groups. At 300°C, all of these bands decrease in intensity as a result of the thermal treatment. In the range between 400 cm^{-1} and 1000 cm^{-1}, where Ti—O bond vibrations occur, some differences are noticed that are assigned to the presence of vanadium in different valence states in the TiO_2 lattice.

UV-Vis absorption spectra (Fig. 3) of compositions V_1 and V_2 were determined for the films deposited on Si wafers and were compared with pure TiO_2 film. Spectral absorption data show the microstructural changes of the system as a function of the V source and of the thermal treatment schedule. The presence of different V sources in the initial compositions results in some changes in the intensity and position of the TiO_2 absorbtion band. No absorption bands for V^{3+} and V^{4+} were noticed, as their characteristic bands overlap with the broad band of TiO_2 [5]. After annealing, the absorption spectra of all the compositions displayed a shift of the absorbance maxima position λ_0 of the charge transfer absorption band towards the UV. The transfer charge band being a measure of the metal-oxygen link, the shift towards the UV implies a shortening of metal-oxygen link, indicating a densification of the film with the increase of the temperature of the thermal treatment.

Based on the results obtained above, solution V_1 was selected for preparation of TiO_2-V^{3+}/C and TiO_2-V^{3+}/Ti electrodes. In order to obtain a suitable thickness of the film (≈1500 Å), three successive depositions were made on Ti and spectral carbon substrates. The redox potential measurements carried out with the TiO_2-V^{3+}/C electrodes did not give reproducible results due to the porosity of the support. Systematic studies were made of TiO_2-V^{3+}/Ti electrode. The electrode has been tested as sensor of redox potential for a large range of potential values (−531 and 293 mV), having in view in the same time the interference of pH in the range of 2.34–13.5.

The measurements of the TiO_2-V^{3+}/Ti electrode were made in comparison with a reference electrode (ECS) and a platinum electrode. The results together with the composition of the redox system are presented in Table 2.

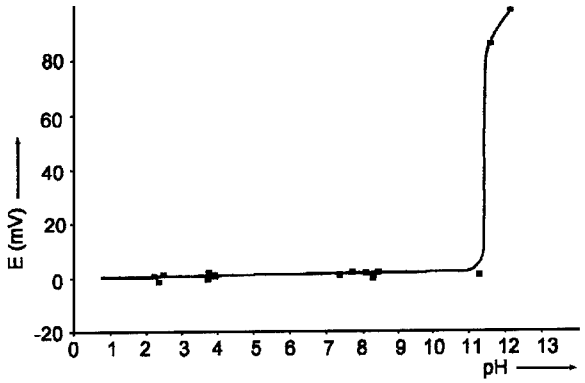

Figure 4. The deviation with pH of the response of the redox potential sensor TiO_2-V^{3+}/Ti, in comparison with a Pt etalon electrode.

A very good indication of the redox potential was obtained, except with highly alkaline systems (pH >11.5), when the TiO_2-V^{3+}/Ti electrode gave large positive deviations from the measurements made with a Pt etalon electrode. These deviations are presented in Fig. 4.

Conclusions

Vanadium doped sol-gel TiO_2 coatings have been produced. The dopant has been included in TiO_2 matrix as V^{3+} or V^{4+}. A TiO_2-V^{3+}/Ti electrode has been produced which was tested as a sensor of redox potential with the functional performances comparable with those of a platinum electrode.

References

1. K. Nagase, Y. Shimizu, N. Miura, and N. Yamazoe, J. Ceram. Soc. Japan **101**, 1032 (1993).
2. H. Hirashima and S. Kamimura, Mat. Res. Soc. Symp. Proc. **121**, 779 (1988).
3. B.E. Handy, M. Maiejewski, and A. Baiker, J. Catal. **134**, 75 (1992).
4. D.P. Partlow, S.R. Gurkovich, K.C. Radford, and L.J. Denes, J. Appl. Phys. **70**, 443 (1991).
5. A.B.P. Lever, *Inorganic Electronic Spectroscopy*, 2nd edition (Elsevier, Amsterdam, 1984), p. 400.

Journal of Sol-Gel Science and Technology 13, 779–782 (1998)
© 1998 Kluwer Academic Publishers. Manufactured in The Netherlands.

Development of Heteropolysiloxane Coatings on Electrogalvanized Steel

M. MAYRAND AND J.F. QUINSON
Groupe d'Etude Métallurgie Physique et Physique des Matériaux, CNRS UMR 5510, INSA, 20 Avenue Albert Einstein, 69621 Villeurbanne Cedex, France

V. ROISNE AND H. GUYON
Groupe d'Etude Métallurgie Physique et Physique des Matériaux, CNRS UMR 5510, INSA, 20 Avenue Albert Einstein, 69621 Villeurbanne Cedex, France; and L.E.D.E.P.P., SOLLAC, 17 Avenue des Tilleuls, 57191 Florange Cedex, France

Abstract. The development of heteropolysiloxane coatings on electrogalvanized steel by sol-gel processing has been studied from the sol state to the solid state using techniques such as ^{29}Si NMR, SIMS, XPS, and the three point flexure test. It was possible, from the results obtained, to propose a simplified model for the coatings which brings into play two layers of differing molecular structure: an extremelly thin internal layer and an outer layer, respectively called the "anchoring" and "volume" layers.

Keywords: heteropolysiloxane coating, electrogalvanized steel, coating development, coating modelling

1. Introduction

Sol-gel coatings on metals [1] present many advantages such as the improvement of the chemical and mechanical properties of metallic substrates. Moreover, coatings prepared from heteropolysiloxanes exhibit specific properties [2–8] due to the incorporation of adapted organofunctional groups in the silica backbone.

Recently, we investigated adhesion promotion and corrosion prevention of heteropolysiloxane coatings, incorporating both amine and methyl functions into their structure on electrogalvanized steel substrates [9]. In the present paper, the formation of these coatings is studied.

2. Experimental Procedure

2.1. Sol Preparation

The coatings were prepared from sols encompassing two precursors, aminopropyltriethoxysilane (APS) and methyltriethoxysilane (MS). Two kinds of sols were selected. Their compositions are given in Table 1.

The "8-3" and "4-7" sols were aged for one hour before use.

2.2. Coating Preparation

The electrogalvanized steel plates were degreased ultrasonically in ethylacetate and dried under warm air. Immediately after cleaning, the electrogalvanized steel plates were dipped in the coating solution and withdrawn at a rate of 10 cm min^{-1}. After deposition, wet coatings were either immediately cured at 100°C for 12 hours in air to preserve the amino and methyl groups, or submitted to an ethanol rinsing prior to curing in order to eliminate physisorbed species on the surface: depending on the procedure used, the coatings are referred to as "8-3" or "rinsed 8-3", and "4-7" or "rinsed 4-7".

3. Results and Discussion

3.1. Sol Characterization

The sols were examined with ^{29}Si NMR. Whatever the sol composition, before deposition species such as T_0^0APS, T_0^0MS, and T_0^1MS or T_0^2APS, attributed

Table 1. Sol compositions.

	APS (mol)	MS (mol)	C_2H_5OH (mol)	H_2O (mol)
Sol "8-3"	0.05	0.95	8	3
Sol "4-7"	0.05	0.95	4	7

respectively to unhydrolyzed and hydrolyzed mononomers, were always present. Moreover, in the case of the "4-7" sol, resonances were observed at higher fields and were assigned to oligomers, T_1, T_2 and T_3.

3.2. *Surface Substrate Characterization*

XPS analysis of the electrogalvanized steel substrate after cleaning with an organic solvent (ethylacetate) or an alkaline solution (NaOH, 1 M), indicates both an oxidized zinc layer and the presence of carbon due to atmospheric pollution. The majority of the carbon was present as hydrocarbons (atomic concentration close to 80%). The fitting of the O_{1s} spectrum reveals the presence of two peaks attributed to O^{2-} and OH^-, respectively. Given the low concentration of carbon-oxygen compounds adsorbed on the surface, it is assumed that the O^{2-} and OH^- peaks represent only contributions from the zinc oxide and hydroxide, respectively, because a large increase in hydroxyl groups on the surface oxidized zinc layer occurs after the alkaline treatment: with the hydroxyl concentration, equal to 46%, after cleaning by ethylacetate, increasing to 72%.

3.3. *Coating Characterization*

Morphology. Secondary electron imaging induced by SIMS was used to investigate the morphology of the coatings (Fig. 1). For "8-3" and "4-7" coatings, the images exhibit clear and dark areas due to charge effects

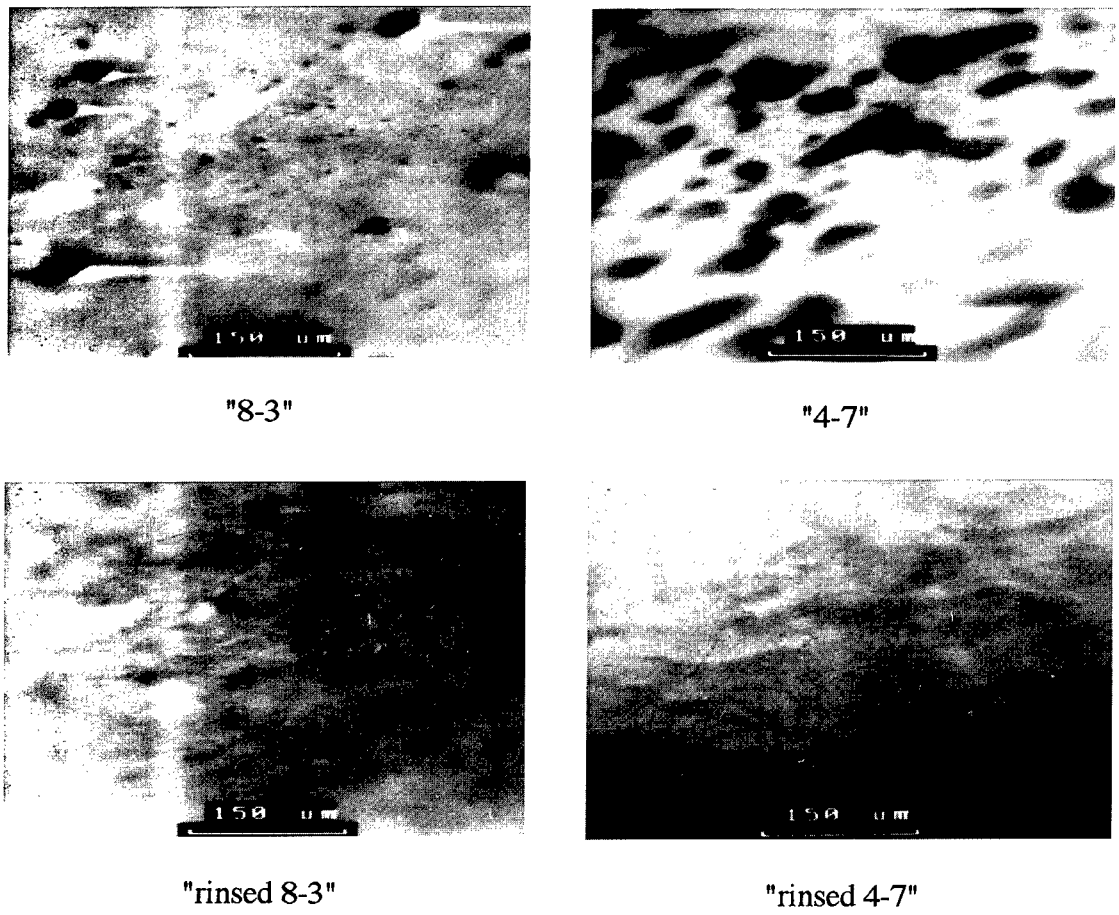

Figure 1. Secondary electron images of "8-3" and "4-7" coatings before and after rinsing.

induced by coating thickness heterogeneity. These regions disappear when the coatings are rinsed with ethanol before curing. Thus, after removal of species weakly incorporated inside the structure, a homogeneous layer, called the "anchoring" layer, remains.

Thickness Estimation and Structure. XPS analysis of the coated electrogalvanized substrate reveals a Zn signal, whichever coating is studied. This result means that the coating thickness is less than the escape depth of photoelectrons, evaluated at 10 nm, and furthermore that the other elements detected (Si, N, ...) originate from the coating. So, the coating thickness, unmeasurable by ellipsometry due to the substrate roughness, can however be estimated through the Si/Zn ratio (Table 2).

Likewise, the Si/N ratio (Table 3) can give information on the respective amounts of APS and MS precursors incorporated in the coating structure, because nitrogen is present only in the APS precursor.

From the data reported in Tables 2 and 3, the following conclusions can be drawn:

Table 2. Si/Zn and Si/N ratios deduced from XPS analysis of coated electrogalvanized substrates.

	Si/Zn	Si/N
"8-3"	3.5	2.3
"4-7"	23.4	6.0
"rinsed 8-3"	0.3	1.8
"rinsed 4-7"	0.3	1.5

Table 3. Identification and quantification of amine forms from N(1s) XPS spectra.

	NH_2	NH_3^+
	Binding energy (eV)	
	Concentration (%)	
"8-3"	399.8	401.5
	78	22
"4-7"	399.8	401.6
	85	15
"rinsed 8-3"	400.3	—
	100	—
"rinsed 4-7"	400.1	—
	100	—

The low values of the Si/Zn and Si/N ratios determined for the "8-3" coating suggest that the unrinsed "8-3" coating is thinner than the unrinsed "4-7" coating, and incorporates less MS precursor into its structure. Moreover, the amino groups are present in two forms, free amine (NH_2) and protonated amine (NH_3^+); the larger amounts free amine are present.

For the "rinsed" coatings, the Si/Zn and Si/N ratios are practically identical and only free amine is detected. It is assumed that the "anchoring" layer, identified previously with the "rinsed" coating, has the same composition whichever sol is used. The extremely low value of the Si/Zn ratio indicates that this layer is very thin. From NMR data concerning the sols, it is obvious that only monomers take part in the "anchoring" layer formation. The subsequent development of the "anchoring" layer to complete the coating structure is realized by incorporating monomers and/or oligomers within another layer, called the "volume" layer.

Adherence. The adherence of the coatings to electrogalvanized steel substrate was characterized using Three point flexure testing [10]. The ultimate deformation of the coated substrate before failure, d_{max}, is used as the adherence measurement. The d_{max} values obtained for coatings deposited onto electrogalvanized steel substrate, previously degreased in ethylacetate, are given in Table 4.

The best adherence is observed in the case of the "8-3" coating. This result suggests that the thinner the coating is, the weaker the internal residual stresses are and/or the stronger the coating cohesive strength.

For both "rinsed" coatings, d_{max} has the same value confirming the commonality of the "anchoring" layer. This layer being extremely thin, the decrease in d_{max} observed is probably due to a low degree of crosslinking.

Moreover, the very strong adherence measured (1.7 mm) between the "8-3" coating and the electrogalvanized steel substrate, previously cleaned by an alkaline solution, is worth noting. Keeping in mind

Table 4. Results of adherence measurements on both "rinsed" and "unrinsed" coatings.

	d_{max} (mm)
"8-3"	1.0
"4-7"	0.8
"rinsed 8-3"	0.7
"rinsed 4-7"	0.7

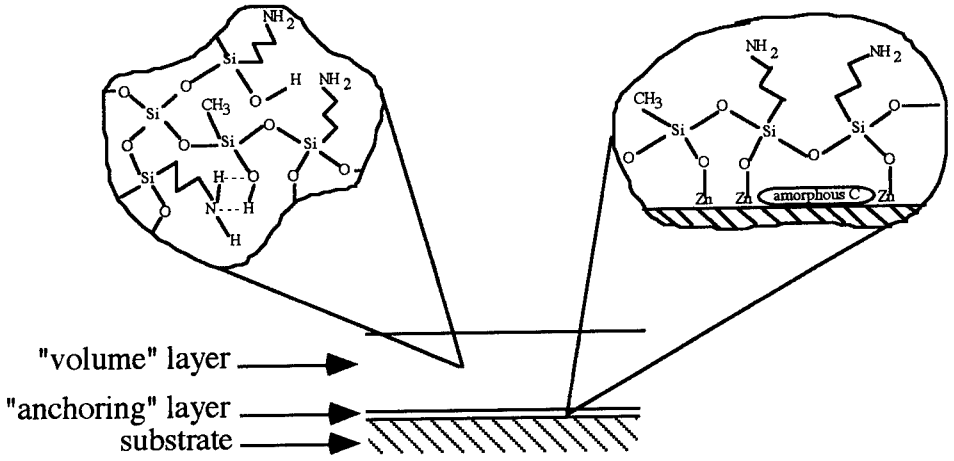

Figure 2. Schematic model of the chemical structure of the heteropolysiloxane coatings.

that the alkaline treatment induces a large increase in hydroxyl groups on the substrate surface, this result suggests direct bond formation between these groups and the silanol or ethoxy groups of the monomers inside the sol during deposition. It also suggests that the carbon layer present on the substrate surface is discontinuous so that the coating can adhere to the substrate via the Si—O—Zn linkages.

4. Conclusion

From data collected in the present investigation, a schematic model of the chemical structure of the heteropolysiloxane coatings deposited onto electrogalvanized steel substrate is proposed.

References

1. M. Guglielmi, J. Sol-Gel Sci. Tech. **8**, 443 (1997).
2. M. Murakami, K. Izumi, T. Deguchi, A. Morita, N. Tohge, and T. Minami, J. Ceram. Soc. Jpn. Inter. Ed. **97**, 86 (1989).
3. S.R. Holmes-Farley and L.C. Yanyo, J. Adhesion Sci. Tech. **5**, 131 (1991).
4. K. Izumi, H. Tanaka, Y. Uchida, N. Tohge, and T. Minami, J. Non-Cryst. Solids **147/148**, 483 (1992).
5. K. Izumi, H. Tanaka, Y. Uchida, N. Tohge, and T. Minami, J. Mater. Sci. Lett. **12**, 724 (1993).
6. R. Kasemann and H. Schmidt, in *Proceedings of the First European Workshop on Hybrid Organic-Inorganic Materials*, edited by C. Sanchez and F. Ribot (C.N.R.S, Bierville, 1993), p. 171.
7. L. Mancinelli Degli Esposti, P. Innocenzi, G. Scarinci, and M. Guglielmi, in *Proceedings of the First European Workshop on Hybrid Organic-Inorganic Materials*, edited by C. Sanchez and F. Ribot (C.N.R.S., Bierville, 1993), p. 229.
8. M. Mayrand, J.F. Quinson, M. Pauthe, M. Lacroix-Repellin, F. Gaillard, and G. de Marignan, in *Proceedings of the First European Workshop on Hybrid Organic-Inorganic Materials*, edited by C. Sanchez and F. Ribot (C.N.R.S., Bierville, 1993), p. 313.
9. M. Mayrand, J.F. Quinson, A. Roche, V. Roisn, and H. Guyon, J. Sol-Gel Sci. Tech., submitted.
10. A. Roche, F. Gaillard, M. Romand, and M. von Fahnestock, J. Adhesion Sci. Tech. **1**, 145 (1987).

Journal of Sol-Gel Science and Technology 13, 783–787 (1998)
© 1998 Kluwer Academic Publishers. Manufactured in The Netherlands.

Multilayer SiO_2-B_2O_3-Na_2O Films on Si for Optical Applications

N. PELLEGRI* E.J.C. DAWNAY†AND E.M. YEATMAN
Department of Electrical and Electronic Engineering, Imperial College, London SW7 2BT, UK.

Abstract. The fabrication of glass by the sol-gel technique has attracted considerable attention in microelectronics, optics and other fields. For applications in integrated optics on silicon substrates, sol-gel offers the possibility of a great variety of compositions and structures. For example, the porosity may allow the insertion of a dopant species, such as nano-crystals for optical non-linearity, into the host glass. Here we have investigated SiO_2-B_2O_3-Na_2O compositions, to obtain low process temperatures, and to prepare SiO_2 guiding layers with a porosity control using the Vycor glass method.

Films of several micron thickness were prepared in many compositions of the SiO_2-B_2O_3-Na_2O system. The process included a two-step method to introduce the water while inhibiting crystal formation, a repetitive spin-coating technique in a humidity-controlled chamber, and rapid-thermal-annealing. The results show good quality in terms of homogeneity, absence of cracks, and versatility in the studied compositions. However, films prepared using rapid thermal annealing show a high residual carbon concentration. This causes strong optical absorption, and inhibits the phase separation and leaching associated with the Vycor technique. Reduction of carbon content has been investigated through adaptation of the heat treatment.

Keywords: Vycor, pyrex, porosity, nanocrystals

1. Introduction

The possibility of manufacturing silica-on-silicon photonic components using sol-gel films and materials giving advanced functionality has been demonstrated, but progress is needed before this technology can be accepted for practical implementation [1]. The sol-gel technique offers potential advantages in that it can be used to produce films with a great variety of composition and structure [2]. Recently, a complete process for the fabrication of SiO_2/Si integrated optic devices using sol-gel has been described [3]. This overcomes the main disadvantage, the difficulty in obtaining sufficient thickness due to shrinkage stresses, by an iterative technique of spin-coating and rapid thermal annealing. The porosity in such materials may allow the insertion of a dopant species, such as nano-crystals for third-order optical non-linearity, into the host glass.

*Permanent address: Laboratorio de Materiales Ceramicos, IFIR, FCEIyA, Universidad Nacional de Rosario, Av. Pellegrini 250, 2000 Rosario, Argentina.
†Present address: Bookham Technology Ltd., 90 Milton Park, Abingdon, Oxfordshire OX14 4RY, UK.

Sodium borosilicate glasses constitute an interesting system for this application because of many thermal and chemical properties. In particular, low process temperatures are possible, and porous glasses of nearly pure silica may be obtained by phase seperation and leaching, i.e., the Vycor technique. Previously, sodium borosilicate monoliths and films have been prepared by the sol-gel method using several precursors and processes [4]. Here we have studied whether such materials may be adapted to the thick film fabrication methods of [3], for applications in integrated optics.

2. Fabrication

Tetraethylorthosilicate (TEOS), triethylborate (TEB) and sodium ethoxide (NaEtox) were used as precursors, and HCl as a catalyst, with compositions and molar ratios as summarized in Table 1. First, TEOS and ethanol were mixed and stirred vigorously for 10 min at room temperature in a molar ratio TEOS/ethanol $= 1:4$. To produce a required pre-hydrolysis of TEOS before the incorporation of the TEB and NaEtox [4], 0.1 M HCl was added gradually until a water to

Table 1. Compositions of the solutions.

	Composition (mol%)				
Sample	SiO_2	B_2O_3	Na_2O	Al_2O_3	R
SBN1	70	20	10	—	1/2.15/10
SBN2	85	10	5	—	1/2.96/10
SBN3	65	26	9	—	1/1.92/10
SBN4	80	15	5	—	1/2.67/6
SBN3′	62.3	28.9	8.8	—	1/1.81/6
SBN5	67.6	23.3	9.1	—	1/2.04/6
SBNA1	62.7	26.9	6.6	3.5	1/1.83/10

R: Final molar ratio of alkoxides (TEOS + TEB + NaEtox + A1IP/H_2O/EtOH).

TEOS molar ratio of 2 was attained. The solution was placed in the refluxing bath immediately after mixing, and the temperature of the bath increased to 70°C in 15 min, while stirring, and kept there for 2 hours. Meanwhile, a solution of TEB and ethanol was prepared and stirred under nitrogen for 30 min. This solution was then added, dropwise, to the TEOS solution under N_2 and refluxed for 90 min. The temperature was decreased to room temperature and the nitrogen was removed. A solution of NaEtox, acetic acid and ethanol was prepared and stirred for 30 min; and further added, dropwise, to the TEOS-TEB solution and stirred at room temperature for 1 hour. Then, more water was added with a suitable quantity of ethanol, to yield the desired concentration or film thickness, stirred for 30 min and used for the films' preparation. All the chemicals were obtained from Aldrich. The sols were dispensed on p-type, 3 in. diameter silicon wafers, through a 0.1 μm filter (PTFE Whatman), and thereafter the substrate was spun at 2000 or 3000 rpm. for 30 s.

For monolayer films the coated substrates were baked in air, at temperatures in the range 100°C to 1000°C, for 30 min, or in the rapid thermal annealer (RTA) in oxygen at the desired temperature for 10 s. Thick layers were built up by repetition of spin-coating, annealing for 10 s in the RTA at 650°C, and cooling by convection [3]. Due to the reactivity of the film with atmospheric humidity, all coatings were made in an atmosphere-controlled chamber, with a relative humidity below 20% [4, 5]. The thickness and refractive index of the samples were measured using a Rudolph AutoEl III ellipsometer, with an operating wavelength of 633 nm, and precisions of about 0.002 and 3 Å in index and thickness, respectively. For microporous films, the measured index is strongly dependent on relative humidity, because of condensation of water in the pores. By measuring the dependence of index on humidity, information about porosity can be obtained [6]. The quality of the films was determined by visual examination and with an optical microscope. To analyze the internal structure and final composition of the films, Infrared (FTIR), Auger and energy dispersion (EDS) spectroscopy were used.

3. Results and Discussions

Water content and the way in which it is introduced are key parameters in obtaining optical quality films. Crystal formation is observed when all the water is introduced with the TEOS solution, and these crystals grow with heat treatment. Their presence was detected by optical microscopy (Fig. 1) and confirmed by X-Ray

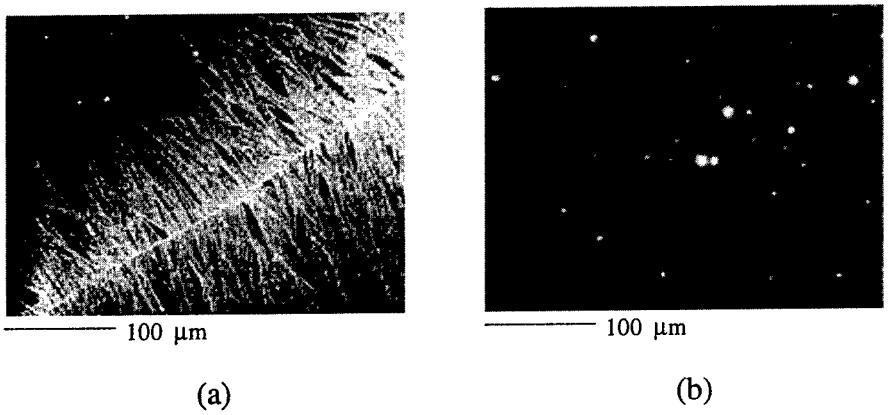

Figure 1. Optical microscope photographs of single-layer coatings on silicon, processed at 1000°C for 30 min, of compositions: (a) SBN3 and (b) SBNA1.

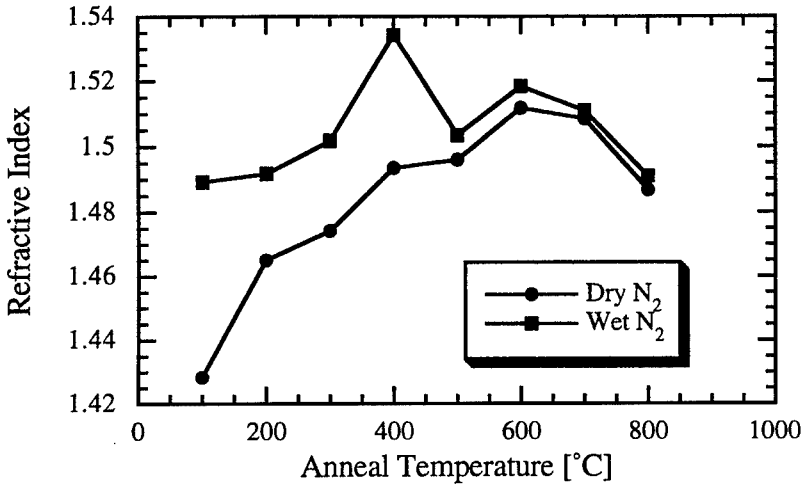

(a)

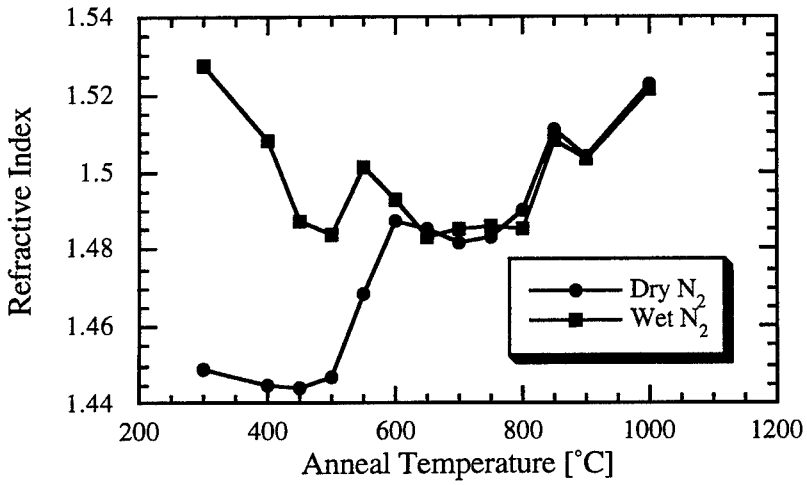

(b)

Figure 2. Film refractive index vs. annealing temperature, measured in dry N_2 and 100% RH atmospheres, for single layer films on silicon: (a) sample SBN3 annealed in conventional furnace for 30 min and (b) sample SBN4 annealed in RTA for 10 s. Lines are for ease of viewing only.

Diffraction. To avoid this devitrification, the two-step hydrolysis method described above was found to be effective. Another approach is to incorporate Al_2O_3 into the glass [7]. We selected aluminum isoproposide in solution with ethanol as the precursor, introduced in the final step of the solution preparation. In Fig. 1 the absence of crystals on an Al_2O_3 co-doped sample is shown, in relation with the non-codoped sample. The SiO_2-B_2O_3-Na_2O films obtained by these two methods showed good quality, in terms of absence of cracks, homogeneity, thickness and versatility in the studied compositions.

Using both techniques described above, film thicknesses of several microns were obtained. To determine the optimum heat treatment, evolution of the thickness and the refractive index with annealing temperature was studied for monolayer samples [8]. Figure 2 displays the evolution of refractive index for SBN3

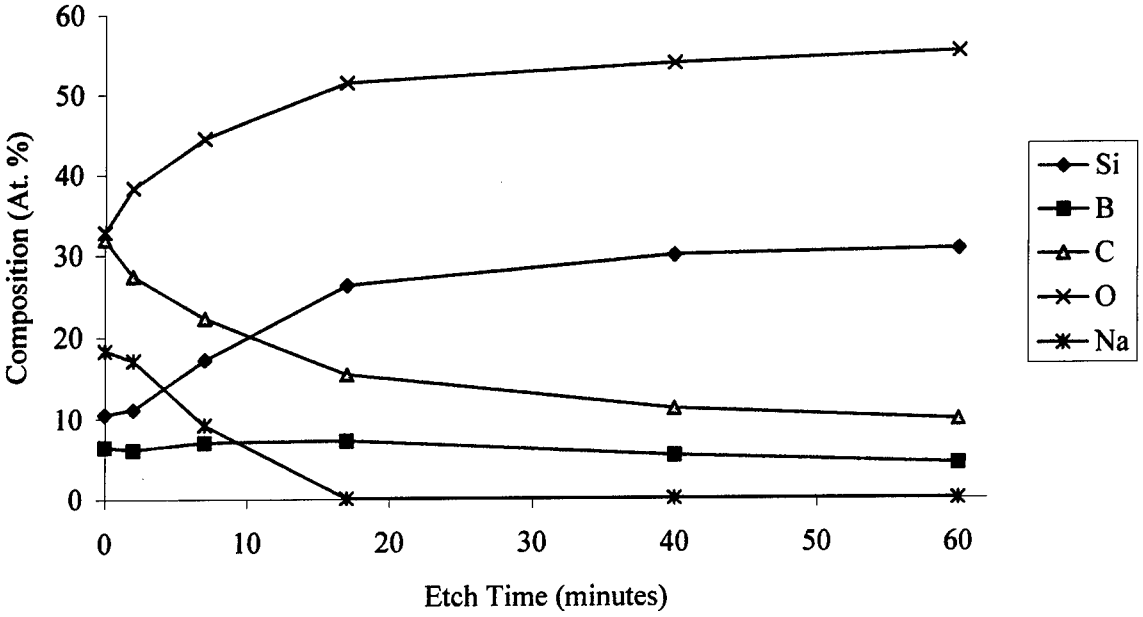

Figure 3. Depth profile through SBN5 sample on silicon vs. electron etching time by the Auger technique.

and SBN4 compositions. Around 600°C complete densification of the films is achieved, as compared to >1000°C for pure SiO_2 films. This reduction in softening temperature greatly eases preparation of waveguides.

The second goal was to prepare guiding layers with a porosity control based on Vycor type glasses. We performed a set of experiments to leach the samples of compositions SBN3′ and SBN5. Several heat treatments (from 0 to 48 hours) at different temperatures (room temperature, 550, 600 and 650°C) were performed to induce phase separation. Then, leaching was attempted with HCl 0.1, 1 and 3 N, for seconds up to several hours, with a further rinse and drying to remove the alkali and boric oxide rich phase [7, 9]. However, refractive index measurements showed that phase separation did not occur.

To obtain information about the internal structure of the films, before and after the leaching treatment, we measured FTIR spectra on films of composition SBN3′ before and after the heat treatment to induce phase separation, and after the leaching with HCl. The spectra were qualitatively similar. Peaks corresponding to Si—O—Si vibrational bonds at 1050, and to O—Si—O at 800 and 470 cm^{-1} were detected, as were peaks for Si—OH vibrations at 960 and 1150 cm^{-1}. All three spectra show a peak which corresponds to the B—O—B bonds at 1380 cm^{-1}, but there is no signal for the B—OH vibration bond [10–12]. There is no clear detection of organic group peaks (C=C, C—O, etc.). Clearly the internal structure is not affected by the two treatments, so the boron rich phase is not eliminated.

Finally, to confirm the existence of a phase separation inhibitor we performed compositional analysis by Auger spectroscopy in several thick samples. The results are semi-quantitative, and the relative elemental compositions should be taken as indicative only. Figure 3 shows the depth profile through an SBN5 sample (2 μm thickness) on silicon as a function of electron etching time by the Auger technique. The maximum etch time (60 min) corresponds to an etch depth of about 1 μm. The remarkable point is the large quantity of carbon in all the studied samples. This appears to decrease with depth, with a corresponding increase in Si and O. A likely cause of this variation is that the etched depth corresponds to about 10 deposited layers, and the lower layers, having undergone more annealing steps, have lost more carbon (some loss of boron with annealing is also suggested). Sodium content appears to drop rapidly with depth, but this we believe is an artefact, caused by charge induced migration of the highly mobile Na^+ ions in reponse to the Auger beam itself.

We infer that the presence of carbon is responsible for the phase separation inhibition, and for the high optical absorption found in thick samples, which makes

the films unsuitable for waveguides. To eliminate the presence of carbon, several heat treatment experiments have been made. Preliminary results show that a reduction of carbon content, detected by optical quality observations, was obtained using an adapted heat treatment, in which the rate of temperature increase was reduced from 15 to 5°C/s.

4. Conclusions

This study has shown that films of several microns thickness, in many compositions of the SiO_2-B_2O_3-Na_2O system, are obtained presenting good quality in terms of homogeneity and absence of cracks. These compositions have the advantage of lowering the necessary process temperatures for the fabrication of planar waveguides. The process included a two-step method to introduce the water while inhibiting crystal formation, a repetitive spin-coating technique in a chamber to control the humidity and rapid-thermal-annealing.

The films, however, showed a high carbon concentration which causes strong optical absorption, and inhibits the phase separation and the leaching process associated with the Vycor technique. We believe that the reduction of softening temperature to levels approaching those of organic decomposition results in organic ligands being trapped within a fully dense matrix, and therefore decomposing without sufficient diffusion of oxygen into the matrix from the annealing atmosphere. Therefore, rapid thermal processing becomes more difficult to implement in such glass compositions.

Acknowledgments

N.P. is grateful for support from Consejo Nacional de Investigaciones Cientificas y Tecnicas, Argentina. Support from the European Commission (ACTS project AC047: CAPITAL) is also acknowledged.

References

1. E.M. Yeatman and E.J.C. Dawnay, J. Sol-Gel Sci. Tech. **8**, 1007 (1997).
2. J.D. Mackenzie and Y.H. Kao, in *Glass Integrated Optics and Optical Fiber Devices*, SPIE **CR53**, 83 (1994).
3. R.R.A. Syms and A.S. Holmes, J. Non-Cryst. Solids **170**, 223 (1994).
4. N. Pellegri, O. de Sanctis, and A. Duran, J. Sol-Gel Sci. Tech. **2**, 519 (1994).
5. N. Tohge and T. Minami, J. Non-Cryst. Solids **112**, 432 (1989).
6. E.M. Yeatman, Mino Green, E.J.C. Dawnay, M.A. Fardad, and F. Horowitz, J. Sol-Gel Sci. Tech. **2**, 711 (1994).
7. *Glass Science and Technology Vol. 1: Glass Forming Systems*, edited by D.R. Ulhmann and N.J. Kreidl (Academic Press, NY 1983), p. 179.
8. M.A. Fardad, Ph.D. Thesis, Imperial College, University of London, 1995.
9. J. Rincon and A. Duran, *Separacion de Fases en Vidrios* (Sociedad Espanola de Ceramica y Vidrio, 1982).
10. D. Niznansky and J.L. Rechspringer, J. Non-Cryst. Solids **180**, 191 (1995).
11. R. Almeida, International J. Optoelec. **9**, 135 (1994).
12. J. Brinker and D. Haaland, J. Am. Ceram. Soc. **66**, 758 (1983).

Journal of Sol-Gel Science and Technology 13, 789–792 (1998)
© 1998 Kluwer Academic Publishers. Manufactured in The Netherlands.

Synthesis of Nanocrystalline, Redispersable Antimony-Doped SnO_2 Particles for the Preparation of Conductive, Transparent Coatings

DETLEF BURGARD, CHRISTIAN GOEBBERT AND RÜDIGER NASS
Institut für Neue Materialien, Im Stadtwald, Geb. 43, D-66123 Saarbrücken, Germany

Abstract. Nanocrystalline, redispersable Sb-doped SnO_2 with Sb contents from 0.1–10 mol% (with respect to Sn) and a primary particle size of about 5 nm was prepared from $SnCl_4$ and $SbCl_3$ in solution by a growth reaction. The aggregation of the particles was avoided by in situ surface modification with amino carbonic acids. The stabilizing effect of the surface modification could be maintained during the following hydrothermal crystallization step (150°C, 10 bar). The resulting nanocrystalline particles are fully redispersable in aqueous suspensions at pH $\geq$ 11; solid contents up to 40 wt% can be achieved.

Such aqueous dispersions were used to prepare transparent, conductive coatings on glass by spin coating. After thermal densification (1 hour at 550°C) transparent coatings of 220 nm thickness were obtained. A minimum specific electrical resistance of $2.5 \cdot 10^{-2}$ Ω cm for Sb contents between 4 and 5 mol% was measured, the transparency in the visible range against air was 90%.

Keywords: SnO_2, nanocrystalline, redispersable, particles, transparent, conductive coatings

Introduction

Transparent conducting oxides (TCO) on glass are important materials in the field of optoelectronic devices such as solar cells, electroluminescence and liquid crystal displays [1–3]. *N*-type semiconductors such as indium tin oxide (ITO), fluorine or antimony doped tin dioxide (FTO, ATO) or alumina or gallium doped zinc oxide (AZO, GZO) are widely used for these applications. For the preparation of the coatings practically all known coating processes are used [4].

SnO_2 : Sb coatings obtained by the sol-gel route show a relatively high resistivity in the range from $3 \cdot 10^{-3}$ Ω cm [5] to $2.1 \cdot 10^{-2}$ Ω cm [6]. However, when compared to the ITO coatings the ATO coatings have a higher mechanical and thermal stability. The reasons for the low conductivity of the SnO_2 : Sb films can be explained by their relatively low density. Aegerter and co-workers [7] examined the influence of deposition techniques on the densification and resistivity of SnO_2 : Sb coatings. They observed that the density of the film obtained after sintering is one of the most important reasons for a high conductivity. Large and closely packed crystallites exhibit higher electron mobility and hence higher electrical conductivity.

From this it can be concluded that the use of already densified nanocrystalline SnO_2 : Sb particles for the preparation of coatings will lead to higher conductivities as a consequence of the higher density/crystallinity of the coatings. This requires the availability of nanocrystalline, redispersable SnO_2 : Sb particles that can be processed to dense, homogeneous coatings. The aim of this work was the preparation of nanocrystalline, redispersable SnO_2 : Sb particles for coating applications. This included particle characterization, optimizing the Sb-content with respect to the electrical conductivity as well as examination of the influence of densification temperature and time on the optical and electrical properties of the prepared coatings.

Experimental

The SnO_2 : Sb powders were prepared by the controlled growth technique [8–10].

A solution of tin(IV)chloride in ethanol containing 0.1–10 mol% of $SbCl_3$ (dopant) was added dropwise to an aqueous ammonia solution containing 10 wt% of the surface modifying agent, β-alanine (with respect to the oxide). The prepared suspensions were treated at 150°C and 10 bar for 3 hours. The resulting powder was isolated by centrifuging and washed with water several times. The powder was dried at 60°C. The powders obtained were characterized by High Resolution Transmission Electron Microscopy (HRTEM) and X-ray diffraction.

Colloidal suspensions of these powders were prepared by dispersing them in water at pH $\geq$ 11 using tetramethylammoniahydroxide as a base. The concentration of the base had a total amount of 0.78 mol/l of water. The solid content of the powder varied from 2 to 40 wt%. After powder addition the resulting suspensions were ultrasonically agitated for 2 min. After this treatment the suspensions were stirred for 1 day. The obtained dispersions were clear and had a yellowish orange color.

To examine the influence of the SnO_2 : Sb particles, a sol which could incorporate a large amount of water was prepared. As a precursor tin(II)chloride in ethanol (0.3 mol/l) with 5 mol% $SbCl_3$ with respect to the oxide was used. As a stabilizer 0.3 mol/l ethylenediamine was added. After stirring for 1 day, a clear solution was obtained. Up to 25 wt% of the SnO_2 : Sb powders were redispersed in this sol.

Conductive coatings on glass were prepared by spin-coating. 5 $\times$ 5 cm^2 borofloat substrates were fixed by vacuum on a chuck. After adding 500 μl of the dispersion on the glass substrate, the chuck was moved to a final speed of 2000 rpm for 15 s. The thermal densification of the film was carried out at temperatures from 400 to 600°C for 0.25 to 8 hours.

Results and Discussion

The synthesis of nano-scale modified particle suspensions was carried out by precipitation in the presence of the surface modifying agent β-alanine as described above. These suspensions were hydrothermally treated at a relatively low temperature and pressure (150°C, 10 bar, 3 hours). The resultant powders were characterized by X-ray diffraction and HRTEM. The phase analysis indicated the SnO_2 structure is cassiterite, the primary particle size ranges from 3 to 5 nm.

The resistivity of the coatings is strongly dependent on the concentration of the dopant [11] in the tin dioxide structure and on the electron mobility and density. In order to find the dopant concentration leading to the lowest resistivities, powders with different dopant levels were produced and the resistivity of the coatings obtained from the particulate sols (particle concentration 20 wt%) as described above, was examined by a Van der Pauw/Hall measurement. This showed the resistivity reaches a minimum (with a resistivity of $5.2 \cdot 10^{-2}$ Ω cm, fired at 550°C, 15 min) at a dopant concentration of 4 mol% with respect to the tin dioxide (film thickness 200 nm). For further investigations the powder with the lowest resistivity and an antimony concentration of 4 mol% was used.

These first experiments showed that electrically conductive coatings can be prepared using dispersed nanocrystalline particles. However, the resistivity is still relatively high. This can be explained by insufficient densification in the particulate coating. Porosity between the particles is responsible for a low mobility of the electrons. It can be assumed that the precursor sol fills the pores in the (green) particulate coating and after firing, the precursor crystallizes so that the pores are filled with crystalline material.

The first step, the examination of the particulate sols, gives information on the properties of the SnO_2 : Sb particles as a coating material and on the best coating conditions. Next the effects of the addition of particles to a sol was studied.

The sol containing $SnCl_2$ as a precursor and doped with 4 mol% antimony was used to obtain transparent conducting coatings using a spin coating process. Because of the low density of the coating from this sol, the resistivity was not very low. The best value for the resistivity was $1.0 \cdot 10^{-1}$ Ω cm and a thickness of 40 nm was obtained after a heat treatment of 550°C for 15 min. With the addition of SnO_2 : Sb particles, the resistivity decreased dramatically. From Fig. 1, it can be seen that the lowest resistivity, $3.7 \cdot 10^{-2}$ Ω cm can be achieved for a particle concentration of 22.4 wt% (the coatings were sintered at 550°C for 15 min). This indicates that the electron mobility can be increased by using particulate coating systems.

Another important influence on the resistivity of the coatings is the heat treatment after the spin coating process. An examination of various sintering temperature from 400 to 600°C and heating times from 0.25 to 8 hours showed that a maximum resistivity of $2.5 \cdot 10^{-2}$ Ω cm and a film thickness of 200 nm was achieved at 550°C with a holding time of 1 hour (Fig. 2). Temperatures above 600°C could not be used because of the softening point of the glass.

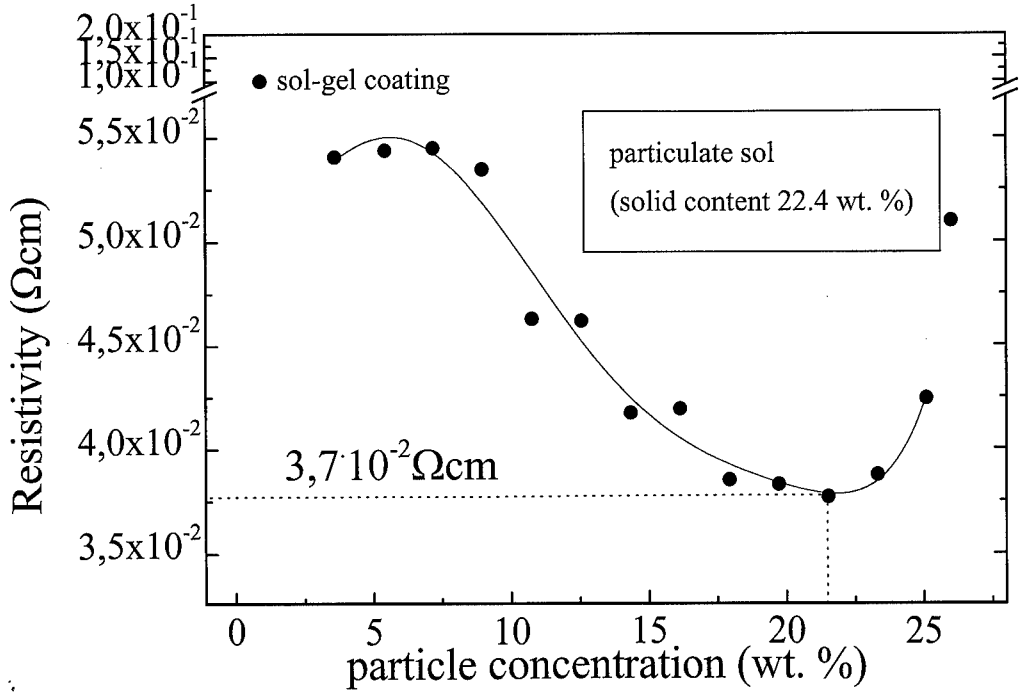

Figure 1. Antimony doped tin dioxide sol (with $SnCl_2$ used as precursor) versus concentration of antimony doped tin dioxide particles added to the sol. The spin coated films were sintered at a furnace temperature of 550°C for 15 min.

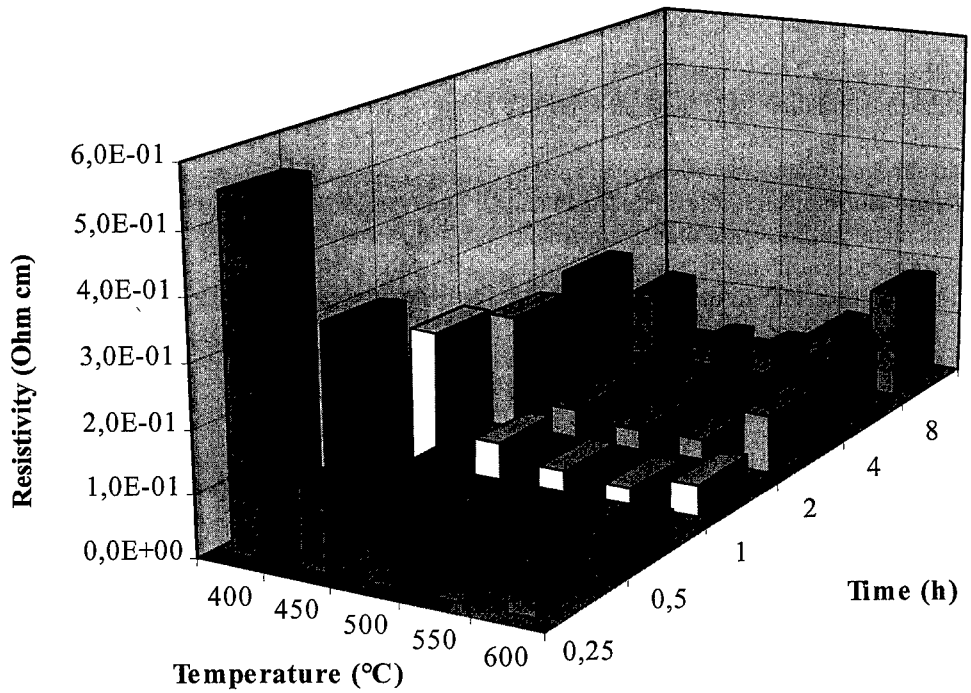

Figure 2. Resistivity vs. sintering temperature and time (films obtained by spin coating process with sol-gel particulate sols (20 wt% particle concentration)).

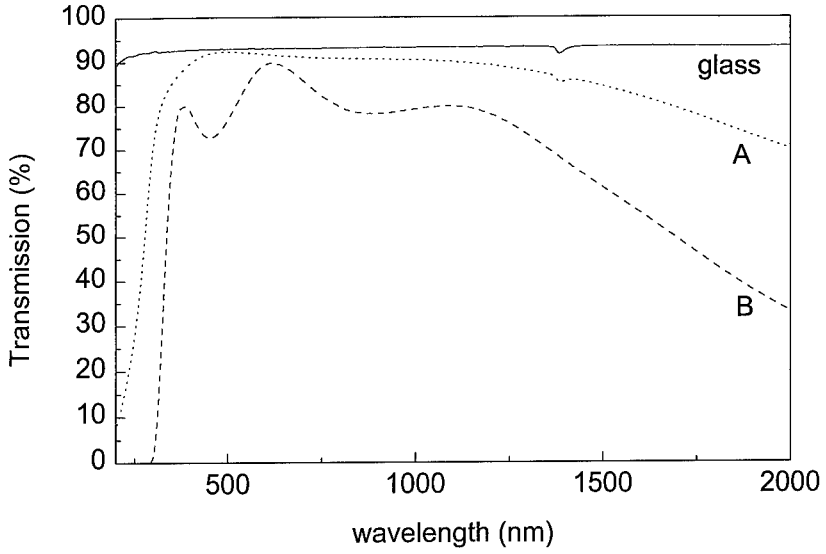

Figure 3. Transmission vs. wavelength of different transparent conductive coatings, A: sol-gel particulate sol with a solid content of 20 wt%, sintered at 550°C for 15 min (thickness: 200 nm), B: sputtered commercial ITO coating on float glass (thickness: 300 nm).

For most applications of transparent conducting coatings a high transmission value in the visible range is important. The transmission is dependent on many different factors. Small particles in the nanometer range, which do not scatter visible light, and a relatively thin layer give a coating with a relatively high transmission. The coatings obtained by sol-gel particulate sols via spin coating show a transmission in the visible range of about 90% (measured against air) as can be seen in Fig. 3.

In the visible range, the coating shows almost the same transmission as the substrate used, the borofloat glass. This is due to the highly homogeneous distribution of the nano-scale particles in the film.

Conclusion

Transparent electrically conducting sol-gel $SnO_2 : Sb$ coatings made by a spin coating process exhibit systematically higher resistivity values than those made by spray pyrolysis (resistivity $1 \cdot 10^{-3}$ Ω cm [4]). However, the use of already dense, crystalline and redispersable antimony doped SnO_2 (with Sb content of 4 mol%) provides a means of producing a denser film. As a result the mobility of the electrons is increased but not obstructed or scattered by small and loosely packed crystalline particles obtained from the sol. Furthermore, the investigation of sintering conditions to achieve a higher density of the coating is important to obtain films with higher conductivities. The use of other dopants such as fluorine would be of interest in further investigations.

References

1. S. Wagner and D.E. Carlson, in *Proc. 10th European Photovoltaic Solar Energy Conference* (Lisbon, 1991), p. 1179.
2. Y. Arai, M. Ishii, H. Shinohara, and S. Yamazaki, IEEE Electr. Dev. Lett. **12**, 460 (1991).
3. S. Kumar and B. Drevillon, J. Appl. Phys. **65**(8), 3023 (1989).
4. K.L. Chopra, S. Major, and D.K. Pandya, Thin Solid Films **102**, 1 (1983).
5. C. Terrier, J.P . Chatelon, R. Berjoan, and J.A. Roger, Thin Solid Films **263**, 37 (1995).
6. W. Lada, A. Deptula, T. Olczak, W. Torbicz, and D. Pijanowska, J. Sol-Gel Sci. Tech. **2**, 551 (1994).
7. G. Gasparro, J. Pütz, D. Ganz, and M.A. Aegerter, *EuroSun '96, Int. Symp. on Optical Materials Technology for Energy Efficiency and Solar Energy Conversion* (1996).
8. D. Burgard, R. Naß, and H. Schmidt, Aqueous Chemistry and Geochemistry of Oxides, Oxyhydroxides and related Materials, MRS **432**, 113–120 (1997).
9. D. Burgard, R. Naß, and H. Schmidt, *Werkstoffwoche, Symp. 6 Werkstoff und Verfah-renstechnik* (DGM Informationsgesellschaft mbH, 1997), pp. 569–577.
10. D. Burgard, C. Kropf, R. Naß, and H. Schmidt, Better Ceramics through Chemistry, MRS **346**, 101–107 (1994).
11. Christian Göbbert, Diplomarbeit, and Saarbrücken, 1996.

Journal of Sol-Gel Science and Technology 13, 793–798 (1998)
© 1998 Kluwer Academic Publishers. Manufactured in The Netherlands.

Improved Conductivity Induced by Photodesorption in SnO_2 Thin Films Grown by a Sol-Gel Dip Coating Technique

LUIS V.A. SCALVI
Departamento de Física, FC, UNESP, Caixa Postal 473, 17033-360 Bauru SP, Brazil

FÁBIO R. MESSIAS
Instituto de Física de São Carlos, U.S.P., Caixa Postal 369, 13560-970 São Carlos SP, Brazil

A.E. SOUZA
Instituto de Química, UNESP, Caixa Postal 355, 14801-907 Araraquara SP, Brazil

M. SIU LI
Instituto de Física de São Carlos, U.S.P., Caixa Postal 369, 13560-970 São Carlos SP, Brazil

C.V. SANTILLI AND S.H. PULCINELLI
Instituto de Química, UNESP, Caixa Postal 355, 14801-907 Araraquara SP, Brazil

Abstract. Thin films of undoped and Sb-doped SnO_2 have been prepared by a sol-gel dip-coating technique. For the high doping level (2–3 mol% Sb) *n*-type degenerate conduction is expected, however, measurements of resistance as a function of temperature show that doped samples exhibit strong electron trapping, with capture levels at 39 and 81 meV. Heating in a vacuum and irradiation with UV monochromatic light (305 nm) improve the electrical characteristics, decreasing the carrier capture at low temperature. This suggests an oxygen related level, which can be eliminated by a photodesorption process. Absorption spectral dependence indicates an indirect bandgap transition with $E_g \cong 3.5$ eV. Current-voltage characteristics indicate a thermionic emission mechanism through interfacial states.

Keywords: thin films, impurities in semiconductors, electronic transport, recombination and trapping

Introduction

Undoped SnO_2 is an *n*-type, wide bandgap semiconductor [1]. A high concentration of antimony as a dopant leads to quasimetallic behaviour while maintaining its transparency [2]. This is an interesting optoelectronic property, exploited in electro-optical devices [3]. Electrical properties of undoped SnO_2 depend mainly on deviation from the stoichiometric composition. Either oxygen vacancies or interstitial tin atoms are expected to be donors in pure SnO_2 [1]. Sb doping increases the *n*-type conductivity since Sb^{5+} is incorporated into the lattice substituting for Sn^{4+} [4]. Another important feature is the mechanism of chemisorption of oxygen on the SnO_2 surface which provides electron transfer from the conduction band to an acceptor level introduced by the adsorbed atoms [5]. Bandgap transitions change electron and hole concentrations at the semiconductor surface [6]. Photoproduced electrons will induce oxygen adsorption, but photoinduced holes will induce oxygen desorption, so that the net effect depends on the

rate constants and on the sample properties in the dark.

By the methods typically used to prepare SnO_2 films it is hard to coat large surfaces and control stoichiometry [7]. Coatings of large and complex-shaped substrates have been obtained by means of the dip-coating sol-gel process, using both organic and inorganic precursors [8–10]. Alkoxides are expensive and sensitive to moisture, producing inhomogeneous SnO_2 layers [8]. The colloidal suspensions prepared via inorganic sol-gel route developed in our laboratory [9] have been the preferred way of making SnO_2 layers by dip coating [10] because these disadvantages are absent. In this communication we show electrical and optical properties of undoped and Sb-doped SnO_2 thin films. Our conclusions help sample preparation and the understanding of electrical transport properties of SnO_2 thin films prepared by a sol-gel dip-coating technique.

Experimental

Films were deposited as follows: borosilicate glass substrates were dipped vertically into a suspension of SnO_2 prepared from the hydrolysis of $SnCl_4 \cdot 5H_2O$ in aqueous solution [9]. Sb doping was obtained by dissolution of $SbCl_3$ in a $SnCl_4$ aqueous solution. The dipping rate was 6 cm/min and the resulting thickness after 30 dips was 300 nm. Samples were annealed at 550°C for 1 hour in air. Films presented 80% transmission in the visible and were uniform over the whole surface, being polycrystalline with an average grain size of 3 nm and porosity of about 35%.

Electrical measurements were performed in a parallel orientation to the coating, using evaporated In electrodes, annealed to 150°C for 30 min. The resistance was measured as a function of temperature in the range 77–300 K using an electrometer and the conductivity (σ) was calculated considering the distance between electrodes and film thickness. Optical absorption coefficients were determined by UV-Vis spectroscopy.

Results and Discussion

Figure 1 shows conductivity as a function of temperature for a Sb-doped (2 mol%) SnO_2 sample, both in the dark and under illumination with $\lambda = 305$ nm monochromatic light. The lower curve represents the measurement carried out in the dark: the sample was taken to 77 K and then the temperature was allowed to increase very slowly. There was a pronounced increase in the sample conductivity as the temperature was raised, suggesting a carrier freezeout of defects. Taking the sample to 77 K again and illuminating steadily with monochromatic light of $\lambda = 305$ nm, the $\sigma \times T$ curve suggests that whatever is causing the carrier freezeout has its concentration decreased by exposure to monochromatic light above the bandgap. It is important to mention that below bandgap light had no effect on the resistance with the same procedure. Repeating several times the procedure of illuminating the sample continuously with $\lambda = 305$ nm as the temperature was increased, resulted in the conductivity keeping on increasing. It seems that there is a tendency for saturation, but at low temperature at least, this saturation has not yet been reached. Subsequently, the temperature was increased to 200°C for about 5 min in a vacuum and cooled to room temperature. Once more the sample was taken to 77 K and the resistance measured during the increase of temperature in the dark. The strong decrease in conductivity, observed in the first measurement in the dark no longer existed and the conductivity dependence with temperature can hardly therefore be associated with deep levels. The cycling procedure had eliminated most of the traps which were present in the beginning. Although Fig. 1 represents data recorded for an Sb-doped sample, the same behavior is also observed for a pure SnO_2 film. The only difference is the absolute value of resistance, which is higher for the pure SnO_2 film than for the Sb-doped sample, as expected. In order to interpret these results we performed the same measurement after annealing the sample to 200°C, but keeping the sample in air this time. Low conductivity and electron trapping behavior was recovered, being quite similar to the curve in the dark shown in Fig. 1.

The inset in Fig. 1 is an Arrhenius plot related to the data of the upper and the lower curves of Fig. 1. Before any photo- or thermal processing, the curve can be approximated by two straight lines with good correlation coefficients. These two regions have activation energy of about 39 and 81 meV, for the lower and higher temperature ranges, respectively, which may be related to two levels: a Sb donor level and an oxygen vacancy level (the deeper one) [11]. Considering that our samples were polycrystalline, the scattering at grain boundaries [12] should contribute to the discrepancies between single crystal data [11] and our data. This change in slope has been predicted by Blakemore [13] for semiconductors dominated by several localized

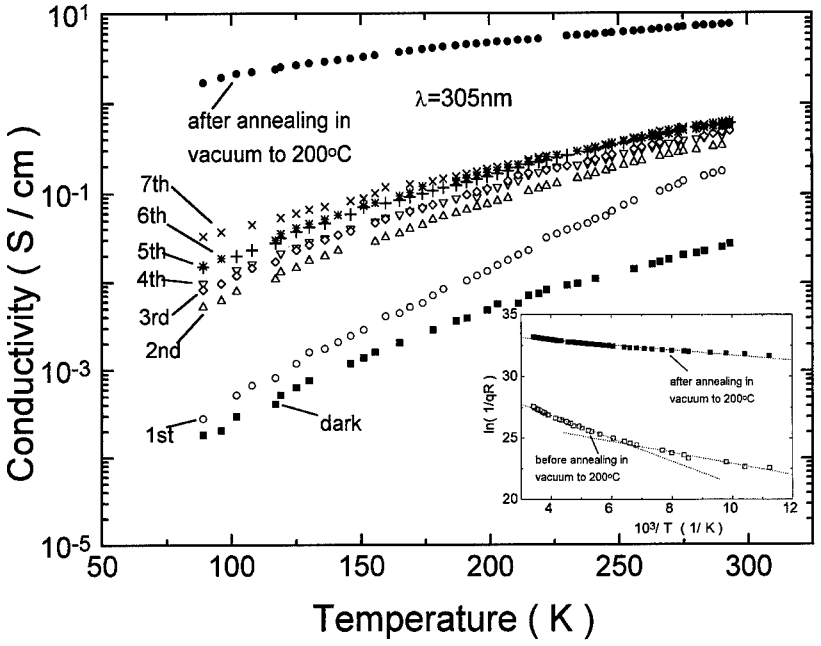

Figure 1. Conductivity of an Sb-doped (2 mol%) SnO_2 thin film as function of temperature in the dark and under steady illumination with $\lambda = 305$ nm monochromatic light during several cycles. The upper curve represents data obtained after annealing in vacuum at 200°C. Inset: Arrhenius plot for the curve obtained in the dark and after all of the cycling process.

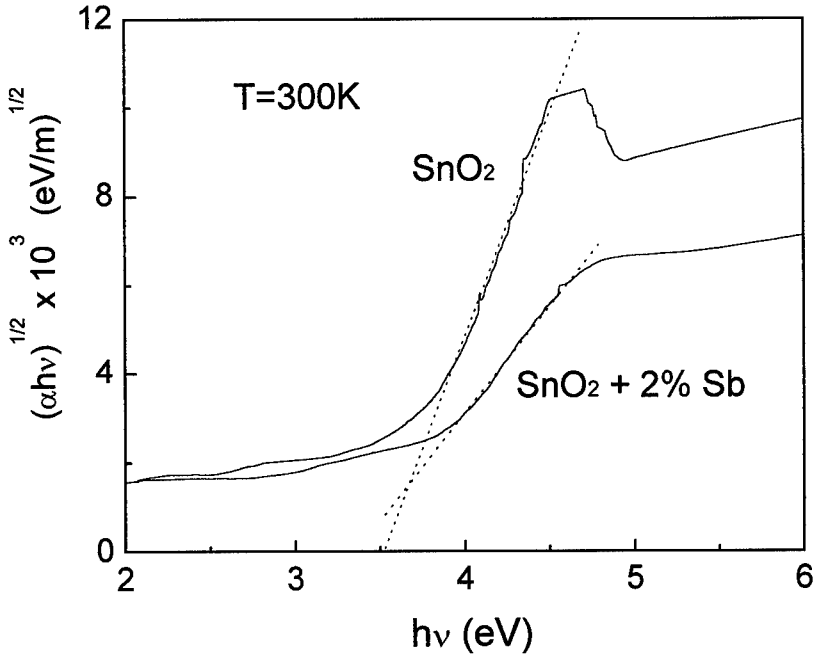

Figure 2. Test for indirect bandgap transition for pure SnO_2 and 2 mol% Sb doped. Data calculated from optical absorption.

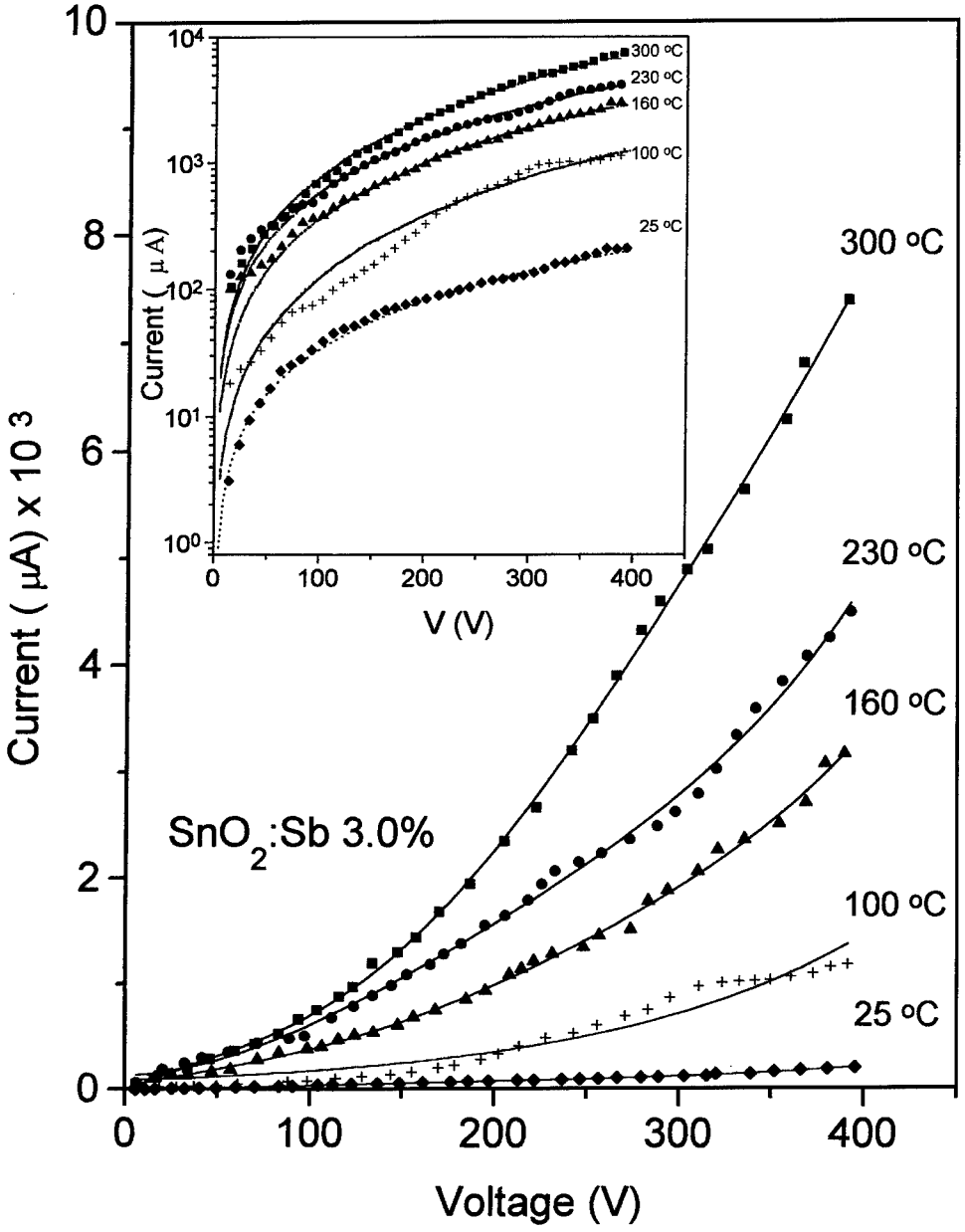

Figure 3. Current-voltage characteristics of a 3 mol% Sb-doped SnO_2 sample at several temperatures. Inset: Test for Poole-Frenkel model for thermionic emission.

levels. As the temperature rises, the upper donor levels release their electrons to the conduction band, and the Fermi level moves downwards to the second level as the shallower level supply becomes exhausted. The dominant donor level changed after the cycling procedure, resulting in a single Arrhenius behavior (upper curve) with an activation energy of about 18 meV, which is rather low.

The continuous variation of the $\sigma \times T$ curve slope with the number of cycles seems to indicate a decrease of the donor level's energy. Since oxygen vacancies act as donors in SnO_2, the observed behavior may be interpreted as a decrease of the donor ionization energy with increasing donor concentration, which has been observed previously [1]. Indeed, it seems consistent to attribute this behavior to the elimination of

traps at grain interface. This can be understood by considering light irradiation above the bandgap on the sample ($\lambda = 305$ nm). Then there is generation of electron-hole pairs, and the existence of some gaseous specimen that is adsorbed or desorbed depending on the cryostat pressure, and has a direct contribution to the carrier concentration. Photo-generated electrons and holes may recombine with this gas [6] leaving net electrons which can conduct the electrical current. This gas is most probably oxygen [5].

From an applications point of view, it is important to notice that the best conductivity value obtained after the treatment is one order of magnitude lower than the best published values [8, 12, 14]. This is mainly related to the small grain size and high layer porosity of the samples studied here. Such microstructural characteristics can be improved by using the multidipping procedure suggested by Park and Mackenzie [8], which should yield precipitation of small particles inside the pores, reducing porosity and promoting grain coalescence. Photo-desorption proposed here, combined with the Park and Mackenzie procedure, probably would yield easier and cheaper processing for high quality material.

We can distinguish between direct or indirect bandgap transitions in SnO_2 samples by studying the spectral dependence of the absorption coefficient [15]. Figure 2 shows the behavior of pure and 2 mol% Sb doped SnO_2 samples filled to the indirect transition model. The absorption coefficient was calculated from absorption spectra measured at 300 K [16]. The indirect bandgap fit, $(\alpha h\nu)^{1/2}$ for the pure SnO_2 sample is better for a wider range, yielding a bandgap transition energy of 3.52 eV. Another strong point to support an indirect bandgap transition is that our measurements, shown in Fig. 1, were collected using 305 nm monochromatic light as the excitation source; this corresponds to about 4.05 eV, which is well above the estimated indirect bandgap transition, but below the value estimated from fitting the direct transition model (4.15 eV, not shown in Fig. 2). The inclusion of Sb doping in SnO_2 decreases the indirect bandgap transition to 3.35 eV. This decrease may be related to the high doping level, which can modify the band structure diagram, or to the electron-impurity interaction which can shift the absorption edge to a lower photon energy [15].

Figure 3 represents current-voltage curves for an SnO_2 sample doped with 3 mol% of Sb. This sample exhibited a high resistivity, which may be explained by this measurement being taken prior to any thermal or photo-processing. The curve is clearly non-linear, which can be explained by the presence of an electron-depleted layer at the grain boundary, and the formation of a potential barrier. The shape of the current-voltage curves is typical of thermionic emission over the barrier. As the temperature was increased, the deviation from ohmic behaviour became more evident. The conductivity through the grain boundary of the doped thin film under the applied electric field came from excitation of the ionized acceptors localized close to the interface. The inset in Fig. 3 represents a test for Poole-Frenkel model for thermionic emission [17], which yields a good fit, indicating that emission from interfacial states is the most probable mechanism. This result also suggests the presence of adsorbed oxygen acting acting as an acceptor state at the grain boundary.

Conclusion

Electrical conductivity of SnO_2 thin films grown by a sol-gel dip-coating technique are strongly influenced by the annealing process. The adsorbed specimen traps electrons, producing electron-depleted space-charge layers at the grain boundary, yielding poor electrical characteristics. Current-voltage measurements show non-linear behavior which can be described by Poole-Frenkel emission through the grain boundary. The conductivity can be raised 4 orders of magnitude by irradiation of above bandgap light plus annealing under vacuum. Spectral dependence of the absorption coefficient indicates an indirect bandgap transition of about 3.5 eV.

Acknowledgments

We acknowledge the Brazilian financial agencies CAPES, CNPq, FAPESP, FINEP and PRONEX 402/96.

References

1. Z.M. Jarzebski and J.P. Marton, J. Electrochemical Society **123**, 199C and 299C (1976).
2. K.C. Mishra, K.H. Johnson, and P.C. Schmidt, Phys. Rev. B **51**, 13972 (1995).
3. G. Sanon, R. Rup, and E.A. Mansingh, Phys. Rev. B **44**, 5672 (1991).
4. C. Terrier, J.P. Chatelon, R. Berjoan, and J.A. Roger, Thin Solid Films **263**, 37 (1995).

5. F. Prado, G. Meyer, and J. Saura, J. Phys.: Condens. Matter **5**, A351 (1993).
6. S.R. Morrison, *The Chemical Physics of Surfaces* (Plenum Press, New York, 1990), p. 341.
7. K. Chopra, S. Major, and D.K. Pandya, Thin Solid Films **102**, 1 (1983).
8. S.S. Park and J.D. Mackenzie, Thin Solid Films **258**, 268 (1995).
9. R.S. Hiratsuka, S.H. Pulcinelli, and C.V. Santilli, J. Non-Cryst. Solids **121**, 76 (1990).
10. B. Orel, U. Laurencie-Stangar, Z. Crnjak-Orel, P. Bukovec, and M. Kosec, J. Non-Cryst. Solids **167**, 272 (1994).
11. C.G. Fonstad and R.H. Rediker, J. Appl. Phys. **42**, 2911 (1971).
12. E. Santhi, V. Dutta, A. Banerjee, and K.L. Chopra, J. Appl. Phys. **51**, 6243 (1980).
13. J.S. Blakemore, *Semiconductor Statistics* (Dover Publications, New York, 1987), p. 159.
14. T.D. Senguttuvan and L.K. Malhotra, Thin Solid Films **289**, 22 (1996).
15. E.A. Johnson, in *Semiconductors and Semimetals*, edited by R.K. Willardson and A.C. Beer (Academic Press, New York, 1967), Vol. 3, p. 153.
16. G. Campet, C. Geoffroy, J.P. Manaud, J. Portier, Z.W. Sun, J. Salardenne, and P. Keou, Materials Sci. and Engr. **B8**, 45 (1991).
17. T.K. Gupta, J. Am. Ceram. Soc. **73**, 1817 (1990).

Journal of Sol-Gel Science and Technology 13, 799–803 (1998)
© 1998 Kluwer Academic Publishers. Manufactured in The Netherlands.

Phase Development in Sol Derived Microporous Membranes for Gas Permselectivity

U. STEFAN BJÖRKERT, DIANE HOLLAND AND MIKE H. LEWIS
University of Warwick, Centre for Advanced Materials, Department of Physics, Coventry CV4 7AL, United Kingdom
U.S.Bjorkert@warwick.ac.uk

Abstract. A sol-gel route has been used to produce a nanoporous membrane for the separation of "greenhouse" gases from power plants at elevated temperatures (700–900 K). The membrane has a controlled pore size distribution and is multiphasic, in order to prevent grain growth and pore coarsening. The alumina/titania diphasic ceramic was obtained from alkoxide precursors with additional magnesium or lanthanum doping to stabilize low temperature phases and to provide possible chemisorption of CO_2. It was found that both Mg and La stabilized the γ-alumina phase to higher temperature by as much as 200 K, although Mg is less effective.

Keywords: sol-gel, thermal stability, Al_2O_3, TiO_2, membranes

Introduction

Removal of "greenhouse" gases from power station emissions requires membranes with permselectivity for these gases, which can work at elevated temperatures (700–900 K). Microporous, metal oxide membranes have the capability to operate at this temperature. However, their efficiency as permselective membranes is dependent on their retaining their pore size and a narrow pore size distribution. Hence, it is necessary to thermally stabilize the microstructure of the membrane material.

This study has been concerned with thermally stabilizing an alumina membrane microstructure with a second titania phase and stabilizing the phase composition by doping with Mg or La which should also have a chemical interaction with CO_2. This paper compares the phase development between the Mg doped and the La doped $Al_2O_3 : TiO_2$.

Experimental Procedures

The La or Mg doped alumina/titania material was produced using Al *sec*-butoxide, Ti(IV) *iso*-propoxide and La nitrate or Mg nitrate as precursors. The Ti-alkoxide and Al-alkoxide sols were made and hydrolyzed separately. The alumina sol was prepared by hydrolysis and peptization, both at 363 K [1]. The molar ratios of water to alkoxide and of HCl to alkoxide were 100 and 0.25, respectively. For the titania sol, only a single hydrolysis step was used (at 353 K) with molar ratios of water to alkoxide and HNO_3 to alkoxide of 300 and 0.5, respectively. The metal ion in the Ti-alkoxide sol was adjusted, with *iso*-propanol, to a concentration of 1.6×10^{-1} mol/l. These two sols were mixed to give 95, 90 and 85 mol% Al_2O_3 in the final pyrolyzed material. La or Mg nitrate was added, to the hydrolysis step of the boehmite sol, so that the ratio of added ions to the sum of original metal ions ($R = n_M/(n_{Al} + n_{Ti})$ where M is La or Mg) would be 0, 0.05, 0.1 and 0.15. The two sols were then mixed and the total metal ion concentration was adjusted to 4×10^{-1} mol/l in all sols, by adding water.

A xerogel was produced by heating the sol in a drying oven at 323 K in air and this was then heated to higher temperature (1°C/min) and held at the final temperature for 3 hours. X-ray diffraction (XRD) and ^{27}Al MAS-NMR have been used to examine the phase

development and the microstructure in these materials. DTA and TGA gave information on crystallization and transformation temperatures.

Results and Discussion

DTA and TGA

The DTA traces showed similar features and identical trends. From TGA it can be seen that only peaks between 400 and 675 K are associated with weight loss. The first peak around 400 K is associated with evaporation of physically bound water. The peak at 500–675 K arises from removal of crystallographic water from pseudo-boehmite giving boehmite and shifts towards higher temperature as doping levels increase, indicating La and Mg ions retard the pseudo-boehmite to boehmite transition. The peak at 700 K is related to the transformation of boehmite to γ-alumina and decreases gradually with increasing La level as a result of chemical interaction between the dopant and boehmite, hence, consuming this phase before transformation to γ-alumina. The peak at 500 K arises from the decomposition of nitrates.

The exothermic peak at high temperature corresponds to the transformation of the γ-alumina to α-alumina. Figure 1 shows that the transformation temperature can be increased by as much as 200 K with La doping but by less with Mg doping. The transformation temperature increases linearly with increasing Mg doping whereas the response is non-linear with La and reaches a saturation level. Transformation temperature also decreases linearly with increasing TiO_2, indicating that TiO_2 either catalyzes the α-alumina transformation or provides convenient nucleation sites.

XRD

XRD data from xerogels (Fig. 2) shows broad peaks from pseudo-boehmite (γ-$Al_2O_3 \cdot 1.3H_2O$) and anatase (TiO_2). In La doped samples, the boehmite peaks broaden even more, indicating either smaller or more

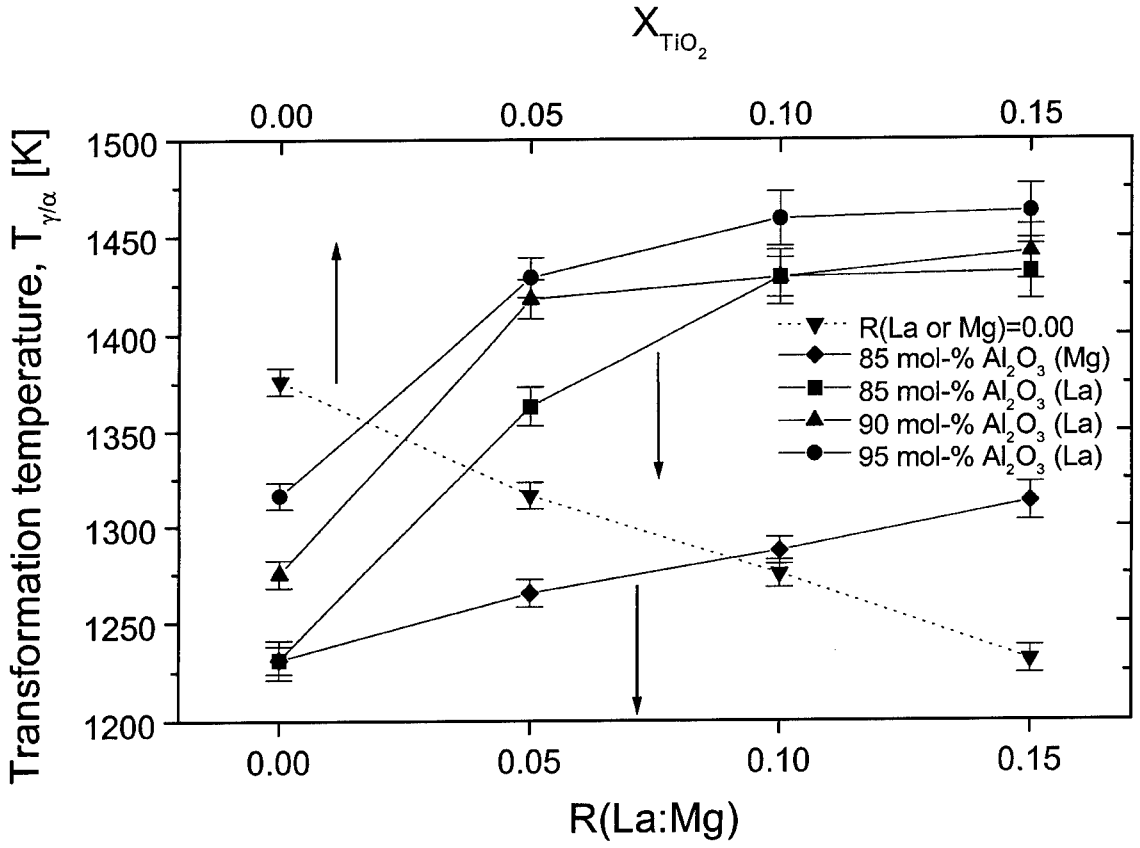

Figure 1. Graph showing the extrapolated onset of α-alumina against doping level (unbroken lines) and against molar ratio TiO_2 of undoped $Al_2O_3 : TiO_2$.

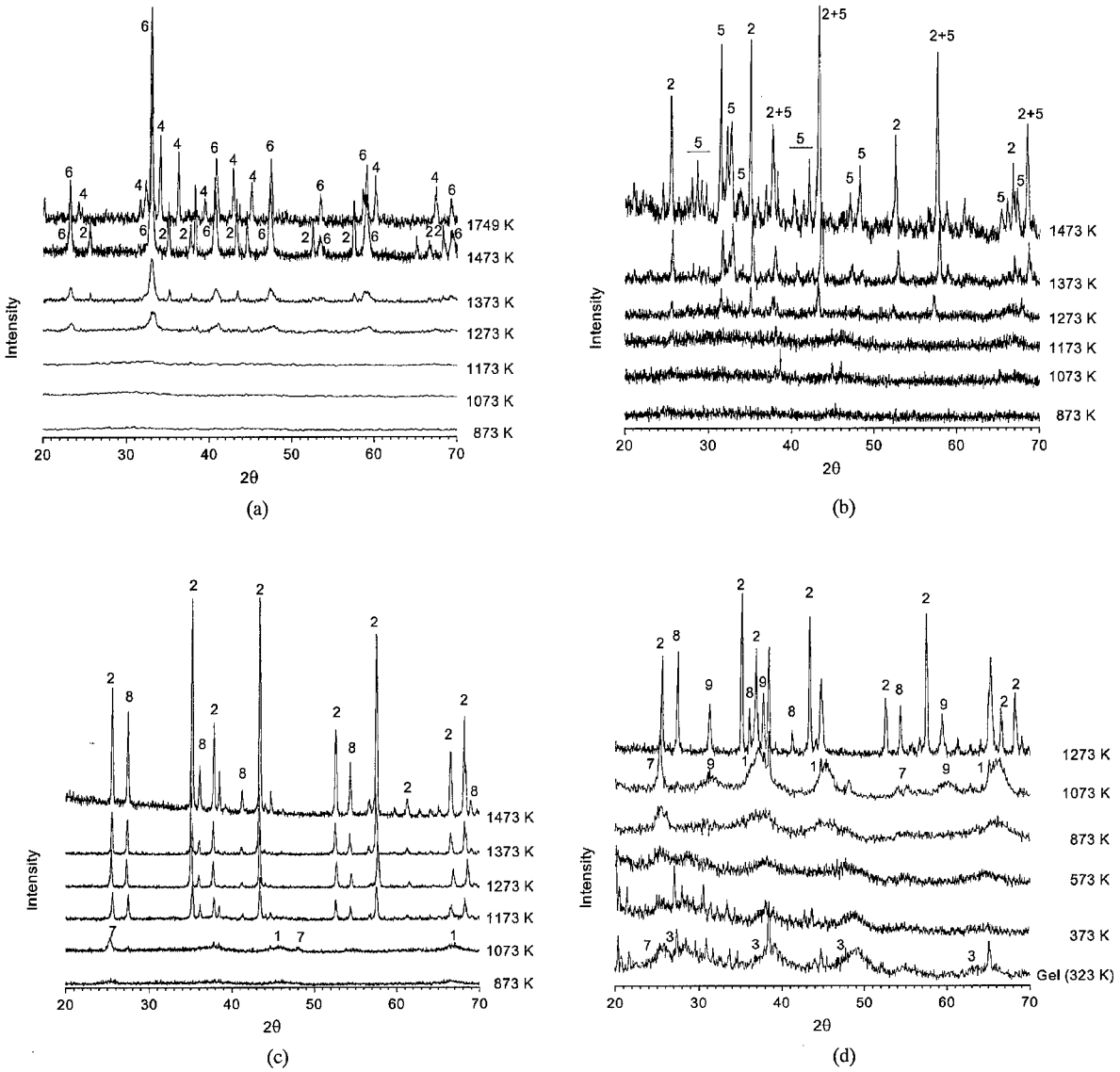

Figure 2. XRD spectra: (a) 85 mol% Al_2O_3 $R(La) = 0.15$, (b) 85 mol% Al_2O_3 $R(La) = 0.05$, (c) 85 mol% Al_2O_3 $R(La : Mg) = 0.00$ and (d) 85 mol% Al_2O_3 $R(Mg) = 0.15$. Key: (1) γ-Al_2O_3, (2) α-Al_2O_3, (3) pseudo-boehmite, (4) $LaAl_{11}O_{18}$, (5) $LaTi_2$ Al_2O_{19}, (6) solid solution; $LaAlO_3 : LaTiO_3$, (7) anatase, (8) rutile, (9) spinel ($MgAl_2O_4$).

disordered boehmite crystals containing La ions. This trend is not observed in Mg doped material.

After heat treatment at 873 K the XRD showed, in addition to anatase, peaks at d-values of 1.40, 1.98 and 2.38 Å, although, in the presence of La, they are very broad. The peak positions and relative intensities match those of γ-alumina and do not provide evidence of intermediate alumina phases as suggested by Wilson [2, 3].

Mg doped samples calcined at 1073 and 1273 K gave identical XRD spectra. At 1073 K we see a narrowing of the lines from γ-alumina and anatase phase reflecting crystal sizes of 14 and 79 nm, respectively, compared with 8 and 22 nm at 873 K. Also, at 1073 K we see the appearance of broad lines assigned to spinel ($MgAl_2O_4$). γ-Alumina and anatase undergo phase transitions between 1073 and 1273 K to form α-alumina and rutile (Fig. 2(d)).

The XRD spectra for La doped material are more complex. For $R(La) = 0.10$ and 0.15 we see an initial transformation of pseudo-boehmite to γ-alumina but the diffraction peaks remain very broad. At 1273 K strong peaks appear corresponding to $LaAlO_3$, with a slight increase in d-spacing indicating solid solution

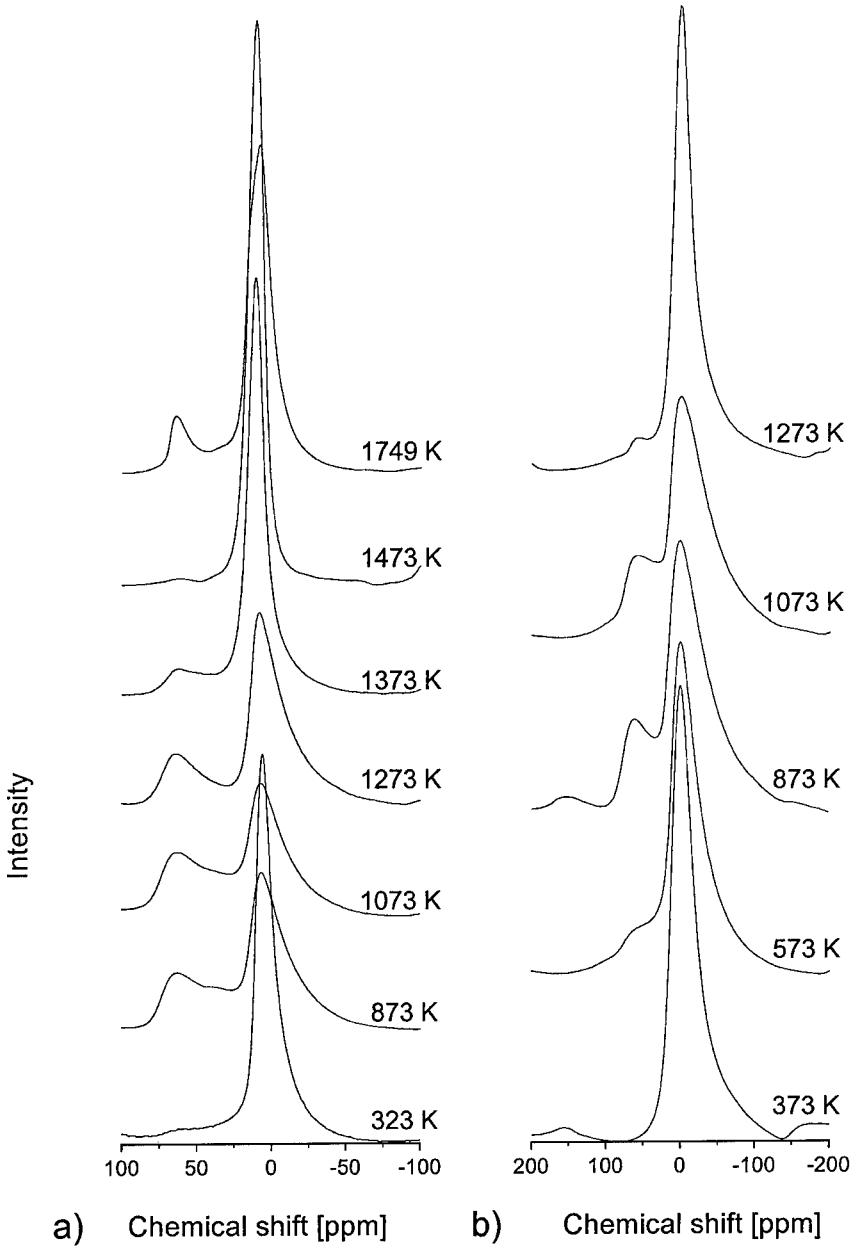

Figure 3. ^{27}Al MAS-NMR spectra of 85 mol% Al_2O_3 with (a) $R(La) = 0.15$ and (b) $R(Mg) = 0.15$. Note the two sets of spectra are collected with different magnetic fields, hence, different line width.

with 30% $LaTiO_3$ [4]. At 1373 and 1473 K α-alumina is also present in the XRD traces. However, this phase is replaced by $LaAl_{11}O_{18}$, which belongs to the β-alumina family, at 1750 K. For $R(La) = 0.05$ at 1273 K there are two phases, α-alumina and $LaTi_2Al_9O_{19}$ [5] and these remained present at higher processing temperature.

^{27}Al MAS-NMR

Below 723 K, all NMR spectra show a broad single asymmetric peak with its maximum at 4 ppm (Fig. 3). This peak corresponds to six co-ordinated aluminum in pseudo-boehmite. The width and asymmetry arise from the interaction between the quadrupolar-moment

of ^{27}Al and the electric field gradient in the asymmetric site created by five oxygen and one hydroxyl nearest neighbors.

Spectra of samples heat treated above the transition to γ-alumina show 6 and 4 co-ordinated ^{27}Al as expected. The 4-CN peak appears at around 64 ppm. A peak at 27 ppm is present in the spectra from La doped samples in the temperature range 873–1073 K but is absent in the Mg doped. A possible explanation for this peak is five co-ordinated aluminum. The presence of five co-ordinated aluminum has been suggested [6, 7] to exist in the bulk and the surface of γ-alumina. However, in this study only La doped alumina showed five co-ordinated aluminum.

At higher temperatures the peak corresponding to four co-ordinated aluminum disappeared and there is a shift in the peak for the six co-ordinated aluminum to around 12 ppm. Furthermore, the peak becomes symmetrical corresponding to the environment in α-alumina. With dopant added to the material four co-ordinated Al appear at lower temperature and are retained to higher temperature.

Overall Discussion

As demonstrated in the DTA and ^{27}Al MAS-NMR, it is possible to thermally stabilize the low temperature phases of alumina by doping it with La or Mg. However, the stabilizing mechanism is different for the two cations. As seen in Fig. 1, the α-alumina transition temperature increases linearly with increasing Mg content. This is radically different from the response of La doping where the transition temperature reaches a limiting value. Oudet et al. [8] suggest that the stabilizing mechanism for La doped alumina is the formation of $LaAlO_3$ on the active nucleation sites on the γ-alumina phase rather than a solid solution of La_2O_3 and Al_2O_3. These active sites would normally be available for the nucleation of α-alumina and hence the presence of $LaAlO_3$ phase will inhibit this nucleation. Such a mechanism would reach a limit when $LaAlO_3$ has occupied all the available active nucleation sites as seen in the DTA results in this study. This would mean that even low levels of La doping would have a great effect on the transformation temperature as seen in the NMR data. However, the XRD data show a less crystalline material for the La doped as compared to the undoped samples. This suggests that a more disordered pseudo-boehmite forms, which contains La ions. The subsequent γ-alumina is also more disordered than the undoped counterpart. This complicates the picture presented by Oudet et al. [8].

The crystal structure of γ-alumina is described as tetragonal disordered spinel and hence it would be expected that a solid solution between Mg spinel and γ-Al_2O_3 can occur freely. This would in turn mean that the stabilizing effect of Mg in γ-alumina comes from the substitution of Mg^{2+} ions for Al^{3+} in the fcc oxygen packing of γ-alumina. This might explain the small, linear effect on the transformation temperature to α-alumina.

Conclusion

This study has shown that the phase composition of $Al_2O_3 : TiO_2$ membrane material is greatly affected by the type of cation used for doping, resulting in different reaction paths depending on the amount and nature of the dopant.

The DTA and the NMR results show that the it is possible to stabilize the low temperature phase of alumina by as much as 200 K with La doping. However, due to different stabilizing mechanisms Mg doping is not as efficient in retaining γ-alumina at high temperature.

Acknowledgment

The authors would like to acknowledge the financial support from Japan Fine Ceramic Center (JFCC).

References

1. B.E. Yoldas, Am. Ceram. Soc. Bull. **54**, 289 (1975).
2. S.J. Wilson, J. Solid State Chem. **30**, 247 (1979).
3. S.J. Wilson, Proc. British Ceram. Soc. **28**, 281 (1979).
4. U.S. Björkert, R. Mayappan, and D. Holland, J. Euro. Ceram. Soc., submitted for publication.
5. P.E.D. Morgan, Mat. Res. Bull. **19**, 369 (1984).
6. F.R. Chen, J.G. Davis, and J.J. Fripiat, J. Catal. **133**, 263 (1992).
7. L.J. Alvarez, L.E. Leon, J.F. Sanz, M.J. Capitan, and J.A. Odriozola, Surface Science **322**, 185 (1995).
8. F. Oudet, P. Courtine, and A. Vejux, J. Catal. **114**, 112 (1988).

Journal of Sol-Gel Science and Technology 13, 805–811 (1998)
© 1998 Kluwer Academic Publishers. Manufactured in The Netherlands.

Study of the Selectivity of SnO_2 Supported Membranes Prepared by a Sol-Gel Route

L.R.B. SANTOS
Instituto de Química, UNESP, PO Box 355, CEP 14 801-970, Araraquara, SP, Brazil; Laboratoire des Matériaux et Procédés Membranaires, ENSCM 8, rue de l'Ecole Normale, 34296 Cedex 5, Montpellier, France

A. LARBOT
Laboratoire des Matériaux et Procédés Membranaires, ENSCM 8, rue de l'Ecole Normale, 34296 Cedex 5, Montpellier, France

C.V. SANTILLI AND S.H. PULCINELLI
Instituto de Química, UNESP, PO Box 355, CEP 14 801-970, Araraquara, SP, Brazil

Abstract. In this work the sol-gel process was used to prepare SnO_2 supported membranes with an average pore size of 2.5 nm. The effects of salt concentration (NaCl or $CaCl_2$) and of the pH of the aqueous solutions used on the flux and selectivity through the SnO_2 membrane were analyzed by permeation experiments and the results interpreted taking account of the zeta potential values determined from the electrophoretic mobility of the SnO_2 powder aqueous dispersion. The results show that the ion flux (Na^+, Ca^{2+} and Cl^-) throughout the membrane is determined by the electrostatic repulsion among these species and the surface charge at the tin oxide-solution interface.

Keywords: SnO_2 membranes, ultrafiltration, selectivity, rejection capacity

1. Introduction

The broadened interest in the membrane field observed during the last decade has been largely the result of the potential of membrane separation processes as the answer to several environmental and biotechnological problems such as atmospheric and water pollution, energy-saving, liquid food treatment, a better controlled release of powerful drugs and desalination of brackish water [1]. The well-developed families of polymer membranes are not able to satisfy the request of high thermal, chemical and microbiological stability desirable for many of these separation processes. In this more demanding environment ceramic membranes are needed [2].

The family of ceramic membranes commercially available consists of several porous layers, the active top-layer being made of alumina, titania or zirconia [3]. These membranes are specially designed for ultrafiltration and microfiltration while ceramic membranes for nanofiltration are not yet available. Consequently, a great deal of work has been put into the development of new ceramic membranes [4, 5].

Recently, we have shown that a SnO_2 layer coated on an α-Al_2O_3 macroporous support could satisfy the demand for a controlled-pore size distribution in all the pore size ranges used for ultrafiltration applications [6, 7]. However, the separation properties of this new membrane have not yet been described. This aspect is considered in this work, more attention being given to the effects of electrolyte concentration and pH of the aqueous solution, to the ion (Na^+, Ca^{2+} and Cl^-) selectivity and retention capacity of the SnO_2 membrane. Emphasis is placed on correlations between the dynamic filtration flux on the SnO_2 membrane and on the surface electric charge of the colloidal oxide in the presence of NaCl and $CaCl_2$ aqueous solutions.

2. Experimental

2.1. *Preparation of SnO_2 Powders and Membranes*

The SnO_2 aqueous colloidal suspension has been prepared as described elsewhere [6, 7], an aliquot of this being used for the preparation of the SnO_2 powder and another one for membrane deposition. For the former, gelation of a fresh suspension has been promoted by partial evaporation of water (60°C) until the critical concentration of sol was reached at which the sol-gel transition occurs. The gel was dried at 110°C, and then fired at 400°C for 1 h. The small fragments of the xerogels were ground for 1 h in an automatic mortar.

The SnO_2 membranes were deposited by slip-casting for 10 min on a tubular α-Al_2O_3 microfilter support with 5.0 nm average pore diameter. Polyvinyl alcohol (3.5 wt%) had been previously added to the solution as a binder, to avoid crack formation. After drying overnight in air, the samples were fired at 400°C for 1 h.

2.2. *Characterization*

The electrophoretic mobility of diluted SnO_2 dispersions (1.0 $g \cdot l^{-1}$) was measured as a function of pH using a Coulter Delsa 440. The dispersions were prepared in aqueous solutions of different electrolytes (NaCl or $CaCl_2$) with ionic strengths (I) of 10^{-3} and 10^{-2} $mol \cdot l^{-1}$ and allowed to equilibrate to their original pH. Subsequently, the pH of the dispersions was adjusted with NaOH and hydrochloric acid. The zeta potentials (ζ) have been calculated by using the Smoluchowski equation [8]. During the measurements, the current intensity, the frequency and the working temperature were fixed at 0.1 mA, 250 Hz and 25°C, respectively.

Permeability tests have been conducted in a laboratory cross filtration pilot system equipped with a tubular membrane (length = 150 mm, inner diameter = 7 mm, outer diameter = 10 mm and filtration area = 26 cm^2), with ionic aqueous solutions (NaCl or $CaCl_2$) of several pH values. The working pressure using the nitrogen gas source and the feed flowing parallel to the membrane were 10 bar and 2.5 $m \cdot s^{-1}$, respectively. The salt concentration of the permeate and of the feed solution were measured by ionic exchange chromatography (Dionex). The temperature was set at 20°C and the membrane was immersed in water 16 hours before the start of testing.

3. Results and Discussion

The curves of zeta potential versus pH for the SnO_2 sol dispersed in NaCl and $CaCl_2$ aqueous solutions are given in Fig. 1(a) and (b), respectively. The values of the pH between 2.5 and 4.0 at the isoelectric point (iep) observed for all the solutions are in agreement with that reported in the literature, which range from pH 3 to 7.7 [9].

It is found that the curves for suspensions with different salt concentrations do not show a common point of intersection at $\zeta = 0$, indicating that the iep depends on the ion surface activity. For $CaCl_2$ the pH_{iep} is almost invariant with the ionic strength. The opposite behavior is observed for NaCl solutions, i.e., the pH_{iep} shifts from 4.3 to 2.5 with increasing I from 10^{-3} to 10^{-2} $mol \cdot l^{-1}$. However, for the two salts a predominant anion adsorption is observed.

SEM micrographs of the SnO_2 membrane are shown in Fig. 2. The lateral fracture surface of the sample (Fig. 2(a)) reveals that the SnO_2 layer has a uniform thickness of about 0.3 μm. It is possible to increase the layer thickness both by ageing the colloidal suspension or by increasing the casting time period, but crack-free membranes are only obtained for layer thicknesses smaller than 0.6 μm. The absence of cracks, or other defects in the surface layer is clear in Fig. 2(b), while the magnified image (Fig. 2(c)) shows a homogeneous porous microstructure with a grain size of about 2.5 nm. The pore size of less than 2.5 nm is in agreement with the average diameter obtained by N_2 adsorption measurements [7].

Filtration experiments allowed investigation of the influence of the pH of the aqueous salt solution on the permeate flux (F) and ion rejection coefficient (R). This coefficient is given by $R = (C_f - C_p)/C_f$, where C_f is the concentration of the ions retained in the feed solution and C_p the corresponding concentration in the permeate.

Typical results obtained for NaCl solution ($I = 10^{-3}$ $mol \cdot l^{-1}$) are show in Fig. 3, in which both the flux and R are plotted as a function of the filtration time. The rejection coefficient increases immediately after starting the experiments while the permeate flux remains practically invariant. This effect is much more remarkable at higher pH for Cl^- rejection and at the extreme values of pH for Na^+ rejection. In this condition, more than one hour is required to reach a constant value of R, the effect being too slow to be explained in terms of the diffusion process of counter-ions. As described

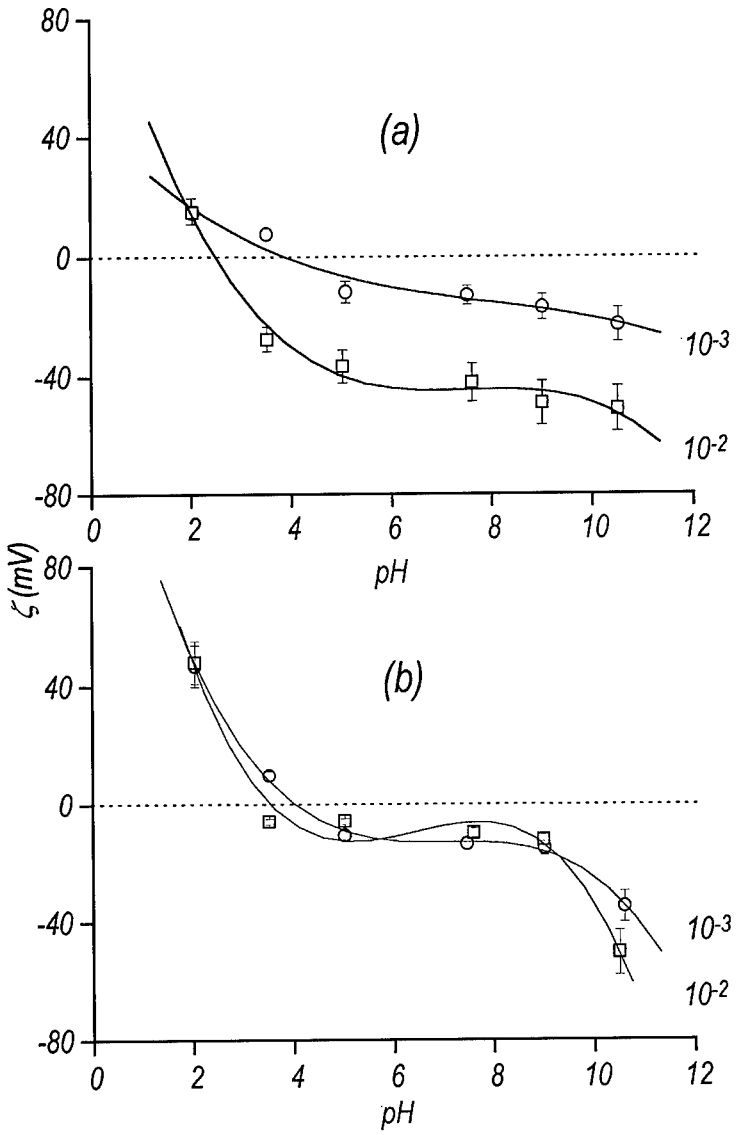

Figure 1. Zeta potential of SnO_2 as a function of the pH of NaCl (a) and $CaCl_2$ (b) aqueous solutions.

by Venida et al. [10] for the case of SnO_2 electrodes, this behavior can be attributed to a slow rate of counter-ion adsorption (including complex formation) at the tin oxide-solution interface. The small rejection coefficient at pH = 2.0 (0.50) can be attributed to the large quantities of hydrochloric acid used in the pH adjustment, making the hydration level decrease and favoring the transfer process of the ions through the membrane.

The interesting aspect that these results reveal is the ion selectivity dependence on the pH. The rejection of Cl^- is high (0.80) at alkaline values of pH, the opposite effect being observed for Na^+, where R is small (0.62) for the same pH interval. This behavior is in agreement with the coloidal chemistry (zeta potential) results (Fig. 1(a)). At acid pH the tin oxide surface has a positive charge causing the cation repulsion. As a consequence, the rejection of Na^+ is increased. At alkaline pH, the opposite behavior is observed, the surface of the membrane being negatively charged and the rejection of the anion being greater than that of the cations.

The effect of the ionic strength of the $CaCl_2$ solution at pH 7.5 on the rejection coefficient and on the permeate flux is shown in Fig. 4. The flux value is practically

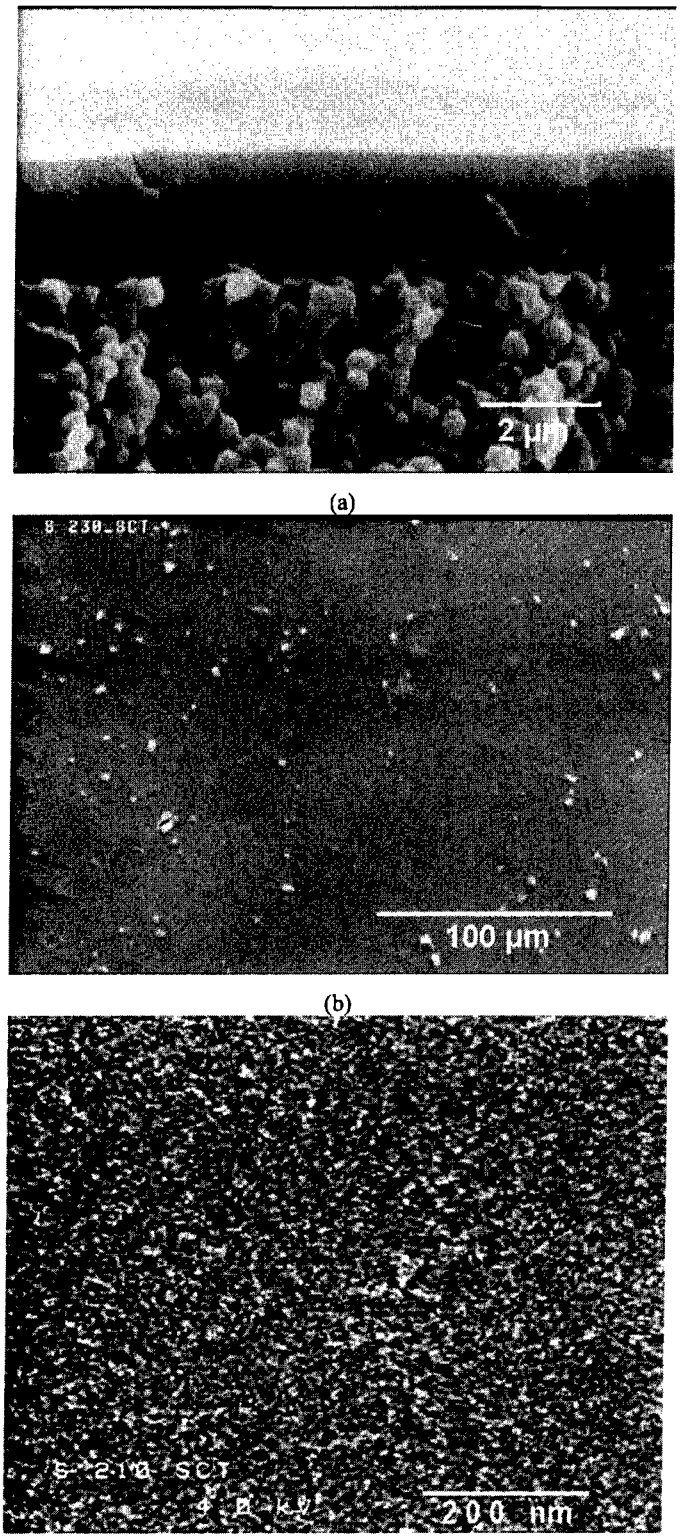

Figure 2. SEM micrographs SnO_2 supported membrane: (a) lateral fracture surface; (b) top surface of membrane; and (c) higher magnification of top surface.

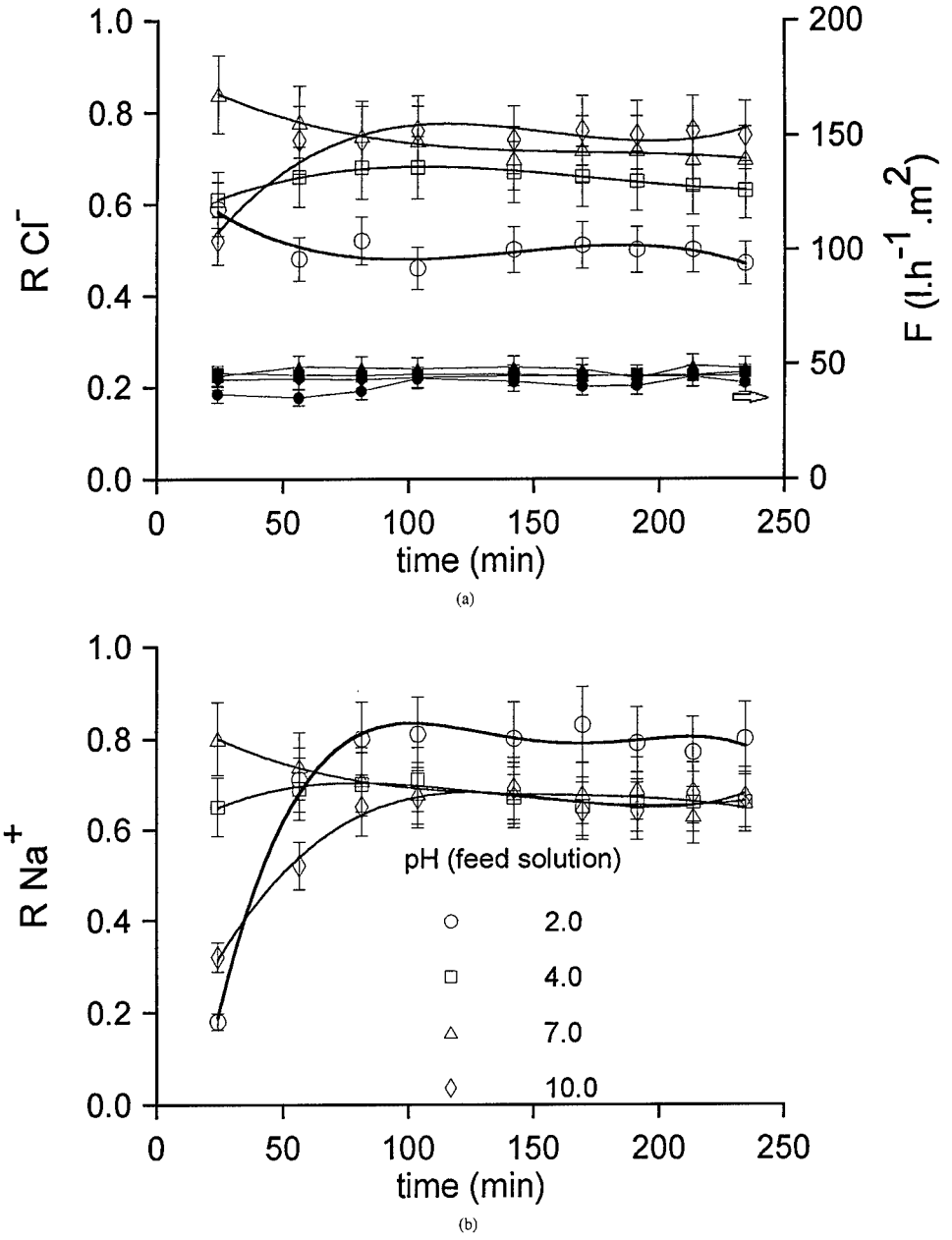

Figure 3. Rejection coefficient (R) and flux (F) versus filtration time of the NaCl solution ($I = 10^{-3}$ mol · l^{-1}) for different values of pH: (a) Cl^- and (b) Na^+ rejection coefficients.

invariant ($501 \cdot h^{-1} \cdot m^{-2}$) with the electrolyte concentration. The R values for Ca^{2+} ions decrease from 0.97 to 0.75 as I increases from 10^{-3} to 10^{-2} mol, while the rejection coefficient of Cl^- remains practically constant at 0.98. This confirms that the ion selectivity of this membrane is dependent on the nature of the surface charge of the tin oxide-solution interface. At pH 7.5 the membrane is negatively charged and anion repulsion is strong at $I = 10^{-3}$ and 10^{-2} mol · l^{-1}.

The Ca^{2+} rejection decreases as the electrolyte concentration increases. This behavior is a consequence of the decrease of the Debye length (diffuse layer) causing an increase of the attraction between the membrane and the Ca^{2+} cations.

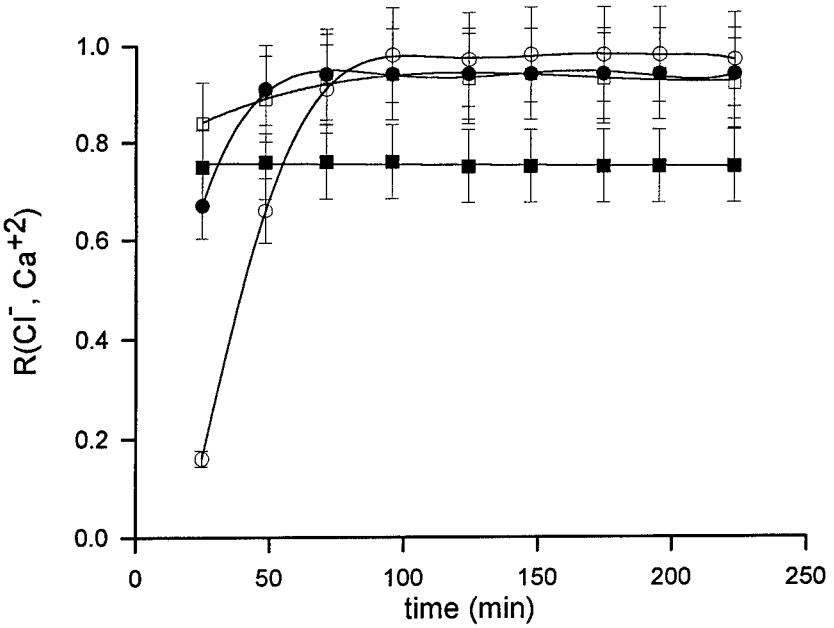

Figure 4. Rejection coefficient (R) versus filtration time of $CaCl_2$ solution (pH = 7.5) for different ionic strengths: Cl^- (○ = 10^{-3} mol · l^{-1}, ● = 10^{-2} mol · l^{-1}) and Ca^{2+} (□ = 10^{-3} mol · l^{-1}, ■ = 10^{-2} mol · l^{-1}).

The rejection of ions can be achieved by one or more mechanisms, namely charge (Coulombic) interactions, hydrated-ion size exclusion or dielectric interaction [11]. The charge pattern of rejection is characterized by the behavior of the co-ions, i.e., those with the same charge as the membrane. The hydration pattern of rejection is characterized by the rejection of large hydrated ions, the larger the hydrated size the more strongly it will be rejected. The hydration effect is reduced as the ion concentration increases; Na^+ and Cl^- form hydrated ions pairs [12].

4. Conclusions

The NaCl and $CaCl_2$ aqueous solution interface with the sol-gel derived SnO_2 powder, which has been used to prepare an ultrafiltration membrane, was characterized. A shift of the pH_{iep} with the ionic strength was observed, typical of active electrolyte.

The preliminary results show that for SnO_2 supported membranes at alkaline pH values, the rejection by charge is predominant and at neutral and weakly acidic pH, the rejection process is governed by the hydration phenomenon.

The dynamic behavior of an ionic solution in terms of ion rejection by the SnO_2 ultrafiltration membrane depends on the surface charge of the pore walls. Positively charged surfaces have a preferential rejection of cations (Na^+, Ca^{2+}) while anions (Cl^-) are rejected by the negatively charged surfaces. A detailed study is needed to understand all the transfer phenomena and interactions existing between the solution and this new membrane.

Acknowledgments

The work has been supported by CAPES/COFECUB and FAPESP.

References

1. E. Drial, Russian Chem. Bull. **42**, 777 (1993).
2. L. Cot, J. Chim. Phys. **88**, 2083 (1991).
3. A.J. Burggraaf, K. Keizer, and B.A. Van Hassel, Solid State Ionics **32/33**, 771 (1989).
4. L. Klein, C. Vu, C. Woodman, and R. Pavlik, Catalysis Today **14**, 165 (1992).
5. C. Guizard, A. Julbe, A. Larbot, and L. Cot, J. Alloys Comp. **188**, 8 (1992).
6. L.R.B. Santos, S.H. Pulcinelli, and C.V. Santilli, J. Sol-Gel Sci. Tech. **8**, 477 (1997).
7. L.R.B. Santos, S.H. Pulcinelli, and C.V. Santilli, J. Memb. Sci. **127**, 77 (1997).

8. R.J. Hunter, *Colloid Science: Zeta Potential in Colloid Science: Principles and Applications* (Academic Press, London, 1981).
9. M.R. Houchin and L.J. Warren, J. Coll. Interface Sci. **100**, 278 (1984).
10. I. Uchida, H. Akahoshi, and S. Toshima, J. Electroanal. Chem. **88**, 79 (1978).
11. S. Alami-Younssi, A. Larbot, M. Persin, J. Sarrazin, and L. Cot, J. Mem. Sci. **102**, 123 (1995).
12. A.G. Fane, A.R. Awang, M. Bolko, R. Macoun, R. Schofield, Y.R. Shen, and F. Zha, Wat. Sci. Tech. **25**, 5 (1992).

Journal of Sol-Gel Science and Technology 13, 813–820 (1998)
© 1998 Kluwer Academic Publishers. Manufactured in The Netherlands.

Ferroelectric PZT Thin Films by Sol-Gel Deposition

IAN M. REANEY
Department of Engineering Materials, University of Sheffield, Sir Robert Hadfield Building, Mappin St., Sheffield, S1 3JD

DAVID V. TAYLOR
Laboratoire de Céramique, Département des Materiaux Ecole Polytechnique Fédérale de Lausanne, Lausanne, CH-1015, Switzerland

KEITH G. BROOKS
Département de Chimie, Ecole Polytechnique Fédérale de Lausanne, Lausanne, CH-1015, Switzerland

Abstract. Sol-gel spin coating has a low "thermal budget," is cheap compared to vacuum-based techniques and is now routinely used to produce dense, pore-free ferroelectric films. $PbZr_xTi_{(1-x)}O_3$ (PZT) is utilized in most applications because it has a large remanent polarization, high piezo- and pyroelectric coefficients and optimized electromechanical coupling factors, depending on precise composition. This paper will review some of the principles and applications of PZT films and highlight using transmission electron microscopy some of the basic problems and solutions involved in producing device-quality material on Si-substrates.

Keywords: ferroelectric, thin film, PZT, platinum

1. Introduction

The use of thin films of high dielectric constant electroceramics gives the possibility of miniaturizing any electronic component which requires the use of a capacitor. In addition, ferroelectric (FE) films offer other usable properties such as switching characteristics that allow the storage of binary data (ferroelecric nonvolatile memories), piezoelectricity (sensors, micropumps and motors) and pyroelectricity (infrared imaging arrays) [1]. The integration of FE films into Si technology would lead to the production of devices in which the control circuitry and active materials are incorporated onto one microchip. One possible method of thin film deposition currently being explored is sol-gel spinning.

The solid solution $Pb(Zr, Ti)O_3$ (PZT) is FE and has a large remanent polarization, high piezo- and pyroelectric coefficients, optimized electromechanical coupling factors, depending on precise composition, and satisfies the requirements of most potential applications [2]. Film thicknesses, however, may vary depending on the application; sensors, micropumps and micromotors require films of 5–10 μm thickness whereas memories need films of around 200 nm. Deposition is usually carried out onto platinized Si/SiO_2 wafers followed by sputtering of a top electrode onto the surface of the film.

A schematic of part of a device, in this case a pyroelectric detector array, is shown in Fig. 1 [3]. Individual sections of ceramic act as thermally and electrically isolated pixels which are used to form a thermal image. This technology currently uses lapped and polished bulk ceramics. The development of an integrated, thin film-based system would dramatically reduce the cost of such imaging arrays leading the way to the exploitation of more commercial markets.

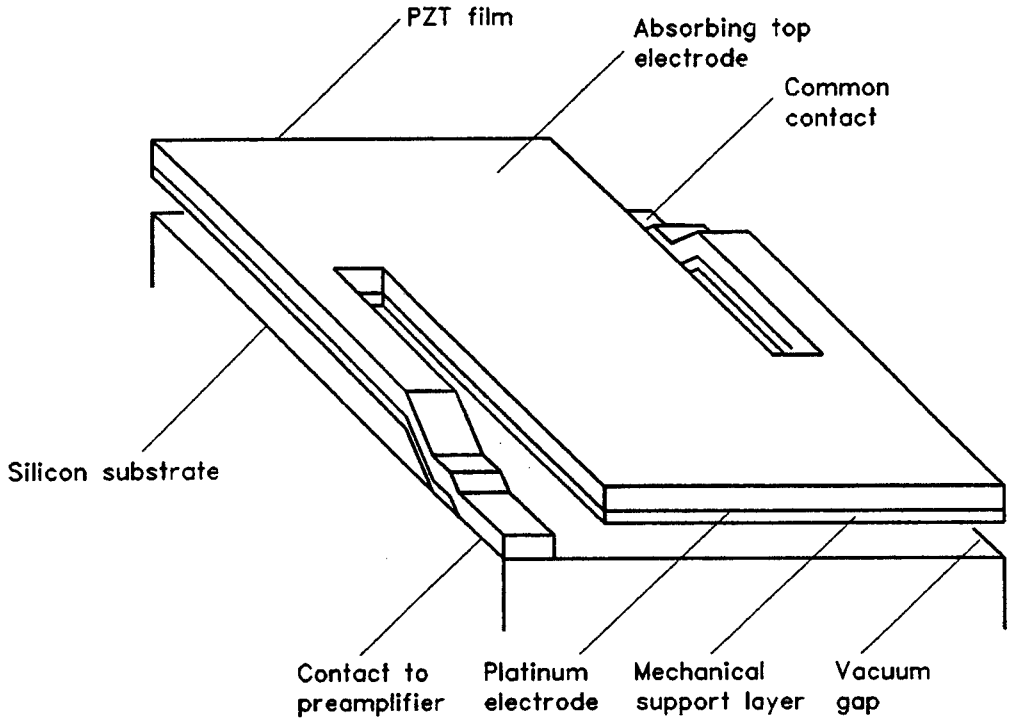

Figure 1. Schematic of part of a FE thin films pyroelectric detector array (after Shorrocks et al. [3]).

2. Film Deposition

Sol-gel spin coating is cheap, since it does not involve a vacuum chamber, and can be used to deposit an even coat of PZT onto a 6 inch electroded Si/SiO_2 wafer. There are several methods for the deposition of films. The differences between them revolve largely around the chemistry of the precursor solutions. Readers are referred to papers by Yu and Milne [4], Whatmore et al. [5] and several papers which are to appear in these proceedings. Here, we will discuss a modified sol-gel route by Brooks et al. [6] which is based on that first reported by Budd and Payne [7]. In the Brooks' process, the organometallic precursor solutions are not prehydrolyzed. Film fabrication involves the preparation of an organometallic precursor solution and its deposition by a multilayer spin coating technique.

The film precursor solution is prepared by dissolution of $Pb(C_2H_4O_2)\cdot 3H_2O$ in 2-methoxyethanol. Vacuum distillation is used to remove the water associated with the hydrated Pb salt. A solution of Zr-*n*-propoxide and Ti-isopropoxide in 2-methoxyethanol is then added to the Pb precursor solution and refluxed for 2 hours. A solution containing the equivalent of 0.4 moles of $Pb(Zr_{0.53}Ti_{0.47})O_3$ per liter of solution is obtained by further distillation. During this vacuum distillation process, other reaction byproducts are also removed from the sol-gel stock solution. A microprocessor controlled vacuum distillation apparatus (Rotavapor EL-141, Buchi Laboratory-Techniques Inc., Flawil, Switzerland) is used to achieve reproducibility of solution preparation. Excess Pb may be added using extra Pb precursor solution.

PZT films may be prepared by spin coating the stock solution onto substrates (described above) at 3000 rpm. for a duration of 30 s. The films are pyrolyzed after each coating application at 350°C or 420°C for 15 seconds. Films of 250–300 nm thickness are prepared by repeated coating. Crystallization of the perovskite phase is achieved by rapid thermal annealing of the resulting amorphous films.

The route described above is reliable and produces high quality films of up to 0.3 μm. Thicker films have been produced by a multideposition step. In effect, the exact same procedure is reproduced on the surface of the already deposited film. However, the more deposition steps there are, the greater the deterioration of the electrode/substrate [8]. Deposition of thick films

(5–10 μm) often results in delamination of the electrode or film from the substrate. The "diol" method devised by Milne et al. [4] has advantages over that described above since the viscosity of the precursor solution is greater and a thicker single deposition film can be produced. However, even with the "diol" route the thickness of a single layer is a maximum of 1 μm and 10 such layers are required to produce material ideal for use as sensors and micropumps.

3. Film Crystallization and Orientation

It has been reported by several authors [6, 9, 10] that the transformation kinetics from amorphous to perovskite along with the orientation of the film are strongly dependent on the temperature of pyrolysis. The following is a comparison using TEM and XRD between two series of films deposited on identical substrates. The substrates used in this study are composed of (111) oriented Pt (0.1 μm thick) e-beam evaporated onto SiO_2/Si. The films were prepared identically except that they were pyrolyzed at either 350°C or 420°C followed in each case by RTA annealing at 600°C for short times.

3.1. *X-Ray Diffraction*

Figure 2 shows a comparison of XRD patterns obtained from films pyrolyzed at 350°C and annealed for 0, 1, 2, 5, 300 and 600 s at 600°C. As the annealing time is increased the PZT peaks become gradually more apparent and their intensity reaches a maximum at around 5 s. In the as-pyrolyzed state, a large diffuse hump is observed at about 29°C. This peak becomes sharper after 1 s and begins to diminish in intensity until it is no longer present after 5 s. This phase has been identified by Brooks et al. as pyrochlore [6]. Figures 3(a) and (b) are XRD patterns comparing the phase evolution in samples pyrolyzed at 350°C and 420°C. Figure 3(a) clearly shows the development of a (111) perovskite peak between 1 and 2 s heat treatment accompanied by a drop in the relative intensity of the pyrochlore peak at 29° which according to Fig. 2 disappears after 5 s. In Fig. 3(b) (420°C pyrolysis), the pyrochlore peak is still present even after 300 s and the orientation of the film is (001).

3.2. *Transmission Electron Microscopy*

Figure 4 shows TEM images of parts of transverse sections from samples heat treated for 2 s but pyrolyzed at (a) 350°C and (b) 420°C. In both images, pyrochlore is observed as a nanocrystalline phase whereas the perovskite is distinctly columnar, growing from the Pt surface. In Fig. 4(a) (350°C), the perovskite has grown through the majority of the film. In Fig. 4(b) (420°C), only nuclei are observed at the Pt surface. Figures 5(a) and (b) are electron diffraction patterns obtained from (a) an as-pyrolyzed film and (b) a purely pyrochlore

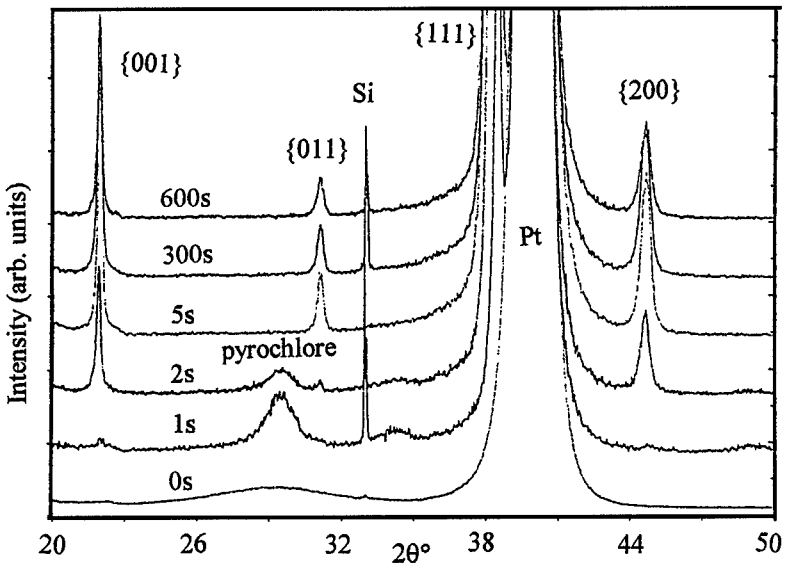

Figure 2. Comparison of XRD patterns obtained from films pyrolyzed at 350°C and annealed for 0, 1, 2, 5, 300 and 600 s at 600°C.

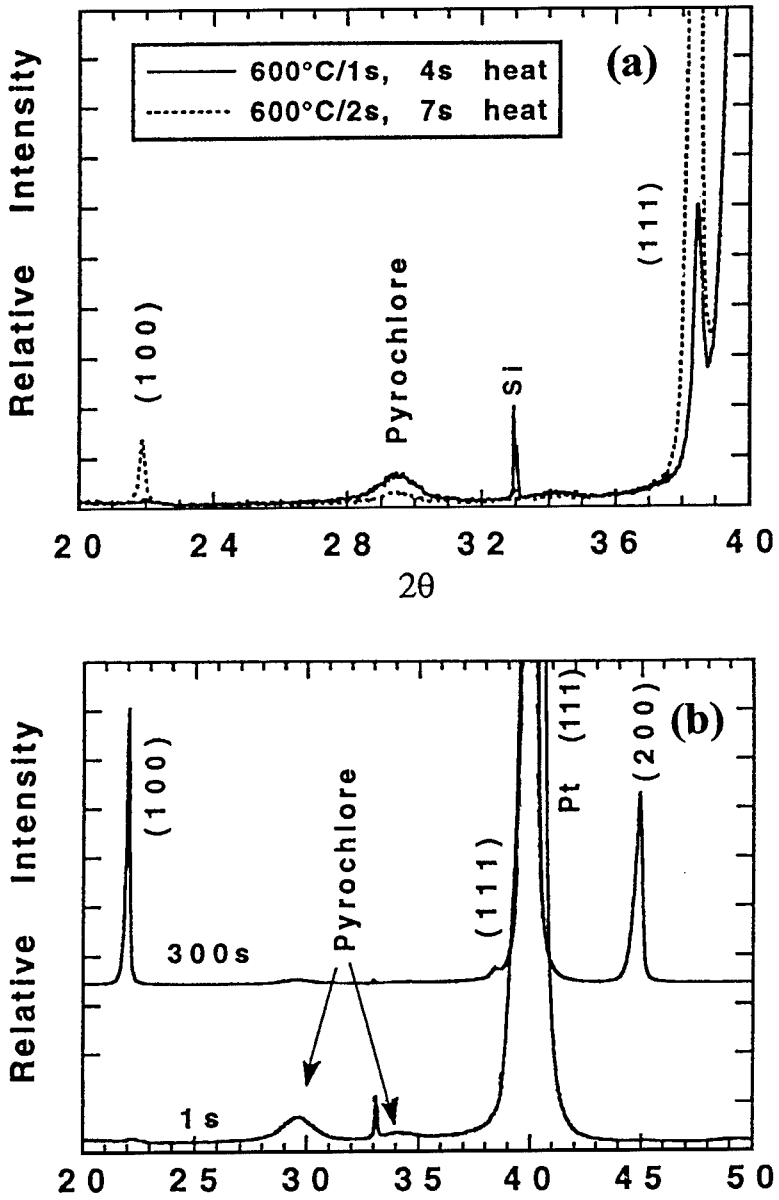

Figure 3. XRD patterns comparing the phase evolution in samples pyrolyzed at 350°C and 420°C.

film. The as-pyrolyzed film gives rise to two broad rings (Fig. 5(a)) whereas the pyrochlore phase exhibits discrete doublets, Fig. 5(b). The position of the doublets from the pyrochlore coincides with diffuse rings in the amorphous halo pattern. This observation agrees with the XRD data shown in Fig. 2 and suggests that the nearest neighbor and next nearest neighbor ions in the amorphous material have similar distributions to those in the pyrochlore phase. Therefore, the transformation from amorphous to pyrochlore is kinetically more favorable than a straight transformation to the thermodynamically stable perovskite phase.

Comparison of the pyrochlore peaks with known structures in the XRD data files indicates that the "best-fit" phase is $Pb_2Ti_2O_6$. This is known to be an oxygen deficient, metastable variant of the more conventional pyrochlore structure. It is believed that Zr^{4+} is able to substitute for Ti^{4+} and that the real macroscopic formula for this phase is $Pb_2(Zr_{53}Ti_{47})_2O_6$. Reaney et al. [11] observed a Pb-deficient and Zr-rich (with respect

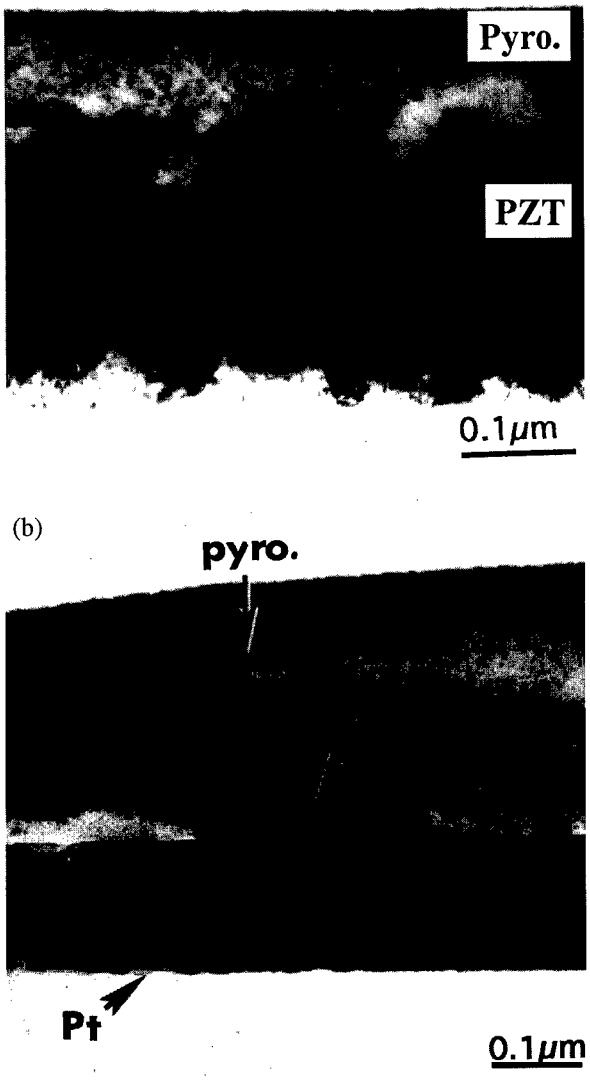

Figure 4. Bright field TEM images of parts of transverse sections from samples heat treated for 2 s but pyrolyzed at (a) 350°C and (b) 420°C.

to the perovskite in the film) pyrochlore-type phase which was at the surface of annealed films either as a continuous layer or as islands and did not transform to perovskite even after heat for long times. The fact that $Pb_2(Zr_{53}Ti_{47})_2O_6$ is metastable and rapidly transforms to perovskite strongly suggests that, in this instance, it is not Pb-deficient. The conclusion therefore is that two pyrochlore phases occur in the system; the metastable intermediate phase and a relatively stable Pb-deficient phase retained at the film surface.

The nanocrystalline phase identified here as a pyrochlore-type phase is considered by some authors to have a structure more similar to that of fluorite, depending on the exact heat treatment [12]. These two descriptions are not mutually exclusive since the pyrochlore (Fd3m) unit cell can be considered as a derivative of the fluorite structure (Fm3m). Largely kinematic diffraction techniques such as XRD should distinguish between these two structures because of the absence of the {200} reflections in pyrochlore arising from the d-glide plane. However, double diffraction effects in electron diffraction may cause this absence to occur.

Aside from the orientation, the most obvious difference between samples pyrolyzed at 350°C and 420°C is the speed with which the pyrochlore phase is able to transform to the perovskite phase. Brooks et al. [6] explained these observations by considering that the intermediate pyrochlore phase was more stable in samples pyrolyzed at 420°C than at 350°C. This was attributed to a higher degree of oxidation of the film which resulted in an increase in the average valence state of the Pb cations. $Pb_2(Zr_{53}Ti_{47})_2O_6$ is a metastable pyrochlore variant in which the valence state of the Pb is 2+. In general, stable pyrochlore structures such as Pb niobate are based on the formula $A_2B_2O_7$. Any increase in the valence state would change the stoichiometry of the metastable pyrochlore from O_6 towards on O_7 phase, possibly increasing its stability with respect to perovskite. The effect that an increase in the stability of the transient phase has on orientation is more difficult to explain. The (111) perovskite orientation arises from a lattice parameter match with the (111) planes of the Pt substrate. However, the (111) facet of the perovskite structure is not its natural growth habit since this plane is charged. Conventionally, perovskites grow along their principal axes forming cuboid single crystals, primarily because the {001} planes are neutral. The increase in the stability of the pyrochlore phase could increase the interfacial energy between itself and the (111) nuclei to the point where they are no longer stable, despite the preferred epitaxial relationship with the platinized substrate. The neutral facets of the {001} nuclei may be the only ones that have a low enough interfacial energy with the 420°C pyrochlore to be stable and grow.

Although the above scenario is difficult to prove, Brooks et al. [6] performed experiments in oxidizing

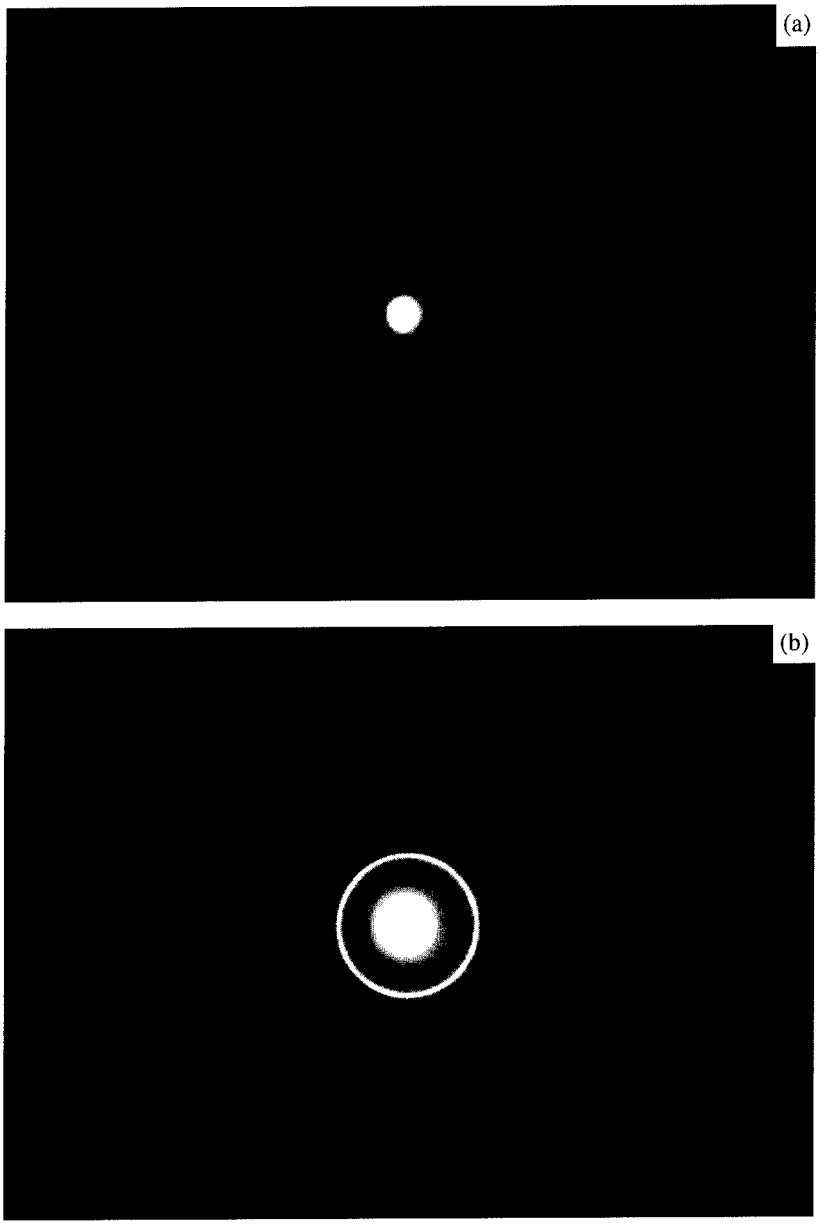

Figure 5. Electron diffraction patterns obtained from (a) an as-pyrolyzed film and (b) a purely pryochlore film.

and reducing atmospheres and showed that a 420° pyrolysis when heat treated in argon reverted back to a (111) orientation lending credence to the idea that reduction and oxidation play a role in the transformation kinetics and orientation. However, Chen and Chen [13] have suggested that the switch in orientation is related to the formation of a Pb-Pt alloy which when present favors a (111) but, if absent, a (001) orientation.

4. Development of Device Quality Material

Figure 6 is a high resolution TEM image showing a small island of pyrochlore at the top electrode/film interface. In general, the quality of the contact between electrode and film strongly influences the switching behavior of the sample. Therefore, the elimination of this phase is desirable. Reaney et al. [11, 14] have shown

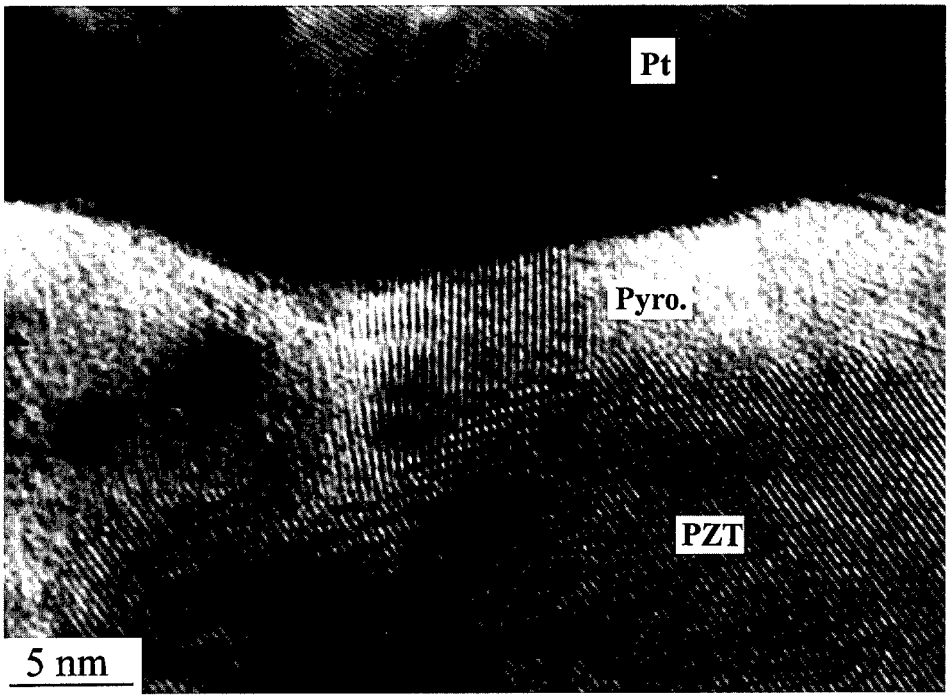

Figure 6. High resolution TEM image showing a small island of pyrochlore at the top electrode/film interface.

Figure 7. TEM image showing a PZT film prepared with a covercoat layer of Pb, Ti-rich material.

that the stable pyrochlore phase, residual on the film surface is Zr rich and Pb deficient compared to the bulk of the film. Furthermore, there is a general increase in the Zr content in the bulk of the film as the distance from the bottom electrode increases. The preferential nucleation and growth of Ti-rich material is thought to be responsible for this phenomenon. Therefore, to eliminate the pyrochlore phase and to redress the

Zr enrichment, a final "covercoat" of Ti- and Pb-rich (<20% exess Pb) material can be deposited onto the surface during spin coating. Figure 7 is a TEM image showing a PZT film prepared in this manner. The surface contains no residual pyrochlore and the final layer can be distinguished by a small change in contrast near the top of the coating. This change in contrast arises because of the small mismatch in lattice parameter between the Zr-enriched bulk and the Ti-rich covercoat layer.

References

1. M.E. Lines and A.M. Glass, *Principles and Applications of Ferroelectrics* (Clarendon Press, Oxford, 1977).
2. B. Jaffe, W.R. Cook, and H. Jaffe, *Piezoelectric Ceramics* (Academic Press, London, 1971).
3. N.M. Shorrocks, A. Patel, M.J. Walker, and A.D. Parsons, Microelectronic Engineering **29**, 59 (1995).
4. Y.L. Yu and S.J. Milne, Brit. Ceram. Proc. **54**, 233 (1995).
5. R.W. Whatmore, P. Kirby, A. Patel, N.M. Shorocks, T. Bland, and M. Walker, in *Proc. NATO Conf. on Sci. and Tech. of Electroceramics Films*, E 284, (1993), p. 383.
6. K.G. Brooks, I.M. Reaney, R. Klissurska, Y. Huang, L. Bursill, and N. Setter, J. Mater. Res. **9**(10), 2540 (1994).
7. K.D. Budd, S.K. Dey, and D.A. Payne, Brit. Ceram. Proc. **36**, 107 (1985).
8. D.V Taylor, private communication, Labo. de Céramique, E.P.F.L., Switzerland.
9. Klee, A. De Veirman, P. Van de Weijer, U. Mackens, and H. Van Hal. Philips Res. Rep. **47**, 263 (1993).
10. S. Hirano, T. Yugo, K. Kikuta, Y. Araki, M. Saitoh, and S. Ogasahara, J. Am. Ceram. Soc. **75**(10), 2785 (1992).
11. Ian M. Reaney, K. Brooks, R. Klissurska, C. Pawlaczyk, and N. Setter, J. Am. Ceram. Soc. **77**(5), 1209 (1994).
12. B.A. Tuttle, H.N. Al Shareef, W.L. Warren, M.V. Raymond, T.J. Headley, J.A. Voigt, J. Evans, and R. Ramesh, Microelectronic Engineering, **29**, 223 (1995).
13. S. Chen and I Chen, IMF Proc. Aug. (1993).
14. I.M. Reaney, T. Maeder, K.G Brooks, and P. Muralt, Brit. Ceram. Proc. **54**, 219 (1995).

Journal of Sol-Gel Science and Technology 13, 821–825 (1998)
© 1998 Kluwer Academic Publishers. Manufactured in The Netherlands.

Preparation of Thick PZT Ceramic Film by an Interfacial Polymerization

MASAYUKI YAMANE
Department of Inorganic Materials, Tokyo Institute of Technology, 2-12-1 Ookayama, Meguro-ku, Tokyo 152, Japan
myamane@ceram.titech.ac.jp

Abstract. The formation of a PZT film of 10–20 μm in thickness via an interfacial polymerization of metal-organic precursors has been studied. A commercially available PZT precursor solution developed for dip- or spin-coating was diluted with hexane containing acetylacetone as chelating agent. The solution was poured on water contained in a teflon reaction container of 88 mm inside diameter. A translucent gel film was formed at the interface of the two immiscible liquids. While floating on water it shrank as the evaporation of solvent proceeded until its diameter decreased to about 45% of its initial value. The dried gel film was almost pore free and its thickness was estimated to be about 10 μm.

Keywords: thick film, sol-gel, PZT, interfacial polymerization

1. Introduction

There is a growing interest in obtaining ceramic films of 10–20 μm in thickness on silicon wafer for the development of electronic and optoelectronic devices such as micro-actuators [1]. However, the method of fabricating such thick films has not yet been established, while there are a wide variety of methods applicable to the formation of thin films with thicknesses below 2 μm [2].

Recently, the author succeeded in forming a silicate glass film of 10–20 μm in thickness on a silica glass substrate using interfacial polymerization of partially hydrolyzed silicon alkoxide [3–6]. In the method, which begins with pouring a precursor alkoxide dissolved in an organic solvent such as hexane on water in a cylindrical reaction container, a gel film of desired thickness is formed at the interface between the two immiscible liquids as a result of the hydrolysis and polycondensation of the precursor. The gel film is then gently placed on a substrate placed near the bottom of the container by draining the liquids. This is followed by a drying process.

In contrast to gel films formed by dip- or spin-coating of an alkoxy derived sol, the film formed by this method can shrink freely while floating on water. This is particularly important for ceramic gel films for which the densification by viscous sintering cannot be expected. Although there may be various issues to overcome, the method should be applicable to non-silicate systems whose precursors are usually sensitive to moisture and easily precipitate as powders rather than develop a three dimensional network of colloid particles.

The present results on the formation of a PZT film of 10–20 μm in thickness on a silicon wafer by interfacial polymerization comprise a basic study of the fabrication of a micro-actuator.

2. Experimental

2.1. Gel Film Formation

The experiment was carried out using as a precursor a commercially available solution containing 0.095 g/ml oxide of the composition $Pb(Zr_{0.53}, Ti_{0.47})O_3$ prepared by Kojundo Chemical for dip- or spin-coating. The modifications made in the experimental conditions used for silica gel film were: (1) the amount of the organic phase was kept at 3 ml so that all the ingredients could change into a gel film and the evaporation of the solvent (hexane) was completed while the gel film was floating on water; (2) no particular catalyst

for the hydrolysis or condensation was added in the inorganic phase because the reactivity of the precursor was sufficiently high; (3) acetylacetone was added as a chelating agent in the organic phase to control the rate of hydrolysis of the precursor.

First, a 100 μl of acetylacetone (AcAc) was mixed with 2 ml of hexane by stirring with a magnetic stirrer for 15 min. Then 1 ml of the coating solution was added and mixed for another 15 min. The hydrolysis and the interfacial polymerization of the precursor was facilitated by pouring the whole solution on the liquid inorganic phase contained in a teflon container of 88 mm inside diameter. The gel formation was tested for two kinds of inorganic phase, distilled water and a mixture of water and *N,N*-dimethylformamide (DMF) at approximately 2 to 1 in volume, in order to see the influence of the properties of the inorganic phase.

The changes in the appearance of the gel film formed by the hydrolysis and condensation of the precursor, onset of fracture, self shrinkage due to capillary forces induced by the evaporation of the volatile solvent, etc., were observed through a window located on the cover of the container.

2.2. *Ageing and Drying*

A gel film, separated from the container wall, was allowed to shrink while floating on water by facilitating the evaporation of the solvent through a small gap between the container and its cover until the change in size became minimal, followed by exposure to ambient atmosphere. The gel film was then placed gently on a glass or silicon substrate placed in advance near the bottom of the container by draining the water. The wet gel film was kept at room temperature for at least 2 days in a tight plastic container of about 80 mm diameter and 2 mm high, in order to avoid the onset of fracture caused by the high shrinking rate due to capillary forces induced by the evaporation of liquid filling micropores of the gel film. Then, the drying was facilitated by opening the cover very slightly until the gel film appearance changed from semi-transparent to translucent with a yellow color.

3. Results

3.1. *Changes in Size and Appearance While Floating*

The hydrolysis and condensation reaction of the PZT precursor took place immediately after pouring the solution on water. The transparent solution spread over the water turned translucent in a few minutes as the result of the gel film formation. The gel film which had been covered with the solvent became exposed to the atmosphere in the container as the evaporation of the solvent advanced, and its diameter began to decrease within about 1 h. The shrinkage continued while the film was floating on water until it became minimal. At this stage, the diameter of the gel film formed by the reaction with distilled water was about 45% of its initial value, while it was about 55% for the reaction with the mixture of water and DMF. The rate of shrinkage was very large until the diameter had decreased to about 1.2 times of the final value in 15–20 h. The changes in size and appearance of the gel film are shown in Fig. 1.

The gel film was very sensitive to the rate of evaporation of the solvent. If it was exposed to ambient atmosphere before the shrinkage became minimal, the onset of cracks was inevitable. Therefore, the pictures in Fig. 1 were taken through the window of the cover of the container.

3.2. *Changes During Drying and Yield*

The gel film remained unfractured while floating, but when placed on the substrate it fractured into several pieces if left in ambient atmosphere without being covered. In order to avoid the fracture at this stage, it was necessary to evaporate the water very slowly.

The appearance of the gel film after drying is shown in Fig. 2. The surface of the dried film was glossy and no porous structure was observed with an optical microscope, suggesting that the gel film is already dense when dried.

The weight of the dried film was about 0.06 g for all the samples. This value is about 60% of the amount expected from the 1 ml precursor solution. Although the detailed analysis of the composition has not yet been made, PZT was the only crystal phase detected by powder X-ray diffraction on a fractured sample heat treated at 1000°C for 2 h.

The diameter after drying of the gel film obtained by the reaction with distilled water was 38 mm, and 46 mm for the one prepared with the mixture of water and DMF. Assuming that the diameter is not changed by the heat treatment, the thickness of the film is estimated to be 5–7 μm from its weight and the density of PZT (8 g/cm^3). This indicates that the desirable thickness for the development of a micro-actuator, about 20 μm, can be obtained from the organic phase of the same composition having a volume three times larger.

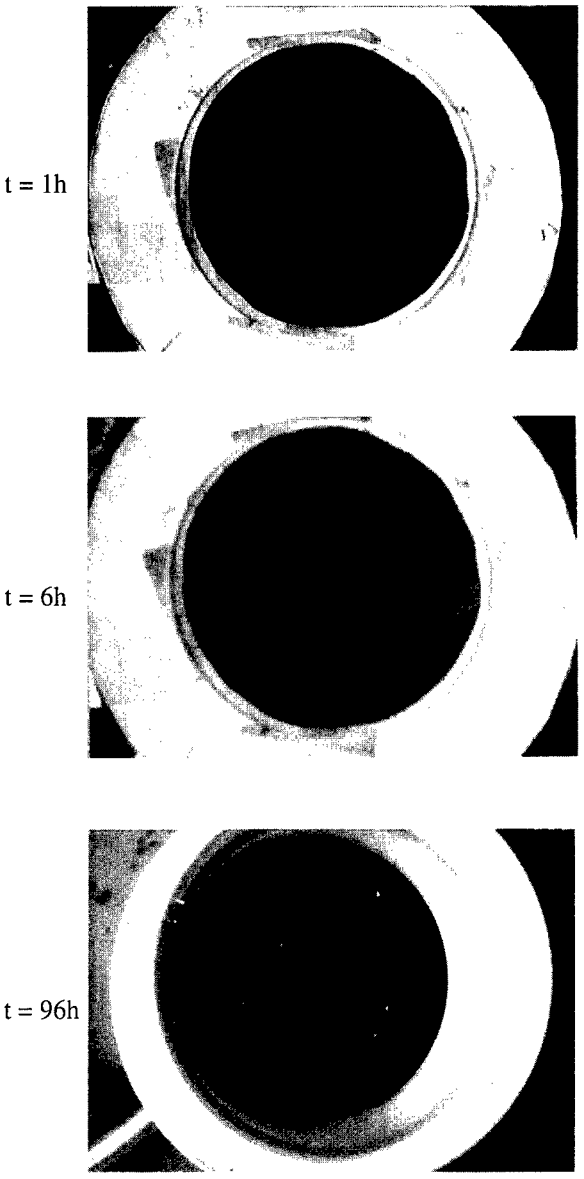

Figure 1. Change in size and appearance of PZT gel film while floating on water.

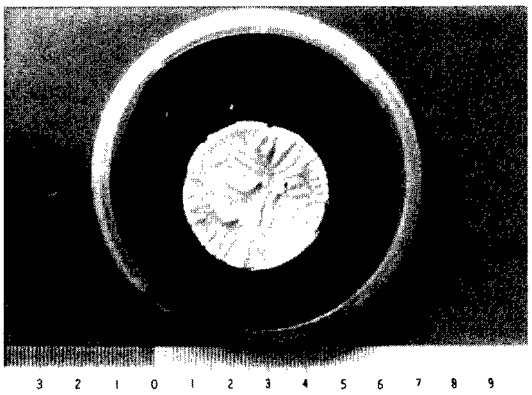

Figure 2. Appearance of dried PZT gel film prepared by the reaction with distilled water.

4. Discussion

4.1. *Influence of the Composition of Organic and Inorganic Phases*

The reaction rate of the hydrolysis of the precursor was greatly influenced by the amount of acetylacetone. In this study, about 2 mol of acetylacetone was used per mol of PZT. If the amount was smaller, the color of the wet gel film, which reflects its thickness, was not uniform. On the contrary, if the amount of acetylacetone was doubled, only a trace of film was observed. The low reaction yield, only about 60%, may be partly attributed to the influence of the chelating agent. In other words, a part of the precursor alkoxide has been completely capped by the acetylacetone and moved across the interface to the lower inorganic phase without being hydrolyzed.

The rate of shrinkage and the time until the shrinkage began was dependent on the amount of hexane. As described above, the shrinkage began after the surface of the gel film had been exposed to the atmosphere of the container. The initial thickness of the organic phase spread over water is about 0.5 mm as estimated from the volume of the solution and the diameter of the container. Therefore, if the whole organic phase was transformed into a gel and the diameter to thickness ratio was kept constant during the shrinkage, the thickness of the 38 mm diameter dried gel film should be about 200 μm. But the estimated thickness of the dried film (5–7 μm) was smaller by more than one order of magnitude. This suggests that the chemical bonds between PZT particles constituting the gel film is very weak. In contrast to a silica gel film formed from partially hydrolyzed silicon ethoxide which extends three dimensionally throughout the organic phase and does not show an appreciable shrinkage during the evaporation of hexane [6], such PZT particles are gradually accumulated near the interface of the two immiscible liquids due to their high density and form a gel film through weak Van der Waals forces rather than develop a three dimensional network through strong chemical

bonds. The drying of such a gel film results in the formation of a densely packed film with much lower thickness to diameter ratio than that of the initial organic phase.

Another fact to be noted is that the diameter of the gel film, when the shrinkage became minimal, was dependent on the composition of the inorganic phase. The shrinkage was larger for the gel formed by the reaction with distilled water than that obtained by the reaction with the mixture of water and DMF. This difference is attributed to the lower vapor pressure and the lower surface tension of DMF than those of water, suggesting that the liquid in the micropores of the wet gel is replaced by the inorganic phase as the evaporation of the solvent proceeds.

Based on this discussion, the process of the gel film formation and its shrinkage while floating is schematically illustrated in Fig. 3.

4.2. *Issues to Overcome*

The main problem obtained during the present study is the development of creases while the gel film shrinks on water due to a nonuniform rate of shrinkage. One of the reasons for a nonuniform shrinkage is the inhomogeneity of the film thickness. Another is the presence of tiny dust particles which hindered the smooth movement of materials. The improvement of the homogeneity of the film thickness may be possible by increasing the amount of hexane. In such a way the reaction rate

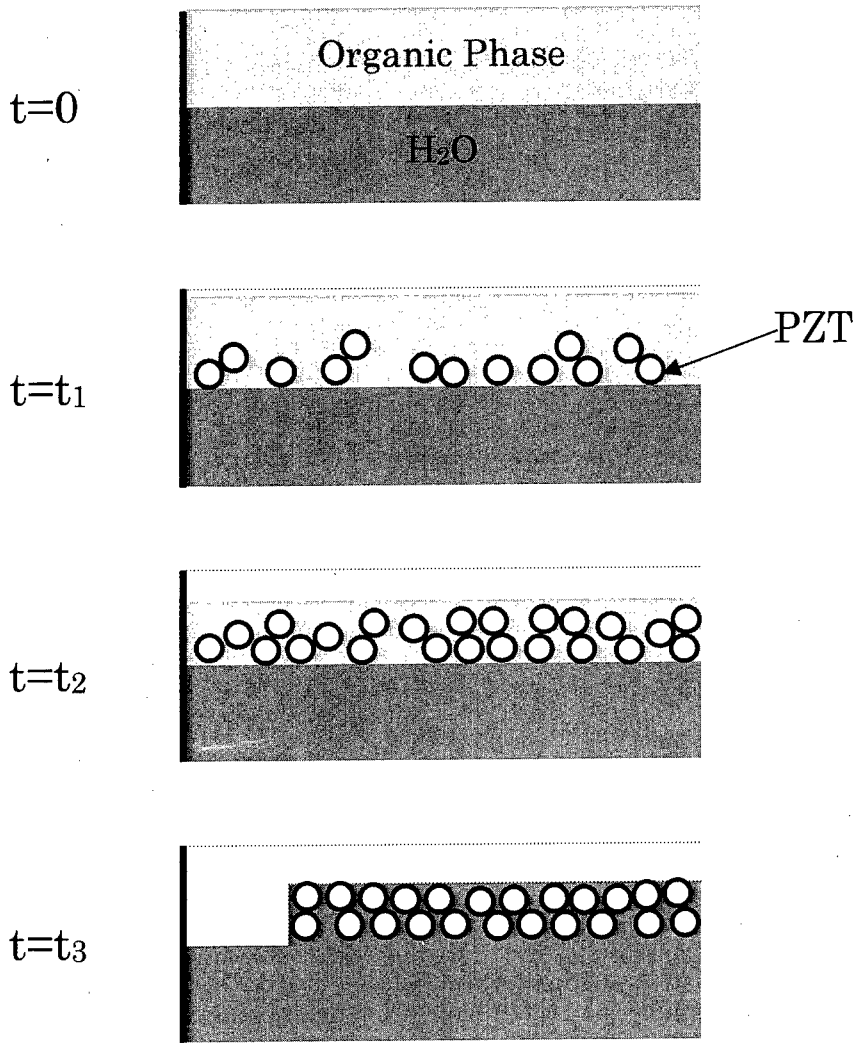

Figure 3. Schematic illustration of the process of PZT gel film formation.

will be slightly reduced and a uniform spread of the organic phase will occur before the reaction takes place. In order to avoid the occurrence of creases attributed to the dust, the film formation should occur in a clean room. In order to offset the influence of dust, it may be also advantageous to introduce a large amount of very fine PZT powder in the organic phase. This powder will act as heterogeneous nucleation sites during the heat treatment to convert the gel into PZT ceramics.

5. Summary

Formation of a PZT ceramic film of 10–20 μm thick via an interfacial polymerization of metal-organic precursors has been investigated. The PZT gel film prepared from a commercially available solution developed for dip- or spin-coating shrank to less than half of its initial diameter while floating on water. The hindrance of development of creases during the shrinkage of the wet gel is essential to obtain a thick flat film. One of the suggested ways to overcome the issue is the addition of fine PZT powder in the organic phase.

Acknowledgment

This work was supported by a Grant-in Aid for Scientific Research from the Ministry of Education, Science and Culture, Japan. The author is also grateful to Prof. T. Tsurumi for invaluable discussion and to Mr. H. Yoshikawa for X-ray diffraction measurement.

References

1. H. Moilanen, J. Lappalainen, and S. Leppavuori, Sensors and Actuators A **43**, 357–365 (1994).
2. G. Teowee, J.M. Boulton, S. Motakef, D.R. Uhlmann, and B.J.J. Zelenski, SPIE **1758**, 236–248 (1992).
3. M. Yamane, S. Shibata, A. Yasumori, T. Yano, and S.Uchihiro, J. Sol-Gel Science and Technology **2**, 457–460 (1994).
4. H. Schulze-Bergkamen, S. Uchihiro, and M. Yamane, in *Advanced Materials in Optics Electro-optics and Communication Technologies*, edited by P. Vincenzini and G.C. Righini (Techna Srl., 1995), pp. 63–71.
5. H. Schulze-Bergkamen and M. Yamane, J. Sol-Gel Science and Technology **5**, 185–191 (1995).
6. M. Yamane, J. Sol-Gel Science and Technology **8**, 483–487 (1997).

Journal of Sol-Gel Science and Technology 13, 827–831 (1998)
© 1998 Kluwer Academic Publishers. Manufactured in The Netherlands.

Lead Zirconate-Titanate Films Prepared from Soluble Powders

PEER LÖBMANN, SUSANNE SEIFERT, STEFAN MERKLEIN AND DIETER SPORN
Fraunhofer-Institut für Silicatforschung, Neunerplatz 2, D-97082 Würzburg, Germany

Abstract. Precursor powders for $Pb(Zr_{1-x}Ti_x)O_3$ (PZT) thin films were produced by the reaction of zirconium- and titanium-*n*-propoxides with acetylacetone and lead acetate trihydrate. The subsequent complete removal of volatile components yielded powders that can be handled in air. The powders are indefinitely stable under ambient conditions.

High molarity (>2m) coating sols were prepared by dissolution of the precursor powders in mixtures of 1,3-propanediol, triethanolamine (TEA) and water. Excess amounts of lead to compensate lead loss during firing were easily introduced into these solutions.

The deposition of these sols on steel substrates and firing at 600°C yielded PZT films. Many physical parameters like film thickness, morphology and electrical performance could be influenced by choice of the solvent mixture composition and oxide content of the sols. Depending on the preparation dielectric permittivities, ε_r of up to 840 were measured at 1 kHz. By hysteresis measurements at 50 Hz and a field amplitude of 50 V/μm a remanent polarization of about 40 $\mu C/cm^2$ and coercivity of about 8 V/μm was obtained. The films were stable against dielectric breakdown up to 70 V/μm.

Keywords: sol-gel, thin films, ferroelectricity, lead zirconate titanate (PZT)

1. Introduction

Perovskite-type ceramics such as lead titanate ($PbTiO_3$, PT) and lead zirconate-titanate ($PbZr_{1-x}Ti_xO_3$, PZT) are widely used due to their ferroelectric and piezoelectric properties. Their reaction upon exposure to an electric field provides numerous applications such as actuators [1] or non-volatile memory devices [2]. Sol-gel processing of these materials enables the fabrication of thin films [3], fibers [4] and aerogels [5] which are not accessible by conventional mixed-oxide routes.

The preparation of PZT films by sol-gel techniques is cheaper, more flexible and less time consuming in comparison to physical deposition methods. High purities and easy doping are further advantages. In contrast to conventional mixed-oxide methods, processing temperatures below 700°C allow the use of metallic substrates such as steel. It is often stated as a drawback though that films exceeding 150 nm thickness are difficult to prepare within one coating step.

In this paper we describe the application of precursor powders of PZT stoichiometry, which readily dissolve in a variety of solvent mixtures to form highly concentrated coating sols. Processing of these solutions yields ceramic films exceeding 5 μm thickness.

2. Experimental Procedure

Soluble powders with a metal content with a stoichiometry $Pb_{1.05}Zr_{0.53}Ti_{0.47}$ were prepared by a method reported previously [6]. The resulting yellow powder has a solid content of 67 mass% with respect to the final ceramic product.

Coating sols were prepared by dissolving the powder in mixtures of 1,3-propanediol, triethanolamine (TEA) and water at 90°C. Excess lead acetate trihydrate was dissolved in the sols; the final composition of the solutions was $Pb_{1.25}Zr_{0.53}Ti_{0.47}$. A solvent mixture denoted 6-1-3 contained 60 mass% propanediol, 10 mass% TEA and 30 mass% water, whereas solvent 0-5-5 contained no propanediol (0%) but equal weight fractions of TEA (50%) and water (50%). In general, solutions were prepared by dissolving 1 g powder in

0.9 g solvent mixture corresponding to a 35% oxide content of the solution. Sols of higher oxide content were prepared with mixture 6-1-3. All sols were passed through an 0.2 μm in-line syringe filter directly before film preparation.

Steel substrates were cleaned with acetone and annealed at 600°C prior to the application of the wet films. The coating solution was applied to the substrate and spun off at 3000 rpm for 30 s. The samples were immediately placed in a preheated furnace at 600°C for 5 min.

In parallel, wet films were made by a doctor-blading technique and annealed under the same conditions. Up to four subsequent coating/firing cycles were performed. Detailed procedures for the characterization of the samples are described elsewhere [6].

3. Results and Discussion

3.1. Film Deposition Technique

PZT films were prepared from sols containing equal weight fractions of TEA and water (0-5-5) by spin coating and doctor blading. A single spin-coating process and subsequent firing yielded ceramic films up to

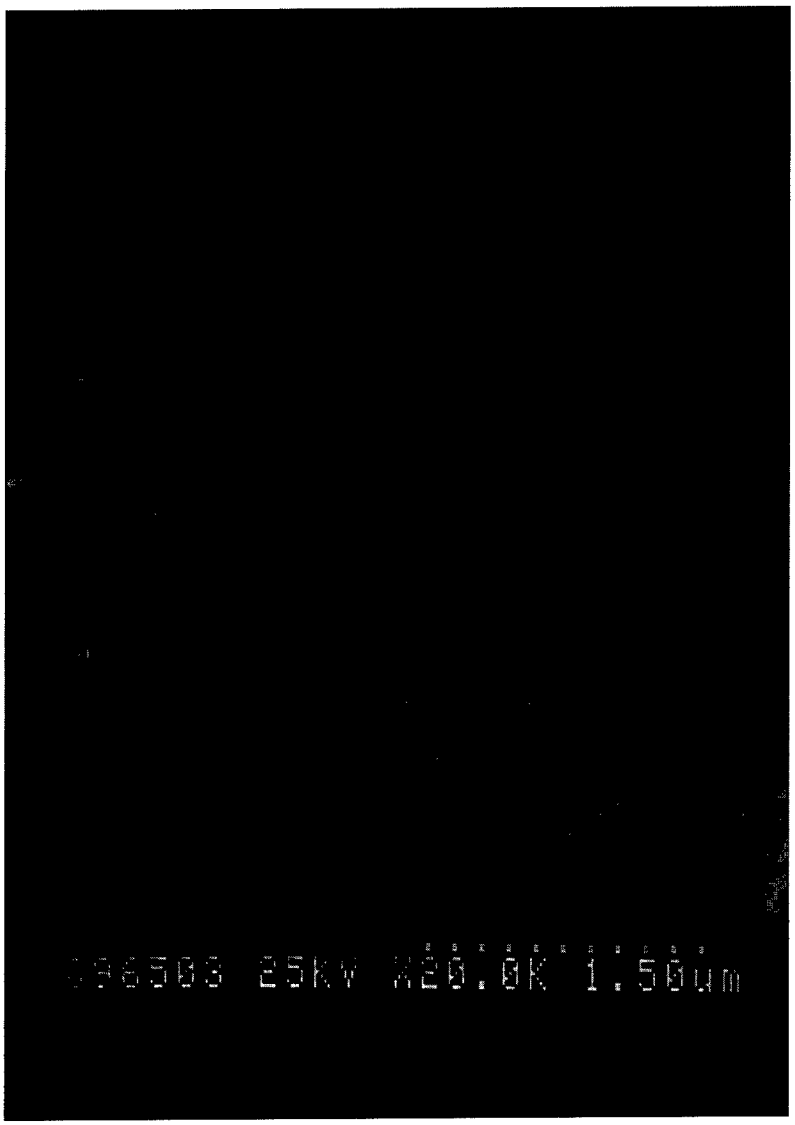

Figure 1. SEM micrograph of a PZT layer derived from a sol with a solvent composition of 0-5-5 prepared by double doctor blading.

1.6 μm thickness, but there were strong local variations in thickness and optical quality. Both thickness and crack density increased towards the edges of the 2 cm × 2 cm steel platelets.

In contrast, the doctor-bladed samples were more homogeneous and by multiple coating/firing cycles high overall film thickness could be achieved more easily. PZT films were doctor bladed on 7 cm × 14 cm steel sheets using the same sol composition as for the spin-coating experiments. During placement of the samples into the furnace ignition of the solvent vapors was often observed. The final stoichiometry of the material after heat treatment, determined by chemical analysis, was $Pb_{1.04}Zr_{0.53}Ti_{0.47}$. Obviously a Pb loss has taken place, even though at the processing temperature of 600°C PbO is not expected to be volatile. But the oxidative decomposition of TEA and residual organics may increase the temperature for a short period of time above 600°C. Details of the lead loss and its impact on the electric performance of the PZT layers will be discussed elsewhere [7].

The doctor-bladed samples had a dense and smooth surface with some porosity in the interior as can be seen from the Scanning Electron Microscopy (SEM) image in Fig. 1. Since the surface of the material is first exposed to the heat of the furnace and the flame of the ignited solvent densification seems to be greater at the outside of the film.

Since the overall quality of films prepared by doctor blading is superior to those derived from spin coating and larger, more homogeneous samples can be obtained, all further films discussed in this paper were prepared by doctor blading.

3.2. *Variation of the Solvent Mixture Composition and Quality of PZT Layers*

PZT sols were prepared by dissolving the powder in different solvent mixtures. The results of the doctor blading experiments are listed in Table 1 with the data from dielectric measurements.

PZT films up to a few microns with good dielectric and ferroelectric properties can be obtained from a number of different solvent mixtures. The use of TEA (e.g., 9-1-0) faciliates the addition of excess lead, but the film quality decreases if the TEA content increases (7-3-0). Moreover, the increasing viscosity of the sols makes the processing difficult. If small amounts of water are introduced into the solvent mixture (4-5-1), the viscosity drops and the sols can easily be doctor bladed again. No ceramic films can be obtained after firing, though the ceramic material delaminates from the substrate. Obviously TEA is necessary to prepare high molarity PZT sols in which excess lead acetate trihydrate can be dissolved, but larger amounts of this solvent diminish the film quality.

When the sols only contain 10 to 20 mass% TEA but considerable amounts of water (6-1-3 and 4-2-4), up to 4 single layers each with smooth surface can be prepared by subsequent coating/firing cycles. The optical quality of these films is significantly higher than those prepared from sols that only contain TEA and water (0-5-5 and 0-3-7).

It is possible to optimize the film preparation parameters by carefully selecting the composition of the solvent mixture. Best results are obtained when the TEA content is kept at 10 mass%.

Table 1. Properties of PZT-layers on steel substrates derived from sols with different solvent compositions. All films were prepared by doctor blading. ε_r: permittivity, P_r: remanent polarization, E_c: coercivity.

Solvent mixture	Sol viscosity (Pa s)	Max. number of coatings[a]	Av. thickness of single layer (μm)	Quality[b]	ε_r	El. breakthrough at (V/μm)	P_r (μC/cm^2) at 50 V/μm	E_c (V/μm) at 50 V/μm
9-1-0	0.55	4	0.72	++	840	>70	40	8
7-3-0	0.94	3	0.95	+	670	ca. 40	—	—
4-5-1	0.42	0		−				
6-1-3	0.05	4	0.89	++	230	>70	30	14
4-2-4	0.08	3	0.72	+	—	35	—	—
0-5-5	0.13	2	0.95	0	—	50	45	22
0-3-7	0.04	3	0.64	+	400	>70	40	17

[a]Maximum number of layers of which electric measurements could be performed.

[b]Quality of the layers was derived from the appearance of the films after consequent deposition/firing cycles: (++) 3-4 layers with smooth surfaces and only minor defects at the sample borders, (+) 2-3 layers with minor defects, (0) 1-2 layers with defects, (−) no satisfactory film formation at all.

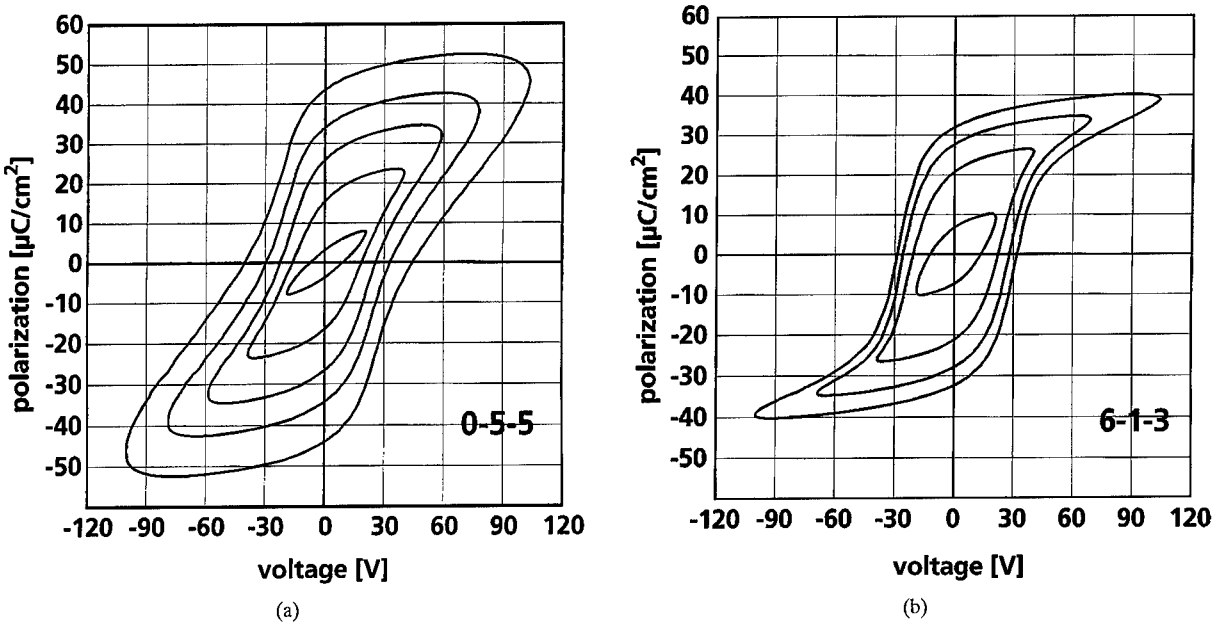

Figure 2. Hysteresis curves for PZT layers derived from sols with a solvent composition of 0-5-5 (a) and 6-1-3 (b) prepared by double doctor blading.

Hysteresis loops obtained on PZT films prepared by double doctor blading and firing of sols with the solvent composition 0-5-5 and 6-1-3 are given in Fig. 2. For both samples a film thickness of about 1.9 μm was measured.

The hysteresis loops of the 0-5-5 sample are broad. With increasing applied field the remanent polarization as well as the coercitivity significantly increased and no saturation of the hysteresis could be found. Even the slope of the hysteresis loop is small. This behavior indicates a large nonswitching element within the sample.

By contrast for the 6-1-3 sample the hysteresis loops show a strong slope of the polarization and smaller coercive field values. Not only the optical film quality but also the electric performance can be influenced by the solvent composition of the sol.

3.3. *Variation of Film Thickness*

Up to four subsequent doctor-blading/firing cycles can be performed using sols with solvent compositions 9-1-0 and 6-1-3, both yielding ceramic films with good electric properties (Table 1). While both sols have the same oxide content (35 mass%), the viscosity of sol 6-1-3 is significantly lower. Therefore, coating solutions with a higher oxide content (45 mass%) could be prepared with this solvent composition. In Fig. 3 the overall film thickness of samples doctor bladed from sols of different solvent content are given as a function of the number of coatings.

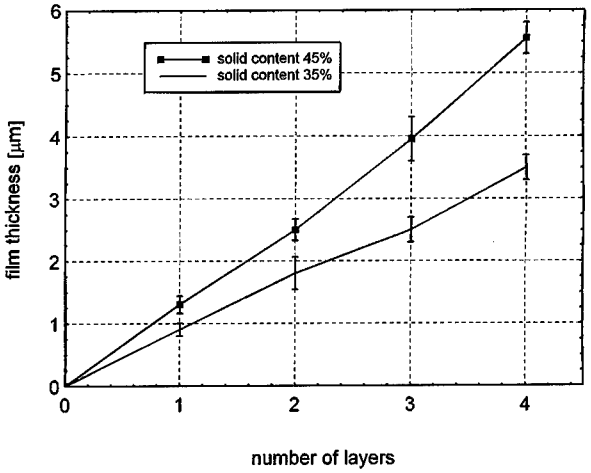

Figure 3. Thickness of PZT ceramic films prepared from sols with a solvent composition of 6-1-3 as a function of the number of layers. The films were doctor bladed using coating sols with solid contents of 35 and 45 mass%, respectively. Lines are drawn as guides for the eye.

As one would expect the film thickness rises with the number of applied layers. Thicker films can be prepared, using sols with a higher solid content, without any decrease in film quality. For an oxide content of 45 mass% after four film preparation processes an overall thickness of 5.5 μm is measured.

4. Conclusions

The use of soluble precursor powders offers a wide range of possibilities to influence the quality, thickness and electrical performance of PZT films by choice of film application technique, solvent composition and solid content.

References

1. U. Dibbern, in *Actuator 94 4th International Conference on New Actuators* (ASCO-Druck, Bremen, 1994), p. 114.
2. R. Jones and S. Desu, MRS Bulletin **21**(6) 55 (1996).
3. Y. Tu and S. Milne, J. Mat. Sci. **30**, 2507 (1995).
4. W. Watzka, H. Scholz, D. Sporn, and K. Franke, in *Fourth Euro-Ceramics*, edited by G. Gusmano and E. Traversa (Gruppo Editiorale Faenza, Editrice, Faenza/Italy, 1995), Vol. 5, p. 189.
5. P. Löbmann, J. Groß, W. Glaubitt, and J. Fricke, J. Non-Cryst. Solids **201**, 66 (1996).
6. D. Sporn, S. Merklein, W. Grond, S. Seifert, S. Wahl, and A. Berger, Microel. Engin. **29**, 161 (1995).
7. S. Seifert, P. Löbmann, and D. Sporn, *2nd European Meeting on Integrated Ferroelectrics* (Jouy-en-Josas, France, 1997), O.I.E.

Journal of Sol-Gel Science and Technology 13, 833–836 (1998)
© 1998 Kluwer Academic Publishers. Manufactured in The Netherlands.

Acetic Acid Based Sol-Gel PLZT Thin Films: Processing and Characterization

BARBARA MALIČ*, NAVA SETTER AND KEITH BROOKS
Laboratoire de céramique, Ecole Polytechnique Fédérale de Lausanne, Ecublens, CH-1015 Lausanne, Switzerland

MARIJA KOSEC AND GORAN DRAŽIČ
Jožef Stefan Institute, 1001 Ljubljana, Jamova 39, Slovenia

Abstract. PLZT 4/65/35 thin films were prepared by the acetic acid based sol-gel route. The choice of lanthanum precursor, i.e., acetate or nitrate, influences the functional group content of formamide modified sols and the microstructure of the thin films. The lanthanum nitrate based PLZT thin film deposited on $Si/SiO_2/TiO_2/Pt/TiO_2$ substrate has a columnar perovskite grain structure, while the lanthanum acetate based one is characterized by a lead-silicon containing reaction layer beneath the platinum electrode. Although lead is depleted from the PLZT thin film the perovskite structure is retained by the use of the top layer with a large excess of PbO.

Keywords: PLZT thin films, processing, acetic acid modified sol-gel

Introduction

Materials based on PLZT ((Pb, La)(Zr, Ti)O_3 solid solution) are promising candidates for a variety of microelectronic and electro-optic applications in thin film form with functional property modifications easily achieved by stoichiometric variations [1].

Acetic acid based sol-gel processing of PZT (Pb(Zr, Ti)O_3), introduced by Yi et al. [2], and later developed by Assink and Schwartz [3] offers a simpler preparation route in comparison to 2-methoxyethanol based sol-gel. The method is based on a reduction of the reactivity of transition metal alkoxides by acetic-acid modification. Essentially, the sol is formed by dissolving lead acetate in the solution of metal alkoxides in acetic acid without a distillation step. For the PLZT sol-gel route lanthanum is usually introduced as lanthanum acetate hydrate [4], however, when a high lanthanum content is needed, lanthanum acetate hydrate may be difficult to dissolve. Therefore, lanthanum nitrate hydrate may also be used; it easily dissolves in simple alcohols.

The paper focuses on the effect of various lanthanum sources (acetate and nitrate) on PLZT 4/65/35 sol thermal decomposition, thin film crystallization and microstructure. It has been shown previously that lanthanum content, i.e., 4, 8 or 10 mol%, has only a minor effect on microstructural features and crystallization in comparison to the influence of lanthanum source [5], therefore only one composition was studied in this work.

Experimental

The formula for PLZT 4/65/35 is calculated by assuming compensation of the charges on B-sites, i.e., $Pb_{1-x}La_x(Zr_{1-y}Ti_y)_{1-x/4}O_3$ with 5 mol% excess PbO. The sols are synthesized by reacting zirconium *n*-propoxide *n*-propanol complex ($Zr(OnPr)_4nPrOH$), titanium *i*-propoxide ($Ti(OiPr)_4$), lead tetraacetate ($Pb(OAc)_4$) in acetic acid (HOAc) and methanol (MeOH) following the procedure of Assink and Schwartz [3]. Dehydrated lanthanum acetate

*On leave from Jožef Stefan Institute, Jamova 39, 1001 Ljubljana, Slovenia.

$(La(OAc)_3)$ or lanthanum nitrate hexahydrate $(La(NO_3)_3 \cdot 6H_2O)$ are used as lanthanum sources. Hereafter, sols and thin films prepared from lanthanum acetate are denominated as LA and those prepared from lanthanum nitrate as LN.

Briefly, the synthesis of LA sols proceeds by adding lanthanum acetate and lead tetraacetate to the solution of zirconium and titanium alkoxides in acetic acid and methanol. Dissolution of both acetates occurs in about 60 min at 90°C. The solution is cooled to room temperature.

LN sols are prepared by first dissolving lead tetraacetate in the acetic acid/methanol solution of zirconium and titanium alkoxides for about 15 min at 90°C. The clear solution is cooled to 50°C and lanthanum nitrate, separately dissolved in methanol, is added. The mixture is heated to 70°C for 15 min and then cooled to room temperature. Experimental details are reported in [5].

4 vol% of formamide ($CHONH_2$) is added to freshly prepared sols at room temperature as a drying control additive [6].

Thin films are prepared by spin-coating the sols on to platinized silicon substrates (Si/SiO_2/10 nmTi/80 nmPt or Si/SiO_2/10 nmTiO_2/80 nmPt/2 nmTiO_2) followed by pyrolysis at 400°C and rapid thermal annealing (RTA) at 650°C, 5 min with a heating rate of 3600°C/min. The films contain three layers of PLZT-5% PbO and a top layer with 30% PbO excess to compensate PbO loss due to evaporation upon thermal processing.

The dried sols are characterized by thermogravimetry, and the films by X-ray diffraction and transmission electron microscopy. Polarization-electric field hysteresis loops are determined with platinum electrodes applied to the top of the films.

Results

Thermal decompositions of LA- and LN-based PLZT sols with 4% formamide, dried at 60°C, are compared in Fig. 1. The LN-PLZT sample gradually loses about 40% weight while LA-PLZT exhibits much greater weight loss of 54% up to 550°C. Up to about 300°C thermal decompositions of both samples proceed similarly, losing about 35% weight. In the range 320 to 420°C, however, LN samples lose only 3% while LA loses almost 20%. Upon heating to 550°C both samples lose a further 3%. Surprisingly, both unmodified sols exhibit weight losses of about 40% up to about 400°C (curves not shown here, but similar to that of LN-PLZT).

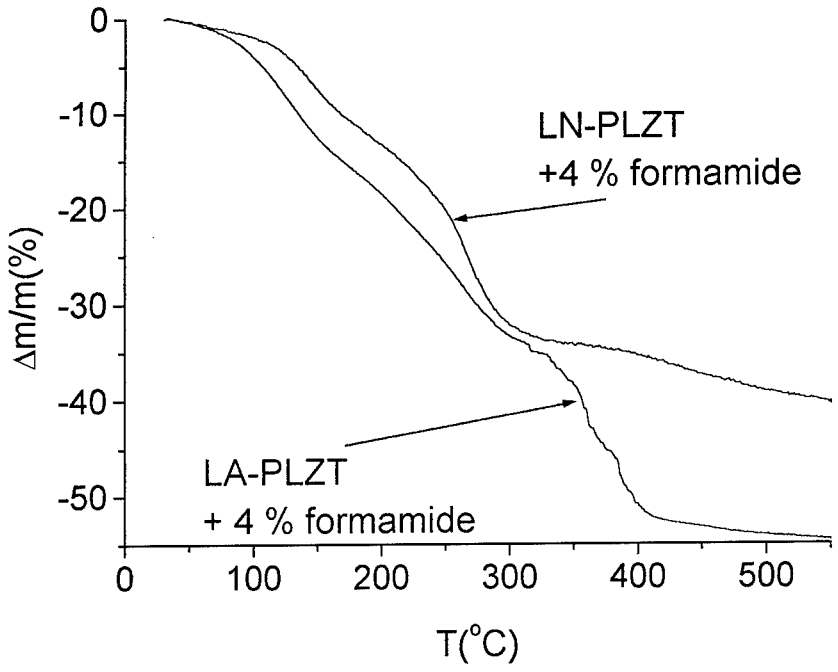

Figure 1. Thermal decompositions of PLZT-5% excess PbO sols, dried at 60°C.

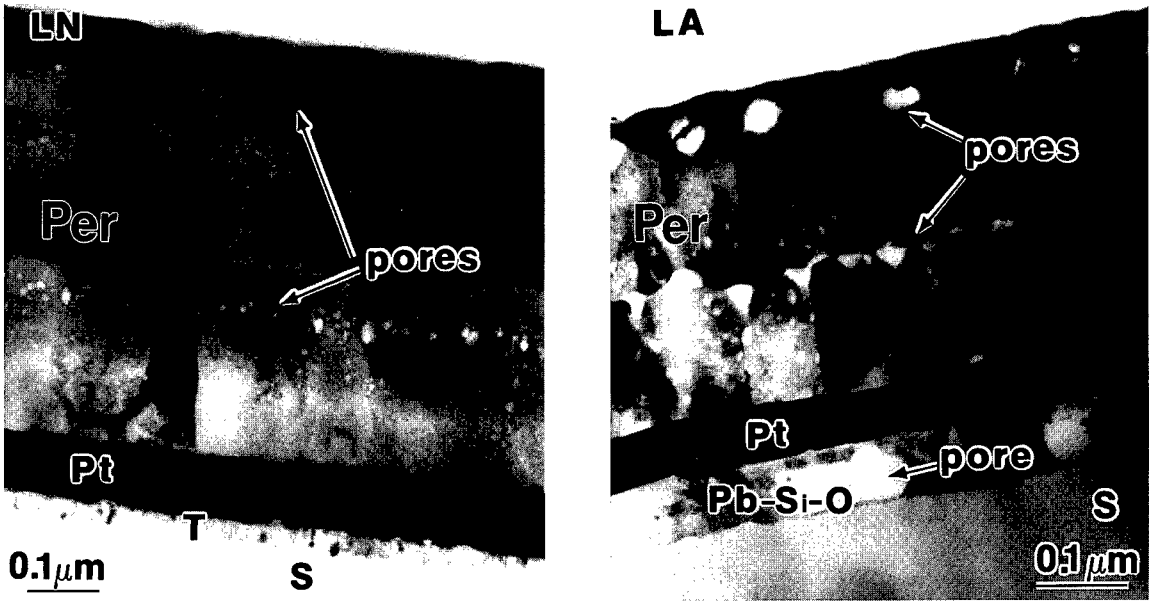

Figure 2. TEM cross-section micrographs of LN-PLZT (left) and LA-PLZT 4/65/35 thin films (right) on $TiO_2/Pt/TiO_2/SiO_2/Si$ substrates after rapid thermal annealing at 650°C, 5 min. Both films were prepared by depositing three layers of PLZT-5% excess PbO sols and the top layer of PLZT-30% excess PbO. Per: perovskite, T: TiO_2, S: SiO_2 (substrate).

The temperature range 320–400°C is typical for acetate group decomposition, as observed in a TGA/EGA study of alkoxide derived lead zirconate [7]. It is tentatively proposed that formamide addition effectively promotes cross-linking of LA-PLZT sol and therefore increases acetate group content.

The LA-PLZT thin film, deposited on a Ti/Pt coated substrate, consists of amorphous phase and of PbPt alloy after pyrolysis on hot plate at 400°C. After RTA at 650°C only a randomly oriented perovskite phase is present. The LN-PLZT thin film on a Ti/Pt substrate is amorphous after pyrolysis and preferentially (111) oriented after annealing at 650°C.

As the presence of the lead-platinum phase in the as-pyrolyzed LA-PLZT thin film indicates a partial reduction of lead, thought to occur during the intensive acetate group decomposition, and therefore dehomogenization, the sols were also deposited on a $TiO_2/Pt/TiO_2$ coated substrate. A slower pyrolysis step, with 10 min to 400°C was also introduced.

Both the LA and LN thin films are amorphous after pyrolysis at 400°C and preferentially (100) and (111) oriented after RTA at 650°C. The films are ferroelectric; LN-PLZT having a wider hytsteresis loop (Pr 10 $\mu C/cm^2$, Ec 60 kV/cm) than LA-PLZT (Pr 8 $\mu C/cm^2$, Ec 40 kV/cm). However, marked differences between the two films were found by cross-sectional TEM analysis (Fig. 2).

A TEM micrograph of the LN-PLZT thin film reveals the columnar structure of perovskite grains on the $Pt/TiO_2/SiO_2$ substrate. The 2 nm thin TiO_2 layer on top of the platinum cannot be discerned. No pyrochlore phase or excess lead oxide was found in the film, so it is thought that at the given conditions of RTA the excess lead oxide in the top layer of the film compensated lead oxide loss due to evaporation. Two fronts of nanometer-sized pores parallel to the substrate plane can be seen in the micrograph. EDS analysis of the perovskite phase and of the pore-containing regions revealed no compositional differences. The origin of the pores is still not clear.

A cross-sectional micrograph of LA-PLZT thin film reveals the perovskite phase on top of platinum electrode. The perovskite grains are smaller than those in LN-PLZT. The columnar structure is interrupted at about half of the film height by a front of 10 nm large pores. About 30 nm beneath the top of the film another front of 10–20 nm sized pores is present. EDS analysis of the bottom and the medium parts of the film revealed only minor compositional fluctuations. The top of the film is slightly titanium rich compared to the rest of the film. No marked lead deficiency or

pyrochlore phase was found. Beneath the platinum electrode the approximately 100 nm thick amorphous layer containing a few 100 nm large pores is identified as lead silicate. Only rare TiO_2 particles are found in place of originally 10 nm thick layer. Note that this film was deposited on a part of the same $TiO_2/Pt/TiO_2$ coated substrate as the LN-PLZT film.

The presence of lead silicate layer below the platinum electrode confirms a massive reaction between lead and silicon oxides. A plausible explanation for the glassy layer is the presence of defects (holes) in the platinum, enabling the reaction upon thermal treatment [8]. However, the reaction layer was not found in LN-PLZT thin films, deposited on the same substrate, therefore a large population of defects in the platinum is not probable. Further, TEM analysis is in progress in order to verify the assumption that LA-PLZT thermal decomposition influences the formation of the reaction layer.

Although some of the lead was depleted from the PLZT phase due to the reaction with the substrate, no lead-deficient pyrochlore phase was observed by TEM. The use of the top layer with high PbO excess, a modification of the procedure introduced by Tani and Payne [9], is evidently sufficient to accommodate even the lead loss caused by reaction with the substrate.

Conclusion

PLZT 4/65/35 thin films were prepared by acetic acid based sol-gel route with lanthanum acetate or nitrate hydrate. The films consisted of three layers of PLZT + 5% excess PbO and a top layer of PLZT with 30% excess PbO.

Various lanthanum salts influence sol thermal decomposition and thin film crystallization on platinized silicon substrates (Ti/Pt or $TiO_2/Pt/TiO_2$).

TEM analysis of lanthanum nitrate based PLZT reveals a columnar structure of perovskite grains and a uniform composition as determined by EDS. Lanthanum acetate based films also consist of perovskite grains, but there are fluctuations in the Zr/Ti ratio.

Acknowledgment

Support by the Ministry of Science and Technology of the Republic of Slovenia within the National Research Program is acknowledged. The work was performed in the frame of COST 514 EU Action on Ferroelectric Thin Films, partially supported by the Ministry of Science and Technology of the Republic of Slovenia.

B. Malič acknowledges the support of the Slovene Science Foundation for the postdoctoral scholarship at the Ecole Polytechnique Fédérale de Lausanne (Switzerland).

References

1. G. Teowee, E.L. Quackenbush, C.D. Baertlein, J.M. Boulton, E.A. Kneer, and D.R. Uhlmann, in *Mat. Res. Soc. Symp. Proc. 361*, edited by B.A. Tuttle, S.B. Desu, R. Ramesh, and T. Shiosaki (MRS, Pittsburgh, 1995), p. 433.
2. G. Yi, Z. Wu, and M. Sayer, J. Appl. Phys. **64**, 2717 (1988).
3. R.A. Assink and R.W. Schwartz, Chem. Mater. **5**, 511 (1993).
4. T. Beltram, M. Kosec, and S. Stavber, Mat. Res. Bull. **28**, 313 (1993).
5. B. Malič, N. Setter, M. Kosec, and K. Brooks, in *Proc. MIEL-SD '96*, edited by I. Šorli, S. Amon, and M. Kosec (MIDEM, Ljubljana, 1996), p. 385.
6. D. Chang, Y. Choh, W. Hsieh, P. Lin, and T. Tseng, J. Mater. Sci. **28**, 6691 (1993).
7. B. Malič, M. Kosec, and B. Orel, Silicates Industriels **60**, 163 (1995).
8. G. Dražič, T. Beltram, and M. Kosec, Ferroelectrics **152**, 49 (1994).
9. T. Tani and D.A. Payne, J. Am. Ceram. Soc. **77**, 1242 (1994).

Journal of Sol-Gel Science and Technology 13, 837–841 (1998)
© 1998 Kluwer Academic Publishers. Manufactured in The Netherlands.

Chemistry-Crystallization-Microstructure Relations of Sol-Gel Derived Lanthanum Modified Lead Titanate Thin Films

M.L. CALZADA, M. ALGUERÓ AND L. PARDO
Inst. Ciencia de Materiales de Madrid (CSIC), Cantoblanco, 28049 Madrid, Spain

Abstract. Lanthanum modified lead titanate thin films have been obtained by the deposition of sol-gel solutions onto platinized (100) silicon substrates. Crystallization of perovskite films was achieved by thermal treatments at 650°C with slow or rapid heatings. Lead oxide excesses were used in the precursor solutions to counterbalance the lead losses produced during the thermal treatment. Rapid heatings and large excesses of lead produce a preferred orientation of the films. These films have more homogeneous and denser microstructures than slow heated films without lead excess.

Keywords: thin films, perovskite, ferroelectric

Introduction

$Pb_{1-3x/2}La_xTiO_3$ thin films on silicon substrates have been prepared by means of rf-magnetron sputtering [1] and spin-on sol-gel processing [2]. Potential applications of these films are mainly related to their use as pyroelectric infrared sensors [2], although their ferroelectric and piezoelectric properties can be also exploited in memory and microactuator devices.

The sol-gel deposition technique has advantages for the fabrication of these films such as compositional homogeneity of the final ceramic layer and low cost. However, lanthanum compounds have low solubility in the organic solvents generally used in the sol-gel method. Therefore, alternative processes that enhance the stability of the sol-gel synthesized solutions containing lanthanum and that preserve homogeneity at molecular level, are technologically important for the preparation of lanthanum lead titanate perovskite films.

In this work, preliminary results are reported on the preparation of (Pb, La)TiO_3 thin films by a sol-gel process, which was previously tested with other modified lead titanate perovskites [3]. Here, the substitution of lead by a small percentage of lanthanum is studied ($Pb_{0.88}La_{0.08}TiO_3$) although perovskite films containing up to a 20 mol% of lanthanum have been already prepared in our laboratory and their properties are now under investigation. Emphasis is given to obtaining single-perovskite films with the appropriate composition and a homogeneous microstructure.

Experimental

$Pb_{0.88}La_{0.08}TiO_3$ precursor solutions containing different excesses of PbO (0, 10 and 20 mol%) were prepared by the sol-gel process of Fig. 1. A lead and titanium sol was first prepared by reacting lead(II) acetate trihydrate, $Pb(OOCCH_3)_2 \cdot 3H_2O$, with titanium diisopropoxide bisacetylacetonate, $Ti(OC_3H_7)_2(CH_3COCHCOCH_3)_2$, in 1,3-propanediol, $HO(CH_2)_3OH$. Then, a water solution of lanthanum(III) acetate hydrate, $La(OOCCH_3)_3 \cdot xH_2O$, with a concentration of ~0.06 M was added to the former sol. Stirring of this mixture for 12 hours yielded a stock solution with a concentration of ~0.50 M and a density of ~1.25 g/cm^3.

Thin films were fabricated by spin-coating the solutions at 2000 rpm for 45 s onto platinized 100-oriented silicon substrates. The wet films were partially pyrolyzed on a hot plate at 350°C for 60 s. The coating and prefiring operations were repeated three times to build up thicker films. Crystallization of the films was achieved at 650°C/12 min, with heating rates of 10°C/min (slow) or 500°C/min (rapid). The rapid heating was obtained by introducing the films quickly into

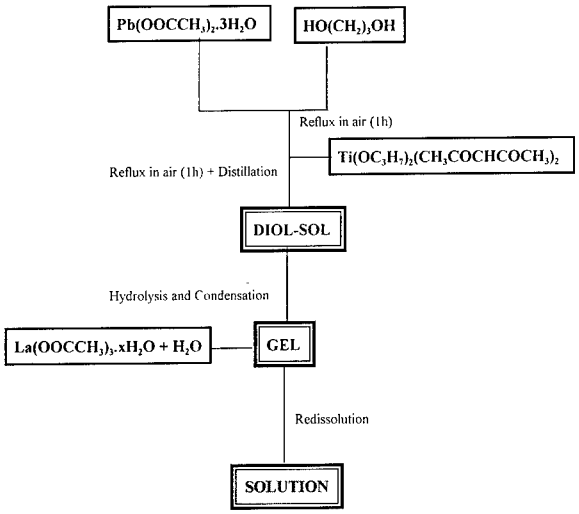

Figure 1. Reaction scheme of the sol-gel preparation of lanthanum modified lead titanate precursor solutions.

the furnace, previously stabilized at 650°C, and maintaining them at this temperature for 12 min. Temperature of the films during this thermal treatment was controlled through a thermocouple placed beside the sample. This treatment did not produce over-shooting of temperature and was reproducible for all the films treated in this way. Slow and rapid heated films were air-quenching down to room temperature. Thickness of the films was measured by means of surface profilometry.

Thermal decomposition of the solutions was monitored by means of thermogravimetric and differential thermal analysis (TGA and DTA). Phase analysis of the crystallized films was performed at room temperature using grazing incidence X-ray diffraction (GIXRD), with an incidence angle of 2°. Scanning electron microscopy (SEM) was used to study the film microstructures. Compositional analysis of the films was made by energy dispersive X-ray spectrometry (EDXS).

Top platinum electrodes of ~0.5 mm in diameter were deposited by sputtering on the films for electrical characterization. Hysteresis loops were measured at 200 Hz with a modified Sawyer-Tower circuit. Poling of the films was made with a train of 1000 square pulses of 2.5 ms width, separated by 2.5 ms and with an amplitude of 250 kV/cm.

Results and Discussion

The TGA and DTA traces of the lanthanum modified lead titanate synthesized solutions are shown in

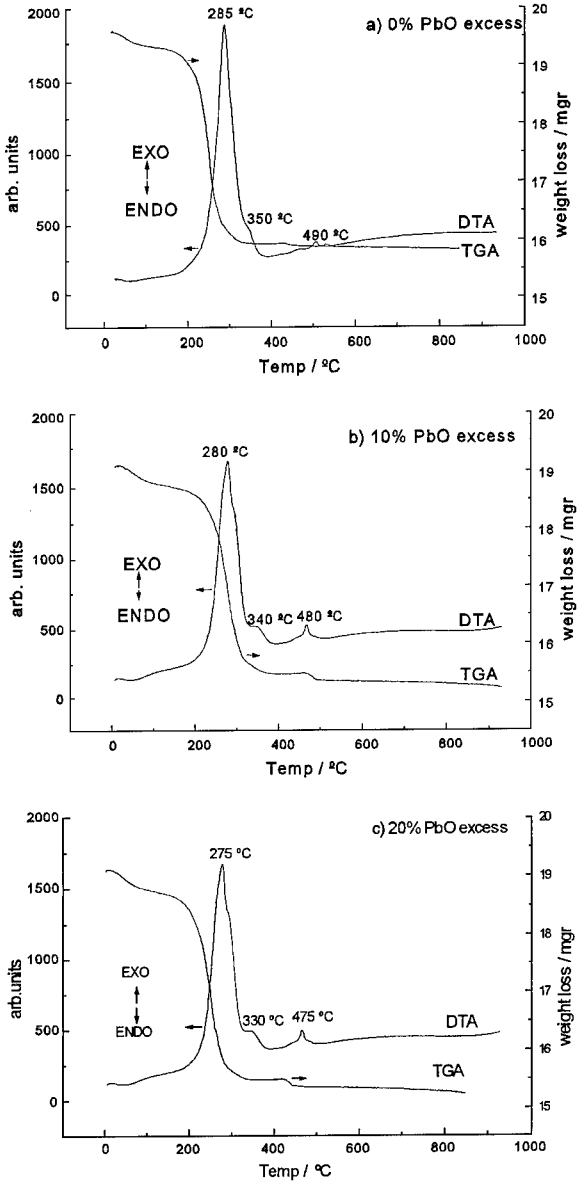

Figure 2. TGA and DTA curves of solutions prepared with different excesses of PbO (mol%) and dried at 100°C for 12 hours. Analyses were monitored in air with a heating rate of 10°C/min.

Fig. 2. In all the solutions, a small weight loss of about 1–2% appears at temperatures lower than 200°C that is due to the evaporation of physically bound water. A second weight loss of about 18–19%, associated to the main exothermic peak, is recorded between 200–400°C. Elimination of the majority of volatiles occurs in this temperature interval. A last step close to 500°C is observed in the curves of Fig. 2, where an exothermic peak and a small weight loss of about 1.0–1.5% are recorded. This exothermic could be assigned to the

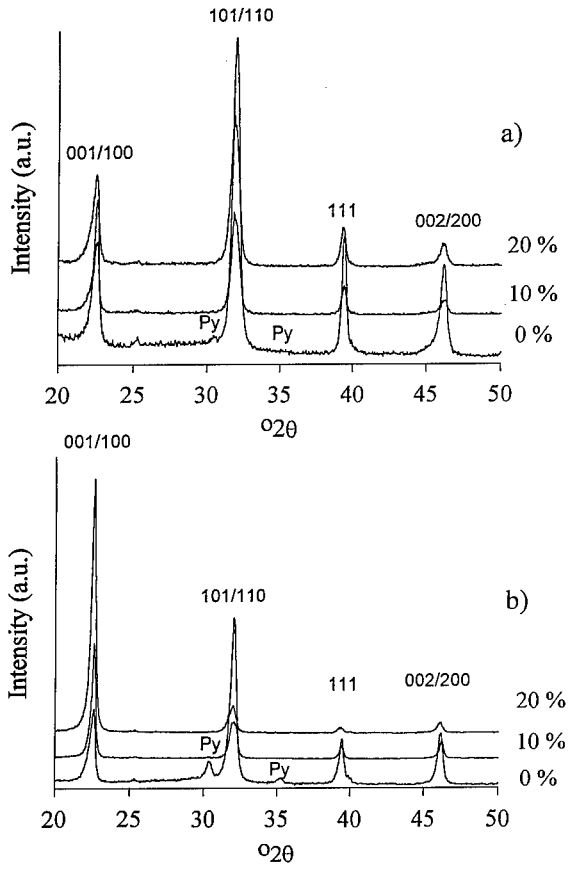

Figure 3. GIXRD of films derived from solutions with different excesses of PbO and crystallized with (a) a heating rate of 10°C/min and (b) a heating rate >500°C/min.

crystallization of the perovskite which occurs at these temperatures [4]. However, the weight losses measured indicate that organic residuals still remain in the material. The thermal decomposition process appears to be complete at ~500°C. Incorporation of lead oxide excess to the solutions produces a slight decrease of the temperature of the exothermic peaks detected by DTA, which may indicate an easier elimination of organics and an easier perovskite crystallization with the lead oxide excess. This could be related to a difficult formation of second lead deficient phases that delay and in some cases hinder the formation of the perovskite. Thus, crystallization of the films has been carried out at 650°C for 12 min. Undesirable pyrochlore-type phases always appear in the X-ray patterns of the films deposited from the stoichiometric solutions (Fig. 3). A diminution of this phase is not observed by using rapid heatings. However, these phases are not detected in the X-ray patterns when a 10 mol% PbO excess is incorporated into the solutions. Slow heating rates during annealing produce the crystallization of randomly oriented perovskites (Fig. 3(a)). On the contrary, rapid heating rates lead to the formation of (001)(100) oriented perovskites (Fig. 3(b)) whenever pyrochlore is not formed. Incorporation of an ~20 mol% PbO excess to the precursor solution compensates the lead losses produced during heating, giving rise to single-perovskite layers with the nominal Pb/Ti ratio (see Table 1) and without other crystalline structures detectable by GIXRD (Fig. 3). A progressive increase of the preferred orientation is obtained with the increase of the excess of PbO, for the rapid crystallized films.

Film surface microstructures are presented in Fig. 4. Stoichiometric solution-derived films prepared with a slow heating develop a complex microstructure (Fig. 4(a)), most likely associated with the two crystalline phases detected by GIXRD. However, the rapid heating of these films leads to a homogeneous surface microstructure although the pyrochlore is still present in the material. Incorporation of lead oxide excesses to the solutions allow crystalline and microstructurally homogeneous films to be obtained. A larger porosity is observed in the conventionally annealed films than in those prepared with the rapid thermal treatment (Figs. 4(c) and (d)) indicating a difference between the bulk densities of the slowly and the rapidly crystallized films containing 20 mol% of

Table 1. Compositional analysis of the films made by EDXS.

		Pb/Ti ratios		
	Mol% of PbO excess	0	10	20
Crystalline (Pb, La)TiO_3 films*	Slowly heated films (10°C/min)	0.80 ± 0.02	0.85 ± 0.02	0.90 ± 0.02
	Rapid heated films (>500°C/min)	0.81 ± 0.02	0.83 ± 0.02	0.90 ± 0.02

*Nominal composition: $Pb_{0.88}La_{0.08}TiO_3$ (Pb/Ti = 0.88).

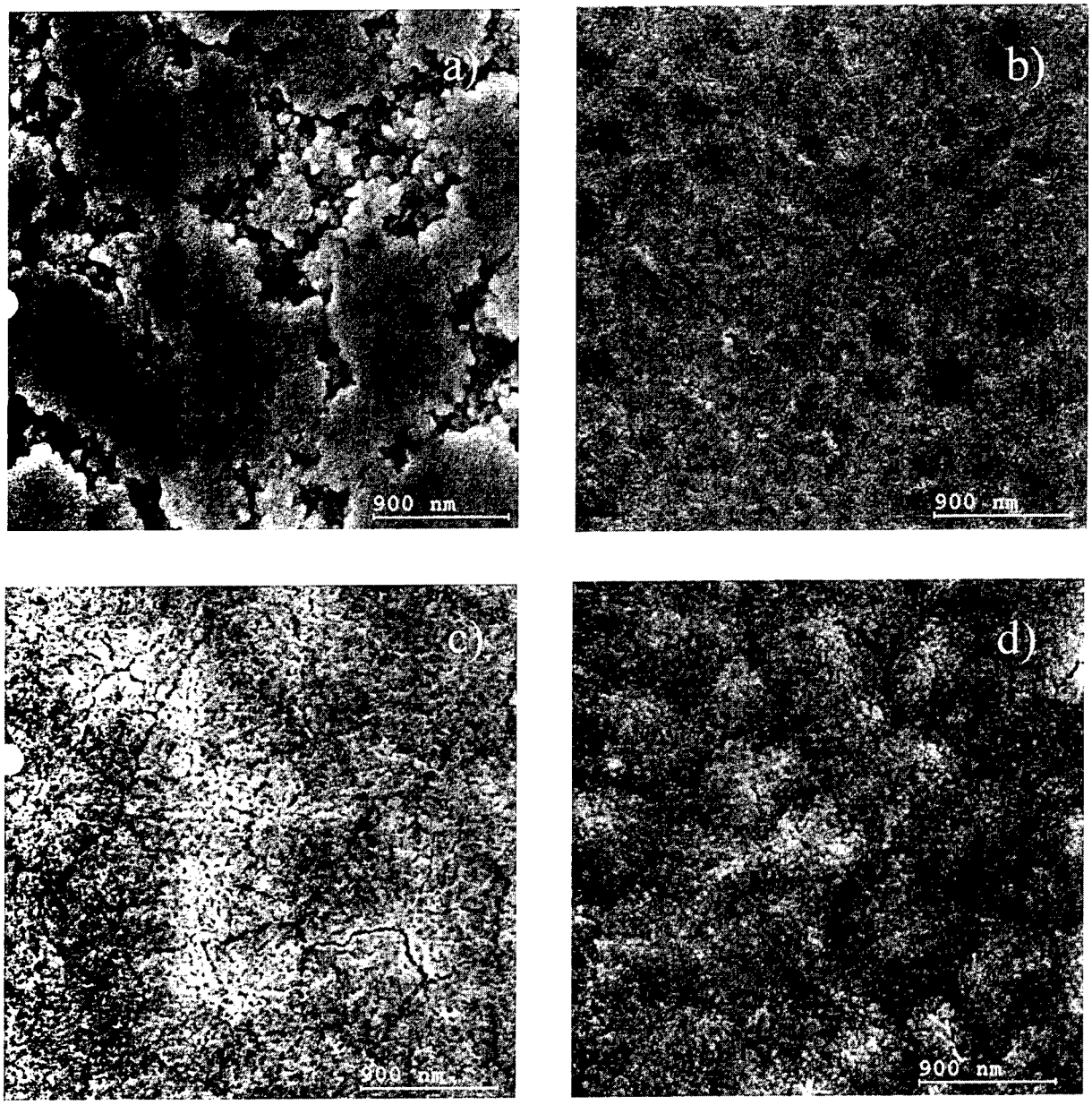

Figure 4. Micrographs of the films, surfaces: (a) without PbO excess and heated at 10°C/min, (b) without PbO excess and heated at >500°C/min, (c) with a 20 mol% excess of PbO and heated at 10°C/min, and (d) with a 20 mol% of PbO and heated at >500°C/min.

excess lead. Their thicknesses also differed (~500 and ~400 nm, respectively).

The stoichiometric solution derived films do not exhibit ferroelectric behavior. The other (Pb, La)TiO_3 films prepared with a 10 and 20 mol% excess of PbO show the characteristic P-E hysteresis loops. The better defined loops with larger remanent polarizations are always obtained for the films prepared with a 20 mol% PbO excess (Fig. 5). It should be noted that there is a slightly larger remanent polarization in the films crystallized with a rapid heating rate than in those slowly heated. This could be related either to preferred orientation of the perovskite [5] or to the formation of film-substrate interfaces in the slowly heated films [6].

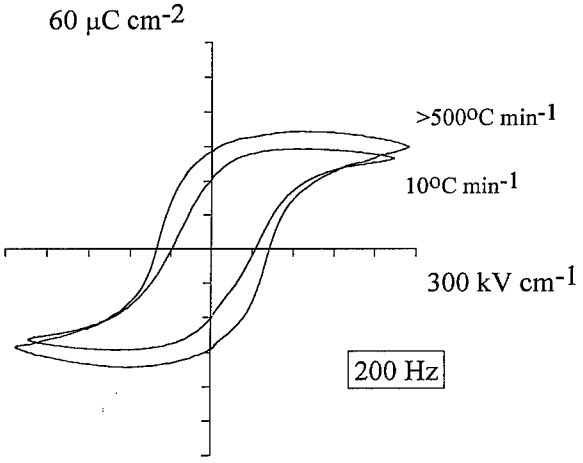

Figure 5. Hysteresis loops of films prepared with a 20 mol% excess of PbO and heated at 10°C/min or at >500°C/min.

Conclusions

1. Stable and precipitate lanthanum modified lead titanate solutions have been synthesized by a sol-gel route where La was incorporated as water soluble acetate, to overcome the low solubility of La-compounds in organic solvents. These solutions were applied to the preparation of thin films.
2. The difficulty of maintaining the lead stoichiometry during the crystallization of the films requires the use of up to a 20 mol% of lead excess in the precursor solutions to obtain perovskite ceramic layers with the nominal Pb/Ti ratio of the $Pb_{0.88}La_{0.08}TiO_3$ composition.
3. The PbO excess of the precursor solution did not modify significantly the main steps in the thermal decomposition of the precursor solutions up to 500°C.
4. Slow heating rates during the film crystallization lead to the formation of randomly oriented perovskites whereas rapid heating rates favor the growth of preferred oriented perovskites.

Acknowledgments

This work has been supported by the EU project ERBCIPACT940236 and the CICyT Spanish project MAT95-0110. The work was performed within the European program on ferroelectric ceramic thin films (COST514).

References

1. N. Nagao, T. Takeuchi, and K. Ijima, Jpn. J. Appl. Phys. **32**, 4065 (1993).
2. J.J. Shyu and K.L. Mo., Jpn. J. Appl. Phys. **34**, 5683 (1995).
3. M.L. Calzada, J. Mendiola, F. Carmona, P. Ramos, and R. Sirera, Mater. Res. Bull. **31**(4), 413 (1996).
4. J.C. Ho, I.N. Lin, and K.S. Liu., J. Mater. Sci. **29**, 1884 (1994).
5. B.A. Tuttle, J.A. Voigt, D.C. Goodnow, D.L. Lamppa, T.J. Headley, M.O. Eatough, G. Zender, R.D. Nasby, and S.M. Rodgers, J. Am. Ceram. Soc. **76**(6), 1537 (1993).
6. M.L. Calzada, M.J. Martín, P. Ramos, J. Mendiola, R. Sirera, M.F. da Silva, and J.C. Soares, J. Phys. Chem. Solids **58**(7), 1039 (1997).

Journal of Sol-Gel Science and Technology 13, 843–847 (1998)
© 1998 Kluwer Academic Publishers. Manufactured in The Netherlands.

Study by Rutherford Backscattering Spectroscopy of the Heterostructure of Lead Titanate Thin Films

M.J. MARTÍN, M.L. CALZADA* AND J. MENDIOLA
Inst. Ciencia de Materiales de Madrid (CSIC). Cantoblanco, 28049 Madrid, Spain

M.F. DA SILVA
Inst. Tecnológico e Nuclear. Departámento de Física. Estrada Nacional no. 10, 2685 Sacavém, Portugal

J.C. SOARES
Centro de Física da Universidade de Lisboa. Av. Prof. Gama Pinto 2, 1699 Lisboa, Portugal

Abstract. A depth profile analysis of modified lead titanate thin films was performed by means of Rutherford Backscattering Spectroscopy (RBS). These films were deposited from sol-gel synthesized solutions onto platinized silicon substrates and crystallized by thermal treatments at temperatures of about 650°C. The chemistry of the solution and the thermal treatment for crystallization affect the heterostructure of the resulting films. Losses of lead and formation of substrate-film interfaces are produced during the crystallization of the films. These film characteristics determine their ferroelectric response.

Keywords: Rutherford backscattering spectroscopy, thin films, lead titanate

Introduction

Microelectronic devices including ferroelectric ceramic thin films integrated with silicon substrates have created much interest during recent years due to the possibility of using their ferro, pyro and piezoelectric properties at the microscale level [1]. Pure and modified lead titanate perovskite films were shown to be good candidates for these applications.

The preparation of films by sol-gel includes two steps. The first step is the synthesis of the precursor solution and the second step is the deposition of this solution onto the substrate and the subsequent crystallization of the ceramic layer. The characteristics of the films obtained are dependent on the fabrication conditions and they strongly affect the electrical properties of the films.

Numerous studies have reported the importance of obtaining lead titanate based films totally crystallized into the perovskite structure [2]. The control of the lead stoichiometry and the possible interdiffusion between the different layers forming the final device are other factors that need to be considered during the preparation of the material.

Rutherford Backscattering Spectroscopy (RBS) is a technique that has been widely used for the characterization of surfaces of single oxides. In this work, this technique is used in the study of multicomponent perovskite films (modified lead titanate) deposited by sol-gel on complex substrates ($Pt/TiO_2/SiO_2/Si$). The results obtained reveal the potential applicability of the RBS technique to the study of this type of materials.

Experimental

Spin-on Sol-Gel Thin Film Preparation

Calcium modified lead titanate thin films with a composition of $Pb_{0.76}Ca_{0.24}TiO_3$ have been deposited from

*Author to whom correspondence has to be addressed.

solutions synthesized by a sol-gel method [3]. Solutions with the nominal composition and with a 10 mol% excess of PbO, to compensate possible lead losses, were prepared. These solutions were deposited by spin-coating onto 1000 Å Pt/500 Å $TiO_2/SiO_2/(100)Si$ substrates. Wet layers were dried on a hot-plate at 350°C/60 s and then crystallized in air at 650°C. Two heating rates of ~8°C/s and ~30°C/s (to 650°C) were used for the crystallization of the ceramic layers. Both types of crystallization thermal treatments led to single-perovskite films without second crystalline phases being detected by X-ray diffraction analysis.

Top platinum electrodes of ~0.5 mm were deposited on the top surfaces of the films to test their ferroelectric response by measuring hysteresis loops at 200 Hz with a modified Sawyer-Tower circuit.

Profile composition of the crystallized films as well as interactions between the substrate and the ceramic layer were studied by RBS, using the procedure explained in the following section.

Rutherford Backscattering Spectroscopy

Figure 1 shows a schematic representation of the RBS technique. This technique is based on the detection of ions that are elastically backscattered by the nuclei of the atoms of a material analyzed. Energy and mass of the projectile atoms are known. Then, the composition of the sample examined is calculated through the measurement of the number of projectile ions backscattered at different energies (backscattered spectrum) [4], and considering the principles of conservation of momentum and energy during the elastic collision of two masses. Equations and constants used for these calculations are included in a computer program called RUMP [5] which simulates the experimental backscattering spectrum as a function of the composition of the material studied.

Data were collected using a 3.1 Van der Graaff accelerator. A 1.6 MeV He^+ beam was collimated and directed on the sample down to an area of 1 mm^2. Backscattered ions were detected by two surface barrier detectors of energy resolutions, of 12 and 18 KeV at 180° and 140° to the beam direction, respectively. Solid angles are 3.8° and 22° for the 180° and 140° detectors. Generally, we used the data obtained from the 140° detector because it has a better energy resolution.

Samples are held in a vacuum chamber perpendicular to or with an inclination angle of θ from the perpendicular position to the ion beam (see Fig. 1). The spectrum recorded with $\theta = 0°$ (perpendicular position) provides general information of the heterostructure of the sample, where the silicon substrate, the buffer TiO_2 layer, the Pt bottom electrode and the ceramic

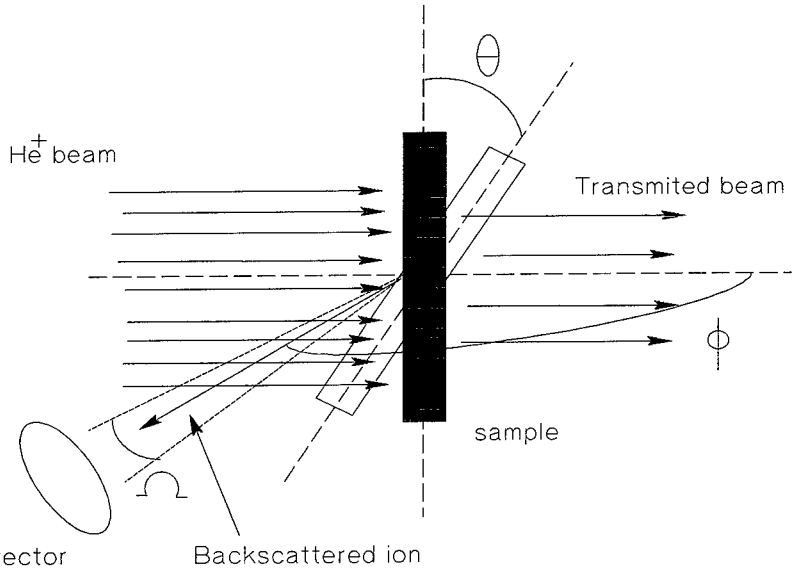

Figure 1. Schematic diagram of the RBS technique; Ω is the detector solid angle placed at an angle ϕ to the ion beam; θ is the angle of inclination of the sample from the perpendicular to the ion beam.

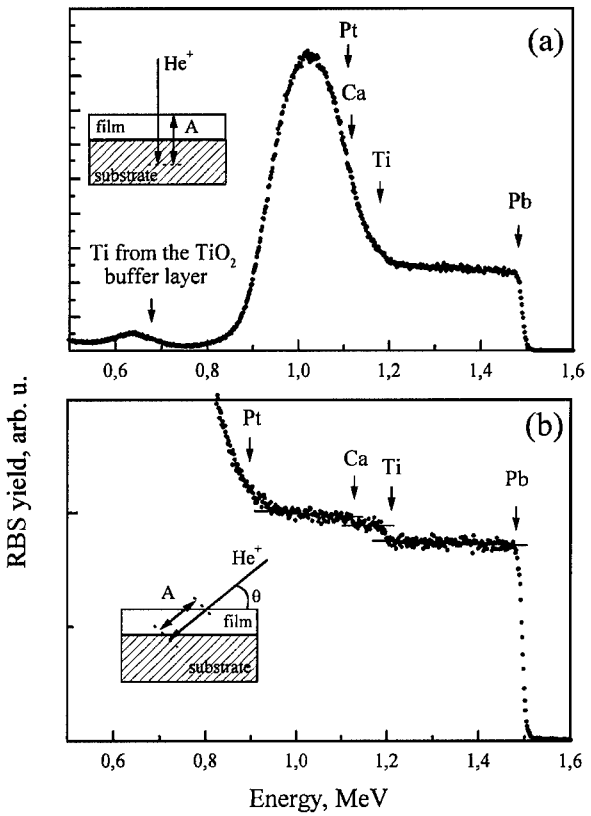

Figure 2. RBS spectra obtained with (a) $\theta = 0°$ or (b) $\theta = 30–40°$. A is the effective thickness of the sample analyzed.

(Pb, Ca)TiO_3 film are detected. The Ca and Ti RBS signals are overlayed on the Pt RBS signal, in this spectrum (Fig. 2(a)). If the sample is tilted an angle θ from the perpendicular to the ion beam, the effective thickness of the film analyzed increases (Fig. 2(b)). Then, these experimental conditions produce a shift of the Pt RBS signal and make possible its separation from the Ca and Ti RBS signals. Therefore, two spectra have been recorded for each sample: one perpendicular ($\theta = 0°$), to get information about the heterostructure of the sample, and another with $\theta = 30–40°$, from which non-overlapped Pb, Ca and Ti RBS signals are obtained. In this spectrum, increments are detected that correspond to the Pb, Ca and Ti signals of the film (see Fig. 2(b)). [Pb]/[Ti] and [Ca]/[Ti] atomic ratios are obtained from these increments, using the following equations:

$$\frac{[\text{Pb}]}{[\text{Ti}]} = \frac{(\text{increment due to Pb})}{(\text{increment due to Ti}) \times \sigma_d(\text{Ti})/\sigma_d(\text{Pb})}$$

$$\frac{[\text{Ca}]}{[\text{Ti}]} = \frac{(\text{increment due to Ca})}{(\text{increment due to Ti}) \times \sigma_d(\text{Ti})/\sigma_d(\text{Ca})}$$

where σ_d are the differential cross sections for each element, which are tabulated in the RUMP program.

The values obtained with these equations correspond to the quantitative atomic ratios for the first atomic layers of the top surface of the films. The projectile ions lose energy as they pass through the analyzed sample. Hence the composition of the bulk films cannot be quantitatively calculated and approximations have to be made taking into account the composition values obtained for the top surface of the films.

The method of analyzing the experimental spectra can be summarized in the following steps:

1. Atomic ratios at the film surfaces are calculated from the increments of the Pb, Ca and Ti signals obtained from the RBS spectra measured with $\theta = 30–40°$.
2. Simulations of the composition of the bulk films are performed on the perpendicular RBS spectra ($\theta = 0°$), considering the composition data of the top surface. The amount of oxygen is matched so that the simulation fits the experimental spectrum of the surface.
3. The thickness of the different layers forming the heterostructure of the material and of the reaction interfaces developed during the preparation are calculated from the simulations assuming the theoretical density of the perovskite.

Results and Discussion

Figure 3 shows the RBS experimental spectra with $\theta = 0°$ obtained for two (Pb, Ca)TiO_3 perovskite films crystallized at 650°C with two different heating rates: a moderate heating rate of ~8°C/s and a rapid heating rate of ~30°C/s. The energy of the backscattered He^+ by the Pt, Pb, Ti and Ca is indicated in the figure. The arrow bars correspond to the elements at the surface, except for Pt that is underneath the film. The Pt signal overlaps the Ti and Ca signals. Thus, as explained above, compositional data cannot be obtained from these spectra ($\theta = 0°$). However, interdiffusion regions among the different layers forming the heterostructure of the material can be deduced from the data of Fig. 3 if a linear decrease of the lead and titanium contents of the film into the platinized substrate is assumed [6]. The larger slopes of the spectrum in the

Table 1. Ferroelectric properties of the (Pb, Ca)TiO_3 films prepared under different conditions.

	Heating rate of the thermal treatment at 650°C			
	~8°C/s		~30°C/s	
PbO excess of the solution (mol%)	Coercive field, E_c (kV/cm)	Remanent polarization, δP_r ($\mu C/cm^2$)	Coercive field, E_c (kV/cm)	Remanent polarization, δP_r ($\mu C/cm^2$)
0	~150 Loop with a large bias field	~2.3 Large leakage currents	No ferroelectric response	
10	~175 Loop with a large bias field	~1.0 Large leakage currents	~82	~20

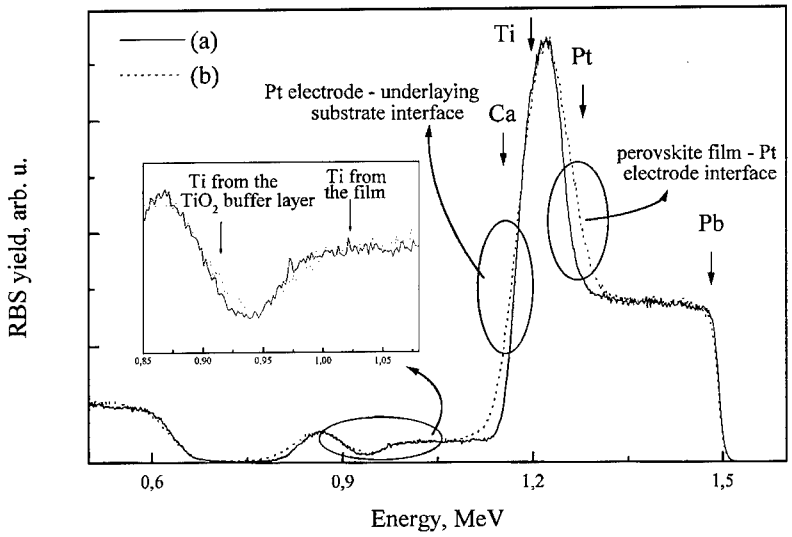

Figure 3. RBS spectra obtained with $\theta = 0°$ for thin films crystallized with heating rates of (a) ~30°C/s and (b) ~8°C/s.

regions between the perovskite film and the Pt electrode, and between this electrode and the underlying substrate, for the films more slowly heated (~8°C/s), are an indication of the thicker reaction interfaces in this film than in that treated at ~30°C/s. Both films develop a single-perovskite phase, as detected by XRD [7], because both heating rates are fast enough to prevent the stabilization of second pyrochlore or fluorite-type phases [8]. However, the formation of these interfaces damages the ferroelectric response of the film, as shown in Table 1.

Compositional deviations from the desired perovskite, $Pb_{0.88}Ca_{0.24}TiO_3$, are also detected in the films by RBS, besides the described interdiffusion and reaction among the different layers of the material. Figure 4 shows the RBS spectra of the films heated to 650°C at 8°C/s, derived from stoichiometric solutions and from solutions with a 10 mol% excess of PbO. The composition of these films at their top surface has been calculated from the spectra with $\theta = 30$–$40°$. Simulations of the complete spectra have been made considering the [Pb]/[Ti] and [Ca]/[Ti] ratios calculated from the former spectra. A good agreement between the experimental and the simulated spectra is obtained for both films. However, it should be noted that only films prepared from solutions with PbO excess have the [Pb]/[Ti] atomic ratio of the perovskite, $Pb_{0.88}Ca_{0.24}TiO_3$. Therefore, although both films have developed a perovskite structure, the desired composition is only obtained in films prepared with lead excess. These films have an improved ferroelectric response compared with the other films (Table 1).

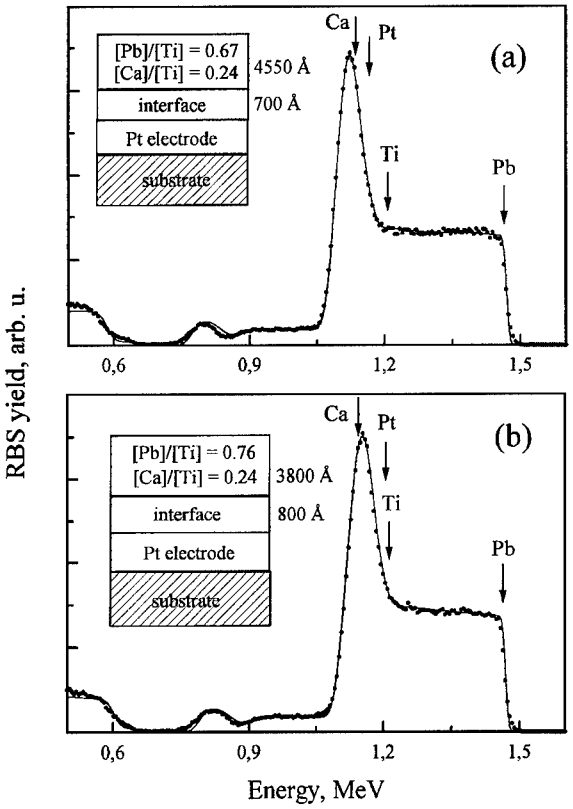

Figure 4. RBS spectra obtained with $\theta = 0°$ for thin films crystallized at 650°C with a heating rate of ~30°C/s and derived from (a) stoichiometric solutions and (b) solutions with a 10 mol% PbO excess.

Conclusions

1. Rutherford Backscattering Spectroscopy is shown to be an appropriate technique to study the composition and heterostructure of ferroelectric thin films integrated with silicon based microdevices.
2. Interfaces developed between sol-gel derived lead titanate perovskite thin films and platinized substrates are a function of the heating rate used during the heat treatment for crystallization. Higher heating rates minimize the formation of these interfaces.
3. Lead oxide excess in the sol-gel synthesized solutions compensates for the lead loss during the annealing and allow lead titanate based films to be obtained with the [Pb]/[Ti] ratio of the perovskite composition.

Acknowledgments

This work has been supported by the CICyT Spanish project MAT95-0110. The work was performed within the European program on ferroelectric ceramic thin films (COST514).

References

1. P.K. Larsen, R. Cuppens, and G.A.C.M. Spierings, Ferroelectrics **128**, 265 (1992).
2. C.C. Hsueh and M.L. Mecartney, J. Mater. Res. **6**(10), 2208 (1991).
3. R. Sirera and M.L. Calzada, Mater. Res. Bull. **30**(1), 11 (1995).
4. W.K. Chu, J.W. Mayer, and M.A. Nicolet, "Backscattering Spectrometry." Ed. Acad. Press., Orlando, 1978.
5. L.R. Doolittle, Nucl. Instrum. Meth. **B9**, 344 (1985).
6. M.L. Calzada, M.J. Martín, P. Ramos, J. Mendiola, R. Sirera, M.F. da Silva, and J.C. Soares, J. Phys. Chem. Solids **58**(7), 1033 (1997).
7. F. Carmona, M.L. Calzada, E. Román, R. Sirera, and J. Mendiola, Thin Solid Films **279**, 70 (1996).
8. E.K.P. Dang and R.J. Gooding, Phys. Rev. Lett. **74**(19), 3848 (1995).

Journal of Sol-Gel Science and Technology 13, 849–853 (1998)
© 1998 Kluwer Academic Publishers. Manufactured in The Netherlands.

A Raman Scattering Study of $PbTiO_3$ and TiO_2 Obtained by Sol-Gel

D. BERSANI AND P.P. LOTTICI
Istituto Nazionale per la Fisica della Materia and Physics Department, University, Viale delle Scienze, 43100 PARMA, Italy

T. LOPEZ
Departamento de Química, Universidad Autonoma Metropolitana-Iztapalapa, A.P. 55-534 México D.F. 09340, México

XING-ZHAO DING
Ion Beam Laboratory, Shanghai Institute of Metallurgy, Chinese Academy of Sciences, 865 Chang Ning Road, Shanghai 200050, People's Republic of China

Abstract. The mechanisms that give rise to the broadening and the shifts of the Raman peaks of titanium dioxide and lead titanate nanocrystals prepared by sol-gel are discussed. Phonon confinement and oxygen deficiency are competitive mechanisms in TiO_2 obtained by different sol-gel preparations whereas pressure effects on the nanocrystals predominate in ferroelectric $PbTiO_3$.

Keywords: Raman, TiO_2, $PbTiO_3$-nanocrystals

Introduction

Titanium dioxide, TiO_2, is a well-known material with a very large number of applications due to its optical, chemical and mechanical properties [1, 2]. Lead titanate $PbTiO_3$ (PT) is a perovskite type ferroelectric material with interesting dielectric, pyroelectric and piezoelectric properties [3]. The size of the nanocrystals observed during the first stages of the sol-gel synthesis of these titanium based oxides influences the functional properties of the materials, determining the specific surface, the amount of defects, the transition temperatures and the stability of the different phases. Raman spectroscopy is sensitive to the various mechanisms (phonon confinement, pressure, stoichiometry) that influence the vibrational dynamics in nanosized systems. In this study we discuss the importance of various effects in determining the Raman lineshapes in sol-gel derived TiO_2 and $PbTiO_3$.

Experimental

TiO_2 powders were obtained by two different sol-gel routes: TiO_2 (A) was prepared using titanium tetraethoxide $Ti(OEt)_4$ as the precursor and ethanol as the solvent. Acid catalysis was obtained by acetic acid. After gelation, the samples were dried in air at 70°C for 12 h and then annealed, at an heating rate of 20°C/min, up to temperatures ranging from 100 to 900°C [1].

TiO_2 (B) samples were prepared starting from tetrabutyltitanate $Ti(O\text{-}Bu)_4$, ethanol was used as the solvent and hydrochloric acid was added to the solution as a catalyst. After gelation, the samples were heat-treated for 2 hours at four different temperatures: 425, 450, 475, and 500°C [4].

$PbTiO_3$ gel was prepared from titanium isopropoxide $Ti[(CH_3)_2CHO]_4$ and lead acetate $Pb(CH_3COO)_2 \cdot 3H_2O$. Hydrochloric acid was added to the solution as a catalyst. The gel was dried at 125°C for 1 h, then

powdered. The powders were laser-annealed at different powers [5].

RT Raman measurements were performed, with the 488 cm^{-1} line, for powdered samples in capillary tubes using a SPEX 1403 double monochromator with a standard photon counting system.

Results and Discussion

The Raman spectra of the TiO_2 (A) powders annealed at different temperatures are reported in Fig. 1. The dried gel showed highly broadened anatase features and the peaks sharpened as the temperature increased. At 600°C a mixed anatase-rutile phase was observed. XRD [1] and TEM measurements [6] indicated that the dried gel was composed of nanosized crystals (5–10 nm), which grew up to 100 nm as the thermal treatments proceeded.

The Raman spectra of the TiO_2 (B) samples are reported in Fig. 2. The broadening and the blue-shift of the anatase peaks were lower than those evidenced for the TiO_2 (A) samples. The line-widths of the XRD patterns [4, 7] indicated that the TiO_2 (B) samples were composed of nanocrystals with mean size: 9.5 nm (for the sample annealed at 425°C); 10.9 nm (450°C); 12.1 nm (475°C) and 13.4 nm (500°C). TEM measurements were in good agreement with these results (Fig. 3).

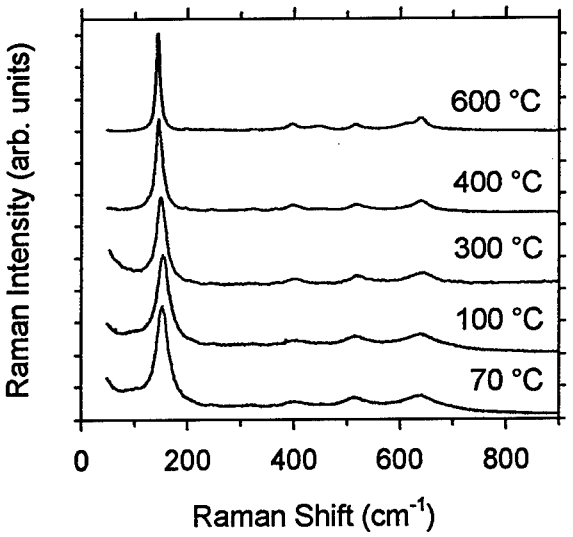

Figure 1. Raman spectra of TiO_2 powders (A) annealed at different temperatures.

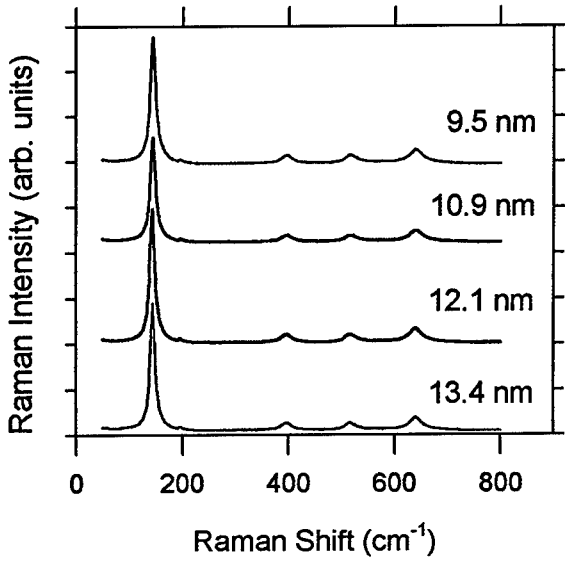

Figure 2. Raman spectra of TiO_2 powders (B) with increasing mean diameters (corresponding to different annealing temperatures).

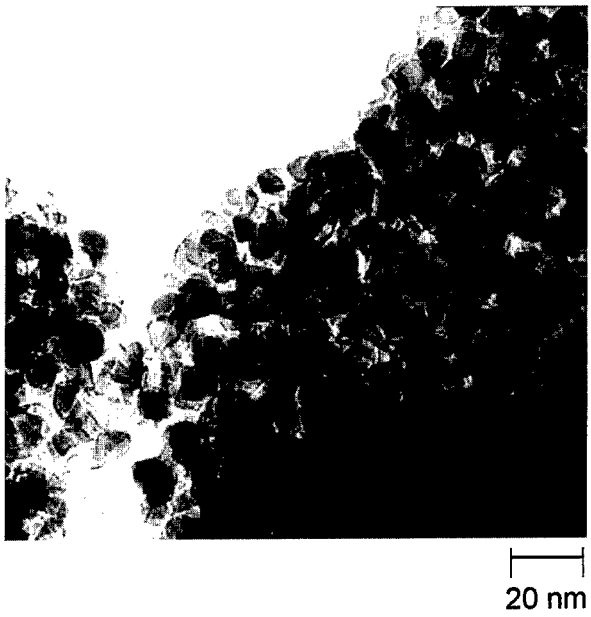

Figure 3. TEM image of TiO_2 powders (B) annealed at 450°C.

The Raman spectra of the $PbTiO_3$ samples annealed at different laser powers (Fig. 4) showed an evolution from an amorphous phase to the pure perovskite one. This was the same behavior observed for samples heat-treated up to 800°C in an electric furnace [5]. As the perovskite phase grew, the main Raman peaks

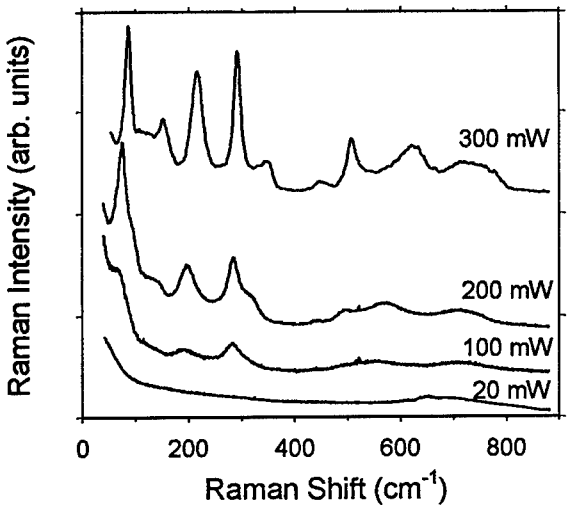

Figure 4. Raman spectra of $PbTiO_3$ powders annealed at increasing laser power.

blue-shifted up to values slightly lower than those found for the bulk.

The observed Raman line broadening for the TiO_2 (B) samples may be explained by a phonon confinement effect, due to the reduced size of the anatase crystals [8, 9]. All the phonons over the Brillouin zone contribute to the first order Raman spectra, and this results in an asymmetrical broadening and a shift of the Raman peaks. Figure 5 shows the shape of the 144 cm^{-1} mode of the anatase calculated [10] for different crystal sizes (diameter 5, 10 and 100 nm). The broadening and blue-shift of the Raman peak fairly describe those observed in nanocrystals of different sizes.

The anatase features in the Raman spectra of the (A) dried gel are much more broadened than in the (B) case: the FWHM of the 144 cm^{-1} is $\approx$27 cm^{-1}. The finite-size effect on the phonons is not adequate to explain this broadening: the most likely origin is the non-stoichiometry of the TiO_2 powders. According to Parker and Siegel [11], oxygen vacancies may cause a high broadening of the Raman bands due to the long-range Coulomb interactions between the titanium atom and the basal oxygens. In the (B) samples, all the organic residues were removed at $T > 400°C$ and a good crystallization of the anatase phase is expected, but in the (A) powders, annealed at 70°C, titanium deficiency and organic residues are present. The pressure acting on the growing nanograins cannot be the main cause of the broadening because this would require larger shifts and, moreover, the pressure-induced shifts are of opposite signs of different phonons, contrary to what was observed.

A comparison between two series of (A) samples annealed in air and in a non-oxidizing (N_2) atmosphere, respectively, shows (Fig. 6) that for both series the FWHM of the anatase main peak decreased with increasing annealing temperature, but for the N_2-annealed samples it remained larger by a few cm^{-1}, at all temperatures. This result confirms that the powders are oxygen deficient and that the broadening of

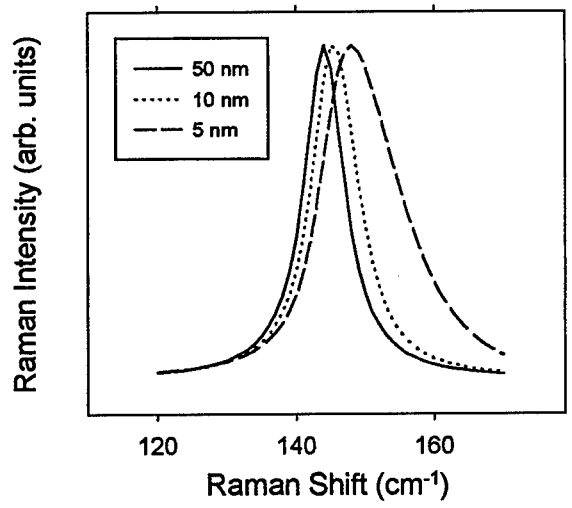

Figure 5. Raman lineshapes calculated [10] with the phonon confinement model for different diameters of the nanocrystals in TiO_2 (B) samples.

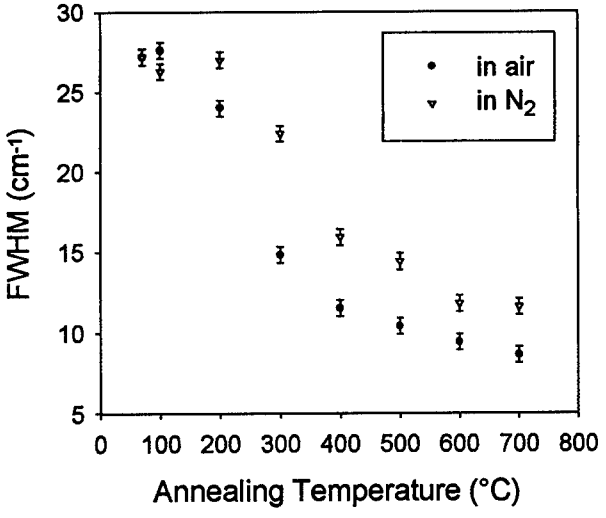

Figure 6. FWHM of the main anatase peak at 144 cm^{-1} in TiO_2 powders (A) annealed at different temperatures in air and in N_2 atmosphere.

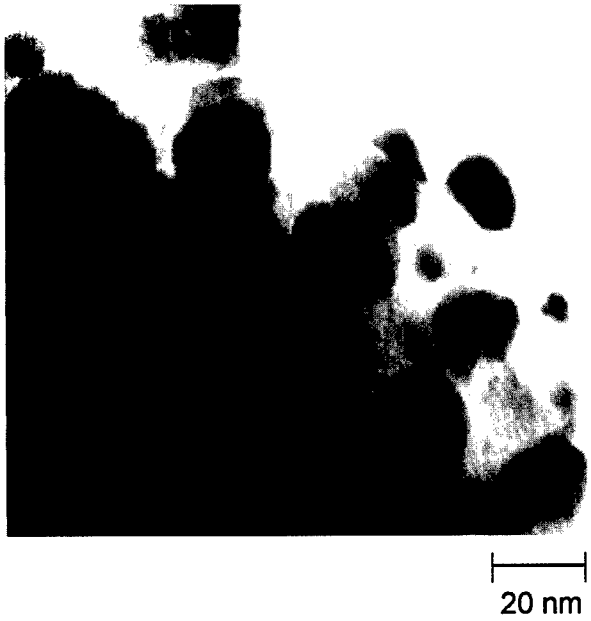

Figure 7. TEM image of $PbTiO_3$ powdered, dried gel.

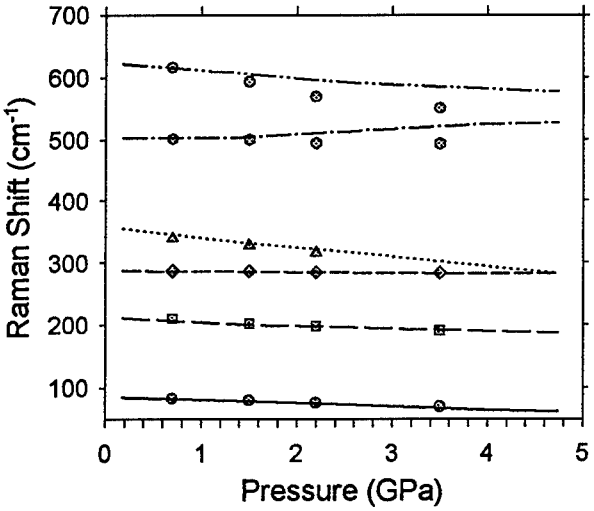

Figure 8. Fit of the changes of the frequencies of the Raman peaks in $PbTiO_3$ at different stages of the crystallization during the laser annealing (symbols) to the changes induced by an external pressure (lines).

the Raman features originated both by this deficiency and by phonon confinement effects. The annealing in a non-oxidizing atmosphere produced only the sharpening of the peaks due to the crystal growth. The residual broadening, of about 3-4 cm^{-1}, may be due to pressure effects or to an inner re-arrangement during the treatments.

For $PbTiO_3$, phonon confinement effects may be excluded, as the TEM images showed large grain sizes (>20 nm) even in the dried gel (Fig. 7). The differences in the Raman frequencies of the final perovskite phase with respect to the bulk crystal were due to pressure effects on PT crystallites [12]. In all sol-gel derived materials, the crystallization generates some stress on the growing nanocrystals. The effect is more pronounced in the early stages of crystallization when the number of the atoms in the stressed interfacial layers of the grains is greater. In the $PbTiO_3$ samples the pressure effects are more important than in TiO_2 due to the ferroelectric transition. The perovskite phase is ferroelectric but is obtained at temperatures higher than the Curie point ($T_c = 490°C$), in the cubic paraelectric state. Cooling to room temperature, the cubic to tetragonal deformation takes place but the micrograins are clamped by neighboring grains with different orientations, leading to high stresses. At high annealing temperatures, the grains become larger, the domains are formed and the stress is released. In Fig. 8 the frequencies of some Raman peaks measured at various stages of the crystallization during the laser-annealing process are reported, together with data [13] for the changes of the frequencies with respect to an external hydrostatic pressure. The overall behavior of the Raman frequencies as the crystallization proceeded fits fairly well with a progressive lowering of the pressure effect on the grains.

Conclusions

The Raman data enabled a discrimination between the different mechanisms that influence the Raman lineshapes in different sol-gel derived materials. The phonon confinement may be regarded as the main cause of the broadening in stoichiometric TiO_2 samples with small nanocrystals (<20 nm diameter). When non-stoichiometry was present, the oxygen deficiency also plays an important role in the determination of the Raman lineshapes. In sol-gel derived $PbTiO_3$, due to the presence of the ferroelectric transition, the pressure effects are the main cause of the shifts of the perovskite Raman peaks.

Acknowledgments

We are indebted to Dr. Lucia Nasi, MASPEC-CNR Institute in Parma for TEM measurements.

References

1. T. Lopez, E. Sanchez, P. Bosch, Y. Meats, and R. Gomez, Mater. Chem. Phys. **32**, 141 (1992).
2. R.J. Gonzalez and R. Zallen, in *NATO-ASI Proceedings, Amorphous Insulators and Semiconductors*, edited by M.F. Thorpe and M.I. Mitkova (Kluwer, 1997).
3. J.S. Wright and L.F. Francis, J. Mater. Res. **8**, 1712 (1993).
4. X. Ding, J. Luo, Z. Qi, and Y. He, Chin. Phys. Lett. **12**, 123 (1995).
5. D. Bersani, P.P. Lottici, G. Gnappi, A. Montenero, and S. Pigoni, J. Mater. Science **31**, 3153 (1996).
6. D. Bersani, G. Antonioli, P.P. Lottici, and T. Lopez, J. Non-Cryst. Solids **234**, 175 (1997).
7. X. Ding, X.H. Liu, and Y. He, J. Mater. Science Lett. **15**, 1789 (1996).
8. H. Richter, Z.P. Wang, and L. Ley, Solid State Commun. **39**, 625 (1981).
9. D. Bersani and P.P. Lottici, Phys. Stat. Sol. (b) **174**, 575 (1992).
10. D. Bersani, P.P. Lottici, and X.-Z. Ding, Appl. Phys. Lett. **72**, 73 (1998).
11. J.C. Parker and R.W. Siegel, Appl. Phys. Lett. **57**, 943 (1990).
12. J.A. Sanjurjo, E. Lòpez-Cruz, and G. Burns, Phys. Rev. B **28**, 7260 (1983).
13. G.J. Exarhos and N.J. Hess, Thin Solid Films **220**, 254 (1992).

Journal of Sol-Gel Science and Technology 13, 855–859 (1998)
© 1998 Kluwer Academic Publishers. Manufactured in The Netherlands.

The Effect of Barrier Layer Composition and Structure on the Crystallization of PZT Coatings on Silicon

D.P. BIRNIE III, M.H. JILAVI, T. KRAJEWSKI AND R. NAß
Institut für Neue Materialien, 66123 Saarbrücken, Germany

Abstract. Recent studies to improve the crystallization of PZT on silicon by using a very thin intermediate barrier layer are presented. Barrier layer compositions which displayed beneficial effects included: $SrTiO_3$, $BaTiO_3$, $BaZrO_3$, $LaAlO_3$ and $NdAlO_3$. X-ray diffraction was performed to monitor the phase transformation using barrier layers. High Resolution Transmission Electron Microscopy (HRTEM) was used to characterize the sample with the $SrTiO_3$ inter-layer. Energy Dispersive X-ray Spectroscopy (EDX) was applied for microchemical analysis and the lead distribution through the film depth was determined with a step-scanning method. Seeding layers which were nanocrystalline and dense were best at promoting PZT microstructure development because of increasing nucleation as well as reducing interdiffusion.

Keywords: crystallization, PZT, barrier layers

Introduction

Lead-zirconate-titanate (PZT) is an interesting and promising ferroelectric material. For various microelectronics applications it is particularly interesting to find ways of optimizing the structure of the PZT when fired in close proximity to either silicon or silicon dioxide surfaces. For example, field effect transistors can be fabricated with ferroelectric material as the gate dielectric, thus making a switchable transistor with hysteresis [1–3]. However, it is often found that direct contact between silicon and PZT during heating interferes with the crystallization process and the desired ferroelectric properties [4–6]. Two key effects are important during these heat treatments: nucleation of PZT into the perovskite phase, and prevention of reaction with the substrate. The present work examines whether chemically derived coatings between the silicon and the PZT could perform these functions.

Using thin interlayers is an important method for controlling the deposition and growth of thin films. For example, earlier studies have shown that lead titanate (PT) layers can be useful for lowering the transformation temperature for PZT on either platinum or sapphire substrates [7–9]. Also, lanthanum doped PT (PLT) was good for nucleating the lanthanum doped PZT analog (PLZT) [10, 11]. However, the PT or PLT layers are still not appropriate for use in direct contact with silicon.

Interlayers which have a marked difference in composition from the ferroelectric layer have also been tested, including MgO, $SrTiO_3$, ruthenium oxide, indium tin oxide, zirconia, $LaNiO_3$, TiO_x, Al_2O_3, the Y-Ba-Cu superconductor and various nitrides [12–20]. Many of these studies tried to take advantage of known epitaxial relationships which the perovskite layers have with various crystalline materials [21–25]. Unfortunately, many of these layers have the drawback that they must be deposited under very restrictive vacuum conditions.

The above studies emphasize that interlayers can have a strong epitaxial seeding effect on the transformation of PZT coatings. Here, chemical techniques are used to deposit very thin perovskite structured layers to determine whether they serve as nucleation layers or diffusion barriers during the conversion of sol-gel derived PZT thin films.

Table 1. Diffraction and structural data for PZT coatings fabricated with selected seeding layer compositions.

	t (nm)	Seeding layer	PZT coating	Comments
(No seeding)	—	—	Pyrochlore only	Lots of cracking
$SrTiO_3$	89	Crystalline	Perovskite only	No cracking
$BaTiO_3$	220	Crystalline	Perovskite only	No cracking
	71	Amorphous	Strong perovskite	No cracking
	45	Amorphous	Good perovskite	No cracking
	27	Amorphous	Good perovskite	Minor cracking
$BaZrO_3$	147	Crystalline	Mostly perovskite	No cracking
	81	Amorphous	Perovskite only	No cracking
	48	Amorphous	Perov/Pyro. mixture	No cracking
$LaAlO_3$	107	Amorphous	Strong perovskite	No cracking
$NdAlO_3$	60	Amorphous	Good perovskite	No cracking
	46	Amorphous	Good perovskite	No cracking
	28	Amorphous	Strong perovskite	No cracking
	20	Amorphous	Strong perovskite	No cracking
$PbTiO_3$	101	Amorphous	Perov/Pyro. mixture	Large cracking

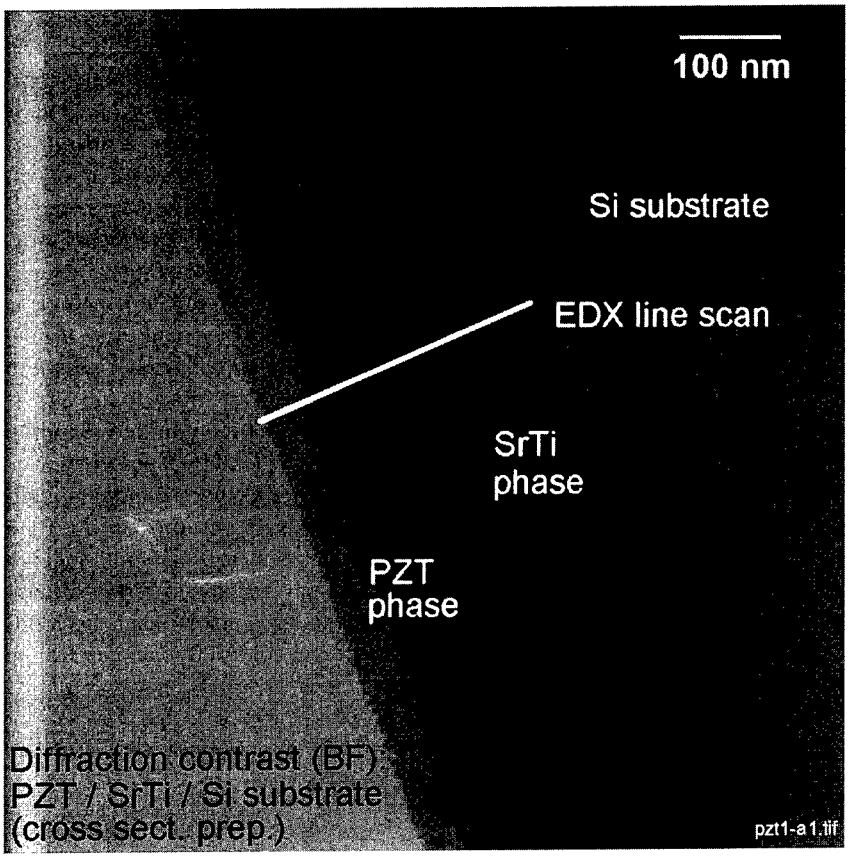

Figure 1. Cross-sectional TEM image of a $SrTiO_3$-seeded PZT coating on silicon. The white line indicates the position used for the EDS scan given in Fig. 2.

Experimental Procedure

The primary target was to generate seeding layers which would easily crystallize into the perovskite crystal structure at moderate temperatures. In keeping with possible integration into a microelectronics circuit fabrication sequence, firing temperatures were kept the same as the temperature which was used for firing the PZT coating itself. Thus, the formation of the seeding layer would not put more limiting "thermal budget" restrictions on the process line than the PZT. Compositions were chosen by careful examination of the ionic radii of elements, their normal stable ionic valences, and relevant phase diagram information [26]. In addition, rational precursors were required which could be used to synthesize the desired materials. The following compositions were tested: $BaTiO_3$, $BaZrO_3$, $PbTiO_3$, $LaAlO_3$, $NdAlO_3$, $SrTiO_3$, $YAlO_3$, $CeAlO_3$, $CeInO_3$, $LaInO_3$, $NdInO_3$, $PrAlO_3$, $PrInO_3$, and $YInO_3$. The titanate and zirconate compositions were made using titanium isopropoxide or zirconium *n*-butoxide as the primary precursors. Barium and strontium were obtained as hydrated hydroxides and dissolved into acetic acid/alcohol mixtures. The water contained in the Ba or Sr precursor provided the only water used for hydrolysis. Some aluminum containing compositions were made using aluminum *sec*-butoxide, while others used aluminum nitrate hydrate. All of the rare earth, and indium, additions were made by dissolving nitrate-hydrates into acetic acid.

Solutions were prepared and coated onto silicon substrates using spin coating and fired in air at 600°C. After forming the seeding layer, one layer of PZT solution was deposited on and fired in air, also for 15 min at 600°C. The sol-gel PZT used was an acetate-based solution having composition of Zr : Ti = 50 : 50 with 10% excess Pb [27]. PZT coating thicknesses were 175 ± 35 nm after firing. Uncoated seeding layers as well as the PZT coated substrates were characterized using XRD with a thin-film attachment allowing grazing-angle analysis (incidence angle = 2°). Broadband optical reflectance spectrum fitting was used to determine coating thicknesses to within 20% accuracy. TEM examination was performed on selected samples. This included careful cross-sectional sample preparation and allowed microcompositional profiling using energy dispersive X-ray spectroscopy.

Results and Discussion

Many of the seeding layers assisted in the transformation of the PZT coating. Table 1 gives the coating transformation results for the most successful samples tested. Although most of the seeding layers failed to transform to their crystalline perovskite structure, they nevertheless were quite beneficial towards helping transform the PZT. However, $SrTiO_3$, $BaTiO_3$, and $BaZrO_3$ were all found to be crystalline if they were thick enough. Of these samples, the $SrTiO_3$ was found to give the best coating quality. Complete transformation of the PZT layer was also achieved for $SrTiO_3$ layers of 56 nm and 39 nm. Thus, further characterization of this interlayer material was carried out using TEM.

Figure 1 shows a cross-sectional TEM image of the $SrTiO_3$-seeded sample listed in Table 1. The image shows that extensive crystallization of the $SrTiO_3$ layer has occurred and that good crystallization has also occurred in the PZT. Because of the nano-scaled grain size of the $SrTiO_3$, it is difficult to verify any particular epitaxial growth behavior. It appears that there is significantly larger grain size in the PZT layer than in the $SrTiO_3$ layer, suggesting that once the PZT has been nucleated by the $SrTiO_3$, then growth in the PZT layer occurs quite rapidly.

The possible interdiffusion processes occurring in this sample have been investigated using EDS line-scanning. Figure 2 shows a compositional profile taken from the same sample. Data were collected for Sr, Zr, Ti and Pb, starting just inside the silicon substrate and moving incrementally outward through the $SrTiO_3$ and the PZT. The data points within the 25–125 nm position range show strong Sr intensity in the $SrTiO_3$ seeding layer. From 125–275 nm both Zr and Pb have strong intensities in the PZT phase. The intensity of each signal gets smaller as the sample edge is approached because of the wedge shape near the ion-thinning perforation. Interdiffusion processes are suggested by (1) the slight enrichment of Zr near the silicon/$SrTiO_3$ interface, (2) the presence of significant Sr within the PZT layer, and (3) Pb within the $SrTiO_3$ layer. No significant amount of Pb has reacted with the silicon substrate material.

When no gel-forming alkoxide was used in the chemistry, then there was substantial difficulty obtaining good wetting and coverage of the silicon wafer before firing. Of these compositions, both $CeAlO_3$ and $CeInO_3$ were observed to crystallize into a defective

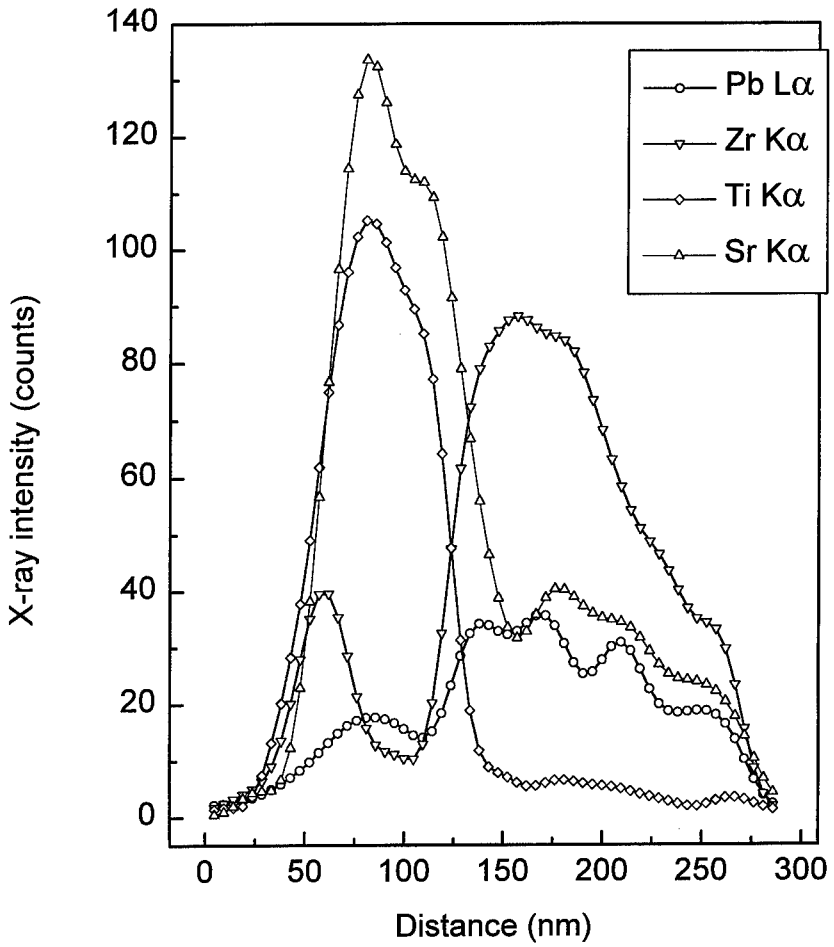

Figure 2. EDS line-scan from the $SrTiO_3$-seeded PZT sample. Scan origin starts within the silicon substrate and moves up through the $SrTiO_3$ and finally into the PZT layer.

CeO_2 structure at 600°C, while all others remained amorphous. In spite of the poor coating quality, two of these compositions ($NdInO_3$ and $LaInO_3$) provided some improved PZT transformation even though still amorphous, probably due to a diffusion barrier effect.

Table 1 also presents data on the general PZT coating quality which resulted after firing. In cases where the transformation has been well seeded by the interlayer, then homogeneous layers have been formed. However, when interdiffusion has occurred between the PZT and the silicon, then cracking of the PZT layer is always found, probably due to out-diffusion of Pb from the PZT layer and subsequent reaction at the silicon surface.

The fact that some of the amorphous materials were also quite successful as interlayers between the PZT and silicon suggests that their action as diffusion barriers is quite important. The TEM results also show that when the barrier layer has been well crystallized, especially fine grained and homogeneous PZT can be formed. This indicates that growth can proceed from the perovskite seeds which have been created underneath the PZT.

Conclusions

Chemically derived barrier layers to help prevent interaction between PZT and silicon have been investigated. The compositions of $SrTiO_3$, $BaTiO_3$, $BaZrO_3$, $LaAlO_3$ and $NdAlO_3$ were all found to provide substantial or complete conversion of the PZT layers for 15 min heat treatments at 600°C. TEM observations of the $SrTiO_3$ sample support the conclusion

that epitaxial effects are helpful in assisting in the PZT perovskite formation process. Amorphous layers were also beneficial since they acted as diffusion barriers between the PZT and the silicon substrate.

References

1. G.G. Teather and L. Young, Solid-State Electronics **11**, 527 (1968).
2. S.Y. Wu, IEEE Trans. on Electr. Dev. ED**21**, 499 (1974).
3. S.Y. Wu, Ferroelectrics **11**, 379 (1976).
4. S.L. Swartz, P.J. Melling, and C.S. Grant, Mat. Res. Soc. Symp. Proc. **152**, 227 (1989).
5. C.J. Chen, E.T. Wu, Y.H. Xu, K.C. Chen, and J.D. Mackenzie, Ferroelectrics **112**, 321 (1990).
6. L.D. Madsen and L. Weaver, J. Electronic Mater. **21**, 93 (1992).
7. S.L. Swartz, S.J. Bright, P.J. Melling, and T.R. Shrout, Ferroelectrics **108**, 71 (1990).
8. C.K. Kwok and S.B. Desu, J. Materials Res. **8**, 339 (1993).
9. C.J. Kim, D.S. Yoon, J.S. Lee, C.G. Choi, and K. No, Jpn. J. Appl. Phys., Part 1, **33**, 2675 (1994).
10. J.S. Lee, J.C. Kim, D.S. Yoon, C.G. Choi, J.M. Kim, and K. No, Jpn. J. Appl. Phys., Part 1, **33** (1A), 260 (1994).
11. J.S. Lee, J.C. Kim, D.S. Yoon, C.G. Choi, and K. No, Jpn. J. Appl. Phys., Part 1, **34** (4A), 1947 (1995).
12. E. Tokumitsu, K. Itani, B.-K. Moon, and H. Ishiwara, Jpn. J. Appl. Phys., Part 1, **34**(9B), 5202 (1995).
13. A. Matsuda, Y. Yamanaka, M. Tazoe, Y. Yonezawa, A. Morimoto, and T. Shimizu, Jpn. J. Appl. Phys., Part 1, **34**(9B), 5154 (1995).
14. N.R. Parikh, J.T. Stephen, M.L. Swanson, and E.R. Myers, Mat. Res. Soc. Symp. Proc. **200**, 193 (1992).
15. D.P. Vijay and S.B. Desu, J. Electrochem. Soc. **140**, 2640 (1993).
16. T. Zheleva, P. Tiwari, and J. Narayan, Mat. Res. Soc. Symp. Proc. **310**, 215 (1993).
17. M.-S. Chen, J.-M. Wu, and T.-B. Wu, Jpn. J. Appl. Phys., Part 1, **34**(9A), 4870 (1995).
18. K. Aoki, Y. Fukuda, K. Numata, and A. Nishimura, Jpn. J. Appl. Phys., Part 1, **34**(1), 192 (1995).
19. C.K. Barlingay and S.K. Dey, Appl. Phys. Lett. **61**, 1278 (1992).
20. G. Yi, Z. Wu, and M. Sayer, J. Appl. Phys. **64**, 2717 (1988).
21. S.H. Rou, T.M. Graettinger, A.F. Chow, C.N. Soble II, D.J. Lichtenwalner, O. Auciello, and A.I. Kingon, Mat. Res. Soc. Symp. Proc. **243**, 81 (1992).
22. K. Iijima, Y. Tomita, R. Takayama, and I. Ueda, J. Appl. Phys. **60**, 361 (1986).
23. R. Takayama and Y. Tomita, J. Appl. Phys. **65**, 1666 (1989).
24. V.E. Wood, J.R. Busch, S.D. Ramamurthi, and S.L. Swartz, J. Appl. Phys. **71**, 4557 (1992).
25. D.S. Yoon, C.J. Kim, J.S. Lee, W.J. Lee, and K. No, J. Mater. Res. **9**, 420 (1994).
26. *Phase Diagrams for Ceramists*, Vols. I–VIII (American Ceramic Society, Columbus, Ohio).
27. R.A. Assink and R.W. Schwartz, Chem. Mater. **5**, 511 (1993).

Journal of Sol-Gel Science and Technology 13, 861–864 (1998)
© 1998 Kluwer Academic Publishers. Manufactured in The Netherlands.

Study of the Lead Environment in Liquid and As-Dried Precursors of PZ, PT and PZT Thin Films

IZTOK ARČON
School of Environmental Sciences, p.p. 301, 5001 Nova Gorica, Slovenia and Jožef Stefan Institute, 1001 Ljubljana, Jamova 39, Slovenia

BARBARA MALIČ AND MARIJA KOSEC
Jožef Stefan Institute, 1001 Ljubljana, Jamova 39, Slovenia

ALOJZ KODRE
Faculty of Mathematics and Physics, University of Ljubljana, Jadranska 19 and Jožef Stefan Institute, 1001 Ljubljana, Jamova 39, Slovenia

Abstract. The environment of lead and zirconium atoms in liquid and as-dried precursors for $PbZrO_3$ (PZ), $PbTiO_3$ (PT) and $Pb_{1.1}Zr_{0.53}Ti_{0.47}O_3$ (PZT) thin film deposition were analyzed by EXAFS. The sols were prepared by 2-methoxyethanol route with lead acetate and lead oxide as lead sources. Pb—O—M (M = Zr and/or Ti, depending on the sol composition) linkages were determined in all sols. The choice of lead source weakly influences the lead environment, and strongly influences that of zirconium in both PZ and PZT sols. By drying lead oxide based sols the Pb—M correlation is moderately reduced in PZ, and PT and is strongly reduced in PZT.

Keywords: PZT thin films, EXAFS, precursors

Introduction

Materials based on Pb(Zr, Ti)O_3 (PZT) are among the most widely studied functional ceramics. Alkoxide based sol-gel processing of PZT prevails in thin film preparation, with a variety of applications in microelectronics and micromechanics that cannot be realized with bulk ceramic materials [1]. Although the short-range structure of the sols and amorphous as-dried precursors is recognized as influencing the crystallization and the microstructure of thin films, only a few structural studies of PZT precursors have been reported to date [2–4]. Using EXAFS, which is a powerful tool for this purpose [5], the environments of lead and titanium atoms in $PbTiO_3$ (PT) amorphous precursor have been found to be weakly dependent on various alkoxide groups (*n*-propoxide or *n*-butoxide). Pentacoordinated titanium atoms, forming a trimeric structure of distorted hexagon rings, with lead atoms bound to titanium atoms by oxygen linkages have been proposed [2]. On the other hand, in the $PbZrO_3$ (PZ) amorphous precursor the choice of alkoxide group (*n*-propoxide or *n*-butoxide) distinctly influences the environment of zirconium atoms [3].

In a similar study of PT, PZ and PZT heat treated amorphous precursors, prepared by 2-methoxyethanol based route, Sangupta et al. [4] showed a preferred homocondensation of titanium and/or zirconium species. For PT and PZT precursors separate networks of Ti—O—Ti and Zr—O—Zr linkages were observed whereas in PZ both Zr—O—Zr and Pb—O—Zr correlations were found. Sangupta et al. concluded that lead cations do not contribute to the polymeric M—O—M framework, but occupy random positions in the amorphous gel.

In this paper the local environment of lead and zirconium atoms in PZ, PT and PZT ($Pb_{1.1}Zr_{0.53}Ti_{0.47}O_3$) sols for thin film deposition are studied. A series of

sols was prepared via the 2-methoxyethanol route with lead acetate and zirconium and titanium *n*-propoxides [6]. A modified route, avoiding the presence of acetate groups in the sol, was introduced by using lead oxide as the source of lead [7]. The lead oxide based sols were also analyzed after drying to 150°C. (It should be noted however that our results cannot be directly compared to those of Sangupta et al. [4]: they studied the local structure of PT, PZ and PZT precursors dried at much higher temperatures, namely 375 to 500°C.) The influence of the lead source and the effect of drying on the local structure of the sols is examined.

Experimental

PZ, PZT and PT sols were prepared by diluting zirconium and/or titanium *n*-propoxides with 2-methoxyethanol (typically 0.1 mole of alkoxides in 200 ml) and adding anhydrous lead acetate or lead oxide in the required quantity. The metal contents of all the compounds were determined gravimetrically. The reaction mixtures were heated to approximately 60°C to get clear solutions. By refluxing for 2 hours the by-products were distilled off and stable 0.5 M sols were obtained. All manipulations were performed in dry argon atmosphere.

The sols were further concentrated to approximately 2 M solutions in order to increase signal to noise ratio in EXAFS measurements. As-dried amorphous samples of the lead oxide based sols were prepared at 150°C.

EXAFS spectra at lead L_3-edge and zirconium K-edge of the precursors (sols and as-dried samples) were measured at the ROEMO station in HASYLAB at DESY (Hamburg, Germany). An Si(311) double-crystal monochromator was used with 2 eV resolution at 18 keV. Harmonics were effectively eliminated by detuning the monochromator crystal using a stabilization feedback control. A liquid absorption cell with lucite windows was used for sol samples, while as-dried samples were prepared on multiple layers of adhesive tape, with the absorption thickness of $\mu d \sim 2$ above the absorption edge of investigated elements. Reference spectra without the samples were taken under identical conditions.

Results

EXAFS spectra were analyzed with the University of Washington analysis programs using FEFF6 code for ab initio calculation of scattering paths [8, 9]. Two distinct shells of neighbors are found in the k^3 weighted Fourier transforms of all the lead and zirconium spectra. Each shell is fitted separately in the k space interval from 3.5 to 12 Å^{-1}. The number and species of neighbor atoms and distances are listed in Tables 1–3 for PZ, PZT and PT precursors, respectively.

Table 1. Parameters of the nearest coordination shells around lead and zirconium atoms in PZ precursors. Type of neighbor atom, average number N, distance R for lead acetate ($Pb(OAc)_2$), lead oxide (PbO) based sols and as-dried (PbO) sample are given. Uncertainty of the last digit is given in parentheses.

	PZ precursors					
	Sol ($Pb(OAc)_2$)		Sol (PbO)		As-dried (PbO)	
	N	R (Å)	N	R (Å)	N	R (Å)
Pb neigh.						
O	1.8(1)	2.28(1)	2.2(4)	2.27(2)	2.2(2)	2.25(1)
Zr	2.4(4)	3.91(2)	1.4(2)	3.80(2)	1.1(2)	3.82(2)
Zr	—	—	1.0(2)	3.95(2)	0.7(1)	3.98(2)
Zr neigh.						
O	2.0(2)	2.09(2)	1.8(2)	2.09(2)	2.0(1)	2.08(2)
O	2.0(4)	2.16(2)	2.0(2)	2.16(2)	2.0(3)	2.16(2)
O	2.1(3)	2.26(1)	1.9(2)	2.27(1)	2.0(3)	2.26(1)
Zr	5.4(8)	3.48(1)	3.4(7)	3.50(1)	3.7(7)	3.45(1)

Table 2. Parameters of the nearest coordination shells around lead and zirconium atoms in PZT precursors. (Same assignations as in Table 1.)

	PZT precursors					
	Sol ($Pb(OAc)_2$)		Sol (PbO)		As-dried (PbO)	
	N	R (Å)	N	R (Å)	N	R (Å)
Pb neigh.						
O	1.0(2)	2.23(1)	1.0(2)	2.20(1)	0.3(1)	2.15(2)
O	1.0(2)	2.38(1)	1.0(2)	2.36(1)	1.7(4)	2.25(2)
Ti	1.0(3)	3.67(1)	0.9(3)	3.73(1)	0.32(5)	3.74(1)
Zr	1.0(3)	3.83(1)	1.0(3)	3.83(1)	—	—
Zr neigh.						
O	2.0(2)	2.08(2)	2.1(2)	2.09(2)	2.0(1)	2.08(2)
O	2.0(2)	2.16(2)	1.9(2)	2.16(2)	2.0(2)	2.17(2)
O	2.2(2)	2.26(1)	2.2(2)	2.27(1)	2.0(1)	2.27(1)
Zr	5.2(8)	3.47(1)	3.0(7)	3.49(1)	2.2(7)	3.45(1)

PZ Precursors

All three PZ precursors have a similar environment around the lead atoms (Table 1). Two oxygen atoms

Table 3. Parameters of the nearest coordination shells around lead atoms in PT precursors. (Same assignations as in Table 1.)

	PT precursors					
	Sol ($Pb(OAc)_2$)		Sol (PbO)		As-dried (PbO)	
	N	R (Å)	N	R (Å)	N	R (Å)
Pb neigh.						
O	0.5(3)	2.21(2)	1.0(3)	2.21(2)	0.9(3)	2.20(2)
O	0.9(3)	2.31(2)	0.9(2)	2.35(2)	1.0(3)	2.33(2)
Ti	0.6(2)	3.34(1)	0.5(2)	3.29(1)	0.8(3)	3.33(1)
Ti	0.6(2)	3.51(1)	0.5(2)	3.45(1)	—	—

are identified in the first shell at the distance of 2.27 Å. In the second shell, at about 3.9 Å, zirconium atoms are clearly identified. Their number is found to decrease from 2.4 to 1.8 between sol and as-dried sample.

Zirconium atoms are octahedrally coordinated with six oxygen atoms in pairs at nonequal distances: 2.09, 2.16 and 2.26 Å. (The three different Zr—O distances can be assigned to three different coordination forms of the alkoxide ligands: terminal, bridging and coordinated, respectively [10].) Zirconium neighbors are found in the second shell of all three PZ precursors at the distance of about 3.5 Å. A significant difference of 2 units in coordination number of zirconium atoms is observed between lead oxide and lead acetate based precursors.

Spectral features beyond 3.5 Å are indicated but they cannot be modelled by a distinct shell. Reliable values for the probable presence of lead neighbors cannot be obtained.

PZT Precursors

Both PZT sols have the same local structure around lead atoms. The first coordination shell consists of two oxygen atoms at nonequal distances of 2.23 and 2.38 Å. In the second shell one titanium and one zirconium atom are identified at 3.7 and 3.8 Å, respectively (Table 2).

The environment of lead atoms in the as-dried sample is significantly different: the oxygens in the first shell are redistributed to 0.3 at 2.15 Å and 1.7 at 2.25 Å. No zirconium atoms are found in the second shell and only 0.3 titanium atoms at the distance 3.74 Å.

The local environment of zirconium atoms is basically the same as in the case of PZ precursors. Zirconium atoms are octahedrally coordinated by six oxygens at nonequal distances, and by zirconium atoms in the second shell.

PT Precursors

In PT precursors lead atoms are coordinated with two oxygens in the first shell: at 2.21 and 2.31 Å. The second shell consists of one titanium atom. In both sols the shell is split equally and two Pb—Ti distances are found: 3.3 and 3.5 Å. In the as-dried sample only one Pb—Ti distance is found (Table 3).

Discussion and Summary of Results

The EXAFS technique has been extended for the first time to the quantitative analysis of $Pb(Zr,Ti)O_3$ precursors in the liquid state. The immediate neighborhood is the same in all cases: two oxygen atoms for lead and six for zirconium. Significant differences introduced by the choice of the lead source and by drying are found in the metal-metal correlation in the second shell. The apparent discord with stoichiometric ratios is most probably compensated in the more distant neighborhood, beyond the sensitivity of the method. However, Pb—O—Ti and Pb—O—Zr linkages in the sols are definitely established for the first time.

Surprisingly the choice of the lead source has almost no influence on the lead atom neighborhood, but affects significantly the Zr—Zr correlation. Only about two thirds of the number of Zr—O—Zr linkages found in lead acetate based precursors is retained in those based on lead oxide.

The process of drying, on the other side, mainly effects the lead EXAFS spectra. Generally, the lead-metal correlation is reduced: the effect is weak in both bimetallic species (PZ and PT) and dramatic in PZT where zirconium neighbors are completely lost from the second shell and titanium neighbors are depleted to one third. The finding is supported by a corresponding change in the oxygen distribution in the first shell. It should be noted, however, that the resulting parameters need not correspond to an equilibrium structure. The drying temperature chosen was intended to expel the solvent and thus was not at a steady TGA point.

Some of the findings can easily be incorporated into the generally known dynamics of the PZT sol-gel precursors. For other findings, however, the interpretation in the form of a structural model is still subject to debate: there have been no reports on zirconium alkoxide liquid oligomers with Zr—Zr correlation in excess of 2 [10, 11]. However, with the technique employed, the development of the metal-metal linkages can in principle be followed throughout the processing from the early liquid phases to the final product.

Acknowledgment

Support by the Ministry of Science and Technology of the Republic of Slovenia within the National Research Program, the Commission of the European Communities within the Community's Action for Cooperation in Science and Technology with the Central and Eastern European Countries (1992) and internationales Büro Jülich (Germany) is gratefully acknowledged. R. Frahm (HASYLAB) provided expert advice on beamline operation.

References

1. P. Muralt, Informacije MIDEM **26**, 266 (1996).
2. B. Malič, I. Arčon, M. Kosec, and A. Kodre, J. Mater. Res. **12**, 2602 (1997).
3. B. Malič, I. Arčon, M. Kosec, and A. Kodre, J. Sol-Gel Sci. Tech. **8**, 343 (1997).
4. S.S. Sangupta, L. Ma, D.L. Adler, and D.A. Payne, J. Mater. Res. **10**, 1345 (1995).
5. D.C. Koningsberger and R. Prins, *X-Ray Absorption* (John Wiley, New York, 1988).
6. K.D. Budd, S.K. Day, and D.A. Payne, Br. Ceram. Proc. **36**, 107 (1995).
7. M. Kosec, U. Delalut, B. Malič, V. Bobnar, and G. Dražič, in *ISAF '96: The Tenth IEEE International Symposium on Applications of Ferroelectrics*, edited by B.M. Kulwicki, A. Amin, and A. Safari (IEEE, Piscataway, NJ, 1996), p. 443.
8. E.A. Stern, M. Newville, B. Ravel, Y. Yacoby, and D. Haskel, Physica B **208/209**, 117 (1995).
9. J.J. Rehr, R.C. Albers, and S.I. Zabinsky, Phys. Rev. Lett. **69**, 3397 (1992).
10. D. Peter, T.S. Ertel, and H. Bertagnolli, J. Sol-Gel Sci. Tech. **5**, 5 (1995).
11. D. Peter, T.S. Ertel, H. Bertagnolli, J. Sol-Gel Sci. Tech. **3**, 91 (1994).

Journal of Sol-Gel Science and Technology 13, 865–868 (1998)
© 1998 Kluwer Academic Publishers. Manufactured in The Netherlands.

Preparation of PZT Film and Powder by Sol-Gel Technique Using Ti- and Zr-Alkoxides and a Novel Pb-Precursor; $Pb(NO_3)_2$1.5EO3

K. LASHGARI AND G. WESTIN
Dept. of Inorganic Chemistry, Arrhenius Laboratory, Stockholm University, S-106 91 Stockholm, Sweden

Abstract. PZT ($PbZr_{0.53}Ti_{0.47}O_3$) films and powders have been prepared by a precursor mixture containing $Pb(NO_3)$1.5EO3 (EO3 = triethylene glycol) and Zr- and Ti-methoxy ethanolates. The gel films have been deposited on Si/Ti/Pt substrates and on glass substrates from which they can easily be removed. The PZT films on the Si/Ti/Pt substrates were prepared with thicknesses up to 200 nm per layer after heating to 700°C. The phase development on heat-treatment of loose gel films to yield PZT was investigated by Powder-XRD, FT-IR, SEM-EDS, TEM-EDS, thermo-mass spectroscopy and DSC and the PZT was found to form in the region 550–700°C. PZT powders of 50–5000 nm sizes were prepared by hydrolysis under basic conditions and washing with water followed by heat-treatment to 650°C.

Keywords: PZT, film, powder, thermal phase evolution, Pb-precursor

1. Introduction

PZT ceramics have the highest piezoelectric coupling constants known and have significant ranges of ferroelectric polarization and dielectric constant [1]. Sol-gel processing has proved to be a potent and versatile technique for preparation of many types of complex oxide films [2]. In the preparation of PZT films however, many difficulties have to be dealt with, e.g., evaporative loss of PbO, reduction of PbO to Pb with alloying of the substrate as result, formation of pyrochlore or fluorite phases and cracking during heat-treatment [3–6]. The temperatures needed for preparation of PZT films are normally in the range 600–650°C, which is higher than for many other perovskites. We are investigating new precursor systems for preparation of relatively thick $Pb(Zr_{0.53}Ti_{0.47})O_3$ films (5–10 μm) for application as actuator elements in micro-motors.

2. Experimental

Preparation of the Precursor Solution and Films and Powders. The synthesis schemes for the Pb-, Zr- and Ti-precursors and the preparation routes for PZT films and powders are shown in Fig. 1. The $Pb(NO_3)_2$, $Ti(OiPr)_4$, 70% $Zr(nOPr)_4$ in nPrOH and EO3 were used as purchased. The methoxyethanol (MOEH) was distilled over CaH_2 before use. All manipulations of chemicals were made under dry, oxygen free N_2 using vacuum-line techniques.

Phase-Development Studies. The changes in weight on heating of loose films to obtain the PZT was studied by thermo-gravimetric analysis (TGA). The reactions occurring on heating were also studied by thermo-mass spectroscopy (TMS) on the gases evolved and by differential scanning calorimetry (DSC) up to 700°C on the heat exchanged with the surroundings on heating. Materials were also quenched in the TG apparatus from different temperatures for analysis of their contents by a scanning electron microscope with an energy dispersive spectrometer (SEM-EDS), a transmission electron microscope with an EDS (TEM-EDS), powder X-ray diffraction (powder-XRD) and Fourier transform infrared (FT-IR) spectroscopy.

3. Results and Discussion

Synthesis of Precursor. $Pb(NO_3)_2$ is a stable, non-hygroscopic compound, but is not soluble in common organic solvents in which Ti and Zr alkoxides are soluble. By complexation with polyglycol ligands it

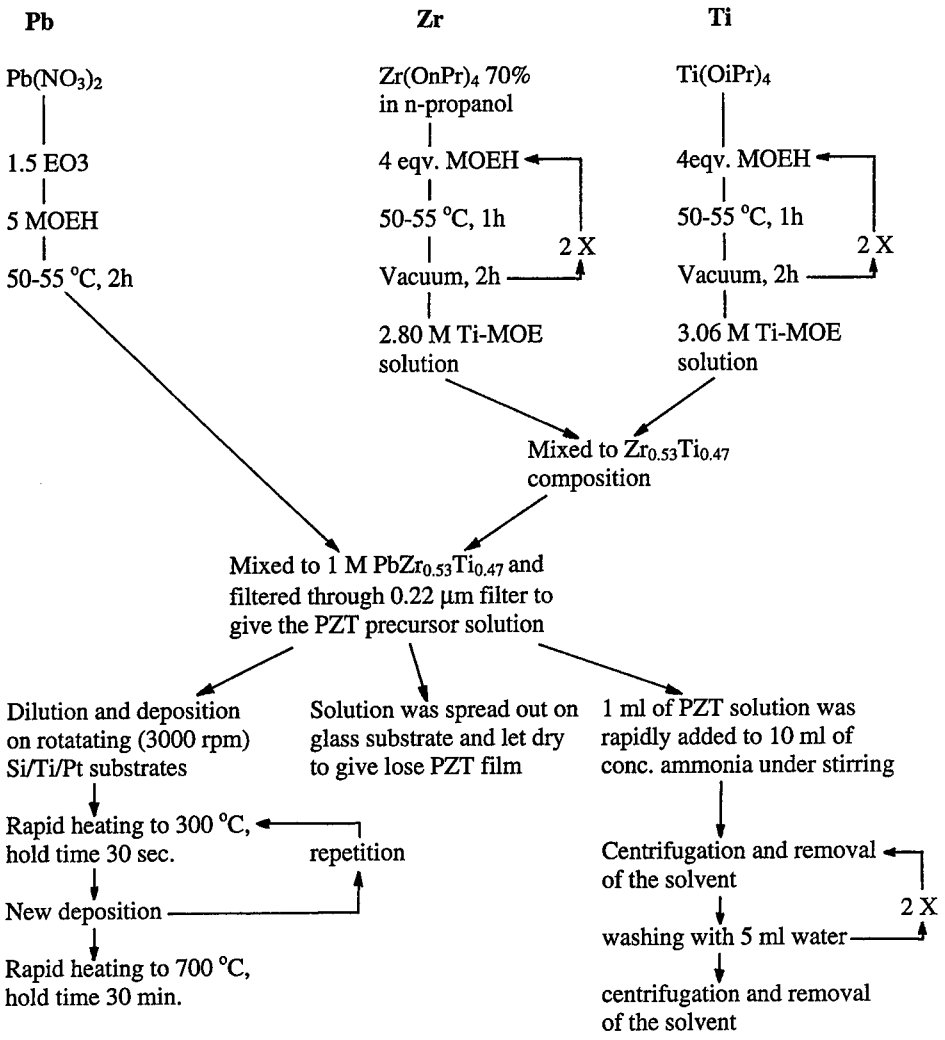

Figure 1. Preparation scheme of the PZT precursor solution and the preparation of films and powders from it.

is possible to obtain a lead nitrate that is soluble in methoxy ethanol. After some initial studies the EO3 chainlength was selected and it was found that a minimum of 1.5EO3 per $Pb(NO_3)_2$ was needed for a good solubility. During our studies using $Pb(NO_3)_2$1.5EO3, the structures of several $Pb(NO_3)_2$ complexes with EOx ligands were reported [7]. The EO3 complex was not reported, but the structure of the $Pb(NO_3)_2$1.5EO4 complex showed that both the NO_3^- and EO4 groups were co-ordinated to the Pb^{2+} atom. We believe that the EO3 complex has a similar structure. Complexation of other ions, e.g., Bi^{3+} and Re^{3+} with EOx groups have also been reported [8, 9] and the Bi^{3+} compound has been used in the preparation of varistors [10]. The solubility of the precursor is low in normal alcohols such as isopropanol, which requires a vacuum treatment to obtain pure methoxy ethanolates, if $Ti(OiPr)_4$ and $Zr(nOPr)_4$ are used as precursors.

Preparation of Loose Gel Films. In order to study the phase evolution when decomposing the hydroxyls and organic groups to form PZT, the precursor solution was deposited on glass substrates, so that the films formed could be removed after drying. The transparent and ca 100 μm thick films were X-ray amorphous and homogeneous in SEM. The IR spectrum of the gel film showed peaks mainly from polyether groups (1250–800 cm^{-1}), H_2O (1630 cm^{-1}) and nitrato groups (1384 cm^{-1}) (see Fig. 2). The gel was virtually free of MOE(H) as is shown by the absence of a peak at 1194 cm^{-1} which was found in MOE(H) only, while the EO3 groups remained, as is shown by the great

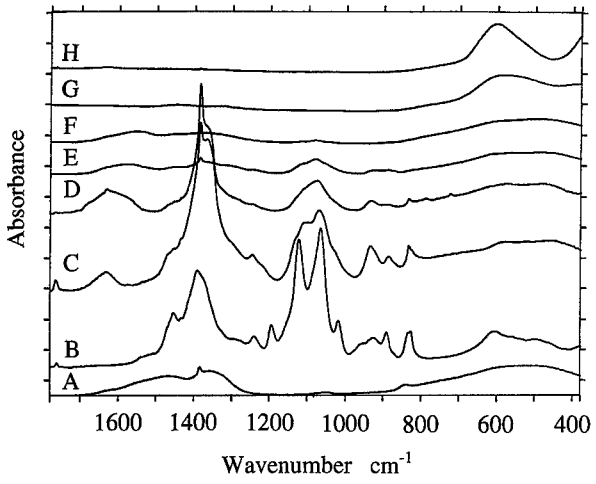

Figure 2. FT-IR spectra of PZT powder (A), PZT precursor solution (B), PZT gel (C), gel heated to 185°C (D), gel heated to 285°C (E), gel heated to 355°C (F), gel heated to 550°C (G) and gel heated to 700°C (H). The heating rate was 5°C/min in air.

similarity of the peaks in the region 1250–800 cm^{-1} to those of EO3. The peak due to the NO_3^- group was quite broad in the precursor solution as well as in the gel, but a small sharp peak at 1384 cm^{-1} had emerged which is probably due to a small amount of uncomplexed $Pb(NO_3)_2$ which has a single, sharp peak at 1384 cm^{-1}.

Thermal Decomposition of Gel Films. The weight loss can be separated into four distinct steps at; 140–185°C, 185–285°C, 285–355°C, and 355–520°C, as is shown in the TG-curve in Fig. 3. The IR spectra of materials quenched from the end of each step are shown in Fig. 2.

In the region 140–185°C, the weight loss is ascribed mainly to evaporation and decomposition of EO3 and to

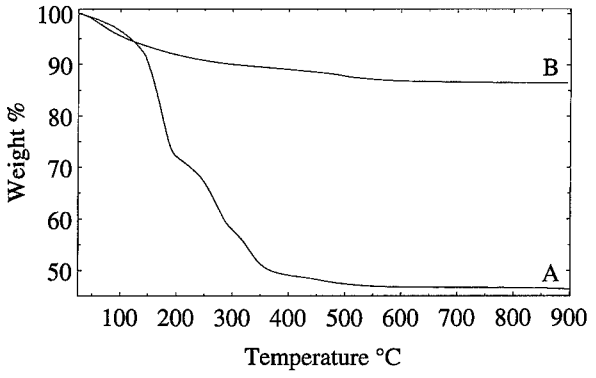

Figure 3. TG-curves obtained at a rate of 5°C/min in air of PZT gel film (A) and PZT powder (B).

a smaller degree NO_3^- groups and masses corresponding to organic groups; NO_x and CO_2 were observed in the thermo-mass spectra. The IR spectrum of a sample quenched from 185°C showed an increased portion of the sharp 1384 cm^{-1} peak, due to crystalline $Pb(NO_3)_2$ and also showed that the amount of EO3 had been reduced. In the TEM, a network of ca 5–10 nm diameter wires of closely sintered particles containing Zr and Ti was observed, while the interpenetrating Pb containing phase was found with parts as crystalline $Pb(NO_3)_2$ (also observed in the powder XRD studies and in line with the IR spectrum). The Pb could easily be heated in the electron beam to form lead particles and leave the network containing Zr and Ti without Pb. This shows that the Pb-NO_3-EO3 did not participate in the network, but only was intermixed with it. The origin of this structure might be found in the different reactivities of the $Pb(NO_3)_2$1.5EO3 which we have shown to remain in the gel and the easily hydrolyzed Zr- and Ti-alkoxides. It is probable that the Zr- and Ti-alkoxides form the network during the hydrolysis and the $Pb(NO_3)_2$EO3 stays in the liquid phase which eventually is dried out.

In the temperature range 185–285°C, most of the remaining NO_3^- groups were exothermically lost together with further organic matter yielding the gaseous hydrocarbons, H_2O, NO_x and CO_2. The remaining material at 285°C was composed of ca 3–5 nm densely packed particles and was amorphous when observed by TEM and by powder-XRD. The analyzed elemental contents over the material, in a 10–15 nm probe, varied little, ca 10%. The IR spectrum showed that almost all of the NO_3^- groups had been removed and that the remainder contained somewhat smaller amounts of EO3 and H_2O compared to the 185°C sample.

In the region 285–355°C most of the remaining MOE(H) and EO3 groups were removed, leaving a very small amount of organic groups and hydroxyls. The sample quenched from 355°C showed weak and broad powder-XRD peaks that could be ascribed to PbO (orthorhombic) and Pb (cubic) and in the TEM, areas with very high Pb contents were found, as well as 5 nm sized Pb containing particles, that might account for the two phases observed by powder-XRD. However, the main part of the material remained amorphous and contained Pb, Zr and Ti.

In the last small step at 355–520°C, removal of all of the remaining hydroxyl and organic groups occurred and the resulting material at 550°C showed powder-XRD peaks mainly from PZT, but also peaks that could be attributed to pyrochlore or fluorite and to a very small extent PbO (tetragonal). TEM showed that the main

part of the material consisted of ca 100–200 nm sized diffuse PZT grains with good diffraction patterns, while the remaining part consisted of ca 10–20 nm sized crystalline particles and amorphous material. The elemental homogeneity had again improved and was of the same magnitude as that observed for the 285°C sample. The crystalline 10 nm particles probably consist of the pyrochlore or fluorite phase observed in the powder-XRD. The particles were too small to be analyzed properly with the EDS in their surrounding material and had too weak and broad XRD peaks to determine the unit cell accurately, but they probably contain Pb, Zr and Ti as the pyrochlore or fluorite phase observed by other groups in other sol-gel derived films [3–6].

After further heat-treatment to 700°C only the PZT phase could be observed with powder-XRD and in the TEM. The PZT crystallites showed as ca 50–300 nm crystals with sharp diffraction patterns of PZT. Heating to 900°C caused the crystallites to grow to 150–400 nm. The M-O peak at 606 cm^{-1} in the IR spectrum was unchanged when the sample was further heated to 900°C showing that the material had reacted to completeness at 700°C. At 550°C, the peak maximum was observed at lower values indicating the presence of other phases, such as the fluorite (or pyrochlore) and PbO ones.

Preparation of PZT Films. PZT films on Si/Ti/Pt substrates were prepared by the spin coating technique as given in Fig. 1. Rapid heating was made to 300°C to ensure that most of the weight losses had occurred and to make a solid base for the next layer. The thickness of each layer was up to 200 nm with the 0.7 M PZT solutions. Thicker layers, up to 500 nm, were obtained with 1 M PZT solutions that could sometimes be prepared crackfree, but often some narrow cracks were obtained in places. When a desired thickness was achieved, the film was rapidly heated to 700°C and annealed for 30 min. The resulting film was covered with ca 1 μm rosettes of the type that has been observed for sol-gel derived PZT films [3–6].

Preparation of PZT Powders. After hydrolysis with an excess of water-ammonia as described in Fig. 1, the IR spectrum of the resulting 50–5000 nm sized and densely agglomerated particles showed that the MOE(H) and EO3 groups were totally removed and that only a very small amount of $Pb(NO_3)_2$ (peak at 1384 cm^{-1}) remained (see Fig. 2). The material was homogeneous in the SEM. The hydroxyls and NO_3^- groups were removed by heating to ca 550°C. Samples quenched from temperatures up to 450°C were all X-ray amorphous. At 650°C, the PZT phase had formed with particles of the same sizes as the gel and the IR M-O band was identical to that of the loose film samples heated to 700 and 900°C, respectively.

4. Conclusions

The preparation of PZT films on Si/Ti/Pt substrates with a new Pb-nitrate precursor was described. Up to 200 nm thick, crackfree oxide layers were obtained in a single deposition and a surface structure typically found for PZT was shown after heat-treatment to 700°C for 30 min. The phase development was studied in loose films and the gel was shown to consist of two phases, Pb-NO_3-EO3 and hydrolyzed Zr- and Ti-alkoxides. The phase evolution occurring on heat-treatment of the loose gel films has been described. The PZT was first found at 550°C together with pyrochlore or fluorite and a very small amount PbO. Pure PZT was obtained at 700°C. These observations are similar to those observed for other sol-gel systems with metal-organic Pb-precursors. Powders produced by treatment with water-ammonia contained a rather small amount of hydroxyls and a very small amount of $Pb(NO_3)_2$, which were removed at 550°C. The material gave the PZT phase at 650°C. Futher studies on the phase development during heat-treatment are in progress with various techniques and a more detailed description of the phase development, including TEM micrographs, will be given elsewhere.

References

1. M. Sayer and K. Sreenivas, Science **247**, 1056 (1990).
2. C.D. Chandler, C. Rogers, and M.J. Hampden-Smith, Chem. Rev. **93**, 1205 (1993).
3. C.D.E. Lakeman, Z. Xu, and D.A. Payne, J. Mater. Res. **10**, 2042 (1995).
4. B.A. Tuttle, T.J. Headley, B.C. Bunker, R.W. Schwartz, T.J. Zender, C.L. Hernandez, D.C. Goodnow, R.J. Tissot, J. Michael, and A.H. Carim, J. Mater. Res. **7**, 1876 (1992).
5. A.H. Carim, B.A. Tuttle, D.H. Doughty, and S.L. Martinez, J. Am. Ceram. Soc. **74**, 1455 (1991).
6. C.D.E. Lakeman and D.A. Payne, J. Am. Ceram. Soc. **75**, 3091 (1992).
7. R.D. Rogers, A.H. Bond, and D.M. Roden, Inorg. Chem. **35**, 6964 (1996).
8. R.D. Rogers, A.H. Bond, and D.M. Roden, J. Am. Chem. Soc. **114**, 2960 (1992).
9. T. Lu, L. Ji, M. Tan, Y. Liu, and K. Yu, Polyhedron **16**, 1149 (1997).
10. Å. Ekstrand, M. Nygren, and G. Westin, J. Sol-Gel Sci. Techn. **8**, 697 (1997).

Journal of Sol-Gel Science and Technology 13, 869–872 (1998)
© 1998 Kluwer Academic Publishers. Manufactured in The Netherlands.

Synthesis and Characterization of Highly Oriented Sol-Gel (Pb, La)TiO_3 Thin Film Optical Waveguides

JUNMO KOO, KWANGSOO NO, AND BYEONG-SOO BAE
Department of Materials Science and Engineering, Korea Advanced Institute of Science and Technology (KAIST), Taejon, 305-701, Korea

Abstract. The preparation and the optical characteristics of highly oriented PLT thin films are investigated. PLT films fabricated on MgO(100) and *c*-plane sapphire substrates have highly grown in (100) and (111) orientations, respectively. PLT films with high La content have a near cubic structure and weak anisotropy of refractive indices. The optical propagation losses of PLT films decrease as the La content of the films increases due to a complex interaction of surface roughness reduction and a reduction in the anisotropy refractive index. However, optical scattering in thicker sol-gel PLT thin film waveguides occurs by the internal scattering mechanism from the defects and the interfaces rather than by the surface scattering mechanism.

Keywords: sol-gel, lead lanthanum titanate, thin film, optical waveguide, optical propagation loss

1. Introduction

Much attention has been paid to lanthanum-modified lead zirconate titanate (PLZT) solid solution systems which are well-known ferroelectric materials for various applications such as high dielectric, pyroelectric, piezoelectric, and electro-optic devices, [1]. Since PLZT ceramics are transparent in the visible and near-infrared regions, and have superior electro-optic characteristics, thin films of this material are especially attractive for the application to integrated optical devices such as optical switches and optical waveguide modulators [1, 2].

Recently, sol-gel processing of PLZT thin films has been reported as giving advantages such as precise composition control and homogeneity, low temperature synthesis, large-area deposition, low cost, and short fabrication times [3–5].

In this paper, highly oriented PLT thin films are prepared by sol-gel processing and their optical waveguiding characteristics such as refractive index and optical propagation loss are investigated. The reason for studying compositions without zirconium is that PLT is known to be better for optical applications due to its finer grain size and higher transparency than PLZT [3].

2. Experimental Procedure

PLT films with the general chemical formula, $Pb_{1-x}La_xTi_{1-x/400}O_3$ (PLTx) where $x = 5$, 10, 15, 20 and 28 mol%, were prepared. A precise procedure for preparing the precursor solution is presented elsewhere [4, 5]. Lead acetate, lanthanum nitrate, and titanium isopropoxide were used as precursors. 5 mol% excess Pb was incorporated to compensate for PbO loss. 2-Methoxyethanol was used as a solvent. The substrates used in this study were MgO(100) and *c*-plane sapphire single crystals. The green films, which were spin-coated, were dried at 400°C on a hot plate for 10 min, yielding about 500 Å thickness per coating. The films were heat-treated with 5°C/min to 700°C holding for 30 min to crystallize them as a single perovskite phase. All the films were cooled at 2°C/min in air to prevent the microcracks from thermal shock during cooling.

The crystalline phase and the orientation of the PLT films were examined using X-ray diffraction. The microstructure and the RMS surface roughness of the films were observed using atomic force microscopy (Park Scientific Instruments, Autoprobe 5M). In order to measure the refractive indices and the optical

propagation losses of the films, a prism coupler with a 632.8 nm wavelength was used [5].

3. Results and Discussion

3.1. Preparation of PLT Thin Films

XRD patterns of a PLT films (≈3500 Å) with a range of La contents, fabricated on MgO(100) single crystal substrates are shown in Fig. 1(a). All the films contain a single perovskite phase without any other noticeable phases, and are highly *a*-axis oriented with small extra peaks of (110) and (111). When the La content is low, both (100) and (001) peaks are observed. Only the (100) peak is detected when the La content increases to above 20 mol% due to the change of the perovskite structure from tetragonal structure to cubic structure [6]. XRD patterns of PLT films, with a range of La contents, fabricated on *c*-plane sapphire substrates are shown in Fig. 1(b). The films are highly oriented on the *c*-plane sapphire substrate, and the main (111) peak and small extra peaks are observed. Since the structure of the film changes from the tetragonal structure to the cubic structure as La content increases, the misfit between the film and the substrate decreases [7]. Therefore, the intensity of main (111) peak increases compared with other peaks, and the peak shifts to a higher 2θ angle and approaches the (0001) peak of the sapphire substrate as the La content increases.

3.2. Characteristics of PLT Thin Film Waveguides

The refractive indices n_o and n_e of the PLT films on MgO(100) substrates, measured using the prism coupler, are shown in Fig. 2. In the tetragonal perovskite PLT films (5 mol% La to 20 mol% La), the extraordinary refractive index, n_e, decreases significantly as La content increases, while the ordinary refractive index, n_o, remains at an almost constant level. However, the refractive indices n_o and n_e of PLT28 are almost the same since the film has a cubic structure. Thus, it is suggested that the anisotropy of the refractive indices decreases with increasing La content.

The optical propagation losses of the PLT films (≈2500 Å) on MgO and sapphire substrates are plotted in Fig. 3. The optical propagation losses of the films decrease with increasing La content for films on both the MgO and sapphire substrates.

Generally, optical propagation loss in the transparent thin film waveguides is considered to occur by scattering, and this scattering mechanism can be divided into surface scattering and non-surface scattering [8]. The non-surface scattering is affected by the defects

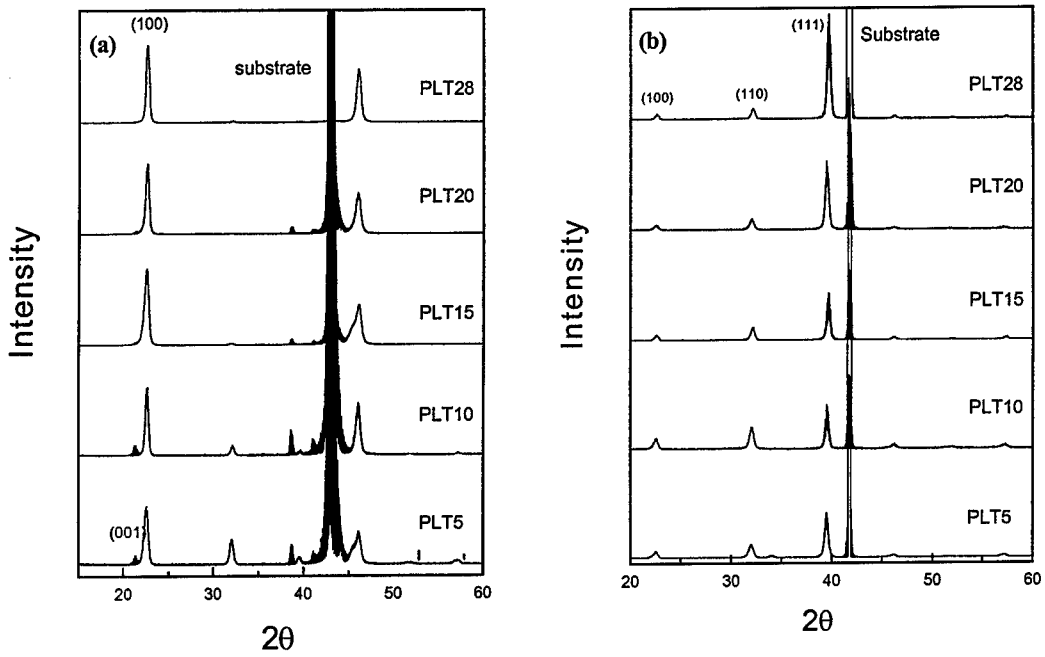

Figure 1. XRD patterns of PLT films on (a) MgO(100) substrates and (b) *c*-plane sapphire substrates as a function of La content.

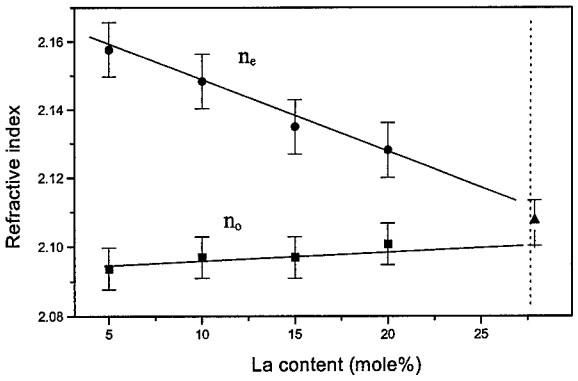

Figure 2. Refractive indices n_e and n_o of PLT films on MgO substrates as a function of La content.

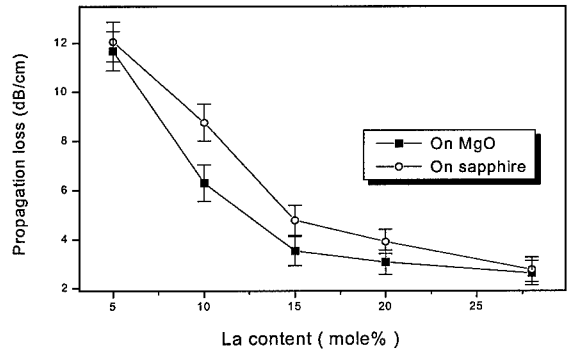

Figure 3. Propagation losses of PLT films fabricated on MgO and sapphire substrates as a function of La content.

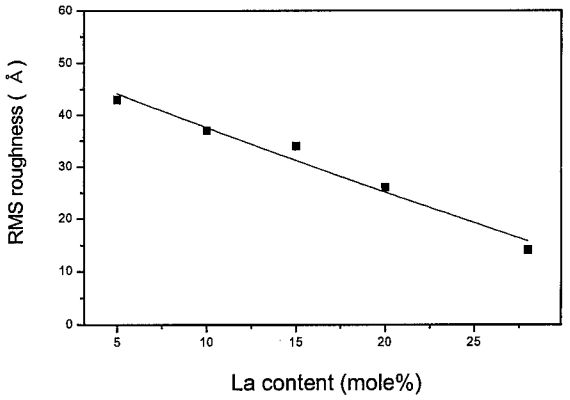

Figure 4. RMS surface roughness of PLT films fabricated on MgO substrates as a function of La content.

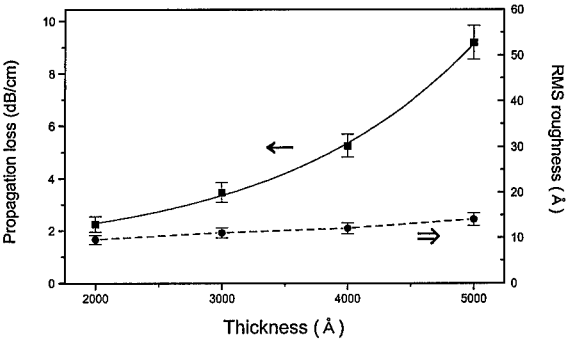

Figure 5. Propagation losses and RMS surface roughness of PLT28 films on MgO substrates as a function of film thickness.

or the anisotropy of refractive indices in the film. The main cause of the surface scattering is known to be surface roughness. AFM shows that the RMS surface roughness of the PLT films decreases linearly with increasing La content of the films as shown in Fig. 4. Since the grain size of the film becomes smaller as the La content increases, the surface roughness of the films is reduced. Therefore, the optical propagation loss decreases with the increase of La content due to a complex effect involving reduction of both non-surface scattering arising from the anisotropy of the refractive indices, and surface scattering due to surface roughness.

To ascertain the main scattering mechanism in the sol-gel PLT films, the optical propagation losses of the films were measured as a function of the film thickness (Fig. 5). The film composition of PLT28 was chosen since it has the lowest optical propagation loss because of its fine grain size and isotropic refractive index. The optical propagation losses increase exponentially with film thickness although the RMS surface roughness of the films is not greatly affected by the film thickness. Since thick sol-gel films are generally obtained by multiple coating, the presence of interfacial layers between coatings and/or the defects such as the pores, organic and nitrate residues in the films enhances the optical scattering. Therefore, internal scattering by unavoidable defects and interfacial scattering in multiple coatings should be reduced to achieve lower optical propagation loss in the sol-gel PLT thin film waveguides with thicknesses greater than 4000 Å.

4. Conclusions

Highly oriented PLT thin films, which exhibit good optical properties, have been prepared on MgO and sapphire substrates by sol-gel processing. X-ray diffraction analyses indicate that the PLT films fabricated on MgO(100) and *c*-plane sapphire substrates

grow preferentially in the (100) and (111) orientations, respectively. The refractive index and the optical propagation losses are affected by the film composition. The optical propagation losses of PLT films decreases with La content since the anisotropy of the refractive indices and the surface roughness of the films are reduced as the La content in the film increases. Thicker films obtained by multiple coatings have higher optical propagation loss regardless, although the film surface roughness is nearly constant. Thus, the main scattering mechanisms in thicker sol-gel PLT films are internal and interfacial scattering rather than surface scattering.

Acknowledgments

This work has been supported by Korea Science and Engineering Foundation (Grant No.: 94-0300-06-01-3).

References

1. G.H. Haertling and C.E. Land, J. Amer. Ceram. Soc. **54**, 1 (1971).
2. H. Adachi, T. Kawaguchi, K. Kentaro, K. Ohji, and K. Wasa, Appl. Phys. Lett. **42**(10), 867 (1983).
3. G. Teowee, Ph.D. Thesis, The University of Arizona, 1992.
4. B.-S. Bae, W.J. Lee, K. No, D.S. Yoon, and S.-U. Kim, in *Thin Films for Integrated Optics Applications*, edited by B.W. Wessels, S.R. Marder, and D.M. Walba (Mater. Res. Soc. Symp. Proc. 392, Pittsburgh, PA, 1995), p. 279.
5. J. Koo, S.-U. Kim, D.S. Yoon, K. No, and B.-S. Bae, J. Mater. Res. **12**(3), (1997).
6. R. Takayama, Y. Tomita, K. Iijima, and I. Ueda, Ferroelectrics **118**, 325 (1991).
7. J. Koo, C. Lee, K. No, and B.-S. Bae, J. Am. Ceram. Soc., submitted.
8. D.K. Fork, F. Armani-Leplingard, J.J. Kingston, and G.B. Aderson, in *Thin Films for Intergated Optics Applications*, edited by B.W. Wessels, S.R. Marder, and D.M. Walba (Mater. Res. Soc. Symp. Proc. 392, Pittsburgh, PA, 1995), p. 189.

Journal of Sol-Gel Science and Technology 13, 873–876 (1998)
© 1998 Kluwer Academic Publishers. Manufactured in The Netherlands.

Preparation of Transparent, Partially-Crystallized $BaTiO_3$ Monolithic Xerogels by Sol-Gel Processing

HIROKAZU SHIMOOKA, KEN-ICHI YAMADA AND SEIJI TAKAHASHI
Kyushu Institute of Technology, 1-1 Sensui-cho, Tobata-ku, Kitakyushu-shi, Fukuoka 804, Japan

MAKOTO KUWABARA
The University of Tokyo, 7-3-1 Hongo, Bunkyo-ku, Tokyo 113, Japan

Abstract. Transparent, partially-crystallized nanostructured barium titanate ($BaTiO_3$) monolithic xerogels (dried at 90°C) have been successfully synthesized via hydrolysis of Ba, Ti alkoxide precursor solutions in a concentration range of $\geq$1.0 mol/l with addition of water with a molar ratio of $H_2O/Ba \geq 6.3$. Transparent monolithic xerogels obtained from a precursor solution of 1.0 mol/l remained transparent even after firing at 500°C in oxygen, although the degree of their transparency was considerably decreased. Firing at temperatures above 500°C yielded translucent ceramics of $BaTiO_3$, and ultimately, firing above 600°C resulted in normal opaque ceramic bodies. Those obtained from a more concentrated precursor solution of 1.2 mol/l were, on the other hand, still transparent after firing at 600°C in oxygen, and turned opaque at 700°C. The results demonstrate that the materials retained their transparency even after pyrolysis of organic compounds involving exothermic oxidation at temperatures in the range of 200 to 400°C. The densification behavior of transparent $BaTiO_3$ monolithic xerogels obtained was found to be excellent; for example, those derived from a 1.0 mol/l precursor solution could be sintered to form monolithic $BaTiO_3$ ceramics with a relative sintered density of about 94% and an average grain size of $\approx$1 μm by firing at 1100°C for 2 h in oxygen.

Keywords: barium titanate, sol-gel method, transparent, partially-crystallized xerogel, low temperature densification

1. Introduction

Ferroelectric barium titanate ($BaTiO_3$) based ceramics are widely used as a main component of high permittivity capacitors. The ferroelectric properties of $BaTiO_3$ ceramics, such as their dielectric constant, Curie temperature, and tetragonality (c/a), are well known to show a certain dependence upon grain size [1–3]. However, the details of grain size dependencies of these properties in $BaTiO_3$ ceramics are not well understood, though many investigations have been made. To throw light on the size effects in $BaTiO_3$ ceramics an attempt to control the three-dimensional structure of the ceramics in the nanometer range may be necessary. In this sense, the sol-gel method that allows the preparation of gel monoliths with three-dimensional gel networks is especially effective to modify the gel structure by chemical procedure in the range of nano-to micrometer scale. In general, however, since the sinterability of crystalline xerogels with a large porosity is very poor [4], there have been only a few studies with respect to the densification of crystalline gel monoliths in the field of electroceramics. Recently, however, we reported a successful attempt [5, 6] to prepare dense $BaTiO_3$ ceramics with a relative sintered density of >95% by sintering the gel monoliths (partially crystallized) at a relatively low temperature of 1100°C. The partially-crystallized monolithic gels of $BaTiO_3$ were synthesized from high concentration Ba, Ti-alkoxide alcoholic solutions. Furthermore, we succeeded in synthesizing transparent, partially-crystallized $BaTiO_3$ gel monoliths using the same

high-concentration sol-gel processing [unpublished work]. The powderless sol-gel route to dense, fine-grained $BaTiO_3$ bulk ceramics developed by us may allow fabricating new ceramic devices made up of nanostructured $BaTiO_3$-based materials with novel electronic functions.

This paper reports the synthesis of transparent $BaTiO_3$ monolithic gels with a high sinterability and the change of their transparency, being influenced by the synthetic condition of the gels, at elevated temperatures during heat-treatment, in which the sinterability and dielectric properties of $BaTiO_3$ ceramics derived from transparent gel monoliths are also mentioned.

2. Experimental

High concentration (1.0 mol/l) Ba, Ti-alkoxide precursor solutions were prepared using exactly the same procedure as that reported in the previous paper [5]. A brief description of the method for preparing and hydrolyzing the precursor solutions is given here. Barium ethoxide and titanium isopropoxide were used as starting materials, and a mixture of methanol and 2-methoxyethanol in a volume ratio of 60/40 was used as the solvent, with which it was possible to dissolve a large amount of the alkoxides to produce high concentration precursor solutions of 1.2 mol/l at room temperature. The precursor solutions (the concentration, q (in mol/l): $0.2 \leq q \leq 1.2$) were hydrolyzed with water vapor at 2°C with stirring, using an apparatus similar to that reported in a previous paper [7]. The quantity of water contained in a sol was estimated using a gas-chromatograph meter from the amount of water trapped in a reservoir kept at a temperature of liquid nitrogen. The sols were aged in sealed containers at 5°C for 3 days; in this period gelation of the solutions occurred. The gels formed were further aged in two steps successively at 30°C for 3 days and then at 50°C for 5 days to allow them to shrink through syneresis (shrinkage of the gel network associated with expulsion of liquid from the pores). The wet monolithic gels obtained of $BaTiO_3$ were finally dried at 90°C in flowing N_2 to prepare their xerogels. The densification behavior of the xerogels was examined by firing them at temperatures in the range of 500 to 1100°C for 2 h in oxygen.

Powder XRD analysis was performed on gel powders as-dried at 90°C and on the powders of sintered gels obtained by pulverizing them using a mortar and pestle. Microstructures of the as-dried gels and gel-derived ceramics were observed using a transmission electron microscope (TEM) and a field emission scanning electron microscope (FE-SEM). Differential thermal analysis (DTA) and thermogravimetric (TG) analysis were performed in the temperature range of 20 to 1000°C to investigate the combustion behavior of organic compounds contained in a xerogel and also to estimate the amount of organics remaining in the gel after firing at 1000°C.

3. Results and Discussion

Figure 1 shows the synthetic conditions of gel materials used in this study, represented in a diagram of alkoxide concentration (q) versus hydrolysis water content (r) plot, in which open and filled circles and squares denote experimental points. All the experimental points yielded wet gels. No powdery gels were formed and no precipitates were generated. This figure indicates that three types of monolithic wet gels were obtained: transparent partially-crystallized gels (indicated by filled circles), opaque partially-crystallized ones (open circles) and opaque amorphous ones (squares). The uppermost experimental points in the q-r diagram indicate the maximum water content reached before gelation started in the respective alkoxide solutions examined. The minimum water content required for formation of crystalline gels decreased with an increase in the q value, and transparent crystalline monolithic gels

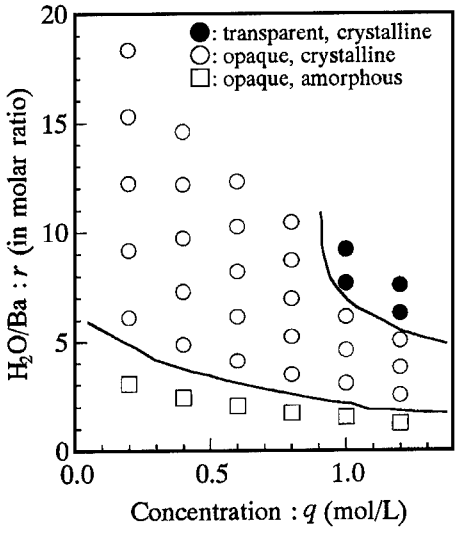

Figure 1. Synthesis conditions of gel materials used in this study, represented in a diagram of alkoxide concentration (q) versus hydrolysis water content (r) plot.

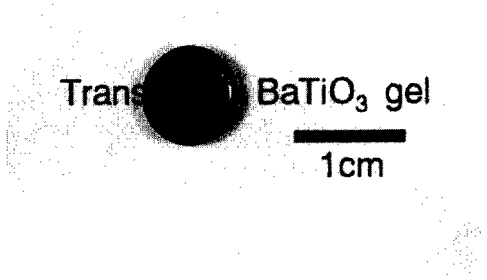

Figure 2. Appearance of an ≈1 mm thick transparent $BaTiO_3$ monolithic gel as-dried at 90°C.

were obtained in a confined region of $q \geq 1.0$ mol/l and $r \geq 6.3$.

Figure 2 shows the appearance of a transparent, partially-crystallized xerogel prepared with $q = 1.0$ and $r = 7.6$ in Fig. 1. The bulk density of the xerogel was 2.7 g/cm^3, and the TEM size of $BaTiO_3$ crystalline particles was in a range of 10 to 15 nm. The xerogel remained transparent after firing at 500°C in oxygen, although the degree of transparency was appreciably degraded. Firing such transparent xerogels at temperatures above 600°C resulted in the usual opaque ceramics. Monolithic transparent gels obtained with $q = 1.2$ and $r = 6.3$, on the other hand, were found to be still transparent (it may be more appropriate to say translucent) even after firing at 600°C in oxygen, and turned opaque at 700°C. This result seems to imply that the retention temperature of transparency for a gel can increase more if we are able to obtain Ba, Ti-alkoxide solutions with a concentration of >1.2 mol/l and to successfully synthesize transparent monolithic xerogels from the solutions. From the DTA-TG analysis for a transparent xerogel (prepared with $q = 1.0$ and $r = 7.6$), shown in Fig. 3, organic compounds present in the gel decomposed at temperatures in a range of 200 to 400°C associated with an exothermic reaction, indicated by a characteristic peak at around 250°C. A significant weight loss of about 17% was observed which ceased at around 600°C. Also, the crystallization of a transparent xerogel was considerably enhanced in the temperature range of 500 to 600°C, as seen from the XRD data of Fig. 4. Figures 3 and 4 may demonstrate that there existed some intergranular phases playing a role in dispersing crystalline particles in the xerogels, and the loss of these phases during heating

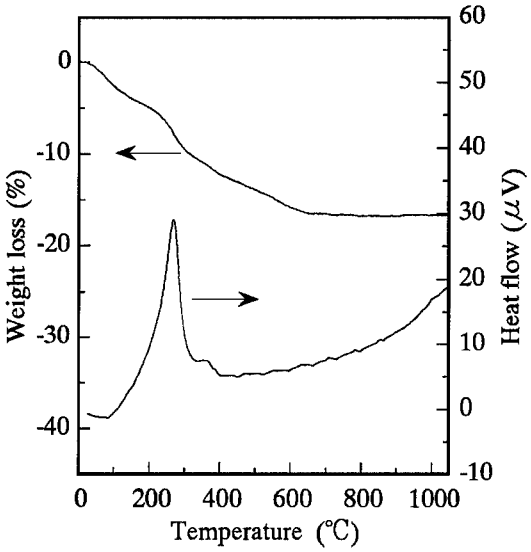

Figure 3. DTA-TG analysis of a transparent xerogel prepared with $q = 1.0$ and $r = 7.6$.

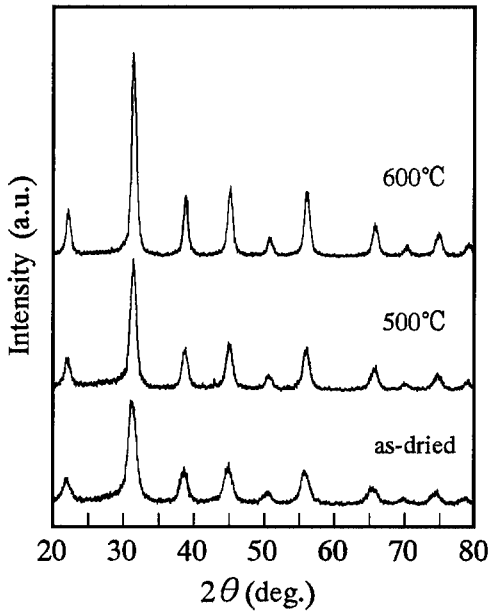

Figure 4. XRD patterns of a transparent gel and the gel derived ceramics fired at 500°C and 600°C in flowing oxygen. The transparent gel was prepared with $q = 1.0$ and $r = 7.6$.

up to 600°C caused an enhancement of the crystallization of the xerogels. As a result, rearrangement or agglomeration of $BaTiO_3$ crystalline particles occurred resulting in opaque bodies. This is a tentative explanation of the loss of transparency for the present materials. Success in preparing transparent

(or translucent), porous $BaTiO_3$ ceramics at 600°C provides two pieces of important information: (1) the existence of organic compounds and amorphous Ba-Ti-O phases in a xerogel is not essential for the material to be transparent, and (2) using a high concentration of alkoxide precursor solutions is very effective in the preparation of transparent monolithic xerogels of $BaTiO_3$.

Finally, the sinterability of the transparent monolithic xerogel obtained from a 1.0 mol/l precursor solution is briefly described. Firing the xerogels at 1100°C for 2 h in oxygen yielded dense, opaque $BaTiO_3$ ceramics with a relative sintered density of about 94% and an average grain size of $\approx 1\ \mu m$.

4. Conclusion

Transparent, partially-crystallized $BaTiO_3$ xerogels were obtained via hydrolysis of Ba, Ti alkoxide precursor solutions in a concentration range of ≥ 1.0 mol/l with addition of water with a value of $H_2O/Ba \geq 6.3$. The opacification temperature of the transparent $BaTiO_3$ gels during thermal treatment in oxygen tended to rise with increasing precursor concentration. The gels obtained from a concentrated precursor solution of 1.2 mol/l were still translucent even after firing at 600°C in oxygen. Firing the xerogels at 1100°C for 2 h in oxygen yielded dense, opaque $BaTiO_3$ ceramics with a relative sintered density of about 94.

References

1. G. Arlt, D. Hennings, and G. de With, J. Am. Ceram. Soc. **58**, 1619 (1985).
2. K. Uchino, E. Sadanaga, and T. Hirose, J. Am. Ceram. Soc. **72**, 1555 (1989).
3. K. Kinoshita and A. Yamaji, J. Appl. Phys. **47**, 371 (1976).
4. C.J. Brinker and G.W. Scherer, *Sol-Gel Science: The Physics and Chemistry of Sol-Gel Processing* (Academic Press, Boston, 1990), p. 675.
5. H. Shimooka and M. Kuwabara, J. Am. Ceram. Soc. **78**, 2849 (1995).
6. H. Shimooka and M. Kuwabara, J. Am. Ceram. Soc. **79**, 2983 (1996).
7. J.S. Smith II, R.T. Dolloff, and K.S. Mazdiyasni, J. Am. Ceram. Soc. **53**, 91 (1970).

Journal of Sol-Gel Science and Technology 13, 877–883 (1998)
© 1998 Kluwer Academic Publishers. Manufactured in The Netherlands.

Sol-Gel Derived Barium-Strontium Titanate Films

V.A. VASILJEV AND K.A. VOROTILOV
Moscow State Institute of Radioengineering, Electronics and Automation (Technical University), 78 Vernadsky prosp., 117454, Moscow, Russia

M.I. YANOVSKAYA AND L.I. SOLOVJEVA
Karpov Institute of Physical Chemistry, 10 Vorontsovo pole, 103064, Moscow, Russia

A.S. SIGOV
Moscow State Institute of Radioengineering, Electronics and Automation (Technical University), 78 Vernadsky prosp., 117454, Moscow, Russia

Abstract. Sol-gel techniques for the preparation of barium-strontium titanate (BST) films are discussed. The evolution of film microstructure during heat treatment, and the dielectric properties of BST films prepared from alkoxide solutions and from alkoxide solutions modified by 2-ethylhexanoic acid were studied. It is shown that the extent of the modification of the precursors by 2-ethylhexanoic acid changes the precursor molecular complexity governing the microstructure of the films and their electrical properties.

Keywords: sol-gel process, ferroelectric thin films, barium-strontium titanate, microstructure, electrical properties

1. Introduction

Barium-strontium titanate (BST) films have been intensively investigated during recent years as high-dielectric constant materials for high density dynamic random access memory devices (256 Mbit/1 Gbit), as well as for millimeter microwave integrated circuits (ICs). The sol-gel method is one of the approaches which is being extensively used for the preparation of complex oxide thin films in IC processing. A key issue of any sol-gel thin film processing is the chemistry of the precursor solution which governs the properties of the final oxide layer. Metal 2-ethylhexanoates are frequently used together with metal alkoxides for the preparation of the precursor solutions for thin film applications [1, 2].

In this project we studied the effect of 2-ethylhexanoic acid modification on the microstructural evolution in the film formation process and dielectric properties of the films.

2. Experimental

Titanium isopropoxide, Sr and Ba were dissolved in methoxyethanol to give a 0.48 M solution with stoichiometry corresponding to $Ba_{0.7}Sr_{0.3}TiO_3$. After the metals had dissolved completely, an excess of 2-ethylhexanoic acid was added, the solution was then heated on stirring, and the solvent was gradually distilled off. The amount of the solvent distilled varied from 0 to 52% of the initial volume. Distillation at ambient pressure allowed elimination of ~40% of the initial volume. In order to increase the extent of distillation, the process was performed under reduced pressure, which allowed elimination of 52% of the initial volume. After cooling of the solution, xylene was added to the residue in an amount equal to the volume of the distilled solvent.

It has been previously shown [3] that the reaction of titanium isopropoxide with 2-ethylhexanoic acid in methoxyethanol performed under distillation of the

solvent results in elimination of ester and formation of oxoisopropoxy-2-ethylhexanoate:

$$\mathrm{Ti(OPr^{\textit{i}})_4 + MeOC_2H_4OH + C_7H_{15}COOH}$$
$$\rightarrow \mathrm{TiO_x(OPr^{\textit{i}})_y(C_7H_{15}COO)_{4-2x-y}}$$
$$+ \mathrm{C_7H_{15}COOC_2H_4OMe} + \textit{i}\mathrm{PrOH}$$

According to the chromatomasspectroscopy and NMR data only the ester of 2-ethylhexanoic acid with methoxyethanol, rather than with ^{i}PrOH was produced and isopropoxide groups are partially preserved in the product. Methoxyethoxide groups which substitute isopropoxide groups on dissolution of $Ti(OPr^{i})_4$ in methoxyethanol [4] are readily eliminated in reaction with 2-ethylhexanoic acid leaving an oxo-atom in the product. Oxoproducts thus formed are oligomers with varying molecular complexity. Distillation under rigid conditions results in enhancement of molecular complexity.

In the case of the trimetallic solutions similar reactions presumably occur. The viscosity of the solutions gradually decreases in the course of distillation, which is due to the consumption of the most viscous component, 2-ethylhexanoic acid; only distillation under vacuum results in increase of viscosity due to enhancement of molecular complexity of the species. The extent of distillation presumably is the main parameter of the process regulating the nature of the species formed in the complex trimetallic solution and thus influencing the film-forming process.

For comparison a metal alkoxide solution containing no 2-ethylhexanoic acid was also prepared by dissolution of the necessary amount of Sr and Ba ($Ba/(Ba + Sr) = 0.7$) metals in the methoxyethoxide solution of $Ti(OPr^{i})_4$.

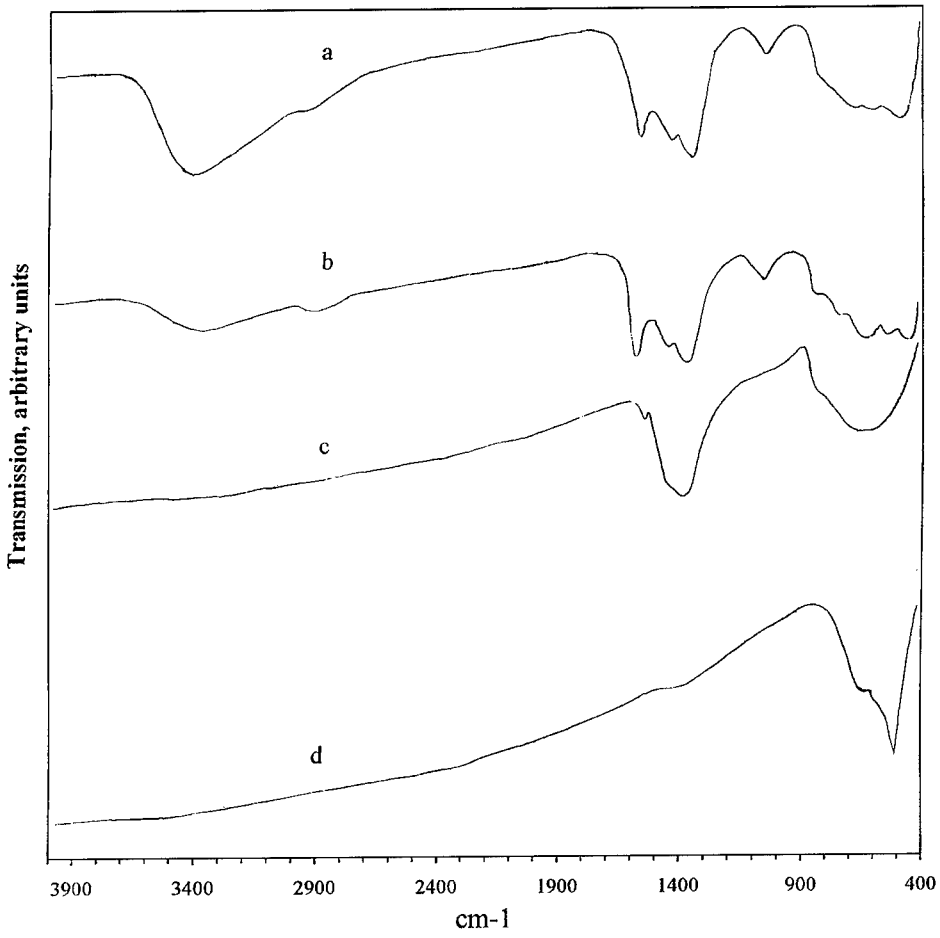

Figure 1. IR spectra of the alkoxide precursor for BST films applied to the KBr single-crystal substrate: as prepared (a); cured at 200 (b), 400 (c), and 600°C, 30 min (d).

The films were prepared by spin-on coating onto Si for optical characterization, $Si/SiO_2/Ti/Pt$ substrates for dielectric and X-ray measurements, and KBr single-crystal plates for IR spectroscopy studies.

The film thickness and refractive indexes were measured by multiangle ellipsometry at 632.8 nm and the incident irradiation angles from 45° to 70° [5]. The shrinkage was determined as the percent change in thickness of the films after the heat treatment:

$$\text{Shrinkage} = (1 - h_T/h_{200}) \times 100\%,$$

where h_{200} is the thickness of the films after drying at 200°C, and h_T is the thickness of the film annealed at the temperature T.

3. IR Spectra of BST Films

Figures 1(a)–(d) show the IR spectra of the BST alkoxide precursor (prepared without addition of the 2-ethylhexanoic acid) cured at various temperatures in air for 30 min. The broad band around 3400 cm^{-1} (Fig. 1(a)) is due to O—H stretching vibrations of the hydroxyls present in the system; it decreases in intensity with increase of the annealing temperature, and disappears after annealing at 400°C. The extremely low intensity of the bands due to C—H stretching vibrations at 2800–3000 cm^{-1} testifies to the very low content of organic radicals in these samples, thus alkoxide groups are mostly eliminated in the course of spinning. These bands completely disappear in the samples annealed

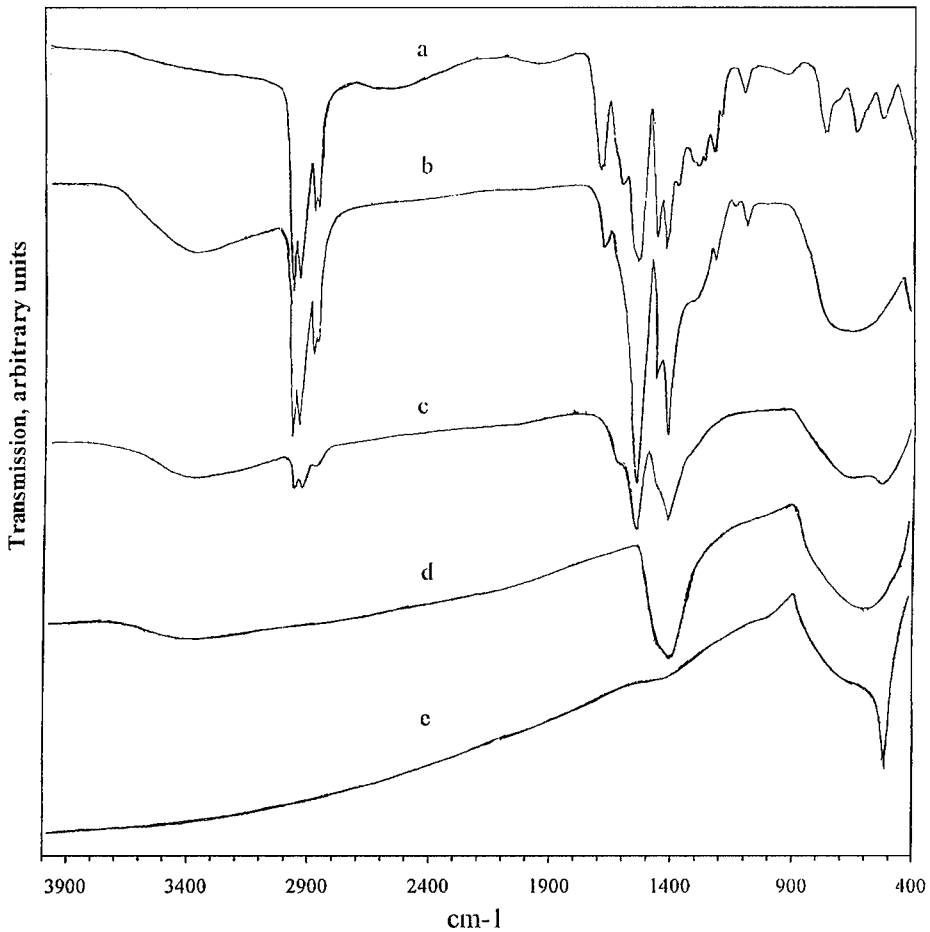

Figure 2. IR spectra of the alkoxide precursor for BST films, modified with 2-ethylhexanoic acid, applied to the KBr single-crystal substrate: as prepared (a); cured at 200 (b), 300 (c), 400 (d), and 600°C, 30 min (e).

at 400°C. It is also interesting to note a quite intense band at 1580 cm^{-1}. It has been previously shown by us that this band frequently appears in the spectra of alkaline and alkaline-earth alkoxides and is due to formation of carboxylate (mostly formate) during oxidative decomposition of the alkoxide radicals by oxygen dissolved in the alcoholic solutions [6], which is especially pronounced in the case of alkaline-earth methoxyethoxides. The broad band in the region of 1400 cm^{-1} registered in the spectra of the samples annealed at 400°C (organic residues by this temperature are already eliminated) needs further investigation, although Kamalasanan et al. [2] attributed it to formation of Ba—O—Ti bond. This band disappears on further annealing and is substituted by the band at 530 cm^{-1}, characteristic of the crystalline $M^{II}TiO_3$ [7].

Figures 2(a)–(e) show the IR spectra of the films coated by the BST precursor solution prepared with addition of 2-ethylhexanoic acid and subsequent elimination of 41% of the solvent by distillation. The spectra in this case have much lower intensity of the O—H stretching vibration bands around 3400 cm^{-1}, but the C—H stretching vibration bands in the range of 2800–3000 cm^{-1} are considerably more intense corresponding to the much higher content of organics in these films. The intensity of the latter bands practically does not change on annealing at 200°C, but decreases drastically in the samples annealed at 300°C and disappears completely in the films annealed at 400°C. Thus, the main loss of organics occurs on thermal treatment of these films in the temperature region of 200–300°C, rather than during spinning. The band at 1700 cm^{-1} in the films which did not undergo any thermal treatment corresponds to the stretching vibrations of the free 2-ethylhexanoic acid. The C—H deformation vibration bands (1300–1500 cm^{-1}), as well as the stretching vibrations of the carboxylate group (1400–1600 cm^{-1}), gradually disappear on heating. However, just as in the previous case, a broad intense band in the region of 1400 cm^{-1} is observed and is especially pronounced in the films annealed at 400°C; it disappears in the crystalline films annealed at 600°C.

4. Evolution of Film Thickness and Refractive Index during Heat Treatment

Evolution of the film microstructure during heat treatment was characterized by the change in film thickness (shrinkage) and refractive index (see Figs. 3(a)–(c)).

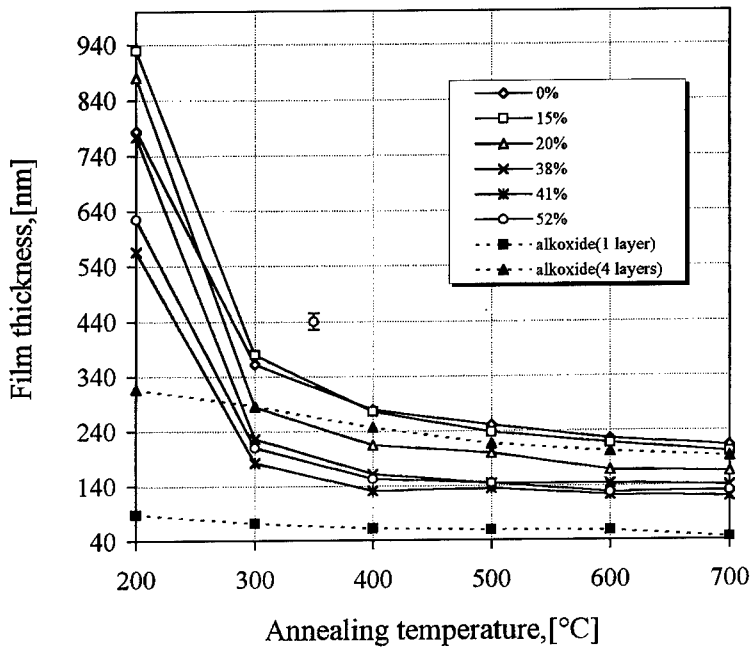

(a)

Figure 3. Thickness (a), shrinkage (b) and refractive index (c) of BST films prepared from alkoxide precursors and modified alkoxide precursors with different extent of solvent distillation as a function of annealing temperature.

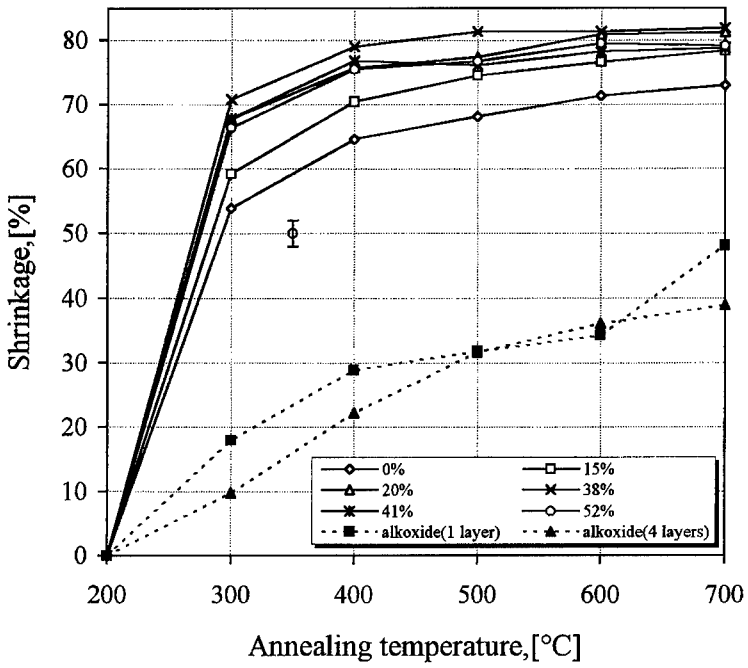

(b)

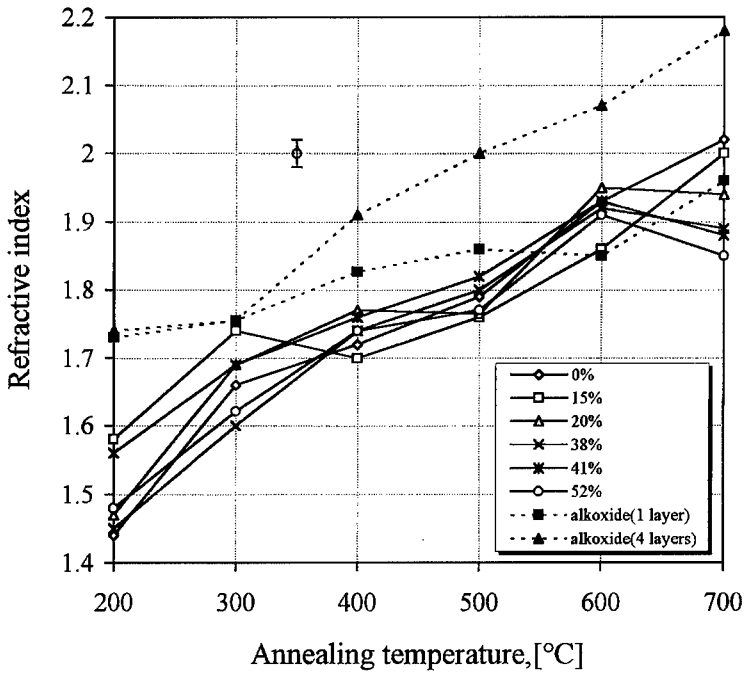

(c)

Figure 3. (*Continued*).

The films prepared from metal alkoxides typically had a thickness of about 60 nm (after drying at 500°C). Preparation of thicker films is hindered by their cracking during drying. Modified metal alkoxide precursors permit preparation of films with greater thickness (140–250 nm) in one application step without cracking. To obtain films with similar thicknesses from metal alkoxides, a four fold spin-on coating with intermediate bake was used. Film thickness decreased with the increase of extent of solvent distillation mainly due to reduction of solution viscosity as mentioned previously.

The films prepared from the metal alkoxide precursor had significantly lower shrinkage (about 30% in the range of 200–500°C), in comparison with that prepared from the modified precursors (70–80%). In the latter case the most pronounced shrinkage occurs in the temperature range 200–300°C and corresponds to the loss of organics as shown by the IR spectra. The higher the extent of distillation and the consequent substitution of the alkoxide groups by 2-ethylhexanoate groups, the greater the shrinkage. Pyrolysis of organics is complete by 400°C; further shrinkage is due to formation of the metal-oxide network, structural relaxation and crystallization. The films prepared from the metal alkoxide solution without addition of 2-ethylhexanoic acid contain no organic residue and the metal-oxide network is formed in the course of spin-on deposition with a subsequent branching during further heating. Films prepared from metal alkoxide precursors have a higher refractive index than films obtained from the modified solutions (see Fig. 3(c)) testifying to their higher density and smaller interatomic spacing. This is also the reason for the lower cracking resistance of the films prepared without the modification process. It should be noted that thicker alkoxide films (prepared by four fold deposition) had lower shrinkage and a higher value of refractive index than those prepared by the one-step application process where structural relaxation is probably hindered by the influence of the substrate.

5. Dielectric Properties

Figure 4 shows the dielectric constant of BST films (annealed at 700°C for 20 min) as a function of voltage bias. The films prepared from alkoxide solutions had relatively low dielectric constants (about 100) with a weak dependence from voltage. The reason for this lies in the formation of a metal-oxide network during the early stages of film formation in the case of the alkoxide precursor. This hinders structural relaxation and causes high mechanical stresses in the films. As a result crystallization starts at lower temperatures, but results in a structure with defects and distortions.

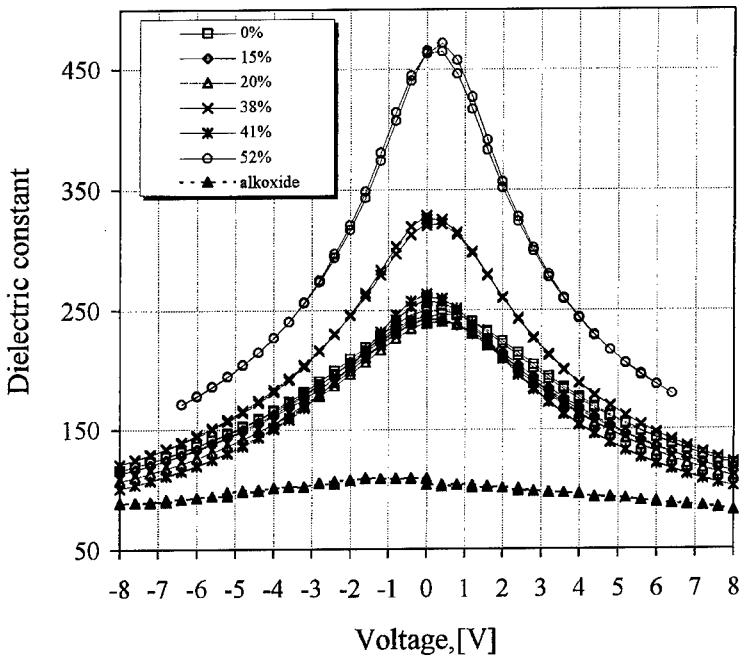

Figure 4. The dependence of dielectric constant of BST films (1 MHz, 20°C) as a function of voltage bias.

By contrast, in the case of modified metal alkoxides precursors the metal-oxide network is created after pyrolysis of organics at higher temperatures when atoms with higher energy and mobility give better conditions for crystallite growth with a porous nonstressed structure.

In general, greater solvent distillation led to a higher value of dielectric constant and more pronounced ferroelectric behavior (the peak dielectric constant increased). The correlation between dielectric properties and crystalline structure of BST films will be discussed in detail elsewhere.

Acknowledgments

This work was partially supported by Russian Foundation for Basic Research grants 96-33553 and 97-02-17822, and State Scientific and Technical Program "Advanced Technologies and Devices of Micro- and Nanoelectronics" grant 218/68/1-2.

References

1. M. Klee, R. Eusmann, R. Waser, W. Brand, and H. Hal, J. Appl. Phys. **72**, 1566 (1992).
2. M.N. Kamalasanan, N.D. Kumar, and S. Chandra, J. Appl. Phys. **78**, 4803 (1994).
3. T.V. Rogova, M.I. Yanovskaya, D.U. Grudtsyna, Yu.D. Grudtsyn, and E.P. Kovsman, Russ. J. General Chem. **67**, (1997).
4. D. Ramamurthi and D.A. Payne, J. Amer. Ceram. Soc. **73**, 2547 (1990).
5. Grigorév, V.I. Petrovsky, and I.A. Shapova, Izmeritelnaja Technicka **1**, 15 (1991) (in Russian).
6. N.Ya. Turova, E.P. Turevskaya, M.I. Yanovskaya, N.M. Kotova, and R.R. Shifrina, Russ. J. Inorg. Chem. **38**, 1055 (1993).
7. J.T. Last, Phys. Rev. **105**, 1740 (1957).

Journal of Sol-Gel Science and Technology 13, 885–888 (1998)
© 1998 Kluwer Academic Publishers. Manufactured in The Netherlands.

$SrBi_2Nb_2O_9$ Ferroelectric Powders and Thin Films Prepared by Sol-Gel

J.H. YI, P. THOMAS, M. MANIER, J.P. MERCURIO, I. JAUBERTEAU AND R. GUINEBRETIÈRE
Laboratoire de Matériaux Céramiques et Traitements de Surface, ESA CNRS no. 6015, Faculté des Sciences, 123 Avenue Albert Thomas, 87060 Limoges Cedex, France

Abstract. Pure $SrBi_2Nb_2O_9$ powders and thin films were obtained using sol-gel synthesis from mixtures of niobium ethoxide, bismuth and strontium 2-ethylhexanoates. Powders crystallized for 2 hours at 700°C had grain sizes of about 100–150 nm. $SrBi_2Nb_2O_9$ thin films were prepared by spin-coating a stable precursor solution onto $Si/SiO_2/TiO_2/Pt$ substrates. Crystallization of pure $SrBi_2Nb_2O_9$ phase occurred at about 500–550°C. Randomly oriented 0.3 μm-thick crack-free films were obtained after 10 successive depositions and heating at 700°C for 2 hours. P-E hysteresis loops have confirmed the ferroelectric behavior of the films: they show a remanent polarization of 2.5 $\mu C/cm^2$ (5 V, 8 ms). No fatigue was observed up to 10^9 full switchings.

Keywords: bismuth oxide layer, ferroelectric, spin-coating, thin films morphology

Introduction

Bismuth oxide layered ferroelectric thin films have attracted considerable attention for application in non-volatile memories and capacitors of dynamic random-access memories due to their reversible spontaneous polarization and their high dielectric constant [1–3]. $SrBi_2Nb_2O_9$ compound is a member of the family of layered bismuth compounds, so-called Aurivillius phases, generally formulated as $Bi_2A_{m-1}B_mO_{3m+3}$. Their crystal structure can be described as a regular intergrowth of $(Bi_2O_2)^{2+}$ layers and $(A_{m-1}B_mO_{3m+1})^{2-}$ perovskite-type slabs [4–6]. In these compounds, A is a mono-, di- or trivalent element with dodecahedral coordination, B is a transition element suited to octahedral coordination and m an integer ($1 \leq m \leq 5$) which represents the number of perovskite-like slabs intercalated between the $(Bi_2O_2)^{2+}$ layers. To date $Bi_4Ti_3O_{12}$ and $SrBi_2Ta_2O_9$ are the only compounds used in thin-film studies of bismuth oxide layered materials. Such thin films have ferroelectric characteristics comparable with PZT films and high fatigue resistance to switching [3, 7–10].

The present paper deals with the sol-gel synthesis of $SrBi_2Nb_2O_9$ powders and spin-coating preparation of $SrBi_2Nb_2O_9$ thin films.

Experimental

A 0.087 mol/l $SrBi_2Nb_2O_9$ precursor solution was prepared by first dissolving strontium 2-ethylhexanoate in 2-ethylhexanoic acid at 120°C, then adding bismuth, 2-ethylhexanoate and finally adding niobium ethoxide diluted in ethanol. These conditions are particularly interesting for the deposition of thin films. In such a case, the viscosity of the sol obtained ($\eta = 3.6\ mm^2\ s^{-1}$) and stored in a glove box in dried air conditions, increases progressively with time ($\eta = 3.65\ mm^2\ s^{-1}$ for 10 days, $\eta = 3.7\ mm^2\ s^{-1}$ for 20 days, $\eta = 3.9\ mm^2\ s^{-1}$ for 40 days) to reach a maximum ($\eta = 4.3\ mm^2\ s^{-1}$) for 80 days. However, even after 80 days of storage, the viscosity of the sol can easily be reduced to $\eta = 3.6\ mm^2\ s^{-1}$ by stirring.

Pure $SrBi_2Nb_2O_9$ powders were obtained after two successive drying steps at 85°C and 230°C to enable separate elimination of ethanol and 2-ethylhexanoic acid and then final crystallization step of 2 hours at 700°C.

Films were obtained by spin-coating the stable precursor solution onto $Si/SiO_2/TiO_2/Pt$ substrates mounted on a Sulzer photoresist spinner. Platinum was chosen as the bottom and top electrodes for hysteresis cycle measurements. The spin-coating conditions were

an acceleration of 7 rpm/s, a rotation speed of 4000 rpm and a rotation time of 30 s. The coating was then dried at 300°C for 10 min to remove the organics. Each coating produced a film about 30 nm thick. Deposition and drying steps were repeated (up to 15 cycles) to prepare thicker films. Pure, well-crystallized $SrBi_2Nb_2O_9$ thin films were obtained after heating to 700°C for 2 hours.

The crystallization of powders and films was followed by temperature-programmed X-ray diffraction at various temperatures ranging from 20 to 800°C, under atmospheric conditions, using a Siemens D5000 diffractometer (θ/θ, CuK_α radiation) fitted out with a high temperature furnace (Anton Paar HTK10, Pt heating sample holder) and an Elphyse Position Detector (aperture: 14°). The powders were observed by transmission electron microscopy (Jeol 2010). The morphology and surface microstructure of the thin films were observed by scanning electron microscopy (Philips XL30) and atomic force microscopy (Digital Instrument Nanoscope II). P-E hysteresis cycles were measured using a Radiant Technologies pulsed testing system (RT 66A).

Results and Discussion

$SrBi_2Nb_2O_9$ powders begin to crystallize at about 450–500°C (Fig. 1). At 700°C well-crystallized powders with grain sizes in the range 100–150 nm were obtained (Fig. 2).

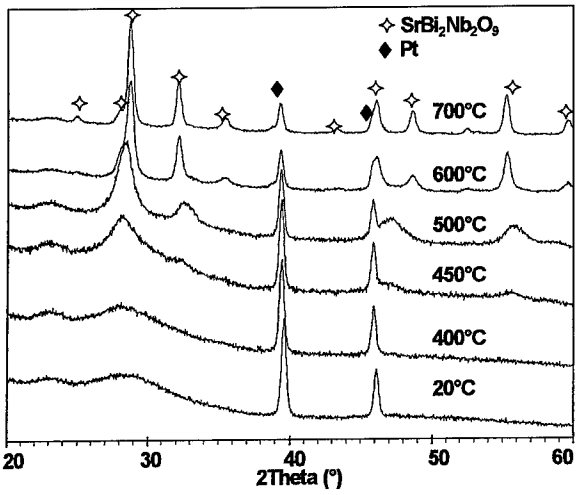

Figure 1. XRD patterns vs. temperature of an $SrBi_2Nb_2O_9$ dried gel (diffraction peaks of platinum are those of the heating sample holder).

Figure 2. TEM micrograph of an $SrBi_2Nb_2O_9$ powder heated for 2 hours at 700°C.

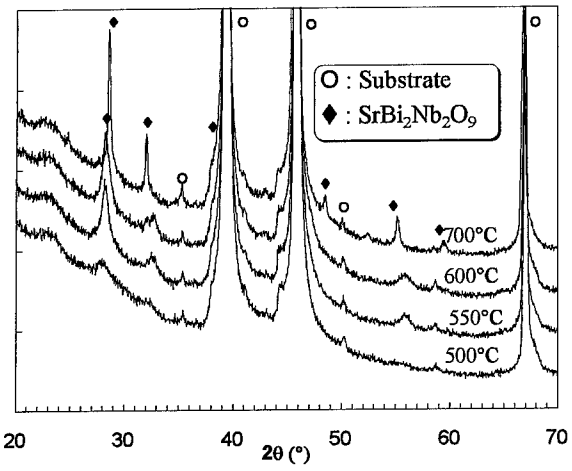

Figure 3. XRD patterns vs. temperature of an $SrBi_2Nb_2O_9$ thin film prepared with 10 coatings on an $Si/SiO_2/TiO_2/Pt$ substrate.

Figure 3 shows X-ray diffraction patterns recorded at various temperatures of an $SrBi_2Nb_2O_9$ thin film prepared with 10 coatings on an $Si/SiO_2/TiO_2/Pt$ substrate. Crystallization of pure $SrBi_2Nb_2O_9$ occurs at about 500–550°C. Randomly oriented $SrBi_2Nb_2O_9$ films on $Si/SiO_2/TiO_2/Pt$ substrates were obtained whatever the

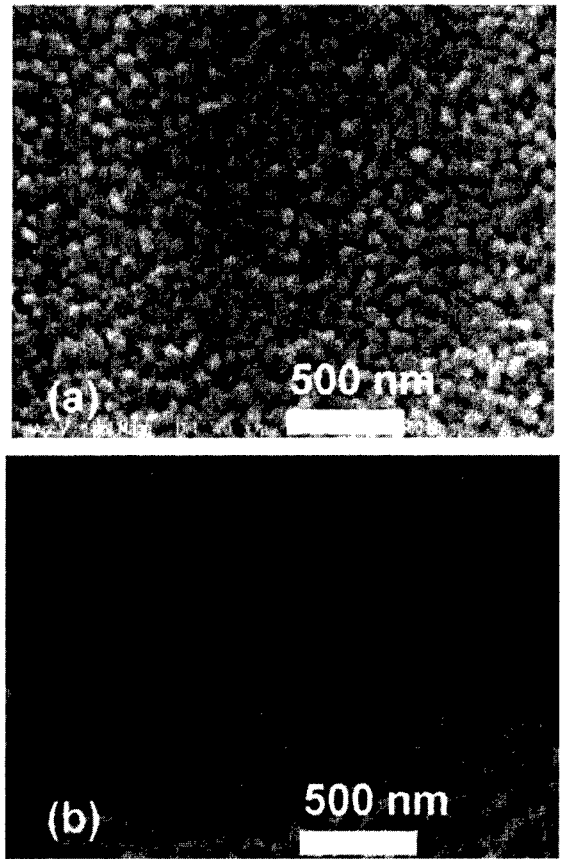

Figure 4. SEM micrographs of $SrBi_2Nb_2O_9$ thin films heat-treated for 2 hours at 700°C and prepared with (a) 1 coating and (b) 5 coatings.

number (1, 3, 5 or 10) of coatings applied. Crack-free films have been obtained using the conditions described previously. The films have a dense (density of about 90%) and homogeneous microstructure and the grain size increases with the number of coatings (Fig. 4).

AFM has been used to study the detailed morphology of the various thin films. Figure 5 shows images of the surface of thin films heat-treated at 700°C for 2 hours and prepared with 1 and 10 coatings. AFM clearly shows that the grain size increases as the number of deposited coatings increases; the grain size is about 50–80 nm for one coating, 100–120 nm for 5 coatings and 150–170 nm for 10 coatings. As previously seen with $Bi_4Ti_3O_{12}$ thin films [8], the surface becomes rougher as the number of coatings increases. The roughness rises from 50 nm for 1 and 5 coatings to 70 nm for 10 coatings. The value of 50 nm for 1 coating can be explained by the presence of some inhomogeneities (such as small island microstructures) on the film surface.

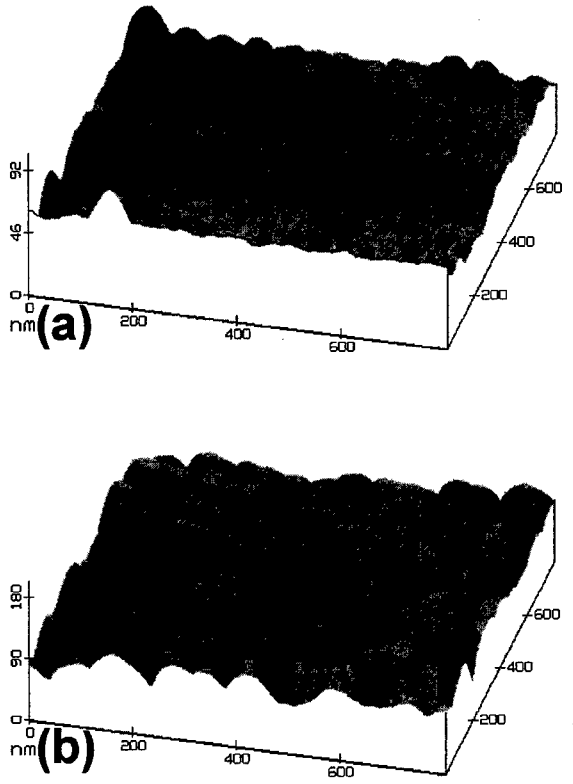

Figure 5. AFM images of the surface of $SrBi_2Nb_2O_9$ thin films heat-treated for 2 hours at 700°C and prepared with (a) 1 coating and (b) 10 coatings.

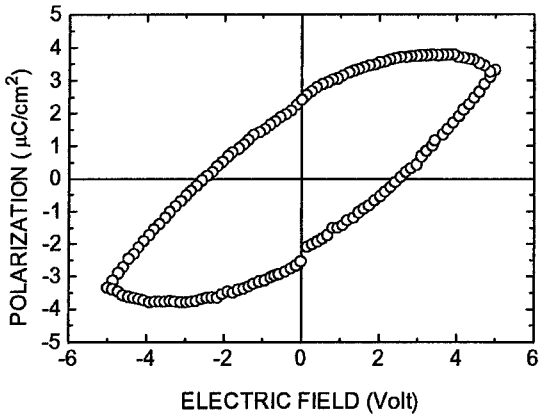

Figure 6. Hysteresis loop of a 0.3 μm-thick (10 coatings) $SrBi_2Nb_2O_9$ thin film.

The electrical properties of $SrBi_2Nb_2O_9$ thin films were measured with pulse measurements using a voltage of 5 V and a pulse of 8 ms. Ferroelectric loops have confirmed the ferroelectric behavior of such films (Fig. 6). The remanent polarization is about

2.5 $\mu C/cm^2$. The $SrBi_2Nb_2O_9$ thin films show no fatigue at room temperature up to 10^9 cycles.

A study of the thin films morphology related to possible crystallographic orientation (films produced on $SrTiO_3$ substrates) and electrical properties is now in progress. X-ray diffraction line broadening analysis will be used to characterize the size and shape of $SrBi_2Nb_2O_9$ powders crystallized at various temperatures.

Conclusion

$SrBi_2Nb_2O_9$ powders were obtained using sol-gel synthesis from mixtures of niobium ethoxide, bismuth and strontium 2-ethylhexanoates. Randomly oriented 0.3 μm-thick crack-free films were obtained after 10 successive depositions of stable precursor solutions on to $Si/SiO_2/TiO_2/Pt$ substrates and heating at 700°C for 2 hours. They show a remanent polarization of 2.5 $\mu C/cm^2$ (5 V, 8 ms). No fatigue was observed up to 10^9 full switchings.

References

1. J.F. Scott and C.A. Araujo, Science **246**, 1400 (1989).
2. S.B. Desu and D.P. Vijay, Mater. Sci. Eng. **B32**, 83 (1995).
3. H. Watanabe, T. Mihara, H. Yoshimori, and C.A. Araujo, Jpn. J. Appl. Phys. **34**, 5240 (1995).
4. B. Aurivillius, Arkiv. Kemi **1**, 463 (1949).
5. B. Aurivillius, Arkiv. Kemi **2**, 519 (1951).
6. E.C. Subbarao, J. Am. Ceram. Soc. **45**(4), 166 (1962).
7. F. Soares-Carvalho, P. Thomas, J.P. Mercurio, B. Frit, and S. Parola, J. Sol-Gel Science and Technology **8**, 759 (1997).
8. F. Soares-Carvalho, I. Jauberteau, P. Thomas, and J.P. Mercurio, J. Phys. III **7**, 1221 (1997).
9. K. Amanuma, T. Hase, and Y. Miyasaka, Appl. Phys. Lett. **66**(2), 221 (1995).
10. P.Y. Chu, R.E. Jones, P. Zurcher, D.J. Taylor, B. Jiang, S.J. Gillespie, Y.T. Lii, M. Kottke, P. Fejes, and W. Chen, J. Mater. Res. **11**(5), 1065 (1996).

Journal of Sol-Gel Science and Technology 13, 889–893 (1998)
© 1998 Kluwer Academic Publishers. Manufactured in The Netherlands.

Ferroelectric Thin Films of Bismuth Strontium Tantalate Prepared by Alkoxide Route

E.P. TUREVSKAYA AND V.B. BERGO
Moscow State University, Department of Chemistry, 119899 Moscow, Russia

K.A. VOROTILOV AND A.S. SIGOV
Moscow State Institute of Radioengineering, Electronics and Automation (Technical University), Vernadsky Prosp., 78, 117454 Moscow, Russia

D. BENLIAN
Universite de Provence, Lab. de Chimie de Coordination, Saint Jerome, 13397 Marseille, Cedex 20, France

Abstract. Study of the interactions in $Bi(OR)_3$-$Ta(OR)_5$-ROH (R = Me, Et, ^{i}Pr) at 20°C show that metal ethoxides are the best of the investigated precursors for the production of bismuth tantalates via alkoxides. Polycrystalline $SrBi_2Ta_2O_9$ (SBTO) and $BiTaO_4$ films on Si-SiO_2-Ti-Pt substrates with thicknesses of 0.4–0.5 μm and 0.4 μm, respectively, have been formed by sol-gel processing. The most stable solutions for film application were obtained by using mixed-metal Bi-Ta ethoxides and solutions of Sr carboxylate (2-ethylhexanoic acid derivative) in 2-ethylhexanoic acid. Films annealed at 700–750°C for 30 min were single-phased. SBTO films demonstrated good ferroelectric properties: remanent polarization ranged from 3.5 to 4.0 $\mu C/cm^2$ and coercive voltage 1.5–2.0 V, whereas $BiTaO_4$ films showed dielectric behavior.

Keywords: sol-gel method, alkoxides, films, bismuth

1. Introduction

Ferroelectric thin films have been intensively investigated during recent years as components of integrated circuits (ICs) [1, 2]. The two main applications of ferroelectrics are related to their physical properties: nonvolatile random-access memory (NVRAM) based on polarization of ferrolectrics and its alteration by external electric field; and dynamic random-access memory (DRAM) in which the extremely high permittivity of ferroelectrics is utilized.

The majority of recent studies have concentrated on lead zirconate titanate (PZT) films for NVRAM. PZT films have a high value of remanent polazrization and relatively low processing temperatures (550–650°C) for the production of the perovskite structure which is suitable for NVRAM technology (e.g., [3]). However, a major problem in the synthesis of PZT films is the volatility of PbO [4], which in many cases determines their crystalline structure and leads to oxygen vacancies and as a result to extensive fatigue in Pt/PZT/Pt capacitor structures. The amount of switchable polarization commonly drops after ferroelectrics are subjected to repeated (about 10^8 cycles) polarization reversals as a result of domain pinning by space charge [5].

There are two major strategies to overcome the fatigue problem: the reduction of charge trapping at the interface by the use of oxide conductive electrodes (e.g., RuO_2, LaSrCoO, etc.) and the control of defect density by vacancy compensation via donors doping or the use of ferroelectrics without volatile components thereby changing stoichiometry [3]. It has been demonstrated that PZT capacitors with oxide electrodes have practically no polarization fatigue up to about 10^{12}

switching cycles, but the use of oxide electrodes gives problems during the integration process (e.g., high resistivity). $SrBi_2Ta_2O_9$ (SBTO) is an alternative to PZT ferroelectric material with superior fatigue behavior which was recently proposed for NVRAM applications [6, 7]. During the past two years SBTO thin films have been prepared by various techniques, including sol-gel. The significant influence of precursor solutions on the properties of thin films formed by this method is well known. The present work represents the results of the studies in the field of precursor solution chemistry for deposition of SBTO. In addition, we have studied the sol-gel synthesis of $BiTaO_4$ films as a candidate material for a seeding layer form in SBTO crystallization, as well as for a dielectric with a high dielectric constant.

2. Experimental

The alcoholic metal derivatives are the most commonly used precursors in sol-gel chemistry. We have studied interactions in $Bi(OR)_3$-$Ta(OR)_5$-ROH systems, where R = Me, Et or ^{i}Pr to identify the most suitable derivatives of Bi and Ta, among the first members of the aliphatic homologous series, for the preparation of the precursor solutions. Bismuth and tantalum alkoxides were prepared according to previously described techniques [6, 7]. Bi carboxylates (2-ethylhexanoic acid derivatives) and mixed-ligand derivatives of Bi and Ta which were prepared by partial substitution of alkoxygroups in $M(OR)_x$ by the action of R′COOH on initial alkoxides have also been used as precursors. Solutions of $Sr(OR)_2$ and $Sr(R'COO)_2$ were prepared by direct reaction of Sr metal with alcohol or acid.

The films were formed by spin-on deposition on Si-SiO_2 (500 nm)-Ti(100 nm)-Pt(300 nm) substrates by four repeated depositions. The films were heat treated after each deposition at 600, 700, 750, 800, 850, or 900°C for 30 min. Final film thickness varied from 450 to 500 nm.

3. Result and Discussion

It was found that metal ethoxides are the best of the investigated precursors of bismuth tantalates via alkoxide route. In the methoxide system Bi-containing solutions cannot be prepared because of insolubility of polymeric $Bi(OMe)_3$ in $Ta(OMe)_5$ solutions. A bimetallic Bi-Ta complex crystallizes from isopropoxide solutions and therefore only solutions of mass concentration less than 10% can be prepared. Only in the ethoxide system can solutions of any concentration and with $Bi/Ta \leq 1.5$ be prepared. Vacuum evaporation of the solvent from solutions of $Bi(OEt)_3$ and $Ta(OEt)_5$ in EtOH results in formation of viscous pastes, which can be stored without noticeable decomposition for several months. Preparation of precursor solutions from these pastes was found to be the most convenient. It was found that quality of formed SBTO coatings significantly depended on precursor solution chemistry.

The various techniques used to prepare precursor solutions are shown in Table 1. By comparison of all studied methods only technique I seemed to be efficient. The following results are observed only for the films prepared from precursor solution I.

For crack-free films the optimal solution concentration was 0.6 mol as a total amount of alkoxides. 15% excess of Bi was used in the precursor solutions for SBTO films.

Table 1. Precursor solutions in $SrBi_2Ta_2O_9$ and $BiTaO_4$ thin film synthesis.

	Components ($R = C_2H_5$, $R' = C_7H_{15}$)			
Technique	Sr	Bi	Ta	Solvent
I	$Sr(R'COO)_2$	Mixed-metal ethoxide ("paste")		R′COOH
II	$Sr(OR)_2$	Mixed-metal ethoxide ("paste")		Ethanol
III	$Sr(OR)_2$	Mixed-metal ethoxide ("paste")		$CH_3OC_2H_4OH$
IV	$Sr(OR)_2$	Mixed-metal ethoxide ("paste")		Toluene
V	$Sr(R'COO)_2$	$Bi(R'COO)_3$	$Ta(OR)_x(R'COO)_{5-x}$	R′COOH
VI	$Sr(R'COO)_2$	$Bi(OR)_3$	$Ta(OR)_x(R'COO)_{5-x}$	R′COOH
VII	$Sr(R'COO)_2$	$Bi(OR)_x(R'COO)_{3-x}$	$Ta(OR)_x(R'COO)_{5-x}$	R′COOH
—	—	$Bi(OR)_3$	$Ta(OR)_5$	R′COOH

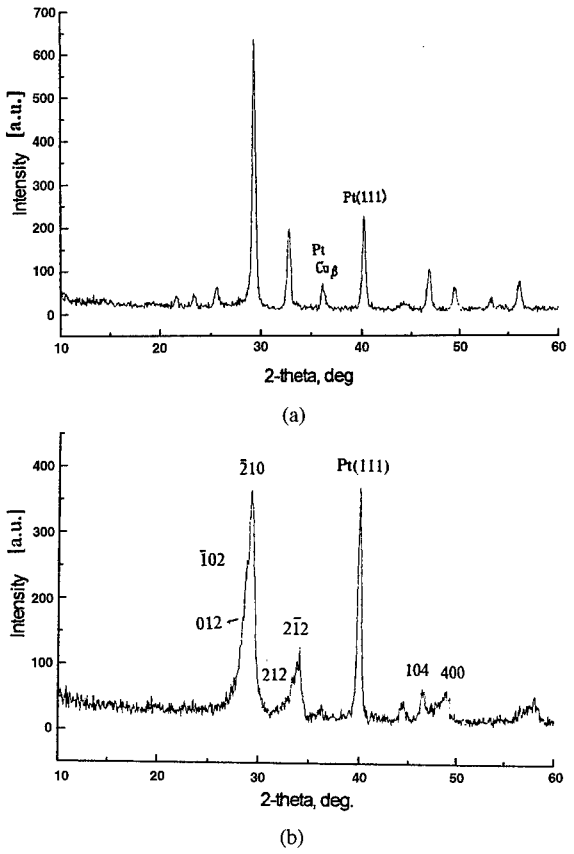

Figure 1. XRD pattern of $SrBi_2Ta_2O_9$ (a) and $BiTaO_4$ (b) films; furnace treatment at 750°C.

XRD showed that annealing at 600°C did not lead to crystallization as only a few rather broad peaks were present in the XRD pattern. However, annealing at 700°C gave single-phase, crystalline, $SrBi_2Ta_2O_9$. Annealing at higher temperatures slightly improved the quality of crystallinity. Reflections of the sample annealed at 750°C; $d(I/I_0)$: 4.13(7), 3.80(7), 3.49(10), 3.04(100), 2.73(32), 2.48(11), 2.24(38), 1.94(16), 1.84(10), 1.72(7), 1.64(13), 1.53(8) corresponded to the set of interplanar spacings reported in [8] and can be indexed, according to the data [8], with an orthorhombic primitive cell with axes $a = 0.582 \pm 0.002$ nm, $b = 2.509 \pm 0.004$ nm and $c = 0.526 \pm 0.002$ nm (Fig. 1(a)). Increasing the heat treatment temperature to 900°C led to the formation of an admixture phase. At the 750°C single-phase $BiTaO_4$ films were formed (Fig. 1(b)) [9].

SEM micrographs of $SrBi_2Ta_2O_9$ and $BiTaO_4$ films prepared at 700°C are shown in Fig. 2. The SBTO film has a well-defined rod-like crystalline structure with crystallites between 100 and 300 nm in size and a porosity of about 10 vol%, probably as a result of using 2-ethylhexanoic acid with a long carbon chain as a solvent (the film structure is similar to one described in [10]). Films of bismuth tantalate consist of large grains with strongly oriented domains.

Electrical properties of SBTO films were dependent on the temperature of their crystallization. Only the films prepared at 700 and 750°C demonstrated good ferroelectric properties (Fig. 3(a)). The coercive field was about 50 kV/cm and the remanent polarization was 7–9 $\mu C/cm^2$ (the films annealed at 750°C had somewhat higher value of remanent polarization than those annealed at 700°C) which is typical for films prepared by sol-gel techniques. The capacitance of SBTO films was 5–7 $fF/\mu m^2$ (corresponding to the values of

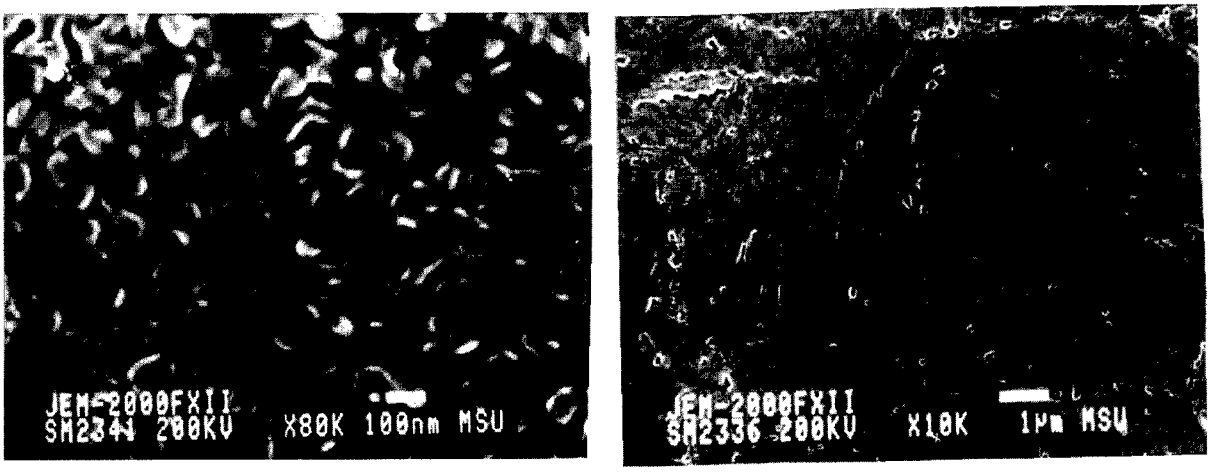

Figure 2. SEM microphotograph of $SrBi_2Ta_2O_9$ (a) and $BiTaO_4$ (b) films.

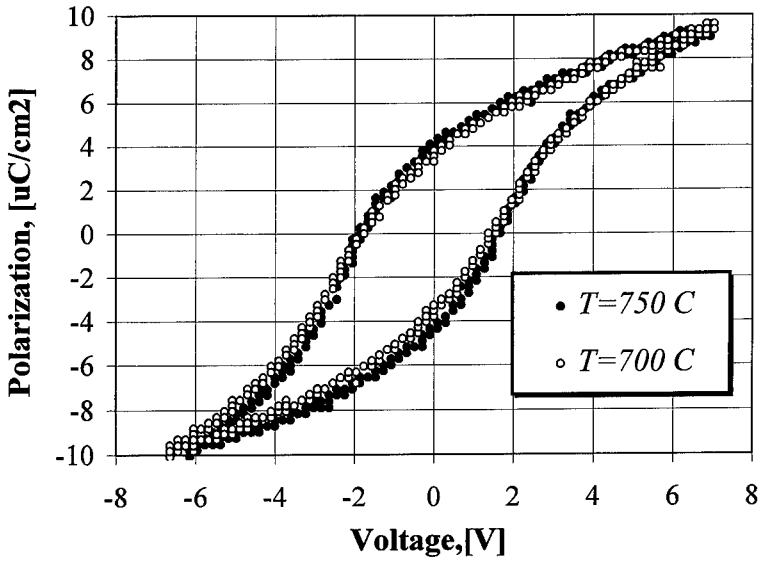

(a)

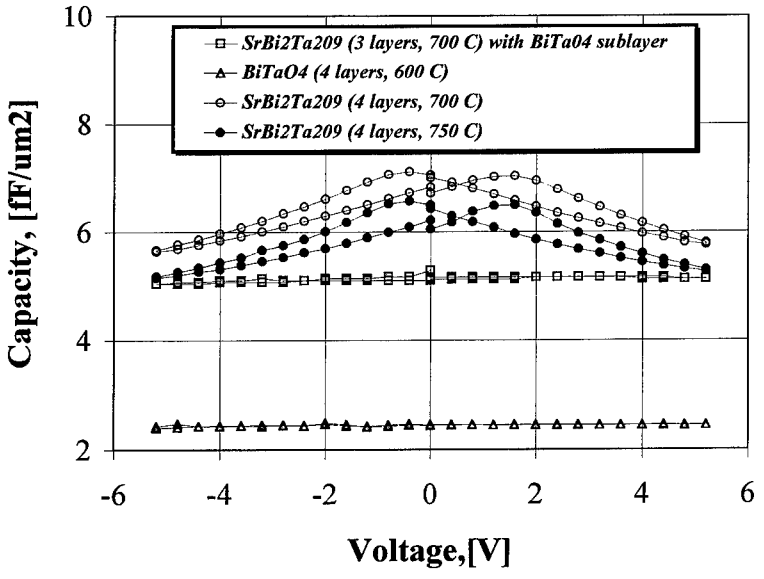

(b)

Figure 3. The hysteresis loop for $SrBi_2Ta_2O_9$ films (a) CV dependences for $SrBi_2Ta_2O_9$ and $BiTaO_4$ capacitor structures (b).

dielectric constant from 230 to 320) and had a nonlinear dependence on voltage with hysteresis. $BiTaO_4$ displayed typical linear dielectric behavior (Fig. 3(b)) with a capacitance of about 2.4 fF/μm^2.

4. Conclusions

SBTO and $BiTaO_4$ films have been obtained by sol-gel processing. The film quality is significantly dependent on the conditions of solution preparation. Films annealed at 700–800°C are single-phase. Annealing at a higher temperature (900°C) leads to second phase formation. The best electrical properties are demonstrated by SBTO films annealed at 700–750°C.

Acknowledgments

This work was supported by INTAS grant 94-771, Russian Foundation for Basic Research grants 96-33553 and 97-02-17822, and State Scientific and

Technical Program "Advanced Technologies and Devices of Micro- and Nanoelectronics" grant 218/68/1-2.

References

1. J.F. Scott, C.A. Paz de Aranjo, and L. D. Macmillan, Condensed Matter News **1**, 16 (1992).
2. A.S. Sigov, V.I. Petrovsky, E.F. Pevtsov, K.A. Vorotilov, and A.S. Valeev, NATO ASI Series, Vol. 284, edited by O. Auciello and R. Waser (Kluwer Academic Publishers, Boston, 1995), p. 427.
3. O. Auciello, Integrated Ferroelectrics **15**, 211 (1997).
4. L.I. Solov'eva, I.E. Obvinteseva, M.I. Yanovskaya, K.A. Vorotilov, and V.A. Vasil'ev, Inorganic Materials **32**, 766 (1966).
5. W.L. Warren, D. Dimos, and R.M. Waser, MRS Bulletin **40**(7), (1996).
6. S.I. Kucheiko, V.G. Kessler, and N.Ya. Turova, Koord. Khimiya **13**, 1043 (1987) (in Russian).
7. N.Ya. Turova, A.V. Korolev, D.E. Tchebukov, A.I. Belokon, A.I. Yanovsky, and Yu.T. Struchkov, Polyhedron **15**, 3869 (1996).
8. M. Klee, U. Mackens, J. Pankert, W. Brand, and W. Klee, in *Science and Technology of Electroceramic Thin Films*, edited by O. Auciello and R. Waser (Kluwer, Dordrecht, 1995), p. 99.
9. M. Roth and A. Waring, Am. Mineral **48**, 1348 (1963).
10. D. Thomas, A.I. Kingon, O. Auciello, R. Waser, and M. Schumacher, Integr. Ferroel. **14**, 51 (1995).

Journal of Sol-Gel Science and Technology 13, 895–898 (1998)
© 1998 Kluwer Academic Publishers. Manufactured in The Netherlands.

Preparation and Characterization of Sol-Gel Derived Y_2O_3 Thin Films

G. TEOWEE, K.C. McCARTHY, F.S. McCARTHY AND T.J. BUKOWSKI
Donnelly Corporation, 4545 East Fort Lowell Road, Tucson, AZ 85712

D.G. DAVIS JR. AND D.R. UHLMANN
Department of Materials Science and Engineering, University of Arizona, Tucson, AZ 85721

Abstract. Sol-gel derived Y_2O_3 thin films have been prepared on platinum coated silicon wafers and fired to temperatures ranging from 400°C to 750°C. Multiple coats were used to obtain films up to 0.5 μm thick with an intermediate firing of 400°C between coatings. Top Pt electrodes were sputtered to form monolithic capacitors. These films exhibited a dielectric constant of 18 and a leakage current of 10^{-11}–10^{-7} A/cm^2, making them attractive candidates for high dielectric constant dielectric films in high density DRAMs.

Keywords: films, yttrium oxide, dielectric, ferroelectric

Introduction

New research into materials for high-density monolithic capacitors in microelectronics is being fueled by the necessity for smaller feature size. Projected applications include elements for use as dynamic random access memory (DRAM) devices, an interlevel dielectric in very large-scale integrated circuits (VLSI), as well as gate dielectrics for thin film transistors. SiO_2 is used as the workhorse dielectric material in today's devices, and exhibits a dielectric constant of only 3.5. High dielectric constant insulators are being sought as an alternative to provide for the capacitance density needed. Y_2O_3, with a bulk dielectric constant of 18 [1], excellent chemical stability and high affinity for oxygen, is a promising candidate.

Y_2O_3 films have been used in applications such as antireflection coatings [2, 3], protection against chemical corrosion [2, 4], phosphor thin film [3, 5] and dielectric layer for electroluminescent devices [6]. Various methods have been used for the production of Y_2O_3 films including; rf magnetron sputtering [7, 6], reactive sputtering [8], sol-gel [5], self-assembling monolayers [9], electrochemical anodization [10, 11], injection-CVD [12], MOCVD [13], plasma-sprayed [4], pulsed laser deposition [3] and electron beam evaporation [2, 14]. Y_2O_3 films exhibit a high electrical breakdown field (>3 MV/cm) [6, 8], low dissipation factor (<0.005) [15], high resistivity (>10^{14} Ω·cm) [16], low leakage current, large band gap (5.8 eV) [3], low bulk trap density of 4–11 × 10^{11}/cm^2 [14] and high refractive index (1.9–2.0) [2, 12], in addition to a large dielectric constant (12–18). The present authors are unaware of previous reports on the dielectric properties of sol-gel derived Y_2O_3 films.

Experimental Procedures

The yttria solution was prepared via sol-gel methods, using yttrium acetate in methanol to form the precursor. Platinum coated silicon wafers were used as the substrates for electrical characterization. The 0.5 M yttrium acetate solution was deposited onto the substrates by means of spincoating, using a Headway Spinner under clean room conditions. The precursor was filtered through a 0.2 μm syringe filter to prevent particulate contamination. The films were spun at 2000 rpm for 30 s, and subsequently fired to 400°C for 1 hour to densify the films between coats. The films were later subjected to a range of temperatures, 450°C–750°C for half an hour. All firing was performed in an oxygen

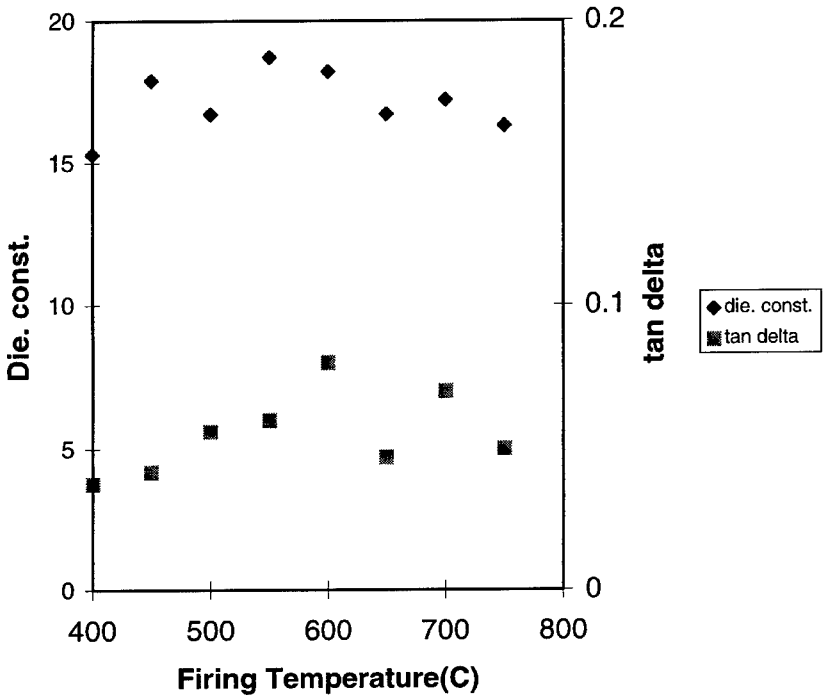

Figure 1. Dielectric constant and tan delta of Y_2O_3 films as a function of firing temperature.

atmosphere. Electrical characterization was performed to determine the dielectric properties. An HP4192A impedance analyzer was used to measure capacitances and dissipation factors at 1 MHz and 1 V rms oscillation voltages. Leakage currents were obtained from 0 V to 3 V at 0.2 V intervals and 60 s delay times using a Keithley 617 programmable electrometer interfaced to a PC. The phase development of the films was determined by X-ray diffraction (XRD), using a Scintag Diffractometer with CuK_α wavelength from $2\theta =$ 20–50°, performed at a scan rate of 10°/min.

Results and Discussions

XRD results indicate that the films are amorphous at 400°C and begin to crystallize at 450°C. It has been reported that e-beam evaporates and sol-gel films crystallize at 400–430°C [1, 14] and 600°C [5], respectively. In the latter films, the higher crystallization temperature is explained by the conversion of the yttrium hydroxide to oxide in the sol-gel precursor at 562°C [5]. As the firing temperature increases, strong crystalline Y_2O_3 peaks develop in the sol-gel derived films, particularly the (222). Reactively evaporated Y_2O_3 films also exhibit (222) texture [8]; the (222) plane has the lowest surface energy.

The values of dielectric constant and dissipation factor in the Y_2O_3 films as a function of firing temperature are shown in Fig. 1. It can be seen that the values of ε_r remains fairly constant at about 18 with firing temperature. ε_r in these films is much higher compared to that found in SiO_2, i.e., 3.5. This agrees well with the value for bulk Y_2O_3 [1, 14], indicative of the high degree of densification achieved in the films. The tan delta values are reasonably low but they tend to increase with firing temperature. This increase can be attributed to the increased degree of crystallization with firing temperature which leads to more grain boundaries and higher conductivity losses.

There have been many proposals for the conduction mechanisms in Y_2O_3 thin films. Leakage currents in these films have been reported due to space charge [10], Poole-Frenkel [1, 14], Schottky [17] and ionic [12, 14] conductions. Leakage currents of the films were also investigated in the study, with the results shown in Fig. 2. The I–V characteristics appear to follow typical Schottky emission. Samples fired at 400°C yielded the best leakage values, i.e., lowest current of only 10^{-11} A/cm^2. This is due to the fact that the films are amorphous at 400°C and so have no grain boundaries to allow for intergrain boundary conduction. Upon crystallization of the films when fired at 450°C and above,

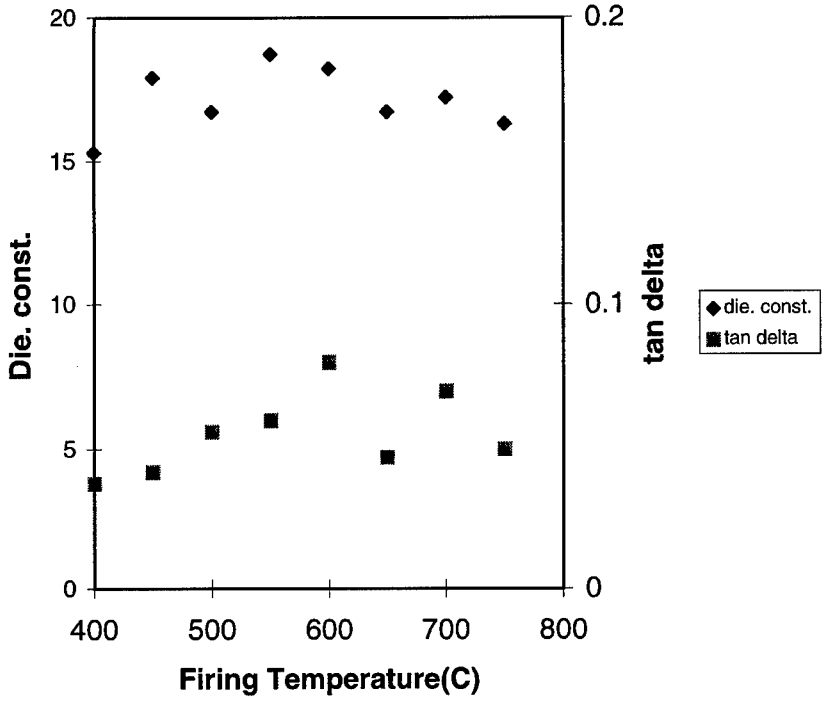

Figure 2. Leakage current in Y_2O_3 films fired to various temperatures.

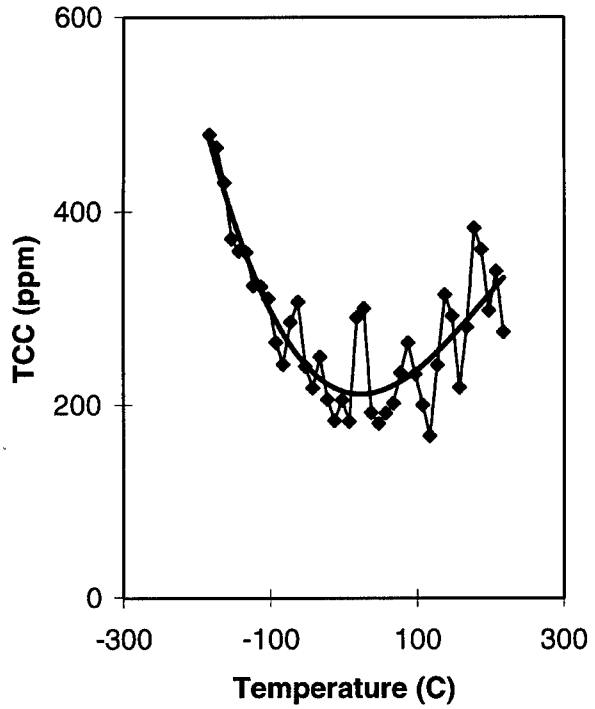

Figure 3. Temperature coefficient of capacitance (TCC) as a function of temperature in Y_2O_3 films fired to 600°C.

the leakage currents increase dramatically to around 10^{-6}–10^{-7} A/cm^2 due to the presence of grain boundaries. Local asperities and grain boundaries have also been reported to result in large leakage currents in evaporated Y_2O_3 films [14].

There is a steady increase in capacitance at higher measuring temperatures, while the dissipation factor increased dramatically above 130°C. Such a sharp increase has also been reported in sputtered Y_2O_3 films and was attributed to enhanced leakage currents [15, 18]. The temperature coefficient of capacitance (TCC) of a sol-gel derived Y_2O_3 film fired to 600°C is shown in Fig. 3, ranging from 200 to 500 ppm/°C. There is a minimum (200 ppm/°C) in the TCC value at 20°C. The TCC of other Y_2O_3 and rare earth oxide thin films reported in the literature are summarized in Table 1. The TCC obtained in the present Y_2O_3 film is among the lowest value reported for Y_2O_3 or other rare earth oxide thin films. Such a value is attractive for monolithic capacitors to minimize large capacitance fluctuations arising from changes in operating temperature. Additionally, the rare earth oxides typically exhibited lower values of ε_r (~14) compared to Y_2O_3 films [18]. Thus, among the rare earth oxide thin films, Y_2O_3 appears to be the best candidate for high quality high ε_r materials.

Table 1. TCC of various Y_2O_3 and rare earth oxide films.

Method	TCC (ppm/°C)	Ref.
Sol-gel Y_2O_3	200	This work
e-beam evap. Y_2O_3	300	[18]
e-beam evap. Y_2O_3	320	[15]
Rf sputtered Y_2O_3	200	[15]
Reactive sputtered Y_2O_3	240	[15]
Anodized Y_2O_3	375	[15]
Evap. Eu_2O_3	560	[19]
Evap. Nd_2O_3	360–560	[20]
Evap. Yb_2O_3	370	[21]
Evap. Er_2O_3	650–2100	[22]
Evap. Sm_2O_3	1000	[23]
Evap. Dy_2O_3	200–800	[24]

Conclusions

Sol-gel derived Y_2O_3 films were prepared on platinized Si wafers. XRD data indicate that the films crystallize at a firing temperature of 450°C. The dielectric properties of these films are excellent; dielectric constant and dissipation factor of the films were measured as 18 and 0.03, respectively, with a leakage current as low as 10^{-11} A/cm^2. The capacitance and dissipation factor of the films increased monotonically with measuring temperature exhibiting a TCC of about 200 ppm/°C at room temperature. Based on high ε_r, low leakage current and low TCC values, these Y_2O_3 films appeared very promising for high density DRAM applications.

Acknowledgments

The financial support of the Donnelly Corporation and the Air Force Office of Scientific Research is greatly appreciated.

References

1. A.C. Rastogi and R.N. Sharma, J. Appl. Phys. **71**, 5041 (1992).
2. A.F. Andreeva, A. Sisonyuk, and E. Himich, Phys. Stat. Sol. **A145**, 441 (1994).
3. S.L. Jones, D. Kumar, R.K. Singh, and P.H. Holloway, Appl. Phys. Lett. **71**, 404 (1997).
4. M. Berkowski, P. Bowen, T. Liechti, and H.J. Scheel, J. Am. Ceram. Soc. **75**, 1005 (1992).
5. R.P. Rao, Sol. State Comm. **99**, 439 (1996).
6. W.M. Cranton, D. Spink, R. Stevens, and C. Thomas, Thin Solid Films **226**, 156 (1993).
7. Ken-ichi Onisawa, M. Fuyama, K. Tamura, K. Taguchi, T. Nakayama, and Y. Ono, J. Appl. Phys. **68**, 719 (1990).
8. J. Hudner, H. Ohlsen, and E. Fredriksson, Vacuum **45**, 967 (1995).
9. M.R. De Guire, H. Shin, R. Collins, M. Agarwal, C.N. Sukenik, and A.H. Heuer, Proc. SPIE **2686**, 33 (1989).
10. S. Kuriki, A. Noya, and G. Matsumoto, Thin Solid Films **48**, 27 (1978).
11. R.M. Goldstein, Electronic Components Conference, 141 (1968).
12. J.P. Senateur, A. Abrutis, F. Felten, F. Weiss, O. Thomas, and R. Madar, Advances in Inorganic Films and Coatings, 161 (1995).
13. M. Pulver and G. Wahl, Advances in Inorganic Films and Coatings, 167 (1995).
14. C.K. Campbell and M. Thewalt, Thin Solid Films **13**, 195 (1972).
15. C.K. Campbell, Thin Solid Films **6**, 197 (1970).
16. T. Tsutsumi, Jpn. J. Appl. Phys. **9**, 735 (1970).
17. P. Meena, C. Balasubramanian, S. Narayandass, and D. Mangalaraj, Phys. Stat. Sol. **A125**, K97 (1991).
18. M. Sayer and S. Martin, Thin Solid Films **6**, R61 (1970).
19. C.R. Dutta and K. Barua, Thin Solid Films **100**, 149 (1983).
20. V.S. Dharmadhikari and A. Goswami, Thin Solid Films **87**, 119 (1982).
21. T. Wiktorczyk and C. Wesolowska, Thin Solid Films **71**, 15 (1980).
22. M.K. Jayaraj and C.P.G. Vallabhan, Thin Solid Films **40**, 16 (1991).
23. A. Goswami and R.R. Varma, Thin Solid Films **28**, 157 (1975).

Journal of Sol-Gel Science and Technology 13, 899–902 (1998)
© 1998 Kluwer Academic Publishers. Manufactured in The Netherlands.

Dielectric and Ferroelectric Properties of Sol-Gel Derived $YMnO_3$ Films

G. TEOWEE, K.C. McCARTHY, F.S. McCARTHY AND T.J. BUKOWSKI
Donnelly Corporation, 4545 East Fort Lowell Road, Tucson, AZ 85712

D.G. DAVIS, JR. AND D.R. UHLMANN
Department of Materials Science and Engineering, University of Arizona, Tucson, AZ 85721

Abstract. There has been considerable interest in ferroelectric (FE) films especially for non-volatile memories and ultra high density DRAM applications. Such FE films typically consist of lead zirconate titanate (PZT) with novel oxide contacts, or layered perovskite such as $Sr_2Bi_2TaO_9$. Recently, there have been reports of sputtered $YMnO_3$ films which exhibit a single polarization axis and do not contain any volatile species of Pb or Bi. Single crystal $YMnO_3$ exhibits satisfactory polarization (6 $\mu C/cm^2$) and low coercive field (<20 kV/cm). Additionally, the dielectric constant of $YMnO_3$ is quite low (<30) which should facilitate ferroelectric switching. In this study, sol-gel derived $YMnO_3$ films were prepared on platinized Si wafers and their dielectric and ferroelectric properties were characterized. Their electrical properties will be discussed with respect to Y/Mn stoichiometry ratio, hexagonal phase development and processing conditions. The potential of $YMnO_3$ as a material in non-volatile memories is evaluated.

Keywords: films, yttrium manganate, dielectric, ferroelectric

Introduction

There has been intense interest in the use of layered perovskite films, notably $SrBi_2Ta_2O_5$ (SBT) [1] and PZT-RuO_2 [2] for applications in non-volatile memories. These films exhibit no or minimal fatigue. But they contain volatile species, i.e., Bi and Pb, which can lead to non-stoichiometry and heterogeneity problems during processing, especially at elevated temperatures. Hence there is a need to explore other FE materials which are fatigue-free and also processing-friendly.

$YMnO_3$ is a hexagonal FE with T_c of 650°C [3] and unipolar axis along the (0001) direction [4] with 180° domain walls [5]. Its conductivity is quite high, and $YMnO_3$ is classified as a *p*-type semiconductor [6]. The spontaneous polarization, coercive field and dielectric constant are fairly low, being 2.5–5.5 $\mu C/cm^2$, 15–20 kV/cm and 20, respectively. Recently, there have been a few reports of $YMnO_3$ thin films obtained using sputtered and pulse laser deposition techniques. The dielectric constant of the films (~8.2) [7–9] is typically lower than that found in bulk (~20) [10, 11].

Experimental Procedures

The yttrium manganate solution was prepared using yttrium acetate, manganese acetate, and methanol as precursors. The relative amount of Y and Mn was varied to ascertain the effect of film stoichiometry on properties. The substrates used for electrical characterization were platinized silicon wafers. The 0.25 molar yttrium manganate solution was spincoated onto the platinum surface, using a Headway Spinner. To prevent particulate contamination of the precursor, a 0.2 μm filter was added to the syringe. The films were spincoated at 2000 rpm for 30 s, and fired at 400°C between coats. To vary the degree of crystallization, the films were subjected to a range of temperatures, 450–800°C for 1/2 hour. All firing was performed in an oxygen atmosphere. Electrical characterization was performed to determine the dielectric properties. An HP4192A impedance analyzer was used to measure capacitance and dissipation factors at 1 MHz and a 1 v rms oscillation voltage. Leakage currents were obtained from 0 to 2 v at 0.2 v intervals at 60 s delay times using

a Keithley 617 programmable electrometer interfaced to a computer. The phase development of the films was determined by X-ray diffraction (XRD), using a Scintag Diffractometer with a CuK_α wavelength from $2\theta = 20$–$50°$, performed at a scan rate of 10°/min.

Results and Discussions

The XRD scans of $YMnO_3$ films indicated that the films were amorphous below firing temperatures of 750°C. Crystallization into the hexagonal phase initiated at 750°C and above 800°C, the films became fully crystallized. No extraneous phase of MnO_2, Y_2O_3 or orthorhombic $YMnO_3$ was detected during phase development. The microstructures of the films fired at 800°C consisted of a very fine grain size (<100 nm).

The dielectric constants of the $YMnO_3$ films fired at various temperatures are shown in Fig. 1. The dielectric constant increased from 16 for films fired below 600°C to 23 when fired to 700°C, and decreased slightly above 750°C, probably indicative of reactions with the Pt substrates. The dielectric constants of these films are higher than reported for sputtered or pulsed laser deposited films (8.2) and is comparable to bulk values (20). The dissipation factors, however, are high (>1.0) especially for films fired above 750°C, indicative of high conductivity films.

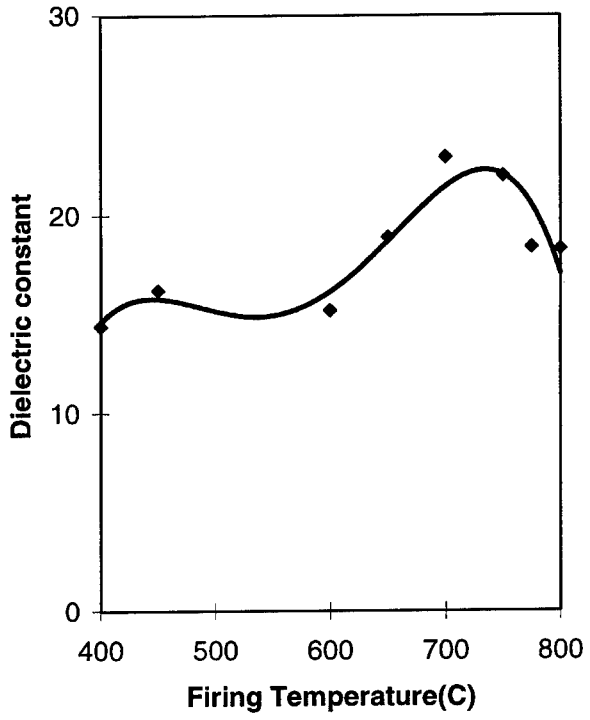

Figure 1. Dielectric constant of $YMnO_3$ films as a function of various firing temperatures.

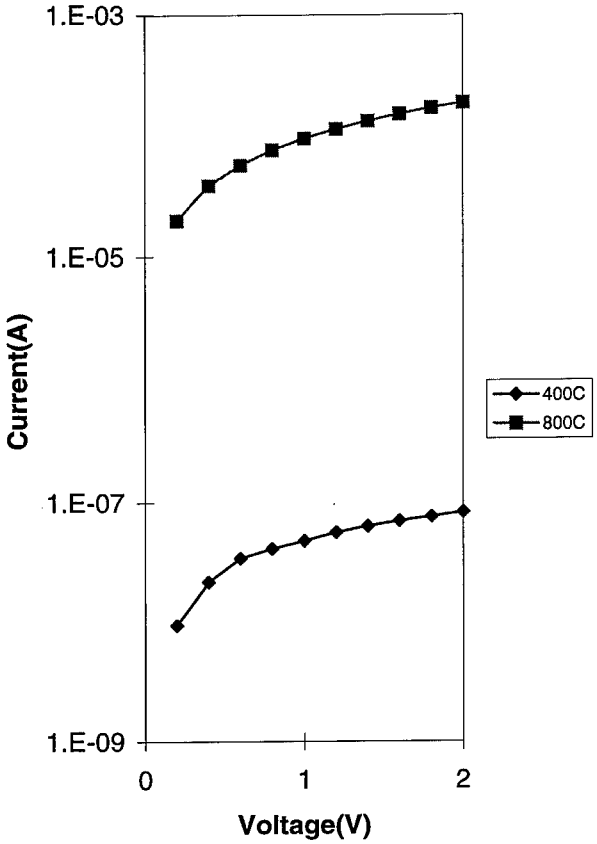

Figure 2. I–V characteristics of $YMnO_3$ films fired to 400 and 800°C.

The leakage characteristics of the films fired to 400 and 800°C are shown in Fig. 2. The leakage currents generally increased at higher firing temperatures, especially when fired above 800°C. The leakage currents followed typical Schottky emission. Even in amorphous films, the leakage currents are already high (10^{-4} A/cm^2) compared to other FE films, e.g., PZT films with leakage currents of 10^{-8}–10^{-9} A/cm^2 [12]. The high conductivity in the films is attributed to Mn^{3+}–Mn^{5+} intervalence electron transfer [8] and to the small grain size of the films which facilitates intergrain boundary conduction. Bulk $YMnO_3$ has also been reported to exhibit enhanced conductivity, especially at high temperatures [4].

The effect of stoichiometry is illustrated in Fig. 3, which shows respectively the effect of Y content, x, on the dielectric constant and leakage current at 2 V for

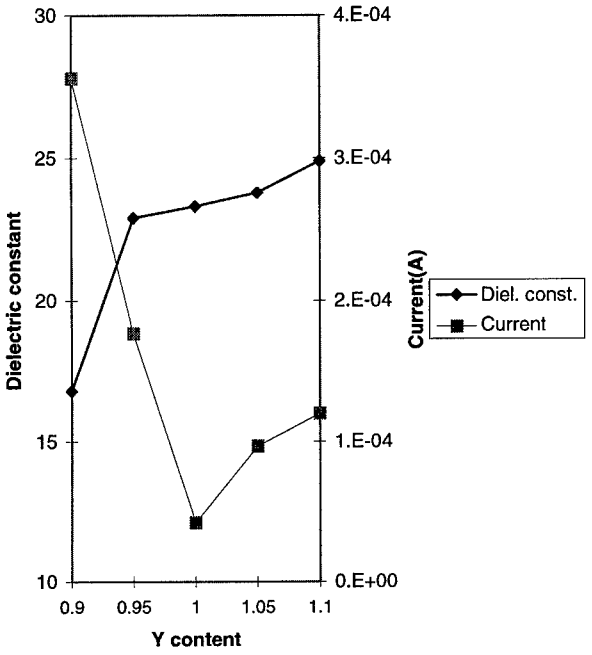

Figure 3. Effect of Y content on the dielectric constant and leakage currents at 2 V of Y_xMnO_3 films fired to 750°C.

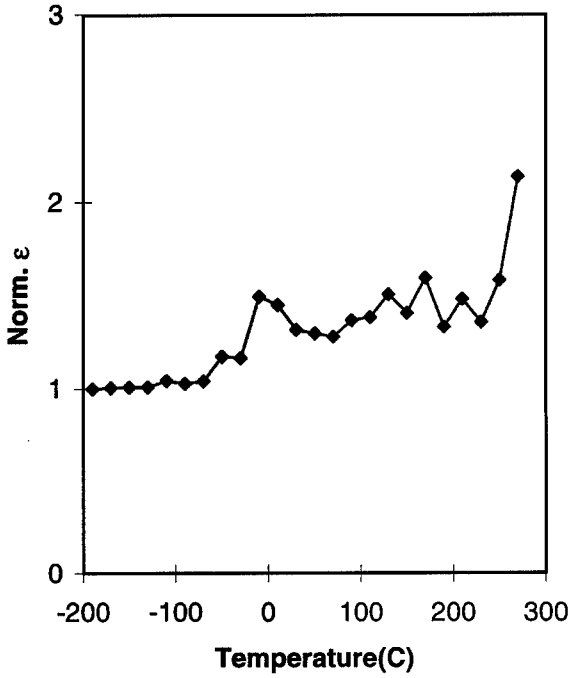

Figure 4. Effect of measuring temperature on normalized dielectric constant of $YMnO_3$ films fired to 750°C.

Y_xMnO_3 films fired to 750°C. The dielectric constant is fairly independent of Y content except at $x = 0.9$ where it falls to 16, but the Y content appears to influence strongly the leakage current. Stoichiometric $YMnO_3$ has the lowest leakage current. This is indicative of enhanced conductivity resulting from incomplete charge compensation in the non-stoichiometric films.

The effect of measuring temperature on normalized dielectric constants in a $YMnO_3$ film fired to 750°C is shown in Fig. 4. It is fairly constant except for a kink near 0°C and at above 230°C when it increases dramatically. These observations can be associated with an A-axis lattice parameter shift at 0°C and a phase transition near 230°C which were reported in bulk $YMnO_3$ [4]. The ferroelectric loop obtained at room temperature is quite lossy and elliptical in all the films due to the conductive nature of the films. Sputtered films also yield very lossy loops [7]. Even in single crystal samples, such loops are also lossy and distorted [10]. At low temperatures, the FE loops become more distinct since the films are less conducting, but the polarization values are quite small. For example, at a measurement temperature of −45°C, the polarization is only about 0.5 $\mu C/cm^2$. This value is much lower than that found in PZT or even SBT, i.e., up to 30 and 10 $\mu C/cm^2$, respectively.

Conclusion

Sol-gel derived $YMnO_3$ films were prepared on platinized Si wafers. The films were amorphous when fired at temperatures below 750°C. At higher firing temperatures, the films became crystalline and appeared very conductive. A dielectric constant of 23 is obtained in these films when fired to 700°C. This is higher than reported literature values for thin films and comparable to the bulk value. Stoichiometric $YMnO_3$ film appeared to yield the lowest leakage current. The FE loop was lossy and elliptical at room temperature but became more distinct at lower measuring temperatures with polarization and coercive fields of 0.5 $\mu C/cm^2$ and 50 kV/cm, respectively, at −45°C. Due to the low polarization and high leakage current characteristics which distort the ferroelectric properties, these films do not appear attractive for application in nonvolatile memories.

Acknowledgments

The financial support of the Donnelly Corporation and the Air Force Office of Scientific Research is greatly appreciated.

References

1. C.D. Gutleben, MRS Symp. Proc. **433**, 109 (1996).
2. B.A. Tuttle, T.J. Headley, H.N. Al-Shareef, J.A. Voigt, M. Rodriguez, J. Michael, and W.L. Warren, J. Mater. Res. **11**, 2309 (1996).
3. I. Ismailzade, Phys. Stat. Sol. **46**, K39 (1971).
4. I. Ismailzade and S. Kizhaev, Soviet Phys. Sol. Stat. **7**, 236 (1965).
5. E. Betraut, F. Forrat, and P. Fang, Bull. American Physical Society **8**, 61 (1963).
6. V.E. Wood, A.E. Austin, E.W. Collins, and K.C. Brog, J. Phys. Chem. Solids **34**, 859 (1973).
7. N. Fujimura, T. Ishida, T. Yoshimura, and T. Ito, Appl. Phys. Lett. **69**, 1011 (1996).
8. N. Fujimura, T. Ishida, T. Yoshimura, and T. Ito, Mat. Res. Soc. Symp. Proc. **433**, 119 (1996).
9. N. Fujimura, S. Azuma, N. Aoki, T. Yoshimura, and T. Ito, J. Appl. Phys. **80**, 7084 (1996).
10. V. Bokov, G. Smolenskii, S. Kizhaev, and E. Myl'nikova, Soviet Physics Solid State **5**, 2646 (1964).
11. Landolt Borstein, Numerical Data and Functional Relationships in Science and Technology **16**, 164 (1981).
12. G. Teowee, unpublished results.

Journal of Sol-Gel Science and Technology 13, 903–907 (1998)
© 1998 Kluwer Academic Publishers. Manufactured in The Netherlands.

Preparation and Dielectric Properties of $YMnO_3$ Ferroelectric Thin Films by the Sol-Gel Method

KIYOHARU TADANAGA, HIROYA KITAHATA, TSUTOMU MINAMI, NORIFUMI FUJIMURA AND TAICHIRO ITO

Department of Applied Materials Science, Osaka Prefecture University, Sakai, Osaka 593, Japan

Abstract. Thin films of $YMnO_3$ are proposed as a new candidate for non-volatile ferroelectric memory devices. They were prepared via solutions through two different processes: thermal decomposition and reflux using yttrium acetate tetrahydrate and manganese acetate tetrahydrate as starting materials. For coatings prepared by thermal decomposition process, the starting materials were dissolved in ethanol containing diethanolamine, and single phase $YMnO_3$ was obtained with heat-treatment at 900°C. When the starting materials were refluxed using 2-ethoxyethanol as a solvent, single phase $YMnO_3$ was obtained with heat-treatment at 800°C. Scanning electron microscopy showed that the 300 nm thick films with a stoichiometric Y/Mn ratio had many pinholes, and a very large dielectric loss, 0.83 at 100 kHz. Inclusion of 5–10% excess of Y in the coating solution produced dense structures with improved dielectric properties. The dielectric constant and loss tangent of the thin films with Y/Mn ratio of 1.00/0.90 were about 20 and 0.05 at 100 kHz, respectively.

Keywords: $YMnO_3$, non-volatile ferroelectric memory devices, reflux, dielectric property

1. Introduction

Thin films of $YMnO_3$ with hexagonal structure are proposed as a new candidate for non-volatile ferroelectric memory devices, especially for Metal-Ferroelectric-Semiconductor (MFS) type devices [1, 2]. $YMnO_3$ films are attractive because they have one polarization axis and low dielectric permittivity, contain a rare earth element which is more easily oxidized than the substrate (e.g., Si) and do not contain volatile elements such as Bi and Pb; the point defects formed by Bi and Pb vacancies affect fatigue and imprint properties. Although epitaxial $YMnO_3$ films on (111)MgO and (0001)ZnO : Al/(0001) sapphire have successfully been obtained using RF magnetron sputtering and pulsed laser deposition [1, 2], it is also important to prepare them via solutions because control of chemical composition is easy, lower firing temperatures are expected, and the cost of fabrication is low. However, the dielectric properties of thin films are closely associated with the microstructure of the films. Consequently, it is important to investigate the effects of the preparation conditions on the microstructure and the dielectric properties. Additionally, in the case of Mn-containing oxides, the control of oxidation states of Mn is important to obtain the desired products. Recently, we have reported the preparation of $YMnO_3$ thin films from solution, and showed that the preparation conditions and the Y/Mn ratios in the starting solution affected the microstructure and dielectric properties of the $YMnO_3$ thin films [3, 4].

$YMnO_3$ thin films have been prepared by sol-gel processing and either thermal decomposition or refluxing. Thin films with several Y/Mn ratios were prepared. The effects of the reflux and the Y/Mn ratio on the microstructure and the electric properties of the $YMnO_3$ thin films are discussed.

2. Experimental [3, 4]

For the thermal decomposition process, yttrium acetate tetrahydrate ($Y(OAc)_3 \cdot 4H_2O$) and manganese acetate tetrahydrate ($Mn(OAc)_2 \cdot 4H_2O$) were separately

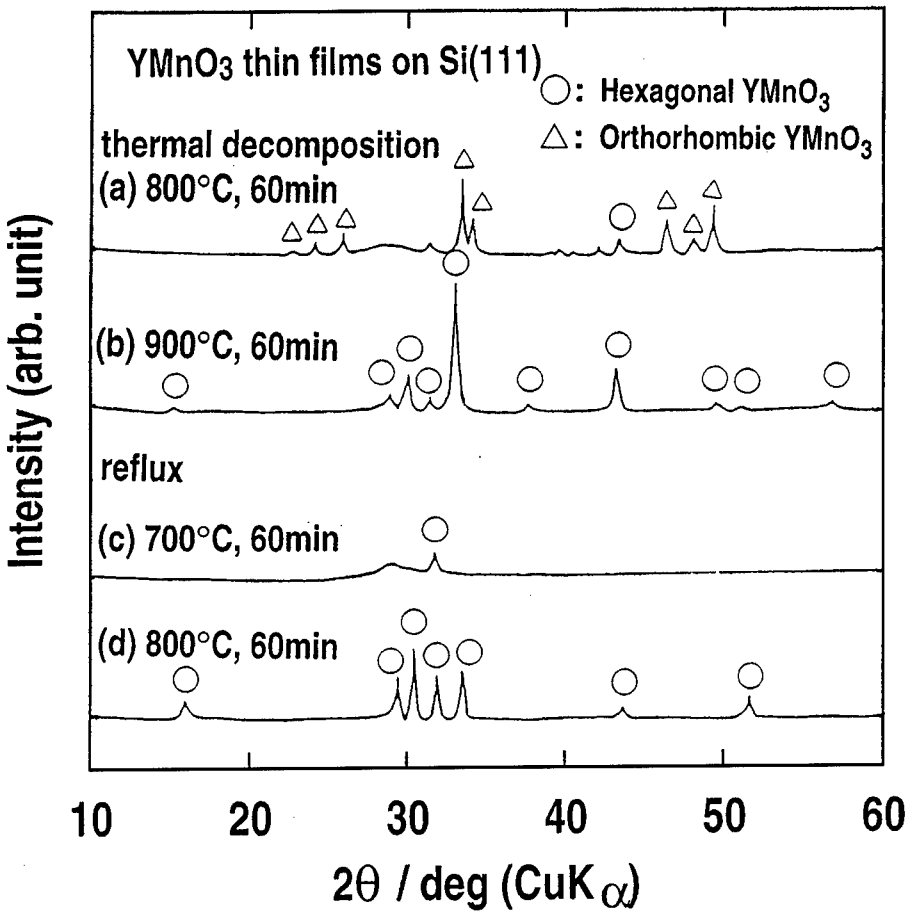

Figure 1. XRD patterns of $YMnO_3$ thin films prepared by thermal decomposition and reflux processes.

dissolved in ethanol (EtOH) containing diethanolamine (DEA). These solutions were then mixed and the solution was stirred for 2 h. For the reflux process, $(Mn(OAc)_2 \cdot 4H_2O)$ was dissolved in 2-ethoxyethanol (2EE), which has a higher boiling point (125°C) than water. The solution was subsequently dehydrated and the dehydrated solution refluxed at 125°C for 3 h. Then, $(Y(OAc)_3 \cdot 4H_2O)$ dissolved in 2EE containing DEA was added, and the solution was again refluxed at 125°C for 5 h. The coatings were applied to Pt, (111)Si, and $Pt/Ti/SiO_2/(100)Si$ substrates by dip-coating. The films obtained were preheated at 400°C for 10 min to decompose any residual organics. These coating and heat-treatment processes were repeated several times to obtain sufficient thickness of the films (about 300 nm). The films were finally heat-treated at 700–900°C for 60 min for crystallization. Thin films with Y/Mn ratios of 1.00/1.05, 1.00/1.00 and 1.00/0.90 were prepared.

3. Results and Discussion

Figure 1 shows X-ray diffraction patterns of $YMnO_3$ thin films prepared by thermal decomposition and by refluxing [3]. The thickness of the films was about 300 nm. In the case of the thermal decomposition process, the films did not crystallize at firing temperatures lower than 700°C. As shown in Fig. 1(a), the films crystallized during the heat-treatment at 800°C; the main phase is not hexagonal $YMnO_3$ but rather is orthorhombic $YMnO_3$, which is the high temperature and high pressure phase (JCPDS#20-732). Heat-treatment at 900°C resulted in the single phase hexagonal $YMnO_3$. In the case of the reflux process, crystallization began at 700°C with the crystallization of hexagonal $YMnO_3$. The film contains some amorphous material because a halo pattern is observed. At 800°C, however, the single phase hexagonal $YMnO_3$ without an amorphous phase is obtained (Fig. 1(d)). Mn—O—Y bonds are

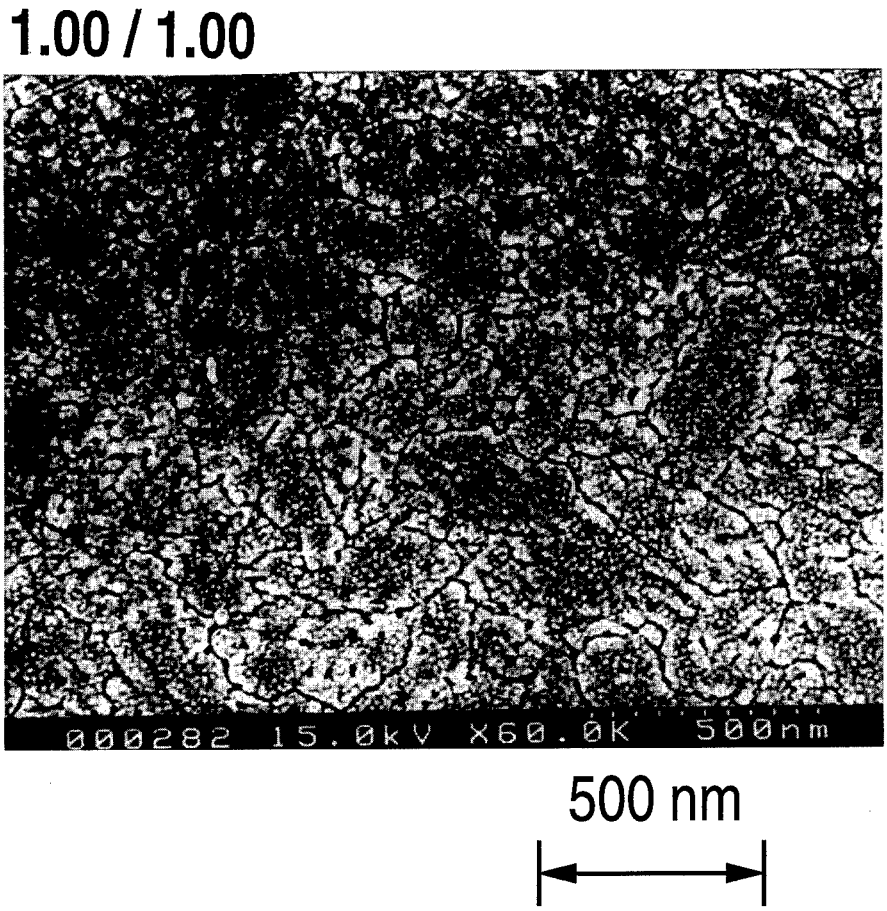

Figure 2. FE-SEM micrograph of the surface of a $YMnO_3$ thin film (Y/Mn = 1.0/1.0) prepared with the reflux process on a silicon (111) substrate.

expected to form during reflux. The formation of these bonds may decrease the firing temperature and prevent the films from forming a metastable phase. Although the temperature is still high for memory device application, the reflux method effectively decreases the heat-treatment temperature.

In the samples synthesized by refluxing and heat-treated at 800°C for 60 min, the dielectric permittivity and dielectric loss of the $YMnO_3$ films with stoichiometric composition were 23.3 and 0.87 at 100 kHz, respectively [3]. Figure 2 shows field emission-type scanning electron microscope (FE-SEM) micrograph of the surface of the $YMnO_3$ thin films prepared with the reflux process from the solution with the Y/Mn ratio of 1.00/1.00. In this film, crystal grains of 200–300 nm in diameter and the small grains, 50–100 nm in diameter, are observed. In addition, large pores are observed at the grain boundaries and their occurrence may be the cause of the large dielectric loss.

To improve the microstructure and dielectric properties, thin films with several Y/Mn ratios were prepared by refluxing [4]. The XRD patterns of the films with Y/Mn ratio from 1.00/1.05 to 1.00/0.90 showed single phase polycrystalline hexagonal $YMnO_3$ in random orientations; excess Mn and Y ions do not form oxides like Mn_2O_3 or Y_2O_3, but are incorporated into the lattice. Figure 3 shows an FE-SEM micrograph of the surface of $YMnO_3$ thin films prepared with the Y/Mn ratio of 1.00/0.90 by refluxing [4]. This film has a fine and uniform structure with grain size of about 50 nm in diameter. The pores, observed in stoichiometric $YMnO_3$ thin films (Fig. 2), are not observed. Since the microstructure of $YMnO_3$ thin films becomes smoother, denser, and finer with an increase in the Y/Mn ratio, the Y ions in excess are assumed to promote the nucleation at the initial stage of the crystallization.

In Fig. 4, the frequency dependence of the dielectric permittivity (ε) and dissipation factor (tan δ) of

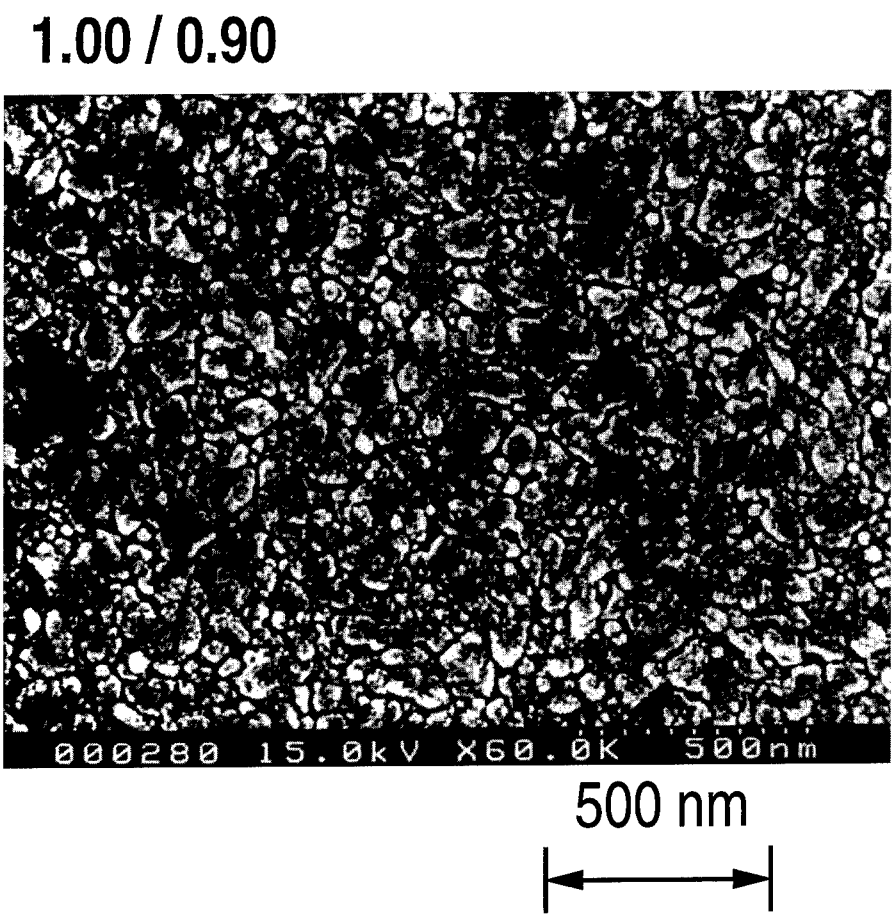

Figure 3. FE-SEM micrograph of the surface of a $YMnO_3$ thin film (Y/Mn = 1.00/0.90 prepared with the reflux process on a silicon (111) substrate.

a $YMnO_3$ thin film with a Y/Mn ratio of 1.00/0.90 is indicated by open and closed circles, respectively [4]. For comparison, ε and tan δ of a film deposited by pulsed laser deposition [2] are also plotted by open and closed triangles, respectively. For frequency greater than 1 kHz, the permittivity of the film is about 20. This value is almost the same as that of bulk $YMnO_3$ ceramics [5] but is larger than that of thin films prepared by pulsed laser deposition. The dissipation factor of $YMnO_3$ thin films, in the range 10^4–10^6 Hz, is about 0.05, and is similar to that of film prepared by pulsed laser deposition. These results indicate that an excess of Y in the coating solution leads to denser structures with improved dielectric properties. The differences in the dielectric properties of the films prepared by the solution method compared to pulsed laser deposition are probably due to differences in crystallinity, degree of *c*-axis preferred orientation, and insufficient heat treatment. The frequency dispersion in the permittivity and dissipation factors is still large in the low frequency region. This seems to be mainly due to interfacial polarization, caused by the grain boundary or space charge of the micropores.

The characteristic hysteresis loop of $YMnO_3$ thin films could not be observed even in the samples with the Y/Mn ratio of 1.00/0.90. The leakage current of the $YMnO_3$ thin film was about 1×10^{-5} A · cm^{-2} at the applied voltage of 1 V [4]; is as large as a ferroelectric material. Although $YMnO_3$ has only one polarization axis, the XRD pattern showed that the film had random orientation with insufficient crystallinity. Thus, the fact that the hysteresis loop could not be observed is probably caused by the large leakage current and random growing orientations with insufficient crystallinity. The Y/Mn ratio causes changes

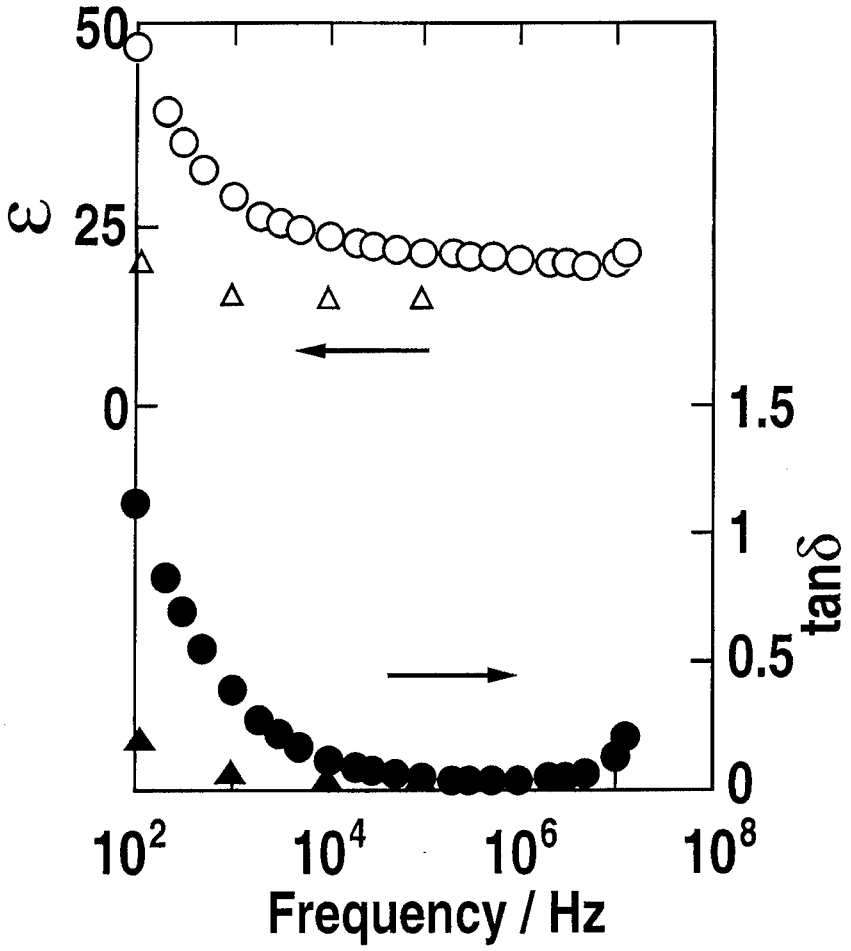

Figure 4. Frequency dependence of the dielectric permittivity (ε) and dissipation factor (tan δ) of a $YMnO_3$ thin film with the Y/Mn ratio of 1.00/0.90 on platinum substrate. Permittivity and dissipation factors of a film prepared by pulsed laser deposition on silicon (111) substrate are plotted by open and closed triangles, respectively, for comparison [2].

in morphology and improvements in the dielectric properties indicating that control of the microstructure of the films, the degree of *c*-axis preferred orientation, and the oxidation state of Mn ions are required to obtain the desired $YMnO_3$ ferroelectric materials.

4. Conclusion

The reflux process effectively decreases the heat-treatment temperature for preparation of $YMnO_3$ thin films. SEM observation showed that the thin films prepared with stoichiometric Y/Mn ratio had many pinholes, and dielectric properties showed very large dielectric loss. 10% excess Y in the coating solution was effective to grow a denser structure and improve the dielectric properties.

Acknowledgments

The present study was supported by a Grant-in-Aid from Ministry of Education, Science, Sports, and Culture of Japan.

References

1. N. Fujimura, T. Ishida, T. Yoshimura, and T. Ito, Appl. Phys. Lett. **69**, 1011 (1996).
2. N. Fujimura, S. Azuma, N. Aoki, T. Yoshimura, and T. Ito, J. Appl. Phys. **80**, 7084 (1996).
3. N. Fujimura, H. Tanaka, H. Kitahata, K. Tadanaga, T. Yoshimura, T. Ito, and T. Minami, Jpn. J. Appl. Phys. Pt. 2-Lett. **36**, L1601 (1997).
4. H. Kitahata, K. Tadanaga, T. Minami, N. Fujimura, and T. Ito, J. Am. Ceram. Soc. **81**, 1357 (1998).
5. G.A. Smolenskii and U.A. Bakov, J. Appl. Phys. **35**, 915 (1964).

Journal of Sol-Gel Science and Technology 13, 909–913 (1998)
© 1998 Kluwer Academic Publishers. Manufactured in The Netherlands.

Investigation of New Ion Conducting Ormolytes Silica-Polypropyleneglycol

K. DAHMOUCHE
Instituto de Química, Universidade Estadual Paulista, Araraquara, Brazil

P.H. DE SOUZA, T.J. BONAGAMBA AND H. PANEPPUCCI
Instituto de Física de São Carlos, Universidade de São Paulo, São Carlos, Brazil

P. JUDEINSTEIN
Laboratoire de Chimie Structurale Organique, Université Paris-Sud, Orsay, France

S.H. PULCINELLI AND C.V. SANTILLI
Instituto de Química, Universidade Estadual Paulista, Araraquara, Brazil

Abstract. Two groups of hybrid organic-inorganic composites exhibiting ionic conduction properties, so called ORMOLYTES (organically modified electrolytes), have been prepared by the sol-gel process. The first group has been prepared from mixture of a lithium salt and 3-isocyanatopropyltriethoxysilane(IsoTrEOS),O,O′-bis(2-aminopropyl)polypropyleneglycol. These materials produce chemical bonds between the organic (polymer) and the inorganic (silica) phases. The second group has been prepared by an ultrasonic method from a mixture of tetraethoxysilane (TEOS), polypropyleneglycol and a lithium salt. The organic and inorganic phases are not chemically bonded in these samples. The Li^+ ionic conductivity, σ, of all these materials has been studied by AC impedance spectroscopy up to 100°C. Values of σ up to $10^{-6}\ \Omega^{-1}\cdot cm^{-1}$ have been found at room temperature. A systematic study of the effects of lithium concentration, polymer chain length and the polymer to silica weight ratio on σ shows that there is a strong dependence of σ on the preparation conditions. The dynamic properties of the Li^+ ion and the polymer chains as a function of temperature between −100 and 120°C were studied using ^7Li solid-state NMR measurements. The ionic conductivity of both families are compared and particular attention is paid to the nature of the bonds between the organic and inorganic components.

Keywords: hybrid material, ionic conductor, solid electrolyte, silica-polypropyleneglycol

Introduction

The technological importance of solid polymer electrolytes [1] is due to their potential applications in batteries, sensors, energy and data storage system [2]. Electrolytes containing additions of lithium offer the most favorable properties [3]. Unfortunately, poor mechanical properties and the low optical transparency of such materials limit their use in many applications such as electrochromic and photochromic devices. Recently, we have prepared and studied [4, 5] a new class of transparent hybrid materials presenting ionic conduction properties called Ormolytes (Organically Modified Electrolytes). They are comprised of an organic phase (poly(ethylene)glycol (PEG)) which acts as a "solid" solvent for lithium ions and a structural silica network which mechanically reinforces the material [6, 7]. The properties are strongly related to the connectivity of the two phases and the mobility of both the structural network and the active species.

This work reports on the preparation and properties of new hybrid ionic conductors SiO_2-

Polypropyleneglycol (PPG) with and without covalent organic-inorganic chemical bonds. Our study emphasizes the electrical properties and their relationships with the texture of the materials and the nature of the bonds between the organic and inorganic components.

Experimental

Commercial chemical reagents were used (Fluka, Aldrich). For the first type of materials equimolar amounts of 3-isocyanatopropyltriethoxysilane (Iso-TrEOS) and O,O′-bis(2-aminopropyl)polypropyleneglycol (NH_2-PPG-NH_2) were stirred together in tetrahydrofuran (THF) under reflux for 6 hours. The THF was evaporated and a pure hybrid precursor $(OEt)_3Si$-PPG-$Si(OEt)_3$ was obtained. 0.5 g of this precursor was mixed with 1 ml of ethanol containing NH_4F ($NH_4F/Si = 0.005$) to which the desired quantity of the lithium salt ($LiClO_4$) was added. Finally, 0.2 ml of water was added upon stirring and a monolithic wet gel was obtained in 4 h. The ethanol was then slowly removed to give a body of rubbery material.

The second group of materials were prepared by an ultrasonic method: 12.5 ml of tetraethoxysilane (TEOS) and 4 ml of water were stirred together under ultrasound to hydrolyze the TEOS. Then the desired quantities of PPG_n (n = molecular weight of the PPG) were added in neutral pH conditions. The lithium salt ($LiClO_4$) was then introduced and dissolved under ultrasound in order to obtain a transparent monophasic liquid. Gelation occurred in a few minutes and the samples were allowed to dry slowly as monoliths.

The electrical properties of the samples were determined by complex impedance spectroscopy between 20 and 100°C with a Solartron 1260 apparatus, from 1 Hz to 10 MHz, with an applied voltage amplitude of 5 mV. The samples were monoliths, about 0.5 mm thick, with surfaces as flat as possible. The contacts were obtained with plastic conductive probes (Altoflex) pressed on the samples. Stable and reproducible values of the ionic conductivity σ were obtained by conditioning the dried samples under vacuum at 90°C for 24 h.

The solid-state NMR spectra of ^7Li, consisting only of the central transition, were recorded between −100 and 120°C at 33 MHz using a TECMAG LIBRA system and a variable temperature double resonance Doty probe. The ^7Li linewidths were measured from the Fourier transform of the Free Induction Decays (FID) obtained by a simple 10 μs $\pi/2$ excitation. Full widths at half maximum (FWHM) were obtained by curve fitting using Lorentzian or Gaussian functions, depending on the temperature ranges.

Results and Discussion

Figure 1 presents the variation of room temperature conductivity (σ_{RT}) for the chemically bonded hybrid silica-PPG_{2000} as a function of the ratio [O]/[Li] (only oxygens of ether type). The maximum of conductivity ($1 \cdot 10^{-6}\ \Omega^{-1}\cdot cm^{-1}$) is observed at an [O]/[Li] ratio of about 15, in contrast with the behavior observed in most polymeric systems, in which σ_{max} occurs for [O]/[Li] = 8 [8, 9]. For pure polymers, the increase of conductivity with the salt concentration is attributed to the increase of the number of cations [10]. The decrease after the maximum is a consequence of the immobilization of the polymer chains by interactions with the Li^+ ions. In our material, this immobilization occurs at a lower concentration of lithium, showing that the PPG chains' mobility is smaller when both networks are chemically bonded. For all samples, the temperature variation of the conductivity follows strictly the Arrhenius law $\sigma = \sigma_o \exp(-E_a/RT)$, as shown in Fig. 2. The variation of the activation energy (E_a) with lithium concentration shows a minimum (0.16 eV) also at an [O]/[Li] ratio of about 15.

In the non-chemically bonded hybrid silica-PPG_{2000} the maximum of conductivity ($5 \cdot 10^{-4}\ \Omega^{-1}\cdot cm^{-1}$) is

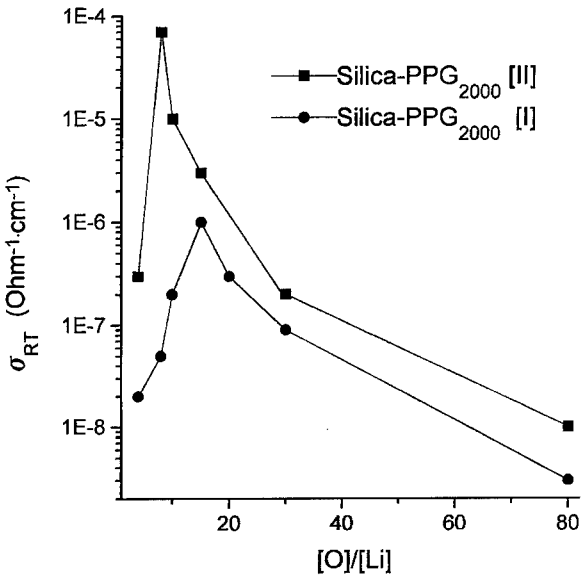

Figure 1. Variation of room temperature conductivity (σ_{RT}) as a function of the ratio [O]/[Li] for the chemically and the non-chemically bonded hybrid silica-PPG_{2000}.

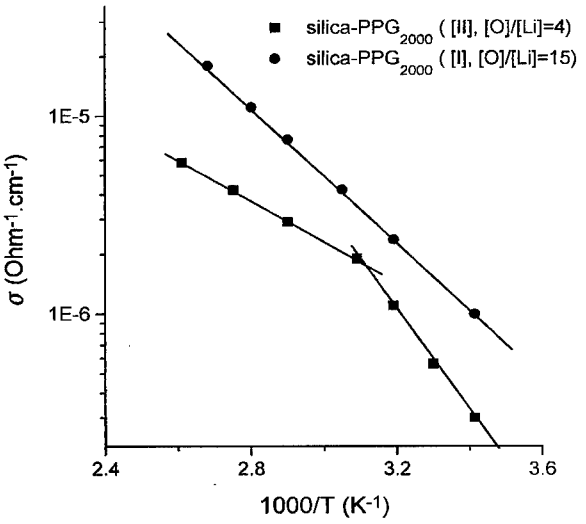

Figure 2. Temperature dependence of conductivity for the chemically bonded hybrid silica-PPG_{2000} ([O]/[Li] = 15) and the non-chemically bonded hybrid silica-PPG_{2000} ([O]/[Li] = 4, PPG/TEOS = 40%).

observed for an [O]/[Li] ratio of about 8 (Fig. 1). This behavior is similar to that observed in most polymer electrolytes [8, 9]. As only weak physical bonds are present between the PPG and the inorganic silica network, the polymer chains have higher mobility than in the chemically bonded materials and their immobilization by interactions with the Li^+ ions occurs at higher lithium concentrations.

Table 1 presents the variation of room temperature ionic conductivity and activation energy as a function of the PPG chain length for both types of hybrids. The values of σ_{RT} for chemically bonded hybrid silica-PPG ([O]/[Li] = 15) increase when the polymer chain length increases. It is well known that conduction in polymer electrolytes occurs via a liquid-like motion of cations through the segmental motion of the neighboring polymer chains [1]. Therefore, the PPG chain mobility increases as the chain length increases. Judeinstein et al. [6, 11] have studied similar silica-PEG or silica-PPG samples by EPR and have shown that the mobility of the polymer chain near the silica clusters is much lower than the mobility of the chain at larger distances. Therefore, a hybrid with short PPG chains offers only a small area of the chain with high mobility, while for longer chains the region of high mobility is much larger. This phenomenon is responsible for the ionic conductivity results. For all samples the activation energy is deduced from the temperature variation of the conductivity which follows strictly the Arrhenius law.

For the non-chemically bonded hybrid silica-PPG ([O]/[Li] = 4) the values of σ_{RT} and therefore the PPG chain mobility increase when the polymer chain length decreases (Table 1). Because of the absence of chemical bonds between the organic and inorganic networks the polymeric phase has a "liquid-like" behavior [6, 7]. With such configuration there are less interactions between the polymer chains themselves, with short chains than with long chains. The mobility of short PPG chains will be higher than that of longer chains. The variation of the conductivity with temperature shows discrepancies with the pure Arrhenius model (Fig. 2). Two slopes are observed, with an intercept around 50°C for all systems. The activation energies are $0.05 < E_{al} < 0.2$ eV for $T > 50$°C and $0.2 < E_{a2} < 0.5$ eV for $T < 50$°C. Such behavior has also been observed in some polymers [12] and composite electrolytes [4, 5, 7, 13] and attributed to a partial crystallization and phase separation below a critical temperature. The chemical stability of non-chemically bonded materials is therefore lower than that of the chemically bonded ones.

Table 2 presents the variation of room temperature ionic conductivity and activation energy as a function of the polymer to silica weight ratio, PPG/TEOS, for the non-chemically bonded hybrid silica-PPG_{2000}

Table 1. Variation of room temperature ionic conductivity (σ_{RT}) and activation energy (E_a) as a function of the PPG chain length for class I ([O]/[Li] = 15) and class II ([O]/[Li] = 4, PPG/TEOS = 40%) hybrids.

	Class I			Class II		
PPG molecular weight	300	2000	4000	425	1000	2000
σ_{RT} (Ω^{-1}·cm^{-1})	$7 \cdot 10^{-8}$	$1 \cdot 10^{-6}$	$3.5 \cdot 10^{-6}$	$4 \cdot 10^{-5}$	$1 \cdot 10^{-6}$	$3 \cdot 10^{-7}$
E_{a1} (eV)	0.5	0.16	0.16	0.05	0.1	0.2
E_{a2} (eV)	—	—	—	0.25	0.3	0.5

Table 2. Variation of room temperature ionic conductivity (σ_{RT}) and activation energy (E_a) as a function of ratio PPG/TEOS (class II, [O]/[Li] = 4, silica-PPG_{2000}).

PPG/TEOS (wt%)	20	40	80	100
σ_{RT} ($\Omega^{-1}\cdot cm^{-1}$)	$8\cdot10^{-8}$	$3\cdot10^{-7}$	$1\cdot10^{-6}$	$6\cdot10^{-6}$
E_{a1} (eV)	0.2	0.2	0.14	0.14
E_{a2} (eV)	0.6	0.5	0.3	0.3

([O]/[Li] = 4). The values of σ_{RT} increase with the polymer concentration. In samples with high PPG concentration the influence of the silica network is negligible for the "liquid-like" polymeric phase. When the volume of PPG decreases, the influence of the interface between organic and inorganic domains becomes predominant and so the mobility of the polymer chain is small. This influences the conductivity values.

Figure 3 shows the typical temperature behavior of the ^{7}Li linewidth for several of the samples investigated. The observed rapid change in the ^{7}Li linewidth reflects the onset of motional narrowing and is associated with the polymer chain motion and, therefore serves to characterize the glass transition temperature, T_g. For this purpose the value of T_g was taken as the temperature at which the maximum rate of change occurs and was obtained by differentiation of the data in Fig. 3. The temperature dependence of the linewidth for the various compositions shows that the effect of the silica structure in raising the glass transition temperature is more pronounced for the chemically bonded composites. Furthermore, for these samples, increasing the ratio [O]/[Li] in silica-PPG_{2000} from 4 to 15 results in the glass transition temperature decreasing from 8 to −13°C, confirming that Li^+ addition favors the immobilization of polymeric chains. The effect of the polymer chain length on T_g is remarkable; T_g decreases from 70 to −15°C as the PPG molecular weight increases from 300 to 2000.

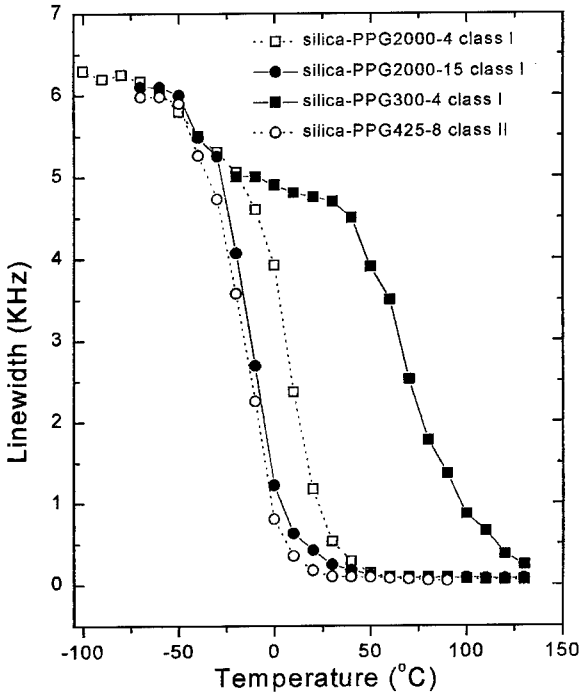

Figure 3. Typical temperature behavior of ^{7}Li linewidth for several of the samples investigated.

Conclusion

We have obtained new ion-conducting Ormolytes Silica-Polypropyleneglycol with high ionic conductivities (up to $10^{-6}\ \Omega^{-1}\cdot cm^{-1}$), which are transparent and flexible, permitting their use in electrochemical devices.

In covalent bonded silica-PPG hybrids the ionic conductivity is a maximum for [O]/[Li] = 15, while for non-chemically bonded hybrids this occurs at [O]/[Li] = 8 as for pure polymer electrolytes. In the bonded materials the mobility of the PPG chains increases with chain length, while the opposite happens with the non-bonded materials. In the latter case we also observed the increase of the ionic conductivity as the polymer to silica weight ratio increased.

The NMR results show that the effect of the silica structure in raising the glass transition temperature of the polymer is more pronounced for the chemically bonded materials. Furthermore, for these materials, increasing the Li concentration or decreasing the polymer chain length increased the glass temperature transition of the organic phase.

Acknowledgments

This work was supported by FAPESP, CNPq and USP-COFECUB.

References

1. F.M. Gray, *Solid Polymer Electrolytes: Fundamental and Technological Applications* (VCH Publishers, New York, 1991).
2. M. Armand, Adv. Mater. **2**, 278 (1990).
3. M.A. Ratner and D.F. Shriver, MRS Bull. **14**, 39 (1989).

4. K. Dahmouche, M. Atik, N.C. Mello, T.J. Bonagamba, H. Paneppucci, M. Aegerter, and P. Judeinstein, Mat. Res. Symp. Proc. **435**, edited by B.K. Coltrain, C. Sanchez, D.W. Schaefer, and G.L. Wilkes (San Francisco, 1996), p. 363.
5. K. Dahmouche, M. Atik, N.C. Mello, T.J. Bonagamba, H. Paneppucci, M. Aegerter, and P. Judeinstein, J. Sol-Gel Sci. and Techn. **8**, 711 (1997).
6. P. Judeinstein, M.E. Brik, J.P. Bayle, J. Courtieu, and J. Rault, Mat. Res. Symp. Proc. **346**, edited by A.K. Cheetham, C.J. Brinker, M.L. McCartney, and C. Sanchez (San Fransisco, 1994), p. 937.
7. P. Judeinstein, J. Titman, M. Stamm, and H. Schmidt, Chem. Mater. **6**, 127 (1994).
8. M. Watanabe, S. Nagano, K. Sanui, and N. Ogata, J. Power Sources **20**, 327 (1987).
9. E. Tsuchida and K. Shigehara, Mol. Cryst. Liq. Cryst. **106**, 361 (1984).
10. J.R. McCallum and A.C. Vincent, in *Polymer Electrolytes Reviews*, edited by J.R. McCallum and A.C. Vincent (Elsevier, London, 1987), p. 23.
11. M. Brik, J. Titman, J.P. Bayle, and P. Judeinstein, J. Polym. Sci. B: Polym. Phys. **34**, 2533 (1996).
12. J.R. Giles, C. Booth, and R. Mobbs, in *Sixth International Symposium on Metallurgy and Materials Science, Transport-Structure Relations in Fast Ion and Mixed Conductors*, edited by F.W. Hessel (1985), p. 329.
13. X. Huang, L. Chen, H. Huang, R. Xue, Y. Ma, S. Fang, Y. Li, and Y. Jiang, Solid State Ionics **51**, 69 (1992).

Journal of Sol-Gel Science and Technology 13, 915–921 (1998)
© 1998 Kluwer Academic Publishers. Manufactured in The Netherlands.

Optical Switching in VO_2 Thin Films

F. BÉTEILLE AND J. LIVAGE
Chimie de la Matière Condensée, Université Pierre et Marie Curie, 4 place Jussieu 75252 Paris, France

Abstract. Vanadium dioxide thin films have been deposited from vanadium alkoxides $VO(OR)_3$. An amorphous film is formed that transforms into crystalline VO_2 upon heating at 500°C under a reducing atmosphere. Optically transparent VO_2 thin films are then obtained that exhibit both electrical and optical switching around 70°C. The switching temperature together with the shape of the hysteresis loop can be modified by doping VO_2 films with foreign cations. Doped M_xVO_2 ($M = W^{6+}$, Nb^{5+}, Ti^{4+}, Cr^{3+} or Al^{3+}) thin films have been prepared under the same conditions by mixing the vanadium alkoxide and a metal salt in an alcoholic solution. The switching temperature decreases when the film is doped with high-valent cations (W^{6+}) and increases with low-valent cations (Al^{3+}, Cr^{3+}). The transition temperature first decreases and then increases when Ti^{IV} is added to the VO_2 film while the width of the hysteresis loop is significantly reduced.

Keywords: vanadium dioxide, thermochromism, sol-gel, optical switching

1. Introduction

Vanadium dioxide VO_2 is known to undergo a reversible semiconductor-metal transition around 70°C associated with a structural phase transformation from monoclinic to tetragonal [1]. The high temperature phase has a tetragonal rutile type structure characterized by chains of edge sharing [VO_6] octahedra along the *c* axis with equidistant vanadium atoms (V-V = 2.88 Å). Vanadium pairing occurs below 70°C giving rise to a monoclinic phase with alternate shorter (2.65 Å) and longer (3.12 Å) V-V distances [2, 3]. This leads to a doubling of the *c* parameter and opens a gap at the Fermi level in the vanadium 3*d* conduction band. Electrical conductivity and IR reflectivity then increase abruptly when going through the transition temperature.

This semiconductor-metal transition has been extensively studied by physicists on single crystals. However, such crystals do not withstand the structural distortions associated with the transition. They usually break after a few cycles and cannot be used for making smart windows, thermal sensors or switching devices. Thin films would be much more convenient for optical applications. They appear to survive stress during a large number of cycles. More than 10^8 cycles, for instance, have been reported for sol-gel deposited VO_2 thin films [4].

VO_2 thin films have been prepared by many different methods including chemical vapor deposition, thermal evaporation or reactive sputtering of V_2O_5. V^{IV} alkoxides such as $V(OBu^t)_4$, have also been used as precursors by Potember et al. [5–8]. However, such alkoxides are not easy to synthesize and are highly reactive toward hydrolysis. Despite the fact that vanadium already has the V^{IV} oxidation sate, they have to be heated under a neutral atmosphere in order to avoid oxidation into V_2O_5. It appears that V^V oxo-alkoxides, $VO(OR)_3$, would be more convenient as molecular precursors [9–14].

This paper reports on VO_2 thin films deposited from $VO(OR)_3$ ($R = Pr^i$, Am^t) alkoxide solutions. Such films can be easily doped and their switching properties can be tailored by adding foreign cations such as W^{VI}, Ti^{IV}, Cr^{III} or Al^{III}.

2. Synthesis of Pure and Doped VO_2 Thin Films

Vanadium alkoxides precursors $VO(OR)_3$ were prepared upon heating under reflux a mixture of ammonium

vanadate and alcohol.

$$NH_4VO_3 + 3ROH \leftrightarrow VO(OR)_3 + 2H_2O + NH_3 \quad (OR = OAm^t)$$

The reaction is carried out in cyclohexane and water is eliminated via azeotropic distillation. The resulting alkoxide is purified by distillation under reduced pressure and dissolved in its parent alcohol ($c \approx 0.7$ mol/l).

Thin films are deposited by spin-coating from a solution of $VO(OAm^t)_3$ in isopropanol Pr^iOH. Transesterification reactions occur leading to the formation of a mixture of $VO(OAm^t)_{3-x}(OPr^i)_x$ mixed alkoxides. ^{51}V NMR experiments show that such a solution contains about 50% of $VO(OPr^i)_3$. However, as both $VO(OPr^i)_3$ and $VO(OAm^t)_3$ alkoxides have the same tetrahedral molecular structure, mixed alkoxides also exhibit a monomeric tetrahedral structure. No water is added to the alkoxide solution before spin-coating. The alkoxide film is left in air so that partial hydrolysis occurs spontaneously due to ambient humidity. The coating is then dried around 80°C with an infrared heater. Thin films are pale yellow but turn green upon drying. This should be due to some reduction arising from the remaining organic components ($V^{IV}/V^V \approx 10\%$).

As deposited thin films appear to be amorphous by X-ray diffraction. They have to be heated for 2 hours at 500°C under a reducing atmosphere (H_2/Ar 5%) in order to obtain crystalline VO_2. Optically transparent thin films about 0.07 μm are formed so that several spin-coating procedures have to be performed in order to have thicker films. Most films have been made with three successive coatings. They are about 0.2 μm in thickness. Different kinds of substrates such as SiO_2, Si or Ge have been used. Glass substrates have to be avoided in order to prevent Na^+ diffusion into the VO_2 layers that would lead to the formation of vanadates instead of VO_2.

Doped M_xVO_2 thin films are prepared following the same procedure. Dopants are just dissolved in the precursor solution of $VO(OAm^t)_3$ in Pr^iOH. Either alkoxides, $Ti(OPr^i)_4$ and $Al(OBu^s)_2(etac)$ (etac = $C_6H_9O_3$) or inorganic salt $WOCl_4$, have been used as precursors for doping. The mixed solution is then spin-coated onto the substrate and heat treated as previously for two hours at 500°C under a reducing atmosphere (H_2/Ar 5%).

3. Optical Properties of Pure VO_2 Thin Films

The optical absorption spectra of crystalline VO_2 thin films, below and above the transition temperature, is quite similar in the visible region ($\lambda < 700$ nm) but the transmittance in the infra-red decreases significantly in the metallic state showing that the film becomes highly reflective above 700 nm [8].

The optical transmission of VO_2 thin films was measured in the infrared region as a function of temperature in order to study their cycling properties. IR transmittance was measured at $\lambda = 2.5$ μm using a Nicolet 550 FTIR spectrometer equipped with a temperature controlled chamber. Experiments were performed up to 110°C at a heating rate of 1°C/mn. VO_2 thin films exhibit a typical hysteresis loop around the transition temperature (Fig. 1). Optical switching upon heating is rather sharp. It occurs around $T_1 = 80$°C. Optical transmittance drops by almost two orders of magnitude in the metallic state and becomes smaller than 1% suggesting that the reflectivity of VO_2 films is quite high. The process is not so sharp when the temperature decreases (Fig. 1(a)). Switching occurs in the 60–40°C range. The increase in optical transmittance is not regular and a small bump is observed between 40°C and 50°C. Such a behavior was already observed with other VO_2 films deposited from alkoxides [7, 10].

It has to be pointed out that the shape of the hysteresis loop strongly depends on the experimental procedure. Much sharper and more regular hysteresis loops have been obtained when the alkoxide film is first heated in air in order to get crystalline V_2O_5 and then reduced under an H_2/Ar atmosphere for 12 h at 550°C (Fig. 1(b)).

4. Optical Properties of Doped VO_2 Thin Films

The thermochromic behavior of VO_2 thin films appears to improve when a small amount of Ti (up to 5%) is added (Fig. 2(a)). The hysteresis loop becomes much sharper. The transition temperature upon heating decreases and the bump observed on the transmittance curve upon cooling disappears. Best results are obtained for Ti/V in the range 5–8% ($\Delta T = 14$°C). Beyond this value, the hysteresis loop becomes smoother and the high temperature state becomes less IR reflecting. The transition temperature increases slightly while the optical contrast between high and low temperature states decreases significantly [15, 16].

High-valent cations W^{VI} have been introduced as chlorides $WOCl_4$ in the alkoxide solution. This leads to the formation of some chloroalkoxides such as $VOCl_x(OPr^i)_y(OAm^t)_{3-x-y}$ that can be seen by ^{51}V NMR. However, Cl^- ions are removed during the thermal treatment and no Cl has been detected in the VO_2 films. The temperature at which the optical switching

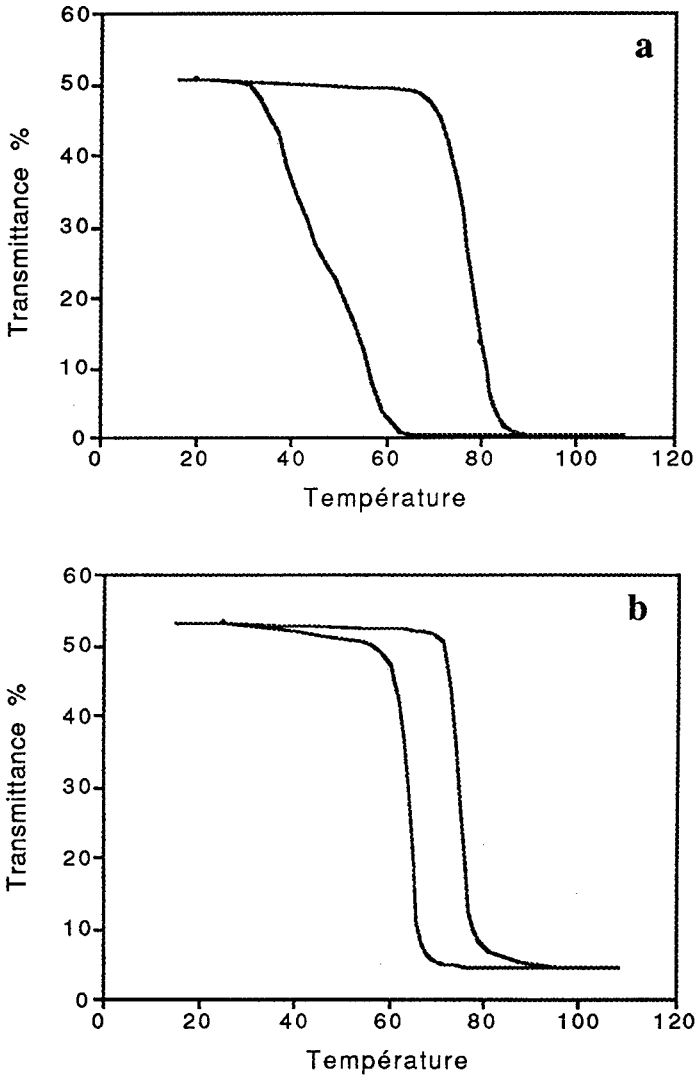

Figure 1. Optical switching and hysteresis loop in VO_2 thin films ($\lambda = 2.5$ μm). (a) VO_2 film obtained via the direct reduction of vanadium alkoxides and (b) VO_2 obtained via the reduction of a V_2O_5 film.

occurs decreases progressively when VO_2 films are doped with W^{VI} (Fig. 2(b)). In the same time, the optical contrast also decreases and the hysteresis loop broadens as for Ti doping [17]. W^{VI} is reported to induce the fastest decrease of the transition temperature in VO_2 [3]. Switching occurs below 40°C when the film is doped with 2% of W^{VI} and transitions close to room temperature can be obtained. However, the optical contrast becomes so weak that the transition is almost no longer visible beyond 4% of W^{VI} [18].

As already reported for single crystals, the transition temperature increases when VO_2 films are doped with trivalent cations (Al^{III}, Cr^{III}) and the optical contrast decreases rapidly (Fig. 3) [19].

5. Conclusion

VO_2 thin films can be easily synthesized from vanadium (V) alkoxides, $VO(OR)_3$ ($R = Pr^i$, Am^t). The experimental conditions to obtain the VO_2 crystalline phase without other vanadium oxides are not too severe so that thin films of good optical quality can be made reproducibly. The process could be scaled up for making large homogeneous optical coatings for thermochromic devices or smart windows. Hysteresis cycles are rather large. A bump is observed on the cooling branch. It could be due to the formation of an intermediate metastable phase called M_2, between the usual monoclinic (M_1) and rutile (R) phases [19].

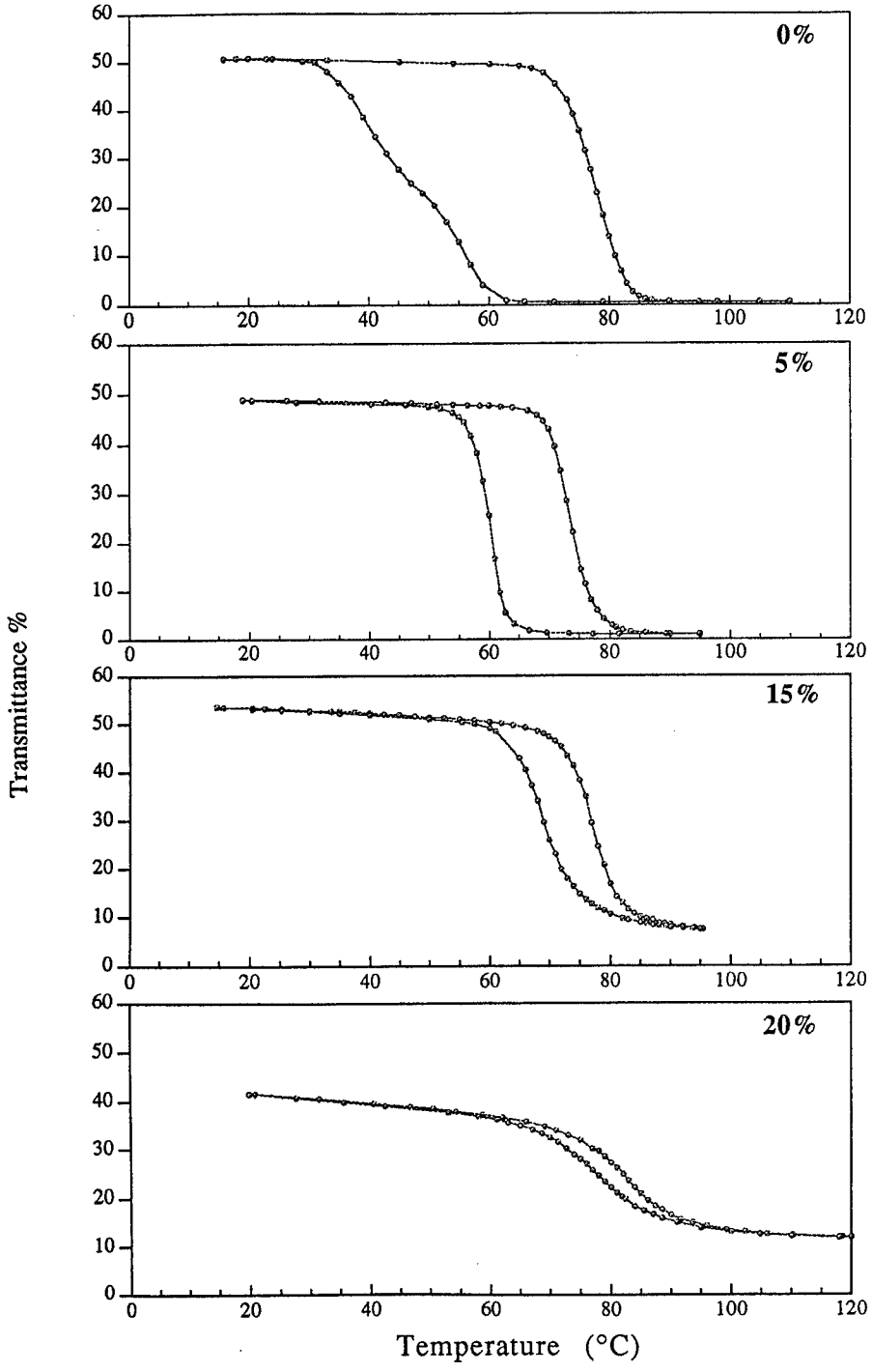

(a)

Figure 2. Optical switching and hysteresis loops of VO_2 thin films doped (a) with Ti^{IV} cations and (b) with high-valent W^{VI} cations.

(*Continued on next page.*)

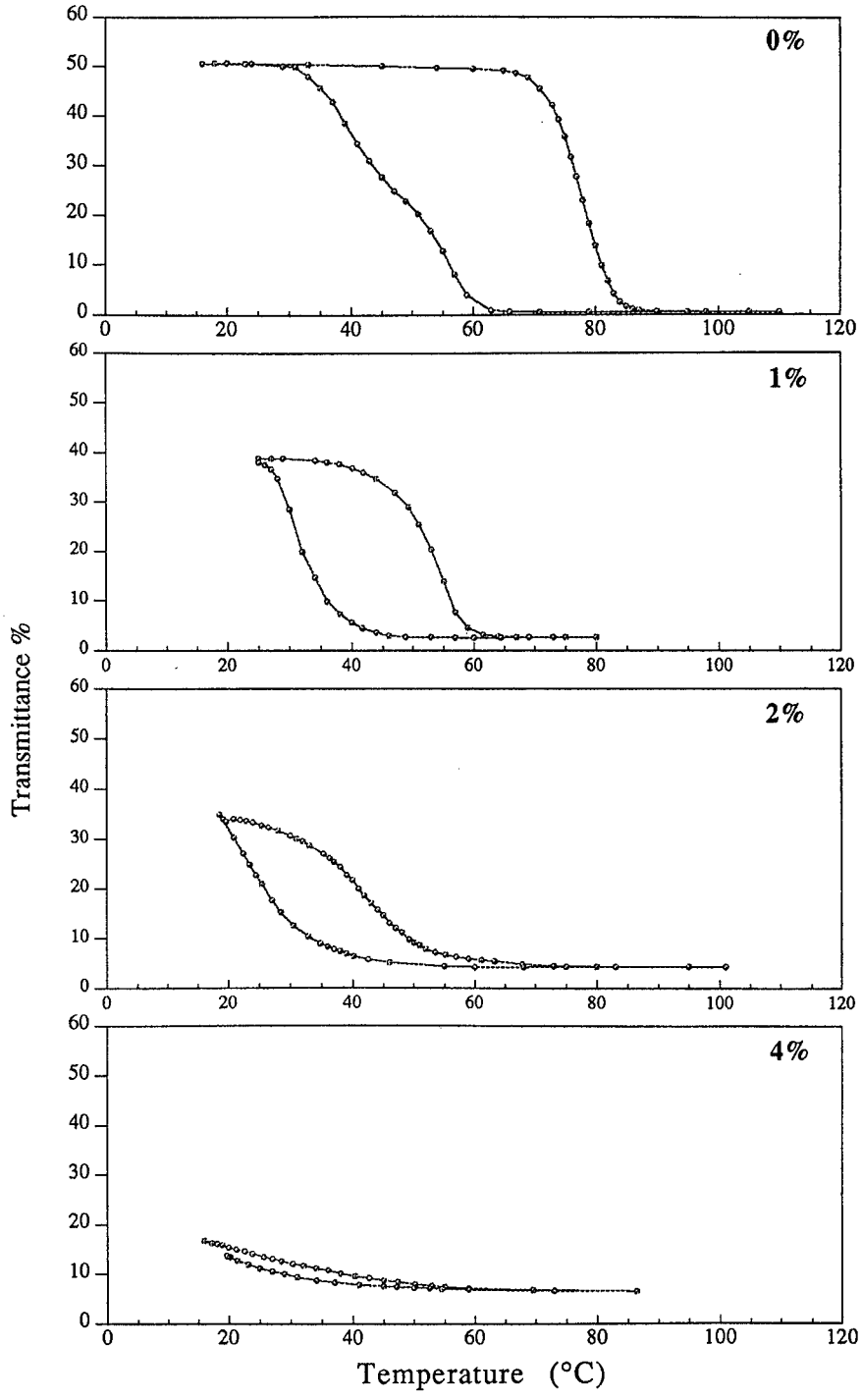

(b)

Figure 2. (*Continued*).

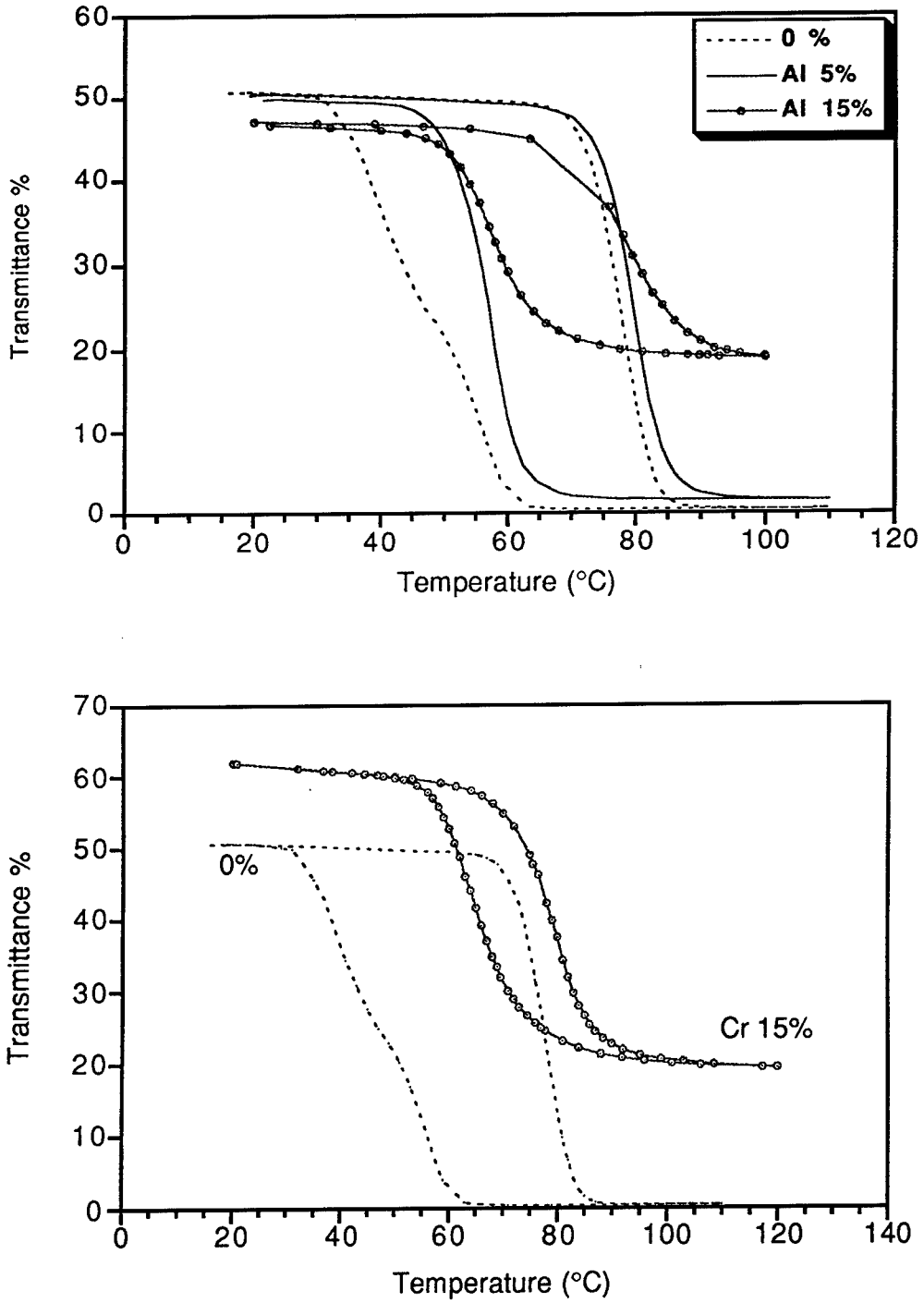

Figure 3. Optical switching and hysteresis loop of VO_2 thin films doped with low-valent cations (a) Al^{III} and (b) Cr^{III}.

Thin films can be easily doped by mixing precursor solutions. As already reported for single crystals, the transition temperature and the hysteresis loop can be modified by doping. Some electron transfer could occur between V^{IV} in VO_2 and doping cations. Low-valent cations behave as electron acceptors whereas high-valent cations behave as electron donors. Charge compensation then leads to the formation of V^{V} or V^{III} ions. Lowering the transition temperature can be easily obtained with tungsten precursors. For low doping ratio, the optical contrast can be kept as high as two orders of magnitude. Introducing doping elements also decreases the width of the hysteresis loop. It is then possible to dope the VO_2 thin films in order to tailor their switching properties according to the desired application. It has to be pointed out that the intensity distribution of the X-ray diffraction peaks of VO_2 thin films suggests some preferred orientation along the $(011)_{monoclinic}$ direction. Such an orientation disappears when VO_2 films are doped. It seems that this observation could be related with the change in the hysteresis loop.

References

1. F.J. Morin, Phys. Rev. Lett. **3**, 34 (1959).
2. J.B. Goodenough, Phys. Rev. **117**, 1442 (1960).
3. J.B. Goodenough, J. Solid State Chem. **3**, 490 (1971).
4. G. Guzman, F. Béteille, R. Morineau, and J. Livage, J. Mater. Chem. **6**, 505 (1996).
5. K.R. Speck, H.S-W. Hu, M.E. Sherwin, and R.S. Potember, Thin Solid Films **165**, 317 (1988).
6. K.R. Speck, H.S-W. Hu, R.A. Murphy, and R.S. Potember, Mater. Res. Soc. Symp. Proc. **121**, 667 (1988).
7. R.S. Potember and K.R. Speck, Sol-Gel Optics, SPIE **1328**, 364 (1990).
8. R.S. Potember and K.S. Speck, Better ceramics through chemistry, Mat. Res. Soc. Symp. Proc. **180**, 753 (1990).
9. C.B. Greenberg, Thin Solid Films **110**, 73 (1983).
10. Y. Takahashi, M. Kanamori, H. Hashimoto, Y. Moritani, and Y. Masuda, J. Mater. Sci. **24**, 192 (1989).
11. D.P. Partlow, S.R. Gurkovich, K.C. Radford, and L.J. Denes, J. Appl. Phys. **70**, 443 (1991).
12. S. Lu, L. Hou, and F. Gan, J. Mater. Sci. **28**, 2169 (1993).
13. S. Lu, L. Hou, and F. Gan, Adv. Mater. **9**, 24 (1997).
14. G. Guzman, R. Morineau, and J. Livage, Mater. Res. Bull. **29**, 509 (1994).
15. T. Hörlin, T. Niklewski, and M. Nygren, J. Phys. **37**, C4 (1976).
16. T. Hörlin, T. Niklewski, and M. Nygren, Acta Chem. Scand. **A30**, 619 (1976).
17. G. Guzman, F. Béteille, R. Morineau, and J. Livage, Eur. J. Solid State Inorg. Chem. **32**, 851 (1995).
18. M.A. Sobhan, R.T. Kivaisi, B. Sternja, and C.G. Granqvist, Solar Energy Mater. Solar Cells **44**, 451 (1996).
19. J.M. Reyes, S.L. Segel, and M. Sayer, Canadian J. Phys. **54**, 1 (1976).

Journal of Sol-Gel Science and Technology 13, 923–927 (1998)
© 1998 Kluwer Academic Publishers. Manufactured in The Netherlands.

Electrochromic Properties of Peroxopolytungstic Acid Thin Films

B. PECQUENARD, H. LECACHEUX, S. CASTRO-GARCIA AND J. LIVAGE
Laboratoire de Chimie de la Matière Condensée, Université Pierre et Marie Curie, 4 place Jussieu, 75252 Paris, France

Abstract. Electrochromic thin films have been deposited from peroxopolytungstic acid aqueous solutions. These solutions are obtained via the dissolution of tungstic acid in hydrogen peroxide. The nature and properties of the films depend on the drying procedure. Amorphous films are formed upon fast drying. They exhibit good electrochromic properties but have to be heat treated in order to become insoluble. Crystalline films are formed upon slow drying. Their electrochromic properties are not very good but better amorphous or crystalline films are then obtained after a thermal treatment above 200°C. In both cases, the reversibility of lithium insertion is not good during the first cycles but improve significantly upon cycling. This should be due to the electrochemical reduction of peroxo groups.

Keywords: electrochromics, peroxopolytungstic acid, film

1. Introduction

WO_3 is a well known electrochromic material and the electrochemical insertion of lithium in tungsten oxides has been studied for many years [1]. Thin films switch reversibly from white to blue upon electrochemical reduction and oxidation [2]. Coloration is due to the double injection of Li^+ and electrons as follows:

$$WO_3 + xLi^+ + xe^- \Leftrightarrow Li_xWO_3$$

A mixed valence Li_xWO_3 oxide is formed in which tungsten ions formally exhibit both W^{6+} and W^{5+} oxidation states. A blue coloration is then observed arising from an optically activated hopping process between both valence states.

The electrochromic properties of WO_3 thin films are strongly influenced by the preparation technique. Amorphous WO_3 thin films are currently used. They exhibit rather short switching times. They can be made by electron beam deposition, sputtering or vapor deposition [1]. They have also been deposited via the sol-gel route from tungsten ethoxide $W(OEt)_6$ or chloride WCl_6 solutions. The alkoxide is obtained by refluxing a benzene solution of WCl_6 and NaOEt [3]. WCl_6 or $WOCl_4$ can also be simply dissolved into an alcohol giving chloroalkoxides solutions that can be easily spin-coated onto the substrate [4, 5]. However, tungsten alkoxides are very sensitive to moisture and aqueous precursors would be more convenient for large scale production. Aqueous solutions of tungstic acids are cheap and easy to handle, but they are not stable and a yellow precipitate of $WO_3{\cdot}2H_2O$ forms spontaneously after a few hours [6]. However, Kudo et al. showed precipitation can be avoided by adding complexing reagents such as H_2O_2 [7]. Stable solutions of peroxopolytungstic acid were obtained by dissolving tungsten metal or tungsten carbide into an aqueous solution of hydrogen peroxide. An amorphous yellow solid forms upon evaporation of the solution that can be dissolved in a polar solvent such as alcohol or water to make thin films [8, 9].

This paper shows that stable solutions of peroxopolytungstic acid could also be obtained via the dissolution of tungstic acid and presents a study of the electrochromic properties of thin films deposited from such solutions.

2. Synthesis of Peroxopolytungstic Acid Films

Peroxopolytungstic acid was obtained via the dissolution of a commercial tungstic acid H_2WO_4 powder in an aqueous solution of hydrogen peroxide (30% H_2O_2). Dissolution is performed at 60°C for few hours under

continuous stirring and leads to a clear pale yellow acid solution (pH $\approx$ 1). These solutions are very stable as long as H_2O_2 remains in excess. They can be kept for months at room temperature without precipitation. Dipping a platinum net into the solution leads to the decomposition of H_2O_2 and the rapid formation of a precipitate.

Thin films, about 0.5 μm thick, are deposited by dip-coating a glass substrate into the H_2WO_4-H_2O_2 solution. The nature of these films strongly depends on the drying process. Fast drying around 100°C leads to amorphous films while the slow evaporation of the solvent at room temperature leads to the formation of a crystalline film. Amorphous films are optically transparent while the crystalline ones are translucent and could therefore be used for reflecting electrochromic devices only.

3. Electrochromic Properties of Thin Films

The electrochromic properties of amorphous and crystalline thin films were studied by cyclic voltammetry, using a classical three electrodes cell with a solution of $LiClO_4$ (1M) in propylene carbonate as an electrolyte. The working electrode is made of the thin film deposited onto a glass substrate covered with a transparent conducting SnO_2/F coating. A platinum grid behaves as the counter electrode and the reference electrode is made of an Ag wire in an $AgClO_4$-propylene carbonate solution.

Cyclic voltammetry curves have been recorded within the -2V/$+1$V range (vs Ag/Ag$^+$) at a scanning rate of 50 mV $\cdot$ s^{-1}. The number of charges Q exchanged during these experiments can be deduced from the surface of cyclic voltammetric curves and the reversibility of one cycle can be expressed by the coulombic ratio $\tau = Q_{ox}/Q_{red}$.

The optical density of the films is measured simultaneously, during cyclic voltammetry runs, using an He-Ne laser beam (λ = 632.8 nm) passing through the electrochemical cell.

3.1. *Amorphous Films*

Amorphous films were obtained via the fast evaporation of the solvent at 100°C. They are still soluble in the electrolyte so that a further heating treatment for ten minutes at 200°C has to be performed. A continuous cyclic voltammogram is observed, typical of an amorphous compound (Fig. 1(a)). The reversibility is not good during the first nine cycles and most of the charge inserted during the electrochemical reduction cannot be removed upon oxidation. However, reversibility improves significantly upon cycling and the coulombic

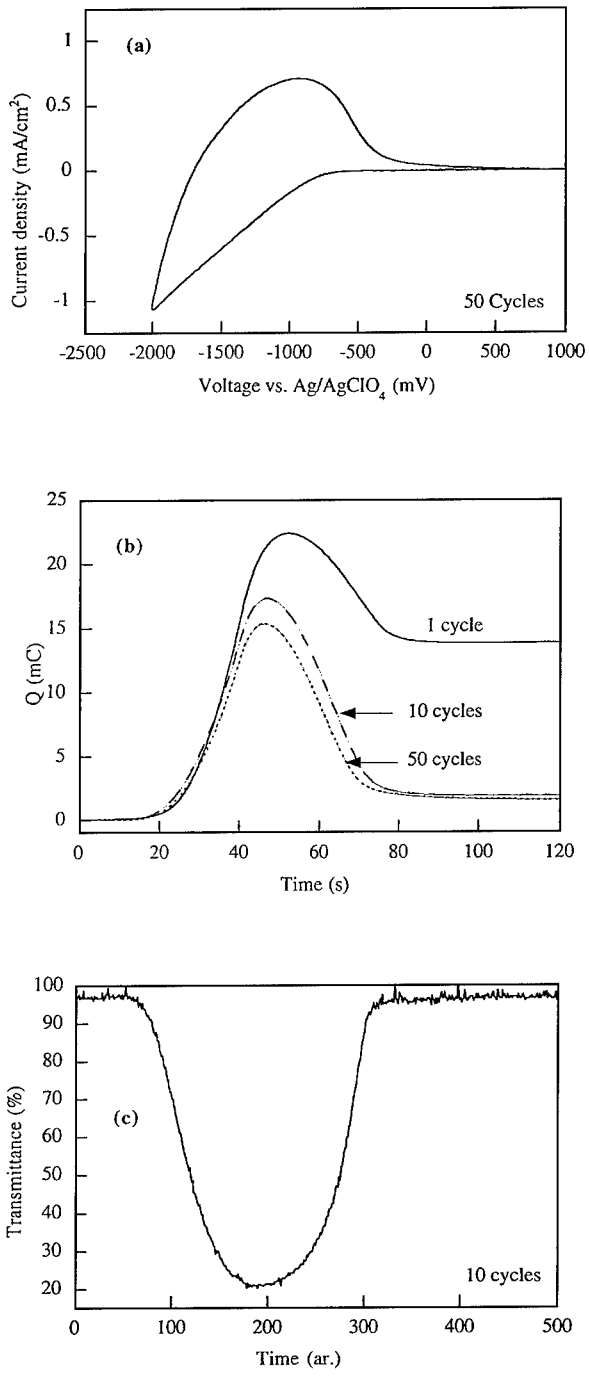

Figure 1. Electrochemical measurements performed on amorphous films deposited from peroxopolytungstic acid solutions: (a) cyclic voltammetry, (b) charge exchanged during one cycle, and (c) optical transmittance at λ = 632.8 nm.

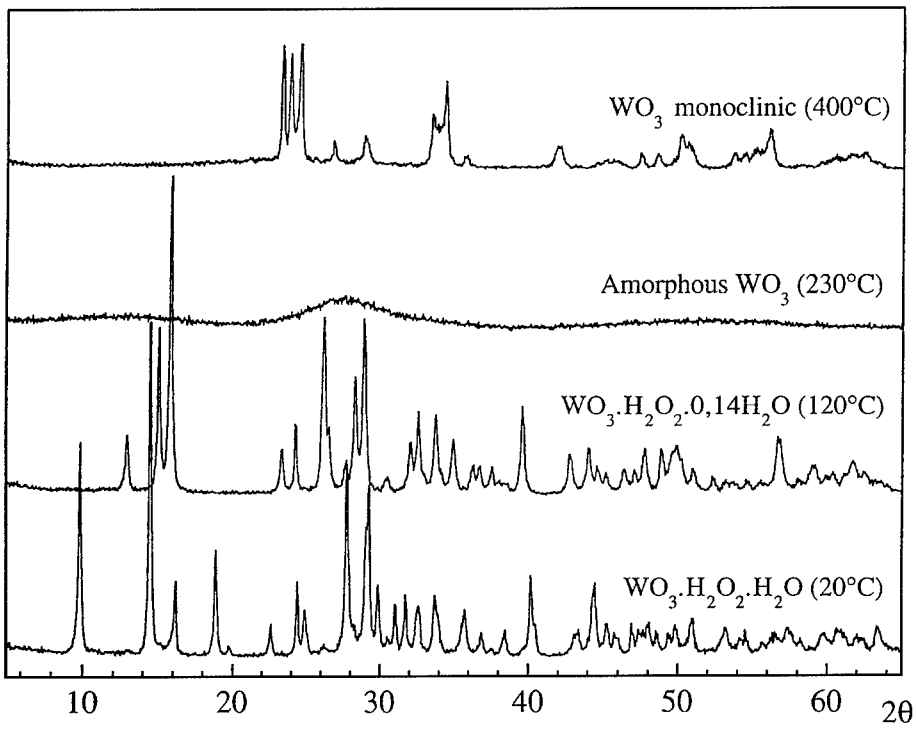

Figure 2. X-ray diffraction patterns of thin films deposited from peroxopolytungstic acid solutions after a thermal treatment at different temperatures.

ratio $\tau = Q_{ox}/Q_{red}$ reaches 95% after ten cycles and the charge exchanged during one cycle is close to 16 mC/cm^2 (Fig. 1(b)). Optical measurements performed during the electrochemical cycles show that the transmittance of the films decreases down to 20% of its initial value (Fig. 1(c)).

3.2. *Crystalline $WO_3 \cdot H_2O_2 \cdot nH_2O$ Films*

Crystalline films are obtained when the film is slowly dried at room temperature (Fig. 2). They correspond to the "$WO_3 \cdot H_2O_2 \cdot H_2O$" phase previously described by Kudo et al. [9]. Partial dehydration is observed upon heating around 120°C and a new crystalline phase is formed corresponding to "$WO_3 \cdot H_2O_2 \cdot 0.14H_2O$" [10]. Further dehydration occurs upon heating at higher temperature giving an amorphous oxide at 230°C and then the usual monoclinic oxide WO_3 above 400°C (Fig. 2).

Crystalline films are rather thick and their thickness is difficult to control. All experiments have then been performed on the same film heated at different temperatures in order to be able to compare the behavior of the different phases. The corresponding cyclic voltammetry curves are reported in Fig. 3. The electrochromic properties of both crystalline peroxo phases "$WO_3 \cdot H_2O_2 \cdot nH_2O$" ($n = 1$ and $n = 0.14$) are not good. Figure 4 and Table 1 show that lithium insertion

Table 1. Charge (mC/cm^2) exchanged during each electrochemical cycle on $WO_3 \cdot H_2O_2 \cdot H_2O$ and $WO_3 \cdot H_2O_2 \cdot 0.14H_2O$ thin films after a thermal treatment at different temperatures. $\tau = (Q_{ox}/Q_{red}) * 100$.

	$WO_3 \cdot H_2O_2 \cdot H_2O$			$WO_3 \cdot H_2O_2 \cdot 0.14H_2O$			Amorphous WO_3			Monoclinic WO_3		
Cycle	Q_{red}	Q_{ox}	τ	Q_{red}	Q_{ox}	τ	Q_{red}	Q_{ox}	τ	Q_{red}	Q_{ox}	τ
1	8.8	0.7	8%	51	3.5	7%	50	3.5	7%	38	28	74%
10	3.7	0.9	24%	24	11	48%	36	21	58%	32	30	95%
50	—	—	—	—	—	—	29	27	92%	32	30	95%
500	—	—	—	—	—	—	—	—	—	30	29	95%

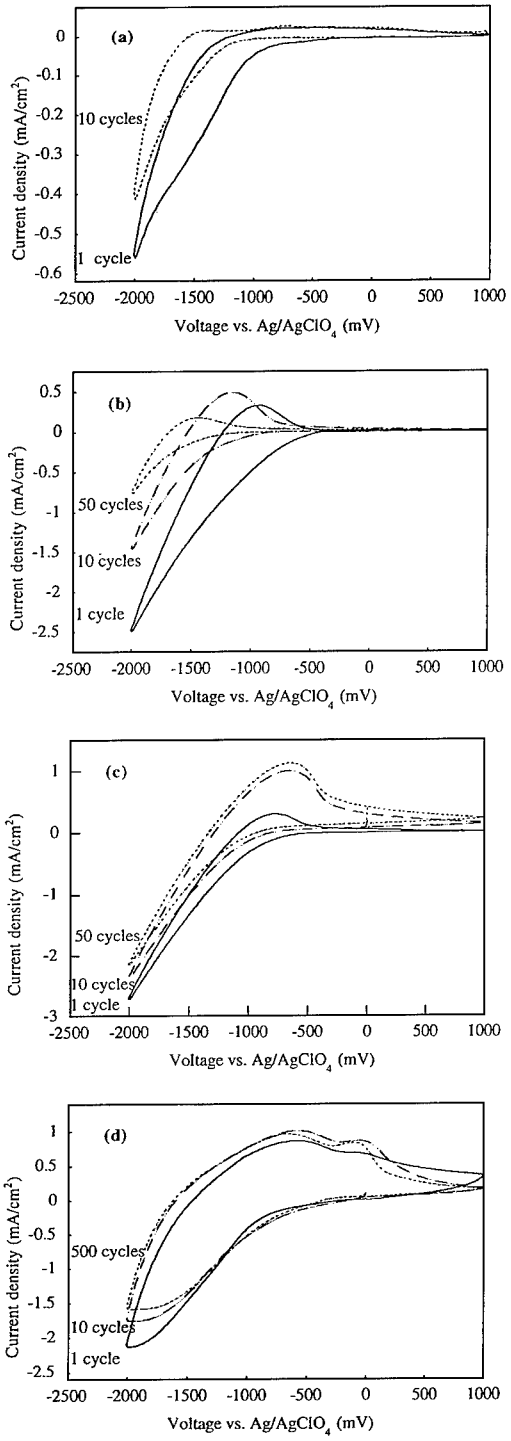

Figure 3. Cyclic voltammetry curves of thin films deposited from peroxopolytungstic acid solutions after a thermal treatment at different temperatures: (a) crystalline $WO_3 \cdot H_2O_2 \cdot H_2O$ ($T = 20°C$), (b) crystalline $WO_3 \cdot H_2O_2 \cdot 0.14H_2O$ ($T = 120°C$), (c) amorphous WO_3 ($T = 230°C$) and (d) monoclinic WO_3 ($T = 400°C$).

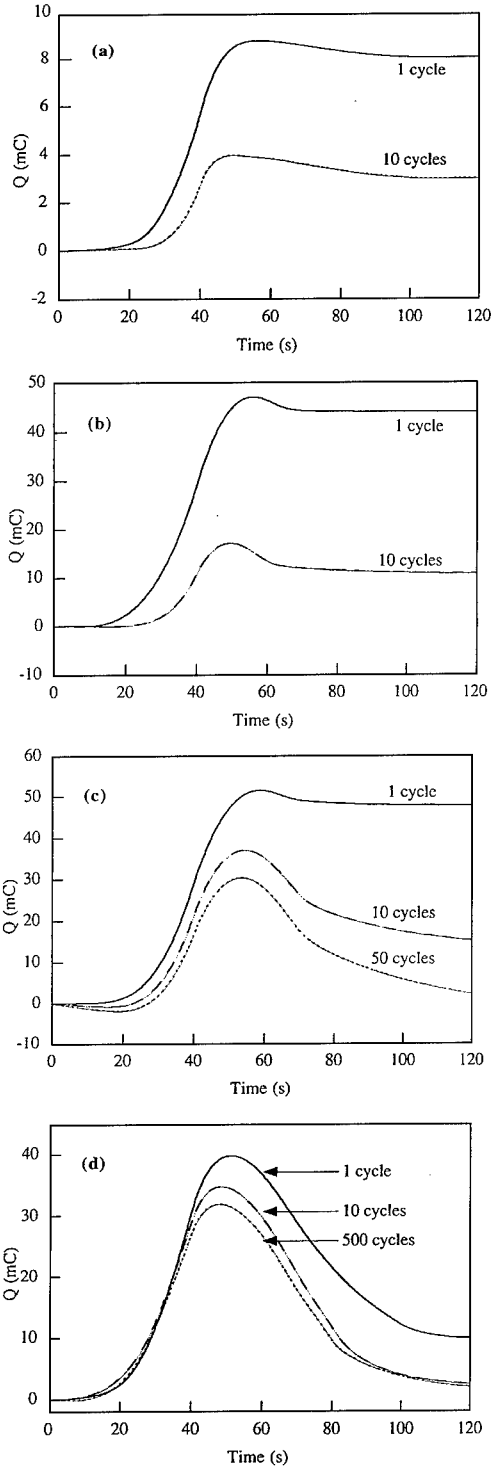

Figure 4. Charge inserted during one electrochemical cycle: (a) crystalline $WO_3 \cdot H_2O_2 \cdot H_2O$ ($T = 20°C$), (b) crystalline $WO_3 \cdot H_2O_2 \cdot 0.14H_2O$ ($T = 120°C$), (c) amorphous WO_3 ($T = 230°C$) and (d) monoclinic WO_3 ($T = 400°C$).

is poorly reversible and less than 10% of the initial charge is recovered after the first cycle. However, reversibility improves upon cycling and almost 50% of the charge is reversibly inserted after 10 cycles for the $WO_3 \cdot H_2O_2 \cdot 0.14H_2O$ film. This might be due to the progressive decomposition of peroxo groups. It has to be pointed out that cyclic voltammetry experiments are performed at a rather high scanning rate (50 mV/s) in order to be close to the switching behavior of an electrochromic device. Kinetic factors due to Li^+ diffusion could then be partly responsible for the low reversibility. The amount of Li^+ ions inserted upon electrochemical reduction remains very small. It is of the order of 2% ($Li/W \approx 0.02$).

Amorphous films formed upon heating at 240°C exhibit much better properties, mainly after several cycles. Their cycling behavior is much more reversible. The coulombic ratio reaches 58% after 10 cycles and becomes close to 90% after 60 cycles (Table 1). Best results have been obtained with the crystalline monoclinic phase formed after heating at 400°C. 74% of the inserted charge is already recovered after the first cycle. This value reaches 95% after 500 cycles.

4. Conclusion

Electrochromic tungsten oxide films can be deposited from aqueous solutions of tungstic acid H_2WO_4. However, oxolation reactions via the condensation of W-OH groups lead to the formation of an oxide network. Aqueous solutions of tungstic acid are not stable and $WO_3 \cdot 2H_2O$ precipitates after few hours. This hydrous oxide exhibits a layered structure built of corner sharing $[WO_6]$ octahedra. We have shown that stable solutions can be obtained in the presence of hydrogen peroxide. The dissolution of tungstic acid in aqueous solutions of H_2O_2 leads to the formation of peroxo-polytungstic acid species such as $[W_2O_3(O_2)_4(H_2O)_2]^{2-}$ [11]. W-OH groups are replaced by peroxo ions $[O_2]^{2-}$ that behave as chelating ligands toward W^{VI}. The functionality of aqueous precursors toward condensation decreases, preventing the precipitation of an oxide network. Stable solutions can be formed as long as peroxo ions remain in excess.

Homogeneous thin films can be deposited from these solutions. They can be amorphous or crystalline depending on the drying procedure. However, they still contain chemically bonded peroxo groups that are reduced during the first electrochemical cycles. Therefore the electrochromic properties of peroxopolytungstic films are not good at the beginning. They have to be cycled several times. Good characteristics are then obtained with the amorphous films which could compete with other films deposited by sputtering or vapor deposition.

References

1. C.G. Granqvist, *Handbook of Inorganic Electrochromic Materials* (Elsevier 1995).
2. B.W. Faughnan, R.S. Crandall, and P.M. Heyman, RCA Rev. **36**, 177 (1975).
3. B. Ohtani, T. Atsumi, S. Nishito, and T. Kagiya, Chem. Letters, 295 (1988).
4. J. Göttsche, A. Hinsch, and V. Wittwer, SPIE **1728**, 13 (1992).
5. J. Livage and P. Judeinstein, J. Mater. Chem. **1**, 621 (1991).
6. A. Chemseddine, R. Morineau, and J. Livage, Solid State Ionics **9–10**, 357 (1983).
7. T. Kudo, H. Okamoto, K. Matsumoto, and Y. Sasaki, Inorg. Chim. Acta **111**, L27 (1986).
8. K. Yamanaka, H. Oakamoto, H. Kidou, and T. Kudo, Japanese J. of Applied Phys. **25**, 1420 (1986).
9. H. Okamoto, K. Yamanaka, and T. Kudo, Mat. Res. Bull. **21**, 551 (1986).
10. H. Okamoto, A. Ishikawa, and T. Kudo, Bull. Chem. Soc. Jpn. **62**, 2723 (1989).
11. M.H. Dickman and M.T. Pope, Chem. Rev. **94**, 569 (1994).

Journal of Sol-Gel Science and Technology 13, 929–932 (1998)
© 1998 Kluwer Academic Publishers. Manufactured in The Netherlands.

Metal (Fe, Co, Ni) Nanoparticles in Silica Gels: Preparation and Magnetic Properties

T. LUTZ, C. ESTOURNÈS AND J.L. GUILLE
I.P.C.M.S. Groupe des Matériaux Inorganiques, UMR 46 CNRS, ULP, ECPM, 23, rue du Loess
B.P. 20/CR, 67037, Strasbourg Cedex, France

Abstract. Metal containing silica gels with an Me/Si molar ratio between 0.01 and 0.2 are submitted to thermal treatment under hydrogen within the temperature range 600 to 1000°C. The changes occurring during these treatments are followed by X-ray diffraction, transmission electron microscopy, Mössbauer spectrometry and static magnetization measurements.

During these treatments, nickel is nearly totally reduced to metal particles, the mean size of which increases from 3 to 10 nm with increasing temperature, but does not vary appreciably with nickel content. These particles exhibit a classical superparamagnetic behavior and are stable towards reoxidation when reexposed to air at room temperature.

Iron and cobalt behave in a notably different manner. First, in both cases, silicates may be formed during the thermal treatment and consequently the reduction to the metallic state is not complete unless it occurs at high temperature (1000°C and above). Secondly, the particles formed are much less stable toward reoxidation, especially in the case of iron. Accordingly, the evolution of the magnetic behavior is much more complex than in the case of nickel.

Keywords: metal, nanoparticles, magnetism, silica, gel

1. Introduction

Nanosized particles of ferromagnetic metals have been widely studied as they present an interest both for fundamental physics and potential applications such as catalysis and magnetic recording. Various chemical methods have been used to produce these particles [1–6]. The most often used is the reduction of a metal oxide, salt or complex dispersed in a supporting material. The case where the matrix is porous, typically a silica gel, has been the subject of various studies. The average particle size as well as the particle size distribution are strongly dependent on various parameters such as composition of the initial mixture, concentration of the reducible species, thermal treatment preceding the reduction and reduction treatment itself. The purpose of the present study is to investigate the phase constitution and the magnetic properties of composites obtained in similar conditions from silica gels containing nickel, iron or cobalt, respectively. These gels were submitted to various thermal treatments and the changes occurring during these treatments were followed by X-ray diffraction, Mössbauer spectrometry, transmission electron microscopy (TEM) and static magnetic measurements.

2. Experimental

2.1. Sample Preparation

Samples were prepared from a mixture of tetraethylorthosilicate, formamide, ethanol and 0.1 N nitric acid aqueous solution, the molar ratios being 1 : 1 : 4 : 4.5. The metal was added in the form of nitrate in order to obtain molar Me/Si ratios ranging from 0.01 to 0.20.

The mixture was stirred for one hour at room temperature, and held at 40°C for 50 hours. Removal of solvents from the resultant gels was performed in two steps: drying under argon atmosphere for 50 hours which allows elimination of most of ethanol and water and heating under reduced pressure to 220°C to eliminate formamide. Finally, the gels were calcined at 500°C for 5 hours.

These xerogels were heated under an argon flow until the desired reduction temperature was reached (600 to 1000°C). Argon was then replaced by hydrogen under atmospheric pressure. After one hour, hydrogen was replaced by argon and the furnace was allowed to cool down to room temperature.

2.2. *Characterization*

The homogeneity of the samples was checked by energy dispersive X-ray analysis, using a JEOL JSM840 scanning electron microscope equipped with a Delta Kevex analyzer. The size of the metal particles was estimated by TEM, using a Topcon EM002B microscope operating at 200 kV. X-ray diffraction patterns were obtained using a D500 Siemens diffractometer equipped with a Co tube. Mössbauer experiments were performed using a constant acceleration spectrometer equipped with a ^{57}Co source and magnetic properties were measured using a vibrating sample magnetometer.

3. Results

3.1. *Nickel Containing Gels*

More detailed results concerning these materials will be published elsewhere [7]. The main features are the following: before reduction X-ray diffraction patterns show that nickel is in the form of NiO particles the diameter of which has been estimated as close to 2 nm; the values of the saturation magnetization show that nickel is totally reduced to the metallic state, whatever the reduction temperature; the magnetic behavior at room temperature is superparamagnetic; the mean particle size, as directly measured by TEM (Table 1) or as determined by fitting the magnetization versus field curves depends mainly on the reduction temperature; increasing the nickel concentration results in a broadening of the size distribution.

Table 1. Average particle size (in nm) of nickel nanoparticles as a function of treatment temperature as determined by TEM.

Temperatures (°C)	Average particle size (nm)
600	3
700	5
800	7
900	10

3.2. *Iron Containing Gels*

Marked differences, with regard to nickel containing gels, have been observed concerning both the phase constitution and the magnetic behavior. In the calcined gels X-ray diffraction shows that no iron containing crystalline phase is present. This is confirmed by Mössbauer spectra which show that even in the most concentrated samples iron is present as Fe^{3+} ions and by magnetization versus field curves which exhibit a classical paramagnetic behavior. In the reduced gels, three cases may be distinguished, depending on the reduction temperature. After treatment at temperatures below 700°C, no crystalline phase is detected whereas Mössbauer spectrometry shows that iron is present as Fe^{2+} and Fe^{3+} ions. In the 700°C to 900°C temperature range metallic iron and fayalite (Fe_2SiO_4) are detected as well as quartz. TEM observations show two particle populations, the mean sizes of which, a few nm and over 20 nm, can be respectively attributed to fayalite and α-Fe. Above 900°C the only remaining crystalline phases are α-Fe and quartz. Corresponding to these structural changes, different magnetic behavior is observed for various samples. In the low temperature range it remains purely paramagnetic. At intermediate temperatures a small hysteresis loop appears, but the magnetization at maximum field remains far below that corresponding to the total reduction of iron. At high temperatures the magnetization is close to that corresponding to total reduction, but the coercive field becomes too small with regard to the magnetometer sensibility. Figure 1 shows the evolution of the 1.5 Tesla magnetization versus reduction temperature and an example of the magnetization versus field curves observed at intermediate temperatures. It is to be noted that the limits of the temperature ranges decrease with increasing iron content.

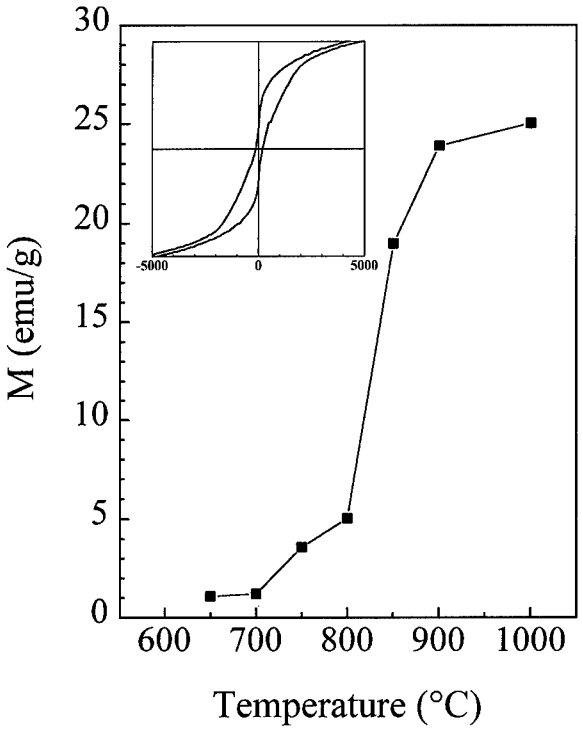

Figure 1. Magnetization (at 1.5 Tesla) of the 20% iron doped gel heated 60 min at various temperatures (insert: hysteresis loop of this gel reduced at 750°C).

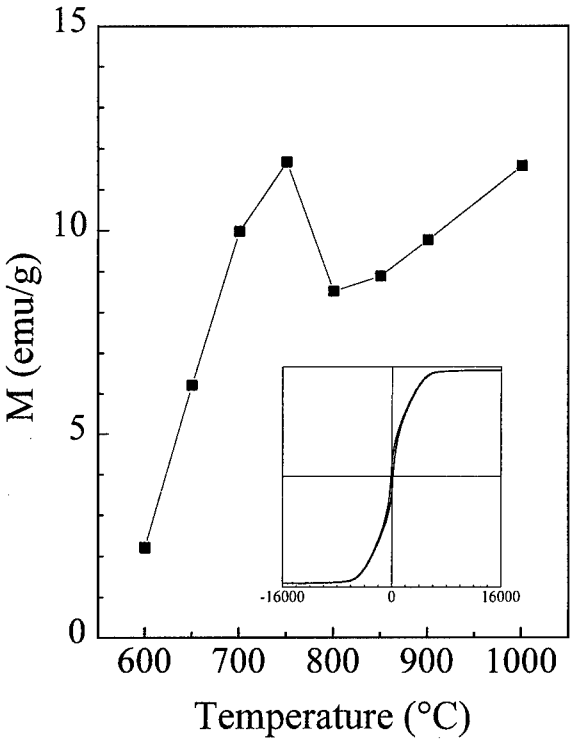

Figure 2. Magnetization (at 1.5 Tesla) of the 20% cobalt doped gel heated 60 min at various temperatures (insert: hysteresis loop of this gel reduced at 1000°C).

3.3. Cobalt Containing Gels

Cobalt containing gels exhibit marked similarities to the preceding ones: cobalt silicate (Co_2SiO_4) is formed at intermediate temperatures while at high temperatures, the metal is totally reduced and the silica crystallizes in the form of quartz. However, some differences appear concerning the phase constitution and the magnetic behavior. First, it has been observed that cobalt silicate may form before reduction if the preceding calcination step is too long whereas fayalite is formed only under reducing atmosphere. Secondly, after hydrogen treatment, metallic cobalt is observed even at the lowest temperature (i.e., 600°C). Concerning the magnetic properties, the main differences are due to the presence of metallic cobalt in all samples. Consequently the 1.5 Tesla magnetization increases much more quickly with increasing temperature than in the case of iron. It decreases in the intermediate temperature range when silicate is present and reaches values close to that corresponding to total reduction at high temperatures (Fig. 2).

4. Summary of Reuslts

The main difference between nickel, on the one hand, and iron and cobalt, on the other hand, is due to the formation of silicates in the second case. In the first case total reduction occurs whatever the temperature and the size of the particles increases continuously with increasing temperature. In the second case, above a given temperature, reduction enters into competition with the formation of silicates, and the total reduction is obtained only at temperatures high enough for the silicates to be reduced. The observed difference between iron- and cobalt containing gels is more surprising. Indeed, the formation of iron nanoparticles in similar systems at temperatures below 700°C has already been mentioned [8–10]. This difference can possibly result from a reoxidation of the very small iron particles formed at low temperature, followed by a redistribution of Fe^{2+} and Fe^{3+} ions in the silica matrix. This reoxidation can be favored by the high porosity of the matrix, the specific surface area of which is close to 600 m^2/g. This assumption is supported, on

the one hand, by the presence of Fe^{3+} ions detected by Mössbauer spectrometry that could not be present after reduction at 600°C without reoxidation, and on the other hand, by the fact that a similar phenomenon has already been observed for copper nanoparticles in the same kind of matrix [11]. The resistance of cobalt particles toward oxidation may be due to the formation of a passivating oxide or silicate superficial layer.

Concerning the magnetic properties, they can be straightforwardly analyzed in the case of nickel where the particles show always a superparamagnetic behavior, but the situation is much more confusing for iron and cobalt. It can be schematically described in the following manner: at low temperatures when the particles are chemically stable (the case of cobalt) a superparamagnetic behavior is once more observed, at intermediate temperatures the existence of a coercive field indicates the presence of stable monodomain particles and at high temperatures the particles are larger and become multidomain and the coercive field decreases.

References

1. S. Gangopadyay, G.C. Hadjipanayis, C.M. Sorensen, and K.J. Klabunde, MRS Symp. Proc. **206**, 55 (1991).
2. A. Gavrin and C.L. Chien, J. Appl. Phys. **73**, 6949 (1993).
3. E.F. Kneller and F.E. Lubrovsky, J. Appl. Phys. **34**, 656 (1994).
4. X.Q. Zhao, Y. Liang, Z.Q. Hu, and B.X. Liu, J. Appl. Phys. **80**, 5857 (1996).
5. S. Roy, B. Roy, and Chakravorty, J. Appl. Phys. **79**, 1642 (1996).
6. C. Estournès, T. Lutz, and J.L. Guille, J. Non-Cryst. Solids **197**, 192 (1996).
7. C. Estournès, T. Lutz, J. Happich, T. Quaranta, P. Wissler, and J.L. Guille, J. Magn. Magn. Mater. **173**, 83 (1997).
8. J.P. Wang and H.L. Luo, J. Magn. Magn. Mater. **131**, 54 (1994).
9. A. Chatterjee and D. Chakravorty, J. Phys. D: Appl. Phys. **22**, 1386 (1989).
10. R.D. Shull, J.J. Ritter, A.J. Shapiro, L.J. Swartzendruber, and L.H. Bennett, J. Appl. Phys. **67**(9), 4490 (1990).
11. N. Cornu, Ph.D. Thesis, University Louis Pasteur, Strasbourg, 1994.

Journal of Sol-Gel Science and Technology 13, 933–936 (1998)
© 1998 Kluwer Academic Publishers. Manufactured in The Netherlands.

Role of Water on Fast Proton Conduction in Sol-Gel Glasses

MASAYUKI NOGAMI, RITSUKO NAGAO, WANG CONG AND YOSHIHIRO ABE
Department of Materials Science and Engineering, Nagoya Institute of Technology, Showa Nagoya, 466, Japan

Abstract. Fast proton-conducting P_2O_5-ZrO_2-SiO_2 glasses were prepared by sol-gel processing of metal alkoxides. Glasses heated to 150 to 400°C exhibited room temperature conductivities of $\sim 10^{-4}$ S/cm, larger by ~ 2 order of magnitude than that of as-prepared gel, $\sim 3 \times 10^{-7}$ S/cm at 30°C. The conductivity increased quadratically with the increasing product of proton and molecular water concentration. These high conductivities were regarded as fast proton transfer accelerated by molecular water bonded with the hydroxyl groups.

Keywords: proton conductor, phosphate glass, sol-gel, water containing glass

1. Introduction

Proton-conductors have a potential for use in clean energy fields, such as hydrogen gas sensors and hydrogen fuel cells. Although some hydrated crystalline compounds, $H_3(PMo_{12}O_{40})\cdot 30H_2O$, $H_3(PW_{12}O_{40})\cdot 30H_2O$, and $HUO_2PO_4\cdot 4H_2O$ are known to show high proton conductivity [1, 2], they are not appropriate for industrial applications because of their instability to humidity. Fast proton-conducting glasses, if developed, do not have the limitations of the above compounds and have potential for various applications. Phosphate glasses, in which protons are very mobile, are considered to exhibit high conductivities due to high proton mobility [3, 4]. However, the P_2O_5 component is lacking in chemical durability; the water lowers mechanical strength and chemical stability. Such disadvantages limit the practical use of these glasses. Recently, using a sol-gel method, we successfully prepared gels and glasses in the P_2O_5-ZrO_2-SiO_2 system with high conductivities of approximately 10^{-4}–10^{-2} S/cm at room temperature [5–7]. The sol-gel method is appropriate for the preparation of the fast protonic P_2O_5-containing glasses. These high conductivities are regarded as the fast proton mobility accelerated by molecular water incorporated in samples. However, the effect of molecular water was not clearly understood at that time. In the previous paper, we elucidated how hydrogen-bonded molecular water contributes to the proton conduction using a porous silica glass [8]. Although the conductivity of silica glass is small, its chemical durability is favorable for examining this topic.

Crack-free glasses containing 25 mol% P_2O_5 were successfully prepared using the sol-gel process. The glasses obtained by heating at 200 to 400°C were chemically stable and exhibit high conductivities of $\sim 10^{-4}$ S/cm at room temperature [7]. In this paper, based on the knowledge of porous silica glasses, we discuss the effect of molecular water on the fast protonic conductivity of the P_2O_5-containing glasses. It is important to understand how molecular water affects proton conduction and to determine the truly effective molecular water for the development of high proton conducting glasses.

2. Experimental

P_2O_5-ZrO_2-$2SiO_2$ (mole ratio) glass was prepared by the hydrolysis of $PO(OCH_3)_3$, $Zr(OC_3H_7)_4$, and $Si(OC_2H_5)_4$. The starting materials were commercially available and used as received. The $PO(OCH_3)_3$ was first heated for 2 h at about 150°C in $(CH_3)_2CHOH$. After cooling to room temperature, $Zr(OC_3H_7)_4$ dissolved in $(CH_3)_2CHOH$, was added in this solution, followed by stirring for 1 h. Then the partially hydrolyzed $Si(OC_2H_5)_4$ was added and stirred for 1 h at room temperature. The resulting homogeneous solution was finally hydrolyzed with H_2O, and left for about 1 month

to form a stiff gel about 1 mm thick. The gel obtained was heated at 1.5°C/min to a given temperature and held for 5 h.

The dc conductivity was determined from Cole-Cole plots by an ac method using Solartron SI 1260 Impedance Analyzer, where silver paste electrodes were used. The Cole-Cole plot consisted of a single semicircle and electrical conductivity was obtained from the intersecting point of the semicircle with a real axis. The conductivity measurements were carried out in constant temperature chamber controlled temperatures between 30 and 90°C and a constant relative humidity of 50%. Thermal analysis (DTA-TGA) of powdered samples with a heating rate of 5°C/min was carried out.

3. Results and Discussion

The dried gel is porous and contains a large amount of water incorporated during gel synthesis. Upon heating, the gel shrinks due to dehydration-condensation of the hydroxyl groups and sintering, which results in the transformation of the gel to glass. The porous structure remains unchanged in glass heated below 800°C. Pore surfaces of the porous glass are terminated with a hydroxyl group and are sensitive to air humidity, so that the porous sample absorbs water. Figure 1 shows the weight change of the P_2O_5-ZrO_2-$2SiO_2$ glass heated to 300°C with exposure time in an ambient air of 50% relative humidity (RH) at 30°C. It is apparent that the adsorption of water takes place within several tens of minutes and approaches a saturated level of ~8 wt%.

Conductivities of glass, heated at 300°C and measured both on exposure to 50% RH and an ambient C_3H_7OH vapor atmosphere at 30°C, are plotted in Fig. 2 as a function of exposure time. The conductivity, measured without exposure to the ambient atmosphere after the heat treatment, was low, $\sim 3 \times 10^{-7}$ S/cm. When exposed to ambient air, the conductivity dramatically increases as the exposure time increases and approaches a constant level of 10^{-5} S/cm. The exposure to C_3H_7OH vapor made no change in the conductivity. These experimental results strongly suggest that the adsorption of water in pores causes the conductivity to increase.

Figure 3 shows the conductivity, measured at 30°C in 50% RH, for the P_2O_5-ZrO_2-$2SiO_2$ glasses heated at temperatures up to 600°C. Note that the conductivities of glasses heated to between 150 and 400°C exhibit room temperature conductivities of 10^{-5}–10^{-4} S/cm; larger by ~2 orders of magnitude than that of the

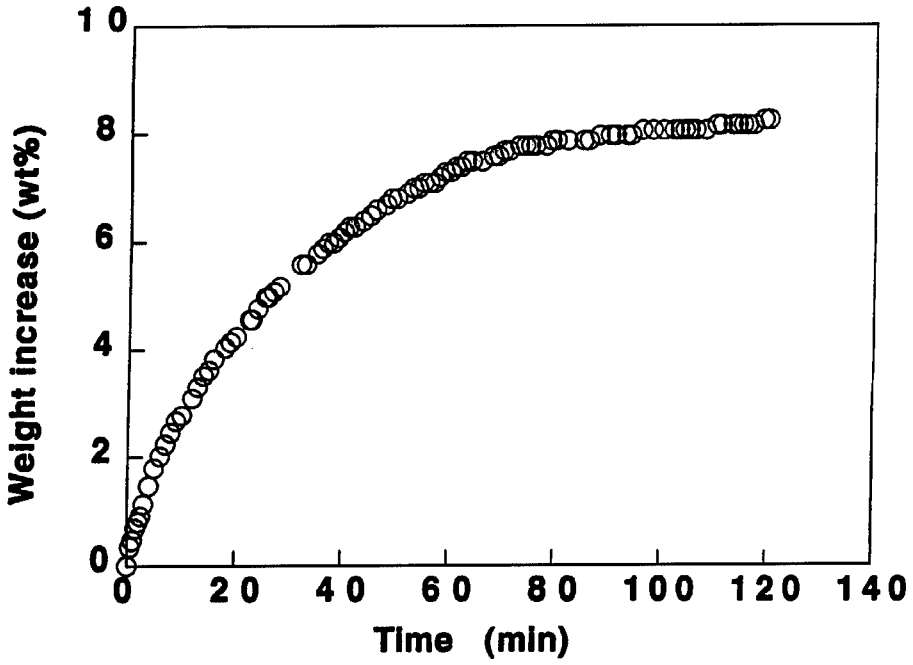

Figure 1. Change in weight of P_2O_5-ZrO_2-$2SiO_2$ glass heated to 300°C exposed in air atmosphere, 30°C and ~50% RH.

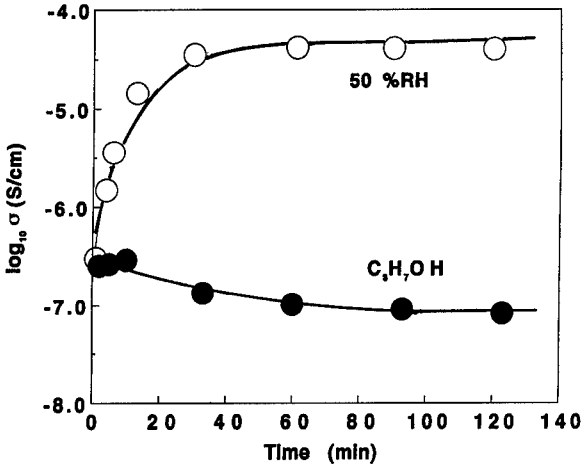

Figure 2. Change in conductivity of P_2O_5-ZrO_2-$2SiO_2$ glass heated to 300°C with exposing in air atmosphere of ~50% RH and C_3H_7OH vapor, at 30°C.

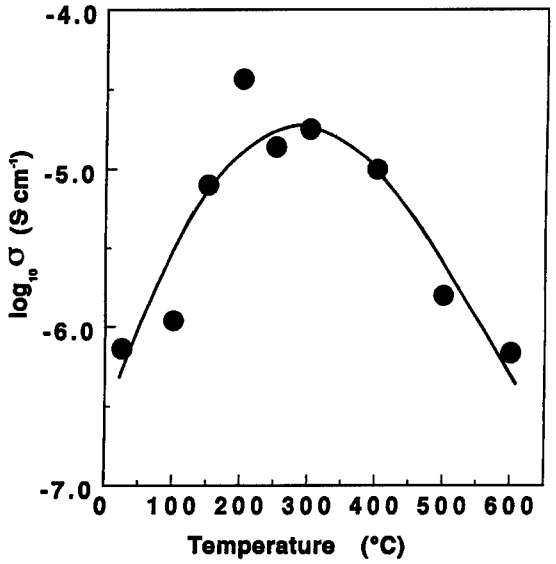

Figure 3. Conductivities, measured at 30°C in 50% RH, of P_2O_5-ZrO_2-$2SiO_2$ glasses annealed at various temperatures.

as-prepared gel. It is interesting to note that high conductivities are achieved in the heated samples although the mechanism of high conductivity in the heated glasses is not clear. The chemical durability of glasses increased as the heat-treatment temperature increased. The glasses heated above 200°C exhibited neither change in the conductivity nor dissolution of any components of the glass after immersion in water for 2 days at room temperature, which is very important for practical applications. When heated above 300°C, the conductivity was observed to decrease with increasing the heat treatment temperature. In our previous paper [8], we proposed that protons in the SiOH groups on the pore surface act as electrical charge carrier and the electrical conduction is associated with the proton hopping between SiOH and water molecule. The conductivity increases with increasing concentration of both protons and adsorbed water. On heating, the dehydration-condensation reaction between the surface MOH (M=Si, P or Zr) bonds takes place: MOH + HOM=M—O—M + H_2O. This reaction reduces the proton concentration as a charge carrier, which might result in the decrease in conductivity, although the water is adsorbed in the pores. The concentrations of protons are calculated assuming that the weight loss in the TG curve is the removal of water by the dehydration-condensation reaction. The proton concentrations are 11.1, 3.83, 1.34, and 0.38 mol/l for glasses heated to 300, 400, 500, and 600°C, respectively. On the other hand, no significant difference was observed in the amount of water adsorbed in glasses heated at 300–600°C. The conductivities shown in Fig. 3 are plotted in Fig. 4 as a function of the proton concentration, where both values are shown in a log-log scale. It is evident that the conductivity increases linearly with increasing proton concentration on a log-log scale. There is no doubt that protons act as electrical charge carriers in the P_2O_5-ZrO_2-SiO_2 glasses. As mentioned above, these glasses absorb water in ambient air, the content of which is about 8 wt%. The absorption is little influenced by the heat treatment temperature. Therefore, the slope of the linear relation in Fig. 4 can be considered to depend on only the proton

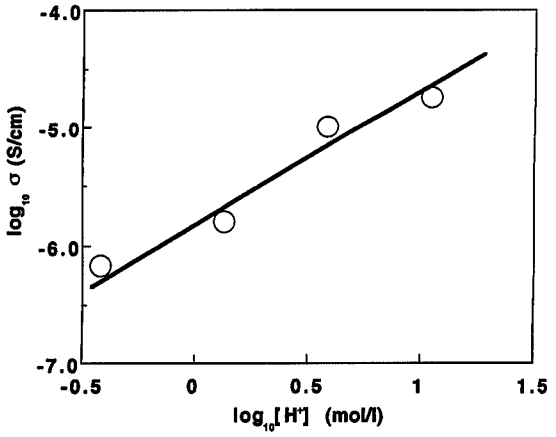

Figure 4. Relation between electrical conductivity, measured at 30°C in 50% RH, and proton concentration of P_2O_5-ZrO_2-$2SiO_2$ glasses heated to 300°C.

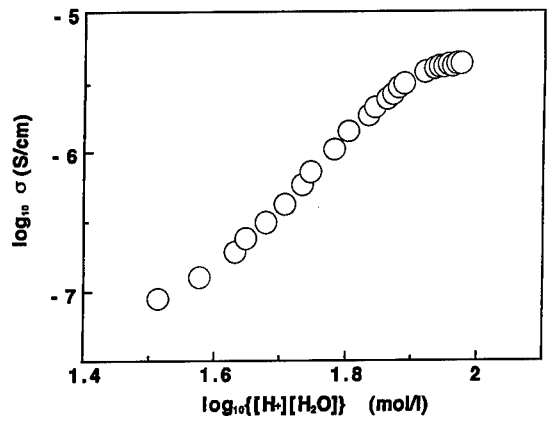

Figure 5. Relation between electrical conductivity, measured at 30°C in 50% RH, and the product of concentration of proton and water molecule of P_2O_5-ZrO_2-$2SiO_2$ glasses heated to 300°C.

concentration. Abe et al. analyzed the proton conductivity using the phosphate glasses prepared by the melting method and concluded that the conductivity at a temperature of 417 K is proportional to the square of the proton concentration [9]. It is interesting to note that for the sol-gel glasses the conductivity increases quadratically with increasing proton concentration, although there are some questions as to whether Abe et al.'s equation can be applied to sol-gel glasses.

Next we consider the effect of the adsorbed molecular water on proton conductivity. As shown in Figs. 1 and 2, the glass prepared in this study is porous and absorbs the water from ambient air, which results in the increase of conductivity. We previously showed that a small amount of absorbed water bonded with SiOH on pore surfaces causing the proton conductivities to increase [8]. The present glass, on the other hand, contains a large amount of water. To study the role of the adsorbed water on the proton conductivity, the conductivities of glass, heated to 300°C, are replotted on a log-log scale as a function of the product of proton and water concentration in Fig. 5, where proton concentration is 11.1 mol/l. It is apparent that the logarithm of conductivities are proportional to logarithm of the product $[H^+] \cdot [H_2O]$. This linearity suggests that protons dissociate from MOH bonds form complex ions such as H_3O^+ in water and transfer by hopping through water molecules. This is a possible mechanism for the fast proton conductivity of glass incorporating both the proton and molecular water, although more quantitative analyses are necessary to clarify the effect of water.

4. Conclusion

In summary, we have successfully prepared crack-free P_2O_5-ZrO_2-$2SiO_2$ glasses by the sol-gel method. The heated glasses exhibit high conductivities of $\sim 10^{-4}$ S/cm at room temperature, which is larger than that of the as-prepared gels. It is concluded that proton mobility is accelerated by molecular water bound with the hydroxyl groups. These fast protonic conductors are chemically stable and have a high potential for practical applications.

Acknowledgment

This work was partly supported by a Grant-in-Aid for Scientific Research (No. 08229229) from the Ministry of Education, Science, and Culture of Japan and New Energy and Industrial Technology Development Organization of Japan.

References

1. O. Nakamura, T. Kodama, I. Ogino, and Y. Miyake, Jpn. Patent no. 76/106683, 1977.
2. M.G. Shilton and A.T. Howe, Mater. Res. Bull. **12**, 701 (1977).
3. Y. Abe, H. Hosono, Y. Ohta, and L.L. Hench, Phys. Rev. B **38**, 10166 (1988).
4. Y. Abe, H. Hosono, W.H. Lee, and T. Kasuga, Phys. Rev. B **48**, 15621 (1993).
5. Y. Abe, G. Li, M. Nogami, T. Kasuga, and L.L. Hench, J. Electrochem. Soc. **143**, 144 (1996).
6. M. Nogami, K. Miyamura, and Y. Abe, J. Electrochem. Soc. **144**, 2175 (1997).
7. M. Nogami, R. Nagao, K. Makita, and Y. Abe, Appl. Phys. Lett. **71**, 1323 (1997).
8. M. Nogami and Y. Abe, Phys. Rev. B **55**, 12108 (1997).
9. Y. Abe, H. Shimakawa, and L.L. Hench, J. Non-cryst. Solids **51**, 357 (1982).

Journal of Sol-Gel Science and Technology 13, 937–943 (1998)
© 1998 Kluwer Academic Publishers. Manufactured in The Netherlands.

Sintering Aerogels

GEORGE W. SCHERER
Princeton University, CEOR/PMI, Eng. Quad. E-319, Princeton, NJ 08544, USA
Scherer@Princeton.Edu

SYLVIE CALAS AND ROBERT SEMPÉRÉ
Lab. des Verres, Univ. Montpellier II, Place E. Bataillon, 34095 Montpellier, France

Abstract. Studies of the densification kinetics and structural evolution of non-crystalline aerogels during sintering are examined in light of theory. In most respects, the theory of viscous sintering is capable of quantitatively accounting for the experimentally observed behavior, as long as the initial pore size distribution is known. Unfortunately, it is difficult to obtain adequate structural information; in particular, measurements using nitrogen desorption and thermoporometry often erroneously indicate the presence of macroporosity. Some authors have claimed that large pores contract more quickly than small pores during sintering; under certain circumstances this is predicted by the theory.

Keywords: sintering, aerogel, pore size distribution, viscosity, characterization (of aerogels)

1. Introduction

Aerogels are dry gel networks with extremely high porosity, but very small pores [1]. They are traditionally prepared by supercritical drying (SCD) of wet gels [2, 3], either by removal of an organic solvent at relatively high temperature (e.g., 240°C for methanol), or carbon dioxide at modest temperature (31°C) [4, 5]. Recently, considerable progress has been made in preparing structurally equivalent materials without SCD, either by chemical passivation [6, 7] or aging in the presence of additional monomer [8].

Aerogels provide a stringent test of theories of sintering [9–13], because they can be prepared at extremely low densities, so changes in density, pore size, and surface area can be followed over a very wide range. Some practical applications of aerogels, such as catalytic substrates [14, 15], require stability at high temperatures; on the other hand, preparation of bulk silica requires complete elimination of porosity [16–19]. Therefore, it is useful to compare experimental results of sintering experiments with theoretical expectations. This review is limited to amorphous aerogels that sinter by viscous flow, because the theory of viscous sintering is well developed and abundant data are available. There is no comparably detailed theory for sintering of low-density crystalline networks, which is unfortunate, because crystalline aerogels are of great importance, particularly in catalysis.

2. Theory of Viscous Sintering

Sintering is a process by which the surface area of a material is decreased by mass transport. In crystalline materials many concurrent processes can occur, including lattice, grain boundary, and surface diffusion; moreover, grain growth can accompany densification. For amorphous materials, only viscous flow is important, because it is much faster than any competing densification process resulting from diffusion [20]. The rate of viscous sintering is calculated using the energy balance concept introduced by Frenkel [9]: the energy dissipated in viscous flow is equal to the energy liberated by reduction in surface area. For a body with a given density, higher surface area means greater surface to

volume ratio, so there is more surface energy to drive the flow of the relatively small volume; therefore, at a given density, a body with smaller pores densifies more rapidly. The sintering rate can be determined from an equivalent formulation in terms of capillary pressure, since the curvature (κ) is related to the surface area (S) and volume (V) of the body by $\kappa = dS/dV$, and the capillary pressure acting on the condensed phase is given by the Laplace equation, $p = -\gamma\kappa$, where γ is the surface tension. Thus, the greater the specific surface area, the greater the capillary pressure driving flow.

To predict the change in density resulting from a given decrease in surface area, it is necessary to choose a microstructural model. Frenkel [9] considered two spheres in contact, and obtained a result that agrees rather well with experiment [21] (but only because of the fortuitous cancellation of serious errors in his analysis [22]); a much more precise (but complicated) treatment of that geometry is now available [23]. Mackenzie and Shuttleworth [10] obtained an exact expression for the rate of contraction of a spherical shell, which is a good approximation for the late stages of densification, when pores become isolated. The most appropriate model for a low-density material, such as an aerogel, is a network with strands of solid phase joined at nodes. Idealized networks have been analyzed, where the unit cell has a cubic [11] or other [12] polyhedral shape, and where an arbitrary distribution of cell sizes is present [13]. In these "cylinder models," the solid phase is represented by cylindrical rods lying along the edges of the unit cell.

For the cylinder model, regardless of the shape of the cell, Eqs. (9) and (31) of [12] indicate that the densification rate is given by

$$\frac{d\rho}{dt} = \frac{\gamma S \rho_b}{2\eta}, \tag{1}$$

where ρ_b is the bulk density of the network, ρ_s is the skeletal density, the relative density is $\rho = \rho_b/\rho_s$, γ is the specific surface energy, S is the specific surface area, and η is the viscosity. The effect of cell shape enters through the dependence of S on ρ. The result of integrating Eq. (1) is a complicated expression of the form [12],

$$f(\rho) - f(\rho_0) = \int_0^t \frac{\gamma n^{1/3}}{\eta} dt, \tag{2}$$

where ρ_0 is the initial relative density and n is the number of pores per unit volume of solid. For a cubic cell with edge length ℓ, given that there is one pore per cell,

$$n = 1/(\rho\ell^3) = 1/(\rho_0\ell_0^3), \tag{3}$$

where ℓ_0 is the initial edge length. For gels, the viscosity may not be constant even during an isothermal experiment, because of the changing hydroxyl content [20]; for aerogels, it seems that η is constant at a given temperature, so Eq. (2) reduces to

$$f(\rho) - f(\rho_0) = \gamma n^{1/3} t/\eta. \tag{4}$$

The time to reach full density is found by setting the left side of Eq. (4) to $f(1) - f(\rho_0)$; since that quantity is on the order of unity, regardless of the value of ρ_0, the time needed to sinter a viscous body is approximately $\tau_s \approx \eta/(\gamma n^{1/3}) = \eta\ell_0\rho_0^{1/3}/\gamma$. Thus, the time to reach full density decreases with pore size (related to ℓ_0) and viscosity; the viscosity of glass is sensitive to moisture in the atmosphere, so sintering in air is faster than in a dry atmosphere [20, 24, 25].

When a pore size distribution is present, the pores with greater surface area shrink faster, which leads to internal stresses in the body. To predict the net densification rate, it is necessary to know the constitutive equation for the network (i.e., the strain rate produced by a given stress applied to the porous body). For a porous viscous material, this equation takes the form [26, 27]

$$\dot{\varepsilon}_x = \dot{\varepsilon}_f + \frac{1}{E}[\sigma_x - \nu(\sigma_y + \sigma_z)], \tag{5}$$

where $\dot{\varepsilon}_x$ is the strain rate in the x direction, $\dot{\varepsilon}_f$ is the free strain rate, E is the uniaxial viscosity, ν is Poisson's ratio, and σ_x, σ_y, σ_z are the principal stresses. For a nonporous viscous material, $E = 3\eta$ and $\nu = 1/2$ [27], but a porous material is more compliant; several models have been developed to predict E and ν (or, equivalently, the shear viscosity G and bulk viscosity K) of porous materials [12, 28–30]. The free strain rate is the linear shrinkage rate due to sintering in the absence of applied stress, $-\dot{\rho}/(3\rho)$, so according to Eq. (1), the free strain rate is

$$\dot{\varepsilon}_f = -\frac{\gamma S \rho_s}{6\eta}. \tag{6}$$

If a compressive stress ($\sigma_x < 0$) is applied, then the densification rate increases; in hot isostatic pressing,

the applied pressure ($\sigma_x = \sigma_y = \sigma_z = -p_A$) is much larger than the capillary pressure [31, 32].

When the pores are not identical, the free strain rate given by Eq. (6) is different for each size; the measured strain rate $\dot{\varepsilon}_x$ must be a weighted average of the free strain rates of all the pores. There are many ways to calculate that average, just as there are many ways to estimate the properties of a composite on the basis of the properties of the components. A good approximation is given by the self-consistent scheme [13, 33].

The preceding analysis leads to a prediction of the densification rate, as well as the change in surface area and pore size, but analytical solutions are possible only for a highly idealized geometry. Recently, a model was proposed to describe the evolution of the microstructure (but not the kinetics) for a fractal material, such as an aerogel [34]. That model was compared to a numerical simulation of an aerogel network (created using an aggregation model) [35]; the predicted scaling behavior was not in good agreement with the simulation, except over a very limited range of density. In contrast, the simulation agreed rather well with the predictions of the cylinder model [12].

3. Aerogel Structure

There is a huge amount of literature on the structure of aerogels, but only a few relevant points can be mentioned here. Silica aerogels made from alkoxides under acidic (A) or neutral (N) conditions are fractal networks with polymeric, rather than particulate, character; when prepared by high-temperature SCD, the surfaces are rough, but they become smooth when oxidized (i.e., when alkoxy groups are burned off) at ~400°C [36]. Base-catalyzed (B) silica aerogels may have primary particles with diameters of ~1–2 nm; the networks have a limited range of fractality, except at very low densities [36, 37]. Where fractal structure exists, it extends over a limited range of length scale with a lower cutoff size b and upper cutoff (known as the mass correlation length) ξ; beyond ξ the mass distribution in the body is uniform. As the density increases, ξ decreases; for an N aerogel, ξ is ~25 nm when $\rho_b = 0.1$ g/cm^3 and ~3 nm when $\rho_b = 0.4$ g/cm^3 [38]; similar correlation lengths have been found using light scattering [39]. The connectivity may have a correlation length much larger than ξ [40]; for example, if large clusters interpenetrate extensively, then ξ can be much smaller than the cluster size, but the connectivity correlation length is equal to the cluster size.

It is sometimes claimed that the structure of an aerogel is hierarchical, with small particles packed into clusters, then clusters arranged into larger clusters, and so on. This picture is consistent with a fractal structure [41], but would be expected to extend only over lengths up to ξ. Bourret [42] used transmission electron microscopy to examine silica aerogels, and observed chains with diameters of ~3 nm linked at nodes where 3–4 chains met; the node spacing was 12–14 nm in B aerogels and ~7 nm in N or A aerogels. He found no evidence of a second level of hierarchy in B with $\rho_b > 0.03$ g/cm^3, nor in A or N with $\rho_b > 0.12$ g/cm^3; at the latter limit he found indications of a second level with a node spacing of ~25 nm. A TEM study of a silica aerogel with extremely low density (0.009 g/cm^3) [43] showed a node spacing of ~60 nm, and no indication of pores much larger than 100 nm.

Three types of studies routinely (and erroneously) indicate the presence of very large pores in aerogels. Nitrogen sorption often detects a small fraction of the total pore volume [44], which can be found from the density:

$$V_p = 1/\rho_b - 1/\rho_s. \tag{7}$$

Since this technique should reveal any cylindrical pores with diameters $\leq$60 nm, it is inferred that most of the pore volume is in much larger pores [44, 45]. There are several reasons to disbelieve these results: (a) the permeability of gels is low [1], and indicates that the mean size of pores is in the mesopore range (<50 nm); (b) condensation of liquid nitrogen in the pores of an aerogel can case significant compression, leading to an underestimate of the pore volume [46]; (c) condensation on a network is qualitatively different from condensation in a cylindrical pore, because most of the solid surface has positive curvature, so the radius of curvature of the adsorbate/vapor interface can be much greater than the pore size [47]; and (d) there is no evidence of a preponderance of large pores indicated by TEM, except when ρ_b is exceptionally low. Another technique that indicates a large volume of macropores is thermoporometry [48, 49], but this method has been shown [46, 50, 51] to cause severe compression of compliant gels; thus, the volume attributed to macropores is actually the volumetric compression. Mercury porosimetry causes severe compression of the gel without entering the pores [44, 52, 53], so use of this method yields a false indication of macroporosity [54]. Recently, a highly original method has been proposed

[55] for extracting the pore size distribution from the compression behavior of an aerogel; however, mercury porosimetry is useful principally for measuring the bulk modulus of aerogels [52].

The difficulty of measuring the initial pore size distribution of an aerogel complicates the problem of predicting sintering behavior. In all of the published analyses of sintering kinetics, the aerogel was assumed to have a uniform pore size, usually found from the hydraulic radius,

$$r_h = 2V_p/S. \tag{8}$$

As we shall see, it is not possible to predict the evolution of surface area or pore size on the basis of this characteristic pore size.

4. Previous Studies of Aerogel Sintering

4.1. Structural Studies

Apparently the first study of the effect of heat treatment on the structure of a silica aerogel was by van Nordstrand et al. [56]. On the basis of the small change in surface area accompanying a substantial change in density, they concluded that the larger pores contracted first during sintering. This conclusion was also reached by Emmerling et al. [57, 58] on the basis of small angle X-ray scattering. It is possible to understand this counter-intuitive conclusion as follows. If one compares two bodies with the same relative density, then the one with a higher surface area has smaller pores, and will sinter faster. However, suppose there are two networks with different densities constructed from cylinders of the same radius, a (i.e., networks differing only in the spacing ℓ of the nodes). In that case, the specific surface area (i.e., area/mass) is greater in the network with *lower* density; the result for a cubic network (calculated using Eq. (8) of [12]) is shown in Fig. 1. The reason for this behavior is that the specific surface area of the cylindrical element is greater than that of the node, so S is greater when the node spacing ℓ is greater. In this case, Eq. (6) indicates that the shrinkage rate is greater in the body with larger cells (higher S).

A recent study [59] used nitrogen adsorption to follow the surface area during sintering of a silica aerogel at 1050°C. The initial pore size distribution was calculated from the adsorption data by using a new model that takes proper account of the network structure [47]. Using the cylinder model for sintering [11], and

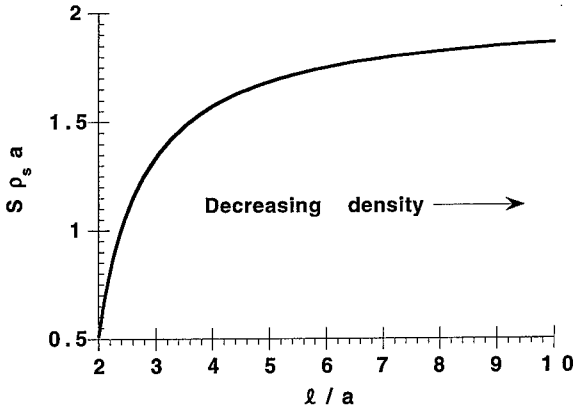

Figure 1. Specific surface area of cubic network as function of node spacing, ℓ, where all networks have the same cylinder radius, a.

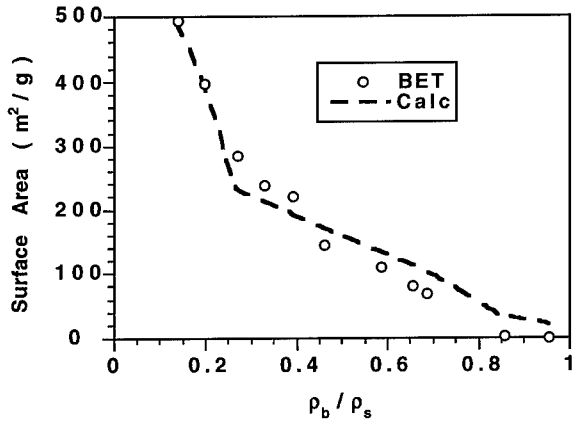

Figure 2. Change in surface area with density during sintering of silica aerogel; symbols are measured data, curve calculated from cylinder model. Results taken from [59].

allowing for the pore size distribution [13], the change in the surface area with density was predicted, and the results are shown in Fig. 2. Evidently, when the pore size distribution is taken into account, the shrinkage of the pores can be accurately predicted.

Small angle scattering of X-rays (SAXS) and neutrons (SANS) has been used to follow structural changes in aerogels during sintering. For B aerogels, Vacher et al. [37] found that the primary particle size increased and the correlation length decreased, while the fractal dimension was unchanged; similar behavior was observed for N aerogels [36]. Schaefer et al. [40, 60, 61] used neutron spin echo (NSE) spectroscopy to demonstrate an increase in short-range connectivity (i.e., on a length scale $\leq$100 nm) in the network upon heating. All of these studies are consistent with expectations, since densification occurs initially on the

smallest length scale; ξ decreases as a consequence of densification of the local structure, which causes a uniform contraction.

A curious observation by Schaefer et al. [40, 60, 61] is that the connectivity seems to *decrease* at long length scales (i.e., on a micron scale). They argue that small structures shrink at the expense of larger structures, causing the opening of large pores, and say that it would be difficult to envision a shrinkage process that would not lead to such an effect. On the contrary, if one imagines a tree-like fractal, then sintering ought to begin by the smallest shoots becoming shorter and thicker (corresponding to growth of the primary particles), forming nodules on the branches, then the next larger branches would contract similarly, and the branches would all contract toward the trunk (corresponding to a decrease in ξ). Such a process would not necessarily lead to breakage of any of the larger branches (reducing connectivity at long length scales). The nature of the process observed by Schaefer et al. is not clear. However, it is clear that the net connectivity increases, since the modulus increases monotonically upon heat treatment [62], and NSE shows that the structure becomes rigid on a scale larger than 0.1 μm [61].

4.2. *Kinetic Studies*

The isothermal densification kinetics of aerogels have been found to fit the cylinder model [57, 63, 64], with the viscosity η as the only fitting parameter. The activation energy is found to be surprisingly low, but this is likely to be an effect of the OH content, since the gels were sintered in air. Onorato (in an unpublished study described in [20]) studied the sintering kinetics of silica aerogels [65] isothermally and at a constant heating rate, and found good agreement with the cylinder model in both cases. Moreover, she showed that the atmosphere has a strong effect on the densification rate, being almost an order of magnitude faster in air than in oxygen; in chlorine, the rate was slower than in oxygen, because of the removal of OH.

Emmerling et al. [58] compared the densification rates of silica aerogels with initial densities of 0.086, 0.145 and 0.235 g/cm^3, and found that the densification rate decreased as the initial density increased (but the actual rates are not given). They claimed that this result contradicted the predictions of the cylinder model. However, inspection of Eq. (1) reveals that there are three factors to be considered: ρ_b, S and η. If the higher initial density is offset by a lower surface area, then the densification rate will decrease as ρ_b increases; more importantly, if the OH content of all the gels is not identical, then η will vary, and this effect may dominate the densification kinetics. In fact, Emmerling et al. used the beam-bending method to measure the viscosity of the porous gel (which measures the viscosity of the network, not the viscosity of the condensed phase, η). If the data are compared at a density of 0.3 g/cm^3 (to remove the effect of porosity and obtain a quantity proportional to η), the viscosities are 2, 7, and 20 times 10^{12} Pa · s for aerogels with initial densities 0.086, 0.145 and 0.235 g/cm^3, respectively. This variation is in the right direction to account for the trend in the observed densification rates; Emmerling et al. claim that the OH content is the same in all of the samples on the basis of the value of the BET C-parameter, but that is not a sensitive measure of hydroxyl content. In these proceedings, Emmerling and Fricke [66] argue that the viscosity measurements indicate a scale-dependent viscosity that controls densification kinetics. This is consistent with the cylinder model, since the network viscosity depends on ρ, which varies with ℓ in cells with a given a; this effect could be quantified if the pore size distribution were known.

When the initial pore size distribution is known, it is possible to predict the densification kinetics and the evolution of the pore size distribution [59]. Figure 3 shows the densification kinetics for a silica aerogel sintered at 1050°C in air, compared with the rate calculated from the cylinder model [11, 13], taking account of the initial pore size distribution. The only fitting parameter is η, which is found to be 2.1×10^{12} Pa · s; given

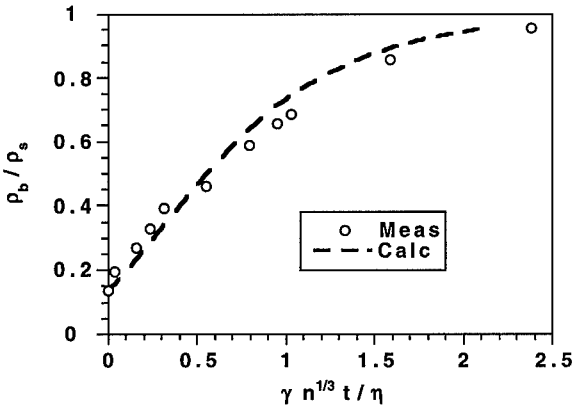

Figure 3. Measured densification kinetics (symbols) for silica aerogel compared to calculation (curve) based on cylinder model, taking account of initial pore size distribution. Data from [59].

that sintered aerogels of this type have been found to contain 3000–5000 ppm OH [16], this viscosity agrees well with data for vitreous silica [67].

4.3. Sintering and Crystallization

No crystallization of silica was reported in any of the studies cited above; given the sensitivity of X-ray diffraction, the volume fraction of crystals (if any) was probably <1%. That amount would not affect the densification kinetics, although it might show up as large scattering centers (and possibly be mistaken for large pores). Substantial crystallization of silica gels during sintering is generally observed only when alkali impurities are present [68]; in that case, it is difficult to achieve full densification, even by hop-pressing [69]. In many systems, crystallization is so fast that it is difficult to densify the aerogel by viscous sintering. Sintering of crystalline materials is much slower [20], and once the crystals percolate, densification is drastically retarded [70, 71]. For example, an amorphous aerogel with the composition of mullite sinters only to a relative density of 0.51 before shrinkage is arrested by crystallization [72]; however, if the gel is crushed and passed into a pellet, it densifies completely (because the denser body requires less time to sinter, so much less crystallinity develops).

5. Conclusions

The densification kinetics and structural evolution of amorphous aerogels during sintering are generally in good agreement with conventional sintering theory: the structures with the highest specific surface area (which are not necessarily the smallest pores) densify fastest, all of the pores shrink, and the rate increases as the viscosity decreases. When the initial structure of the aerogel is adequately characterized, it is possible to account quantitatively for the changes in density, pore size, and surface area. When crystallization occurs, the rate of densification is retarded, and shrinkage effectively stops when the crystals percolate. Unfortunately, understanding of the sintering behavior of crystalline materials is less well developed than for glasses.

References

1. J. Phalippou, G.W. Scherer, T. Woignier, D. Bourret, and R. Sempéré, J. Non-Cryst. Solids **186**, 64–72 (1995).
2. S.S. Kistler, J. Phys. Chem. **36**, 52–64 (1932).
3. J. Fricke and A. Emmerling, in *Chemistry, Spectroscopy and Applications of Sol-Gel Glasses*, edited by R. Reisfeld and C.K. Jørgensen (Springer, Berlin, 1992), pp. 37–87.
4. P.H. Tewari, A.J. Hunt, and K.D. Lofftus, Mater. Lett. **3**(9, 10), 363–367 (1985).
5. A.A. Bartlett and H.P. Burstyn, *Scanning Electron Microscopy/1975, Part I* (IIT Res. Inst., Chicago, IL, 1975), pp. 305–316.
6. D.M. Smith, D. Stein, J.M. Anderson, and W. Ackerman, J. Non-Cryst. Solids **186**, 104–112 (1995).
7. S.S. Prakash, C.J. Brinker, A.J. Hurd, and S.M. Rao, Nature **374**, 439–443 (1995).
8. M.-A. Einarsrud and S. Hæreid, J. Sol-Gel Sci. Tech. **2**, 903–906 (1994).
9. J. Frenkel, J. Phys. (Moscow) **9**(5), 385–391 (1945).
10. J.K. Mackenzie and R. Shuttleworth, Proc. Phys. Soc. London **62**(12B), 833–852 (1949).
11. G.W. Scherer, J. Am. Ceram. Soc. **60**(5/6), 236–239 (1977).
12. G.W. Scherer, J. Am. Ceram. Soc. **74**(7), 1523–1531 (1991).
13. G.W. Scherer, J. Am. Ceram. Soc. **71**(10), C447–C448 (1988).
14. R.A. van Nordstrand, W.E. Kreger, and H.E. Ries, Jr., J. Phys. Colloid Chem. **55**, 621–638 (1951).
15. M.A. Cauqui and J.M. Rodríguez-Izquierdo, J. Non-Cryst. Solids **147/148**, 724–738 (1992).
16. T. Woignier, J. Phalippou, and M. Prassas, J. Mater. Sci. **25**, 3118–3126 (1990).
17. Y. Sano, S.H. Wang, R. Chaudhuri, and A. Sarkar (Sol-Gel Opt.) SPIE **1328**, 52–61 (1990).
18. G.W. Scherer and J.C. Luong, J. Non-Cryst. Solids **63**, 163–172 (1984).
19. R. Clasen, J. Non-Cryst. Solids **89**, 335–344 (1987).
20. C.J. Brinker and G.W. Scherer, *Sol-Gel Science* (Academic Press, NY, 1990), chap. 11.
21. W.D. Kingery and M. Berg, J. Appl. Phys. **26**(10), 1205–1212 (1955).
22. G.W. Scherer, in *Mechanics of Granular Materials and Powder Systems*, edited by M.M. Mehrabadi (ASME, New York, 1992), pp. 1–18.
23. A. Jagota and P.R. Dawson, J. Am. Ceram. Soc. **73**(1), 173–177 (1990).
24. G.M. Tomilov, N.V. Solomin, and T.V. Smirnova, Inorganic Mater. **14**(1), 145–146 (1978), (Eng. transl.).
25. T.Y. Tseng and J.J. Yu, J. Mater. Sci. **21**, 3615–3624 (1986).
26. G.W. Scherer, J. Non-Cryst. Solids **34**, 239–256 (1979).
27. R.K. Bordia and G.W. Scherer, Acta Metallurgica **36**(9), 2393–2397 (1988).
28. R.K. Bordia and G.W. Scherer, Acta Metallurgica **36**(9), 2399–2409 (1988).
29. A. Jagota, K.R. Mikeska, and R.K. Bordia, J. Am. Ceram. Soc. **73**(8), 2266–2273 (1990).
30. V.C. DuCamp and R. Raj, J. Am. Ceram. Soc. **72**(5), 798–804 (1989).
31. P. Murray, E.P. Rodgers, and A.E. Williams, Trans. Brit. Cer. Soc. **53**, 474–510 (1954).
32. J. Zarzycki, J. Non-Cryst. Solids **48**, 105–116 (1982).
33. V.V. Skorokhod, Powder Metallurgy **12**, 188–200 (1963).
34. R. Sempéré, D. Bourret, T. Woignier, J. Phalippou, and R. Jullien, Phys. Rev. Lett. **71**, 3307 (1993).
35. N. Olivi-Tran, R. Jullien, and G.W. Cohen-Solal, Europhys. Lett. **30**(7), 393–398 (1995).

36. R. Vacher, T. Woignier, J. Phalippou, J. Pelous, and E. Courtens, Rev. Phys. Appl. **24**(4), C4-127–C4-131 (1989).
37. R. Vacher, T. Woignier, J. Phalippou, J. Pelous, and E. Courtens, J. Non-Cryst. Solids **106**, 161–165 (1988).
38. R. Vacher, T. Woignier, J. Pelous, and E. Courtens, Phys. Rev. B **37**(11), 6500–6503 (1988).
39. P. Wang, W. Körner, A. Emmerling, A. Beck, J. Kuhn, and J. Fricke, J. Non-Cryst. Solids **145**, 141–145 (1992).
40. D.W. Schaefer, B.J. Olivier, C.S. Ashley, D. Richter, B. Farago, B. Frick, L. Hrubesh, M.J. van Bommel, G. Long, and S. Krueger, J. Non-Cryst. Solids **145**, 105–112 (1992)
41. J. Zarzycki, in *Science of Ceramic Chemical Processing*, edited by L.L. Hench and D.R. Ulrich (Wiley, NY, 1986), pp. 21–36.
42. A. Bourret, Europhys. Lett. **6**(8), 731–737 (1988).
43. G.C. Ruben, L.W. Hrubesh, and T.M. Tillotson, J. Non-Cryst. Solids **186**, 209–218 (1995).
44. J. Fricke and G. Reichenauer, J. Non-Cryst. Solids **95/96**, 1135–1142 (1987).
45. G. Schuck and W. Dietrich, in *Aerogels*, edited by J. Fricke (Springer-Verlag, Berlin, 1986), pp. 148–153.
46. G.W. Scherer, D.M. Smith, and D. Stein, J. Non-Cryst. Solids **186**, 309–315 (1995).
47. G.W. Scherer, Adsorption in sparse networks: I. Cylinder model, J. Colloid Interface Sci., submitted.
48. J.L. Rousset, A. Boukenter, B. Champignon, E. Duval, J.F. Quison, M. Chatelut, J. Dumas, and J. Serughetti, Rev. Phys. Appl. **24**(4), C4-163–C4-166 (1989).
49. F. Ehrburger-Dolle, J. Dallamano, E. Elaloui, and G.M. Pajonk, J. Non-Cryst. Solids **186**, 9–17 (1995).
50. G.W. Scherer, J. Non-Cryst. Solids **155**, 1–25 (1993).
51. J.F. Quinson, M. Repellin Lacroix, M. Pauthe, A. Roche, and G.W. Scherer, J. Sol-Gel Sci. Tech. **2**(1–3), 239–244 (1944).
52. G.W. Scherer, D.M. Smith, X. Qiu, and J.M. Anderson, J. Non-Cryst. Solids **186**, 316–320 (1995).
53. A.R. Minihan, D.R. Ward, and W. Whitby, in *The Colloid Chemistry of Silica*, edited by H.E. Bergna (Am. Chem. Soc., Washington, DC, 1994), pp. 341–355.
54. J. Iura, H. Hishikura, N. Taneda, and T. Kawaguchi, Asahi Garasu Kenkyu Hokoku, **38**(1), 15–30 (1988).
55. R. Pirard and J.P. Pirard, J. Non-Cryst. Solids **212**, 262–267 (1997).
56. R.A. van Nordstrand, W.E. Kreger, and H.E. Ries, Jr., J. Phys. Colloid Chem., **55**, 621–638 (1951).
57. A. Emmerling, J. Gross, R. Gerlach, R. Goswin, G. Reichenauer, J. Fricke, and H.G. Haubold, J. Non-Cryst. Solids **125**, 230–243 (1990).
58. A. Emmerling, W. Lenhard, J. Fricke, and G.A.L. van de Vorst, J. Sol-Gel Sci. Tech. **8**, 837–842 (1997).
59. S. Calas, R. Sempéré, and G.W. Scherer, Densification kinetics and structural evolution during sintering of silica aerogel, J. Non-Cryst. Solids, submitted.
60. D.W. Schaefer, C.J. Brinker, D. Richter, B. Farago, and B. Frick, Phys. Rev. Lett. **64**(19), 2316–2319 (1990).
61. B.J. Olivier, D.W. Schaefer, B. Frick, D Richter, B. Farago, C.S. Ashley, and W.A. Kamitakahara, Trans. Am. Cryst. Assoc. **27**, 199–210 (1991).
62. T. Woignier, J. Phalippou, and r. Vacher, J. Mater. Res. **4**(3), 688–692 (1989).
63. T. Woignier, J. Phalippou, and M. Prassas, J. Mater. Sci. **25**, 3118–3126 (1990).
64. A. Emmerling, R. Gerlach, R. Goswin, J. Gross, G. Reichenauer, J. Fricke, and H.G. Haubold, J. Appl. Cryst. **24**, 781–787 (1991).
65. S.R. Su and P.I.K. Onorato, in *Better Ceramics Through Chemistry II*, Mater. Res. Soc. Symp., Pittsburgh, PA, 1986), pp. 237–244.
66. A. Emmerling and J. Fricke, Scale-length dependent viscosity controls isothermal sintering of base-catalyzed silica aerogels, these proceedings.
67. R. Brückner, J. Non-Cryst. Solids **5**, 177–216 (1971).
68. C. Zhu, J. Phalippou, and J. Zarzycki, J. Non-Cryst. Solids **82**, 321–328 (1986).
69. J. Zarzycki, *Advances in Ceramics* (Am. Ceram. Soc., Columbus, OH, 1982), Vol. 4, pp. 204–216.
70. G.W. Scherer, in *Better Ceramics Through Chemistry IV*, edited by B.J.J. Zelinski, C.J. Brinker, D.E. Clark, and D.R. Ulrich (Mat. Res. Soc., Pittsburgh, PA, 1990), pp. 503–514.
71. P.C. Panda, W.M. Mobley, and R. Raj, J. Am. Ceram. Soc. **72**(12), 2361–2364 (1989).
72. M.N. Rahaman, L.C. de Jonghe, S.L. Shinde, and P.H. Tewari, J. Am. Ceram. Soc. **71**(7), C338–C341 (1988).

Journal of Sol-Gel Science and Technology 13, 945–949 (1998)
© 1998 Kluwer Academic Publishers. Manufactured in The Netherlands.

Silicon Oxycarbide Glasses Derived from Polymer Precursors

K. EGUCHI AND G.A. ZANK
Dow Corning Asia Ltd., Research and Information Center, 603 Kishi Yamakita, Kanagawa 258-01, Japan

Abstract. This paper describes a new predictive model to estimate compositions of ceramic materials from the structure of the preceramic polymer. The polymers are prepared by sol-gel methods and have M and T silicone functionality. The ceramic predictive model works well for highly branched silsesquioxanes, which are some of the most common ceramic precursors. This report describes the control of ceramic SiOC compositions which in turn make the materials useful as: (1) matrices for ceramic matrix composites and; (2) anodes for rechargeable lithium ion batteries.

Keywords: silsesquioxane, preceramic, silicon oxycarbide glasses

Introduction

The composition or stoichiometry of a ceramic dictates many of the properties of the ceramic material. For example, in employing a polymer as a binder for the sintering of ceramic powders, it is important that the polymer provides sufficient excess or free carbon if sintering to high density is desired [1]. For SiC_x precursors a nearly linear dependence has been shown between the amount of phenyl groups in the polymer and the amount of carbon in the ceramic [2]. For SiOC materials the stoichiometry has been shown to influence the stability of the ceramic towards oxidation [3]. This has allowed the formation of oxidatively resistant ceramic fiber reinforced ceramic matrix composites based on SiOC matrices [4]. Recently, we have explored the use of these SiOC ceramics as anodes for rechargeable lithium ion batteries. Our results indicate that the composition, or stoichiometry, of the SiOC material has great influence over the performance of the anode and subsequently the utility of the rechargeable battery [5–7].

A number of workers have probed both the chemistry and the structures of SiOC glasses derived from polymeric silsesquioxane based precursors. There have been studies directed at the preparation of these glasses with low O/Si ratios [8] or with high levels of Si—H to reduce the overall amount of excess carbon present in the SiOC [9]. Others have examined the pyrolysis chemistry of precursors that give "ultrahigh" ceramic yields [10] or employed elegant precursors such as block and graft copolymers [11] or precursors that contained preformed polyhedral silsesquioxane cages [12]. However, all of this work has shown that the initial chemical environment around the silicon in a siloxane polymer is only maintained up to 500°C. The results of these studies are perhaps best summarized by one of the investigators: "Further heating results in a scrambling of the silicon environment" [12]. Indeed this redistribution of elements (C and O) bound to silicon has been observed by MAS-NMR and these insights into the SiOC materials documented by a number of workers [2, 13–16]. Other techniques have been employed to look at the micro/nanostructure of SiOCs. The pore structure has been probed by BET analysis [17] and a number of authors have augmented the MAS-NMR studies with X-ray diffraction and TEM analysis [2, 18–20]. Others have also employed FTIR [21] and XPS spectroscopy [22] to provide information about the bonding at the silicon in these SiOC glasses.

All of this work has provided insights to the environment locally about the silicon in these SiOC glasses and, to some extent, what effect this environment has on the broader nano and micro structure. The conclusions are that the environment of the Si in the glass is determined by the Si to O ratio in the precursor. This, however, does not mean that the overall structure of the glass depends on the Si to O ratio. For example,

materials with the same Si to O ratio but with different amounts of carbon exhibit different X-ray diffraction patterns [6], have different stabilities in air [3] and have different electrochemical behavior [6]. We believe that these properties, which are key to many applications of the materials, are controlled by the overall stoichiometry and structure of the glass and not strictly by the local environment about the silicon. That is why it is important to control the SiOC stoichiometry and hence structure of the glass by control of the polymer precursor.

Experimental

All polymer formulations were determined by ^{1}H and ^{29}Si NMR (Bruker 400 MHz) and were used in the subsequent calculations. All of the ceramic elemental analyses were performed at Dow Corning Corporation utilizing the following procedures: The ceramic was ground into a fine powder prior to elemental analysis. The CHN analyses were carried out on a Perkin Elmer 2400 combustion analyzer. Oxygen analyses were done on a Leco oxygen analyzer (model R0-316) equipped with an oxygen determinator 316 (model 783700) and an electrode furnace EF100. Silicon analyses were determined by a fusion technique which consisted of converting the solid to a soluble form and analyzing the solute for total silicon by Arl 3580 ICP-AES analysis.

Polymer Synthesis

The following detailed description is representative of the procedures followed for all of the polymers studied. In a 5-l three necked round bottom flask fitted with an internal thermometer, a reflux condenser and an overhead stirrer: phenyltrimethoxysilane (77.0 g), methyltrimethoxysilane (742 g), 1,1,3,3-tetramethyl-1,3-divinyldisiloxane (192 g), trifluoromethanesulfonic acid (5.0 ml) and deionized water (50 g) were placed. This mixture was then heated to reflux with stirring for 2 hours. Toluene (1.5 l) and deionized water (410 ml) were added to the mixture and the reaction mixture heated to reflux for an additional two hours. Calcium carbonate (10 g) was added, the reflux condenser replaced with a distillation head and the reaction distilled to a vapor head temperature of 85°C. Aqueous 3 wt% potassium hydroxide (50 ml) was added, the distillation head replaced with a Dean-Stark trap and reflux condenser and the water azeotropically removed. After the reaction mixture was dry of water (internal temperature above 105°C), the mixture was cooled and chlorodimethylvinylsilane (50 ml) was added. After stirring, the mixture was filtered through a sintered glass fit with filter-aid. The solvent was removed from the filtrate in vacuum affording a greater than 95% isolated yield.

Ceramic Preparation

Aliquots of all of the polymers studied were cured by mixing the polymer with 1% by weight Lupersol™ 101 peroxide and heating the mixture to 175°C for 30 minutes under Ar. Aliquots of the cured polymers were then converted to ceramics by pyrolysis in a Lindberg Model 54434 tube furnace fitted with Eurotherm temperature controllers. The pyrolysis was conducted under High Purity Ar gas at a purge rate sufficient to prevent decomposition and redeposition of the vapors that were evolved during the pyrolysis (ca. 30 turnovers per hour). The samples were placed in alumina boats, and transferred to the pyrolysis tube which was then sealed from the atmosphere and flushed with argon for 30 minutes prior to beginning the pyrolysis. The temperature was raised at 5°C/minute to the hold temperature of 1200°C and held one hour. Samples were weighed before and after the pyrolysis to calculate the ceramic conversion (char) yield.

Results and Discussion

Three series of preceramic silsesquioxane based polymers were synthesized, of the general formula:

Series I $(PhSiO_{1.5})_x(MeSiO_{1.5})_{.75-x}(Me_2ViSiO_{.5})_{.25}$ where x is from 0 to 0.75 in 0.05 increments

Series II $(PhSiO_{1.5})_x(ViSiO_{1.5})_{.75-x}(Me_2ViSiO_{.5})_{.25}$ where x is from 0.05 to 0.75 in 0.1 increments

Series III $(ViSiO_{1.5})_x(MeSiO_{1.5})_{.75-x}(Me_2ViSiO_{.5})_{.25}$ where x is from 0.05 to 0.75 in 0.1 increments

The stoichiometry of the polymer was rarely identical to that intended, most likely due to the formation of small amounts of silicate gels which were removed in the work-up. The actual formulations were obtained by NMR (both ^{1}H and ^{29}Si) analysis.

Each of the polymers were crosslinked at temperatures between 150 and 200°C with Lupersol™ 101

peroxide, 1 wt%, as a catalyst. Some insight into the pyrolysis process of these cured polymers is provided by TGA/RGA [23]. From this RGA work we can conclude the following:

- The cured polymers show thermal stability up to 400°C.
- The vinyl or silethylene functionality has the lowest thermal stability.
- Only "organic" decomposition by-products are observed.
- The "backbone" Si and O elements are retained "quantitatively" in the 1200°C ceramic.

All of the polymer precursors were pyrolyzed in bulk (ca. 5.0 g quantities) to ceramics. In general, the elemental analyses total greater than 95% and with only a few exceptions the totals are also less than 98%. It is our experience that the greatest error in the elemental analysis of these ceramics is in the Si analysis. Since this analysis depends on a chemical digestion of the SiOC it is very common to have incomplete digestion of the ceramic and for the analysis to be low compared to the actual Si content.

The predictive carbon content model for SiOC glasses developed here is based on multiple linear regression derived from the experimental percent carbon analysis and organic functional groups present in the precursors. The wide range of variation for the content of the considered functionalities in the precursors allows one to develop a robust model. The types of precursors included in this study covers highly branched, or networked, silsesquioxane systems. One assumption in this model is that all Si and O elements which constitute the backbone of the polymeric precursors quantitatively remain in the SiOC ceramic. This assumption is based on the RGA results that detected no silicon or oxygen containing species in the volatile by-products [23].

The model developed here for the carbon content of the SiOC ceramics is based on evaluation of the carbon remaining in the ceramic material after pyrolysis of the precursor, as a function of the mole fraction of each functional group. This then provides a quantitative relationship of the efficiency of carbon transfer for

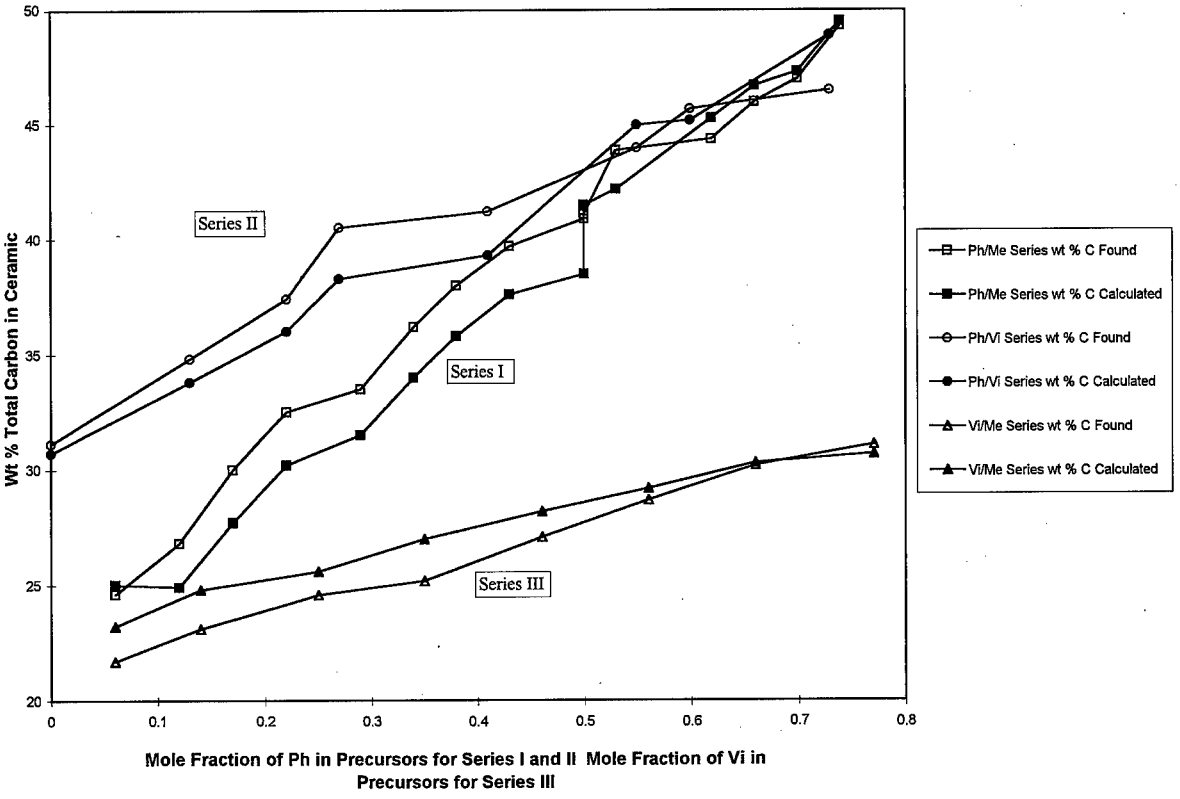

Figure 1. Comparison of calculated and found total wt% carbon in SiOC ceramics derived from the precursors studied here.

each functional group. This evaluation was performed by multiple linear regression analysis without intercept employing a SAS statistical computer package for the 37 data points examined. This resulting relationship is given in Eq. (1)

$$\begin{aligned}\text{moles of C} = {} & 3.94 \times (\text{mole fraction Ph-T}) + 1.52 \\ & \times (\text{mole fraction Vi-T}) + 0.59 \\ & \times (\text{mole fraction Me-T}) + 2.746 \\ & \times (\text{mole fraction Vi-M}) \\ r^2 = {} & 0.9976 \text{ for the 37 points examined}\end{aligned} \quad (1)$$

The comparison of the actual and predicted values obtained from this model are shown in Fig. 1. Based on this study we feel that this mathematical model can be used to predict the compositions of ceramic derived from polysiloxanes and further aid in the design and development of polymers targeted to desired SiOC stoichiometries.

Conclusions

This work has resulted in a mathematical model to help guide the preparation of preceramic polymers for applications that require specific SiOC ceramic stoichiometries. This mathematical relationship holds for highly branched silsesquioxane based polymer systems that allow one to predict the ceramic composition based on the precursor polymer's chemistry and structure.

One assumption in this model is that all Si and O elements which constitute the backbone of the polymeric precursors quantitatively remain in the SiOC ceramic. This assumption is supported by RGA results that detected no silicon or oxygen containing species in the volatile by-products and appears to be a valid assumption based on the limits of the experimental error used to quantify these elements. The carbon content of the ceramics is a more difficult problem since it is not a backbone element in the polymeric precursor and it is known from the RGA results that some carbon is lost during the pyrolysis. Evaluation of the carbon analyzed in the ceramic material after pyrolysis of the precursors as a function of the mole fraction of each functional group provides a quantitative relationship of the efficiency of carbon transfer for each functional group. The results of this analysis is shown in Eq. (1) and Fig. 1.

This model indicates that the most efficient functionality is vinyl while the least efficient is methyl. More specifically, the efficiency of each of the functional groups considered in this study is:

- 75% of the vinyl groups will stay and contribute two carbons to the ceramic
- 69% of the dimethylvinyl groups will stay and contribute four carbons to the ceramic
- 67% of the phenyl groups will stay and contribute six carbons to the ceramic
- 60% of the methyl groups will stay and contribute one carbon to the ceramic

While the current model provides a predictive tool for the elemental composition of the ceramic material, based on the chemical structure of the precursor, the true chemical structure and the morphology of the ceramic material is not covered by this model and is the focus of our ongoing research.

References

1. W.H. Atwell, G.T. Burns, and G.A. Zank, in *Inorganic and Organometallic Polymers and Oligomers*, edited by J.F. Harrod and R.M. Laine, (Kluwer Academic Publishers, Dordrecht, Netherlands, 1991).
2. G.T. Burns, R.B. Taylor, Y. Xu, A. Zangvil, and G.A. Zank, Chemistry of Materials **4**, 1313–1323 (1992).
3. R.H. Baney, K. Eguchi, and G.A. Zank, The Society of Silicon Chemistry of Japan **8**, 23–27 (1996).
4. R.Y. Leung and M. Glazier, Ceramic Engineering Society Proceedings **16**, 209–216 (1995).
5. W. Xing, A.M. Wilson, G.A. Zank, and J.R. Dahn, Solid State Ionics **93**, 239–244 (1997).
6. W. Xing, A.M. Wilson, K. Eguchi, G.A. Zank, and J.R. Dahn, Journal of the Electrochemical Society **144**, 2410–2416 (1997).
7. A.M. Wilson, G.A. Zank, K. Eguchi, W. Xing, and J.R. Dahn, J. Power Sources **2549**, (1996), in press.
8. V. Belot, R.J.P. Corriu, D. LeClercq, P.H. Mutin, and A. Vioux, Journal of Non-Crystalline Solids **176**, 33–44 (1994).
9. G.D. Soraru, G. D'Andrea, R. Campostrini, F. Babonneau, and G. Mariotto, Journal American Ceramics Society **78**, 379–387 (1995).
10. G.D. Soraru, R. Campostrini, S. Maurina, and F. Babonneau, Journal American Ceramics Society **80**, 999–1004 (1997).
11. K.A. Youngdahl, M.L. Hoppe, R.M. Laine, J.A. Rahn, and J.F. Harrod, Applied Organometallic Chemistry **7**, 674–754 (1993).
12. R.A. Mantz, P.F. Jones, K.P. Chaffee, J.D. Lichtenhan, J.W. Gilman, I.M.K. Ismail, and M.J. Brumeister, Chemistry of Materials **8**, 1250–1259 (1996).
13. V. Belot, R.J.P. Corriu, D. LeClercq, P.H. Mutin, and A. Vioux, Journal of Non-Crystalline Solids **147/148**, 52–55 (1992).
14. F. Babonneau, L. Bois, and J. Livage, Journal of Non-Crystalline Solids **147/148**, 280–284 (1992).
15. F. Babonneau, L. Bois, C.-Y. Yang, and R.M. Laine, Chemistry of Materials **6**, 51–57 (1994).

16. L. Bois, J. Maquet, F. Babonneau, H. Mutin, and Bahloul, Chemistry of Materials **6**, 796–802 (1994).
17. C. Liu, H. Zhang, S. Komarneni, and S.G. Pantano, Journal of Sol-Gel Science and Technology **1**, 141–151 (1994).
18. F.I. Hurwitz, P. Heimann, S.C. Farmer, and D.M. Hembree, Journal of Materials Science **28**, 6622–6630 (1993).
19. M. Hammond, E. Breval, and C.G. Pantano, Ceramic Engineering Society Proceedings **14**, 947–954 (1993).
20. E. Breval, M. Hammond, and C.G. Pantano, Journal of American Ceramic Society **77**, 3012–3018 (1994).
21. A.K. Singh and C.G. Pantano, Journal of Sol-Gel Science and Technology **8**, 371–376 (1997).
22. R.J.P. Corriu, D. LeClercq, P.H. Mutin, and A. Vioux, Journal of Sol-Gel Science and Technology **8**, 327–330 (1997).
23. A.M. Wilson, G.A. Zank, K. Eguchi, W. Xing, B. Yates, and J.R. Dahn, Chemistry of Materials **9**, 1601–1606 (1997).

Journal of Sol-Gel Science and Technology 13, 951–956 (1998)
© 1998 Kluwer Academic Publishers. Manufactured in The Netherlands.

Crystallization of Gels in the Apatite-Mullite System

B. SAMUNEVA, V. DIMITROV, S. KALIMANOVA AND E. GATTEF
University of Chemical Technology and Metallurgy, Sofia, Bulgaria

R. HILL
University of Limerick, Ireland

Abstract. Crystallization processes in gels of the apatite-mullite system were studied to obtain information for the synthesis of bioglass-ceramics and composite materials. SiO_2-sol, $Al(NO_3)_3 \cdot 9H_2O$, $Ca(NO_3)_2 \cdot 4H_2O$, $(NH_4)_3PO_4 \cdot 3H_2O$ and CaF_2 were used as precursors. CaF_2 was added before and after gelation. Mixtures of mullite gel-glass and fluorapatite in the range 10 to 90 mol% were investigated for synthesis of composites. All the samples were heat treated at different temperatures in the range 950–1250°C and the structural changes were established using X-ray diffraction and IR-spectroscopy. When the gels were treated at 1050°C and at 1150°C, the main crystalline phases found were fluorapatite and mullite independent of the CaF_2 content and the manner of its addition. At 1250°C the relative amounts of fluorapatite and mullite decrease and gehlenite appears. Composite materials containing fluorapatite and mullite as main crystalline phases can be obtained only when the content of mullite gel-glass in the initial mixture is more than 60 mol%.

Keywords: sol-gel synthesis, biomaterials, apatite-mullite system, glass-ceramics, composites

Introduction

Apatite-mullite glass-ceramics with good mechanical properties for dental applications were synthesized using traditional technology by Hill and Wood [1–3] and Dimitrova-Lukacs [4]. Using sol-gel processing these glass-ceramics can be obtained by direct crystallization of gel-glasses with suitable compositions [5] or by sinter crystallization of composite gels, containing mullite gel-glass and fluorapatite. Glass-ceramics, ceramics and composite materials can be obtained by direct crystallization of gels or gel-glasses without melting. The rate of nucleation and crystallization of glasses made from gels is much higher than those made from mixtures of oxides [6]. Uhlmann et al. [7] have summarized the published results about crystallization of glasses prepared by sol-gel method and by melting. Many articles about the synthesis and the properties of glass ceramic materials prepared by the sol-gel route have been published recently [8–19], and some of them describe the synthesis of bioglass-ceramics [14–19]. In particular, sol-gel synthesis of mullite is of great interest both for understanding the processes taking place and because of its good mechanical and chemical properties [20–25].

The main purpose of the present work is to study the crystallization of the gels in the apatite-mullite system during heat treatment and to establish the dependence of the crystallization processes on the type of the precursors and the way of the gel preparation.

Experimental

Gels of composition $1.5SiO_2 \cdot 0.5P_2O_5 \cdot 1Al_2O_3 \cdot 1CaO \cdot 0.5CaF_2$ [1] have been synthesized using appropriate amounts of the following precursors: SiO_2-sol, $Al(NO_3)_3 \cdot 9H_2O$, $Ca(NO_3)_2 \cdot 4H_2O$, $(NH_4)_3PO_4 \cdot 3H_2O$ and CaF_2 (powder). SiO_2 was introduced by SiO_2-sol, because it has been shown that by using TEOS mullite was not the main crystalline phase present [5].

Solutions of the precursors were mixed for 1 hour and CaF_2 powder was added to the mixture either before or after gelation of the samples.

Fluorapatite and mullite gel-glass were synthesized as the first stage of synthesizing composite materials. TEOS, $Al(NO_3)_3 \cdot 9H_2O$ and $Ca(NO_3)_2 \cdot 4H_2O$ were used as starting materials to synthesize mullite gel-glass. The gels, obtained without gelation catalysts, were dried at 100°C for 24 hours and after that were heated for 2 hours at 400°C, 600°C, 800°C, 950°C, 1050°C, 1150°C or 1250°C. Mullite gel-glass, heated at 600°C, was used for synthesis of composite materials in the mullite-apatite system. The fluorapatite $[Ca_5(PO_4)_3F]$ was synthesized from hydroxyapatite $[Ca_5(PO_4)_3OH]$ and ammonium fluoride (NH_4F) by heating to 500°C for 2 hours. Samples were prepared by mixing and homogenization of fluorapatite and mullite gel-glass in the concentration range from 10 to 90 mol%. All gels were dried at 100°C for 24 hours and than heated to 950°C, 1050°C, 1150°C or 1250°C for 1 hour. Lower firing temperatures (<950°C) led to largely amorphous products.

Phase formation was followed by means of X-ray diffraction (Diffractometer DRON-UM1, CuK_α radiation) and IR-spectroscopy (Spectrometer Specord M-80).

Results and Discussion

XRD traces of heat treated $1.5SiO_2 \cdot 0.5P_2O_5 \cdot 1Al_2O_3 \cdot 1CaO \cdot 0.5CaF_2$ gels are presented in Fig. 1(a) and (b). It was established that crystallization begins at 950°C and that the main crystalline phases are apatite and mullite. It has previously been found that in materials with similar starting compositions, the formation of crystals within the amorphous matrix starts at 950°C and that the sizes of the crystals vary from 0.05 to 1 μm [5]. For samples in which the CaF_2 was added before gelation, peaks of fluorite are absent after the heat treatment at 950°C. For the sample in which the CaF_2 was added after gelling, these peaks are present after the heat treatments at 950°C and at 1050°C. After higher temperature heat treatments the intensity of the mullite and fluorapatite peaks decreases and gehlenite peaks appear. In both cases at 1250°C, the anorthite also appears as one of the main crystalline phases. It is seen that the best apatite-mullite glass-ceramics can be synthesized from gels prepared with addition of

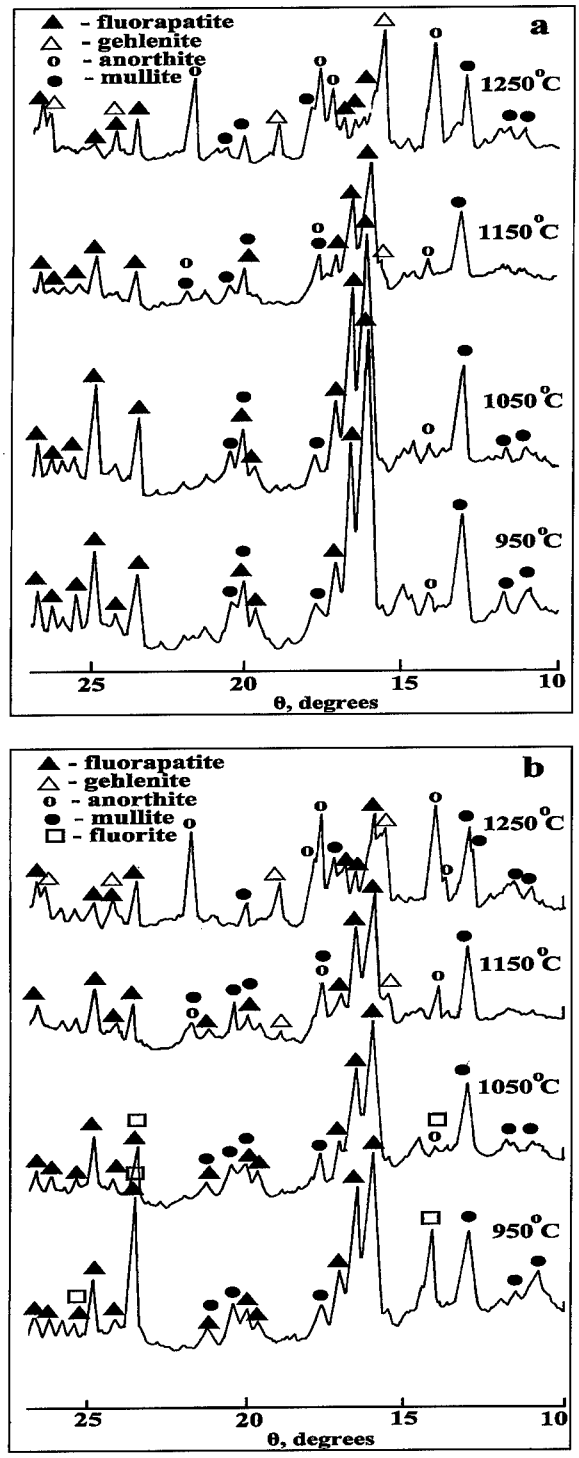

Figure 1. X-ray patterns of heat treated gels with composition: $1.5SiO_2 \cdot 0.5P_2O_5 \cdot 1Al_2O_3 \cdot 1CaO \cdot 0.5CaF_2$: (a) addition of CaF_2 before gelling; (b) addition of CaF_2 after gelling.

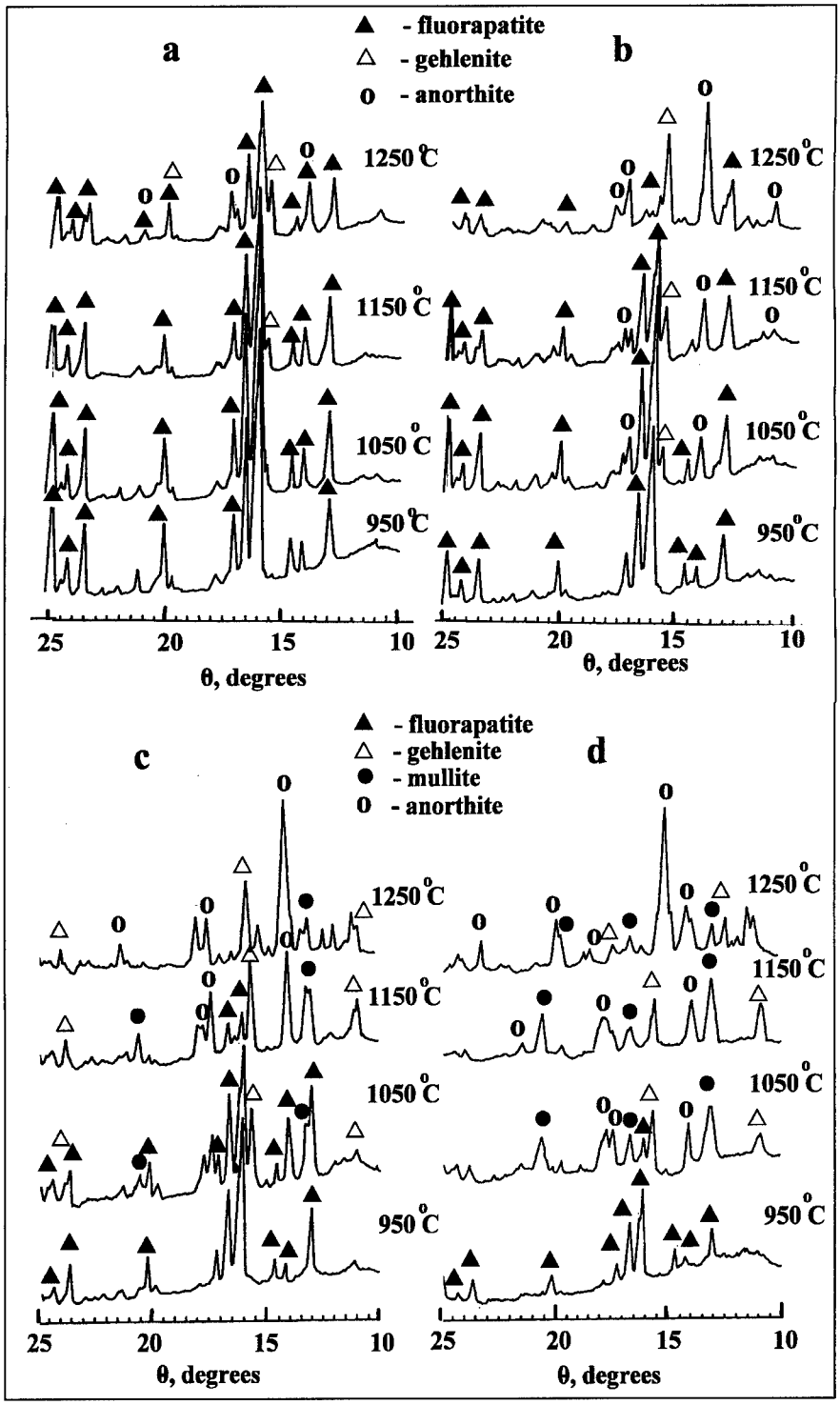

Figure 2. X-ray patterns of heat treated composite gels: (a) 20 mol% mullite gel-glass; (b) 40 mol% mullite gel-glass; (c) 60 mol% mullite gel-glass; (d) 80 mol% mullite gel-glass.

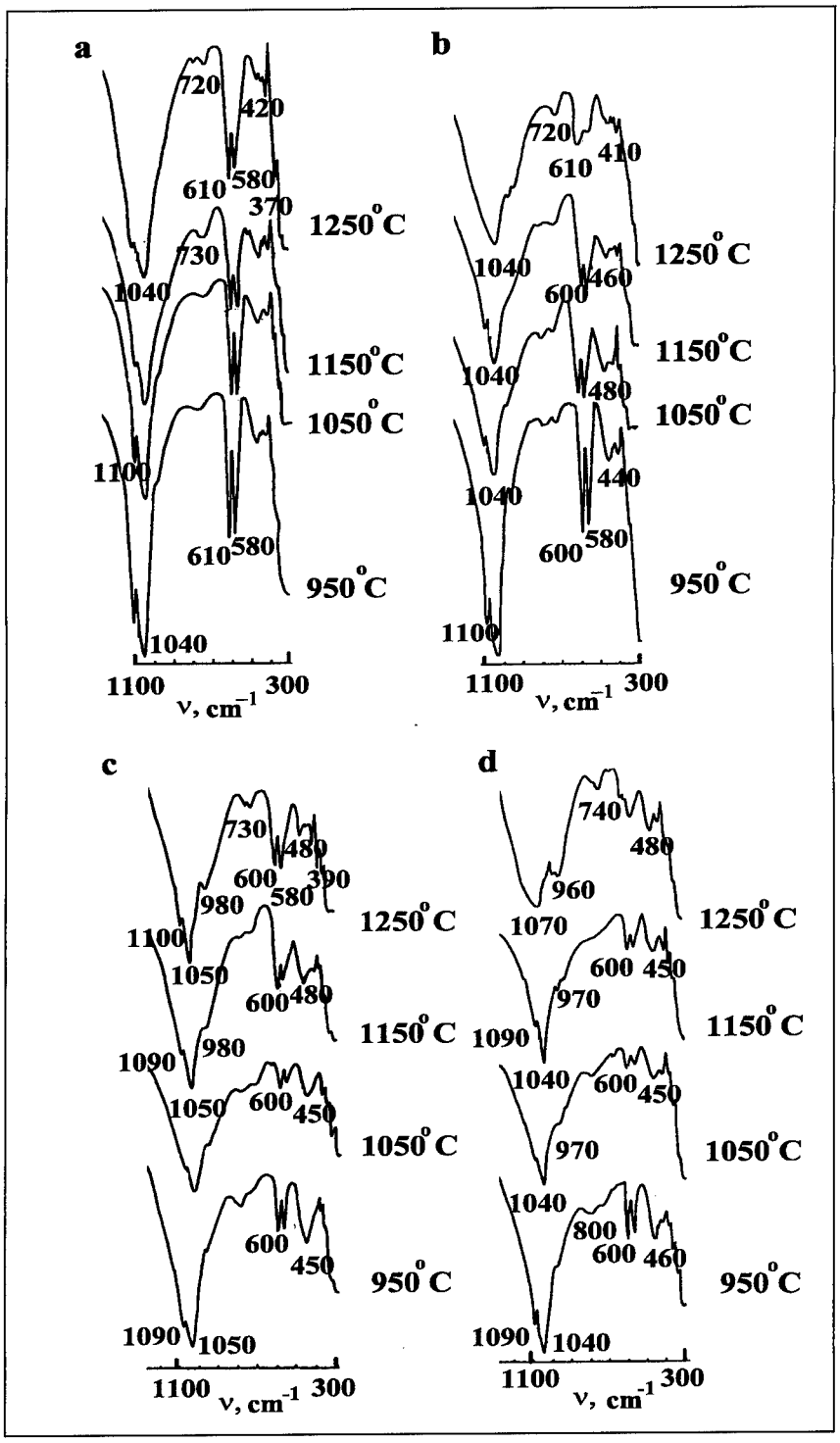

Figure 3. IR spectra of heat treated composite gels: (a) 20 mol% mullite gel-glass; (b) 40 mol% mullite gel-glass; (c) 60 mol% mullite gel-glass; (d) 80 mol% mullite gel-glass.

CaF_2 before gelation and heated to 950°C and 1050°C (Fig. 1(a)).

XRD of the synthesized fluorapatite heat treated at elevated temperature show that this phase is stable till 1250°C. The result is quite different if the mullite gel-glass is added to fluorapatite Fig. 2. In the sample, that contains 20 mol% amorphous mullite, fluorapatite is the only crystalline phase after heat treatment at 950°C and 1050°C. At 1250°C the amount of the fluorapatite decreases and gehlenite and anorthite are present as well (Fig. 2(a)). The fluorapatite is also the main crystalline phase in the 40 mol% mullite sample heat treated at 1150°C (Fig. 2(b)); in the 60 mol% mullite sample heat treated at 1050°C (Fig. 2(c)) and in the 80 mol% mullite sample heat treated at 950°C (Fig. 2(d)). At temperatures higher than the temperatures cited above three crystalline phases predominate—gehlenite, anorthite and mullite. In these cases P_2O_5 and fluor probably remain in the amorphous phase. For example, in the sample containing 70 mol% mullite gel-glass and heat treated at 1250°C it is possible to obtain glass-ceramic materials only with one crystalline phase which is the anorthite. XRD shows that crystalline mullite is only formed in the samples that contain 60 mol% or more mullite gel-glass (Fig. 2(c) and (d)). It is noteworthy that in all samples, including the 90 mol% mullite gel-glass sample, only fluorapatite exists at 950°C, while in pure amorphous mullite composition crystalline mullite is formed at the same temperature.

The IR spectrum of pure fluorapatite is characterized by a triple band at 1100, 1050, 970 cm^{-1} and a well defined absorption double band at 607, 577 cm^{-1} [26]. These bands are related to the stretching and bending vibrations of the PO_4-tetrahedra in the fluorite structure. IR spectra of the investigated samples are presented in Fig. 3. IR spectra of the sample with 20 mol% mullite (Fig. 3(a)) show that for the whole temperature range studied fluorapatite is the main crystalline phase. With increasing mullite content the main bands of fluorapatite remain in IR spectra of samples heat treated at temperatures up to 1150°C (Fig. 3(b), (c), and (d)). A considerable change occurs in the spectra of the samples heat treated at 1250°C. The high frequency maximum in the range 900–1200 cm^{-1} expands and a new well defined band at 960–940 cm^{-1} appears. This expansion and the appearance of the new band in this frequency range could be connected with the formation of new silicate phases. One of them is anorthite, because the absorption band at 960 cm^{-1} is typical for this phase. The IR spectral results are in good agreement with the X-ray data.

Conclusions

During crystallization of gels of composition 1.5 $SiO_2 \cdot 0.5P_2O_5 \cdot 1Al_2O_3 \cdot 1CaO \cdot 0.5CaF_2$ at 950–1150°C fluorapatite and mullite are formed as main phases. At 1250°C the amount of fluorapatite decreases and gehlenite and anorthite are also present in the samples.

XRD and IR analysis of the composite gels show that three main types of glass-ceramic materials can be synthesized depending on the chemical composition and the thermal treatment of the samples: (1) glass-ceramics containing only one crystalline phase, fluorapatite, and an amorphous phase of mullite composition; (2) glass-ceramics containing two or three crystalline phases—fluorapatite, gehlenite and anorthite or mullite; (3) glass-ceramics containing one, two or three crystalline phases, without crystalline fluorapatite. In these case the P_2O_5 and the fluor are included in the amorphous phase.

Acknowledgment

We would like to acknowledge the financial support from the EU under the COPERNICUS Project No. ERB3512PL940583, Contract No. CIPA-CT94-0145.

References

1. R. Hill, M. Patel, and D. Wood, in *Bioceramics*, edited by W. Bonfield, G. Hastings, and K. Tanner (Butterworth Heinemann London, 1991), Vol. 4, p. 79.
2. R. Hill, C. Goad, and D. Wood, J. Amer. Cer. Soc. **75**, 778 (1992).
3. A. Clifford and R. Hill, J. Non-Cryst. Solids **196**, 346 (1996).
4. M. Dimitrova-Lukacs and L. Gillemot, *Third Euro-Ceramic*, Spain (1993), Vol. 3, p. 179.
5. B. Samuneva, R. Hill, V. Dimitrov, and S. Kalimanova, in *Proc. Intern. Symp. on Glass Problems*, edited by R. Akcakaya, N. Erinc, G. Albayrak, and S. Isevi, Istanbul, Turkey (1996), Vol. 2, p. 244.
6. S. Mukherjee, I. Zarzycky, and J. Traverse, J. Mat. Sci. **11**, 341 (1976).
7. D. Uhlmann, M. Weinberg, and G. Teowee, J. Non-Cryst. Solids **100**, 154 (1988).
8. M. Nogami, J. Matt. Sci. **21**, 5313 (1986).

9. M. Nogami, K. Nagasaka, K. Kadono, and T. Ishimoto, J. Non-Cryst. Solids **100**, 298 (1988).
10. M. Chen, W.E. Lee, and P.F. James, J. Non-Cryst. Solids **147/148**, 532 (1992).
11. B. Unger, H. Jancke, R. Muller, B. Peplinski, and M. Hahnert, Glastech. Ber. Glass Sci. Technol. **67C**, 448 (1994).
12. B. Samuneva, Y. Dimitriev, V. Dimitrov, Y. Ivanova, E. Kashchieva, and P. Djambaski, in *Proc. 11th Inter. Congress on Glass*, Leningrad (1989), Vol. 2a, p. 26.
13. B. Samuneva, V. Dimitrov, E. Kashchieva, V. Chernev, and P. Hinkov, Glastech. Ber. Glass Sci. Technol. **67C**, 440 (1994).
14. P. Li, K. de Groot, and T. Kokubo, *Third Euro-Ceramics*, Spain (1993), Vol. 3, p. 101.
15. P. Li and K. de Groot, J. Sol-Gel Sci. Technol. **2**, 797 (1994).
16. P. Li, C. Ohtashki, and T. Kokubo, J. Amer. Cer. Soc. **75**, 2094 (1992).
17. Y. Ivanova, E. Spasova, Y. Dimitriev, B. Samuneva, and E. Kashchieva, J. Sol-Gel Sci. Technol. **2**, 819 (1994).
18. Bulg. Patent No. 51696/11.07.1994.
19. K. Cholewa and M. Zaczka, in *Proc. Intern. Symp. on Glass Problems*, edited by R. Akcakaya, N. Erinc, G. Albayrak, and S. Isevi, Istanbul, Turkey (1996), Vol. 2, p. 89.
20. D. Hoffman, R. Roy, and S. Komarmeni, J. Amer. Cer. Soc. **67**, 468 (1984).
21. S. Sakka and K. Kamiya, J. Non-Cryst. Solids **42**, 40 (1980).
22. M. Fukuoka, Y. Onoda, S. Inoue, K. Wada, A. Nukui, and A. Makihita, J. Sol-Gel Sci. Technol. **1**, 47 (1993).
23. I. Jaymes and A. Douy, J. Amer. Cer. Soc. **75**, 3154 (1992).
24. I. Jaymes, A. Douy, M. Gervais, and J.P. Coutures, J. Sol-Gel Sci. Tech. **8**, 415 (1997).
25. Y. Dimitriev, B. Samuneva, D. Wood, E. Kashchieva, and E. Gattef, in *Proc. Intern. Symp. on Glass Problems*, edited by R. Akcakaya, N. Erinc, G. Albayrak, and S. Isevi, Istanbul, Turkey (1996), Vol. 2, p. 314.
26. R.Y. Zinuk, A.G. Balikov, I.B. Gavrilenko, and A.M. Sheviakov, *IR-Spectroscopy in Inorganic Technology* (Chimia, Leningrad, 1983), p. 147, in Russian.

Journal of Sol-Gel Science and Technology 13, 957–960 (1998)
© 1998 Kluwer Academic Publishers. Manufactured in The Netherlands.

Structural Efficiency and Microstructural Modeling of Wet Gels and Aerogels

JOACHIM GROSS AND GEORGE W. SCHERER
Princeton University, Department of Civil Engineering and Operations Research, E-Quad E-228, Princeton, NJ 08544, USA
joegross@phoenix.princeton.edu

Abstract. We present a microstructural model of aerogels that includes the effect of particle necks, tortuosity and dangling ends on the scaling of elastic moduli with density. Relative neck radii can be determined for sintering series of silica aerogels and for Resorcinol Formaldehyde (RF) aerogels produced with different catalyst concentrations. The density of elastically ineffective dangling ends and the tortuosity can be estimated using information from thermal conductivity and elastic modulus measurements in silica aerogels. Typical values for the load bearing mass range from >50% for high density and heat treated aerogels to <10% of the total mass for low density wet-gels.

Keywords: elastic modulus, aerogels, microstructure, structural efficiency

Introduction

The elastic properties of sol-gel materials play an important role both during production and in the application, e.g., during drying of gels [1] or to withstand influences from a rough industrial environment [2]. Inorganic aerogels suffer specifically from their low moduli and brittleness. This inhibits their use in many cases even though their other properties seem to set them apart as ideal candidates. It must be noted that many macroporous (metallic, polymeric or even ceramic) foams of comparable or even lower relative density are stronger by an order of magnitude.

This apparent weakness of low density sol-gel materials was mentioned before and attributed to a low mechanical efficiency of the random gel network [3], but no attempt was made to quantify it and to relate it to specific microstructural features. The scaling of elastic modulus M with density ρ of the form

$$\frac{M}{M_o} = \left(\frac{\rho}{\rho_o}\right)^{\alpha} \tag{1}$$

(α is the scaling exponent) in gels and aerogels was the subject of numerous publications, e.g., [4–6]. In a recent paper the elastic properties of resorcinol formaldehyde gels and aerogels were analyzed and their elastic efficiency was discussed in greater detail [7]. This work applies the same principles to data published for gels in other systems, including organic, silica and carbon aerogels.

Theory

It has been shown that the elastic moduli of three-dimensional cellular materials, like foams, scale with the second power of relative density. This scaling behavior is quite independent of the details of the microstructure and mainly relies on the assumption that bending of the members is the predominant deformation mechanism. While it was derived for low densities only, experimental results for foams showed that it approximately holds up to fully dense, nonporous materials [8]. In contrast to gels, foams tend to have a fairly ideally connected structure, with basically straight members. This is due to the action of surface tension during growth of bubbles in the viscous polymer melt. Gels grow in a much more statistical manner and deviate from this elastically rather effective

structure in several ways: The connection between nodes is not straight (tortuosity t), their diameter is not uniform (string-of-beads with relative neck radius a) and there is elastically ineffective mass (dead ends connected to the network on one end only). In the following we start from an elastically effective, foamlike structure assumed to be located on a scaling line with slope 2 in a log modulus versus log density plot. The derivation of the scaling relationship in detail will be published separately [9].

The string-of-bead like structure of aerogels is obtained by removing material from the cylindrical members such as to mimic spherical particles fused together. The relative neck radius a, defined as $a = r_{\min}/r_{\max}$, will be considered as the only variable because the length of the indentations is related to their depth. Because of this relation the bending stiffness of an indented member scales as a^2, not as a^4 as was previously assumed [10]. The mass is not dramatically changed by introducing the necks. It varies approximately as

$$\frac{m}{m_s} = \frac{2}{3} + \frac{1}{3}a^3, \tag{2}$$

which approaches 1 for $a = 1$ and 2/3 for $a = 0$ (in the case of sintering aerogels, the relation of modulus and density is a little different, because the mass in the structure is constant, but the cell size changes). The reduction of modulus M below the scaling line and the evolution of the density as a function of a have the approximate form

$$\frac{M}{M_s} = \left\{\frac{3a}{2+a^3}\right\}^2, \quad \frac{\rho}{\rho_o} = \left\{\frac{2+a^3}{3}\right\}^3, \tag{3}$$

where the subscript s denotes the modulus on the scaling line at the density ρ. The first relation is plotted in Fig. 1.

A very rough approximation yields the result that the modulus scales as t^{-1}, where t is the tortuosity factor defined as the ratio of the length of the member and the distance between its end points ($t > 1$). The basic argument is that the bending moment (and therefore also the bending angle) is proportional to the distance between a given segment of a tortuous member and the line of force. The total compliance, integrated over the length of the member, can thus be expected to roughly scale with its total length. The density obviously increases proportional to the tortuosity. Introducing tortuosity therefore increases the density while it decreases the stiffness of the network.

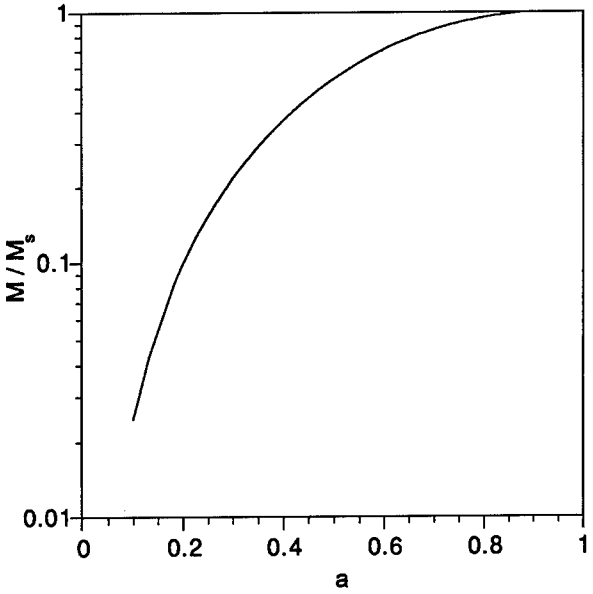

Figure 1. Relative elastic modulus M/M_s during initial sintering as function of relative neck radius a according to Eq. (3).

The last alteration with respect to an ideally connected foam structure is the addition of elastically inefficient mass. During gelation "fuzzy" clusters grow in solution until they become large enough to touch and intertangle, creating random connections between each other. It can be expected that only part of the strings do in fact connect while a large fraction remains attached to only one cluster and therefore does not carry any load upon deformation of the network. This part of the structure with density ρ_d only contributes to the total density, not to the modulus.

All of the above scaling relationships are also correct for a combination of tortuosity, necks and dangling mass. Figure 2 shows the scaling of modulus versus density as result of the structural features. All of them cause gels to be less elastically efficient than foams. In the next section we will try to quantify realistic ranges for the parameters a, t and ρ_d.

Parameters from Experiments

Two aerogel systems allow estimation of the relative neck radii, namely sintering series of silica aerogels and Resorcinol Formaldehyde (RF) aerogels synthesized with different catalyst concentrations.

During the earliest stage of sintering lightly connected spherical particles develop a larger neck area.

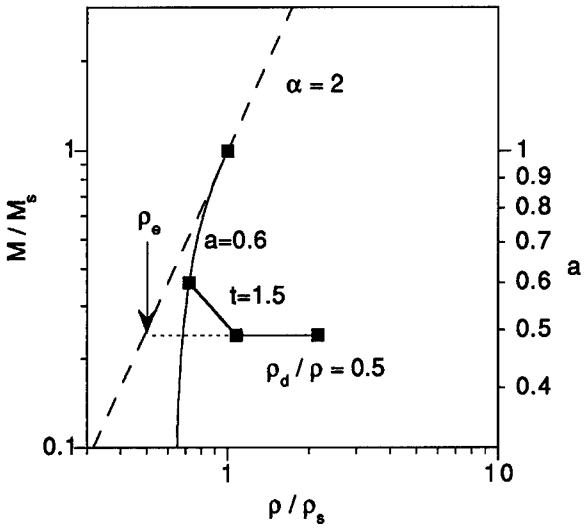

Figure 2. Relative modulus M/M_s as function of the relative density ρ/ρ_s. The influence of necks (relative neck radius a), tortuosity t and density of dangling mass ρ_d, on modulus and density of aerogels. ρ_s and M_s are the density and modulus of a gel with straight, cylindrical members without dangling mass. ρ_e is the elastically effective density and the dashed line represents the foam scaling with exponent 2.

This leads to a rapid increase of the elastic moduli. After the necks have disappeared, the members of the network become shorter and thicker [11]. In the framework of this model that would lead to a scaling exponent for the modulus of 2.0. However, increased connectivity (scaling of ρ_d) can lead to a higher scaling exponent [5]. It is therefore advisable to establish a scaling line from samples of the same series with supposedly no necks and evaluate the reduction of the modulus of necked samples below that scaling line. Reexamination of the data in [10] along these lines yields values for the relative neck radius a of 0.52 and 0.64 for the samples with initial density 122 and 256 kg m^{-3}, respectively (to be compared to δ in Table 1 of that paper, 0.68 and 0.83). The lower values obtained with the new analysis are consistent with the weaker scaling of the modulus with a, and are also closer to values around 0.5, determined from strength and moduli of silica aerogels [12]. It has to be noted here that due to other possible stiffening effects during initial sintering (e.g., increased crosslinking) the neck radii obtained here are probably lower bounds for the actual values.

RF aerogels produced with different monomer to catalyst (RC) ratio exhibit a continuous transition between polymerlike, smooth chains (low RC) and a distinctly beadlike structure. RC 50 aerogels are about seven times stiffer than RC 300 at the same density. The scaling exponents are independent of the RC ratio, indicating a similar network structure [13]. TEM micrographs of RC 50 aerogels do not show necks ($a = 1$). The modulus at a given density scales with a^2, therefore, the relative neck radii are directly given by

$$a_{\mathrm{RC}} = \sqrt{\frac{M_{\mathrm{RC}}}{M_{50}}}. \tag{4}$$

The result is $a_{200} = 0.58$ and $a_{300} = 0.37$ for RC 200 and 300, respectively. The modulus values were obtained by calculating the modulus at a density of 100 kg m^{-3} from the scaling parameters given in Table 1 of [14]. TEM micrographs of RC 300 RF aerogels (e.g., Fig. 4.7 in [13]) reveal necking that is compatible with the obtained value for a_{300}.

To our knowledge no explicit values have been published for the network tortuosity (not to be confused with the pore tortuosity). However, a combined geometrical constant ("pathway constant p") for thermal conductivity of silica aerogels was derived [15]. It allows to estimate the tortuosity to be between 1.5 and 2 for aerogels with relative densities between 0.05 and 0.15.

The mass in dangling ends is most difficult to quantify since it depends on the connectivity of the gel structure. We will discuss its contribution after introducing the elastic efficiency in the next section.

Elastic Efficiency

It was mentioned above that foams are elastically efficient and exhibit a scaling exponent $\alpha = 2.0$. An intuitive measure of the elastic efficiency of gels and aerogels is the ratio of the elastically effective density ρ_e and the measured density ρ. It can be obtained from

$$\frac{\rho_e}{\rho} = \frac{\rho_0}{\rho}\sqrt{\frac{M}{M_0}}, \tag{5}$$

where the subscript 0 refers to the skeleton material [7]. Figure 2 indicates how ρ_e can be determined graphically and Fig. 3 shows some values for wet gels and aerogels. As was shown for RF gels in [7] the efficiency of most the gels decreases with density. However, for extremely low density silica aerogels the trend seems to slow down. This might be due to the fact that

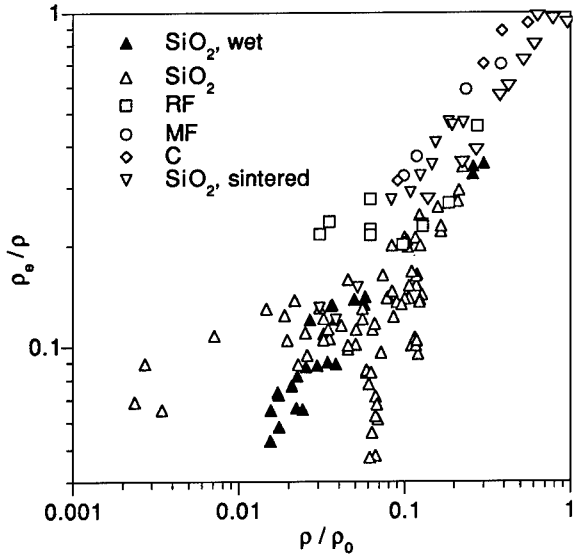

Figure 3. Fraction of elastically effective density, ρ_e/ρ, as function of relative density ρ/ρ_0 for aerogels of various materials, and some wet silica gels. The sintering series denoted by big triangles was adapted from Fig. 9 of [5].

a minimum stiffness of the gels is necessary to stay monolithic during the drying process, therefore weak low density aerogels might simply not exist. It is also interesting to note that organic and carbon aerogels seem to be more efficient than silica aerogels. For the formation of RF aerogels spinodal decomposition rather than cluster-cluster aggregation was suggested as the growth process [16]. It can be expected that this would lead to a higher connectivity because in this process phase boundaries do play a role, in accordance with the higher structural efficiency we find. As was noted before for RF gels [7], wet silica gels are usually also less efficient than aerogels, probably due to continued crosslinking and increased connectivity during supercritical drying with respect to methanol. This is even true for partially dried gels of relatively high densities. It fits into this picture that CO_2 dried silica aerogels have the lowest efficiency (<0.1) at moderate relative densities around 0.06.

The loss of elastic efficiency due to various structural features can be estimated from Fig. 2 from the horizontal distance between the solid lines and the dashed scaling line. For the combination of $a = 0.6$ and $t = 1.5$, which can be considered typical for relative densities around 0.1, ρ_e is about half of the total density ($\rho_e/\rho = 0.45$). Figure 3 shows that the fraction of effective density is between 0.1 and 0.3 in this area, so the dangling mass accounts for 50 to 80% of the total mass in these specimens.

Conclusion

We have shown in this paper that the influence of several non-ideal features of sol-gel materials on elastic moduli can be quantified from a theoretical point of view. The main advantage of the approach taken here is that it does not rely on calculating elastic moduli based on highly idealized structural models, but instead studies the change of modulus and density upon alterations to the network. In certain series of gels it is possible to estimate the contribution of specific features. We arrive at relative neck radii between 0.5 and 0.6 in accordance with published results obtained by different methods. The most important factor that keeps the elastic efficiency of aerogels low is the mass in dangling ends, or the low connectivity. Further attention should be addressed to the tortuosity of the network. Our guesses are rather inaccurate, but could be improved by including thermal conductivity into the analysis.

References

1. G.W. Scherer, J. Non-Cryst. Solids **145**, 33 (1992).
2. O. Krauss, R. Gerlach, and J. Fricke, Ultrasonics **32**(3), 217 (1994).
3. J.D. LeMay, Mat. Res. Soc. Symp. Proc. **207**, 21 (1991).
4. R.W. Pekala, L.W. Hrubesh, T.M. Tillotson, C.T. Alviso, J.F. Poco, and J.D. LeMay, Mat. Res. Soc. Symp. Proc. **207**, 197 (1991).
5. T. Woignier, J. Phalippou, H. Hdach, and G.W. Scherer, Mat. Res. Soc. Symp. Proc. **180**, 1087 (1990).
6. J. Groß and J. Fricke, NanoStructured Materials **6**, 905 (1995).
7. J. Gross, G.W. Scherer, C.T. Alviso, and R.W. Pekala, J. Non-Cryst. Solids **21**, 132 (1997).
8. L.J. Gibson and M.F. Ashby, Proc. R. Soc. London **A382**, 43 (1982).
9. J. Gross, J. Non-Cryst. Solids, submitted.
10. A. Emmerling, J. Gross, R. Gerlach, R. Goswin, G. Reichenauer, J. Fricke, and H.-G. Haubold, J. Non-Cryst. Solids **125**, 230 (1990).
11. G.W. Scherer, S. Calas, and R.Sempéré, *Sintering of Aerogels*, this volume.
12. T. Woignier and J. Phalippou, J. Non-Cryst. Solids **100**, 404 (1988).
13. J.D. LeMay, R.W. Hopper, L.W. Hrubesh, and R.W. Pekala, MRS Bulletin **XV**(12), 19 (1990).
14. R.W. Pekala, C.T. Alviso, and J.D. LeMay, J. Non-Cryst. Solids **125**, 67 (1990).
15. P. Scheuerpflug, M. Hauck, and J. Fricke, J. Non-Cryst. Solids **145**, 196 (1992).
16. D.W. Schaefer, R.W. Pekala, and G. Beaucage, J. Non-Cryst. Solids **186**, 159 (1995).

Journal of Sol-Gel Science and Technology 13, 961–967 (1998)
© 1998 Kluwer Academic Publishers. Manufactured in The Netherlands.

Laser Sintering of SnO_2 : Sb Sol-Gel Coatings

D. GANZ, G. GASPARRO AND M.A. AEGERTER
Institut für Neue Materialien—INM, Im Stadtwald, Gebäude 43, D-66123 Saarbrücken

Abstract. Sb doped sol-gel SnO_2 single layers (thickness ≈100 nm) were prepared from alcoholic solution and deposited via a dip coating process on fused silica substrates. The coatings have been sintered at a typical rate of 10–15 cm^2/s by CO_2 laser irradiation. The laser spot was scanned in one direction at a speed of 15,000 cm/s and the sample was moved in a perpendicular one at a speed up to 250 mm/s. The temperature of the topmost 10 μm layer was monitored by a fast pyrometer (μs resolution). The following properties of the coatings have been determined: the electrical resistivity ρ, the carrier density n, and mobility μ, the structure, the thickness, the mesoscopic and micromorphology and the density. The sintering by CO_2 laser radiation is mainly a thermal driven process. At $T \approx 500°C$ it allows to obtain coatings with a smaller resistivity (6.8×10^{-3} Ω cm) than those produced by conventional furnace firing ($\rho_{el} \approx 2.9 \times 10^{-2}$ Ω cm). The results are discussed in terms of particle size and packing density.

Keywords: sol-gel, thin film, SnO_2 : Sb, transparent conducting coatings, laser densification, electrical properties, morphology

1. Introduction

The sol-gel process enables homogeneous oxide films to be obtained using the dip or spin coating technique. The coatings are usually dried and fired in two separate processes in a furnace [1, 2]. The high temperature needed for the densification of the coatings, usually ≈500°C, and the repetition of the deposition and thermal processes necessary to produce thick coatings are drawbacks as the major speed-limiting factor of the coating process is the substrate/coating cooling rate.

During the last decade several attempts have been made to overcome these disadvantages by using electromagnetic radiation (EM) such as UV, visible or IR radiation as a densification energy source. In this process the EM radiation is absorbed either in the film or the substrate and converted locally into heat. Several authors densified films by scanning a low power laser spot at low speed (up to 2 cm/s) across the surface, resulting in a surface firing speed of 0.2 cm^2/s [3–8].

This work presents data on the densification of electronic conductive transparent sol-gel SnO_2 : Sb (5 mol%) films fired at high speed (up to 15 cm^2/s) by a CO_2 cw laser. Comparison between laser fired and conventionally furnace fired coatings is also addressed.

2. Experimental

Sb doped sol-gel SnO_2 : Sb films were prepared from alcoholic solution and deposited via a dip coating process (one layer only) with a drawing speed of 5 mm/s on 5×2 cm^2 fused silica substrates. The thickness of the coatings dried at 25°C, measured with a Tencor P 10 Surface Profiler, was 158 nm for all samples. The preparation procedure of the sols [9] and the description of the laser setup [10] is given elsewhere. Some of the samples were fired in a furnace in air at 550°C for 15 min and the others were subjected to CO_2 laser densification reaching the same temperature.

The local temperature of the coatings is monitored by a fast pyrometer measuring in the spectral range of 7.3 to 9.3 μm with a detector rise time of 3 μs and a spatial resolution $d_{spot} = 0.5$ mm.

In the *fast scan* mode the laser beam is focused onto a rotating 14 plane mirrors polygon scanner and

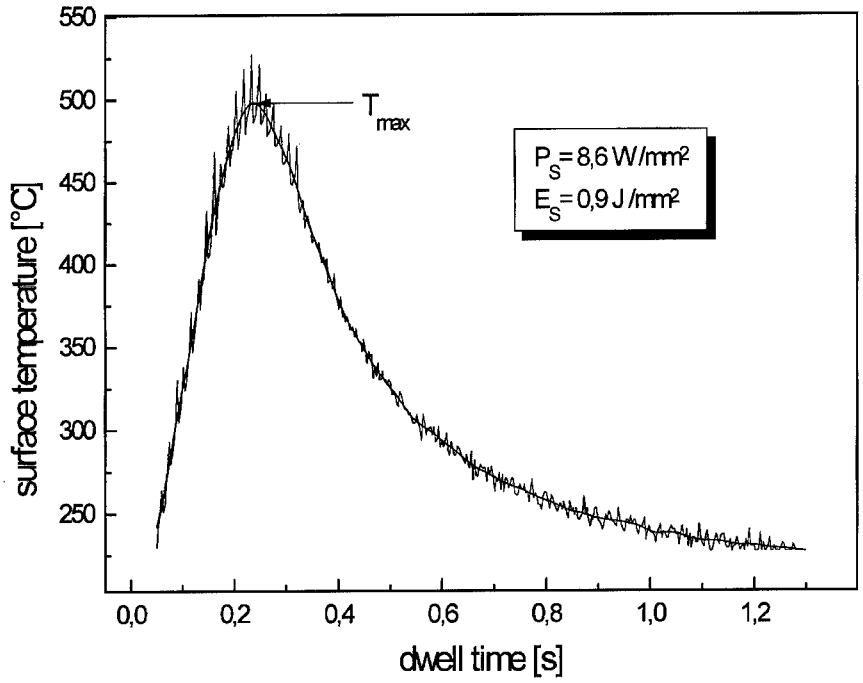

Figure 1. Typical surface temperature recorded during a fast scan mode. The smooth line is a Fast Fourier Transform of the data drawn to better determine T_{max}.

scanned in the y direction at a very high speed (up to ≈20,000 cm/s) resulting in a laser streak as small as 0.1 mm in width. This streak can be moved along a perpendicular direction at a speed up to 250 mm/s. In this way, areas can be densified at a typical rate of 10–15 cm^2/s, a much larger value than those previously reported [11]. The focused beam integral output power delivers up to 560 kW/cm^2 to the samples.

The coatings have been characterized by several methods. The electrical properties of the coatings (resistivity ρ, carrier density n, electron mobility μ, and sheet resistance R) have been determined using a van der Pauw-Hall equipment (MMR Technology). The coating structure has been determined by X-ray diffraction (XRD) at glancing incidence using a Siemens D500 equipment and a high resolution transmission electron microscope (HRTEM, Philips CM 200 FEG). The surface morphology of the films has been observed by scanning electron microscopy (SEM) (JEOL 6400 F). The coating thickness was measured with a surface profiler (Tencor P10) and the density by X-ray total reflection (XTR) and Rutherford back scattering (RBS).

3. Results and Discussion

The typical time variation of the temperature measured at a fixed spot during the laser firing is shown in Fig. 1. It exhibits spikes which are due to the many passages of the laser along the y direction as the substrate moves along the x direction. The effective surface temperature maximum (T_{max}) of the samples was defined as the maximum of the temperature curve smoothed by a fast Fourier transform (Fig. 1). Temperatures T_{max} as high as 1000°C were obtained.

In Fig. 2 the resistivity is depicted as a function of the effective surface temperature T_{max} for different laser power densities I_{st}. It decreases with increasing temperature for all laser power densities until ≈400°C and then increases rapidly at higher temperatures with a slope that increases with the power density. For $I_{st} = 5$ W/mm^2 the resistivity reaches a minimum value $\rho_{el} \approx 8 \times 10^{-3}$ Ω cm at about 500°C. For $I_{st} = 15$ W/mm^2 the minimum is $\rho_{el} \approx 6.8 \times 10^{-3}$ Ω cm and lies at $T_{max} = 375$°C. The corresponding resistivity of the furnace fired coatings gradually decreases with temperature to a minimum value $\rho_{el} \approx 9 \times 10^{-3}$ Ω cm at 700°C (Fig. 2).

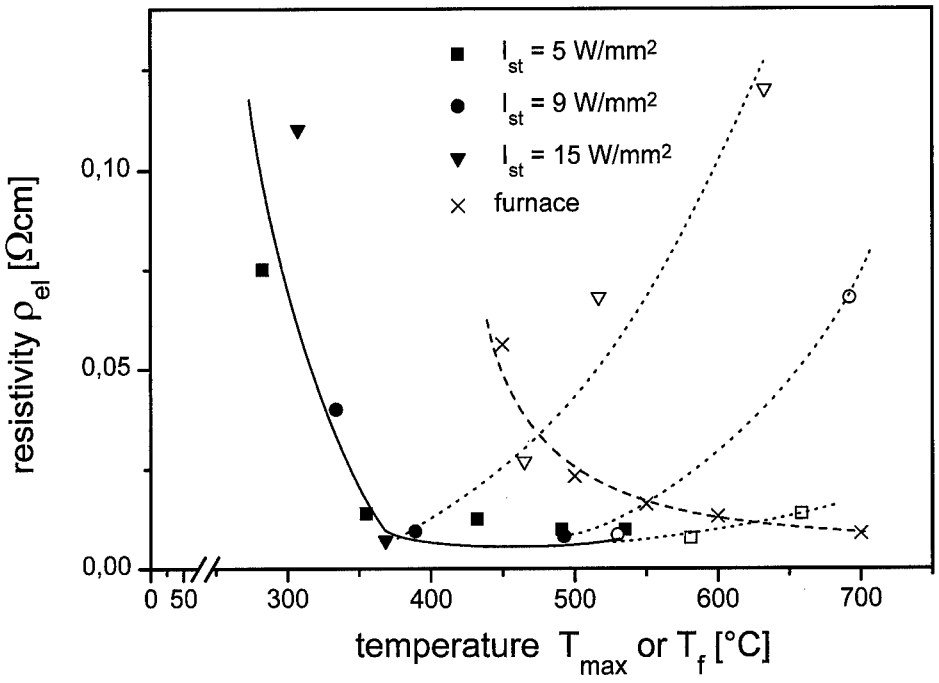

Figure 2. Variation of the resistivity ρ_{el} vs. the sintering temperature. The lines drawn are guides for the eye.

This behavior can be understood by analyzing the temperature dependence of the carrier density n and the electron mobility μ. The carrier density increases monotonically with T_{max} (Fig. 3) and saturates at a temperature of 600°C at a value of $n \approx 3 \times 10^{20}$ cm^{-3} for all heat treatment processes. For the laser treated samples the slope of the curves increases with power density. As the temperature increases the network formation due to chemical reactions occurring in the coatings increases, which leads to an increase of the carrier concentration. However at 600°C all chemical reactions are completed so that the carrier density cannot be increased any longer and reaches a maximum value ($n \approx 3 \times 10^{20}$ cm^{-3}).

The electron mobility (Fig. 4) shows a behavior complementary to that of the resistivity. It increases with increasing temperature for all laser power densities up to a certain temperature and then decreases. This decrease is faster the greater the power density is. Each curve has a maximum at a different temperature.

The behavior of μ for the samples heat treated in a furnace is different. The overall values are smaller and only slightly increase with the temperature.

The fact that the electron mobilities of all laser fired samples follow the same temperature dependence up to ≈420°C is essentially due to the network formation. At higher temperatures the crystallite size starts to increase (Fig. 5) leading to an increase of the mobility (Fig. 4).

The individual decrease for each power density is due to the formation of cracks by strong temperature gradients (Fig. 8). These cracks do not appear in furnace fired samples. The difference in the temperature dependence of the laser and furnace fired samples can be understood in terms of densification and crystal growth. The high heating rates (up to 7000 K/s) during laser firing cause a densification rather than a nucleation of the films [12]. The films are highly densified with a small number of nuclei. These nuclei grow larger as the temperature rises and the morphology of the layer is formed by large and densely packed crystallites (Figs. 6 and 7). This leads to a high electron mobility in the laser fired samples. In a furnace the coatings are fired at a low heating rate. This creates many nuclei and no significant densification. With rising temperature the large number of nuclei increases slightly resulting in a porous layer composed of small crystallites [12].

This was confirmed by Rutherford back scattering measurements [13] which gave a value of 4.8 and 3.2 g/cm^3 for the samples fired at $T = 550$°C by laser and furnace respectively, and by the HRTEM analysis (Figs. 6 and 7).

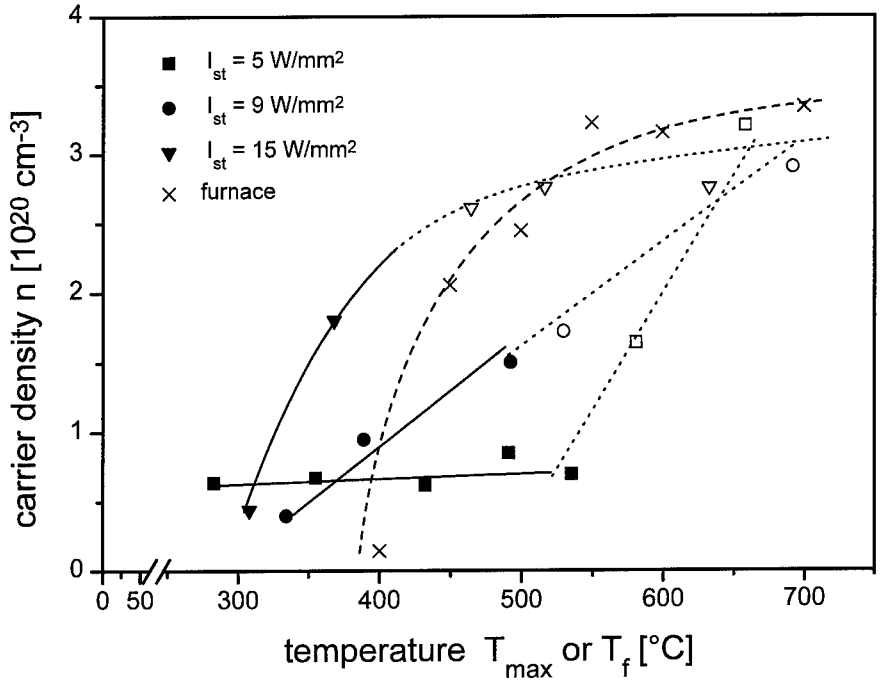

Figure 3. Variation of the carrier density n vs. the sintering temperature. The lines drawn are guides for the eye.

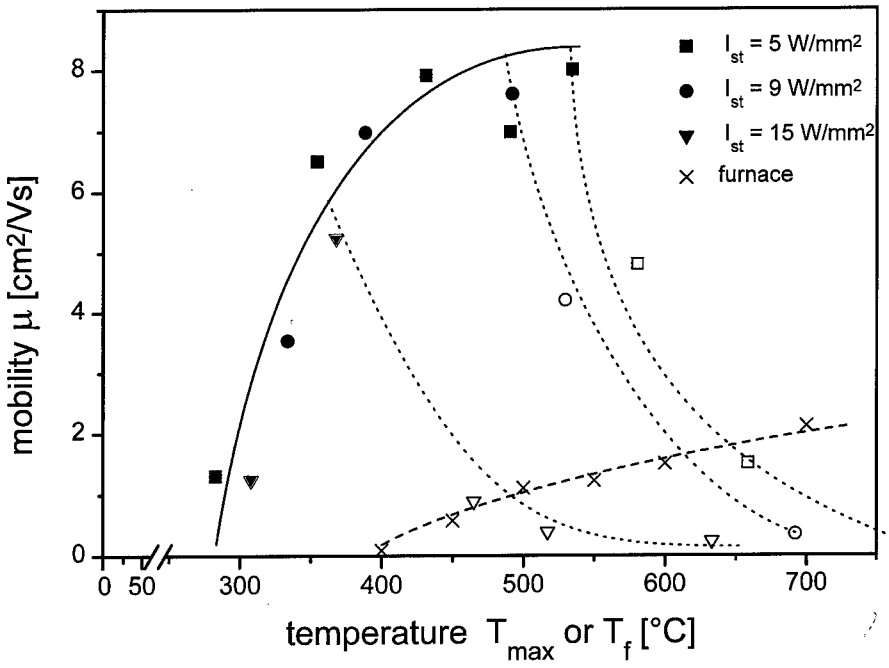

Figure 4. Variation of the electron mobility μ vs. the sintering temperature. The lines drawn are guides for the eye.

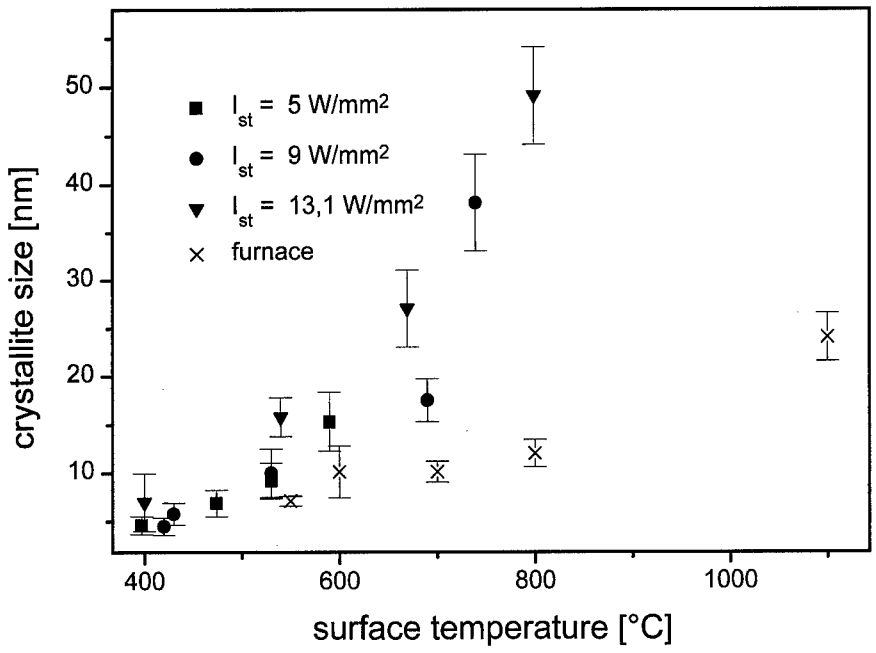

Figure 5. Temperature dependence of the crystallite size.

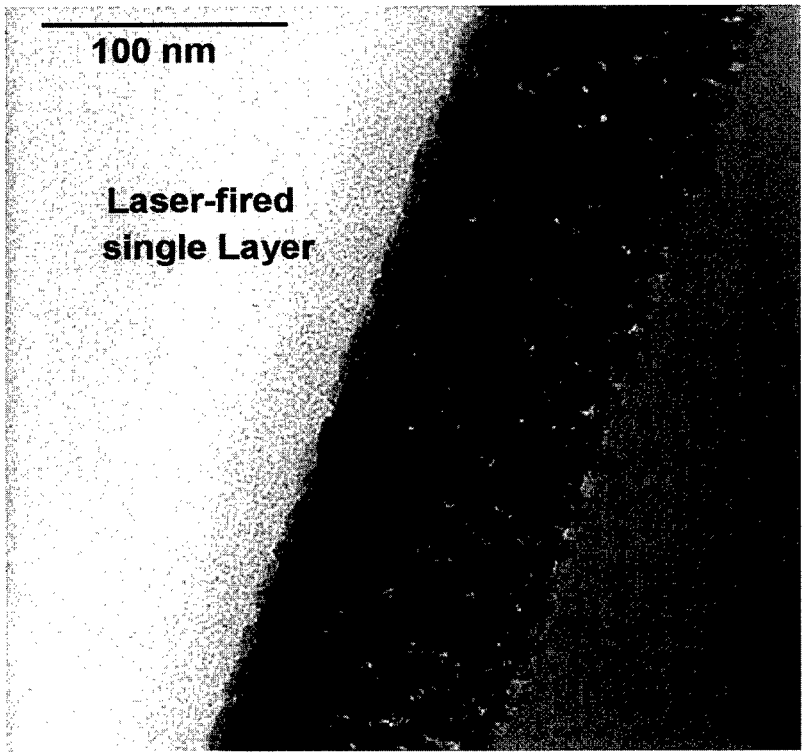

Figure 6. HRTEM cross section of a SnO_2 : Sb coating sintered at 380°C, $I = 9$ W/mm^2.

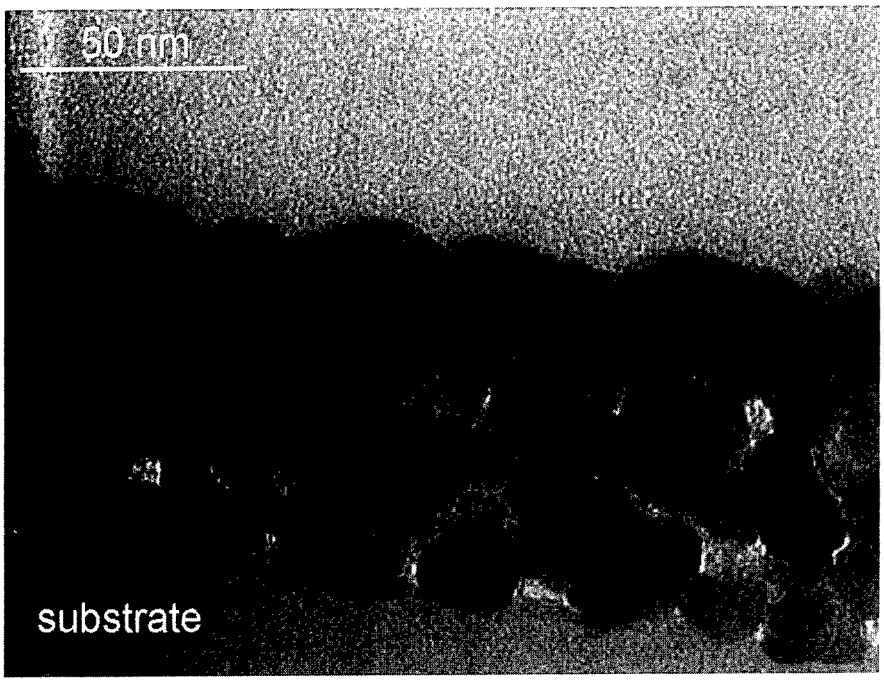

Figure 7. HRTEM cross section of a SnO_2 : Sb coating sintered at 700°C, $I = 9$ W/mm^2.

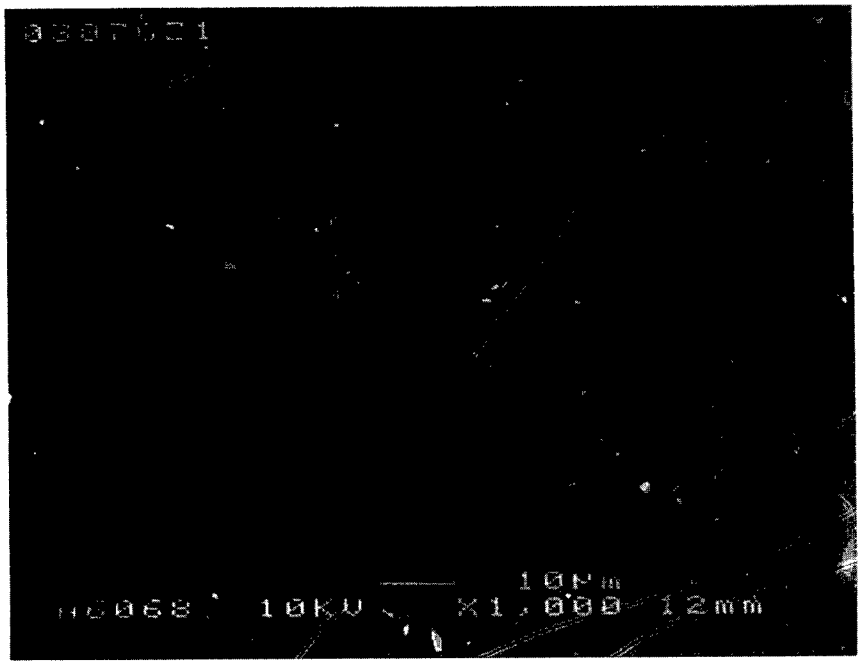

Figure 8. SEM micrograph of the surface of a SnO_2 : Sb coating sintered at 700°C, $I = 9$ W/mm^2.

4. Conclusion

Fast CO_2 laser sintering is mainly a temperature driven process. The important parameter is the effective maximum temperature. Laser firing produces denser layers with larger crystallites than those obtained by furnace firing at the same temperature. This sintering process leads to coatings that show lower resistivities than conventionally furnace fired ones. There exists a threshold for the appearance of cracks that depends on the laser power density, and which reduces the electron mobility and consequently increases the resistivity. CO_2 laser irradiation therefore appears to be an interesting way to sinter single layers of $SnO_2:Sb$ conducting coatings. Sheet resistances as low as $R_\square = 780\ \Omega_\square$ can be obtained at 500°C with a 100 nm thick coating.

References

1. H. Dislich, in *Sol-Gel Technology for Thin Films, Fibers, Preforms, Electronics and Special Shapes*, edited by L. Klein (Noyes publications, 1988), p. 50.
2. H. Schröder, in *Physics of Thin Films*, edited by E.T.G. Hass (Academic Press, 1969), Vol. 5, p. 87.
3. D.J. Taylor, B.D. Fabes, and M.G. Steinthal, Mat. Res. Soc. Symp. Proc. **180**, 1047 (1990).
4. T.C. Zaugg, Submolecular Glass Chemistry and Physics, SPIE **1590**, 27 (1991).
5. D.P. Birnie, S.M. Melpolder, B.D. Fabes, B.J.J. Zelinski, M.J. Hanrahan, D.J. Taylor, and L. Weisenbach, Sol-Gel Optics II, SPIE **1758**, 630 (1992).
6. B.D. Fabes, B.J.J. Zelinski, D.J. Taylor, L. Weisenbach, S. Boggavarapu, and D.Z. Dent, Sol-Gel Optics II, SPIE **1758**, 227 (1992).
7. N.-J. Arfsten, Patent No. 37 44 368, DE, 1989.
8. N.-J. Arfsten, B. Lintner, M. Heming, O. Anderson, and C.R. Ottermann, Mat. Res. Soc. Symp. Proc. **271**, 449 (1992).
9. G. Gasparro, D. Ganz, J. Pütz, and M.A. Aegerter, J. of Non Crystalline Solids, (1997), in press.
10. D. Ganz, G. Gasparro, J. Otto, A. Reich, N.-J. Arfsten, and M.A. Aegerter, Journal of Material Science Letters **16**, 1233 (1997).
11. B.D. Fabes, in *Sol-Gel Optics, Processing and Application*, edited by L. Klein (Kluwer Academic Publisher, 1994), p. 483.
12. J.L. Keddie and E.P. Giannelis, J. Am. Ceram. Soc. **74**, 2669 (1991).
13. M. Guglielmi, E. Menegazzo, M. Paolizzi, D. Ganz, G. Gasparro, J. Pütz, and M.A. Aegerter, to be published.

Journal of Sol-Gel Science and Technology 13, 969–974 (1998)
© 1998 Kluwer Academic Publishers. Manufactured in The Netherlands.

Silica Gels and Gel Glasses Containing Silver and Platinum Metal Particles

B. SAMUNEVA, Y. DIMITRIEV, V. DIMITROV, E. KASHCHIEVA AND G. ENCHEVA
University of Chemical Technology and Metallurgy, blvd. Kl. Okhridski 8, Sofia 1756, Bulgaria

Abstract. Silica gels containing between 0.05 and 20.0 mol% Ag_2O and between 0.1 and 1.0 mol% PtO_2 have been synthesized using TEOS, C_2H_5OH, H_2O, HNO_3, HCl, $AgNO_3$ and $PtCl_4$ as precursors. The gels obtained with Ag_2O are colorless, while the gels containing PtO_2 are yellow. The gels have been heat treated in the 25–1000°C temperature range. The processes of structural evolution of gels have been studied by means of IR-spectroscopy, X-ray diffraction analysis, transmission electron microscopy (TEM) and transmission electron microdiffraction (TEMD). It has been established that the temperature of gel to gel-glass transition decreases when the Ag_2O content of the gels increases. The same tendency was established for the gel to gel-glass transition in the SiO_2-PtO_2 system.

Special attention was paid to the formation of silver and platinum metallic particles in amorphous materials. The microstructure of the gels has been observed and the sizes of the metal particles were determined to be from 3 to 25 nm.

The crystallization processes in the gels heat treated at 1000–1200°C have been examined and besides the silver and platinum particles α-cristobalite was formed.

It has been shown that nanocomposite materials containing ultrafine silver and platinum particles in SiO_2 amorphous or polycrystalline matrixes can be obtained.

Keywords: silica gel, nanocomposite, silver, platinum

Introduction

Using sol-gel technology nanocomposites with high homogeneity and high purity containing metal particles can be obtained. There is considerable interest in such materials because of their high third-order nonlinear optical susceptibility, selective optical absorption, reflection properties, catalytic effects and photochromic properties.

In recent years sol-gel synthesis of nanocomposites containing ultrafine particles of noble metals (Au, Ag, Pt and Pd) in oxide matrices (SiO_2, TiO_2, V_2O_5 and WO_3) has been rapidly developed [1–9]. Many authors have studied the preparation and properties of coating films of these materials containing Ag and Pt particles [10–16]. They have shown that such coatings are suitable for nonlinear optical applications.

The purpose of this paper is to examine the production of bulk gels in the SiO_2-Ag_2O and SiO_2-PtO_2 systems over a wide composition range and to study the structural and phase evolution with increasing temperature.

Experimental

SiO_2-Ag_2O and SiO_2-PtO_2 gels were prepared using TEOS, C_2H_5OH, H_2O, HCl, HNO_3, $AgNO_3$ and $PtCl_4$ as precursors. Volume ratios of the main precursors TEOS : C_2H_5OH : H_2O : HCl(HNO_3) was 1 : 0.72 : 0.77 : 0.33. The content of Ag_2O in the gel composition was: 0.05, 0.1, 0.2, 0.5, 1.0, 2.0, 3.0, 5.0, 10.0 and 20.0 mol%. The content of PtO_2 in the gel composition was: 0.1, 0.2, 0.5 and 1.0 mol%.

It was accepted conditionally that the content of silver and platinum can be expressed as oxide forms. Other chemical bonds may in fact form and therefore the systems studied are more complicated than assumed.

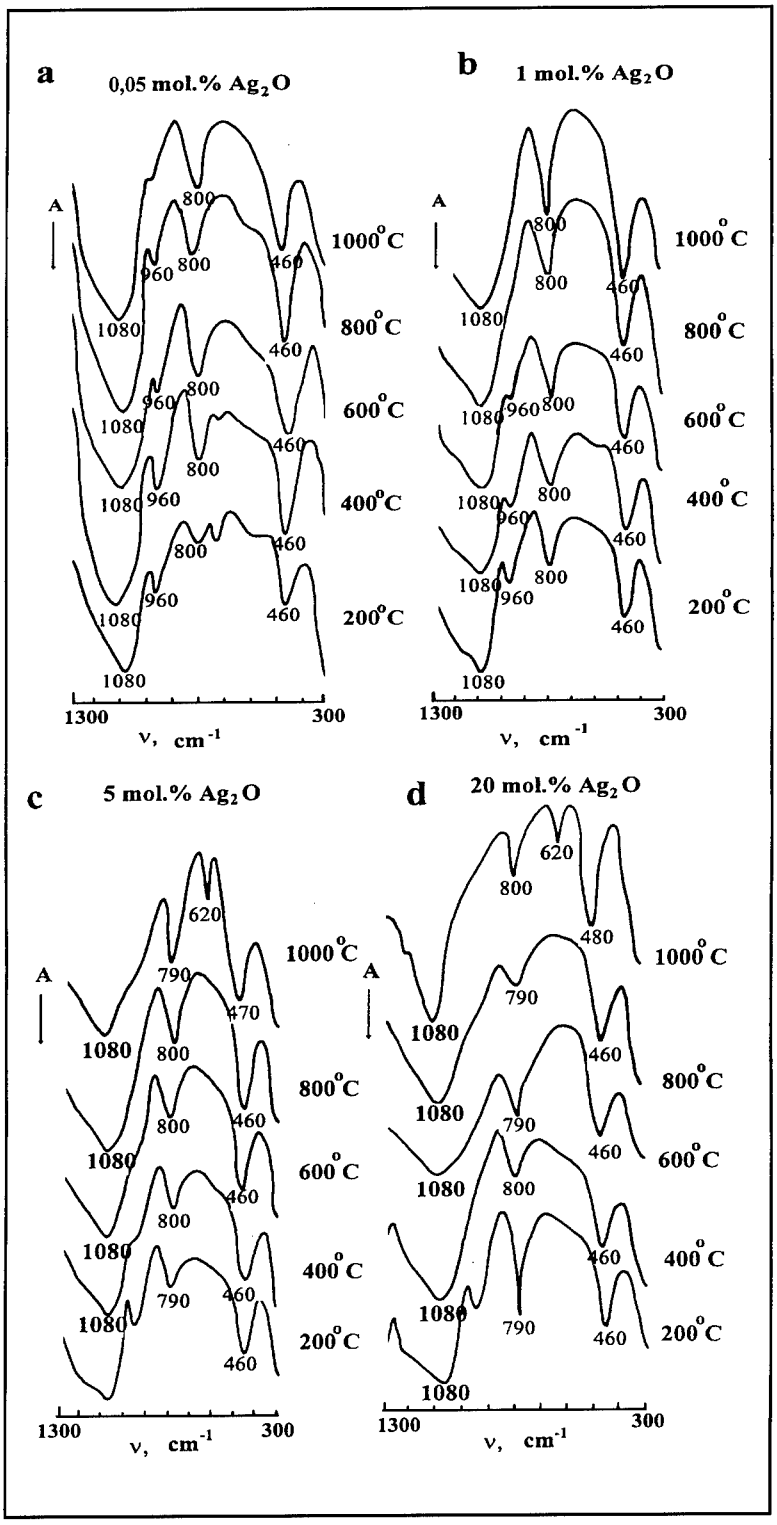

Figure 1. IR-spectra of silica gels containing 0.05 mol% Ag_2O (a), 1 mol% Ag_2O (b), 5 mol% Ag_2O (c), and 20.0 mol% Ag_2O (d) after heat treatment in the 200–1000°C temperature range.

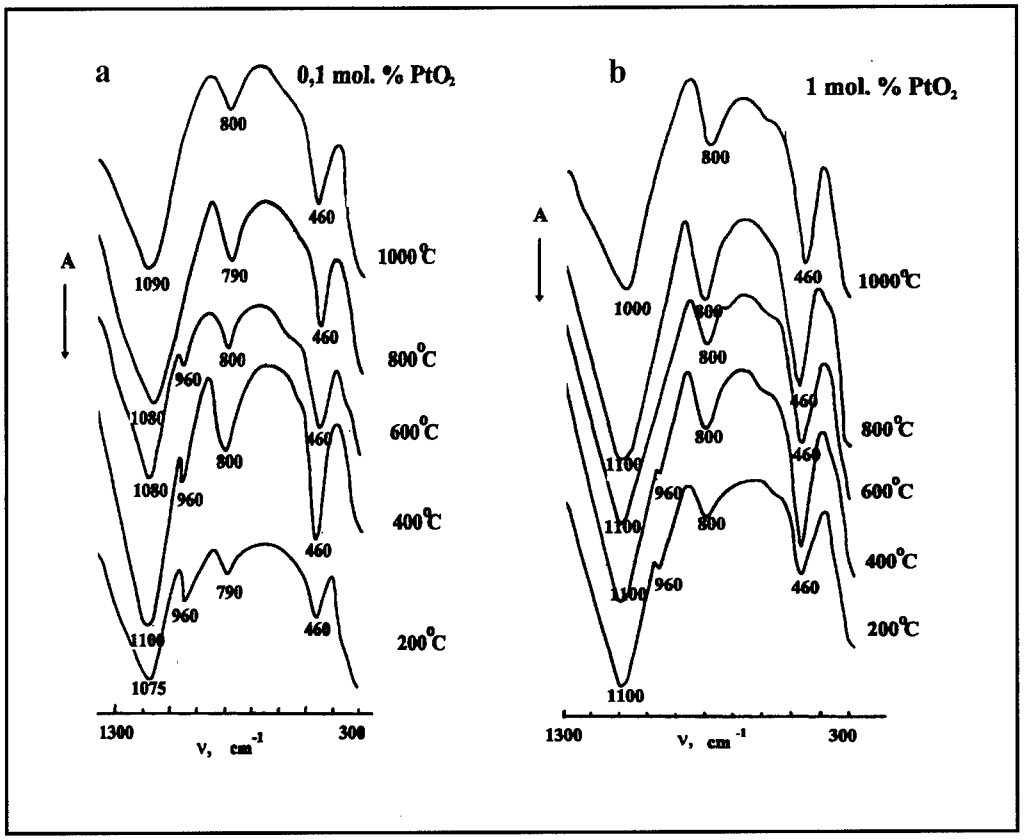

Figure 2. IR-spectra of silica gels containing 0.1 mol% PtO_2 (a) and 1 mol% PtO_2 (b) after heat treatment in the 200–1000°C temperature range.

The starting solutions were obtained by the sequential addition and stirring of TEOS and C_2H_5OH, H_2O and HCl and solutions of $AgNO_3$ or $PtCL_4$. For the preparation of homogeneous $AgNO_3$-containing sols it was necessary to add HNO_3 by drops. The gelling time was from 1 to 8 days depending on the metal oxide concentration. It was established that the gelling time increases with increasing metal oxide content. The gels were heat treated at 100°C for 12 hours and at 200°C, 400°C, 600°C, 800°C, 1000°C and, only for the gels containing Pt, 1200°C for two hours.

IR-spectra were recorded by a SPECORD-M-80 spectrophotometer for the 1300–300 cm^{-1} range. The specimens were photometered in liquid paraffin.

X-ray diffraction patterns were obtained using a DRON-IM diffractometer (CuK_α-radiation, Ni-filter).

The microstructure of the gels was studied using Philips EM-400 electron microscope. Powder specimens for electron diffraction and carbon-platinum replicas from fresh-fractured surfaces were examined.

Results and Discussion

Colorless silica gels containing up to 20.0 mol% Ag_2O and light yellow colored gels containing up to 1 mol% PtO_2 were synthesized. The gelation time varied from 1 day to 8 days. During the heat treatment the color of the gels changed from yellow to dark gray for the Ag-containing gels and from yellow to brown and black for Pt-containing gels.

Figure 1 shows IR-spectra of four samples containing 0.05, 1, 5 and 20.0 mol% Ag_2O. In all cases bands at 1080 cm^{-1}, 800 cm^{-1} and 460 cm^{-1} are seen in the IR-spectra. These bands are assigned to ν^{as}_{SiO}, ν^{s}_{SiO} and δ_{SiO}. The band at 960 cm^{-1}, due to the Si—OH vibration, disappears at 1000°C in the gel with 0.05 mol% Ag_2O. With increasing Ag_2O content in the gels the band at 960 cm^{-1} disappears at lower temperatures. For the gel containing 20.0 mol% Ag_2O this band, which is connected with the network formation and the gel to gel-glass transition, is seen in the IR spectrum only at

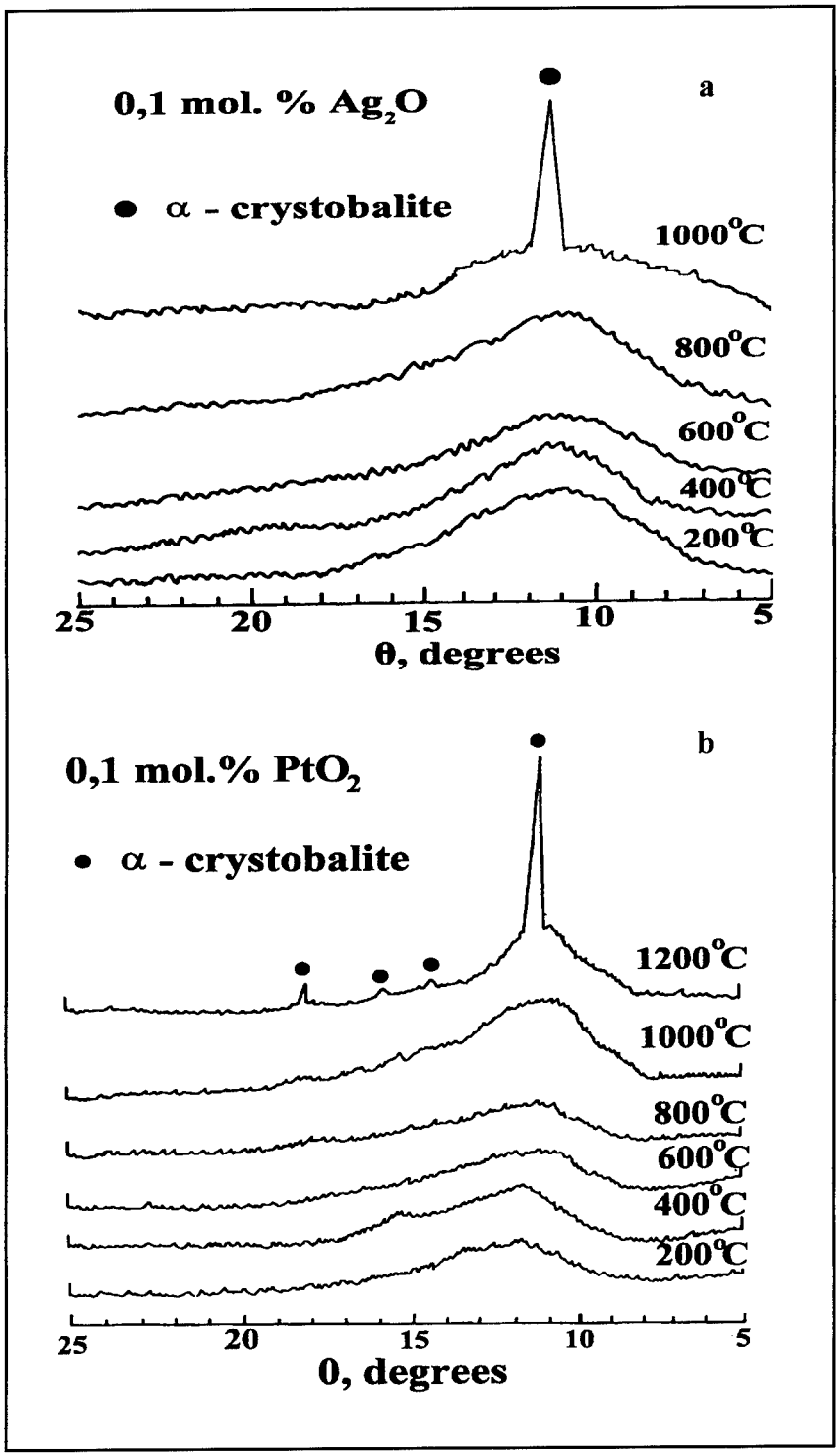

Figure 3. X-ray diffraction patterns of gel containing 0.1 mol% Ag_2O (a) 0.1 mol% PtO_2 (b) after heat treatment in the 200–1200°C temperature range.

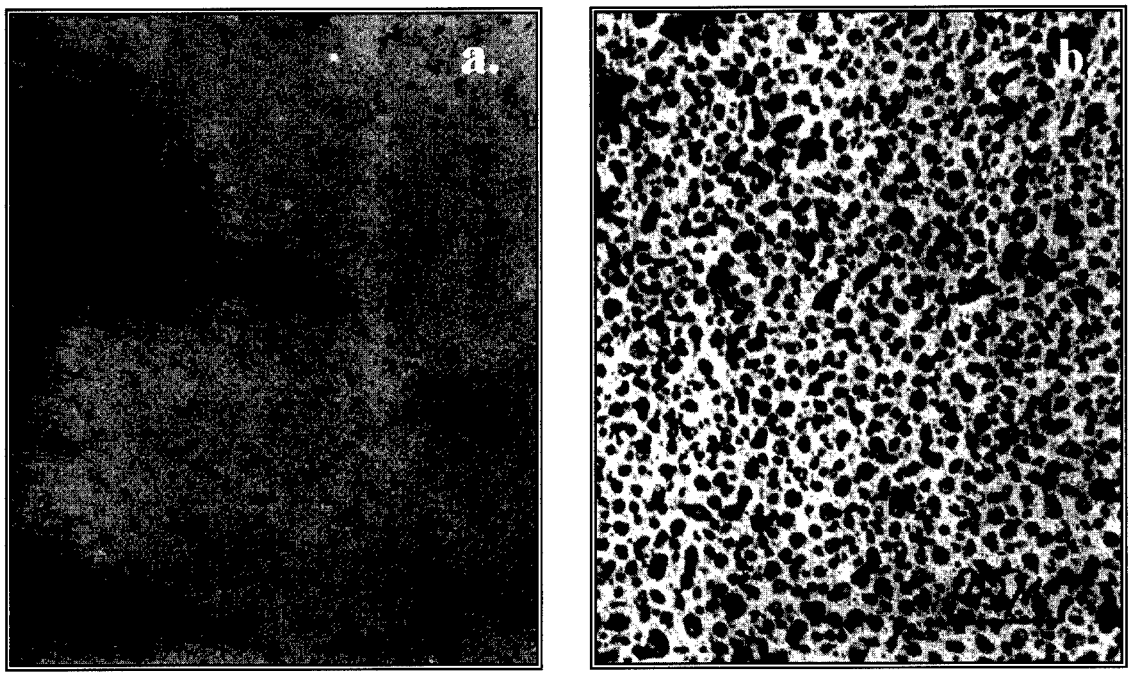

Figure 4. TEM micrographs of silica gels containing 2.0 mol% Ag_2O after heat treatment at 100°C (a) and 200°C (b).

200°C. The band at 620 cm^{-1} due to cristobalite is observed only in the spectra of the gels containing 5.0 and more mol% Ag_2O heat treated at 1000°C.

Similar conclusions about the structural changes and about the gel-glass transition during the heat treatment can be established from the IR-spectra of gels containing platinum (Fig. 2).

X-ray patterns of silica gels containing 0.1 mol% Ag_2O and 0.1 mol% PtO_2 are shown in Fig. 3. It can be seen that this concentration of Ag particles present in silica gel induce α-cristobalite formation at lower temperatures (1000°C) than Pt particles (1200°C). XRD also showed that at higher concentrations of Ag_2O the formation of a crystalline silver phase is observed at lower temperatures. When the concentration of Ag_2O was 1 mol% or more the crystalline silver phase was seen at 200°C. Such results were also obtained for the sample containing 1 mol% PtO_2. This proves that platinum does not react with the SiO_2 matrix [17].

The microstructure of some gels, observed by TEM, are given in Fig. 4. In the sample containing 2.0 mol% Ag_2O at 100°C (Fig. 4(a)) silver particles were observed in the C + Pt replicas. The increase of the temperature up to 200°C leads to the increase of the concentration and the size of the silver particles (Fig. 4(b)). It was found that the particle size in this case is between 3 and 10 nm. At higher concentrations of Ag_2O the size of the silver particles increases to 25 nm. These results are in agreement with the data published recently by De et al. [13].

Conclusion

Silica gels containing from 0.05 to 20.0 mol% Ag_2O and from 0.1 to 1.0 mol% PtO_2 have been obtained at room temperature using TEOS, C_2H_5OH, H_2O, HCl, HNO_3, $AgNO_3$ and $PtCl_4$ as precursors. It was found that the gel to gel-glass transition temperature decreased with increasing metal oxide concentration. Silver stimulates the formation of α-cristobalite phase at lower temperatures than platinum when 0.1 mol% metal oxide was present.

The XRD results show that silver and platinum crystalline phases are found at lower temperatures (200°C) when the concentration of metal oxide is 1 mol% or more. It was established using TEM that metal silver particles are formed and uniformly distributed in matrix. The size of the particles is in the 3–25 nm range and depends from the initial concentration of the silver oxide and the heat treatment temperature.

Acknowledgment

We are grateful to the National Research Fund for the financial support under grant X-437/1994.

References

1. R. Reisfeld, M. Eyal, and D. Brusilovsky, Chem. Phys. Lett. **153**, 210 (1988).
2. A. Tour, S. Pendalwar, and J. Cooper, Chem. Mater. **2**, 647 (1990).
3. Z. Spanhel, M. Mennig, and H. Schmidt, in *Proc. of 17th Inter. Congress on Glass*, Vol. 7 (Madrid, 1992), p. 9.
4. M. Mennig, Z. Spanhel, H. Schmidt, and S. Bedholz, J. Non-Cryst. Sol. **147/148**, 326 (1992).
5. D. Korvin, and Z. Pye, Glastech. Ber. **67C**, 296 (1994).
6. T. Tsuchiya, T. Sei, Y. Watanabe, M. Mori, and T. Kineri, J. Sol-Gel Sci. Technol. **8**, 685 (1997).
7. H. Kozuka, and G. Zhao, Bull. Inst. Chem. Res., Kyoto Univ. **72**, 209 (1994).
8. P. Innocenzi, H. Kozuka, and S. Sakka, J. Sol-Gel Sci. Technol. **1**, 305 (1994).
9. H. Kozuka and S. Sakka, Chem. Mater. **5**, 222 (1993).
10. H. Kozuka, G. Zhao, and S. Sakka, J. Sol-Gel Sci. Technol. **2**, 741 (1994).
11. S. Sakka, H. Kozuka, and G. Zhao, in *Proc. of Sol-Gel Optics III*, SPIE-2288 (San Diego, 1994), p. 108.
12. B. Breitscheidel, J. Ziedel, and M. Schubert, Chem. Mater. **3**, 559 (1991).
13. G. De, A. Licciulli, C. Massaro, L. Tapher, M. Catalano, G. Battaglin, C. Meneghini, and P. Mazzoldi, J. Non-Cryst. Sol. **194**, 225 (1996).
14. G. Battaglin, G. De Marchi, F. Caccavale, F. Gonella, G. Matei, P. Mazzoldi, F. Spizzo, A. Quaranta, F. Garrido, and G. De, in *Proc. Intern. Symp. on Glass Problems*, Vol. 1, edited by R. Akcakaya, N. Erinc, G. Albayrak, and S. Isevi (Istanbul, Turkey, 1996).
15. M. Suzuki and Y. Taga, J. Non-Cryst. Sol. **150**, 148 (1992).
16. B. Ritzer, M. Villegas, and J. Fernandez Navarro, J. Sol-Gel Sci. Technol. **8**, 917 (1997).
17. R. Pretorius, J.M. Harris, and M.-A. Nicolet, J. Solid State Electr. **21**, 667 (1978).

Journal of Sol-Gel Science and Technology 13, 975–979 (1998)
© 1998 Kluwer Academic Publishers. Manufactured in The Netherlands.

Crystallization Behavior of SiO_2-TiO_2 Ceramics Derived from Titanosiloxanes on Pyrolysis

T. GUNJI, T. KASAHARA AND Y. ABE
Department of Industrial Chemistry, Faculty of Science and Technology, Science University of Tokyo, 2641 Yamazaki, Noda, Chiba 278 Japan
gunji@ci.noda.sut.ac.jp

Abstract. The crystallization behavior of SiO_2-TiO_2 *ceramics derived from* titanosiloxanes was investigated in relation to the structure of the precursor and the pyrolysis temperature. The titanosiloxanes, $[Si(OBu^t)_2OTi(acac)_2O]_2$, $[(Bu^tO)_3SiO]_2Ti(OPr^i)_2$, and $[(Bu^tO)_3SiO]_3Ti(OPr^i)$, were pyrolyzed in an air atmosphere to form *SiO_2-TiO_2 ceramics which* crystallized to anatase at 600–650°C, 700–750°C, and 800–850°C, respectively. The crystallization temperature decreased with increased *titanium content* of the precursor. The average crystallite size of anatase increased with increased pyrolysis temperature and the titanium content. The crystallization temperature and the crystallite size for SiO_2-TiO_2 ceramics is controlled by the precursor structure, which may enable control of the physical properties of the ceramic materials.

Keywords: titanosiloxane, SiO_2-TiO_2, crystallization, precursor method, crystallite size

Introduction

Polymetalloxanes or polymetallosiloxanes are promising polymer precursors for ceramic materials since they easily provide SiO_2-M_xO_y ceramics on pyrolysis because the main chain is a metallosiloxane bond. These precursors are useful for producing ceramic fibers [1–5], and thin films [6, 7], as well as bulk bodies [8], which are difficult to prepare by conventional processes.

The transformation of metalloxanes to oxide ceramics is attractive for investigation because it features a new route to control the ceramic microstructure. The thermal and mechanical properties of the ceramic materials are significantly affected by the microstructure of the precursor metal-containing polymers, especially the sequence in the backbone structure and/or the main chain. However, previous studies have been hindered by the difficulty in the syntheses of precursors with a well defined structure.

The SiO_2-TiO_2 system is a good candidate for the investigation of the relationship between the structure of precursor and the crystallization behavior based on the phase separation of SiO_2 and TiO_2 [9] on pyrolysis. Recently, Almeida and Christensen [10] reported formation of SiO_2-TiO_2 thin films on a silicon wafer by a sol-gel process using $Si(OEt)_4$ and $Ti(OPr^i)_4$ and observations of the crystallinity and composition of the titania. In this work, the transformation of titanosiloxanes with a well defined backbone structure was investigated according to Eqs. (1) to (4) to clarify the relationship between the microstructure of the precursors and the phase separation behavior of the ceramic materials on pyrolysis.

$$2Si(OBu^t)_2(OH)_2 + 2Ti(acac)_2(OPr^i)_2 \xrightarrow{\text{Benzene}} \underset{\text{CTS}}{[Si(OBu^t)_2OTi(acac)_2O]_2} + 4\ Pr^iOH \quad (1)$$

$$n\,Si(OBu^t)_3OH + Ti(OPr^i)_4 \xrightarrow[(n=2,3)]{\text{Benzene}} \underset{\text{TS2}(n=2),\ \text{TS3}\ (n=3)}{[(Bu^tO)_3SiO]_nTi(OPr^i)_{4-n}} + nPr^iOH \quad (2)$$

$$\underset{\text{CTS}}{[Si(OBu^t)_2OTi(acac)_2O]_2} \xrightarrow{\Delta} SiO_2\text{-}TiO_2 \quad (3)$$

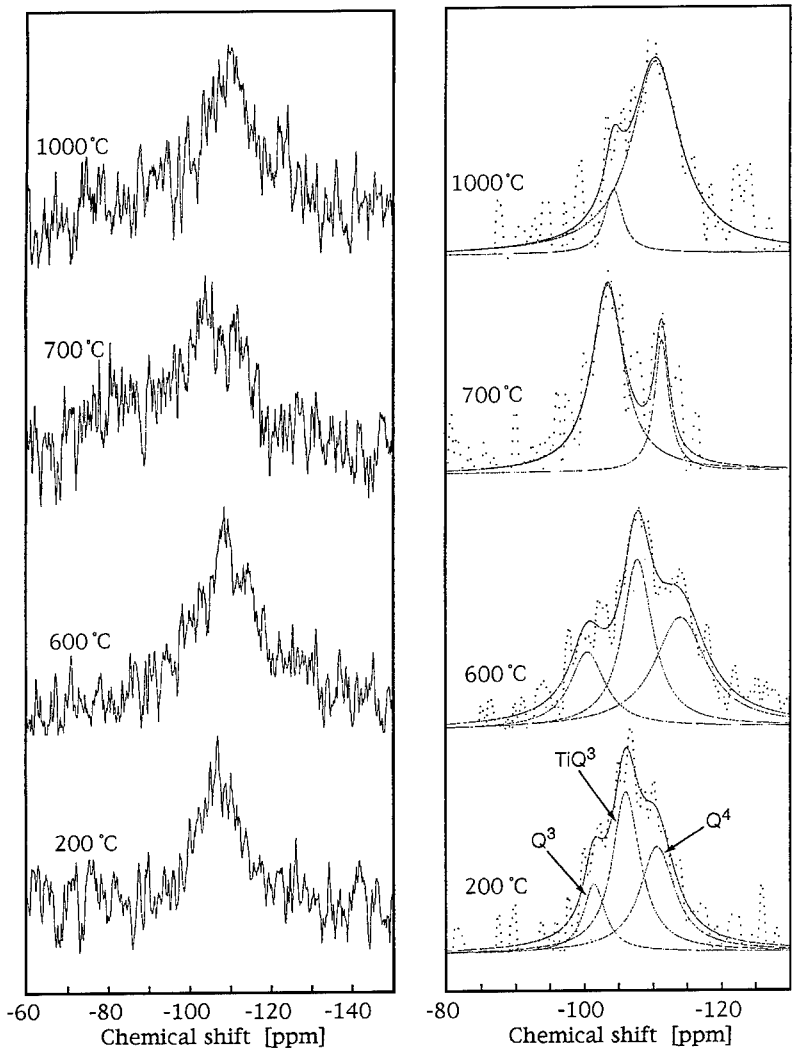

Figure 1. ^{29}Si DD/MAS NMR spectra of CTS on pyrolysis (left) and their deconvoluted spectra (right) Ref.: Polydimethylsilane).

$$[(Bu^tO)_3SiO]_nTi(OPr^i)_{4-n} \xrightarrow{\Delta} nSiO_2\text{-}TiO_2 \qquad (4)$$

TS2 ($n = 2$), TS3 ($n = 3$)

Experimental

Preparation of Cyclotitanosiloxane (CTS)

Into a benzene (10 ml) solution of di-*t*-butoxysilanediol (2.08 g (0.01 mol)), a benzene (10 ml) solution of bisacetylacetonatotitanium diisopropoxide (3.64 g (0.01 mol)) was added dropwise with stirring. The reaction mixture was heated to 50°C for 1 h followed by removal of solvent under reduced pressure. CTS was isolated as a yellowish-white powder by a reprecipitation method using benzene and hexane; mp : 115°C (decompostion), yield: 85%.

Preparation of Bis(tri-t-butoxysiloxy) diisopropoxytitanium (TS2)

Into a benzene (25 ml) solution of tetraisopropoxytitanium (4.26 g (0.015 mol)), a benzene (25 ml) solution of tri-*t*-butoxysilanol (7.93 g (0.03 mol)) was added with stirring. The reaction mixture was refluxed for 0.5 h followed by distillation under reduced pressure. TS2 was isolated as a transparent liquid by distillation, bp : 135–136°C/0.02 Torr., yield: 58%.

Preparation of Tris(tri-t-butoxysiloxy) isopropoxytitanium (TS3)

Into a benzene (15 ml) solution of tri-*t*-butoxysilanol (7.93 g (0.03 mol)), a benzene (10 ml) solution of tetraisopropoxytitanium (2.84 g (0.01 mol)) was added with stirring. The reaction mixture was refluxed for 1 h followed by distillation under reduced pressure. TS3 was isolated as a transparent crystalline solid by recrystallization from hexane; mp : 115°C (decomposition), yield: 73%.

Measurements and Analyses

^{29}Si dipolar decoupling/magic angle spinning nuclear magnetic resonance (DD/MAS NMR) spectra were obtained on a JEOL JNM-EX400. Infrared (IR) spectra were obtained on a HITACHI 260-50 by means of the carbon tetrachloride solution method or the KBr disc method. Thermogravimetry-differential thermal analysis (TG-DTA) was obtained on a RIGAKU Thermoflex under an air atmosphere. X-ray diffraction was carried out on a RIGAKU CN-2013. The silicon and titanium contents were analyzed by wet and dry methods, respectively.

Results and Discussion

Pyrolysis of CTS, TS2, and TS3

The transformation of titanosiloxanes to SiO_2-TiO_2 ceramics was investigated by means of TG-DTA analysis. The TG-DTA trace of CTS showed that CTS decomposed in three steps: the elimination of organic groups at 120–180°C with a small endothermic peak, the combustion of organic groups at 180–520°C, and the combustion of free carbon at over 950°C. On the other hand, TS2 and TS3 decomposed in two steps: elimination of organic groups and then combustion of organic groups.

The ceramic yields of CTS, TS2 and TS3 were calculated based on the total weight losses at 1400°C. The observed and calculated ceramic yields of CTS, TS2, and TS3 were 31.3% (30.7%), 26.4% (28.9%), and 29.1% (29.0%), respectively (the calculated values are shown in parentheses). The difference between the observed and calculated values for TS2 was due to vaporization of TS2 during the pyrolysis, since the elemental analysis of the residue showed that the relative molar ratio was $SiO_2 : TiO_2 = 2.02 : 1.00$. As a result, it was confirmed that the SiO_2-TiO_2 ceramics were formed quantitatively by the pyrolysis of CTS, TS2, and TS3, according to Eqs. (3) and (4).

The pyrolysis of CTS was monitored by IR and ^{29}Si DD/MAS NMR spectra. In the IR spectra, disappearance of the absorption peaks due to organic groups and ν_{SiOTi} and increased peak intensity due to ν_{SiOSi} and ν_{TiOTi} were observed with increasing pyrolysis temperature. Interestingly, an absorption peak due to ν_{SiOH} appeared at 200°C and then weakened during the pyrolysis. Figure 1 shows the ^{29}Si DD/MAS NMR spectra of CTS on pyrolysis. These spectra were deconvoluted by using PeakFit™ software. When CTS was pyrolyzed at 200°C and 600°C, the ceramics mainly consisted of the siloxane units Q^3 ($ROSi(OSi)_3$), TiQ^3 ($TiOSi(OSi)_3$), and Q^4 ($Si(OSi)_4$). On the other hand, after pyrolysis at 700°C and 1000°C, the unit TiQ^3 disappeared. Table 1 summarizes the percentages of the siloxane units. Up to 200°C and 600°C, the units Q^3 and Q^4 increased gradually with decrease of TiQ^3. At 700°C, TiQ^3 disappeared to produce the unit Q^3. At 1000°C, Q^4 was the main unit. These IR and NMR changes indicate combustion of the organic groups and crystallization of TiO_2 with cleavage of the Si—O—Ti linkages. The same features were observed for TS2 and TS3 on pyrolysis.

Scheme 1 represents a model for the pyrolysis of CTS to produce the phase separated SiO_2-TiO_2 ceramic materials. The precursor, CTS, consists of an eight membered ring in the center of the molecule with *t*-butoxy and acetylacetonate groups on the silicon and titanium atoms, respectively. On pyrolysis of CTS below 600°C, the *t*-butoxy and acetylacetonate groups are eliminated with the redistribution of titanosiloxane bonds to siloxane and titanoxane bonds and the formation of silanol groups, resulting in formation of seeds for the crystallites of titania. When CTS is pyrolyzed at over 700°C, TiO_2 groups combine and crystallize in

Table 1. Siloxane units of CTS on pyrolysis[a].

Temperature (°C)	Siloxane unit (%)		
	Q^3	TiQ^3	Q^4
200	16	46	38
600	20	39	41
700	75	0	25
1000	11	0	89

[a]Calculated from ^{29}Si DD/MAS NMR after deconvolution.

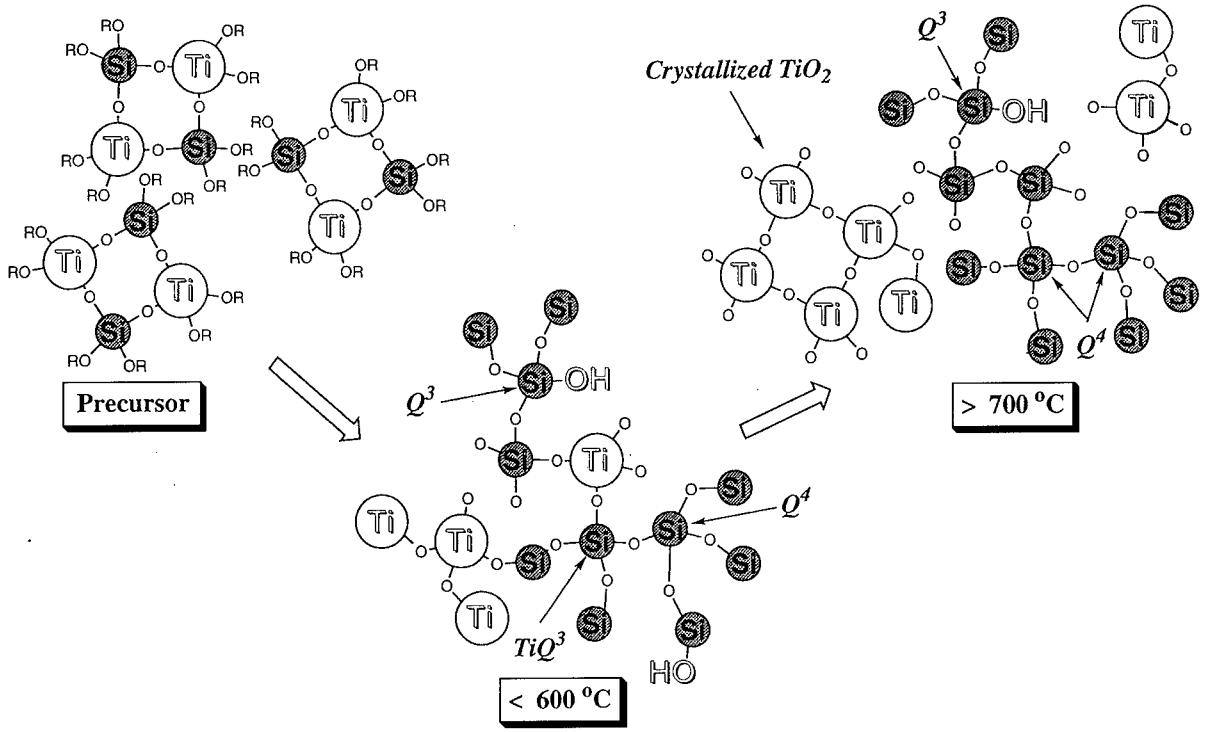

Scheme 1. A model for the rearrangement of CTS on pyrolysis.

anatase form to provide the phase separated ceramic materials of titania and silica.

Formation of Titania Crystallites

Figure 2 shows the X-ray diffractograms of CTS on pyrolysis. The crystallization temperature was determined as "the pyrolysis temperature when the diffraction pattern was observed beyond the background in the diffractogram," by which the crystallization temperature for CTS was determined as 600–650°C. The same procedure was applied for TS2 and TS3; crystallization appeared at 700–750°C and 800–850°C, respectively. With increasing pyrolysis temperature, the peak width for crystallization of titania in the anatase form narrowed with an increase of the peak intensity. On the other hand, the rutile form was observed for CTS and TS2 on pyrolysis at 1000°C and 1100°C, respectively. The decrease of the crystallization temperature with the increase of titania content suggests the possibility of controlling the crystallization temperature by the titania content and/or the sequence of Si–O–Ti bonds in the precursor molecule.

Table 2 summarizes the average crystallite sizes of CTS, TS2 and TS3 on pyrolysis. The average crystallite size of the anatase increased with increase of the pyrolysis temperature and the titania content, which increased in the order of TS3, TS2 and CTS. Hence, the crystallization temperature and the crystallite size for SiO_2-TiO_2 ceramics is controlled by the precursor structure.

Table 2. Crystal form[a] and the average crystallite size[b] of CTS, TS2 and TS3 on pyrolysis.

	CTS		TS2		TS3	
Temp. (°C)	Form	Size (A)	Form	Size (A)	Form	Size (A)
600	—	—	—	—	—	—
700	A	30	—	—	—	—
800	A	39	A	40	—	—
900	A	72	A	54	A	39
1000	A+R	121	A	78	A	60
1100	A+R	217	A+R	155	A	109

[a]Amorphous, A: Anatase, R: Rutile.
[b]Calculated from Scherrer's equation.

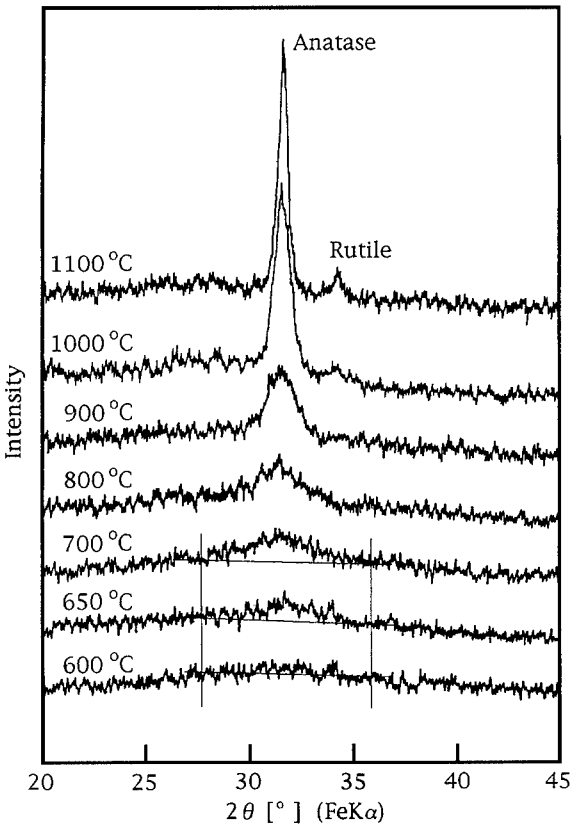

Figure 2. X-ray diffractograms of CTS on pyrolysis.

Conclusions

The titanosiloxanes, $[Si(OBu^t)_2OTi(acac)_2O]_2$, $[(Bu^tO)_3\ SiO]_2Ti(OPr^i)_2$, and $[(Bu^tO)_3SiO]_3Ti(OPr^i)$ crystallized at 600–650°C, 700–750°C and 800–850°C, respectively. The crystallization temperature decreased with increased titanium content. The average crystallite size of anatase increased with increase of the pyrolysis temperature, and the titania content. The crystallization temperature and the crystallite size for SiO_2-TiO_2 ceramics is controlled by the precursor structure, which may enable control of the physical properties of the ceramics.

Acknowledgment

This work was supported by the financial support from Futaba Memorial Foundation.

References

1. Y. Abe, T. Gunji, M. Hikita, Y. Nagao, and T. Misono, *Yogyo Kyokai Shi* **94**, 1243, (1986).
2. T. Gunji, Y. Nagao, T. Misono, and Y. Abe, J. Non-Crystal. Solids **107**, 149 (1989).
3. Y. Abe, Y. Nagao, and T. Misono, Kenkyu Hokoku—Asahi Garasu Kogyo Gijutsu Shoreikai **51**, 129 (1987).
4. T. Gunji, Y. Nagao, T. Misono, and Y. Abe, J. Polym. Sci. Part A: Polym. Chem. **29**, 941 (1991).
5. T. Gunji, I. Sopyan, and Y. Abe, J. Polym. Sci. Part A: Polym. Chem. **32**, 3133 (1994).
6. A. Kasgöz, T. Misono, and Y. Abe, Seramikkusu Ronbunshi **100**, 763 (1992).
7. A. Kasgöz, K. Yoshimura, T. Misono, and Y. Abe, J. Sol-Gel Sci. Tech. **1**, 185 (1994).
8. Y. Abe, N. Sugimoto, Y. Nagao, and T. Misono, J. Non-Crystal. Solids **104**, 164 (1988).
9. R.C. DeVries, R. Roy, and E.F. Osborn, Trans. Brit. Ceram. Soc. **53**, 531 (1954).
10. R.M. Almeida and E.E. Christensen, J. Sol-Gel Sci. Tech. **8**, 409 (1997).

Journal of Sol-Gel Science and Technology 13, 981–985 (1998)
© 1998 Kluwer Academic Publishers. Manufactured in The Netherlands.

β-Eucryptite by a Sol-Gel Route

WAFA I. ABDEL-FATTAH
National Research Centre, Tahrir, St. Dokki, Cairo, Egypt

M.SH. FAYED, SH.R. GOODA AND W.F.F. MEKKY
Armed Force of Egypt

Abstract. β-Eucryptite solid solution (LAS) $Li_2O : Al_2O_3 : 3SiO_2$(113) was prepared via a sol-gel route. Complex solutions of lithium or aluminum salts in ethanol/water mixtures were catalyzed by inorganic acids (catalyst/alkoxide ratio 0.1). Different ratios of H_2SO_4 catalyst were also used.

TGA showed that the maximum % yield of LAS 113 occurred using H_2SO_4 catalyst. Above 400°C exothermic peaks occurred in DSC followed by the glass transition. XRD and IR showed a high crystallinity of β-eucryptite solid solution using all acids at the 0.1 ratio with the highest crystallinity for the 0.05 H_2SO_4 ratio. SEM revealed similar grain sizes in spite of higher acid concentrations. XRD data indicated a change to a tetragonal modification with higher catalyst ratio.

Keywords: β-eucryptite, crystallization, effect of catalyst

1. Introduction

Lithium aluminosilicates have potential application in regenerator cores that salvage waste heat for improved fuel consumption [1]. Porous β-eucryptite (LAS 1 : 1 : 2) was characterized for use as a humidity sensor [2]. Among the factors affecting the performance of ceramic sensors are uniformity, internal stress and phase stability [3]. Stress-free bodies of LAS (1 : 1 : 3) ratio, have been obtained by conventional ceramic techniques [4]. Here the preparation of the same composition was investigated via sol-gel, to develop a multi-functional device and exploit its properties for several applications. The use of the sol-gel technique provides the possibility of generating a multiphase nanostructured material.

The present work deals with the preparation of β-eucryptite LAS (1 : 1 : 3) using alcoholic solutions of aluminum nitrate and lithium chloride with a silicon alkoxide. The influence of sol parameters, acid catalyst type or ratio and percentage of solid yield were followed by TGA and DSC. Crystallinity of the calcined powders was studied qualitatively using XRD peak heights supplemented by IR band width and SEM.

2. Materials and Methods

Ethanolic solutions of $LiCl{\cdot}H_2O$ (Koch-light) and $Al(NO_3){\cdot}9H_2O$ (Fisher) were mixed and added to TEOS [$Si(OC_2H_5)_4$] (Aldrich). [The effect of a molar ratio of catalyst to TEOS of 0.1 was studied by using as HCl, HNO_3, H_2SO_4, or $H_3PO_4{\cdot}H_2SO_4$ was chosen to follow the effect of different acid ratios (0.01, 0.05 and 0.15).] The precursors were refluxed for 1 hour at 85°C. After cooling, the hydrolyzed products were added to TEOS along with a drying agent (formamide). Formamide, (NH_2CHO, FA Prolabo) a Lewis base like ammonia, was added in molar amount equal to the alcohol to form a monolithic sample by controlling the drying. The TEOS/water/ethanol molar ratio was 1/10/5. Stable gels were obtained at ambient conditions within 3–5 days, aged for one week, and then dried at 120°C until no further weight change occurred.

TGA (Netzch TG 209) and DSC (Netzch DSC 200) were employed (10 K/min) to follow the decomposition of the dried gels. Phase analysis of the gels calcined at 900°C was performed using X-ray diffraction (Philips, PW 1390, 2°(2θ)/min and CuK_α radiation). Infrared analysis with the KBr disc technique (Philips PU 9712

spectrophotometer) and scanning electron microscopy (SEM, JEOL JSM. T20) was also used.

3. Results and Discussion

3.1. Effect of Catalyst Type

3.1.1. Thermal Analysis. The weight loss is a single reaction step and is almost complete at $260 \pm 2°C$ in all samples and is attributed to the dissociation of organics. The order for highest percent of solid yield as a function of catalyst is $H_2SO_4 > HNO_3 > HCl > H_3PO_4$ (Table 1). The decomposition of H_2SO_4 dried gels occurred at the lowest temperature. A lower % yield implies that hydrolysis of OR groups to form $Si(OH)_4$ is small and so the condensation reaction starts before the complete hydrolysis of $Si(OR)_4$ to $Si(OH)_4$ [5]. The lower % yield in the presence of HCl and HNO_3 catalyst is attributed to the common ion effect with the precursors and to differences in their dissociation constants.

The DSC traces revealed one exothermic-peak at $270 \pm 3°C$ with a shoulder at 268°C due to oxidation of organics. Glass transition end points are recorded above the weight loss temperatures. The values of ΔC_p were a function of catalyst and followed the order $H_3PO_4 > H_2SO_4 > HCL > HNO_3$ corresponding to the relative ease of protonation of the negatively charged alkoxide group. Acid catalyzed condensation is directed towards the ends rather than the middle of the chains, resulting in less highly branched polymers yielding monolithic gels [6].

3.1.2. Structural Data. XRD characteristic peaks for β-eucryptite solid solution with hexagonal structure were recorded at the lattice spacings 4.6, 4.5, 2.61, 2.08, 1.88, 1.74, 1.45 and 1.42 Å for all the acid-derived dried gels with negligible differences in their intensities except for the H_3PO_4-derived gel.

The IR spectra confirmed the XRD findings. In the 4 samples there were great similarities in band widths and wave number positions except for the H_3PO_4 sample which had a lower intensity. The band at 3432 cm^{-1} is assigned to (O-Li) or H^+ ions formed by the dissociation of $2H_2O \rightarrow OH^- + H_3O^+$ and is in the position formerly occupied by H_2O. The well defined band recorded at 1010 cm^{-1} is assigned to Si-O-str. Bands at 550 and 420 cm^{-1} along with 820 cm^{-1} shoulder are assigned to Al-O.

3.2. Ratios of H_2SO_4 Catalyst

3.2.1. Thermal Analysis. Thermogravimetric data revealed that the percentage of solid yield increased with increasing acid concentration (Table 1). Weight loss temperatures due to organic dissociation are similar for 0.01 and 0.1 ratios of acid ($\simeq$257°C) and are higher for the 0.05 and 0.15 ratios.

DSC traces with main exothermic-peaks are similar for the 0.05 and 0.15 ratios recorded at $727 \pm 2°C$ (Fig. 1). The energy released due to organic combustion increased with the catalyst ratios is as follows: $0.01 < 0.1 < 0.15 < 0.05$, indicating degree of condensation in the same order. The lowest ratio 0.01, has three exothermic peaks at 268, 271.6 and 274.8°C.

Table 1. Thermal data of dried gels with acid catalysts.

	TGA		DSC			
Acid	Loss temp. (°C)	Yield (%)	T_g end point (°C)	ΔC_p (J/g K)	Exothermic-peak (°C)	ΔH exo (J/g)
HCl	263.5	91.00	328	2.72	269–272	710.1
HNO_3	261.1	92.77	313	1.88	274.0	661.8
H_2SO_4	256.6	96.77	326	2.99	273.0	596.1
H_3PO_4	262.3	88.29	330	3.32	273.7	693.1
Ratios			H_2SO_4			
0.01	257.2	91.63	331	3.03	271	590.6
0.05	265.3	95.39	314	1.84	270	679.7
0.10	256.6	96.44	326	2.99	273	596.1
0.15	261.9	99.36	341	0.73	272–263	645.69

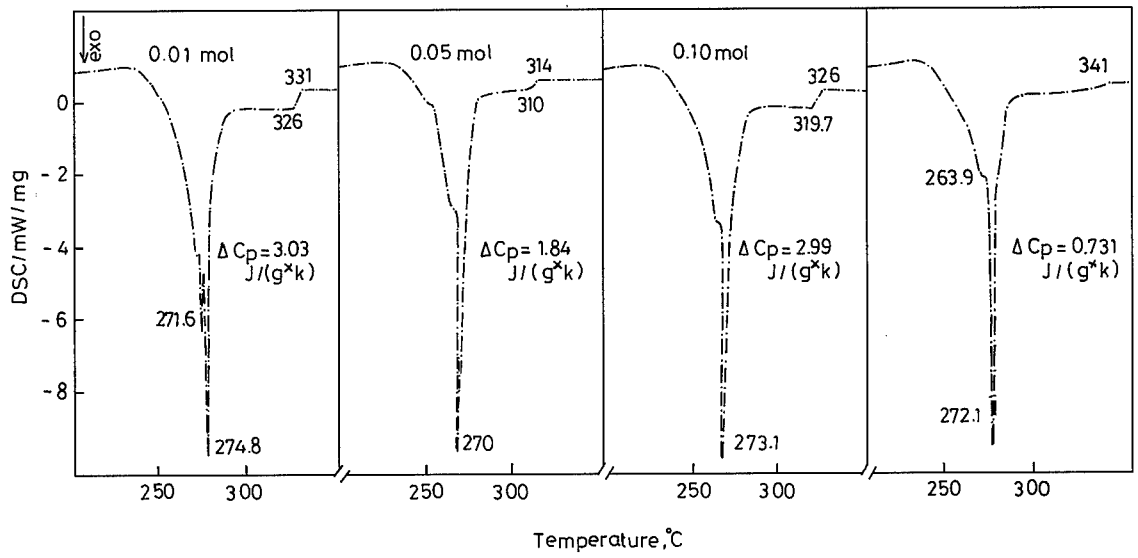

Figure 1. Differential scanning calorimetry traces of LAS dried gels with H_2SO_4 acid catalyst with 4 ratios.

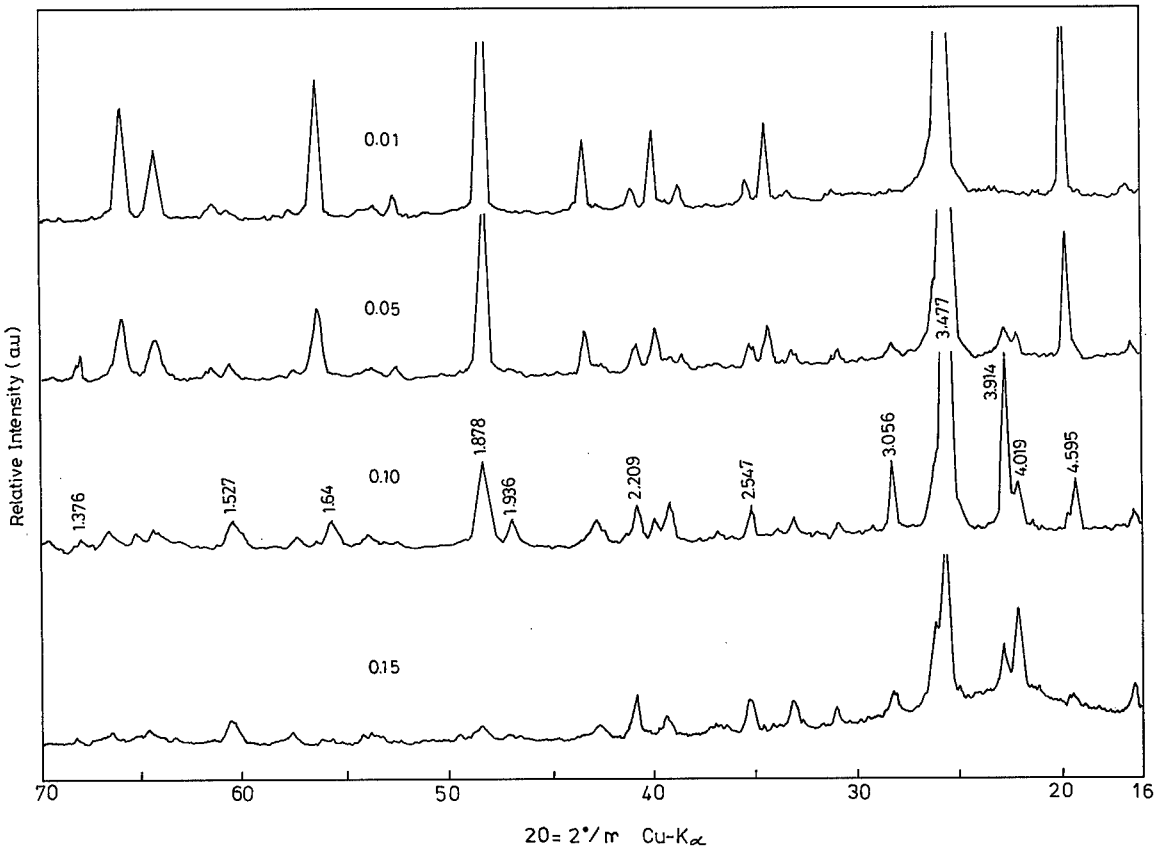

Figure 2. X-ray diffraction patterns of LAS gels calcined at 900°C as a function of H_2SO_4 acid catalyst.

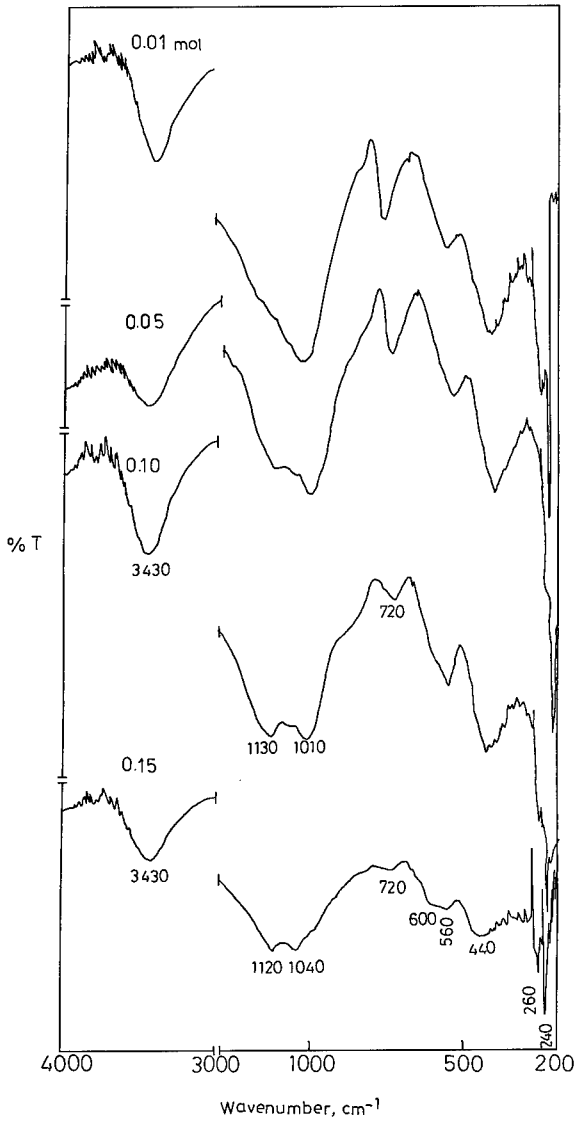

Figure 3. Infrared spectra of LAS gels calcined at 900°C with H_2SO_4 acid catalyst.

3.2.2. Structural Analysis. The XRD peaks for higher catalyst ratios above 0.05 indicated lower crystallinity as some peaks grew diffuse with reduced peak height. Peaks characteristic of β-eucryptite solid solution recorded at 4.2, 2.6, 1.77 and 1.47 Å disappeared. Other peaks at 4.09, 3.91, 3.05 and 1.93 Å appear due to a change to the tetragonal structure of β-spodumene (Fig. 2).

The IR spectra (Fig. 3) exhibited similar bands to those for the other acids especially for the ratio 0.01. With higher ratios, the 1010 cm^{-1} band became a doublet and a band at 1030 cm^{-1} can be assigned to the (O-Si)-O antisymmetric vibration in the SiO_4 tetrahedra. The large width of this band suggests that the silica network is open and disordered. This corresponds to the lower degree of crystallinity from XRD. The triplet recorded at 1120, 1040 and 980 cm^{-1} and assigned to Al-O-Al^4, Si-O td, Si(Al)-O str and Al^6-O-Al^6, respectively, for the highest acid ratio confirm the change to tetragonal β-spodumene. The shoulder at 820 cm^{-1} disappears. The band at 720 cm^{-1} grows smaller and more diffuse. The splitting of 1010 cm^{-1} band and shift of the 750 cm^{-1} band to 720 cm^{-1} coincide with the disappearance of peaks at high XRD 2θ values indicating structural rearrangement, and reorientation of ions upon increasing the acid catalyst ratio.

3.3. Grain Morphologies

SEM of the LAS gels prepared with various acids shows a non-uniform particle size distribution with some neck areas joining particles (Fig. 4). A few long laths are observed (Fig. 4(a)) with the HNO_3 catalyzed gels. Similar particle size with long laths and a more homogenous texture is obtained with H_2SO_4 catalyst ratio of 0.01 (Fig. 4(b)). With the lowest catalyst ratio (0.01), small aggregates of small particles are clearly observed with many long laths (Fig. 4(c)). Increasing the catalyst ratio to 0.05 (not shown) a more uniform distribution results, although some domains with a different grain size are observed. With the highest acid ratio (0.15) the grains appear larger (Fig. 4(d)). The larger grain size in spite of the higher acid ratio [7] is a consequence of a shift away from the stoichiometric $1:1:3\ Li_2O:Al_2O_3:SiO_2$.

4. Conclusion

The formation and crystallinity of the β-eucryptite solid solution was not affected significantly by catalyst type but was reduced with higher H_2SO_4 ratios. IR spectra for high catalizer ratios showed splitting of the bands and their shift and/or disappearance with the reorientation to tetragonal symmetry. A fine grained microstructure was obtained for the highest ratio of H_2SO_4 catalyst.

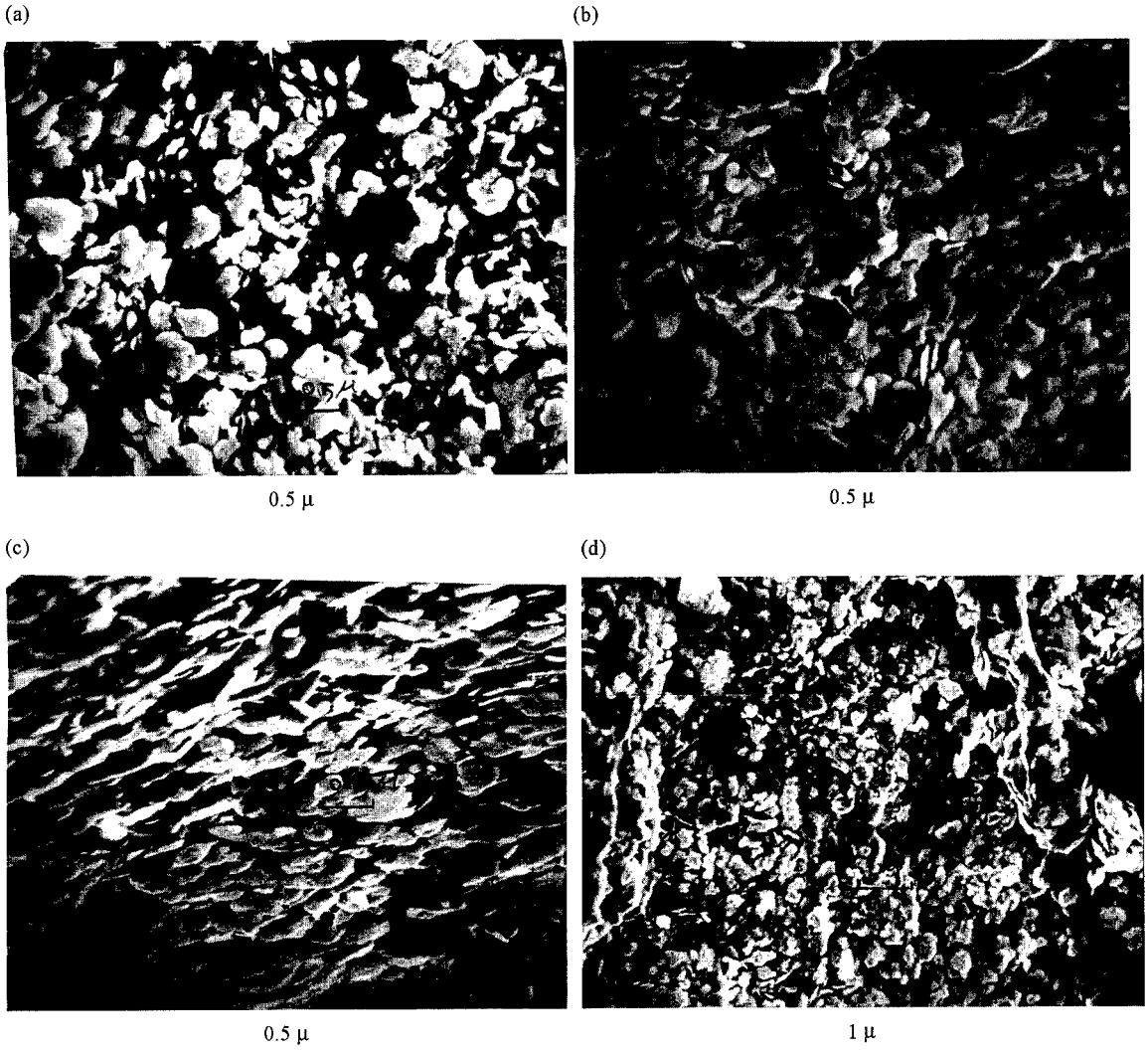

Figure 4. Microstructures of LAS calcined gels.

References

1. M.R. Poscucci and R.N. Katz, Interceram. **42**(2), 71–78 (1993).
2. N. Susumn, K. Hiroshi, S. Yoshihiko, and S. Yoshiro, J. Ceram. Soc. Japan **100**, 968–971, 1163 (1992).
3. K.Lisa, Am. Ceram. Soc. Bull. **68**(4), 860–865 (1989).
4. W.I. Abdel-Fattah and R. Abdellah, Ceramics Inter., (1997), in press.
5. R. Aelion, A. Loebel, and F. Erich, J. Am. Chem. Soc. **72**, 5705–5712 (1950).
6. B.E. Yoldas, J. Mater. Sci. **21**, 1087 (1986).
7. C. Aoki, T. Ban, Sh. Hayashi, and K. Okada, *Third Euro Ceramics* (Faenza Editrice Iberica, S.L., 1993), Vol. 1, p. 389.

Journal of Sol-Gel Science and Technology 13, 987–990 (1998)
© 1998 Kluwer Academic Publishers. Manufactured in The Netherlands.

Role of MnO on the Mullitization Behavior of Al_2O_3-SiO_2 Gels

M.G. FERREIRA DA SILVA
Departamento de Engenharia Cerâmica e do Vidro, Universidade de Aveiro, 3800 Aveiro, Portugal

Abstract. Gels were synthesized from solutions of tetraethylorthosilicate (TEOS) and aluminium nitrate (with and without manganese nitrate).

The structural evolution of the gels as a function of manganese content and heat-treatment temperature was studied by visible spectrophotometry (VIS), electron paramagnetic resonance (EPR), X-ray diffraction (XRD) and scanning electron microscopy (SEM). The results show that the presence of manganese can induce mullitization at lower temperatures. However, the effect of manganese depends on its content and how it enters into the mullite structure.

Keywords: mullite, MnO, crystal structure, electronic paramagnetic resonance (EPR), sol-gel chemistry

1. Introduction

Mullite ceramics have attracted considerable research interest, mainly due to their promising properties, such as an excellent creep resistance, high chemical and thermal stability and good dielectric properties.

The preparation of a mullite precursor using the sol-gel method can provide good mixing of starting materials, chemical homogeneity of the products and lower sintering temperatures [1].

The transformation behavior of a gel to a mullite ceramic may be dependent on the presence of transition metal cations. For example, manganese is believed to be incorporated into mullite as Mn^3. The incorporation induces strain. This strain is correlated with the substitution of octahedrally bound Al^{3+} by Mn^{3+}. The replacement of Al^{3+} by Mn^{3+} causes a deformation of the oxygen octahedra. This may be explained by the repulsion of the d_z^2 manganese(III) electron from the electrons of the oxygen ligands (Jahn-Teller distortion). In fact, the $3d^4$ electrons of Mn^{3+}, in an octahedral crystal field, are split from the energetic ground state to the high spin state $(t_{2g})^3$ $(e_g)^1$ and the e_g electron occupies the d_z^2 orbital [2].

The purpose of the present study is to compare the mullitization behavior of manganese doped and undoped monolithic Al_2O_3-SiO_2 materials prepared by the sol-gel method.

2. Experimental

Manganese doped and undoped Al_2O_3-SiO_2 gels were prepared as summarized in Table 1. The solutions were stirred for 1 hour at room temperature and converted to a gel by heating at a temperature near 60°C. However, the 2AETOH and 2AMnETOH samples were prepared by mixing TEOS, ethanol and the 1^aphase water and, after a previous hydrolysis of 1 hour at room temperature, the aluminum and manganese nitrates dissolved in water were added. The resulting solutions were stirred for 1 hour at room temperature and converted to a gel at a temperature near 60°C. All the samples were dried at 60°C. The dried gels were heat-treated between 900 and 1300°C in ambient air conditions. The structural evolution of the samples was examined using several techniques. UV-VIS diffuse reflectance spectra were obtained in the range 240–800 nm using a UV-VIS-IV_p Shimadzu UV-2101/3101PC spectrophotometer. The EPR measurements were carried out at room temperature in a Brücker ESP 300E spectrometer operating at the X-band frequency. The modulation frequency was 100 KHz. XRD analysis was performed in a Rigaku XDMAX diffractometer. The X-ray source was CuK_α radiation. The microstructures of the samples was determined by SEM, using a Hitachi S4100-1 electron microscope.

Table 1. Manganese undoped and doped samples.

Samples	Composition (wt%)				
	$Al(NO_3)_3 \cdot 9H_2O$	H_2O	TEOS	EtOH	$Mn(NO_3)_2 \cdot 4H_2O$
Gel A	44.84	44.84	8.49	1.83	Undoped
Gel AMn	44.84	44.84	8.49	1.83	1.04/100 of A solution*
Gel AETOH	44.84	33.56	6.36	26.52	Undoped
Gel AMnETOH	33.56	33.56	6.36	26.52	0.15/100 of A solution*
Gel 2AETOH	33.56	0.59 (1^aphase) + 33.36 (2^aphase)	6.32	26.37	Undoped
Gel 2AMnETOH	33.36	0.59 (1^aphase) + 33.36 (2^aphase)	6.32	26.37	1.12/100 of A solution*

*The A solution is formed by $Al(NO_3)_3 \cdot 9H_2O + H_2O + TEOS + EtOH$.

3. Results and Discussion

The Gel A and Gel AMn samples before gelation showed some phase separation and flocculation and after drying at 60°C a foam-like texture. The solutions for samples AEtOH, AMnETOH, 2AETOH and 2AMnETOH had a transparent appearance and after gelation and drying at 60°C showed a rubbery texture. All the gel samples dried at 60°C showed a white color. The samples without Mn maintained the white color at temperatures higher than 60°C. The Mn-containing samples exhibited intense purple-brown colors at temperatures higher than 60°C. The colors of the Mn-containing samples are related to the presence of manganese as Mn(II), Mn(III) or Mn(II) and Mn(III).

The diffuse reflectance and electron paramagnetic resonance spectra (Fig. 1A) confirm that the Gel 2AMnETOH at 60°C contains Mn(II) octahedrally coordinated. The sample shows a diffuse reflectance spectrum without bands that can be explained by the fact that d-d transitions of a d^5 system are forbidden in spin and parity [3]. However, it may be seen that the EPR spectrum at room temperature (Fig. 1A) has a poorly resolved hyperfine structure and a resonance signal around $g = 2.00$. This means that the sample contains Mn(II) in an octahedral environment. The diffuse reflectance and EPR spectra of the Gel 2AMnETOH samples (Fig. 1B, C and D), heat-treated at higher temperatures than 60°C, reveal the presence of Mn(II) and Mn(III). In fact, the diffuse reflectance spectra present a broad band centered around 480 nm that can be attributed to the presence of high-spin Mn(III) compounds [3] and the EPR spectra show broad single lines due to the presence of Mn(II) octahedrally coordinated. The different appearance of the EPR spectra lines can be related to changes in the Mn(II) concentration and environment. Thus, the broad single lines observed between 1000 and 1300°C may be due to the immobilization of manganese(II) in certain sites [4]. This interpretation is in accordance with the transformation of aluminosilicate gels (that contain a high level of residual —OH groups and organics) into organized mullite structures.

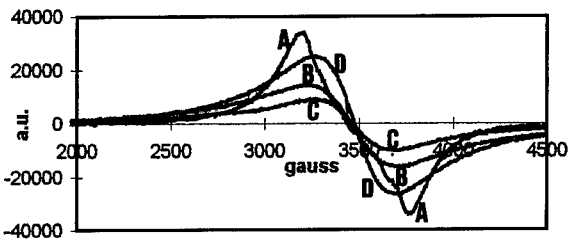

Figure 1. EPR spectra of 2AMnETOH samples at: (A) 60°C; (B) 1000°C; (C) 1200°C; and (D) 1300°C.

The incorporation of manganese(II) into the aluminosilicate samples does not produce strain because this cation has a stable d^5 configuration with a spherically symmetric charge distribution [5]. As mentioned in the introduction it is the manganese incorporated as Mn(III) that induces strain.

The influence of Mn(III) on the orthorhombic mullite (o-mullite) formation was studied by XRD and SEM. The XRD patterns of the Gel AETOH and

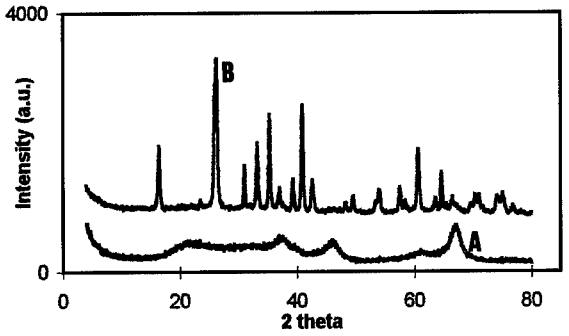

Figure 2. X-ray diffraction patterns for 2AETOH (A) and 2AMnETOH (B) samples heat-treated at 1000°C.

Gel AMnETOH samples at 1000°C show the presence of cubic mullite (Si-Al spinel of a composition similar to 3:2 mullite) [6] and a glassy phase. At 1200°C o-mullite was formed. Also the microstructure of these samples appeared very similar. This means that manganese oxide has no apparent effect on the temperature of formation of o-mullite. However, this effect was observed when the amount of MnO was increased. Thus, the XRD patterns of the Gel 2AEtOH-1000°C and Gel 2AMnETOH-1000°C are different (Fig. 2A and B). Gel 2AETOH-1000°C shows the formation of cubic mullite and Gel 2AMnETOH-1000°C the formation of o-mullite. These samples also show different microstructures (Fig. 3(a) and (b)). The Gel 2AETOH-1000°C shows a fine textured fractured surface (Fig. 3(a)). However, the microstructure of Gel 2AMnETOH-1000°C (Fig. 3(b)) contains many needle-like mullite crystals [7]. The Gel 2AETOH and Gel 2AMnETOH samples heat-treated at higher temperatures than 1000°C (1200 and 1300°C) show similar X-ray diffractograms with sharp and intense peaks of o-mullite (Fig. 4). However, the XRD patterns of Mn-containing samples also show α-Al_2O_3 as an incipient phase. Nevertheless, scanning electron micrographs of these samples (at 1300°C) exhibit considerable differences. The microstructure of Gel 2AETOH-1300°C is characterized by a cross-linked structure formed by abundant tabular mullite crystals, while the microstructure of Gel 2AMnETOH-1300°C appears similar to that of a fused-mullite refractory with some dispersed crystals (probably of α-Al_2O_3). This shows that MnO has an important role in the microstructural evolution of these samples.

The Gel 2AMnETOH-1000°C sample and all the samples heat-treated at temperatures higher than

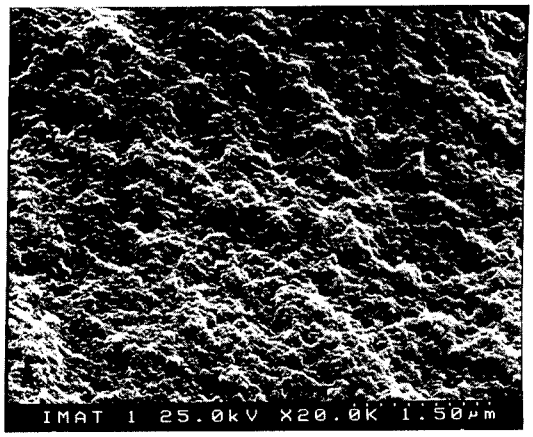

(a)

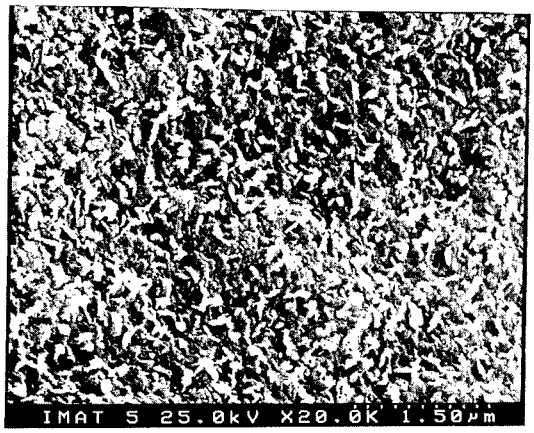

(b)

Figure 3. Electron micrographs of the 2AETOH-1000°C (a) and 2AMnETOH-1000°C (b) samples.

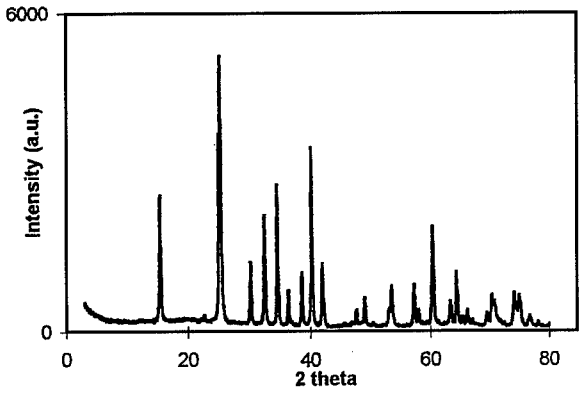

Figure 4. X-ray diffraction pattern for 2AMnETOH sample heat-treated at 1200°C.

1000°C exhibit very intense and sharp diffraction peaks and this indicates that an amorphous phase is not present [8].

4. Conclusions

From the diffuse reflectance spectra, XRD patterns and SEM of the aluminosilicate gels prepared without MnO and with different amounts of MnO it was concluded that:

- it is possible to obtain, using an easy preparation method, o-mullite samples with good chemical homogeneity and at low sintering temperatures.
- in the samples with ca. 0.8 mol% of MnO the incorporation of Mn(III) appears not to induce strain in the aluminosilicate structure and samples with and without MnO have the same behavior after heat treatment.
- the incorporation of manganese(III) induces strain in the aluminosilicate network and samples with and without MnO show different behavior with heat treatment. The strain has an effect on the temperature of formation of o-mullite and on the microstructure of the samples.
- the sample with ca. 6 mol% of MnO shows complete mullitization at 1000°C.

Acknowledgments

The authoress thanks the Physics Department of Aveiro University for EPR measurements.

References

1. Y. Zhou, J. Vleugels, T. Laoui, and O. Van Der Biest, J. Mater. Sci. **13**, 1089 (1994).
2. H. Scnneider, K. Okada, and J.A. Pask, *Mullite and Mullite Ceramics* (John Wiley & Sons, Chichester, 1994).
3. F.A. Cotton and G. Wilkinson, *Advanced Inorganic Chemistry* (Interscience Publishers, John Wiley & Sons, New York, 1972).
4. N. Abidi, B. Deroide, J.V. Zanchetta, D. Bourret, H. Elmkami, and P. Rumori, Phys. Chem. Glasses **37**, 149 (1996).
5. H. Scheneider, in *Mullite and Mullite Matrix Composites*, edited by S. Somiya, R.F. Davies, and J.A. Pask (The American Ceramic Society, Inc., Westerville, 1990).
6. A.K. Chakravorty, J. Mat. Sci. **29**, 6131 (1994).
7. B.E. Yoldas, Ceramic Bulletin **59**, 479 (1980).
8. R.X. Fisher, H. Schneider, and D. Voll, J. Eur. Ceram. Soc. **16**, 109 (1996).

Journal of Sol-Gel Science and Technology 13, 991–994 (1998)
© 1998 Kluwer Academic Publishers. Manufactured in The Netherlands.

Ultraviolet-Laser-Induced Crystallization of Sol-Gel Derived Indium Oxide Films

HIROAKI IMAI, ATSUSHI TOMINAGA AND HIROSHI HIRASHIMA
Faculty of Science and Technology, Keio University, 3-14-1 Hiyoshi, Kohoku-ku, Yokohama 223, Japan

MOTOYUKI TOKI AND MAMORU AIZAWA
Kansai Research Institute, Kyoto Research Park 17, Chudoji Minami-machi, Shimogyo-ku, Kyoto 600, Japan

Abstract. Modification of sol-gel derived indium oxide thin films using ultraviolet lasers was investigated. Irradiation by an ArF excimer (6.4 eV) and the fourth harmonic generation of a Nd : YAG laser (4.7 eV) was found to be effective in crystallization with a loss of hydroxyl groups and a decrease in the sheet resistance of the sol-gel films. Transparent crystalline indium oxide films were successfully obtained by 6.4 eV laser irradiation at fluences below 20 mJ/(cm^2 · shot), whereas degradation of the films was induced by a relatively high-fluence beam.

Keywords: sol-gel, indium oxide, ITO, crystallization, ultraviolet laser

1. Introduction

Indium oxide (In_2O_3) and tin-doped indium oxide (ITO) films are conducting and highly transparent to visible radiation. Thus, these films are useful for a variety of applications, such as heat mirrors and electrodes for solar cells and liquid crystal displays. In recent years, a low-temperature fabrication process for crystalline ITO thin films has been required for the coating on substrates which have a restricted thermostability, such as polymer films and color filters.

Although the sol-gel process is one of the candidates for the fabrication method of ITO films, a subsequent heat-treatment at a relatively high temperature is needed for crystallization and removal of residual organic and hydroxyl groups [1]. Recently, various irradiation techniques using energetic ions [2–4] and ultraviolet (UV) light [5–8] were applied to modification of sol-gel films as an alternative to conventional heat-treatments. These studies revealed that collisional atomic displacements and electronic excitations could densify sol-gel derived films at low temperatures. However, transformation into a crystalline phase was not achieved by these techniques. Although photo-enhanced annealing using infrared and visible lasers was investigated for densification [9] and crystallization [10, 11] of sol-gel films, these structural changes were ascribed to thermal effects induced by a focused beam. Irradiation of UV lasers at fluences exceeding 100 mJ/(cm^2 · shot) was also reported to be effective in modifying thin films and surfaces [12–14], whereas degradation of sol-gel films was caused by the powerful laser beam [15]. However, UV laser beams are expected to be useful for modification of thin films even at a low fluence because only chemical bonds in a surface layer are directly excited by the energetic photons.

Here we report on the crystallization of sol-gel derived In_2O_3 thin films promoted by UV laser irradiation. Transparent, crystalline In_2O_3 films with a low sheet resistance were successfully obtained by the UV laser beams at a relatively low fluence.

2. Experimental

Starting sols were prepared by hydrolysis of indium tri-secondary-butoxide. Tin tetra-secondary-butoxide was used for the tin doping. The sample films were prepared on polished and cleaned silicon wafers and silica glass

plates by dipping. After drying at 100°C in air, the samples were subjected to an ArF laser (6.4 eV) and the second harmonic generation (SHG) (2.3 eV) and the fourth harmonic generation (FHG) (4.7 eV) of a Nd : YAG laser in air at room temperature. The ArF and the Nd : YAG lasers were operated at 1–10 Hz with a 20 ns pulse width and at 10 Hz with a 5 ns pulse width, respectively. The fluence of the laser pulse was varied from 3 to 30 mJ/(cm^2· shot). Heat treatments of the samples were carried out in an electric furnace from 100 to 600°C in air.

X-ray diffraction (XRD) measurements were made using CuK$_\alpha$ radiation with a rotating sample holder for thin films. Fourier transform infrared (FTIR) absorption spectra and UV and visible transmission spectra were obtained using an FTS-65 spectrometer (BIO RAD) and an UV-2500PC spectrometer (Shimadzu), respectively. The surface of the samples was observed using a JEOL JSM-5200 scanning electron microscope (SEM). Sheet resistance of the films was measured with the four probe method.

3. Results and Discussion

Figure 1 shows that the transmission for an as-dried In_2O_3 film decreased in UV region above ~4 eV. Thus, the UV laser beams (4.7 and 6.4 eV) are absorbed in the dried gel films, whereas absorption at 2.3 eV is negligible. Figure 2 shows the XRD patterns for In_2O_3 gel films as-dried, heated at 400°C and irradiated with the 6.4-eV laser at a fluence of

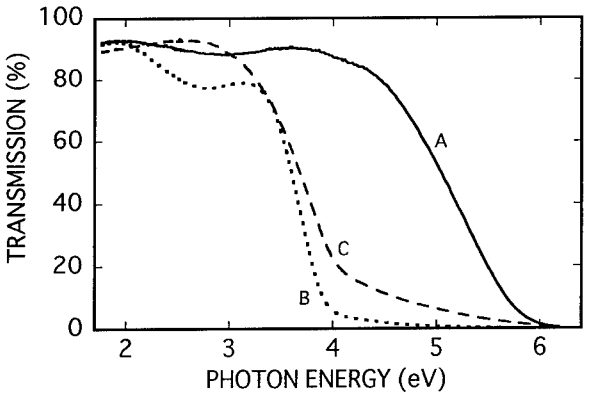

Figure 1. Transmission in the visible and ultraviolet regions of sol-gel derived In_2O_3 films on a silica glass substrate: (A) as-dried, (B) heated in air at 400°C, (C) irradiated by a 6.4-eV laser (18 mJ/(cm^2 · shot), 1000 shots). The thickness of as-dried In_2O_3 gel films was estimated to be about 100 nm using an ellipsometer.

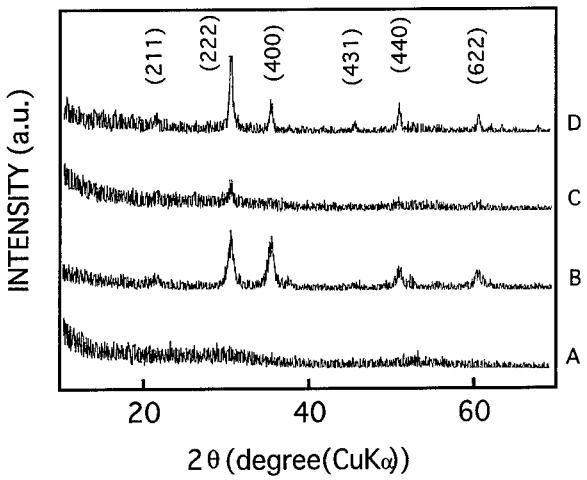

Figure 2. XRD patterns for sol-gel derived In_2O_3 films on a silicon substrate: (A) as-dried, (B) heated in air at 400°C, (C) irradiated with a 6.4-eV laser (21 mJ/(cm^2 · shot), 10 shots), (D) irradiated by a 6.4-eV laser (21 mJ/(cm^2 · shot), 1800 shots).

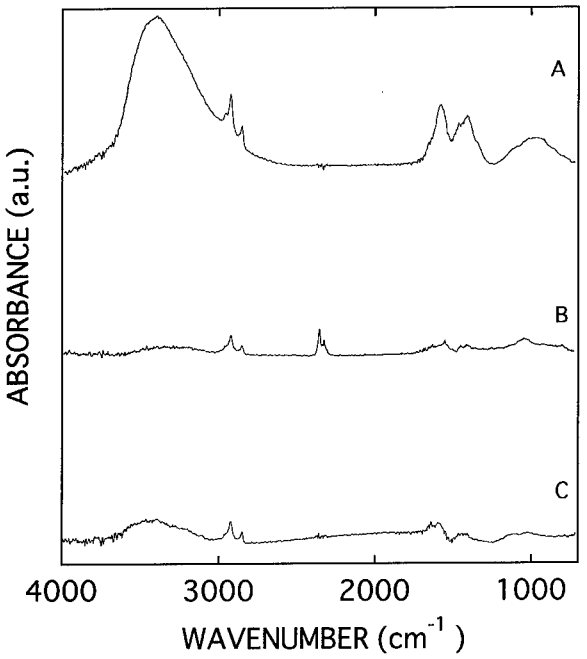

Figure 3. FTIR spectra for sol-gel derived In_2O_3 films on a silicon substrate: (A) as-dried, (B) heated in air at 400°C, (C) irradiated by a 6.4-eV laser (21 mJ/(cm^2 · shot), 1800 shots).

21 mJ/(cm^2 · shot). The diffraction peaks due to the crystalline In_2O_3 were observed both for the heated and the irradiated films. Figure 3 shows that the broad absorption around 3400 cm^{-1} due to hydroxyl groups and several absorption bands around 1500 and 2900 cm^{-1}

associated with organic groups decreased with the heating and the laser irradiation. Thus, crystallization with a reduction of hydroxyl and organic groups was induced by the laser irradiation in a similar manner as in conventional heat-treatments. Since the diffraction peaks in Fig. 2 almost agree with the powder pattern of crystalline In_2O_3, the laser-induced crystal grains were not oriented in the films. The diffraction peaks were not observed at fluences below ~11 mJ/(cm^2 · shot). The 4.7-eV laser beam at a fluence of 30 mJ/(cm^2 · shot) also led to the crystallization of the films, whereas the 2.3-eV laser beam at almost the same fluence did not induce any changes. These results indicate that the structural changes are attributable to direct absorption of the energetic photons.

The sheet resistance of the sol-gel In_2O_3 films was decreased by the laser irradiation. The changes in the sheet resistance and the peak intensity of XRD have a saturating tendency with irradiation higher than 100–1000 shots. Figure 4 shows the sheet resistance of the 6.4 eV laser-irradiated sol-gel In_2O_3 films as a function of the laser fluence. The lowest value of the resistance achieved at a fluence around 15 mJ/(cm^2 · shot) was smaller than that obtained by a conventional heat-treatment at 600°C. In the case of tin-doped samples (In : Sn = 95 : 5 in mol), however, the resistance of the laser-irradiated films was higher than that of the heated one at 500°C. Szörényi et al. [16] studied the changes in the surface of DC sputtered ITO films with laser irradiation using X-ray photoelectron spectroscopy (XPS).

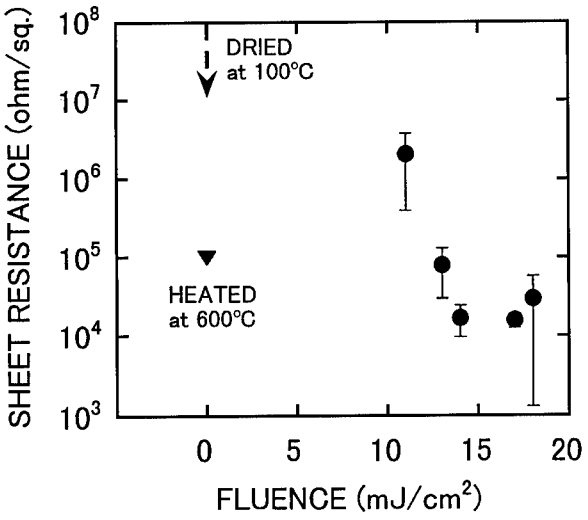

Figure 4. Sheet resistance of sol-gel derived In_2O_3 films as dried, heated in air at 600°C and irradiated by a 6.4-eV laser (5000 shots).

An increase in oxygen-deficient region associated with oxygen displacement was suggested as being induced by irradiation with a KrF excimer laser (5.0 eV) at fluences exceeding 300 mJ/(cm^2 · shot). Thus, the low resistance of the laser-irradiated sol-gel In_2O_3 films is assumed to be due to an increase in carrier density due to the oxygen deficiency. The XPS analysis also indicated segregation of tin atoms with the laser irradiation. Thus, the high resistance of the irradiated tin-doped films is related to segregation of tin. These differences in resistance between the laser-irradiated and the annealed films suggest that atomic displacements are promoted even by a relatively low-fluence laser beam. Therefore, the laser induced crystallization is presumed not to be caused by a simple annealing effect.

Figure 1 shows the transmission in UV region for In_2O_3 gel films heat-treated above 400°C and laser-irradiated at 6.4-eV with a fluence of 18 mJ/(cm^2 · shot). Laser irradiation with a low fluence pulse is found to promote crystallization of the sol-gel films without a decrease in transmission in the visible region. An increase in absorption around 4 eV is attributed to the crystallization of the films. On the other hand, irradiation at fluences above ~20 mJ/(cm^2 · shot) decreased the transmission in visible region. Unevenness of film surfaces subjected to relatively high laser beam fluences was observed using scanning electron microscopy. Thus, the decrease in the transmission in the visible region was deduced to be due to the degradation of the surface. The degradation of the tin-doped samples was induced at a lower fluence than that for the non-doped films. Van de Leest et al. [15] showed that UV laser irradiation with a pulse of about 100 mJ/cm^2 led to cracking and delamination of sol-gel films. Since the ablation of sputtered ITO films via sublimation was reported to be induced by UV laser irradiation at fluences above 200 mJ/cm^2 [17], the degradation is not ascribable to sublimation. A relatively high-fluence beam is assumed to cause a surface stress leading to the degradation of the films.

In order to evaluate the UV-laser-induced effects, estimation of the maximum temperature at the irradiated films is important. Numerical calculations on In_2O_3 films [18], indicated that the increase in temperature at the film surface irradiated by a KrF laser pulse at a fluence of 190 mJ/cm^2 was about 2000°C. On the other hand, the crystallization of the sol-gel films was observed at fluences in 11–20 mJ/cm^2. These results suggest that the laser-enhanced crystallization occurred at a relatively low temperature, whereas heating

above 300°C is required for crystallization of the sol-gel In_2O_3 films. Thus, UV-laser-induced crystallization may be ascribed to dense electronic excitations induced by coherent UV beams. However, this estimate cannot be directly applied to our study because the thermal properties of In_2O_3 used for the calculation must be different from those of the "In_2O_3 gel film." Further investigations are needed to reveal the process of the UV-laser-induced structural changes including crystallization and atomic displacements.

4. Summary

Crystallization of sol-gel derived indium oxide films was found to be promoted by irradiation using 6.4- and 4.7-eV laser beams. Transparent crystalline indium oxide films with a low sheet resistance were successfully fabricated using the laser beams with a relatively low fluences. The difference in the sheet resistance between the laser-irradiated and thermally crystallized films suggests that atomic displacements were induced by irradiation.

Acknowledgments

The authors are grateful to A. Nakajima (Keio University), K. Nagasawa and Y. Sakurai (Shonan Institute of Technology) for the irradiation experiments using an ArF excimer laser and a Nd : YAG laser.

References

1. D.M. Mattox, Thin Solid Films **204**, 25 (1991).
2. N. Moriya, Y. Shacaham-Diamand, and R. Kalish, Appl. Phys. Lett. **57**, 108 (1990).
3. T.E. Levine, J.L. Keddie, P. Revesz, J.W. Mayer, and E.P. Giannelis, J. Am. Ceram. Soc. **76**, 1369 (1993).
4. H. Hirashima, K. Adachi, and H. Imai, Mater. Res. Soc. Symp. Proc. **346**, 183 (1994).
5. S. Maekawa and T. Ohishi, J. Non-Cryst. Solids **169**, 207 (1994).
6. H. Imai, H. Hirashima, K. Awazu, and H. Onuki, Proc. SPIE-Int. Soc. Opt. Eng. **2288**, 71 (1994).
7. H. Imai, M. Yasumori, H. Hirashima, K. Awazu, and H. Onuki, J. Appl. Phys. **79**, 8304 (1996).
8. R.E. Van de Leest, Appl. Surf. Sci. **86**, 278 (1995).
9. D.J. Taylor and B.D. Fabes, J. Non-Cryst. Solids **147/148**, 457 (1992).
10. G.J. Exarhos, N.J. Hess, and S. Wood, Proc. SPIE-Int. Soc. Opt. Eng. **1624**, 444 (1991).
11. K. Kikuta, Y. Isobe, T. Yogo, S. Ono, and S. Hirano, J. Am. Ceram. Soc. **79**, 2289 (1996).
12. Y. Morita and T. Noguchi, Jpn. J. Appl. Phys. **28**, 309 (1989).
13. H. Kuriyama, S. Kiyama, S. Noguchi, T. Kuwahara, S. Ishida, T. Nohda, K. Sano, H. Iwata, M. Osumi, S. Tsuda, S. Nakano, and Y. Kuwano, Jpn. J. Appl. Phys. **30**, 3700 (1991).
14. L.D. Laude, K. Kolev, M. Brunel, and P. Deleter, Appl. Surf. Sci. **86**, 368 (1995).
15. R.E. Van de Leest and F. Roozeboom, Mater. Res. Soc. Symp. Proc., in press.
16. T. Szörényi, L.D. Laude, I. Bertóti, Zs. Geretovszky, and Z. Kántor, Appl. Surf. Sci. **96–98**, 363 (1996).
17. T. Szörényi, Z. Kántor, and L.D. Laude, Appl. Surf. Sci. **86**, 219 (1995).
18. T. Szörényi, L.D. Laude, I. Bertóti, Z. Kántor, and Zs. Geretovszky, J. Appl. Phys. **78**, 6211 (1995).

Journal of Sol-Gel Science and Technology 13, 995–999 (1998)
© 1998 Kluwer Academic Publishers. Manufactured in The Netherlands.

Sol-Gel Synthesis and Microstructural Characterization of Silicon Oxycarbide Glass Sheets with High Fracture Strength and High Modulus

N. SUYAL, T. KRAJEWSKI AND M. MENNIG
Institut für Neue Materialien GmbH, 66123 Saarbrücken, Germany

Abstract. A synthesis route to silicon oxycarbide glass sheets (thickness 40 to 1000 μm and area up to 20×35 cm^2) has been developed for the first time starting from a methyl modified sol containing nano-particulate SiO_2 and having a solid content of ~70 wt%. The gel sheets obtained by casting and drying of this sol were sintered in N_2 atmosphere at temperatures between 900–1650°C. Only by the incorporation of colloidal silica (0.10–0.35 mole per mole alkoxide) to the sol could crack-free, large area glass sheets be obtained. Fracture strength (three point bending) was found to attain a maximum (200–300 MPa) for the sheets sintered at 1000°C. Young's modulus attained a peak value between 120 and 130 GPa for the sheets sintered at 1200°C. HR-TEM studies showed an amorphous and homogeneous matrix up to a sintering temperature of 1200°C, whereas at 1450°C and 1650°C, crystallites of SiC and lamellar graphite were formed. It is concluded that addition of colloidal silica to the sol does not lead to inhomogeneities after sintering and therefore does not decrease the strength and elastic modulus.

Keywords: sol-gel synthesis, thin glass sheets, silicon oxycarbide glass, mechanical properties

Introduction

The existence of metastable silicon oxycarbide (stoichiometrically SiC_xO_{2-2x}) phase where both Si—O— and Si—C≡ bonds exist to the same silicon atom is well known [1, 2]. Heating of silica with carbon [3, 4] allows a maximum incorporation of 2–3 wt% of carbon as oxycarbide phase in the glass structure [4], because under equilibrium conditions the stable Si—C and SiO_2 phases are preferred. The synthesis of oxycarbide glasses by the sol-gel route allows the incorporation of up to 10 wt% of carbon as SiC_xO_{2-2x} [5–7] and a tailoring of the composition by using different Si-precursors. The O/Si ratio of the precursors and the temperature of pyrolysis determine the distribution of SiC_xO_{4-x} units in the final glass [8]. Free carbon has also been found to exist inevitably along with the oxycarbide phase [6] irrespective of the precursors chosen, giving the black color to the glasses.

Oxycarbide glasses have a thermal expansion coefficient of around 3.14×10^{-6}/K [1], a dielectric constant of around 4.4 in the frequency range from 10 to 10^7 Hz [1], a fracture strength in the range from 150 ± 84 to 550 ± 230 MPa [9], and a sintering temperature of around 1000°C [9]. These values suggest their suitability for applications like microelectronic packaging. But beside polycarbosilane derived fibers (Nicalon™ and Tyranno™), no bulk forms like sheets or plates are in use.

The objective of the present work was to prepare thin sheets of silicon oxycarbide glasses, which could have an application potential as substrates for microelectronic packaging and for laminates with high elastic modulus. A method for the synthesis of thin (40–1000 μm), large area (up to 35×20 cm^2) gel sheets has been developed [10] by the present authors. Conversion of these gel sheets to silicon oxycarbide glass sheets, determination of their mechanical properties and the study of their microsructure is reported here.

Experimental

For the synthesis of gel sheets (details will be reported elsewhere [10]), 0.9 mole methyltriethoxysilane (MTEOS) and 0.1 mole tetraethoxysilane (TEOS)

were mixed with 4.5 moles of ethanol and 0–0.35 mol of a colloidal silica sol (30 wt% SiO_2 in methanol, Nissan Chemicals) were added to it. 4 mole NH_3-water (5×10^{-3} moles of NH_3/mole water) was used for hydrolysis. This mixture was reacted at 80°C for 96 h under reflux conditions. For the reaction a two step process with 96% reflux for the first 48 h followed by 93% reflux for another 48 h was chosen. The sol thus obtained was cast on polystyrol substrates using the doctor blade method and kept at 50°C for 15 h for gelation and drying.

Dried gel sheets were placed between two Al_2O_3 substrates with spacers of appropriate thickness, heated under N_2, up to different temperatures between 900 and 1650°C (heating rate 75 K/h, holding time 0.5 h) and finally cooled to room temperature in the closed furnace. Helium pycnometry was used for the determination of densities of the glass sheets. Rectangular sheet samples (length ~35 mm, width 5–8 mm and thickness ~300 μm) were used for the determination of fracture strength (three point bending test, traverse speed 0.75 mm/min and span 20 mm) after polishing of the edges. Weibull statistical analysis was performed using fifteen samples for each data point and the characteristic Weibull strength (σ_0) and Weibull modulus (m) were determined. 95% of confidence limits for σ_0 was determined using the values of σ_0 and m [11]. Young's modulus was determined by an impulse echo method using time of flight measurements of ultrasonic waves.

A Siemens diffractometer (40 kV, 25 mA, LiF monochromator and CuK_{α_1} radiation) was used for recording X-ray diffraction (XRD) patterns from the crushed glass powders. Samples for electron microscopy (diameter 3 mm) were prepared by Ar^+ ion milling. Electron micrographs and diffraction patterns were recorded using a high resolution transmission electron microscope (HR-TEM, CM 200 FEG, Philips) on these samples. Glass sheets containing 0, 0.10, 0.25 and 0.35 moles of colloidal silica per mole alkoxide are named as MTC00, MTC10, MTC25 and MTC35 in the further discussion.

Results and Discussion

Remarkable differences were observed in the sintering behavior of the gel sheets with and without colloidal silica sol. Gel sheets obtained from MTEOS and TEOS sol without colloidal silica (i.e., MTC00) showed many cracks (~3–4/cm^2) along the whole length and width of the sheets after sintering, whereas MTC10, MTC25 and MTC35 gel sheets could be sintered to flat, black and crack-free oxycarbide glass sheets under the same conditions. The addition of colloidal silica was found to increase the density, specific surface area (SSA) and pore volume of the dried gels sheets [10]. An addition of 0.25 mole colloidal silica per mole alkoxide increases the density from 1.34 to 1.48 g/cm^3, SSA from 0.55 to 4.48 m^2/g and the pore volume from 0.003 to 0.026 cm^3/g [10]. It is assumed that this facilitates the outgassing of organic residuals during sintering resulting in crack-free sintered sheets. Figure 1 shows one of the glass sheets (MTC25) of dimensions ~11 cm × 12 cm × 350 μm sintered at 1000°C.

The question was whether the addition of colloidal silica to the sol could lead to inhomogeneities after sintering, which could have an influence on the mechanical properties. Therefore, the fracture strength and the Young's modulus of the glass sheets were measured as a function of colloidal silica content and the sintering temperature. Figure 2 shows the Weibull strength (σ_0) of the sheets as a function of colloidal silica content (the error bars represent the 95% level of confidence for σ_0). The values for Weibull modulus (m) ranged between 3.3 and 6.6. It can be seen that for a sintering temperature of 1000°C, a maximum strength between 230 MPa (95% confidence limits, 197–267) and 309 MPa (95% confidence limits, 268–357) is obtained. A significant influence of the colloidal silica content cannot be detected from these data. The strength values are significantly higher than the practical strength of fused silica (110 MPa [12]) and are comparable with data reported for silicon oxycarbide glass bars prepared using silicone resins [1] and rods prepared from organosilanes [9]. This indicates sintering to a dense oxycarbide matrix with low defect density. MTC25 derived oxycarbide glass sheets sintered at 1000°C had a density of 2.26 g/cm^3 (silica 2.20 g/cm^3 [12]), which also suggests sintering to a dense matrix. It is known that the metastable oxycarbide (SiC_xO_{4-x}) units have a statistically random distribution at around 900–1000°C and on increasing the temperature this metastable phase tends to separate to equilibrium SiO_2 and SiC phases [8]. A random distribution of oxycarbide units is expected to lead to improved fracture strength. This may be a reason for the maximum in fracture strength at 1000°C.

The dependence of the Young's modulus on sintering temperature and colloidal silica content is shown in Fig. 3. Again a significant influence of the colloidal

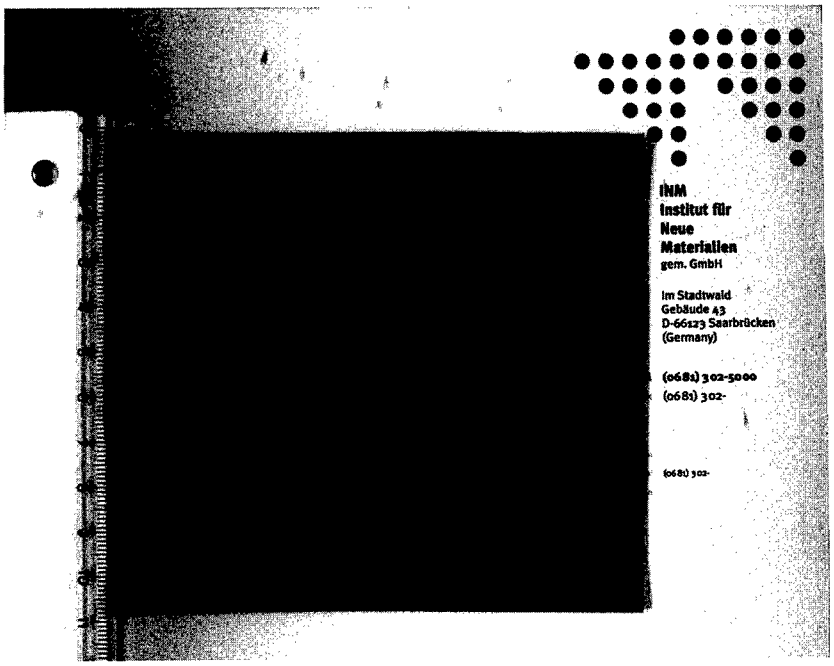

Figure 1. A photograph of an oxycarbide glass sheet (11 cm × 12 cm × 350 μm) obtained by sintering an MTC25 gel sheet at 1000°C under N_2.

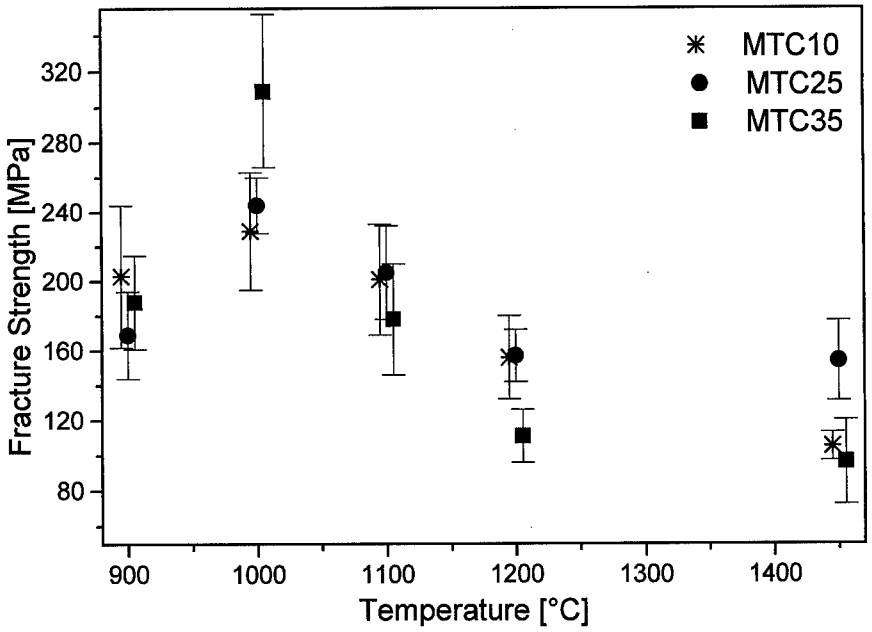

Figure 2. Weibull strength of oxycarbide glass sheets as a function of sintering temperature and colloidal silica content determined using three point bending method (MTC10 and MTC35 data points have been given an offset of −5 and +5°C, respectively along X-axis for better visibility).

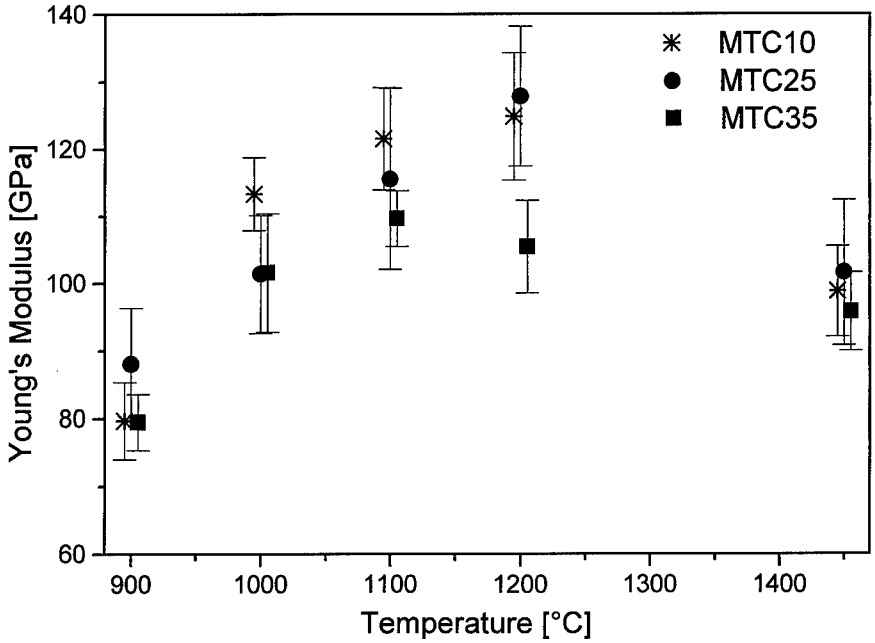

Figure 3. Young's modulus of oxycarbide glass sheets as determined by the impulse echo method as a function of sintering temperature and colloidal silica content. (MTC10 and MTC35 data points are shown with an offset of −5 and +5°C, respectively along X-axis).

silica content cannot be identified, but a maximum of the Young's modulus for sintering temperatures of about 1200°C is obvious, where values of about 120 GPa are reached. This is considerably higher compared to the reported value in the literature of 70 GPa for fused silica glass [12]. This value of Young's modulus is also higher as compared to the known values for silicon oxycarbide glass bars derived from silicone resin [1] and for rod-like glasses derived from organosilanes [9].

The Young's modulus is a function of the type of bonds existing in the material and is strongly influenced by any defect or mismatch between the boundaries of the prevailing phases. Therefore, the influence of the sintering temperature on the microstructure of the glass sheets was investigated by HR-TEM for MTC00 and MTC25 samples. MTC25 was chosen as representative for colloidal silica containing samples, keeping in view the fact that no remarkable effect of the addition of colloidal silica on the mechanical properties is observed. Glass sheets heat treated up to a temperature of 1200°C were found to be amorphous and homogeneous. However, the samples sintered at 1450°C showed uniformly dispersed crystalline zones less than 5 nm in diameter. Electron diffraction patterns showed two types of crystalline entities with d-spacing of around 0.34, 0.21, 0.15 nm, and 0.25, 0.15, 0.13 nm, which could be assigned to crystalline graphite and silicon carbide, respectively. Figure 4 shows a HR-TEM picture from a MTC25 sample sintered at 1650°C. Graphite and SiC crystallites could be identified by Fourier transformation processed images (see FT1 and FT2 in Fig. 4).

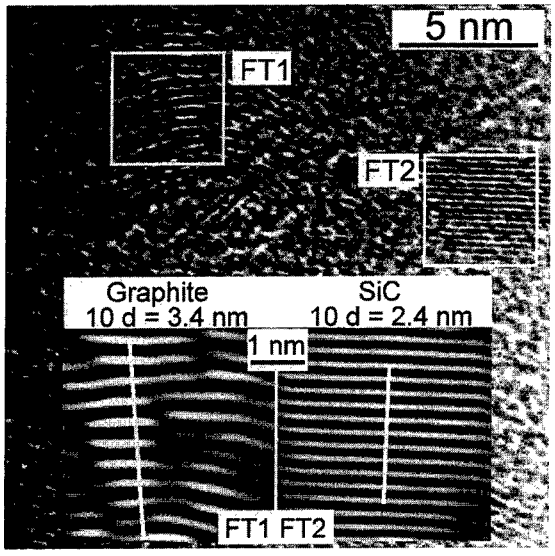

Figure 4. HR-TEM micrograph of the silicon oxycarbide glass heat treated at 1650°C/N_2 (insets show the FT-processed images of regions FT1 and FT2, showing SiC and graphite crystal planes).

Analysis of 10 different micrographs showed that rectangular lamellar graphite crystallites around 20 nm long and around 10 nm wide and silicon carbide crystallites 5–10 nm in diameter were formed. The electron diffraction patterns support the presence of hexagonal (2H or 4H) silicon carbide, though an exact assignment was difficult. Any influence of colloidal silica on the microstructure could not be identified.

The formation of the SiC phase may be caused by a redistribution reaction of SiC_xO_{4-x} units to SiO_4 and SiC_4 units [6] and by carbothermal reduction of SiO_2 with free carbon, resulting in the formation of gaseous CO [13]. These phase separation processes are assumed to be responsible for the decrease of the Young's modulus for sintering temperatures above 1200°C, as it is already known from silicon carbide fibers [14].

Conclusions

A method for the synthesis of thin, large area oxycarbide glass sheets with high fracture strength and high Young's modulus has been developed for the first time. The key was the incorporation of colloidal silica in the synthesis route. By this way the density and the porosity of the gel sheets can be increased, which is necessary for a crack-free sintering. Since the colloidal silica sol consists of non agglomerated 10 nm sized SiO_2 particles, the preparation of homogeneous silicon oxycarbide glass sheets with high fracture strength and Young's modulus is possible as a result of the dissolution of the silica particles during sintering. Further investigations with NMR will be carried out in the future in order to study the exact distribution of various oxycarbide units as a function of sintering temperature.

References

1. G.M. Renlund, S. Prosazka, and R.H. Doremus, J. Mat. Res. **6**, pt I: 2717; pt. II: 2723 (1991).
2. G.D. Soraru, G. D'Andrea, R. Compostrini, F . Babonneau, and G. Mariotto, J. Amer. Ceram. Soc. **78**(2), 379 (1995).
3. J. Homeny and S.H. Risbud, Mater. Lett. **3**(11), 432 (1985).
4. J. Homeny, G.G. Nelson, S.W. Paulik, and S.H. Risbud, J. Amer. Ceram. Soc. **70**(5), C-114 (1987).
5. H. Zhang and C.G. Pantano, J. Am. Ceram. Soc. **73**(4), 958 (1990).
6. G.D. Soraru, J. Sol-Gel Sci. and Tech. **2**, 843 (1994).
7. E. Breval, M. Hammond, and C.G. Pantano, J. Amer. Ceram. Soc. **77**(11), 3012 (1994).
8. R.P.J. Corriu, D. Leclercq, P.H. Mutin, and A. Vioux, Mat. Res. Soc. Symp. Proc. **346**, 351 (1994).
9. G.D. Soraru, E. Dallapiccola, and G. D'Andrea, J. Ceram. Soc. **79**(8), 2074 (1996).
10. N. Suyal, M. Mennig, and H. Schmidt, to be communicated to J. Non-Crystalline Solids.
11. Metals Handbook, Vol. 8: *Mechanical Testing* (Amer. Soc. for Metals, Ohio, 1985) pp. 628, 714. OR Deutsche Norm, DIN 51 110 Teil 3 (Deutsches Institut fuer Normung e.V. Berlin, Sept. 1993), pp. 2–16.
12. M.B. Wolf, *Chemical Approach to Glass* (Glass Science and Technology 7, Elsevier, 1984), pp. 152–154.
13. T. Shimbo, H. Chen, and K. Okamura, J. Ceram. Soc. Japan, Int. Edition **100**, 48 (1991).
14. T. Yamamura, T. Hurushima, M. Kimoto, T. Ishikawa, M. Shibuya, and T. Iwai, *High Tech Ceramics*, edited by P. Vincenzini (Elsevier Science Publishers B.V., Amsterdam, 1987), p. 737.

Journal of Sol-Gel Science and Technology 13, 1001–1004 (1998)
© 1998 Kluwer Academic Publishers. Manufactured in The Netherlands.

Sol-Gel Synthesis and Structure of Borosilicon Oxycarbide Glasses

A.M. WOOTTON AND M.H. LEWIS
Centre for Advanced Materials, University of Warwick, Coventry CV4 7AL, UK

Abstract. Existing sol-gel polymerization/pyrolysis routes employing two separate boron containing metal alkoxide precursors have been applied to form multi-component silicon oxycarbide glasses based on a borosilicon oxycarbide (B—Si—O—C) system. ^{29}Si and ^{11}B magic angle spinning nuclear magnetic resonance (MAS-NMR) was used to characterize the atomic structure of the gels, glasses and glass ceramics. Structural changes such as glass formation and crystal nucleation were identified by X-ray diffraction (XRD). Transmission electron microscopy (TEM) provided images of crystal nucleation and growth.

Keywords: structure, borosilicon, MAS-NMR, oxycarbide, multi-component

Introduction

The process of making anionic substitutions into conventional glass network structures has been used for some time [1]. The incorporation of carbon bonding to four silicon cations in the glass network can result in a high degree of cross linking, tightened network and strengthened molecular structure [2]. Fabrication routes employing the sol-gel process offer a more reliable method for the preparation of carbon containing glasses [3]. This route was first suggested by evidence of amorphous silicon oxycarbide species ($SiC_{4-x}O_x$) in polycarbosilane derived fibers such as Nicalon [4].

Using alkoxysilane precursors the required Si—C bonds can be retained through the hydrolysis, polymerization, and inert atmosphere pyrolysis yielding black glasses with bonded carbon $\leq$18 wt% [5]. These black glasses typically exhibit combinations of the four $SiC_{4-x}O_x$ bond types found around the silicon nucleus [6–8].

Methods and Materials

Methyltrimethoxysilane, trimethylborate [$B(OCH_3)_3$] and a boron containing aromatic precursor were used for the B—Si—O—C glasses, trimethylborate being one of the most frequently used borosilicate glass precursors [9].

Borosilicon Oxycarbide Gel Preparation

Partial hydrolysis of the less reactive siloxane component followed by the addition of boron containing precursors has been a frequently applied method for the preparation of ordinary borosilicate gels [9]. A B—Si—O—C solid, porous xerogel containing 30 mol% B_2O_3 was successfully prepared by applying similar reaction parameters. Methyltrimethoxysilane was partially hydrolyzed using a H_2O : silane ratio of 2 : 1 at room temperature for an hour under acidic (pH 2–3) conditions with ethanol as solvent (30 vol% addition). The trimethylborate with the remaining H_2O requirement was then added and the stirred solution held at 60°C for another hour for further hydrolysis and polymerization. The sols were gelled and aged at room temperature between 5 and 21 days and were dried at 60°C for 3 days (heating rate 5°C/h).

The above experimental procedure was successfully applied to the boron containing aromatic precursor to produce dry, porous xerogels containing 20 mol% B_2O_3.

The dried xerogels were transformed into glasses and crystallized by pyrolysis in a tube furnace under flowing argon between 800°C and 1600°C.

Structural Characterization

^{29}Si and ^{11}B magic angle spinning nuclear magnetic resonance (MAS-NMR) experiments were carried out on a spectrometer (Bruker MSL 360) operating at 8.45 T. Line broadening of 50 Hz for the gel and 200 Hz for the glasses was applied to the ^{29}Si spectra to obtain adequate signal to noise ratios.

X-ray powder diffraction (XRD) studies were carried out using a horizontal diffractometer (Philips PW1130/00) with a CuK_α X-ray source [10].

Both dark and bright field transmission electron microscopy (TEM) and selected area diffraction (SAD) analysis was carried out (Jeol 2000FX) on the most crystalline (1600°C) samples [10].

Results and Discussion

Trimethylborate Derived B—Si—O—C Glasses and Glass Ceramics

The ^{29}Si and ^{11}B MAS-NMR spectra provided a detailed characterization of the B—Si—O—C gel and glass structures.

The ^{29}Si MAS-NMR traces for the 30 mol% B_2O_3 containing gel and glasses shown in Fig. 1 demonstrate the continual modification of the silicon environment between 1000°C and 1600°C. The xerogel exhibits a predominant peak at −65.0 ppm which can be assigned to $[H_3CSiO_3]$ species. The slight shoulder apparent on this main peak at −56.5 ppm is attributed to $[H_3CSiO_2OH]$. The spectrum of the glass sample pyrolyzed at 1000°C shows the structural changes involved in the gel to glass conversion. The main peak is now assigned to $[SiO_4]$ at −110.0 ppm with a smaller $[CSiO_3]$ peak being apparent at −69.0 ppm, indicating that Si—C bonds have been formed and retained during pyrolysis. The 1300°C spectra shows the formation of $[C_2SiO_2]$ groups at −37.0 ppm and $[SiC_4]$ groups at −11.0 ppm. At the peak pyrolysis temperature (1600°C) all Si—C bonding has transformed to the $[SiC_4]$ group at 13.0 ppm.

The ^{11}B MAS NMR spectra for the same 30 mol% B_2O_3 containing xerogel and glass system are shown in Fig. 2. The isotropic chemical shift is observed at the left edge of the peak at 10 ppm. The characteristic BO_3 doublet lineshape is exhibited by the gel and 1300°C samples. For the 1000°C and 1600°C samples the upfield lineshape intensity has been increased giving a more symmetrical spectra. This can be attributed to a narrow BO_4 Gaussian lineshape being superimposed over the second order doublet at approx. −4 ppm. This small intensity increase indicates the existence of <5% BO_4 species.

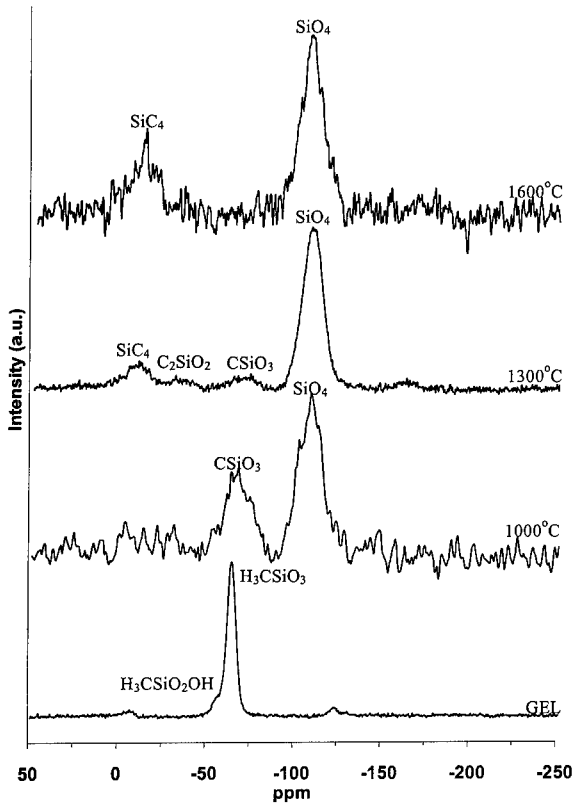

Figure 1.

The XRD spectra provided complementary findings to the MAS-NMR data for the 30 mol% B—Si—O—C gels and glasses:

- gel to glass conversion occurs at 1000°C.
- crystallization of the glasses commences at 1300°C in the form of nanosized β-SiC crystallites.
- reflections become stronger >1300°C indicating an increased volume of β-SiC crystallites.

TEM investigations of B—Si—O—C glasses pyrolyzed at 1600°C demonstrated limited, localized β-SiC crystallization (5–20 nm sized crystallites) within an amorphous matrix.

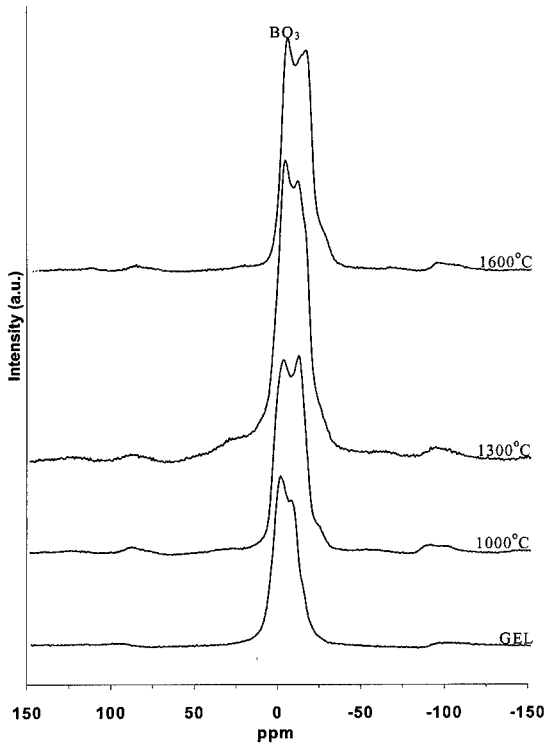

Figure 2.

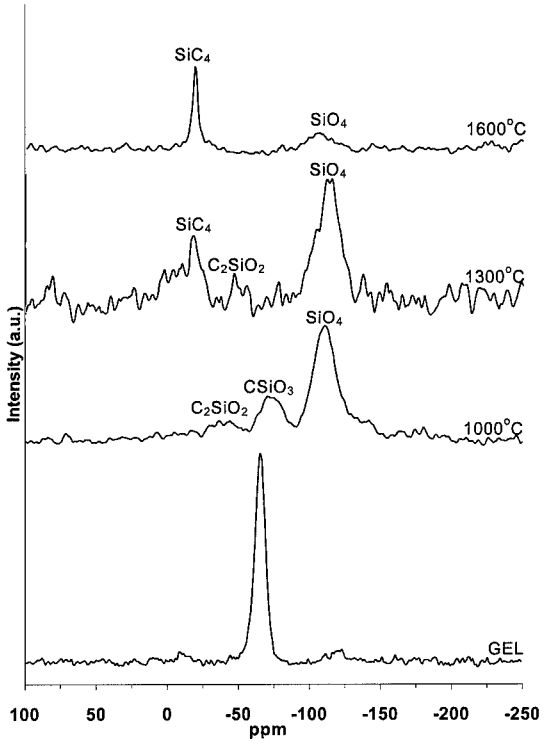

Figure 3.

Aromatic Boron Derived B—Si—O—C Glasses and Glass Ceramics

A 20 mol% B_2O_3 containing gel was successfully produced by the sol-gel process using the aromatic boron precursor. ^{29}Si and ^{11}B MAS-NMR spectra characterized the atomic structure of the B—Si—O—C gel and glasses.

Figure 3 shows the ^{29}Si MAS-NMR spectra for the 20 mol% B_2O_3 containing glass system. The spectrum of the glass sample pyrolyzed at 1000°C shows a predominant [SiO_4] peak at −110.0 ppm with a smaller [$CSiO_3$] peak apparent at −69.0 ppm. A small, broad peak at approx. −37.0 ppm is attributed to [C_2SiO_2] species. These sites indicate the formation and development of Si—C bonds at substantially lower temperatures than the trimethylborate precursor. The 1300°C spectra displays the initial development of [SiC_4] species at approx. −17.0 ppm. At the peak pyrolysis temperature (1600°C), [SiC_4] species in the form of β-SiC predominate, demonstrated by the tall, narrow peak at approx. −17.0 ppm. The remaining [SiO_4] species are evident by the small, broad peak at −110.0 ppm. This indicates Si atoms being consumed by available C atoms forming [SiC_4] species with accompanying B-SiC crystallization at the expense of amorphous [SiO_4] species. The carbon contained in the benzene ligand appears to have remained stable throughout the sol-gel process and has become readily available to form Si—C species between 1000°C and 1600°C. The XRD spectra confirm a substantial increase in volume of β-SiC crystallization between 1300°C and 1600°C. TEM investigations of samples pyrolyzed at 1600°C again displayed randomly oriented β-SiC crystallites between 5–20 nm in size.

The ^{11}B MAS-NMR spectra are shown in Fig. 4. The 1000°C spectra exhibits two characteristic shoulders on the downfield BO_3 curve indicating possible carbon-boron bonding. The 1300°C spectra displays >95% trigonally co-ordinated B^{III} species at −12.0 ppm with a small amount (<5%) of tetrahedrally co-ordinated B^{IV} at −25.0 ppm. However, the sample pyrolyzed at 1600°C shows evidence of increased upfield lineshape intensity giving a more symmetrical spectra. This can be attributed to a possible increase in the amount of B^{IV} co-ordinated species with the narrow Gaussian lineshape being superimposed over the second order doublet at approx. −22.0 ppm. This increase in BO_4 could

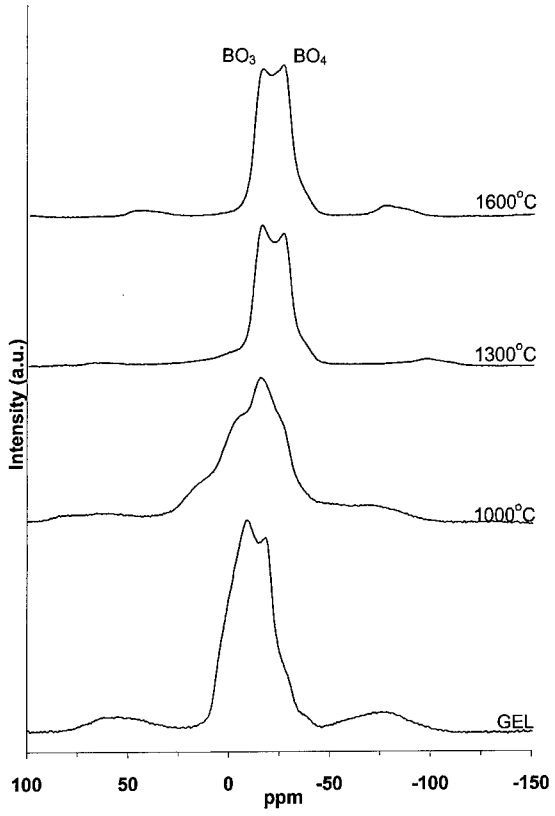

Figure 4.

be due to increased available oxygen due to the reduction in $[SiO_4]$ species.

Summary and Conclusions

Borosilicon oxycarbide glasses have been successfully prepared by sol-gel methods using two differing boron containing metal-organic precursors namely, trimethylborate and a boron containing aromatic.

^{29}Si MAS-NMR of samples pyrolyzed at 1000°C has shown direct evidence of C atoms bonded to the glass network in the form of $[CSiO_3]$ and $[C_2SiO_2]$ groups. The local environment of silicon atoms in B—Si—O—C glass systems has been shown to contain a random combination of four of the five possible $SiC_{4-x}O_x$ metastable tetrahedral sites.

For trimethylborate based precursor samples at temperatures >1300°C the exothermic crystallization of β-SiC results in the re-distribution of the Si local environment into $[SiC_4]$ and $[SiO_4]$ species. The ^{11}B MAS-NMR spectra indicated predominantly B^{III} trigonally co-ordinated species.

The aromatic based precursor displayed Si—C bond formation at temperatures ~1000°C with a considerable increase in β-SiC formation at 1600°C than the trimethylborate precursor. Trigonal B^{III} co-ordination sites were observed with an increase in tetrahedrally co-ordinated B^{IV} species at 1600°C.

No boron crystalline species were evident in XRD studies at elevated temperatures.

References

1. P.W. McMillan, *Glass Ceramics*, 2nd edition (Academic Press, London, 1979).
2. J. Homeny, G.G. Nelson, S.W. Paulik, and S.H. Risbud, J. Am. Ceram. Soc. **70**, C-114–C-116 (1987).
3. H. Zhang and C.G. Pantano, J. Am. Ceram. Soc. **73**, 958 (1990).
4. L.C. Sawyer, R.T. Chen, F. Haimback, P.J. Harget, E.R. Prack, and M. Jaffe, Ceram. Eng. Sci. Proc. **7**, 914 (1986).
5. F.K. Chi, Ceram. Eng. Sci. Proc. **4**, 704 (1983).
6. G.M. Renlund, S. Prochazka, and R.H. Doremus, J. Mater. Res. **6**, 2723 (1991).
7. F. Babonneau, L. Bois, and J. Livage, J. Non-Cryst Solids **147/148**, 280 (1992).
8. R.J.P. Corriu, D. Leclercq, P.H. Mutin, and A. Vioux, J. Mater. Sci. **30**, 2313 (1995).
9. B.E. Yoldas, J. Mater. Sci. **14**, 1843 (1979).
10. A.M. Wootton, M. Rappensberger, M.H. Lewis, S. Kitchen, A.P. Howes, and R. Dupree J. Non-Cryst. Solids. **204**, 217 (1996).

Journal of Sol-Gel Science and Technology 13, 1005–1010 (1998)
© 1998 Kluwer Academic Publishers. Manufactured in The Netherlands.

Influence of the Heating Rate on the Microstructure and on Macroscopic Properties of Sol-Gel SnO_2 : Sb Coatings

J. PÜTZ, D. GANZ, G. GASPARRO AND M.A. AEGERTER
Institut für Neue Materialien—INM, Department of Coating Technology, Im Stadtwald, D-66123 Saarbrücken

Abstract. Sol-gel dip-coated films of transparent conducting antimony-doped tin oxide (SnO_2 : Sb) have been heat treated with heating rates varying from 0.2 to 4300 K/s using either a furnace or cw CO_2 laser irradiation. The final sintering temperature of 540°C was maintained for up to 15 min. The sheet resistance of the coatings decreases with increasing heating rate. A decrease of the sheet resistance with the sintering time at constant temperature can be observed for low heating rates but the final values are higher than those obtained with higher heating rates. It is assumed that the densification of the coatings is determined by a competition between the nucleation at low temperatures and the growth of the crystallites at high temperatures. The microstructure of the coatings has been investigated by high resolution TEM cross-sections, X-ray diffraction, and Rutherford back scattering (RBS) and has been correlated to the resulting electrical properties measured by 4 point technique. Different mechanisms of heating arise with the furnace and the cw CO_2 laser.

Keywords: SnO_2 : Sb, transparent conducting coating, sol-gel process, sintering, heating rate

1. Introduction

Transparent conducting coatings like antimony-doped tin oxide (ATO) are widely used as a basic component in optoelectronic applications [1]. Compared to SnO_2 : Sb coatings prepared by vapor deposition techniques [2, 3], sol-gel based films heat treated in a conventional furnace have resistivities which are at least one order of magnitude higher [4, 5]. To some extent this can be attributed to the microstructure of the sol-gel films, i.e., the smaller crystallite size and their high porosity of up to 50–60% [5]. These structural differences can be explained by a competition between nucleation and crystal growth occurring in the early stages of heat treatment as was observed during the rapid thermal annealing (RTA) of TiO_2 [6] and ZrO_2 [7].

In this paper it is shown for single layers of sol-gel SnO_2 : Sb that the thermal treatment of the films and, especially the initial heating rate, substantially influences its film microstructure and therefore determines the electrical properties of the films. The heating rates were varied over a large scale (0.2–4300 K/s) surpassing those typically achieved with rapid thermal annealing [6].

2. Experimental

Single layer SnO_2 : Sb films were dip coated from 0.5 M ethanolic solution of $SnCl_2(OAc)_2$ with 5 mol% $SbCl_3$ onto fused silica substrates. The films were treated in a furnace with a heating rate of 0.2 K/s or by cw CO_2 laser irradiation [8] with heating rates ranging from 8 to 4300 K/s, respectively. While the highest rates have been performed in a fast scanning mode [8], heating rates from 8 to 500 K/s were realized with a single laser spot by adjusting the power density of the beam [9]. The time τ_r to reach the final sintering temperature of 540°C was used to calculate the average heating rate for the laser treated samples. The substrate temperature was determined using a calibrated fast pyrometer [10]. After the initial heating ramp the temperature was kept constant for a period τ_s of up to 15 min leading to a total sintering time of $\tau_t = \tau_r + \tau_s$.

In another series of measurements the samples have been put directly into the preheated furnace at $T_s = 540$°C. For these samples the corresponding heating rate could not be determined but it is estimated to be about 1 K/s. Hence, a distinction between the ramp and sintering phase is not possible.

HRTEM cross-sections, X-ray diffraction, and Rutherford back scattering have been used to investigate the morphology of the samples. The sheet resistance has been obtained from 4 point measurements. The film thickness was determined with a surface profiler (Tencor P10).

3. Results and Discussion

The variation of sheet resistance with the heating rate is given in Fig. 1 where the first values in each series corresponds to the ramp time τ_r. The sheet resistance decreases with increasing heating rate from about 5 $k\Omega_\square$(0.2 K/s) to 800 $k\Omega_\square$ (4300 K/s). The influence of the sintering time τ_s on the sheet resistance depends on the heating rates. For high heating rates of 100 to 500 K/s the sheet resistance stays nearly constant in time whereas the sheet resistance for furnace fired samples with a heating rate of 0.2 K/s slightly decreases. The final sheet resistance therefore is dependent on the heating rate.

The variations in sheet resistance cannot be attributed to a change in film thickness (see Fig. 2) but arise from differences in the microstructure of the coatings. The initial thickness of the gel film of 158 nm is reduced to about 140 nm for a heating rate of 0.2 K/s (furnace) and to 107 nm for a heating rate of 4300 K/s (laser treated sample). The furnace treated samples have a shrinkage of less than 10% indicating that the porous structure of the gel film is largely retained while the laser treated samples with a higher shrinkage of about 30% should have a denser structure. As the total mass of the films has to be the same, this can only reflect a large difference in the sintered film density which is confirmed by RBS density measurements. The densities are 3.2 and 4.8 $g \cdot cm^{-3}$ for the furnace and laser treated sample, respectively, which corresponds to porosities of 50 and 30%, respectively, assuming a theoretical density of 7.0 $g \cdot cm^{-3}$ for pure SnO_2.

This difference in morphology is clearly seen in the HRTEM cross-sections of two samples both heat treated at 540°C at a rate of 0.2 and 2600 K/s, respectively (Figs. 3 and 4). For the furnace treated sample with the low heating rate (Fig. 3) a loose structure of small crystallites, intercepted by numerous pores, can be seen. In contrast, the laser treated sample (Fig. 4) is denser and consists of larger crystallites in a less porous structure [5].

A similar trend of densification with increasing heating rate is evidenced by the crystallographic grain size.

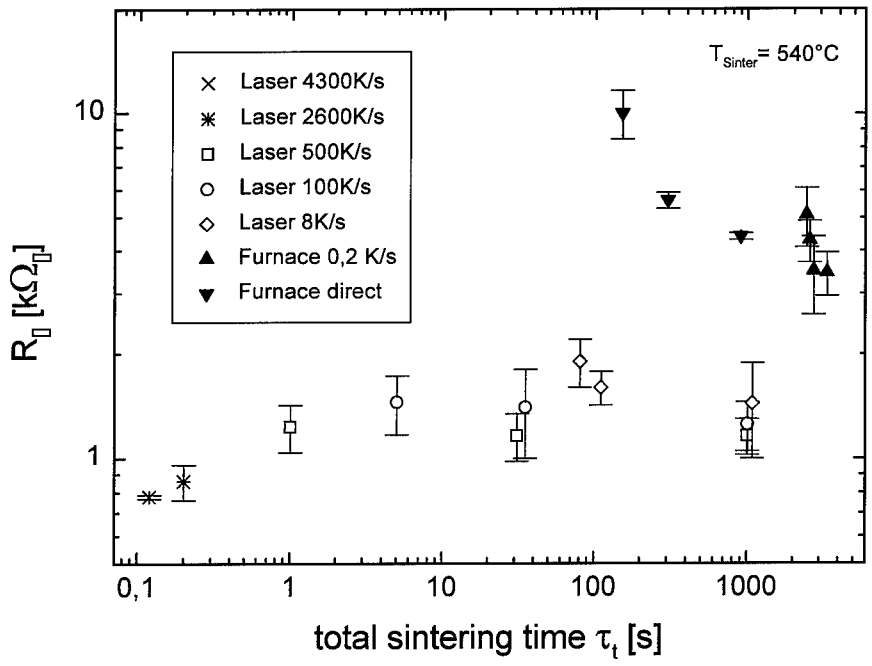

Figure 1. Sheet resistance of SnO_2 : Sb coatings prepared with different heating rates using either a furnace or a cw CO_2 laser at a final sintering temperature of 540°C.

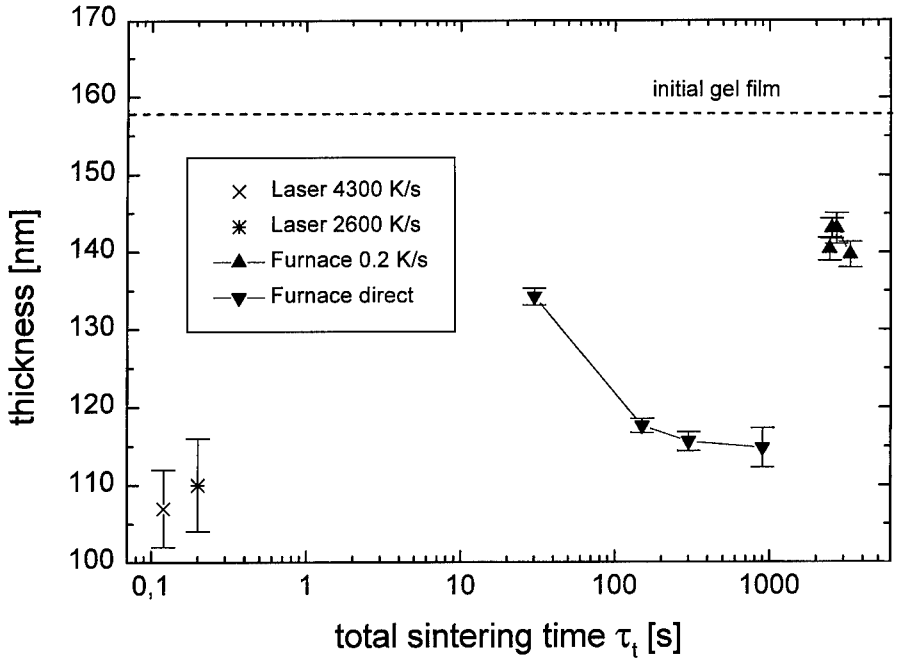

Figure 2. Film thickness of samples heat treated with different heating rates at a final sintering temperature of 540°C. The thickness of the initial gel film is 158 nm.

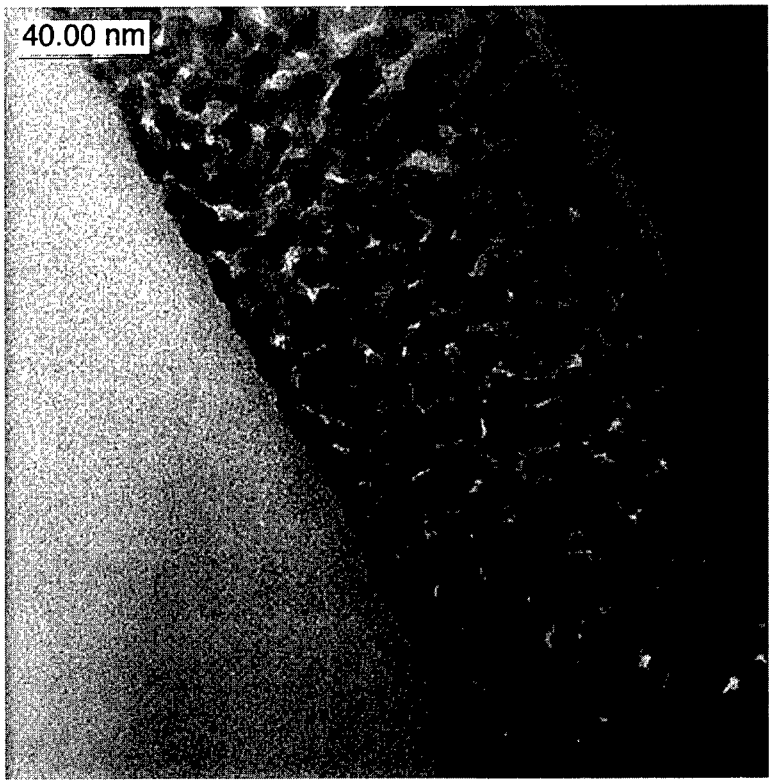

Figure 3. HRTEM cross-section of an SnO_2 : Sb coating heat treated in a furnace at a heating rate of 0.2 K/s.

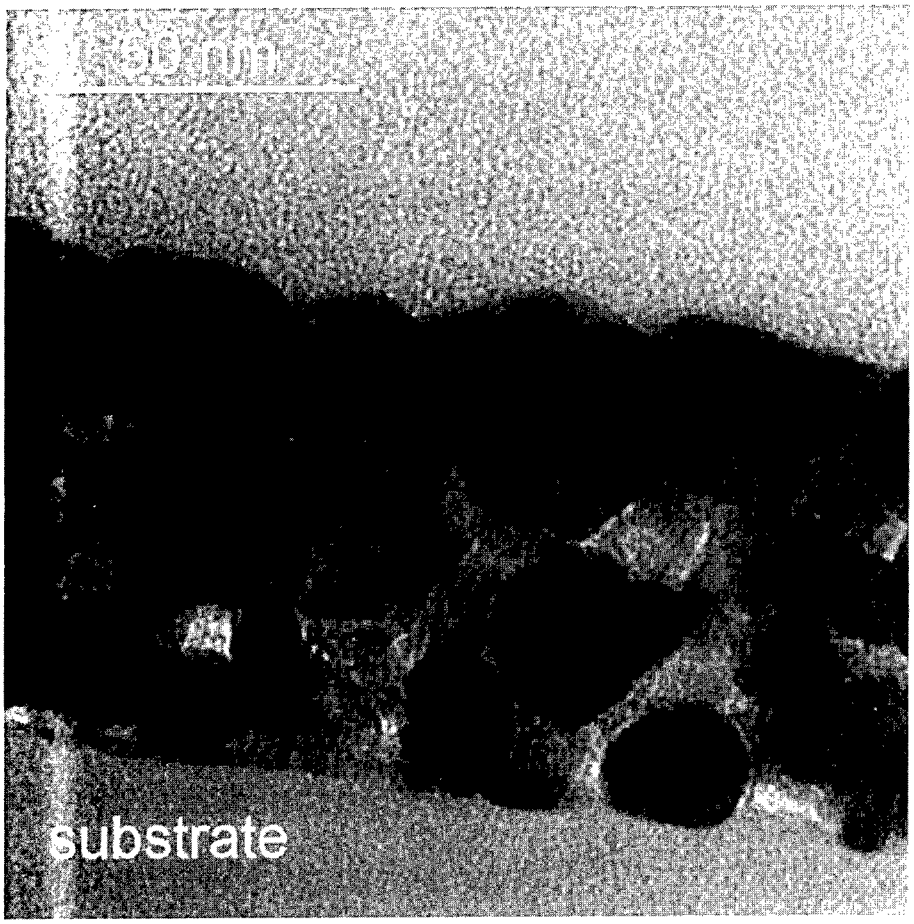

Figure 4. HRTEM cross-section of an SnO_2 : Sb single layer heat treated with a cw CO_2 laser and a heating rate of 2600 K/s.

The furnace treated samples typically have crystallite sizes of 5–6 nm whereas higher heating rates lead to crystallites of 8 nm (2600 K/s) and 12 nm (4300 K/s). The crystal structure of all investigated samples corresponds to natural cassiterite.

The results lead to the conclusion that a competition between nucleation and crystal growth is responsible for the differences in the densities. At lower temperatures a nucleation process takes place whereas at higher temperatures crystallite growth can be observed [11]. Low heating rates favor the formation of numerous nuclei. By the use of high heating rates this nucleation process is passed through very quickly leading to few nuclei that can grow more easily because of shorter diffusion pathways.

The series of samples fired in a pre-heated furnace shows a different behavior, with a higher decrease in sheet resistance from 800 to 4.4 $k\Omega_{\square}$ after 15 min (Fig. 1). The final thickness of the film is 115 nm (Fig. 2) which is smaller than that of the slowly heated furnace samples but only slightly higher than that obtained with laser treated samples. This higher densification in a pre-heated furnace compared to more slowly furnace fired films is due to the formation of a dense surface layer [5], which is shown in Fig. 5.

An explanation for this could be different mechanisms of heating for pre-heated and slow furnace firing, respectively, and for CO_2 laser treatment. For the low heating rates in the furnace a uniform temperature profile through the sample can be assumed. The slow increase in temperature allows for a complete escape of volatile compounds during film formation. The structure of the coatings is homogeneous and porous, reflecting the loose structure of the gel film. The film is formed by the aggregation of small crystallites, which results in a high sheet resistance, due to a large number

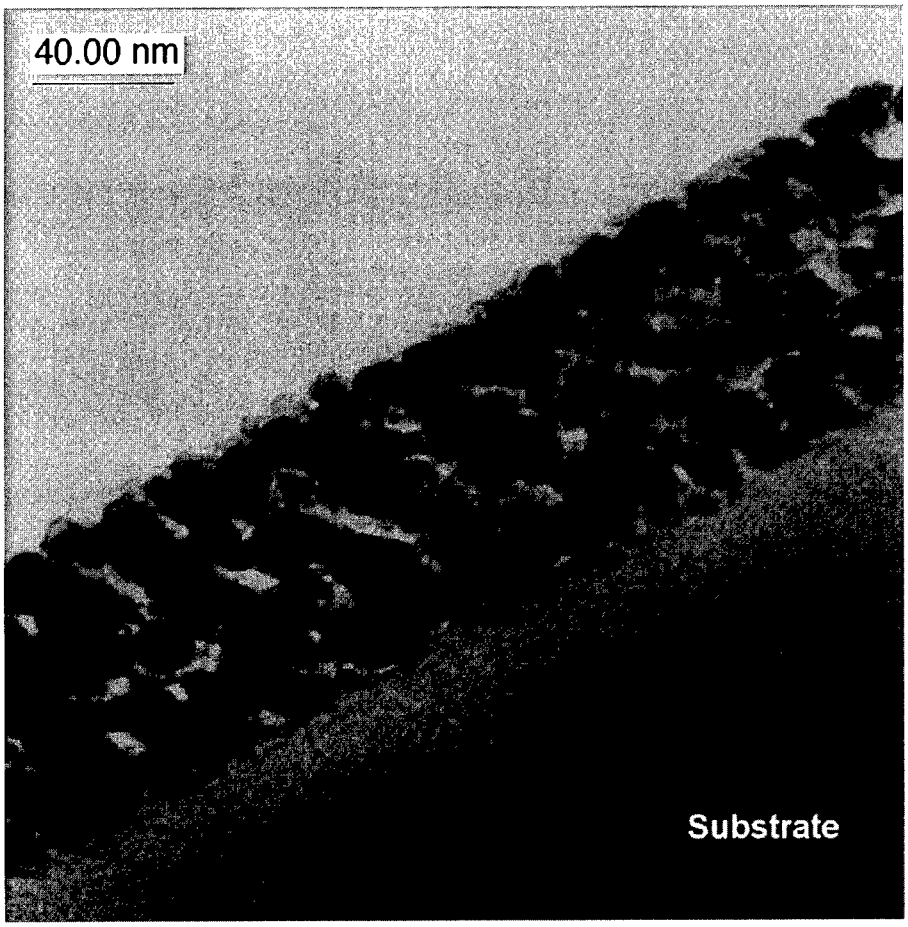

Figure 5. HRTEM cross-section of a SnO_2 : Sb coating prepared by firing in a pre-heated furnace with a heating rate of ca. 1–2 K/s.

of grain boundaries. With pre-heated furnace firing (rate ~1 K/s) the heat has to be conducted from the film surface to the substrate. The upper film surface is heated quickly leading to a thin dense layer which seals the film bulk. Thus, the evaporation of residues from the gel film is impeded and further heating is retarded as the conductive surface layer reflects heat radiation and the sample has to be heated mainly by heat conduction. As a consequence the film bulk exhibits a structure similar to that observed with slow furnace firing. The sheet resistance in both films is about the same as the crystallite sizes are similar, but for the pre-heated furnace fired sample this is obtained with a lower film thickness. This implies a higher overall density for these films.

In contrast, the laser treated samples are mainly heated from the substrate side as the gel film practically does not absorb at 10.6 μm. The sintering of the films proceeds from the substrate towards the film surface. As the transport of heat through the thin film is fast and hence the heating is high, the low number of nuclei that is formed in this time allows a growth of larger crystallites. This leads to a homogeneous structure with a higher density and consequently to a better sheet resistance due to a reduced number of grain boundaries.

4. Conclusions

Heat treatment of SnO_2 : Sb thin films with different heating rates from 0.2 to 4300 K/s at a sintering temperature of 540°C has shown that the heating rate decisively determines the film morphology. It is proposed that this is caused by a competition between nucleation at lower temperatures and the growth of the formed nuclei at higher temperatures. Whereas slowly heated

samples present a porous structure of small crystallites, the laser samples are denser and consist of significantly larger crystallites with few pores. The porosity and the limited crystallite size of sol-gel processed SnO_2 : Sb thin films can therefore be overcome if heating rates in the order of 10^4 K/s, which can only be obtained by high power laser irradiation are closer. In this way a sheet resistance as low as 250 $\Omega_\square$ in 120 nm thick coatings (resistivity of $3 \times 10^{-3} \Omega \cdot$ cm) [5] has been obtained. Due to the high energy density and the fact that CO_2 laser irradiation, unlike rapid thermal annealing, can heat glass substrates directly, this method seems favorable for the investigation of sintering processes with heating rates in the range from 0.1 to 10^4 K/s.

Acknowledgments

Dr. Th. Krajewski is gratefully acknowledged for the preparation of the HRTEM cross-sectional images and C. Battaglin for the RBS measurements performed at the Department of Physics of the University of Padova.

References

1. K.L. Chopra, S. Major, and D.K. Pandya, Thin Solid Films **102**, 1 (1983).
2. H.S. Randhawa, M.D. Matthews, and R.F. Bunshah, Thin Solid Films **83**, 267 (1981).
3. E. Shanti, V. Dutta, A. Banerjee, and K.L. Chopra, J. Appl. Phys. **51**, 6243 (1980).
4. C. Terrier, J.P. Chatelon, R. Berjoan, and J.A. Roger, Thin Solid Films **263**, 37 (1995).
5. G. Gasparro, D. Ganz, J. Pütz, and M.A. Aegerter, in *Proc. of 1st International Conference on Coatings on Glass, ICCG (1996)* (Saarbrücken, Germany, 1996), to be published in J. Non-Cryst. Solids (1997).
6. J.L. Keddie and E.P. Giannelis, J. Am. Ceram. Soc. **74**, 2669 (1991).
7. R. Pascual, M. Sayer, C.V.R.V. Kumar, and L. Zou, J. Appl. Phys. **70**, 2348 (1991).
8. D. Ganz, G. Gasparro, A. Reich, and M.A. Aegerter, in *Proc. of PacRim 2* (Cairns, Australia, 1996), to be published.
9. D. Ganz, G. Gasparro, J. Otto, A. Reich, N.J. Arfsten, and M.A. Aegerter, J. Mater. Sci. Lett. (1997), in press.
10. D. Ganz, A. Reich, and M.A. Aegerter, in *Proc. of 1st International Conference on Coatings on Glass, ICCG (1996)* (Saarbrücken, Germany, 1996), to be published in J. Non-Cryst. Solids, (1997).
11. M. Avrami, J. Chem. Phys. **9**, 177 (1941).

Journal of Sol-Gel Science and Technology 13, 1011–1016 (1998)
© 1998 Kluwer Academic Publishers. Manufactured in The Netherlands.

Production of Titanate Microspheres by Sol-Gel and Spray-Drying

E. SIZGEK AND J.R. BARTLETT
Materials Division, Australian Nuclear Science and Technology Organisation, Private Mail Bag 1, Menai NSW 2234, Australia

M.P. BRUNGS
School of Chemical Engineering and Industrial Chemistry, The University of New South Wales, Sydney 2052, Australia

Abstract. Porous titanate precursor microspheres (20–60 μm in diameter), with a high sorption capacity for radioactive wastes from nuclear reprocessing plants, have been produced on a 50 kg scale by spray-drying precursor sols. Well-dispersed, stable sols were produced by hydrolyzing acetic acid modified tetraisopropyltitanate and peptizing the titania hydrolysate with acidic zirconia sol. The resulting TiO_2/ZrO_2 sols were routinely concentrated to 900 g dm^{-3} (oxide basis) and exhibited excellent stability. These sols were subsequently mixed with dispersible alumina powder and partially aggregated by adding calcium and barium nitrate salts. The resulting sols were spray-dried to produce microspheres with controlled porosity and morphology. The properties of the spray-dried powder were very dependent upon the chemical properties of the precursor sol. In particular, hollow spheres were produced from well-dispersed sols, whereas solid spheres could be produced from partially-aggregated sols.

Keywords: microspheres, sol-gel, titania, Synroc, spray-drying

Introduction

Synroc is a multi-component titanate ceramic, designed to immobilize high level liquid waste (HLLW) from nuclear fuel reprocessing plants [1]. The Synroc concept involves immobilizing the elements present in HLLW within an assemblage of mutually compatible, thermodynamically stable mineral phases, namely hollandite, zirconolite and perovskite. These minerals are formed during calcination and hot-pressing of a precursor powder containing TiO_2, ZrO_2, Al_2O_3, BaO and CaO in relative mass abundances of 71.4, 6.6, 5.4, 5.6 and 11.0%, respectively.

Various technological aspects of HLLW processing make the use of free-flowing, dust-free and highly sinterable precursor powders desirable. Such multi-component titanate powders have been produced by spray-drying colloidal precursors, yielding microspherical particles with controlled morphology [2]. This paper discusses the preparation of the microspherical precursor particles by spray-drying of sols, and investigates the influence of sol aggregation and drying rate on the morphologies of the microspheres.

Experimental

Preparation of Well-Dispersed $TiO_2/ZrO_2/Al_2O_3$ (TZA) Sol. Equivalent molar quantities of glacial acetic acid (42.2 kg, Ajaxchem, Australia) and tetraisopropyltitanate (200 kg, TPT, Hüls AG, Germany) were mixed in a stirred and cooled chemical reactor. The resulting alkoxyacylate was rapidly added to a large excess of deionized water at ambient temperature, producing large flocs of titania hydrolysate which settle rapidly. The settled product was washed with water to remove isopropyl alcohol and isopropyl acetate liberated during hydrolysis.

About half of the total required quantity (10.8 kg) of zirconium basic carbonate (Magnesium Electron

Ltd., UK, ~40 wt% ZrO_2) was added to 4.45 dm^{-3} of concentrated nitric acid ($[H^+]/[Zr(IV)] = 2$). The resulting solution was diluted with 5 dm^{-3} of deionized water and the remaining zirconium basic carbonate was added. The mixture was heated at 70°C for ca. one hour. The final sol was transparent and extremely stable.

The titania hydrolysate was peptized by adding the acidic zirconia sol, yielding a TiO_2/ZrO_2 (TZ) sol with an acid-to-titania mole ratio of ~0.1. The resulting translucent TZ sol was concentrated to over 900 g dm^{-3} (oxide basis) by evaporation. The stoichiometric quantity of fumed δ-Al_2O_3 (Degussa Aluminum Oxid-C) was dispersed in the concentrated TZ sol using a high-shear mixer, yielding a well-dispersed TZA sol.

Preparation of Partially-Aggregated Sols. The well-dispersed TZA sols were aggregated, prior to spray-drying, by adding appropriate quantities of aqueous barium and calcium nitrate solutions to produce $TiO_2/ZrO_2/Al_2O_3/BaO/CaO$ (TZABC) multi-component sols. In some cases, aqueous aluminum nitrate solution was used to aggregate the TZ or TZA sols for rheology investigations. The degree of aggregation was controlled by the amount of electrolyte added, and monitored by measuring the viscosity of the sols.

Production of Powders. Free-flowing TZA and TZABC powders were produced on a 50 kg batch scale from the appropriate sols by spray-drying (Niro Production Minor). The spray-drying experiments were carried out using both rotary disk and ultrasonic atomizers. The water evaporation rate was typically 1 to 10 kg per hour, while the inlet air temperature was maintained between 100°C and 210°C. The spray-dried powders were then calcined at 450°C, in air, to decompose nitrate compounds and residual organic species and improve the mechanical strength of the microspheres.

Characterization of Sols and Gels. Scanning electron micrographs (SEM) of the gel microspheres were obtained using a JEOL JXL-840 microscope. The particle size distributions and viscosities of the sols were determined with a Malvern Autosizer IIC and a Brookfield RVTDV-IICP viscometer, respectively. The total oxide content of the sols was measured by thermogravimetry.

Results and Discussion

Peptization of titania hydrolysate with an acidic zirconia sol produced a well-dispersed TZ sol with a particle size of <30 nm. The resulting sols were readily concentrated by conventional evaporation methods, and exhibited viscosities of <100 mPa·s at solids content of 900 g dm^{-3}. The viscosity of the well-dispersed sols exhibited Newtonian-like rheology.

In contrast, addition of aqueous aluminum or calcium nitrate solutions to the TZ sols yielded non-Newtonian (shear-thinning) dispersions (Fig. 1). Increasing concentrations of electrolyte resulted in an increase in the viscosity of the sol, due to an increase in the extent of aggregation [3]. As expected, the degree of aggregation is very sensitive to the concentration of solids; sols with concentrations exceeding 800 g dm^{-3} aggregated immediately following addition of very small amounts of electrolyte.

Spray-Drying and Particle Morphology. SEM micrographs of the gel microspheres produced by spray-drying well-dispersed and partially-aggregated TZA sols are illustrated in Figs. 2 and 3, respectively. Well-dispersed sols invariably yielded hollow and toroidal particles. In contrast, under certain conditions, "solid" microspheres were produced from the partially-aggregated sols. The characteristics of the particles produced from well-dispersed and aggregated sols are summarized in Fig. 4 as a function of droplet drying conditions.

Spray-Drying of Well-Dispersed Sols. During spray-drying of well dispersed sols, a gel layer initially forms at the surface of the drops due to rapid evaporation of water from the drop's surface. This gel layer is semi-permeable to water/vapor flow and reduces the rate of evaporation of the solvent. DLVO calculations for the net interaction potential between the colloidal aggregates (ca. 25 nm diameter) indicate that the barrier-to-aggregation in these sols is relatively high (>30 kT) [4]. Hence, gelation occurs by a reaction-limited process, producing a relatively dense microporous gel layer with correspondingly low permeability.

The reduced evaporation rate through the gel layer results in a temperature increase, which at high air inlet temperature leads to "ballooning." When the droplets are ejected from the atomizer through the heated air, one side of the droplet always is exposed to hotter

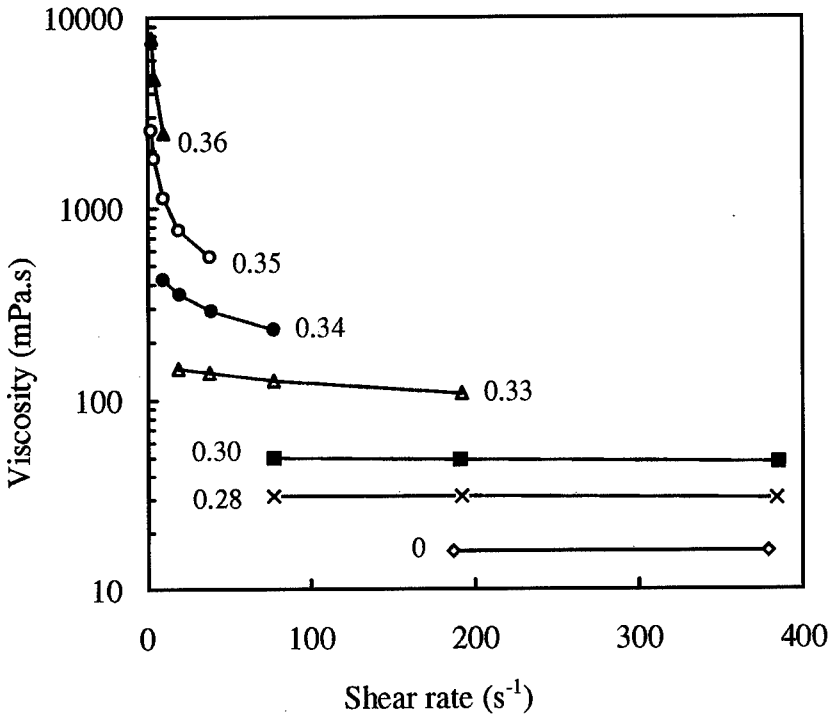

Figure 1. Viscosity of TZA sol (solids content = 550 g dm^{-3}) as a function of shear rate and $Al(NO_3)_3$ concentrations (mol dm^{-3}).

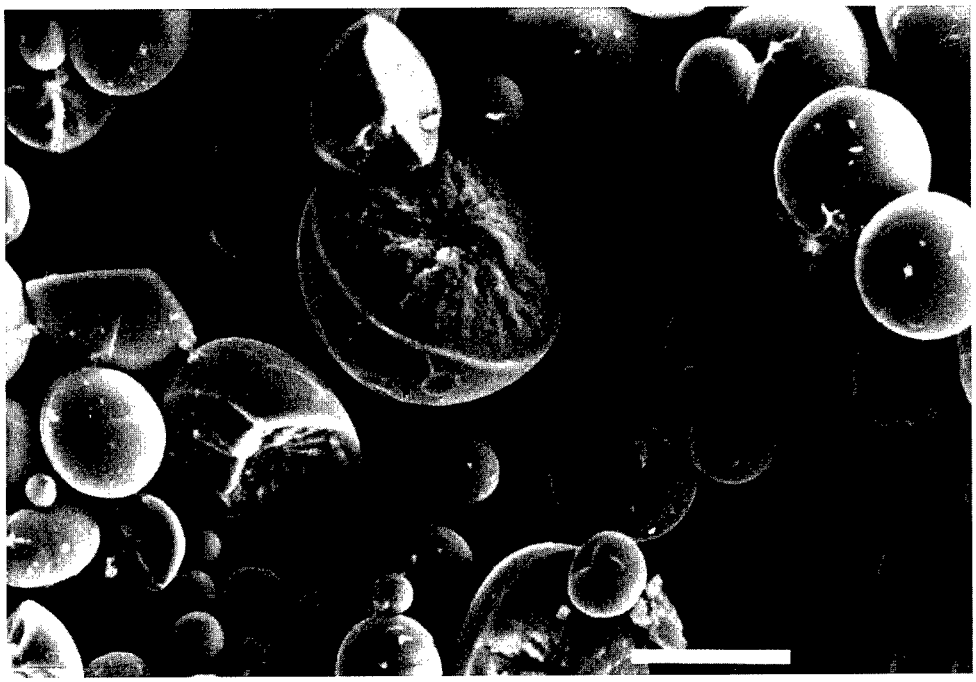

Figure 2. Spray-dried TZA powder produced from well-dispersed sol. $[Al(NO_3)_3] = 0$ mol dm^{-3} (solids content = 740 g dm^{-3}). Bar = 10 μm.

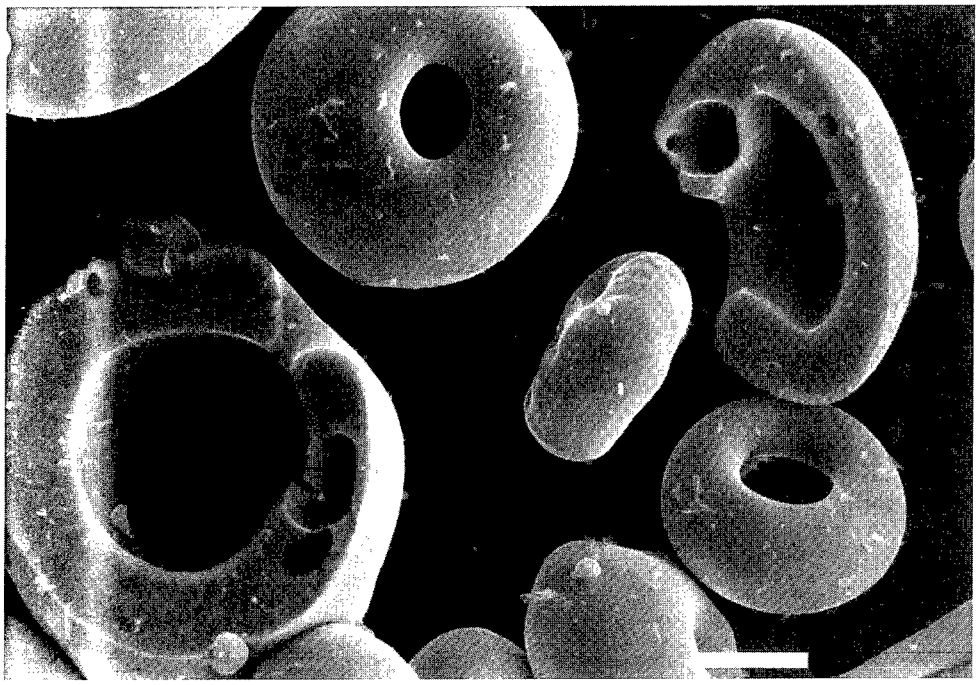

Figure 3. Spray dried TZA powder produced from partially-aggregated sol. $[Al(NO_3)_3] = 0.15$ mol dm^{-3} (solids content $= 700\,g\,dm^{-3}$). Bar $= 10\,\mu m$.

air stream and a skin forms on the hotter side. The cooler side is wetter and drawn inward and "doughnuts" (Fig. 2) are produced.

At low air inlet temperatures the well-dispersed colloids in the drop remain relatively mobile as water evaporates through the gel layer at the surface of the drop, producing a diffusion-gradient towards the surface. As liquid flows to the drop surface, with accompanying solids, a gradual growth of the solid shell occurs, leaving a void in the center of the particle. Apart from the effect of the drying rate, the shell thickness varies with the solids' concentration of the spray-dried feedstock. Dilute sols produce thin-walled particles, while concentrated sols yield thick-walled particles.

Spray-Drying of Partially-Aggregated Sols. The DLVO theory indicates that the addition of free electrolyte to a well-dispersed TZA sol reduces the interparticle potential-energy barrier to aggregation and a slow aggregation process commences above a critical electrolyte concentration. During spray-drying of such a metastable sol, the ionic strength within the atomized droplet increases rapidly as water evaporates from the surface. This process produces a corresponding further decrease in the barrier to aggregation in the droplet. After a certain degree of water evaporation, the ionic strength reaches a critical concentration at which there is no repulsive barrier to aggregation and the colloids within the droplet rapidly flocculate and the droplet gels. This sudden, volume gelation immobilizes the colloidal particles and prevents the formation of central voids in the microspheres (Fig. 3).

Computational fluid dynamics (CFD) simulations of the spray-drying of partially-aggregated sols revealed that the formation of solid spheres was also occurring through another complex mechanism. Differences in the coupled heat, momentum and mass transfer rates in droplets of different diameters leads to the formation of hollow spheres from droplets larger than a critical size (e.g., 30 μm). The CFD simulations reveal that increasing droplet size leads to a corresponding decrease in the drying rate [5], as expected. In addition, when the droplet trajectories and temperature isotherms in the spray drier were plotted from the simulation calculations, it was observed that smaller droplets are exposed to the hotter zone of the air stream in the drying chamber, which leads to a further increase in the relative drying rate of the smaller droplets. Thus, under identical drying conditions, larger drops require more drying time to reach the critical flocculation concentration. Hence, it is concluded that for a relatively large drop, the constant rate drying period should be extended.

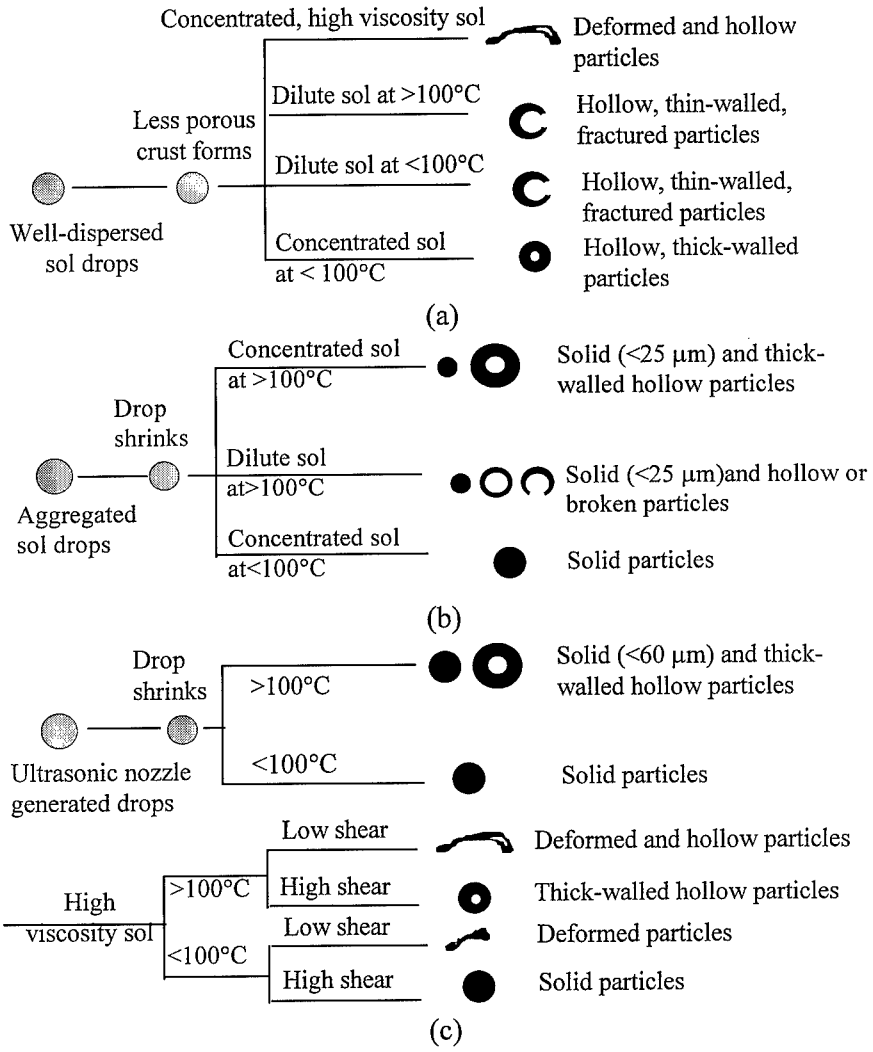

Figure 4. Effect of drying temperature and sol concentration on morphology of the particles produced from (a) well-dispersed and (b) aggregated sols. (c) The effect of shear treatment on morphology of particles produced from aggregated sols.

This allows the drop to shrink, until it reaches the critical flocculation concentration, without forming a crust on the surface. Therefore, in addition to the partial aggregation of sols, the effect of the drying rate on the morphology of the particles must be considered. The experiments revealed that under slow drying conditions, "solid" spheres as large as 80 μm in size can be produced from partially-aggregated sols.

Conclusions

It has been demonstrated that multi-component TiO_2-based sols can be produced consistently by a hybrid sol-gel process on a pilot-plant scale. The resulting sols demonstrated excellent stability over a period of three years and could be concentrated to in excess of 900 g dm^{-3}.

Experiments on spray-drying of sols have qualitatively shown that the droplets of electrokinetically stabilized sols follow more complicated drying mechanisms than ordinary water-solid mixtures or slurries. Spray-drying experiments revealed that in general hollow microspheres were produced from well-dispersed sols, while partially aggregated sols produced solid particles. It is concluded that the drying rate of the droplets also influences particle morphology. The increased rate of drying for the partially aggregated sols may result in

the formation of hollow particles over a certain particle size.

References

1. A.E. Ringwood, S.E. Kesson, K.D. Reeve, D.M. Levins, and E.J. Ramm, in *Radioactive Waste Forms for the Future*, edited by W. Lutze and R.C. Ewing (Elsevier Science, 1988), p. 233.
2. E. Sizgek, Production of Titanate Microspheres by Sol-Gel and Spray-Drying, Ph.D. Thesis, The University of New South Wales, Australia.
3. C.J. Brinker and G.W. Scherer, *Sol-Gel Science: The Physics and Chemistry of Sol-Gel Processing* (Academic Press, Boston, 1990).
4. J.R. Bartlett and J.L. Woolfrey, in *Chemical Processing of Advanced Materials*, edited by L.L. Hench (John Wiley & Sons, NY, 1992), p. 247.
5. D. Sizgek, unpublished data.

Journal of Sol-Gel Science and Technology 13, 1017–1021 (1998)
© 1998 Kluwer Academic Publishers. Manufactured in The Netherlands.

Preparation of Mullite Fibers by the Sol-Gel Method

K. CHANG SONG
Department of Chemical Engineering, Konyang University, Nonsan, Chungnam 320-030, Korea

Abstract. Mullite fibers were synthesized from an aqueous solution of aluminum isopropoxide, aluminum nitrate and tetraethylorthosilicate by the Sol-Gel method. The starting solution was prepared by adding aluminum isopropoxide and tetraethylorthosilicate simultaneously to an aluminum nitrate aqueous solution. The spinnability of the starting solution was investigated by varying the molar ratio of aluminum isopropoxide/aluminum nitrate in the solution. Gel fibers were obtained from solutions in a composition range of aluminum isopropoxide/aluminum nitrate of 3 to 5. Gels obtained from spinnable solutions appeared to have high homogeneity in the mixing of the Al/Si components, leading to a sharp 980°C exothermic peak in the DTA curve and a mullitization temperature of 1000°C. However, in the case of gels obtained from unspinnable solutions, a small 980°C exothermic peak was detected, and the mullitization temperature was as high as 1200°C, probably due to greater heterogeneity in the mixing of the Al/Si components.

Keywords: mullite fibers, sol-gel method, spinnability, DTA curves, XRD analysis

1. Introduction

Mullite ($3Al_2O_3 \cdot 2SiO_2$) fibers have attracted considerable attention because of their excellent high temperature strength and creep resistance, thermal and chemical stability, low thermal expansion coefficient and good dielectric properties [1].

There have been many reports describing successful methods for preparing mullite fibers by the Sol-Gel method [2–4]. For preparation of mullite fibers by the Sol-Gel method, tetraethylorthosilicate (TEOS) and aluminum alkoxide have generally been used as starting materials. However, the hydrolysis rate of aluminum alkoxide is much faster than that of TEOS, resulting in a poor level of chemical homogeneity in the gel fibers. This chemical heterogeneity has a weakening effect on the high temperature properties of the mullite fibers, especially creep resistance [4]. To circumvent this problem, many methods, including prehydrolysis of the silicon alkoxide [5], and modification of the aluminum alkoxide [6], have been used.

In this paper, the author reports a new synthesis method for the preparation of mullite fibers from the homogeneous gels obtained from aqueous solutions of aluminum isopropoxide, aluminum nitrate and TEOS. The conditions for obtaining a spinnable solution were investigated. The molecular structures of gel fibers were also studied.

2. Experimental

Aluminosilicate gels with the stoichiometric mullite composition (Al : Si = 3 : 1) were prepared as follows. Aluminum isopropoxide and aluminum nitrate were used as the alumina sources. TEOS was also used as the silica source. A 0.5 M aqueous solution was prepared from aluminum nitrate nonahydrate. To this solution, aluminum isopropoxide and TEOS were added simultaneously and stirred vigorously at room temperature for 24 h. Synthesized sols were aged in a dry oven maintained at 60°C until the solutions were spinnable. Spinnability of the sols was determined from the capability of fiber formation by immersing a glass rod of approximately 8 mm in diameter into the sols, then pulling it up quickly by hand. Drawn gel fibers were dried at room temperature for 2 days, then heated in air at a heating rate of 5°C/min in a range from 600 to 1200°C.

The thermal behavior of the gel fibers was investigated at a heating rate of 10°C/min in flowing air by DTA/TGA (STD2960, TA instruments). An X-ray diffractometer (D/MAX-IIIC, Rigaku) was used for identification of crystalline phases in the heated fibers. Ni-filtered CuK_α radiation was used as the X-ray source, and measurement was performed for diffraction angles between 10 and 70° in 2θ.

Table 1. Spinnability of mullite sols.

Sample number	$\frac{Al(OPr)_3}{Al(NO_3)_3}$	Initial state of solution	Spinnability of solution
1	0	Clear sol	No
2	1	Clear sol	No
3	3	Silver-gray clear sol	Yes
4	5	Silver-gray clear sol	Yes
5	7	Gray opaque sol	No

3. Results and Discussion

Table 1 shows characteristics of mullite sols prepared by dissolving various amounts of $Al(OPr)_3$ powder in the 0.5 M aluminum nitrate solution. All sols were prepared with the stoichiometric mullite composition. The spinnability of the sols is remarkably dependent on the content of dissolved $Al(OPr)_3$ powder. Gel fibers can be obtained from viscous solutions in a composition range of $Al(OPr)_3/Al(NO_3)_3$ molar ratio of 3 to 5 (samples 3 and 4). The more $Al(OPr)_3$ powder is dissolved, the more opaque and the more viscous the initial state of the solutions becomes.

In order to compare the difference between the thermal behavior of gels from spinnable solutions and those of gels from unspinnable solutions, the DTA/TGA curves of sample 4 and sample 2 in Table 1 are given in Figs. 1 and 2, respectively. In the data on sample 4 in Fig. 1, the TGA curve shows that most weight loss occurs below 600°C and total weight loss

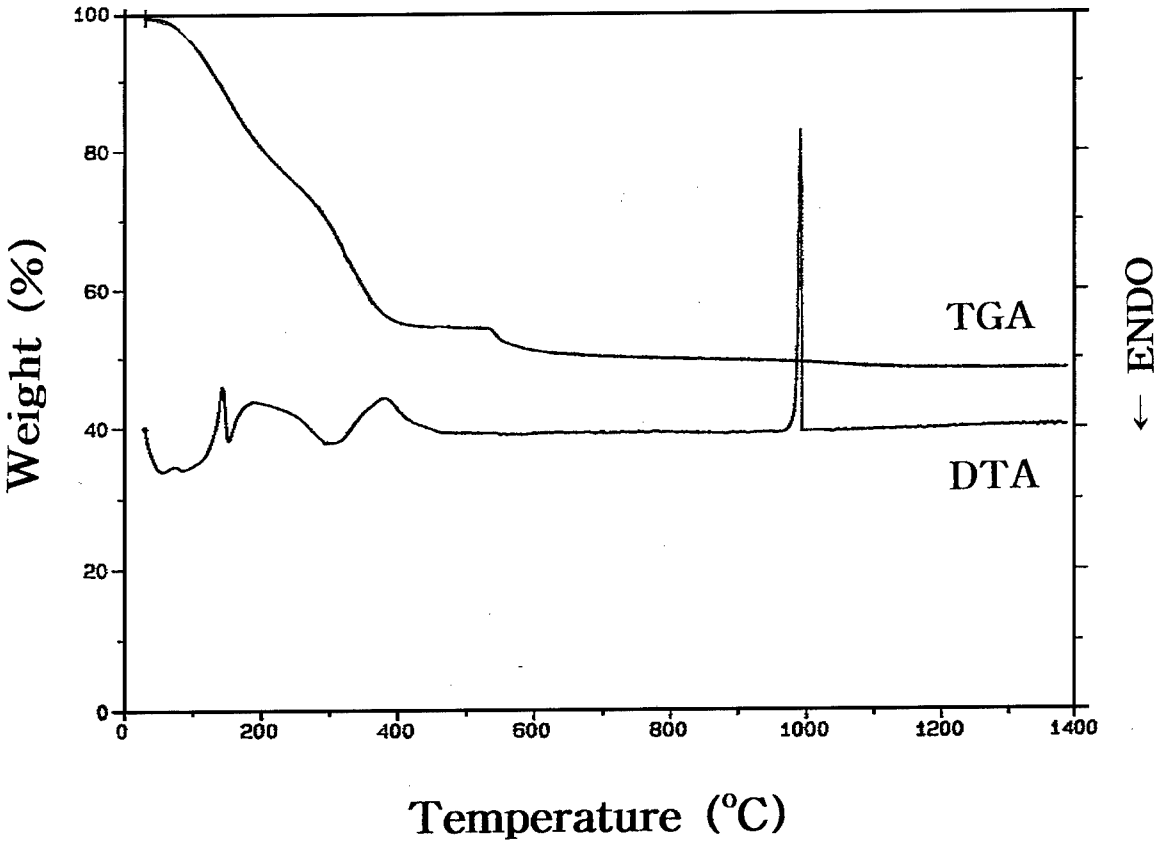

Figure 1. DTA/TGA curves of gel fibers prepared from sample 4 in Table 1.

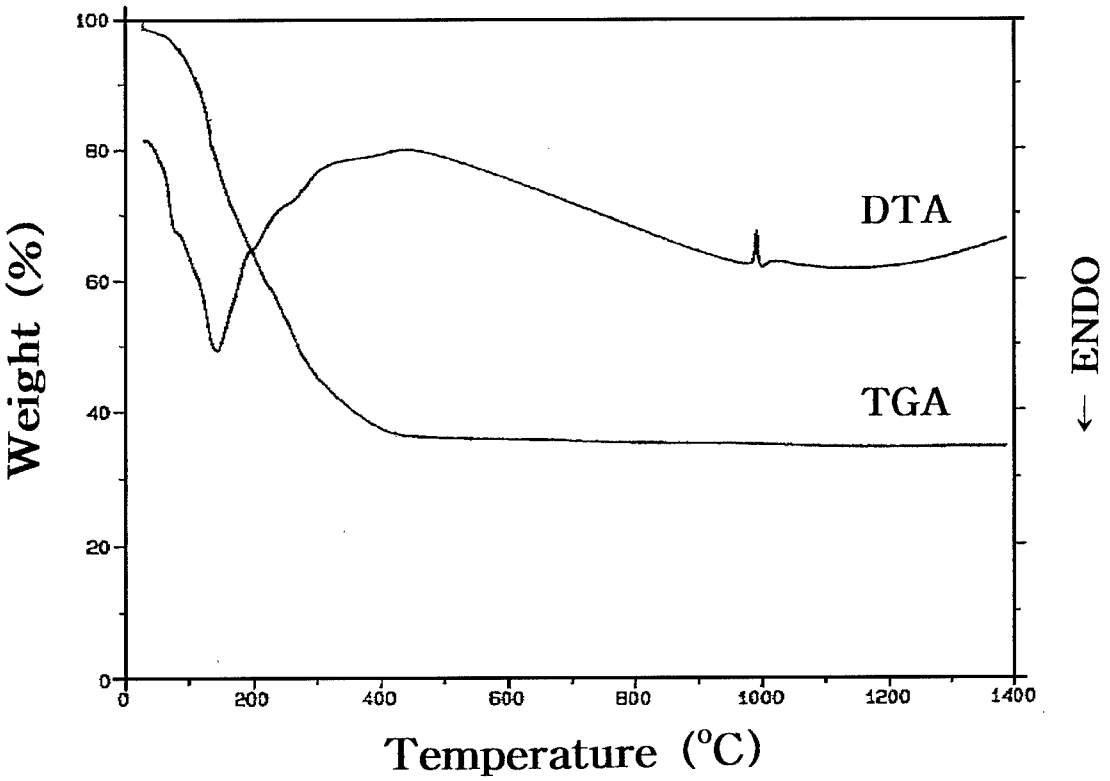

Figure 2. DTA/TGA curves of gel prepared from sample 2 in Table 1.

is 50%. In the DTA curve, two endothermic peaks observed below 200°C are due to the evaporation of absorbed water, while the exothermic peak at 400°C relates to burning of organics [7]. A strong exothermic peak is shown at about 980°C. On the other hand, the TGA curve of sample 2 in Fig. 2 indicates that there is a weight loss of 63% between 30 and 500°C, and no additional significant weight loss is seen up to 1400°C. In the DTA curve, the endothermic peak observed below 200°C is also attributed to the evaporation of absorbed water. A weak exothermic peak is observed at 980°C.

In the above thermal analysis, the most interesting feature is the intensity of the DTA exothermic peak at 980°C. The occurrence and intensity of this exothermic peak are closely related to the intimacy and homogeneity of the Al-Si components in the gels [8]. A sharp and strong 980°C exothermic peak indicates a better homogeneity in the degree of mixing of the Al and Si components in the gels. The DTA curve of the gel fibers in Fig. 1 shows a sharp exothermic peak at 980°C, while that of the gels obtained from the unspinnable solution shown in Fig. 2 exhibits only a small peak. Thus, the homogeneity in the mixing of Al and Si components in the gels is deemed to be a necessary condition for obtaining spinnability of solutions.

Figure 3 shows the XRD patterns of the gel fibers obtained from sample 4 in Table 1 at various calcination temperatures. The gel fibers show an amorphous phase at 400°C and crystallize directly to mullite at temperatures as low as 600°C. However, complete transformation to mullite is observed at 1000°C, which corresponds to the exothermic peak in the DTA curve at 980°C. The XRD patterns in the gel from sample 2 in Table 1 show some differences, as observed from the data in Fig. 4. At 600 and 800°C, no crystalline phase is detected. When the temperature is increased to 1000°C, mullite and Al-Si spinel are simultaneously observed. At 1200°C, only mullite is observed, complete mullitization having taken place.

The mullitization temperature is considered to be an important criterion in the assessment of the mixing scale of the Al and Si components in the gels. Sacks et al. [9] pointed out that temperatures in the range of 1600–1700°C are required to achieve complete

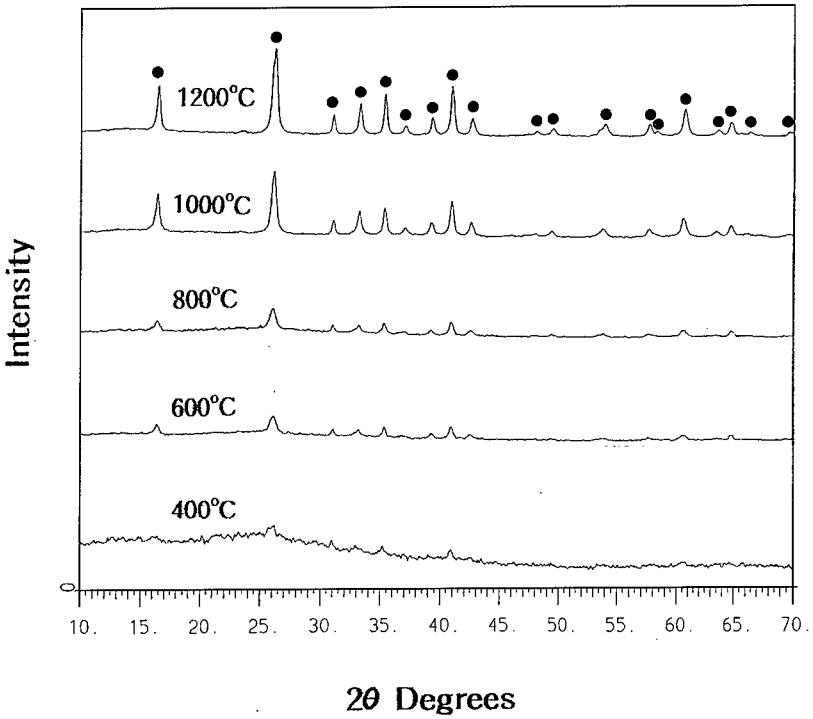

Figure 3. XRD patterns of gel fibers from sample 4 in Table 1 at various calcination temperatures. Marks indicate assignment of the peaks: (•) Mullite.

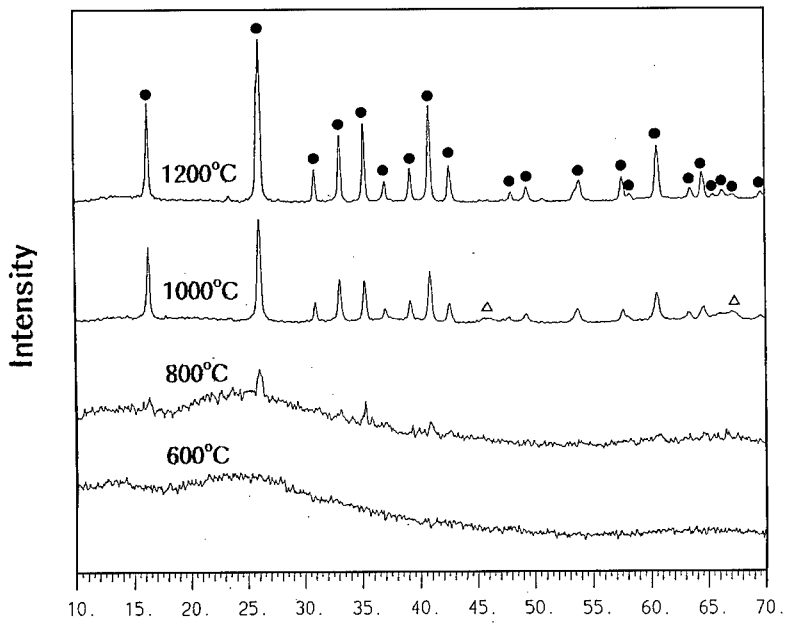

Figure 4. XRD patterns of the gel from sample 2 in Table 1 at various calcination temperatures. Marks indicate assignment of the peaks: (•) Mullite and (Δ) Al-Si spinel.

mullitization when alumina and silica particles are mixed in the micrometer size range. If the mixing scale is at the molecular level, mullitization temperatures of 1000–1100°C can be achieved. In Fig. 3, the gel fibers crystallize directly from the amorphous phase to mullite at 1000°C. Such a low mullitization temperature is indicative that all the Al and Si components in the gel fibers are mixed at the molecular level. However, in gels from the unspinnable solution of sample 2, Al-Si spinel occurs at 1000°C and a higher temperature (1200°C) is needed for complete mullitization. These results are attributed to the heterogeneity in the mixing scale of the Al-Si components in the gels.

4. Conclusion

Gels obtained from spinnable solutions are shown to have homogeneity in the mixing scale of the Al-Si components, leading to a sharp 980°C exothermic peak in the DTA curve and a mullitization temperature of 1000°C. On the other hand, for gels from unspinnable solutions, a small 980°C exothermic peak was detected, and the mullitization temperature was as high as 1200°C, probably due to the heterogeneity in the mixing scale of the Al-Si components. Thus, the homogeneity in the mixing of Al and Si components in the gels is deemed to be a necessary condition for obtaining spinnability of solutions.

Acknowledgments

This paper was supported by Non Directed Research Fund, Korea Research Foundation 1996.

References

1. I.A. Aksay, D.M. Dabbs, and M.J. Sarikaya, J. Am. Ceram. Soc. **74**, 2343 (1991).
2. D.S. Tucker, J.S. Sparks, and D.C. Esker, Ceramics Bulletin **69**, 1971 (1990).
3. K. Kamiya, S. Sakka, and N. Tashiro, Yogyo-Kyokai-Shi **84**, 614 (1976).
4. L. Chen, B. Wang, S. Lin, and Y. Yan, J. Am. Ceram. Soc. **79**, 1494 (1996).
5. B.E. Yoldas and D.P. Partlow, J. Mat. Sci. **23**, 1895 (1988).
6. R. Nass and H. Schmidt, J. of Non-Crystal. Solids **121**, 329 (1990).
7. G.D. Kim, D.A. Lee, H.I. Lee, and S.J. Yoon, Mat. Sci. Eng. **A167**, 171 (1993).
8. A.T. Chakravorty, J. Mater. Sci. **29**, 1558 (1994).
9. M.S. Sacks, H.W. Lee, and J.A. Pask, *Ceramic Transactions: Mullite and Mullite Matrix Composites* (American Ceramic Society, Westerville, OH, 1990), Vol. 6, p. 167.

Journal of Sol-Gel Science and Technology 13, 1023–1026 (1998)
© 1998 Kluwer Academic Publishers. Manufactured in The Netherlands.

Synthesis and Characterization of PZT Fibers via Sol-Gel

O. BINKLE AND R. NASS
Institut für Neue Materialien gem. GmbH, Im Stadtwald, Gebäude 43, 66123 Saarbrücken, Germany

Abstract. A fiber forming PZT gel containing 58.5 wt% PZT was synthesized by using zirconium-*n*-propylate, titanium-iso-propylate, lead acetate and butoxyethanol. Unseeded PZT gels and gels containing 0.5 wt% PZT perovskite seeds (Ø = 200–300 nm) could be extruded through a monofilament nozzle (Ø = 100 μm) at pressures between 50 and 150 bar, whereas PZT gels, containing 1 and 2 wt% PZT particles, were pressed through the nozzle at higher pressures (200–300 bar). The microstructure of unseeded and seeded (0.5, 1, 2 wt% PZT) PZT fibers was characterized by SEM. Unseeded fibers had three different shells at 450°C: an external dense shell (approx. 200 nm thick), a middle shell consisting of a porous structure (1.5 μm thick) and the center of the fiber, characterized by a matrix containing globular particles. At 700°C, a 200–250 nm thick and dense external shell and a porous fiber interior were be observed. 2 wt% of PZT seeds was necessary to densify the fiber completely. The seeds were located in the center of each PZT perovskite rosette.

Keywords: PZT fibers, piezoelectric fibers, sol-gel, fibers

Introduction

A new trend in the field of ceramic fiber synthesis is the synthesis of fibers which can play an active role in composites. Among these are the piezoelectric lead zirconate titanate (PZT) fibers which can be used for the production of sensor and actuator composites. The synthesis of PZT fibers has been reported before [1–5]. But there no reports of the relationship between fiber formation, crystallization of the perovskite phase and development of the microstructure.

Experimental

Synthesis of Spinnable PZT Gels

Fiber forming PZT gels containing 58.5 wt% PZT were obtained via sol-gel processing as reported in detail elsewhere [6], using zirconium-*n*-propylate, titanium-iso-propylate, leadacetate and butoxyethanol. The PZT sols were hydrolyzed with a water content of $W = 6$ ($W = [H_2O]/[Pb + Zr + Ti]$) at $pH = 3(HNO_3)$. The sols were concentrated until a solid content of 58.5 wt% was achieved.

Extrusion Process

58–61 wt% PZT gels were filled into special extrusion equipment with a fine monofilament nozzle ($Ø = 100$ μm). The pressure during the fiber forming process ranged between 50–300 bar.

Microstructure

The gelfibers (seeded and unseeded) were first dried at room temperature and than treated for 1 h at different temperatures ranging from 230°C to 700°C. The development of the microstructure of cross sections of fibers was investigated by SEM.

Phase Development

The development of the crystalline phase of PZT powders, treated at 360, 480, 510 and 650°C for 1 h was investigated by X-ray diffraction. The powders were synthesized from spinnable sols, which were the basis of PZT fiber production.

Seeding of the Fibers

PZT seeds were obtained by milling sol-gel-derived PZT perovskite powders. The particle size of the PZT seeds ranged between 200 and 300 nm. The seeds were homogenously mixed into the concentrated spinnable PZT gels by using a roller mill. The PZT gels were seeded with 0.5, 1 and 2 wt% PZT perovskite particles.

Results and Discussion

Process of Fiber Extrusion

In order to produce continuous PZT fibers it was necessary to extrude the fibers. 58–61 wt% PZT gels were pressed through a monofilament nozzle with a diameter of 100 μm. Unseeded PZT gels and PZT gels, containing 0.5 wt% seeds, could be extruded at pressures between 50–150 bar. The fibers were dried at room temperature. PZT gels, seeded with 1 and 2 wt% PZT particles, clogged the nozzle up so that an extrusion pressure of 200–300 bar was necessary to obtain a gel fiber. This high pressure made it difficult to collect the fibers during the extrusion process. Further investigations are necessary in order to optimize the rheological behavior of the PZT gel, especially the gels with 1 and 2 wt% seeds, for use in the extrusion process. Lower pressures were needed to enable collection of the fibers during the forming process.

Phase Development and Microstructure

The phase development of the PZT fibers was characterized by X-ray diffraction. At 510°C both the pyrochlore and the perovskite phase could be detected. The pure perovskite phase crystallized at 650°C.

A controlled microstructure PZT fiber is a basic requirement for good mechanical and piezoelectric properties in PZT fibers and ceramics. In order to understand how to achieve a dense and crack-free fiber, research on the development of the fiber structure during thermal treatment (step-by-step investigation from 230°C to 700°C) was undertaken using SEM.

At 230°C, a homogenous and dense microstructure could be observed. The removal of the organics started at 270°C, as shown by microcracks (200 nm long, 1–10 nm thick) in the fiber structure. At 310°C, two different areas could be detected: a shell close to the fiber surface, rich in microcracks, and a more globular structure inside of the fiber. At 450°C, three different "shells" could be observed (see Fig. 1). The external

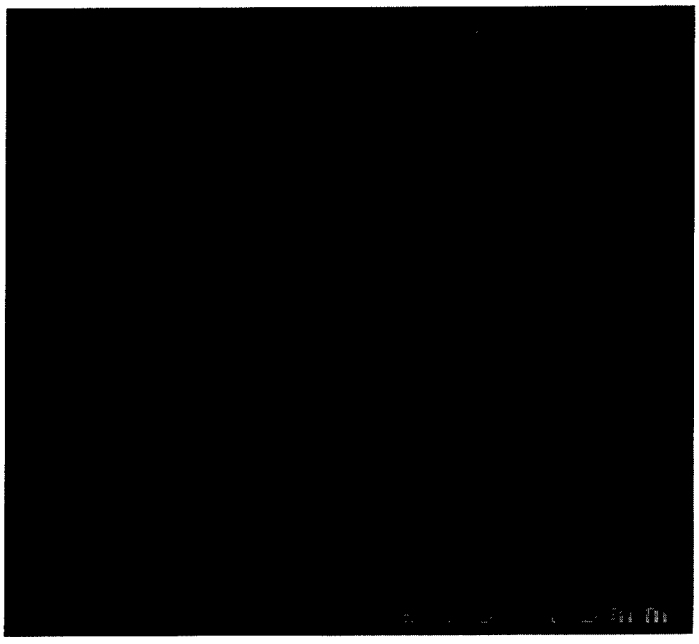

Figure 1. Cross section of a PZT fiber after 1 h calcination at 450°C. Three different "shells" could be observed: a dense external shell, a porous middle shell and the inside of the fiber, characterized by a globular structure.

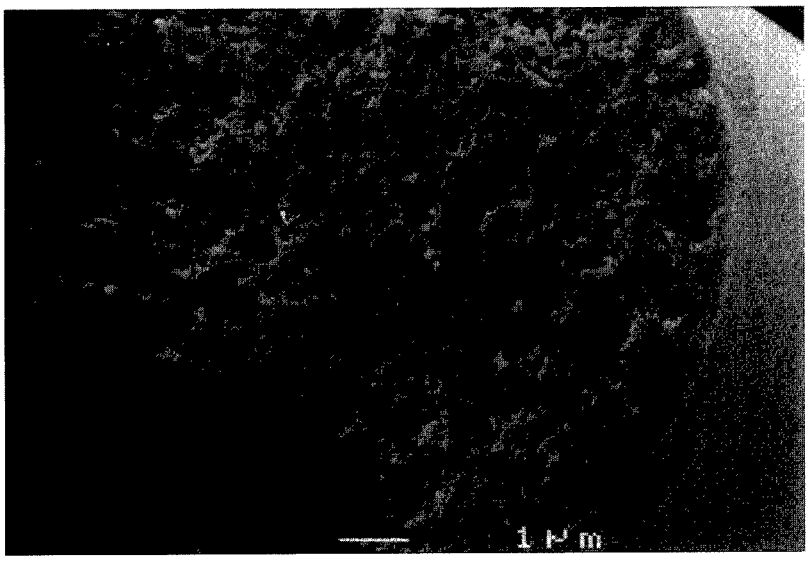

Figure 2. Cross section of a PZT fiber after 1 h sintering at 700°C. A 200–250 nm thick, dense external shell and a porous structure inside of the fiber could be observed.

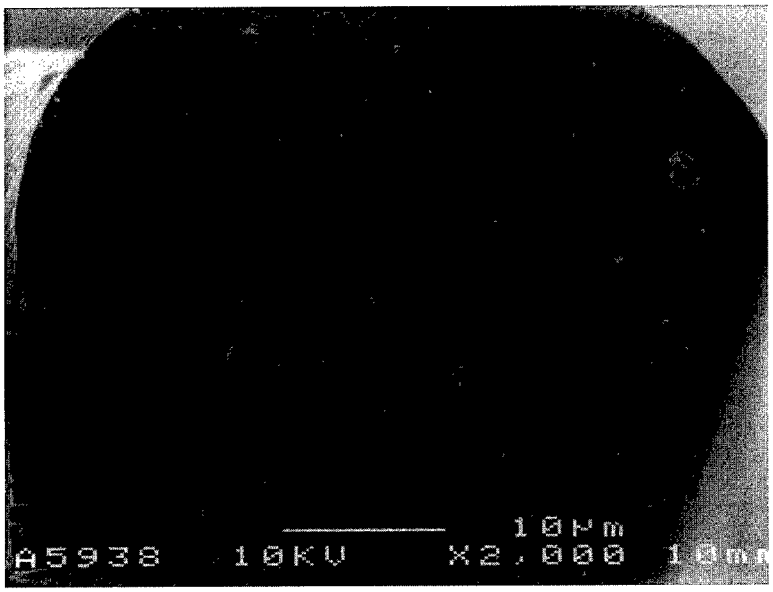

Figure 3. Microstructure of a sintered (1 h at 700°C) PZT fiber which was seeded with 2 wt% PZT seeds.

shell has an approx. 200 nm thick and dense structure. The following 1.5 μm thick area is characterized by a porous structure and the central area is a matrix containing globular particles.

At 700°C a 200–250 nm thick, dense external shell and a porous structure on the inside of the fiber could be observed (see Fig. 2). The diameter of the pores ranged between 100–200 nm.

The dense external shell is the result of a diffusion of the burnout products. In the area closer to the fiber surface, the distance covered by the burnout products while diffusing is shorter than the one from the center

of the fiber to the outside. Diffusion therefore leads to quicker densification in the area close to the fiber surface. With the external region being densified, it is not possible to achieve a completely dense structure in the center of the fiber without cracking. The development of such a porous microstructure is a well known phenomenon in the field of sol gel chemistry caused by insufficient nucleation during thermal treatment and burnout of organic species.

Microstructure of Seeded PZT Fibers

The seeding of PZT fibers should improve nucleation during thermal treatment. After sintering a PZT fiber seeded with 2 wt% PZT perovskite particles for 1 h at 700°C, a completely dense microstructure could be observed by SEM characterization. The seeds were located in the middle of each PZT perovskite rosette (see Fig. 3).

Nucleation was improved by the incorporation of PZT perovskite seeds. In addition these seeds probably supported the diffusion processes and therefore gave a homogenous densification of the PZT fiber.

Conclusions

The production of continuous PZT fibers by an extrusion process through a monofilament nozzle was described. It was shown that the incorporation of 2 wt% PZT perovskite seeds led to a complete densification of the fiber after sintering for 1 h at 700°C. Further investigations are necessary in order to improve the rheological behavior of the seeded gels in the forming process.

References

1. V.K. Seth and W.A. Schulze, Ferroelectrics **112**, 283 (1990).
2. U. Selvaraj, A.V. Prasadarao, S. Komarneni, K. Brooks, and S. Kurtz, J. Mater. Res. **7**, 992 (1992).
3. D. Sporn, Sprechsaal **126**(10), 612 (1993).
4. V.K. Seth, Nanofabrication, characterisation and electrical properties of sol-gel derived ferroelectric PLZT 7/65/35 ceramic thin films and fibers, Dissertation: Alfred University, New York, 1989.
5. D. Sporn, Materials Edge **65**, 6 (Oct. 1995).
6. O. Binkle, Dissertationsschrift, Universität des Saarlandes, Saarbrücken, 1997, to be published.

Journal of Sol-Gel Science and Technology 13, 1027–1031 (1998)
© 1998 Kluwer Academic Publishers. Manufactured in The Netherlands.

Effect of Solvent Diols and Ligands on the Properties of Sol-Gel Alumina-Silicas

FUJIO MIZUKAMI*, YOSHIMICHI KIYOZUMI, TSUNEJI SANO†, SHU-ICH NIWA, MAKOTO TOBA AND SHIGEMITSU SHIN‡

National Institute of Materials and Chemical Research, 1-1 Higashi, Tsukuba, Ibaraki 305, Japan

Abstract. Amorphous alumina-silicas were prepared from a tetra-alkoxysilane and anhydrous aluminum trichloride or an aluminum alkoxide by a sol-gel process using 2-methyl-2,4-pentanediol, pinacol, 1,2-propanediol, 2,3-butanediol or ethylene glycol as the solvent or complexing agent, and the effect of diols and alkoxy groups on the physical and chemical properties of the alumina-silicas was examined. When the diol or the alkoxy group was bulky, the alumina-silicas had relatively larger micropores, a larger pore volume and higher surface areas. In the conversion of methanol catalyzed by the alumina-silicas, the bulkier diols and alkoxides gave catalysts that produced dimethyl ether in higher yield and hydrocarbons in lower yield. Thus, when ethylene glycol was used as the diol, the best catalyst for the production of hydrocarbons, especially the production of olefins such as ethylene, propylene and butene, was obtained. Furthermore, in comparison with alumina-silica prepared by a traditional kneading process, it was found that the sol-gel alumina-silica could efficiently convert methanol to dimethyl ether and hydrocarbons, but the material prepared by kneading had a very low conversion of methanol to other compounds.

Keywords: alumina-silica, methanol conversion, pore design, sol-gel

1. Introduction

Alumina-silica is one of the most popular catalysts, and its catalytic properties are closely related to its physical properties such as homogeneity, pore size distribution and surface area. On the other hand, it is well known that physical properties of a sol-gel derived metal oxide are greatly affected by a solvent and complexing agent used in the sol-gel process [1–3]. Thus, we investigated here the effect of solvent diols and ligands used in the sol-gel process on the physical and catalytic properties of the sol-gel alumina-silicas, while comparing the performance for methanol conversion with that of conventional catalysts.

*Author to whom correspondence should be addressed.
†*Present address:* Japan Advanced Institute of Science and Technology, Asahidai, Tatsunokuchi, Nomi-gun, Ishikawa 923-12, Japan.
‡*Present address:* Advanced Technology Laboratory, Kubota Corporation, 5–6 Koyodai, Ryugasaki, Ibaraki 301, Japan.

2. Experimental

2.1. *Preparation of Alumina-Silicas*

All chemicals employed were of reagent grade and used without further purification. The alumina-silicas were prepared as follows. Aluminium trichloride anhydride (ATCA, 2.6 g) was dissolved in 15 g of ethanol. To this were added 148.5 g of 2-methyl-2,4-pentanediol (hexylene glycol, HG) and 100.6 g of tetraethoxysilane (TEOS), and the solution was stirred at 353 K for 3 h. Then, 36 g of water was added dropwise to the solution. The solution became viscous and finally coagulated in agar. The coagulum was dried under reduced pressure at 373 K and finely powdered. The powder was calcined at 823 K for 12 h. This 3.3 wt% Al_2O_3-SiO_2 is given as sample 1 in Table 1.

In similar manner, samples 2–5 in Table 1 were prepared by using 2,3-dimethyl-2,3-butanediol(pinacol), 1,2-propanediol (1,2-PD), 2,3-butanediol (2,3-BD), 1,2-ethanediol (ethylene glycol, EG), respectively,

Table 1. Properties of various alumina-silicas prepared by sol-gel procedure.

Sample[a] No.	Al_2O_3 Content (wt%)	Si/Al_2	Preparation of sample			Number of pulses absorbed[b]			S.A. (m^2/g)	P.V. (10^{-2} cm^3/g)
			Starting materials		Solvent	*n*-HEX	3-MP	2,2-DMB		
1	3.3	50	TEOS	ATCA	HG	21	21	2	530	30.3
2	3.3	50	TEOS	ATCA	Pinacol	13	5	2	422	12.7
3	3.3	50	TPOS	ATCA	1,2-PD	12	6	3	465	5.73
4	3.3	50	TEOS	ATCA	2,3-BD	13	5	3	438	4.67
5	3.3	50	TEOS	ATCA	EG	>25	6	0	352	3.70
6	6.3	25	TEOS	ATCA	EG	5	5	0	282	3.72
7	25.3	5	TEOS	ATCA	EG	>25	11	0	460	39.3

[a]Calcined at 823 K for 12 h, [b]one pulse: 2 dm^3 (*n*-HEX + 3-MP + 2,2-DBM)/0.1 g of sample; the ratio of the isomers, 1 : 1 : 1 (v/v). S.A.: specific surface area, P.V.: pore volume, TPOS: tetra-*n*-propylorthosilicate, ATCA: alminum trichloride anhydride.

instead of HG, and samples 6 and 7 in Table 1 were obtained by changing the ratio of TEOS/$AlCl_3$ in the preparation of sample 5.

2.2. *Measurements*

Specific surface areas and pore size distributions of the alumina-silicas were obtained by measuring the nitrogen adsorption and desorption isotherms at 77 K, using micro-BET apparatus (an AccuSorb 21000–01 of Micromeritics). A pulse absorption technique [4, 5] was also applied to estimate the pore size of the alumina-silicas.

Ammonia temperature-programmed desorption (TPD) spectra were recorded using a conventional apparatus [6] to evaluate the acidity of the alumina-silicas in the following manner. An alumina-silica (0.3 g) was packed in a tube heated in a stream of helium at 773 K for 2 h, and cooled to 373 K. At this temperature, ammonia was repeatedly injected to the packed tube together with a helium stream. When ammonia was detected in the effluent gas, the injection of ammonia was stopped and the alumina-silica was allowed to stand in a helium stream at the same temperature for 0.5 h. Then, the TPD spectrum was obtained by heating the packed tube at a rate of 5°/min from 373 to 873 K.

The alumina-silicas (dry gels) before calcination were analyzed in air with a Shimadzu thermogravimeter TG-30.

X-ray diffraction patterns of the alumina-silicas were recorded on a Philips PW 1700 diffractometer equipped with a curved graphite monochrometer. With CuK_α radiation, the samples were scanned over the range $2\theta = 5$–$60°$.

2.3. *Methanol Conversion*

A fixed-bed continuous flow micro reactor with 2 cm^3 of an alumina-silica was used in methanol conversion. Gaseous methanol was mixed directly with the argon flow to achieve the desired space velocity and was fed on the alumina-silica bed heated at the desired temperature. The mixed gas was composed of 50 mol% methanol and 50 mol% argon, and 2 h^{-1} in LHV. The reaction products were analyzed by gas chromatography. The methanol conversion and carbon-based selectivity were calculated on the basis of the concentration of argon used as the internal standard.

3. Results and Discussion

3.1. *Physical Properties*

All the alumina-silicas prepared, samples 1–7, showed no distinct lines in X-ray diffraction and were found to be amorphous.

In the thermogravimetric analysis, all the dry gels of samples 1–7 showed the weight losses not only at lower temperatures but also at higher temperatures than the boiling points of the diols used in gel preparation. In particular, the gels obtained using EG showed clear weight losses below and above 471 K, which is the boiling point of EG. The weight losses observed above the boiling points of the diols have been related to the release of the organic residues derived from the diols used [5]. From this, it is considered that the organic residues, or diols used, will greatly affect the network structure of the final alumina-silicas [1, 3, 5]. Thus, the pore structure and surface area were examined (Table 1).

It was found from the nitrogen adsorption results that all the seven alumina-silicas have micropores below 2 nm. The size of the micropores was further examined by the pulse absorption technique [4, 5] using three hexane iomers of *n*-hexane (*n*-HEX), 3-methylpentane (3-MP) and 2,2-dimethylbutane (2,2-DMB) whose kinetic diameters are assumed to be 0.31, 0.56 and 0.70 nm, respectively. None of the alumina-silicas (samples 5–7) obtained using EG absorbed 2,2-DMB which is the largest molecule among the three hexane isomers, but all the alumina-silicas prepared using bulkier diols than EG could absorb 2,2-DMB. From the comparison in pore volume between samples 1–5, it is found that when the diols and the alkoxy group of the $Si(OR)_4$ are bulky, the alumina-silicas show larger pore volumes. This suggests that the size and structure of pores in the alumina-silicas may be designed by the selection of the diol used in the sol-gel process.

3.2. *Chemical Properties*

Figure 1 shows NH_3 TPD spectra of the amorphous alumina-silicas and of a crystalline aluminosilicate, ZSM-5. All the amorphous alumina-silicas did not show distinct NH_3 TPD peaks above 700 K. On the other hand, ZSM-5 gave a clear NH_3 TPD peak above 700 K in addition to a peak near 520 K. This indicates that the alumina-silicas prepared here do not have as strong acidic sites as ZSM-5. Among the sol-gel alumina-silicas, samples 1–5 showed similar NH_3 TPD patterns, having a peak in the 450–500 K region and a shoulder near 650 K. Thus, from the NH_3 TPD spectra, it is difficult to deduce the effects of the diols and silicon alkoxides used on the acidity of the alumina-silicas. However, as for the alumina-silicas obtained using EG, the NH_3 TPD shoulder peaks appear to slightly shift to the higher temperature region compared with the other alumina-silicas, and all the peaks tend to become clear as the alumina content increases. This indicates that the acidic properties also depend on the alumina content, as can be expected.

Tables 2 and 3 show the conversions of methanol with different alumina-silicas and crystalline aluminosilicates. The methanol conversion reaction, roughly considered, proceeds by two steps of dehydration, the formation of dimethyl ether from methanol (first step; $CH_3OH \rightarrow CH_3OCH_3$) and then the conversion of dimethyl ether to hydrocarbons (second step; $CH_3OCH_3 \rightarrow C_nH_{2n} + C_nH_{2n+2}$).

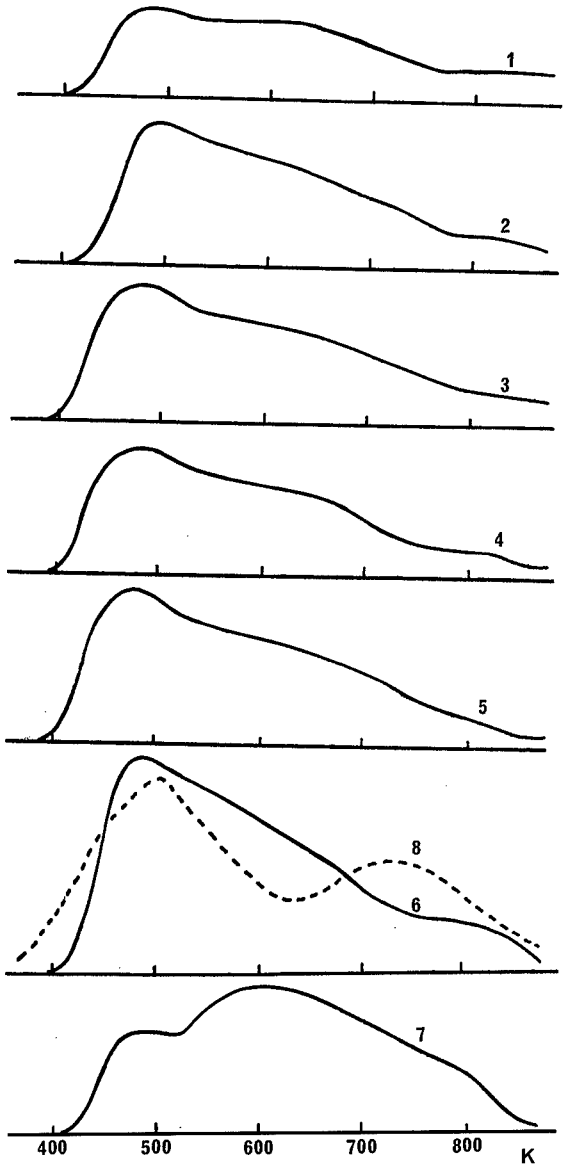

Figure 1. NH_3 TPD spectra of the sol-gel alumina-silicas (1–7 correspond to samples 1–7, respectively) and ZSM-5 (8).

First, it is found that there are major differences in performance between the catalysts. The alumina-silica prepared by kneading has a very low conversion of the methanol. Also the commercially available alumina-silica can only produce hydrocarbons in a low yield below 5%. On the other hand, ZSM-5 can completely convert methanol to hydrocarbons, and FCC and the sol-gel alumina-silicas have conversion percentages higher than the commercial alumina-silica and lower than ZSM-5. This will be related to the "acid strength"

Table 2. Methanol conversion with various alumina-silicas and aluminosilicates at 633 K.

	ZSM-5 ($Si/Al_2 = 40$)	FCC (MRZ-204)	Nikki (N632HN)[a]	Sol-gel alumina-silicas 1	2	3	4	5	6	7
MeOH conv. (%)	99.7	83.7	85.0	83.9	83.8	84.5	85.1	85.7	85.3	84.6
DME yield (%)[b]	0.0	72.9	80.5	79.6	74.6	74.3	63.5	62.6	63.4	74.7
Total HC yield (%)[b]	99.7	10.8	4.5	4.3	9.2	10.2	21.6	23.1	21.9	9.9
Selectivity (%)[b]										
Methane	0.6	4.3	0.9	0.8	1.0	0.7	0.6	0.7	0.5	1.0
Ethylene	2.5	9.8	0.4	1.3	7.9	6.2	7.5	8.3	6.3	2.4
Ethane	0.3	0.4	0.0	0.0	0.1	0.1	0.1	0.1	0.1	0.1
Propylene	3.8	16.8	0.0	0.0	0.0	9.7	10.9	11.8	0.0	0.0
Propane	8.9	0.8	0.0	0.4	0.8	0.7	0.8	0.7	0.6	0.7
Butene	12.0	5.9	0.0	0.0	3.6	5.4	3.3	7.4	2.4	1.1
i-Butane	16.6	3.7	0.0	0.8	5.5	5.1	6.8	7.5	4.8	1.6
n-Butane	4.0	0.0	1.6	0.0	0.3	0.0	0.1	0.2	0.0	0.0
Pentene	0.3	0.0	0.0	0.5	0.3	4.6	1.2	0.0	0.2	0.5
Pentane	0.8	0.1	0.0	0.0	2.3	0.0	0.0	0.0	0.5	0.7
Others[c]	50.2	58.2	97.1	96.2	78.2	67.5	68.7	63.3	84.6	91.9

LHSV = 2 h^{-1}; Ar/MeOH, 50/50 (mol/mol). [a]28 wt% alumina-silica, [b]based on carbon, [c]mainly toluene, xylene, hexane and heptenes, HC: hydrocarbon, DME: dimethyl ether.

Table 3. Methanol conversion with various alumina-silicas and aluminosilicates.

		593 K[a]			633 K[a]			653 K[a]		
			Yield (%)			Yield (%)			Yield (%)	
Catalyst	Si/Al_2	Methanol conv. (%)	T.H.C.	C2′ + C3′	Methanol conv. (%)	T.H.C.	C2′ + C3′	Methanol conv. (%)	T.H.C	C2′ + C3′
Sol-gel silica-alumina										
1	50	83.6	3.8	0.0	83.9	4.3	0.1	83.5	4.4	0.1
2	50	86.3	5.2	0.1	83.8	9.2	0.7	82.9	11.5	2.7
3	50	86.1	5.8	0.1	84.5	10.2	1.6	83.9	13.8	2.6
4	50	85.9	12.7	1.3	85.1	21.6	4.0	84.0	26.2	5.7
5	50	85.8	14.2	1.8	85.7	23.1	4.6	84.6	27.2	6.1
6	25	85.9	10.2	0.1	85.3	21.9	1.4	85.0	31.2	3.6
7	5	85.7	8.3	0.1	84.6	9.9	0.2	84.0	10.7	0.3
Kneading	50	1.9	1.9	0.0	3.0	3.0	0.0	3.3	3.3	0.0
Nikki (N632HN)	4.4	85.8	4.3	0.0	85.0	4.5	0.0	83.4	4.4	0.1
FCC (MRZ-204)	—	84.3	13.1	2.9	83.7	10.8	2.9	83.2	8.5	1.5
ZSM-5	40		No data		99.7	99.7	6.3	99.7	99.7	7.2

[a]Reaction temperature, T.H.C.: total hydrocarbons, C2′: ethylene, C3′: propylene.

of the catalysts, because it is deduced that the "acid strength" is in the order of ZSM-5 > FCC ~ sol-gel alumina-silicas > purchased alumina-silica > kneading alumina-silica [6].

Secondly, it can be seen that the catalytic properties of the sol-gel alumina-silicas are remarkably affected by the diols used in the sol-gel process (samples 1–5) and the ratios of SiO_2/Al_2O_3 (samples 5–7). From the results, the alumina-silicas obtained using bulky diols or from a bulky alkoxysilane gave relatively low hydrocarbon and olefin yields, and samples 4 and 5, which were prepared using small diols and the highest silica

content, showed comparable ability for the formation of olefins to the crystalline aluminosilicates, FCC and ZSM-5 having strong acidic sites.

References

1. F. Mizukami, S. Niwa, M. Toba, T. Tsuchiya, K. Shimizu, S. Imai, and J. Imamura, Stud. Surf. Sci. Catal. **31**, 45 (1987).
2. M. Toba, F. Mizukami, S. Niwa, T. Sano, K. Maeda, and H. Shoji, J. Mater. Chem. **4**, 1131 (1994).
3. M. Toba, F. Mizukami, S. Niwa, T. Sano, K. Maeda, A. Annila, and V. Komppa, J. Mol. Catal. **91**, 277 (1994).
4. K. Suzuki, Y. Kiyozumi, S. Shin, K. Fujisawa, H. Watanabe, K. Saito, and K. Noguchi, Zeolites **6**, 290 (1986).
5. S. Niwa, F. Mizukami, S. Isoyama, T. Tsuchiya, K. Shimizu, S. Imai, and J. Imamura, J. Chem. Tech. Biotechnol. **36**, 236 (1986).
6. K. Fujisawa, T. Sano, K. Suzuki, H. Okado, K. Kawamura, Y. Kohtoku, S. Shin, H. Hagiwara, and H. Takaya, Bull. Chem. Soc. Jpn. **60**, 791 (1987).

Journal of Sol-Gel Science and Technology 13, 1033–1036 (1998)
© 1998 Kluwer Academic Publishers. Manufactured in The Netherlands.

Application of ZrO_2-Al_2O_3 Aerogels to Catalysts

K. KOHAMA, H. IMAI AND H. HIRASHIMA
Faculty of Science and Technology, Keio University, 3-14-1, Hiyoshi, Kohoku-ku, Yokohama, 223 Japan

H. HAMADA AND M. INABA
National Institute of Materials and Chemical Research, 1-1, Higashi, Tsukuba, 305 Japan

Abstract. ZrO_2-Al_2O_3 aerogels were prepared by hydrolysis of metal alkoxides in alcoholic solutions and supercritical drying in order to obtain an improved de-NO_x catalyst with high activity in a wide temperature range. The aerogels have about 20–50% higher activity than the xerogels in the range 300–600°C. The higher activity of aerogels may be attributed to the higher effective gas diffusivity in them, estimated to be about 20–60 times higher than that of the xerogels, because of their high porosity and large pore size. The catalytic activity of aerogels containing 4–10 mol% ZrO_2 is more than 20% higher than that of Al_2O_3 aerogels at temperatures <450°C.

Keywords: aerogel, catalyst, ZrO_2-Al_2O_3, selective reduction of NO_x

1. Introduction

Air pollution by automobile exhaust gas, especially NO_x, is still an important problem. Removal of NO_x in an oxidizing atmosphere, e.g., in diesel and lean-burn engine exhaust gases, is difficult without toxic NH_3 addition. Recently, it has been reported that NO_x could be reduced under high oxygen partial pressures using oxide catalysts and hydrocarbons [1–4]. Catalysts are a potential application of aerogels with high porosity and large surface area. We have reported the high catalytic activity of Al_2O_3 aerogels for selective reduction of NO using C_3H_6 under an oxidizing atmosphere [5]. However, its activity rapidly decreases with decreasing temperature when <500°C. On the other hand, ZrO_2 has a higher activity at lower temperatures [4]. In this study, ZrO_2-Al_2O_3 aerogels have been prepared in order to obtain a better de-NO_x catalyst with a high activity in a wide temperature range.

2. Experimental Procedures

ZrO_2-Al_2O_3 wet gels were prepared by hydrolysis of $Zr(C_4H_9O)_4$ and $Al(C_4H_9O)_4$ in ethylacetoacetate/ethanol mixed solutions. The wet gels were supercritically dried in an autoclave, at 250°C and 210 atm, to obtain aerogels [5]. The wet gels were also dried at 90°C in air to prepare the xerogels. The microstructure of the gels was observed by transmission electron microscopy (TEM). The crystallization behavior of the gels was investigated by X-ray diffraction (XRD) after heat treating at various temperatures up to 500°C. The specific surface areas and pore size distributions of the aero- and xerogels, heat treated at 500°C for 4 h, were determined by N_2 adsorption. The catalytic activities of dried gels were determined for the selective reduction of NO with addition of C_3H_6 in the temperature range from 300 to 600°C using a fixed-bed type flow reactor [2]. The solid acidity, which is known to affect the catalyst activity for the selective reduction of NO [4], was studied by NH_3-TPD (Temperature-programmed desorption) measurements.

3. Results

The porosities of the aerogels and xerogels were higher than 90% and about 50%, respectively. It was shown by TEM that Al_2O_3 aerogels consisted of needle-like

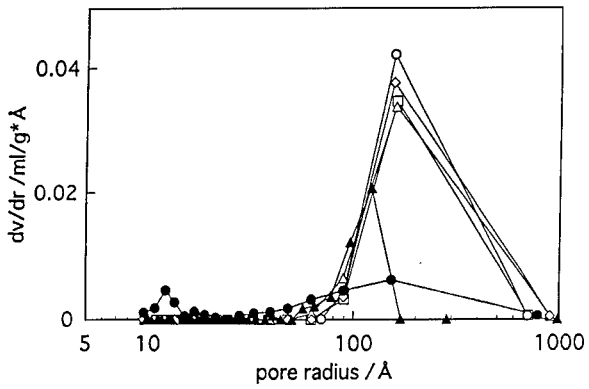

Figure 1. Pore size distributions for ZrO_2-Al_2O_3 aerogels heat treated at 500°C for 4 h. (ZrO_2-content; □ 0, ○ 3.9, △ 9.5, ◇ 18.2, ● 66.7 and ▲ 100 mol%.)

particles, about 20 nm long, and ZrO_2 aerogels consisted of spherical particles, less than 10 nm in diameter. ZrO_2-Al_2O_3 aerogels contained both needle-like and spherical particles. The mean pore radius of ZrO_2-Al_2O_3 aerogels, estimated by the BJH method, was about 20–30 nm and 10 times larger than that of the xerogels. The specific surface area of the aerogels, about 300 $m^2\ g^{-1}$, as well as the pore size distribution of the aerogels, was hardly changed by addition of 0 to 18 mol% of ZrO_2 (Fig. 1). The xerogels containing up to 66.7 mol% ZrO_2 were shown to be amorphous by XRD after heat treatments at 500°C. The diffraction peaks of Boehmite and tetragonal ZrO_2 were observed for the as-prepared aerogels. After heat treating at 500°C, diffraction peaks of γ-Al_2O_3 and monoclinic ZrO_2 were observed for the aerogels.

The aerogels have about 20–50% higher activity for NO reduction than the xerogels in the temperature range 300–600°C (Figs. 2(a) and (b)). The catalytic activity of aerogels containing 4–10 mol% ZrO_2 is more than 20% higher than that of Al_2O_3 aerogels at temperatures lower than 450°C (Fig. 2(a)). The peak temperatures of NH_3-TPD curves, related to the strength of solid acidity, for the aerogels and xerogels containing 0 to 18 mol% ZrO_2 are almost the same, about 220°C (Fig. 3). The amounts of desorbed NH_3 are also almost constant, about 650 μ mol g^{-1}, for the aerogels and the xerogels in the same composition range.

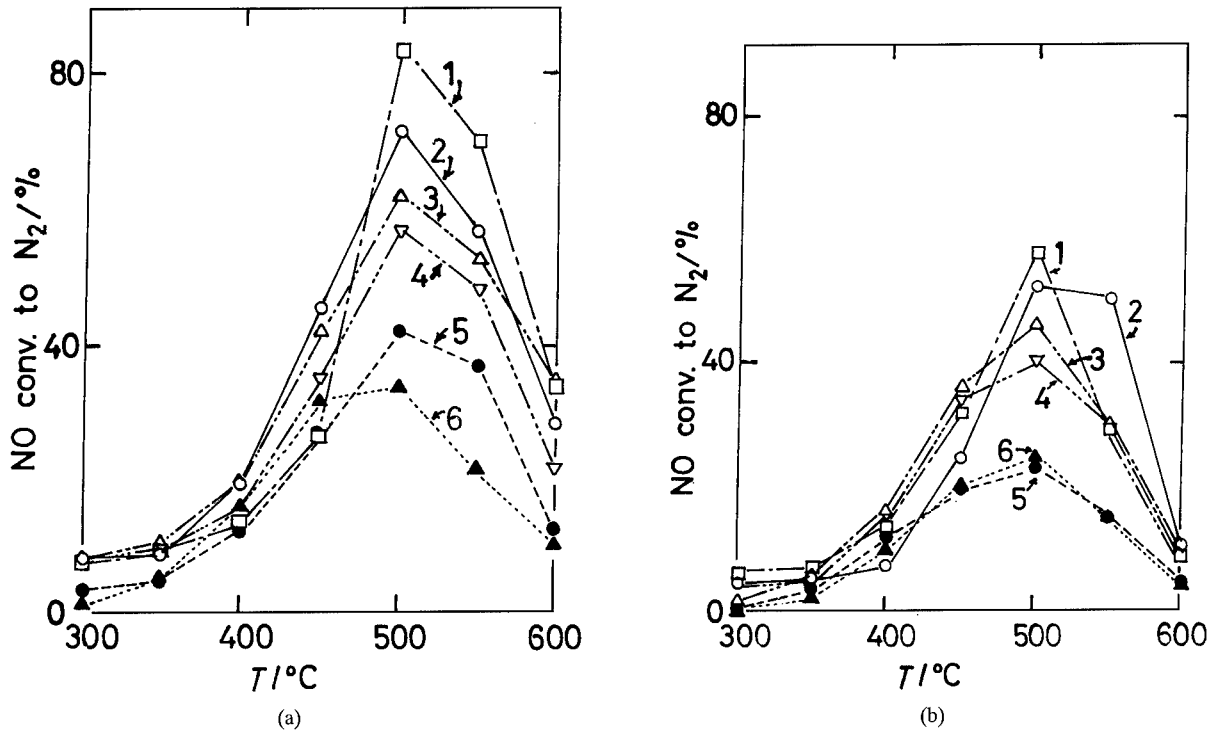

Figure 2. Catalytic activities for ZrO_2-Al_2O_3 aerogels (a) and xerogels (b). (ZrO_2-content; (1) 0, (2) 3.9, (3) 9.5, (4) 18.2, (5) 66.7, and (6) 100 mol%.)

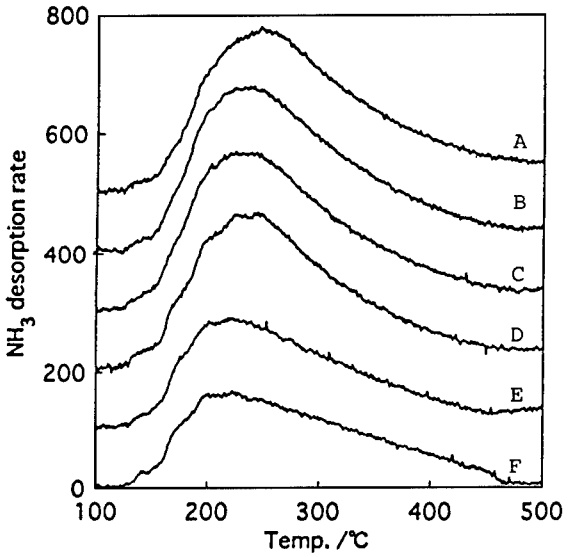

Figure 3. NH_3-TPD curves for ZrO_2-Al_2O_3 aerogels. (ZrO_2-content; A = 0, B = 3.9, C = 9.5, D = 18.2, E = 66.7, and F = 100 mol%.)

4. Discussion

The specific surface areas of the aerogels and the xerogels, about 300 $m^2\,g^{-1}$ and 200–300 $m^2\,g^{-1}$, respectively, are not significantly different. However, the catalytic activities of the aerogels are higher than those of the xerogels. The xerogels are amorphous and the aerogels are crystalline at 500°C, but the difference in the acidities of the solid surfaces, determined by NH_3-TPD, is also not significant. On the other hand, the porosity and pore size of the aerogels are much larger than those of the xerogels. The activity of the porous catalysts may depend not only on the surface area but on the diffusivity of gases in the small pores. In this case, the pore radius, about 20–30 nm for the aerogels and 2 nm for the xerogels, is smaller than the mean free path of C_3H_6, which is about 100 nm at 500°C. The effective diffusivity, $D_e = pD_K/\tau$, of C_3H_6 in the pores can be estimated using the Knudsen diffusion constant, $D_K = 3.067r(T/M)^{1/2}$, where r = pore radius, p = porosity, T = temperature, M = molecular weight and τ = tortuosity factor (usually 3–6) (Table 1). The effective diffusivities for the aerogels are 20 to 60 times larger than those of the xerogels. The higher activity of the aerogels may be attributed to the higher effective gas diffusivity of the aerogels, because of their high porosity and large pore size.

Table 1. Knudsen diffusion constant, D_K, and effective diffusivity, D_e, of C_3H_6 for ZrO_2-Al_2O_3 dried gels.

ZrO_2 (mol%)	r (nm)	p	D_K ($m^2\,s^{-1}$)	τD_e ($m^2\,s^{-1}$)
Aerogels				
0	27	0.95	1.11×10^{-5}	1.05×10^{-5}
3.9	26	0.96	1.09×10^{-5}	1.04×10^{-5}
66.7	20	0.95	8.32×10^{-6}	7.91×10^{-6}
100	18	0.91	7.63×10^{-6}	6.85×10^{-6}
Xerogels				
0	2.5	0.48	1.04×10^{-6}	4.99×10^{-7}
3.9	2.7	0.34	1.12×10^{-6}	3.81×10^{-7}
66.7	1.1	0.25	4.58×10^{-7}	1.14×10^{-7}
100	2.7	0.32	1.12×10^{-6}	3.58×10^{-7}

The catalytic activity of aerogels containing 4–10 mol% ZrO_2 is more than 20% higher than that of Al_2O_3 aerogels at temperatures lower than 450°C (Fig. 2(a)). ZrO_2 is a better catalyst for oxidation of hydrocarbons at low temperatures, e.g., the conversion of C_3H_6 into CO_x at 450° with the ZrO_2 aerogel catalyst and with the Al_2O_3 aerogel catalyst are about 80% and 20%, respectively. The selective reduction of NO is considered to proceed by the reaction with partially oxidized hydrocarbons. Then, addition of small amounts of ZrO_2 enhanced reduction of NO, but the addition of a larger amount, 18 mol% or more, enhanced oxidation of hydrocarbons and reduced the NO conversion.

5. Conclusions

The ZrO_2-Al_2O_3 aerogels have about 20–50% higher activity for NO reduction than the xerogels in the range 300–600°C. The higher activity of aerogels may be attributed to the higher effective gas diffusivity in them. The catalytic activity of aerogels containing 4–10 mol% ZrO_2 is more than 20% higher than that of Al_2O_3 aerogels at temperatures <450°C. The effects of ZrO_2-addition on the catalytic activity of the aerogels were discussed.

Acknowledgments

The authors gratefully acknowledge Profs. Masayuki Yamane, Shuichi Shibata and Atsuo Yasumori of Tokyo Institute of Technology for their help in

preparation of the aerogels and measurements of N_2 adsorption.

References

1. W. Held, A. Koenig, T. Richter, and L. Puppe, SAE Paper, 900496 (1990).
2. Y. Kintaichi, H. Hamada, M. Tabata, M. Sasaki, and T. Ito, Catal. Lett. **6**, 239 (1990).
3. M. Iwamoto and H. Hamada, Catalysis Today **10**, 57 (1991).
4. H. Hamada, Catalysis Today **22**, 21 (1994).
5. H. Hirashima, C. Kojima, and H. Imai, J. Sol-Gel Sci. Technol. **8**, 843 (1997).

Journal of Sol-Gel Science and Technology 13, 1037–1041 (1998)
© 1998 Kluwer Academic Publishers. Manufactured in The Netherlands.

Preparation of Layer Structure-Controlled Ru-Sn-Al_2O_3 Catalysts and Their Reactivity

M. TOBA, S. TANAKA, S. NIWA AND F. MIZUKAMI
National Institute of Materials and Chemical Research, Tsukuba 305, Japan

Z. KOPPÁNY AND L. GUCZI
Institute of Isotopes of the Hungarian Academy of Sciences, P.O. Box 77, Budapest, Hungary H-1525

Abstract. In order to achieve functional group selective hydrogenation, the layer structure of Ru-Sn-Al_2O_3 catalysts was controlled by using sol-gel, powder impregnation and combined sol-gel impregnation methods. The properties of the catalysts and effectiveness in hydrogenation of dimethyl terephthalate were examined. The surface Sn contents of the catalysts characterized by X-ray photoelectron spectroscopy depended on the preparation method, in spite of almost the same bulk Ru and Sn compositions measured by X-ray fluorescence analyses. TPR and CO adsorption of the catalysts also depended on the preparation method. With regard to the conversion rate of dimethyl terephthalate and the rate of product conversion from methyl 4-hydroxy methylbenzoate to *p*-xylene via methyl *p*-toluate, Ru impregnation catalysts had higher rates than the other catalysts.

Keywords: hydrogenation, ruthenium-tin-alumina, catalyst preparation, dimethyl terephthalate, X-ray photoelectron spectroscopy

1. Introduction

It is known that the surface structure of a catalyst has a great influence on its catalytic activity and selectivity [1–3]. So, control of the layer structure is very important in realizing a selective reaction by functional groups.

We have reported the development of new Ru-Sn-Al_2O_3 catalysts prepared by a complexing agent-assisted sol-gel method, which selectively hydrogenate unsaturated or aromatic carboxylic acid and ester to the corresponding unsaturated or aromatic alcohol [4–7]. These previous results suggested that the method of catalyst preparation has a large effect on the catalytic properties. However, the relationship between the layer structure, catalytic performance and preparation method is not clear. In this work, we have attempted to control the layer structure of Ru-Sn-Al_2O_3 catalysts by using sol-gel, powder impregnation and combination methods, and examined their properties and hydrogenation of dimethyl terephthalate.

2. Experimental

Five types of 2 wt% Ru-4.7 wt% Sn-Al_2O_3 catalysts were prepared by sol-gel, powder impregnation and combination methods. $Ru(NO)(NO_3)_3$ solution (Ru = 6.8 wt%, N.E. Chem. Cat. Co.), $Sn(O^nBu)_4$ (Ko-jundo Kagaku Co.) and aluminum isopropoxide (Kawaken Fine Chemicals Co.) were used as raw materials.

(i) *Catalyst A* (*Ru, Sn(sol-gel)*). 74.8 g of aluminum isopropoxide and 86.7 g 2-methylpentane-2,4-diol were mixed at room temperature and then heated at 383 K for 3 h while stirring. Alcohols which were produced by the ligand exchange reaction between alkoxide and diol were removed in vacuo. 5.88 g of $Ru(NO)(NO_3)_3$ solution was evaporated to remove excess nitric acid and then the residue was dissolved in 60 g of ethanol. 3.25 g of $Sn(O^nBu)_4$ was dissolved in 80 g of 1-butanol. Both solutions were added to the aluminum-diol

mixture and stirred for 2 h. After removing alcohols, 123 g of water was added to the mixture. The gel formed was aged and dried in a rotary evaporator at 423 K.

(ii) *Catalyst B (Ru (sol-gel), Sn (imp.) combination).* Ru-Al_2O_3 was prepared in a similar manner to that above except that the tin solution was not added. The tin solution was added to the Ru-Al_2O_3 powder, which had been previously degassed at 473 K for 3 h in vacuo. Solvent was removed and the powder obtained was dried at 423 K.

(iii) *Catalyst C (Ru (imp.), Sn (sol-gel) combination).* Sn-Al_2O_3 was prepared in a similar manner to that above except that the ruthenium solution was not added. The ruthenium solution was added to the Sn-Al_2O_3 powder, which had been previously degassed at 473 K for 3 h in vacuo. Solvent was removed and the powder obtained was dried at 423 K.

(iv) *Catalyst D (Ru(imp.1), Sn(imp.2) impregnation).* Sol-gel alumina was prepared in a similar manner to that above except that the ruthenium and tin solutions were not added. The ruthenium solution was added to alumina powder, which had been previously degassed at 473 K for 3 h in vacuo. Solvent was removed and the power obtained was dried at 423 K. The tin solution was then added to the powder impregnated with Ru, and the mixture was dried as before.

(v) *Catalyst E (Ru (imp.2), Sn (imp.1) impregnation).* The procedure for this catalyst was the same as that described for catalyst D, except that the sequence of impregnation of Ru and Sn was reversed.

All catalysts were activated in a hydrogen atmosphere at 673 K for 4 h before characterization and hydrogenation.

Ru-4.7 wt% Sn-Al_2O_3 catalysts were characterized by X-ray fluorescence (SEIKO SEA-2010), X-ray photoelectron spectra (XPS, Perkin-Elmer ESCA5500) and hydrogen and carbon monoxide adsorption (Institute of Isotopes of the Hungarian Academy of Sciences SORBST AR200). Bulk Sn/Ru ratios of the catalysts were measured by the X-ray fluorescence analysis. Sampling time and X-ray irradiation diameter were 100 s and 10 mm, respectively. The X-ray photoelectron spectra were obtained with a monochromatic MgK_α source. The binding energies of elements were referenced to the C_{1s} line at 285 eV.

The hydrogenation of dimethyl terephthalate was carried out in a 500 cm^3 batch reactor (stainless autoclave) equipped with pressure regulator. The reactor was charged with 20 g of dimethylphthalate, together with 2 g of catalyst and 180 g of *n*-undecane (solvent), and purged with hydrogen four times at different pressures (1, 2, 4, 4 MPa) to remove the air. The reactor was then heated to 523 K and pressurized with hydrogen to 8 MPa. Samples were drawn during the course of reaction for analysis. The reaction products were analyzed by gas chromatography and GC-MS with a 0.25 mm × 60 m TC-1 capillary column (GL Science Co).

3. Results and Discussion

X-Ray Fluorescence Analyses and X-Ray Photoelectron Spectroscopy (XPS)

The results of X-ray fluorescence analysis are shown in Table 1. Observed bulk Sn/Ru compositions of all catalysts are almost same. These results indicate that the bulk composition of the catalyst does not depend on the preparation method.

The results of X-ray photoelectron spectroscopy (XPS) are shown in Table 1. From the results of the survey spectra, the peaks of O_{1s}, Sn_{3d}, C_{1s}, Ru_{3d}, Al_{2s}, Al_{2p} and some small peaks were observed. The surface Ru contents of the catalysts could not be determined because the peaks of Ru_{3d} and C_{1s} overlapped each other. The surface Sn contents of the catalysts characterized by XPS depended on the preparation method, that is, the surface on the catalyst B (Ru (sol-gel) → Sn (imp.)) and catalyst D (Ru (imp.) → Sn (imp.)) had

Table 1. X-ray fluorescence analyses and X-ray photoelectron spectroscopy of 2 wt% Ru-4.7 wt% Sn-Al_2O_3.

Catalyst	Sn/Ru (wt%/wt%)[a]	(Sn/Al) × 100 (%)[b]
A	2.3	5.15
B	2.5	7.62
C	2.7	3.93
D	2.6	7.24
E	2.5	2.12

[a]Bulk Sn/Ru compositions, Sn/Ru (wt%/wt%) were measured by X-ray fluorescence analyses.
[b]The surface Sn contents of catalysts, (Sn/Al) × 100 (%) were measured by X-ray photoelectron spectroscopy.

a higher content of tin than that of the catalyst C (Sn (sol-gel) → Ru (imp.)) and catalyst E (Sn (imp.) → Ru (imp.)). The surface tin content of the catalyst A (Ru-Sn (sol-gel)) showed a value intermediate between the other catalysts. These results suggest that surface metal element contents of the catalysts depend on the preparation method and can be controlled by a combination of the sol-gel technique and the order of impregnation.

Hydrogen Adsorption, Temperature Programmed Reduction (TPR) and Carbon Monoxide Adsorption

Table 2 shows hydrogen adsorption, temperature programmed reduction (TPR) and carbon monoxide adsorption of 2 wt% Ru-4.7 wt% Sn-Al_2O_3 catalysts. All catalysts did not show hydrogen adsorption. TPR and CO adsorption depended on the catalyst preparation method. Catalyst A showed two TPR peaks. However, the other catalysts showed only one TPR peak. The temperature of the TPR peak increases in the order of D (Ru (imp.) → Sn (imp.)) < B (Ru (sol-gel) → Sn (imp.)) ≈ E (Sn (imp.) → Ru (imp.)) < C (Sn (sol-gel) → Ru (imp.)). Apart from catalyst A, the quantities of hydrogen which are required for reduction of the catalysts decrease in the order of D > B > E > C. From the XPS, catalysts D and B have tin-rich surfaces. These results suggest that catalysts with tin-rich surfaces are reduced more easily. The adsorbed amounts of CO on catalysts D and E which were prepared by impregnation were larger than those of catalysts B and C which were prepared by a combination method. Compared with the two combination catalysts, the amount of CO adsorbed on catalyst B was larger than that on catalyst C. Compared with the two impregnation catalysts, the amount of CO adsorbed on catalyst D was larger than that on catalyst E. These results indicate that the preparation method and the sequence of addition of metal elements have a large influence on the adsorption characteristics of the catalyst surface.

Table 2. Hydrogen adsorption, temperature programmed reduction (TPR) and carbon monoxide adsorption of 2 wt% Ru-4.7 wt% Sn-Al_2O_3.

Catalyst	H_2 ads. (mmol/g)	TPR (mmol/g)	TPR (K)	CO ads. (mmol/g)
A	0	109	393, 423	17
B	0	99	423	8
C	0	59	457	<5
D	0	140	411	26
E	0	90	423	13

Hydrogen and carbon monoxide adsorptions were measured at room temperature.
TPR: carrier gas, its flow rate and heating rate were 1% H_2-Ar, 1.8 dm^3/h, 10 K/min, respectively.

Hydrogenation of Dimethyl Terephthalate

As shown in Fig. 1, dimethyl terephthalate(1) gave several kinds of products in the hydrogenation. The main products are methyl 4-hydroxymethylbenzoate(2), methyl *p*-toluate(4) and *p*-xylene(5). The parallel reactions *a* and *b* are the first step of the hydrogenation of (1). The reaction products, methyl 4-methoxymethylbenzoate(3) from reaction *a* and methyl 4-hydroxymethylbenzoate(2) from reaction *b*, can be further hydrogenated to methyl *p*-toluate(4) via reactions *e* and *f*. (4) can be also hydrogenated to *p*-xylene(5) via reaction *h*.

Table 3 shows the conversion of dimethyl terephthalate and the selectivities and yields of the main products in the hydrogenation with various catalysts. In terms of the conversion rate, catalysts C and E were higher than the other three catalysts. These results mean that catalysts with a ruthenium rich surface have a high hydrogenation activity. The selectivities of methyl 4-hydroxymethylbenzoate(2) decreased. The behavior of catalysts C and E is slightly different

Table 3. Hydrogenation of dimethyl terephthalate.

Catalyst	Conv. (%)	Selectivity (%) (2)	(4)	(5)	Yield (%) (2)	(4)	(5)
		Reaction time: 5 h					
A	22	50	32	9	11	7	3
B	22	50	27	9	11	6	2
C	40	35	30	20	14	12	8
D	18	61	11	6	11	2	1
E	37	49	22	11	18	8	4
		Reaction time: 20 h					
A	68	26	44	19	18	23	13
B	67	21	36	13	14	24	9
C	78	13	29	33	10	23	26
D	53	32	25	8	17	13	4
E	84	11	31	24	9	26	20

Temperature, 523 K; hydrogen pressure, 8 MPa; catalyst, 2 g; dimethyl terephthalate, 20 g; solvent (*n*-undecane) 180 cm^3.

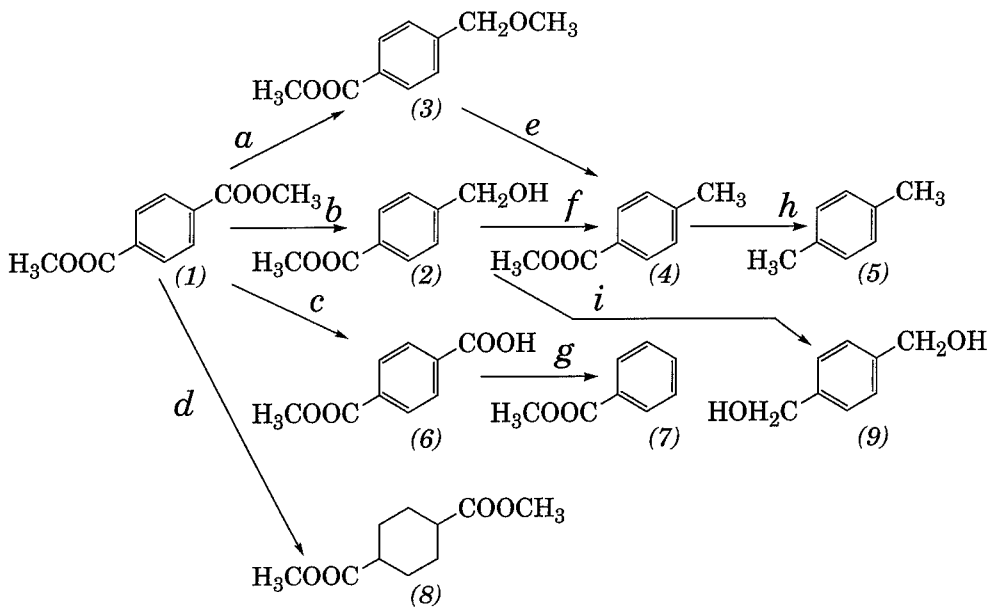

Figure 1. Hydrogenation products of dimethylterephthalate.

from that for the other three catalysts, i.e., the yield of methyl 4-hydroxymethylbenzoate(2) has a maximum value during the initial stage of the reaction and then decreases with reaction time. As the reaction time continues, catalysts C and E gave undesirable over-hydrogenated products such as methyl *p*-toluate(4) and *p*-xylene(5), in quantity. These results indicate that methyl 4-hydroxymethylbenzoate is more easily hydrogenated on the ruthenium-rich surface of catalysts C and E.

As also shown in Fig. 1, dimethyl terephthalate(1) gave undesirable by-products, methyl benzoate(7) via reaction *c* and *g*, and dimethyl 1,4-cyclohexyldicarboxylate(8) from reaction *d*. As we previously reported, tin had a large influence on the hydrogenation of C=O groups while preserving the aromatic ring. Therefore, the yields of (8) were depressed to values of only less than 2%. On the other hand, (7) is easily formed from monomethyl terephthalate(6) by the decarboxyl reaction *g* under high temperature conditions. When hydrogenation of the C=O bond, followed by hydrogenolysis of the C—OH or C—OCH_3 bonds occurs, products (2) and (3) are obtained. However, when only hydrogenolysis of the O—CH_3 bond occurs, (6) is the main product.

In these reactions, *p*-xylylene glycol(9) was not observed. This result suggests that hydrogenation of two methoxy carbonyl groups occurs consecutively and hydrogenation of the hydroxymethyl group is much faster than that of the methoxy carbonyl group. From these results, it was found that the catalyst properties given by the different preparation methods have an influence on the reaction steps, such as *a–i*, and the product distributions.

4. Conclusions

The layer structure of Ru-Sn-Al_2O_3 catalysts could be controlled by choosing the preparation method. The preparation method and the sequence of addition of metal elements have a large influence on the catalyst properties, especially the adsorbed characteristics of the catalyst surface and reactivity. With regard to the reaction rate of dimethyl terephthalate and methyl 4-hydroxymethylbenzoate, Ru impregnation catalysts had a higher rate than the other catalysts. The favorable combinations of catalysts and reaction conditions to obtain methyl 4-hydroxymethylbenzoate are Catalysts C and E (Ru rich surface catalysts) with a short period of reaction, or Catalysts B and D (Sn-rich surface catalysts) with a long period of reaction.

Acknowledgment

We thank Dr. Hiromichi Shimada (NIMC) for help in the XPS analyses.

References

1. T. Narita, H. Miura, K. Sugiyama, and T. Matsuda, Journal of Catalysis **103**, 492 (1987).
2. C.S. Narasimhan, V.M. Deshpande, and K. Ramnarayan, Applied Catalysis **48**, L1 (1989).
3. S. Galvagno, A. Donato, G. Neri, and R. Pietropaolo, Catalysis Letters **8**, 9 (1991).
4. K.-Y. Cheah, T.-S. Tang, F. Mizukami, S. Niwa, M. Toba, and Y.-M. Choo, Journal of American Oil Chemists' Society **69**, 410 (1992).
5. T.-S. Tang, K.-Y. Cheah, F. Mizukami, S. Niwa, and M. Toba, Journal of American Oil Chemists' Society **71**, 501 (1994).
6. K. Ishii, F. Mizukami, S. Niwa, M. Toba, and T. Sato, Catalysis Letters **30**, 297 (1995).
7. K. Ishii, F. Mizukami, S. Niwa, M. Toba, H. Ushijima, and T. Sato, Journal of American Oil Chemists' Society **73**, 465 (1996).

Journal of Sol-Gel Science and Technology 13, 1043–1047 (1998)
© 1998 Kluwer Academic Publishers. Manufactured in The Netherlands.

Evidence for Lewis and Brønsted Acid Sites on MgO Obtained by Sol-Gel

T. LÓPEZ AND R. GÓMEZ
Universidad Autónoma Metropolitana, Iztapalapa, CBI-Química, P.O. Box 55-534, México, D.F. 09340, Mexico

J. NAVARRETE AND E. LÓPEZ-SALINAS
Instituto Mexicano del Petróleo, STI, P.O. Box 14805, México, D.F. 07730, Mexico

Abstract. Traditionally, magnesium oxide has been considered a typical basic catalyst, catalyst carrier and/or adsorbent. In this study MgO was prepared using Mg-ethoxide dissolved in ethanol and hydrolyzed with various aqueous inorganic acids and bases. We have found that it is possible to induce Brønsted and Lewis acid sites depending on the method of preparation and, more specifically, on the type of inorganic acids used in the hydrolysis stage. In the FTIR spectra of adsorbed pyridine on MgO obtained using aqueous HCl (pH = 3), the bands corresponding to Lewis (1603, 1496 and 1444 cm^{-1}) and Brønsted (1550 cm^{-1}) acid sites are observed. The fact that upon vacuum and high temperature treatment, i.e., at 773 K, the above mentioned bands are clearly distinguishable indicated that the acid sites are very strong. On the other hand, the MgO materials obtained using aqueous acetic acid as a hydrolysis catalyst (pH = 5), and that without any catalyst (pH = 7) showed only Lewis acid sites which decreased markedly upon higher temperature treatment. When aqueous NH_4OH (pH = 9) was used as the hydrolysis catalyst, the MgO obtained showed only Lewis acid sites. In all cases the number of Lewis acid sites was greater than that of Brønsted sites.

Keywords: magnesium oxide, sol-gel, magnesia acidity, pyridine adsorption

Introduction

Alkaline earth metal oxides are well known for their basic properties. Even though MgO shows the least basic properties of this group, no acid characteristics have ever been examined in detail [1]. Accordingly, the adsorption of CO_2 on a series of alkaline earth oxides indicates that the base strength decreases in the following order: BaO > SrO > CaO > MgO [2]. CO_2 adsorbs on MgO as a bidentate and monodentate species at low and high coverings, respectively, while on CaO it adsorbs as a bidentate species, regardless of the degree of covering. On the other hand, the profiles of CO_2-temperature programmed desorption on MgO are made up of three well defined peaks which indicate the presence of three different base sites [3]. The relative distribution of these sites depends on the thermal treatment. FTIR studies indicate that CO_2 adsorbs on MgO not only as bidentate and monodentate species, but also forming carbonates and bicarbonates [4]. These results suggest that the remaining OH groups on MgO react as a base with acidic CO_2 molecules. Hence, four types of basic sites were proposed for MgO: (i) surface hydroxy groups and three types of O^{2-} sites located on (ii) edges, (iii) vertex and (iv) pits on the surface of the material [5].

When alkaline earth metal oxides are used as catalysts, the reaction is initiated by the withdrawl of a proton from the reactant to form anionic intermediates. In this case, surface O^{2-} groups remove the proton while the metal cation stabilizes the anionic intermediates. For instance, in the isomerization of 1-butene the variation in the activity and selectivity (towards *cis/trans* 2-butene) is directly dependent on the thermal treatment of MgO [6]. A high *cis/trans* ratio is characteristic of the double bond isomerization of olefins using base

catalysts. In the decomposition of alcohols, MgO catalyzes the reaction towards the dehydrogenation mechanism (i.e., ketone formation), opposite to the case of acid catalysts which favor the dehydration products (i.e., olefin formation).

In this study we show that, depending on the preparation methods, it is possible to induce acid sites (both Brønsted and Lewis type) on MgO with predominant basic characteristics. The sol-gel method is used in this study to obtain MgO with both acid and basic characteristics.

Experimental

Preparation of MgO. A proper amount of magnesium diethoxide $Mg(OEt)_2$ (0.05 mol, 98% purity), deionized water (0.25 mol) and anhydrous ethanol (0.85 mol) were mixed with constant stirring and kept for 10 min at room temperature. After this, the hydrolysis catalyst was added to the mixture in the following amounts: (a) 0.02 mol of HCl (38 wt%); (b) 0.02 mol of acetic acid; (c) 0.02 mol of oxalic acid; (d) 0.02 mol of ammonium hydroxide (29 mol%); and (e) no catalyst addition. The solutions were kept under reflux conditions at about 353 K until gel formation. After this, the gels were dried for 12 h at 343 K under vacuum and then calcined in flowing air for 4 h at 873 K. Table 1 summarizes the conditions and samples used in this study.

Characterization. Self supported wafers of the dried MgO samples were placed in a pyrex cell furnished with CaF_2 windows and heat-treated in situ under reduced pressure (1×10^{-6} Torr) from ambient temperature to 773 K. The samples thus treated were cooled to ambient temperature and exposed to D_2O vapor for 10 min. In a separate analysis, self supported wafers of previously calcined MgO samples (at 873 K) were prepared in a similar way as described above and activated at 673 K for 2 h. After this and at ambient temperature, the wafer was exposed to pyridine vapor for 30 min. The FTIR analysis was carried out in a NICOLET 710 spectrophotometer.

Table 1. Magnesium oxide obtained under various conditions.

Sample	pH	Hydrolysis catalyst	Gelation time/(h)
MgO-1	3	HCl	89
MgO-2	5	Acetic acid	48
MgO-3	5	Oxalic acid	67
MgO-4	9	NH_4OH	21
MgO*	—	—	—

*Commercial MgO.

Results and Discussion

All dried MgO samples showed amorphous X-ray diffraction patterns as reported by Bokhimi et al., where the evolution of the crystalline structure is chiefly related to the calcination temperature and the type of hydrolysis catalyst employed [7]. In general all dried MgO samples show a characteristic behavior when calcined at 773 K. It has been proposed that the preparation of metal oxides by sol-gel methods leads to highly hydroxylated materials, especially when the condensation mechanism proceeds by olation reactions [8]. From the FTIR spectra of a MgO-4 sample in Fig. 1 (all MgO samples showed similar behavior) a very broad and intense band at about 3450 cm^{-1} can be observed which is ascribed to fundamental ν_{OH} stretching vibrations from residual water and water of crystallization, residual alcohol and surface OH groups. However, when the treatment temperature increases above 573 K, MgO crystallization into periclase occurs [7].

The spectra of the samples calcined at 773 K contain no more residual water and ethanol and instead structural OH groups can be observed as two well defined bands at 3570 and 3729 cm^{-1}. Accordingly, Anderson et al. have reported that hydration water fixes to crystalline MgO by two different mechanisms: the first one involves the formation of surface OH groups directly attached to the cation (band at 3752 cm^{-1}) which are able to interact with other polar substrates by means of hydrogen bonds, and the second one where interstitial OH groups are shared between two adjacent Mg^{2+} cations (band at 3610 cm^{-1}) [9]. All of our calcined samples showed these bands shifted to lower energy, which is probably related to a different phase transition pathway towards crystalline MgO. When these materials were exposed to D_2O vapor at different temperatures, an isotopic D/H-exchange occured even at room temperature (Fig. 1). Particularly in MgO-1, the band at 3729 cm^{-1} almost disappeared and was replaced by a narrow band at 2743 cm^{-1} ($\Delta\nu = 986$ cm^{-1}), which remained almost unaltered below 773 K. This behavior is quite different from that of commercial MgO (MgO*) and that of MgO-4 where the intensity of the band indicates a lower isotopic transfer degree. The isotopic shift values for the OH groups are in agreement with

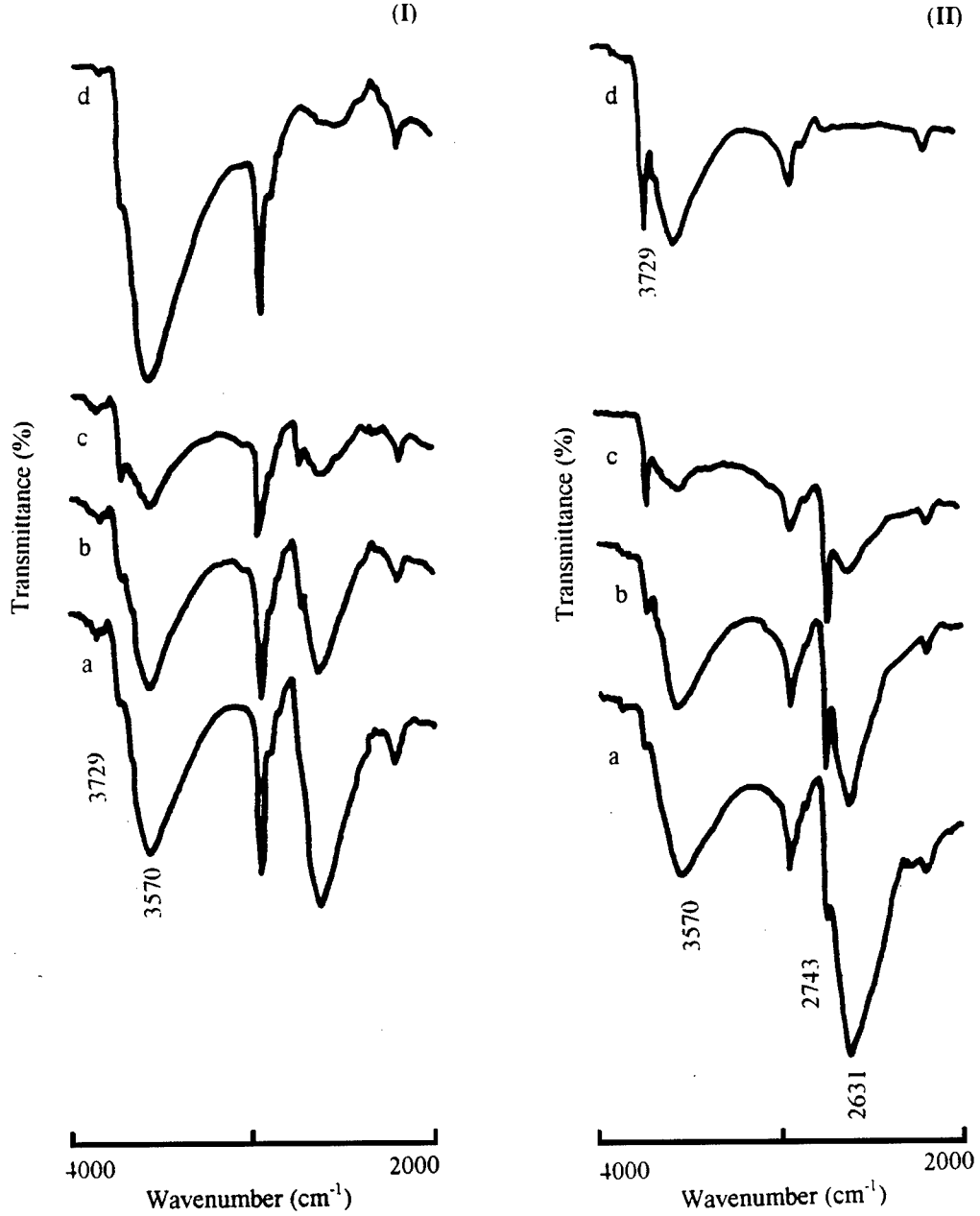

Figure 1. FTIR spectra of D_2O adsorbed on MgO samples in the OH and OD stretching region. (I) MgO* (commercial), (II) MgO-1 calcined at 873 K. (a) Room temperature, (b) 373 K, (c) 573 K, and (d) activated sample before exposure to D_2O.

those reported by Kazanski et al. [10] and agree with the band assignments of Anderson et al. [9]; they suggest that surface OH groups (ca. 3729 cm^{-1}) are more labile than those in the bulk (ca. 3594 cm^{-1}). Proton lability, evidenced during the isotopic exchange, suggested that besides the existence of Lewis acid sites in these solids, generated by charge unbalance of the framework, the presence of Brønsted acid sites could be possible.

The adsorption of pyridine on solid catalyst or materials and its analysis by FTIR has been widely used to distinguish the presence of Lewis and/or Brønsted

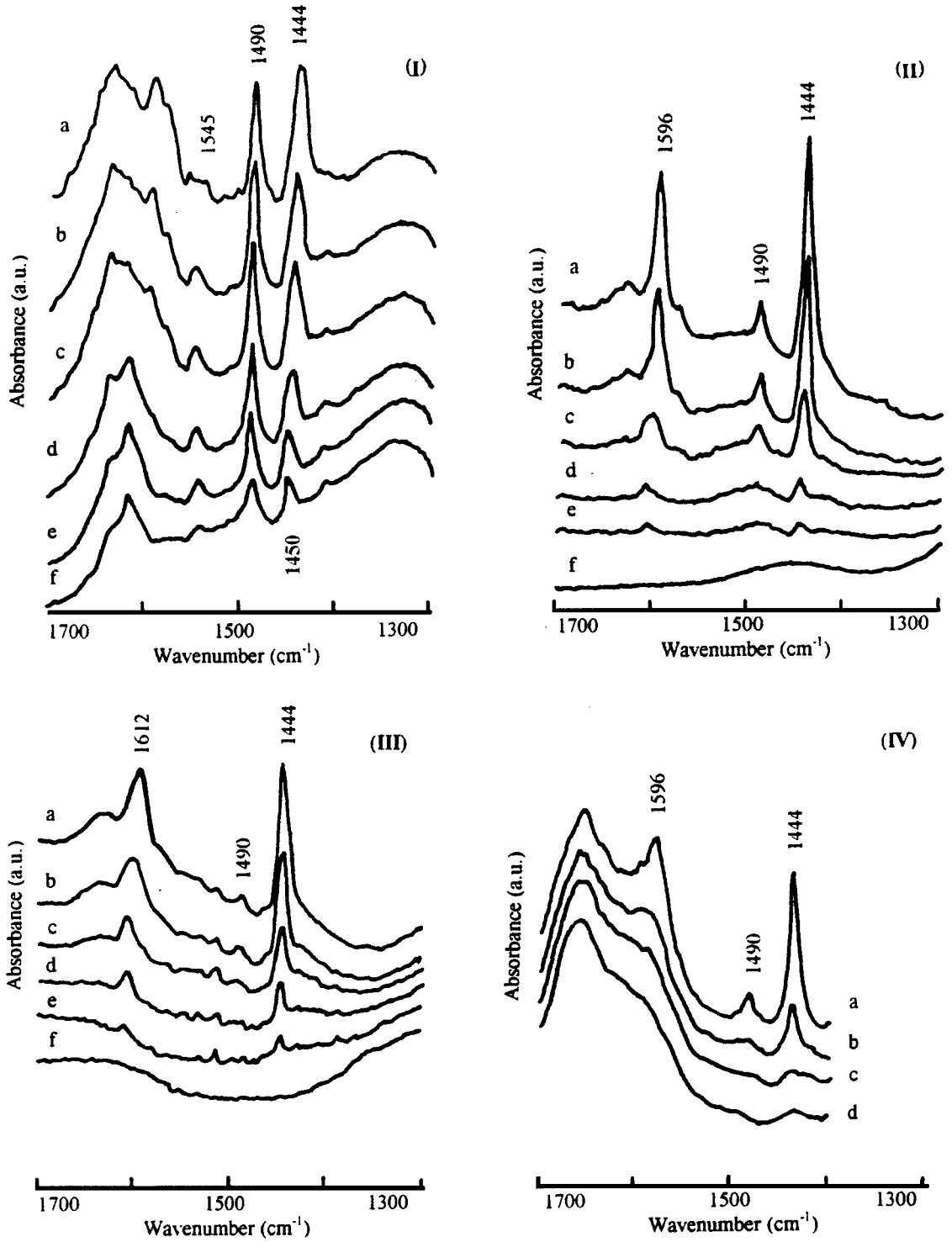

Figure 2. FTIR spectra of pyridine adsorbed on MgO samples. (I) MgO-1, (II) MgO-3, (III) MgO-4, and (IV) MgO* (commercial sample). (a) Room temperature, (b) 373 K, (c) 473 K, (d) 573 K, (e) 673 K, and (f) 773 K.

acid sites. The infrared spectrum of adsorbed pyridine, recorded in the region of the aromatic ring vibrations (modes 19b and 8a, according to Kline and Turkevich notation [11]), has been studied in detail. These two modes have been assigned to: (i) hydrogen-bonded pyridine (1440–1447 and 1580–1600 cm^{-1}); (ii) the pyridinium ion (1535–1550 and 1640 cm^{-1}) and (iii) coordinated pyridine (1447–1460 and 1600–1634 cm^{-1}). The FTIR spectra of the MgO samples show a wide and intense band between 1440 and 1450 cm^{-1}, which grew when the heat-treatment temperature rose from ambient to 773 K. At room temperature this band is made up of physisorbed pyridine, which was removed at 473 K, and chemisorbed pyridine on Lewis sites (band at 1450 cm^{-1}). This band disappeared above 673 K. The corresponding band at 1603 followed a similar behavior. A band of variable intensity at 1496 cm^{-1} can be clearly observed in all spectra and is related to the extent of interaction of the adsorbate with both Lewis and Brønsted sites. These bands, which appear for all MgO samples, and differ only in intensity, behave in a similar way with the treatment (Fig. 2).

However, MgO-1, which was prepared using aqueous HCl as the hydrolysis catalyst, shows special behavior. Though the presence of Lewis sites can be explained in terms of a charge unbalance generated by defects in the metal oxide network which form electrophilic sites, the presence of Brønsted sites for this particular MgO should involve a different mechanism. Here, the chloride ion may adsorb on the surface of Mg^{2+} cations where inductive effects originating on the chloride ion may act on adjacent OH groups increasing the proton lability. The FTIR spectra of pyridine adsorbed on MgO-1 (in Fig. 2) show bands which corroborate the above explanation. It can also be observed that the intensity of the bands discussed above is greater and that two new bands appear at 1545 and 1641 cm^{-1}, ascribed to pyridinium ion formation $[Py\text{-}H]^+$. Note in these spectra, the marked increase in the intensity and stability of the band at 1490 cm^{-1} associated with the pyridinium ion ring vibrations due to interactions with Brønsted and Lewis acid sites. Worthy of mention is the fact that the thermal stability of the adsorbate-adsorbant interaction has been modified because the bands of both acid sites can be observed even above 773 K. These results suggest the presence of very strong Lewis and Brønsted sites.

Conclusions

The pH of hydrolysis during the sol-gel synthesis of MgO leads to materials with very different characteristics from those of MgO prepared by traditional methods. The hydrolysis catalyst itself, used to control pH, is able to affect the final physicochemical properties of MgO. In particular, the use of aqueous HCl results in a MgClOH intermediate which is able to modify the surface structure of MgO yielding an acid-base bifunctional MgO. The application of MgO as a catalyst should take into account the history of preparation in order to understand better the catalyst performance.

References

1. F.A. Cotton and G. Wilkinson, *Advanced Inorganic Chemistry*, 4th edition (John Wiley and Sons, 1988).
2. G. Zhang, H. Hattori, and K. Tanabe, Appl. Catal. **36**, 189 (1989).
3. G. Wang and H. Hattori, J. Chem. Soc. Farady Trans. I **80**, 1039 (1984).
4. J.V. Evans and T.L. Whateley, Trans. Faraday Soc. **63**, 2769 (1967).
5. H. Hattori, Materials Chem. Phys. **18**, 533 (1988).
6. H. Hattori, K. Shimazu, N. Yoshii, and K. Tanabe, Bull. Chem. Soc. Jpn. **49**, 96 (1976).
7. Bokhimi, A. Morales, T. López, and R. Gómez, J. Solid State Chem. **115**, 411 (1995).
8. C.J. Brinker and G.W. Scherer, *Sol-Gel Science: The Physics and Chemistry of Sol-Gel Processing* (Academic Press, 1990).
9. P.J. Anderson, R.F. Horlock, and S.F. Oliver, Trans. Faraday Soc. **61**, 2754 (1995).
10. V.B. Kazanski, A.M. Gristov, V.M. Adreev, and G.M. Shidomirov, **72**, 149 (1989).
11. C.H. Kline and J. Turkevich, J. Chem. Phys. **12**, 300 (1944).

Journal of Sol-Gel Science and Technology 13, 1049–1055 (1998)
© 1998 Kluwer Academic Publishers. Manufactured in The Netherlands.

Chemical Microengineering in Sol-Gel Derived Fluoride and Lanthanide Modified Ceria Materials

PHILIP G. HARRISON, ADAM KELSALL AND JOHN V. WOOD
Departments of Chemistry and Materials, Engineering and Materials Design, University of Nottingham, University Park, Nottingham NG7 2RD, UK

Abstract. The effect of the incorporation of rare earth cations and fluoride anions into the ceria fluorite lattice has been studied. Ternary Ln-Ce-O (Ln = La, Pr, Nd) oxide gels of target Ln : Ce ratios of 1 : 4, 1 : 1.86 and 1 : 1, with and without added fluoride ion, have been prepared, and the oxide materials obtained after calcination at 1223 K examined. Incorporation of Ln results in the formation of Ln/CeO_2 solid solutions at low Ln levels, but a microscopic mixture of two cubic phases, pure ceria and a Ln-Ce-O phase of composition $Ce_{0.35}La_{0.65}O_{1.67}$, is obtained when a 1 : 1 ratio is employed. With fluoride pure CeO_2 and LaF_3 are the only phases present and no mixed Ln-Ce-O phase is formed. TEM shows that the microstructure of this material is complex. The nature of analogous Pr- and Nd-substituted ceria materials is also described.

Keywords: ceria, fluoride doping, lanthanides, powder X-ray diffraction, transmission electron microscopy

Although lanthanide oxides including ceria have been shown to be active catalysts for a number of processes, the activity of the pure oxide materials can be improved by the incorporation of other ions in the lattice [1–3]. In addition, the conductivity of ceria can be enhanced by doping with trivalent lanthanides [4], and these materials have applications in solid oxide fuel cells [5]. The preparation of these materials is usually effected by sol-gel methods followed by a calcination procedure before use. Both the presence of fluoride and the particular rare earth cation influence profoundly the constitutional and microstructural nature of the materials obtained, which will inevitably lead to changes in their performance. Here we examine the nature of ternary Ln-Ce-O (Ln = La, Pr, Nd) oxide materials with and without added fluoride ion.

Ternary Ln-Ce-O (Ln = La, Pr, Nd) oxide materials of target Ln : Ce ratios of 1 : 4, 1 : 1.86 and 1 : 1, with and without added fluoride ion, were obtained by adding concentrated aqueous ammonia (0.880) to a vigorously stirred aqueous solution containing $Ln(NO_3)_3$ and $Ce(NO_3)_3$ in the appropriate molar ratios in the presence of hydrogen peroxide. The source of fluoride was NH_4HF_2 which was added to the mixtures at a level of 5 wt%. Subsequently, the gel materials obtained were calcined at 1223 K for 1 h. The physical appearance of the resulting materials together with both target and experimentally determined elemental analysis (X-ray fluorescence) as well as pertinent XRD (Phillips PW 3020 Diffractometer, CuK_α radiation $\lambda = 1.54050$ Å) are summarized in Table 1. Samples of pure ceria and fluoride-doped ceria were also prepared in the same way. The presence of fluoride in the materials has a noticeable effect on the color; those with fluoride being significantly paler.

Prior to calcination, all the materials are gel-like, only differing in color, and exhibiting very broad lines in the XRD spectrum characteristic of very small crystallite ceria. Low resolution XRD spectra for all the calcined La-Ce-O materials exhibited peaks characteristic of single-phase solid solutions possessing the fluorite structure. However, a high resolution spectrum of the 50 : 50 material shows quite clearly (Fig. 1(A)) the presence of two phases, both of the fluorite structure but with different lattice parameter values. Rietveld analysis shows one spectrum to be due to pure ceria and the other to a Ln-Ce-O phase of composition $Ce_{0.35}La_{0.65}O_{1.67}$ in the ratio 47.5% : 52.5%,

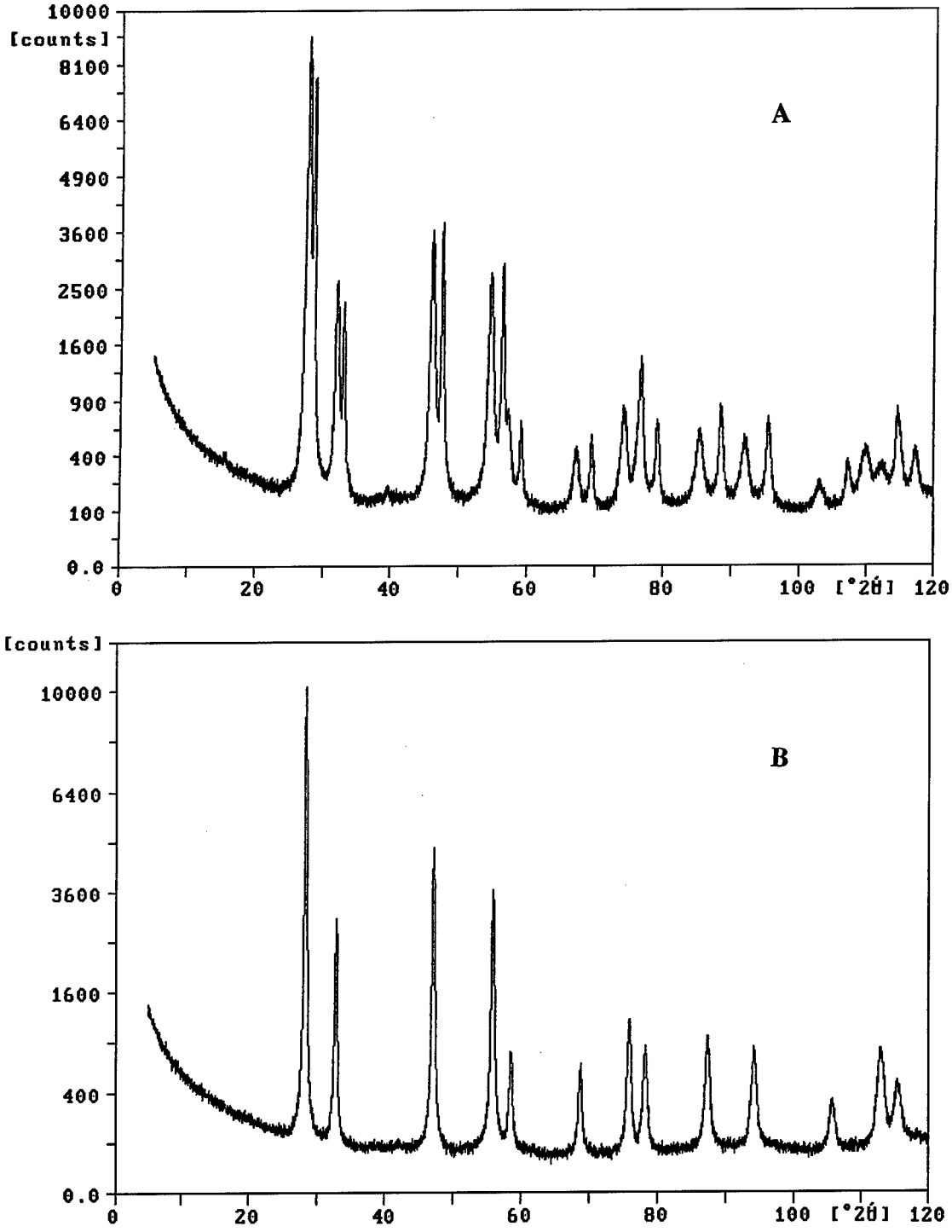

Figure 1. Powder XRD diffractograms for (A) the 50 : 50 La/Ce/O gel calcined at 1273 K, (B) the 50 : 50 Nd/Ce/O gel calcined at 1273 K, (C) fluorine-doped 50 : 50 La/Ce/O gel calcined at 1273 K, and (D) fluorine-doped 50 : 50 Nd/Ce/O gel calcined at 1273 K.

(*Continued on next page.*)

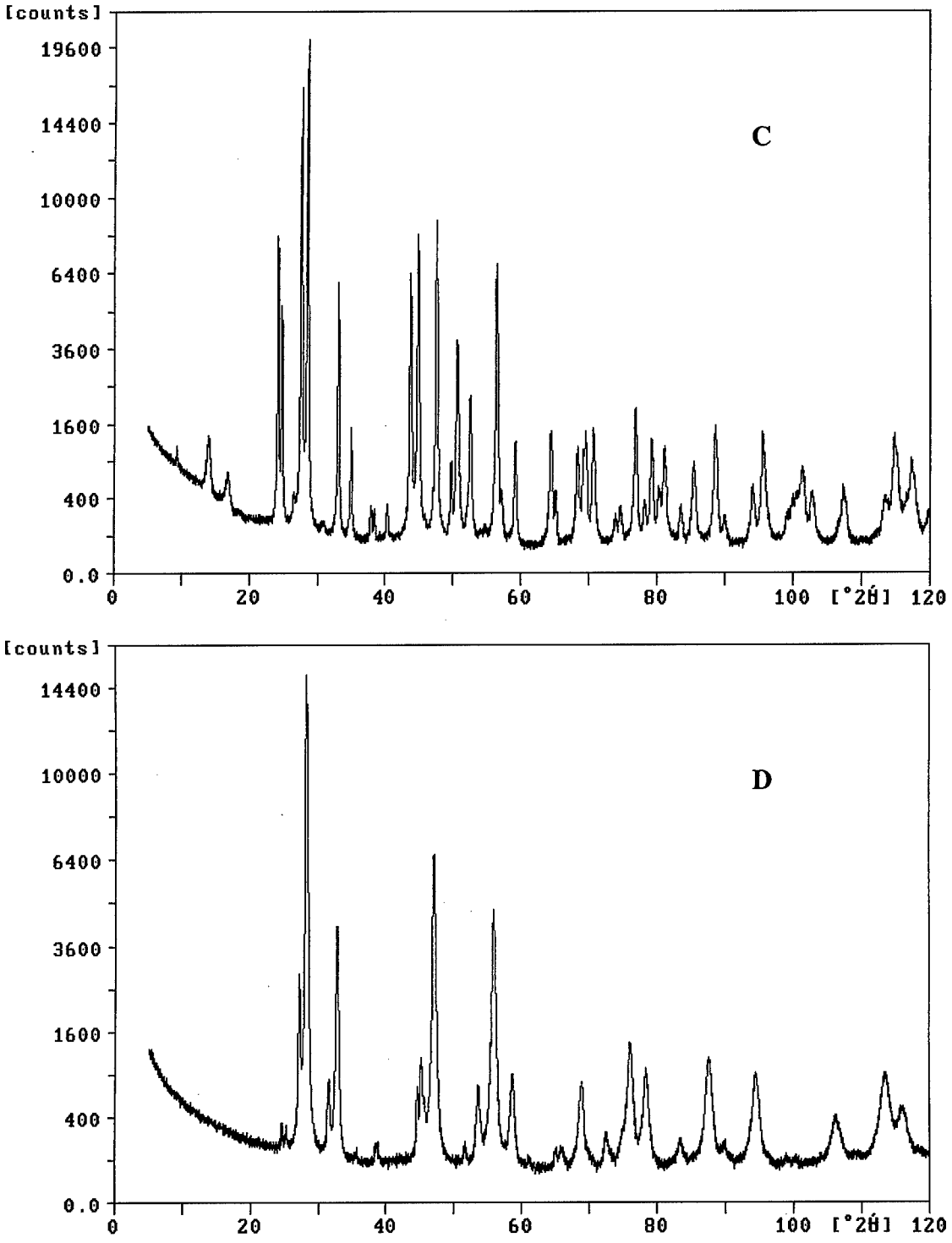

Figure 1. (*Continued*).

Table 1. Analytical and X-ray data for materials obtained after calcination of lanthanide- and fluoride-doped ceria.

Material	Ln : Ce atomic ratio[a]	Wt% F	Color	Phases present	Fluorite lattice parameter a (Å)	Mean crystallite size (nm)
CeO_2	—	—	Pale yellow	CeO_2	5.4127	195
F/CeO_2	—	2.15	White	CeO_2	5.4136	1295
				CeOF (minor)	—	—
La/CeO_2	1.07	—	Salmon pink	CeO_2	5.4178	289 (353)[b]
				$Ce_{0.35}La_{0.65}O_{1.67}$	5.5777	158 (426)[b]
$F/La/CeO_2$	1.13	15.3	Pinky off-white	CeO_2	5.4115	817
				LaF_3	—	—
Pr/CeO_2	0.99	—	V. dark chocolate	CeO_2	5.4313	274
				Pr_6O_{11}, $(Pr,Ce)O_2$	—	—
$F/Pr/CeO_2$	1.02	6.1	Dark brown	CeO_2/Pr_6O_{11}	5.4322	304
				CeOF		
Nd/CeO_2	0.57	—	Pale grey green	$Ce_{0.64}Nd_{0.36}O_{1.71}$	5.4735	284
$F/Nd/CeO_2$	0.55	3.9	Greyish off white	$Ce_{0.64}Nd_{0.36}O_{1.71}$	5.4620	249
				CeOF (minor)[c]	—	—

[a]Target atomic ratio in all cases was 1 : 1.
[b]Values after further calcination at 1273 K for 24 h.
[c]Also traces of NdF_2 and NdF_3 present.

respectively. In spite of comprising two phases, a transmission electron micrograph of this material (Fig. 2, top left) shows it to appear homogeneous, both phases appearing as small (ca. 20 nm) cubes and are indistinguishable from one another. Further calcination at 1273 K for 24 h had negligible effect on the compositional nature of the two phases, although the average particle size of each increased somewhat.

In the case of Ln = Pr, the XRD trace exhibited a pattern due to a single phase with the fluorite structure, Riedvelt analysis of which indicated a solid solution of composition $Ce_{0.53}Pr_{0.47}O_{1.99}$. However, TEM/EDX analysis showed that three types of particle are present: very large rectangular particles containing only praseodymium and oxygen, small particles containing only cerium and oxygen, and other particles which contain both cerium and praseodymium in addition to oxygen. Unlike the case of Ln = La or Pr, the loading of neodymium in the Nd-Ce-O materials appears to reach a maximum value at ca. 36 wt%, and target metal atom ratios greater than this were not achievable. At this level of neodymium loading, Rietveld analysis of the XRD data show the phase which is formed to be $Ce_{0.64}Nd_{0.36}O_{1.71}$, very similar to the known phase $Ce_{0.75}Nd_{0.25}O_{1.83}$ [6] (Fig. 1(B)).

The effect of fluoride on the constitutional nature and microstructure of the materials is very dependent on the particular rare earth. Gels containing only cerium ions in the presence of added fluoride followed by calcination leads to the incorporation of only 2.2 wt% of fluoride, and the XRD shows the presence of pure ceria together with a minor cerium oxyfluoride phase, probably CeOF (or $Ce_3O_4F_3$). In contrast, incorporation of fluoride in the gel obtained from solutions containing both lanthanum and cerium cations increases linearly with lanthanum content (20.3% La, 6.0% F; 33.7% La, 11.7% F; 43.9% La, 15.3% F). These data correspond to F : La atom ratios of 2.53, 2.98 and 2.98, respectively. XRD showed that for all La : Ce ratios examined pure CeO_2 and LaF_3 were the only phases present (Fig. 1(C)). Thus, it would appear that, in the presence of lanthanum all the fluoride segregates as LaF_3, and no mixed Ln-Ce-O phase is formed at all. This observation is corroborated by TEM/EDX analysis and electron diffraction. However, these show that the microstructure of this material is complex. Individual particles of both ceria and LaF_3 are seen. Figure 3 (top left) shows a ceria particle (for which EDXa confirms the absence of lanthanum and fluorine) with its characteristic cubic electron diffraction pattern (Fig. 3,

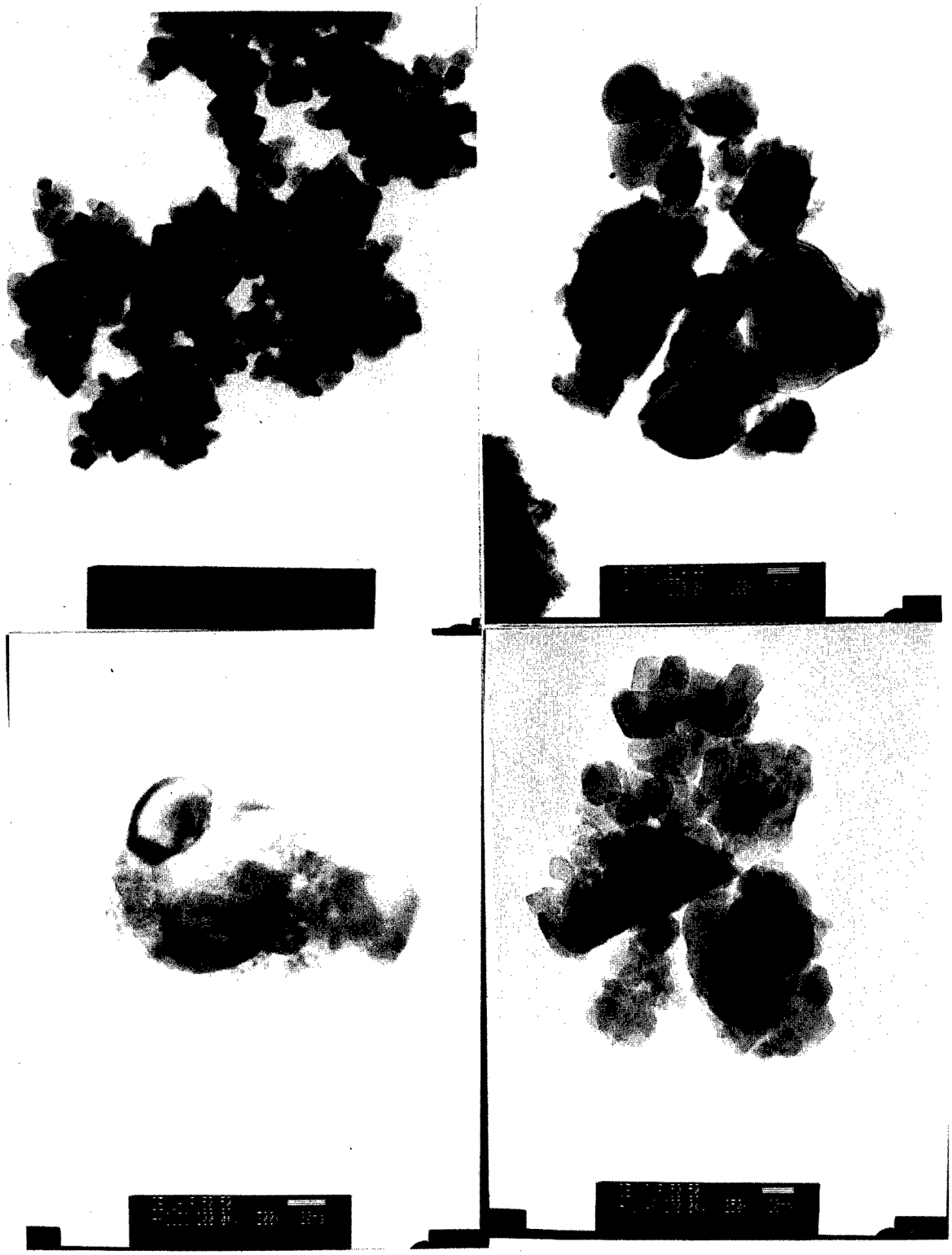

Figure 2. Transmission electron micrographs for (top left) the 50 : 50 La/Ce/O gel calcined at 1273 K (scale bar 50 nm), (top right) fluorine-doped 50 : 50 La/Ce/O gel calcined at 1273 K (scale bar 50 nm), (bottom left) fluorine-doped 50 : 50 La/Ce/O gel calcined at 1273 K (scale bar 20 nm), and (bottom right) fluorine-doped 50 : 50 Nd/Ce/O gel calcined at 1273 K (scale bar 20 nm).

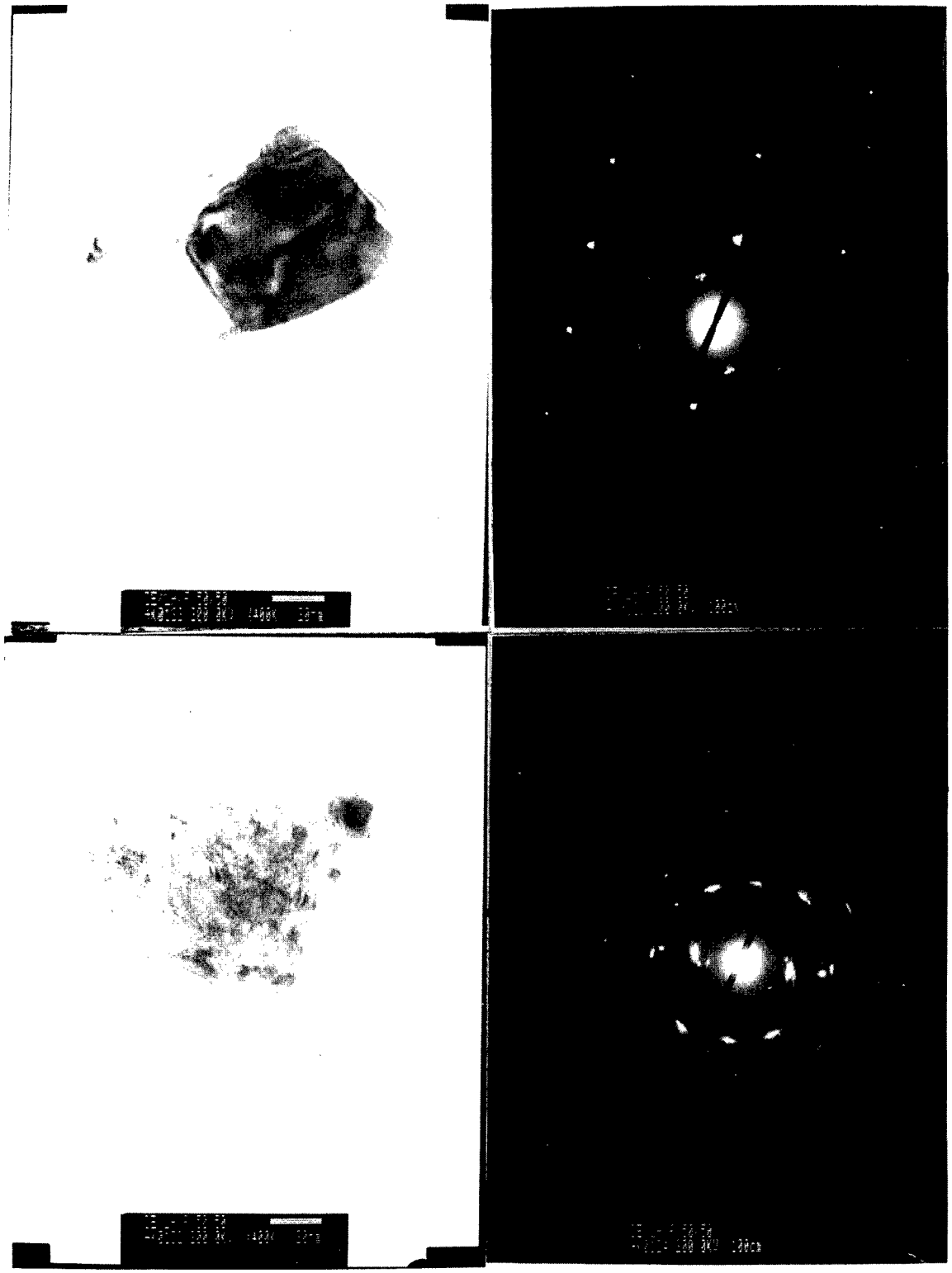

Figure 3. Transmission electron micrographs for (top left) a ceria particle and (top right) a LaF_3 particle present in the fluorine-doped 50 : 50 La/Ce/O gel calcined at 1273 K (scale bar 20 nm in both). The corresponding electron diffraction patterns are shown in the top right and bottom right, respectively.

top right). Figure 3 (bottom left) illustrates a particle free from cerium and oxygen exhibiting a hexagonal electron diffraction pattern expected for LnF_3 (Fig. 3, bottom right). In addition to both of these are particles of ceria on the surface of which are "seaweed" type growths of LnF_3 (Fig. 2, bottom left), and other aggregates of ceria particles which are adhered together by LnF_3 (Fig. 2, bottom right).

Fluoride incorporation in both the Pr-Ce-O and Nd-Ce-O systems is much lower. At the highest Pr : Ce ratio (ca. 45%) only 3–4% fluoride is incorporated, all of which is present as PrF_2. Other phases present in this material are CeO_2 and Pr_6O_{11}. Only 3% fluoride is incorporated at the highest Nd : Ce ratio. However, in this case the fluoride is present as cerium oxyfluoride, CeOF, together with the neodymium fluorides NdF_2 and NdF_3, and the neodymium forms the ternary $Ce_{0.64}Nd_{0.36}O_{1.82}$ phase (Fig. 1(D)). The transmission electron micrograph of this material (Fig. 2, bottom right) shows it to comprise mainly ceria crystallites together with minor neodymium fluoride phases.

In conclusion, both the presence of fluoride and the particular rare earth cation influence profoundly the constitutional and microstructural nature of the materials obtained after calcination of the homogeneous gels formed by sol-gel techniques from aqueous solution containing these ions.

Acknowledgments

We thank the OST Division of London and Scandinavian Ltd. and the EPSRC for support.

References

1. R.J.H. Voorhover, *Advanced Materials in Catalysis* (Academic Press, New York, 1973), p. 129.
2. Y. Okomoto, K. Adachi, T. Imanaka, and S. Teranishi, Chem. Letters, 241 (1974).
3. Y. Osada, S. Koike, T. Fukushima, S. Ogasawara, T. Shikada, and T. Ikariya, Appl. Cat. **59**, 59 (1990).
4. R. Gerhardt and A.S. Nowick, J. Am. Ceram. Soc. **69**, 641 (1988).
5. H. Yahiro, K. Eguchi, and H. Arai, Solid State Ionics **36**, 71 (1989).
6. Smith and McCarthy, JCPDS Grant in Aid Report, 1975, Penn. State University, University Park, Penn., USA.

Journal of Sol-Gel Science and Technology 13, 1057–1060 (1998)
© 1998 Kluwer Academic Publishers. Manufactured in The Netherlands.

Structural and Chemical Modification of Polydiene Latexes by Gel Derived Silica

I.A. TOUTORSKI AND T.E. TKACHENKO
Department of Colloid Chemistry, Moscow Academy of Fine Chemical Technology, Vernadsky pr., 86, 117571 Moscow, Russia

N.I. MALIAVSKI
Department of General Chemistry, Moscow University of Civil Engineering, Yaroslavskoe sh., 26, 129337 Moscow, Russia

Abstract. Latex-silicate compositions and unsupported films (green and vulcanized) were prepared by mixing natural Qualitex and synthetic butadiene-styrene (SKSS) latexes with an aqueous solution of sodium silicate modified with a zinc tetrammine complex. The mechanism and efficiency of the inorganic modification of latex structures were investigated by UV-vis and IR spectrophotometry, rotational viscometry of liquid and gelled mixtures as well as by tensile testing of the prepared films. Measurements showed an increase of elastic modulus and tensile strength with silica concentration for all composite films except for the green SKSS-based ones. The improvement of mechanical properties can be related to the formation of interpenetrating organic and silicate networks linked by Zn atoms that can also participate in the vulcanization process.

Keywords: hybrid material, latex, sodium silicate, zinc

1. Introduction

Sol-gel method is an attractive approach for the preparation of silica-reinforced rubbers [1]. For this purpose, alkoxide derived silica is usually used, for example, by hydrolyzing tetraethoxysilane (TEOS) incorporated in green or vulcanized rubbers by swelling. Silica-reinforced poly(dimethylsiloxane) [2], polyisobuthylene [3], butadiene-styrene [4] and epoxidized natural rubbers [5] have been obtained by this method. Recently, silica-reinforced natural and synthetic latex films have been prepared from corresponding latexes mixed with aqueous emulsions of TEOS [6]. The properties of the hybrid nanocomposites obtained, depend on interpenetration of organic and inorganic networks formed in the materials.

In this work, hybrid latex-silica nanocomposites were prepared by sol-gel synthesis directly in latex, a water-soluble silica precursor being used. Zinc was incorporated in the precursor mix to promote a chemical interaction of the latex and silicate networks. The preparation of water-soluble zinc-silicate precursors has been described previously [7, 8] and is based on the high stability of zinc-diamino and zinc-amino (as ethylenediamine, ethanolamine, etc.) complexes. Among possible systems, the system SiO_2-Na_2O-ZnO-NH_3-H_2O was selected as the most promising for industrial applications due to low costs of components and ease of synthesis.

2. Experimental

An aqueous solution of sodium silicate $Na_2O/2.9SiO_2$, with a total mass concentration of oxides of 39.6%, was used as the silica route. Zinc oxide and aqueous ammonia (28 wt% NH_3) were added at molar ratios $ZnO/SiO_2 = 0.11$ and $NH_3/ZnO = 4.2$. The suspension obtained was stirred at room temperature for 2–3 h until complete dissolution of ZnO had been reached.

The clear solution of (SNZ) so prepared at pH = 12.7 was stable if stored in a closed container (to prevent escape of ammonia).

The natural latex (Qualitex, stabilized with ammonia, mass concentration 40%, pH = 10.9) and the synthetic butadiene-styrene latex (SKSS, stabilized with potassium oleate, pH = 9.8) were used as the organic components. The compositions were made by mixing latexes with SNZ at mass ratios from 120 : 1 to 6 : 1 that corresponded to silica/rubber mass ratios (S/R) from 0.005 to 0.1. The standard vulcanizing composition containing sulfur, ZnO and zinc diethyl dithiocarbamate, was added to some part of the prepared mixtures. All the compositions prepared at S/R higher than 0.03 (SKSS-SNZ) and 0.06 (Qualitex-SNZ) were gelled 1–2 h after the preparation. Composite 1-mm thick films were then obtained by pouring the calculated quantities of as-prepared liquid mixtures (at S/R = 0–0.05) into glass dishes, drying at room temperature for 5 days and peeling off the formed films from the glass substrate. The films prepared from the mixtures containing vulcanizing additives were heated at 90°C for 30 min.

Rheological properties of the modified latexes were studied at 20°C by the rotational viscometer "Polymer RPE-2M." The polymer structure parameters of the silicate anions in solution and gels were measured by the UV-vis spectrophotometric molybdate method [9, 10] using a bimodal approximation to characterize the molecular mass distribution, as in the work [11]. For every polyanion fraction (low oligomers and high polymers) the statistical weights (g_1 and g_2) and the values of the mass averaged polymerization grade for the fractions (n_1 and n_2) and for the whole sample (n) were calculated according to well-known relations [9].

Infrared spectra of latex films deposited on silicon wafers were measured at 400–4000 cm^{-1} using a Specord M82 apparatus. Tensile strength and moduli at tensile extents 20–500% were determined from standard tensile tests carried out for all prepared films on an Instron mechanical testing machine.

3. Results and Discussion

Figure 1 shows flow curves (shear rate versus shear stress) for several equilibrium compositions SKSS-SNZ at different S/R. The curves for the compositions at S/R = 0.01–0.03 are similar to those for the pure latex. At silica concentrations higher than 3% the compositions gelled and their flow curves showed a non-zero yield stress and two regions corresponding to the pseudoplastic and viscous flows.

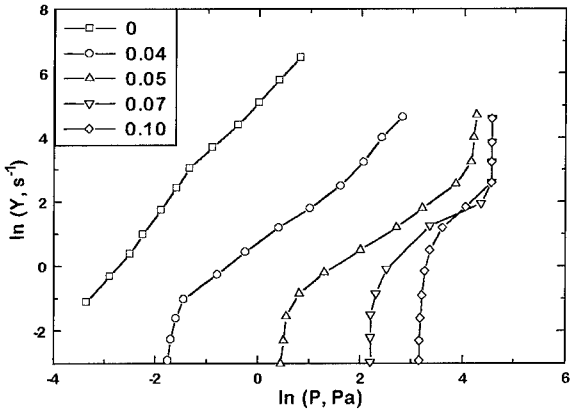

Figure 1. Flow curves for the mixtures of butadiene-styrene latex SKSS with zinc-silicate solutions at different silica/rubber ratios (S/R).

This behavior of low silica concentrations is probably connected with thixotropic properties of an inorganic zinc-hydroxide network formed in the systems because of decreasing ammonia concentrations (20–60 times, due to the dilution of the SNZ solution), according to the equation:

$$[Zn(NH_3)_4]^{2+} + 2OH^- + 4H_2O \rightarrow Zn(OH)_2 + 4NH_4OH \quad (1)$$

The gel probably consists of $Zn(OH)_2$ globules connected by donor-acceptor and hydrogen bonds.

In Table 1 the yield stress values are displayed for the precursor solution diluted by water and latexes (the S/R values for the SNZ-water system mean that the solutions were prepared at the same silica/water ratio as the corresponding latex/SNZ compositions). It can be seen that pure SNZ solutions gelled in the same way when diluted 6–13 times. Hence, weak gels were formed with low yield stresses (0.5–1.5 Pa) which decreased with increased S/R above 0.05. On the contrary, in the SKSS-SNZ system yield stress increased with an increase of the silica content in the whole of the region studied. It is evident that in this system there is a continuous transition from zinc-hydroxide to a siloxane structure. The latter is generally characteristic of silicate-organic mixtures [12] and results in rather strong gels cross-linked with covalent bonds. In fact, the concentrated SKSS-SNZ gels had yield stresses up to 22 Pa.

Unlike SKSS-SNZ, the system Qualitex-SNZ was less disposed to gelling. Here the non-zero values of

Table 1. Some rheological and polymerization parameters of the sodium-zinc-silicate solutions and their mixtures with latexes.

	MMD parameters for the systems SNZ-H_2O						Yield stress for SNZ-A; A=		
S/R	pH	n_1	g_1	n_2	g_2	n	H_2O	SKSS	Qualitex
0.01	11.5	2	0.67	900	0.33	298	0	0	0
0.03	12.0	2	0.69	150	0.31	48	0.5	0	0
0.05	12.2	4	0.71	170	0.24	52	1.5	1.8	0
0.07	12.3	5	0.69	170	0.31	56	0.08	11	0.25
Undiluted	12.7	5	0.58	140	0.42	62	0	—	—

yield stress appear only above S/R = 0.06 (see Table 1). In this system, dilution of SNZ is not connected with a significant decrease of the ammonia concentration (the latex contains NH_3 as a stabilizer) and therefore no zinc-hydroxide structuring took place. In addition, the siloxane gels formed were less strong than in the previous system (yield stresses were less than 5 Pa) probably due to higher pH values (12.3–12.5 against 11–12 in the SKSS-SNZ system) disturbing the polycondensation process:

$$\equiv Si{-}O^- + OH{-}Si\equiv \leftrightarrow OH^- + \equiv Si{-}O{-}Si\equiv \quad (2)$$

The siloxane network must be formed in both latex-silicate systems (also at low S/R) as a result of drying due to the increase of the general silica concentration that displaces equilibrium (2) to the right.

Some principal characteristics of the molecular-mass distribution for SNZ and its diluted aqueous solutions are shown in Table 1. It can be seen that dilution of SNZ to S/R = 0.03–0.07 (accompanied by gelation) resulted in some depolymerization of silicate anions, mainly due to the decrease of n_1 and g_2. This fact confirms the assumption of $Zn(OH)_2$-caused gelation in diluted SNZ solutions. Only the most diluted solution (S/R = 0.01) exhibited a different behavior, displaying a significantly higher polymerization degree of the high-polymer fraction. This disproportionation was probably connected with a low pH value (11.5). This effect was also reproduced in the SKSS-SNZ composition at the same S/R where $n_1 = 3$, $n_2 = 2200$ and $n = 1520$.

Mechanical properties of green latex films are determined by their organic networks based on the hydrophobic interactions of latex globules. Since the latex-silicate films were dried for a rather long period (5 days), we suppose that their structures were formed at equilibrium conditions and the interpenetrating latex

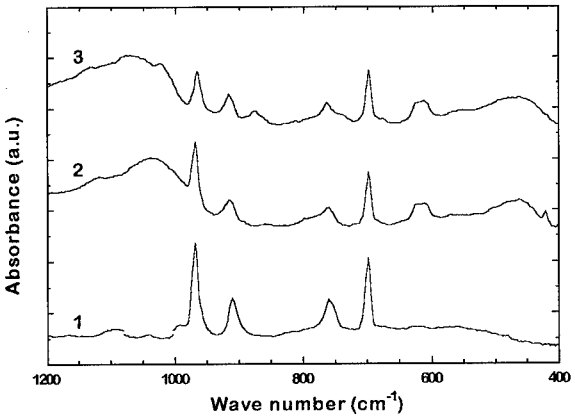

Figure 2. Infrared spectra of: green SKSS (1) green SKSS-SNZ (S/R = 0.1) and vulcanized SKSS-SNZ (S/R = 0.1) latex films.

and siloxane networks may be reduced after having been destroyed due to the shrinkage. Infrared spectra of the SKSS-SNZ films (in the characteristic region 400–1200 cm^{-1}) are shown in Fig. 2 and compared with that of the corresponding pure latex film. The presence of the siloxane network in binary films is evident from the intensive broad peaks centred at 1040–1070 and 460 cm^{-1} and assigned to the Si—O—Si stretching and rocking vibrations, respectively. The strong double peak at 610–625 cm^{-1} is probably due to the $Si{-}O{-}Zn^{IV}$ stretching vibration because its position and shape are close to those of the corresponding peak in the spectrum of villemite [13]. Tetrahedrally coordinated Zn atoms may be formed in the silicate structure according to the reaction:

$$2(\equiv Si{-}ONa) + [Zn(NH_3)_4]^{2+} + 2OH^- + 2(HO{-}Si\equiv) \rightarrow (\equiv Si{-}O)_4Zn^{2-} \cdot 2Na^+ + 2H_2O + 4NH_3 \quad (3)$$

Other Zn atoms can interconnect the latex and silicate networks through the bond $\equiv Si{-}O{-}Zn{-}O{-}CO{-}C\equiv$.

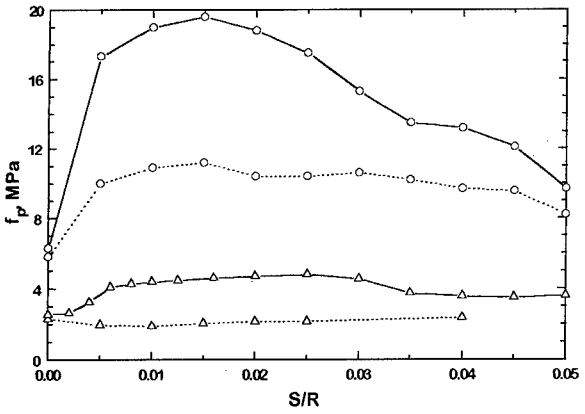

Figure 3. Tensile strengths versus S/R for the green (dot lines) and vulcanized (solid lines) Qualitex/SNZ (circles) and SKSS/SNZ (triangles) latexes.

The carboxyl groups are present on the surface of globules due to the stabilizers (hydrolyzed lipids and proteins in Qualitex, potassium oleate in SKSS).

The reinforcement effect in the systems studied can be demonstrated by the positive dependence of the film modulus and tensile strength on S/R. We observed a monotonous increase of modulus versus S/R for both composite systems except the SKSS-SNZ films at high tensile stress in the S/R range 0.015–0.025.

However, the differences between the two systems are more evident when considering the dependence of tensile strength on S/R shown in Fig. 3. Among green films, all Qualitex-SNZ films were notably stronger (up to 1.9 times) than those of pure latex. In contrast, in the SKSS/SNZ system the composites showed lower (or equal) strengths than pure latex. This effect can be explained by the difference in shape of the globules of Qualitex and SKSS: whereas the former consists of spherical globules of 0.5–1 μm diameters [14], the latter contains irregular agglomerated globules of smaller dimensions (about 0.1 μm [15]). In the Qualitex structure the silicate network could be located (at low silica concentrations) in narrow channels between close-packed spherical globules; this structure would promote interaction of the networks. On the other hand, the agglomerated SKSS globules should adsorb significant quantities of polysilicate anions on their internal surface and the formation of a continuous silicate network in the interglobular space would be difficult.

All composite vulcanized films displayed higher tensile strengths than the pure latex films, especially in the S/R range 0.5–3. The maximum increase grades are 3.1 for Qualitex-based films and 1.8 for SKSS-based films. Since this effect does not appear in latex films reinforced with alkoxy-derived silica [6], it is probably connected with the well-known role of Zn^{2+} ions as efficient vulcanization activators. During the heat treatment at 90°C, some of the Zn^{2+} ions form additional silicate—globular and interglobular cross-links, for example: ≡Si—O—Zn—S—C≡. At higher silica content (S/R > 1.5 for Qualitex-SNZ and S/R > 2.5 for SKSS/SNZ) the siloxane network becomes too bulky and distorts the hydrophobic-bonded organic network; this may explain the observed decrease of strengths with increased S/R.

4. Conclusions

The use of the water-soluble Zn-containing silica precursor allows composite latex-silicate films to be prepared based on natural Qualitex and synthetic butadiene-styrene latexes. This inorganic reinforcement notably improves mechanical properties of vulcanized latex films over green ones. Zinc ions contained in the precursor seem to ensure the interconnection between the organic and inorganic networks as well as participating in the process of vulcanization cross-linking.

References

1. J.E. Mark, J. Appl. Polym. Sci.: Appl. Polym. Symp. **50**, 273 (1992).
2. G.B. Sohoni and J.E. Mark, J. Appl. Polym. Sci. **45**, 1763 (1992).
3. C.C. Sun and J.E. Mark, J. Polym. Sci., B: Polym. Phys. **25**, 1561 (1987).
4. S. Kohjiya, A. Yajima, C. Yoo, and I. Ineda, J. Soc. Rubber Ind. (Jap.) **67**, 859 (1994).
5. A.S. Hashim, N. Kawabata, and S. Kohjiya, J. Sol-Gel Sci. Technol. **5**, 211 (1995).
6. I.A. Toutorski, O.A. Dulina, and A.M. Zatevalov, Elastomers Production and Use (Rus.), (2), 16 (1997).
7. N. Maliavski and M. Guglielmi, in *Ultrastructure Processing of Advanced Ceramics*, edited by J.D. Makenzie and D.R. Ulrich (John Wiley & Sons, N.Y., 1988), p. 315.
8. A.N. Khripunkov, N.I. Maliavski, and V.I. Sidorov, Sov. J. Appl. Chem. **62**, 656 (1989).
9. R.K. Iler, *The Chemistry of Silica*, chap. 3 (Wiley, N.Y., 1979).
10. N. Maliavski, E. Tchekounova, and O. Dushkin, J. Sol-Gel Sci. Technol. **2**, 503 (1994).
11. B. Unger, H. Jancke, M. Hahnert, and H. Stade, J. Sol-Gel Sci. Technol. **2**, 51 (1994).
12. R.K. Iler, *The Chemistry of Silica*, chap. 2 (Wiley, N.Y., 1979).
13. Chung-Chern Lin and Pouyan Shen, J. Non-Cryst. Solids **171**, 281 (1994).
14. *Natural Rubber Science and Technology*, edited by A.D. Roberts, chap. 4 (Oxford Univ. Press, 1988).
15. L.N. Erkova and O.S. Tchechik, *Latexes* (Rus., Chimija, Moscow, 1983), p. 102.

Journal of Sol-Gel Science and Technology 13, 1061 (1998)
© 1998 Kluwer Academic Publishers. Manufactured in The Netherlands.

Thematic Index

Sol-Gel Chemistry and Structure 17
Applications and New Directions 133
Biomaterials and Biomimetics 237
Aerogels/Xerogels 299
Hybrids 371
Sol-Gel Optics and Optoelectronics 509
Coatings and Membranes 673
Electrical/Magnetic Properties 813
Drying, Sintering, Crystallization and Pyrolysis 937
Powders, Catalysts, Fibers and Composites 1011

Journal of Sol-Gel Science and Technology 13, 1063–1068 (1999)
© 1999 Kluwer Academic Publishers. Manufactured in The Netherlands.

Author Index

A

Abbas, A.F., 753
Abbas, B., 647
Abdel-Fattah, W.I., 981
Abdelghani, A., 569
Abe, Y., 541, 933, 975
Adeogun, M.J., 27
Aegerter, M.A., 177, 679, 961, 1005
Ahmad, M.M., 517
Ahmed, A.A., 753
Aizawa, M., 991
Akiyama, Y., 421
Alaoui, A.H., 365
Algueró, M., 839
Almeida, R.M., 51
Amberg-Schwab, S., 141
Andrew, J.E., 757
Antonioli, G., 667
Apsel, F., 89
Arčon, I., 861
Armelao, L., 213
Armellini, C., 599
Atkins, G.R., 103
Atkinson, A., 133
Aubonnet, S., 593
Avnir, D., 17

B

Babonneau, F., 75
Badenes, J., 347
Bader, H., 141
Bae, B.-S., 409, 869
Baratto, C., 667
Bartlett, J.R., 113, 1011
Bazin, N., 757
Becker, C., 397, 499
Bekiari, V., 95
Benatsou, M., 529
Ben-dor, L., 229
Benlian, D., 889
Bergo, V.B., 889
Berková, D., 569, 617
Bernards, T.N.M., 71, 749
Berquier, J.M., 739
Bersani, D., 667, 849
Bescher, E.P., 371
Beteille, F., 915
Bhagat, M., 45
Bharathi, S., 241
Biehl, S., 177
Bilmes, S.A., 341
Binkle, O., 1023
Birnie, D.P., III, 855
Björkert, U.S., 799
Blacher, S., 415
Blanco, E., 451
Boilot, J.P., 61
Bonagamba, T.J., 909
Bonhomme, C., 65
Böttcher, H., 89, 277
Bouazaoui, M., 529
Bouhedja, L., 65
Boukos, N., 503
Brányik, T., 283
Bray, K.L., 605
Brooks, K.G., 815, 833
Brungs, M.P., 1011
Brusatin, G., 535, 717
Bukowski, T.J., 895, 899
Burgard, D., 789
Büttgenbach, L., 679

C

Calas, S., 937
Calzada, M.L., 839, 843
Campero, A., 651, 657, 663
Cantoni, M., 229
Cao, G., 305
Capoen, B., 529
Carr, S.W., 31
Carturan, G., 273
Castro-Garcia, S., 923
Chaïeb, A., 439
Chaput, F., 457
Chaudhuri, S.R., 311
Chaumont, D., 353
Chen, Y., 735
Chmelka, B.F., 75
Chomát, M., 569
Chopin, T., 119

Collins, D., 553
Colombo, P., 195, 213
Cong, W., 933
Cooke, R.G., 171
Costa, L., 679
Costa, V.C., 605
Coudray, P., 523
Craeivich, A., 353
Crisan, D., 775
Crisan, M., 769, 775
Cros, F., 457

D

Da Costa, P.T., 251
Da Silva, M.F., 843
Dahmouche, K., 427, 909
Dal Monte, R., 273
Damborenea, J.J., 717, 723
Danzebrink, R., 177
Davidson, K., 553
Davis, D.G., Jr., 895, 899
Dawnay, E.J.C., 783
De La Rosa-Fox, N., 629
De Souza, P.H., 909
De Souza Nóbrega, M.C., 251
Deichmann, A., 183
Del Longo, L., 599
Deligiannakis, Y., 503
Demnerová, K., 283
Deng, C.S., 489
Dimitriev, Y., 255, 969
Dimitrov, V., 951, 969
Dimitrova-Lukacs, M., 255
Ding, X.-Z., 849
Djambaski, P., 255
Dostálek, P., 289
Dražič, G., 833
Du, Y., 763
Dubois, Ph., 415
Durán, A., 679, 717, 723
Durand, B., 119

E

Eguchi, K., 945
Einarsrud, M.-A., 317
Eisenberg, N., 547
Eleinen, O.A., 753
Ellis, B., 695
Emmerling, A., 299
Encheva, G., 969
Eo, Y.-J., 409
Esquivias, L., 629
Estournès, C., 929
Etienne, P., 523

F

Fabrizio, M., 213
Fairclough, J.P.A., 27
Fave, J.-L., 439
Fayed, M.SH., 981
Ferrari, M., 599
Ferreira, J.M.F., 201
Ferreira da Silva, M.G., 987
Ferrer, M., 95
Fick, J., 535
Fidalgo, A., 433
Fiorello, A., 517
Forest, L., 329
François, N., 341
Fricke, J., 299
Frischat, G.H., 763
Fujimura, N., 903
Fukuda, Y., 485

G

Gaboriaud, F., 353
Gacoin, T., 61
Gago-Duport, L., 629
Galliano, P., 723
Gan, F., 559
Ganz, D., 679, 961, 1005
Garcia, M.A., 651
Garcia Macedo, J., 657, 663
García-Hernández, M., 451
Gardlund, Z., 553
Gasparro, G., 679, 961, 1005
Gattef, E., 951
Gaulandris, V., 75
Gazeau, D., 113
Geiger, F., 473
Geiter, E., 397
Georgi, U., 295
Gerber, T., 323
Gessler, M., 141
Gharbi, N., 439
Gibbons, G.J., 379
Gibiat, V., 329
Gilath, I., 547
Ginzberg, B., 341
Glaubitt, W., 269
Gnappi, G., 667
Godhwani, J., 45
Goebbert, C., 789
Gomes, L.C.F.L., 251
Gómez, R., 1043
Gooda, SH.R., 981
Göttlicher, J., 85
Gouin, J.F., 207
Graebner, H., 295

Green, M., 509
Greenspan, D.C., 245
Griffoni, M., 195
Gross, J., 957
Guczi, L., 1037
Guglielmi, M., 535, 679, 717
Guille, J.L., 929
Guilment, J., 129
Guinebretière, R., 885
Gulik-Krzywicki, 99
Gun, J., 189, 241
Gunji, T., 975
Guth, J.-L., 119
Guy, I., 575
Guyon, H., 779

H

Haddow, D.B., 261
Hähnert, M., 81
Hall, C., 391
Hamada, H., 1033
Hammett, F., 171
Hand, R.J., 15, 695
Hanquet, B., 353
Harris, B., 171
Harrison, P.G., 391, 1049
Haruvy, Y., 547
Hasegawa, I., 485
Hay, J.N., 27, 109
Hayakawa, S., 237
Hayer, M., 617, 729
Heinrichs, B., 335
Hench, L.L., 245
Hill, R., 951
Himmel, B., 85
Hirashima, H., 991, 1033
Hodgson, S.N.B., 219
Hoebbel, D., 37
Hofacker, S., 385, 479
Hoffmann, M., 141
Hoinkis, E., 629
Holland, D., 379, 799
Holmes, A.S., 509
Horiuchi, S., 229
Horowitz, F., 707
Howes, A.P., 379
Huang, W., 509
Hubert-Pfalzgraf, L., 679

I

Ibusuki, T., 691
Ilharco, L., 433
Imai, H., 991, 1033
Inaba, M., 1033
Ion, R., 775
Ishizuka, M., 229
Ito, S., 587
Ito, T., 903
Ivanova, Y., 255
Iwasaki, M., 587
Izutsu, H., 421

J

Jackson, D., 359
Jacquiod, C., 739
Jaffrezic-Renault, N., 569
James, P.F., 15, 261, 359, 489, 495
Janicke, M.T., 75
Jansen, J.A.J., 749
Jasiorski, M., 585
Jauberteau, I., 885
Jérôme, R., 415
Jilavi, M.H., 855
Jiménez-Riobóo, R., 451
Jin, L., 735
Jordan, R.M., 171
Judeinstein, P., 909
Jung, G., 635, 685

K

Kaddami, H., 499
Kajiwara, M., 485
Kalfat, R., 439
Kalimanova, S., 951
Kaňka, J., 617
Kasahara, T., 975
Kashchieva, E., 969
Kašík, I., 569, 617
Katayama, S., 445
Kelsall, A., 1049
Kiefer, W., 385
Kim, D.-J., 409
Kirkbir, F., 311
Kitahata, H., 903
Kiyozumi, Y., 421, 1027
Kodre, A., 861
Kohama, K., 1033
Koo, J., 869
Koppany, Z., 1037
Korb, J.-P., 457
Kordas, G., 503
Kosec, M., 833, 861
Kozuka, H., 701
Krajewski, T., 855, 995
Krämer, S., 673
Kritikos, M., 125
Kron, J., 183
Krug, H., 397, 499, 673

Kucernak, A., 189
Kuncová, G., 283, 289
Kuraki, J., 587
Kursawe, M., 269
Kutsch, B., 499, 685
Kuwabara, M., 873

L

Lacroix, M., 569
Lana, S.L.B., 461
Langlet, M., 743
Larbot, A., 805
Lashgari, K., 865
Lavin, P., 641
Lecacheux, H., 923
Lee, T.-Y., 409
Legendziewicz, J., 611
Lev, O., 189, 241
Lewis, M.H., 799, 1001
Lianos, P., 95
Lischewski, R., 89
Lisowski, M., 585
Livage, J., 65, 915, 923
Llusar, M., 347
Löbmann, P., 827
López, T., 849, 1043
López-Salinas, E., 1043
Lottici, P.P., 667, 849
Loza, P., 657
Lu, S., 685
Lutz, T., 929

M

MacCraith, B.D., 207, 641
Mackenzie, J.D., 371
Maeda, K., 421
Majdoub, M., 439
Maliavski, N.I., 1055
Malič, B., 833, 861
Malier, L., 61, 457
Manier, M., 885
Maniewictz, M., 547
Manolache, M., 775
Marignan, J., 99
Martin, D., 129
Martín, M.J., 843
Martucci, A., 535
Maruszewski, K., 585, 611
Marx, J., 89
Mascia, L., 405
Masters, A.F., 103
Matějec, V., 569, 617, 729
Mayrand, M., 779
McCarthy, F.S., 895, 899
McCarthy, K.C., 895, 899
McCarthy, O., 579
McDonagh, C.M., 207, 641
McEvoy, A.K., 207
Mcinnes, H.A., 757
Mehrotra, R.C., 45
Mekky, W.F.F., 981
Mendiola, J., 843
Mendonça, A.M.R., 201
Menegazzo, E., 679
Mennig, M., 397, 635, 685, 717, 995
Mercurio, J.P., 885
Merklein, S., 827
Messias, F.R., 793
Metz, R., 575
Meyers, D., 311
Michels, A.F., 707
Minakuchi, H., 163
Minami, T., 903
Miranda Salvado, I.M., 201
Mitchell, G.R., 647
Mitchell, M.B.D., 359
Mitrikas, G., 503
Mizukami, F., 421, 1027, 1037
Modesti, M., 195
Mohseni, M., 495
Mondragon, M.A., 657
Monrós, G., 347
Montagna, M., 599
Montenero, A., 667
Moreau, Y., 523
Moustiakimov, M., 125
Munro, B., 673
Murata, H., 311
Muševič, I., 769

N

Naß, R., 855
Nacken, M., 37
Nagao, R., 933
Nagase, T., 223
Nakanishi, K., 163
Nass, R., 789, 1023
Navarrete, J., 1043
Negishi, N., 691
Nilsen, E., 317
Nitzsche, R., 81
Niwa, S., 1027, 1037
No, K., 869
Nogami, M., 541, 933
Nonat, A., 353

O

Ogasawara, T., 251
Ohtsuki, C., 237

Okada, T., 485
Oliveira, P., 177
Ortega, R., 657
Osaka, A., 237
Ou, D.L., 31, 623

P

Páca, J., 283
Paneppucci, H., 909
Panitz, J.-C., 473
Pankratov, I., 241
Paolizzi, M., 679
Pardo, L., 839
Pascual, C., 679
Pascual, M.J., 723
Patzák, M., 289
Pecquenard, B., 923
Peeters, M.P.J., 71
Pellegri, N., 783
Pelli, S., 535
Pentinghaus, H.J., 85
Perry, C.C., 593
Pevzner, S., 189
Phalippou, J., 365
Piñero, M., 629
Pirard, J.P., 335, 415
Pirard, R., 335
Pita, K., 517
Poncelet, O., 129
Porcar, L., 99
Porque, J., 523
Pospišilová, M., 729
Pressi, G., 273
Prieto, R.L.C., 451
Pucker, G., 599
Pulcinelli, S.H., 427, 793, 805, 909
Pütz, J., 679, 1005
Puyané, R., 575

Q

Quinson, J.F., 779

R

Rabinovich, L., 241
Rädlein, E., 763
Ramirez J.E., 657
Ramírez-del-Solar, M., 451
Raval, H.M., 109
Ray, A.K., 219
Reaney, I.M., 815
Regev, O., 189
Renteria, V.M., 663
Ribeiro, C.A., 427
Ribeiro, S.J.L., 427
Riegel, B., 385
Righini, G.C., 535
Roche, A., 171
Roewer, G., 295
Roisne, V., 779
Romdhane, S., 439
Rose, K., 729
Rottman, C., 17
Ryan, A.J., 27

S

Saenger, D.U., 635, 685
Sagoo, P., 599
Sakaguchi, K., 421
Sakane, K., 223
Sakka, S., 701
Sampath, S., 241
Samuneva, B., 255, 951, 969
Sano, T., 1027
Santilli, C.V., 427, 793, 805, 909
Santos, A., 629
Santos, L.R.B., 805
Sato, M., 421
Scalvi, L.V.A., 793
Schelle, C., 717
Scherer, G.W., 365, 937, 957
Schmidt, H.K., 37, 397
Schnabel, R., 89
Schneider, V.M., 509
Schottner, G., 183, 385, 479
Secondin, S., 273
Seddon, A.B., 15, 461, 623, 695
Sedlář, M., 569
Segal, D.L., 133
Seifert, S., 827
Sempéré, R., 937
Setter, N., 833
Shields, A.M., 207
Shimooka, H., 873
Shin, S., 1027
Sigov, A.S., 467, 877, 889
Singh, A., 45
Siu Li, M., 793
Sizgek, E., 1011
Slowik, P., 277
Smy, E., 233
Soares, J.C., 843
Sobolevsky, M.V., 467
Soga, N., 163
Sohling, U., 685
Sokolnicki, J., 611
Solovjeva, L.I., 877
Sommerdijk, N.A.J.M., 565

Song, K.-C., 409, 1017
Song, S.-W., 409
Souza, A.E., 793
Sporn, D., 827
Statham, M.J., 171
Stathatos, E., 95
Stefanova, S., 255
Strȩk, W., 585, 611
Strohhöfer, C., 535
Süß, W., 277
Sullivan, A.C., 31
Suratwala, T., 553
Suyal, N., 995
Syms, R.R.A., 509
Szilva, J., 289

T

Tadanaga, K., 903
Takahasi, S., 873
Takeuchi, K., 691
Tanaka, N., 163
Tanaka, S., 1037
Tanaka, Y., 229
Tang, T., 405
Taylor, D.V., 815
Tchana, W., 529
Tena, M.A., 347
Teowee, G., 153, 895, 899
Teyssedre, L., 739
Thierauf, A., 269
Thomas, I.M., 713
Thomas, P., 885
Tian, D., 415
Tian, H., 305
Tkachenko, T.E., 1055
Toba, M., 1027, 1037
Toki, M., 991
Tominaga, A., 991
Toutorski, I.A., 1055
Tracey, S.M., 219
Trapalis, C.C., 503
Tsuru, K., 237
Turevskaya, E.P., 889
Turniansky, A., 17

U

Uhlmann, D.R., 153, 553, 895, 899
Unger, B., 81

V

Valero, R., 119
Van Bommel, M., 679
Van Bommel, M.J., 71, 749
Van Cantfort, O., 335
Van Noort, R., 261
Vannucci, A., 517
Vasconcelos, W.L., 605
Vasiljev, V.A., 467, 877
Vautey, C., 743
Verza, P., 273
Vicent, J.B., 347
Vilcot, J.P., 529
Vorotilov, K.A., 467, 877, 889

W

Wacławek, W., 585
Wada, H., 223
Wang, F.H., 695
Westin, G., 125
Weston, G., 865
Wheeler, D.L., 245
Wieslaw, S., 585
Wijk, M., 125
Willems, H.X., 679
Winkler, R.-P., 397
Woignier, T., 329, 365
Wolf, G., 295
Wood, J.V., 1049
Woolfrey, J.L., 113
Wootton, A.M., 1001
Wright, J.D., 565
Wright, P.V., 489, 495
Wu, Z., 241

X

Xie, Y., 735

Y

Yamada, K.-I., 873
Yamada, N., 445
Yamane, M., 821
Yanovskaya, M.I., 877
Yeatman, E.M., 517, 579, 707, 783
Yi, J.H., 885
Yoldas, B.E., 147
Yoshinaga, I., 445
Youssof, I.M., 753

Z

Zaharescu, M., 769, 775
Zank, G.A., 945
Zapp, P., 673
Zemb, Th., 113
Zha, C., 103

Journal of Sol-Gel Science and Technology 13, 1069–1091 (1999)
© 1999 Kluwer Academic Publishers. Manufactured in The Netherlands.

Subject Index

A
Abrasion resistance, of ormosils, 375
Absorption spectroscopy
  of CdSe doped ormosils, 623
  of Mn^{2+} doped ZnS, 685
Acetic acid
  on lead crystal glass, 753
  on particle formation, 713
  in sol-gel route, 833
  in titanate microsphere production, 1011
Acetylacetone, for PZT thick film drying, 821
Acid catalyst, on two-step sol-gel process, 749
Acid step, of sol-gel process, 71
Acid-catalyzed silica sols, 81
Acoustical measurements, 329
Adhesion
  on coating strength, 695
  of heteropolysiloxane coatings, 779
  VTES on, 409
Adhesive(s)
  barrier, 141
  nanocomposites in, 397
Adsorption
  of aqueous solution dopants, 579
  of pyridine, 1043
Aerial oxidation, of tetraethylorthosilicate (TEOS), 713
Aerogel(s)
  characterization of, 937
  drying pressures on, 311
  isostatic compression on, 365
  production techniques for, 299
  sintering of, 937
  structural efficiency of, 957
  subcritical preparation of, 323
  of ZrO_2-Al_2O_3, 1033
Aeromosils, 375
Aerosol-gel process, 743
AES depth profile, for mirror coatings, 757
Aggregation
  of metallic tetrasulphophthalocyanines, 651
  of sulfide gels, 61
  tendency, in thermoplastic nanocomposites, 499
Aging
  of acid-catalyzed silica sols, 81
  on aerosol-gel process, 743
  of neodyium-doped silica gel-glasses, 593
  of silica gels in monomer solutions, 317
Air pollution
  elimination of, 691
  NO_x in, 1033
Alcogel structure, 329
Alkali silicate gelation process, colloidal, 233
Alkaline ions, on silicate entities, 353
Alkali-silica reaction (ASR), 353
Alkaloid production, 273
Alkane perfluoroether oligomer, 405
Alkoxides
  for bismuth strontium tantalate production, 889
  co-hydrolysis of, 113
  Er-containing, 125
  in forsterite xerogel, 359
  in PZT film preparation, 865
Alkoxysilane
  in alumina-silica gels, 1027
  in hydrolysis reactions, 75
Al_2O_3
  in gas permselectivity membranes, 801
  in optical fiber doping, 617
  in ZrO_2-Al_2O_3 aerogel catalysts, 1033
AlO(OH) matrix, in ink jet printing, 147
Al-O-PDMS hybrids, 445
Al_2O_3-TiO_2-SiO_2, atomic force microscopy of, 764
Alumina, in mullite-alumina composites, 201
Alumina-silica gels, solvent diols and ligands on, 1027
Alumina/titania diphasic ceramics, 801
Aluminosilicate
  films, 529
  glasses, 541
Aluminum
  as dopant, 580
  reactivity of, 109
Aluminum isopropoxide, in mullite fiber preparation, 1017
Aluminum nitrate
  in Al_2O_3-SiO_2 gels, 987
  in mullite fiber preparation, 1017
Aluminum substrates, in nanocomposite protective coatings, 735
Ambient pressure drying, 305
Amine hardener, in glass coatings, 695
Amino acid-doping, 585

Amino- (APTM) silanes, 588
3-Aminopropyltriethoxysilane, 553
Aminopropyltriethoxysilane (APTS)
  in GTPS/APTS system, 385
  on tetraethoxysilane base sol, 295
3-Aminopropyl(trimethoxy)silane, 623
Aminosilanes, water soluble colloids from, 553
Ammonia catalyzed hydrolysis, 713
Amorphization, in superconductor materials, 229
Amorphous materials, silver and platinum particles in, 969
Amorphous powders, 31
Anhydrous system, 103
Annealing process, 793
Annealing temperature, of barium-strontium titanate films, 877
Anorthite, in apatite-anorthite system, 255
Antimony doping
  of SnO_2 particles, 789
  for SnO_2 : Sb coatings, 961
  of tin oxide, 679
Antireflective coatings, 713
AOT/H_2O/heptane, 623
Apatite, 237
  in apatite-anorthite system, 255
  formation of, calcium silicophosphate on, 726
Apatite-mullite system, gel crystallization in, 951
Applications, of ormosils, 371
Aqueous sol-gel processing, 133
Aqueous solution, ion adsorption from, 579
Arrester, 575
ATD-TG analysis, 348
Atomic force microscopy (AFM)
  of Al_2O_3-TiO_2-SiO_2, 764
  of aluminosilicate planar waveguides, 529
  of photocurable coatings, 526
  of PLT film waveguides, 870
  of reversing gels, 554
  of TiO_2 films, 769
  of TiO_2 thin film photocatalyst, 691
Aurivillius phases, 885
Azo dyes, 17
Azomethine, 295

B
Barium titanate, 873
Barium-strontium titanate films, 877
Barrier layers, on PZT coating crystallization, 855
Barrier properties, of inorganic-organic polymers, 141
Benzene, 31
  on phenyl-group doped porous layers, 572
Benzyl alcohol, on porous layer coatings, 571
BET surface area
  in alumina-silica gels, 359
  in forsterite xerogels, 359
  in inorganic-organic cubane copolymers, 391
  in monolithic aerogel drying, 313
  in organically modified silica xerogels, 473
  in organic/inorganic hybrids, 305
  in TiO_2 films, 769
  in TiO_2 thin film photocatalyst, 691
Biaxially oriented polypropylene (BOPP) films, 144
Binding characteristics, of entrapped receptors, 565
Bioactive coatings
  of calcium phosphate, 261
  of glass, for metallic prosthesis, 723
  of vinyltrimethoxysilane, 237
Bioactivity
  molecular control of, 245
  in vinyltrimethoxysilane gel coatings, 237
Bioceramics, and hydoxyapatite nucleation, 251
Biodegradable material, silica fibers as, 267
Biodegradation. *See also* Degradation
  of phenol, 283
Biomaterials. *See also* Bioactive coatings
  apatite-mullite ceramics as, 951
Biosensors, glucose, 241
Biosorbents, for heavy metal, 289
Biotechnology, and hybrid sol-gels, 273
Biot's theory, 329
Bismuth 2-ethylhexanoates, 885
Bismuth oxide, 213
Bismuth oxide layer, 885
Bismuth silicate, 213
Bismuth strontium tantalate, 889
Bisphenol-A
  in epoxy resin, 405
  in nanocomposite protective coatings, 735
1,4-Bis(trichlorosilylmethyl) benzene, 31
Bis(tri-t-butoxysiloxy)diisopropoxytitanium, 976
$BiTaO_4$ films, 889
Boehmite
  in nanocomposite protective coatings, 735
  powder of, 397
Bone growth, 245
BOPP (biaxially oriented polypropylene films), 144
Borosilicate
  protection coatings of, 717
  in sol-gel, 103
Borosilicon, 1001
Bragg peaks, in lamellar phase, 99
Brillouin spectroscopy, of sono-ormosils, 451
Brønsted acid sites, 1043
Buckling model, 335
Butadiene-styrene latex, 1057
n-Butanol
  on aerogel esterification, 323
  in ormosil production, 467
1-Butanol, on porous layer coatings, 571

Butoxyethanol, in PZT fibers, 1023
By-products, in lithium chloroboracite preparation, 223

C
^{13}C MAS-NMR
  of CdSe doped ormosils, 623
  of copolymer (PEPPV), 440
  of d-fructose SiO_2 composites, 422
Ca. *See* Calcium
Cadmium sulfide nanocrystals, 61
Cadmium-selenium, 623, 629
Calcination
  of inorganic oxides, 109
  of mesoporous thin film, 739
Calcium
  as dopant, 580
  incorporation of, 237
Calcium ions, on silico-alkaline sol, 353
Calcium silicophosphate coatings, 723
Calorimetry, 295
Candida tropicalis, 283
Capacitors, monolithic, 895
Carbide, 485
Carbon dioxide sensitivity, 729
Carbon tetrachloride. *See* CCl_4
Carbon-silicate electrodes, 241
Carbonyl stretching frequencies, infrared, 391
Carbothermal reduction, 485
Carboxylic acids, binding detection of, 565
Casting, in artistic applications, 233
Catalyst(s)
  on β-Eucryptite, 981
  for inorganic oxides, 109
  MgO as, 1043
  microporous pillared clays as, 133
  preparation of, 1037
  Ru-Sn-Al_2O_3 as, 1037
  ZrO_2-Al_2O_3 in, 1033
Catharantus alkaloids, production of, 273
Cathodoluminescent phosphor powders, 133
Cationic alkoxometallate components, 45
CCl_4
  in GeO_2-SiO_2 waveguides, 535
  on porous layer fiber coatings, 572
CdS nanocrystals, 629
CdSe doping, 623
CdSe nanocrystals, 629
Ce^{3+}, for doping, 588
Cell cultures, 273
Cell encapsulation. *See also* Encapsulation
  into silica gel, 283
  with SiO_2, 273
Ceramers, 405
Ceramic composite gels, in mullite-alumina system, 201
Ceramic fiber synthesis, 1023
Ceramic gel films, 821
Ceramic pigments, 133
Ceramic powders, for varistor discs, 575
Ceramic predictive model, 945
Ceramics
  alumina/titania diphasic, 801
  barium titanate in, 873
  freeze-gelation on, 171
  as material precursors, 45
  of mullite, 987
  preceramic polymer predictive model for, 945
Cerenkov detection, 302
Ceria, 1049
Cerium, for doping, 588
Cetyltrimethyl ammonium bromide (CTAB)
  in methyl red entrapment, 17
  in transparent matrices, 95
  in transparent mesoporous film, 739
Chalcogenide ormosils, 559
Chalcogenide systems, 61
Channel waveguides, 523
Characterization, of aerogels, 937
$CHCl_3$, on phenyl-group doped porous layers, 572
Chelation, on aggregate formation in glasses, 611
Chemical changes, of alcogels, 329
Chemical homogeneity, 51
Chemical sensing
  and entrapment matrix, 565
  porous layers and, 569
Chemistry
  coordination, 593
  precursor (*See* Precursor chemistry)
  sol-gel (*See* Sol-gel chemistry)
  zeolite, 27
Chip coupling, nanocomposites for, 397
Chirality, dopant-induced, 585
Chloride alkoxide systems, 45
Chloro- (CPTM) silanes, 588
Chromatography
  liquid, 163
  materials for, 189
  for silicate based electrodes, 241
Chromophores, 439
Clays, pillared, 133
Cluster shell polyvanadates, 65
Coatings
  of Al_2O_3-TiO_2-SiO_2, 764
  antireflective, 713
  barrier properties of, 141
  bioactive, 237
  calcium silicophosphate as, 723
  conductive, 789
  for corrosion protection, 717

development of, 779
dip, 91 (*See also* Dip coating(s))
doped porous polysiloxane as, 569
glass-like, 717
hard, of nanocomposites, 397
heteropolysiloxane, 779
high purity, 713
for 316L steel, sol-gel in, 723
for lead leaching inhibition, 753
of Mn^{2+} doped ZnS, 685
modeling of, 779
noble metal colloids in, 701
ORMOCER as, 489
ormosil for glass strengthening in, 695
of photocurable sol-gel, 523
of silica sols, properties of, 89
SnO_2 : Sb sintering in, 961
and sol-gel technology, 154
TEOS/VTES as, 409
transparent conducting, 961
Cobalt nanoparticles, in silica gels, 929
Co-condensation, 75
Co-hydrolysis, 75
Colloidal alkali silicate gelation process, 233
Colloidial nanoparticles, 113
Colloids
from aminosilanes, 553
minimum-contrast points for, 113
of noble metals, in coating films, 701
of silver, thermochromic properties of, 663
Color, of gels, 969
Color fastness, in ink-jet printing, 151
Column sorption, 289
Commercial applications, 153
Complex impedance method, 223
Complex-forming precursors, in silica gels, 605
Complexing agents, 565
Composite(s)
in apatite-anorthite system, 255
in apatite-mullite system, 951
carbon-silicate electrodes as, 241
in controlled drug delivery, 277
fluorescence probing of, 95
matrix effects and chemical sensing in, 565
mullite-alumina in, 201
of saccharide-silica, 421
Compression, isostatic, on aerogels, 365
Concerted European Action (CEA) project, 679
Concrete, degradation of, 353
Condensation
of GTPS and Ti-alkoxides, 37
with O-NMR, 71
in polytetrahydrofuran preparation, 433
of silicic acid, 85
of trialkoxysilyl moieties, 385
Condensation reaction
alkoxysilanes and, 75
of metal chlorides, 109
of SiOH groups in aerogel drying, 323
Conductive coatings, 789
Conductivity
of lithium chloroboracite, 223
of ormolytes, 909
of phosphate glasses, 933
in SnO_2 thin films, 793
Conductors, transparent, 679
Confinement, in MTEOS xerogels, 457
Conjugated polymer, polyetherpolyphenylenevinylene (PEPPV) as, 439
Continuous wave EPR measurements, 503
Contrast variation, in multicomponent nanoparticles, 113
Controlled release, 277
Coordination chemistry, 593
Copolymerization, rhodium complex on, 391
Copper, 565
Corrosion
by NaOH, 764
and ormosils, 375
Corrosion protection coatings, for stainless steel, 717
Covalent entrapment, 17
CR 39, 397
Cracking, in micro-optical arrays, 547
Critical transition temperature, 229
Crosslinked epoxy resins-silica hybrids, 405
Cross-linking, 379
Crystal glass, lead leaching from, 753
Crystal glassware, decoration of, 183
Crystal growth, II-IV, 629
Crystal structure, of Al_2O_3-SiO_2 gels, 987
Crystalline materials
of alkaline-earth, 129
low temperature modification of, 125
in varistor discs, 575
Crystallite size, of SiO_2-TiO_2 ceramics, 975
Crystallization
of apatite-mullite system, gels in, 951
of borosilicon oxycarbide glasses, 1001
in β-Eucryptite solid solution, 981
in indium oxide films, 991
of PZT coatings, 855
silver and platinum particles on, 969
and sintering, 942
of SiO_2-TiO_2 ceramics, 975
of sol-gels, 51
of $SrBi_2Nb_2O_9$, 885
of zircon, mechanism for, 119
CTAB (cetyltrimethyl ammonium bromide). *See* Cetyltrimethyl ammonium bromide (CTAB)
Cu^{2+}, on Eriochrome Cyanine R (ECR), 565
Cubane copolymers, 391

CuTSPc, 651
Cyclopentadienlrhodium dicarbonyl, 391
Cyclotitanosiloxane, 976

D
Degradation. *See also* Biodegradation
  of concrete, 353
Dendrimer, in matrix effects, 565
Densification
  of aerogels, 365
  of barium titanate xerogel, 873
  kinetics of, in aerogel sintering, 937
  of PZT fibers, 1023
Depassivation, 61
Deposition
  multilayer, for GeO_2-SiO_2 waveguides, 535
  vapor, for bismuth oxide coatings, 213
Depth profiling
  of lead titanate films, 843
  of mirrors coating structure, 757
Derjaguin-Landau-Verwey-Overbeek (DLVO) theory, 553
d-Fructose silica, 421
Diamino diphenyl sulphone (DDS), 405
Dichlorodimethylsilane (DCDMS), 379
Dichlorodimethylvinylsilane (DCMVS), 379
Dielectric matrix, 629
Dielectric properties
  of barium-strontium titanate films, 877
  of $BiTaO_4$ films, 889
  of yttrium manganate films, 899, 903
  of yttrium oxide films, 895
Diethanolalmine, 903
Differential scanning calorimeter (DSC), of TiO_2
  thin film photocatalyst, 691
Diffusion, interpore translational, 457
β-Diketones, as lanthanide salt precursors, 611
Dimer formation, in metallic tetrasulphophthalocyanine
    gels, 651
Dimethyl terephtalate, 1037
Dimethylformamide, 651
Diols, on alumina-silica gels, 1027
Dip coating(s)
  of Al_2O_3-TiO_2-SiO_2, 763
  bioactivity of, 238
  for bismuth oxide coatings, 213
  of borosilicate glass in SnO_2, 793
  of Er^{3+} doped-aluminosilicate, 529
  for mirrors, 757
  modified silica sols in, 91
  for stainless steel, 717
  for TiO_2 thin film photocatalyst, 691
  of vanadium doped TiO_2 films, 775
  for WO_3 layers, 673
Direct wiring, of enzymes, 241
Dishwashing resistance, 183
Disperse Red 1, 647
Dispersibility, surface modification on, 397
Dispersion fluid, 82
Dissolvable substrates, 233
Dissolved oxygen, 207
  quenching of, ormosil film sensors in, 641
DLVO theory, 553
Doping
  with amino acid, 585
  with antimony, 789
  CdSe in, 623
  Ce^{3+} in, 588
  with erbium, 529
  with fluoride, 1049
  with lanthanum, 801
  with magnesium, 801
  Mn^{2+} in, 635, 685
  and nanoporous films, 579
  neodymium in, 593
  and nonlinear optical effects, 559
  with Pr^{3+}, 599
  with rare-earths, 617
  Sb doped SnO_2 films in, 961
  Sb-doped tin oxide in, 679
  tin-doped indium oxide in, 991
  vanadium in, 775
  of vanadium oxide films, 915
Double C=C bonds, on film shrinkage, 467
Double-pore silica, 163
DRAMs
  yttrium manganate films for, 899
  yttrium oxide films for, 895
Drop-on-demand ink-jet process, 177
Drug delivery, controlled, 277
Drug production, 273
Drying process
  ambient pressure process in, 305
  gel drying in, molecular guest dynamics of, 457
  for monolithic aerogels, 311
  for monolithic glass samples, 233
  for neodyium-doped silica gel-glasses, 593
  for peroxopolytungstic acid films, 923
  for PZT thick film, 821
  for titanate microspheres, 1011
  for varistor powders, 575
DSC
  in β-Eucryptite solid solution, 981
  in PZT film preparation, 865
DTA-TG analysis
  of barium titanate xerogels, 873
  of mullite fibers, 1017
Durability improvement, 753
Dye immobilization, 147

Dye leaching
of anthraquinone dye, 473
of methyl red dyes, 17
in optical-based sensor, 207
Dyes, organic
for optical colored layers, 479
photodegradation of, 657
Dynamic light scattering, 81
Dynamic mechanical thermal analysis (DMTA), 695

E
Effective Mass Model, 623
Elastic modulus. *See* Modulus, elastic
Elastic properties, of aerogels, 365
Electrical equipment, 575
Electrical properties
of barium-strontium titanate films, 877
of lithium chloroboracite, 223
of ormosil films, 467
of PLZT materials, 833
of Sb-doped tin oxide, 679
of SnO_2 : Sb coatings, 961
Electrochemical properties
of ORMOCER coatings, 489
of vanadium doped TiO_2 films, 775
Electrochromic properties, of peroxopolytungstic acid films, 923
Electrochromism, of WO_3 layers, 673
Electrodes, silicate based, 241
Electrogalvinized steel, 779
Electroinduced second harmonic generation, 559
Electrolyte, solid, 909
Electron microscopy. *See* specific types
Electron paramagnetic resonance spectroscopy, 503
Electronic paramagnetic resonance (EPR), 987
Electronic transport, 793
Electronics, sol-gel processing for, 156
Electrons, trapping of, 793
Electrostatic repulsion, 805
Ellipsometry
of nanoporous films, 581
of ormosil film, 467
Elongation, 445
ELS, of silica-alkaline sol, 353
Emslie, Bonner and Pack (EBP) model, 709
Encapsulation. *See also* Cell encapsulation
of metallic tetrasulphophthalocyanines, 651
of polysaccharides, 289
vs. tethering, 391
Energy dispersive X-ray analysis (EDX)
of inorganic oxides, 109
of perovskite film, 841
of PZT coatings, 855
Entrapment
of chiral amino acids, 585
on molecular recognition, 565
pH indicators in, 17
of rare-earth elements, 617
Enzyme immobilization, 295
Epichlorohydrin, 289
Epoxy resin, in glass coatings, 695
Epoxy resins-silica hybrids, 405
Epoxysilane, in nanocomposite protective coatings, 735
EPR measurements, continuous wave, 503
Er-alkoxides, 125
Erbium doping
for aluminosilicate waveguides, 529
for GeO_2-SiO_2 waveguides, 535
for optical amplifiers, 517
for optical fiber, 617
Eriochrome Cyanine R (ECR), 565
Esterification, in sodium water glass aerogel drying, 323
Ethanol
on hydrolyzed TMOS system, 71
on silver colloids, 663
2-(2-ethoxyethoxy)ethanol, 691
2-Ethylhexanates, in $SrBi_2Nb_2O_9$ powders, 885
2-Ethylhexanoic acid
on bismuth strontium tantalate films, 889
on film formation microstructural evolution, 877
Ethyltriethyloxysilane (ETEOS), in oxygen sensors, 207
Eu^{3+}
in luminescence spectroscopy, of hydrid xerogels, 427
for optical probes, 611
for silica gels doping, 605
β-Eucryptite, 981
Europium. *See* Eu^{3+}
Evanescent-wave detection, 569
Evaporation, on spin coating, 707
Exciton quantum confinement level, 629
Extrusion process, for PZT fibers, 1023

F
Fast sol-gel method, 547
Fe_2O_3, 667
Fermentation industry, 289
Ferroelectric memory devices, non-volatile, 903
Ferroelectric properties
of barium-strontium titanate films, 877
of lanthanum modified $PbTiO_3$, 839
of lead titanate films, 843
of PZT thin films, 815
of $SrBi_2Nb_2O_9$ powders, 885
of yttrium manganate films, 899
of yttrium oxide films, 895
Ferroelectricity, and PZT precursor powders, 827
Fiber optic sensor, 729
Fibers
biodegradable, 267
lignin-silica-titania hybrids for, 485

of mullite, 1017
optical (*See* Optical fibers)
porous layers in, 569
PZT in, 1023
rare-earth doped, 617
Film(s). *See also* Thin film(s)
of Al_2O_3-TiO_2-SiO_2, 763
of barium-strontium titanate, 877
of bismuth strontium tantalate, 889
calcium silicophosphate as, 723
coatings in, for noble metal colloid films, 701
crack-free, 739
2-ethylhexanoic acid on, 877
Fe_2O_3 in, 667
ferroelectric, 815
hydrophobicity of, in ormosil films, 641
of indium oxide, 991
lanthanum modified $PbTiO_3$ in, 839
for lead leaching inhibition, 753
lead zirconate titanate (PZT) in, preparation of, 865
in mirror production, 757
multilayer SiO_2-B_2O_3-Na_2O in, 783
of peroxopolytungstic acid, 923
of PLZT, 833
polytetrahydrofuran in, 433
Sb-doped tin oxide in, 679
SC-RTA process for, 509
shrinkage in, 467
of silica sols, modified, 89
of SnO_2, conductivity of, 793
of SnO_2 : Sb, 961, 1005
swelling of, in ink-jet printing, 150
of vanadium dioxide, 915
vanadium doped TiO_2 in, 775
of yttrium manganate films, 899
of yttrium oxide, 895
Flavor barrier, 141
Flexible molding, artistic applications of, 233
FLN spectra
of organoeuropium-doped silica gels, 605
of Sm^{2+}-doped glass, 542
Fluorapatite, 255, 951
Fluorescence, 95
in organoeuropium-doped silica gels, 605
Fluorescence excitation spectroscopy, of metal ion center structures, 611
Fluorescence line narrowing, 541
Fluoride doping, 1049
Fluoride material synthesis, 129
Fluoride medium, in zircon synthesis, 119
Fluorine, 405
on water removal, 605
Fluoroalkoxides, 129
4-Fluorophenythiol, 61
Foams
of macroreticular materials, 189
open cell, 195
in silicate based electrodes, 241
Formic acid-alkoxide route, 473
Forsterite xerogels, 359
Fractal clusters, in sodium water glass aerogels, 323
Fractional distillation, of TEOS, 713
Fracture strength, of silicon oxycarbide glass, 995
Fracture stress, 174
Freeze fracture, 99
Freeze-gelation, 171
FTIR spectroscopy. *See also* Infrared (IR) spectroscopy
of adsorbed pyridine on MgO, 1043
of aerosol-gel process layers, 743
of Er-alkoxides, 125
of GeO_2-SiO_2 waveguides, 535
of HF on two-step sol-gel process, 749
of indium oxide film, 991
of lignin-silica-titania hybrid fibers, 487
of mesoporous thin film, 740
of micro-optical arrays, 548
of neodyium doped silica gel-glasses, 593
of polytetrahydrofuran, 433
of polyviologen, 27
of Pr_2O_3-SiO_2 xerogels, 599
of PTEGM and coatings, 489
of PZT films, 865
of RTA compositions, 519
of TEOS/VTES hybrid, 409
of vanadium-based hybrids, 495
FTO coated glass, 673
FT-Raman spectroscopy
of aluminosilicate planar waveguides, 529
of fluoroalkoxides, 129
of glycidoxypropyltrimethoxysilane/aminopropyltriethoxysilane, 385
Fullerene, 599
Functionalized silane, in Ce^{3+}-doped hybrids, 588
Fused silica, XRD patterns for, 461

G
G modulus, aging on, 317
Gas permselectivity membranes, 801
Gas-phase quenching, 643
GC mass spectroscopy, for oxidation product identification, 713
Gel coatings, bioactive, 237
Gel color, 969
Gel dissolution, in zircon synthesis, 119
Gel drying. *See also* Drying
molecular guest dynamics of, 457
Gelation
alkaline ions on, 353

in anhydrous systems, 103
colloidal alkali silicate process in, 233
HF on, 749
inorganic, 99
non-oxide, 61
of silica alcogels, 329
siloxane bonds in, 553
Gelation time
in colloidal alkali silicate route, 233
estimation of, 81
in modified silica sols, 89
and photo-induced poling, 649
of titania in reverse micelles, 341
Gelling time. *See* Gelation time
Gels
Al_2O_3-SiO_2 mullitization behavior of, 987
crystallization of, 951
in mullite-alumina system, 201
wet, structural efficiency of, 957
GeO_2-SiO_2 waveguides, 535
Geyserites, 85
Glancing angle X-ray diffraction (GA-XRD), of bismuth oxide thin films, 213
Glass(es)
artistic forming of, 233
of borosilicon oxycarbides, 1001
coloration of, 183
ITO/FTO coating for, 673
low temperature modification of, 125
ormosil coating strengthening of, 695
phosphate, 933
rare-earth doped, 605
of silicon oxycarbide, 945, 995
Sm^{2+}-doped, 541
sodium borosilicate in, 783
surface flaws in, 695
thermochromic, 663
Glass bioactive coatings, for metallic prosthesis, 723
Glass-ceramics
in apatite-anorthite system, 255
in apatite-mullite system, 951
Glass-like sol-gel coatings, 717
Glucose biosensors, 241
Glucose-oxidase, 295
3-Glycidoxypropyltrimethoxysilane, in nanocomposite protective coatings, 735
Glycidoxypropyltrimethoxysilane (GPTS). *See* GPTS (^{3}glycidoxypropyltrimethoxysilane)
Glycidyloxy- (GPTM) silanes, 588
Gold, in noble metal colloid films, 701
GPTS (^{3}Glycidoxypropyltrimethoxysilane)
in GPTS/aminopropyltriethoxysilane system, 385
and hybrid pigments, 479
titanosiloxane bonds in, 37
Grain boundary response, 223
Grain size
on ferroelectricity of barium titanate xerogels, 873
on liberation rate, 277
Graphite-ormosil materials, 241
Grazing incidence X-ray diffraction. *See also* X-ray diffraction (XRD) spectroscopy
of perovskite film, 841
in spectroscopy of sol-gel systems, 51
Guest-host system, 647
Guinier approximation, 353

H
Hafnia, 757
Halides, reactivity of, 109
Hard coatings
of nanocomposites, 397
ormosils as, 375
Heat treatment. *See also* Temperature; Thermal analysis
on lead leaching, 755
Heating rate, on SnO_2 : Sb coatings, 1005
Heavy metal biosorbents, 289
Height Equivalent to Theoretical Plate (HETP), 167
Hematite, 667
Heterocondensation, 51
Heterometal bond, 37
Heterometallic alkoxide precursors, 45
Heterometallic alkoxides, 125
Heterometallic glycolates, 45
Heteropolysiloxane coatings, 779
Heterostructures, 219
HF, on two-step sol-gel process, 749
High level liquid waste, 1011
High performance liquid chromatography (HPLC), 163
High resolution transmission electron microscopy (HR-TEM). *See* Transmission electron microscopy (TEM)
Highly porous hybrids, 305
High-Tc Bi-based superconductors, 229
Hole burning, persistent spectral, 541
Homogeneity
chemical, 51
from hetero-bimetallic alkoxides, 125
HPLC (high performance liquid chromatography), 163
Hyalites, 85
Hybrid(s)
for chemically sensitive coatings, 729
crosslinked epoxy resins-silica as, 405
crystalline network in, 65
for fibers, 485
films of (*See also* Film(s))
films of, silica gel-polytetrahydrofuran as, 433
gels, silica-polyethyleneglycol as, 427
in GPTS/APTS systems, 385
highly porous hybrids in, 305
inorganic-organic cubane copolymers as, 391

ioene polymers as, 27
latex-silica nanocomposites as, 1057
matrix of, in nanocomposite protective coatings, 735
nanocomposites as, 65
optical nonlinearity of, 559
organic-inorganic glasses as, porosity studies for, 457
organic-inorganic sols as, 177
organic-inorganics as, 305
ormolytes silica-polypropylenenglycol as, 909
ormosil coatings in, strengthening with, 695
pigments as, 479
silica xerogels as, 75
sol-gel coating as, 183
sol-gel material as, 479
thermoplastic nanocomposites as, 499
vanadium-based organic-inorganics as, 495
Hybrid materials. *See* Hybrid(s)
Hydoxyapatite coatings, 251
Hydrocarbon sensitivity, 729
Hydrofluoric acid, in doped porous polysiloxane coatings, 570
Hydrogen peroxide decomposition, 189
Hydrogenation, 1037
Hydrolysis
alkoxysilanes and, 75
ammonia catalyzed, 713
in anhydrous TEOS, mechanism of, 103
for barium titanate xerogel, 873
of fluoroalkoxides, 129
of GPTS, 385
in GPTS system, titanosiloxane bonds in, 37
in MgO synthesis, 1043
in nanoparticle production, 113
in siliceous prepolymer synthesis, 289
TEOS/TMOS and, 71
Hydrolysis reactions. *See* Hydrolysis
Hydrolytic durability, of glass coatings, 695
Hydrolytic precipitation, 31
Hydrolytic stability, 37
Hydrophobicity, in ormosil film oxygen sensing, 641
Hydrothermal synthesis
of polyoxovanadates, 65
of zircon, 119
Hydroxyapatite, and calcium phosphate coatings, 261
2-Hydroxyethylmethacrylate (HEMA), in thermoplastic nanocomposites, 499
Hydroxypropyl cellulose (HPC), 685
Hysteresis loop, 34
in vanadium oxide films, 915

I
Ibuprofen, 565
II-IV Crystal growth, 629
Image transfer, 147
Imidazol catalyst, in nanocomposite protective coatings, 735
Immobilization
of glucose-oxidase, 295
on phenol degradation, 283
Impedance method, complex, 223
Implant materials, 237
corrosion protection for, 723
Impurity
acetate as, 713
in semiconductors, 793
Indium oxide films, 991
Infrared carbonyl stretching frequencies, 391
Infrared (IR) spectroscopy. *See also* FTIR spectroscopy
of apatite-mullite system, 951
of barium-strontium titanate film, 877
of $\mathcal{B}$-Eucryptite solid solution, 981
of nanocomposite protective coatings, 737
of OH^- mode detection, 611
of ormosil films, 467
of polydiene latex, 1057
of sol-gel systems, 51
of vanadium doped TiO_2 films, 775
Ink-jet, 147
Ink-jet coating, 147
Ink-jet printing
aqueous sol-gel processing in, 133
sol-gel coating media for, 147
Ink-jet process, for microlens fabrication, 177
Inorganic gelation, 99
Inorganic networks, 27
Inorganic oxide, 109
Inorganic sol-gel process, 61
Inorganic-organic composite, saccharide-silica as, 421
Inorganic-organic copolymers, 391
Inorganic-organic hybrids. *See also* Hybrid(s); Organic-inorganic hybrids
Ce^{3+} doping for, 588
poly(ε-caprokactone) (PCL) as, 415
TEOS/VTES as, 409
with various inorganic compounds, 445
Inorganic-organic polymers, 141
Integrated optics
and dopant adsorption control, 579
multilayer SiO_2-B_2O_3-Na_2O in, 783
photocurable coatings for, 523
SC-RTA process for, 509
waveguides for, 517
Interfacial polymerization, 821
Interferometric monitoring, of spin coating, 707
Inter-penetrating polymer network (IPN) materials, 379
Interpore translational diffusion, in MTEOS xerogels, 457
Ionene polymers, 27
Ionic conductor, 909
IR. *See* infrared
Iron. *See also* Fe
Iron diffusion, coatings for, 723

Iron nanoparticles, in silica gels, 929
Iron(III) chloride, as inorganic oxide catalyst, 109
Irradiation, on crystallization, 991
Isobestic-point behavior, 17
3-Isocyanatopropyltriethoxysilane (IPTS), in hybrid pigments, 480
Isomerization, and photo-induced poling, 647
Isopropoxometallate components, 45
Isostatic compression, on aerogel, 365
Isotopic substitution, 391
ITO coated glass, 673
ITO films, 991

K
Kinematic viscosity, in spin coating, 707
Kinetics, of silico-calco-alkaline gel, 353
Kohlrausch-Williams-Watts equation, 649

L
Lamellar phase, 99
Laminating agent, 141
Lanthanide fluoride, 129
Lanthanides
  in metal ion centers, 611
  microengineering of, 1049
Lanthanum
  in doping, 801
  on PLT film optical propagation, 870
  in PLZT thin film, 833
LAS, 981
Lasers
  damage from, 757
  for densification, 961
  power-fusion with, 713
  in sintering, 961
  ultraviolet, crystallization induction with, 991
Lasers, YAG
  crystallization with, 991
  mirrors for, 757
  on rare-earth doped fibers, 617
  on SiO_2 : Rh B gels, 657
Latex, polydiene, 1057
Layer structure, of Ru-Sn-Al_2O_3 catalysts, 1037
Layered structures, 65
Leaching
  of anthraquinone dye, 473
  inhibition of, 753
  of methyl red dyes, 17
  in optical-based sensor, 207
Lead
  as dopant, 580
  leaching of, 753
Lead crystal glass, lead leaching from, 753
Lead lanthanum titanate (PLT) films, 870
Lead phthalocyanine, 219
Lead precursor, in PZT film preparation, 865
Lead release, 183
Lead titanate
  Raman scattering study of, 849
  Rutherford backscattering spectroscopy (RBS) of, 843
Lead zirconate titanate (PZT)
  in ferroelectric thin films, 815
  precursor powders for, 827
  synthesis and characterization of, 1023
Lead zirconate titanate (PZT) films
  lanthanum-modified, 833
  lead environment in, 861
  preparation of, 865
  thick, 821
  thin, 815
Leadacetate, in PZT fibers, 1023
Lewis acid sites, 1043
^{7}Li NMR, 909
Liberation rate, 277
Ligand, in Ce^{3+}-doped hybrids, 588
Ligands, on alumina-silica gels, 1027
Light scattering studies, 81
Lignin, in silica-titania hybrids, 485
Line narrowing, fluorescence, 541
Liquid chromatography, 163
Lithium
  in β-Eucryptite, 981
  in ormolyte preparation, 909
  in peroxopolytungstic acid films, 923
  on silicate entities, 353
  on WO_3 layers, 673
Lithium boracite, 223
Lithium perchlorate, 489
Lithium salt doping, 495
Lithium-ion conductor, 223
Low surface energy systems, 405
Low temperature densification, of barium titanate xerogel, 873
Luminescence
  Mn^{2+} doping in, 685
  photodegradation of, 657
  of solids, 635
Luminescence spectroscopy
  of Mn^{2+} doped ZnS, 685
  of Pr_2O_3-SiO_2 xerogels, 599
Lyotropic lamellar phase, 99
Lyotropism, 27

M
Macroreticular materials
  hydrogen peroxide decomposition for, 189
  in silicate based electrodes, 241
Magnesia acidity, 1043
Magnesium
  in corrosion protection coatings, 717
  in doping, 801

Magnesium diethoxide, in forsterite xerogels, 359
Magnesium ethoxide, in fractional distillation, 713
Magnesium oxide
  Lewis and Brønsted acid sites on, 1043
  in PLT film fabrication, 870
Magnesium silicate coatings, 717
Magnesium-SiO_4 gels, 359
Magnetism, in metal nanoparticles, 929
Magnetization, in superconductor materials, 229
Manganese doping, 635, 685
Manganese oxide, on Al_2O_3-SiO_2 gels, 987
Manufacture, net-shape method of, 171
MAS-NMR spectroscopy
  of alkoxysilanes condensation/hydrolysis reactions, 75
  of Al_2O_3, 804
  of borosilicon oxycarbide glasses, 1001
  of inorganic-organic copolymers, 391
Matrix(ces)
  amorphous, on polarized light, 585
  in chemical sensing, 565
  dielectric, 629
  siloxane-based glassy, 547
  transparent, 95
Mechanical properties, of silicon oxycarbide glass, 995
Membranes
  in aqueous sol-gel processing, 133
  for gas permselectivity, 801
Menshutkin reaction, 27
Mercury porosimetry, 335
Mesophases, 65
Mesoporous materials, 739
Metal
  biosorbents of, 289
  chelate compounds of, 421
  ethoxides of, 889
  nanoparticles of, in silica gels, 929
Metallic prosthesis, bioactive glass coatings for, 723
Metallic silver nanoparticles, 503
Metallic tetrasulphophthalocyanines, 651
Metalloxanes, 975
Metal-O-PDMS hybrids, 445
Metal-organic chemical vapor deposition (MOCVD), for bismuth oxide coatings, 213
Metavanadates, 67
Methacryloxypropyltrimethoxysilane (MPTS), 178
Methanol, on TEOS system, 74
Methanol conversion, 1027
2-Methoxyethanol, 667
Methyl nadic anhydride (MNA), 405
Methyl red indicators, 17
Methyldiethoxysilane, 75
Methylmethacrylate (MMA), in thermoplastic nanocomposites, 499
Methyl-methyl cross-linking, 379
Methyl-modified silicate films, 467
Methyl-modified SiO_2 coatings, in corrosion protection coatings, 717
Methyltriethoxysilane (MTES)
  on ormosil sensor behavior, 641
  in ruthenium oxygen sensors, 207
  in sol-gel carrier systems, 277
  for thick silica films, 723
Methyltrimethoxysilane (MTMS)
  in borosilicon oxycarbide glasses, 1001
  in micro-optical arrays, 548
  in ormosil preparation, 461
  on ormosil sensor behavior, 641
Mg_2SiO_4 gels, 359
Micelles, in AOT/H_2O/heptane, 623
Microbial cell encapsulation, 283. *See also* Cell encapsulation; Encapsulation
Microemulsion, 341
Microlens fabrication, 177
Micro-optics, 547
Microporous pillared clays, 133
Micro-Raman spectroscopy, 51
Microscopy. *See* specific types
Microspheres, of titania, 1011
Microstructure
  of barium-strontium titanate films, 877
  of geyserites and hyalites, 85
  in high-Tc Bi-based superconductors, 229
  PZT fibers, 1023
  of silicon oxycarbide glass, 995
  of SnO_2 : Sb coatings, 1005
  of sono-ormosils, model of, 451
  of wet gels and aerogels, 957
Mie theory, 81
Minimum-contrast points, for colloids, 113
Mixed oxide colloids, 113
Mn^{2+} doping
  properties of, 635
  ZnS nanoparticles in, 685
Mode confinement, in silica-on-silicon fabrication, 517
Moderate pressure drying process (MPD), 311
Modulus, elastic
  of inorganic-organic hybrids, 445
  of silicon oxycarbide glass, 995
  of wet gels and aerogels, 957
Molecular diffusion, in composite matrices, 95
Molecular guest dynamics, 457
Molecular recognition, 421, 565
Molecular templating, 739
Molecular weight, on epoxy resin, 405
Monitoring, of spin coatings, 707
Monofilament nozzle, 1023
Monolithic gel
  barium titanate xerogel as, 873
  metallic tetrasulphophthalocyanines in, 651

Monoliths
  Ce^{3+}-doped hybrid, 588
  hydrogen peroxide decomposition for, 189
  from non-oxide gelation, 61
  production of, 311
  sol-gel processing of, 154
Monomer solutions, 317
Monometal glycolates, 48
Morphology
  of Al_2O_3-TiO_2-SiO_2 coatings, 764
  of lithium chloroboracite, 223
  of SnO_2 : Sb coatings, 961
  of $SrBi_2Nb_2O_9$ powders/films, 885
  of titanate microspheres, 1011
Mössbauer spectrometry, of metal nanoparticles, 929
MTEOS xerogels, 457
Mullite
  on Al_2O_3-SiO_2 gels, 987
  fibers of, 1017
  in mullite-aluminia composites, 201
Mullite-alumina composites, 201
Mullitization behavior, 987
Multicomponent borosilicon oxycarbide glasses, 1001
Multilayer SiO_2-B_2O_3-Na_2O film, 783
Multilayered dense coatings, 723

N
N_2 adsorption-desorption isotherms, 27
Nanocomposites
  hybrid, 65
  optical and mechanic properties of, 397
  optical nonlinearity of, 559
  organic-inorganic, for protective coatings, 735
  in photocurable coatings, 523
  of silver and platinum, in gels, 969
  sol-gel processing of, 155
  thermoplastic, 499
Nanocrystalline
  antimony-doped SnO_2 particles as, 789
  in WO_3 layers, 673
Nanocrystallization, of sol-gels, 51
Nanocrystals
  of cadmium sulfide, 61
  in multilayer SiO_2-B_2O_3-Na_2O film, 783
  of $PbTiO_3$, 849
  semiconductor, 629
Nanofiltration membranes, 133
Nanoparticles
  CdSe as, 623
  and hybrid matrix protective coatings, 735
  of metal, in silica gels, 929
  of silver, 503
  of titania, 341
  of titania/zirconia, 113
  ZnS in, 635
  ZnS with Mn^{2+} doping as, 685
Nanoparticulate sols, in corrosion protection, 717
Nanoporous sol-gel films, 579
Nanosized particles, hybrid matrix protective coatings and, 735
Nanostructure, of materials
  aerogels in, 299
  ZnS particles in, doped, 635
Nanotechnology, for WO_3 layers, 673
NaOH corrosion, 764
Natural hydrous silica, 85
NBO species, 53
n-Butanol. *See* Butanol
Nd^{3+}, for optical probes, 611
Near-infrared spectroscopy. *See also* Infrared (IR) spectroscopy of CdSe doped ormosils, 623
Nematic liquid crystals, 65
Neodymium, 593
  for optical probes, 611
Net-shape manufacture, 171
Nickel nanoparticles, in silica gels, 929
Nifedipine, 277
Niobium ethoxide, 885
NIR adsorption spectroscopy, of Pr_2O_3-SiO_2 xerogels, 599
Nitric acid, in mirror production, 757
Nitrogen adsorption
  in low density xerogels, 338
  in organically modified silica xerogels, 473
  in sono-ormosils, 451
Nitrogen adsorption-desorption technique, 415
Nitrogen desorption, 937
Nitrogen oxides, 691
Nitrogen sorption measurements, 31
NMR. *See* Nuclear magnetic resonance (NMR) spectroscopy
Noble metal colloids, in coating films, 701
Non-hydrolytic sol-gel process, 109
Nonlinear optical effects
  in CdSe doped ormosils, 623
  in guest-host system, 647
  in hybrid and nanocomposite materials, 559
Non-oxide gelation, 61
Non-volatile ferroelectric memory devices, 903
NO_x, selective reduction of, 1033
Nozzle, 1023
Nuclear fuel, 1011
Nuclear magnetic resonance (NMR) spectroscopy
  for alkoxysilane hydrolysis reactions, 75
  for anhydrous sol-gel systems, 103
  of organic probes, 457
  for silicate amorphous powder, 31
  for sulfide gels and films, 61
Nuclear magnetic resonance (NMR) spectroscopy, ^{13}C MAS-NMR in

of copolymer (PEPPV), 440
of d-fructose SiO_2 composites, 422
Nuclear magnetic resonance (NMR) spectroscopy, ^{17}Li-NMR in, 909
Nuclear magnetic resonance (NMR) spectroscopy, MAS-NMR spectroscopy in
of alkoxysilanes condensation/hydrolysis reactions, 75
of borosilicon oxycarbide glasses, 1001
of inorganic-organic copolymers, 391
Nuclear magnetic resonance (NMR) spectroscopy, ^{17}O-NMR in
for alkoxysilanes hydrolysis, 75
and Si-O-Ti bonds, 37
for TEOS/TMOS sol-gel processes, 71
Nuclear magnetic resonance (NMR) spectroscopy, ^{29}Si-NMR in
for alkoxysilanes, 75
of glucose-oxidase, 295
of GPTS, 37
of hybrid pigments, 479
of silico-alkaline sol, 353
of TEOS/VTES hybrid, 409
vs. ^{17}O-NMR, 71
Nuclear magnetic resonance (NMR) spectroscopy, solid state
of CdSe doped ormosils, 623
of cross-linked organopolysiloxanes, 379
Nuclear magnetic resonance (NMR) spectroscopy, solution NMR in, 75
Nucleation, of hydoxyapatite, 251

O
OH content, Pr^{3+} doping on, 599
OH^- mode detection, 611
(OH)AITSPc, 651
^{17}O-NMR
for alkoxysilanes hydrolysis, 75
and Si-O-Ti bonds, 37
for TEOS/TMOS sol-gel processes, 71
Opacification temperature, of barium titanate xerogel, 873
Open-air sol-gel processing, 707
Open-cell ceramic foams, 195
Optical activity, in amino acid-doped xerogels, 585
Optical components, 177
Optical fibers
organopolysiloxanes coatings for, 729
polysiloxane-doped porous layers in, 569
rare-earth doping in, 617
Optical nonlinearity
in CdSe doped ormosils, 623
in hybrid and nanocomposite materials, 559
Optical probes, 427
Optical propagation loss, of PLT films, 870
Optical properties
of Ce^{3+}-doped hybrids, 588
of doped ZnS nanoparticles, 635
of PLZT materials, 833
of power-fusion lasers, 713
of Sb-doped tin oxide, 679
of silver colloids, 663
Optical resolution, saccharide-silica composites in, 421
Optical sensors, 207
Optical spectroscopy, of doped ZnS nanoparticles, 635
Optical switching, 915
Optical viscometry, 707
Optical waveguides
amplifiers for, 535
highly oriented, 870
strip-loaded high-confinement, 517
Optics
of aluminosilicate planar waveguides, 529
applications for, 51
colored-layer fabrication in, 479
integrated, 509
integrated, dopant adsorption control in, 579
micro-optical arrays in, 547
nanocomposites and, 397
ormosils in, 374
for signal processing, 623
and sol-gel technology, 156
Optospinography, 707
Organic dyes
for optical colored layers, 479
photodegradation of, 657
Organically modified silica gels, 473
Organically modified silicates, 467
Organic-inorganic hybrids. *See also* Hybrid(s); Inorganic-organic hybrids
ambient pressure processing for, 305
crosslinked epoxy resins-silica as, 405
lignin-silica-titania as, 485
optical nonlinearity in, 599
vanadium-based, 495
Organic-inorganic matrix, photo-reduction for, 701
Organic-inorganic nanocomposites, for protective coatings, 735
Organobridged silicates, 31
Organoeuropium-doped silica gels, 605
Organopolysiloxanes
as chemically sensitive coatings, 729
simple cross-linked, 379
ORMOCER coatings, 489
Ormolytes silica-polypropylenenglycol, 909
Ormosil films
for chromatography, 190
with different organics, 467
for optical sensor applications, 641
for oxygen sensing, 207
Ormosils
amine-functionalized, 623
CdSe doping for, 623

coating of, in glass strengthening, 695
in composite carbon-silicate electrodes, 241
optical nonlinearity of, 559
sol-gel processing of, 155
structure and properties of, 371
X-ray diffraction studies of, 461
Osteoconduction, 245
Overvoltage transient, Zinc oxide varistors in, 575
Oxide films, temperature on, 701
Oxide systems, 61
Oxidoreductase enzymes, 241
Oxophilicity, 45
Oxycarbide
in borosilicon oxycarbide glasses, 1001
gel precursors, 75
silicon oxycarbide glass as, 945, 995
Oxygen
barrier, 141
bridge, in ormosils, 461
detection of, 207
sensors, ormosil film optimization for, 641

P
Palladium, in noble metal colloid films, 701
Palladium-Ag/SiO_2 xerogels, 335
PAMAM dendrimer, 565
Partially crystallized xerogel, 873
Particles. *See also* Nanoparticles
complexation of, 62
redispersable, 789
size of, on optical performance, 713
Passivation, 61
Patterning, in micro-optical arrays, 547
Pb. *See* Lead
PCB biodegradation, 283
Pd. *See* Palladium
2,4-Pentanedionate, 485
PEO-based polymers, 489
Peptizing, in multicomponent nanoparticle production, 113
Perceramics, 945
Perfluoroether oligomer, 405
Permeation rates, of barrier materials, 141
Perovskite grain structure
in lanthanum modified $PbTiO_3$ film, 839
of lead titanate films, 843
in PLZT, 833
Peroxopolytungstic acid films, 923
Peroxotungistic acid, 673
Persistent spectral hole burning (PSHB), 541
Perylene dicarboxylic acid (PDA), 480
PET (polyethyleneterephthalate), barrier
properties of, 144
pH
on GPTS/APTS systems, 385
on MgO hydrolysis, 1043
on organic/inorganic pore volume, 305
on zircon synthesis, 119
Phase development, 801
in PZT fibers, 1023
Phase evolution, in PZT film preparation, 865
Phase formation, in apatite-anorthite system, 255
Phase separation, 163
Phenol biodegradation, 283
Phenyl-groups
chemical capping with, 623
doping with, 569
Phenyl-modified silicate films, 467
Phenyltriethoxysilane (ThTS), 569
Phonon confinement, 849
Phosphate glass, 933
Phosphors, 133
Photobleaching, 207
of SiO_2 : Rh B gels, 657
Photocatalyst, dip-coating for, 691
Photochemical
oxidation, of Mn^{2+} doped ZnS, 685
stabilization, of organic dyes, 479
Photocurable sol-gel coatings, 523
Photodegradation, of luminescence, 657
Photodesorption, 793
Photoinduced
poling, 647
second harmonic generation, 559
Photoluminescence, of polysiloxane gel, 439
Photopolymerization, 523
Photo-reduction, for noble metal colloid films, 701
Photostability, 657
Photovoltaic devices, 219
Phthalocyanine, 219
Physical entrapment, 17
Piezoelectric fibers, 1023
Pigments
ceramic, 133
hybrid, 479
Pillared clays, 133
Planar lightwave circuit, 509
Planar waveguides, 529
Plant cell immobilization, 273
Plasticity, of aerogels, 365
Platinized substrates, and lead titanate film, 843
Platinum
in ferroelectric PZT films, 815
in noble metal colloid films, 701
in silica gels, 969
in yttrium manganate film preparation, 899
in yttrium oxide film preparation, 895
PLT, 870
PLZT thin films, 833
PMH copolymer, 499
Polar order, and photo-induced poling, 647

Poling, photo-induced, 647
Pollution, air, 691, 1033
Polycarbonate, nanocomposite coatings for, 397
Polydiene latex, 1057
Polydimethylsiloxane (PDMS)
  in metal-O-PDMS hybrids, 445
  in organopolysiloxanes, cross-linked, 379
  on ormosil hardness, 371
Poly(ε-caprokactone), in porous silica preparation, 415
Polyetherpolyphenylenevinylene (PEPPV), 439
Polyethyleneglycol (PEG)
  in sol-gel drug delivery, 277
  in TiO_2 photocatalyst, 691
  in transparent matrices, 95
Polyethyleneterephthalate (PET), barrier properties of, 144
Poly(4-hydroxystrene) (PHS), 409
Polymer electrolytes, 427
Polymeric films, barrier properties of, 141
Polymerization
  inorganic, 99
  interfacial, 821
Polymerization-induced phase separation, 163
Polymetalloxanes, 975
Polymethylvinylsiloxane, 379
Polyoxovanadates, controlled condensation of, 65
Polypropylene, in dip-coating, 237
Polypropylenenglycol, in ormolytes, 909
Polysaccharide encapsulation, 289
Polysiloxane gel, photoluminescence of, 439
Polysilsesquioxane, 31
Poly(tetraethylene glycol malonate) (PTEGM), 489
Polytetrafluorotheylene, in dip-coating, 237
Polytetrahydrofuran (PTHF), 433
Polyurethane
  in cell immobilization, 283
  for ceramic foams, 195
Polyvanadates, cluster shell, 65
Polyviologens, 27
Pore design, in alumina-silica gels, 1027
Pore size
  on cell growth, 283
  in Ia-doped gels, 565
  mercury pressure on, 335
  in organically modified silica xerogels, 473
Pore size, distribution of
  in aerogel sintering, 937
  bimodal, 189
  in double-pore silica, 163
Pore systems, 27
Porosimetry, 335
  in aerogel isostatic compression, 365
Porosity
  of aerogels, 299
  of AlO(OH) film, 149
  in bioactive sol-gel glasses, 245
  Biot's theory on, 329
  freeze-gelation on, 171
  of hybrid organic-inorganic glasses, 457
  in MTEOS xerogels, 457
  of organic/inorganic hybrids, 305
  in ormosil film sensor applications, 641
  in porous silica, 415
  in sol-gel systems structure, 51
  of titanate microspheres, 1011
  Vycor glass method for, 783
Porous layers, in optical fibers, 569
Porous materials, 31
Porous media, mesodimensioned, 99
Porous silica, 415
Powder
  PZT, preparation of, 865
  sol-gel processing of, 154
  X-ray diffraction of, 1049
Power-fusion lasers, 713
Pr^{3+} doping, 599
Preceramic polymers, 195
Precursor chemistry
  and alkoxysilanes, 75
  and glucose-oxidase, 295
Precursor method, for SiO_2-TiO_2 ceramics, 975
Precursors
  complex-forming, in silica gels, 605
  heterometallic oxide as, 45
  lead as, in PZT film preparation, 865
  of PZT thin films, 861
Pre-gelation effect, 94
Prehydrolysis, in forsterite xerogels, 359
Printing, 177. *See also* Ink-jet
Probing, fluorescence, 95
Processing
  of acetic acid based PLZT film, 833
  sol-gel method of, overview of, 154
Production kinetics, 273
Profilometry, of polytetrahydrofuran, 433
Protective coatings
  organic-inorganic nanocomposites as, 735
  for stainless steel, 717, 723
Proton conductor, 933
Pseudomonas species 2, 283
Pulsed EPR, 503
Pulverization, of aerosol, 743
Pyrex, 783
Pyridine
  adsorption of, 1043
  on metallic tetrasulphophthalocyanines, 651
Pyrolysis
  of barium titanate xerogel, 873

of silica-PCL hybrid, 415
in SiO_2-TiO_2 ceramics crystallization, 975
PZT. *See* Lead zirconate titanate (PZT)

Q
Qualitex, 1057
Quantum confinement level, 629
Quantum dots
CdSe doping for, 623
CdSe/CdS crystal growth in, 629
Quenching, of dissolved oxygen, 641

R
Radiative decay rates, in Eu^{3+}, 427
Radioactive wastes, 1011
Raman spectroscopy. *See also* FT-Raman spectroscopy
of Fe_2O_3 films, 667
of lead titanate ($PbTiO_3$), 849
of Pr_2O_3-SiO_2 xerogels, 599
of titanium dioxide, 849
Rapid thermal annealing process, 517
for SnO_2 : Sb coatings, 1005
Rare-earth doping
for glasses, 605
for optical fibers, 617
Reactive ion etching, 517
Recombination, 793
Redispersable particles, 789
Redox
potential measurement, 775
silicate biosensors, 242
Reducing atmosphere, on noble metal colloids, 701
Reesterification, in aerosol-gel process, 743
Reflectivity, of mirror, 757
Reflux, for yttrium manganate films, 903
Refractive index
acid-catalyzed silica sols, 82
of barium-strontium titanate films, 877
of doped porous polysiloxane, 569
in nanoporous films, 582
nonlinear, 559
of PLT films, 870
Refractive microlens fabrication, 177
Rejection capacity, 805
Relaxation effect
in aerogels, 365
spin lattice, 503
Replication, for micro-optical arrays, 547
Resorbable materials, 267
Resorcinol formaldehyde aerogels, 957
Reticular methyl-silicate materials, 189
Reverse micelles, 341
Reversible gel, 553
Review, of ormosils, 371
Rheology, of silica sols, 89
Rhodamine B, 657
Rhodium complex, on copolymerization, 391
Ribbon-like structure, 65
Room temperature densification, of aerogels, 365
Rotation axis, in spin coating, 707
Rubbery ormosils, 371
Ruthenium
in ormosil film sensors, 641
in oxygen sensors, 207
Ruthenium-tin-alumina, 1037
Rutherford backscattering spectroscopy (RBS)
of lead titanate film, 843
of SnO_2 : Sb coatings, 963, 1005

S
Saccharide-silica composites, preparation of, 421
Saccharomyces cerevisiae, 289
Salt concentration, on membrane selectivity, 805
Salt-spray test, 717
Samarium-doped glass, 541
Sapphire substrates, in PLT waveguides, 870
SAXS. *See* Small angle X-ray scattering (SAXS)
Sb-doped tin oxide films, 679. *See also* Antimony doping
SBTO films, 889
Scanning electron microscopy (SEM)
of aerogel, 326
of Al_2O_3-SiO_2 gels, 987
of aluminosilicate planar waveguides, 529
of amorphous organobridged powders, 31
of apatite crystals, 239
of Bi(Pb) speciums, 230
of calcium phosphate coating, 263
of cured nanocomposite coating (Al_2O_3), 738
of β-Eucryptite solid solution, 984
of freeze-cast fracture surface, 173
of geyserite and hyalites, 85
of hydrothermal zircon, 120
of hydroxyapatite formation, 252
of NH_4Cl, 225
of PDA-Si doped pigment, 482
of polytetrahydrofuran, 433
of preceramic foams, 198
of PZT films, 865
of PZT layer, 828
of reticular silicates, 191
of SI-Ti-C fiber, 487
of SnO_2 membrane, 808
of SnO_2 : Sb coatings, 966
of Tb : YAGG phosphor particles, 137
of TZA powder, 1013
of yttrium manganate films, 903
of zircon lattice, 351
Scintillators, fast light-output, 213
SC-RTA process, 509
Second harmonic generation, 559

Secondary ion-mass spectrometry (SIMS)
of bismuth oxide thin films, 213
of heteropolysiloxane coatings, 779
Selective reduction, of NO_x, 1033
Selectivity, of SnO_2 membranes, 805
Semiconductors, impurities in, 793
Sensors. *See also* Chemical sensing
fiber optic, 729
vanadium doped TiO_2 films in, 775
Sheet resistance, 991, 1005
Short-range structure, 51
Shoup method, 233
Shrinkage
of films, 467
in large monolith production, 311
in micro-optical arrays, 547
Si-alkoxides, in drug production, 273
Si-H bonds, 75
Silane
functionalized, 588
in glass coating strength, 695
Silanols, 72
Silianol groups, 237
Silica
cation adsorption on, 579
coatings, for metallic prosthesis, 723
colloidal, ammonia catalyzed hydrolysis of, 713
in controlled drug delivery, 277
cores, properties of, 617
crack-free drying of, 311
fibers of, 267
fused, 461
glass of, 71
layers of, from aerosol-gel process, 743
in lignin-silica-titania hybrids, 485
matrix of, CdS/CdSe semiconductors in, 629
in mirrors, 757
nanoparticles of, 499
natural hydrous, 85
network of, in ormosils, 371
particle size of, optical performance in, 713
porous, 415
synthesis of, 27
water soluble, 553
Silica aerogels, structural efficiency of, 957
Silica alcogels, acoustical properties of, 329
Silica gels, 163
CdS/CdSe crystal growth in, 629
Eu^{3+}-doped, 605
hydoxyapatite nucleation on, 251
metal nanoparticles in, 929
organically modified, 473
photodegradation of luminescence in, 657
with silver and platinum particles, 969
Silica sols, rheological and coating properties of, 89
Silica xerogels
anthraquinone dye leaching in, 473
with dopant-induced chirality, 585
in large monolith production, 311
Pr^{3+} doping on, 599
silica-polyethyleneglycol as, 427
Silica-on-silicon
optical waveguides in, 517
SC-RTA process in, 509
Silica-polyethyleneglycol xerogels, 427
Silica-polypropylenenglycol, 909
Silica-surfactant composites, 95
Silicate
alkaline ions on, 353
based electrodes, 241
Silica-titania
films, 51
in silica-on-silicon components, 517
Silicic acid, forced condensation of, 85
Silico alkaline gel, 353
Silico-calco-alkaline gel, 353
Silicon, reactivity of, 109
Silicon acetates, on particle formation, 713
Silicon compounds, in mesoporous film, 739
Silicon dioxide (SiO_2)
coatings of, for 316L steel, 723
compounds of (*See* SiO_2-)
gels of, silver colloids in, 663
layers of, for glucose-oxidase immobilization, 295
matrices, probing of, 95
in SiO_2-B_2O_3-Na_2O film, 783
Silicon oxycarbide, 195
Silicon oxycarbide gel precursors, 75
Silicon oxycarbide glasses, 79, 945, 995
Silicon tetramethoxide, and lamellar phase, 99
Silicone resin, thermosetting, 195
Siloxane-based glassy matrices, 547
Silsesquioxanes, 391, 945
Silver
colloids of, thermochromic properties of, 663
nanoparticles of, 503
in noble metal colloid films, 701
particles of, in silica gels, 969
Single dip-coating process, for WO_3 layers, 673
^{29}Si-NMR
of alkoxysilanes, 75
of CdSe doped ormosils, 623
of glucose-oxidase, 295
of GPTS, 37
of heteropolysiloxane coatings, 779
of hybrid pigments, 479
of silico-alkaline sol, 353
of TEOS/VTES hybrid, 409
vs. ^{17}O-NMR, 71

Sintering
of aerogels, 937
by laser, of SnO_2 : Sb coatings, 961, 1005
of silicon oxycarbide glass, 995
SiOC compositions, 945
SiO_2-CaO-P_2O_5 coatings, 723
SiO_2 : Rh B gels, luminescence photodegradation in, 657
SiO_2-TiO_2, thin film oxide gels and, 51
SiO_2-TiO_2 ceramics, crystallization of, 975
SiOH groups, in aerogel drying, 323
SiO_x-coated films, 141
Si-SiO_2-Ti-Pt substrates, 889
Small angle X-ray scattering (SAXS)
of biodegradable silica fibers, 268
of geyserite and hyalites, 85
of ionene polymers, 27
and lamellar phase, 99
of Mn^{2+} doped ZnS, 685
of porous silica, 415
of reticular silicates, 193
of silica-alkaline sol, 353
of sodium water glass aerogels, 323
of sulfide gels, 61
of thermoplastic nanocomposites, 499
Small-angle neutron scattering (SANS)
of CdS/CdSe crystals, 629
of titania/zirconia nanoparticles, 113
Sm^{2+}-doped glass, 541
Smectic order, 99
SnO_2, 961
SnO_2 membranes, selectivity of, 805
SnO_2 particles, antimony-doped, 789
SnO_2 thin films, conductivity of, 793
SnO_2 : Sb coatings
heating rate on, 1005
sintering of, 961
Sodium borosilicate glasses, for optical applications, 783
Sodium ethoxide, 783
Sodium silicate, 1057
Sodium water glass solution, 323
Sol coatings, optical viscometry for, 707
Solar cells, 219
Solar energy, aerogels in, 302
Sol-gel
fluorescence probing of, 95
metallic tetrasulphophthalocyanines in, 651
in mirror refraction, 757
in photocurable coatings, 523
Sol-gel biotechnology, 273
Sol-gel chemistry
in Al_2O_3-SiO_2 gels, 987
of doped ZnS nanoparticles, 635
of fluoroalkoxides, 129
HF in, 749
for TEOS and TMOS, 71
Sol-gel coatings
of Al_2O_3-TiO_2-SiO_2, 764
glass-like, 717
hybrid, 183
for ink-jet printing, 147
on 316L steel, 723
for lead leaching inhibition, 753
TEOS/VTES as, 409
Sol-gel entrapment, 17
on molecular recognition, 565
Sol-gel films
dopant adsorption control in, 579
as oxygen sensors, 207
Sol-gel glass
bioactivity of, 245
and SC-RTA process, 509
Sol-gel kinetics, of GPTS/APTS systems, 385
Sol-gel method. *See* Sol-gel process
Sol-gel process
acetic acid in, 833
acid step in, 71
and AFM study of TiO_2 films, 769
for alumina-silica gels, 1027
at ambient pressure, 305
aqueous, 133
for barium titanate xerogels, 873
for barium-strontium titanate films, 877
for bismuth oxide thin films, 213
for bismuth strontium tantalate films, 889
in CdSe doped ormosils, 623
current state and future prospects of, 153
in drug production, 273
for Er^{3+} doped-aluminosilicate films, 529
fast, 547
for gas permselectivity membranes, 801
for gel crystallization, in apatite-mullite system, 951
in GeO_2-SiO_2 waveguides, 535
for heavy metal biosorbents, 289
for indium oxide films, 991
inorganic, 61
for Lewis and Brønsted acid sites on MgO, 1043
and microbial cell encapsulation, 283
for mullite fibers, 1017
for nanocomposite protective coatings, 735
for noble metal colloid films, 701
open-air, 707
and optical nonlinearity of materials, 559
for optical waveguides, highly oriented, 870
for phosphate glasses, 933
for polysiloxane-doped porous layers, 569
for polysiloxane/PEPPV gel film, 439
for PZT (lead zirconate titanate) film, thick, 821
for PZT precursor powders, 827
for PZT synthesis, 1023
for rare-earth doped optical fibers, 617

rheological and coating properties in, 89
of silica fibers, 267
for silica-polyethyleneglycol xerogels, 427
of silicon oxycarbide glass, 995
for Sm^{2+}-doped glass, 541
for SnO_2 : Sb coatings, 961, 1005
in solid solution differentiation, 347
for superconducting materials, 229
for thin film deposition, 743
for titanate microspheres, 1011
in TMOS/MTMS ormosils, 461
two-step acid-base process in, 305
two-step process in, acid catalyst on, 749
for vanadium dioxide thin films, 915
vanadium doped TiO_2 films in, 775
for vanadium-based hybrids, 495
for WO_3 layers, 673
for xerogels with dopant-induced chirality, 585
Sol-gel silica synthesis, 27
Sol-gel silicates, with metal ion centers, 611
Sol-gel SiO_2, in drug production, 273
Sol-gel synthesis, in organopolysiloxanes coatings, 729
Sol-gel systems
for controlled drug delivery, 277
and spectroscopy, 51
Sol-gel transition
in MTEOS xerogels, 457
of sulfide gels and films, 61
of titania, 341
Solid electrolyte, 909
Solid impregnation, 347
Solid solution, 347
Solid state NMR
of alkoxysilanes, 75
of CdSe doped ormosils, 623
of cross-linked organopolysiloxanes, 379
Solid state spectroscopy, 31
Solution NMR, 75
Solvent Blue 59, 473
Solvent-free systems, 109
Sono-ormosils, 451
Sorbitol, 277
Spectral hole burning, 541
Spectral shifts, 17
Spectrophotometry
of matrix effects and chemical sensing, 565
of TiO2 thin film photocatalyst, 565
Spectroscopy, 51. *See also* specific types
Spherical *vs.* non-spherical particles, 81
Spin coating
for ferroelectric films, 815
for mesoporous film, 739
for mirrors, 757
monitoring of, 707
for nanocomposite protective coatings, 735
optical viscometry of, 707
optical waveguides in, 517
of polytetrahydrofuran films, 433
rotation axis in, 707
of Sb-doped SnO_2, 789
SC-RTA in, 509
of $SrBi_2Nb_2O_9$ powders, 885
for yttrium oxide films, 895
Spin lattice relaxation, 503
Spinnability
of biodegradable silica fibers, 267
of lignin-silica-titania hybrids, 485
of mullite fibers, 1017
Spray-drying
for pigments, 479
for titanate microspheres, 1011
for varistor discs, 575
Spraying procedure, in glassware decoration, 183
$SrBi_2Nb_2O_9$ powders, ferroelectric properties of, 885
$SrBi_2Ta_2O_9$ films, 885
Stainless steel
corrosion protection for, 717
corrosion protection for, 316L samples in, 723
Static oxidation test, 717
Steady state water concentration, 71
Steel
electrogalvinized, 779
stainless (*See* Stainless steel)
Stiffness, of low density xerogels, 335
Storage modulus, 445
Strengthening, of glass, 695
Strip-loaded high-confinement waveguides, 517
Strontium. *See also* Sr
carboxylate, 889
2-ethylhexanoates, 885
Structural development, 81
Structural efficiency, of wet gels and aerogels, 957
Structural properties
of doped ZnS nanoparticles, 635
of ormosil films, 467
Structure
of aluminosilicate planar waveguides, 529
of borosilicon oxycarbide glasses, 1001
control of, 27
of Er-alkoxides, 125
of low density xerogels, 335
of multicomponent nanoparticles, 113
of ormosils, 371
of sodium water glass aerogels, 323
studies of, 31
Subcritical
aerogel preparation, 323
conditions, in monolith drying, 311
Sucrose consumption kinetics, 273
Sulfide gels and films, 61

Supercapacitor, aerogels as, 299
Superconductors, 229
Surface energy, 405
Surface flaws, in glass, 695
Surface modification
  with amino carbonic acids, 789
  in nanocomposites, 397
  in thermoplastic nanocomposites, 499
Surface passivation, in corrosion protection, 717
Surface plasmon resonance
  of Ib-doped gels, 565
  of silver colloid gels, 663
Surface techniques, in bismuth oxide thin film synthesis, 213
Surfactant composites, 95
Surfactants, 17
Swinging in behavior, 673
Syneresis, 63
Synroc, 1011

T
Tantalum, 445
Ta-O-PDMS hybrids, 445
Temperature. *See also* Thermal treatment
  on aluminosilicate planar waveguides, 529
  on apatite-anorthite system, 255
  on barium titanate xerogels, 873
  on borosilicate glasses, 103
  on fast CO_2 laser sintering, 961
  on film structure, 467
  on fluoroalkoxide hydrolysis, 129
  on gelling times, 91
  on liberation rate, 277
  on metal colloid precipitation, 701
  on mullite-alumina system, 201
  on organopolysiloxanes, 382
  on silver colloid gel color, 663
  on surface adsorption, 579
  on TiO_2 films, 769
  on ZnS absorption spectra, 635
Temperature-programmed desorption,
  of alumina-silica gels, 1027
Temperature-programmed reduction,
  of Ru-Sn-Al_2O_3 catalysts, 1037
Template, surfactants as, 739
Temporal aging, of silica gels, 317
Tensile strength, 445
TEOS (tetraethylorthosilicate).
  See Tetraethylorthosilicate (TEOS)
Tetraethoxysilane, in ormosil production, 467
Tetraethyleneglycoldimetacrylate (TEGDMA), 178
Tetraethylorthosilicate (TEOS)
  aerial oxidation of, 713
  in aerosol-gel process, 743
  in aging of silica gels, 317
  ammonia catalyzed hydrolysis of, 713
  in boric acid-ethanol system, 103
  in cell immobilization, 283
  in doped porous polysiloxane layers, 569
  in forsterite xerogels, 359
  HF on, 749
  for lead leaching inhibition, 753
  in monolithic aerogel drying, 311
  in mullite fiber preparation, 1017
  in mullite precursors, 987
  in mullite-alumina composites, 201
  in nonlinear optical materials, 559
  ^{17}O-NMR of, 71
  in optical oxygen sensors, 207
  in ormolyte preparation, 909
  on ormosil sensor behavior, 641
  for polytetrahydrofuran, 433
  with saccharide, 421
  and silica sol coatings, 90
  in sodium borosilicate glasses, 783
  in sol-gel spectroscopy, 52
  in sol-gel spectroscopy and structure, 52
  in TEOS/VTES hybrid, 409
  for thick silica films, 723
  ultrasound-assisted polycondensation of, 451
Tetraisopropyltitanate, 1011
Tetramethoxysilane (TMOS)
  and Eriochrome Cyanine R entrapment, 565
  in isostatic compression studies, 365
  and methyl red entrapment, 17
  in micro-optical arrays, 548
  ^{17}O-NMR of, 71
  in orientationally ordered glasses, 647
  in ormosil preparation, 461
  on ormosil sensor behavior, 641
  reversing gels and water soluble colloids from, 553
  in transparent matrices, 95
Tetrapropyl orthotitanate (TPOT), 691
Tetrasulphophthalocyanines, metallic, 651
Textural features, of sono-ormosils, 451
Texture characterization, 415
Thermal
  aging, of silica gels, 317
  applications, of sol-gel processing, 156
  decomposition, for yttrium manganate films, 903
  densification, of Sb-doped SnO_2, 789
  insulant, aerogels as, 299
  phase evolution, in PZT film preparation, 865
  reduction, for noble metal colloids, 701
  stability, of gas permselectivity membranes, 801
Thermal analysis
  of ArO_2 and HfO_2, 757
  dynamic mechanical, 695
  of β-Eucryptite solid solution, 981

for nanocomposite protective coatings, 736
of TiO_2 films, 769
of vanadium-based hybrids, 495
Thermal phase evolution, in PZT film preparation, 865
Thermal treatment. *See also* Temperature
of lead titanate films, 843
of perovskite films, 839
of vanadium doped TiO_2 films, 775
Thermochromic glasses, 663
Thermochromism, 915
Thermodynamic explanation, 251
Thermodynamics, solvent structure on, 565
Thermo-optic switches, 509
Thermoplastic matrices, and hybrid pigments, 479
Thermoporometry, 937
Thermosetting silicone resin, 195
Thick films, 821
Thin film(s). *See also* Film(s)
of barium-strontium titanate, 877
bismuth oxide in, 213
crack-free, 739
deposition process for, 743
dopant adsorption control in, 579
Fe_2O_3 in, 667
ferroelectric, 815, 877
of indium oxide, 991
lanthanum modified $PbTiO_3$ in, 839
mesoporous, 739
in mirror production, 757
from non-oxide gelation, 61
ormosil with different organics as, 467
oxide gels in, 51
of peroxopolytungstic acid, 923
photocatalyst for, 691
PLT synthesis in, 870
of PLZT, 833
polytetrahydrofuran in, 433
PZT precursor powders in, 827
Rutherford backscattering spectroscopy (RBS) of, 843
Sb-doped tin oxide in, 679
shrinkage in, 467
SnO_2 as, conductivity of, 793
of SnO_2 : Sb, 961
of vanadium dioxide, 915
of yttrium oxide, 895
Thin glass sheets, of silicon oxycarbide, 995
Thin interlayers, as barrier layer, 855
Thiols, 61
Three point flexure test
for heteropolysiloxane coatings, 779
for silicon oxycarbide glass, 995
Tin. *See also* SnO_2
in indium oxide doping, 991
Ti-O-PDMS hybrids, 445
Titanate microspheres, 1011
Titania. *See* Titanium dioxide
Titanium
in ORMOCER coatings, 489
in PZT film preparation, 865
on SiO_2-TiO_2 crystallization, 975
Titanium dioxide (TiO_2)
coatings of, vanadium doped, 775
crystallites of, 978
crystallization and corrosion mechanisms of, 763
films of, atomic force microscopy of, 769
in gas permselectivity membranes, 801
gels of, 341
in lignin-silica-titania hybrids, 485
microspheres of, 1011
nanocrystals of, 341
nanoparticles of, 113
in optical fiber doping, 617
in photovoltaic cells, 219
Raman scattering study of, 849
in thin film photocatalyst, 691
in TZA sol, 1011
Titanium isopropoxide
in doped porous polysiloxane layers, 569
in ORMOCER coatings, 489
in spectroscopy and study of sol-gel, 52
Titanium isopropylate, in PZT fibers, 1023
Titanium oxide, doping with, 569
Titanium oxide-zirconium sols, 1011
Titanium tetrakis, 485
Titaniumtetraethoxide, 37
Titanosiloxanes
bonds of, 37
crystallization behavior of, 975
TMOS (tetramethoxysilane).
See Tetramethoxysilane (TMOS)
Toluene, on phenyl-group doped porous layers, 572
Tortuosity, 957
TPOT (titanium isopropoxide), 52
Transesterification, of siliceous prepolymers, 289
Transmission electron microscopy (TEM)
of ceria materials, 1049
of ferroelectric PZD films, 815
of hydrothermal zircon, 121
of metal nanoparticles, 929
of Mn^{2+} doped ZnS, 685
of silver and platinum gel particles, 969
of sodium water glass aerogel, 326
of WO_3 layers, 673
Transparencies, and ink-jet printing, 147
Transparent
adhesives, nanocomposites in, 397
barium titanate xerogels, 873
conducting coatings, 961, 1005
conducting oxides, 789
conductors, 679

films, indium oxide as, 991
matrices, 95
mesoporous film, 739
stiff gels, 61
Transverse optic component, 52
Trapping, of electrons, 793
Tree-structured power splitters, 509
Tricalcium phosphate, 261
Trichlorosilylmethyl benzene, 31
Triethoxysilane, 75
Triethylborate, 783
Trifluoro- (TFTM) silanes, 588
Trimethylborate, 1001
Tungsten oxide, 673
Tunneling electron microscopy (TEM)
of Bi(Pb) specimens, 231
of borosilicon oxycarbide glasses, 1001
of buckling model constant *vs.* geometric diameters, 338
of coating structure, of mirrors, 757
of epoxy ceramer, 407
of forsterite xerogels, 359
of metal-O-PDMS hybrids, 445
of PLZT, 835
of PZT films, 865
of silicon oxycarbide glass, 995
of silver nanoparticles, 503
of SnO_2 : Sb coatings, 965, 1005
of $SrTiO_3$-seeded PZT coating, 855
of thermoplastic nanocomposites, 499
of titanium dioxide, 850
Turkish blue pigment, 347
Two-step acid-base process, 305
Two-step sol-gel process, acid catalyst on, 749

U
Ultrafiltration, 805
Ultrasonic pulverization, of aerosol, 743
Ultraviolet lasers, 991
UV irradiation, for noble metal colloids, 701
UV spectroscopy
of Mn^{2+} doped ZnS, 685
of neodymium doped silica gel-glasses, 593
UV-curing, of organopolysiloxanes coatings, 729
UV-induced polymerization, 141
UV-Vis spectra
of polydiene latex, 1057
of vanadium doped TiO_2 films, 775

V
Vanadates, 65
Vanadium
based hybrids, 495
doped TiO_2 films, 775
oxide gels, 65
pentoxide, 69
in zircon lattice, 347
Vanadium dioxide, optical switching in, 915
Vapor deposition, for bismuth oxide coatings, 213
Varistor discs, 575
Veratrylaldehyde, 295
Vinyltriethoxysilane (VTES), in TEOS hybrid, 409
Vinyltrimethoxysilane (VTMS),
in bioactive gel coatings, 237
Viscometry, optical, 707
Viscosity
in acid-catalyzed silica sols, 83
in aerogel sintering, 937
in ink-jet printing, 148
kinematic, in spin coating, 707
and rheological and coating properties, 89
Visible spectrophotometry, of Al_2O_3-SiO_2 gels, 987
Visible spectroscopy, of CdSe doped ormosils, 623
VLSI, 895
Voltage suppression, 575
Vulcanization, 1057
V^v precursors, 65
Vycor, 783

W
Washburn's equation, 335
Waste water decontamination, 283
Water
absorption of, in ink-jet printing, 147
containing glass, 933
on fast proton conduction, 933
molecules of, clustering processes of, 611
resistance, in ink-jet printing, 147
soluble silica, 553
vapor barrier, 141
Water glass
in subcritical aerogel preparation, 323
TEOS solution aging on, 317
Waveguides
of Er^{3+} doped-aluminosilicate, 529
GeO_2-SiO_2 erbium-doped, 535
highly oriented, 870
for photonic applications, 517
in SC-RTA process, 509
Wet gels, structural efficiency of, 957
Wetting, poly(4-hydroxystrene) (PHS) on, 409
Wetting angle, 305
Wide angle X-ray scattering (WAXS)
of geyserite and hyalites, 85
of ionene polymers, 27
WO_3 layers, 673

X
Xerogels
anthraquinone dye leaching in, 473

of barium titanate, 873
with dopant-induced chirality, 585
of forsterite, 359
hybrid silica as, 75
matrices of, 95
mercury porosimetry for, 335
MTEOS in, 457
partial crystallization of, 873
Pr^{3+} doping on, 599
silica-polyethyleneglycol as, 427
thermal and temporal aging of, 317
transparency in, 873
X-ray absorption fine structure, of Fe_2O_3 films, 667
X-ray diffraction (XRD) spectroscopy
of Al_2O_3-SiO_2 gels, 987
of alumina-silica gels, 1027
of anhydrous sol-gel systems, 103
of apatite-anorthite system, 255
of apatite-mullite system, 951
of borosilicon oxycarbide glasses, 1001
of calcium phosphate/hydroxyapatite coatings, 261
of ceria materials, 1049
of coating structure, of mirrors, 757
of d-fructose SiO_2 composites, 422
of $\mathcal{B}$-Eucryptite solid solution, 981
of Fe_2O_3 films, 103
of ferroelectric PZD films, 817
of forsterite xerogels, 359
of GeO_2-SiO_2 waveguides, 535
of indium oxide film, 991
of lignin-silica-titania hybrid fibers, 488
of mesoporous thin film, 739
of metal nanoparticles, 929
of MgO, 1043
of mullite fibers, 1017
of mullite-alumina composites, 201
of ormosils, 461
of pillared clays, 136
of PLT film waveguides, 870
of PZT coatings, seeded layer compositions in, 855
of PZT fiber, 1023
of PZT films, 865
of Sb-doped tin oxide, 680
of silver and platinum gel particles, 969
of SnO_2 : Sb coatings, 1005
of stainless steel corrosion, 717
of TiO2 films, 769
of TiO_2 thin film photocatalyst, 691
of vanadium doped TiO_2 films, 775
of xerogels for gas permselectivity, 801
of yttrium manganate films, 899, 903
of yttrium oxide films, 895
of zircon lattice, 347
of zircon synthesis, 119
X-ray photoabsorption spectroscopy, 51
X-ray photoelectron spectroscopy, of PTEGM, 489
X-ray photoelectron spectroscopy (XPS)
of bismuth oxide thin films, 213
of coating structure, of mirrors, 757
of heteropolysiloxane coatings, 779
of micro-optical arrays, 548
of Ru-Sn-Al_2O_3 catalysts, 1037
X-ray photoemission spectroscopy, 51
X-ray scattering, 27

Y
YAG laser
crystallization with, 991
mirrors for, 757
on rare-earth doped fibers, 617
on SiO_2 : Rh B gels, 657
Yb, in GeO_2-SiO_2 waveguides, 535
Yeast cells, 289
Young's modulus, 445
of silicon oxycarbide glass, 995
Yttrium manganate films
dielectric and ferroelectric properties of, 899
preparation of, 899
Yttrium oxide, films of, 895

Z
Zeolite chemistry, 27
Zero-shrinkage ceramic bodies, 171
Zeta potential, 805
Zinc
oxide powder, for varistor discs, 575
in polydiene latex, 1057
Zinc sulfide (ZnS) nanoparticles
with Mn^{2+} doping, 685
optical/structural properties of, 635
Zircon, hydrothermal synthesis of, 119
Zircon lattice, 347
Zirconia
in mirrors, 757
in nanofiltration membranes, 133
nanoparticles of, 113
Zirconium, in PZT film preparation, 865
Zirconium-*n*-propylate, 1023
ZrO_2-Al_2O_3 aerogel catalysts, 1033

Journal of Sol-Gel Science and Technology

INSTRUCTIONS FOR AUTHORS

Authors are encouraged to submit high quality, original work that not appeared in, nor is under consideration by, other journals. Papers which have previously appeared in conference proceedings will also be considered, and this should be so indicated at the time of submission.

PROCESS FOR SUBMISSION

1. Authors should submit four copies of their final manuscript to:

Judith A. Kemp
JSST—Editorial Office
Kluwer Academic Publishers
101 Philip Drive, Assinippi Park
Norwell, MA 02061 USA

PH: 781 871 6600
FX: 781 878 0449
EM: jkemp@wkap.com

For prompt attention, all correspondence can be directed to this address.

2. Enclose with each manuscript, on a separate page, from three to five key words. Some typical key word examples are: precursor chemistry, gelation mechanism, optical solids, hydrolysis.
3. Enclose originals for the illustrations, see "Style for Illustrations" for one copy of the manuscript. Photocopies of the figures may accompany the remaining copies of the manuscript. Alternatively, original illustrations may be submitted after the paper has been accepted.
4. Enclose a separate page giving the preferred address of the contact author for correspondence and return of proofs. Please include a telephone number, a fax number, and an e-mail address if available.
5. The refereeing is done by anonymous reviewers.

ELECTRONIC FORM

Upon acceptance of publication, *the preferred format of submission is the Kluwer LaTeX journal style file.* The style file may be accessed through a WWW site by means of the following commands:

WWW URL: http://www.wkap.nl/

- Choose "Author Instructions/Stylefiles"
- Choose "Journals Listed Alphabetically"
- Choose appropriate journal listing
- Choose "Stylefiles" from list of options

Authors are encouraged to read the "readme" file.

If you do not have access to WWW or have questions, please send e-mail to:

dthelp@wkap.com

The Kluwer LaTeX journal style file *is the preferred format,* and we urge all authors to use this style for existing and future papers; however, we can accept almost any word processing format (e.g., WordPerfect, Microsoft Word, etc.) as well as ASCII (text only) files. Note, it is also helpful to supply both the source and the ASCII files of a paper. Please submit encapsulated PostScript files for figures. An encapsulated PostScript figure file should be named after its figure number, e.g., fig1.eps or circle1.eps.

ELECTRONIC DELIVERY

Please send only the electronic version (of ACCEPTED paper) via one of the methods listed below. Note, in the event of minor discrepancies, the electronic file will be used as the final version.

Via electronic mail

1. Please e-mail electronic version to:

KAPfiles@wkap.com

2. Recommended formats for sending files via e-mail:
   a. Binary files - uuencode or binhex
   b. Compressing files - compress, pkzip, or gzip
   c. Collecting files - tar

3. The e-mail message should include the author's last name, the name of the journal to which the paper has been accepted, and the type of file (e.g., LaTeX or ASCII).

Via anonymous FTP

ftp: ftp.wkap.com
cd: /incoming/production

Send e-mail to KAPfiles@wkap.com to inform Kluwer electronic version is at this FTP site.

Via disk

1. Label a 3.5-inch floppy disk with the operating system and word processing program along with the authors' names, manuscript title, and name of journal to which the paper has been accepted.
2. Mail Disk to:

Kluwer Academic Publishers
Desktop Department
101 Philip Drive
Assinippi Park
Norwell, MA 02061

Any questions about the above procedures please send e-mail to:

dthelp@wkap.com

We hope that these electronic procedures will encourage the submission of manuscripts to this journal as well as improve the publication schedule.

TRADITIONAL STYLE FOR MANUSCRIPT

1. Typeset, double or 1 1/2 space; use one side of sheet only (laser printed, typewritten, and good quality duplications acceptable). Our LaTeX style file offers a draft mode for this purpose.
2. Use an informative title and provide an informative 100 to 250 word abstract at the head of the manuscript. The abstracts are printed with the articles. The abstract should be a carefully worded description of the problem, the key ideas introduced, and the results.
3. Provide a separate double-spaced sheet listing all footnotes, beginning with "Affiliation of author" and continuing with numbered footnotes. Acknowledgment of financial support may be given if appropriate.
4. References should appear in a separate bibliography at the end of the paper. References should be complete, in the following style:

   Style for papers: Author(s) initials followed by last name for each author, publication name, volume number in boldface, page number, and year in parentheses.
   For Example: J.X. Doe, W.T. Smith, and T. Wang, Physical Review **37**, 2961 (1942).

Style for books: Author(s) initials followed by last name, title of book (in italics), publisher, city, year, page or chapter number. Publisher, city and year should all be enclosed in a set of parentheses.
For Example: C.J. Brinker and G.W. Scherer, *Sol-Gel Science: The Physics and Chemistry of Sol-Gel Processing* (Academic Press, San Diego, 1990), p. 601.
Style for articles in proceedings or edited book: Author(s) initials followed by last name, publisher, city, year, page. Publisher, city and year should be enclosed in parentheses.
For Example: J. Livage, F. Babonneau, and C. Sanchez, in *Sol-Gel Optics: Processing and Applications*, edited by L.C. Klein (Kluwer Academic Publishers, Boston, 1994), p. 371.

The references should be cited in the text using numbers, for example [7].

5. Type or mark mathematical expressions exactly as they should appear in print. Journals style for letter symbols is as follows: variables, italic type (indicated by an underline); constants, roman text type; matrices and vectors, boldface type (indicated by wavy underline). In word-processor manuscripts, use appropriate typeface. It will be assumed that letters in displayed equations are to be set in italic type unless you mark them otherwise. All letter symbols in text discussion must be marked if they should be italic or boldface. Indicate best breaks for equations in case they will not fit on one line.

STYLE FOR ILLUSTRATIONS

1. Originals for illustrations should be sharp, noise-free, and of good contrast. We regret that we cannot provide drafting or art service.
2. Line drawings should be in laser printed output or in India ink on paper. Use 8 1/2 $\times$ 11 inch size sheets if possible to simplify handling of the manuscript.
3. Each figure should be mentioned in the text and numbered consecutively using Arabic numerals. Specify the desired location of each figure in the text, but place the figure itself on a separate page following the text.
4. Number each table consecutively using Arabic numerals. Please label any material that can be typeset as a table, reserving the term "figure" for material that has been drawn. Specify the desired location of each table in the text, but place the table itself on a separate page following the text. Type a brief title above each table.
5. All lettering should be large enough to permit legible reduction.
6. Photographs should be glossy prints, of good contrast and gradation, and any reasonable size.
7. Number each original on the back.
8. Provide a separate sheet listing all figure captions, in proper style for the typesetter, e.g., "Fig. 2. XRD pattern of 5CeZr gel isothermally heat treated at 1273, 1373, and 1473 K at different holding times."

PROOFING

Page proofs for articles to be included in a journal issue will be sent to the contact author for proofing, unless otherwise informed. The proofread copy should be received back by the Publisher within 72 hours.

COPYRIGHT

It is the policy of Kluwer Academic Publishers to own the copyright of all contributions it publishes. To comply with the U.S. Copyright Law, authors are required to sign a copyright transfer form before publication. This form returns to authors and their employers full right to reuse their material for their own purposes. Authors must submit a signed copy of this form with their manuscript.

OFFPRINTS

Each group of authors is entitled to 25 free offprints of their paper. Additional reprints may be ordered from the Publisher prior to publication. An order form will be sent to authors with page proof.

Introduction to Sol—Gel Processing

By:
Alain C. Pierre
Université Claude Bernard-Lyon I, France

THE KLUWER INTERNATIONAL SERIES IN SOL—GEL PROCESSING:
Technology & Applications 1

Introduction to Sol-Gel Processing introduces undergraduate and graduate students to the field of colloids applied to materials processing, better known as sol-gel processing. It is written for Engineering or Science students in the fields of Chemical Engineering, Materials Processing, Ceramics Engineering, Colloid Science and Mineral Chemistry. *Introduction to Sol-Gel Processing* does not intend to be exhaustive on the research done in this field. However the most important facts about the most recent developments, including mixed organic—inorganic sol-gels known as hybrid materials and the use of surfactants and micelles, are addressed. More precisely, the book focuses on gathering the main theories related to sol-gel processing in a comprehensive manner, so as to provide the most important scientific basis to students. *Introduction to Sol-Gel Processing* is organized in such a way that each chapter corresponds to one of the main steps in a chronological order of application of sol-gel techniques to the synthesis of materials. The book first presents elementary solvent chemistry, in particular the partial charge model theory. Next, theories on the nucleation and growth of particles and on the steric or electrostatic stabilization (also known as D.L.V.O. theory) of colloidal suspensions, are gathered in a chapter on colloidal particles. Another chapter is devoted to the theories on gelation. Gels, their structure and properties at large such as their swelling, shrinkage or drying behavior, also constitute an important chapter. After drying, gels become almost traditional ceramic materials and they are often submitted to thermal treatments during which they can phase-transform and sinter. Two chapters offer an opportunity to gather the main theories related to these two fields. Finally, the main applications are reviewed according to the domains of application, particularly for coatings, filtering membranes, and catalysts.

Contents:

Preface. **1.** General Introduction. **2.** The Chemistry of Precursors Solutions. **3.** Colloidal Particles and Sols. **4.** Gelation. **5.** Gels. **6.** New Types of Sol-Gel Derived Materials. **7.** Phase Transformations. **8.** Sintering Sol-Gel Ceramics. **9.** Applications of Sol-Gel Processing. Appendix.

1998 **ISBN 0-7923-8121-1**
408 pp./Hardbound
NLG 330.00/USD 145.00/GBP 98.60

P.O. Box 322, 3300 AH Dordrecht, The Netherlands
P.O. Box 358, Accord Station, Hingham MA 02018-0358, U.S.A.

http://www.wkap.nl

Kluwer
academic
publishers

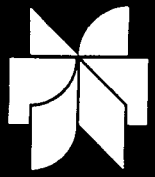

JOURNAL OF SOL-GEL SCIENCE AND TECHNOLOGY

AIMS AND SCOPE

Advances in high performance materials for structural and functional applications depend on the development of materials processing which allows for the regulation of phenomena and structures at atomic, molecular, nanoscale and micrometer scale levels. Sol-gel processing provides such materials in an efficient manner, and tremendous opportunities are now open for developing and producing novel high technology materials.

The primary objective of the **JOURNAL OF SOL-GEL SCIENCE AND TECHNOLOGY** is to provide an international forum for the dissemination of scientific and technical information and knowledge about sol-gel processed materials. The materials of interest include gels, gel-derived glasses and ceramics in bulk, fiber, film or powder form. Gel-processed composites of all types are also included. Optical, electronic, magnetic, mechanical, chemical, environmental and biomedical functions and applications of the resultant materials are of interest.

The Journal will publish original research papers and occasionally invited overview papers on scientific and technical issues in the emergent field of sol-gel materials.

The following are major topics of the Journal:

- Chemistry, physics, materials science and technology of sol-gel synthesis and processing;
- Characterization of sol-gel derived gels, glasses, ceramics and composites;
- Properties, performance and applications: optical, electronic, magnetic, mechanical, chemical, environmental and biomedical.

Governed by an international advisory board, the Journal will serve as an international forum for the field of sol-gel science and technology.

Journal of Sol-Gel Science And Technology

Editor-in-Chief
Sumio Sakka

Guest Editors
Russell Hand
Peter James
Angela Seddon

Volume 13, Nos. 1/2/3, 1998

Proceedings of the Ninth International Workshop on Glasses and Ceramics from Gels, August 31–September 5, 1997, Centre for Glass Research, The University of Sheffield, UK

Kluwer Academic Publishers

0928-0707(1998)13:1/3;1-Q